

Lecture Notes in Civil Engineering

Sheila Belayutham ·
Che Khairil Izam Che Ibrahim ·
Anizahyati Alisibramulisi ·
Hazrina Mansor · Muntasir Billah *Editors*

Proceedings of the 5th International Conference on Sustainable Civil Engineering Structures and Construction Materials

SCESCM 2020

 Springer

Lecture Notes in Civil Engineering

Volume 215

Series Editors

Marco di Prisco, Politecnico di Milano, Milano, Italy

Sheng-Hong Chen, School of Water Resources and Hydropower Engineering,
Wuhan University, Wuhan, China

Ioannis Vayas, Institute of Steel Structures, National Technical University of
Athens, Athens, Greece

Sanjay Kumar Shukla, School of Engineering, Edith Cowan University, Joondalup,
WA, Australia

Anuj Sharma, Iowa State University, Ames, IA, USA

Nagesh Kumar, Department of Civil Engineering, Indian Institute of Science
Bangalore, Bengaluru, Karnataka, India

Chien Ming Wang, School of Civil Engineering, The University of Queensland,
Brisbane, QLD, Australia

Lecture Notes in Civil Engineering (LNCE) publishes the latest developments in Civil Engineering - quickly, informally and in top quality. Though original research reported in proceedings and post-proceedings represents the core of LNCE, edited volumes of exceptionally high quality and interest may also be considered for publication. Volumes published in LNCE embrace all aspects and subfields of, as well as new challenges in, Civil Engineering. Topics in the series include:

- Construction and Structural Mechanics
- Building Materials
- Concrete, Steel and Timber Structures
- Geotechnical Engineering
- Earthquake Engineering
- Coastal Engineering
- Ocean and Offshore Engineering; Ships and Floating Structures
- Hydraulics, Hydrology and Water Resources Engineering
- Environmental Engineering and Sustainability
- Structural Health and Monitoring
- Surveying and Geographical Information Systems
- Indoor Environments
- Transportation and Traffic
- Risk Analysis
- Safety and Security

To submit a proposal or request further information, please contact the appropriate Springer Editor:

- Pierpaolo Riva at pierpaolo.riva@springer.com (Europe and Americas);
- Swati Meherishi at swati.meherishi@springer.com (Asia - except China, and Australia, New Zealand);
- Wayne Hu at wayne.hu@springer.com (China).

All books in the series now indexed by Scopus and EI Compendex database!

More information about this series at <https://link.springer.com/bookseries/15087>

Sheila Belayutham ·
Che Khairil Izam Che Ibrahim ·
Anizahyati Alisibramulisi · Hazrina Mansor ·
Muntasir Billah
Editors

Proceedings of the 5th International Conference on Sustainable Civil Engineering Structures and Construction Materials

SCESCM 2020

 Springer

Editors

Sheila Belayutham
School of Civil Engineering, College
of Engineering
Universiti Teknologi MARA
Shah Alam, Selangor, Malaysia

Che Khairil Izam Che Ibrahim
School of Civil Engineering, College
of Engineering
Universiti Teknologi MARA
Shah Alam, Selangor, Malaysia

Anizahyati Alisibramulisi
School of Civil Engineering, College
of Engineering
Universiti Teknologi MARA
Shah Alam, Selangor, Malaysia

Hazrina Mansor
School of Civil Engineering, College
of Engineering
Universiti Teknologi MARA
Shah Alam, Selangor, Malaysia

Muntasir Billah
Department of Civil Engineering
Lakehead University
Thunder Bay, ON, Canada

ISSN 2366-2557

ISSN 2366-2565 (electronic)

Lecture Notes in Civil Engineering

ISBN 978-981-16-7923-0

ISBN 978-981-16-7924-7 (eBook)

<https://doi.org/10.1007/978-981-16-7924-7>

© The Editor(s) (if applicable) and The Author(s), under exclusive license to Springer Nature Singapore Pte Ltd. 2022

This work is subject to copyright. All rights are solely and exclusively licensed by the Publisher, whether the whole or part of the material is concerned, specifically the rights of translation, reprinting, reuse of illustrations, recitation, broadcasting, reproduction on microfilms or in any other physical way, and transmission or information storage and retrieval, electronic adaptation, computer software, or by similar or dissimilar methodology now known or hereafter developed.

The use of general descriptive names, registered names, trademarks, service marks, etc. in this publication does not imply, even in the absence of a specific statement, that such names are exempt from the relevant protective laws and regulations and therefore free for general use.

The publisher, the authors and the editors are safe to assume that the advice and information in this book are believed to be true and accurate at the date of publication. Neither the publisher nor the authors or the editors give a warranty, expressed or implied, with respect to the material contained herein or for any errors or omissions that may have been made. The publisher remains neutral with regard to jurisdictional claims in published maps and institutional affiliations.

This Springer imprint is published by the registered company Springer Nature Singapore Pte Ltd.

The registered company address is: 152 Beach Road, #21-01/04 Gateway East, Singapore 189721, Singapore

Preface

In current times, the civil engineering field has developed in many ways, especially on the technologies and materials, in riding along the waves of Industry 4.0. Alongside the current developments and state-of-the-art affairs, the construction industry has also been very engaging in regard to sustainability, as construction academics and practitioners all around the world strive to embed sustainability in all aspects of construction, in order to sustain the balance in the environment for the next generation. The concept of high efficiency and effectiveness of human resources and the use of materials with low or minimal impact to the environment should be implemented in the design, construction and maintenance phase of civil engineering structures/buildings. Thus, the series of International Conference on Sustainable Civil Engineering Structures and Construction Materials has been conceived to spread the latest information, scientific findings and achievements of civil engineers around the world in regard to the applications of sustainability in all aspects of civil engineering and infrastructure facilities. This series of conference was initiated by the Civil and Environmental Engineering Department of Gadjah Mada University, in cooperation with Hokkaido University, Japan, and Karlsruhe Institute of Technology, Germany, with the organization of the inaugural first Sustainable Civil Engineering Structures and Construction Materials (SCESCM) International Conference in 2012 in Yogyakarta, Indonesia, with the theme “Enhancing the Role of Civil Engineering for Sustainable Environment”. This scholarly platform of network building and information sharing has since been routinely organized every two years (biennial) to support the agenda of sustainability in civil engineering and construction. The biennial conference is now at its fifth series (SCESCM 2020), which was virtually held from Malaysia, in December 2020. The main organizer for the fifth series is Universiti Teknologi MARA, in collaboration with Gadjah Mada University, Indonesia, Hokkaido University, Japan, and Karlsruhe Institute of Technology, Germany. The theme for the fifth SCESCM was “Transforming the World, Foster the Sustainable Development Goals (SDGs)”, aimed to explore and demonstrate the range of issues, novel findings, as well as developments in the area of civil and infrastructure, conforming to the SDGs. The inclusion of SCESCM 2020 in the Lecture Notes in Civil Engineering (LNCE) highlights the latest developments in civil engineering

with research that spans across different fields in civil engineering, from structures, materials, geotechnic, environment, water resource, construction management to smart cities and built environment. The blend of various fields in civil engineering that were grounded to the theme of sustainability within the context of SDGs makes this book a comprehensive referral point for civil engineering academics, as well as practitioners in general. All the papers included in this book have been carefully reviewed and selected with approximately 75% rate of acceptance.

This book represents the blood, sweat and tears of many, and we would like to sincerely thank the SCESCM 2020 organizing committee and scientific committee for their relentless effort, commitment and invaluable contribution. Our appreciation also goes to the dedicated reviewers, authors and participants for their active role in contributing to the wealth of knowledge and advocacy on sustainability in civil engineering.

Our sincere gratitude also goes to Mr. Ramesh Kumaran and Dr. Ramesh Nath Premnath, Publishing Editors at Springer for their immense assistance and support in materializing the book.

Finally, we hope that the readers would find the book beneficial for their current tasks, as well as the source of inspiration in expanding the plethora of knowledge in future works.

Shah Alam, Malaysia
Shah Alam, Malaysia
Shah Alam, Malaysia
Shah Alam, Malaysia
Thunder Bay, Canada

Sheila Belayutham
Che Khairil Izam Che Ibrahim
Anizahyati Alisibramulisi
Hazrina Mansor
Muntasir Billah

Contents

Structural and Material Engineering

Practical Measurement Method for Dynamic Structural Large Displacement Using a High-Speed Camera	3
Ashar Saputra and Aries Putra Purba	
Finite Element Analysis of CRTS III Slab Track Model	17
Mughtar Sufaat, Ali Awaludin, Iman Satyarno, Andreas Triwiyono, Akhmad Aminullah, Mukhlis Sunarso, and Guntar Muria Adityawarman	
Effect of Partial Replacement of Cement with Volcanic Ash on Mechanical Behaviour of Mortar	33
Md. Shahjalal, Jesika Rahman, Afia Farzana Haque, Lutful Habib, Khadiza Binte Jalal, and Mohd Mezanur Rahman	
Lateral Load–Displacement Behaviors of Reinforced Geopolymer-Concrete Column Using Finite Element Analysis	45
Kukuh Kurniawan Dwi Sungkono, Iman Satyarno, Henricus Priyosulistyo, and Indra Perdana	
Optimal Sensor Placement for Accelerometer in Single-Pylon Cable-Stayed Bridge	63
Akhmad Aminullah, Bambang Suhendro, and Raka Bagus Panuntun	
Seismic Performance of Instant Steel Frame House for Post Earthquake Reconstruction	81
Widatar Sutrisno, Iman Satyarno, Ali Awaludin, Ashar Saputra, and Angga Fajar Setiawan	
Nonlinear Numerical Model of Glued-Laminated Petung Bamboo Under Flexural Test Based on ASTM D 143-94	99
Abdul Widayat Abzari, Inggar Septhia Irawati, and Bambang Suhendro	

Numerical Simulation Reinforcement of RC T-Beam with Carbon Fiber Reinforced Polymer (CFRP)	119
A. Mahendra, Muslikh, and A. S. Fajar	
Development Experimental Investigations of Truss Bridge Model for Vibration-Based Structural Health Monitoring	137
Sukamta, Angga Alfiannur, Susilo Adi Widyanto, and Han Ay Lie	
Parameter Identification of Bouc-Wen Model Using Firefly Algorithm	155
Richard Frans, Yoyong Arfiadi, and Junaedi Utomo	
Mechanical Properties of Fly Ash Bottom Ash (FABA) Geopolymer Hybrid Concrete Using Portland Cement	173
Monita Olivia, Rizky Noviandri, Gunawan Wibisono, and Iskandar Romey Sitompul	
Investigation of Confined Masonry Using Non-standard Quality of Concrete and Reinforcement	187
Andreas Triwiyono, I. Gusti Lanang Bagus Eratodi, Dian Eksana Wibowo, and Suprpto Siswosukarto	
Prospective of Passive Control Structural Devices for Existing Low-Rise Building at Earthquake-Prone Region of Developing Countries: A Literature Review	201
Yenny Nurchasanah, Bambang Suhendro, and Iman Satyarno	
Numerical Modelling of Concrete-Filled Steel Tube Columns Under Eccentric Loading	221
Joarder Md. Sarwar Mujib, Avijit Pal, Ibriju Ibrahim, and Tanvir Mustafy	
Maturity Method to Predict Strength Development of Concrete Made of Portland Cement Composite (PCC)	241
G. Turuallo, H. Mallisa, N. Rupang, and Z. Mallisa	
Study on Partial Replacement of Cement with Limonite in Mechanical Strength of Mortar	255
Md. Shahjalal, Jesika Rahman, Afia Farzana Haque, Lutful Habib, Khadiza Binte Jalal, and Mohd Mezanur Rahman	
Development of Numerical Model for Highly-Flowable Strain Hardening Fiber Reinforced Concrete (HF-SHFRC) Columns Subjected to Lateral Displacement Reversals and High Axial Loading Level	269
Wisena Perceka, Wen-Cheng Liao, and Li-Wei Tseng	

Mechanical Properties of Eco-Friendly Self-consolidating Concrete Containing Ground Granulated Blast Furnace Slag and Calcined Dolomite	285
Herry Suryadi Djayaprabha, Ta-Peng Chang, Jeng-Ywan Shih, and Hoang-Anh Nguyen	
An Overview of the Development of Replaceable Links in Eccentrically Braced Frame Steel Structures	297
Naomi Pratiwi, Helmy Hermawan Tjahjanto, and Muslinang Moestopo	
The Evaluation of Six Indonesian Hardwood Species According to SNI 7973:2013	311
Wiryanto Dewobroto, Christian Gerald Daniel, Ricky Weinata Kurniawan, and Au Chuenliana Audi	
Image Analysis of the Color Change on Concrete Surface Under the Change of Temperature and Humidity	329
Naoki Tosaka, Deng Pengru, and Takashi Matsumoto	
Dynamic Formation of Spontaneous Corrugation on Sand Surface Due to Repeated Loading of Moving Vehicle	349
Shunji Kanie, Hao Zheng, Kai Hashimoto, and Risa Endo	
Assessment and Back Analysis of a Swaying-Jetty in Dumai Indonesia	363
Merdeka Sandi Tazakka, M. Adecar Nugroho, and Budiwan Adi Tirta	
Seismic Assessment of Reinforced Concrete Frame with Unreinforced Masonry Infill Walls in Malaysia	379
Nurbaiah Mohammad Noh, Nur Izzah Aznin, Muhamad Hafizi Mohamed Zin, Muhammmad Azamuddin Mohd Ghari, Muhammad Ammar Zahari, and Muhammad Faiz Rushdi	
High Temperature Performance of Concrete Incorporating Recycled Glass Powders	391
Joarder Md Sarwar Mujib, Nayeem Ahmed Shuvo, Abu Bakar Siddique Ishmam, and Tanvir Mustafy	
The Effect of Palm Oil Fuel Ash (POFA) and Steel Fiber Addition to the Mechanical Properties of Ultra High Performance Concrete (UHPC)	405
Hafizuddin Zakare, Anizahyati Alisibramulisi, Muhd Norhasri Muhd Sidek, Aidan Newman, Nadiyah Saari, Suraya Hani Adnan, and Norshariza Mohd Bhkari	

Investigation on Fire Resistance of Concrete Incorporating Recycled Ceramic Fine Aggregate 417
 Joarder Md. Sarwar Mujib, Md. Maruf Hasan, Md. Rasel Molla, Tahsin Md. Zahid, and Tanvir Mustafy

Image Analysis on the Deformation Behaviors of RC Beams with Simulated Deteriorations Under Moving Wheel Load Fatigue 435
 Takamasa Nagai, Ko Kakuma, Hiroaki Nishi, Pengru Deng, and Takashi Matsumoto

Investigation of Catalyzed Biomass Thermoelectric Concrete with Palm Oil Fuel Ash 451
 Hoong-Pin Lee, Wan-Foong Chak, Kar-Loke Teow, Wen-Zhang Lee, Nurharniza Binti Abdul Rahman, and Abdullah Zawawi Awang

Examination on the Processes of Structural Performance Evaluation of SRC Deep Beams by FEA with NDT Results 465
 Motonori Yasui, Deng Pengru, and Takashi Matsumoto

Development of Time Histories Based on Shallow Crustal Earthquake Sources Considering the New Version of the Indonesian Earthquake Map 483
 Wisnu Erlangga, Mochamad Teguh, and Imam Trianggoro Saputro

Bamboo Reinforced Concrete Beam 497
 Nurharniza Abdul Rahman, Choo Li Rong, and Lee Hoong Pin

Shear Strength Parallel to Grain for Selected Malaysian Tropical Timber According to BS EN408 511
 M. B. Norshariza, W. C. Lum, Z. Ahmad, A. Alisibramulisi, and M. S. Nordin

Effect of Pineapple Leaf Fibre as Additional Material in Concrete Mixture 525
 Siti Khadijah Che Osmi, Mohamad Asrul Zamuddin, Noor Aina Misnon, Suriyadi Sojipto, and Hapsa Husen

Flexural Behavior of SCC Beams with Different Shear Span to Effective Depth Ratio 539
 Oh Chai Lian, Mohd Raizamzamani Md Zain, Norrul Azmi Yahya, Lee Siong Wee, and Balqis Md Yunos

Flexural Strength and Ductility of Green Engineered Cementitious Composites Containing High Volumes of Fly Ash 553
 Siong Wee Lee, Mohd Raizamzamani Md Zain, Chai Lian Oh, Norrul Azmi Yahya, and Nadiah Saari

An Experimental Study on the Influence of Ground Granulated Blast-Furnace Slag (GGBS) on Bending Strength of Green Engineered Cementitious Composites 565
 Mohd Raizamzamani Md Zain, Siong Wee Lee, Chai Lian Oh, Ching Hua Goh, and Norrul Azmi Yahya

The Correlation Between Split Tensile and Flexural Strength with Compressive Strength of Crumb Rubber-Rice Husk Ash Concrete 581
 Habib Abdurrahman, Gunawan Wibisono, Iskandar Romey Sitompul, and Monita Olivia

Finite Element Dynamic Analysis of Double-Span Steel Beam Under an Instantaneous Loss of Support 593
 Nur Ezzaryn Asnawi Subki, Hazrina Mansor, Yazmin Sahol Hamid, and Gerard A. R. Parke

Effect of Replacement Area Ratio on Bearing Capacity Improvement of Peat Soil Columns Stabilized Using MUF-P Polymer Resin 611
 Mohd Nazrin Mohd Daud, Nik Norsyahariati Nik Daud, and Jestin Jelani

Ettringite: Influence of Steam Curing and Excessive Sulphate Content 625
 M. Y. Balqis, H. M. K. Saiful, and M. M. Z. Raizamzamani

Geoforensic Investigation of Cavity and Settlement for Abutment Bridge Using Electrical Resistivity Imaging 639
 A. S. A. Rahman and I. B. M. Jais

Strength Predictions of Normal Concrete Beam with Corner Notch 653
 Hilton Ahmad and Noor Yasmin Zainun

Structural Condition Assessment of a Log Bridge Under Heavy Traffic Load (Case Study: 105 Tons Gas Engine Delivery in Central Borneo Project) 669
 Angga T. Yudhistira, Angga S. Fajar, Irfani N. Hud, Budi Suanda, and Ali Awaludin

The Application of Inserted Steel Pipe as an Alternative Confinement Design in Reinforced Concrete Column Plastic Hinge Regions 685
 Johanes Januar Sudjati, Iman Satyarno, Andreas Triwiyono, Bambang Supriyadi, and Angga Fajar Setiawan

Influence of Solvable Connections on the Life Cycle Assessment of a Facade System 705
 Leonie Scheuring, Melanie Werner, Franziska Rehde, and Bernhard Weller

Seismic Performance Comparison of Pile Supported Slab Viaduct with PHC Pile and RC Bored Pile in South Part of Java Island 719
 Muhamad Fauzi Darmawan, A. S. Fajar, Iman Satyarno, Ali Awaludin, and Bonifacius Adiguna Yogatama

Finite Element Analysis for Developing Multi-direction Crossing Web Type Shear Panel Damper 735
 N. U. Bagas, I. Satyarno, A. S. Fajar, A. Awaludin, and M. A. Guntara

Numerical Model of Finned Tubular Shear Panel Damper for Multi-direction Seismic Excitation 751
 A. M. Emilidardi, A. S. Fajar, A. Awaludin, I. Satyarno, and M. Sunarso

Investigation of Fast Connection (Clamped Pocket Mechanics) for Modular Instant Steel House with Finite Element Analysis: Back to Build Post-disaster 767
 A. S. Fajar, A. Saputra, I. Satyarno, and L. Himawan

Method Assessment of Bridge Conditions Using Vibration Mode Patterns 787
 Sukamta, Bagus Acung Billahi, Susilo Adi Widyanto, and Han Ay Lie

Quantification of Bacteria Self-healing Efficiency on Concrete Cracks 803
 M. S. Hamidah, H. Noor Hana, K. M. G. Iqmal, and K. Kartini

Feasible Design Tensile Capacity of Post-installed Anchors Based on the New Eurocode 2: Part 4 (2018) 819
 L. T. Ng, E. S. W. Wong, and D. T. W. Looi

The Maximum Allowable Peak Ground Acceleration of a Six Storey Building Based on Micro Tremor and Numerical Analysis 837
 Agustinus Sri Pandu and Henricus Priyosulistyo

The Bond Strength and Damping Properties of Mortar Joint Using Rubber Tire Crumbs 857
 Restu Faizah, Henricus Priyosulistyo, and Akhmad Aminullah

Using Calcium Oxide and Accelerator to Control the Initial Setting Time of Mortar in 3D Concrete Printing 871
 Antoni Antoni, David Christian Widjaya, Alexander Ricardo Koentjoro Wibowo, Jimmy Chandra, Pamuda Pudjisuryadi, and Djwantoro Hardjito

Numerical Simulation of Spalling and Moisture Evaporation in Concrete Tunnel Linings Exposed to Fire 881
 Zobaer Saleheen and Renga Rao Krishnamoorthy

Optimization on Geometry Design of Double-Layer Space Trusses 895
 Yazmin Sahol Hamid and Nurul Najihah Abd Rahim

Numerical Investigation of Structural Behavior of Timber-Glass Composite Wall Panel 911
 M. A. N. Abuzaid, M. K. Kamarudin, and M. Yussof

Effect of Palm Oil Bottom Ash (POBA) on Concrete Mechanical Properties of Fresh and Hardened Ultra High Performance Concrete (UHPC) 929
 Izzani Farhana Baharudin, Nurul Huda Suliman, Sakhiah Abdul Kudus, and Nuradila Izzaty Halim

Impacts of Steel LNG Tank Aspect Ratio on Seismic Vulnerability Subjected to Near-Field Earthquakes 941
 N. Sharari, B. Fatahi, A. Hokmabadi, and R. Xu

Load–Displacement Behavior of Soil–Pile Interaction Under Lateral Action 957
 Thevaneyan K. David and Renga Rao Krishnamoorthy

Shear Failure of Pile in Clay Due to Soil–Structure Interaction 973
 Thevaneyan Krishta David, Syahrie Safri Peter, and Renga Rao Krishnamoorthy

RC Beams Strengthened with Near Surface Mounted Carbon Fiber Reinforced Polymer Plate at Short Term Saltwater Exposure 987
 Amiruddin Mishad, Mohd Hisbany Mohd Hashim, Azmi Ibrahim, Mohammad Hazizi Jamal, and Dicken Anak Baboh

Assessment on Bonding Strength of Cross Laminated Timber Made from Light Red Meranti Manufactured by Vacuum Press Method 999
 M. S. Nordin, M. B. Norshariza, W. C. Lum, N. S. Zainal, and Z. Ahmad

Effect of Kenaf Core to the Physical Properties of Cement-Sand Brick for Non-load Bearing Walls 1013
 Mohd Fadzil Arshad, Nurul Aini Salehuddin, Zakiah Ahmad, Mohd Zaim Mohd Nor, and Abdul Hadi Hassan

Bond Strength of Different Mechanically Rebar-Spliced Embedded in Concrete Under Pull Out Test 1027
 Nursafarina Ahmad, Nur Fitriah Mohd Rohzi, N. S. N. Ain Fatimah Nik Mahmood, and M. Hadri Hamidun

Construction Management

Construction Supply Chains for Strategic Materials of Building Contractors in the Greater Bandung Areas 1045
 I. Made Bhisma Pranandya, F. S. C. S. Maisarah, and Muhamad Abduh

Social Sustainability in Education: An Insight into the Civil Engineering Curricular 1063
 Nurul Elma Kordi, Sheila Belayutham, Che Khairil Izam Che Ibrahim, and Nur Shuhada Nor Shahrudin

Legacy of the Games: Portable Architecture Transforming the Host City—The Pre-game, Game and Post-game Phase 1077
 Shivangi Varma and Himanshu Sanghani

Cost Structure Identification for Third-Party Logistics Services in Construction Projects 1107
 Fauziah S. C. S. Maisarah and Muhamad Abduh

Constraint and Fault Tree Analysis in Safety Construction System Integration 1119
 N. Fitri, A. Bhaskara, and A. Purbiantoro

Identifying Competency of Housing Construction Personnel in Indonesia 1137
 Albani Musyafa’, Dhanoe Seto Nugroho, and Nelly Buldan Afifa Hidayati

Experiment to Determine Worker Needs Index in Brick Work with Space Mold Tools 1151
 Albani Musyafa’, Irsyad Hanif Ansori, and Muchammad Rizky Anugrah

Development of Entry Mode Assessment Criteria (EMAC) Model for Malaysian Construction Companies to Sustain in International Operations 1161
 Norizzati Ibrahim and Che Maznah Mat Isa

Development of Automated Web-Based Condition Survey System for Heritage Monuments Using Deep Learning 1179
 Lukman E. Mansuri and D. A. Patel

Developing Indicators of Green Operation and Maintenance of Green Supply Chain Management in Construction Industry 1193
 Mochamad Agung Wibowo, Naniek Utami Handayani, and Nur Farida

Proposed Workflow of 3D Modelling Conversion and Enhancement in Quantity Surveying Profession 1207
 Lam Tatt Soon, Hasnanywati Hassan, Nazirah Zainul Abidin, Myzatul Aishah Kamarazaly, Boon Tik Leong, and Kenn Jhun Kam

Industry 4.0 in the Malaysian Construction Industry and Its Adoption Challenges 1223
 Mohd Afiq Azinuddin Bin Tayib, Nor Azmi Bakhary, and Che Khairil Izam Che Ibrahim

Customers’ Interests in Sustainable Townships and Smart Housing Features in Malaysia 1235
 Sahithi Ajjarapu, Che Maznah Mat Isa, Divya Ganesan, Nur Kamaliah Mustaffa, Ahmad Yazed Yahaya, and Christopher Nigel Preece

Technology? Financial Viability or What? Challenges and Benefits of Eco and Reflective Roof in Malaysia 1251
 Boon Tik Leong, Cheng Fern Tey, Lam Tatt Soon, Kenn Jhun Kam, and Fuey Lin Ang

Reviewing Quality Control Management of Road Construction Projects 1261
 Debby Willar, Anak Agung Diah Parami Dewi, and Febriane P. Makalew

Review of Previous Research Methods in Evaluating BIM Investments in the AEC Industry 1273
 Jeri Adin Ardani, Christiono Utomo, Yani Rahmawati, and Cahyono Bintang Nurcahyo

Sustainable Built Environment

Seismic Performance Evaluation of Horseshoe Tunnel on Weathered-Sedimentary Rock Formation 1289
 J. R. K. Nur Aji, A. S. Fajar, T. F. Fathani, and W. Wilopo

Sustainable Construction and Its Challenges 1305
 Adhilla Ainun Musir, Siti Rashidah Mohd Nasir, Siti Hafizan Hassan, Nur Farah Asyikin Abdul Rahim, and Nurul Farah Afiqah Harun

Removal of Nutrients, Organic Matter and Total Suspended Solids from River Water by Adsorption on Chicken Eggshell 1319
 Wen-Pei Low, Fung-Lung Chang, and Shwu Ying Loo

Effect of Roofing Material on the Quality of Harvested Rainwater	1335
Nordila Ahmad, Muhammad Faiz, Zuliziana Suif, Maidiana Othman, and Siti Khadijah Che Osmi	
Impact of Proposed Bus Rapid Transit (BRT) Peshawar on Modal Shares of Private Modes	1347
Jawad Mehmood, Sameer-Ud-Din, Muhammad Jawed Iqbal, and Nasir Ali	
Design of Groundwater Filter Media Using Activated Carbon for Emergency Purpose	1357
Zuliziana Suif, Siti Khadijah Che Osmi, Maidiana Othman, Nordila Ahmad, and Adam Muhammad Ezzat Aripin	
Prediction of HMA Mixture Performance from Rheological and Rutting Evaluation of Nanopolymer Asphalt Binder	1371
Ekarizan Shaffie, Ahmad Kamil Arshad, Juraidah Ahmad, Wardati Hashim, Ramadhansyah Putra Jaya, Khairil Azman Masri, Mohd Amin Shafii, and Haryati Yacoob	
Study on Nitrogen Removal Capability of Selected Regional Sewage Treatment Plants in Klang Valley, Malaysia	1385
Suzana Ramli, Jurina Jaafar, and Raja Baharudin Raja Mohamad	
Sustainable Use of Plastic Waste on Laterite Soil as Stabilizer	1397
Nurul Ain Binti Ibrahim, Tan Jia Jun, Muhammad Irfan Shahrin, and Nur'Ain Mat Yusof	
Exploration of Palm Kernel Use in Construction: A Review	1411
Donald Kwabena Dadzie, A. K. Kaliluthin, and D. Raj Kumar	
Evaluation of the Physical and Mechanical Properties of Concrete with Partial Replacement of Coarse Aggregates with Epoxy-Based E-Waste (EBEW)	1425
Joseph Berlin Juanzon and Jaime Aquino	
The Potential of Plastic Waste as Building Material	1441
Chong Lih Yen, Myzatul Aishah Kamarazaly, Soon Lam Tatt, Nurulhuda Hashim, Shirley Chin Ai Ling, and Azrina Md. Yaakob	
Identification Characteristic of Energy Efficient Timber House	1465
Febriane Paulina Makalew, Rilya Rumbayan, and Novatus Senduk	
The Effect of Dominant Rainfall Duration on the Planning of Dimensions of Infiltration Well and the Reduction of Surface Runoff	1477
Sri Amini Yuni Astuti and Dinia Anggraheni	

Evaluation of Hot Mix Asphalt Mixtures Design Modified with Hydrate Lime 1493
 Noorfaizah Hamzah, Nur’ Ain Mat Yusof, Adnan Derahman, and Mustaqiim Mohamad

Effectiveness of Waste Glass as Filler in Hot Mix Asphalt 1507
 Noorfaizah Hamzah, Nur’ Ain Mat Yusof, Adnan Derahman, and Ahmad Hafizi Rosely

Evaluating the Impact of Junction Type on Emissions Level 1531
 Masria Mustafa and Nur Amirah Mohammad Noor

Structural and Material Engineering

Practical Measurement Method for Dynamic Structural Large Displacement Using a High-Speed Camera



Ashar Saputra and Aries Putra Purba

Abstract Structural health and monitoring systems for built infrastructure became more important at this time. During the measurement of large displacements, such as displacement of a long-span bridge, some difficulties arise. Measurements using sophisticated technology such as accelerometers with high accuracy Global Positioning System (GPS), in many cases, are not affordable. For example, a 50 m span of a steel truss bridge does not necessarily require a degree of accuracy to 10^{-2} mm of equipment since the displacement could reach 60 mm, which is $1/800$ of the span. This research contains an initial proposal for a practical and affordable dynamic measurement of displacement using a high-speed camera. The study used two high-speed cameras to record five light-emitting diodes (LEDs) on a scaled masonry house. The model laid on an R-1-1-H-1.5 MTS shake table, which accommodates three earthquakes; El Centro, Kobe, and Yogyakarta. An accelerometer was placed near the targeted position to calibrate the displacement from the camera record. TRACKER software was utilized to produce a time-displacement curve. Four time-displacement curves were compared, which are made from the shake table input and the accelerometer, and the other two are produced using two different cameras. Analysis results showed that the curve constructed from the video camera is closed to the curve from the input and accelerometer. The results imply that the initial affordable method of measurement has a good opportunity for further development.

Keywords Dynamic measurement · Graphic analysis · Displacement · High-speed camera

A. Saputra (✉) · A. P. Purba

Department of Civil and Environmental Engineering, Faculty of Engineering, Gadjah Mada University, Yogyakarta, Indonesia

e-mail: saputra@ugm.ac.id

1 Background

Recently, a lot of infrastructure development is being carried out in Indonesia. Therefore, it is also necessary to monitor the performance of the built infrastructure. Structural health and monitoring systems (SHMS) are becoming more critical, and their needs are increasing. Many approaches are needed so the SHMS can be carried out at various levels of technological readiness.

In structures with large spans such as bridges, static or dynamic deformation may occur at large sizes, at least up to a scale of dozens of cm. For dimensions of this size, several alternatives can be used for measurement. The best method is to use an accelerometer that is installed at a specific point. Another approach is to use an accurate global positioning system (GPS) device. Also, it is possible by using radio waves or laser light-based technology. However, all these systems are sometimes unavailable or unaffordable in certain conditions and environments. The aspects of cost, safety, and security may determine the success of the monitoring process.

The load acting on a structure may consist of static and dynamic loads, or more frequently, are the combination of several types of loading. Loading parameters include the magnitude, direction, and position of the load. A static load is a load for which the loading parameters are fixed. The dynamic load parameters vary accordingly to the time function. Loading parameters on dynamic analysis that are more complex than static makes it more challenging to obtain internal forces and displacement of a structure on a time series.

In addition to structural modelling, dynamic testing can be carried out using accelerometer sensors placed at dedicated points of structure. These sensors are then connected to a computer for data reading and recording. Of course, this sensor provides a more accurate structural response because it is tested directly in the field with actual structural conditions.

The use of an accelerometer sensor brings several challenges. This sensor has a significant magnitude, particularly in mass, so a strong adhesive or anchoring is needed to joint this sensor to the structure. In terms of the proper operation, this sensor must be installed carefully, bearing in mind that the connecting cable between the sensor and the analog-to-digital (AD) converter is relatively thin and prone to breaking if it experiences a large tensile force. Besides, the AD converter also requires a reliable power source, so testing will be difficult for structures in open environments that do not have electricity. While in terms of cost, a set of sensors and converters can reach tens of millions of rupiah.

The objective to be achieved through this research is to measure the displacement of a dedicated point in the structure using high-speed video recordings. This research is expected to provide an overview and initial information to determine the movement of a point in the structure using video recordings and graphic analyzing software.

2 Literature Review

Xia et al. [1] conducted a study on traffic flow data collection by tracking and analyzing vehicle trajectories through video image processing. This study aims to develop the previous method, namely the Adaptive Mean Shift (CAMShift) method, prone to target mismatches and color disturbances in heavy traffic flows. The first development carried out is to reduce the brightness level of the observed video background so that it can automatically detect and select vehicle targets. The subsequent development is to use the estimation method to estimate the next vehicle's motion and predict the new location of the vehicle. The later and the former developments were then combined to obtain a new approach that could be used to track the vehicle's position in each video frame.

This proposed method shows better results when compared to the old CAMShift process. This method produces much more accurate tracking results and is not distracted by color distraction in heavy traffic, although it takes a little longer than the older CAMShift method.

Tracking labor and equipment in a construction work area in Quebec, Canada, using a video camera placed statically at a certain point in the area have been done by Zhu et al. [2]. The study conducted in [2] was done to determine the level of productivity, security monitoring, and layout planning in the work area. Visual tracking with a video camera is compared with Real-Time Locating Systems (RLTSs) equipment that is physically installed on workers and equipment in the work area.

The MATLAB R2014b software is used for visual tracking and installed on a 64-bit computer operating system using Microsoft Windows 7 Enterprise. The results of visual tracking using a video camera compared to RLTSs equipment show a difference of between 50–78%. The weakness of the tracking system with this video camera is that tracking cannot be carried out for several objects in one video at the same time.

Hockicko et al. [3] introduced the Tracker program to students as a new and creative teaching method in physics. These students are divided into two groups: the first group uses computer modeling (in this case, using the Tracker program), and the next group uses traditional teaching methods. The results show that the ability of students to read kinematics charts in the first group (using the Tracker program) is better than the second group using traditional teaching. Video analysis helps students understand the basic principles of science and natural phenomena related to physics.

Kang et al. [4] use the Tracker program as a pedagogy to understand the movement of an object. The work presented in [4] is done to overcome several misunderstandings between existing hypotheses and modeling in real life analyzed by video. Through gradual and iterative research, the approach published by Kang et al. can improve the discovery of models that are better at studying the movement of an object in physics so that it is more fun in connecting concepts received through learning and examples in the real world.

Sirisathitkul et al. [5] used the Tracker program in video analysis to observe the movement of objects in a free fall position in the air and liquid (glycerol). Experimental results are compared with basic equations in mechanics to verify the displacement. In the case of free fall in the air, g -values with high accuracy are obtained. Also, the average speed of video analysis can represent the instantaneous velocity of the object. However, the camera's distance and the contrast between the observed object and the background significantly impact its accuracy. Whereas in the case of a fall in glycerol, the results obtained follow Stokes's law from average speed to the terminal speed.

Testing procedures performed by Sirisathitkul et al. [5] were started by manually releasing objects and captured by a digital camera (Sony DSC-W350, 14.1 megapixels, 720p) in video mode. Based on a jpeg file of 30 consecutive images per second, the ball's movement is followed frame by frame with a time interval of 33 ms using Tracker 3.1. A marker in the program identifies the pixel's position in the center of the object in each frame, and its coordinates are recorded as a free-fall function. Errors can occur due to the position of the marker. Besides, the center of the object may not coincide with individual pixels but fall between pixels. The uncertainty in marking and finding the center of an object depends more on the moving object's appearance. Before recording each experiment, the image plane is carefully aligned to be parallel to the plane of motion to minimize systematic error from the projection. Apart from the distance between the camera and the plane of motion, the height of the walls is also measured concerning the length scale in the image.

Simple equipment consisting of a digital camera and video analysis software, Tracker, is used to analyze falling objects' movement. The experimental results are then compared with fundamental equations in mechanics to verify the method used. In the case of a falling object in the air, the motion can be approached as free fall, and a value of g with high accuracy is obtained. Also, the average velocity derived from digital analysis can adequately represent the ball's instantaneous velocity being thrown and bouncing. However, the accuracy of an experiment is greatly affected by the camera distance and the contrast between the sphere and the background.

3 High-Speed and High-Resolution Video

3.1 High-Speed Video

For video recording, the frame rate is the number of images (frames) per second (fps) that a camera can capture, generally expressed in frames per second or fps. From a practical perspective, the frame rate can be seen as individual pictures being taken per second [6]. The motion pictures' standard rate was set as 24 fps, a value slightly above the perceptual limit. For this research, the video recording speed rate was set to be a minimum of 60 fps.

3.2 High-Resolution Video

Resolution is the number of pixels or picture elements arranged in a digital image. Resolution is determined by the number and set of pixels that make up the photographic image. The quantity of dots in the field of the image dramatically determines the quality of the image. Pixels are the most diminutive image dimensions in digital form. Resolution is one of the determinants of digital image quality because the resolution is directly proportional to the image's quality. The higher the resolution, the better quality of the picture. Conversely, the lower the resolution, the lower the image quality.

The sharpness and smoothness of the image are some of the main parameters in digital image processing. The sharper the image displayed, the more detailed the information presented. Usually, getting more detailed information about an image can be done directly by enlarging the image to get a more informative picture. This enlarged image can cause the image to be prone to disturbance. The image is not smooth and cannot provide accurate information, and sometimes it is difficult to evaluate.

In common practices, cameras for surveillance purposes are needed to obtain recordings and facilitate surveillance from a long distance. However, the cameras used for surveillance are generally low resolution. The surveillance camera has a resolution between QVGA (320×240 pixels) to a maximum of 2 megapixels. This low resolution is intended to transmit image data over the network quickly with minimum delay if the recording must be accessible simultaneously. Also, with this low resolution, the resulting image data can be saved with a minimum of storage. The resulting image quality is low due to the camera's low quality, especially the lack of image detail received from the recording. The low-quality image could hinder an investigation into the contents of the tapes. Therefore, a system that can clarify low-resolution video footage from the camera is needed so that the details of the images that were not visible become clearer.

4 Research Methods

4.1 Research Procedure

The one-third scale of a wall structure made of red brick was placed on the shake table machine. The movements of the wall will be recorded using two video cameras (see Fig. 1). Four light-emitting diodes (LEDs) are glued on the four corners of the one-third scale wall, and one LED is placed at the center of the wall. The model is laid on an R-1-1-H-1.5 MTS shake table, which accommodates three earthquake time history records; El Centro, Kobe, and Yogyakarta. Two high-speed video cameras are used to record the movements. One accelerometer is placed near the targeted

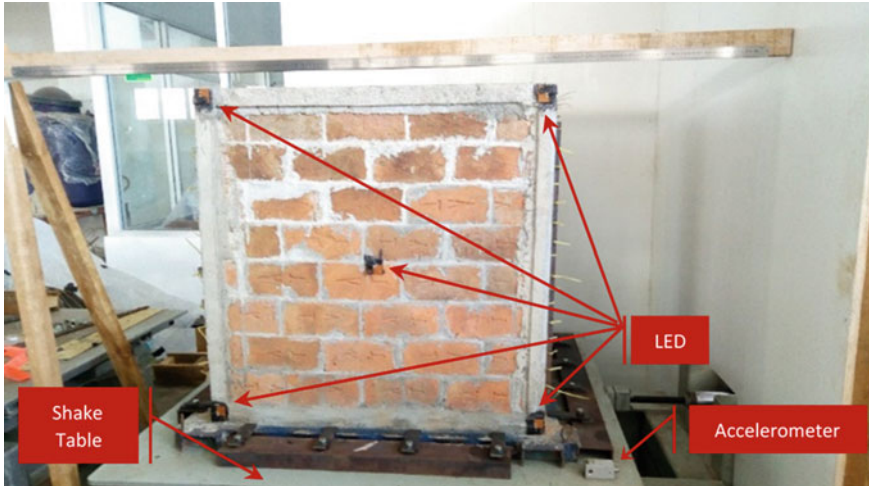


Fig. 1 One-third scaled of a wall structure laid on a shake table

position (see Fig. 1) to calibrate the displacement recorded by the camera and the displacement calculated from the analysis software.

4.2 Analysis Using Tracker Software

Firstly, the test was performed by inserting the time history data into the shake table machine. The video cameras were used to record the motion pictures. Finally, the motion pictures were analyzed using the Tracker software. The Tracker software is an OSP (Open Source Physic) software that can be downloaded for free on the web page: <https://physlets.org/tracker> (Copyright (c) 2021 Douglas Brown, Wolfgang Christian, Robert Hanson).

4.3 Shake Table Calibration

The shaking table must be calibrated prior to the test to verify that the vibration on the table aligns with the input on the computer. The calibration process is an iterative procedure that must be performed until the vibration on the table matches the computer's input data, and the shake table machine can accommodate earthquake time history records.

4.4 Recording Process and Analysis

The test specimen is a one-third scaled house brick wall. This specimen is vibrated to simulate the wall receiving three types of earthquake records. The first simulation uses the El Centro earthquake in Imperial Valley, California, on October 15, 1979. The second simulation uses the Hyogoken-Nanbu earthquake in Kobe, Japan, in 1995. The third simulation uses an earthquake record in the Yogyakarta area, which is calculated based on the spectrum response method on an Indonesian Earthquake Code SNI 1726: 2012.

During the process, the test objects were recorded using 2 (two) digital cameras, namely the Nikon Coolpix L320 and CANON EOS M10. The Nikon Coolpix L320 camera records one of the light points located at the top of the wall, which will then be analyzed using video analysis software, Tracker. The reason for choosing the top light point is to get the most significant deviation and also to compare it to the physical ruler attached to the top of the wall. Meanwhile, the Canon EOS M10 camera will record the wall as a whole to visually observe how the shake occurs on the specimens.

To simulate the Yogyakarta earthquake in a shaking table machine, it is necessary to first calculate the response spectrum in the Yogyakarta area using the spectrum response method on SNI (Indonesia National Standard) 1726: 2012 and using the Indonesia earthquake map 2017. The building has a design service life of 50 years and an earthquake risk of 2%, and a return period of 2500 years. The S_S soil acceleration parameter, namely the short period base rock acceleration of 0.2 s, is 1.25 g. Soil acceleration parameter S_1 is the base rock acceleration for 1 s period of 0.5 g. The classification of sites in the Yogyakarta area was taken as S_D (medium soil). The F_a site coefficient can be determined following the values in the SNI 1726: 2012.

The SPECTIME software produced by the ANCO Engineers, Inc. used to calculate the Yogyakarta time history earthquake input. The initial display of this ANCO software can be seen in Fig. 2.

In Fig. 2, Box 1 (one) is used to fill in the spectral response of an earthquake, which is then translated into time history data. Box 1 (one) contains the frequency and acceleration of the spectrum response. The spectral response data was calculated based on SNI 1726: 2012 in periods, and accelerations must first convert the period data into frequency data with the relation formula: $f = 1/T$.

Furthermore, the frequency and acceleration data are filled in the appropriate input box, followed by the desired earthquake duration data. In this section, the earthquake duration specified is the same as the El Centro earthquake duration, 53 s. Following the input of the earthquake duration, the Multiple Iterations command is used to perform the iteration process (Fig. 3).

After the iteration process is completed, the time history data is obtained according to the response spectrum, as can be seen in Fig. 4 (box no.5). The time history data then saved for further processing in the DANCE EQ software that runs the shaking table machine. Figure 3 shows the findings of the time history data gathered using the SPECTIME software.

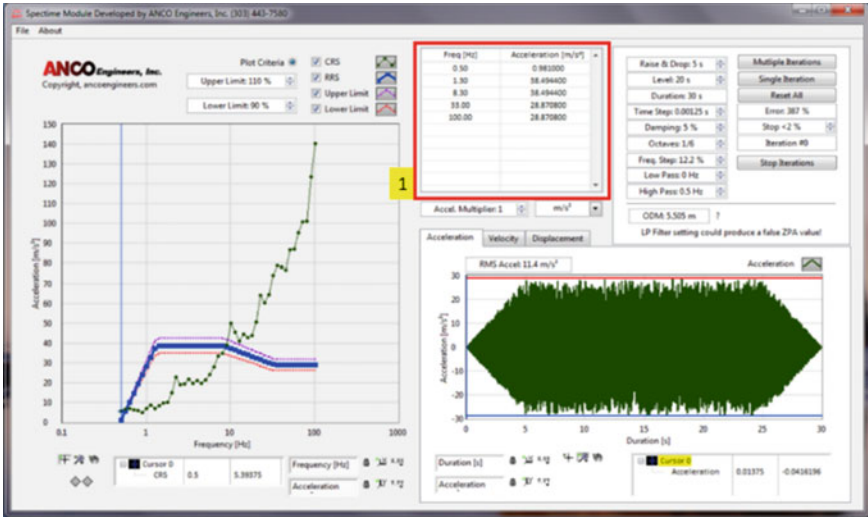


Fig. 2 Initial display of ANCO software

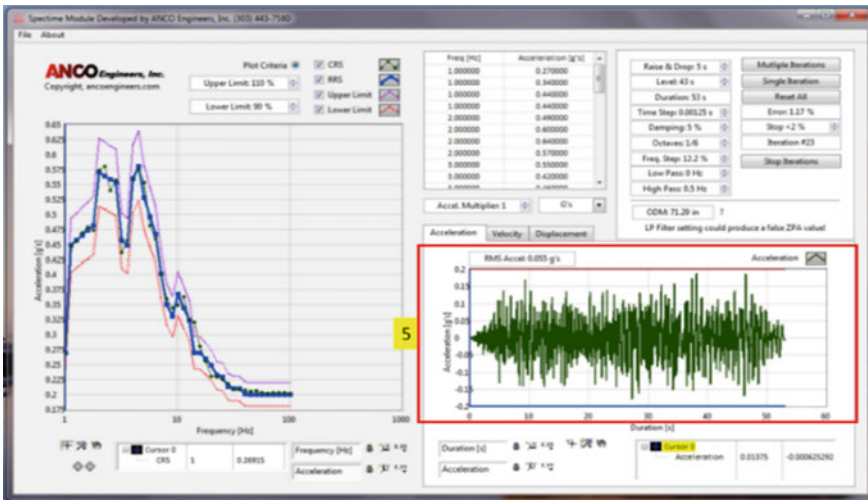


Fig. 3 Time history data obtained from the iteration process

5 Results

As shown in Figs. 4, 5 and 6, all of the video recording frames are examined to produce a Tracker software's time-displacement relationship graph. The graphs show the results of both the shake table and the Trackers software analysis.

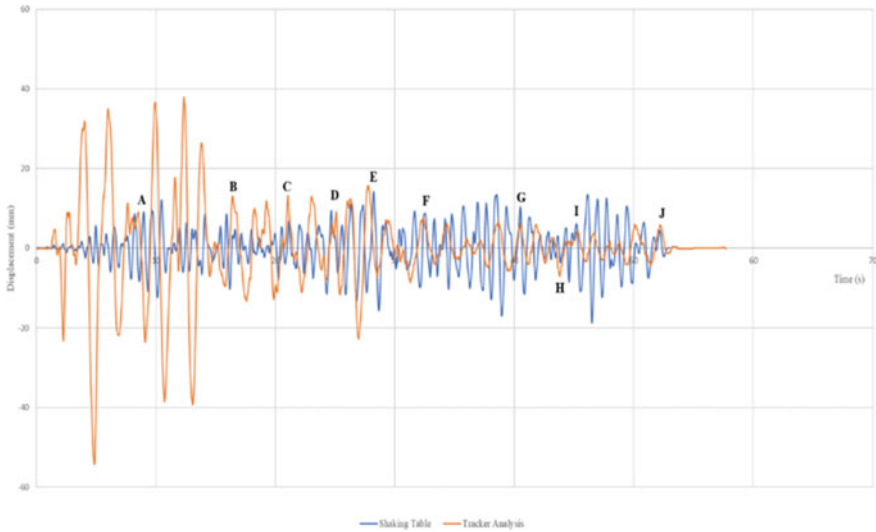


Fig. 4 Displacement–time recorded by tracker software versus shake table displacement for El-centro input

The study’s findings were presented in two ways: the first was comparing the software’s and the shake table machine’s time-displacement curves, and the second was a comparison of the measured deflection from the software analysis and the physical ruler measurement.

After the dedicated review points are analyzed using the Tracker software (as shown in Fig. 7), the displacement is compared between the analysis results using the software and the ruler installed on top of the LED light sensor. The results can be seen in Tables 1 and 2.

The shaking table machine used in this study cannot run an earthquake based on spectrum response but must use time history data. To get time history data, software on the shaking table machine computer, called SPECTIME, is used. This software will iterate until it finds a time history that matches the spectrum response data that will be the vibration input. The results of this SPECTIME software can then be used to run an earthquake on the shake table machine.

6 Discussion

Dynamic displacement measurements have been presented. Some inaccuracy has been found in those initial proposal methods due to several aspects: vibration input, the sensitivity of accelerometer, and video software analysis. Figure 3 shows an example of inaccurate results. In Fig. 5, there are significant differences in the outcome between Tracker software and input data from the shaking table machine.

Table 1 Comparison of readings on Tracker software and physical ruler for the El centro earthquake

Reference points	Deflection on video (mm)	Deflection measured with a physical ruler (mm)	Deviation (mm)	Error (%)
A	9.006	8	1.006	11.170
B	11.818	13	1.818	15.383
C	13.187	12	1.187	9.001
D	5.131	5	0.131	2.553
E	15.618	17	0.382	2.446
F	6.955	7	0.045	0.647
G	5.131	5	0.131	2.553
H	6.875	7	0.125	1.818
I	3.156	3	0.156	4.943
J	4.827	4	0.827	17.133
Average				6.867
Standard deviation				5.242

Table 2 Comparison of readings on Tracker software and physical ruler for the Yogyakarta earthquake

Reference points	Deflection on video (mm)	Deflection measured with a physical ruler (mm)	Deviation (mm)	Error (%)
A	17.955	18	0.045	0.251
B	41.609	40	1.609	3.867
C	46.058	45	1.058	2.297
D	40.749	40	0.749	1.838
E	13.865	12	0.865	6.239
F	39.557	40	0.443	1.120
G	51.797	50	1.797	3.469
H	47.260	48	0.74	1.566
I	25.569	26	0.431	1.686
J	54.138	55	0.862	1.592
K	47.252	47	0.252	0.533
L	35.694	35	0.694	1.944
M	68.264	69	0.736	1.078
N	41.208	40	1.208	2.931
Average				2.687
Standard deviation				3.262

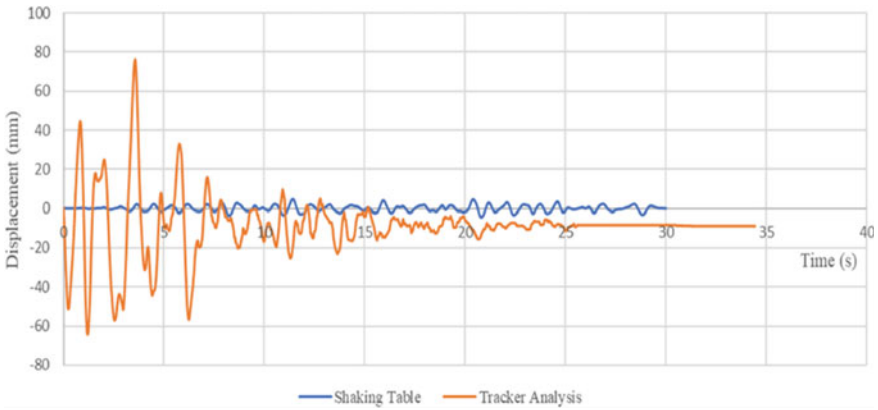


Fig. 5 Displacement–time recorded by tracker software versus shake table displacement for Hyogo-Ken-Nanbu input

This discrepancy can be caused by the input data on the shaking table machine between acceleration and time, not data between displacement and time.

The better result of vibration input d video analysis can be seen in Fig. 4 and Table 2. Both information from Fig. 6 and Table 2 showed high suitability between shake table movement and video analysis. From Table 2, it can be seen that the maximum discrepancy is 6.2%, with an average of about 2.7%. If these values can be taken as indicators, then the initial dynamic measurement proposal using high-speed video can be further developed.

Analysis regarding the high different result shown in Fig. 4 is due to the displacement data and time compared with the results of data analysis using the Tracker software. The input incorporating SPECTIME software that has been installed on the computer is used to drive the shaking table engine. To get this data, SPECTIME

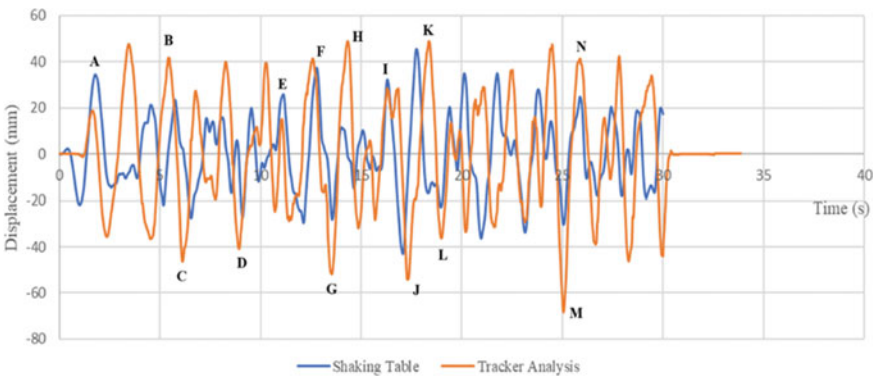


Fig. 6 Displacement–time recorded by tracker software versus shake table displacement for Yogyakarta input

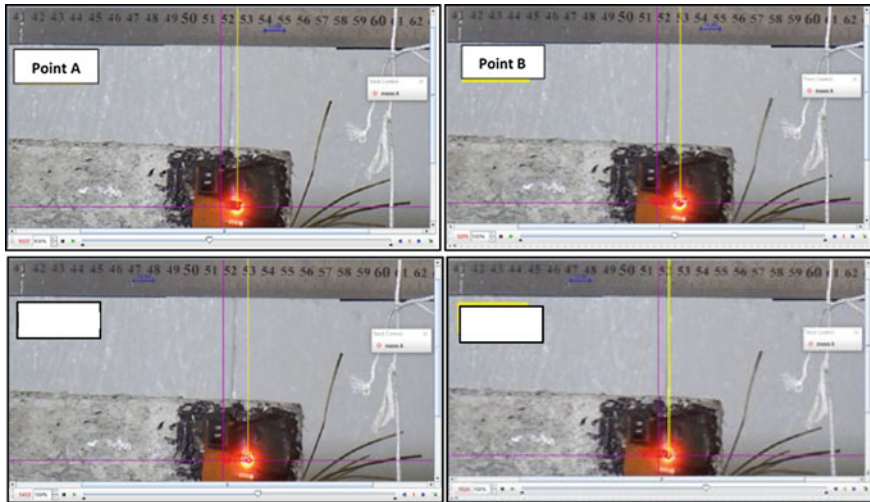


Fig. 7 Tracker software analysis for point A to point D

iterates through input data in the form of acceleration and time to get displacement and time data with an error rate of 5%. Several displacement iterations and time outcomes for the Hyogo-ken-Nanbu Earthquake must be tried one by one to get a pattern comparable to the generated data on the shaking table.

7 Conclusion

Structural and health monitoring systems are becoming more important in supporting infrastructure performance to ensure that design life is met and improved user safety. Many methods have been proposed, but an appropriate method is still needed in certain conditions and environments. The success of monitoring implementation is determined by the characteristics of cost-effective performance, operational costs, and safety in the monitoring process. Using information technology and high-speed cameras and developing graphical analysis software, an appropriate method is proposed to measure deflection in structures with large deflection values.

A study to propose the initial practical dynamic measurement method for large structural displacement has been presented. Analysis results showed that the curve produced from the video camera is closed to the curve from the input and accelerometer for certain earthquake records. The displacement analysis results using Tracker software show displacement charts that resemble the displacement graphs generated by the shaking table machine. Also, the displacement value obtained from visual measurements compared to the physical ruler placed above the measured point compared with the Tracker software analysis shows relatively close results.

Problems related to the synchronization between earthquake records and the shake table movement become the primary issue to be solved.

Further research is needed to improve the accuracy and sensitivity of the camera's accuracy and other video analyzing software. The influence of distance, level of brightness, frequency of the movement also needs to be addressed as keys variables for further study.

References

1. Xia J, Rao W, Lu Z (2012) Automatic multi-vehicle tracking using video cameras: an improved CAMShift approach. *KSCE J Civil Eng*
2. Zhu Z, Ren X, Chen Z (2012) Visual tracking of construction Jobsite workforce and equipment with particle filtering. *J Comput Civil Eng*
3. Hockicko P (2012) Video analysis of motions proceedings. Department of Physic Faculty of the Electrical Engineering University of Zilina, Slovakia
4. Wee LK, Chew C, Goh GW, Tan S, Lee TL (2015) Using tracker as a pedagogical tool for understanding projectile motion. *J Phys Educ*
5. Sirisathitkul C, Glawtanong P, Eadkong T, Sirisathitkul Y (2013) Digital video analysis of falling objects in the air and liquid using Tracker. *Revista Brasileira de Ensino de Fisica*
6. Pueo B (2016) High-speed cameras for motion analysis in sports science. *J Human Sport Exercise*

Finite Element Analysis of CRTS III Slab Track Model



Muchtar Sufaat, Ali Awaludin, Iman Satyarno, Andreas Triwiyono, Akhmad Aminullah, Mukhlis Sunarso, and Guntar Muria Adityawarman

Abstract This paper evaluated the mechanical properties of a ballastless track system using the finite element model developed in ABAQUS. The CRTS III ballastless track model was chosen, composed of steel rails, fasteners, prefabricated concrete slabs, and intermediate and base layers. The track model has a 16.8 m length in the longitudinal direction, and the analysis computation was limited to static analysis and linear-elastic material stress–strain relation. In this numerical analysis, steel rails were modeled as beam elements, fasteners were modeled as spring connectors, and prefabricated slabs, intermediate layer, and base layer were modeled as 3D solid elements. Soil support was represented as an elastic foundation throughout the length of the track model. Contact condition between track components was facilitated through surface contact elements having frictionless type. Load model LM-71 suggested by EN 1991-2 was applied to the track model through a load factor (k_1), and soil elastic foundation coefficient (k_s) varied from 0.01 to 0.06 N/mm³. Initially, patch test analysis to ensure convergence of the numerical solution was conducted and perform simple analysis using one point load acting on the track model to compare the numerical results with the calculation given by Zimmermann and Westergaard's methods provided by EN 16432-2 (2017). The numerical results indicated that the axial fastener force and flexural stress steel rail has a linear function with respect to k_1 , while the deflection of steel rail, flexural stress of prefabricated concrete slab, intermediate layer and the base layer is best described by $\alpha(k_s)^\beta k_1$ where α and β are constants. As the minimum subgrade modulus stiffness required by EN 16432-1 (2017) is 60 N/mm², which is equivalent to a subgrade modulus reaction k_s of 0.0153 N/mm³, a load factor k_l of 1.28 will result in steel rail deflection of 6 mm,

M. Sufaat · A. Awaludin (✉) · I. Satyarno · A. Triwiyono · A. Aminullah
Universitas Gadjah Mada, Yogyakarta, Indonesia
e-mail: ali.awaludin@ugm.ac.id

I. Satyarno
e-mail: imansatyarno@ugm.ac.id

M. Sunarso · G. M. Adityawarman
PT. Wijaya Karya Beton, Jakarta, Indonesia
e-mail: guntara@wika-beton.co.id

which is the allowable value recommended by the American Railway Engineering and Maintenance-of-Way Association.

Keywords CRTS III ballastless track · Load model 71 · Subgrade modulus · Reaction · Finite element analysis · Railway

1 Introduction

Indonesia is currently developing high-speed railway plans in which one of which is a railway plan connecting Jakarta city and Surabaya city in Java Island. In general, railway tracks are divided into two-track systems: ballasted track system, known as conventional track, and ballastless track system or slab track. In the ballastless track system, the concrete slab replaces the traditional function of ballast. The load acted above the train rail was distributed to the slab track through the fasteners. According to Esveld [1], the ballastless track system has become a popular choice in many countries. This track system has higher service life and less regular maintenance cost than the ballasted track system.

Many studies presented analytical or numerical approaches to evaluate the mechanical behavior of a slab track, including the stresses developed on the concrete slab under a given load model. The analytical approaches proposed by Zimmermann and Westergaard found in EN 16432-2 [2] were limited to one single concrete slab and a simple concrete slab model. A condition where a load model applied to more than one concrete slab was not able to take into consideration in their approaches. In this case, numerical approaches based on the finite element model will become a better choice to explore and simulate the mechanical behavior of slab track. Yen and Lee [3] utilized the ABAQUS program to numerically modeled slab track in 3D shell and solid elements. The train rails were assumed as beam elements, while the fasteners were assumed as spring elements and the resulted stress versus deformation then normalized using a closed-form solution.

In 2012, Xu and Li [4] evaluated mechanical characteristics of slab track connecting Suining to Chongqing in China using ANSYS. In their evaluation, the deadweight of slab track and train and temperature influence was taken into account. The results show that the load position significantly affects the longitudinal stress of the slab and concrete base. Furthermore, the proportion of the longitudinal stress and longitudinal moment of the slab and concrete base due to distributed load, temperature load, and local settlement was 45, 35, and 20%, respectively. While the proportion of transversal stress of the slab and concrete base developed by distributed load, temperature load, and local settlement was 60, 35, and 5%, respectively.

Sun et al. in 2013 [5] conducted a static analysis of CRTS III ballastless track using a finite element model developed using ABAQUS. The track was simulated on top of a soil embankment and a bridge. The result shows that the rail deformation and stress at the concrete were higher when the load was applied in the slab's critical position (in the slab end position). In 2017, Raja et al. [6] evaluated Continuously

Reinforced Concrete Pavement (CRCP) ballastless track based on a finite element model developed in SOFisTik and the analytical model proposed by Zimmermann and Westergaard. The load assigned in the rail was based on the LM-71 model with some modification factors depending on the loading condition.

This study aims to provide a database of the mechanical behavior of slab track evaluation based on the finite element model under different soil conditions and the magnitude of the selected load model. CRTS III ballastless track was chosen for this study, and the numerical analysis was performed using ABAQUS. The analysis focused on flexural stress and deformation of steel rail, fastener’s axial forces and flexural stress concrete slab of CRTS III track system where linear stress–strain relations was assumed for both concrete and steel materials. Numerical analysis was conducted to evaluate the short term response of the structure under the LM-71 load model.

2 Ballastless Track Model

Figure 1 provides some examples of ballastless track models used in different countries where in general, they can be categorized into discrete rail support type and continuous rail support type [7]. CRTS III ballastless track used in this study are included in a discrete rail support system. It is composed of steel rails at the top, fasteners that connect steel rail to concrete slab, prefabricated concrete slabs, base layer or (cast-in-place) concrete roadbed at the bottom, and an intermediate layer

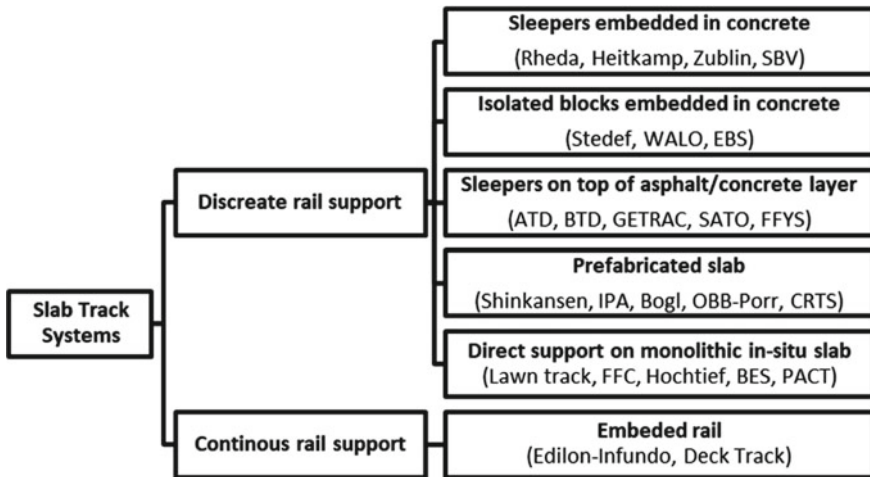


Fig. 1 Classification of ballastless track system [7]

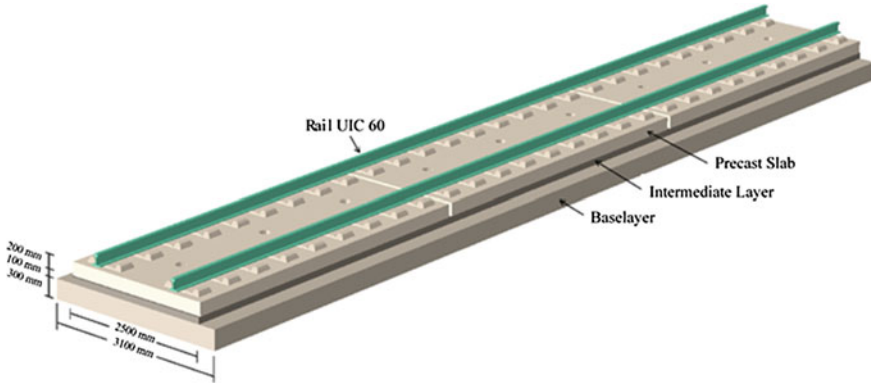


Fig. 2 CRTS III ballastless track model used in this study

between prefabricated concrete slab and base layer. Figure 2 shows the CRTS ballastless track model used in our numerical study, where it has three connected units of prefabricated concrete slabs of equal length 5600 mm.

According to the ballastless track system classification presented in Fig. 1, CRTS III can be classified as a prefabricated slab type. CRTS III was the development of CRTS I (developed and applied in Japan) and CRTS II (developed and applied in Germany).

CRTS III was later developed in China and applied since 2011 [8]. The precast slab was pre-stressed in both longitudinal and lateral directions of the concrete slab. Moreover, the intermediate layer of CRTS III was made of self-compacted concrete (SCC) layer to replace the Concrete Asphalt mortar (CAM) layer commonly used in the CRTS I and CRTS II. The design of the slab track is similar to the rigid pavement design.

Figure 2 shows the CRTS ballastless track model used in our numerical study, where it has three connected units of prefabricated concrete slabs of equal length 5600 mm. Pre-stressed and non-pre-stressed steel reinforcement bars were placed inside the concrete slab track. For non-prestressed reinforcement, 8 mm steel bars were used, placed at the top and the bottom of the concrete slab. Sixteen (16) steel bars were arranged longitudinally, while 34 steel bars were arranged transversely. The pre-stress reinforcements bars, tendon effective area of 54.84 mm^2 were also placed inside the concrete slab. Eight (8) longitudinal pre-stressed tendons were arranged in each top and bottom of the concrete slab. In addition, twenty-four (24) pre-stressed lateral tendons were placed inside the concrete slab in one layer.

As shown in Fig. 2, the base layer of the selected CRTS III model's width is 3100 mm, with a concrete thickness of 300 mm. The intermediate layer located above the base layer has a width and thickness of 2500 and 100 mm. The width of the concrete precast slab is 2500 mm with a 200 mm thickness. The cross-sectional area of the steel rail UIC 60 placed above the slab track is 3038.3 cm^2 .

2.1 Soil-Structure Interaction

Soil-structure interaction was modeled by elastic springs where the only vertical direction was considered in the analysis. The spring constant, or often called subgrade modulus reaction, is expressed by Eq. (1).

$$ks = q \delta \quad (1)$$

where ks is the subgrade modulus reaction (N/mm^3), q is the pressure (N/m^2), and δ is the vertical displacement (mm).

2.2 Finite Element Model

The weighted residual method was utilized in the numerical analysis based on the finite element model. ABAQUS software was used to perform this analysis. This weighted residual method in an approximate technique for solving boundary value problems that utilize trial functions to satisfy the existing boundary conditions. ABAQUS program facilitates various types of elements required to generate many engineering structures. Those elements are 3D solid elements, shell elements, infinite elements, rigid elements, spring and dashpot elements, and truss elements.

Equation (2) was commonly used to solve the boundary value problem in the finite element method.

$$\underline{KU} = \underline{F} \quad (2)$$

where \underline{K} , \underline{U} , and \underline{F} Represent the stiffness, nodal displacement, and nodal force of each element. The definition of the geometric equation component was shown in Eq. (3), followed by the constitutive formula presented in Eq. (4) [9].

$$\underline{\varepsilon} = \underline{\frac{\partial u}{\partial x}} \quad (3)$$

$$\begin{Bmatrix} \varepsilon_x \\ \varepsilon_y \\ \varepsilon_z \\ \gamma_{xy} \\ \gamma_{yz} \\ \gamma_{xz} \end{Bmatrix} = \begin{bmatrix} \frac{\partial}{\partial x} & 0 & 0 \\ 0 & \frac{\partial}{\partial y} & 0 \\ 0 & 0 & \frac{\partial}{\partial z} \\ \frac{\partial}{\partial y} & \frac{\partial}{\partial x} & 0 \\ 0 & \frac{\partial}{\partial z} & \frac{\partial}{\partial y} \\ \frac{\partial}{\partial z} & 0 & \frac{\partial}{\partial x} \end{bmatrix} \begin{Bmatrix} u \\ v \\ w \end{Bmatrix}$$

$$\underline{\sigma} = \underline{C}\underline{\varepsilon}$$

$$\begin{Bmatrix} \sigma_{xx} \\ \sigma_{yy} \\ \sigma_{zz} \\ \tau_{xy} \\ \tau_{yz} \\ \tau_{xz} \end{Bmatrix} = \frac{E}{(1+\nu)(1-2\nu)} \begin{bmatrix} (1-\nu) & \nu & \nu & 0 & 0 & 0 \\ \nu & (1-\nu) & \nu & 0 & 0 & 0 \\ \nu & \nu & (1-\nu) & - & 0 & 0 \\ 0 & 0 & 0 & \frac{1-2\nu}{2} & 0 & 0 \\ 0 & 0 & 0 & 0 & \frac{1-2\nu}{2} & - \\ 0 & 0 & 0 & 0 & 0 & \frac{1-2\nu}{2} \end{bmatrix} \begin{Bmatrix} \varepsilon_x \\ \varepsilon_y \\ \varepsilon_z \\ \gamma_{xy} \\ \gamma_{yz} \\ \gamma_{xz} \end{Bmatrix} \quad (4)$$

In Eq. (3), u , v , and w refer to the nodal translation in x , y , and z -direction. In addition, ε , γ , σ , and τ refer to the strain, rotation, axial stress, and shear stress in the specified direction.

Through the ABAQUS model, the prefabricated concrete slab, intermediate layer, and base layer were modeled as 3D solid elements. The steel rail was modeled as a beam element, and the fasteners were model as elastic spring connectors. The pre-stressed and non-prestressed steel reinforcement bars were modeled as truss elements. Contact problems between two adjacent components were facilitated via contact surface element having a frictionless type. Under the base layer or concrete roadbed, soil support is modeled as an elastic foundation with a single value of modulus subgrade reaction coefficient (k_s).

The American Railway Engineering and Maintenance-of-way Association (AREMA), in their document, indicated that for slab track design, the maximum vertical deflection of steel rail is 6 mm, and the longitudinal stress created in the steel rail due to bending shall not exceed 77 MPa [10]. In addition, EN 16432 (2017) gives the minimum stiffness modulus of the substructure of the slab track system should not exceed 60 N/mm². The acceptance criteria of the slab track component should also consider its maximum compressive and tensile stress capacity. The safety factor of the material's capacity is usually taken as 0.5 [14].

The accuracy of the FEA results was affected by several aspects, including the assumption and simplification conducted in the FE model and the meshing size. Therefore, before proceeding with further analysis, a patch test was conducted for some parameters of the FE model listed in Table 1 to ensure that solutions given by the FEA numerical method converge to the exact solutions. For this case, one-third of the ballastless track model shown in Fig. 2 was isolated for the numerical calculation. Its numerical results were then compared to the analytical solutions given by Zimmermann and Westergaard method. Mesh size of 50 mm in longitudinal and lateral directions was found reasonable, as indicated in Table 1, owing to know that a smaller size less than 50 mm would increase significantly computer memory size as well as computation time. The analysis was carried out on a PC with 32 GB of RAM. In this patch test, the element of the prefabricated slab, intermediate layer, and base layer was divided into six layers (of equal mesh thickness) per each.

Table 1 Results of patch test with a mesh size of 50 mm

Observation		Error mesh (%)	Theory/numeric	
Rail deflection		0.41	–	
Slab deflection		1.27	–	
Fastener’s axial force		0.10	0.97	
Rail flexural stress		0.28	1.22	
		Error mesh (%)	Westergaard	Zimmermann
<i>Precast Slab</i>	Longitudinal Stress	9.45	0.97	1.36
	Lateral Stress	10.03	1.64	–
<i>Intermediate Layer</i>	Longitudinal Stress	–	1.68	2.35
	Lateral Stress	–	2.78	–
<i>Base Layer</i>	Longitudinal Stress	5.78	1.15	1.30
	Lateral Stress	4.73	2.73	–

2.3 Parametric Study

The CRTS III ballastless track model was statically analyzed using the load model LM-71 defined by EN 1991-2 [11], as illustrated in Fig. 3. The load model was applied for two steel rails so that half of it was applied to one steel rail. This loaded model LM-71 was symmetrically applied to the track model shown in Fig. 2, thus all point load components of this LM-71 were applied on the middle prefabricated concrete slab, while the uniformly distributed load component of this LM-71 was applied on both left and right side of the prefabricated concrete slabs. This load model was applied to the track model through load factor (k_1) equals to 1.0, 2.0, 3.0, and 4.0.

Steel rail UIC 60 type was used in this study, and the soil layer beneath the base layer was modeled through sub-grade modulus reaction coefficient (k_s) that varies from 0.01 to 0.06 N/mm³. Fasteners connected steel rails to prefabricated concrete slab was represented by spring connector having a spring constant of 40 kN/mm. The longitudinal spacing of the fastener was set into 630 mm.

Figure 4 shows the material model for concrete and steel where linear-elastic stress–strain relation idealization was assumed during the computation. The Young modulus of the concrete was obtained using the empirical formula provide by SNI

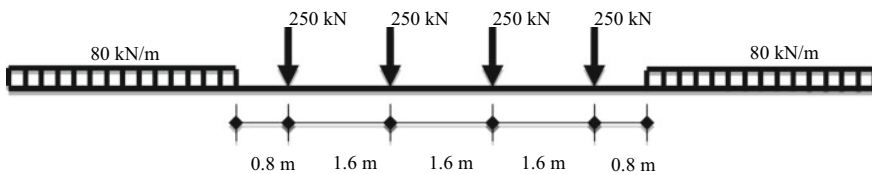


Fig. 3 Load model LM-71 (EN 1991-2, 2003)

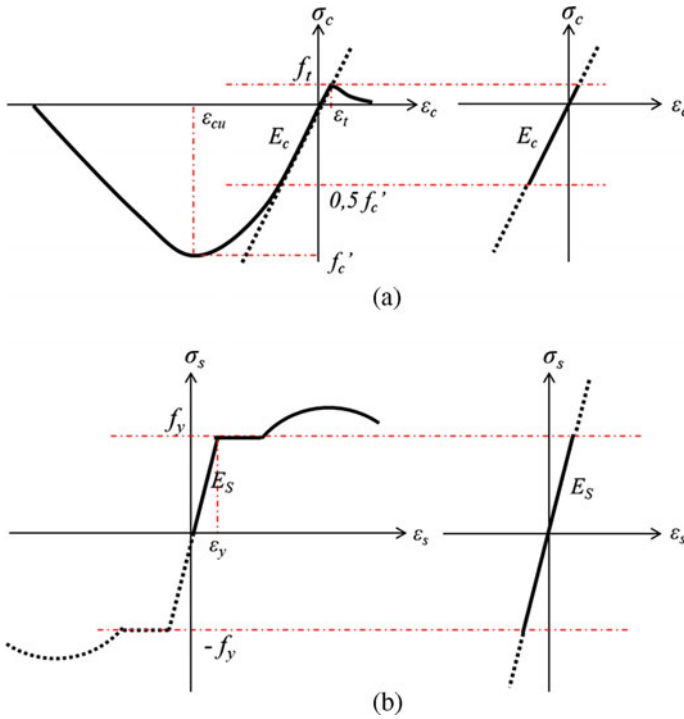


Fig. 4 Linear-elastic stress–strain relation and its idealization: **a** concrete material; **b** steel material

2847-2013 [12], as expressed in Eq. (5). According to SNI 2847-2002 [13], the tensile strength of the concrete can be derived from its compressive strength, as shown in Eq. (6).

$$E_c = 4700\sqrt{f'_c} \tag{5}$$

$$f_r = 0.7\sqrt{f'_c} \tag{6}$$

where E_c is the young modulus of the concrete, f'_c is the concrete compressive strength, and f_r is the concrete tensile strength.

Material properties of concrete for the precast slab is as follows: compressive strength of 60 MPa, Poisson’s ratio of 0.2, Young Modulus of 36,000 MPa, the density of 24 kN/m³. Material properties of steel rail are Poisson’s ratio of 0.3, Young Modulus of 210,000 MPa, the density of 78 kN/m³. The material properties of steel reinforcement of the precast concrete slab are Poisson’s ratio of 0.2, Young Modulus of 210,000 MPa, yield stress 400 MPa, and yield stress of 1700 MPa for the pre-stressed steel wires. The compressive strength of the intermediate layer and base layer is 50 MPa and 25 MPa, respectively. The Young modulus of the intermediate

layer and base layer is 33,200 MPa and 23,500 MPa, respectively. The numerical analysis was conducted to obtain the structure's short-term responses due to train load in static and linear conditions.

3 Results and Decision

Mechanical properties of the ballastless track model investigated in this study were limited to steel rail deflection, steel rail flexural stress, fastener's axial forces, and flexural stress of the concrete slab component. Allowable deflection of steel rail of a ballastless track of 6 mm is required by American Railway Engineering and Maintenance-of-Way Association (AREMA) [10]. Figure 5 shows the vertical displacement of the ballastless track model under load factor (k_1) equals 1.0 and subgrade-modulus reaction (k_s) equals to 0.025 kN/mm³ where the maximum displacement was located at middle steel rail.

In Fig. 5, deflection of the steel rail will surely be slightly higher as contribution of axial deformation of the fastener, caused by an axial force developed during loading, must be considered. Axial deformation of the fasteners can be calculated based on the information of axial forces in the spring connector provided by the numerical results (see Fig. 6) and spring constant-coefficient set in the calculation, which is 40 kN/mm. The distance between two adjacent fasteners is 630 mm.

The deflection of the ballastless track model for the various magnitude of load factor and sub-grade modulus reaction is presented in Fig. 7. Vertical deflection of the ballastless track model has a linear relationship with load factor k_1 , where deflection increases as load factor increases. Higher coefficient of subgrade modulus reaction caused smaller deflection of the ballastless track model. The relation between steel rail deflection (δ_{rail}) and load factor (k_1) or subgrade modulus reaction coefficient (k_s) can be written as follows:

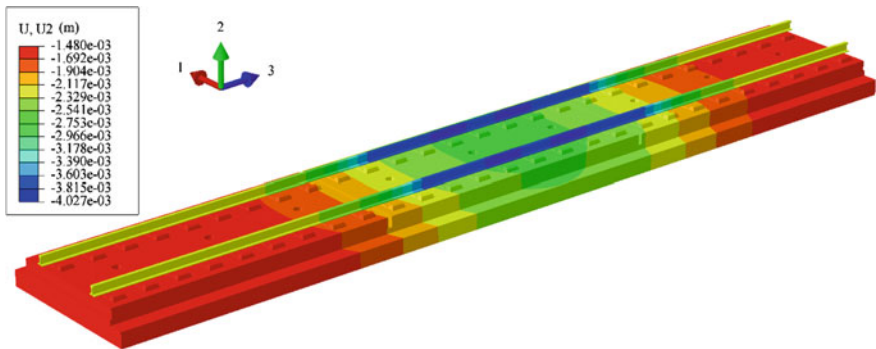


Fig. 5 Vertical displacement of the ballastless track model ($k_1 = 1.0$, $k_s = 0.025$ N/mm³)

Fig. 6 Axial forces in fasteners of the ballastless track model ($k_1 = 1.0$, $k_s = 0.025 \text{ N/mm}^3$)

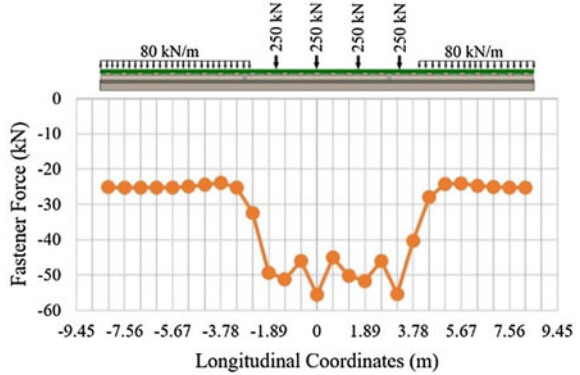
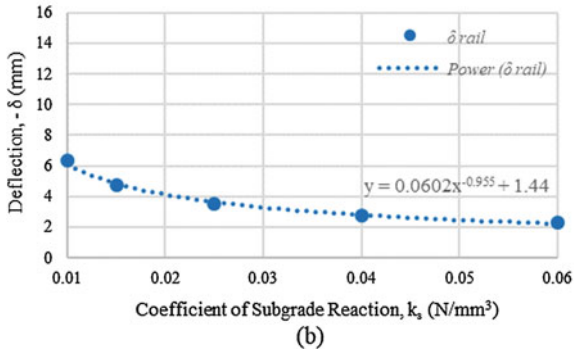
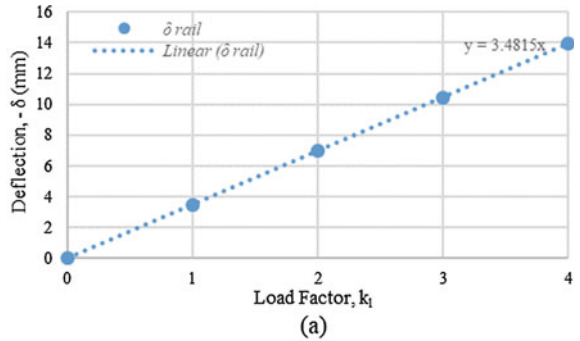


Fig. 7 Deflection of ballastless track model: **a** different value of load factor k_1 ; and **b** different value of subgrade modulus reaction k_s

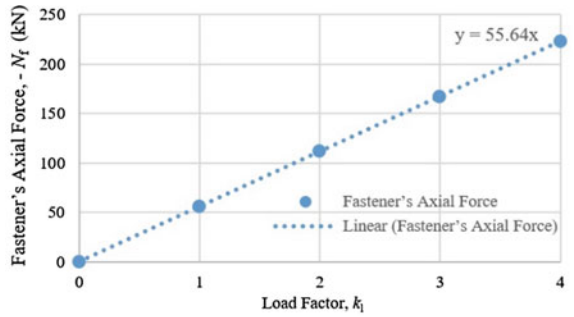


$$\delta_{rail} = 3.4815 k_1 \tag{7}$$

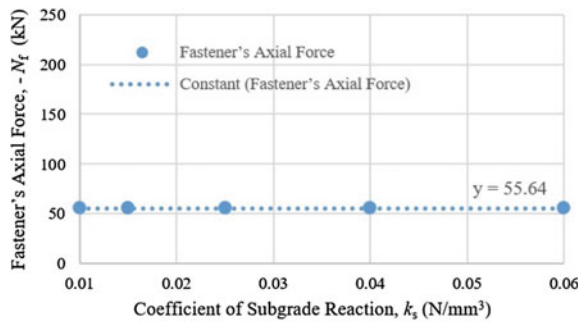
$$\delta_{rail} = 0.0602 k_s^{-0.955} + 1.44 \tag{8}$$

Fastener's axial force linearly increases concerning load factor (k_1) as shown in Fig. 8a, but it is nearly constant no matter the magnitude k_s changes (see Fig. 8b).

Fig. 8 Relation between fastener’s axial force and load factor k_1 **a**; or subgrade modulus reaction coefficient k_s **b**



(a)



(b)

The relation between the fastener’s axial force (N_f) and load factor (k_1) can be written as follows:

$$N_f = 55.64 k_1 \tag{9}$$

The distribution of flexural stress of steel rail at the bottom side obtained from the numerical analysis is shown in Fig. 9 in which maximum flexural stress occurs at the middle rail, specifically beneath the application of point loads. Under the condition of k_1 and k_s , respectively, equal to 1.0 and 0.025 N/mm³, the maximum flexural stress of steel rail was found comparable to 50 MPa. This maximum flexural stress is still less than the allowable limit requested by AREMA [10], which is 77 MPa. Figure 10 shows the distribution of flexural stress in both the longitudinal axis and lateral axis of the prefabricated concrete slab (CS), the intermediate layer (IL), and the base layer (BL) under the condition of k_1 equal to 1.0 and k_s similar to 0.025 N/mm³. AREMA [10] suggested that the tensile stress must not exceed 50 percent of the tensile strength of the concrete (f_r), which can be calculated based on Eq. 6 given by Indonesia National Standard SNI 2847 [13].

Thus, allowable tensile stress for prefabricated concrete slab, intermediate layer, and the base layer are as follows:

Fig. 9 Distribution of flexural stress of steel rail ($k_1 = 1.0$, $k_s = 0.025 \text{ N/mm}^3$)

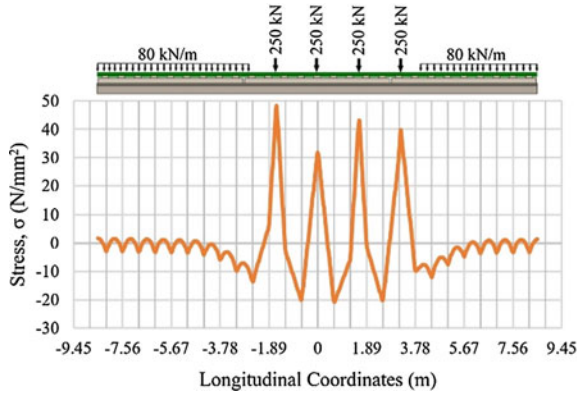
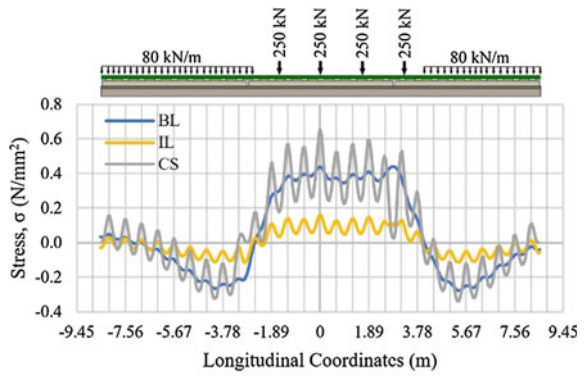
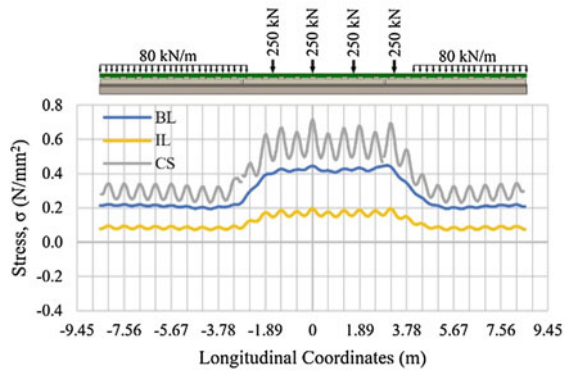


Fig. 10 Distribution of flexural stress in the prefabricated concrete slab (CS), intermediate layer (IL), and base layer (BL) under $k_1 = 1.0$ and $k_s = 0.025 \text{ N/mm}^3$: **a** longitudinal direction; **b** lateral direction



(a)



(b)

Prefabricated concrete slab: $0.5 \times 0.7\sqrt{60} = 2.71$ MPa
 Intermediate layer: $0.5 \times 0.7\sqrt{50} = 2.48$ MPa
 Base layer: $0.5 \times 0.7\sqrt{25} = 1.75$ MPa.

Evaluation of maximum flexural stress of the prefabricated concrete slab, intermediate and base layers in both longitudinal and lateral directions, and maximum flexural stress of steel rail for the different magnitude of k_1 and k_s are described in Fig. 11. Increment of load factor k_1 causes an increase in flexural stress of steel rail, prefabricated concrete slab, and intermediate and base layers. Flexural stresses of steel rail and flexural stresses of prefabricated concrete slab, intermediate and base layers in the lateral direction are constants though the magnitude of k_s changes.

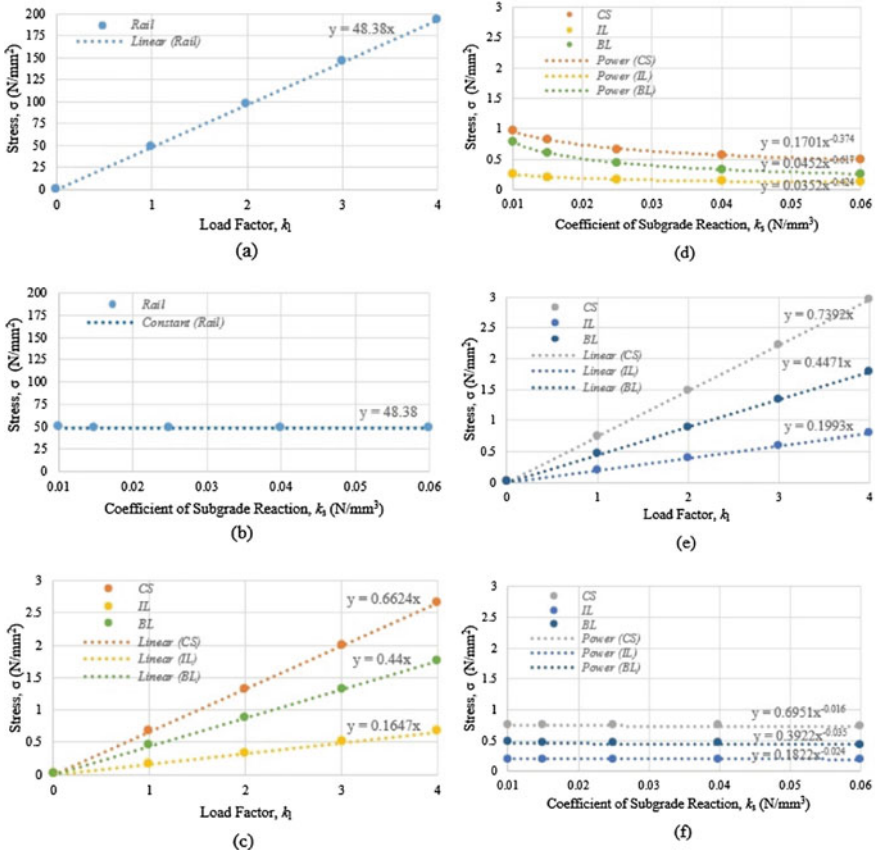


Fig. 11 Relation of maximum flexural stress for different magnitude of k_1 and k_s : **a** flexural stress of steel rail versus k_1 ; **b** flexural stress of steel rail versus k_s ; **c** longitudinal flexural stress of CS, IL, and BL versus k_1 ; **d** longitudinal flexural stress of CS, IL, and BL versus k_s ; **e** lateral flexural stress of CS, IL, and BL versus k_1 ; **f** lateral flexural stress of CS, IL, and BL versus k_s

Table 2 Equations to calculate mechanical properties of the ballastless track model

No	Ballastless track component	Equation	
1	Steel rail		
	Deflection, d_{rail} , (mm)	$(0.0602 k_s^{-0.955} + 1.44) k_1$	(10)
	Flexural stress (MPa)	$48.38 k_1$	(11)
2	Fastener		
	Axial force, N_f , (kN)	$55.64 k_1$	(12)
3	Prefabricated concrete slab		
	Longitudinal flexural stress (MPa)	$0.1701 k_s^{-0.374} k_1$	(13)
	Lateral flexural stress (MPa)	$0.6951 k_s^{-0.016} k_1$	(14)
4	Intermediate layer		
	Longitudinal flexural stress (MPa)	$0.0352 k_s^{-0.424} k_1$	(15)
	Lateral flexural stress (MPa)	$0.1822 k_s^{-0.024} k_1$	(16)
5	Base layer		
	Longitudinal flexural stress (MPa)	$0.0452 k_s^{-0.617} k_1$	(17)
	Lateral flexural stress (MPa)	$0.3922 k_s^{-0.016} k_1$	(18)

However, the flexural stress of prefabricated concrete slab, intermediate and base layers in longitudinal direction decreases as k_s value increases.

Combining factors of k_1 and k_s into one equation that defines the mechanical properties of the ballastless track model is necessary for practical and quick evaluation. In this regard, the following general equation is used where R is the targeted mechanical properties α and β the constants.

$$R = \alpha(k_s)^\beta(k_1) \quad (9)$$

These equations are summarized in Table 2 as follows.

EN 16432-1 [11] recommended a minimum sub-grade stiffness Modulus of 60 N/mm^2 for high-speed railways, equivalent to subgrade modulus reaction coefficient k_s of 0.0153 N/mm^3 . Utilizing this information that $k_s = 0.0153 \text{ N/mm}^3$ together with the Eq. 10 in Table 2 and set steel rail deflection (δ_{rail}) equals to 6 mm (as suggested by AREMA, [10]), then the value of load factor k_1 will be equal to 1.28.

4 Conclusions

Numerical evaluation of mechanical properties of CRTS III ballastless track system using finite element model developed in ABAQUS was carried out in this study. The load model LM-71 given by EN 1991-2 [11] was adopted, and the analysis was limited to linear-elastic material stress–strain relation. This study found that a load factor of

1.28 caused steel rail deflection of 6 mm, which is the maximum deflection allowed by the American Railway Engineering and Maintenance-of-Way Association [10]. A further study considering dynamic analysis is required to consider the train speed effect on the mechanical properties of the investigated ballastless track model.

Acknowledgements This study was conducted under partnership research between the Civil and Environmental Engineering Dpt., Faculty of Engineering, Universitas Gadjah Mada and PT. Wijaya Karya Beton in 2018.

References

1. Esveld C (2010) Recent developments in slab track. In: First international conference on road and rail infrastructure, Holand
2. EN 16432-2 (2017) System design, subsystems and components—Ballastless track systems. British Standards Institution, London
3. Yen ST, Lee YH (2007) Parameter identification and analysis of a slab track system using 3D ABAQUS program. *J Transp Eng* 133:288–297
4. Xu Q, Li B (2012) Study on spatial mechanical characteristic of high-speed railway Ballastless slab track on subgrade. In: Advanced material research, Switzerland
5. Sun L, Duan YF, Yang X (2013) Static response analysis of CRTS III type slab Ballastless track. *J Railway Eng Soc* 16(11):32–39
6. Raja MNA, Rashid U, Sajjad U (2017) Comparative analysis of Ballastless track system design using analytical and numerical tools. *Technical Journal UET, Taxila*
7. C4R (2012) Design requirements and improved guidelines for design. European Union's Seventh Frame Work for Research, Paris
8. Yuan X, Tian G, Wang K, Zhai W (2016) Analysis on the dynamic performance of a high-speed train running on different. In: International conference on transportation and development. ASCE, Chengdu, pp 434–445
9. Moharos I, Oldal I, Szekrényes A (2012) Finite element methode. Szent István University Faculty of Mechanical Engineering, Budapest, Hungaria
10. AREMA (2017) Chapter 8, Part 27—concrete slab track. American Railway Engineering and Maintenance of Way Association, Landrover
11. EN 1991-2 (2003) Traffic load on bridge—actions on structures. British Standards Institution, London
12. Standard Nasional Indonesia, Persyaratan Beton Struktural untuk Bangunan Gedung (SNI 2847-2013). Jakarta: Badan Standardisasi Nasional, 2013. In Bahasa
13. Standard Nasional Indonesia, Persyaratan Beton Struktural untuk Bangunan Gedung (SNI 2847-2002), Jakarta: Badan Standardisasi Nasional, 2002. In Bahasa
14. EN 16432-1 (2017) General requirements—Ballastless track systems. British Standards Institution, London

Effect of Partial Replacement of Cement with Volcanic Ash on Mechanical Behaviour of Mortar



Md. Shahjalal, Jesika Rahman, Afia Farzana Haque, Lutful Habib, Khadiza Binte Jalal, and Mohd Mezanur Rahman

Abstract Portland Composite Cement (PCC) has so far been the most used binding material worldwide. However, it is also one of the significant sources of carbon dioxide emitters leading to global warming. It is, therefore, of utmost importance nowadays in developing nations that a sustainable cementitious material is developed. Volcanic ash (VA) is the debris found after volcanic eruptions. VA shows pozzolanic properties upon reacting with calcium hydroxide, which is given off during cement hydration. This paper represents the effect of VA on the physical and mechanical properties of mortar. VA is used to replace PCC by 5, 10, 15 and 20% by weight. The results of the mechanical properties are represented in terms of compressive strength, whereas the physical properties are illustrated through its specific gravity, fineness, setting time and consistency. This study shows that the compressive strength of the hardened mortar increases as the replacement is increased up to 15% by weight and then decreases as the replacement with VA is greater. Lastly, this study suggests the potential of VA as a partial substitute for cement to fabricate green concrete structures.

Keywords Volcanic ash · Cement replacement · Mortar · Compressive strength

1 Introduction

The use of supplementary cementitious materials (SCM) today is vital to maintain the stability of the environment. Concrete production remains one of the most prominent causes of global warming, and the concern has reached an alarming stage as

Md. Shahjalal (✉) · J. Rahman · A. F. Haque · L. Habib
Military Institute of Science and Technology, Dhaka, Bangladesh
e-mail: shahjalal@ce.mist.ac.bd

J. Rahman
e-mail: jesikarahman547@ce.mist.ac.bd

K. B. Jalal · M. M. Rahman
University of Texas, Arlington, USA

modernization continues. The production of Portland cement alone contributes to about 6% anthropogenic CO₂ emission, increasing the greenhouse effect worldwide [1]. The intensive technology undertaken for the manufacturing of cement poses a severe threat to the natural reservoirs. Sometimes referred to as mineral admixtures [2], the SCMs are generally industrial by products that do not have pozzolanic properties inherently, but when added to Portland cement, they react to form pozzolanic compounds. Typical examples of SCM include fly ash, blast furnace slag, silica fume and natural pozzolans such as volcanic ash (VA). Upon replacing even, a small percentage of cement with these SCMs can significantly reduce the load on natural resources by using less energy and protecting the environment. Previously, several studies have been carried out to observe the Effect of replacing Portland cement partially by rice husk, blast furnace slag, fly ash, fuel ash and silica fume [3–7]. It is observed that such additives do produce concrete strength similar to those produced from Portland cement. These low-cost alternatives for general-purpose Portland cement provide many scopes, such as self-sufficient means of shelter for the developing nations. Other benefits of concrete made of SCMs include strength and durability enhancements compared to conventional Portland cement concrete [8–10]. Self-consolidating concrete mixture is prevalent to be used in complex and massive concrete structures. Previous researchers have found that self-consolidating concrete mix combined with fly ash and limestone can increase the workability of concrete and high resistance to chloride penetration [8]. Using silica in SCM can influence the hydrates in concrete and causes a change in volume, porosity, and materials [9]. Several types of research have been conducted for decades to understand the impact of SMCs in increasing long term concrete strength and lowering concrete cost [8–10].

Djayaprabha et al. demonstrated the effectiveness of blast furnace slag and calcined dolomite as the cementitious binder [11]. At 20% optimal amount of dolomite mixed with slag resulted in maximum compressive strength. The slag-dolomite paste was observed to have lower thermal conductivity than the average cement specimen. A comprehensive study was conducted by Singh et al. [12] to find out the utilization of by product from marble industry called marble slurry as partial replacement of cement. It was observed that incorporation of dried marble slurry up to 15% replacement of cement could improve the mechanical strength of concrete. Degirmenci et al. [13] aimed to determine the use of diatomite as a partial replacement of cement in cement mortar. The investigation pointed out that the increase in diatomite content decreased the compressive and flexural strength. With 15% diatomite content in mortar, the water absorption rate was reduced.

Volcanic eruptions are common in many parts of the world, and VA is derived from pulverized rock or magma thus formed. Frequent eruptions cause environmental degradation, and reusing the VA can significantly reduce the burden on the waste disposal authorities. Concrete production from VA and hydrated lime originated from the Romans about 2000 years ago [14]. It is since being prime attention to the cement industry worldwide for the production of greener binding materials. Celik et al. [2] investigated the effect of basaltic volcanic ash and limestone powder as partial replacement of Portland cement. They found that both the materials decreased the

workability and the compressive strength of the resulting concrete. Another study by Patil et al. [15] reported that where up to 50% Ordinary Portland Cement is replaced by volcanic ash, it is observed that by providing a proper mix design considering the volcanic ash composition to obtain the optimum mechanical strength, the embodied energy can be reduced by approximately 16% when compared to traditional building materials. Hossain [16] investigated the suitability of using volcanic ash and pumice as partial substitutions for Portland cement and discovered that the compressive strength decreases as the percentage substitution by VA increases, with up to 20% substitution of cement by VA providing optimum compressive strength, normal consistency, and setting time values. In another study, Hossain [17] made different concrete specimens with type I, II and V cement and observed the Effect on specimens under marine environment. The investigation obtained that mixing type I and II cement with volcanic ash showed better seawater resistance than type V cement. The precast concrete with type I cement mixed with VA 10% to 20% range was found to be suitable for chloride and porosity resistance. Also cement mixed with VA reduces long-term chloride ion diffusion coefficient and thus increases the corrosion resistance of concrete material [18]. The density and compressive strength of lateralized concrete can be decreased with increased VA content [19]. Sierra et al. [20] mentioned the characterization and pozzolanic reactivity of VA used as white binder.

Upon reviewing previous literature, it is seen that most of the pozzolanic materials under study have provided optimal results when the replacement levels are in the range of 10–20% [11–13, 16]. This study investigates the effect of VA replacement at four different percentage cement levels, namely 5, 10, 15, and 20%. The effect of the percentage VA replacement on the physical properties of volcanic ash, cement and sand, and the short- and long-term mechanical properties of mortar, thereby evaluating the possibility of using it as a commercial source of building material.

2 Experimental Investigation

The experimental study constitutes the determination of physical properties of VA, cement and sand in terms of chemical composition, normal consistency, initial and final setting time, fineness, specific gravity, workability and mechanical properties of the mortar mixtures like compressive strength, Strength activity index.

2.1 Materials

Materials for mortar mixtures include fine natural aggregate (NFA), PCC (Portland Composite Cement) and VA (volcanic ash). PCC is used in this study as it is cheaper than Ordinary Portland Cement, and it is more readily available in developing countries. The VA used in this study, as shown in Fig. 1, is obtained from a shield volcano of the Democratic Republic of Congo (DRC) named Nyamuragira, Africa's and one

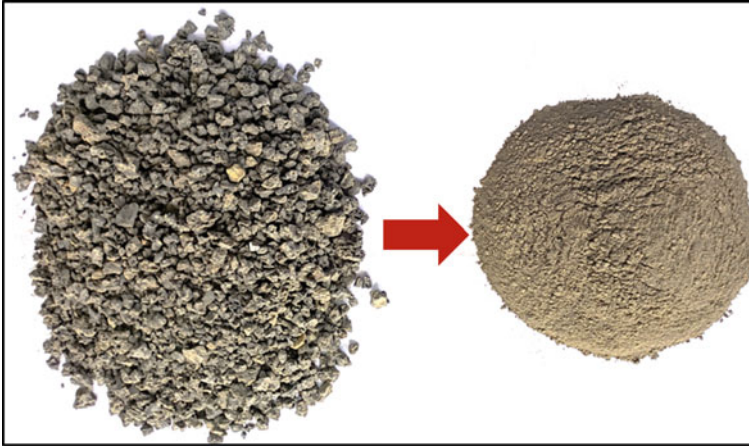


Fig. 1 VA sample collected and ground for the current study

of the world's most active volcano. It erupts roughly every two years, producing large fluid lava flows. The VA collected is dried in the open area for about three weeks to eliminate the moisture present in them. The VA is then ground and sieved through a seventy-five (75) μm sieve at the laboratory. The chemical composition of VA and PCC is determined through X-Ray Fluorescence, and their physical properties used in this investigation are shown in Table 1. Unlike Portland cement, whose primary

Table 1 Chemical and physical properties of VA and portland cement

Component	VA (%)	PCC (%)
<i>Chemical composition</i>		
SiO ₂	52.34	19.8
Al ₂ O ₃	15.67	3.98
Fe ₂ O ₃	8.49	4.67
CaO	7.43	64.79
MgO	6.19	2.32
K ₂ O	1.15	0.4
Na ₂ O	3.86	0.35
P ₂ O ₅	0.71	0.19
TiO ₂	2.43	0.2
MnO	0.26	
Loss on ignition (LOI)	1.19	1.31
<i>Physical properties</i>		
Specific gravity	2.89	3.13
Fineness (m ² /kg)	257.95	320
Bulk density (kg/m ³) (Oven-dry basis)	1890	–

Table 2 Physical properties of NFA

Variables	NFA
Apparent specific gravity	2.47
Bulk specific gravity (SSD)	2.41
Bulk specific gravity (OD)	2.36
Absorption capacity (%)	1.8
Fineness modulus	2.39
Loose condition unit weight (kg/m ³)	1455.44
Compact condition unit weight (kg/m ³)	1579.25
Loose condition % of voids	38.3
Compact condition % of voids	33.0

component is CaO, the sample of VA used in this study is mainly composed of silica. According to ASTM C618 [21], the VA sample can be classified as N-type ash as the total percentage level of silicon oxide (SiO₂), aluminium oxide (Al₂O₃), and ferric oxide (Fe₂O₃) is more than the minimum of 70%. Also, the total amount of alkali present in the sample is 5.01% greater than Portland cement (2.6%). The VA has a lower fineness than Portland cement, which explains the increase in setting time described in the subsequent section of this study. Locally manufactured ASTM Type 1 Portland cement is used in this study. A locally available well graded natural sand with a nominal maximum grain size of 4.75 mm is used in this study. All the physical properties of NFA are determined according to the ASTM standards and is presented in Table 2. The gradation curve of NFA, presented in Fig. 2, shows a well-fitting curve within the ASTM range (ASTM C136) [22].

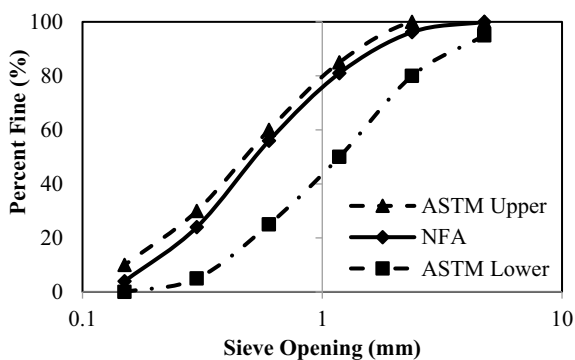
Fig. 2 Gradation curve of natural fine aggregate

Table 3 Mix proportions of materials per cubic meter

Sample designation	w/c ratio	Water (kg)	Cement (kg)	VA (kg)	Fine aggregate (kg)
100PC	0.48	234.1	482.5	–	1326.7
95PC-5VA	0.48	234.1	458.3	24.1	1326.7
90PC-10VA	0.48	234.1	434.2	48.2	1326.7
85PC-15VA	0.48	234.1	410.1	72.4	1326.7
80PC-20VA	0.48	234.1	386.0	96.5	1326.7

2.2 Mixture Proportions

Four different replacement levels of VA, namely 5, 10, 15 and 20% by weight of cement and a control mixture (no volcanic ash), in total five mortar mixtures are prepared for this study. The cement to sand ratio is 1:2.75, and a water-cement ratio of 0.48 is fixed throughout the mix design to eliminate the effects of water on mortar properties. The control mixture was proportioned with a target strength of 35 MPa at 28 days. The mixed proportions of materials per cubic meter can be seen in Table 3. Each mix design is designated with a unique name for ease in referencing within the text. They are denoted as 100PC, 95PC-5VA, 90PC-10VA, 85PC-15VA and 80PC-20VA, where the first number signifies the percentage levels of Portland composite cement and the second one represents the percentage level of VA. For example, V15 means that 15% of cement is replaced by volcanic ash and the rest 85% is the percentage of cement content.

2.3 Specimens

A total of 75 mortar cube specimens of 50 mm side length were prepared following the ASTM C305 [23] standard. After casting, the specimens are initially cured 24 h within the mould in a moist room and then demolded and kept at a controlled temperature in a constant condition under fresh water for 28 days.

2.4 Testing Procedure

The specimen mixtures are tested for normal consistency in the fresh state according to ASTM C187 [24]. The initial and final setting times are also determined in accordance with ASTM C191 [25]. As a measure of the mortar mix workability, flow value is determined following the standard procedure by ASTM C1437 [26]. The compressive strength at different ages (3, 7, 28, 56 and 120 days) is determined according to ASTM C109 [27] standard. The test set up for compressive strength of

Fig. 3 Test set up for compressive strength of mortar



mortar is shown in Fig. 3 where a constant loading rate of 1.80 KN/s is used. The strength activity index (SAI) test is done on the cube specimens at 7 and 28 days using a slightly modified version of the ASTM C311 [28] standard specifications. The control mixture is prepared with 500 g of ASTM Type 1 Portland cement, 1375 g of standard sand and 242 ml of water. For comparison, 5, 10, 15 and 20% of the Portland cement is replaced by VA for the SAI test and the resulting cube specimens are cured in saturated lime water until the day of testing.

3 Results and Discussion

3.1 Normal Consistency and Setting Times

It is necessary to determine the consistency of binder materials because the amount of water used in mortar or concrete affects the setting time of the cement. So, the correct proportion of water to binder materials must be known to achieve proper strength while using it in structure. This can be found by knowing the standard consistency of binder paste. The results of normal consistency and setting times of the specimens are shown in Fig. 4. It is seen that the normal consistency decreases with an increase in percentage levels of volcanic ash as was identified by the author in [16]. This reduction refers to the fact that the amount of water needed to form the

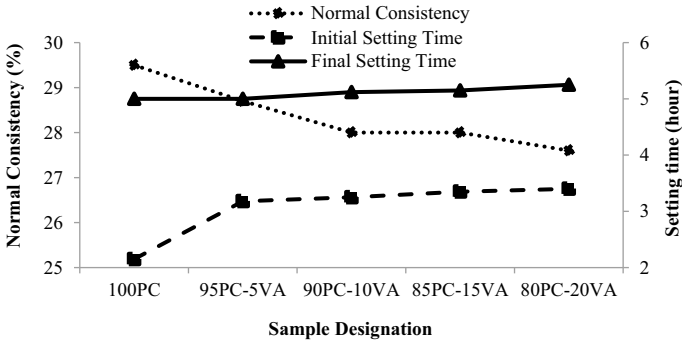


Fig. 4 Effect of VA on normal consistency and setting time

same consistency has increased for different percentages of into the mixture. As the specific gravity of volcanic ash is less than that of Portland Composite Cement, a higher volume of volcanic ash is required to replace the cement as the substitution is designed by mass. The initial and final setting times show an increasing trend as the volcanic ash levels increase. The lower specific gravity can again be held responsible for this phenomenon as this value indicates a lower surface area of the volcanic ash particles. For this reason, the hydration reaction takes longer hence the greater setting times. Higher setting times can allow subsequent lower heat of hydration than that of Portland cement.

3.2 Workability

One of the most important properties of a mortar mixture is its workability. It must be free-flowing without the segregation of water or other constituents in the mix. But too much water in mortar impairs its strength. So, it is important to know the right amount of water so that proper workability can be ensured. The workability of the mortar samples decreases as the percentage replacement by volcanic ash increases, as presented in Fig. 5. This is in correspondence with the results obtained by previous authors [19, 20]. With the control sample 100PC having the highest flow value (108%), the lowest value is found in sample 80PC-20VA which is 31.5% less than the value obtained in the 100PC sample. This could be attributed to the fact that the density of the volcanic ash particles is less than that of the PCC particles, and so it settles less than PCC in the flow table test as described in ASTM C1437 [26].

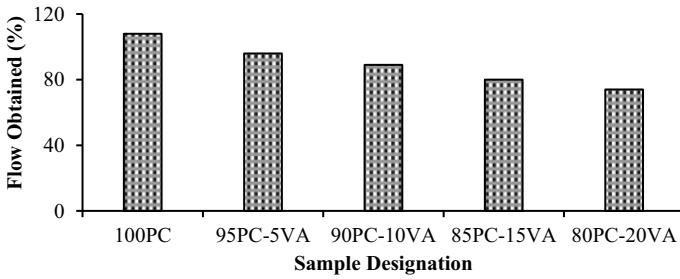


Fig. 5 Flow table test results

3.3 Compressive Strength

Compressive strength is one of the most important properties of concrete and mortar. Therefore, the strength of the binder has a significant effect on the performance characteristics of the mixture and ensures the overall quality of the finished product. The Effect on compressive strength due to the incorporation of volcanic ash at different levels is shown in Fig. 6, where the results are the average of three test specimens. Compressive strength is increased up to 15% replacement level of cement by volcanic ash for all ages, which is also more than the control specimen’s strength and then starts to decrease for 20% replacement combination. The compressive strength at 28 days increased by 27.7, 7.8 and 4.3% when the amount of volcanic ash increased from 5 to 15%, respectively. On the other hand, the compressive strength at 28 days decreased by 27.4% when the percentage of volcanic ash is 20%. This might be due to the fact that the cement content has been reduced, thus lowering the binding capacity of the mortar. However, this trend is also observed for 56 days and 120 days compressive strength. Thus, in terms of short- and long-term durability, the samples containing 15% volcanic ash content can be regarded as an optimum level of incorporation in the mortar mixture. The failure pattern of different mortar mixtures is shown in Fig. 7. The specimens containing volcanic ash shows a brittle failure compared to control specimens.

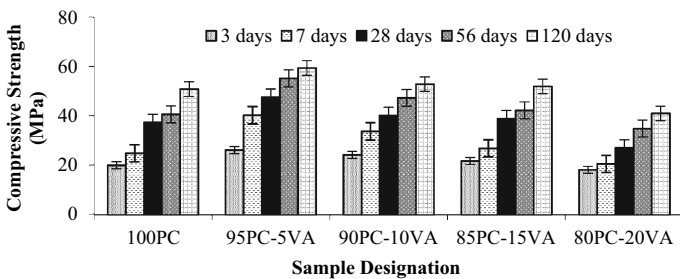


Fig. 6 Effect of VA on compressive strength of the mortar samples

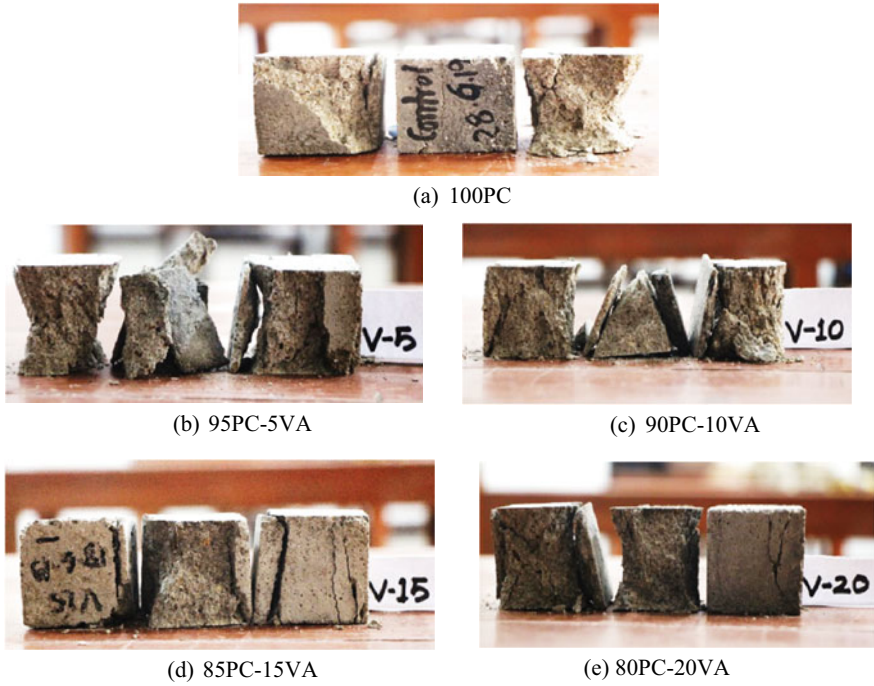


Fig. 7 Mortar cube specimens after crushing

3.4 Strength Activity Index (SAI)

The strength activity index is the ratio of the strength of the volcanic ash–cement mortar to the strength of the reference mortar (purely cement-based mortar) at each specific curing time under a special curing process. A separate mix is used for this test, and the results are shown in Table 4, which reveals the average value of SAI of three test samples each. The SAI value as per the requirement in ASTM C618 [21] is a minimum of 75%, and based on that, the SAI value at 7 and 28 days for the 5,

Table 4 Effect on SAI due to VA content in mortar cubes

Sample designation	Percentage replacement by VA	Average compressive strength (MPa)		SAI (%)	
		7 days	28 days	7 days	28 days
100PC	0	27.7	38.4	100	100
95PC-5VA	5	42.4	48.3	153.1	125.8
90PC-10VA	10	35.3	41.7	127.4	108.6
85PC-15VA	15	28.5	40.0	102.8	104.2
80PC-20VA	20	19.5	26.2	70.4	68.2

10 and 15% replacement combinations are found to be more than 75%. On the other hand, the SAI values for 20% replacement of cement by volcanic ash are seen to be 70.4 and 68.2% at 7 and 28 days, respectively, which is much lower than the required level. Thus, it can be said that the samples 95PC-5VA, 90PC-10VA and 85PC-15VA can behave as a natural pozzolan.

4 Conclusion

The current study on partial substitution of Portland cement by volcanic ash shows that the volcanic ash content affects the resulting mortar mix's fresh and hardened properties. According to the specified code, volcanic ash has the potential to be used as a pozzolona in mortar mixes. The normal consistency, setting times and workability are taken into consideration at the fresh state, whereas compressive strength and SAI are considered as the hardened state properties of the specimens under this investigation. Based on the experimental findings, the following conclusions can be drawn:

1. The normal consistency decreased with the increasing replacement level of cement by volcanic ash; on the contrary, the setting times increase with the mix's volcanic ash content, thus providing scope for the possible advantages of lower heat of hydration during construction.
2. The compressive strength increases as the replacement percentage of cement by volcanic ash is up to 15% as an alternative binder and then decreases.
3. The SAI value is well within the specified limit for the samples up to 15% replacement level. From these results, it is evident that the conventional Portland cement can be replaced by up to 15% with volcanic ash without having any discrepancies. Therefore, this study suggests that a cement blend with 15% volcanic ash content can be used for mortar mixes with a target strength of 35 MPa.

Acknowledgements This research project is undertaken at the Concrete Lab of Civil Engineering Department, Military Institute of Science & Technology (MIST), Dhaka, Bangladesh. The authors would like to acknowledge the start-up fund provided by MIST and laboratory technicians of Concrete Lab, who helped during the experimental program.

References

1. Olivier JG, Schure K, Peters J (2017) Trends in global CO₂ and total greenhouse gas emissions. PBL Netherlands Environmental Assessment Agency, pp 5
2. Celik K et al (2019) Effect of volcanic ash pozzolan or limestone replacement on hydration of Portland cement. *Constr Build Mater* 197:803–812

3. Al-Ani M, Hughes B (1989) Pulverized-fuel ash and its uses in concrete. *Mag Concr Res* 41(147):55–63
4. Mehta PK (1977) In: Properties of blended cements made from rice husk ash. *J Proc*
5. Swamy R (1983) In: New concrete materials. vol 1. Surrey University Press
6. Swamy R (1986) In: Concrete technology and design, Volume 3, cement replacement materials. London, UK, Surrey University Press, First publication
7. Bilodeau A, Malhotra VM (2000) High-volume fly ash system: concrete solution for sustainable development. *Mater J* 97(1):41–48
8. Celik K et al (2015) Mechanical properties, durability, and life-cycle assessment of self-consolidating concrete mixtures made with blended portland cements containing fly ash and limestone powder. *Cement Concr Compos* 56:59–72
9. Lothenbach B, Scrivener K, Hooton R (2011) Supplementary cementitious materials. *Cem Concr Res* 41(12):1244–1256
10. Juenger MC, Siddique R (2015) Recent advances in understanding the role of supplementary cementitious materials in concrete. *Cem Concr Res* 78:71–80
11. Djayaprabha HS et al (2017) Mechanical properties and microstructural analysis of slag based cementitious binder with calcined dolomite as an activator. *Constr Build Mater* 150:345–354
12. Singh M, Srivastava A, Bhunia D (2017) An investigation on effect of partial replacement of cement by waste marble slurry. *Constr Build Mater* 134:471–488
13. Degirmenci N, Yilmaz A (2009) Use of diatomite as partial replacement for Portland cement in cement mortars. *Constr Build Mater* 23(1):284–288
14. Brandon CJ et al (2014) In: Building for eternity: the history and technology of Roman concrete engineering in the sea. Oxbow Books
15. Kupwade-Patil K et al (2018) Impact of embodied energy on materials/buildings with partial replacement of ordinary portland cement (OPC) by natural Pozzolan volcanic ash. *J Clean Prod* 177:547–554
16. Hossain KMA (2003) Blended cement using volcanic ash and pumice. *Cem Concr Res* 33(10):1601–1605
17. Hossain KMA (2005) Performance of volcanic ash based precast and in situ blended cement concretes in marine environment. *Environ J Mater Civil Eng* 17(6):694–702
18. Hossain KMA (2003) Chloride diffusivity of volcanic ash blended hardened cement paste. *Adv Cem Res* 15(2):83–90
19. Olawuyi B, Olusola K (2010) Compressive strength of volcanic ash/ordinary portland cement laterized concrete. *Civil Eng Dimension* 12(1):23–28
20. Sierra OM et al (2015) Characterization and Pozzolan reactivity of a volcanic ash from Guatemala to be used in white binders. In: The international conference of NOCMAT2015: Winnipeg, Canada
21. ASTM C618–19 (2019) Standard specification for coal fly ash and raw or calcined natural Pozzolan for use in concrete. ASTM International, West Conshohocken, PA
22. ASTM C 136 (2014) Standard test method for sieve analysis of fine and coarse aggregates. ASTM, ASTM International, West Conshohocken, PA
23. ASTM C305–14 (2014) Standard practice for mechanical mixing of hydraulic cement pastes and mortars of plastic consistency. ASTM International, West Conshohocken, PA
24. ASTM C187–16 (2016) Standard test method for amount of water required for normal consistency of hydraulic cement paste. ASTM International, West Conshohocken, PA
25. ASTM C191–19 (2019) Standard test methods for time of setting of hydraulic cement by vicat needle. ASTM International, West Conshohocken, PA
26. ASTM C1437–15 (2015) Standard test method for flow of hydraulic cement mortar. ASTM International, West Conshohocken, PA
27. ASTM C109 / C109M-16a (2016) Standard test method for compressive strength of hydraulic cement mortars (Using 2-in. or [50-mm] Cube Specimens). ASTM International, West Conshohocken, PA
28. ASTM C311 / C311M-18 (2018) Standard test methods for sampling and testing fly ash or natural Pozzolans for use in portland-cement concrete. ASTM International, West Conshohocken, PA

Lateral Load–Displacement Behaviors of Reinforced Geopolymer-Concrete Column Using Finite Element Analysis



Kukuh Kurniawan Dwi Sungkono, Iman Satyarno, Henricus Priyosulistyo, and Indra Perdana

Abstract Today the use of environmentally friendly building materials in construction is considerably important, such as geopolymer concrete. Geopolymer concrete uses by-product material, such as fly ash instead of cement. Some aggressive materials in the environment, such as seawater and soil with high sulfate content, attack ordinary reinforced concrete structures. In such aggressive environments, structures on the basis of geopolymer reinforced concrete are preferable because previous studies showed that geopolymer reinforced concrete has ability to survive in those corrosive environments. This paper discusses finite element analyses on a reinforced geopolymer concrete column to predict their lateral load–displacement behavior using ABAQUS software. Mechanical properties of geopolymer concrete such as stress–strain relation, modulus of elasticity, and Poisson Ratio need to be determined as an input in the finite element analyses. For the validation purpose of the analyses, a previous experimental test result of a reinforced geopolymer concrete column having a cross-section of 175 square mm, 1500 mm high and of slender type was used. Three types of eccentric load were examined. It is found that by appropriate determination of the geopolymer properties, the finite element analyses using ABAQUS can predict the lateral load–displacement behavior of the slender column significantly.

Keywords Geopolymer concrete column · Finite element analyses · ABAQUS · Lateral load–displacement

K. K. D. Sungkono (✉) · H. Priyosulistyo
Department of Civil and Environmental Engineering, Gadjah Mada University, Yogyakarta, Indonesia
e-mail: kukuhkurniawan@mail.ugm.ac.id

I. Satyarno
Department of Civil Engineering, Tunas Pembangunan University, Surakarta, Indonesia

I. Perdana
Department of Chemical Engineering, GadjahMada University, Yogyakarta, Indonesia

1 Introduction

At present, climate change is a priority in reducing carbon dioxide emissions. Construction materials are starting to look for alternative material and binders for concrete to reduce these emissions. Research on the use of fly ash as a binder in concrete is mostly done. The geopolymer technology proposed by Davidovitz promises its application as a substitute for binders for Portland Cement in concrete. The technology reduces CO₂ emission caused by the cement and aggregates industries by 80% [1].

The durability of concrete, especially in aggressive environments, is an important requirement for structural performance. Acid resistance is an important property of concrete as a structural element. Acid attack is known to cause significant degradation of reinforced concrete structures. In this case, reinforced concrete structural elements that function as foundations and piles are at risk from aggressive environmental conditions. Concrete in an aggressive environment experiences various chemical reaction such as those involving sulfate, chloride and magnesium ions.

The durability of geopolymer concrete is better than Portland cement. Ca(OH)₂ in Portland cement that reacts with MgCl₂ produces CaCl₂, which causes porous in concrete. In comparison, the reaction in geopolymer concrete is the polymerization of Aluminum (Al) and Silica (Si) to produce polymer bonds to solidify the concrete. The study of the permeability of geopolymer concrete also shows that the level of porosity is small. So that the geopolymer concrete is able to protect the steel reinforcement from chemical attacks (water, chloride, and other chemicals) that enter the concrete.

Many studies have been carried out on the strength of geopolymer concrete materials. This study was conducted to obtain the optimal compressive strength and durability of concrete. Fly ash-based geopolymer mortar (class C) can produce compressive strength up to 60 MPa by curing at room temperature [2]. Geopolymer based concrete fly ash (Class C) which has been exposed to the marine environment for 3 (three) years, has increased compressive strength. This increase varies based on the amount of NaOH solution (molarity 8–16 M). The increase in the compressive strength of geopolymer concrete after exposure to the marine environment is 7–26% [3]. The utilization of geopolymer concrete as the building foundation has the advantage of being resistant to aggressive environmental conditions (e.g. marine environment, industrial building, and peat soil). Therefore, the use of geopolymer concrete as material on piles is recommended in aggressive environments. Hence, it is necessary to analyze the strength of the structural elements using the FE simulation. This paper aim to discusses the simulation of finite element of reinforced geopolymer concrete columns compared to the experimental results conducted by Sumajouw et al.

2 Review of Previous Studies

2.1 Durability Geopolymer Concrete

Concrete durability is the ability of concrete to withstand weather, chemical attacks, abrasion or other damaging processes. Thus, the durability of concrete will maintain the concrete to remain in its original form, maintaining the quality and ability of concrete services to environmental conditions.

The study of the durability of high calcium fly ash-based geopolymer concrete and Portland cement concrete exposed to 2% sulfuric acid solution and 5% magnesium sulfate for 45 days showed satisfactory results [4]. The decrease in compressive strength due to exposure to sulfuric acid in Portland cement concrete ranged from 18 to 28%, while for geopolymer concrete, about 12–20%. While the decrease in strength due to exposure to magnesium sulfate is in the range of 5–25% for Portland cement concrete and 5–12% in geopolymer concrete.

The study on the durability of reinforced geopolymer concrete in corrosive marine environments compared to ordinary Portland concrete has been carried out [5]. A series of geopolymer concrete beams were tested for accelerated corrosion exposure with dry and wet cycles in artificial seawater and induced currents. The behavior and properties of geopolymer concrete are more homogeneous and have a good bond on the aggregate (observed from the failure surface), compared to OPC concrete. Excellent resistance of geopolymer concrete to chloride attack, with a longer time for corrosion relative to Portland cement concrete. A sudden increase in current intensity caused by specimen cracking is an indication of the durability.

The rate of chloride that enters the small geopolymer concrete is caused by the polymerization reaction, which causes leaching of Si and Al, which then reacts with alkaline activators (NaOH and SiO₂/Al₂O₃). The high concentration of NaOH increases the leaching of Si and Al from fly ash to produce a higher level of geopolymerization [3]. This leads to the dense matrix and increased ability to resist chloride ions penetration in geopolymer concrete [6].

2.2 Stress–strain Relationship of Geopolymer Concrete

Experimental results the stress–strain relationship of fly ash-based geopolymer concrete have been reported [7]. The test results obtained strains at peak stress in the range 0.0024 to 0.0026. These values are similar to strains in Portland cement concrete. The stress–strain relation of OPC concrete proposed by Collins et al. [8] in compression can be predicted using the following expression:

$$\sigma_c = f_{cm} \frac{\varepsilon_c}{\varepsilon_{cm}} \frac{n}{n - 1 + (\varepsilon_c/\varepsilon_{cm})^{nk}} \quad (1)$$

Table 1 Experimental from stress–strain curves [7]

Mixture No	Compressive strength (MPa)	Strain at peak stress	Modulus of elasticity (GPa)
23	64	0.0025	30.6
24	61	0.0026	30.8
26	41	0.0024	24.7

where

f_{cm} : peak stress

ϵ_{cm} : strain at peak stress

n : $0.8 + (f_{cm}/17)$

k : $0.67 + (f_{cm}/62)$ when $\epsilon_c/\epsilon_{cm} > 1$

k : 1.0 when $\epsilon_c/\epsilon_{cm} \leq 1$.

The stress–strain relationship of the three mixtures and predicted using Eq. (1) is shown in Table 1 and Fig. 1 [7]:

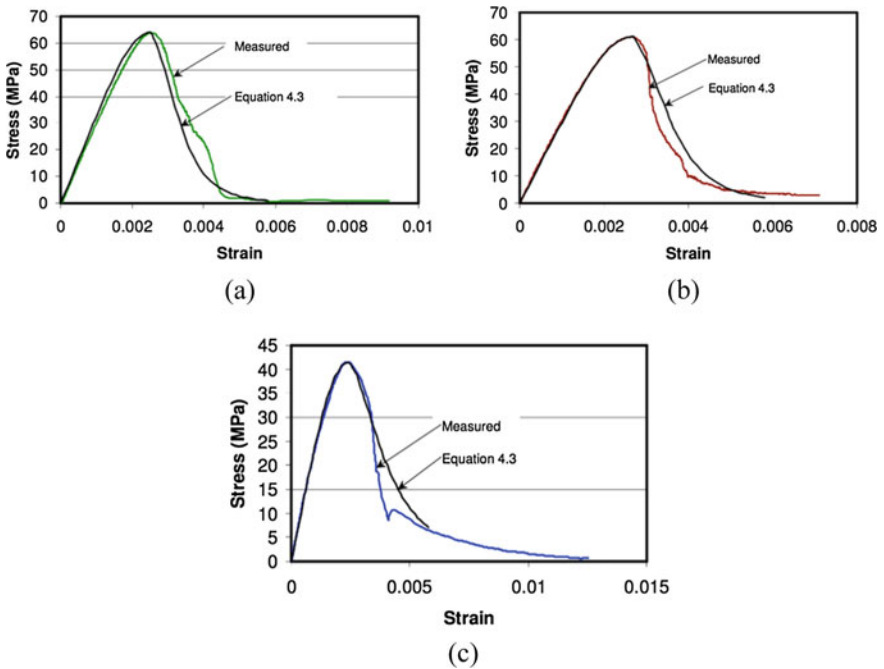


Fig. 1 a Prediction and test stress–strain relations for concrete made from a Mixture 23, b Mixture 24, c Mixture 26 [7]

2.3 *The Experiment of Structural Element*

Currently, there are many studies on the behavior of geopolymer concrete as a structural element. Even geopolymer concrete can be designed using design codes for conventional reinforced concrete, such as American Concrete Institute (ACI) and Australian Standard. In general, the failure behavior of reinforced geopolymer concrete studies on the structural elements similar to conventional reinforced concrete.

The study of the behavior of reinforcing bond strengths in OPC and geopolymer concrete on variations in the diameter of steel rebar has been carried out [9]. Geopolymer concrete in this study is based on fly ash class F, and alkali activators are Sodium Hydroxide (NaOH) and Sodium Silicate (Na_2SiO_3). The test results show that the bond strength of geopolymer concrete is two times higher than OPC concrete. The failure mechanism of all OPC and geopolymer specimens is characterized by shear failure.

Studies on structural elements of reinforced geopolymer concrete (RGPC) beams have been carried out to determine flexural behavior [10]. In this study, fly ash-based geopolymer concrete low calcium and alkali activators (Na_2SiO_3 and NaOH) are used. The concentration of sodium hydroxide solution was 8 Molar (M). The stress–strain curve in compression was obtained from a cylinder geopolymer concrete test. Strain at the peak stress occurs between 0.0016 to 0.0023. It is observed that the stress–strain curve in compression for geopolymer concrete is similar to conventional concrete. Reinforced geopolymer concrete beams were tested to measure the mid-span deflection and flexural crack patterns. Crack patterns occur in the mid-span as the load increases.

The studies of load-carrying capacity, load–deflection characteristics and failure modes of slender reinforced geopolymer concrete columns were carried out [11]. In this study, low-calcium fly ash is used as a binder for geopolymer concrete which is reacted with sodium hydroxide solution and sodium silicate solution. Twelve reinforced concrete samples with various eccentric loading were applied to the geopolymer concrete column. The load capacity of the test column matches the value calculated using the design provisions of the Australian Standard AS3600 and the American Concrete Institute Building Code ACI 318–02.

In general, initial cracks in mid-height columns occur due to surface tension. Existing cracks propagate, and new cracks appear along the surface of the stress and spread as the load increases. Loading increases cause existing cracks to propagate and new cracks to form along the stress surface. The design provisions contained in current standards and codes can be used to design geopolymer concrete products.

The study of the behavior of geopolymer concrete slabs on impact resistance capacity has been reported [12]. This geopolymer concrete is based on fly ash and GGBS (Ground Granulated Blast furnace Slag), with variations of 100%: 0%, 75%: 25%, and 50%: 50%. The alkaline solution consists of a solution of NaOH and Na_2SiO_3 . The molarity of the NaOH solution used varied, namely 8, 12, and 16 M. Specimens in this study use slabs of dimensions of 600 mm (length), 600 mm (width)

and 60 mm (thickness). The curing oven is applied at 60 °C for 24 h. Impact test by dropping a solid ball was weighing 75.50 N as high as 700 mm. From the drop weight impact test, the result is that the energy absorption capacity of geopolymer concrete is more than normal concrete. Increasing NaOH molarity and increasing GGBS content can increase the ultimate impact strength of geopolymer concrete slabs.

3 Finite Element Model

3.1 General

To investigate the behavior of these structural elements, a numerical analysis of reinforced geopolymer concrete columns was performed using the finite element ABAQUS tool. Material behavior, which is related to concrete material, steel material, and other boundary conditions, were obtained from experimental results.

ABAQUS contains an extensive library of elements that can model almost any geometry. Also, able to be used for modeling different materials to simulate the behavior of most engineering materials, one of them is reinforced concrete. ABAQUS contains a solid element library for two-dimensional and three-dimensional applications. Two-dimensional elements allow modeling of symmetrical fields and axes and include extensions to common plane strains. Material descriptions of three-dimensional solid elements can consist of several different materials in different orientations to analyze laminated composite solids.

In the analysis phase, geometry and boundary conditions, element types, material properties, and nonlinear analysis are determined.

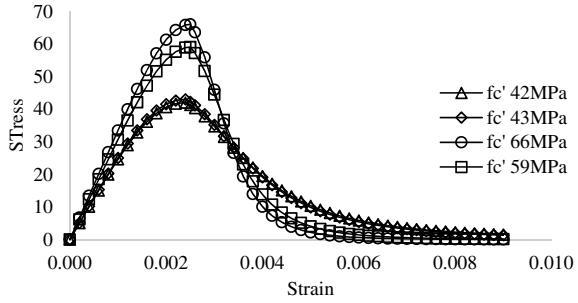
3.2 Stress–strain Relationship

In the analysis, the average compressive strength of geopolymer concrete is 42, 43, 66, and 59 MPa. Based on observations by Hardjito and Rangan [7] concerning the prediction of stress–strain geopolymer concrete proposing the equation presented by Collins et al. [8]. While the empirical equation given in the following equation was used to compute the modulus of elasticity of geopolymer concrete provided by Hardjito et al. [13].

$$E_c = 2707\sqrt{f'_c + 5300} \quad (2)$$

The stress–strain curve calculated using Eq. (1) is shown in the following Fig. 2.

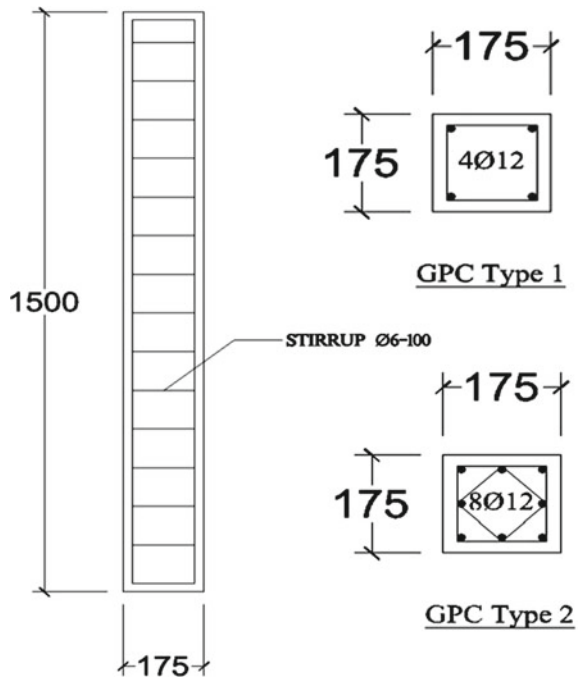
Fig. 2 Prediction stress–strain relations for geopolymer concrete for finite element model



3.3 Finite Element Model, Boundary Conditions and Loading

The cross-section and height of reinforced geopolymer concrete columns are 175 mm square and 1500 mm high, respectively, as shown in Fig. 3. The reinforced geopolymer concrete column was modeled in three dimensions. An 8-node linear brick reduced integration with hourglass control (3D C3D8R) solid elements were used to model concrete elements in ABAQUS. The rebar element was modeled using a 2D truss element named T3D2 (a 2-node linear 3D truss). Embedded region constraints were used to determine the bond of reinforcing steel with concrete which

Fig. 3 Detail of reinforced geopolymer concrete columns [11]



limits the reinforcement element nodes to compatible degrees of freedom (DOF) of the region element (concrete).

The model was discretized into a finite element to the concept of meshing before loading applied of loading conditions. The mesh size of the element obtained by 20 mm indicates acceptable convergence to produce the desired accuracy. Static loading was applied at the top of mid-height reinforced geopolymer concrete columns with displacement control techniques to identify the pattern of lateral load–displacement relationships. The displacement applied to the column is 20 mm and at an eccentric distance determined from the center of the specimen.

Twelve concrete geopolymer columns with two types of reinforcement and four concrete compressive strengths are modeled in ABAQUS. Three types of eccentricity loading (15, 35, and 50 mm) are given in each column to study lateral load–displacement behavior. Details of material characteristics and load of all column specimens are shown in Table 2.

Experimental data on the concrete plasticity of geopolymer concrete are very limited in the literature. Parameters for the concrete plasticity was selected as recommended by the ABAQUS user manual [14]. In this study, the dilation angle (ψ) of 30° , the plastic potential eccentricity of concrete (ϵ) of 0.1, the ratio of compressive stress in the biaxial state to the compressive stress in the uniaxial state (σ_b/σ_c) of 1.16, the shape factor of the yielding surface in the deviatoric plane (K_c) of 0.667, and viscosity parameter of 0.005.

Longitudinal and lateral reinforcement diameters used are 12 and 6 mm. The steel reinforcement material used in grade N500 with yield strength and ultimate tensile strength is 550 and 650 MPa, respectively. The column reinforcement ratio is 1.47 and 2.95%.

Table 2 Detail material and load eccentricity of column specimen [11]

Column No	Concrete strength (MPa)	Load eccentricity (mm)	Longitudinal reinforcement	
			Bars	Ratio (%)
GCI-1	42	15	4D12	1.47
GCI-2	42	35	4D12	1.47
GCI-3	42	50	4D12	1.47
GCI-4	43	15	8D12	2.95
GCI-5	43	35	8D12	2.95
GCI-6	42	50	8D12	2.95
GCI-1	66	15	4D12	1.47
GCI-2	66	35	4D12	1.47
GCI-3	66	50	4D12	1.47
GCI-4	59	15	8D12	2.95
GCI-5	59	35	8D12	2.95
GCI-6	59	50	8D12	2.95

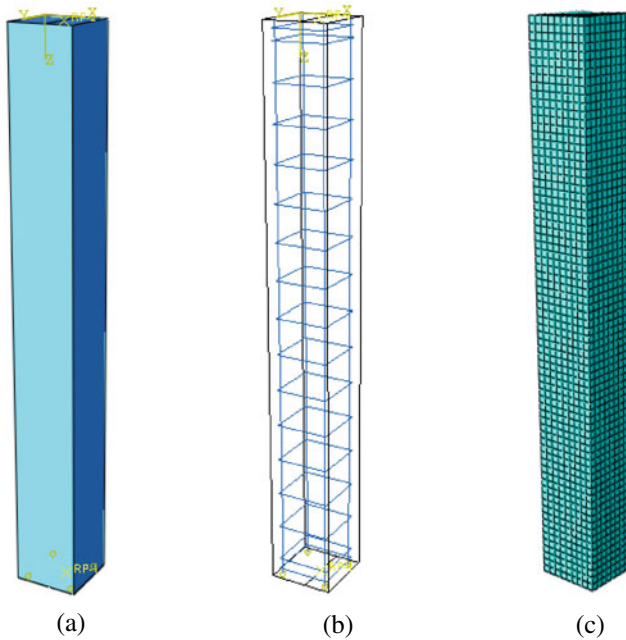


Fig. 4 Modelling of reinforced geopolymer concrete column **a** geometry, **b** steel reinforcement, **c** Finite element meshing

Details of the geometry and finite element modeling of reinforced geopolymer concrete columns are shown in Fig. 4.

4 Analysis of Results

4.1 Lateral Load–Displacement

The results of the finite element method of 12 (twelve) reinforced geopolymer concrete column specimens are shown in Table 3. GCI 1–6 models show the tendency of FEM failure load under an experimental failure load of 5%. However, the tendency for FEM failure load to exceed the experimental failure load by 12% is shown by the GCI1-6 model.

Figure 5a presents the lateral load–displacement between experimental and FEM in reinforced geopolymer concrete columns of GCI 1 to 3, at compressive strengths of 42 MPa. GCI-1 simulation results show higher failure load and lateral displacement than experimental. However, the differences are shown in GCI-2, and GCI-3 simulations show similarities between experimental and FEM patterns. The difference in failure load and lateral displacement for GCI-2 and GCI-3 is 7 and 3%, respectively.

Table 3 Comparison between experimental and finite element analysis failure loads

Column No.	Concrete strength (MPa) [f'c]	Load Eccentricity (mm) [e]	Result						Ration failure load Exp/FEM	
			Experimental [11]		Rangan [11]	AS3600 [11]	ACI 318-02 [11]	FEM simulation		
			Failure load (kN)	Mid-Disp (mm)				Failure load (kN)		Mid-Disp (mm)
GCI-1	42	15	940	5.44	988	962	926	997.48	6.73	0.94
GCI-2	42	35	674	8.02	752	719	678	725.35	8.60	0.93
GCI-3	42	50	555	10.31	588	573	541	594.14	10.45	0.93
GCI-4	43	15	1237	6.24	1149	1120	1050	1251.91	7.29	0.99
GCI-5	43	35	852	9.08	866	832	758	882.09	9.18	0.97
GCI-6	43	50	666	9.4	673	665	604	705.58	9.55	0.94
GCI-1	66	15	1455	4.94	1336	1352	1272	1145.75	6.37	1.27
GCI-2	66	35	1030	7.59	1025	1010	917	925.86	8.35	1.11
GCI-3	66	50	827	10.7	773	760	738	728.32	9.57	1.14
GCI-4	59	15	1559	5.59	1395	1372	1267	1363.66	6.28	1.14
GCI-5	59	35	1057	7.97	1064	1021	911	994.20	8.20	1.06
GCI-6	59	50	810	9.18	815	800	723	834.39	9.90	0.97

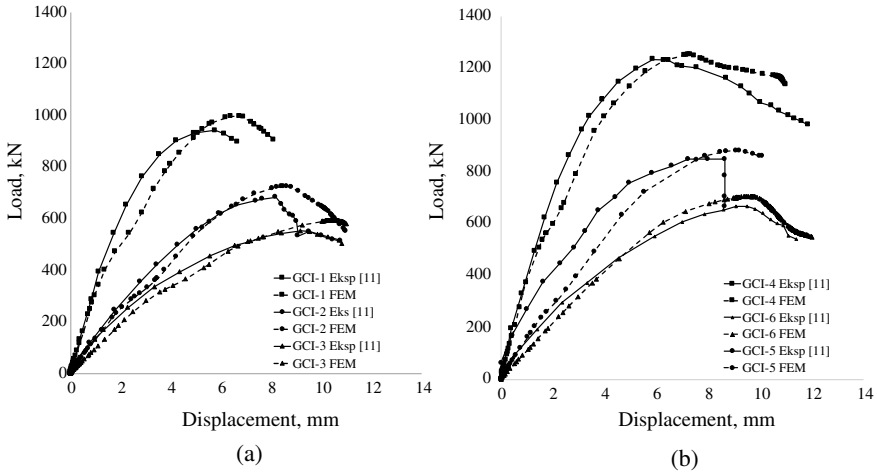


Fig. 5 Experimental and FEM lateral load–displacement results **a** GCI 1–3 (f_c' 42 MPa), **b** GCI 4–6 (f_c' 43 MPa)

The failure load results from FEM approached predictions based on calculations proposed by Rangan [15], Australian Standard AS3600 [16] and ACI 318 [17].

The reinforced geopolymer concrete column of GCI-4, GCI-5 and GCI-6 have more reinforcement ratios than GCI 1–3, which is 2.47%. Therefore, the capacity of the GCI-1 to 3 columns is smaller than the GCI-4 to 6. Similar to the conventional concrete columns, reinforced geopolymer concrete columns with a large reinforcement ratio will produce a large column capacity. In Fig. 5b it can be seen that the experimental and FEM tests have similar lateral load–displacement patterns.

Figure 6a is a comparison of experimental and finite element models of reinforced geopolymer concrete columns of type GCII-1 to 3. Finite element analysis shows significant differences with the experimental results, for column lateral load capacity and displacement the differences are 27 and 22%, respectively. GCII-1 specimens in experimental tests showed failure was brittle. GCII-2 and GCII-3 specimens show more similar lateral load–displacement results between experimental and FEM

The lateral load–displacement behavior in GCII-4 to 6 specimens shown in Fig. 6b between experimental and FEM results is similar. FEM simulation shows expected results because the behavior of reinforced geopolymer concrete columns is similar to conventional concrete columns. Where the column load capacity is influenced by the strength of the concrete material, reinforcement ratio, and the load. Column load capacity increases when material strength and reinforcement ratio increase.

Column load capacity is influenced by the compressive strength of concrete, seen in the reinforcement ratio 1.47% between concrete compressive strength of 42 and 66 MPa gives different column load capacity results. The columns with the same compressive strength have different reinforcement ratios (type GCI and GCII), and the maximum column load capacity is produced from a large reinforcement ratio. In GCII columns 1–3, the concrete compressive strength of 66 MPa and reinforcement

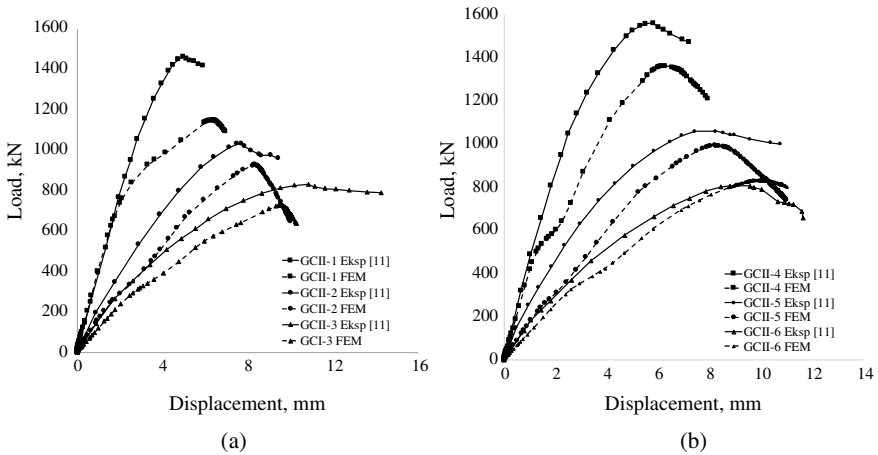


Fig. 6 Experimental and FEM lateral load–displacement results **a** GCI 1–3 (f_c ' 66 MPa), **b** GCII 4–6 (f_c ' 59 MPa)

ratio of 1.47% results in a smaller column load capacity, compared to GCII 4–6 with the compressive strength of 59 MPa and reinforcement ratio of 2.95%.

4.2 Stress–strain of Elements

The results of the FEM stress of the geopolymer reinforced concrete columns from GCI-1 to 3 are shown in Fig. 7. Stress and strain distribution due to different eccentricity loads at the top of the column.

The study shows that the maximum stress values obtained from the GCI-1, GCI-2, and GCI-3 models are 4.13, 3.52, and 2.58 MPa respectively. The cracked concrete condition results in a positive maximum principal plastic strain (PE) occurring in the mid-height column and the largest PE value at the corner of the column. The PE values for GCI-1, GCI-2, and GCI-3 are 0.2658, 0.2453, and 0.2132, respectively.

Figure 8 shows the maximum stress values obtained by the GCI-4, GCI-5, and GCI-6 models are 3.964, 3.866, and 2.696 MPa, respectively. While the value of plastic strains (PE) is 0.3488, 0.2326 and 0.2126.

Figure 9 shows the maximum stress values obtained by the GCII-1, GCII-2, and GCII-3 models are 9.125, 3.970, and 3.888 MPa, respectively. While the value of plastic strains (PE) is 0.3488, 0.2404 and 0.211. In the GCII-1 type column model, stress and strain concentrations appear in the mid-height column with a distance of 200 mm.

Figure 10 shows the maximum stress values obtained by the GCII-4, GCII-5, and GCII-6 models are 5.560, 4.537, and 3.932 MPa, respectively. While the value of plastic strains (PE) is 0.3125, 0.2089 and 0.1564.

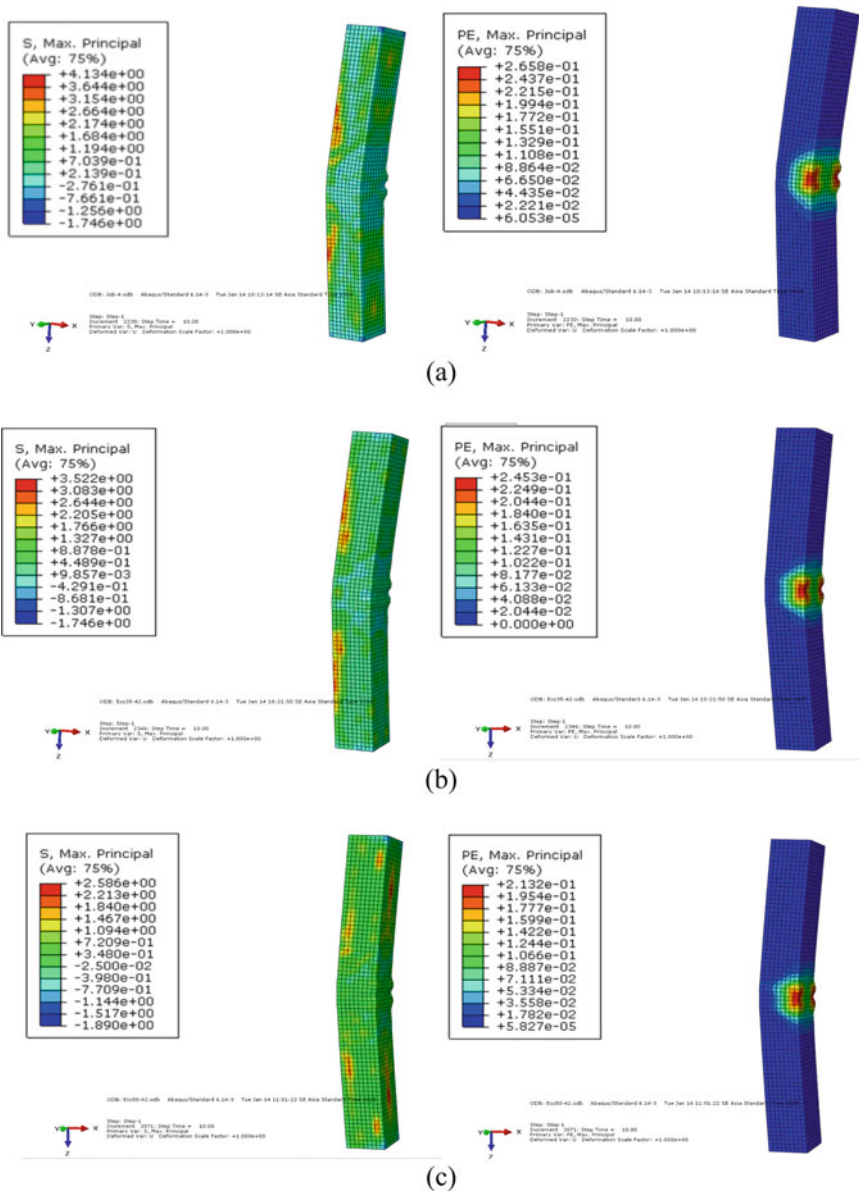


Fig. 7 Stress and crack patterns in the geopolymer column **a** GCI-1 (eccentricity 15 mm), **b** Column GCI-2 (eccentricity 35 mm) and **c** GCI-3 (eccentricity 50 mm)

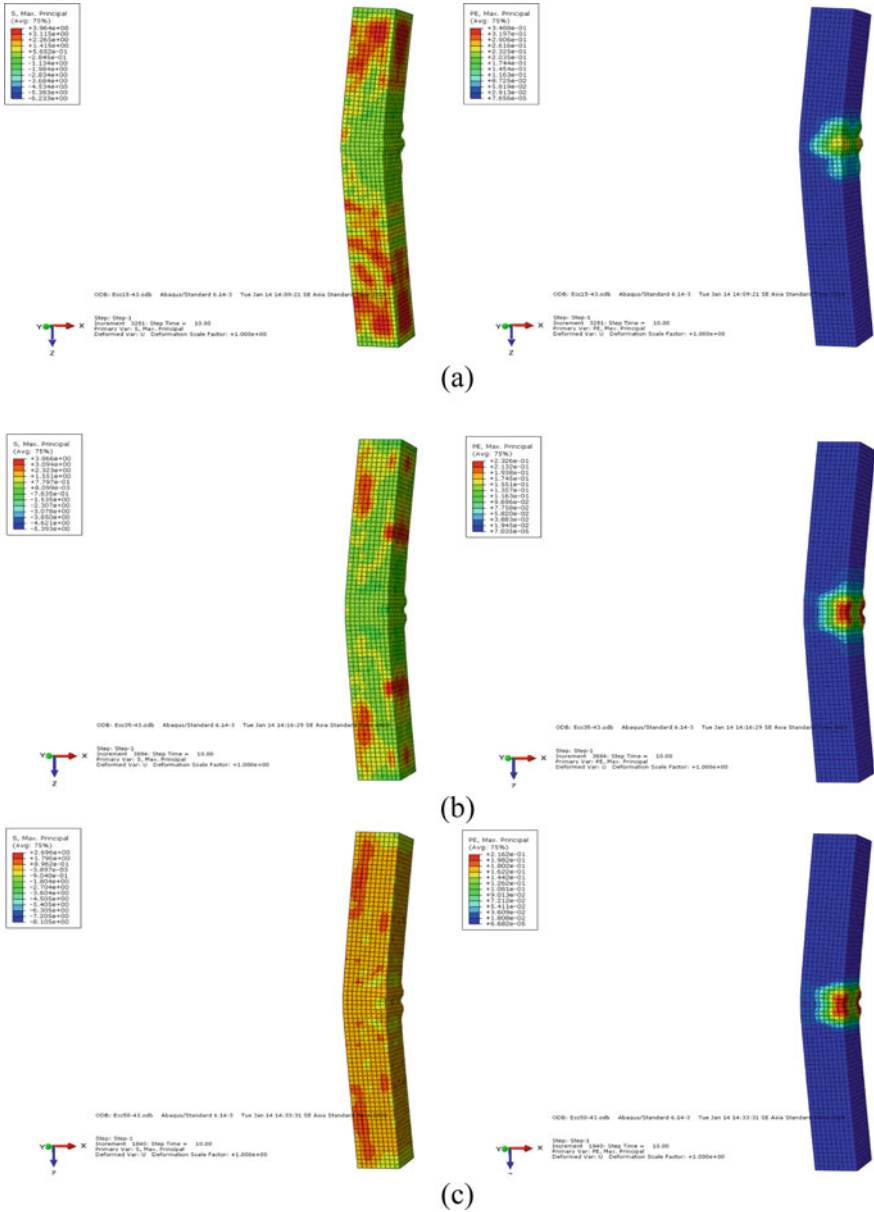


Fig. 8 Stress and crack patterns in the geopolymer column **a** GCI-4 (eccentricity 15 mm), **b** GCI-5 (eccentricity 35 mm) and **c** GCI-6 (eccentricity 50 mm)

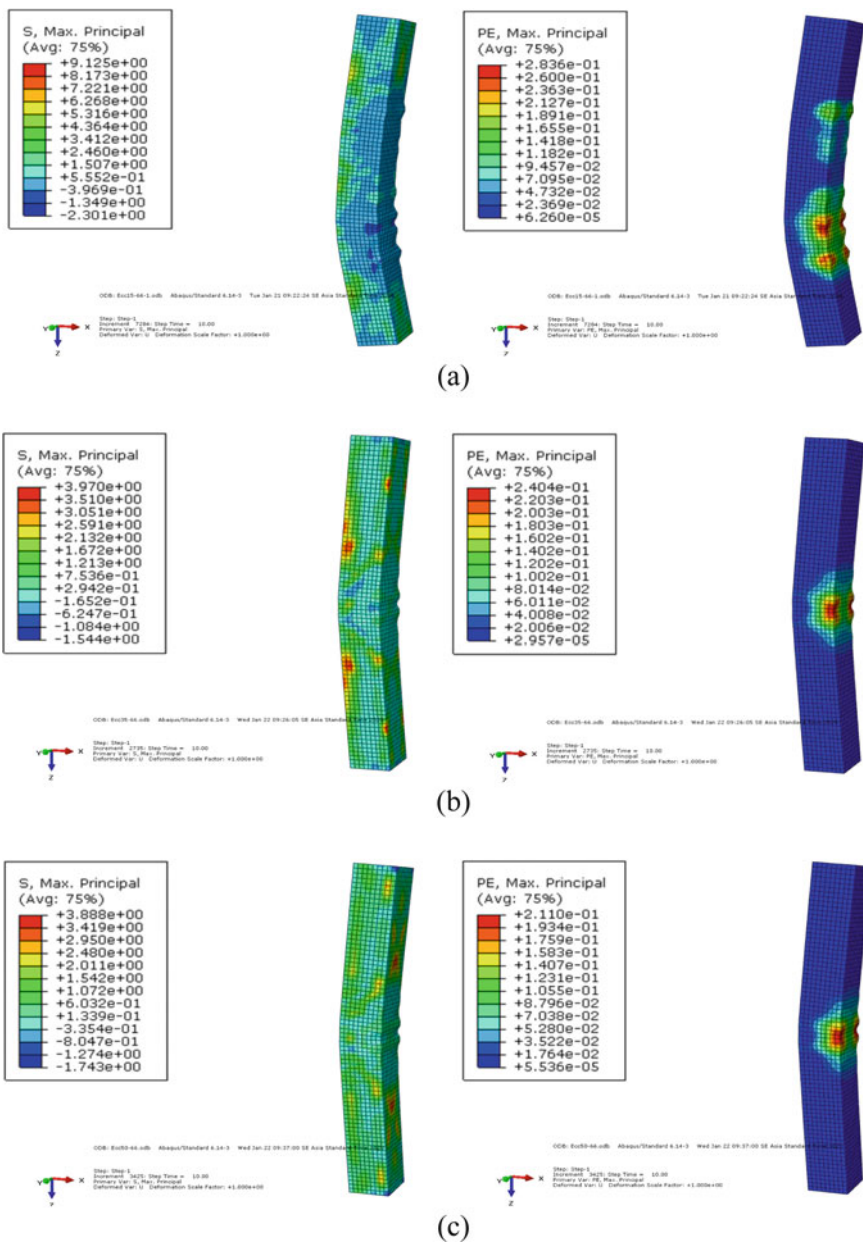


Fig. 9 Stress and crack patterns in the geopolymer column **a** GCII-1 (eccentricity 15 mm), **b** GCII-2 (eccentricity 35 mm) and **c** GCII-3 (eccentricity 50 mm)

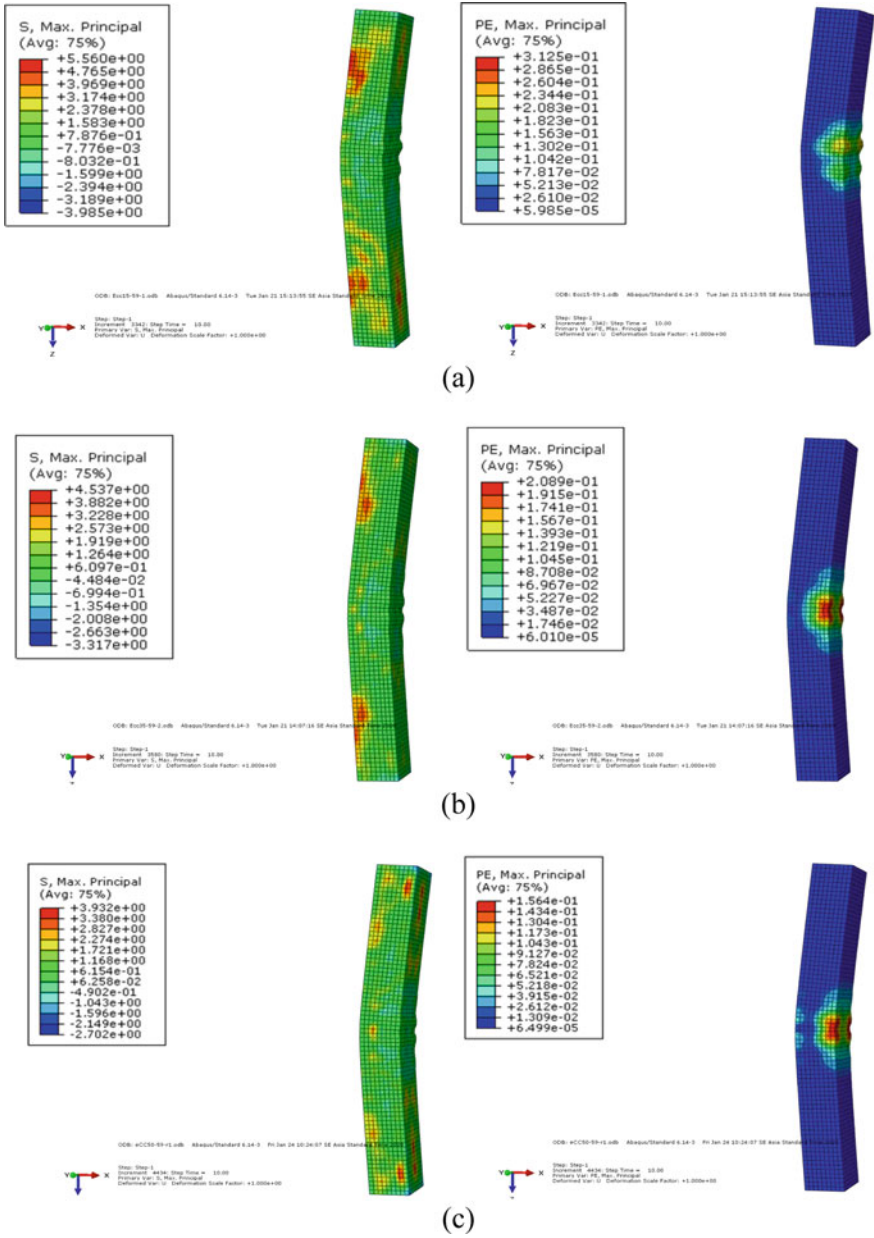


Fig. 10 Stress and crack patterns in the geopolymer column **a** Gcii-4 (eccentricity 15 mm), **b** Gcii-5 (eccentricity 35 mm) and **c** Gcii-6 (eccentricity 50 mm)

Column failure occurred in the mid-height column or occurred at the top or bottom of the mid-height column at a distance of 250 mm [11]. This condition is due to the difference in load eccentricity in the column. The strain on the finite element model indicates that the column pressure area has occurred spalling.

5 Conclusion

This study presents finite element analysis using ABAQUS to predict the behavior of 12 (twelve) reinforced geopolymer concrete columns with eccentric loads.

1. Load–displacement behavior from the results of FE and experimental modeling shows a similar pattern. While the failure load shows the results of a small ratio of the experimental results, and mid-deflection also similar.
2. The stress–strain equation recommended by Collins et al. in Hardjito et al. is more in line with the experimental results.
3. The higher compressive strength of geopolymer concrete, ductility decreases but stiffness increases.

Acknowledgements We sincerely thank LPDP, Ministry of Finance, Republic of Indonesia for funding education through the Education Scholarship program.

References

1. Davidovits J (1994) Global warming impact on the cement and aggregates industries. 6(2):263–278
2. Cornelis R, Priyosulistyo H, Satyarno I, Rohmadi (2019) Workability and Strength properties of class C fly ash-based geopolymer mortar. *Int Conf Sustain Civ Eng Struct Constr Mater (SCESCM 2018)* 258:6
3. Chindaprasirt P, Chalee W (2014) Effect of sodium hydroxide concentration on chloride penetration and steel corrosion of fly ash-based geopolymer concrete under marine site. *Constr Build Mater* 63:303–310
4. Lavanya G, Jegan J (2015) Durability study on high calcium fly ash based geopolymer concrete. *Adv Mater Sci Eng* 2015:1–7
5. Reddy DV, Edouard J, Sobhan K (2013) Durability of fly ash–based geopolymer structural concrete in the marine environment. *J Mater Civ Eng © ASCE* 781–787
6. Sung G, Bok Y, Taek K, Soo Y (2015) The mechanical properties of fly ash-based geopolymer concrete with alkaline activators. *Constr Build Mater* 47(2013):409–418
7. Hardjito D, Vijaya RB (2005) Development and properties of low-calcium fly ash-based geopolymer concrete
8. Collins MP, Mitchell D, MacGregor JG (1993) Structural design considerations for high-strength concrete.pdf. *Concr Int* 15(5):27–34
9. Nuroji, Primadyas DH, Nurhuda I, Muslikh (2017) The comparison of bond strength between geopolymer concrete and OPC concrete for plain reinforcing bars, *Int J Conf Adv Eng Technol (IJCAET 2017) Int Symp Adv Mech Power Eng (ISAMPE 2017)* 159

10. Khoa Tan N, Tuan Anh L, Kihak L (2016) Experimental study on flexural strength of reinforced geopolymer concrete beam. *Int Sch Sci Res Innov* 10(4):516–520
11. Sumajouw DMJ, Hardjito D, Wallah SE, Rangan BV (2007) Fly ash-based geopolymer concrete: Study of slender reinforced columns. *J Mater Sci* 42(9):3124–3130
12. Kiran T, Zai SAK, Reddy S (2015) Impact test on geopolymer concrete slabs. *IJRET Int J Res Eng Technol* 04(12):110–116
13. Hardjito D, Wallah SE, Sumajouw DMJ, Rangan BV (2005) The stress–strain behaviour of fly ash-based geopolymer concrete. vol 2.
14. Raza A, Khan QZ, Ahmad A (2019) Numerical investigation of load-carrying capacity of GFRP-reinforced rectangular concrete members using CDP model in ABAQUS. *Adv Civ Eng* 2019
15. Rangan BV (1990) Strength of reinforced concrete slender columns. *ACI Struct J* 87(1)
16. AS3600 (2001) Concrete structures code. Standards Association of Australia
17. ACI318–02 (2002) Building code requirements for structural concrete. ACI Committee

Optimal Sensor Placement for Accelerometer in Single-Pylon Cable-Stayed Bridge



Akhmad Aminullah, Bambang Suhendro, and Raka Bagus Panuntun

Abstract The construction of Indonesian cable-stayed bridges is developing nowadays. The most common approach for detecting bridge damage is the Structural Health Monitoring System (SHMS). The SHMS uses instrumentation equipment to monitor actions in the structure, including the cable-stayed bridge. In this study, the writer uses a single-pylon cable-stayed bridge as a case study, which is Soekarno Bridge in Manado, Indonesia. The accelerometer is one of the major sensors used in SHMS, as it can determine the bridge's frequencies, damage detection, and the deterioration of the structures. This study exclusively reviews accelerometer sensors for bridge deck and only discusses vertical vibration since the vertical modes dominate this type of bridge. Optimal Sensor Placement (OSP) is a method to optimize the number and sensor position. The OSP processes the bridge's participation vector mode using several methods such as the Effective Independence Method, Eigenvalue Component Product, and Mode Shape Summation Plot Method, in which the accelerometer's number and position are decided. The result shows that the Effective Independence Method has the most optimum number and sensor position based on the Fisher Information Matrix (FIM). The optimal number of accelerometers for the Soekarno Bridge deck is four (4) placed along the bridge deck.

Keywords Structural health monitoring system · Accelerometer · Optimal sensor placement · Cable-stayed bridge

A. Aminullah (✉) · B. Suhendro · R. B. Panuntun
Universitas Gadjah Mada, Yogyakarta, Indonesia
e-mail: akhmadaminullah@ugm.ac.id

B. Suhendro
e-mail: bsuhendro@ugm.ac.id

R. B. Panuntun
e-mail: raka.bagus.p@ugm.ac.id

1 Introduction

1.1 Background

The bridge is one of the important infrastructures. Bridges connect roads that are separated by rivers, valleys, and other traffic crossings. Travel time is significantly reduced by the presence of a bridge, which positively impacts the country's economy. Long-span cable-stayed bridge commonly has a design lifetime of more than 100 years. In that long time, the bridge will be suffering short-term and long-term environmental [1]. As a result, the bridge will deteriorate all the time. There are at least eight (8) factors that cause the bridge to be degraded, for instance: dynamic properties of vehicle loads, overloads, cyclic thermal loading, fatigue, corrosive and aggressive environments, wind and earthquake forces, ageing, flooding, and scouring [2].

The manual physical assessment is one of the actions taken to prevent the bridge from deteriorating. This method can be done by observing the bridge directly on-site. This assessment is usually conducted periodically around six (6) months or every twelve (12) months. However, in complex bridges such as long-span bridges, the manual assessment is not enough. This type of bridge has a complex structural response due to the actions that occur. It is also difficult to carry out inspections on long-span bridges since the size and the environmental difficulties will increase the cost of inspections. To overcome the issues of manual monitoring of the bridge, monitoring the condition of the bridge structure can be done by placing sensors on the bridge, which can be monitored continuously [3]. The monitoring system using a sensor can read structural responses and actions that occur on the bridge. This system is needed to complement the existing assessment manual. This system does not require any field testing and does not have to stop the traffic operation of the bridge [1]. Several monitoring technologies are implemented to reduce the risk of deterioration and improve bridge safety [4].

Structural Health Monitoring System (SHMS) is a popular method for damage detection for bridges using sensors. This method uses sensors to detect actions on structures, for instance, structural behavior, traffic loads, environmental actions, and early damage detection [5]. There are many objectives of the SHMS, for example, to collect environmental data as an early warning for bridge users and to notify the owner if there is a structural problem. In Japan, SHMS is also being developed to improve stock management efficiency and prevent structural failure [4].

Several studies on structural health monitoring systems have been conducted. Research on SHMS for bridges in the United States shows that SHMS is a powerful method for detecting damage and assessing conditions as part of the decision-making process [6]. Several SHMS studies have been conducted for individual bridges, such as the Tamar Bridge [7], which has been shown to be severely affected by temperature fluctuations that produce sagging. Besides, the Akashi Kaikyo Bridge [8] is considered the pioneer case study for real-time bridge monitoring systems. FEA calculation was carried out for the Danube Bridge [9], and the FEA results matched with the SHMS results. Furthermore, a study conducted on the Hammersmith Flyover

[10] successfully detected damage to the prestressing tendon cable with the help of SHMS. While, a study conducted on the Ricollo Viaduct Bridge [11], Sutong Bridge [12] and Tsing Ma Bridge [1] proves that the SHMS data is not for bridge health monitoring purposes but also as a platform to collect other data for research purposes.

Soekarno Bridge is a bridge inside Manado City to support the traffic network and as a tourist attraction [13]. Soekarno Bridge is a single-pylon cable-stayed bridge that passes through Manado's harbor. The bridge was originally built in 2003; however, it was delayed due to technical constraints during the construction and was completed in 2015. It has a 62.8 m height pylon and 240 m long span with a 17 m deck width. There are several shape types of cable-stayed bridge, harp, fan, and radial. Based on the classification of the three types of cable-stayed bridge configurations, most of the cable-stayed bridges built are harp types. Meanwhile, fan types are mostly used for longer spans [14]. Hence, Soekarno Bridge uses the fan-type as its cable configurations.

The SHMS sensors have been installed to monitor the structural condition of the Soekarno Bridge. Nine types of sensors are equipped on the Soekarno Bridge which are accelerometer (7 units), anemometer biaxial (1 unit), anemometer triaxial (2 units), ATRH (4 units), seismic sensor (1 unit), temperature sensor (4 units), strain transducer (48 units), tiltmeter (22 units), and EM sensor (12 units) [15]. The collected data are saved to a server and accessible online as a Soekarno Bridge evaluation material. The SHM on the Soekarno Bridge aims to monitor the bridge's health by recording the environmental load. The recorded data would be beneficial in a decision-making process in terms of long-span bridge maintenance in Indonesia.

One of the sensors that are important for SHMS is the accelerometer. Accelerometers must be mounted on pylons and girders to measure vibrations and characteristics of the main part of the structure, such as natural frequencies, damping ratio, and mode shape. Other than that, the use of accelerometers is wide. The accelerometer can be used to obtain the bridge displacement [16], identify the damage location [17], and also it can be used to obtain the value of cable force [18]. Hence, the need for an accelerometer to be planted on the bridge is essential, especially for the long-span bridges.

There are several methods for determining the number of accelerometers needed and where they should be located on. First, it can be determined by copying how to install the sensor on the other bridge that has the same characteristics. This method is better for a typical bridge, for example, girder bridge. Second, the sensor location and number can be obtained by using SHMS code. If the country where the bridge is located does not have the code, another nation code can be used. Third, the number of sensors and their position can be determined through dynamic analysis and mode analysis. There are several formulas to obtain the optimum sensor placement, which will be described in this paper.

This research evaluates the SHMS in Soekarno Bridge by analyzing the number and position of the planted accelerometers. This research is expected to be one of the references for designing the SHMS for other cable-stayed bridges in Indonesia.

2 Optimal Sensor Placement Technique

A sensor is an electronic device that is attached to a structure to obtain detailed information about the response of the structure, the source of loading, and the environmental situation around the structure. Since data acquisition expenses are expensive, the main factor in data acquisition using sensors is the number of sensors to be installed. Problems with sensor accessibility have now been reduced with the introduction of wireless sensors. However, its application is limited due to energy source and time synchronization issues. The number of sensors must be optimized because the price of each sensor is quite expensive [19]. This paper concern about the placement technique for the accelerometer.

The location of the sensor is usually determined from previous experience regarding the vibration event. In most cases of structural health monitoring, analysis of measured data is required to obtain immeasurable results. Therefore, optimal sensor placement is needed to get better accuracy. There are several methods for determining the optimal amount of accelerometer required for health monitoring.

1. Effective Independence Method
2. Eigenvalue Component Product
3. Mode Shape Summation Plot Method
4. Effective Independence—Drive Point Residue Method

Through the iteration technique, each sensor placement candidate is evaluated for its contribution so that the candidate with the smallest contribution is eliminated until the desired number of sensors is achieved [20].

2.1 Effective Independence Method

Effective Independence Method (EI) is to select measurement positions that make the mode shapes of interest as linearly independent as possible while containing sufficient information about the target modal responses in the measurements [21]. To obtain the *Fisher Information Matrix* (FIM) determinant $[A]$, Eq. (1) is used.

$$[A]_{M \times M} = [\Phi]_{M \times N}^T [\Phi]_{N \times M} = \sum_{i=1}^N ([\Phi]_i^T [\Phi]_i) \quad (1)$$

where

N = Number of *Degree of Freedom* (DOF)

M = Number of *Mode Shape*

Φ = *Vibration vector of mode shape*

$[\Phi]_i$ = $[\Phi_{i1}, \Phi_{i2}, \Phi_{i3}, \dots, \Phi_{in}]$ Vector vibration for the i th DOF

Firstly, maximizing A by using the following eigenvalue Eq. (2)

$$([A] - [\lambda]_i [I])[\psi]_i = 0 \quad (2)$$

where

λ_i = Eigenvalue A of the ith DOF
 ψ_i = Eigenvector A of the ith DOF

Matrix A is positive and symmetric. The eigenvalue λ of A is a positive real number and eigenvector ψ is orthogonal. Optimal Sensor Placement conditions are obtained when A determinant is maximum. This process is done by trial and elimination of nodes. To obtain the maximum value, an algorithm was developed by evaluating Effective Independence Distribution (EI_D) of each candidate sensor location in Eq. (3)

$$EI_D = (\Phi\psi)^2 \lambda^{-1} \{1\}_k \quad (3)$$

where

$\{1\}_k$ = Column vector with all element of 1
 EI_D = EI_D factor

The iteration should be conducted to obtain the maximum value of A determinant the candidate sensor location with the least EI_D should be eliminated.

2.2 Eigenvalue Component Product

The Eigenvalue Component Product (ECP) method computes the absolute products of each row vector [22]. In ECP, the sensor positions with large ECP index values are selected as candidate sensor positions [23]. ECP has shown in Eq. (4) as follows.

$$ECP_i = \prod_{k=i}^M |\Phi_{ik}| \quad (4)$$

where

i = Number of DOFs
 k = Number of mode shapes
 ECP_i = ECP index for the ith DOFs

This technique selects sensor positions with larger ECP indices ECP and has the I advantage to prevent deploying sensors at or near nodes of selected modes. However, the ECP tends to cluster sensors in a small area and is not able to capture global mode shapes with clustered sensors.

2.3 Mode Shape Summation Plot Method

By the *Mode Shape Summation Plot* (MSSP) method, the components of a mode shape corresponding to a sensor position (a row in the mode shape matrix) are drawn in a graph, and the absolute summation is calculated for each row (candidate sensor positions). The positions with large MSSP indices are selected as sensor positions as follows. MSSP method shown in Eq. (5) as follows.

$$MSSP_i = \sum_{k=1}^M |\Phi_{ik}| \quad (5)$$

where,

- i = Number of DOFs
- k = Number of mode shape
- $MSSP_i$ = MSSP index for the i th DOF

The MSSP method has the advantage to graphically show the contributions of candidate sensor positions to the total responses of a structure and is easy to compute [24].

2.4 Effective Independence—Drive Point Residue Method

The EI-DPR method is a combination of the EI and DPR methods. The EI method in the previous section allows selecting the location of sensors with low energy levels. This can cause the information obtained by sensors at that location to be less than optimal. Through the EI-DPR method, the problem is solved by multiplying the contribution to the EI method by the DPR coefficient. The DPR coefficient is formulated in Eq. (6) as follows:

$$DPR_i = \sum_{k=1}^M \frac{\Phi_{ik}^2}{\omega_k} \quad (6)$$

where,

- ω_k = Frequency in k th mode shape
- DPR_i = DPR coefficient for the i th DOF

Therefore, the EI_D factor became:

$$EI_D = (\Phi\psi)^2 \lambda^{-1} \{1\}_k DPR_i \quad (7)$$

The formula above shows that the DPR coefficient is used as a coefficient factor for the value of the EI factor. This allows the method to focus on position sensors with large energy values.

3 Methods

3.1 Finite Element Model

In modeling Soekarno Bridge, software based on Finite element analysis is used. Finite element analysis is a numerical calculation method that is widely used in the civil engineering field. Finite element analysis has progressed to the point where it is now used in a variety of software, including Midas.

In this research, a numerical model was made based on the finite element using Midas Civil 2011 software. The finite element model of the Soekarno Bridge is done to verify the sensor measurement so that it can be appropriately interpreted. The main span model on the Soekarno Bridge is shown in Fig. 1.

The model of Soekarno Bridge in Midas Civil uses the following assumptions.

1. The foundation of the pylon is modelled as a fixed support above the pile cap.
Instead of modeling the whole pile cap and the bore pile, the research uses fixed support as the foundation for simplification. The pile cap is shown in Fig. 2.
2. The relationship of the cross beam with the girder is fixed.
3. The support of both ends of the girders is pinned.

Both ends piers of the main span were idealized as pinned supported. The parameters obtained from this modeling are deflection at point, shape mode, and participation mode vector [15]. These parameters are compared with the Soekarno Bridge load test report issued by the Ministry of Public Works and Public Housing.

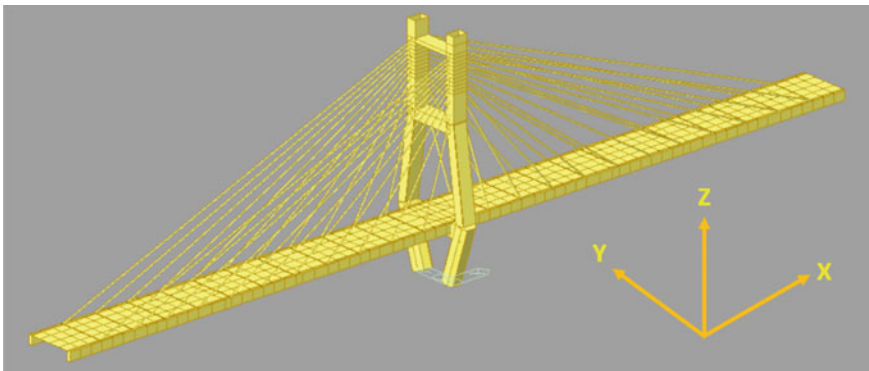


Fig. 1 Finite element model of Soekarno bridge

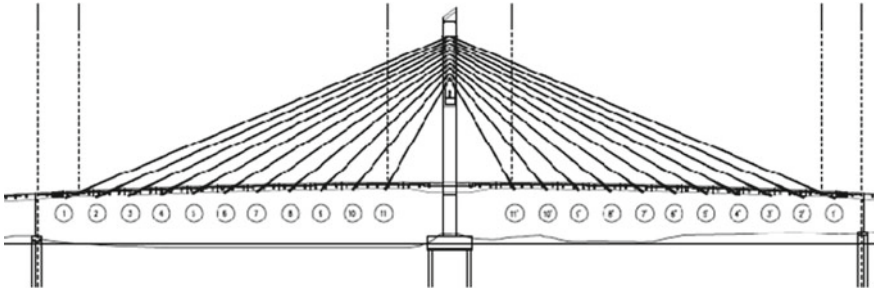


Fig. 2 Detail engineering design (DED) of Soekarno bridge

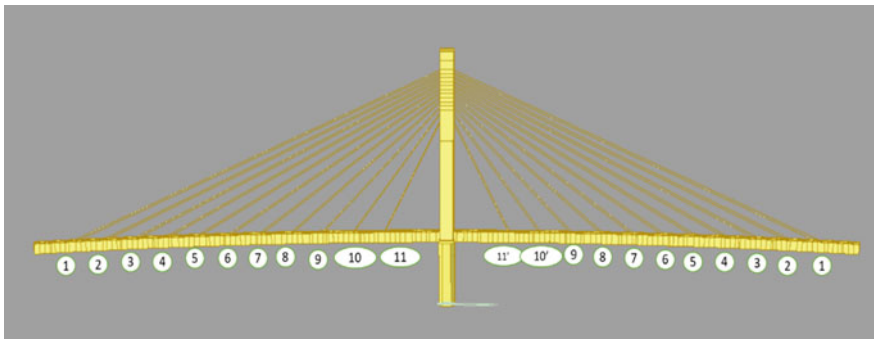


Fig. 3 Measured deflection location

The measured deflection is vertical deflection (U_z), vertical mode shape, and natural frequencies. The measured deflection location is shown in Fig. 3. The validation results of the Soekarno Bridge model in Midas Civil will be presented later in this paper.

3.2 Optimal Sensor Placement

The sensors' location is usually obtained based on the experience or by using code provided by other countries like China [25]. However, to obtain the best result on how the accelerometer configuration, the calculation is needed by using the following methods:

1. Effective Independence Method
2. Eigenvalue Component Product Method
3. Mode Shape Summation Plot Method
4. Effective Independence Method—Driving Point Residue

The flowchart of obtaining number and accelerometer sensor location of Soekarno Bridge shown in Fig. 3.

4 Results

4.1 Validation

Soekarno Bridge model is modeled in Midas Civil 2011 Trial Edition. The model is compared to the load test result to determine the quality of the model. The load test consists of 2 phases, a full loading test and a half loading test. Below is the outcome of comparing the loading test from the Midas Civil Soekarno Bridge model to the actual loading test.

1. The maximum error of the full-load loading test is 44%, the maximum difference is 30.47 mm.
2. The maximum error of the half-load loading test is 36%, the maximum difference is 35.78 mm.

From these results, the bridge model is considered quite close to the original bridge in terms of vertical displacement.

The mode shape and natural frequencies of the bridge also need to be validated. The first mode is shown in Fig. 4, which has a natural frequency of 0.7079 Hz, the second mode is shown in Fig. 5, and the third mode is shown in Fig. 6 are all vertical bending. The comparison between measured frequency and model frequency are described in Table 1.

The model of Soekarno Bridge satisfies the displacement validation (static), and frequency validation (dynamic) which means the model can be used for the next analysis.

4.2 Accelerometer Position

There are four methods to evaluate sensor placement:

1. Eigenvalue Component Product (ECP),
2. Mode Shape Summation Plot (MSSP),
3. Effective Independence (EI), and
4. Effective Independence—Drive Point Residu (EI-DPR).

The factor of each method is calculated to obtain the optimal result for each OSP method. The results are compared using the FIM determinant to determine the best sensor configuration.

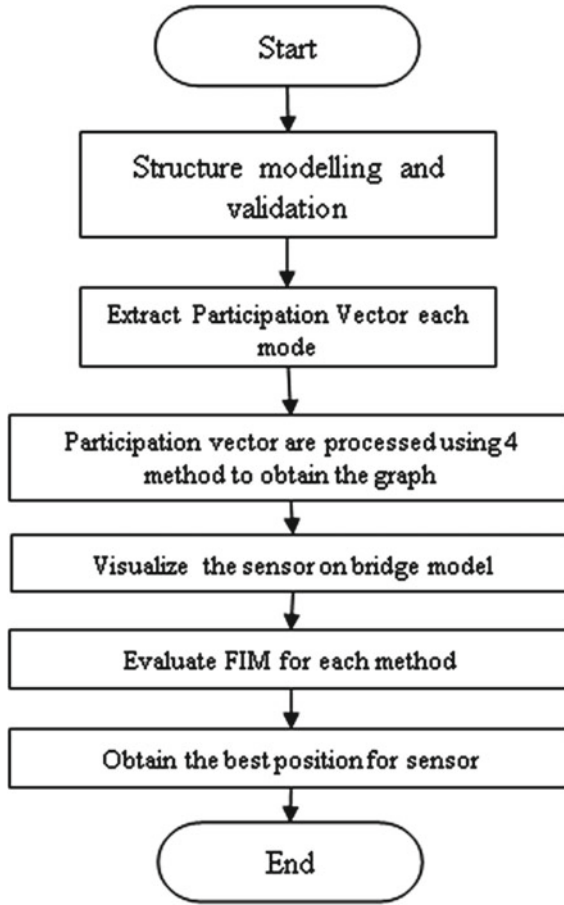


Fig. 4 Flowchart of optimal sensor placement method

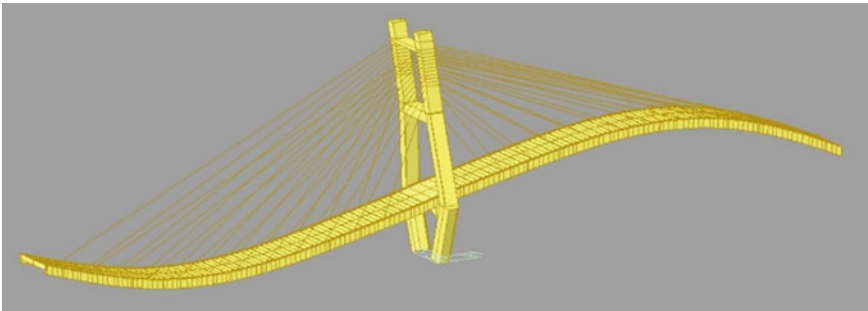


Fig. 5 Mode 1 ($f = 0.7079$ Hz)

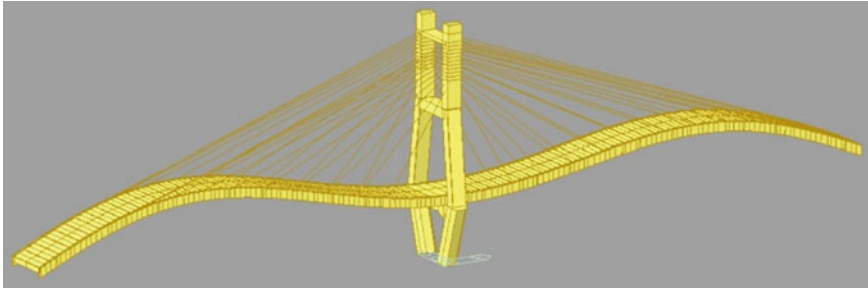


Fig. 6 Mode 2 ($f = 1.2212$ Hz)

Table 1 Model mode shape and measurement comparison

Mode	Measurement		Model	
	Frequency (Hz)	Mode shape	Frequency (Hz)	Mode shape
1	0.67	Vertical bending	0.7079	Vertical bending
2	1.22	Vertical bending	1.2212	Vertical bending
3	1.27	Vertical bending	1.2735	Vertical bending

By using the Eigenvalue Component Product (ECP) method, the sensor candidate is determined by the ECP factor. Figure 7 shows the ECP factor of the Soekarno Bridge. The position of sensors according to ECP is on -72 m and 72 m from the pylon which is shown by Figs. 8 and 9.

By using the Mode Shape Summation Plot method, the sensor candidate is determined by the MSSP factor. Figure 8 shows the MSSP factor of the Soekarno Bridge. The position of sensors according to MSSP is on -75 and 75 m from the pylon which is shown by Fig. 10.

EI method using EI factor to determine sensor location. The higher EI factor means the signal is stronger. Therefore, the maximum value will be chosen as the sensor location. Figure 11 shows the EI factor of the Soekarno Bridge. According

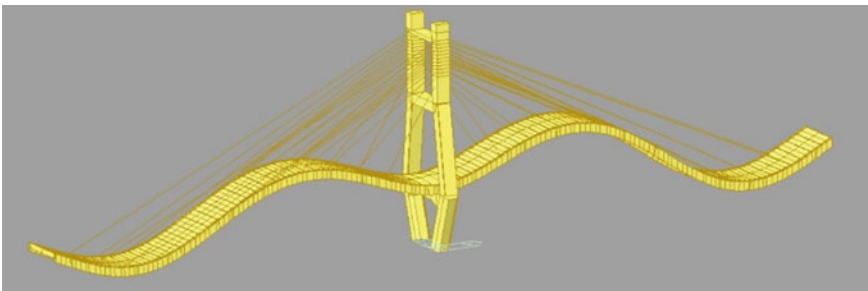


Fig. 7 Mode 3 ($f = 1.2735$ Hz)

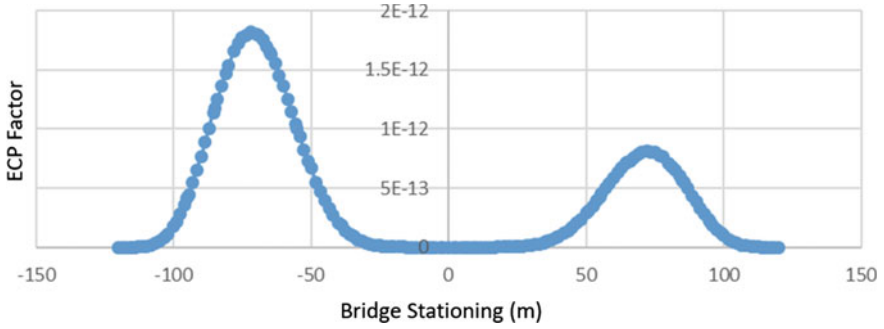


Fig. 8 ECP factor

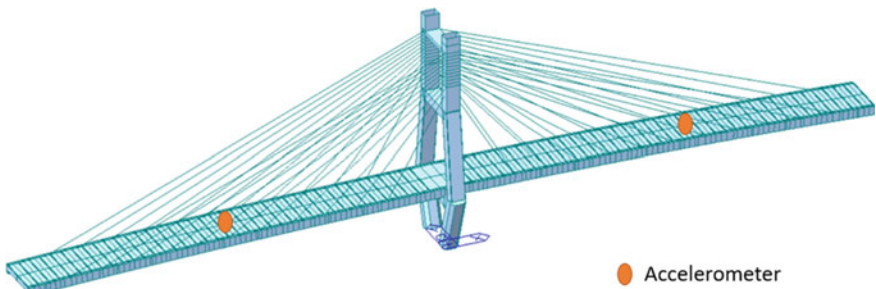


Fig. 9 The position of accelerometers according to the ECP method

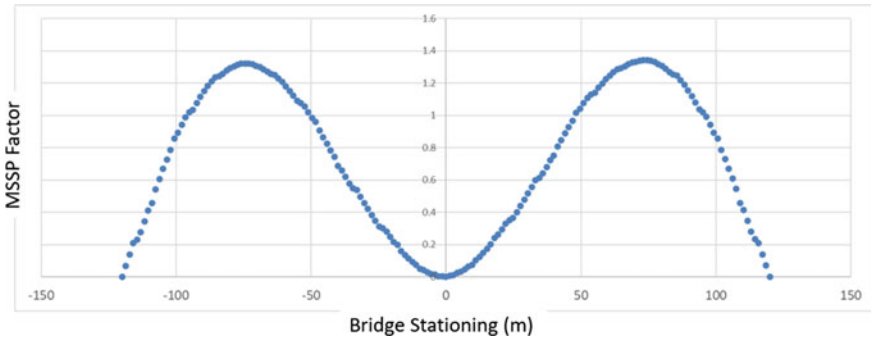


Fig. 10 MSSP factor

to the EI method, the position of sensors is on -102 , -57 , 57 , and 102 m from the pylon, shown by Fig. 12.

EI method using the EI-DPR factor to determine sensor location. The higher EI-DPR factor means the signal is stronger. Therefore, the maximum value will be chosen as the sensor location. Figure 13 shows the EI-DPR factor of the Soekarno

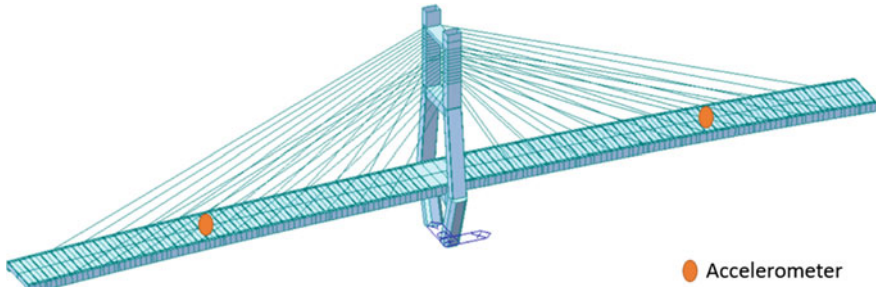


Fig. 11 The position of accelerometers according to the MSSP method

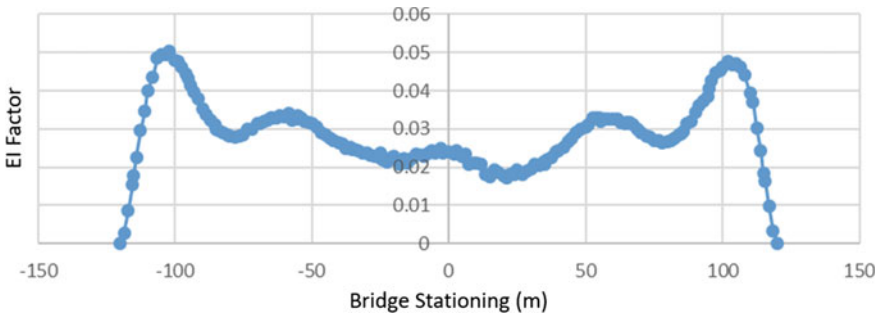


Fig. 12 EI factor

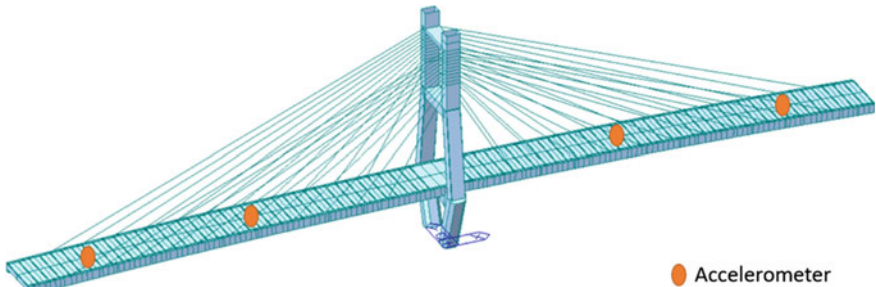


Fig. 13 The position of an accelerometer according to the EI method

Bridge. According to the EI-DPR method, the position of sensors is on -87 , -66 , 66 , and 87 m from the pylon, shown by Fig. 14 and 15

The best sensor candidates have the highest factor value. In the EI and EI-DPR methods, each iteration gives different factor values so that the factor scores of each candidate are not always the same.

The parameter is evaluated by the value of the Fisher Information Matrix (FIM) determinant. The determinant of the FIM matrix is calculated in each calculation of

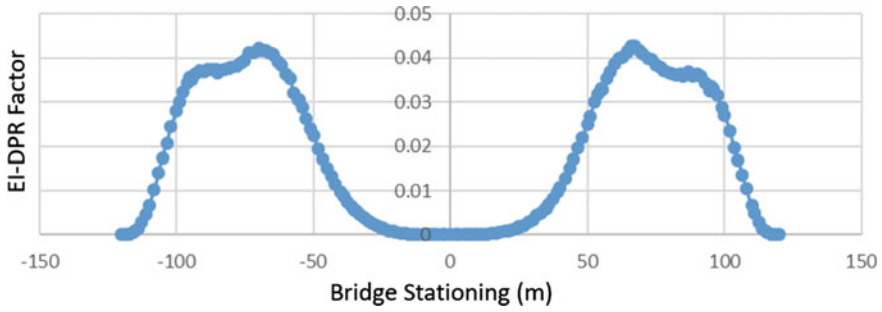


Fig. 14 EI-DPR factor

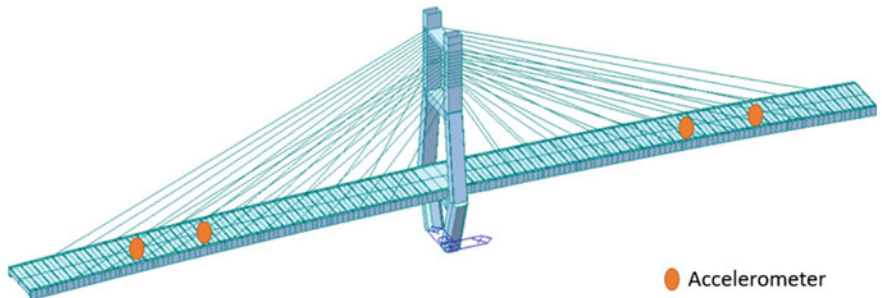


Fig. 15 The position of an accelerometer according to the EI-DPR method

the combination of the number of sensors for each method. Each determinant value is divided by the largest determinant value so that a comparison between methods is obtained in the form of a percentage [26]. The higher determinant value shows the performance of each method. Figure 16 shows the comparison of FIM for each method.

Based on these results, it was found that the EI method provides better performance compared to other methods. With the same number of sensors, the EI method has a

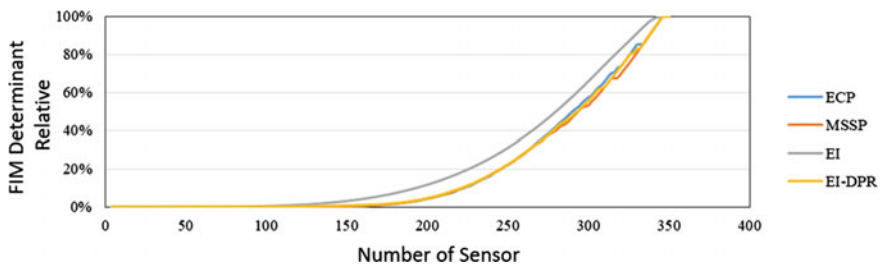


Fig. 16 FIM determinant comparison

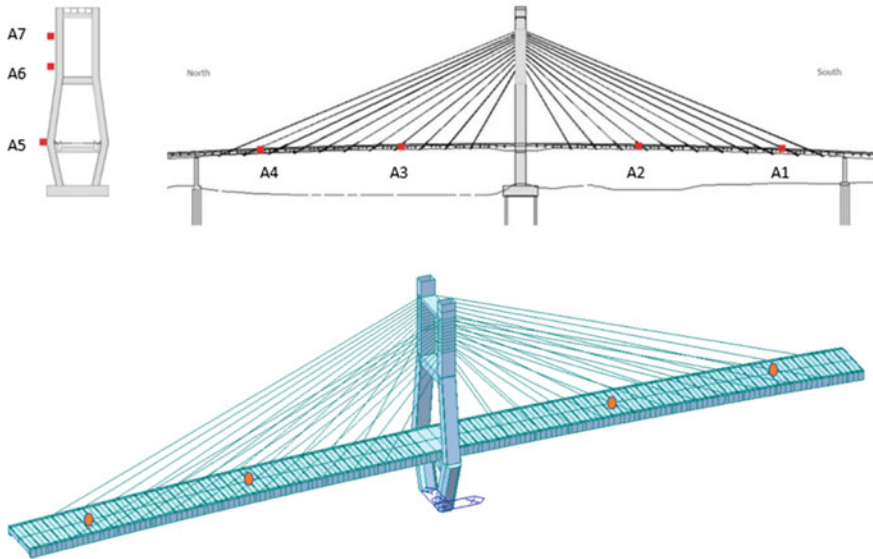


Fig. 17 Existing accelerometer Locations comparing to optimum sensor locations

higher FIM determinant than other methods. The comparison chart shows that the EI method has better performance, followed by the EI-DPR, ECP, and MSSP methods.

4 Accelerometer sensors on Soekarno Bridge are installed on the deck of the Soekarno Bridge. Figure 17 shows the position of the accelerometer on the Soekarno Bridge comparing to the optimum sensor position based on the analysis. From the two images, the position of the accelerometer is the same, so it can be concluded that the position of the accelerometer sensor on the Soekarno Bridge is optimal.

5 Conclusion

The study regarding Structural Health Monitoring System in Soekarno Bridge has been done in term of optimal sensor placement for the accelerometer. There are several conclusions:

1. The finite element model of Soekarno Bridge fulfilled the displacement and frequency validation based on the loading test report of Soekarno Bridge.
2. To determine the needs of the accelerometer in a single-pylon cable-stayed bridge. The optimum sensor placement method is conducted. The Effective Independence Method is the best method to determine the number and the position by having the highest FIM Determinant Relative comparing to the other methods.

3. According to the Effective Independence Method, the existing accelerometers in the Soekarno Bridge are optimal, with four accelerometers on the deck.

References

1. Xu Y, Xia Y (2007) Structural health monitoring of long-span suspension bridges. *Isis* 1:65310–65311
2. Suhendro B (2012) The role of structural health monitoring in sustainability of civil engineering structures. In: International conference on sustainable civil engineering structures and construction materials. pp 16
3. Li J et al (2015) Optimal sensor placement for long-span cable-stayed bridge using a novel particle swarm optimization algorithm. *J Civ Struct Heal Monit* 5(5):677–685. <https://doi.org/10.1007/s13349-015-0145-4>
4. Fujino Y, Siringoringo DM (2011) Bridge monitoring in Japan: the needs and strategies. *Struct Infrastruct Eng* 7(7–8):597–611. <https://doi.org/10.1080/15732479.2010.498282>
5. Modares M, Waksanski N (2013) Overview of structural health monitoring for steel bridges. *Pract Period Struct Des Constr* 18(3):187–191. [https://doi.org/10.1061/\(ASCE\)SC.1943-5576.0000154](https://doi.org/10.1061/(ASCE)SC.1943-5576.0000154)
6. Nagarajaiah S, Erazo K (2016) Structural monitoring and identification of civil infrastructure in the United States. *Struct Monit Maint* 3(1):51–69. <https://doi.org/10.12989/smm.2016.3.1.051>
7. Koo KY, Brownjohn JMW, List DI, Cole R (2013) Structural health monitoring of the Tamar suspension bridge. *Struct Control Heal Monit* 20:609–625. <https://doi.org/10.1002/stc>
8. Sumitoro S et al (2001) Long span bridge health monitoring system in Japan. In: 6th annual international symposium NDE healing monitoring diagnostics. vol 4337. pp 517–524. <https://doi.org/10.1117/12.435628>
9. Ároch R et al (2016) Structural health monitoring of major danube bridges in bratislava. *Procedia Eng* 156:24–31. <https://doi.org/10.1016/j.proeng.2016.08.263>
10. Webb GT et al (2014) Analysis of structural health monitoring data from hammersmith flyover. *J Bridge Eng* 19(6):1–11. [https://doi.org/10.1061/\(ASCE\)BE.1943-5592.0000587](https://doi.org/10.1061/(ASCE)BE.1943-5592.0000587)
11. Glišić B et al (2008) Structural health monitoring method for curved concrete bridge box girders. *Sensors Smart Struct Technol Civil Mech Aerosp Syst* 6932:693204. <https://doi.org/10.1117/12.778643>
12. Wang H et al (2014) Full-scale measurements and system identification on sutong cable-stayed bridge during typhoon Fung-Wong. *Sci World J* 2014. <https://doi.org/10.1155/2014/936832>
13. Wijayanto A et al (2017) Evaluasi Integritas Sistem Struktur Jembatan Dr. Ir. Soekarno 24(2):125–138. <https://doi.org/10.5614/jts.2017.24.2.3>
14. Bannazadeh B et al (2012) A study on cable-stayed bridges. *Appl Mech Mater* 193–194:1113–1118. <https://doi.org/10.4028/www.scientific.net/AMM.193-194.1113>
15. Panuntun RB (2019) Evaluasi structural health monitoring system pada Jembatan cable-stayed single-pylon (Studi Kasus: Jembatan Soekarno). Universitas Gadjah Mada
16. Sekiya H et al (2016) Technique for determining bridge displacement response using MEMS accelerometers. *Sensors (Switzerland)* 16(2):1–15. <https://doi.org/10.3390/s16020257>
17. Dessi D, Camerlengo G (2015) Damage identification techniques via modal curvature analysis: overview and comparison. *Mech Syst Signal Process* 52–53(1):181–205. <https://doi.org/10.1016/j.ymssp.2014.05.031>
18. Hidayat I et al (2018) Validation value of cable force using the accelerometer. *IOP Conf Ser Earth Environ Sci* 195(1). <https://doi.org/10.1088/1755-1315/195/1/012022>
19. Beal JM et al (2008) Optimal sensor placement for enhancing sensitivity to change in stiffness for structural health monitoring. *Optim Eng* 9(2):119–142. <https://doi.org/10.1007/s11081-007-9023-1>

20. Tong KH et al (2014) Optimal sensor placement for mode shapes using improved simulated annealing. *Smart Struct Syst* 13(3):389–406. <https://doi.org/10.12989/sss.2014.13.3.389>
21. Kammer DC (1991) Enhancement of on-orbit modal identification of large space structures through sensor placement. *J Sound Vib* 171(1):119–139. <https://doi.org/10.1006/jsvi.1994.1107>
22. Heylen W, Sas P (1998) In: *Modal analysis theory and testing*. Belgium
23. Larson CB et al.(1994) A comparison of modal test planning techniques: excitation and sensor placement using the NASA 8-bay truss. *SPIE—Int Soc Opt Eng* 205–211
24. Li D (2012) Sensor placement methods and evaluation criteria in structural health monitoring. *Siegen*
25. Moreu F et al (2018) Technical specifications of structural health monitoring for highway bridges: new chinese structural health monitoring code. *Front Built Environ* 4(March):1–12. <https://doi.org/10.3389/fbuil.2018.00010>
26. Ly A et al (2017) A tutorial on fisher information. *J Math Psychol* 80:40–55. <https://doi.org/10.1016/j.jmp.2017.05.006>

Seismic Performance of Instant Steel Frame House for Post Earthquake Reconstruction



Widarto Sutrisno, Iman Satyarno, Ali Awaludin, Ashar Saputra,
and Angga Fajar Setiawan

Abstract Earthquakes in Indonesia revealed that the majority of the destroyed buildings were community dwellings. For instance, the 2006 Yogyakarta earthquake itself caused 390,077 houses collapsed. The recent earthquakes in 2018 that happened in Lombok and Palu again caused 83,392, and 68,451 houses collapsed, respectively. Those collapsed houses were dominated by brick masonry wall type houses, which caused thousands of casualties in each major earthquake. This is due to the fact that the dwellings were not built properly, and this type of system is considered brittle. The casualties were caused mainly by the falling debris of the brick masonry walls. Recently new types of houses are introduced for the reconstruction after the earthquakes to satisfy the slogan Built Back Better. One of the newly introduced types of houses is called Instant Steel Frame House with the Indonesian acronym RISBA that can be built only within several days. The main steel frames of RISBA are made of double canal CNP $95 \times 33 \times 10 \times 1.8$ profile. This paper discusses the seismic performance of RISBA by using pushover analysis with SAP 2000 software. To take into account the material non-linearity, flexural plastic hinges were inserted in the frames. Pushover analysis results show that RISBA will respond almost elastically even in the very high seismic region like Palu City in Indonesia. In 2018 experience

W. Sutrisno (✉) · I. Satyarno · A. Awaludin · A. Saputra · A. F. Setiawan
Department of Civil and Environment Engineering, Universitas Gadjah Mada, Yogyakarta,
Indonesia
e-mail: widartosutrisno@mail.ugm.ac.id

I. Satyarno
e-mail: imansatyarno@ugm.ac.id

A. Awaludin
e-mail: ali.awaludin@ugm.ac.id

A. Saputra
e-mail: saputra@ugm.ac.id

A. F. Setiawan
e-mail: angga.fajar.s@ugm.ac.id

W. Sutrisno
Department of Civil Engineering, Universitas Sarjanawiyata Tamansiswa, Yogyakarta, Indonesia

a big earthquake because especially the RISBA is very light. It is noted that adequate anchorages must be provided in the tie beams to prevent the locking mechanism.

Keywords Built back better · Brittle · Ductile · Plastic hinge · Pushover analysis · Seismic performance · Steel frame

1 Introduction

1.1 Brittle Structure

Located at the edge of The Eurasian Plate, Pacific Plate and Indo–Australian Plate, Indonesia have a high degree of tectonic activity. Earthquakes have caused the collapse of many non-designed and engineered buildings [1], with the majority of the collapsed buildings being non-engineered community dwellings. For instance, the 2006 Yogyakarta earthquake itself caused 390,077 houses collapsed [2]. The recent earthquakes in Lombok and Palu in 2018 caused 67,875 [3] and 65,733 [4] houses to collapse, respectively. According to the most recent National Agency for Disaster Countermeasure (BNPB) data, 83,392 and 68,451 houses collapsed, respectively [5]. Those collapsed houses were dominated by brick masonry wall type houses, which caused hundreds of victims in each severe earthquake and exposed the highest economic losses [6]. This is because the houses were not properly built while this house system is considered very brittle [7].

The seismic stability of a building is determined by the materials used. Brittle materials result in brittle structures, which would cause the building to collapse rapidly if an earthquake occurred [8]. If the structural load exceeds elastic strength in brittle structures, the structure will be damaged or collapse suddenly, even in low seismic regions [9].

The most damage in earthquake disasters in the housing sector that remain particularly vulnerable to hazard [10] and general brittle failure mechanisms can be broadly similar [11, 12]. Yet, the government of Indonesia release the newest earthquake map zone in order to minimize vulnerability [13] (Figs. 1 and 2).

1.2 Masonry Wall

Houses made of brick walls are particularly popular because homeowners feel more at ease living in them. The well-isolated object saves energy for heating, which is environmentally sound [14]. However, during the earthquake, most casualties were caused by the falling debris of the brick masonry walls. It is generally known that in seismically active areas, buildings formed of masonry can be quite harmful if not correctly constructed [15]. The danger is that masonry brick walls can interfere with

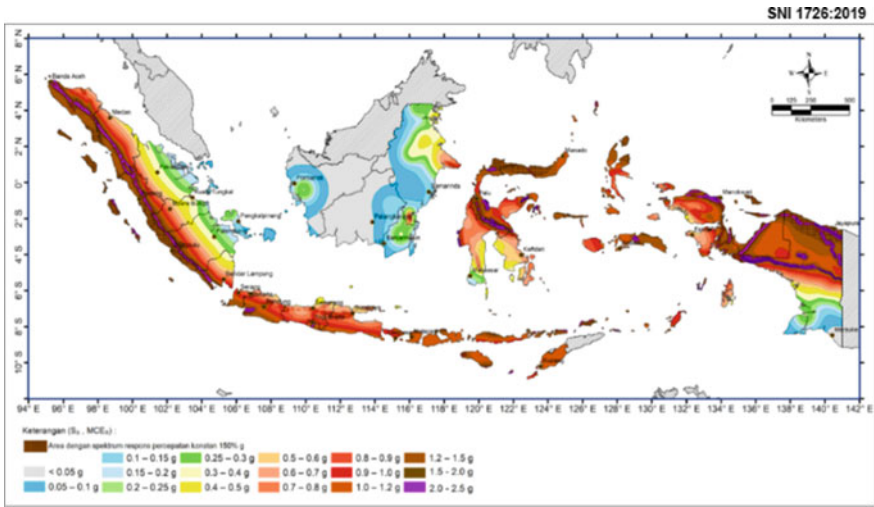


Fig. 1 Indonesian earthquake S_s -zone [13]

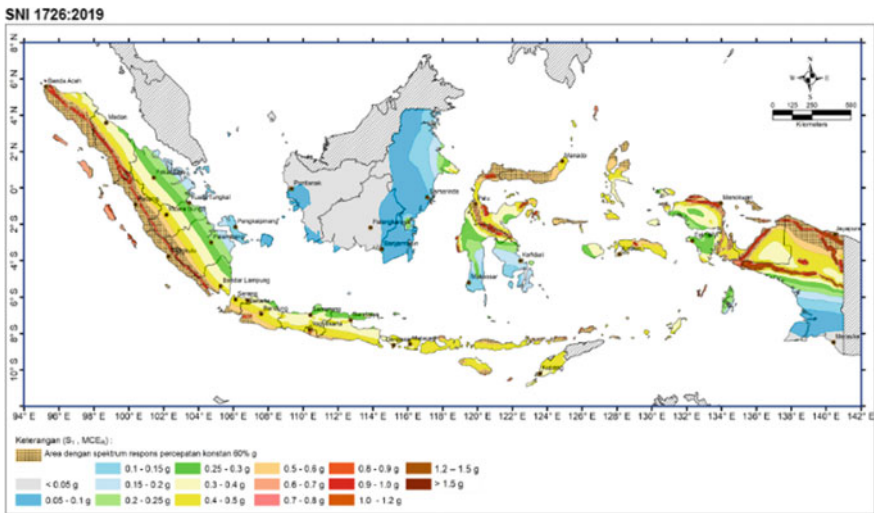


Fig. 2 Indonesian earthquake S_1 -zone [13]

the structure's ability to deform optimally [16]. The brittle behavior of brick masonry also makes it very sensitive to support settlements [17].

Among the factors that contribute to the vulnerability of the typical brick masonry community houses in Indonesia are listed as follows [18].

Fig. 3 Low quality of mortar bed joint [18]



Low materials quality

Mortar and concrete are two primary materials utilized to construct brick masonry wall houses. Mortar functions as a bed joint in a brick wall comprised of water, cement, and sand. Concrete is made of water, cement, sand, and aggregate used for wall confinement frames such as columns, ring beams, and plinth beams. The water-cement ratio refers to the amount of cement and water used in the mix to control the quality of these components. In the case of concrete, improper fabrication, such as insufficient compaction and curing procedure, frequently results in poor concrete quality (Fig. 3).

The wall elements strength becomes very low if such low materials quality used in the wall houses.

Absence of critical structural element

Critical elements such as reinforced concrete columns, reinforced concrete plinth beam or tie beam, ring beam, gable roof frames, wind bracing, and wall plaster must be designed to seismic proof. The crucial elements play as confinement element to increase the house robustness under a major earthquake (Fig. 4).

Poor Reinforcement Details

Under earthquake load, the house robustness greatly depends on the reinforcement details like stirrup and reinforcement joints between elements. Poor reinforcement detail causes the joint parts to be separated from one another during an earthquake (Fig. 5).

Modification of Traditional House

The most popular type of traditional house features a solid wood frame with woven bamboo walls. Without proper connection details, the community replaces the woven bamboo wall with a brick masonry wall, far more brittle than the woven bamboo.

Fig. 4 Brick masonry without crucial elements collapsed [18]



Fig. 5 Brick masonry with poor detailing of stirrup reinforcement [18]



The seismic stress increases because the self-weight of the brick masonry wall is now significantly more than the self-weight of the woven bamboo wall (Fig. 6).

Unstable Ground Condition

The most difficult challenge to solve is the unstable ground condition. The only thing that might be done is to carry out a relocation program, which is also challenging to undertake (Fig. 7).

Fire and Others

The fall of cooking stoves can potentially start a fire during an earthquake. However, how to secure stoves in kitchens to prevent fire during an earthquake is rarely covered (Figs. 8 and 9).

Fig. 6 Replacement of woven bamboo wall with brick masonry [18]



Fig. 7 The damaged house built on unstable ground [18]



Fig. 8 Damaged houses due to fire during earthquake [18]





Fig. 9 Brick masonry collapsed in Lombok 2018 **a** full collapsed (<https://nasional.kompas.com>); **b** wall collapsed (<https://tirto.id>)

1.3 Built Back Better

After the earthquake, the government provided household assistance to rebuild any collapse houses. Because construction practices create vulnerability to housing, the government stated the need to “build back safer” or “build back better” [19]. To achieve the recovery goal, houses must be designed and built in a way that reduces the risk of damage and destruction, with safe and simple structural modifications and implements hazard-resistant housing design and construction [20].

This paper discusses alternative houses for reconstruction, namely RISBA (Instant Steel Frame House). For this purpose, a performance point for the Palu and Lombok demand curves is proposed for generating seismic performance (Fig. 10).

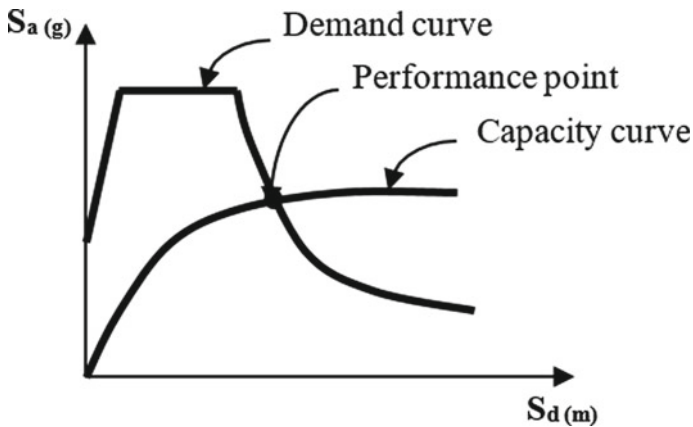


Fig. 10 Performance point [21]



Fig. 11 RISBA house [23]

1.4 Instant Steel Frame House

To meet the slogan “Built Back Better,” new forms of houses have recently been introduced for reconstruction after earthquakes. Steel has a high strength-to-weight ratio and is ductile, making it a safe alternative material for superior structural performance in seismic zones [22].

Instant Steel Frame House, also known as RISBA in Indonesia, is a newly introduced form of a house built in a couple of days. The main steel frames of RISBA are made of double canal CNP $95 \times 33 \times 10 \times 1.8$ profile [23] (Fig. 11).

RISBA is intended to be designed and built quickly. Based on real simulations in the field, RISBA can be completed in 5 days with a workforce of 5 people per day. RISBA is being constructed in the former premises of old houses destroyed by the earthquake to help speed up development. A lightweight RISBA does not require a foundation like a heavy building structure [23].

RISBA is made of ductile, robust, and resilient steel that does not easily break under seismic forces, reducing potential casualties in future earthquakes. The CNP steel is the main structure of RISBA, and it was coated with at least two layers of corrosion-resistant coating substance [23].

RISBA is also built to allow for natural cooling. To achieve this, RISBA employs a steeply sloping roof, which allows the air space under the roof cover to be large enough to withstand heat from the roof [23].

1.5 RISBA Detailing

RISBA connections were designed to behave elastically even after the frame has reached/surpass it plastic capacity/yield point due to the applied load [23]. To prevent

the rocking mechanism, adequate anchorages must be provided in the tie beams once it works as a shear connector.

In this work, the RISBA structure was modelled and analysed using finite element analysis software SAP2000. The novelty is that the RISBA house was analysed based on the proposed generated demand spectrum for Palu and Lombok's earthquake. A three-dimensional (3D) frame model of the RISBA house was developed in SAP2000. The analysis is intended to predict the seismic performance level of the RISBA house. This study broadens the possibility of offering an earthquake-resistant and quick-construction frame building in Indonesia and other nations with a similar community-dwelling design (Figs. 12 and 13).

For this purpose, a performance point from the capacity RISBA structure according to the demand curve of Palu and Lombok determined by pushover analysis.

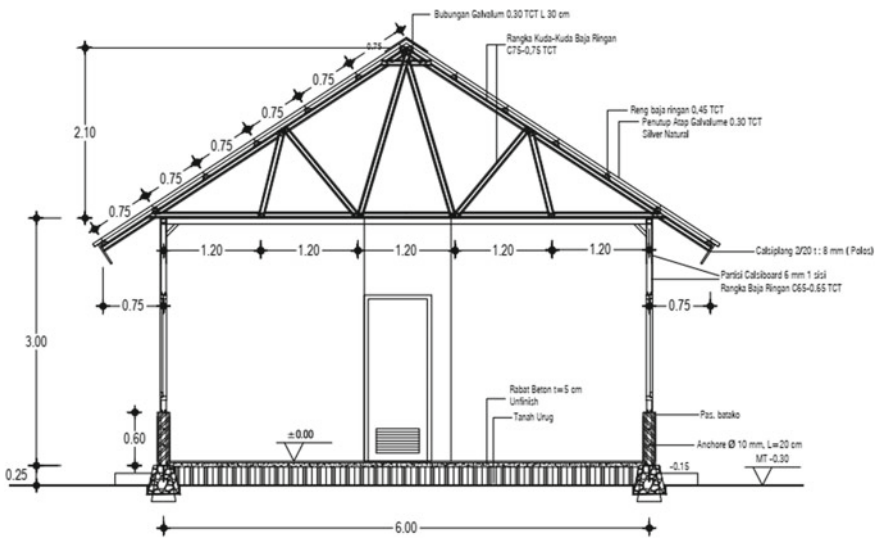


Fig. 12 Cross of RISBA house design [23]

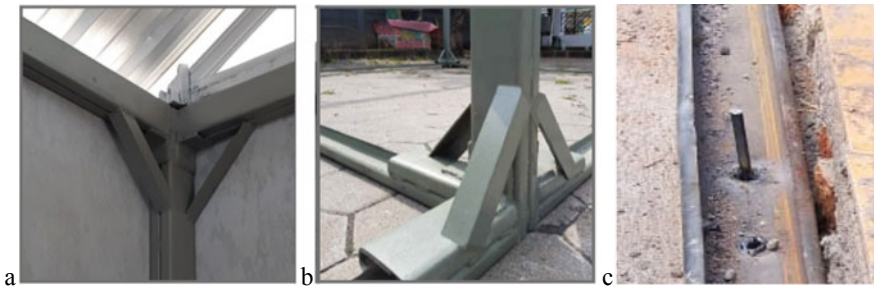


Fig. 13 a Beam column connection; b Sloof column connection; c Sloof shear connector [23]

2 Pushover Analysis

2.1 Performance-Based Design

The performance-based design is carried out via a non-linear static analysis known as a non-linear static pushover analysis that utilized more straightforward analytical tools than non-linear time history analysis [24–30]. The performance-based design used while strength-based design cannot explain non-linear criteria with relative ease to predict structure performance against lateral loads. In strength-based design, structural performance is only guaranteed at two level, in small earthquakes (serviceability limit state) and in large earthquakes (safety limit state) and cannot explain building performance in a state of moderate earthquake.

In this method, the static load was applied in the lateral direction, whose magnitude is increased incrementally until the structure reaches the assigned displacement target or collapse load. The correlation between base shear and roof displacement can be plotted as a structural capacity curve. The structural capacity curve depicts the structure's behaviour during the elastic and plastic condition and till the structural elements collapse.

In the SAP2000 program, input for pushover analysis is performed by idealizing the structure as follows:

1. The M3 hinge properties were assigned to all of the beams.
2. The P-M2-M3 hinge properties was assigned for the bottom column, which means plastic joints occur because of axial forces and moments.
3. The load for the static pushover analysis is a joint load in the lateral direction given to the beam column joint in the center of the building
4. Plastic joint lengths in pushover analysis can only be expressed as fixed lengths of 45 mm (1/2 h profile), which means plastic joints are located 45 mm from joints of beams and columns.

2.2 RISBA Modelling

The SAP2000 pushover analysis was employed in this study to analyze the seismic performance of the RISBA house, which was designed in compliance with FEMA [31]. The material non-linearity is considered by inserting the flexural plastic hinges in the frames. The characteristic of the hinges used is taken from the auto hinge FEMA available in the SAP2000 software. The permissible plastic hinge rotation angle is the main parameter, indicated by the damage performance level (immediate occupancy, life safety, and collapse prevention) [32].

The three-dimensional (3D) RISBA house was analyzed with 100% earthquake load applied on the weak axis in the y axis direction and 30% earthquake load on the strong axis in the direction of the x-axis. The analysis results generated by the

pushover analysis is plotted, and the demand capacity curve was presented (Figs. 14 and 15).

Under seismic load, the frame structure can experience different levels of damage with potentials for hinge formation in structural elements, depending on the level of stringency in design. Therefore, the seismic behavior and performance of buildings, which depend on the structural system and the degree of irregularities in the structural system, must be analyzed.

The first yield point is defined as the point on the ($M - \phi$) curve when the flens furthest from the neutral axis attains the first yield. The last point of the ($M - \phi$) curve represents the failure to reach the ultimate strain in CNP Plastic Hinge. From the picture shown that canal CNP profile used have a good moment curvature behavior.

The curvature ductility was determined based on the area under the moment–curvature curves of the CNP, where the ductility represents the ratio of the area under the $M - \phi$ curve up to the ultimate curvature, to the area under the $M - \phi$ curves up to the yield curvature. The curvature ductility (energy absorption capability) is

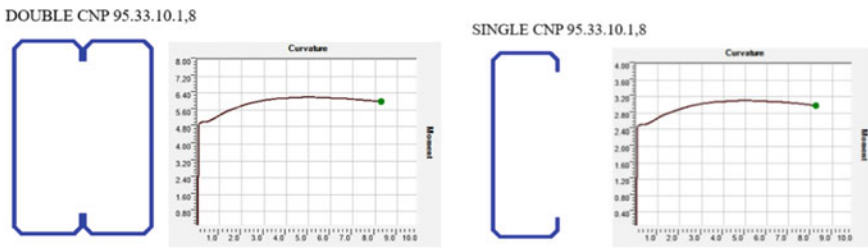


Fig. 14 Moment curvature curve (kN ~ m) in CNP plastic hinge

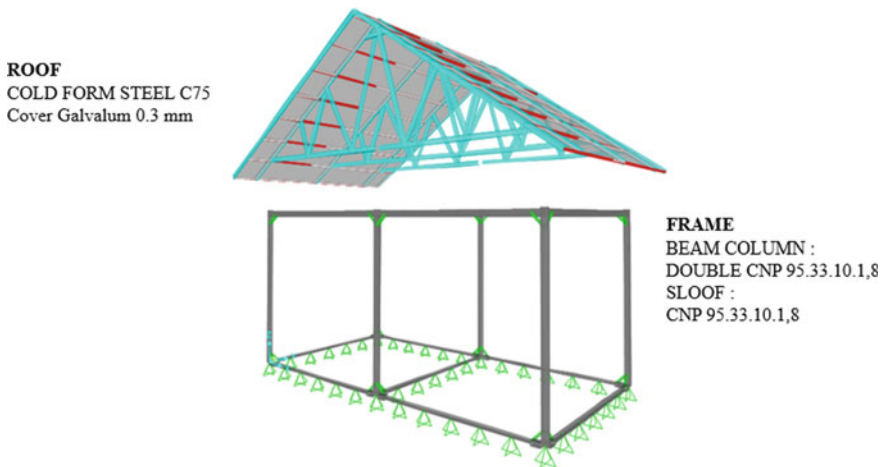


Fig. 15 RISBA modelling in SAP2000

considered one of the principal measurements to assess the structural performance of CNP profile under any earthquake loads.

It was observed that using double canal CNP profile for the RISBA frame resulted in an increase of approximately twice in the maximum moment capacity of the profile and in the future application will be able to composite with local material [33].

3 Analysis Result

The capacity curve analysis results were first determined. The capacity curve is a curve that describes the capacity of structures with lateral load centered on the roof, which gradually increased to deformation limits set. The capacity curve resulting from the pushover analysis shows the relationship between the primary shear force (base shear) and roof displacement due to lateral loads applied to the structure with a specific loading pattern to the expected ultimate conditions or expected transition (Fig. 16).

From the capacity curve shown in Fig. 16, the RISBA base reaction achieves a target of about 1,8 ton-force. Meanwhile, the horizontal displacement reaches almost 100 mm.

The maximum tension from the SAP2000 joint reaction about 13.891 N can be handled with shear connector anchors. The rocking mechanism will not occur when Ø10 mm reinforcement steel bar along 20 cm can provide maximum tension (T_{max}) 45.740 N. The value is obtained from $T_{max} = \mu l_d \pi d_b$ (μ = mortar bonding, l_d = 20 cm, π = 3,14 and d_b = 10 mm) [34].

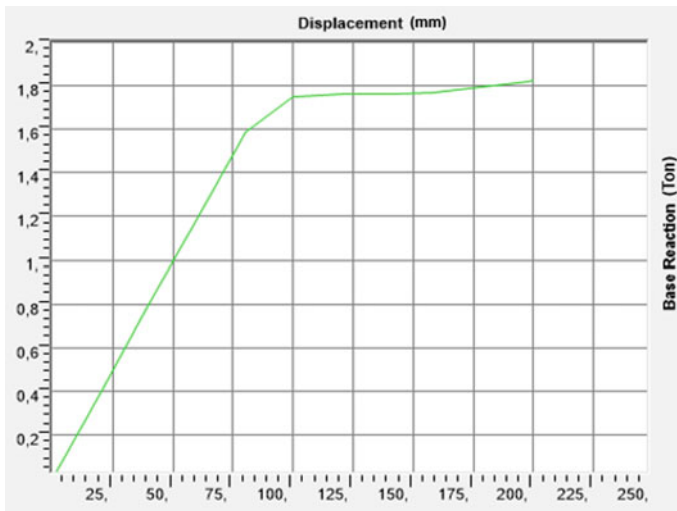


Fig. 16 Capacity curve

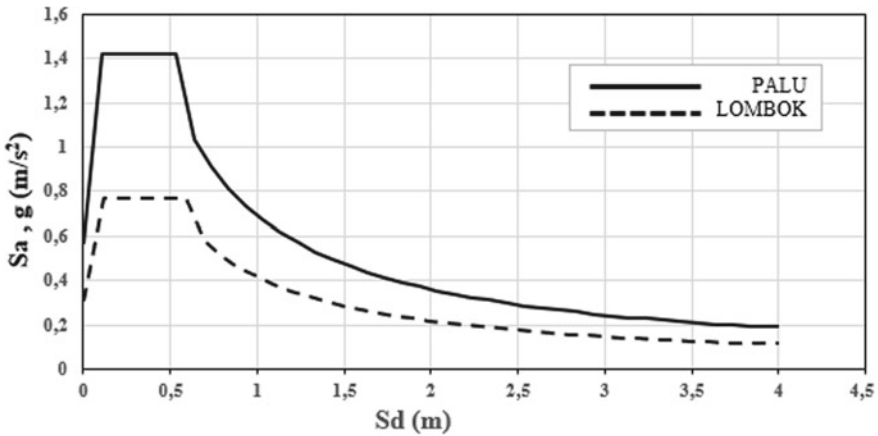


Fig. 17 Demand spectrum curve

The next step is to generate the spectrum response curve according to SNI 1726–2019 into the curve ADRS with existing methods on ATC-40 [35] (Fig. 17).

Figure 18 shows Palu has a higher peak of spectral acceleration intensity against Lombok (Fig. 19), as indicated in the Indonesian earthquake maps zone. The design spectrum is smooth and conservative. However, the spectrum curve of any actual earthquake ground motion is usually quite irregular. In this work, both spectrum curves provide a reasonable range of intensity that every earthquake might frequently happen in Indonesia. They will intersect RISBA’s capacity curve at each point of peak response displacement and acceleration. The peak spectral displacement is then used to cross-examine damage state probabilities.

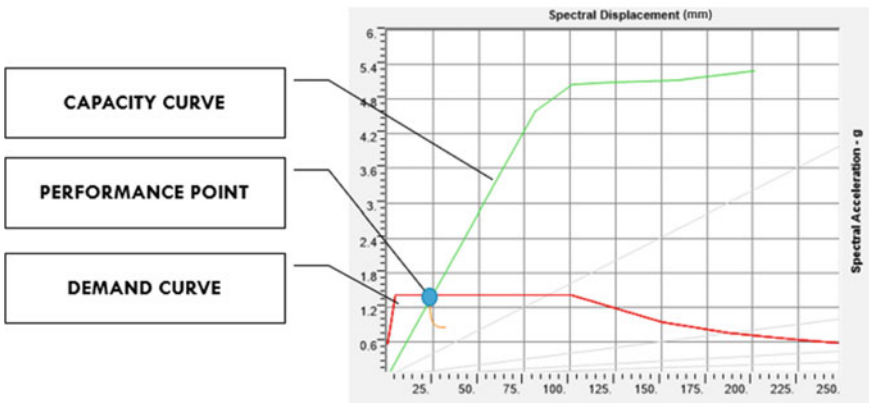


Fig. 18 RISBA performance point at palu

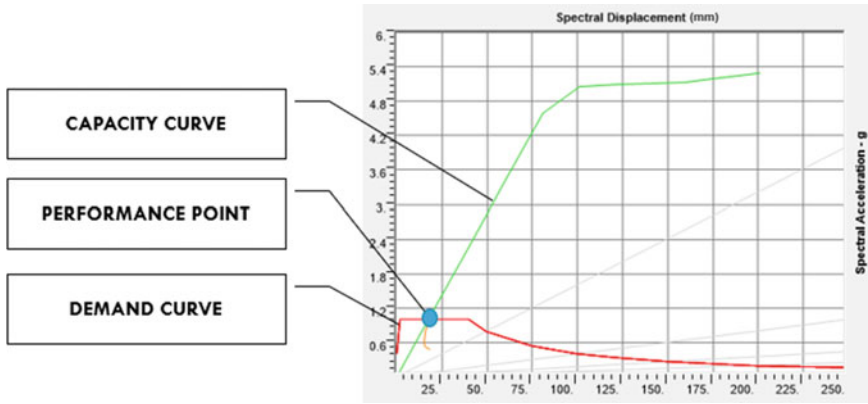


Fig. 19 RISBA performance point at lombok

The intersection point of the demand spectrum and the building capacity curve indicated the seismic response of the building. Results of non-linear pushover analysis in SAP2000 show that RISBA is still in elastic condition and guarantee that RISBA performance. At the same time, the earthquake that happened is satisfied and safe as long as it is done with adequate engineering supervision and application. This condition of performance can happen because of the CNP profile used and the total weight of RISBA’s frame, and the roof is very light, about 4.416 kN, which is equivalent to 450.5 kg. RISBA has proven to be strong and flexible enough against Palu and Lombok seismic loads.

Based on the design philosophy, building structure performance due to earthquake plans is Life Safety. Even though the building structure suffers from a relatively severe level of damage, occupant safety is maintained because the building structure does not collapse. The output of the performance graphic showed that RISBA has a long linear response that can cover the demand spectrum of Palu and Lombok. The systems have no problems carrying the generated seismic loads.

Knowing the structure’s behavior from the elastic limit until its collapse and the different type of construction used [36] can be planned and simulated the expected collapse pattern, which can minimize the number of victims at the time of the earthquake.

The RISBA capacity curve showed that RISBA will maintain elastic conditions up to more higher ground motion acceleration that might happen in Indonesia. The straight-long curve also showed that RISBA could meet the needs of the ability instant frame house to withstand earthquakes all over in Indonesia.

Modal analysis results generated from the SAP2000 show that RISBA has a natural frequency of about 3075–1519 Hz higher than the dominant natural frequency of ground surface at Palu about 0,47–1,97 Hz [37] and 0,13–10,96 Hz at Lombok [38]. RISBA at Palu have no potential to resonate and will have no potential for damage in the event of an earthquake. At Lombok, RISBA has little potential to resonate and will have little potential for injury in the event of an earthquake.

Hereafter, when Palu have a higher peak of spectral acceleration intensity against Lombok as indicate in the Indonesian earthquake maps zone, RISBA will be a good alternative to build back safer, immediately leave the tent to go back home and built back better.

4 Conclusion

In this study, RISBA design of steel frames under earthquake loading was studied. For this purpose, a performance point for the Palu and Lombok demand curves is proposed. Structural analysis in the proposed method is carried out using pushover analysis with SAP2000. The non-linear pushover analysis results in relatively realistic and accurate evaluations of structural responses. Using the non-linear pushover analysis as the structural analysis method can be done relatively precisely and cost-effectively computationally. This research shows that RISBA will respond almost elastically even in the very high seismic region like Palu City in Indonesia in 2018 experience a big earthquake because especially the RISBA is very light. It is noted that adequate anchorages must be provided in the tie beams to prevent the rocking mechanism. In future research, time history analysis can be studied for the RISBA optimization problem under earthquake load.

References

1. Satyarno I (2019) Seismic risk of important buildings (Case: Hospitals In Indonesia Recent Earthquake) (2019). <https://www.researchgate.net/publication>. Last Accessed 30 Oct 2019
2. Kompas Homepage (2019). <https://kilaskementerian.kompas.com>. Last Accessed 10 Oct 2019
3. Republika Homepage (2019). <https://www.republika.co.id>. Last Accessed 10 Oct 2019
4. Wikipedia Homepage (2019). <https://id.wikipedia.org>. Last Accessed 10 Oct 2019
5. BNPB Homepage (2019). <http://www.bnpb.go.id>. Last Accessed 09 Dec 2019
6. Aulady MFN, Fujimi T (2019) Earthquake loss estimation of residential buildings in Bantul regency Indonesia. *Jambá J Disaster Risk Stud* 11(1):a756. <https://doi.org/10.4102/jamba.v11i1.756>
7. Faizah R, Satyarno I, Priyosulistyo H, Aminullah A (2018) Improving the masonry brick ductility using mortar bed joint from rubber tire crumbs: a review. *J Phys Sci* 29(Supp. 2):117–132
8. Abdullah B (2017) Mubarak: precast panel (BeRi-C) for housing in Indonesia. Universitas Syah Kuala
9. Murty CVR, Goswami R, Vijayanarayanan AR, Mehta VV (2012) Some concepts in earthquake behaviour of buildings. Gujarat State Disaster Management Authority, Government of Gujarat
10. Ahmed I, Charlesworth ER (2015) An evaluation framework for assessing resilience of post-disaster housing. *Int J Disaster Resil Built Environ* 6(3):300–312
11. Chian SC, Wilkinson SM, Whittle JK, Mulyani R, Alarcon JE, Pomonis A, Saito K, Fraser S, Goda K, Macabuag J, Offord M, Hunt-Raby AC, Sammonds P, Franco G, Stone H, Ahmed B, Hughes FE, Jirouskova NK, Kaminski S, Lopez J (2011) Lessons learnt from the 2009 Padang Indonesia. 2011 Tohoku Japan and 2016 Muisne Ecuador Earthquakes, *Frontiers in Built Environment*

12. Saghafi MH, Shariatmadar H, Kheyroddin A (2019) Seismic behavior of high-performance fiber-reinforced cement composites beam-column connection with high damage tolerance. *Int J Concrete Struct Mater*. <https://doi.org/10.1186/s40069-019-0334-3>
13. BSN (2019) Tata cara perencanaan ketahanan gempa untuk struktur bangunan gedung dan nongedung. Badan Standarisasi Nasional
14. Premrov M, Kuhta M (2009) Influence of fasteners disposition on behaviour of timber-framed walls with single fibre-plaster sheathing boards. *Constr Build Mater* 23:2688–2693
15. Torratsi T (2001) In: Seismic design of timber structures. VTT Tiedotteita, Espoo, Finland
16. Leksono RS, Iranata D, Kristijanto H (2012) Studi Pengaruh Kekuatan dan Kekakuan Dinding Bata Pada Bangunan Bertingkat. *JURNAL TEKNIK ITS* 1(1). ISSN:2301–9271
17. Ozen GO (2006) Comparizon of elastic and inelastic behaviour of historic masonry structures at the low load levels. Middle East Technical University, Thesis
18. Satyarno I (2019) Vulnerability of Indonesian community houses to earthquake disaster. <https://www.researchgate.net/publication>. Last Accessed 30 Oct 2019
19. Clinton W (2006) Lessons learned from Tsunami recovery: key propositions for building back better. United Nations, New York
20. Venable C, Will AJ, Liel A (2018) Built back better? an analysis of perceived performance of post disaster housing. In: 16th engineering project organization conference: EPOC 2018—(Re)organizing in an uncertain climate. pp 348–366
21. Sutrisno W, Fajar AS, Satyarno I (2019) Sebuah Gambaran Respon Beban Gempa : ADRS (Acceleration-Displacement Response Spectra). In: Civil engineering and environmental symposium
22. Anuj D, Kalurkar LG (2018) Seismic analysis of RCC and steel frame structure by using ETABS. *IOSR J Mech Civil Eng (IOSR-JMCE)* 15(2):Ver. II PP 38–42. e-ISSN: 2278–1684, p-ISSN: 2320–334X
23. Setiawan AF, Saputra A (2019) RISBA Rumah instan struktur baja, Bimbingan Teknis Penerapan Teknologi Rumah Tahan Gempa Mataram. NTB
24. Ginsar IMB, Lumantarna B (2019) Seismic performance evaluation of building with pushover analysis. https://nanopdf.com/download/seismic-performance-evaluation-of-building-with-faculty-e_pdf. Last Accessed 28 Mar 2019
25. Shanker BJU, Sreenu R (2019) Seismic behaviour of reinforced concrete frame with different infills. *Int J Civil Struct Environ Infrastruct Eng Res Develop (IJCSEIERD)* ISSN (P): 2249–6866; ISSN (E): 2249–7978
26. Astariani NK, Sudika IGM (2018) Perbandingan Perilaku Struktur Gedung Beton Bertulang dengan Pelat Lantai Beton Konvensional dan Pelat Lantai Kalsi. *Media Komunikasi Teknik Sipil* 24(2):176–183
27. Wiranata IGK, Bagiarta IKY, Jawat IW (2016) Perbandingan Perilaku Struktur Beton Bertulang Analisis Sistem Dinding Bata Sebagai Strut dengan Sistem Open Frame. *Paduraksa* 5(2): 24–45. ISSN: 2303–2693
28. Nugroho F (2016) Penerapan Analisis Pushover Untuk Menentukan Kinerja Struktur Pada Bangunan Eksisting Gedung Beton Bertulang. *Jurnal Momentum* 18(2): 19–25. ISSN:1693–752X
29. Vijay A, Vijayakumar K (2013) Performance of steel frame by pushover analysis for solid and hollow sections. *Int J Eng Res Develop*. 8(7):05–12. e-ISSN: 2278–067X, p-ISSN: 2278–800X
30. Hashmi AK, Madan A (2008) Damage forecast for masonry infilled reinforced concrete framed buildings subjected to earthquakes in India. *Current Sci* 94(1)
31. Dewobroto W (2006) Evaluasi Kinerja Bangunan Baja Tahan Gempa dengan SAP2000. *Jurnal Teknik Sipil* 3(1)
32. Faridmehr I, Tahir MM, Lahmer T, Osman MH (2017) Seismic performance of steel frames with semirigid connections. *Hindawi J Eng*. <https://doi.org/10.1155/2017/5284247>
33. Tualaka SP (2019) Alternatif Rumah Tetap Yang Lebih Aman Bagi Masyarakat Berpenghasilan Rendah Di Kabupaten Timor Tengah Selatan. Thesis, UGM
34. Mandolang RR, Pandaleke R, Windah R (2016) Pemeriksaan Tegangan Lekat Beton Dengan Variasi Luas Tulangan. *Jurnal Sipil Statik* 4(4):279–285. ISSN: 2337–6732

35. ATC 40 (1996) Seismic evaluation and retrofit of concrete buildings. Redwood City, California, USA
36. Satyarno I (2020) Evaluasi Kerentanan Bangunan Rumah Masyarakat Terhadap Gempa Bumi Di Desa Wisata Bugisan Kecamatan Prambanan Kabupaten Klaten, https://simantu.pu.go.id/personal/img-post/superman/post/20181130101333_F_KMS_STUDI_20180725105707.pdf. Last Accessed 05 Feb 2020
37. Kurniawan M, Brotopuspito KS, Setianto A (2016) Studi Kerentanan Seismik Tanah Terhadap Frekuensi Alami Bangunan di Kota Palu Berdasarkan Analisis Data Mikrotremor, Proceeding, Seminar Nasional Kebumihan Ke-9, 6–7 Oktober
38. Azmiyati U, Brotopuspito KS, Dibiyosaputro S (2016) Building vulnerability to earthquake in Mataram City West Nusa Tenggara. *Jurnal Riset Kebencanaan Indonesia* 2(1):77–84

Nonlinear Numerical Model of Glued-Laminated Petung Bamboo Under Flexural Test Based on ASTM D 143-94



Abdul Widayat Abzarih, Inggar Septhia Irawati, and Bambang Suhendro

Abstract This paper presents the non-linear orthotropic material model of glued-laminated (glulam) bamboo under the flexural bending test. The purpose of modeling was to simulate the non-linear flexural behavior of glulam bamboo in a radial and tangential direction. Glulam bamboo was made of Petung Bamboo (*Dendrocalamous Asper*). Bamboo properties used for creating a numerical model and validation were obtained from secondary data. The non-linear numerical model was developed based on the flexural test of ASTM D143, Hooke's Law, Yield Criterion of *Tsai-Hill*, and Associated Flow Rule for orthotropic material. However, the surface interaction property, hardening function, and damage types have not been defined yet. The 3-dimensional analysis was applied with the total element were 121.600 elements. The result depicts that the flexural behavior of the non-linear numerical model sufficiently meets the result of the experimental study, either in the radial or tangential direction.

Keywords Orthotropic material · Non-linear numerical model · Glued-laminated bamboo · Flexural behavior

1 Introduction

Petung Bamboo (*Dendrocalamous Asper*) is one of the natural orthotropic materials which has high potential to be used as a wood substitute material to reduce the number of illegal logging. Petung Bamboo is easily found in all regions of Indonesia

A. W. Abzarih (✉)

Department of Civil Engineering, Faculty of Engineering, Universitas Dayanu Ikhsanuddin, Jalan Dayanu Ikhsanuddin No 124, Baubau, Indonesia
e-mail: widayat.abzarih@unidayan.ac.id

I. S. Irawati · B. Suhendro

Department of Civil and Environmental Engineering, Faculty of Engineering, Universitas Gadjah Mada, Jalan Grafika No 2, Sleman, Yogyakarta, Indonesia
e-mail: inggar_septhia@ugm.ac.id

B. Suhendro

e-mail: bsuhendro@ugm.ac.id

[1]. Compared to the other bamboo species grown in Indonesia, Petung Bamboo has a greater bamboo culm dimension. It has an outer diameter dimension of 70–180 mm. The wall thickness is 8–20 mm. Due to its dimension, Petung bamboo is commonly used as an alternative building material [2, 3]. However, because the bamboo shape is a non-prismatic hollow tube, it is more difficult to install the bamboo structure in the field. Technological innovations are required to solve the bamboo application constraint in the construction industry [4]. Subsequently, experimental and numerical researches are necessary to characterize bamboo behavior.

Previous experimental and numerical studies on engineered bamboo products have been carried out. Dongsheng [5] conducted an experimental study on the non-linear bending of parallel strand bamboo beams. Sinha [6] conducted a research on the structural performance of glulam bamboo beams. Sharma [4] conducted a research on engineered bamboo for structural applications. Dongsheng [5] also conducted a numerical study on the non-linear bending of parallel strand bamboo beams. Eratodi [7] performed a numerical study of the beam-column joint using steel plate and bolts. However, the numerical study of the non-linear behavior of glulam Petung bamboo under radial and tangential lateral load has not been conducted yet. This research is very important because glulam bamboo is very potential to be used as beam elements. Moreover, it has a different mechanical behavior under tensile and compressive tests parallel to grain [5]. It also has different behavior in three main axes directions, called an orthotropic material [3, 3].

Based on the previous background, this study aims to develop a non-linear numerical model that simulates the mechanical behavior of glulam Petung bamboo beams during static loading. In this research, the dimension of the numerical model was defined referring to ASTM D143 bending test sample dimension [8]. Hooke's law was used to define the relationship of the stress–strain in elastic condition. *Tsai-Hill* yield criterion was applied to determine the yield point in the compressive condition and tensile material condition. *Associated Flow Rule* was used to define the behavior of plastic material behavior [9]. The 3-dimensional analysis of the bending load toward the radial and tangential direction was applied. The surface interaction property, hardening function, and type of material damage have not been considered in this study.

2 Problem Statement

Glulam Petung bamboo is a material that has different properties in the main three axes directions (orthotropic material). It also has different properties under compressive and tensile loading. The compressive behavior of Petung bamboo is non-linear, but tensile behavior is linear. The modulus of elasticity Petung bamboo under tensile load differs from that under compressive load. As a result, calculating using a finite element computer program is preferable.

As previously described, this study aims to develop a nonlinear glulam bamboo numerical model. The 3-dimensional model was created by using Abaqus. However,

there is a lack of information in modeling the non-linear orthotropic material using Abaqus. The default Abaqus program is only capable of modeling a linear orthotropic material. In the case of a non-linear orthotropic material, it is required UMAT subroutine. The problem is how to model the non-linear orthotropic material glulam Petung bamboo beams by using Abaqus and applying UMAT subroutine.

3 Finite Element Method

Simulation of the nonlinear orthotropic material behavior by using Abaqus was performed by considering three methods, as follow:

- i. Hooke's Law
- ii. Tsai-Hill yield criterion
- iii. Associated flow rule

3.1 Hooke Law for Orthotropic Material

Glulam bamboo is an orthotropic material which has symmetric property at least 2 orthogonal areas. Orthotropic material has 9 stiffness matrix constants, as follows:

$$\begin{pmatrix} \sigma_{11} \\ \sigma_{22} \\ \sigma_{33} \\ \sigma_{12} \\ \sigma_{13} \\ \sigma_{23} \end{pmatrix} = \begin{bmatrix} C_{1111} & C_{1122} & C_{1133} & 0 & 0 & 0 \\ \dots & C_{2222} & C_{2233} & 0 & 0 & 0 \\ \dots & \dots & C_{3333} & 0 & 0 & 0 \\ \dots & \dots & \dots & C_{1212} & 0 & 0 \\ \dots & \dots & \dots & \dots & C_{1313} & 0 \\ \dots & \dots & \dots & \dots & \dots & C_{2323} \end{bmatrix} \begin{pmatrix} \varepsilon_{11} \\ \varepsilon_{22} \\ \varepsilon_{33} \\ \varepsilon_{12} \\ \varepsilon_{13} \\ \varepsilon_{23} \end{pmatrix} \quad (1)$$

Equation (1) above is the stress-strain relationship of the orthotropic material [10]. However, Hooke's law only applies to an elastic condition.

The stiffness matrix for orthotropic material can be obtained by using Eq. (2) up to Eq. (10).

$$C_{1111} = \frac{1 - v_{23}v_{32}}{E_2 E_3 \Delta} \quad (2)$$

$$C_{1122} = \frac{v_{21} + v_{23}v_{31}}{E_2 E_3 \Delta} \quad (3)$$

$$C_{2222} = \frac{1 - v_{13}v_{31}}{E_1 E_3 \Delta} \quad (4)$$

$$C_{1133} = \frac{v_{31} + v_{21}v_{32}}{E_2 E_3 \Delta} \quad (5)$$

$$C_{2233} = \frac{v_{32} + v_{21}v_{31}}{E_1 E_3 \Delta} \quad (6)$$

$$C_{3333} = \frac{1 - v_{12}v_{21}}{E_1 E_2 \Delta} \quad (7)$$

$$C_{1212} = G_{23} \quad (8)$$

$$C_{1313} = G_{31} \quad (9)$$

$$C_{2323} = G_{12} \quad (10)$$

where:

$$\Delta = \frac{(1 - v_{12}v_{21} - v_{23}v_{32} - v_{13}v_{31} - 2v_{21}v_{32}v_{13})}{(E_1 E_3 E_3)} \quad (11)$$

and

E_1 : The modulus of elasticity in a longitudinal direction

E_2 : The modulus of elasticity in a radial direction

E_3 : The modulus of elasticity in a tangential direction

v_{12} : The Poisson ratio in longitudinal-radial plane

v_{21} : The Poisson ratio in radial-longitudinal plane

v_{13} : The Poisson ratio in longitudinal-tangential plane

v_{31} : The Poisson ratio in tangential-longitudinal plane

v_{23} : The Poisson ratio in radial-tangential plane

v_{32} : The Poisson ratio in tangential-radial plane

G_{23} : The shear modulus in radial-tangential plane

G_{31} : The shear modulus in tangential-longitudinal plane

G_{12} : The shear modulus in longitudinal-radial plane.

3.2 Hill's 1948 Yield Criterion

Hill's 1948 yield criterion is the yield criterion for an orthotropic material. Hill's 1948 yield criterion is the advance criterion of Von Mises' yield [11]. In Hill 1948 yield criterion, the compressive elastic modulus is equal to the tensile elastic modulus. Besides that, the compressive yield stress is equal to the tensile yield stress. Subsequently, Hill 1948 yield criterion is developed into Tsai-Hill's yield criterion. In Tsai-Hill's yield criterion, the compressive elastic modulus and the compressive yield stress have been separated from the tensile elastic modulus and the ultimate

tensile stress. Because the property of glulam Petung bamboo (the modulus of elasticity and the yield stress) under compression parallel to grain loading differs from that under tensile parallel to grain loading, it is proper to use Tsai-Hill's yield criterion compared to Hill 1948 yield criterion.

The Hill 1948 yield criterion is presented in the quadratic Eq. as described in Eq. (12) [11].

$$f(\sigma_{ij}) = (F(\sigma_{22} - \sigma_{33})^2 + G(\sigma_{33} - \sigma_{11})^2 + H(\sigma_{11} - \sigma_{22})^2 + 2L\sigma_{12}^2 + 2M\sigma_{13}^2 + 2N\sigma_{23}^2)^{\frac{1}{2}} - 1 = 0 \quad (12)$$

where f is the compressive yield stress or the ultimate tensile stress condition; F , G , H , L , M , and N are special constant for an anisotropic material; 1, 2, and 3 are the principal axes of an anisotropic material. In this research, axis 1, 2, and 3 presents the beam longitudinal axis, radial axis, and tangential axis, respectively. If the ultimate stress (for tensile element) or the yield stress (for compressive element) in the principal axis direction of an anisotropic material is denoted as A , B , and C , Eq. (13) is written as following [11]:

$$\frac{1}{A^2} = G + H; \quad \frac{1}{B^2} = H + F; \quad \frac{1}{C^2} = F + G \quad (13)$$

Regarding Eq. (13), coefficient F , G , and H can be obtained from uniaxial stress by using simple mathematical calculations [11].

$$2F = \frac{1}{B^2} + \frac{1}{C^2} - \frac{1}{A^2} \quad (14)$$

$$2G = \frac{1}{C^2} + \frac{1}{A^2} - \frac{1}{B^2} \quad (15)$$

$$2H = \frac{1}{A^2} + \frac{1}{B^2} - \frac{1}{C^2} \quad (16)$$

If R , S , and T are the ultimate shear stress in axis 1, 2, and 3, thus [11]:

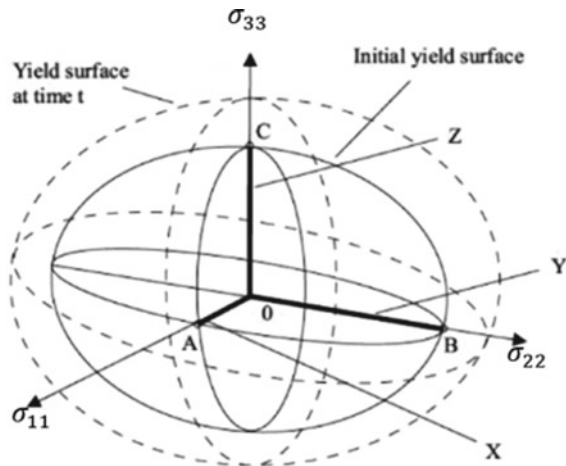
$$2L = \frac{1}{R^2} \quad (17)$$

$$2M = \frac{1}{S^2} \quad (18)$$

$$2N = \frac{1}{T^2} \quad (19)$$

According to Eq. (14) up to Eq. (16), there is only one parameter F , G , H which could be negative. But, this condition rarely happens in practice because this condition

Fig. 1 Hill's yield criterion [1]



will cause huge differences among stresses. Condition F is greater than G ($F > G$) if and only if A is greater than B ($A > B$). L , M , and N will always be positive. Consequently, to give a complete picture from an anisotropic material, six ultimate stresses that consist of the tensile ultimate stresses, the compressive yield stresses and the shear stress (A , B , C , R , S , and T) must be known for an anisotropic principle axis [11].

Yield criteria can be interpreted as the surface of which the six stress components can be seen in Fig. 1. A point that is located on the inner side of the surface represents the elastic condition of a material, while a point that is located on the surface represents a plastic condition.

As previously described, due to different behavior between tension and compression, the *Tsai Hill* yield criterion is suitable to define the compressive yield stress or the tensile stress of glulam Petung bamboo material. When compressive stress occurs, the *Tsai Hill* yield criterion is used to define a yield criterion. When tensile stress occurs, the *Tsai Hill* criterion is used to define a failure criterion regarding that the grain does not undergo plastic condition.

3.3 Associated Flow Rule

The associated flow rule is developed based on the Levy–Mises flow rule. Levy–Mises flow rule describes the stress–strain relationship that is applied for idealizing plastic conditions on the solid element. In plastic condition, the elastic strain can be ignored, and then the strain equation can be written as Eq. (20) [11].

$$d\varepsilon_{ij}^p = d\lambda\sigma_{ij} \tag{20}$$

where, $d\varepsilon_{ij}^p$ is the plastic strain of material, $d\lambda$ is the hardening function, and σ_{ij} is the stress function. The plastic multiplier can be determined through the hardening rule. Equation (20) can be rewritten in a more general form as shown in Eq. (21) [11].

$$d\varepsilon_{ij}^p = d\lambda G_{ij} \tag{21}$$

where G_{ij} is the stress function. G_{ij} stress function is symmetric because the strain is symmetric.

The plastic behavior of the material generally can be modeled in Eq. (22) [11].

$$d\varepsilon_{ij}^p = d\lambda \frac{\partial g}{\partial \sigma_{ij}} \tag{22}$$

where g is the scalar function. When the scalar function is divided into the stress, it will give the plastic strain. This is called the potential plastic which is known as the non-associated flow rule.

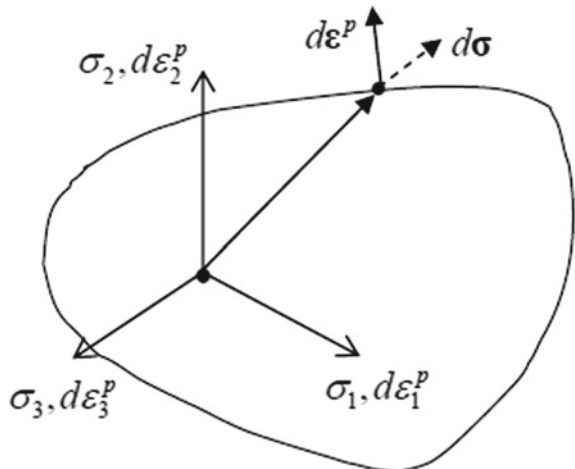
Considering that subclass of material which has plastic potential with yield function $f = g$, Eq. (22) can be rewritten as in Eq. (23) [11].

$$d\varepsilon_{ij}^p = d\lambda \frac{\partial f}{\partial \sigma_{ij}} \tag{23}$$

This flow rule is known as the associated flow rule because it relates to a certain failure criterion [11]. Yield criteria of the surface have been reached based on Eq. (12), when $f(\sigma_{ij})$ the function is equal to 0 ($f(\sigma_{ij}) = 0$).

In Fig. 2, the main stress axis and the main plastic strain are considered to coincide. The normal force against yield surface is parallel to $\frac{\partial f}{\partial \sigma_{ij}}$ so that associated flow rule

Fig. 2 Yield surface [10]



related to Eq. (23) can be defined as the plastic strain increment vector that is normal to the yield surface.

To solve the differentiation more easily, Eq. (23) can be stated in the principal stress, as described in Eq. (24) [11].

$$d\varepsilon_i^p = d\lambda \frac{\partial f}{\partial \sigma_i} \quad (24)$$

Equation (24) can be rewritten into Eq. (25) [9].

$$d\varepsilon_i^p = d\lambda \frac{\partial f}{\partial \sigma_i} = \frac{d\lambda}{f} \Phi \quad (25)$$

where

$$\Phi = \begin{bmatrix} -G(\sigma_{33} - \sigma_{11}) + H(\sigma_{11} - \sigma_{22}) \\ F(\sigma_{22} - \sigma_{33}) - H(\sigma_{11} - \sigma_{22}) \\ -F(\sigma_{22} - \sigma_{33}) + G(\sigma_{33} - \sigma_{11}) \\ 2N\sigma_{12} \\ 2M\sigma_{31} \\ 2L\sigma_{23} \end{bmatrix} \quad (26)$$

In the case of modeling glulam Petung bamboo, the tensile behavior of glulam bamboo does not undergo the plastic phase. Thus, the associated flow rule was only applied for the compressive stress and not applied for the tensile stress.

4 Implementation of Finite Element Simulation

4.1 Abaqus CAE Numerical Model

In this research, the glulam Petung bamboo beam had a cross-sectional dimension of 50 mm × 50 mm and a length of 760 mm. The dimension was defined based on the ASTM D143-94 test standard. Glulam Petung bamboo beam model was arranged from 20 Petung bamboo strips that have a cross-section dimension of 5 mm × 20 mm and 10 Petung bamboo strips that has the cross-section dimension of 5 mm × 10 mm. The beam was assumed as a simple beam. The three points bending static loading system was applied. The distance between the bearings was 710 mm.

Glulam Petung bamboo was modeled as an orthotropic material. The three principal axes on Petung bamboo strips can be seen in Fig. 3, where L is a longitudinal axis, R is a radial axis, and T is a tangential axis.

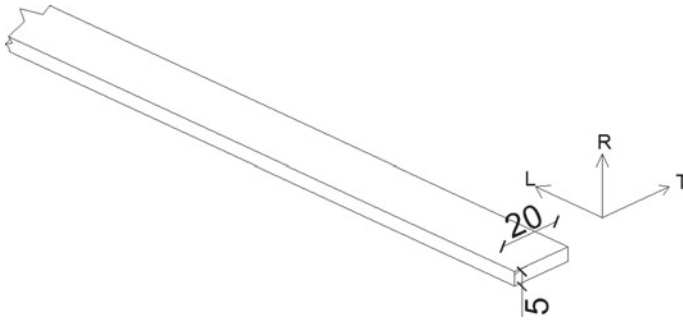


Fig. 3 The principle axis of the beam

In this model, the longitudinal, radial and tangential axes were parallel to the X, Y, Z axes, respectively. These axes directions were defined to simplify the analysis because local axes were parallel to the global axes. As a result, the transformation matrix can be ignored. The 3D solid analysis was conducted by using *Abaqus CAE/Standard* software.

In this research, there were two types of flexural loading modeled, named radial load (RF) and tangential load (TF). The radial and tangential load direction can be seen in Figs. 4 and 5, respectively. The radial load was applied parallel to the radial axis of the beam. The tangential load was applied parallel to the tangential axis of the beam.

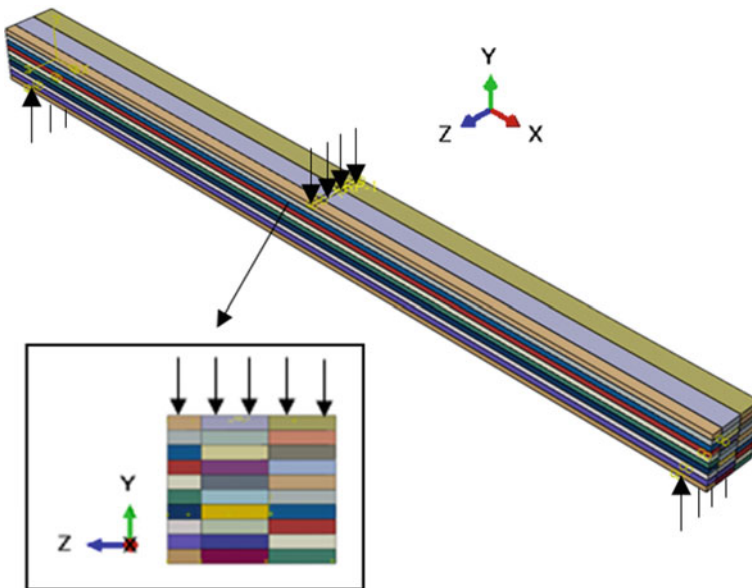


Fig. 4 Flexural loading in the radial direction of the beam

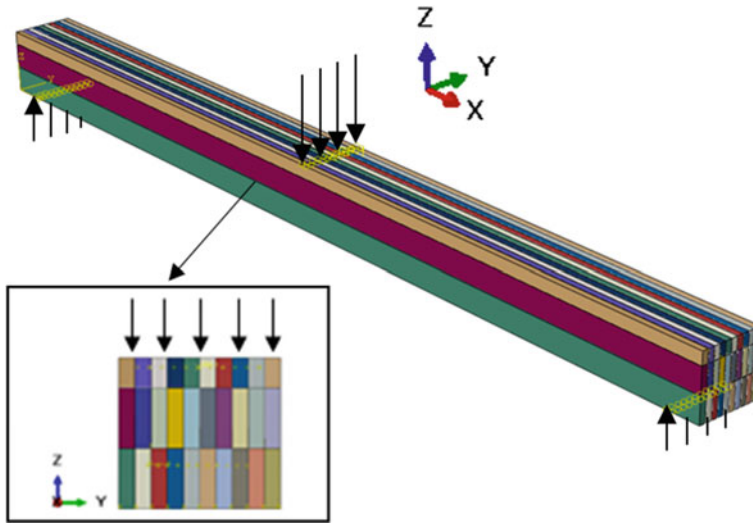


Fig. 5 Flexural loading in the tangential direction of the beam

Considering that the glulam Petung bamboo beams were modeled as an orthotropic material and the bamboo tensile properties differ from the bamboo compressive properties, the 27 bamboo properties (as seen in Table 1 and Table 2) were needed to define. Table 1 presents the properties of an orthotropic stiffness matrix for glulam Petung bamboo. Table 2 presents the properties of the *Tsai Hill* failure yield criterion for glulam Petung bamboo. Bamboo material properties used in this research were obtained from research result conducted by Eratodi [7], where:

- E_{1c} : The compressive elastic modulus in a longitudinal direction
- E_{2c} : The compressive elastic modulus in a radial direction
- E_{3c} : The compressive elastic modulus in a tangential direction
- E_{1t} : The tensile elastic modulus in a longitudinal direction
- E_{2t} : The tensile elastic modulus in a radial direction
- E_{3t} : The tensile elastic modulus in a tangential direction
- ν_{12} : The Poisson ratio (radial expansion due to longitudinal compression)
- ν_{21c} : The Poisson ratio (longitudinal expansion due to radial compression)
- ν_{21t} : The Poisson ratio (longitudinal contraction due to radial tension)
- ν_{13} : The Poisson ratio (tangential expansion due to longitudinal compression)
- ν_{31c} : The poisson ratio (longitudinal expansion due to tangential compression)
- ν_{31t} : The poisson ratio (longitudinal contraction due to tangential tension)
- ν_{23} : The Poisson ratio (tangential expansion due to radial compression)
- ν_{32c} : The poisson ratio (radial expansion due to tangential compression)
- ν_{32t} : The poisson ratio (radial contraction due to tangential tension)
- G_{12} : The shear modulus of a longitudinal plane in the radial direction loading
- G_{13} : The shear modulus of a longitudinal plane in the tangential direction loading
- G_{23} : The shear modulus of a radial plane in the tangential direction loading

Table 1 The properties of the stiffness matrix for glulam bamboo [7]

No	Symbol	Magnitude	Unit
1	E_{1c}	9545	MPa
2	E_{2c}	511	MPa
3	E_{3c}	814	MPa
4	E_{1t}	25,450	MPa
5	E_{2t}	75	MPa
6	E_{3t}	59	MPa
7	ν_{12}	0.1870	–
8	ν_{21c}	0.0100	–
9	ν_{21t}	0.0005	–
10	ν_{13}	0.2290	–
11	ν_{31c}	0.0195	–
12	ν_{31t}	0.0005	–
13	ν_{23}	0.2310	–
14	ν_{32c}	0.3680	–
15	ν_{32t}	0.1799	–
16	G_{23}	239	MPa
17	G_{13}	619	MPa
18	G_{12}	412	MPa

Table 2 The properties *Tsai-Hill* yield/failure criterion for glulam bamboo [7]

No	Symbol	Magnitude	Unit
1	σ_{y1}	40	MPa
2	σ_{y2}	2.556	MPa
3	σ_{y3}	2.556	MPa
4	σ_{u1}	180	MPa
5	σ_{u2}	2.63	MPa
6	σ_{u3}	2.85	MPa
7	τ_{u12}	8.46	MPa
8	τ_{u13}	7.74	MPa
9	τ_{u23}	8.63	MPa

- σ_{y1} : The compressive yield stress in a longitudinal direction
- σ_{y2} : The compressive yield stress in a radial direction
- σ_{y3} : The compressive yield stress in a tangential direction
- σ_{u1} : The tensile ultimate stress in a longitudinal direction
- σ_{u2} : The tensile ultimate stress in a radial direction
- σ_{u3} : The tensile ultimate stress in a tangential direction
- τ_{u12} : The ultimate shear stress of longitudinal plane due to radial load
- τ_{u13} : The ultimate shear stress of longitudinal plane due to tangential load

τ_{u23} : The ultimate shear stress of a radial plane due to tangential load.

4.2 *Abaqus CAE Numerical Model*

A load increment for the orthotropic elastoplastic model of glulam Petung bamboo beams can be seen in Fig. 6.

5 Result and Discussion

5.1 *Non-linear Behavior*

The non-linear behavior of glulam beams was obtained by investigating glulam bamboo beam load–deflection. The investigation was conducted on the element located in the middle span of the beam that has critical deflection. The load–deflection curve resulted from a numerical analysis of the flexural model in the radial direction (RF Num) and tangential direction (TF Num) can be seen in Fig. 7.

Figure 7 and Table 3 show that the glulam beam subjected to tangential lateral loading is stiffer than that subjected to radial lateral loading. It is caused by the differences of glulam bamboo elastic modulus in the tangential and radial direction. The tangential compressive elastic modulus of the glulam beam is higher than the radial compressive elastic modulus. The compressive elastic modulus highly dominates the flexural behavior of glued-laminated Petung bamboo because the compressive property of glued-laminated Petung bamboo was lower than its tensile properties. As a result, for obtaining the equilibrium condition of the glulam beam, the compressive stress occurs in most of the beam cross-section.

The comparison between the load–deflection curve obtained from numerical analysis result and that obtained from the previous experimental study [7] can be seen in Fig. 8 and Fig. 9 for the flexure numerical model in a radial direction (RF) and the tangential direction (TF), respectively.

Based on Figs. 8 and 9, the load–deflection curve of numerical analysis results can be categorized as a bilinear curve. It is different from the load–deflection curve resulted from the experimental study. The differences might be caused by the unidentified hardening function, softening, and the damage model of glulam bamboo in the ABAQUS CAE program.

Figures 8, 9, and Table 3 depict that the deflection under maximum radial and tangential flexural loading resulted from the numerical analysis is 27.47 mm and 25.88 mm, respectively. The experimental result shows that the deflection under maximum radial and tangential flexural loading is 28.02 mm and 29.07 mm, respectively. The error value between numerical and experimental study is 1.96% and 10.97% for beam subjected lateral radial and tangential direction, respectively.

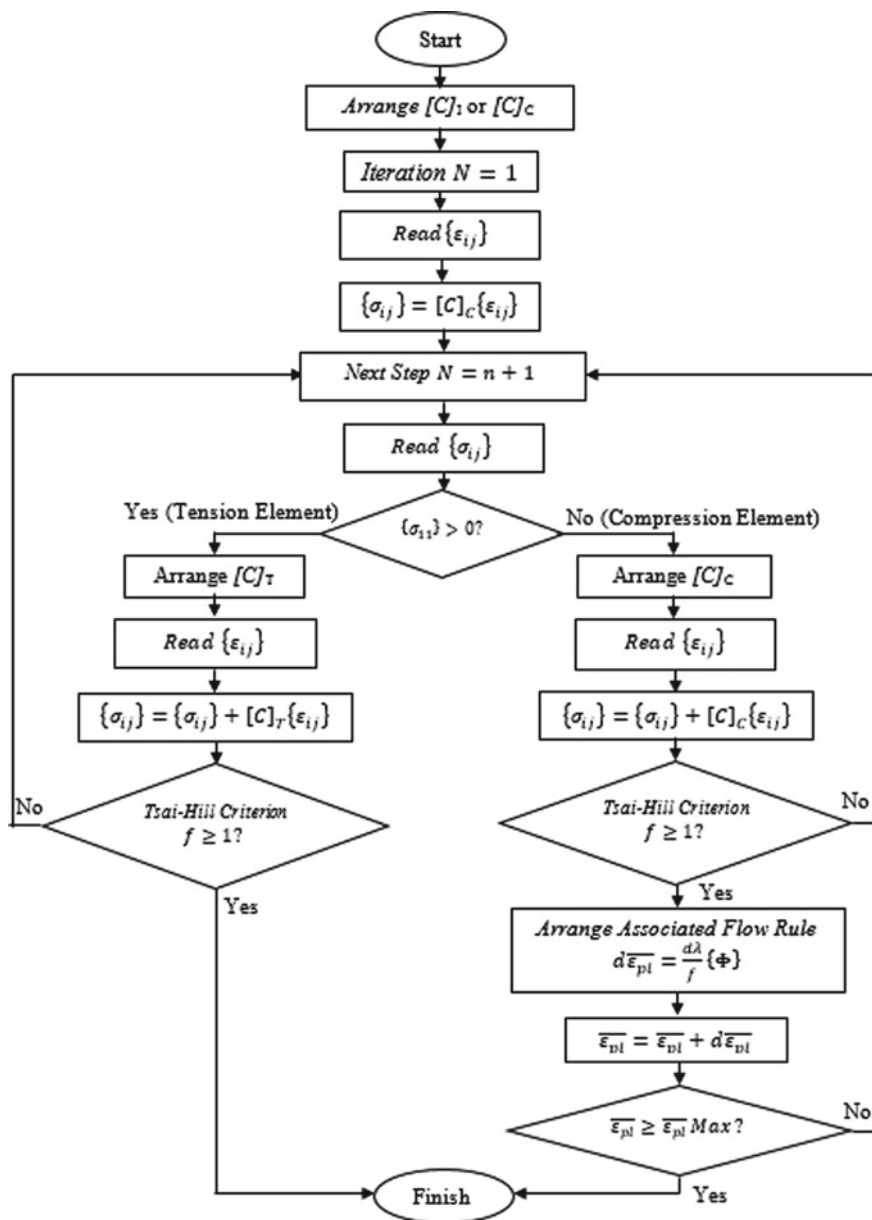


Fig. 6 Load increment for elastoplastic modeling of glued-laminated bamboo

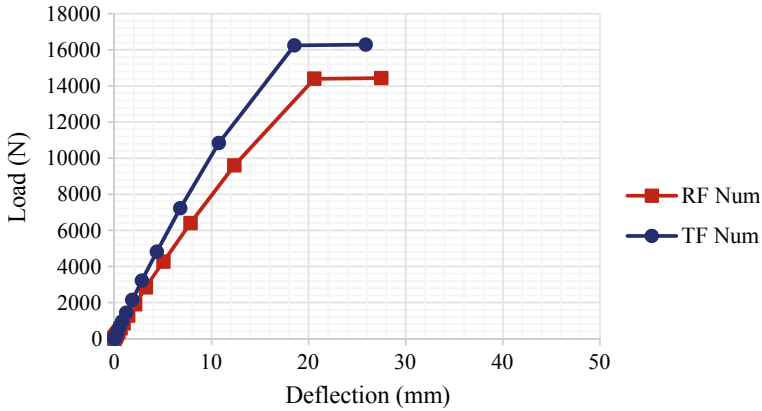


Fig. 7 Flexural load–deflection graph in tangential direction

Table 3 Numerical analysis results

Model	Elastic maximum load	Elastic maximum deflection	Ultimate load	MoE ^a	Maximum deflection	MOR ^b	Ultimate tensile stress ^c
	(MPa)	(MPa)	(N)	(MPa)	(mm)	(MPa)	(MPa)
RF Num	14,398	20.59	14,434	10.011	27.47	122.98	178
TF Num	16,247	18.53	16,288	12.553	25.88	138.78	186

^aMOE is calculated based on elastic maximum load and deflection resulted from the non-linear numerical analysis

^bMOR is calculated based on ultimate resulted from the non-linear numerical analysis and by using assumption that neutral plane is located in one-half the beam height

^cUltimate tensile stress is directly obtained from numerical analysis data

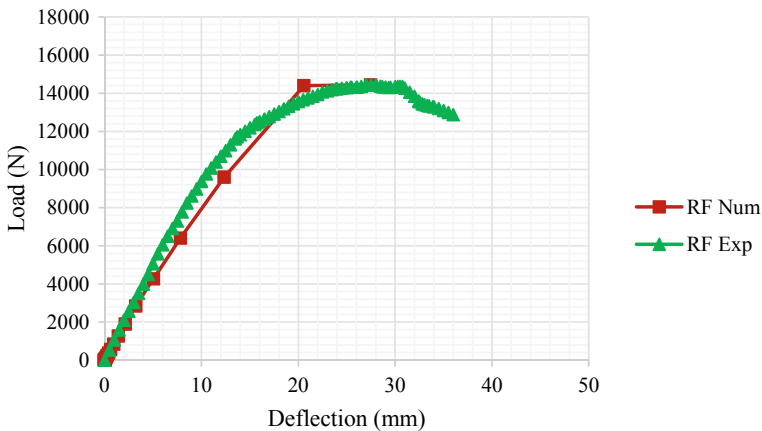


Fig. 8 Validation of load–deflection relationship of glulam Petung bamboo under radial lateral load

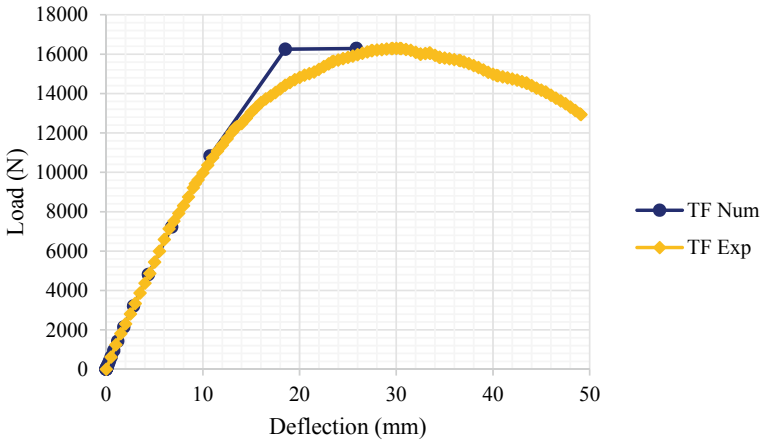


Fig. 9 Validation of load–deflection relationship on loading in tangential flexure

5.2 Modulus of Elasticity, Modulus of Rapture, and Ultimate Tensile Stress

The modulus of elasticity (MoE) and the modulus of rupture (MoR) of glulam bamboo beams resulted from the numerical analysis can be observed by using Fig. 7. The results can be seen in Table 3. The comparison between MoE and MoR obtained from the numerical analysis conducted in this research and that obtained from an experimental study performed by Eratodi [7] can be seen in Table 4.

As shown in Table 4, the error value of MoE in the radial and tangential direction is 17.0% and 1.07%, respectively. These comparison results are clearly illustrated in Figs. 8 and 9. The load–deflection curve of the beam model tangentially loaded coincides with the load–deflection curve of the beam specimen tested in tangential loading.

The error values of MoR of the beam flexural radially and tangentially loaded are 0.55% and 5.95% that indicates the small error. However, as shown in Figs. 8 and 9, the plastic behavior of the glulam beam obtained from the numerical study has not satisfied the plastic behavior of the glulam beam obtained from the experimental

Table 4 The comparison between MoE and MoR obtained from the numerical and experimental study

Model	MoE	MoE	Error	MOR	MoR	Error
	Num	Exp		Num	Exp	
	(MPa)	(MPa)		(MPa)	(MPa)	
RF	10,011	12,070	17.06	123	122	0.55
TF	12,553	12,420	1.07	139	131	5.95

study. It might be caused by the hardening function and damage mode that has not been defined yet.

5.3 Stress–Strain Distribution

Observing the material behavior on the beams is not enough when it is only focused on the load–deflection curve. The distribution of the normal stress–strain needs to be observed because it can prove whether the model created is well run and be able to give results in accordance with the expectations. Investigating the stress–strain distribution over the cross-section of the beam can define the neutral axis position on each loading step.

The normal stress distribution of the numerical model on the radial direction and the tangential direction can be seen in Figs. 10 and 11, respectively. It is shown that the pattern of stress–strain distribution along the beam subjected radially is similar to that subject tangentially. The detailed stress–strain distribution located in the mid-span of the beam model radially and tangentially loaded can be seen in Figs. 12 and 13, respectively.

When the beam is radially subjected to 14,434 N, the compressive and tensile stresses are -98 MPa and 178 MPa, respectively. When the beam is tangentially subjected to 16,288 N, the compressive and tensile stresses are -124 MPa and 186 MPa, respectively. The applied load of 14,434 and 16,288 N is the maximum load applied in radial and tangential direction conducted by Eratody [7].

The neutral axis location of beams in each loading step 15, 20, and 24 can be seen in Figs. 14 and 15 for radially and tangentially loading, respectively. For radial direction flexural, the lateral load applied in loading step 15; 20; and 24 are 560 N;

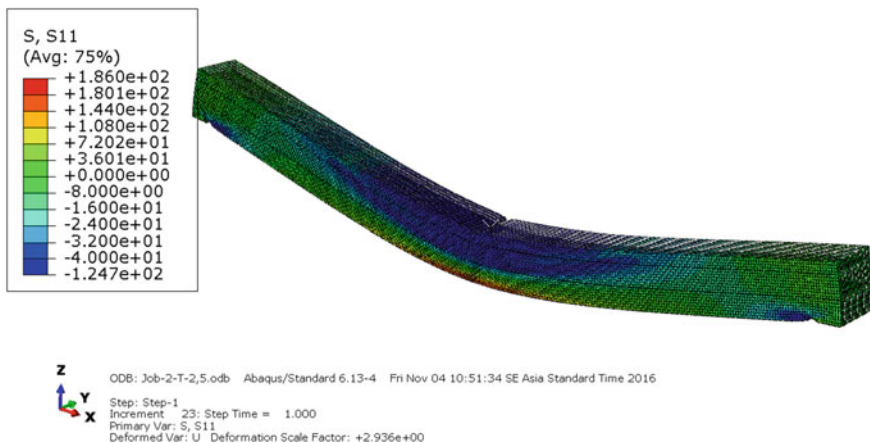


Fig. 10 The normal stress distribution along the beam loaded in a radial direction

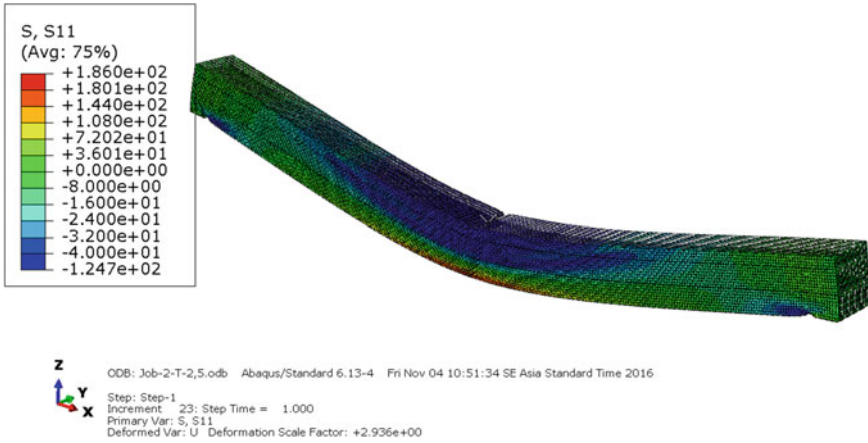


Fig. 11 The normal stress distribution along the beam loaded in the tangential direction

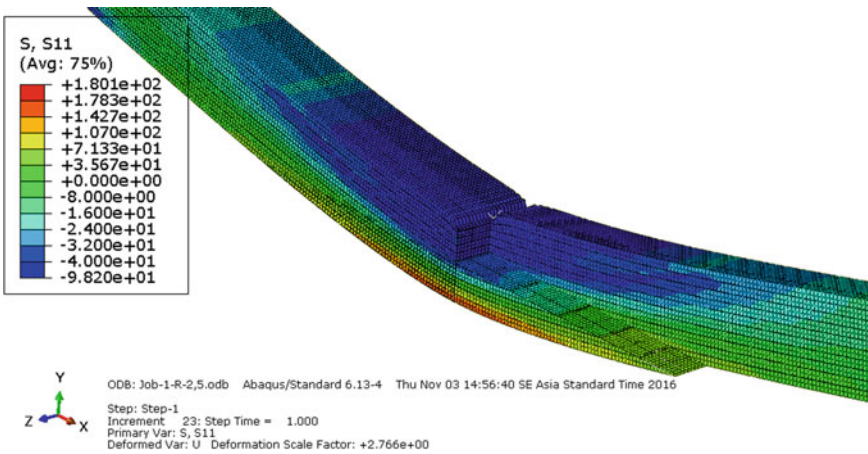


Fig. 12 The details of the normal stress distribution along the beams loaded in the radial direction

4,265 N; 14,434 N, respectively. For Tangential direction flexural, the lateral load applied in loading step 15; 20; and 24 are 632 N; 4,813 N; 16,288 N, respectively. It can be seen that the neutral axis location change for different lateral loading. It caused by the differences in glulam behavior under compressive and tensile loading.

As previously discussed, the plastic behavior of the glulam beam obtained from the numerical study has not satisfied the plastic behavior of the glulam beam obtained from the experimental study because of the hardening function and damage mode that has not been defined yet. As a result, the compressive stress–strain distribution cannot accurately depict the actual compressive stress–strain distribution when the compressive stress exceeds 40 MPa.

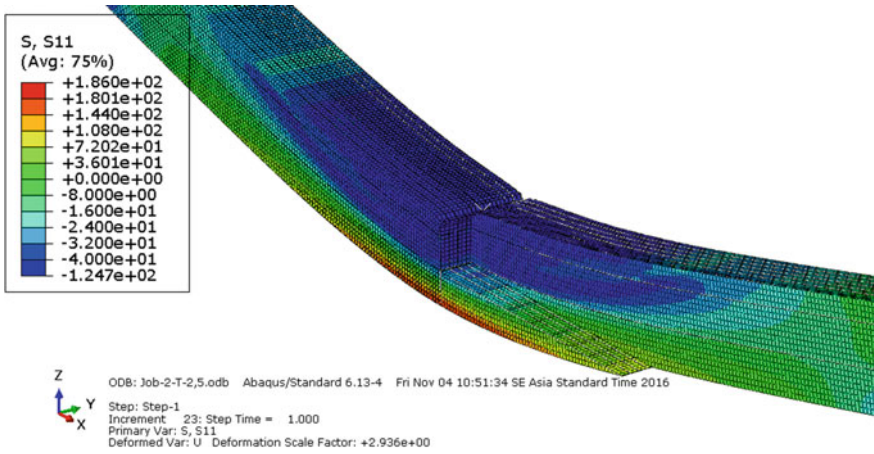


Fig. 13 The details of the normal stress distribution along the beams loaded in the tangential direction

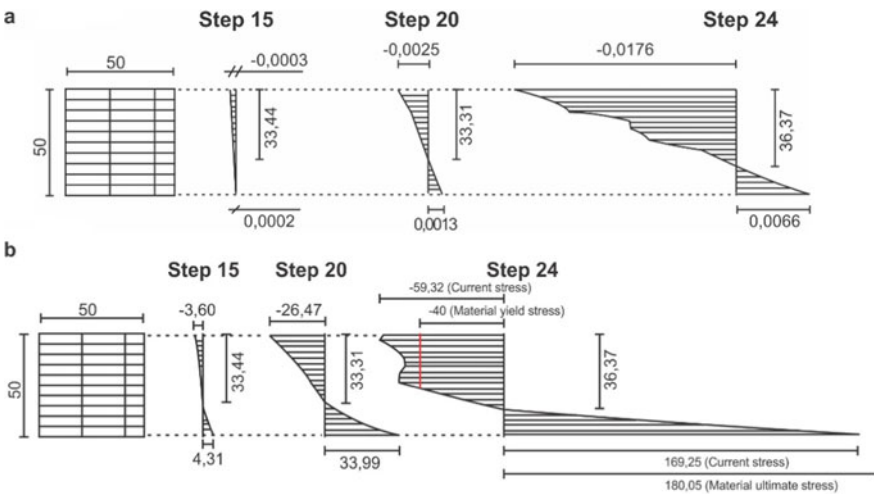


Fig. 14 The stress–strain distribution over the cross-section located at a distance of 375 mm from the bearing when the beam is loaded in radial direction: **a** strain distribution, **b** stress distribution (Unit in mm and MPa)

6 Conclusion

Based on the research results, it can be concluded that:

1. The load–deflection curves resulted from numerical analysis and experimental study are similar. The error value of maximum deflection resulted from the

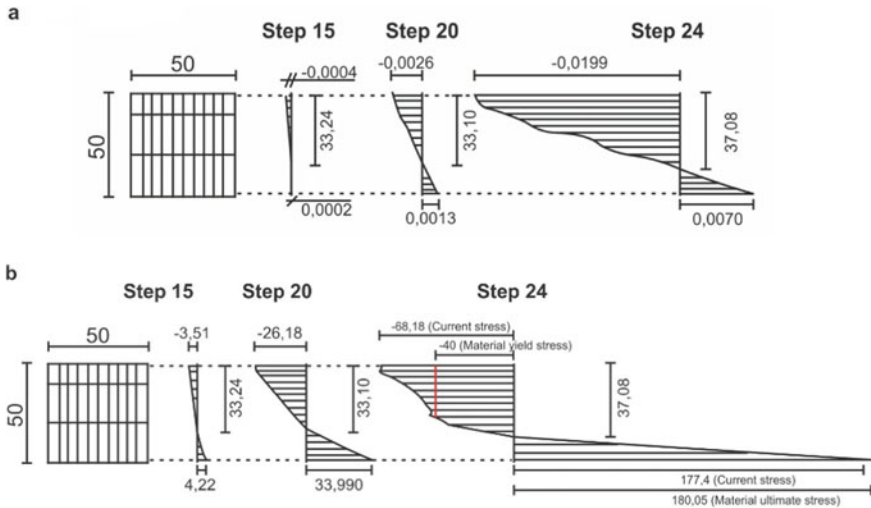


Fig. 15 The stress–strain distribution over the cross-section located at a distance of 375 mm from the bearing when the beam is loaded in tangential direction: **a** strain distribution, **b** stress distribution (*Unit in mm and Mpa)

numerical and experimental study is 1.95% and 10.96% for beam subjected radial and tangential direction, respectively.

2. The error value of MoE in radial and tangential direction is 17.0% and 1.07%, respectively. It indicates that the numerical model can represent the experimental model.
3. The error values of MoR of the beam flexural radially and tangentially loaded are 0.55 and 5.95% that indicates the small error.
4. The neutral axis location change for different lateral loading. It caused by the differences in glulam behavior under compressive and tensile loading.
5. The plastic behavior of the glulam beam obtained from the numerical study has not satisfied the plastic behavior of the glulam beam obtained from the experimental study because of the hardening function and damage mode that has not been defined yet.

References

1. Widjaya E (1999) State of the art of Indonesian Bamboo. In: Proceedings of a training course cum workshop on bamboo conservation, diversity, ecogeography, germplasm, resource utilization, and taxonomy. Kunming and Xishuanbanna, Yunnan-China
2. Silviana, Kareth S, Petermann M (2014) Durability assessment and physical properties investigation of modified Petung bamboo (*Dendrocalamus asper*) as resulted in acetylation, assisted by supercritical CO₂. In: International conference and workshop on chemical engineering UNPAR 2013, ICCE UNPAR 2013, vol 9. Elsevier B.V. Semarang, pp 273–283

3. Correal JF, Echeverry JS, Ramirez F, Yamin LE (2014) Experimental evaluation of physical and mechanical properties of glued laminated *Guadua Angustifolia* Kunth. *Constr Build Mater* 105–112
4. Sharma B, Gatoo A, Bock M, Ramage M (2015) Engineered bamboo for structural applications. *Constr Build Mater* 66–73
5. Dongsheng H, Aiping Z, Yuling B (2013) Experimental and analytical study on the nonlinear bending of parallel strand bamboo beams. *Constr Build Mater* 585–592
6. Sinha A, Way D, Mlasko S (2014) Structural performance of glued laminated bamboo beams. *J Struct Eng ASCE* 1–8
7. Eratodi IG, Triwiyono A, Awaludin A, Prayitno TA (2014) Sambungan Balok Kolom Menggunakan Pelat Baja Dikarter dan Baut. Universitas Gadjah Mada, Yogyakarta
8. ASTM Committee (1994) Standard method of testing small clear specimen of timber. Designation D143-94. Annual Book of ASTM Standard
9. Dassault Systèmes Simulia (2013) Abaqus Documentation 6.13. Providence, Rhode Island-USA, Dassault Systèmes
10. Kaw AW (2005) *Mechanics of composite materials*, 2nd edn. Taylor and Francis Group, Boca Raton
11. Kelly (2008) *Solid mechanics part II*. The University of Auckland, Auckland-New Zeland

Numerical Simulation Reinforcement of RC T-Beam with Carbon Fiber Reinforced Polymer (CFRP)



A. Mahendra, Muslikh, and A. S. Fajar

Abstract Many infrastructures damaged are due to environmental, inadequate maintenance, and natural disaster like an earthquake. Some structures in Indonesia were built using the old code design, which was unsafe when compared to the new code. The structure needs to be strengthened to increase the safety level and extend its service period. One solution to the problem is to enhance the structure using synthetic wraps or Carbon Fiber-Reinforced Polymeric (CFRP). This research simulates the reinforced concrete T-beam with CFRP by numerical analysis following the predecessor experimental study. The numerical analysis of reinforced T-beam with CFRP was modeled using finite element method. The concrete damage plasticity model for the concrete material was adopted to idealize the concrete material. Also, the interaction property between the CFRP and concrete to be idealized as a perfect bond that is constraint-tie and Hanshin damage for CFRP properties that applied as a composite layup. The numerical analysis results achieve a good agreement with the predecessor's experiments in the term load–displacement curve, bending moment capacity, and failure mode. Although the finite element generated more less similar results with the experiment, the T-beam's failure mode was slightly different in experimental compared with the finite element results. The possible reason might be the experimental study has a failure mode of debonding between interface concrete and CFRP. However, the result of the finite element has a similar failure mode with a normal specimen with a positive post-yield stiffness. In future work, the effect of bond interaction between the CFRP and concrete need to be idealized as contact, or epoxy should be modeled between the CFRP and the concrete.

Keywords CFRP · Numerical simulation · Finite element analysis · RC T-beam

A. Mahendra · Muslikh (✉) · A. S. Fajar
Civil and Environmental Engineering, Gadjah Mada University, Yogyakarta, Indonesia
e-mail: muslikh_jtsl@ugm.ac.id

A. Mahendra
e-mail: andhikamahendra@ugm.ac.id

A. S. Fajar
e-mail: angga.fajars@ugm.ac.id

1 Introduction

Indonesia is known located in a ring of fire. Many disasters, especially earthquakes, happened in Indonesia, triggering many buildings to collapse, making the safety level decrease. In fact, many occupants are unaware of the building's falling safety rating after a disaster and continue to utilize it as usual. As a result, it is important to repair/retrofit the cracked structure in order to improve its performance. Furthermore, there are some factors that make the structure getting weak. Among the factors is the use of old code design among engineers, which is believed to be outdated and poor maintenance, impacting the structure's strength. The effective method to reinforce the structure is by using carbon fiber reinforced polymer (CFRP). Many previous studies have concentrated on experimental research and finite element analysis models in Abaqus software that have been subjected to FRP reinforcement of beam and column. However, no research study on T-beams has been conducted. It is critical to do so in Indonesia because practically all structures in the country are built with T-beams. As a result, both numerical and experimental investigation of the performance of reinforced T-beam with CFRP wrap is required.

Lundqvist et al. [5] in this study, there are experimental and numerical analyses of researches. It would do an experimental study of CFRP strengthening and then analyze numerical with Abaqus software. The techniques used were externally bonded plates, CFRP sheets, and Near Surface Mounted Reinforcement (NSMR) also, there are three different anchorage lengths, they are 100, 200, and 500 mm. As a result, the experiment showed that the critical length is less than 200 mm. Extending the anchorage length make safety level increased, but it does not enhance the load-carrying capacity. The numerical results are fracture energy, the tensile strength, and the shape of the softening response for the concrete. It is necessary to have accurate methods and material parameters for finite element analysis. And it can conclude that when material properties and geometry are changed, it will also change the critical lengths [8]. In this research, the numerical study predicted structural behavior, especially concrete members, strengthened with FRP sheets or plates. For predicting the debonding failure between FRP and epoxy, it used the concept of damage band or crack band. In order to validate the numerical simulation, it would be compared with experimental. The experimental study was to test concrete blocks and reinforced with FRP. The result of the numerical simulation was verified with experimental. Also, it presented the concept of the crack band was accepted when modeling concrete-epoxy interfaces under general states of stresses [7]. The paper studied experimental reinforcement concrete with FRP, and it's numerical using Abaqus 6.10.1 software. The numerical simulation was to validate the experimental study. The result of this study was numerical and experimental curves had a similar response. It was shown that the average experimental ultimate load was 70.7 kN while the numerical result was 73.8 kN, there was 4.6% of the difference [10]. In this research, the study of numerical simulation concrete-to-FRP bond behavior had been done. A concrete damage plasticity model was applied in this study. As a result, the numerical result has closed an agreement with test data, and it was validated. This finite element model can predict

that an increased bond length be able to enhance loading capacity [6]. The important study is to reinforce T-beam with FRP. The test of this research was a loading test, but the T-beam was not tested like usual because its monolith plate was below, and the beam was above since it searched the pure bending moment for this study. The result was the combination FRP flexural and u-shaped shear FRP strengthening be able to increase the capacity load of the T-beam [4]. The main object of this paper was to study and investigate the behavior of strengthened and repaired concrete with FRP. The finite element analysis was with Abaqus software, and there are four patch lengths of the variation of this research. Isotropic concrete damage plasticity was applied for the behavior of concrete and repair material. Linear elastic–plastic and linear elastic isotropic were applied for steel and FRP. The result of this numerical simulation had a good agreement with the experimental. Yu et al. [9] researched about finite element modeling of debonding behavior of FRP-to-concrete subject to mixed-mode loading with using a peeling test of FRP. The parameters that investigated were peeling angle, interfacial parameters, and the coupling of mode I and mode II. The result was the mode I component role a critical role in the debonding failure even when the peeling angle was very small. Therefore, this research about numerical simulation T-Beam has not been done in the past as this research is needed to do.

2 Parameters and Properties

There are many parameters and properties that we need to model in Abaqus software. The parameters include material properties, geometry, interaction with each part, and others. The paper that will be followed is not shown the complete parameters. Therefore, the parameters which is used from the other paper that has similar properties. The parameters include material properties and interaction with each other. But for geometry parameters and dimensions, this study is based on an experimental study from the paper which is published before. For geometry and dimension of the beam that we will model is based on experimental research, which has been done by Tudjono et al. [6] (Figs. 1 and 2).

2.1 Concrete

This study is to make a model T-beam. T-beam is the monolith from the beam and plate above; this construction is well-known to do. In the construction of T-beam, the flange and web of the beam have to be one or monolith each other effectively. The theory for T-beam is the shape of this beam is “T,” and it is for adding flanges to increase the compression area. The thickness of the flange has to have half from the width of the web beam, and the effective flange is not allowed to be four times the width of the web beam. And the effective width of the slab is not permitted to

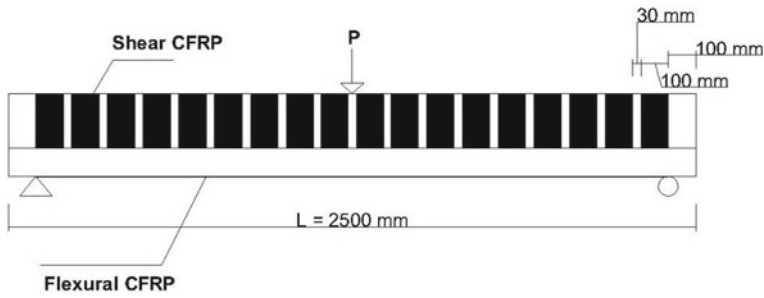
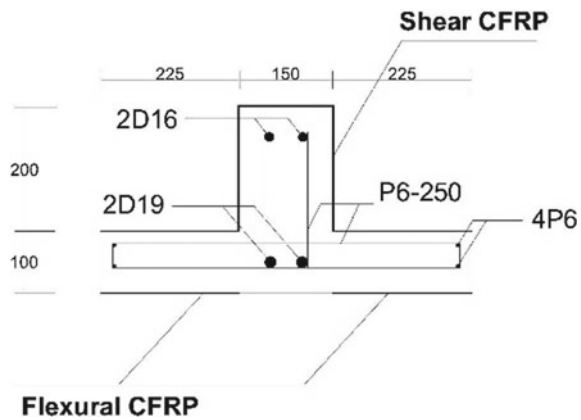


Fig. 1 T-Beam model [6]

Fig. 2 Cross section T-beam model [6]



longer than a quarter of the length beam. If the main flexural steel in the slab as the flange of T-beam, the perpendicular steel to the beam has to be available at the top of the slab. Transversal steel has to be designed to carry the load, which has a factor on flange width, and it is assumed as a cantilever. Because of that, the study is making a model for T-beam. Since the T-beam consists of many parameters, there is the dimension of T-beam, concrete, and steel. The main parameters like that have to be designed in Abaqus software to make a closed enough to actual behavior or the experimental test. The concrete model is the main parameter that has to be designed because concrete has a plasticity behavior.

Concrete is a mixture of the Portland cement and the other hydraulic cement, fine aggregate, coarse aggregate, water, and with or without admixture [14]. For modeling concrete in Abaqus software, it needs to have some parameters and material properties. The parameters of concrete are included young modulus, compressive strength, and tensile strength. For this study, it is used elastic and plasticity behavior for concrete. Those parameters are concrete damage plasticity (CDP) in Abaqus software.

The compressive behavior needs to be modeled. It is about a stress–strain model for this concrete. A stress–strain model is applied for concrete, and it is tested to uniaxial compressive loading and reinforcing steel confinement. The stress–strain of the concrete parameter is very important because it showed the plasticity damage behavior of the concrete. There are many equations to get the closed behavior of the concrete in finite element to the experimental or actual behavior of the concrete.

Based on [12] that early investigators present the strength and the corresponding longitudinal strain at the strength of concrete confined by a hydrostatic pressure that can be followed with relationships Eqs. (1–2). Where, f'_c = the maximum concrete stress and ϵ'_c = the concrete strain at the maximum stress. f and ϵ are unconfined concrete strength and strain [12]. After that, the compressive behavior of this concrete is like what in graphics display Fig. 3.

$$f = f'_c x r / (r - 1 + x^r) \tag{1}$$

$$x = \epsilon / \epsilon'_c \quad \text{and} \quad r = E / (E - (f'_c / \epsilon'_c)) \tag{2}$$

In this study, there are three variation of compressive and tension concrete behavior. These variations are to find the right parameter of concrete. And then, it can be validated with the result of laboratory test.

The tensile behavior of the concrete in this study has followed the behavior like Fig. 4 from Abaqus manual [1]. This research, the fracture energy cracking criterion to be adopted in simulating tensile behavior. The type of concrete tension stiffening is GFI input. Based on Abaqus manual, that is a relationship’s curve between tension and strain in fracture energy theory. Typical values of G_f range from 40 N/m until 120 N/m. It depends on f'_c that is from 20 to 40 MPa. After that, the tensile behavior of this concrete is shown in Fig. 5.

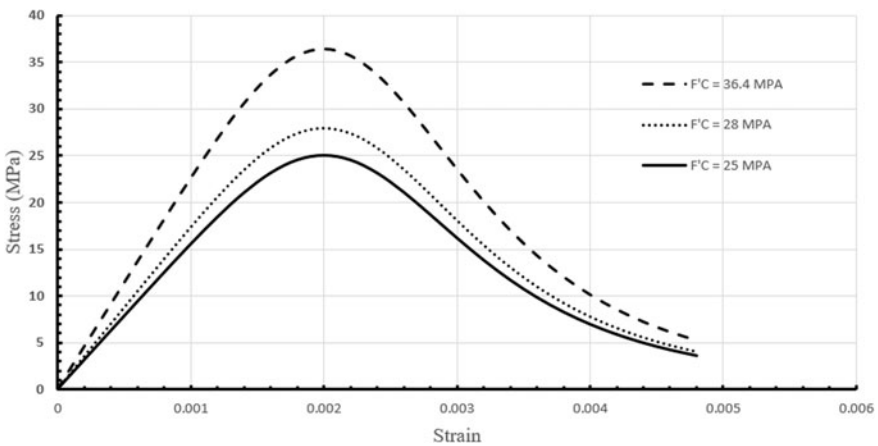


Fig. 3 Compressive concrete behavior

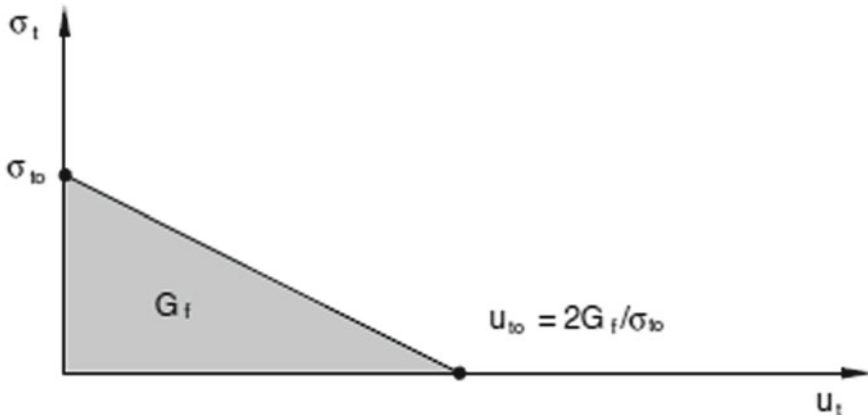


Fig. 4 Concrete tension stiffening, Type = GFI Input

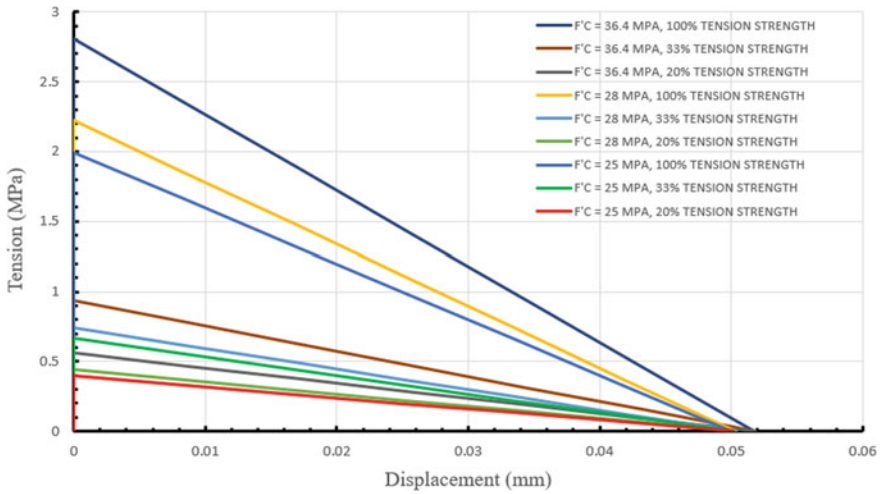


Fig. 5 Tensile concrete behavior

2.2 Steel

In this study, there are two characteristics of steel. They are the steel that has a yield stress of 240 and 400 MPa. Steel which has yield stress of 240 MPa is a diameter of steel less than 10 mm. And the other steel that has a diameter of more than 10 mm, it will be characterized as yield stress of 400 MPa. For ultimate stress will be followed like Eq. (3). So, the properties of steel can show in Table 1. Also, the behaviors of two characteristics of steel are in Figs. 6 and 7.

Table 1 The parameters of steel

Parameters	Explanation (MPa)
E	200,000
f_y (diameter < 10 mm)	240
f_y (diameter > 10 mm)	400
f_u (diameter < 10 mm)	300
f_u (diameter > 10 mm)	500
ϵ_{sh}	0.02
ϵ_{su}	0.2

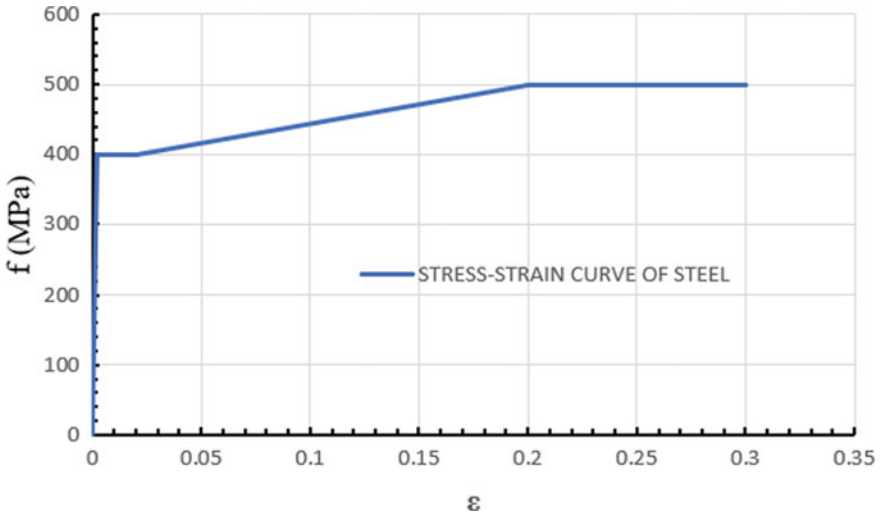


Fig. 6 The behavior steel with yield stress of 400 MPa

$$f_u = 1.25 f_y \tag{3}$$

The interaction of steel rebar with concrete in Abaqus is idealized as an embedded region. It is a perfect bond between rebar steel and concrete. Also, it implements that rebar steel has a region that is concrete.

2.3 CFRP

Implementation CFRP in the concrete structural member has been established to hold the load bigger than design load, to repair the strength decrease, and to increase a safety level in the buildings. It is made from composite material, which is fiber include resin polymer. It is known as an alternative method for reinforcement that

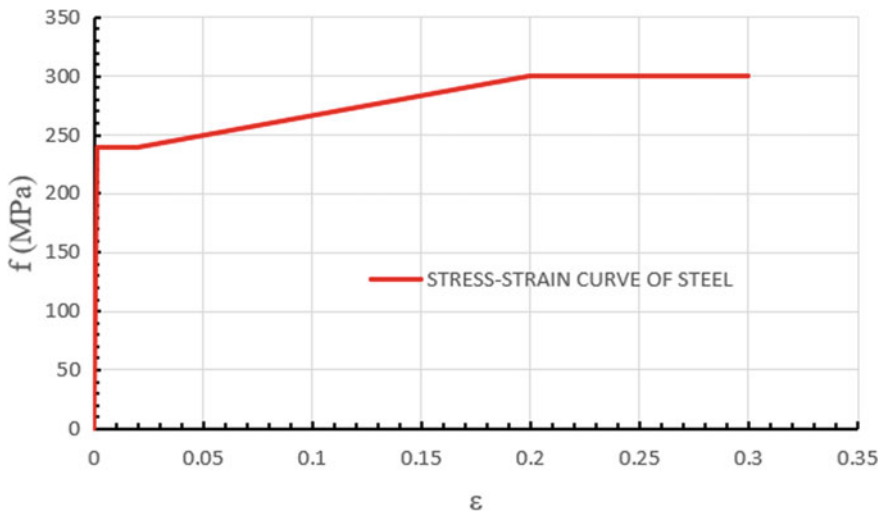


Fig. 7 The behavior steel with yield stress of 240 MPa

is to repair and to rehabilitate the structure. The system of CFRP is described as fiber and resin used to make composite lamina to protect concrete and to strengthen it. The CFRP materials have characteristics as lightweight, thin, not corrosive, and have high tensile strength. It has many shapes, sizes, and it is made a dried sheet for applying in geometry that we want [2]. So, CFRP is a known method to repair the structure and make a safety level increase. It makes CFRP is so applicable and easy to use. Many countries use CFRP for reinforcement. Sometimes, the reinforcement is not about cracked because of disaster, but it is because of the wrong construction and problems in the field area during the construction.

In this study, the parameter of CFRP is followed a paper. And in that paper, it is studied about finite element analysis, which was searching about the characteristics CFRP if it is tested with unidirectional drilling. The parameter is got from that study are like Tables 2 and 3 [3, 13]. And the interaction property between the CFRP and concrete to be idealized as a perfect bond. In Abaqus software, the perfect bond interaction is constraint-tie input and for the properties of CFRP is idealized as Hanshin damage input and applied with a composite layup.

Table 2 The parameters of CFRP [3]

Parameters	Explanation (MPa)
E_1	65,402
E_2	5876
E_3	5876
Longitudinal tensile strength	894
Longitudinal compressive strength	779

Table 3 The parameters of CFRP [13]

Parameters	Explanation
G_{12}	4500 MPa
G_{13}	4500 MPa
G_{23}	3000 MPa
Y_t	84 MPa
Y_c	250 MPa
S_{12}	60 MPa
S_{23}	60 MPa
ν_{12}	0.3
ν_{13}	0.3
ν_{23}	0.3

Where Y_t and Y_c are the transverse tensile (compressive) strength, S_{12} and S_{23} show shear strength and transverse shear strength.

3 Finite Element Model

The finite element is used to solve problems in engineering analysis and design. The problem is like an existing structure or some components that be carried the load. For practical engineering problems, the finite element is used with the digital computer or program. Because two properties are effective and applicability in engineering analysis are theory and practical computation, so the finite element is a good method for engineering problems [11].

In this research, Abaqus software is used to do the finite element, and the models are RC T-Beam without CFRP and RC T-Beam with CFRP-reinforcement. Abaqus software is chosen because the software can model 3D performance like Figs. 6 and 7. Also, Abaqus is able to do micro-analysis. For the specimen with CFRP, there are flexural CFRP and shear CFRP. And the assumption of the loading test is displacement-load control. Because it will be more compatible and we can know about the maximum load until reach the displacement that we control. The shape of the loading test is a cylinder of steel. It is used because the cylinder of steel can be approached with the experimental loading test (Figs. 8 and 9).

4 Result and Discussion

The purpose of this paper is to make a finite element with Abaqus software about T-Beam, which is reinforcement by CFRP and without reinforcement. The behavior

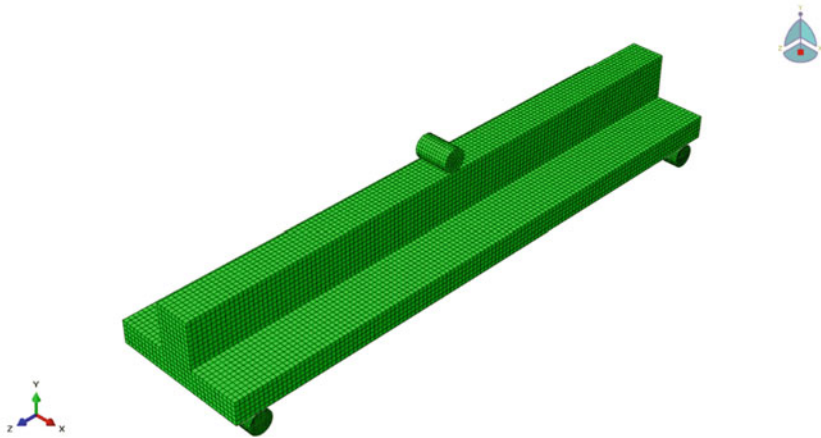


Fig. 8 T-Beam finite element model without reinforcement

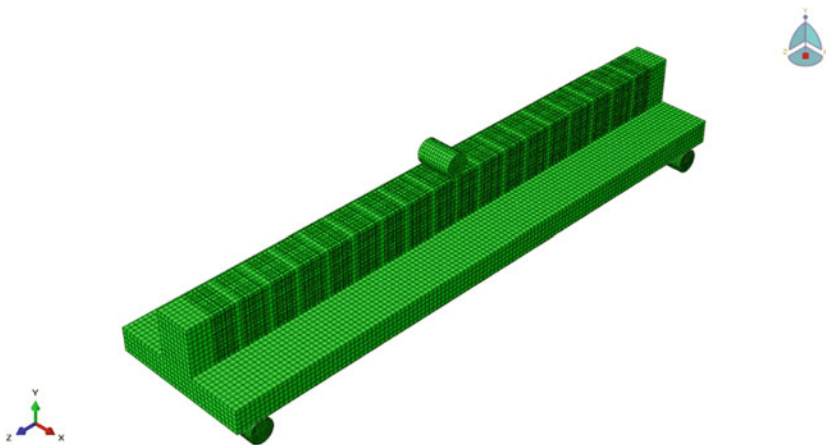


Fig. 9 T-Beam finite element model with reinforcement

will be investigated the load–displacement curve, the bending moment capacity, and failure mode.

For validation of this finite element, it will be compared the result of the finite element and experimental. And it will be compared to three behaviors above. The validation is if three behaviors are similar to the experimental specimen.

4.1 Load–Displacement Curve

Based on the load–displacement relationships Fig. 10, the parameter is maximum load and similarity of skeleton curve. The maximum load is to know the bending moment capacity of each specimen. The result skeleton curve from some variations of compressive and tension strength can be seen in Fig. 10. Maximum load and percentage of difference between laboratory test and finite element are able to be taken from that relationship shown in Table 4.

From those skeleton curves and the result of maximum load, it can be concluded that parameter of concrete which is validated between similarity of experimental and

Fig. 10 The result of load–displacement skeleton curve: **a** $f'_c = 36.4$ MPa **b** $f'_c = 28$ MPa **c** $f'_c = 25$ MPa

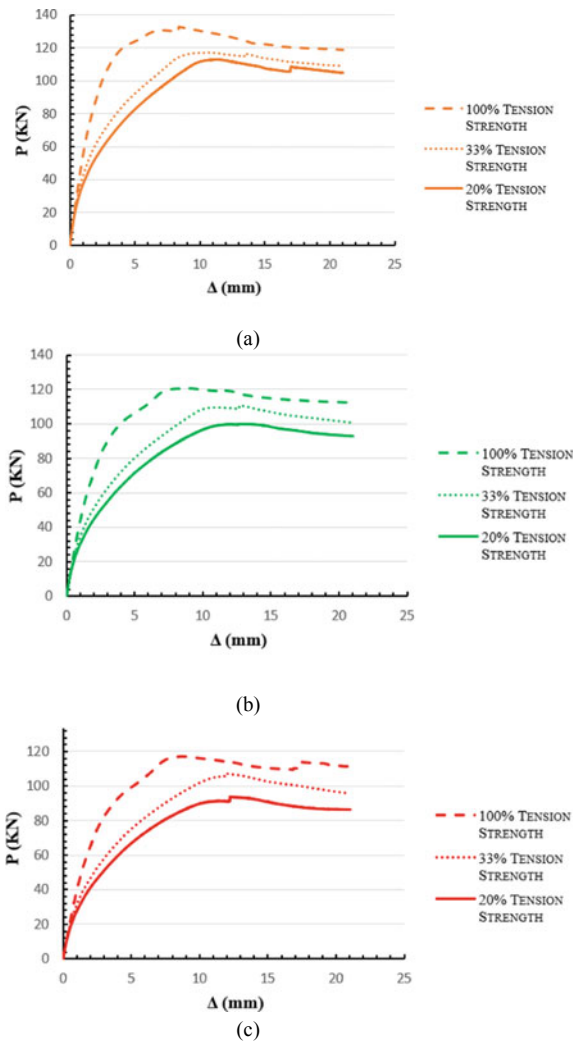


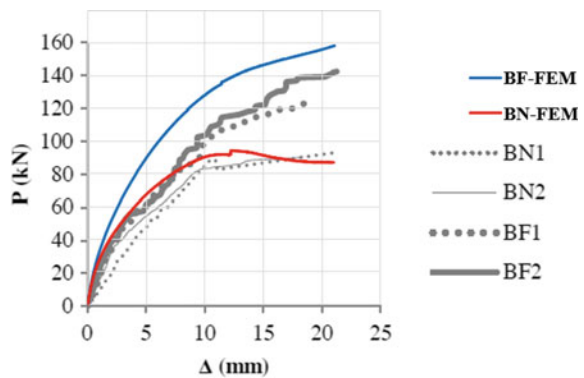
Table 4 Maximum load of variations skeleton curve

Compressive strength specimen (MPa)	Percentage of tension strength (%)	P max (kN)	Laboratorium test, P max (kN)	The difference from experimental specimen (%)
36.4	100	132.899	93.6	41.986
	33	117.313	93.6	25.334
	20	113.139	93.6	20.875
28	100	120.606	93.6	28.853
	33	110.598	93.6	18.160
	20	99.8772	93.6	6.706
25	100	117.245	93.6	25.262
	33	107.039	93.6	14.358
	20	93.7805	93.6	0.193

finite element method load displacement skeleton curve. The parameter of concrete is $f'_c = 25$ MPa and tension strength reduced until 80%. Because the difference between experimental and finite element method maximum load is 0.193%. It is closed enough than other variations. The comparison load–displacement curve of experimental work and finite element method can be seen in Fig. 11.

From the graphic of load–displacement, we can see the RC T-beam without CFRP reinforcement and RC T-beam with CFRP reinforcement have a good agreement. And it can be validated because the behavior of the experimental study and the result analysis from the finite element method with Abaqus software is similar. And the percentage of difference from the experimental specimens is not far.

Fig. 11 The comparison load–displacement curve of experimental work and finite element method



4.2 Bending Moment Capacity

In this study, for making a good agreement and validating the experimental result with finite element result. It will be shown the bending moment capacity each beam. And there are some equations to get the bending moment capacity, which is manual section calculation of bending moment capacity, plasticity analysis, and from the maximum load that can be held. The manual calculation is the one way to find the capacity moment. It is calculated from the section area that is had by the beam. For this study, the beam shape is “T”. So, the calculation of inertia moment is important to do and has to care because it makes a difference for the result. And for the manual calculation, it is followed the Eqs. (4–5) from [14]

$$M_n = 0.85 f'_c b w a (d - a/2) \tag{4}$$

$$M_n = PL/4 \tag{5}$$

The bending moment capacity from the maximum load is like a simple analysis structure. Because the beam that is modeled is simple beam, it has two supports. So, it can be analyzed with a simple analysis structure. And the bending moment capacity from the maximum load has followed this Equation. As a result of the calculation bending moment capacity from equations above, it can be seen in Table 3.

From Table 5 we can see the RC T-beam without CFRP reinforcement and RC T-beam with CFRP reinforcement have a good agreement. And it can be validated because the bending capacity moment and maximum load are similar between model Abaqus and experimental study. And the percentage of difference from the experimental specimen is not far.

Where BN-Experimental is a specimen of the experimental research, BN-FEM is the specimen for finite element study. BF-Experimental is a specimen for reinforcement beams, while BF-FEM is the specimen of reinforcement beam in finite element. A column, difference from the experimental specimen is the percentage difference between BN-FEM with BN-Experimental and BF-FEM with BF-Experimental.

Table 5 The result of comparison experimental work and finite element method (FEM)

Specimen	Compressive strength (MPa)	P max (kN)	Mn (KNm)	The difference from experimental specimen (%)
BN-Experimental	36.4	93.6	53.820	–
BF-Experimental	36.4	142.2	81.770	–
BN-FEM	25	93.7805	53.924	0.193
BF-FEM	25	158.594	91.192	11.529

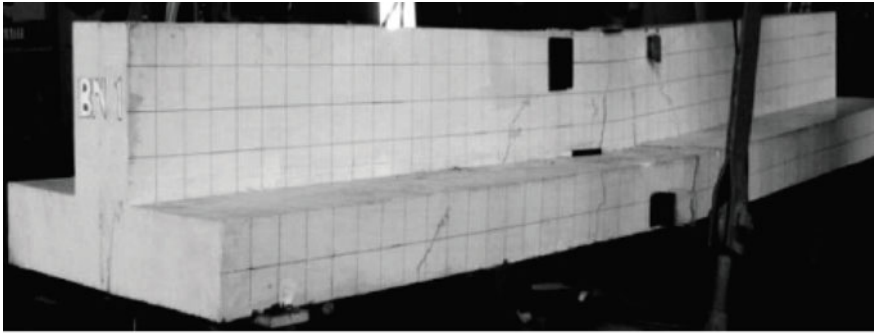
4.3 Failure Mode

The failure mode in this study is about to make matching the crack pattern between experimental study and finite element method. On Abaqus software, the crack pattern can be shown with DAMAGET output. The comparison of experimental study and finite element method can be seen in Figs. 11 and 12. From Fig. 11, we can see the similar crack between experimental study and Abaqus analysis. Then, the cracks are in the bottom of T-beam and web beam section. Therefore, flexural CFRP and shear CFRP are needed to apply to T-Beam. And Fig. 12, there is a different cracking. In an experimental study, the failure is because of debonding the CFRP. In Abaqus model, the failure is the same with normal specimen but load capacity increase than the normal specimen. Because the model uses a perfect bond between CFRP and T-beam (Fig. 13).

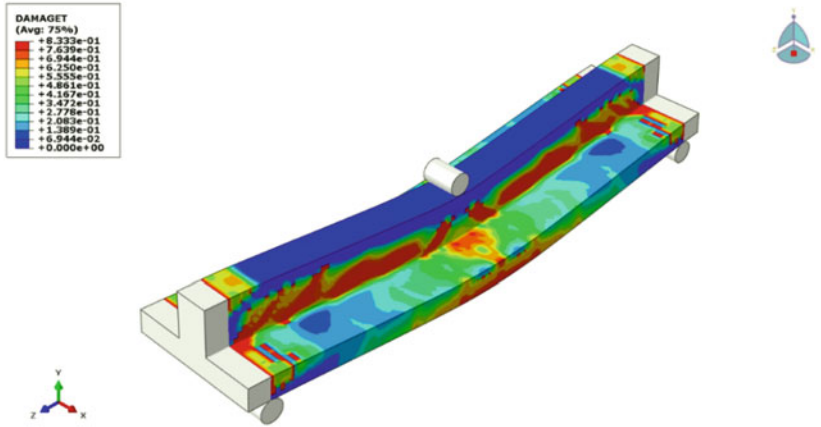
5 Conclusion

In this research, the finite element method is developed for RC T-beam and RC T-beam with reinforcement by CFRP. There are two models in this study. The model about CFRP is used in this research because it is important to do. For remaining, in Indonesia has many disasters so, the reinforcement is one of the best options to repair the buildings than rebuilding because it needs high cost than the reinforcement does. And the purpose of this study is to make a good agreement between the experimental and finite element methods. To model the concrete, it is used the concrete damage plasticity for its behavior. And to make a model CFRP this is used the elasticity-orthotropic and Hanshin damage behavior. The interfaces between CFRP and concrete applied is constraint-tie. The behavior of concrete is followed by the Eqs. (1–2) and research from paper studied [12]. It is because the parameters of the concrete in a paper which is followed present not enough for modeling the T-beam in Abaqus. For the parameters and behavior of the CFRP is followed the parameters that showed in paper studied [13] and it is applied with a composite layup in Abaqus software. The parameter of concrete that can be validated is $f'_c = 25$ MPa and tension strength reduced until 80% also leaving 20% tension strength.

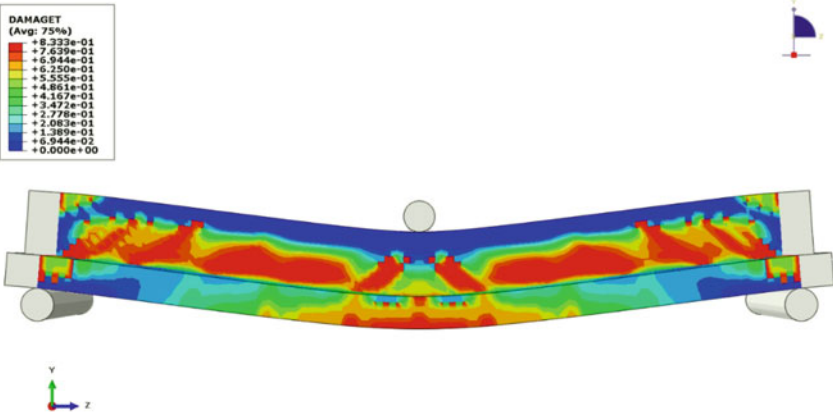
The result from finite element methods is models in Abaqus have a good agreement than experimental study and it can be seen in three parameters above. The models have a similar results and behavior than the experimental study. The most important using this finite element is about to know the right behavior of concrete materials, meshing the parts, right support, and interface between concrete and CFRP. Because they make a good result and close enough than experimental do. The advantage using the finite element method is the cost not high because after we can model the experimental study to the finite element method in Abaqus, we are able to test with a different conditions and different tests like first we test in static load. After we find the right model, we can test in dynamic load.



(a)

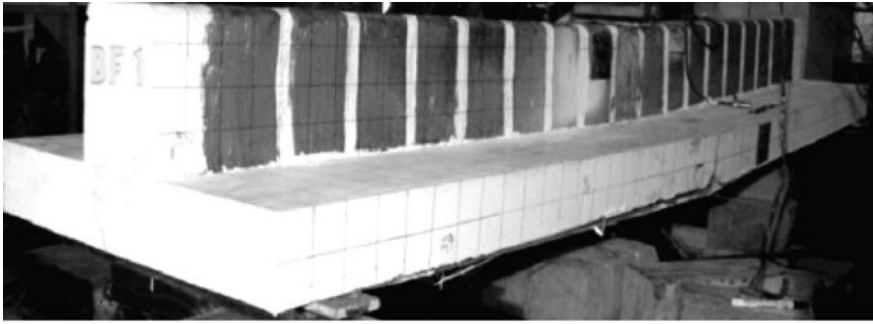


(b)

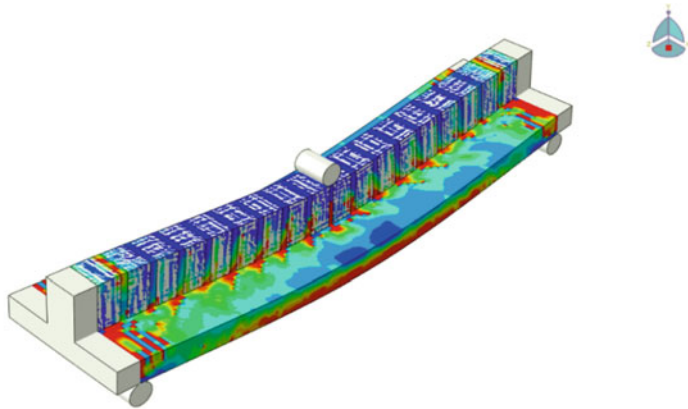
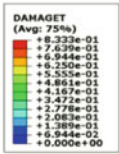


(c)

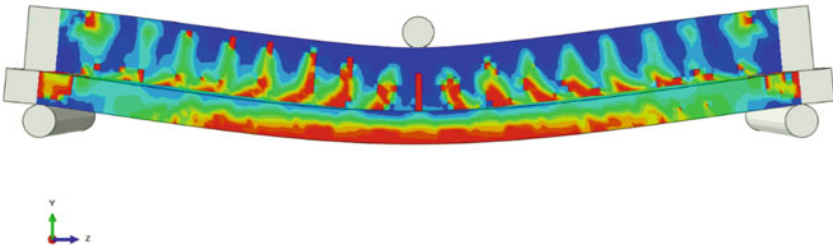
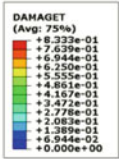
Fig. 12 Failure mode of RC T-Beam specimen. **a** An experimental study, **b** Abaqus in 3D model, **c** Abaqus in YZ cross section



(a)



(b)



(c)

Fig. 13 Failure mode of RC T-Beam with CFRP specimen. **a** An experimental study, **b** Abaqus in 3D model, **c** Abaqus in YZ cross section and CFRP released

References

1. Abaqus User's Manual Volume III: Materials Version 6.4. (2003), Abaqus Inc.
2. American Concrete Institute(2005) Guide for the design and construction of externally bonded FRP systemXs for strengthening concrete structures. ACI 440.2R-08, Detroit
3. Eamon CD, Wu H-C, Makkawy AA, Siavashi S (2014) Design and construction guidelines for strengthening bridges using fiber reinforced polymers (FRP). MDOT reference number: OR10-039: Final Report
4. Salathiel M, Mbereyaho L, Moyo P (2016) Finite element modeling of reinforced concrete beam patch repaired and strengthened with fiber-reinforced polymers. *Int J Eng Techn Res (IJETR)* 4(3):47–54 ISSN: 2321-0869 (O) 2454-4698 (P)
5. Lundqvist J, Nordin H, Taljsten B, Olofsson T (2005) Numerical analysis of concrete beams strengthened with CFRP- a study of anchorage lengths. In: Chen, Teng (eds) Proceedings of the international symposium on bond behaviour of FRP in structures (BBFS 2005), International Institute for FRP in Construction. pp 239–246
6. Tudjono S, Lie H, Hidayat B (2015) An experimental study to the influence of fiber reinforced polymer (FRP) confinement on beams subjected to bending and shear. In: The 5th international conference of Euro Asia civil engineering forum (EACEF-5). *Procedia Engineering*, vol 125. pp 1070–1075
7. Minouei M (2013) Finite element analysis of bond characteristics at the FRP-concrete. McGill University, Montreal. Canada
8. Coronado C, Lopez M (2010) Numerical modeling of concrete-frp debonding using crack band approach. *J Composite Construct ASCE* 14:11–21
9. Yu H, Bai Y, Dai J, Gao W (2017) Finite element modeling for debonding of FRP-to-concrete interfaces subjected to mixed-mode loading. *Polymers*. <https://doi.org/10.3390>
10. Tao Y, Chen J (2015) Concrete damage plasticity model for modeling FRP-To-concrete bond behavior. Queen's University, United Kingdom (UK)
11. Bathe K (2014) In: Finite element procedures. 2nd edn. United States of America
12. Mander J, Priestley N, Park R (1988) Theoretical stress strain model for confined concrete. *J Struct Eng ASCE* 114(8):1804–1826
13. He Y, Zhang G, Xue J (2014) Finite element analysis on drilling of unidirectional carbon fiber reinforced plastic (CFRP). *Appl Mech Mater* 455:228–231
14. Standar Nasional Indonesia Persyaratan Beton Struktural untuk Bangunan Gedung (2013) SNI 2847:2013, Indonesia

Development Experimental Investigations of Truss Bridge Model for Vibration-Based Structural Health Monitoring



Sukamta, Angga Alfiannur, Susilo Adi Widyanto, and Han Ay Lie

Abstract In recent years the need for Structural Health Monitoring (SHM) has become increasingly important. Given current technological developments, a visual inspection can no longer be a reference due to inaccurate accuracy levels. In this case, there is a need for an early warning in detecting fast and accurate damage compared to visual inspection. This study proposes a vibration-based structural health monitoring analytical framework by introducing a modal analysis approach based on the bridges structural response. The test begins with making a small-scale model of a steel frame type bridge using the similarity model theory to project a prototype bridge. In this research, a damage simulation is given to the model to project damage to the structure. Static and dynamic tests are carrying to obtain the response characteristics of the structure. The assessment has delayed consequences exhibit that the variety of the supported discharge shows that contrasts look like the bend of the predominant recurrence that influences the FFT bend. Output values in natural frequency, mode shapes, and capital damping ratios were adopted as damage indicators. As a comparison, we are testing the model using FE simulation with a tolerance level of 10%. This research is using to build an SHM database system of the existing bridge structure model.

Keywords Vibration-based health monitoring · Steel bridges · Modal analysis · Small scale model

Sukamta (✉) · H. A. Lie

Department of Civil Engineering, Diponegoro University, Semarang, Indonesia

H. A. Lie

e-mail: hanaylie@live.undip.ac.id

A. Alfiannur

Master Program in Civil Engineering, Diponegoro University, Semarang, Indonesia

S. A. Widyanto

Department of Mechanical Engineering, Diponegoro University, Semarang, Indonesia

1 Introduction

Structural health monitoring (SHM) in recent years has become very important. Along with current technological developments and the many requests for monitoring, structural health monitoring such as bridges caused by deteriorating structural conditions due to age and damage due to natural disasters. Vibration-based SHM has become one of the efforts that have received attention in recent years to detect a malfunction [1, 2].

Damage detection methods are currently the most widely used visual observations made by bridge experts. This method is inaccurate and requires a long time, mainly if the observed bridge is locating in a difficult-to-reach location with large dimensions. Visual inspection is very dependent on the examiner's condition and, in certain conditions, can endanger the examiner itself. Also, structural damage is observing on exposed surfaces, and it is difficult to observe the damage that is hiding in nature, so it is not easily observed directly [3].

The vibration-based SHM technique requires identifying the dynamic characteristics of the bridge through field vibration measurements. Taking advantage of modern technology capabilities, such as vibration data, is obtained remotely, which allows for real-time monitoring of bridge conditions [4]. Damage that occurs in the structure causes changes in the stiffness and damping properties of the global structure so that it affects dynamic characteristics such as mode shape, natural frequency, and damping ratio [3, 5, 6]. The method of detecting damage using the vector shape mode as a feature generally analyzes the difference between the modal vectors measured before and after the damage. The mode shape vector is a spatially distributed number, and the data is using to detect damage [7].

The proposed vibration-based SHM approach can promise the ability to detect damage at the local level when problems related to sensitivity, low frequency, and mode shape result from local damage. Damage detection by changing the stiffness parameter using an updated finite element model utilizes data from a large number of sensors [1]. Time–frequency analysis is significant for damage detection because it is more sensitive to damage when the dynamics change from various conditions [8]. Another thing to note is that the optimal experimental design method refers to an algorithm to optimize the structures location and many sensors. The measurement data obtained contains the most important information for structural identification purposes.

In this study, the proposed framework uses a vibration mode in the form of deterministic vibrations. The amount of dynamic excitation (force or motion) acting on the system can be adjusting according to the need. The raw data from these vibrations are processed using Fast Fourier Transform to obtain the time domain signals vibration spectrum and determine the damaged structures natural frequency. The next process is to analyze the damping ratio to determine the degree of change in the structures attenuation characteristics when there is damage.

In these studies, structural testing in the Laboratory often requires a scaled model for testing. Bridges generally have large dimensions and heavy loads. Therefore, they

require a scale to suit laboratory facilities, costs, and testing schedules. However, the model scale is not an easy procedure, requiring the fulfilment of special requirements stemming from the same analysis. A steel truss bridge is using with the case study of Sendang Mulyo Bridge, Semarang Indonesia.

This research is the initial stage of SHM testing based on vibration, where this study models the actual bridge (Prototype) on a small scale. It aims to gain theoretical insight into global damage detection causes, leading to practical and useful vibration-based SHM.

2 Vibrate Mode

2.1 Fast Fourier Transform (FFT)

An appropriate numerical way for computers to determine the frequency and time domains response is the fast Fourier transform (FFT) [9]. With a single degree of freedom due to a force, the systems response is given by Eq. (1), which is expressed as an exponential function.

$$A(j) = \sum_{n=0}^{N-1} A^{(0)}(n) W_N^{jn} \tag{1}$$

where

$$W_N = e^{2\pi i/N} \tag{2}$$

The evaluation of addition will be more effective if the number of time increments of N, the divisor in period T, is a square number.

$$N = M^2 \tag{3}$$

M is an integer; in this case, the integers *j* and *n* were expressing in the “binary” form. As an illustration, consider a simple condition in which the load period is divide into eight increment intervals: N = 8, M = 3. In this situation, the indices have a binary form,

$$\begin{aligned} j &= j_0 + 2j_1 + 4j_2 \\ n &= n_0 + 2n_1 + 4n_2 \end{aligned} \tag{4}$$

and Eq. (3) can be written as

$$\begin{aligned}
A(j) &= \sum_{n_2=0}^1 \sum_{n_1=0}^1 \sum_{n_0=0}^1 A^{(0)}(n) W_8^{(j_0+2j_1+4j_2+)(n_0+2n_1+4n_2)} \\
W_8^{jn} &= W_8^{8(j_1n_2+2j_2n_2+j_2n_1)} W_8^{4n_2j_0} W_8^{2n_1(2j_1+j_0)} W_8^{n_0(4j_2+2j_1+j_0)} \quad (5)
\end{aligned}$$

It might be seeing that the principal factor on the privilege is worth one in light of Eq. (2).

$$W_8^{8I} = e^{2\pi i(8/8)I} = \cos 2\pi I + i \sin 2\pi I = 1 \quad (6)$$

where $I = j_1n_2 + 2j_2n_2 + j_2n_1$ is an integer. Therefore, only three factors remain that need to be considered in the summation.

These summations can be carried out accurately and persistently by introducing a new notation that indicates the addition process is the correct step. The first step that is showing is.

$$A^{(1)}(j_0, n_1, n_0) = \sum_{n=1}^1 A^{(0)}(n_2, n_1, n_0) W_8^{4n_2j_0} \quad (7)$$

where $A^{(0)}(n_2, n_1, n_0) = A^{(0)}(n)$ in Eq. (3) in the same way, do it for $M = 2$ and $M = 3$.

2.2 Half Power Bandwidth Method for Damping Analysis

The bandwidth method is the difference between two frequencies concerning the same amplitude response related to attenuation in a system [9]. The curved shape of the amplitude of a frequency is obtained experimentally for an ordinary damped structure. In the evaluation of damping, it is appropriate to measure the bandwidth at $1/\sqrt{2}$ times the amplitude given by Eq. (8) that is,

$$\frac{y_{st}}{\sqrt{(1-r^2)^2 + (2r\xi)^2}} = \frac{1}{\sqrt{2}} \frac{y_{st}}{2r\xi} \quad (8)$$

It is solving by squaring the two sides to give the frequency ratio.

$$r^2 = 1 - 2\xi\sqrt{1+\xi^2} \quad (9)$$

Finally, the damping ratio is giving almost half the difference between the frequency ratios of the two “half-powers,” that is,

$$\zeta = \frac{\omega b - \omega a}{2\omega n} \text{ a tau } \zeta = \frac{fb - fa}{2fn} \quad (10)$$

3 Experimental Program

3.1 Small Scale Bridge Bride for Model Fabrication

In this research, the case study (prototype) is the Sendang Mulyo Bridge, a steel-frame bridge built-in 1996 over a river for road traffic. Overall, the sections on the Sendang Mulyo Bridge consist of 3 parts, namely the side/horizontal part, the upper part (wind tie), and the lower part (deck), with a total length of the bridge of 53 m, a width of 9.3 m and a bridge height of 5 m. The type of steel profile used on the primary side is IWF 300.300.10.25, the upper side uses IWF 300.300.10.15, the upper (wind bond) uses 200.200.8.12, and the lower part (deck) uses IWF 300.300.10.15. The bridge consists of a composite deck of steel beams and reinforced concrete slabs with a thickness of 35 cm.

The prototype bridge was made into a small-scale bridge based on Pi Theorem Buckingham theory to get the bridges same characteristics [7]. The bridge model structure uses a 1:23 scale geometry determined based on the availability of types and profiles available in the market. In this study, the bridge model structure uses hollow steel 15×15 mm with 1.2 mm thickness. The connection between modules uses a steel plate with a 2 mm thickness using a steel bolt connection sized M4. To represent the road plane, the bridge model uses a 2 mm thick plate. In the deck, a welding connection system is using. Figure 1 shows the results of the small-scale model of the bridge.

3.2 Vibration Measurement Instruments

In this study, to simulate the load of vehicles passing the bridge, a dynamic loading system is used in the form of a rotating unbalance mass. The working system of an unbalance or excitation mass generator is a force generated from centrifugal force. The characteristics of the vibrations caused by excitation are deterministic (periodic) vibrations. The excitation forces magnitude was vibrated equal to the structure's natural frequency using the bump test method on a small-scale bridge model. Table 1 shows the specifications of the unbalance mass.

This study, accelerometer sensor uses a 3 Axis-ADXL 355 type sensor with a sensitivity of each axis (X, Y, Z) max is 330 mV / g. Each vibration sensor unit uses an accelerometer with a power system, signal conditional, and transmitter system. Two

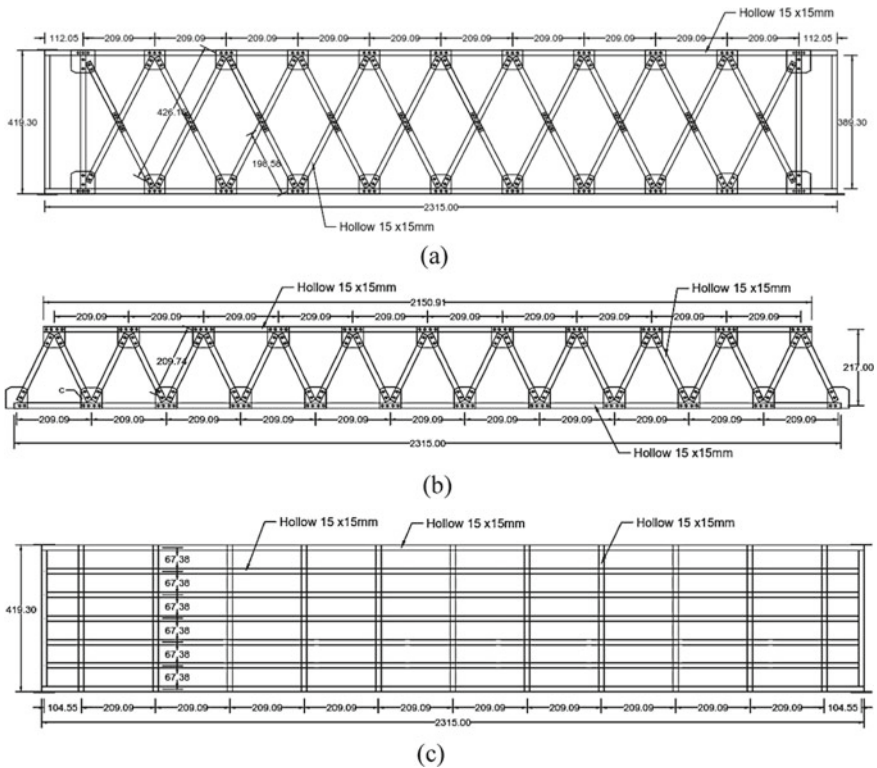


Fig. 1 Scale model 1:23: **a** Top view; **b** Side view; **c** Bottom view

Table 1 Specifications of unbalance mass

Specification	Unit	Value
Unbalance mass	g	5
Force	N	1064
Frequency	Hz	39–40
Turning radius	mm	10

accelerometer sensors are placed on the side diagonal bars to record the vibrations of the structure.

3.3 Simulation of Damage and Test Preparation

Table 2 presents the various damage simulations performed. The damage was simulating with two methods: the first method by performing the bar release (V-B) on the diagonal bar element. The second method is to reduce the bar inertia by 50% on the

Table 2 Damage simulation variations

Variation	Damage simulation position				Information
	V1	V2	V3	V4	
N	–	–	–	–	Normal
V-B	✓	✓	✓	✓	Bar release
V-50%	✓	✓	✓	✓	Bar inertia reduction 50%

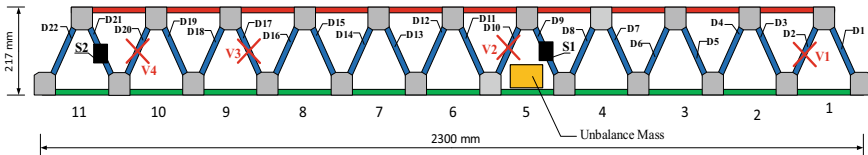


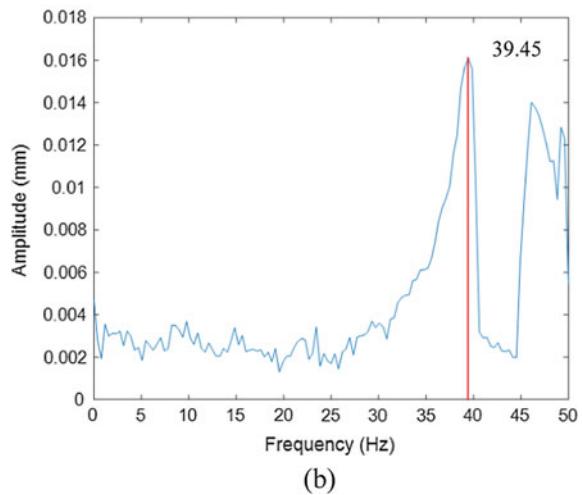
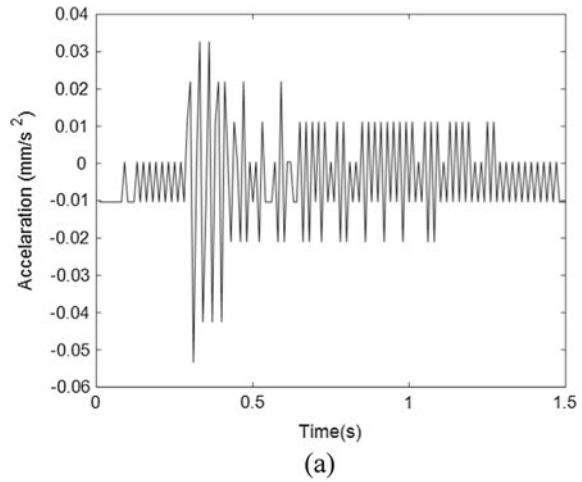
Fig. 2 Sensor position, excitation, and damage position

diagonal bar element (V-50%). The damage representation simulates a real-world vibration monitoring problem, where the location and size of the damage are both unknown. This study uses a variation of the V-B damage due to the software limited ability to compare experimental results with FE simulation. Damage simulation is useful for seeing the magnitude of changes in the vibration characteristics of the bridge model (Fig. 2).

Figure 3 presents the layout of the test settings and damage simulation. The sensor installation location considers the sensitivity of the sensor in detecting damage by paying attention to the position of the damaged bar and the mass load (excitation) on the bridge model. The dynamic excitation placement on the bridge deck is located on element 5. Sensor 1 (S1) is located close to the excitation/vibration source, namely on the diagonal rod element D9, and sensor 2 (S2) is located on the diagonal bar element D21 from the source of the vibration.

The initial process of testing the vibration mode is to perform a short test under Normal (N) conditions. In this condition, the bridge is new or not damaged. After getting the natural frequency from condition N, the next step is to test the damage simulation in the bar release condition (V-B). The simulation of V-B damage starts from position V1 to position V4. The position of V1 is on the diagonal bar D2, and then the rod will be released for vibration recording to be carried out. After obtaining the vibration mode data in condition V1, the diagonal bar D2 is again installed in its position and continued with V2, which is on the D10 bar for vibration mode recording. This process is valid until the position of V4 on the diagonal bar of D20. In the V-50% damage simulation, one new diagonal bar has reduced the inertia in the cross-section, replacing the diagonal bar installed at each damage simulation position. The stages of recording the vibration mode data in the V-50% condition is the same as during the V-B conditions.

Fig. 3 The results of the bump test on the bridge model: **a** Time-domain; **b** Frequency-domain



3.4 Data Processing

During the recording process, the data obtained is the time domain structure-acceleration (time-domain). The domain response is then transformed into a frequency-amplitude domain using the Fast Fourier Transform (FFT) method. The FFT transformation will see that the natural frequency of the structure is indicated by the frequency of the peak value of the frequency—amplitude (frequency domain) curve.

Data is usually seen on the frequency—amplitude curve on the response to vibration and structural disturbances (noise). Identification is needed to ensure that the

Table 3 Simulation model results for frequency

Variation	Frequency (Hz)
Normal	41.908
V1	42.191
V2	41.962
V3	40.529
V4	40.232

peak amplitude responds to structural vibrations, which will later obtain the structures natural frequency. The half-power bandwidth method is used to determine the vibration damping ratio. The final step is to simulate the bridge model using FE to get the theoretical natural frequency, which helps validate the bridge model experimental test results against the structures natural frequency.

4 Result and Discussion

4.1 Identification Natural Frequency FE Model

Table 3 shows the results of testing natural frequencies on the FEA and bar release variations. Modal analysis in the FEA model produces a natural frequency, wherein this study, the first mode form used for comparison with experimental model testing. In this mode, the type of vibration obtained is transverse bending.

The results of global vibration identification produce different frequency values. In the N condition, the natural frequency is 41.908 Hz. Natural frequency tends to decrease after damage simulation is carried out in a row from conditions V1, V2, V3, and V4 of 42.191, 41.962, 41.529, and 41.232 Hz. Changes in frequency occur due to deformation changes, which result in stress concentrations in the bridge model structure.

4.2 Natural Frequency of Bridge Model Structures

The natural frequency value of the bridge model is obtained using the bump test method. A bump test using a 12 N object dropped 10 cm into the bridge model deck center. The test results can be seen in Fig. 3.

From the results of the graphical FFT analysis shown in Fig. 3b, it can be seen that the natural vibration frequency of the structure is at a frequency of 39 to 40 Hz with a peak of 39.45 Hz. The natural frequency obtained is used to reference the vibrations magnitude, given by the excitation/signal generator.

4.3 V-B Vibration Mode Measurement

Before measuring the vibration on the bridge model structures condition, it is necessary to measure the frequency generated by excitation. Unbalance mass setting at a rotational speed of ± 2340 RPM or around 39–40 Hz. It was recorded in vibration mode for 10 s with a sampling rate of 100 samples/second. Especially for the V–B damage simulation, data collection is carried out on N, V1, V2, V3, and V4 for S1 and S2. The natural frequency analyzed by Fast Fourier Transform (FFT) between S1 and S2 produces a similar frequency. The difference occurs in the amplitude value of the vibration.

. At the resulting peak amplitude, not all of them can be identified as the natural frequency of the structure because there is noise such as the new peak amplitude, as shown in Fig. 4. To be able to identify which is a natural frequency or noise, repeated checking is done, which is the highest peak amplitude appears on every measurement or not. If the highest peak occurs at each measurement, the amplitude-frequency is the natural frequency of the structure.

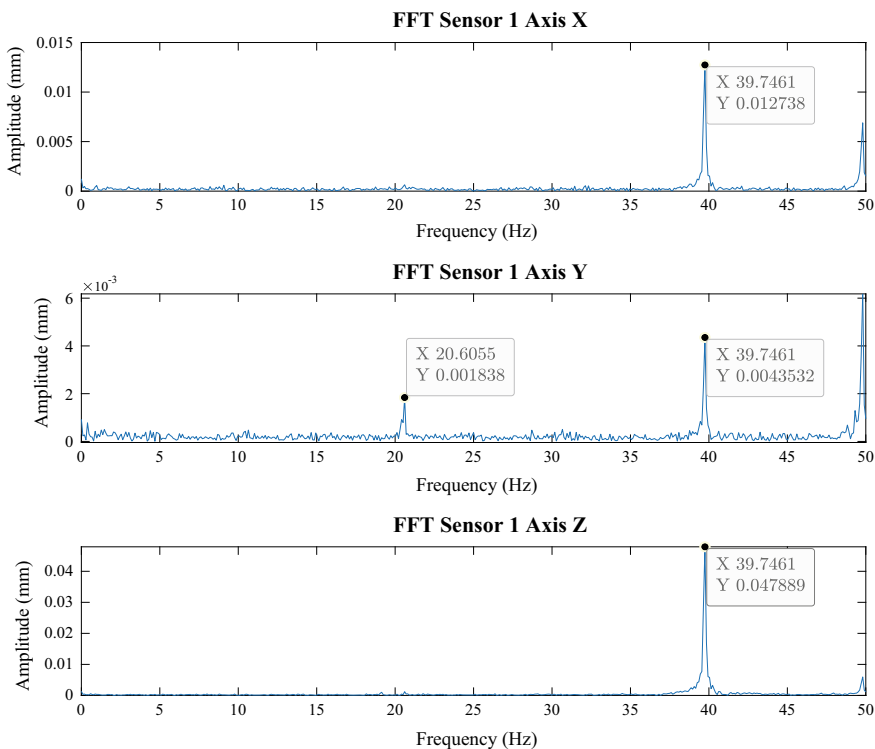


Fig. 4 The vibration mode test sample on sensor 1

Table 4 The natural frequency results (V-B)

Variation	Frequency (Hz)
N	39,746
V1	39,258
V2	39,648
V3	39,063
V4	39,648

The data from the measurement results of the vibration mode in Table 4 shows that the simulated damage affects the natural frequency of the structure. The frequency obtained in N conditions for normal conditions is 39,746 Hz. The V-B damage simulation displays condition frequency V1, V2, V3, and V4, respectively 39,258, 39,648, 39,063, and 39,648 Hz.

Figure 5 shows a graph comparing the amplitude results on each axis recorded on sensor 1. The comparison results show that the amplitude value has increased compared to the N or “normal” condition, with the Z-axis largest deviation. The higher the amplitude was resulting from the vibration, the greater the disturbance/damage to the structure.

The location of the excitation also affects the high amplitude as a source of vibration. The position of V2, which is close to the vibration source, produces the highest vibration amplitude with a value of 0.0722 mm. The position of V4 farthest from the source of the vibration produces the lowest amplitude with a value of 0.0272 mm.

Figure 6 shows a graph comparing the amplitude results on each axis recorded on sensor 2. Based on the observations, the S2 sensor’s location, far from the excitation, results in a much smaller amplitude than the S1 sensor. The largest deviation is on the Z-axis, with the highest amplitude occurring in condition V2, namely 0.0390 mm, and the lowest amplitude occurring in condition V4 with a value of 0.0191 mm.

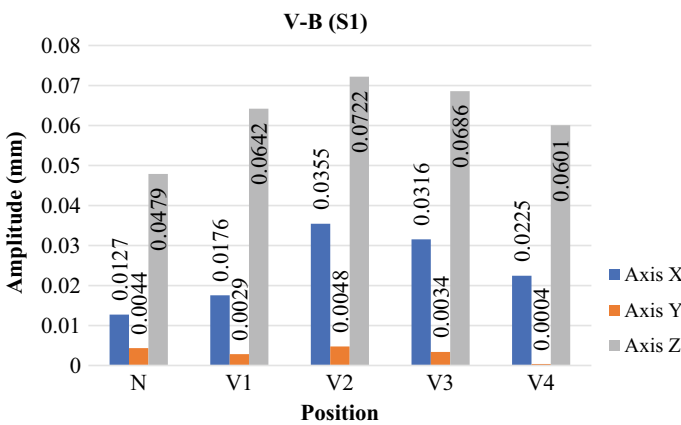


Fig. 5 Comparison of V-B (S1) amplitudes on each axis

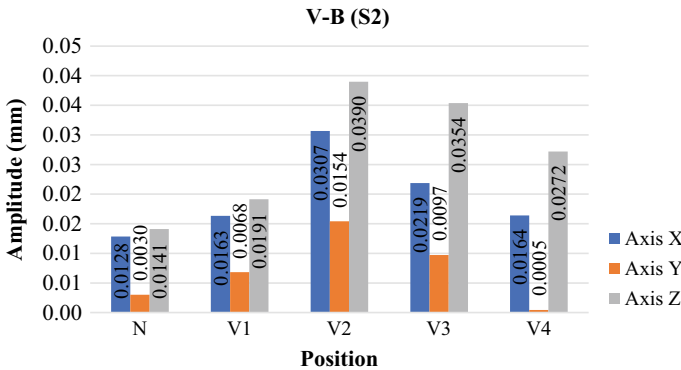


Fig. 6 Comparison of V-B (S2) amplitudes on each axis

4.4 V-50% Vibration Mode Measurement

Table 5 shows the natural frequency of the V-50% damage simulation. The damage simulation V-50% of data collection is at positions on V1, V2, V3, and V4. The natural frequency analyzed by Fast Fourier Transform (FFT) produces natural frequencies in a row from conditions V1, V2, V3, and V4 are 39.648, 39.551, 39.746, and 39.746 Hz.

Figure 7 shows the results of the amplitude comparison of the results of the FFT analysis at S1. The test results show that the dominant amplitude is on the Z-axis for S1. Position V2 provides the highest amplitude with a value of 0.0618 mm for S1. Simultaneously, the lowest value is in the V4 position, with a value of 0.0487 mm. The reason occurs because the position of V2 is close to the source of the vibration. Inversely proportional to the position of the V4, which is far from the source of the vibration.

Figure 8 shows the results of the amplitude comparison of the results of the FFT analysis on S2. The test results on S2 show the same amplitude characteristics as in S1. Position V2 provides the highest amplitude with a value of 0.0219 mm for S1. Simultaneously, the lowest value is in the V4 position, with a value of 0.0138 mm. The reason occurs because the position of V2 is close to the source of the vibration. Inversely proportional to the position of the V4, which is far from the source of the vibration.

Table 5 The natural frequency results (V-50%)

Variation	Frequency (Hz)
V1	39,648
V2	39,551
V3	39,746
V4	39,746

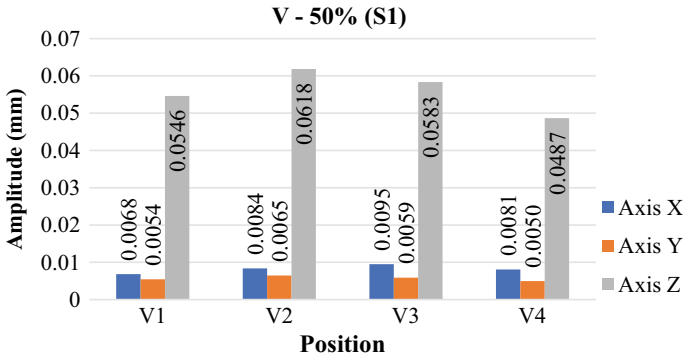


Fig. 7 Comparison of V-50% (S1) amplitudes on each axis

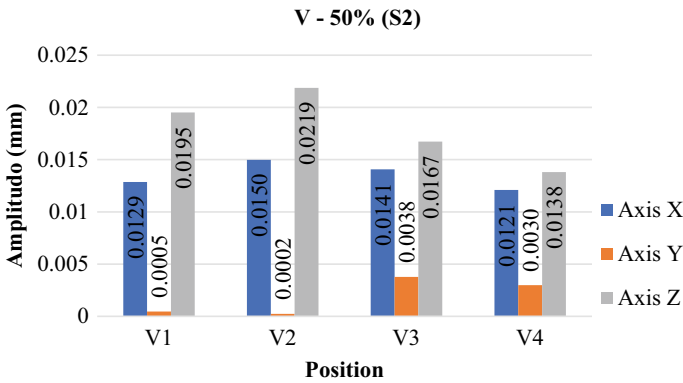


Fig. 8 Comparison of V-50% (S2) amplitudes on each axis

4.5 Comparison of FE Modeling Results versus Bridge Model

Comparing the natural value of the measured frequency due to dynamic load in the FEA model and the experimental model shows relatively good value. The difference resulting from the natural frequency is relatively small, with an error rate of below 10%.

Table 6 compares the natural frequency values in the FE and experimental models. The experimental model shows the highest error rate of 7% at position V2 with a frequency value of 42,191 Hz for the FE model and 39,258 Hz for the experimental model. The lowest error rate is 4% at position V4. This proves that the designed bridge model has a reasonably high similarity in structural characteristics to the FE model simulation.

Table 6 Comparison of frequency results

Position	Frequency (Hz)		Error (%)
	FE	Experimental	
N	41,908	39,746	5
V1	42,191	39,258	7
V2	41,962	39,648	6
V3	41,592	39,063	6
V4	41,232	39,648	4

Table 7 V-B case damping ratio

Position	Sensor 1 (%)	Sensor 2 (%)
V1	0.224	0.229
V2	0.098	0.098
V3	0.145	0.144
V4	0.276	0.283

Table 8 V-50% case damping ratio

Position	Sensor 1 (%)	Sensor 2 (%)
V1	0.096	0.094
V2	0.088	0.087
V3	0.107	0.107
V4	0.282	0.278

4.6 The Damping Ratio of the Great Model

In this damping ratio analysis using the highest amplitude on the Z-axis, then by using Eq. 10, the damping ratio of the structure is obtained, as shown in Tables 7 and 8.

The structural damping ratio analysis on the V-B and V-50% damage simulations above show that the damage simulation performed on the V-B case produces a better damping ratio than the V-50% case. Thus, the damage simulation will affect the damping that occurs in the bridge model due to the decreased structural stiffness.

4.7 Evaluation

In the three-damage simulation model, the bridge model produces varying amplitudes. Figure 9 compares the amplitude results based on three simulations of the damage change in amplitude. The highest amplitude value is used, namely on the Z-axis.

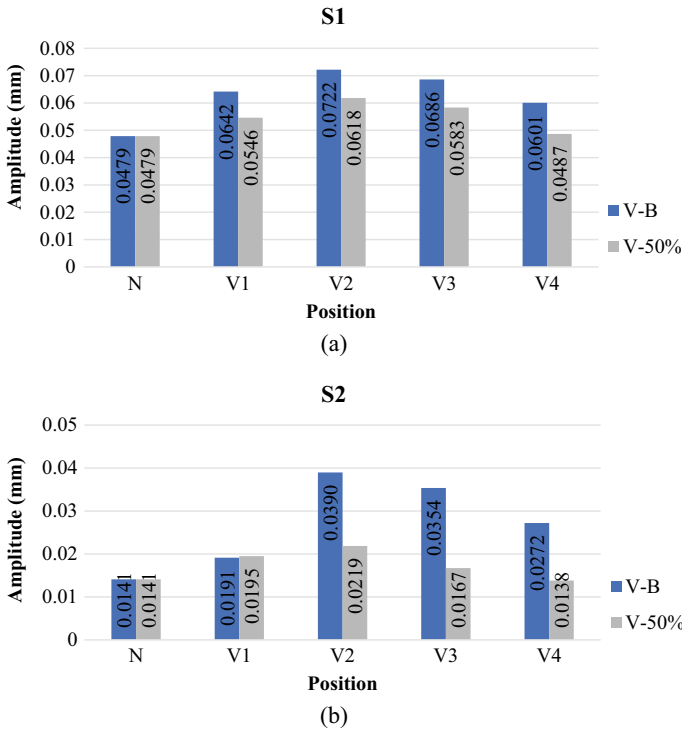


Fig. 9 Comparison of amplitude at V-B and V-50% damage simulation model: **a** sensor 1; **b** sensor 2

Figure 9 shows the comparison of the damage simulation results, namely V-B and V-50% for S1 and S2. The change in amplitude that occurs in the case of V-B damage simulation shows a significant increase. The normal condition (N) comes from the damage simulation V-B, wherein in this condition, the bridge model is in good condition, and then the vibration mode measurements are taken. The level of change in the amplitude of S1 to the damage condition shows that the average increase for the V-P case compared to when the N condition is 38%, and for the V-50% case, it is 17%. For S1, the average increase in the V-B case compared to the N condition was 114%, and for the V-60% case, it was 27%.

Overall, this test succeeded in detecting structural damage locally by looking at amplitude changes based on frequency changes under normal conditions (N) and after damage simulations. When the condition is new or in good condition, the characteristics of the bridge model structure will change characteristics if there is damage to the structure. As a result, the vibration mode generated on the bridge in the form of amplitude tends to increase. Amplitude is a characteristic that shows how much damage has been done. The higher the amplitude obtained, the greater the disturbance/damage that occurs in the structure. The test results [10] show that the differences in natural frequency and amplitude give different responses to vibration mode

and component deformation; this is due to deflection that occurs due to material type, configuration, defects, and others.

5 Conclusion

In this study, the approach taken for monitoring the health of the bridge structure is to use a vibration-based method, which is then carried out by small-scale modeling of the bridge prototype for laboratory testing. The main conclusions of this study are as follows:

1. The natural structure frequency is 39–40 Hz from the vibration test results, with a peak of 39.45 Hz.
2. The natural frequency resulting from normal conditions and four damage positions against the V-B damage simulation in the FE model and the experimental model shows an error rate of below 10%. The most significant error value of 7% in condition V1, and the lowest value of 4% in condition V4.
3. Comparing amplitude measurements in V-P and V-50% shows an increase in amplitude after simulating damage to normal conditions.
4. The characteristics of the bridge model structure when the condition is new or in good condition will change characteristics if there is damage to the structure. As a result, the vibratory mode generated on the bridge in the form of amplitude tends to increase. The amplitude itself is a characteristic that shows how much damage has occurred. The higher the amplitude is showing, the greater the disturbance/damage that occurs in the structure.

The proposed vibration-based SHM approach successfully detects structural damage locally by looking at amplitude changes based on frequency changes under normal conditions (N) and after damage simulation. However, in actual structural conditions, the damage can be caused by various factors such as natural conditions and types of damping. Therefore, this research is still in its early stages. Further, development is needed to model structural damping and change factors in amplitude to identify defects more precisely.

Acknowledgements The author would like to thank the Diponegoro University Structure and Materials Laboratory and the Diponegoro University CNC production process and Laboratory for their assistance in completing this research.

References

1. Mustafa S, Matsumoto Y, Yamaguchi H (2017) Vibration-based health monitoring of an existing truss bridge using energy-based damping evaluation. *J Bridg Eng* 23(1):04017114. [https://doi.org/10.1061/\(asce\)be.1943-5592.0001159](https://doi.org/10.1061/(asce)be.1943-5592.0001159)

2. Feng D, Feng MQ (2016) Output-only damage detection using vehicle-induced displacement response and mode shape curvature index. *Struct Control Heal Monit* 23(8):1088–1107. <https://doi.org/10.1002/stc.1829>
3. Adi Widyanto S, Widodo Sukamta A, Suprihanto A, Yusuf Tornado F, Nugroho C (2014) Karakteristik peredaman getaran konstruksi model jembatan untuk pengembangan sistem diagnosis pola gagal. pp 776–785
4. Ntotsios E, Papadimitriou C, Panetsos P, Karaiskos G, Perros K, Perdikaris PC (2009) Bridge health monitoring system based on vibration measurements. *Bull Earthq Eng* 7(2):469–483. <https://doi.org/10.1007/s10518-008-9067-4>
5. Mustafa S, Matsumoto Y (2017) Bayesian model updating and its limitations for detecting local damage of an existing truss bridge. *J Bridg Eng* 22(7):1–14. [https://doi.org/10.1061/\(ASCE\)BE.1943-5592.0001044](https://doi.org/10.1061/(ASCE)BE.1943-5592.0001044)
6. Abdo MA-B (2014) In: *Structural health monitoring history, applications and future*. 1st edn. New York, Open Science
7. Farrar CR, Doebling SW, Nix DA (2001) Vibration-based structural damage identification. *Philos Trans R Soc A Math Phys Eng Sci* 359(1778):131–149. <https://doi.org/10.1098/rsta.2000.0717>
8. Pan H, Azimi M, Yan F, Lin Z (2018) Time-frequency-based data-driven structural diagnosis and damage detection for cable-stayed bridges. *J Bridg Eng* 23(6):1–22. [https://doi.org/10.1061/\(ASCE\)BE.1943-5592.0001199](https://doi.org/10.1061/(ASCE)BE.1943-5592.0001199)
9. Paz M (1993) In: *Dinamika Struktur Teori & Perhitungan*, 2nd edn. Jakarta, Erlangga
10. Ofrial MTA, Noerochim L, Hidayat MIP (2017) Analisis Numerikal Frekuensi Natural Pada Poros low pressure boiler feed pump PT.PJB UP Gresik. *J Tek ITS* 6(1). <https://doi.org/10.12962/j23373539.v6i1.21080>

Parameter Identification of Bouc-Wen Model Using Firefly Algorithm



Richard Frans, Yoyong Arfiadi, and Junaedi Utomo

Abstract Bouc-Wen (BW) model is widely used in civil engineering applications, especially for assessing the nonlinear behavior of structural elements. In structural engineering, the BW model is used to explain the hysteretic behavior of systems in a simple mathematical form. This model is well-known because of its versatility in producing a variety of hysteretic characteristics of systems. The basic idea of the BW model is to match the data obtained from the experimental test or analytical solution with the model's output by using a curve fitting technique. Generally, four parameters need to be identified in the BW model. To obtain the parameters of the BW model, the optimization technique is used. One of the most suitable methods that give an excellent result to obtain the optimized variables is the firefly algorithm (FA). The theory of FA is based on firefly behavior that consists of two important variables, i.e., attractiveness and variation of the light intensity. This paper presents FA method to identify the parameters of the BW model based on the finite element analysis results. The objective function is the root mean square error (RMSE) between finite element results and the predicted model. The data used for curve fitting in this paper are force and displacement that are obtained from finite element analysis. In the present work, several types of structural elements are considered, i.e., steel dampers, castellated beams, and composite castellated beams. The results show a good agreement between the finite element results and the identified model from the optimization.

Keywords Bouc-Wen model · Parameter identification · Hysteretic behavior · Optimization · Firefly algorithm

R. Frans (✉)

Department of Civil Engineering, Universitas Atma Jaya Makassar, Makassar, Indonesia

Y. Arfiadi · J. Utomo

Department of Civil Engineering, Universitas Atma Jaya Yogyakarta, Yogyakarta, Indonesia

e-mail: yoyong.ar@uajy.ac.id

1 Introduction

The nonlinear behavior of structures is very important to be established. With the nonlinear behavior, the strength, stiffness, or collapse mechanism of a structure can be accurately predicted. However, formulating a mathematical model of the nonlinear behavior is a challenging task. Many mathematical models were recently developed to fit nonlinear behavior, such as the Masing model, the pseudo elastic constitutive model, and the Bouc-Wen model [1]. One of the most mathematical models that is very simple, precise, and easy to construct the nonlinear behavior is the Bouc-Wen (BW) model [2–4]. Because of its ability, the BW model becomes more popular than others and has been widely developed by many researchers in various applications. Modified Bouc-Wen model by Wang and Wen, normalized Bouc-Wen model, Bouc-Wen-Baber-Noori model, and asymmetric hysteresis are examples of the enhanced BW models [5–8].

BW model is used to predict the structure's nonlinear behavior, including determining the energy dissipation of each cycle of structural systems. These include determining the energy dissipation of dampers (metallic damper, MR-damper, passive damper, active damper, semi-active damper, and hybrid damper), beam-column joint, reinforced concrete structure and steel structure performance, especially against cyclic loading (earthquake loading or wind loading), and many more. With the mathematical formulation of BW model, the energy dissipation can be accurately and easily obtained. This formulation can be also considered as the alternative to calculate energy dissipations, in addition to the theory of energy-based model proposed by Climent [9].

This paper presents the determination of hysteresis parameters of BW model using the firefly algorithm (FA) with the root mean square error (RMSE) as the objective function. Three cases of steel dampers and one model of composite castellated beams subjected to a quasi-static loading are considered in this paper.

2 Survey of the Literature

Kwok et al. used Genetic Algorithm to obtain the model parameters of a non-symmetrical Bouc-Wen model. The Genetic Algorithm that used in this research was improved with the absorption of the selection stage into the crossover and mutation operations. Besides, the crossover and mutation operations were made adaptive corresponding to the fitness value such that no need for user specified. To satisfy the parameters identification results, experimental data was compared with the proposed approach [10].

Charalampakis and Dimou conducted a comparison study of Differential Evolution (DE), Particle Swarm Optimization (PSO), and Genetic Algorithms (GA) in order to identify the Bouc-Wen model parameters. Full-scale bolted-welded steel connection conducted by Popov and Stephen was considered as the case study. The

objective function used was the Mean Square Error (MSE) of the predicted and reference time history. The results show that DE outperforms PSO and GA [11, 12].

Zhu and Lu used BW to model the load–displacement curve of mild steel damper that has been experimentally conducted by Xu. The mild steel damper was subjected to a cyclic loading using a displacement control with triangle signal where the frequency equals to 0.01 Hz. Five parameters of BW, i.e., k_x , k_y , ρ , σ , and n , were needed to be identified. The result shows the experimental model fits with the predicted BW model [13, 14].

Sengupta and Li presented an analytical approach based on the modified Bouc-Wen-Baber-Noori (BWBN) model to predict the hysteresis behavior of reinforced concrete beam-column joint with limited transverse reinforcement. The resulted BWBN is able to predict the characteristics of non-seismic beam-column joints, i.e., stiffness, strength degradation, and pinching. To solve the differential equation of the BWBN model and to obtain the hysteresis parameters associated with the BWBN model, the combinations of Livermore Solver for Ordinary Differential Equations (LSODE) and GA have been employed. The objective function used is the RMSE of the response. The analytical BWBN model was calibrated with the experimental result considering interior and exterior beam-column joints from several pieces of literatures. There were 14 hysteresis parameters of BWBN model (α_0 , ω_0 , ξ_0 , β , γ , n , δ_v , δ_η , ζ_s , q , p , ψ , δ_ψ , λ) have to be identified. The results showed that there are strong correlations between the shear force and horizontal deflection obtained from the experimental and the BWBN model for any type of beam-column joint (interior and exterior). Moreover, the hysteresis parameters can be instantly estimated without using any system identification; and the hysteresis of a beam-column joint can be obtained using the estimated hysteresis parameters with any kind of solver [7, 15].

Wang and Lu identify the parameters of BW hysteretic model using time-domain measured data. The parameters were treated as an optimization problem using least square method as the objective function. An enhanced response sensitivity approach was adopted to solve the optimization problem. Several numerical tests were conducted for verifying the proposed identification approach, with measurement noise of 0 and 5%. The result shows that all parameters were well identified using the proposed approach [16].

Solovoyov et al. considered the “efficiency” of linear viscous, nonlinear viscous, and hysteretic dampers which based on BW model. The results show that the hysteretic damper has high efficiency both in and outside of the resonance region compared to the other dampers [17].

Bartkowski et al. used a modified BW hysteresis model to describe the nonlinear properties of cylindrical samples made of vacuum-packed particles. Seven parameters were considered in this study. All parameters of BW model were identified using Genetic Algorithm (GA). Although the proposed model is found to be in good agreement with the experimental results, for an accurate calibration of the BW model, more GA should be performed. It also requires supplementary experimental research for enhancing the uniqueness of the solution and for ensuring the correctness of the identification process [18].

Zhang et al. investigated the asymmetric hysteretic characteristic piezoelectric ceramic actuators. To obtain the parameters of BW model and to make a comparison, the optimization techniques, i.e., GA, PSO, and GA-PSO, were used in this paper. The modified BW model used to be the hysteretic model, where seven parameters, i.e. k_1 , k_2 , α , β , g , n , δ , need to be found using the algorithms. Six different iteration numbers were taken (80, 100, 150, 200, 250, and 300) to see the convergence characteristics of the algorithms. The objective function was to minimize the root mean square error (RMSE) of displacement measured by experimental and the displacement computed using BW model. The result shows that PSO results in the highest objective function, followed by GA. The lowest value is obtained from GA-PSO. This concludes that the GA-PSO algorithm was more accurate compared to GA or PSO. This is caused by the features strong searching ability both in the local or global condition of GA-PSO compared to the PSO, which is easily trapped in the local extremum [19].

Negash et al. proposed a novel genetic algorithm (nGA) to estimate the Bouc-Wen parameters for magnetorheological (MR) fluid dampers. To obtain the Bouc-Wen parameters, simulation output forces was compared with the magnetorheological (MR) forces generated by experimental testing. The performance evaluation considered three variables such as the mean absolute error, standard deviation and number of generations for convergence. The result shows that the accuracy obtained using nGA was increase 46.67% compared to the ordinary Genetic Algorithm (GA) [20].

3 Bouc-Wen Model Representation

The Bouc-Wen (BW) model is widely used to describe the nonlinear hysteretic system. This model was first proposed by Bouc [2, 3] and extended by Wen [4]. The advantage of the BW model is because it is versatile in producing variations of hysteretic patterns. It can represent smooth, bi-linear, softening, hardening, pinching, strength/stiffness degradations, as well as asymmetrical hysteretic curves [2–4, 8].

The mathematical formulation of BW models is based on a nonlinear differential equation. Considered the equation of motion of single degree of freedom (SDOF) as follows:

$$m\ddot{u}_{(t)} + c\dot{u}_{(t)} + F_{(t)} = f_t \quad (1)$$

where, m is mass, c is linear viscous damping coefficient, $\ddot{u}_{(t)}$ is acceleration based on time- t , $\dot{u}_{(t)}$ is velocity based on time- t , $F_{(t)}$ is restoring force based on time- t , and f_t is excitation force based on time- t .

According to the BW model, the restoring force $F_{(t)}$ is represented by:

$$F_{(t)} = a \frac{F_y}{u_y} u_{(t)} + (1 - a) F_y z_{(t)} \quad (2)$$

where F_y is yield force, u_y is yield displacement, a is ratio of post yield stiffness to pre yield stiffness, and $z_{(t)}$ is hysteretic displacement which obeys the nonlinear differential equation with initial condition is zero. The restoring force can also be decomposed into an elastic part (first term) and hysteretic parts (second term) which is like two springs connected in parallel.

$$F_{(t)} = F_{(t)}^{elp} + F_{(t)}^{hlp} \tag{3}$$

The equation of hysteretic displacement follows:

$$\dot{z}_{(t)} = A\dot{u}_{(t)} - \beta|\dot{u}_{(t)}||z_{(t)}|^{n-1}z_{(t)} - \gamma\dot{u}_{(t)}|z_{(t)}|^n \tag{4}$$

where A , β , γ , and n are dimensionless quantities to control the patterns of the hysteretic curve. These four variables can be determined using experimental input and output data; and can be accomplished using system identification techniques such as Extended Kalman Filter, Genetic Algorithms, Particle Swarm Optimization, Differential Evolution, etc. By taking the root mean square error between the observed and actual data as the objective function, all variables involved in the model can be determined. For the illustration, the hysteresis patterns of BW model are shown in Fig. 1.

4 Firefly Algorithm (FA)

Firefly Algorithm (FA) is based on the behavior of firefly and was first proposed by Yang. In the FA, two factors, i.e. attractiveness and variation of the light intensity, are very significant to achieve the objective. The attractiveness is controlled by the brightness of the firefly that corresponds to the objective function [21].

The basic equation in FA is to determine the movement of a firefly i that is attracted by another. More attractive (brighter) firefly j is obtained by using:

$$x_i^{t+1} = x_i^t + \beta_0 e^{-\gamma r_{ij}^2} (x_j^t - x_i^t) + \alpha \varepsilon_i^t \tag{5}$$

where the second term composed of β_0 , i.e., the attractiveness at zero distance ($r = 0$), and $e^{-\gamma r_{ij}^2}$ is due to attraction; while the third term contains α is the randomization parameter (mutation parameter), and ε_i^t is a random vector numbers based on Gaussian distribution or uniform distribution at time t .

In general, the basic step of the firefly algorithm (FA) can be summarized as follow:

1. Initiate an initial population of n fireflies x_i^t ($i = 1, 2, 3, 4, \dots, n$).
2. Determine the light intensity I_i at x_i which is according to the objective function, $f(x_i^t)$.

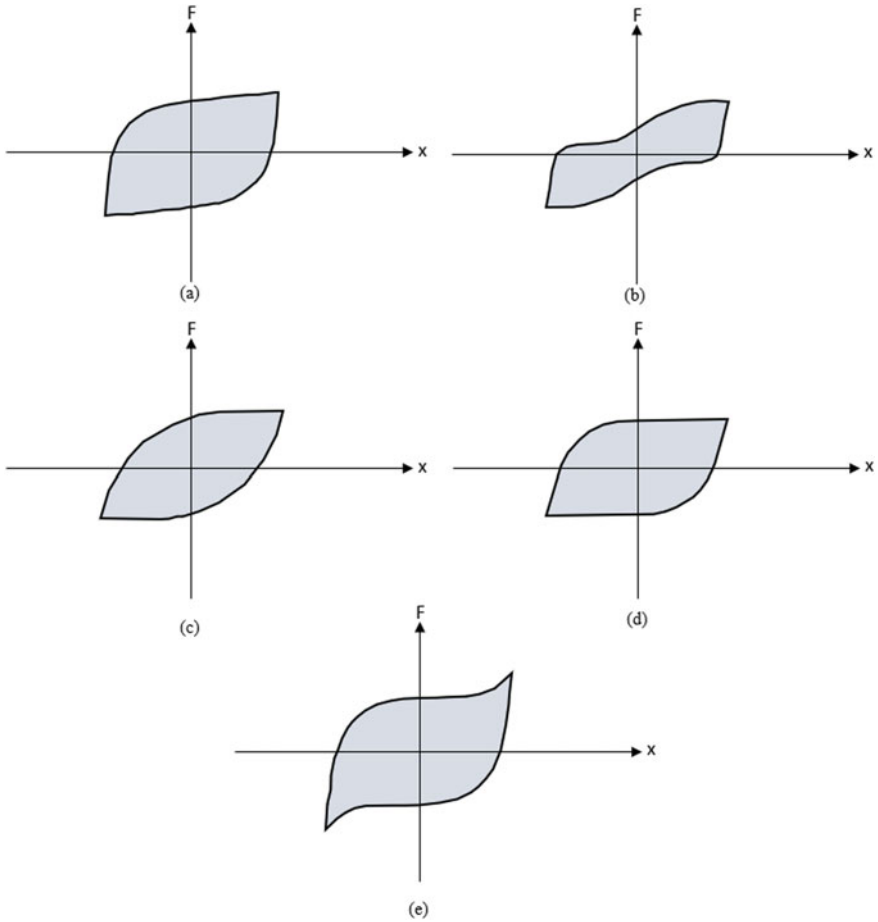


Fig. 1 **a** Basic hysteresis loop, **b** Pinching, **c** Stiffness deterioration, **d** Asymmetric yield force, **e** Strain hardening [11]

3. Define light absorption coefficient γ .
4. For $i = 1:n$ (all fireflies)
 - For $j = 1:n$ (all fireflies)
 - If $I_i < I_j$
 - Moving the firefly from i to j using equation (5)
 - end if
 - Evaluate new solutions and update the light intensity
 - end for loop j
 - end for loop i
5. Rank the fireflies and find the current global best g^* .

6. Post process results and visualization.

FA is a special algorithm that can be considered as a more general algorithm that can turn into Differential Evolution (DE), Simulated Annealing (SA), and Accelerated Particle Swarm Optimization (APSO), as discussed in [20]. Its general form and ability are shown in Eq. (5). FA will become a variant of DE when γ is very small ($\gamma \rightarrow 0$) and $\alpha = 0$. If γ is very large, the second term in Eq. (5) becomes negligible, and the FA becomes SA. Furthermore when x_i^t is replaced by g^* , FA will become APSO. Therefore, FA can be considered as a combination of three algorithms; hence it becomes more efficient than other algorithms such as Genetic Algorithm (GA) and Particle Swarm Optimization (PSO) [22].

5 Fitness Value and Objective Function

In order to obtain the hysteretic parameters of Bouc-Wen model (A, β, γ, n), the root mean square error (RMSE) was chosen as the objective function. Because the optimization problem is to minimize the value of the RMSE, the fitness equation of objective function as follows

$$fitness = \sqrt{\sum_{i=1}^N \frac{(F_{BW} - F_{EXP})^2}{N}} \tag{6}$$

where F_{BW} is the restoring force from BW model, F_{EXP} is restoring force from experimental data, and N is number of data considered.

According to Eq. (6), the lower fitness value means the better agreement between experimental results and the BW model. Otherwise, the higher fitness value obtained means that the experimental results and the BW model will not fit one to another.

The coding of FA, calculation and optimization process were done using MATLAB software [23, 24].

6 Case Studies

There are 4 case studies considered in this paper which are circular hollow steel damper (CHSD), hexagonal hollow steel damper (HHSD), Vertical steel pipe damper and composite castellated beam. In order to identify four Bouc-Wen parameters (A, β, γ and n) of each case study, the FA algorithm was used. The parameters were represented as the firefly. To find out the four parameters, the objective function used was to minimize the RMSE value of the force–displacement curve obtained from finite element analysis and predicted model (BW model) using the curve fitting technique.

6.1 Circular Hollow Steel Damper (CHSD)

A circular hollow steel damper CHSD, where the section geometry is shown in Fig. 2 with the thickness of 20 mm was considered. The material properties of the CHSD can be found in Table 1. The material was modelled to follow elastic–full plastic behavior. ABAQUS was used to model the CHSD [25, 26].

A quasi-static loading of the triangular form was used as the displacement applied to the structure, with the maximum displacement of 60 mm. Only one cycle loading was considered as shown in Fig. 3. The optimization parameters used in this problem can be seen in Table 2.

Figure 4 shows the comparison of the load–displacement curve of CHSD obtained from the numerical model and BW model; while Fig. 5 shows the comparison of the load-time curve obtained by numerical model and BW model. The hysteretic parameters obtained for BW model using FA are $A = 0.8238$, $\beta = 0.0256$, $\gamma = 0.3885$, and $n = 0.0067$.

From Figs. 4 and 5, it can be seen that the result of BW model fits the numerical model for the load–displacement curve as well as the load-time curve.

Fig. 2 Section geometry of CHSD

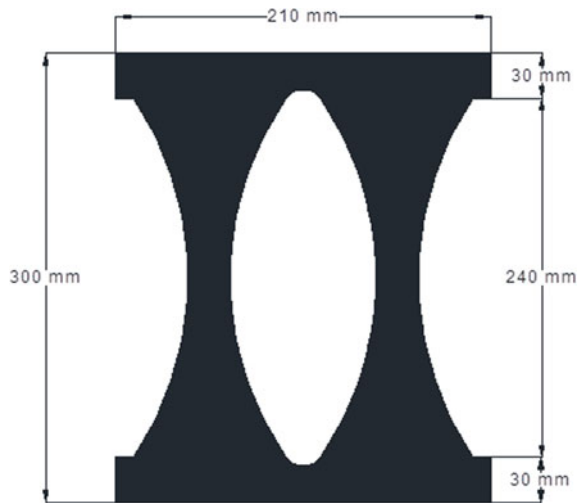


Table 1 Material properties of CHSD

Material properties		
Modulus of elasticity (E)	200,000	MPa
Yield stress (F_y)	330	MPa
Poisson ratio (ν)	0.3	

Fig. 3 Loading pattern of CHSD

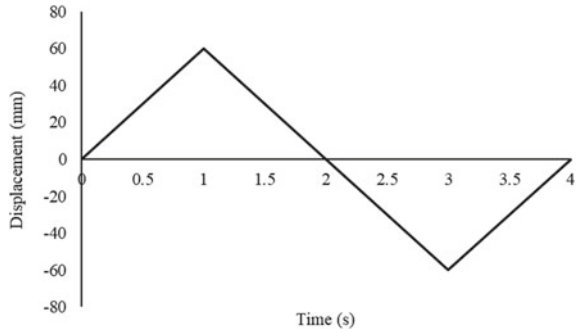


Table 2 Optimization parameters of FA

Maximum iterations	400
Number of fireflies	5
Light absorption coefficient (γ)	0.3
Mutation parameter (α)	0.2
Lower bound	0
Upper bound	1

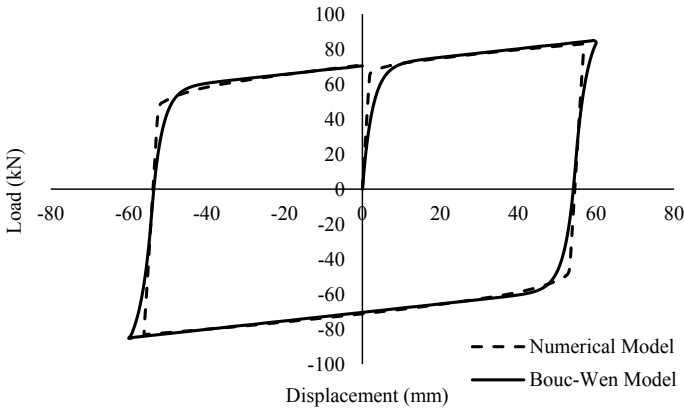


Fig. 4 Comparison the load–displacement curve of CHSD for numerical model and BW model

6.2 Hexagonal Hollow Steel Damper (HHSD)

The second case damper considered in this paper is similar to the first case but with different geometry. In the first case, the opening is an elliptical shape, while in the second case is a hexagonal shape as a hexagonal hollow steel damper (HHSD). The material properties and the loading history are taken the same as in the previous case.

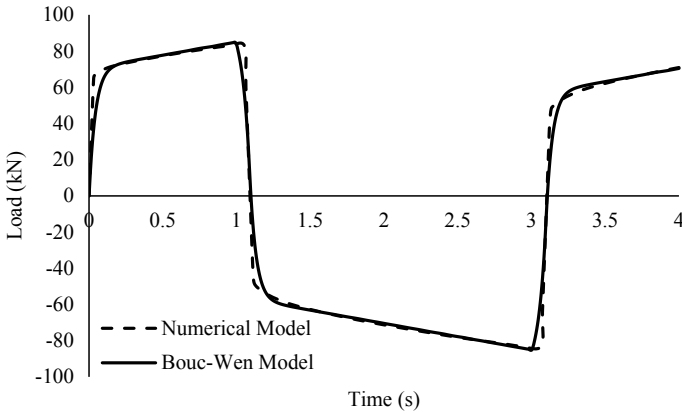


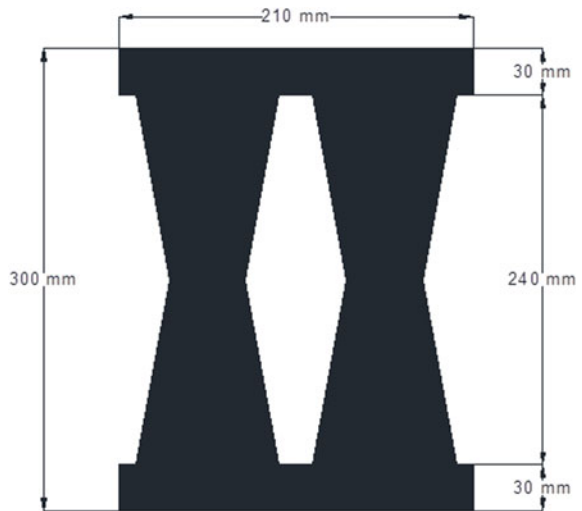
Fig. 5 Comparison the load-time curve of CHSD for numerical model and BW model

(Table 1 and Fig. 3). The geometry of HHSD can be found in Fig. 6. The optimization parameters also follow Table 2.

Figures 7 and 8, respectively, are the load–displacement curve and the load-time curve of HHSD subjected to the same quasi-static loading.

According to Figs. 7 and 8, there is no significant difference between the load–displacement curve and the load-time curve obtained from both numerical and BW model. It can be considered that the BW model fits the numerical model. The hysteresis parameters obtained for the second case are $A = 0.8435$, $\beta = 0.2360$, $\gamma = 0.0436$, and $n = 0.0021$.

Fig. 6 Section geometry of HHSD



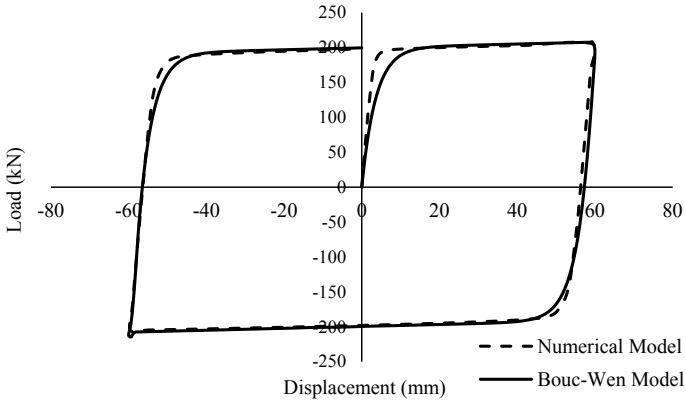


Fig. 7 The load–displacement curve for numerical model and BW model of HHSD

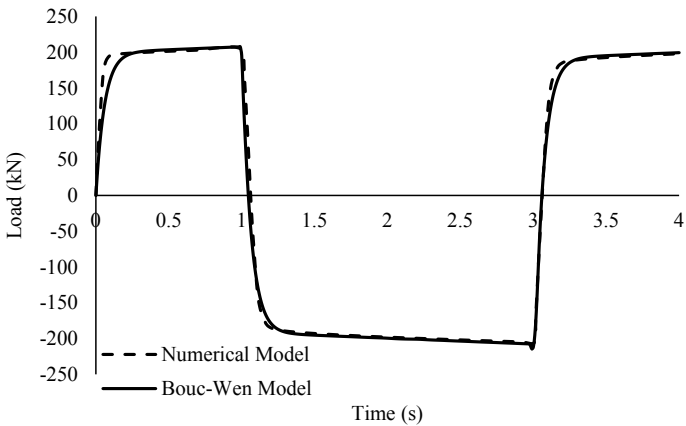


Fig. 8 The load-time curve for numerical model and BW model of HHSD

6.3 Vertical Steel Pipe Damper

For the third case, the hysteretic behavior of a vertical steel pipe damper was considered. The metallic dampers, especially steel pipe dampers, have been developed extensively [25–27], where experimental and numerical simulation has been conducted to vertical steel pipe dampers strengthened by trapezoidal plates and inner rings or horizontal steel pipe damper strengthened by outer rings, etc. [27–29]. But only one type of steel damper is considered in this paper that is vertical steel pipe damper. Figure 9 shows the vertical steel pipe dampers considered in this paper.

The material properties of vertical steel pipe damper can be found on Table 3. ABAQUS was chosen to model and analyze the behavior of vertical steel pipe damper.

Fig. 9 Vertical steel pipe damper

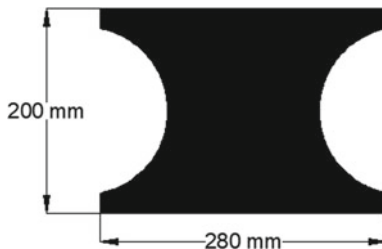


Table 3 Material properties of vertical steel pipe damper

Density (ρ)	7850 kg/m ³	
Modulus of elasticity (E)	210,000	MPa
Yield stress (F_y)	320	MPa
Poisson ratio (ν)	0.3	

In the original paper, the vertical steel pipe damper has been subjected to ultra-low cycle fatigue (ULCF) with four loading conditions to find the hysteretic behavior of the vertical steel pipe damper, especially its energy dissipation. In this paper, only one cycle loading is considered to illustrate the BW model. The maximum displacement used is 30 mm, where the same triangular loading was used in the simulation. The loading history can be seen in Fig. 10. The optimization parameters of FA are taken the same as before.

Figures 11 and 12 show the load–displacement curve and the load-time curve of the numerical model and the BW model, respectively.

The results show the parameters obtained for the BW model are $A = 0.8617$, $\beta = 0.1358$, $\gamma = 0.1781$, and $n = 0.0012$. It can be seen from Figs.11 and 12 that both load–displacement and load-time curves fit each other, except for the yield and the

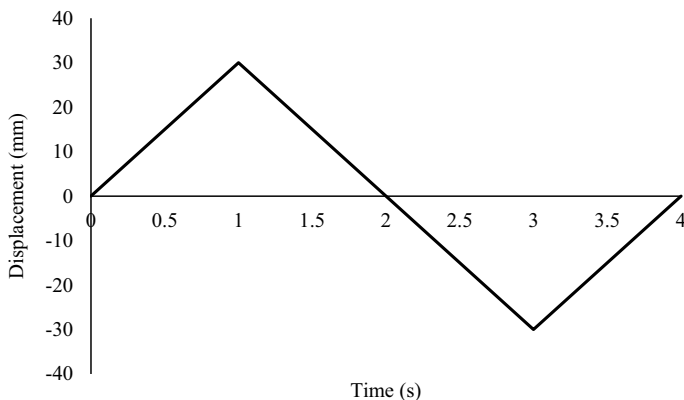


Fig. 10 The loading history of vertical steel pipe damper subjected to triangle cyclic loading

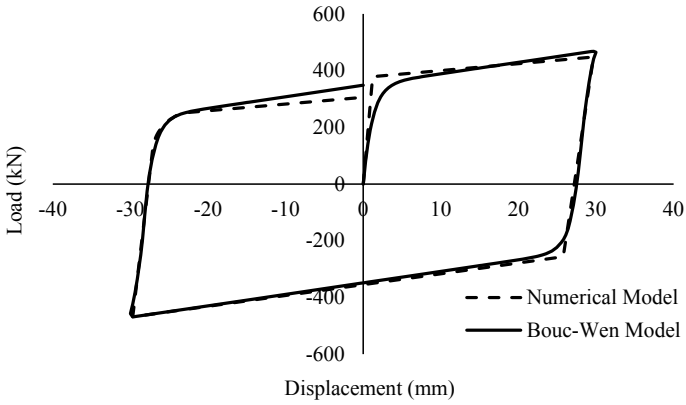


Fig. 11 Comparison the load–displacement curve of vertical steel pipe model for numerical model and BW model

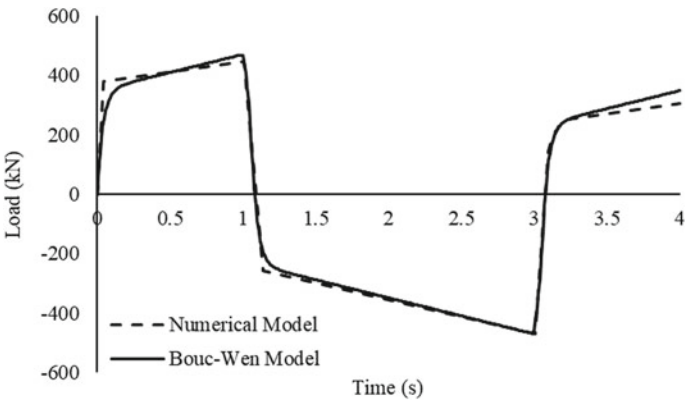


Fig. 12 Comparison the load-time curve of vertical steel pipe model for numerical model and BW model

last points. For the yield point, the numerical model shows a linear behavior from the initial condition to the yield point; while for the BW model, the behavior is nonlinear from the initial condition to the yield point due to the continuity function used in the BW model. For the last point of loading, when the displacement went back to zero, the restoring forces for numerical and BW models are, respectively, 305.883 kN and 348.6257 kN. These differences are due to the asymmetric behavior obtained in the numerical model that has not been considered in the current BW model. To obtain a better result, an asymmetrical hysteresis BW model is suggested to be used. If the asymmetric BW model is used, it will cause more computational time since more hysteresis parameters are presents in the model.

Table 4 Material properties of composite castellated beam

Steel profile		
Modulus of elasticity (E)	210,000	MPa
Yield stress (F_y)	300	MPa
Ultimate stress (F_u)	420	MPa
Poisson ratio (u)	0.3	
Mass density	7850	kg/m ³
Steel rebar		
Modulus of elasticity (E)	210,000	MPa
Yield stress (F_y)	415	MPa
Ultimate stress (F_u)	550	MPa
Poisson ratio (u)	0.3	
Mass density	7850	kg/m ³
Concrete		
Modulus of elasticity (E)	30,000	MPa
Compressive strength (f_c')	41	MPa
Poisson ratio (u)	0.2	
Mass density	2400	kg/m ³

6.4 Composite Castellated Beam

The fourth case study considered here is a composite castellated beam. The composite castellated beam is a composite beam structure with a combination of steel beam and reinforced concrete slab. The composite castellated beam in this study is taken from Frans et al. [30], where numerical analysis using shell element via finite element analysis (ABAQUS) were conducted. The original model was taken from Prakash et al. [31] that observed the behavior of a composite beam subjected to a monotonic loading and made a comparison between the result obtained from numerical and experimental tests [30, 31]. The only difference is that the composited castellated beam was performed under monotonic loading in the previous research, while in the present study, the composite castellated beam is subjected to cyclic loading. The material properties of steel, rebar, and concrete are shown in Table 4. Figure 13 shows the composite castellated beam used to be observed. The loading history is shown in Fig. 14.

The hysteresis parameters obtained are $A = 0.9764$, $\beta = 0.0413$, $\gamma = 0.0739$, and $n = 0.0734$. The load–displacement and the load-time history are shown in Figs. 15 and 16, respectively. Refer to Figs. 15 and 16, the load–displacement curve and the load-time history for both model (numerical and BW models) match to each other.

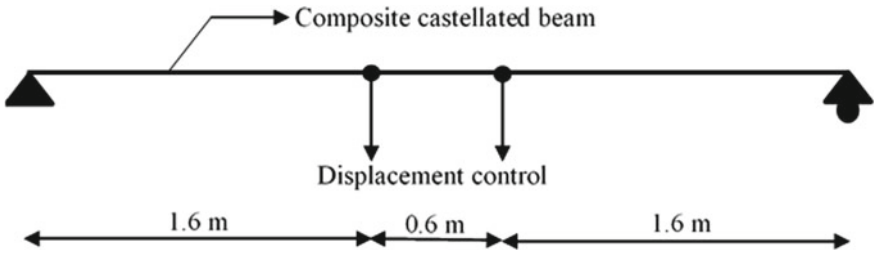


Fig. 13 Composite castellated beam

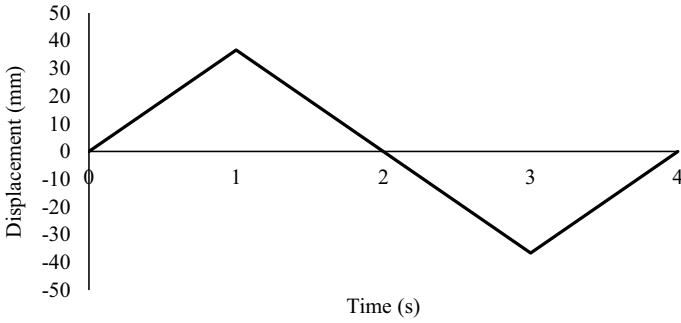


Fig. 14 Loading history of the composite castellated beam

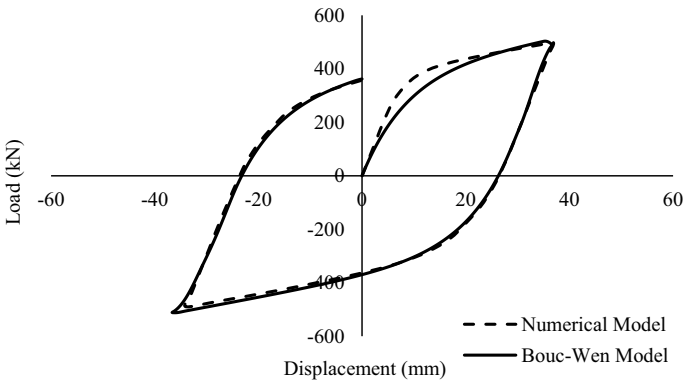


Fig. 15 Comparison the load–displacement curve of composite castellated beam for numerical model and BW model

7 Conclusions

In this present study, a FA is employed to identify the hysteresis parameters of several structural elements. A simple BW model is used, where four hysteresis parameters

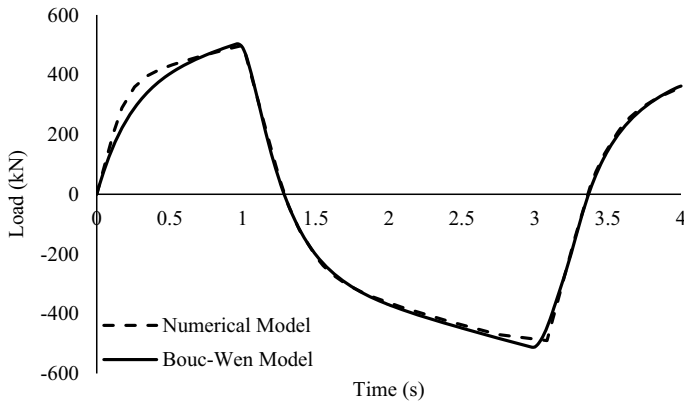


Fig. 16 Comparison the load-time curve of composite castellated beam for numerical model and BW model

are needed to be obtained (A , β , γ , and n). The objective function is to minimize the RMSE of the restoring force between the numerical model and BW model. The results showed that FA can satisfactorily be used and has the ability to identify the hysteresis parameters for all study cases that can be seen from the load–displacement curve and load-time history between the numerical and BW models.

References

1. Lacarbonara W, Vestroni F (2012) Nonlinear phenomena in hysteretic systems. In: IUTAM symposium on 50 years of chaos: applied and theoretical on Procedia IUTAM 5. Elsevier, Kyoto-Japan, pp 69–77
2. Bouc R (1967) Forced vibration of mechanical systems with hysteresis. In: Proceedings of the fourth conference on nonlinear oscillation. Prague, Czechoslovakia, pp 315
3. Bouc R (1971) Modèle mathématique d'hystérésis: application aux systèmes à un degré de liberté". *Acustica* 24:16–25
4. Wen YK (1976) Method for random vibration of hysteretic systems. *J Eng Mech* 102(2):249–263
5. Wang CH, Wen YK (2000) Evaluation of pre-northridge low-rise steel buildings. I: Model J *Struct Eng* 126(10):1–39
6. Ikhouane F, Rodellar J (2005) On the hysteretic Bouc-Wen model. *Nonlinear Dyn* 42:63–78
7. Baber TT, Noori MN (1985) Random vibration of degrading, pinching systems. *J Eng Mech* 111(8):1010–1026
8. Song J, Kiureghian DA (2006) Generalized Bouc-Wen model for highly asymmetric hysteresis. *J Eng Mech* 132(6):610–618
9. Climent B (2007) An energy-based damage model for seismic response of steel structures. *Earthquake Eng Struct Dynam* 36:1049–1060
10. Kwok NM, Ha QP, Nguyen MT, Li J, Samali B (2007) Bouc-Wen model parameter identification for a MR fluid damper using computationally efficient GA. *ISA Trans* 46(2):167–179
11. Charalampakis AE, Dimou CK (2011) A comparison of differential evolution, particle swarm optimization and genetic algorithms for the identification of Bouc-Wen hysteretic systems.

- In: Proceedings of the second international conference on soft computing technology in civil, structural and environmental engineering, vol 48. Civil-Comp press, Scotland, pp 1–16
12. Popov EP, Stephen RM (1972) Cyclic loading of full-size steel connections. Center for cold-formed steel structures library, United States
 13. Zhu X, Lu X (2011) Parametric identification of Bouc-Wen model and its application in mild steel damper modelling. *Proc Eng* 14:318–324
 14. Xu CE (2008) Study on energy dissipation and seismic mitigation performance of HADAS damper. MSc Thesis. Tongji University
 15. Sengupta P, Li B (2013) Modified Bouc-Wen model for hysteresis behavior of RC beam-column joints with limited transverse reinforcement. *Eng Struct* 46:392–406
 16. Wang L, Lu ZR (2017) Identification of Bouc-Wen hysteretic parameters based on enhance response sensitivity approach. In: 12th international conference on damage assessment of structures in IOP conference series: journal of physics: conf. series, vol 842. IOP Publishing, Japan, pp 1–8
 17. Solovyov AM, Semenov ME, Meleshenko PA, Barsukov AI (2017) Bouc-Wen model of hysteretic damping. In: 3rd international conference “information technology and nanotechnology” on procedia engineering, vol 201. Elsevier, Russia, pp 549–555
 18. Bartkowski P, Zalewski R, Chodkiewicz P (2019) Parameter identification of Bouc-Wen model for vacuum packed particles based on genetic algorithm. *Archiv Civil Mech Eng* 19:322–333
 19. Zhang Q, Dong Y, Peng Y, Luo J, Xie S, Pu H (2019) Asymmetric Bouc-Wen hysteresis modelling and inverse compensation for piezoelectric actuator via a genetic algorithm-based particle swarm optimization identification algorithm. *J Intell Mater Syst Struct* 00:1–13
 20. Negash BA, You W, Lee J (2020) Parameter identification of Bouc-Wen model for magnetorheological (MR) fluid damper by a novel genetic algorithm. *Adv Mech Eng* 12(8):1–12
 21. Yang XS (2010) Nature-inspired metaheuristic algorithm, 2nd edn. Luniver Press, United Kingdom
 22. Yang XS (2014) Nature-inspired metaheuristic algorithm, 1st edn. Elsevier, London
 23. MathWorks (2015) MATLAB: primer, Version 8.6. The Mathworks, Inc, United States
 24. MathWorks (2015) MATLAB: programming fundamental, Version 8.6. The Math-works, Inc., United States
 25. Inc A (2016) ABAQUS analysis user’s guide. Dassault Systemmes Corp, USA
 26. Abaqus (2005) Inc.: User’s Manual I-III. Version 6.5. Dassault Systemmes Corp, USA
 27. Utomo J, Moestopo M, Surahman A, Kusumastuti D (2015) Estimating the ultimate energy dissipation capacity of steel dampers. In: The 5th international conference of euro asia civil engineering forum in procedia engineering, vol 125. Elsevier, Indonesia, pp 1101–1107
 28. Utomo J, Moestopo M, Surahman A, Kusumastuti D (2015) Studi eksperimental perilaku siklus pendisipasi energi pipa tegak. In: Konfrensi nasional teknik sipil 9 in Proceedings of Konfrensi nasional teknik sipil 9, BMPPTSSI, Indonesia, pp 831–838
 29. Utomo J (2017) Pengembangan pendisipasi energi dari pipa baja untuk proteksi seismik bangunan. PhD Dissertation. Institut Teknologi Bandung, Indonesia
 30. Frans R, Parung H, Muhiddin AB, Irmawaty R (2017) Finite element modelling of composite castellated beam. In: Euro asia of civil engineering forum 2017 on MATEC web of conferences. EDP Sciences, Seoul-South Korea, vol 138. pp 1–9
 31. Prakash AN, Anandayalli NCK, Madheswaran CK, Rajasankar JN, Lakshmanan N (2011) Three dimensional FE model of stud connected steel-concrete composite girders subjected to monotonical loading. *Int J Mech Appl* 1:1–11

Mechanical Properties of Fly Ash Bottom Ash (FABA) Geopolymer Hybrid Concrete Using Portland Cement



Monita Olivia, Rizky Noviandri, Gunawan Wibisono,
and Iskandar Romey Sitompul

Abstract The accumulation of fly ash bottom ash (FABA) as solid waste from coal power station has increased each year significantly; hence, one of the immediate solutions is to use FABA as a cement replacement material. The FABA could be stabilized/solidified by activating the FABA with the alkaline activator to produce a geopolymer. The geopolymer concrete usually undergoes a fast reaction at a high temperature curing with excellent mechanical properties and low early shrinkage values. The geopolymer hybrid is produced by combining the geopolymer material with Portland cement (Portland Composite Cement) in a certain percentage to assist a fast strength gain at ambient curing. In this paper, the mechanical properties and shrinkage of the FABA geopolymer hybrid concrete were presented. A control mix was the Portland Composite Cement (PCC) concrete. Compressive strength, tensile strength and flexural strength are studied at 7, 28 and 91 days. The shrinkage values recorded up to 28 days were also determined. The results show the optimum mix consisted of 12 M NaOH, Ms ratio of 2.5, and PCC of 15%. Samples were mixed, cast and cured until the testing date (28 days) at room temperature. The FABA geopolymer hybrid concrete showed a significant change in strength by 29.5% than the PCC concrete by 13.77% at 28 days. At 91 days, the strength of PCC and the geopolymer hybrid were changed by 33.57% and 37.93%, respectively. In general, both tensile and flexural strength of the FABA geopolymer hybrid concrete followed the same trend from compressive strength. The FABA geopolymer hybrid cured at the ambient temperature had significantly higher shrinkage than that of the PCC concrete. This condition leads to an early fine crack observed in the FABA geopolymer hybrid although it has comparable mechanical properties with the PCC concrete.

M. Olivia (✉) · R. Noviandri · G. Wibisono · I. R. Sitompul
Department of Civil Engineering, Universitas Riau, Pekanbaru, Indonesia

R. Noviandri
e-mail: rizky.noviandri@student.unri.ac.id

G. Wibisono
e-mail: g.wibisono@eng.unri.ac.id

I. R. Sitompul
e-mail: iskandar.romey@lecturer.unri.ac.id

Keywords Fly ash bottom ash · Geopolymer hybrid · Mechanical properties · Shrinkage · Portland cement

1 Introduction

Demand for materials by construction industries have increased substantially in the past decades. Solid waste from industrial by-products become a potential substitute as a solution to overcome a shortage of raw binder materials in nature. The activated solid waste such as fly ash with the alkaline solution was applied as a substitute binder of cement particles in concrete. A mix of sodium hydroxide and sodium silicate was an activator to react and bind the silicate in the source materials. This method is known as geopolymerization and the product is called fly ash-based geopolymer [1]. Previous studies have stated that physical properties, mechanical properties, and durability of the geopolymer concrete are comparable or higher than the conventional concrete [2–5].

The geopolymer uses a high temperature curing to assist reaction and hardening process. However, high-temperature curing is more energy-consuming and more suitable for precast concrete compared to ambient temperature curing. In one study, the geopolymer cured at the ambient temperature could be produced by modifying fly ash reactivity, mineralogical composition, and sodium silicate quantity [6]. Other researchers have added Portland Cement (PC), slag, and nano-silica, into the geopolymer mixtures to improve fresh properties, mechanical properties and durability at ambient temperature [7–9]. The material is known as the geopolymer hybrid because it contains a mineral additive that acts as a catalyst to increase the geopolymerization at the ambient temperature. It usually has a fly ash content of 70–80 wt % and a low OPC clinker content (20–30 wt %). The produced geopolymer hybrid gels are known as (C, N)–A–S–H or N–(C)–A–S–H from a reaction of OPC cement and fly ash geopolymer [10–12].

Portland cement (PC) as an additive or replacement material on geopolymer hybrid was investigated in some studies [13–17]. The Portland cement used was in the range of 0–50% in an increment of 10% of the fly ash by weight. Inclusion of PC improves setting time, workability, durability, and mechanical strengths of geopolymer concrete at room temperature. The properties of the geopolymer concrete are considered suitable for application. Workability dropped, however, the compressive strength slightly increased when PC content increased in the mixture. Nath and Sarker [16] reported that addition of PC content up to 6% in geopolymer has increased the flexural strength. However, Young's Modulus of Elasticity value dropped by 25–30% than that of the OPC concrete, and showed no difference in values between ambient and high-temperature curing. The Portland cement improved the strength due to a fast reaction by the calcium that promotes the geopolymerization because of the exothermic reaction in the system [18]. The optimal Portland cement content clearly defines the strength gain and development of the geopolymer at room temperature.

Approximately 5.2 million tonnes of by product or fly ash and bottom ash from the energy industry was produced in Indonesia annually [19]. A mix of fly ash bottom ash (FABA) as a mean of efficiency by the industry could be used as a cement replacement material and geopolymer primary material. The FABA consists of fly ash (80%) and bottom ash (20%). Previous studies related to FABA as a cement replacement material in blended, high volume and geopolymer concrete were conducted [20]. Findings show although it has a low quality, the early strength properties of the FABA concrete imposed in peat water was excellent. Characteristics of the FABA geopolymer hybrid has been studied, and leaching of heavy metals in peat water was reported by Wijaya et al. [21]. The heavy metals' leaching was significantly lower than the permissible limit of heavy metals in complying with USEPA (The United States Environmental Protection Agency) and the PP (Indonesian Government Regulations) limits. Although the FABA geopolymer hybrid concrete has been studied for its physical and environmental characteristics, there was a limited report of tensile strength, flexural strength, and shrinkage. In this study, the mechanical properties of FABA geopolymer hybrid and drying shrinkage were determined by study its characteristics and to gain more acceptance in the application.

2 Materials and Methods

2.1 Materials

Fly ash bottom ash (FABA) as the main ingredient of the geopolymer was taken from Ombilin region in West Sumatra, Indonesia. The ashes have dark-grey particles because of the high carbon content of 18.89%. The FABA particles could be seen in Fig. 1.

Fig. 1 Fly ash bottom ash (FABA) used in this study



Table 1 The chemical composition of PCC and FABAs

Oxides (%)	Portland composite cement (PCC) [23, 24]	Fly ash bottom ash (FABA)
SiO ₂	23.04	59.25
Al ₂ O ₃	7.40	29.25
Fe ₂ O ₃	3.36	5.45
MgO	0.63	0.31
CaO	57.38	1.54
Na ₂ O	–	0.68
K ₂ O	–	2.23
Na ₂ O + 0.658K ₂ O	0.52	–
P ₂ O ₅	–	0.04
SO ₃	1.78	0.29
LOI	–	–
Others	5.89	0.84

Chemical composition of the FABAs and PCC is presented in Table 1. The FABAs particles have 59.25% of SiO₂, 29.25% of Al₂O₃ and 5.45% of Fe₂O₃. Based on the ASTM C618-9 [22], the FABAs is Class F. The alkaline activator used was a mix of commercially available Na₂SiO₃ (sodium silicate) and NaOH (sodium hydroxide). The Na₂SiO₃ has SiO₂ of 31.71%, Na₂O of 14.56%, total solid of 46.27%, the mol ratio of 2.26, a density of 1.56 g/mL and the Baume scale of 52. Coarse aggregates from Kampar Regency, Riau Province, had a specific gravity of 2.61 and water absorption of 3.35%. Fine aggregates from the same quarry were used with a specific gravity of 2.76 and water absorption of 3.63%. Portland Composite Cement (PCC) produced in West Sumatra as an accelerator for curing at ambient temperature. A high range water reducer superplasticizer with a quantity of 1% by cement weight was used in the mixture to increase the workability of the geopolymer hybrid.

2.2 Preparation, Casting, and Curing of Test Specimens

The optimum parameters for FABAs geopolymer hybrid (FABAs-GP) mixtures were taken from a previous study by Wijaya et al. [21]. The studied parameters were 10, 12, and 14 M NaOH, Ms ratio (Na₂SiO₃/NaOH) of 2, 2.5 and 3.0 and percentage of PCC cement of 10, 15 and 20% of FABAs by weight. In this study, the PCC cement was used to replace FABAs in the mix. According to the study, the optimum values of the parameters to produce moderate strength were 12 M NaOH, Ms ratio of 2.5, and 15% of PCC. Based on the optimum parameters, the FABAs-GP was calculated. The mix had an alkaline activator/FABAs ratio of 0.60 and used extra water of 80 kg/m³. The PCC concrete is a control mix with a 28 days target strength of 20 MPa. The PCC and the FABAs-GP concrete mix design was presented in Table 2.

Table 2 A mix design of PCC and FABAs geopolymers hybrid concrete

Ingredients	Type of concrete	
	PCC (kg/m ³)	FABA-GP (kg/m ³)
FABA	–	446.25
Fine aggregates	660.34	546
Coarse aggregates	1014	1014
NaOH	–	90
Na ₂ SiO ₃	–	225
Superplasticizer	–	7.88
Cement	410	78.75
Extra water	195.88	80

The initial step in producing FABAs-GP was to blend all the dry ingredients for few minutes. The dry ingredients were coarse aggregates, fine aggregates and fly ash. The alkaline activator was a mix of NaOH, sodium silicate and superplasticizer. Subsequently, after the dry ingredients were uniformly mixed, the activator solution was poured slowly to the mix. The mix was blended for 5 min, and the PCC cement was added into the mix to produce the FABAs-GP concrete.

The slump values of the PCC concrete were 100 mm, while the FABAs-GP was 125 mm. The PCC concrete samples were cast and cured in a pond for 28 days before its dried in an ambient temperature before the testing date. The FABAs-GP concrete samples were air-cured until the testing days. The compressive strength specimens were cast in 105 mm × 210 mm cylinders. Samples of tensile strength and shrinkage tests used were 150 mm × 300 mm cylinders. The flexural strength test used beams with a size of 150 mm × 150 mm × 600 mm. Triplicate samples were used for each variation. Data was reported as the average of three samples.

2.3 Testing of Specimens

Triplicate specimens were tested at 7, 28 and 91 days to measure the tensile strength, flexural strength and shrinkage. Specified strength at 91 days was taken to accommodate a slow strength gain of FABAs-GP concrete. The slump test was carried based on SNI 1972:2008 [25]. The compressive strength and tensile strength were determined using SNI 1974:2011 and SNI 2941:2014 [26, 27]. The flexural strength test was conducted based on SNI 4431:2011 [28]. The shrinkage measurement was taken with ASTM C157/C157M-08 [29].

2.4 Predicted Tensile and Flexural Strength Equations

The predicted tensile and flexural strength was calculated based on the approximate relationship between those experimental properties with compressive strength values. Based on ACI Code 318-14 [30], the relationship between the compressive strength and the tensile strength (f_t) is defined as:

$$f_t = 0.56\sqrt{f'c} \quad (1)$$

where $\sqrt{f'c}$ is the specified compressive strength.

The characteristic flexural strength ($f_{ct,f}$) according to ACI Code 318-14 can be calculated as follows:

$$f_{ct,f} = 0.62\sqrt{f'c} \quad (2)$$

where $\sqrt{f'c}$ is the specified compressive strength.

3 Results and Discussion

3.1 Slump, Density and Compressive Strength

Table 3 shows the slump, density and compressive strength values of PCC and FABAGP concrete at 7, 28 and 91 days. The workability of FABAGP was approximately 16.7% lower than the PCC mix. This could be due to a very low extra water content, a sticky nature of sodium silicate and a PCC content in the mixture. It could be seen the density of the FABAGP concrete was below the range of the PCC concrete. The density of the PCC concrete was between 2.3397 and 2.5526 g/cm³. FABAGP samples had lower density than PCC samples with values between 2.0016 to 2.0366 g/cm³. The FABAG replacement in the mixture has changed the density, and

Table 3 Slump, density and compressive strength of PCC and FABAGP concrete

Mix	Slump (mm)	Concrete age (days)	Density (g/cm ³)	Compressive strength (MPa)	SD
PCC	±150	7	2.5526	19.35	0.60
		28	2.2776	22.44	1.05
		91	2.3397	26.69	0.89
FABAGP	±125	7	2.0366	12.66	0.63
		28	2.0016	17.95	0.60
		91	2.0221	19.06	0.57

made the FABAs-GP lighter than the PCC concrete. The number of fine aggregates in the FABAs-GP mix was 17.10% lower than the PCC mix could also determine the final concrete density.

Table 3 also shows the compressive strength of both PCC and FABAs-GP concrete. In general, both concrete had approximately $\pm 10\%$ difference than the target strength of 20 MPa. The compressive strength of the PCC mix was higher than that of the FABAs-GP concrete. The strength of the PCC was about 20% higher than the FABAs-GP mix at 28 days. This could be due to a different mechanism of the FABAs-GP that contains more silicate and slow geopolymerization process to develop strength at ambient temperature. Ideally, the geopolymerization needs a room temperature curing (rest period) and a high temperature curing to enhance the compressive strength [31]. Although the PCC has been included in the FABAs-GP mix, the cement itself contains pozzolanic materials that could delay the strength gain at early ages. Zhang et al. [31] stated that the strength in the geopolymer mixture using cement is weaker than high-temperature curing, but still beneficial for cast-in-situ method. Another factor that influences the final strength of the FABAs-GP was w/b (water to binder ratio) in the mix. The strength probably could be improved by decreasing the water to binder ratio; however it was not achievable for a large batch pouring in this study. This could be a reason a lower strength of the FABAs-GP than the control mix at 28 and 91 days in this study.

A comparison of strength development percentage between PCC and FABAs-GP concrete at 7, 28 and 91 days is presented in Fig. 2. In general, the strength percentage was higher for the FABAs-GP than the PCC mix. The compressive strength of FABAs-GP concrete at 28 days was 41.79% and increased to 50.55% at 91 days. However,

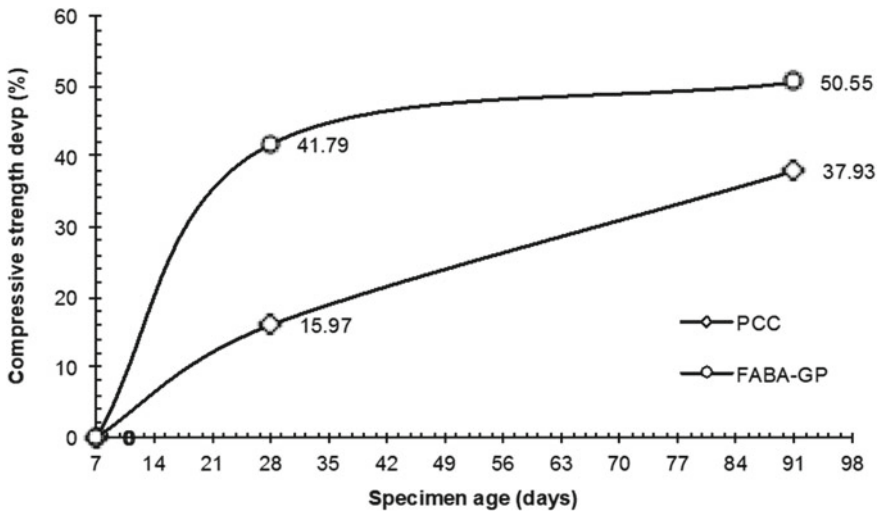


Fig. 2 Compressive strength development of PCC and FABAs-GP concrete at 7, 28 and 91 days

the strength development percentage of PCC concrete was lower than the FABA-GP with approximately 15.97% and 37.93% at 28 and 91 days, respectively. This condition probably due to a more complete and stable PCC hydration mechanism reaction compared to the FABA-GP mix at ambient temperature. It could be seen that geopolymer concrete mixed with Portland cement cured at ambient temperature performed high strength development because of evaporation of expelled water continues at a high degree during geopolymerization. Furthermore, Assi et al. [32] stated that the Portland cement improves the early strength of due to the existence of $\text{Ca}(\text{OH})_2$ (calcium hydroxide) that increases fly ash reaction rate in the absence of high temperature curing.

3.2 Tensile Strength

The experimental tensile strength and the predicted values based on the ACI 318-14 of the PCC and FABA-GP concrete at 7, 28 and 91 days could be seen in Table 4. In general, the tensile strength increases as the age of concrete like following the compressive strength's trend. In this study, the PCC showed a higher tensile strength property than the FABA-GP mix. Generally, the geopolymer concrete has higher elastic properties than the conventional concrete because of a small transition zone between cement matrix and aggregates surface [33]. A similar finding was also reported by Shi et al. [34] for geopolymer recycled concrete. According to Phoo-ngernkham et al. [35], the Ca^{2+} ion in the geopolymer mix supposedly reduces the interface zone due to the additional hydration product in the area. However, in this study, there was a slightly lower bonding between the geopolymer binder with Ca^{2+} from Portland Cement that eventually reduce the tensile strength of the FABA-GP concrete.

By using the Eq. (1), the prediction values were somewhat higher than the experimental tensile strength values for the PCC and FABA-GP concrete. The difference

Table 4 Compressive strength, experimental and calculated tensile strength of PCC and FABA-GP concrete

Mix	Concrete age (days)	Compressive strength (MPa)		Experimental tensile strength (MPa)		Predicted tensile strength (MPa) ^a	
		f'_c (MPa)	SD	f'_t (MPa)	SD	$f'_{ct,f}$ (MPa)	SD
PCC	7	19.35	0.60	1.85	0.18	2.46	0.04
	28	22.44	1.05	2.39	0.12	2.65	0.06
	91	26.69	0.89	2.76	0.24	2.89	0.05
FABA-GP	7	12.66	0.63	1.38	0.11	1.99	0.05
	28	17.95	0.60	1.78	0.13	2.37	0.04
	91	19.06	0.57	1.79	0.13	2.44	0.04

^aEq. (1) ACI 318-14

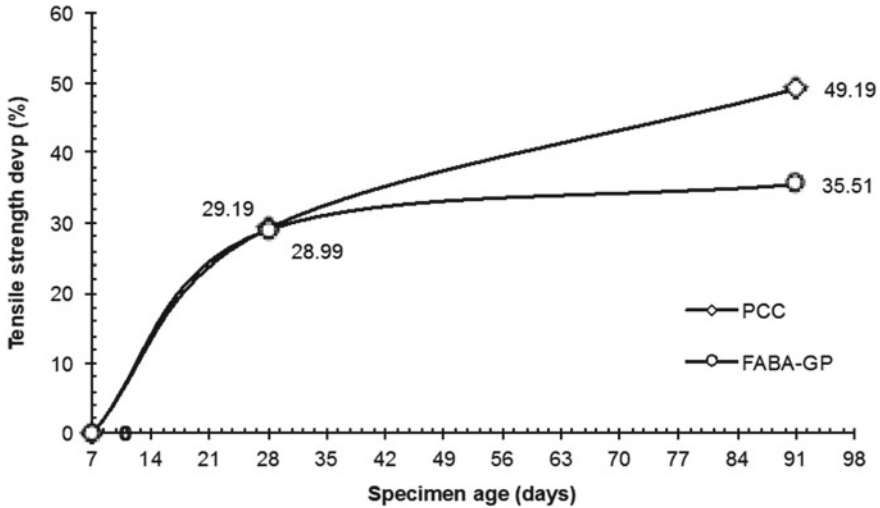


Fig. 3 Tensile strength development of PCC and FABA geopolymer hybrid concrete at 7, 28 and 91 days

between the predicted tensile strength between both types of concrete was very significant (more than 25%). Usually, the predicted values from a code of standard were lower than the experimental values; however, in this research, the prediction values were overestimating the experimental values. Some possible reasons for this behavior are different concrete mechanism, adhesion between aggregates and matrix, and the formation of a brittle material that induce microcracks in the matrix.

In Fig. 3, the tensile strength of the PCC concrete increased gradually to 49.19% at 91 days. On the contrary, the FABA-GP concrete had a steady development from 29.99% and 35.51% at 28 days and 91 days, respectively. A complete hydration reaction has increased bonding between the PCC matrix and aggregates, especially after 28 days. However, slow development of the FABA-GP’s tensile strength possibly due to a slow degree geopolymerization reaction that resulted in a weaker matrix and low elastic properties. This could also be due to the quality and carbon content of FABA used in this study.

In this study, the tensile strength did not develop well, with a slight increase by 15.54% in the tensile strength development at 91 days. In the geopolymer system, tensile strength is usually higher than the conventional concrete. This is because the geopolymer matrix with the aggregates has a strong bonding since there is no transition zone between the geopolymer matrix and the aggregates. The fact that a good reaction due to high-temperature curing could also be a reason for this behavior, according to Assi et al. [32]. However, possibly because the low-quality FABA in the geopolymer hybrid system, then a weak bonding was developed between the geopolymer matrix and aggregate. Although the tensile strength of FABA-GP in this study was approximately 25% lower than the PCC concrete, but the concrete strength mix is still viable for cast-in-situ in the application.

3.3 Flexural Strength

The compressive strength, the experimental and calculated flexural strength of PCC and FABAGP concrete during testing time are listed in Table 5. In general, the experimental flexural strength increased with curing time for both types of concrete. However, the flexural strength of FABAGP concrete was lower than the PCC concrete by 23.28%, 28.48% and 31.17% at 7, 28 and 91 days, respectively.

Flexural strength followed the trend of compressive strength values for both concrete. As the compressive strength increased, the flexural strength of both concrete has also increased at 91 days. The flexural strength development of the FABAGP concrete was 57.61%, which was higher than the PCC concrete, with only 41.39% from 7 to 91 days. The flexural strength of both concrete was not proportionally compatible with the compressive strength development of the PCC and FABAGP concrete by 37.93% and 50.55%, because of a different mechanism in both types of concrete.

Based on the ACI 318-14 prediction, flexural strength values at 7, 28, and 91 days can be determined. It seems that the ACI 318-14 prediction is more conservative compared to the PCC and FABAGP concrete experimental study. Both concrete showed higher flexural strength than the calculated ACI values. This might be due to different elastic properties calculation and flexible nature of the geopolymer hybrid [34].

The flexural strength development is shown in Fig. 4 where the PCC and FABAGP concrete displayed a gradual increase in flexural strength with the specimen age. A higher flexural percentage was shown by the FABAGP concrete than the PCC concrete after 28 days by 26.45% and 57.61% at 91 days. The elastic properties of concrete depend on the hydration mechanism and adhesion at the transition zone between the aggregates and matrix. The geopolymer hybrid has a fast strength development that was due to high drying shrinkage in concrete. Inclusion of Portland

Table 5 The compressive strength, experimental and calculated flexural strength of PCC and FABAGP concrete

Mix	Concrete age (days)	Compressive strength (MPa)		Experimental flexural strength (MPa)		Predicted flexural strength (MPa) ^a	
		f'_c (MPa)	SD	f'_l (MPa)	SD	$f'_{cl,f}$ (MPa)	SD
PCC	7	19.35	0.60	4.01	0.48	2.72	0.04
	28	22.44	1.05	4.88	0.22	2.94	0.07
	91	26.69	0.89	5.67	0.14	3.20	0.05
FABAGP	7	12.66	0.63	2.76	0.44	2.21	0.06
	28	17.95	0.60	3.49	0.10	2.63	0.05
	91	19.06	0.57	4.35	0.27	2.71	0.04

^aEq. (2) ACI 318-14

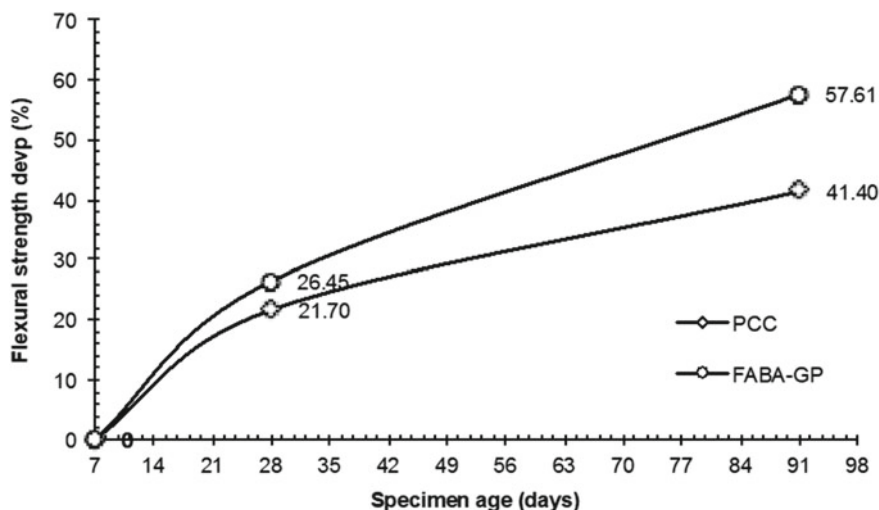


Fig. 4 Flexural strength development of PCC and FABA geopolymer hybrid concrete at 7, 28 and 91 days

cement in FABA-GP has changed the workability and strength of the geopolymer hybrid concrete. Previous researchers have also reported similar findings [32, 35].

The Portland Cement (PC) in the geopolymer system has reduced the workability and permeability, but increased setting time, early strength, and elastic modulus. This because the Ca^{2+} increased exothermic temperature, formed new hydration product with the geopolymer that improves the microstructure and pore development of the concrete. Other studies highlighted the benefit of using PC as additive or replacement of the fly ash in the range of 5–15% [35]. According to Mehta and Siddique [15], the increase of the Portland cement content in the geopolymer mixture of more than 20% could not significantly improve the strength of geopolymer hybrid. The resultant mix was more brittle and elastic properties reduced significantly.

3.4 Shrinkage

Shrinkage is a long-term property that determines the dimension stability of the concrete specimen. Figure 5 shows the shrinkage of PCC and FABA geopolymer hybrid concrete measured at 28 days. The PCC concrete had smaller shrinkage values than the FABA-GP concrete. In a system that contains pozzolanic material where usually the hydration process is much slower than the conventional OPC concrete, hence the shrinkage of PCC is usually bigger than the OPC concrete. In this study, the shrinkage values of the PCC concrete were less than $100 \mu\text{m}$. This is because at the hydration rate of the PCC concrete, although it is very slow but the formation of micropores is well developed in the matrix.

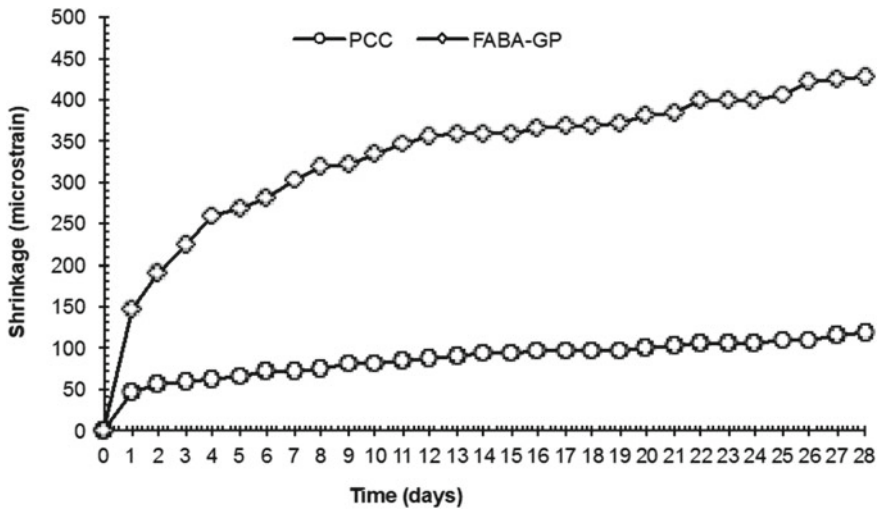


Fig. 5 Shrinkage of PCC and FABAGP geopolymer hybrid concrete

As shown and confirmed in Fig. 2, there was a very fast strength gain for the FABAGP that has a negative impact on shrinkage because drying of moisture in the concrete was faster than in the PCC concrete. The geopolymer concrete cured in a high temperature of more than 60 °C usually had small shrinkage of approximately 200 μm [36]. This value is considered very low for concrete. In a conventional geopolymer system without Portland cement, using heat curing is beneficial for early-age strength of the concrete. Curing at ambient temperature using an additive such as Portland cement, slag or high calcium fly ash were not creating the same impact to curing at high temperature, especially for drying shrinkage.

Since the FABAGP used Portland cement as a curing agent and without high temperature curing the concrete, the shrinkage is much higher than the ordinary geopolymer concrete. This is due to a prolonged exothermic heat released by the Portland cement to induce high early strength below 28 days. Despite the condition, loss of moisture in the concrete was very fast because the strength gain of FABAGP at 28 and 91 days was approximately 2.6 and 1.3 times higher compared to the PCC concrete. The condition is beneficial at an early age; however, the risk of a high rate of drying shrinkage in the samples could be a problem in the long term. Drying shrinkage is usually due to evaporation of water in the matrix. A previous study has highlighted this condition and used a little extra water as a precaution to a fast-drying shrinkage [37].

4 Conclusions

Compressive strength, tensile strength and flexural strength (mechanical properties) of the FABA-GP were investigated. The PCC concrete was the control mix. The FABA-GP has considerably lower compressive strength values, but a higher strength development than the PCC concrete. The tensile strength development of the FABA-GP, on the other hand, was lower than the PCC concrete. Moreover, the flexural strength development of the FABA-GP was much higher than the PCC concrete. The values were probably due to different hydration and elastic properties mechanism than the conventional concrete. Based on ACI 318-11 prediction values, a quite significant discrepancy between the predicted and calculated values could be due to many factors included concrete mechanism, adhesion between matrix and aggregates, the carbon content of the fly ash and water content in the matrix. Shrinkage of the FABA-GP at the ambient temperature was significantly higher than the PCC concrete.

Acknowledgements This research was funded by World Class Research, Direktorat Riset dan Pengabdian Masyarakat Kementerian Riset Teknologi dan Pendidikan Tinggi (Kemenristekdikti) Republic of Indonesia.

References

1. Pacheco-Torgal F, Castro-Gomes J, Jalali S (2008) Alkali-activated binders: a review Part 1. Historical background, terminology, reaction mechanisms and hydration products. *Constr Build Mater* 22:1305–1314
2. Singh NB, Middendorf B (2020) Geopolymers as an alternative to Portland cement: an overview. *Constr Build Mater* 237:117455
3. Diaz-Loya EI, Allouche EN, Vaidya S (2011) Mechanical properties of fly ash based geopolymer concrete. *ACI Mater J* 108:300–306
4. Topark-Ngarm P, Chindapasirt P, Sata V (2015) Setting time, strength and bond of high calcium fly ash geopolymer concrete. *J Mater Civ Eng* 27:04014198
5. Kupwade-Patil K, Allouche EN (2013) Examination of chloride-induced corrosion in reinforced geopolymer concretes. *J Mater Civ Eng* 25:1465–1476
6. Bignozzi MC, Manzi S, Natali ME, Rickard WDA, van Riessen A (2014) Room temperature alkali activation of fly ash: the effect of $\text{Na}_2\text{O}/\text{SiO}_2$ ratio. *Constr Build Mater* 69:262–270
7. Mehta A, Siddique R (2017) Properties of low calcium fly ash based geopolymer concrete incorporating OPC as partial replacement of fly ash. *Constr Build Mater* 150:792–807
8. Aydin S, Baradan B (2012) Mechanical and microstructural properties of heat cured alkali activated slag mortars. *Mater Des* 35:374–383
9. Deb PS, Sarker PK, Barbhuiya S (2015) Effects of nano-silica on the strength development of geopolymer cured at room temperature. *Constr Build Mater* 101:675–683
10. Palomo A, Fernandez-Jimenez A, Kovalchuk G, Ordóñez LM, Naranjo MC (2007) OPC-fly ash cementitious system. Study of the gel binders produced during alkaline hydration. *J Mater Sci* 42:2958
11. Garcia-Lodeiro I, Maltseva O, Palomo A, Fernandez-Jimenez A (2012) Hybrid alkaline cements: Part I. Fundamentals. *Romanian J Mater* 42:330–335
12. Garcia-Lodeiro I, Fernandez-Jimenez A, Palomo A (2015) Cements with a low clinker content: versatile use of raw materials. *J Sustain Cement-Based Mater* 4:140–151

13. Suwan T, Fan M (2014) Influence of OPC replacement and manufacturing procedures on the properties of self-cured geopolymer. *Constr Build Mater* 73:551–561
14. Palomo A, Fernandez-Jimenez A, Kovalchuk G, Ordenez LM, Naranjo MC (2007) OPC-fly ash cementitious systems: study of gel binders produced during alkaline hydration. *J Mater Sci* 42:295–2966
15. Mehta A, Siddique R (2017) Properties of low-calcium fly ash based geopolymer concrete incorporating OPC as partial replacement of fly ash. *Constr Build Mater* 150:792–807
16. Nath P, Sarker PK (2017) Flexural strength and elastic modulus of ambient-cured blended low-calcium fly ash geopolymer concrete. *Constr Build Mater* 130:22–31
17. Saraswathy V, Song H-W (2007) Effectiveness of fly ash activation on the corrosion performance of steel embedded in concrete. *Mag Concr Res* 59:651–661
18. Hongen Z, Feng J, Qingyuan W, Ling T, Xiaoshuang S (2017)
19. Amino GK (2018) Hasil pembakaran batu bara PLN bakal diserap semen Indonesia. BUMN Track. Available at <https://bumntrack.com/berita/hasil-pembakaran-batu-bara-pln-bakal-diserap-semen-indonesia>
20. Olivia M, Wibisono G, Saputra E (2019) Early strength of various fly ash based concrete in peat environment. *Matec Web Conf* 276:01022
21. Wijaya MF, Olivia M, Wibisono G, Saputra E, Wang S (2019) Characteristics of geopolymer hybrid concrete in peat water. *IOP Conf Ser Mater Sci Eng* 615:012120
22. ASTM C618-19 (2019) Standard specification for coal fly ash and raw or calcined natural pozzolan for use in concrete. ASTM International, West Conshohocken, PA
23. Salain IMAK (2009) Pengaruh jenis semen dan jenis agregat kasar terhadap kuat tekan beton. *Teknologi dan Kejuruan* 32:63–70
24. PCC specification brochure. PT Semen Padang, Padang
25. SNI 1972:2008 (2008) Cara Uji Slump Beton. Badan Standardisasi Nasional, Jakarta
26. SNI 1974:2011 (2011) Cara Uji Kuat Tekan Beton dengan Benda Uji Silinder. Badan Standardisasi Nasional, Jakarta
27. SNI 2491: 2014 (2014) Metode uji kekuatan tarik belah spesimen beton silinder. Badan Standardisasi Nasional, Jakarta
28. SNI 4431:2011 (2011) Cara Uji Kuat Lentur Beton Normal dengan Dua Titik Pembebanan. Badan Standardisasi Nasional, Jakarta
29. ASTM C157/C157M-08 (2008) Standard test method for length change of hardened hydraulic cement mortar and concrete. American Society for Testing and Materials, West Conshohocken
30. ACI 318-14 (2014) Building code requirements for structural concrete. American Concrete Institute, Farmington Hills
31. Zang H, Shi X, Wang Q (2018) Effect of curing condition on compressive strength of fly ash geopolymer concrete. *ACI Mater J* 115:191–196
32. Assi L, Ghahari SA, Deaver E, Leapart D, Ziehl P (2016) Improvement of the early and final compressive strength of fly ash-based geopolymer concrete at ambient conditions. *Constr Build Mater* 123:806–813
33. Olivia M (2011) Durability related properties of low calcium fly ash based geopolymer concrete. PhD thesis of School of Civil and Mechanical Engineering, Department of Civil Engineering, Curtin University of Technology, Perth, Western Australia
34. Shi XS, Collins FG, Zhao XI, Wang QY (2012) Mechanical properties and microstructure analysis of fly ash geopolymeric recycled concrete. *J Hazard Mater* 237–238:20–29
35. Phoo-ngernkham T, Chindaprasirt P, Sata V, Pangdaeng S, Sinsiri T (2013) Properties of high calcium fly ash geopolymer pastes with Portland cement as an additive. *Int J Miner Metall Mater* 20:214–220
36. Olivia M, Nikraz H (2012) Properties of fly ash geopolymer concrete designed by Taguchi method. *Mater Des* 36:191–198
37. Pangdaeng S, Phoo-ngernkham T, Sata V, Chindaprasirt P (2014) Influence of curing conditions on properties of high calcium fly ash geopolymer containing Portland cement as additive. *Mater Des* 53:269–274

Investigation of Confined Masonry Using Non-standard Quality of Concrete and Reinforcement



Andreas Triwiyono, I. Gusti Lanang Bagus Eratodi, Dian Eksana Wibowo, and Suprpto Siswosukarto

Abstract Masonry structure is a common type of residential house in several regions. A significant number of guidelines were issued to enhance the resistance of such house against earthquakes. The International Association for Earthquake Engineering (IAEE) published a Guideline for Non-Engineered Earthquake Resistant Construction. Referring to this guideline by adjusting to local conditions, the Indonesian Ministry of Public Works has developed a guideline on how to build dwellings, especially for houses made of bricks masonry, confined by reinforced concrete (RC) frames. However, despite the availability of the guidelines, field observation on masonry construction practices shows that the qualities of concrete are still inadequate, and the steel reinforcement configurations were different compared to those on the guidelines. An experimental study was conducted to obtain the effect of concrete quality disparity and reinforcement configuration of the RC frame on the brick masonry wall performance. The wall specimens made of brick masonry were loaded cyclically, from the top of the wall in the plane direction up till failure. The test results suggest that the nonstandard quality of concrete contributes no significant effect on the stiffness, strength, deformation ability, and ductility of the walls. Early damage of all specimens occurs in the bottom end of the RC column before reaching the load capacity. Strong anchorage is needed by continuing the longitudinal column reinforcement to the foundation of the wall.

A. Triwiyono (✉) · S. Siswosukarto
Civil and Environmental Engineering Department, Universitas Gadjah Mada, Yogyakarta,
Indonesia

e-mail: andreas.triwiyono@ugm.ac.id

S. Siswosukarto

e-mail: suprpto.siswosukarto@ugm.ac.id

I. Gusti Lanang Bagus Eratodi

Civil Engineering Department, Universitas Pendidikan Nasional, Denpasar, Indonesia

e-mail: eratodi@undiknas.ac.id

D. E. Wibowo

Civil Engineering and Planning Education Department, Universitas Negeri Yogyakarta,
Yogyakarta, Indonesia

Keywords Anchorage · Disparity · Guideline · Masonry · Nonstandard quality

1 Introduction

In several regions, brick masonry is a common type of residential house. It is a kind of construction with individual units of bricks, bound with mortar. Usually, using mortar as binding material is made of cement, lime, or other cementitious material mixed with sand. Brick masonry is known to be durable, economical and exhibits adequate strong construction, where it is used as a partition or load-bearing wall. Usually, houses are built without a structural design process, classified as non-engineered structures. Evaluation of the effect of earthquakes has showed that these kinds of structures were easily damaged, leading to life and material losses. Based on these experiences, various types of strengthening of the masonry wall to improve its performance to reduce losses are proposed [1–3]. One of them is called confined masonry, which is confined by a reinforced concrete (RC) frame. Strengthening of masonry walls can be done by adding steel reinforcement or polypropylene/pp-band [4, 5].

Confined brick masonry consists of a masonry wall made of clay brick confined by reinforced concrete frames consisting of horizontal and vertical RC members surrounding its four sides. The vertical and horizontal elements are known as “tie-columns” and “tie-beams.” These confining members function as ties or bands for the wall to create a better resistance to tensile stresses [3]. In practice, the bricks are arranged first per one meter height, followed by the pouring of the columns. This method is repeated and enclosed on their upper ends with tie beams to confine the wall. This system anchors the wall to the bottom beam and transfers the loads to the foundation.

Various guidelines have been prepared and endorsed and are generally applicable for various regions with a variation in earthquake zone regions. Guidance for safer permanent houses, especially for houses made of confined masonry, has been published by IAEE [1], by the Gujarat State Disaster Management Authority [6], and the Swiss Agency for Development and Cooperation Earthquake Engineering Research Institute [7]. These standards require adaptation to incorporate the use of local materials, workman capacities, codes, and local regulations. Hart and Brzev reported an overview of confined masonry design and construction developed by the Confined Masonry Network under the auspices of the Earthquake Engineering Research Institute, the International Association for Earthquake Engineering, and other organizations [8]. CSIR-Central Building Research Institute [9] and the Department of Public Works Indonesia and Japan International Cooperation Agency [2] have published design guidelines specially designated for confined masonry buildings. The guidelines are specifically for masonry construction work. These guidelines present the manner and explanation in a step-by-step manner with clear illustrations, the sequences on how to build houses, and steel reinforcement detailing, including material quality assessment requirements.

The good or standard quality is based on the key requirements for the masonry building published by the Ministry of Public Works and Japan International Cooperation Agency (JICA) [2]. The concrete quality requirements for the RC frame are specified in the mix proportion of materials, expressed in the volume of the mixture between aggregate: sand: cement: water-cement ratio. The ratio required for a good concrete mixture is 3: 2: 1 with a 0.5–0.75 water-cement ratio, while for mortar, the sand to cement proportion is either 4:1 or 5:1.

The strength of the confined frame depends not only on the material quality but also reinforcement assembly of the RC members. Overall experiences in Indonesia showed that house failure often occurs due to disparities in material qualities, poor steel reinforcement detailing, and inadequate working methods [10, 11]. Typical examples of these material discrepancies are the poor concrete quality and deficiencies in the reinforcement configuration or material properties.

Based on the variation in the implementation in the field, this paper reports on the study of brick masonry walls experimental testing with a variation in the RC frame quality. The variations are in the concrete compressive strength, the dimensions of the tie-column, tie-beam diameter of the longitudinal steel reinforcement, and spacing of the stirrup of the two members. The study discussed part of the studies undertaken by the JICA-research team [12] by focusing on some parameters such as poor qualities of clay bricks, mortar, and concrete coupled with numerical-based studies. These variations of inadequate qualities are originated by nonconformity of requirements and may lead to failures and damages of the house structures under lateral seismic loads. The purpose of the study is to find out whether these quality variations will significantly affect the behavior of the wall. The study covered brick masonry walls confined by reinforced concrete frames, cyclically loaded by applying horizontal loads in the direction of the wall plane.

2 Experimental Testing Program

2.1 General

The experimental testing program was started with the testing of the material quality of bricks, the mortar, the concrete. The full-scale confined brick masonry wall specimens were manufactured where its dimensions and detailing of the reinforcements were checked after the completion of the curing time of 28 days. Afterward, the preparation of testing equipments and initial condition were conducted. This is followed by full experimentally testing of the structural aspects by cyclic monotonic loading on the specimens of the full-scale confined brick masonry wall system.

2.2 Wall Specimens

Some general practice building was constructed by not following the requirements, whereas the columns have small dimension, small reinforcement, high stirrup spacing, poor quality of brick and mortar etc., see Table 3.1. The arrangement of the anchorage, longitudinal and lateral reinforcement for the wall specimens is also shown in the figures.

The wall specimens were manufactured in the following steps:

- i. Installation of the reinforcement of the foundation, anchorages and longitudinal reinforcement of the two tie-columns, molding attachment and concrete pouring. Steel reinforcements used as anchorage between foundation and bottom tie-beam has a diameter of 16 mm.
- ii. Reinforcement assembly for RC frame members (bottom tie-beam, tie-columns, and top tie-beam). Longitudinal reinforcement in the RC frame members is a plain bar with a diameter of 10 mm, except wall pattern 4 with a diameter of 8 mm.
- iii. Installation of strain gauges on several reinforcing bars and anchors. Strain gauges were installed on anchorages, longitudinal and lateral rebars to determine the strain and to check whether the rebars have experienced yielding during testing.
- iv. Concrete pouring for bottom tie-beam. The beam was anchored to the foundation.
- v. Horizontal anchor installation that is placed on every six layers of bricks
- vi. Bricklaying. The bricklaying arrangement is controlled to ensure straightly in the horizontal and vertical direction. The bricklaying in the vertical direction were done in three steps. Only one step can be installed in one day. Each step has a height of 1 m.
- vii. Concrete pouring of the tie-columns. Concrete pouring was done in three steps, after laying of the bricks.
- viii. Releasing the mold and checking the results of casting concrete
- ix. Plaster application of the wall surface. The walls are finished with plaster on one side to obtain a finished product
- x. Painting of wall surfaces dan concrete.

The wall specimens and test methods were similar to the specimens and test methods described in previous studies [4]. This study focuses on the variations of the quality of concrete, dimensions, and reinforcement details of RC frames, which confine the brick masonry walls.

In practice, some residence houses were constructed by not following the requirements of the guideline [2], especially the quality of concrete is poor, and steel reinforcement details do not match the guideline. In this study, the wall specimens were made of local materials. The dimension of bricks was $22 \times 10 \times 5.5$ cm and manually produced in the area near Bandung in the West Java Province. The brick masonry walls with dimensions of 3.0×3.0 m were confined by RC frame in all

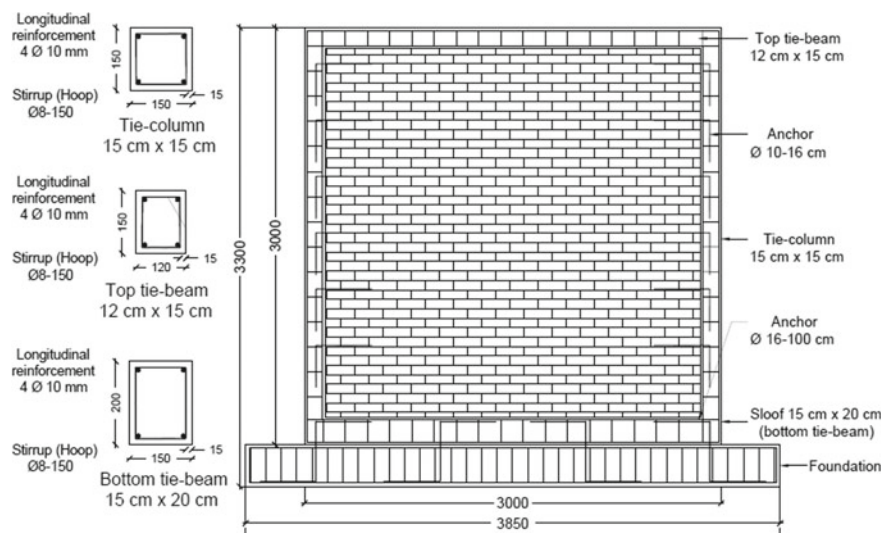


Fig. 1 Typical wall pattern

surrounding perimeters and constructed based on the key requirements published by the Department of Public Works Indonesia-JICA [2]. The horizontal anchors to connect between the RC frame and the brick masonry were provided on the level of every six bricklayers. They lay in mortar layers between bricks.

Figure 1 shows the configuration, dimension of the members, steel reinforcement detailing, and anchorages between the bottom tie-beam and foundation of the 5 brick masonry wall patterns. During the loading test, the foundation was anchored to the strong floor, thus providing support for the walls.

Table 1 shows the variation of the concrete quality of the RC frame. All walls have the same quality of brick and mortar. Wall pattern 1 is called a control or

Table 1 Wall patterns

Wall Pattern	Concrete	Tie column dimension	Reinforcement	
			Longitudinal	Stirrup
1 (control)	Good (1:2:3:0.8)	150 mm × 150 mm	4φ10 mm	φ8-150
2	Poor (1:2:3:1.2)	150 mm × 150 mm	4φ10 mm	φ8-150
3	Good (1:2:3:0.8)	100 mm × 100 mm	4φ10 mm	φ8-150
4	Good (1:2:3:0.8)	150 mm × 150 mm	4φ8 mm	φ8-150
5	Good (1:2:3:0.8)	150 mm × 150 mm	4φ10 mm	φ8-250

standard wall pattern. It was made based on the standard of concrete quality, RC frame dimensions, and steel reinforcement arrangement where it was constructed based on the key requirements for the masonry building published by the Ministry of Public Works and Japan International Cooperation Agency (JICA) [2]. The other walls were constructed by not following the requirements. They have poor or nonstandard concrete quality (wall pattern 2), smaller dimension tie columns (wall pattern 3), smaller diameter longitudinal steel reinforcement (wall pattern 4), and longer stirrup spacing (wall pattern 5).

2.3 Test Setup

Figure 2 shows the test setup of the wall specimen. The horizontal cyclic loads were applied on the five points along the top tie-beam in the direction of the strong axis of the wall through the steel box. The load is gradually increased and terminated after the structure reached a degradation degree of approximately 25% to the maximum load, or alternately when the drift ratio reached 2%. Figure 3 shows elevated view of the schematic of cyclic load based on ASTM, E 2126-02a [8]. For each displacement target, three cycles were applied, with a smaller cycle in between these three cycles. The lateral cyclic loads were applied using a controlled hydraulic actuator.

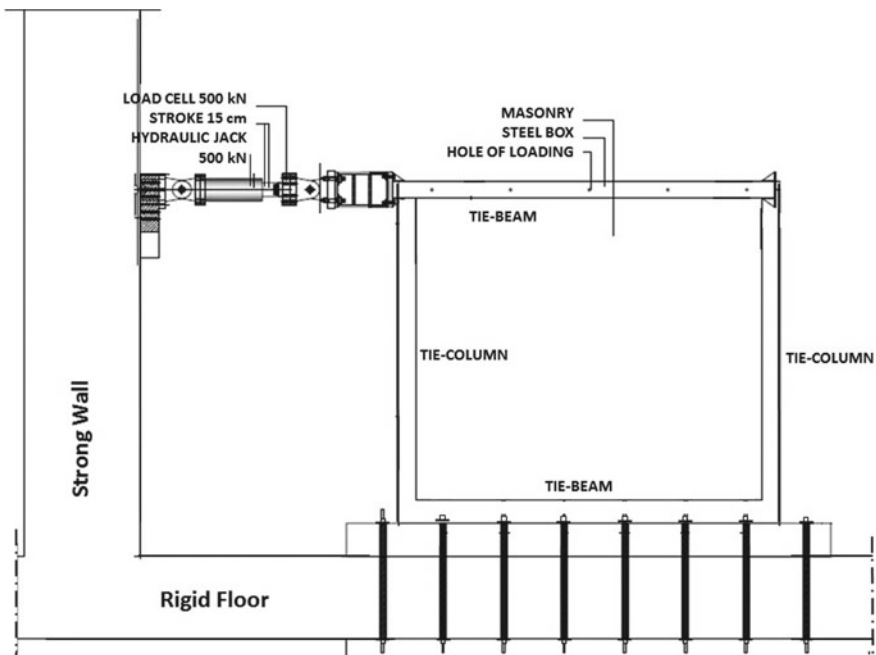


Fig. 2 Test setup of the wall

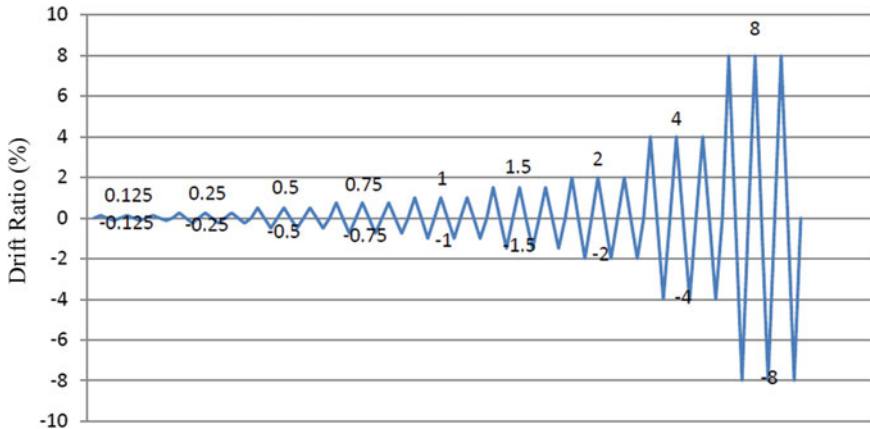


Fig. 3 Loading pattern based on ASTM, E 2126-02a [8]

2.4 Data Collection

The displacement of each load was monitored and recorded using Linear Variable Differential Transformer (LVDT) on the top of the wall specimen. The strains in the reinforcing steel bars were measured using strain gauges. The data were collected from the data acquisition system (data logger) used in the experiment. Cracks of the wall and RC frame are clarified by making lines on the wall surface at each load stage with different colors in the push or pull directions. Documentation is carried out at each stage of loading.

3 Test Results and Discussion

3.1 Material Properties

The bricks are known to be of good quality with an average compressive strength of 3.25 MPa. The test of the compressive strength of brick is based on the Specification and Testing Method for Red Brick of Indonesian Industrial Standard. The specimens were made of 2 layers of brick attached by 1 cm thick mortar. The compressive strength of the mortar used for brick with ratio cement: sand of 1:4 was 8.94 MPa. The test of the compressive strength of mortar was carried out using Universal Testing Machine (UTM) based on Indonesia Standard of a Testing method for Compressive Strength of Mortar. The test specimen of mortar is a cube with a size 50 mm × 50 mm × 50 mm. The mortar mixture composition used in the specimens is 1:4 for the ratio of cement and sand.

The average compressive strength of concrete with a proportion of aggregate: sand: cement: water-cement ratio was 3:2:1:0.8 and 3:2:1:1.2 for representing good and poor-quality concrete. The resulting compressive strengths were 19.08 MPa and 15.48 MPa, respectively. The compressive strength of concrete is obtained from a standard cylinder test with a height of 300 mm and a diameter of 150 mm. Tensile strength test of reinforcing steel bars for the longitudinal reinforcement, stirrup and anchorage is conducted by using a Universal Testing Machine (UTM) based on the Indonesian code of Tensile Testing Methods of Reinforcing Steel. The specimens were taken with the sampling method from reinforcement steel to be used in the wall. At least 3 pieces of bar with the length of each at least 600 mm should be tested for each type of diameter. Tests were conducted by pulling the test object until fracture. The average values of yield strength of plain steel bar $\Phi 8$, $\Phi 10$ were 405.56 MPa, 386.37 MPa, and the tensile strengths of both diameters were 506.86 MPa, 550.32 MPa, respectively.

3.2 Cracks Patterns

Formation and propagation of cracks on the walls were observed during the loading process. For all walls, the first crack generally occurred in the brick masonry area horizontally at the bottom left and right side near the bottom end corner of the wall. The next cracks mostly occurred in the wall area near the left and right columns. These cracks were indicated as flexural cracks. These secondary cracks were longer and wider in size at the bottom side of the masonry. The following cracks occur in the reinforced concrete (RC) frame area at the bottom corner external side. The cracks distribution on the bottom side of the wall was more intense when compared to the top side. The new cracks were recognized to have formed within the elastic range. This is evident until the drift ratio of 0.27% was reached. At larger drift ratios, the cracks progressed faster and became longer and wider quickly in dimension. At the drift ratio of 1%, the concrete cover started spalling, and the bottom tie beam separated from the foundation. Figure 4 shows the crack patterns at the ultimate load.

At a drift ratio of around 2%, the cracks between the bottom tie-beam and foundation have widened and become more pronounced. These cracks indicate a separation between both components. It shows that the anchorages between the tie-beam and foundation are not adequate to withstand the tension force between the wall and the foundation. Wall pattern 2 with a different concrete quality of the tie-columns and tie-beams, the cracks occur similar to wall pattern 1 as a control wall. Compared to wall pattern 1, cracks on wall pattern 3 (smaller dimension of RC frame) were observed to be wider and run continuously from the brick masonry to the RC frame. Cracks on the wall patterns 4 and 5 occurred earlier compared to the control wall and two other walls. The number of cracks in the tie-columns was greater than that of the control wall. These cracks affected the degradation strength rapidly.

The followings are additional report and discussion about cracks especially in the base of the walls as shown in Fig. 5. The cracks width between the bottom

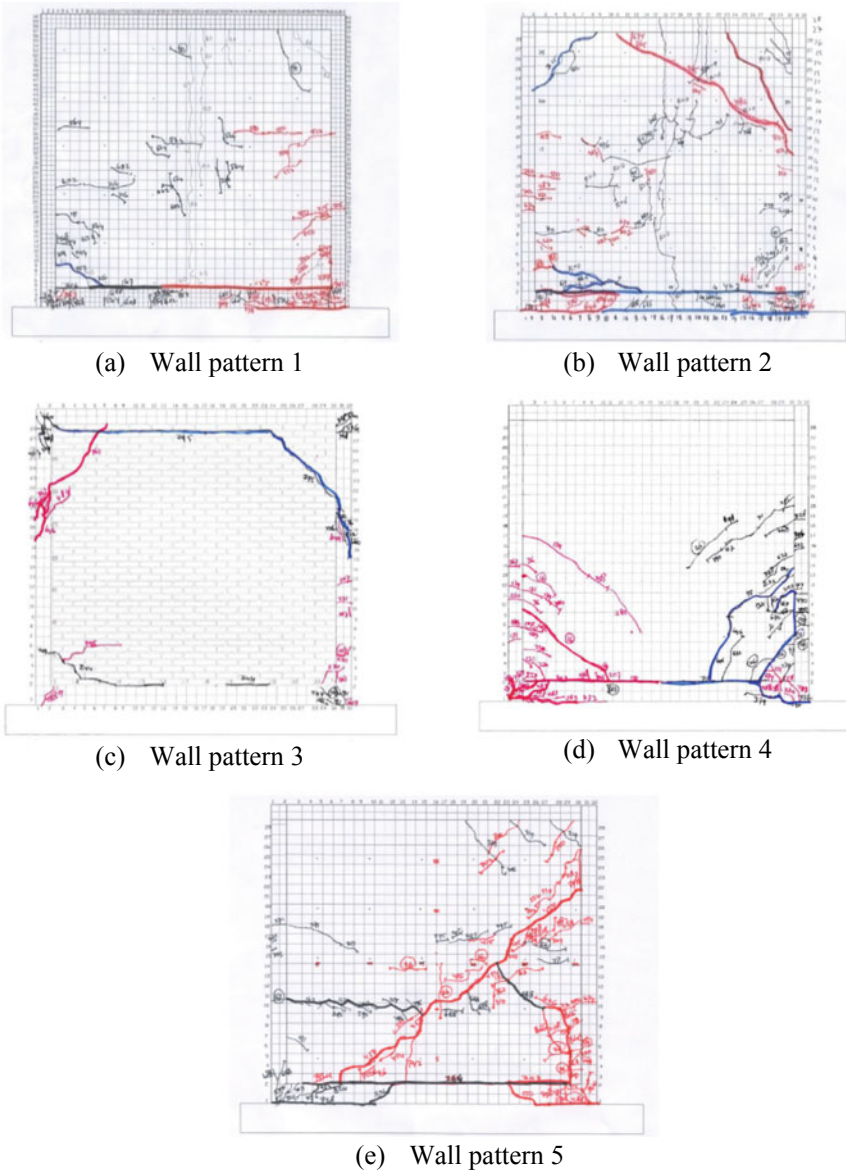


Fig. 4 Crack patterns of the walls

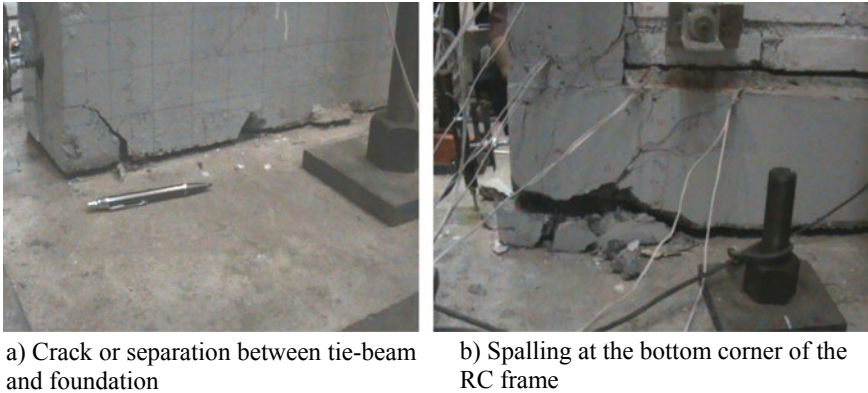


Fig. 5 Crack and failure under the bottom tie-beam

tie-beam and foundation become bigger and it indicated a separation between the both components. The separation between the tie-beam and foundation is about 1 m horizontal long. The crack occurred between the first and the second anchors. Small cracks happened in the top area of the wall and RC frame. It seems that the wall can support higher load, but it is restricted by the crack between tie-beam and foundation and by capacity of the anchorage. Until the load capacity of the wall, the stress of all reinforcement bars did not reach the yield stress.

The load capacity of the specimen is determined by the maximum load capacity of anchorage. Because of cracks and spillings, there is a slip between bottom corner anchorage and concrete. This slip happened before the strain of the anchorage reach yield. The maximum load occurred and then the strength of the wall was reduced rapidly.

3.3 Hysteresis Curves

From the lateral cyclic loading, the response of the wall was presented in load-displacement hysteretic loop. The displacements were obtained from LVDT reading on top of the specimen, whereas applied loads were obtained from the load actuator. From the hysteretic loop, several key parameters of the structure can be evaluated, namely, maximum lateral load carrying capacity, displacement at maximum load, stiffness, yield capacity and ductility.

It is interesting to discuss the hysteresis curves to obtain the earthquake resistance of the walls, especially to investigate the capacity of the wall to withstand horizontal loads. Figure 6a shows the hysteretic loop of the wall pattern 1, known as the control or standard wall. The curves of the other wall patterns are illustrated in Fig. 6b–e. The curves are drawn to the same vertical and horizontal scales to allow comparison among the specimens. The curves were stable and exhibit almost linear-elastic range

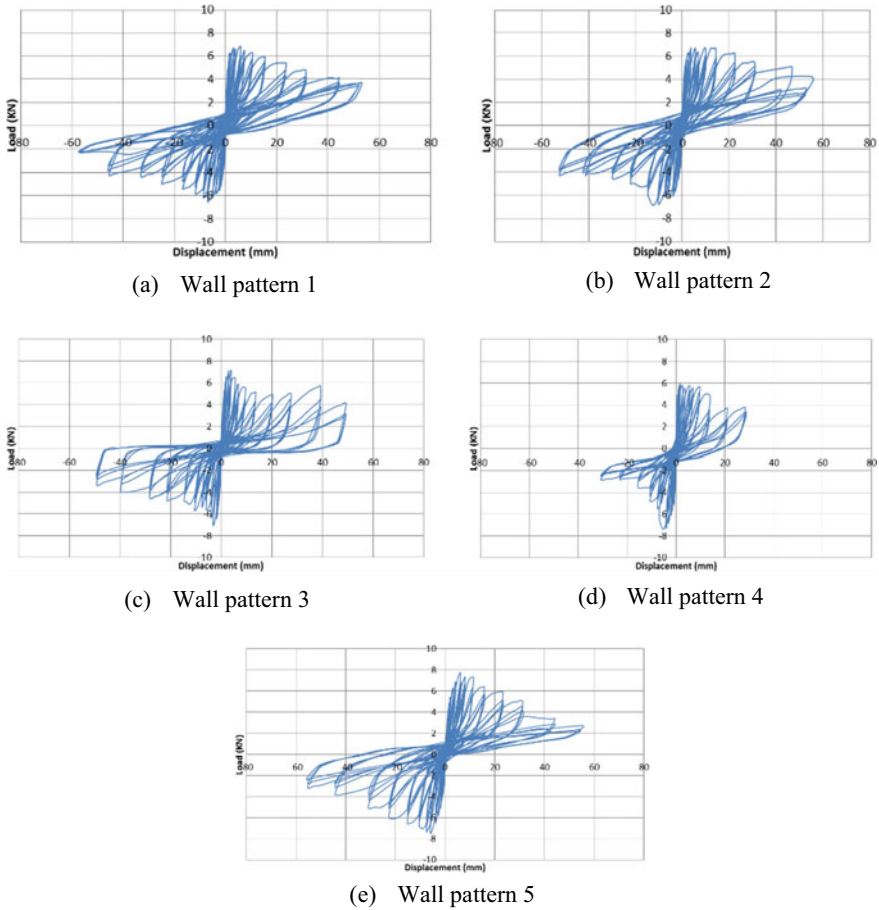


Fig. 6 Hysteresis curve of the walls

until the horizontal deflection of 1.5 mm (drift ratio of 0.05%). Then the stiffness is downwards after reaching the horizontal deflection of 6–10 mm (drift ratio of 0.2–0.33%).

The curves indicate that the collapse did not fall in a brittle mode under the lateral load. Slow degradation of the walls is observed from the curves after reaching its capacity. These are caused by degradation in bond strength of the anchorages in the bottom tie-beam. The strain gauge recording indicated that the longitudinal steel did not yield at this condition. When the load degraded and reached about 75% of its capacity, the lateral deformation achieved up to 55–60 mm, a drift ratio of 1.8–2%.

Compared to the control or standard wall (wall pattern 1), the load capacity of other walls approaches the same value. The average load capacity of the pull and push loads of each wall is 6.67 ton, 6.78 ton, 6.39 ton, 6.58 ton, and 7.58 tons respectively.

From the crack patterns, hysteretic curves, the several variations, the wall can be evaluated by these behaviors, namely maximum lateral load capacity, and ductility. Wall pattern 2 with different quality of concrete of the RC frame, behaves similarly to wall pattern 1. The poor quality of concrete did not significantly affect the stiffness of the wall in the elastic range, as well as the strength and the degradation curve after reaching maximum capacity. Compared to the control wall, cracks on wall pattern 3 (smaller dimension of RC frame) were observed to be wider and run continuously from the brick masonry to the RC frame. The maximum load of wall pattern 3 was about 4% lower than that of the standard wall. From the crack pattern, cracks in wall pattern 4 occurred early in the testing. The number of cracks was greater than that of the standard wall. More cracks occur in the tie-column and affect on the strength degradation rapidly. However, the wall had a similar load capacity as the other walls. By using larger stirrups spacing than that of the standard wall, wall specimen 5 still behaved ductile and also had a load capacity close to the standard wall.

From these phenomena, it is recommended that the anchorage between the beam and the foundation has to be made stronger by using more anchor bars. Alternately, the column reinforcements should be continued into the foundation base, so that it can also be functioning as anchorages.

4 Conclusions

Results of the study of confined brick masonry walls using non-standard quality of the reinforced concrete frame can be concluded as following:

1. The guideline of confined brick masonry wall provides enough strength. The walls can deflect to a 1.8–2% drift ratio without collapsing. The strength of the anchorage limits the maximum load capacity of the walls.
2. Wall pattern 2 with a different quality of concrete of the RC frame behaved similarly to the control wall (wall pattern 1). The low concrete quality of the RC frame did not significantly affect the strength and ductility of the wall.
3. Compared to the control wall, cracks on wall pattern 3 (smaller dimension of RC frame) were observed to be wider and run continuously from the brick masonry area to the RC frame. The maximum load of wall pattern 3 was approximately 4% below the standard wall.
4. Cracks in column 4 occurred earlier, and the number of cracks was greater than that of the control wall. More cracks occurred in the tie-column, thus degrade the strength of the wall. This may lead to rapid disintegration of the wall.
5. By using longer stirrup spacing, wall pattern 5 had wider cracks in the brick masonry area, continuing to the tie-columns. The load capacity was close to the control wall.

It is recommended that the anchorage between the beam and the foundation has to be made stronger by using more anchor bars. Alternately, the column reinforcements

should be continued into the foundation base, so that they can also be functioning as anchorages.

References

1. International Association for Earthquake Engineering (IAEE): Guidelines for Earthquake Resistant Non-Engineered Construction, Gakujutsu Bunken Fukyu-Kai, Tokyo (1986)
2. Department of Public Works Indonesia, and Japan International Cooperation Agency (JICA): Basic Requirements for Safer Houses, Masonry Building with Reinforced Concrete Frame, Jakarta (2009)
3. Arya AS, Boen T, Ishiyama Y (2012) Revised of IAEE guidelines for earthquake engineered construction, 15 WCEE, Lisboa
4. Triwiyono A, Neo F, Ardianto J, Pratama GM, Sugijopranto A (2016) Experimental Investigation on the flexural performance of Brick Masonry wall retrofitted using PP-band meshes under cyclic loading. *Appl Mechanics Mater* 845:175–180
5. JICA Team Research: report of the survey of construction method, peoples awareness and so on experiment and numerical study of Masonry confined wall (2012)
6. Iyer K, Kulkarni SM, Subramaniam S, Murty CVR, Goswami R, Vijayanarayanan AR (2012) Built a safe house with confined Masonry House, Gujarat State Disaster Management Authority, Government of Gujarat Sept 2012
7. Swiss Agency for Development and Cooperation Earthquake Engineering Research Institute (2015) guide book for building earthquake-resistant houses in confined Masonry revised version Aug 2015
8. ASTM, E 2126–02a, Standard test methods for cyclic (Reversed) load test for shear resistance of walls for buildings. USA (2003)
9. CSIR-Central Building Research Institute: design guidelines for confined Masonry buildings, India (2017)
10. Triwiyono A, Eratodi IGLB (2019) Investigation of brick Masonry with using of bad quality of bricks and reinforced concrete frame. *MATEC Web Conf* 258:04008
11. Triwiyono A, Arif SB, Nugroho ASB, Firstyadi AD, Ottama F (2015) Flexural strength and ductility of concrete Brick Masonry wall strengthened using steel reinforcement. *Procedia Eng* 125:940–947
12. Hart TM, Brzev S (2014) The confined Masonry network's design and construction guidelines. In: Tenth U.S. national conference on earthquake engineering frontiers of earthquake engineering July 21–25 2014

Prospective of Passive Control Structural Devices for Existing Low-Rise Building at Earthquake-Prone Region of Developing Countries: A Literature Review



Yenny Nurchasanah, Bambang Suhendro, and Iman Satyarno

Abstract In terms of earthquake disaster mitigation, one thing that needs attention in structural engineering is developing concepts to improve structural performance and safety level of existing building due to earthquakes. This study combines findings among the effectiveness of passive, active and semi-active controls systems. The first part of this paper describes the seismicity in Asian region, the second part discusses methods of energy dissipation, and the third part focus on low-rise building with dampers. It was found from references that the behavior of the semi-active control system shows better performance in seismic protection when compared to the passive control and active control systems. Passive control devices, when integrated into the structure will partially dissipate the input energy, thereby reducing the need for energy reduction in the main structural elements and reducing the structural damage. Base isolator can provide a good foundation for large and heavy structures that are located on hard ground against earthquakes. Base isolators and viscous dampers that work in a hybrid system can behave well under strong earthquakes. Semi-active control is the best in energy dissipation, but for easier and cheaper the purposes that are appropriate for Asian developing countries, passive control is more suitable for implementation. In addition, for the purpose of improving the performance of existing buildings, passive control is the best system applied to old and low rise buildings, that were built referred to old seismic code, without having to make major improvements to structural elements. Further numerical analysis and experimental programs specifically for existing buildings with recommended damping systems are needed in order to obtain verification for further application purposes.

Y. Nurchasanah (✉) · B. Suhendro · I. Satyarno
Civil and Environmental Engineering, Universitas Gadjah Mada, Yogyakarta, Indonesia
e-mail: yenny.nurchasanah@ums.ac.id

B. Suhendro
e-mail: bsuhendro@ugm.ac.id

I. Satyarno
e-mail: imansatyarno@ugm.ac.id

Y. Nurchasanah
Civil Engineering, Universitas Muhammadiyah Surakarta, Surakarta, Indonesia

Keywords Existing building · Damper · Earthquake · Passive control

1 Introduction

In the latest science of earthquakes, in addition to the potential for earth shaking, the existence of humans who live on earth is also considered, how far humans are exposed and vulnerable to shaking due to earthquakes in various regions of the world. At the moment, what needs more attention is how vulnerable are the safety of people who are at home, at school and at work, how crowded the population is in earthquake-prone areas, and, how many deaths have been caused by the earthquake. It is very important to find as much information as possible by collaborating with public, private, and academic institutions about the design of structures, populace, potential death, potential harm, and financial losses in detail.

According to the Council of Tall Buildings and Urban Habitat (see Fig. 1), of the 50 buildings with damper applications studied, as many as 4% of hotel buildings use structures accompanied by damper technology. While the percentage of office buildings with dampers is 22%, and residential buildings are 26%. The remaining 48% are buildings that are used for various purposes. According to this data, only 30% of the 20 skyscrapers in the world use damper technology to reduce shocks [1].

The use of dampers as enhancements to buildings in Asia, especially in developing countries, is not yet widespread, although in Asia many regions are exposed to earthquake hazards. In Indonesia, not many buildings have been specifically designed to be given an additional energy dissipation device, especially buildings designed with old regulations that have not yet applied earthquake regulations. It is necessary to investigate the existing buildings built before earthquake regulations exist so that performance improvements can be made to resist the earthquake forces.

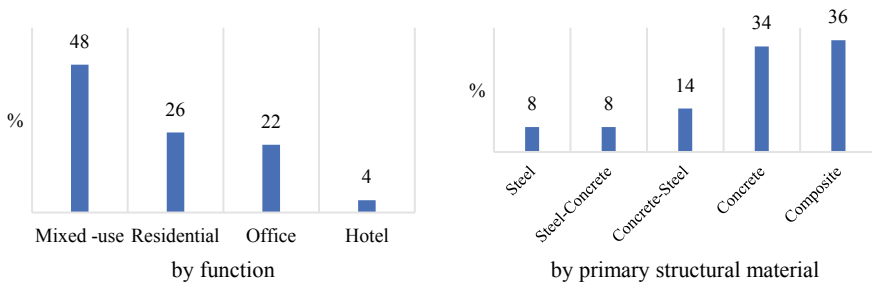


Fig. 1 Tallest 50 buildings with dampers, by function and by primary structural material [1]

2 Earthquakes and Building Dampers in Asia

China is one of the countries often hit by earthquakes with a fairly high earthquake strength. This region is at the intersection of several minor plates of the world that are quite active. As a result, earthquakes have become commonplace even though they have not caused tsunamis like those in Japan and Indonesia. China which is seismically active and is accompanied by the largest population in the world, China contributes about half of the total number of deaths from earthquakes. Be it for the last 50 years or 500 years, China has recorded half of the total fatalities worldwide due to the earthquake.

With more than 1.3 billion population, the potential number of deaths and property is huge. The largest earthquake in China had a 7.5 magnitude earthquake that struck Tangshan in 1976 and caused the death of 242,769 residents. The earthquake in China has an average of 6–8 SR. However, the number of fatalities is usually large. For example, the earthquake in Sichuan (see Fig. 2a), China in 2008 ago. The 7.9 magnitude quake left 69,000 people dead. Earlier in 1927 an earthquake in Gulang also caused 41,000 people to die horribly.

Shanghai Tower is the tallest building in the world that applies a damper to its building structure (see Fig. 2b). With a height of 632 m, someone who is at the top level of the building will feel dizzy. This happens because the shake that the building receives is very fast and wide. To overcome this problem, a damper is needed. In addition to reducing the shake caused by the earthquake, this damper can also make the building stable when hit by strong winds. Damper is located at the top of the building, precisely at an altitude of 581 m or on the 126th floor. The damper type is Tuned Mass Damper (TMD). This system uses a similar device with a 1000-ton pendulum where the pendulum serves to reduce mechanical vibration. This tool will make the building more stable when hit by shocks. The damper at Shanghai Tower works automatically like clockwork with a drift as far as two meters in all directions. The damping system used makes the occupants inside do not feel any movement when shocks occur.

The device which is able to increase the stability of the building is opened to the public (see Fig. 2c), has several supporting facilities such as the fastest elevator in



Image: AsiaNews/Agencies

(a)



Image: Bloomberg

(b)



Image: <http://www.smartshanghai.com/>

(c)

Fig. 2 a Sichuan earthquake effect [2], b Shanghai Tower [3], c Tuned Mass Damper [4]

the world that can run at a speed of 18 m per second. With this speed, visitors can reach the highest peak of the building from the lowest floor in just 55 s.

Japan is located in one of the most dynamic quake zones in the world, the Pacific Ring of Fire. Seismic alerts in this nation are best in the world. Japan began a framework in 2007 that detected the initial shock wave through a system of more than 1000 seismometers throughout the country. The system then signals telephones, TVs and radios throughout the country, as well as stopping trains and giving everyone an extra few second to prepare for the vibrations.

The Ring of Fire is a tectonic plate belt located in the Pacific Ocean and passes the coast of Japan, New Zealand, to North and South America. The Pacific Ring of Fire is a tectonic plate in the valley at the bottom of the Pacific Ocean and causes about 90% of the total cases of earthquakes in the world. Throughout this region, high and low scale earthquakes occur frequently.

In one year, Japan experienced more than 1500 earthquakes and even up to 3000 earthquakes. In addition, Japan is also in the Pacific plate which is actively shifting. As a result, earthquakes with very high strength often occur. On April 14, 2016 Japan was again shaken by an earthquake with a magnitude of 6.2 in Kumamoto. As a result of this earthquake 9 people died and many buildings were damaged. Before this major earthquake occurred, Japan had experienced a large earthquake several times, some even causing a very large tsunami in 2011 such as Tohoku earthquake (see Fig. 3) and Kanto high earthquake 1923.

Japan is certainly one of the role models with a variety of technologies and uniqueness. Buildings that are environmentally friendly and earthquake resistant make this country a place of learning for those who want to design earthquake safe buildings like those in Japan.



Image: Matthew M. Bradle

Fig. 3 Tohoku Earthquake and Tsunami, Japan 2011 [5]

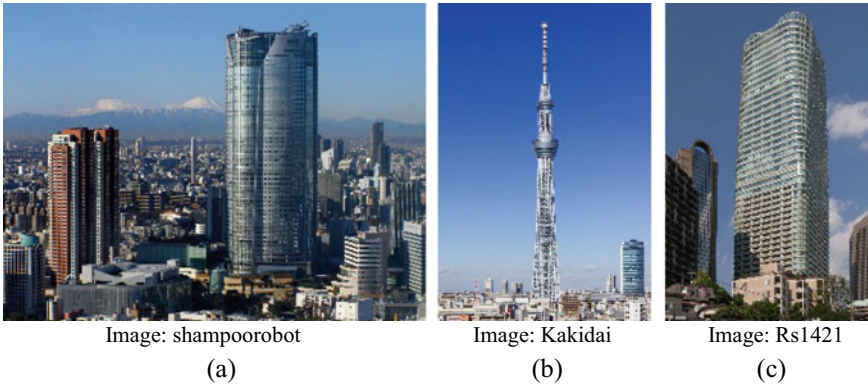


Fig. 4 Buildings in Japan with earthquake resistant structures [6]: **a** Roppongi Hills, **b** Tokyo Skytree, **c** Ark Hills Sengokuyama Mori Tower

The country which is often hit by earthquakes certainly designs their buildings to withstand shocks from small to large ones. Architects and experts also of have found a variety of ways so that their buildings have structures that are stable and resistant to earthquakes. Each type of building has a different structure so that it can withstand shocks. Here are some structures in Japan with some seismic safe structures applied.

Roppongi Hills, the 54-storey building, located in Roppongi, Minato, Tokyo, is one of the tallest buildings in Tokyo with a height of 238 m (see Fig. 4a). The building which is used as an office, restaurant and retail is become one of the earthquake resistant buildings in Japan. The structure is similar to that applied in the Taipei 101 building. In addition to steel pipe reinforcement, the shock absorber technology, namely oil damper, is also used. The building is equipped with 192 vibration dampers that contain liquid dampers. The semi-active damper contains viscous oil, when the building starts to vibrate, the damper will balance the building. Oil in the damper slips in the opposite direction from the direction of the earthquake or wind vibration so that it fights and minimizes shaking in the building.

Tokyo Skytree (see Fig. 4b) is a television and radio signal transmitter tower also functions as an observation tower. Located in Sumida, Tokyo, this building has a height of 634 m. This tower is the tallest structure after the Burj Khalifa. This building has a triangular base plan that turns into a circle on it. The triangular shape of the plan is indeed considered sturdy and can maintain the stability of buildings and circles located at the top can anticipate wind gusts at heights from various directions.

Tokyo Skytree also uses an oil damper located at a height of 125 m from the bottom of its central column. This central column functions as a counterweight so that the outside frame of the building can move when an earthquake occurs. While the vibration damper system will keep the gravity of the tower so that it is always balanced at the top with the bottom. Besides the existence of this column, the foundation of the building is also designed to withstand earthquakes with four piles and reinforced concrete at a depth of 50 m below the ground so that it has a strong foundation.

Ark Hills Sengokuyama Mori Tower (see Fig. 4c). This multi-functional building in Tokyo also uses oil damper technology that is commonly found in skyscrapers in Japan. But in addition to using vibration dampers, this building is also reinforced with steel plates mounted on each floor. This plate is attached to the upper wall cavity while the lower part of the wall is attached to the vibration damper. In addition, there is also a V-shaped column structure mounted on the floor of the building so that the building load is transferred in all directions, not directly to the bottom of the building. This is because column V has a function with a triangular frame that divides the load in all directions.

The Philippines is also located in the Pacific Ring of Fire which is on the border of the Pacific plate, an active seismic zone. The danger posed by the earthquake in Manila will be three times greater. What is more, this country is also crossed by the Pacific Ring of Fire, making the Philippines not only prone to earthquakes, but also volcanic eruptions. These two combinations made the Philippines often experience quite devastating earthquakes and caused many deaths. The 7.2 SR earthquake that struck the Bohol region of the central Philippines on October 15, 2013 was the deadliest earthquake and very severe infrastructure damage with the energy released equivalent to 32 Hiroshima atomic bombs (see Fig. 5a). An earthquake with a magnitude of 7.9 magnitude also occurred in 1976 which caused the death of up to 8000 people. The average earthquake in the Philippines has a magnitude of 6–8 SR and can be felt almost every year.

The Grand Hyatt building in Manila (see Fig. 5b), has almost the same height as the St Francis Shangri-La Place building in the same city. The St Francis Shangri-La Place (see Fig. 5c) at Mandaluyong City in Metro Manila is the tallest private elevated structure in the nation. This building involves two towers, each rising 60 stories to 217 m high. A total of 32 dampers was applied, 16 for each tower. These dampers are similar that applied at Millennium Bridge over the River Thames in London. Different with St Francis Shangri-La, The Grand Hyatt building only apply



Image: REUTERS/Erik De Castro

(a)



Image: Lawrence Ruiz

(b)



Image: Rob J. Smith

(c)

Fig. 5 a The Philippines earthquake 2013 [7], b Grand Hyatt Metrocenter, Manila [8], c Damper installation of St Francis Shangri-La, Manila [8]

the outrigger damper in only one direction and additional 4 dampers with 2MN capacity.

India has the second highest population after China, which means the potential loss of death if there is an earthquake is also large of a number. The area around New Delhi is located close to the Indian tectonic plate and make it have a high risk. Shifting tectonic plates at speeds reaching 47 mm per year often results in large earthquakes. Indian territory is divided into 5 zones based on the acceleration of plate movements. The city of Gujarat in India has experienced the third most destructive earthquake in history in the world. Many brick buildings that can easily collapse and hit the occupants in it. Brick buildings dominate damage and fatalities. The average annual cost due to an earthquake in New Delhi reaches US \$ 150 million.

Delhi ATC is the first building in India to apply TMD, which is positioned at an altitude of 91 m (see Fig. 6b). The new ATC tower is not only vulnerable to strong winds but can also face massive damage in the event of an earthquake. ATC Delhi is the most unique in the world because it has a shape that changes from the bottom to the roof. The top two levels of the tower are steel, the rest is built using high strength reinforced concrete. The tower steps on a raft as deep as 3.0 m and is supported by 32 piles with a diameter of 1.5 m.

Pakistan, the mountains in Pakistan are also prone to earthquakes. In 2005, an earthquake in the mountains of the country killed more than 76,000 people. Pakistan stands on both the Indian and Eurasian plates, which are often seen to shake. The northern region of the country, whose land is filled with highland cities like Muzaffarabad, is most at risk. Geologically, Pakistan is in the Indus-Tsangpo Suture Zone. This zone has the highest level of seismic activity and the biggest earthquake in the Himalayan region. Because of plate movements in the Himalayas, Pakistan carries a large seismic risk and can ‘eliminate’ the country in one big shock.

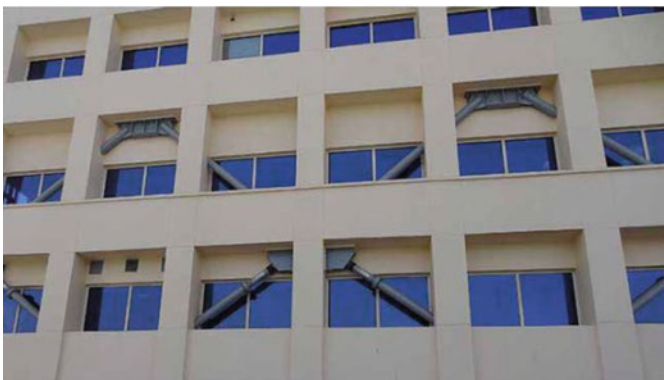


Image: Sandeep Donald Shah

(a)



Image: BuroHappold engineering and HOK

(b)

Fig. 6 a India’s Delhi international airport administration building with Damper, b ATC building with damper in New Delhi airport [9]

Nepal is located in the Himalayan mountains, which make it an earthquake hotspot. The existence of a mountain range in Nepal makes this country earthquake-prone. These mountains arise due to the Indian tectonic plates pressing under the Central Asian region. These two plates move closer to 4–5 cm per year. It can be said, the population of Nepal has the potential loss of life due to an earthquake greater than the population in other regions of the world. Buildings in Nepal started to adjust strategies to make homes and schools more secure from earthquakes. Traditional buildings that use brick material do not have to be replaced with steel and reinforced concrete, because they can make earthquake-safe buildings using bricks and mortar.

As for Indonesia, it is almost the same as Japan, this country is basically surrounded by most of the earth's subduction zones, making the ocean reproducing volcano from Sumatra to the Nusa Tenggara region so that volcanic earthquakes often occur. Indonesia is in a precarious area given its vulnerability to earthquakes and other natural disasters. The capital of Indonesia, Jakarta is also in a dangerous area. Not only in the pacific ring of fire, but also this metropolitan city is lower than sea level and has soft land. Thus, the impact caused by an earthquake will be more massive. As a result of plate movements, large earthquakes often shake Indonesia. Some of them cause quite severe tsunamis, such as earthquake in Aceh on December 26, 2004. This earthquake caused a tsunami and caused 200,000 people to die. In addition to the earthquake in Aceh there are still a series of other earthquakes such as the Nias Earthquake (2005) and the Yogyakarta Earthquake (2006).

International joint workshop 2018 at Bandung Indonesia, Wijanto and Montgomery has introduced a design called Jakarta Signature Tower (Fig. 7a). The importance of this building as a reflection for Indonesia and Southeast Asia as the developer has carried out in-depth research on the use of a damping system that will be applied to protect buildings in Southeast Asia in the future. Viscoelastic Coupling Dampers (VCDs) systems (Fig. 7b) are used for reasons such as reduced building structure costs because of the benefits of having a VCDs [10]. VCDs are well integrated into building structures. VE material has the longest performance record of all dampers (1969) and has no maintenance, monitoring or replacement requirements.

3 Energy Dissipation Methods

Damper and isolator function to protect the structure from shocks. This technology is generally used in machine transmissions, car engines, and buildings. In the construction field, it is used to control the movement of buildings by reducing the velocity and distance of buildings displacement.

To achieve a satisfactory earthquake response of a structure, there are three methods that can be applied practically and efficiently, namely:

- **Base Isolation**, is the earliest and tested technology with applications that are quite extensive compared to the other two systems.

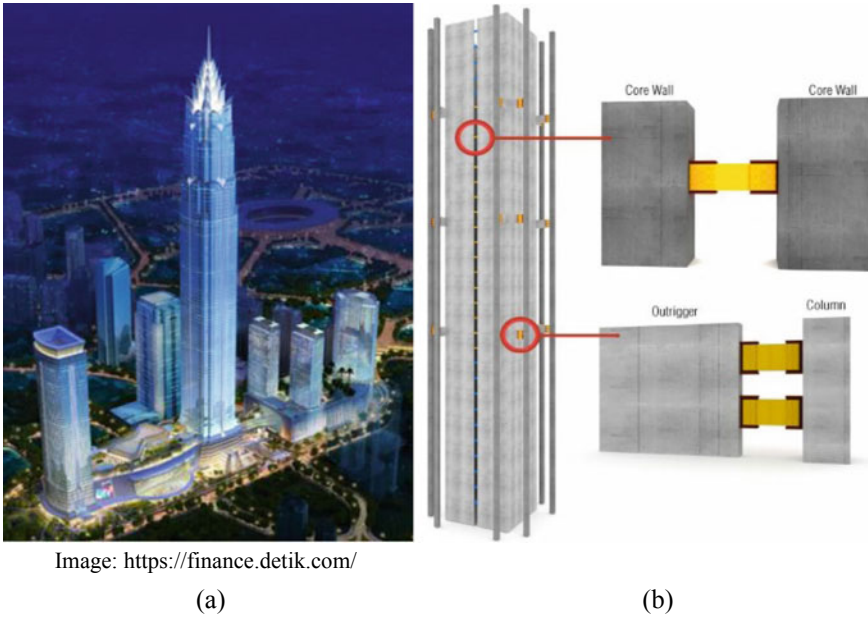


Fig. 7 **a** Design of Jakarta Signature Tower 2018, **b** Viscoelastic Coupling Dampers proposed for Jakarta Signature Tower [10]

- **Passive Energy Dissipation**, energy absorption in plastic joints, this system includes various materials and tools to increase damping, stiffness and strength. This system can be used as earthquake hazard mitigation and also for rehabilitation of structures that are not feasible anymore.
- **Active, Hybrid and Semi-active Structural Control**, use of mechanical devices as structural controls. It is an evolution of passive control technology, and it make it possible with a hybrid system between passive and active systems.

3.1 *Passive Energy Dissipation*

The main principles to use passive energy dissipation devices in a structure is to limit damaging deformations in structural components. Simplified at Fig. 8, effect of incorporating passive energy dissipation systems in structures when subjected to a single historical earthquake record. Basically, the main concept of the use of structural control devices is the response parameters, both in passive control, active control and semi-active control. In passive control, systems will work without needing a power supply. The behavior seen in the structure is eliminating energy and ultimately reducing responses. Some devices that are included in the passive control structure include friction damper, yield damper, viscous damper, visco-elastic damper.

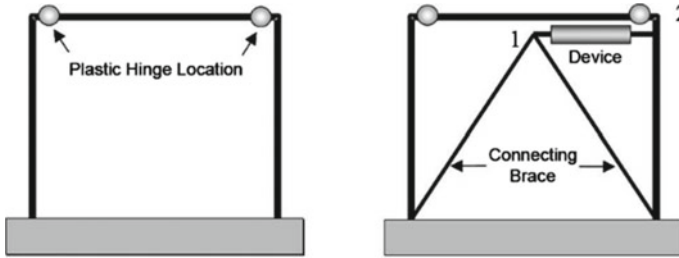


Fig. 8 Frame without and with energy dissipation device [11]

Low frequency and amplitude are applied to structures with a passive control system to modify the vibration characteristics of the structure [12]. Soong 1994 has reviewed a lot of damper systems and their behavior in responding to earthquakes in structures [13]. Symans 2007 has also been reviewed specifically on Semi active control systems [11] and passive hybrid control systems have been reviewed by Makris [6]. In 1996, Housner conducted research with its application to the US Panel on Structural Control and some of the applications of passive devices in structures in Japan are also covered [14].

Currently the device most widely used to control the vibrations of buildings during seismic attacks is passive control damper devices for earthquake energy dissipation. There are already many types of dampers currently available on the market, using a variety of materials and designs to obtain varying degrees of stiffness and damping. Some of these include viscous dampers, hysteresis dampers, viscouelastic dampers, and friction dampers (see Fig. 9), the use a variety of materials to obtain various

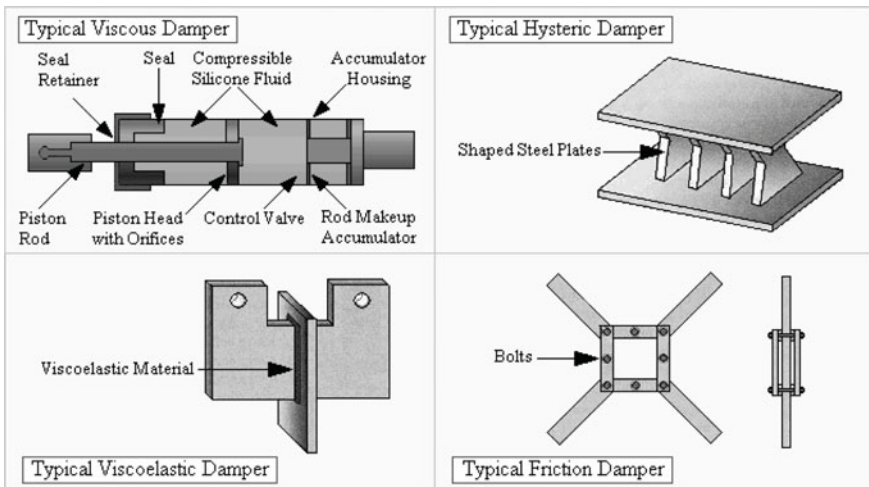


Fig. 9 Types of Passive Energy Dissipation [15]

levels of stiffness and damping. These dampers have been reviewed in Soong and Dargush (1997) [15].

Several passive energy dissipation devices have been suggested and used for wind and earthquake loads. The devices are categorized according to how they operate. Following is a brief discussion of the application of each device:

Dampers are usually installed between two structural elements (walls or columns) for the new construction to be built. In existing buildings dampers can be installed between shear walls or between columns. An effective damping system can produce a higher level of safety and comfort.

Passive energy dissipation devices are commonly classified as follows:

- The dissipated energy depends on the relative displacement between each end of the systems called Displacement Dependent Devices DDD or hysteretic devices (friction devices, metallic, yielding devices), and
- Depends on its relative velocity called Velocity Dependent Devices VDD (solid, viscoelastic and fluid viscous dampers).

These classifications are used in Chap. 18 of ASCE 7–16.

Fluid Viscous Dampers Sample. Viscous Fluid Dampers (VFDs) devices have begun to be developed, including viscous walls developed by the Sumitomo Construction Company, which consists of plate elements that move in thin steel shrouds filled with VFDs. VFDs damper generally consists of a piston in a chamber filled with silicon material or similar to oil, and on the piston, there are a number of small holes through which liquid can pass from one side of the piston to the other side, which are called orifices (see Fig. 10).

Viscous Fluid Dampers (VFDs) provide the optimal method for reinforcing historic and important buildings. Because of the importance of these buildings, these structures must be preserved and need to meet seismic performance requirements during an earthquake.

Hysteretic Damper. Also known as Metallic Dampers utilize the hysterical behavior of metals in the inelastic area, so the strength of the damper depends on the nonlinear stress–strain characteristics of the metal material. Various types of metallic damper have been examined in a review of the sliding area, bending, and material in the plastic range. The most important characteristics of this device are its stable hysteresis behavior, long-term reliability, and insensitivity to temperature changes. This device is also relatively inexpensive, and its material properties are stable over the life of

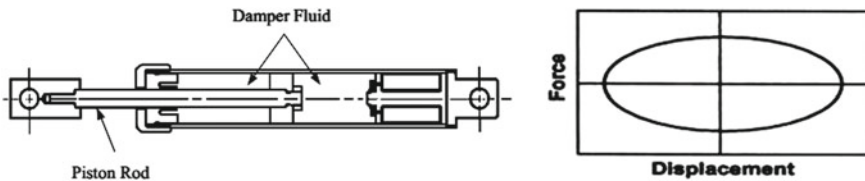


Fig. 10 Design and hysteresis behavior of VFDs [16]

the structure. The disadvantage of this device is the limited number of work cycles and its non-linear response.

The most widely used type of metallic damper is X-shaped plate dampers (see Fig. 11a). The design is in the form of a series of X-shaped steel plates which were introduced by the Bechtel Power Corporation. Experimental studies of this device have been carried out by Bergman et al., (1987) and Whittaker et al., 1991 [3] (see Fig. 11b). Several applications of non-linear structural analysis for building frameworks that apply metal dampers are also carried out by Xia and Hanson (1992), Jara et al., (1993). X-shaped plate dampers show good performance and prove stable under large axial loads.

Viscous-elastic Damper. Viscous-elastic damper (VED) has the characteristic of shifting forces that occur at the relative speed at the tip of the damper and the frequency of movement. However, the response of this device may also be a function of relative displacement. VED shows stiffness and damping coefficients that are frequency dependent. In addition, the damping strength of this device is proportional to the speed, whose behavior is viscous. Research and development of VED for seismic applications began in the early 1990s. During the last few years experimental research has been designed and applied to steel frames and reinforced concrete frames [18] and the Design and Hysteresis behavior of Viscous-elastic Damper see Fig. 12. VED is mostly used in structures that are predominantly subjected to shear deformation.

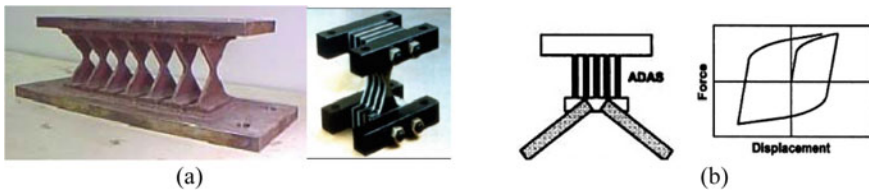


Fig. 11 a X-shaped plate dampers [17], b Design and Hysteresis behavior of Hysteretic Damper [11]

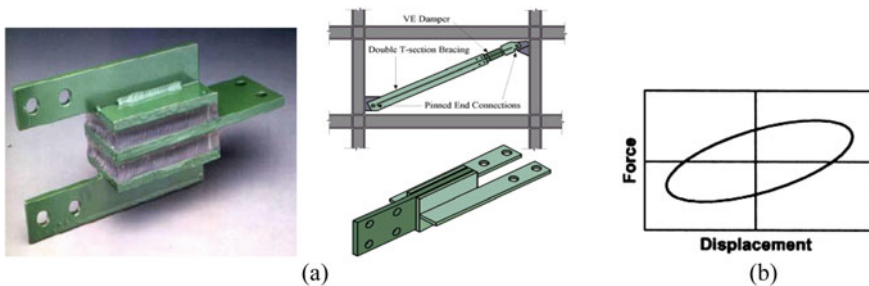


Fig. 12 Design and Hysteresis behavior of Viscous-elastic Damper [18]

Friction Damper. Various friction dampers designs have been developed and applied to building structures. Friction dampers are able to anticipate large amounts of energy, have good performance characteristics and are not affected by load frequencies, number of load cycles, or temperature changes. X-bracing damper was investigated by Pall et al. [19] (see Fig. 13), idealized hysteretic behavior of friction jointed brace see Fig. 14. In this type, bracing devices as frictional devices are able to hold moments in the frame. When a load is applied to this damper, a tension occurs in one of the braces that slips the connection so that all four links compresses.

Tuned Mass Damper. Tuned mass dampers (TMDs) are the most passive control system used to improve building performance against vibrations (see Fig. 15).

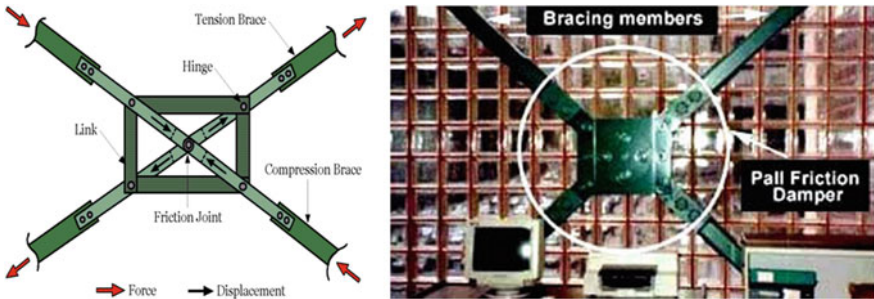


Fig. 13 Design Pall Friction Damper [20]

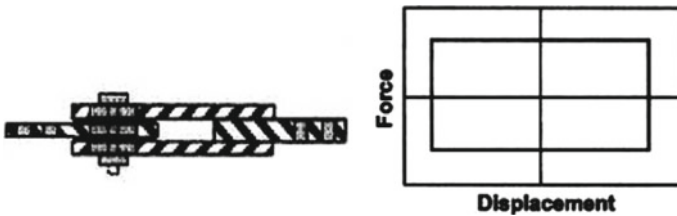
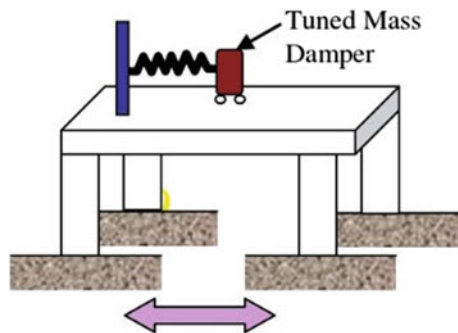


Fig. 14 Basic Design and Hysteresis behavior of Friction Damper [19]

Fig. 15 SDOF frame with Tuned mass damper [21]



Because of its simplicity and efficiency, it has become the most practical application used by tall buildings in the world.

Wu and Chen in 2000 [22] introduced the Multiple Tuned Mass Damper (MTMD) system with several variable number of oscillators. Li continued in 2002 [23] and was able to measure parameters in an optimal MTMD such as frequency range, average attenuation ratio, tuning frequency ratio, mass ratio, and the total number of MTMD tools by controlling for maximum displacement and acceleration factors.

Even though there have been many studies on the structure applied by MTMD with numerical earthquake loads, the application of TMD to the structure has been done only to withstand wind vibrations. In 1989, the use of an active mass damper type in order to anticipate earthquake loads was applied to the 11-story Kyobashi Seiwa Building in Tokyo [24].

4 Low-Rise Building with Damper

In the past, there were not too many tall buildings in most of country, especially in Asia for public buildings such as school, shop-house and meeting-hall, which is at present almost all these buildings are not feasible anymore if evaluated according to the latest earthquake regulations. It is become the main requirement to do an innovation on the current building so that it can improve its seismic performance.

Soda and Iwata has conducted research on viscous damper application on low rise buildings [25]. Viscous damper as seismic control installed at first story in order to rise the performance of low-rise building. Model of 5-DOF with seismic response analyzed to validate and compare the behavior of model at experimental result. In Fig. 16, the hysteresis loops between three model, that are un-control (UC), viscous damper (VD) and semi-active control (SAC), proven that the large displacement concentrate on first story that causing building will collapse. The larger displacement happens at UC building and can reduce by VD and SAC, on the other hand they can reduce the acceleration response in the upper stories.

Das and Choudhury studied the Tuned Liquid Damper (TLD) for low-rise buildings [26], by applying a variable ratio of water depth to tank width, variation in excitation frequency and amplitude. TLD application is carried out on a reinforced concrete building model scale 3/4 and tested in a shaking table. The TLD is mounted on the roof of the model building and applies dynamic response to models without TLD and models with TLD. Another variable is comparing normal water use with a sugar-water solution. It can be seen that the TLD on the flat rectangular type can control the vibration response of low-rise building models better and satisfactorily. Also, sugar-water solutions provide better responses (see Fig. 17).

Kaur 2012, corresponding peak top floor displacement and peak top floor acceleration of the three structures for different number of stories and earthquakes are shown in Tables 1 [27]. It is observed that in the brace frame (BF), owing the increase as compared to that in case of the moment resisting frame (MRF). In the friction damper frame (FDF), due to slip across the friction damper, the peak top floor displacement

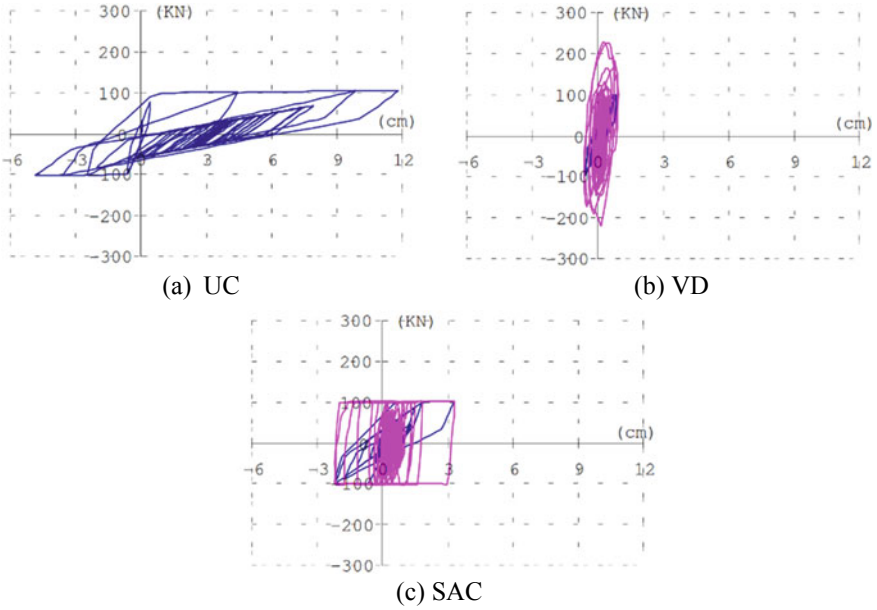


Fig. 16 Hysteresis loops comparison between un-controlled, viscous damper and semi active control [25]

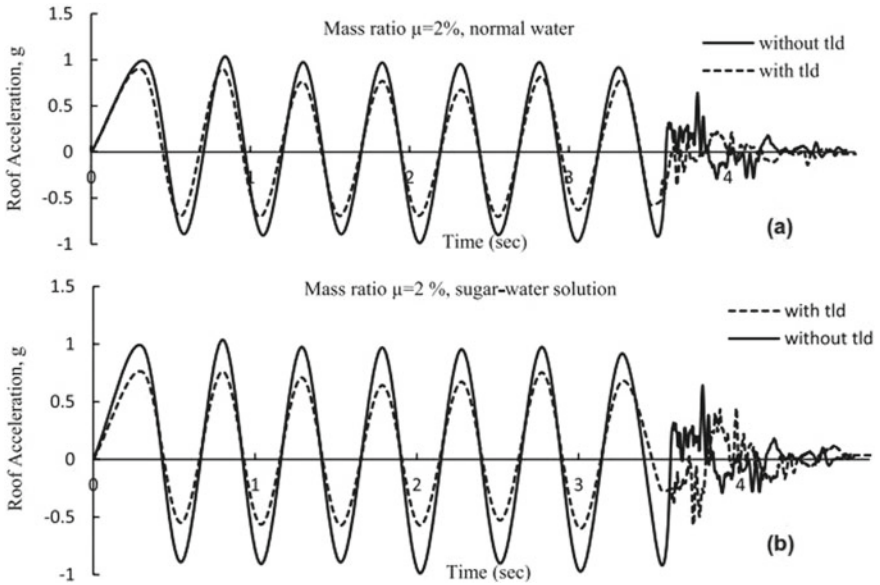


Fig. 17 Acceleration response reduction at roof [26]

Table 1 Roof Displacement response at different stories [27]

Number of stories	Displacement at roof (mm) Kobe earthquake, 1995		
	MRF	BF	FDF
5	12.05	8.21	8.56
10	47.45	22.54	41.77
15	25.31	49.16	23.44
20	36.68	33.28	27.09

is amplified as compared to that in case of the BF. However, the values are still lesser than that in case of the MRF.

It is observed that for 15 stories building, the FDF provides a seismic response reduction of 23.21% in the top floor displacement, whereas the BF provides a reduction of 70.41% in the seismic response, both compared to the top floor displacement of the MRF. In the FDF, peak top floor acceleration reduces as compared to that in case of the MRF due to energy dissipation by the friction dampers [27].

Liyanage 2012 and Garivani 2018. Metallic yielding dampers are passive control energy dissipation devices that are designed to reduce earthquake energy in building structures. This damper is made of metal, is one device that is very efficient because it can reduce seismic energy through hysteretic behaviour (see Fig. 18). This research uses ETABS software to analyse the performance of three metal dampers. X-shaped Metallic Damper, Double X-Shaped, and Comb Teeth Damper. The parameter reviewed is the response at each level shown by the analysis of the shear story [28, 29].

Liyanage 2018 analyse building structure with Added damping and stiffness devices (ADAS) for 5 stories and 20 stories. The analysis shows that both ADAS and Comb teeth dampers perform well when subjected to both high frequency and low frequency earthquakes. ADAS dampers made from steel performed better than the other ADAS dampers. For the two ADAS type dampers the performance level was high for higher number of plates. Comb teeth dampers made from aluminium showed better results than dampers made from steel. It was observed that the number

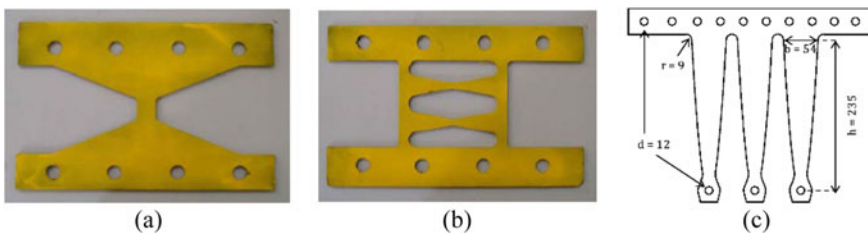


Fig. 18 Metallic yield dampers **a** X-shaped [28], **b** Double X-shaped [28], **c** Comb Teeth Damper [29]

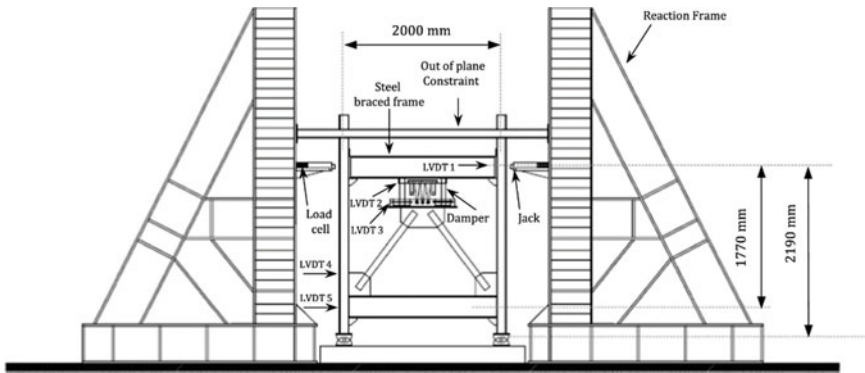


Fig. 19 Test set up of Garivani’s experimental research [29]

of teeth affected the performance of these dampers. The lesser the number of teeth, the better the performance will be [28].

Garivani 2019 conducted numerical and experimental studies of steel frames reinforced concentrically with the Chevron bracing model and placed the damper the bracing on the side close to the beam [29] (see Fig. 19). Two model of frames are analysed, namely a low-rise building with five floors and a high-rise building with twenty floors. Site location for both structures is in the California region of the United States. The structure is analysed by referring to the two earthquakes Loma Prieta and San Fernando which represent the two major earthquakes that struck California in the nineties.

Espinoza 2018, has conducted research by studying the behaviour, especially in low-rise buildings with tuned mass damper applications as well as considering the soil parameters that exist under the structure. Seismic excitation frequencies content uses two earthquake recordings and two artificial earthquakes which correspond to the Chilean code NCh2745 with high frequency and earthquakes similar to the 1985 Mexico earthquake with low frequency characteristics. the results show that TMD is able to optimally and efficiently control the response of all soil type variables [30].

5 Summary

Conventional building design will no longer be suitable when the building being designed is required that the structure must be able to survive its functions after earthquake. For this purpose, structures must be designed with sufficient strength and ductility so that inelastic deformation can be reduced. Comparison of the effectiveness of passive, active, and semi-active control systems shows that semi-active systems have better behavior for seismic protection when compared to active and passive control systems. Base Isolators provide a foundation that performs well for large structures located on hard ground against earthquakes. Base Isolators and

viscous dampers that work in hybrids will behave very well under strong earthquakes. Although semi-active controls are the best in energy dissipation, passive damper energy dissipation is more suitable for implementation as it is more readily available, accessible and cheaper. For the purpose of improving the performance of existing buildings, passive control is the best system applied to old and low rise buildings, that were built referred to old seismic code, without having to make major improvements to structural elements.

6 Suggestions

Laboratory experiments that are preceded by numerical model simulating existing buildings performance are needed for more applicative purposes so that the proposed system will be more useful and can be applied immediately, especially for low-rise buildings in disaster-prone areas of developing countries.

References

1. Safarik D, Wood A, Panseri S, Jory J, Jory J (2018) Construction of tall buildings. no. iii, [Online]. Available: <https://store.ctbuh.org/journal/209-2018-journal-issue-iii.html>
2. Kelly, Luke, Dhaval, and Tim, Sichuan Earthquake 2008. <https://earthpbl.wordpress.com/sichuan-earthquake-2008-kelly-luke-dhaval-and-tim/>.
3. Al-Kodmany K, Ali MM, Zhang T (2013) Importing urban giants: Re-imaging shanghai and Dubai with skyscrapers. *Archnet-IJAR* 7(2):22–42. <https://doi.org/10.26687/archnet-ijar.v7i2.153>
4. Kayabekir AE, Bekdaş G, Nigdeli SM, Geem ZW (2020) Optimum design of PID controlled active tuned mass damper via modified harmony search. *Appl Sci* 10(8):1–16. <https://doi.org/10.3390/APP10082976>
5. Zaré M, Ghaychi Afrouz S (2012) Crisis management of Tohoku; Japan earthquake and tsunami, 11 March 2011. *Iran J Public Health* 41(6):12–20
6. Spencer BF, Nagarajaiah S (2003) State of the art of structural control. *J Struct Eng* 129(7):845–856. [https://doi.org/10.1061/\(ASCE\)0733-9445\(2003\)129:7\(845\)](https://doi.org/10.1061/(ASCE)0733-9445(2003)129:7(845))
7. Lagmay AMF, Eco R (2014) Brief communication: on the source characteristics and impacts of the magnitude 7.2 Bohol earthquake, Philippines. *Nat Hazard* 14(10):2795–2801. <https://doi.org/10.5194/nhess-14-2795-2014>
8. Smith R (2016) The damped outrigger—design and implementation. *Int J High-Rise Build* 5(1):63–70. <https://doi.org/10.21022/ijhrb.2016.5.1.63>
9. Ho S, McCormick F, Sheppard J, De Sá Caetano E (2013) The Delhi air traffic control tower: engineering, architecture and design with TMD for the tallest ATCT in India. *IABSE Congr Rep* 18(2):1927–1934. <https://doi.org/10.2749/222137912805112680>
10. Pant DR, Montgomery M, Christopoulos C, Xu B, Poon D (2017) Viscoelastic coupling dampers for the enhanced seismic resilience of a Megatall building. In: 16th World Conference Earthquake Engineering, no. Dec 2016 pp 1–9
11. Symans MD et al (2007) Energy dissipation systems for seismic applications: current practice and recent developments. *J Struct Eng* 134(1):3–21. [https://doi.org/10.1061/\(asce\)0733-9445\(2008\)134:1\(3\)](https://doi.org/10.1061/(asce)0733-9445(2008)134:1(3))

12. Ian B (1993) Seminar on seismic isolation, passive energy dissipation, and active control. In: Proceedings of ATC-17-1 seminar, pp 435–446
13. Soong TT (1994) Constantinou MC Passive and active structural vibration control in civil engineering, 345th ed. Springer, Wien
14. Housner et al (1997) Structural control: past, present, and future. *J Eng Mech* 123(9):897–971. [https://doi.org/10.1061/\(ASCE\)0733-9399\(1997\)123:9\(897\)](https://doi.org/10.1061/(ASCE)0733-9399(1997)123:9(897))
15. Soong TT, Dargush GF (1997) Passive energy dissipation systems in structural engineering 1st edition, 1st edn. Wiley, US
16. Tsuji M, Nakamura T (1996) Optimum viscous dampers for stiffness design of shear buildings. *Struct Des Tall Build* 5(3):217–234. [https://doi.org/10.1002/\(SICI\)1099-1794\(199609\)5:3%3c217::AID-TAL70%3e3.0.CO;2-R](https://doi.org/10.1002/(SICI)1099-1794(199609)5:3%3c217::AID-TAL70%3e3.0.CO;2-R)
17. Hameed A, Qazi A-U, Rasool AM (2014) Seismic performance of low to medium rise reinforced concrete buildings using passive energy dissipation devices. *J Engg Appl Sci* 14(January):1–16
18. Shen KL, Soong TT (1995) Modeling of viscoelastic dampers for structural applications. *J Eng Mech* 121(6):694–701. [https://doi.org/10.1061/\(ASCE\)0733-9399\(1995\)121:6\(694\)](https://doi.org/10.1061/(ASCE)0733-9399(1995)121:6(694))
19. Engr P, Group TSNC, Desjardins C, Studies B (1982) Pall, Avtar S., and Cedric Marsh. ‘Response of friction damped braced frames.’ *Journal of Structural Engineering* 108.9 (1982): 1313–1323.,” vol. 108, no. June, 1982.
20. Pall AS, Pall RT (2004) Performance-based design using pall friction dampers - an economical design solution. In: 13th world conference earthquake engineering, no. 1955, p. Paper No. 1955 (2004), [Online]. Available: https://www.iitk.ac.in/nicee/wcee/article/13_1955.pdf
21. Parulekar YM, Reddy GR (2009) Passive response control systems for seismic response reduction: A state-of-the-art review. *Int J Struct Stab Dyn* 9(1):151–177. <https://doi.org/10.1142/S0219455409002965>
22. Wu J, Chen G (2000) Optimization of multiple tuned mass dampers for seismic response reduction. *Proc Am Control Conf* 1(June):519–523. <https://doi.org/10.1109/acc.2000.878954>
23. Li C (2002) Optimum multiple tuned mass dampers for structures under the ground acceleration based on DDMF and ADMF. *Earthq Eng Struct Dyn* 31(4):897–919. <https://doi.org/10.1002/eqe.128>
24. Kobori T (1996) Future direction on research and development of seismic-response-controlled structures. *Comput Civ Infrastruct Eng* 11(5):297–304. <https://doi.org/10.1111/j.1467-8667.1996.tb00444.x>
25. Soda S, Iwata N (2000) Seismic design of low to mid-rise building with a soft first storey subject to semi-active viscous damping control. In: Proceeding 12th World Conference Earthquake Engineering Auckland, New Zealand, vol. Paper No., pp 1–8
26. Das S, Choudhury S (2017) Seismic response control by tuned liquid dampers for low-rise RC frame buildings. *Aust J Struct Eng* 18(2):135–145. <https://doi.org/10.1080/13287982.2017.1351180>
27. Kaur N (2012) Earthquake response of mid-rise to high-rise buildings with friction dampers. *Int J High-Rise Build* 1(4):311–332. <https://doi.org/10.21022/IJHRB.2012.1.4.311>
28. Liyanage UDD, Perera TN, Maneetes H (2018) Seismic analysis of low and high rise building frames incorporating metallic yielding dampers. *Civ Eng Archit* 6(2):41–53. <https://doi.org/10.13189/cea.2018.060201>
29. Garivani S, Aghakouchak AA, Shahbeyk S (2019) Seismic behavior of steel frames equipped with comb-teeth metallic yielding dampers. *Int J Steel Struct* 19(4):1070–1083 (2019), [Online]. Available: <https://doi.org/10.1007/s13296-018-0188-6>
30. Espinoza G, Benedetti F, Alvarez-Mendoza P, Bonilla E (2018) Influence of the seismic excitation frequencies content on the behavior of a tuned mass damper in low-rise building considering soil-structure interaction. *Lat Am J Solids Struct* 15(8). <https://doi.org/10.1590/1679-78254868>

Numerical Modelling of Concrete-Filled Steel Tube Columns Under Eccentric Loading



Joarder Md. Sarwar Mujib, Avijit Pal, Ibriju Ibrahim, and Tanvir Mustafy

Abstract Concrete-filled steel tubular (CFST) columns have been widely adopted in structural engineering. It is used most often for tall building structures and bridge piers construction processes to enhance and modify the structural behaviors. CFST columns are a form of composite construction that comprises of concrete-filled into a steel tube. The purpose of using a steel tubular structure is to provide necessary confinement to the concrete core of the construction. This confinement eventually leads to the increment of deformation capacity and compressive strength for the inherent material property of the concrete. Under the concentric loading phenomenon, compressive loading on CFST columns has been studied, and constitutive models were developed. But there is still a lack of data on the eccentric loading mechanism of the CFST columns. In this paper, compressive loading on CFST columns under both concentric and eccentric conditions have been simulated using ABAQUS based on experimental data and a numerical modelling approach has been developed. Experimental data have been used for numerical modelling comparison. Load–deflection behavior, failure modes, and ultimate strength have been investigated. A new strain hardening/softening function is developed for accurately simulating the damaged plasticity material model of the concrete structures. The results indicated that the response of the models in the plastic zone is greatly influenced by the dilation angle and the ratio of the second stress variant on the tensile meridian. Also, the contact stress between the steel and concrete responds sensitively with the eccentric ratios, which indicate a profound effect of the steel tube confinement of the considered structure.

Keywords CFST columns · Eccentric loading · Finite element analysis · Stress–strain model

J. Md. Sarwar Mujib · A. Pal (✉) · I. Ibrahim · T. Mustafy
Military Institute of Science and Technology, Dhaka, Bangladesh

T. Mustafy
e-mail: mustafy@ualberta.ca

T. Mustafy
University of Alberta, Edmonton, Canada

1 Introduction

In recent years, the limited land area encouraged the erection of high-rise buildings. This type of construction requires the structural capacity to be increased. Due to passive confinement of concrete-filled steel tube (CFST) columns, CFST columns can bear a tremendous amount of load, which makes it suitable for high-rise buildings. In general, the steel tube of a CFST column provides confinement to the concrete, and the concrete core prevents early local buckling of the steel tube [1].

So far, numerous experimental and numerical investigations have been conducted on the behavior of CFST columns under axial load, whereas research on concrete-filled steel tubular columns under eccentric loading is still quite limited. A finite element (FE) analysis using the commercial software ABAQUS was performed by Tao et al. [2] to analyze the non-linear behavior of circular and square CFST stub columns under axial loading. An experimental and numerical study was performed by Lee et al. [1] on circular CFST columns under eccentric loading to find the strength behavior of the short columns where they modeled the concrete as confined as well as unconfined conditions. The variation of specimen parameters was the D/t ratio and eccentricity ratio. The experiment showed the relation between stiffness, axial stiffness, and flexural ductility with the D/t ratio. The variation between experimental and fiber element analysis result was satisfactory. Evirgen et al. [3] performed an experimental and finite element study to investigate ultimate load, axial stress, ductility, and buckling behavior on circular, hexagonal, rectangular, and square sections where parameters used were b/t ratio and compressive strength of concrete under axial compression. Circular sections showed excellent performance than other sections in terms of axial stress and ductility values. However, FE analysis results varied a lot from the experiments. An extensive study was done by Gupta et al. [4] on circular columns with various parameters such as slenderness ratio and D/t ratio under concentric loading. They found the results of the analytical model partially matching with the experimented results. Uy et al. [5] studied box columns with different b/t ratios and concrete strength. The aim was to find out the local buckling of the box columns, and experimental results differed a lot in the inelastic region from the model but can predict the behavior quite accurately in the elastic region. An experimental and numerical investigation was carried out by Wang et al. [6] for square columns having different slenderness ratio under axial compression to study the static behavior of CFST columns. The study showed that the FE analysis results agree reasonably well with the experimental results being on the safe side. Xiong et al. [7] had done a numerical study on CFST columns under axial compressive load considering initial stresses. They found a moderate variation of numerical results and experimental results.

This paper aims to develop a refined FE model using ABAQUS, which can predict the behavior of the CFST column under concentric as well as eccentric loading accurately. To accomplish this task, this study was performed with varying various parameters of concrete damage plasticity, and a new strain hardening/softening rule was developed. There was a total of 23 experimental data that had been collected

from various research papers and used to compare the numerical result with the test result. A parametric study was also carried out numerically with different shapes, eccentricity, slenderness ratio, steel ratio, the tensile strength of steel, the compressive strength of concrete to investigate the behavior of the CFST column.

2 FE Modeling

2.1 General

To model the CFST columns for simulation, finite element program ABAQUS 6.14 [8] was used. Four node shell element S4R was adopted to model the steel tubes of the CFST members. This was explained by Lai et al. [9], These elements have: (i) six degrees of freedom per node, and (ii) reduced integration in the plan of the elements, and (iii) five-section points to compute the stress and strain variations through the thickness. The elements model thick shell behavior but converge to Kirchhoff's thin plate bending theory with reducing thickness. The concrete infill of CFT members was modeled using eight-node solid elements with reduced integration (C3D8R). These elements have three degrees of freedom per node and reduced integration to calculate the stresses and strains in the elements. The C3D8R elements are computationally useful for modeling concrete cracking.

To model the columns, mesh convergence was adopted from [2], element size across the cross-section was chosen as $B/15$ for a square column or $D/15$ for a circular column, where B and D are the overall width and diameter of the square and circular tube and, respectively. For a typical specimen, the mesh contains a total of over 4000 elements.

The interaction between the concrete infill and the surrounding steel tube was simulated by using surface-to-surface contact. In the normal direction of the contact between steel inner and concrete outer surface, the "hard contact" pressure-overclosure relationship was used, where the separation of the interface in tension and no penetration of that in compression is allowed. For tangent contact between two surfaces, the Coulomb friction model was used. In the current model, the friction coefficient was adopted to be 0.25.

The Poisson's ratios for concrete and steel were taken as 0.2 and 0.3, respectively. These values have been used widely in FE numerical simulation [2].

Initial geometric and local imperfection, as well as residual stresses, were ignored, as they have minimum influence in the presence of concrete filling inside the steel tube. This was explained in [2].

2.2 *Boundary Conditions*

Columns under Concentric Loading. As explained in [2], for stub columns with welded end plates and/or stiffeners, there is no need to include the endplates or stiffeners in the model. Instead, the top and bottom surfaces of the steel tube and concrete can be fixed against all degrees of freedom except for the displacement at the loaded end (clamped end condition). The result obtained is the same as that of the model with end plates and/or stiffeners. So, to model the columns under concentric loading condition, the displacement load ($U1 = U2 = UR1 = UR2 = UR3 = 0$) was placed at the middle load point (reference point) at the top of the column. All the nodes of the steel tube and elements of concrete core were constrained with the reference point. The constraint of the reference points was modeled as MPS type beam constraint which acts as the stiffeners or welded plates. The bottom of the column was fixed against all degrees of freedom ($U1 = U2 = U3 = UR1 = UR2 = UR3 = 0$).

Columns under Eccentric Loading. The eccentricity is defined along the x-axis, which allows the section to rotate about the y-axis. As the eccentric load was applied on the x-axis of the CFST sections, constraining ($UR1 = UR3 = 0$) at the top and bottom of the column significantly reduces the time consumption of the simulation without compromising the accuracy of the FE analysis. To apply the displacement load at the middle load point of the column reference point was constrained as $U1 = U2 = 0$ and the bottom load point of the column was constrained as $U1 = U2 = U3 = 0$. To simulate actual conditions, reference points were kept at the same distance as the experimental scenarios.

2.3 *Material Modeling of Steel*

Square Sections. Square sections exhibit easier local buckling which provides less confinement to the infill concrete. Again, square sections seldom show strain hardening behavior. This is why an elastic-perfectly plastic model of the steel is used for square sections which provide a better prediction of the stress–strain curve in the plastic region without including the strain hardening behavior.

Circular Sections. Circular sections provide better confinement to the infill concrete which also gives better protection against local buckling than square sections. Strain hardening is observed more in normal strength steel than high strength steel. Tao et al. [10] proposed a σ – ϵ model for structural steel under 500 °C. This model is valid for the range of f_y from 200 to 800 Mpa. This model was used to simulate the steel material of the circular CFST column. But in this current model, the outer range was extended from 800 to 900 Mpa, which also gives a better prediction of the behavior of the CFST column. This model is expressed like the following.

$$\sigma = \begin{cases} E_s \varepsilon & 0 \leq \varepsilon < \varepsilon_y \\ f_y & \varepsilon_y \leq \varepsilon < \varepsilon_p \\ f_u - (f_u - f_y) \cdot \left(\frac{\varepsilon_u - \varepsilon}{\varepsilon_u - \varepsilon_p} \right)^p & \varepsilon_p \leq \varepsilon < \varepsilon_u \\ f_u & \varepsilon \geq \varepsilon_u \end{cases} \quad (1)$$

where E_s is the modulus of elasticity, f_y is the yield strength, f_u is the ultimate strength, ε_y is the yield strain $\varepsilon_y = f_y/E_s$, ε_p is the strain at the onset of strain hardening, ε_u is the ultimate strain at ultimate strength; p is the strain-hardening exponent, which can be found by the following equation,

$$p = E_p \cdot \left(\frac{\varepsilon_u - \varepsilon_p}{f_u - f_y} \right) \quad (2)$$

where E_p is the initial elastic modulus of elasticity at the onset of strain-hardening.

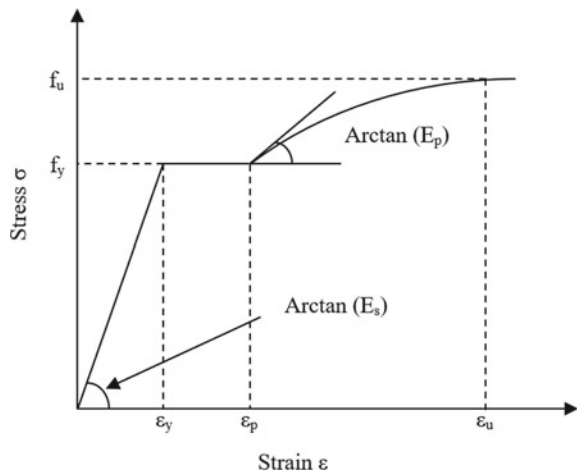
$$E_p = 0.02E_s \quad \text{for structural steel} \quad (3)$$

$$\varepsilon_p = \begin{cases} 15\varepsilon_y f_y \leq 300MPa \\ [15 - 0.018(f_y - 300)]\varepsilon_y, 300MPa < f_y \leq 800MPa \end{cases} \quad (4)$$

$$\varepsilon_u = \begin{cases} 100\varepsilon_y f_y \leq 300MPa \\ [100 - 0.15(f_y - 300)]\varepsilon_y, 300MPa < f_y \leq 800MPa \end{cases} \quad (5)$$

Figure 1 shows the full range of stress–strain relationship can be generally divided into four different stages: (1) elastic stage; (2) plastic stage; (3) strain hardening stage; (4) necking and failure stage. In this case, only three parameters will be needed to

Fig. 1 σ - ε model proposed by Tao et al. [10] for structural steel



generate the curve, i.e. yield strength (f_y), ultimate strength (f_u), modulus of elasticity (E_s). In the absence of reported E_s value, it can be assumed as 200,000 MPa. Furthermore, if f_u is also unavailable, it can be calculated from the following equations,

$$f_u = \begin{cases} [1.6 - 2 \times 10^{-3}(f_y - 200)]f_y & 200MPa \leq f_y \leq 400MPa \\ [1.2 - 3.75 \times 10^{-4}(f_y - 400)]f_y & 400MPa < f_y \leq 800MPa \end{cases} \quad (6)$$

2.4 Material Modeling of Concrete

In general, concrete fails by cracking in tension and crushing in compression. These failures are plastic in nature which means irreversible deformations as well as reduction of material stiffness. In the case of unconfined concrete, tension and compression lead to strain softening, i.e. decreasing stress under increasing strain. Extensive plastic volumetric happens when strain softening occurs. In highly confined compression, on the other hand, the stiffness degradation and the inelastic volume expansion are significantly reduced [11]. As concrete failure mode is a combination of plastic deformation and strain hardening, this damage is called anisotropic damage. Concrete is a brittle material, which makes it difficult to apply anisotropic damage model directly. It is a complex process and structural analysis with this model is not straight forward [12].

Concrete Damaged Plasticity Model. ABAQUS offers a default damaged plasticity model for concrete. As this paper deals with monotonic loading conditions, the only plasticity is considered for modeling nonlinearity. The input variables for the damaged plasticity in ABAQUS were dilation angle (Y), ratio of the second stress invariant on the tensile meridian to that on the compressive meridian (K_c), flow potential eccentricity (e), ratio of the compressive strength under biaxial loading to uniaxial compressive strength (f_{b0}/f_c'), strain hardening/softening rule, viscosity parameter and tensile behavior of concrete, modulus of elasticity of concrete (E_c). Constant values of $K_c, f_{b0}/f_c', e$ and Y were adopted by Li et al. [13], which were 2/3, 1.16, 0.1, 40° respectively. Though these values work fine with unconfined concrete, in case of confined concrete like in CFST column where steel tube provides confinement to concrete and application of damaged plasticity model cannot be a straight forward process, this paper suggests these parameters as variables which differ with the change of concrete strength and confinement factor. But default values of flow potential eccentricity and viscosity parameter works fine because these two have negligible influence in the prediction accuracy.

This default value of e indicates that the dilation angle in the p–q (hydrostatic pressure–deviatoric stress) plane converges to Y reasonably quickly with increasing hydrostatic compression pressure (p) [9].

Modulus of elasticity of concrete (E_c) is calculated from the empirical equation suggested by ACI 318 [14] where only the value of f_c' (in MPa) is needed to be known.

$$E_c = 4700\sqrt{f_c'} \quad (7)$$

The value of the ratio of the compressive strength under biaxial loading to uniaxial compressive strength (f_{bo}/f_c') is calculated from the following equation which is suggested by Kappos et al. [15] and also used by Tao et al. [2].

$$f_{bo}/f_c' = 1.5(f_c')^{-0.075} \quad (8)$$

where f_{bo}/f_c' depends on the value of f_c' which is in MPa. The increase in the value of f_c' decreases the value of f_{bo}/f_c' . But it was investigated by Tao [2] that, decrease in the value of f_{bo}/f_c' has a negligible effect on the ultimate strength of the specimen. So in this paper Eq. (8) is used.

To define the damaged plasticity of concrete in ABAQUS, the tensile behavior of concrete needs to be defined. The value of the tensile strength of concrete was calculated $0.1f_c'$ in [2]. This tensile strength is reached linearly but the tensile softening response which is also known as fracture energy (G_F). The following equation was used to calculate the value of G_F (in MPa),

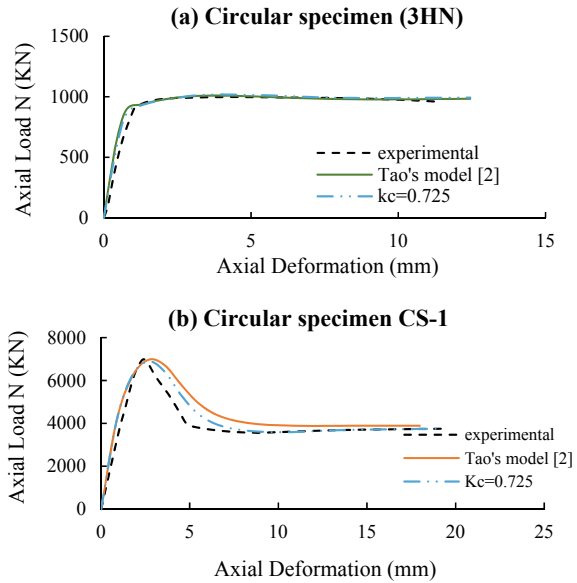
$$G_F = a \cdot \left(f_c' / 10 \right)^{0.7} \times 10^{-3} \quad (9)$$

$$a = 1.25d_{max} + 10 \quad (10)$$

Here d_{max} is the maximum particle diameter (in mm) of the aggregate which is used for concrete. Tao [2] suggested the value of d_{max} be assumed 20 mm if it is unavailable.

Value of K_c . Various researchers have used a constant value of the ratio of the second stress invariant on the tensile meridian to that on the compressive meridian (K_c) to model concrete damaged plasticity in ABAQUS which is $2/3$. But Tao [2] mentioned that the value of K_c influences the stress–strain curve of concrete after crossing the yield point. That means, in the plastic zone, K_c holds an important role in determining the behavior of CFST columns. Yu et al. [16] proposed the value of K_c to be 0.725. In the sensitivity analysis in Fig. 2 shows that with the increase in the value of K_c , the trend line of the inelastic zone shifts from upward to downward. Tao et al. [2] proposed a formula for K_c which relates it with the value of f_c' where an increase in the value of f_c' decreases the value of K_c . Using the model proposed by Tao [2] and the value suggested by Yu et al. [16] then comparing them with the test data shows that, though varying the K_c value with the variation of f_c' gives better result when the value of f_c' is in the lower side, but in case of high strength concrete it gives poorer result than using the constant value suggested by Yu et al. [16]. In this

Fig. 2 Influence of K_c on the load-deformation curve



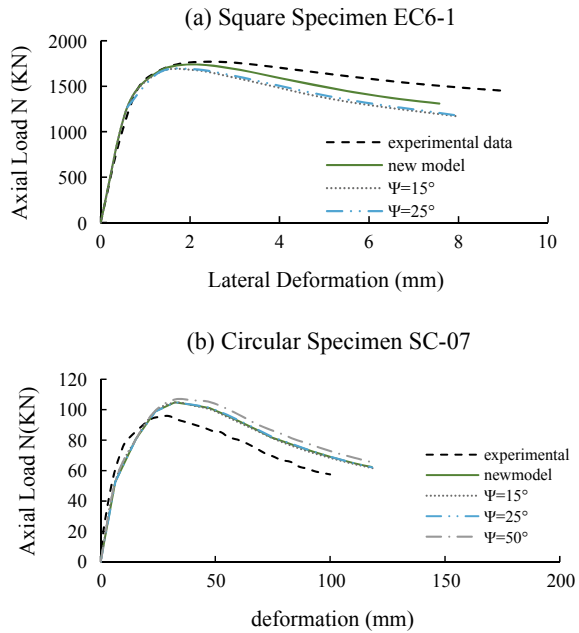
paper, the value of K_c is adopted to be 0.725 as it gave good agreement with the test data.

Value of Y . The available dilation angle (Y) ranges from 0 to 56° in ABAQUS. For unconfined concrete $15\text{--}30^\circ$ was used for the value of Y by many researchers. Increasing the dilation angle (Y) above 15° will result in larger volumetric dilation of the concrete and potentially better but unrealistic effects of confinement on the strength and ductility [9]. But in the CFST column, the concrete is confined by the steel tube. Increasing the value of Y increases the interaction between the concrete and the steel tube, which increases the confining stress in the inelastic zone. Figure 3 shows that, different Y values result in different load-deformation curves for CFST columns. But it is only affected in the inelastic zone, before the yield point, all the values of Y gives similar results. In the case of a rectangular column, this phenomenon is not seen for all Y values. Many researchers suggested value of 40° for rectangular columns. Rectangular columns are more prone to local buckling which lowers the confining stress provided by the steel tube in the inelastic zone. Tao et al. [2] suggested determining the value of Y by using Eq. (11) where Y is the function of the confining factor (ξ_c). This was proposed because of the increasing confining stress with the increase in the value of Y .

$$\psi = \begin{cases} 56.3(1 - \xi_c) & \text{for } \xi_c \leq 0.5 \\ 6.672e^{\frac{7.4}{4.64 + \xi_c}} & \text{for } \xi_c > 0.5 \end{cases} \quad (11)$$

$$\xi_c = \frac{A_s f_y}{A_c f_c'} \quad (12)$$

Fig. 3 Influence of Ψ on the load-deformation curve



Strain Hardening/Softening Rule. Han et al. [17] proposed a strain hardening/softening rule for unconfined concrete. But as the concrete reaches its yield point a sudden drop in the stress–strain curve occurs as no confinement effect is in consideration. In the CFST column, the concrete is in the highly confined situation and the steel jacket around the concrete increases the ductility. In the initial loading stage, the interaction between concrete and steel is negligible. This initial stage can be considered as the unconfined stage for the concrete. The Poisson’s ratio of concrete and steel is different, and concrete expands quickly in the lateral direction than steel. When the load is increased, the lateral expansion concrete doesn’t match with the steel tube, which makes the interaction between the concrete and steel and the confinement effect increase. Tao et al. [2] proposed a three-stage stress–strain model that defines the strain hardening/softening rule of the CFST column. In Fig. 4, the ascending branch of the curve (OA) represents the unconfined stage of concrete, which can be determined by the model proposed by Han et al. [17].

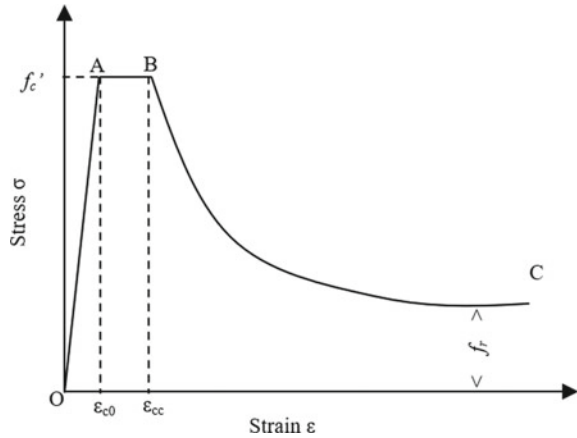
$$y = 2x - x^2 (x \leq 1) \tag{13}$$

where,

$$y = \frac{\sigma}{f_c'} \tag{14}$$

$$x = \frac{\varepsilon}{\varepsilon_0} \tag{15}$$

Fig. 4 Stress–strain curve of confined concrete



$$\epsilon_{c0} = \epsilon_c + 800\xi_c^{0.2} \times 10^{-6} \quad (16)$$

$$\epsilon_c = (1300 + 12.5f'_c) \times 10^{-6} \quad (17)$$

The flat part of the curve (AB) represents the changing stage of concrete from unconfined to confined, where strain increases without increasing the load. The strain at point B (ϵ_{cc}) is calculated by the following equation proposed by Samani et al. [18].

$$\frac{\epsilon_{cc}}{\epsilon_{c0}} = e^k \quad (18)$$

$$k = (2.9224 - 0.00367f'_c) \left(\frac{f_B}{f'_c} \right)^{0.3124 + 0.002f'_c} \quad (19)$$

Tao et al. [2] proposed the value of f_B (confining stress provided to concrete at point B) to be calculated from the following equation.

$$f_B = \begin{cases} \frac{(1+0.027f_y) \cdot e^{-0.02\frac{D}{t}}}{1+1.6e^{-10} \cdot (f'_c)^{4.8}} (\text{circular section}) \\ \frac{0.25(1+0.027f_y) \cdot e^{-0.02\sqrt{(B^2+D^2)}}}{1+1.6e^{-10} \cdot (f'_c)^{4.8}} (\text{rectangular section}) \end{cases}$$

The descending part (BC) of the curve represents the strain-softening rule of concrete, where the concrete is highly confined. This curve can be determined by the following equation proposed by Binici et al. [19].

$$\sigma = f_r + (f'_c - f_r) \exp \left[- \left(\frac{\epsilon - \epsilon_{cc}}{\alpha} \right) \right]^\beta \quad \epsilon \geq \epsilon_{cc} \quad (20)$$

Here f_r = residual stress; α and β are the parameters to determine the shape of the curve. f_r and α can be calculated from the following equations proposed by Tao et al. [2],

$$f_r = \begin{cases} 0.7(1 - e^{-1.38\xi_c}) f'_c \leq 0.25 f'_c & (\text{circular section}) \\ 0.1 f'_c & (\text{rectangular section}) \end{cases} \quad (21)$$

$$\alpha = \begin{cases} 0.04 - \frac{0.036}{1 + e^{6.08\xi_c - 3.49}} & (\text{circular section}) \\ 0.005 + 0.0075\xi_c & (\text{rectangular section}) \end{cases} \quad (22)$$

β can be taken as 1.2 and 0.92 for circular and rectangular columns, respectively [2].

Method of Analysis. As discussed in [9], The fracture behavior of concrete in tension makes it virtually not possible to get converged results using standard (predictor–corrector) nonlinear solution methods like full Newton or modified Newton–Raphson iteration approaches. Even arc-length-based techniques just like the modified-Riks ways cannot offer converged results because of the brittle fracture behavior of concrete in tension. Implicit dynamic analysis strategies also become unstable and cannot give results after significant cracking. Therefore, the explicit dynamic technique was used to conduct the analysis. The first reason for using this technique is that it will find results up to failure, particularly when brittle materials (like concrete in tension) and failure modes are concerned. The explicit dynamic analysis methodology was used to perform quasi-static analyses simulating the experiments.

3 Verification of the FE Model

3.1 Specimen Parameters of Experimental Data

From the study of various researchers, N– Δ curves of 12 circular, 10 square and specimens were collected and used to verify the proposed FE model. The parameters of these specimens are summarized in Tables 1 and 2 for circular and square specimens, respectively, where D is the overall diameter of a circular section, B is the overall width of a square sections, L is the total length of the specimen, e is the eccentric distance from the center of the specimen. The 22 tests in total given in Tables 1 and 2 are from the mentioned references. It is worth noting that the majority of the above references have received extensive citations. For the circular columns shown in Table 1, the ranges of different parameters are: $f_y = 271\text{--}853$ MPa; $f'_c = 28.7\text{--}163$ MPa; $D = 76\text{--}219$ mm and $e/D = 0\text{--}0.5$. The parameter ranges for the square columns in Table 2 are: $f_y = 300.1\text{--}779$ MPa; $f'_c = 27.8\text{--}157$ MPa; $D = 120\text{--}250$ mm and $e/B = 0\text{--}0.43$. As can be seen, the parameter ranges of the collected data are very broad and cover the current practical ranges. Figure 5 shows example of failure modes of specimen.

Table 1 Summary of test data of circular CFST columns

Specimen name	D (mm)	t (mm)	L (mm)	f_y (MPa)	f_c' (MPa)	e/D	Source
3HN	150	3.2	450	287.4	28.7	0	Tomii et al. [20]
CC8-A-8	108	6.47	324	853	77	0	Sakino et al. [21]
S16CS80A	190	1.52	664	306	80.2	0	O'Shea et al. [22]
CS-1	219	6.3	600	300	163	0	Liew et al. [23]
SC-0	76	2.2	802	435	49.3	0.19	Kilpatrick et al. [24]
SC-7	76	2.2	2402	435	49.3	0.19	Kilpatrick et al. [24]
SC-9	101.7	2.4	1947	410	49.3	0.09	Kilpatrick et al. [24]
SC-15	101.7	2.4	1947	410	49.3	0.5	Kilpatrick et al. [24]
ZC-16	160.3	5.1	2000	271	85.9	0.05	Zeghiche et al. [25]
ZC-17	160.1	4.97	2000	281	86.7	0.1	Zeghiche et al. [25]
ZC-18	159.8	5.02	2000	280	85.9	0.15	Zeghiche et al. [25]
ZC-19	159.7	5.02	2000	276	85	0.2	Zeghiche et al. [25]

Table 2 Summary of test data of square CFST columns

Specimen name	B (mm)	t (mm)	L (mm)	f_y (MPa)	f_c' (MPa)	e/B	Source
3MN	150	3.2	450	300.1	27.8	0	Tomii et al. [20]
sczs2-1-4	120	5.86	360	321	43.6	0	Han et al. [26]
UNC-H	250	2.5	750	338	41.8	0	Tao et al. [27]
SSH-1-2	150	8	450	779	157	0	Liew et al. [28]
EC1-1	150	4	450	434.56	102	0.13	Li et al. [13]
EC2-1	150	4	450	434.56	102	0.23	Li et al. [13]
EC3-1	150	4	450	434.56	102	0.33	Li et al. [13]
EC4-1	150	4	450	434.56	102	0.43	Li et al. [13]
EC5-1	150	5	450	433.1	102	0.33	Li et al. [13]
EC6-1	150	6	450	436.9	102	0.33	Li et al. [13]

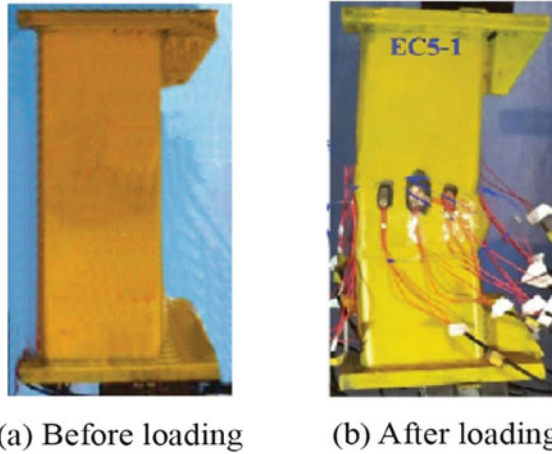


Fig. 5 Example of failure modes of specimen (Li et al. [13])

3.2 Comparison of Experimental and FE Results

Ultimate Load Carrying Capacity. The predicted ultimate strengths (N_{num}) from the current FE model is compared with the measured ultimate strengths (N_{ex}) of all collected data in Tables 3 and 4 for square and circular sections, respectively. Table 5 shows both the mean value (Mean) and standard deviation (STD) of the ratio of N_{ex}/N_{num} for specimens with different cross-sections.

For the current FE model, the mean values of N_{ex}/N_{num} are 1.0358 and 1.0141 for circular and square columns, respectively; whereas the standard deviations of N_{ex}/N_{num} are 0.0759 and 0.0339, respectively. As can be seen, slightly conservative predictions are obtained from the current FE model but with reasonable accuracy.

Table 3 The ultimate strength predicted and ultimate strength measured for square sections

Specimen name	N_{ex} (kN)	N_{num} (kN)	N_{ex}/N_{num}
3MN	1121.44	1152.39	0.973
sczs2-1-4	1367.25	1385.12	0.987
UNC-H	3198.96	3159.51	1.012
SSH-1-2	6743.59	6166.83	1.094
EC1-1	2127.19	2139.04	0.994
EC2-1	1841.70	1770.93	1.040
EC3-1	1446.90	1452.05	0.996
EC4-1	1248.44	1246.28	1.002
EC5-1	1633.72	1594.88	1.024
EC6-1	1769.62	1738.35	1.018

Table 4 The ultimate strength predicted and ultimate strength measured for Circular sections

Specimen name	N_{ex} (kN)	N_{num} (kN)	N_{ex}/N_{num}
3HN	999.27	1061.45	0.941
CC8-A-8	2728.4	2531.14	1.078
S16CS80A	2570.11	2558.18	1.005
CS-1	6993.79	6899.64	1.014
SC-0	245.23	227.34	1.079
SC-7	95.91	104.84	0.915
SC-9	361.25	354.32	1.02
SC-15	159.5	170.4	0.936
ZC-16	1698.78	1494.66	1.137
ZC-17	1403.71	1291.37	1.087
ZC-18	1214.72	1116.58	1.088
ZC-19	1100.61	972.9	1.131

Table 5 Comparison of FE predictions with measured ultimate strength

Section type	Number of specimens	Current model	
		Mean	STD
Circular	12	1.0358	0.0759
Square	10	1.0141	0.0339

The standard deviation signifies that for square sections the FE model predicts quite accurately than the circular sections (Table 5).

Axial Load Versus Axial Displacement Curve. $N-\Delta$ curve of experiment and FE model for both concentric and eccentric loading condition was plotted together to observe the prediction accuracy of the FE model.

Specimens under Concentric Loading. From Fig. 6 it can be seen that current FE model gives a reasonable prediction for circular CFST columns under concentric loading. It is observed in Fig. 6 that the current model predicts the $N-\Delta$ curve accurately in the elastic as well as in the plastic zone. The use of this current model predicts an accurate $N-\Delta$ curve for high strength concrete and steel.

In Fig. 6 the circular specimen CC8-A-8 has steel whose yield strength is 853 MPa which is high strength steel. In this case, the current model predicted the $N-\Delta$ curve reasonably well in the plastic zone but underestimated the values in the plastic zone. But it follows the measured data.

It is observed in Fig. 7 that for square sections the current model predicts the $N-\Delta$ curve accurately in the elastic as well as in the plastic zone. The use of this current model predicts an accurate $N-\Delta$ curve for high strength concrete and steel.

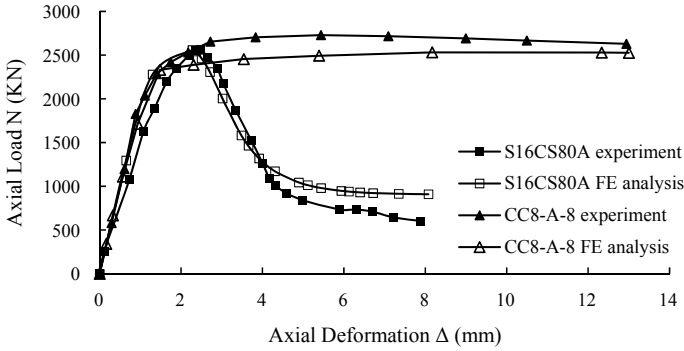


Fig. 6 Comparison between predicted and measured N-Δ curves for circular specimen under concentric loading

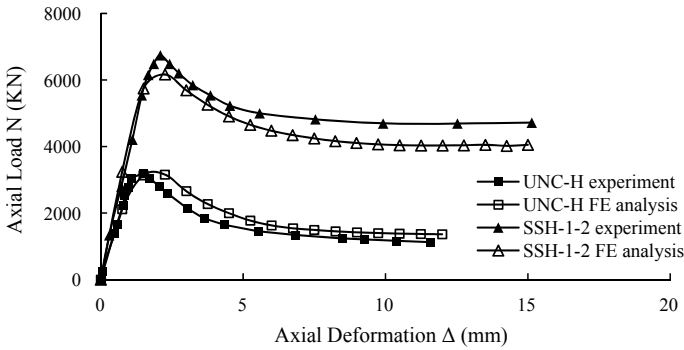


Fig. 7 Comparison between predicted and measured N-Δ curves for square specimen under concentric loading

Figure 8 shows a comparison of ultimate strength, where it can be seen that, for both types of sections under concentric loading conditions, the FE model underestimates the ultimate strength than the measured data. This makes the current FE model more conservative.

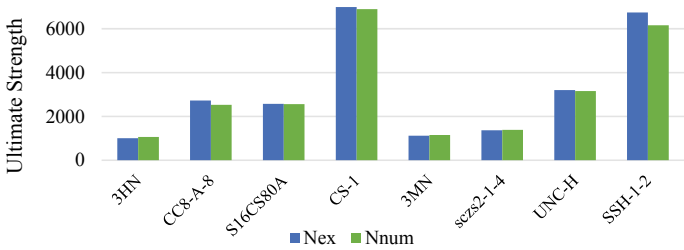


Fig. 8 Comparison between current FE model and measured ultimate strength of columns under concentric loading

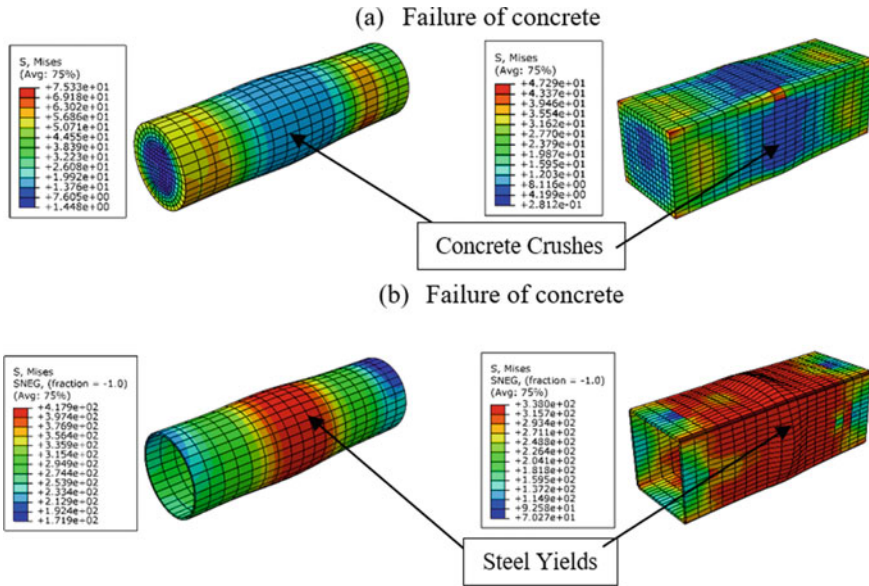


Fig. 9 Failure of columns under concentric loading

Figure 9a, b shows the failure mode of concrete and steel respectively for circular and square sections. Concrete failed by crushing and steel exhibit failure in tension by yielding.

Specimens under Eccentric Loading. The prediction accuracy for eccentric load-mid-height lateral deformation curves can be showed in Figs. 10 and 11 of the current FE model for circular and square CFST columns respectively.

In Fig. 10 for circular specimen SC-9 the current FE model predicts the eccentric load- mid-height lateral deformation curve accurately both pre-peak and post-peak

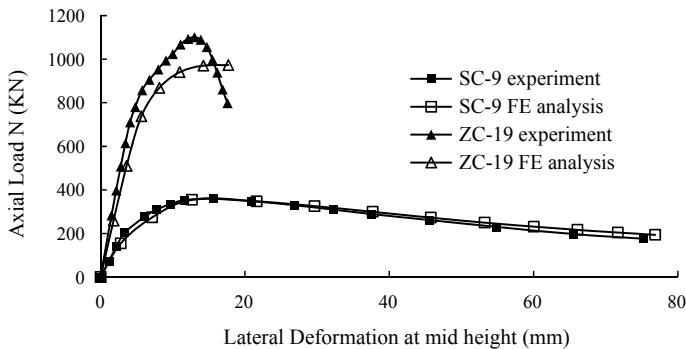


Fig. 10 Comparison between predicted and measured eccentric load- mid-height lateral deformation curves for circular specimen under eccentric loading

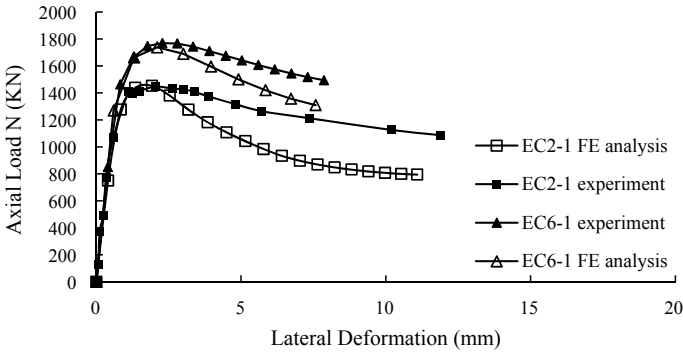


Fig. 11 Comparison between predicted and measured eccentric load- mid-height lateral deformation curves for square specimen under concentric loading

stage. Up to peak, the predicted curve matches with measured data. But after the peak, the prediction slightly overestimates the measured data. It was mentioned in the experimental paper that, displacement control was exercised during the loading process which enables the opportunity of getting stable post-peak load–deflection curves in the experimental process.

For circular specimen ZC-19, the prediction of the current FE model for eccentric load- mid-height lateral deformation curve is reasonably accurate up to the pre-peak stage. Up to the peak point, the predicted curve underestimates the measured data. But the post-peak stage doesn't match. In this regard, it should be noted that load control was exercised during the loading process but quite possibly the specimens failed due to prescribed load was applied to each specimen at the point of failure which apparently caused the unstable and unreliable post-peak load-deformation curve.

In the case of square sections, the prediction of the model in the pre-peak stage of the section mentioned in Fig. 11 matches the experimental data very well. But after the peak point of the load, the predicted curve goes downward than the measured curve. This phenomenon of miss matching decreases in EC6-1, where the thickness of the steel tube is higher. This means in the case of eccentric loading with higher confinement of square sections, the model predicts the curve quite accurately. This also may have been happened due to easier local buckling of square sections in which under eccentric load the joints of the steel section may have failed which caused the mismatch of the curve.

Figure 12 shows the comparison of predicted and measured the ultimate strength of the columns under eccentric loading condition. From the comparison study, it can be observed that the current FE model underestimates the measured ultimate strength in all the cases thus being in the conservative state of prediction.

Figure 13a, b show the failure mode of concrete and steel respectively. Concrete failed by crushing and steel exhibit failure in tension by yielding as defined

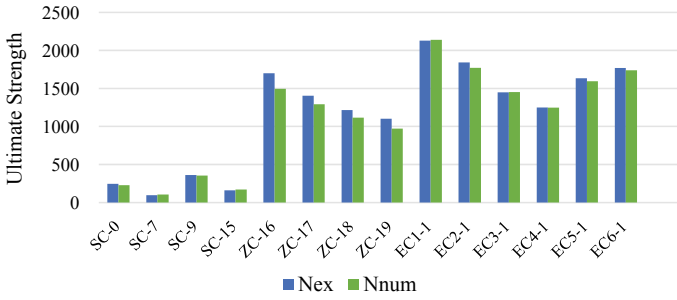


Fig. 12 Comparison between current FE model and measured ultimate strength of circular columns under eccentric loading

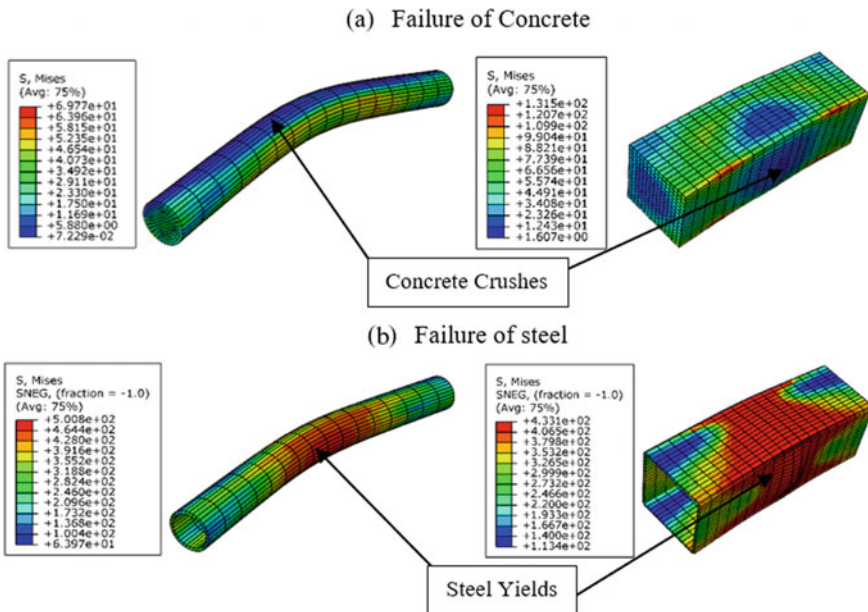


Fig. 13 Failure of Sections under eccentric Loading

4 Conclusions

Extensive numerical investigations were conducted to study the behavior of circular and square CFST columns under concentric and eccentric loading. The data of these columns were collected from various research papers where researchers have done experimental studies to produce those data. For the columns, the compressive strength of concrete and yield strength of steel tube varied from normal strength to very high strength. The model was created and simulated in Finite Element package

ABAQUS/Standard. For eccentrically loaded columns, the eccentricity varied from 0 to 0.5D. This study investigates the difference in the load-deformation curve, failure mode, and the ultimate strength of the columns.

The following conclusions found from the verification of the FE model:

1. The FE model developed in this study was found to be able to predict the load-deformation curve reasonably well with good accuracy with small and large cross-sections, different shapes of cross-sections, normal and high strength steel, and concrete and also concentric and eccentric loading conditions.
2. The numerical model can predict the peak load quite well with a mean value of N_{ex}/N_{num} of 1.03 and 1.01 for circular and square sections respectively. This result shows the excellent performance of the numerical model in predicting the ultimate strength of CFST columns.
3. The FE model underestimates the load-deformation curve after the peak for columns having smaller confining factor x and overestimates the curve after the peak for columns having higher confining factor x .

Acknowledgements The all out research program counted on the patronage of the department of Civil Engineering, Military Institute of Science and Technology (MIST). The authors would like to share the profound gratitude and acknowledge all of the technical supports and sufficient fund provided by the authority (MIST).

References

1. Lee S, Uy B, Kim S, Choi Y, Choi S (2011) Behavior of high-strength circular concrete-filled steel tubular (CFST) column under eccentric loading. *J Constr Steel Res* 67(1):1–13. <https://doi.org/10.1016/j.jcsr.2010.07.003>
2. Tao Z, Wang Z, Yu Q (2013) Finite element modelling of concrete-filled steel stub columns under axial compression. *JCSR* 89:121–131. <https://doi.org/10.1016/j.jcsr.2013.07.001>
3. Evirgen B, Tuncan A, Taskin K (2014) Structural behavior of concrete filled steel tubular sections (CFT/CFSt) under axial compression. *Thin-Walled Struct* 80:46–56. <https://doi.org/10.1016/j.tws.2014.02.022>
4. Gupta PK, Sarda SM, Kumar MS (2007) Experimental and computational study of concrete filled steel tubular columns under axial loads. 63:182–193. <https://doi.org/10.1016/j.jcsr.2006.04.004>
5. Uy B (2000) strength of concrete filled steel box columns. Mar 2000, pp 341–352
6. Wang Q, Zhao Z, Shao Y, Li Q (2017) “crossmark,” *Thin Walled Struct* 110:106–122 Oct 2016. <https://doi.org/10.1016/j.tws.2016.10.019>
7. Xiong D, Zha X (2007) A numerical investigation on the behaviour of concrete-filled steel tubular columns under initial stresses. 63:599–611. <https://doi.org/10.1016/j.jcsr.2006.07.002>
8. “Abaqus V (2014) Abaqus standard user’s manual, Version 6.14. Providence, RI (USA): Dassault Systèmes Corp.
9. Lai Z, Varma AH, Zhang K (2014) Non-compact and slender rectangular CFT members: experimental database, analysis, and design. *J Constr Steel Res* 101:455–468. <https://doi.org/10.1016/j.jcsr.2014.06.004>
10. Tao Z, Wang X, Uy B, Asce M (2013) Stress-strain curves of structural and reinforcing steels after exposure to elevated temperatures. pp 1306–1316 Sept 2013. [https://doi.org/10.1061/\(ASCE\)MT.1943-5533.0000676](https://doi.org/10.1061/(ASCE)MT.1943-5533.0000676)

11. Grassl P (2006) Damage-plastic model for concrete failure. 43:7166–7196. <https://doi.org/10.1016/j.ijsostr.2006.06.032>
12. Carol I, Rizzi E, Willam K (2001) On the formulation of anisotropic elastic degradation. II. Generalized pseudo-Rankine model for tensile damage. *Int J Solids Struct* 38(4):519–546. [https://doi.org/10.1016/S0020-7683\(00\)00031-7](https://doi.org/10.1016/S0020-7683(00)00031-7)
13. Li G, Chen B, Yang Z, Feng Y (2018) Thin-walled structures experimental and numerical behaviour of eccentrically loaded high strength concrete filled high strength square steel tube stub columns. *Thin Walled Struct* 127(Nov 2017):483–499. <https://doi.org/10.1016/j.tws.2018.02.024>
14. ACI 318R, ACI 318R-14.pdf. 2014
15. Papanikolaou VK, Kappos AJ (2007) Confinement-sensitive plasticity constitutive model for concrete in triaxial compression. *Int J Solids Struct* 44(21):7021–7048. <https://doi.org/10.1016/j.ijsostr.2007.03.022>
16. Yu T, Teng JG, Wong YL, Dong SL (2010) Finite element modeling of confined concrete-I: Drucker-Prager type plasticity model. *Eng Struct* 32(3):665–679. <https://doi.org/10.1016/j.engstruct.2009.11.014>
17. Han LH, Yao GH, Tao Z (2007) Performance of concrete-filled thin-walled steel tubes under pure torsion. *Thin-Walled Struct* 45(1):24–36. <https://doi.org/10.1016/j.tws.2007.01.008>
18. Samani AK, Attard MM (2012) A stress-strain model for uniaxial and confined concrete under compression. *Eng Struct* 41:335–349. <https://doi.org/10.1016/j.engstruct.2012.03.027>
19. Binici B (2005) An analytical model for stress-strain behavior of confined concrete. *Eng Struct* 27(7):1040–1051. <https://doi.org/10.1016/j.engstruct.2005.03.002>
20. Tomii M, Yoshimura K, Morishita Y (1977) Experimental studies on concrete filled steel tubular stub columns under concentric loading. In: *Proceedings of the international colloquium on stability of structures under static and dynamic loads*. Washington DC, USA, pp 718–41
21. Sakino K, Nakahara H, Morino S, Nishiyama I (2004) Behavior of centrally loaded concrete-filled steel-tube short columns. *J Struct Eng ASCE* 130(2):180–8
22. O'Shea M, Bridge R (1998) Tests on circular thin-walled steel tubes filled with medium and high strength concrete. *Aust Civ Eng Trans* 40:15–27
23. Liew J, Xiong D (2010) Ultra-high strength concrete filled columns for highrise buildings. In: *Proceedings of the 4th international conference on steel & composite structures*. Sydney, Australia, pp 82–93
24. Kilpatrick A, Rangan B (1999) Tests on high-strength concrete-filled steel tubular columns. *ACI Struct J* 96(2):268–74
25. Zeghiche J, Chaoui K (2005) An experimental behaviour of concrete-filled steel tubular columns. *J Constr Steel Res* 61(1):53–66
26. Han L, Zhao X, Tao Z (2001) Test and mechanics model for concrete-filled SHS stub columns, columns, and beam-columns. *Steel Compos Struct* 1(1):51–74
27. Tao Z, Uy B, Han L, Wang Z (2009) Analysis and design of concrete-filled stiffened thin-walled steel tubular columns under axial compression. *Thin-Walled Struct* 47(12):1544–56
28. Liew J, Xiong D, Zhang M (2011) Experimental studies on concrete filled tubes with ultra-high strength materials. In: *Proceedings of the 6th international symposium on steel structures*. Seoul, Korea, pp 377–84

Maturity Method to Predict Strength Development of Concrete Made of Portland Cement Composite (PCC)



G. Turuallo, H. Mallisa, N. Rupang, and Z. Mallisa

Abstract This study aims to evaluate whether the maturity method suggested by Nurse-Saul (ASTM C 1074-19) could be applied on the concrete using Portland Cement Composite (PCC) cement in a country with high temperature such as Indonesia. The method was developed using concrete specimens produced from Original Portland Cement (OPC) and cured in cold countries with lower temperature. The cement used in this research was manufactured by PT Semen Tonasa Indonesia. At the same time, the fine aggregate was taken from the Palu river, and the coarse aggregate was stone crushed aggregate produced by PT Meriba Palu. The targeted strength of concrete used in this research was 25 MPa at age 28 days. The concrete strengths at the ages 1, 3 and 9-days were predicted using the Nurse-Saul method and then compared to their actual strength at the same ages. The outcomes of this study indicated that the maturity method suggested by Nurse-Saul was acceptable to anticipate the strength of concrete. The discrepancies of the estimated strengths and their actual strengths are 1.95%, 3.73%, and 2.40% for the strengths of concrete at the ages of 1, 3, and 9-days respectively, where the errors of the predicted concrete strengths are less than 4% different.

Keywords Maturity method · Predicted strength · Actual strength and reasonably good

1 Introduction

There are numerous methods for estimating the strength growth of concrete at a specific age; nonetheless, it occasionally produced incorrect or inappropriate findings. The inaccurate results might be due to various cement and curing temperature, which are applied in an actual field. The maturity is the compound of curing temperature with time history, and the method was firstly introduced by McIntosh in 1949 [1]. McIntosh estimates the strength development of concrete by preparing cube samples

G. Turuallo (✉) · H. Mallisa · N. Rupang · Z. Mallisa
Civil Engineering Department, Tadulako University, Palu, Central Sulawesi, Indonesia

under electrical curing. The concrete strengths resulting from the electrical curing were compared to concrete with a similar mixture cured under normal condition. Furthermore, he expanded a parameter called ‘*basic age*’ to combine the effects of time and curing temperature. He recommended applying a datum temperature of $-1.1\text{ }^{\circ}\text{C}$ to consider the influences of maturity on the strength development of concrete.

Saul reported his experimental results at the Research Station Cement and Concrete in 1951 [2]. The term ‘*maturity*’ was first introduced as an indication of strength obtained, which relied on concrete’s age and temperature curing. Like McIntosh, Saul proposed that the maturity should be counted with notice to a ‘datum temperature’ lower than the temperature. As the cement reaction will not take place, there will be no growth in strength. He added that once the concrete has set, the strength of concrete would be continuously increased even the temperature below $0\text{ }^{\circ}\text{C}$. Furthermore, a datum temperature of $-10.5\text{ }^{\circ}\text{C}$ was proposed, which was later amended by McIntosh [3] in his 1956 article by using a datum temperature of $-10\text{ }^{\circ}\text{C}$.

In 1951, Saul [4] introduced the ‘maturity rule’ as follow:

“Concrete of the same mix at the same maturity (reckoned in temperature-time) has approximately the same strength whatever combination of temperature and times go to make up that maturity.”

Nurse and Saul then prompted the maturity function as below [5–7]:

$$M = \sum_0^t (T - T_0) \Delta t \quad (1)$$

where: M is the maturity or the temperature–time factor at age t ($^{\circ}\text{C}$. days or $^{\circ}\text{C}$. hours), t is the age of concrete (days or hours), Δt is a time-lapse (days or hours), T is the average temperature of the concrete throughout a time-lapse Δt ($^{\circ}\text{C}$), and T_0 is an initial temperature ($^{\circ}\text{C}$) of cement to hydrate, below this temperature, the strength of concrete will cease to develop. Furthermore, Saul encouraged applying the maturity method to estimate the strength of concrete, which was cured below $50\text{ }^{\circ}\text{C}$ in the initially two hours or about $100\text{ }^{\circ}\text{C}$ in 6 h after mixing [6].

The inability to accurately forecast the strength development of concrete at the early stages of building operations resulted in two outcomes: (i) Contractors either spend too much time on the following task, such as removing formwork, which is costly owing to delays in completing a work item, or the concrete acts prematurely, which may cause the building to crack. These two consequences would result in future durability and performance difficulties, as well as structural collapse.

This work proposed to evaluate whether the maturity method suggested by Nurse-Saul could be applied on the concrete using PCC cement in a country with high temperature such as Indonesia.

2 Literature Review

The maturity method is an appropriate approach to estimate the early age strength gain of concrete, using the principle that the concrete strength is directly related to the hydration temperature history of cementitious paste. Most construction sites conduct test field-cured concrete samples for strength at various ages within the first week after the concrete is poured. Such testing was carried out as a basis for determining whether or not to remove the formwork. The maturity method is built on the basic principle of a specific relationship between the maturity index and the strength of concrete. Therefore, concretes with the same mixtures and maturity will produce a similar strength, even though the temperature and curing period of the concretes are different.

The concept of the method can be applied to define the strength development of a specific concrete mixture cured at different curing temperatures. The maturity theory was developed initially in the late 1940s and early 1950s in England when various publications dealing with the accelerated curing procedure were published. Many studies were conducted to estimate the strength development of concrete at early and later ages using the maturity method. There were also numerous studies on the prediction of concrete’s setting time using the method. The combined effects of time history and temperature, called maturity index, could predict the strength of concrete [8].

The concept of the maturity method can be used to estimate the strength development of a concrete mixture cured at different temperatures. Furthermore, if the concrete is cured in either lower or higher temperatures have the same value of maturity, then the strength of the concrete should be the same as seen in Fig. 1.

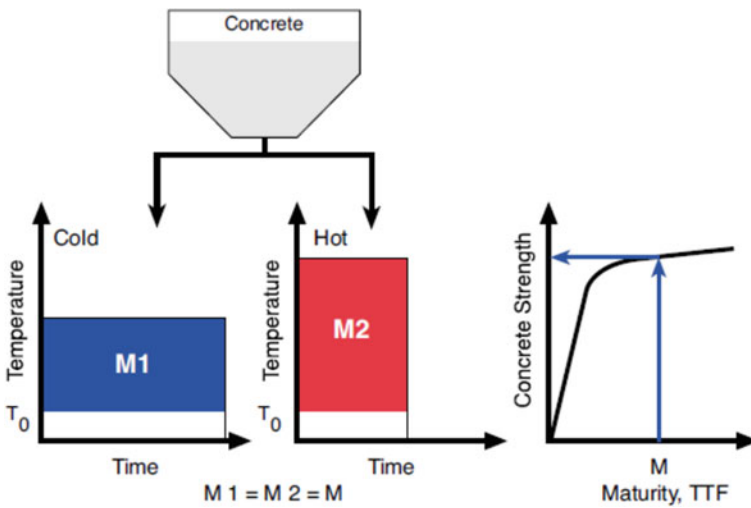


Fig. 1 Saul’s maturity rule using temperature–time factor [9]

Figure 1, which is presented by Kehl et al. [9] explains the concept of maturity method for concrete, which is cured at different temperatures, i.e. lower and higher temperatures. They noted that if concretes with the same mixture, which is cured at different curing temperatures, will achieve the same maturity when the temperatures-time areas are the same as shown in the above figure. When the areas of M1 and M2 are the same, then it could be explained that for the same concrete mixture, a certain maturity will be achieved quicker from the concrete cured at the higher temperature than that of cured in the lower temperature. Therefore, period required to achieve the equal maturity for both the curing conditions will also diverse.

2.1 Equivalent Age Concept

The equivalent concept of age was firstly proposed by Rastrup in 1954 [10] shown in Eq. 2, which referred to Saul's work, and it was called '*temperature time-factor*'.

$$t_e = \sum 2^{(T-T_r)/10} \times \Delta t \quad (2)$$

It was more palpably clarified in ASTM C-1074-19 [5] as 'the period that is needed to cure the concrete at a reference temperature after casting, in order to attain a maturity index, which is equal to that of obtained from the same concrete, cured at a temperature other than the reference temperature during a time interval, ' Δt .'

Nurse-Saul [7] calculated the equivalent age based on the Eq. (1) above as the following equation:

$$t_e = \frac{\sum(T - T_0)}{(T_r - T_0)} \times \Delta t \quad (3)$$

where: t_e = the equivalent age (hour or day), T_r = reference temperature, normally it is applied as 20 °C in Europe ambient temperature. The Eq. (3) above then can be written as follow:

$$t_e = \sum \beta \Delta t \quad (4)$$

β is defined as the age conversion factor that is calculated as follow:

$$\beta = \frac{(T - T_0)}{(T_r - T_0)} = \frac{k}{k_r} \quad (5)$$

k and k_r are the rate constant at temperature T and T_r , respectively (hours^{-1} or days^{-1}). The age conversion factor β can be applied to calculate the time period, Δt at curing temperature T , where t_e is the equivalent age at the reference temperature T_r .

In 1977, Freiesleben-Hansen and Pedersen [11, 12] found a more accurate equation to calculate the equivalent age. They found that maturity is exponentially dependent on the curing temperature. This method is known as the equivalent age method, which is developed from the Arrhenius equation, which was taken to explain temperature's influence on the rate of chemical reaction, as presented in the following equation:

$$t_e = \sum e^{-Q\left(\frac{1}{T} - \frac{1}{T_r}\right)} \times \Delta t \quad (6)$$

Q is calculated as follow:

$$Q = \frac{E_a}{R} \quad (7)$$

where: E_a is apparent activation energy (J/mol), R is the universal gas constant (8.314 J/mol.K).

Furthermore, Carino and Lew [7] suggested Eq. (8) to determine the equivalent age at the reference temperature. The equation is slightly more straightforward than that proposed by Freiesleben-Hansen and Pedersen above as follows:

$$t_e = \sum e^{B(T-T_r)} \times \Delta t \quad (8)$$

where B is the temperature sensitivity factor, T and T_r are the average and reference temperature, respectively.

Two decades later, in 1971, Waver and Seagrove offered a way to reckon the equivalent age for Portland cement concrete using the following equation:

$$t_e = \sum \left(\frac{T + 16}{T_r + 16} \right)^2 \times \Delta t \quad (9)$$

2.2 The Relationship Between Strength and Maturity

The ASTM C-1074-19 defined a method to expand the relationship between strength and maturity. The mixture proportion and ingredient of the concrete, which will be estimated its strength should be the same as that of reference concrete has. The concrete cubes should be prepared to be tested their strength at certain ages, such as at 1, 3, 7, 14 and 28 days. After calculating the maturity index of the concrete at each age, the next step then is to set up a graph, which presents the relation between the maturity and strength of the concrete as follow.

Fig. 2 Strength-maturity relationship [13]

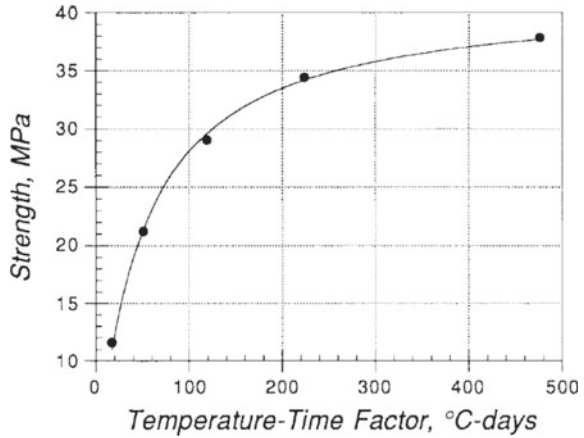


Figure 2 can be applied to estimate the strength of concrete with the same mixture and ingredients once the concrete’s maturity is known. Tank and Carino [8] proposed the equation for calculating the strength based on the maturity of concrete as follow:

$$S = S_{\infty} \frac{K(M - M_0)}{1 + K(M - M_0)} \tag{10}$$

S_{∞} is assigned as ultimate strength (N/mm^2), M is the concrete maturity ($^{\circ}C$ -hours or $^{\circ}C$ -days), the rate constant, and the maturity when the concrete start to have the strength ($^{\circ}C$ -hours or $^{\circ}C$ -days), are expressed by K and M_0 , respectively.

2.3 The Relationship Between Strength and Ages

The strength-age relationship was introduced by Carino and Tank [8, 14] as the given equation below:

$$S = S_{\infty} \frac{k_T(t - t_0)}{1 + k_T(t - t_0)} \tag{11}$$

S and S_{∞} are the strength and the ultimate strength (N/mm^2) respectively, t and t_0 are the curing age and the age when the strength of concrete is expected to start (hours or days). The rate constant k_T is calculated by using the Arrhenius formula as follow:

$$k_T = Ae^{-\left[\frac{E_a}{R(T+273)}\right]} \tag{12}$$

where A is a constant (days^{-1} or hours^{-1}), the average temperature of the concrete during the time period Δt , is expressed by T ($^{\circ}\text{C}$). Furthermore, they found that the rate constant and temperature have the relationship as follows:

$$k(T) = CT + D \quad (13)$$

where the curing temperature ($^{\circ}\text{C}$) is T , C and D are the regression constant.

Freiesleben and Pedersen proposed another strength-ages relationship as the equation given below [6, 12, 15–17]:

$$S = S_{\infty} e^{(-\frac{t}{\tau})^a} \quad (14)$$

where: τ is the characteristic time constant (hours^{-1} or days^{-1}), S is the strength at age t (MPa), a is a shape parameter.

Precise concrete strength estimates can be useful for engineers in arranging job after concrete jobs in a project. To obtain an exact estimation of the concrete strength, engineers have to grasp precisely the hardening process of concrete, particularly at early ages. Both the maturity methods proposed by Nurse-Saul and Arrhenius did not count the influences of the curing temperatures at very earlier ages on the ultimate strength; therefore, both methods conscientiously estimate the strength of concrete, particularly at later ages.

3 Materials and Experimental Works

3.1 Materials

The materials utilized in the experiment, such as sand, coarse aggregate, and PCC cement, were from a single batch. The cement was Portland Composite Cement, which was Type I, produced by PT Semen Tonasa, with a density of 3.1. The absorption, density, and sieve analysis of coarse and fine aggregates were measured in the laboratory and met the requirements needed.

The fine aggregate was fine sand taken from the Palu River and the coarse aggregate was a crushed aggregate produced by the stone crusher industry with an interval granule size between 5 and 20 mm. Both the fine and coarse aggregates were in air-dry states; therefore, some water was supplemented for absorption to reach their saturated service dry (SSD) state.

3.2 Experimental Work

The strength of 25 MPa was plotted to achieve at age 28-days. The mix proportions per m³ of concrete consist of 353 kg of Portland Cement Composite (PCC), 219 kg of water, 748 kg and 1079 kg of fine and coarse aggregates, respectively.

For each test age, three cubes of concrete cured at room temperature i.e. 25 °C, were provided. They were tested at age 1, 2, 3, 7, 14, 21 and 28 days. To find out the concrete's datum temperature, a number of concrete cube specimens, which were cured at the temperature of 35 and 50 °C, were also provided. There were three cubes for each testing age at 1, 3, 5 and 7 days for both mixes.

To rate the exactness of the maturity function used in estimating concrete strength; therefore, a concrete slab with the size of 60 × 40 × 12 cm for its length, width and thickness, respectively, was prepared. The slab was placed outside the concrete laboratory and the cube specimens placed alongside the concrete slab. A thermocouple cable was embedded in the concrete slab, which was connected to a maturity meter to record the temperature history inside the concrete slab. It is then used to calculate the maturity of the concrete during the experiment (Fig. 3). The concrete mix of the concrete slab with the cube specimens was exactly the same with that of concrete cured at 25, 35, and 50 °C above to produce the maturity curve from the same mixture.

The maturity meter recorded the temperature history in the concrete slab specimen, which was used to produce maturity of concrete cured at ambient temperature. The

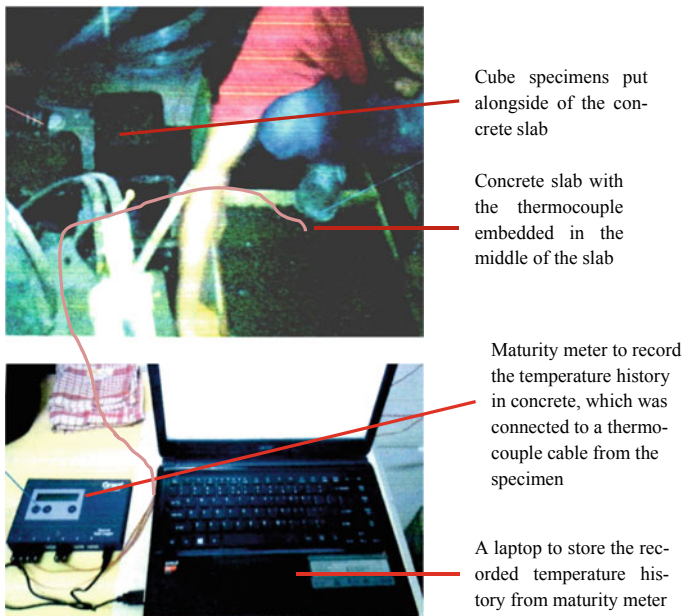


Fig. 3 Setting specimens and maturity meter equipment to measure temperature history in concrete slab

calculated maturity was then utilized to predict the concrete’s strength. The cube specimens, which were put beside the slab specimen, were used to check or validate the predicted strength of the concrete slab using the maturity function.

4 Results and Discussions

Table 1 shows the compressive strengths of concrete cured at reference temperature (25 °C), 35 and 50 °C. There were three cubes provided for every testing of concrete at a certain age. The average strength of the three cubes then presented in the table below.

The concrete compressive strength data presented in Table 1 was plotted against the testing age, as shown in Fig. 4. The graph shows that at earlier ages, concrete with higher curing temperature gained higher strength. However, concretes that were maintained at higher temperatures get lower strength at later ages. This circumstance is called “*crossover effect*” [17–20]. The “*crossover effect*” is due to the forming of congested hydrated layers that wrap the cement granules that are not hydrated yet, thus preventing further hydration reactions. The higher treatment temperatures result in greater pores in the microstructure of the concrete because the results of hydration reactions are not distributed well. The deleterious effects on the strength growth of concrete that were treated at a lower temperature were less than those concretes cured at a higher temperature. Moreover, the growth of concrete strength, particularly the concrete cured at room temperature, still went up and did not show if there was a detrimental on its strength development.

Furthermore, the graph shows that the higher the curing temperature, the higher the detrimental effect on the strength of concrete at later ages. The higher the curing temperature earlier, the more un-hydrated cement produced.

The regressions linear of the concrete strength cured at the three different curing temperatures (Fig. 4) were conducted using Eq. (11) to obtain the parameters as shown in Table 2 and Fig. 5.

Table 1 Compressive strength of concrete cured at different temperature

Age (days)	Compressive strength (MPa)		
	25 °C (standard)	35 °C	50 °C
1	4.2220	5.1110	5.1110
2	7.6300		
3	9.6110	9.7780	10.6850
5		12.2220	14.4440
7	16.1330	16.4650	16.0000
14	19.0220		
21	23.8220		
28	25.3330		

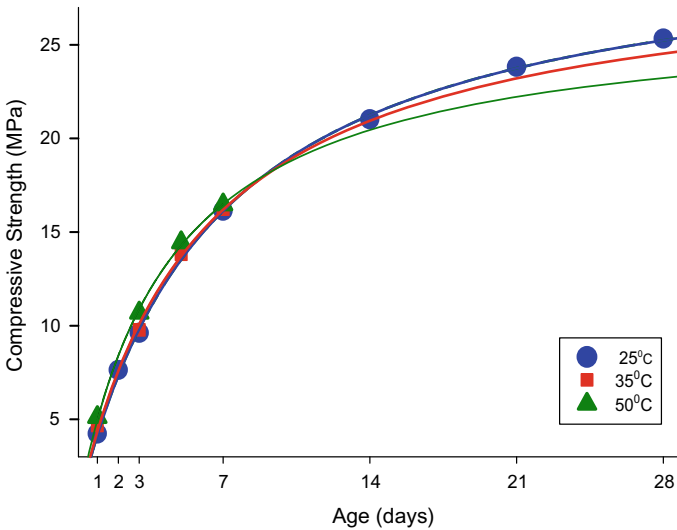


Fig. 4 Strength development of concrete cured under different curing temperatures

Table 2 Results of regression linear of the concrete strength cured at three different curing temperatures

Parameter	Curing temperature		
	25 °C (standard)	35 °C	50 °C
S_{∞}	30.5248	28,9555	26.8849
K	0.1529	0.1672	0.2270
t_0	2.2462×10^{-9}	1.1730×10^{-11}	9.0003×10^{-11}
R^2	0.9842	0.9775	0.9989

The parameters rate constant $k(T)$, which were obtained from the regression before, were then plotted against the curing temperature as shown in the following graph;

A datum temperature, t_0 is the temperature, where below the temperature, no reactions have occurred. A regression linear using Eq. (13) was done by plotting $k(T)$ values and the curing temperatures. This is done to find out the value of t_0 . The regression linear gives the values of C and D of 0.003 and 0.0707 respectively. Therefore, Eq. (13) can be rewritten as follows:

$$k(T) = 0.003T + 0.0707 \tag{15}$$

By taking the value of the rate constant $k(T)$ is equal zero, the above Eq. (15) then gives the value of T or the datum temperature, t_0 of -23.6 °C.

The temperatures of the concrete cubes cured under reference temperature were recorded for 28 days. These temperatures data were then used to compute the maturity value of the concrete, as presented in Table 3.

Fig. 5 Rate constant k against curing temperature

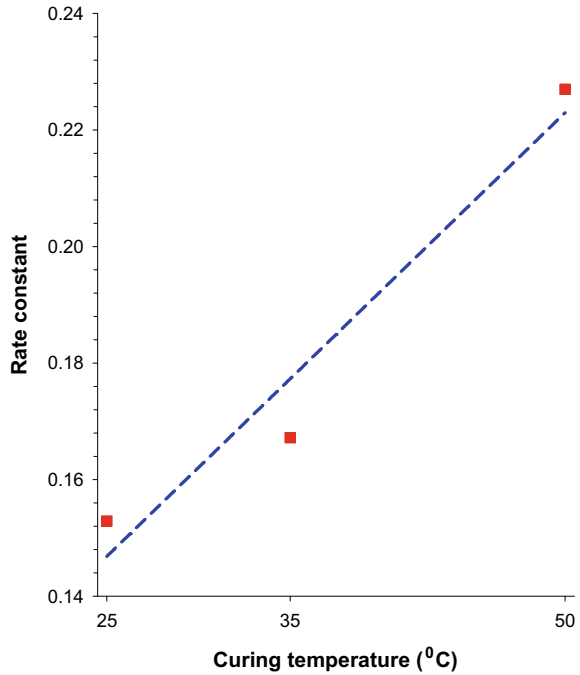


Table 3 The maturity value for concrete cured at standard curing (25 °C)

Concrete age (days)	Average Temperature (°C)	Datum temperature (°C)	Maturity (°C.days)
1	28.1		51.7
2	28.2		103.6
3	28.4		156.0
7	26.9	-23.6	353.5
14	26.7		704.2
21	25.5		1031.1
28	25.4		1372.0

The relationships between the compressive strengths against the maturity values of the concrete treated at reference temperature (25 °C) are illustrated, as pointed in Fig. 6. A regression linear then is performed on the plotted graph using Eq. (10) to obtain the value of parameters of S_{∞} , K and M_0 ; which are 31.5864 N/mm², 0.0029 and 2.869×10^{-8} °C-days, respectively, which would be used to develop the predicted strength equation based on the Eq. (10) above. The predicted strength equation shown in Fig. 6 can then be adopted to estimate the strength of concrete applying its maturity value.

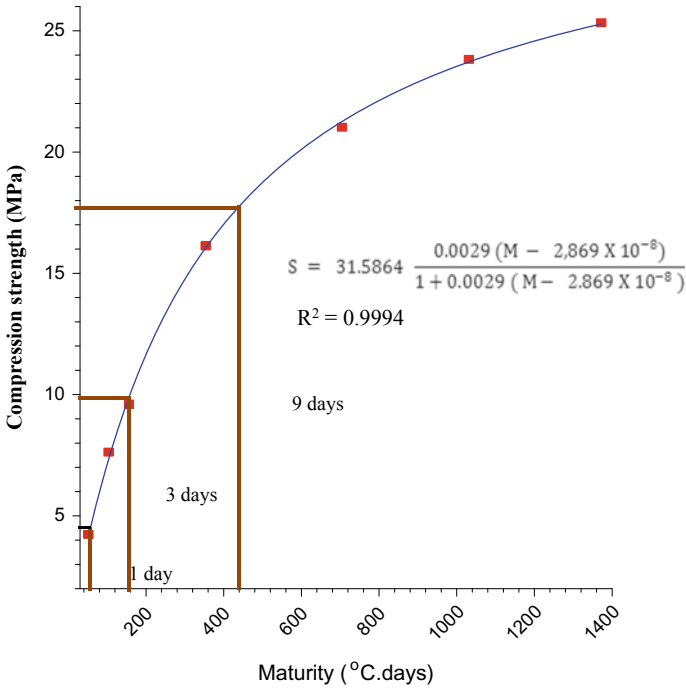


Fig. 6 Graph relationship between the strength against maturity of concrete

The maturity of the concrete slab was then calculated firstly using Eq. (1) above for each age 1, 3 and 5 days as presented in Table 4. Table 4 also shows the strengths of concrete cubes cured alongside the concrete slab that were evaluated at 1, 3, and 9 days. The predicted strengths of the concrete slab at the ages were then compared to their actual strengths at each age. The predicted strength of concrete at an earlier age, such as one day, was very close to the actual strength, which is different, only 1.95%.

Table 4 presents the predicted concrete strengths at ages 1, 3 and 9 days using the predicted strength equations, which were developed based on the linear regression. It was made on the concrete treated under standard curing temperature.

Table 4 Comparison between the actual and predicted strengths of concrete

Age (days)	Temperature (°C)	Maturity (°C.days)	Actual Strength (MPa)	Predicted Strength (MPa)	Differences (%)
1	27.9	51.5	4.026	4.100	1.95
3	29.2	158.4	9.585	9.940	3.73
9	26.4	450.0	17.483	17.880	2.40

Although the maturity method proposed by Nurse-Saul overestimate the strength of concrete until the age of 9-days, this method however, predicted the strength of concrete reasonable good. The differences between predicted and actual strength for the three testing ages are lower than 4%.

5 Conclusion

The curing temperature affects the strength growth of concrete for both earlier and later ages. The concretes treated at higher temperature result in higher strength at earlier ages than that of concrete cured at a lower temperature.

The Nurse-Saul maturity function predicts the concrete strength more accurately at earlier ages than at later ages, where the errors value is 1.95% compared to the ages 3 and 9 days i.e. 3.73% and 2.4%, respectively. The method could not predict the strength development of concrete well as it does not account for the impact of taller temperature at earlier ages on the strength of concrete later on.

The maturity formula, which Nurse-Saul proposed, predicted the strength of concrete accurately enough up to the age of 9 days; although the method predicts the strength of concrete higher than their actual strength till the age, it still looks reasonably good results as the differences between the actual and predicted strengths are lower than 4%. The results appear to be a little more accurate compared to when this method applied to estimate the strength growth of OPC concrete conducted in European countries, which have lower curing standard temperature. The errors were higher than 5% as reported in a previous work [14], where conducted in the UK.

References

1. McIntosh JD (1949) Electrical curing of concrete. *Mag Concr Res* 1(1):7
2. Saul AG (1951) Principles underlying the steam curing of concrete at atmospheric pressure. *Mag Concr Res* 2(6):13
3. McIntosh JD (1956) The effects of low-temperature curing on the compressive strength of concrete. In: *Proceedings*
4. Carino NJ, Lew HS (1984) The maturity method: from theory to application. *Cem Concr Aggr* 6(2):12
5. ASTM-C-1074, Standard practice for estimating concrete strength by the maturity method, in *Annual Book of ASTM Standards* 2019
6. Malhotra VM, Carino NJ (2004) *Handbook on nondestructive testing of concrete*. ASTM International
7. Carino N, Lew H (2001) *The maturity method: from theory to application*. Structures Congress & Exposition. Washington (DC)
8. Tank RC, Carino NJ (1991) Rate constant functions for strength development of concrete. *ACI Mater J* 88(1)
9. Kehl RJ, Constantino CA, Carrasquillo RL (1998) Match-cure and maturity: taking concrete strength testing to a higher level. Bureau of Engineering Research University of Texas at Austin, Center for Transportation Research

10. Rastrup E (1954) Heat of hydration in concrete. *Magazine of Concrete Research*, pp 13
11. Hansen PF, Pedersen EJ (1977) Maturity computer for controlled curing and hardening of concrete
12. Turuallo G (2015) Using GGBS for partial cement replacement in concrete: effects of water-binder ratio and GGBS level on activation energy. *Int J Technol* 6(5):9
13. Austin SA, Robins PJ, Issaad A (1992) Influence of curing methods on the strength and permeability of GGBFS concrete in a simulated arid climate. *Cem Concr Compos* 14(3):10
14. Turuallo G (2013) Early age strength development of GGBS concrete cured under different temperatures in engineering. Liverpool, UK, pp 588
15. Hansen PF, Pedersen EJ (1984) Curing of concrete structures
16. Brooks AG, Schindler AK, Barnes RW (2007) Maturity method evaluated for various cementitious materials. *J Mater Civ Eng* 19(12):8
17. Turuallo G, Mallisa H (2019) Sustainable cementitious materials: the effect of fly ash percentage as a part replacement of portland cement composite (PCC) and curing temperature on the early age strength of fly ash concrete. In: MATEC web of conferences. 2019. EDP Sciences
18. Soutsos MN et al (2009) The effect of temperature on the rate of strength development of slag cement. *ACI Spec Publ* 263:15
19. Barnett SJ et al (2006) Strength development of mortars containing ground granulated blast-furnace slag: Effect of curing temperature and determination of apparent activation energies. *Cem Concr Res* 36(3):7
20. Turuallo G (2015) Sustainable development of concrete using GGBS: effect of curing temperatures on the strength development of concrete. *Appl Mech Mater* 776:6

Study on Partial Replacement of Cement with Limonite in Mechanical Strength of Mortar



Md. Shahjalal, Jesika Rahman, Afia Farzana Haque, Lutful Habib, Khadiza Binte Jalal, and Mohd Mezanur Rahman

Abstract With the increasing population worldwide, main concerns are not limited to accessing sustainable living spaces but also managing waste disposal and greenhouse emissions. The supplementary cementitious materials (SCM) therefore play a vital role in providing an economical solution towards a greener environment, especially in the developing countries. The pozzolanic properties of limonite are studied in this paper to identify its potential to be used as an SCM. This study is aimed at utilizing limonite as a partial replacement of cement in the mortar by 5%, 10%, 15% and 20% of its weight. The pozzolanic properties of the limonite are traced through the results of compressive strength and the physical properties are also investigated in the form of specific gravity, setting time, consistency and fineness. Conventional cement mortar is also included for comparison. The results indicate that up to 10% replacement of cement by limonite allows an increase in the compressive strength of the mortar by 27% at 28 days. However, upon further increasing the percentage replacement, limonite had a significant effect in the mortar specimens. Lastly, this paper suggests that a reliable design guideline can be developed which will promote the use of limonite in wider implementations.

Keywords Limonite · Cement replacement · Mortar · Compressive strength

1 Introduction

Affordable building construction practice in the developing nations is increasing its popularity since the cost of construction materials is on the rise every day. Among

Md. Shahjalal (✉) · J. Rahman · A. F. Haque · L. Habib
Military Institute of Science and Technology, Dhaka, Bangladesh
e-mail: shahjalal@ce.mist.ac.bd

J. Rahman
e-mail: jesikarahman547@ce.mist.ac.bd

K. B. Jalal · M. M. Rahman
University of Texas at Arlington, Arlington, USA

the constituents of traditional concrete, cement is the most expensive one and so reducing the demand of cement eventually reduces the cost of producing concrete. Converting waste products into useful ones through substitution of the conventional raw materials in cement composition plays a vital role in increasing the affordability of building construction. In this way the non-renewable resources are saved leading to reduced environmental degradation. Portland cement production is responsible for emitting an estimated amount of 5% of the global CO₂ emission which is why even a small percentage of reduction in the cement consumption significantly reduces the greenhouse effect [1]. Pozzolans, as defined by ASTM C125 [2], are siliceous materials which obtain binding properties when they are added to Portland cement in finely divided form. Adding mineral in optimum quantity can work as filler material to reduce the voids in concrete mixtures and improve the mechanical strength of mortar.

Widely known industrial wastes used as alternative raw materials in binders are ceramic wastes, steel slag and sludge ash [3–6]. Such an industrial waste is also the iron ore tailings (IOT) which is produced from the extraction of iron ore. With the ever increasing industries worldwide, there are over 300 million tons of IOT released per year as the solid waste generated during the processing of iron and steel. Luo et al. [7] investigated the likelihood of utilizing iron ore tailing as raw material for producing Portland cement clinker. The results showed that using iron ore in producing clinker can improve the reactivity and burn ability of cement clinker. This has led to a considerable perturbation in environmental stability as the waste are dumped in on the landfills and with a recycling rate of merely 10% [8, 9]. With a view to minimize the problem of waste disposal and secondary pollution Chen et al. [9] tried to prepare an eco-friendly construction brick using hematite tailing from western Hubei province of China. The produced bricks were conformed well to the Chinese standard. Utilization of IOTs in building materials offer cost effective solution of the resource recovery and waste management problems [10, 11]. Researches in the past were made on the utilization of IOT as additives in clinker [12], high strength construction materials [13]. Substitution of aggregates in concrete with ferrous mill tailing was investigated by Cai et al. [14]. The result showed that concrete workability and strength can be increased by replacing fine or coarse aggregates with ferrous mill tailing. The chemical and minerals present in iron ore has made it applicable as raw material to prepare environment friendly composite ceramics [15]. Various iron ore derived products such as hematite (Fe₂O₃) and magnetite (Fe₃O₄) can be used to make different types of high strength concrete that can be used in special purposes [16, 17]. Abo-El-Enein et al. [16] revealed that high performance heavy density concrete made from ilmenite and air-cooled slag was suitable for gamma-ray shielding purpose. Adding 10% silica fume with cement and using ilmenite as coarse aggregate can give better physical and mechanical properties of concrete. Similar study was conducted by Ouda [17] to obtain heavy density high performance concrete using magnetite, goethite, barite and serpentine as coarse and fine aggregates. The concrete mixture with magnetite as fine aggregate was found to be efficient and suitable to protect against gamma-ray. Another product is the limonite (2Fe₂O₃·3H₂O), a hydrous iron ore formed after weathering

of hematite and magnetite, also used as aggregates in heavy weight concrete to shield nuclear radiation [18]. Past studies indicate the suitability of limonite as aggregates in concrete [19–21]. In radiation shielding limonite mixed concrete perform well but concrete compressive and flexural strength decreases with an increase in water absorption capacity [20]. Iron ore tailing can be used as partial replacement of cement in mortar with satisfactory compressive strength [22]. Huang et al. [23] used powder formed iron ore tailing as partial replacement of cement to develop greener engineered cementitious composites. The studies done on IOT signify its potential to be used as additives in cement blend to produce effective binders [22–24]. To the authors knowledge, no studies has yet been performed on the use of limonite as cement replacement in mortar or concrete.

This study investigates the pozzolanic characteristics of limonite by replacing Portland cement partially in the amounts of 5%, 10%, 15% and 20% respectively in mortar specimens. Previous researches on pozzolanic materials have been concluded that cement replacements of 10% to 20% with alternative binders provide good results which is why such replacement levels by limonite are undertaken by the authors in the current study [22, 25, 26]. In this paper, the physical and chemical properties are determined accordingly and the short and long term mechanical properties determined are also discussed in the subsequent sections. This utilization of waste limonite would reduce the burden on the waste management authorities as well as provide a sustainable solution to the costly methods of building constructions in the less developed nations.

2 Experimental Investigation

The experimental study constitutes the determination of physical properties of limonite, cement and sand in terms of chemical composition, normal consistency, initial and final setting time, fineness, specific gravity, workability and mechanical properties of the mortar mixtures like compressive strength and strength activity index.

2.1 Materials

The materials used for mortar specimens in this paper are Portland Composite Cement (PCC), limonite, natural fine aggregate (NFA) and water. PCC is used in this study as it is cheaper than Ordinary Portland Cement and it is more readily available in developing countries. The limonite used in the investigation as shown in Fig. 1 is collected from Congo. This limonite was dried in air for about three weeks, ground manually and sieved through 75 μm sieve at the laboratory. The chemical composition of limonite determined through X-Ray Fluorescence and the physical properties are shown in Table 1. The chemical analysis shows that limonite is primarily

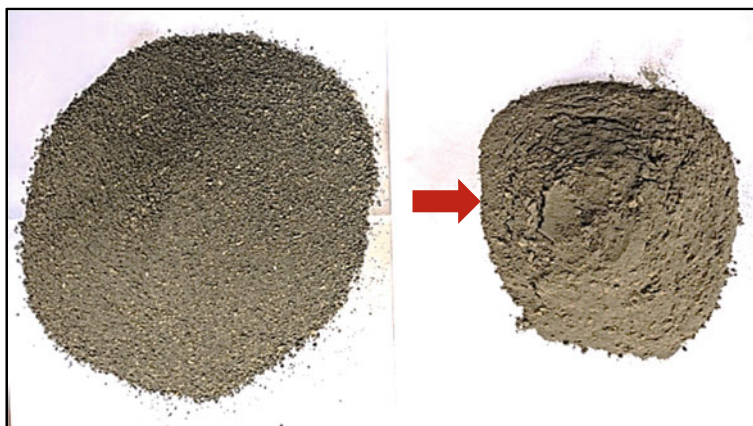
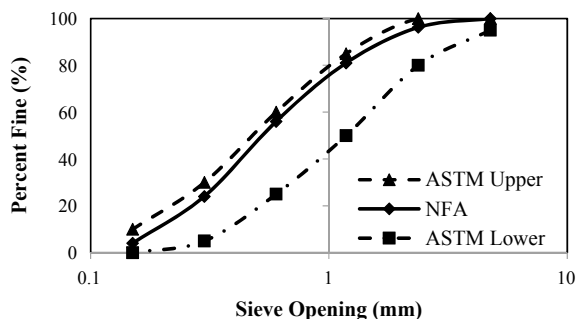


Fig. 1 Limonite sample collected and ground for the current study

Table 1 Chemical and physical properties of limonite and Portland Composite Cement

Component	Limonite (%)	PCC (%)
<i>Chemical Composition</i>		
SiO ₂	22.58	19.8
Al ₂ O ₃	12.59	3.98
Fe ₂ O ₃	41.08	4.67
CaO	10.89	64.79
MgO	5.63	2.32
K ₂ O	0.31	0.4
Na ₂ O	1.13	0.35
P ₂ O ₅		0.19
TiO ₂	0.49	0.2
MnO		
Loss on ignition (LOI)	2.21	1.31
<i>Physical Properties</i>		
Specific Gravity	2.66	3.13
Fineness (m ² /kg)	219.18	320
Bulk Density (kg/m ³) (Oven-Dry Basis)	2120	–

composed of silica which is unlike Portland cement where major component is CaO. The amounts of silicon oxide (SiO₂), aluminum oxide (Al₂O₃) and ferric oxide (Fe₂O₃) compounds in limonite sample used sums upto 75% hence it can be denoted as a class N-type ash material according to ASTM C618 [27]. The alkali present in the limonite sample is less than 2.6% which is the maximum limit in Portland cement [28]. Limonite (fineness of 219 m²/kg) is found to be much coarser than Portland

Fig. 2 Gradation curve of natural fine aggregate**Table 2** Physical properties of NFA

Variables	NFA
Apparent Specific Gravity	2.47
Bulk Specific Gravity (SSD)	2.41
Bulk Specific Gravity (OD)	2.36
Absorption Capacity (%)	1.8
Fineness Modulus	2.39
Loose Condition Unit Weight (kg/m^3)	1455.44
Compact Condition Unit Weight (kg/m^3)	1579.25
Loose Condition % of Voids	38.3
Compact Condition % of Voids	33.0

cement whose fineness is $320 \text{ m}^2/\text{kg}$, which may lead to an increase in setting time. The NFA used in this study is locally available well graded natural sand with a nominal maximum grain size of 4.75 mm. The gradation curve of NFA, presented in Fig. 2, shows a well-fitting curve within the ASTM range which is determined according to the ASTM C136 [29] standard. Besides, all the physical properties of NFA are also determined according to the ASTM standard presented in Table 2.

2.2 Mixture Proportions

The cement used in this investigation is replaced by 5, 10, 15 and 20% with limonite by weight basis and thus there are four different mixtures of limonite and one control mix (with no limonite). The water to cement and cement to sand ratios in the mixes are 0.48 and 1:2.75 respectively without using any admixtures. A target strength of 35 MPa at 28 days for the control mix was set for this study. The mix proportions of materials per cubic meter can be seen in Table 3. For aid in referencing within this paper, the samples are denoted as CC for control mix, L5, L10, L15 and L20 where the number refers to the percentage replacement and the preceding letter as limonite.

Table 3 Mix proportions of materials per cubic meter

Sample designation	w/c ratio	Water (kg)	Cement (kg)	Limonite (kg)	Fine aggregate (kg)
CC	0.48	234.1	482.5	–	1326.7
L5	0.48	234.1	458.3	24.1	1326.7
L10	0.48	234.1	434.2	48.2	1326.7
L15	0.48	234.1	410.1	72.4	1326.7
L20	0.48	234.1	386.0	96.5	1326.7

For example, L10 means that 10% cement is replaced by limonite and the rest 90% is the percentage of cement content.

2.3 Specimens

A total of 75 mortar cube specimens of 50 mm length are prepared according to ASTM C305 [30]. The specimens are initially cured for 24 h within the mold in a moist room and cured at a controlled temperature in a constant condition under fresh water for 28 days after demolding.

2.4 Testing Procedure

The normal consistency along with the initial and final setting times are determined following the ASTM C187 [31] and ASTM C191 [32] standards respectively. Workability of the mortar specimens were determined through flow table test as described in ASTM C1437 [33]. The compressive strength at different ages (3, 7, 28, 56 and 120 days) is determined according to ASTM C109 [34] standard. The test set up for compressive strength of mortar is shown in Fig. 3 where a constant loading rate of 1.80 KN/s is used. The mortar specimens are tested for their strength activity indices (SAI) following a slightly modified version of the ASTM C311 [35]. The control mixture is prepared with 500 g of ASTM Type 1 Portland cement, 1375 g of standard sand and 242 ml of water. For the purpose of comparison, all the percentage levels as used in the study (5, 10, 15 and 20%) for the SAI test and the resulting cube specimens are cured in saturated lime water until the day of testing.

Fig. 3 Test set up for compressive strength of mortar



3 Results and Discussion

3.1 Normal Consistency and Setting Times

It is necessary to determine consistency of binder materials because the amount of water used in mortar or concrete affects the setting time of the cement. So, correct proportion of water to binder materials is required to be known to achieve proper strength while using it in structure. This can be found out knowing standard consistency of binder paste. As depicted in Fig. 4, the normal consistency decreases with increase in replacement levels. This trend is similar to the behavior of mortar samples containing other cementitious binders such as volcanic ash and blast furnace slag [36]. The setting times indicated in the same figure shows that as the percentage levels increase so does the initial and final setting times. These two phenomenon observed in the test samples might be due to the lower specific gravity and fineness than those of Portland cement. The lower surface area of the limonite particles elongates the time required for hydration reaction thus leading to longer setting times. This can be regarded as advantageous as higher setting times allow lower heat of hydration consequently.

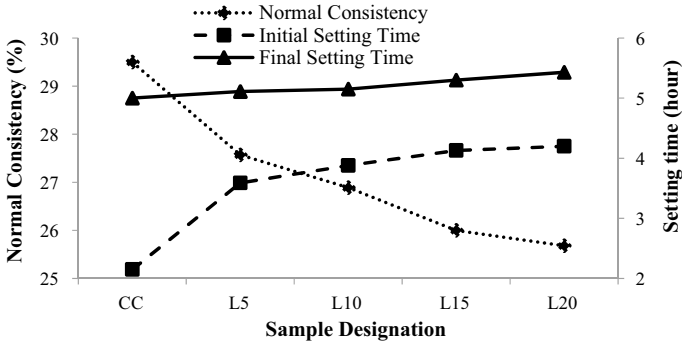


Fig. 4 Effect of limonite on normal consistency and setting time

3.2 Workability

One of the most important property of a mortar mixture is its workability. It must be free flowing without the segregation of water or other constituents in the mix. But too much water in mortar impairs its strength. So it is important to know the right amount water so that proper workability can be ensured. Workability of the mortar mixes were measured following the ASTM C1437 standard [33]. From the results as shown in Fig. 5, the control mix was superior to that of the mixes containing limonite. It is seen that the flow value decreased with increase in percentage replacement by limonite, with L20 having the lowest by 44.4% less than that obtained in sample CC. This suggests that limonite might have higher water absorption capacity than that of the Portland cement.

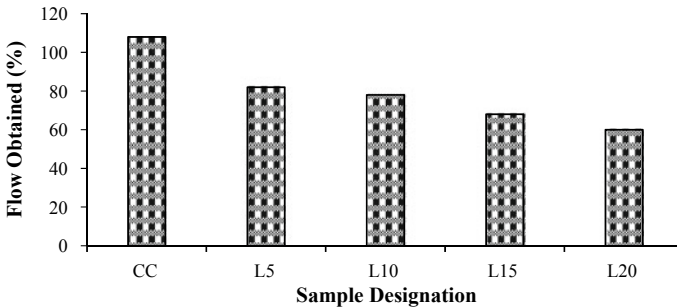


Fig. 5 Flow table test results

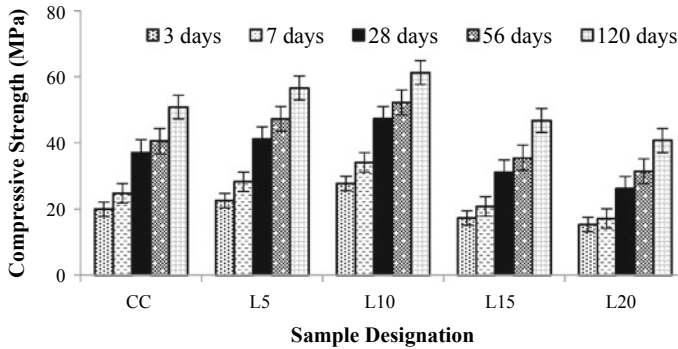


Fig. 6 Effect of limonite on compressive strength of the mortar samples

3.3 Compressive Strength

Compressive strength is one of the most important properties of concrete and mortar. The strength of the binder therefore has a significant effect on the performance characteristics of the mixture and ensures the overall quality of the finished product. The compressive strength at different batches is shown in Fig. 6, where the results are the average of three test specimens. It is observed that the compressive strength of all the samples in general increased with the age. The mortar specimens with 5% and 10% limonite replacement present greater compressive strength than the control samples. This increment might be due to the fact that the silica present in the limonite is finely divided to react with the calcium to form calcium silicates in the presence of water, results a higher value of compressive strength. However, it is seen that for all ages the compressive strength starts to decrease for 15% and 20% limonite specimens. The compressive strength at 28 days increased by 10.5% and 27% when the amount of limonite increased from 5 to 10% respectively. On the other hand, the compressive strength at 28 days decreased by 16.2% and 29.5% when the percentage of limonite are 15% and 20%, respectively. This might be due to the fact that the cement content has been reduced thus lowering the binding capacity of the mortar. Similar trend is also observed for 3, 7, 56 and 120 days compressive strength. Thus in terms of short and long term durability the substitution by limonite more than 10% is not suggested so that the compressive strength is not compromised. The failure pattern of different mortar mixtures is shown in Fig. 7. The specimens containing limonite shows a brittle failure compared to control specimens.

3.4 Strength Activity Index (SAI)

The strength activity index is the ratio of the strength of the limonite–cement mortar to the strength of the reference mortar (purely cement based mortar) at each specific

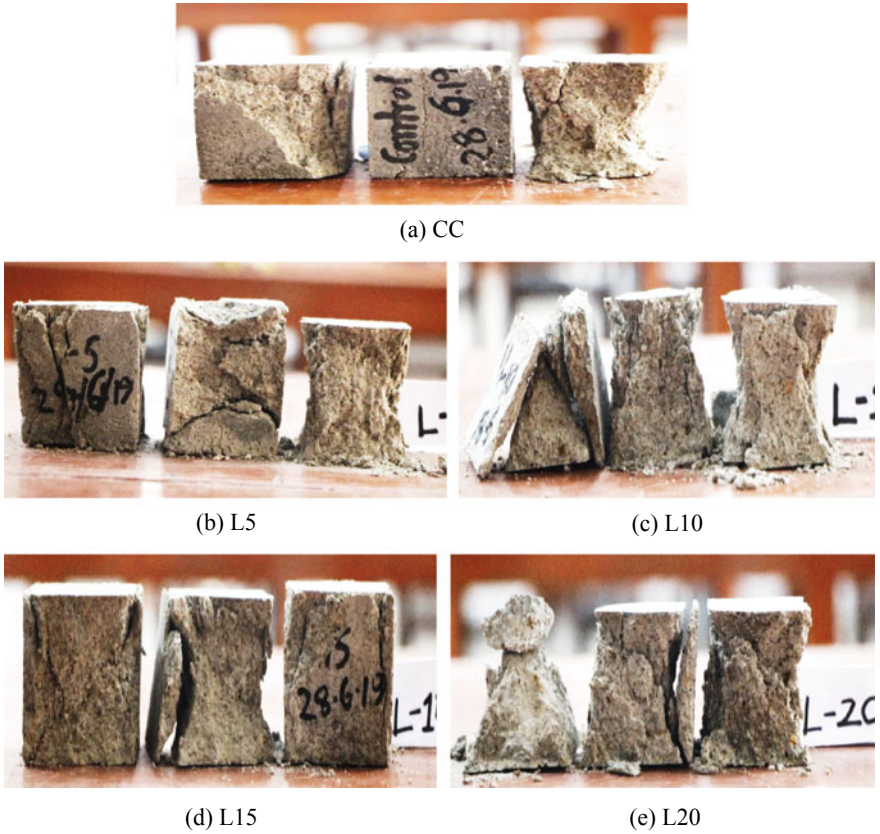


Fig. 7 Mortar cube specimens after crushing

curing time under a special curing process. A separate mix is used for this test and the results are shown in Table 4 which reveals the average value of SAI of three test samples each. According to the specifications by ASTM C618 [27], a natural

Table 4 Effect on SAI due to limonite content in mortar cubes

Sample designation	Percentage replacement by limonite	Average Compressive strength (MPa)		SAI (%)	
		7 days	28 days	7 days	28 days
CC	0	25.40	39.20	100	100
L5	5	29.50	43.40	116	111
L10	10	33.20	48.30	131	123
L15	15	18.50	29.10	73	74
L20	20	15.20	25.30	60	65

pozzolanic material must have an SAI value of a minimum of 75%. The corresponding values at 7 and 28 days for the 5% and 10% replacement levels are more than the minimum requirement. However, the SAI value for 15% and 20% limonite is less than 75% for both 7 and 28 days. Therefore, it is safe to suggest that limonite can perform as a natural pozzolan when their content in the mortar mixes are up to 10% of the weight of Portland cement.

4 Conclusion

This study investigates the effect of partial replacement of cement by limonite on both fresh and hardened properties of mortar. The normal consistency, setting times and workability are taken into consideration at the fresh state whereas compressive strength and SAI are considered as the hardened state properties of the specimens under this investigation. Based on the experimental findings, the following conclusions can be drawn:

1. With the increasing percentage of limonite, the value of normal consistency decreases but the setting time increases thus providing scope for the possible advantages of lower heat of hydration during construction.
2. The compressive strength increases as the replacement of cement by limonite as an alternative binder is up to 10% of the weight of cement and then starts to decrease.
3. Up to 10% replacement of cement by limonite, the SAI value is greater than 75% which is within the specified limit. Thus up to 10% limonite can be used as a replacement of Portland cement without having any discrepancies. Therefore, this study suggests that a cement blend having 10% limonite content can be used for mortar mixes with a target strength of 35 MPa.

Acknowledgements This research project is undertaken at Concrete Lab of Civil Engineering Department, Military Institute of Science & Technology (MIST), Dhaka, Bangladesh. Also a special thanks to MIST for the financial support.

References

1. Worrell E et al (2001) Carbon Dioxide emissions from the global cement industry. *Annu Rev Energy Env* 26(1):303–329
2. ASTM C125-19 (2019) Standard Terminology Relating to Concrete and Concrete Aggregates. ASTM International, West Conshohocken, PA
3. Puertas F et al (2008) Ceramic wastes as alternative raw materials for Portland cement clinker production. *Cement Concr Compos* 30(9):798–805
4. Tsakiridis PE et al (2008) Utilization of steel slag for Portland cement clinker production. *J Hazard Mater* 152(2):805–811

5. Lin K-L, Lin C-Y (2005) Hydration characteristics of waste sludge ash utilized as raw cement material. *Cem Concr Res* 35(10):1999–2007
6. Vangelatos I, Angelopoulos G, Boufounos D (2009) Utilization of ferroalumina as raw material in the production of Ordinary Portland Cement. *J Hazard Mater* 168(1):473–478
7. Luo L, Zhang Y, Bao S, Chen T (2016) Utilization of iron ore tailings as raw material for Portland cement clinker production. *Adv Mater Sci Eng*
8. Li C, Sun H, Bai J, Li L (2010) Innovative methodology for comprehensive utilization of iron ore tailings: Part 1. The recovery of iron from iron ore tailings using magnetic separation after magnetizing roasting. *J Hazard Mater* 174(1–3):71–77
9. Chen Y et al (2011) Preparation of eco-friendly construction bricks from hematite tailings. *Constr Build Mater* 25(4):2107–2111
10. Das SK, Kumar S, Ramachandrarao P (2000) Exploitation of iron ore tailing for the development of ceramic tiles. *Waste Manage* 20(8):725–729
11. Huang X et al (2013) Development of green engineered cementitious composites using iron ore tailings as aggregates. *Constr Build Mater* 44:757–764
12. Wang J, Wu C (2000) Effect of energy saving and formation of Portland cement clinker using iron-tailings as raw materials. *J Shenyang Arch Civ Eng Inst* 16(2):112–114
13. Zheng Y et al (2010) Mechanochemical activation of iron ore tailings and preparation of high-strength construction materials. *J Univ Sci Technol Beijing* 32(4):504
14. Cai JW, Zhang SB, Hou GX, Wang CM, Feng XX (2009) Effects of Ferrous Mill Tailings as aggregates on workability and strength of concrete. *J Wuhan Univ Technol* 7
15. Liu M, Xu LH, Zhang XM, Hao HS, Di YP (2009) Preparation of eco-friendly composite ceramic from iron ore tailings. In: *Materials Science Forum. Trans Tech Publ.*
16. Abo-El-Enein SA et al (2014) Physico-mechanical properties of high performance concrete using different aggregates in presence of silica fume. *HBRC Journal* 10(1):43–48
17. Ouda AS (2015) Development of high-performance heavy density concrete using different aggregates for gamma-ray shielding. *Prog Nucl Energy* 79:48–55
18. Makarious AS, El-Kolaly MA, Bashter II, Kansouh WA (1989) Radiation distribution through ilmenite—limonite concrete and its application as a reactor biological shield. *Int J Rad Appl Instr Part A. Appl Radiat Isot* 40(3):257–260
19. Oto B et al (2015) Neutron shielding qualities and gamma ray buildup factors of concretes containing limonite ore. *Nucl Eng Des* 293:166–175
20. Esen Y, Doğan ZM (2018) Investigation of usability of limonite aggregate in heavy-weight concrete production. *Prog Nucl Energy* 105:185–193
21. Davis HS, Witter FLBHC (1956) Properties of high-density concrete made with iron aggregate. In: *Journal proceedings*
22. de Magalhães LF, de Souza Morais I, dos Santos Lara LF, de Resende DS, Menezes RM, Aguilar MT, da Silva Bezerra AC (2018) Iron ore tailing as addition to partial replacement of Portland Cement. In: *Materials Science Forum. Trans Tech Publ.*
23. Huang X, Ranade R, Li VC (2012) Feasibility study of developing green ECC using iron ore tailings powder as cement replacement. *J Mater Civ Eng* 25(7):923–931
24. Li C et al (2010) Innovative methodology for comprehensive utilization of iron ore tailings: Part 2: the residues after iron recovery from iron ore tailings to prepare cementitious material. *J Hazard Mater* 174(1–3):78–83
25. Osinubi K, Yohanna P, Eberemu A (2015) Cement modification of tropical black clay using iron ore tailings as admixture. *Transp Geotech* 5:35–49
26. Yi Z-L et al (2009) Iron ore tailings used for the preparation of cementitious material by compound thermal activation. *Int J Miner Metall Mater* 16(3):355–358
27. ASTM C618-19 (2019) Standard specification for coal fly ash and raw or calcined natural pozzolan for use in concrete. ASTM International, West Conshohocken, PA
28. Hossain KMA (2005) Volcanic ash and pumice as cement additives: pozzolanic, alkali-silica reaction and autoclave expansion characteristics. *Cem Concr Res* 35(6):1141–1144
29. ASTM C136/C136M-14 (2014) Standard test method for sieve analysis of fine and coarse aggregates. ASTM International, West Conshohocken, PA

30. ASTM C305-14 (2014) Standard practice for mechanical mixing of hydraulic cement pastes and mortars of plastic consistency. ASTM International, West Conshohocken, PA
31. ASTM C187-16 (2016) Standard test method for amount of water required for normal consistency of hydraulic cement paste. ASTM International, West Conshohocken, PA
32. ASTM C191-19 (2019) Standard test methods for time of setting of hydraulic cement by Vicat Needle. ASTM International, West Conshohocken, PA
33. ASTM C1437-15 (2015) Standard test method for flow of hydraulic cement mortar. ASTM International, West Conshohocken, PA
34. ASTM C109/C109M-16a (2016) Standard test method for compressive strength of hydraulic cement mortars (Using 2-in. or [50-mm] Cube Specimens). ASTM International, West Conshohocken, PA
35. ASTM C311/C311M-18 (2018) Standard test methods for sampling and testing fly ash or Natural Pozzolans for use in Portland-Cement Concrete. ASTM International, West Conshohocken, PA
36. Hossain KMA (2003) Blended cement using volcanic ash and pumice. *Cem Concr Res* 33(10):1601–1605

Development of Numerical Model for Highly-Flowable Strain Hardening Fiber Reinforced Concrete (HF-SHFRC) Columns Subjected to Lateral Displacement Reversals and High Axial Loading Level



Wisena Perceka, Wen-Cheng Liao, and Li-Wei Tseng

Abstract Highly-flowable strain hardening fiber reinforced concrete (HF-SHFRC) is one of the advanced concrete material technologies. This material has good workability in the fresh state and exhibits strain-hardening and multiple cracking characteristics of high-performance fibre-reinforced cementitious composites (HPFRCC) in the hardened state. The use of steel fibers in a reinforced concrete column can replace the number of transverse reinforcement without reducing column strength and deformation capacity. Several experimental studies on the cyclic behavior of HF-SHFRC columns were carried out to capture the big picture of the feasibility study of steel fibers to substitute the transverse reinforcement. However, information regarding the numerical model of steel fibers reinforced concrete column, particularly column subjected to displacement reversals, is very limited. In this paper, an analytical macro model for HF-SHFRC columns subjected to lateral displacement reversals and high axial loading level is developed. The steel fibers are converted into transverse reinforcement in order to obtain equivalent confinement. In general, the cyclic behavior of the HF-SHFRC column could be predicted.

Keywords Toughness ratio · Equivalent confinement · Fiber effectiveness factor · Equivalent bond strength · Highly-flowable strain hardening fiber reinforced concrete (HF-SHFRC) · Buckling spring · Shear spring

W. Perceka (✉)

Parahyangan Catholic University, Bandung, West Java 40141, Indonesia

e-mail: wperceka@unpar.ac.id

W.-C. Liao · L.-W. Tseng

National Taiwan University, Taipei 10617, Taiwan

1 Introduction

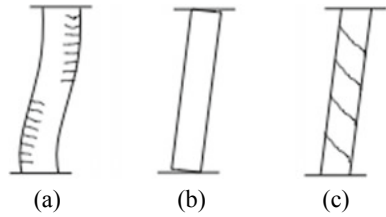
By using high-strength concrete (HSC) with compressive strength of 70 MPa and high-strength steel (HSS) with yield stress of 685 MPa or greater, the member cross-section size and the volume of concrete and steel reinforcing bars for the entire building structure can be reduced [1]. Owing to lower water-to-cementitious materials ratio of the HSC, the concrete is more durable [2]. However, the brittle behavior of high strength reinforced concrete during fracturing is still a primary concern despite wide application in the construction industry. This failure behavior can be disastrous for countries located in moderate to high seismic region. Since earthquakes are frequent and unpredictable and consequently, structures must be constructed to meet minimum ductility standards [3].

Traditional techniques to increase the compressive strength and ductility of reinforced concrete columns rely on increasing the amount of transverse reinforcement in the column. However, constructability decreases due to increase of the amount of transverse reinforcement. Therefore, new materials are required to be applied to reinforced concrete structures in hopes of leading a reinforced concrete member to maintain design strength without associated losses in constructability. Previous studies showed that adding short and discontinuous steel fiber to reinforced concrete improved the ductile behavior of concrete [4, 5]. In steel fiber reinforced concrete (SFRC), the presence of steel fibers substituting the transverse reinforcement can replace the number of transverse reinforcement without reducing column strength and deformation capacity [5].

Additionally, during fracturing, the steel fibers serve a bridging role and provide more tensile strength during fracturing than solid concrete. This behavior inhibits the formation of fractures and distributes the fractures to other regions of the concrete member. Concrete fails once the steel fibers either break or are completely pulled out from the concrete. As the result, the fibers reduce early flaking of the thin outer cover and help preventing sudden catastrophic failure. On the other hand, the presence of steel fibers reduces the workability of fresh concrete. This obstacle may become barrier for extending the application of steel fibers to reinforced concrete structures. Therefore, for cast in place purpose, Liao et al. in 2017 proposed highly-flowable strain hardening fiber reinforced concrete (HF-SHFRC) [6].

Highly-flowable strain hardening fiber reinforced concrete (HF-SHFRC) is one of advanced concrete material technologies, where this material has good workability in the fresh state and exhibits strain-hardening and multiple cracking characteristics of high-performance fiber reinforced cementitious composites (HPFRCC) in the hardened state. The tensile strain-hardening behavior prevents concrete cover to experience spalling early after cracking. Several experimental studies on the cyclic behavior of HF-SHFRC columns were carried out to capture the big picture of the feasibility study of steel fibers to substitute the number of transverse reinforcement [7, 8]. Although the experimental results are available, to the authors' knowledge, information regarding the numerical model of steel fibers reinforced concrete column, particularly column subjected to displacement reversals (cyclic loading), is very

Fig. 1 Lateral deformation of a RC column due to: **a** flexural, **b** slip, **c** shear



limited. This paper is aimed at developing an analytical macro model to predict the cyclic behavior of the SFRC columns under high axial loading level. The finite element software (OpenSees) was used to build the model of SFRC column in order to observe the response of SFRC columns. During earthquake, the column undergoes deformation, which is comprised of three components; flexural deformations, reinforcement slip deformation, and shear deformations, as shown in Fig. 1. In this study, the analysis is focused on SFRC columns experiencing flexural or flexure-shear failure only.

2 Constructed Analytical Model

The Open System for Earthquake Engineering Simulation (OpenSees) is a software framework for simulating the seismic response of the structural and geotechnical system that has been developed as the computational platform for research on performance-based earthquake engineering at the Pacific Earthquake Engineering Research Center [9]. OpenSees library provides several element commands, where the force-based beam-column element is usually used for constructing a reinforced concrete beam or column. In addition, the beam or column element is combined in series with zero-length element, where this zero-length element depends on the spring behavior. In order to construct behavior of concrete and steel reinforcement, the uniaxial material command providing both monotonic and cyclic uniaxial material behavior can be used. Section flexural response is modeled using fiber section command. The modeling procedure in this study refers to a composed analytical model proposed by Liu et al. [10]. The double-curvature column may be reduced to the equivalent cantilever column. By referring to PEER structural database manual, Perceka in 2019 and Liao in 2010 reported that reducing double-curvature large-scale column model to equivalent cantilever could compare column behavior consistently for a wide range of the testing configuration [11, 12]. For a double-curvature column, the lateral deformation of the large-scale model is multiplied by half ($1/2$) since the length of the equivalent cantilever is half of the length of the large-scale double-curvature column. This is because the contra-flexure point of the double-curvature column is assumed to always occur at the half-length of the large-scale double-curvature column model [13]. For the lateral strength, the lateral strength of the equivalent cantilever remains the same as that of the large-scale double-curvature column

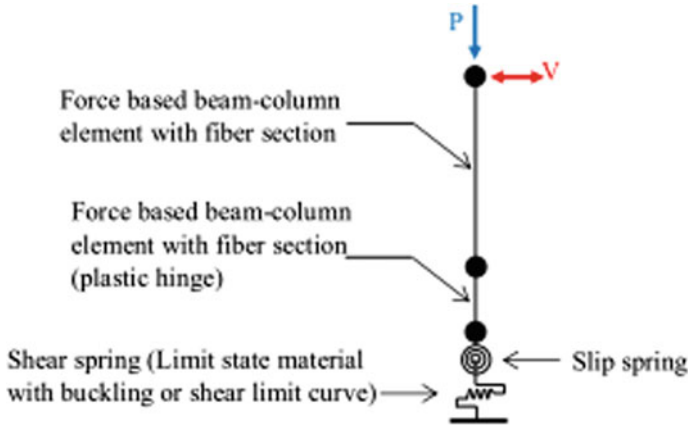


Fig. 2 A numerical model for SFRC column constructed by OpenSees

model. Figure 2 presents the analytical model of the column that is constructed in OpenSees (Fig. 2).

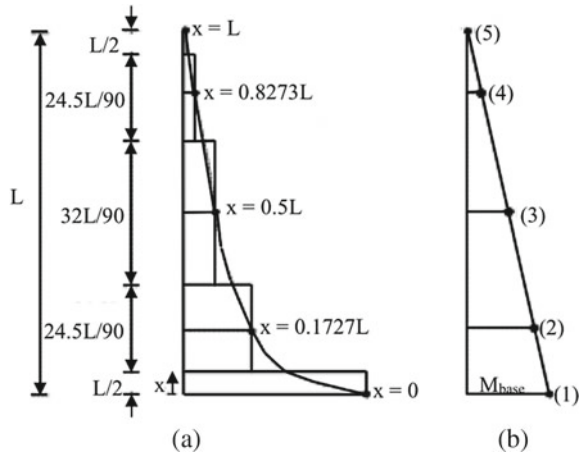
2.1 Forced-Based Beam-Column Element

The model of the column element is built using a force-based beam-column element. According to Teng et al. in 2016 [14], this element allows the nonlinear deformation of structural members in frames to be taken with a very coarse discretization. The forced-based beam-column element was used in the simulation of seismic performance of RC bridge columns, RC columns, or RC columns confined by fibre-reinforced polymer (FRP) in recent years [10, 14]. The force field is interpolated along with the element, as a result, element equilibrium is satisfied in a strict sense. For a member without distributed loads, typically, only one element is needed to perform a structural member in a frame. The Gauss–Lobatto integration scheme can be used, accordingly, since it has two integration points at the element ends where the maximum bending moments commonly occur. A schematic diagram of the five-point Gauss–Lobatto integration scheme for the sectional curvature of a cantilever column, which has also been shown by Teng et al. [14], is re-presented in Fig. 3.

2.2 Fiber Section

Fiber section is the section discretized based on fibers that collectively define section response. The stress–strain response of fibers is integrated to determine resultant behavior. A fiber section has a general geometric configuration formed by sub-regions

Fig. 3 The schematic diagram of the five-point Gauss–Lobatto for: **a** Curvature diagram, **b** Moment distribution for a force-based-beam-column element [14]



of simpler, regular shapes (quadrilateral, circular, and triangular regions), called patches. The steel reinforcement can be assigned by layer subcommand in order to construct the section of RC member.

2.3 Material Model

The fiber sections of concrete cover are assigned using the constitutive stress–strain model of concrete referring to ‘Concrete04’ and ‘Concrete02’, where this command is provided in uniaxial material command library. In order to show the steel fibers effect, the stress–strain model parameters of ‘Concrete04’ is defined based on the constitutive stress–strain model for steel fiber reinforced concrete in compression proposed by Liao et al. in 2015 [2]. Also, the parameters of tension part of ‘Concrete04’ are determined based on the constitutive stress–strain model for steel fiber reinforced concrete in tension proposed by Vianthy in 2015 [15]. The fiber sections of concrete core are assigned using the constitutive stress–strain model for confined concrete proposed by Cusson and Paultre [16]. The mechanical properties for confined concrete calculated by using Cusson and Paultre equation was assigned to ‘Concrete04’ to define behavior of column core. Since information regarding stress–strain model for confined concrete with steel fibers is very limited, the steel fibers shall be converted to transverse reinforcement. In 2016, Perceka et al. [4] proposed equations to calculate confinement efficiency of steel fiber reinforced concrete column confined by high strength transverse reinforcement. Those equations were proposed based on test results obtained from compression behavior of columns subjected to uniaxial concentric compression load. The confinement efficiency is expressed in term of toughness ratio that is the function of steel fiber and confinement parameters.

The ‘Hysteretic’ material model provided in uniaxial material command in OpenSees is selected to define the fiber sections of steel reinforcing bars. Liu et al. in 2014 performed iterative procedures to set the Pinchx and Pinchy parameters in the steel model [10]. It was reported that the Pinchx and Pinchy, respectively, were set as 0.5 and 0.4. Furthermore, it was reported that the post-yielding ratio of the steel should be adjusted to avoid negative stiffness in the beam-column element response and guarantee that a unique solution could be generated when the shear limit state material model was activated [10]. Also, the range of post-yielding ratio was varied from 0.5 to 2.5% of Young’s modulus of steel [10]. In this study, the Pinchx and Pinchy are set as 0.5 and 0.4, respectively.

2.4 Spring in Zero-Length Element

It is worth mentioning that the behavior of the zero-length element depends on the spring behavior. Two zero-length elements are available at the bottom of column. Two different spring models are required to represent slip and shear behavior of the HF-SHFRC column, while flexural behavior depends on concrete and steel reinforcement materials assigned for beam-column element.

Rotational slip spring. The rotational slip spring was selected to consider the additional rigid body rotation that was caused by longitudinal reinforcement slip. The reinforcement slip is assumed to occur in tension reinforcement only. According to Liu et al. [10], the contribution of the bond-slip was kept to remain at the elastic level to conserve the model unpredictability. This approximation was selected after considering the high degree of nonlinearity in the proposed model. This elastic rotational stiffness can be determined using an equation proposed by Elwood and Eberhard in 2009 [17]. The rotational stiffness of slip spring, K_{slip} , is expressed in Eq. 1.

$$K_{\text{slip}} = [8.u/(d_{\text{bl}}.f_{\text{yl}})].EI_{\text{flex}} \quad (1)$$

where d_{bl} is longitudinal reinforcement diameter, f_{yl} is longitudinal reinforcement yield stress, EI_{flex} is flexure stiffness of column section ($EI_{\text{flex}} = M_y/\phi_y$), u is the bond stress of embedded longitudinal bar, and d_{bl} is diameter of longitudinal reinforcement.

Buckling spring element. In order to simulate the behavior of HF-SHFRC columns experiencing flexural failure, the buckling spring is used. Similar to the analytical study conducted by Liu et al. [10], the buckling spring element shall be defined using the shear spring with the shear limit state proposed by Elwood [12]. Also, the nonphysical parameters of the spring, such as pinchx, pinchy, damage1, damage2, and beta can be set as 1.0, 1.0, 0.0, 0.0, 0.4, respectively [10]. In contrast, the pinchx and pinchy in this study are set as 0.5 and 0.4, respectively. Furthermore, Liu et al. [10] reported that the shear spring at the bar buckling failure point could be activated by shifting the original shear limit curve to the buckling point. The bar buckling limit, which is expressed as the ratio of delta-to-element length, can

be calculated using the equation proposed by Berry and Eberhard [18], as given in Eq. 2.

$$\Delta_{bb}/L (\%) = 3.25 (1 + K_{ebb} \cdot \rho_{eff} \cdot d_{bl}/D) \cdot (1 - N_u/[A_g \cdot f'_c]) \cdot (1 + L / 10D) \quad (2)$$

where Δ_{bb}/L is the drift ratio corresponding with the bar buckling failure, K_{ebb} is a coefficient that is equal to 40, 150, or 0 for rectangular-reinforced columns, spiral-reinforced columns, columns with a ratio of transverse reinforcement spacing-to-diameter of transverse reinforcement greater than 6, respectively, ρ_{eff} is a ratio of the volumetric transverse reinforcement ratio multiplied by the ratio of yield strength of transverse reinforcing bar-to-concrete compressive strength ($\rho_{eff} = \rho_s \cdot f_{yt}/f'_c$), f_{yt} and f'_c , respectively, are the yield strength of transverse reinforcement and concrete compressive strength. Also, L is the distance from the one of column ends to the point of contra flexure, D is the column section depth, N_u is axial load acting on column cross-section, and A_g is the area of column cross-section.

Once the bar buckling failure is detected, the shear strength of the column decreases up to all shear strength capacity losses. The collapse displacement is adjusted to be twice displacement at bar buckling failure detected. Therefore, the degrading slope of the total response can be calculated using Eq. 3.

$$k_{deg}^l = V_u/(\Delta_c - \Delta_{bb}) = V_u/\Delta_{bb} \quad (3)$$

The degrading slope of the shear spring response was empirically set as fifty percent of the degrading slope of the total response. Additionally, the symbol V_u in Eq. 3 denotes the shear strength of the column.

Shear spring element. It is known that as the displacement ductility decreased, shear failure governs. This condition causes the column to fail in shear prior to bar buckling. If the shear failure occurs after the yielding of longitudinal reinforcement, the failure mode is called flexure-shear failure. As mentioned, the bar buckling failure is calculated based on the original shear limit curve proposed by Elwood [18]. To simulate the HF-SHFRC column failing in flexure-shear, the shear limit curve is defined in Eq. 4.

$$\Delta_s/L = 3/100 + 4\rho'' - v_u/(40 \cdot \sqrt{f'_c}) - N_u/(40 \cdot A_g \cdot f'_c) \geq 1/100 \quad (4)$$

where Δ_s/L is the drift ratio at shear failure, ρ'' is the transverse reinforcement ratio and v is the nominal shear stress that is the sum of shear strength provided by concrete and transverse reinforcement.

Like modeling for a column experiencing flexural failure, once the shear failure point is reached, the column's shear strength decreases until the column loses its shear capacity. According to Elwood [19], based on the intersection of total response and shear limit curve corresponding to detected shear failure, the degrading slope for the total response that is function of shear strength, displacement at shear failure detected, and displacement at axial failure detected, is expressed in Eq. 5.

$$k_{deg}^I = V_u / (\Delta_a - \Delta_s) \tag{5}$$

It shall be noted that Δ_a is displacement at axial failure, as given in Eq. 6.

$$\Delta_a / L = (4/100) \left[\frac{1 + (\tan \theta)^2}{\tan \theta + N_u \cdot [s / (A_s \cdot f_{yt} \cdot d_c \cdot \tan \theta)]} \right] \tag{6}$$

where d_c is the depth of the column core from the center line to center line of the ties, and s is the spacing of the transverse reinforcement.

2.5 Toughness Ratio

Toughness ratio, TR, is the ratio of the toughness of the concrete material or column under uniaxial compression to the toughness of the rigid material. Perceka et al. [4] described toughness as an area under the stress–strain or load–strain curve of SFRC column under uniaxial concentric load up to strain of 0.0154. Figure 4 presents the compressive stress–strain curve of the concrete material or column and that of rigid material. Perceka et al. [4] proposed a TR equation in term of transverse reinforcement and steel fiber parameters to quantify confinement efficiency of HF-SHFRC column under uniaxial compression by regressing 69 TRs of high strength concrete column without steel fibers and 27 TRs of high strength concrete column with steel fibers [2]. The TR of high strength concrete and HF-SHFRC column are given in Eqs. 7 and 8, respectively.

$$T_{R,HSC} = 0.48(T_{IT})^{0.18} \tag{7}$$

$$T_{R,HF-SHFRC} = 0.48(T_{IT} + 0.62T_{If})^{0.18} \tag{8}$$

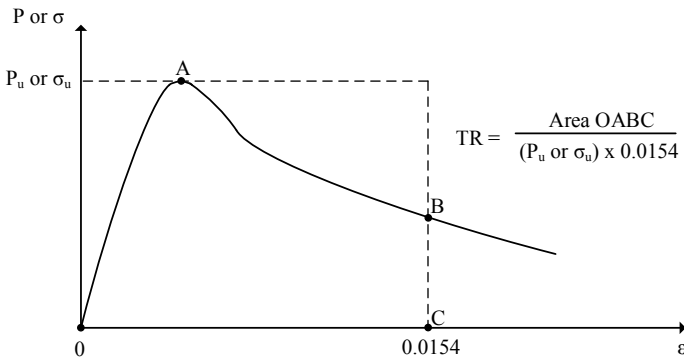


Fig. 4 Toughness ratio TR of RC column under uniaxial compression

where $T_{R,HSC}$ is TR of high strength concrete column, $T_{R,HF-SHFRC}$ is TR of high strength SFRC column, T_{It} is effective confinement index, and T_{If} is confinement index steel fibers. T_{It} and T_{If} are given in Eqs. 9 and 10, respectively.

$$T_{It} = k_e \cdot \rho_s \cdot f_{yt} / (f'_c \cdot k_n) \quad (9)$$

$$T_{If} = V_f \cdot (L_f / d_f) \cdot \tau_{eq} / f'_c \quad (10)$$

Equations 11 through 13 are provided to calculate the transverse reinforcement ratio in HF-SHFRC column.

$$\rho_s = 2A_{sh} / (s \cdot b_c) \text{ (square column)} \quad (11)$$

$$\rho_s = [A_{shx} / (s \cdot h_c) + A_{shy} / (s \cdot b_c)] \text{ (rectangular column)} \quad (12)$$

$$k_n = n_l / (n_l - 2) \quad (13)$$

where A_{sh} is the total cross-section area of transverse reinforcement perpendicular to one direction, A_{shx} is the total cross-section area of transverse reinforcement perpendicular to the x-axis, A_{shy} is the total cross-section area of transverse reinforcement perpendicular to the y-axis, b_c is the side dimension of concrete core parallel to the x-axis, h_c is the side dimension of concrete core parallel to the y-axis, k_e is confinement effectiveness coefficient, k_n is confinement effectiveness factor, n_l is the number of longitudinal bars around the perimeter of the column core that are laterally supported by the corner of close-hoops or conventional ties having 135° hooks anchored into the concrete core, f_{yt} is the yield stress of transverse reinforcement, V_f is fiber volume fraction, L_f is steel fiber length, d_f is steel fibers diameter, and τ_{eq} is the bond strength between steel fibers and the surrounding matrix.

The yield stress of transverse reinforcement for calculation shall not exceed 700 MPa. By using TR equation, the steel fibers can be treated as shear reinforcement, and the equivalent total shear reinforcement can be obtained.

2.6 Shear Strength Prediction Equation

Prior to this study, no equation is available for shear strength design or prediction of the steel fibers reinforced concrete column. Moreover, despite many shear strength equations proposed by other authors for designing or predicting the shear strength of a beam with steel fibers, no equation expresses concrete and steel fiber parameters in one term. Perceca et al. in 2019 [5] proposed an equation for predicting the shear strength of SFRC beam, where the concrete and steel fiber parameters are put in one

term. They also slightly modified the shear strength equation proposed in ACI 318–19 [20] by multiplying shear strength equation and fiber effectiveness factor. Since the equations for shear provided in ACI 318–19 [20] is applicable to both beam and column, the analytical shear strength of shear spring for HF-SHFRC column model can be predicted. Equations 14 and 15 are ACI equations that have been slightly modified by Perceka et al. [5]:

$$V_{c,SF} = [0.17\text{sqrt}(f'_c) + N_u/(6A_g)] \cdot F_{\text{eff}} \cdot b_w \cdot d \quad (14)$$

$$V_{c,SF} = [0.66(\rho_w)^{1/3} + N_u/(6A_g)] \cdot F_{\text{eff}} \cdot b_w \cdot d \quad (15)$$

where b_w is column section width, d is column effective depth, and ρ_w is the ratio of tension reinforcement, and F_{eff} is fiber effectiveness factor.

According to ACI 318–19 [20], if the amount of provided shear reinforcement is greater than the minimum requirement for shear reinforcement, either Eq. 14 or Eq. 15 can be used. For analysis and design, it is recommended to use the smallest of Eqs. 14 and 15. There are three equations for RC member provided in ACI 318–19 [20]; however, the third equation is provided for the reinforced concrete member with shear reinforcement less than the minimum requirement. The third equation is neglected in this study by assuming the fiber volume fraction of 0.75% equal to minimum reinforcement for SFRC beam. Equation 16 was proposed by Perceka et al. [15] to account for the fiber effectiveness factor that represents the steel fibers contribution in an SFRC beam.

$$F_{\text{eff}} = 1 + [(\tau_{\text{eq}} \cdot V_f \cdot L_f / d_f) / (0.75 \cdot \text{sqrt}(f'_c))] \quad (16)$$

The shear strength provided by transverse reinforcement can be determined by using Eq. 17. As reported by Perceka in 2019 [12], in order to calculate the shear strength provided by high strength transverse reinforcement, the yield stress shall not be greater than 600 MPa.

$$V_s = A_v \cdot f_{yt} \cdot d / s \quad (17)$$

3 Benchmark Specimens

The selected column specimens that are referred to verify the numerical model constructed in this study are columns tested by Tseng in 2014 [21] and Perceka et al. in 2016 [3]. Table 1 and Fig. 5 present the parameters and section detailing for both specimens, respectively. Both S90-0.75 and S130-1.0 were made of HF-SHFRC material with specified concrete compressive strength of 100 MPa. However, the concrete compressive strength assigned in OpenSees is in accordance with the

Table 1 Parameters of HF-SHFRC column specimens

ID	$f'_{c,spec}$ [$f'_{c,test}$] in MPa (V_f [%])	longitudinal bars SD685 n_1-d_{bl} ($f_{y,test}$ [MPa])	Transverse bars SD785		$\frac{p}{A_g f'_c}$
			d_{bt} ($f_{y,test}$ [MPa])	S (mm)	
S90-0.75	100 [82.7] (0.75%)	8D32 (734), 8D25 (723)	D16 (816)	90	0.42
S130-1.00	100 [81.2] (1.00%)	8D32 (734), 8D25 (723)	D16 (816)	130	0.42

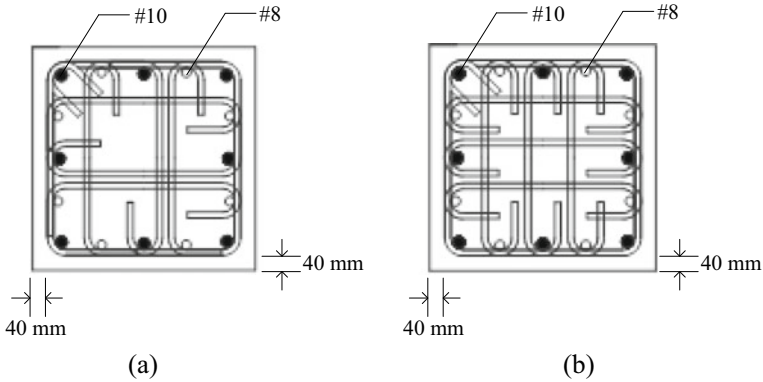


Fig. 5 Detail section for specimen: **a** S90-0.75 [21], **b** S130-1.0 [3]

compressive strength of cylinders tested on the same day with column specimens. The symbol S denotes column specimens, while two number following the S character denote transverse reinforcement spacing and fiber volume fraction, respectively. Those specimens were subjected to displacement reversals and a constant axial compression force ratio of 0.42.

Both specimens have the same cross-section design and similar longitudinal and transverse reinforcement layout. Specimen S90-0.75 has the transverse reinforcement with a single close hoop supporting longitudinal bars on the corners of the hoop and hooked end bent at 135° at one corner, crossties with a 90° at one end and 180° on the opposite end, and transverse reinforcement spacing of 90 mm. Unlike S90-0.75, specimen S130-1.0 has transverse reinforcement spacing of 130 mm, with all crossties having hooked end bend at 180° at both ends.

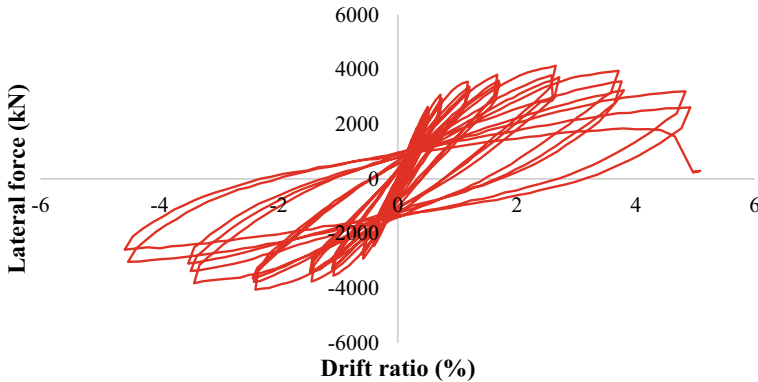


Fig. 6 The hysteresis loops for specimens S90-0.75 [21]

4 Benchmark Specimens

4.1 Specimen S90-0.75

In specimen S90-0.75, the transverse reinforcement with single close hoop supporting longitudinal bars on the corners of the hoop and having hooked end bent at 135° at one corner and cross-ties with a 90° at one and 180° on the opposite end. Both specimens were subjected to constant high axial compression force with an axial load ratio of 0.42. The hysteresis loops for specimens S90-0.75 is plotted in Fig. 6. The peak lateral strength was reached once the drift ratio was 2.65% that corresponded with the maximum lateral strength of 4135 kN. The ultimate drift ratio (UDR) (drift ratio corresponding to 80% maximum lateral capacity) of S90-0.75 was 4.23%, where the UDR was greater than 3%. Specimen S90-0.75 failed once the drift ratio was 4.59%.

4.2 Specimen S130-1.0

Like specimen S90-0.75, specimen S130-1.0 was subjected to constant axial compression force with an axial load ratio of 0.42. The transverse reinforcement spacing in S130-1.0 is one-fourth of effective column depth ($d/4$). Figure 7 presents the hysteresis loops for specimen S130-1.0. At a 1% drift ratio, the stiffness of specimen S130-1.0 began to decrease. The lateral strength and the corresponding drift ratio to peak strength were 3856.25 kN and 2.26%, respectively. The 3.78% drift ratio was reached once the ultimate strength dropped by about 20%. Therefore, the ultimate drift ratio was greater than the minimal acceptance drift ratio (3%). Notably, at a drift ratio of 4%, the lateral strength of the specimens rapidly decreased. Once a

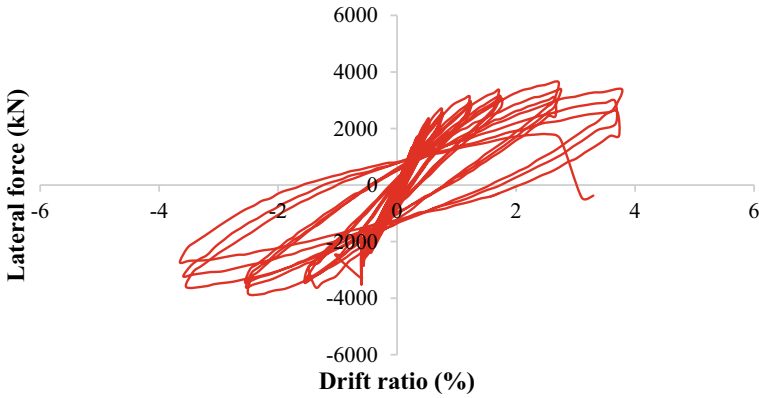


Fig. 7 The hysteresis loops for specimens S130-1.0 [3]

4% drift ratio was reached during the 3rd hysteresis loop, the specimen failed under axial loading.

5 Comparison Between Experimental and Numerical Model

Figures 8 and 9 present the comparison of experimental and predicted response of column tested by Tseng in 2014 [21] for S90-0.75 and Perceka et al. in 2016 for S130-1.0 [3]. As shown in both figures, the drift response for both experimental and numerical model is in the range of -4.5 to $+5.0\%$. From both experimental and numerical model, it can be known that the column was able to maintain the lateral

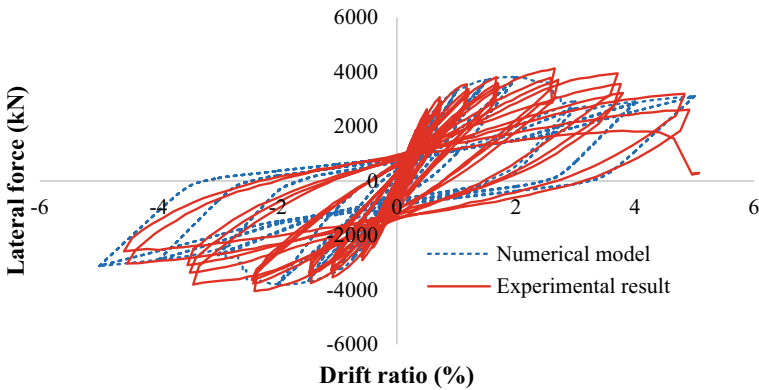


Fig. 8 Comparison between experimental and numerical model for specimen S90-0.75

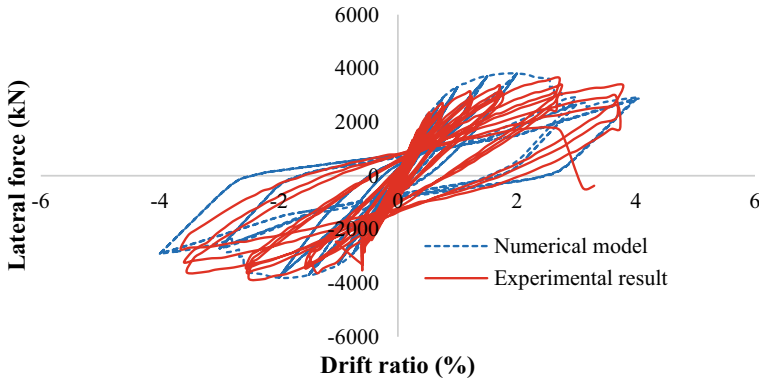


Fig. 9 Comparison between experimental and numerical model for specimen S130-1.0

strength at a large drift ratio, despite under high axial loading level. The maximum lateral strength of the numerical model for S90-0.75 was 3820 kN, where this value was slightly less than that of the experimental result. From a comparison between the experimental and numerical model for specimen S130-1.0, the difference between the experimental and numerical model for lateral strength was only 40.1 kN, where the lateral strength of experimental was slightly higher than that of the numerical model. The initial lateral stiffness of the numerical model for both specimens was almost similar to that of the experimental model. However, it can be seen in both comparison figures that the drift ratio corresponding to the peak strength of the experimental was greater than that of the numerical model. Since a numerical model for RC column consisted of beam-column element and buckling or shear spring, the column response highly depends on those elements. Once the shear failure in shear or buckling spring was detected, the degrading slope tended to follow the post-peak response of spring prior to degradation of the beam-column element. The response of slip of longitudinal reinforcement was assumed to be constant, while in the real test, the slip response affected the behavior of the column. In general, the hysteretic curves resulted from the numerical model can capture the peak strength and strength decay in columns. However, the overall response was not predicted well in many cycles.

6 Conclusions

An analytical macro model has been developed in order to simulate the cyclic behaviour of high strength concrete columns with high strength steel reinforcement and steel fibre. Since no stress-strain model for steel fibre concrete confined by high strength reinforcing is available, particularly high strength steel fibre reinforced concrete confined by high strength transverse reinforcement, the steel fibers shall be

converted into transverse reinforcement. Therefore, the equivalent confinement can be obtained. Once the equivalent transverse reinforcement is obtained, the parameters of the traditional stress–strain model for confined concrete can be adopted to develop a stress–strain curve based on uniaxial material “Concrete04” in OpenSees. Although the overall response could not be well predicted in many cycles, the hysteretic curves resulted from the numerical model could still capture the peak strength and strength decay in columns. Therefore, in general, the cyclic behavior of the HF-SHFRC column could still be predicted.

References

1. Lee HJ, Chen JH (2014) Testing of mechanical splices for grade 685 steel reinforcing bars. TTK Report, NCREE
2. Liao WC, Perceka W, Liu EJ (2015) Compressive stress-strain relationship of high strength steel fiber reinforced concrete. *J Adv Concr Technol* 13(8):378–392
3. Perceka W, Liao WC, Tseng LW (2016) Application of highly-flowable strain hardening fiber reinforced concrete in NEW RC Columns. In: Maekawa K, Kasuga A, Yamazaki J (eds) *Proceeding of The 11th fib international PhD symposium in civil engineering*. The University of Tokyo, Tokyo, Japan
4. Perceka W, Liao WC, Wang YD (2016) High strength concrete columns under axial compression load: hybrid confinement efficiency of high strength transverse reinforcement and steel fibers. *Materials* 9(4)
5. Perceka W, Liao WC, Wu YF (2019) Shear strength prediction equations and experimental study of high strength steel fiber reinforced concrete beams with different shear span-to-depth ratios. *Appl Sci* 9(22)
6. Liao WC, Perceka W, Yu LC (2017) Systematic mix procedures for highly flowable-strain hardening fiber reinforced concrete (HF-SHFRC) by using tensile strain hardening responses as performance criteria. *Sci Adv Mater* 9(7):1157–1168
7. Kimura H, Ishikawa Y, Kambayashi A, Takatsu H (2007) Seismic behavior 200 MPa ultra-high-strength steel-fiber reinforced concrete columns under varying axial load. *J Adv Concr Technol* 5(2):193–200
8. Lee HH (2007) Shear strength and behavior of steel fiber reinforced concrete columns under seismic loading. *Eng Struct* 9:1253–1262
9. OpenSees Homepage, <https://opensees.berkeley.edu>. Last Accessed 29 Apr 2020
10. Liu K, Witarto W, Chang K (2014) Composed analytical models for seismic assessment of reinforced concrete bridge columns. *Earthq Eng Struct Dynam* 44(2):265–281
11. Liao WC (2010) Performance-based plastic design of earthquake resistant reinforced concrete moment frames. PhD Dissertation. Department of Civil and Environmental Engineering, University of Michigan, Ann Arbor, Michigan
12. Perceka W (2019) Shear behavior of high strength steel fiber reinforced concrete columns. Doctoral Dissertation. College of Engineering-Department of Civil Engineering, National Taiwan University, Taiwan
13. Berry M, Parrish M, Eberhard M (2004) PEER structural performance database user’s manual (Version 1.0)
14. Teng JG, Lam L, Lin G, Lu JY, Xiao QG (2016) Numerical simulation of FRC-jacketed RC columns subjected to cyclic and seismic loading. *J Compos Constr* 20(1)
15. Vianthly A (2015) Analytical study of shear capacity and behavior of highly flowable strain hardening steel fiber reinforced concrete panel. Master Thesis. College of Engineering-Department of Civil Engineering, National Taiwan University, Taiwan

16. Cusson D, Paultre P (1995) Stress-strain model for confined high-strength concrete. *J Struct Eng* 121(3):468–477
17. Elwood KJ, Eberhard MO (2009) Effective stiffness of reinforced concrete column. *ACI Struct J* 106(4):476–484
18. Elwood KJ (2004) Modelling failures in existing reinforced concrete columns. *Can J Civ Eng* 31:846–859
19. Berry M, Eberhard MO (2005) Practical performance model for bar buckling. *J Struct Eng* 131(7):1060–1070
20. ACI Committee 318 (2019) Building code requirement for structural concrete (ACI 318-19) and commentary. American Concrete Institute: Framington Hills, MI, USA
21. Tseng LW (2014) Feasibility study of steel fibers as a substitute for transverse reinforcement in new RC columns. Master Thesis. College of Engineering, Department of Civil Engineering, National Taiwan University, Taipei, Taiwan (2014). (In Chinese)

Mechanical Properties of Eco-Friendly Self-consolidating Concrete Containing Ground Granulated Blast Furnace Slag and Calcined Dolomite



Herry Suryadi Djayaprabha, Ta-Peng Chang, Jeng-Ywan Shih,
and Hoang-Anh Nguyen

Abstract During recent decades, the aim of transferring ground granulated blast furnace slag (GBFS) from a waste material into an advantageous construction material has received significant attention. In this study, natural dolomite, $\text{CaMg}(\text{CO}_3)_2$, powder burned at a complete decarbonation temperature (about $900\text{ }^\circ\text{C}$) is referred to as calcined dolomite (CD). This powder could be used as an activator for the GBFS to form an eco-friendly cementitious material. From the previous study, the optimum amount of CD as slag activator was found at 20 wt%. This study explored both of the fresh and hardened properties of self-consolidating concrete (SCC) of two mixtures prepared by mixing weight ratio of CD:(CD + GBFS) in a percentage equal to 10 and 20 wt% and one ordinary Portland cement (OPC) based mixture with equivalent strength as a control set. The mechanical properties of SCCs including workability, compressive strength, splitting tensile strength, the volume of permeable voids, and water absorption. The results showed that the mixture with 20 wt% of CD reached the 28-day compressive strength of 35.75 MPa, which was lower by 12.39% compared with OPC-based SCC. Based on Vicroads classification for the computed volume of permeable voids, the mixture with 20 wt% of CD can be classified as good concrete. Therefore, the eco-friendly SCC with 20 wt% of CD has exceeded

H. S. Djayaprabha (✉)

Department of Civil Engineering, Parahyangan Catholic University, Bandung, Indonesia
e-mail: herry.suryadi@unpar.ac.id

T.-P. Chang

Department of Civil and Construction Engineering, National Taiwan University of Science and Technology (NTUST) (Taiwan Tech), Taipei, Taiwan, ROC
e-mail: tpchang@mail.ntust.edu.tw

J.-Y. Shih

Department of Chemical Engineering, Ming Chi University of Technology, New Taipei City, Taiwan, ROC

H.-A. Nguyen

Department of Rural Technology, College of Rural Development, Cantho University, Cantho City, Viet Nam
e-mail: hoanganh@ctu.edu.vn

the minimum compressive strength requirement for concrete structural application with satisfactory durability.

Keywords Calcined dolomite · Ground granulated blast furnace slag · Self-consolidating concrete · Volume of permeable voids · Water absorption

1 Introduction

Concrete with Portland cement as a binding ingredient becomes the most dominant world's construction material due to its excellent mechanical, thermal, and durability properties [1]. A significant amount of carbon dioxide (CO₂) was emitted to the atmosphere for every kilogram production of Portland cement. On the other hand, the most energy consumption is both clinker and cement manufacture [2]. Many researchers tried to find a clinkers binder as an alternative for replacing Portland cement. One of the most popular industrial waste material that commonly used for replacing Portland cement is ground granulated blast furnace slag (GBFS). GBFS is a byproduct obtained in the production of pig iron in the blast furnace. Due to the fact that GBFS is of great benefit to concrete, considerable attention has been paid in recent decades to shift GBFS from waste material to the valuable construction material [3]. GBFS reacts slowly with water [4]; therefore, concrete made with pure GBFS as binding material is never used as a construction material. GBFS has been found to demonstrate excellent hydraulic properties when the activator is used. Widely available commercially chemical solutions, such as sodium hydroxide (NaOH), sodium silicate (Na₂SiO₃), potassium hydroxide (KOH), sodium carbonate (Na₂CO₃), sodium sulfate (Na₂SO₄) were generally used as GBFS activator [5]. On the other hand, the reactive earth metal oxides such as calcium oxide (CaO) could be used as an alternative GBFS activator [6, 7].

Dolomite, a type of calcium magnesium carbonate, which is represented by a stoichiometric chemical composition of CaMg(CO₃)₂ with alternate layers of calcium carbonate (CaCO₃) and magnesium carbonate (MgCO₃). Calcium magnesium carbonate could be decomposed into calcium oxide when subjected to elevated temperature. When a rising temperature exposed to dolomite, it could be decomposed into two stages. The first stage, calcium carbonate and magnesium oxide were formed at a lower temperature (about 550–765 °C) as shown in Eq. (1), whereas calcium carbonate was decomposed to form calcium oxide at higher temperature (about 900–960 °C) as shown in Eq. (2) [8].



The feasibility of calcined dolomite (CD) with reactive calcium oxide acted as a GBFS activator has been proven in construction material with excellent mechanical properties and durability in binder [9–11] and mortar [12]. Therefore, CD is a potential activator for GBFS for producing no-cement binder, mortar, and concrete.

Self-consolidating concrete (SCC) was first invented in 1988 to produce a concrete structure with satisfactory quality and durability [13]. SCC becomes the most preferable material due to its high flowability and adequate capacity of flowing, passing, and filling the formwork under its own weight without any vibration [14–16]. Due to the environmental issue, many researchers tried for producing eco-friendly SCC by utilizing GBFS as based material, with the most common activator used is sodium hydroxide and sodium silicate mixture solution [17, 18]. The mixture solution of sodium hydroxide and sodium silicate has been proven to be effective to produce no-cement binder; however, those chemicals are harmful to human. Therefore, this study aims to produce eco-friendly self-consolidating concrete with CD as GBFS activator that have a less toxicity levels. Besides that, the application of GBFS based eco-friendly SCC with CD as an activator still lack of studies. Thus, this study seeks the development of GBFS based eco-friendly SCC with CD as an activator in the amount of 10 and 20 wt%. The associated mechanical properties were explored such as fresh properties, compressive strength, splitting tensile strength, water absorption, and volume of permeable voids.

2 Experimental Studies

2.1 Material Properties

Ground Granulated Blast Furnace Slag (GBFS) and Calcined Dolomite (CD).

GBFS and CD powders were used as binding ingredients of eco-friendly self-consolidating concrete (SCC). The GBFS had Blaine fineness and specific gravity of 6000 cm²/g and 2.83, respectively. From the microstructural investigation using Scanning Electron Microscope (SEM), it can be revealed that GBFS grain has an angular and irregular shape, as exhibited in Fig. 1a. With a specific gravity of 2.85, the CD powder was produced in the laboratory by burning the natural dolomite powder in a muffle furnace. The heating rate is determined at 5 ± 0.2 °C/min from ambient temperature in stagnant air to reach the decarbonization condition at 900 °C and burned for 1 h [11] with heating and cooling regime as shown in Fig. 2. The SEM micrograph of CD powder is demonstrated in Fig. 1b.

The mean particle size of CD powder was 20 μm, which being determined by a laser diffraction particle size analyzer (Mastersizer 2000). The X-ray diffraction (XRD) patterns of both GBFS and CD were exhibited in Fig. 3. The XRD pattern of GBFS (Fig. 3a) showed that a hump angle (2θ) approximately between 25 and 35° expressed that GBFS is an amorphous state [19]. The XRD pattern of CD (Fig. 3b) revealed the presence of calcium carbonate, calcium oxide, and magnesium oxide as

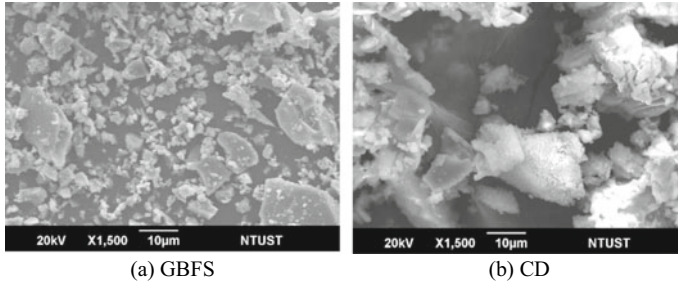
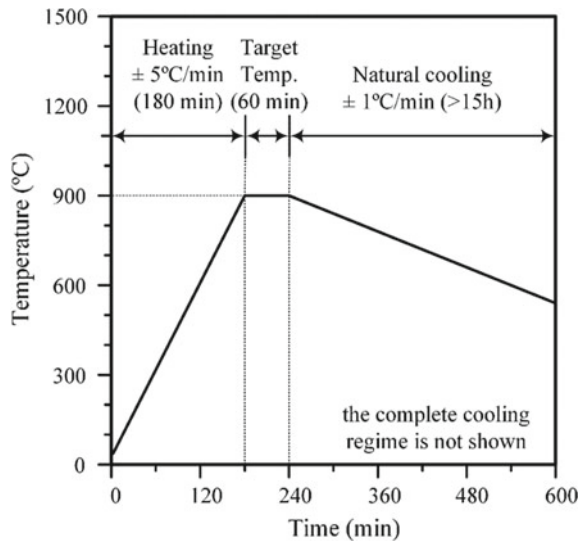


Fig. 1 SEM micrographs of the materials

Fig. 2 Dolomite calcination heating and cooling regime

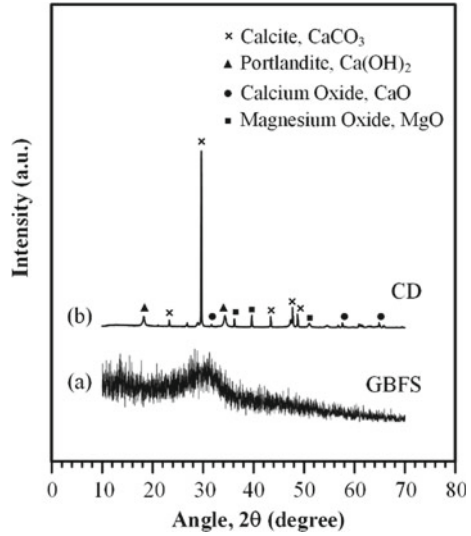


the consequence of thermal decomposition of natural dolomite. In addition, the peak of portlandite ($\text{Ca}(\text{OH})_2$) indicates that calcium oxide reacted with vaporized water ($\text{H}_2\text{O}(\text{g})$) in air.

Fine and coarse aggregates.

The aggregates were the river sand passing the #4 sieve (< 4.75 mm) with fineness modulus (FM) of 2.99 and river gravel with a maximum diameter of 19 mm. In order to eliminate silt and clay content, the aggregates were carefully washed under running water. Before mixing, the aggregates were dried in an oven for at least 24 h at a temperature of 110 ± 5 °C. The specific gravity and absorption capacity of the fine aggregate were 2.72 and 0.779%, respectively, which was conducted using ASTM C128 [20]. While the specific gravity and absorption capacity of the coarse aggregate was 2.75 and 0.619%, respectively, being tested in accordance with ASTM C127 [21].

Fig. 3 X-ray diffraction (XRD) pattern of **a** GBFS, **b** CD



2.2 Mixture Proportions

The mixture proportions of the SCC were determined based on the absolute volume method, which assumes that the sum of the absolute volumes of all ingredients of the mixture is equal to 1 cubic meter. Two eco-friendly SCC mixtures were prepared by different amounts of CD in weight percentage equal to 10 and 20 wt% and one SCC mixture of ordinary Portland cement (OPC) based with equivalent strength as a control set. The weight percentage of GBFS (α) and CD (β) was calculated using Eqs. (3) and (4), respectively, where W_{GBFS} and W_{CD} are the quantities by mass of GBFS and CD powders.

$$\alpha = W_{GBFS} / (W_{GBFS} + W_{CD}) \tag{3}$$

$$\beta = W_{CD} / (W_{GBFS} + W_{CD}) \tag{4}$$

Three mixture proportions of SCC used in this study were presented in Table 1. In order to produce the SCC with high flowability, the binder content was fixed at 0.37, as suggested by Nguyen et al. [22]. The amount of fine and coarse aggregates were previously determined by the method of the highest packing density of blended aggregates. It was discovered that the optimum fraction of fine aggregate was 51 wt% of the total of blended aggregate.

Table 1 Mixture proportions of SCCs

Mixture code*	Ingredients (kg/m ³)						SP [†] (%)
	GBFS	CD	OPC	Water	FA	CA	
S90D10	447	50	–	198	868	853	0.30
S80D20	396	99	–	198	868	853	0.58
OPC	–	–	453	226	868	853	0.19

*S = ground granulated blast furnace slag; D = calcined dolomite; the numbers in mixture code denote the weight percentages of each powder; OPC = ordinary Portland cement

†SP = superplasticizer (in the percentage of total binder weight). water-to-binder ratio (w/b) of eco-friendly SCC was fixed at 0.4; water-to-cement ratio (w/c) of OPC as control set was 0.5

2.3 Specimens Preparation and Testing Methods

The fresh properties of SCC were designed in accordance with ASTM C1611/1611 M [23]. The exact amount of type F superplasticizer (SP) was added to the fresh concrete mixture in order to establish the expected flowability. Immediately after mixing, the Abrams cone in an upright position was filled with freshly mixed concrete without tamping, and then the mold was raised. The slump flow diameter (d) and flowing time (T_{50}) were recorded. The slump flow diameter (d) was measured by taking the average of two measurements of the diameter of the circular spread of freshly mixed SCC, as shown in Eq. (5).

$$d = (d_1 + d_2)/2 \quad (5)$$

where d_1 is the largest diameter and d_2 is the diameter at approximately perpendicular to d_1 . In addition, the freshly mixed concrete was visually observed, and the visual stability index was determined according to ASTM C1611/1611 M [23]. The flowing time (T_{50}) necessary for slump flow diameter reaching 500 mm by using Abrams cone tests was recorded by using a digital stopwatch. Shortly after fresh properties testing, the freshly mixed concrete was cast in a cylindrical mold with 100 mm in diameter and 200 mm in height for making a cylindrical specimen, which conform to ASTM C192/C192M [24]. The cylindrical specimens were demolded after 24 h then they were cured in the saturated lime water at the temperature of 25 ± 2 °C. Compressive strength tests were investigated at the ages of 7 and 28 days in accordance with ASTM C39 [25]. The 28-day splitting tensile strength tests were explored at 28 days in accordance with ASTM C496 [26]. Water absorption and volume permeable voids at 28 days were tested by using ASTM C642 [27] on specimens with 100 mm in diameter and 50 mm in thickness which was cut from a cylindrical specimen. According to ASTM C642 [27], the water absorption (W_A) and volume of permeable voids (V_{PV}) could be determined by using Eq. (6) and (7), respectively.

$$W_A = \left(\frac{w_s - w_i}{w_i} \right) \times 100\% \quad (6)$$

Table 2 Workability characteristics of SCCs

Mixture code	d	T_{50}	VSI value*	Criteria
	(mm)	(s)	based on ASTM C1611/C1611M [23]	
S90D10	650	2	1 = Stable	No evidence of segregation and slight bleeding observed as a sheen on the concrete mass
S80D20	680	2	1 = Stable	
OPC	650	2	1 = Stable	

*VSI = Visual Stability Index

$$V_{PV} = \left(\frac{w_b - w_i}{w_b - w_w} \right) \times 100\% \quad (7)$$

where w_i and w_s are the oven-dry mass and saturated mass of the specimen, respectively. The saturated mass after boiling (w_b) of the specimen was measured in boiled specimen for 5 h. After immersion and boiling, the apparent mass (w_w) was measured as the mass of specimens suspended in water.

3 Results and Discussion

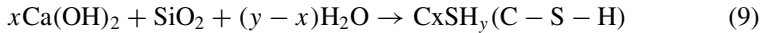
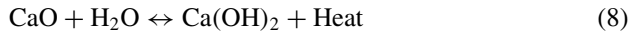
3.1 Workability of Freshly Mixed SCC

The fresh properties both of eco-friendly and OPC based SCCs were designed with satisfactory workability in accordance with the ASTM C1611/1611 M [23]. Table 2 demonstrated the workability characteristics of freshly mixed SCCs in the term of slump flow diameter (d), flowing time (T_{50}), and visual stability index which was determined by visual observation. All SCC mixtures had satisfactory workability with slump flow diameter in the range of 650–680 mm and flowing time to reach a diameter 500 mm in two seconds. In addition, all mixtures were passed the requirement of self-consolidating concrete with the stable category, which was evaluated based on visual stability index (VSI) based on ASTM C1611/1611 M [23].

3.2 Compressive Strength

The influence of CD by the amount of 10 and 20 wt% on the compressive strength of eco-friendly SCC concretes were carried out at the ages of 7 and 28 days. The results, exhibited in Fig. 3, showed that the mixture with the CD amount of 10 and 20 wt% induced the 28-day compressive strength of 26.58 and 35.75 MPa. The early age compressive strengths of eco-friendly SCC with the amount of 10 and 20 wt% at the age of 7 days were approximately 80.76 and 88.57% of that the age of 28 days. The

compressive strength evolution of eco-friendly SCC was attributed to the hydration mechanism of the GBFS and CD. Initially, the dissolution of CD occurred, leading to the aqueous mixtures of the binder with a significant increase of alkalinity attributed to the precipitated portlandite, as shown in Eq. (8). In addition, the hydration reaction between silica (SiO_2) and portlandite to form calcium silicate hydrate (C-S-H) was obtained, as described in Eq. (9) [28].



Based on ACI 318 M-14 [29] (Sec. 19.2.1.1), the minimum 28-day compressive strength (f_c) for structural concrete is 17 MPa. Therefore, the utilization of CD as a slag activator as low as 10 wt% was feasible for producing eco-friendly SCC, which could be applied for structural concrete. Comparing with the OPC based SCC, the 28-day compressive strength of eco-friendly SCC with CD amount of 10 and 20 wt% was lower by 34.87 and 12.39%.

3.3 Splitting Tensile Strength

The splitting tensile strength test of eco-friendly SCC was investigated by using cylindrical specimens 100 mm diameter and 200 mm in height. According to ASTM C496 [26], the tensile stress on the specimen's plane occurred from the compressive loading acting on the length sides of a concrete cylinder. As tabulated in Table 3, the 28-day splitting tensile test results of eco-friendly SCC with CD amount of 10 and 20 wt% were 2.22 and 3.00 MPa, respectively, whereas the splitting tensile strength of the OPC based SCC was 3.01 MPa.

The correlation between splitting tensile strength (f_{ct}) and compressive strength (f_c) as expressed in Eq. (10) has been commonly used. ACI 318 M-14 [29] explained that the theoretical coefficient for normal weight concrete is $k = 0.56$. From the experimental work, the coefficients of k for eco-friendly SCC were found in the range of 0.43–0.50, whereas the OPC based SCC had a coefficient equal to 0.47, as shown in Table 3. From the results, it could be found that the k coefficient of all SCC mixtures had a lower value than the theoretical coefficient.

Table 3 Compressive and splitting tensile strength of SCCs at the age of 28 days

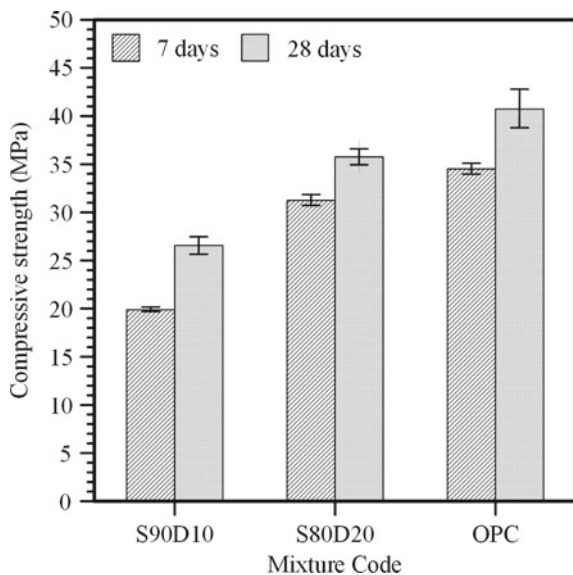
Mixture Code	f_c	f_{ct}	$k = f_{ct} / \sqrt{f_c}$
	(MPa)	(MPa)	
S90D10	26.58	2.22	0.43
S80D20	35.75	3.00	0.50
OPC	40.82	3.01	0.47

$$f_{ct} = k\sqrt{f_c} \tag{10}$$

3.4 Water Absorption and Volume of Permeable Voids

The water absorption (W_A) and volume of permeable voids (V_{PV}) values were used as the durability-related indicators of the hardened concretes. The variations of W_A and V_{PV} of eco-friendly SCC with CD contents of 10 and 20 wt% are illustrated in Fig. 4. The results confirm that the eco-friendly SCC with a CD amount of 20 wt% has lower water absorption comparing with that of 10 wt%. It possibly due to pore reduction induced by physical and chemical effects that contributed to the optimized particles size distribution of the CD powder and pozzolanic reaction between GBFS particles and reactive CaO from CD. Comparing with the OPC based SCC, the water absorption of the eco-friendly SCC is higher by 30.54 and 16.41% for CD contents of 10 and 20 wt%, respectively. The water absorption properties of concrete indirectly revealed the porosity and provided comprehension of the volume of permeable pore [30]. The value of the volume of permeable voids (V_{PV}) was used for determining the total porosity of concrete, which indicates the ease of liquid penetration into the concrete through gel pores, capillary pores, voids, and microcracks [31]. The computed V_{PV} values of the eco-friendly SCC with 10 and 20 wt% of CD amount were 14.21 and 13.16%, respectively, which are well consistent with the water absorption results. Vicroads [32] (Concrete Institute of Australia) determined the classification for concrete durability in the term of volume of permeable voids

Fig. 4 Compressive strength of eco-friendly and OPC SCCs at the ages of 7 and 28 days



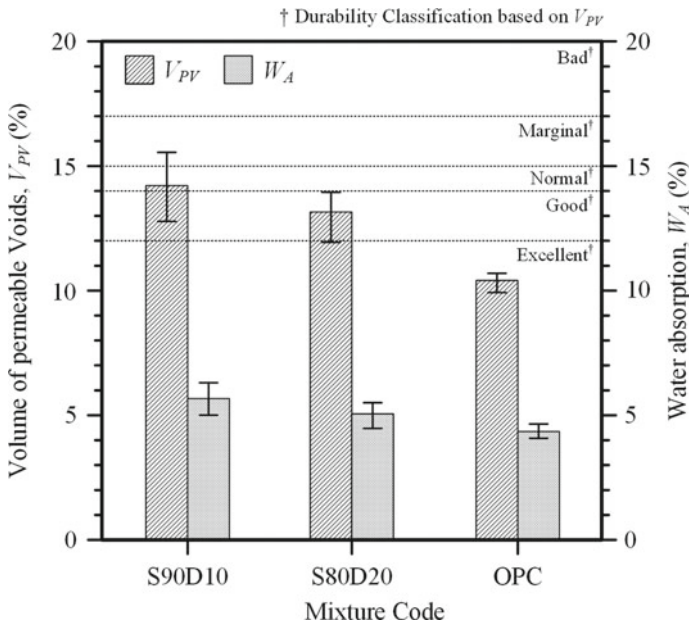


Fig. 5 Variation of the volume of permeable voids and water absorption of eco-friendly and OPC SCCs at the age of 28 days

(V_{PV}). The V_{PV} value of eco-friendly SCC with 10 wt% of CD can be classified as “normal” concrete. Moreover, the eco-friendly SCC with a CD amount of 20 wt% has better durability and can be classified as a “good” concrete. The OPC based SCC has the best durability, comparing with those of eco-friendly SCC, with the classification of “excellent” concrete (Fig. 5).

4 Conclusions

The eco-friendly self-consolidating concrete (SCC) mixes were successfully developed with the base cementitious material made of the industrial steel waste, ground granulated blast furnace slag (GBFS) and calcined dolomite (CD) as an activator. The natural dolomite, which was burned at decarbonation temperature at 900 °C for 1 h, has to be found as an effective GBFS activator. The fresh properties of SCC mixtures are shown to be satisfying the ASTM C1611/1611 M with excellent workability without any indication of segregation. The hydration reaction between GBFS and CD led to the increment of compressive strength of eco-friendly SCC. By comparing with OPC based SCC, the 28-day compressive strength showed that the mixture with 10 and 20 wt% of CD had lower compressive strength by 34.87 and 12.39%, respectively. On the other hand, the splitting tensile strength of OPC based

SCC at the age of 28 days, the eco-friendly SCC with CD amount of 10 wt% had 26.24% lower splitting tensile strength, whereas eco-friendly SCC with CD amount of 20 wt% has a comparable splitting tensile strength when compared with OPC based SCC. The eco-friendly SCC with CD dosage of 20 wt% has exceeded the minimum compressive strength requirement for concrete structural application with good concrete durability classification.

References

1. Zhang HY, Kodur V, Qi SL, Cao L, Wu B (2014) Development of metakaolin–fly ash based geopolymers for fire resistance applications. *Constr Build Mater* 55:38–45
2. Van Oss HG, Padovani AC (2002) Cement manufacture and the environment part I: chemistry and technology. *J Ind Ecol* 6(1):89–105
3. Özbay E, Erdemir M, Durmuş Hİ (2016) Utilization and efficiency of ground granulated blast furnace slag on concrete properties—a review. *Constr Build Mater* 105:423–434
4. Mindess S, Young JF, Darwin D (2008) *Concrete*. 2nd edn. Pearson Education, Taiwan
5. Kim H-S, Park J-W, An Y-J, Bae J-S, Han C (2011) Activation of ground granulated blast furnace slag cement by calcined alunite. *Mater Trans* 52(3):210–218
6. Kim MS, Jun Y, Lee C, Oh JE (2013) Use of CaO as an activator for producing a price-competitive non-cement structural binder using ground granulated blast furnace slag. *Cem Concr Res* 54:208–214
7. Jeong Y, Park H, Jun Y, Jeong JH, Oh JE (2016) Influence of slag characteristics on strength development and reaction products in a CaO-activated slag system. *Cem Concr Compos* 72:155–167
8. Maitra S, Choudhury A, Das HS, Pramanik MJ (2005) Effect of compaction on the kinetics of thermal decomposition of dolomite under non-isothermal condition. *J Mater Sci* 40:4749–4751
9. Gu K, Jin F, Al-Tabbaa A, Shi B (2014) Activation of ground granulated blast furnace slag by using calcined dolomite. *Constr Build Mater* 68:252–258
10. Gu K, Jin F, Al-Tabbaa A, Shi B (2016) Evaluation of sulfate resistance of calcined dolomite activated ground granulated blast furnace slag. *J Mater Civil Eng* 28(2):04015135
11. Djayaprabha HS, Chang T-P, Shih J-Y, Chen C-T (2017) Mechanical properties and microstructural analysis of slag based cementitious binder with calcined dolomite as an activator. *Constr Build Mater* 150:345–354
12. Djayaprabha HS, Chang T-P, Shih J-Y (2018) Comparison study of dynamic elastic moduli of cement mortar and no-cement slag based cementitious mortar activated with calcined dolomite with impulse excitation technique. *MATEC Web of Conferences* 186:1–5
13. Okamura H, Ozawa K, Ouchi M (2000) Self-compacting concrete. *Struct Concr* 1(1):3–17
14. Long G, Gao Y, Xie Y (2015) Designing more sustainable and greener self-compacting concrete. *Constr Build Mater* 84:301–306
15. Dinakar P, Sethy KP, Sahoo UC (2013) Design of self-compacting concrete with ground granulated blast furnace slag. *Mater Des* 43:161–169
16. Nguyen H-A, Chang T-P, Shih J-Y, Djayaprabha HS (2018) Enhancement of low-cement self-compacting concrete with dolomite powder. *Constr Build Mater* 161:539–546
17. Manjunath R, Narasimhan MC (2018) An experimental investigation on self-compacting alkali activated slag concrete mixes. *J Build Eng* 17:1–12
18. K NV, Babu DLV (2018) Assessing the performance of molarity and alkaline activator ratio on engineering properties of self-compacting alkaline activated concrete at ambient temperature. *J Build Eng* 20:137–155
19. Zhang M, Yang C, Zhao M, Yang K, Shen R, Zheng Y (2017) Immobilization potential of Cr(VI) in sodium hydroxide activated slag pastes. *J Hazard Mater* 321:281–289

20. ASTM C128-15 (2015) Standard test method for relative density (specific gravity) and absorption of fine aggregate. West Conshohocken, PA 19428-2959, USA
21. ASTM C127-15 (2015) Standard test method for relative density (specific gravity) and absorption of coarse aggregate. West Conshohocken, PA 19428-2959, USA
22. Nguyen H-A, Chang T-P, Shih J-Y, Chen C-T, Nguyen T-D (2016) Engineering properties and durability of high-strength self-compacting concrete with no-cement SFC binder. *Constr Build Mater* 106:670–677
23. ASTM C1611/C1611M (2014) Standard test method for slump flow of self-consolidating concrete. West Conshohocken, PA 19428-2959, USA
24. ASTM C192/C192M (2016) Standard test method for making and curing concrete test specimens in the laboratory. West Conshohocken, PA 19428-2959, USA
25. ASTM C39/C39M (2017) Standard test method for compressive strength of cylindrical concrete specimens. West Conshohocken, PA 19428-2959, USA
26. ASTM C496/496M (2017) Standard test method for splitting tensile strength of cylindrical concrete specimens. West Conshohocken, PA 19428-2959, USA
27. ASTM C642 (2013) Standard test method for density, absorption, and voids in hardened concrete. West Conshohocken, PA 19428-2959, USA
28. Dung NT, Chang T-P, Chen C-T (2015) Circulating fluidized bed combustion fly ash-activated slag concrete as novel construction material. *ACI Mater* 112:105–114
29. ACI 318M-14 (2014) Building code requirements for structural concrete. Farmington Hills, MI 48331, USA
30. Khotbehsara MM, Miyandehi BM, Naseri F, Ozbakkaloglu T, Jafarie F, Mohseni E (2018) Effect of SnO₂, ZrO₂, and CaCO₃ nanoparticles on water transport and durability properties of self-compacting mortar containing fly ash: experimental observations and ANFIS predictions. *Constr Build Mater* 158:823–834
31. Saha AK, Sarker PK (2018) Durability characteristics of concrete using ferronickel slag fine aggregate and fly ash. *Mag Concr Res* 70(17):865–874
32. Vicroads TN 089 (2007) Test methods for the assessment of durability of concrete. Australia

An Overview of the Development of Replaceable Links in Eccentrically Braced Frame Steel Structures



Naomi Pratiwi, Helmy Hermawan Tjahjanto, and Muslinang Moestopo

Abstract Recently, other than possessing good seismic performance, structures should be designed and constructed in sustainable and resilient manners. It means that buildings are able to function as immediately as possible after an earthquake without major reconstruction and/or demolition works. Eccentrically braced frame (EBF) steel structures have good seismic performance with high ductility and good lateral stiffness. EBFs utilize links as energy dissipation devices, and for the structures to be sustainable, the links are made as sacrificial yet replaceable elements in the structures. This paper summarizes the development of replaceable links in EBF structures that have been applied and evaluated to date. The research was conducted by reviewing previous studies on EBF links and evaluating the advantages and the disadvantages of different replaceable link types with the considerations of their seismic performance as well as the difficulties and the risks in the replacement methods. Recommendations on the types of EBF links that are the potential to be further developed or improved are proposed.

Keywords Resilient structures · Replaceable links · Eccentrically braced frame · Steel structures · Seismic energy dissipation device

1 Introduction

1.1 Background of Seismic Resistant Steel Structures

Recently, it has been common to understand structural engineering practices that preventing loss of life as an objective for seismic performance of a building is simply not sufficient [1]. Buildings, especially those serving a vital purpose, need to be

N. Pratiwi (✉) · H. H. Tjahjanto
Parahyangan Catholic University, Bandung, Indonesia
e-mail: naomi.pratiwi@unpar.ac.id

N. Pratiwi · M. Moestopo
Bandung Institute of Technology, Bandung, Indonesia

designed and constructed in sustainable and resilient manners. It means that structures must be able to withstand earthquake load as well as to recover quickly after the disaster. It does not only refer to the choice of using sustainable material but also structural systems and design methods, which allow the buildings to behave in a desirable manner, one of which is to localize the damage and thus easier to repair the structure for it to serve its function, as immediate as possible.

Steel has become the main choice of construction material due to its strength and efficiency. Moreover, it is also known that steel has better ductility compared to other materials. In the context of structural engineering, a ductile material is one that is capable of undergoing large inelastic deformations without losing its strength [2]. Ductile structural systems will allow significant deformation to exceed its elastic deformation limit, which then increase the ability to dissipate the seismic energy during an earthquake.

It is indeed possible to design a structure to remain elastic during a strong earthquake; however, it is not economical as it will require larger and heavier cross-sections. Alternatively, a structure should be allowed to deform and experience some damage without complete collapse during a strong earthquake. This practice will reduce the seismic design forces and therefore reduce construction cost and make the structure more constructible, although this usually creates more complexity in the detailing. In nearly all buildings designed today, building survival in large earthquakes depends directly on the ability of their framing system to dissipate energy hysteretically while undergoing relatively large inelastic deformations.

There are at least three most commonly used earthquake-resistant ductile structural steel systems, namely moment-resisting frames (MRF), concentrically braced frames (CBF), and eccentrically braced frames. Although provided architects and building owners with open-space floors, MRF has a higher construction cost compared to braced frames [3]. Braced frames, concentric or eccentric, use bracings to provide lateral stiffness of the structures. Concentrically braced frames (CBF) have large lateral stiffness, but the energy dissipation is hindered by the possibility of brace buckling (braces in compression). Eccentrically braced frames (EBF) is introduced in Japan in early 1970 [4]. EBF combines both high elastic stiffness and high ductility at large story drifts. The seismic energy is dissipated by shear and/or flexural yielding in a small segment of the beam called links. The ductile action is achieved through plastic deformation of the links.

1.2 The Need for a Replaceable Link

The issue of sustainability and resilience of structures is rising due to the fact that even if the structures are designed and proved to withstand the seismic load, they are still required major reconstruction, repair, and probably some demolition works before they can resume their function. The development of a replaceable shear link is motivated by the fact that it is highly possible to localize the damage to a certain element of the structures and thus to repair/replace that certain part only. Thus,

avoiding major reconstruction works, which will expedite the structures to resume their function.

With increasing emphasis on performance-based design, replaceable links have also been explored [5]. The replaceable links are suitable for providing sustainable and resilient structures by localizing the damage in the seismic resistant structures and replacing the damaged element for the structures to function as immediately as possible. In order to be easily replaced, the shear link has to be connected to the mainframe by bolts. The degree of replaceability will depend on the assurance that while the links are designated to be damaged after an event of an earthquake, all other elements are still in their elastic state and can be returned to their initial condition.

2 Development of EBF and Shear Link

2.1 Early-Stage of EBF Development (1970–1990s)

EBFs (K-braced frame) was first introduced in Japan [4] as systems that combine the benefits of large lateral stiffness and high ductility at large story drift. Links in the beam will act as fuses and energy dissipation elements by controlled shear/flexural yielding while maintaining all other members in an elastic state. Figure 1 shows the typical bracing arrangement for EBFs.

Further experimental testing was conducted to understand the inelastic behavior of short wide-flange steel beams used as links in EBF [6]. The design inelastic rotation capacity of 0.08 rad was recommended. The test specimens were subjected to severe cyclic loading with stiffening arrangements to increase the capacity by preventing web buckling. The previous study shows that most link elements fail by web buckling.

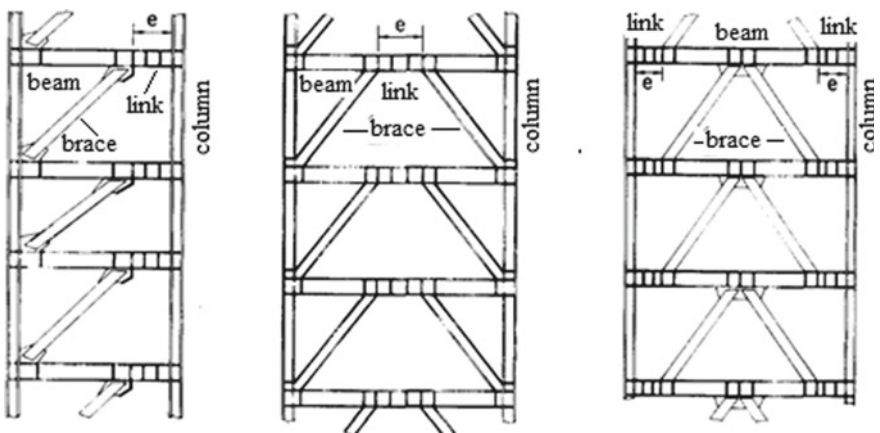


Fig. 1 Typical bracing arrangements for EBFs [4]

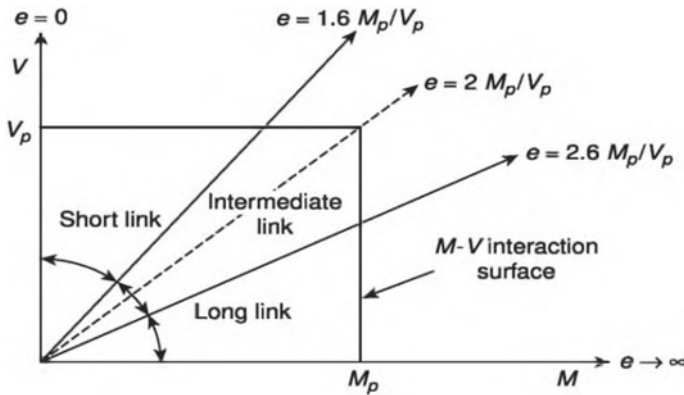


Fig. 2 Classification of link based on its length [7]

It was found that the length of link elements determines its yielding mechanism, whether it yields due to shear and/or moment [7]. Cyclic tests were performed to investigate the behavior of link specimens. The effects of axial force in link elements were also observed. The length of the link is recommended to be less than $1.6 M_p/V_p$ to ensure that shear yielding will govern. This length is considered able to reduce the moment hinge rotation demand throughout cyclic loading by keeping the end moment relatively smaller than M_p , where M_p is the full plastic moment of the link section and V_p is the shear resisted by the yielding of the web. The classification of links based on their length is presented in Fig. 2.

A comprehensive overview of the design and behavior of seismic resistant EBF was presented after ten years of its development [8]. The emphasis of this overview is on the behavior and design of shear links, including the detailing of their stiffener. All the studies carried out in this period led to the design provisions stipulated in 1988 UBC [9] and 1990 AISC [10].

2.2 Further Development of EBF and Study of Link Inelastic Behavior (1990–2000s)

Ramadan and Gobarah rigorously researched the performance of link elements in EBF in the 1990s [11–14]. Both numerical studies with finite element models and experimental testing to verify the results were carried out. The effect of the axial load was also studied. When the link elements are subjected to axial forces, both load-carrying capacity and ductility were observed. Furthermore, the effect was found to be adverse when the link elements have the length close to their critical shear link length limit, which is about 37% of the values of maximum link deformation angle and ductility, whereas, for short links and very long moment links, the effects were small [11]. Their study also concluded that the performance of short shear

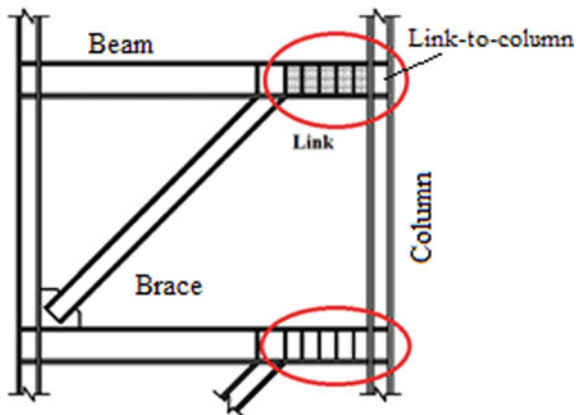
links in terms of maximum deformation angle and ductility is better than the long links [12]. Although the long links in EBF led to a smaller deformation angle and less damage to the non-structural elements, it also reduced ductility, which is undesirable. The performance of EBF with long links would be improved by increasing the flange thickness of the link elements. However, this would only be economical and practical for links up to $1.4e_{crit}$, with e_{crit} is the critical value of the link length.

Cyclic behaviour of links in EBF was further investigated to reevaluate the flange slenderness limits and overstrength factor by Okazaki, 2005 [15]. A total of 23 tests were conducted for links made of A992 ASTM steel. This research concluded that the flange slenderness limit of for short/ shear link could be relaxed from the AISC 2002 limit of $0.3 (E/F_y)^{\frac{1}{2}}$ to $0.38 (E/F_y)^{\frac{1}{2}}$. The overstrength factor was found to be at an average of 1.41 for the shear link as compared to 1.5 in AISC 2002. AISC imposed a reasonable overstrength factor for typical rolled wide-flange sections; however, a higher overstrength factor was recommended for built-up sections.

The previous design standards are responsible for the poor performance of the EBF structures in 1994 Northridge and 1995 Kobe earthquake due to the link-to-column connections. Thus, the performance of various link-to-column (Fig. 3) connections was experimentally studied to understand the performance of each connection by Okazaki, 2006 [16]. A total of 12 large-scale link-column specimens were tested with varied welded connection types with three different link lengths, including the pre-Northridge connection detailing. The performance of the link-to-column connections depended strongly on the link length, with the inelastic link rotation capacity decreases significantly with the increase in the link length. The majority of link-column specimens failed by fracture of the link flanges near the groove weld.

While all earlier studies employed welded links in EBFs, Ghobarah, 1994 [13] investigated bolted links for the first time and their study is limited to the link-to-column connection. The proposed bolted connection showed no degradation in both strength and stiffness compared to the welded connection between the link and column. The bolts must be designed adequately to resist the high shear forces

Fig. 3 Link connected to the structural column in EBF [16]



developed by the shear links. The previous design formulae for bolts in AISC, as presented in Tsai and Popov, 1988 [17], were under-designed. It was also concluded in this study that the thickness of the endplates affected the performance of the links. The recommended thickness of the ends plate was formulated herein.

The development of bolted link elements in EBFs supported the idea of having removable and replaceable energy dissipation elements in the structures. These elements are meant to experience deformation due to seismic load, and to be damaged. Bolted connections are considered to be the easier and faster type of connections to be removed and replaced. Experimental investigations proved the feasibility of this connection type [18] by performing tests on both bolted and welded links to floor beams. The performance of the structures showed that although bolted links experienced reduced stiffness of 25% of the conventional (welded) link, which resulted in the increase of lateral drift and inelastic deformation demand in the links, the global structural performance was satisfactory in terms of serviceability, ultimate and collapse prevention limit states [19, 20]. The intention of having bolted links is to limit the requirement to repair the structures after a moderate to strong earthquake by only replacing the bolted links.

By having the links bolted to the floor beam sections, it was possible to use different sections or steel grades for the links. The links can be designed as required without being dependent to the steel grade or the dimension of the beam outside the links. This motivated the development of the “dog-bone” concept for links in EBFs as the energy dissipation devices which would undergo inelastic deformation due to seismic load [21]. The dog-bone links could be made of wide-flange steel sections or double-channel steel sections; both are bolted to the beams, as shown in Fig. 4a, b.

The results of those studies were then set forth in AISC 314 [22, 23], which contains seismic provisions for the EBF structural systems. AISC regulates the maximum inelastic rotation angle of the coupling elements based on their length, which determines the yielding mechanism, whether in shear or bending or the combination of the two actions. The yielding mechanism of the link elements can also be used to compute the design strength of the link elements. The use of stiffeners on the link element is also regulated in AISC 314.

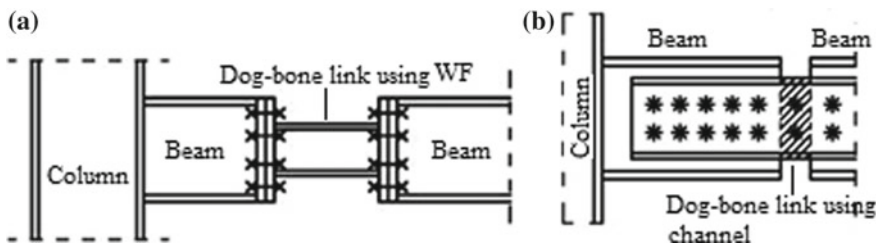


Fig. 4 Dog-bone link using wide-flange section **a** and double-channel section **b** bolted to the beam [21]

2.3 Research of Replaceable Links in EBF Structure in the Last Decade (2010–Present)

Replaceable links mean decoupling the yielding links from the rest of the structures. Decoupling the yielding links would create the flexibility of choosing the link sections regardless of the floor beam sections. The links could use built-up sections with thin webs and thick flanges or any other section with lower yield strength materials than the rest of the structural elements.

After the 2010 and 2011 Christchurch earthquakes, the repair and retrofit of the EBF system became more important. This led to an even deeper need to study the possibility of adopting replaceable energy-dissipating elements in steel structures.

The research for EBF structures with replaceable links became more popular during this period. Experimental tests were conducted using specimens of both welded and bolted links [5]. The results proved that replaceable links could achieve the minimum rotation of 0.08 rad, which satisfies the inelastic link rotation demand as prescribed in AISC 341-10. The on-site replaceability is confirmed even in the presence of residual deformation of 0.5% drift. While the bolted links were easier to handle and erect, welded links provided greater flexibility and ease to position the replacement links.

Another experimental test was carried out on half-scale test specimens for both bolted and welded links [24]. The results showed that the bolted links provide only slightly different performance from the welded links. Then bolted links were then replaced by the new one and tested once again, and the result showed a similar level of performance as the original one.

Numerical studies were performed to investigate the practical feasibility of the link replacement procedure regarding the order in which bolted links need to be replaced [25]. The result in the study showed that there is negligible redistribution of forces among stories; thus, it can be performed on a story-by-story basis, starting from the least to the most loaded ones (upper story toward the lower story). It was recommended that prior to the link removal, tie rods are installed at the moment-resisting bays. The mounting of some temporary tie braces is also necessary for safety measures during the link removal procedure. The damaged links were removed by unbolting the link-beam connection; thus, the forces locked in links were smoothly transferred to the temporary bracing system.

More study on the replaceable link in terms of the bolt design was carried out to investigate the overstrength factor and its response to seismic load [26]. Finite element analyses were carried out on the EBFs with replaceable links. Several parameters such as the type of pre-loadable bolts, the level of bolt clamping force, the boundary conditions, and the presence of constructional tolerances were investigated. The results showed that the type of high strength bolts had limited influence on the response of detachable links. The level of bolt clamping force also did not affect the link overstrength. The response of the link is not affected much by the boundary condition in terms of stiffness and yield shear force. However, the overstrength and axial force developed in the link are dependent on the restraining condition. The

constructional tolerances for the end-plate also affect the link by reducing the shear overstrength and increasing axial force.

If the links are constructed with the concrete slab (composite links), the composite action resists the shear distortion together with the links. This led to a higher overstrength, larger than the recommended value of $V_u/V_p = 1.5$. A study was conducted to compare the performance of two types of short links, one was uncoupled from the slab and the other was where the slab and the link were connected (composite). Results from the finite element analyses showed that the internal forces in the links in the composite link-slab system are very close to those developed by uncoupled link-slab. Hence, the design of the link connection is not influenced by the slab. However, the composite action might cause more damage to the slab than when the link and slab are uncoupled.

The link-to-column connection proposed earlier in the previous research [16] did not satisfy the criteria stipulated in AISC 341-10. Several welded moment connection details developed after the 1994 Northridge earthquake for special moment frames still experienced brittle fracture in the link flange groove welds. Thus, two additional connection details were developed and examined through a combined analytical and experimental research program [27, 28], as shown in Fig. 5.

Abebe, 2016 [29] further improved the dog-bone links proposed by Balut and Gioncu, 2003 [21]. In this more recent study, replaceable links with reduced web sections were introduced, and design equations were suggested. Instead of using smaller sections for the link, which might lead to some disadvantages such as the difference in yielding strength and difficulties in construction, reduced web sections of the links were proposed by introducing holes (open areas) in the web of the links. Non-linear finite element analyses were conducted in order to evaluate the proposed links. The analysis results of the reduced web link sections satisfy the shear rotation limit recommended by AISC 341-10 for the shear link. The effect of open areas on both hysteresis characteristics and deformation modes showed that the plastic rotation capacity decreases as the proportion of the open area increase.

From this recent research conducted on the performance of replaceable links in EBF structures, it can be concluded that this option is feasible to be adopted in the

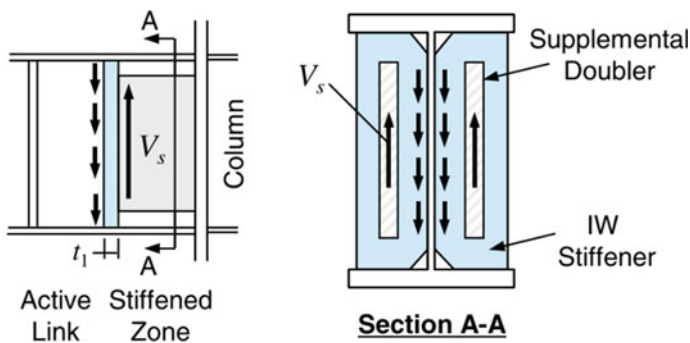


Fig. 5 Link-to-column connection with supplemental doubler plate [27]

design of seismic-resistant structures. The use of replaceable links will provide more sustainable and resilient structures by replacing the damaged elements, which are already localized to the link elements. This will also provide a faster and relatively easier rehabilitation effort after earthquakes.

The recent research also contributes to the updates in the provisions of AISC 341-16 [30]. This code becomes the prevailing code that is currently used in Indonesia.

2.4 Challenges in Adopting Replaceable Link

However, the concept of replaceable links, despite having some advantages, also faces another challenge. The link replacement is not a straightforward process due to the amount of residual frame deformations. Among the replaceable link details developed in the past research, as shown in Fig. 6, only the one with the web-connected links (Fig. 6c) is suitable for replacement under residual frame drift. However, the web-connected link exhibited a pinched hysteretic behavior under cyclic loading [5]. The replacing links might not fit into the remaining space between the beams after the frames undergo large lateral deformation and leave residual frame deformation. The replacement links were then recommended to be smaller in size, with the gap between the beams and the end-plate of the links eventually filled in.

Alternative forms of replaceable link were explored to enhance the existing details [31, 32]. Instead of applying the bolted connection for the links in between the beams, the connections were proposed to be applied as spliced braces and/or beams, as shown in Fig. 7. These details provided easier replacement procedures and eliminated the need for hydraulic jack operation.

Consequently, another type of replaceable links was also studied recently [33]. The proposed type requires splicing of the links at their mid-length, as shown in Fig. 8. These details accommodated vertical offset between the two ends of the links. Bolted connections with standard holes, long slotted holes and welded connections were studied under residual frame drifts of 0.5% and 0.7% to demonstrate the potential application of this detail. The test results showed that all the specimens satisfied the inelastic link rotation capacity required by AISC 341-10.

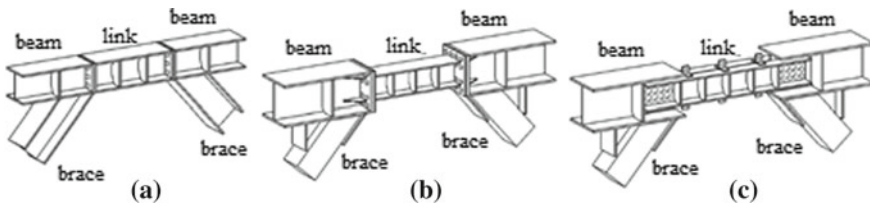


Fig. 6 Replaceable link details **a** bolted-flushed end plate, **b** bolted extended-end-plated, **c** web connected [32]

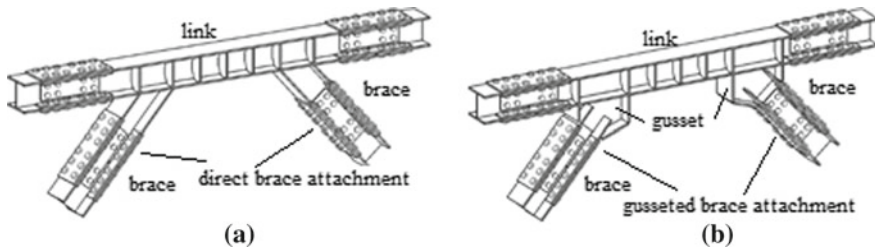


Fig. 7 Replaceable link details **a** with direct brace attachment, **b** gusseted brace attachment [32]

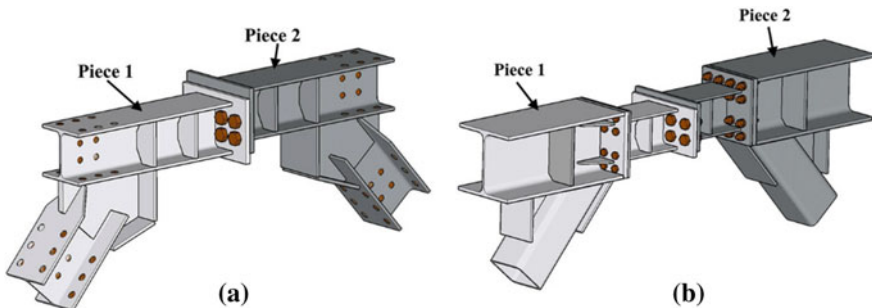


Fig. 8 Proposed replaceable link details **a** spliced link with gusseted brace attachment, **b** bolted extended end-plated spliced link [33]

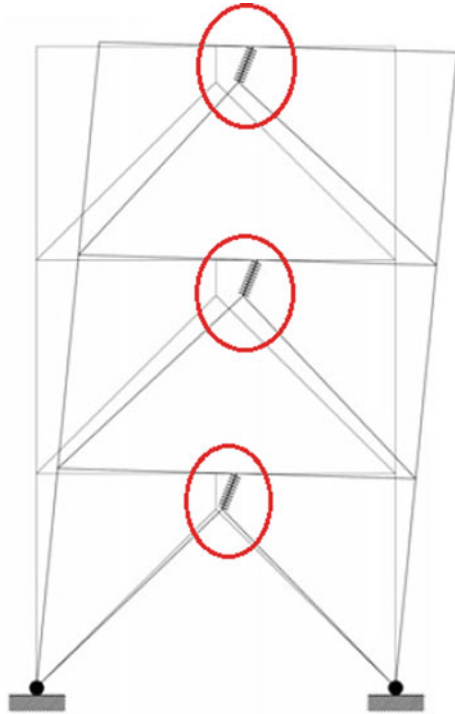
2.5 Research of Vertical Links in EBF Structure

Studies of horizontal links have been carried out by many researchers, both the links connected to the columns and the links at the mid-span of the beam. On the other hand, there are still few studies on vertical links (Fig. 9). Research on welded vertical links in EBF is limited, while the research on bolted vertical links is even scarcer [34].

An experimental study on the behavior of vertical shear links in normal (steel sections with and without stiffener) and composite (steel section with concrete located at the area limited to web and flanges of the section) configurations was conducted [35]. The tests were conducted on full-scale specimens under quasi-static loading. The experimental results show a remarkable increase in shear capacity and ductility of the composite links as compared to the normal specimens. The existence of stiffeners causes the web shear buckling to be postponed and contributes to the increase of specimen ductility. Concrete composite links can delay web buckling and improve the seismic performance of the structures.

Another experimental research utilized a higher grade of steel for vertical links in EBF [36]. This configuration reduces the amount of steel consumed for structures in seismic areas. The force–displacement hysteretic curves exhibited good plastic deformation behavior and did not generate the pinching phenomenon. The maximum

Fig. 9 EBF with vertical link and its yield mechanism [34]



story drift ratio and maximum ductility factor on the first story reached 1/40 and 2.5, respectively. However, severe instability and damage were observed at the maximum story drift angle. The plastic deformation occurs mainly due to the shear deformation of the link webs and the flexural deformation of the link flanges at the link-to-beam connection in the first story.

An analytical model for EBF with vertical links was developed to investigate the inelastic cyclic response of the structure [37]. Experimental results showed that the ultimate shear strength of the vertical links is more than two times of the yielding strength. The analytical models showed accurate results with an upper bound for yielding surface to the vertical link, by using the kinematic-isotropic strain hardening model for shear and only the kinematic strain hardening model for flexure.

The advantage of using vertical links than horizontal links is that the links are not directly connected to the slab. That would mean that during rehabilitation or the replacement of the damaged links, fewer disturbances would be caused to the structural floor system compared to the replacement of horizontal link.

The nature of vertical structural elements to experience axial load would also need to be considered when designing vertical links. The effect of the axial load has been studied previously, and it was concluded that the vertical action in the links decreases the load-carrying capacity as well as reduces the ductility. The effect of link length is taken to be the same for both horizontal and vertical link to determine if the link

would experience yield in shear, in bending, or in both. This has to be verified in order to understand further the behavior of vertical link and their performance. Thus, future research opportunity is still very widely opened in this area.

3 Concluding Remarks

Application of replaceable links in EBF can contribute to the development of sustainable structures. There are still challenges in how to make the concepts applicable considering some aspects: simplicity in design and construction; replacement methods; post-replacement structural behavior, etc. Therefore, further research on the type and application of replaceable link is worth to be looked into further. This includes both horizontal and vertical link, including its connection to the mainframe, which would create a feasible replaceability.

Acknowledgements The author would like to thank the Indonesia Endowment Fund for Education (LPDP), Ministry of Finance, Republic of Indonesia for their financial support in her research and doctoral study.

References

1. Bruneau M, MacRae G (2017) Reconstructing Christchurch : a seismic shift in building structural systems. Quake Cent Rep
2. Bruneau M, Uang CM, Sabelli R (2011) Ductile design of steel structures, 2nd edn. The McGraw-Hill Companies Inc., New York
3. Uang CM, Bruneau M (2018) State-of-the-art review on seismic design of steel structures. *J Struct Eng (United States)* 144(4):1–24
4. Fujimoto M, Aoyagi T, Ukai K, Wada A, Saito K (1972) Structural characteristics of eccentric K-braced frames. *Trans Archit Inst Japan* 195:39–49, 97
5. Mansour N, Christopoulos C, Tremblay R (2011) Experimental validation of replaceable shear links for eccentrically braced steel frames. *J Struct Eng* 137(10):1141–1152
6. Popov EP (1983) Recent research on eccentrically braced frames. *Eng Struct* 5(1):3–9
7. Kasai K, Popov EP (1986) General behaviour of WF steel shear link beams. *J Struct Eng (United States)* 112(2):362–382
8. Popov EP, Engelhardt MD (1988) Seismic eccentrically braced frames. *J Constr Steel Res* 10(1):321–354
9. ICBO (International Conference of Building Officials) (1988) Uniform building code. Whittier, CA
10. American Institute of Steel Construction (1990) Seismic provisions for structural steel buildings: load and resistance factor design. Chicago
11. Ghobarah A, Ramadan T (1990) Effect of axial forces on the performance of links in eccentrically braced frames. *Eng Struct* 12(2):106–113
12. Ghobarah A, Ramadan T (1991) Seismic analysis of links of various lengths in eccentrically braced frames. *Can J Civ Eng* 18(1):140–148
13. Ghobarah A, Ramadan T (1994) Bolted link-column joints in eccentrically braced frames. *Eng Struct* 16(1):33–41

14. Ramadan T, Ghobarah A (1995) Analytical model for shear-link behaviour. *J Struct Eng* 121(11):1574–1580
15. Okazaki T, Arce G, Ryu HC, Engelhardt MD (2005) Experimental study of local buckling, overstrength, and fracture of links in eccentrically braced frames. *J Struct Eng* 131(10):1526–1535
16. Okazaki T, Engelhardt MD, Drolia A, Schell E, Hong JK, Uang CM (2006) Experimental investigation of link-to-column connections in eccentrically braced frames. *J Constr Steel Res* 132:1201–1211
17. Tsai KC, Popov EP (1988) Steel beam-column joints in seismic moment resisting frames
18. Stratan A, Dubina D (2004) Bolted links for eccentrically braced steel frames. In: *Connections in steel structures V*, pp. 223–232
19. Stratan A, Dogariu A, Dubina D (2007) Bolted links for eccentrically braced frames: Influence of link stiffness. *Proc. 3rd International Conference Steel Composite Structures ICSCS07—Steel Composite Structures*, pp 847–853
20. Dubina D, Stratan A, Dinu F (2008) Dual high-strength steel eccentrically braced frames with removable links. *Earthq Eng Struct Dyn* 37(15):1703–1720
21. Balut N, Gioncu V (2003) Suggestion for an improved ‘dog-bone’ solution. In: *Proceedings of the conference on behaviour of steel structures in Seismic areas*, pp 129–134
22. American Institute of Steel Construction (2005) Seismic provisions for structural steel buildings, AISC 314-05. American Institute of Steel Construction
23. American Institute of Steel Construction (2010) Seismic provisions for structural steel buildings, AISC 314-10. American Institute of Steel Construction, Illinois
24. Moestopo M (2012) On improved performance of eccentrically braced frames with replaceable shear link. In: *15th world conference on earthquake engineering*
25. Ioan A, Stratan A, Dubina D (2013) Numerical simulation of bolted links removal in eccentrically braced frames. *Pollack Period* 8(1):15–26
26. Zimbru M, D’Aniello M, Stratan A, Landolfo R, Dubina D (2017) Finite element modelling of detachable short links. In: *COMPADYN 2017—proceedings of the 6th international conference on computational methods in structural dynamics and earthquake*, vol 1. pp 790–801
27. Hong JK, Uang CM, Okazaki T, Engelhardt MD (2015) Link-to-column connection with supplemental web doublers in eccentrically braced frames. *J Struct Eng (United States)* 141(8):1–8
28. Okazaki T, Engelhardt MD, Hong JK, Uang CM, Drolia A (2015) Improved link-to-column connections for steel eccentrically braced frames. *J Struct Eng (United States)* 141(8):1–8
29. Abebe DY, Gwak G, Jeong S, Choi J (2016) Replaceable reduced web link section for link-to-column connections in EBFs
30. American Institute of Steel Construction (2016) Seismic provisions for structural steel buildings, AISC 341-16. American Institute of Steel Construction. Chicago, Illinois
31. Bozkurt MB, Topkaya C (2017) Replaceable links with direct brace attachments for eccentrically braced frames. *Earthq Eng Struct Dyn* 46(13):2121–2139
32. Bozkurt MB, Topkaya C (2018) Replaceable links with gusseted brace joints for eccentrically braced frames. *Soil Dyn Earthq Eng* 115:305–318
33. Bozkurt MB, Kazemzadeh Azad S, Topkaya C (2019) Development of detachable replaceable links for eccentrically braced frames. *Earthq Eng. Struct Dyn* 48(10):1134–1155
34. Saravanan M, Goswami R, Palani GS (2018) Replaceable fuses in earthquake resistant steel structures: a review. *Int J Steel Struct* 18(3):868–879
35. Shayanfar MA, Rezaeian AR, Zanganeh A (2014) Seismic performance of eccentrically braced frame with vertical link using PBD method. *Struct Des Tall Spec Build* 23(1):1–21
36. Wang F, Su M, Hong M, Guo Y, Li S (2016) Cyclic behaviour of Y-shaped eccentrically braced frames fabricated with high-strength steel composite. *J Constr Steel Res* 120:176–187
37. Bouwkamp J, Vetr MG, Ghamari A (2016) An analytical model for inelastic cyclic response of eccentrically braced frame with vertical shear link (V-EBF). *Case Stud Struct Eng* 6:31–44

The Evaluation of Six Indonesian Hardwood Species According to SNI 7973:2013



Wiryanto Dewobroto, Christian Gerald Daniel, Ricky Weinata Kurniawan, and Au Chuenliana Audi

Abstract In Indonesia, a new timber engineering standard called SNI 7973:2013 was recently introduced to replace the old standard (PKKI 1961) established in 1961. The 1961 standard classified timber products solely based on their species names. Meanwhile, the SNI7973:2013 is designed to distinguish the grades by the respective elastic modulus (MOE) value of the timber yielded from the non-destructive bending test. The objective of this research is then set to employ the given norm as the means to identify the grade of six Indonesian hardwood species, namely Camphor, Nyatoh, Mahogany, Sengon, Meranti, and White Jabon tree originated from Indonesia. Simultaneously, this research also attempts to compare the design values given in the norm and the actual test results according to ASTM D198. A four-point bending test is carried out to examine and compare the values of MOE and bending strength (MOR) of the timbers to achieve such goals. The tests are carried out in accordance with ASTM D198, which states that the MOR obtained from the tests must be adjusted using a specific conversion factor provided by ASTM D1990 to meet the 5-percentile value of forty test results, which is the minimum number of test specimens required by EN384:2004. The results show that the adjusted bending strength is twice as large as the design values provided by the national norm after cross-matching the grade of the timbers to the respective MOE. In conclusion, SNI 7973:2013 has the potential to become the means to identify the proposed six types of timber species, with rather conservative design values that can be safely used during the design stage of timber construction.

Keywords Timber grading · Indonesian hardwood · SNI 7973:2013 · MOE · Bending strength

W. Dewobroto · C. G. Daniel (✉) · R. W. Kurniawan · A. C. Audi
Department of Civil Engineering, Pelita Harapan University, Tangerang, Indonesia
e-mail: christian.daniel@uph.edu

W. Dewobroto
e-mail: wiryanto.dewobroto@uph.edu

1 Introduction

The use of timber in building construction in Indonesia has been relatively overshadowed by its counterparts, i.e. concrete and steel. According to the data taken from National Statistical Bureau, the volume of wood production in 2018 was estimated at around 53 million ton, with only about 12% were manufactured as sawn and laminated timber that is generally used as a construction product [1]. In contrast, the major parts (approximately 80%) of raw wood were used in the pulp and paper industry [2]. However, recent development has suggested timber as a sustainable material for construction. Timber is viewed as the producer of oxygen, and thus, an eco-friendly construction material. Therefore, timber can be used as a structural part in small as well as massive-scale constructions [3].

In Indonesia, the most recent norm regarding the application of timber as a construction material was declared in 2013, namely by SNI 7973-2013: Design Specification for Wood Construction [4], equipped with the means to classify any timber products based on its elastic modulus (E) value, which is a direct adaptation from the most up-to-date norm in the USA, called National Design Specification for Wood Construction, 2012 Edition [5]. The standard has been proposed to replace the old norm, called Indonesian Timber Construction Norm (PKKI 1961), which was invented back in 1961 and grouped the timber according to its species and strength class [6]. Moreover, there was also a norm developed prior to SNI 7973-2013, namely RSNI 3 PKKI NI-5 in 2002 [7], that attempted to group timber products according to elastic modulus as well, with a difference in the means of obtaining the value. The 2002 code incorporated the timber species and density in the determination of E-value, made it similar to PKKI 1961, whereas SNI 7973-2013 highlights the importance of the non-destructive bending test to classify the product. However, the approach seemed unsuccessful back then due to the change in design paradigm, from allowable or elastic to the ultimate state design approach, without remarkable improvement in practice [8]. Hence, PKKI 1961 has been able to maintain its popularity in the construction industry [9].

Naturally, there is a notable difference between the material properties of Indonesian and American timber, hence comes a difference in the norm of both countries. Therefore, this research aims to evaluate the impact of the variation in timber species on the design process. Several timber species are incorporated to the observation, namely Camphor (*Cinnamomum camphora*), Nyatoh (*Palaquium spp.*), Mahogany (*Swietenia mahagoni*), Sengon (*Paraserianthes falcataria*), Meranti (*Shorea spp.*) and White Jabon (*Anthocephalus cadamba*).

2 Background Theory

2.1 Grading System in SNI 7973-2013

There is a considerable distinction between the old (PKKI 1961) and the new (SNI 7973-2013) timber engineering norm. The approach in the former is based on certain parameters, namely specific gravity and the name of a wood species, after which the timber products can be grouped into a specific strength grading system. In contrast, the latter is mainly based on the value of Elastic Modulus (Modulus of Elasticity—MOE), as shown in Table 1.

The old grading system incorporates ASTM D2395-07 (*Standard Test Methods for Specific Gravity of Wood and Wood-Based Materials*) to develop the material for testing [10]. Such unique material shape described in the code has limited the practicality of the method. Meanwhile, the new norm only requires a non-destructive bending test to obtain elastic modulus according to ASTM D198-09 (*Standard Test*

Table 1 Timber grade classification according to SNI 7973-2013 [4]

Grade code	Prescribed design values (MPa)					Elastic modulus (MPa)	
	F _b	F _t	F _c	F _v	F _{cl}	E	E _{min}
E25	26.0	22.9	18.0	3.06	6.11	25,000	12,500
E24	24.4	21.5	17.4	2.87	5.74	24,000	12,000
E23	23.2	20.5	16.8	2.73	5.46	23,000	11,500
E22	22.0	19.4	16.2	2.59	5.19	22,000	11,000
E21	21.3	18.8	15.6	2.50	5.00	21,000	10,500
E20	19.7	17.4	15.0	2.31	4.63	20,000	10,000
E19	18.5	16.3	14.5	2.18	4.35	19,000	9500
E18	17.3	15.3	13.8	2.04	4.07	18,000	9000
E17	16.5	14.6	13.2	1.94	3.89	17,000	8500
E16	15.0	13.2	12.76	1.76	3.52	16,000	8000
E15	13.8	12.2	12.00	1.62	3.24	15,000	7500
E14	12.6	11.1	11.1	1.48	2.96	14,000	7000
E13	11.8	10.4	10.4	1.39	2.78	13,000	6500
E12	10.6	9.4	9.4	1.25	2.50	12,000	6000
E11	9.1	8.0	8.0	1.06	2.13	11,000	5500
E10	7.9	6.9	6.9	0.93	1.85	10,000	5000
E9	7.1	6.3	6.3	0.83	1.67	9000	4500
E8	5.5	4.9	4.9	0.65	1.30	8000	4000
E7	4.3	3.8	3.8	0.51	1.02	7000	3500
E6	3.1	2.8	2.8	0.37	0.74	6000	3000
E5	2.0	1.7	1.7	0.23	0.46	5000	2500

Methods of Static Tests of Lumber in Structural Sizes). This implies that the newest grading system can directly be applied to classify any timber products without breaking it, thus establishing it as a better approach.

The value of MOE obtained from 3 the bending test is compared to the value of MOE given in Table 1 to obtain the classification of the timber product. The design strength values, e.g. bending strength (in Table 1 is written as F_b), can then be obtained with respect to the grading scale. Such values can be applied directly to the design stage without the need to perform actual tests to get them, thus may cut any unnecessary cost and waste materials off the calculation. Generally, bending strength values are directly proportional to the elastic modulus, or the grade, of the timber, meaning that the increase of the stiffness will result in a stronger timber product.

2.2 Specification of Bending Test and the Determination of Design Values

Both non-destructive and destructive bending tests are executed to evaluate the value of elastic modulus and bending strength. The accuracy of the grading system in SNI 7973-2013 depends on the testing equipment. Both two-point and center-point bending tests are performed using rectangular shape beam specimens with a width-to-depth ratio of 11–15 in accordance with ASTM D198-09 (*Standard Test Methods of Static Tests of Lumber in Structural Sizes*) [11].

In each non-destructive test, the loading is applied to the specimen in several stages, where the displacement at the midspan is recorded in every phase. The force–displacement curves can then be constructed based on each timber species; hence the mean value of elastic modulus can be obtained by considering the proportional elastic limit from respective curves.

In the next phase of this research, the destructive tests are performed on the test specimens to get the value of bending strength to be compared to the design values according to the respective grade of each species. The actual bending strength for further calculation is taken as the 5th percentile frequency value from the series of results for each species. However, a specific modification factor is necessary to convert the actual test results so that the final conversion is comparable to the values given in Table 1. The conversion factor is provided by ASTM D1990-07 [12].

In order to verify the eligibility of the result, each timber specimen is required to have a maximum moisture content of 19%, with an optimum content of 15%. Otherwise, another particular reduction factor given in ASTM D1990-07 needs to be taken into the calculation.

Lastly, the number of 40 specimens per species are employed for both the non-destructive and destructive tests to meet the minimum requirement of testing frequency given in NEN 384:2004 [13] to ensure the statistical accuracy of the results.

3 Research Methods

3.1 Development of Testing Specimens

There are six types of timber species selected for this research: Camphor, Nyatoh, Mahogany, Sengon, Meranti, and White Jabon. Each specimen must undergo two stages of preparation, from cutting to smoothening, to construct the desired test samples, as given in Fig. 1.

The dimension of each test specimens is $23 \sim 25 \times 85 \times 800 \sim 1500$ mm, depending on the availability of the raw materials. Different measurements are situated according to the availability of the testing apparatus. The complete list is shown in Table 2

The moisture content of each specimen must be checked prior to the mechanical test. This test can be done through a digital AMTAST MD010 moisture meter with an accuracy of $99\% \pm 0.5\%$ [14]. In comparison, a standardized test according to ASTM D4442—16 has also been performed, which employs small, clear-cut specimens [15] to find out the moisture content of Camphor, Nyatoh and Mahogany in this research.

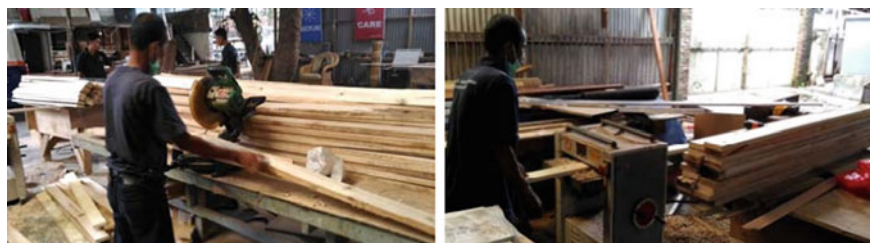


Fig. 1 (Left) The cutting of raw timber and (Right) smoothening timber beam surface

Table 2 The specification of testing specimens

No	Species	Dimension (mm)	Num. of sample	Test setup
1	Sengon (A)	$23 \times 85 \times 1500$	50	Panter
2	Sengon (B)	$23 \times 85 \times 1000$	40	UTM
3	White Jabon (A)	$25 \times 85 \times 1500$	40	Panter
4	White Jabon (B)	$25 \times 85 \times 1000$	40	UTM
5	Meranti (A)	$25 \times 85 \times 1500$	40	Panter
6	Meranti (B)	$25 \times 85 \times 1000$	40	UTM
7	Camphor	$25 \times 85 \times 1000$	80	UTM
8	Nyatoh	$25 \times 85 \times 1000$	80	UTM
9	Mahogany	$25 \times 85 \times 800$	80	UTM



Fig. 2 (Left) Panter machine, (Middle) analogue UTM and (Right) digital UTM



Fig. 3 The scheme of (left) two-point bending and (right) three-point bending test [all units in mm]

In this study, several testing apparatus is used for bending tests. The first tests are carried out at the Forestry Department’s Research and Development Center (Puslitbang) in Bogor, using two machines: (a) a mechanical device (Panter) invented by Prof Surjono Surjokusumo and the IPB team, and (b) an Analogue Universal Testing Machine (UTM). Furthermore, the tests are carried out with the aid of a digital UTM. Figure 2 depicts each instrument.

Specimens are subjected to the center-point loading in the Panter machine apparatus, while two-point loading is applied to the specimen using both analogue and digital UTM. The configurations of both setups are illustrated in Fig. 3.

3.2 Development of Testing Specimens

The output of the bending test is presented in the series of force–displacement relationship. Such plots can be used to derive the elastic limit that lies between the linear proportion of force and displacement field, which can be estimated as up to 40% of the peak load. Figure 4 depicts the force–displacement curve resulted from bending test.

Both force and displacement values from each curve are converted to the elastic modulus of each specimen through the following equations for centre-point and two-point loading, respectively:

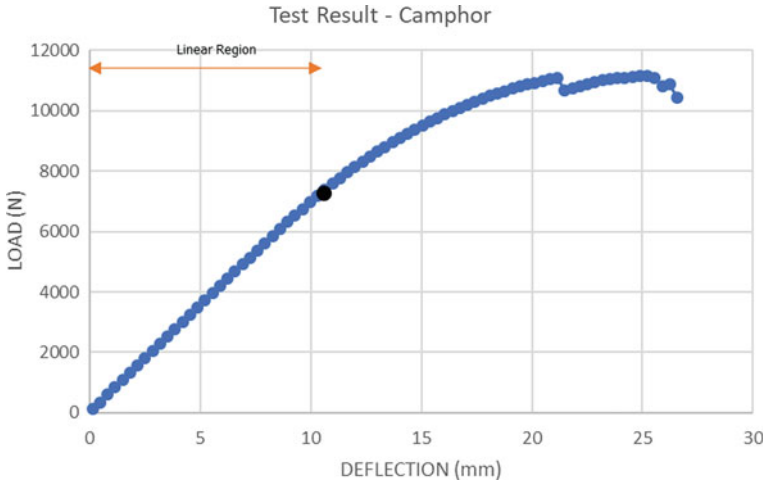


Fig. 4 Force–displacement curve and determination of elastic limit. *Source* Author

$$E = \frac{PL^3}{4bh^3 \Delta} \tag{1}$$

$$E = \frac{Pa(3L^2 - 4a^2)}{4bh^3 \Delta} \tag{2}$$

where:

- P Load within elastic limit (approximately 30–40% from maximum load)
- L Distance between supports
- Δ Displacement at midspan at subjected load
- b Width of cross-section (flatwise)
- h Height of cross-section (flatwise)
- a Distance between load to support

The value of elastic modulus must be adjusted to a specific correction factor in the case of the Panter device test [16]. Such adjustment on elastic modulus has raised concerns about its impact on the accuracy of the test results compared to the result obtained from the standard equation given by ASTM D198-09 without any correction factor needed (Fig. 5). This issue is worth addressed and so has been discussed in this research. Such an attempt is remarked by comparing Panter test results and the results from UTM to find the correlation between them. The information holds significant importance to determine if the Panter apparatus remains a reliable means to examine any timber product grade according to SNI 7973-2013.

The bending strength tests are carried out directly after the specimens’ elastic limits have been determined. However, the test can only be done using UTM apparatus. Furthermore, the analogue system’s loading test is only applied to one type of the selected timber (Sengon) due to the difficulties of having an accurate reading and



Fig. 5 (Left) Load test in progress using Panter and (Right) deflectometer for load and displacement reading

constructing the complete force–displacement curve. Therefore, the majority of the tests are performed by employing the digital UTM (Fig. 6).

During the bending test, the specimens were finally loaded until their breaking point to find the actual peak load of the specimens. The bending strength of the specimen is calculated using the following expressions—Eqs. (3) and (4)—for two and center-point bending test, respectively.

$$F_{b,2point} = \frac{3 \times P_{max} \times a}{bh^2} \quad (3)$$

$$F_{b,centre} = \frac{3 \times P_{max} \times L}{2bh^2} \quad (4)$$

The bending strength of the selected 40 samples for each specimen is then collected to construct a frequency-based statistical analysis. The frequency-based statistical analysis was conducted to determine the 5th percentile value, which then is selected for allowable bending strength of the timber species and compared with the values from the table according to the specific grading class.



Fig. 6 (Top) Bending test execution using analogue UTM; (Bottom) test using digital UTM

4 Results and Discussions

4.1 Moisture Content Examination

Moisture content is an important characteristic that affects the stiffness, and thus, the strength of a timber product; consequently, moisture content needs to be controlled in such a way to maintain the quality of timber that is used in this research. Moisture content itself has been one parameter that is prescribed in the newest norm (SNI 1973-2013) such that the upper limit is 19%. Therefore, the moisture content of each sample is tested utilizing a digital moisture meter and validated using the manual examination according to ASTM D4442 [15].

The average moisture content is approximately 11.5%, both by digital moisture meter and manual measurement, with the maximum being recorded at 15%. The deviation is recorded at 1.5%. Consequently, the moisture content of every specimen meets the criterion of SNI 7973-2013 and, therefore, may be subjected to further mechanical experiments.

4.2 Elastic Modulus Final Result

The mean value from the data set of 40 test specimens is selected as the apparent elastic modulus, with the result shown in Table 3.

The coefficient of variation is determined as the ratio between the deviation and the mean value of each data set. Judging from the result, it is visible that the variation of elastic modulus ranges from 6.5 to 31%, which is deemed normal due to the heterogeneous properties of each timber product. Furthermore, the variations resulted from the Panter test result are quite comparable to that of the results of UTM, proving that Panter device is reliable enough to become the means of elastic modulus determination. Lastly, Meranti is found out to be the stiffest timber, while Sengon becomes the least stiff timber out of the six species. Traditionally, this means that Meranti and Sengon will have the highest and lowest bending strength, respectively, which must be confirmed by the result of destructive test results in the latter part of this paper. An interesting finding is that Sengon while having the elastic modulus of around 5500 MPa, might still be categorized as E5 as well as E6 in Table 4. This is possible due to the invariance of testing results available, hence making it ambiguous. In conclusion, further effort is compulsory to clarify to which group Sengon belongs.

Table 3 Apparent elastic modulus (MOE) for six timber species

Wood type	E	COV (%)	Grade	Apparatus
Camphor	11,677	6.52	E11	Digital UTM
Nyatoh	9040	7.33	E9	Digital UTM
Mahogany	7062	6.85	E7	Digital UTM
Sengon	5284	31.10	E5–E6	Panter
	5470	19.00		Analogue UTM
White Jabon	6299	26.00	E6	Panter
	5765	27.10		Digital UTM
Meranti	13,387	22.60	E13	Panter
	12,195	22.30		Digital UTM

Table 4 Comparison between the test result and the national standard (SNI 7973:2013)

Wood type	Grade	Design bending strength		Efficiency (%)
		Allowable	SNI 7973-2013	
Camphor	E11	36.9	9.1	25
Nyatoh	E9	15.7	7.1	45
Mahogany	E7	13.5	4.3	32
Sengon	E6	10.8	3.1	29
White Jabon	E6	12.95	3.1	24
Meranti	E13	24.38	11.8	48

4.3 Elastic Modulus Final Result—Comparison with Other Research Outcomes

Timber is known as a heterogeneous material, and thus, such an attempt of categorization will be a complicated process as it needs a vast amount of data. To address this difficulty, the results obtained are compared to the results of other publications to verify and validate if each species was classified in the correct grade in the previous section. The comparison has been made for three species, namely Sengon, White Jabon and Meranti, shown in Figs. 8, 9, and 10.

According to Fig. 8, the test results by the authors exhibit slightly higher performance than the other sources. Nonetheless, the results still lie within the acceptable range ($\pm 33\%$), considering many factors possessed by each wood specimen that could potentially deviate from the results. Conclusively, White Jabon can safely be classified as E6 according to SNI 7973-2013, thus confirming the result in Table 3.

As depicted in Fig. 9, the range of elastic modulus for Sengon is about $\pm 36\%$. Therefore, the test results can be accepted as the means to determine the grade of Sengon. Consequently, Sengon can be given the E6 category, which lies at the same category as White Jabon, and confirms the result in Table 3. The elastic modulus given by both Panter and UTM apparatus herein is relatively conservative or smaller than the other values.

Among the tested species, Meranti holds the title as the stiffest material (Fig. 10). The findings are further supported by comparing with other sources, with a range of roughly 30%. The results given by Panter and UTM tests are relatively higher than their predecessors. Nonetheless, as the range can be considered as a standard

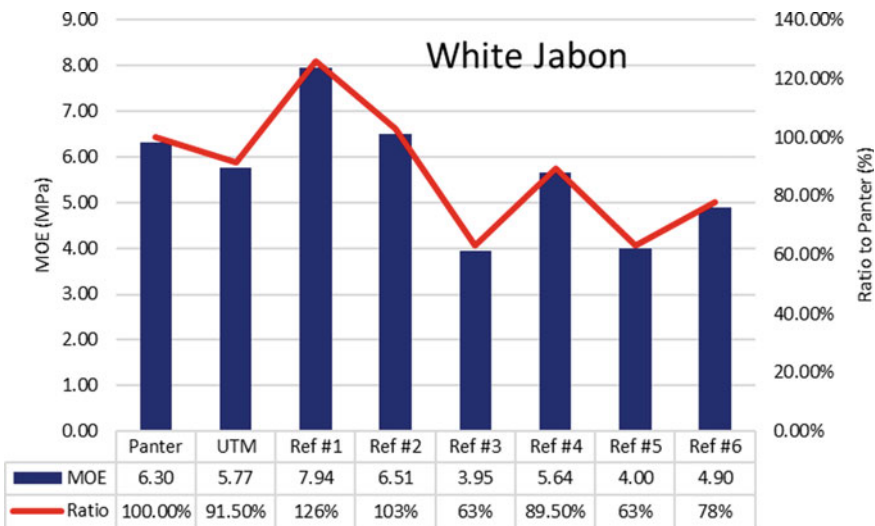


Fig. 8 White Jabon test results compared with various sources [1–6, 17–22], respectively

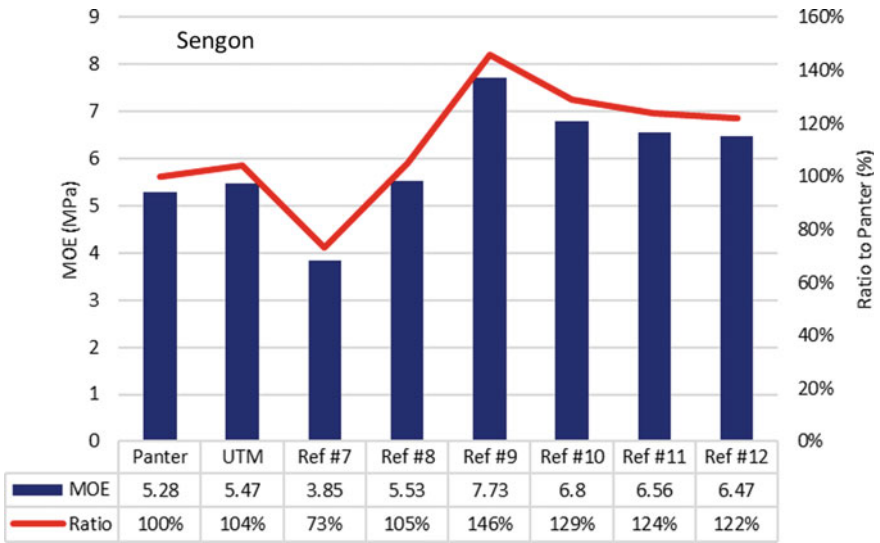


Fig. 9 Sengon test results compared with various sources [7–12, 23–28], respectively

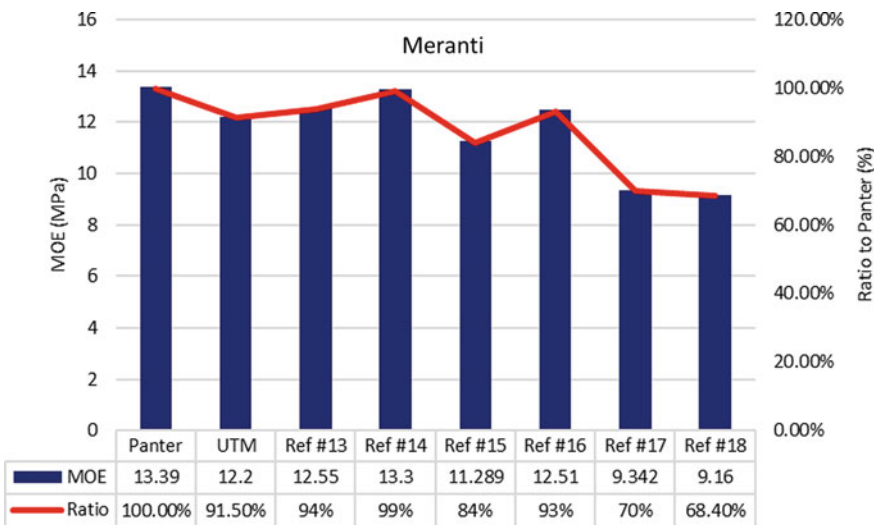


Fig. 10 Meranti test results compared with various sources [13–18, 29–34], respectively

deviation, so can the grade of Meranti be determined as E13. Hence, it confirms the result in Table 3.

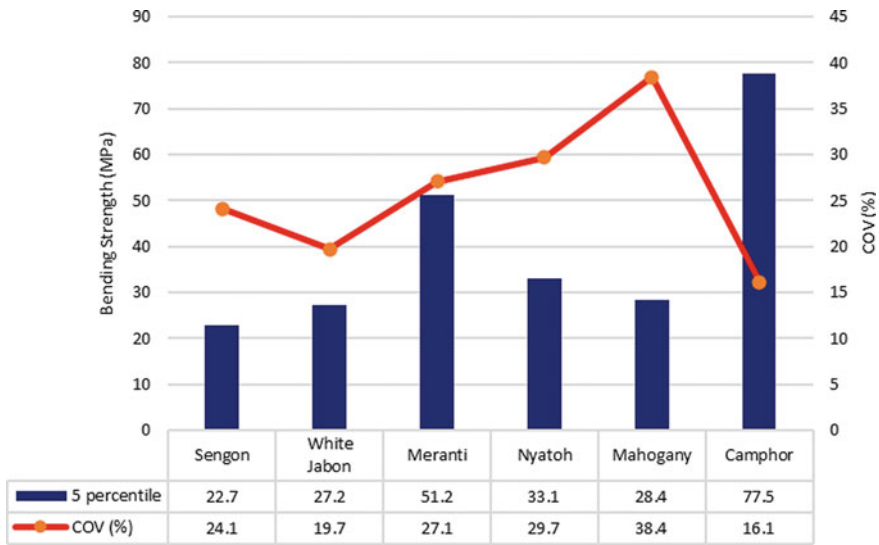


Fig. 11 Actual bending strength (MOR) and coefficient of variation of each species

4.4 Actual Bending Strength (Modulus of Rupture—MOR)

The test results illustrated in Fig. 11 indicate that Camphor is the species that has the highest bending strength, followed by Meranti. Meanwhile, Sengon is the species with the lowest strength. These values follow the pattern of the timber grades obtained from Table 3, indicating that the stiffness of the timber is directly proportional to its bending strength. Interestingly, there is a slight difference in the upper class, as the bending strength of Camphor is higher than Meranti, albeit being less stiffer. This phenomenon is worth to be examined further.

On the other hand, the coefficient of variation of each species shows a relatively well distribution, indicating the accuracy of the results.

4.5 Comparison Between the Test Result and SNI 7973:2013

The final step in the research was to compare the allowable bending strength from the test results to the design values (Fb) specified by the national standard (SNI 7973:2013) for the respective grades. The value of the allowed bending strength of each species is obtained by simply dividing the ultimate bending strength from the previous section with the reduction factor taken from ASTM D1990-07, which in this case will be 2.1. Such comparison is described in Table 4.

The efficiency in Table 4 is defined as the intended bending strength (Fb) ratio specified in SNI 7973-2013 to the previously lowered allowable bending strength. It

comes as no surprise that the design bending strength shown in the national standard SNI 7973:2013 are remarkably smaller than the allowable bending strength from the test result. It implies that SNI 7973-2013 provides a relatively conservative bending parameter, or similarly, a very safe approach. Conversely, safe practice here could also indicate a non-efficient system.

In conclusion, based on the respective elastic modulus and bending strength, Camphor and Meranti are the best timber materials to use in a construction project, whereas Sengon is the least desirable alternative. Furthermore, the results presented here have also been adequate to classify Sengon as E6, based on its permitted bending strength, which exceeds the E6 bending strength criteria outlined in SNI 7973-2013. Since the given values in the standard can be considered highly conservative, it is safe to say that Sengon is suitable for E6 group.

4.6 Comparison Between Test Results and SNI 7973:2013 and PKKI 1961

An attempt is performed to check the difference between the elastic modulus obtained from the actual test (consequently, SNI 7973:2013) and the result from the PKKI 1961 standard based on the specific gravity of each species. Such comparison becomes critical because the timber industry in Indonesia nowadays remains mainly accustomed to PKKI 1961. In contrast, the most recent standard (SNI7973:2013) has yet to be fully established and implemented throughout the entire chain of the timber sector. Therefore, this paper can become a means to exhibit the suitability of both codes and hence, promote the application of the new standard. Firstly, the grade of each species is determined, and the elastic modulus is given in Table 5.

Based on the predecessor standard (PKKI 1961), Camphor is classified in class II, whereas both Nyatoh and Mahogany are put into class III. For each standard class, PKKI 1961 has prescribed a distinct value of elastic modulus that can be used to design timber. These values are compared with the design bending strength taken from the newest standard (SNI 7973-2013). Evidently, the result presented in Table 5 concludes that only Mahogany can be precisely estimated by PKKI 1961, while the other two deviates approximately 15 and 20%, respectively. This result suggests that the old Indonesian standard provides an even more conservative but less efficient parameter; yet, SNI 7973:2013 can still classify the grade of the six timber products within the conservative limit.

Table 5 The determination of timber grade based on PKKI 1961

Wood type	Grade (PKKI 1961)	E (MPa)	
		PKKI 1961	SNI 7973-2013
Camphor	II	9807	11,677
Nyatoh	III	7845	9040
Mahogany	III	7845	7062

5 Conclusion

This research has attempted to classify the grade of six local timber species, namely Camphor (*Cinnamomum camphora*), Nyatoh (*Palaquium* spp.), Mahogany (*Swietenia mahagoni*), Sengon (*Paraserianthes falcataria*), Meranti (*Shorea* spp.) and White Jabon (*Anthocephalus cadamba*) using the newest standard of timber engineering in Indonesia, so-called SNI 7973-2013. The examination of the moisture content of each specimen prior to the mechanical testing has proven that all samples are fit to the standard for further testing, with the maximum and average moisture content of 15% and 11.5%, respectively. Furthermore, numerous non-destructive bending tests have been performed using three different types of equipment, namely Panter, analogue and digital UTM apparatus, to obtain the elastic modulus of each species. Meranti and Camphor are found out to be the stiffest material (giving them the highest grades—E13 and E11, respectively), whereas Sengon has the lowest elastic modulus, and consequently, the lowest grade—E6. More experiments conducted using destructive bending tests in UTM have compared allowable bending strength based on the actual test and the design values given in the norm corresponding to each grade. The results comparison conclude that the former is significantly larger than the latter values. Conclusively, the outcome that design values given in SNI 7973-2013 are relatively conservative, and hence, safe to be used in the calculation. However, the bending strength of Camphor is relatively larger than that of Meranti, even though their grades are in the reversing order. Another important finding is the probability to find an ambiguous case, such as Sengon, which can be firmly classified as E6 after comparing it to other research outcomes and after obtaining sufficient proof in the form of bending strength. An extra comparison to the predecessor norm (PKKI 1961) shows a similar result to strengthen the hypothesis. To sum up, this research has presented the shreds of evidence that the design values given in SNI 7973-2013 are primarily conservative and provide a safe range to be used in the design. Nonetheless, further research needs to be conducted to compare other local timber species to the code to examine the conservativeness of each design value given in the newest norm relative to the allowable design values provided by the test results.

References

1. Badan Pusat Statistik (2018) Badan Pusat Statistik. [Online]. Available <https://www.bps.go.id/indicator/60/167/1/produksi-kayu-hutan.html>. Accessed 01 10 2020
2. Koalisi Anti Mafia Hutan (2015) Kesenjangan Persediaan Kayu Legal dan Implikasinya terhadap Peningkatan Kapasitas Produksi Industri Kehutanan di Indonesia: Sebuah Kajian Peta Jalan Revitalisasi Industri Kehutanan, Fase 1. DKI Jakarta
3. Ramage MH, Burrige H, Busse-Wicher M, Fereday G, Reynolds T, Shah DU, Wu G, Yu L, Fleming P, Densley-Tingley D, Allwood J, Dupree P, Linden PF, Scherman O (2017) The wood from the trees: the use of timber in construction. *Renew Sustain Energy Rev* 68:333–359

4. Badan Standarisasi Nasional (2013) SNI 7973-2013: Spesifikasi desain untuk konstruksi kayu. Badan Standarisasi Nasional
5. American Forest & Paper Association (2005) National design specification for wood construction ASD/LRFD. American Wood Council
6. Departemen Pekerjaan Umum Indonesia (1961) Peraturan konstruksi kayu Indonesia NI 5 PKKI 1961. Departemen Pekerjaan Umum Indonesia
7. Badan Standarisasi Nasional (BSN) (2002) Tata cara perencanaan konstruksi kayu Indonesia (PKKI NI-5), DKI Jakarta
8. Dewobroto W, Kurniawan R (2018) EVALUASI TEGANGAN IJIN HASIL UJI EMPIRIS TIGA JENIS KAYU TROPIS TERHADAP NILAI DESAIN ACUAN SNI 7973:2013. In: Konferensi Nasional Teknik Sipil (KonTeks) 12, Batam
9. Hernadi A, Prasetya N, Aidil R (2017) Borneo Engineering: Jurnal Teknik Sipil 1(2):63. ISSN 2581-1134 (Online) Analisis Kuat Tarik Kayu Menggunakan PKKI 1961 dan SNI 7973:2013. Borneo Engineering: Jurnal Teknik Sipil 1(2):63–67
10. ASTM International (2007) ASTM D2395-07: standard test methods for specific gravity of wood and wood-based materials. ASTM International
11. ASTM International (2009) ASTM D198-09: standard test methods of static tests of lumber in structural sizes. ASTM International
12. ASTM International (2007) ASTM D1990-07: standard practice for establishing allowable properties for visually-graded dimension lumber from in-grade tests of full-size specimens. ASTM International
13. European Committee for Standardization (2004) EN 384:2004 Structural timber—determination of characteristic values of mechanical properties and density
14. Mandiri CJ (2016) Distributor Alat Uji dan Alat Ukur Berkualitas: Alat Ukur Kadar Air Kayu AMTAST MD010. [Online]. Available <https://alat-ukur-indonesia.com>. Accessed 10 01 2020
15. ASTM International (2016) ASTM D4442-16: standard test methods for direct moisture content measurement of wood and wood-based materials. ASTM International
16. Surjokusumo S, Nugroho N, Karlinasari L, Priyono J, Suroso A (2003) Buku Petunjuk Penggunaan Mesin Pemilah Kayu—Versi Panter MPK 5. Bogor
17. Sari Y, Massijaya M, Hadjib N (2011) Characteristic of glulam from two species of community wood: Pine (*Pinus merkusii* Jungh.et de Vriese) and Jabon (*Anthocephalus cadamba* Lamk.). Departemen Hasil Hutan Fakultas Kehutanan Institut Pertanian Bogor
18. Savitri R (2011) Pengujian Sifat Fisis Dan Mekanis Kayu Jabon [*Anthocephalus cadamba* (Roxb.) Miq.]. Departemen Hasil Hutan, Fakultas Kehutanan, Institut Pertanian Bogor
19. Hadi, Rahayu, Danu (2013) Physical and mechanical properties of methyl methacrylate impregnated. *J Indian Acad Wood Sci* 10(2):77–80
20. Darmawan N, Rahayu F, Marchal (2013) Determination of juvenile and mature transition ring for fast growing Sengon and Jabon wood. *J Indian Acad Wood Sci* 10(1):39–47
21. Lestari, Hadi, Hermawan, Santoso (2018) Physical and mechanical properties of glued laminated lumber of pine (*Pinus merkusii*) and Jabon (*Anthocephalus cadamba*). *J Korean Wood Sci Technol* 46(2):143–148
22. Yunianti D, Suhasman S, Sahriyanti S (2015) Basic properties and nanostructure of wood from four fast growing species from a community forest. *J Indian Acad Wood Sci* 12:94–98
23. Marsoem SNA, Pujiwinarko A (2005) Comparison for the physical and mechanical properties of Sengon (*PARASERIANTHES FALCATA* (L) NIELSEN) wood of seed trees and off-shoot trees. In: International seminar on plantation forest research and development
24. Suryawan, Poerwodihardjo (2007) Sifat-Sifat Fisika dan Mekanika Kayu Keruing-Sengon. *Teodolita* 8:39–44
25. Nordahlia, Lim, Hamdan, Anwar (2014) Wood properties of selected plantation species: *Tectona grandis* (Teak), *Neolamarckia Cadamba* (Kelempayan/Laran), *Octomeles Sumatrana* (Binuang) and *Paraserianthes Falcataria* (Batai). *Timber Technology Bulletin* No. 54
26. Nandika D, Darmawan W, Arinana (2015) Peningkatan Kualitas Kayu Sengon (*Paraserianthes Falcataria* (L) Nielsen) Melalui Teknik Kompregnasi. *Jurnal Teknologi Industri Pertanian* 25(2):125–135

27. Eratodi I, Bagus, Awaludin A (2017) Bending capacity of non-prismatic LVL beams *Paraserianthes falcataria*. *Procedia Eng* 171:1362–1369
28. Ishiguri, Eizawa, Saito, Iizuka, Yokota, Priadi, Sumiasri, Yoshizawa (2007) Variation in the wood properties of *Paraserianthes Falcataria* planted In Indonesia. *IAWA J* 28(3):339–348
29. Malaysian Timber Industry Board, 100 Malaysian Timbers, 1994
30. Wahab M, Jumaat M, Khaidzir M (2012) Statistical technique for grouping tropical timbers into similar strength groups. *Modern Appl Sci* 6(3)
31. Fernandes, Saridan (2013) Sifat Fisik Dan Mekanik Kayu *Shorea Macroptera* ssp. *Sandakanensis* (Sym.) Ashton Sebagai Bahan Baku Mebel. *JURNAL Penelitian Dipterokarpa* 7(1)
32. Toong et al (2014) Wood anatomy and property. *Bio Resour* 9(3):5184–8197
33. Pranata, Kristianto, Pattipawaej (2015) Pengujian Non-destruktif Modulus Elastisitas (MoE) Kayu Penyusun Sambungan Join Balok-Kolom. In: *Seminar Nasional ReTII*
34. Noh, Ahmad (2017) Heat treatment on Keruing and light red Meranti: the effect of heat exposure at different levels of temperature on bending strength properties. *IOP Conf Ser Mater Sci Eng* 271
35. Badan Pusat Statistik (2018) Badan Pusat Statistik Republik Indonesia. [Online]. Available <https://www.bps.go.id/indicator/60/502/1/produksi-kayu-bulat-menurut-jenis-kayu.html>. Accessed 01 10 2020
36. Badan Pusat Statistik (2016) Statistik Produksi Kehutanan 2016. Badan Pusat Statistik, DKI Jakarta

Image Analysis of the Color Change on Concrete Surface Under the Change of Temperature and Humidity



Naoki Tosaka, Deng Pengru, and Takashi Matsumoto

Abstract Today, concrete is used as a major construction material all over the world. Maintenance of concrete structures is getting important increasingly, and there is a need to inspect huge amount of concrete structures. It is required to develop labor-saving maintenance technologies and methods. Concrete is known as a porous material. The surface color changes correspondingly to the environmental temperature and humidity change. If concrete absorbs moisture, the color becomes dark. On the other hand, if it releases moisture, the color becomes bright. By establishing the relationship between environment-dependent color change and current concrete quality, it might be possible to inspect which part of concrete is poor quality. As a preliminary step towards the development of this inspection method, the purpose of this paper is to investigate the relationship between the color and the environment in an environmental chamber. A concrete specimen which has a damage was examined by image analysis. Since concrete changes brightness depending on the environment, observing the luminance values is useful to evaluate the color change. With time-lapse videos, these values are calculated in each frame. Comparing the temperature and humidity when color change happens, it is shown that both have a positive correlation. To distinguish between sound and unsound concrete, it is necessary to observe more specimens which have various deterioration in.

Keywords Image analysis · Maintenance · Deterioration · Repair

N. Tosaka

Graduate School of Engineering, Hokkaido University, Kita 13 Nishi 8, Kita-ku, Sapporo, Japan
e-mail: tosaka@eis.hokudai.ac.jp

D. Pengru · T. Matsumoto (✉)

Faculty of Engineering, Hokkaido University, Kita 13 Nishi 8, Kita-ku, Sapporo, Japan
e-mail: takashim@eng.hokudai.ac.jp

D. Pengru

e-mail: pengrudeng@eng.hokudai.ac.jp

1 Introduction

Today, concrete is used as a major construction material all over the world. Maintenance of concrete structures is getting important increasingly, and there is a need to inspect huge amount of concrete structures. It is required to develop labor-saving maintenance technologies and methods [1, 2]. Concrete is known as a porous material. In Koshiwa's report, it is indicated that the water penetrability into concrete changes correspondingly to the environmental change [3]. When water in concrete is in equilibrium state with the environment and, concrete absorbs moisture, it becomes wet and the surface color changes dark. On the other hand, if concrete releases moisture, it becomes dry and the surface color changes bright. The water content is different between wet process and dry process even a same humidity [4–6]. Furthermore, the permeability of concrete becomes larger, if a crack grows up between aggregates and cement paste and leads water to inside concrete. Cracks have a great effect on the permeability [7–9]. Therefore, it is possible that we understand what happened to concrete such as corrosion induced cracks and water leakages by making a connection between the color and the environment.

As a preliminary step towards the development of this inspection method to observe the surface color on real concrete structures, the first purpose of this paper is to investigate the relationship between temperature and humidity when color change happens. One specimen is prepared and observed in an environmental chamber. The judgement when the color change happen is made by human's visual sense. As a second step towards the development, the second purpose of this paper is to investigate the difference of color change between cracked and sound concrete in the chamber. Three concrete specimens are observed and one of them is prepared with a crack. Since the surface color changes chronologically, image analysis which digitizes the surface color at any time can detect the color change. Comparing analysis results of three specimens, the difference of color change between them will be evaluated.

This paper consists of five chapters. Chapter 1 mentions background, previous studies and purposes. Chapter 2 shows the overview, results and discussions about the preliminary experiment, the purpose of which is to investigate the relationship between temperature and humidity when color change happens in an environmental chamber. Chapter 3 shows the overview and method of image analysis about the experiments, the purpose of which is to investigate the difference of color change between cracked and sound concrete in an environmental chamber (hereinafter, referred to as Experiment 1, 2 and 3). Chapter 4 shows the analysis results and discussions about Experiment 1, 2 and 3. Chapter 5 mentions conclusions of this paper.

2 Preliminary Experiment

One preliminary experiment was conducted to investigate the relationship between temperature and humidity when color change happens on the specimen in an environmental chamber. In this chapter, overview, observation method, results and discussions about the preliminary experiment are described.

2.1 Observation of Concrete

Specimen One concrete specimen was prepared and called specimen A hereinafter. The length, width and thickness of specimen A are 160 mm, 150 mm and 33 mm, respectively (see Fig. 1).

Experimental Devices for Observation of Concrete Figure 1 shows the devices for the preliminary experiment. This experiment was conducted in an environmental chamber. A time-lapse camera and a thermo-hygrometer were used to record color change, temperature and humidity history in the chamber. In Fujiwara's report, it is indicated that water penetrability into concrete is differs greatly between liquid water and water vapor [10]. In actually, the surface color didn't change when dry concrete was observed while changing temperature and humidity. To emphasize color change in response to temperature and humidity change, the specimen was soaked in water. Because the water evaporation was not controlled, the water depth went down from 50 to 30 mm while the chamber worked.

Image capture was conducted with the digital time-lapse camera, Brinno TLC200 Pro, which can capture videos of 1280 * 720 pixels (921,600 pixcels) in an .avi

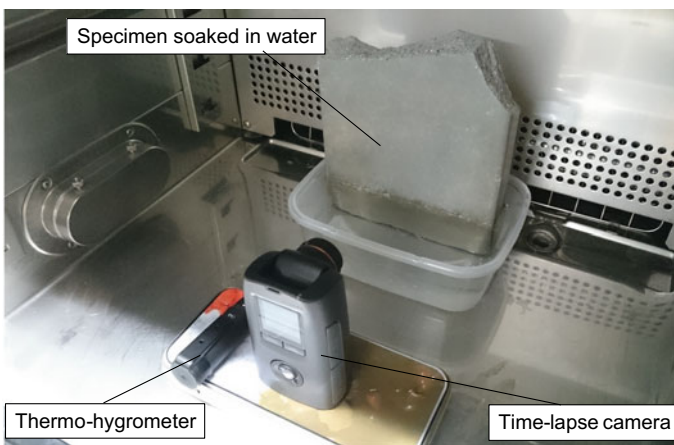


Fig. 1 Experimental devices in the preliminary experiment

Table 1 Condition cases and setting conditions in preliminary experiment

Condition case	Setting condition in the environmental chamber	
	Temperature (°C)	Humidity (%)
Condition A	5	50
Condition B	5	70
Condition C	15	50
Condition D	15	70

video file. To record the surface color clearly, the sharpness was set to minimum. Thermo-hygro measurement was conducted with a temperature and humidity data logger, EL-USB-2 which can record the temperature and humidity in a .txt file. Image capture and thermo-hygro measurement were conducted at every 15 min.

Setting Conditions. Table 1 shows the list of condition cases in the preliminary experiment. In Condition A, setting temperature and humidity were 5 °C and 50% respectively. In Condition B, C and D, 5 °C and 70%, 15 °C and 50%, and 15 °C and 70%, respectively. In Kudo's report, it is indicated that the amount of water in concrete changes hardly two days after concrete absorbs water [11]. To make the specimen be in equilibrium state, the environmental chamber worked for 48 h. In the first 24 h, temperature and humidity in the chamber was changed to setting temperature and humidity from room temperature and humidity. In the next 24 h, those were kept in the setting condition. During the chamber working, there was no color change on the specimen surface. This is because the fan in the chamber was running. Therefore, the specimen was observed after the chamber stopped. 0 h is defined as the moment when the chamber was stopped. Just after stopped, the temperature and humidity in the chamber changed rapidly because the chamber went through a cooling-down process. After that process, they increased gradually because the lamp in the chamber emitted heat. Because the specimen was observed continually, the lamp was needed and kept on throughout. The window of the chamber was covered by a shed and the specimen was illuminated constantly by only the lamp in the chamber.

2.2 Observation Results

Figure 2 shows the history of temperature and humidity in the environmental chamber until color change happens. Green, yellow, blue, orange shows the history in Condition A, B, C and D, respectively. The judgement when color change happens is made by human's visual sense from the time-lapse video. In Condition A, the color change happened at 17.5 °C, 82.5%, and 17 h. In Condition B, it happened at 18.0 °C, 81.5%, and 23 h. In Condition C, it happened at 19 °C, 79.5%, and 13 h. In Condition D, it happened at 19.5 °C, 84.5% and 10 h. Comparing Condition A and Condition B, the lower the setting humidity in the environmental chamber, the earlier color change

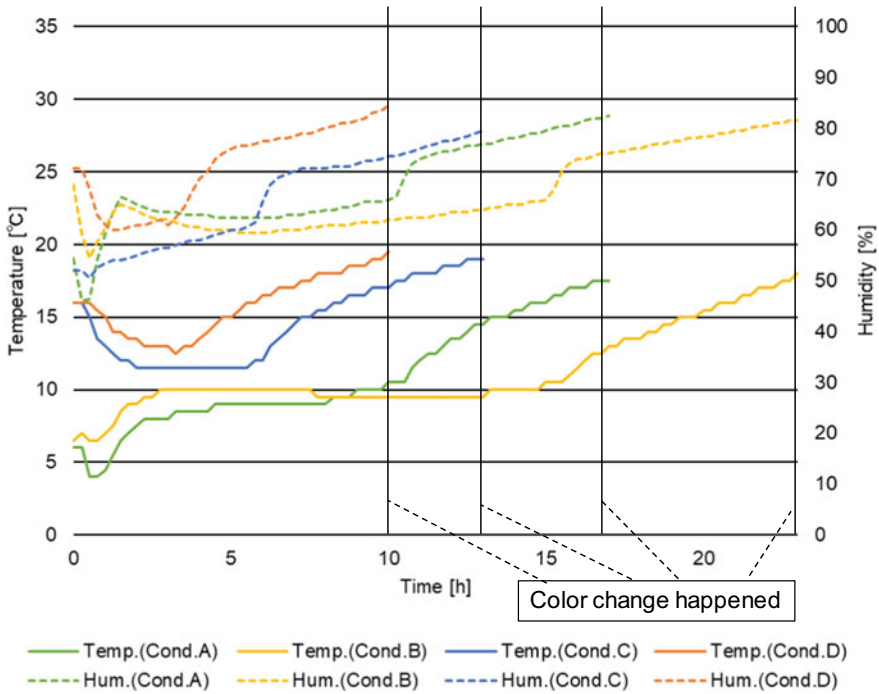


Fig. 2 Temperature and humidity history in the preliminary experiment

happen. Comparing Condition C and Condition D, the higher the setting humidity in the environmental chamber, the earlier color change happen. There was not the effective relationship between temperature, humidity and time when color change happened.

Then the relationship between temperature and humidity in the chamber before color change happened is shown in Fig. 3 except for time axis. Green, yellow, blue, and orange line show the behavior of temperature and humidity in Condition A, B, C and D, respectively.

2.3 Discussions

From Fig. 3, the temperature and humidity in the environmental chamber at 0 h were different in four conditions. However, the behaviors of temperature and humidity in the chamber became similar gradually in four conditions. This is because the chamber went through a cooling process. As a result, the temperature and humidity in the chamber when color change happened were all similar. All color change happened at around 17–20 °C and 80–85%. Color change is caused by the water content in

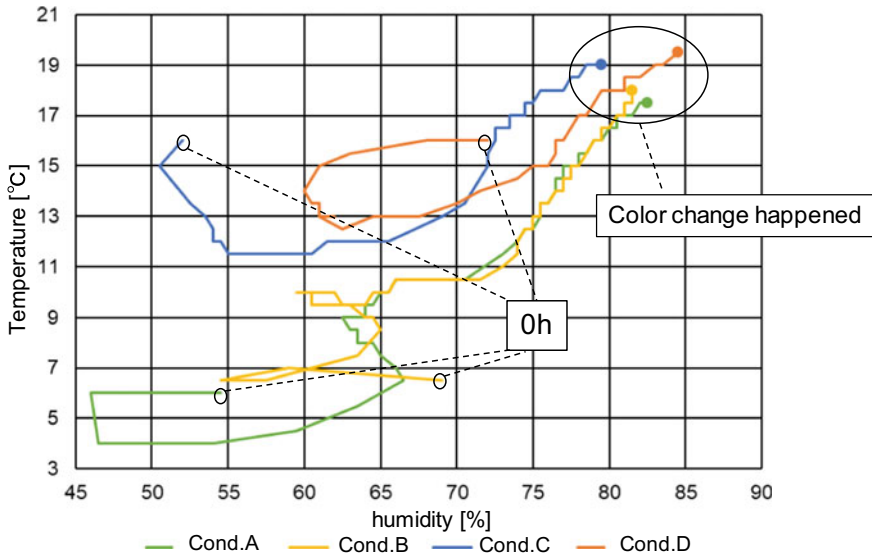


Fig. 3 Relationship between temperature and humidity when color change happened in the preliminary experiment

concrete. In Ryu's report, it is indicated that the water content is influenced by temperature and humidity [12]. However, there was not the effective relationship between temperature and humidity in the chamber when color change happened. Therefore, finding the relationship between them was unsuitable in the current devices and method. Following the result in this preliminary experiment, how the surface color changes are focused on in Chaps. 3 and 4.

3 Observation of Cracked and Sound Concrete

Three experiments were conducted to investigate the difference of color change between cracked and sound concrete in an environmental chamber. In this chapter, the overview about these experiments is described.

3.1 Specimens

Figure 4 shows the list of specimen names, their dimensions and cracked region. The length, width, and thickness of Specimen L and CL are 125 mm, 199 mm, 39 mm, and those of Specimen R are 135 mm, 199 mm, 33 mm, respectively. Specimen R was not made by the same form as Specimen L. After Experiment 1 (see Sect. 3.2),

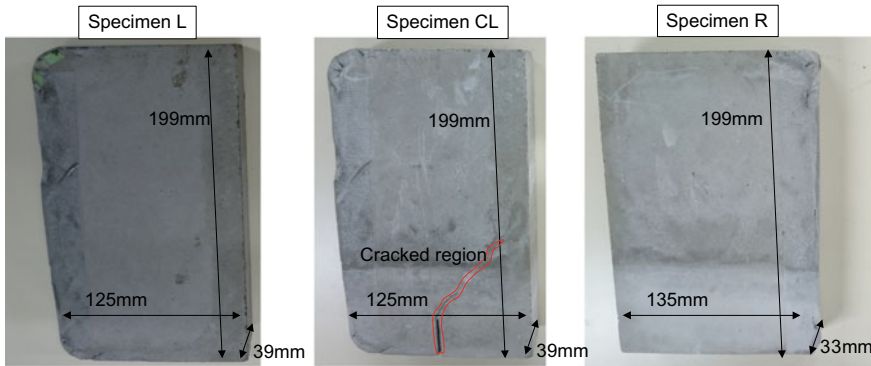


Fig. 4 Specimens in Experiment 1, 2, and 3

Table 2 Concrete mix of specimen L, CL, and R

Water	Cement	Coarse aggregate	Fine aggregate
175 kg/m ³	417 kg/m ³	699 kg/m ³	1156 kg/m ³

a crack was made on Specimen L by a concrete cutter and a wedge, and Specimen CL was made from Specimen L. Therefore, Specimen CL has the same dimension as Specimen L. The length of crack is 80 mm. Table. 2 shows the concrete mix of Specimen L, CL and R. The weight of water, cement, coarse aggregate and fine aggregate per unit volume were 175 kg/m³, 417 kg/m³, 699 kg/m³ and 1156 kg/m³, respectively. These three specimens were made of the same mix.

3.2 Experimental Devices for Observation of Concrete

Figure 5 shows the experimental devices in those three experiments. All experiments are conducted in an environmental chamber. A time-lapse camera and a thermo-hygro meter were used to record color change, temperature and humidity history in the chamber. To emphasize color change in response to temperature and humidity change, the specimens were soaked in water. Because the water evaporation was not controlled, the water depth went down from 50 to 30 mm while the chamber worked.

Image capture was conducted with the digital time-lapse camera, Brinno TLC200 Pro, which can capture videos of 1280 * 720 pixels (921,600 pixels). Image capture was conducted at every 5 min and recorded the video in an .avi video file. To record the surface color clearly, the sharpness was set to minimum. Thermo-hygro measurement was conducted with a temperature and humidity data logger, EL-USB-2. Thermo-hygro measurement was conducted at every 5 min and recorded the temperature and humidity in a .txt file.

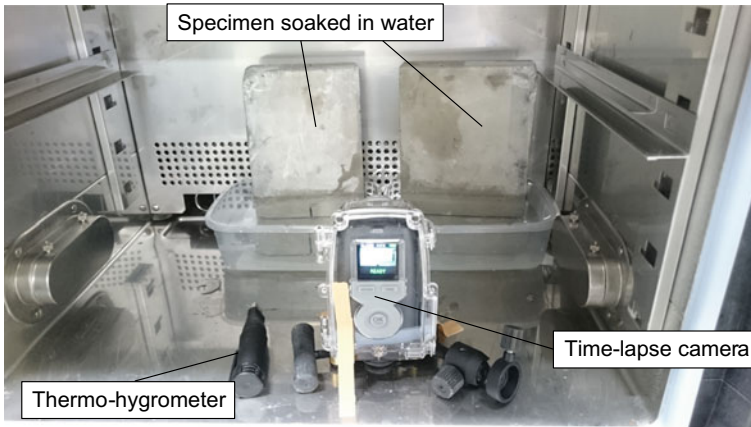


Fig. 5 Experimental devices in Experiment 1, 2, and 3

3.3 Setting Condition

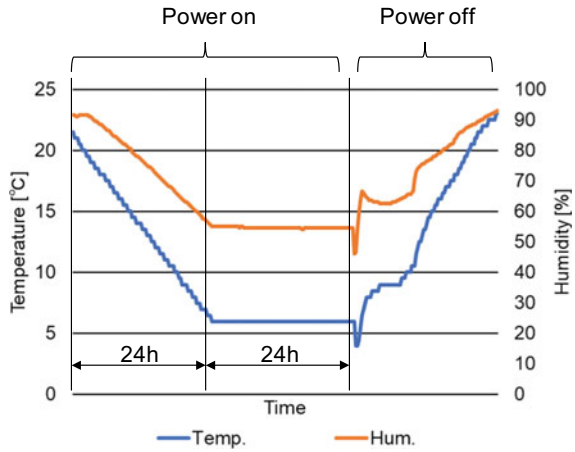
Table 3 shows the list of experiment cases, specimens which were observed, setting conditions of three experiments. In Experiment 1, Specimen L and Specimen R were observed. In Experiment 2 and 3, Specimen CL and Specimen R were observed. The thickness of Specimen R is not the same as Specimen L and CL. Before Experiment 2 and 3 (comparing Specimen CL and R), Experiment 1 was done to confirm that Specimen L and R have the same color change trend although they have different thickness.

To make specimens be in equilibrium state, the environmental chamber worked for 48 h. In the first 24 h, temperature and humidity in the chamber was changed to setting temperature and humidity from room temperature and humidity. In the next 24 h, those were kept in the setting condition (see Fig. 6). During the chamber working, there wasn't color change on the specimen surface. This is because the fan in the chamber was running. Therefore, specimens are observed after the chamber stopped. 0 h is defined as the moment when the chamber was stopped. Just after stopped, the temperature and humidity in the chamber decreased rapidly because the chamber was the cooling-down processing. After that process, they increased rose

Table 3 Experiment case and setting conditions

Experiment case	Specimens which observed	Setting condition in the environmental chamber	
		Temperature (°C)	Humidity (%)
Experiment 1	L and R	5	50
Experiment 2	CL and R	5	50
Experiment 3	CL and L	15	50

Fig. 6 Setting conditions of the environmental chamber



gradually because the lamp in the chamber emitted heat. Because the specimen was observed continually, the lamp was needed and kept on throughout. The window of the chamber was covered by a shed and the specimen was illuminated constantly by only the lamp in the chamber.

4 Method of Image Analysis

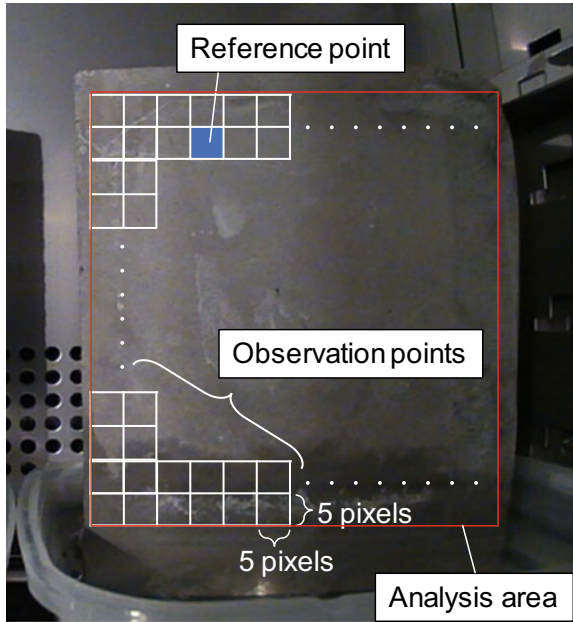
At first, all frames of a video were converted from an .avi file to a .bmp files by the video editing software, AviUlt. The following analysis is executed by the formula manipulation system, Mathematica. All conducted codes are shown in appendices.

4.1 Grayscale Convert

Figure 7 shows the target of image analysis. That area is divided into 5 * 5 pixels, and that 25 pixels areas are named observation points. To estimate the luminance of the points, the RGB values are converted to grayscale ones on the basis of Eq. 1 [13, 14]. Those coefficients are determined from the sensitivity of human’s visual sense. To reduce an influence of the image noise, the luminance value at some observation point is determined from the average grayscale value of 25 pixels [15]. By converting grayscale, the concrete color can be evaluated in a form close to human’s visual sense.

$$Y = 0.2126 * R + 0.7152 * G + 0.0722 * B \tag{1}$$

Fig. 7 Example of analysis area, observation points and reference point

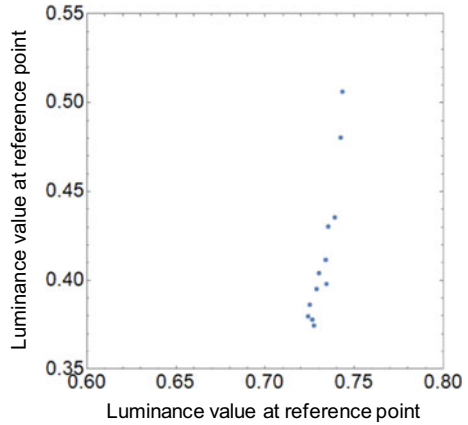


where Y is a grayscale value, R is a R value in RGB color space, G is G value in it, and B is B value in it. All ranges of R , G and B are 0–1. Hence, the range of Y is 0–1. It is completely black when Y is 0. It is completely white when Y is 1. For example, Y is 0.33357 when R is 0.3608 and G is 0.3255 and B is 0.3333.

4.2 Calculate Correlation Coefficient

The observation point which doesn't have the color change are established as the reference point (see Fig. 7). Figure 8 shows the relationship of the luminance value at the observation point and the reference point for one observation point. Its vertical axis is luminance value at observation point and horizontal axis is luminance value at the reference point. The number of dots is equal to analysis frames (12 dots in this paper). That scatter graph is output as many as the number of observation points. Finally, the correlation coefficients are calculated by the graph each observation point.

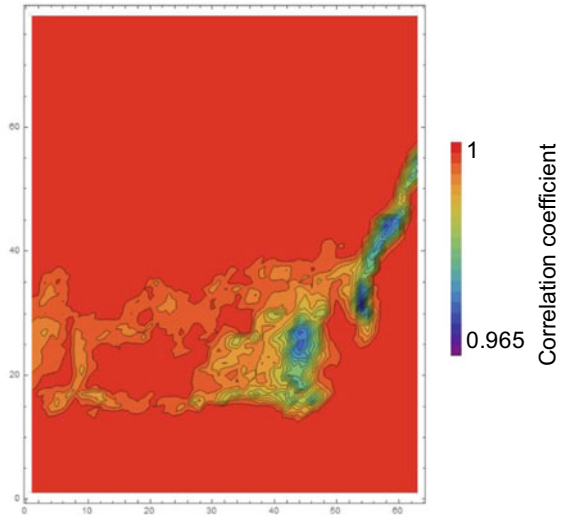
Fig. 8 Example of the relationship of luminance value between the observation point and the reference point



4.3 Distribution of Correlation Coefficients

Figure 9 shows the distribution of the correlation coefficients in analysis area. This figure is output by arranging correlation coefficients in a Fig. 7 layout. The high correlation coefficient area has correlation with the reference point and the low correlation coefficient area does not have correlation with the reference point. It means that the color change in the high correlation coefficient area is alike with the reference point. In contrast, the color change in the low correlation coefficient area is not alike with the reference point.

Fig. 9 Example of the correlation coefficient distribution



5 Results and Discussions of Image Analysis

In this section, the results and discussions of image analysis in Experiment 1, 2, and 3 are described. At first, the relationship of the luminance value at the observation point and the reference point at 0–1 h are described. Here, the observation point A to F are assigned as in Figs. 11, 14 and 17. Then, the distributions of correlation coefficient at 0–1 h are shown second. This is because the clearest color change happened at 0–1 h in Experiment 1, 2, and 3. After that, the chronological areas with the value of correlation coefficient less than 0.999 or 0.9996 (hereinafter, referred to as a color-changing band) are shown.

There was no color change at the reference point in all experiments. This means the surface color in high correlation coefficient area has a correlation with the reference point. On the other hand, the surface color in the low correlation coefficient area does not have a correlation with the reference point. In other words, high area shows non-color-changing area and low area shows color-changing area. By this image analysis, how the color changes can be understood. Finally, discussions are described on the basis of the analysis result.

5.1 Analysis Results

Experiment 1. Figure 10 shows the relationship of the luminance value at the observation point A, B and the reference point at 0–1 h. The vertical axis shows the luminance value at the observation point and the horizontal one shows that value at the reference point.

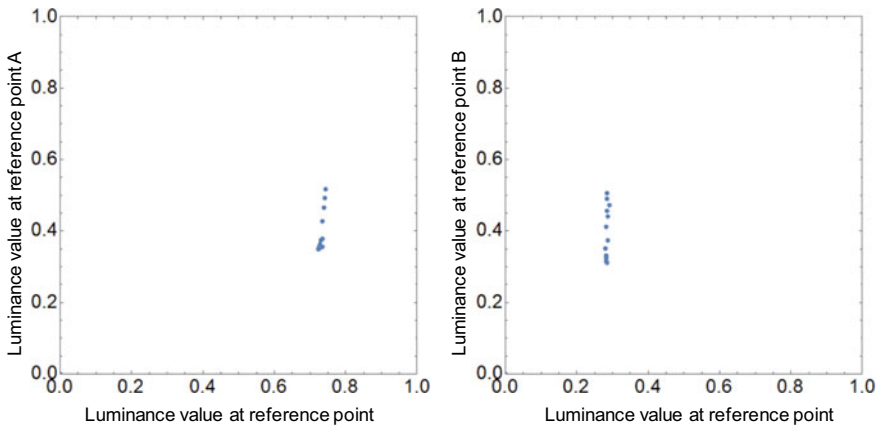


Fig. 10 Relationship of the luminance value between the observation point A, B and the reference point at 0–1 h in Experiment 1

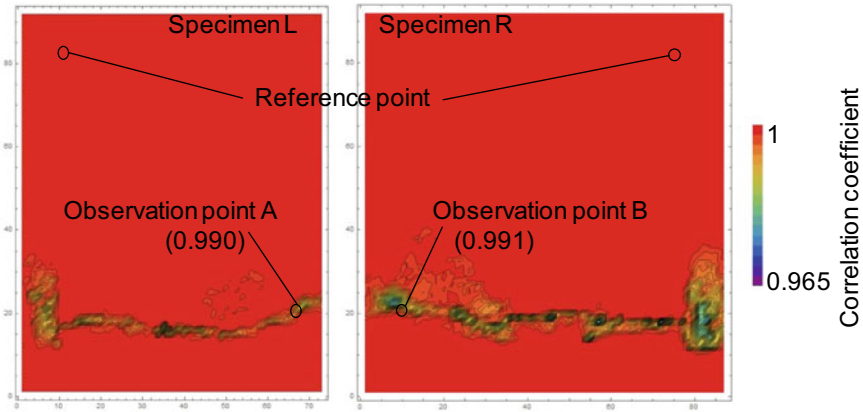


Fig. 11 Distribution of correlation coefficient at 0–1 h in Experiment 1

Both axis ranges are 0–1. The value of correlation coefficient in the observation point A and B were 0.990 and 0.991 respectively. Figure 11 shows the distribution of correlation coefficient in Experiment 1. The analysis time is 0–1 h and the value range of color bar is 0.965–1. Figure 12 shows the chronological areas with correlation coefficient less than 0.999. The time range of color bar is 0–24 h. From Fig. 12, there are some color-changing bands in both specimens. Under the 0–1 h’s band, the specimen had been wet and dark through Experiment 1. On the other hand, over the 23–24 h’s band, the specimen had been dry and bright through Experiment 1.

Left specimen was Specimen L and right one was Specimen R in Figs. 10, 11 and 12. In Specimen L, the analysis area was set to 360 pixels (570–210) in width and 380 pixels (520–140) in height from the original 1280 * 720 image. In Specimen R,

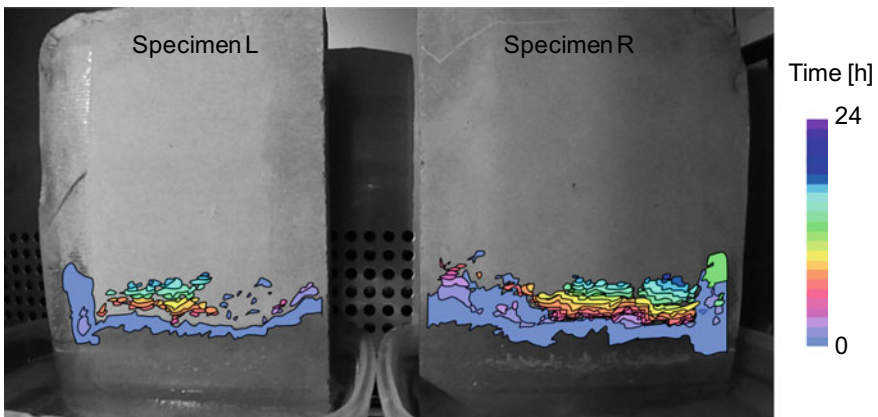


Fig. 12 Areas with correlation coefficient less than 0.999 in Experiment 1

the analysis area was the analysis area was set to 430 pixels (1150–720) in width and 380 pixels (520–140) in height from the original 1280 * 720 image.

Experiment 2. Figure 13 shows the relationship of the luminance value at the observation point C, D and the reference point at 0–1 h. The vertical axis shows the luminance value at the observation point and the horizontal axis shows that value at the reference point. Both axis ranges are 0–1. The value of correlation coefficient in the observation point A and B are 0.968 and 0.988 respectively. Figure 14 shows the distribution of correlation coefficient in Experiment 2. The analysis time is 0–1 h and the value range of color bar was 0.965–1. Figure 15 shows the chronological areas with correlation coefficient less than 0.999. The time range of color bar is 0–24 h.

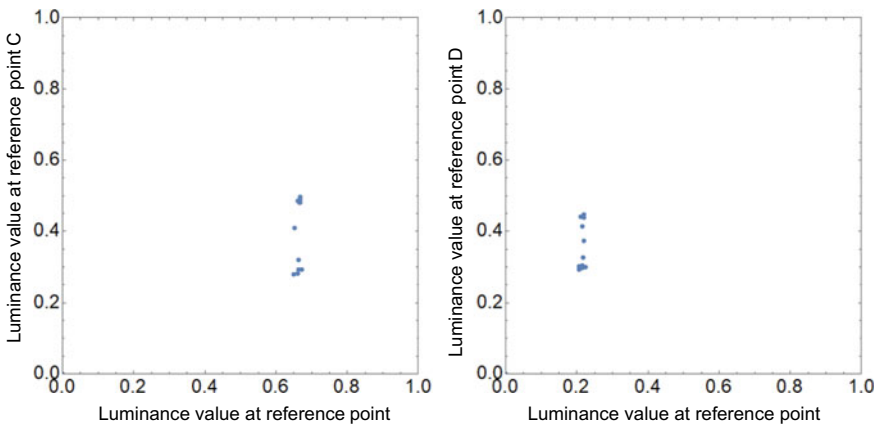


Fig. 13 Relationship of the luminance value between the observation point C, D and reference point at 0–1 h in Experiment 2

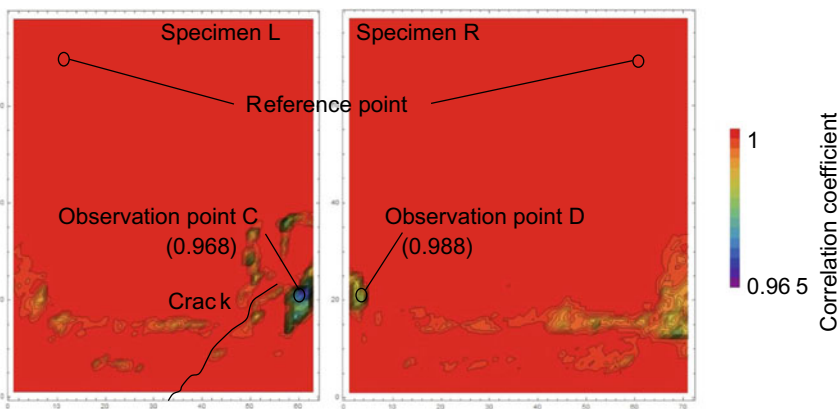


Fig. 14 Distribution of correlation coefficient at 0–1 h in Experiment 2

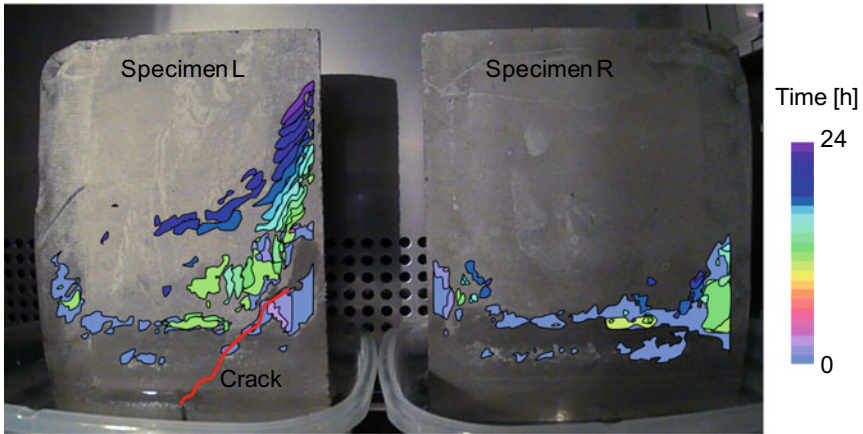


Fig. 15 Areas with correlation coefficient less than 0.999 in Experiment 2

From Fig. 15, there were some color-changing bands in both specimens. Under the 0–1 h’s band, the specimen had been wet and dark through Experiment 1. On the other hand, over the 23–24 h’s band, the specimen had been dry and bright through Experiment 1.

Left specimen was Specimen CL and right one was Specimen R in Figs. 13, 14 and 15. In Specimen CL, the analysis area was set to 310 pixels (470–160) in width and 385 pixels (480–95) in height from the original 1280 * 720 image. In specimen R, the analysis area was the analysis area was set to 350 pixels (960–610) in width and 385 pixels (470–85) in height from the original 1280 * 720 image.

Experiment 3. Figure 16 shows the relationship of the luminance value at the observation point C, D and the reference point at 0–1 h. The vertical axis shows the

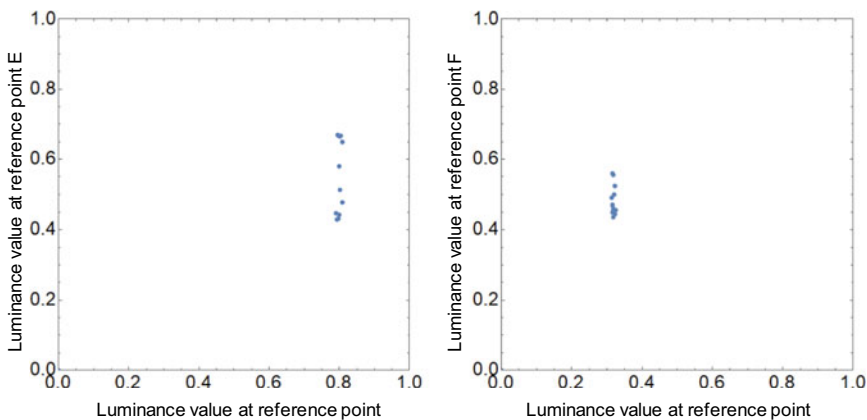


Fig. 16 Relationship of the luminance value between observation point E, F and the reference point at 0–1 h in Experiment 3

luminance value at the observation point and the horizontal axis shows that value at the reference point. Both axis ranges are 0–1. The value of correlation coefficient in the observation point A and B are 0.984 and 0.997 respectively. Figure 17 shows the distribution of correlation coefficient in Experiment 3. The analysis time is 0–1 h and the value range of color bar was 0.965–1. Figures 18 and 19 show the chronological areas with correlation coefficient less than 0.9990 and 0.9996 respectively. The time range of color bars is 0–24 h. Under the 0–1 h's band, the surface color was black always. From Fig. 19, there was some color-changing bands in both specimens. Under the 0–1 h's band, the specimen had been wet and dark through Experiment 1. On the other hand, over the 23–24 h's band, the specimen had been dry and bright through Experiment 1.

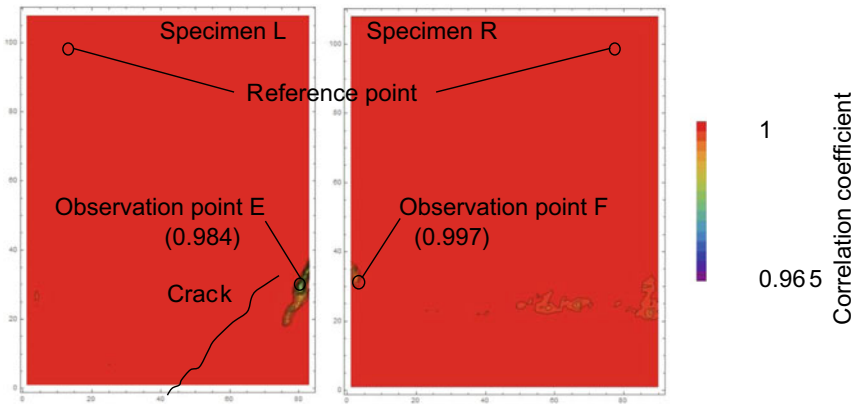


Fig. 17 Distribution of correlation coefficient at 0–1 h in Experiment 3

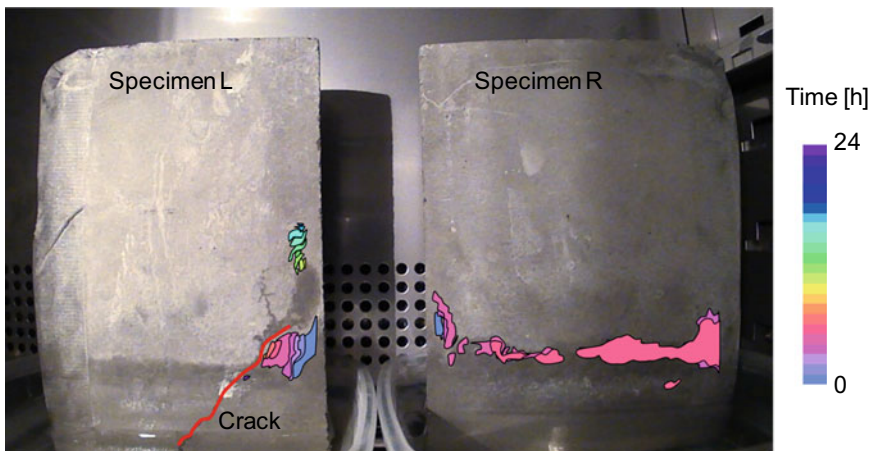


Fig. 18 Areas with correlation coefficient less than 0.9990 in Experiment 3

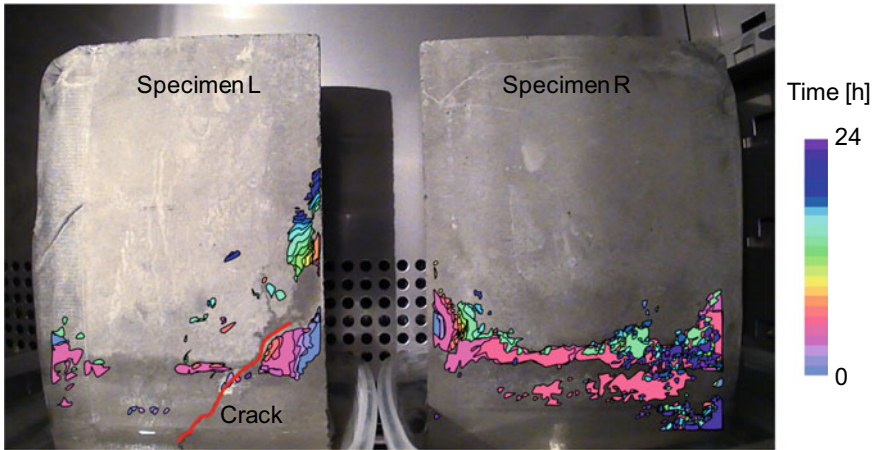


Fig. 19 Areas with correlation coefficient less than 0.9996 in Experiment 3

Left specimen was Specimen CL and right one was Specimen R in Figs. 16, 17, 18, and 19. In specimen CL, the analysis area was set to 410 pixels (550–140) in width and 535 pixels (640–105) in height from the original 1280 * 720 image. In Specimen R, the analysis area was the analysis area was set to 445 pixels (1170–725) in width and 535 pixels (640–105) in height from the original 1280 * 720 image.

5.2 Discussions

Experiment 1

In Figs. 10 and 11, the value and location of low correlation coefficient were almost the same. In Fig. 12, specimen L and R changed its color simultaneously and the behaviors of color-changing bands were the same. Based on the above, it is summarized the specimens whose mix are the same change color alike. Furthermore, it is considered the decision value of the correlation coefficient, 0.999 was enough to distinguish between color-changing area and non-color-changing area.

Experiment 2

In Fig. 13 and, the value and location of low correlation coefficient were quite different. That value of specimen CL was lower than R and that location was near the crack. In Fig. 15, specimen CL and R changed its color, but the behaviors of color-changing bands were different between two specimens. Color-changing bands of specimen CL went up parallelly to the crack. It is assumed that the specimen absorb water from the crack. Based on the above, it is summarized the crack had an influence on the surface color. Furthermore, it is considered the decision value of the

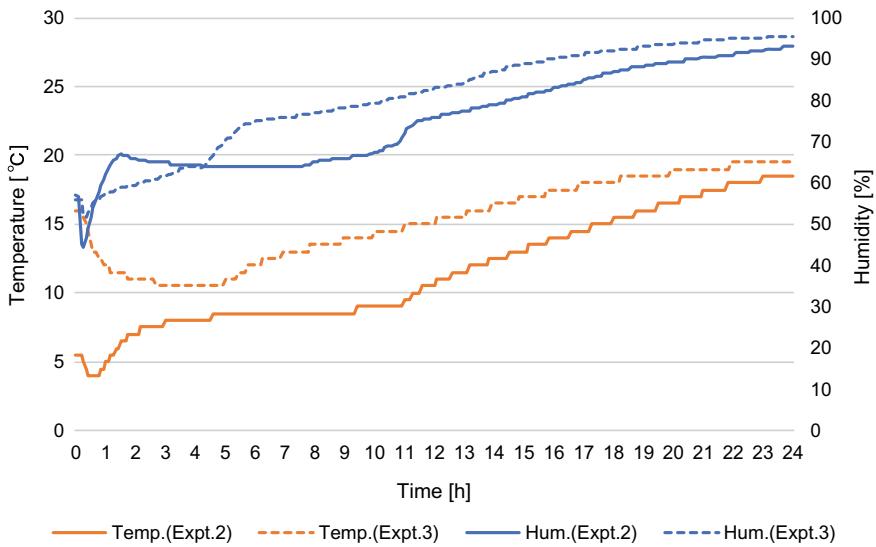


Fig. 20 Temperature and humidity history in Experiment 2 and 3

correlation coefficient, 0.999 was enough to discriminate between color-change area and non-color-changing area.

Experiment 3

In Figs. 16 and 17, the value and location of low correlation coefficient were quite different. That value of specimen CL was lower than R and that location was near the crack. In Fig. 18, there were not clear hierarchical color-changing bands like Figs. 12 and 15. On the other hand, in Fig. 19, there were hierarchical color-changing bands. Therefore, it is assumed the threshold value needs adjustment to distinguish between color-changing area and non-color-changing area. Figure 20 shows temperature and humidity history in Experiment 2 and 3.0 h means the moment when the environmental chamber was stopped. The changing gradient of temperature in Experiment 3 was gentler than that in Experiment 2. On the above, it is considered the gentler the changing gradient of temperature, the higher the decision value. However, the noise near the water surface was detected, too due to the high decision value. Furthermore, in Fig. 20, it is shown the crack had an influence on the surface color like Experiment 2.

6 Conclusion

In this study, four experiments; preliminary, Experiment 1, 2 and 3 were conducted and analyzed. The purpose in the preliminary experiment is to investigate the relationship between temperature and humidity when color change happens in an environmental chamber. One specimen was prepared and observed in the chamber. The judgement when the color change happens is made by human's visual sense. On the other hand, the purpose in Experiment 1, 2 and 3 is to investigate the difference of color change between cracked and sound concrete in the chamber. Three specimens were prepared and one of them were prepared with a crack. These specimens were observed while changing the temperature and humidity and compared about the behavior of color-changing bands by the use of image analysis. The results of four experiments are as follows:

1. The preliminary experiment yields that all color changes happened at around 17–20 °C and 80–85%. However, there is not the effective relationship between temperature and humidity when color change happened. The behaviors of temperature and humidity in all conditions were alike gradually as time goes on because the environmental chamber went through a cooling process. As a result, temperature and humidity when color change happened were all similar.
2. Experiment 1 yields that two specimens whose mix are the same have a similar trend of color change. Therefore, the sound specimens whose mix are the same change color alike.
3. Experiment 2 and 3 yield that the surface color changes parallelly to the crack. The cracked specimens have quite different trend of color change. Therefore, the crack has an influence on the surface color.
4. Experiment 3 yields that the unsuitable decision value of correlation coefficient cannot discriminate between color-changing area and non-color-changing area. The decision value needs adjustment according to the environmental condition. Furthermore, the gentler the changing gradient of temperature, the higher the decision value.

Since this paper is limited to analysis of the color change on cracked and non-cracked concrete, how to determine the decision value and the analysis on other deteriorated concrete will be studied in the future. Besides, the analysis to detect what deterioration happen on the concrete by the use image analysis will also be carried out.

References

1. Konkurito kouzoubutu no hosyu · hokyo hensyuiinkai (Maintenance of Concrete Structure Committee) (2016) Repair reinforcement of concrete structures. Industrial Technology Service Center, pp 13–17

2. Public Works Research Institute Nippon Structural Inspection and Technology Association (2003) Hihakaishiken womotita doboku konkurito kozobutsu no kenzendo shindan manyuaru (Soundness diagnosis manual of concrete structure by nondestructive testing). Gihodo Publishing
3. Koshikawa S, Ogihara Y (1991) Method of testing capillary infiltration of concrete. *J JSCE* 426(V-14), 188–189
4. Iwasaki I (1975) *Konkurito no tokusei* (The character of concrete). Kyoritsu Publishing, pp 123–126
5. Akita H, Fujiwara T, Ozaka Y (1990) Water movemet within mortar due to drying and wetting. *J JSCE* 426(V-13):62–63
6. Kusuhaawa C, Ishida T, Maekawa K (2004) Semento koukakai tyuni sonzaisuru ekijosuiryo no ondoizonsei to jikankoka (Temperature dependence and time effect of liquid water content in hardened cement paste). *J Japan Concr Inst* 26(1):580–582
7. Iwasaki N (1975) *Konkurito no tokusei* (The character of concrete). Kyoritsu Publishing, pp 142–143 (1975).
8. Ogino K, Ujike I (2000) Hibiwarebu no tosuisei oyobi toukisei ni eikyo wo oyobosu yoin ni kansuru kenkyu (Study on the factor that influences water and air permeability around crack). *J Japan Concr Inst* 22(2):812–816
9. Hayano H, Noguchi T, Tochigi N (2007) Influence of surface roughness of crack on water tightness of concrete. *J Struct Constr Eng AIJ* 615(25–30):26–29
10. Fujiwara T, Ishida H, Sato K, Konishi T (1989) *Konkurito tyuno suibunidou niyobosu kankyo-ojyoken oyobi haigo no eikyo* (The effect of environment and mixture propotion on water transfer in concrete). *J Japan Concr Inst* 1989(11–1):225–226
11. Kudo M, Simomura T (2019) *Konkurito buzai heno mizu no shintou kansou ni oyobosu hibiware no eikyou ni kansuru jikken to sutikaiseki* (Experiment and numerical analysis on the effect of cracks on water penetration and drying of concrete members). *J JSCE-E2* 75(3):196–207
12. Ryu DW, Ko JW, Kanematsu M, Noguchi T (2007) Study on the moisture distribution in concrete associated with change of environmental conditions. *J Struct Constr Eng AIJ* 612:5–6
13. Stokes M, Anderson M, Chandasekar S, Motta R (1996) A standard default color space for the internet—sRGB, <https://www.w3.org/Graphics/Color/sRGB.html>. Accessed 2020/10/14
14. International Telecommunication Union: Parameter values for the HDTV standards for production and international programme exchange. https://www.itu.int/dms_pubrec/itu-r/rec/bt/R-REC-BT.709-6-201506-I!!PDF-E.pdf. Accessed 2020/10/14
15. Kishino F, Sato T, Yokoya N, Aizawa K, Arikawa M (2000) *Gazo to Kukan no Johosyori* (The date processing of images and spaces). Iwanami Publishing, pp 48–49

Dynamic Formation of Spontaneous Corrugation on Sand Surface Due to Repeated Loading of Moving Vehicle



Shunji Kanie, Hao Zheng, Kai Hashimoto, and Risa Endo

Abstract Washboard road on snowy-icy road in Hokkaido is a well-known phenomenon. It spontaneously appears several times a year due to moving vehicles. However, the formation mechanism has not yet been verified physically and mathematically. The authors developed their original experimental apparatus to reproduce the spontaneous corrugation on dry-sand condition in laboratory. Through the experiments, we confirmed that the running velocity of vehicle is one of the dominant factors for the formation of corrugation and the amplitude of the wave increases with the velocity of vehicle. In addition to the dynamic formation experiments, the authors carried out a static penetration test to obtain a relationship between the vertical settlement of surface material and the force given by the wheel. As a result, the relationship between the settlement and the force can be expressed as an almost linear function for loading and unloading. However, the residual settlement after loading is relatively large and the material shows an inelastic behaviour. The dynamic motion of the oscillator is simulated by a time-domain technique with a simple model of single degree of freedom. By introducing the plastic deformation of the surface material based on the penetration test, we successfully constructed a numerical model for imitating the corrugation process even if it may need some modification on the movement of surface material for more precise simulation. We believe that the accumulation of knowledge on the spontaneous corrugation with dry sand leads to the elucidation of formation mechanism of the phenomenon on snowy-icy road.

S. Kanie (✉) · H. Zheng
Faculty, Hokkaido University, Sapporo 0608628, Japan
e-mail: kanie@eng.hokudai.ac.jp

H. Zheng
e-mail: zhenghao@ec.hokudai.ac.jp

K. Hashimoto · R. Endo
Hokkaido University, Sapporo 0608628, Japan
e-mail: kai81@eis.hokudai.ac.jp

R. Endo
e-mail: lisa-mame33@eis.hokudai.ac.jp

Keywords Spontaneous corrugation · Formation · Moving vehicle · Indoor experiment

1 Introduction

In winter Hokkaido, appearance of washboard road on snowy-icy road is broadly known as a mysterious phenomenon. It spontaneously emerges on snowy-icy road several times a year due to moving vehicles, and it endangers motor drivers and pedestrians because of loss of sufficient friction between road surface and tires. Figure 1a shows a typical example of washboard road on snowy-icy road observed in Hokkaido. However, the formation mechanism has not yet been verified physically and mathematically as well as the formation process. Therefore, it is almost impossible to predict the occurrence and to apply some effective countermeasures for prevention. In order to establish a maintenance technology for washboard road, the authors are investigating this phenomenon with an indoor reproduction experiment [1] and field observation by time-lapse cameras [2]. This paper aims to introduce the results of indoor experiments with a simple numerical model to understand the fundamental mechanism of spontaneous corrugation on dry sand.

The phenomenon of spontaneous formation on unpaved road has been known for long time. Figure 1b) shows an example of washboard road on dry gravel road [3]. In Japan, Takeshita et al. [4] reported their observation results about the corrugation appeared on unpaved road in 1954 with the phrase of ‘Soroban (Abacus in Japanese) road’. They considered that the washboard road is likely to happen when the road surface is in dry condition. For example, corrugation on unpaved road is frequently observed during summer because moisture in soil easily evaporates into the air. They also mentioned the phenomenon is caused by both of external and internal factors. One of the formers is the natural frequency of vehicle which is decided by the spring coefficient and the damping constant equipped on a vehicle. On the other hand, the material properties of surface are the latter. It can be easily imagined that dry and fine sand is easily rolled up and blown off by the centrifuge of rotating wheel, whereas



(a) Snowy Icy Road



(b) Unpaved Road [3]

Fig. 1 Examples of corrugation patterns

cohesive moist clay is not likely to scatter. The mobility of surface material is thought as an important factor of the formation.

Similarly, in Europe, various researchers have studied the phenomenon with empirical and theoretical approaches [5, 6, 7]. Interesting is that similar corrugation pattern also appears on farmland when an agricultural tractor drags plow or hoe [8]. The authors developed their original experimental apparatus to reproduce the phenomenon in laboratory. Since the model scale of the experiment including the model vehicle is rather small, we adopted fine granular sand as a surface material and investigated the growing process of corrugation. In this paper, we introduce some interesting findings in the experiments as well as our numerical model to explain the formation process on dry sand surface.

2 Indoor Reproduction Experiment

The authors introduce here the indoor reproduction experiment with dry sand. We have understood that the physical mechanism of the formation on dry sand cannot sufficiently explain the occurrence of corrugation on snowy-icy road because the formation on snowy-icy road is caused by some thermochemical reactions among ice, snow and water. Therefore, we may have to learn those physical and thermochemical interaction including the formation of penitentes [9], for example. However, we believe that fundamental knowledge on the physical process should be accumulated through the experiments with dry sand.

2.1 Experimental Setup

The experimental apparatus is shown in Fig. 2. It consists of a self-rotating track (Fig. 2a) and a seesaw-shaped oscillator (Fig. 2b). The radii of the outer and the inner boundaries of the track are 50 and 41 cm respectively. The surface material is filled between those two circular boundaries. The authors adopted Toyoura sand, which is designated as a fine granular sand with an average particle size of 0.2 mm

Fig. 2 Experimental apparatus

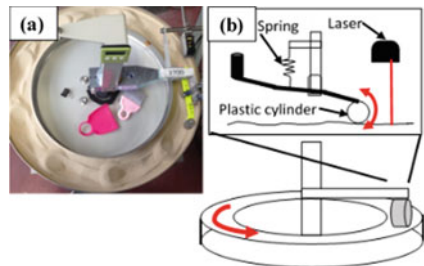
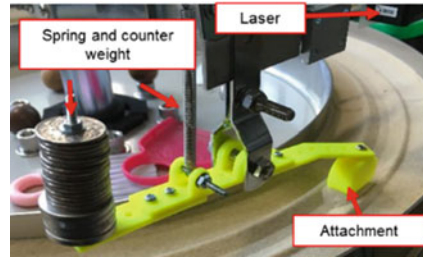


Fig. 3 Seesaw-shaped oscillator



by the Japanese Industrial Standard. The rotation velocity of the rotating truck can be controlled arbitrarily and precisely from 0 to 20.0 rounds per minute (rpm). The maximum velocity of the rotating track at 20.0 rpm is about 0.5 m/s. The seesaw-shaped oscillator is fixed at the end of a cantilever beam extending from the rotational axis of the track. A laser displacement sensor set just behind the oscillator records time-dependent change in height of the surface material with a sampling frequency of 100 Hz (Fig. 3).

The total length of the seesaw-shaped oscillator is 14.2 cm. A soft spring is equipped at the midst of the arm to allow oscillation. An attachment imitating a wheel is mounted at one end of the arm and pendulum is loaded at the other end. It becomes possible to control the natural frequency of the oscillator as well as the loading magnitude at the contact with surface material by changing the weight of pendulum. In this experiment, the attachments do not roll unlike a real wheel and are dragged on the road surface. It is obvious that the oscillator plays an important role in our reproduction experiments.

The procedure of experiment starts with flattening the road surface. The self-rotating track revolves at a slow velocity of 2–3 rpm for several minutes to scour the surface by a fixed scraper. After confirming the surface roughness with monitoring the record by the laser sensor, the rotating velocity is increased to a target speed, and the track keeps rotation constantly and continuously for 7 min. The change in height of the road surface measured by the laser displacement sensor is recorded in a data logger.

2.2 *Experimental Results*

We thought that the running velocity of vehicle is one of the dominant factors. Then, we conducted experiments with various velocities of the track rotation increased from 10 to 19.5 rpm. Figure 4 shows running spectrums of corrugation in which the colors indicate the height of surface. The horizontal axis of the figure represents the location of track, and the vertical axis stands for the number of rotations with time. At the beginning of the rotation located at the bottom of the vertical axis, for example, the horizontal zones along the axis are colored with light green in any cases. It means that the height of surface is almost flat at any location of the

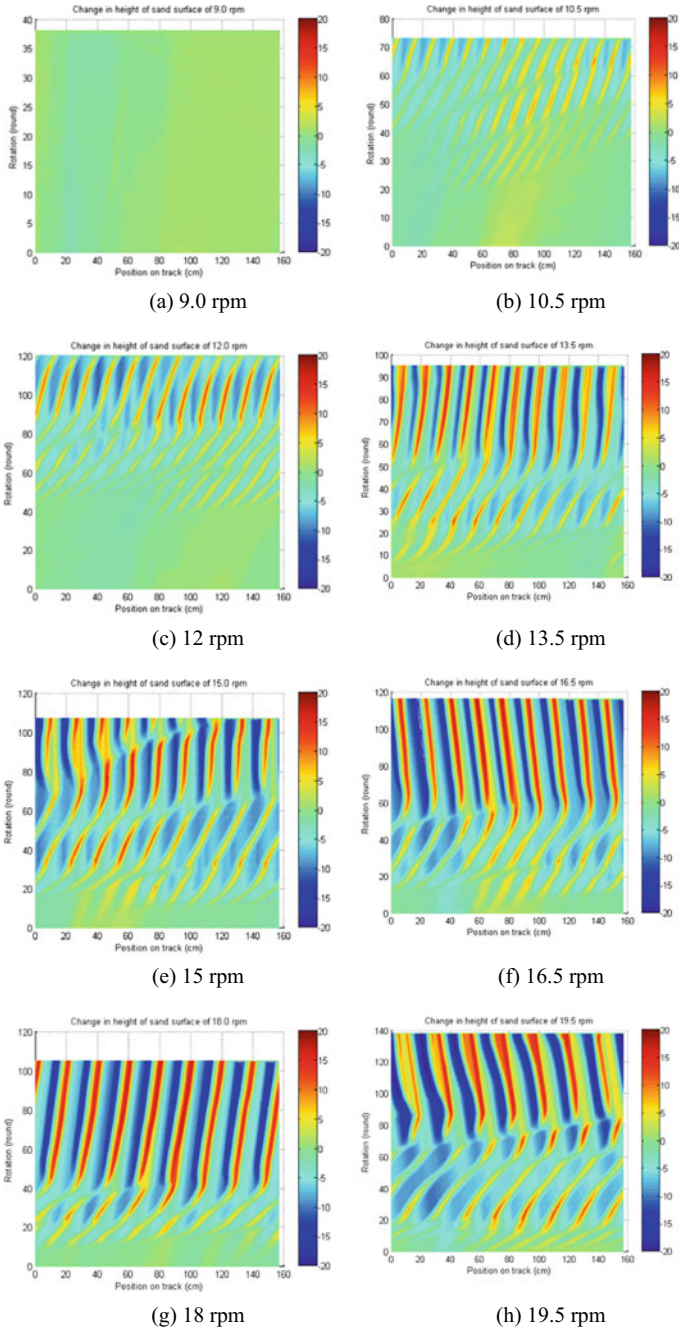


Fig. 4 Running spectrum of each track rotation velocity

Table 1 Comparison of experimental corrugation

Velocity (rpm)	Wave number	Max amplitude (mm)	Peak frequency (Hz)
10.5	14	11.77	2.25
12.0	12	12.66	2.34
13.5	10	16.17	2.25
15.0	9	19.01	2.25
16.5	9	20.41	2.44
18.0	8	20.07	2.44
19.5	7	19.37	2.25

rotating track. By keeping the experimental velocity of rotation, the road surface gradually fluctuates from the initial flat condition. Accumulating the number of rotations towards upward direction in the figure, the areas are colorized with red and blue because the corrugation gradually grows. By those figures, the growing processes of corrugation are visualized. Interesting is that the convex part of the corrugation slowly shifts in backward or in forward, and the shifting directions are depending on the rotation velocity. In addition, the maximum height of the wave is increasing with the rotation velocity. At the rotation velocity of 9.0 rpm shown in Fig. 4a, the surface was kept flat throughout the experiment and no waves were observed. As the rotation velocity increases, the amplitude of the wave is gradually increased.

Table 1 shows the experimental results at the end of each experiment, such as the number of waves formed on the track, the maximum amplitude of the road surface and the frequency of the wave on road surface. We used an oscillator with a natural frequency of 1.66 Hz in those experiments. It is found that the faster the track rotation velocity is, the earlier the formation of wave begins. From this table, it is recognized that the maximum amplitude of the wave gradually increases with the rotation velocity, and it converges to around 20 mm at the rotation velocity of 16.5 rpm or larger. As the rotation velocity of the track increases, the wavelength also increases while the wave number on the track decreases. As a result, the peak frequency of the wave shown on the track is kept constant at approximately 2.25–2.44 Hz, and it is larger than the natural frequency of the oscillator. From those above, it can be said that the occurrence of corrugation is significantly depending on the rotation velocity of the track.

2.3 Effects of Shapes and Surface Materials

The shape effect of the attachment on the formation of corrugation is very interesting as a physical phenomenon. Then, we prepared several different shapes of the attachments as shown in Fig. 5 in addition to the cylindrical one. Three attachments in

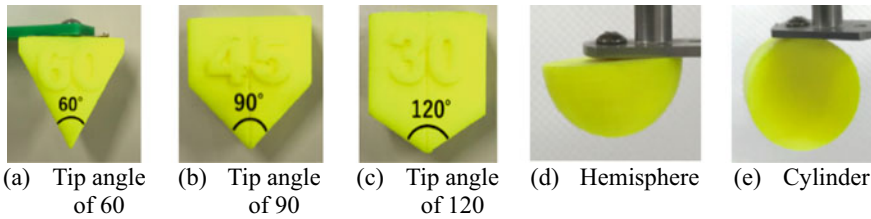


Fig. 5 Various shapes of attachment

triangular shape have different tip angles of 60, 90 and 120 degrees, and a hemisphere is another type of the attachment. All the attachments are made of acrylonitrile butadiene styrene plastic. According to our literature survey, washboard road appears not only on unpaved road with sand or gravel but also on farmland by dragging plow or hoe. The attachments in triangular shape are modelling plows with different contact angles to the surface. The authors thought that the contact angle to the surface along the longitudinal direction is one of the important factors to decide the shape of corrugation. Similarly, the contact angle to the surface in the transverse direction might give some effect on the shape. Then, a hemisphere-shaped attachment was provided in addition to the standard type of attachment in cylindrical shape. We conducted the reproduction experiments using those attachments.

At the same time, the authors thought that the material property of surface is another factor to determine the formation of corrugation. We changed the moisture content of sand from dry to over saturated conditions. Since there are plenty of combinations with shape of attachment, material property and rotating velocity, we summarized the results in Table 2 as an example of comparison. The tip angle of triangular attachment shown in this table is fixed at 90 degrees and the results for moisture content of 70% is compared with those under dry and over saturated conditions. The figures in the table are indicating the wave numbers on the track after the convergence.

When the surface material includes moisture, the triangular attachment is likely to generate corrugation on the road surface by comparing with those by cylindrical

Table 2 Wave numbers under different conditions

Sand condition		Shape of attachment	Rotation velocity (rpm)	
			12 rpm	15 rpm
Dry		Cylinder	11	8
		Triangular	10	8
Wet	Around 70%	Cylinder	Slightly	Slightly
		Triangular	13	10
	Over saturated	Cylinder	None	None
		Triangular	13	9

attachments. In addition, it can be said that spontaneous corrugation is likely to occur under less moist condition of the surface material and this fact endorses the findings by Takeshita et al. [4]. In Fig. 6, the running spectrums of the experimental results are shown to compare the effect of moisture content. The shape of the attachment for those is a cylindrical one.

Based on the study above, it became obvious that the deformation ability of surface material is very important as well as the shape of attachment. For example, dry sand is more deformable than that in wet condition under a same force magnitude. In order to propose a mathematical model for spontaneous corrugation, the authors decided to verify the deformability of material by a penetration test described in the next section.

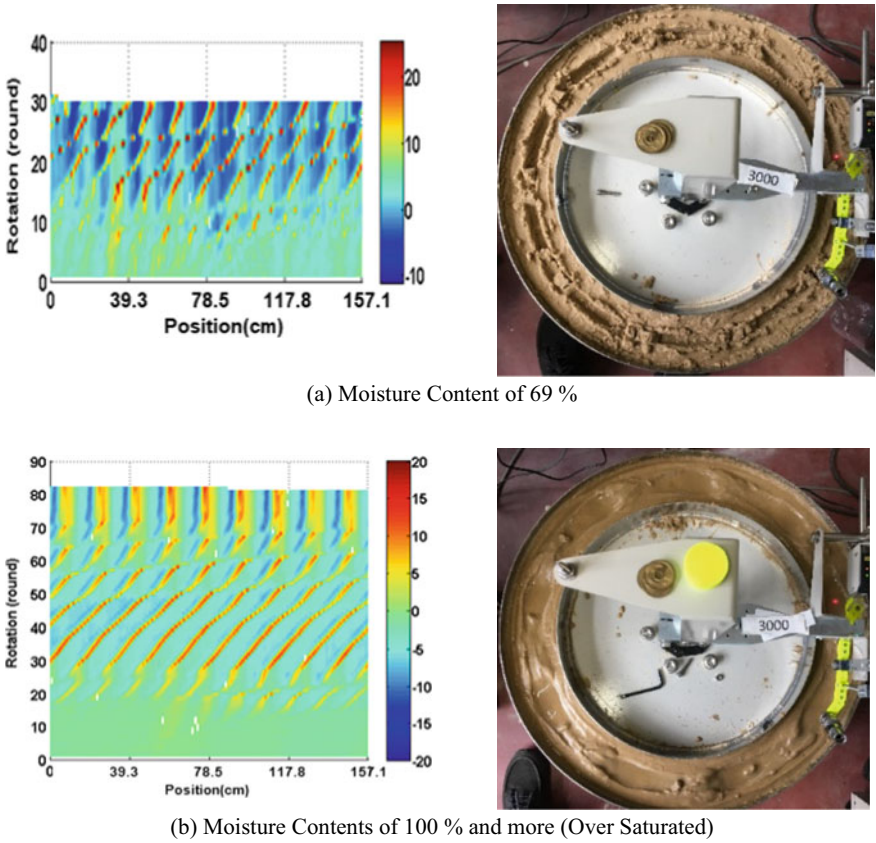


Fig. 6 Experimental results with different road surface condition

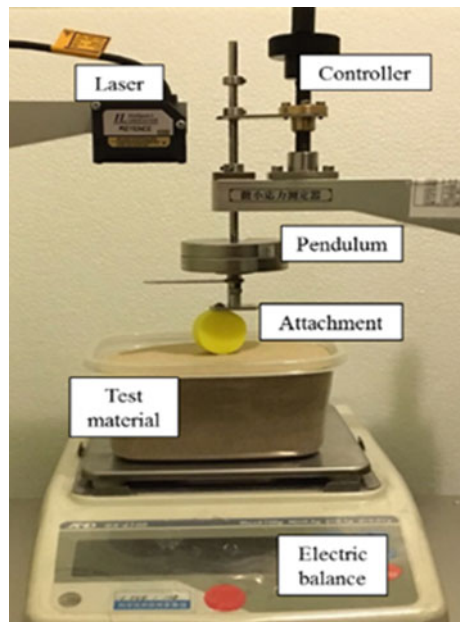
3 Penetration Test

Due to some dynamic action of force transmitted by wheel, the surface material settles, bounces and migrates. As a result, it finally causes the formation of washboard road. Therefore, it is obviously important to know the interaction between the wheel and the surface based on the deformation ability of surface material. The authors provided a static penetration test device to confirm the deformation ability of sand.

3.1 Experimental Setup

The penetration test device is shown in Fig. 7. An attachment imitating a wheel is fixed at bottom end of a metal rod, and a weight of 5 N is loaded at the top to apply downward force to the surface material through the attachment. As a fine sand material representing road surface, we adopted Toyoura standard sand which is same as the material used in the reproduction experiments. Toyoura standard sand is one of typical fine sands in Japan with an average granular size of 0.2 mm. By controlling the vertical displacement measured with a laser displacement sensor, the attachment gradually settles down into the surface material put on an electronic balance. The real interactive force between the attachment and the surface material is recorded by the electronic balance. When the attachment penetrates to the deepest position under a maximum load magnitude given to the top of the rod, the loading phase is ceased. In

Fig. 7 Penetration test instrument



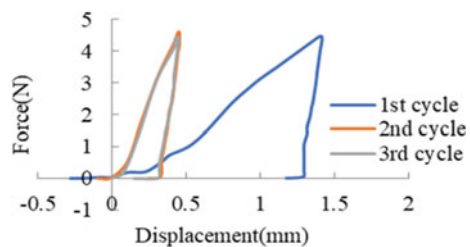
the unloading phase, however, a displacement-control procedure cannot be applied because the surface material shows an inelastic behaviour and the major part of the vertical displacement given by the loading phase is thought as a residual settlement. Therefore, the unloading is completed when the loading magnitude gets back to almost 0 N. We repeated loading and unloading three times in this manner for each experiment and the relationship between the penetration depth and the magnitude of interactive force was investigated.

3.2 Experimental Results

Figure 8 illustrates the relationship between the penetration depth and the downward force magnitude for the cylindrical attachment with dry sand. In the loading phase, the displacement linearly increases with the force magnitude regardless of the number of repetitions. The increment in the penetration depth for the first cycle is much larger than those of second and third cycles because the surface material is not sufficiently compacted and migrated in the first cycle. Therefore, the increment in the penetration depth for the second and third cycles becomes smaller than that in the first cycle. In other words, the deformation ability of the material is largest in the first cycle and it becomes lessened with the repetition. After the first cycle of loading and unloading, it seems that the sand surface has already been deformed in inelastic range. In the unloading phase, the displacement shows a slight recovery from the deepest position of settle down. It means that the major part of the deformation due to loading remains as a residual deformation. Then, the authors considered that the deformation of the material has already been in a plastic range and this behavior is introduced in our mathematical model.

For comparison of shape effect, Fig. 9 shows the experimental results of the relationship between the penetration depth and the force magnitude in their first cycles. It is found that the rate of increase in the displacement due to force strongly depends on the shape of attachment. Those results seem very natural since the steepness of the tip angle has a significant effect on the penetration ability of the attachment. For example, the steepest one with a tip angle of 60 degrees easily settles down with the least force magnitude. When the tip angle becomes larger from 60 to 120 degrees, greater force is required to obtain a same penetration depth. Similarly, we

Fig. 8 Relation between depth and force magnitude



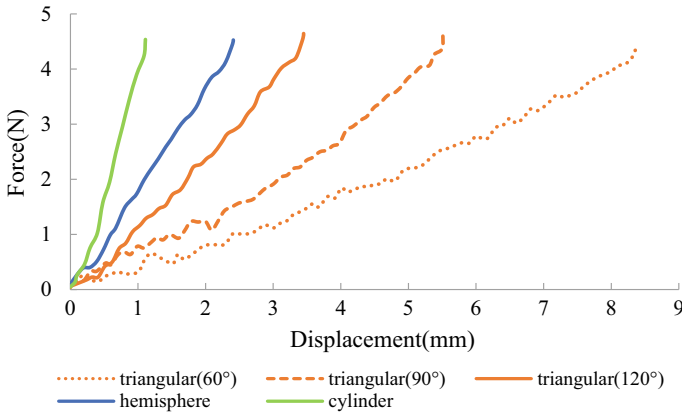


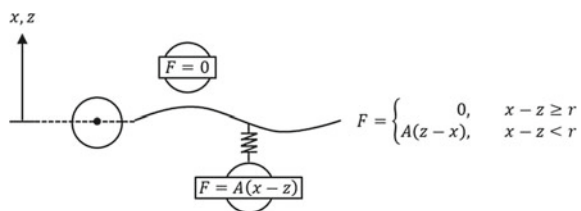
Fig. 9 Relationship between displacement and force for different shapes of attachment

also found clear difference between the cylindrical and the hemisphere attachments. The difference in their rates of increase is caused by the shape effect in the transvers direction to the driving track. From those results, it is concluded that the steeper the tip angle of the attachment becomes, the larger the force magnitude to induce a same penetration is.

4 Numerical Model and Analysis

The dynamic motion of the oscillator can be described by a simple equation for single degree of freedom as shown in Eq. (1). The oscillator has a counterweight representing m at the tail and a spring with a spring coefficient of k near the middle of the arm. We set a damping coefficient of suspension as c . The height of the attachment is expressed as x , and the external force applied to the attachment from the road surface is given as F . As shown in Fig. 10, the top surface of the road is assumed as z and the reaction force from the road material is assumed to work only when the attachment touches the road surface. The magnitude of the force is estimated as a function of $(z-x)$ and the linear constant of A is decided by the penetration test. Since the road surface deforms plastically in the experiment, the deformation of the

Fig. 10 Setting of external force F



road surface caused by F never behaves elastically and it is assumed that the height of surface keeps its deformed position after unloading.

$$m\ddot{x} + c\dot{x} + kx = F(t) \tag{1}$$

In the numerical model, it is necessary to give some initial roughness on the surface to promote the spontaneous corrugation. We adopted a sinusoidal wave with an amplitude of 1 mm. In order to confirm the effect of initial condition, we gave different wave frequencies of 1, 2, 4 and 8 Hz as an initial roughness. Figure 11 shows the calculation results with different initial conditions. However, the formation processes of those look very similar regardless with the initial roughness, and the model satisfactorily imitates the formation process. Figure 12 compares the relationships between the rotation velocity of the track and the wave number on the road surface by the numerical analysis with those observed by the experiments. The natural frequencies of the oscillators are 1.49 Hz for the analysis and 1.46 Hz for the experiments. The wave numbers of those are similarly decreasing with increase in the rotation velocity of the track. Even though the analytical solution slightly underestimates the wave numbers observed in the experiments, those difference comes from the evaluation in the migration of surface material due to the plastic deformation and it can be improved by the modification in the migration modelling of surface material.

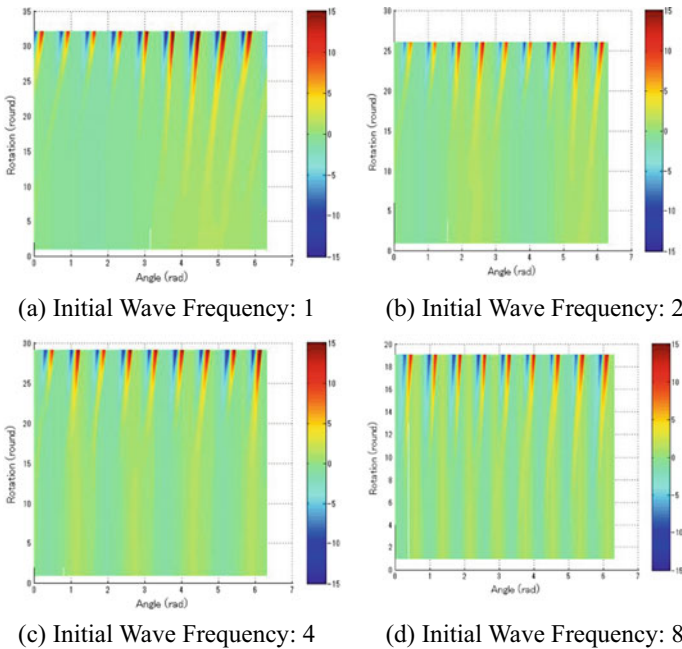
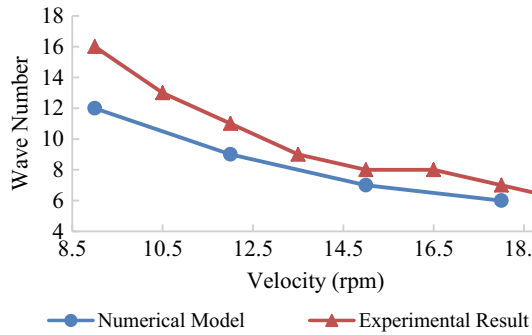


Fig. 11 Comparison of running spectrums with different initial fluctuation

Fig. 12 Relationship between track rotation velocity and wave number



The authors are convinced of that the numerical model we proposed is practically applicable for the estimation of the formation process.

5 Conclusions

We investigated the spontaneous corrugation patterns of dry sand on the self-rotating track formed by the oscillator. It is confirmed that the rotation velocity of the track is one of the dominant factors for the formation of corrugation and the amplitude of the wave increases with the rotation velocity. The effect of the shape of the attachment is also verified by the experiments as well as the effect of the moisture content of surface material. By the penetration test, relationship between the vertical displacement driven into the test material and the force applied from the attachment was discussed. As a result, the relationship between the displacement and the force can be expressed as a linear function for loading and unloading but the behaviour of the material shows an inelastic property. The dynamic motion of the oscillator is calculated by a time-domain technique with a simple model of single degree of freedom. By introducing the plastic deformation of the surface material based on the penetration test, we successfully constructed a numerical model for imitating the corrugation process even if it may need some modification on the movement of surface material for more precise simulation. The authors are now improving the oscillator which has a revolving attachment like a real wheel and are investigating the phenomenon more realistically. We believe that the accumulation of knowledge on the spontaneous corrugation with dry sand leads to the elucidation of formation mechanism of the phenomenon on snowy-icy road and it contributes to the establishment of road management technology in winter Hokkaido.

Acknowledgements This work was supported by KAKENHI Grants No. 16K01278 of Japan. The authors would like to express our gratitude to Yasuhiro Kaneda and Yasuhiro Nagata of Hokkaido development engineering center (DEC) as well as Mr. Teeranai Gartoon Srimahachota, a doctoral candidate of our school.

References

1. Srimahachota T, Zheng H, Sato M, Kanie S, Shima H (2017) Dynamics of washboard road formation driven by a harmonic oscillator. *Phys Rev E* 96(6):062904
2. Kanie S, Zheng H, Yokomise D, Kaneda Y, Nagata Y, Masaki Y (2016) A study on a growing process and its conditions of Soroban road based on observation with fixed point cameras (in Japanese). In: Proceedings of Hokkaido chapter of the Japan society of snow and ice, annual report on snow and ice studies in Hokkaido, vol 35. pp 55–58
3. Mays DC, Faybishenko BA (2000) Washboards in unpaved highways as a complex dynamic system. *Complex* 551–560
4. Takeshita H, Kobayashi K (1954) Soroban road: corrugation of roads with gravel (in Japanese). *Road Eng Manage Rev* 54(2):69–71
5. Both JA, Hong DC, Kurtze DA (2001) Corrugation of roads. *Physica A* 301: 545-559. Elsevier
6. Taberlet N, Morris S, McElwaine J (2007) Washboard road: the dynamics of granular ripples formed by rolling wheels. *Phys Rev Lett PRL* 99:068003. The American Physical Society. <https://doi.org/10.1103/PhysRevLett.99.068003>
7. Bitbol A, Taberlet N, Morris SW, McElwaine JN (2009) Scaling and dynamics of washboard roads. *Phys Rev E* 79:061308. The American Physical Society. <https://doi.org/10.1103/PhysRevE.79.061308>
8. Percier B, Manneville S, McElwaine JN, Morris SW, Taberlet N (2011) Lift and drag forces on an inclined plow moving over a granular surface. *Phys Rev E* 84:051302, The American Physical Society. <https://doi.org/10.1103/PhysRevE.84.051302>
9. Claudin P, Jarry H, Vignoles G, Plapp M, Andreotti B (2015) Physical processes causing the formation of penitents. *Phys Rev E* 92:33015, The American Physical Society

Assessment and Back Analysis of a Swaying-Jetty in Dumai Indonesia



Merdeka Sandi Tazakka, M. Adecar Nugroho, and Budiwan Adi Tirta

Abstract A Jetty structure was constructed as a berthing facility for 50,000 DWT vessels at Dumai, Indonesia. After the construction finished, the main jetty tended to sway frequently, and this was easily noticed by people who stand on the top of the deck. An investigation had been carried out to identify what causing this problem to check the performance of the jetty. A full review of design and construction documentation, direct observation of existing structures included the field vibration measurement tests, and new soil investigation campaign had been carried out as part of the investigation. After the new soil investigation, the soil profile at the jetty location was found to be worse than expected, since the borehole used for design was located 90 m distance from the main jetty and hence could not represent the actual condition. This finding led to a main concern on the global stiffness of the structure. Remodelling was conducted accordingly to evaluate the actual performance of the main jetty. The result showed a good agreement with data from field measurements (e.g., vibration test) and confirmed the earlier concern, whereas this jetty has structural stiffness issue in which may result in sway effect. The structural analysis indicated that the existing main jetty may experience an excessive displacement of more than 100 mm allowable displacement under SLS condition, and hence mitigation measures are needed to be taken.

Keywords Jetty assessment · Back analysis · Swaying jetty · Marine structure vibration test

M. S. Tazakka (✉) · M. A. Nugroho · B. A. Tirta
PT. Witteveen+Bos, Port and Geotechnics Department, Jakarta, Indonesia

M. A. Nugroho
e-mail: Adecar.Nugroho@witteveenbos.com

B. A. Tirta
e-mail: Budiwan.Tirta@witteveenbos.com

1 Background

Dumai district is one of Indonesia's central industrial area for oil and crude palm oil that is located in Riau Province in Sumatra Island. Many ports are built here to support the growth of industries. Dumai district, which is located on the Dumai Strait, is bounded by tectonic faults [1]. It is known that these faults have shaped the Dumai Strait in combination with erosion during a period of low sea level. During the sea-level rise, this trough has been filled with thick covers of sediment [2]. According to the research by Rifardi [3], Dumai Strait was becoming a deposit area of sediments that were transported from both the Indian Ocean and the South China Sea, lead to quite some thickness of the soft deposit layer dominating the top layer of the seabed in the area.

In 2016, a jetty structure was constructed for a berthing facility of a maximum 50,000 DWT vessel. After the construction finished, this jetty was supposed to be directly operated by the project owner, at least in early 2017. However, prior to the operation, the jetty tended to sway and seemed unstable. The main jetty was found to sway not only during the high water spring event (HWS) but also during the low water spring event (LWS). The intensity of the sways was considered unusual compared to a normal jetty (before service condition). The sways were noticeably by the people standing on top of the deck.

An investigation was carried out, which consisted of new soil investigation on the constructed jetty area along with direct observational data of the jetty to identify the problems. The acquired data was then used as an input for back analysis to assess the condition, and field instrumentation of natural vibration test were used to calibrate the model. Sways problem in jetty is known to occur due to the lack of the stiffness of the structural components. The sways problem can also relate to the global stiffness of the structure itself due to the bad soil-structure interaction.

2 Existing Jetty Structure Configuration

2.1 Jetty Configuration

The main jetty is connected to the land via trestle and equipped with four mooring dolphins, four berthing dolphins, and one platform, as presented in Fig. 1. The main jetty is an island type of open pile structure with berthing elements. The berthing elements are three massive concrete blocks, each supported by a pile group of 8 piles. Beam and floor systems are installed in between these blocks. The longitudinal beam and top slab are precast concrete structures. The finishing of the top slab is in-situ concrete with 15 cm thick topping. The as-built length of the main jetty is approximately 100.5 and 17 m width.

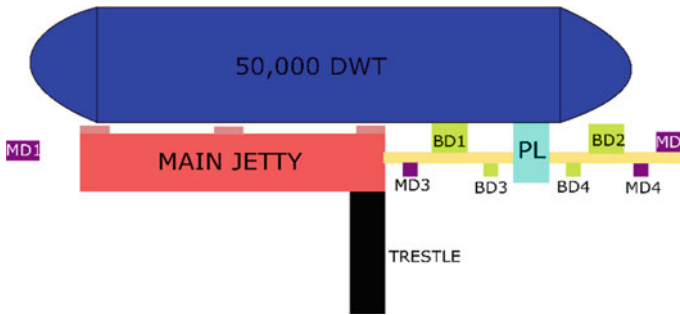


Fig. 1 Jetty structures layout configuration sketch

2.2 Pile Configuration of the Main Jetty

The main jetty’s foundations are configured as nine grids total, and each grid is installed with a series of piles. The main jetty has three grids as berthing elements with eight inclined piles each berthing elements’ pile group. Other than the berthing elements grids, each grid has three installed piles per-grid. In general, the main jetty grids’ piles have a transverse center to center distance of 3500 mm and have 11,500 mm center to center distance in the longitudinal direction. The deck design elevation is +5 m LWS, and the top pile main jetty is +3 m LWS.

3 Main Jetty Design

3.1 Pile Design of the Main Jetty

The jetty was designed using an initial site investigation consisted of 5 boreholes and lab tests data. Those five boreholes were located far from the main jetty. BH-1, the closest borehole of all that had a distance of 90 m, was used to design the main jetty piles. The surface level at the executed boreholes was in the range of +3 to -10 m LWS, while the jetty location had a seabed level of about -24 to -27 m LWS.

The 40 m borehole of BH-1 indicated that a dense sand layer with silt mixture was found in the depth of 21 m below the seabed level. BH-1 borehole was executed at -10 m LWS seabed and only had 40 m boring depth; thus, the dense sand information stopped at 40 m. Based on the design, this BH-1 soil profile was used for the main jetty design, although the main jetty seabed level was located at -24 to -27 m LWS, and it was assumed that this dense silty sand would extend to a very deep layer in the design.

As per design calculation based on BH-1, one pile in the main jetty that was located on the -27 m LWS actual seabed level would have a free length of 30 m from the total length of 62 m. Thus, it was supposed to have 32 m penetration depth,

and the piles were supposed to be installed into 21 m stiff layer of fine-grained soils overlying ~ 11 m dense silty sand layer with SPT more than 40 N-Value. The piles were designed as end-bearing piles and relied significantly on this ~ 11 m hard layer as lateral and vertical bearing capacity.

Prior to construction, there was no static pile loading conducted to confirm the geotechnical design assumption for the jetty area. Although some PDA tests were conducted during the installation of piles, those PDA tests were executed on the trestle piles and not exactly at the main jetty location.

On the berthing elements of the main jetty, the piles were inclined to increase the structural stiffness. The raking piles were designed to have a uniform inclination of 1:5 (H:V) for all structures.

4 Geotechnical Assessment of the Main Jetty

4.1 Actual Soil Condition

Additional soil investigations consisted of 6 new additional boreholes (AB1 to AB6) were proposed to confirm the actual soil condition exactly on the jetty location during the assessment process.

Based on the new site investigation, it indicates that the top 1–2 m dominated by thick clay deposits with some gravel and sand in certain areas. The next 5–7 m consists of a medium to stiff clay layers. The clay layer is considered as clay with high plasticity since the PI is 43 [4]. It is followed with a medium-dense gravelly sand layer with a thickness of about 5 m. Below the gravelly sand layer, medium stiff to hard clays with high plasticity layer are presented until 90 m below the seabed layer, with another sand lenses of medium dense relative density are found at depth 20 to 40 m that varies in thickness. The mentioned stiffness consistency of all cohesive soils and the relative density of all granular soils are according to Peck and Terzaghi [5]. The long section of AB1 to AB6 is presented in Fig. 2.

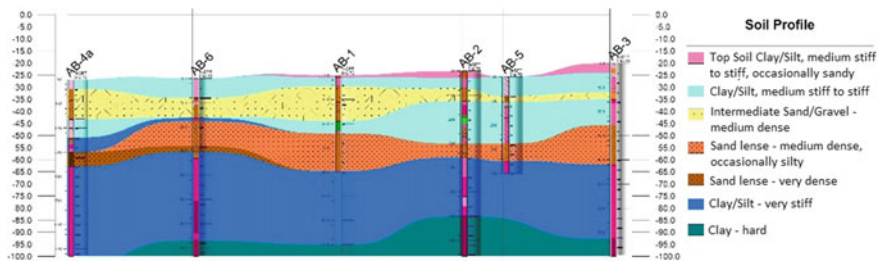


Fig. 2 Long section of the new boreholes

Table 1 PDA test result of pile TRES-37 in the project

Pile number	Bearing capacity (kN)			
	PDA	CAPWAP		
		Total	Friction	Toe
TRES-37	3508	3508	2878	630

4.2 Comparison of Actual Soil Condition Versus Initial Site Investigation with Respect to Pile Bearing Capacity

The new site investigation has brought a completely different view of the geotechnical condition on the main jetty area. The silty sand layer at depth 21 m to 40 m found in BH-1 (initial SI) is later known as a local lens. The assumption that the dense silty sand layer would extend to a very deep layer is incorrect, confirmed by the new site investigation. BH-1, as used in the design, cannot represent the actual condition due to the inhomogeneity of soil profiles in the waterfront area [6].

Before having the new site investigation data, the performance of piles can be checked via construction documentation such as the PDA test and CAPWAP analysis. Data from PDA and CAPWAP analysis, as presented in Table 1, shows that the highest bearing capacity contribution is from shaft capacity. Pile number TRES-37, which is located on the trestle and is considered to be the closest PDA test point to the main jetty, shows a total bearing capacity of 3508 kN with the shaft friction capacity of 2878 kN and an end bearing capacity of 630 kN. The contribution of end bearing capacity is only 18 percent out of the total pile capacity. This result shows a friction pile in which the shaft contribution is quite high, and the pile bearing capacity relies significantly on the friction instead of end-bearing.

It is given side by side overview comparing new borehole AB-4 and BH-1 in Fig. 3. Clearly that until the depth of 40 m below seabed level, the dominant soil layers are medium to very stiff clay, and in the 21 m or deeper, any dense silty sand layer is barely found except at depth 30–36 m in which a sand layer is found at the new borehole. If the pile stops at –32 m depth, it means only 2 m of pile toe will be covered with sand layer, either dense or medium dense layer, and it will not give any significant impact to the lateral or vertical bearing capacity. Although the gravelly sand layer is found in the main jetty location, this type of soil will not give a higher friction capacity to the piles compared to the cohesive soils layer with the same SPT value. The SPT value of this layer is ranging from very low to very high SPT, 10 to 50, and the thickness will vary as well in the whole main jetty area.

4.3 Seabed Level Evaluation from 2013 to 2016

During the initial design phase in 2013, prior to the construction phase, the deepest seabed level in the main jetty location based on the bathymetric survey was at

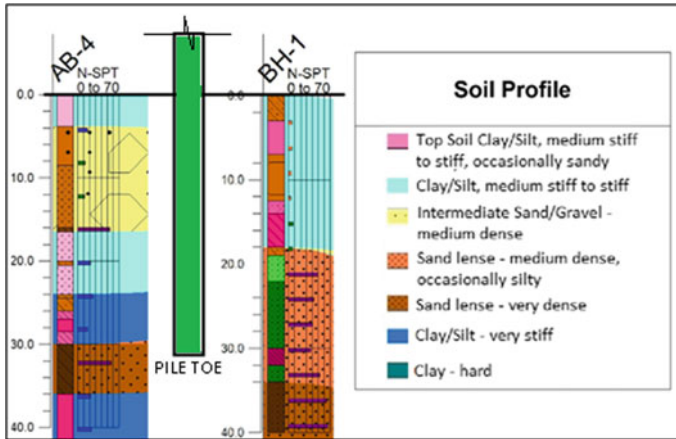


Fig. 3 Side by side comparison of AB-4 versus BH-1 (initial site investigation)

–25 m LWS. During the construction from 2013–2014, it was recorded on the piling records that the seabed levels can reach up to –26 m LWS. It could be seen that during a period of one year, there was erosion in the seabed level.

During the assessment of the jetty in 2016, a measurement of the seabed level was conducted. Based on the latest measurements by the divers, the main jetty location was dominantly located on the –26 to –27 m LWS. Hence, the seabed was eroded about 1–2 m thick during the three years period.

Some areas in the jetty location had topsoil of clay with sand and gravel mix. Based on laboratory tests conducted from new boreholes, the first 7 m had the mean particle size (D50) in the range of 0.04–1.5 mm. Although in this project, no comprehensive sediment transport analysis has been carried out due to the lack of time and data, the seabed erosion causes might be preliminary identified. It was recorded in the area that the maximum near-surface current speed was 1.2 m/s. The seabed erosion might be caused by the relatively high current on the floor area with respect to mean grain size [7] as well as the critical shear stress on the bed [8]. Another possibility is that the sediments are transported due to the combination of waves and current [9].

5 Structural Assessment

5.1 Field Instrumentation Using the Accelerometer

The vibration test was carried out to the structure by producing initial excitation by hitting the structure with a small tugboat. The natural vibration properties of the structure were measured by putting accelerometer instruments to record the response of the structure during the collision. One of the vibration properties, the natural

frequency, is useful information to identify the structure’s stiffness. In this project, the natural frequency obtained from the test would be compared with the remodeling result.

The mission of this investigation is to answer whether the main jetty can be operational or otherwise, and hence, it was needed to evaluate the main jetty performance, especially during the berthing of 50,000 DWT vessels. The instrumentation data was used as a benchmark for the product of the back analysis model. A close value between the back analysis model and field measurement would bring a good confidence level to conduct further predictive analysis.

5.2 Finding on Layout Configuration and Actual Structure Stiffness

It can be seen on the main jetty layout presented in Fig. 4, the longitudinal pile spacing of 11.5 m (approximately 12.6D) is considered too large. The consequences of having an excessive spacing between piles resulting in insufficiency on the number of piles to withstand design loads as follow:

- High displacement of upper structures
- Result in pile overstressed.

The required maximum pile distance was determined through structural analysis. Since it was known that the actual soil condition is much worse than determined on

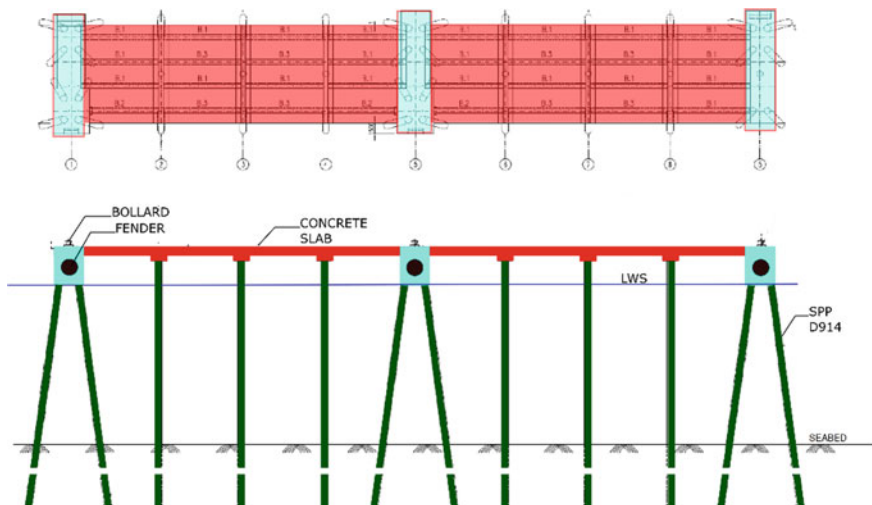


Fig. 4 Main jetty configuration sketch

the design; therefore, 12.6D was simply considered insufficient to withstand loads proven with the back analysis result that is further discussed in Sect. 7.

5.3 Actual Raking Pile Inclination Versus Design Inclination

Based on the conducted underwater inspection, the condition of inspected piles was generally reasonable. There was no indication of deflection, buckling, and ripped. All HDPE (High-Density Poly Ethylene) wrap protection was in good condition, and cathodic protection was also in good condition. However, the inclinations of the raking piles were not similar to the designs. The piles were installed steeper than what was suggested in the design. Most of those piles could not achieve the designed inclination of 1:5 (H:V) rake and had an inclination of 1:10 (H:V), which was steeper than the design. The raking piles were meant to increase the jetty structures' stability mainly due to horizontal loads such as berth loads, wave loads, etc.

The cause of this inclination problem was most likely due to the slenderness of the piles that were not able to maintain its orientation during pile driving. The pile tended to bend by its self-weight when the pile was being installed. The consequence of having lower pile inclination is discussed in Sect. 7.

6 Remodeling of the As-Built Main Jetty

6.1 Structural Parameter for Modelling

Structural analysis on the main jetty was carried out by modelling structure using 3D FEM (Finite Element Method) with a software called Nemetschek SCIA Engineer version 14. The geometry of the structure (Fig. 5) was developed based on the actual geometry of the as-built structure. Loads and load combinations had been applied in the model accordingly and were chosen based on the appropriate/relevant condition. Load combinations are further discussed in Sect. 7.2.

The as-built main jetty had a 100.5 m long and 17 m wide structure with pile foundations. The representative seabed level was at -26 m LWS, and the representative piles' toe elevation was taken at -59.0 m LWS. The pile tips were connected to the pile cap/beam at their center lines at a level of approximately $+3.00$ m LWS.

The longitudinal and transverse beams were precast concrete elements with a rigid connection to the pile cap/beams. The slab was modelled as a 2D member. The connections between beam and slab were modelled as a rigid connection, and the beams themselves were modelled as continuous beams.

A formation of 6 vertical piles and 76 inclined (1:10) piles with 914 mm diameter and 14 ~ 16 mm thickness was used in the model. The inclination of piles in the model was based on actual field measurement. The jetty consisted of a 300 mm thick

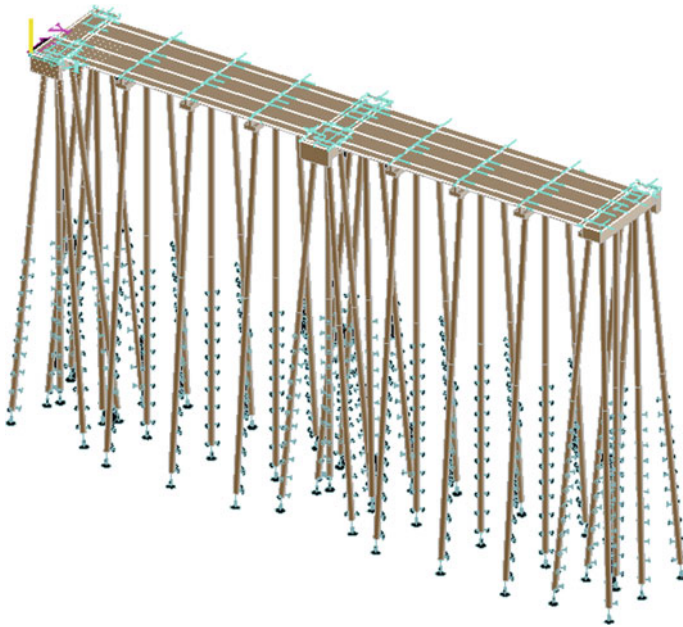


Fig. 5 Structural geometry of the back analysis model of the main jetty

concrete slab (150 mm precast and 150 mm in-situ) supported by grids of concrete beams.

6.2 Soil Parameter for Structural Modelling

The spring stiffness method was used to model the soil-structure interaction. The general method, such as the fixity point method, is not applicable to estimate the true deformation of the structure. Although both methods have their unique limitations, the spring stiffness method is more conservative than the fixity point method; however, it is more realistic since the plastic state of the soil due to horizontal loading can be implemented with modification to the linear springs. The horizontal spring stiffness that is determined by using the Menard-Brinch Hansen method [10], will provide a linear response and the plastic state of the soil. Besides that, the vertical spring is based on API RP 2A [11]. Soil horizontal and vertical stiffness are presented in Tables 2 and 3, respectively.

In the structural model, two different soil stiffness values were taken into account to calculate the interaction of pile and soil to get the worse effect of the structure. Two models were developed to determine the force distribution in the structure. These models were distinguished by the value of soil lateral stiffness (k_H and k_V , horizontal and vertical stiffness, respectively) as follow:

Table 2 Horizontal spring stiffness for back analysis

Soil type	Depth		$k_{hor;Menard}$	
	Top	Bottom	Low	High
	[m]	[m]	[kN/m ³]	[kN/m ³]
Top soil: clay/silt—medium stiff to stiff, occasionally sandy	0	4	3000	5600
Clay/silt—medium stiff to stiff	4	11	3000	5600
Intermediate Sand/gravel—medium dense	11	16	13,000	45,000
Clay/silt—medium stiff to stiff	16	30	3000	12,000
Sand lense—medium dense	30	33	12,000	30,000
Clay/slt—very stiff	33	67	7000	12,000
Clay—hard	67	90	12,000	17,000

Table 3 Vertical spring stiffness for back analysis

Pile type	Pile diameter	Thickness	Vertical spring stiffness (k_v)	
			Low	High
	[mm]	[mm]	[MN/m]	[MN/m]
Steel pipe pile	914	14–16	105	170

- i. The higher value of soil lateral stiffness was used to introduce maximum internal forces to the pile;
- ii. The lower value of soil lateral stiffness was used to get maximum deformation.

7 Back Analysis Result

7.1 Discussion on Jetty Structure’s Stiffness

Structural element resists lateral loads subject to horizontal displacement and deforms within their elastic limit. The lateral motion of the jetty structure by external excitation (e.g., mooring, berthing force, and ground motion during an earthquake) generates initial displacement then released and permitted to vibrate freely. The structure will vibrate back and forth about its initial equilibrium position. The displacement occurs with differentiation of acceleration and velocity with regards to time.

Based on BS 6439 Part 1–4 [12], this project’s jetty structure shall be classified as a rigid structure since all the horizontal loadings are carried by direct compression or tension action of the piles. Rigid structure, by this definition, shall have high stiffness, thus has a high natural frequency and should not experience large amplitude deflections due to dynamic loadings.

Table 4 Comparison of natural frequency obtained from initial design, field measurement, and back analysis result

Jetty structure	Back analysis (Hz)		Field measurement (Hz)	Initial design (Hz)
	Low	High		
Main jetty	0.31	0.32	0.4	0.66

The dynamic analysis had been performed by using a three-dimensional FEM model structure. The dynamic analysis result from the back analysis was compared with the vibration field test result. The comparison results are presented in Table 4.

The natural frequency f_n represents the stiffness of the structure—the lower of f_n , the lower the structural stiffness. From Table 4, the natural frequency of the main jetty from the analysis was in the range of field measurement results. The frequencies obtained from the analysis between low and high stiffness soil had no significant difference (0.31 versus 0.32 Hz) since it only checked the superstructure stiffness itself. The “zero displacement level” on the structural model was about at the same level for both soil stiffness.

The higher natural frequency in the initial design means that the structure is more rigid in theory, but not in reality. This issue can be understood since the initial structure was modelled and analysed based on the ideal geometry as designated (e.g., correct pile raking 1:5, with the ideal free length of piles). The structure was initially designed using the fixity point method, in which the pile zero displacement level was very shallow; hence, it was very optimistic. In the actual situation, many piles were not raking as designated and had longer free length due to deeper eroded seabed. Besides the superstructure structural rigidity, the interaction between the structure and the ground is also important. In this project, the weak ground condition will support the superstructure badly, resulting in a deeper actual zero displacement level. This can be explained that soil behaviour plays an important role in determining the zero-displacement level (fixity point) in the actual condition. Under a certain load, the soil will still behave elastically until a specific load has been reached, making the soil enter a plastic state. Once the soil enters a plastic state, theoretically, the strength contribution will be given by the passive soil pressure of the soil itself [10]. After the load relief, in short term condition, the soil condition will not revert back to the initial condition due to the excessive strains occurred. In other words, the pile loses the grips on the plastic zone. In long-term condition, the seabed erosion will increase the normative bending moment since the free length of the pile is longer. Hence the actual fixity point will be shifted downward, resulting in a deeper point than before. This condition is simply illustrated in Fig. 6.

These multiple issues affect the global stiffness of the structure. The structure will deform relatively high even with a small load (e.g., < 10 kN), and if it is repetitive loads, such as wave and current, the swaying effect may occur.

A swaying or vibrating structure due to dynamic loads does not mean that the structure is unsafe. Furthermore, the aim of this investigation is to answer whether

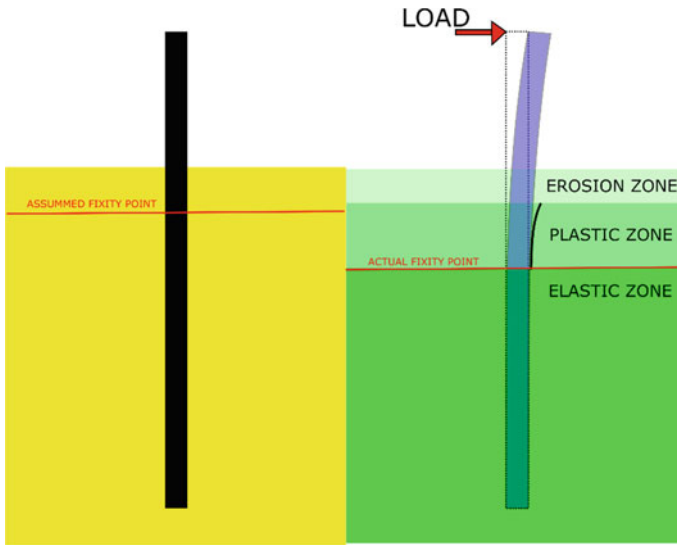


Fig. 6 Actual deeper fixity point resulting in higher displacement and bending moment

the jetty can be operational due to the berthing or mooring vessels. The operational condition or the service condition could be predicted by doing an additional structural analysis using the current structure strength/condition. A close value of natural frequency parameter between the back analysis model and field measurement (0.31/0.32 versus 0.4 Hz) brought a good confidence level to conduct further predictive analysis.

7.2 Predicted Displacement Due to 50,000 DWT Berthing and Pile Stress Ratio on the Main Jetty

The maximum displacement in-service limit state (SLS) of the structure for two chosen load combinations based on BS-6349 [12] in the transverse direction is presented in Table 5. The first scenario was environmental loading, which included self-weight with superimposed dead load and live load on the main jetty. The second

Table 5 Structure deflection result of back analysis and initial design under SLS condition

Load combination	Back analysis (low soil stiffness)	Initial design
	[mm]	[mm]
DL + LL + Environmental load	Lower than 20 mm	Lower than 15 mm
DL + LL + Environmental load + Berthing load	More than 200 mm	Lower than 25 mm

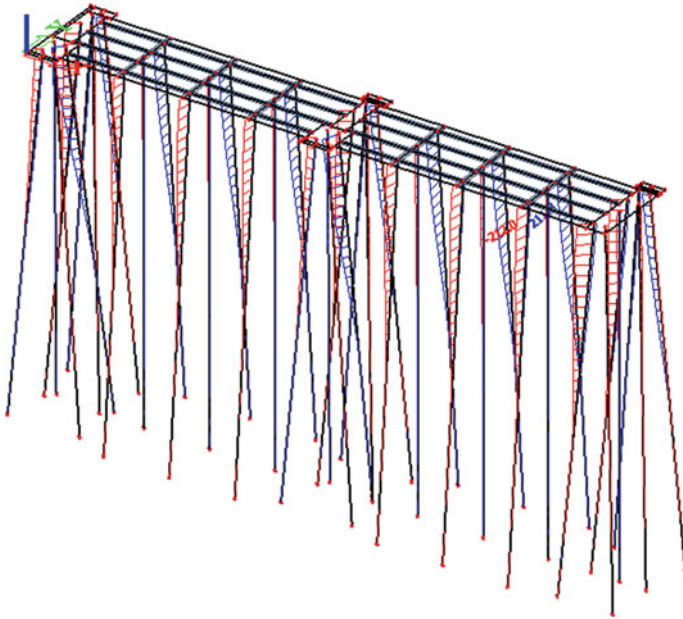


Fig. 7 Maximum deflection in Y direction under SLS condition with berthing load

scenario was similar to scenario one but included with berthing load. Both of the scenarios did not include seismic forces. The allowable deflection (δ) was set to 100 mm.

Based on the two scenarios, the deflection criteria in SLS condition with berthing load was unsatisfied, and therefore mitigation measures such as additional jetty reinforcement needed to be planned if necessary. The deflection result of more than > 200 mm under SLS condition occurred in transverse (Y) direction parallel with the berthing line, this deflection result is illustrated in Fig. 7.

For jetty structure, having some raking piles are essential for most cases or projects. Raking piles will be designed to have a certain inclination angle, and the inclined angle is up to the designer. The consequence of having a steeper actual inclination than the design is that the bending moment of the pile tends to be higher. The lateral loads resist by the rake piles primarily in axial compression and tension action. With steeper inclination or near-vertical pile, a high bending moment is induced due to the inability of the pile to transfer the lateral load into compression and tension action. The piles tend to absorb the lateral load by its bending moment capacity, and at the same time, the internal forces are being transferred to the ground due to soil-structure interaction. If the bending moment is high, then the lateral displacement will be high as well. In this jetty case, the displacement obtained from structural modelling was found to be excessive.

Excessive displacement produced by a high bending moment will result in overstressed pile conditions. From structural modelling, the pile stress ratio was ranging

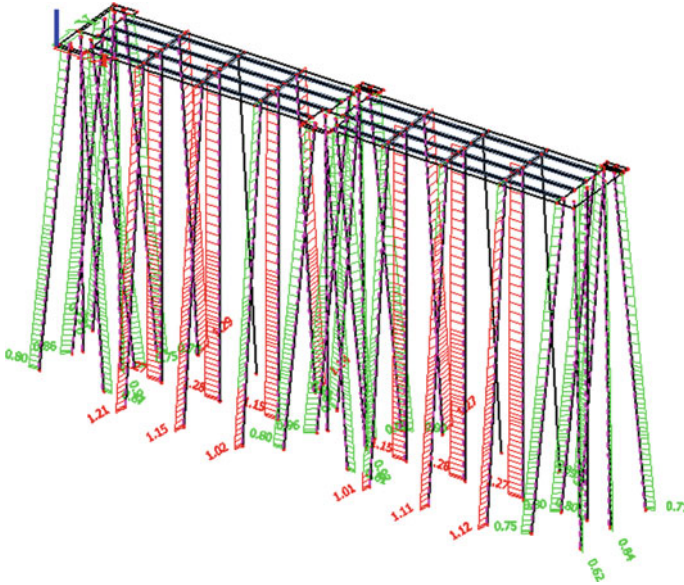


Fig. 8 Pile stress ratio in SLS condition with berthing load

from 0.8 to 1.3 maximum (Fig. 8). According to Eurocode 3 [13], the maximum allowable pile stress ratio is 1, and obviously, some piles were in overstressed condition. The stress ratio of 1 means that the occurred stress is equal to the yield of steel. In short-term condition, allowing a stress ratio to equal to 1 is fine. However, this is unfavourable for the long-term situation since the steel thickness will decrease over time due to corrosion; hence, corrosion thickness allowance needs to be considered to accommodate the future stress induced on the pile.

8 Conclusion

The initial borehole used for the design cannot represent the actual jetty condition due to no small distance (e.g., BH-1 with 90 m). In the waterfront area, especially Dumai, the inhomogeneity of soils is high, and designers shall carefully estimate the representative soil profile for design boundary condition [6].

In this location, from 2013 to 2016, the seabed elevation was eroded about up to 2 m. This reduction of topsoil will negatively impact the overall structure stiffness since the piles' free length increases. Most of the rake piles in this project were installed with steeper inclination than the designated. Rake piles have a better carrying capacity of lateral loads than vertical piles, particularly when piles have large free length and when the lateral loads are high (e.g., berthing vessel load). Also, the new boreholes data showed that the actual soil strength and stiffness are significantly

weaker. Accumulating all the issues found in the actual condition, these conditions drastically reduce the stiffness of the structure and, thus, introduce significant horizontal displacement even with small loads. If the loads are occurring periodically, such as waves and current, the jetty may sway.

In most jetty design cases, the fixity point method will be used as a method to determine the pile zero displacement level. However, using this method at a deep seabed level (e.g., 20 m or more) with weak ground strength (e.g., average NSPT ≤ 8) and highly erodible seabed are not practically recommended unless a high safety factor in fixity point level is applied. Designers shall be aware that the fixity point method does not consider the fact that the soil will deform plastically at a particular load. Once the soils are deformed plastically, the piles' free length will increase; thus, the bending moment will be higher. Assumption of the future seabed level changes due to seabed erosion is also needed during the design process, in order to accommodate the increases of the bending moment due to deeper seabed. This assumption is similar to sheet pile design practice, whereas morphological changes due to hydraulic condition need to be considered, such as lowering the passive side ground of the sheet pile [14].

From the remodeling result of the existing structure, the 50,000 DWT berthing vessel would induce more than 200 mm displacement to the main jetty. This displacement exceeds the displacement criteria of 100 mm. A reinforcement effort of the existing structure can be implemented in order to make the jetty operational. The reinforcement can be carried out, especially on the right side of the main jetty, whereas space is available to conduct additional pilling works to create the new berthing structures.

References

1. Cameron NR (1982) Geologic map of the Dumai and Bagansiapiapi quadrangles, Sumatra Peta geologi lembar Dumai dan Bagansiapi-api, Sumatra. Geological Research and Development Centre, Bandung
2. Vries Ld (2017) Pile foundation in challenging soft soil conditions. Importance of Geotechnol Geolog Knowl
3. Rifardi R (2001) Study on sedimentology from the Mesjid River Estuary and its environs in the Rupert Strait, the East coast of Sumatera Island. *J Coastal Zone Manage* 4(2):87-98
4. Burmister DM (1949) Principles and techniques of soil identification. In: Proceedings of annual highway research board meeting national research council, Washington, D.C., pp 402-34
5. Terzaghi K, Peck RB, Mesri G (1996) Soil mechanics in engineering practice, 3rd edn. John Wiley & Sons, New York
6. Nugroho A, Tazakka MS, Tirta BA (2019) Pentingnya Pelaksanaan Penyelidikan Tanah yang Tepat untuk Proyek Geoteknik di Kawasan Waterfront Area, Studi Kasus Jetty Dumai, Sumatera, Indonesia. Seminar Nasional Rekayasa dan Teknologi, TAU, Jakarta, pp 122-8
7. Hjulström F (1935) Studies of morphological activity of rivers as illustrated by the River Fyris. *Upsala Mineral. Geologis Inst Bull* 25:222-527
8. Shields A (1936) Anwendung der Aehnlichkeitsmechanik und der Turbulenzforschung auf die Geschiebebewegung. PhD Thesis. Technical University Berlin, Berlin
9. Van Rijn LC, Nieuwjaar MW, Van Der Kaay T, Nap E, van Kampen A (1993) Transport of fine sands by currents and waves. *J Waterw Port Coast Ocean Eng* 119(2):123-143

10. Deltares (2014) D-Sheet piling user manual. Deltares, Delft
11. API (2014) Planning, designing and constructing fixed offshore platforms—working stress design
12. BSI (2013) BS 6349–1–4: Maritime structures. General code of practice for materials. BSI, London
13. CEN (2005) Eurocode 3: design of steel structures—Part 1–1: General rules and rules for buildings. CEN, Brussels
14. CUR (2008) Damwandconstructies. SBRCURnet Publication, vol 166. CUR, Gouda

Seismic Assessment of Reinforced Concrete Frame with Unreinforced Masonry Infill Walls in Malaysia



Nurbaiah Mohammad Noh, Nur Izzah Aznin,
Muhamad Hafizi Mohamed Zin, Muhammmad Azamuddin Mohd Ghari,
Muhammad Ammar Zahari, and Muhammad Faiz Rushdi

Abstract This paper addresses the seismic performance of reinforced concrete frame structures constructed in Malaysia. Even though Malaysia is far from the destructive events of earthquakes triggered by plate tectonics, the country has experienced many serious earthquakes, especially from the Sumatran subduction zone, occurring on the nearest active plate boundaries. This study examines two families of RC buildings consisting of four-story and eight-story RC office building structures, including bare RC frames and masonry infilled RC frames. The nine regular office RC frame buildings are designed according to Eurocodes 2 provision that only considers gravity load effect (non-ductile building) and Eurocode 8 provision to consider ductility in seismic design (ductile building). Two different seismic building designs are considered, including ductility class medium and ductility class low, to examine entirely the implication of buildings performance subjected to seismic effect. Nonlinear static pushover analysis conducted through ETABS software is used to evaluate the structural response. The results indicate that the presence of the URM infill walls influence the overall behavior of the RC frame structure. The contribution of the infill panels improved the ultimate lateral strength and initial stiffness of the RC frame buildings. However, as the number of the story increased from 4-story to 8-story buildings, it reduced the ultimate building displacement. Compared to non-ductile RC frame buildings, Ductility Class Low and Medium RC frame buildings demonstrate a higher performance, which is affected by the reinforcement detailing of the building components.

Keywords Reinforced concrete · Unreinforced masonry wall · Eurocode · Non-ductile · Ductility

N. M. Noh (✉) · N. I. Aznin · M. H. M. Zin · M. A. M. Ghari · M. A. Zahari · M. F. Rushdi
School of Civil Engineering, College of Engineering, Universiti Teknologi MARA (UiTM),
40450 Shah Alam, Selangor, Malaysia
e-mail: nurbaiah@uitm.edu.my

1 Introduction

Reinforced concrete (RC) frame buildings are widely used in structural systems around the world. Lessons learned from previous earthquakes have shown that due to insufficient lateral stiffness to withstand lateral forces, RC structures suffered an extreme loss of stiffness and strength [1, 2]. Many RC buildings designed based on gravity-load only, so-called non-ductile RC frame, may suffer severe damage immediately after major shocks failure [1]. RC frame building damage caused by the earthquake may also cause damage to other non-structural components, such as unreinforced masonry (URM) wall. The failure of non-structural components may become a hazard to people. However, previous research has shown that the RC frame without the URM infill wall suffers more significant damage than the RC frame buildings with URM infill wall [3–5].

URM infill walls are commonly used for both interior and exterior walls in buildings but the URM infill wall is generally regarded as a non-structural element. The seismic response of these structures is highly influenced by the presence of the masonry infill walls, as demonstrated by damage observed during earthquakes such as in Algeria, China, Italy, Mexico, Turkey, Taiwan, and India [6, 7]. Experience during past earthquakes has shown the beneficial impacts of the presence of infill masonry walls as well as the negative impacts. For instance, it may increase lateral initial stiffness, strength, and energy dissipation capacity of the bare RC frame [8–10]. The detrimental effects derive from the fact that the frame may have an unpredicted distribution of forces and result in local collapse due to the involvement of the URM infill wall [11]. These effects depend on the geometrical arrangement of the infills in plan and elevation, infill mechanical properties, infill aspect ratio, the configuration of openings, and the construction methods [12–19]. URM infill walls in the RC frame were exposed to severe earthquakes and were seriously damaged due to some improper design. In many cases, the rigidity of the infill wall in the RC design is not concluded. Therefore, when assessing existing or new RC buildings to know the actual behavior of the structure, it is important to incorporate the effect of the infill wall into the seismic study.

The RC frame with URM infill walls building is the most common type of buildings built in Malaysia. The majority of RC frame buildings in Malaysia are designed by considering the gravity and or wind loads only, which no seismic design input since Malaysia is located at the low-risk hazard of the earthquake [20]. Besides, no specific design requirements for the URM infill walls have been considered. However, in recent years, earthquakes have also happened in Malaysia. These seismic events in Malaysia are mainly triggered by regional and remote seismic events in the Sumatera region which have two important sources of Sundra Arc slip fault offshore. From 2008 to 2010, there were a series of weak earthquakes in Bukit Tinggi in Peninsular Malaysia that were tracked to Bukit Tinggi's fault. Malaysia's most destructive earthquake is the Ranau earthquake that occurred on 5th June 2015. These earthquakes have caused much damage to the RC building structures, such as schools, mosques, temples, and commercial buildings. Building damage would have a significant effect

on both the country/region and its community, as sudden earthquakes will instantly lead to severe damage. Thus, the assessment of the seismic performance of these buildings can provide some practical guidelines for the reduction of any losses caused by earthquakes.

In this study, an assessment on ductile and non-ductile RC frame buildings with URM infill walls in Malaysia was conducted to determine which behavior of frame structure undergoes a better seismic performance. A static-pushover analysis is implemented using ETABS software as the main tool to assess the seismic response of the selected RC frame buildings. The method is used to monitor the performance and collapse pattern of the structural component and the entire building and the development of the global capacity curve of the structure. The structures are analyzed for two cases: (1) RC frame building designed as non-ductile buildings and (2) RC frame building designed as ductile (Low and Medium) buildings. Finally, the results are discussed concerning the yield load, ultimate load, and displacement.

2 Description of the Buildings

Nine RC frame buildings representing office buildings, divided into three categories, are considered to complete the objectives described above: a set of three 4-story and two 8-story regular frames, which both buildings have been designed and built to represent RC structures with no seismic detailing, and four 4-story regular frames designed with ductility class low (DCL) and medium (DCM), respectively. Within each group, two configurations of URM infill wall (Fully and Partially) lead to the four cases mentioned above. The selection of four cases for each set is inspired by the necessity to evaluate and compare the efficiency of structures design according to a ductility class set of rules but with different story height and infill configuration.

The RC office building has 7–6 m typical bays in N-S direction and three typical bays in the E-W direction consisting of 2–9 m and a bay (Fig. 1). The story height for each level is 4.0 m. Each building in groups one and two is designed by considering only gravity loads to meet the Eurocode 2 [21]. In contrast, the last group has been designed and detailed by Eurocode 8 [22], Parts 1–1 to 1–3, as a representative of the seismic design code. Typical superimposed loads from roof floor finishes and services are assumed to be 1.0 and 0.5 kN/m², respectively. The office floor live load of 3.0 kN/m² is considered. The same floor plan is used at all levels, as illustrated in Fig. 1. Concrete compressive strength, f_c' , and concrete modulus of elasticity, E_c , were taken as 30 and 24,700 MPa. High yielding strength deformed rebar is used with yield strength, $f_y = 460$ MPa. ETABS 2015, which has the option of current Eurocode 8, analyzes and designs a three-dimensional RC structure system. Figure 1 illustrates the configuration in plan and elevation of the buildings.

The buildings in group three, which includes four 4-story regular frames designed with ductility class low (DCL) and ductility class medium (DCM), are designed based on the Eurocode 8 seismic design provision. The seismic base shear force F_b for each horizontal direction determined by Eq. 1 (Clause 4.3.3.2.2 (1)) [22]

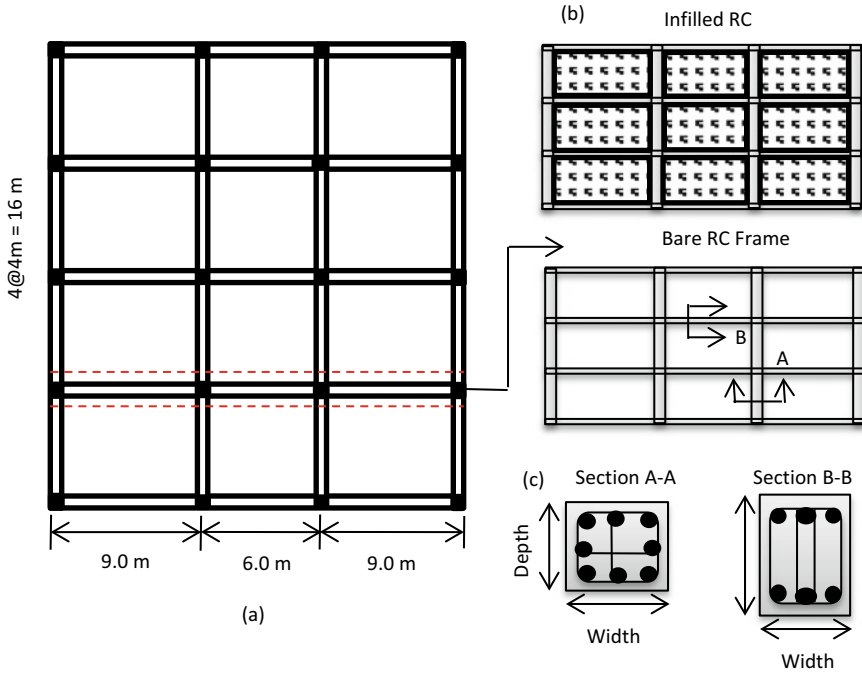


Fig. 1 RC frame buildings; **a** Frame plan, **b** Frame elevations and types and **c** Typical columns and beams detailing

$$F_b = \lambda \cdot m \cdot S(T_1) \tag{1}$$

where m is the total mass of the building, λ is correction factor (used 0.85), $S_d(T)$ is the design spectrum associated with the period of vibration, which can be determined by Eq. 2,

$$S_d = a_g S \frac{2.5 T_C}{q T_1} \tag{2}$$

The fundamental time period, T was obtained using Eq. 3 (Clause 4.3.3.2.2(3)) [22]

$$T_1 = 0.085 H^{0.75} \tag{3}$$

where H is the total story height. T_C is the period at the end of the constant-acceleration part of the design response spectrum.

Each building is designed with an importance factor, $\gamma_1 = 1.2$, on medium soil type ‘B’ of EC8 and assumed fixed at ground level. Two different ductility factors, which are DCL ($q = 1.5$) and DCM ($q = 2.0$), are also considered.

Table 1 Summary of design for ductile and non-ductile RC frame

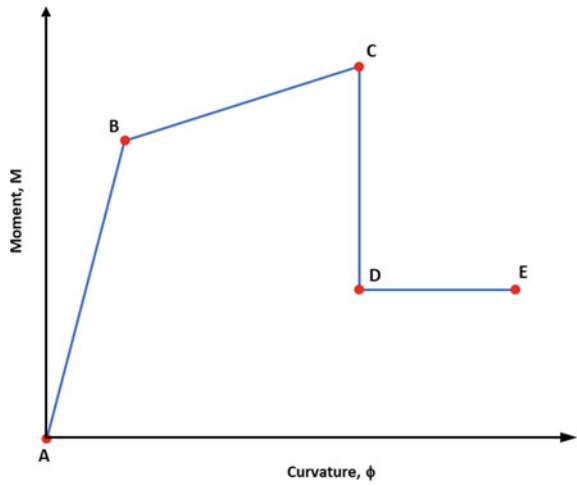
Structure ID	Ductility class	Infill	Beam size (mm)	Column size (mm)
4S_ND_NI 4S_ND_I 4S_ND_PI 8S_ND_NI 8S_ND_I	Non-ductile	No infill Full infill Partially Infill No infill Full infill	400 × 600	450 × 450
4S_LD_NI 4S_LD_I	Ductile class low (DCL)	No infill Full infill	400 × 600	450 × 450
4S_MD_NI 4S_MD_I	Ductile class medium (DCL)	No infill Full infill	400 × 600	450 × 450

Table 1 summarizes the design characteristics and the definition of the set of structures under consideration. The interior and exterior column is 450 × 450 mm. The columns are assumed fixed at the base with ignoring soil-structure interaction. All buildings are assumed to be founded on medium soil type ‘B’ of EC8. The beams of both the N-S and E-W frames are 400 wide × 600 mm deep for the whole stories. The two-way slab floor system consists of a 200 mm thick slab. For the infilled-RC frame buildings, the URM infill walls are considered as a non-structural element and neglected in the structural design process. The thickness and compressive strength of infill panels are 150 mm and 2.1 MPa, respectively.

3 Modeling Approaches for RC Frames and URM Infill Walls

Three-dimensional models of RC frame buildings with and without URM infill walls were developed using the ETABS software. To determine the performance of the structural system and the overall lateral load behavior of the structure through nonlinear static pushover analysis requires the formation of the moment-rotation curve for the critical sections of beams and columns. The moment-rotation in flexure is derived from the reinforcement details and cross-section properties, and next, the hinge properties are assigned for both beams and columns. The plastic hinge properties described in FEMA 356 have been assigned to the computer model in ETABS V.9.6.0. Default flexural hinges (M3) are assigned to the beams at two ends. Simultaneously, interactive (P-M2-M3) frame hinges type, a coupled hinge property, is assigned to all columns at the upper and lower ends of the members. Figure 2 shows the force–deformation relationship of the plastic hinge. The force–deformation relationship is under elastic stage from the initial point A to yield point B, followed by post yielding condition to point C. Then, the development of plastic hinge continued from C to D indicates post-maximum capacity, and D to E is the residual strength state. User-defined hinge properties options usually involve moment–curvature analysis, material properties, plastic hinge length, and information reinforcement of each

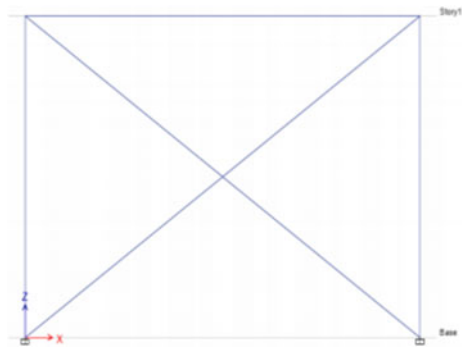
Fig. 2 Moment–curvature relationship defining the flexural plastic hinge



structure element. Moment curvature values are identified based on a concrete and steel material model.

In the case of URM infill walls, an equivalent diagonal strut model developed by Burton and Deierlein [23] was considered to determine the strength and stiffness of URM infill walls. Two opposing pairs of diagonal compression-only struts in each direction are used to simulate the performance of the URM infill wall subject to the in-plane effect (Fig. 3). In this approach, the URM infill wall is replaced by a pin-jointed diagonal strut. The strut width and strength of the infill model are calculated by the equations introduced by Priestley and Calvi [24] and Paulay and Priestley [25].

Fig. 3 Equivalent diagonal strut model



3.1 Verification of the Analytical Model

A set of experimental tests conducted by Stylianidis [17] was considered to evaluate the accuracy and ability of the simulation model. Quasi-static cyclic experiments on 1/3 scaled single story-single bay bare and infilled RC frames were carried out in this experiment work. The infill walls have been made of $190 \times 63 \times 90$ mm perforated clay bricks units and a 7.5 mm thick mortar. The samples of the first program in this study were selected for comparison: FBN (bar frame) and F1N (masonry infilled framework).

The loading program, with increasing displacement up to 30 mm, is focused on displacement controlled load cycles. The columns were given an axial compressive load of 0 kN and 80 kN (14% of the column strength). The experiment was reproduced as two-dimensional models.

The validation of the model is based on the comparison of numerical and experimental results for the total base shear and top displacement curve. The comparison of the analytical model with experimental data is shown in Fig. 4. It can be seen

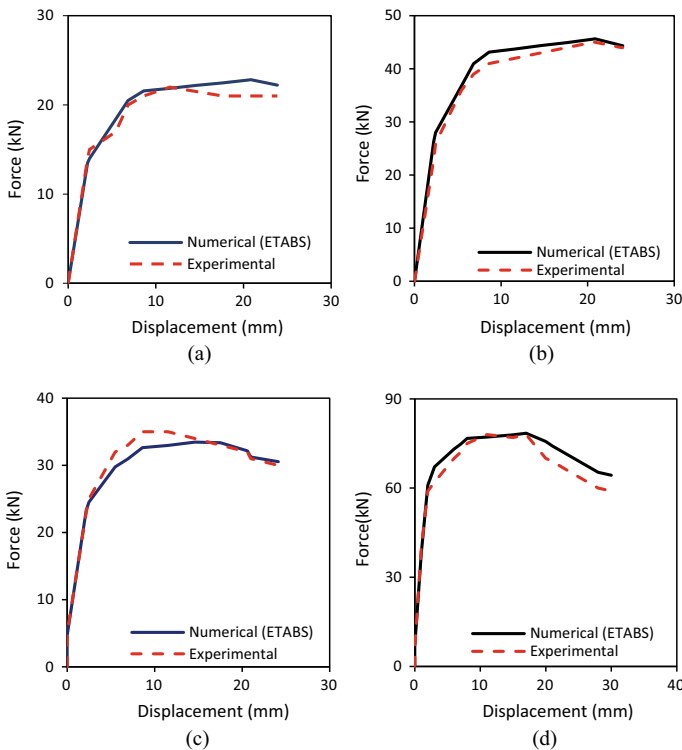


Fig. 4 Force–displacement comparison of bare RC frame and Infilled RC frame model: **a** Bare Frame with 0 kN axial load, **b** Bare frame with 80 kN axial load, **c** Infilled frame with 0 kN axial load, and **d** Infilled frame with 80 kN axial load

that a good agreement is obtained between the two until the yield point. However, a small significant difference is found, which starting at post yielding point until failure state. The factors that probably lead to the difference is due to the design code used to the model during the design stage. The analytical model was designed based on Eurocode, while the experiment result was based on the Indian standard. Overall, it can be said that the models are capable of capturing the response of the experimental sample, in which the difference between the analytical model and experimental results are not exceeding the 5% difference. Therefore, the model is used further to simulate the behavior of the selected buildings.

4 Result and Discussion

The seismic performance of the structural system is assessed through a nonlinear pushover analysis. A series of nonlinear static pushover analyses is carried out by the displacement control method, with the target displacement 4% of the total height of the building as per Eurocode 8. The pushover analysis is carried out by a gradually increasing displacement controlled lateral load. The pushover analysis results provide a relationship between the base shear force and top displacement. From the force–displacement curve, the yield and maximum displacement at the roof and base reaction of the structure during displacement controlled analysis can be obtained. Figures 5 and 6 show pushover results for the 4- and 8-story RC frame buildings designed with and without seismic provision. While Table 2 shows the yield and ultimate displacement and base shear of each model building.

In the first phase of pushover analyses, a comparison is made considering a non-ductile RC frame with and without URM infill walls for 4- and 8-story buildings. As shown in Table 2, it is confirmed that the RC frame designed for the 8-story building has a high base shear force than the 4-story RC frame. The yield force of 4- and

Fig. 5 Force–displacement comparison of 4- and 8-story Non-ductile bare RC frame and Infilled RC frame

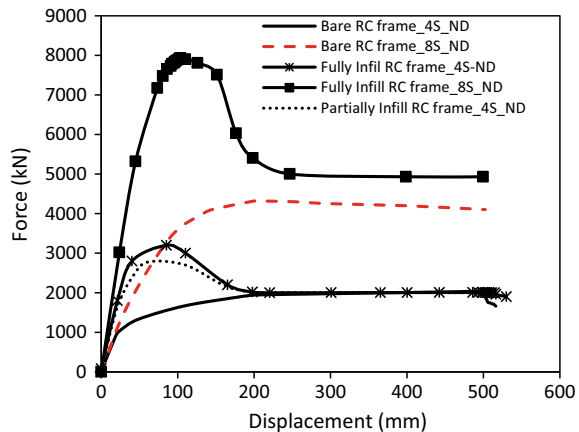


Fig. 6 Force–displacement comparison of 4-story Bare RC frame and infilled RC frame with different ductility class

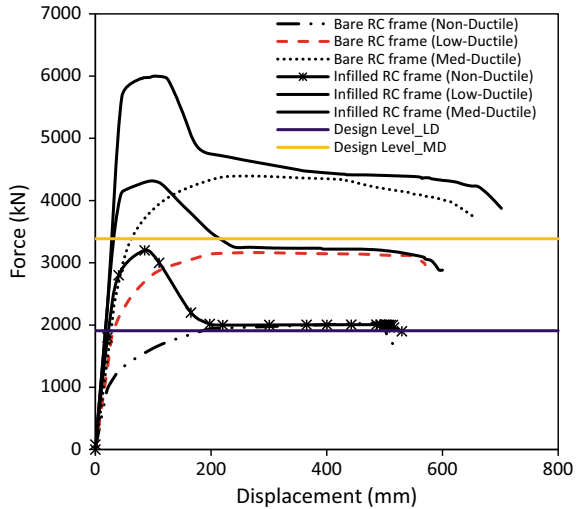


Table 2 Summary of displacement and shear at yield and ultimate point

Specimen	Displacement (mm)		Base shear (kN)	
	Yield	Ultimate	Yield	Ultimate
4S_ND_NI	32.2	295.6	1593.6	2004
4S_ND_I	40.2	85.3	2800	3200
4S_ND_PI	41.5	61.9	2420	2780
8S_ND_NI	132.3	251.1	3988.1	4301.4
8S_ND_I	80.65	109.9	7473	7901.3
4S_LD_NI	107.9	194.8	2190.9	3237.5
4S_LD_I	44.1	121.1	4098.6	4294
4S_MD_NI	117.3	260.5	2352.5	4393.9
4S_MD_I	45.7	101.6	5667.5	5998.7

8-story bare RC frame buildings were found to be 1593.6 kN, and 3988.1 kN and the corresponding capacity obtained from the fully infilled RC frame buildings are 2800 kN and 7473 kN, respectively. The ultimate roof displacement for both 4- and 8-story bare RC frame buildings were 295.6 mm and 251.1 mm, and for infilled RC frame buildings were 85.3 and 109.9 mm, respectively. However, the ultimate base shear for a partially URM infill wall is 2780 kN which is less than a fully infilled RC frame. The result shows that the configuration of the infill also may affect the overall performance of the buildings. Figure 5 revealed that the presence of the infill wall into the RC frame buildings increases the initial stiffness and the ultimate strength of both buildings. However, the base shear is decreased significantly due to damage or

collapse of infill walls, and then the buildings continued to function as a bare frame at later times.

In the second phase of analyses, pushover curves of the RC frame, designed with different ductility class (DCL and DCM), are presented in Fig. 8 and is compared with the design valued. The design base shear following Eurocode 8 is determined as 1908.8 kN and 3387.01 kN for DCL and DCM, respectively. As presented in Table 2 and Fig. 6, the yield and ultimate shear capacity of the DCL RC frame is defined as 2190 kN and 3237.5 kN, respectively, at a displacement corresponding to 107.9 and 194.8 mm. In contrast, for the DCM RC frame building, the yield and ultimate shear capacity of the DCL RC frame is defined as 2352.5 and 4393.94 kN, respectively. The yield and ultimate displacement were defined at 117.3 and 260.5 mm, respectively. Form the yield and ultimate displacement results give ductility ratio of 1.8 and 2.22 for both DCL and DCM RC frame buildings. From Fig. 6, it is observed that the RC frame designed with DCL and DCM resist the lateral load effect longer than the non-ductile RC frames. Besides, the inclusion of the ductility design towards the building will increase the strength of the RC frame. However, as reported above, the DCL RC frame shows less deformation as compared with the DCM RC frame due to a lack of a weak beam-strong column mechanism.

Concerning the effect of the infill walls in the seismic performance of the RC frame, Fig. 6 shows that the infilled RC frame building for DCM has the highest yield shear capacity with 5667.5 kN, followed by the infilled RC frame designed with DCL 4098.6 kN and 2800 kN for non-ductile infilled RC frame. The yield shear value corresponds to the displacement value of 45.7, 44.1, and 45.7 mm, respectively. The results show that lateral strength and initial stiffness is increased due to the presence of infill panels but reduce the ultimate displacement of the building. This result showed a similar pattern to the case in phase 1 and confirmed that the infill walls enhance the lateral resistance of the frames and their initial rigidity.

5 Conclusion

The seismic behaviors of RC frame buildings are assessed by conducting nonlinear pushover analysis. The preliminary work has been done by verifying the simulation model developed in commercial software ETABS v.9 with available experimental data in terms of total base shear force and top displacement. The infill wall is modeled using a single strut element in both the diagonal directions. The developed model provides good agreement with the experimental results. The verified model has been used further to assess the seismic performance of RC frame buildings. The seismic behavior of RC frames is studied based on three different cases: (1) different height (4- and 5-story building), (2) different infill configuration (partially and fully URM infill wall), and (3) different ductility class (Low and medium). The following conclusion can be drawn based on the above result and discussion:

1. The increase in the height of the building has a greater impact on the base shear of the structure.
2. The presence of the infill wall increased the initial stiffness and ultimate strength of the RC buildings compared to the bare RC frame.
3. The overall performance of the RC frame with URM infill walls offers better performance than the bare RC frame. The configuration of the infill wall plays a major role in the seismic efficiency of the RC frame.
4. The ductile RC frame endures large lateral displacement under pushover loading compared to the non-ductile RC Frame. The low and medium ductile RC frame performed very well under pushover loading due to weak beam-strong column considerations.
5. Overall, the presence of URM infill walls and consideration of ductility design in the RC buildings contribute to higher resistance against the lateral load on the buildings.

In conclusion, this study successfully evaluates the global response of RC frame buildings with URM infill walls under in-plane lateral loads. The results presented from this study help comprehend the overall performance of buildings in Malaysia. However, further studies can be carried out by considering the effect of opening and configuring the URM infill walls in the buildings and developing a seismic fragility curve that can assess the seismic vulnerability of infilled frame buildings in Malaysia.

References

1. Siswosukarto S, Sulisty D, Priyosulistyo H, Triwiyono A, Ashar S, Siswanto F (2012) Lesson learned from the damage of academic buildings due to earthquake in Padang, Sumatera. In: 1st international conference sustainable civil engineering structuring construction material lesson, no. September 2018
2. Adel E, Abdelnaby (2012) Multiple earthquake effects on degrading reinforced concrete structures, pp 1–223
3. Sattar S, Liel AB (2016) Seismic performance of non-ductile reinforced concrete frames with masonry infill walls—II: collapse assessment. *Earthq Spectra* 32(2):819–842
4. Papailia A (2011) Seismic fragility curves for reinforced concrete buildings, University of Patras
5. Choopool N, Boonyapinyo V (2011) Seismic performance evaluation of reinforced concrete moment resisting frames with various ductility in low seismic zone. 4(1):17–36
6. Mosalama KM, Günay S (2014) Progressive collapse analysis of RC frames with URM infill walls considering in- plane/out-of-plane interaction. *Prof J Earthq Eng Res Inst* 1–26
7. Sezen H, Elwood KJ, Whittaker AS, Mosalam KM, Wallace JW, Stanton JF (2000) Structural engineering reconnaissance of the August 17, 1999 earthquake: Kocaeli (Izmit), PEER Rep. 2000/09, Turkey
8. Asteris PG, Antoniou ST, Sophianopoulos DS, Chrysostomou CZ (2011) Mathematical macromodeling of infilled frames: state of the art. *J Struct Eng* 137(12):1508–1517
9. Campione G, Cavaleri L, Macaluso G, Amato G, Di Trapani F (2015) Evaluation of infilled frames : an updated in-plane-stiffness macro-model considering the effects of vertical loads. *Bull Earthq Eng* 2265–2281
10. Martinelli E, Lima C, De Stefano G (2015) A simplified procedure for nonlinear static analysis of masonry infilled RC frames. *Eng Struct* 101:591–608

11. Asteris PG, Giannopoulos IP, Chrysostomou CZ (2012) Modeling of infilled frames with openings. *Open Constr Build Technol J* 6(1):81–91
12. Al-chaar GK (1998) Non-ductile behavior of reinforced concrete frames with masonry infill panels subjected to in-plane loading, University of Illinois at Chicago
13. Angel R, Abrams DP (1994) Out-of-plane strength evaluation of URM infill panels.pdf. In: Proceedings from the NCEER workshop on seismic response of masonry infills, in: Technical Report. Presented at the NCEER workshop on seismic response of masonry infills, national center for earthquake engineering research, pp 9–14
14. Bell DK, Davidson BJ (2001) Evaluation of earthquake risk buildings with masonry infill panels. In: 2001 technical conference, future directions: a vision for earthquake engineering in New Zealand
15. Flanagan RD, Bennet RM (1999) Bidirectional behavior of structural clay tile infilled frames. *125(3):236–244*
16. Fiorato AE, Sozen MA, Gamble WL (1970) An investigation of the interaction of reinforced concrete frames with masonry filler walls
17. Hashemi SA, Mosalam KM (2007) Seismic evaluation of reinforced concrete buildings including effects of masonry infill walls. PEER Rep. 2007/100
18. Mehrabi AB, Shing PB, Schuller MP, Noland JL (1996) Experimental evaluation of masonry infilled RC frames 89:228–237
19. Pires F, Carvalho EC (1992) The behavior of infilled rc frames under horizontal cyclic loading. In: 10th world conference on earthquake engineering, pp 3419–3422
20. Adiyanto MI, Majid TA (2013) Influence of behaviour factor on seismic design of two storey reinforced concrete building in malaysian seismic region. *Aust J Basic Appl Sci* 7(8):411–419
21. Narayanan RS (2001) EN1992 Eurocode 2: design of concrete structures. *Civ Eng* 144(6):23–28
22. CEN (2003) EN8–1 General rules, seismic actions and rules for buildings Eurocode, vol. 3(121124)
23. Burton H, Deierlain G (2013) Simulation of seismic collapse in non-ductile reinforced concrete frame buildings with masonry infills. *J Struct Eng* 140(8):A4014016
24. Priestley MJN, Calvi GM (1991) Towards a capacity-design assessment procedure for reinf. concrete frames. *Earthq Spectra* 7(3):413–437
25. Paulay T, Priestley MJN (1992) Seismic design of reinforced concrete and masonry buildings. John Wiley, New York

High Temperature Performance of Concrete Incorporating Recycled Glass Powders



Joarder Md Sarwar Mujib, Nayeem Ahmed Shuvo,
Abu Bakar Siddique Ishmam, and Tanvir Mustafy

Abstract In this study, it was investigated the performance of recycled glass powders (GP) incorporated concrete subjected to elevated temperature as a partial replacement for sand material. Different portions of GP were used with sand for preparing 8 working mix conditions, i.e., 5, 10, 15, 20, 25, 30, 35 and 40 wt%. A total of 48 cylinders were prepared ($n = 6$ for each group). 10 cylinders were prepared without any GP percentage for comparison. One-third of the cylinders from each group were tested before the fire treatment. Cylinders were tested under compressive loading at certain temperatures (600, 700, and 800 °C) after 28 days of curing. Thermo-couple and data logger was used to calibrate the furnace temperature. X-ray fluorescence (XRF) analyses were conducted on the corresponding samples to extract the chemical composition under elevated temperature. At temperatures below 700 °C, concrete containing GP percentage of 35 wt% exhibited the best performance at high temperature, incurring an average strength loss of 21% compared to 39% strength loss in reference samples. Calcium hydroxide (CH) content was found to be reduced for the samples with GP. The strength loss that occurred at a lower temperature range marked below 700 °C could have been resulted from the dehydration process of CH. Hence, a reduction in CH content was observed for the lower strength concrete samples. The measured strength loss was found to be 56% and 35% for the GP concrete and reference samples, respectively under an elevated temperature range of 700–800 °C. The inherent property of glasses i.e. softening phenomenon, might have contributed to the shrinkage of GP concrete comparatively more than the counterparts. And the shrinkage property of glasses under elevated temperature coupled with sand particle expansion might have contributed to the higher strength loss of GP concrete at elevated temperature.

J. M. S. Mujib · N. A. Shuvo (✉) · A. B. S. Ishmam · T. Mustafy
Military Institute of Science and Technology, Dhaka, Bangladesh

T. Mustafy
e-mail: mustafy@ualberta.ca

T. Mustafy
University of Alberta, Edmonton, Canada

Keywords High temperatures · Compressive strength · Recycled glass powder · Microstructure

1 Introduction

The damage caused by devastating fire to engineering structures and infrastructure is probably one of the most well-known natural disasters that humanity has been facing for thousands of years. Fire accident, a sensitive problem, damage structures in different dimension and a liable safety issue for human lives and economy. Reducing the degree of damages for fire accidents and reconstruction of concrete structures is a concerning issue. Though Concrete has a resistance in high temperature but due to fire but there are remarkable changes in its mechanical, chemical & physical properties. With disintegration of cement paste, the disparity in thermal expansion behavior between cement paste and aggregates, and degradation and phase decomposition (and/or transition) of aggregates under high temperature are considered as main factors impacting the mechanical properties of concrete [1]. The behavior of nonhomogeneous concrete at high temperature is the result of simultaneously interacting factors [2]. According to Bostami et al. Types of aggregate and sand has significant impacts on concrete in different temperature and noticeable changes in color, microcracking and spalling at 800 °C is observed [3]. Phan et al. stated that concrete loses its capacity up to 60% when it is heated up to 600 °C [4]. The researchers and professionals give emphasis to improve the material quality in thermal expansion and try to develop the proper strategy to incorporate the delay mechanism of concrete at high temperature.

Waste glass, a low thermal stuff, is one of the non-decaying harmful materials for the environment & ecological balance directly or indirectly. Recycled Glass powder (RGP) was used for concrete casting. This recycling help to reduce the burdens on environment and can attain sustainable development. The purpose of this research is mainly to investigate the properties and behavior of concrete at high temperature after burning hence the prime focus is on the RGP (partially replaced with sand weight %), Sand, Coarse aggregate and binding material. The performance of concrete, casted with recycled GP, is better than the normally casted concrete with sand after fire burning. As GP is low heat consuming material, so the compressive strength of concrete is satisfactory enough. It is observed that heat rises comparatively slow in the experimented concrete samples which were casted with RGP partially replaced with sand weight. The compressive strength of normal concrete at high temperature (500, 600, 700 and 800 °C) is determined to compare with strength of RGP mixed specimen. The changes of minerals and chemical composition of concrete specimen at high temperature carried out by the experiment.

It is very complex to detect the concrete behavior at elevated temperature because heat do not spread to the inner side or the whole surface in systematized progression and the behavior may vary depending upon the properties of materials. In general,

the concrete surface is significantly affected by the detrimental fire effect or by any fire accident.

2 Background of the Research

Fire, in any kind of structure can have a serious impact on safety and the human economy. When a fire occurs, structural elements such as beams, columns and slabs that fired along the entire area and heat uniformly and the severity of the fire cannot be accurately determined the motivation of this research was to find a way by which can minimize the impact of fire accident to structures. After proper inspection of fire hazard structures, it was found that the structural members which were covered by tiles have been less affected in comparison which have not been covered by tiles. So, tiles covered concrete as well as non-tiles covered concrete can be tested to find out the strength after heat episode. Therefore, it is studied that the risk of fire and discovered ways to reduce its impact. This research will be helpful to reduce the loss of life and property during the fire incident as well as in the rescue operation of fire incidents.

3 Desk Study for the Research

At the very beginning of the research, firstly the primary data was collected from the structures which burned in fire accident for different reasons. The common reasons were electric short circuit problem and the reason for massive fire accident was liquid chemical storage in any kind of structures. The chemicals can become very much combustible during fire accident and it may damage the structures, lives as well as the economy.

Specially, in the garments building or in large factory, fire can be exposed from the friction of the heavy machineries or the equipment which is used for production. Hence, the storage of jute or neat in garments is a sensitive part of the factory. So, the main theme of the experiment is to reduce the degree of damage to the structures as well as the live and economy, so the structures can be more sustainable due to fire accident.

4 Aim of the Experiment

The variation of compressive strength in different RGP mixed concrete specimen at high temperature is the main objective of this research. Determination of the compressive strength of normal concrete at high temperature (500, 600, 700 and 800 °C) and compare with strength of glass mixed specimen at elevated temperature. The changes

of minerals and chemical composition of concrete specimen at high temperature are also carried out by the experiment. This research work mainly appries to know the behavior of concrete cylinders under fire exposure and to make the fire more delayed so that the structures made with concrete faces less losses in different degree of dimensions and it can be more be suitable to reduce the economic and lives losses.

5 Recycled Glass Powder (RGP) and Environmental Sustainability

Glass powder (GP) will become a good recycling material when it will use in casting concrete for the different element of the structure like column because column is the sensitive part of a building. The waste glasses which is thrown in the environment is very harmful for the ecological balance and if the wastes are thrown in the like sea or river or pond, then it can be very harmful for aquatic ecosystem and geo texture. On the other hand, waste glasses can be very much harmful for the Phytoplankton and aquatic plants under water. For this reasons the water can be polluted. So, it is better to recycle the waste glass and it can be capable of being sustained the process of development.

6 Materials

6.1 Recycled Glass Powder (RGP)

RGP has high heat insulating capacity. Clear glass, brown glass and green glass all of them have high melting point about 1400–1600 °C.

Clear glass is used for casting concrete samples. It is mentionable that 10.3 is the pH of waste glass, it is environmental friendly. RGP doesn't involve in any harmful activity to environment. Los Angeles Machine was used to make glass powder from the waste glass. RGP was used as fine aggregate. RGP is very sharp element in replacement of fine sand. RGP makes a strong bonding to the mortar and it provides better interlocking system among the mixture.

When glass powder added to concrete structure it exhibits a remarkable strength. Glass mixed concrete are able to retain a significant amount strength against fire. The following table represent the chemical composition of glass which is demonstrated in Table 1

Material Characterization Black stone of 12.5 and 9.5 mm was used as coarse aggregate (CA). To identify the strength of aggregate Los Angeles Abrasion test was introduced. Los Angeles Abrasion test value was 35%, which was in between reasonable range.

Table 1 Chemical composition of RGP before burning with XRF

Chemical composition (%)	Clear glass
SiO ₂	71.42
Al ₂ O ₃	1.46
TiO ₂	0.037
Cr ₂ O ₃	0.002
Fe ₂ O ₃	0.07
CaO	11.45
MgO	0.33
Na ₂ O	13.67
K ₂ O	0.34
SO ₃	0.20

*XRF = X-ray Fluorescence Spectrometer

Sand and Glass powder was use as fine aggregate (FM = 2.8) and Ordinary Portland Cement (OPC) (Bulk density 3.15) was used as binding materials in accordance with the reference ASTM C 136 Table 2 (see Fig. 1) [5] Material properties

Table 2 Material properties

Properties	Materials			
	Coarse aggregate	Fine Aggregate	Glass powder	Cement
Specific gravity	2.84	2.62	2.55	3.15
Water absorption capacity (%)	0.85	3.31	5.7	0.08
Unit weight (kg/m ³)	1569	1635	2500	1400
FM	7.13	2.62	2.8	-

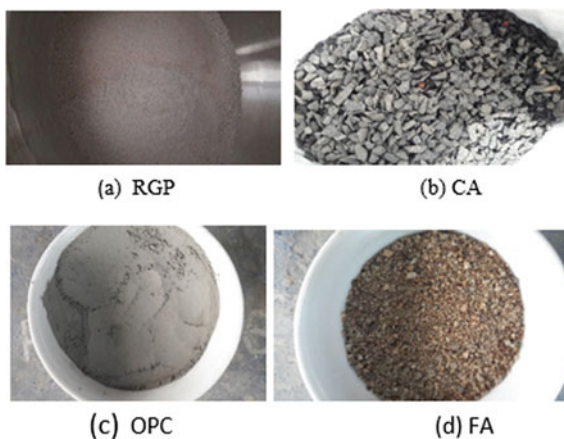
Fig. 1 Materials used for casting

Table 3 Sieve analysis of RGP

Sieve no	RGP retained (gm)	% of RGP retained	Cumulative and of retained	FM of RGP
#4	0	0	0	
#8	35	7	7	
#15	77.5	15.5	22.5	
#30	202.5	40.5	63	2.81
#50	130	26	89	
#100	55	11	100	
Total			281.5	

is described in the following and the materials are exhibited in the following (see Fig. 1). Sieve analysis of RGP is given in Table 3.

7 Experimental Procedure

7.1 Concrete Sample Preparation for Experiment

For casting the Cylindrical samples, the selected materials were mixed with recycled GP (partially replaced with sand in different weight percentage and 0.42 w/c ratio) and after well mixing for 2 min they were poured in to metallic mold having diameter 100 and height 200 mm in reference with ASTM C470/C470M (see Fig. 2) [6]. Slump tests were varying in between 98 to 110 mm with the reference of code ASTM C 143 and AASHTO T 119. Slump test is mainly done to identify the condition of the concrete mortar with respect to water ratio. [7] All the samples were kept in room temperature (25–30 °C) for 24 h when they were casted. After 24 h, All the specimen in the steel mould were ready for curing (23 °C was measured) for 28 days [8]. When curing is done then the concrete samples were kept in the laboratory for 24 h (room

Fig. 2 Cylindrical molds and casted concrete





Fig. 3 Gas furnace

temperature 23 °C) for further compression test and identifying the way of behaviour of concrete at post-burning phase.

Configuration of Mixtures Coarse aggregate (CA), Fine aggregate (FA), Ordinary Portland cement (OPC) & RGP with adequate water was used in the concrete mortar mixture in reference to ASTM C33 / C33M—18. Total 135 cylindrical sample were casted incorporating with (RGP) in partial replacement of fine sand. The percentage of replacement of fine sand is 0, 5, 10, 15, 20, 25, 30, 35 and 40%. Each group has 15 sample specimens. Total 108 samples (Each group has 12 samples) were taken to investigate the post fire burning properties at elevated temperatures of 25, 500, 600, 700 and 800 °C for approximately 60 min and the undesirable consequences of concrete. Burning procedure was done in a gas furnace (See Fig. 3). Thermocouple and data logger were used to observe the temperature of the furnace.

Temperature Calibration The furnace contains two gas burners. Thermocouple and data logger was use to calibrate the inside temperature of the furnace. It takes 100 ~ 120 min to reach the height temperature of 800 °C which was found from the calibration result and the temperature increase rate was 7.5°/min (see Fig. 4).

8 Result

The materials like stone chips, sand, cement and RGP undergoes in a significant and noticeable change in elevated temperature up to 800 °C. At the post burning phase (for 1 h), the strength of the specimen is gradually increased by the increasing of RGP (at different temperature). But a specific percentage of glass powder (35%) the specimen reach maximum strength, after that it the specimen loss it's strength by increasing the percentage of glass powder and Slump test result was varying in between 98 to 110 mm with reference to ASTM C 143 or AASHTO T 119 (see Fig. 5) and. The maximum strength (MPa) is observed in the sample which was casted with 35% of RGP at 800 °C and it is 26.43 MPa. This strength is comparatively better than the strength of other samples and strength reduces almost 55% for 800 °C for

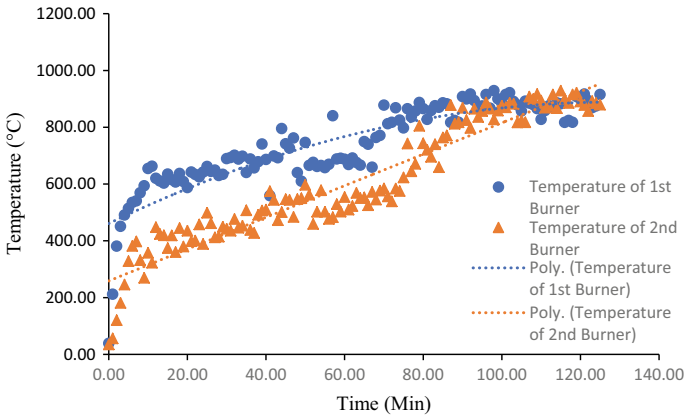
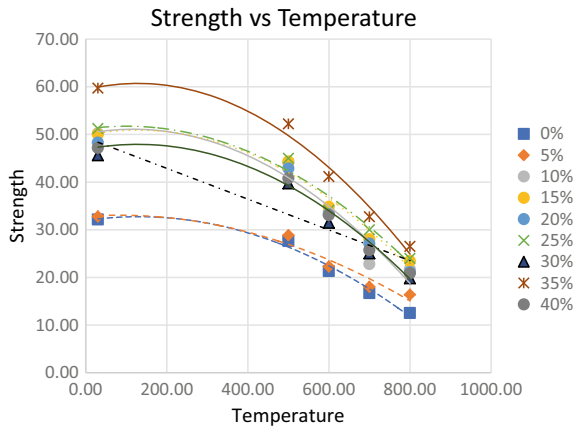


Fig. 4 Temperature calibration of gas furnace

Fig. 5 Strength (MPa) versus temperature (°C) curve of concrete at different temperature with different % of RGP



35% of RGP is partially used. Hence the reduction of the compressive strength of other samples also (Table 4).

Relation between temperature and strength Average strength of concrete (in partial replacement with sand) at different temperature is given below Table 5. The strength of concrete decrease with the increase of temperature and sand 35% RGP which was partially replaced with sand gives the most satisfying result.

Strength Reduction. It is observed that strength reduction percentage of concrete sample is increased with the increase of temperature. The percentage of strength reduction at elevated temperature is given below Table 6. Concrete loses its compressive strength up to 61% at 800 °C incorporating with 35% of RGP and there is a significant loss found at different temperature. The Table 6 and the graph (see Fig. 5) represents the percentage of reduction of the strength of the concrete at 500 and 800 °C.

Table 4 Relation between compressive strength, % RGP, and temperature

(%) GP in the mixture	Average strength (MPa) at different temperature					
	Value of slump test (mm)	30 °C	500 °C	600 °C	700 °C	800 °C
0	110	32.16	27.65	21.34	16.72	12.54
5	106	32.80	28.86	22.30	18.04	16.40
10	105	50.25	44.04	33.82	22.81	21.74
15	102	50.06	44.34	34.81	28.02	23.44
20	102	48.29	42.87	33.25	27.10	21.11
25	101	51.24	45.01	34.10	30.01	24.00
30	100	45.64	39.74	31.48	25.07	19.82
35	100	59.72	52.23	41.18	32.74	26.53
40	98	47.18	40.79	33.09	25.74	20.87

Table 5 Strength of samples at elevated temperatures with respect to different % of GP

% of GP	At 500 °C	At 600 °C	At 700 °C	At 800 °C
0	14	33.64	48	61
5	12	32.01	49.02	50
10	12.35	32.01	54.60	56.73
15	11.42	32.69	44.02	53.17
20	11.23	31.14	43.88	56.28
25	12.17	33.45	41.43	53.16
30	12.92	31.02	45.07	56.57
35	12.54	31.04	45.18	55.57
40	13.54	29.85	45.16	55.76

Table 6 % of strength reduction of RGP mixed concrete with different temperature with respect to standard compressive strength corresponds to 30 °C

Temperature (°C)	Average strength at different % of RGP in MPa								
	0	5	10	15	20	25	30	35	40
30	32.16	32.80	50.25	50.06	48.29	51.24	45.64	59.72	47.18
500	27.65	28.86	44.04	44.34	42.87	45.01	39.74	52.23	40.79
600	21.34	22.30	33.82	34.81	33.25	34.10	31.48	41.18	33.10
700	16.72	18.04	22.81	28.02	27.10	30.01	25.07	32.74	25.74
800	12.54	16.40	21.74	23.44	21.11	24.00	19.82	26.53	20.87

Crack patterns of concrete Specimens are heated at different temperatures ranges from 500 to 800 °C. At low temperatures no significant changes in color of concrete was seen. But when the heat rises over 600 °C it started to show slight visual color changes.

Losses of weight of the concrete samples at post burning phase with the increasing heat the mass of the specimens was getting lower and slight variation with weight of specimen at normal condition occurs. This might be caused by the driving out of moisture and concrete hydration due to high temperature. The weight loss varies in between 100 to 600 gm at elevated temperature. Normally weight loss is maximum at 800 °C and it was varying for the different percent of RGP. The chemical composition of the RGP decreasing with the increase of high temperature.

9 Discussion

Strength of the cylindrical concrete samples are reduced by increasing the temperature (at any % of specimen), which was shown in Table 5 and (see Fig. 6) But in Table 6 strength is randomly increase by increasing the percentage of RGP. The strength was increase up to a certain percentage (35%) of RGP then it again falls. By increasing the temperature, percentage of strength reduction was increased which was represent by the Table 5 and Fig. 6. At 800 °C (as concern about high temperature) 5% RGP had less reduction but initial strength was less compare to other. But in 35% GP the result was suitable compare to other percentage of RGP. After the analysis a point can be arise that the use of 35% GP can be the better option than the other percentage of RGP. The crack patterns of the samples are significant enough. Cracks varies with the increase of temperature (see Fig. 7).

9.1 Challenges Faced During the Research Experiment

1. Sometimes it was difficult to test the specimens keeping at the instant temperatures due to the reason that the sample to get out and it to be placed inside

Fig. 6 % of Strength reduction verrsus % of GP

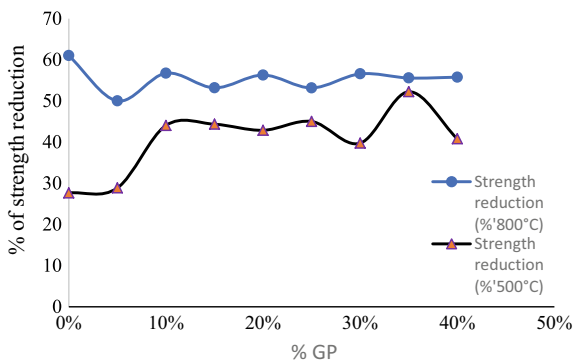




Fig. 7 Various aspects and crack formation of concrete (35% RGP) at prescribed temperatures

the compressive testing machine. During this set up, time elapsed and cylinder sample got cooled down a bit.

2. Insulation could not be assured 100% for the gas burning furnace and desired maximum temperature condition could not be obtained thus.
3. There were difficulties to test the specimen for instant heating condition as the furnace was installed in an open field, from where it was not possible to carry the specimen keeping the hot condition constant to test instant compressive strength.

10 Recommendation

The research is only done with the compressive test of cylindrical concrete for residual strength as well as the strength at high temperature. But there are few experiments which is not done and the experiment can be covered like splitting test, modulus

of elasticity test pre-burning and post burning phase, impact loading test of beam or column at post burning condition, permeability test of concrete before and after burning state, in situ test on concrete, concrete pull over test etc. with various incorporating percentage of RGP. On the other hand, various concrete mix like 80 or 100% of RGP can be used to cast concrete in replacement of fine sand which was not done. And also fly ash can be used for casting.

In this research scheme, the concrete samples were tested only up to 800 °C to find out the properties of concrete. But from the desk study, it is identified that temperature of fire accident mostly vary in between 600 to 800 °C and more temperature can rise for different purpose like sources of fire accident, weather or climate condition of different locality. So, another experiment can be done with the concrete specimen heating them up to 1000 °C or more. By this experiment the performance and behavior of concrete can be determined for higher and higher temperature. The fire furnace was slightly reintegrated. As a results the temperature may slightly vary. If it was properly insulated higher temperature can be measured properly.

This research aimed to investigate the residual strength of concrete after heat episode for fire accident. In pursuance of such demand this research has been conducted to discover improved construction mechanism to build better fire endurable structure. Covering concrete with tiles can be a technique suggested to build more fire resistive structure. Different types of materials can be used; fly ash can be used partially in place of cement to check whether the fire resistance capacity improves or not. On the side, different type of coarse aggregate like white stone, brick chips can be used for this experiment to investigate the properties and performance of concrete. For the cylinder samples with different aggregate types the residual strength and compressive strength of concrete after immediate burning as well as the mentioned test can be done in order to observe the strength reduction and the behavior. All these studies and experiment can be brought out a good number of findings.

References

1. Shahzada K, Gencturk B, Wei J, Tufail M (2016) Effect of elevated temperature on mechanical properties of limestone, quartzite and granite concrete. *Int J Concrete Struct Mater* 1–2
2. Hong SW, Kang S-G (2003) Behavior of concrete members at elevated temperatures considering inelastic deformation. Springer, pp 2
3. Bastami M (2011) Performance of high strength concretes at elevated temperatures. *Scientia Iranica* 3
4. Phan LT, Carnio NJ (2000) Fire performance of high strength concrete: research need. *ASCE/SEI Struct Congress* 2–3
5. ASTM (2014) Active standard of material. In: Standard test method for sieve analysis of fine and coarse aggregates, West Conshohocken, ASTM, pp 50–62
6. ASTM (2003) Advance concrete technology. In: Standard specification for molds for forming concrete test cylinders vertically, West Conshohocken, Butterworth-Heinemann, pp 41–42

7. AASHTO (2018) Standard test method for slump of hydraulic-cement concrete, North Capitol Street NW
8. Don brogan SF (2008) In: Guide to curing concrete, Farmington Hills, ACI

The Effect of Palm Oil Fuel Ash (POFA) and Steel Fiber Addition to the Mechanical Properties of Ultra High Performance Concrete (UHPC)



Hafizuddin Zakare, Anizahyati Alisibramulisi, Muhd Norhasri Muhd Sidek, Aidan Newman, Nadiyah Saari, Suraya Hani Adnan, and Norshariza Mohd Bhkari

Abstract Over a period of time, Ultra High Performance Concrete (UHPC) has been innovated more and more. Since it has high performance and durability, thus it is deemed to be expensive due to the material used in the recipe. High cement content due to low water cement ratio and high production cost are a few of UHPC disadvantages. Therefore, a new innovation and alternative to this solution is needed. Incorporating waste material such as Palm Oil Fuel Ash (POFA) in UHPC could be the new innovation, since POFA is abundantly available. Other than that, POFA is proven to improve conventional concrete performance, hence it could also be used to enhance UHPC. Therefore, this paper emphasizes the effect of POFA and steel fiber inclusion to the mechanical properties of UHPC using modified cube method and four-point bending test. Non Destructive Testing (NDT) using Ultrasonic Pulse Velocity (UPV) method was also conducted. The POFA percentages used were 5, 10, and 15% whereas, steel fiber percentage was only 1% by weight of OPC cement. The Test specimen dimension used was 500 mm × 100 mm × 100 mm. The testing

H. Zakare · A. Alisibramulisi (✉) · M. N. M. Sidek · A. Newman · N. Saari · N. M. Bhkari
School of Civil Engineering, College of Engineering, Universiti Teknologi MARA (UiTM),
40450 Shah Alam, Selangor, Malaysia
e-mail: aniza659@uitm.edu.my

M. N. M. Sidek
e-mail: muhdnorhasri@uitm.edu.my

N. Saari
e-mail: nadia903@uitm.edu.my

N. M. Bhkari
e-mail: nshariza@uitm.edu.my

A. Alisibramulisi · M. N. M. Sidek · N. M. Bhkari
Institute for Infrastructure Engineering and Sustainable Management (IESM), Universiti
Teknologi MARA (UiTM), 40450 Shah Alam, Selangor, Malaysia

S. H. Adnan
Department of Civil Engineering Technology, Universiti Tun Hussein Onn Malaysia (UTHM),
84600 Pagoh, Johor, Malaysia
e-mail: suraya@uthm.edu.my

in this study was done at a concrete age of 28 days by following the standard of the American Society of Testing and Material (ASTM). Based on the result, the addition of 15% POFA gave the highest flexural strength, while 5% POFA plus 1% steel fiber gave the highest compressive strength. UPV highest value result was obtained from 15% POFA. It is recommended that the optimum addition level of POFA is 15% for good results of both flexural and compressive strength.

Keywords Palm oil fuel ash (POFA) · Steel fiber · Ultra high performance concrete (UHPC) · Compressive strength · Flexural strength · Ultrasonic pulse velocity (UPV)

1 Introduction

Structures constructed may be made of different concrete materials and each has a certain characteristic feature. Concrete is a vital material and is often used in construction as a part of building materials. Nowadays some modern functional technologies and some innovative application methodologies have been introduced. The usage of recycled material as an alternative for originally concrete components such as aggregates, fine, and cement has resulted in many innovative works.

Thereafter another new concrete material is also widely released to give more strength to the concrete mechanical properties. Because of this, a variety of concrete types have been created that have specific requirements in terms of origin and operation for each concrete. Ultra-High-Performance Concrete (UHPC) is typically one of its types, which can be accomplished by incorporating or replacing new materials from conventional concrete materials such as chemicals or waste products.

Ultra-High-Performance Concrete (UHPC) is one of the latest building materials. Compared to ordinary concrete it has superior mechanical strength, durability, and impact resistance as the name suggests. The extremely low porosity increases the uniformity of the mixture and helps the concrete to achieve extreme properties with a more homogeneous stress distribution [1]. Ultra-High-Performance Fiber Reinforced Concrete (UHPFRC) is a composite material based on cement with distinctive properties such as compressive and flexural strength ranging from 150 to 30 MPa [2].

On the other hand, palm oil ash is one of the choices for the re-use of palm oil goods. Palm oil is derived from soil materials used in the palm oil crop. After the extraction process, earlier lunches are scorched as biomass fuel into bubble water, e.g. palm oil filaments, shells, and void organic material, which produces steam for energy and extraction in palm oil plants. The result is heavy waste factor palm oil fuel debris (POFA), which by weight is around 5%. Calcium hydroxide ($\text{Ca}(\text{OH})_2$) can degrade the silica oxide content of POFA to concrete, and pozzolanic reactions produce more calcium silicate hydrate (C-S-H), a gel compound that decreases the calcium hydroxide measurement. Thus, this contributes to the strength of the concrete

thus producing stronger and denser concrete as well as enhancing the durability of the concrete [3].

The usage of POFA as building material could improve the performance of UHPC and reduce pollution to the environment at the same time. AS palm oil production increases, the amount of POFA also increases [4]. Since the wastage is abundant, POFA is disposed of in landfill. About 5% of ash is produced from solid waste, POFA due to limited application has been disposed of in landfill and could lead to environmental problems [5]. Therefore, this research aims to use POFA to be incorporated in building materials instead of disposing of it in the landfill. This can help to improve the performance of conventional UHPC to be more sustainable and greener, as well as saving the environment from pollution.

2 Methodology

2.1 Materials

Palm Oil Fuel Ash (POFA)

The POFA was dried up in the oven for 24 h during processing to reduce the moisture content. Then, the raw POFA collection is sieved passing 212 μm to remove the husk and shell of Palm Oil and the coarse and fine particles using a Sieve Shaker or by hand. Only POFA in the form of a filler was used to give effect to the compressive strength of the concrete. Alternatively, the sieved POFA was placed inside the container and stored in a dry, airtight humidity-controlled space within the laboratory. The POFA’s chemical composition used in this research is tabulated in Table 1.

Table 1 Chemical composition

Chemical Composition	% in POFA
MgO	8.1241
Al ₂ O ₃	3.2178
SiO ₂	36.2926
P ₂ O ₅	4.0987
SO ₃	1.6632
K ₂ O	6.8238
CaO	36.3689
TiO ₂	0.2677
MnO	0.2736
Fe ₂ O ₃	2.8696

Cement

For this study, Ordinary Portland cement (OPC) obtained from Tasek Corporation Berhad was used with the cement strength category of 42.5 N.

Aggregate Preparation

The coarse and fine aggregate were sieved manually using a sieved tool device. Coarse aggregate was collected from the retained 2 mm sieve and 10 mm passing. While for fine aggregate was taken from passing 2 mm sieve.

Admixture

Master-Glenium ACE 8538 superplasticizer was used in this research to increase the strength and durability of concrete. This was also used to boost the early strength performance of the concrete. The flow and water reduction operation of the Master-Glenium ACE 8538 allows for the effective and direct formulation of self-compacting concrete. It can be put in without vibration. It was added after the water mixing process in the concrete.

Steel Fiber

The steel fiber form used in this research was a hooked end with a fiber length of 30 mm and a diameter of 0.5 mm. The fiber aspect ratio is the ratio of its length to its diameter and the aspect ratio usually varies from 30 to 150 and here the aspect ratio of the steel fiber is 60.

2.2 Mix Proportion and Specimens

Six different batches were examined in this study. In this research, only 5% POFA was added with the inclusion of steel fiber based on the previous study done in optimizing the results. Table 2 tabulates the mix proportion of UHPC with and without the addition of POFA and steel fiber. Since there is no specific design mix for a UHPC, the design mix used in this analysis was determined by comparison to previous research measurement and formula in a series of trial mixes [6].

The prism specimens' sizes are 100 mm × 100 mm × 500 mm. Numbers of prism specimens produce: 3 for each mix.

2.3 Testing

Flexural strength

Generally, the flexural strength is known as a material property that is defined as the stress experienced within a material just before it yields. It is also known as modulus of rupture. Knowledge of a material's flexural nature is very important to understand

Table 2 Mix proportion of UHPC with additions of POFA and steel fibers

Mixes material	OPC	5% POFA	10% POFA	15% POFA	OPC + 1% SF	5% POFA + 1% SF	Unit
Coarse aggregate (800 kg/m ³)	15.6	15.6	15.6	15.6	15.6	15.6	kg
Fine aggregate (433 kg/m ³)	8.44	8.44	8.44	8.44	8.44	8.44	kg
Cement (OPC) (800 kg/m ³)	15.6	15.6	15.6	15.6	15.6	15.6	kg
Water (160 kg/m ³)	3.12	3.12	3.12	3.12	3.12	3.12	kg
Admixture (16 kg/m ³)	0.31	0.31	0.31	0.31	0.31	0.31	kg
Steel fibers ($V_f = 1\%$)					0.156	0.156	kg
POFA		0.78	1.56	2.34		0.78	kg

the quality of structural members under different loading conditions, which in turn depends on the deciding factors such as the materials used in the preparation, the mixed model adopted, and the fiber content [2].

The flexural strength was conducted on the prism with dimensions of 100 mm × 100 mm × 500 mm in a four-point bending configuration. This test measured concrete flexural strength indirectly for the prism specimen at 28 days of age according to the UHPC flexural strength ASTM C1609 standard [7] using Universal Testing Machine (UTM). The speed rate of 0.20 kN/s was applied. For this experiment, the sample was located horizontally over two touch points or support points. Two loading points were the pressure to be applied on top of the specimen before the sample failed. The four-point flexural will yield greater tension. Three samples were prepared for each mixture and the experiment was carried out for 28 days. Figure 1 shows the setting up and testing of concrete prisms.

Compressive strength

The research protocol for Concrete Compressive Strength Using Portions of Broken Beams in Flexure for this compression test was carried out in accordance with the ASTM C116-90 standard [8] using Compression Testing Machine 3000 kN. The strength was recorded for 28 days of concrete age. The average reading of the tested broken beam was recorded as the concrete strength. The load was applied at the frequency of speeds 3.0 kN/s. The ultimate strength was then recorded.

In this study, concrete compressive strength determination and assessment were performed using portions of flexure-broken beams called the Modified Cube Method. Using standard concrete specimens and procedure, the results obtained from this test are approximately equal to, and on average may be up to five percent greater than those obtained by the compressive strength test. The Modified Cube Method is



Fig. 1 Flexural test setting up (left) and sample testing (right)

performed instead of normal compressive test for the reason that to minimize wastage. Figure 2 shows the modified cube method testing on a compression machine.

Ultrasonic Pulse Velocity

Non-destructive testing (NDT) is characterized as the process in which materials, parts, or assemblies are inspected, checked, or evaluated without compromising the part or system’s serviceability. NDT seeks to determine the quality and reliability of materials, parts, or assemblies without compromising the ability to fulfill their

Fig. 2 Broken beam set up in compression machine



intended functions [9]. There are several NDT methods such as Ultra Pulse Velocity (UPV) and the Rebound Hammer (RH) techniques are two of the most widely used in in-situ applications. The UPV approach is based on the measurements of the velocity of an ultrasonic pulse that an electro-acoustic transducer produces through concrete. The concrete structure can be measured alongside its thickness and any cracks or faults based on the velocity measurements [10].

Ultrasonic Pulse Velocity (UPV) testing was done with the same flexural strength measurement prism. The UPV was calculated using ASTM C 597 standard [11]. A non-destructive test was conducted for checking or evaluating the quality of UHPC concrete with the addition of POFA and steel fiber. The ultrasonic pulse velocity (UPV) test using an indirect approach is the non-destructive test tool applied in this analysis. The purpose of this test was to determine the quality of the concrete without damaging the surface and the performance. Using a transducer, the ultrasonic pulse velocity passes through the concrete with a particular length was observed as the output.

In this study, the UPV method used was an indirect method on concrete prism samples. UPV calculations were done for each concrete sample at 4 locations which were at long surfaces, and the average values were determined. UPV was measured as the ratio of path length to flight time. Figure 3 shows the prism set up for the UPV test.



Fig. 3 Concrete prism marking (left) and UPV device calibration (right)

3 Result and Analysis

3.1 Flexural Strength Test

In addition to the compressive strength, UHPC's flexural strength was also investigated in this research with a different percentage of additional Palm Oil Fuel Ash (POFA), which is 5, 10, and 15%, and inclusions of 1% of steel fibers. The results are given in Table 3.

The maximum flexural strength in UHPC was indicated from the results of 18.988 MPa for 5% POFA addition with 1% inclusion of steel fibers and 20.085 MPa for 15 percent POFA addition respectively. The flexural strength of concrete for beams with 1% steel fibers was observed to be slightly more than from the beam without steel fibers for UHPC with an addition of 5 and 10% of POFA. The percentage increase in flexural strength for beams with 5% POFA inclusion with 1% steel fibers compared to the 5% POFA without steel fibers beams is +8.58%.

From the observations, it can be seen that the application of POFA and steel fibers can improve the flexural strength of concrete or its mechanical properties. This can be because of the steel fibers' presence by contributing its tensile strength by effectively holding the concrete mass. The steel fibers also act as anchorage between the coarse aggregate. When the binders harden, it will also enhance the anchorage points of the overall concrete structure, hence improve the flexural strength. Other than that, for specimens without steel fibers, as the POFA percentage increases, the flexural strength also increases. This is probably due to the pozzolanic reaction of POFA react with water and superplasticizer. This pozzolanic reaction could improve the bondage between aggregates since it can produce Calcium Silicate Hydrate (CSH) gel from calcium hydroxide (CaOH) produced by cement powder reaction with water.

It is therefore recommended to use steel fibers by concrete volume to get the maximum benefit in enhancing flexural strength. Since the purpose of this study is to assess the effect addition of UHPC POFA using a 4-point bending test, it can be observed that with additional POFA in cement content, the flexural strength of concrete also increases.

Table 3 Flexural strength test result (4-point bending) at 28 days age

Concrete mix	Pace rate (kN/s)	Flexural strength (MPa)
OPC	0.2	16.798
5% POFA	0.2	15.988
10% POFA	0.2	17.382
15% POFA	0.2	20.085
OPC + 1% SF	0.2	17.598
5% POFA + 1% SF	0.2	18.988

3.2 Compressive Strength Test

The findings obtained from the test performed are shown below in Table 4. The compressive strength was investigated using portion of broken beam in flexure. The compressive strength was observed for all mixes at 28 days of water curing since all tests showed a compressive strength value above 120 MPa.

The result indicates that the compressive strength appears to decrease with the addition of 10% POFA relative to other tests with additional POFA for 5 and 15% as well as the result for a concrete mix for control 1% steel fiber and additional 5% POFA with 1% steel fiber. This is probably due to the agglomeration of POFA particles in the mix. Agglomerate POFA particles happen when the mix is not blended well during preparation. Hence, this will affect the strength of the concrete produced. Agglomerate POFA will not be able to react completely since only the outer layer of the agglomerate POFA can react to produce the CSH gel. This resulted in the inner layer to be intact, hence no reaction occurs leaving the POFA to be as it is. This will influence the overall concrete strength since there will be void due the unreacted POFA powder in the structure.

The maximum compressive strength was recorded at 224.35 and 234.45 MPa with a 1% inclusion of steel fibers. The highest compressive strength value is UHPC's concrete mixture with 5% POFA plus 1% steel fiber applied. The addition of POFA and the inclusion of steel fiber in UHPC mixes have, therefore, increased the compressive strength values over the control mix. It showed that the strength of UHPC mixes increased as the POFA percentage increased by comparing the control specimen of UHPC with the addition of 5% POFA as well as with the inclusion of steel fiber. The inclusion of steel fiber does not only improve flexural strength but also the compressive strength of concrete. This is because when applied to compressive loading, UHPC tends to burst when failing. With the steel fiber inclusion, there is some resistance to the bursting failure effect.

Table 4 Compressive strength test results at age 28 days

Concrete mix	Pace rate (kN/s)	Compressive strength (MPa)
OPC	3.0	134.50
5% POFA	3.0	184.15
10% POFA	3.0	158.30
15% POFA	3.0	189.25
OPC + 1% SF	3.0	224.35
5% POFA + 1% SF	3.0	234.45

Table 5 UPV test result (indirect method) at 28 days age

Concrete mix	Path length (m)	Ultrasonic pulse velocity (m/s)
OPC	0.2	3601.34
5% POFA	0.2	3809.67
10% POFA	0.2	3727.48
15% POFA	0.2	3830.43
OPC + 1% SF	0.2	3520.74
5% POFA + 1% SF	0.2	3563.12

3.3 Ultrasonic Pulse Velocity (UPV)

The results obtained from the test done are shown in Table 5. The results of the UPV test conducted in the laboratory, shows that there is a different value for the concrete mixtures that have POFA and steel fibers added.

The results indicate that the control sample, which is without the addition of POFA and steel fibers, has the lowest UPV value, followed by 10, 5 and 15%. Such findings showed that UHPC's compressive strength can be improved with the addition of POFA due to the POFA's fineness which can serve as a filler to close the voids. When POFA pozzolanic reactions improve filler and binder effect, it improves the concrete quality altogether. This in turn makes the concrete denser, therefore less defects such as voids. As observed in a compressive strength test where 10% addition has slightly lower strength compared to 5% addition due to the effect of POFA agglomeration. This also affects the quality of concrete as shown by the UPV test. The quality is shown to have a slight defect since there is void due to the POFA agglomeration effect during mixing.

On the other hand, the inclusion of steel fibers tends to further decrease the UPV reading as shown in the figure. Although it is proven in flexural tests and compressive tests that the inclusion of steel fiber increases the performance of concrete, UPV shows the opposite result. This is probably due to the steel fibers reflecting the ultrasonic pulse when emitted through the structure itself, hence reducing the UPV reading. However, steel fiber specimens showed an increasing result in the 5% POFA plus 1% steel fiber specimen compared to the OPC plus 1% steel fiber. This shows that the POFA once again improves the quality although the UPV reading is interfered by the presence of steel fibers.

All the specimens tested at 28 days of curing are classified in a good category using the indirect method. The classification of concrete quality can be referred to in Table 6. From the results obtained, it can be concluded that UHPC has the highest pulse velocity value with a percentage of 15% addition of POFA. The UHPC control specimen showing the lowest value of OPC.

Table 6 Classification of concrete quality [8]

Ultrasonic pulse velocity (m/s)	Quality of concrete
Above 4500	Excellent
3500–4500	Good
3000–3500	Medium
Below 3000	Poor

4 Conclusion

This study emphasizes the performance of UHPC when cement is partially replaced by POFA and the inclusion of steel fibers. The performance is measured by conducting flexural test, compressive test and ultrasonic pulse velocity test. Based on the test conducted, here are the findings.

1. In flexural tests, addition of POFA indeed improves the flexural strength of UHPC beam. The inclusion of steel fiber will further enhance the performance of UHPC with POFA.
2. In the compressive strength test, the addition of POFA does improve the compressive strength of UHPC. With the inclusion of steel fibers, the performance is improved up to 127%. However, the agglomeration of POFA particles could affect the compressive strength of UHPC since it resulted in voids inside the structure.
3. In ultrasonic pulse velocity, it is seen that POFA does improve the quality of concrete by its pozzolanic reaction, which resulted in higher pulse reading. However, the inclusion of steel fiber tends to interfere with the pulse velocity reading resulting in lower pulse reading. On the other hand, the effect of POFA agglomeration can also be seen on the UPV test since it can indicate there are defects such as voids inside the specimen.

Overall, the addition of POFA and steel fiber in this study shows promising results in increment of flexural and compressive strength as compared to conventional concrete mixture. The pozzolanic reaction of POFA plays a vital role in affecting these mechanical properties. Thus, it is recommended that the optimum addition level of POFA is 15% for good results of both flexural and compressive strength. Whereas, inclusion of steel fiber should be studied further.

Acknowledgements The authors would like to acknowledge the financial support for this study from Ministry of Higher Education—Fundamental Research Grant Scheme of 600-IRMI/FRGS 5/3 (178/2019) and other supports from Institute of Research Management & Innovation (IRMI), Institute for Infrastructure Engineering and Sustainable Management (IIESM) and School of Civil Engineering, UiTM Shah Alam, Selangor. The authors would also like to acknowledge industrial support from United Palm Oil Sdn Bhd Penang for providing POFA in this study. These supports are gratefully acknowledged.

References

1. Sierens Z, Joseph M, Vandevyvere B, Li J (2018) High quality recycled concrete aggregates in UHPC: a preliminary study 1–7
2. Reddy GKG, Ramadoss P (2017) Flexural behavior of ultra-high-performance steel fiber reinforced concrete: a state-of-the-art review. 4(9):89–99
3. Sooraj VM (2013) Effect of palm oil fuel ash (POFA) on strength properties of concrete. *Int J Sci Res Publ* 3(6):2250–3153. Retrieved from www.ijsrp.org
4. Hamada HM, Jokhio GA, Yahaya FM, Humada AM, Gul Y (2018) The present state of the use of palm oil fuel ash (POFA) in concrete. *Constr Build Mater* 175:26–40
5. Alsubari B, Shafiqh P, Jumaat MZ (2016) Utilization of high-volume treated palm oil fuel ash to produce sustainable self-compacting concrete. *J Clean Prod* 137:982–996
6. Muhd Norhasri MS, Hamidah MS, Mohd Fadzil A, Megawati O (2016) Inclusion of nano metakaolin as additive in ultra-high-performance concrete (UHPC). *Constr Build Mater* 127:167–175. <https://doi.org/10.1016/j.conbuildmat.2016.09.127>
7. ASTM C1609/C1609M-19 (2019) Standard test method for flexural performance of fiber-reinforced concrete (Using Beam with Four-Point Loading). ASTM International, West Conshohocken, PA
8. ASTM C116-90 (1990) Test method for compressive strength of concrete using portions of beams broken in flexure (withdrawn 1999). ASTM International, West Conshohocken, PA
9. Helal J, Sofi M, Mendis P (2015) Non-destructive testing of concrete: a review of methods. *Electron J Struct Eng* 14(1):97–105
10. Lampropoulos A, Tsioulou O, Paschalis S (2012) Combined non-destructive method for evaluating the mechanical performance of ultra high performance fibre reinforced concrete (UHPFRC). 131:66–77
11. ASTM (2009) ASTM C 597: Standard test method for pulse velocity through concrete

Investigation on Fire Resistance of Concrete Incorporating Recycled Ceramic Fine Aggregate



Joarder Md. Sarwar Mujib, Md. Maruf Hasan, Md. Rasel Molla, Tahsin Md. Zahid, and Tanvir Mustafy

Abstract The paramount importance of the fire resisting competency of a fire exposed concrete, which has a significant impact on civil engineering structures, has been an influential segment of this research work. In this study, it was investigated the performance of recycled ceramic fine aggregate (RCFA) incorporated concrete subjected to elevated temperature as a partial replacement for sand material. Different portions of RCCA were used with sand for preparing 8 working mix conditions, i.e., 5, 10, 15, 20, 25, 30, 35, and 40 wt%. A total of 135 cylinders were prepared ($n = 15$ for each group). 15 cylinders were prepared without any RCFA percentage for comparison. Cylinders were tested under compressive loading at certain temperatures (500, 600, 700, and 800 °C) after 28 days of curing. X-ray fluorescence (XRF) analyses were conducted on the corresponding samples to extract the chemical composition under elevated temperature. At 600 °C, concrete containing RCFA percentage of 40 wt% exhibited the best performance at high temperature, incurring an average strength loss of 30.87% compared to 33.86% strength loss in reference samples. The measured strength was noted to be retained by 4.78% more of the total strength for RCFA percentage of 40 wt% reference normal concrete samples, respectively under an elevated temperature range of 700–800 °C. Mixes with high contents of RCFA displayed better post-fire behavior, mostly because of the similarities between the coefficient of thermal expansion of RCFA, compared to the natural fine aggregates, the coefficient of thermal expansion of the mortar that induced less internal thermal stresses and less cracking at high temperatures and the intrinsic higher stability of the recycled ceramic aggregates at high temperature compared to natural fine aggregate.

J. Md. S. Mujib · Md. Maruf Hasan (✉) · Md. Rasel Molla · T. Md. Zahid · T. Mustafy
Military Institute of Science and Technology, Dhaka, Bangladesh

T. Md. Zahid
e-mail: tahsin.zahid@ce.mist.ac.bd

T. Mustafy
e-mail: mustafy@ualberta.ca

T. Mustafy
University of Alberta, Edmonton, Canada

Keywords High temperature · Compressive strength · Recycled ceramic fine aggregate · Microstructure

1 Introduction

Safety management regarding fire hazard and the structural competency of complete concrete construction has been a widespread global catastrophic issue today. Risks due to domestic or industrial fire is a very concerning fact and has a rampant effect on economic, social and industrial sectors. Necessary precaution must be required for the structural safety and serviceability that may prevent unexpected casualties of livelihoods. Generally the physical, chemical and thermal properties of a structural element control the impact of fire resistance behavior. Thermal competency of the concrete mostly depends on the concrete volume per square foot or square meter, aggregate properties and free moisture content, the design mix ratio of concrete etc. Several influential factors dominate the performance of a concrete structure such as lateral restraint behavior, clear cover around the reinforcing bars, induced stress–strain level of both concrete and steel, the tendency to spalling by the trapped moisture content in concrete and aggregate used etc.

Concrete exposed to fire shows magnificent upshot and acts as a constitutive part being a shield agent against fire. Generally, the enormous fire effect induced in the infrastructural project is more drastic than typical building fires that may result in very high temperatures within a few minutes [1]. The cracking and spalling pattern followed by different concrete construction has been a troublesome fact that has to be determined with the varying temperature regimes. Many statistical analysis showed that concrete structures have a trend to lose the compressive strength within the temperature range 300–600 °C, ironically which seems tremendously difficult to maintain over 600 °C [2]. The damage pattern in concrete cylinder specimen incorporating rubber crumb that melted inside the concrete during the fire was found to be disturbing at elevated temperature (600 °C) and regarded as more susceptible to significant cracking [3]. Several fire investigations were conducted to evaluate the overall structural ability of concrete construction as concrete is predominantly a good fire resistant against fire exposure. Residual strength was noted to be decreased after suffering from fire exposure to temperatures above 400 °C for fiber concrete, whereas residual fracture energy was found higher prior to heating procedure [4]. The overall fire performance of concrete construction, mostly depends on the size, type and output of fire [1].

Investigating the post-fire performance regimes of concrete structure incorporating the alkali-activated fly ash cements at successively higher temperatures (600–700 °C) had been reported to be significantly deteriorated [5]. Porous concrete contains trace amount of entrapped moisture content in it which eventually starts to vaporize when the temperature exceeds 100–140 °C causing a pressure build-up in the neighboring concrete skeleton. When the temperature exceeds 400 °C beyond the moisture plateau, the calcium hydroxide $[\text{Ca}(\text{OH})_2]$ in the cement will begin to

dehydrate producing more water vapor resulting a significant compressive strength reduction of concrete. In determining the mechanical properties and compressive strength of concrete incorporating hematite component, concrete was subjected to heating up to 800 °C showed a better result, but that eventually result in failure of hematite-concrete mixture homogeneity [6]. As the temperature increases, residual compressive strength of the concrete follows a notable decline. At 400 °C residual compressive strength of the concrete seems to fall 60% and it is below 10% at 800 °C [7]. The compressive and flexural strength degradation pattern of concrete structure begins with a cracking mechanism in the carbon textile concrete matrix due to preheating at 600 °C [8]. The residual strength of reactive powder concrete (RPC) shows better out-turn in comparison with ordinary concrete (OC) as well as high-performance concrete (HPC) at 500 ± 50 °C [9]. Up to 950 °C, a mixture of waste ceramic powder (WCP) with alkali-activated mortars shows a significant increase in resistance capacity in concrete construction [10].

Due to the heat effect, concrete structures undergo physical as well as chemical changes abruptly. There is a complex relation between fire and concrete, mostly due to the varying composition of the concrete. In this research, varying proportions of recycled ceramic fine aggregate (RCFA) replacing with sand has been used to reveal the overall residual structural strength of concrete in comparison to the conventional ordinary concrete (OC) after preheating to various temperatures (500, 600, 700, and 800 °C). To reveal the overall residual compressive strength after a heating mechanism to concrete, these phenomena entail the requirement of a detail investigation of RCFA mixed concrete at successively higher temperatures. Ceramic waste powder (CWP) as a landfill, has an extreme effect on the environment that significantly help in polluting the groundwater and underlying soil strata. Ultra hardness, chemical inertness and mechanical strength of RCFA play a vital role in the formation of concrete specimen matrix which is pronounced to be eco-friendly material.

2 Research Significance

Out of many scientific explorations and advancements in technological sectors worldwide, structural integrity and safety, serviceability and design competency regardless of structure types has been a term of great importance. The inclusion of RCFA in concrete could be a pragmatic research program as it has sufficient structural strength which acts like an electrical and thermal insulator during fire attack. Due to higher endurance capability and mechanical stability of RCFA investigation at higher temperatures i.e. 800 °C requires more area of interest and importance. Sustainability is a matter of great concern in concrete construction and for the engineers associated with it. Compressive strength of RCFA incorporated with concrete needs to be identified for pre-firing and post-firing behavior which is investigated in this paper. General properties of the materials incorporated in building construction characterized by the structural element that has the ability to withstand fire or to continue

Table 1 Features of CA, FA and RCFA

Features	Materials		
	CA (Stone chips)	FA (Sand)	RCFA
Specific gravity	2.80	2.60	2.45
Water absorption capacity (%)	0.9	3	5
Unit weight (kg/m ³)	1550	1633	1610
Fineness modulus	7.21	2.81	2.66

CA—Coarse Aggregate, FA—Fine Aggregate, RCFA—Recycled Ceramic Fine Aggregate

to carry out structural functions or both governed by ACI 216 [11]. Moreover, RCFA exhibits the desired the compatibility needed for structural performance.

3 Experimental Program

3.1 Material Features

Ordinary Portland Cement with a relative density of 3.15 and bulk density ranging from 830 to 1650 kg/m³ considered as cementitious material, was used in this experiment. Sieve analysis of RCFA, coarse aggregates and fine aggregates were conducted in accordance with the reference given by ASTM C136 [12]. In order to reveal the strength of coarse aggregates Los Angeles Abrasion test was conducted and the L.A. abrasion value of coarse aggregate reported to be 32% (acceptable range lies between 10 and 40%) [13]. Notably, maximum coarse aggregate size (stone chips) was used 19 mm. Recycled ceramic is made of 50% clay materials, 25% silica and 25% feldspar (aluminum silicate Al₂SiO₅, Na⁺, K⁺ and Ca⁺). Constituent materials of different varieties have been used are discussed in Table 1.

3.2 Morphology of RCFA

Inorganic, metallic or nonmetallic crystalline ceramics having a density of 2–6 gms/cm³ both ionic and covalent bonds have high melting point ranging from 1000 to 1600 °C or even more. Ceramics demonstrate tremendous structural strength when added to concrete structures and sufficient hardness as well. They are typically formed to withstand high temperatures and imparts no harmful chemical residue inside the concrete during heating. The chemical morphology of ceramics is depicted in Table 2.

Table 2 Various chemical composition of ceramic powder and residue published in [14]

Chemical components (%)	Ceramic powder (%)	Residue (%)
SiO ₂	63.36	64.20
Al ₂ O ₃	18.20	18.32
Fe ₂ O ₃	2.77	0.65
CaO	1.74	1.09
Na ₂ O	0.34	1.95
K ₂ O	3.87	1.84
MnO	0.02	0.06
TiO ₂	0.80	0.26
MgO	2.04	6.63
P ₂ O ₅	0.05	0.06
PF	6.80	4.96

3.3 Mix Proportioning

The candidate RCCA replacing with the weight of fine sand taken as 5, 10, 15, 20, 25, 30, 35 and, 40%, a total of 96 concrete cylinder specimens ($n = 15$ for each group) were prepared in order to investigate the post-fire behavior at elevated temperatures (500, 600, 700, and 800 °C) for about an hour and its detrimental effect on the concrete structure.

For further comparison with the normal concrete compressive strength, a group of additional 15 cylinders was made without RCFA. Mix proportioning of the candidate materials CA, FA (fine sand), Ordinary Portland Cement (OPC), RCFA with sufficient water content was conducted in a concrete mixer in accordance with ASTM C 192 [15]. RCFA mixed concretes were conducted to attain the required workability and stability needed for the construction. The external appearance of the candidate materials is displayed in (see Fig. 1).

3.4 Preparation of Specimen

In a concrete mixer, the candidate materials were mixed with varying RCFA compositions using one-third of the water content. Since the primary mixing period that lasted for 2 min, remaining water content was used for further mixing procedure for 1.5–2 min more. Prepared concrete mixes were then poured into the steel cylinder molds having diameter and height of successively 100 and 200 mm. The slump test measurement was conducted for ensuring the concrete mix workability with a reference to ASTM C 143 [16] and the related average slump test value was recorded 103.33 mm.



(a) Coarse aggregates



(b) Recycled ceramic fine aggregates



(c) Ordinary Portland Cement



(d) Fine aggregates (fine sand)

Fig. 1 Appearance of construction candidate materials

After the concrete casting being done, all the specimens in the cylinders were kept inside the laboratory at room temperature 20~25 °C for next 1 day (24 h). 24 h later of casting, specimens were finally ready for curing procedure under still water at 23 °C for the next 4 weeks (28 days). Candidate specimens were taken out of the still water and left in a chamber for 1 day at room temperature (25 °C) in order to make the specimens ready for introducing into the heating furnace for identifying the post-fire behavior.

3.5 Experimental Procedure

After the curing procedure and post-curing task being accomplished, normal compressive strength of the 27 candidate concrete cylinder specimens (CCCS) was evaluated at 25 °C using compression testing machine whereas 3 cylinders from group of makes a total of 24 cylinders of varying RCFA proportions (5, 10, 15, 20, 25, 30, 35, and 40%) and 3 cylinders of ordinary concrete having no RCFA proportion. Compressive strength test with a compression machine was conducted according to the standards given ASTM C 39 [17] with a 2000 KN capacity. This evaluation of compressive strength prior to heating was carried out to use as a reference for the analysis of post-fire behavior.

For further investigation to identify the post-fire behavior 96 cylinders, 12 CCCS of ordinary concrete and 96 CCCS having the proportions of RCFA from each groups were taken to the gas furnace for heating at prescribed temperatures (500, 600, 700, and 800 °C) for 1 h positively. Mud coating over the entrance was used to seal the possible apertures so that excess air cannot enter into the furnace that may cause unexpected complications during heating. There was a setup of a tiny gateway aperture so that the water vapor can easily escape during heating from the gas furnace (see Fig. 2). Structural steel rebars with a high melting point of 1370 °C (2500 °C) were used to hold the specimens during the heating period inside the conventional gas furnace (see Fig. 3).

Fig. 2 Conventional gas furnace

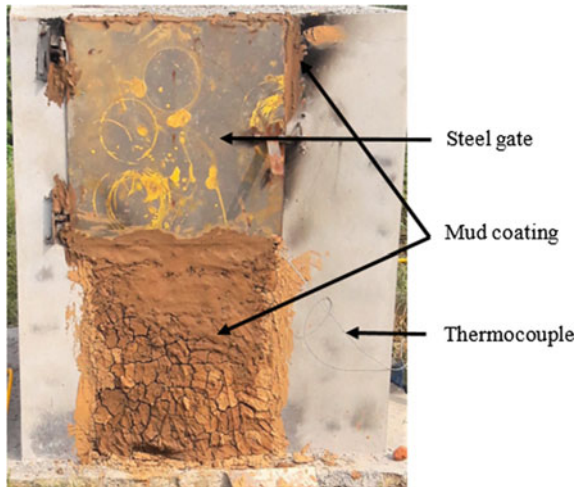
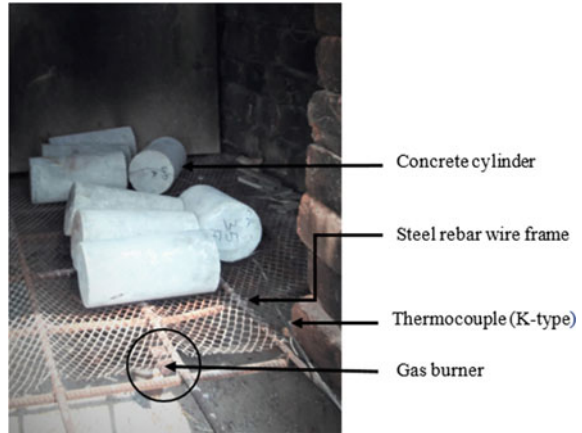


Fig. 3 Specimens inside the gas furnace



4 Analysis Via Visual Inspection

4.1 External Change of Color and Appearance

At room temperature (25°) concrete specimens were seen gray or slightly light gray and with the temperature being raised inside the gas furnace, specimens start to change their external appearance. This change is caused as the concrete specimens were suffering from heating extremely at higher temperatures that finally result in the subsequent change in the chemical and physical composition of neighboring concrete specimens. When the temperature is 500 °C the concrete specimens turned light yellowish-grey. Discoloration to slightly reddish at 600 °C and eventually it turned to dark color at 800 °C.

4.2 Spalling and Crack Pattern

With the increasing temperature regimes up to target temperature (800 °C), several numbers of micro-cracks were developed on the surface of the candidate concrete specimens without RCFA. This seems a gradual decline in cracking patterns with the successive incorporation of recycled ceramics into the concrete specimens. This is to be noted that existing investigation has already shown that concrete specimens without RCFA suffered from higher temperatures developed internal pressure or stresses within the constituent materials inside the concrete. Spalling is generally caused by the development of interior water vapor which is the result of moisture content in concrete [18]. Cracking was the result due to thermal expansion, drying shrinkage of concrete and water vaporization at elevated temperatures [19]. An

overall crack pattern including the change of external appearances being negotiated in Table 3.

5 Result and Discussion

5.1 Trend of Temperature–Time Curves

Temperature–time trend is used in portraying the overall fire exposing nature of concrete inside the gas furnace. Materials inside the concrete associated with this experiment underwent chemical, physical and mechanical changes due to the extreme heat impact at a rate of 8 °C/min for 1 h at targeted temperatures. Concrete specimens inside the gas furnace were heated at a rate of 8 °C/min determined from the graphical illustration (see Fig. 4). Less significant spalling was observed at the time of heating whereas other studies have experienced few micro-cracks with explosive spalling while being heated at elevated temperatures [20].






5.2 States of Compressive Strength

After 1 h heating period, concrete specimens underwent an instantaneous physical change with their compressive strength. It is observed from Table 4 that having 40% RCFA with concrete replacing sand retains most of the strength even after suffering from high temperatures i.e. 800 °C comparing with different RCFA proportions. For normal concrete without RCFA mix displayed less compressive strength 33.86 MPa whilst it was recorded 12.93 MPa at the highest prescribed temperature 800 °C in this experiment. Comparatively better result came out when increasing proportions of RCFA was added to the concrete. For RCFA-5, strength increased slightly higher than the normal concrete at different prescribed temperatures. RCFA-5 has literally no significant effect on strength increment. At 800 °C, RCFA-40 showed better strength 21.49 MPa which is larger than other mixing proportions at that temperature.

At room temperature (25 °C), 47.64% of the compressive strength was observed to be increased with RCFA-40 whereas only trace amount of (1.57%) strength was increased by RCFA-5 at 25 °C illustrated in Table 5.

66.16% strength increased for RCFA-40 at 800 °C in comparison with the normal concrete which is the best approximate result found comparing with other RCFA proportions (Fig. 5).

Table 3 External appearance and crack patterns at prescribed temperatures

Temperature	25 °C	500 °C	600 °C	700 °C	800 °C
Specimen					
W/C ratio	0.42	0.42	0.42	0.42	0.42
Crack pattern	No crack	No significant crack	Crack begins to appear	Significant crack appears	Large crack

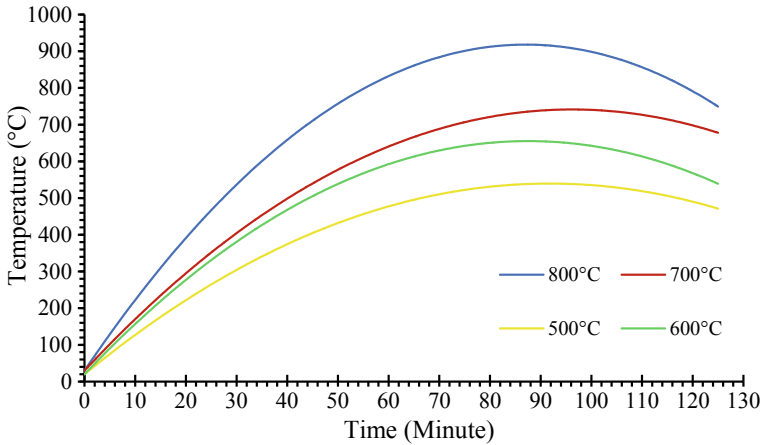


Fig. 4 Temperature–time curves at prescribed temperatures

Table 4 Compressive strength for normal and RCFA concrete

Mix	Slump value (mm)	Compressive strength (MPa)				
		25 °C	500 °C	600 °C	700 °C	800 °C
NC-0	108	33.86	29.08	21.83	17.60	12.93
RC-5	104	34.4	30.16	22.49	17.88	15.52
RC-10	104	37.21	32.24	24.30	19.53	15.31
RC-15	103	37.92	33.21	25.22	20.09	16.61
RC-20	103	41.03	36.02	27.43	21.86	17.71
RC-25	103	40.16	34.91	26.33	21.73	16.75
RC-30	102	43.16	37.58	28.95	23.85	19.11
RC-35	102	44.66	39.04	30.36	24.08	18.95
RC-40	101	50	43.04	34.56	27.27	21.49

NC—Normal concrete, RC—Recycled ceramics (Fine aggregate)

5.3 Elastic Modulus of Different Concretes

According to the standard specified by ACI 363 committee, elastic modulus for lightweight concrete having a unit weight of 145 lb/ft³ (2323 kg/m³) was evaluated in Table 6.

At room temperature (25 °C), elastic modulus of normal concrete (NC-0) without RCFA was 26.61GPa which was increased by 15.86% when 40% RCFA was introduced where the least increment was found out to be 0.60% for 5% RCFA and 3.57% for 10% RCFA which had literally no significant effect compared with the normal concrete (see Fig. 6). At the highest temperature (800 °C) the increment in elastic modulus was noted 18.31% for 40% RCFA in comparison with normal concrete.

Table 5 Strength increment in comparison with normal concrete

Mix	Strength increment comparing with normal concrete (%)				
	25 °C	500 °C	600 °C	700 °C	800 °C
NC-0			0.00		
RC-5	1.57	3.72	3.04	1.57	20
RC-10	9.89	10.87	11.31	10.98	18.40
RC-15	11.97	14.19	15.53	14.15	28.45
RC-20	21.16	23.84	25.65	24.22	36.98
RC-25	18.60	20.06	20.63	23.48	29.56
RC-30	27.46	29.23	32.61	35.48	47.76
RC-35	31.89	34.25	39.05	36.81	46.52
RC-40	47.64	48.01	58.32	54.91	66.16

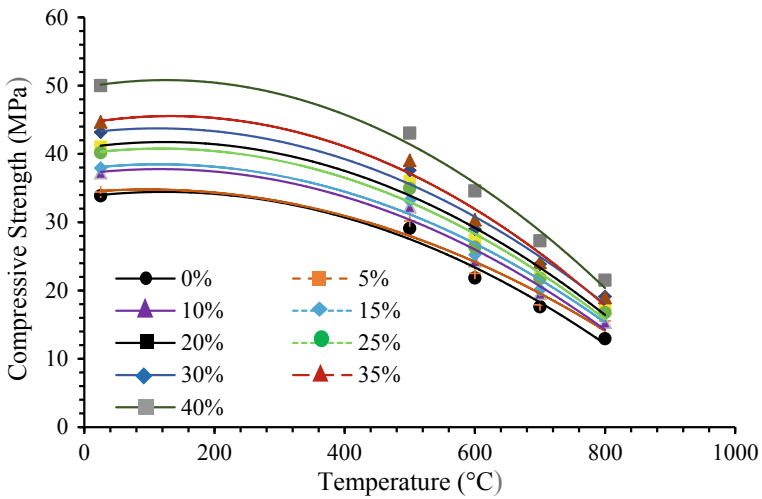


Fig. 5 Compressive strength-temperature relation

For normal concrete (NC-0) 28.15% reduction in elasticity was noted within the temperature range from 25 to 800 °C where 26.60% reduction for both RCFA-35 and RCFA-40 was recorded within this temperature region.

With the increment in including the RCFA with the concrete mix, the modulus of elasticity of the concrete gradually grows upward trend. Concrete strength mainly depends on the aggregate elasticity. As temperature increases, the detrimental effect on the constituent materials appears that may also be the reason behind the loss of subsequent rigidity of concrete.

Table 6 Elastic modulus of concrete at prescribed temperatures

Mix	Elastic modulus (GPa)				
	25 °C	500 °C	600 °C	700 °C	800 °C
NC-0	26.61	25.17	22.75	21.14	19.12
RC-5	26.77	25.50	22.98	21.25	20.28
RC-10	27.56	26.14	23.61	21.89	20.19
RC-15	27.75	26.42	23.93	22.11	20.74
RC-20	28.59	27.23	24.65	22.76	21.18
RC-25	28.36	26.91	24.29	22.71	20.80
RC-30	29.14	27.66	25.13	23.46	21.73
RC-35	29.52	28.06	25.57	23.54	21.67
RC-40	30.83	29.11	26.81	24.60	22.62

$$E_c = \left(\frac{w_c}{2300} \right)^{1.5} (3320\sqrt{F_c} + 6900) \text{ (MPa) [21]}$$

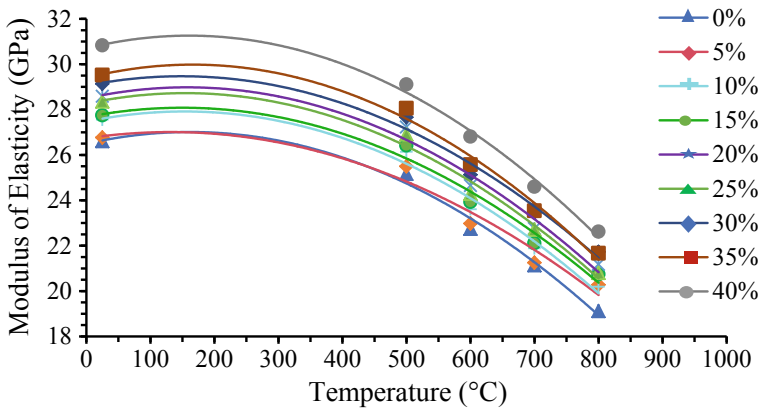


Fig. 6 Elastic modulus of concrete

5.4 Failure Patterns of Concrete

Destructive damages of the concrete at which concrete fails in compression test prior to heating becomes more severe due to post-fire effect of the concrete. This happens as the constituent chemical properties of the concrete begins to lose their stability with the increasing temperature. In contrast to the incorporation of RCFA i.e. 5, and 10%, no significant changes appeared in this experiment. Higher RCFA proportions showed comparatively better-withstanding capacity against compression in comparison with the normal concrete. Recycled ceramics provide sufficient hardness to concrete having a better interlocking characteristic with other constituent

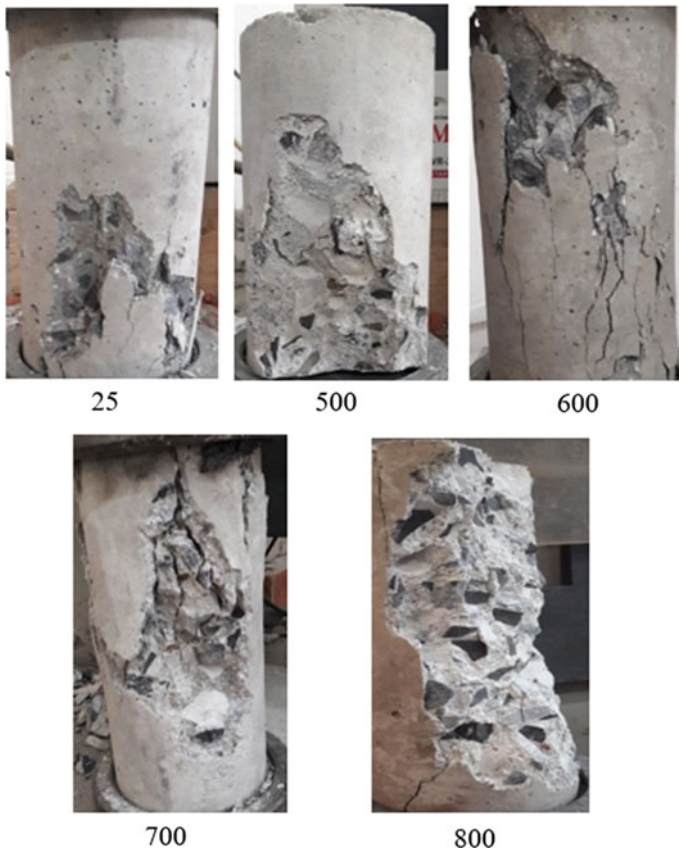


Fig. 7 Failure patterns of RCFA-40 at elevated temperatures

cementing materials in concrete. For instance, the failure pattern of RCFA-40% at high temperatures is depicted in the following (see Fig. 7).

5.5 Weight Loss

Weight loss of the concrete specimens was observed to be changed in a curv fashion in this paper (see Fig. 8). At 500 °C and 600 °C, highest losses were recorded i.e. 3.77 and 7.15% for 25% RCFA which showed a different trend with the highest losses i.e. 10.86 and 11.74% for 5% RCFA at 700 °C and 800 °C. The least weight losses for which 35% RCFA concrete underwent a significantly less change i.e. 10.32% in its chemical and physical deterioration after exposing to 800 °C.

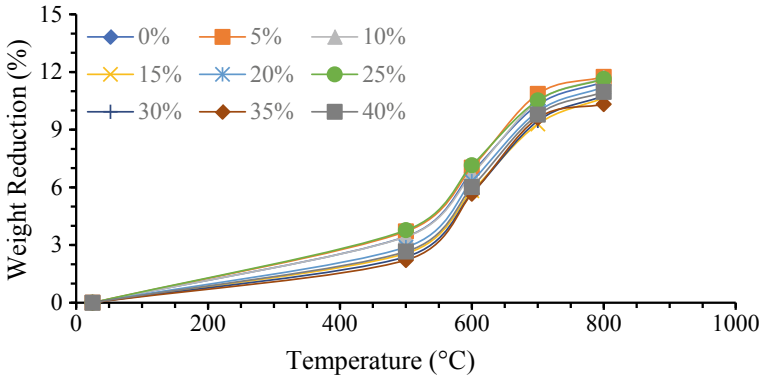


Fig. 8 Weight losses of both normal and varying RCFA mixed concrete

5.6 X-ray Fluorescence (XRF) Spectrometer Test on RCFA

Non-destructive chemical analysis known as X-ray fluorescence (XRF) spectrometer test was conducted to determine the overall chemical composition needed to determine the pre-fire and posterior-fire behavior illustrated in Table 7.

Highest accuracy (99.7%) in measuring the routine chemical test of recycled ceramics at room temperature and 800 °C was ensured by introducing 3 sigma (standard deviation) in the generalized calculation. Experimental analysis has revealed that less change occurred in most of the constituent elements in ceramic after suffering from 800 °C for 1 h. It proved the overall posterior-fire resistivity of the ceramic materials against fire exposer. A detailed representation of a routine X-ray fluorescence spectrometry on ceramic explained that manganese (Mn) was completely vanished

Table 7 Routine X-ray fluorescence spectrometer test of recycled ceramics

Pre-fire state (25 °C)			Posterior-fire state (800 °C)		
Element	%	$\pm 3\sigma$	Element	%	$\pm 3\sigma$
Al	23.5	1.3	Mg	2.7	2.5
Si	75.7	1.3	Al	18.77	0.95
S	0.22	0.21	Si	77.9	2.2
Mn	0.035	0.024	S	0.15	0.11
Fe	0.382	0.048	Fe	0.176	0.022
Cu	0.005	0.005	Cu	0.005	0.003
Zn	0.137	0.014	Zn	0.003	0.002
Zr	0.006	0.002	Zr	0.0035	0.0008
Pb	0.005	0.003	Pb	0.002	0.001
Bi	0.007	0.003	Bi	0.002	0.001

after heating at 800 °C whereas copper (Cu) and silicon (Si) was found to be approximately unchanged even after heating at the same temperature. Aluminium content decreased by 4.73% due to heat exposure to 800 °C. A more precise result could be obtained if the recycled ceramics were of coarser aggregates instead of finer form. It is observed from the X-ray test that aluminium (Al) and silicon (Si) content plays vital role in the formation of ceramic aggregate regardless of calcium (Ca) content.

6 Conclusions

A rigorous experimental study has evaluated the effectiveness of incorporating recycled ceramics into the concrete at successively higher temperatures. Authors suggested the recycled ceramic incorporation with concrete, have been investigated exhaustively according to the compression test conducted specified by ASTM standard. After strenuous analysis, a vivid prospect outlining the succeeding closures came out (see Fig. 9). Compressive strength was observed to be increased linearly different temperatures for varying RCFA proportions in concrete mix.

1. Comparatively RCFA concrete showed different characteristics at different temperatures. 87.69% of the compressive strength was retained by RCFA-5 at 500 °C whereas 65.4%, 51.98%, and 45.12% was recorded at successively 600, 700 and 800 °C.
2. With a swift loss pattern, 61.81% of the compressive strength decreased for normal concrete after exposing to 800 °C while for RCFA-35 and RCFA-40 those were 57.57 and 57.02% which are discussed in Table 8. With the increasing RCFA replacing sand proportions in concrete showed less strength reduction delaying the loss pattern for a while.
3. Lower RCFA in concrete i.e. 5 and 10% increased the modulus of elasticity by 6.07 and 5.59% where higher RCFA i.e. 30, 35, and 40% increased the elasticity

Fig. 9 Compressive strength of normal and varying RCFA mixed concrete at elevated temperatures

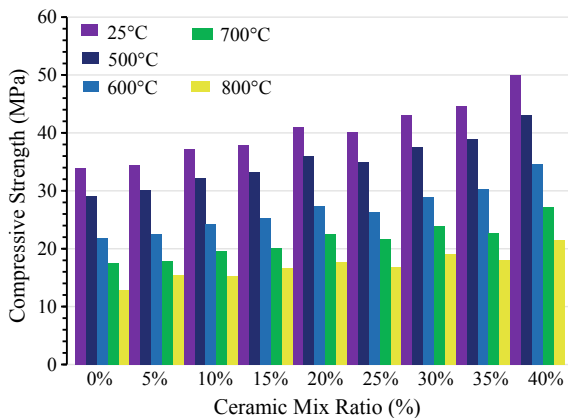


Table 8 Strength decrease comparison of various concrete mix

Mix	Strength decrease at prescribed temperatures (%)				
	25 °C	500 °C	600 °C	700 °C	800 °C
NC-0	0	14.12	35.53	48.02	61.81
RC-5		12.31	34.60	48.02	54.88
RC-10		13.36	34.69	47.51	58.85
RC-15		12.42	33.48	47.00	56.19
RC-20		12.23	33.14	46.71	56.82
RC-25		13.07	34.43	45.88	58.28
RC-30		12.93	32.93	44.75	55.73
RC-35		12.59	32.03	46.08	57.57
RC-40		13.91	30.87	45.46	57.02

successively by 13.65, 13.34, and 18.31%. Thus, it proved to be useful using higher RCFA proportion in concrete that eventually strengthens the concrete in adverse temperature regimes.

- Eventually it can be brought to light that inclusion of higher RCFA-40 retains 4.78% more of the compressive strength in comparison to the normal concrete at 800 °C. To investigate the failure mechanism and strength retaining competency with the inclusion of RCFA further pragmatic approach with the existing research needs to be studied in future.

Acknowledgements The all out research program counted on the patronage of the department of Civil Engineering, Military Institute of Science and Technology (MIST). The authors would like to share the profound gratitude and acknowledge all of the technical supports and sufficient fund provided by the authority (MIST). Special gratitude towards the Structural Engineering Lab, Solid Mechanics Lab, and Nuclear Science Engineering Lab who put their remarkable contribution accomplishing this research.

References

- Kodur VKR, Phan L (2007) Critical factors governing the fire performance of high strength concrete systems. *Fire Saf J* 42:482–488
- Peng G-F, Chan SYN, Song QM, Yi QX (2006) Effect of high temperature on concrete: a review. *Key Eng Mater* 302–303:138–149
- Guo Y, Zhang J, Chen G, Xie Z (2014) Compressive behaviour of concrete structures incorporating recycled. *J Cleaner Prod* xxx:1–11
- Peng G-F, Yang W-W, Zhao J, Liu Y-F, Bian S-H, Zhao, L-H (2006) Explosive spalling and residual mechanical properties of fiber-toughened high-performance concrete subjected to high temperatures. *Cement Concr Res* 36(4):723–727
- Fernández-Jiménez A, Pastor JY, Martín A, Palomo A (2010) High-temperature resistance in Alkali-activated cement. *J Am Ceramic Soc* 3411–3417

6. Gencil O (2012) Fire and materials. 15 June 2012. [Online]. Available wileyonlinelibrary.com
7. Lee J, Choi K, Hong K (2009) Color and material property changes in concrete exposed to high temperatures. *J Asian Archit Build Eng* 8(1):175–782
8. de AndradeSilva F, Butler M, Hempel S, Filho RDT, Mechtcherine V (2014) Effects of elevated temperatures on the interface properties of carbon textile-reinforced concrete. *Cem Concr Compos* 48:26–34
9. Liu C-T, Huang J-S (2009) Fire performance of highly flowable reactive powder concrete. *Constr Build Mater* 23:2072–2079
10. Huseien GF, Sam ARM, Mirza J, Tahir MMd, Asaad MA, Ismail M, Shah KW (2018) Waste ceramic powder incorporated alkali activated mortars exposed to elevated temperatures: performance evaluation. *Constr Build Mater* 187:307–317
11. ACI (2007) Code requirements for determining fire resistance of concrete and masonry construction assemblies. American Concrete Institute, Farmington Hills MI 48331
12. ACI (2016) Aggregates for concrete. American Concrete Institute, Farmington Hills, MI 48331
13. Kekeç B, Bilim N, Dünder S (2017) Abrasion properties of some building stone wastes and usability for sustainability. *Sustainable Development in the Minerals Industry*, Beijing, China
14. Effting C, Folgueras MV, Güths S, Alarcon O (2010) Microstructural characterization of ceramic floor tiles. *Mater Res* 13(3):319–323
15. A. C192 (2006) Standard practice for making and curing concrete test specimens in the laboratory. American Society for Testing Material, West Conshohocken, U.S.A
16. A. C143 (2015) Standard test method for slump of hydraulic-cement concrete. ASTM International, West Conshohocken, PA
17. A. C39 (2018) Standard test method for compressive strength of cylindrical concrete specimens. ASTM International, West Conshohocken, PA
18. Chan SYN, Peng G-F, Anson M (1999) Fire behavior of high-performance concrete made with silica fume at various moisture contents. *Mater J* 96(3):405–409
19. Son KS, Hajirasouliha I, Pilakoutas K (2011) Strength and deformability of waste tyre rubber-filled reinforced concrete columns. *Constr Build Mater* 25(1):218–226
20. Hertz K (2003) Limits of spalling of fire-exposed concrete. *Fire Saf J* 38(2):103–116
21. Committee A (1984) State-of-the-air report on high-strength concrete. *ACI J* 81(4):364–411
22. Tufail M, Shahzada K, Gencturk B, Wei J (2010) Effect of elevated temperature on mechanical. *Int J Civil Environ Eng IJCEE-IJENS* 1–6
23. A. 216.1-07 (2007) Code requirements for determining fire resistance of concrete and masonry construction. American Concrete Institute, Farmington Hills MI 48331
24. A. C143 (2015) Standard test method for. ASTM International, West Conshohocken, PA

Image Analysis on the Deformation Behaviors of RC Beams with Simulated Deteriorations Under Moving Wheel Load Fatigue



Takamasa Nagai, Ko Kakuma, Hiroaki Nishi, Pengru Deng,
and Takashi Matsumoto

Abstract Using an image analysis method, the fatigue deformation behaviors of two RC beams which were artificially damaged to simulate the freeze–thaw deteriorations are investigated under a moving wheel loading condition. The two beams were loaded with a moving wheel under dry and wet surface condition, respectively, to investigate the effects of water. Pictures were taken at noticeable deterioration stages when cracks occurred and propagated. Those pictures were then analyzed by an image analysis method to obtain two-dimensional displacement fields. The analytical results indicate that the water accelerates RC beam fatigue damages. Under dry condition, shear crack is formed along the line from the edge of center loading block on top surface to the support during the moving wheel load test. Under wet condition, shear crack is also observed at the same location. Additionally, significant local compressive strain accumulates in the upper side surface. That indicates the disintegration of concrete due to water. It is confirmed that the disintegration affects the direction of diagonal crack propagation. In summary, the image analysis successfully captures the progressive damage of artificially damaged zone with the presence of water.

Keywords RC beam · Image analysis · Simulated deterioration · Moving wheel load fatigue

T. Nagai

Graduate School of Engineering, Hokkaido University, Sapporo, Japan
e-mail: nagai-t@eis.hokudai.ac.jp

K. Kakuma

Hokkaido Regional Development Bureau, Kushiro, Japan
e-mail: kakuma@ceri.go.jp

H. Nishi

Civil Engineering Research Institute for Cold Region, Sapporo, Japan
e-mail: h-nishi@ceri.go.jp

P. Deng · T. Matsumoto (✉)

Faculty of Engineering, Hokkaido University, Sapporo, Japan
e-mail: takashim@eng.hokudai.ac.jp

P. Deng

e-mail: pengrudeng@eng.hokudai.ac.jp

1 Introduction

In cold and snowy regions of Japan, the combined deterioration of RC deck slab due to water, frost attack and fatigue is observed in some bridges. This deterioration leads to the top surface disintegration of RC deck slab concrete. The disintegration occurs due to the elution of the cement matrix, thereby aggregates are exposed in the final form. These deterioration cases have been reported in CERI monthly reports [1, 2] and some researchers have investigated the effects of combined deterioration [3]. However, its processes have not been systematically understood and at the same time it is hard to detect the combined deterioration from outer surface in early stage.

Therefore, to understand this combined deterioration processes, this study investigates the fatigue deformation behaviors of RC beams by first artificially damaging to simulate real deteriorated conditions and then by loading under a moving wheel load. The two specimens, which were initially deteriorated by introducing an expansive agent to simulate the frost attack, were tested under a repetitive moving wheel load. In addition, two surface conditions are set as a difference between the two specimens. One surface condition is wet condition, and the other one is dry condition.

This study mainly discusses about water effect by using image analysis. DIC (Digital Image Correlation), which enables us to observe the strain field of a specimen visually, is adopted as a method. DIC has already been applied to measure the displacement and strain of deformed objects in Matsumoto's studies [4, 5], and they show effective results.

The purpose of this study is to analyse the deformation behaviors of RC beams with simulated deterioration under a moving wheel load by using the image analysis. Besides, the analytical results of this research provide an understanding of the combined deterioration in early stage.

2 Approach

2.1 Moving Wheel Load Test

The tested RC beams are 1500 mm in the longitudinal direction, 600 mm in the transverse direction and 180 mm in the thickness direction, having a span of 1110 mm (Fig. 1). As shown in Fig. 1, the beams are reinforced with D13 in the transverse direction and D19 in the longitudinal direction on the top side. On the bottom side, they are reinforced with D19. Specimens are artificially damaged in upper half by mixing an expansive agent and upper transverse reinforcements lead artificial damage in the horizontal direction to imitate real frost damage (Fig. 2). The moving wheel load test was executed on Specimen D and W at the same time (D stands for dry surface condition, W stands for wet surface condition) until the damage reaches about 40 mm from top surface in either D or W. When the deterioration reaches 40 mm from top surface, the wheel load is not able to run on the specimens, so the test has

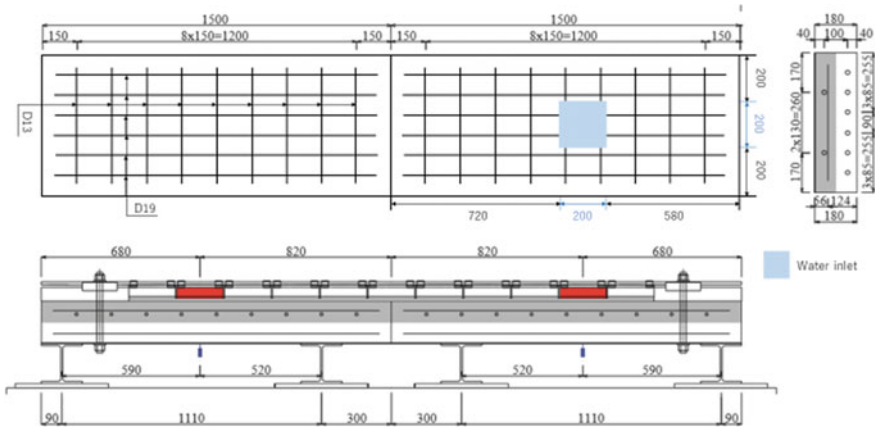
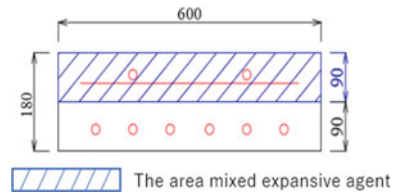


Fig. 1 Test set up: specimen dimensions

Fig. 2 Test set up: simulated deteriorations



to end at that situation. The 100 kN wheel load was moved on these two specimens and moving length was 2000 mm in the longitudinal direction (Fig. 3). The load was moved on blocks that were 500 mm in the transverse direction and 200 mm in the longitudinal direction. The specimens were supported with H steel elastic supports. The both ends of the specimens are fixed to the supports by anchor bolts to prevent them from slipping and uplifting. The procedure of the wheel loading test is below. Firstly, wheel loading was executed on specimen D and W simultaneously. Then,

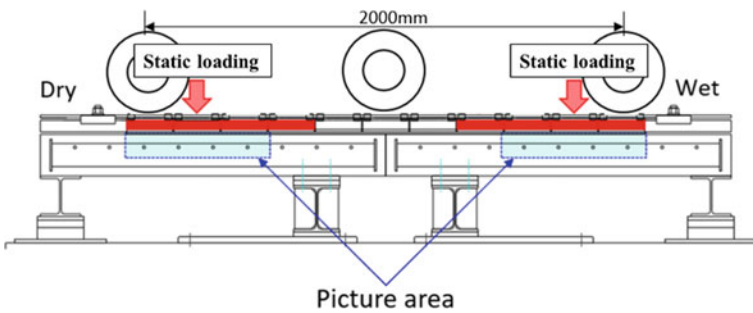


Fig. 3 Test set up: moving wheel load and static load area

when specific cracks were observed in a specimen, moving loading was interrupted and the static loading was applied at the center of each specimen. Next, pictures were taken for analysis. This procedure was continued until the wheel load could no longer run on the specimens due to deterioration. Finally, the test was ended after 120,000 cycles of loading.

2.2 Image Capture

Image capture was conducted with a digital camera, Nikon D3100, which is able to capture image of 4608×3072 pixels. Figure 3 shows the target area of image analysis. Random pattern was made on the specimens by using spray in order to apply digital image correlation method to the specimens. The images were captured before and after the static loading.

2.3 Image Analysis

An RGB color image of the specimen is converted to a grayscale image, and furthermore to a binary image. The measurement points for the image correlation are set as follows. Figure 4 shows the investigated area where the measurement points are

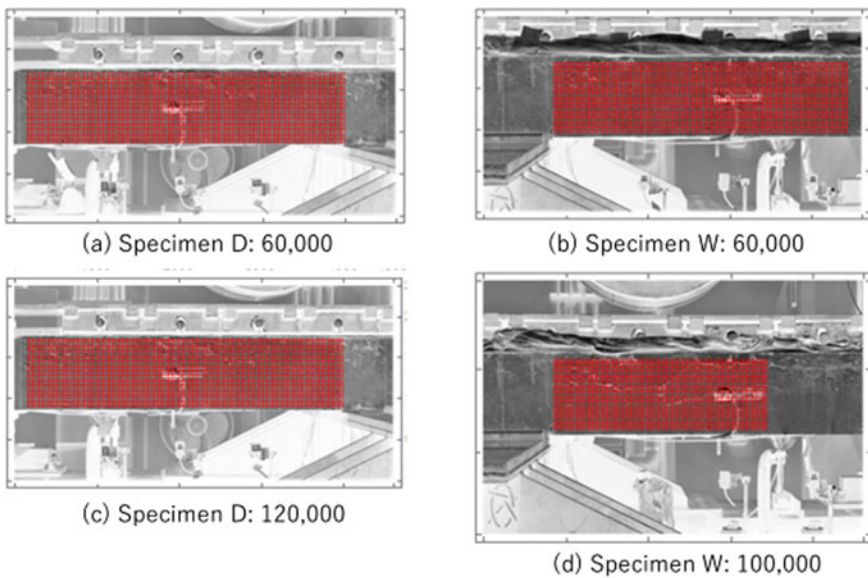


Fig. 4 Allocated measurement points

allocated. On specimen D, 154 points in the horizontal direction and 34 points in the vertical direction are allocated at the interval of 25 pixels. In terms of specimen W, as the random pattern was washed off due to water, so the investigated area was narrowed with increasing loading cycles. Therefore, the two settings were applied on specimen W. Firstly, at 60,000 cycles, 144 points in the horizontal direction and 35 points in the vertical direction were allocated at the interval of 25 pixels. Secondly, at 100,000 cycles, 104 points in the horizontal direction and 35 points in the vertical direction were allocated at the interval of 25 pixels. After allocation of the measurement points, a mask image (128×128 pixels) is clipped out around a measurement point from the image which was captured before loading, and similarly, a region image (256×700 pixels) is clipped out from the image which is captured after loading as well. And then, the displacement of measurement points is calculated to track the mask image in the region image. The cross-correlation is calculated about the mask image and region image. The position with the maximum cross-correlation value is regarded as the measurement point after deformation.

Binalize image

In this study, a captured image stored in JPEG format is converted into a 256-level grayscale image, and then that image is converted into a binary image using Otsu's method. Otsu's method is applied to determine the threshold by discriminant analysis. Firstly, this method calculates the variance of inter-class distribution between the two classes of luminance that are divided by every luminance value. Then, the luminance value that shows the maximum variance is determined as the optimal threshold.

Image correlation method

The process to obtain the displacement of the measurement points by cross-correlation is explained in this section. If the clipped region from the image before and after deformation are given as $g(i, j)$ and $f(i, j)$ respectively, the cross-correlation function is expressed as Eq. (1).

$$(f * g)(k, l) = \sum_{i=1}^p \sum_{j=1}^p \overline{f(i, j)} g(i + k, j + l) \quad (1)$$

When Fourier transform is applied to Eq. (1), the right side is expressed as the product of the Fourier transform of f and g . After calculating this product, an inverse correlation was applied to calculate the cross-correlation coefficient. Then, the position with the maximum cross-correlation value is regarded as the measurement point after deformation. The displacement obtained by this section's method is in pixel unit.

Sub-pixel measurement

The displacement that is obtained by the above image correlation method is expressed the integer value (unit: pixel). However, the actual displacement value should contain sub-pixel value (Sub-pixel means the value that is smaller than 1 pixel). Therefore, the

sub-pixel values are necessary to obtain accurate displacement values. In this study, the displacement of less than 1 pixel is obtained by using both of the value of the maximum correlation point and correlation about the surrounding 8 points. First, the coordinates and correlation coefficient are obtained about the maximum correlation point in integer unit by the image correlation method. Next, the correlation coefficients are calculated about the eight points around the maximum correlation point. Using these values and the following Eq. (2), approximate the elliptic paraboloid is obtained. The vertex of the paraboloid is regarded as the maximum correlation point in Sub-pixel level and that is defined as the coordinate of the measurement point in Sub-pixel level.

$$ax^2 + bx + cy^2 + dy + e = 0 \tag{2}$$

2.4 Calculation of Strain

The normal and shear strains are calculated via the X direction strain and the Y direction strain from the horizontal and vertical displacement of four measurement points, where the four measurement points form a square element. The used formulae are shown below. The four measurement points in the grid are defined as shown in Fig. 5, the side length in the X direction is L_x , the side length in the Y direction is L_y , the displacement of the point i in the X direction is u_i , and the displacement in the Y direction is v_i . Furthermore, principal strains are calculated. The equations are shown below as (3)–(7).

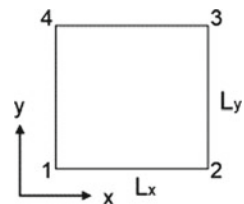
X direction strain

$$\varepsilon_{xx} = \frac{1}{L_x} \left(\frac{u_2 + u_3}{2} - \frac{u_1 + u_4}{2} \right) \tag{3}$$

Y direction strain

$$\varepsilon_{yy} = \frac{1}{L_y} \left(\frac{v_3 + v_4}{2} - \frac{v_1 + v_2}{2} \right) \tag{4}$$

Fig. 5 Strain calculation



XY direction shear strain

$$\gamma_{xy} = \frac{1}{L_y} \left(\frac{u_2 + u_3}{2} - \frac{u_1 + u_4}{2} \right) + \frac{1}{L_x} \left(\frac{V_3 + V_4}{2} - \frac{V_1 + V_2}{2} \right) \tag{5}$$

Maximum principal strain

$$\varepsilon_1 = \frac{\varepsilon_{xx} + \varepsilon_{yy}}{2} \sqrt{\left(\frac{\varepsilon_{yy} - \varepsilon_{xx}}{2} \right)^2 + \frac{\gamma_{xy}^2}{4}} \tag{6}$$

Minimum principal strain

$$\varepsilon_2 = \frac{\varepsilon_{xx} + \varepsilon_{yy}}{2} \sqrt{\left(\frac{\varepsilon_{yy} - \varepsilon_{xx}}{2} \right)^2 + \frac{\gamma_{xy}^2}{4}} \tag{7}$$

3 Results of Image Analysis

The wheel loading test was ended at 120,000 loading cycles, because the wheel load could no longer run on the specimen W due to deterioration. During the wheel loading test, the images were taken several times. As shown in Table 1, this study discusses about the two stages about the specimens after 60,000 cycles loading. At these stages, the specimens showed significant damage in its appearance. The observations have been reported by CERI as well [6], where the two same specimens as this study were investigated experimentally. According to the CERI report, the deflection of specimen W experienced a jump at around 60,000 cycles of loading. On the other hand, the deflection of specimen D was in the range of theoretical deflection from initial condition to the end of experiment. Therefore, in this study, image analysis focuses on the condition after 60,000 cycles of loading.

Image analysis was conducted about the two images which are taken before and after static loading, respectively. The static loading point is shown in Fig. 1.

Table 1 Targets of image analysis

Dry surface condition (D)	Wet surface condition (W)
60,000 cycles loading	60,000 cycles loading
120,000 cycles loading	100,000 cycles loading

3.1 Specimen D at 60,000 Cycles of Loading

Figure 6 shows the maximum principal strain and vector map about Specimen D when it was applied the static loading after 60,000 cycles of wheel loading. The diagonal crack was observed at middle part of this specimen and it was on the line from the right edge of center loading block on top surface to the support. This diagonal crack was opening at middle part of specimen where it was not directly below the loading point and the open direction vector was vertical. In addition, the bending cracks were observed. Both of diagonal crack and bending crack showed roughly same strain value.

Figure 7 shows the minimum principal strain and vector map. From the directly below loading point, a high magnitude of strain was observed along the diagonal crack. The direction of this strain vector was vertical, whereas this direction was reversed from just below the loading point to the other area.

In the above results, the two kinds of cracks were observed. One was the diagonal crack which was observed over both of maximum principal and minimum principal strain map. Upper half of it was observed in minimum principal strain and rest of it appeared in the maximum principal strain map. That indicates the specimen still had stress transfer across the diagonal crack and the stress transfer affected the behavior of the diagonal crack. The other one was the bending crack which was observed only in the maximum principal strain map, so they were simply opening due to loading.

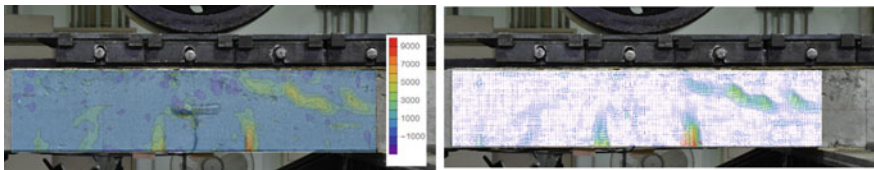


Fig. 6 Specimen D 60,000 cycles: maximum principal strain and vector

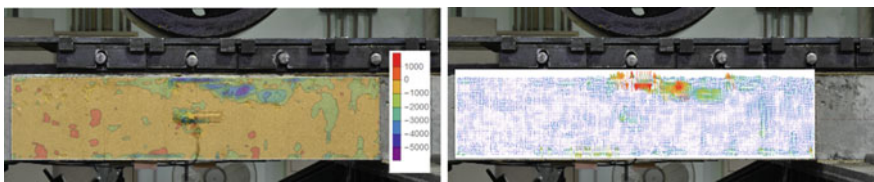


Fig. 7 Specimen D 60,000 cycles: minimum principal strain and vector

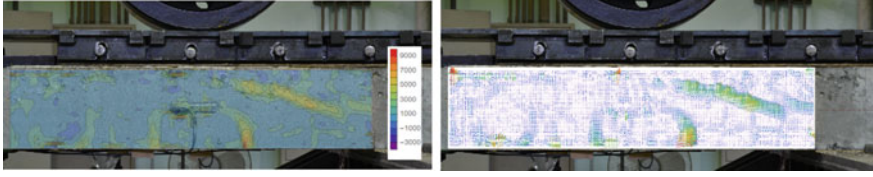


Fig. 8 Specimen D 120,000 cycles: maximum principal strain and vector

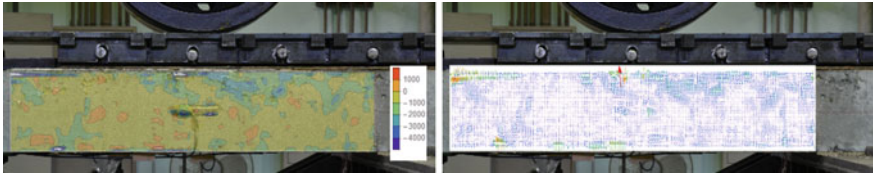


Fig. 9 Specimen D 120,000 cycles: minimum principal strain and vector

3.2 *Specimen D at 120,000 Cycles of Loading*

Figure 8 shows the maximum principal strain and vector map about Specimen D when it was applied the static loading after 120,000 cycles of wheel loading. The diagonal crack was observed at middle part of the specimen and it is on the line from the edge of center loading block on top surface to the support. The bending cracks were also observed in this map. These cracks had already been observed at 60,000 cycles and significant progress of the cracks was not confirmed.

Figure 9 shows the minimum principal strain map. This map also shows similar trend to the map at 60,000 cycles of loading. From the point directly below load, a localized high magnitude of strain was observed along the diagonal crack. The strain vector direction was vertical.

According to the above, the specimen still had stress transfer across the diagonal crack and the grip force affected the behavior of the diagonal crack. Besides, the bending cracks are not propagating.

3.3 *Specimen W at 60,000 Cycles of Loading*

Figure 10 shows the maximum principal strain and vector map about Specimen W when it applied the static loading after 60,000 cycles of wheel loading. A localized high magnitude of strain was observed in the left side of this specimen. This strain indicates the diagonal crack. This diagonal crack was along the line from the left edge of center loading block on top surface to the support. As shown in vector map, this crack was opening vertically. The bending cracks were also observed in this map, but the diagonal crack was more remarkable than the bending cracks. At this loading

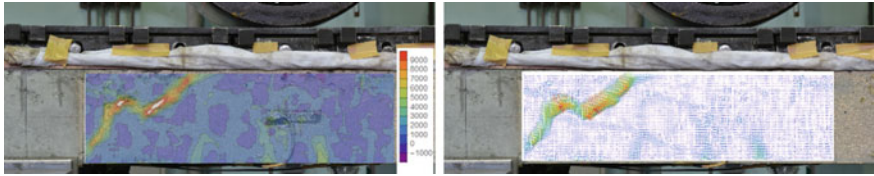


Fig. 10 Specimen W 60,000 cycles: maximum principal strain and vector

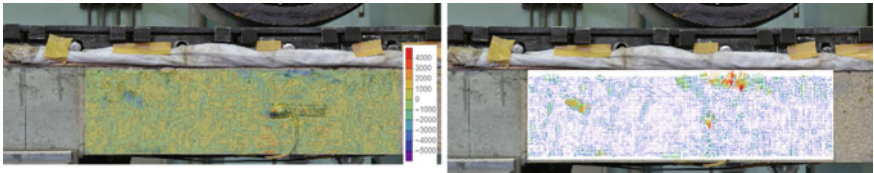


Fig. 11 Specimen W 60,000 cycles: minimum principal strain and vector

cycle, a significant increase of deflection has been reported in CERI report [6]. It is considered that this is due to the propagation of the diagonal crack according to this result.

Figure 11 shows the minimum principal strain and vector map. At directly below the loading point, compressive strain was observed slightly. The area was spreading horizontally.

From the above results, the diagonal crack was the most important feature about this specimen at 60,000 cycles of loading. This crack propagated along the line from the edge of center loading block on top surface to the support and opened vertically. In terms of compressive strain, the strain area was located just below the loading point and not related with the diagonal crack.

3.4 Specimen W at 100,000 Cycles of Loading

Figure 12 shows the maximum principal strain and vector map about Specimen W when it applied the static loading after 100,000 cycles of wheel loading. A high

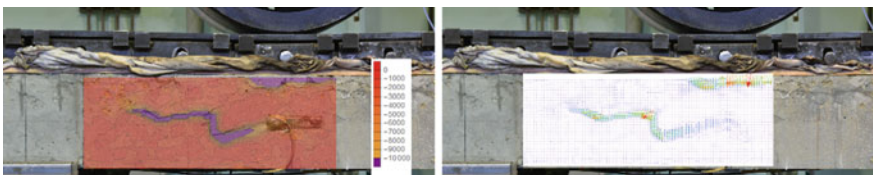


Fig. 12 Specimen W 100,000 cycles: maximum principal strain and vector

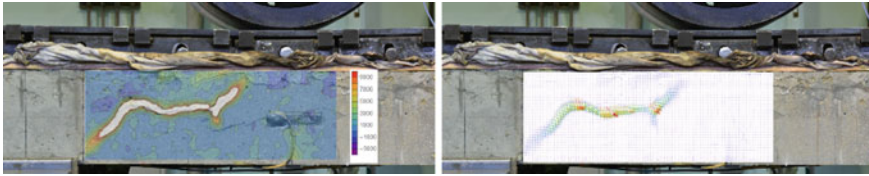


Fig. 13 Specimen W 100,000 cycles: minimum principal strain and vector

magnitude of tensile strain was observed along the diagonal crack. Comparing with the maximum principal strain map at 60,000 cycles of loading, the upper half of diagonal crack was clearly changed. At 60,000 cycles, the diagonal crack was basically on the line from the left edge of center loading block on top surface to the support, but in this case, the diagonal crack propagated horizontally at the middle of the specimen and reached areas closer to the center surface than in the 60,000 cycles case. In addition, the previous tensile strain disappeared at the upper half of this specimen. About vector map, the diagonal crack was opening vertically. This trend was the same as 60,000 cycles.

Figure 13 shows the minimum principal strain and vector map. A high magnitude of compressive strain appeared in two areas. First one was directly below the loading block. This strain was only observed in the minimum principal strain map and the top end of the diagonal crack nearly reached this area. It is assumed that this area of the specimen was disintegrated due to the water. Second one was located at middle of this specimen and spreading horizontally. The middle part of this area was also observed in maximum principal strain map. However, the right end of this area was only observed in the minimum principal strain map. In terms of the area near the left support, minimum principal strain was not confirmed around the diagonal crack. Therefore, those strains were due to the crack opening and closing.

According to the above results, the high magnitude of compressive strain area that appeared at 10,000 cycles loading affected the diagonal crack behavior. In particular, the diagonal crack propagated horizontally at the middle part of this specimen and the top end of the crack reached the area with the high magnitude of compressive strain.

4 Discussions

Due to the difference of surface conditions, three points were observed among results.

4.1 *Diagonal Crack*

A diagonal crack was observed both of Specimen D and W from 60,000 cycles of loading. According to this result, the diagonal crack was not due to water, but due to the loading condition.

Water accelerates deterioration of Specimen W, so there was a difference about propagation speed between D and W. The diagonal crack was basically on the line from the edge of center loading block on top surface to support. In addition, as the number of loading cycles increased, the opening and closing of the cracks increased and that vector was vertical. According those facts, the diagonal crack is considered as a punching shear crack. In this study, the loading condition was not the same as general wheel loading test that simulates a punching shear crack, in particular wheel running direction. However, the dimensions about Specimen D and W were similar to a part of beamed slab which is in the processes of punching shear failure. In general case, under wheel loading, a slab is divided by each 400–500 mm in right angle of wheel running direction due to cracks. Then, each part of slab behaves as individual beam which is reinforced by main reinforcements of the slab [7]. The specimens which were investigated in this study have a span of 600 mm in transverse direction. That span is near to 400–500 mm and reinforcement condition is similar to a beamed slab. According these reasons, it is considered that the specimens behaved like a part of the beamed slab and then punching shear crack appeared in this study.

4.2 *Propagation of Diagonal Crack*

As mentioned above, a diagonal crack was observed in both of D and W. About Specimen D, the diagonal crack appeared at the middle of the specimen and did not propagate to other areas. However, about Specimen W, the diagonal crack appeared at the middle part at 60,000 cycles of loading, then it propagated horizontally until 100,000 cycles loading. According to this, the diagonal crack shape was not the same between 60,000 and 100,000 cycles. In the maximum principal strain maps about W (Fig. 12), the bottom end of the diagonal crack did not change from 60,000 to 100,000, but top end of the crack shifted toward center of the specimen. Simultaneously, the previous top end of the crack that was observed at 60,000 cycles disappeared. Those fact indicates the area where tensile stress was worked was sifted due to the water-related deterioration. This phenomenon was only observed in Specimen W. the water-related deterioration was confirmed from the minimum principal strain map at 100,000 cycles loading about Specimen W (Fig. 13) and that deterioration is considered as the disintegration due to the elution of the cement matrix. The disintegration was also investigated by CERI [6] and that area was 320 mm of width and 30–40 mm of depth when the wheel load test ended at 120,000 cycles loading. Therefore, the effective height of the Specimen W was decreased due to the water. Based on that fact, it is assumed that the deterioration processes about the Specimen



Fig. 14 Influence of decreasing of effective height

W are as follows. Firstly, a diagonal crack occurred at the middle part of the specimen and the crack propagated along the line from the edge of center loading block to the support. This step of process was the same as Specimen D. Secondly, as the number of loading cycles increased, a disintegration proceeded from top surface. This disintegration led to a decreasing of the effective height. Then, the diagonal crack propagated toward the disintegration area and reached the deteriorated surface. In addition, this punching shear crack behavior was mentioned in “The Study to Improve Durability of Reinforcement Concrete Decks in Snowy and Cold Region” [8]. After the effective height decreasing, it is assumed that the area which was mainly affected by the static loading was narrowed as shown in Fig. 14. Due to this effect, the top end of the diagonal crack disappeared between 60,000 and 100,000 cycles of loading. According to the above, the durability of RC beam which is deteriorated by disintegration should be considered about the relationship between a punching shear crack and the decrease of effective height.

4.3 Local Compressive Strain About Specimen W

As shown in Fig. 11, a local compressive strain was obtained in the area which was around the top surface just below loading point at 100,000 cycles of loading in W (Fig. 13). Nevertheless, the maximum principal strain map did not have significant change in that area. In terms of the Specimen D, this phenomenon was not observed at any cycles. That means that the area did not deform elastically. Thus, it is confirmed that the top surface area was disintegrated due to water. In that area, water eliminated the cement matrix from top surface of specimen W. Therefore, it is also assumed that a volume reduction occurred at the top part of Specimen W. The disintegration was not clearly observed in Specimen W at 60,000 cycles of loading, so in this study, it is concluded that the large deflection of Specimen W that reported at 60,000 cycles of loading by CERI was not due to the decreasing effective height but the diagonal crack. On contrary, the local compressive strain that was observed at the middle part of Specimen W at 100,000 cycles loading was compatible with the maximum principal strain map (Fig. 12), so the volume reduction did not occur at middle of Specimen W.

5 Conclusion

This study investigated the deformation behaviors of RC beams by firstly introducing simulated deteriorations and then by loading under repetitive moving wheel load to understand the combined deterioration processes. Two specimens were deteriorated using an expansive agent to simulate the frost attack beforehand. Then a moving wheel loading was applied on the two specimens where one had dry surface and the other one had wet surface. Three points were observed on the deterioration processes of the two specimens as follows.

As for the influences of the experiment settings, following phenomena occurred over the deterioration processes of Specimen D and W:

1. A punching shear crack was observed on the line from the edge of center loading block on top surface to support of both Specimen D and W. This crack opened vertically. As the number of loading cycles increased, the extent of crack opening and closing increased.

In terms of the influences of water, following processes were observed in Specimen W:

2. A disintegration occurred from top surface, which led to a decreasing of the effective height. This phenomenon occurred from top surface which was subjected to the water. As a result, the area volume reduction also occurred.
3. The punching shear crack propagated and reached disintegration area, which affected the durability of structure. Therefore, it is of great significance to consider the relationship between the punching shear crack and the decreasing effective height in relevant future studies.

The achievements of this study were obtained based on the image analyses of the images of the specimens loaded statically at the midspan. In the future, it is needed to consider about the behaviors about those specimens which are subjected to other loading conditions by using image analysis.

References

1. Nakamura T, Kakuma K, Morita K, Kasai S, Nishi H (2019) Investigation of disintegration of RC bridge deck slabs in Hokkaido. CERI monthly report (796), pp 2–10, Japan
2. Kakuma K, Satou K, Nishi H (2017) Investigation case of RC slab of steel bridge subjected to combined deterioration in Hokkaido [Hokkaidou ni oite fukugourekka wo uketa koukyou RC syouban no chousa jirei]. CERI monthly report (770), pp 13–18, Japan
3. Sawamatsu T, Okada S, Yamazaki T (2013) Destruction of Slab about Shisunagawa bridge on route 275 [ippan kokudou 275gou shisungawa-basi no syouban kanbatsu ni tsuite]. 2012 Technical Research Presentation, Japan
4. Matsumoto T, Sakuraba H (2011) Flexural behavior of CFRP box and strain measurement by image analysis. J JSCE-A2 67(2):I.793-I.800, Japan
5. Sakai T, Matsumoto T, Hayashikawa T, He X (2008) Study on the precision improvement of displacement measurement in digital image analysis. J JSCE Hokkaido Branch 64, A-1, Japan

6. Kakuma K, Nishi H (2019) Wheel load running test of RC beams with simulated layered crack [mogiteki na soujyou hibiware wo dounyuusita RC buzai no rinkajyuu soukou shiken]. CERI monthly report (792), pp 28–33, Japan
7. Matsui S (2007) Road bridge slab design, construction and maintenance [dourokyou syouban sekkei sekou to ijikanri], 1st ed. Morikita Publishing, Japan, p 49
8. Adachi Y, Nishi H, Fujikawa M, Matsui S (2005) The study to improve durability of reinforcement concrete decks in snowy and cold region. J JSCE Hokkaido Branch 62, I-61, Japan

Investigation of Catalyzed Biomass Thermoelectric Concrete with Palm Oil Fuel Ash



Hoong-Pin Lee, Wan-Foong Chak, Kar-Loke Teow, Wen-Zhang Lee, Nurharniza Binti Abdul Rahman, and Abdullah Zawawi Awang

Abstract Numerous studies have focused on promoting sustainability using renewable resources across various industries. This is especially important in the construction industry where the production process of concrete serves as a challenge to the global environment especially since its major component, cement, contributes largely to the harmful environmental effects through the emission of CO₂. Thus, there is a need for new breakthrough in concrete manufacturing, with hopes to incorporate a more environmentally friendly perspective with partial cement replacement to enhance the concrete's properties and reduce in environmental pollution. This study builds on the idea of reconciling two pre-existing research by mixing palm oil fuel ash (POFA) as partial cement replacement and chemicals which serve as a catalyst for electricity generation, without effecting the strength of the structure. It aims to investigate the effect of POFA on the strength of concrete as well as ability to generate electricity under different scenarios of surrounding temperature. The volume of the chemicals were set fixed and biomass-cement content was make varied throughout the study with a 5% increment starting from 5 to 25%. The size of sample concrete in the study was kept constant at 50 mm × 50 mm × 20 mm for voltage testing while for compressive strength test, it was conducted on a concrete specimen sized 150 mm × 150 mm × 150 mm. The experiment had successfully shown that POFA as a partial cement replacement has reflected positively. Higher POFA content in concrete improved its ability to generate electricity in all surrounding temperatures as observed from increased voltage readings at higher POFA content.

H.-P. Lee (✉) · W.-F. Chak · K.-L. Teow · W.-Z. Lee · N. B. A. Rahman
Department of Civil Engineering, Faculty of Engineering and Quantity Surveying, INTI
International University, Nilai, Negeri Sembilan, Malaysia
e-mail: hoongpin.lee@newinti.edu.my

W.-Z. Lee
e-mail: i1601127@student.newinti.edu.my

N. B. A. Rahman
e-mail: nurharniza.rahman@newinti.edu.my

A. Z. Awang
School of Engineering, Universiti Teknologi Malaysia, Skudai, Malaysia
e-mail: abdullahzawawi@utm.my

An interesting outcome was that at higher temperatures, the electricity generating ability also increased for all POFA content. 5% POFA reflected an increase from 64 to 222 mV (an increase of 246%) when temperature is increased from 0 to 100 °C. As for 25% POFA, voltage readings increased from 111 to 375 mV, reflecting an increase of 238%. This experiment also reinforced our belief that the incorporation of POFA in cement has the ability to generate electricity while maintaining a reasonable strength.

Keywords Catalysed biomass concrete · Biomass Renewable energy · Sustainable construction · Thermoelectric concrete · Electricity generation

1 Introduction

Concrete is an indispensable conventional material that remains an integral part of modern construction. However, the inherent problems accompanying concrete production continue to haunt efforts to drive down global carbon footprint and overcome exhaustion of non-renewable resources [1].

The major environmental problem caused by concrete production lies in the unavoidable need to use fossil fuels at the current stage to power commercial production plants. This adverse contribution to climate change and pollution [7] is further aggravated by the fact that the concrete and building sector has been identified by the United Nations Environment Programme [1, 8–10] as the largest energy consumers worldwide. The present energy consumption rate stands at about 40% of the global reported rate and is expected to increase over time due to higher housing demand to support the growing population. Hence, it is inevitable that more sustainable and environmentally friendly alternative renewable energy source must be developed to alleviate the current situation and prepare us for the future.

A solution could exist in the development of an alternative renewable source using lignocellulosic biomass. This technology is already available in the market and at present covers raw material such as cellulose, poplar, lignin, POFA, switch grass, pozzolanic materials and etc. Timothy et al. [2] defines palm oil fuel ash or POFA as a by-product created from burning the husk and shell of palm oil that is usually disposed in landfills; this again contributes to another environmental problem in relation to increased demand for landfill areas [3]. Nevertheless, as highlighted by Hamada et al. [1], the issue can be overcome by blending POFA with construction material. In fact, its commercial deployment is within the foreseeable future, as a significant number of studies conducted on the subject matter have successfully demonstrated its feasibility. From an engineering perspective, the concrete incorporated with POFA has shown remarkable improvement in resistance to chloride attack [4], reduction in heat development, the drying shrinkage of concrete, [5] and finally resistance towards sulphate attack [6].

On top of the afore-mentioned improvements in concrete incorporated with POFA, a ground-breaking discovery has been made recently in the potential of generating

charges from the concrete. Although still at its infancy, the untapped potential is promising. Firstly, a number of studies [11–17] have shown that it is possible to electrify biomass at a lower temperature than that currently required to generate electricity through combustion and gasification of non-renewable fuels at a commercial scale. Secondly, the power-generating process using biomass is also cleaner, easier, and carbon-neutral, making it a versatile energy source for many applications. Thus far, the electricity generated by these biomass cells has a power density of about 0.72 mW/cm^2 ; this is notably near to the results of the best microbial cell available. Thirdly, with an addition of activated catalyst, followed by some exposure to heat or solar energy, lignocellulosic biomass with external circuit can harness the surrounding oxygen particles to generate electricity. This is an interesting discovery that warrants further research and development efforts. However, the largest barrier to overcome is that lignocellulosic biomass is generally not efficient enough to be directly used as any conductor in any conventional way. It needs to be mediated with catalyse in order to convert biomass to electricity through solar or thermal means.

The efforts made thus far to incorporate biomass into concrete production is fundamentally driven by a desire to develop innovative and sustainable material with cementitious properties to replace the conventional Portland cement. This may seem contradictory at first, as construction is itself destructive to our environment. However, studies done by forward-looking researchers such as Hamada et al. [1] and others [18–25] have proven that concrete containing biomass is able to emit lesser carbon dioxide (CO_2) gas during its production. Furthermore, the compressive strength, durability, chemical resistance properties, heat development and other mechanical properties of such concrete have been proven to be better than ordinary Portland cement alone. Biomass like POFA, sugar cane bagasse ash, rice husk ash, wood saw ash, bamboo leaf ash, maize ash and etc. have also been identified as possessing cementitious properties and thus, highly suitable for concrete mix [26]. Based on these findings, it is clear that a paradigm shift is required—the question is no longer about “can a sustainable concrete be produced?”, but “how to produce sustainable concrete in a large scale for a sustainable future?”

The potential of biomass in concrete is yet to be fully explored. At the INTI International University, active researches [27–30] are continuously being conducted, utilizing a variety of biomasses and special catalyst to produce good quality concrete and generate electricity at the same time. In this paper, POFA is used as biomass to enhance the concrete’s properties, focusing on areas such as compressive strength and potential in conductivity. The final product has been termed the “catalysed lignocellulosic biomass thermoelectric concrete” or CBC.

2 Experimental Program

The objectives of the experimental program can be addressed in two aspects. The first was to explore the effect of replacing cement with POFA at a range of 5–25% of total cement content on the compressive strength of the CBC concrete. The second

was to understand the effect of temperature difference to the conductivity of the CBC concrete. Thus, the varying POFA content, beginning from 5% of total cement content and increased at a 5% interval until 25% as well as the temperature difference from 0 to 100 °C were the independent factors in this study. The dependent factors were the resultant compressive strength and electricity conductivity respectively. In all cases, the concrete samples were expected to achieve target compressive strength of class M30. The constants were the type of raw material (POFA, cement and aggregates) and water-cement ratio. An undisclosed catalyst was also added to the concrete mix in this study to act as photochemical and thermochemical agent that carries charges under thermal difference. This is important to ensure charges are delivered to the pre-installed circuit.

2.1 Material and Sample Preparation

Preparatory works began with setting up moulds with a dimension of 150 mm × 150 mm × 150 mm to produce the concrete cubes for compressive strength testing. For voltage test, formworks with dimensions of 50 mm × 50 mm × 20 mm were prepared.

The concrete design mix is shown in Table 1. Since there is no guidance on the density of a CBC concrete, the density was assumed to be 2400 kg/m³. The DoE design method for M30 concrete was adopted in this study. With a water cement ratio of 0.5, the strength of concrete was expected to meet M30 class within a standard deviation of 5 and tolerance factor of 1.65. The target mean strength was 38.2 N/mm².

POFA was used to replace the cement content at an interval of 5% of total cement content from 5 to 25%. The different samples were identified based on the identification code tabulated in Table 2. A total of 54 cubes were produced, segregated into six series based on the POFA content and finally sub-divided into three groups for compressive strength testing on the 7th, 28th and 56th day.

During the concrete-mixing process, an undisclosed catalyst was added intermittently during the mixing process. After that, the wet mix was subjected to slump test, conducted based on the requirement of ASTM C143-78 to test the workability of the fresh concrete. The target slump height was expected to fall within the range of 10–30 mm. Once done, the wet mix was poured into the mould, stirred to ensure uniform distribution, compacted 25 times, and cured following the typical method to produce conventional concrete. Right after casting, the wet mixes were oven-dried for 24 h at 90 °C to facilitate the hydration and pozzolanic processes as well as to liquefy the powder form catalyst.

The steps to produce all concrete, regardless of mould sizes, were similar. The only difference lies in the water-curing process, whereby the samples prepared in the 50 mm × 50 mm × 20 mm moulds were not placed in water tanks for curing, but only oven-dried. The concrete cubes prepared in the 150 mm × 150 mm × 150 mm moulds were removed from the moulds after 24 h and subjected to water-curing for a period of 7–56 days. Tests were conducted on the 7th, 28th and 56th day. For the

Table 1 Mix proportion

Materials/properties	Details	Unit
Concrete grade	30	
Cement type	Ordinary Portland cement	
Standard deviation	5	
Tolerance factor	1.64	
Target mean strength	38.2	MPa
Aggregate type	Uncrushed coarse and fine aggregate	
Water cement ratio	0.515	
Assumed slump	10–30	mm
Maximum aggregate size	20	mm
Water content	180	kg/m ³
Cement content	350	kg/m ³
Volume occupied by aggregate	0.709	m ³
Density of aggregate	2600	kg/m ³
Total aggregate content	1843.5	kg/m ³
% of fine aggregate	35	%
% of coarse aggregate	65	%
Fine aggregate content	645.2	kg/m ³
Coarse aggregate content	1198.3	kg/m ³

Table 2 Identification code for the concrete specimens with varying POFA content

POFA content (% of total cement content)	Identification code
0	CBC-C30-Conc
5	CBC-C30-5%POFA
10	CBC-C30- 10%POFA
15	CBC-C30- 15%POFA
20	CBC-C30- 20%POFA
25	CBC-C30- 25%POFA

rectangular concrete specimens prepared in the 50 mm × 50 mm × 20 mm moulds, conductivity testing was conducted right after demoulding.

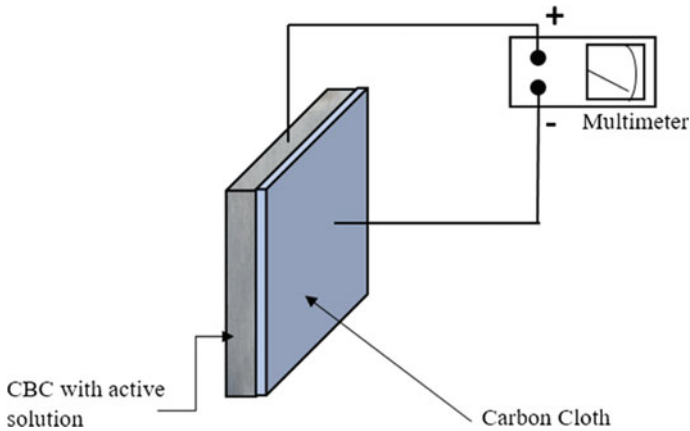


Fig. 1 External circuit setup for CBC with active solution

2.2 Setup for External Circuit

Figure 1 illustrates the configuration of the external circuit for the concrete samples to extract charges generated under thermal difference. This circuit was installed on the specimens measuring 50 mm × 50 mm × 20 mm right after oven curing. It should be noted here that, if more intense curing effort is required, then it is best to install the circuit after the curing is complete. In this circuit, the carbon cloth was the anode while the concrete was the cathode. The charges generated and extracted are measurable using a multi-meter, the probes were attached firmly on the anode and cathode to ensure the efficiency of the extraction. It is important to make sure the contact surface is as flat as possible so the voltage extracted will more consistent.

2.3 Setup for Conductivity Test

The specimens with complete circuit generate charges when it is exposed to thermal difference. This setup was tested under different circumstances to examine its conductivity and efficiency. However, it should be reminded that there is no standard of practice for the design of a concrete specimen conductivity test. The test conducted here was based on the temperature range commonly seen in daily life, which are 0–20 °C (cold condition), 20–60 °C (normal condition) and finally 60–100 °C (hot condition). The cold condition was simulated by placing the CBC setup in a refrigerator or covering it with ice. To achieve higher temperature, the setup was tested under room temperature, in an oven, and in boiling water. The multi-meter's probes were only connected after a desired temperature had been reached. Then, the reading was taken after it has stabilized. For each condition, 10 readings were taken at an

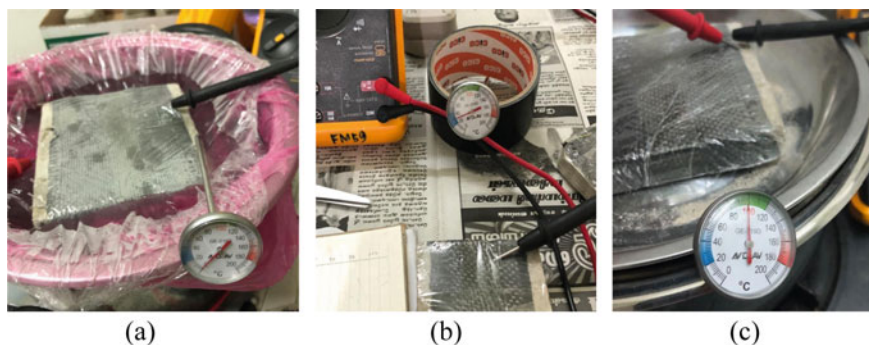


Fig. 2 Conductivity test for **a** cold condition, **b** normal condition and **c** hot condition

interval of 10 °C. Figure 2a–c show the conductivity test for CBC with complete circuit in cold, normal and hot conditions.

2.4 Compressive Load Test

The compressive strength of the concrete specimens was tested under the uniaxial compression test following ASTM C39/C39M. The specimens were loaded until failure right after water curing (compliance to ASTM C192) at the 7th, 28th, and 56th day. The concrete density was recorded individually before testing. The cracking and failure behaviour were observed during test. And the ultimate compressive strength was recorded when the specimen reached its peak capacity.

3 Findings and Discussion

3.1 Slump Test

The slump test was conducted based on the requirements of ASTM C143-78. The results are tabulated in Table 3, which show that all slump heights were within the targeted slump height of 30–60 mm. For the control specimen with 0% POFA content, the slump height was 45 mm. The lowest slump height of 31 mm was recorded for the specimen with the highest POFA content at 25% of total cement content. This is translated into a difference of approximately 30% from the slump height of the control specimen. However, since the slump height was still within the target range, it was concluded that the incorporation of POFA up to 25% of total cement content would not cause the fresh concrete mix to become unworkable.

Table 3 Slump test results for all concrete mixes

Specimen sets	Slump height (mm)
CBC-C30-Conc	45
CBC-C30-5% POFA	40
CBC-C30-10% POFA	39
CBC-C30-15% POFA	35
CBC-C30-20% POFA	33
CBC-C30-25% POFA	31

3.2 Compressive Strength Test

The compressive test was conducted based on the requirement of ASTM C39/C39M. All specimens were uniaxially loaded until failure immediately after water curing as stipulated in ASTM C192. The test was conducted on the 7th, 28th and 56th day. The concrete density was recorded for each cube before testing. During testing, the cracking and failure behaviour of all cubes were observed and recorded. The peak compressive strength of the cubes was taken at the point of failure. Since there were three specimens for each series, an average was computed and taken as the “ultimate compressive strength” for the series.

Figure 3 shows the results of the compressive test on the concrete cubes. A general trend depicts a decrease in compressive strength with every 5% increase in POFA content. On the 7th day, all specimens had yet to achieve the target mean strength of 38.2 MPa, but all specimens with POFA content depicted lower compressive strength than the control specimen. For the control specimen, the compressive strength had achieved almost 50% of the target mean strength on the 7th day while the compressive strength of the concrete with 25% POFA content was only 9.61 MPa or 25% of the target mean strength.

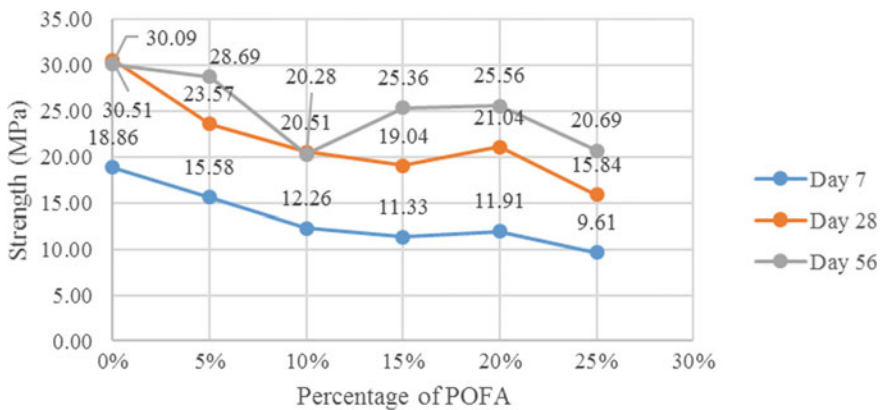


Fig. 3 Compressive strength of various percentage of POFA concrete at Day 7, 28 and 56

On the 28th day, the compressive strength of all specimens had increased, but at a similar trend whereby the control specimen continued to depict the highest strength while the specimen with 25% POFA had the lowest strength. The control specimen had achieved 80% of the target strength at this point of time, recorded at 30.51 MPa. Ironically, for the specimen with 25% POFA, the achieved strength was not even comparable to that of the control specimen on the 7th day. The strength was a mere 15.84 MPa, almost 42% below the target mean strength and 16% below the control specimen's compressive strength on the 7th day. However, it is worth noting that the specimen with 20% POFA content depicted a reasonable strength development that only became obvious on the 28th day. The strength increased from 11.91 MPa on the 7th day to 21.04 MPa on the 28th day. Within 21 days, the strength had increased from 31 to 55% of target mean strength—the highest increment among all specimens with POFA content.

The increase in compressive strength at the later stages could be attributed to the reaction between the SiO_2 present in the POFA and the $\text{Ca}(\text{OH})_2$ in the concrete, forming more calcium silicate hydrate (C–S–H) that improved the bonding of concrete paste and aggregates. On the 56th day, the compressive strength of most specimens continued to grow except for the control specimen and the specimens with 10% POFA. However, both were negligible since the decrease was about 1% only compared to the strength on the 28th day. For the rest, the specimens with only 5% POFA had the highest compressive strength at 28.69 MPa, followed by the specimens with 20% POFA at 25.56 MPa. The corresponding strength growth from the 7th day to the 56th day based on the target mean strength was only 1% different for both series; the series with 5% POFA recorded 34.3% growth while the series with 20% POFA recorded 35.7% growth.

Based on the compressive strength test results, the series with 20% POFA was determined as the optimum mix. Although the compressive strength was lower than the control specimens and the series with 5% POFA content, in general it was comparable and have ample room for enhancement. To achieve 30 MPa, for example, a plausible solution may lie in adjusting the initial strength design for the concrete with 20% POFA content to 35.22 MPa (a 1.174 factor).

3.3 Voltage Test

Figure 4 shows the average voltage reading when the voltage test was conducted in the range of 0–100 °C. The coloured lines represent samples with different POFA content.

Generally, the graph depicts an obvious relationship between the POFA content and the average voltage whereby the higher the POFA content, the higher the voltage reading. A positively linear relationship is also observed between temperature difference and voltage reading. However, since the experiment was limited to 25% POFA, the relationship might not necessarily hold above 25% POFA content; further research is still required to establish such property in totality.

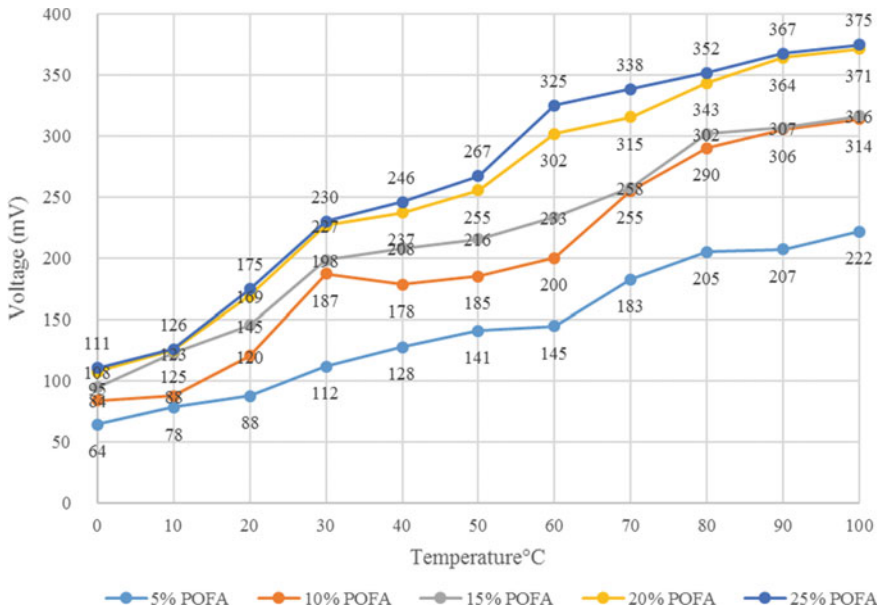


Fig. 4 Voltage generated at different exposing temperature by Catalyzed Biomass Concrete with various percentage of POFA

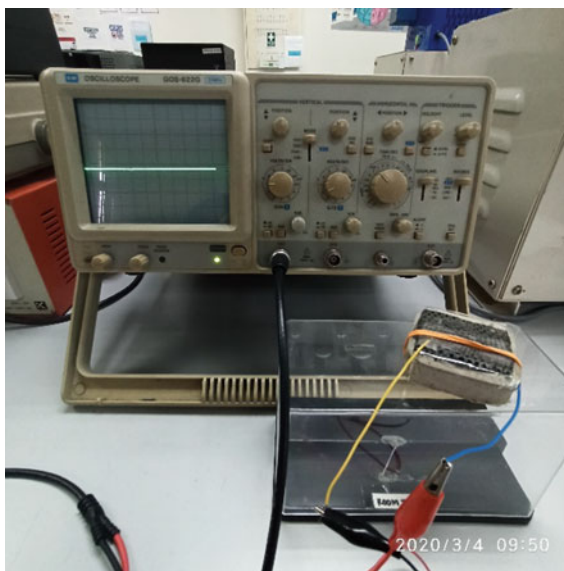
At 0 °C, At 5% POFA content, the average voltage recorded was 64 MV while the voltage for 25% POFA was 73% higher at 111 MV. At an ambient temperature of approximately 20°C, the voltage readings for 5% POFA increased to 88MV while that for 25% POFA increased to 175MV, indicating a 31.3% and 57.7% increase, respectively. At 40°C, the average voltage for 5% POFA remained relatively flat at 112 MV while that for 25% POFA continued to show increment to 230 MV. Beyond 70 °C, the increase in voltage was not as steep as previously recorded. At 70 °C, 5% POFA recorded 183 MV while 25% POFA recorded 338 MV. At 100 °C, 5% POFA recorded 222 MV whilst 25% POFA recorded 375MV. This reflects an increase in voltage reading of 21.3 and 10.9% within this 30 °C temperature range.

The waveform of the electrical signal was analysed using the oscilloscope shown in Fig. 5. Although the generated voltage was low, the pulsating direct current had been stable. The voltage can be potentially boosted with a proper amplifier circuit, but this is not the main topic of this paper and thus, will not be discussed in detail.

4 Conclusion

This experimental study has examined the electricity generation and compressive strength of five series of CBC incorporated with POFA. The mixtures were tested and

Fig. 5 The oscilloscope for electrical signal's waveform study



evaluated under workability test, uniaxial compressive strength test and conductivity test. Based on the test results, several conclusions have been drawn:

1. The specimen with 25% of POFA replacement achieved the highest average voltage reading amongst the various percentage biomass content consistently from 0 to 100 °C. The positive relationship between temperature and electricity generation ability was also verified by samples with different POFA content.
2. Specimen with 20% POFA demonstrated the most reasonable strength when measured using a compressive test. Although other concrete samples did indicate better performance than the 20% POFA at Day 7 and Day 28, the results at Day 56 were taken as being more conclusive given that overall strength for all samples had improved due to the improved chemical bonds between POFA and the concrete mixture.
3. All concrete specimens had generated stable direct voltage. However, the voltage per sample is relatively small and a booster circuit is needed for practical application.

Acknowledgements The research described in this paper is supported by the FRGS 2020-1 under Vot FRGS/1/2020/TK0/INTI/02/1 and FYP Funding by INTI International University. Laboratory testing of the specimens were performed in the Concrete Laboratory, INTI International University, Nilai. Assistance from the dutiful technicians were very much acknowledged.

References

1. Hamada HM, Jokhio GA, Yahaya FM, Humada AM (2018) The present state of the use of palm oil fuel ash (POFA) in concrete. *Constr Build Mater* 175:26–40
2. Timothy ZHT, Matthew ZYT, Muhammad ER, Vikram P (2019) Palm oil fuel ash: innovative potential applications as sustainable materials in concrete. *Ref Module Mater Sci Mater Eng*
3. Chindaprasirt P, Homwuttivong S, Jaturapitakkul C (2007) Strength and water permeability of concrete containing palm oil fuel ash and rice husk-bark ash. *Constr Build Mater* 21(7):1492–1499
4. Chindaprasirt P, Rukzon S, Sirivivatnanon V (2008) Resistance to chloride penetration of blended Portland cement mortar containing palm oil fuel ash, rice husk ash and fly ash. *Constr Build Mater* 22(5):932–938
5. Weerachart T, Jaturapitakkul C (2010) Strength, drying shrinkage, and water permeability of concrete incorporating ground palm oil fuel ash. *Cement Concr Compos* 32(10):767–774
6. Jaturapitakkul C, Kraiwood K, Weerachart T, Tirasit S (2007) Evaluation of the sulfate resistance of concrete containing palm oil fuel ash. *Constr Build Mater* 21(7):1399–1405
7. Ma T, Østergaard P, Lund H, Yang H, Lu L (2014) An energy system model for Hong Kong in 2020. *Energy* 68:301–310
8. Luo Y, Ling Z, Liu Z, Wang Y, Meng F, Jing W (2016) Thermal performance evaluation of an active building integrated photovoltaic thermoelectric wall system. *Appl Energy* 177:25–39
9. Armin RA, Sumper A, Davarpanah A (2019) Development of sustainable energy indexes by the utilization of new indicators: a comparative study. *Energy Rep* 5:375–383
10. Salvo M et al (2015) Biomass ash as supplementary cementitious material (SCM). *Adv Appl Ceram* 114:3–10
11. Zhao X, Liu W, Deng Y, Zhu JY (2017) Low-temperature microbial and direct conversion of lignocellulosic biomass to electricity: advances and challenges. *Renew Sustain Energy Rev* 71:268–282
12. Wu W, Liu W, Mu W, Deng Y (2016) Polyoxymetalate liquid-catalyzed polyol fuel cell and the related photoelectrochemical reaction mechanism study. *J Power Sour* 318:86–92
13. Zhao X, Liu W, Deng Y, Zhu J (2015) Lignocellulosic biomass-energized fuel cells: cases of high-temperature conversion. Momentum Press
14. Liu W, Mu W, Liu M, Zhang X, Cai H, Deng Y (2014) Solar-induced direct biomass-to-electricity hybrid fuel cell using polyoxometalates as photocatalyst and charge carrier. *Nat Commun* 5:3208
15. Georgia Institute of Technology (2014) Hybrid fuel cell produces electricity directly from biomass. *Phys Org* 1–5
16. Vanita KS (2014) A newer approach to green earth—solar-induced hybrid biomass fuel cell. *Am Int J Res Formal Appl Nat Sci* 14(278):141–142
17. Evans A, Strezov V, Evans TJ (2014) Sustainability considerations for electricity generation from biomass. *Renew Sustain Energy Rev* 14(5):33–52
18. Ul-Islam MM, Mo KH, Alengaram UJ, Jumaat MZ (2016) Durability properties of sustainable concrete containing high volume palm oil waste materials. *J Clean Prod* 137:167–177
19. Velay-Lizancos M, Azenha M, Martínez-Lage I, Vázquez-Burgo P (2017) Addition of biomass ash in concrete: effects on E-modulus, electrical conductivity at early ages and their correlation. *Constr Build Mater* 157:1126–1132
20. Warid MH, Khairunisa M (2009) Properties of palm oil fuel ash cement based aerated concrete panel subjected to different curing regimes. *Malaysian J Civ Eng* 21(1):17–30
21. Timothy TZH, Matthew TZY, Muhammad RE, Vikram P (2019) Palm oil fuel ash: innovative potential applications as sustainable materials in concrete. *Refer Module Mater Sci Mater Eng*
22. Chindaprasirt P, Rukzon S, Sirivivatnanon V (2008) Resistance to chloride penetration of blended Portland cement mortar containing palm oil fuel ash, rice husk ash and fly ash. *Constr Build Mater* 22(5):932–938

23. Chindapasirt P, Homwuttiwong S, Jaturapitakkul C (2007) Strength and water permeability of concrete containing palm oil fuel ash and rice husk-bark ash. *Constr Build Mater* 21(7):1492–1499
24. Weerachart T, Jaturapitakkul C (2010) Strength, drying shrinkage, and water permeability of concrete incorporating ground palm oil fuel ash. *Composites* 32(10):767–774
25. Jaturapitakkul C, Kraiwood K, Weerachart T, Tirasit S (2007) Evaluation of the sulphate resistance of concrete containing palm oil fuel ash. *Constr Build Mater* 21(7):1399–1405
26. Aprianti E, Shafigh P, Syamsul B, Nodeh Farahani J (2015) Supplementary cementitious materials origin from agricultural wastes—a review. *Constr Build Mater* 74:176–187
27. Wan-Foong C, Hoong-Pin L (2019) Catalyst biomass concrete using palm oil fuel ash (POFA). INTI International University, Malaysia
28. Zhen-Xiang P, Hoong Pin L (2019) The effect of catalyst biomass concrete with sawdust ash on different content of activated catalyst. INTI International University
29. Chee-King G, Hoong-Pin L (2019) The effect of biomass in generating electricity for catalyst biomass concrete. INTI International University
30. Kuan-Sheng L, Hoong-Pin L (2019) Different type of biomass material uses in concrete essential for generating electricity. INTI International University

Examination on the Processes of Structural Performance Evaluation of SRC Deep Beams by FEA with NDT Results



Motonori Yasui, Deng Pengru, and Takashi Matsumoto

Abstract Maintenance of bridges is becoming increasingly important in Japan. In the maintenance of bridges, it is necessary to evaluate the current load carrying capacity of a deteriorated structure by the use of design equations or numerical analyses. However, the design drawings are often missing, thereby input parameters such as material properties and internal reinforcement arrangements for the equations and analyses are not available. In such a case, it is necessary and important to determine the input parameters by destructive or non-destructive tests (NDT) or rational judgments and to estimate the load carrying capacity of a deteriorated structure with a rational analytical model. In this study, using NDT results, the structural performance of SRC deep beams is evaluated by FEA, where the evaluation processes are examined as well. Considering that the material properties from NDT has some ranges and may contain errors, their values are adjusted referencing the design of similar beams from some papers and then input for FEA. In terms of concrete, a nonlinear stress–strain relation is employed for compression. Under tension, the concrete is assumed to behave linear elastically before the tensile strength is reached. After that, a linear softening behavior is assumed for cracked concrete. As for steel reinforcements, i.e. embedded I-beam and rebars, the stress–strain relation is assumed as elasto-plastic. The steel/concrete interface is regarded as rigidly connected. In addition to FEA, hand calculation using empirical equations is conducted as well to examine the predictions. Finally, the predictions such as internal structure, material properties and load carrying capacity are compared with their corresponding experimental results which have been closed until this step. From this comparison, the employed performance evaluation processes are examined.

Keywords Maintenance · Structural performance evaluation · SRC · Deep beam · FEA · NDT

M. Yasui (✉)

Graduate School of Engineering, Hokkaido University, Kita 13 Nishi 8, Kita-ku, Sapporo, Japan
e-mail: motonori@eis.hokudai.ac.jp

D. Pengru · T. Matsumoto

Faculty of Engineering, Hokkaido University, Kita 13 Nishi 8, Kita-ku, Sapporo, Japan

1 Introduction

Nowadays, existing bridges are required to be inspected once every five years. In Japan, the number of infrastructures which are over 50 years old is increasing. It is reported by the Ministry of Land, Infrastructure, Transport and Tourism of Japan that the ratio occupied by such structures will be 60% in the upcoming 20 years [1]. Therefore, it is of great importance to provide effective maintenance and evaluation for those structures.

Unfortunately, the design drawings are lost for some existing structures. Thus, to evaluate the performance of these structures, one has to obtain or estimate the values of the material properties and the structural type and arrangement of the internal structures including concrete, reinforcement rebar and members based on destructive or non-destructive tests or rational predictions. Even though the structural performance can be evaluated easily using appearances such as the degree of cracking, the evaluations are rather rough and the reliability of these evaluations can hardly be checked and verified. However, theoretically, as the status of an existing structure can be reflected on some structural characteristics including the geometrical dimensions, material properties and behaviors under some given loads, a more mechanical sound and accurate performance evaluation can be provided by inputting the data from in-situ inspection, measurement and NDTs into a numerical model of the structures and then conducting analysis. So far, the process of these prediction and evaluation has not been established yet. Nowadays, the process depends on the judgment skill of engineers.

As one of the evaluation methods for such structures, “Blind Performance Evaluation” is currently under consideration at the Committee on Hybrid Structures, Japan Society of Civil Engineers. We also decided to work on blind performance evaluation. The Blind Performance Evaluation is to predict the internal structure of the structure from the data obtained by inspection and measurement of the structure with unknown internal structure, and then evaluate the structure performance including future behavior. Blind performance evaluation has 4 steps. The first step is inspection and measurement. The second step is prediction and analysis of the structure from data of first step. The third step is evaluating the structure. The fourth step is comparing the prediction and the experimental results of the actual specimen. Therefore, the performance of an SRC beam is evaluated with the developed method as well as hand calculation using empirical equations. At the meanwhile, the process of structural performance evaluation by conducting FEA of the structure predicted with data from NDTs is examined, which is the primary purpose of this research.

2 The Procedure of Blind Performance Evaluation

As shown in Sect. 1, the blind performance evaluation has 4 steps. The first is inspection and measurement. In this study, this step contains two phases. The first phase is

only inspection of the structure, such as dimensions and cracking procedure during loading experiment. The second phase is measurement by non-destruction testing (NDT) techniques. The data obtained from NDT includes the prediction of material property and internal structure arrangement. The second step is prediction and analysis the structure. From the data of first step, the specimen is predicted referring other papers of which specimen is close to this study to determine material property and internal structure arrangement. Then, following this prediction, the analysis is conducted using hand calculation and FEA by MSC/MARC. In this analysis, the behavior is analyzed, such as procedure of cracking, failure mode and the maximum load capacity. The third step is evaluation. In this step, the future behavior of the specimen after damaged is evaluated from data of first step and prediction and analysis of second step. The fourth step is comparison the prediction and actual structure and loading experiment.

3 The Data from Inspection and Measurement

The inspection and measurement has two phases. The first phase of inspection and measurement is to obtain the dimensions of the specimen. Figure 1 shows the geometric information of the specimen. As the reinforcement condition is not available from these information, one can only assume the specimen as a regular reinforced concrete (RC) beam as this structural type is most commonly employed. The second phase of inspection and measurement is to conduct non-destruction test (NDT) to get material property and internal steel arrangement. The arrangement of internal structure determined from NDT is shown in Fig. 1. In terms of the NDT, a microwave radar was used for prediction of steel arrangement and a hammer test was adopted for determining the range of compressive strength of concrete. It is found that the tested specimen may be a steel reinforced concrete beam rather than a normal reinforced concrete beam. Tables 1 and 2 show ranges of material properties of concrete and

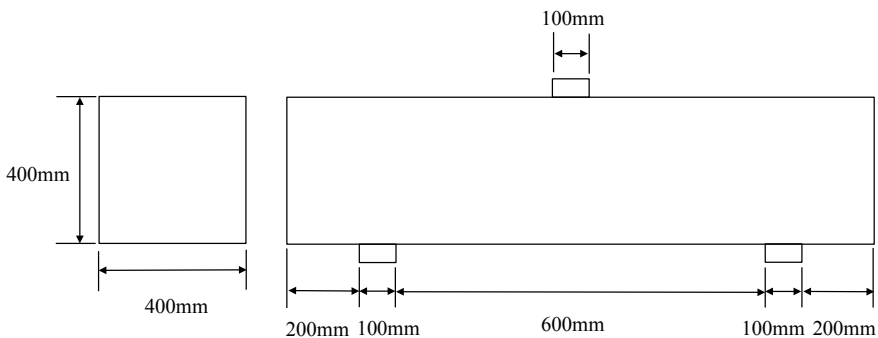


Fig. 1 The data of size of specimen

Table 1 The data of concrete from NDT

Compressive strength	26.8–40.7 MPa
Tensile strength	2.06–2.72 MPa
Young's modulus	26.4–31.1 GPa

Table 2 The data of steels from NDT

Diameter of rebar in compressive zone	D16 or D19
Diameter of rebar in tensile zone	D19 or D22
Diameter of stirrups	D13, D16 or D19

**Fig. 2** Picture of the specimen after cracking

steels from NDTs. To investigate the dependence of the accuracy of the proposed method on the completeness and richness of the data from inspection and measurement, prediction of the specimen details is conducted after each phase. The specimen is named as first prediction from the data of the first phase. The specimen is named as second prediction from the data of the second phase (Figs. 2 and 3).

4 Prediction of Material Properties and Internal Arrangements

In this study, the paper written by Muhammad SAFDAR [2] is referenced, where a non-linear analysis software MSC/Marc was used to analyze RC beams and slabs repaired with Ultra-high performance fiber reinforced concrete (UHPFRC). In this paper, the same software, MSC/Marc, is used as well. In SAFDAR's paper, it is showed that the method developed in MSC/Marc can provide an accurate prediction of behaviors including load–displacement of mid-span curve of the tested structures

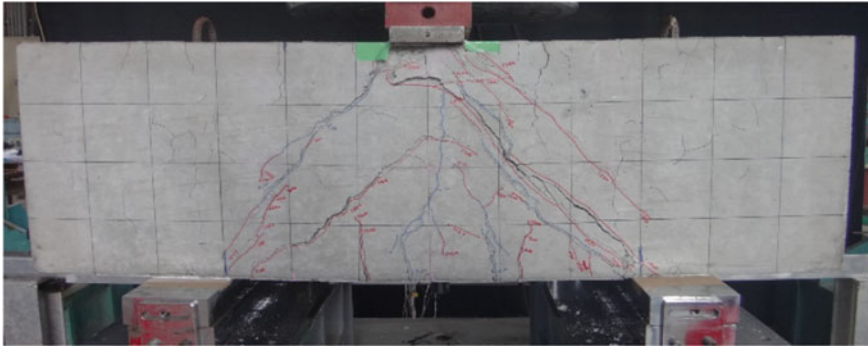


Fig. 3 Picture of the specimen after failure

compared to experiment. Therefore, the same theories adopted in SAFDAR’s paper are adopted in this study as well.

4.1 Concrete

In this study, two assumptions are employed on the material properties of concrete. The first assumption is that concrete is homogenous and initially isotropic. The second assumption is that the uniaxial compressive stress–strain relationship for the concrete model shown in Fig. 4 is obtainable following the multi-linear equations for concrete proposed by MacGegor 1992 [3].

According to first phase of data, i.e. the dimensions of specimen, no information about the concrete was provided. The material properties have to be predicted based on experiences and existing related knowledge, such the design specifications, standard design cases, as the specimen should satisfy the requirements of the design specification and should not be too special. Then two papers were referenced [4, 5]. The dimensions of the specimens which were used on these two papers were close to the specimen which are used in this research. From these two papers, it is showed that

Fig. 4 Uniaxial compressive stress–strain curve for concrete

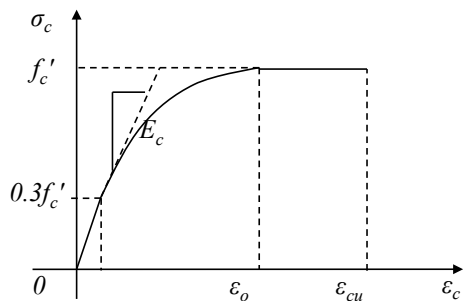
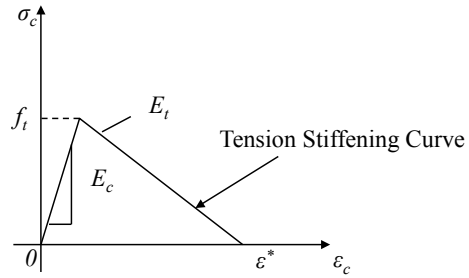


Fig. 5 Tension stiffening model for concrete



the maximum compressive strength and Young’s modulus of the concrete, f'_c , and, E_c , are close to 30 MPa and 28 GPa. Therefore, in this research, 30 MPa and 28 GPa were adopted for the compression strength and Young’s modulus of the concrete of the specimen named as the first prediction.

According to the second phase of data, it was found that the uniaxial compressive strength and Young’s modulus of concrete vary in 26.8–40.7 MPa and 26.4–31.1 GPa, respectively, as shown in Table 1. These ranges include the values, which are predicted at first phase. Under uniaxial compression, the concrete strain, ϵ_o , corresponding to the peak stress, f'_c , is assumed as 0.002 which is commonly used. The crushing strain, ϵ_{cu} , of concrete is defined as 0.003 as suggested by ACI committee 318. The Poisson’s ratio of concrete is assumed to be 0.2. In terms of the tensile properties of concrete, it is generally accepted that the uniaxial tensile strength, f_t , varies from 2.06 MPa to 2.72 MPa. In this study, the tensile strength is calculated based on Eq. (5) using the compression strength. Under tension, a linear elastic relation is used for the stress and strain of concrete before cracking, i.e. until the tensile strength of concrete, f_t , is reached. Once the cracking of concrete takes place, a discrete model is used to represent the macro cracking behavior. It is known that cracked concrete of RC member can still carry the tensile stress in the direction normal to the crack, which is known as tension stiffening [6]. In this study, a linear softening model as shown in Fig. 5 is adopted to capture the tension-stiffening phenomenon. The softening modulus, E_t , is selected as 2.55 GPa and corresponding strain, ϵ^* , at which tension stiffening stress reduces to zero is 0.001. During the post-cracking stage, the cracked concrete can still transfer the shear forces through aggregate interlocking or shear friction, which is termed as shear retention. The shear retention is modeled by introducing the shear retention factor, which is an input parameter to reduce the shear modulus after cracking. Numerous analytical results have demonstrated that shear retention factor has value between 0 and 1 [7]. The shear retention factor is selected as 0.4 in this analysis.

$$f_c = \epsilon E_c \quad 0 \leq \epsilon \leq \epsilon_1 \tag{1}$$

$$f_c = \frac{\epsilon E_c}{1 + \left(\frac{\epsilon}{\epsilon_o}\right)^2} \quad \epsilon_1 \leq \epsilon \leq \epsilon_o \tag{2}$$

$$f_c = f'_c \quad \varepsilon_o \leq \varepsilon \leq \varepsilon_{cu} \tag{3}$$

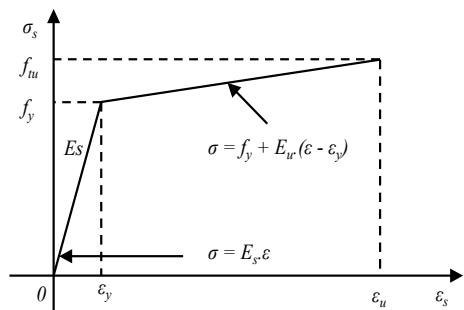
$$\varepsilon_o = \frac{2f'_c}{E_c} \tag{4}$$

$$f_t = 0.23(f'_c)^{2/3} \tag{5}$$

4.2 Reinforcing Rebar

On first phase of data, any information of internal structure was not given. On second phase of data, material properties of steel include only prediction of range of diameter, no maximum tensile strength, f_{tu} , and yield strength, f_y , and stress–strain curve. Thus, these material properties were predicted according to normal design. Figure 6 shows the constitutive law of reinforcing bar and I-Beam. In this research, a linear elasticity is used for $0 \leq \sigma_s \leq f_y$, and a linear hardening elastoplastic model is applied until a specified ultimate strain is reached under tension and compression. The yield strength and ultimate strength of all reinforcing bar are provided with 345 MPa and 545 MPa respectively. These values are from construction criteria of steel. The ultimate strain ε_u used in this study is 240,000 μ . The Poisson’s ratio and elastic modulus, E_s , of 0.3 and 200 GPa for both steels are used in this study considering that these values are generally used. Diameter of each reinforcing bar is determined to ensure that the steel ratio of the specimens in this study is similar to the steel ratios used in KOSA’s and TANIMURA’s papers [4, 5] because the specimens in these papers possess dimensions and material properties approximate to the data from the inspections and measurement in this study. In these papers, the steel ratio of the specimen is 2% in tensile zone and 0.4% in shear zone at the first phase. The diameter of rebar in compressive zone is not important because the rebars in compressive are exploited to facilitate the installation of the stirrups and the compressive stress of rebar is quite small compared to the concrete which has much larger area. According

Fig. 6 Stress–strain model for steel



to the above considerations, the diameter of rebars in compressive zone, tensile zone and stirrups are finally determined as D13, D29 and D10 respectively at the first prediction as shown in Fig. 7. However, at the second prediction, it is found that these steel ratios are not included in the data of NDTs. Thus, diameters which can provide steel ratios approximate to 2% and 4% were adopted. Finally, at the second prediction, the diameter of rebar in compressive zone, tensile zone and stirrups are determined as D13, D29 and D10 respectively as show in Fig. 8. Table 3 shows the determined diameters of each rebar.

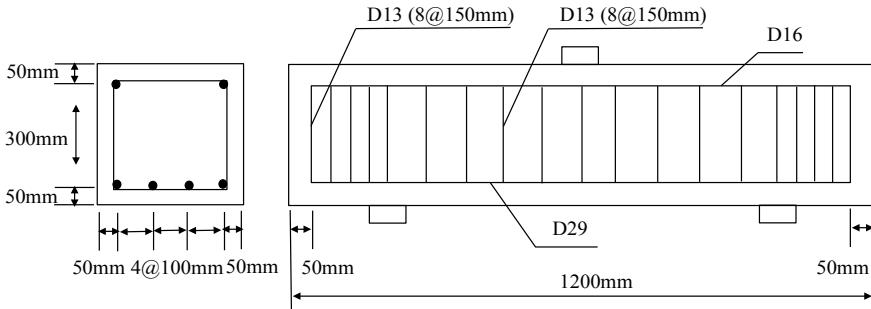


Fig. 7 First prediction

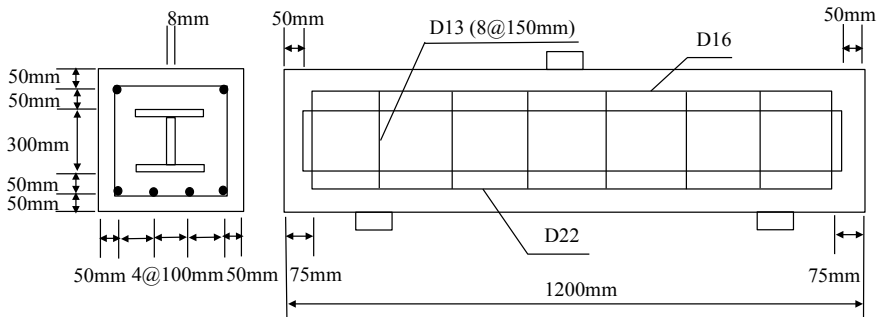


Fig. 8 Second prediction

Table 3 Diameter of rebar

	Rebar of compressive	Rebar of tensile	Stirrups
First prediction	D13	D29	D10
Second prediction	D22	D22	D13

4.3 *I-beam*

At the first prediction, the specimen is predicted as a simple RC beam as no internal information was available after the first phase and the RC beam is the most widely employed structural type. However, it is revealed that the specimen has a steel I-beam as internal reinforcement according to the data of NDT. The beam may be a steel-reinforced concrete (SRC) beam. In a relevant paper presented by MURATA, it is found that the yield strength, f_y , of the steel I-beams may vary over a wide range, from 271.6 to 527.6. In this paper, the yield strength of the I-beam of the specimen which is close to the specimen of this research was 351.2 MPa. It is close to the value of rebars, i.e. 345 MPa. In that paper, as no information of other material properties, such as young's modules and maximum tensile strength are available, the material properties of the steel rebar are exploited for the steel I-beam as well for the SRC beam.

4.4 *Discussion*

Figures 7 and 8 show the first prediction and second prediction, respectively, following Sects. 4.2 and 4.3. In this chapter, i.e. Chap. 4, material properties and internal arrangement are predicted. From only picture of cracking and size, it is too difficult to predict internal arrangement with confidence. Actually, the specimen is predicted as RC beam at the first phase, but it is revealed that the specimen is SRC from NDT at the second phase. Therefore, it is quite important to conduct NDTs for predict internal arrangement and the accuracy of the prediction depend greatly on the richness and completeness of the data from NDTs. With the predicted structural type and material properties, a finite element model of the tested specimen will be developed in Chap. 5 to predict the maximum load capacity and also check the influences of NDT on the accuracy of the method.

5 Analysis of the Predicted Structure

5.1 *FEA*

Finite element analysis is performed by using a nonlinear FEA software, i.e. MSC/Marc. The steel reinforcement is idealized using truss elements with the node points defined such that each rebar element is sharing common nodes with the concrete solids. This approach is called discrete idealization of rebar with concrete. Figures 9 and 10 shows analysis model on MSC/Marc on each prediction phase. Figure 11 shows load–displacement of mid-span curves by FEA of each prediction. It is found that the maximum load capacities are 1003 kN and 1593 kN for the first

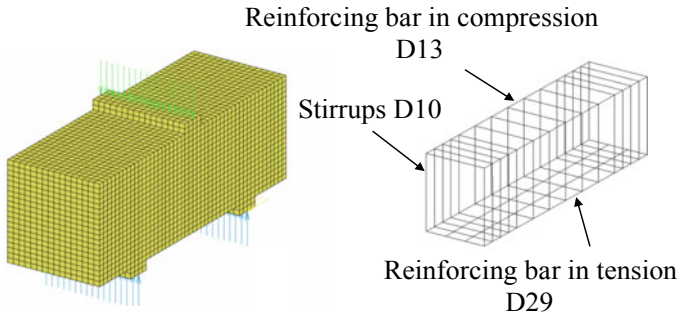


Fig. 9 Boundary conditions, mesh and internal arrangement at first prediction

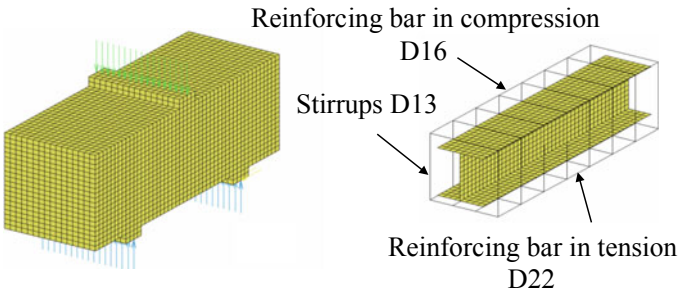
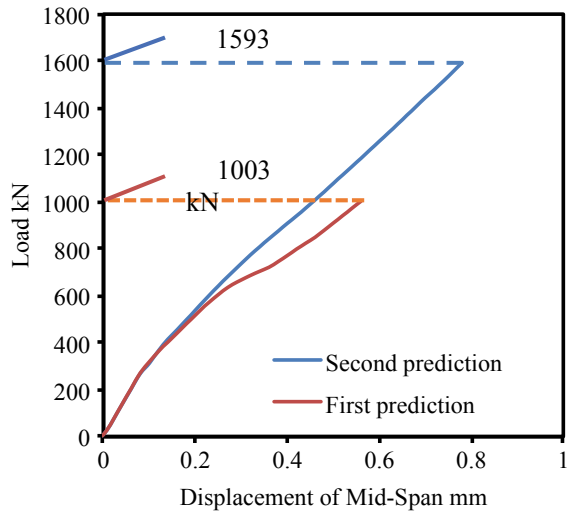


Fig. 10 Boundary conditions, mesh and internal arrangement at second prediction

Fig. 11 Load–displacement relation of the specimens at mid-span from FEA



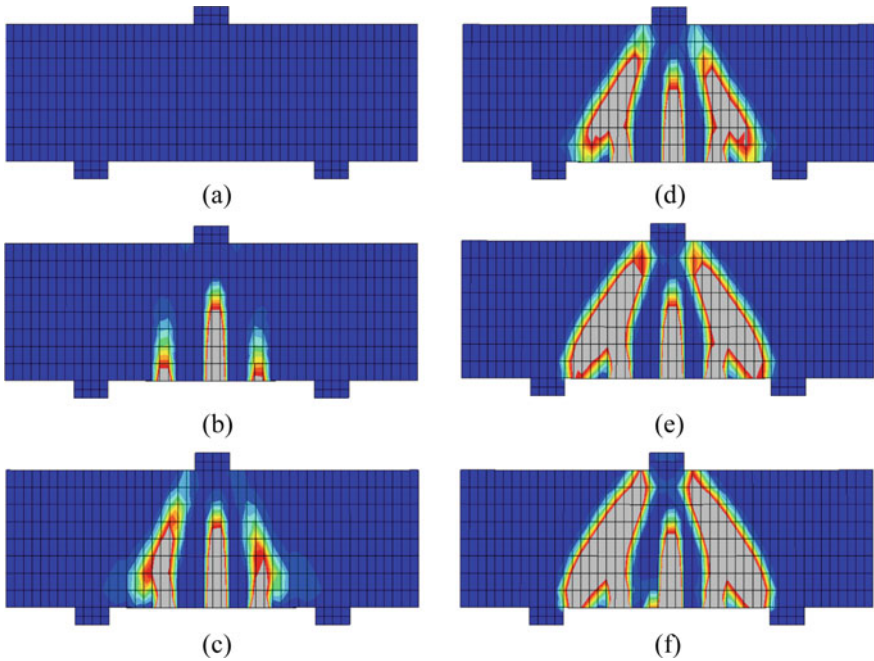


Fig. 12 Maximum principal strain of first prediction on Marc

and second predicted specimens, respectively. From FEA, it is generally recognized that the shear failure is difficult to be reproduced output. However, according to TANIMURA’s paper [5], the procedure of cracking can be reproduced. In this study, to facilitate the investigation of the cracking procedure, it is defined that a major crack forms once the strain exceeds ϵ^* , i.e. 0.001, (see Fig. 5). Besides, the shear failure would be defined as once the major shear crack determined according to the definition reaches from bottom side to top side as shown in Figs. 12f and 13f, where the gray zones indicate the concrete with tensile strain larger than 0.001.

From the analysis of the first prediction, it is found that the simple RC beam cannot reproduce the procedure of cracking. The cracking process of the first prediction can be divided into 4 steps as follows. Step 1: one flexural crack initiates in tensile zone. Step 2: two flexural cracks initiate adjacent to the crack initiated in step 1 in the tensile zone. Step 3: those two cracks expand to the direction of shear cracking. Step 4: those two shear cracks reach both of the bottom and top sides. And then the shear failure happens according to the definition.

In terms of the analysis of the second prediction, it is found that the procedure of cracking is successfully reproduced by the SRC beam. The cracking process of the second prediction can be divided into 4 steps as follows. Step 1: two flexural cracks initiate in tensile zone. Step 2: two cracks initiate adjacent to the two initiated flexural cracks in step 1. Step 3: these two cracks expands to the direction of shear cracking. Step 4: these two shear cracks reach both of bottom side and top side. And

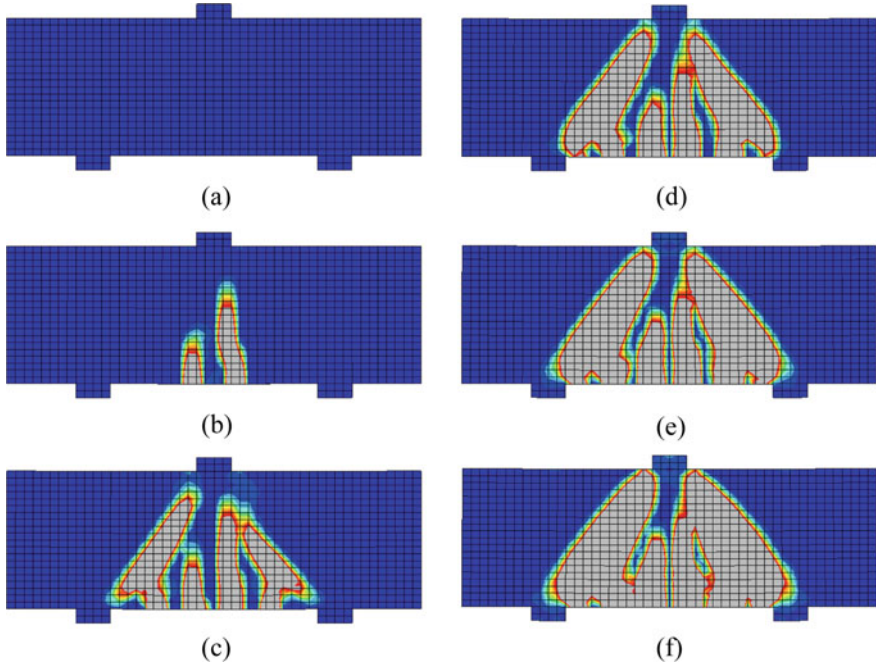


Fig. 13 Maximum principal strain of second prediction on Marc

then, the shear failure happens according to the definition in this research. Figure 11 shows the load-displacement curve of the specimen at mid span.

5.2 Hand Calculation

In this research, the hand calculation using empirical equations was conducted for prediction the maximum load capacity and cross check with the results from FEA. In these equations, the assumption is adopted that the maximum load capacity is a summation of the load capacity of each material, such as concrete, stirrups and I-beam. Table 4 shows the calculation result of the first prediction and the second prediction.

Table 4 Maximum load capacity by FEA and hand calculation

	FEA (kN)	Hand calculation (kN)
First prediction	1003	957
Second prediction	1593	1298

$$V_{cal1} = \frac{0.24 f'_c (1 + \sqrt{100 p_t}) \cdot (1 + 3.33 r/d)}{1 + (a/d)} b_w \cdot d \quad (6)$$

where, V_{cal1} is the load capacity of RC without stirrups (N). f'_c is compressive strength of concrete (N/mm²). p_t is the steel ratio in tensile zone. d is the effective height (mm). b_w is the width (mm). r is the length of loading plate (mm). a is the shear span.

$$V_{cal2} = V_{cal1} + \varphi \cdot V_s \quad (7)$$

$$\varphi = -0.17 + 0.3a/d + 0.33/(100p_w) \quad (8)$$

$$V_s = A_w \cdot f_{wy} \cdot Z/S_s \quad (9)$$

where, V_{cal2} is the load capacity of RC with stirrups (N). V_s is the load capacity of stirrups (N). p_w is $A_w/(b \cdot S_s)$. A_w is the amount of area of stirrups in S_s (mm²). f_{wy} is the yield strength of stirrups (N/mm²). S_s is the interval of stirrups (mm). Z is $d/1.15$.

$$V_{cal3} = V_{cal2} + V_{sy} \quad (10)$$

$$V_{sy} = f_{vy} \cdot t_w \cdot Z_w \quad (11)$$

where, V_{cal3} is the load capacity of SRC (N). V_{sy} is the load capacity of I-Beam (N). f_{vy} is the yield strength of I-Beam (N/mm²). t_w is the thickness of I-Beam (mm). Z_w is the height of I-Beam (mm).

5.3 Discussion of Prediction of Behavior on Loading Experiment

Table 4 shows the result of prediction of load capacity by FEA and hand calculation. As the first prediction shown, the results from FEA and hand calculation are close to each other. From these results, if the prediction of first step of the specimen is correct, the results would be close to the experimental results. However, as the actual specimen is an SRC beam, the results of the specimen from the first prediction should not be close to the experimental results. As shown in the results of the second prediction, the gap between FEA and hand calculation is relatively large. This may be due to the setting of node at FEA. As shown in Sect. 5.1, in this analysis, the rigid connection is adopted. This is considered as a reason of gap of prediction of

maximum load capacity of the specimen. On the real specimen, the slip between I-beam structure and concrete happens. However, in this analysis, the slip is ignored. As comparison of first prediction shows, without I-beam, the gap of prediction of maximum load capacity is much larger. Therefore, the connection of concrete and rebar may not have a remarkable effect compared to the connection of concrete and steel I-beam. As a future work, the connection between I-beam structure and concrete may have to be deliberated.

6 Comparison of Prediction and Actual Specimen

6.1 Arrangement of Internal Structure

Figure 14 shows the actual design drawing of the specimen. Comparing the second prediction, the steel arrangement is similar to the actual design drawing. The difference of the second prediction and the actual design is the rebar diameters and the length of steel I-Beam. Table 5 shows the actual diameter of all types of rebars. It is found that the diameter of the tensile rebar of the second prediction is larger than in the tested specimen.

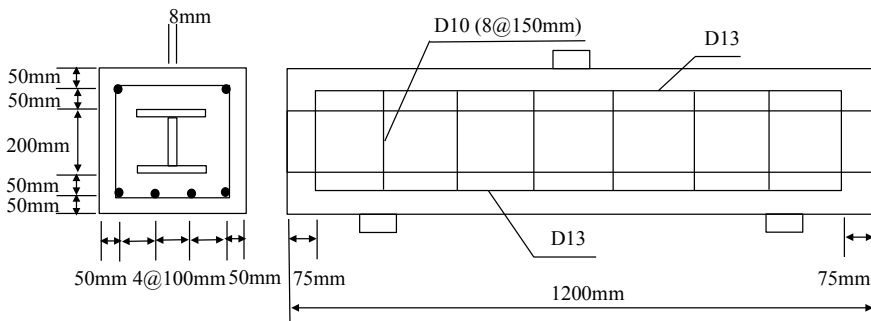


Fig. 14 Actual design drawing of the specimen

Table 5 Each actual diameter of rebar

	Rebar of compressive	Rebar of tensile	Stirrups
Actual diameter of rebar	D13	D13	D10

6.2 Load–displacement Curve

Figure 5 shows the load—displacement curves of the specimen at mid-span from FEA and experiment. In the experiment, the maximum load capacity is 1758 kN. This value is larger than value of FEA and hand calculation. Error is -9.4% for FEA and -26.1% of hand calculation, respectively. Therefore, FEA is reliable in the range. It could be considered that this gap may come from the error of the predicted material property of I-Beam structure. From the comparison between the predictions and actual design drawing, it is found that all diameters of rebar of actual structure are smaller than the predictions. However, the maximum loading capacity from experiment is larger than the load capacity from prediction. Therefore, this gap may come from the error of the material property of I-beam in the predicted specimen.

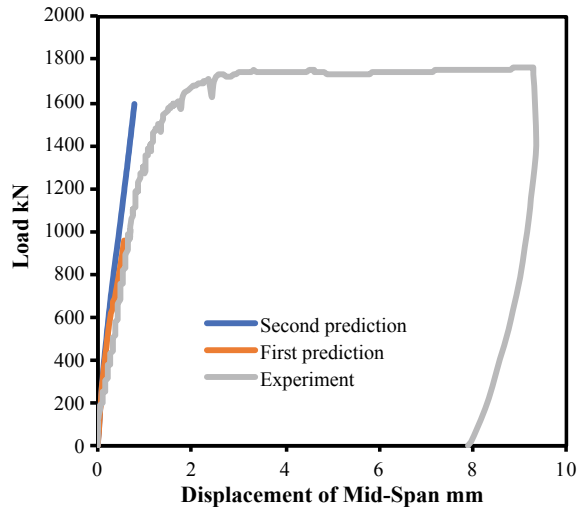
6.3 Procedure of Cracking of Actual Structure and FEA

From Sect. 5.1, the cracking procedure of the second prediction is got. Comparing to the actual structure, it is found that the second prediction reproduces the actual procedure of cracking reasonably well. As shown on the picture of the actual structure after damage (Fig. 2), the specimen has two tensile micro cracking and two micro shear cracking. As shown on the picture of the actual specimen after failure (Fig. 3), the shear cracking expands and leads to a shear failure finally. Comparing this experimental cracking procedure with the analytical cracking procedure using FEA (see Fig. 13), it is found that the FEA using data from NDTs can provide an accurate prediction of the actual cracking procedure and damages.

6.4 Discussion from Comparison

In this section, a comparison between the behaviors of the specimen from FEM and from experiment is conducted. As for the first prediction, it is very different from the actual specimen as no internal information from NDTs was provided until this prediction. This prediction has to be conducted by only referring other papers. Consequently, it was impossible to predict the internal structure or in other words whether the beam is an RC or SRC beam. In this prediction, the specimen was predicted as RC, however actual structure was SRC. In terms of the second prediction, the internal steel arrangement is predicted appropriately using the data from NDTs. The gap of the maximum load capacity between FEA of second prediction and the actual specimen is 163 kN which is only 9.4% of the experimental load capacity. This gap may be due to the difference of diameter of rebar, I-beam material property and concrete material property. However, the gap of maximum load capacity of between

Fig. 15 Comparison of FEA and experiment



hand calculation of second prediction and the actual specimen is 460 kN, which is much larger than the FEA. Thus, the hand calculation has a room of improvement and can be used as a rough cross check of the FEA. Therefore, it would be demonstrated that the process of predicting the structure details by jointly using data from NDTs and referring related experiences and knowledge and then conducting FEA of the predicted structure can provide a structural performance evaluation with good accuracy (Fig. 15).

7 Conclusion and Future Work

In this research, a process, namely blind performance evaluation, is conducted to predict and evaluate the structural performance of a beam using data from NDTs. The process can be described as follows. Firstly, a prediction of the details of the tested beam is conducted using data from inspection, measurement, and NDT technique together with referencing to related experiences and knowledge including standards, and academic article. Secondly, a nonlinear numerical analysis is conducted on the predicted structure based on FEM. Finally, the analytical behaviors of the structure are compared with the corresponding experimental behaviors to examine the proposed process for structural performance evaluation. Main findings can be concluded as follows:

1. The accuracy of the predictions depends greatly on the richness and completeness of the data from inspection, measurement, and NDTs. For example, the tested SRC beam was predicted incorrectly as an RC beam incorrectly with only pictures and dimensions and correctly as an SRC beam with additional

data from NDTs. Besides, referencing to related experiences and knowledge can be a helpful supplementary for an appropriate prediction.

2. As the data from NDTs, such as material properties, may vary over wide ranges, it is of great significance to consider the effects of the obtained data on the behaviors of the structures.
3. For the SRC beam which is predicted using NDTs, a numerical analysis based on nonlinear FEA and a hand calculation based on empirical equations are conducted to predict the load capacity. Comparing with the experimental load capacity, it is found that the FEA can provide a good accuracy which is much higher than the hand calculation. This observation demonstrates the reliability and applicability of the proposed method and process. Nevertheless, the empirical equation can be a cross check of the FEA.
4. In addition, the experimental cracking procedure and shear failure mode are reproduced by the nonlinear FEA as well. Superior to the experiment and hand calculation, the FEA could provide a more detailed investigation of the structure.
5. In this research, the gap between FEA and the experiment may be from the modeling of the interface of rebar/concrete and I-beam/concrete. In this study, the materials or components are rigidly connected. As a future work, it may need to be improved.

Acknowledgements This work is carried out as a part of committee activities (H216 committee) of Japan Society of Civil Engineers.

References

1. Ministry of Land, Infrastructure, Transport and Tourism of Japan Homepage, https://www.mlit.go.jp/sogoseisaku/maintenance/02research/02_01.html. Last accessed 2020/01/11
2. Muhammad S (2016) Finite element analysis of RC beams and slabs repaired with ultra-high performance fiber reinforced concrete (UHPFRC)
3. MacGREGOR JG (1992) Reinforced concrete mechanics and design. Prentice-Hall, Inc., Englewood Cliffs, NJ
4. Kenji K (2006) Effect of shear span ratio on the fracture of deep beams. J JSCE 62(4):798–814
5. Yukihiro T (2004) Shear Strength of deep beams with stirrups. J JSCE 2004(760):29–44
6. Hu HT, Lin FM, Jan YY (2004) Nonlinear finite element analysis of reinforced concrete beams strengthened by fiber-reinforced plastics. J Compos Struct 63:271–281
7. Hu HT, Schnobrich WC (1999) Nonlinear analysis of cracked reinforced concrete. ACI Struct J 87(2):102–118

Development of Time Histories Based on Shallow Crustal Earthquake Sources Considering the New Version of the Indonesian Earthquake Map



Wisnu Erlangga, Mochamad Teguh, and Imam Trianggoro Saputro

Abstract Earthquake disasters are widespread in Indonesia, and one of the areas that frequently experiences earthquakes is Yogyakarta. Many buildings have experienced minor to severe damage during an earthquake. Given this reason, the building design should consider earthquake loads from spectral responses; however, there is the difficulty of getting time history data. In the latest earthquake map, the return period earthquake changes from the 475 to 2475 years made the old buildings comply with the new code. A research object that was selected in this study is the Alana Yogyakarta Hotel. This study examines the changes in time history's value based on shallow crustal earthquake sources using Probabilistic Seismic Hazard Analysis (PSHA). Earthquake events around Yogyakarta were collecting from various sources. In hazard analysis requires the distinction between the mainshock, foreshock, and aftershock. This study's attenuation function was selected based on the similarity of Indonesia's geological and tectonic conditions. A reference to select the time history data is the dominant distance and dominant magnitude from hazard deaggregation analysis. The spectral matching process was carried out to equalize the spectral response value in the study area of time history. The resulting time history is artificial. The results showed that the old code's peak acceleration value is smaller than in the new code.

Keywords Shallow Crustal · Hazard deaggregation · Time History

1 Background

Indonesia is a country that is very vulnerable to earthquake disasters. The data noted that in recent years in Indonesia's territory, there were many earthquakes with large

W. Erlangga (✉) · M. Teguh

Department of Civil Engineering and Disaster Risk Management, Islamic University of Indonesia, Yogyakarta, Indonesia

I. T. Saputro

Department of Civil Engineering, Politeknik Katolik Saint Paul, Sorong, Indonesia

magnitudes causing losses and casualties. The number of earthquakes in Indonesia is caused by Indonesia's geographical location, which is located between 3 active tectonic plates, namely the Eurasian plate, Pacific plate, and Indo-Australian plate. The three tectonic plates' movement causes seismic activity with small to large magnitudes scale [1]. A large number of earthquakes in Indonesia cause the need to make earthquake maps for Indonesian territory. The earthquake map was made by experts who show different earthquake risks for each region in Indonesia [2].

Yogyakarta is one of the regions in Indonesia that has moderate-high earthquake intensity. The large number of earthquakes that occur is due to Yogyakarta's area close to the subduction zone of the Indo-Australian plate to the Eurasian plate [3]. These plates' movement results in the formation of tectonic elements, which are characteristic of subduction systems, such as the benioff zone, sea troughs, active fault distribution, and volcanoes [4]. Figure 1 presents the tectonic setting cross-section of the Java subduction zone. Besides, in 2006 a major earthquake with a magnitude of 6.3 R occurred in Yogyakarta. The earthquake source comes from a tectonic activity that occurs in the Opak fault (shallow crustal). Previously, Yogyakarta's area rarely experienced large-scale earthquakes, but after the 2006 Bantul earthquake, the level of earthquake risk in the Yogyakarta area increased. Special Region of Yogyakarta also has a relatively large population, which causes a high level of risk for earthquake disasters. The earthquake caused damage to buildings and fatalities. The majority of collapsed buildings are residential houses built and designed not according to regulations, especially in the Bantul Regency area. One way to reduce the risk of disaster is to plan and build buildings by considering seismological, geological, geotechnical, and structural aspects to be resistant to the earthquake [5, 6].

An earthquake is a natural event that, until now, cannot be predicted when and where it will occur and can cause substantial losses, both property, and casualties. Until now, the earthquake is a disaster that cannot be prevented and cannot be accurately estimated at both the time, place, and magnitude. In the process of making earthquake hazard maps, there are changes to the latest earthquake maps. The old

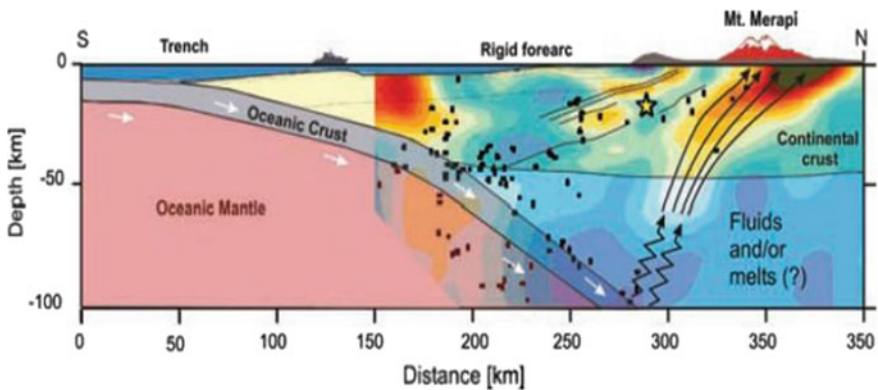


Fig. 1 Tectonic setting cross-section of Java subduction zone [5]

regulation using probability exceeded 10% (when the earthquake returned 475 years) to 2% in 50 years (when the earthquake returned 2475 years). One of the high-rise buildings in Yogyakarta is the Alana Yogyakarta Hotel, designed using the old regulation, namely SNI 1726-2002 [7]. Changes in earthquake risk design parameters where the earthquake risk in the new regulation SNI 1726-2012 [8] is greater than the old regulation causes further research on areas built of buildings with old regulations. High-level building occupants want a safe place to live without the need to worry about risks when an earthquake occurs. On one-story dwellings may not be a big problem because the risk is smaller compared to high-rise dwellings. That is because the evacuation process during an earthquake in a multi-story building takes longer, especially in the building's upper levels. Thus high-rise buildings in Yogyakarta must be resistant to earthquakes. Research on the value of time history on the old rules and new regulations needs to be known to determine how much the design earthquake forces change. The use of time history in building designs is very rarely done because of the difficulty of getting time history data in Indonesia.

This study uses the PSHA (Probabilistic Seismic Hazard Analysis) method to analyze earthquake hazards in an area [9]. The PSHA method is used to calculate the effect of the uncertainty factor in the analysis. Besides, it can also consider the uncertainty of the size, location, and frequency of earthquakes. The advantage of the PSHA method can integrate the hazard of a location with various earthquake sources [10–13]. This method has not been able to provide information on the dominant magnitude and dominant distance. The dominant magnitude and dominant distance are obtained from hazard deaggregation analysis, making it easy to determine the earthquake time history data used. This research resulted in time history acceleration from the response spectra's matching process in the bedrock at the study area. The effect of the earthquake analyzed came from the shallow crustal earthquake source. Time history acceleration on bedrock is propagated vertically to obtain time history acceleration data on the surface. Time history acceleration on the surface needs to be known to determine the amplification factor caused by the soil layer's type and thickness in the area [13–16].

2 Research Method

2.1 Research Instrument

In this study, to facilitate the data analysis process, four software were used as follows:

1. SR Model Software used for seismic hazard analysis using the PSHA method and for deaggregation analysis [17]
2. SeismoMatch Software used to match the response spectrum of time history data to get ground motion data on bedrock.
3. NERA Software (Nonlinear Earthquake Site Response Analysis) was used to process earthquake wave propagation on the bedrock to the ground surface.

Table 1 Reviewed faults

No	Fault
1	Semangko
2	Cimandiri
3	Lembang
4	Baribis
5	Bumiayu
6	Opak fault
7	Pati
8	Lasem
9	Flores back arc
10	SC sunda

4. Microsoft Excel Software used for data processing in this research.

2.2 Identification of the Earthquake Fault Source (Shallow Crustal) and Earthquake Source Modeling

The earthquake hazard source that is taken into account is the earthquake fault source, which is located on Java island and its surroundings (Table 1). Earthquake source modeling used is a three-dimensional earthquake source model (3D Source). The earthquake zone of the earthquake source calculated includes 10 (ten).

2.3 Determination of Earthquake Source Parameters and Attenuation Function

The determination of earthquake parameters in this study is based on previous studies of shallow crustal fault [18–20]. These parameters can later be used for hazard analysis. In contrast, the attenuation equation's determination is taken from other countries' attenuation function based on the similarity of tectonic and geological conditions in Indonesia. This equation is because there is no attenuation function in Indonesia, which requires many ground acceleration data to be made where the amount of data is minimal in Indonesia.

2.4 Logic Tree

Logic trees are used to provide a weighting of parameters used in hazard analysis. Weighting indicates a level of confidence in the parameters used. This logic needs to be done, considering that there are uncertainty factors that must be taken into account in hazard analysis. This weighting is carried out on each attenuation function used.

2.5 Earthquake Hazard Analysis and Hazard Deaggregation Analysis

Seismic hazard analysis was performed using the total probability theory [21]. In the analysis process, the distance probability is used to consider the effect of earthquake source geometry on a particular site. The prediction of each source's probability, causing an earthquake at an absolute magnitude, is obtained from the magnitude probability value. The probability theory also considers the uncertainty of parameter magnitude, distance, and intensity exceeded in the analysis process. The earthquake hazard analysis's final results in this study are the maximum earthquake acceleration on the rock bottom for a probability of exceeding 10% in 50 years (475 years earthquake return period) and 2% in 50 years (2475 years earthquake return period). Dominant magnitude (M) and dominant distance (R) from the earthquake source to the site reviewed were obtained from hazard deaggregation analysis and used in determining ground motion acceleration design at the building site.

2.6 Ground Motion

Synthetic ground motion on bedrock is obtained from matching ground motion acceleration design with a uniform hazard response spectrum appropriate to the Alana Yogyakarta Hotel's location. The matching process is performed by using SeismoMatch software.

2.7 Analysis of Soil Dynamic Response

Analysis of soil dynamic response in this research propagates earthquake waves from the bedrock vertically to the surface using the theory of one-dimensional wave propagation (1D) with NERA software's help. The process begins by entering synthetic ground motion data and calculating soil dynamic parameters according to the location borlog data being reviewed (N-SPT data).

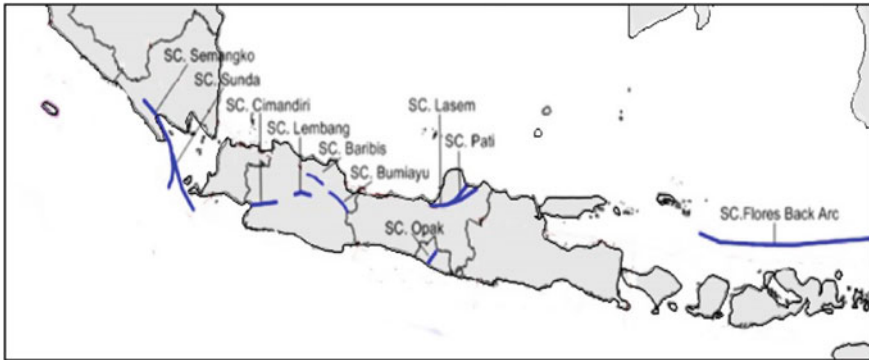


Fig. 2 Modeling of shallow crustal earthquake sources in Java and surrounding areas

3 Results and Discussion

3.1 Identification and Earthquake Source Modeling

The earthquake source zone is divided into 2 (two) parts, including the subduction source zone (megathrust and benioff) and the transformation zone (shallow crustal). However, this research only discusses the shallow crustal earthquake source modeling zone. Earthquake source modeling used in the earthquake hazard analysis of the Java region and its surroundings with shallow crustal earthquake sources using a three-dimensional (3D) model adjusting to the specifications required by the SR Model software. Figure 2 shows the modeling of the shallow crustal earthquake sources.

3.2 Characteristics of Earthquake Sources

The characterization of earthquake sources is determined based on geological and seismotectonic conditions in the study area. The earthquake source characteristic produces parameters used in seismic hazard analysis, such as the b-value, maximum magnitude, and slip rate, as shown in Table 2. A maximum magnitude is a measure of the most significant earthquake value that can occur in an area. This value is obtained based on the magnitude of the most massive earthquake that has happened or based on geologists' research. Simultaneously, the slip rate is the speed of movement of a plate or fracture relative to a nearby plate or fault. Both of these values are very important in analyzing seismic hazard. The parameters a and b are generated based on the regression results to earthquake data using the recurrence model based on the Gutenberg Richter method. Also, the mechanism of the earthquake source occurrence is essential in earthquake hazard analysis. Each earthquake zone

Table 2 Parameter shallow crustal earthquake sources [18–20]

Fault	Slip rate (mm/year)	Mmax (history)	b-value	a-value	Rate(ν)	Source
Semangko	10	7.2	1	4.756	0.570	Mechanism
Cimandiri	10	7.6	1	4.828	0.673	Strike-slip
Lembang	2	7.2	1	4.057	0.114	Strike-slip
Baribis	2	6.6	1	3.949	0.089	Strike-slip
Bumiayu	0.2	6.8	1	2.985	0.010	Strike-slip
Opak fault	0.2	6.8	1	2.985	0.010	Strike-slip
Pati	0.2	6.8	1	2.985	0.010	Strike-slip
Lasem	0.5	6.8	1	3.383	0.024	Strike-slip
Flores back arc	0.5	6.5	1	3.329	0.021	Strike-slip
SC sunda	14	7.8	1	5.010	1.024	Strike-slip

has a different earthquake mechanism. This mechanism can be identified based on geologist research on the movement of the earthquake source.

3.3 Attenuation Function and Logic Tree

The attenuation function is used to determine the earthquake peak acceleration, which is decreased due to distance influence. This function connects the magnitude of the earthquake magnitude and the distance to the epicenter's location with ground motion parameters. This study's attenuation function derives the attenuation equation studied by experts under Indonesia's geological and tectonic conditions. The following is the attenuation function used for shallow crustal earthquake zones:

1. Boor-Atkinson attenuation function (2006-NGA) [22],
2. Sadigh attention function (1997) [23], and
3. Chiou-Young attenuation function (2006-NGA) [24].

Based on the attenuation function, a logic tree will be created, which is used to overcome the uncertainty of the parameters used and the inaccuracy in selecting the model when conducting a seismic hazard analysis. The use of logic trees will provide a more appropriate framework for improving seismic hazard analysis results by weighting each model calculated in the hazard analysis. Figure 3 explains the logic tree used in this study with shallow crustal earthquake sources. Weighting carried out is a value of the level of confidence of the model or parameter being interpreted. In the recurrence model section, the earthquake characteristic value is given a weighting value of 0.66, while the Gutenberg Richter (exponential model) is weighted at 0.34. This characteristic model gives greater weight because geological evidence shows that characteristic earthquakes occur more frequently than earthquakes are estimated from extrapolating the Gutenberg-Richter recurrence model.

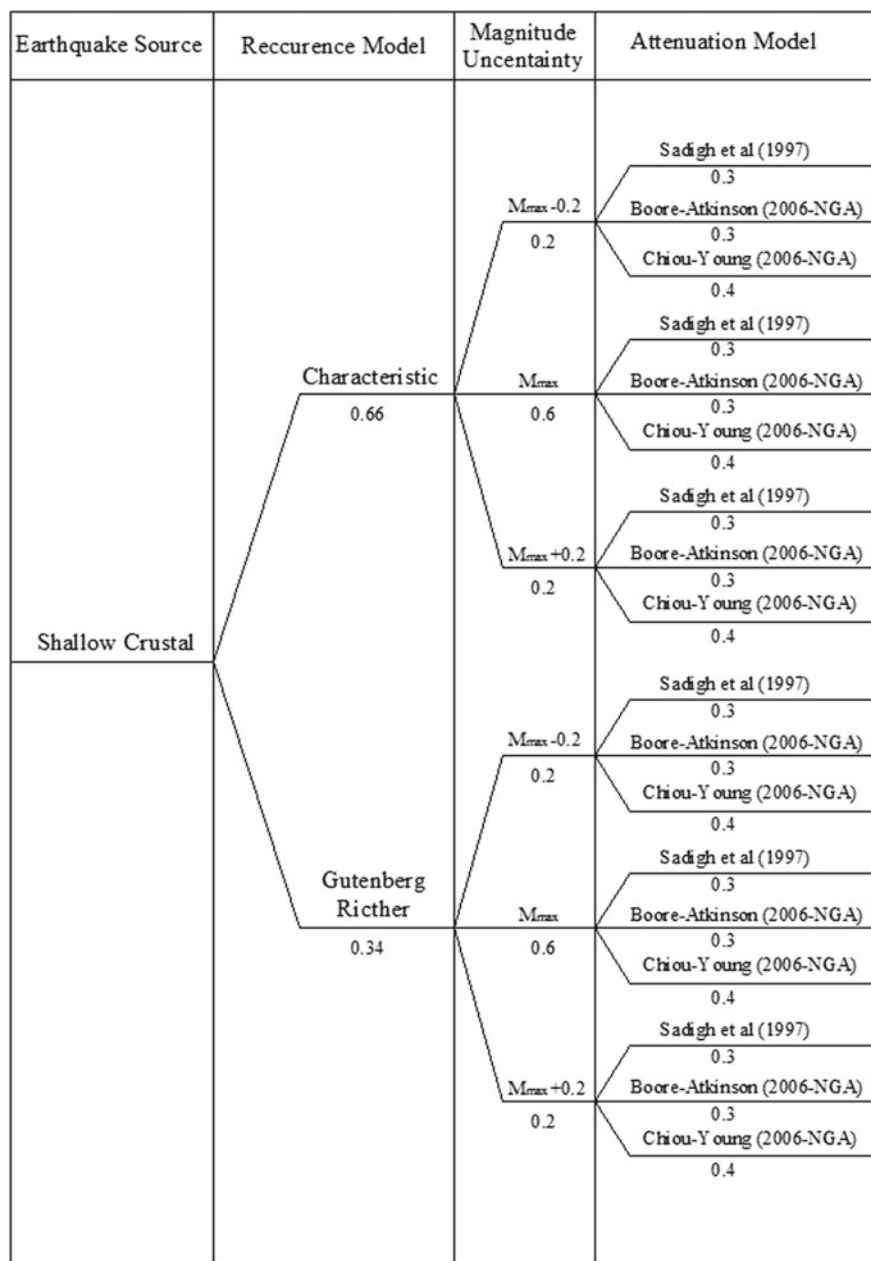


Fig. 3 Logic tree

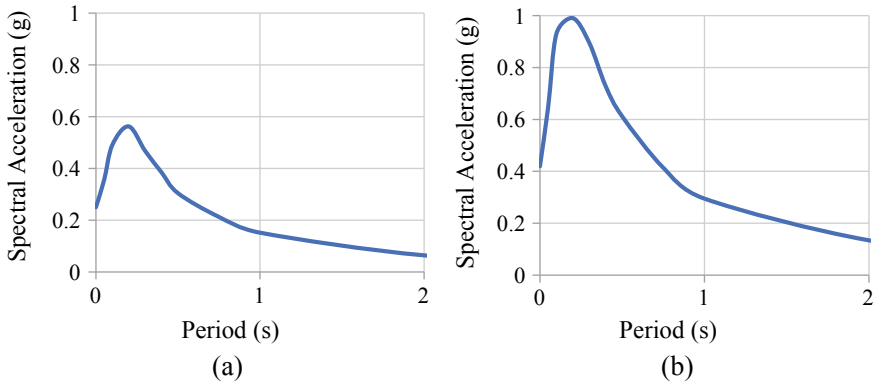


Fig. 4 Graph of the uniform hazard response spectrum **a** probability of 10% exceeded in 50 years **b** probability of 2% exceeded in 50 years

3.4 Results of Earthquake Hazard Analysis

Earthquake hazard analysis in this study uses the probabilistic method (PSHA), which produces a uniform hazard response spectrum (Fig. 4). The 0 s period is known as PGA (Peak Ground Acceleration). PGA value in bedrock at the study site at a probability of 10% exceeded in 50 years of 0.2502 g, and a probability of 2% exceeded in 50 years of 0.4198 g. From the results of earthquake hazard analysis it can be concluded that the earthquake load when the PGA in an earthquake with a return scale of 475 years is smaller than the PGA in an earthquake with a return scale of 2475 years. This causes a significant difference in seismic load between the old earthquake load regulations and the new earthquake load regulations. It can be seen the effect of using a different earthquake load when an earthquake occurs, many old buildings are more affected than new buildings.

3.5 Hazard Deaggregation

Hazard deaggregation is the process of analyzing various sources of earthquake hazards that affect a location by predicting the magnitude of the dominant distance and dominant magnitude. Based on Fig. 5, the dominant distance (R) that can affect the study location is 19.5 km, with a dominant magnitude (M) of 6.3. The deaggregation process resulted that the dominant earthquake source that influenced the research location was sourced from the Opak fault with the hazard contribution given to reach 99.9%. From the results of the deaggregation, earthquake data were chosen following the location of the study, San Fernando, in 1971, which was recorded at the Pasadena—Old Seismo Lab earthquake recording station. This earthquake has a magnitude of 6.61, with a distance of 21.5 km.

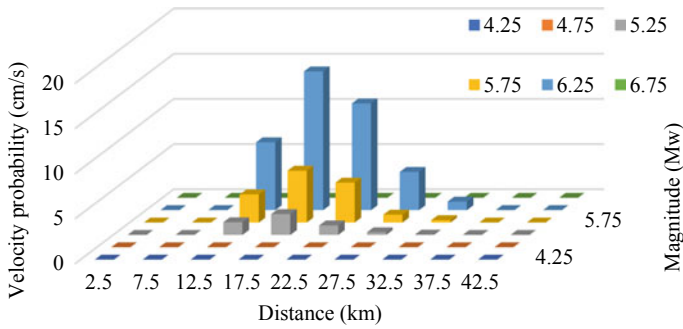


Fig. 5 Hazard deaggregation result

3.6 Spectral Matching

The time history data used is adopted based on earthquake recordings from other regions, so a matching process needs to be performed to match the study site’s conditions. Time history can be scaled through matching the response spectra of the target at the location under study. In this study, the target spectra used is the spectra’s response in the bedrock of the shallow crustal earthquake source, as presented in Fig. 5. The target spectra will be used as a reference in spectral matching analysis for this study’s time history. The spectral matching analysis process uses the help of SeismoMatch software. This software works to equalize the appropriate time history based on the hazard deaggregation with the response spectrum of the used target.

Figure 6 shows a comparison of time history before and after the matching process. The resulting peak acceleration is increased from the previous one (at a probability of 10% exceeded in 50 years from 0.2049 to 0.2711 g and 2% exceeded in 50 years from 0.2049 to 0.4039 g). The thing that influences this result is the spectrum’s response, which is adjusted based on its value. This process can be seen in the spectral response’s matching results from the initial conditions to the target presented

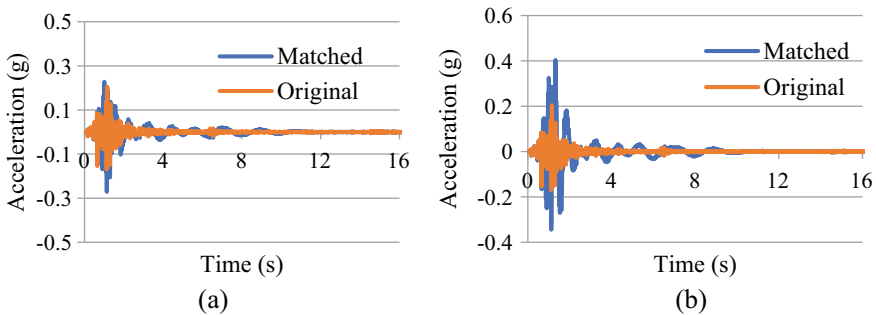


Fig. 6 Comparison of time history acceleration on bedrock **a** probability of 10% exceeded in 50 years **b** probability of 2% exceeded in 50 years

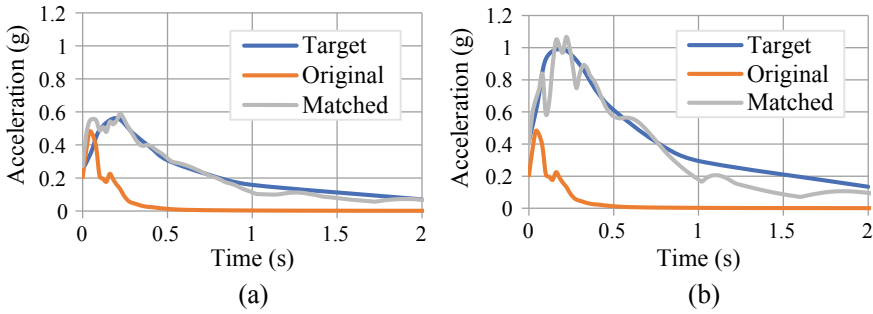


Fig. 7 Response spectrum **a** probability of 10% exceeded in 50 years **b** probability of 2% exceeded in 50 years

in Fig. 7. The spectral response matching process in Fig. 7 is one of the outputs of SeismoMatch, where the actual is the initial acceleration response from the 1971 San Fernando earthquake. The response spectrum target is the response spectrum acceleration obtained from the seismic hazard analysis process at the location reviewed, the Alana Yogyakarta Hotel. The Seismosoft software performs a matching process to obtain an artificial scaled response spectrum based on the two-response spectrum acceleration.

3.7 Analysis of Soil Dynamic Response

Soil dynamic response analysis is carried out to determine the value of earthquake acceleration at the surface, including the determination of soil dynamic parameters and wave propagation from the bedrock to the ground surface. The soil parameters used are maximum shear modulus (G_{max}), and shear wave propagation velocity (V_s) obtained from soil test results in the form of borlog data. This analysis process is carried out using NERA's help (Nonlinear Earthquake site Response Analysis) software. Soil dynamic parameters are obtained from borlog data correlations in N-SPT using equations that have been studied by geologists.

Soil dynamic parameters help the process of earthquake wave propagation on bedrock to the surface with NERA software's help. The process has several stages of filtering the time history data on bedrock, then scaling the acceleration value and the filtered acceleration until the time history acceleration data on the surface is obtained. Each region produces a different propagation value because the type of subsoil influences the time history acceleration on the surface.

Based on the results of wave propagation, the peak acceleration value on the surface is greater than the peak acceleration on the bedrock (Fig. 8). This increase is influenced by local site soil conditions and is commonly referred to as the amplification factor. This study obtained different amplification values at the time of the earthquake return. When the probability of 10% exceeded in 50 years, the peak

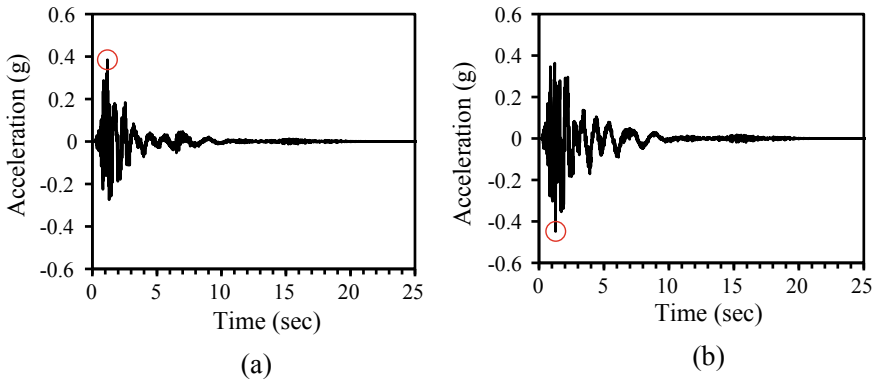


Fig. 8 Time history acceleration on surface **a** probability of 10% exceeded in 50 years **b** probability of 2% exceeded in 50 years

acceleration value of time history acceleration on the bedrock is 0.2711 g. The peak acceleration of time history acceleration on the surface has increased to 0.384 g. Whereas the probability of 2% exceeded in 50 years, the peak acceleration value of the time history acceleration on the bedrock, which was initially 0.4039 g, becomes 0.448 g on the surface. It can be concluded that the magnitude of the amplification factor in the study area is 1.416 for 475 years earthquake return period and 1.11 for 2475 years earthquake return period. A significant gap in the value of peak acceleration between new regulations and old regulations makes it necessary to do further research on buildings designed using the old regulations.

4 Conclusion

According to the results of the analysis, there are several conclusions generated from this study. The results of the hazard deaggregation analysis conducted at the Alana Yogyakarta Hotel location produced a dominant magnitude (M) of 6.31 with a dominant distance (R) of 19.49 km. The most significant hazard to the research location for earthquakes originating from shallow crustal earthquake sources is the earthquake caused by the Opak fault activity. Based on the results of hazard deaggregation analysis, earthquake data used to perform spectral matching analysis. They can be recommended to represent synthetic ground motion in bedrock due to shallow crustal earthquake sources at the study site in the 1971 San Fernando earthquake. The peak acceleration value of the time history acceleration on the bedrock and the surface for the new regulations is greater than the old regulations. In bedrock, the peak acceleration of the probability of 2% exceeded in 50 years is 0.4039 g and the probability of 10% exceeded in 50 years is 0.2711 g. While on the surface, the peak

acceleration value of 2475 years earthquake return period at 1.167 times the peak acceleration value of 475 years earthquake return period.

References

1. Aldiamar F (2007) Earthquake risk analysis and making of design spectra response for Suramadu Bridge with 3D earthquake source modeling. Thesis, Postgraduate Program in the Faculty of Civil Engineering and Planning, ITB, Bandung
2. Widodo P (2012) Seismology engineering & earthquake engineering. Pustaka Pelajar. Yogyakarta
3. Hamilton W (1979) Tectonics of the Indonesia region. U.S. Geological Survey professional paper, vol 1078, p 345. Washington
4. Wagner D, Koulakov I, Rabbel W, Luehr BG, Wittwer A, Kopp H, Bohm M, Asch G (2007) The MERAMEX scientists: joint inversion of active and passive seismic data in Central Java. *Geophys J Int* 170:923–932
5. Mahesworo RP (2008) Ground motion proposal for four big cities in sumatra region based on the results of seismic hazard analysis using 3-dimensional earthquake source model. Thesis, Postgraduate Program in the Faculty of Civil Engineering and Planning, ITB, Bandung
6. Irsyam M, Sengara IW, Adiamar F, Widiyantoro S, Triyoso W, Natawidjaja DH, Kertapati E, Meilano I, Suhardjono Asrurifak M, Ridwan M (2010) Summary of study results by the revised earthquake map team of Indonesia, Bandung
7. SNI 1726-2002 (2002) Earthquake resistance planning standards for building structures. Department of Settlement and Regional Infrastructure, Bandung
8. SNI 1726-2012 (2012) Earthquake resistant planning procedures for building and non-building structures. National Standardization Agency (BSN), Jakarta
9. Cornell CA (1968) Engineering seismic risk analysis. *Bull Seismol Soc Am* 58:1583–1606
10. Fauzi UJ (2011) Map of Indonesian deaggregation based on probability analysis with three dimensional earthquake sources. Thesis, Postgraduate Program in the Faculty of Civil Engineering and Planning, Institut Teknologi Bandung, Bandung
11. Erlangga W (2018) Evaluation of structural response of multi-story building using FEMA 310 and ATC-40 based on the time history of seismic hazard analysis. Thesis, Department of Civil Engineering, Islamic University of Indonesia, Yogyakarta
12. Imam TS (2016) Response evaluation of multi-story building structures using time history in shallow crustal earthquakes sources based on the PSHA method. Thesis, Department of Civil Engineering, Islamic University of Indonesia, Yogyakarta
13. Mochamad T, Wisnu E (2019) Comparison of bedrock and surface time histories subjected to subduction earthquake in a selected location of Yogyakarta. *J Geomate* 17(63):77–86
14. Idriss IM (1985) Evaluating seismic risk engineering practice. In: Proceedings of the international conference on soil mechanics and foundation engineering, San Francisco, vol 1, pp 255–320
15. Kramer SL (1996) Geotechnical earthquake engineering, Prentice-Hall, New Jersey
16. Wisnu E, Mochamad T, Lalu M (2019) The analysis of performance level on an existing multi-story building structure using the time history based on the subduction earthquake source. In: 4th ICEEDM
17. Lalu M (2009) Development of hazard deaggregation map for Indonesia through making software with three-dimensional earthquake modeling
18. Asrurifak M (2010) Indonesian spectra response map for earthquake-resistant building structures planning with three-dimensional source models in probabilistic analysis. Dissertation. Institut Teknologi Bandung, Indonesia
19. Firmansyah J, dan Irsyam M (1999) Development of seismic hazard map for Indonesia. In: Proceedings of the national seismic engineering conference in Indonesia, ITB, Bandung, Indonesia

20. Kertapati EK (1999) Probabilistic estimates of seismic ground-motion hazard in Indonesia. In: Proceedings of the national seismic engineering conference in Indonesia, Bandung, Indonesia
21. McGuire RK (1976) Fortran computer program for seismic risk analysis. U.S. Geol Surv Open-File Rept 67-76
22. Boore DM, Atkinson GM (2006) Ground motion prediction equations for the average horizontal component of PGA, PGV, and 5% damped PSA at spectral periods between 0.01 s and 10.0 s: Earthq Spectra 24(1)
23. Sadigh K, Chang CY, Egan JA, Maksidi F, Young RR (1997) Attenuation relationship for shallow crustal earthquake based on California Strong motion data. Seismol Res Lett 68. Seismological Soc Am
24. Chiou BS-J, Youngs RR, Youngs C (2006) PEER-NGA empirical ground motion model for the average horizontal component of peak acceleration, peak velocity, and pseudo-spectral acceleration for spectral periods of 0.01–10 sec. Interim report submitted to PEER

Bamboo Reinforced Concrete Beam



Nurharniza Abdul Rahman, Choo Li Rong, and Lee Hoong Pin

Abstract The demand of steel is increasing especially in developing countries has made the price rose tremendously. It has made the cost of production of this material rise and at the same time, the milling process had brought critical issues to the environment. This issue has created an interest to the researchers to investigate on new potential material to replace the conventional reinforcement. Based on thorough literature review has shown the potential of bamboo to be replaced steel bar in concrete structure. Thus, this research is focusing on bamboo as a replacement to steel reinforcement in concrete beam. In total nine concrete cubes grade 30 were test under compression test for 7, 14 and 28 days. Moreover, six beams had been prepared, three for bamboo reinforced concrete beam (BRCB) and three for normal steel reinforced concrete beam (SRCB). SRCB had used T10 steel bar for longitudinal bar and R6 for shear reinforcement. On the other hand, the 10 mm diameter of bamboo slats had been use for longitudinal bar and the 6 mm thickness of bamboo slats were use as shear reinforcement in BRCB. The beams were test under four-point bending. Based on the test had shown the potential of bamboo to be used as reinforcement. However, it is recommended to use bamboo pole instead of slats as the durability of bamboo might been affected when the properties had been modified. Further investigation is required to improve the strength and the durability of bamboo as reinforcement replacement in concrete beam.

Keywords Concrete beam · Bamboo slat · Reinforcement

N. A. Rahman (✉) · C. L. Rong · L. H. Pin
INTI International University, Persiaran Perdana BBN, Putra Nilai, 71800 Nilai, Negeri Sembilan, Malaysia
e-mail: nurharniza.rahman@newinti.edu.my

© The Author(s), under exclusive license to Springer Nature Singapore Pte Ltd. 2022
S. Belayutham et al. (eds.), *Proceedings of the 5th International Conference on Sustainable Civil Engineering Structures and Construction Materials*, Lecture Notes in Civil Engineering 215, https://doi.org/10.1007/978-981-16-7924-7_32

497

1 Introduction

1.1 General

The overall sustainable economic growth, productivity, and the well-being of the nation is depending on the functionality, consistency, and durability of construction technologies. Apart from the environmental and operational condition, the constituent materials accounting for the increasing cases of structural deficiency and functional obsolescence are recorded in the built environment [1]. As the demand of steel reinforcement is very high, it has created the need of steel replacement material in construction industries [2]. Thus it make the researchers start to investigate on the new properties of material to be used as steel replacement without jeopardizing the strength and the safety of the structure. On the other hand, the increasing of steel price is another factor to push the need of steel replacement in construction industries. Many researchers have conducted research on the engineering properties of bamboo and found out bamboo is suitable to be used as substitution for steel although it has a little less strength than steel [1–3]. Srimathi et al. [2] for example has reviewed few research studies on bamboo reinforced concrete beam which shown that the square bamboo cross section reinforcement obtained good load carrying capacity, deflection, flexural and shear strength. The tensile strength and modulus of elasticity of bamboo is one half and one third of steel strength. Similar to a study by Naznin and Chetia [4] has found that bamboo beam will able to perform better under flexural load with the increase in number of reinforcements, diameter of the bars and addition of shear links to the bamboo reinforced beams.

The parts of bamboo like the stem and culm can be made into various products ranging from domestic household products to industrial applications [5]. In China and Hong Kong for example, bamboo has been widely used by the developers as scaffolding and bridges [5]. Apart from that, bamboo is also widely used as it is one of the most sustainable yet economical materials where it also able to meet the extensive need for economical housing. Due to the distinctive rhizome-dependent system, bamboo is one of the fastest-growing plants in the world and their growth is three times faster than other species of plants. Bamboo can be easily cut into various sizes, can be handled and repositioned without any equipment or special tools. From the growing process until it becomes any kind of usable product, bamboo does not produce any polluted materials to environment. On the other hand, Mahzuz et al. [6] had highlighted that the production per ton of steel releases over two tons of CO₂ which this condition could be harmful to the environment.

Bamboo is a great potential substitute for production of composite materials and components which is much more cost effective [3, 5]. With hollow section and circular form, bamboo is a light building material which is easier to be handled, transported and stored. With technologies and the advancement of science today, bamboo shall be processed in a more advanced way in order to make it as a more durable and sustainable construction material [5, 7]. It is frequently had been referred

as a highly renewable and high-strength alternative material to timber [7]. Occasionally, it is also has been referred as a ‘strong-as-steel’ reinforcement for concrete structure [6]. Through some research investigation, bamboo has good potential to be used for structural and non-structural activities in construction. With the mechanical properties of bamboo, it is considered as high tensile strength that been used for a decade as main reinforcement in structural component for the low cost houses [3]. The tensile strength of bamboo is relatively high and can reach 370 MPa [8, 9]. It is somehow depends on the species or types of bamboo and the origin of the bamboo had been grow as different location will have different weather. The maximum strength at 3–4 years is the best age to reach maximum strength as the strength of bamboo increase with its age before its start to decline in years later [9].

However, there are few weaknesses or disadvantages about bamboo. The previous research by Hector [7] had found out that bamboo as brittle material especially in longitudinal tension-dominated failure modes. Bamboo is particularly weak in the direction perpendicular to the fibre [7]. Thus some treatment is required to increase the strength of bamboo to make bamboo reinforcement more sustainable and strong [6]. The epoxy-based adhesive is one of the materials can be applied to improve the bonding strength of bamboo. The average bond stresses for pull-out test for bamboo splints had increased more than 100% when Sikadur 32 adhesive was used to coat the splints [6].

2 Methodology

British Standard Mix Design (DOE) method was used to design the beam and the concrete in this research. Concrete was design for Grade 30 with slump target of 10–30 mm and concrete was designed for normal concrete density 2400 kg/m³ as this study is aiming to focus on the effect of bamboo as the reinforcement replacement in concrete beam as shown in Table 1. Ordinary Portland cement (OPC) Type 1, fine aggregate, coarse aggregate was used for concrete in this study. Table 2 shows quantities of raw materials for concrete grade M30 in this research.

On the other hand, the 10 mm bamboo sticks, 6 mm bamboo slats, R6 steel bars, T10 steel bars were been prepared for concrete beam. There are few criteria should be considered in the selection of bamboo culms for use as reinforcement in concrete structures. The bamboo culm required at least 3 years and above before it can be cut into bamboo stick. Green color bamboo is considered as fresh bamboo, seasoning process changed the color of bamboo into brown color. The whole culms of green or unseasoned bamboo should not be used. The longest large diameter culms available should be selected. During seasoning, bamboo should be properly arranged to avoid any bending and it need to seasoning for at least three to four weeks.

Further notes to be reminded, bamboo should be protected from rapid changes in moisture content. That is mean bamboo should not be exposed too long under the hot sun as this will cause bamboo to crack. Another important point to take note is bamboo cut in spring or early summer should be avoided as this season has make

Table 1 Concrete mix design with DOE method

Stage 1	
Grade of concrete	M30
Type of cement	Ordinary portland cement (OPC)
Standard deviation, σ	5
Tolerance factor, t	1.65
Target mean strength, f_t	$30 + (5 \times 1.65) = 38.25$ Mpa
Cement strength class	52.5
Coarse and fine aggregate type	Crushed
Free water cement ratio	0.5
Stage 2	
Slump	60–180 mm
Maximum aggregate size	20 mm
Free water content	225 km/m ³
Stage 3	
Cement content	$225/0.5 = 450$ kg/m ³
Stage 4	
Relative density of aggregate (SSD)	2.7
Concrete density	2400 kg/m ³
Total aggregate content	$2400 - 225 + 450 = 1725$ kg/m ³
Stage 5	
Grading of fine aggregate	50%
Proportion of fine aggregate	40%
Density of fine aggregate	690 kg/m ³
Density of coarse aggregate	1035 kg/m ³

Table 2 Quantities of raw materials for concrete grade M30

Quantities	Cement (kg)	Water (L)	Fine aggregate (kg)	Coarse aggregate (kg)
Per m ³	450	225	690	1035
0.151	67.95	33.975	104.19	156.285

bamboo weaker due to increased fiber moisture content. Moreover, the storage area should be in good ventilation and should also be avoided from direct contact with soil surface. This precaution is important to protect bamboo from fungal and insect’s attacks.

Bamboo sticks and bamboo slats used for this study were been purchased from the bamboo supplier, Bamboo Malaysia. Where the bamboo product has undergo treating process: cutting, pointed, selecting, antiseptis, anti-mildew and fumigation. This company has supply treated bamboo sticks and bamboo slats. The bamboo slats

Fig. 1 Details of bamboo reinforcement



have been cut and smoothed into a straight shape ideal for aligning into uniform panels. This slat is suitable to be drilled a hole onto it thus it has been used as shear reinforcement in this project. Semantan bamboo species has been used for this project. Figure 1 shows the detail arrangement of bamboo reinforcement.

The 10 mm bamboo sticks had been used as longitudinal bar and the 6 mm thickness of bamboo slats as link or shear reinforcement. The holes were drilled on the bamboo slat then the longitudinal reinforcement which made from bamboo stick had been slot in through this hole.

In total nine cubes with size $150 \times 150 \times 150$ mm had been cast and 6 beams with size $150 \times 150 \times 750$ mm had been prepared for Flexural Test. There are two types of beams had been prepared, normal concrete beam as control sample which used steel reinforcement and bamboo reinforced concrete beam which had fully utilized bamboo as total replacement to steel reinforcement. The cube and beam samples were kept at room temperature for 24 h before it been demolded and soak in waster for curing process. The compression test was done to test the strength of concrete by using compression machine at 7 days, 14 days and 28 days. Whilst, the beams specimens were test for Flexural Test at 28 days to get the flexural capacity of bamboo reinforced concrete beam.

2.1 Laboratory Test

Slump Test: This test was used to indicate the degree of wetness and measure the consistency of fresh concrete. As normal procedure on concrete material study, the slump test (Fig. 2) was conducted to test the workability of concrete. Based on BS

Fig. 2 Slump test

EN 12,390-2 [10], only true slump is permissible where the concrete is intact and having a spherical shape with 0.5 water cement ratio.

Compression Test: Compressive strength had measured through the compression test on concrete cubes using compression testing machine according to BS1881-116:1983 [11]. The cubes were removed from curing tank and weighted before the cubes had been placed for compressive strength test (Fig. 3). The specimens were then loaded to failure in a compression testing machine. The load was set with constant rate of loading to prevent sudden failure and in order to obtain the maximum concrete compressive load. The maximum load sustained was recorded and compressive strength of the concrete was been determined.

Flexural Test: This test was done to determine the flexural strength of beam. 4 points flexural bending machine was used in this research. Flexural test is also known as tensile strength test which the load was applied to concrete beam (Fig. 4) after 28 days curing. This test was done to test the ability of concrete to withstand failure in bending. The beam was designed according BS8110 [12] with size of specimen was cast for $150 \times 150 \times 750$ mm dimension. Please take note that the test machine must make sure cleaned, and the specimen should be aligned with the machine. The

Fig. 3 Cube test



Fig. 4 Flexural test



Table 3 Slump test

Slump test	Height (mm)
First mixed	78
Second mixed	80
Third mixed	83
Fourth mixed	77

loading and roller support should be in even contact with the specimen. The load was applied continuously at constant rate until failure. The data was recorded, analyzed and discussed.

Tensile Test: This test was done to determine the strength of material by using Universal Testing Machine (UTM). 10 mm thickness bamboo and T10 steel bar had been test in this research. Specimen was placed in UTM and tensile load was being applied until rupture. Elongation was measured at regular interval of applied tensile load.

3 Results and Discussions

3.1 Slump Test

The slump test had been done as per designed. Based on the design accordance of BS EN 12,390-2 [10], the slump should be in range 60–180 mm. Table 3 shows the Slump Tests results which in average value is 79.5 mm. Thus it shows that the slump has met the design requirement for normal concrete design grade 30.

3.2 Compression Test

In total 9 cubes with the size of 150 × 150 × 150 mm had been test for compressive strength by using compression testing machine after 7 days, 14 days and 28 days curing respectively. Table 4 shows the compression result for 9 cubes. The result shows concrete strength had achieved 70% of the strength at 7 days curing. Whilst,

Table 4 Cube test result for concrete cube

	Cube 1 (MPa)	Cube 2 (MPa)	Cube 3 (MPa)	Average (MPa)
Day 7	19.4	22.7	21.3	21.13
Day 14	23.4	23.7	25.2	24.10
Day 28	33.5	32.8	34.7	33.67

the average compressive concrete strength at 28 days was 33.67 MPa. Thus it shows that the concrete strength had met the design strength for grade 30 concrete according to BS1881-116:1983 [11].

3.3 Flexural Test

In total 6 beams were cured inside water tank and tested on day 28. Load is increasing slowly; maximum flexural stress and displacement width had been recorded in Table 5. While, Fig. 5 shows the load comparison between bamboo and steel reinforced beam. The results has shown that bamboo reinforced concrete beam is 7% lighter than steel reinforced concrete beam. It shows that the usage of bamboo as the replacement to the reinforcement in concrete beam does not really affect the weight of the beam. The results also shows that the usage of bamboo as reinforcement replacement has not really help to increase the stress capacity of the concrete beam.

Figure 5 clearly showed that the load capacity for steel reinforced concrete beam increase higher than bamboo reinforced concrete beam. The average ultimate load of steel reinforced concrete beam is 53 kN with an average displacement of 13 mm. On the other hand, bamboo reinforced concrete beam has an average ultimate load at 14kN with an average displacement at 7 mm. The low displacement has shown that bamboo has low shear capacity [5]. Thus it mean bamboo reinforced concrete beam has 74% lower strength with 46% lower displacement compared to steel reinforced concrete beam. This condition may cause due to natural behavior of bamboo which have high water absorption due to repeat cycles of expansion and contraction. Bamboo also may shrink larger and faster than concrete may lead to quick debonding between bamboo and concrete. Thus it may show that bamboo not really suitable to be used as replacement to the reinforcement.

The laboratory test result has shown that bamboo reinforced concrete beam had achieved about 45% of load design. The load capacity of bamboo reinforced concrete structure has shown reasonable tensile strength, which suggests that it can be used as reinforcement in reinforced concrete structure especially for low cost housing projects [5]. Previous study had also proven that bamboo can be sustained better if

Table 5 Flexural test result for bamboo and steel beam at 28 days

Sample	Weight (kg)	Stress (Mpa)	Load (kN)	Displacement (mm)
Bamboo 1	37.79	0.12	13.74	8
Bamboo 2	38.12	0.11	13.04	6
Bamboo 3	38.36	0.12	14.41	7
Steel 1	39.5	0.47	53.94	14
Steel 2	42.24	0.46	52.68	13
Steel 3	41.22	0.46	52.78	13

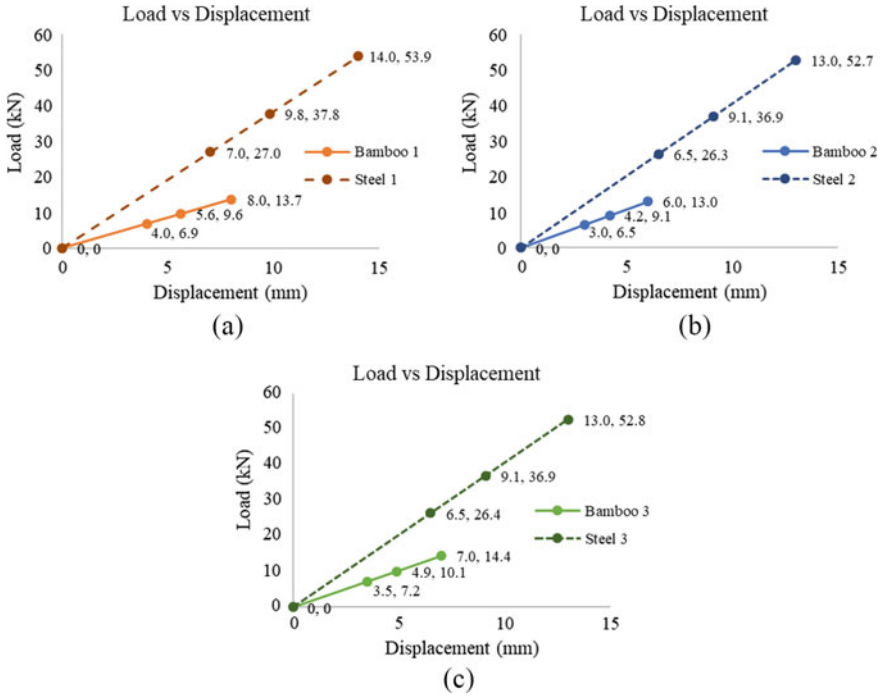


Fig. 5 Comparison of bamboo beam and steel beam; a sample 1, b sample 2, c sample 3

used with bamboo nodes. The bamboo nodes can help to divide or transverse wall that maintains strength and allows bending thus preventing rupturing when bent [2].

3.4 Tensile Test

The bamboo and steel reinforcements were then been test for tensile strength test. It is to test the tensile resistance for these two different types of reinforcement. Three (3) 10 mm bamboo sticks and three (3) T10 steel bars had been test for this research.

Table 6 shows the tensile test results between 10 mm bamboo sticks and T10 steel bar. The average tensile strength of bamboo sticks is 226.67 MPa and average tensile strength of steel bar is 472.77 MPa. Thus, it shows that the strength of bamboo

Table 6 Tensile test for 10 mm bamboo sticks and T10 steel bar

Tensile strength	Sample 1 (MPa)	Sample 2 (MPa)	Sample 3 (MPa)	Average (MPa)
Bamboo reinforcement	190.0	274.0	216.0	226.67
Steel reinforcement	474.3	472.0	472.0	472.77

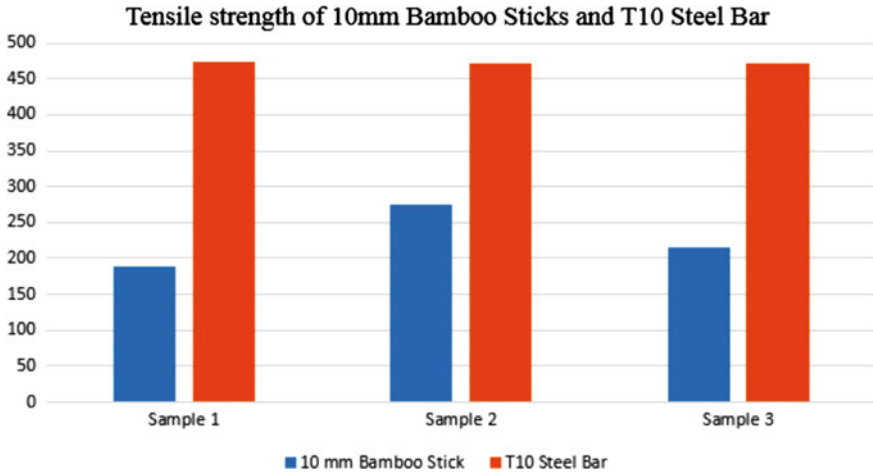


Fig. 6 Tensile strength of 10 mm bamboo sticks and T10 steel bar

sticks is 47.94% lower compared to steel bar strength. As the tensile strength had achieved 50% of the strength of steel mild reinforcement. Figure 6 shows more clear comparison for tensile test results for bamboo stick versus steel bar for diameter size 10 mm. Thus the results prove that bamboo has potential to be used as reinforcement in reinforced concrete structure. Bamboo reinforcement has shown reasonable tensile strength, which suggests that it can be used as reinforcement in reinforced concrete structure such as floor, roof, beam, wall-panel, column and etc. [5]. For some cases, the researchers have found that the tensile strength of bamboo may reach the tensile strength of mild steel [8, 9, 13]. This makes bamboo as an alternative of reinforcement in structure. However, it is depends on the species of bamboo that been used [13].

4 Conclusions

Bamboo may be considered as the replacement to the reinforcement in concrete. Its may achieve the strength of mild steel for some cases, however, it is depends on the species that been used. Semantan Bamboo was been used as reinforcement replacement in concrete beam for this study. The tensile strength results for 10 mm Bamboo sticks shows that the strength is much lower than T10 steel bar. However, it has achieved half of the strength of mild steel. In order to have a better strength of bamboo, make sure the bamboo structure was made from bamboo age 3–4 years. Too young or too matured may affect the strength of the bamboo.

On the other hand, the flexural test for steel reinforced concrete beam is three times stronger than bamboo reinforced concrete beam therefore bamboo is not able completely replace steel bar as main structure member in building or others heavy engineering works but it can used in lightweight engineering construction which

there is not heavy-load-bearing. It can be proved economical option for columns of compound walls as bamboo is good under compression force [5]. Thus it shows that both physical and mechanical characteristics may vary with respect to diameter, length, age, type, position along culm and moisture content of bamboo. Bamboo is also having high water absorption and this condition has affect the bonding with concrete. To make the condition worse, previous study had found that bamboo have low fire resistance [13].

Moreover, bamboo have few others factored may be considered as high concerned in considering bamboo as a replacement to reinforcement in reinforced concrete structure. Treated bamboo is high recommended as bamboo have high risk towards fungal and insect attack. It is because bamboo is considered natural sourced thus it is containing high nutrient which may attract to these fungal and insect. Thus bamboo need to be treated in order to protect from pest, temperature and moisture to improve the durability of bamboo to be used as reinforcement replacement.

5 Recommendations

1. Determine the tensile strength for different species of bamboo through tensile test, choose the highest tensile strength of bamboo for further research.
2. Raw material like cement, coarse and fine aggregate will affect the concrete strength, choose those raw material where those are in good condition. Besides, make sure concrete machine and testing machines had been calibrated before using.
3. Choose 10 mm bamboo pole instead of 10 mm bamboo stick, bamboo pole having better strength compare with bamboo sticks. Rahman et al. [9] had found that bamboo reinforced concrete beam can be performed better than concrete reinforced concrete beam for 2 times for singly reinforced concrete beam and 2.5 times for doubly reinforced concrete beam. But have to make sure a proper preparation process of bamboo reinforcement before the casting. The best performance for bamboo to be applied as reinforcement replacement is for the bamboo to undergo the treatment process as same process as timber structure.
4. Instead of drilled hole on bamboo slats, use rattan or strapping rope to tie bamboo slats and bamboo pole together. Drilled hole or damage bamboo material will disturb and weaken the behavior of bamboo.
5. In order to have a good ductility bamboo reinforcement, it is highly recommended to make sure that only treated bamboo will be choose as reinforcement in order to protect it from temperature, moisture and pest.

References

1. Adewuyi AP, Otukoya AA, Olaniyi OA, Olafusi OS (2015) Comparative studies of steel, bamboo and rattan as reinforcing bars in concrete: tensile and flexural characteristics. Federal University of Agriculture, Abeokuta, Nigeria
2. Srimathi S, Dinesh S, Preetha R, Reshmi R (2016) A review of bamboo as a reinforcement material in modern construction. *Int J Sci Technol Eng* 3(5)
3. Naznin F, Nayanmoni C (2015) A study on bamboo reinforced concrete beam. *Int J Sci Appl Inf Technol (IJSAIT)* 4(3):49–53
4. Naznin F, Chetia N (2015) A study on bamboo reinforced concrete beams. *Int J Sci Appl Inf Technol (IJSAIT)* 4(3):49–53
5. Rayadu SV, Akshay PR, Ishwar KG (2017) Study of bamboo as reinforcement in concrete. *Int Adv Res J Sci Eng Technol (IARJSET)* 4(11)
6. Mahzuz HMA, Mushtaq A, Ashrafuzzaman M, Rejaul K, Raju A (2011) Performance evaluation of bamboo with mortar and concrete. *J Eng Technol Res* 3(12):342–350
7. Hector A, Sebastian K, David T, Edwin ZE, Kent AH (2018) Bamboo reinforced concrete: a critical review. *J Mater Struct* 51(102)
8. Eldin MM, Eman ET (2016) Validity of using bamboo as reinforcement of concrete beams. In: *Proceeding of the international conference on advances in civil, structural and construction engineering (CSCE)*
9. Rahman MM, Rashid MH, Hossain MA, Hasan MT, Hasan MK (2011) Performance evaluation of bamboo reinforced concrete beam. *Int J Eng Technol (IJET-IJENS)* 11(04)
10. British Standard (BS EN 12390-3:2002): Testing hardened concrete—Part 3: Compressive strength of test specimens
11. British Standard (BS 1881-116:1983): Methods of testing concrete. Method for determination of compressive strength of concrete cubes (AMD 6097) (AMD 6720)
12. British Standard (BS 8110-1:1997): Structural use for concrete—Part 1: Code of practice for design and construction
13. Adom-Asamoah M, Afrifa OR (2011) A Comparative study of bamboo reinforced concrete beams using different stirrup materials for rural construction. *Int J Civil Struct Eng* 2(1):1420–1436

Shear Strength Parallel to Grain for Selected Malaysian Tropical Timber According to BS EN408



M. B. Norshariza, W. C. Lum, Z. Ahmad, A. Alisibramulisi, and M. S. Nordin

Abstract In order to develop shear strength data for limit state design as stated in Eurocode 5, the strength properties need to be determined using large size structural specimens. However, the specific data for Malaysian tropical hardwood were not available for the moment. Thus, shear strength parallel to the grain for structural specimens from seven Malaysian tropical hardwood timbers was determined in this research. The timber species were selected from different strength group (SG) according to MS 544: Part 2. The timber species studied were Balau (*Shorea* spp.), Kempas (*Koompassia malaccensis*), Resak (*Cotylelobium* spp.), Keruing (*Dipterocarpus* spp.), Mengkulang (*Heritiera simplicifolia*), Light Red Meranti (*Shorea leprosula*) and Geronggang (*Cratoxylum aborescens*). The strength determination of the specimens was carried out according to the BS EN408. The nominal dimension of the specimen was 33 mm in thickness, 56 mm in width and 303 mm in length. The loading rate was set at 0.6–1.2 mm/min for all the specimens to achieve failure during the time stipulated in the standard. The results show that Kempas (SG 2) has the highest shear strength which is 6.46 N/mm². On the other hand, Resak (SG 4) exhibits the lowest shear strength which is 3.04 N/mm². It is worth noting that, the values of shear strength for this study are higher compared to the values of shear strength from MS 544: Part 2 and MS 544: Part 3. To better justify the results, further testing is needed for more timbers species with a higher number of replicates.

Keywords Shear strength · Structural timber · Tropical timber · Hardwood · Green material

M. B. Norshariza (✉) · W. C. Lum · A. Alisibramulisi
Institute for Infrastructure Engineering and Sustainable Management, Universiti Teknologi MARA Malaysia, 40450 Shah Alam, Selangor, Malaysia
e-mail: nshariza@uitm.edu.my

M. B. Norshariza · Z. Ahmad · A. Alisibramulisi · M. S. Nordin
School of Civil Engineering, College of Engineering, Universiti Teknologi MARA (UiTM), 40450 Shah Alam, Selangor, Malaysia

M. S. Nordin
Malaysian Timber Industry Board, Level 13-17, Menara PGRM, No 8, Jalan Pudu Ulu, 56100 Kuala Lumpur, Cheras, Malaysia

1 Introduction

Trees and wood-based products have been utilized for construction and building material for thousands of years before modern materials such as concrete and steel are used. In Japan the oldest timber structure, the three-story Pagoda, which had been built since the seventh century is a typical historical timber building still standing today [1]. The oldest existing timber bridge is a 222 m long chapel bridge in Luzern, Switzerland that was built in year 1333 and acknowledge as traveler attraction [2]. Today, timber is well-known as a renewable building material compared with concrete and steel. Timber is considered as green and sustainable construction material if sourced from sustainably and responsibly managed forest and plantation. Basic structural properties of timber are different among timber species or even within similar species [3]. Timber has variable degree of natural durability and is suitable to be used as exterior construction materials [4].

In Malaysia, the design value for solid timber is determined in accordance with MS 544: Part 2 [5], meanwhile the design value for engineered timber products is determined according to MS 544: Part 3 [6]. However, the design values given in MS 544: Part 2 [5] was developed using small clear specimens and the values stated in MS 544: Part 3 [6] was adopted from BS 5268: Part 2 [7]. As more countries have started to embrace Eurocode 5 (EC 5) [8], it is crucial that local designers follow suit as well [9]. In order to move to EC 5 [8], the data for the design values must be derived from large size specimens. Furthermore, the basics of EC 5 [8] for timber structures are based specifically on the limit state design. According to the design system, the characteristic strength of timber is needed during the designing stage of timber structures. Therefore, in order to comply with EC 5 [8], there is a need to provide strength data from Malaysian tropical timber tested using large size specimen based on BS EN 408 [10] so that limit state design can be applied.

Strength properties of timber are described as the ultimate resistance of the timber specimens when subjected to sustain load. It is known that the strength properties of timber differ in the three main directions. However, there are only very slight differences between the tangential and radial planes. Therefore, most studies on the mechanical properties of timber were only focused on the directions parallel and perpendicular the grain. According to BS EN 338 [11] the strength properties are derived using structural size specimens. The strength table established in BS EN 338 [11] includes bending strength, compression strength parallel and perpendicular to grain, tensile strength parallel and perpendicular to grain and also shear strength parallel to grain. The values for modulus of elasticity and shear modulus are also given.

In recent years, to determine the strength properties of timber for structural use, the samples size has evolved from small clear specimen to structural size specimen where most of the testing methods were based on BS EN 408 [12–15]. The materials tested involved solid timber and also engineered timber products. The mechanical

properties studied include flexural, compression, tension and shear strength properties. However, the shear strength properties of tropical hardwood timber determined using EN408 is still very limited [16].

Thus, this study focused on the shear strength parallel to the grain of selected Malaysian tropical hardwood. The seven timber species selected were Balau (*Shorea* spp.), Kempas (*K. malaccensis*), Resak (*Cotylelobium* spp.), Keruing (*Dipterocarpus* spp.), Mengkulang (*H. simplicifolia*), Light Red Meranti (*S. leprosula*), Geronggang (*C. aborescens*) and Sesendok (*Endospermum malaccense*). These data on the shear strength of tropical timber in structural size will lead to a better understanding and subsequently a better application of Malaysian timbers in the building and construction industry.

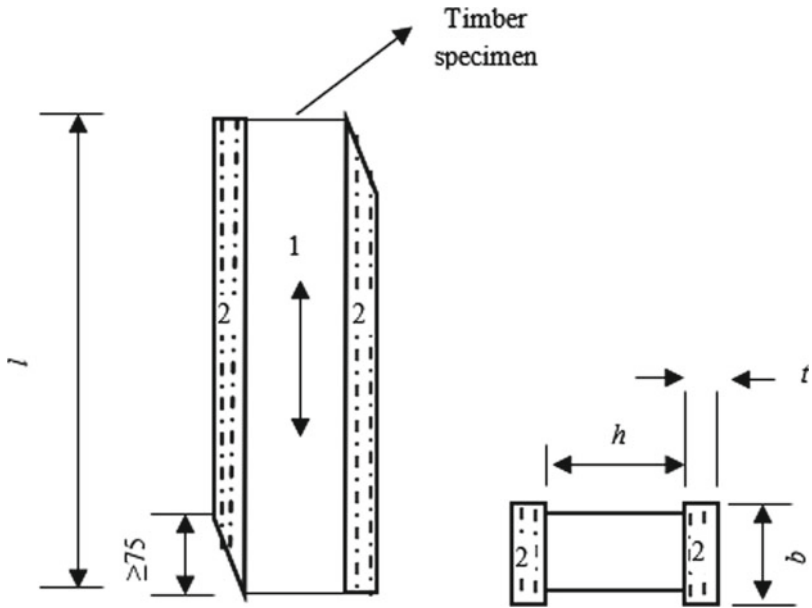
2 Materials and Method

2.1 Materials

The timber used in this study were supplied from Woodsfield Timber Industries Sdn. Bhd. Seven timber species Balau (*Shorea* spp.), Kempas (*K. malaccensis*), Resak (*Cotylelobium* spp.), Keruing (*Dipterocarpus* spp.), Mengkulang (*H. simplicifolia*), Light Red Meranti (*S. leprosula*), Geronggang (*C. aborescens*) and Sesendok (*E. malaccense*) were used for this research. Ten samples parallel to the grain for each timber species were prepared. The nominal dimension of samples used was (33 × 55 × 300) mm.

2.2 Sample Preparation

The timber samples prepared were glued to steel plate according to the illustration given in BS EN 408 [10] (Fig. 1). The real test pieces of Kempas timber glued to steel plate is shown in Fig. 2. The adhesive that had been used was two-part epoxy Sikadur-30. The adhesive comprised of two components which is component A (resin) and component B (hardener). The ratio used for component A and component B was in the ratio of 3:1. The adhesive used acted as a bonding agent between the timber sample and steel plates. The steel plates were tapered as shown in Fig. 2. The steel plates were sandblasted prior to the application of the adhesive to improve the bonding performance between the test pieces and the steel plate. This was crucial to ensure that the failure occurred in the timber test pieces. After the application of adhesive, the test samples together with the steel plate were stored for seven days before the shear strength test was conducted to allow the adhesive to fully cure.



Legend

1: grain direction; 2: steel plate l : (300 ± 2) mm; b : (32 ± 2) mm; h : (55 ± 2) mm; t : (10 ± 1) mm

Fig. 1 Schematic diagram of timber test piece glued to steel plate according to BS EN 408 [10]

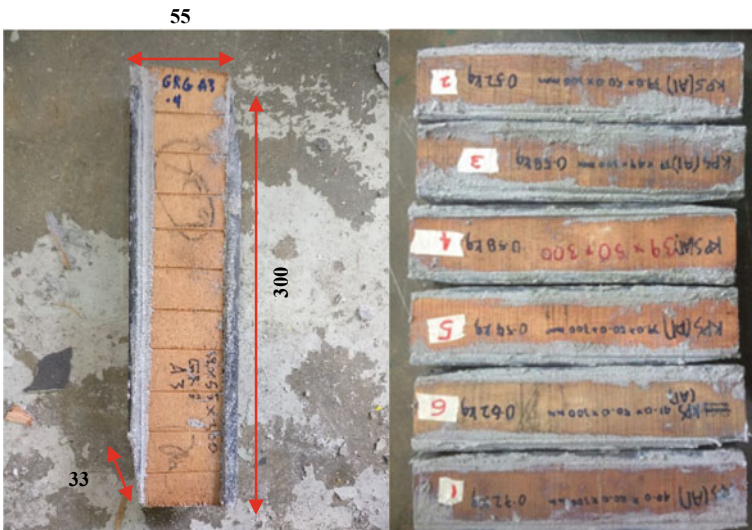


Fig. 2 Kempas timber specimens for the determination of shear strength parallel to grain in accordance with BS EN 408 [10]

2.3 Shear Strength and Failure Modes Evaluation

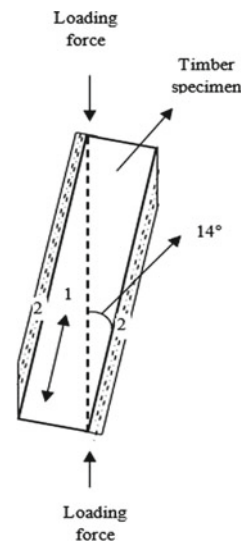
The shear strength of the samples was determined using 100 kN capacity Universal Testing Machine (UTM). Prior to testing, the loading rate for each timber species was determined by using 3 trials specimens. The loading rate for the seven species timber species is tabulated in Table 1. In order to ensure that the timber specimens reach the break point between 180 and 480 seconds, the loading rate for all the specimens was set at the range of 0.6–1.2 mm/min.

The test procedures were conducted according to the specifications stipulated in BS EN 408 [10] (Fig. 3). The machine set up is shown in Fig 4. From the test that had been conducted, the failure modes of the specimens were also observed and recorded.

Table 1 Loading rate for different species of timber specimens

Species	Loading rate (mm/min)
Balau	0.6
Kempas	1.2
Resak	0.6
Keruing	1.2
Mengkulang	0.9
Light Red Meranti	0.9
Geronggang	1.2

Fig. 3 Schematic diagram of loading arrangement according to BS EN 408 [10]



Legend

1: grain direction; 2: steel plate

Fig. 4 Test set-up for the determination of shear strength according to BS EN 408 [10]



The shear strength of the specimens tested was calculated by the equation to an accuracy of 1%. The equation for shear strength is shown in Eq. (1).

$$f_v = \frac{F_{\max} \cos 14^\circ}{lb} \quad (1)$$

where f_v = Shear Strength (N/mm^2), F_{\max} = max loading applied (N), l = length of the sample (mm), b = width of the sample (mm)

2.4 Determination of Density and Moisture Content

The moisture content (MC) of the timber specimens were determined using two methods, one during test and one after testing. During testing, the MC of the specimens was measured moisture meter (GANN Hydromette M 2050). Fig. 5a shows the probe was placed on the sample where the reading of the MC was recorded by the receiver. Figure 5b shows the complete set of the moisture meter equipment.

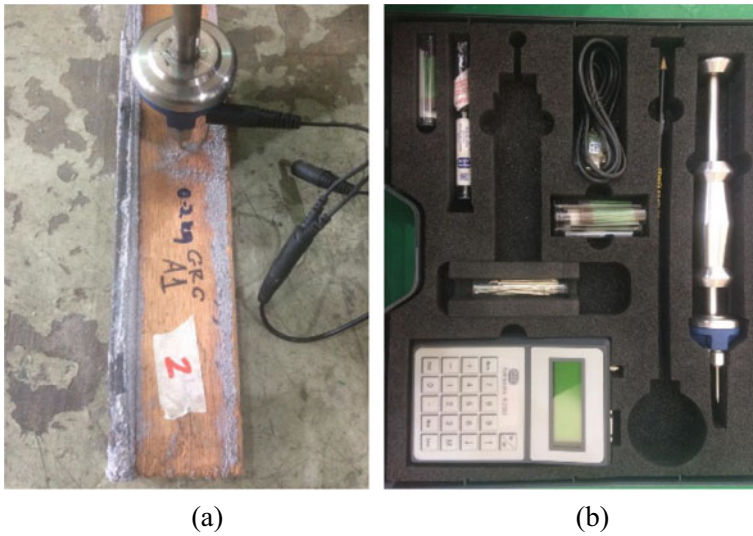


Fig. 5 Moisture content measurement by moisture meter, **a** taking MC measurement and **b** GANN Hydromette M 2050

After the timber specimens had been subjected to load until failure, two samples with the dimension of (25 × 50 × 100) mm were cut toward the grain of the timber band and was cut as near as possible to the location of fracture of the timber. MC of the timber specimens was determined using oven dry method in accordance with MS 837: 2006 [17]. After sample cutting, the samples were weighted and put into the oven immediately in order to ensure the accuracy of the mass values. The initial weight of the sample was taken using a weighing machine as shown in Fig. 6a. After weighing the samples, the samples were placed in the oven for 24 hours (Fig. 6a). Then the oven dry weight of the samples was measured after 24 hours and subsequent readings were taken every two hours until the mass of the samples was constant.

The moisture content and density of the samples were calculated using Eqs. (2) and (3).

$$\text{Moisture Content, } \omega = \frac{m_i - m_o}{m_o} \times 100\% \tag{2}$$

where ω = Moisture content (%), M_i = Mass of specimen before drying (g), M_o = Mass of specimen after drying (g)

Density, ρ is a measure of relative compactness or how heavy an object is relative to its size. Density is defined as mass (m) in a given unit volume (V).

$$\text{Density, } \rho \text{ kg/m}^3 = \frac{m}{V} \tag{3}$$

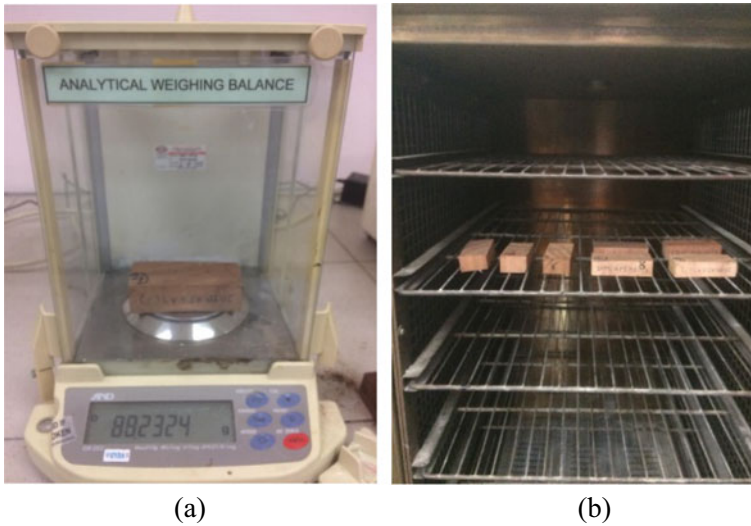


Fig. 6 Moisture content measurement; **a** drying sample in the oven and **b** weight the sample

where; ρ = density (kg/m^3), m = mass of specimen initially weight (kg), V = volume of specimen (m^3)

The moisture content (MC) of every sample was recorded because the moisture content is one of the main factors affecting the shear strength of timber specimens. It was stated in the standard that only timber specimens with the MC below 19% were considered valid for testing. It is worth noting that the reading of MC from moisture meter might be higher than the actual MC of the timber by using the standard test method for MC which is by oven dry method. Therefore, two methods were used to determine the MC in this study and the results from oven dry method were recorded and tabulated in this study.

3 Results and discussion

3.1 Shear Strength Properties

The data obtained from the test were used to calculate the shear strength of every sample. The average shear strength of the ten samples that had been tested for each timber species was determined and recorded.

The results of laboratory testing for the determination of shear strength parallel to the grain of large specimen has provided new information on the shear strength value of Malaysian tropical timber for the development of strength class in accordance with BS EN 338 [11]. MS 544: Part 2 [5] also recorded the shear strength values

Table 2 Summary of the mean shear strength for seven species of Malaysian hardwood timber

Species	Shear strength (N/mm ²)	Density (kg/m ³)	Moisture content (%)
Balau	5.28 ± 1.27	937 ± 15.54	14.04 ± 0.50
Kempas	6.46 ± 0.63	943 ± 113.05	13.23 ± 8.89
Resak	3.04 ± 0.41	1011 ± 70.04	14.13 ± 0.60
Keruing	4.40 ± 0.84	836 ± 68.49	16.32 ± 0.52
Mengkulang	4.43 ± 0.97	665 ± 50.24	17.90 ± 0.70
Light Red Meranti	4.20 ± 0.66	558 ± 41.90	13.43 ± 0.50
Geronggang	3.68 ± 0.49	472 ± 23.74	16.25 ± 0.44

*Note value after ± is standard deviation

of the selected species used in this study namely Balau, Kempas, Resak, Keruing, Mengkulang, Light Red Meranti and Geronggang. The shear strength stated in MS 544 Part 2 [5] was used to compare with the strength value obtained from this study by laboratory testing in accordance to BS EN 408 [10].

The shear strength values for all the samples within the same timber species only shows slight difference with Balau showing the highest standard deviation which is 1.27. As expected, the shear strength among different species is more significant. With the loading rate selected for this study, most of the samples tested fulfil the requirement stipulated in BS EN 408 [10] which stated that the timber specimens subjected to shear load must fail within be 300 ± 120 seconds and the failure must at least occur partially in the glued area of the test piece or steel plate interface.

Based on Table 2, Mengkulang exhibits the highest moisture content which is 17.9%. Keruing and Geronggang display the second highest moisture content which is 16.32% and 16.25% respectively. On the other hand, Resak, Balau, Light Red meranti has the moisture content of 14.13%, 14.04% and 13.42% respectively. Kempas has the lowest moisture content which is 13.23%. From the data obtained, it can be concluded that the moisture content of all specimens falls below 19% which satisfy the requirement stated in the BS EN 408 [10].

As observed in Table 2, Kempas has the highest shear strength (6.46 N/mm²), while Resak has the lowest shear strength (3.04 N/mm²). Balau exhibits the second highest shear strength which is 5.18 N/mm². Keruing, Mengkulang and Light Red Meranti all have similar shear strength which is 4.40 N/mm², 4.43 N/mm² and 4.20 N/mm² respectively. The results from this study suggest that the higher the density of the specimens the higher the shear strength, except for Resak. Figure 7 shows the relationship between shear strength and the density for selected Malaysian tropical hardwood timber. These results are similar to the findings by Ravenshorst et al. [16] which found out that the shear strength of Massaranduba timber species was closely related to its corresponding density.

According to Fig. 7, the shear strength of all the timber specimens tested is closely dependant to its corresponding density. Pearson correlation analysis was performed to further evaluate the correlation between shear strength and density. Generally, a

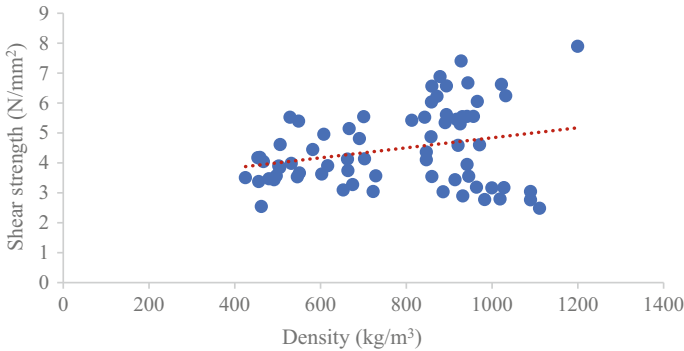


Fig. 7 Relationship between the shear strength and the density for selected Malaysian tropical hardwood timber

significant positive correlation ($r = 0.266$; $p = 0.026$) was observed which indicate that the shear strength of Malaysian tropical hardwood increased along with increasing wood density. However, this correlation is only valid for timber species with density below 1000 kg/m^3 . Kempas with the high density of 943 kg/m^3 displays the shear value of 6.46 N/mm^2 . Contrarily, Geronggang with the low density of 472 kg/m^3 exhibits the shear value 3.68 N/mm^2 . Resak with the highest density (1011 kg/m^3) exhibits the lowest shear strength (3.04 N/mm^2). This might due the facts that majority of the tested specimens for Resak failed near to or on steel plate. Therefore, the adhesive used for this high-density timber ($>1000 \text{ kg/m}^3$) needs to be investigated thoroughly and some modifications might be needed in order to make sure that the bonding strength between the timber surface and steel plate is sufficient.

3.2 Comparison with MS 544: Part 2 and MS 544: Part 3

Table 3 shows the shear strength value from the standard MS 544: Part 2 [5] (small clear specimen), MS 544: Part 3 [6] (structural size specimen) and laboratory testing. The shear strength values of dry timber from the standard grade given in MS 544: Part 2 [5] were used for the purpose of comparison. On the other hand, the shear strength values in MS 544: Part 3 [6] were adopted directly from BS 5268: Part 2 [7]. Contrarily, the shear strength values parallel to the grain for the seven timber species tested was calculated from the formula given in BS EN 408 [10].

Based on Table 3, it can be concluded that the value of shear strength parallel to the grain are much higher compared to the value of shear strength as stated in both the MS 544: Part 2 [5] and MS 544: Part 3 [6]. This finding is aligned with the finding by Gamper [18] which stated that the shear strength from experimental work was higher than the values given in BS EN 338 [11] which was derived using formula.

For Light Red Meranti specimens, the mean shear value from experimental work is 4.20 N/mm^2 while the value from MS 544: Part 2 [5] is 0.86 N/mm^2 . The value

Table 3 Comparison of shear strength values from MS 544: Part 2 [5], MS 544: Part 3 [6] and experimental values

Timber species	Shear strength parallel to the grain (N/mm ²)		
	MS 544: part 2	MS 544: part 3	Experimental value
Balau	2.28	2.8	5.28
Kempas	1.97	2.3	6.46
Resak	1.55	–	3.04
Keruing	1.55	1.7	4.4
Mengkulang	1.71	1.7	4.43
Light Red Meranti	0.86	1.1	4.2
Geronggang	0.96	–	3.68

obtained in this study is about 388% higher than the value given in MS 544: Part 2 [5] which is the highest among the seven timber species. In contrast, the mean shear value for Resak from experimental work is 1.55 N/mm² while the value from MS 544: Part 2 [5] for standard grade dry timber is 3.04 N/mm². The value obtained in this study for Resak is roughly 96% higher than the value given in MS 544: Part 2 [5], which is the lowest for all species tested. It is worth noting that the material size for which MS 544: Part 2 [5] was based on was small clear specimen while in this study, large size timber specimens with the dimension of (33 × 55 × 300) mm were used. Even then, the value obtained in this research is still far higher.

According to Table 3, the shear value of Light Red Meranti from experimental work is about 281% higher than the value given in MS 544: Part 3 [6] which is the highest difference in percentage. Meanwhile, the shear value of Balau is about 88% higher than the value given in MS 544: Part 3 [6] which is the lowest difference in percentage. From the data obtained in this study, it is safe to assume that the shear strength values of Malaysian tropical hardwood have been underestimated by a large margin in MS 544: Part 3 [6]. Thus, the data obtained by experimental work is more relevant to be used in the designing of timber structure. It is because shear strength determined by actual large size specimens parallel to the grain is more accurate than the values given in MS 544: Part 3 [6] which are adopted from BS 5268: Part 2 [7].

3.3 Failure Patterns

After the large specimen sample has reached its peak, the sample will fail after continuous loading applied on it. Eventually, most of the specimen that had reaches its maximum loading has experienced a reduced in loading imposed to it before the sample fails. There are two way to characterize the sample failure which is one, fail near to steel plate and fail in timber sample. To choose whether the species fails on steel plate or in the timber is by choosing the most ways of failure of sample. The 70 samples that fail had been analysed for seven species namely Balau, Kempas,

Table 4 Number of specimens and the failure patterns of the timber specimens tested

Species	Failure near to steel plate	Failure in timber specimen
Balau	4	6
Kempas	2	8
Resak	6	4
Keruing	3	7
Mengkulang	3	7
Light Red Meranti	7	3
Geronggang	8	2



Fig. 8 Failure near to steel plate

Resak, Keruing, Mengkulang, Light Red Meranti and Geronggang. The results are displayed in Table 4.

Table 4 shows the failure patterns of all the timber specimens tested according to BS EN 408 [10]. Based on Table 4, it can be concluded that Balau, Kempas, Keruing and Mengkulang fail in timber specimen. On the other hand, Resak, Light Red Meranti and Geronggang fail near to steel plate. The failure patterns varied for all the specimen tested. However, the shear strength values were considered to be valid because less than 20% of the timber failure occurred near the area of steel plate for all the specimens tested. Figures 8 and 9 show the failure near to steel plate and failure in timber specimen respectively.

4 Conclusion

Shear strength of seven species of Malaysian timber species were determined according to BS EN 408 [10]. The following are the summary of conclusions for this study:

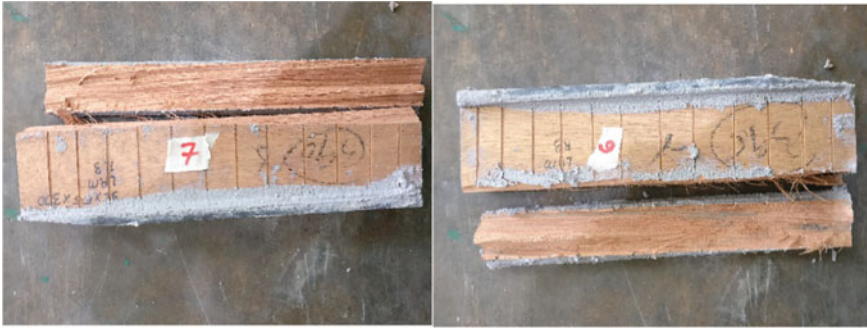


Fig. 9 Failure in timber specimen

1. The shear strength of the specimens is closely dependent on its corresponding density. The higher the density, the higher the shear strength value.
2. Kempas has the highest shear strength which is 6.46 N/mm^2 ; while Resak has the lowest shear strength which is 3.04 N/mm^2 .
3. Shear value of Light Red Meranti obtained in this study is 388% higher than the value given in MS 544: Part 2 [5] which is the highest percentage among the seven species tested. Shear value of Resak obtained in this study is 96% higher than the value given in MS 544: Part 2 [5] which is the lowest percentage among the seven species tested.
4. The shear strength values given in MS544: Part 3 [6] does not represent the real shear strengths of the selected Malaysian hardwood timber. The shear strength values from experimental works are much higher for all the timber species tested. Therefore, the shear strength values stated in MS 544: Part 3 [6] should be revised based on laboratory experiment with large size specimens.

Results from this study revealed that the shear strength values of the tested specimens from selected Malaysian tropical hardwood are higher than that specified in MS 544: Part 2 [5] and MS 544: Part 3 [6]. In order to developed the shear strength values of tropical timber according to BS EN 408 [10], a broader study involving larger number of timber species with larger number of replicates is needed in order to obtain a more accurate data.

Acknowledgement Special thanks to the Malaysia Timber Industry Board (MTIB) for the funding of research grant and Faculty of Civil Engineering, Universiti Teknologi MARA, Malaysia in providing the experimental facilities.

References

1. Yasemura M (2000) Seismic performance of timber structures in Japan. In: Cecotti A, Thelandersson S (eds) Proceedings of COST E5 workshop, timber frame building systems. Venice, Italy

2. Stadelmann W (1990) *Holzbrücken der Schweiz – ein Inventar*. Verlag Bundner Monatsblatt, Chur
3. Lavers GM (1966) The strength properties of timbers. *Forest Prod Res Bull* 50. Ministry of Technology
4. Panshin AJ, De Zeeuw C (1980) *Textbook of wood technology*. Part 1. Formation, anatomy, and properties of wood 11–404
5. MS 544 (2001) Code of practice for structural use of timber: Part 2: Permissible stress design of solid timber, MS (Malaysia Standards), Malaysia
6. MS 544 (2001) Code of practice for structural use of timber: Part 3: Permissible stress design of glued laminated timber, MS (Malaysia Standards), Malaysia
7. BS 5268: Part 2 (2002) Code of practice for permissible stress design, materials and workmanship, BS (British Standards), England
8. BS EN 1995-1-2 (2004) Eurocode 5: design of timber structures, BS (British Standards), England
9. Sheikh S, Yusof A (2015) Flexural timber design to eurocode 5 and the malaysian timber code MS 544: 2001. *Malay J Civil Eng* 27
10. BS EN 408 (2012) Timber structures—structural timber and glued laminated timber—determination of some physical and mechanical properties, BS (British Standards), England
11. BS EN 338 (2010) Structural timber-strength classes. BS (British Standard), England
12. Christovasilis IP, Brunetti M, Follesa M, Nocetti M, Vassallo D (2016) Evaluation of the mechanical properties of cross laminated timber with elementary beam theories. *Construct Build Mater* 122:202–213
13. Ibitolu BJ, Jimoh AA (2017) Characterization and grading of some potential Nigerian Timbers species in accordance to Eurocode EN 338: 2009
14. He M, Sun X, Li Z (2018) Bending and compressive properties of cross-laminated timber (CLT) panels made from Canadian hemlock. *Construct Build Mater* 185:175–183
15. Chuan DE, Abd Ghafar N, Boon K (2020) Behaviour of post-tensioned kempas timber beam with two tendon types. In: *IOP conference series: materials science and engineering*, vol 713, no 1, p 012022. IOP Publishing
16. Ravenshorst G, Gamper N, Vries PD, Van de Kuilen JWG (2016) Determination of the shear strength of tropical hardwood timber. In: *Proceedings of 14th world conference on timber engineering (WCTE 2016)*, Vienna, Austria, pp 23–25
17. MS 837 (2006) Solid timber—determination of moisture content (First revision). MS (Malaysia Standard), Malaysia
18. Gamper N (2015) Determination of the shear strength of tropical hardwood timber. Minor thesis, Delft University of Technology

Effect of Pineapple Leaf Fibre as Additional Material in Concrete Mixture



Siti Khadijah Che Osmi, Mohamad Asrul Zamuddin, Noor Aina Misnon, Suriyadi Sojipto, and Hapsa Husen

Abstract Recently, the usage of agricultural waste received special attention from many engineering fields. The wastes have been used in the concrete mixture either as a replacement material for producing lightweight concrete or as new additional material for improving the mechanical properties of the concrete. In this study, the effect of pineapple leaf fiber as a new additional material in concrete was investigated. Pineapple leaf fiber (PALF) was chosen because it has a low thermal conductivity and bulk density. Three percentage of the PALF; 0.1, 0.2 and 0.3% was added in concrete grade C30. The results were reported for both fresh and hardened state of concrete with fiber. For fresh concrete state, the slump test results showed that all batches of the concrete mixtures yielded the true slump height with a value range from 42 to 57 mm. Meanwhile, the mechanical properties of the concrete were investigated by performing three tests in the hardened state, i.e. compression, splitting tensile and flexural. The results showed that the addition of PALF was successfully improved the mechanical properties of the concrete. It is found that the addition of PALF in concrete improves the mechanical properties of the concrete. The highest strength was achieved when 0.3% of the fiber added in the concrete mixture. Alternatively, this study provides a potential way of converting the abundant of agriculture waste to wealth.

Keywords Agricultural waste · Pineapple leaf fibre · Concrete mixture · Additional material · Mechanical properties

1 Introduction

Concrete has been widely used in construction fields since ancient times because it offers excellent stability and flexibility for constructing civil engineering structures. In general, concrete has high compressive strength, good heat resistance and promise

S. K. Che Osmi (✉) · M. A. Zamuddin · N. A. Misnon · S. Sojipto · H. Husen
Department of Civil Engineering, Faculty of Engineering, Universiti Pertahanan Nasional
Malaysia, Kem Perdana S. Besi, 57000 Kuala Lumpur, Malaysia
e-mail: sitikhadijah@upnm.edu.my

© The Author(s), under exclusive license to Springer Nature Singapore Pte Ltd. 2022
S. Belayutham et al. (eds.), *Proceedings of the 5th International Conference on Sustainable Civil Engineering Structures and Construction Materials*, Lecture Notes in Civil Engineering 215, https://doi.org/10.1007/978-981-16-7924-7_34

525

minimum maintenance cost; although, it has a low tensile stress resistance. A significant number of researches have been conducted to improve the tensile strength of concrete by incorporating different types of fiber; for instance, synthetic and natural fiber. Established research on the use of synthetic fiber such as steel, carbon and glass fiber proved that the synthetic fiber might improved the strength of the concrete structures [1–3]. Similarly, the utilization of natural fiber in concrete also has been developed by several researchers, e.g. [4–6], whereby the addition of such fiber increased the energy absorption and tensile strength of the concrete.

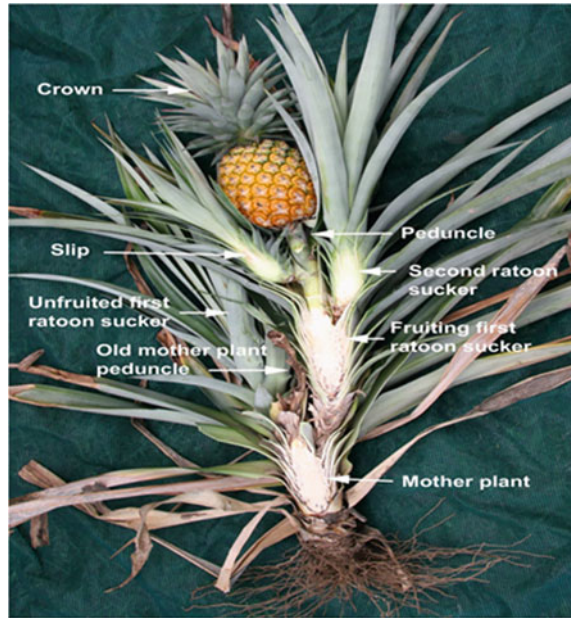
Most of the natural fiber is extracted from agricultural waste such as kenaf, coconut, and flax which can be found easily and cheap. Previous studies (i.e. [7–9]) reported that the natural fiber was successfully bridging the crack of the concrete samples. Besides, Ali et al. [7] revealed that coconut fiber reinforced concrete (CFRC) performed well in both mechanical and dynamic properties when 5% of the fiber with the optimum length of 5 cm is added in the concrete mixture. The effectiveness of CFRC in improving the tensile strength and toughness of concrete properties was revealed by Purnachandra Sai et al. [10]. On the other hand, oil palm trunk fiber (OPTF) is another type of agro-waste that possess high tensile strength, i.e. 300–600 N/mm². In previous works conducted by Ahmad et al. [11] in the year 2010, the OPTF was used to minimize the cracking behavior of concrete. It is highlighted that 1% of OPTF was found as the optimum amount to be added in concrete which successfully increased the compressive, flexural and splitting tensile strengths of the concrete approximately by 29.8%, 18.4% and 25% in respectively relative to normal concrete [11].

Previous evidence proved that the utilization of agriculture waste in construction material received special attention from many engineering fields. The wastes have been used in concrete mixture either as a replacement material for producing lightweight concrete or as new additional material for improving the mechanical properties of the concrete. In addressing the inherent benefit of natural fibers, the effect of pineapple leaf fiber (PALF) as additional material in concrete mixture was investigated. In this study, the PALF was chosen because it has a low thermal conductivity and bulk density. Three percentage of the PALF; 0.1, 0.2 and 0.3% was added in concrete grade C30. The results are reported for both fresh and hardened state of concrete with fiber. The outcome of this study was expected to provide a better improvement in the quality and mechanical properties of the new PALF reinforced concrete. Alternatively, the PALF reinforced concrete might promise the best solution to tackles the abundant of agriculture waste by converting the waste to new green and sustainable concrete material.

2 Pineapple Leaf Fiber (PALF)

Pineapple leaf characterized as a long, trough-shaped, horizontal wide at the base and tapered at the tip. The leaves are arranged spirally around the stump, which allows the pineapple to receive more sunlight for photosynthesis and retained water

Fig. 1 Morphology of a Pineapple plant [12]



during rainy, thereby, avoids loss of moisture. Figure 1 shows the morphology of the pineapple plant, which consist of four crucial parts of the plant, i.e. slips, collars, side suckers or stem shoots, and crown [12]. The pineapple leaf fiber (PALF) is made from the outer leaves of the pineapple plant because it is stronger and provide much better mechanical properties compared to the inner leaf.

According to Vijayan and Krishnamoorthy [13], pineapple leaf fibers are usually obtained by beating, rasping and stripping the leaf before soaking in water for 24-hours. The chemical reagent is added in the water to boost the activity of microorganism and to digest the unwanted tissue [14]. The fiber then is washed clean and left dried under the sun. Figure 2 illustrates the image of the physical properties of the PALF under the scanning electron microscope (SEM) [14].

According to Table 1, the investigation on the physical and mechanical properties of the PALF have been conducted by previous researchers [14–16]. They concluded that the PALF is one type of natural fibers which exhibits good mechanical properties with high tensile strength values. The researches highlighted that the PALF indicates that the fiber is suitable to be incorporated in the concrete mix. In this study, the pineapple leaf fiber is added as a part of concrete constituents. The effect on mechanical properties of concrete with the fiber is reported in the next sections.

Furthermore, the chemical properties PALF is presented in Table 2. Generally, pineapple leaf fibers contain several chemical substances such as cellulose, holocellulose and lignin, as discussed by previous researchers, e.g. [12, 14, 18].

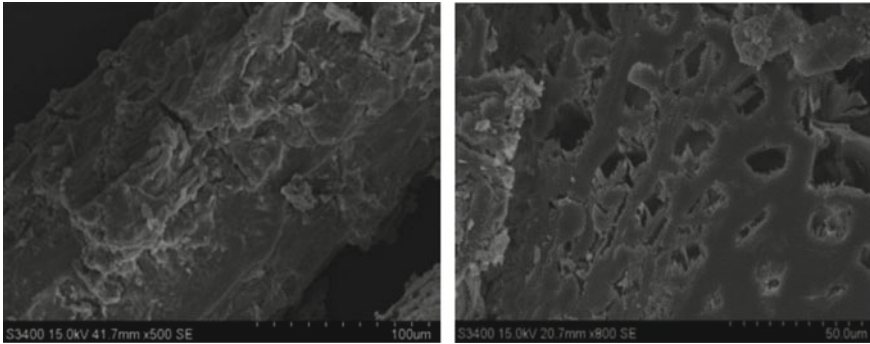


Fig. 2 Image of physical properties of the PALF under the SEM [14]

Table 1 Physical and mechanical properties of PALF [14, 15, 17]

Properties	Arib et al. [15]	Mishra et al. [14]	Devi et al. [17]
Density (g/cm ³)	1.07	1.44	1.526
Tensile strength (MPa)	126.60	413–1627	170
Elongation at break (%)	2.2	1.6	–
Young's modulus (MPa)	4405	34.5–82.51	6210

Table 2 Chemical properties of PALF [12, 14, 18]

Chemical composition	Value
Extractive (%)	5.5
Holocellulose (%)	80.5
α -cellulose (%)	73.4
Lignin (%)	10.5
Ash (%)	2.0

3 Materials and Mix Design

In this study, a concrete grade C30 was selected in accordance to BS 5328: Part 2: 1997 [19] with water-cement ratio (w/c) of 0.5. As shown in Table 3, the standard mix ST5 was chosen for calculation of concrete design mix proportion of cube, cylinder and beam samples. The standard concrete mix design presents the total weight of cement, fine and coarse aggregate for 1 m³ volume of sample.

Table 3 Standard concrete mixes according to BS 5328—Part 2:1997 [19]

Standard mix	Characteristic compressive strength at 28 days (N/mm ²)	Constituents (Cement and Total aggregate) (kg)	Maximum size of aggregate			
			40 mm		20 mm	
			Workability Medium	Workability High	Workability Medium	Workability High
ST1	7.5	Cement	180	200	210	230
		Aggregate	2010	1950	1940	1880
ST2	10	Cement	210	230	240	260
		Aggregate	1980	1920	1920	1860
ST3	15	Cement	240	260	270	300
		Aggregate	1950	1900	1890	1820
ST4	20	Cement	280	300	300	330
		Aggregate	1920	1860	1860	1800
ST5	25	Cement	320	340	340	370
		Aggregate	1890	1830	1830	1770
Workability – slump (mm)			50–100	80–170	25–75	65–135

Three different shapes and size of the sample was prepared depending on the type of experiments; there are; (1) cube sample size is $0.15 \times 0.15 \times 0.15 \text{ m}^3$ for the compression test, (2) cylinder size is $\pi \times 0.075 \times 0.3 \text{ m}^3$ for tensile test, and (3) beam size is $0.5 \times 0.1 \times 0.1 \text{ m}^3$ for the flexural test. The ordinary Portland cement (OPC) which complied with Malaysian Standard (MS) MS 522: Part 1:2003 [20] was used with the maximum size of coarse and fine aggregate was limited to 20 mm and 5 mm respectively. Both aggregates were kept under the roof to maintain the moisture.

Meanwhile, the concrete mix proportion used for cube, cylinder and beam samples which include the weight of cement, coarse aggregate, fine aggregate, water and PALF is presented in Table 4. It is shown that the weight of each sample increased depending on the volume of the sample itself. The production of PALF was prepared according to the literature survey (e.g. [14, 18, 21]), the fresh pineapple leaf was scrubbed to extract the fibre from the leaf. Afterwards, it was dried under room temperature to remove any substances for a few days. When the fibre was completely dried, the fibre was cut into 5 cm length.

In this study, the percentages of PALF were chosen based on the previous researches conducted by Mathew et al. [22], Roselin et al. [23] and Hisana et al. [24]. In their study, [22] and [24] investigated the mechanical properties of concrete by adding a few ranges of 0–0.25% of the PALF in concrete samples. Both researchers highlighted better agreement that the optimum strength of concrete was achieved when 0.1% of PALF was added in the concrete mixture. However, Roselin et al. [23] proved that the maximum strength of concrete samples was achieved when 0.75% PALF was added in the concrete mixture. Based on previous researches, the concrete samples were prepared in this present study with three different percentages of the PALF i.e. 0.1, 0.2 and 0.3% were added into concrete mixture depending on the

Table 4 Concrete mix proportion for one sample

Constituent volume	ST5	Cube	Cylinder	Beam
	1 m ³	Cube size: (0.15 × 0.15 × 0.15) m ³ = 0.0034 m ³	Cylinder size: (π × 0.075 × 0.3) m ³ = 0.0053 m ³	Beam size: (0.5 × 0.1 × 0.1) m ³ = 0.005 m ³
Cement (kg)	340	1.16	1.802	1.7
Coarse aggregate (kg)	1190	4.046	5.95	5.95
Fine aggregate (kg)	640	2.176	3.2	3.2
Water (kg)	170	0.578	0.901	0.85
<i>PLAF</i>				
0.1%	–	0.048	0.037	0.035
0.2%	–	0.095	0.074	0.070
0.3%	–	0.140	0.112	0.140

volume of samples of each laboratory tests. Meanwhile, the samples with 0% of PALF were prepared as a control sample for validation purposes.

As presented in Table 5, a total of 48 samples were tested in two states of the concrete stage, i.e. fresh concrete and hardened concrete. In fresh concrete, the workability or consistency of concrete mixture was measured by conducting the slump test. Meanwhile, three mechanical properties of concrete were determined by performing the compression, splitting tensile and flexural strength tests at the hardened state of concrete. The results of each laboratory tests are taken from the average of three samples prepared with different percentages of PALF.

Table 5 Total number of sample for each test

Sample	Compression test cube size: (0.15 × 0.15 × 0.15) m ³		Tensile test cylinder size: (π × 0.075 × 0.3) m ³	Flexural test beam size: (0.5 × 0.1 × 0.1) m ³
	Curing days			
	7	28	28	–
0% (control)	3	3	3	3
0.1%	3	3	3	3
0.2%	3	3	3	3
0.3%	3	3	3	3
Total	12	12	12	12

4 Experimental setup

The properties of the fresh and hardened state of concrete were carried out to find out the effect of PLAF on concrete. The fresh state was involved slump test to check the workability of concrete mix. The slump test was conducted according to BS 1881-102:1983 [25]. On the contrary, the hardened states consist of the compressive test, splitting tensile test and flexural test. The tests were conducted following BS EN 12390 (Part 3, Part 5 and Part 6) [26–28]. Figure 3 shows the apparatus used to test the concrete samples in a hardened state.

According to [29–31], the samples were tested at the age of 7 and 28 days using the compressive machine with the maximum load rate of 15 NM/m²/min (i.e. 150 kg/cm²/min) until the samples fail. The laboratory test was done to find the ultimate compressive strength of samples under the applied compressive load. During the experiment, the maximum load, F (N) was recorded (after the sample break), and the contacted surface area of the sample, A_c (mm²) was calculated. According to BS EN 12390-3:2001 [26], the compressive strength (f_c) is determined based on equation shown in Eq. (1) as stated below.

$$f_c = F/A_c \quad (1)$$

Instead, the purpose of splitting tensile test is to measure the shear failure of the concrete samples based on the recorded splitting tensile strength, STS (f_{ct}). In this study, the samples were tested at the age of 28 days. The STS is calculated using Equation in Eq. (2) as stated in BS EN 12390-6:2000 [28];

$$f_{ct} = (2 \times F)/(\pi \times L \times d) \quad (2)$$

where F is the maximum load applied on the sample (N), L is the length of the line of contact of the sample (mm), and d is designated diameter of the sample (mm).



Fig. 3 Experimental setup for, **a** compression test, **b** splitting tensile test, **c** flexural test

Finally, the flexural test was conducted to define the ability of concrete to withstand the bending force. The measurement of maximum force was recorded when the samples failed. This failure is known as ‘Modulus of Rupture’ (MOR) with unit psi or MPa. Eq. (3) is used to determine the flexural strength, f_{cf} (N/mm^2) of samples according to BS EN 12390-5:2009 [19];

$$f_{cf} = (F \times l)/(d_1 \times d_2^2) \quad (3)$$

where F is the maximum load applied (N), l is the distance between support rollers (mm), d_1 and d_2 are the lateral dimensions of the specimens (mm).

5 Result and Discussion

5.1 Slump test

The result of the slump test was decreased from 57 to 42 mm with increment amount of PLAF in the concrete mix, as illustrated in Fig. 2. It is noted that a 0.3% amount of fiber gives the lowest slump value of 42 mm. It might be due to the capability of the fiber to hold the materials in the concrete mix. However, the slump test showed a good agreement with BS 5328—Part 2:1997 [19] as described in Table 3. It is recommended that for standard concrete mixes type ST5 and maximum coarse aggregates of 20 mm, the fresh concrete mixture may experience two types of slump workability, i.e. medium and high workability for the slump in range of 25–75 mm and 65–135 mm respectively. It can be concluded that the concrete samples are classified under true slump type with medium workability [19] (Fig. 4).

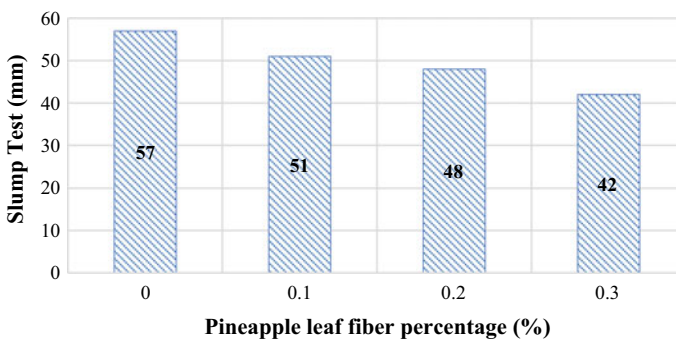


Fig. 4 Slump test for a different amount of fibre content

5.2 Compressive strength, f_c

The compression test is conducted to obtain the compressive strength of the concrete sample after added with different percentage of PALF. Figure 5 shows the results of compressive strength, f_c of concrete samples with four different percentages of PALF after 7 days and 28 days of the curing process. As can be seen, the f_c after 7 days curing is 22.98 N/mm² for control samples. Meanwhile, the f_c increased slightly to 24.09 N/mm², 25.11 N/mm² and 27.86 N/mm² after added with 0.1%, 0.2% and 0.3% of PALF respectively.

However, after 28 days of the curing process, the f_c of each concrete samples increased significantly up to grade 40 concrete (i.e. more than 40 N/mm²), although was initially designed as concrete grade 30. The lowest strength was recorded for concrete with 0.1% PALF, i.e. 42.04 N/mm², while the highest strength of 44.73 N/mm² was obtained when 0.3% PALF was added in concrete samples. It is found that there is a significant increase of f_c when comparing concrete curing after 7 days and 28 days, whereby the increment is approximately 46% for plain concrete and 60–75 % for concrete reinforced with fiber.

It is interesting to remark that the addition of PALF in concrete was able to increase the f_c to high compressive strength concrete of more than 40N/mm² within a short time (i.e. 28 days of curing process). The increment of strength is might be due to the ability of fiber to increase the initial compressive strength of the concrete and withstand the applied load.

Further investigation was done by comparing the obtained results of compressive strength, f_c after 28 days curing process with a previous study conducted by Mathew et al. [22], Roselin et al. [23] and Hisana et al. [24]. As shown in Fig. 6, the present study shows a similar agreement with works done by Roselin et al. [23]. It is noted that the f_c increased with the increment of PALF in concrete, although the present study produced relatively better strength compared to previous literature. However,

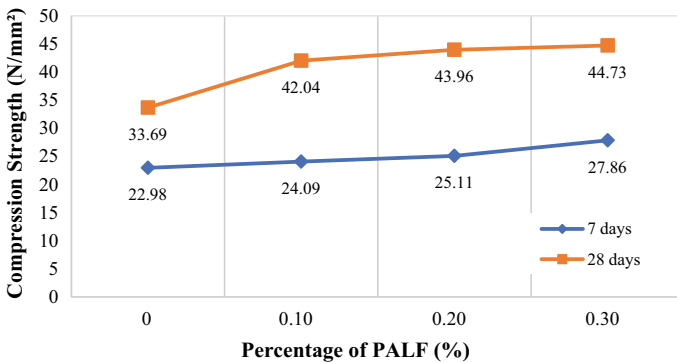


Fig. 5 The compression strength of concrete samples with addition of PALF

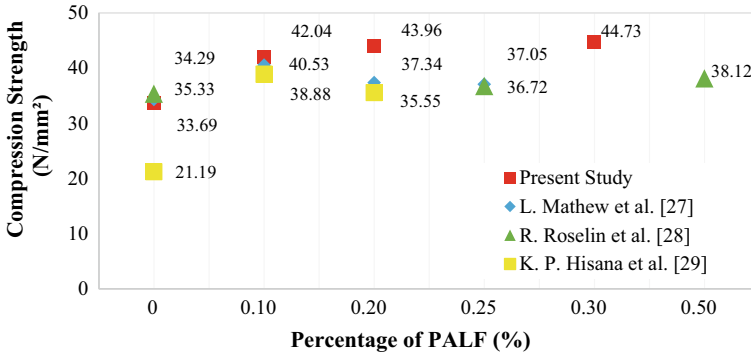


Fig. 6 Comparison of compression strength of concrete samples after 28 days curing process

it can be seen that studies conducted by Mathew et al. [22] and Hisana et al. [24] experienced the reduced in strength when 0.2% of PALF is added in concrete samples.

In overall, the results depict the favorable contribution of PALF towards the strength improvements of the concrete at 28 days. The maximum compressive strength was attained for the concrete containing 0.3% PALF, which was measured to be 32% higher than the reference concrete (i.e. control sample). The results proved that PALF is capable of strengthening the concrete and providing same as earlier hypotheses for previous literature.

5.3 Splitting Tensile Strength, f_{ct}

The splitting tensile test was carried out after 28 days to determine the capability of samples to resist the tensile load. Fig. 7 shows the splitting tensile strength, f_{ct} of

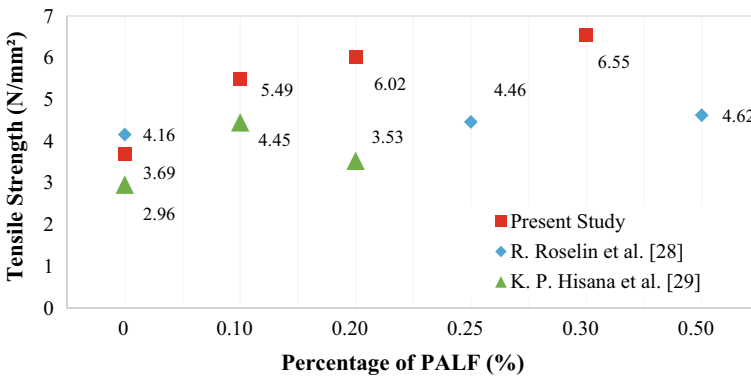


Fig. 7 Comparison of the tensile strength of concrete after 28 days of the curing process

the specimens of the present study compared with the previous study performed by Roselin et al. [23] and Hisana et al. [24]. The tensile strength of the sample without the addition of PALF is 3.69 N/mm² was used as the reference value. The highest f_{ct} of 6.55 N/mm² was achieved when 0.3% of PLAF is added in concrete; however, the lowest was 5.49 N/mm² for samples with 0.1% of PALF. A similar trend of f_c was experienced by present and previous studies conducted by Roselin et al. [23], whereby the f_{ct} was increased with increment percentage of PLAF in concrete.

It is noted that the f_{ct} in present study produced relatively better strength compared to previous literature. However, it can be seen that studies conducted by Hisana et al. [29] experienced the reduced in strength when 0.2% of PALF is added in concrete samples. The f_{ct} increased slightly when compared to plain concrete, whereby the percentage difference is approximately 49, 63 and 78% when 0.1, 0.2 and 0.3% of PLAF was added in concrete, respectively. Improvement of f_{ct} indicates that the specimens with PLAF could resist the shear failure due to the presence of fibre which is able to bridge the crack within the concrete materials.

5.4 Flexural Strength, f_{cf}

The flexural strength, f_{cf} of the specimens after 28 days of the curing process is shown in Fig. 8. The figure highlights that 0.3% of fibre resulted in the highest f_{cf} of 4.06 N/mm² which increased from the strength of plain concrete, i.e. 3.43 N/mm². The specimens of the present study were compared with a previous study conducted by Roselin et al. [23] and Hisana et al. [24]. Previous studies agreed that the addition of PALF in concrete would increase the flexural strength of the concrete, although the present study experienced the lowest f_{cf} compared to the previous literature. The improvement of f_{cf} showed that concrete with PLAF could resist the bending load better than normal concrete. The consistency of the increment might result from well distribution of fibre in the concrete mix.

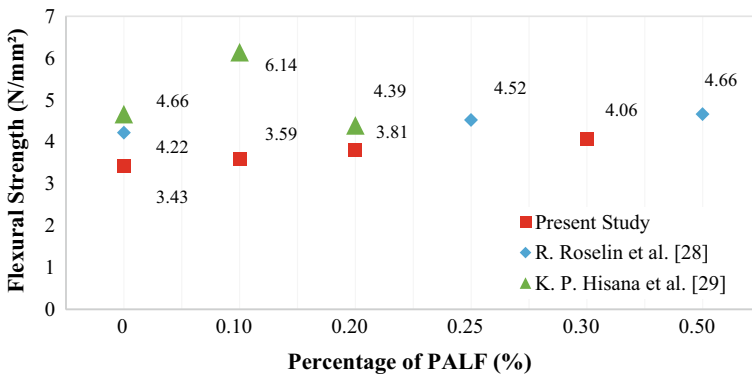


Fig. 8 Comparison of flexural strength of concrete samples after 28 days curing process

6 Conclusion

In this study, incorporating PLAF in concrete successfully improved the mechanical properties of the concrete. As a conclusion, an increasing percentage of PLAF in concrete improved the compressive strength, flexural strength and splitting tensile strength. It is found that 0.3% of PLAF was performed well with the highest value of the mechanical properties of concrete. The outcome of this study provides better improvement in the quality and mechanical properties of the new PALF concrete. Alternatively, the PALF reinforced concrete might promise the best solution to tackle the abundant of agriculture waste by converting the waste to new green and sustainable concrete material.

Acknowledgement The authors gratefully acknowledged the Universiti Pertahanan Nasional Malaysia (UPNM) for the opportunity to conduct this research.

References

1. Meier U (1995) Strengthening of structures using carbon fibre/epoxy composites. *Constr Build Mater* 9(6):341–351
2. Chung DDL (2000) Cement reinforced with short carbon fibres: a multifunctional material. *Compos Part B Eng* 31(6–7):511–526
3. Hao Y, Hao H, Chen G (2015) Experimental tests of steel fibre reinforced concrete beams under drop-weight impacts. *Key Eng Mater* 626(8):311–316
4. Petrone G, Rao S, De Rosa S, Mace BR, Franco F, Bhattacharyya D (2013) Behaviour of fibre-reinforced honeycomb core under low velocity impact loading. *Compos Struct* 100:356–362
5. Akil H, Zamri MH (2013) Performance of natural fiber composites under dynamic loading. Woodhead Publishing Limited
6. Mo KH, Yap SP, Alengaram UJ, Jumaat MZ, Bu CH (2014) Impact resistance of hybrid fibre-reinforced oil palm shell concrete. *Constr Build Mater* 50:499–507
7. Ali M, Liu A, Sou H, Chou N (2012) Mechanical and dynamic properties of coconut fibre reinforced concrete. *Constr Build Mater* 30:814–825
8. Aziz MA, Paramasivam P, Lee SL (1981) Prospects for natural fibre reinforced concretes in construction. *Int J Cem Compos Light Concr* 3(2):123–132
9. Fuqua MA, Huo S, Ulven CA (2012) Natural fiber reinforced composites. *Polym Rev* 52(3–4):259–320
10. Sai PP, Murali K, Kumar GS, Teja KV (2018) Study on properties of natural fibre reinforced concrete made with coconut shells and coir fibre. *Int J Civ Eng Technol* 9(1):416–422
11. Ahmad Z, Saman HM, Tahir PM (2010) Oil palm trunk fiber as a bio-waste resource for concrete reinforcement. *Int J Mech Mater Eng* 5(2):199–207
12. Pandey S (2005) Pineapple leaf fibers
13. Vijayan R, Krishnamoorthy A (2019) Review on natural fiber reinforced composites. *Mater Today Proc* 16:897–906
14. Mishra S, Mohanty AK, Drzal LT, Misra M, Hinrichsen G (2004) A review on pineapple leaf fibers, sisal fibers and their biocomposites. *Macromol Mater Eng* 289(11):955–974
15. Arib RMN, Sapuan SM, Ahmad MMHM, Paridah MT, Khairul Zaman HMD (2006) Mechanical properties of pineapple leaf fibre reinforced polypropylene composites. *Mater Des* 27(5):391–396

16. Chuan VVB (2010) Effect of concrete compressive strength with various natural additives fiber for green environment
17. Devi LUMA, Bhagawan SS, Thomas S (1996) Mechanical properties of pineapple leaf fiber-reinforced, pp 3–7
18. Asim M, Abdan K, Jawaid M, Nasir M, Dashtizadeh Z, Ishak MR, Hoque ME, Deng Y (2015) A review on pineapple leaves fibre and its composites. *Int J Polym Sci* 2015
19. British Standards Institute (1997) BS 5328: part 2: 1997 concrete part 2: methods for specifying concrete mixes. BSI Standards Publication
20. Department of Standards Malaysia (2003) MS 522: part 1: 2003 Portland cement (ordinary and rapid-hardening) specification (Second Revision) (3)
21. Todkar SS, Patil SA (2019) Review on mechanical properties evaluation of pineapple leaf fibre (PALF) reinforced polymer composites. *Compos Part B Eng* 174(5):106927
22. Mathew L, Paul MM (2017) Mechanical properties of pineapple fibre reinforced concrete subjected to high temperature. *GRD J Glob Res Dev J Eng* 2(5):200–205
23. Roselin R, Ravikumar MS (2018) Experimental investigation on pineapple fibre reinforced cement concrete. *Int J Civ Eng Technol* 9(6):1479–1484
24. Hisana KP, Parathodika MS, Ajeesh K (2019) Experimental study on pineapple leaf fiber reinforced RCC beams. *Int J Eng Res Gen Sci* 6(3):2018–2020
25. British Standards Institute (2005) BS 1881-102: 1983 testing concrete—part 102: method for determination of slump, no 12
26. British Standard Institute (2001) BS EN 12390-3:2001 testing hardened concrete—part 3: compressive strength of test specimens
27. British Standards Institute (2009) BS EN 12390-5:2009 testing hardened concrete—part 5: flexural strength of test specimens, no 8
28. British Standards Institute (2000) BS EN 12390-6:2000 testing hardened concrete—part 6: tensile splitting strength of test specimens, vol 3, no 1
29. Mali S, Pachpande T, Jogi A (2015) Effect of rate of loading on compressive strength of concrete. *Int J Innov Emerg Res Eng* 2(4):20–25
30. Xiao Y, Shan J, Zheng Q, Chen B, Shen Y (2009) Experimental studies on concrete filled steel tubes under high strain rate loading. *J Mater Civ Eng* 21(10):569–577
31. Rossi P, Van Mier JGM, Toutlemonde F, Le Maou F, Boulay C (1994) Effect of loading rate on the strength of concrete subjected to uniaxial tension. *Mater Struct* 27(5):260–264

Flexural Behavior of SCC Beams with Different Shear Span to Effective Depth Ratio



Oh Chai Lian, Mohd Raizamzamani Md Zain, Norrul Azmi Yahya, Lee Siong Wee, and Balqis Md Yunos

Abstract Self-compacting concrete (SCC) is a self-consolidating concrete which does not require any compaction. Innovation in SCC adopting waste materials has become one of the research trends worldwide. This study presents experimental results on flexural behavior of SCC beams containing 10% eggshell as partial cement replacement. A total of three reinforced SCC beams with size of $150 \times 200 \times 1200$ mm were tested under four-point bending test. Flexural characteristics such as load–deflection relationship and failure modes of the SCC beams were evaluated considering different shear span to effective depth ratio (a/d) of 1.0, 1.5 and 2.0. The ultimate flexural strength of the SCC beams was compared with the theoretical values proposed by Eurocode 2. It is found that the beam SCCB1.0 failed in shear whereas SCCB1.5 and SCCB2.0 in shear–flexural mode, respectively. When a/d ratio increase, the beam failure changed from brittle to ductile manner.

Keywords Self-compacting concrete · Flexural · Eggshell · Shear span

1 Introduction

Self-compacting concrete (SCC) was first introduced in Japan at 1980s. SCC has an excellent flowing characteristic, consolidates under its own weight and achieves full compaction without vibration. Excellent flow ability of SCC makes the concrete completely fills the formwork even in the presence of congested reinforcement. Such concrete could be applied in large structures such as long span bridges and earth retaining systems.

O. C. Lian (✉) · M. R. Md Zain · N. A. Yahya · B. Md Yunos
School of Civil Engineering, College of Engineering, Universiti Teknologi MARA (UiTM),
40450 Shah Alam, Selangor, Malaysia
e-mail: chailian@uitm.edu.my

L. S. Wee
School of Civil Engineering, College of Engineering, Universiti Teknologi MARA (UiTM), Johor
Pasir Gudang Campus, 81750 Masai, Johor, Malaysia

Many researchers have interests in producing greener and innovative concretes by utilizing waste materials [1, 2]. Innovation in SCC adopting waste materials has become one of the research trends worldwide. Utilization of wastes such as oil palm shell, fly and bottom ash in construction industry reduces allocation of landfill sites. Owing to high calcium, magnesium carbonate (lime) and protein, food wastes particularly eggshells are dried and used as a source of calcium in many countries. Pliya and Cree [3] found that the brown eggshell contains composition of more than 96% calcium carbonate. Following this, the fine-grained powder sieved to the required sizes was also incorporated in concrete at a suitable eggshell to cement ratio. Oh, Lee and Mohd Raizamzamani (2020) reported that the addition of 15% eggshells in SCC mix replacing cement has increased the compressive strength up to 29% as compared to the control mix.

Flexural behavior of green concrete can be obtained experimentally through bending test on large scaled reinforced concrete beam specimens. For instance, Oh et al. [4] compared the structural performance of six high strength concrete beams incorporated with and without recycled concrete aggregates. The flexural characteristics particularly ultimate capacity, load–deflection relationship and failure modes were examined. Rahman et al. [5] investigated foamed concrete beam specimens incorporated with palm oil fuel ash and eggshell powder. The experimental work showed the beam specimens with combination of 20% palm oil fuel ash and 5–10% eggshell powder achieved 13–14% higher ultimate load capacity but more severe cracking compared to control beams (without palm oil fuel ash and eggshell powder). Specifically in the field of SCC, Perumal et al. [6] investigated flexural behavior of SCC beams of $230 \times 230 \times 1000$ mm utilizing coconut husk under both three and four-point bending tests. Slight increment in the ultimate load carrying capacity of the beams was observed when the fly ash was replaced by coconut husk in both bending tests. Ofuyatan et al. [7] studied the properties of SCC developed using 10, 20 and 30% eggshell powder as partial cement replacement. All the mixes with eggshell powder showed comparable compressive strength and flexural strength compared to the control mix (without eggshell powder). Mahmud et al. [8] evaluated the flexural performance of fourteen reinforced SCC beams containing various percentage of steel fiber. The experimental results were compared with ACI 318 code. It was found that the flexural strength in beams increases with increasing concrete compressive strength, longitudinal steel rebar ratio, and fiber amount. Zhang et al. [9] investigated flexural behavior of twelve reinforced SCC beams containing steel fiber, macro polypropylene fiber, micro polypropylene fiber, and their combinations. A calculation method for ultimate bearing capacity of flexural SCC beams considering effect of fibers at room temperature was proposed. Mohammed and Najim [10] determined the compressive strength, flexural strength and modulus of elasticity of series of SCC incorporating recycled coarse aggregate, recycled fine aggregate and superplasticizer at different percentages of replacement. The outstanding four mixes were used in the investigation of flexural behavior of eight $100 \times 150 \times 1200$ mm reinforced concrete beams under four-point bending test. Decrement in hardened properties and the flexural stiffness and toughness after application of recycled concrete aggregate was found.

Many experimental works on reinforced concrete beams containing wastes have been found, however, investigation on the effect of shear span-effective depth ratio on flexural behavior of SCC beams containing eggshell is limited. Khatab et al. [11] determined the effect of shear span-to-depth ratio of 0.8 and 1.7 in eight two-span self-compacting concrete (SCC) deep beams. The predictions using the strut-and-tie model suggested by ACI 318 M-11, EC2 and CSA23.4–04 are conservative results compared to the experimental shear capacities of the beams. Different from Khatab, this paper presents an experimental work on three reinforced SCC beams containing 10% eggshell as partial cement replacement in the mix. The effects of shear-span to effective depth ratio of 1.0, 1.5 and 2.0 on the flexural behavior of the beams were evaluated. The experimental results were further compared with Eurocode 2. The study also presents the fresh properties and compressive strength of the SCC mix incorporating eggshells.

This paper is organized as follows. Section 2 presents the experimental program for investigation of flexural strength of SCC beam containing eggshell. Section 3 presents and discusses the results inclusive the compressive strength of SCC mixes and flexural behavior of the SCC beams loaded with different shear span to effective depth ratio. This section also shows the predicted values of flexural strength from Eurocode 2. Finally, our work for this paper is summarized in the last section.

2 Method

This section presents the experimental program in investigating flexural strength of SCC beam specimens containing eggshell replacing cement. The experimental program is described in three parts: (1) preparation of SCC mix, (2) testing for fresh properties and (3) testing for flexural strength of SCC beam specimens.

2.1 Preparation of SCC Mix

Table 1 shows a mix composition for SCC with eggshell replacing cement. Main materials such as Ordinary Portland Cement, water, fine aggregates, coarse aggregates, eggshell powder and admixture were used in the SCC mix:

Table 1 The material composition of the SCC mix

Cement (kg/m ³)	Water (L/m ³)	Fine aggregate (kg/m ³)	Coarse aggregate (kg/m ³)	Eggshell (kg/m ³)	Superplasticizer (L/kg/m ³)
463.5	215	644	966	51.5	5.15

Table 2 Properties of cement and master GLENIUM 8784

Chemical composition (%)		
Compositions	Cement	Eggshell
SiO ₂	21.28	16.278
Al ₂ O ₃	5.60	2.917
Fe ₂ O ₃	3.36	4.369
CaO	64.64	71.765
MgO	2.06	NA
SO ₃	2.14	2.604
Total alkalis	0.05	0.045
Insoluble residue	0.22	NA
Loss on ignition	0.64	NA
Physical properties of Master GLENIUM 8784		
Relative density	1.10 ± 0.01 at 25 °C	
pH	>6	
Chloride ion content	<0.2%	

Cement. The Ordinary Portland cement conforming Malaysia Standard MS522 was used. The chemical compositions of the cement are shown in Table 2.

Aggregates. Coarse aggregates from gravel of size 6 mm and fine aggregates from local sand of size with range of 0.3–0.8 mm were used. Good combination of aggregate sizes can ensure appropriate workability of SCC and decrease the possibility of segregation in the concrete mix. Fine to coarse aggregate ratio of 0.67 were considered.

Water. In order to provide an optimum strength and stability, water-cement ratio of 0.42 was used.

Eggshells. The eggshell were collected from various local restaurant and street vendors. Eggshells were cleaned and left dried at natural condition under direct sunlight. Then, the eggshells were put in the oven for 24 h for further removal of moisture content. Grinder machine (as shown in Fig. 1) was used to grind the eggshell into fine powder. Eggshell was used at weightage of 10% to partial replacing cement.

Admixture. The superplasticizer Master GLENIUM 8784 certified under ASTM C494 Types G was used. The physical properties of the superplasticizer are shown in Table 2. The amount of superplasticizer added to the mix was 1% from the amount of cement.



Fig. 1 Testing machines (left) grinder (right) compression machine

2.2 Testing for Fresh Properties

Slump flow test, L-Box test and sieve segregation test were conducted in accordance with the European Guidelines for Self-Compacting Concrete, (EFNARC 2005) to assess the fresh properties of SCC mix.

Slump Flow Test

The slump flow test was carried out to assess the flowability of SCC in the absence of obstructions. A truncated cone conforming to EN 12,350–2 was used. The apparatus has height of 300 mm, internal diameter of 200 mm and 100 mm at base and top, respectively. The SCC flowed out from the cone was measured its final diameters in two perpendicular directions. The average of these two measured diameters were calculated as slump flow. Viscosity of ECC was assessed by recording T500 time during the slump flow test, when the diameter of flow reaches 500 mm.

L Box Test

L Box test was conducted to determine the filling and passing ability of SCC. Passing through the apparatus L Box with three bars, the SCC was measured the height at the end of the horizontal box (H1) and the height at the gate side (H2), near the vertical box. The passing ability was measured in ratio of H2/H1. The whole test was performed within 5 min accordance to EFNARC, (2005).

Sieve Segregation Test

The sieve segregation test was performed to assess the resistance of SCC to segregation. With the sieve and receiver on the weighing machine, 5 kg SCC was poured into the sieve. The actual mass of the SCC on the sieve was recorded as W_c in gram. The sieve was removed at least after 2 min, the mass of the receiver and SCC that has passed through the sieve was recorded as W_{ps} in gram. The sieve receiver was weighted and recorded as W_p in gram. The segregated portion SR in percentage was calculated as in the following equation:

$$SR = (W_{ps} - W_p) \times 100 / W_c \% \tag{1}$$

2.3 Testing for Hardened Properties

A total of six $100 \times 100 \times 100$ mm SCC cubes were cast based on the mix in Table 1 and tested for the compressive strength. The compression test was conducted for the cubes at ages 7 and 28 days based on BS-EN:12,390-3 [12]. At the same time, three beam specimens were cast, to investigate the flexural strength at their age of 28 days. All SCC beam specimens with size of $150 \times 200 \times 1200$ mm were designed with both top and bottom rebars of diameter 10 mm. The effective depth of the beams is 160 mm. The high yield deformed longitudinal rebar has characteristics strength of 460 N/mm^2 . The link of 6 mm diameter was provided at 200 mm spacing along the beam, and with characteristics strength of 250 N/mm^2 . Both cubes and beams were cured in water curing tank before the testing day.

Figure 2 shows the experimental set up of a four-point bending test and the distance of shear span a . The beam specimens were loaded to fail under a load test

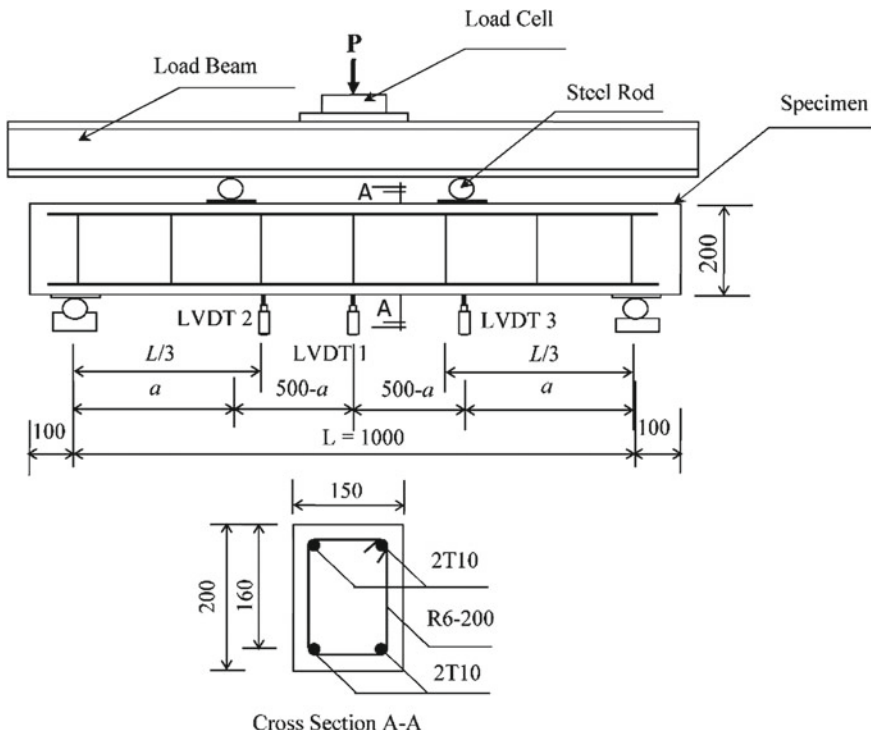


Fig. 2 Experimental set up for four-point bending test (elevation view)

with different shear span to effective depth ratio a/d . Specifically, beam SCCB1.0, SCCB1.5 and SCCB2.0 denote the beams loaded with shear span a of 160 mm and 240 mm and 320 mm, respectively. The linear variable differential transformers LVDT 1, LVDT 2 and LVDT 3 were placed at the bottom of the beams. LVDT 1 was placed at the middle while, LVDT 2 and LVDT 3 at one-third of span length from each support. The load was exerted on the beam with the control criteria using displacement rate of 0.01 mm/s.

3 Results and Discussion

This section presents the fresh properties of SCC, compressive strength for the SCC cubes and flexural strength for the SCC beam specimens containing 10% eggshell as partial cement replacement.

3.1 Fresh Properties

Table 3 shows the results of fresh properties from the slump flow, L-box and sieve segregation tests. All the tests for flexural properties confirmed the mix in the study are within the acceptable limits set by EFNARC. Slump flow and time T500 were recorded as 590 mm and 7 s, respectively. The SCC can be classified as SF1 with the typical applications such as for housing slabs and small diameter piles as recommended by EFNARC. From the viscosity result, classed under VS2, the SCC is generally appropriate for most applications.

For L-Box test, the heights $H_1 = 110$ mm and $H_2 = 100$ mm were recorded. The passing ability measured from L-Box test is 0.91, indicating SCC is type PA2 according to EFNARC. This type of SCC is suitable for civil engineering structures like walls and columns applications. On the other hand, the segregated portion SR was calculated as 14%. EFNARC suggested this type of SCC, category SR2 may be used for tall vertical application with flow distance more than 5 m and confined gap is less than 80 mm. The results of fresh properties of the SCC in this study are comparable to the trend of results in ESP10 (mix incorporated 10% of eggshell) from Ofuyatan et al. [7].

Table 3 Properties of cement and Master GLENIUM 8784

Test	Slump flow		L-Box	Sieve segregation
Unit	D (mm)	T ₅₀₀ (s)	$P_1 = H_2/H_1$	SR (%)
SCC10	590	7	0.91	14

Table 4 Compressive strength at 7 and 28 days

Specimens	Compressive strength at 7 days (MPa)			Compressive strength at 28 days (MPa)		
	Cube	Mean	Standard deviation	Cube	Mean	Standard deviation
Cube 1	45.93	44.13	1.30	55.54	56.66	3.15
Cube 2	43.56			53.48		
Cube 3	42.90			60.95		

3.2 Compression Strength

The SCC mix was initially designed to achieve the targeted compressive strength 30 MPa at 28 days. Table 4 shows the compressive strength for the SCC mix at ages 7 and 28 days. The mean compressive strength was determined based on the compressive strength of three cubes. It is shown that the mean compressive strength for the SCC mix at 7 days (i.e. 44.13) reached about 78% of the compressive strength at 28 days (i.e. 56.66 MPa). The standard deviations of the compressive strength at 7 days and 28 days are 1.30 and 3.15, respectively. The average compressive strength for the SCC mix at 28 days has achieved compressive strength greater than the targeted.

3.3 Flexural Behavior of SCC Beam Specimens Containing Eggshell

Under four-point bending test, all the beams were loaded gradually until reaching the ultimate load. The results on the flexural behavior of SCC beam specimens containing 10% eggshell as partial cement replacement were presented in terms of load–deflection relationship and failure modes. Effects of shear span to effective ratio on flexural behavior of SCC beams were discussed in this section. Lastly, the experimental flexural strengths were compared with the theoretical values recommended by Eurocode 2.

Load–deflection relationship. Figures 3, 4 and 5 presents the load–deflection curves for SCCB1.0, SCCB1.5 and SCCB2.0 obtained from LVDT 1, LVDT 2, and LVDT 3 respectively. Generally, all the load–deflection curves demonstrate linear elastic pattern at load of range 6–8 kN (the first crack loads) before advancing to plastic manner (i.e. crack development region).

The load–deflection curves for SCCB1.0 demonstrates an increasing nonlinear in the plastic region whereas for SCCB1.5 and SCCB2.0, the curves are almost flat until the beams failed at ultimate load. Beam SCCB1.0 clearly show higher ultimate load (i.e. 20.0 kN) compared to SCCB1.5 (i.e. 10.0 kN) and SCCB2.0 (i.e. 9.0 kN). Maximum deflections at failure loads recorded are 23 mm, 33 mm and 39 mm for SCCB1.0, SCCB1.5 and SCCB2.0, respectively.

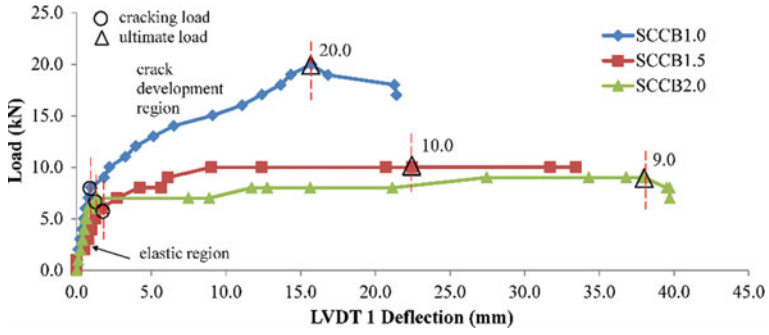


Fig. 3 Load-deflection for LVDT 1

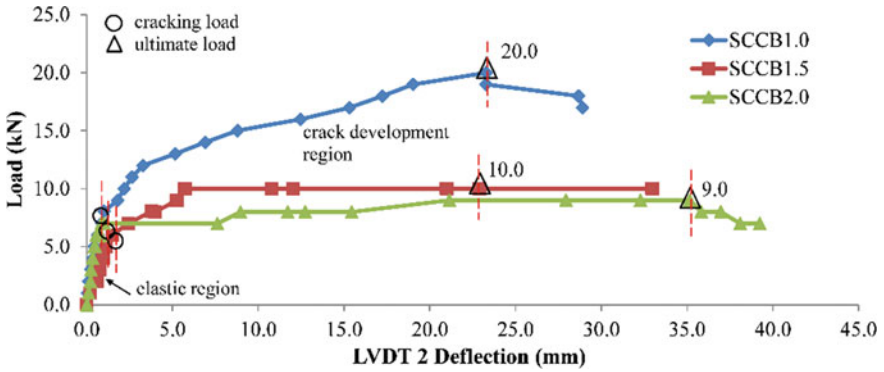


Fig. 4 Load-deflection for LVDT 2

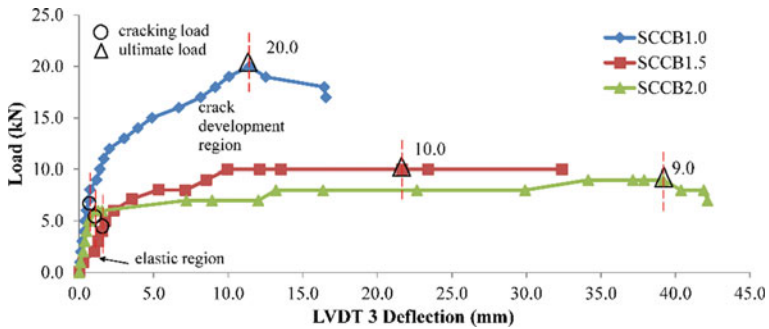


Fig. 5 Load-deflection for LVDT 3

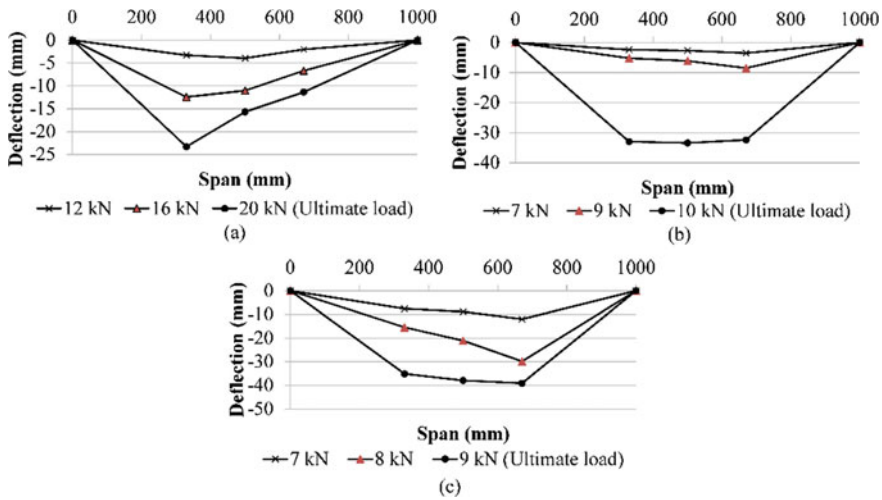


Fig. 6 Deflections along the beam, a SCCB1.0, b SCCB1.5 and c SCCB2.0

Figure 6 shows the deflections along beam specimens SCCB1.0, SCCB1.5 and SCCB2.0 at various load applications. The loads were chosen randomly to illustrate the changes of beam deflections upon loading during the test. It could be seen that the beam SCCB1.0 exhibited obvious deflection at one-third span length from the left support (LVDT2) than mid-span at load insertion of 16 kN onwards. Oppositely, beam SCCB2.0 showed the highest deflection at one-third span length from the right support (LVDT2). On the other hand, the beam SCCB2.0 showed maximum deflection approximately at mid span throughout the test.

From Figs. 3, 4, 5 and 6, it is noted that with lesser *a/d* ratio (or when the loads were placed near to supports, i.e. SCCB1.0), beam can sustain greater load with better deflection control. For beam with *a/d* of 1.0, the decrease in the maximum deflection at failure was 30.30%, and 41.02% compared to beams with *a/d* of 1.5 and 2.0, respectively. In addition, the beam with *a/d* of 1.0 resulted in an obvious increase in the ultimate load of 100.00% and 122.22% compared to beams with *a/d* of 1.5 and 2.0, respectively. Acting differently, SCCB1.5 and SCCB2.0 obviously show longer strain hardening curve compared to SCCB1.0 (i.e. 40% and 150% longer for SCCB1.5 and SCCB2.0, respectively), indicating better ductile behavior. Beam SCC1.0 (*a/d* of 1.0) has good agreement with the result from Khatab, Ashour, Sheehan, and Lam (2017) who reported all beams with *a/d* ratio of 0.8 and 1.7 failed in brittle manner. To add up the gap, the beams with *a/d* 1.5 and 2.0 demonstrated increasing ductility behavior. Generally, when *a/d* ratio increase, the beams failure changed from brittle to ductile manner.

3.4 Failure Modes

Figure 7 shows the failure mode of beams SCCB1.0, SCCB1.5 and SCCB2.0. During the exertion of loads, the development of cracks in SCC beams was observed and noted constantly. The first crack was observed at the tension zone near the mid span for both beams. As the load was increased, obvious shear cracks spread from supports of the beam SCCB1.0, moved further upward to the steel rods that inserted point loads.

With further loading penetrations, more shear cracks continued to be developed until the compression area especially under the point load started to crush. Spalling was observed on the beam surfaces as the shear cracks became obvious. The beams SCCB1.5 and SCCB2.0 acted almost the same as SCCB1.0 however demonstrated more flexural cracks at the tension zone near the mid-span of the beam. Besides, the beam SCCB1.0 failed clearly in shear mode whereas SCCB1.5 and SCCB2.0 in

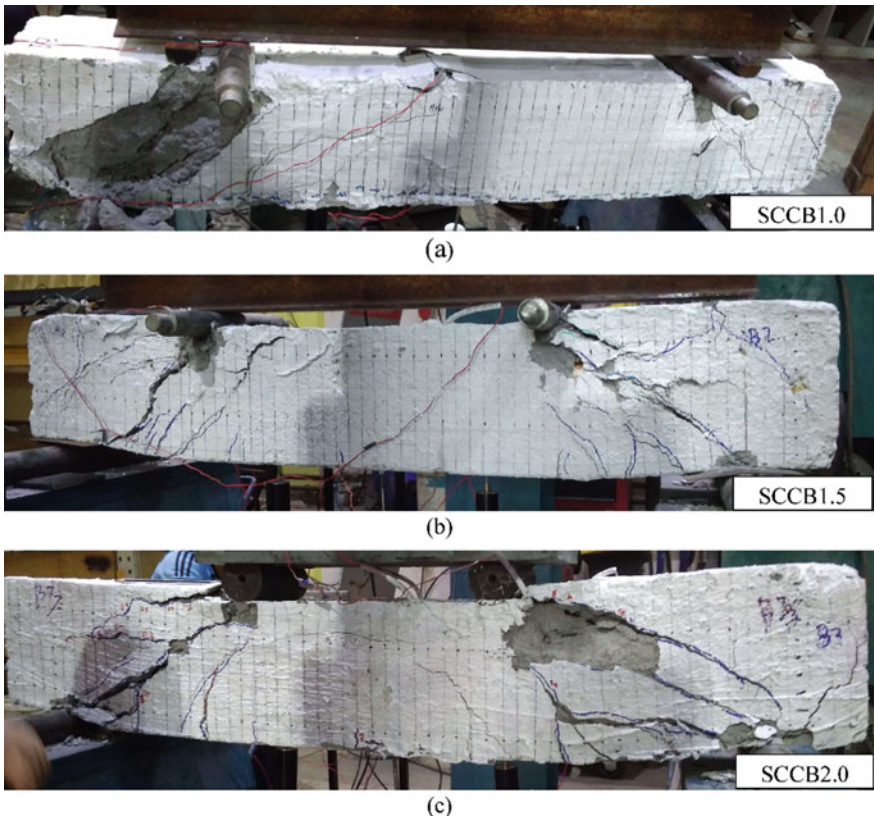


Fig. 7 Failure modes: a SCCB1.0, b SCCB1.5 and c SCCB2.0

Table 5 Prediction of flexural strength from Eurocode 2

Beam	Bending capacity (kNm)		$M_{Exp}/M_{Predict}$
	M_{Exp}	$M_{Predict}$	
SCCB1.0	1.60	11.17	0.14
SCCB1.5	1.20	11.17	0.11
SCCB2.0	1.44	11.17	0.13

shear-flexural mode. This also reveals that when the a/d increase, the beam behavior change from shear to flexural mode.

3.5 Prediction of Flexural Strength of SCC Beams

The flexural strength of the beam specimens was predicted using Eurocode 2. The stress distribution in the concrete using rectangular-parabolic stress block was chosen and the predicted flexural strength for a singly reinforced section of concrete with grade below C50/60 could be calculated as:

$$M_{Predict} = A_s f_{yk} d \left[1 - (0.513 A_s f_{yk} / b d f_{ck}) \right] \quad (2)$$

where f_{ck} is the characteristic cylinder crushing strength of concrete (MPa), f_{yk} is the characteristic strength of rebars (MPa), A_s is the cross-sectional area of steel rebars, b is the width (mm) and d is the depth (mm) of the beam specimens. According to Table 3.1 in EN-1992-1-1 [13], the characteristic cylinder crushing strength of concrete converted from cube strength obtained from the experimental (refer Table 4) for the SCC mix is 46.66 MPa.

Table 5 shows the comparison between the experimental M_{Exp} and predicted flexural strength $M_{Predict}$ in terms of ratio $M_{Exp}/M_{predict}$ for beam SCCB1.0 and SCCB2.0. The ratios $M_{Exp}/M_{Predict}$ for both beams are considered low. This reveals that the Eq. (2) may not predict well the SCC beam containing eggshell in this case.

4 Conclusions

This paper presents results on an experimental work with the main aim to evaluate the flexural behavior of the SCC beams containing 10% eggshell as partial cement replacement. The compressive strengths of SCC cubes at age 7 and 28 days were found greater than the targeted compressive strength. The flexural strength of beam specimens loaded with shear span to effective depth ratio of 1.0, 1.5 and 2.0 were investigated and compared with the predicted value suggested from Eurocode 2. Based on the experimental results, the following conclusions can be drawn:

1. The fresh properties of the proposed mix with 10% eggshell partial replacing cement are within the acceptable limits set by EFNARC, (2005). The recommended specific categories for the flowability, viscosity, passing ability and segregation resistance of SCC (i.e. SF1, VS2, PA2 and SR2) has indicated its potential applications in housing slabs, and vertical applications such as columns, walls, and piles.
2. Beam SCCB1.0 failed in shear whereas SCCB1.5 and SCCB2.0 in shear-flexural mode, respectively. When a/d ratio increase, the beams failure changed from brittle to ductile manner.
3. When the shear span to effective depth ratio increase, reduction in the ultimate load and flexural strength of beam and increment in maximum deflection were recorded.
4. The ratio experimental and predicted flexural strength, $M_{Exp}/M_{Predict}$ reveals that the Eq. (1) may not effectively predict the flexural strength of SCC beam containing eggshell in this study and required corrections prior to the properties of the new concrete with eggshell.

Acknowledgements The authors would like to acknowledge the Ministry of Higher Education under Fundamental Research Grant Scheme (FRGS) (600-IRMI/FRGS 5/3 (378/2019)) for providing the financial support to perform this study. The authors gratefully acknowledge undergraduate student Ainina Yusriani binti Mohd Yusof in assisting laboratory works. The authors would also like to thank to Laboratory of Heavy Structure, Faculty of Civil Engineering MARA, Shah Alam, Selangor.

References

1. Lee S, Oh C, Zain M, Yahya N (2018) The use of oil palm fiber as additive material in concrete. In: IOP conference series: materials science and engineering, vol 431, no 4. IOP Publishing, p 042012
2. Lee SW, Oh CL, Zain MRM (2018) Evaluation of the design mix proportion on mechanical properties of engineered cementitious composites. In: Key engineering materials, vol 775. Trans Tech Publ, pp 589–595
3. Pliya P, Cree D (2015) Limestone derived eggshell powder as a replacement in Portland cement mortar. *Constr Build Mater* 95:1–9
4. Oh CL, Lee SW, Mohd Asha'ari M, Goh CH (2013) Experimental Study on Shear behaviour of high strength reinforced recycled concrete beam. *Pertanika J Sci Technol* 21(2)
5. Rahman AF, Goh W, Jhatial A (2019) Flexural study of reinforced foamed concrete beam containing palm oil fuel ash (POFA) and eggshell powder (ESP) as partial cement replacement. *Int J Sustain Construct Eng Technol* 10(1)
6. Perumal K, Kumar A, Lingshwaran N, Susmitha S (2020) Experimental studies on flexural behaviour of self compact concrete beam. *Materials Today: Proceedings*
7. Ofuyatan OM, Adeniyi AG, Ijje D, Ighalo JO, Oluwafemi J (2020) Development of high-performance self compacting concrete using eggshell powder and blast furnace slag as partial cement replacement. *Construct Build Mater* 256:119403
8. Mahmood M, Hanoon AN, Abed HJ (2018) Flexural behavior of self-compacting concrete beams strengthened with steel fiber reinforcement. *J Build Eng* 16:228–237

9. Zhang C, Han S, Hua Y (2018) Flexural performance of reinforced self-consolidating concrete beams containing hybrid fibers. *Constr Build Mater* 174:11–23
10. Mohammed SI, Najim KB (2020) Mechanical strength, flexural behavior and fracture energy of recycled concrete aggregate self-compacting concrete. *Structures* 23:34–43. Elsevier
11. Khatab MA, Ashour AF, Sheehan T, Lam D (2017) Experimental investigation on continuous reinforced SCC deep beams and comparisons with code provisions and models. *Eng Struct* 131:264–274
12. BS-EN:12390-3 (2009) Testing hardened concrete. Part, vol 3
13. EN-1992-1-1 (2004) Eurocode 2: design of concrete structures—part 1–1: General rules and rules for buildings

Flexural Strength and Ductility of Green Engineered Cementitious Composites Containing High Volumes of Fly Ash



Siong Wee Lee, Mohd Raizamzamani Md Zain, Chai Lian Oh, Norrul Azmi Yahya, and Nadiah Saari

Abstract In the current study, compressive strength and flexural properties of green engineered cementitious composites (ECC) containing high volumes of fly ash have been investigated. A green ECC was developed by employing Portland cement, high volume of fly ash, recycled concrete fines (RCF), polypropylene (PP) fiber, water and superplasticizer (SP). The effect of sand to binder ratio (0.2 and 0.4) was studied in the different content of fly ash (70 and 80% as cement replacement). Thus, a total of four design mixes of green ECC were employed in this study. Compression test and three-point bending test were carried out for green ECC specimens after 28 days of curing. Test results show that the compressive strengths for green ECC containing higher volume of fly ash (80% as cement replacement) decreased compared to green ECC containing fly ash (70% as cement replacement). However, performances of green ECC in terms of flexural strength and ductility were improved when the amount of fly ash increased from 70 to 80%. On the other hand, increasing RCF to binder ratio (from 0.2 to 0.4) has brought negative impact to both compression and flexural properties of green ECC. Therefore, the use of RCF to binder ratio (R0.2) is considered optimum for the design of this series of green ECC. The choice of fly ash content whether 80% or 70% as cement replacement in developing green ECC depends on the targeted performance of green ECC corresponding to its application.

Keywords Engineered cementitious composite · Compressive strength · Flexural strength · Ductility · Multiple-cracking

S. W. Lee (✉) · N. Saari

School of Civil Engineering, College of Engineering, Universiti Teknologi MARA (UiTM), Johor Pasir Gudang Campus, 81750 Masai, Johor, Malaysia
e-mail: leesiongwee@uitm.edu.my

M. R. Md Zain · C. L. Oh · N. A. Yahya

School of Civil Engineering, College of Engineering, Universiti Teknologi MARA (UiTM), 40450 Shah Alam, Selangor, Malaysia

1 Introduction

Engineered cementitious composite (ECC) is characterized as a sub-group of high-performance fiber reinforced composites (HPFRC) which can demonstrate superior deformation capacity, multiple cracking behavior and damage tolerance. Unlike high strength concrete (HSC), ECC demonstrates moderate or slightly high compressive strength compared to normal concrete (NC) without featuring nature brittle failure as shown in HSC or NC. ECC is superior in terms of its tensile ductility, tensile strain capacity exceeded 4% associated with the tensile strength of 4.5 MPa can be obtained in early study by Li et al. [1]. One of the advantages of ECC is it only uses low-moderate volume fraction (1.5–2.0%) of short and randomly distributed fibres in the mixture design to achieve excellent tensile strain capacity and exhibit strain-hardening behaviour. Some fibre reinforced concretes (FRCs) made of high-volume fraction (5–20%) of fibres such as slurry infiltrated fibre concrete (SIFCON) or slurry-infiltrated mat concrete (SIMCON) have performed excellently in their mechanical properties but their application may be hindered by the special processing requirement due to their high fibre volume fractions and they are often restricted to precast members [2]. In addition, high volume fraction of fibres used in cementitious matrix can increase the weight of structures and lead to higher cost of construction. Therefore, ECC is currently emerging as a popular concrete material that offers flexible processing in which it can be used in both precast and cast- in-place applications with low-moderate volume fraction of fibres.

Applications on the structural use of ECC is triggered by the recommendations for design and construction of HPFRC published by Japan Society of Civil Engineers [3]. In US, full scale ECC link slab was practically used to join the precast slab panels. While in Japan, ECC coupling beams were employed in the construction of 60-storey Kitahama Building. Due to the tensile ductility and damage tolerance behavior, ECC was greatly explored by researchers specifically in the field of earthquake resistance structures [4–7]. ECC also exhibits multiple cracking behaviors which contribute to tensile ductility when overloaded. These micro cracks have tight width below 100 μm , which is very important feature in contributing to self-healing mechanism of ECC as can be seen in previous studies [8–10].

Material cost of ECC is more expensive than normal concrete due to the inclusion of fibers into cementitious matrix, therefore ECC are generally incorporated in certain critical regions in structures which require large inelastic deformation especially when subjected to earthquake. For instance, beam-column connections, squat walls, coupling beams, as well as in regions of flexural members subjected to large inelastic deformations combined with high shear, such as column and structural wall bases, and selected beam plastic hinge regions in frame structures [7]. Parra-Montesinos et al. [4] tested two large beam-column sub-assemblages with HPFRC under reverse cyclic loads and found out that HPFRC beam -column connections performed satisfactory despite no transverse reinforcement was provide in the beam plastic hinge region. Minor damage of the joint core was observed at the end of the test, indicating damage tolerance of HPFRC. In another study by Lee et al. [5], the

use of ECC significantly changed the behavior of the joint from brittle to ductile and ECC specimens exhibit superior damage tolerance, with limited shear distortion and multiple fine cracks in the joints even though no transverse reinforcement was provided in the joint. It is worthy to mention that in both tests [4, 5], ECC was incorporated in the critical region of beam-column sub-assembly. ECC is also well known in terms of having good bond with the embedded steel reinforcement. Previous research [5, 11] revealed that enhanced bond strength could be developed by ECC compared to normal concrete and thus can relax anchorage length requirement as stipulated in design codes. Similar finding can be seen in study by Parra-Montesinos et al. [4], no signs of bond deterioration in beam longitudinal bars passing through the connection were observed.

Typical ECC is made of cement, fly ash, silica sand, polyvinyl alcohol (PVA) fibers, water and superplasticizer. Most of the studies employed PVA fibers in developing ECC, very limited research performed the use of polypropylene (PP) fibers in ECC mixtures despite PP fibers are cheaper if compared to PVA fibers. Hence, this study aims to replace PVA fibers with PP fibers since PP fibers are more environmentally friendly and cost saving. In previous works [12–17], mechanical properties of PP-ECC were convinced through the compression and direct tensile tests. But the data set is rather limited due to only few ECC mixtures were tested. Even though Lee et al. [13, 14] have investigated the mechanical performances of PP-ECC through direct tensile as well as flexural tests, but the results are lack of consistency. Moreover, ground granulated blast-furnace slag (GGBS) was employed instead of fly ash in the ECC mixtures. Therefore, there is a need to investigate the compatibility of PP-fly ash in the matrix composition of ECC. Meanwhile, the effectiveness of PP fibres in developing ECC can be evaluated.

Due to the absence of coarse aggregates in ECC, the amount of cement used in the design mixture is greater than that in normal concrete. In a standard design mix of ECC (M45), even though 55% of cement is replaced by fly ash but the cement content is still considered greater than that in normal concrete grade C30/37. When the environmental concerns are getting important nowadays, research on development of green ECC are overwhelming. Green ECC developed by Zhu et al. [15] and Meng et al. [16] demonstrated excellent mechanical behaviours under compression, tension, and bending tests. Green ECC can be achieved when the amount of cement used in ECC is largely reduced i.e. replace cement with high volume of fly ash (equal or more than 70%). Other than the amount of cement, green ECC also can be developed by the use of recycle concrete fines (RCF) instead of silica sand. Li and Yang [17] pointed out that RCF is viable to be used in the production of RCF-ECC due to the decent compressive strength and tensile strain capacity from their test result.

Other than compressive strength, tensile strain ductility is commonly accepted as important criteria to justify properties of ECC. Direct tensile test is the best method to confirm the tensile properties of ECC, however its test set-up required complicated instruments and tools. Thus, four-point or three-point bending test can be treated as another alternative to replace direct tensile test to demonstrate flexural ductility as well as multiple crackings of ECC [18–22]. This study performs experimental investigations on both compression and flexural properties of green ECC made with

PP-fly ash along with recycled concrete fines (RCF). The objectives were to study the effect of fly ash content and the RCF to binder ratio in the compressive strength and flexural properties of green ECC made with PP-fly ash and RCF.

2 Experimental Program

2.1 Materials

A new version of green ECC is developed using cement, fly ash, PP fibres, recycled concrete fines (RCF), water and superplasticizer (SP). In order to make the ECC more sustainable, the amount of cement used need to be comparable or lesser that the amount used in normal concrete mixture. Thus cement replacement at 70 and 80% were employed in this study. In addition, the greenness of ECC mixture was further enhanced by the use of RCF in this study. Table 1 shows the design mix proportion and the ingredients used in the study. Overall a total of four mixtures of green ECC and one control (normal concrete) have been designed. As can be seen from Table 1, the amount of cement used for green ECC mixtures was lesser than that in control except green ECC F70R0.2. The cement content was 415 kg/m³ in control mix whereas it was 429 kg/m³ in green ECC F70R0.2. Designation F70 represented 70% of cement replaced by fly ash while R0.2 indicated the ratio of RCF to binder was 0.2. Binder is defined by the combination of cement and fly ash. The water to binder ratio was fixed at 0.27 and the amount of SP was controlled at ± 10 kg/m³ for each of the green ECC mixture. For control mix, water to cement ratio was 0.47. The content of PP fibers was constant at 2.5% in volume fraction, i.e. 23 kg/m³. PP fibers has a density of 910 kg/m³ with diameter of 19.5 μ m and length of 6 mm.

Table 1 Design mix proportion of normal concrete and green ECC

Mixture	Unit weight (kg/m ³)							Remark
	Cement	Fly ash	Binder	Sand	Water	PP fibers	Aggregate	
Control	415	–	–	605	195	–	1135	Normal concrete
F70R0.2	429	1001	1430	286*	386	23	–	Green ECC
F70R0.4	385	900	1285	518*	350	23	–	Green ECC
F80R0.2	286	1143	1429	286*	358	23	–	Green ECC
F80R0.4	257	1028	1285	518*	350	23	–	Green ECC

*RCF was used to replace sand

2.2 Method

For the purpose of compression test (7 and 28 days), three repetitive cubic specimens with the size of 50 mm × 50 mm × 50 mm were prepared for each mixture of green ECC while size 100 mm × 100 mm × 100 mm cubic specimens were used for normal concrete. Therefore, a total thirty specimens were prepared for compression test after 7 and 28 days of curing.

On the other hand, flexural test of green ECC was carried out for the plate specimens with the size of 300 mm × 75 mm × 12 mm after 28 days of curing. For each green ECC mixture, three repetitive specimens were cast to ensure consistency of the test result. Mixing of green ECC was carried out by using a standard mixer in the concrete laboratory. Mixing process started with the main raw ingredients such as cement, fly ash and RCF placed into the mixer, and the first mixing process took about 2 min to ensure all dry ingredients were well mixed. Water which have already incorporated SP were then carefully added to the mix, mortar was formed during this stage. Mixing process was continued until achieve uniformity and fluidity, normally it took approximately 4–5 min. When the mortar appeared to be in uniform state, PP fibers can be inserted slowly and gently until all fibers were evenly distributed to the cementitious matrix. Precaution needs to be taken on the possibility of fibers balling that can lead to an inaccurate result.

Compression test was carried out by using 300 kN Universal Testing Machine (UTM) while flexural test (three-point bending test) was carried out by employing 50 kN UTM as shown in Fig. 1. A displacement control method was adopted at

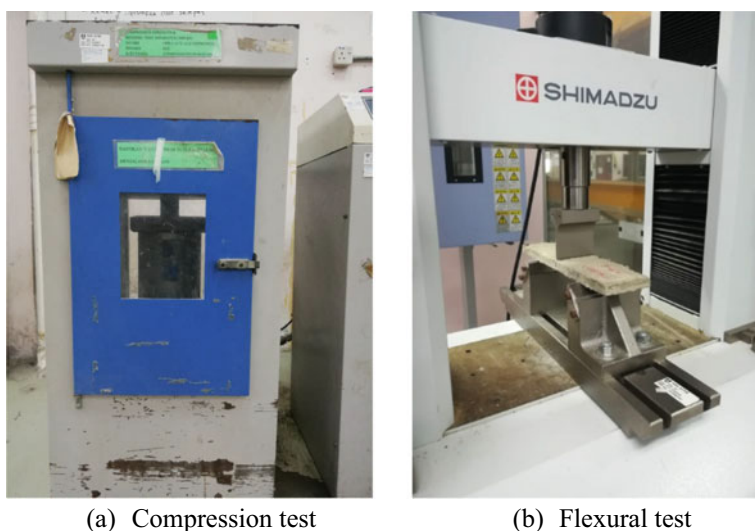


Fig. 1 Test set-up

loading rate of 0.4 mm/minute during three-point bending test and this test was terminated when the load carrying capacity started to decrease.

3 Results and Discussion

3.1 Compressive Strength

Table 2 shows the compressive strength recorded in every tested cube specimen after 7 days and 28 days of curing, respectively. Normal concrete that served as control yields an average compressive strength of 25.33 MPa at 28 days. Generally, all tested specimens gained more compressive strength over the period of curing i.e. from 7 to 28 days as expected. Obviously, the highest compressive strength is achieved by green ECC F70R0.2 with average of 58.06 MPa at 28 days. It is followed by the mixture that contained the same amount of fly ash but more RCF sand content (F70R0.4), in which 10% of reduction in compressive strength can be quantified. When the amount of fly ash increased to 80% as cement replacement, the average 28 days compressive strengths were dropped by 14 and 25% compared to their counterparts (F70R0.2 and F70R0.4). It is observed that similar pattern occurs in ECC F80, increasing RCF content (from R0.2 to R0.4) reduced the compressive strength to 39.13 MPa at 28 days. The enhancement factor of compressive strength in green ECC can be found in Fig. 2. It is worthy to mention that the enhancement factor is calculated based on the compressive strength achieved by control specimens at 7 and 28 days. It can be seen that group ECC F70 performed slightly better than group ECC F80, with the enhancement factor of compressive strength greater than 2.00 in both 7 and 28 days. Group ECC F80 yields enhancement factor of 1.41 to 1.95 for 7 and 28 days. Result of compressive strength demonstrates that increasing fly ash and RCF content in ECC mixtures has negative impact in compressive strength. It could be possibly due to the reduction amount cement used when fly ash F70 changed to F80 and R0.2 changed to R0.4. Another possible reason could be attributed to increased amount of interface transition zones (ITZ) with more RCF content, which makes the composites less resistant under compressive loads [17]. Li and Yang [17] also pointed out that

Table 2 Compressive strength of green ECC at 7 and 28 days

Mixture	Compressive strength at 7 days (MPa)				Compressive strength at 28 days (MPa)			
	sample 1	sample 2	sample 3	Average	Sample 1	Sample 2	Sample 3	Average
Control	22.62	23.88	23.50	23.33	24.30	27.26	25.03	25.53
F70R0.2	44.13	48.30	49.49	47.31	60.68	58.86	54.64	58.06
F70R0.4	46.22	49.37	48.08	47.89	50.62	54.45	51.11	52.06
F80R0.2	42.52	34.57	35.11	37.40	53.04	47.88	48.65	49.86
F80R0.4	34.23	32.97	31.28	32.83	39.31	39.44	38.65	39.13

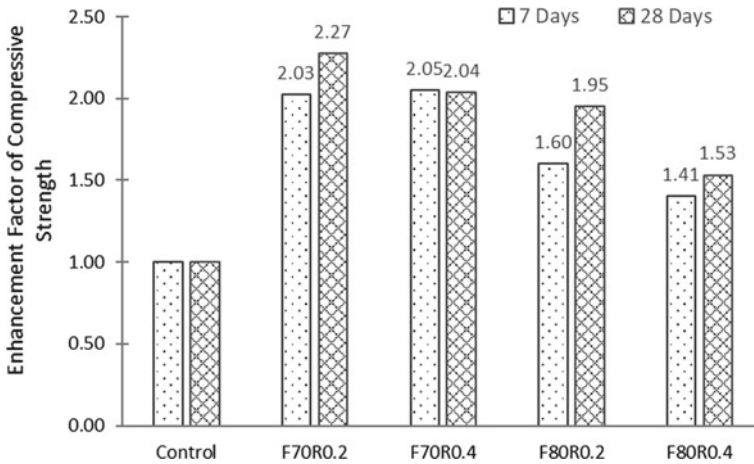


Fig. 2 Enhancement factor of compressive strength in green ECC

the porous adhered old mortar on the RCF surface can induce higher porosity, which also contributes to lower compressive strength of the composite.

3.2 Behaviors of Green ECC Under Bending Test

Three-point bending tests were conducted on green ECC plate specimens after 28 days of curing. Typical flexural behavior of green ECC from each mixture can be explained by Fig. 3. As expected, control (normal concrete) demonstrates a brittle failure under bending test. The specimen experienced a sudden failure upon obtained a flexural strength of 4.39 MPa while the displacement was merely at 0.21 mm. There is no strain-hardening demonstrated in the curve shown by control specimen in Fig. 3. Overall, green ECC specimens exhibited more ductile flexural behavior compared to normal concrete. Green ECC specimens able to undergo large displacement after obtaining peak strength and able to maintain the strength when subjected to the increment of displacement. The modulus of toughness is defined by the area under the flexural stress-displacement curves. Due to the tensile ductility of ECC, the modulus of toughness of all green ECC specimens under bending load is significantly improved as shown in Fig. 3. When the first cracking strength was achieved by green ECC specimens, flexural stress dropped without increment of displacement due to the opening crack occurred in green ECC specimens. However, flexural stresses rose again until another crack opened under the increasing point load. This pattern kept repeating until a maximum load (flexural strength) is reached. This phenomenon defines the flexural ductility and multiple cracking behavior of ECC specimens. Test results indicate the flexural ductility of green ECC specimens and improved displacement capacity if compared to normal concrete. Apparently, increasing fly ash content

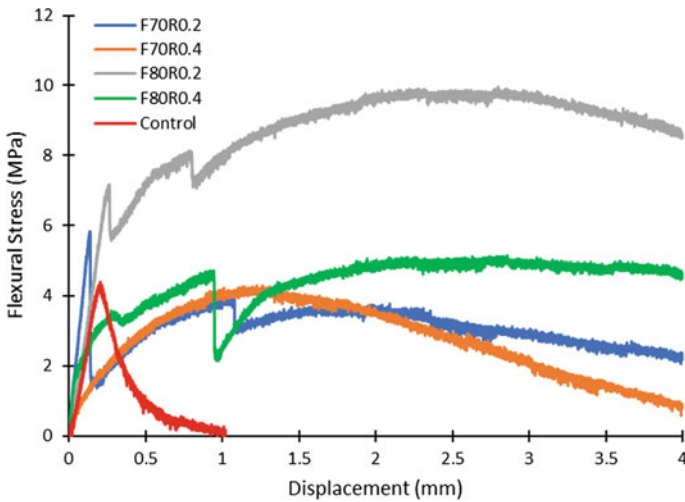


Fig. 3 Flexural stress-displacement of ECC

to 80% as cement replacement yields better performance in terms of bending. This observation agrees with previous study [18], increasing fly ash content in the cementitious matrix can improve the interface of frictional bond and lead to higher deflection capacity.

As can be seen from Fig. 3, ECC F80R0.2 performed excellently good with the ultimate flexural strength of 9.86 MPa and the corresponding displacement is 2.87 mm. However, when RCF to binder ratio adjusted to 0.4 (F80R0.4), ultimate flexural strength decreased around 50% while the corresponding displacement is nearly same with F80R0.2. ECC F70 series exhibited lower flexural strength compared to F80 series. In this series, even though both mixtures obtained flexural strength around ± 4 MPa with the corresponding displacements of 1.11–1.17 mm. But the post-peak behaviors are significantly different in which F70R0.4 experienced softening of the flexural stress-displacement after reaching its peak load while F70R0.2 was able to remain its flexural stress up to a displacement of around 2.3 mm. Therefore, flexural test result indicates that increasing RCF content has brought detrimental effect on flexural ductility of ECC regardless the amount of fly ash. This finding is in line with previous investigation [17], both the flexural strength and strain capacity decreased with increasing RCF content.

In summary, green ECC with 80% of fly ash as cement replacement (F80) with the RCF to binder (R0.2) is the best mix among all to show flexural ductility of ECC under bending test.

3.3 Failure Mode of Green ECC Plates

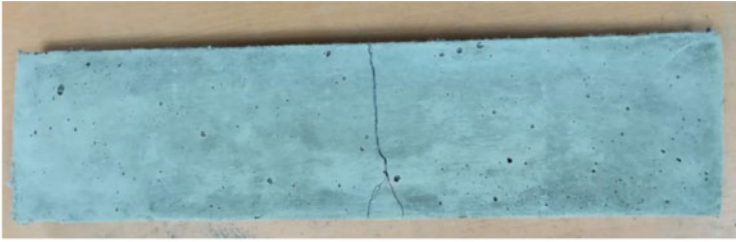
Under three-point bending tests, control specimens failed in a single wide crack due to the nature brittleness of normal concrete. On the other hand, all green ECC specimens failed in the mode of flexural cracks at the middle region of plate specimens as shown in Fig. 4. As described in Sect. 3.2, the more ductile of ECC, the more flexural cracks will be appeared on ECC plate specimens. The crack width also plays important part in assessing ductility of ECC. Among the four green ECC mixture, ECC F80R0.2 yields more fine cracks compared to other mixtures as shown in Fig. 4c because its flexural ductility behavior was greater than others as demonstrated in Fig. 3.

4 Conclusion

A new series of green ECC with high volume of fly ash combined with PP fibers and RCF is developed. The effects of fly ash content and RCF to binder ratio in compressive strength and flexural properties were investigated through compression and three-point bending tests. Based on the test results, the following conclusions can be drawn.

1. Generally, all green ECC mixtures yield enhancement factor of 1.4 to 2.3 in compressive strength and greater flexural behaviors (strength and ductility) compared to normal concrete.
2. Increasing fly ash content as cement replacement material in the mixtures reduce compressive strength of green ECC but enhance the flexural strength and ductility of green ECC.
3. Increasing RCF to binder ratio has brought detrimental effect on both compressive strength and flexural properties (strength and ductility) of green ECC.

Therefore, the use of RCF to binder ratio (R0.2) is considered optimum for the design of green ECC. The choice of fly ash F80 or F70 in developing green ECC depends on the targeted performance of green ECC corresponding to its application. This study suggests that more experimental tests are needed to further confirm the material properties of this version of green ECC. In future, compression test and bending test after 90 days of curing can be added in the study to examine the strength development of green ECC.



(a) F70R0.2



(b) F70R0.4



(c) F80R0.2



(d) F80R0.4

Fig. 4 Cracking patterns of ECC plates

Acknowledgements The authors gratefully acknowledge the financial support by Universiti Teknologi MARA under grant Research Entity Initiative (REI) 600-IRMI/REI 5/3 (012/2018).

References

1. Li VC, Wang S, Wu C (2001) Tensile strain-hardening behavior of polyvinyl alcohol engineered cementitious composite (PVA-ECC). *ACI Mater J-Am Concrete Inst* 98(6):483–492
2. Li VC (1998) Engineered cementitious composites (ECC)-tailored composites through micromechanical modeling. *Fiber Reinf Concr: Present Future* 64–97
3. Rokugo K (ed) (2008) Recommendations for design and construction of high performance fiber reinforced cement composites with multiple fine cracks (HPFRCC). Japan Society of Civil Engineers Concrete Committee, Japan
4. Parra-Montesinos GJ, Peterfreund SW, Shih-Ho C (2005) Highly damage-tolerant beam-column joints through use of high-performance fiber-reinforced cement composites. *ACI Struct J* 102(3):487
5. Lee SW, Tan KH, Yang EH (2018) Seismic behaviour of interior reinforced-concrete beam-column sub-assemblages with engineered cementitious composites. *Mag Concr Res* 70(24):1280–1296
6. Said SH, Razak HA, Othman I (2015) Flexural behavior of engineered cementitious composite (ECC) slabs with polyvinyl alcohol fibers. *Constr Build Mater* 75:176–188
7. Parra-Montesinos GJ (2015) High-performance fiber-reinforced cement composites: an alternative for seismic design of structures. *ACI Struct J* 102(5):668
8. Wu M, Johannesson B, Geiker M (2018) A review: self-healing in cementitious materials and engineered cementitious composite as a self-healing material. *Const Build Mater* 28(1):571–83
9. Zhang Z, Qian S, Ma H (2014) Investigating mechanical properties and self-healing behavior of micro-cracked ECC with different volume of fly ash. *Constr Build Mater* 52:17–23
10. Zhang Z, Zhang Q, Li VC (2019) Multiple-scale investigations on self-healing induced mechanical property recovery of ECC. *Cement Concr Compos* 103:293–302
11. Lee SW, Kang SB, Tan KH, Yang EH (2016) Experimental and analytical investigation on bond-slip behaviour of deformed bars embedded in engineered cementitious composites. *Constr Build Mater* 127:494–503
12. Zhang R, Matsumoto K, Hirata T, Ishizeki Y, Niwa J (2015) Application of PP-ECC in beam-column joint connections of rigid-framed railway bridges to reduce transverse reinforcements. *Eng Struct* 86:146–156
13. Lee SW, Oh CL, Zain MR, Yahya NA, Ali RA (2019) Mechanical performances of green engineered cementitious composites incorporating various types of sand. *Key Eng Mater* 821:512–517
14. Wee LS, Lian OC, Zain MR (2019) Mechanical properties of engineered cementitious composites using local ingredients. *J Mech Eng* 16(2):145–157
15. Zhu Y, Yang Y, Yao Y (2012) Use of slag to improve mechanical properties of engineered cementitious composites (ECCs) with high volumes of fly ash. *Constr Build Mater* 36:1076–1081
16. Meng D, Huang T, Zhang YX, Lee CK (2017) Mechanical behaviour of a polyvinyl alcohol fibre reinforced engineered cementitious composite (PVA-ECC) using local ingredients. *Constr Build Mater* 141:259–270
17. Li J, Yang E-H (2017) Macroscopic and microstructural properties of engineered cementitious composites incorporating recycled concrete fines. *Cement Concrete Compos* 78:33–42 (2017).
18. Sherir MA, Hossain K, Lachemi M (2015) Structural performance of polymer fiber reinforced engineered cementitious composites subjected to static and fatigue flexural loading. *Polymers* 7(7):1299–1330

19. Meng D, Lee CK, Zhang YX (2017) Flexural and shear behaviours of plain and reinforced polyvinyl alcohol-engineered cementitious composite beams. *Eng Struct* 151:261–272
20. Hind MK, Özakça M, Ekmekyapar T (2016) Numerical and parametric studies on flexural behavior of ECC beams by considering the effect of fly-ash and micro-PVA fiber. *J Adv Res Appl Sci Eng Tech* 1(3):48–66
21. Pakravan HR, Jamshidi M, Latifi M (2018) The effect of hydrophilic (polyvinyl alcohol) fiber content on the flexural behavior of engineered cementitious composites (ECC). *J Text Inst* 109(1):79–84
22. Muktadir MG, Alam MF, Rahman A, Haque MR (2020) Comparison of compressive strength and flexural capacity between engineered cementitious composites (Bendable Concrete) and conventional concrete used in Bangladesh. *J Mater Eng Struct* 7(1):73–82

An Experimental Study on the Influence of Ground Granulated Blast-Furnace Slag (GGBS) on Bending Strength of Green Engineered Cementitious Composites



Mohd Raizamzamani Md Zain, Siong Wee Lee, Chai Lian Oh, Ching Hua Goh, and Norrul Azmi Yahya

Abstract This paper provides an experimental study into the efficacy of Ground Granulated Blast-furnace Slag (GGBS) on green engineered cementitious composites (ECC). This study has used ECC made out of Portland cement, recycled concrete fines (RCF), GGBS, water, superplasticizer (SP) and polypropylene (PP) fibers. Thirty-six (36) mixtures of ECC with a water-cement ratio of 0.27 were assessed. Twenty-four (24) ECC mixtures comprising GGBS by differing sand to binder ratio (0.2 and 0.4) of various cement-to-GGBS combinations tested under compressive loading and twelve (12) other mixtures tested under bending after 7 and 28 days of curing period. The mechanical characteristics were evaluated on ECC cubes (50 mm × 50 mm × 50 mm) and ECC plates (300 mm × 75 mm × 12 mm) employing compression and flexural test machines, respectively. Experimental findings showed that the compressive strengths of the ECC incorporating GGBS tend to reduce with an expanding sand to binder ratio. ECC's flexural performance, with 70 per cent and 80 per cent of GGBS used as a partial replacement for cement, dropped considerably when sand content was increased. All green ECC plates exhibited flexural characteristics with a greater ductility compared to conventional concrete. This is due to the tendency of the plates to deform with enormous capacity after undergoing the first crack.

Keywords Engineered cementitious composites · Recycled concrete fines · Ground granulated blast-furnace slag · Compressive strength · Bending strength

M. R. Md Zain (✉) · C. L. Oh · C. H. Goh · N. A. Yahya
School of Civil Engineering, College of Engineering, Universiti Teknologi MARA (UiTM),
40450 Shah Alam, Selangor, Malaysia
e-mail: raizam@uitm.edu.my

S. W. Lee
School of Civil Engineering, College of Engineering, Universiti Teknologi MARA (UiTM), Johor
Pasir Gudang Campus, 81750 Masai, Johor, Malaysia

1 Introduction

The advent of Engineered Cementitious Composites (ECC) with ultra-high ductility has become prominent over the last few decades to overcome the brittleness of concrete. ECC is superior owing to its unique characteristics in tensile ductility and its multiple cracking behavior contributing to a wide variety of applications. The structural use of ECC is taking place by the endorsements for design and construction of high-performance fiber reinforced composites (HPFRC) issued by Japan Society of Civil Engineers [1]. Under tension, ECC undergoes strain –hardening, together with sequential cracks. Its maximum tensile strain can be as high as 5% while its maximum width of cracks is below 100 μm [2]. This favorable behavior provides strong consideration for it to be used in structures in earthquake-prone areas [3].

In comparison with normal concrete, ECC has a smaller elastic modulus when compressed, owing to its lower coarse aggregate content [4]. On the other hand, it achieves its compressive strength at a larger strain. Again, the performance of ECC-based structures is improved seismically as a result of its larger compressive strain. In addition, ECC is desirable in critically confined beam-column connections of earthquake-resistant structures because ECC is well-confined as revealed in post-peak response. Hence, ECC makes an excellent material in earthquake-zone structures from its both compressive and tensile behaviors.

Many attempts on experimental investigation were made to evaluate the flexural performance of ECC [5–7]. The performance behavior of ECC with high capacity of palm oil fuel ash (POFA) were investigated under four-point bending test [5]. The researchers demonstrate that larger content of POFA was found to concurrently enhance the flexural-deflection capacity. Li et al. [8] conducted a series of testing on ECC beams containing glass fiber-reinforced polymer (GFRP) to estimate its flexural characteristics. Results revealed that there is an increase in bending strength, deformation and ductility of ECC beams. Thus, the bending performance of cement-based materials is reliant on their tensile features [9]. In general, the bending response of ECC reflects its tensile ductility [9].

Typical ECC is composed of all the ingredients of a normal concrete (cement, sand, water and superplasticizer) minus coarse aggregates and is reinforced with fibers. Nevertheless, cement manufacturing needs a huge amount of energy and tends to lead to rising temperatures caused by carbon dioxide production [10]. Cement production seems to have an effect on the environment at all levels of the process. Emissions of air pollution in the environment, excessive noise during the activity of the machines and equipment and in the first stage in the manufacture of cement, which may be noticeable from vast distances through the blasting of the face quarries and the limestone quarries and may permanently alter the local climate.

The key environmental health concerns caused by the manufacture of cement were its emission of gas to the atmosphere and the quantity of energy utilized. Processing of cement requires a significant number of non-renewable materials, like raw materials and fossil fuels. As a result of cement manufacturing, it's been reported that the greenhouse gas, which is carbon dioxide generated by human operations is at around

5–6% [11]. Gasses formed by combustion in the furnace encompass oxygen, nitrogen oxides (NO_3), water, carbon dioxide and tiny amounts of dust, Sulphur dioxide, fluorides, carbon monoxide, chlorides, and low amounts of organic chemicals that are not environmentally friendly lead to environmental concerns.

Modern tech has been built in every sector over time to make life more comfortable, healthier and smoother. Not to be overlooked, the construction industry is also striving to create better buildings in all respects, including longevity, efficiency, convenience, service life and commercial benefit. The main materials used throughout construction were mostly non-renewable materials, such as cement, steel and aggregates, and thus advanced innovation was needed to replace such materials not completely, but at least in some part, in order to perpetuate or raise the efficiency of construction. This contributed to the need for green material as a substitute for cement [12].

Concrete with the inclusion of green materials have higher strength for long-term period of time. In addition, by mixing the source material Portland cement with green materials of almost the same composition and function, it has worked to boost the mechanical characteristics of concrete throughout all areas. Owing to the abundance and cost-effective of ground granulated blast-furnace slag (GGBS) in Malaysia, this green material was used as a substitute to replace the standard ingredients of ECC. GGBS can lead to increasing the performance and resilience of concrete at the same time. Its production is basically free from carbon dioxide (CO_2). However, its main benefits were towards the sustainable construction that have a small effect on the environment and the high-quality of the concrete is still remained. Substitution of cement via 35–40% of GGBS in concrete has enhanced durability characteristics such as improved resilience to sulphate attacks, alkali silica reactions and decreased chloride ions resulting in increased resistance to corrosion [13]. Life span of concrete can be improved by a significant value of durability. Causes and effects from the degradation of concrete may be intrinsic and extrinsic hostile environments. This demonstrates that GGBS is a good material to boost service life even in the most sensitive atmosphere and to improve fire resistance.

In addition, when the amount or quantity of cement used in ECC is largely reduced such by equal or more than 70% [14, 15], then, ECC with this compositions can be called as green ECC. Meng et al. [14] and Zhu et al. [15] had conducted experimental investigations on green ECC and the results from their studies had demonstrated excellent mechanical behaviors under tension, compression and bending tests.

Thus, in consideration of these and taking into account the benefit of the use of industrial waste products such as GGBS, a new version of the ECC was worth investigating. In which raw ingredients are much more sustainable and affordable but also ability to endure earthquake loading without some kind of brittle failure. In addition, the bending feature plays a vital role in ECC's overall performance as it can represent the tensile ductility without undertaking a direct tensile test. The set-up and implementation process for bending or flexural testing are much simpler than direct tensile testing. Flexural testing (under three-point bending) was therefore performed to evaluate the mechanical properties of green ECC plates and to assess the generation of their failure mechanism.

2 Experimental Program

The aim of the experimental program was to assess the compressive strength, bending strength and failure mode of the green ECC specimens. Information on the details of the test specimen, the mixing ingredients and the proportions, the mixing procedure and the test set-up were expanded on the following sub-topics.

2.1 Details of Test Specimen

This experimental investigation deals with the performance of green ECC consisting of GGBS as partial substitute to cement. It was performed at the Concrete Laboratory, Civil Engineering Faculty, Universiti Teknologi MARA (UiTM), Shah Alam, Selangor. Thirty-six (36) mixtures of ECC with a water-cement ratio of 0.27 were utilized. Twenty-four (24) ECC mixtures and twelve (12) other mixtures incorporating GGBS by differing ratio of sand to binder (0.2 and 0.4) with various cement-GGBS combinations were experimentally evaluated subjected to compressive loading and bending after 7 and 28 days of curing age, respectively.

2.2 Mix Constituents and Proportions

In this study, ECC made of Portland cement, water, GGBS, superplasticizer (SP), polypropylene (PP) fibers and recycled concrete fines (RCF) were utilized. The views of all dry materials used are displayed in Fig. 1.

In order to investigate the bending strength and the possible mode of failure, two (2) sequence of green ECC mixture were considered. The first sequence included Portland cement, 70% GGBS and RCF with different ratio of sand to binder (0.2 and 0.4). While, the second sequence included Portland cement, 80% GGBS and RCF with different ratio of sand to binder (0.2 and 0.4).

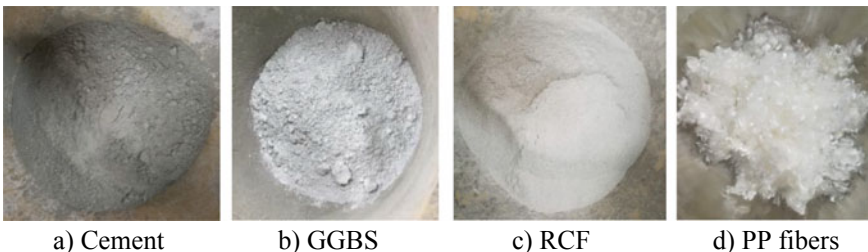


Fig. 1 Dry materials

Table 1 Chemical compositions of cement

Chemical composition	By weight (%)
CaO	77.53
SiO ₂	12.80
Al ₂ O ₃	2.13
SO ₃	2.69
MgO	0.96
K ₂ O	0.53
Fe ₂ O ₃	3.12
TiO ₂	0.18
MnO	0.06
P ₂ O ₅	< LOD (Low on density)

Binder denotes as the combination of cement and GGBS. The chemical compositions of Ordinary Portland Cement (OPC) is displayed in Table 1. In addition, the chemical composition and physical features of GGBS were presented in Table 2. Furthermore, for fine aggregate, recycled concrete fines (RCF) was used. The greenness of ECC mixture was further enhanced with the use of RCF. PP fibers with

Table 2 GGBS Chemical compositions and physical properties

By weight (%)	
<i>Chemical compositions</i>	
CaO	43.68
SiO ₂	35.67
Al ₂ O ₃	10.15
SO ₃	3.80
MgO	4.03
K ₂ O	0.29
Fe ₂ O ₃	1.61
TiO ₂	0.58
MnO	0.19
P ₂ O ₅	<LOD (Low on density)
<i>Physical properties</i>	
*LOI (%)	1.6
*ρ (g/cm ³)	2.85
SSA (m ² /kg)	430
SAI at 28 days (%)	89

*LOI denotes the loss of ignition
 ρ denotes the density
 SSA represents the specific surface area
 SAI represents the strength activity index

diameter of 19.5 μm and length of 6 mm were employed to acquire the distinctive strain hardening performance of green ECC. The amount of PP fibers was constant at 2.5% in volume fraction. The dosage of SP (superplasticizer) was regulated at around 10 kg/m^3 and been applied to boost workability. Table 3 demonstrates the green ECC's mix design proportions employed in this study. As displayed in Table 3, specimen designation G70 denotes as 70% GGBS as substitute to cement and R0.2 represent the ratio of RCF to binder (0.2). The normal concrete mix proportion per m^3 without any GGBS is also presented in Table 4 and used as a benchmark for all the GGBS specimens.

2.3 *Mixing Procedures and Test Methods*

Each green ECC mixture was prepared and tested prior to failure subjected to compression test with three repetitive cubic specimens 50 mm \times 50 mm \times 50 mm (at 7 days and 28 days). Meanwhile, bending test was performed for the ECC plate specimens (300 mm \times 75 mm \times 12 mm in size) after 28 days of curing. In total 24 cubic and 12 plate specimens were casted for each mix design. A standard mixer was used to prepare all specimens. In order to produce good results, the mixing process must follow procedures as displayed in Table 5.

Then, the specimens were cast into into 50 mm \times 50 mm \times 50 mm \times 50 mm ECC cubes and 300 mm \times 75 mm \times 12 mm ECC plate and tested under compressive loading and bending. Prepared specimens were dismantled and cured at room temperature after 24 h in the mould. Experimental testing was carried out when the specimens were at 7 and 28 days testing ages for compression test and at 28 days testing age for bending test.

Under compression, the test was performed using 300 kN Universal Testing Machine (UTM) as shown in Fig. 2. There are several procedures that need to be followed before the specimens can be tested such by cleaning the bearing plate of the compression testing machines. The cube was then placed on the lower bearing plate and the top part of the specimen was altered to be just about in contact with the upper bearing plate. The position of the cube was located in the central part of the spherical head thrust. The cubic specimen was loaded continually prior to failure. The compressive strength and any crack deformities on the cube specimen was observed and recorded.

Under flexural, the three-point bending test was conducted using 50 kN UTM machine as shown in Fig. 3. A displacement control system was applied at the loading rate of 0.4 mm/min. The specimen was mounted on the machine carefully in order not to cause early cracks.

Table 3 Green ECC Mix design proportions

Specimen designation	Unit weight (kg/m ³)										Remark on mixture
	Cement	GGBS	Binder	RCF	Water	PP fibers	SP	Coarse Agg			
G70R0.2	429	1001	1430	286	386	23	10	–			Green ECC
G70R0.4	385	900	1285	518	350	23	10	–			Green ECC
G80R0.2	286	1143	1429	286	358	23	10	–			Green ECC
G80R0.4	257	1028	1285	518	350	23	10	–			Green ECC

Table 4 Normal concrete mix proportion per m³

Cement (kg/m ³)	Water (kg/m ³)	Coarse aggregate (kg/m ³)	Sand (kg/m ³)
415	195	1135	605

Table 5 Mixing process

Mixing process	
1	Add all dry materials such as cement, RCF and GGBS into a mixer
2	Mix all materials for 2–3 min
3	Subsequently add water while mixing and add SP based on the state of workability of the blend
4	Continue the mixing process for 4–5 min until reach uniformity and fluidity
5	Add PP fibers and mixed until consistently dispersed
6	Continue the mixing until no apparent of clumping off fibers and the mixture was workable



Fig. 2 Experimental set-up for compressive test

3 Results and Discussion

Thirty-six mixtures of ECC containing GGBS by varying ratio of sand to binder with differing cement-GGBS combination were prepared and tested prior to failure under compressive loading and bending. The following describes outcomes of compressive and bending load tests of the green ECC specimens.

Fig. 3 Test set-up for bending test



3.1 Compressive Strength

Experimental findings of compressive strength of the green ECC cubic specimens at both 7 and 28 days were tabulated and presented in Table 6 and Fig. 4. As displayed in Fig. 4, the compressive strength of each mix enhanced over time compared to normal concrete.

The highest compressive strength of green ECC was attained by cubic specimen denotes as G70R0.2. The average compressive strength for this specimen after 28 days of curing age was recorded as 51.47 MPa. Then, followed by the mixture denotes as G70R0.4 (same quantity of GGBS with more than double amount of RCF), where it averages compressive strength was recorded as 50.478 MPa (2% drop compared to G70R0.2). Meanwhile, when the quantity of GGBS was increased to 80% as substitute to cement, the average compressive strength of the specimens denotes as G80R0.2 and G80R0.4 were decreased to 8.4 and 22.2% compared to the highest compressive strength of ECC specimen. Similar trends were observed for both series (70 and 80% cement replacement), where at 28 days, by increasing the content of RCF, compressive strength were recorded as slightly lower. It is comparable with the research conducted by Wee et al. [16] and [17], which reveal that by providing a higher quantity of sand, the amount of binder in the ECC matrix was reduced and thereby the compressive strength was lessened. The enhance factor of green ECC cubic specimens are displayed in Table 7.

Table 7 indicates the enhance factor in compressive strength of green ECC cubic specimens at different ages (7 and 28 days). Substantial patterns were found for both series (70% and 80% of cement substitute) where at 7 and 28 days, an increase in RCF content was observed as a slight reduction in the enhancement factor in compressive strength.

Table 6 The compressive strength (MPa) of green ECC cubic specimens under compression test

Mixture ID	Compressive strength (MPa)	Ave. compressive strength (MPa)	Compressive strength, (MPa)	Ave. compressive strength (MPa)
	7 days		28 days	
Normal	22.62	23.36	24.30	25.53
	23.88		27.26	
	23.50		25.03	
G70R0.2	38.53	40.86	52.10	51.47
	41.95		53.40	
	42.11		48.90	
G70R0.4	38.19	37.25	50.21	50.48
	37.59		51.34	
	35.96		49.90	
G80R0.2	40.75	42.28	48.57	47.13
	43.96		44.97	
	42.14		47.86	
G80R0.4	27.67	29.03	32.73	40.02
	31.84		45.15	
	27.57		42.17	

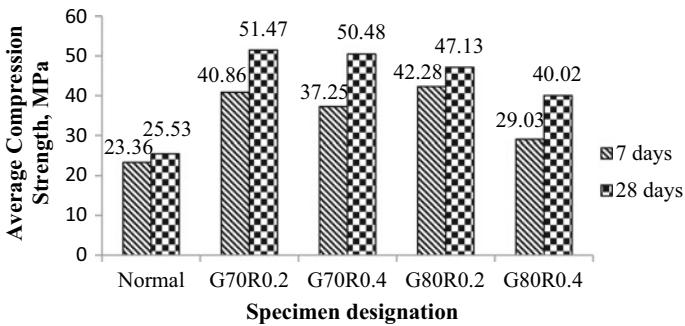


Fig. 4 Average compressive strength of green ECC cubic specimens at 7 and 28 days

Table 7 Enhance factor of compressive strength of green ECC cubic specimens

Mixture designation	ECC/normal	
	7 days	28 days
G70R0.2	1.75	2.02
G70R0.4	1.59	1.98
G80R0.2	1.81	1.85
G80R0.4	1.24	1.57

3.2 Bending Strength

The performance behavior such as flexural strength (maximum stress) of green ECC plate specimens and its failure generation were evaluated based on the experimental investigations performed under three-point bending test. Figure 5 illustrates the bending/flexural strength (MPa) versus displacement (mm) values for green ECC specimens containing GGBS as partial substitute to cement (70 and 80 percent) with two different sand to binder ratios (0.2 and 0.4). The optimum bending stress is characterized as the flexural strength as displayed by the curves in the flexural stress-displacement graph. Flexural stress, σ was calculated on the basis of the standard formula as follows:

$$\sigma = \frac{3PL}{2bd^2} \tag{1}$$

In which, P denotes the pressure applied to the specimen, L embodies the length between the two supports, b represents the specimen width and h as the height of specimen. The results of maximum flexural strength and first cracking strength were presented in Table 8 and Fig. 5. As depicted in Fig. 5, green ECC specimens

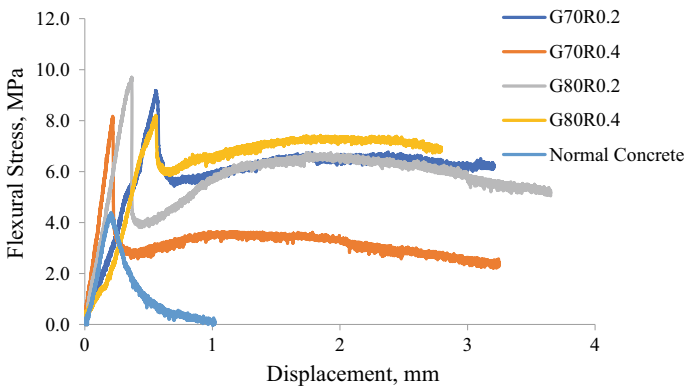


Fig. 5 Flexural stress-displacement curve of ECC plate specimens

Table 8 The ultimate flexural stress of green ECC plate specimens

Mixture ID	Force, P (N)	Ultimate flexural stress, σ (MPa)	Displacement, δ (mm)	Ratio of ECC/Normal
Normal	210.94	4.3945	0.205	
G70R0.2	440.63	9.1797	0.559	2.0889
G70R0.4	392.19	8.1706	0.218	1.8593
G80R0.2	465.63	9.7005	0.306	2.2074
G80R0.4	393.75	8.2031	0.556	1.8667

denotes as G80R0.2 gave the highest maximum value of flexural strength (9.70 MPa) with a displacement value of 0.306 mm. The maximum flexural strength for green ECC denotes as G80R0.4 reduced around 15% compared to G80R0.2, when RCF to binder ratio been altered to 0.4. The lowest value of flexural strength was recorded as 8.1706 MPa with displacement value of 0.218 mm for green ECC specimens denotes as G70R0.4. Meanwhile, for green specimen denotes as G70R0.2, the maximum flexural strength increased around 11% compared to G70R0.4.

Results revealed that the trend for all green ECC specimens exhibited the similar behaviors and the peak of the curve indicate the maximum bending stress where the specimen can withstand before start to drop without increment of displacement due to the occurrence of opening crack and then, continues to rise (slightly) until break down. All green ECC specimens able to undergo huge displacement after gaining peak strength. The vibration projected as can be seen in Fig. 5 denotes as the sequential development of multiple cracking after first cracking.

Increasing GGBS content to 80% as substitute to cement produce better performance in terms of bending. In addition, the bending strength decrease with increasing the amount of RCF. It has found that this experimental result is comparable and agrees with the previous literature search, where adding more amount of RCF able reduce the flexural strength of ECC and ascribed to rise matrix toughness [18]. Thus, the addition of RCF may change the flexural performance and brought unfavorable effects on flexural behavior of green ECC.

3.3 Failure Mechanism of ECC Plates

Twelve (12) ECC plate specimens have been tested up to failure under three-point bending test. The failure of ECC plates occurs when the forces applied on top of it exceeded the strength of ECC. At 28 days after three-point bending test, the type of failure modes that have been observed is in the forms of flexural cracks, which occurs at the middle part of all ECC plate specimens. It has found that this observation is comparable with previous literature search [6, 15, 19–21] where the multiple cracks been observed at the middle region of the ECC specimens, as shown in Fig. 6.

As depicted in Fig. 6a, b, cracks were formed at the middle of the plate specimen and cracks width of these two samples are quite similar. Meanwhile, small multiple cracks width was observed at the middle of the G80R0.2 and G80R0.4 plate specimens as shown in Fig. 6c, d. Combination of RCF and higher amount of green material (GGBS) as substitute to cement (80% of total cementitious materials) in ECC plate specimen has few effects on improving the crack width of green ECC. GGBS has substantial influence to expand ductility of ECC, that is ascribed to decreasing the amount of PP fiber, which useful to the development of cracks.

The distribution of PP fibers of the plate specimen in a ruptured section after bending test is displayed in Fig. 7. As can be observed in Fig. 7, the fibers spread consistently in the mix and demonstrate good bridging action.

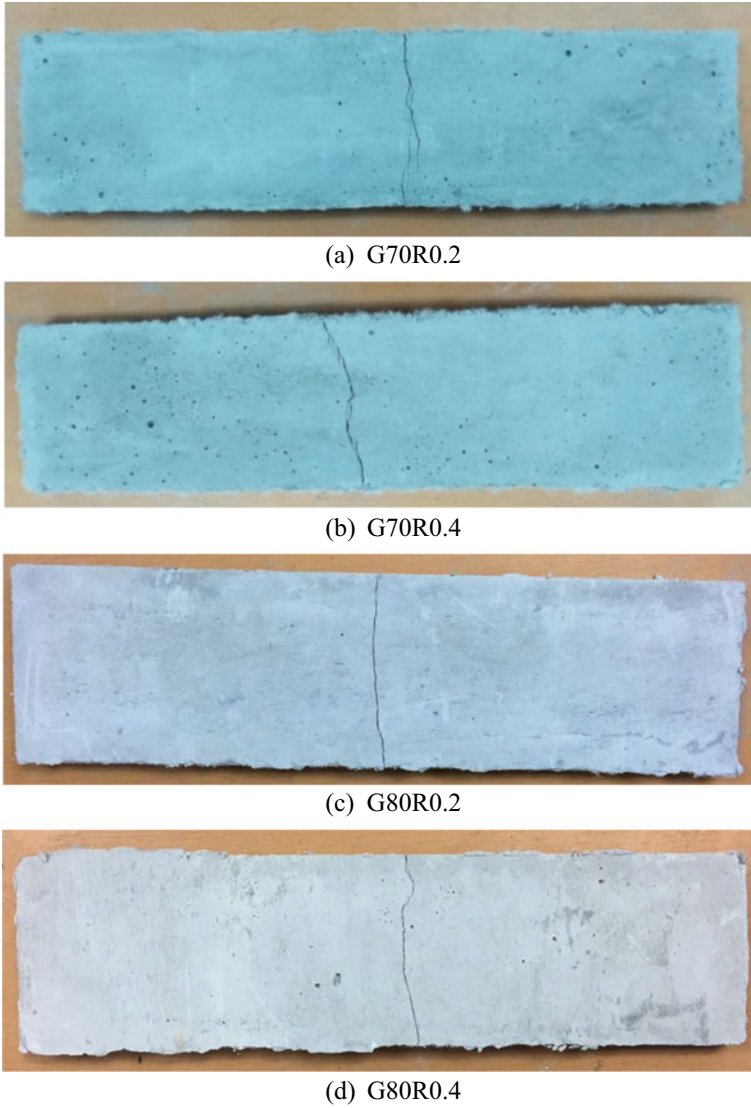


Fig. 6 Mode of failure (crack patterns) of ECC Plates

4 Conclusion

This study explored the influence of GGBS as cement substitute including the usage of RCF as sand replacement in the manufacturing of ECC. Experimental investigations were performed to evaluate the compressive and flexural strength of green ECC. The following conclusion could be obtained:

Fig. 7 PP fibers distribution on the fractured section of the ECC plate specimen



1. Increasing GGBS content (70–80%) of the same sand to binder ratio as substitute to cement in the mixtures lessens the compressive strength of green ECC, nevertheless, gives greater value to the flexural strength of green ECC.
2. Improving the ratio of sand to binder (0.2–0.4) of the same GGBS content reduces the flexural strength of the green ECC. Attributed to the rise in sand content, the amount of binder (a blend of cement and GGBS) was lessened in the ECC matrix and thereby lost its flexural strength.
3. The higher quantity of RCF lowered the binder amount in the ECC matrix and in doing so decreased the compressive strength.
4. The presence of RCF may alter the flexural performance and brought unfavorable effects on flexural behavior of green ECC.
5. GGBS has a significant influence on the expansion of the ductility of ECC, which is ascribed to a drop in the amount of PP fiber, which beneficial to the development of cracks.

It is found that the presence of RCF and GGBS can impact the behavior of ECC specimens. Thus, for a thorough understanding of ECC 's mechanical and ductility efficiency with recycled concrete fines (RCF) as a sand substitute and GGBS as a cement substitute, deeper exploration on an interfacial micro level will be required to evaluate the enhancement in the strength of the ECC matrix.

Acknowledgements The Ministry of Higher Education's financial support under the Fundamental Research Grant Scheme (FRGS) (600-IRMI/FRGS 5/3(378/2019)) is gratefully acknowledged. The authors would particularly like to thank Miss Nurul Shafida binti Ibrahim, who was closely engaged in this study. Similarly, thanks to all the laboratory technicians in civil engineering laboratories, Universiti Teknologi MARA (UiTM), Shah Alam for their valuable assistance during this study.

References

1. Rokugo K (ed) (2008) Recommendations for design and construction of high performance fiber reinforced cement composites with multiple fine cracks (HPFRCC). Japan Society of

- Civil Engineers Concrete Committee, Japan
2. Li VC, Wang S, Wu C (2001) Tensile strain-hardening behavior of polyvinyl alcohol engineered cementitious composite (PVA-ECC). *Mater J* 98(6):483–492
 3. Lee SW, Tan KH, Yang EH (2018) Seismic behaviour of interior reinforced-concrete beam–column sub-assemblages with engineered cementitious composites. *Mag Concr Res* 70(24):1280–1296
 4. Fischer G, Li VC (2003) Deformation behavior of fiber-reinforced polymer reinforced engineered cementitious composite (ECC) flexural members under reversed cyclic loading conditions. *ACI Struct J* 100(1):25–35
 5. Nurdeen MA, Megat Johari MA, Saiyid Hashim SF (2012) Flexural performance of green engineered cementitious composites containing high volume of palm oil fuel ash. *Constr Build Mater* 37:518–525
 6. Said SH, Razak HA, Othman I (2015) Flexural behavior of engineered cementitious composite (ECC) slabs with polyvinyl alcohol fibers. *Constr Build Mater* 75:176–188
 7. Yanhua G, Huaqiang YX, Zhi G, Yongjie H, Shuai L, Renjuan S (2018) Flexural properties of ECC-concrete composite beam. *Adv Civ Eng* 1–7
 8. Li VC, Wang S Flexural behaviors of glass fiber-reinforced polymer (GFRP) reinforced engineered cementitious composite beams. *ACI Mater J–Am Concr Inst* 99(1):11–21
 9. Maalej M, Li VC (1994) Flexural/tensile-strength ration in engineered cementitious composites. *J Mater Civ Eng* 6(4):513–528
 10. Magudeaswaran P, Eswaramoorthi P, Pradeep Kumar D (2015) Green high performance concrete using eco sand and industrial wastes. *Int J Chem Sci* 13(2):661–671
 11. Potgieter JH (2012) An overview of cement production: how “green” and sustainable is the industry? *Environ Manage Sustainable Dev* 1(2):14–37
 12. Gadpalliar SK, Deotale RS, Abhijeet RN (2017) Study on the partial replacement of cement by GGBS & RHA and natural sand by quarry sand in concrete. *J Eng Technol (IRJET)* 4(3):69–77
 13. Saranya P, Nagarajan P, Shashikala AP (2018) Eco-friendly GGBS concrete: a state-of-the-art review. *IOP conference series: materials science and engineering* 330(1)
 14. Meng D, Huang T, Zhang YX, Lee CK (2017) Mechanical behaviour of a polyvinyl alcohol fibre reinforced engineered cementitious composite (PVA-ECC) using local ingredients. *Constr Build Mater* 141:259–270
 15. Zhu Y, Yang Y, Yao Y (2012) Use of slag to improve mechanical properties of engineered cementitious composites (ECCs) with high volumes of fly ash. *Constr Build Mater* 36:1076–1081
 16. Wee LS, Lian OC, Zain MR (2019) Mechanical properties of engineered cementitious composites using local ingredients. *J Mech Eng* 16(2):145–157
 17. Wee LS, Lian OC, Zain MRM (2018) Evaluation of the design mix proportion on mechanical properties of engineered cementitious composites. *Key Eng Mater* 775:589–595
 18. Junxia L, En-Hua Y (2017) Macroscopic and microstructural properties of engineered cementitious composites incorporating recycled concrete fines. *Cement Concr Compos* 78:33–42
 19. Jian Z, Shunzhi Q (2010) Development of engineered cementitious composites with limestone powder and blast furnace slag. *Mater Struct* 43:803–814
 20. Lining W, Farhad A, Iman H, Emmanuel R (2020) Ultra-lightweight engineered cementitious composites using waste recycled glass microspheres. *J Clean Prod* 249:1–14
 21. Soe KT, Zhang YX, Zhang LC (2013) Material properties of a new hydrib fibre-reinforced engineered cementitious composites. *Constr Build Mater* 43:399–407

The Correlation Between Split Tensile and Flexural Strength with Compressive Strength of Crumb Rubber-Rice Husk Ash Concrete



Habib Abdurrahman , Gunawan Wibisono , Iskandar Romey Sitompul, and Monita Olivia

Abstract This research aimed to investigate the correlation between split tensile and flexural strength of crumb rubber-rice husk ash concrete with its compressive strength at the age of 28 days. The crumb rubber was added to the concrete mixture as much as 5% by its fine aggregates volume, while the rice husk ash was added to concrete 10% by its cement volume. The target compressive strength was 35 MPa. The specimens were cast in 105×210 mm cylinders for compressive strength, 150×300 mm cylinders for splitting tensile strength, and $150 \times 150 \times 600$ mm beam for flexural strength. The concretes were cured at a water pond for 28 days. The correlation coefficient between splitting tensile strength and compressive strength was determined by using the least square approximation method with a minimum sum of squares of errors. The correlation coefficient of flexural strength and compressive strength was also determined using this method. From the test result, it was obtained that the concrete had an average value of compressive strength by 32.05 MPa, splitting tensile strength by 3.43 MPa, and flexural strength by 4.84 MPa. By using the method, it could be seen that the concrete had a correlation coefficient of 0.61 and 0.86, respectively for splitting tensile strength and flexural strength.

Keywords Correlation · Splitting tensile · Flexural · Compressive · Crumb rubber · Rice husk ash

H. Abdurrahman · G. Wibisono (✉) · I. R. Sitompul · M. Olivia
Department of Civil Engineering, Universitas Riau, Pekanbaru, Indonesia
e-mail: g.wibisono@eng.unri.ac.id

H. Abdurrahman
e-mail: habib.abdurrahman@student.unri.ac.id

I. R. Sitompul
e-mail: iskandar.romey@lecturer.unri.ac.id

1 Introduction

Concrete is known as an essential material in construction due to its higher strength in bearing loads. However, since concrete is a brittle material, the concrete has a weakness in withstanding massive tensile stress that could lead the fine cracks to occur in the concrete surfaces. These fine cracks will gradually develop over time, causing the concrete to become damaged. Therefore, several studies have been done to improve the concrete ability in bearing the tensile loads and prevent the fine cracks from being appeared. This ability could be improved by adding materials such as fibres into the concrete mixtures instead of using steel reinforcement [1–3].

Waste tires are a non-biodegradable material and have become a critical problem in current environmental pollution issue. It is estimated that 1 billion waste tires are produced every year worldwide and more than half of it are disposed of in the landfill causing the toxic chemical substances to dissolve and pollute the land and nearby water source. These waste tires are expected to reach 1.2 billion by 2030 and will bring serious environmental and health issues if it remains disposed of or not properly recycle [4, 5].

The highly flammable properties of waste tires cause them to be difficult to extinguish if burnt. Also, the fire releases a thick dark smoke contains carbon monoxide and other toxic substances causing the air pollution [6]. Therefore, the disposal of waste tires needs to be managed effectively by recycling it into a new, environmentally friendly material.

In civil engineering area, the waste tires have been used as an additive in asphalt or concrete pavement to increase its toughness and ductility. Several researchers have studied the waste tire in many forms such as chip, shredded, crumb, fiber, and ash [7–10]. The waste tires are usually used as partial replacement of aggregate or added in concrete pavement mixture as reinforcement in the form of crumb rubber.

Crumb rubber was produced by removing the fibers and steel from waste tires and grinding it into the smaller size with an average size between 0.075 and 4.75 mm. Because of its average size, the crumb rubber often used as a partial replacement of fine aggregate. Many researchers have studied the effects of adding crumb rubber in the concrete mixture. It was reported that adding crumb rubber in optimum value could increase the hardened concrete properties such as compressive strength, tensile strength, flexural strength and would likely to decrease after reaching its optimum value. The loss in strength was due to poor adhesion between crumb rubber and cement paste [11]. Also, the elastic properties from crumb rubber made the fresh concrete mixture less compacted and increased the amount of void thus result in reduced of concrete strength. A high reactive fine material such as rice husk ash is used to prevent the loss in strength, to fill the void formed by crumb rubber and improve the strength of concrete.

Rice husk ash is waste from rice milling processing that comes in the form of fine ash due to the burning process of rice husk. The rice husk is used as a fuel to generate steam for the boiling process in the rice mills. Due to the difficulties involved in

its disposal, the rice husk ash also becomes an environmental issue. Therefore, the solutions are needed to reduce its amount as well as solving ecological problems.

The rice husk ash has been commonly used as a supplementary cementing material in concrete. Its high silica content around 80–90% is useful in increasing the concrete strength through the pozzolanic reaction [12–15]. The hydration product from pozzolanic reaction named Calcium Silicate Hydrate (CSH) could fill the voids in the concrete and improve the concrete pores structure thus result in denser concrete mixture and increase its strength [16]. Therefore, incorporating rice husk ash in crumb rubber concrete is expected to prevent the loss in concrete strength by filling the voids that caused by lack of proper bonding between crumb rubber and cement past.

Several studies have been done to examine the concrete strength containing crumb rubber and pozzolanic materials. However, the results come in varies [17]. This varies results happened because concrete is made of various materials with different physical and chemical properties. Also, the addition of crumb rubber and rice husk ash that has specific characteristic changes the concrete behaviors, making it hard to predict its strength, especially its splitting tensile and flexural strength. To predict concrete behavior, modelling through regression is used.

In recent years, analyzing the concrete properties using prediction modelling through regression or artificial intelligence tools is increasing due to its accurate prediction and effectiveness. Several empirical models have been developed to predict the splitting tensile and flexural strength of crumb rubber concrete based on its compressive strength. American Concrete Institute (ACI) also has provided the equation models in the form of square root relationship to predict the splitting tensile and flexural strength of normal weight concrete [18]. However, the equation is mostly unfit when compared to the experimental results. Hence, in this research, the compressive, splitting tensile, and flexural strength of crumb rubber and rice husk ash concrete are examined through experimental tests and the relationship between them are analyzed and calculated to obtain the correlation coefficients using the linear regression equation. The coefficients then will be compared with the coefficients provided by the American Concrete Institute (ACI).

2 Materials and Methods

In this research, the concrete specimens were mixed using Portland Composite Cement (PCC) from Padang, Indonesia, as the main binder. Crumb rubber was taken from the local tire industry, and rice husk ash was taken from Kampar Regency, Riau. The chemical composition of PCC and rice husk ash are shown in Table 1. The specific gravity of coarse and fine aggregates were 2.59 and 2.55 with water absorption by 0.28 and 3.62%. The water-cement ratio (w/c) was set at 0.30 as the concrete was designed to reach the compressive strength value of 35 MPa and flexural strength of 4.5 MPa.

Crumb rubber and rice husk ash were added as an enhancement to concrete mechanical properties such as compressive, tensile, and flexural strength. The crumb

Table 1 Chemical composition of PCC and rice husk ash

Oxides (%)	Portland composite cement	Rice husk ash
SiO ₂	23.04	86.92
Al ₂ O ₃	7.40	1.41
Fe ₂ O ₃	3.36	0.48
MgO	0.63 [20, 21]	1.01
CaO	57.38	1.77
Na ₂ O	–	0.05
K ₂ O	–	0.98
Na ₂ O + 0.658K ₂ O	0.52 [20, 21]	–
P ₂ O ₅	–	0.05
SO ₃	1.78 [20, 21]	0.46
LOI	–	7.63
Others	5.89	–

rubber was added by 5% of fine aggregates volume, and rice husk ash was added by 10% of cement volume. Superplasticizer was also used as much as 1% of cement weight to obtain a slump of 8 cm. These values were determined according to the optimum mixture that was obtained through a parametric study by Abdurrahman et al. [19]. The plain concrete without crumb rubber and rice husk ash were also cast as a control mix. The mixture composition of crumb rubber rice husk ash concrete per m³ is shown in Table 2.

The specimens were cast into 105 × 210 mm cylinders for compressive strength test, 150 × 300 mm cylinders for splitting tensile strength, and 150 × 150 × 600 mm beams for the flexural strength test. Before testing, the specimens were cast and cured in the water for 28 days. Subsequently, the samples were tested according to the Indonesian National Standard at the age of 28 days.

The correlation coefficient between compressive strength of the crumb rubber-rice husk ash concrete with its splitting tensile and flexural strength was determined by modifying the values into the linear equation and calculated using the least square method. The linear equation was formed following ACI 318-05/318R-05 [18]. It is stated in ACI 318-05/318R-05 that splitting tensile strength (f_{ct}) and flexural strength (f_r) for normal weight concrete has a correlation with compressive strength (f'_c) as shown in Eqs. 1 and 2 below.

Table 2 The mixture composition of crumb rubber rice husk ash concrete per m³

Type of concrete	Coarse Agg. (kg)	Fine Agg. (kg)	Cement (kg)	Water (kg)	Crumb rubber (kg)	RHA (kg)	Super-plasticizer (kg)
CR-RHA	886.16	621.67	666.67	218.36	6.61	4.64	6.67
PCC	886.16	621.67	666.67	218.36	0.00	0.00	6.67

$$f_{ct} = 6.7 \sqrt{f'_c(\text{psi})} \text{ or } f_{ct} = 0.56 \sqrt{f'_c(\text{MPa})} \tag{1}$$

$$f_r = 7.5 \sqrt{f'_c(\text{psi})} \text{ or } f_r = 0.62 \sqrt{f'_c(\text{MPa})} \tag{2}$$

It can be seen that both equations are in the form of Eq. 3.

$$Y = a * X \tag{3}$$

where Y is the splitting tensile (f_{ct}) or flexural strength (f_r) value, a is correlation coefficient, and X is the square root of compressive strength. To determine the correlation coefficient for crumb rubber-rice husk ash concrete (a) the equation is calculated using the least square method. The best (a) value is the one that gives the least error (E) in the equation. Therefore, the error's value had to be obtained first using the sum of squares of errors (SSE) method, as shown in Eqs. 4 and 5.

$$E_i = a \cdot X_i - Y_i \tag{4}$$

$$SSE = \sum_{i=1}^n (a \cdot X_i - Y_i)^2 \tag{5}$$

The sum of squares of errors (SSE) value will be minimum if it approaches 0, to achieve that the SSE value has to be differentiated by a, as shown in Eq. 6. Then the correlation coefficient (a) value will be determined using Eq. 7.

$$\frac{d(SSE)}{d(a)} = 0 \tag{6}$$

$$\frac{d(SSE)}{d(a)} = \sum_{i=1}^n 2(a \cdot X_i - Y_i) \cdot X_i = 0$$

$$a \sum (X_i)^2 - \sum (X_i \cdot Y_i) = 0$$

$$a = \frac{\sum (X_i \cdot Y_i)}{\sum (X_i)^2} \tag{7}$$

Table 3 The compressive strength of CR-RHA and PCC concrete

Type of concrete	Sample no	Compressive strength, f'_c (MPa)					
		7 days	SD	14 days	SD	28 days	SD
CR-RHA	1	17.79		26.80		30.02	
	2	23.80	4.08	27.25	1.12	31.66	2.25
	3	25.58		28.91		34.47	
PCC	1	28.29		27.29		36.14	
	2	30.03	4.17	34.39	3.82	36.26	0.56
	3	22.10		28.40		37.11	

3 Results and Discussion

3.1 Compressive Strength

The results of the compressive strength test for crumb rubber-rice husk ash concrete (CR-RHA) are given in Table 3. It can be seen that both concretes were gaining strength until the age of 28 days due to the hydration process of cement and the pozzolanic reaction of rice husk ash. However, the CR-RHA concrete had lower compressive strength than PCC concrete at all ages due to the lack of proper bonding between crumb rubber and cement paste [7, 22]. Also, the presence of crumb rubber in the concrete mixture made it less compacted since rubber had a high elasticity, thus increasing the amount of the pores in the concrete and reduced its strength [9, 23]. The pozzolanic reaction from rice husk ash could improve the pore structure by filling the interfacial transition zone between crumb rubber and cement paste. It turns out that crumb rubber has a more significant effect on changes in concrete compressive strength than rice husk ash [24]. Similar research also found that the cracks occurred rapidly around the interfacial transition zone (ITZ) between crumb rubber and cement paste during the time of loading [25].

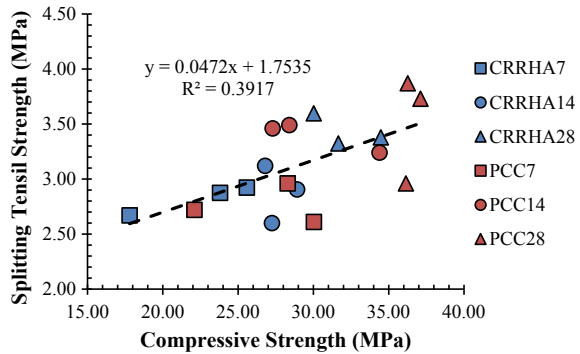
3.2 Splitting Tensile Strength

The splitting tensile strength of CR-RHA concrete is shown in Table 4. From the table, it can be seen that the splitting tensile strength for both types of concretes was also getting higher as the concrete ages increased. The splitting tensile tests had similar results with compressive strength as the CR-RHA concrete had a lower value than PCC concrete. This similar result could happen since both compressive and splitting tensile tests were using the same method to obtain its value by applying a distributed load to the area of concrete until failure occurred. The lower value in splitting tensile strength of CR-RHA concrete was also due to the lack of bonding between crumb rubber and cement paste that made the cracks formed rapidly during

Table 4 The splitting tensile strength of CR-RHA and PCC concrete

Type of concrete	Sample no	Splitting tensile strength, f_{ct} (MPa)					
		7 days	SD	14 days	SD	28 days	SD
CR-RHA	1	2.67		3.12		3.60	
	2	2.87	0.13	2.60	0.26	3.32	0.14
	3	2.92		2.91		3.38	
PCC	1	2.96		3.46		2.96	
	2	2.61	0.17	3.24	0.14	3.87	0.49
	3	2.72		3.49		3.73	

Fig. 1 The correlation between compressive strength and splitting tensile strength



the loading, thus fail to occurred immediately [7, 25]. Other findings also showed a similar result that concrete incorporated with crumb rubber would likely have a lower in splitting tensile strength value than normal concrete [26–31].

Figure 1 shows the correlation between compressive strength and splitting tensile strength for both types of concrete. The splitting tensile strength increased with compressive strength at all ages. However, the CR-RHA concrete had a slightly lower value in compressive and splitting tensile strength compared to the PCC concrete.

3.3 Flexural Strength

Table 5 shows the flexural strength test results for CR-RHA and PCC concrete. The flexural strength test was conducted using the two-point loading method, according to the Indonesian National Standard (SNI). As can be seen, the flexural strength for both types of concretes was gradually increased with age due to the hydration process from cement. The results showed that the CR-RHA concrete had a different strength development in flexural strength compared to compressive and splitting tensile strength. The CR-RHA concrete had a higher flexural strength compared to PCC concrete at all ages. This result was likely due to the characteristic of crumb

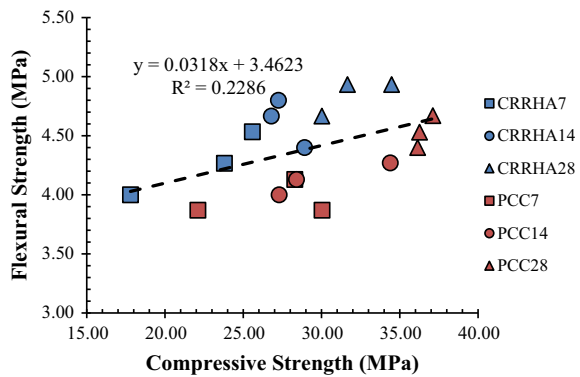
Table 5 The flexural strength of CR-RHA and PCC concrete

Type of concrete	Sample no	Flexural strength, f_r (MPa)					
		7 days	SD	14 days	SD	28 days	SD
CR-RHA	1	4.00		4.80		4.93	
	2	4.27	0.13	4.40	0.26	4.93	0.14
	3	4.53		4.67		4.67	
PCC	1	4.13		4.00		4.40	
	2	3.87	0.15	4.27	0.13	4.53	0.49
	3	3.87		4.13		4.67	

rubber that acted as a reinforcement and absorbed the impact during the loading and prevented the immediate failure after the early cracks occurred [32]. Other researchers also obtained similar results that adding crumb rubber into the concrete mixture gives concrete a higher value in flexural strength compared to normal concrete [22, 33].

The correlation between compressive and flexural strength for CR-RHA and PCC concrete can be seen in Fig. 2. From the figure, it was shown that the compressive and flexural strength for both types of concrete gradually increases with age until 28 days. Unlike the splitting tensile strength, the flexural strength shows a different trend for CR-RHA concrete. While it shows that the compressive strength value of CR-RHA concrete is lower compared to the PCC concrete, it turns out that CR-RHA concrete has a higher value in the flexural strength. This result was likely due to crumb rubber that acted as reinforcement to prevent the concrete beams from immediate failure after the early cracks occurred [32].

Fig. 2 The correlation between compressive strength and flexural strength



3.4 Correlation Coefficient

In order to determine the correlation coefficient between compressive strength with splitting tensile and flexural strength of CR-RHA concrete, the calculation was done using the least square root with a minimum sum of squares of errors method in the formed of a linear regression equation. The equation was formed in Eq. 3.

According to Eqs. 1 and 2 that was given by ACI 318-05, the equations were used to predict the splitting tensile and flexural strength based on the compressive strength values obtained through experimental at 28 days. The splitting tensile and flexural strength of CR-RHA concrete according to the equations by ACI 318-05 were shown in Table 6. As can be seen, the splitting tensile and flexural strength values were significantly different compared to the experimental results. In conclusion, the equations by ACI 318-05 were only used to predict the plain concrete strength at the age of 28 days.

Furthermore, in order to determine the correlation coefficient between compressive strength with splitting tensile and flexural strength of CR-RHA concrete, the calculation was carried out using the data from experimental results of CR-RHA concrete strength at the age of 28 days. The data taken was at least square root with a minimum sum of squares of errors method in the formed of linear regression equation as formed in Eq. 3.

Using Eq. 7 the correlation coefficient for splitting tensile and flexural strength were calculated as shown respectively in Tables 7 and 8 where X is the square root

Table 6 The CR-RHA concrete strength at age of 28 days

Sample no	CR-RHA concrete Strength by experimental (MPa)			ACI 318-05 (MPa)	
	Compressive strength, f'_c	Splitting tensile strength, f_{ct}	Flexural strength, f_r	Splitting tensile strength, f_{ct}	Flexural strength, f_r
1	30.02	3.60	4.93	3.07	3.40
2	31.66	3.32	4.93	3.15	3.49
3	34.47	3.38	4.67	3.29	3.64

Table 7 The correlation coefficient of compressive and splitting tensile strength for CR-RHA concrete

No	$X (\sqrt{f'_c})$	$Y (f_{ct})$	$X \times Y$	X^2
1	5.48	3.60	19.71	30.02
2	5.63	3.32	18.70	31.66
3	5.87	3.38	19.83	34.47
Sum (Σ)	16.98	10.30	58.24	96.15
$a (\Sigma X \times Y) / (\Sigma X^2)$				0.61

Table 8 The correlation coefficient of compressive and flexural strength for CR-RHA concrete

No	X ($\sqrt{f'_c}$)	Y (f_r)	X × Y	X ²
1	5.48	4.93	27.03	30.02
2	5.63	4.93	27.76	31.66
3	5.87	4.67	27.40	34.47
Sum (Σ)	16.98	14.53	82.19	96.15
a ($\Sigma X \times Y$)/(ΣX^2)				0.86

of compressive strength, Y is the splitting tensile or flexural strength, and a is the correlation coefficient.

From Tables 7 and 8, it was obtained that the CR-RHA concrete with 5% crumb rubber and 10% rice husk ash in this research had a correlation coefficient of 0.61 and 0.86, respectively for splitting tensile strength and flexural strength. Therefore, the equation to predict the splitting tensile and flexural strength of CR-RHA concrete are shown respectively by Eqs. 8 and 9.

$$f_{ct} = 0.61 \sqrt{f'_c}(\text{MPa}) \tag{8}$$

$$f_r = 0.86 \sqrt{f'_c}(\text{MPa}) \tag{9}$$

4 Conclusion

The mechanical properties of concrete with the addition of 5% crumb rubber and 10% rice husk ash (CR-RHA) was examined to obtain its correlation coefficient between splitting tensile and flexural strength with its compressive strength. According to ACI 318-05/318R-05, the correlation coefficient and the equation has been provided to predict the splitting tensile and flexural strength of concrete using the compressive strength value obtained from an experimental study. However, the results were shown significantly different. Therefore, the correlation coefficients of CR-RHA concrete were determined using the least square with the minimum sum of squares of errors method in the form of a linear regression equation. The equation was formed according to ACI 318-05. Based on the method, it was obtained that the concrete had a correlation coefficient of 0.61 and 0.86, respectively for splitting tensile strength and flexural strength.

Acknowledgements This work was funded by the Penelitian Unggulan Perguruan Tinggi 2019 DIPA LPPM (Research Institute) Universitas Riau, Contract no. 980/UN.19.5.1.3/PT.01.03/2019.

References

1. Dutra VFP, Maghous S, Filho AC (2013) A homogenization approach to macroscopic strength criterion of steel fiber reinforced concrete. *Cem Concr Res* 44:34–45
2. Ding Y, Azevedo C, Aguiar JB, Jalali S (2012) Study on residual behaviour and flexural toughness of fibre cocktail reinforced self compacting high performance concrete after exposure to high temperature. *Constr Build Mater* 26(1):21–31
3. Curosu I, Mechtcherine V, Millon O (2016) Effect of fiber properties and matrix composition on the tensile behavior of strain-hardening cement-based composites (SHCCs) subject to impact loading. *Cem Concr Res* 82:23–25
4. WBCSD (2010) End-of-life tires: a framework for effective management systems. Conches-Geneva
5. Siegle L (2006) *Recycle the essential guide*. Black Dog Publishing, London
6. Reschner K (2008) *Scrap tire recycling: a summary of prevalent disposal and recycling methods*. Berlin
7. Sgobba S, Borsa M, Molfetta M, Marano GC (2015) Mechanical performance and medium-term degradation of rubberized concrete. *Constr Build Mater* 98:820–831
8. Girskas G, Nagrockiene D (2017) Crushed rubber waste impact of concrete basic properties. *Const Build Mater* 140:36–42
9. Bisht K, Ramana PV (2017) Evaluation of mechanical and durability properties of crumb rubber concrete. *Constr Build Mater* 155:811–817
10. Kardos AJ, Durham SA (2015) Strength, durability, and environmental properties of concrete utilizing recycled tire particles for pavement applications. *Const Build Mater* 98:832–845
11. Eldin NN, Senouci AB (1993) Rubber-tire particles as concrete aggregate. *J Mater Civ Eng* 5(4):478–496
12. Swaminathan AN, Ravi SB (2016) Use of rice husk ash and metakaolin as Pozzolans for concrete: a review. *Int J Appl Eng Res* 11(1):656–664
13. Mahmud HB, Bahri S, Yee YW, Yeap YY (2016) Effect of rice husk ash on the strength and durability of high strength performance concrete. *World Acad Sci Eng Technol* 10(3):375–380
14. Foong KY, Alengaram UJ, Jumaat MZ, Mo KH (2015) Enhancement of the mechanical properties of lightweight oil palm shell concrete using rice husk ash and manufactured sand. *J Zhejiang Univ-Sci A (Appl Phys Eng)* 16(1):59–69
15. Bansal NS, Antil Y (2015) Effect of rice husk on compressive strength of concrete. *Int J Emerg Technol* 6(1):144–150
16. Yu Q, Sawayama K, Sugita S, Shoya M, Isojima Y (1999) The reaction between rice husk ash and Ca(OH)₂ solution and the nature of its product. *Cem Concr Res* 29(1):37–43
17. Muntohar AS, Hashim R (2002) Silica waste utilization in ground improvement: a study of expansive soil treated with LRHA. In: 4th international conference on environmental geotechnics (ICEG). *Geoteknik & Geo-Hazards, Rio de Janeiro*, pp 11–16
18. ACI Committee 318 (2005) Building code requirements for structural concrete (ACI 318-05) and commentary (ACI 318R-05). American Concrete Institute, USA
19. Abdurrahman H, Wibisono G, Qoryati M, Sitompul IR, Olivia M (2019) Mechanical properties of crumb rubber-rice husk ash concrete as a rigid pavement material. In: *IOP conference series: materials science and engineering*, vol 615
20. PCC Specification Brochure Padang: PT Semen Padang
21. Koliass S, Georhiou C (2005) The effect of paste volume and of water content on the strength and water absorption of concrete. *Cement Concr Compos* 27:211–216
22. Sofi A (2017) Effect of waste tyre rubber on mechanical and durability properties of concrete—a review. *Ain Shams Eng J* 9(4):2691–2700
23. Gupta T, Chaudary S, Sharma RK (2014) Assessment of mechanical and durability properties of concrete. *Constr Build Mater* 73:562–574
24. Guneyisi E, Gesoglu M, Ozturan T (2004) Properties of rubberized concretes containing silica fume. *Cem Concr Res* 34:2309–2317

25. Mendis ASM, Al-Deen S, Ashraf M (2017) Behaviour of similar strength crumbed rubber concrete (CRC) mixes with different mix proportions. *Constr Build Mater* 137:354–366
26. Ganjian E, Khorami M, Maghsoudi AA (2009) Scrap-tyre-rubber replacement for aggregate and filler in concrete. *Constr Build Mater* 23:1828–1836
27. Mohammadi I, Khabbaz H, Vessalas K (2014) In-depth assessment of Crumb Rubber Concrete (CRC) prepared by water-soaking treatment method for rigid pavements containing waste rubber tire as fine aggregate. *Constr Build Mater* 71:456–471
28. Onuaguluchi O, Panesar DK (2014) Hardened properties of concrete mixtures containing pre-coated crumb rubber and silica fume. *J Clean Prod* 8:125–131
29. Gupta T, Chaudary S, Sharma RK (2016) Mechanical and durability properties of waste rubber fiber concrete with and without silica fume. *J Clean Prod* 112:702–711
30. Gerges NN, Issa CA, Fawaz SA (2018) Rubber concrete: mechanical and dynamical properties. *Case Stud Const Mater* 9
31. Aslani F, Ma G, Wan DLY, Le VXT (2018) Experimental investigation into rubber granules and their effects on the fresh and hardened properties of self-compacting concrete. *J Clean Prod* 172:1835–1847
32. Yilmaz A, Degirmenci N (2009) Possibility of using waste tire rubber and fly ash with Portland cement as construction materials. *Waste Manage* 29:1541–1546
33. Mohammed BS, Adamu M (2018) Mechanical performance of roller compacted concrete pavement containing crumb rubber and nano silica. *Constr Build Mater* 159:234–251

Finite Element Dynamic Analysis of Double-Span Steel Beam Under an Instantaneous Loss of Support



Nur Ezzaryn Asnawi Subki , Hazrina Mansor, Yazmin Sahol Hamid, and Gerard A. R. Parke

Abstract This paper aims to provide a unified approach of the finite element analysis (FEA) modelling technique in validating experimental work related to progressive collapse study using ABAQUS software version 6.14. The Finite Element Model (FEM) in simulating the experimental study on the dynamic response of a flush end-plate connection under the effect of sudden support (column) removal is shown herein. The double-span beam and the end plate were modelled using the first-order shell element with reduced integration (S4R). The plastic hinge meshing scheme was utilized on the double-span beam geometry with finer mesh modelled for part of the beam with higher bending behavior and vice versa. A simplified modelling approach for the modelling of the flush endplate connection was introduced. The endplate, which was welded to the cross-section of the beam, was idealized via tie-constraint interaction. A translator-type connector element was used to represent the bolt behavior and the Coulomb friction model was enforced for the surface interaction between the endplate and the column flange. The Holzier material model was used to define the nonlinear properties of the hot-rolled steel sections. The nonlinear *Dynamic, Explicit* analysis procedure was adapted in simulating the loading scheme given in the experiment and the Rayleigh model was enforced in the analysis to introduce the effect of damping. The analysis output was successfully verified against the experimental results from previous research. It was concluded that the simplified FEA modelling method proposed in this work can simulate actual dynamic response of the flush-end connection. The proposed alternative finite element model able to predict the maximum dynamic displacement of the double-span beam with 0.83% error.

N. E. A. Subki · H. Mansor (✉) · Y. Sahol Hamid
School of Civil Engineering, College of Engineering, Universiti Teknologi MARA (UiTM) Shah Alam, Selangor, Malaysia
e-mail: hazrina4476@uitm.edu.my

G. A. R. Parke
Department of Civil and Environmental Engineering, University of Surrey, Guildford, UK

Keywords Non-linear modelling · Dynamic analysis · Progressive collapse · Sudden column-removal simulation · Finite element analysis · Steel connection modelling

1 Introduction

Progressive collapse can be simulated by instantaneously removing a column and assuming that such column-removal scenario will exhibit a highly non-linear dynamic reaction that eventually led to the collapse of the overall structure. Such complex progressive collapse behavior is not feasible to conduct experimentally due to the high costs involved. A finite element analysis (FEA) is an alternative approach to examine the action of the remaining structure subject to a sudden column removal scenario. Even so, studies on the behavior of structural collapse require a reliable finite element model. Without an in-depth understanding and significant practical experience, the findings of the FEA may be useless. To simulate the sudden column removal scenario, one can utilize different element complexity ranging from 1-Dimensional (1D) elements such as line element, 2-Dimensional (2D) elements such as shell or plate elements and 3-Dimensional (3D) elements such as continuum elements. Researches conducted in [1–4] have highlighted that the different range of element complexity would either yield to extra computational efforts, various options of output results generated and detail component view of the studied structure.

Many previous studies focus on the evaluation of the effect of sudden column removal utilizing the finite element model [4–8]. However, their findings are mostly limited to the 1D element, which is best suited to the macro model (global) structure. Simulating an experimental work in modelling a beam-to-column connection is quite challenging. Yang and Tan [9, 10] have developed a component-based model that simulates the behavior of bolt angle connections with high deformation stress resistance. Their work has been carried out using ABAQUS software and a 3D numerical model developed, which was validated by comparison with the experimental response. The findings reported by [9, 10] are valuable as the results indicated that utilizing the 3D element will provide alternative results such as capability in capturing stress distribution and buckling effect due to sudden column loss scenario. Meanwhile, Liu et al. [11] have utilized the FEA using continuum element (i.e. 3D element) to simulate the effect of sudden column removal of flush-end plate connection. In their model, only a quarter of the specimen was modelled using symmetric boundary conditions. Such symmetrical modelling offered reduction in the computational effort requires for the analysis and simulation of the actual experimental set-up. However, extra effort and advance modelling skill are needed to establish the flush-end connection model using 3D element, which involves surface-to-surface interaction properties between components (e.g. End-plate to column flange), non-linear contact behavior of bolt and bolt hole, and others.

This paper aims to enlighten and provide a unified simplification of the geometrical modelling approach in validating the experimental work conducted by Liu et al. [11].

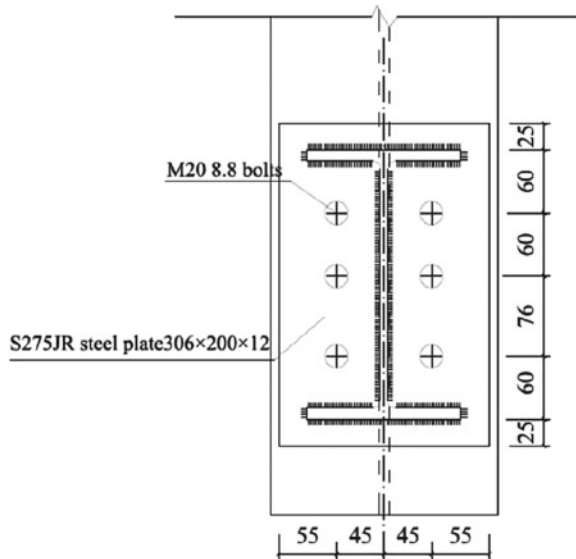
A shell element (i.e. 2D element) was used in this paper to model the experimental work in Liu et al. [11]. It is interesting to compare numerically the different effects produced if the experimental set-up of the double-span beam is being developed utilizing shell element as compared to the continuum element used in Liu et al. [11]. This paper will provide an insight on to what extent should the model be simplified so it can still generate accurate and reliable predictions of the dynamic response caused by instantaneous loss of column support published in the experimental results.

2 Experimental Details

Liu et al. [11] have conducted a dynamic test on a flush end-plate connection to study the structural performance of the flush end-plate connection under an instantaneous loss of support (column). In their experimental work, the flush end-plate connection consists of a 12 mm thick plate welded to the UB254 × 146 × 37 beam as shown in Fig. 1. Six M20 bolts of 8.8-grade were used to connect the plate to the UC203 × 203 × 71 column. The S355 steel was used for the beam and column sections while S257 was used for the end-plate. The EN1993-1-8 [12] was used to design the flush end-plate connection as in Fig. 1, which has been classified as a semi-rigid connection [11].

Liu et al. [11] have adopted the simplified experimental set-up proposed by Yang and Tan [13] for the dynamic test. As shown in Fig. 2, a nominally pinned joint (hinge) was used at each end-span of the beam assembly to replicate the contra-flexure point. This test set-up focuses on the behavior of the connections in the middle span and

Fig. 1 The flush end-plate connection (Figure taken from Yang and Tan [13])



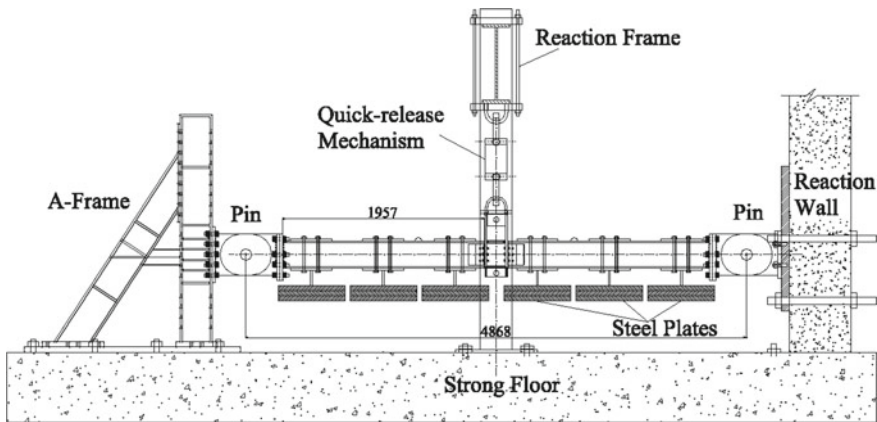


Fig. 2 The experimental set-up for the dynamic test [11]

excludes the end-span connection of the double-span beam [13]. A total beam span length of 4868 mm was used and the beam assembly was horizontally restrained by the steel A-frame and strong wall (See Fig. 2).

The double-span beam assembly was loaded using metal plates hung beneath the beam (See Fig. 2), which creates a uniformly distributed load (UDL) in the structural system [11]. The metal plates were first loaded onto the beam assembly while it was being supported at the central column joint by a quick-release mechanism hook (Refer to Fig. 2). A total of 101.72kN of applied load (UDL; $w = 22.03$ kN/m) was imposed on the beam assembly and about 61.28 kN of upward force (P_c) was required at the center of the beam assembly to support the applied load.

The hook was instantaneously released from the beam assembly to imitate sudden loss of support. The vertical displacement of the central column was then measured on a time-history basis as depicted in Fig. 3. It can be observed in Fig. 3 that the

Fig. 3 The dynamic vertical displacement from the experimental work and finite element analysis using continuum (C3D8R) element [11]

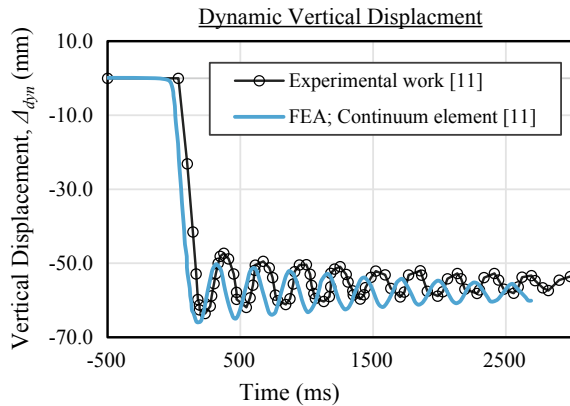


Fig. 4 The failure of the flush-end plate connection [11]

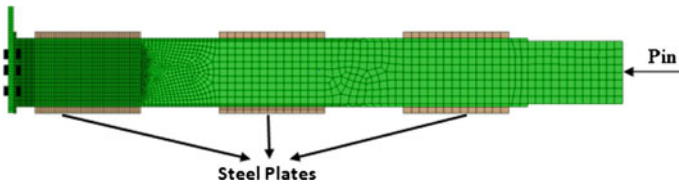


Fig. 5 The finite element model using C3D8R element [11]

double-span beam deformed at the maximum dynamic displacement of $\Delta_{dyn, max} = 64.95$ mm when the support was instantaneously removed. The end-plate was reported to yield as the beam assembly reached structural equilibrium as depicted in Fig. 4. However, no yielding of the bolts was observed during the experiment [11].

Liu et al. [11] have established a finite element model using 8-noded continuum element with reduced integration (C3D8R) as a quarter-span beam (Refer to Fig. 5). They managed to manipulate the boundary condition of the model in order to replicate actual restraints of the beam assembly in the experimental work. Their model has been validated with experimental work and showed consistency with the experimental result as depicted in Fig. 3. The maximum dynamic displacement of $\Delta_{dyn, max} = 65.90$ mm was estimated from their finite element analysis [11], which yields the percentage different of 3.61%.

Note that the flush-end connection (See Fig. 5) was modelled in detailed using the continuum element. This modelling approach of the connection involves contact nonlinearity and various interactions between surfaces (e.g. plate to column flange, bolt and bolt hole, etc.), which is a highly non-linear problem. Essentially, the analysis using this modelling approach is prone towards convergence problem if unsuitable analysis procedure and incrementation setting were chosen.

3 Finite Element Modelling Technique

The alternate version of finite element model for the dynamic test is presented herein. The ABAQUS software version 6.14 was used for the dynamic analysis of the double-span beam. The finite element modelling techniques include the geometrical modelling, material modelling, loading scheme and analysis procedure, and model meshing.

3.1 Geometrical Modelling

The geometrical modelling of the double-span beam with flush end-plate connections as in Fig. 2 can be divided into two parts; the double-span beam modelling and the flush end-plate modelling, which are discussed in the following section.

3.1.1 Double-Span Beam Modelling

The main structural members (i.e. beams, column and stiffeners) in the beam specimen were modelled using the first-order shell element with reduced integration (S4R), as depicted in Fig. 6. The S4R element is selected for the geometry of the main structural members as it was best suited for large strain (i.e. large deformation) simulation [14].

At each end of the beam specimen (See Fig. 6), an analytical rigid surface was added to represent the center of the pinned support. The rigid surface was allowed to rotate about the z-axis or UR3 (See Fig. 6) to replicate the pinned condition of the end-support. The tie-constraint interaction was implemented to connect the beam geometry to the rigid surface. In the analysis, the stiffness of the supporting systems

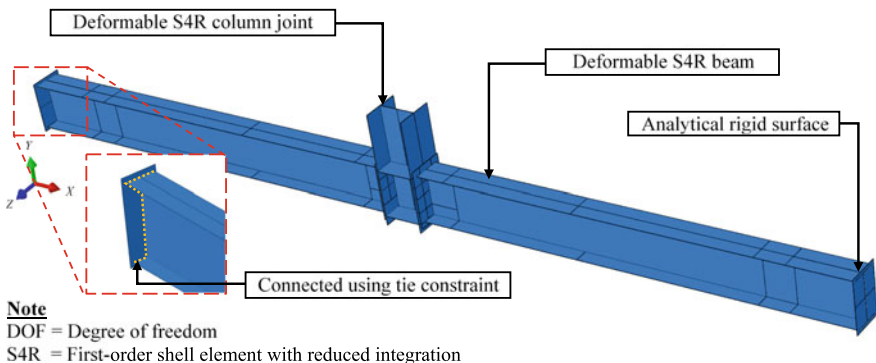


Fig. 6 Geometrical modelling of the beam specimen

(i.e. steel A-frame and strong reaction wall) was assumed to be very rigid. To achieve this condition in the finite element model, the rigid surface's degree of freedom (DOF) was restrained against all translations (i.e. U1, U2 and U3), and rotation about the x -axis (i.e. UR1) and y -axis (i.e. UR2). The lateral-restraining system was also included in the finite element model by restricting the lateral movement of the beam specimen in the z -direction (i.e. U3).

3.1.2 Flush End-Plate Modelling

The end-plate was modelled using the deformable-type S4R element and it was connected to the beam section by using the tie-constraint interaction (See Fig. 7). The Translator connector-element was used to represent the M20 bolts in Fig. 1 that connects the end-plate to the column flange. For the flush end-plate connection model in Fig. 7, the movement the Translator was permitted in the x -direction (i.e. U1) only.

The elastic stiffness of the Translator in the x -direction (i.e. D11) was defined based on the axial stiffness of the bolt (k_b). The axial bolt stiffness is given as follows [15]:

$$k_b = \frac{E_b A_b}{l} \tag{1}$$

As given in Eq. (1), E_b is the Young's modulus of bolt, A_b is the cross-sectional area of the bolt and l is the bolt length. The nominal diameter ($d_c = 20$ mm) of the bolt (Refer to Fig. 8) is used to calculate the cross-sectional area (A_b) of M20 bolt. The bolt length (l) can be taken as the total thickness of the clamped material as shown in Fig. 8 [15]. Assuming that the bolt hole is unthreaded, the total thickness of the clamped material is the summation of column flange thickness ($t_f = 17.3$ mm) and the end-plate thickness ($t_p = 12$ mm). Hence, the bolt length for the flush end-plate

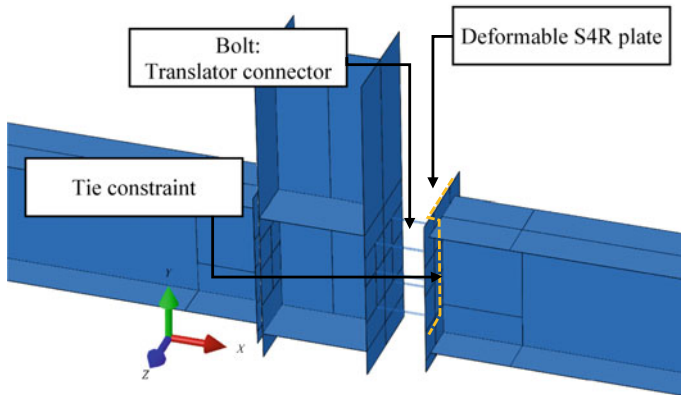


Fig. 7 Modelling of the flush end-plate connection at the central column joint

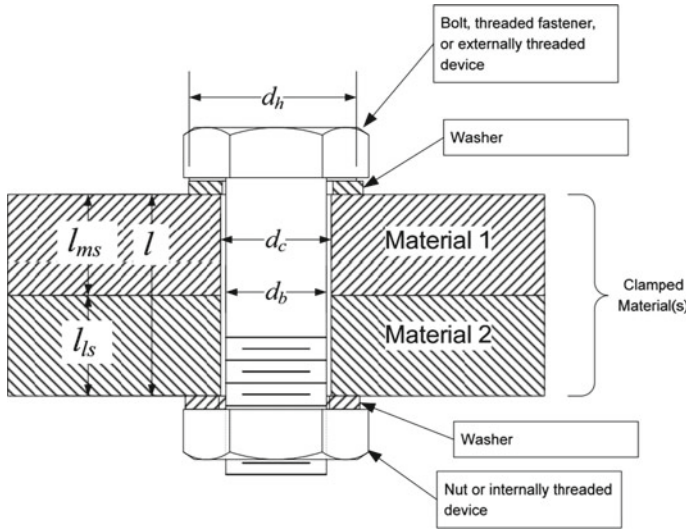


Fig. 8 The bolt nomenclature [15]

connection is $l = 29.3$ mm. By considering $E_b = 210$ GPa, the elastic stiffness for each bolt as calculated using Equation (1) is 2.25×10^6 kN/m. The plastic behavior of the bolts is not included in the analysis as no bolt yielding was reported from the dynamic test [11]. Other sources of bolt stiffness, such as bolt grip stiffness, are not considered in the Translator and are assumed rigid.

The contact between the end-plate and the column flange is simulated by assigning the General Contact interaction to the model. The contact interaction properties for this analysis consist of two behaviors; “Hard” contact and Penalty contact. Based on ABAQUS Analysis User’s Manual, the Penalty contact interaction properties use the Coulomb friction model to simulate friction behavior between surfaces [16]. The Coulomb friction model is given as follows [16]:

$$\tau_{crit} = \mu P \tag{2}$$

Given that τ_{crit} is the critical shear stress for sliding to occur, μ is the coefficient of friction, and P is the normal pressure. The coefficient of friction (μ) is required in the data input for the Penalty properties, which is commonly taken as 0.3 for steel-to-steel surface contact [17–19].

3.2 Material Modelling

There are three parameters that defined the elastic behavior of a hot-rolled steel in the simulation; Young’s modulus (E), Poisson ratio (ν) and density (ρ_{steel}). According

Table 1 The material properties of S275 and S355 hot-rolled steel from [25]

Steel grade	Yield stress f_y (MPa)	Ultimate stress f_u (MPa)	Yield strain ε_y (%)	Ultimate strain ε_u (%)	Material hardening strain ε_{sh} (%)
S275	275.0	430.0	0.13	21.63	1.50
S355	355.0	490.0	0.17	16.53	1.70

to EN1993-1-1:2005 [20], the Young's modulus was taken as $E = 210$ GPa, the Poisson ratio was taken as $\nu = 0.3$ and steel density is taken as $\rho_{steel} = 7850$ kg/m³. The engineering stress–strain plot of hot-rolled steel was established using the Holzer et al. [21] material model, which is given as follows:

$$f = E\varepsilon \quad 0 \leq \varepsilon \leq \varepsilon_y \quad (3)$$

$$f = f_y \quad \varepsilon_y \leq \varepsilon \leq \varepsilon_{sh} \quad (4)$$

$$f = f_y \left(1 + \left(\frac{\varepsilon - \varepsilon_{sh}}{\varepsilon_u - \varepsilon_{sh}} \right) \left(\frac{f_u}{f_y} - 1 \right) e^{\left(1 - \left(\frac{\varepsilon - \varepsilon_{sh}}{\varepsilon_u - \varepsilon_{sh}} \right) \right)} \right) \quad \varepsilon_y \leq \varepsilon \leq \varepsilon_u \quad (5)$$

where ε is strain, f is stress, f_y is yield stress, f_u is ultimate stress, ε_y is yield strain, ε_u is ultimate strain, ε_{sh} is the strain at the beginning of material hardening. The material properties as given in Table 1 were used to establish the stress–strain curve for the S275 and S355 hot-rolled steel. Researchers commonly adapt the true stress–strain plot in an analysis to simulate actual connection behavior [11, 22–24]. The engineering stress (f) and engineering strain (ε) can be converted to true stress (f_{true}) and true strain (ε_{true}) by using the Eqs. (6) and (7) respectively.

$$f_{true} = f(1 + \varepsilon) \quad (6)$$

$$\varepsilon_{true} = \ln(1 + \varepsilon) \quad (7)$$

The engineering stress–strain plot and true stress–strain plot for the S275 and S355 hot rolled-steel are given in Fig. 9.

3.3 Loading Scheme and Analysis Procedure

Liu et al. [17] loading scheme for the sudden column-loss simulation was adapted for this paper. As illustrated in Fig. 10, the sudden column-loss simulation can be divided into three stages; quasi-static preloading ($0 - t_I$), maintaining structural equilibrium

Fig. 9 The stress–strain plot of S275 and S355 hot-rolled steel

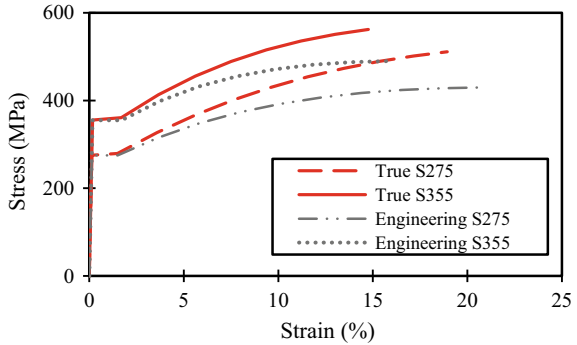
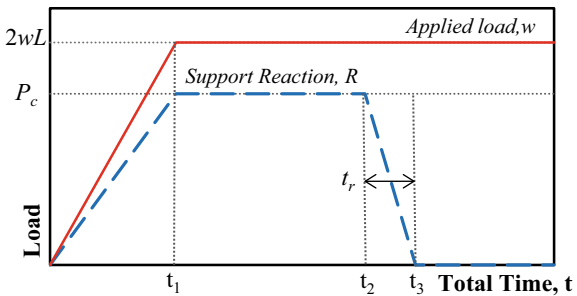


Fig. 10 The loading sequence for the sudden column-removal simulation [17]



$(t_1 - t_2)$, and sudden loss of support $(t_2 - t_3)$. The external forces acting on the beam assembly must first be defined before explaining the load scheme in Fig. 10.

There were two types of external force acting on the beam assembly throughout the analysis, which are the applied load (w) and the upward support reaction (R). The applied load (w) was assigned along the beam span length (L) as a uniformly distributed load, whereas the upward support reaction (R) was assigned at the bottom of the central column joint (Refer to Fig. 11). It should be noted that the R represents the reaction provided by the quick-releasing hook (See Fig. 2) before it was released instantaneously from the beam assembly. The self-weight of the beam assembly was

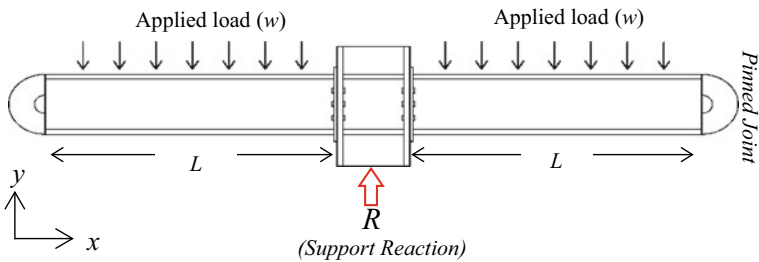


Fig. 11 The external loads' assignment in the double-span beam assembly

included in the finite element model by assigning the gravity acceleration of $g = 9.81 \text{ m/s}$ to the negative y -direction (See Fig. 11).

In the first stage of loading, the applied load (w) and the support reaction (R) were linearly increased to the full magnitude at a slow loading rate (Refer to Fig. 10). To achieve a quasi-static condition, the loading time should be in between 100 to 1000 ms [26]. Liu et al. [11] suggest the time interval for the quasi-static loading to be 200 ms ($t_l = 200 \text{ ms}$). For the second stage, the forces were then maintained for some time interval to ensure the beam assembly has achieved structural equilibrium. The time interval for the static equilibrium was taken as 300 ms ($t_2 = 500 \text{ ms}$) [11]. At the final stage of loading, the magnitude of R is reduced linearly to zero at the time interval of t_r ($t_3 = 500 \text{ ms} + t_r$) to simulate the abrupt removal of support. The parameter t_r is known as the load release time. It is essential to select an appropriate value for t_r as the dynamic structural responses are sensitive to loading rate [27]. Researchers have proven that the dynamic responses are not affected by loading rate if the load release time is equal or less than one-tenth of the natural period ($t_r \leq 0.1 T$) [1, 26]. Hence, as recommended by [28, 29], the load release time for this analysis was taken as one-tenth of the natural period ($t_r = 0.1 T$) corresponded to the vertical motion of vibration.

The support reaction (R) and the natural period of the beam specimen (T) were predetermined before executing the sudden column-loss simulation. To estimate the support reaction (R), a nonlinear static analysis was executed on a double-span beam in its intact state. In this analysis, the double-span beam was statically loaded by the applied load (w) and the support reaction force was determined. The *Static, General* analysis procedure was employed for the non-linear static analysis.

The modal analysis was executed to determine the natural period (T) of the double-span beam. In ABAQUS, modal analysis can be performed by using the *Frequency* analysis procedure.

The output of this analysis procedure is the natural frequency (ω) and its corresponding vibration mode shape. The estimated natural frequency can be converted to a natural period as follows [27]:

$$T = \frac{1}{\omega} \quad (8)$$

The *Dynamic, Explicit* analysis procedure was employed to carry out the sudden column-removal simulation with the loading sequence shown in Fig. 10. The Rayleigh damping model was assigned to introduce damping into the analysis. The Rayleigh damping model is given as follows [16]:

$$\xi = \frac{\alpha_R}{2\omega} + \frac{\beta_R\omega}{2} \quad (9)$$

Given that ξ is the damping ratio, α_R is the mass proportional damping factor, β_R is the stiffness proportional damping factor, and ω is the natural frequency. The two damping factors (α_R and β_R) are required to be defined in the analysis. According to

ABAQUS Analysis User's Guide [16], low-frequency responses are dampened by the factor α_R while high-frequency responses are dampened by the factor β_R . Li et al. [30] claim that the responses of steel structure under a column-loss state are mainly of lower frequency. Hence, only the factor α_R was considered in this analysis as the factor β_R will not significantly affect the analysis output. By employing the damping ratio of $\xi = 1.8\%$, as recommended by Li et al. [30], the factor α_R can be calculated as follows:

$$\alpha_R = 0.036\omega \quad (10)$$

3.4 Model Meshing

In this simulation, bending behavior is expected for the double-span beam after the removal of central support. The analysis is prone towards the hourglass error if coarser mesh density is employed [14], in which it may cause the double-span beam to be softer than its actual behavior. The *Getting Started with ABAQUS: Interactive Edition* [14] suggested the use of finer mesh density for the S4R element to resolve the hourglass error. However, employing finer mesh density on the whole model will increase the analytical burden significantly. To optimize the finite element analysis, varying mesh density is enforced to the geometrical model in Fig. 6.

Each beam geometry was partitioned into two segments as illustrated in Fig. 13. Segment 1 experienced the highest bending stress as compared to Segment 2 (See Fig. 13) and plastic hinge formed at Segment 1. A finer mesh density is implemented to Segment 1 and coarser mesh density for Segment 2. The extent of Segment 1 was determined based on the plastic hinge length, L_p (see Fig. 13). According to the Plastic theory [31, 32], the plastic hinge length (L_p) of a pinned-fixed condition beam is given in Eq. (11).

$$L_p = L \left(1 - \frac{1}{S} \right) \quad (11)$$

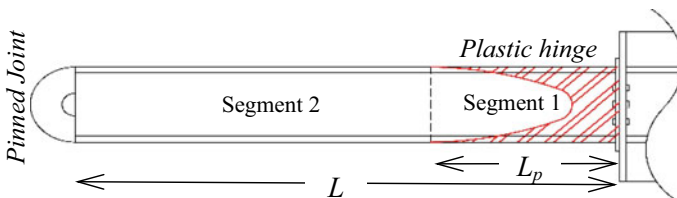
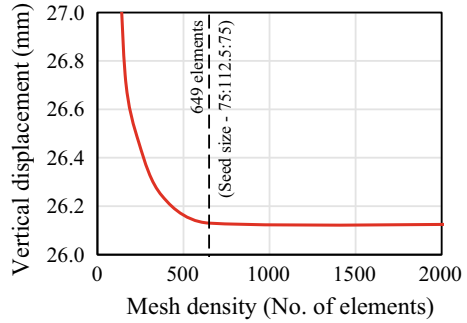


Fig. 13 Segmentation of the beam geometry on a single span prior to meshing

Fig. 14 Mesh sensitivity analysis of the flush end-plate double-span beam



Given that L_p is the plastic hinge length, L is the beam span length, and S is the shape factor. The shape factor is the ratio of plastic section modulus (W_{pl}) to elastic section modulus (W_{el}) and may vary from 1.12 to 1.17 for a universal beam. The recommended value of shape factor for a universal beam is 1.14 [31]. By taking $L = 2434$ mm, the plastic hinge length calculated using Eq. (11) yielded $L_p = 298.9$ mm.

The mesh sensitivity analysis was executed to obtain the optimum mesh density for the double-span beam geometry. From the sensitivity analysis in Fig. 14, the beam response showed consistency for mesh density higher than 649 elements. The mesh density of 649 elements (i.e. seeding size of 75:112.5:75) was concluded as the optimum mesh density for the double-span beam geometry. For the flush end-plate geometry, the seeding size of 75 mm was employed.

4 Verification of the Finite Element Model

4.1 Preliminary Analysis

A preliminary analysis was executed to determine the support reaction (R) and the natural period (T) of the finite element model before the sudden column-loss simulation was executed.

4.1.1 Modal Analysis

The first three vibration modes of the double-span beam and their respective natural frequency are given in Fig. 15. As depicted in Fig. 15, the first vibration mode involved the translation of the whole beam assembly in the y -direction with a natural frequency of 30.29 Hz ($T = 33.0$ ms). The second vibration mode was the translation of each beam span in the y -direction with an estimated natural frequency of 175.4 Hz ($T = 5.7$ ms). The third vibration mode consisted of the rotation of individual beam span about the x -axis with the natural frequency of 182.3 Hz ($T = 5.5$ ms). Note

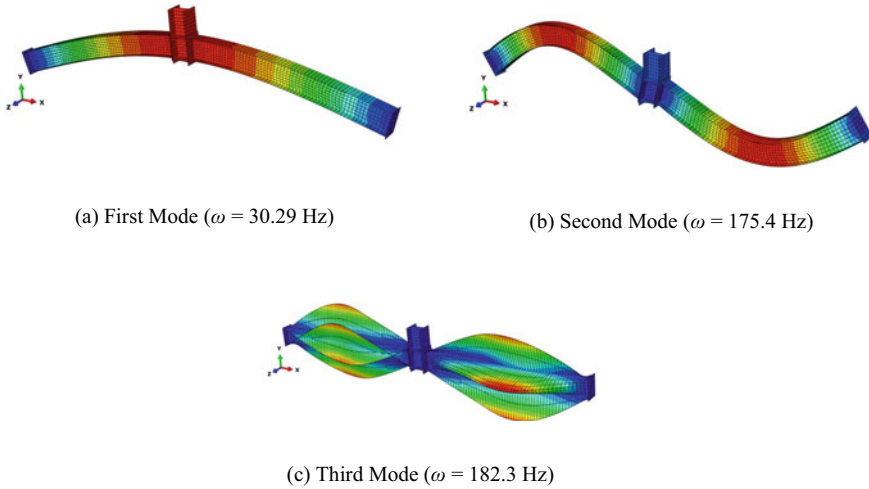


Fig. 15 The first three vibration mode of the flush-end plate beam

that no vibration mode in the z -direction was estimated as the beam assembly was restrained in translation at the z -direction.

To determine the suitable load release time (t_r), one-tenth of the natural period (T) for the first vertical vibration mode was used [28, 29]. Hence, the load release time for this simulation was $t_r = 3.30$ ms. Similarly, the natural frequency of the first vibration mode was used to estimate the Rayleigh damping factor (α_R). The α_R factor was calculated by using Eq. (10), which yield the value of $\alpha_R = 0.1090$.

4.1.2 Non-linear Static Analysis

From the finite element analysis, it was estimated about 56.6kN of upward support reaction (R) was needed at the central column joint to support the applied load (w) of 22.03kN/m. Hence, in the dynamic analysis, the upward support reaction (R) was removed instantaneously at the rate of $tr = 3.30$ ms to initiate the dynamic effect on the model. The complete loading scheme for the sudden column-removal simulation of the flush end-plate double-span beam is depicted in Fig. 16.

4.2 Sudden Column-Removal Simulation (Non-Linear Dynamic Analysis)

The dynamic vertical displacement of the flush end-plate double-span beam is depicted in Fig. 17. Based on Fig. 17, it showed that the finite element model can accurately simulate the dynamic response of the double-span beam. The maximum

Fig. 16 The complete loading scheme for the flush end-plate double-span beam

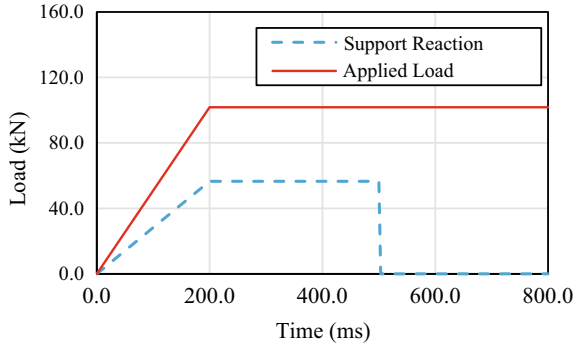
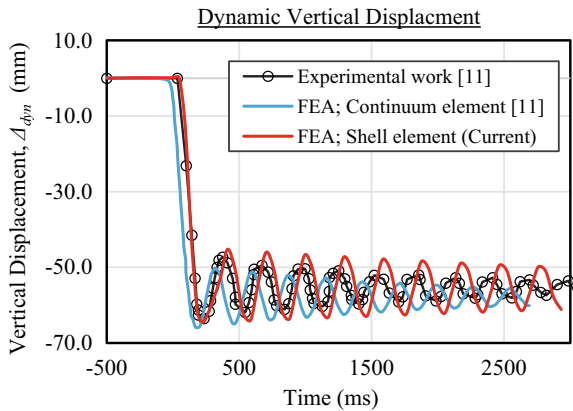


Fig. 17 Comparison of dynamic vertical displacement between current work with previous research in Liu et al. [11].



dynamic displacement of the double-span beam estimated by the finite element analysis was $\Delta_{dyn, max} = 64.41$ mm, which is 0.83% lower than Liu et al. [11] experimental results. Interestingly, the proposed finite element model in this paper yielded lower percentage different as compared to Liu et al. [11] model (i.e. 3.61% different). However, the damping behavior of the double-span beam was comparatively higher than the experimental results. A trial-and-error method must be executed to determine the suitable value of Rayleigh damping factor (α_R) for the proposed finite element model, which is not covered in this paper.

The equivalent plastic strain (PEEQ)¹ contour plot (Refer to Fig. 18) showed that the end-plate has yielded after the instantaneous removal of the upward support reaction (R). Similar failure mechanism was reported with Liu et al. [11] experimental test as shown in Fig. 4. Essentially, the finite element modelling techniques, as presented in Sect. 3, were reliable to simulate the sudden column-removal test.

¹ Equivalent Plastic Strain (PEEQ) is a scalar quantity that measures all plastic strain components at one node or element [16], which is commonly used to indicate the yielding state of the model.

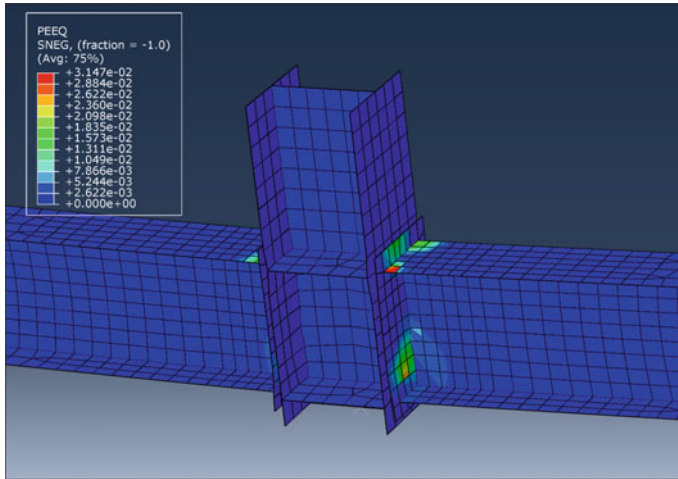


Fig. 18 The PEEQ contour plot showing the yielding state of the flush end-plate connection

5 Conclusion

This paper presents the finite element modelling approach to evaluate the sudden column-removal analysis using the ABAQUS software. The results from the experimental work of the double-span beam published by Liu et al. [11] have been validated herein. In contrast to the finite element modelling technique proposed in Liu et al. [11], this paper proposes to use the first-order shell element with reduced integration (S4R) analysis. The finite element modelling technique presented in this work acquired less computational modelling effort and significantly reduced the geometrical complexity in the modelling process. The analysis output from the finite element analysis is successfully verified against the experimental results of the prior study [11]. The proposed alternative finite element model able to predict the maximum dynamic displacement of the double-span beam with 0.83% percentage different, hence can serve as an alternative FEA modelling technique option in validating the establish experimental work in Liu et al. [11]. In conclusion, it is worth noting that the actual dynamic response of the experimental results published in Liu et al. [11] is successfully be predicted via the use of a reduced geometrical complexity modelling technique and sources of nonlinearity (i.e. contact non-linearity). Also, this work enlightens a nonlinear dynamic analysis procedure in simulating the sudden effect of a column removal of a double span beam. The finite element modelling approach for the sudden column-removal analysis using the ABAQUS software has been introduced in this paper.

Acknowledgements The Authors would like to show gratitude to Ministry of Higher Education Malaysia and UiTM Research Management Centre (RMC) for providing financial support through *Fundamental Research Grant Scheme for Research Acculturation of Early Career Research*, FGRS-RACER (File no: 600-IRMI/FRGS-RACER 5/3 (114/2019)).

References

1. Mansor H, Disney P, Parke G (2011) Evaluation of progressive collapse analysis using beam and shell elements. In: 35th annual symposium of international association for bridge and structural engineering (IABSE). Zurich
2. Sadek F, Main JA, Lew HS, El-Tawil S (2013) Performance of steel moment connections under a column removal scenario. II: analysis. *J Struct Eng* 139(1):106–119. [https://doi.org/10.1061/\(ASCE\)ST.1943-541X.0000617](https://doi.org/10.1061/(ASCE)ST.1943-541X.0000617)
3. Li H, El-Tawil S (2014) Three-dimensional effects and collapse resistance mechanisms in steel frame buildings. *J Struct Eng* 140(8):A4014017. [https://doi.org/10.1061/\(ASCE\)ST.1943-541X.0000839](https://doi.org/10.1061/(ASCE)ST.1943-541X.0000839)
4. Kwasniewski L (2010) Nonlinear dynamic simulations of progressive collapse for a multistory building. *Eng Struct* 32(5):1223–1235. <http://dx.doi.org/10.1016/j.engstruct.2009.12.048>
5. Stephen D, Lam D, Forth J, Ye J, Tsavdaridis KD (2019) An evaluation of modelling approaches and column removal time on progressive collapse of building. *J Constr Steel Res* 153:243–253. <https://doi.org/10.1016/j.jcsr.2018.07.019>
6. Rahnavard R, Fard FFZ, Hosseini A, Suleiman M (2018) Nonlinear analysis on progressive collapse of tall steel composite buildings. *Case Stud Constr Mater* 8:359–379. <https://doi.org/10.1016/j.cscm.2018.03.001>
7. Mansor H, Disney P, Parke G (2017) Performance criterion for selecting column removed in the Alternate Load Path (ALP) analysis for progressive collapse assessment. In: Global civil engineering conference (GCEC2017). Kuala Lumpur
8. Szyniszewski S, Krauthammer T (2012) Energy flow in progressive collapse of steel framed buildings. *Eng Struct* 42:142–153. <http://dx.doi.org/10.1016/j.engstruct.2012.04.014>
9. Yang B, Tan KH (2012) Robustness of bolted-angle connections against progressive collapse: Experimental test of beam-column joints and development of component based models. *J Struct Eng* 139(9):1498–1514. [https://doi.org/10.1061/\(ASCE\)ST.1943-541X.0000749](https://doi.org/10.1061/(ASCE)ST.1943-541X.0000749)
10. Yang B, Tan KH (2013) Robustness of bolted-angle connections against progressive collapse: mechanical modelling of bolted-angle under tension. *Eng Struct* 57(12):153–168. <https://doi.org/10.1016/j.engstruct.2013.08.041>
11. Liu C, Fung TC, Tan KH (2015) Dynamic performance of flush end-plate beam-column connections and design applications in progressive collapse. *J Struct Eng* 142(1):04015074. [https://doi.org/10.1061/\(ASCE\)ST.1943-541X.0001329](https://doi.org/10.1061/(ASCE)ST.1943-541X.0001329)
12. British Standard Institution (2004) Eurocode 8: Design of structures for earthquake resistance—Part 1: General rules, seismic actions and rules for buildings. British Standard Institution, London
13. Yang B, Tang KH (2013) Behavior of composite beam-column joints in a middle-column-removal scenario: experimental tests. *J Struct Eng* 140(2):04013045. [https://doi.org/10.1061/\(ASCE\)ST.1943-541X.0000805](https://doi.org/10.1061/(ASCE)ST.1943-541X.0000805)
14. ABAQUS (2014) Getting started with ABAQUS: interactive Edition. Dassault Systèmes. Available: <http://abaqus.software.polimi.it/v6.14/books/gsa/default.htm>. Accessed 20 Sept 2017
15. Brown KH, Morrow C, Durbin S, Baca A (2008) Guideline for bolted joint design and analysis: Version 1.0. United State Department of Commerce, New Mexico & California
16. ABAQUS (2014) ABAQUS Analysis User's Guide. Available: <http://dsk.ippt.pan.pl/docs/abaqus/v6.13/books/usb/default.htm>
17. Liu C, Tan KH, Fung TC (2013) Dynamic behaviour of web cleat connections subjected to sudden column removal scenario. *J Constr Steel Res* 86:92–106. <https://doi.org/10.1016/j.jcsr.2013.03.020>
18. Meng B, Zhong W, Hao J, Tan Z (2019) Improved steel frame performance against progressive collapse with infill panels. *J Constr Steel Res* 158:201–212. <https://doi.org/10.1016/j.jcsr.2019.03.022>

19. Zhong W, Meng B, Hao J (2017) Performance of different stiffness connections against progressive collapse. *J Constr Steel Res* 135:162–175. <http://dx.doi.org/10.1016/j.jcsr.2017.04.021>
20. British Standard Institution (2005) Eurocode 3: design of steel structures—Part 1–1: general rules and rules for buildings. EN 1993–1–1. British Standard Institution, London
21. Holzer SM, Melosh RJ, Barker RM, Somers AE (1975) Singer: a computer code for general analysis of two-dimensional concrete structures. National Technical Information Service (NTIS), Virginia
22. Dimopoulos CA, Freddi F, Karavasilis TL, Vasdravellis G (2020) Progressive collapse resistance of steel self-centering MRFs including the effects of the composite floor. *Eng Struct* 208:109923. <https://doi.org/10.1016/j.engstruct.2019.109923>
23. Wang H, Yang B, Zhou XH, Kang SB (2016) Numerical analyses on steel beams with fin-plate connections subjected to impact loads. *J Constr Steel Res* 124:101–112. <http://dx.doi.org/10.1016/j.jcsr.2016.05.016>
24. Yang B, Tan KH (2012) Numerical analyses of steel beam–column joints subjected to catenary action. *J Constr Steel Res* 70:1–11. <http://dx.doi.org/10.1016/j.jcsr.2011.10.007>
25. Xiang Y, Gardner L (2017) Stress-strain curves for hot-rolled steels. *J Constr Steel Res* 133:36–46. <http://dx.doi.org/10.1016/j.jcsr.2017.01.024>
26. Yu H, Burgess IW, Davison JB, Plank RJ (2008) Numerical simulation of bolted steel connections in fire using explicit dynamic analysis. *J Constr Steel Res* 64(5):515–525. <https://doi.org/10.1016/j.jcsr.2007.10.009>
27. Biggs JM (1964) Introduction to structural dynamics. McGraw-Hill, New York
28. Department of Defense (DoD) (2016) Unified facilities criteria: design of buildings to resist progressive collapse. UFC 4–023–03. Department of Defense, Washington
29. General Services Administration (GSA) (2016) Alternate path analysis and design guidelines for progressive collapse resistance. General Services Administration, Washington
30. Li GQ, Li LL, Jiang B, Lu Y (2018) Experimental study on progressive collapse resistance of steel frames under a sudden column removal scenario. *J Constr Steel Res* 147:1–15. <https://doi.org/10.1016/j.jcsr.2018.03.023>
31. Baker J, Horne MR, Heyman J (1956) The steel skeleton: plastic behaviour and design, vol 2. Cambridge University Press
32. Neal BG (1963) The plastic methods of structural analysis. Wiley

Effect of Replacement Area Ratio on Bearing Capacity Improvement of Peat Soil Columns Stabilized Using MUF-P Polymer Resin



Mohd Nazrin Mohd Daud, Nik Norsyahariati Nik Daud, and Jestin Jelani

Abstract Generally, performance of stabilized soil foundation of the treated soil using soil column method can be evaluated based upon bearing capacity and settlement behavior of the footing. The evaluation of bearing capacity improvement of treated peat soil is also commonly studied based on replacement area ratio of stabilized columns. In this study, a physical model for scale-down laboratory model has been developed and simulated for load bearing test using various soil column models for peat soil medium treated with melamine urea formaldehyde (MUF) polymer resin. Soil columns were treated with designated maximum MUF-P proportion under wet curing method before tested for load test at various depths for end-bearing foundation application. Overall, the result suggested that the stabilization of peat soil using MUF-P resin polymer had significantly improved the strength properties and compressibility behavior of peat within designated 72 h of curing period. Reinforcement of peat medium using soil columns method with 350 kg/m^3 MUF-P binder had indicated that improvement of bearing capacity ratio (BCR) has increased proportionally to the increase of replacement area ratio, α from 14.1 to 23.6%. It is noticeable that improvement of bearing capacity within rapid curing period is significant for a longer footing model which was attained at 56 and 68 kPa for $\alpha = 9.4\%$ and $\alpha = 14.1\%$ respectively. Effect of α and L/D values has also demonstrated that BCR improvement is greatly dependable to geometry of footing.

Keywords Soil stabilization · Replacement area ratio · Bearing capacity

M. N. M. Daud (✉) · J. Jelani
Universiti Pertahanan Nasional Malaysia, 57000 Kuala Lumpur, Malaysia
e-mail: nazrin@upnm.edu.my

J. Jelani
e-mail: jestin@upnm.edu.my

N. N. N. Daud
Universiti Putra Malaysia, 43300 Serdang, Malaysia
e-mail: niknor@upm.edu.my

1 Introduction

In general, performance of stabilized soil is greatly related to bearing capacity and settlement behavior of the treated soil after mixed with binder. However, performance of stabilized peat soil in terms of bearing capacity ratio (BCR) improvement is not commonly defined as there were also various other parametric studies has yet to be studied and adopted sufficiently. Performance of stabilized soil columns is also related to bearing capacity and settlement behavior of treated soil. Unlike properties of others common stabilization method which is considerably well established, bearing capacity improvement based upon BCR of newly stabilized material particularly using non-standard has yet to be defined sufficiently.

Essentially, effect of replacement area ratio and columns length on improving bearing capacity can be analyzed using bearing capacity ratio (BCR) by many researchers based on geometrical characteristic of soil—column footings [1]. Increase in the ultimate bearing capacity due to the existing of stone columns was considered through a non-dimensional parameter, the bearing capacity ratio (BCR), which is defined as follows [2]:

$$\text{BCR} = q_{ur}/q_{uo} \quad (1)$$

where q_{ur} is the ultimate bearing capacity of the reinforced soil, and q_{uo} is the ultimate bearing pressure of unreinforced soil at the same settlement level. According to Broms [3], the ultimate bearing capacity of a ground improved by end bearing columns is the sum of two independent terms that is q_1 and q_2 . The first term corresponds to the creep resistance of columns located under the footing. While, the second term, denoted as q_2 represents the bearing capacity of the soft soil where local shear failure is assumed [4]. In addition, in a research on laboratory scaled three-dimensional models constructed using remoulded soft clay improved by soil cement columns [5] indicated that bearing capacity by Broms' method [6] tends to be underestimated if the cohesion ratio becomes greater than 30. Thus, it is obvious that the need to define bearing capacity improvement correctly based on consideration of multiple engineering and design factors including type of binder has yet to be seen as an essential evaluation parameter.

According to Rashid et al. [7], further increase of area replacement ratio greater than 17.3% had no significant effect on attainable failure load even after being treated and cured between 7 to 28 days. Other researcher [8] used replacement area ratios of 17, 26 and 35% for parametric investigation, while other employed replacement area ratios of 21.7, 32.5, and 43.4% with column heights of 50 and 100 mm [1]. Previous researchers, including [7] also targeted α that is commonly designed less than 25% for soil columns footing, while other used three area replacement ratios of 13.1, 19.6, and 26.2% with length to depth ratios of 0.25, 0.5, and 0.75 [9].

On the other hand, soft soil stabilization employing various types of chemical and polymer binders has been widely studied over past few decades. Over the years, cement and lime have consistently been found to be among the most effective

stabilisers for road and airfield applications [10]. Chemical stabilisation of soil has become one of the useful solutions to treat the soft soils to achieve the required engineering properties and specification so that structures can be placed safely without susceptible to foundation failure or undergoing large settlements. The use of admixture such as lime, cement, oils and bitumen are among the most common method for improving soil. Obviously, these conventional techniques of lime and cement treatment which have been developed over the years might considered as not practically suitable for certain engineering application which requires rapid improvement of the soils.

Polymer resin such as MUF resin which is certified as low emission formaldehyde had recently found a new application for rapid soil soft soil treatment. Considerable amount of melamine content added into formaldehyde resin that subsequently make the resin less emission, has promoted for a new fresh look of the material for different field of engineering application. MUF is also considered as low emission polymer to be used commonly in construction industry [11]. Studies by Nik Daud and Daud [12] indicated that MUF resin in liquid form had effectively improved the unconfined compressive strength (UCS) of peat soil using air curing method. Later, study using various type of MUF had indicated that dry mixing method using powdered MUF-P has essentially improved strength characteristic of peat soil of high moisture content [13].

Malaysia has significant amount of wetland area in which about 30% of its land area covered by alluvium soil of soft soil medium. Additionally, peat soil which is also considered as problematic soil commonly overlaid by deep soft clay medium made up about 8% of 3 million hectares of total land area in Malaysia. This figure becomes even more significant in East Malaysia which account for about 30% of total land area [14, 15]. Commonly, soft and compressible soil can be improved using conventional method of lime and cement of pozzolanic materials or unconventionally using other types of material binders. Typical traditional stabilizer commonly used in peat soil treatment including quick lime, fly ash and ordinary Portland cement with the range of 2 to 20% proportions [16, 17]. Evidently, various type of binder pozzolanic binder has been a prime focus of research and, also commonly applicable and practically used for soil improvement method over the past few decades. However, research on soil columns stabilisation over compressible soft soil in Malaysia is very limited in which commonly focused on single column or limited numbers of group columns design [18, 19] without further determining other important parametric studies.

2 Material Properties

Specifically, polymeric binder used in the mixture was powdered MUF (MUF-P) resin polymer. It is a powdered type MUF resin that was supplied by Al-Asia Chemical Sdn. Bhd with generic code MUF 907-P. Properties of polymer resin used for a dry mixing process is described in Table 1. MUF-P proportion used in the mixture is defined as the optimum proportion of 350 kg/m³ preliminary designed to achieved

Table 1 Properties of MUF-P polymer resin (AI Asia Chemical Sdn. Bhd.)

Polymer resin	MUF-P907
Generic name	Melamine Urea Formaldehyde (Powder)
Melamine content	10%
Appearance	White powder
pH @ 30 °C	8.5–9.5
Viscosity	1750–3250 cP (mixed at 1:0.4 water ratio)
Percentage volatile	> 3%
Solubility	Soluble in water

Table 2 Engineering properties of untreated peat

Properties	Values
Depth of sampling	0.25–1.0 m
Moisture content, w	296–632%
Wet unit weight	10.3 kN/m ³
Specific gravity, Gs	1.24
Physical classification (von Post)	H5
Liquid limit, LL	153.80%
Plasticity index, PI	47.7
Organic content	76%
Ash content	24%
pH	2.9–3.3 (high acidity)

targeted UCS strength at maximum 3 days of curing period. It was initially to replicate minimum requirement of rapid curing process commonly designated for rapid application purposes. Additionally, peat soil properties used in this study is presented in Table 2. Engineering properties shown in the table were determined and obtained from various laboratory tests using undisturbed and disturbed peat samples.

After the mixing process, all moulded precast columns of treated peat samples were immediately placed vertically on rack stands that made of thick Plexiglass in which holes were drilled to specified diameter to hold the steel tubes. Consequently, 200 g of cylindrical steel plate was loaded onto the precast mixture for each tube. This amount of surcharge that is equivalent to 18 kPa was transferred onto the moulded sample using a cylinder which is also made of Plexiglass. After that, sufficient amount of water was then poured into the curing tank up to 50 mm height to mark the curing period. During wet curing procedure, water was added to resemble on-site wet curing process of naturally high moisture content peat medium which is commonly submerged below water table. All the samples were then left for 3 days to allow curing process to take place.

3 Soil Columns Modelling

Generally, all experiments were carried out on a 20 mm diameter soil column surrounded by peat soil deposits in a rectangular chamber of 350 mm height, 600 mm width and 200 mm length. The soil columns were preliminary made of precast columns of treated peat soil using optimum proportion of MUF-P binder and cured for 3 days. Additionally, the soil columns footing of various depth (L) was constructed and rested on 60 mm sand layer at the bottom.

Figure 1a and b show schematic diagram of physical model and plan views of footings that also show arrangement of footing, α and dimension of rack stand. In this study, columns footings were arranged rectangularly at uniform spacings between the columns. The α shown in the figure are represented for each type of footing of various depths between 100 to 200 mm respectively.

Additionally, provision of boundary condition for footing model has also been assigned sufficiently. The peat soil columns are assumed to be homogeneous and isotropic continuum, in which their resistance is governed by Tresca's criterion [20]. Based on this assumption, they are assumed to be purely cohesive materials. The stress reaching the lateral distance from the center of footing was also defined to be equals to $(d + l)/2$. Width of the Plexiglass chamber is extended to 600 mm to minimize boundary effect on each side of longitudinal axis of the footing model. However, maximum depth of the footing was fixed to 200 mm and d equals to 20 mm. In addition, lateral movement during installation and loading that might possibly occur was reduced by introducing steel brace at every corner of the box (rectangular chamber). Essentially, this braces also worked as a steel casing in which Plexiglass chamber was placed inside it.

4 Load—Settlement Test

4.1 Construction of Foundation

In this study, scaled model of soil deposit was prepared in a rigid rectangular box made of Plexiglass material with a width of 200 mm, length of 600 mm and depth equal to 350 mm. The peat soil used in test was mixed with specified amount of water to obtain the equivalent shear strength between 5 to 10 kPa. Preliminarily, the homogeneous peat slurry was poured into the chamber overlaying 60 mm thick drainage layer of sand at the bottom of the chamber. Consequently, the soil was packed carefully in layers of thickness of about 30 mm or less and gradually added until the layer reached the targeted final height between 100 to 200 mm thick equivalent to a depth of specified footing construction. Each layer was essentially pushed lightly to remove or minimize the entrapped air.

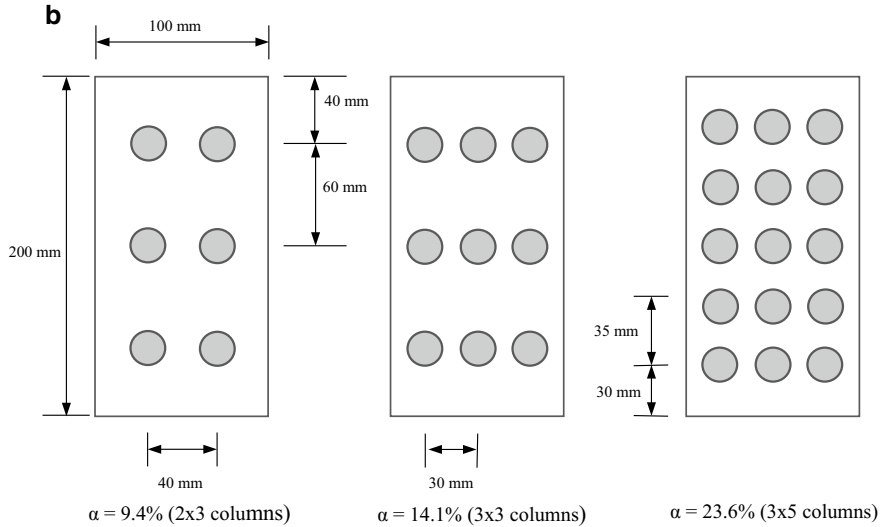
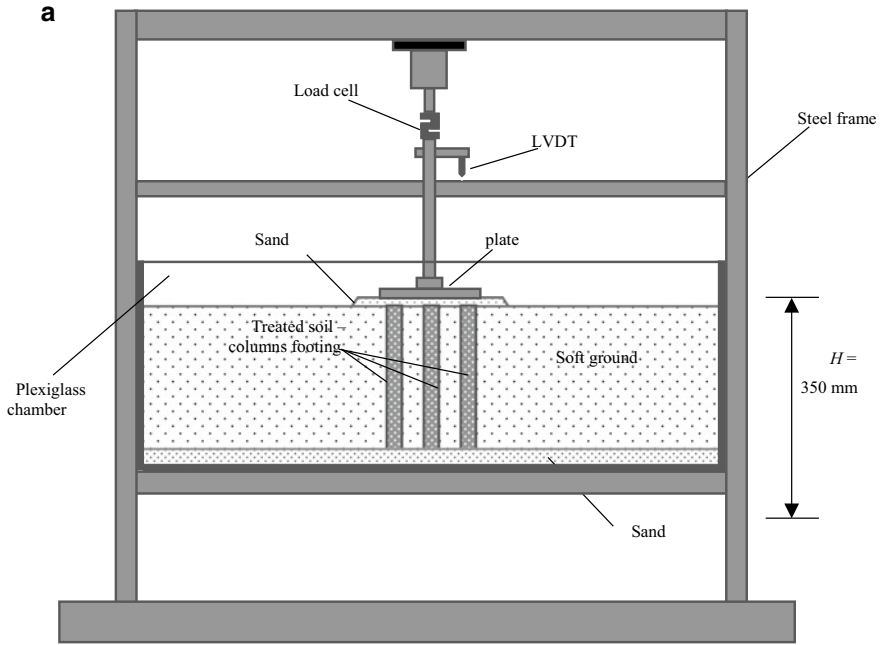


Fig. 1 a Schematic diagram of physical model for load bearing test on improved ground. b Area replacement ratio of reinforced footings and dimension of rack stands (plan views)

4.2 Soil Columns Installation

For installation procedure, group of columns which were still attached inside the steel casing were driven into peat soil medium before extruded slowly by extracting casing from the peat soil medium afterwards. Stand rack was firmly fixed to the transfer rod so that enough care was taken to keep the casing cylinder in vertical position during installation procedure. The extraction for the steel casing was applied at a constant rate of 2 mm/min to ensure smooth transition movement between the casing and precast column which was consequently left inside peat soil medium. A total of nine footings configuration based on area replacement ratio (9.4 to 23.6%) were installed in peat soil medium at various depths. The columns were extended from minimum 100 mm to the full depth of 200 mm, so that L/D ratio (length of column/width or diameter of the column) achieved a minimum of 5 which was required to develop full limiting axial stress on the column.

4.3 Loading Tests

Preliminarily, settlement and attainable failure load of group columns were determined by static load test. The loading test equipment included high capacity electric motor, load cell, data logger, settlement gauge, load displacement transducer (LDVT) and rectangular Plexiglass chamber. Campbell Scientific CR800 Series datalogger was used to record reading from the LDVT attached inside the load cell. After the installation of group of columns, rectangular plate was placed on group columns and attached to transfer rod. Subsequently, both load cell and settlement gauge were connected to a data logger for reading of the applied load and settlement during loading test. The load was applied repetitively at a constant displacement rate of 1 mm/min through a strain-gage type load cell in a vertical direction.

5 Results and Analysis

The results of the analyses, shown in Figs. 2 and 3, show load—settlement with different depth of footing. The figures also simultaneously compare the effect of area replacement ratio between 9.4 to 23.6% for their respective designated depth. For ease of analyses, in each graph the soil columns footing embedded at 200 mm depth are shown as dashed green lines, while those embedded at 150 and 200 mm depth are shown as dashed line colored in blue and red respectively. Additionally, unreinforced peat is shown in straight orange line in each graph. For adding of clarity, longer dashed line represents greater depth of soil columns while, solid line represents unreinforced soil medium that is also differentiated by different colors. Each number of footing configurations that is also representing area replacement

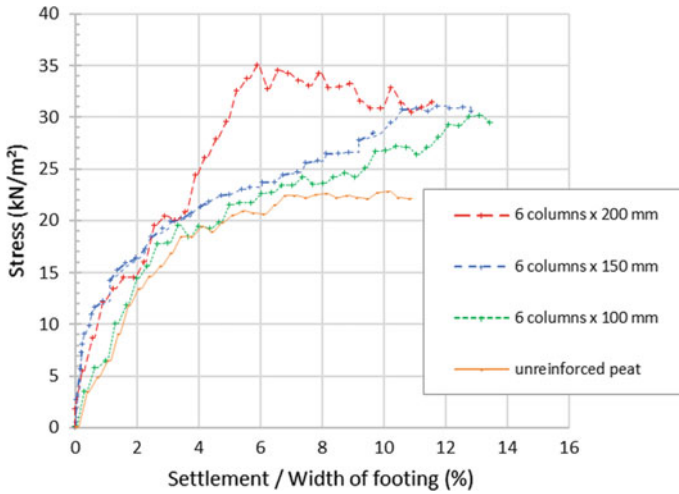


Fig. 2 Stress versus settlement—width of footings for 100 to 200 mm depth of peat medium reinforced with 6 treated peat soil columns

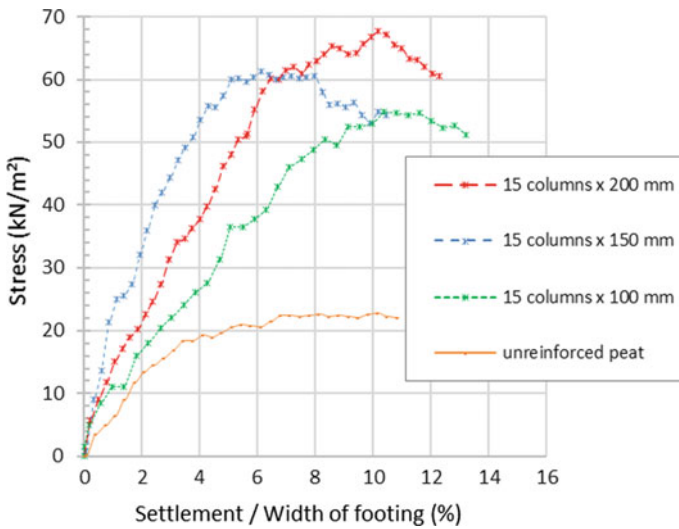


Fig. 3 Stress versus settlement—width of footings for 100 to 200 mm depth of peat medium reinforced with 15 treated peat soil columns

ratio is marked with different type of markers regardless of any footing depth. On the other hand, Figs. 5 and 6 shows stress versus settlement for 100 and 200 mm depth of footing with respect to various area replacement ratio. BCR improvement of treated peat soil using soil columns method is illustrated in Fig. 6 which is analyzed

based upon columns length to width ratio and also against replacement area ratio, respectively.

5.1 Load - Settlement Analyses

Effect of columns length. Figures 2 and 3 demonstrate how numbers of stabilized peat columns embedded in peat soil medium performed against different lengths of columns to that of unreinforced peat medium of similar length. In Fig. 2, the results show stabilized peat medium with 6 soil columns model of longest columns (200 mm) noticeably fails at highest peak attained at 35 kPa. It is about 1.5 times of the original failure stress of unreinforced soil. Additionally, there are insignificant improvements of bearing capacity for 100 and 150 mm length reinforced soil columns footings against unreinforced peat medium which are recorded at 30 and 31 kPa respectively. The improvement of peak strength might be expectedly low due to insufficient reinforcement effort using only 6 soil columns ($\alpha = 9.4\%$) of various lengths. Noticeably, settlement of both 100 and 150 mm columns almost equivalently similar with longest columns model shows peak stress failure at less than 10% of vertical displacement.

Figure 3 shows effect of columns length on footing reinforced with 15 peat soil columns. The result shows that 100 mm length soil columns model attains its peak-failure stress at 11% settlement to width footing ratio of normalized vertical stress compared to others column's length. However, it attains its failure strength slightly lower than others. Additionally, footing with longer span column noticeably acquires its peak-failure stress higher than the unreinforced soil medium by more than 2 folds if compared to that of 100 mm columns footing. Based on the figure, it also indicates that the footing with maximum 15 columns configuration used in this study exhibits brittle material behavior for all column lengths.

Effect of area replacement ratio. According to Fig. 4, it is observed that the failure load of treated columns for each footing represented by area replacement ratio, α increased if compared to unreinforced peat medium. It was found that failure load of footing of equivalent length (100 mm) increased as α increased from initially 9.4 to 23.6% as compared to original unreinforced medium. Combination of six columns settings ($\alpha = 9.4\%$) has resulted in the increase up to 35 kPa and further increase to 61 kPa as α increased to 23.6%. However, it is noticeable that lower α value has resulted in lower bearing capacity of footings with only a slight improvement (24 kN/m^2) over unreinforced peat medium.

In Fig. 5, relationship between applied stress and normalized settlement to width of footings for 200 mm depth reinforced soil columns are shown for $\alpha = 0\%$, $\alpha = 9.4\%$ and $\alpha = 14.1\%$. It can be noticed in the figure that bearing capacity of all footings increases as settlements increase. The results also show that improvement of bearing capacity is significant for a long footing model embedded in deep peat medium which is attainable at 56 and 68 kPa for $\alpha = 9.4\%$ and $\alpha = 14.1\%$ respectively. In contrast, higher bearing capacity improvement is unattainable using footing model constructed

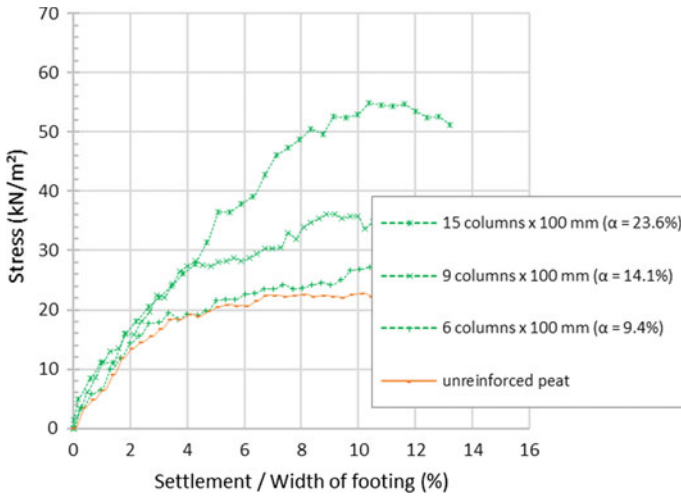


Fig. 4 Stress versus settlement—width of footings for 100 mm depth peat medium reinforced with treated peat soil columns

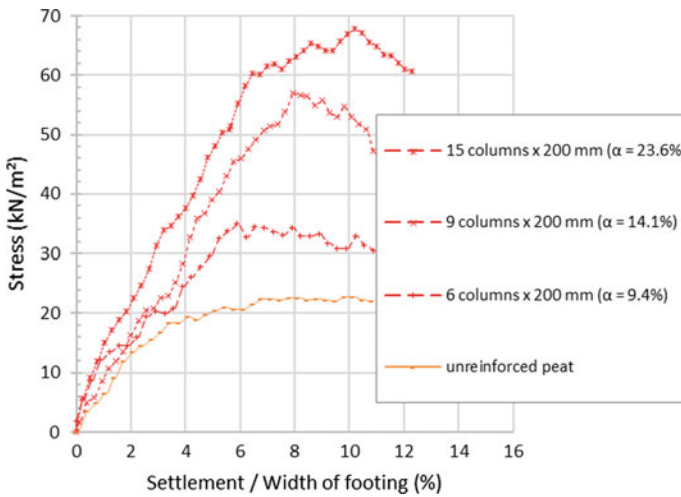
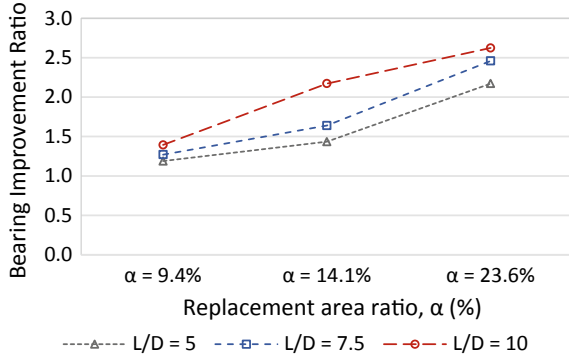


Fig. 5 Stress versus settlement—width of footings for 200 mm depth peat medium reinforced with treated peat soil columns

in depth below 200 mm with α less than 14.1% as described in the previous findings in this study.

Fig. 6 BCR improvement against replacement area ratio, area replacement ratio, α for $L/D = 5.0$, $L/D = 7.5$ and $L/D = 10$



5.2 Improvement of Bearing Capacity Ratio

In Fig. 6, BCR of stabilized columns against area replacement ratio for various column length to width ratio from physical modelling test result. As a result, it shows noticeable incremental value of BCR as length to width ratio increase from 5 to 10. Similarly, improvement pattern also can be noticed as area replacement ratio, α increase. The result shows that noticeable improvement of BCR occurs on footing model with highest replacement area ratio ($\alpha = 23.6\%$). Generally, it can be noticed that BCR increases proportionally to the increase of replacement area ratio from 14.1 to 23.6%. Also, improvement of BCR values affected simultaneously by geometrical parameter of L/D . According to Sunnetcioğlu [21], and Farouk and Shahien [8], effect of columns length on reducing settlement can be analyzed using bearing improvement ratio that are based on geometrical characteristic of soil column footings.

6 Conclusions

As for conclusion, the analyses of the study show that the improvement of bearing capacity for shorter columns of footings seems less significant compared to that of longer footings. It also shows that footings with the least number of columns at any depths do not significantly affect attainable peak failures of the reinforced footings, at least for the application of rapid curing method of stabilization. However, improvement of bearing capacity is significant for a longer footing model which was attained at 56 and 68 kPa for $\alpha = 9.4\%$ and $\alpha = 14.1\%$ respectively.

In this study, the problematic peat soil also has been given a new fresh look by consideration of polymeric material as a potential binder particularly for rapid stabilization purposes. Also, important approaches of analyses in this study that is BCR of soil columns footing constructed as end bearing foundation have sufficiently addressed to promote a better understanding on the performance and improvement

of bearing capacity of treated peat soil using MUF-P polymeric binder. Additionally, study on deep stabilization method also has produced important relationship between α and depth of footing for determination of BCR with respect to the type of load—settlement analyses observed on end bearing footing of soil columns constructed on peat soil medium.

References

1. Nissa KMS, Rashid AAS, Osouli A, Latifi N, Yunus MNZ, Ganiyu AA (2019) Settlement evaluation of soft soil improved by floating soil cement column. *Int J Geomech* 19(1):04018183-1-15. [https://doi.org/10.1061/\(ASCE\)GM.1943-5622.0001323](https://doi.org/10.1061/(ASCE)GM.1943-5622.0001323)
2. Choobbasti AJ, Noorzad R, Zahmatkesh A (2011) Performance of stone columns in soft clay: numerical evaluation. *J Geotech Geol Eng* 29(5):675–684
3. Broms BB (2000) Keynotes lecture: lime and lime/columns. Summary and visions. In: *Proceedings from 4th international conference on ground improvement geosystems*. Helsinki, Finland, pp 3803–3802
4. Bergado DT, Anderson LR, Miura N, Balasubramaniam AS (1996) *Soft ground improvement in lowland and other environments*. ASCE Press, New York, US
5. Porbaha A, Bouassida M (2004) Bearing capacity of foundations resting on soft ground improved by soil cement columns. In: *Proceedings of international conference on geotechnical engineering*. University of Sharjah, UAE
6. Broms BB (2003) *Lectures in deep soil stabilisation, design and construction of lime and lime/cement columns*. Royal Institute of Technology, Stockholm, Sweden
7. Rashid A, Safuan A, Ahmad K, Hisham M (2017) Behaviour of soft soil improved by floating soil–cement columns. *Int J Phys Model Geotech* 18:1–22
8. Farouk A, Shahien MM (2013) Ground improvement using soil-cement columns: experimental investigation. *Alex Eng J* 52(4):733–740
9. Dehghanbanadaki A, Ahmad K, Ali N (2016) Experimental investigations on ultimate bearing capacity of peat stabilized by a group of soil–cement column: a comparative study. *Acta Geotech* 11:295–307
10. Rafalko SD, Brandon TL, Filz GM, Mitchell JK (2008) Rapid chemical stabilisation of soft clay soils. *J Transp Res Board* 2026:39–46
11. LEED (2019) *Version 4 for building design and construction manual—ballot version*. Green Building Inc., Vermont, US
12. Nik Daud NN, Daud MNM (2015) Characterisation of peat soil treated with polymer resin by unconfined compressive strength test. *J Adv Civ Eng Pract Res Ababil Publisher* 1(1):11–17
13. Daud MNM, Nik Daud NN (2018) Effect of wet and dry conditions of MUF polymers on strength properties of treated peat soil. In: Pradhan B (ed) *Proceeding of global civil engineering conference*. Springer International Publishing AG, Switzerland, pp 1235–1246
14. Kalantari B (2010) *Stabilisation of fibrous peat using ordinary Portland cement and additives* (Doctoral dissertation). University of Putra Malaysia
15. Mesri G, Ajlouni M (2007) Engineering properties of fibrous peats. *J Geotech Geoenviron Eng* 133(7):850–866
16. Kolay PK, Taib SNL (2018) Physical and geotechnical properties of tropical peat and its stabilization. In: Topcuoğlu B, Turan M (ed) *Peat*. IntechOpen Limited, U.K., pp 93–105. <https://doi.org/10.5772/intechopen.74173>
17. Talib MKM (2016) *Effectiveness of Sugarcane Bagasse Ash (SCBA) Utilization in Peat Stabilization* (Doctoral dissertation). Kyushu University Fukuoka, Japan.
18. Kalantari B (2013) Civil engineering significant of peat. *Glob J Res Eng* 13(2):26–28

19. Hashim R, Islam S (2008) Engineering properties of peat soils in peninsular Malaysia. *J Appl Sci* 2008(17):1–5
20. Salençon J (1990) An introduction to the yield design theory and its applications to soil mechanics. *Eur J Mech A Solids* 9(5):477–500
21. Sunnetcioğlu ME (2012) A laboratory model study on settlement reduction of stone columns in soft clay (Master dissertation). Middle East Technical University, Turkey.

Ettringite: Influence of Steam Curing and Excessive Sulphate Content



M. Y. Balqis, H. M. K. Saiful, and M. M. Z. Raizamzamani

Abstract Most of IBS manufacturers adopt steam-curing method for rapid hydration process, in which evolves cracking features due to the formation of ettringite and caused expansion at early age. This paper investigates the ettringite formation under the excessive sulphate content and effects of high temperature of steam curing. The preparation of standard mortar prisms of dimensions $40 \times 40 \times 160$ mm made from ordinary Portland cement, sand, water and gypsum was based on EN-196. Specimens were cured under different steam curing temperature of 55, 75 and 90 °C with varies amount of 2, 5 and 7% of gypsum added. The length and compressive strength of the mortar specimens due to the creation of ettringite at different high temperatures of steam curing and excessive sulphate content have been measured and discussed. The ettringite mineral was detected by Scanning Electron Microscope (SEM) and the chemical composition was examined by Energy Dispersive X-ray (EDX). Results showed that the high temperature of steam curing had increased the rate of hydration process and at the same time produced higher population of ettringite.

Keywords Ettringite · Steam curing · Sulphate attack · Precast concrete · DEF · Hydration process

1 Introduction

Pre-fabricated building component has become popular in the last few decades in the construction industrial to speed up the construction process. This environmentally friendly building operations is termed as Industrialised Building System (IBS) by the industry and government in Malaysia. In addition to that, taking into account the time reduction factor and efficiency of manufacturing, most of precast concrete

M. Y. Balqis (✉)

School of Civil Engineering, College of Engineering, Universiti Teknologi MARA (UiTM), Shah Alam, Malaysia

e-mail: balqis1157@uitm.edu.my

H. M. K. Saiful · M. M. Z. Raizamzamani

Ling & Wong Perunding SDN. BHD, Johor, Malaysia

producers choose a steam curing process for rapid hydration. Steam curing method is a thermal process and has been used for quite few years to enhance the growth of concrete products. As the hydration rate of cement increases with an increase in temperature, the increase in strength can be boosted by curing concrete in steam [1]. The steam curing process involves four different stages: the precuring stage, the heating stage, the thermostatic stage, and the cooling stage [2, 3]. However, precast concrete products with higher steam curing temperature were reported to crack after several years [4, 5]. Similar results were reported by other researcher observed defects such as microcracks and porosity enlargement due to the formation of ettringite as compared with concrete cured under room temperature [6, 7].

The technology of steam curing has been primarily utilized for ordinary Portland cement concrete rather than blended cement and concrete with a large portion of mineral admixtures, i.e., gypsum [8, 9]. The sulphate present in Portland cement under normal conditions will react to produce hydrated sulphoaluminate compounds (ettringite). Ettringite was a mineral crystallization which has hexagonal shape. The formation of ettringite is normal product in concrete at its early age heating that occurred from the reaction between sulphate, aluminium and calcium. This predominant ettringite creation is believed to be durable, stable and advantageous for fresh concrete during the time of its initial strength. In the presence of water, ettringite decomposes to calcium monosulphoaluminate. This reaction is difficult to prevent because aluminium, sulphate and calcium were initial chemical composition present in cement. Nevertheless, it is possible to control and reduce the creation of ettringite throughout its initial stage from being more intricate and then converts to the secondary ettringite formation which acts as an expansive compound [10–12]. In the initial stage, ettringite is seen as a positive effect because it enables the setting regulation and gradual stiffness development until the maximum compressive strength of concrete is achieved. However, a damaging role is often attributed by massive secondary ettringite formation in hardened concrete or widely acknowledged as delayed ettringite formation (DEF). DEF is a subdivision of the sulphur threat on internal concrete in which it is classified as a part of harmful mineral which might cause cracking [12]. Several variables have an effect on the growth of DEF and it can be divided into two categories namely those related to the composition of concrete and those linked to the environment [13].

DEF seems to be a rising issue in practise. The existence of DEF in steam-cured concrete, particularly in steam-cured railway sleepers and IBS components, has been continually documented. The fundamental principles of DEF processes can be correlated with prior freezing, ASR cracking or perhaps even shrinkage [14]. More to the point, DEF is a consequence of improper heating during the curing process of the concrete. Primary ettringite was considered to be in steady state in concrete until the curing temperature become too high (above 70 °C–80 °F) and suppressed the primary ettringite formation [15]. During this period, the sulphate concentration in the pore liquid is increased for an unusually long period of time in the hardened concrete. In response to that, the sulphate will react with aluminium and calcium in the cement paste and the cement paste starts to expand. Due to this expansion, the gaps are formed around the aggregate. Based on free energy consideration, ettringite

nucleation will take place preferentially near crack tips. The growth of ettringite crystal will contribute to the spread and opening of the crack [14]. This ultimately initiates micro-cracking and follows by macro-cracking which cause an open space in concrete [16]. The crack system triggers an extreme loss of dynamic elastic modulus, that has significant structural consequences. Local expansive stresses at the tip of the crack can also embody a very high stress intensity factor.

In order to make sure that the concrete fulfils its expected lifespan, it's indeed vital to minimize the propagation of micro-cracking before the creation of macro-cracking. The cracks may remain empty or later be partly or even filled with ettringite. In addition to ambient temperature of curing, the continuous water supply existence at room temperature of water curing process and excessive of sulphate and alkali content have also been reported to contribute to the formation of DEF [17]. High-temperature steam curing can indeed exacerbate visceral reactions to Alkali-Silica (ASR) in certain reactive aggregates that then encouraged the creation of DEF in concrete [14].

The use of gypsum in cement manufacturing process has been permitted to control "setting of cement". Gypsum is a mineral and is hydrated calcium sulphate in chemical form with the chemical formula CaSO_4 . In general, gypsum has water associated in the molecular structure ($\text{CaSO}_4 \cdot 2\text{H}_2\text{O}$). It is also being added to concrete mix to control the rate of hardening of the concrete. However, excess gypsum in the cement would possibly increase cement paste expansion due to DEF [18, 19]. The effect of cement composition on DEF is not fully understood. Some factors correlate strongly but the causes are not clear. For example, the sulphates are added to Portland cement to avoid flash set of concrete. At the same time, there is no consent as to what the critical ratio of sulphates to aluminates is. It should be noted that the sulphate and aluminate content may meet the specified limits for individual components, but the ratio may indicate high risk of developing DEF damage.

In the case of present study, the causes of DEF formation were limited to the combination of excessive sulphate content at elevated temperatures of steam curing. The influence of different steam curing temperature on cement mortars was evaluated. Furthermore, the length of expansion of cement paste (mortar) attributed to the generation of ettringite was measured and observed. This work aimed to enhance the performance of precast concrete under the process of steam curing and minimize defects in precast concrete for the future development of construction, specifically in Malaysia.

2 Materials and Methods

An experimental program was carried out to examine the expansion of mortar specimens and the influence of various steam-curing applications on the growth of the compressive strength of concrete. Descriptions such as the preparation of test specimens, the pre-conditioning of mortar specimens, the set-up of the test and the optical

observations of ESEM and stereomicroscopy were discussed and elaborated in the following sections.

2.1 Materials and Preparation of Test Specimens

Thirty-six (36) standard mortar prisms of dimensions $40 \times 40 \times 160$ mm made from ordinary Portland cement (CEM I 42.5), CEN Standard Sand and 0.5 water to cement ratio in accordance with EN196-1:2005 were prepared in three different batches. The three mortar batches were then added with 2, 5 and 7% of gypsum respectively. Three (3) repetitive prisms were prepared under each steam curing temperature as depicted in Table 1.

Table 2 shows the oxide chemical composition of ordinary Portland cement and Table 3 summarizes the composition for production of three replicate test specimens. Each batch of mixture was subjected to three different temperature of steam curing of 55, 75 and 90 °C respectively.

The amount of fine aggregate (CEN Standard Sand) passing via a sieve is provided in percentage terms as shown in Table 4. In addition, for all mortar samples, it was necessary to follow the standard for the standardizing of its characteristic strength and chemical composition.

The cement and water were brought into contact at a lower speed in a mixer bowl to avoid the loss of water or cement due to splash. After 30 secs of mixing, the sand and gypsum were added to the paste and continue mixing for another 30 secs at the same speed rate. The mixing speed was immediately increased after the 30 secs for another 30 secs and was left in rest condition for another 90 secs. The mixing was continued at higher speed for another 60 secs in which complete the 240 secs of mixing duration in order to ensure all the materials were completely mixed and achieved standard mortar workability outlined by EN-196.

2.2 Pre-conditioned of Mortar Specimens

The mortar prisms were kept for 24 h curing at room temperature before being un moulded and placed in the water pond for 5 h pre-curing process at room temperature. Then, the samples were immediately brought into the autoclave machine for steam curing at different temperature of 55, 75 and 90 °C according to different percentage of gypsum added for 15 h. After 15 h of steam curing, the samples were cooling down gradually for another 5 h. After cooling, the length of each sample was determined and counted as the initial length of the sample. Finally, the samples were placed back in the water pond at room temperature for normal curing for the next 70 days.

Table 1 Details configuration of mortar specimens

Specimen designation	Percentage of gypsum (%)	Steam curing temperature (°C)	Water curing temperature (°C)
M1-En-P2-T0	2	0	25
M2-En-P2-T0			
M3-En-P2-T0			
M1-En-P2-T90		90	25
M2-En-P2-T90			
M3-En-P2-T90			
M1-En-P2-T55		55	25
M2-En-P2-T55			
M3-En-P2-T55			
M1-En-P2-T75		75	25
M2-En-P2-T75			
M3-En-P2-T75			
M1-En-P5-T0	5	0	25
M2-En-P5-T0			
M3-En-P5-T0			
M1-En-P5-T90		90	25
M2-En-P5-T90			
M3-En-P5-T90			
M1-En-P5-T55		55	25
M2-En-P5-T55			
M3-En-P5-T55			
M1-En-P5-T75		75	25
M2-En-P5-T75			
M3-En-P5-T75			
M1-En-P7-T0	7	0	25
M2-En-P7-T0			
M3-En-P7-T0			
M1-En-P7-T90		90	25
M2-En-P7-T90			
M3-En-P7-T90			
M1-En-P7-T55		55	25
M2-En-P7-T55			
M3-En-P7-T55			
M1-En-P7-T75		75	25
M2-En-P7-T75			
M3-En-P7-T75			

Table 2 Chemical composition of ordinary Portland cement

Oxide	Chemical formula	Content %
Lime (C)	CaO	64.73
Silica (S)	SiO ₂	21.20
Alumina (A)	Al ₂ O ₃	5.22
Iron Oxide (F)	Fe ₂ O ₃	3.08
Others	MgO, NaO, K ₂ O, SO ₃	6.0

Table 3 Composition of mortar mix required for three test specimens

Compound	Weight (g)
Cement (CEM I, 42.5)	450
CEN standard sand	1350
Water	225

Table 4 Sieve analysis of CEN standard Sand used in experiments

Sieve size (mm)	% cumulative retained	% of retained	Total mass (g)	Mass retained (g)	Units	Total mass (g)
2	0	0		0		0
1.6	7	7		94.5		1134
1	33	26		351		4212
0.5	67	34	1350	459	12	5508
0.16	87	20		270		3240
0.08	99	13		175.5		2106
Total	100			1350		16,200

2.3 Testing of Samples

DEF may cause swelling of the hardened concrete and subsequent cracking (if unrestrained) has been known for many years. This reaction can take sometimes before it significantly effects the properties of hardened concrete [20]. A test series were conducted to measure the expansion of mortar samples. Initially, Vernier Caliper was used to estimate the length of each sample. The samples were also weighed by using analytical balance to record the change of samples volume. The expansion and volume change of the samples were recorded in every 7 days within the period of 70 days. After curing period of 70 days, the samples were tested against its compressive strength.

2.4 Ettringite Precipitation Observations

DEF, in which individual needle-like crystals cannot easily be observed with the aid of an ordinary optical microscope. In order to conclude that the ettringite formation can be attributed to the high temperature of steam curing, additional measurements were carried out. Microanalysis and electron imaging were done by means of Environmental Scanning Electron Microscopy (SEM) and Energy Dispersive X-Ray (EDX). The microstructural features characteristically associated with DEF provide useful information. The crushed samples from the compression test were examined under SEM at magnification between 20 to 40 times to observe ettringite formation in the micro voids or cracks of the cement matrix. The observed mineral formation was mapped on the enlarged image.

3 Results and Discussions

3.1 Expansion of Mortar

There were no significant changes of expansion of mortar were observed in all specimens by 70 days. The percentage of expansion is determined on the basis of the following formulation.

$$\text{Percentage of expansion}(\%) = \frac{(\text{Final length} - \text{Initial length})}{(\text{Initial Length})} \times 100 \quad (1)$$

The reason of that can be due to the short period of time of test exposure. Within this time, the unstable growth of ettringite was not strong enough to cause internal forces and change in volume that may fracture the hardened cement paste. The other reason can be possibly explained by less sensitivity of Vernier calliper employed. The significant effect of the ettringite at this stage can only be seen on compressive strength development as the growth really much affected the chemical reaction and hydration process of the cement.

3.2 Compressive Strength Development

Table 5 displayed the ultimate compressive strength of mortar samples with different percentages of gypsum at 70 days. The comparison between the strength development of 70 days of standard mortars after steam curing and the strength development of steam-cured mortars containing different percentage of gypsum is shown

Table 5 Ultimate compressive strength of mortar with 2, 5 and 7% gypsum content

Specimen designation	Percentage of gypsum (%)	Steam curing temperature (°C)	Ultimate compressive strength (MPa)	Ave. ult. Compressive strength (MPa)	
M1-En-P2-T0	2	0	36	31.43	
M2-En-P2-T0			34.9		
M3-En-P2-T0			23.4		
M1-En-P2-T90		90	90	34.76	33.56
M2-En-P2-T90				34.48	
M3-En-P2-T90				31.45	
M1-En-P2-T55		55	55	28.05	27.78
M2-En-P2-T55				29.89	
M3-En-P2-T55				25.39	
M1-En-P2-T75	75	75	37.92	38.83	
M2-En-P2-T75			35.26		
M3-En-P2-T75			43.32		
M1-En-P5-T0	5	0	17.19	17.18	
M2-En-P5-T0			19.06		
M3-En-P5-T0			15.3		
M1-En-P5-T90		90	90	38.48	34.15
M2-En-P5-T90				33.09	
M3-En-P5-T90				30.87	
M1-En-P5-T55		55	55	18.54	20.26
M2-En-P5-T55				24.09	
M3-En-P5-T55				18.15	
M1-En-P5-T75		75	75	26.36	29.36
M2-En-P5-T75				34.86	
M3-En-P5-T75				26.86	
M1-En-P7-T0	7	0	8.84	8.98	
M2-En-P7-T0			9.06		
M3-En-P7-T0			9.04		
M1-En-P7-T90		90	90	8.15	8.32
M2-En-P7-T90				7.09	
M3-En-P7-T90				9.73	
M1-En-P7-T55		55	55	13.22	12.23
M2-En-P7-T55				10.85	
M3-En-P7-T55				12.61	
M1-En-P7-T75		75	75	20.18	19.66
M2-En-P7-T75				21.86	
M3-En-P7-T75				16.95	

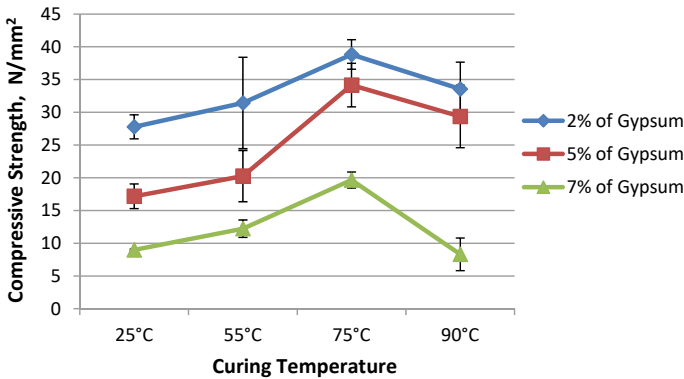


Fig. 1 Compressive strength of mortar at 70 days with different steam curing temperatures and gypsum percentages

in Fig. 1. The increased of gypsum added in mortar specimens resulted in a significant decreased of compressive strength. Mortars with 55 and 75 °C of steam curing temperature indicated a positive development of its compressive strength.

At 75 °C temperature, the strength was increased by almost 40 and 99% in mortar with 2 and 5% gypsum added respectively in comparison to mortar under normal curing process. However, the strength starts to decrease considerably at 90 °C of steam curing by 15% in comparison to 75 °C samples. Additionally, the strengths observed in 90 °C sample were still higher than in normal cured specimens except mortar with higher percentage of gypsum added. Apparently the decreased of compressive strength can possibly be explained by higher steam curing temperature applied which may decompose the primary ettringite into calcium aluminate monosulphate when reacted with tricalcium aluminate (C_3A).

Both effects of high gypsum content and temperature of steam curing apparently result in reduction on compressive strength development of mortar specimen. In addition, another study found that heat treatment seems to be important contributing factors leading to DEF, in which the optimum temperature of the curing process ought to be less than 70 °C in order to minimize the possibility of DEF [18]. Additionally, according to Fridrichova et al. [15], ettringite was found in concrete subject to a temperature of 65 °C and deformation starts at a temperature of 93 °C. In certain cases, it has been found that the DEF creation is also affected by the addition of excessive sulphate in fresh concrete [21].

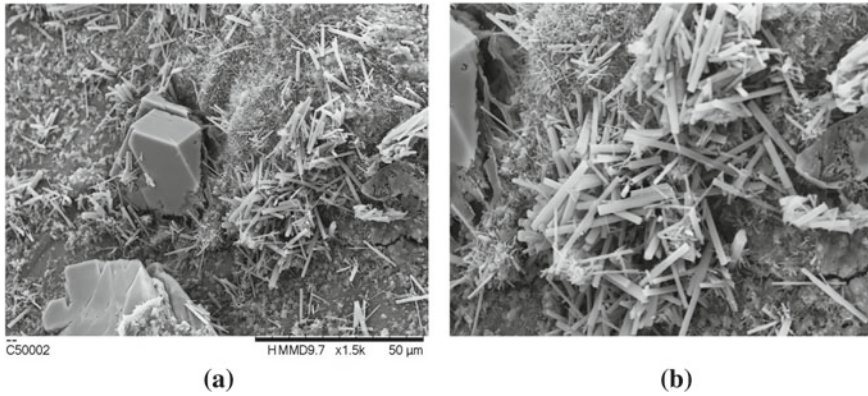


Fig. 2 ESEM images (sample M2-En-P7-T90) of **a** ettringite in microcracks and **b** zooming of ettringite in the form of long crystal

3.3 Microscopic Observation of Ettringite Formation by Using SEM and EDX

The influence of gypsum and steam curing on calcium hydroxide (CH) crystallization of cement mortar was studied using SEM and EDX. Figure 2 indicates the crystal morphology of ettringite formed due to high content of gypsum at higher steam curing temperature. Results showed that the reduction in cement mortar strength was related to formation of ettringite as no observation of ettringite were able to spot in samples with 55 and 75 °C of steam curing temperature. Also according Scrivener and Taylor [22], the initial ettringite discovered after steam curing and exposure to a moist climate emerged to be microcrystalline ettringite closely intermingled with the inner CSH element. It was believed that only later ettringite crystals were discovered to be noticeably different by SEM. In addition to that, the recrystallized ettringite in air voids and in paste cracks and as well as other open spaces is deemed to be mechanically passive and considered to be benign [23].

In the 90 °C of mortar sample, copiousness of “needle-like” crystal structure was observed on pore spaces in the mortar what indicates the nucleation of calcium sulphoaluminate in the form of ettringite. Figures 2a and 3a show a deposition of ettringite with several bright crystals of calcium hydroxide (CH) were presented as well. On the other hand, ettringite was obviously detected across every image taken, which indicates a great evidence of ettringite development in those kind of environments. This mean, in the latter case they may become unstable depending on the amount of sulphates present and can cause serious damage to concrete structures. Figure 2b displays scanning electron micrograph taken at high magnification, revealing that the individual crystals are most often high aspect ratio elongated rods or needles.

The circled area in Fig. 3b has been inspected by EDX as well as its identity has been confirmed. In terms of mineralogy, ettringite is made up of Ca, Si, Al, and

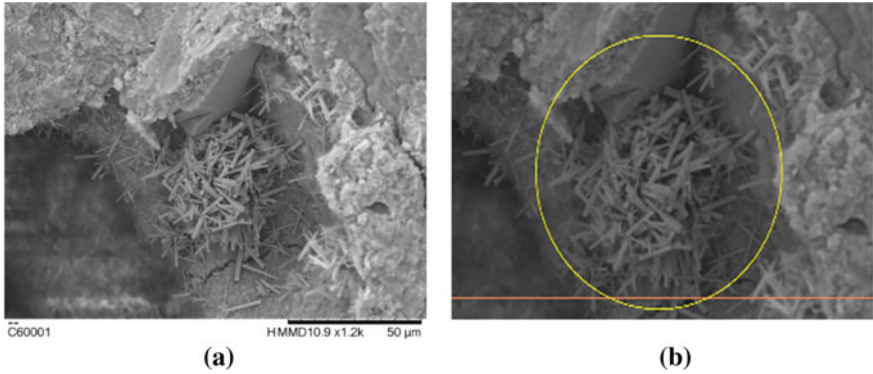


Fig. 3 ESEM images (sample M3-En-P7-T90) of **a** ettringite accumulated in the pore spaces and **b** zooming of ettringite in the form of long crystal

O. These elements were verified, and all components related to ettringite composition were presented as depicted in Fig. 4. Qualitative chemical analysis also shows significant peaks of element contents for calcium sulfoaluminate mineral or widely acknowledged as ettringite.

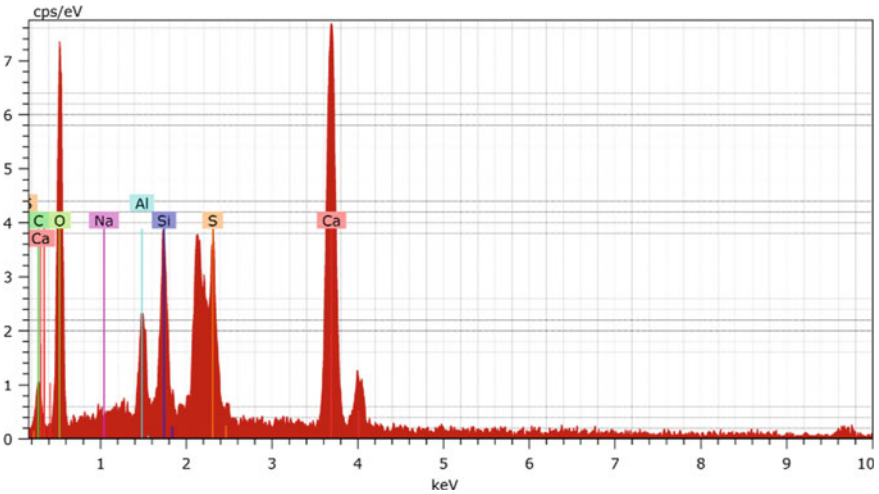


Fig. 4 Micro-structure of ettringite in sample M2-En-P7-T90 generated via EDX analysis

4 Conclusions

The influence of steam curing on mortar containing gypsum was investigated under different of temperature and gypsum percentage used respectively. The compressive strength development of mortar specimens was also characterized in this experimental study. Based on the results presented, it was concluded that the steam curing process facilitated the development of mortar strength in comparison to mortar under normal curing process. However, above temperature 75 °C, it was revealed that the mortar strength drastically drops in all specimens. Subsequent to that, evidence was found that the copiousness presence of ettringite only in the case of higher temperature of steam curing sample with a higher gypsum percentage. The EDX study revealed that the “needle-like crystal” structure was rich in oxygen, calcium, aluminium and sulphur as calcium sulfoaluminate. Nevertheless, the observed ettringite was found not to contribute in the significant expansion of mortar samples at early ages in within 70 days. Based on the experimental study described above, the result contributes better understanding of steam curing method of concrete to the pre-cast concrete industry.

Acknowledgements The authors gratefully acknowledge all staff in Concrete, Fabrication and Heavy Structures laboratories, Faculty of Civil Engineering and Faculty of Applied Science, Universiti Teknologi MARA (UiTM), Shah Alam, Selangor for their strong support and assistance in completing these experimental works.

References

1. Turkel S, Alabas V (2005) The effects of excessive steam curing on Portland composite cement concrete. *Cem Concr Res* 35:405–411
2. Won I, Na Y, Kim JT, Kim S (2013) Energy-efficient algorithms of the steam curing for the in situ production of precast concrete members. *Energy Build* 64:275–284
3. Cassagnabère F, Escadeillas G, Mouret M (2009) Study of the reactivity of cement/metakaolin binders at early age for specific use in steam-cured precast concrete. *Constr Build Mater* 23(2):775–784
4. Sahu S, Thaulow N (2004) Delayed ettringite formation in Swedish concrete railroad ties. *Cem Concr Res* 1675–1681
5. Hime G (1996) Delayed ettringite formation—a concern for precast concrete. *Precast Concr Inst* 26–30
6. Kunlin M, Guangcheng L, Youjun X (2017) A real case of steam-cured concrete track slab premature deterioration due to ASR and DEF. *Case Stud Constr Mater* 63–71
7. Escadeillas G, Aubert JE, Segerer M, Prince W (2007) Some factors affecting delayed ettringite formation in heat-cured mortars. *Cem Concr Res* 37(10):1445–1452
8. Castellano CC, Bonavetti VL, Donza HA, Irassar EF (2016) The effect of w/b and temperature on the hydration and strength of blastfurnace slag cements. *Constr Build Mater* 111:679–688
9. Poon CS, Lam L, Wong YL (2000) Study on high strength concrete prepared with large volumes of low calcium fly ash. *Cem Concr Res* 30(3):447–455
10. Peiyu Y, Feng Z, Jiang P, Xiao Q (2004) Relationship between delayed ettringite formation and delayed expansion in massive shrinkage-compensating concrete. *Cem Concr Compos* 26:687–693

11. Mehta P (1973) Mechanism of expansion associated with ettringite formation. *Cem Concr Res* 1–6
12. Oh BH (2010) Reproduction of delayed ettringite formation (DEF) in concrete and relationship between DEF and alkali silica reaction. *Fract Mech Concr Concr Struct* 1024–1029
13. Pichelin A, Carcasses M, Cassagnabere F, Multon S, Nahas G (2020) Sustainability, transfer and containment properties of concrete subject to delayed ettringite formation (DEF). *Cem Concr Compos* 113:103738
14. Diamond S, Ong S (1994) Combined effects of alkali silica reaction and secondary ettringite deposition in steam cured mortars. In: Gartner EM, Uchikawa H (eds) *Cement technology*. Ceramic transactions vol 40, Amer. Ceram. Soc., Westerville, OH, pp 79–90
15. Fridrichova M, Dvorak K, Gazdik D, Mokra J, Kulisek K. Thermodynamic stability of ettringite formed by hydration of Ye'elimité Clinker. *Adv Mater Sci Eng* 1–10
16. Dayarathne WHRS, Galappathi GS, Perera KES, Nanayakkara SMA (2013) Evaluation of the potential for delayed ettringite formation in concrete. In: National engineering conference. Sri Lanka: 19th ERU Symposium, Faculty of Engineering, University of Moratuwa
17. Mc Donald D (1998) Delayed ettringite formation and curing implications of the work of Kelham. *Cem Concr Res* 29(12):1827–1830
18. Horkoss S, Escadeillas G, Rizk T, Lteif R (2016) The effect of the source of cement SO₃ on the expansion of mortars. *Case Stud Constr Mater* 4:62–72
19. Bing T, Cohen MD (2000) Does gypsum formation during sulfate attack on concrete lead to expansion? *Cem Concr Res* 30:117–123
20. Stark J, Bollmann K (2000) Delayed ettringite formation in concrete. *Nordic Concr Res Publ* 23:4–28
21. Fu Y, Ding J, Beaudoin JJ (1997) Expansion of Portland cement mortar due to internal sulfate attack. *Cem Concr Res* 27(9):1299–1306
22. Scrivener K, Taylor HFW (1993) Delayed ettringite formation: a microstructural and microanalytical study. *Adv Cem Res* 5:139–145
23. Diamond S (1996) Delayed ettringite formation—processes and problems. *Cem Concr Compos* 18(3):205–215

Geoforensic Investigation of Cavity and Settlement for Abutment Bridge Using Electrical Resistivity Imaging



A. S. A. Rahman and I. B. M. Jais

Abstract Geoforensic investigation of cavity and settlement for abutment bridge using electrical resistivity imaging was conducted at Federal Highway FT02 Sect. 12.00 Klang. The objective of the investigation is to identify the cause of undulation occurred beneath the abutment bridge and cause discomfort to the road users and in the same time proposed rehabilitation method to solve the problems. Electrical resistivity imaging and JKR probe were used to identify the subsoil profile properties and the occurrence of water seepage. Findings reveal that by using the electrical resistivity imaging, the water seepage were clearly tabulated beneath the subsoil of the investigated areas and in clearly indicated that the soil is in weak conditions. This fact was also supported by the data of JKR probe recorded at the same location of the electrical resistivity imaging. Thus, the rehabilitation of the problems was proposed to overcome the settlement of the site.

Keywords Geoforensic · Electrical resistivity imaging · JKR Probe · Geological formation

1 Background of the Problem

The Federal Highway located in Klang Valley which is a controlled-access highway connecting the city of Kuala Lumpur and Klang in Selangor with the total length of 45 km. This highway starts from Seputeh in Kuala Lumpur to Klang, Selangor and is the busiest highway in the Klang Valley. It is a three and four lane carriageway providing links to the booming towns in the Klang Valley [1]. The section FT 02 stretch which is from Bandar Klang to Sungai Rasau measures 5.7 km was upgraded to 6 lanes which has completed in 1993 by PLUS Expressway Bhd [2]. Figure 1 illustrates the overview of the Federal Highway stretch from Kuala Lumpur to Klang in Selangor.

A. S. A. Rahman (✉) · I. B. M. Jais
School of Civil Engineering, College of Engineering, Universiti Teknologi MARA (UiTM),
40450 Shah Alam, Selangor, Malaysia
e-mail: abdulsamad@uitm.edu.my



Fig. 1 An overview of the Route FT02 Federal Highway [3]

The abutment approach on the viaduct section just right after Sungai Rasau experienced settlement and undulation. This problem has occurred numerously, thus the only solution is to regulate and resurface the settled section with additional premix to realign vertically from the bridge approaches with the transition earth fill embankment. Due to the settlement issues experienced on site, the contractor has appointed the geotechnical specialist to carry out the geoforensic investigation where one of the objective is to acquire geological information at the site so as to provide data in the evaluation of subsequent rehabilitation of the proposed rehabilitation works at sites, to assess the subsurface condition at the proposed site using JKR Probe and to identify the causes of failure and assessment of settlement using Electrical Resistivity Imaging (ERI) method.

The abutment approach on the viaduct section just right after Sungai Rasau experienced settlement and undulation. This problem has occurred numerously, thus the only solution is to regulate and resurface the settled section with additional premix to realign vertically from the bridge approaches with the transition earth fill embankment. Due to the settlement issues experienced on site, the contractor has appointed the geotechnical specialist to carry out the geoforensic investigation where one of the objective is to acquire geological information at the site so as to provide data in the evaluation of subsequent rehabilitation of the proposed rehabilitation works at sites, to assess the subsurface condition at the proposed site using JKR Probe and to identify the causes of failure and assessment of settlement using Electrical Resistivity Imaging (ERI) method.

2 Site Geomorphology and Geology

2.1 Site Geomorphology

This geoforensic investigation was performed at bridge FT02 Sect. 12.00 at KM5.6 East Bound and West Bound at Federal Highway near Taman Sungai Rasau, Klang as shown in Fig. 2 and Fig. 3. The location of the project is situated at $03^{\circ}03'31.9''N$ $101^{\circ}28'32.6''E$ along the Federal Highway. Generally, the site topography consists of flat terrain surrounded by commercial building and housing areas.



Fig. 2 Site location of FT02 Sect. 12.00 near Taman Sungai Rasau, Klang



Fig. 3 Close-up location of FT02 Sect. 12.00 near Taman Sungai Rasau, Klang

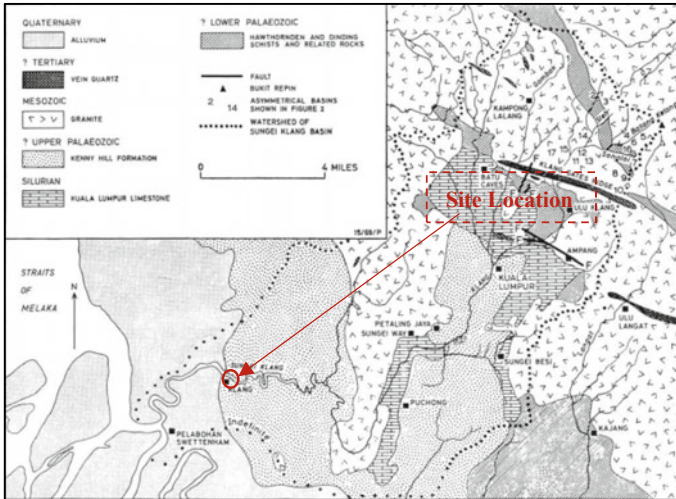


Fig. 4 Geological formation of the site location at Sungai Rasau, Klang [5]

2.2 Site Geomorphology

The geology of the Peninsular Malaysia area has been well documented. The geological formation found in most of the site location situated in Sungai Rasau, Klang area consists of Kenny hill formation [4]. Furthermore, the geological formation in this area is dominated by phyllite, slate, shale, sandstone, peat, humid clay and silt. Moreover, the site location also consists argillaceous rocks which are mostly carbonaceous with locally prominent development of limestone as illustrated in Fig. 4. In general, the presence of this type of materials exhibits soft soil phenomenon due to its high-water content derived from high water table of the lowland areas [5].

It is observed that the proposed project site is located on the Kenny Hill Formation with mixed quaternary deposit (alluvium) based on the geological map of Peninsular Malaysia, 1985 and Quaternary geological map of Peninsular Malaysia, 1989. Towards the coast, quaternary marine deposits formed during the period of Holocene [6].

3 Geoforensic Investigation and Method of Analysis

3.1 Field Investigation

Electrical resistivity imaging (ERI) was used to evaluate the ground settlement in local scale at bridge FT02 at Sect. 12.00 East Bound and West Bound at Federal Highway near Taman Sungai Rasau, Klang. ERI results were used to interpret the

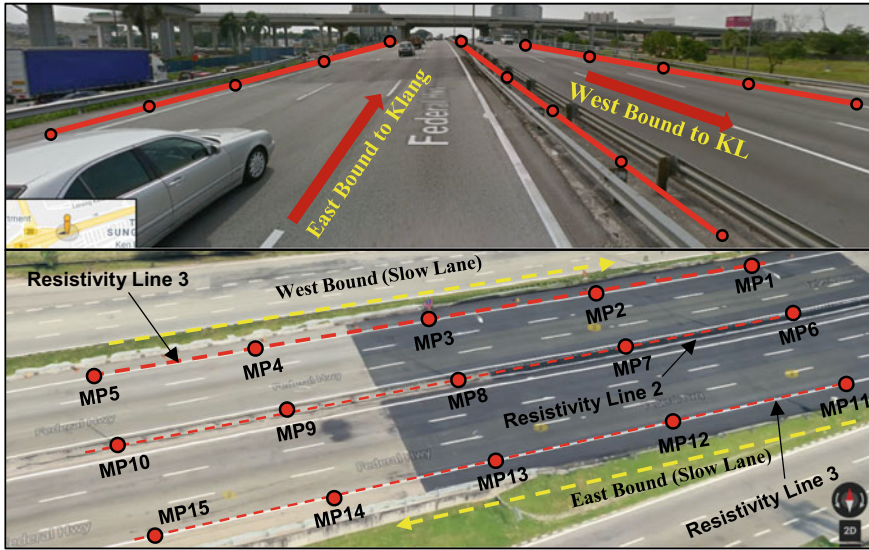


Fig. 5 Layout location plan of JKR Probe and Resistivity Line at the proposed site

condition of the problematic subsurface profile due to its differential stiffness. Electrical resistivity of the subsurface profile was measured using ABEM SAS4000 equipment. The heterogeneous of the subsurface material presented using integrated analysis of ERI and borehole data enabled ground settlement in this area to be evaluated. This is the major factor in evaluating ground instability in the local scale. The result was applicable to assist in planning a strategy for sustainable ground improvement of local scale in fast, low cost, and large data coverage.

Three (3) lines of resistivity were proposed namely Line 1 for West Bound (Slow lane bound to Klang), Line 2 for West Bound (Fast lane bound to Klang) and Line 3 for East Bound (Slow lane bound to Kuala Lumpur) with each line consists of five (5) JKR Probe points with a total of 15 points of JKR Probe carried out at the proposed site. The location of the test positions is shown in the layout plan in Fig. 5. The geoforensic investigation were carried out in accordance with the JKR specifications and guidelines.

4 Results and Analysis

4.1 JKR Probe Analysis

Results of the JKR Probe for the proposed above-mentioned project were stipulated in JKR Probe MP1—MP15 for Lines 1, 2 and 3 and it also illustrate the ground density profile given in Figs. 6, 7 and 8. Based on the results of the JKR probes

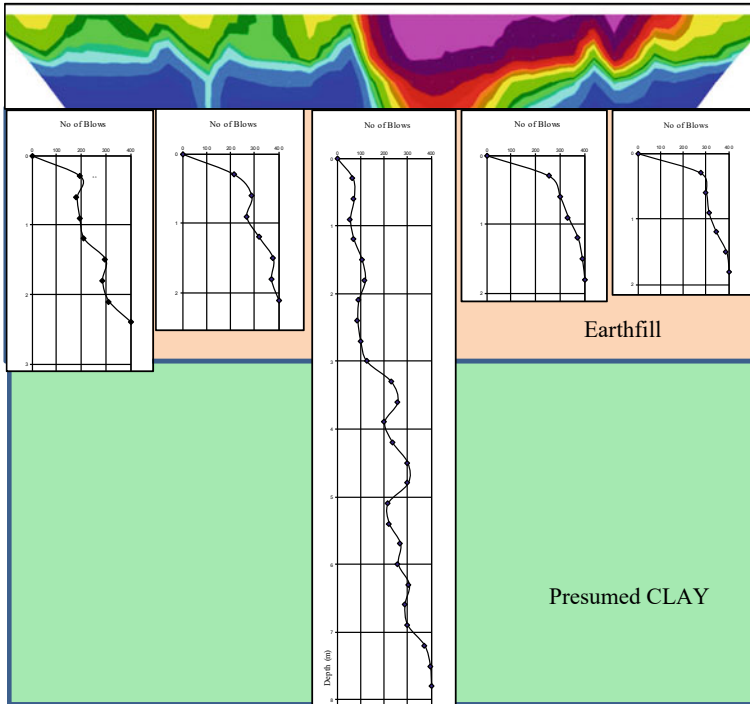


Fig. 6 Subsoil profile for Line 1 at MP1 to MP5

shown in Fig. 6, for MP1 to MP5 (Line 1), the first 0.3 m, the soil is considered to be dense with the no. of blows ranging between 197 and 277 blows/300 mm especially for MP1, MP2, MP4 and MP5. Furthermore, as it reaches only at 1.5 m depth, the soil becomes very dense with blows exceeding 400/300 mm for MP4 and MP5. This is assumed that the cone tip has reached the piled embankment slab since the blows is consistent at 400 blows/300 mm. In addition, for MP1 and MP2, the soil become very dense with blows exceeding 400/300 mm when it reaches at depth of 2.1 m 1.8 m consecutively, However, for MP3 the soil considered to be medium dense for the first 1.2 m and then the number of blows started to increase when the rod penetrated deeper into the ground. The soil becomes very dense when it reaches at a depth of 7.5 m with number of blows exceeding 400/300 mm. The critical point to be observed is at MP3 especially at the depth from 0.3 m 2.7 m where the number of blows were inconsistent for each number of blows/mm. For the first point, the number of blows consistently increase gradually for the first 0.6 m until 1.5 m and then it start to decrease gradually at the depth of 1.8 m until 2.4 m. Finally, the soil condition become stronger and very dense when it reach at depth of 7.5 m. It shows that at MP3, the soil condition is very weak compared to other MP points.

Figure 7 shows the JKR Probe data for Line 2 located at the East Bound Fast Lane to Klang. About five (5) points were recorded namely MP6, MP7, MP8, MP9 and

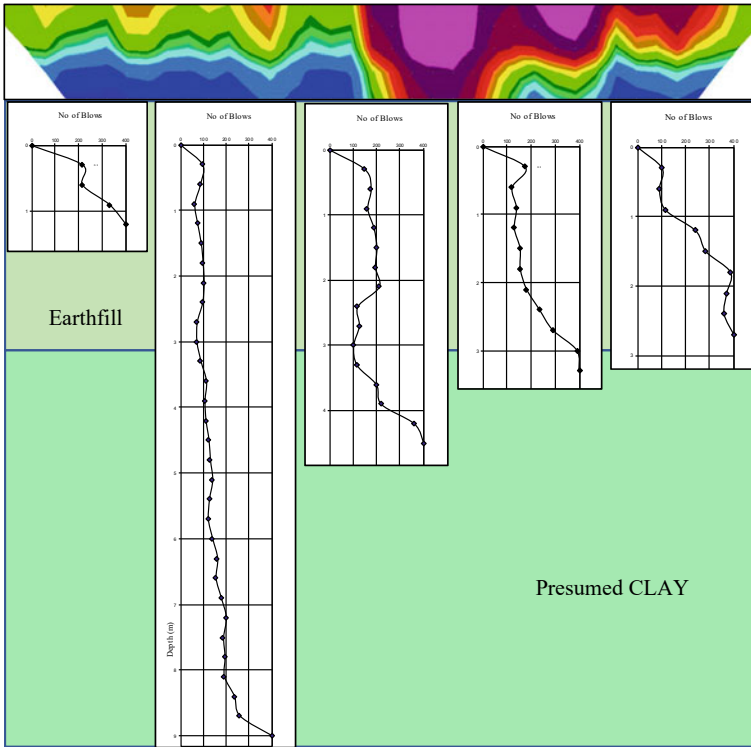


Fig. 7 Subsoil profile for Line 2 at MP6 to MP10

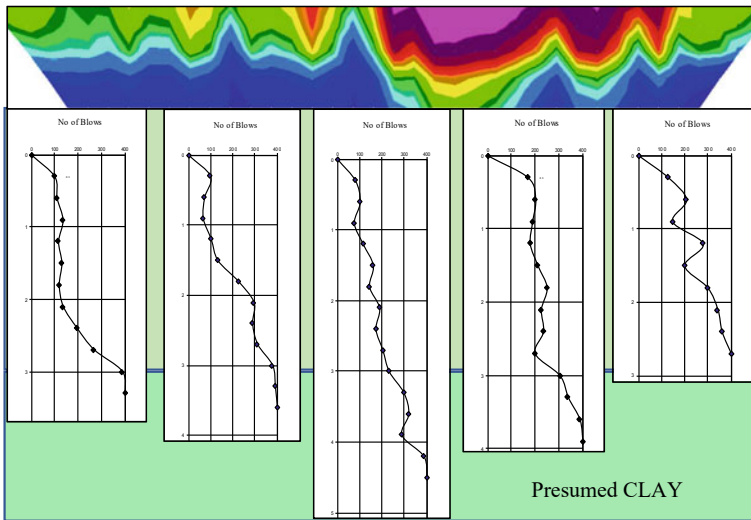


Fig. 8 Subsoil profile for Line 2 at MP11 to MP15

MP10. Results indicates that at MP6 the layer is very dense where the number of blows exceeded 400/300 mm at the depth of 0.9 m. The first 0.3 m depth has indicated that the soil condition is dense where the number of blows reach at 217/300 mm. Meanwhile, for MP8, MP9 and MP10, the soil becomes very dense with blows exceeding 400/300 when it reaches at depth of 4.2 m, 3.0 m and 2.4 m consecutively. However, results from MP9 indicates that the soil becomes very dense where the number of blows exceeded 400/300 mm as it reaches at depth of 8.8 m. This indicated that in MP9, the soil condition is dense for the first 600 mm depth and becomes loose when it reached a depth of 3.0 m and then the values started to increase in until it reaches to a depth of 8.8 m. The critical point to be observed is at MP9 especially at the depth of 2.4 to 3.3 m where the number of blows were only at 71/300 mm to 88/300 mm. It shows that at this particular depth, the sand is in loose state where the void is higher at this point. There is a possibility that the piled embankment was constructed up to this length (Approximately 25 m from the centre line of the resistivity Line 2) or there is rupture at the piled embankment. Then the strengths increase gradually over depth until it reaches to the final depth at 8.8 m. It is likely that the subsurface material in Line 2 especially in MP9 experienced weakening due to the existence of water seeping beneath the subgrade layer or there is rupturing of the piled embankment causing the probe to penetrate easily into the ground.

Figure 8 shows the JKR Probe data for Line 3 located at the West Bound Slow Lane to Shah Alam. About five (5) points were recorded namely MP11, MP12, MP13, MP14 and MP15. Results indicated that the soil condition is very dense where the number of blows exceeded 400/300 mm which differ for each point of MP where for examples at MP11, MP12, MP14 and MP15, the number of blows exceeded 400/300 mm were at 3, 4.2, 3.6 and 2.4 m consecutively. Nevertheless, the first 0.6 m depth the soil condition for all the MP except for MP13 were at dense state where the number of blows exceeded 100/300 mm. However, results from MP13 indicated that the soil becomes very dense where the number of blows exceeded 400/300 mm when it reaches at depth of 3.3 m. This indicated that in MP12, the soil condition is loose state for the first 1.2 m depth and increase gradually until it reaches at a depth of 3.3 m. The critical point to be observed is at MP12 especially at the depth of 0 to 1.2 m where the number of blows were only at 98/300 mm to 101/300 mm. It shows that at this particular depth, the sand is in loose state where the void ratio is higher at this point. Then the strengths keep increasing gradually over depth until it reaches to the final depth at 3.3 m. It is likely that the subsurface material in Line 2 especially in MP7 was weakening due to the existence of water seeping beneath the subgrade layer.

According to the observation and probing executed, the summary of geotechnical subsurface can be divided into 3 lines. As for Line 1, the subsurface were dense and suitable to carry load except for the MP3 which is in the middle of the section. At this point, the soil condition is critically weak because of seepage beneath the subgrade and/or the earth fill material has migrated into the voids beneath the piled embankment. However, for Line 2, the subsurface condition is not as good as in Line 1. There are weak spots of the ground along point MP9 and followed by MP8 which is located in the middle of the section in Line 2. The soil condition in MP9 is much

critical compared to MP8 thus this area needs extra rehabilitation work. Weakening of the subgrade has occurred in this section due to the settlement of the foundation soil beneath the piled embankment, hence the compacted soil has migrated beneath the piled embankment due to the existence of voids, thus weaken the middle section of every line. However, there is a suspected slab rupture at point MP7 since the probe could penetrate pass the 2.5 m mark where it is assumed to have a piled embankment slab constructed. For line no. 3, the subsoil is also in the medium dense state where most of the soil is medium hard. However, there is a slight weakening of the fill material at a depth of 2.0 m due to the migration of the fill into the void area created beneath the piled embankment, as the foundation soil settles. The maximum depth where the no. of blows exceeded 400/300 mm were at depth of 4.2 m. It shows that on that particular location, the soil is very dense beneath the pavement structure. Results of the probing for the rest of the lines, especially in the first and third lines showed that the sand was compacted to specification and the presumed clay has experienced 90% consolidation for Lines 1 and 3.

4.2 Electrical Resistivity Imaging

The problematic subsurface profile due to ground settlement was investigated using electrical resistivity imaging (ERI). The geometry and electrical resistivity anomaly distribution has been determined by analysing ERI data obtained along the settlement zones and the results show good correlation with the JKR probe data. ERI successfully mapped the ground instability which is able to extend the surface information observed during the physical mapping. The information from the ERI will provide suggestion for decision making with regards to the location of the weak layer underneath the pavement structure. This geophysical method is suitable for sustainable ground investigation since it can reduce time, money and compliment other conventional method especially by its 2D surface technique of investigation.

The application of ERI in conjunction with the JKR probe points and geological information was effectively being applied to the evaluation of the ground settlement due to its ability to detect the weak layer within the subsurface profile. Figure 9 through Fig. 14 provide the ERI for the lines as indicated previously.

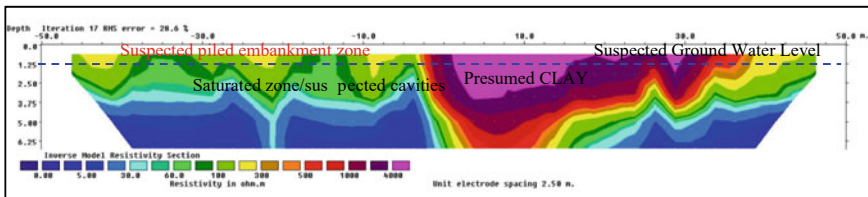


Fig. 9 Shallow electrical resistivity image for Line 1

According to the image given in Fig. 9, at the section closed beneath the suspected piled embankment, there is a potential weakening and seepage. There is potential weakening and cavity causing settlement of the soil. It is clearly seen that the resistivity reading becomes less than 30 below approximately 2.5–3 m suggesting that there is a piled embankment from 0 to –50 m and the soil beneath the piled embankment is fully saturated. At this section, there is potential cavities causing the fill material to migrate below the piled embankment. Therefore, it is advised that the section where the cavities are present, rehabilitation works need to be executed immensely to ensure that the fill transition approach does not settle excessively. It is suggested that if any rehabilitation work is to be conducted, the voids must be plugged to avoid migration of the soil underneath the piled embankment. However, from 0 to 50 m towards the earthfill, the material has been compacted to 90% and close to the transition between earthfill embankment and piled embankment the clay has experienced 90% consolidation.

Figure 10 provides deeper electrical resistivity imaging to give a clear picture of the ground conditions investigated. It is clearly seen that below the piled embankment (0 to –50 m) there are potential cavities, weakening and seepage. While from 0 to 50 m the clay is saturated and there is possible seepage below 5 m since there is a presence of water ponding next to the highway. However, at the top layer of this section, the fill is compacted at 90% as indicated by the resistivity reading more than 500 ohms.

Figure 11 shows the control Line 2 located at the median section where there is potential cavities caused by settlement of the soil underneath the piled embankment and settlement due to migration of the soil at the transition between earthfill and piled embankments. However, the section is rather weak since the ERI values are rather low. At this section, reports of accidents are frequent due to the build-up of sudden road

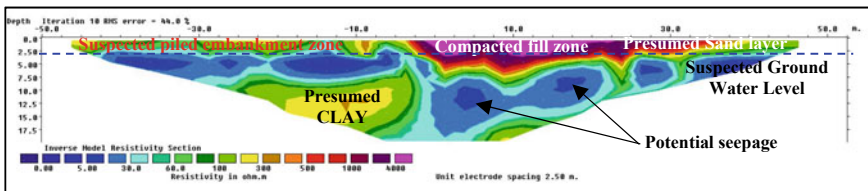


Fig. 10 Deep electrical resistivity image for Line 1

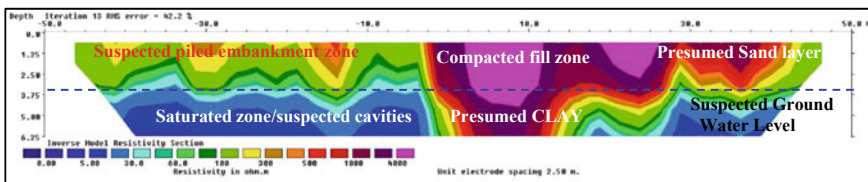


Fig. 11 Shallow electrical resistivity image for Line 2

humps in the middle lane. This problem causes traffic users to break suddenly and accidents occur due to sudden shock. The ground condition at this section is critical due to the presence of potential voids/saturated zones and it must be rehabilitated to reduce the migration of the sand material towards the voids underneath the piled embankment. However, based on the probe data, at MP9, there is potential slab rupture since the MP probe could penetrate down to a depth of 9 m until it is terminated at 400 no. of blows. It is expected that this rupture is minor since there is no settlement experience at this point. In fact, the fill material is compacted to specification. In comparison to the earth fill Sect. (0–50 m) the compacted material is dense and it is suspected that the clay has undergone 90% consolidation. Therefore, potential consolidation settlement is minimal and that the area now is experiencing secondary compression, a gradual and small settlement due to the reorientation of the soil particles.

Figure 12 illustrates deeper electrical resistivity image to give a glimpse of median section. According to the ERI, the potential cavities/seepage is below the piled embankment, therefore it is advised that the section is plugged with lightweight material. The purpose of using lightweight material is to reduce the effect of additional overburden and imposed load. Therefore, the application of lightweight injection using PU foam/resin is advised since it does not provide additional overburden from the current behaviour. At this section, the layer beneath the piled embankment is less than 50 ohms since it is suspected that the voids exist due to settlement of the clay layer.

According to the image shown in Fig. 13, the settlement occurred rather excessive and the voids are directly below the piled embankment. The resistivity image even showed that the ground has weakened. This image showed that cavities are eminent directly below the piled embankment and if it is not treated immediately, continuous

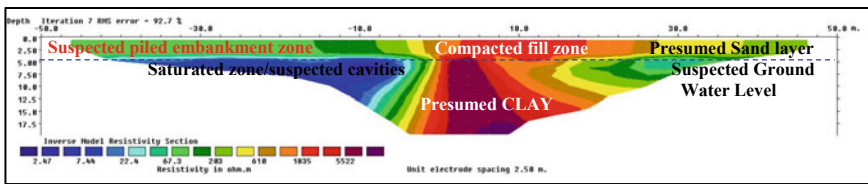


Fig. 12 Deep electrical resistivity image for Line 2

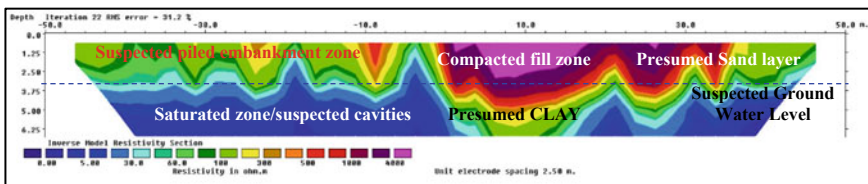


Fig. 13 Shallow electrical resistivity image for Line 3

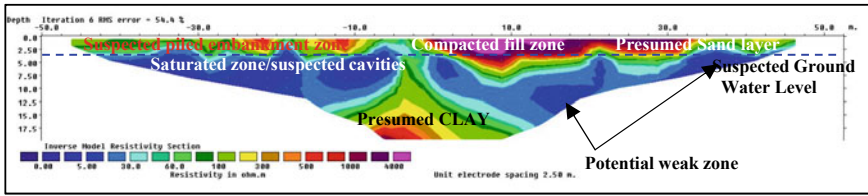


Fig. 14 Deep electrical resistivity image for Line 3

appearance of voids will occur. The fill has been compacted to specification based on the resistivity readings, which is more than 100 ohms. However, since there is a main drain next to the highway eastbound to Kuala Lumpur, there might be a potential seepage above the piled embankment slab since the reading are ecstatic at several points above the piled embankment.

Figure 14 confirms the reading from Fig. 13 with the potential cavity and seepage area is much larger in comparison to Lines 1 and 2. Moreover, beneath the compacted fill the clay is undergoing settlement since it is still saturated and the resistivity reading is below 50 ohms. The transition section will be plugged with PU foam using injection procedure to reduce the migration of the compacted sand towards the potential cavity/seepage zone. It is advised that below the compacted earth fill zone, ground treatment countermeasures need to be proposed to stabilised the ground and reduce the rate of consolidation.

As a summary, the ERI shown critical sections of the settlement occurrence, which is at the transition zone between the piled embankment and the earth fill embankment where the potential voids/saturated zones are below the piled embankment which could cause the earth fill material to migrate towards this zone. The section where it is assumed to be constructed on piled embankments does not experience massive settlement based on the resistivity image. Beneath the piled embankment, cavities start to appear causing the fill material at the transition zone migrated into the cavities, causing settlement and sudden road humps. This transition section underneath the piled embankment will be treated with PU injection to plug the voids and prevent the soil from migrating underneath the piled embankment.

5 Conclusions and Recommendations

5.1 Conclusions

Based on the geoforensic investigation conducted, the conclusions are given below:

1. The existing ground condition consist of 2.5–3 m thick of compacted fill/sand layer, underlain by approximately 10–15 m thick of soft to firm CLAY layer. This

was obtained from the published information, geological map and interpretation supported by the JKR probe and ERI results.

2. Results of the probing for the rest of the lines showed that there is presence of weak layer due to migration of the material into the cavity. The JKR probe values for the lines showed intermediate values less than 100 blows/300 mm. In addition, there were evidence of cavities/seepage since adjacent to the carriageway, the guard rail settled excessively and there is water ponding next to the highway.
3. Results of the ERI for the rest of the lines showed that the soil layer has experienced weakening with rather low resistivity values below the suspected piled embankment suggesting that migration of compacted material has taken place. This justified, the existence of cavities/seepage from the ERI. The presence of cavities promotes to migration of compacted fill material into it and promotes to settlement on the carriageway.

As a summary, the settlement occurred due to the presence of voids and cavities beneath the piled embankment and the migration of the earth fill material towards the cavity zone. From the geoforensic investigation conducted, it is observed that the main problem is the presence of voids beneath the piled embankment due to settlement of the foundation soil below. If this element is not mitigated, future settlement and cavities will develop and cause more problems, not only to the concessionaire but the public as a whole.

5.2 Recommendation for the Proposed Remediation Works

For the geoforensic investigation conducted at FT02 Sect. 12.00 at KM 5.6 East Bound and West Bound at Federal Highway near Taman Sungai Rasau, Klang, the proposed remediation work is given below:

- i .For cavity filling at the piled embankment, it is suggested to inject PU foam/resin for void filling since the existing foundation soil experience settlement, creating cavities beneath it. This will plug the void area and prevent migration of the fill material into the cavities created from the settlement of the ground. Since PU foam/resin is lightweight, it does not impose additional overburden pressure to the soil.

References

1. Inventori Rangkaian Jalan Utama Persekutuan Semenanjung Malaysia. Kuala Lumpur: Malaysian Ministry of Works. pp. 66–69 (2009)
2. Wikipedia Homepage, http://www.en.wikipedia.org/wiki/Malaysia_Federal_Route_2#cite_ref-jkr--inventori_3-2. Last Accessed 18 Jan 2020
3. Klia2.info Homepage, <http://www.klia2.info/trips/highways/federal-highway>. Last Accessed 18 Jan 2020

4. Anuar UM, Nordiana MM (2018) Aquifer detection using 2-D resistivity method and porosity calculation. *J Teknologi (Sci & Eng)* 80(6):149–158
5. Morgan RP (1990) C: an analysis of basin asymmetry in Klang Basin. Selangor. *Geol Soc Malays Bull* 3:17–26
6. Ismail MAM, Majid TA, Goh CO, Lim SP, Tan CG (2019) Geological assessment for tunnel excavation under river with shallow overburden using site investigation data and electrical resistivity tomography. *J Meas Sci Dir* 144:260–274

Strength Predictions of Normal Concrete Beam with Corner Notch



Hilton Ahmad and Noor Yasmin Zainun

Abstract Concrete beam are made by mixing aggregates, water and cement of typical design strength of 30–40 MPa to perform excellent bending resistance, usually tested under flexural test. Presence of notch in concrete beams is associated with stress concentration at the notch tip and reduces its load-carrying capacity. Strength predictions of beam made from concrete is not straightforward due to complex failure morphologies, but advancement of computing technology has led to evolution numerical modelling approaches within finite element analysis (FEA) framework. Modelling of crack is extremely complicated as notch tip exhibited singular stress to require very finely mesh around the crack tip. Incorporation of a constitutive model driven by energetic approach simplifies the modelling technique to perform strength prediction independence of mesh refinements. A traction–separation relationship can be incorporated to perform strength prediction of concrete beam with stress concentration. The main objective of the current project is to perform strength prediction of concrete beam with corner notch with a variation of concrete mixture following experimental work performed by Zhang and Liu. Extended Finite Element Modelling (XFEM), Cohesive Zone Modelling (CZM) and Virtual Crack Closure Techniques (VCCT) techniques were employed to perform strength prediction work using traction–separation relationship. The material properties used in constitutive model were independently determined as reported in the respective literature. 2-D modelling was idealized to take into advantage of geometry symmetries and self-similar behavior cracks using ABAQUS CAE Version 6.14 where meshing was refined at the vicinity of the notch tip. Good agreement predicted from XFEM result contributes by incorporating actual crack path following experimental observation reported from the literatures. Less good agreements from CZM and VCCT techniques were obtained where the simplified crack path as a straight-line was modelled, not accordance to actual crack path as modelling restrictions.

H. Ahmad (✉) · N. Y. Zainun

Faculty of Civil Engineering and Built Environment, Universiti Tun Hussein Onn Malaysia, 86400 Parit Raja, Batu Pahat, Johor, Malaysia
e-mail: hilton@uthm.edu.my

N. Y. Zainun

e-mail: nryasmin@uthm.edu.my

Keywords Concrete beam · Corner notch · Finite element modelling · Extended finite element modelling (XFEM) · Cohesive zone modelling (CZM) · Virtual crack closure techniques (VCCT)

1 Introduction

Concrete is the most prominent engineering materials used in construction industries, partly due to strong and durable materials. It is regarded as composite materials comprised of cement, water, crushed gravel and sand, however in design this material is assumed as a homogeneous material. Beam is a primarily structural components in building system that must be critically design to resist applied load. In typical beam design, the beam is regarded as a solid beam where the beam has no discontinuities. However, design of beams with discontinuities (in the form of notches, cut-out and cracks) are unavoidable due to certain requirements such as piping for cable installation especially in tall building structures. Moreover, aesthetic drawing from architects requested these types of beam design. Study on beam with discontinuities is quite complex due to exhibition of stress concentrations at the notch tip. This stress concentration is associated with reducing loading capacity.

Crack formations and associated micro-cracks usually initiated at largest stress concentration area. In notched concrete structures, crack development can be represented by state-of-the-art fracture mechanics fundamental. From fracture mechanics concept, as energy of the applied load exceed fracture energy of the materials leading to crack initiation of the material. In structures with notches, crack formation usually occurred at the notch tip (associated to stress singularity) and propagated perpendicularly to the applied load. There are three basic modes in fracture mechanics, i.e., opening mode (Mode I), shearing mode (Mode II) and tearing mode (Mode III). Most failures governing in opening mode (Mode I) or mixture of opening and shearing modes (Mode I and II). Failures in beam structures with stress concentration is clear, the prominent crack initiates at the notch-tip and propagates vertically until it reached the top surface. Specimen was preliminarily cracked through a vertical notch starting from the bottom extreme fibers of the specimen with largest tensile bending stress. According to Zhang and Liu [1] a visible crack appears from the crack tip, and progressive micro-cracks presence within fracture process zone (FPZ). At any position of the fictitious crack surface, the energy dissipated to open the crack width can be defined as the local fracture energy G_c which is an important fracture parameter.

Formerly, laborious and expensive experimental set-up was required to study the structure behavior. Zhang and Liu [1] adopted a reversed analysis method based on cohesive crack model to determine the cohesive stress-crack opening relationship taken from bending test. Initially, they considered a central pre-notched concrete beam under three-point bending and found that direction of crack propagation were perpendicular to maximum principal stress. It is well-accepted that the crack path in concrete beam under flexural is known in advance, i.e., crack from the notch tip

developed and grows upwards to the compression top beam parallel to its applied load. Prior to catastrophic fracture, fictitious crack tip is defined as the point where the principal tensile stress attains the cracking strength σ_{fc} and the crack opening at this point is equal to zero.

Advancing computing technology has emerged FEA modelling as the most powerful available numerical tools by incorporation of constitutive model. One of the properties that may provide better physical representation of any engineering material is fracture energy which can be incorporated within FEA framework. These properties can be implemented within constitutive (material) model based from state-of-the-art fracture mechanics fundamental. In order to promote better modelling representation, independently material properties (here, these properties were taken from available literatures) can be used. Lee and Ahmad [2] has developed CZM and VCCT modelling framework to predict delamination failures within adhesive layers in hybrid bolted-bonded joints. Anders et al. [3] and Supar et al [4] have performed XFEM techniques to predict strength predictions in woven fabric kenaf composite joints associated to stress concentration at the notch edge. Good agreements were reported from their modelling framework with experimental datasets.

In general, when brittle engineering material such as concrete is applied as a structural element, fracture energy becomes one of the important material properties that requires further investigations. Fracture energy is a paramount factor that governs crack initiation, fracture and progressive damage of brittle materials. Therefore, fracture energy can be simply understood as total work needed to completely break the specimen per unit ligament area. This definition relies on the assumption that all the required energy to break the specimen is transformed into surface energy. In major cases, fracture energy is influenced by several factors to include the type of concrete, the size of the specimen, test methods and characteristics strength as highlighted by Bazant [5].

From reviews of past studies, there is few investigations on the fracture energy of foamed concrete. In general, it was found that the conventional concrete has fracture energy around 75–100 N/m depend on concrete compressive strength as reported by Muralidhara et al. [6]. However, fracture energy of cellular concretes is lower than the conventional concrete in the range of 30–50%. Nevertheless, foamed concrete is expected to gain similar value of fracture energy exhibited by cellular concrete. Since the characteristic strength of foamed concrete mainly depends on its plastic density which is varies from 800 kg/m³ to 1800 kg/m³, hence the fracture energy may also vary significantly.

The strength prediction work is adopted in concrete beams, both has similarity in exhibition of stress concentration at the notch tip as previously investigated by previous researchers [2–4]. Incorporation of constitutive model associated to fracture mechanics only requires few independent material properties to provide reliable and good predictions. FEA modelling frameworks were carried out which comprised of pre-processing, processing and post-processing stages. 2-D modelling is chosen as the crack exhibited during experimental observations [7] was regarded as self-similar cracks where damages were takes place.

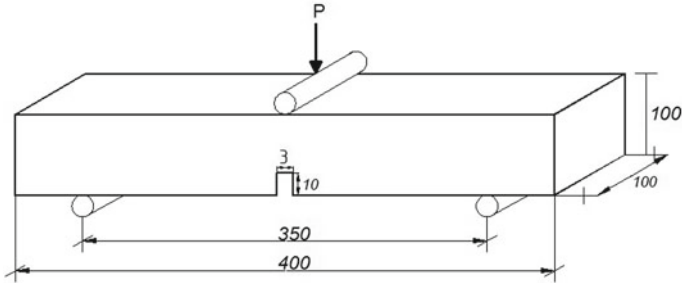


Fig. 1 The dimension of notched normal concrete beam under three-points bending test

2 Finite Element Modelling

The steps involved in pre-processing stage are described further in the following sub-sections.

2.1 Generation of Material and Geometry Properties

Current work implemented 2-D modeling framework to conserve simplicity and allows the analysis to run on a normal processor power to yield reliable results. Finite element model for the notches beam of normal concrete consists of three parts, beam, support and loading. The geometric and dimension are shown in Fig. 1. Beam geometrical parameters are given as D , b and L are height, width and length of the tested beams. In additions, a notch was introduced at the mid-span, given as a notch height and w_n as notch opening width. The elastic and material properties were assigned according to values reported in the respective literatures Zhang and Liu [1].

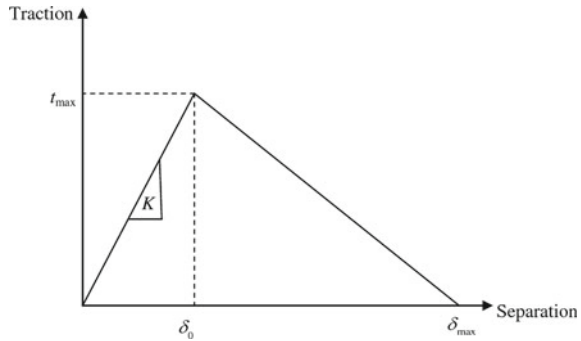
2.2 Testing Series

Testing series investigated followed experimental work conducted by Zhang and Liu [1] to investigate the influence of coarse aggregate on bending performance under three-point bending test. Three concrete mixes with different ratio between sand and the sum of sand and stone were adopted as given in Table 1.

Table 1 Testing series of normal concrete beam investigated in current work following Zhang and Liu [1]

Concrete designations	Concrete mixture <i>water:binders:sand:stone</i>
Mix 1	1:2.27:2.6:5.19
Mix 2	1:2.27:3.88:3.88
Mix 3	1:2.27:5.16:2.58

Fig. 2 Traction–separation constitutive material law used in the current analysis [8, 9]



2.3 Incorporation of Traction–Separation Relationship

In this work, three methods for modelling the damage were identified, namely the extended finite element method (XFEM), cohesive zone model (CZM) and Virtual Crack Closure Techniques (VCCT). Three methods used the same traction–separation material model, illustrated schematically in Fig. 2. This constitutive model was used by Ahmad et al. [8, 9] to predict notched strength of open hole [8] and bolted joints [9] woven fabric carbon fiber polymer composites plates. The material model behaves in a linear manner until the stress reaches a critical value (strength parameter) and then unloads with increasing displacement dissipating the fracture energy, G_c in the process.

2.4 Extended Finite Element Method (XFEM)

The extended Finite Element Modelling (XFEM) region was assigned within a cracked region as seen in Fig. 3 to provide better convergence and computational efforts. XFEM formulations allowed the crack to be visualized during post-processing output. In total, XFEM modelling has five parts, addition to a pre-defined crack. Pre-defined crack was assigned as diagonal crack from the right corner notch tip. Damage stabilization coefficient adopted was chosen from sensitivity study to provide reliable and reasonable strength prediction. Maximum Principal Stress, $MaxPS$ was adopted here as damage failure criterion.

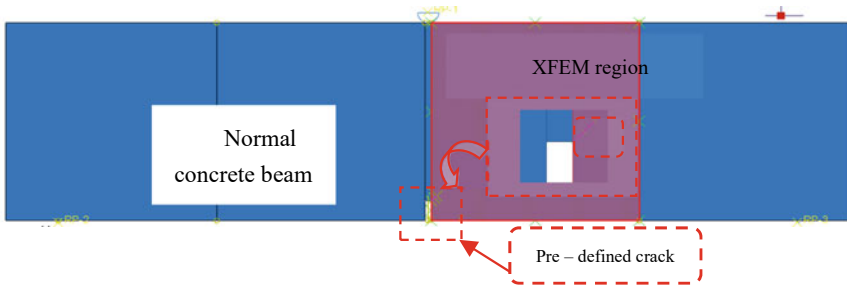


Fig. 3 XFEM region and pre-defined crack

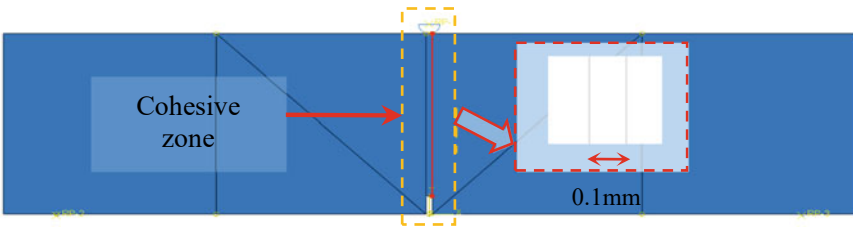


Fig. 4 CZM modelling crack path

Table 2 Normal and shear stiffness properties implemented in CZM models

Traction properties	K_{nn} (kN/m)	K_{ss} (kN/m)
	5000	3000

2.5 Cohesive Zone Modelling (CZM)

CZM technique requires infinitely small cohesive element thickness normal to the applied load from sharp corner notch edge as shown in Fig. 4. The size of cohesive elements 0.1 mm located at notch beam until the top of the beam. Failure criterion used in CZM technique is Maximum Stress Criterion (abbreviated as *MAXS*). Cohesive element was adopted with element designation code as COH2D4 with structured mesh. CZM requires traction properties given in Table 2.

2.6 Virtual Crack Closure Technique (VCCT)

The VCCT is based on the assumption that two separated parts are bonded by crack surfaces to require fracture energy to open the crack surfaces. Separations of both parts were governed by interaction surface properties from two separated parts. Initially two parts were modeled which based on separation of concrete beam

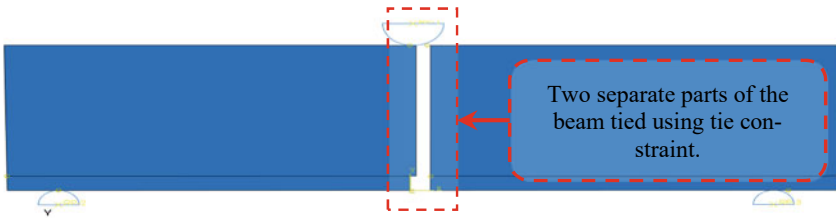


Fig. 5 Two-part of the beam bonded by tie constraint

Table 3 Fracture energies used with respective to different failure modes

	G_{IC}	G_{IIC}	G_{IIIc}
Mix 1	0.185	0.231	0.231
Mix 2	0.165	0.206	0.206
Mix 3	0.108	0.135	0.135

after failure as given in Fig. 5. Both concrete beam parts assigned with tie constraints to bond two cracked surfaces. The fracture criterion used in VCCT technique is for mixed-mode delamination taken from Benzeggagh-Kenane (BK) fracture criterion given in Table 3. Fracture energy value in shear and tearing modes (G_{IIC} and G_{IIIc}) were taken as 25-times larger than fracture energy in opening mode (G_{IC}), agrees values reported in Bažant and Pfeiffer [10]. Bear in mind that the fracture energy values in opening mode, G_{IC} is similar to fracture energy G_c used in former two techniques.

3 Results and Discussions

3.1 Post-processing from XFEM Frameworks

From line (o)-(a), there was no crack was formed as the stress developed is lower than maximum cohesive stress of the respective concrete. At point (a), a diagonal crack was initiated at the corner of the notch beam due to high stress concentration developed at the notch edge. The inclined crack is formed due to shear stress developed as load was applied at the center of top beam. Within line (a)-(b), micro-damage cracks were developed associated to progressive fracture and damage ahead of the notch tip. It is expected that the micro-cracks in concrete beams subjected to flexural load are developed within interfacial zones between cement paste and aggregates, simultaneously crack bridging arrest the crack growth which represented by fracture energy values of concrete assigned. At point (b), ultimate load was obtained corresponds to reach damage zone length. Ahead of damage zone length, catastrophic failure occurred. As seen from Fig. 6, it can be deduced that Point (b)-(c) occurred

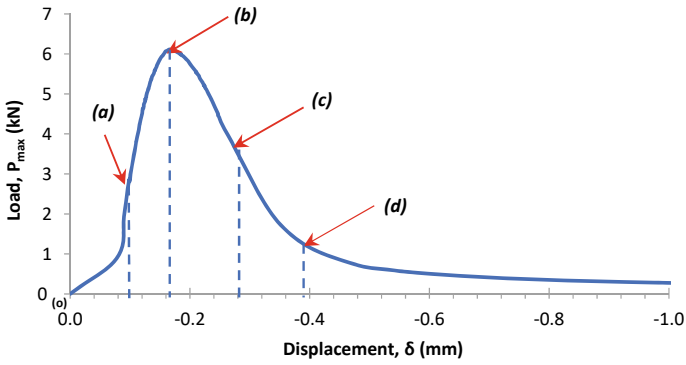


Fig. 6 Typical load–displacement curve of three-point bending from XFEM techniques (from Mix 2 of testing series)

in a very short time due to drastic drop at peak load was reached. Point (d) associated with full crack separation to divide the concrete beam into halves.

Figures 7 and 8 show the damage plots of specific locations as labeled in Fig. 6. The crack was started at (a) step 34 from the step timeframe where the crack occurs as

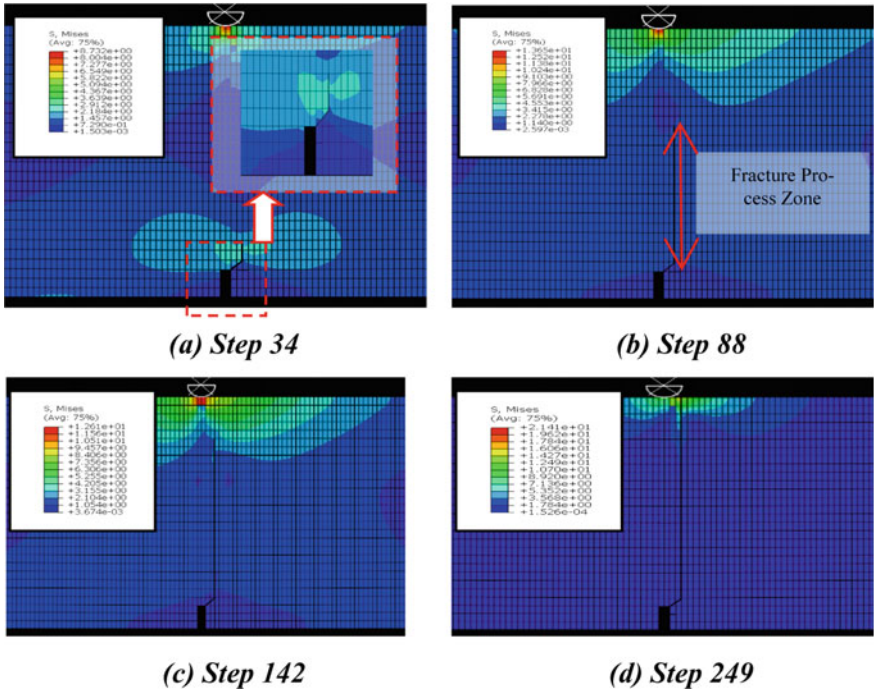


Fig. 7 Von-Mises damage plot at specified location taken from load–displacement curve in Fig. 6

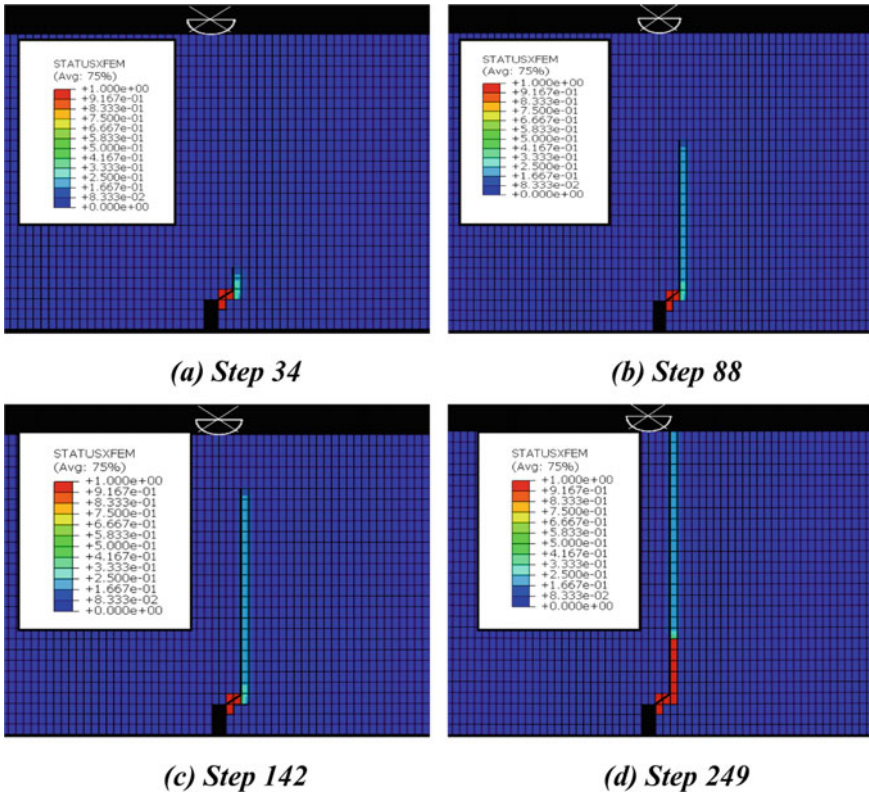


Fig. 8 XFEM status damage plot at specified location taken from load–displacement curve in Fig. 6

the applied fracture energy is larger than fracture energy of the concrete mixture ($G_C = 0.165 \text{ kJ/m}^2$). Subsequent load increment leading to larger crack length where the crack propagates diagonally and push upwards normal to applied load (given as step 88) until the crack reached the ultimate load. Exceeding step 88 leads to catastrophic failures where it occurs at a very small crack separation interval as given in step 142 prior to full separation at step 249.

Validations Against Experimental Works

Excellent strength predictions of tested concrete series under three-points bending were found, less than 10% discrepancies were obtained as depicted in Table 4. Current modelling work used independently determined material properties (σ_o and G_C) from similar concrete mixture of similar author were reported as a series of their research findings.

Table 4 Comparison of peak load between experimental dataset and XFEM modelling

Mixture designations	Peak load from experiment, $P_{\max, \text{exp}}$ (kN)	Strength prediction from XFEM, $P_{\max, \text{XFEM}}$ (kN)	Error (%)
Mix 1	7.8	7.9	1.0
Mix 2	6.6	6.1	7.0
Mix 3	4.8	4.4	7.0

3.2 Post-processing from CZM Techniques

The load–deflection plot in Fig. 9 comprised of three behavior stages. In the first phase, point 0–A the deflection increases linearly with the load with the notch is opened but does not extend. A fracture process develops during the second phase (B–C) where micro-cracks form and slow crack growth is noticeable. In the third phase (C–D), known as strain softening, rapid crack growth is more apparent.

Figure 10a where Von-Mises stress was given as 47.9 N/mm^2 . Then, crack initiation promotes stress alleviation to reduce the stress concentration at the sharp notch. At step 17, failure load was given as it reached damage zone length at slightly reduced maximum applied stress of 3.04 N/mm^2 . Consequently, additional applied load propagates the crack (associated to exceeding concrete fracture energy) to promote crack propagation at step 23 and beam separation at step 26. Figure 11 represented damage variable SDEG where the value is ranging from 0 to 1 where the value of one meant element failure and crack formation and consequently crack separation has taken place. SDEG contours turns red as crack was formed and element deletion to show cracks surface has separated. SDEG damage plot was labelled at steps 14, 17, 23 and 26 given in Fig. 11. At step 14, no crack was visible but stress is concentrated

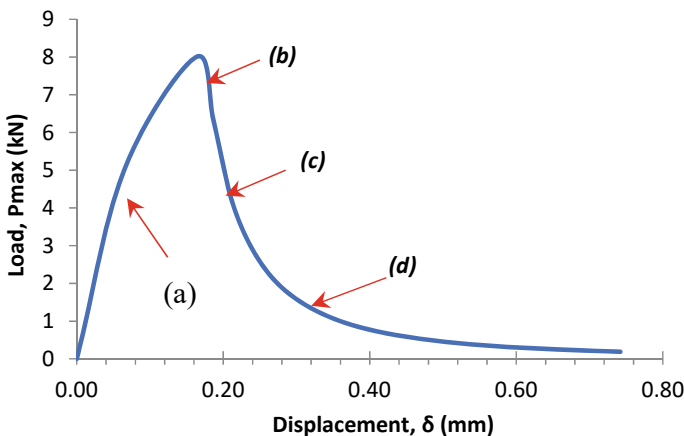


Fig. 9 Typical load–displacement curve of three-point bending from CZM techniques (from Mix 2 of testing series)

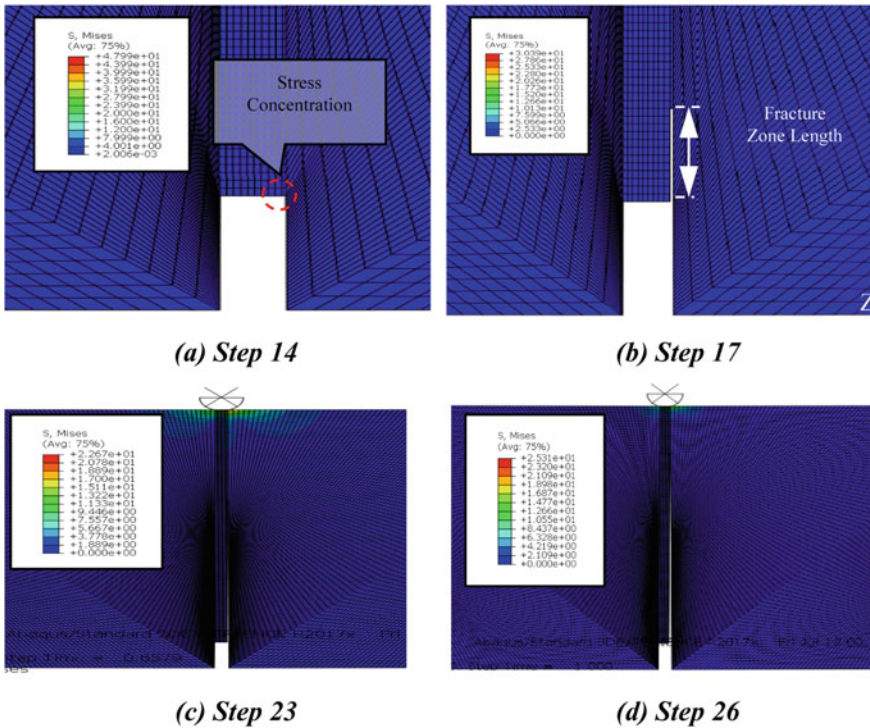


Fig. 10 Von-Mises damage plot at specified location taken from load–displacement curve in Fig. 9. (Note that **a–d** are enlarged at notch vicinity for visual clarity)

at notch tip. Then, at damage zone length of approximately similar to notch height, twelve elements were disappeared. Noting that at step 23 and 26, number of element deletions has increased tremendously from 80 to 106 elements. From step 14 to step 26 occur at a very short time interval to represent catastrophic failure.

Validations Against Experimental Works

Table 5 shows the discrepancies of strength prediction between CZM modelling techniques and experimental datasets. It was found that discrepancies between 20 and 31% were found. Bear in mind that the crack path within CZM framework does not follows experimental observations as current approach only allows crack locations to be modeled in a straight line. Nevertheless, the strength prediction in CZM showing reasonable prediction, in average of 25% discrepancies.

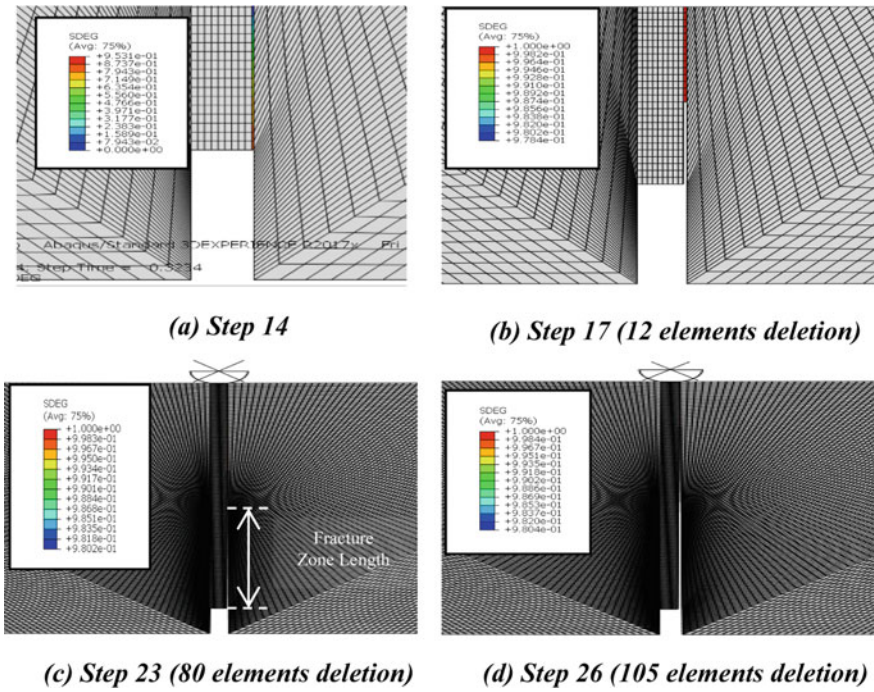


Fig. 11 SDEG status damage plot at specified location taken from load–displacement curve in Fig. 9. (Note that SDEG = 1 denotes element failures)

Table 5 Comparison of peak load between experimental dataset and CZM modelling

Mixture designations	Peak load from experiment, $P_{max, exp}$ (kN)	Strength prediction from CZM, $P_{max, CZM}$ (kN)	Error (%)
Mix 1	7.8	9.8	25.0
Mix 2	6.6	7.9	20.0
Mix 3	4.8	6.3	31.0

3.3 Post-processing from VCCT Techniques

A typical load–displacement curve is given in Fig. 12, Mixture 3 was chosen for further discussion. It was found that similar physical patterns with the former two techniques were found to suggest this model agrees on the physical beam behaviour as subjected to applied bending load. However, it is noticeable that the displacements (associated with crack separation) are relatively small. This may due to this approach is initially bonded between two tie surfaces and separation occurs as applied load (associated with applied cohesive stress) is higher than maximum traction stress

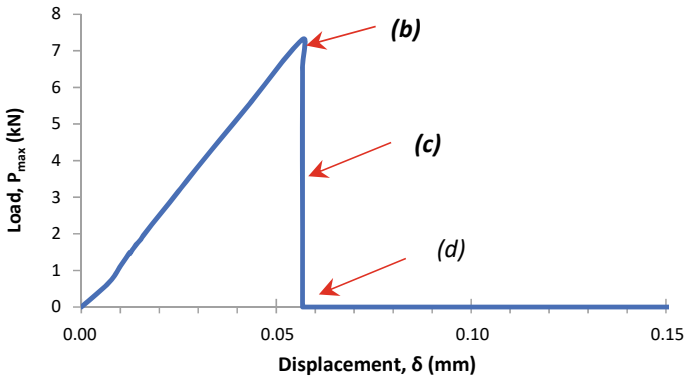


Fig. 12 Typical load–displacement curve of three-point bending from VCCT technique (from Mix 3 of testing series)

(also known as maximum cohesive stress, σ_0). Therefore the displacement is not well represented in this model.

Figure 13 shows Von-Mises stress contour from VCCT technique. As the applied stress reached point (a) step 45, the crack has initiated. Subsequent step (step 46) demonstrated that ultimate load was exhibited. It was found that fracture zone length is relatively shorter than the previous two techniques. From step 46–76, it was found that no crack displacement was much recorded to suggest VCCT model only capture linear deformation in their modelling approach.

Strength Predictions Compared to Experimental Datasets

Validation works have been carried out in all series of VCCT modelling investigated and given in Table 6. Generally, it was found that large discrepancies were found as compared to experimental datasets ranging between 30 and 52%. It is partly due to current modelling approach only ties between two cracks parts and separates as load increased.

4 Comparison of Strength Predictions in All Techniques Implemented

The compilation of load–displacement profiles of Mixture 2 among all techniques incorporated are given in Fig. 14, validated against experimental datasets reported in [1]. From the respective figure, good correlations were seen in XFEM and CZM models, but less good in VCCT techniques.

Overall, XFEM technique performed the best strength prediction than the other two techniques. This is because XFEM able to visual the crack from orthogonally from adopted here based on maximum principal stress (MaxPS). XFEM gives

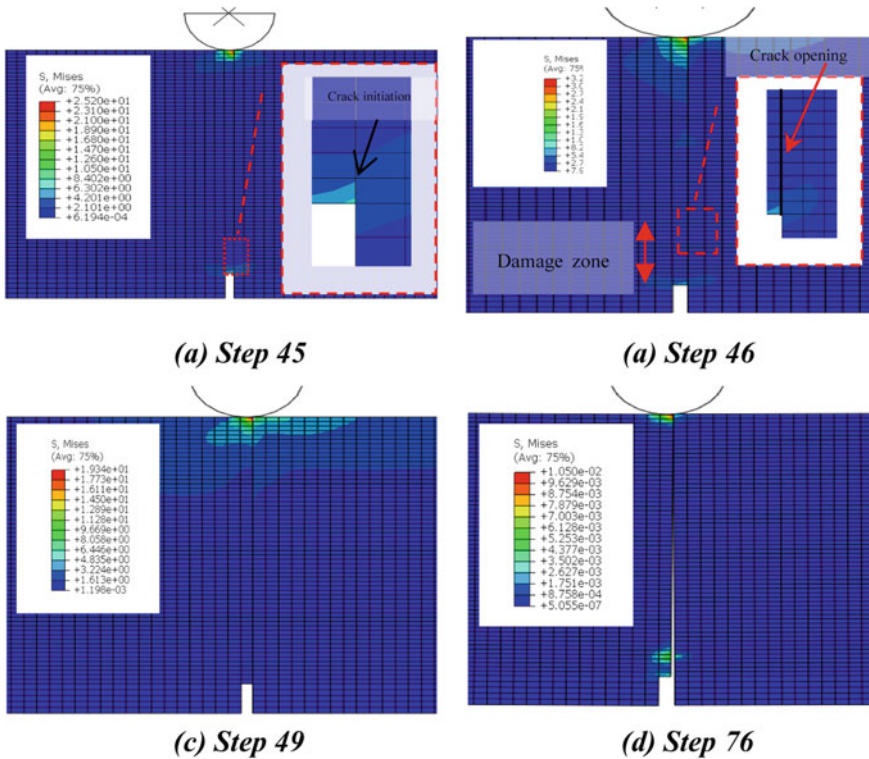


Fig. 13 Von-Mises damage plot at specified location taken from load–displacement curve in Fig. 12

Table 6 Comparison of peak load between experimental dataset and VCCT modelling

Mixture designations	Peak load from experiment, $P_{max, exp}$ (kN)	Strength prediction from VCCT, $P_{max, VCCT}$ (kN)	Error (%)
Mix 1	7.8	10.2	30.0
Mix 2	6.6	9.3	40.0
Mix 3	4.8	7.3	52.0

the discrepancies of less than 7% discrepancies were obtained (average of 4%), good agreement is partly due to implementation of independent determined material properties to be incorporated within constitutive model (σ_0 and G_c).

In CZM techniques, the crack propagation was defined following experimental observation crack path but the crack path has to be modelled infinitely small with small element thickness. CZM techniques mostly exhibit over-predictions between 20 and 31%.

Nevertheless, VCCT techniques displays the curve profile differently from former two modelling approach, i.e., XFEM and CZM. Large discrepancies were seen

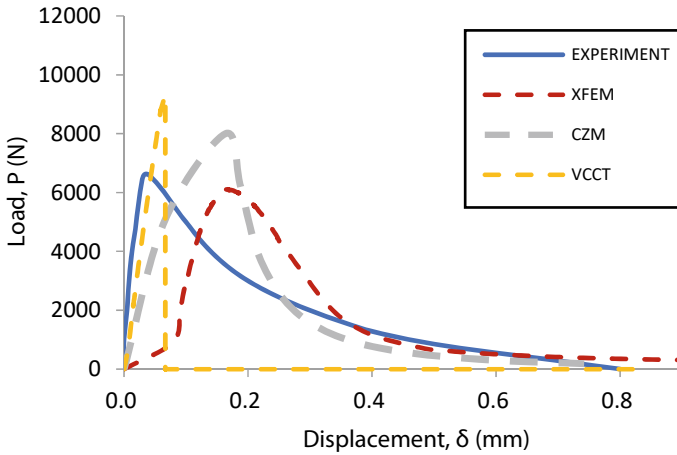


Fig. 14 Load–displacement curve of all techniques implemented compared to experimental curves (from Mix 2 of testing series)

between 30 and 52%, largely due to implementation of tie-constant within two crack surfaces and the formulation adopted in VCCT only covers linear elastic deformation. Likewise, CZM, the tie-constraints between two adjacent crack surfaces were made normal to applied load started from right edge notch.

5 Conclusion

XFEM technique provides the best agreement with experimental datasets to give less than 7% discrepancies than other techniques implemented. This is partly contributed by incorporating actual crack path following experimental observation reported from the literatures. The fracture and failure initiated from the right corner tip notch-tip and propagates normally to applied load until reaching the top beam surface. XFEM allows the model to perform the crack where the crack grows orthogonally to the maximum principal stress. CZM and VCCT techniques required the crack path to be modeled in a straight line, here the cracks path need to be known beforehand. As current approach only allows crack locations to be modeled in a straight line, modelling simplicity idealization is required. From validation work, CZM gives discrepancies of between 20 and 31% and VCCT provides between 30 and 52% of all testing series investigated. Less good agreement compared to XFEM technique, largely due to simplification implemented where crack is assigned from crack tip parallel to applied load. Furthermore, least good in VCCT as this approach only provide linear deformation as load applied (with two separated crack surfaces are assigned with tie-constraint).

References

1. Zhang J, Liu Q (2003) Determination of concrete fracture parameters from a three-point bending test. *Tsinghua Sci Technol* 8(6):726–733
2. Lee SY, Ahmad H (2019) XFEM modelling of single-lap Kenaf fibre composite hybrid joints under quasi-static loading. *Plast, Rubber Compos* 48(2):48–56
3. Romanye A, Ahmad H (2017) XFEM modelling of single-lap woven fabric kenaf composites bolted joints with temperature action. *J Eng Appl Sci* 12(10):2687–2991
4. Supar K, Ahmad H, Yusoff M (2019) XFEM modelling in multi-bolted joints using a unified bolt preload. *Latin Am J Solid Struct* 16(1):1–10
5. Bažant ZP, Xi Y (1991) Statistical size effect in quasi-brittle structures: II. Nonlocal theory. *J Eng Mech* 117:2623–2640
6. Muralidhara S, Prasad BKR, Karihaloo BL, Singh RK (2011) Size-independent fracture energy in plain concrete beams using tri-linear model. *Constr Build Mater* 25(7):3051–3058
7. Yang ST, Hu XZ, Wu ZM (2011) Influence of local fracture energy distribution on maximum fracture load of three-point-bending notched concrete beams. *Eng Fract Mech* 78(18):3289–3299
8. Ahmad H, Crocombe AD, Smith PA (2014) Strength prediction of notched woven composite plates using a cohesive zone approach. *Adv Mater Res* 845:199–203
9. Ahmad H (2014) Strength prediction of double-lap woven cfrp bolted joint incorporating material softening. *Appl Mech Mater* 541–542:234–238
10. Bažant ZP, Pfeiffer PA (1986) Shear fracture tests of concrete. *Mater Struct* 19(2):111–121

Structural Condition Assessment of a Log Bridge Under Heavy Traffic Load (Case Study: 105 Tons Gas Engine Delivery in Central Borneo Project)



Angga T. Yudhistira, Angga S. Fajar, Irfani N. Hud, Budi Suanda, and Ali Awaludin

Abstract Heavy equipment transportation has become the biggest challenge in the implementation of a powerplant project in Central Borneo, Indonesia. The road structure composition was subgrade only, and a simple log bridge only connected several river crossings. One of the longest bridges was Palili Bridge, with a 29-m span. The existing Palili bridge was used for logging trucks with operation load 50–60 ton. While the heaviest equipment in the powerplant project is a Gas Engine with a weight of 105 tons, the structural modification shall be done. The log girder span was modified to be 18.00 m so that a couple of 5.50 m cantilever log abutment was constructed. Also, the main span and abutment improvement were conducted to resist 105 tons of load. The objectives of this research were to investigate the structural performance of the strengthened Palili Bridge under 105 tons of vehicle load with the safety criteria. In the structural investigation, direct loading test under static and dynamic load was conducted. Bridge displacement was monitored at half and a quarter of span. Furthermore, a numerical analysis of the Palili Bridge was conducted by using SAP2000 software to verify the testing result. As the direct loading test result, both static and dynamic fulfilled the corresponded regulation. Based on the log girder span displacement monitoring, and the numerical analysis result, the bridge could resist the loads with safety factor 3.57 on the main span and 2.46 on the cantilever abutment. The computed maximum displacements considering composite action were 7.72 and 8.79 mm for static and dynamic load, respectively, less than the limit of 40.28 mm ($L/360$). Based on the result, the design and concept of the log bridge were proved to be feasible and could be applied in any other similar site condition.

Keywords Log bridge · Heavy traffic load · Structural analysis · Direct loading test

A. T. Yudhistira (✉) · B. Suanda
PT PP Persero, Jakarta, Indonesia
e-mail: angga.trisna@pp-epc.com

A. S. Fajar · I. N. Hud · A. Awaludin
Civil and Environmental Engineering, Universitas Gadjah Mada, Yogyakarta, Indonesia
e-mail: angga.fajar.s@ugm.ac.id

1 Introduction

Nature always delivers challenges for human activity, especially in project construction. Not only because the obstacle varies in different locations, but also the required solution to be more effective and efficient way possible. A project site based on isolated areas usually encounters a more difficult problem such as difficult access, bad soil condition, and so forth. Every problem needs to be solved by engineering study; therefore, an analytical approach is necessary. The recent continuation of the Gas Engine Power Plant Project by PT. PP has faced a unique problem concerning its access.

Located in Bangkanai, Central Borneo, Indonesia, this project was conducted on an uncivilized nature. The access road was subgrade only and was crossed by several rivers. By then, accommodating access through the river, a simple log bridge connecting Karendan (project site) and Luwe (a village located approximately 3 h from the site by car) was constructed, which can be seen in Fig. 1. The existing bridge was used for timber logging truck with 50–60 tons operation load. The structural

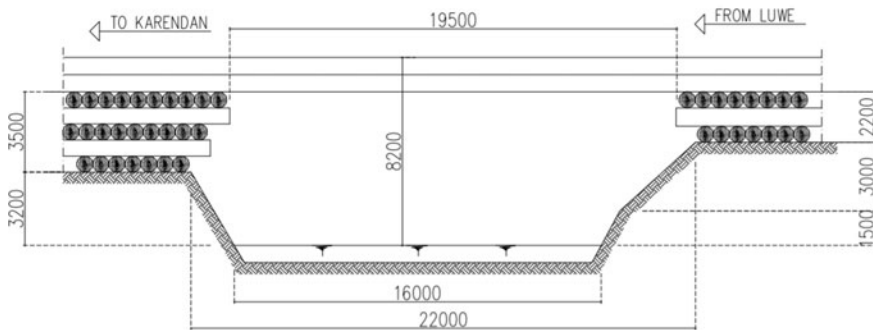


Fig. 1 Documentation and structural sketch of Palili bridge before redesign (2014)

sketch for the existing bridge can be seen in Fig. 1. Considering this bridge was the only access, the contractor decided to modify the structure of the bridge so that it could be used to mobilize heavier load, specifically the 105 Tons weighing Powerplant Engine. In order, considering the aging factor and any heavier load cored to the previous design, a proper analytical and experimental study must be performed before the operation of the log bridge.

Research Studies on log bridge stringers have been conducted in the previous time. One of them as studied by Moody et al. [1] about Strength of Log Bridge Stringers After Several Year's Use in Southeast Alaska. The study concluded that after 12 years, untreated log stringers would encounter strength reduction about 25% compared to fresh logs due to decay. Another study was from Sanders et al. [2] regarding the behaviour of Alaskan Native Log Stringer Bridges. In this study, the researcher compared the analytical method, direct load test method, and Laboratory model-test. From them, ultimate bending stress for log stringers could be calculated more accurately and more realistic. Tinambunan [3] has written a journal entitled Simple Log Bridges Construction Practices at several forest concessions in Kalimantan. It delivered conclusions and suggestions that useful guidance from the government in term of forest bridge planning, construction, and maintenance was strongly needed in order to reduce excessive use of natural resources (logs), to maintain proper bridge function for a longer period and to minimize environmental disturbance. For this purpose, the involvement of civil engineers in handling various forest engineering problems and pacing of research activities are then urgently needed.

Those basics theories encouraged to be continued in different findings, so that, this research paper brave to focused on the implementation of a traditionally constructed log bridge for heavy load supported by log counterweight cantilever abutment. Along its span, the logs were fastened by using wire rope slings, then was piled up by the soil, as suggested by Lohuji [4]. The abutment was designed by controlling the resisting and overturning moment from each layer of the log. The implementation of the cantilever beam in the abutment concept could shorten the superstructure span; as a result, the load-bearing capacity rises.

This bridge has been modified twice. The bridge has also been used to mobilize 105 tons of powerplant engines twice, in 2015 and 2019. In 2015, the contractor modified the span of the bridge from 29 to 18 m, as shown in Fig. 2. In 2019, the contractor added reinforcement of wood girders in the upper layer. Thereby, these increased the capacity and stability of the bridge against heavy equipment loads. The final stage of the bridge design then became the subject of numerical and experimental studies.

The study has aim for investigating the structural performance of the strengthened Palili Bridge under 105 tons of vehicle load with the safety criteria. This conceptual design and the assessment method could lead the application of solution to other similar cases project located in isolated access location. Furthermore, the benefit of the simple, fast, and economical construction could give additional benefit to the contractor.

This study consists of analytical analysis and experimental of the loading test. The analytical analysis including collecting the material properties and geometric

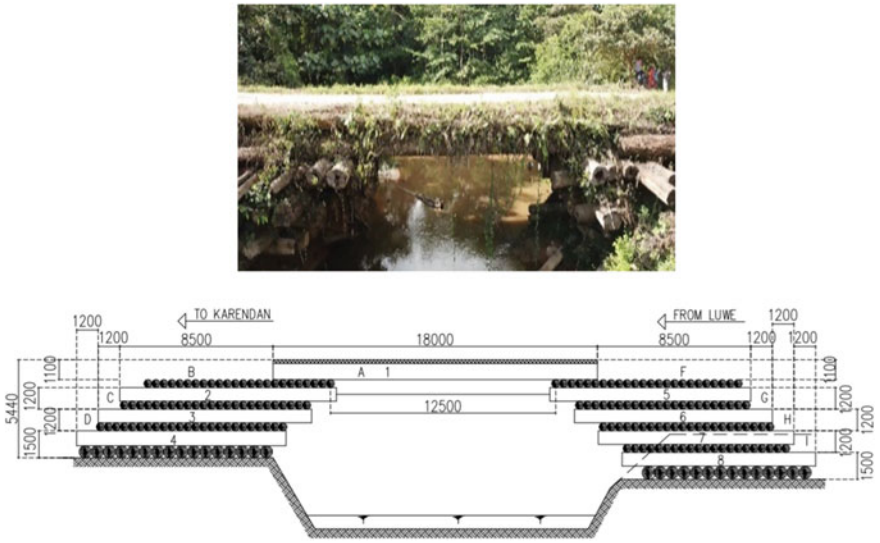


Fig. 2 Documentation and structural sketch of Palili bridge after 1st modification (2018)

data of the log bridge. Continued by the structural analysis, the numerical model was developed by a frame element to calculate the log bridge span displacement and the log's cross-section stress. The point load with the same configuration of the planned heavy vehicle to be subjected to the frame element. Further, the stability of the counterweight abutment was analyzed by using static stability analysis. Experimental studies were conducted twice; the first step made the bridge was loaded with 141.23 tons of static load characteristic contained by heavy equipment and wooden log. In the second experimental study, the bridge was loaded with 100.3 tons jumbo bag cement on multi-axle with dynamic characteristics.

2 Method

There were three conducted steps to show how the log bridge worked according to the study case. These were considering factors for the design approach and validation of the research. The steps were explained below:

2.1 The Concept of the Log Bridge Structure

The main idea of the structural concept raised from the project efficiency demand which structural design should solve the challenge on making time and resources were

efficient. Based on the field survey and the several discussions among the engineering team, construction project team, and professional consultant engineer, shortening the span of the existing superstructure was a concept to enhance structural capacity in supporting the heavy vehicle load. The shorter span of superstructure was expected to achieve smaller deflection and bending stress of the log member. As a result, the log bridge which composed of existing and addition of one type of materials could achieve stiffness, strength, and stability criteria in resisting the heavier vehicle load. The counterweight wooden abutment cantilever was proposed to shorten the superstructure span while the hydraulic radius of the river section to remain.

The main span was a simple beam constructed by winding arranged logs and the abutment stacked perpendicularly by layers of logs in the horizontal plane. The abutment structure was based on the concept of cantilever structure, wherein execution, the edge of each stacking reached closer to the middle span, the higher it got, as shown in Fig. 2. This was chosen to increase the bridge load capacity by shortening its span.

2.2 Structural Design

During the design process of the log bridge, the contractor, the professional engineering consultant, and the expert engineer were involved in solving the demand of log bridge structure under heavy vehicle load. At first, the sketch concept design to be drawn in detail with CAD software. Then, the structural analysis to be conducted by taking stability static analysis and by developing a numerical model with SAP2000 software. Material properties of wood material were already tested at the laboratory, the results can be seen in Table 2. New layers of the log were added on the upper structure and abutment to enhance the strength and stiffness of the bridge, as shown in Fig. 3. In-between the adjustment of new logs on the upper structure, their connections were fastened using 12 mm diameter wire steel sling to ensure that the logs acted as a uniform section.

The loading methods used for the numerical and analytical studies were different from the National Standard of Indonesia 1725–2016 [5]. On this case, the actual direct loading set up was adopted to simulate the realistic heavy loading condition. The seismic load was not considered due to the probability seismic intensity was very low, according to Seismic Hazard Map of Indonesia 2017 [6].

2.3 Loading Test Scenario

The loading test was performed in static and dynamic ways in which both deflections were monitored using the auto-level. There were 3 monitored deflection points acrossed the bridge, as shown in Fig. 8. During the load test, the aerial view was observed using a drone.

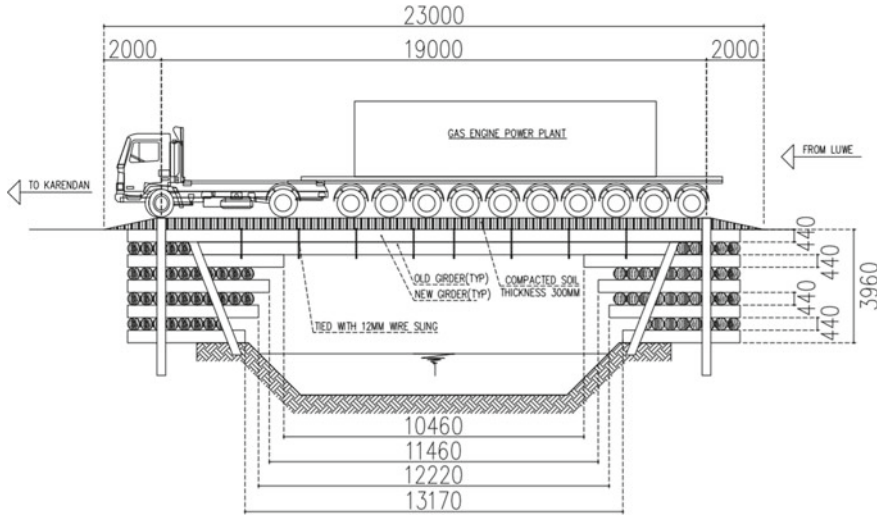


Fig. 3 Structural design Palili bridge under 105 Tons gas engine load

Dummy load for static test consisted of a PC 200 Excavator, a Logging Truck, and timber logs. This test was handling a species of timber namely Meranti Batu, a local material which had around 1.0 ton/m^3 weight. The total static load placed on top of the span was 141.34 tons and remained idle for 30 min to simulate the static load characteristic. The load placements for the static test could be seen in Fig. 4. Under the dynamic test, a multi-axle dummy weight around 100.3 tons were accumulated from 99 bags of cement represented the engine load. The load was moving slowly to the bridge with an average speed of 4–5 km/h.

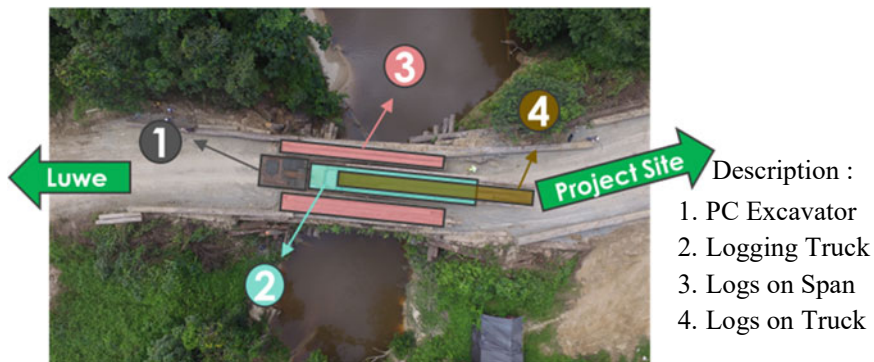


Fig. 4 Load position for static loading test (no scale)

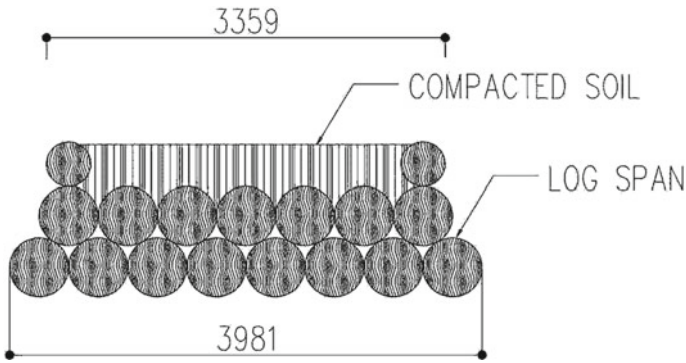


Fig. 5 Log bridge span cross section (length in mm)

2.4 The Idealization of the Superstructure Cross-Section

Log bridge cross-section was wondrously arranged from local logs, as seen in Fig. 5. Furthermore, to analyze this type of section, a model was proposed as an analytical approach that corresponded to the detail engineering design. In reality, the composed section would work uniformly instead of independently. This effect of uniform behavior was called monolithic action, which would also influence the moment of inertia. Theoretically, the moment inertia of a single frame would be different if it was a compiled section. For a solid cylinder frame section, the moment of inertia was calculated by Eq. 4. Whereas, for the compiled cylinder section, the formula would require the distance from each independent area section to the center of mass. This resulted a stiffer frame section than a single one. The formula can be seen in Eq. 1.

$$I = \frac{1}{4}\pi r^4 + A \cdot c^2 \tag{1}$$

where A is the area section of rectangular and c is the distance from the center of mass of independent section to the global center of mass in the corresponding direction.

To analyze this bridge section, it required a complex numerical model that embodies the monolithic action. Further, by the assumption of insignificant composite action in the log bridge, the numerical model used for this study was a single beam with a reduced load.

2.5 The Deflection and Stress of Upper Structure

Common parameter control of timber bridge structure analysis was stress and deflection. Checking the maximum deflection is necessary to fulfill structure comfort

criteria, as stated by Ritter [7]. The deflection limit was shown in Eq. 2.

$$\delta_{\max} = \frac{1}{360}L \quad (2)$$

where δ_{\max} is the notation for deflection limit, and L is the length of span in the meter.

Lauren W. McKeen [8] explained that, for the simply supported structural beam, on the upper surface of the bending beam, there was a compression, while on the bottom surface, there was tension. The two areas were divided by the neutral axis, where there was zero stress. The bending stress (σ) is defined by Eq. 3.

$$\sigma = \frac{M \times c}{I} \quad (3)$$

where c and M are the value of the distance from the neutral axis and moment, respectively, notation of I is the moment of inertia, which formulas varied depending on the shape of the beam. For rectangular shape, the formula is as seen in Eq. 3.

$$I = \frac{1}{4}\pi r^4 \quad (4)$$

In achieving the necessary level of performance, the desired stress value from Eq. 3 has to be below the available strength that has been divided by the safety factor, as written in Eq. 5. The required safety factor for the timber bridge is 1.5, according to the Wisconsin Department of Transportation [9].

$$\sigma < \frac{\sigma_{cap}}{SF} \quad (5)$$

2.6 Abutment Stability

The concept of study used for abutment stability was moment equilibrium, where the ratio of the stabilizing moment to de-stabilizing moment was calculated and limited by a minimum value of Safety Factor. The formula was written in Eq. 6. The state of moment equilibrium was controlled for every layer of logs in the abutment. The axis of rotation was in line with the farthest transversal log from the land side. The scheme of this analysis can be seen in Fig. 6.

$$SF = \frac{\text{Resisting Moment}}{\text{Overturning Moment}} \quad (6)$$

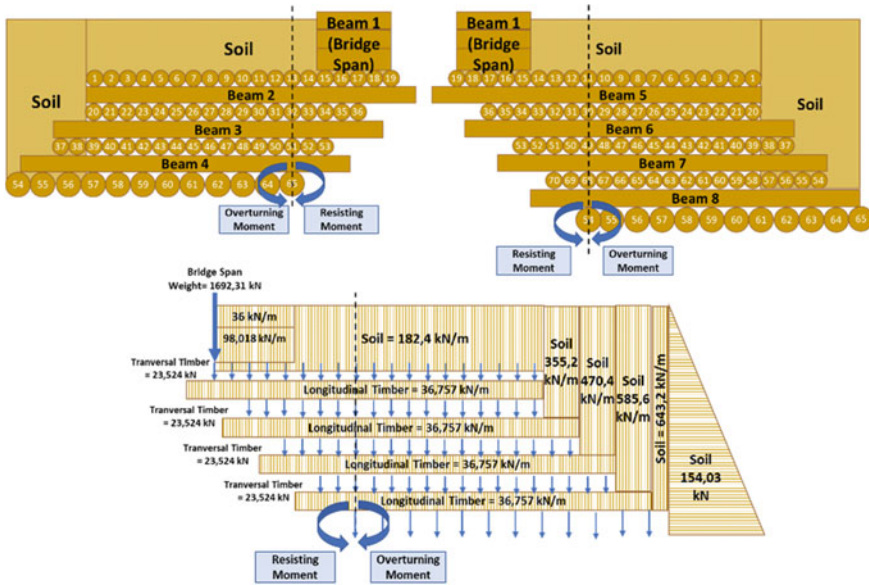


Fig. 6 Internal force idealization for the analytical study of abutment stability

Based on the IBC 2018 [10] section 1807.2.3, the minimum safety factor of 1.5 was needed to define a stable performance from the interaction between resisting and overturning moments. The state of the safety factor in each layer of the log is shown in Table 1 (the number of the layer are represented in Fig. 6). The directions were each pointed to the project location and nearest village access. The safety factor in each layer was remained above the minimum requirement of 1.5. So, the new abutment design has fulfilled with the stability criteria.

Table 1 The safety factor found by analytical study

Direction	Layer number	Safety factor
Karendan (project site)	2	5.587
	3	3.359
	4	2.61
Luwe	5	5.539
	6	4.758
	7	2.609
	8	2.052

Table 2 The lab testing result of various Bengkirai timber (*Shorea laevis*) specimens

Sample number	Max. load (kg)	Bending strength (MPa)	Modulus of elasticity (MPa)
1	12.04	102.61	15,571.99
2	11.56	98.49	15,166.84
3	9.05	77.11	12,715.86
4	13.15	112.04	14,675.78
5	10.15	86.48	13,325.74
6	12.40	105.65	13,632.11

3 Numerical Modeling

The numerical element modeling of the log bridge was performed by using SAP2000. The actual bridge was simplified into a single frame; therefore, the load design was also divided by the total amount of logs used in the redesigned span. The critical span length and diameter of the timber were 14.5 m and 0.6 m, respectively.

Previous researchers have discovered the true natures of timber. Awaluddin (2005) [11] stated that the strength and tension on timber were highly related to the time or duration of loading, so the behavior of timber was time-dependent. J. Bodig (2013) [12] divided these time-dependent phenomena into load dependent phenomena, such as creep, and load-independent phenomena, such as various forms of biological degradation. Furthermore, he introduced random process loads, which was called as Gaussian Process, and was filtered as Poisson Process to model these loads. However, in order to make it simpler, a similar approach by Hoyle (1978) [13] was chosen. He stated that the total load that was able to be resisted by timber in the next ten years would be equal to a load that caused stress of 60% from its initial stress strength, which was acquired from 5 to 10 min of lab testing.

Using the suggested concept by Hoyle, the stress strength was assumed to be linear with the moment of inertia. Therefore, the frame geometries were modified using a reduction factor of 0.8 to assume the reduction of timber quality due to aging. The reduction factor was acquired by assuming that the quality of the first layer of timber or the older one has been reduced to 60%. In the assumption, the bridge was strengthened by applying new layers of timber with 100% of its strength. The overall calculation is as written in Eq. 7.

$$60\% + \frac{(100 - 60)\%}{2} = 0.8 \quad (7)$$

The material properties were 12,716 MPa for Young's Modulus and 77 MPa for maximum bending strength. These numbers were achieved through lab testing from various similar specimens of Bengkirai Timber (*Shorea laevis*). Among the 6 results, the lowest grade was chosen. The results were shown in Table 2.

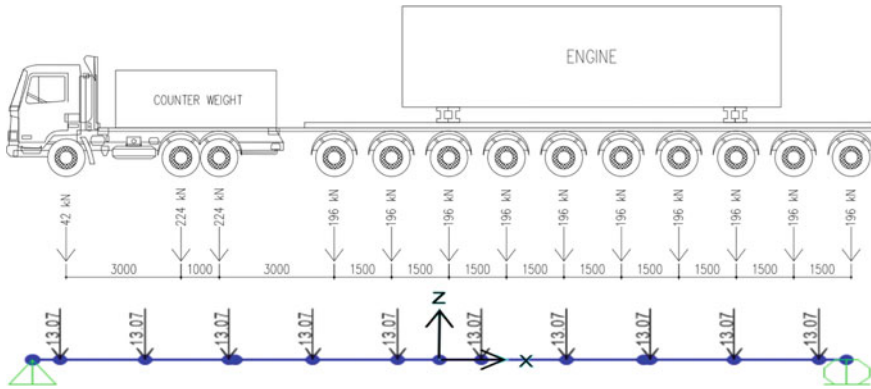


Fig. 7 Logging truckload distribution along with the bridge model in kN (length in mm)

The loading mechanisms for the numerical model were static and dynamic. For the static test, the applied load was multiplied by 1.4 (Dynamic Factor). Loading points placement along the bridge were according to the load distribution of the logging truck, as shown in Fig. 7. Therefore, to achieve the maximum bending moment, the load distributions were placed into a particular way, as shown in Fig. 7.

4 Experimental Studies

The experimental test was conducted into 6 steps and lasted for 8 days. These steps were including the mobilization of timbers, excavation of soil, adding new layers of timber, soil backfilling, preparation for loading test, and finally, the loading test. The loading test was performed in static and dynamic ways, with each one conducted on a different day. The measurement was conducted at three points, as marked by letter a, b, and c for static load test and number 1, 2, and 3 for dynamic load test in Fig. 8. The highest recorded deflection was chosen as the final result. Both types of tests required deflection monitoring using the auto level, as shown in Fig. 9.

The static loading test was conducted gradually in two phases. First phase weights around 57.84 tons and the second 141.34 ton. The deflection result for the static loading test was shown in Table 3. Even though all three deflection points were monitored in the middle span, the gap range between point a to the other two points was quite high due to possible local settlement. As the final result, the highest monitored deflection was 17.00 mm of the total value. Furthermore, the average displacement was 7.50 mm. This result was then considered safe as it was below the limit of 40.278 mm (following the Eq. 2).

The dynamic loading test was performed by mobilizing a total load of 100.35 tons on multi-axle. The average speed for the moving load was around 4–5 km/h. The deflection acquired from this test were shown in Table 4. The highest deflection



Fig. 8 Experimental static load test and dynamic load test

was recorded at the middle span was 8.00 mm, far below the maximum limit of 40.278 mm.

As seen in Tables 3 and 4, the maximum deflection from each loading, 17.00 mm and 8.00 mm for static and dynamic loading respectively, were far below the result of maximum deflection acquired from the preliminary numerical analysis, 24.7 mm and 18.149 mm for static and dynamic loading, respectively. This happened because the model didn't fully resemble the monolith behavior of multilayer timbers as it only considers the global bending moment and shear effect of a single frame. Based on research conducted by Fuentes [14], the modeling must include all independent components of the timber structure, which consist of the frame (1); the connector (2); the contact action between each frame (3); and the contact action between frame and connector (4). Therefore, to prove this effect, an additional analysis was performed. Based on the comparison of the measured deflection under static and dynamic loading



Fig. 9 Displacement measurement using auto-level

Table 3 Deflection results under static loading test

Phase	Deflection in mm			
	a	b	c	Average
1	15.00	5.00	0.00	6.67
2	17.00	7.00	1.00	8.33
Average				7.50

Table 4 Deflection results under dynamic loading test

Point(s)	Deflection (mm)
1	5.00
2	8.00
3	5.00

Table 5 Deflection comparison under static and dynamic test

Point	Deflection (mm)		Difference relative
	Static	Dynamic	
2	7.50	8.00	6.67%

in Table 5 both recorded deflection result has almost equal value with the relative different 6.67%.

On the other hand, the maximum stress for the static load test was 7.974 Mpa (according to Eq. 3). This result was below 51.3 MPa, the allowable stress (1/1.5 times of the bending strength). By using the vehicle load design in Fig. 7, the moving load could be simulated in the numerical model with the result of 3.421 MPa stress. Both results showed adequate performance as the values were still below the allowable stress limit of 51.3 MPa.

As stated before, the preliminary numerical bridge span model used for this study was simplified as a single beam, whereas the actual structure probably to be a monolith of two layers log sections (see Fig. 5). In order for the achievement of the valid numerical model, the section property was readjusted. An analytical approach was conducted to determine the value of inertia moment with monolith idealization. The new moment of inertia then used as a section property modifier for the new model in the numerical study. The load design used for this updated model was the lumpsum (equal with real field implementation value), as seen in Fig. 7.

The updated numerical model result showed that the maximum deflection in the middle span for static and dynamic loading was 7.72 mm and 8.79 mm, respectively. Both deflections have differences relative to the testing results (static and dynamic) with a value of 2.96% and 9.85%, respectively, as shown in Table 6. While the preliminary numerical model achieves a difference relative to the testing results (static and dynamic) with a value of 229.33% and 126.86%, respectively. The updated numerical model that idealized as a monolith cross-section of the superstructure has better accuracy than the preliminary analysis that idealized as individual cross-section action.

Table 6 Deflection comparison after considering monolith action

Loading type	Maximum deflection in mm				
	Experimental results	Numerical results (neglecting monolith action)	Difference relative (%)	Numerical results (considering monolith action)	Difference relative (%)
Static	7.50	24.70	229.33	7.72	2.96
Dynamic	8.00	18.15	126.86	8.79	9.85

5 Conclusion

Based on the analytical, numerical, and experimental tests, which all showed adequate results, this research managed to conclude several points. First, the numerical result of the preliminary model (non-monolith) under both static and dynamic loading showed a maximum deflection of 24.7 mm and 18.149 mm, respectively, which proven to be safe according to standard by A. Ritter [10] that had limits at 40.278 mm. Second, the maximum bridge stress acquired from the analytical and numerical study was 7.974 MPa and 6.453 MPa for the static and dynamic test, respectively. These nominals were still below the allowable stress of 51.5 MPa. Therefore, the strength capacity of span was sufficient for the direct load. Third, the lowest overturning stability ratio in the abutment was 2.052, which still below the safety requirement of 1.5 regulated by the International Building Code 2018 [10]. The abutment was also proven to be stable based on the experimental test. Fourth, in the numerical modeling of the log bridge super-structure, it was found that the implementation monolith action of the cross-section in each log could achieve better agreement result than the individual cross-section action in each log. Finally, the result of this study is expected to provide guidance to projects in remote locations that require temporary access using log bridges to mobilize heavy traffic above 100 tons.

References

1. Moody RC, Eslyn WE, Muchmore FW (1979) Strength of log bridge stringers after several year's use in Southeast Alaska. United States Department of Agriculture Forest Service, Research Paper FPL 346
2. Sanders WW, Muchmore FW, Tuomi RL (1978) Behaviour of Alaskan native log stringer bridges, transportation research board. National Research Council, Washington, DC
3. Tinambunan D (1990) Praktek Pembuatan Jembatan Kayu Bulat Sederhana di Beberapa Koneksi Hutan di Kalimantan. Jurnal Penelitian Hasil Hutan 8
4. Lohuji PL, Taumas R, Gampilok R, Anthony R, Gan BK (2009) Code of practice for forest harvesting in Sabah, Malaysia (3rd edn). Sabah Forestry Department, Sandakan
5. Standar Nasional Indonesia, Badan Standardisasi Nasional (2016) Pembebanan untuk jembatan. BSN, Jakarta
6. Pusat Studi Gempa Nasional, Pusat Litbang Perumahan dan Permukiman (2017) Seismic hazard maps of Indonesia
7. Ritter MA (1990) Timber bridges: design, construction, inspection, and maintenance. U.S. Department of Agriculture, Forest Service, Engineering Staff, Washington, DC
8. McKeen LW (2009) Fatigue and tribological properties of plastics and elastomers, 2nd edn. William Andrew, New York
9. Wisconsin Department of Transportation (2006) Impact of railcar weight change on bridges of the State of Wisconsin owned railroad system. Wisconsin Department of Transportation, Wisconsin
10. International Code Council (2017) International building code 2018 (1st edn). International Code Council, Incorporated, Falls Church, Va.
11. Awaludin A, Irawati IS (2005) Konstruksi Kayu (2nd ed). Biro Penerbit Teknik Sipil UGM, Yogyakarta

12. Bodig J (2013) Reliability-based design of engineered wood structures. (Nato Science Series E:). Springer, Netherlands
13. Hoyle RJ (1978) Wood technology in the design of structures. Mountain Press Pub. Co, Michigan
14. Fuentes S, Eric F, Clermont-ferrand P, Bouchair A (2014) Semi rigidity of traditional timber floors -Modelling aspects of horizontal diaphragms for seismic loading. In: World conference on timber engineering 2014, Canada

The Application of Inserted Steel Pipe as an Alternative Confinement Design in Reinforced Concrete Column Plastic Hinge Regions



Johanes Januar Sudjati, Iman Satyarno, Andreas Triwiyono, Bambang Supriyadi, and Angga Fajar Setiawan

Abstract Plastic hinges in the base of columns cannot be avoided in the seismic ductile design of reinforced concrete structures. Therefore, the adequate amount of transverse reinforcement must be provided in the base of column plastic hinge regions to achieve a ductile failure mechanism. There are two objectives of providing an adequate amount of transverse reinforcement in the column plastic hinge regions. Firstly, is to prevent the shear failure mechanism and secondly is to provide adequate confinement, especially if the axial load in the columns is high. In some cases, the need for transverse reinforcement amounts is very high that makes them difficult to construct. To reduce the difficulty in constructing the transverse reinforcement, 90° hook steel bars are also used. It is known that these 90° hook steel bars are not so effective for confinement, make more congestion, and there are ineffective steel bars volumes for the hooks. This paper discusses an alternative method of conventional transverse reinforcement (CTR) to provide confinement in the column plastic hinge regions by inserting steel pipe in plastic hinge regions to reduce the amount of transverse reinforcement (CTRSP). The moment–curvature relationships and the interaction diagram for CTR and CTRSP were compared numerically. The result showed that the inserted steel pipe reduced the moment capacity deterioration

J. J. Sudjati (✉) · I. Satyarno · A. Triwiyono · B. Supriyadi · A. F. Setiawan
Department of Civil and Environmental Engineering, Universitas Gadjah Mada, Yogyakarta,
Indonesia
e-mail: januar.sudjati@uajy.ac.id; januarsudjati@mail.ugm.ac.id

I. Satyarno
e-mail: imansatyarno@ugm.ac.id

A. Triwiyono
e-mail: andreas.triwiyono@ugm.ac.id

B. Supriyadi
e-mail: bambang.supri@ugm.ac.id

A. F. Setiawan
e-mail: Angga.fajar.s@ugm.ac.id

J. J. Sudjati
Department of Civil Engineering, Universitas Atma Jaya Yogyakarta, Yogyakarta, Indonesia

significantly and increased the ductility of the column so that CTRSP was more effective for confinement than CTR. Moreover, less steel material was needed by CTRSP than CTR as no ineffective steel bars for the hooks were needed in CTRSP.

Keywords Plastic hinges · Confinement · Inserted steel pipe

1 Introduction

Building structures built in earthquake-hazard areas must meet the provisions of earthquake-resistant structural systems. In the principle of planning earthquake-resistant building structures, earthquake loads may be reduced based on the level of structural ductility [1]. When a strong earthquake occurs, certain structural elements can suffer damage so that earthquake energy can be dissipated. This energy dissipation mechanism aims to limit the earthquake forces received by building structures.

The damaged structural elements are called plastic hinges. Plastic hinges at the base of the column cannot be avoided. Therefore, the adequate amount of transverse reinforcement must be provided in the base of column plastic hinge regions to achieve ductile failure mechanism, especially if the structures are subjected by high axial loads. A high axial compressive load will reduce the ductility of the column if there is no adequate confinement. Plastic hinges can occur in the base of building columns or bridge pillars (Fig. 1). Damage to the plastic hinge in the base of a column causes the structure to become unstable, especially on a single pillar of the bridge.

The transverse reinforcement serves to prevent the shear failure mechanism in the column, provides adequate confinement on the concrete core so that the plastic hinge has ductile properties, and prevents buckling of the longitudinal reinforcement. For a column that carries a small axial load, transverse reinforcement is more intended to prevent shear failure. In ACI code, the concrete shear strength is eliminated if



Fig. 1 Plastic hinges in Imperial Valley Services Building during the 1979 Imperial Valley Earthquake [2]

the column is subjected by an axial load of less than $0.05 A_g f'_c$ [3]. However, for a column that carries a large axial load, transverse reinforcement will be more intended to provide confinement on the concrete core so that the column behaves in ductile behavior and prevents buckling of the longitudinal reinforcement.

The failure of the transverse reinforcement leads to the buckling of longitudinal reinforcement, then the degradation of the load-carrying capacity of the column will occur rapidly, and the column will collapse. In high levels of earthquake hazard areas, the need for transverse reinforcement amounts is very high that makes them difficult to construct. The ACI code permits the use of 90° hooks [3] to reduce the difficulty in constructing the transverse reinforcement. It is known that these 90° hook steel bars are not so effective for confinement, make more congestion, and there are ineffective steel bars volumes for the hooks.

Many researchers used outer steel tubes or steel pipes instead of transverse reinforcement to provide confinement on concrete. The behavior of concrete-filled stainless steel tube (CFSST) subjected to constant axial load combined with lateral cyclic load was investigated [4]. The parameters were cross-sectional configuration, steel ratio, and axial load ratio. The result showed that the square specimens had lower ductility compared to the circular specimens. Concrete-filled steel tube columns were compared to concrete-encased steel columns using high-strength steel and high-strength concrete to investigate the effect of various sectional shapes [5]. The steel tube could restrain early concrete crushing and developed its full plastic stress. Another research, a stiffened concrete-filled slender steel tube column (S-CFT) was investigated [6]. The welded longitudinal bars successfully restrained local buckling of the slender steel tube. Thin-walled rectangular concrete-filled tubular (RCFT) columns were investigated to study the effects of a high-strength steel slender section on the overall eccentric compression capacity [7]. The specimens strengthened with vertical stiffeners exhibited enhanced strength and ductility. Square and circular concrete-filled steel tube (CFT) made with high-strength and conventional steel were investigated [8]. CFT columns with high-strength steel had greater elastic deformation capacity and delay the local buckling compare to CFT columns with conventional steel.

Some researchers investigated column with double steel tubes in their experiments. Outer steel tube and inserted inner steel tube were used for concrete-filled double-skin steel tubes (CFDST) specimens [9]. The experiment result showed a stiffer inner tube would delay local buckling effectively and reduce the deterioration in moment capacity. Concrete-filled double-skin steel tubes (CFDST) were also used as a substitute to reinforced concrete columns for bridge piers [10]. CFDST had good energy dissipation capacity and had ductile behavior up to failure. The inner tube in CFDST served as a dowel that effectively prevented the direct shear failure of the section.

Other researchers investigated fiber-reinforced polymer (FRP)-concrete-steel double-skin tubular columns (DSTC) with an outer FRP tube and an inner steel tube. The presence of a concrete filling inside the inner steel tube significantly influenced the seismic behavior of DST columns [11], increased the ultimate axial stress

[12], and increased the compressive strength of confined concrete [13]. The experimental results indicated the DSTC could possess excellent ductility even when high-strength concrete was used [14]. The DSTC also behaved in a ductile manner under blast loading [15, 16]. The bending strength of the DCTC would increase if the diameter-to-thickness ratio of the steel tube decreased [17].

Concrete-filled steel tube columns encased with thin precast concrete was also tested to investigate the load-carrying capacity [18, 19]. The concrete-filled steel tube could maintain the residual moment capacity of the specimens. The structural performances of the specimen using corrugated steel plates were comparable to or even higher than the reinforced concrete specimen.

Based on the previous researches, a steel pipe can be used to reduce the congestion of the transverse reinforcement in the plastic hinge region. This paper discusses an alternative method of conventional transverse reinforcement to provide confinement in the column plastic hinge regions by inserting steel pipe to reduce the amount of transverse reinforcement. In this study, the roles of the inserted steel pipe to maintain or increase the ductility and the load-carrying capacity of the columns were investigated numerically.

2 Concrete Stress–Strain Relationship

For a slow strain rate and monotonic loading, the compression concrete stress f_c can be calculated by Mander formula [20].

$$f_c = \frac{f'_{cc} x r}{r - 1 + x^r} \quad (1)$$

$$f'_{cc} = k f'_{co} \quad (2)$$

$$x = \frac{\varepsilon_c}{\varepsilon_{cc}} \quad (3)$$

$$\varepsilon_{cc} = \varepsilon_{co} [1 + 5(k - 1)] \quad (4)$$

$$r = \frac{E_c}{E_c - E_{sec}} \quad (5)$$

$$E_c = 5000 \sqrt{f'_{co}} \quad (6)$$

$$E_{sec} = \frac{f'_{cc}}{\varepsilon_{cc}} \quad (7)$$

where:

f'_{cc} = compressive strength of confined concrete, k = strength incremental factor, f'_{co} = compressive strength of unconfined concrete, ϵ_c = compressive concrete strain, ϵ_{cc} = compressive strain of the confined concrete corresponding to f'_{cc} , ϵ_{co} = compressive strain corresponding to f'_{co} , E_c = elasticity modulus of unconfined concrete, E_{sec} = secant modulus of confined concrete.

Strength incremental factor can be calculated by the following equation [20].

$$k = \left(-1.254 + 2.254 \sqrt{1 + \frac{7.94 f_l}{f'_{co}}} - 2 \frac{f_l}{f'_{co}} \right) \tag{8}$$

$$f_{lx} = k_e \rho_x f_{yh} \tag{9}$$

$$f_{ly} = k_e \rho_y f_{yh} \tag{10}$$

For rectangular stirrups, k_e can be calculated by the following equation [20].

$$k_e = \frac{\left(1 - \sum_{i=1}^n \frac{(w'_i)^2}{6b_c d_c} \right) \left(1 - \frac{s'}{2b_c} \right) \left(1 - \frac{s'}{2d_c} \right)}{1 - \rho_{cc}} \tag{11}$$

$$\rho_x = \frac{A_{sx} b_c}{b_c d_c s} = \frac{A_{sx}}{s d_c} \tag{12}$$

$$\rho_y = \frac{A_{sy} d_c}{b_c d_c s} = \frac{A_{sy}}{s b_c} \tag{13}$$

where: k = strength incremental factor, f_l = effective lateral confining stress, k_e = confinement effectiveness coefficient, ρ_x and ρ_y = volumetric ratio of transverse reinforcement in x and y directions, f_{yh} = yield stress of the transverse reinforcement, w'_i = clear distance between adjacent longitudinal bars, s' = clear vertical spacing between transverse reinforcement, b_c and d_c = core dimensions to centerlines of perimeter hoop in x and y directions, ρ_{cc} = ratio of area of longitudinal reinforcement to area of core of section, A_{sx} and A_{sy} = total area of transverse reinforcement in x and y directions, s = vertical spacing between transverse reinforcement.

If $f_{lx} = f_{ly}$, k can be calculated by the previous equation, but if $f_{lx} \neq f_{ly}$ k must be calculated by the following equation [21].

$$k = k_l + (k_h - k_l) \sqrt{\frac{\left(\frac{f_{l2}}{f'_{co}} - \frac{f_{l1}}{f'_{co}} \right)}{\left(0.3 - \frac{f_{l1}}{f'_{co}} \right)}} \tag{14}$$

$$k_h = 1.3 + 5.55 \frac{f_{l1}}{f'_{co}} - 7.5 \left(\frac{f_{l1}}{f'_{co}} \right)^2 \tag{15}$$

$$k_l = \left(-1.254 + 2.254 \sqrt{1 + \frac{7.94 f_{l1}}{f'_{co}}} - 2 \frac{f_{l1}}{f'_{co}} \right)$$

where: f_{l1} = smaller lateral confining stress, f_{l2} = larger lateral confining stress.

3 Research Methodology

Rectangular columns of specimens were analyzed using fiber model in this study. The column had 600 mm width and 600 mm height, contained sixteen D25 longitudinal reinforcements providing a reinforcement ratio of 2.18% of the cross-sectional area of the column. The compressive strength of the unconfined concrete was 25 MPa and the yield stress of the steel bar was 414 MPa (A615 Gr 60). The columns were subjected by axial loads with the variety of the $P/(f'_c A_g)$ ratio as follows: 0; 0.05; 0.10; 0.15; 0.20; 0.25; 0.30; 0.35; 0.40; 0.45; 0.50; 0.55; and 0.60. Transverse reinforcement requirements in plastic hinge regions were calculated based on ACI 318M-14 code [3] and the results are listed in Table 1 and shown in Fig. 2. In Table 1, CTR is a column with conventional transverse reinforcement, the numerical value of the specimen denotes the number and spacing of the stirrups, and ρ is the volumetric ratio of transverse reinforcement to concrete core, measured center-to-center of perimeter ties.

Table 1 Column with conventional transverse reinforcement

Axial load ratio	Specimen	Longitudinal reinforcement	Transverse reinforcement	ρ_{actual}
0–0.35	CTR4-150	16D25	4D13-150	0.0140
0.40–0.45	CTR5-150	16D25	5D13-150	0.0175
0.50–0.55	CTR5-125	16D25	5D13-125	0.0209
0.60	CTR5-100	16D25	5D13-100	0.0262

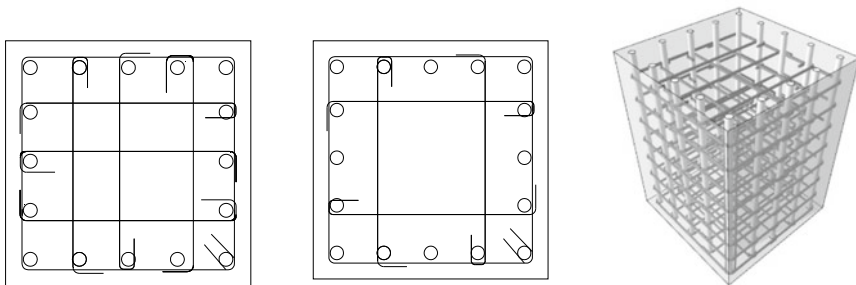


Fig. 2 Cross-section of CTR specimens

Table 2 Column with transverse reinforcement and steel pipe

Axial load ratio	Specimen	Longitudinal reinforcement	Transverse reinforcement	Steel pipe	ρ_{actual}
0–0.35	CTRSP2	16D25	2D13-150	D = 350 mm t = 2 mm	0.0155
0.40–0.45	CTRSP3a	16D25	2D13-150	D = 350 mm t = 3 mm	0.0198
0.50–0.55	CTRSP3b	16D25	2D13-125	D = 350 mm t = 3 mm	0.0212
0.60	CTRSP4	16D25	2D13-100	D = 350 mm t = 4 mm	0.0276

As an alternative of CTR, a steel pipe was inserted in the center of the column cross-section in plastic hinge regions to reduce the number of transverse reinforcements. The steel pipe was put on the top of the foundation. The yield stress of the steel pipe was 290 MPa. The new configuration of specimens is listed in Table 2 and shown in Fig. 3. In Table 2, CTRSP is a column with conventional transverse reinforcement and steel pipe, the numerical value of the specimen denotes the thickness of the steel pipe, D is the diameter of the steel pipe, ρ is the volumetric ratio of confinement reinforcement to concrete core, and t is the thickness of the steel pipe.

The volumetric ratio of the confinement reinforcement of CTR and CTRSP were nearly the same. For CTRSP, the volumetric ratio consisted of the volume of the perimeter transverse reinforcement and steel pipe. The effectiveness of steel pipes in providing confinement on the concrete core was considered by comparison of moment–curvature and interaction diagrams between the CTR and CTRSP specimens. The moment–curvature and interaction diagrams were calculated using fiber model. Both specimens were also compared to UC specimens to examine the performance increase of the confined column. UC specimen was a column without confinement and contained sixteen D25 longitudinal reinforcements, similar to CTR and CTRSP. The analysis was done with SAP 2000 software version 20.0.0.

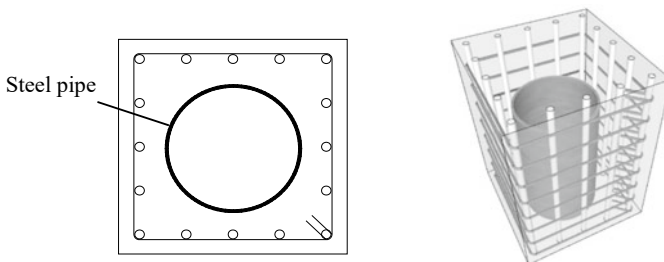


Fig. 3 CTRSP specimens

4 Results and Discussions

4.1 Stress–Strain Relationship

Figure 4 shows the unconfined concrete, the effectively and ineffectively confined core for CTR specimens and CTRSP specimens. The stress–strain of concrete was calculated based on Mander’s model. The arching action, containing the ineffectively confined concrete, is assumed to occur vertically between layers of transverse reinforcements and horizontally between longitudinal reinforcements [20]. CTRSP specimens had two types of effectively confined concrete that were the confined concrete outside the steel pipe and the confined concrete inside the steel pipe.

The stress–strain relationship for unconfined concrete based on Mander’s model is shown in Fig. 5. The unconfined concrete reached up to 0.002219 strain (ϵ_{co}) at

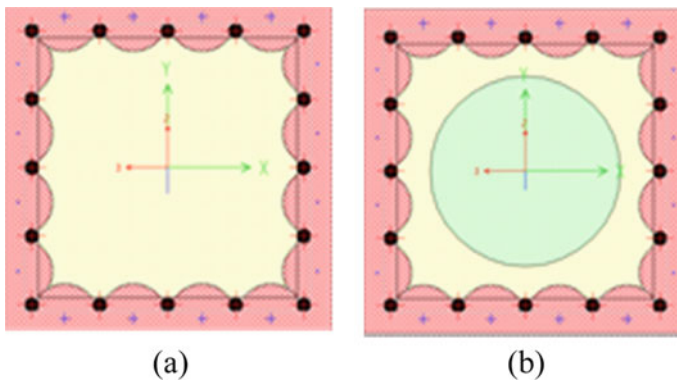


Fig. 4 Effectively and ineffectively confined core: **a** CTR specimens, and **b** CTRSP specimens

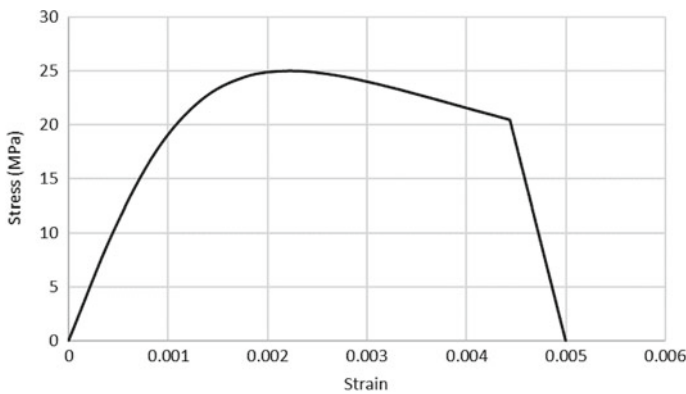


Fig. 5 Stress–strain relationship of unconfined concrete

its peak stress of 25 MPa. After 0.004438 strain ($2\epsilon_{co}$) was attained, the curve was assumed to be a straight line that reached zero stress at the 0.005 spalling strain. Figure 6 shows the stress–strain relationship for the steel bar. The yield stress of the steel bar was 414 MPa and the yield strain was 0.00207. The strain hardening of the steel occurred after the strain reached 0.01 and the ultimate strain was 0.09 at its ultimate stress of 621 MPa.

The comparison of the stress–strain relationship of confined concrete based on Mander’s model in CTR specimens is shown in Fig. 7 and Table 3. In Table 3, f'_{cc} = the compressive strength of confined concrete provided by the conventional transverse reinforcement, ϵ_{cc} = compressive strain of the confined concrete corresponding to f'_{cc} , ϵ_{cu} = ultimate compressive strain of the confined concrete. It can be seen that by increasing the amount of transverse reinforcement, the compressive strength of the concrete will be increased.

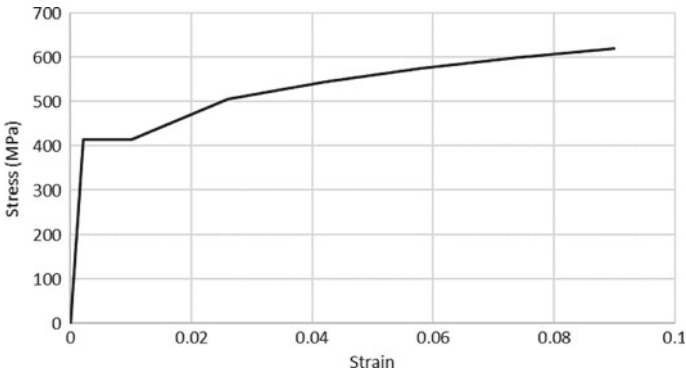


Fig. 6 Stress–strain relationship of steel bar

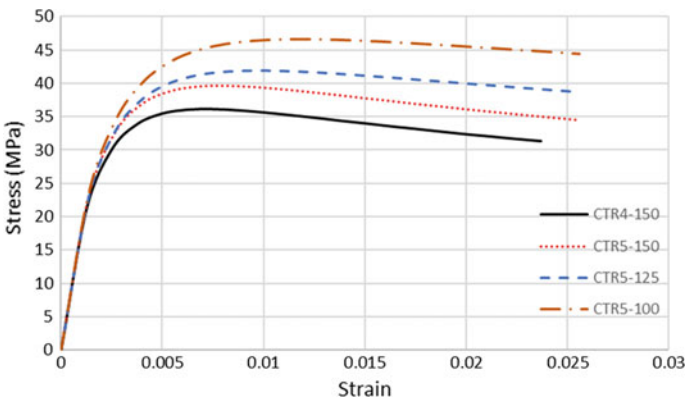


Fig. 7 Stress–strain relationship of confined core in CTR specimens

Table 3 Compressive strength (f'_{cc}) and ultimate strain (ϵ_{cu}) of confined core in CTR specimens

Specimen	Transverse reinforcement	f'_{cc} (MPa)	ϵ_{cc}	ϵ_{cu}
CTR4-150	4D13-150	36.103	0.0075	0.0237
CTR5-150	5D13-150	39.603	0.0081	0.0256
CTR5-125	5D13-125	41.964	0.0094	0.0256
CTR5-100	5D13-100	46.652	0.0121	0.0256

The comparison of the stress–strain relationship of confined concrete based on Mander’s model outside the steel pipe in CTRSP specimens is shown in Fig. 8 and Table 4. The perimeter stirrups provide the compressive strengths of confined concrete in this area.

The stress–strain relationship of confined concrete based on Mander’s model inside the steel pipe in CTRSP specimens is shown in Fig. 9 and Table 5. In Table 5, f'_{cp} is the compressive strength of confined concrete provided by the steel pipe and ϵ_{cp} is the compressive strain of the confined concrete corresponding to f'_{cp} . The compressive strength of concrete will be increased by increasing the thickness of the steel pipe.

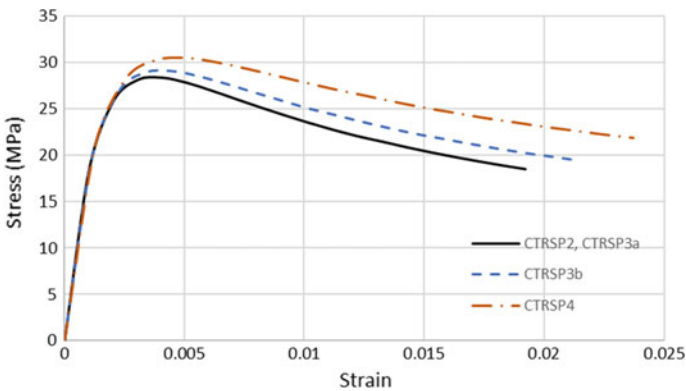


Fig. 8 Stress–strain relationship of confined concrete outside the steel pipe in CTRSP specimens

Table 4 Compressive strength (f'_{cc}) and ultimate strain (ϵ_{cu}) of confined core outside the steel pipe

Specimen	Transverse reinforcement	f'_{cc} (MPa)	ϵ_{cc}	ϵ_{cu}
CTRSP2	2D13-150	28.374	0.0040	0.0192
CTRSP3a	2D13-150	28.374	0.0040	0.0192
CTRSP3b	2D13-125	29.030	0.0045	0.0214
CTRSP4	2D13-100	30.527	0.0050	0.0237

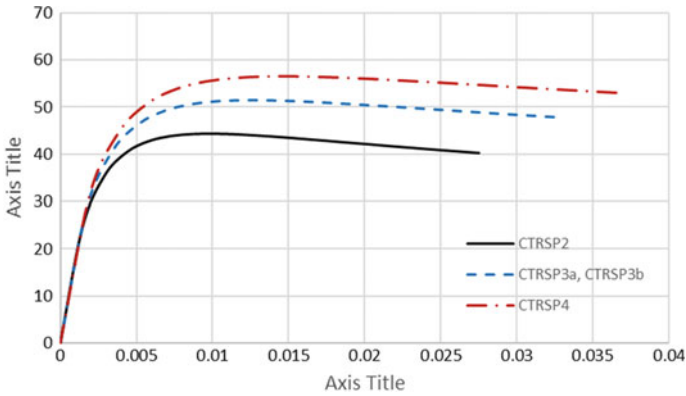


Fig. 9 Stress–strain relationship of confined core inside the steel pipe in CTRSP specimens

Table 5 Compressive strength (f'_{cp}) and ultimate strain (ϵ_{cu}) of confined core inside the steel pipe

Specimen	Steel pipe	f'_{cp} (MPa)	ϵ_{cp}	ϵ_{cu}
CTRSP2	D = 350 mm t = 2 mm	44.427	0.0101	0.0275
CTRSP3a	D = 350 mm t = 3 mm	51.478	0.0120	0.0327
CTRSP3b	D = 350 mm t = 3 mm	51.478	0.0120	0.0327
CTRSP4	D = 350 mm t = 4 mm	56.553	0.0154	0.0366

4.2 Moment–Curvature Relationship

The moment–curvature relationships for the specimens subjected by axial loads with the variety of the $P/(f'_c A_g)$ ratio from 0 until 0.60 are shown in the following figure. In these figures, point A means the cover concrete reached 0.005 spalling strain, point B means the concrete core in CTR or the concrete core outside the steel pipe in CTRSP reached the ultimate strain, and point C means the steel bar reached the ultimate strain. All the specimens showed similar behavior at the initial loading until 0.005 spalling strain of cover concrete was attained. After the spalling of the cover concrete (point A), the moment capacity deterioration occurred, then the curve was increased again because of the strain-hardening of the steel bar. The confined columns (CTR and CTRSP) showed better performance compare to the unconfined concrete column (UC) for all the level of axial load.

In Figs. 10 and 11, CTR4-150 and CTRSP2 show a similar behavior until the ultimate strain of steel was attained (point C) then the rapid deterioration occurred.

Figure 12 until Fig. 14 show the comparison of the moment–curvature between UC, CTR, and CTRSP specimens for $P/(f'_c A_g)$ ratio from 0.10 until 0.20 (Fig. 13).

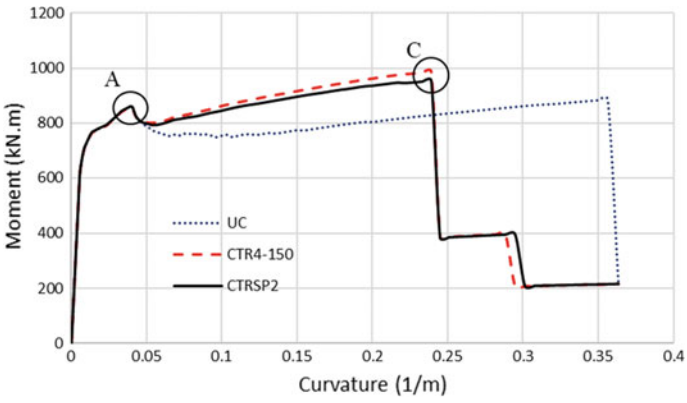


Fig. 10 Moment–curvature curve for $P/(f'_c A_g)$ ratio = 0

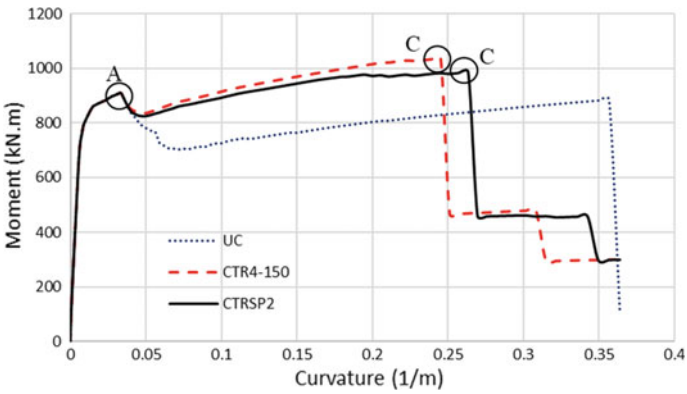


Fig. 11 Moment–curvature curve for $P/(f'_c A_g)$ ratio = 0.05

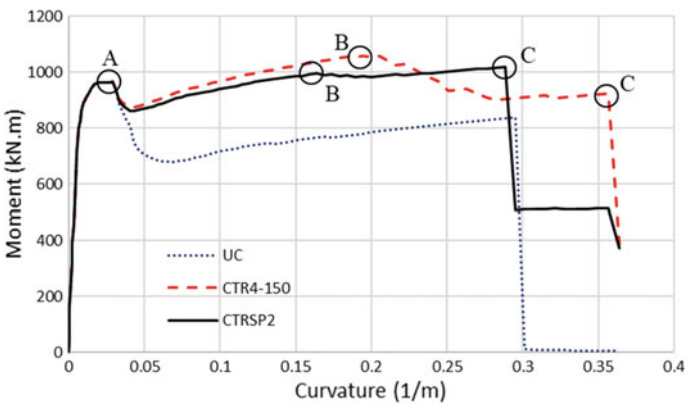


Fig. 12 Moment–curvature curve for $P/(f'_c A_g)$ ratio = 0.10

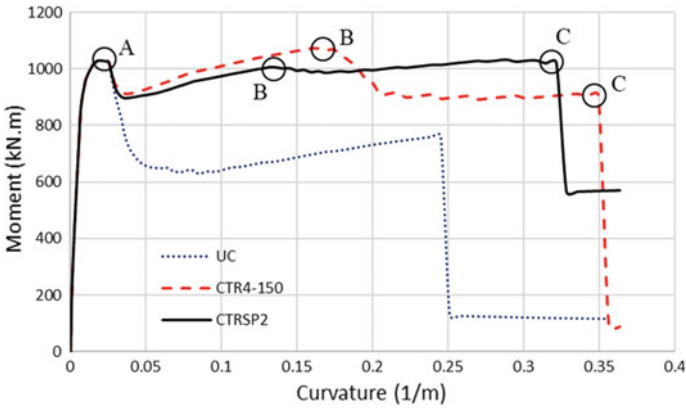


Fig. 13 Moment–curvature curve for $P/(f'_c A_g)$ ratio = 0.15

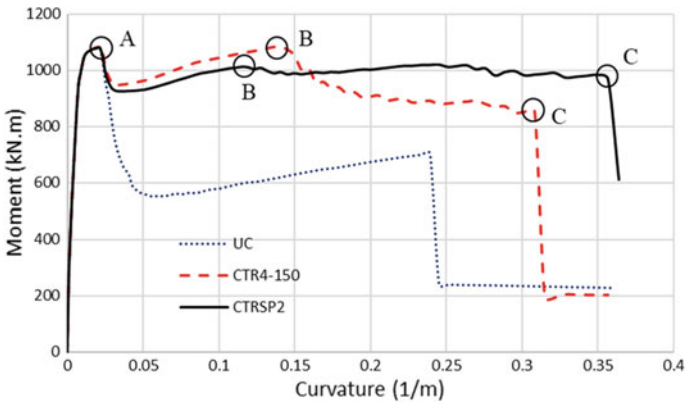


Fig. 14 Moment–curvature curve for $P/(f'_c A_g)$ ratio = 0.20

After the spalling of the cover concrete (point A), the moment capacity deterioration occurred. The steel bar reached the strain-hardening, so the moment capacity was increased until the concrete core reached the ultimate strain (point B). The compressive strength of concrete core in CTR specimen was greater than the concrete core outside the steel pipe in CTRSP specimen so that the moment capacity of CTR specimen was greater than the CTRSP specimen until it reached the ultimate strain of concrete core. After this condition, the moment capacity in CTR specimen was reduced then rupture after the steel bar reached the ultimate strain (point C). But for CTRSP specimens, the moment capacity was still relatively constant because the concrete core inside the steel pipe still resisted the moment until the ultimate strain in the steel bar was attained (point C).

In Fig. 15 until Fig. 22, similar to the previous diagram, the capacity moment for all the specimens was reduced after the spalling of the cover concrete (point A).

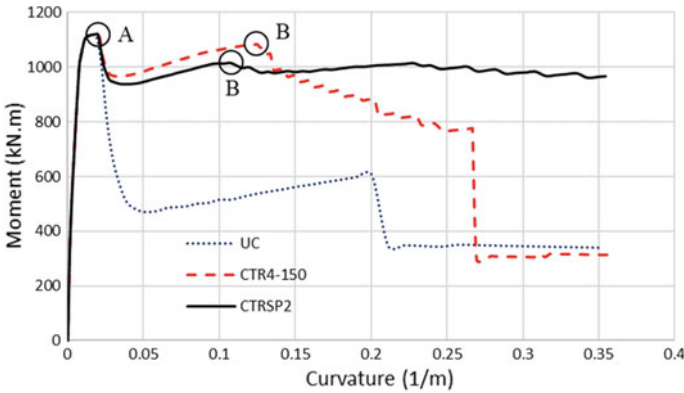


Fig. 15 Moment–curvature curve for $P/(f'_c A_g)$ ratio = 0.25

The moment capacity of UC specimens was reduced rapidly after this spalling. The moment capacity of the CTR specimen was greater than the CTRSP specimen until the ultimate strain of the concrete core was attained. After this, the moment capacity deterioration occurred until the rupture of the column. The increasing axial load significantly increased the deterioration of the moment capacity in CTR specimens. The descending curve after point B in CTR specimen was steeper when the axial load was increased. The CTRSP specimen showed a stable capacity moment even though it had exceeded the ultimate strain of the concrete core outside the steel pipe. The results proved that the ductility of the CTRSP specimens is higher than the CTR specimens. The concrete core inside the steel pipe gives a significant contribution to resisting the moment after the crushing of the concrete outside the steel pipe (Figs. 16, 17, 18, 19, 20 and 21).

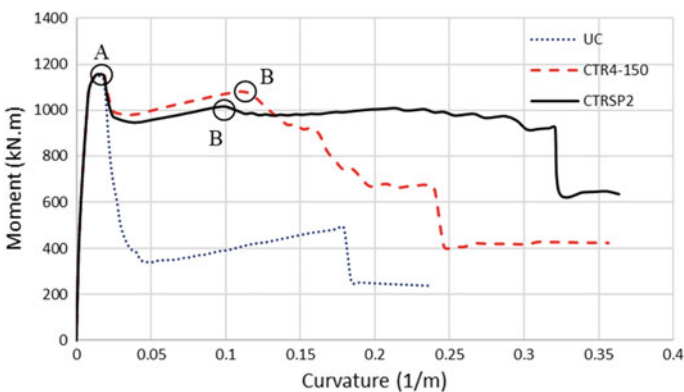


Fig. 16 Moment–curvature curve for $P/(f'_c A_g)$ ratio = 0.30

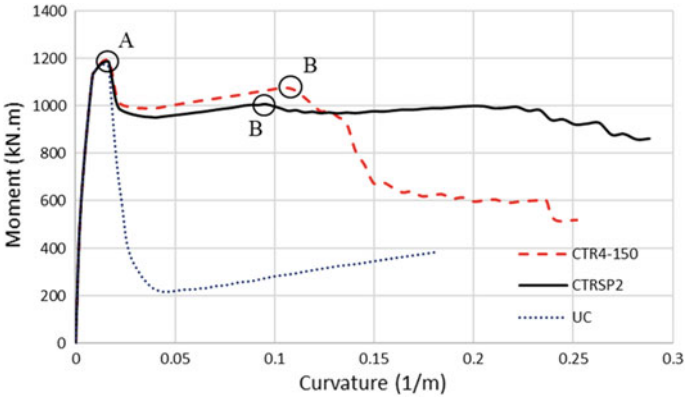


Fig. 17 Moment–curvature curve for $P/(f'_c A_g)$ ratio = 0.35

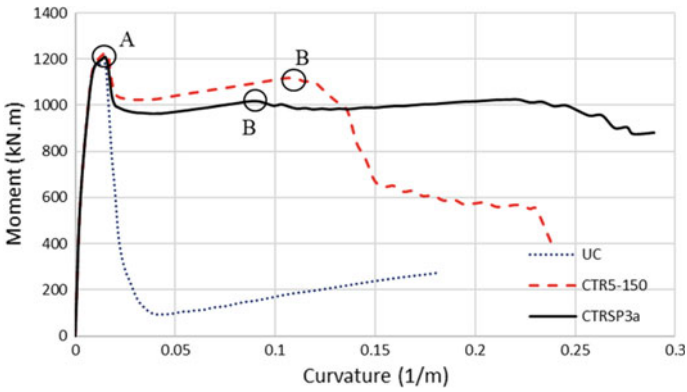


Fig. 18 Moment–curvature curve for $P/(f'_c A_g)$ ratio = 0.40

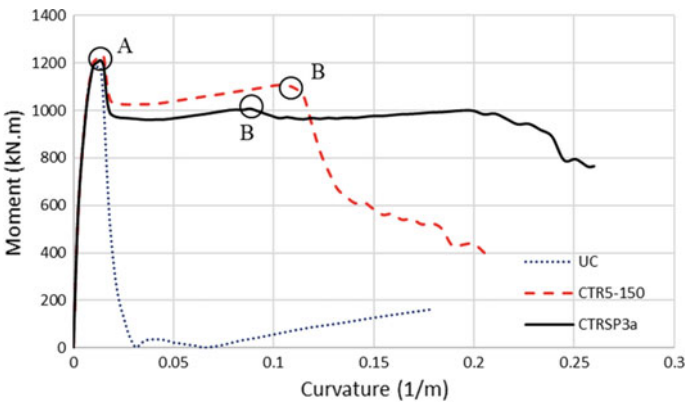


Fig. 19 Moment–curvature curve for $P/(f'_c A_g)$ ratio = 0.45

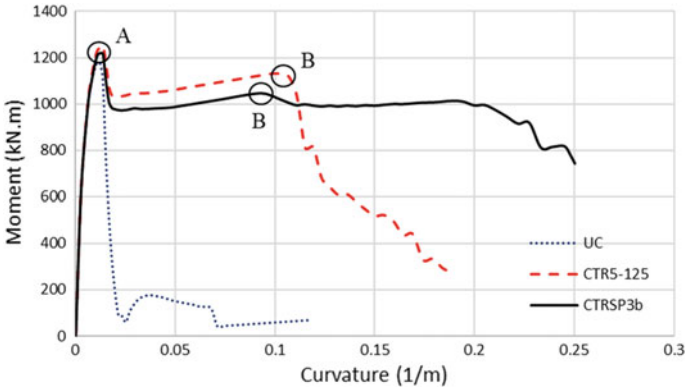


Fig. 20 Moment-curvature curve for $P/(f'_c A_g)$ ratio = 0.50

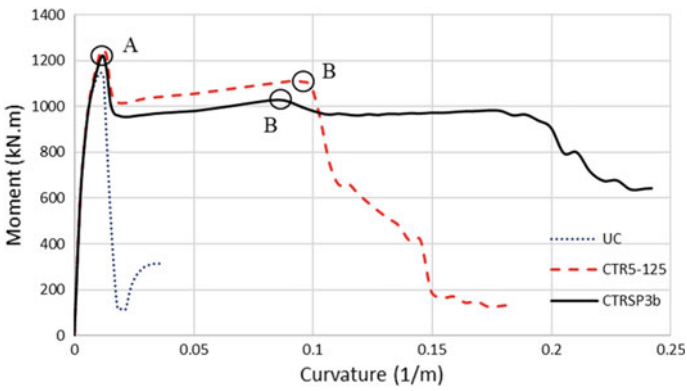


Fig. 21 Moment-curvature curve for $P/(f'_c A_g)$ ratio = 0.55

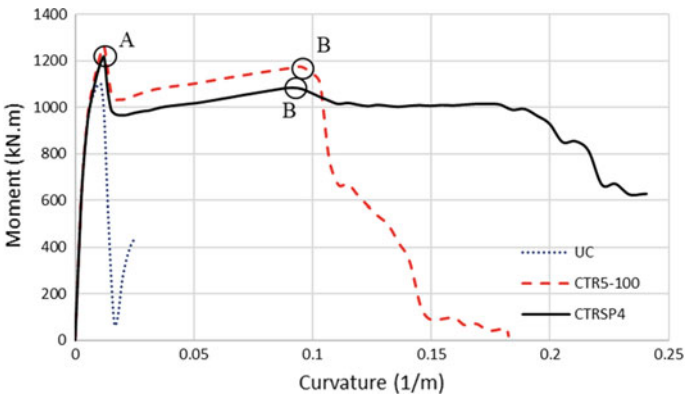


Fig. 22 Moment-curvature curve for $P/(f'_c A_g)$ ratio = 0.60

4.3 Interaction Diagram

The numerical interaction diagrams using fiber model were calculated to study the comparison of the load-carrying capacity of the specimens, in which the confinement effect was considered. The interaction diagrams from UC, CTR, and CTRSP specimens are shown in Fig. 23 until Fig. 26. For all specimens, the confined columns (CTR and CTRSP) had better performance compare to the unconfined concrete column (UC). Confinement increases the compressive strength of the concrete so that the load-carrying capacity of the confined columns is higher compared to the unconfined column, especially at the compression-controlled region. The higher the axial compressive load on the column will increase the area of compressive concrete of the column cross-section so that the flexural capacity of the column is more dependent on the contribution of the concrete compressive stress [20].

The load-carrying capacity of the CTRSP specimen was greater than CTR in the compression-controlled region for a high axial load. CTR5-150 and CTRSP3a specimens had a similar load-carrying capacity near the balanced condition point (Fig. 24). Figures 25 and 26 show that the load-carrying capacity of CTR5-125 and CTR5-100 specimens were slightly higher compared to CTRSP3b and CTRSP4 respectively near the balanced condition point. The compressive strength of the concrete core in CTR specimens was increased due to the increase in the amount of transverse reinforcement. For CTRSP specimens, the compressive strength of the concrete core outside the steel pipe was not increased significantly because its confinement was provided only by the perimeter stirrups. The high compressive strength was attained at the concrete core inside the steel pipe which was located at the center of the column cross-section. Based on this condition, the increasing rate of the load-carrying capacity in the CTR specimens is higher than the CTRSP specimens when the amount of transverse reinforcement is increased.

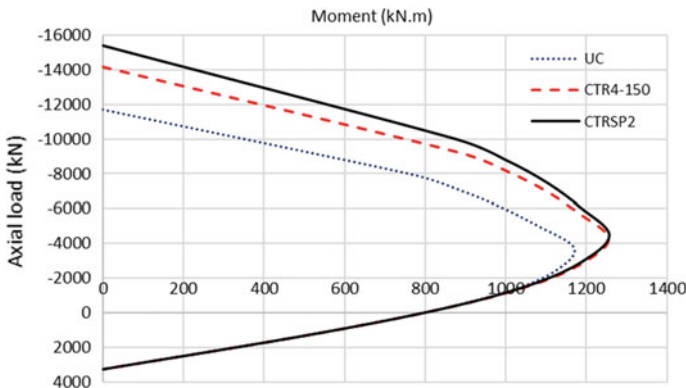


Fig. 23 Interaction diagram UC, CTR4-150, CTRSP2

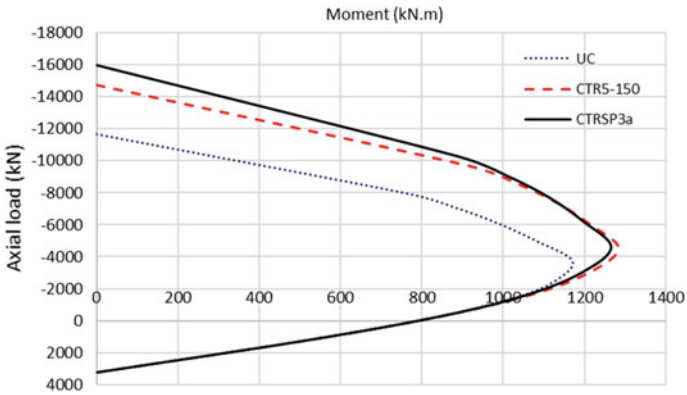


Fig. 24 Interaction diagram UC, CTR5-150, CTRSP3a

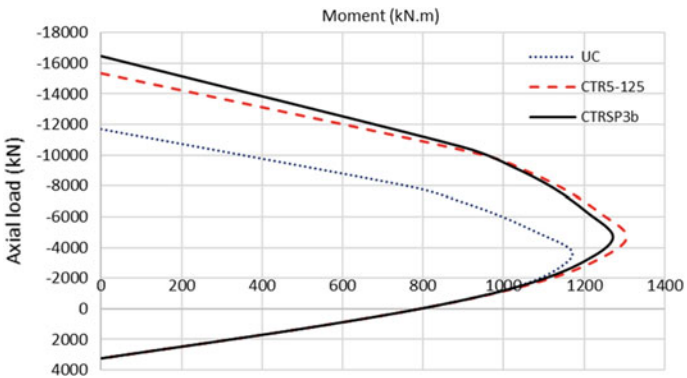


Fig. 25 Interaction diagram UC, CTR5-125, CTRSP3b

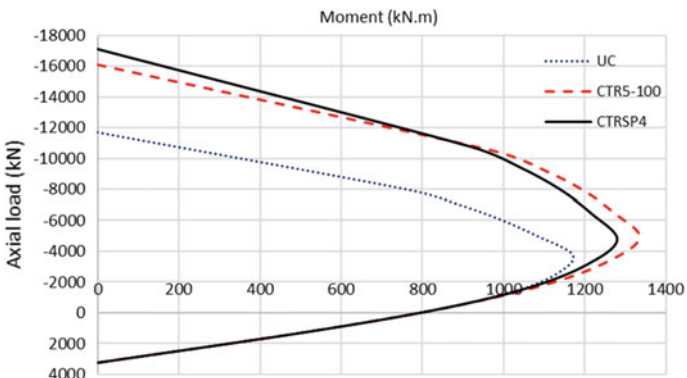


Fig. 26 Interaction diagram UC, CTR5-100, CTRSP4

Table 6 Comparison of the volume of the confinement reinforcement

Conventional column		Column with steel pipe		Difference (%)
Specimen	Volume (mm ³)	Specimen	Volume (mm ³)	
CTR4-150	993,882.24	CTRSP2	619,749.55	37.64
CTR5-150	1,169,882.22	CTRSP3a	702,216.36	39.98
CTR5-125	1,169,882.22	CTRSP3b	702,216.36	39.98
CTR5-100	1,169,882.22	CTRSP4	729,705.29	37.63

4.4 Volume Comparison of Confinement Reinforcement

Table 6 shows the comparison of the volume of the confinement reinforcement between CTR specimens and CTRSP specimens.

For CTR specimen, the volume of confinement reinforcement consists of volume of rectangular hoops, cross ties, include volume of the seismic hook based on ACI code. For the CTRSP specimen, volume of confinement reinforcement consists of volume of rectangular hoops includes the seismic hook and volume of steel pipe. The volume of transverse reinforcement and steel pipe in CTRSP is less than volume of transverse reinforcement in CTR because the volume of the hook in CTRSP is less than CTR.

5 Conclusion

Based on the analysis result, the following conclusions can be reached.

1. The steel pipe increases the compressive strength of the concrete core significantly. The use of 2 mm, 3 mm, and 4 mm thickness of steel pipe increased the compressive strength from 25 MPa to 44.427 MPa, 51.478 MPa, and 56.553 MPa respectively.
2. The CTR and CTRSP specimens (confined column) showed better performance compare to the UC (unconfined column) because of the enhancement of the compressive strength and the ductility.
3. The insertion of a steel pipe reduces the moment capacity deterioration significantly and increases the ductility of the column.
4. The load-carrying capacity of the CTRSP specimen was higher than CTR in the compression-controlled region, especially for a high axial load.
5. The steel material amount for CTRSP was less than CTR due to the reduction of ineffective steel bars for the hooks.
6. This study gives an alternative method of confinement reinforcement in the column plastic hinge regions by inserting steel pipe.

References

1. Thomas P, Priestley MJN (1992) Seismic design of reinforced concrete and masonry buildings. John Wiley & Sons
2. Saatcioglu M. Structural damage caused by earthquakes. https://link.springer.com/reference/workentry/10.1007%2F978-1-4020-4399-4_346
3. ACI 318M-14 (2015) Building code requirements for structural concrete. American Concrete Institute
4. Yang YF, Hou C, Liu M (2018) Experimental study and numerical analysis of CFSST columns subjected to lateral cyclic loading. *J Struct Eng* 144(12): 04018219
5. Kim CS, Park HG, Chung KS, Choi IR (2014) Eccentric axial load capacity of high-strength steel-concrete composite columns of various sectional shapes. *J Struct Eng* 140(4): 04013091
6. Kim CS, Park HG, Lee HJ, Choi IR, Chung KS (2017) Eccentric axial load test for high-strength composite columns of various sectional configurations. *J Struct Eng* 143(8):04017075
7. Lee HJ, Choi IR, Park HG (2017) Eccentric compression strength of rectangular concrete-filled tubular columns using high-strength steel thin plates. *J Struct Eng* 143(5): 04016228
8. Skalomenos KA, Hayashi K, Nishi R, Inamasu H, Nakashima M (2016) Experimental behavior of concrete-filled steel tube columns using ultrahigh-strength steel. *J Struct Eng* 142(9):04016057
9. Hsiao PC, Kazuhiro Hayashi K, Nishi R, Lin XC, Nakashima M (2015) Investigation of concrete-filled double-skin steel tubular columns with ultrahigh-strength steel. *J Struct Eng* 141(7):04014166
10. Fouché P, Asce AM, Bruneau M, Asce F, Chiarito V, Asce M (2017) Dual-hazard blast and seismic behavior of concrete-filled double-skin steel tubes bridge pier, vol 143, issue 12, p 04017155
11. Ozbakkaloglu T, Idris Y (2014) Seismic behavior of FRP-high-strength concrete-steel double-skin tubular columns. *J Struct Eng* 140(6):04014019
12. Ozbakkaloglu T, Fanggi BL (2014) Axial compressive behavior of FRP-concrete-steel double-skin tubular columns made of normal- and high-strength concrete. *J Compos Constr* 18(1):04013027
13. Albitar M, Ozbakkaloglu T, Louk Fanggi BA (2015) Behavior of FRP-HSC-steel double-skin tubular columns under cyclic axial compression. *J Compos Constr* 19(2): 04014041
14. Zhang B, Teng JG, Yu T (2017) Compressive behavior of double-skin tubular columns with high-strength concrete and a filament-wound FRP tube. *J Compos Constr* 21(5): 04017029
15. Wang W, Wu C, Li J (2018) Numerical simulation of hybrid FRP-concrete-steel double-skin tubular columns under close-range blast loading. *J Compos Constr* 22(5): 04018036
16. Ritchie CB, Packer JA, Seica MV, Zhao XL (2018) Flexural behavior of concrete-filled double-skin tubes subject to blast loading. *J Struct Eng* 144(7): 04018076
17. Abdelkarim OI, Elgawady MA (2015) Analytical and finite-element modeling of FRP-concrete-steel double-skin tubular columns. *J Bridg Eng* 20(8): B4014005
18. Park HG, Lee HJ, Choi IR, Kim SB, Park SS (2015) Concrete-filled steel tube columns encased with thin precast concrete. *J Struct Eng* 141(12): 04015056
19. Kim CS, Lee HJ, Park CK, Hwang HJ, Park HG (2017) Cyclic loading test for concrete-filled hollow precast concrete columns produced by using a new fabrication method. *J Struct Eng* 143(4): 04016212
20. Mander R, Priestley JB, Park MJN (1989) Theoretical stress-strain model for confined concrete, vol 114, issue 8, pp 1804–1826
21. Zhao X, Wen F, Chan TM, Cao S (2019) Theoretical stress-strain model for concrete in steel-reinforced concrete columns. *J Struct Eng* 145(4): 04019009

Influence of Solvable Connections on the Life Cycle Assessment of a Facade System



Leonie Scheuring, Melanie Werner, Franziska Rehde, and Bernhard Weller

Abstract In the building industry, environmental protection and the ecological use of resources can be achieved, among other measures, through the choice of building components. During their manufacture, the components of a building emit greenhouse gases, they use primary energy and they contribute to the acidification of the earth, to name just a few of the effects on the environment. This paper deals with ways to reduce the environmental impact of facade systems, more specifically of a louver window system. For two possibilities—an exchange of the used materials and the use of solvable connections in the construction—the influence on the life cycle assessment of the louver window system is quantified. For the exchange of materials, the focus is on the frame profile materials. Plastic is compared with wood, wood-plastic composites (WPC), recycled plastic and glass-fiber reinforced plastic (GFRP). The influence of solvable connections, i.e. a construction option that allows individual components of the facade system to be replaced individually, is also investigated with these aforementioned material variants. The investigations were carried out in accordance with DIN EN ISO 14044. It turned out that the use of solvable connections in the louver window system could improve the negative impact on the environment by 34 % and that replacing plastic as a frame profile material with WPC resulted in an improvement of 84 %.

Keywords Life cycle assessment · Louver window · Solvable connections

1 Introduction

In order to comply with the international climate policy goals anchored in the Paris Climate Treaty and to minimize global warming, it is not only necessary to reduce the energy demand in building operations but also the energy required for the production, maintenance and disposal of building materials. However, it is not always possible to choose the building materials freely with respect to ecological aspects.

L. Scheuring (✉) · M. Werner · F. Rehde · B. Weller
Technische Universität Dresden, 01062 Dresden, Germany
e-mail: leonie.scheuring@tu-dresden.de

© The Author(s), under exclusive license to Springer Nature Singapore Pte Ltd. 2022
S. Belayutham et al. (eds.), *Proceedings of the 5th International Conference on Sustainable Civil Engineering Structures and Construction Materials*, Lecture Notes in Civil Engineering 215, https://doi.org/10.1007/978-981-16-7924-7_46

705

The choice depends strongly on the local conditions, static requirements and the desired aesthetics. This applies in particular to the statically supporting building parts. In earthquake-prone areas, for example, a reinforced concrete structure may be preferable to a masonry construction, and in hot climates a solid structure might be favored over a lightweight construction. For standardized building components such as window systems, where the choice of materials does not influence the static properties or the heat storage capacity of the entire building, the choice of materials can be made considering their impact on the environment. In addition, for building components composed of several materials—as it is the case for window systems—the question arises as to whether solvable connections between the several materials result in an ecological advantage. These composite components are made of materials that may have different lifetimes. If the connections are designed to be non-solvable, the entire component must be disposed of when the material with the shortest life span needs to be replaced. If the connections of the materials are designed to be solvable, the materials with a shorter life span can be replaced while the remaining materials can be used further. Whether this represents a considerable improvement in the life cycle assessment has to be determined. In the following, the impact of solvable material connections and the effect of different window frame materials on five different environmental problem areas, including the Global Warming Potential and the Acidification Potential, will be examined using a louver window system.

2 Case Study

2.1 Base Model

The investigations are carried out for a louver window system as shown in Fig. 1. The louver window consists of three louvers that open outwards. Each of the louvers consists of a triple insulating glazing unit designed as a structural sealant glazing system. The frame of the base system is composed of an aluminum half-shell profile combined with a plastic profile and a transom and mullion profile made of aluminum. To investigate the influence of different frame materials, the material of the plastic profile is varied. All other materials, for instance for the fittings, sealants, glazing, the aluminum half-shell profile and the mullion and transom profile, remain unchanged (Table 1). The tests are carried out on louver windows with a size of 1.50 m in height and 2.00 m in width. It is divided into three louvers, each with a height of 50 cm.

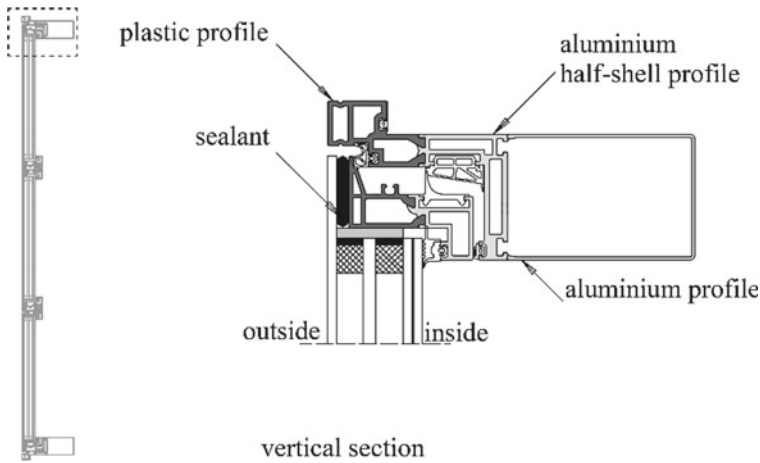


Fig. 1 Base model for the investigation—detail of the upper part of the louver window system (vertical section)

Table 1 Specification of the investigated louver window system

Component	Specification
Glazing	Triple insulated glazing unit 8/12/4/12/44.2
Mountings	Aluminum mounting
Sealants	Polypropylene/polyethylene
Inner half-shell profile	Aluminum
Outer half-shell profile	Material variation is part of the investigation

2.2 Variations of the Base Model

In addition to the base model, four other materials are investigated for the outer half-shell profile: recycled plastic, wood-plastic composites (WPC), wood and glass-fiber reinforced plastic (GFRP). Each frame material variation is based on the basic principle of the louver window: a composite frame with an inner aluminum half-shell profile and an outer half-shell profile. The inner aluminum half-shell profile is retained, while the outer profile is varied with the five different materials mentioned above. Static tests were carried out in advance to ensure the load-bearing capacity of the different materials for the outer profile and, if necessary, to alter the cross-section of the outer half-shell profile.

For each material, two variants are investigated. Firstly, it is of interest how the life cycle assessment turns out if the window is completely replaced at the end of the lifespan of one of the materials. In this case, the window consists of non-solvable

Table 2 Investigated variants

Variant	Material
1	Polyamide PA 66—solvable connections
2	Polyamide PA 66—non-solvable connections
3	Polyamide PA 66 recycled—solvable connections
4	Polyamide PA 66 recycled—non-solvable connections
5	Wood-plastic composites (WPC), with 50% wood flour and 50% plastic PA 66—solvable connections
6	Wood-plastic composites (WPC), with 50% wood flour and 50% plastic PA 66—non-solvable connections
7	Pine—solvable connections
8	Pine—non solvable connections
9	Glass-fiber reinforced plastic (GFRP) made of 35% GFRP and 65% plastic PA 66—solvable connections
10	Glass-fiber reinforced plastic (GFRP) made of 35% GFRP and 65% plastic PA 66—non-solvable connections

connections. Secondly, the life cycle assessment is examined using individual materials that can be replaced independently when their service life is exceeded. Thus, the window consists of solvable connections. This results in a total of ten investigated variants (see Table 2). The first variant represents the base system from Fig. 1 but with solvable connections. In the second variant, the base system is used. For the third and fourth variant, the plastic profile is replaced with a recycled plastic profile. The fifth and sixth system uses a material that is new in window systems: wood-plastic composites (WPC). The geometry of the half-shell profile of these two materials is the same as in the base system. A wood profile is chosen as a seventh and eighth variant. The external dimensions of the wooden profile correspond to those of the plastic profile. However, static calculations showed the necessity of a modified profile cross-section. Thus, a solid wood profile is used instead of the hollow profile to guarantee the load-bearing capacity. The wood used is pine. The last investigated material for variants nine and ten is glass-fiber reinforced plastic (GFRP). The profile shape of the base system is retained in the GFRP profiles.

In the following, the framework materials on which the life cycle assessment is based are described in detail and examined with regard to their advantages and disadvantages.

Plastic. The plastic-aluminum profile is the standard profile used. The plastic used is a polyamide—PA 66—from the group of thermoplastics whose main advantages are the resistance to weathering and the low thermal conductivity. The high resistance to weathering results in low maintenance requirements during use since no additional protective layers need to be applied, as is necessary with wooden frames, for example. The static properties are poor but can be increased by a steel frame reinforcement. The combination with an inner aluminum half-shell, as intended, also improves the

Table 3 Characteristics of PA 66 [1]

Characteristic	Value
Thermal conductivity	0.23 W/mK—high
Durability	Weathering—high
Young’s modulus	1100 MPa—low

Table 4 Characteristics of WPC FIBREX [1, 2]

Characteristic	Value
Thermal conductivity	0.17 W/mK—high
Durability	Weathering—high
Young’s modulus	5000 MPa—middle

static properties of the overall system. The exact values of PA 66 are shown in Table 3. For the sustainability assessment, PA 66 and additionally PA 66 as a recycled plastic is examined.

WPC. WPC (Wood-plastic composite) refers to a composite material made of plastic with wood flour. By combining the plastic with wood flour, the load-bearing capacity is increased, as it achieves a higher stiffness than pure plastic. In addition, compared to the pure plastic variant, the thermal conductivity is improved. In contrast to a pure wood variant, the wood-plastic composite material is characterized by good weather resistance (Table 4). For the life cycle assessment investigations, a WPC made of 50% wood flour and 50% plastic as polypropylene is considered. The profile cross-section corresponds to the standard profile cross-section of the plastic half-shell.

Wood. The wood variant uses the pine wood native to Germany. Wood is characterized by its high thermal insulation properties and good static properties. A significant disadvantage is its poor weather resistance (Table 5). A wooden frame needs a protective coating, which must be renewed in regular intervals. While the standard plastic frame uses a hollow profile, the wooden frame is designed as a solid profile for static reasons.

GFRP. Glass-fiber reinforced plastic (GFRP) is a plastic composite material in which glass-fibers are added to the plastic. There are two different variations. Firstly, the so-called fiber composites use glass fibers from 25 mm in length. Secondly, the so-called short-fiber reinforced thermoplastics use glass fibers which are between 0.1 and 10 mm long. The long fibers from 25 mm length upwards usually result in wall thicknesses of 20–30 mm. This would mean that the standard profile of the

Table 5 Characteristics of pine wood [3]

Characteristic	Value
Thermal conductivity	0.13 W/mK—high
Durability	Weathering—low
Young’s modulus	11,000 MPa (parallel to the fiber)—high

Table 6 Characteristics of GFRP with PA 66 and 35% glass fibers [1]

Characteristic	Value
Thermal conductivity	0.27 W/mK—middle
Durability	Weathering—high
Young's modulus	8500 MPa—middle

base system cannot be used. The higher wall thicknesses would result in additional material consumption, which has a negative effect on the life cycle assessment. Hence, the short fiber-reinforced variant was chosen in which a composite is used that consists of 35% glass fibers and 65% PA 66. This significantly increases the modulus of elasticity from 1100 to 8500 MPa, while the thermal conductivity remains almost unchanged (Table 6). The profile considered in the life cycle assessment corresponds to the hollow profile of the plastic half-shell of the base system. Thus, the amount of material to be applied is identical.

The quantity of the materials is determined according to [4] and is identical for all investigated variants except for the wood frame variant. The wood frame variant uses a solid wood profile instead of a hollow chamber profile.

3 Methodology

3.1 Life Cycle Stages

The impact of the louver window on the environment is determined through the principles of the life cycle assessment according to DIN EN ISO 14,044. The following life cycle stages are examined for the investigations:

With regard to the stages A Production, B Use, C End of life and D Benefits, it is important to consider the estimated service life of the louver window and its components. The life cycle assessment is carried out according to DIN EN ISO 14,044 for a period of 50 years. If one component has a service life of less than 50 years, this component has to be renewed and it undergoes the life cycle stages again. If it does not need to be renewed within the period of 50 years, these stages will only occur once. If, as for example in phase B4 Replacement, the component is to be considered several times due to its service life, a time factor is added. Assuming that the house in which the louver windows are installed will last longer than the observation period of 50 years and one component is replaced after 30 years, the newly installed component is taken into account with a time factor of 20/30, both for production and for disposal and recycling. Thus, 10/30 of the production, disposal and recycling is shifted to the time after the period under consideration (50 years plus). This allows the advantage of different lifetimes of components to be taken into account in the LCA. As a result, the service life of the louver window and its

components must first be determined for the investigation because it has a strong impact on the results. These results are found in chap. 4.1.

For the maintenance stage of the window, various studies [5–10] assume that aluminum, plastic and wood-aluminum (aluminum considered as the exterior part of the window frame) require no or only minor maintenance and repair work during their lifetime. With wood, painting work is necessary. The intervals are between five and eight years and solvent-based paints are used in varying degrees.

3.2 Indicators

The life cycle assessment is carried out for each of the life cycle stages described in Table 7 for different indicators. The investigated indicators are divided into two parts: the ones which have an environmental impact and the ones that consider a resource use. The investigated indicators are shown in Table 8.

The impact of the louver window variants on each of these indicators is considered through the principles of the life cycle assessment. The indicators in Table 8 are calculated, summarized and compared for the ten variants of the louver window described in Table 2 (five different frame materials, and for each material one variant with solvable connections and one without solvable connections). As a result, each variant has seven values (GWP, POCP, etc.) indicating its life cycle assessment. If a comparison between the 10 different window variants is needed, the seven different values have to be summed up for each variant.

It should be noted that different reference values are used for the quantitative assessment depending on the specification of the indicators (see Table 8); while the CO₂ equivalent is included in the assessment of the global warming potential, the phosphate equivalent is included in the eutrophication potential, for instance. Thus, to be able to calculate the total of all seven specifications of the indicators, these different reference values have to be standardized to a common reference value. For this paper, a standardization method is suggested which converts every quantitative

Table 7 Life cycle stages considered for the investigation

Main life cycle stage	Sub life cycle stage
A Production	A1 Raw material supply
	A2 Transport
	A3 Manufacturing
B Use	B2 Maintenance
	B4 Replacement
C End of Life	C3 Waste processing
	C4 Disposal
D Benefits and loads beyond the system boundary	D Re-use—recovery

Table 8 Investigated indicators

Indicators	Specification of the indicators	Abbreviation	Reference value
Environmental impact	Global Warming Potential	GWP	kg CO ₂ equiv/FU
	Photochemical Ozone Creation Potential	POCP	kg Ethene equiv/FU
	Acidification Potential	AP	kg SO ₂ equiv/FU
	Eutrophication Potential	EP	kg (PO ₄) ³ equiv/FU
Resource use	Total use of non-renewable primary energy resources	PENRT	MJ/FU
	Total use of primary energy resources	PE total	MJ/FU
	Ratio of renewable primary energy use to total primary energy use	PERT/PE total	–

value to a value between zero and one. Moreover, it evaluates where exactly the value for the investigated variant is situated between the best and the worst value of all investigated values. For example, 0.5 as a result for one window variant for the global warming potential would mean that the investigated window variant is in the middle of the best and the worst value of all investigated window variants. A higher value indicates a higher impact on the environment and, therefore, a worse result. Thus, low values are favorable. The values are calculated according to Formula (1). The term *ideal value* corresponds to the best value obtained, whereas the term *anti ideal value* stands for the worst value obtained.

It should be noted that the individual values are not presented in equal parts in the overall assessment. For example, the global warming potential should have a higher priority in the life cycle assessment. This is taken into account via weighting factors as can be seen in Formula (2). This way, each indicator of Table 8 for a window variant can be added together and every window variant can be compared with each other using the value obtained. Formula (2) shows the calculation approach on which the results are based. The weighting factors used are given in Table 9.

$$Indicator_{i,normalized} = \frac{|realvalue - idealvalue|}{|idealvalue - antiidealvalue|} \quad (1)$$

$$LCA_{normalized} = \sum Indicator_{i,normalized} \times weightingfactor_i \quad (2)$$

The values for the indicators are taken from two databases: *Ökobaudat* [12] and the *GaBi* database [13]. These databases comply with the principles of DIN EN 15,804—Sustainability of construction works—Environmental product declarations.

Table 9 Weighting factors for the investigated indicators [11]

Specified indicators	Abbreviation	Weighting factor (%)
Global Warming Potential	GWP	40
Photochemical Ozone Creation Potential	POCP	10
Acidification Potential	AP	10
Eutrophication Potential	EP	10
Total use of non-renewable primary energy	PENRT	15
Total use of primary energy resources	PE total	10
Ratio of renewable primary energy use to total primary energy use	PERT/PE total	5

4 Results

4.1 Service Life

For the purpose of this paper—the investigation of the influence of a solvable construction—it is important to know the service life of each component of the window. Knowing this, the influence of a solvable construction on the life cycle assessment can be investigated.

The service lives of various types of windows can be defined using studies by the German Federal Institute for Research on Building, Urban Affairs and Spatial Development. For windows made of aluminum, wood-aluminum, treated hardwood and plastic-aluminum, a service life of more than 50 years is specified [10]. For softwood and plastic, 40 years are specified [10]. However, these service lives consider the window as a whole; the various components of the window are not specified further. Therefore, it was necessary to conduct a literature review on the service lives of the different window materials. The results are shown in Table 10.

Service life of window materials. One reviewed study [5] is based on a survey of 22 county councils/municipalities in the UK, thus, including real life data. Another study [8] is purely based on existing literature. Thereby, the mean value is based on various literature sources. A further study [14] deals exclusively with lifetimes

Table 10 Literature review on the service life for window frame materials

Material	Service Life [years]					Average value	Weighted value
	[6]	[10]	[5]	[8]	[14]		
Aluminum	40	50	43.6	50	47	46	47
Aluminum-wood	40	–	46.7	51	–	46	49
Wood	40	50	39.6	40	36	41	39
Aluminum-plastic	–	–	–	42	–	42	42
Plastic	40	50	24.1	37	38	38	36

and has carried out both a literature evaluation and a survey. Manufacturers, experts, facility management companies and service providers were interviewed. Both [8] and [14] present mean values from various sources. Evaluating these studies and choosing one service lifetime for each window type, the results of the studies were first evaluated by the average value and then evaluated by a weighted value (see Table 10). This results in the fact that [8] and [14] present data from various sources, whereas [5] only presents data from one survey. Therefore, for the weighted value in Table 8, studies [8] and [14] are rated higher than study [5].

The lifetimes of frames made of wood, aluminum and wood-aluminum are estimated to be between 40 and 60 years by the various studies. Depending on the study, the service life of plastic frames is estimated to be between 25 years [5] and 50 years [10].

In the case of frame profiles with material combinations—as is the case for the investigated louver window system (a combination of an aluminum half-shell profile and a varying outer profile)—it should be noted, however, that the lifetimes from the studies in Table 8 can only be adopted if the same material mentioned there forms the outer part. For wood-aluminum windows, aluminum is usually the outer weather-resistant part and wood is used for the inner part. As the wood is on the outside of the wood-aluminum louver window, the value of the wood-aluminum window in the literature review cannot be adopted. In this case, the lifetime of the wood mentioned in Table 10 should be used. WPC and GFRP are to be classified as plastics with regard to their durability. However, even with the plastic-aluminum combination, the aluminum is used on the outside as weather protection. Therefore, for the combinations of plastic-aluminum, WPC-aluminum and GFRP-aluminum, the life span of the plastic window is assumed for the variants of plastic, recycled plastic, WPC and GFRP.

This service life consideration refers only to the frame material. The glazing, fittings, etc. have shorter lifetimes than the window frame. According to the product category rules for environmental product declarations [15], a maximum reference service life of 30 years is assumed for multiple-pane insulating glass. Table 11 summarizes the service lives used for the investigations.

Table 11 Service lives for the window components used for the investigations

Material	Service life (years)
Plastic-aluminum frame	36
WPC-aluminum frame	36
GFRP-aluminum frame	36
Wood-aluminum frame	39
Insulated glazing unit	30

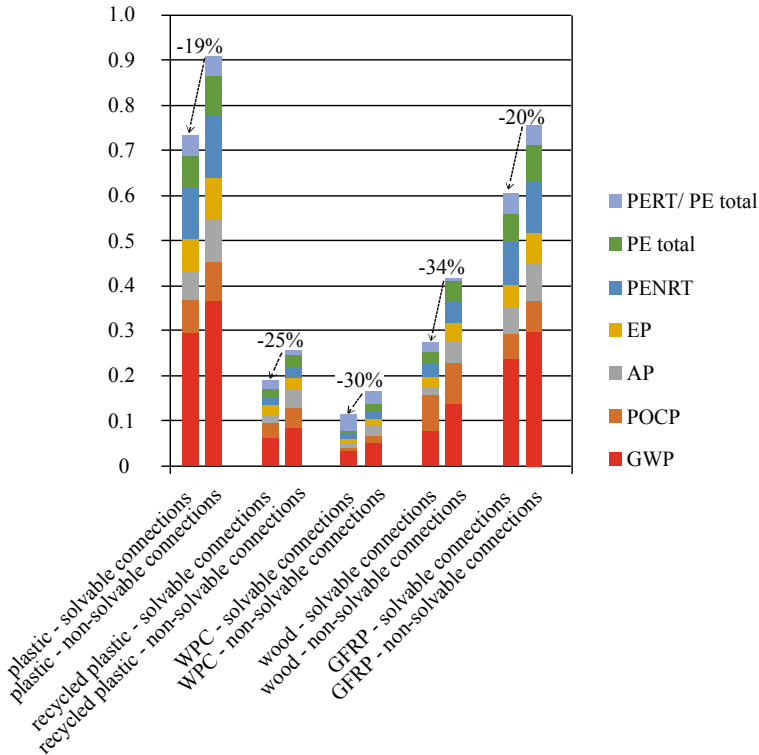


Fig. 2 Normalized life cycle assessment results for the louver window system with five different outer frame materials with and without solvable connections

4.2 Life Cycle Assessment

Figure 2 shows the results of the life cycle assessment with the weighted normalized values according to the method described in chap. 3.2. The ten investigated variants are plotted on the x-axis organized in five blocks. Every block describes one material with and one without solvable connections. Every first variant shown in Fig. 2 presents the results with solvable connections, meaning that the insulated glazing unit can be replaced, independent from the frame. The second variant for each material shows the results assuming that no component can be replaced individually; the window will be replaced in its entirety after its 30-year service life. The y-axis shows the percentage of the worst values reached. A high value is thus associated with a poor life cycle assessment. The percentage of the indicators explained in Sect. 3.2 Table 9 is shown in different colors for each material. The abbreviations for the indicators are explained in Sect. 3.2 Table 8.

Comparing non-solvable connections with solvable connections, it can be seen that an improvement between 19 % and up to 34 % can be achieved. The highest

improvement is seen for the wood variant (34 %), which can be explained by the fact that wood is the only investigated material that has 39 years of service life instead of 36 years. With wood, the advantage of solvable connections can therefore be utilized more than for the other variants. Between the variants with a service life of 36 years (plastic, recycled plastic, WPC and GFRP), WPC shows the biggest improvement (30 %) when using solvable connections instead of non-solvable connections. WPC is also the material with the best life cycle performance (85 % better than plastic). Thus, it can be assumed that the impact of solvable connections is higher when the life cycle performance is already good.

In the following, the different materials are compared. Regarding the variants with solvable connections, it is clearly visible that the louver window with the outer plastic half-shell profile has the worst life cycle assessment, followed by the GFRP profile. The recycled plastic, WPC, wood and GFRP perform more than twice as well. The WPC variant is clearly the best variant. This shows how important it is to take a closer look at the materials and which effect an alternative frame variant might have on the sustainability of the louver window system.

Considering the five material variants with non-solvable connections, the following results were obtained. The ranking of the materials remains the same—WPC as the best variant, then recycled plastic, wood, GFRP and as the worst variant plastic.

It can be deduced that the possibility of an individual replacement of each component can result in an improvement of up to 34 % (wood non-solvable to wood solvable connections) and that solvable connections for the louver window system should therefore be sought out. The choice of material can result in an improvement of up to 85% (plastic solvable connections to WPC solvable connections). The plastic profile made of PA 66 has been identified as the worst variant, the chosen WPC profile as the best variant. However, a significant improvement of 74 % for the LCA results could also be achieved simply by replacing the plastic with a recycled plastic.

5 Conclusion

The life cycle assessment was analyzed and evaluated during the stages of production, maintenance, renewal, disposal and recycling for the different frame variants. For this purpose, it was first necessary to determine the service lifetimes of the frame variants. Therefore, data obtained from the reviewed literature was used as a basis. The environmental impact and resource use for the frame variants were determined mainly with *ÖkobaDat*. The *GaBi database* was used for the GFRP variant. Since no frame variant is better than the other variants with regard to all environment indicators, an evaluation scheme was developed that allows a comparison across the seven investigated indicators. For this purpose, the values for the indicators were normalized using a distance function and then weighted according to DGNB 2018. It turned out that the WPC/aluminum variant is the most ecologically favorable,

followed by recycled plastic/aluminum, wood/aluminum, GFRP/aluminum, and, as the worst variant, plastic/aluminum.

The following principles for sustainable louver windows can be derived from the study: when using plastic, recycled plastic should be used wherever possible. Furthermore, solvable connections can notably decrease the environmental impact and resource use; and the lower the environmental impact, the higher the percentage improvement.

References

1. Domininghaus H, Elsner P, Eyerer P, Hirth T (2012) *Kunststoffe: Eigenschaften und Anwendungen*. 8. edn., Springer, Heidelberg
2. Pech A, Pommer G, Zeininger J (2005) *Fenster*. Springer, Wien
3. Niemz P (2007) Untersuchungen zur Wärmeleitfähigkeit ausgewählter einheimischer und fremdländischer Holzarten. In: *Bauphysik*, vol. 29(4), pp 311–312. Ernst & Sohn, Berlin
4. EuroLam GmbH. Systemschnitt EAL als CAD-Datei, https://www.eurolam.de/fileadmin/user_upload/Systemechnitte/Systemdatenblatt_EAL.dwg. Last Accessed 17 Jan 2020
5. Asif M, Davidson A, Muneer T (2002) Life cycle of window materials—a comparative assessment. School of Engineering, Napier University, Edinburgh (U.K.)
6. Institut für Kunststoffprüfung und Kunststoffkunde: *Ganzheitliche Bilanzierung von Fenstern und Fassaden*. Frankfurt (1998)
7. Künniger T, Richter K (2014) *Ökologische Bewertung von Fensterkonstruktionen*. Verband Fenster und Fassade, Frankfurt am Main
8. Popp M, Waltenberger L (2015) *Fensterwerkstoffe im Vergleich: Lebenszykluskosten und Ökobilanz im Wohnbau: eine Potenzialanalyse aus wirtschaftlicher und ökologischer Sicht*. Aluminium-Fenster-Institut, Wien
9. Richter K, Brunner K, Künniger T (1997) *Ökologischer Vergleich von Fenstern: Rahmenkonstruktionen und Verglasungen*. Eidgenössische Materialprüfungs- und Forschungsanstalt (EMPA), Dübendorf (Schweiz)
10. von Houwald B (2012) *Entwicklung von Umweltproduktdeklarationen für transparente Bauelemente - Fenster und Glas - für die Bewertung der Nachhaltigkeit von Gebäuden*. Abschlussbericht. Fraunhofer-IRB-Verl, Stuttgart
11. Braune A, Ruiz Durán C, Gantner J (2018) *Leitfaden zum Einsatz der Ökobilanzierung*, 2nd edn. Deutsche Gesellschaft für Nachhaltiges Bauen e.V, Stuttgart
12. Bundesministerium des Innern, für Bau und Heimat: ÖKOBAUDAT Datenbank Version 2017-I vom 27.11.2017. <https://www.oekobaudat.de/datenbank/browser-oekobaudat.html>. Last Accessed 17 Jan 2019
13. thinkstep AG (2018) *GaBi Education database 2018*: thinkstep AG, Leinfelden-Echterdingen
14. Ritter F (2011) *Lebensdauer von Bauteilen und Bauelementen: Modellierung und praxisnahe Prognose*. Inst. für Massivbau, Darmstadt
15. Deutsches Institut für Normung e.V.: *DIN EN 17213 Entwurf Fenster und Türen - Umweltproduktdeklarationen - Produktkategorieeregeln für Fenster und Türen*. Berlin: Beuth Verlag GmbH, Berlin (2018)

Seismic Performance Comparison of Pile Supported Slab Viaduct with PHC Pile and RC Bored Pile in South Part of Java Island



Muhamad Fauzi Darmawan, A. S. Fajar, Iman Satyarno, Ali Awaludin, and Bonifacius Adiguna Yogatama

Abstract At present, infrastructures of Indonesia are developed rapidly to enhance economic growth. One of them is in terms of an elevated structure to support highway and railway infrastructures. Pile-supported slab viaduct (PSSV) with pre-stressed hollow concrete (PHC) piles has been widely used in the development of both infrastructures. The structural configuration just contains a pile as a pier, pile head, and slab. So that, quick construction time and lower cost are amongst the consideration of that type selection. Considering that the Indonesian country is mostly in the earthquake zone, the development of the high seismic performance of PSSV structures becomes a necessity. Previous researches showed that PHC piles without additional treatment have low ductility and energy dissipation. On the other hand, reinforced concrete (RC) columns could achieve medium ductility for a stand-alone seismic lateral resistance. In this study, a seismic performance comparison between PSSV with spun pile column and PSSV with RC bored pile column that designed as a medium ductility concept to be conducted with a numerical model by using OpenSees software. A non-linear beam-column element with hinge and fiber section was adopted to simulate the plastic hinge behavior of the pile element. Cyclic loading following ACI 374.1-05 loading protocol was implemented to quantify structural drift-energy dissipation. Then, to evaluate the seismic performance of the proposed structures, a set of scaled ground motion provided by the Japan Road Association (JRA) was generated. The target acceleration spectra based on SNI 2833-2016, the Indonesia seismic load provision for bridge design, for Kulonprogo, Yogyakarta Province. The result of this study concluded that utilizing RC bored pile as the piers of the PSSV structure could produce higher energy dissipation than the one with PHC pile column under cyclic loading. Also, PSSV structure with RC pile column had a better response against the seismic excitation than the one with the PHC column, even though slightly over the

M. F. Darmawan · A. S. Fajar (✉) · I. Satyarno · A. Awaludin
Department of Civil and Environmental Engineering, Universitas Gadjah Mada, Yogyakarta, Indonesia
e-mail: angga.fajar.s@ugm.ac.id

B. A. Yogatama
Geotechnical/Earthquake Engineer, Menard Asia, Subang Jaya, Malaysia

ultimate capacity. However, the PSSV with PHC column had significant over-limit deformation under some ground motion excitation.

Keywords Pile-supported slab viaduct · PHC pile column · Bored pile column · Energy dissipation · Seismic performance

1 Introduction

The Indonesia infrastructure are being developed rapidly to enhance economic growth [1]. Highway and railway become one of the infrastructures currently being constructed by the Indonesia government in some regions of Indonesia. Pile-supported slab viaduct (PSSV) has been generally utilized to support these infrastructures. Figure 1 shows an example of the application of the PSSV structure in railway infrastructure, and Fig. 2 illustrates the typical configuration of the PSSV structure for a double track of railway. Typical PSSV structure just contains pile groups as the pier as well as the foundation, pile head, and concrete slab. It can be constructed segmentally or continuously. Pre-stressed hollow concrete (PHC) pile is commonly preferred to be used as the piers of the viaduct structure due to its economical cost and fast construction. Controlled and consistent off-site fabrication also becomes an additional advantage of using PHC piles [2]. However, an experimental study



Fig. 1 Application of the PSSV structure of Adi Soemarmo Airport Railway Track

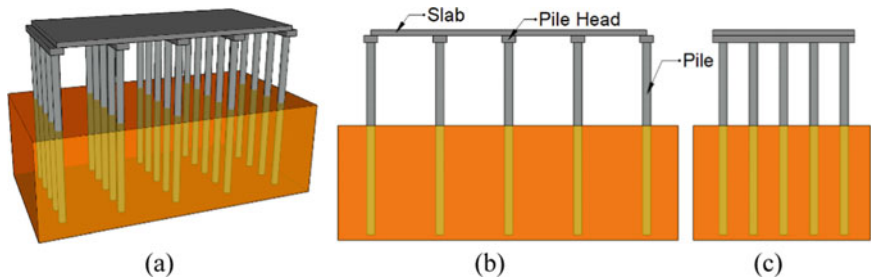


Fig. 2 Typical configuration of PSSV structure: a 3D view, b side view and c front view

conducted by Budek et al. showed that hollow pre-stressed piles without a treatment have low energy dissipation, low ductility, and behave suddenly and violently brittle failure [3]. Furthermore, the axial force effect due to the pre-stressing will indeed increase a pile or column capacity carrying the gravity loads. However, on the contrary, this will decrease the ductility of the structure [4]. Considering that the Indonesia country is mostly located in the earthquake zone, the development of the high seismic performance of PSSV structures becomes a necessity. Based on the brittle behavior of the PHC pile, PSSV structure using that pile is feared to have low seismic performance, so a breakthrough to develop the higher seismic performance of PPSV becomes a need. On the other hand, PSSV structural design conducted by some experts or researchers in Indonesia used medium ductility concept [5]. So that PSSV structure supported by PHC piles will have a high risk in brittle collapse due to major earthquake.

In this study, a segment of PSSV structure as an elevated railway track supported by PHC pile groups (denoted as PSSV1) and Reinforced Concrete (RC) bored pile groups (denoted as PSSV2) as the column were numerically modeled using OpenSees. Each of PSSV structure segments is supported by 25 piles that to be designed as medium ductility concept. Then, the behavior and the seismic performance of both structural types were investigated and compared to each other. Utilizing RC bored pile as the column of the PSSV structure were expected to give better seismic performance than the commonly used PSSV structure in Indonesia, i.e., PHC pile-supported PSSV. The PSSV structures in this study were assumed specifically to be located at the South Part of Java Island due to the railway track of Yogyakarta International Airport (YIA) construction planning at that location. Then, to evaluate the seismic performance of the proposed structures, a set of scaled ground motion provided by Japan Road Association (JRA) was generated. The target acceleration spectra based on SNI 2833-2016, the Indonesia seismic load provision for bridge design, for Kulonprogo, Yogyakarta Province. Elastic structural analysis and design using static equivalent and spectrum response analysis was performed before with SAP2000 to make the preliminary structural design.

2 Numerical Analysis Method

2.1 Determination of Pile Section

Three dimensional of a PSSV structural model carrying the gravity, wind, and earthquake load was analyzed using SAP2000. Dynamic analysis due to the earthquake load was performed using static equivalent analysis and spectrum response method referring to SNI 2833-2016, an Indonesia seismic design provision for the bridge structure. The structure model had four bays in both X and Y axes direction with 5000 mm and 2200 mm length of the span, respectively. The pile head, PHC pile, and RC bored pile element modeled as fiber section using section designer. The

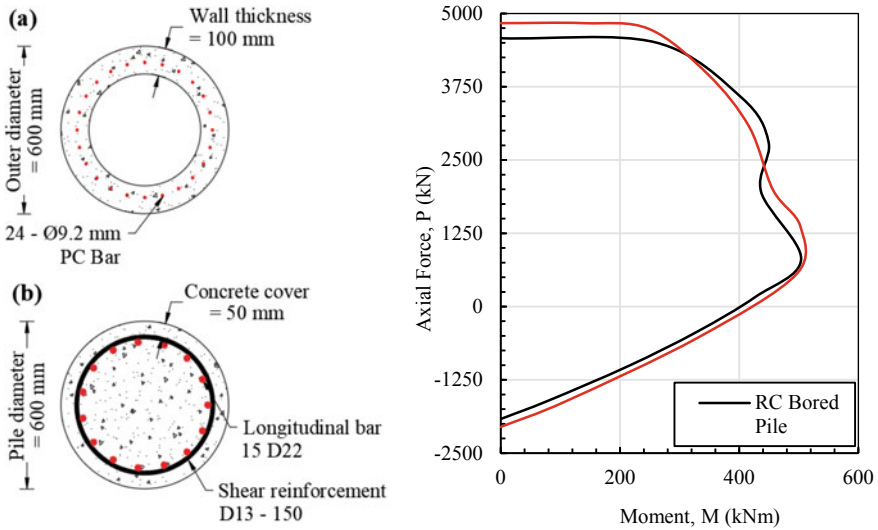


Fig. 3 The cross-section and interaction diagram of a PHC and b RC bored pile

400 mm thickness slab concrete was modeled as a shell element. Piles were assumed to be fixed at the eight meters depth of the pile. PHC pile section and the minimum compressive strength of concrete at 28 days of 60 MPa are referred to [6]. The Prestressed Concrete (PC) bar material of the PHC pile section follows the PC bar tensile test conducted by [7]. Then, the RC bored pile section had 30 MPa of compressive strength of the concrete and 400 MPa and 525 of deform bar yield stress and ultimate stress, respectively. The reduction factor, $R = 3$, was considered following the medium ductility concept for bridge substructure in Indonesia, which commonly to be adopted for the PSSV structure design method. The PHC and RC piles configuration that obtained from this analysis and each interaction diagram of the pile section can be seen at Fig. 3. The maximum demand/capacity (D/C) ratio of the PSSV structure with both type of piles was in range 0.7–0.9.

2.2 Structural Idealization

Two numerical models of PSSV structure were built in a three-dimensional model with six degrees of freedom, as illustrated in Fig. 4, similar to the preliminary structural design. The total height (free height and fixity length) of the column is assumed to be 8 m height. The column elements were idealized as a force-based beam-column element. Modified Radau Hinge Integration [8] was implemented in each hinge region of the pile end. Then, a linear elastic concrete model was utilized for the element interior. The 1.4D plastic hinge length was defined for the PHC pile element following a previous numerical PHC pile simulation done by Fajar et al. [9], which

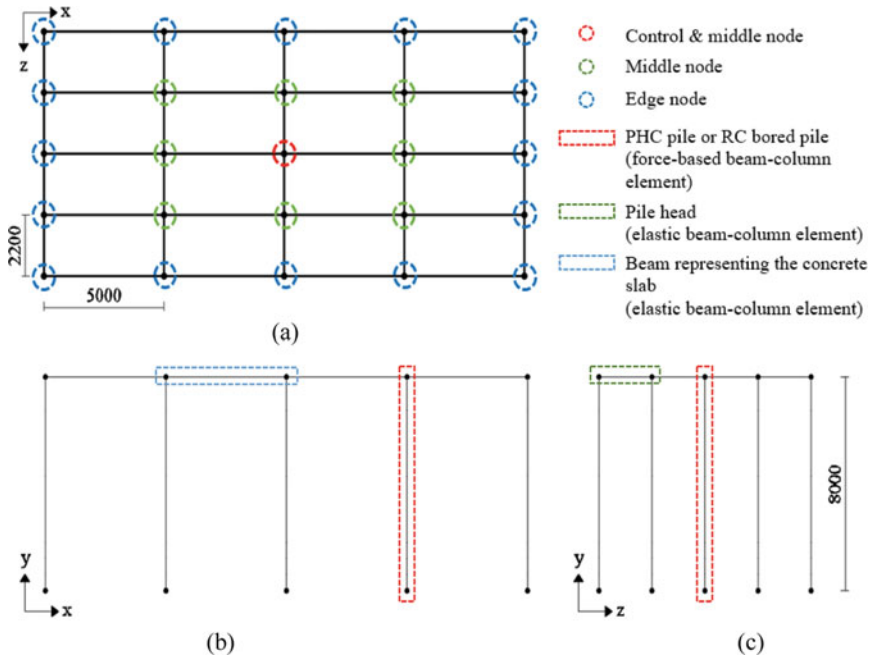


Fig. 4 Structural idealization of PSSV structure: **a** top view, **b** side view and **c** front view

refers to the actual plastic hinge length of $0.85\text{--}1.45D$ observed by Budek et al. [3]. Furthermore, $0.5D$ plastic hinge length was implemented for RC bored pile element proposed by Priestly [10].

The section of both piles was constructed utilizing the fiber section, i.e., circular patch and circular layer, as depicted in Fig. 5 following. The circular concrete patch of both piles was divided into 72 subdivisions/wedges in the circumferential direction. While, in the radial direction, the PHC pile concrete patch and the confined and unconfined concrete RC bored pile were divided into 20, 25, and 5 subdivisions/rings, respectively. The pile head and beams representing the 400 mm of the concrete slab were implemented using the elastic beam-column element with section properties stated in Table 1. The pile elements were assumed to be fixed in the lowest node following the previous preliminary structural design. Nodal masses assigned to all top nodes of the piles were 32 tons. RigidDiaphragm command was utilized to constraint all the nodes on the slab could move together only perpendicular in $x\text{--}z$ plane only.

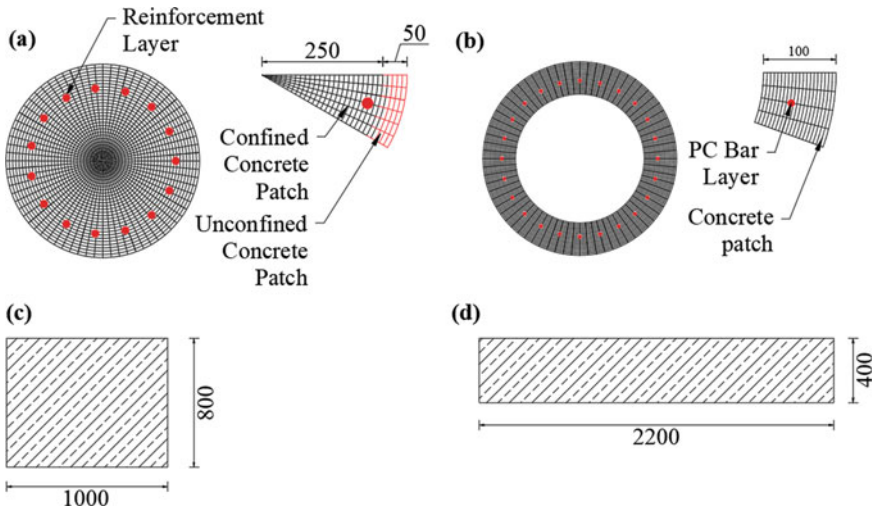


Fig. 5 a RC bored pile fiber section, b PHC pile fiber section, c pile-head elastic section and, d beam elastic section representing the concrete slab

Table 1 Connecting beam element section properties

Parameter	Unit	Pile head element	Beam element representing the concrete slab
A	mm ²	800,000	880,000
E	MPa	36,084.0359	36,084.0359
G	MPa	15,035.016	15,035.016
J	mm ⁴	8.757E + 10	4.156E + 10
I_z	mm ⁴	6.667E + 10	3.549E + 10
I_y	mm ⁴	4.267E + 10	1.173E + 10

Note A = Cross-sectional area of element, E = Young's modulus, G = Shear modulus, J = Torsional moment of inertia, I_z = Moment inertia about the local z-axes, I_y = Moment inertia about the local y-axes [11]

2.3 Concrete and Steel Parameter of the Pile Section

Kent and Park concrete model with linear tension softening adopted in Concrete02 was implemented to model the PHC pile and RC bored pile concrete material. The parameters of Concrete02 were compressive strength at 28 days (f_{pc}), concrete strain at maximum strength (ϵ_{psc0}), concrete crushing strength (f_{pcu}), concrete strain at crushing strength (ϵ_{psU}), the ratio between unloading slope at e_{psc0} and initial slope (λ), tensile strength (f_t) and tension softening stiffness (E_{ts}) [11]. The compressive fracture energy of concrete was considered and estimated by adjusting the strain at

Table 2 Input parameter of Concrete02 for PHC pile and RC bored pile concrete

Parameter	Unit	A	B	C
f_{pc}	MPa	60.00	30.00	32.18
ε_{psc0}	–	0.002	0.002	0.0021
f_{pcu}	MPa	12	6	6.436
ε_{psU}	–	0.002853	0.00583	0.0272
λ	–	0.1	0.1	0.1
f_t	MPa	3.873	2.738	2.738
E_{ts}	MPa	6000	3000	3000

Note: **A** Unconfined PHC pile concrete, **B** Unconfined RC bored pile concrete, **C** Confined RC bored pile concrete

crushing concrete with Eq. (1) proposed by Zhang and Tien [12]. The fracture energy of concrete (G_f^c) for confined and unconfined RC bore piled section were assumed to be 25 N/mm and 150 N/mm, respectively. While, G_f^c of 50 N/mm was implemented for PHC pile concrete material. Elastic modulus of the concrete denoted as E_c was calculated using Eq. (2) [11]. L_{IP} denotes the plastic hinge length as stated before. Concrete crushing strength was taken as $0.2f_{pc}$. Table 2 listed the parameters of Concrete02 in this study. There were two different concrete model of RC bored pile section i.e. confined concrete and unconfined concrete.

$$\varepsilon_{psU} = \frac{G_f^c}{0.6f'_cL_{IP}} - \frac{0.8f'_c}{E_c} + \varepsilon_{psc0} \tag{1}$$

$$E_c = \frac{2f_{pc}}{\varepsilon_{psc0}} \tag{2}$$

Steel02 material based on Giuffre-Menegotto-Pinto model was adopted to construct the behavior of the PC bar and longitudinal reinforcement of the RC bored pile. The input parameters were yield strength (f_y), initial elastic tangent (E_0), strain-hardening ratio (b), and the parameters to control the transition from elastic to plastic branches (R_0, cR_1, cR_2) [11]. Table 3 resumed the steel material parameter.

Table 3 Input parameter of Steel02 for PC bar and deform bar

Parameter	Unit	PC bar	Deform bar
f_y	MPa	1387	400
E_0	MPa	220,267	200,000
b	–	0.05	0.05
R_0	–	10	10
cR_1	–	0.925	0.925
cR_2	–	0.15	0.15

Initial stress material was adopted to develop the PC bar pre-tensioning effect with magnitude 1101 MPa.

2.4 Ground Motions Input

In this study, time history analysis was performed to investigate the studied structure under earthquake excitation. Six ground motions data recorded from Level 2 earthquake ground motion provided by Japan Road Association (JRA) [13] was used following previous non-linear time history analysis done by Fajar [14]. Generally, there are two types of recorded earthquake ground motion. Type 1 is recorded from the 2003 Tokachi-Oki Earthquake representing a large-scale interpolate earthquake with low frequency of occurrence, while Type 2 was recorded from the 1995 Hyogo-ken Nanbu Earthquake representing an inland crustal earthquake with low probability of occurrence. Every type of earthquake used in this study consists of three ground motions based on the three different ground types (hard, medium, and soft) chosen from JRA seismic design specification for highway bridge structure [13]. Hard ground motion type has the shortest period and the soft one has the longest period.

All acceleration time histories (recorded and synthetic) were scaled for Kulonprogo, Yogyakarta Province area by adopting Kalkan and Chopra guidance [15] to match the design response spectrum as suggested by SNI 2833-2016 [16]. The waveform and response spectrum of the processed ground motions are presented in Figs. 6 and 7, respectively.

2.5 Structural Performance Investigation Method

The structural behavior of the PSSV was observed using non-linear cyclic loading analysis. Then, dynamic non-linear time history analysis (NLTH) was performed to investigate the structural performance due to seismic excitation. Several dynamic uniform earthquake ground motions had been prepared to perform the time history analysis, and the result was graphed with the limit states of concrete and steel material. The transient analysis was performed to conduct all of the analysis utilizing modified Newton algorithm and Newmark method integrator. The only longitudinal direction of the PSSV structure was considered in this study due to the lowest degree of redundancy. Eigenvalue analysis for obtaining the natural period (T_n) of the structure and gravity analysis in the form of a constant nodal load pattern in the gravity direction were carried out before. A cyclic loading protocol following ACI 374.1-05 loading protocol without the transition cycles [17] showed in Fig. 8 was applied to the control node to conduct the cyclic loading analysis. The equal damping ratio of PSSV structure was calculated, referring to Jacobsen's method [18] during cyclic loading.

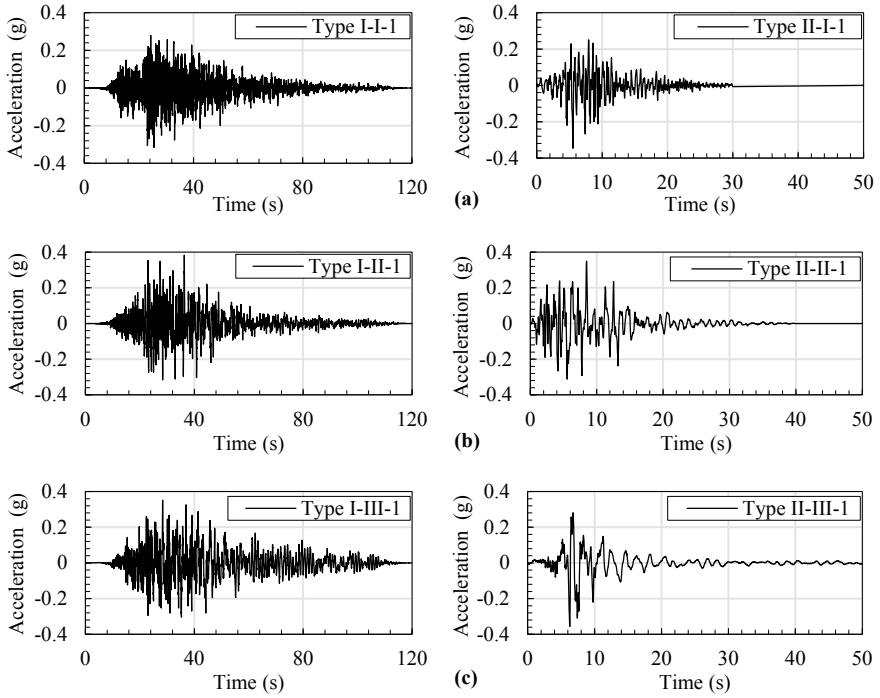


Fig. 6 Scaled ground motion to perform the nonlinear time history analysis: **a** subduction-hard, **b** subduction-medium, **c** subduction-soft

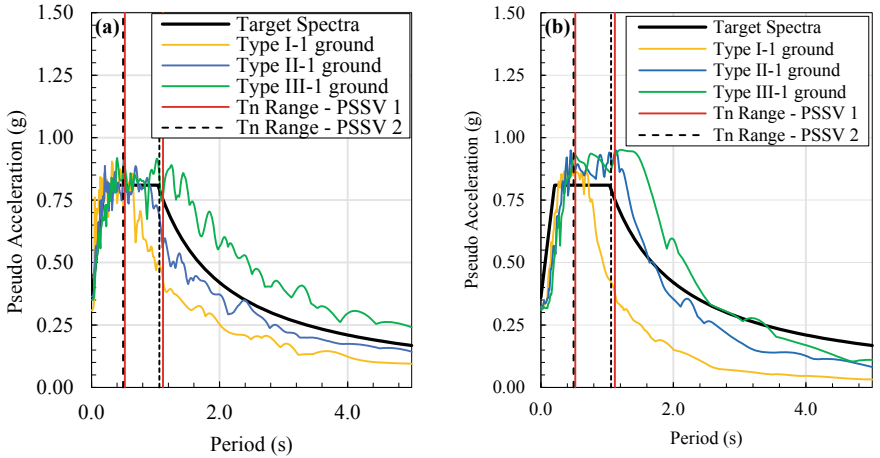


Fig. 7 Design response spectrum and spectral acceleration of **a** Type 1 and **b** Type 2 considered ground motion

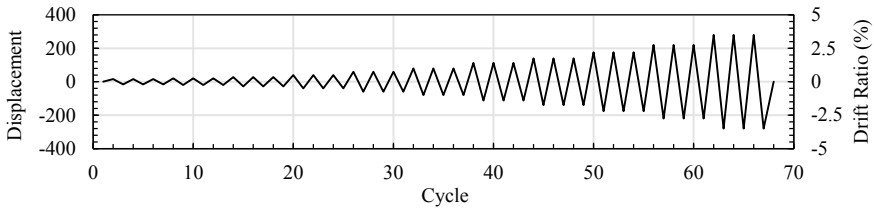


Fig. 8 The cyclic loading protocols

In order to capture the performance limit states of the structure, backbone curves developed from the cyclic hysteretic loop was also figured with the material limit states and the maximum response of the structure due to all of the considered ground motion. The working stages of the PHC pile behaviors introduced by Zhang [19] were adopted in this study for both PSSV structures. The initial elastic stage in which linear behavior occurs until the first crack at pile root is characterized from point O to point A, as shown in Fig. 9. The yield strength in the tensile strength of the pile is achieved at point B after gradually horizontal flexural crack propagates diagonally at the bottom pile. Finally, the strength and stiffness of the pile are decreased rapidly at point C, and then pile failure happens by tensile fracture of the steel bar or concrete crushing. A stable condition was shown at PSSV 2 skeleton curve till the end of the cyclic analysis. So, the end response of the PSSV 2 cyclic analysis is assumed to be the C limit of the PSSV 2 structure. All of those point at the backbone curve of each PSSV structure is shown in Fig. 9 and the displacement of the structures corresponding to each point are summarized in Table 4.

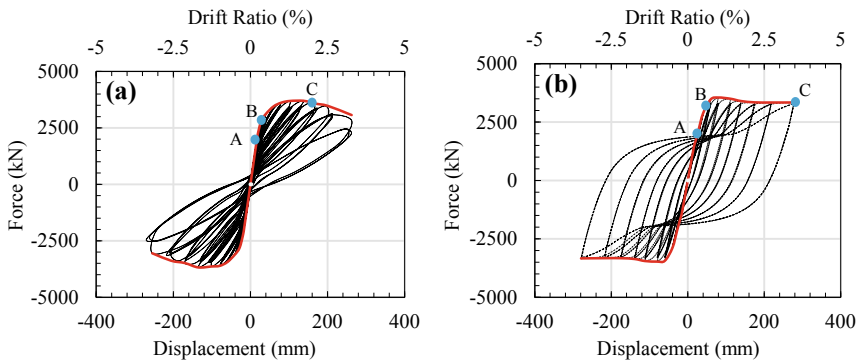


Fig. 9 The cyclic hysteretic and backbone curve of **a** PSSV1 and **b** PSSV2

Table 4 Displacement of the structures at each limit point

Type	Displacement of the structures at each limit point (mm)		
	A Initial elastic limit	B Yielding limit	C Strength degradation
PHC Pile	16	28	150
RC Bored Pile	20	40	277

3 Result and Discussion

3.1 Structural Behavior

Based on eigenvalue analysis, PSSV1 had higher stiffness seen from the smaller natural period. The natural period of PSSV1 obtained from the eigenvalue analysis was 0.520 s and 0.494 s for first and second mode, respectively. While, PSSV2 had 0.526 s and 0.547 s natural period in the first and second mode, respectively. Furthermore, the second stiffness of both PSSV1 and PSSV2 obtained by calculating the second slope of the hysteresis loop graphed in Fig. 10 was utilized to investigate the other natural period of the structure in the longitudinal direction. The results were 1.117 s and 1.059 s for PSSV1 and PSSV2, respectively. The shaded part showed in Fig. 7 shows the natural period range of the structures. The hysteresis loop obtained from the cyclic loading analysis graphed in Fig. 9 shows that PSSV structure utilizing RC bored pile as the piers has a much plumper curve. The more pinching curve shown at PSSV1 hysteresis loops indicates smaller energy dissipation of the structure. Furthermore, Fig. 10 points out that PSSV2 also has higher hysteresis damping compared to PSSV1. The maximum equal damping ratio calculated with Jacobsen’s method was 11% and 29% for PSSV using PHC pile and RC bored pile, respectively. It also emphasizes that the PSSV structure using PHC pile as the piers had lower dissipation energy compared to the RC bored pile PSSV structures.

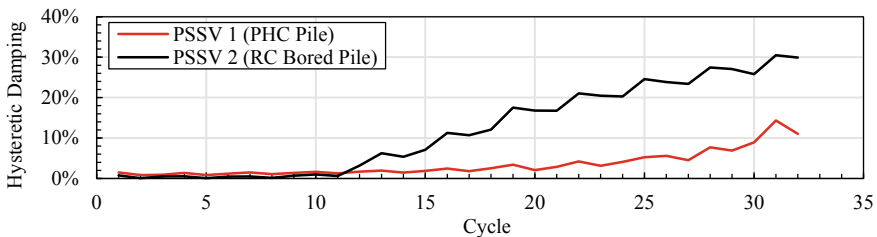


Fig. 10 The hysteretic damping curve of **a** PSSV1 and **b** PSSV2

3.2 Seismic Performance of Both Structure

The maximum response of both PSSV1 and PSSV2 structure under all ground motions shaking are plotted at the skeleton curve shown in Fig. 11. While, the force and deformation relation of the PSSV structure response under seismic excitation including the limit state of each material, are shown in Fig. 11 and Fig. 12. It can be observed that the initial elastic deformation limit of the pile was exceeded under all ground motion excitations. The lowest responses of both PSSV 1 and PSSV 2 are captured under recorded motion Type I-I-1 and Type II-I-1. That was because the recorded ground motion gave the lowest acceleration corresponding with the period enter the natural period range of both structures, as shown in Fig. 7.

In general, the PSSV1 structure had higher structural deformation than the PSSV2 under all cases unless Type I-III-1 seismic excitation. The B limit of both PSSVs was slightly exceeded under Type I-II-1 and Type II-II-1 ground motion excitation. The strength degradation (Limit C) of the pile was exceeded only in PSSV 1 response under Type II-II-1 motions. Based on Figs. 11, 12, and 13, the maximum displacement resulted from the PSSV1 structure was up to 209 mm under Type II-II-1 seismic motion, while the PSSV2 structure exceeded the displacement up to 110 mm under the same seismic excitation. It can be concluded that PSSV using RC bored pile could achieve a smaller response under a designed earthquake than the PSSV with

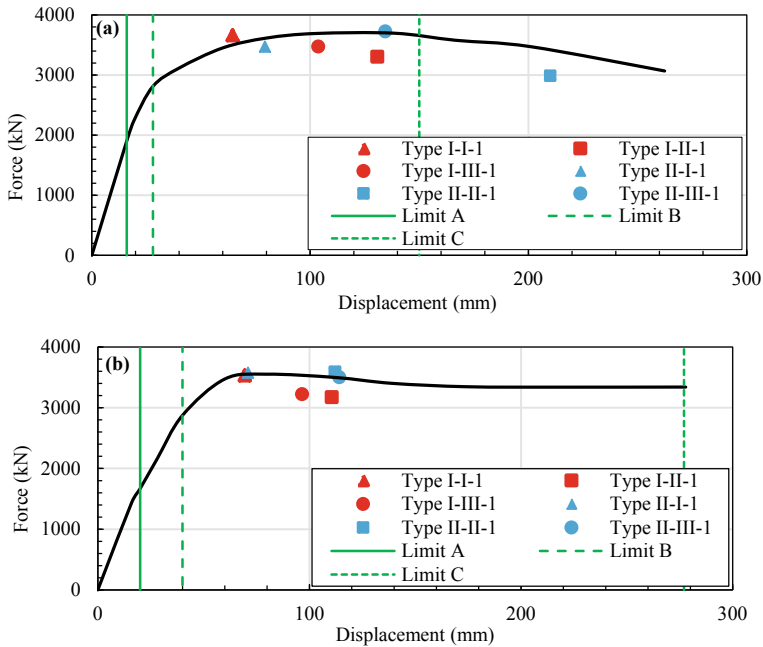


Fig. 11 The skeleton curve and the limit state under static pushover analysis: **a** PSSV1 and **b** PSSV2

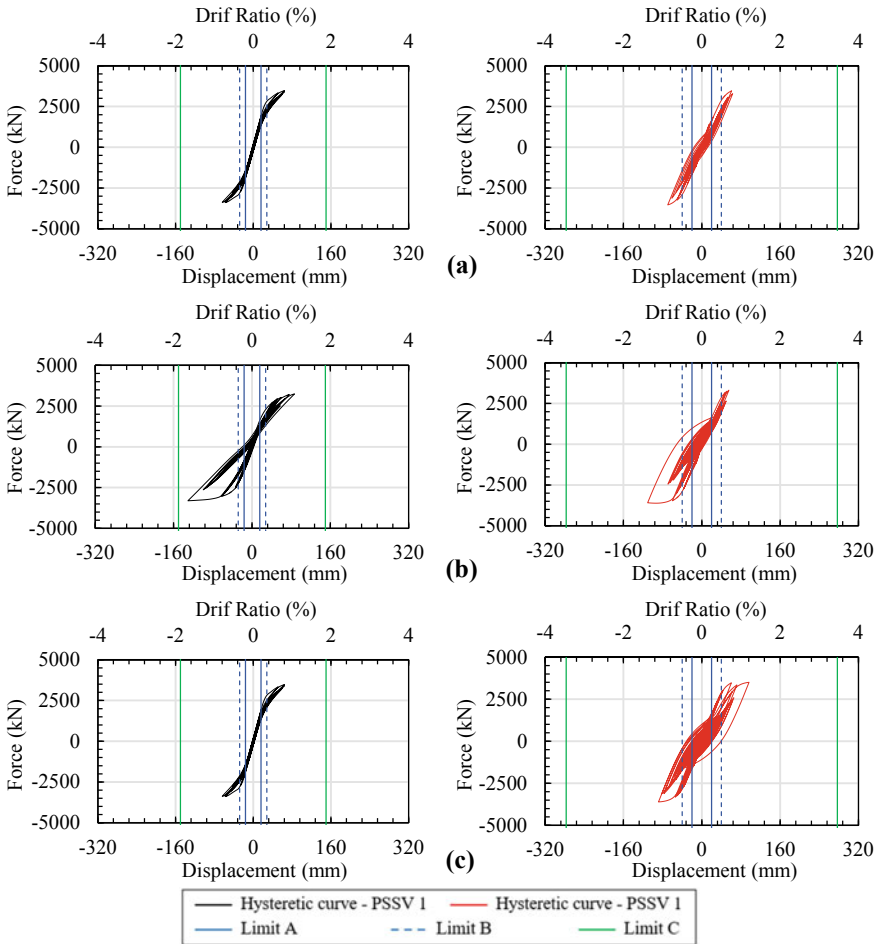


Fig. 12 The force and displacement seismic response under seismic ground motion: **a** Type I-I-1, **b** Type I-II-1, and **c** Type I-III-1

spun pile. It was probably occurred due to the larger energy dissipation achievement of the PSSV 2, as depicted in Figs. 12 and 13. So that utilizing RC bored pile as the pier of PSSV structure is expected to enhance the seismic performance of the structure.

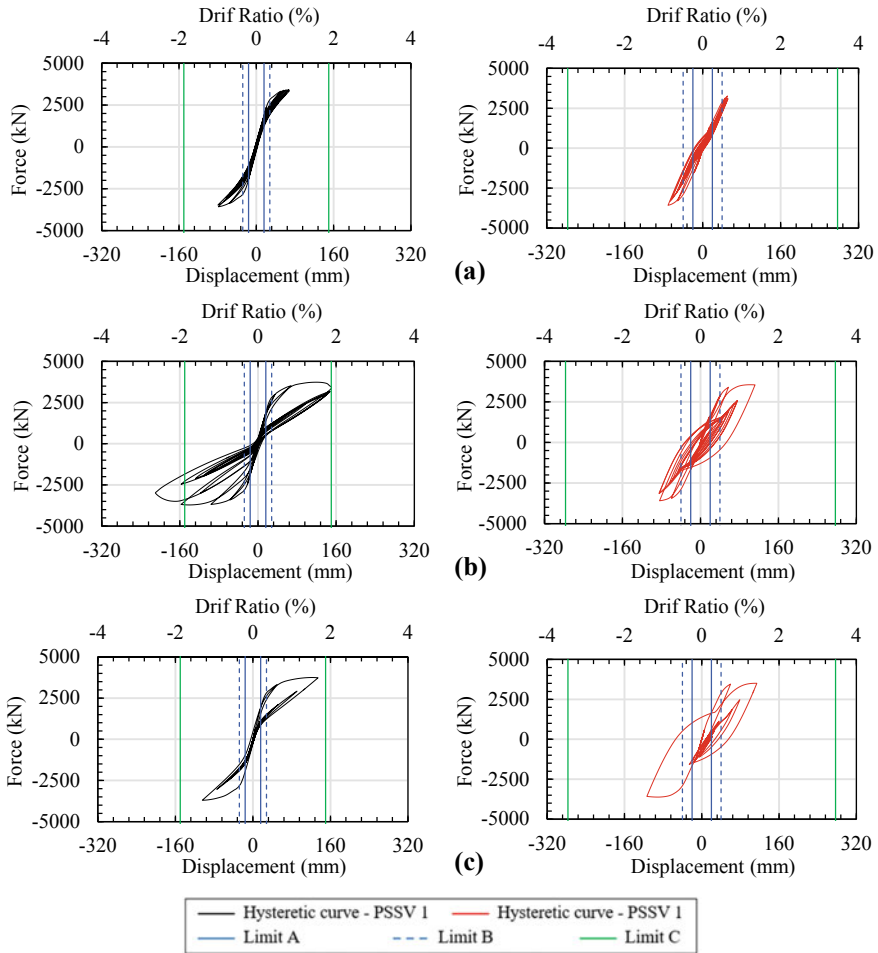


Fig. 13 The force and displacement seismic response under seismic ground motion: a Type II-I-1, b Type II-II-1, and c Type II-III-1

4 Conclusion and Recommendation

4.1 Conclusion

Numerical analysis of both PSSV structure with PHC pile and RC bored pile had been performed. Based on the numerical analysis results, including eigenvalue, pushover, cyclic loading, and dynamic time history analysis using six scaled JRA ground motions with target spectra based on Indonesian seismic bridge provision, both of the structure had the following behaviors and performances:

1. PSSV structure with PHC pile had higher stiffness compared with the RC bored pile-supported one. The natural period range of PSSV1 and PSSV2 structure was 0.520 s–1.117 s and 0.657 s–1.059 s, respectively.
2. Based on the cyclic loading numerical analysis, PSSV 2 structure had the plumper hysteretic curve and achieved 29% of equal damping ratio, which is higher than PSSV 1, i.e., 11%. It indicated that the PSSV structure using RC bored pile as the piers had much higher energy dissipation than the PSSV structure supported by the PHC pile.
3. The strength degradation (Limit C) of the pile was exceeded only in PSSV 1 response under Type II-II-1 motions. Moreover, PSSV 2 could achieve a smaller response under a designed earthquake than the PSSV 1. It was probably occurred due to the larger energy dissipation achievement of the PSSV 2. So that utilizing RC bored pile as the pier of PSSV structure is expected to enhance the seismic performance of the structure.
4. The medium ductility design of both PSSV structure resulted in PHC, and RC bored pile could resist the design load combination. However, based on the non-linear time history analysis result showed that the PSSV 1 structure response due to seismic excitation could significantly exceeded the strength degradation limit (Limit C). So that, middle ductility consideration is not appropriate to be used in the PSSV design utilizing PHC piles as the piers.

4.2 Recommendation

If medium and high ductility concept to be implemented on PSSV structure with PHC pile, a supplemental energy dissipation device need to be added to the structural system to enhance the seismic performance of the structures. The next research related to this study is the effect of soil-structure interaction, liquefaction, and the shear failure effect of PHC Pile.

Acknowledgements The author gratefully acknowledged Directory of Research, Universitas Gadjah Mada that had the support and funded this research.

References

1. Setkab RI (2017) Infrastructure development aims to create higher economic growth, President Jokowi Says, 2017. [Online]. Available: <https://setkab.go.id/en/infrastructure-development-aims-to-create-higher-economic-growth-president-jokowi-says/>
2. Budek AM, Priestley MJN (2005) Experimental analysis of flexural hinging in hollow marine prestressed pile shafts. 47(1):1–20
3. Benzoni G, Budek AM, Priestley MJN (1997) Experimental investigation of ductility of in-ground hinges in solid and hollow prestressed piles, no. Nov 1997
4. Pawirodikromo W (2012) Seismologi Teknik & Rekayasa Kegempaan, 1st ed. Yogyakarta: Pustaka Pelajar

5. Kurniadi A, Rosyidin IF, Indarto H, Atmono ID (2015) Desain struktur slab on pile. *J Karya Tek Sipil* 4(4):57–68
6. WIKA CLT (2015) PC Piles Catalog. WIKA CLT, Batam
7. Irawan C, Djamaluddin R, Raka IGP, Suprobo P (2018) Confinement behavior of Spun Pile using low amount of spiral reinforcement—an experimental study, no. January 2018, 2019
8. Scott MH (2011) Numerical integration options for the force-based beam-column element in OpenSees. 18(19):1111–1120
9. Setiawan AF, Darmawan MF, Ismanti S, Sunarso M, Adityawarman GM (2019) Numerical model for investigating seismic performance of Prestressed Hollow Concrete (PHC) piles with Fiber section element. In: 4th ICEEDM 2019, vol 0. pp 1–9
10. Priestley MJN (2000) Flexural behavior of circular hollow columns with a single layer of reinforcement under seismic flexural behavior of circular hollow columns with a single layer of reinforcement under seismic loading. no. 59
11. Mazzoni S, McKenna F, Scott MH, Fenves GL (2006) OpenSees command language manual. *Pacific Earthq Eng Res Cent* pp 451
12. Zhang Y, Tien I (2020) Methodology for regularization of force-based elements to model reinforced concrete columns with short lap Splices. *J Eng Mech* 146(7):04020073
13. Japan Road Association (2012) Specification for highway bridge: part V seismic design. Tokyo
14. Setiawan AF, Takahashi Y (2018) A high seismic performance concept of integrated bridge pier with triple RC columns accompanied by friction damper plus gap. *J Japan Soc Civ Eng Ser A1 (Structural Eng Earthq Eng* 74(4):I_131–I_147
15. E. Kalkan and A. K. Chopra, “Practical Guidelines to Select and Scale Earthquake Records for Nonlinear Response History Analysis of Structures,” 2010.
16. Badan Standarisasi Nasional Indonesia (2016) “Perencanaan Jembatan Terhadap Beban,” pp. 1–70
17. ACI Comitte (2005) Acceptance criteria for moment frames based on structural testing and commentary
18. Jacobsen LS (1930) Steady forced vibrations as influenced by damping. *Trans* 52(15):169–181
19. Zhang X, Niu S, Yan JB, Zhang S (2019) Seismic behaviour of prestressed high-strength concrete piles under combined axial compression and cyclic horizontal loads. *Adv Struct Eng* 22(5):1089–1105

Finite Element Analysis for Developing Multi-direction Crossing Web Type Shear Panel Damper



N. U. Bagas, I. Satyarno, A. S. Fajar, A. Awaludin, and M. A. Guntara

Abstract Shear panel damper (SPD) has been implemented for supplementary energy dissipation in a wide range of structures. SPD is a kind of wide flange (WF) cross-section steel where the yield strength of the web (LY225) is much lower than the yield strength of the flanges (S355). The beneficial aspects of SPD are high energy dissipation capacity, sufficient ductility, and economical cost. Currently, the SPD is designed to work in one direction of deformation only. However, in real structures such as bridges or viaducts with lead rubber bearing (LRB) or high damping rubber bearing (HDRB) as seismic devices, both LRB and HDRB work in multi-direction of deformation in moving plane. This paper discusses a numerical analysis study using the finite element method (FEM) where the SPD can work at multi-directions of movement in the moving plane. In this study, the proposed multi-direction SPD model was simulated under one selected Crossing Web shape type. In realizing nonlinear material behavior, the metal plasticity material model with combined isotropic and kinematic hardening was adopted in the FEM model using ABAQUS software. Moreover, to measure structural ductility and energy dissipation, static cyclic loading was subjected to the SPD model in four different angle directions relative of the web plane axis, i.e., 0°, 15°, 30°, and 45°. The FEM simulation result found that the proposed

N. U. Bagas · I. Satyarno · A. S. Fajar (✉) · A. Awaludin
Department of Civil and Environmental Engineering, Universitas Gadjah Mada, Yogyakarta,
Indonesia

e-mail: angga.fajar.s@ugm.ac.id

N. U. Bagas

e-mail: Bagas.n.u@mail.ugm.ac.id

I. Satyarno

e-mail: imansatyarno@ugm.ac.id

A. Awaludin

e-mail: ali.awaludin@ugm.ac.id

M. A. Guntara

PT. Wijaya Karya Beton Tbk, North Sumatra, Indonesia

e-mail: guntara@wika-beton.co.id

SPD with load direction from 0° to 45° tends to show increased hysteresis parameters as the load direction angle increases. Furthermore, the SPD with a thickness of 8 mm at the load direction 0° resulting in larger resistance capacity associated with the displacement ductility. This multi-direction shear panel damper can generally be used and applied to bridge structures in particular. However, further research needs to observe the multi-direction SPD's behavior and the bridge structure together.

Keywords Multi-direction shear panel damper · Finite element analysis · Low yield strength steel · Energy dissipation

1 Introduction

Shear panel damper (SPD) has been implemented as a supplemental damper not only building structure but also for the bridge structure. Under shear load in the plane direction of the web panel, it can produce significant energy dissipation due to the yielding of shear deformation [1]. Also, the superiority of the SPD is the achievement of early yielding in small deformation. SPD has unique mechanical characteristics that distinguish it from the other devices, which has good ductility so that it can be used and applied to structural systems that accept cyclic loads such as earthquakes [2]. Shear panel damper, especially SPD, which uses low yield steel can be dissipating energy very well even; naturally, low yield steel SPD is the best device to be dissipating energy from the cyclic load [3].

Generally, in the frame system of the building structure, which has high structural redundancy, SPD can be installed on the frame bays with a bracing system to improve stiffness and energy dissipation. On the other hand, in the bridge pier system, which the seismic resistance system just supported directly with the column element, this system has small energy dissipation and low ductility. Additional SPD in the bridge structure could enhance significant supplemental energy dissipation to cover the low ductility of the bridge pier. In the implementation in the bridge system, a supplemental SPD device is installed to connect the pier system and the superstructure system in the lateral direction. When under seismic event, the SPD transfer the inertia force of the superstructure to the structural pier system while the shear deformation of SPD induces the yielding of web panel steel material to produce energy dissipation. Most of the types of shear panel damper that have been implemented in the bridge structure or the building structure or have been investigated today are one direction load shear panel damper type. As for this research, it will discuss related the multi-direction shear panel damper type.

The first objective of this research is to analyze, confirm, and compare the hysteretical behavior of this multi-direction shear panel damper with one direction shear panel damper (regular SPD) when loaded with cyclic loads. It can be seen by analyzing hysteretic energy and equivalent hysteretic damping. The second objective of this research is to observe the behavior of multi-direction shear panel damper compared to one direction shear panel damper specifically related to ductility

behavior. It can be seen by calculating and analyzing the displacement ductility and yield displacement. The third objective of this research is to observe and clarify the behavior of the multi-direction shear panel damper that is loaded with different cyclic load directions. It also can be seen by analyzing hysteretic energy, equivalent hysteretic damping, displacement ductility, and even yield displacement.

2 Review of Literature

Several studies on SPD have been conducted. Study about strain distribution measurement of a shear panel damper developed for the bridge structure. The digital image processing technology investigated the strain distribution properties of the shear panel damper under cyclic loading. Based on the investigation, the shear panel damper was improved to achieve a high deformation capacity, which contributes to making it possible to be a horizontal bridge bearing [1].

Study about shear panel damper using low yield strength steel applied to reinforced concrete buildings using two types of tests. The first test is an experiment of reinforced concrete beam-support column assemblies with a shear panel damper subjected to horizontal reversed cyclic loads. The second test is an experiment of a shear panel damper with a vertical displacement slide device subjected to horizontal reversed cyclic loads. This research shows that the shear strength of SPD remains stable until 0.25% drifts, and the hysteretic curve remains stable until 2.5% drifts [4]. The lightweight design of a seismic low yield strength steel of shear panel damper is also one of several studies about SPD. In this study, five types of material that used in this study, aluminum, carbon steel, stainless steel, and low yield steel (LYS) with three types LYS225, LYS160, and LYS100, with yield strengths of 225 MPa, 160 MPa, and 100 MPa. Low yield steel is the most optimal material among all the considered metallic damping materials for achieving the lightweight design goal of seismic dampers [5]. A nonlinear finite element of Shear panel damper using low yield point steel (SYP120) has also been analyzed by ANSYS LS-Dyna version 12.0. Besides that, The numerical analysis was verified by an experimental test using static load with a quasi-static loading test. The parameters observed were maximum shear strength, dissipation energy, and hysteretic behavior [6]. In addition to the rectangle shear panel damper, the other form of shear panel damper has also been investigated, one of which is an analytical analysis of circular shear panel damper. In this study, observations were made related to the variation in the ratio of the diameter to the thickness (D/t) of the circular shear panel damper. This study is also the same as the study mentioned earlier that the shear panel damper observed was only a one-way SPD type [7].

Based on the mentioned above, the shear panel damper was installed to improve seismic performance structure just considering under one direction loading. Adopting a seismic isolation device that considering multi-directions of seismic loading, the development of the multi-direction shear panel damper needs to be conducted. In the preliminary study, a numerical model of the multi-direction shear panel damper

was proposed with finite element analysis. The multi-direction shear panel damper model subjected cyclic loading following the AISC testing method for steel element member. Then, the hysteretic loop characteristics (nonlinear stability and hysteretic energy) of multi-direction shear panel damper model under several angle directions (0° , 15° , 30° , and 45°) of cyclic loading were monitored. Also, as a comparison, the regular shear panel damper (one direction) model cyclic loading analysis to be conducted.

2.1 Parameters of Hysteresis Loop

A system or structure that is loaded with the cyclic load will produce a hysteresis loop curve. This curve shows the structure's seismic behavior due to being cyclic burdened. Each peak point of force on each cyclic or step load when connected will form an S-shaped curve called a skeleton curve [8]. Under seismic excitation, hysteretic damping and energy are essential parameters of a hysteretic loop for the structural system. Hysteretic damping in a hysteretic loop of a system that is loaded with cyclic loads can be written as follows [9], as expressed in Eq. (1). Hysteretic energy dissipation of the system (E_{hys}) is the total area in the hysteretic loop curve due to cyclic load. Elastic displacement energy (E_{el}) determined based on the maximum force and displacement of the system, as expressed in Eq. (2). Elastic displacement can be calculated in the following way. Where x_j is the maximum displacement, and y_j is the maximum force.

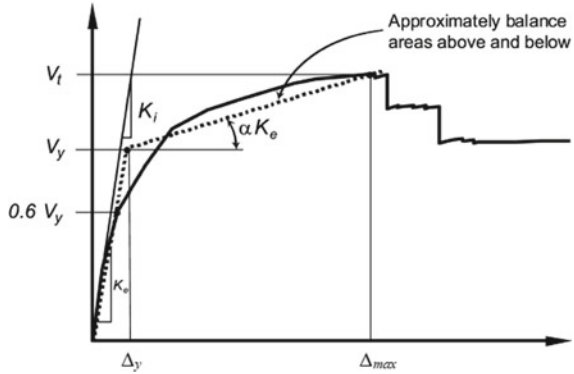
$$\zeta_{hys} = \frac{E_{hys}}{4\pi E_{el}} \quad (1)$$

$$E_{el} = 0,5x_1y_1 \quad (2)$$

2.2 Displacement Ductility

Based on the curve graph of the relationship between displacement and load, the seismic behavior of a structure can be observed and determined by calculating and analyzing the structural ductility of a structure. Displacement ductility is a parameter used to measure the ability of a structure to deform due to cyclic loading. A structure if it has a large displacement ductility, then this shows that the distance between the yield point and the ultimate strength point is far, thus implying that the structure is ductile. As for the opposite, if the displacement ductility of a structure is small, the distance of yield point and the ultimate strength point is too close even coincide; this shows that the structure is brittle. Displacement ductility of the material can be calculated by the following Eq. (3) [10]. Where Δ_{max} is the displacement of

Fig. 1 Displacement ductility calculation [11]



the structure when it reaches the maximum force (V_t). The Δ_y is yield displacement obtained with an idealized force–displacement curve relationship between base shear and displacement to calculate the effective lateral stiffness (K_e) and effective yield strength (V_y). This relationship shall be bilinear with initial slope (K_e) and post-yield slope α . The effective lateral stiffness calculated at a base shear force equal to 0.6 of the effective yield strength. As for the elastic lateral stiffness symbolize K_i . The line segment shall be located using an iterative graphical to approximate the area above and below the curve are balanced [11]. The displacement ductility calculation scheme, as shown in Fig. 1.

$$\mu = \frac{\Delta_{max}}{\Delta_y} \tag{3}$$

2.3 Low Yield Strength Steel

Low yield strength as the name implies steel has a very low yield strength, so it is suitable for use in the shear panel damper system as the primary material. Both are used in earthquake areas that have large magnitude or on small earthquakes. Another thing that is the reason why low yield steel is suitable for use in shear panel dampers is that it has more uniform strength compared to ordinary steel. On the other hand, a low yield steel shear panel damper is used in the structure of a bridge or building to obtain the first yield section is the shear panel damper before yielding in the primary structure [12]. The behavior of low yield strength steel, which is loaded with cyclic or monotonic loads, has been carried out. LY225 testing with monotonic load shows very high ductility, as shown in Fig. 2a [13]. Besides monotonic load, LY225 seismic behavior after being loaded with a cyclic load can also be shown in Fig. 2b [14]. As for seeing the very significant difference in ductility between low yield strength steel and mild steel, for example, LYS100 and SS400 in Fig. 2c [15].

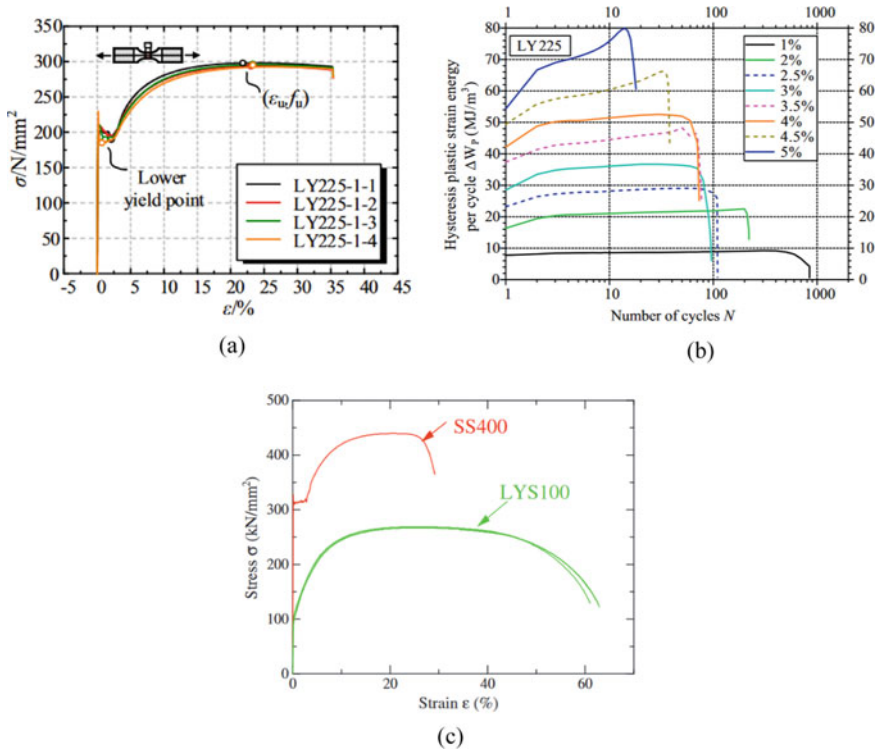


Fig. 2 Behavior of low yield strength steel: **a** monotonic load [13], **b** cyclic load [14], and **c** comparison with mild steel [15]

2.4 Finite Element Analysis

The Chaboche constitutive model has been widely used and applied to numerical analysis software algorithms including in Abaqus software. The plastic-elastic theory that material is loaded with cyclic loads underlies the Chaboche constitutive Model [16]. The plastic elastic theory in the model is defined by the critical state, yield surface, flow, and hardening rule. However, the Chaboche constitutive model was later calibrated by von Mises and is now also being used in Abaqus software [13].

3 Research Methods

In this study, a numerical model of multi-direction shear panel damper was proposed with finite element analysis. In the finite element analysis, the continuum shell element was adopted by considering nonlinear of steel material and geometry. Numerical models of the multi-direction sheal panel damper were proposed without

vertical restrained. The top base plate is free, the only bottom part of the base plate to be fixed restrain. In the application, the multi-direction shear panel damper to be idealized as the stopper of the bridge superstructure, as illustrated in Fig. 3.

The numerical models of multi-direction SPD are modeled with the finite element method using Abaqus Software. There are two shear panel damper models analyzed, SPD-A with a thickness of 8 mm and SPD-B with a thickness of 3 mm. Each numerical model is burdened with four types of load directions 0°; 15°; 30°; and 45° and also the regular SPD (one direction) as a comparison. The load applied to this SPD is a cyclic load. The cyclic load applied refers to the AISC 341–05 about Seismic Provisions for Structural Steel Buildings, as illustrated in Fig. 4 [17].

The shear panel damper consists of four components, three additional components modeled by structural steel S355 and one main part implemented by low-yield steel LY225. The three other parts are baseplate (15 mm and 10 mm thick), flange (12 mm and 5 mm thick), and rib (8 mm and 3 mm thick) and their dimensions in Fig. 5.

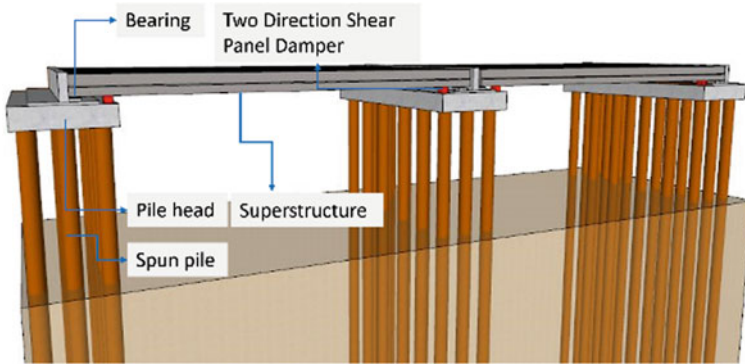


Fig. 3 Implementation two-direction SPD in a pile group supported voided slab system

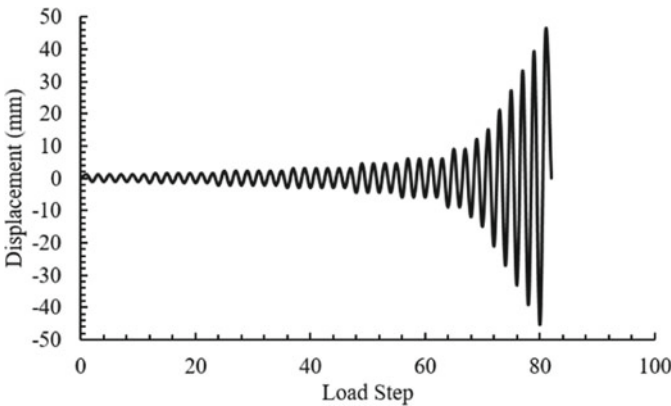


Fig. 4 The cyclic load according to AISC 341–05 [17]

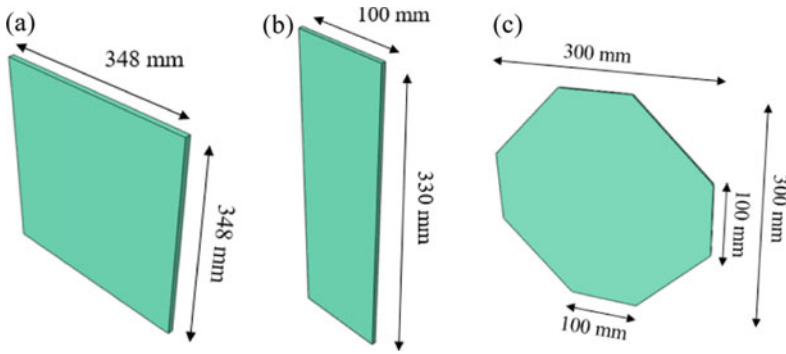


Fig. 5 Three additional components: **a** baseplate, **b** flange, and **c** rib

The main part is crossing web type of shear panel damper (8 mm and 3 mm thick, as shown in Fig. 6).

The elastic and plastic parameters of the LY225 and S355 materials, according to [13] and [16] were analyzed in Abaqus software as the following Table 1.

Where E is elastic modulus; σ^{-0} is yield stress at zero plastic strain; C_1 , C_2 , C_3 , and C_4 are kinematic hardening modulus; γ_1 , γ_2 , γ_3 , and γ_4 are the rate of the kinematic hardening modulus decrease with increasing plastic deformation. The Poisson’s ratio (ν) of this shear panel damper from both LY225 and S355 materials is 0.3.

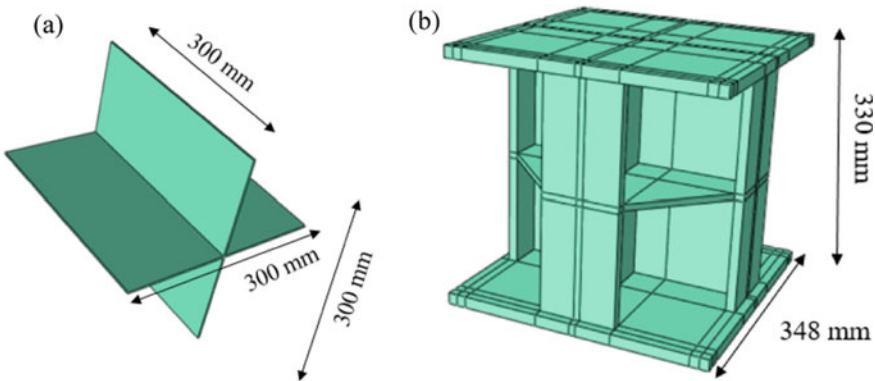


Fig. 6 The main component of shear panel damper and **b** complete structure

Table 1 Material parameters of shear panel damper in the finite element model

No	Material	E (MPa)	σ^{-0} (Mpa)	C_1	γ_1	C_2	γ_2	C_3	γ_3	C_4	γ_4
1	LY225	202,500	191	3041	126	1028	170	890	224	260	1
2	S355	185,000	386	5327	75	1725	16	1120	10	0	0

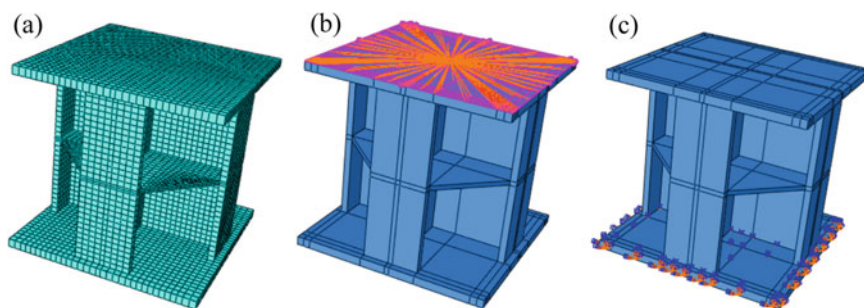


Fig. 7 Numerical model using Abaqus software: **a** mesh, **b** constraints, and **c** boundary condition

In modeling using finite elements with Abaqus software, the mesh size used in the structure of the shear panel damper is around 10 mm. It was used in previous numerical studies, namely research conducted by [18]. The results of the meshing shear panel damper can be seen in Fig. 7a. The interaction in the upper baseplate using MPC tie type constraints, as shown in Fig. 7b. The boundary condition on the bottom baseplate used pin support where the displacement and direction rotation 1, 2, and 3 are equal to 0, as in Fig. 7c.

4 Result and Discussion

Furthermore, an analysis of the multi-direction shear panel damper is performed according to the cyclic load, and the parameters mentioned previously using the Abaqus program. Based on the result of SPD analysis using the Abaqus program, the hysteretic behavior of SPD with a thickness of 8 mm (SPD-A) and 3 mm (SPD-B) without vertical restrained under cyclic loading are obtained, as illustrated in Figs. 8 and 9.

Based on Figs. 8 and 9f skeleton curve comparison from each typical load and the regular SPD, it can be seen that the load direction 45° can achieve the highest force followed by the load direction 30° , 15° , 0° and the regular SPD. It can also be seen that the difference of skeleton curve between multi-direction shear panel damper and one direction shear panel damper is quite significant. This skeleton curve represents a hysteretic loop curve. So that if the skeleton curve is erect and higher as in the load direction 45° , it could produce an area in the loop hysteretic curve that is getting bigger. So the skeleton curve can also be seen as the amount of hysteresis energy from the SPD. The skeleton curve at SPD-A tends to increase with increasing displacement, while the skeleton curve at SPD-B decreases after reaching the maximum force with a displacement around 6–9 mm. It can also be seen that the hysteresis energy of SPD-A is higher than SPD-B because the dimensions of SPD-B are too thin compared to SPD-A, it causes buckling on the web that reduces the strength of SPD-B. Besides, hysteretic energy and damping can be calculated as

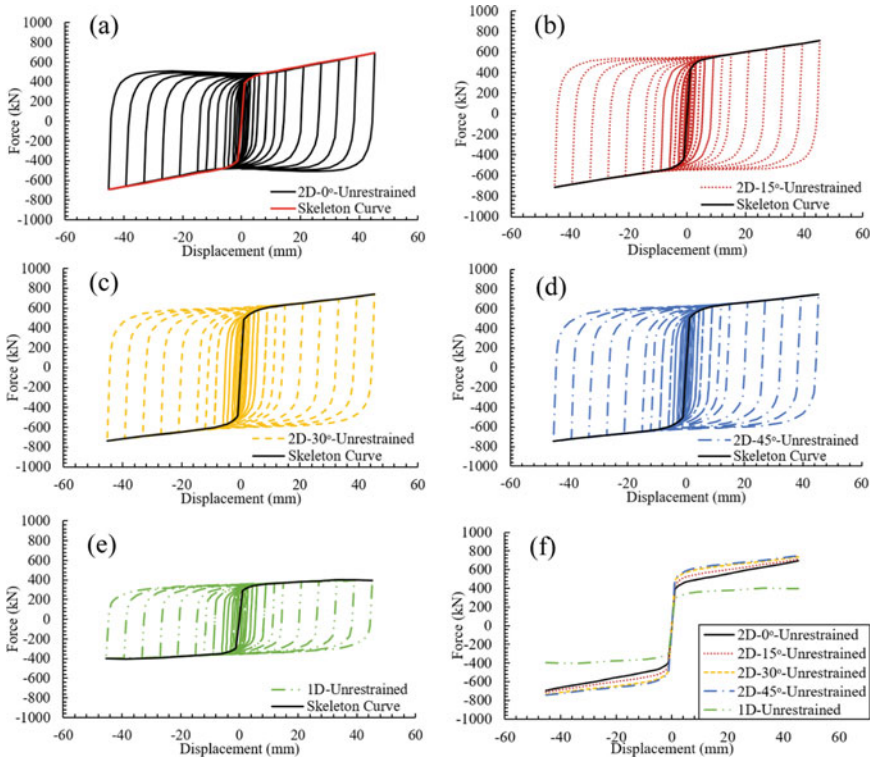


Fig. 8 The behavior of SPD-A with vertical under cyclic loading: **a** 2D-0°, **b** 2D-15°, **c** 2D-30°, **d** 2D-45°, **e** 1D, and **f** skeleton curve comparison

the energy Eqs. (1) and (2) previously stated. The following results are obtained in Figs. 10 and 11.

Figures 10 and 11a show that hysteretic energy increases with increasing displacement or the number of cycles for each type of load direction and the regular SPD. In the initial stages of the cyclic load starts from 0 to 20 n-cycle, the hysteretic energy of each kind of load directions, and the regular SPD are relatively the same. The largest hysteretic energy of SPD 8 mm can reach up to 112.137 kNm at the load direction 45°. The largest hysteretic energy of SPD 3 mm can reach up to 25.788 kNm at the load direction 30°. The smallest hysteretic energy of SPD 8 mm is 61.690 kNm, and SPD 3 mm is 15.509 kNm, both of which occur at the regular SPD type. It also can be seen that the difference of relation hysteretic energy and N-cycle curve between multi-direction shear panel damper and one direction shear panel damper is quite significant. This is because the multi-direction shear panel damper has a crossing web stiffener in the other direction so that the effective length is reduced by half and also reduces the potential for buckling. Besides, it is also influenced by the presence of flanges on the crossing web in another direction which helps resist shear forces.

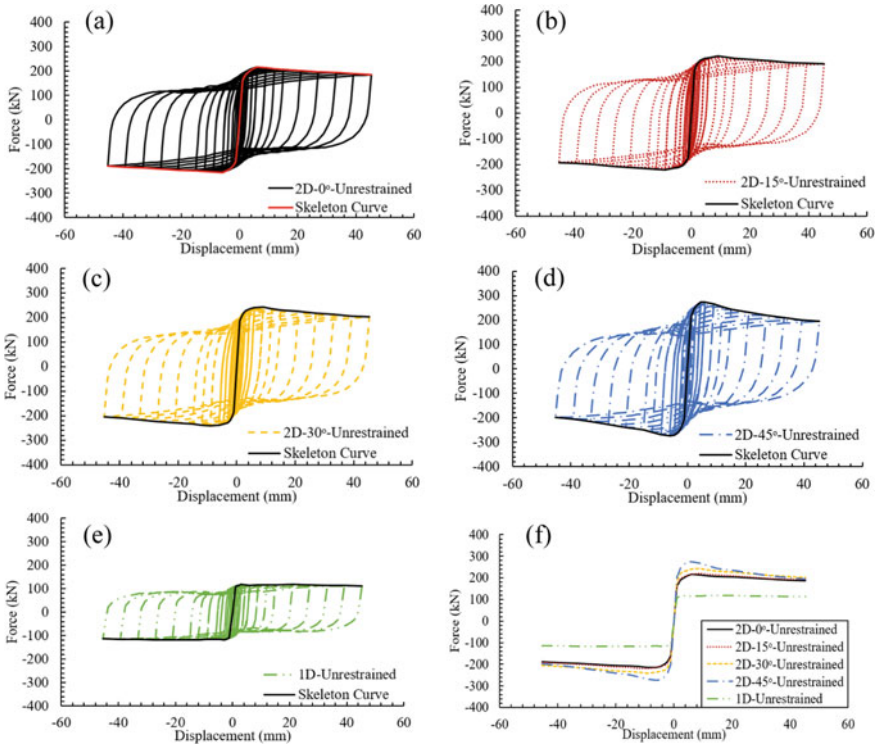


Fig. 9 The behavior of SPD-B with vertical under cyclic loading: **a** 2D-0°, **b** 2D-15°, **c** 2D-30°, **d** 2D-45°, **e** 1D, and **f** skeleton curve comparison

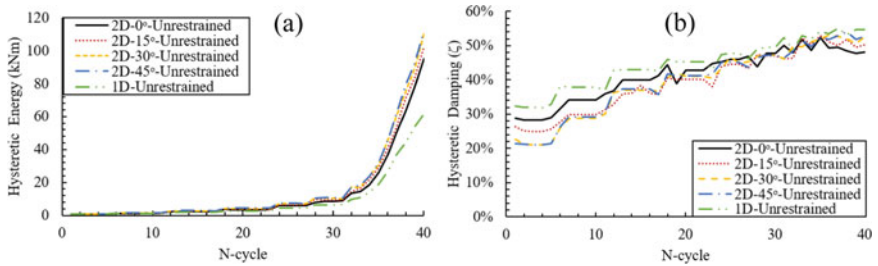


Fig. 10 The hysteretic energy achievement of SPD-A with vertical under cyclic loading: **a** energy and **b** equivalent hysteretic damping

Based on Figs. 10 and 11b, hysteresis damping tends to increase until the end of the cyclic load. The load direction 45° SPD is the most significant increase in the hysteresis damping curve. The largest hysteresis damping of both SPD models can reach 55% and 50% in the regular SPD type, even though it is only 1% and 2% different from the load direction 45°. The smallest hysteresis damping of SPD-A was

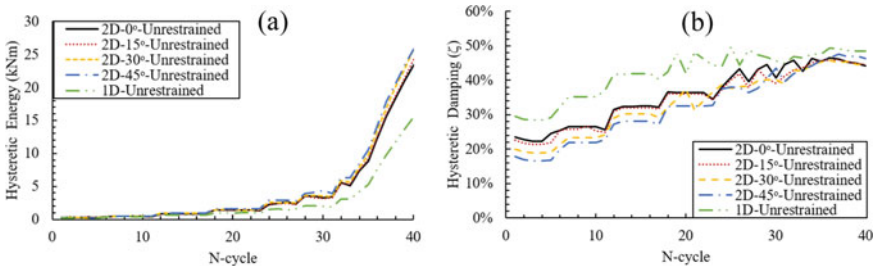


Fig. 11 The hysteretic energy achievement of SPD-B with vertical under cyclic loading; **a** energy and **b** equivalent hysteretic damping

found to occur in the load direction 0°, while for the SPD-B was found in the load direction 15° and 30°.

Furthermore, the von Mises stress contour and deformed shape of SPDs under cyclic loading when the maximum displacement in the last cycle of the cyclic load condition illustrated in Figs. 12 and 13. These stress contours and deformed shapes represented by maximum stress limit 225 MPa.

Displacement ductility (μ) and yield displacement (Δ_y) are calculated using Eq. (3) and based on the illustration in Fig. 1. Table 2 shows the recapitulation of the calculation results for each parameter from SPDs under cyclic loading, i.e., displacement ductility dan displacement yield. The largest yield displacement reaches 1.367 mm at SPD-A with a load direction of 15°, while the smallest yield displacement obtained is 1.127 mm at the regular SPD-B. Furthermore, the largest displacement ductility can reach 34.803 at SPD-A with a load direction of 0°, and

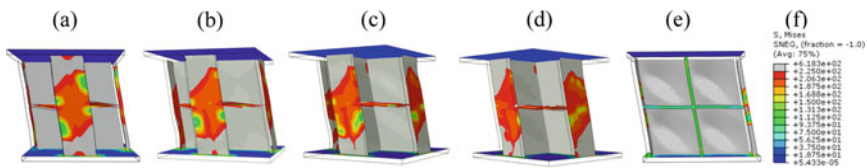


Fig. 12 Stress contour and deformed shape of SPD-A under cyclic loading when maximum displacement condition **a** 2D-0°, **b** 2D-15°, **c** 2D-30°, **d** 2D-45°, **e** 1D and **f** contour scale

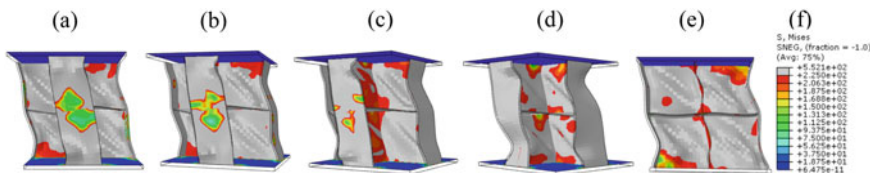


Fig. 13 Stress contour and deformed shape of SPD-B under cyclic loading when maximum displacement condition **a** 2D-0°, **b** 2D-15°, **c** 2D-30°, **d** 2D-45°, **e** 1D and **f** contour scale

Table 2 Recapitulation of the calculation result

SPD		ζ_{max}	Hysteretic energy max (kNm)	H_u (kN)	Δ_y (mm)	μ
SPD-A	2D-0°	52%	95.135	693.583	1.303	34.803
	2D-15°	53%	102.173	712.799	1.367	33.161
	2D-30°	54%	110.365	738.065	1.323	34.277
	2D-45°	54%	112.137	747.272	1.327	34.179
	1D	55%	61.690	400.006	1.311	25.277
SPD-B	2D-0°	47%	23.387	215.882	1.274	4.709
	2D-15°	46%	24.200	222.207	1.326	6.788
	2D-30°	46%	25.788	242.036	1.351	6.663
	2D-45°	48%	25.777	273.912	1.341	4.473
	1D	50%	15.509	118.179	1.127	2.663

also The smallest displacement ductility obtained is 2.663 at the regular SPD-B. The displacement ductility of SPD-A is greater than SPD-B because the positive second stiffness of SPD-A is longer due to not buckling like SPD-B.

5 Conclusion

Based on the numerical analysis that has been done on the shear panel damper with several load directions and types as before, we get several conclusions as to the following points.

1. The multi-direction SPD has greater hysteretic energy than the same dimension of one direction SPD (regular SPD).
2. The displacement ductility and yield displacement of the multi-direction SPD are greater than the regular SPD. It shows that the multi-direction SPD is more ductile than the regular SPD, so it is able to work better, especially due to cyclic loads in the form of earthquake loads.
3. The effect of the loading angle on SPD is very significant. Generally, SPD with load direction from 0 to 45° tends to show an increased hysteresis parameter as the load direction angle increases.
4. The short shear panel damper has greater hysteretic energy and displacement ductility than the slender shear panel damper.
5. This multi-direction shear panel damper can generally be used and applied to bridge structures in particular by looking at the hysteresis and ductility behavior above. However, the equivalent value of hysteresis damping obtained, which around 50%, is still the value of the damping shear panel damper itself and is not included after being installed in the main structure. Therefore, further research needs to be done on the behavior of the multi-direction shear panel

damper that has been installed on the main structure and to find better and more appropriate dimensions to be used on the main structure.

Acknowledgements The author gratefully acknowledges to Ministry of Research, Technology, and Higher Education, Indonesia, and also PT. Wijaya Karya Beton Tbk has supported and funded this research. The discussed seismic device has been registered in a patent.

References

1. Liu Y, Aoki T, Shimoda M (2013) Strain distribution measurement of a shear panel damper developed for bridge structure. *J Struct* 2013(September):1–11. <https://doi.org/10.1155/2013/615275>
2. Tanaka K, Sasaki Y (2000) Hysteretic performance of shear panel dampers of ultra low- yield-strength steel for seismic response control of buildings. 1–8
3. Takaku T (2019) Seismic lens-type shear panel damper for bridges and buildings: innovation and optimization in nature and design to engineering fields. *Syst Res Behav Sci* 36(5):617–620. <https://doi.org/10.1002/sres.2630>
4. Ohta Y, Kaneko H, Kibayashi M, Yamamoto M (2004) In: 13 th World conference on earthquake engineering study on shear panel dampers using low yield strength steel applied to reinforced concrete buildings assemblies with a shear panel damper subjected to horizontal. *Concrete*, no. 2228
5. Zhang C, Zhu J, Wu M, Yu J, Zhao J (2016) The lightweight design of a seismic low-yield-strength steel shear panel damper. *Materials (Basel)* 9(6). <https://doi.org/10.3390/ma9060424>
6. Choi J, Abebe DY (2014) Hysteresis characteristics of shear panel damper using SLY120. *APCBEE Procedia* 9:370–375. <https://doi.org/10.1016/j.apcbee.2014.01.065>
7. Abebe DY, Choi J (2014) Analytical evaluation on hysteresis performance of circular shear panel damper. 8(June):744–750
8. Xu LY, Nie X, Fan JS (2016) Cyclic behaviour of low-yield-point steel shear panel dampers. *Eng Struct* 126:391–404. <https://doi.org/10.1016/j.engstruct.2016.08.002>
9. Zhang Q, Wei ZY, Gong JX, Yu P, Zhang YQ (2018) Equivalent viscous damping ratio model for flexure critical reinforced concrete columns. *Adv Civ Eng* 2018. <https://doi.org/10.1155/2018/5897620>
10. Park R (1988) Ductility evaluation from laboratory and analytical testing. In: *Proceeding ninth world conference earthquake engineering*, vol 8, pp 605–616
11. FEMA (2000) *Prestandard and commentary for the seismic rehabilitation of buildings*. Rehabil Requir 1:1–518
12. Chen Z, Bian G, Huang Y (2013) Review on web buckling and hysteretic behavior of shear panel dampers. *Adv Steel Constr* 9(3):205–217
13. Shi G, Gao Y, Wang X, Zhang Y (2018) Mechanical properties and constitutive models of low yield point steels. *Constr Build Mater* 175:570–587. <https://doi.org/10.1016/j.conbuildmat.2018.04.219>
14. Shi G, Gao Y, Wang X, Cui Y (2018) Energy-based low cycle fatigue analysis of low yield point steels. *J Constr Steel Res* 150:346–353. <https://doi.org/10.1016/j.jcsr.2018.08.026>
15. Zhang C, Zhang Z, Zhang Q (2012) Static and dynamic cyclic performance of a low-yield-strength steel shear panel damper. *J Constr Steel Res* 79:195–203. <https://doi.org/10.1016/j.jcsr.2012.07.030>
16. Narendra PVR, Prasad K, Krishna EH, Kumar V, Singh KD (2019) Low-Cycle-Fatigue (LCF) behavior and cyclic plasticity modeling of E250A mild steel. *Structures* 20(February):594–606. <https://doi.org/10.1016/j.istruc.2019.06.014>

17. AISC (2005) Seismic provisions for structural steel buildings (Including Supplement No. 1)
18. Deng K, Pan P, Li W, Xue Y (2015) Development of a buckling restrained shear panel damper. J Constr Steel Res 106:311–321. <https://doi.org/10.1016/j.jcsr.2015.01.004>

Numerical Model of Finned Tubular Shear Panel Damper for Multi-direction Seismic Excitation



A. M. Emilidardi, A. S. Fajar, A. Awaludin, I. Satyarno, and M. Sunarso

Abstract The earthquake has become a problem in many countries in the world, especially triggering loss of infrastructure due to damage or collapse. In the bridge structure, the critical part that provokes structural damage or collapse occurrence is the plastic hinge of the pier. The main problem is the pier of the bridge has limited ductility, so they are not able to resist a significant earthquake. The application of a passive energy dissipation device is one solution alternative to solve the problem, i.e., shear panel damper (SPD). Currently, SPD is designed to damp seismic forces only in one direction. However, in the real case, the seismic force that works on SPD installed in bridge structure works in multi-direction. This paper discusses an analytical study of two-directional finned tubular shear panel damper (FTSPD) as energy dissipation and resistance devices in the pier of bridges. The beneficial aspects of FTSPD are high energy dissipation capacity, high strength, sufficient ductility, and economical cost. In this study, FTSPD is designed into four models, namely, without fins, four vertical fins, six vertical fins, and eight vertical fins. For this purpose, finite element software (ABAQUS) was conducted to investigate the energy dissipation capacity, damping capacity, ductility, and strength of FTSPD. The main component of the models is tubular steel, which uses low-yield strength LY225, but its plates and fins using S355. In realizing non-linear material behavior, metal plasticity with combined isotropic and kinematic hardening was adopted. Moreover, to calculate the nominal energy dissipation and damping capacity of each model, forty-cyclic

A. M. Emilidardi · A. S. Fajar (✉) · A. Awaludin · I. Satyarno
Civil and Environmental Engineering, Universitas Gadjah Mada, Yogyakarta, Indonesia
e-mail: angga.fajar.s@ugm.ac.id

A. M. Emilidardi
e-mail: andika.emilidardi@mail.ugm.ac.id

A. Awaludin
e-mail: ali.awaludin@ugm.ac.id

I. Satyarno
e-mail: imansatyarno@ugm.ac.id

M. Sunarso
PT. Wijaya Karya Beton Tbk, North Sumatra, Indonesia

loadings on the top of FTSPD were used. The FEM simulation result found that inelastic buckling occurred in TSPD, which not uses fins. On the other hand, FTSPD, which employs more fins, could achieve more high dissipation energy and ductility. This study shows that the implementation of fins can delay buckling occurrence and improve energy dissipation capacity, damping capacity, and ductility of FTSPD. With those achievements of FTSPD, the structural bridge damage under severe earthquake excitation expected could be reduced by implementing FTSPD on a bridge structure.

Keywords Finned tubular shear panel damper · Finite element analysis · Energy dissipation · Damping capacity

1 Introduction

The earthquake is one of the main problems which damaged the bridge pier. In the bridge structure, the critical part that provokes structural damage or collapse occurrence is the plastic hinge of the pier. This matter can happen in a conventional piers system which adopts the concept of weak column [1]. In this concept, a plastic hinge occurred at the bottom of the pier. In a major earthquake, cracking and residual deformation can occur at the plastic hinge when the ductility and strength of the pier able to resist an earthquake demand [2]. However, if the ductility and strength of the pier could not resist an earthquake demand, the pier could collapse [1]. The impact is expensive cost and long downtime demand for the repair and reconstruction process. Highway and railway bridge that implemented as the high importance infrastructure, limited damage during a severe earthquake should be realized to ensure immediate operational after earthquake occurrence. Since the earthquake in Japan in 1995, earthquake-resistant building design standards have been set up to reduce damage or risk due to the earthquake [3]. There are several methods used to solve problems in the bridge pier caused by the earthquake. One such method is the use of hysteresis damper. Hysteresis damper is a device that absorbs earthquake energy that is used to change the shape of the damper device. At present many hysteresis dampers have been developed as examples: Tada's device [4], shear panel damper (SPD) [5], multi-directional torsional hysteretic damper (MTHD) [6].

In fact, the bridge which only supports by rubber bearing has less energy dissipation. One method to increase bridge ductility, stiffness, strength, and energy dissipation is SPD [5]. The implementation of SPD on the bridge pier is placed parallelized with the rubber bearing (RB). Conceptually, the SPD is designed only to hold the seismic force while the RB function is to hold the vertical force of the superstructure, which is passed on to the bridge pier. Seismic forces that occur in the real cases are from all directions. In accommodating this, a two-directional SPD device design needs to be conducted.

Tubular shear panel damper (TSPD) is one of among shape of two-directional SPD. The tubular shape makes it an advantage over other models because it can resist forces from all directions. The capacity of TSPD devices is influenced by

a diameter-to-thickness ratio (D/t). On-device, which has a diameter-to-thickness ratio of $D/t > 27.8$ yieldings with buckling and strength degradation, occurs [3]. In other studies, TSPD with the addition of fins (FTSPD) has developed. Two fins were added to 180 degrees surrounding TSPD. The focus of that studies was to measure the ability of FTSPD steel with a high yielding point of 330 MPa. Besides, the device only added two fins with the direction of loading in the direction of the fins following the ATC-24 testing method. FTSPD was successful in reducing the seismic response of the building due to strong earthquakes. Seismic energy, which converted to dissipation energy, was concentrated in damper, thus maintain other structures that remain elastic [7]. But on the other hand, FTSPD could increase story shear, acceleration, and member forces around the damper [8].

In this study is focussed on designing TSPD, which has a D/t ratio of 50 with additional fins to increase TSPD capacity and prevent strength degradation. For this purpose, finite element analysis in which the use of a continuum shell was conducted by considering non-linear of steel material and geometry. Then, to calculate the nominal energy dissipation and damping capacity of FTSPD, the loading methods used AISC testing methods for steel element member. The FTSPD was expected to gain more energy dissipation and damping capacity than TSPD without fins so that it can support pier structure to resist against the seismic excitation.

2 Numerical Analysis of FTSPD

2.1 FTSPD Configuration

The TSPD consisted of hollow tubular steel as an SPD device which made of low-yield strength named LY225 bonded with an ordinary steel-strength material named S355. TSPD had a height of 120 mm, a diameter of 120 mm, and a thickness of 2.4 mm, and 12 mm thick plates were placed on the top and bottom of TSPD. Then additional fins made of S355 were added surrounding tubular steel to increase the TSPD capacity named FTSPD (see Fig. 1). The dimensions of the fins were 120 mm high and 4.8 mm thick. In realizing non-linear materials behavior, metal plasticity with combined isotropic and kinematic hardening was adopted. LY225 is low yield steel, which has excellent dissipation energy capability. Based on this steel study, when cyclic loading has a low ultimate stretch value, this is due to the cumulative damage to the material by cycle loads [9]. S355 steel commonly used as a pipeline, ship hull, and earthquake-resistant steel framing [10]. The non-linear parameters combined isotropic and kinematic hardening material (NLCHM) LY225 and S355, as shown in Table 1. In ensuring the efficient result comparing the use of materials with its capacity, FTSPD was designed into four models, namely, four vertical fins (V4), six vertical fins (V6), eight vertical fins (V8), and without fins. Each of which was loaded in major direction (0°) toward the X-axis and minor direction (45° for V4, 60° for V6) degrees toward to the X-axis. The presence of fins were expected to

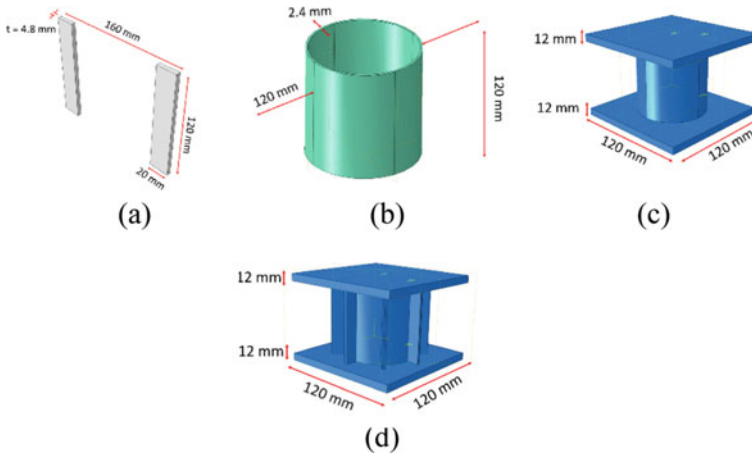


Fig. 1 Numerical device model: **a** Fins S355, **b** Tubular SPD LY225, **c** TSPD (120 × 120 × 2.4), **d** FTSPD (120 × 120 × 2.4)

act as vertical stiffeners so that it can resist buckling on FTSPD caused by seismic excitation.

2.2 Constraint and Loading Condition

The constraint was determined to adapt the models to real conditions. In this study, the reference point was added at the center of the top plate as a control point. The FTSPD models were restrained at the bottom part as fixed restraint, while the top base was freely or unrestrained. In the real case, FTSPD is implemented as the stopper of the bridge structure. The cyclic load, which had eighty one-steps, was added at the top center of FTSPD following the AISC testing methods for steel element members, as shown in (see Fig. 2) [11]. The cyclic loading occurred in X-direction. This study used finite element software called ABAQUS to investigate the energy dissipation, damping capacity, ductility, and strength of FTSPD.

Variations in the testing of tubular shear panel damper devices consist of six devices. The D/t variable is made the same for all devices to compare each device's behavior—the details, as shown in Table 2.

Table 1 NLCHM model parameter of LY225 and S355 [8, 9]

Metallic Material	No. Of backstress	σ_0 (MPa)	$C_{k,1}$ (MPa)	γ_1	$C_{k,2}$ (MPa)	γ_2	$C_{k,3}$ (MPa)	γ_3	$C_{k,4}$ (MPa)	γ_4
LY225	4	191	3041	126	1028	170	890	224	260	1
S355	3	386	5327	75	1725	16	1120	10	-	-

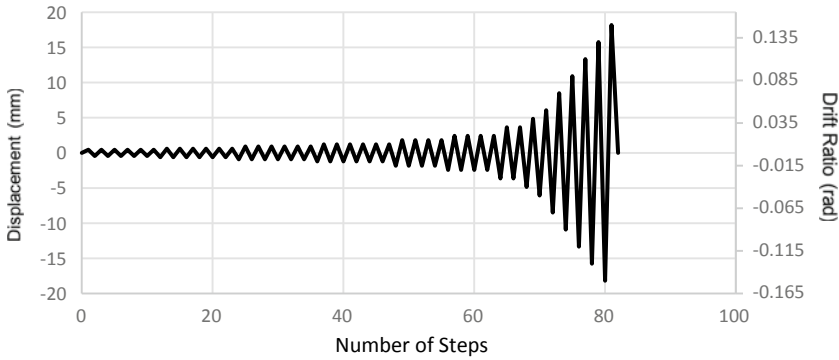


Fig. 2 Loading protocol

Table 2 Devices variations and load degrees

D (mm)	h (mm)	h/D	t (mm)	D/t	Fins	Load Degrees
120	120	1	2.4	50	–	0
120	120	1	2.4	50	4 V	0
120	120	1	2.4	50	4 V	45
120	120	1	2.4	50	6 V	0
120	120	1	2.4	50	6 V	60
120	120	1	2.4	50	8 V	0

2.3 The Structural Performance Investigation Method

Damping Capacity

This study analyzes the ability of the FTSPD model for four variables, namely energy dissipation, damping capacity, ductility, and strength. Damping capacity is the ability of the device to reduce vibrations caused by seismic excitation. Damping capacity was calculated by Jacobsen’s approach, which is formulated into Eq. 1 [12].

$$\zeta = \frac{1}{2\pi} \frac{A_{hyst}}{A_0} \tag{1}$$

where A_{hyst} is the energy dissipation of a loading cycle expressed as the full area in the hysterical loading cycle. Whereas A_0 is the elastic energy displacement, which is the area of the maximum force to the maximum displacement. The results of equal damping of each cycle were plotted into the graph to determine the damping capacity of each model.

Ductility

Ductility is the ability of a material to deform before experiencing damage due to load. Materials that have high ductility will be able to maintain stable stiffness. Devices that have high ductility tend to be more stable in holding force during the loading process than those that have small ductility. Instead, brittle material strength will immediately decrease sharply after reaching peak strength [13]. Ductility is one of the parameters to determine the stability of the structure when it is loaded. In this case, the ductility was calculated based on Eq. 2 [14].

$$\mu = \frac{\Delta u}{\Delta y} \tag{2}$$

where Δu is the ultimate displacement when the force reaches the peak, while Δy is the yield displacement. The yield displacement was obtained by referring to FEMA 356 [15], which in theory states that yield conditions can be obtained as seen (see Fig. 3).

Strength

Strength becomes an essential element for the structure or device in holding force. The higher the power of a device, the greater the force that can hold and vice versa. In this study, the strength of the device obtained from the ultimate force (f_u), which read from the skeleton curve. The strength of the device is also related to stiffness and ductility. The strength and stiffness relationship is, the more rigid the device is, the higher the holding capacity of the force and vice versa. Besides getting the model ductility, the skeleton curve also shows the strength of each model, which is

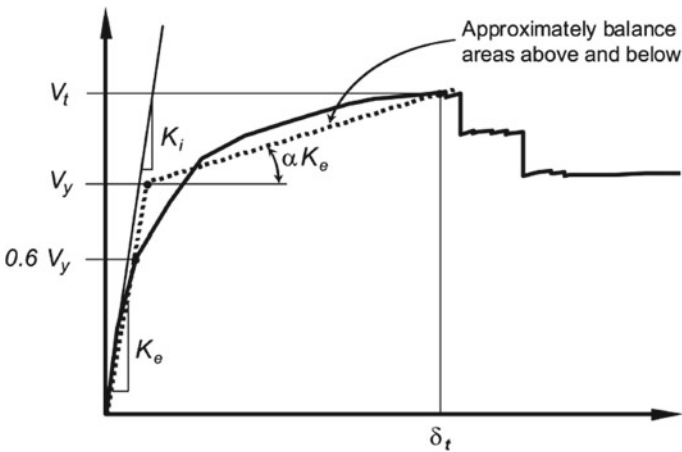


Fig. 3 Definition of yield displacement and ultimate displacement [15]

the value of the ultimate force (f_u). Strength capacity is the maximum capacity of the device to withstand the force imposed on the device.

Energy Dissipation Capacity

Dissipation energy was sought by calculating the area of the hysteresis graph of one loading cycle. The energy of each cycle was plotted into an energy hysteresis graph to determine the energy dissipation capacity of each model. In quantifying the energy dissipation of the devices, the energy dissipation coefficient is used by JGJ 101—2015 [16]. The energy dissipation coefficient can be calculated easily by Eq. 3.

$$E_p = \sum_{i=0}^n \frac{(F_{(i+1)} + F_i)}{2} x (\Delta_{(i+1)} - \Delta_i) \quad (3)$$

where F is the force that occurs while Δ is the displacement or strain that occurs, to find the area, a numerical approach is carried out by dividing the area into small plots, which are then added together. The result of the total area is the amount of dissipation energy in one cycle.

3 Result and Discussion

3.1 Device Behaviour

TSPD and FTSPD devices, which have four vertical fins, turned out to experience stiffness degradation. Stiffness degradation was caused by an inelastic buckling on the device when given a cyclic load as indicated by the stress contour at ultimate displacement, as shown in (see Fig. 5a–f). On the stress contour, it was seen that TSPD had a reasonably severe buckling at the end of loading. However, the addition of 4.8 mm thick vertical fins in TSPD was able to inhibit the inelastic buckling device. On the other hand, the figure (see Fig. 4a–f) shows the stress contour of each model when it reaches its yield point. When it reached yield, the stress that occurred on the device turns out to vary did not form a relationship. For example, in TSPD, the peak stress reached 276.3 MPa, while in FTSPD V8, it reached 382 MPa. However, the stress during yield had increased in models V4 and V6 517.5 MPa and 466.5 MPa, respectively. Among the four models, V4 had the highest stress when the yield achieved.

The dissipation energy of each model increases with the addition of cycle loads on the model. However, in the 30th cycle, TSPD decreased dissipation energy compared to FTSPD types. This is as shown in (see Fig. 6) based on the hysteresis energy graph, TSPD only reached the energy dissipation of 2641.95 Nm significantly different from the FTSPD model which had the lowest dissipation energy value, namely V4 minor axis direction (45°) which obtained dissipation energy of 5031.81 Nm. While the

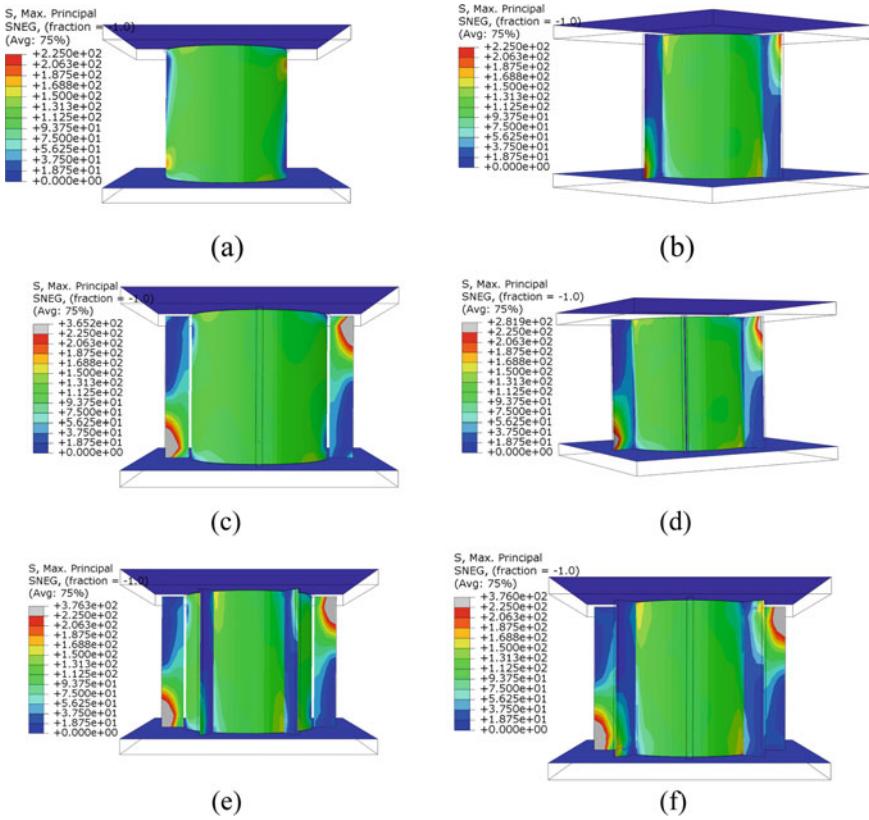


Fig. 4 Stress Contour: **a** TSPD yield displacement, **b** FTSPD V4 minor yield displacement, **c** FTSPD V4 major yield displacement, **d** FTSPD V6 minor yield displacement, **e** FTSPD V6 major yield displacement, **f** FTSPD V8 yield displacement

largest energy dissipation was achieved by FTSPD V8, which was 7889.72 Nm followed by FTSPD V6 major at 6932.55 Nm, FTSPD V6 minor at 6332.44 Nm, FTSPD V4 major at 5362.77 Nm, FTSPD V4 minor at 5031.81 Nm and TSPD V6 minor at 6332.44 Nm, FTSPD V4 major at 5362.77 Nm, FTSPD V4 minor at 5031.81 Nm and TSPD at 2641.95 Nm. Thus the addition of fins to TSPD can increase the dissipation energy capacity of the device.

Based on the skeleton curve (see Fig. 7), it was found that TSPD without vertical fins had the lowest yield displacement point compared to FTSPD devices. This means that when loaded with the same load, models without vertical fins subjected to yielding more quickly than those given vertical fins. So that, TSPD easier to be plastic than FTSPD. The more fins added to the device had a higher-yield displacement. Ultimate displacement obtained from displacement during the ultimate force. Based on Eq. 2, the displacement ductility value of each model obtained from the ultimate displacement divided by yield displacement. From the calculation results obtained,

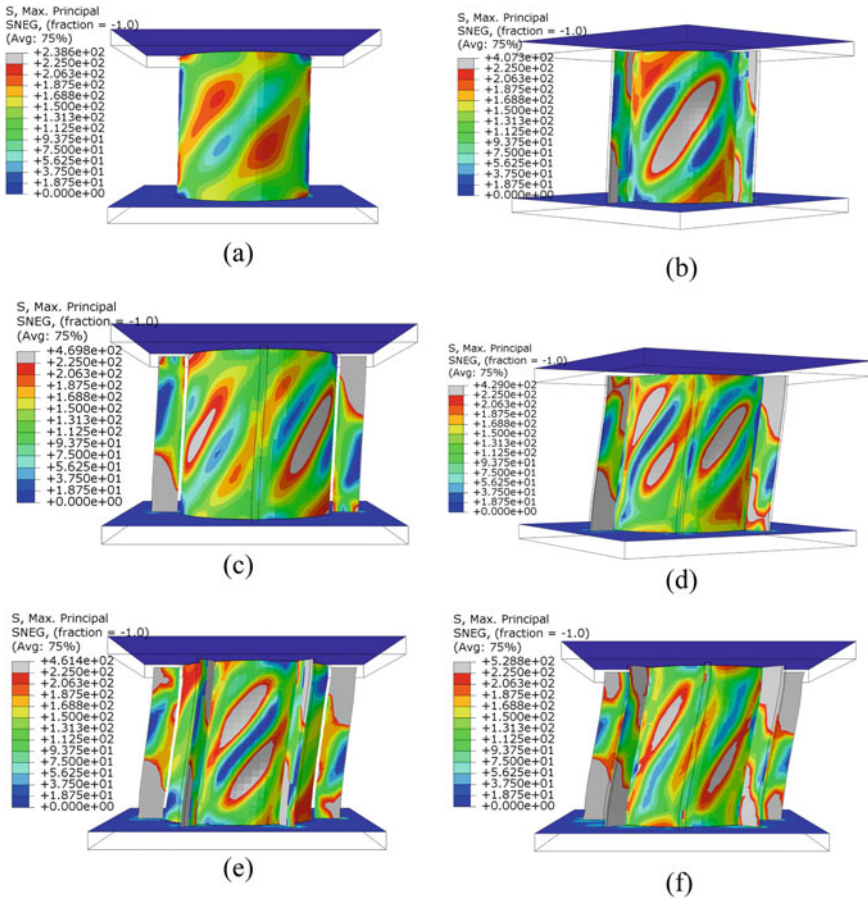


Fig. 5 Stress Contour: **a** TSPD ultimate displacement, **b** FTSPD V4 minor ultimate displacement, **c** FTSPD V4 major ultimate displacement, **d** FTSPD V6 minor ultimate displacement, **e** FTSPD V6 major ultimate displacement, **f** FTSPD V8 ultimate displacement

ductility values for each model. Ductility achieved by FTSPD is quite significant compared to TSPD. TSPD only achieved ductility of 5.11, while the average FTSPD was able to reach 19.66. The pattern shows that the addition of vertical fins also affects the increase in the value of ductility in the model. Ductility was the ability of the device to withstand stability due to loading. The skeleton curve (see Fig. 9) shows that TSPD was only able to be stable up to a force of 69.08 kN while the stability of the FTSPD device can be maintained, even on the V8 model able to maintain ductility until the end of loading.

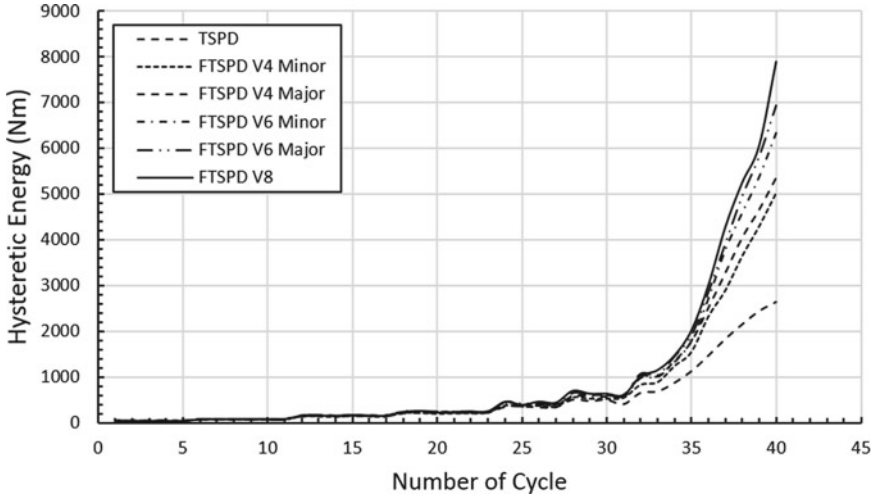


Fig. 6 Hysteritic energy curve

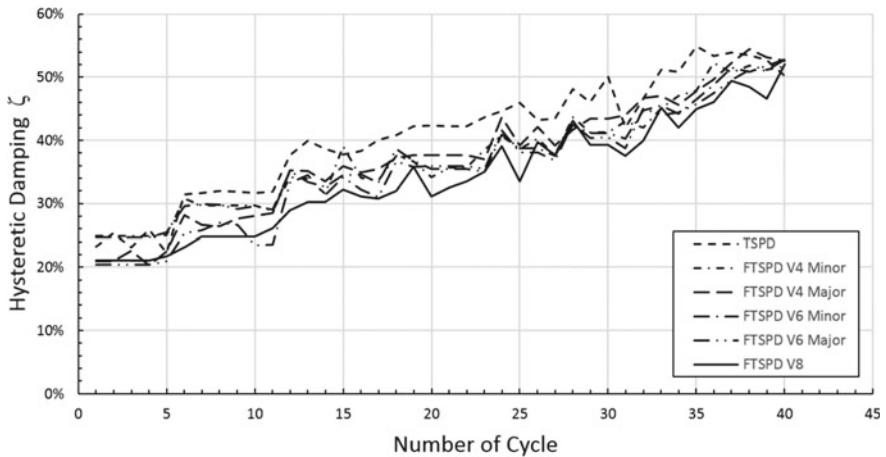


Fig. 7 Hysteritic damping curve

3.2 Seismic Device Performance

Damper device performance in holding damping can be known from equal damping. On the equal damping graph (see Fig. 7), TSPD can attain attenuation of 55%. This shows that TSPD was quite capable of being a damper device on the bridge structure. However, TSPD has low strength and ductility compared to FTSPD. The damping capability of FTSPD was still lower compared to TSPD. In comparison, FTSPD V8, which had the highest strength and stability, was only able to reduce by 52%. But all

specimen achieve almost equal value where in the range of 52–55%. However, the seismic performance of a device was not only determined by the damping capacity, but also by the energy dissipation, ductility, and strength of the device.

Hysteretic curve results show that the use of vertical fins (S355) was able to increase strength and dissipation energy in TSPD as shown in (see Fig. 8a–f). This was because vertical fins can reinforce TSPD devices when horizontal force occurred. As shown by the increasing number of vertical fins added to TSPD with the same loading, the device’s energy dissipation increases. However, under minor axis load, there was

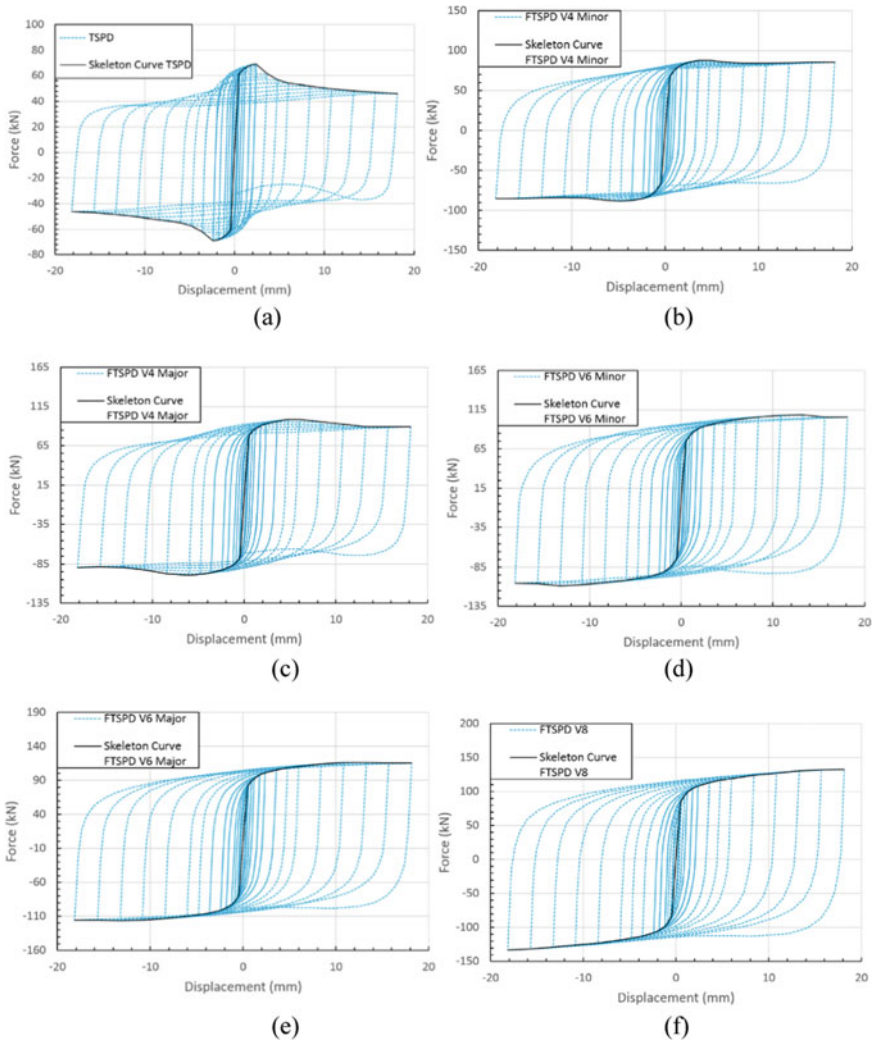


Fig. 8 Hysterical loops and skeleton curve of numerical model: **a** TSPD, **b** FTSPD V4 minor, **c** FTSPD V4 major, **d** FTSPD V6 minor, **e** FTSPD V6 major, **f** FTSPD (V8)

a decrease in dissipation energy, as shown in Table 3. The table shows that for FTSPD V4, major devices have higher dissipation energy, which was 5362.77 Nm than the FTSPD V4 minor, which only reaches 5031.8 Nm. Neither with the FTSPD V6 major and minor. Among all the devices that had the highest energy dissipation was the V8 for 7889.72 Nm. Besides, the V8 device did not occur buckling and strength degradation. FTSPD V8 has achieved energy dissipation of 198.7% compared with the TSPD.

Based on the skeleton curve shown in (see Fig. 9) shows that some modeling can reach the expected target, such as V8 and V6 major. Both devices can maintain strength and more stable than another modeling. In TSPD devices without vertical fins, strength degradation occurs after 2.4 mm displacement. Besides, the

Table 3 TSPD and FTSPD performances

Model	Yield displacement (mm)	Ductility	Strength (kN)	Damping Capacity (%)	Energy Dissipation (Nm)
TSPD	0.47	5.12	69.08	55	2641.94
FTSPD V4 Minor	0.54	8.89	87.83	52	5031.81
FTSPD V4 Major	0.52	11.55	98.73	55	5362.77
FTSPD V6 Minor	0.56	23.67	108.51	53	6332.44
FTSPD V6 Major	0.55	24.10	116.14	53	6932.55
FTSPD V8	0.60	30.23	132.95	52	7889.72

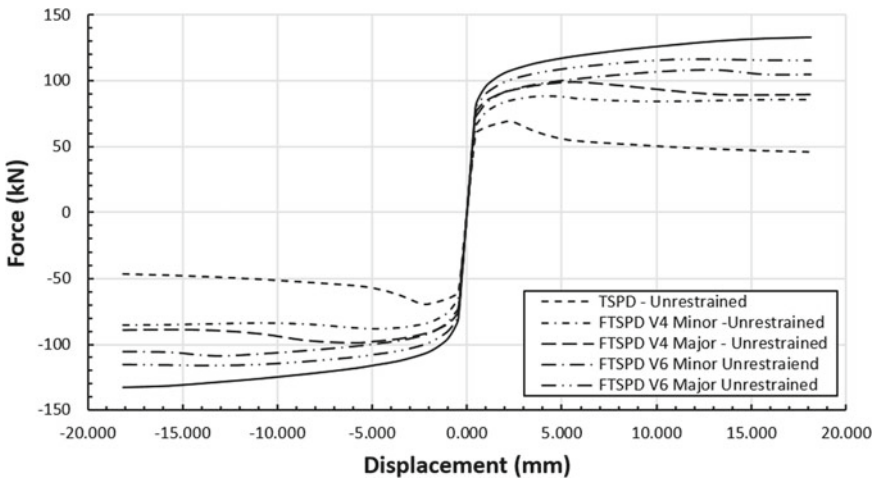


Fig. 9 Skeleton curve

strength achieved was also lower compared to devices that were added vertical fins. As a comparison, TSPD was only able to reach a strength of 69.08 kN significantly different from the FTSPD model, which had the lowest ultimate force (f_u), namely V4 minor axis direction (45°), which obtains f_u of 87.83 kN while the device that had the highest strength was the V8, which can reach 132.95 kN. However, when the FTSPD device was loaded with a minor axis, the strength of the FTSPD decreases. This decrease was not very influential approximately only 7–12% for FTSPD V6 and V8.

Although TSPD had a higher damping capacity than FTSPD, TSPD had significantly lower strengths than FTSPD. When TSPD gave a repetitive loading, TSPD was only able to maintain its stiffness up to 69.08 kN compared to FTSPD, especially V8, which can maintain stiffness up to 132,946 kN. The power possessed by FTSPD, in particular, the V8, was almost twice that of TSPD. While the damping capacity of the two is close to 55% and 52%, respectively. This result shows that to withstand an earthquake force of 130 kN requires two TSPD devices, whereas when using FTSPD, especially V8, requires only 1 FTSPD device. Of course, this can save costs incurred to produce and install dampers on the structure. A comparison of the results of each device, as shown in Table 3 below.

4 Conclusion and Recommendation

4.1 Conclusion

TSPD device with SPD fins addition called FTSPD performed well successfully. These proposed devices could achieve much higher energy dissipation and seismic performance compared to the TSPD. Based on the numerical analysis result, the proposed structure had the following behavior and performances:

1. FTSPD had a higher yield displacement than TSPD. FTSPD has a yield displacement of 0.52–0.60 mm, while TSPD has a yield displacement of only 0.47 mm. The appearance of the fins improved device yield displacement. So that TSPD was swifter to be yield than FTSPD.
2. FTSPD could achieve higher ductility than TSPD. FTSPD V8 achieved the largest FTSPD ductility with the ductility of 24.171. Whereas TSPD only had 10.094. The limit of ductility was determined by TSPD's deformation when buckling occurred. The fins contribute to improve the ductility of the device.
3. The additional fins could enhance the devices strength. FTSPD V8, FTSPD V6 major, FTSPD V6 minor, FTSPD V4 major, and FTSPD V4 minor model could achieve 92%, 68%, 57%, 43%, and 27%, respectively, compared with the TSPD.
4. In the term of equal damping achievement, all specimen achieves almost equal value where in the range of 52–55%.

5. FTSPD had much higher energy dissipation than TSPD. It was indicated by the higher value of the hysteretic energy curve of the FTSPD compared to TSPD. FTSPD can achieve energy dissipation of 198.7% compared with the TSPD.
6. FTSPD loading of the minor axis direction has lower performance approximately 7–12% than the loading of the major axis direction.
7. The capacity produced by FTSPD is almost twice higher than TSPD so that in resisting certain earthquake forces, the number of FTSPD installations will be less than twice that of TSPD. This will save costs, both production costs and installation costs.
8. The results of this study indicate that the addition of vertical fins to TSPD can significantly improve the seismic performance of the device. So that FTSPD could, achieve higher strength, ductility, energy dissipation capacity, and stiffness than TSPD.

4.2 Recommendation

Further research related to this study maybe can improve the performance of proposed finned tubular shear panel damper (FTSPD):

- i .In obtaining optimal results, experiments using FTSPD test objects need to be done.
- i .The implementation of the proposed FTSPD on bridge pier needs to be studied to verify its behavior and performance.
- ii .The strength and thickness relationships of the fins on the FTSPD need to do in order to determine the optimal thickness of the fins.

Acknowledgements The authors gratefully acknowledge to Department of Civil and Engineering, Universitas Gadjah Mada, PT. Wijaya Karya Beton, and Ministry of Research and Technology that had support and funded this research. The discussed seismic device has been registered in a patent.

References

1. Moehle JP, Eberhard MO (2000) Bridge engineering handbook : earthquake damage to bridges. Boca Raton: CRC Press
2. Setiawan AF, Takahashi Y (2018) A high seismic performance concept of integrated bridge pier with triple RC columns accompanied by friction damper plus gap. J Jpn Soc Civil Eng 131–147
3. Abebe DY, Kim JW, Gwak G, Choi JH (2019) Low-Cycled hysteresis characteristics of hollow circular steel damper subjected to inelastic behavior. Int J Steel Struct 157–167
4. Yeh CH, Lu LY, Chung LL, Huang CS (2004) Test of a full-scale steel frame with TADAS. Earthq Eng Eng Seismolog 1–16
5. Takahashi Y, Takemoto Y, Takeda T Takagi M (1973) Experimental study on thin steel shear walls and particular steel bracings under alternative horizontal load their stiffness is so rigid that structure designed by static analysis. Tech Rep Ohbayashi-Gumi Ltd, Tokyo

6. Dicleli M, Milani AS, Multi-directional hysteretic damper with geometrically hardening post-elastic stiffness for seismic protection bridges. Department of Engineering Sciences METU, Ankara.
7. Utomo J, Moestopo M, Surahman A, Kusumastuti D (2017) Applications of vertical steel pipe dampers for seismic response reduction of steel moment frames. EACEF
8. Utomo J, Antonious (2018) Improving resilience of moment frames using steel pipe dampers, ICRMCE
9. Shi G, Gao Y, Wang X, Zhang Y (2018) Mechanical properties and constitutive models of low yield point steels. *Constr Build Mater* 175:570–587
10. Narendra PV, Prasad K, Krishna EH, Kumar V (2019) Low-Cycle fatigue (LCF) behaviour and cyclic plasticity modeling of E250A mild steel. *Structures* 20:594–606
11. American Institute of Steel Construction (2005) ANSI/AISC 341–16 seismic provisions for structural steel buildings. AISC
12. Jacobsen LS (1930) Steady forced vibrations as influenced by damping. *Trans* 52(15):169–181
13. Pawirodikromo W (2012) *Seismologi Teknik, Rekaya Kegempaan*, Yogyakarta: Pustaka Pelajar
14. 2000 Edition NEHRP recommended provisions for seismic regulations for new buildings and other structures
15. United States, Agency FEM (2000) FEMA prestandard and commentary for the seismic rehabilitation of buildings. FEMA, Washington, DC
16. JGJ 101-2015 (2015) Specification for seismic test buildings. China Architecture & Building Press, Beijing

Investigation of Fast Connection (Clamped Pocket Mechanics) for Modular Instant Steel House with Finite Element Analysis: Back to Build Post-disaster



A. S. Fajar, A. Saputra, I. Satyarno, and L. Himawan

Abstract During the post-earthquake disaster in Lombok and Palu, tens of thousands of houses were collapsed, causing hundreds of thousands of people to become homeless. Currently, the instant steel house (RISBA) has been developed in order back to build in substituting the collapsed house. However, based on the real field application, the construction of RISBA takes time around 5 to 7 days of work time due to the on-site welding connection system of the structural joint. The welding system consumes a long time, but it also causes low construction quality due to limited human resources. This study proposes the fast connection system of RISBA with a clamped pocket mechanism (CPM) connection system. That connection system expected could accelerate the construction time of RISBA to be shorter (around one day) than the conventional one. In this preliminary study, the proposed connection system's numerical model was developed with the finite element method by using Abaqus software. As the focus study, we simplify a T-joint connection for the beam-column joint's steel pipe with cantilever beam idealization. In the numerical model, the CPM was installed in the middle of the T-joint to be tested with a pull-out test and lateral cyclic loading test under displacement control. The CPM pocket's appropriate development depth is examined by varying the steel pipe's embedment with 1.5, 2, 2.5, and 3 times of diameter. Based on the pull-out test simulation, the connection's tensile capacity is around 10% of the element member yield strength. The CPM pocket's appropriate development depth was 2.5 times of steel pipe diameter or larger than it. Furthermore, in a proper development depth of the pocket, the

A. S. Fajar (✉) · A. Saputra · I. Satyarno · L. Himawan
Department of Civil and Environmental Engineering, Universitas Gadjah Mada, Yogyakarta,
Indonesia

e-mail: angga.fajar.s@ugm.ac.id

A. Saputra

e-mail: ashar.saputra@ugm.ac.id

I. Satyarno

e-mail: imansatyarno@ugm.ac.id

L. Himawan

e-mail: lava_himawan@ugm.ac.id

proposed connection system stiffness could achieve fully-restrained (FR) criteria. Moreover, the inter-story drift angle capacity could exceed the special moment-resisting (SMF) criteria. However, in the case of insufficient development depth of the pocket (less than $2.5D$), lack of bending moment strength and pinching behavior of the hysteresis loop with small hysteretic energy occurred. Finally, this numerical simulation result of the proposed CPM type for RISBA could be the basis for the fast connection development visibility.

Keywords Instant steel house · Fast connection · Clamped pocket mechanism · Finite element analysis · Steel pipe Introduction

1 Introduction

Many houses collapsed and severely damaged, triggering thousands of victims under several big earthquakes that occurred in Indonesia in the last decade. Indonesia, located in the megathrust zone, has around 13 extended subduction zones in the Southeast and Northeastern regions of Indonesia with the potential for earthquakes from 7.8 to 9.2 Mw. Also, there are 251 active faults in almost all Indonesia regions, except Kalimantan, causing earthquakes from 6.0 to 8.1 Mw. The most recent earthquake was the Lombok earthquake (7.0 Mw), which occurred in August 2018, which killed up to 555 people and damaged 32,129 houses. Then, the Palu Earthquake (7.4 Mw) in September 2018 claimed 2045 lives and damaged 66,926 houses, and the most recent was the Halmahera Earthquake (7.2 Mw) in July 2019, which damaged 500 houses and claimed 14 lives. Majority of the houses collapsed were due to the lack of reinforcement and the structural element configuration were not up to the design common standard, as shown in Fig. 1. Furthermore, during the post-earthquake, thousands of families had to be homeless. Even though the government has conducted the build-back for reconstruction programs, some technical problems remain to inhibit



Fig. 1 The collapse of houses under; **a** Lombok Earthquake 2018 [6], and **b** Palu Earthquake 2018 [7]

these programs. One of them is developing fast constructed houses with high-seismic performance but not applicable in the field. Therefore, a construction technology that is practical and can be built fast with high-seismic performance in post-earthquakes needs to be developed.

The risk of disasters caused by the earthquake in Indonesia needs to be reduced by developing earthquake-resistant housing. Around 60% of the Indonesian population still lives in the non-engineered house category, which means that approximately 150 million people can become victims of houses damaged by the earthquake. If this happens, during the rehabilitation and reconstruction period, rapid construction methods are needed. Instant steel structure house (RISBA) [1] is an option of the type of reconstruction house that can be carried out quickly. So that earthquake victims can immediately inhabit the reconstruction houses. In the post-earthquake housing reconstruction of Lombok to date, RISBA house structure technology has been applied to around 2000 houses, as shown in Fig. 2. The application of RISBA in Lombok (Lombok Post-Earthquake 2018). Those show the existence of acceptance from the community with RISBA technology. Based on the RISBA development team's observation, the average duration of the construction process of the main structure of RISBA is around three days. Based on field observations in North Lombok Regency, there is a high demand for housing reconstruction, but the number of workers is limited. Be-sides, the connection system between structural elements in the form of welding is quite difficult for some craftsmen to do, for example, as shown in Fig. 3. The existing design and construction methods of RISBA need to be optimized to fasten the construction demand of RISBA.

Several predecessor studies about modular steel construction (MSC) have been conducted. Deng (2018) once examined the connection of bolts with the addition of a welded cover plate that is categorized as a semi-rigid steel connection system [2]. Then, Chen (2017) also proposed another type of modular steel connection system, but the formation of the gaps in the joint resulting early stiff-ness and strength degradation when tested under a monotonic load [3, 4]. Dai (2019) also developed a connection with the self-lock plug-in system and gave good ductility and energy



Fig. 2 The application of RISBA in Lombok (Lombok Post-Earthquake 2018)

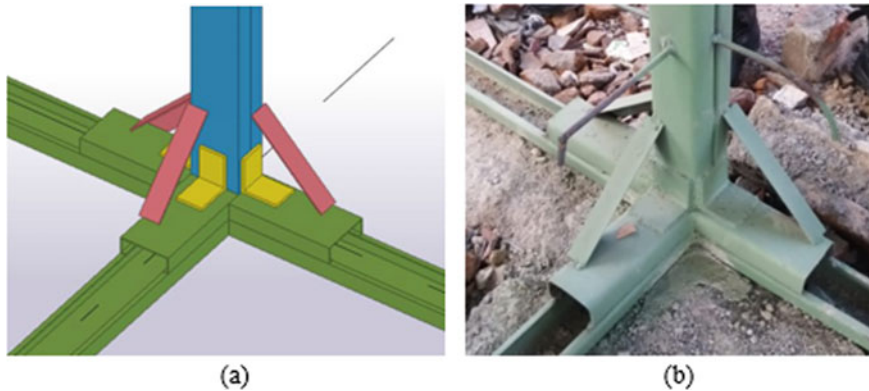


Fig. 3 The existing connection system of RISBA structural element member

dissipation results [5]. However, the modular steel construction connection system discussed above might be very complex to re-construct simple post-disaster housing in rural areas where there is a limited number of human construction resources. Therefore, a simpler connection system of the instant modular house needs to be developed.

In this preliminary study, a numerical model of clamped pocket mechanics (CPM) connection system is proposed to improve the RISBA construction process faster. The CPM is designed to connect the beam and column with the steel pipe section. It contains a steel pipe pocket with a fastener bolt, as illustrated in Fig. 5. The steel pipe section with black/white steel following the BS 1387 standard was adopted as the beam and column element member, which are affordable to be supplied. Using the connection system, assembling RISBA structural elements in the field is expected to be faster, more accessible, more practical, and less require of human resources. Indeed, the designed strength, stable stiffness, sufficient energy dissipation, and ductility under earthquake load should be fulfilled with codes and standards. Therefore, several stages of analysis and testing need to be conducted. This paper focuses on the numerical model in the CPM connection system's visibility study and preparing the experimental test. Finite element analysis to be conducted to examine the CPM connection performance and behavior, i.e., pull out capacity and bending strength under cyclic loading. The finite element model of CPM was developed in three-dimensional with the implementation continuum shell element for the steel pipe and solid element for the bolt in Abaqus software. Metal plasticity with combined isotropic and kinematic hardening was adopted to simulate the non-linear material of steel. The force deformation relation of the CPM under pull-out tests and cyclic bending tests to be examined. Finally, the finite element analysis expected could examine the visibility CPM connection system and experimental study preparation.

2 Structural Performance Requirement

In the seismic performance criteria, the structure should fulfill the recognized code. The structure should achieve sufficient strength under seismic demand with adequate ductility and hysteretic energy. In this numerical study, the proposed connection of the CPM system to be examined based on the AISC 341-16 [8], FEMA-273 [9], and FEMA-350 [10] provisions.

2.1 Strength, Stiffness, and Rotation Capacity

In the strength criteria of the connection system of steel structure, the connection system should have sufficient strength achievement (minimum 80% of nominal bending moment strength) under plastic deformation with limit 0.04–0.02 rad of rotation for the special moment-resisting frame (SMF) and inter-mediate moment-resisting frame (IMF), respectively [8, 10]. Furthermore, the beam-column connection stiffness should reach 85% of fully rigid connection or more to be classified as a rigid connection [11]. Moreover, the more strict stiff-ness requirement of FEMA-273 [9] that the rotation contribution of the connections system should be less than 5% of the total rotation. Those mean that the beam and connection system should be stiffer than 95% of beam end stiffness it-self.

Several predecessor studies [12–14] simplified the backbone of moment-rotation or force–displacement relation of a steel connection system with the bilinear model following FEMA-356 [15]. In this study, the regularized skeleton curve is also determined based on the FEMA-356 provision, as illustrated in Fig. 4. However, the regularizing of the hysteretic curve backbone was conducted just until the ultimate strength. Because this study only focused on the peak strength and ultimate deformation capacity achievement. The regularizing of the backbone curve benchmark point, is to be expressed as the Eqs. 1–9. In the definition, $M_{y,FEM}$, $M_{n,FEM}$, $V_{y,FEM}$, $V_{n,FEM}$ are the yielding moment, moment nominal, yielding lateral force, and nominal

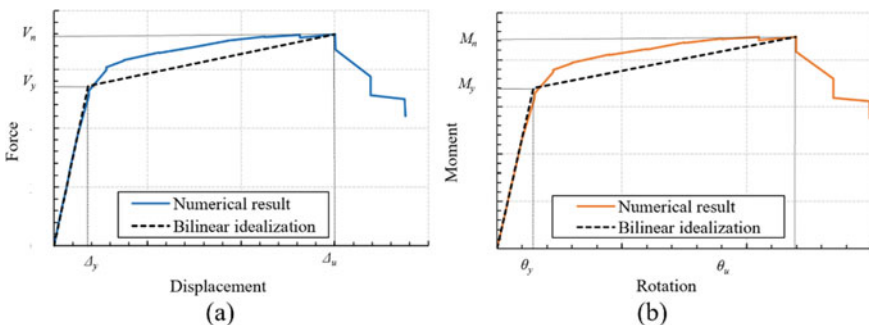


Fig. 4 Strength and ductility idealization

lateral strength based on the FEM results, respectively. Then, $\Delta_{y,FEM}$, $\Delta_{u,FEM}$, $\theta_{y,FEM}$, $\theta_{u,FEM}$, and θ_{sda} are the yielding displacement, ultimate displacement, yielding rotation, ultimate rotation, and rotation inter-story drift angle based on the FEM results, respectively. $\Delta_{y-1,FEM}$, $\Delta_{y+1,FEM}$ and $V_{y-1,FEM}$, $V_{y+1,FEM}$ are the one step of displacement point below and above the yielding displacement and lateral force point below and above the yield strength of the numerical analysis skeleton curve, respectively. Furthermore, $M_{y,anl}$, $M_{n,anl}$, Z_e , Z_p , and f_y are the yielding moment, moment nominal, elastic modulus of a section, plastic modulus of a section, and yield strength of material based on the analytical results, respectively. Moreover, L_m , L , and H are the moment arm length, the total length of the numerical beam specimen, and the pocket connection depth, which monitored from FEM results, respectively.

$$M_{n,FEM} = V_{n,FEM} \cdot L_m \quad (1)$$

$$L_m = L - H \quad (2)$$

$$M_{y,FEM} = M_{n,FEM} \cdot \frac{M_{y,anl}}{M_{n,anl}} \quad (3)$$

$$M_{y,anl} = Z_e \cdot f_y \quad (4)$$

$$M_{n,anl} = Z_p \cdot f_y \quad (5)$$

$$\theta_{y,FEM} = \frac{\Delta_{y,FEM}}{L_{me}} \quad (6)$$

$$\theta_{u,FEM} = \theta_{y,FEM} + \frac{\Delta_{u,FEM} - \Delta_{y,FEM}}{L_m} \quad (7)$$

$$\Delta_{y,FEM} = \Delta_{y-1,FEM} + (\Delta_{y+1,FEM} - \Delta_{y-1,FEM}) \cdot \frac{V_{y,FEM} - V_{y-1,FEM}}{V_{y+1,FEM} - V_{y-1,FEM}} \quad (8)$$

$$V_{y,FEM} = V_{n,FEM} \cdot \frac{M_{y,anl}}{M_{n,anl}} \quad (9)$$

$$\mu_\theta = \frac{\theta_{y,FEM}}{\theta_{u,FEM}}; \mu_\Delta = \frac{\Delta_{y,FEM}}{\Delta_{u,FEM}} \quad (10)$$

$$\theta_{sda} = \theta_{u,FEM} + 0.01 \quad (11)$$

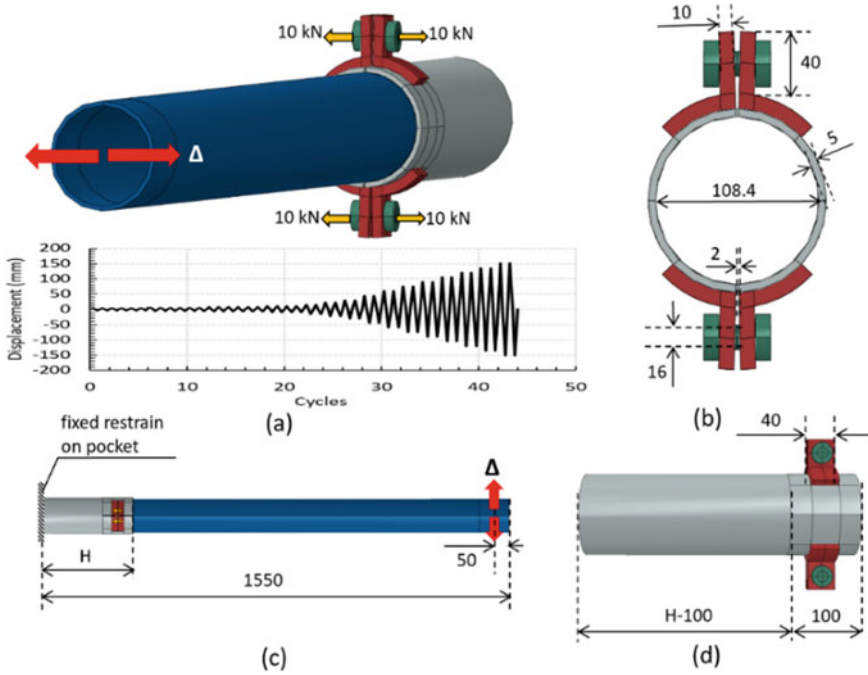


Fig. 5 The numerical model of CPM with FEM; **a** cyclic loading set up, **b** CPM cross-section, **c** longitudinal configuration of CPM, and **d** detail of CPM connection pocket

2.2 Ductility and Hysteretic Energy

The structural element members' connection system should produce sufficient ductility to realize stable resisting force under inelastic deformation during earthquake occurrence. The ductility is the indicator of the inelastic deformation capacity of the structural element member that denotes as Eq. (10). Some predecessors study [13, 16–18] have examined the steel connections system with ductility criteria to observe the seismic performance. Hysteretic energy achievement is also an essential aspect of the role of absorbing seismic energy during an earthquake. In the study of the references [13, 16–18], the effect of the hysteresis loop shape effect due to pinching, stiffness decrement, and strength degradation could be quantified with the hysteretic energy.

3 Numerical Analysis

3.1 Structural and Material Parameters

In the numerical analysis of both the pull-out test and lateral cyclic loading test, the CPM connection system to be tested with a 1500 mm span of cantilever beam set up (half size of the RISBA beam span length). The fixed restraint to be placed on the butt surface of the pocket, as illustrated in Fig. 5. Then, the connected beam cross-section has 100 mm of internal diameter and 4.2 mm of thickness. The BS 1387 steel pipe material [19] has 195 MPa of minimum yield strength and 320 MPa of minimum ultimate strength to be adopted for material affordability.

3.2 CPM Parameters

The critical state of the CPM connection system contains the resisting tension force and bending moment resistance. The appropriate geometric configuration should be tested to achieve structural strength and stiffness criterion. The pocket has 108.4 mm of internal diameter, 5 mm of thickness, and the dept to be variable, which is shown in Table 1. The 16 mm diameter of two-bolts (A325) to be installed on the pocket fastener holder, as illustrated in Fig. 5.

In the axial tension loading, the connection system's friction force action was triggered by the two-bolt clamping force that suppresses the pocked fastener holder. Then, the pocket tightens the steel pipe beam resulting in friction force resistance. Based on the references [20–22], the friction coefficient of each steel surface that is coated with the epoxy zinc-rich material is assumed to be 0.3. Furthermore, bolt pretension load to be assigned to the pocked fastener holder with a magnitude of 10 KN force, as shown in Fig. 5 and Table 1.

Table 1 Variable of the CPM parameters

Numerical specimen name	CPM depth (H, mm)	Friction coefficient (f)	Bolt pretension load (kN)
H150	150.0	0.3	10.0
H200	200.0	0.3	10.0
H250	250.0	0.3	10.0
H300	300.0	0.3	10.0
NS	–	–	–

3.3 Loading Set up

In the pull-out test, 50 mm of longitudinal displacement load to be subjected to the free tip of steel pipe beam in parallel direction of the beam length. The non-linear static analysis with displacement load control was implemented. Then, the reaction force to be measured to monitor the resistance force of the friction force. The relation of the friction force resistance and slip deformation to be plotted in a graph.

Also, in the lateral cyclic loading test, the non-linear static displacement load control to be implemented on the free tip of the steel pipe beam. The cyclic loading protocol is given 44 cycles until 10% of structural drift following the AISC 341-16 provision, as shown in Fig. 5a). Then, the force and deformation curve to be plotted to show the hysteresis loops. Furthermore, every cycle's hysteretic energy is calculated to measure each CPM connection's energy dissipation achievement with different development depths of pocket. Moreover, the stress contour and the plastic hinge formation during cyclic loading to be captured.

where E is elastic modulus; σ^0 is yield stress at zero plastic strain; $Ck_{,1}$ and $Ck_{,2}$ are kinematic hardening modulus; γ_1 and γ_2 are the rates of the kinematic hardening modulus decrease with increasing plastic deformation. The Poisson's ratio (ν) of the steel pipe and clamped pocket of both with BS 1387 material and Elastic materials are 0.3.

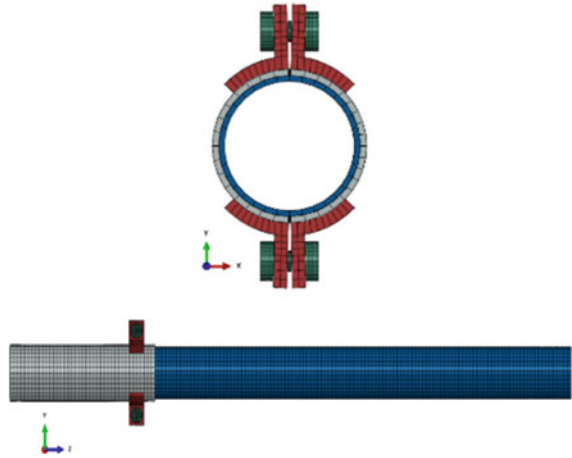
3.4 Numerical Model Parameters

The CPM's numerical model to be developed with 3D FEM analysis by implementing a continuum element for the pocket, steel pipe beam, and pocket fastener holder. The non-linear metal plasticity material to be adopted to those parts with combined isotropic and kinematic hardening following the Chaboche plasticity concept [23]. Due to limited data, BS 1387 metal plasticity's parameter in-put following the study from Narendra et al. [23], who reviewed the several kinds of specification mild steel hardening parameters. Hence the input parameter of the metal plasticity parameters in this study is shown in Table 2. Then, the bolt part of being idealized as an elastic solid hexahedral element. The discretization of the CPM meshing in the numerical model to be illustrated in Fig. 6. Moreover, the interaction between both pocket to steel pipe beam and bolt to pocket fastener holder to be idealized as hard contact

Table 2 Steel material parameters in the finite element model

Metallic Material	Elastic Modulus (MPa)	No. of backstress	σ^0 (MPa)	$Ck_{,1}$ (MPa)	γ_1	$Ck_{,2}$ (MPa)	γ_2
BS 1387	207,000	2	158	2500	50	210	8
Elastic	200,000	–	–	–	–	–	–

Fig. 6 Mesh discretization of the CPM system numerical model.



with friction. The last, the interaction between the pocket to pocket fastener holder, is idealized as tie constraints to as-sume the welding connection.

4 Results and Discussion

Based on the numerical simulation of the clamped pocket mechanism connection with the pocket's varied development depth parameter using finite element analysis, the results could be explained.

4.1 Pull-Out Test Simulation

Based on the numerical analysis of the pull-out test, all numerical specimens have slightly different friction-tension resistance, the ultimate resistance force between 33 and 44 KN, as shown in Fig. 7. Compared to the steel pipe member's yield strength under tension load (347 KN), the pulled strength of the CPM connection system could achieve about 10% yield strength. The more extended pocket depth resulted in stronger friction-tension strength. The reason might be that the longer pocket achieves a larger area on grip pressure influence under bolt pretension load. This argument could be supported by the stress contour distributions that are shown in Fig. 8. Typically, in sticky conditions, elastic behavior occurred until the peak friction-tension strength. Then, under slip conditions, it decreased gradually, almost linear relation with the slip displacement. The strength decrement might be triggered by the reduction friction-contact area during slip.

Fig. 7 Force and deformation curve of pull-out test simulation

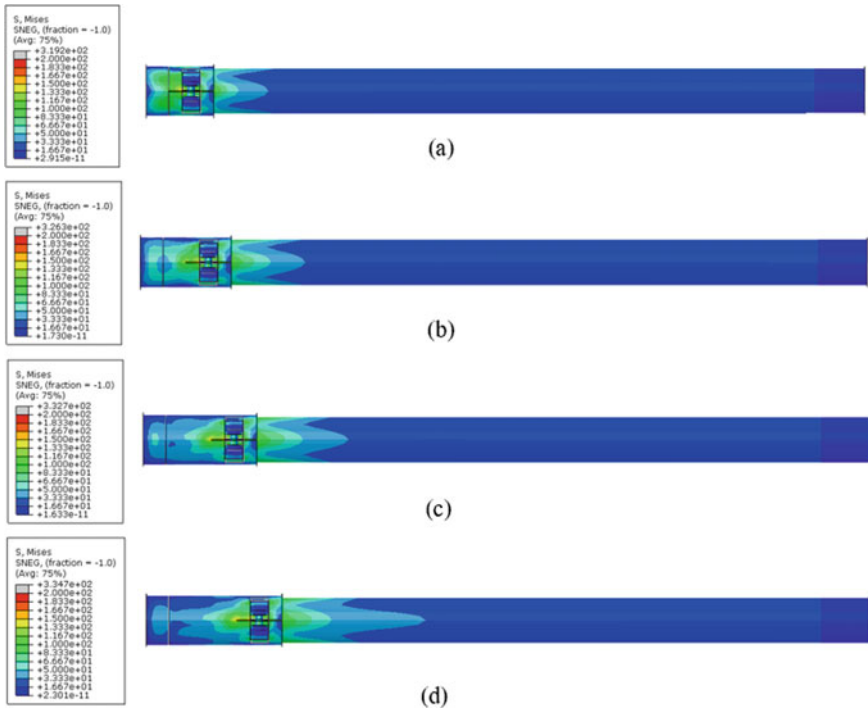
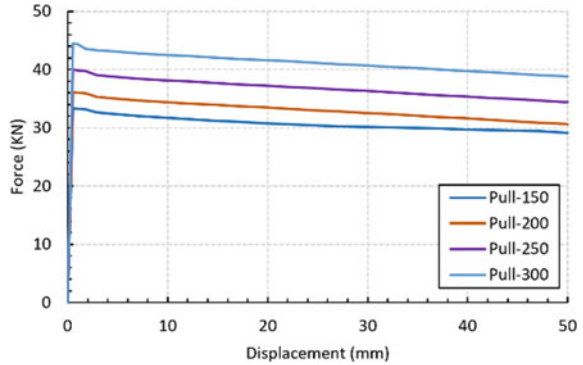


Fig. 8 Stress distribution of the CPM system under pull-out test simulation

4.2 Lateral Cyclic Loading Test Simulation

Based on the hysteresis loop monitoring under cyclic loading test simulation, the numerical specimens' lateral strength capacity ranges from 6.00 to 7.50 kN. Then, the deeper development depth of the pocket resulting in the larger lateral strength, as shown in Fig. 9. The numerical specimen H300, H250 and, H200 occurred plastic

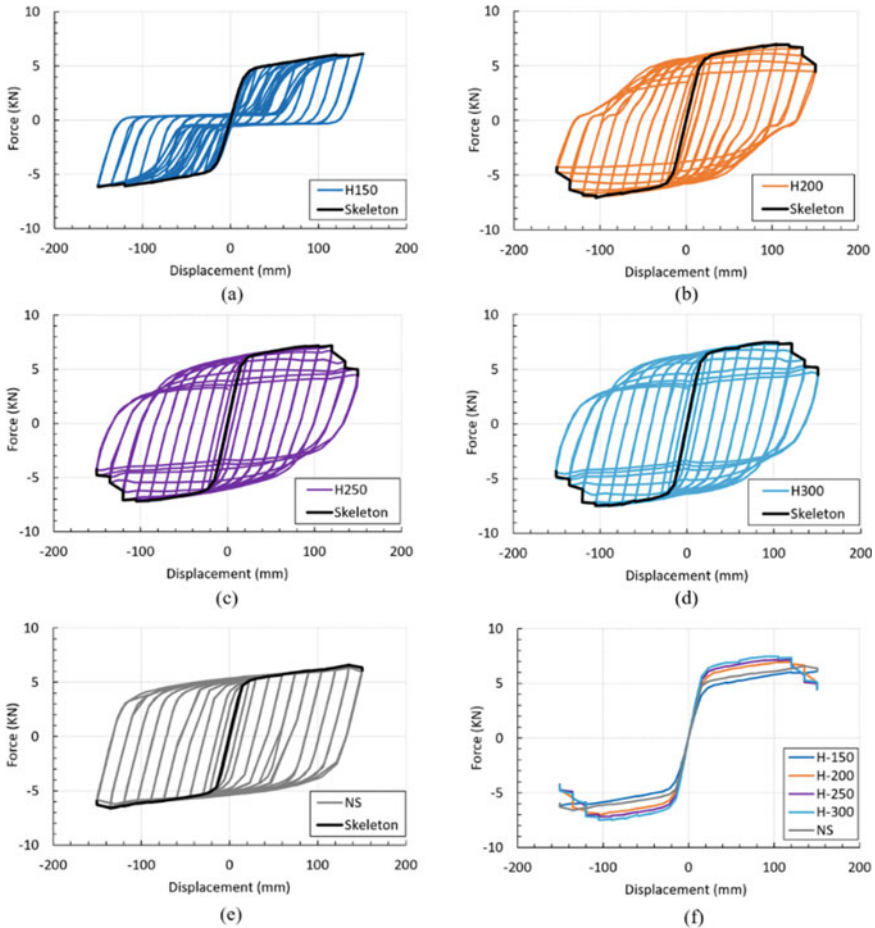


Fig. 9 Force and deformation curve; **a** hysteresis loop of H-400, **b** hysteresis loop of H300, **c** hysteresis loop of H200, **d** hysteresis loop of H150, **e** hysteresis loop of NS and **f** skeleton curve comparison

hinge on pipe located outer part of its pocket entirely, resulting in the shorter moment arm (the distance of the lateral load to the plastic hinge) under plastic deformation, as shown in Table 3 and Fig. 10. However, the H150 numerical specimen plastic hinge formation is located in the pocket grip accompanied by plastic behavior of pocket. The reason might be the pocket insufficient capacity to confine the pipe rotation. Indeed, the NS numerical specimen occurred plastic hinge in the base tip of the cantilever.

However, the pocket’s deeper development depth has consequences resulting in the earlier strength degradation (lower ductility), as shown in Fig. 9. The strength degradation related to ultimate displacement achievement decreased with the increasing of the pocket development depth, as shown in Table 4. That occurred

Table 3 Comparison of FEM and analytical result

Specimens	M_y (KMm)			M_x (KMm)			θ_y (rad)			arm (mm)	
	FEM	Analytic	RD	FEM	Analytic	RD	FEM	Analytic	RD	H	L_m
H150	6.23	7.07	-11.85%	8.25	9.35	-11.85%	0.012	0.009	-28.19%	150	1350
H200	6.84	7.07	-3.21%	9.05	9.35	-3.21%	0.012	0.008	-32.42%	200	1300
H250	6.79	7.07	-3.97%	8.98	9.35	-3.97%	0.012	0.008	-32.81%	250	1250
H300	6.78	7.07	-4.10%	8.97	9.35	-4.10%	0.012	0.008	-36.31%	300	1200
NS	7.46	7.07	5.54%	9.87	9.35	5.54%	0.012	0.009	-2.21%	0	1500

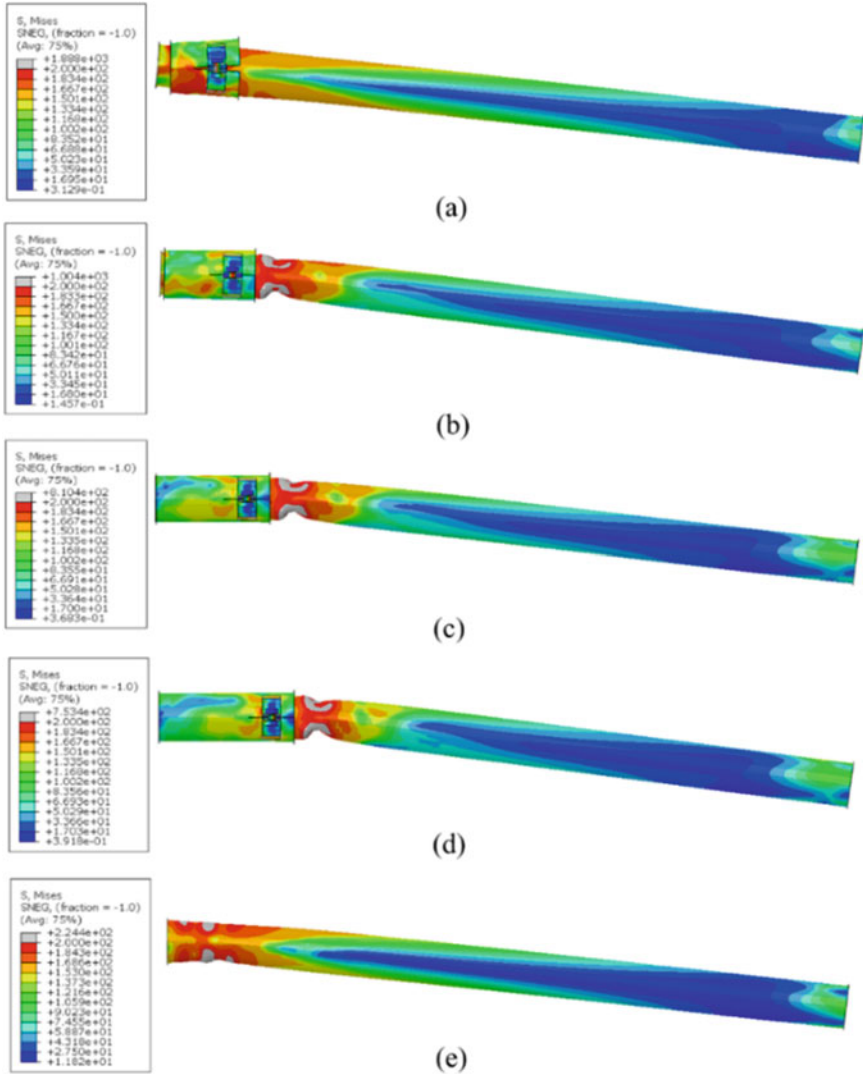


Fig. 10 Misses stress and plastic hinge formation of CPM numerical model of; **a** H150, **b** H200, **c** H250, **d** H300, **e** NS

due to the shorter moment arm under plastic deformation forming more extreme plastic hinge rotation formation on steel pipe, as shown in Fig. 10. Even though H300 enreached the less ductility, it remains achieved sufficient ductility (around 6). While the H150 could achieve the largest ductility (around 9), the plastic hinge rotation remains below a fully plastic rotation limit. The plastic rotation of steel pipe members in H150 is accompanied by plastic behavior of pocket due to insufficient confinement grip to the steel pipe member.

Table 4 Stiffness and ductility of the numerical specimens

Specimens	Elastic stiffness		$K_{in} K_{el}$	Rotation (rad)			Displacement (mm)			Pinching occurrence	Category	$\Sigma E(KJ)$		
	K_{el}	$K_{el}/K_{el,NS}$		Category	θ_y	θ_u	μ_θ	θ_{sda}	Δ_y				Δ_u	μ_Δ
H150	381.74	0.84	PR	0.029	0.012	0.111	9.38	0.121	16.00	150.48	9.41	0.017	OMF	8.58
H200	441.72	0.79	PR	0.043	0.012	0.081	6.66	0.091	15.77	105.09	6.67	0.058	SMF	24.73
H250	490.18	1.08	PR	0.034	0.012	0.096	8.18	0.106	14.66	120.12	8.19	None	SMF	26.33
H300	524.46	1.16	PR	0.046	0.012	0.075	6.30	0.085	14.25	89.93	6.31	None	SMF	28.03
NS	453.73	1.00	PR	0.029	0.010	0.09	9.31	0.100	14.50	135.36	9.33	None	SMF	26.47

In converted moment and rotation ($M-\theta$) of numerical specimen hinge following the Eqs. (1–9), all proposed CPM connection system slightly achieved less moment capacity compared to the analytical plastic moment strength; the details are shown in.

Table 3. Except, the H150 numerical specimen achieved significantly smaller moment strength compared to the analytical result. However, the NS numerical specimen slightly enriched larger moment capacity than the analytical plastic moment strength. Furthermore, the yielding rotation of all proposed CPM connections larger (in the range 30%) than the analytical result. The reason might be the CPM stiffness contributed to add the rotation. Even though the pocket connection exceeded rotation up to 30%, it will be discussed in next paragraph in terms of lateral stiffness.

On the other hand, the shorter development depth of the pocket resulted in more pinching hysteresis loops on the reloading stage, as shown in Fig. 9. The H150 numerical specimen behaves significant pinching on reloading since inelastic deformation occurred. Then, the H200 numerical specimen behaved pinching on reloading since it reaches at 0.058 radians of inter-story drift angle [based on Eq. (11)]. In contrast, the H250 and H300 numerical specimens could achieve firm reloading stiffness directly after unloading in all loading cycles. The pinching effect in the reloading stage of H150 and H200 numerical specimens might be triggered by insufficient bearing capacity (plastic deformation exceeded) of the pocket under the rotation of steel pipe beam pressure.

RD is the relative difference between FEM analysis results and the analytical results.

The deeper development depth of pocket resulted in the larger hysteretic energy achievement, as shown in Fig. 11 and Table 4. Under early to middle plastic deformation, the H300 and H250 numerical specimens could achieve more significant hysteretic energy increment than the other numerical specimens. The larger lateral strength takes the main role of the larger hysteretic energy achievement. However, the H200 and H150 numerical specimens achieved a smaller energy dissipation achievement than the NS numerical specimen. The pinching hysteretic loop of the H200

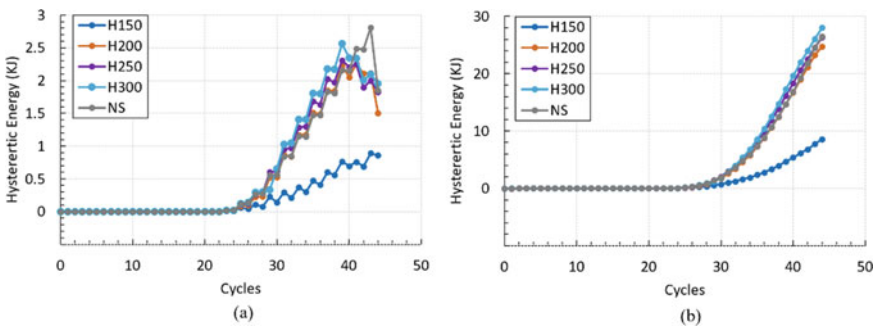


Fig. 11 Hysteretic energy achievement; a in a cycle and b cumulative

and H150 numerical specimen was the main reason for the small energy dissipation achievement. The increment of hysteretic energy achievement of all numerical models decreased beyond the displacement ductility. It was triggered by the strength degradation, as mentioned previously.

4.3 The CPM Connection Performance

In terms of the connection rigidity based on the FEMA-273, all numerical specimens are categorized as fully restrained (FR) moment connection, except the H150, as shown in Table 4. The H150 elastic stiffness achieved only 84% of NS numerical specimen. As a result, the H150 to be categorized as a partially restrained (PR) moment connection. Moreover, all numerical specimens' post-yield stiffness was positive,

In the case of moment-resisting structural system criteria, all specimens could achieve stable inelastic bending moment strength under an inter-story drift angle larger than 0.04 radians, as the requirement of the AISC 341-16 and FEMA-350. However, even though the H150 also achieved the mentioned requirement inelastic rotation capacity, the pinching hysteresis loop occurred on early inelastic deformation. As a result, the writer concluded that the H300, H250, and H200 numerical specimens to be classified as the special resisting-moment frame (SMF). Then, the H150 to be categorized as the ordinary moment-resisting frame (OMF). From this preliminary study with FEM analysis, the author suggests using the pocket dept ratio 2.5 to fulfill the code requirement and sufficient energy dissipation achievement in the CPM connection system design.

5 Conclusion

The numerical modeling of the proposed clamped pocket mechanism (CPM) connection system for steel pipe element members of modular steel houses (RISBA) has been conducted with finite element analysis. It can be concluded that the proposed connection system capable of resisting sufficient friction-tension load. Furthermore, the sufficient development depth (2.5 times of diameter or more) of the pocket could achieve fully-restrained (FR) based on the FEMA-273 and special moment-resisting (SMF) criteria, according to AISC 341-16 and FEMA-350 standard code. Finally, the numerical analysis of the proposed CPM connection system could be the basic study for the development of a fast construction RISBA house.

6 Recommendation

For future work, the CPM connection system's numerical model needs to be improved with the T-joint model, which is composed of beam and columns. Also, in the next step of research, the experimental program of the CPM connection system in the T-joint specimen should be conducted to verify the CPM connection system's real behavior. Furthermore, a study about the prototype and a global numerical model of modular RISBA house with the proposed CPM connection system need to be conducted.

Acknowledgements The author gratefully acknowledges to Department of Civil and Engineering, Universitas Gadjah Mada, that had the support and funded this research.

References

1. Saputra A, Himawan L (2018) RISBA (Rumah Instan Struktur Baja). Fakultas Teknik UGM, Yogyakarta, p 2
2. Deng EF, Zong L, Ding Y, Dai XM, Lou N, Chen Y (2018) Monotonic and cyclic response of bolted connections with welded cover plate for modular steel construction. *Eng Struct* 167(November):407–419
3. Chen Z, Liu J, Yu Y, Zhou C, Yan R (2017) Experimental study of an innovative modular steel building connection. *J Constr Steel Res* 139:69–82
4. Chen Z, Liu J, Yu Y (2017) Experimental study on interior connections in modular steel buildings. *Eng Struct* 147:625–638
5. Dai XM, Zong L, Ding Y, Li ZX (2019) Experimental study on seismic behavior of a novel plug-in self-lock joint for modular steel construction. *Eng Struct* 181(November):143–164
6. Mataram K, Septia K (2018) BNPB: 32.129 Rumah Rusak akibat Gempa Lombok Sudah Diverifikasi Artikel ini telah tayang di Kompas.com dengan judul 'BNPB: 32.129 Rumah Rusak akibat Gempa Lombok Sudah Diverifikasi', <https://regional.kompas.com/read/2018/08/29/12074971/bnpb-32129-rumah-ru>," Kompas.com, p 4
7. Pipit (2018) 800 Rumah Hancur di Kecamatan yang Terdampak Gempa dan Tsunami Palu Terparah, Kompas.com, p 3
8. AISC (2016) Seismic provisions for structural steel buildings. American Institute of Steel Construction, Chicago
9. FEMA-273 (1997) Nehr guidelines for the seismic rehabilitation of buildings, no October. FEMA-273, California
10. FEMA-369 (2001) NHEPR recommended provisions for seismic regulations for new buildings and others structures, 2000th ed., no March. Building Seismic Safety Council, Virginia
11. Faridmehr I, Osman MH, Tahir MM, Nejad AF, Azimi M (2015) Seismic and progressive collapse assessment of new proposed steel connection. *Adv Struct Eng* 18(3):39–452
12. Serror MH, Abdelmoneam MN (2018) Seismic performance evaluation of Egyptian code-designed steel moment resisting frames. *HBRC J*. 14(1):37–49
13. Ye J, Mohammad S, Hajirasouliha I (2019) Seismic performance of cold-formed steel bolted moment connections with bolting friction-slip mechanism. *J Constr Steel Res* 156:122–136
14. Forum CE et al (2012) Plastic analysis of steel frame structure. *J Civ Eng Forum XXI(May):1217–1226*
15. FEMA-356 and ASCE (2000) Prestandard and commentary for the seismic rehabilitation of buildings, 2000th ed., no November. FEMA-356, Washington, D.C

16. Deng E, Zong L, Ding Y, Luo Y (2018) Thin-Walled Structures Seismic behavior and design of cruciform bolted module-to-module connection with various reinforcing details. *Thin Walled Struct* 133(April):106–119
17. Lee S, Park J, Shon S, Kang C (2018) Seismic performance evaluation of the ceiling-bracket-type modular joint with various bracket parameters. *J Constr Steel Res* 150:298–325
18. Song QY, Heidarpour A, Zhao XL, Han LH (2017) Performance of flange-welded/web-bolted steel I-beam to hollow tubular column connections under seismic load. *Thin-Walled Struct.* 116(March):250–264
19. Cotco-SV (2018) BS 1387 : 1985 welded steel pipes. p 2
20. Kulak GL, Fisher JW, Struik JHA (2001) Guide to design criteria for bolted and riveted joints, 2nd ed., vol 2, no 1. American Institute of Steel Construction, Inc., Chicago
21. Cruz A, Simões R, Alves R (2012) Slip factor in slip resistant joints with high strength steel. *J Constr Steel Res* 70(March):280–288
22. Anzar M, Morris H, Smith T (2011) Assessment of coatings for friction-type connections. 11:096
23. Narendra PVR, Prasad K, Krishna EH, Kumar V, Singh KD (2019) Low-Cycle-Fatigue (LCF) behavior and cyclic plasticity modeling of E250A mild steel. *Structures* 20(February):594–606

Method Assessment of Bridge Conditions Using Vibration Mode Patterns



Sukamta, Bagus Acung Billahi, Susilo Adi Widyanto, and Han Ay Lie

Abstract The current bridge structure maintenance method is done by visual observation only, this often has limitations and the results obtained are less accurate. This research was conducted to obtain a vibratory mode data base which will be used as a basis for compiling the failure patterns of the bridge structure. Vibration mode measurements are carried out on the prototype and the bridge model using an accelerometer sensor mounted on the bridge structure. Accelerometer installed at several points to get variations in the vibrate mode. Dynamic load frequency variations are given to get vibrational mode variations. The results of the vibration mode measurement analysis show the similarity between the prototype and the model, so that the bridge model can be used to study structural failure patterns.

Keywords Dynamic characteristics · Prototype model · Scale model · Vibrate mode · Experimental analysis

1 Introduction

The development of bridge technology has continued to experience rapid increases over the last few years in line with the increasing demand for land and air transportation. This can be seen from the increase in bridge plan load classes, understanding of bridge construction planning/implementation technology, and the use of various kinds of software to support statistical analysis and dynamics of bridge structures. A maintenance system is needed to see and ensure that the bridge is still fit for use or

Sukamta (✉) · H. A. Lie
Department of Civil Engineering, Diponegoro University, Semarang, Indonesia

H. A. Lie
e-mail: hanaylie@live.undip.ac.id

B. A. Billahi
Master Program in Civil Engineering, Diponegoro University, Semarang, Indonesia

S. A. Widyanto
Department of Mechanical Engineering, Diponegoro University, Semarang, Indonesia

commonly known as Structural Health Monitoring. Bridge performance needs to be considered over its service life. The old bridge structure, the uncertain environmental conditions, and the increasing load of the vehicles in its path must be monitored for bridge maintenance.

Bridge detection monitoring is needed to determine structural deformations caused by regular operation or environmental impacts such as temperature, humidity, and heavy vehicle loads. It is also necessary to monitor the entire structure after extreme conditions, such as earthquakes. A system that can measure the performance of structures, especially truss bridges, is Structural Health Monitoring (SHM). The current maintenance system can be used and is considered an interesting topic because it can be carried out by routine monitoring and evaluation of civil construction's integrity through the use of sensor network technology, both wired and wireless. Structural Health Monitoring System refers to the in-service monitoring process embedded to effectively manage structured systems with various possible failures. The goal of a Structural Health Monitoring (SHM) system is to reduce security operating costs by providing more accurate condition-based maintenance [1].

Currently, the Structural Health Monitoring System is still limited to data collection and direct testing of structural elements, so it is time-consuming and relatively expensive. The bridge itself, has not yet developed an automatic monitoring system and a more accurate and efficient maintenance system. The main requirement for monitoring that is currently needed is an effective method to collect data from a structure and process the data for the benefit of performance measures such as the health level of a bridge, which correlates with its vibration mode. An automatic vibration sensor system is required, without the need for constant monitoring by human operators. The use of an accelerometer measuring device is very suitable for maintenance or maintenance with a vibration-based structural health monitoring system on this bridge structure. The accelerometer device will generate vibration mode data, which will later be converted from an analog signal to a digital signal, for easy reading. The obtained vibration mode signal will be processed using Fast Fourier Transform (FFT) analysis, which will obtain a graph of the frequency relationship to changes in amplitude. Through this graph, the bridge structure failure pattern can be analyzed, with several variations in the condition of the bridge structure. Variation of several dynamic load positions related to the condition of the bridge structure will be carried out.

According to this study's type of structure, a single degree of freedom system is used, meaning that mass or objects are limited in motion to only one axis, namely the x-axis or the y-axis. The vibration system used in this research is forced vibration with damping, which means that there is an excitation force (F), which is a sine function with amplitude (F_0) and frequency (ω) as shown in Fig. 1 [2]. The equation for the motion of mass m in response to this force can be determined from the analysis of the force acting on mass m when its position deviates by (x) from its position of static equilibrium [3]. Under conditions of dynamic equilibrium, Eq. 1 can be constructed.

$$m \ddot{x} + c \dot{x} + kx = F_0 \sin \omega t \quad (1)$$

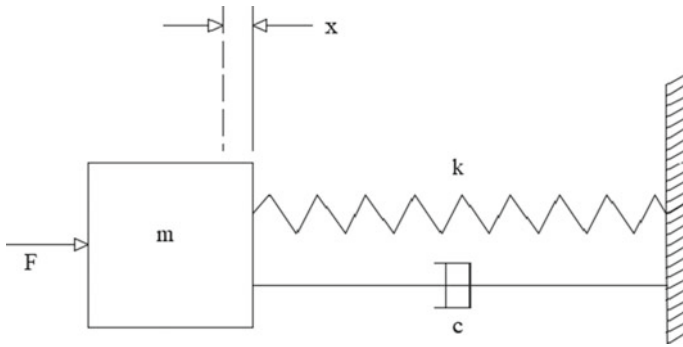


Fig. 1 Schematic forced vibration with damping

where

- $m\ddot{x}$ Inertia force (N)
- $c\dot{x}$ Viscous Damping
- kx Spring force (N)
- F_0 Centrifugal force (N).

The centrifugal force is obtained from Eqs. 2 and 3 as follows:

$$F = m\omega^2 r \tag{2}$$

$$\omega = (2\pi n)/60 \tag{3}$$

where

- F Centrifugal force (N)
- m Mass unbalance (kg)
- ω Angular speed (rad/s)
- r Turning radius (m).

Using the model’s scale analysis calculations, we can combine the variables to become “comfortable” groups, called “Piterms”, and result in a subtraction from the number of unknowns involved in the problem. Buckingham’s Pi theorem says any homogeneous equation involving a specific physical quantity can be reduced to an equivalent equation involving a complete set of dimensionless products. In general, the theory states that Eq. 4 is below:

$$F(X_1, X_2, \dots X_n) = 0 \tag{4}$$

Can be expressed equivalently in the form of Eq. 5:

$$G(\pi_1, \pi_2, \dots \pi_m) = 0 \tag{5}$$

The pi terms are dimensionless product of the physical quantities X_1, X_2, \dots, X_n , a complete set of dimensionless product are the $m = n - r$ independent product that can be formed from the physical quantities X_1, X_2, \dots, X_n . Generally, it can be stated that the number of dimensionless products (m) is equal to the difference between the number of physical variables (n) and the number of fundamental measure (r) that are involved. Buckingham’s Pi theorem occupies a very important place in the theory of dimensional analysis. Before moving on to dimensional analysis applications, the next section discusses some details of the procedures used to get the dimensionless product that goes into Buckingham’s Pi Theorem equation [4].

Analysis of the scaling model aspects calculated using the Pi Buckingham Theorem results in the scaling aspect for dynamic loads or vibration loads used in the bridge prototype and bridge models. Classification of the resulting vibration or dynamic load is one type of deterministic vibration, where the excitation quantity or load frequency can be known at a specific time. Vibration or dynamic load both work based on frequency, understanding the dynamic load frequency can certainly prevent resonance in the prototype structure or bridge model which is related to natural frequencies. The results of the Pi Buckingham theorem analysis for the load scale aspects given for the bridge model and bridge prototype are compiled in Eq. 6:

$$W_m = \left(\frac{\rho_m \cdot \ell_m^3}{\rho_p \cdot \ell_p^3} \right) W_p \tag{6}$$

where

- W_m The dynamic load of the bridge model
- W_p The dynamic load of the bridge prototype
- ρ_m Density of the material bridge model
- ρ_p Density of the material bridge prototype
- ℓ_m Length of the bridge model
- ℓ_p Length of the bridge prototype.

Studies on the dynamic characteristics of structures have been carried out by several practitioners such as Wei-Xin et al. [5]. Wei-Xin et al. study on the vibration testing, which carried out on bridge cables in Fuzhou China. The study is related to dynamic response, particularly in constructing these structures. The research was conducted in 2 ways, namely by using modal analysis and experimental analysis to obtain the natural frequency of the structure, aiming for the health of the structure. The analytical capital analysis was carried out with a 3-dimensional finite element program, namely ANSYS. Experimental analysis of direct vibration vibrations on the bridge, installed a total of 180 accelerometer sensors that are placed in separate places. The experimental analysis will perform three vibration tests: vibration, free vibration and ambient vibration. The vibration test uses force, impulse, weight loss, and electrodynamic excitation.

The free vibration test is carried out by releasing a load or mass suddenly. Test for ambient vibrations caused by wind, traffic, and pedestrians. The test results show

that the analytical and experimental vibration tests have been tested on the bridge prototype. The results of the analysis are created a good correlation between analytic capital and experimentally tested directly in the field. The natural frequency produced in the direct vibration test is 0.36 Hz for the longest cable and 1.97 Hz for the shortest cable [5].

Seno et al. tested the structural response system based on dynamic response structures using wireless sensor networks. The parameters tested for vibration are the natural frequency and shape of the bridge vibrational mode. The test is carried out on a prepared model and then validated using finite element method software (FEM). The method used to validate the success of the system is used two ways, namely using the FEA as a standard reference to determine the behavior of the structure and analysis of the Capital Assurance Criterion (MAC). Analysis of the finite element method was carried out using the CSi Bridge 2015 software to measure the natural frequency of the test-bed bridge built. The finite element method analysis results showed that the natural frequency of the test-bed bridge was 22.24 Hz, while the system developed to measure the average natural frequency of the bridge was 20.26 Hz. It is concluded that the value obtained by the finite element method analysis is close to the value obtained from the measurement system that has been built. The second way is to use it. MAC has calculated the correlation between the shape modes obtained from the finite element method analysis with those obtained by the system being developed. If the MAC value is close to one, both calculations have a strong correlation, so that the data obtained from the measurement system from the wireless sensor used is valid. The MAC value for finite element analysis (FEA) and measurement by the wireless sensor system is 0.8, so it is concluded that the two measurement parameters have a strong correlation [6].

Cristian et al. conducted research related to the Structural Health Monitoring System of Bridges on one of Romania's bridges. Visual inspection and incorporating several sensors were carried out for integrated monitoring of the bridge's durability. Some aspects observed were steel corrosion, concrete carbonation, freeze-liquid cycle, chemical reactions, mechanical damage, and changes in structural behavior such as deformation, strain, cracking, vibration. The success of the Structural Health Monitoring System depends on two stages of the procedure, namely design and implementation. By creating a dynamic sign database for all bridges, the conclusion is that enabling the Structural Health Monitoring (SHM) system to provide complete, accurate, and real-time data on the feasibility of the entire bridge network being monitored [7].

Cristiano et al. examined the dynamic response of a small-scale bridge model that is subjected to running loads. The basis of modeling is Buckingham's theory, which states that any homogeneous dimensional equation that involves a certain physical quantity can be reduced to an equivalent equation involving a dimensionless series of products known as the term pi terms.

Physical variables that involve modeling here are length (l), flexural stiffness (EI), mass density (p), load ($P = mg$) and longitudinal velocity ($v = \zeta$). Several parameters are determined through analysis, such as the transverse deflection (w) and the natural frequency of vibration ($f_r = \omega r / 2\pi$) by defining the pi terms [8].

This paper presents the correlation between vibration response in the form of vibration mode on the prototype bridge structure with a 1: 23 scale bridge model.

2 Material and Method

2.1 Prototype and Model

The truss bridge used as a prototype is the steel frame bridge Sendangmulyo Rowosari, located on Jl. Rowosari Raya, Semarang City, Indonesia. The prototype bridge structure has a total length of 53 m, a width of 9.3 m, and a bridge height of 5 m shown in Fig. 2. The thickness of the gusset plate is 21 mm and uses M24 bolts. The top, side, and bottom steel profile types are IWF 300.300.10.15, then for the upper bracing section use the type IWF 200.200.8.12.

The 1:23 model scale is selected and produces the dimensions of the bridge structure model scale (Fig. 3) as follows: 2315 m long, 0.389 m wide, and 0.217 m high. The bridge model's scale is 1:23, and is made using a hollow profile steel structure of 15 × 15 mm. The structural components are bolted by using M4 bolts, to represent the road area, the bridge model uses a 2 mm thick plate and is coated with a 2 mm thick rubber sheet.

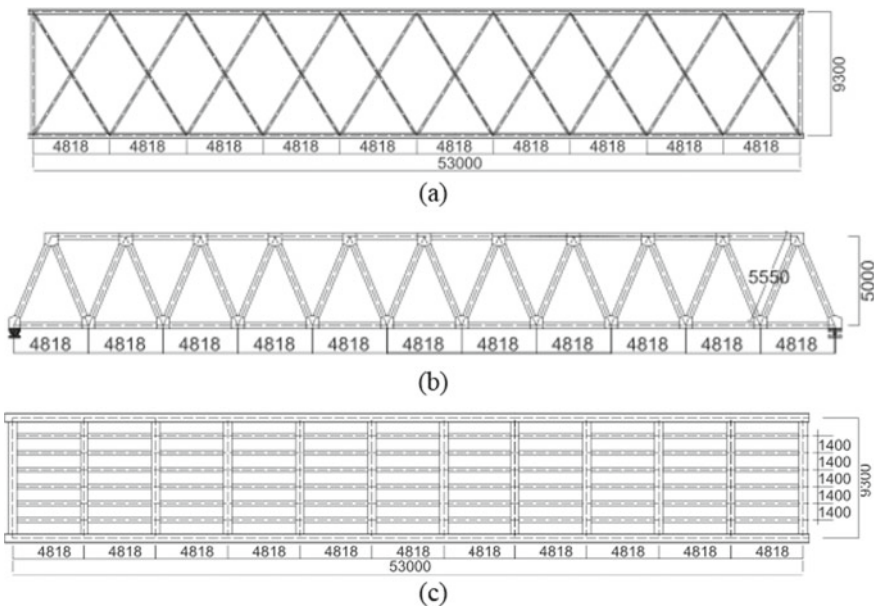


Fig. 2 Prototype bridge: a top view, b side view, c bottom view

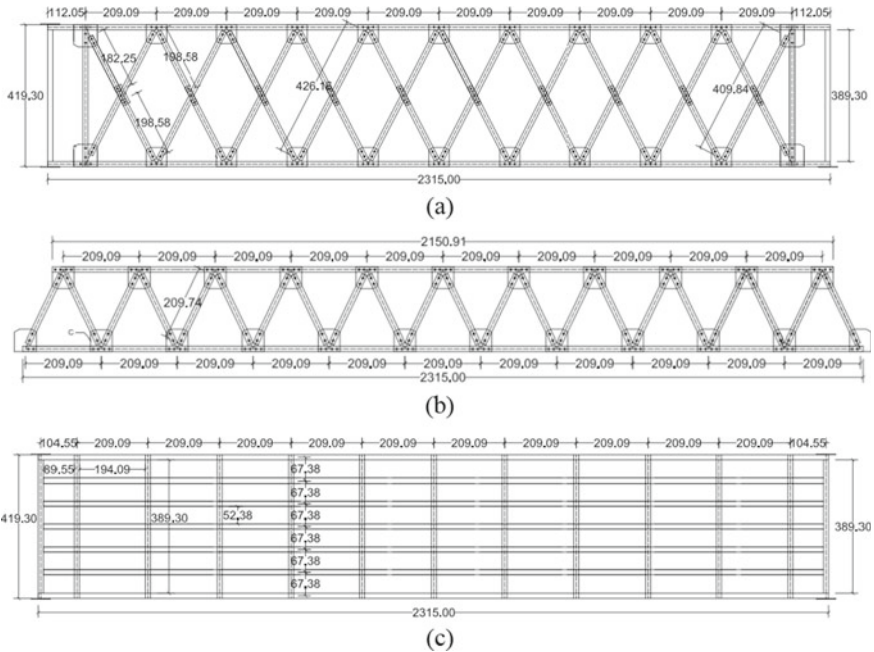


Fig. 3 Model bridge: a top view, b side view, c bottom view

2.2 Dynamic Loading System Prototype and Model Bridge

The dynamic loading of the bridge prototype uses a tamping rammer machine with 12,209 N impact force, as shown in Fig. 4. The dynamic loading model data from the tamping rammer machine can be seen in Table 1 [9].

The tamping rammer produces a deterministic vibration output whose value or amount of excitation can be known at a specific time and has a particular frequency to be used as test analysis. The tamping rammer works based on the rotor’s centrifugal force, which is present in the machine. The direction of the excitation issued is vertical, the vibration can be adjusted to produce the desired frequency as a test basis for the prototype bridge.

The dynamic loading of the model uses the rotating unbalance mass (Fig. 5). The characteristics of unbalanced mass are as in Table 2.

2.3 Sensor Accelerometer

The accelerometer used is the ADXL 335 brand with a sampling rate of 100 Hz. This sensor is of type small, low power, 3-Axis as shown in Table 3.

Fig. 4 Tamping rammer machine

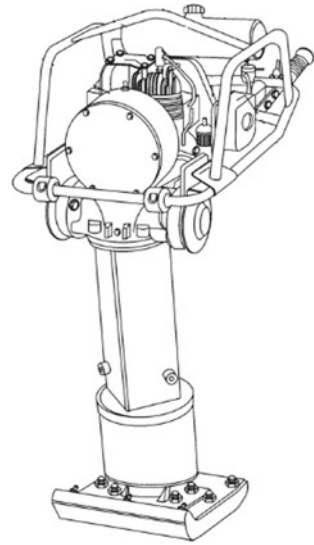


Table 1 Dynamic load testing data for prototype bridge structures

Experimental data	Value	Unit
Weight	74	kg
Force	12,209	N
Frequency	30	Hz
Jumping stroke	50–70	mm

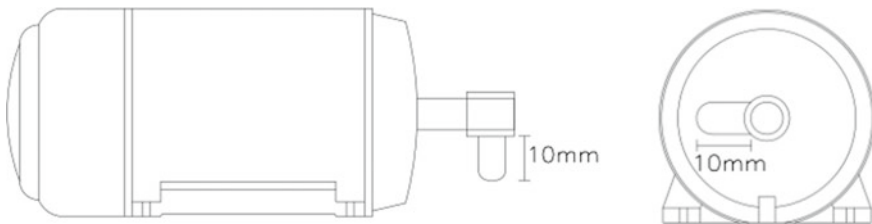


Fig. 5 Mass unbalance

Table 2 Unbalance mass characteristics

Experimental data	Value	Unit
Mass <i>unbalance</i>	3	g
Force	1.064–1.449	N
Frequency	30–35	Hz
Turning radius mass <i>unbalance</i>	10	Mm

Table 3 Spesifikasi accelerometer

Size: $4 \times 4 \times 1.45$ mm
3-axis sensing and single-supply operations: 1.8–3.6 V
Full scale measurement range can beset to ± 3 g
Low power: 350 μ A (typical)

2.4 Experimental Set Up

The test set-up circuit is shown in Fig. 6. In Fig. 6a is the test set-up used to determine the correlation of the prototype bridge structure and the bridge model structure. Figure 6b is the test set up used to determine the response due to frequency variations. The test was carried out at five position points, which later obtained the vibration mode results, which was used to determine the condition of the bridge structure. The resulting vibration mode will be measured and processed using fast Fourier transform (FFT) analysis, then a frequency domain graphic pattern is generated for changes in amplitude that can represent the feasibility of the structure.

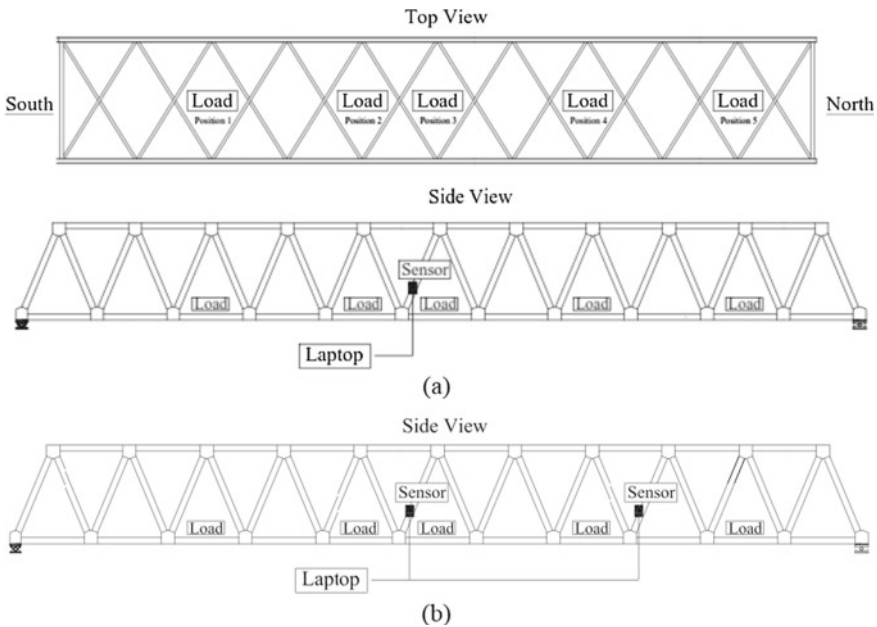


Fig. 6 Experimental set up

2.5 Research Stages

1. Identify problems regarding the vibration mode using the vibration-based Structural Health Monitoring (SHM) method on the bridge's upper structure as in the problem formulation. Prepare literature and theories related to the method of measuring the vibration mode on bridges. Collecting bridge data such as structural geometry, girder dimensions that will be used as a reference for making the bridge model scale.
2. Testing due to dynamic loads on the prototype bridge structure and model scale can be done when the test object has been completed. Tests will be carried out with several variations of dynamic load frequency and dynamic load position variations to obtain the actual vibration mode data of the bridge structure and the scale of the model. Vibration data is read through data acquisition software, from the software is obtained a graph that is still in the form of a vibration measurement curve that will be processed again.
3. Processing the measured data with data acquisition software, data processing using a program with the Fast Fourier Transform (FFT) analysis method. The results of the data processing produced a graph of the frequency domain relationship to changes in amplitude. Through the graph of the frequency domain relationship to changes in amplitude, the failure pattern of the bridge structure can be analyzed.

3 Results and Discussion

3.1 Dynamic Prototype Bridge Load Response

The test results of the bridge prototype structure due to dynamic load at position 1 can be seen through the FFT graph in Fig. 7, and the test results in other positions can be seen in Table 4. Variations in dynamic load positions are carried out to determine the variation in the vibration mode. The Z-axis is chosen as a reference for the variation of the vibrating mode, because the direction of the dynamic load is vertical.

From Fig. 7 and Table 4, it can be seen that the magnitude of the amplitude value is influenced by variations in the placement of dynamic load positions.

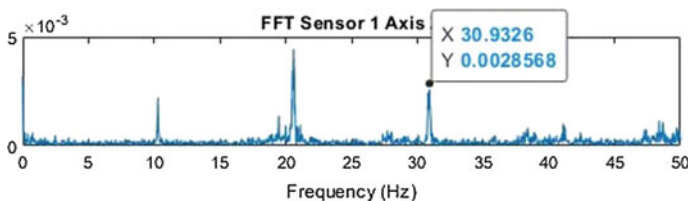


Fig. 7 Position 1

Table 4 Experimental result

Position	Frequency value (Hz)	Amplitude value (mm)
1	30.932	0.00285
2	30.957	0.00383
3	30.639	0.00668
4	30.908	0.00337
5	30.468	0.00247

The largest amplitude value of 0.00668 mm occurs in position 3, where position 3 is the position of the dynamic load closest to the accelerometer sensor. The smallest amplitude value of 0.00247 mm occurs in position 5 which is the farthest position from the accelerometer sensor. This shows that the position of the dynamic load has an effect on the value of the resulting amps. The closer the dynamic load position of the accelerometer sensor, the greater the resulting amplitude value, while the farther the dynamic load position from the accelerometer sensor the smaller the resulting amplitude value. The results of the FFT graph from all dynamic load positions also show that there are frequencies other than the excitation frequency given to the structure, namely frequencies between 20 and 50 Hz, which means that it can be seen that the condition of the prototype bridge structure has been damaged at several points of the structure.

Dynamic Load Response of Bridge Models

The results of testing the structure of the bridge model due to dynamic load at position 1 can be seen through the FFT graph in Fig. 8 and for the results of testing at other positions can be seen in Table 5.

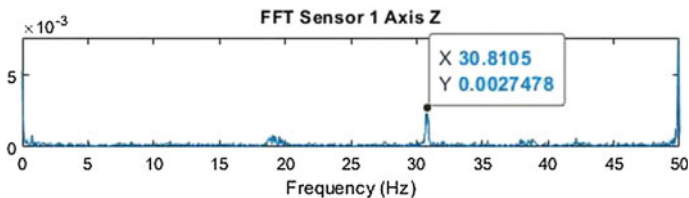


Fig. 8 Position 1

Table 5 Experimental result

Position	Frequency value (Hz)	Amplitude value (mm)
1	30.810	0.00274
2	30.127	0.00370
3	30.957	0.00628
4	30.957	0.00359
5	30.615	0.00254

The largest amplitude value with a value of 0.00628 mm occurs in position 3, where position 3 is the dynamic load position closest to the accelerometer sensor. The smallest amplitude value with a value of 0.00254 mm occurs in position 5 which is the furthest position from the accelerometer sensor.

Analyses

The comparison of the vibration mode response measurement results due to dynamic loads on the prototype of the bridge structure and the bridge model is quite good, the difference in amplitude values is relatively small, and the error shown is still below 10% as shown in Table 6 and Fig. 9.

The comparison of the amplitude value of the bridge prototype structure and the bridge model shows that the highest error value is 6.128% in position 4 with the amplitude value of the prototype bridge structure 0.00337 mm and the amplitude value of the bridge model structure 0.00359 mm. The comparison of the amplitude value of the prototype bridge structure and the model scale bridge shows that the lowest error value is 2.756% in position 5 with the amplitude value of the prototype bridge structure 0.00247 mm and the amplitude value of the model scale bridge structure 0.00254 mm.

Table 6 Comparison of the prototype bridge vibration mode and model scale

Position	Amplitude of bridge prototype (mm)	Amplitude of bridge scale model (mm)	Error (%)
1	0.00285	0.00274	3.860
2	0.00383	0.00370	3.394
3	0.00668	0.00628	5.988
4	0.00337	0.00359	6.128
5	0.00247	0.00254	2.756

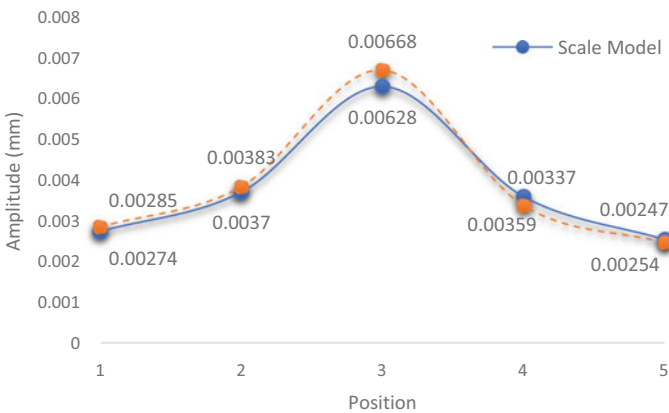


Fig. 9 Comparison of vibration mode response graph prototype model and scale model

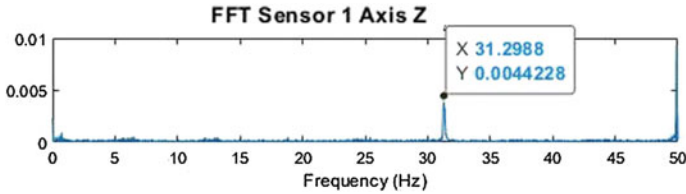


Fig. 10 Position 1

The amplitude value of the prototype structure and the bridge model shows similarities because previously the scaling model aspect has been calculated between the prototype structure and the bridge model using Buckingham's theory.

Frequency Variations in Bridge Model

Vibration mode testing with dynamic load frequency variations in the bridge model structure is done after the similarity of the vibration mode measurement results between the model and prototype is obtained. Unbalance mass frequency is set 31–35 Hz. The test results with a frequency of 31 Hz in position 1 are shown in Fig. 10. And for the results of testing in the frequency and other positions recap in Table 7.

The amplitude value that occurs can be determined from the analysis of the force acting on the mass (m), when the position of the mass deviates as far (x) from its balanced position. The force exerted is in the form of centrifugal force which is related to the rotation frequency of a machine [2]. The relationship between load frequency variations and amplitude values shows that if the greater the load frequency is given, the resulting amplitude will be greater as well. The dynamic load frequency that has increased, automatically the calculation of the centrifugal force load also increases so that the response of the structure will also be different, that is, it is certain to have an increase in the amplitude value as well. This can be proven from the load frequency of 31 Hz to the load frequency of 35 Hz, from the output of the accelerometer sensor number 1 and the accelerometer sensor number 2.

The lowest amplitude value for position 1 is at a frequency of 31 Hz, namely 0.00442 mm for sensor number 1 and 0.00409 mm for sensor number 2, while the highest amplitude value for position 1 is at a frequency of 35 Hz, namely 0.01893 mm for sensor number 1 and 0.01838 for sensor number 2. The lowest amplitude value for position 2 is at a frequency of 31 Hz, which is 0.00659 mm for sensor number 1 and 0.00714 mm for sensor number 2, while the highest amplitude value for the position is at a frequency of 35 Hz, namely 0.01391 mm for sensors number 1 and 0.01128 for sensor number 2. The lowest amplitude value for position 3 is at the 31 Hz frequency, namely 0.00797 mm for sensor number 1 and 0.00602 mm for sensor number 2, while the highest amplitude value for the position is at a frequency of 35 Hz, namely 0.02219 mm for sensor number 1 and 0.02136 for sensor number 2. The lowest amplitude value for position 4 is at a frequency of 31 Hz, which is 0.00471 mm for sensor number 1 and 0.00491 mm for sensor number 2, while the highest amplitude value for the position is at a frequency of 35 Hz, namely

Table 7 Experimental data

Position	Frequency value (Hz)	Amplitude value (S1) (mm)	Amplitude value (S2) (mm)
<i>Frequency 31 Hz</i>			
1	31	0.00442	0.00409
2	31	0.00659	0.00714
3	31	0.00797	0.00602
4	31	0.00471	0.00491
5	31	0.00319	0.00367
<i>Frequency 32 Hz</i>			
1	32	0.00845	0.00647
2	32	0.00917	0.00743
3	32	0.01796	0.01571
4	32	0.007163	0.00716
5	32	0.007413	0.00869
<i>Frequency 33 Hz</i>			
1	33	0.01177	0.00881
2	33	0.01091	0.00924
3	33	0.01508	0.01211
4	33	0.00908	0.00624
5	33	0.00939	0.00876
<i>Frequency 34 Hz</i>			
1	34	0.01316	0.01010
2	34	0.01119	0.01077
3	34	0.01781	0.01441
4	34	0.00845	0.00687
5	34	0.01009	0.01122
<i>Frequency 35 Hz</i>			
1	35	0.01893	0.01838
2	35	0.01391	0.01128
3	35	0.02219	0.02136
4	35	0.00968	0.00774
5	35	0.01485	0.01933

0.00968 mm for sensor number 1 and 0.00774 for sensor number 2. The lowest amplitude value for position 5 is at frequency 31 Hz, which is 0.00319 mm for sensor number 1 and 0.00367 mm for sensor number 2, while the highest amplitude value for the position is at a frequency of 35 Hz which is 0.01485 mm for sensor number 1 and 0.01933 for sensor number 2.

4 Conclusion

The results of the analysis of the vibration mode measurement show the similarities between the prototype and the model, so that the bridge model can be used to study structural failure patterns. A comparison of the amplitude value of the bridge prototype structure and the scale of the bridge model shows that the error that occurs is less than 10% at all given load positions. Variations in the dynamic load position in the bridge model structure indicate that the amplitude value can change due to the load position's influence on how close to the accelerometer sensor position. The amplitude value will be greater if the load position is closer to the accelerometer sensor position, and vice versa, the amplitude value will be smaller when the load position is far from the accelerometer sensor.

The variation of the dynamic load frequency in the bridge model structure shows that the greater the dynamic load frequency given, the greater the resulting amplitude value. The value of the centrifugal force increases when the dynamic load frequency value increases, so that the structural response results in an increasing amplitude value as the load frequency increases. The situation is different when it comes to natural frequency structures, because the highest amplitude values are at the moment of resonance which corresponds to the natural frequency.

References

1. Farrar CR, Worden K (2007) An introduction to structural health monitoring. *J Eng* 365:303–315. <https://doi.org/10.1098/rsta.2006.1928>
2. Harris C, Piersoll A (2002) *Harris shock and vibration handbook*, 5th edn. McGraw-Hill, New York
3. Faisal YT (2017) Analisis Frekuensi Respon Getaran Model Struktur Jembatan Dengan Prototype Exciter Statik. Tugas Akhir. Diponegoro University, pp 19–21
4. Harry GH, Gajanan MS (1999) *Structural modeling and experimental techniques*. CRC Press
5. Wei-Xin R, Xue-Lin P, You-Qin L (2005) Experimental and analytical studies on dynamic characteristics of a large span cable-stayed bridge. *J Eng Struct* 27:535–548
6. Seno AP, Gede AA, Adi TN, Abikarami A, Pratama B, Wijayanto, Bambang RT, Muhammad R (2018). Sistem Penilaian Kondisi Jembatan Menggunakan Respons Dinamik dengan Wireless Sensor Network. *J Civ Eng Environ* 3:338–343
7. Cristian CC, Nicolae T, Gheorghita B, Maria CS (2017) Structural health monitoring system of bridges. *J Civ Eng* 199:2054–2059
8. Cristiano B, Lawrence AB, Daniel K (2004) Experimental investigation of a small-scale bridge model under a moving mass. *J Civ Eng*. 130:799–804. [https://doi.org/10.1061/\(ASCE\)0733-9445\(2004\)130:5\(799\)](https://doi.org/10.1061/(ASCE)0733-9445(2004)130:5(799))
9. Mikasa tamping rammer manual operation book (2001)

Quantification of Bacteria Self-healing Efficiency on Concrete Cracks



M. S. Hamidah, H. Noor Hana, K. M. G. Iqmal, and K. Kartini

Abstract Use of a biological repair technique such as Microbial Induced Calcite Precipitation (MICP) has proven its success by previous research works. Previous studies concluded each bacteria has different healing capability depending on its population rate and width of crack to be healed. In this study, *Sporosarcina pasteurii* (*S. pasteurii*) was prepared in NH₄ YE media with additional of 5 g/L of filter sterilised urea solution. Three (3) series of specimens with artificial cracks were used for the application of bacteria taken from three (3) different highest population rate onto the cracks and one (1) control cracked specimen without bacteria. The number of live cells in the *S. pasteurii* population over a period of time was examined at hour 24, 33 and 48. Bacterial cell concentrations consisted of 207×10^6 cfu/ml at hour 24 (Specimen 1), 835×10^6 cfu/ml at hour 33 (Specimen 2) and 2.88×10^9 cfu/ml at hour 48 (Specimen 3) were dropped into the crack created on each specimen by using a 1 ml pipette/dropper. The formation of filling material was verified using Scanning Electron Microscopy (SEM). The results indicated that the crack created on Specimen 3 which was injected with bacteria concentration of 2.88×10^9 cfu/ml taken at highest population rate growth exhibited highest healing efficiency (HE). The crack was 100% fully healed after 28 days applying the bacteria broth solution. Meanwhile, it showed that those with higher bacteria concentration marked higher healing efficiency capacity. Calcium carbonate (calcite) formation as the crack filling material was confirmed by SEM examination. The results indicated that *S. pasteurii* in broth form has great potential to be used as crack remediation agent in concrete.

M. S. Hamidah (✉) · K. Kartini
School of Civil Engineering, College of Engineering, Universiti Teknologi MARA (UiTM),
40450 Shah Alam, Selangor, Malaysia
e-mail: hamid929@uitm.edu.my

H. Noor Hana
Faculty of Applied Sciences, Universiti Teknologi MARA (UiTM), 40450 Shah Alam, Selangor,
Malaysia

K. M. G. Iqmal
Executive Project, Al Jufri Integrated, Automobile Complex, Section 15, 40200 Shah Alam,
Selangor, Malaysia

Keywords MICP · *Sporosarcina pasteurii* · *S. pasteurii* · Bacterial cell concentrations · Self-healing crack

1 Introduction

Cracking of concrete is a common phenomenon due to the relatively low tensile strength and its low ductility. Durability of concrete is impaired by these cracks since they provide an easy path for the transportation of liquids and gasses that potentially contain harmful substances. If micro-cracks grow and reach the reinforcement, not only the concrete itself may be attacked, but also the reinforcement will be corroded. Therefore, it is important to control the crack width and heal the cracks within a very short time. Even though reinforcement bars have positive effect on crack width restriction by controlling plastic shrinkage, however, they cannot prevent crack formation.

Without immediate and proper treatment, cracks in concrete structures tend to expand further and eventually require costly repairs. Remediation of cracks in concrete has been the subject of research for many years. Even though a variety of techniques has been introduced for remediation of cracks, the traditional repair systems have a number disadvantageous aspects such as different thermal expansion coefficient compared to concrete, environmental and health hazards, and the techniques are still considered expensive because most of them are chemical based.

Recently, with new approach, bioconcrete appears to be emerging technology between biology and engineering which is known in many names such as microbial concrete or bacteria concrete. Bioconcrete can be an alternative and high quality concrete sealant which is cost-effective, environmental friendly, and eventually leads to improvement in the durability of building materials. Bioconcrete refers to an improved concrete that undergoes microbiological induced calcium carbonate precipitation (MICP) via biomineralisation process from bacteria. The precipitation helps to fill the micro cracks in concrete and can be an alternative and environment-friendly way to improve the strength of the concrete [1–10].

Urease positive bacteria have been found to influence the precipitation of calcium carbonate (calcite) by the production of urease enzyme. This enzyme catalyzes the hydrolysis of urea to CO_2 and ammonia, resulting in an increase of the pH and calcite precipitation in the bacterial environment. Ureolytic bacteria are able to precipitate calcite (CaCO_3) in their micro-environment by conversion of urea into ammonium and carbonate. The bacterial degradation of urea locally increases the pH and promotes the microbial deposition of carbonate as calcium carbonate in a calcium rich environment. These precipitated crystals can thus fill the cracks [2, 8, 11–16]. Thermogravimetric analysis showed that bacteria able to precipitate CaCO_3 crystals inside the cracks [11]. The potential of bacteria as a self-healing agent in concrete has evidenced to be a promising solution.

Thus, the success of Microbial Induced Carbonate Precipitation (MICP) has sought the interest to apply bacteria in crack to initiate the self-healing process. In

this study, *S. pasteurii* was used to examine the suitability and capability to remedy crack in concrete within shortest time. *S. pasteurii* is a gram-positive bacterium able to survive in highly alkaline environments (pH ~ 10) [17]. This is due to the fact that *S. pasteurii* has the unique ability to secrete copious amounts of the enzyme urease and has been identified as a possible agent for inducing significant volumes of MICP under certain conditions [2, 17–20]. Several researches on MICP reported on using this type of bacteria with various methods such as immobilised the whole cell of *Bacillus pasteurii* into Polyurethane (PU) foam [21], bacteria mixed with sand and packed into a column [22], bacteria mix with fly ash and silica fume concrete [23, 24]. In this study, the production of precipitation in remediating crack was increased whereof more urea consisting of 5 g per liter (5 g/L) was added to Yeast Extract (YE) broth. Despite many studies on *S. pasteurii* have been conducted, the present work has explored ways to increase the production of precipitation in remediating cracks. Extra urea was added to Yeast Extract (YE) broth during the cultivation process of bacteria to increase the production of urease. The number of live cells in *S. pasteurii* population over a period of time was examined at hour 24, 33 and 48. This method makes this present study unique and different from the previous one.

There are numerous self-healing using multiple species of bacteria have been reported to remedy cracks. Each bacteria has different capability in terms of time and the width of crack healing. Wiktor and Jonkers [4] used *Bacillus alkalinitrilicus* showed that the complete crack healing after 100 days of treatment and the widest crack to be healed is only 0.2 mm. Krishnapriya et al. [25] used four (4) species of bacteria such as *Bacillus megaterium* BSKAU, *Bacillus licheniformis* BSKNAU, *Bacillus flexus* BSKNAU and *Bacillus Megaterium* MTCC 1684. They observed the self-healing process completed within 81 days. The conclusion from both researches indicated that the time taken for cracks to be completely healed is too long and the widest crack to be healed is very small.

This study is to identify the efficiency of *S. pasteurii* taken at highest population rate of its growth as self-healing agent to heal the cracks in concrete. The time taken to complete crack healing was observed. Thus, this study will be benefited in terms of accelerating crack healing time through using *S. pasteurii* at its highest population rate of growth with additional urease during the cultivation process. If feasible, the durability of concrete structures could be improved and prolong the service life of the concrete structure.

2 Materials and Methods

2.1 Preparation of Bacteria

A thermophilic bacterium namely *S. pasteurii* used in this study was obtained from Next Gene Scientific Sdn. Bhd. (Code DSM 33, Brand: DSMZ, Germany) (Fig. 1). The bacteria were cultured and grown in the Microbiology Laboratory, Faculty

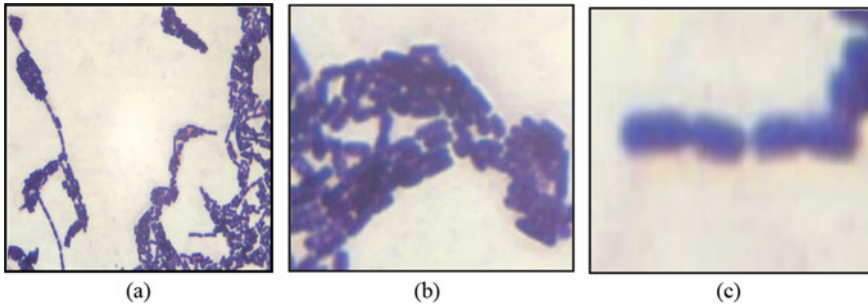


Fig. 1 **a** Image of *S. pasteurii* 1000× magnification under light microscope (Leica); **b** the morphology of *S. pasteurii* vegetative cells in short chain; **c** the morphology of *S. pasteurii* vegetative cells in single form

of Applied Sciences, Universiti Teknologi MARA (UiTM) Shah Alam, Selangor, Malaysia. *S. pasteurii* was inoculated into NH_4YE broth (Fig. 2) and incubated for 24 h at 30 °C (Fig. 3). *S. pasteurii* isolation was reconfirmed with Gram stain and urea test. To determine possibility of producing calcium carbonate by isolates, the spores were grown on a B4 media (2.4 g/L of calcium acetate powder, 4.0 g/L of yeast extract powder, 10 g/L of glucose and 20 g/L of bacteriological agar powder). During revival process, *S. pasteurii* pallet was placed into Yeast Extract (YE) broth so that the pallet revolved into broth. Extra urea was added to YE broth during the cultivation process of bacteria to increase the production of urease.

The bacterial culture was taken in shaking incubator at 30 °C to stimulate the bacterial growth. Spectrophotometer (Model: Genesys 20) was used to measure the bacterial cultured samples and the cell mass, so that the growth curve of *S. pasteurii* can be identified based on the optical density (OD) data. In order to determine colony forming units per ml of culture (cfu/ml), the colony formation of the bacteria in each OD data was counted by plating *S. pasteurii* cells using the serial dilution process.

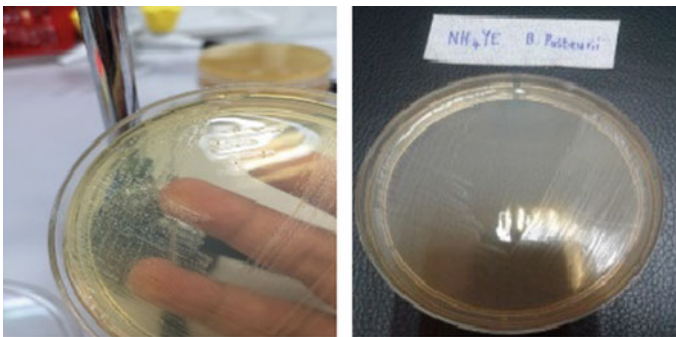


Fig. 2 *S. pasteurii* in NH_4YE broth media

Fig. 3 Image of *S. pasteurii* after 24 h incubation in urea agar



Table 1 The mix proportion of Grade 30 concrete (in kg/m³)

Quantities (in kg/m ³)	Cement	Water	Fine aggregate	Coarse aggregate	
				10 mm (1 part)	20 mm (2 parts)
Per m ³ (nearest 5 kg)	375	205	680	385	770

The OD data with regards to the colony forming inferring the population growth of the bacteria will be discussed in Sect. 3.

2.2 Preparation of Materials and Mix Proportion for Concrete Specimens

In this study, concrete Grade 30 was used which consists of Portland cement, crushed aggregate size 10 and 20 mm, fine aggregate (sand) and water. Two (2) types of coarse aggregate sizes were adopted to ensure the uniformity and particle packed mix. All these materials were prepared at Concrete Laboratory, School of Civil Engineering, UiTM Shah Alam, Selangor, Malaysia. The mix proportion for Grade 30 concrete 1 m³ with water cement ratio of 0.55 was determined using Department of Environment (DOE), UK method and is shown in Table 1.

2.3 Preparation of Concrete Specimens

The concrete specimens were prepared in cylinder shape, size Ø100 mm × 200 mm. Slump test was conducted to determine the degree of workability of the concrete mixture. After the workability of the mix was satisfied (targeted 75 mm slump), the

concrete mix was immediately poured into the moulds. The surface of the moulds was oiled prior to the pouring. The vibrator machine was used to compact the concrete, minimizing air pores and control the honey-comb conditions that formed in hardened concrete.

2.4 Curing and Compressive Strength of Specimens

The concrete specimens were cured in water for 28 days. The concrete specimens were immersed in water pond at Concrete Laboratory of School of Civil Engineering, UiTM Shah Alam. The compressive strength of the specimens was conducted for the specimens at 7, 14 and 28 days of ages. The reading rate of the loading was obtained by conducting test in the laboratory by using a 3000 kN compression machine. The compressive machine was operated at a pacing rate of 3.0 kN/s.

2.5 Creation of Cracks

The cracks were created by applying load to the cylinder specimens using Universal Testing Machine (UTM) Type 1000 at Concrete Laboratory of School of Civil Engineering, UiTM Shah Alam. The concrete specimen was placed between the grips and a suitable jig with an increasing load at the rate of 0.083 kN/s on the concrete specimen. The load (kN) was recorded throughout the conducted test by control system and its associated software. Later, the widths of crack between 0.1 and 0.3 mm were created.

2.6 Applying Bacteria Broth onto Cracked Specimens

S. pasteurii formerly known as *Bacillus pasteurii* was used as a self-healing agent to remedy the cracks. *S. pasteurii* in broth form taken from three (3) different highest population rate based on the OD reading were dropped into pre-determined points of crack by using pipet size 1 ml.

2.7 Quantification of Healing Efficiency (HE)

The study area or point of crack was observed to visualize the healing process by using stereomicroscope camera Dino Capture 2.0. The stereomicroscope camera equipped with Dino Lite software was used to capture the images of the cracks before and after healing. The crack healing was quantified based on the reduction width of the crack.

Furthermore, the average data of healing was obtained from the crack healing ratio. The crack healing ratio was determined using Eq. 1 as suggested by Wang et al. [26] as follows:

$$\text{Healing ratio (\%)} = (C_{wi} - C_{wf}/C_{wi}) \times 100\% \quad (1)$$

where

C_{wi} initial crack width

C_{wf} final crack width.

2.8 Examination on Filling Up Materials

Scanning Electron Microscopy (SEM) was used to verify the crack filling materials is calcite precipitation by confirming the shape and morphology of filling materials in the cracks.

3 Results and Discussion

3.1 Bacteria Identification and Urease Production

Isolation of *S. pasteurii* was reconfirmed with Gram stain (Fig. 1) and urea test (Fig. 3). The morphology of *S. pasteurii* on NH_4YE agar is circular, creamy, smooth, entire, glistening and opaque as illustrated in Figs. 1 and 2. The urease test showed *S. pasteurii* is capable of hydrolysing urea to produce ammonia and carbon dioxide. Urease is a constitutively expressed enzyme that hydrolyses urea to carbon dioxide and ammonia. The colour changed from yellow (pH 6.8) to bright pink (pH 8.2) due to the production of ammonia and increase in pH.

The extraction of calcium carbonate (calcite) was performed by fermentation of *S. pasteurii* in B4 media for 2 weeks. The appearance of crystals was observed by light microscope. From the result, the precipitation of crystals was formed after 2 weeks of incubation at 30 °C on B4 media and no formation of crystal at B4 media without calcium carbonate (Fig. 4). This process showed that the crystals were mainly composed of inorganic minerals. This is verified that *S. pasteurii* was able to produce calcium carbonate (calcite).

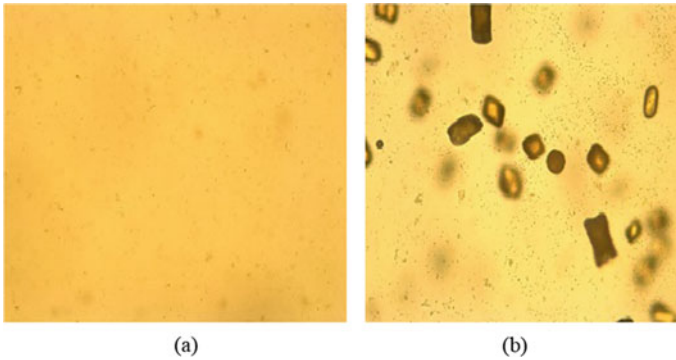


Fig. 4 Image of no formation of crystals on B4 media **a** without calcium carbonate and **b** formation of crystals for the one incubated in B4 media after 2 weeks of incubation at 37 °C

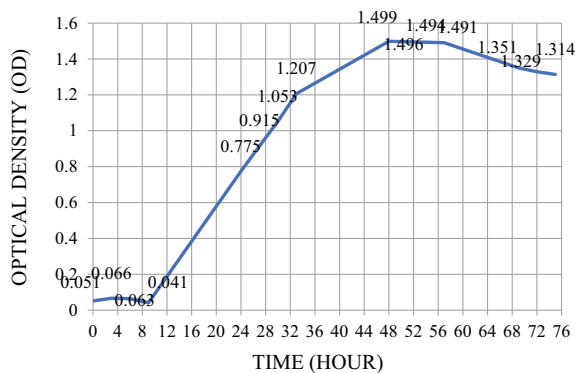
3.2 *Determination of Growth Curve and Colony Forming Unit*

The growth of bacteria shown in Fig. 5 can be determined by OD reading. The higher reading of OD indicated the higher number of bacteria growths. The growth of bacteria ended at certain hours.

The OD data is plotted to determine four (4) characteristic phases of bacterial growth curve. From Fig. 5, it shows that lag phase occurred in hour zero (0) until nine (9), while exponential phase was observed in hour nine (9) until 48. Meanwhile, the stationary phase occurred in hour 48 until 57 and death phase starting from hour 57.

From each hour with known OD, 1 ml of sample was taken from the bacteria cultured in YE broth and dropped into the plate with YE agar. The sample went through serial dilution for 10 times. Then, 1 ml of each time of dilution was taken and dropped in YE agar plate. Later, the YE agar plate was incubated for 24 h.

Fig. 5 *S. pasteurii* bacterial growth curve with respect to OD measured versus time after incubation



Later, numbers of colony that appeared in plate was counted to determine the colony forming unit per ml (cfu/ml).

Three (3) series of bacteria cell concentration at known OD readings were selected consisting of 0.775 for 207×10^6 cfu/ml bacterial cell concentrations at hour 24, 1.207 for 835×10^6 cfu/ml bacterial cell concentrations at hour 33 and 0.775 for 2.88×10^9 cfu/ml bacterial cell concentrations at hour 48.

First and second bacterial cell concentrations attained at exponential phase were selected because at this phase the number of new bacteria appearing is proportional to the present population. If the growth continues, doubling will continue at a constant rate so both the number of cells and the rate of population increase doubles with each consecutive time period [27]. Third bacterial cell concentration at stationary phase was chosen because at this phase, growth rate and death rate of bacteria were equal. The number of new cells created is limited by the growth factor and as a result, the rate of cell growth matches the rate of cell death [2]. These three (3) series of bacterial cell concentrations were investigated its healing capability.

3.3 Compressive Strength

Initially, the design concrete strength has been set was 30 N/mm^2 at age 28 days and targeted compressive strength is 42 N/mm^2 . It showed the compressive strength were 40.96 N/mm^2 at day 7, 41.8 N/mm^2 at day 14 and 46.87 N/mm^2 at day 28 (Fig. 6) and it is shown that the targeted compressive strength was achievable and the concrete was used to monitor the healing of crack after spraying the crack with the bacteria broth. The compressive strength attained at 7 days is higher in comparison with the normal percentage (75%) gained with reference to the compressive strength

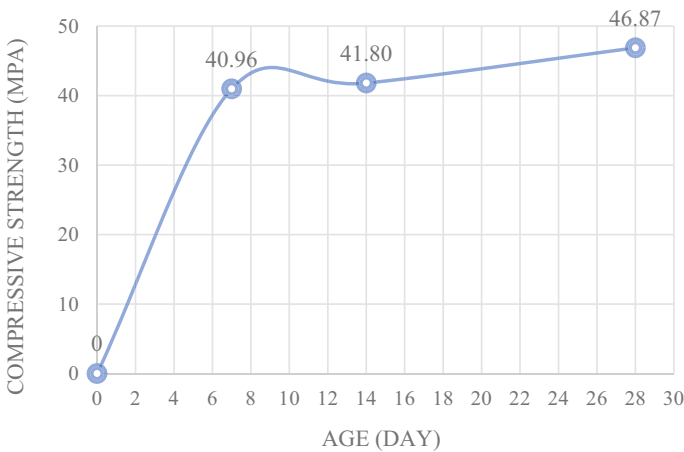


Fig. 6 The compressive strength of concrete specimens used for crack healing investigation

at 28 days. At 7 days, the compressive strength recorded was 40.96 MPa, which is 87% from that of 28 days. The slowing down of hydration process is the main reason of a slight drop of the compressive strength at 8–10 days of age, most possibly due to the hardening process and reduction in water content.

3.4 Quantification of Healing Efficiency

The images of healing effect for each specimen are shown in Figs. 7, 8 and 9 for Specimen 1, Specimen 2, and Specimen 3 respectively. Figure 10 shows healing effect on crack created for control specimen.

Figure 11 shows healing efficiency (HE) ratio for cracked specimens filled up with broth containing different concentrations of bacteria (broth) including control. It appears that higher bacterial concentration of 2.88×10^9 cfu/ml (48 h) hold a greater HE ratio as compared to those cracks that treated with other levels of bacteria concentration. In other words, the HE was improved when the bacteria cell concentration used to heal the cracks increased [8, 9, 28]. HE has a direct proportion on the formation of calcium carbonate (CaCO_3), in which rate of CaCO_3 precipitation influenced by the cell concentration of bacteria [9, 29, 30]. Copious amount of CaCO_3 only can be produced at high cell concentration or when the growth of bacteria achieved at highest rate which is associated with OD measurement. The low bacteria cell concentrations reduce the overall efficiency of the self-healing process because it decreases the potential of bacteria to produce CaCO_3 [31].

Figures 12, 13 and 14 portray the crack and crack filling materials for Specimens 1, 2 and 3.

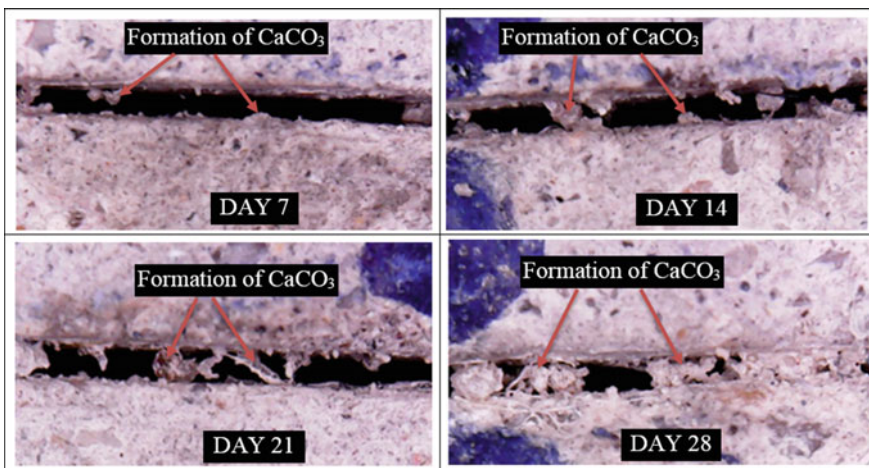


Fig. 7 Healing efficiency (HE) captured for Specimen 1 at 7, 14, 21 and 28 days

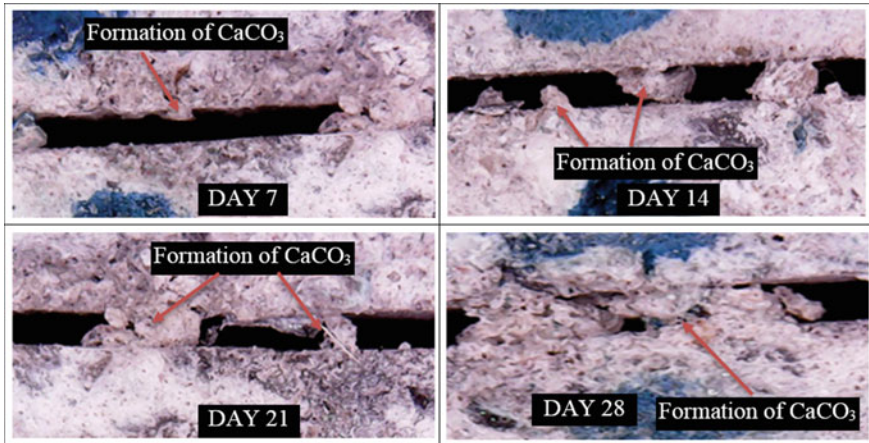


Fig. 8 Healing efficiency (HE) captured for Specimen 2 at 7, 14, 21 and 28 days

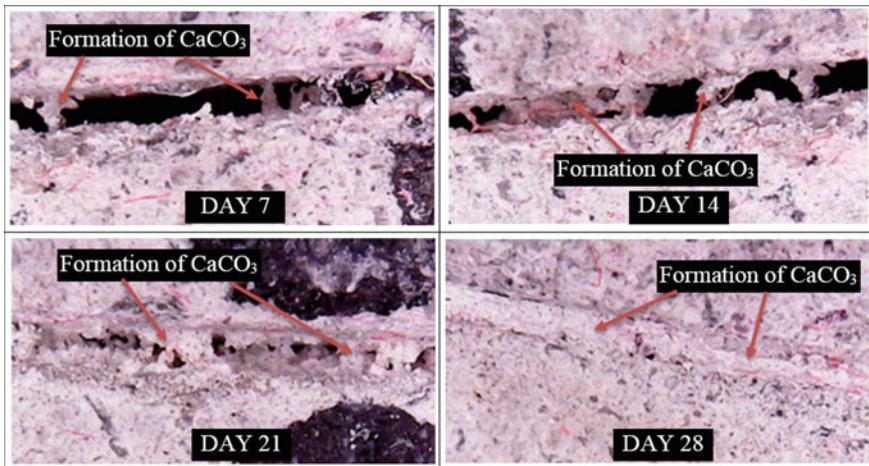


Fig. 9 Healing efficiency (HE) for Specimen 3 at 7, 14, 21 and 28

4 Conclusions

In this present study, more urea was added into YE broth as nutrient to increase the production of calcite precipitation. The live cells of *S. pasteurii* attained at highest population rate at hour 24, 33 and 48 based on OD measurement were adopted. The formation of *S. pasteurii* induced calcite precipitation on the filling-up material was verified. The following conclusions can be drawn from the experimental works carried out in this research:

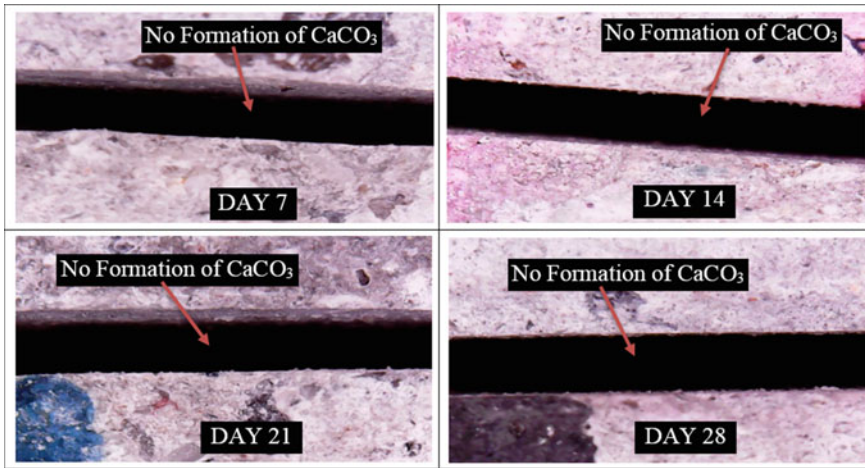


Fig. 10 The crack of control specimen is not filled up captured at the age of 7, 14, 21 and 28 days

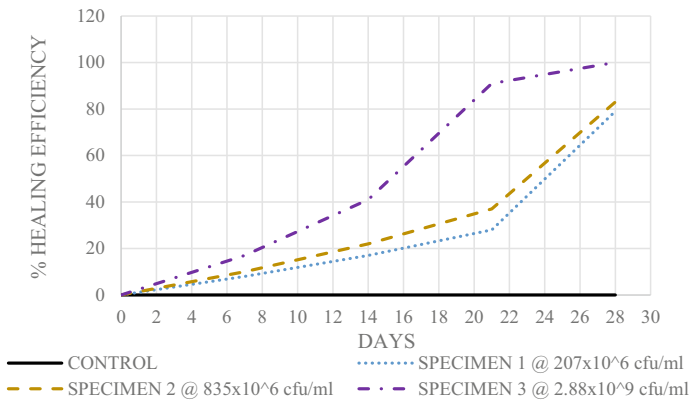


Fig. 11 Healing efficiency (HE) ratio for cracked specimens filled up with solution containing different concentrations of bacteria (broth)

1. The higher bacterial cell concentration of 2.88×10^9 cfu/ml (48 h) hold a greater healing efficiency (HE) as compared to those treated with other concentration levels of bacteria. The exponential phase of *S. pasteurii* growth ended in hour 48 and stationary phase started after that. Even though the bacteria cells were taken within the exponential phase of growth at hour 24 and hour 33 and showed healing efficiency (HE) when used to treat the cracks, HE ratio was found to be lesser as compared to those taken at highest growth rate at hour 48.
2. The shortest time of the crack to be fully healed was found to be 28 days by using bacterial cell concentration of 2.88×10^9 cfu/ml (48 h). Meanwhile, the

Fig. 12 No formation of calcite captured by SEM in the crack on control specimen

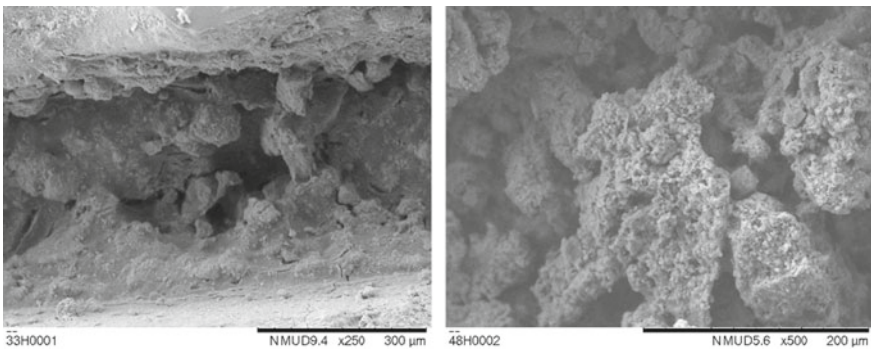
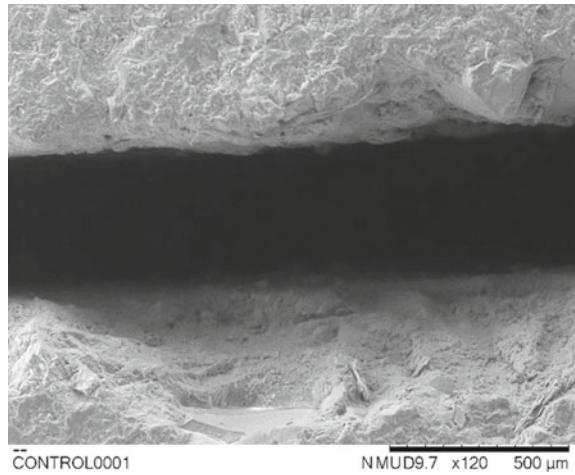


Fig. 13 SEM micrographic of calcite by shape taken on the filling material from the crack created on the concrete specimen that applied with 835×10^6 cfu/ml *S. pasteurii* growing after 33 h

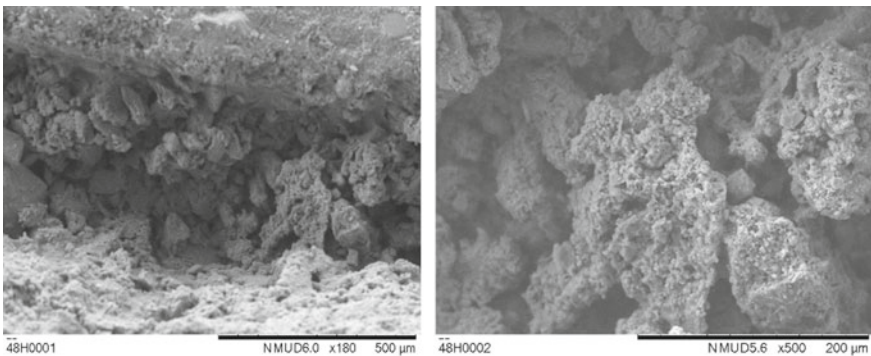


Fig. 14 SEM micrographic of calcite by shape taken on the filling material from the crack created on the concrete specimen that applied with 835×10^6 cfu/ml *S. pasteurii* growing after 48 h

healing begins as early as 7 days of age after treating the cracks with three (3) different cell concentrations of bacteria.

3. It was confirmed by SEM that the crystals precipitated in the crack composed of calcite. This proved the potential of *S. pasteurii* in broth form to be a crack remediation agent.

Acknowledgements The author would like to acknowledge Zacklim Floor Specialist Sdn. Bhd. for providing the grant, Faculty of Applied Sciences and Faculty of Civil Engineering, Universiti Teknologi MARA, Shah Alam, SELANGOR, MALAYSIA for providing the facilities to accomplish the experimental work for this research.

References

1. Wiktor V, Jonkers HM (2015) Field performance of bacteria-based repair system: pilot study in a parking garage. *Case Stud Constr Mater* 2:11–17
2. Gupta S, Pang SD, Kua HW (2017) Autonomous healing in concrete by bio-based healing agents—a review. *Constr Build Mater* 146:419–428
3. De Belie N, De Muynck W (2008) Crack repair in concrete using biodeposition. In: Proceedings of the international conference on concrete repair, rehabilitation and retrofitting (ICRRR), Cape Town, South Africa, pp 291–292
4. Wiktor V, Jonkers HM (2011) Quantification of crack-healing in novel bacteria based self-healing concrete. *Cem Concr Compos* 33(7):763–770
5. Muynck W, Debrouwer D, De Belie N, Verstraete W (2008) Bacterial carbonate precipitation improves the durability of cementitious materials. *Cem Concr Res* 38(7):1005–1014
6. Mostafa S, Ali KS, Aydin B (2016) Bioconcrete: next generation of self-healing concrete. *Appl Microbial Biotechnol* 100:2591–2602
7. Sandip M, Palash D, Arun KC (2017) Application of bacteria in concrete. *Mater Today Proc* 4:9833–9836
8. Kunamineni V, Meena M, Shirish VD (2017) Bacteria based self healing concrete—a review. *Constr Build Mater* 152:1008–1014
9. Van Tittleboom K, De Bellie N, De Muynck W, Verstraete W (2010) Use of bacteria to repair cracks in concrete. *Cem Concr Res* 40(1):157–166
10. De Muynck W, Cox K, De Belie N, Verstraete W (2008) Bacterial carbonate precipitation as an alternative surface treatment for concrete. *Constr Build Mater* 22(5):875–885
11. Krishnapriya S, Venkatesh BDL, Prince AG (2015) Isolation and identification of bacteria to improve the strength of concrete. *Microbiol Res* 174:48–55
12. Amir S, Rebecca G, Filippo G (2019) Is concrete healing really efficient? A review. *Constr Build Mater* 205:257–273
13. Fischer-Stocks S, Galinat JK, Bang SS (1999) Microbiological precipitation of CaCO₃. *Soil Biol Biochem* 31(11):1563–1571
14. Ramachandran SK, Ramakrishnan V, Bang SS (2001) Remediation of concrete using micro-organisms. *ACI Mater J* 98:3–9
15. Bang SS, Galinat JK, Ramakrishnan V (2001) Calcite precipitation induced by polyurethane—immobilized *Bacillus pasteurii*. *Enzyme Microb Technol* 28:404–409
16. Mitchell A, Feris F (2006) The influence of *Bacillus pasteurii* on the nucleation and growth of calcium carbonate. *Geomicrobiol J* 25:213–226. <https://doi.org/10.1080/01490450600724233>
17. Sarah L, William S, Mary JK, Raisa DF (2017) Influence of concrete-related environmental stresses on biomineralizing bacteria used in self-healing concrete. *Constr Build Mater* 139:611–618

18. Santosh K, Ramachandran SK, Ramakrishnan V, Bang SS (2001) Remediation of concrete using microorganisms. *Am Concr Inst Mater J* 98:3–9
19. Day JL, Ramakrishnan V, Bang SS (2003) Microbiologically induced sealant for concrete crack remediation. In: 16th engineering mechanics conference, Seattle, 16–18 July 2003
20. Ramakrishnan V, Panchalan RK, Bang SS (2005) Improvement of concrete durability by bacterial mineral precipitation. In: Proceedings of 11th international conference on fracture, Turin, 20–25 Mar 2005
21. Bang SS, Galinat JK, Ramakrishnan V (2001) Calcite precipitation induced by polyurethane-immobilized *Bacillus pasteurii*. *Enzyme Microbiol Technol* 28:404–409
22. Gollapudi U, Knutson C, Bang S, Islam M (1995) A new method for controlling leaching through permeable channels. *Chemosphere* 30(4):695–705
23. Chahal N, Siddique R, Rajor A (2012) Influence of bacteria on the compressive strength, water absorption and rapid chloride permeability of fly ash concrete. *Constr Build Mater* 28(1):351–356
24. Achal V, Pan X, Özyurt N (2011) Improved strength and durability of fly ash-amended concrete by microbial calcite precipitation. *Ecol Eng* 37(4):554–559
25. Krishnapriya S, Babu DLV, Prince Arulraj G (2015) Isolation and identification of bacteria to improve the strength of concrete. *Microbiol Res* 174:48–55
26. Wang JY, Soens H, Verstraete W, De Belie N (2014) Self-healing concrete by use of microencapsulated bacterial spores. *Cem Concr Res* 56:139–152
27. Abir AT, Litina C, Ginnarous P, Kanellopoulos A, Livia S (2019) First UK field application and performance of microcapsule-based self healing concrete. *Constr Build Mater* 208:669–685
28. Achal V, Mukerjee A, Reddy MS (2013) Biogenic treatment improves the durability and remediates the cracks of concrete structures. *Constr Build Mater* 48:1–5
29. Pei R, Liu J, Wang S, Yang M (2013) Use of bacterial cell walls to improve the mechanical performance of concrete. *Cem Concr Compos* 39:122
30. Andalib R, Muhd Zairni AM, Mohd Warid H, Mohanadoss P, Ali K, Jahangir M, Han-Seung L (2016) Optimum concentration of *Bacillus megaterium* for strengthening structural concrete. *Constr Build Mater* 118:180–193
31. Khaliq W, Ehsan MB (2016) Crack healing in concrete using various bio influenced self-healing techniques. *Constr Build Mater* 102:349–357

Feasible Design Tensile Capacity of Post-installed Anchors Based on the New Eurocode 2: Part 4 (2018)



L. T. Ng, E. S. W. Wong, and D. T. W. Looi

Abstract Anchor fastening is commonly used in construction of steel-to-concrete connections. These anchors can be pre-embedded and cast in place or post-installed. It is noted that post-installed anchors are used more often nowadays in concrete structure construction, mainly because it can minimise misalignment issue during installation. This paper describes a methodology to simplify the complex equations in the new Eurocode 2: Part 4 (2018) into feasible design tensile capacity regions for design check of single post-installed anchor (mechanical anchor and bonded anchor). The design tool is demonstrated with an example of C30/37 cracked concrete for a 125 mm thick slab with downward hanging non-structural members, e.g. suspended ceiling, that are subjected to vertical action and installed on the soffit of slab. Parametric study was performed for commonly available anchor sizes (M8, M10, M12, M16, M20 and M24) by using the empirical equations proposed in the new code. The authors foresee that the design tools developed using the methodology in this paper are useful for practicing engineers in quick estimation of anchor resistance.

Keywords Post-installed anchors · Mechanical anchors · Bonded anchors · Tensile capacity

1 Introduction

Anchor fastening technology has been widely used in steel-to-concrete connection. Anchors are typically divided into two categories according to its installation method: (1) pre-embedded to cast in place, and (2) post-installed anchors. For cast in place method, anchors are arranged before concreting while for post-installed method, the anchors are installed after concrete is hardened.

L. T. Ng · D. T. W. Looi (✉)
Swinburne University of Technology, Sarawak, Malaysia
e-mail: dlooi@swinburne.edu.my

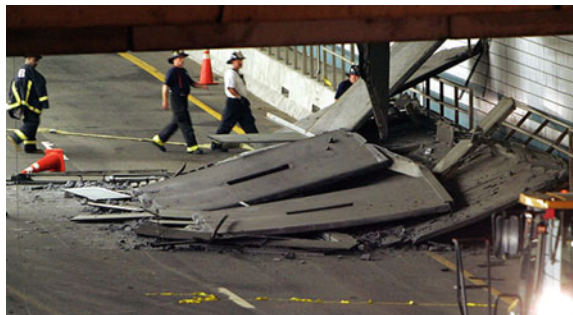
E. S. W. Wong
Konsortium Malaysia, Sarawak, Malaysia

Post-installed anchors are now commonly practiced in concrete structure construction due to ease of installation as drilling technology advances. It is also noted that post-installed anchors can minimize misalignment issue during construction. Post-installed anchors include mechanical type (e.g. undercut anchors, screw anchors and expansion anchors) and bonded anchors. Undercut anchor features mechanical interlock load transfer mechanism between the anchor and concrete. Expansion anchor features friction load transfer mechanism between the anchor and side wall of the drilled hole. These mechanical anchors are efficient if immediate loading is required. On the contrary, bonded anchor features bond transfer mechanism to concrete through adhesives. The adhesives can be grout or chemical based material. Grouted anchors consist of a smooth-shanked anchor embedded in cementitious based bonding material, while chemical anchors consist of threaded rod installed in a drilled hole with polymer-based adhesive.

Steel-to-concrete connections in structures are mainly dependent on the use of fastened anchors. Thus, these anchors must be prequalified by European Assessment Document (EAD), EAD 330232 [1] for mechanical anchors and EAD 330499 [2] for bonded anchors, designed to Eurocode 2: Part 4 (2018) and installed by trained workers with proper drilling machine. A study conducted by González et al. [3] showed that the drilling machine has a major impact on the capacity of the anchor. Unqualified, improperly designed or poorly installed anchors may cause collapse failure of structural or non-structural members, which may lead to human life casualty. Figure 1 shows an example of collapsed ceiling at the Boston's Big Dig tunnel. The anchor failure due to creep under sustained load caused the collapse of ceiling panel and crushed a car, a passenger died in the accident.

Numerous experimental and numerical studies had been performed to predict the failure mechanisms and capacity of anchors subjected to pull-out force [5–7]. These background work has led to empirical equations proposed in design standard, e.g. ETAG 001 which is superseded by the new Eurocode 2: Part 4 (2018) (officially known as BS EN 1992-4: 2018 [8]). In engineering practice, commercial software provided by vendors (e.g. Hilti PROFIS Anchor [9]) is used to estimate the capacity of the anchors based on selected design codes. However, the design solution gives only one point of result after going through the rather complex empirical equations. This process can be time-consuming for engineers who are new to anchor design and

Fig. 1 Collapse of ceiling panel at the Boston's Big Dig tunnel due to anchor failure [4]



iterating the process without getting an overview of the feasible solutions. Hence, this paper recommends a methodology to develop a tool (simplified chart) to estimate the feasible design tensile capacity of single post-installed anchor (mechanical anchor and bonded anchor) associated with possible failure modes against embedment depth ratio, according to the new Eurocode 2: Part 4 (2018).

2 Design Methodology of Eurocode 2: Part 4 (2018)

2.1 Typical Failure Mechanisms of Anchors Subject to Tension Force

In Eurocode 2: Part 4 (2018), post-installed anchors exhibit failure modes under tension load which include steel failure, concrete cone failure, pull-out failure, combined pull-out and concrete cone failure, concrete splitting failure, and concrete blow-out failure. Figure 2 shows the schematic diagrams of the aforementioned failure modes for post-installed anchors under tension load.

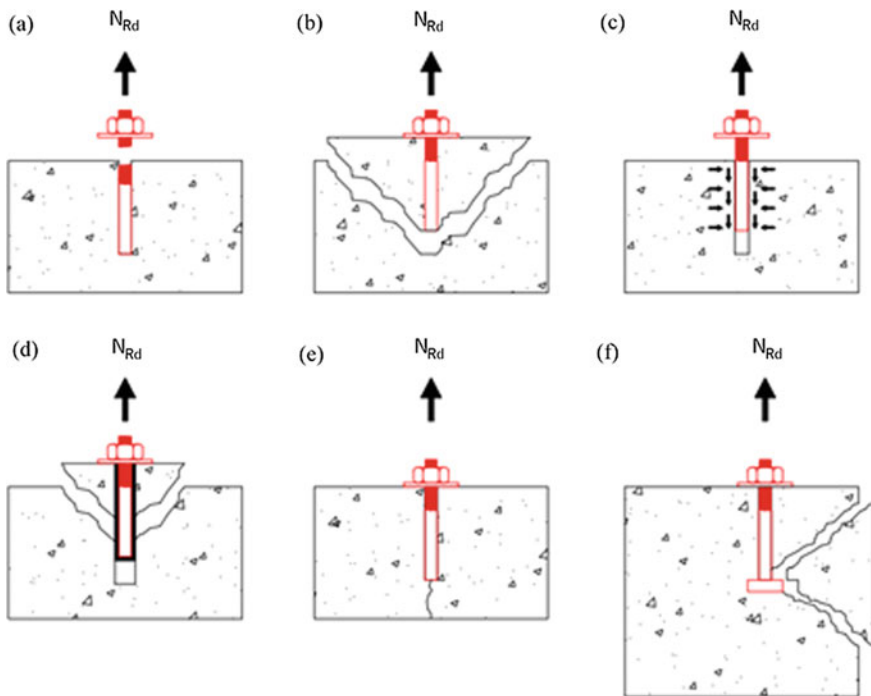


Fig. 2 Typical failure modes of post-installed anchors under tension load: **a** steel failure, **b** concrete cone failure, **c** pull-out failure, **d** combined pull-out and concrete cone failure, **e** concrete splitting failure, and **f** concrete blow-out failure

Table 1 Possible failure modes checks for mechanical and bonded anchors in tension

Failure mode	Mechanical anchor	Bonded anchor
Steel failure	Required	Required
Concrete cone failure	Required	Required
Pull-out failure	Required	Not required
Combined pull-out and concrete cone failure	Not required	Required
Concrete splitting failure	Required	Required
Concrete blow-out failure	Depend on anchor types	Not required

Steel failure occurs due to yielding and rupture of anchors where the maximum capacity of anchor is reached. Concrete cone failure is characterized by the formation of shallow cone-shaped fracture in the concrete when the full tensile capacity of the concrete is reached. Anchors with shallow embedment depth are susceptible to this mode of failure. The primary factors affecting this type of failure are the embedment depth of anchor, tensile strength of concrete and diameter of anchor head [10]. Pull-out failure is characterized by the anchor being pulled out from the drilled hole. This type of failure is only applicable for post-installed mechanical anchor or headed anchor as stated in Eurocode 2: Part 4 (2018). For post-installed bonded anchor, the failure would be the combined pull-out and concrete cone failure. Concrete splitting failure is characterized by vertical plane cracking of the base material concrete passing through the anchor, because of tension stresses. Anchor installed in relatively thin concrete member, very close to adjacent anchors or very near to concrete free edge are the possible causes of concrete splitting failure [7, 10, 11]. Concrete blow-out failure occurs when the anchor is installed close to concrete free edge. This type of failure is only applicable for headed anchor or post-installed mechanical undercut anchor acting as headed anchor if an edge distance equal or less than 0.5 times the embedment depth ($\leq 0.5h_{ef}$) as per requirement of Eurocode 2: Part 4 (2018). Table 1 summarizes the possible failure modes for mechanical and bonded anchors in tension according to Eurocode 2: Part 4 (2018).

2.2 Design Theories

The characteristic tensile resistance of anchor is calculated based on the various failure modes. The lowest resistance of anchor among the failure modes is dominant. This paper focuses on concrete cone failure, combined pull-out and concrete cone failure, concrete splitting failure, pull-out failure and steel failure. It is noted that the characteristic resistance of the pull-out failure is dependent on different load transfer mechanism and mechanical properties of the anchors. Also, the characteristic resistance of the steel failure is dependent on the mechanical properties of the anchors, which can be obtained from the relevant European Technical Assessment (ETA) reports. Therefore, readers are advised to refer to ETA reports. Equations (1)–(14)

are the characteristic tensile resistance equations for relevant failure modes adopted from Eurocode 2: Part 4 (2018).

(a) **Concrete cone failure ($N_{Rk,c}$)**

$$N_{Rk,c} = N_{Rk,c}^0 \left(\frac{A_{c,N}}{A_{c,N}^0} \right) (\varphi_{s,N}) (\varphi_{re,N}) (\varphi_{ec,N}) (\varphi_{M,N}) \tag{1}$$

where $N_{Rk,c}^0$ is the characteristics resistance of a single anchor placed in concrete without the influence of geometry or load eccentricity. It can be calculated using Eq. (2).

$$N_{Rk,c}^0 = k_1 (\sqrt{f_{ck}}) (h_{ef})^{1.5} \tag{2}$$

where k_1 is taken as 7.7 for cracked concrete and 11.0 for uncracked concrete. f_{ck} is the characteristic cylinder strength of concrete. h_{ef} is the embedment depth of the anchor. $A_{c,N}^0$ is the theoretical influencing area, which can be calculated as $s_{cr,N}^2$, where $s_{cr,N}$ is the characteristic spacing of anchor and it is considered as $3h_{ef}$. $A_{c,N}$ is the actual influencing area which can be calculated using Eq. (3).

For single reinforcement,

$$A_{c,N} = (c_1 + 0.5s_{cr,N})(c_2 + 0.5s_{cr,N}) \tag{3}$$

where c_1 and c_2 are defined in Fig. 3.

$\varphi_{s,N}$ is the effect of distribution stress due to edge which can be calculated using Eq. (4).

$$\varphi_{s,N} = 0.7 + 0.3 \left(\frac{c}{c_{cr,N}} \right) \leq 1 \tag{4}$$

where c is the smallest edge distance and $c_{cr,N}$ is the characteristic edge distance and it is considered as $1.5h_{ef}$.

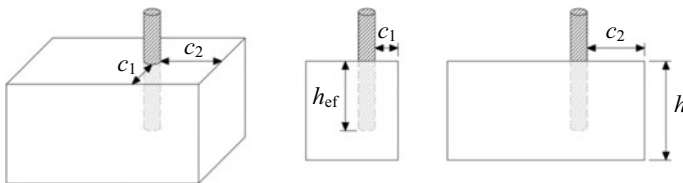


Fig. 3 Nomenclature explanation for c_1 and c_2

$\varphi_{re,N}$ is the shell spalling factor for dense reinforcement with embedment depth less than 100 mm. It can be calculated using Eq. (5).

$$\varphi_{re,N} = 0.5 + \frac{h_{ef}}{200} \leq 1 \quad (5)$$

$\varphi_{re,N}$ shall be taken as 1 if the spacing of the reinforcement provided is more than 150 mm for reinforcement size with any diameter or spacing of the reinforcement provided is more than 100 mm for reinforcement size with diameter of 10 mm or smaller.

$\varphi_{ec,N}$ is the factor to cater for different tension loads applied on the group anchors. It is taken as 1 if there is no eccentricity of the loading, otherwise it shall be calculated using Eq. (6).

$$\varphi_{ec,N} = \frac{1}{1 + 2(e_N/s_{cr,N})} \leq 1 \quad (6)$$

where e_N is the eccentricity of resultant tension force of tension anchors in respect to the centre of gravity of the tensioned anchors.

(b) **Concrete splitting failure ($N_{Rk,sp}$)**

$$N_{Rk,sp} = N_{Rk,sp}^0 \left(\frac{A_{c,N}}{A_{c,N}^0} \right) (\varphi_{s,N}) (\varphi_{re,N}) (\varphi_{ec,N}) (\varphi_{h,sp}) \quad (7)$$

where $N_{Rk,sp}^0 = \min \{N_{Rk,p}; N_{Rk,c}^0\}$ in case of mechanical anchor, and $N_{Rk,sp}^0 = \min \{N_{Rk,p}^0; N_{Rk,c}^0\}$ in case of bonded anchor. $A_{c,N}$, $A_{c,N}^0$, $\varphi_{s,N}$, $\varphi_{re,N}$ and $\varphi_{ec,N}$ shall be calculated according to the aforementioned Eqs. (3)–(6) as concrete cone failure, however the values $c_{cr,N}$ and $s_{cr,N}$ shall be replaced by $c_{cr,sp}$ and $s_{cr,sp}$. $c_{cr,sp}$ is depending on type of anchor and $s_{cr,sp} = 2c_{cr,sp}$.

$\varphi_{h,sp}$ is the influence of the actual member thickness on the splitting resistance which can be calculated using Eq. (8).

$$\varphi_{h,sp} = \left(\frac{h}{h_{min}} \right)^{2/3} \leq \max \left\{ 1; \left(\frac{h_{ef} + 1.5c_1}{h_{min}} \right)^{2/3} \right\} \leq 2 \quad (8)$$

where h_{min} is the minimum allowed thickness of concrete member.

(c) **Combined concrete cone and pull-out failure ($N_{Rk,p}$)**

$$N_{Rk,p} = N_{Rk,p}^0 \left(\frac{A_{p,N}}{A_{p,N}^0} \right) (\varphi_{g,Np}) (\varphi_{s,Np}) (\varphi_{re,Np}) (\varphi_{ec,Np}) \quad (9)$$

where $N_{Rk,p}^0$ is the characteristics resistance of a single bonded anchor without the influence of geometry or load eccentricity. It can be calculated using Eq. (10).

$$N_{Rk,p}^0 = (\pi)(D)(h_{ef})(\tau_{Rk})(\varphi_{sus}) \quad (10)$$

where D is the diameter of the anchor. τ_{Rk} and φ_{sus} are product dependent factors. τ_{Rk} is the characteristic bond strength in either uncracked or cracked concrete whereas φ_{sus} is the sustained load factor on bond strength as per Eq. (11).

$$\varphi_{sus} = \varphi_{sus}^0 + 1 - \alpha_{sus} \leq 1 \quad (11)$$

where φ_{sus}^0 can be taken from ETA or 0.6 as suggested in Eurocode 2: Part 4 (2018) for design life of 50 years with long term concrete temperature of 43 °C. α_{sus} is the ratio between sustained load and total load at ultimate limit state. $A_{p,N}$, $A_{p,N}^0$, $\varphi_{s,Np}$, $\varphi_{re,Np}$ and $\varphi_{ec,Np}$ shall be calculated according to the aforementioned Eqs. (3)–(6) as concrete cone failure, however the values $c_{cr,N}$ and $s_{cr,N}$ shall be replaced by $c_{cr,Np}$ and $s_{cr,Np}$, where $s_{cr,Np}$ is calculated using Eq. (12).

$$s_{cr,Np} = 7.3(D)\sqrt{(\varphi_{sus}) \times \tau_{Rk,ucr}} \leq 3h_{ef} \quad (12)$$

where $\tau_{Rk,ucr}$ is the characteristic bond strength in uncracked concrete for C20/25.

$\varphi_{g,Np}$ is a factor to account for the effect of closely packed fasteners which can be obtained by using Eq. (13).

$$\varphi_{g,Np} = \varphi_{g,Np}^0 - \left(\frac{s}{s_{cr,Np}}\right)^{0.5} \times (\varphi_{g,Np}^0 - 1) \geq 1 \quad (13)$$

$$\varphi_{g,Np}^0 = \sqrt{n} - (\sqrt{n} - 1) \times \left(\frac{\tau_{Rk}}{\frac{k_3}{\pi D} \sqrt{h_{ef}(f_{ck})}}\right)^{1.5} \geq 1 \quad (14)$$

The n represents the number of bonded anchors. k_3 is defined as 7.7 and 11.0 for cracked and uncracked concrete, respectively. The rest of the symbols are consistent with previously defined text.

3 Methodology Framework to Develop the Design Tool

In this paper, single anchor is considered for a 125 mm thickness slab. Slab member is chosen as typically it is vertically loaded with hanging structural or non-structural members at the soffit. A common grade of concrete, i.e. C30/37 cracked concrete is chosen to perform the analysis. It should be noted that cracked concrete should be considered as bending cracks tend to occur at the soffit of the slab. The edge distances are ranged from $2D$ to c_{cr} (i.e. characteristic edge distance).

3.1 Selecting Parameters

Tables 2 and 3 show the range of parameters adopted from various ETA reports [12–18] for post-installed mechanical anchors and bonded anchors, respectively. Based on Tables 2 and 3, typical anchor sizes of M8, M10, M12, M16, M20 and M24 are selected in this research. The embedment depth ratio (h_{ef}/D) will range from 4 to 14.

For mechanical anchors, the minimum allowed thickness of the concrete member is taken as the maximum of 100 mm or 2 times of the embedment depth of anchor ($2h_{ef}$) for mechanical anchors. As mentioned earlier, the characteristic edge distance ($c_{cr,sp}$) is dependent on the type of anchor. From Table 2, it is observed that different types of anchors feature different ranges of characteristic edge distance, hence $c_{cr,sp}$ of $1.5h_{ef}$, $2.5h_{ef}$ and $3.5h_{ef}$ are selected to perform the analysis in order to monitor the effect of characteristic edge distance on various failure modes.

For bonded anchors, the minimum allowed thickness is selected based on the anchor type. Table 3 summarizes some of the parameters for different types of anchor according to ETA-16/0143 [16], ETA-15/0882 [17] and ETA-12/0084 [18].

Table 2 Range of parameters for post-installed mechanical anchors

ETA	Anchor size	h_{ef}/D	h_{min}	$c_{cr,sp}$
ETA-02/0027 [12]	M6, M8, M10, M12	4–6.7	max (100 mm; $2h_{ef} - 2.2h_{ef}$)	$1.5h_{ef} - 1.7h_{ef}$
ETA-99/0009 [13]	M10, M12, M16, M20	10–12.5	$1.4h_{ef} - 1.8h_{ef}$	$1.5h_{ef}$
ETA-02/0042 [14]	M8, M10, M12, M16, M20, M24	6.3–12.5	$1.9h_{ef} - 2.5h_{ef}$	$1.75h_{ef} - 3.3h_{ef}$
ETA-98/0001 [15]	M8, M10, M12, M16, M20, M24	4–6	max (100 mm; $1.9h_{ef} - 2h_{ef}$)	$1.5h_{ef} - 2.1h_{ef}$

Note D is the diameter of anchor, h_{ef} is the embedment depth of anchor

Table 3 Range of parameters for post-installed bonded anchors

ETA	Anchor size and type	h_{ef}/D	h_{min}	$c_{cr,sp}$
ETA-16/0143 [16] ETA-15/0882 [17] ETA-12/0084 [18]	M8–M30 (threaded rod/meter rod)	4–20	$D < 16$: $h_{min} = \max(100 \text{ mm}; h_{ef} + 30)$ $D \geq 16$: $h_{min} = h_{ef} + 2D_0$	Depend on member thickness to embedment depth ratio
	M12–M24 (tension anchor)	8–20	$h_0 + 2D_0$	$h/h_{ef} \geq 2$, $c_{cr,sp} = h_{ef}$ $2 > h/h_{ef} > 1.3$, $c_{cr,sp} = 4.6h_{ef} - 1.8h$
	M8–M20 (internal threaded sleeve)	10.3–20	$13.5D - 15D$	$h/h_{ef} \leq 1.3$, $c_{cr,sp} = 2.26h_{ef}$

Note D is the diameter of anchor, D_0 is the diameter of the drill hole, h_{ef} is the embedment depth of anchor, h_0 is the depth of drilled hole

For anchor diameter of less than 16 mm, the minimum thickness of the concrete member is equal to maximum of 100 mm or embedment depth of the anchor (h_{ef}) plus 30 mm, while for anchor diameter of equal to or greater than 16 mm, the minimum thickness of the concrete member is equal to embedment depth of the anchor (h_{ef}) plus 2 times the diameter of the drill hole ($2D_0$). The characteristic edge distance ($c_{cr,sp}$) is shown in Table 3. The characteristic adhesive bond strength (τ_{Rk}) is acquired from relevant ETA reports according to the anchor type and anchor size. Hence, a specific adhesive product, Hilti HIT RE-500 V3, is selected to perform the analysis as it is commonly used in construction.

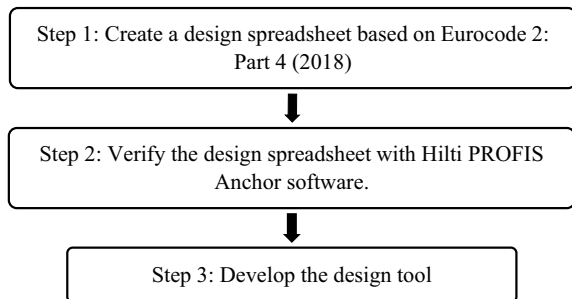
3.2 Developing the Design Tool

The conceptual flowchart for developing the design tool is as shown in Fig. 4. First, a design spreadsheet to estimate the characteristic tensile capacity of anchors for each failure modes is created. The calculation is based on the equations found in Eurocode 2: Part 4 (2018). The spreadsheet is verified by using Hilti PROFIS Anchor software [9]. An example of the results comparison (e.g. Expansion anchor (mechanical anchor) for C30/37 concrete with sizes of M8, M10, M12, M16, M20 and M24, and thickness of concrete member, h equals to $2.5h_{ef}$, with edge distance (c_1 and c_2) follows the minimum requirements from ETA) between the spreadsheet and Hilti PROFIS Anchor software [9] is shown in Fig. 5, where the results are matching perfectly.

The lowest resistance of anchor among all the failure modes will be the dominant resistance. Figure 6 shows the methods to develop the design tool for a single set of parameters (i.e. Mechanical anchor for 125 mm thick C30/37 concrete with size of M8 and edge distance (c_1 and c_2) equals to $c_{cr,N}$). Figure 6a shows the tensile resistance capacity for each failure modes (cone, splitting and steel). The design tool is formed by taking the lowest boundary line of all the resistance capacities, as shown in Fig. 6b. The same steps are repeated for other sets of parameters.

Figure 6 shows the effects of tensile capacity by varying the embedment depth (h_{ef}) alone. It should be noted that edge distance (c_1 or c_2) presents another dimension

Fig. 4 Flowchart of developing the design tool



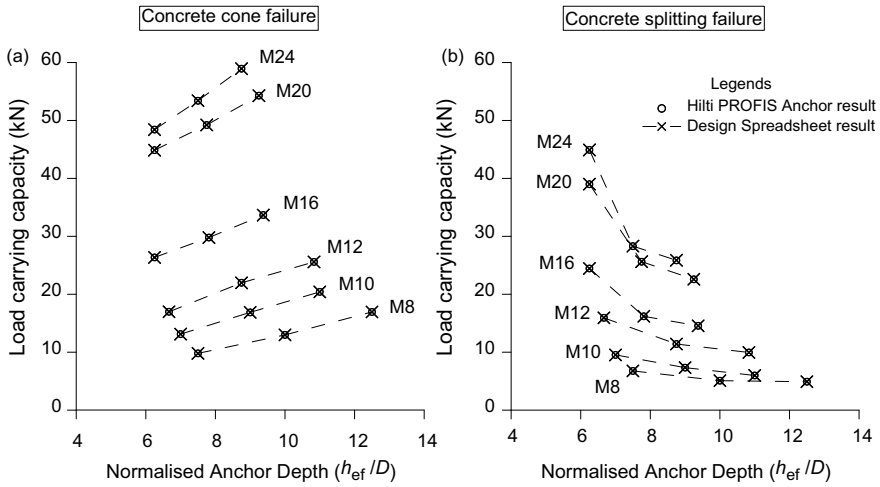


Fig. 5 Results comparison between design spreadsheet and Hilti PROFIS Anchor software for expansion anchor: **a** concrete cone failure, and **b** concrete splitting failure (with consideration of pull-out failure)

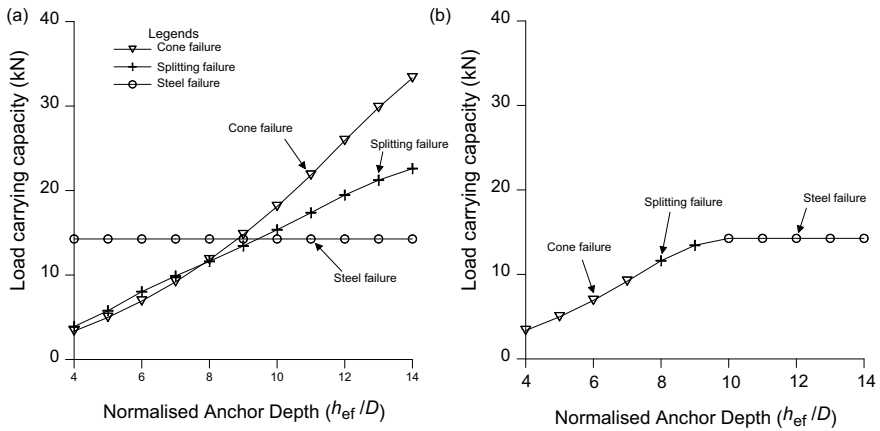


Fig. 6 An example of the development of the design tool: **a** tensile resistance capacity for each failure modes, and **b** the lowest boundary line to form the design tool

of effect on the tensile capacity. Figure 7a shows a three-dimensional graph featuring the embedment depth axis, edge distance axis and the resulting tensile capacity axis. This 3D graph can be simplified into a two-dimensional graph by overlaying the minimum edge distance (taken as $2D$) and the maximum edge distance (c_{cr}).

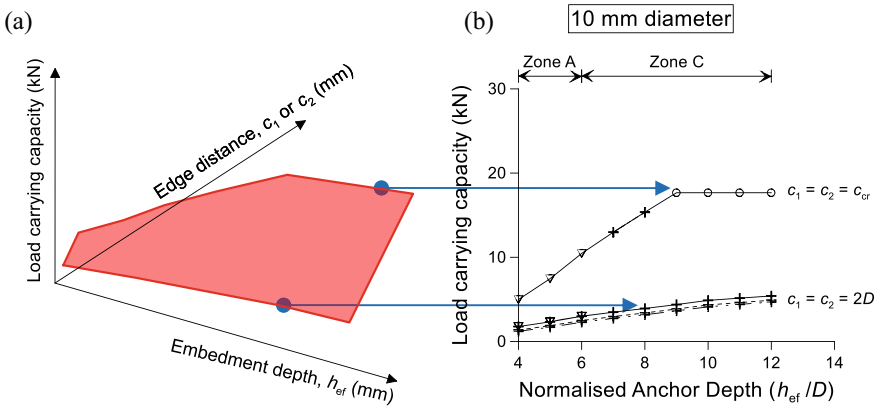


Fig. 7 An example of the development of the design tool considering embedment depth and edge distance: **a** the three-dimensional graph, and **b** overlay on a two-dimensional graph

4 Results and Discussions

4.1 Mechanical Anchors

Adopting the methodology explained in Figs. 6 and 7. Figure 8 shows the characteristic tensile resistance capacity against the embedment depth-to-anchor diameter ratio (h_{ef}/D) for mechanical anchors of 8, 10, 12, 16, 20 and 24 mm. Interestingly, two zones featuring different failure modes can be observed. In Zone A, concrete cone failure and concrete splitting failure are observed for the case when edge distance in both directions (c_1 or c_2) is less than the characteristic edge distance (c_{cr}) and the characteristic edge distance for concrete splitting failure ($c_{cr,sp}$) is same as the characteristic edge distance for concrete cone failure ($c_{cr,N}$). This is because of the equations for concrete cone and concrete splitting failures are similar in Eurocode 2: Part 4 (2018). However, there is possibility that concrete splitting failure is dominant in Zone A. This happens when the characteristic edge distance for the concrete splitting failure ($c_{cr,sp}$) is greater than the characteristic edge distance for concrete cone failure ($c_{cr,N}$), or the characteristic resistance for pull-out failure ($N_{Rk,p}$) is considered. Besides, it can be observed that concrete splitting failure dominates when edge distance in both directions (c_1 and c_2) reach the maximum, i.e. greater than the characteristic edge distance (c_{cr}).

In Zone C, concrete splitting failure and steel failure are observed. The occurrence of concrete splitting failure is likely due to long embedment depth of anchor installed in thin concrete member (e.g. slab). The insufficient distance between the tip of the anchor and the remaining concrete member thickness before reaching the surface, causes concrete to crack due to tensile stresses (see Fig. 8e). Furthermore, it can be seen that the capacity of the anchor reduces with the increase of characteristic edge distance for concrete splitting failure ($c_{cr,sp}$) for the case when edge distance

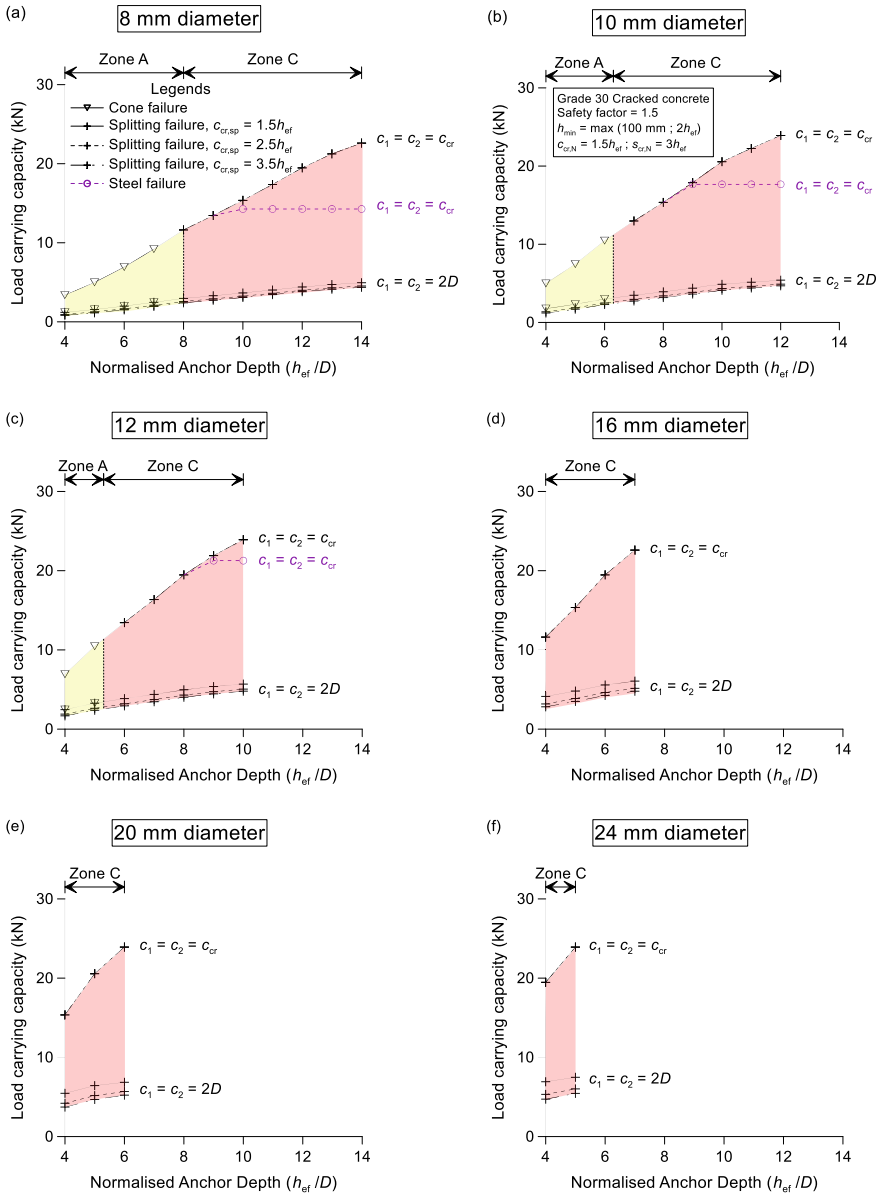


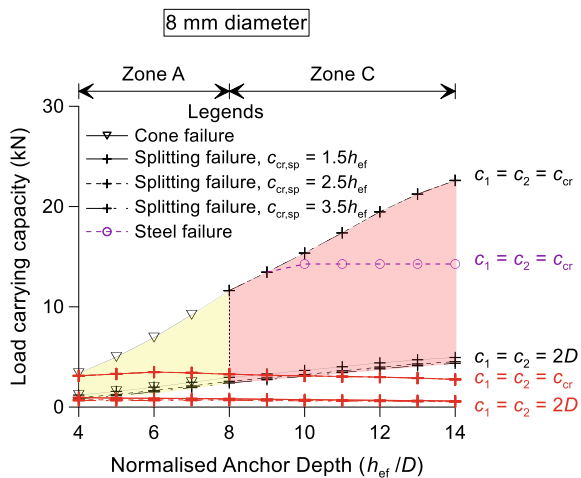
Fig. 8 Load carrying capacity against embedment depth ratio for mechanical anchors: **a** 8 mm, **b** 10 mm, **c** 12 mm, **d** 16 mm, **e** 20 mm, and **f** 24 mm anchor diameter. *Note* The characteristic resistance of steel failure is dependent on the mechanical properties of the anchors. Pull-out failure has not been considered. Material partial safety factor of 1.5 is applied

(c_1 or c_2) is less than the characteristic edge distance (c_{cr}). However, the increase of characteristic edge distance ($c_{cr,sp}$) will not affect the capacity of the anchor when the edge distance in both directions (c_1 and c_2) is greater than the characteristic edge distance ($c_{cr,sp}$). Note that under the same case, steel failure (yielding) was observed for the anchor diameter less than 16 mm. The occurrence of steel failure is dependent on the mechanical properties of the mechanical anchors, which may produce a lower resistance in Zone C at larger c_1 or c_2 .

In Fig. 8, it should be noted that pull-out failure has not been considered. Figure 9 shows an example of results (e.g. Expansion anchor (mechanical anchor) for C30/37 concrete with size of M8) with consideration of characteristic resistance for pull-out failure ($N_{Rk,p}$). From Fig. 9, it can be seen that the pull-out resistance is significantly affecting the capacity of the anchor. Concrete splitting failure are observed and dominated Zone A and Zone C when the characteristic resistance for pull-out failure ($N_{Rk,p}$) is considered. This is only applicable for mechanical anchor features friction grip load transfer mechanism, i.e. expansion anchor. However, for mechanical anchor features mechanical interlock load transfer mechanism, i.e. undercut anchor, the characteristic resistance for concrete splitting failure ($N^0_{Rk,sp}$) is conservatively calculated as the characteristic resistance for concrete cone failure ($N^0_{Rk,c}$) as indicated in Eq. 7. This is due to this anchor type is not governed by pull-out failure. Therefore, it is recommended to use mechanical anchor features mechanical interlock load transfer mechanism when large load carrying capacity is required.

From the foregoing results, it can be concluded that concrete cone failure is more likely to occur for small diameter anchor ($D \leq 12$ mm) with short embedment depth. As the diameter of the anchor or embedment depth increases, the occurrence of concrete cone failure reduces and eventually will be dominated by concrete splitting failure. Steel failure may occur only for small anchor diameter. Even though, large anchor diameter and deep embedment depth increase the capacity of the anchor [19], but it is recommended to avoid using large anchor diameter in thin concrete

Fig. 9 The effect of pull-out resistance on the capacity of the anchor



member. The characteristic edge distance (c_{cr}) is an important parameter as it affects the capacity of mechanical anchors. As the characteristic edge distance for concrete splitting failure ($c_{cr,sp}$) increases, the capacity of anchor reduces. In addition, pull-out resistance has a major impact on the capacity of the anchors, therefore readers are advised to refer to ETA reports.

4.2 Bonded Anchors

Figure 10 shows the estimated load carrying capacity with the possibly failure modes against the embedment depth-to-anchor diameter ratio (h_{ef}/D) for bonded anchors. From Fig. 10, it can be seen that the dominant failure modes are different, depending on the diameter of the bonded anchor. Four categories of anchor diameters are grouped for ease of discussion.

(i) $D \leq 10$ mm

Two types of failure modes are observed for diameter of anchor less than or equal to 10 mm, as shown in Fig. 10a, b. In Zone B, combined pull-out and concrete cone failure is observed, while in Zone C concrete splitting failure was observed. For a small diameter anchor with short embedment depth, combined pull-out and concrete cone failure is observed instead of concrete cone failure. This is likely due to adhesive bond fails first before concrete reaches its tensile capacity. As the pull-out resistance of bonded anchor is dependent on the circumference surface and adhesive bond resistance as indicated in Eq. 10, therefore the characteristic bond resistance of small diameter anchors is relative low (due to smaller circumference surface) which causes combined pull-out and concrete cone failure instead of concrete cone failure.

Concrete splitting failure (Zone C) is observed when the embedment depth reaches certain limit. The same observations and explanations as in mechanical anchors apply, i.e. due to insufficient distance between the tip of anchor and the remaining concrete member thickness before reaching the surface, which causes concrete to crack. It is noted that steel failure (yielding) was observed for 8 mm diameter anchor in the case when edge distance (c_1 or c_2) reaches the characteristic edge distance (c_{cr}). A transition zone (Zone T) is identified, where the occurrence of combined pull-out and concrete cone failure is inconsistent with respect to different edge distances (c_1 and c_2).

(ii) $D = 12$ mm

For 12 mm diameter anchor, there are three zones of controlling failure modes as observed, and shown in Fig. 10c. Concrete cone failure occurs at short embedment depth (see Zone A). As the embedment depth increases, the failure modes are dominated by combined pull-out and concrete cone failure (Zone T) and followed by concrete splitting failure (Zone C) for the case of large edge distance is provided. However, only two types of failure modes were observed when the anchor is placed near to the edge (for the case of $c_1 = c_2 = 2D$). Concrete cone failure was observed at

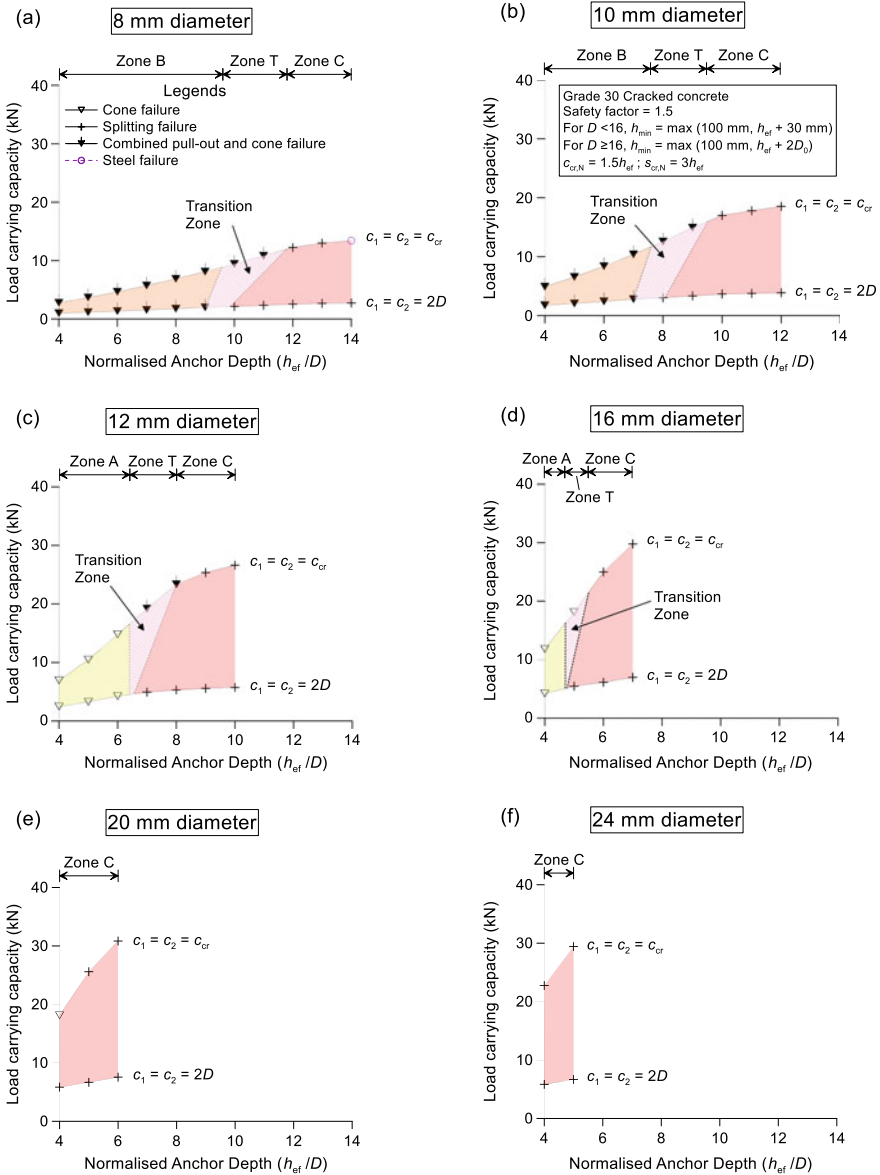


Fig. 10 Load carrying capacity against embedment depth ratio for bonded anchors: **a** 8 mm, **b** 10 mm, **c** 12 mm, **d** 16 mm, **e** 20 mm, and **f** 24 mm anchor diameter. *Note* The characteristic resistance of steel failure is dependent on the mechanical properties of the anchors. Material partial safety factor of 1.5 is applied

short embedment depth, and followed by concrete splitting failure when the embedment depth of the anchor increases. The failure modes in the transition zone (Zone T) for edge distances (c_1 and c_2) between $2D$ and c_{cr} behaved differently with respect to different edge distances. The failure modes are possibly dominated by: (i) concrete cone failure and followed by concrete splitting failure, and (ii) concrete cone failure, then combined pull-out and concrete cone failure, and followed by concrete splitting failure.

(iii) **$D = 16 \text{ mm}$**

Two types of failure modes (Zones A and C) are observed, as shown in Fig. 10d. Concrete cone failure is observed at short embedment depth, and followed by concrete splitting failure when the embedment depth of the anchor increases. As compared to smaller diameter anchor ($D \leq 12 \text{ mm}$), the occurrence of concrete splitting failure is observed at small embedment depth ratio. Noted that the occurrence of concrete cone failure is inconsistent with respect to different edge distances (c_1 and c_2) in transition zone (Zone T).

(iv) **$D \geq 20 \text{ mm}$**

The failure modes are mainly dominated by concrete splitting failure. But, for anchor diameter of 20 mm, there is possibility of concrete cone failure at short embedment depth for the case when edge distance is greater or equal to characteristic edge distance (c_{cr}).

From the foregoing results, it can be concluded that small diameter of bonded anchor ($D \leq 10 \text{ mm}$), combined pull-out and concrete cone failure occurs more frequently at short embedment depth, and followed by concrete splitting failure when the embedment depth increases. Steel failure may possibly occur, only for smaller anchor diameters. For medium size anchors ($D = 12 \text{ mm}$), concrete cone failure happens at short embedment depth, and followed by combined pull-out and concrete cone failure, and concrete splitting failure for the case of large edge distance. As the diameter of anchors increases, the occurrence of concrete cone failure reduces, combined pull-out and concrete cone failure will be eliminated and will be dominated by concrete splitting failure. Similar to mechanical anchor, it is recommended to avoid using large anchor diameter in thin concrete member even though the large anchor diameter and deep embedment depth increase the adhesive areas between the concrete and anchor according to Wang et al. [20].

5 Conclusion

This paper describes the latest design procedure of post-installed anchor subject to tensile action as per Eurocode 2: Part 4 (2018). A methodology to simplify the complex empirical equations in the code into feasible design tensile capacity regions is presented using an example of C30/37 cracked concrete for a 125 mm thick slab. The controlling failure mechanisms were found to vary according to types of anchors

(mechanical or bonded) and the diameter of anchor. Importantly, it is recommended to avoid using large anchor diameter in thin concrete member. The authors foresee that the design tools developed using the methodology in this paper are useful for practicing engineers in quick estimation of anchor resistance. For non-gravity-controlled type of applications (other than structural or non-structural components hanging on soffit of slab assumed in this paper), shear resistance of anchors should be included in the design of anchors [21–23]. The interaction of shear and tension should be carefully considered in the design.

References

1. Mechanical fasteners for use in concrete. European Assessment Document, EAD 330232-00-0601 (2016)
2. Bonded fasteners for use in concrete. European Assessment Document, EAD 330499-00-0601 (2017)
3. González F, Fernández J, Agranati G, Villanueva P (2018) Influence of construction conditions on strength of post-installed bonded anchors. *Constr Build Mater* 165:272–283
4. Wald ML (2007) Collapse of big dig ceiling in Boston is tied to glue. *The New York Times*. <https://www.nytimes.com/2007/07/11/us/11bigdig.html>. Accessed 2020/03/11
5. Goto Y, Obata M, Maeno H, Kobayashi Y (1993) Failure mechanism of new bond-type anchor bolt subject to tension. *J Struct Eng* 119(4):1168–1187
6. McVay M, Cook RA, Krishnamurthy K (1996) Pullout simulation of postinstalled chemically bonded anchors. *J Struct Eng* 122(9):1016–1024
7. Eligehausen R, Mällée R, Silva JF (2006) Anchorage in concrete construction, 1st edn. Ernst & Sohn GmbH & Co. KG, Germany
8. European Standard (2018) Design of concrete structures—part 4: design of fastenings for use in concrete. BS EN 1992-4:2018. British Standard Institution, United Kingdom
9. Hilti (2019) Hilti webpage. PROFIS Anchor. https://www.hilti.com.my/c/CLS_CUSTOMER_SOFTWARE/CLS_SOFTWARE_FASTENING_SYSTEMS/r2755?itemCode=2097332. Accessed 2019/10/09
10. Ashour AF, Alqedra MA (2005) Concrete breakout strength of single anchors in tension. *Adv Eng Softw* 36(2):87–97
11. Nilforoush R, Nilsson M, Elfgren L (2018) Experimental evaluation of influence of member thickness, anchor-head size, and orthogonal surface reinforcement on the tensile capacity of headed anchors in uncracked concrete. *J Struct Eng* 144(4):04018012-1–14
12. European Technical Assessment (2018) Hilti HSC undercut anchor, ETA-02/0027
13. European Technical Assessment (2015) Hilti HDA undercut anchor, ETA-99/0009
14. European Technical Assessment (2017) Hilti HSL-3 expansion anchor, ETA-02/0042
15. European Technical Assessment (2018) Hilti HST3 expansion anchor, ETA-98/0001
16. European Technical Assessment (2019) HIT-RE 500 V3 injection mortar, ETA-16/0143
17. European Technical Assessment (2019) HIT-RE 100 injection mortar, ETA-15/0882
18. European Technical Assessment (2019) HIT-HY 200-R injection mortar, ETA-12/0084
19. Kim JS, Jung WY, Kwon MH, Ju BS (2013) Performance evaluation of the post-installed anchor for sign structure in South Korea. *Constr Build Mater* 44:496–506
20. Wang D, Wu D, Ouyang C, Zhai M (2016) Performance and design of post-installed large diameter anchors in concrete. *Constr Build Mater* 114:142–150

21. Çalışkan Ö, Yılmaz S, Kaplan H, Kırac N (2013) Shear strength of epoxy anchors embedded into low strength concrete. *Constr Build Mater* 38:723–730
22. Epackachi S, Esmaili O, Mirghaderi SR, Behbahani AAT (2015) Behavior of adhesive bonded anchors under tension and shear loads. *J Constr Steel Res* 114:269–280
23. Takase Y (2019) Testing and modelling of dowel action for a post-installed anchor subjected to combined shear force and tensile force. *Eng Struct* 195:551–558

The Maximum Allowable Peak Ground Acceleration of a Six Storey Building Based on Micro Tremor and Numerical Analysis



Agustinus Sri Pandu and Henricus Priyosulistyo

Abstract It is widely known that the natural frequency of building structures can be determined by analyzing Fourier transforms from micro vibrational records. This research was conducted in the structural laboratory of the Department of Civil and Environmental Engineering of UGM, which is a six-storey building. The aim of this study is to verify if maximum ground acceleration of the building in accordance to SNI: 1726-2012 can be approximated by means of analysing amplitudes of microtremor data of the building at resonance. In addition, a numerical calculation is also presented using SAP 2000 for a comparison purpose. The accelerometers were positioned alternately in the direction of N-S and E-W, at the lower end of the columns, close to the center of gravity of the building, on each floor. One of the PCB-Piezotronics accelerometers was placed at the bottom end of the ground floor column while the other one was placed at the bottom end of the consecutively above floor columns. Natural frequencies of the building, resulting from the site measurement, were utilized for validation of the model. The results of this measurement indicate that the first natural frequencies in the direction of N-S and E-W are respectively 2.2473 and 2.1496 Hz. Based on Nakamura theorem (Clear identification of fundamental idea of Nakamura's technique and its applications, 2000 [1]), the highest vulnerability index occurs in the N-S direction, on the 4th story but for the E-W direction it does in the 3rd story. The predicted maximum allowable ground accelerations, based on the minimum acceptable acceleration at the drift ratio between floors at 1% of resonance, are 216.576 cm/s² (gal) and 177.037 cm/s² (gal) in the N-S and E-W directions respectively. If the lowest value binds, the maximum allowable ground acceleration of the building is 177.037 cm/s². The bi-axial analysis on column K1 at 4th and 3rd story approves that the column cannot withstand peak

A. S. Pandu

Department of Civil and Environmental Engineering, Faculty of Engineering, Universitas Gadjah Mada, Yogyakarta, Indonesia

H. Priyosulistyo (✉)

Structural Engineering of Department of Civil and Environmental Engineering, Faculty of Engineering, Universitas Gadjah Mada, Yogyakarta, Indonesia

e-mail: priyo_ugm@ugm.ac.id

ground acceleration at resonance with amplitude of 216.576 cm/s^2 (gal). The numerical comparison using SAP 2000 and sinusoidal function at the resonance frequency of 2.1705 Hz in the N-S direction, shows that the maximum allowable acceleration is of 241.33 cm/s^2 (gal) which is similar to the experimental results in the same direction. On the other hand, the numerical analysis using a sinusoidal frequency at out of resonance (4 Hz) in the E-W direction predicts allowable ground acceleration of 943.643 cm/s^2 (gal). Such a prediction is 533% greater than the results of site measurement. This concludes that if there is no resonance to occur during the earthquake shake, the building can accept significantly higher ground acceleration.

Keywords Resonance frequency · PGA · Allowable acceleration · Predicted maximum ground acceleration

1 Introduction

Indonesia is located between three main plates namely, the Australian, the Eurasian, and the Pacific Plates. This is one of some factors that causes Indonesia to become an earthquake-prone area. Earthquakes can cause a structure to damage or to collapse due to the decrease of its stiffness and strength. The structure will suffer great damage if a resonant frequency occurs to the building [2], where one of frequencies of earthquake vibration is close to the natural frequency of the structure. If these conditions occur, the building structure will become more vulnerable to damage.

One way to predict structural damage upon the earth can be carried out by measuring micro vibration of the horizontal to vertical amplitudes ratio at the related natural frequency [1, 3]. The natural frequency of structures in buildings used to be determined by measuring large vibrations resulting from dynamite explosion which was buried down the earth. Nowadays, such a method is no longer permitted since it may cause damage and injury to people at surrounding. The invention of very sensitive sensors has made the recording of very low vibrations possible. Measurement of vibrations in structures using the accelerometer is a method that does not damage structures because it can be done by recording ambient vibrations [4–7]. This research was carried out to investigate the compliment to SNI 1726-2012, after Bantul Earthquake in 2006, using H/V spectral ratio. The Nakamura theorem [1, 3] had indicated that the maximum allowable acceleration of the building (98 cm/s^2) did not comply with the SNI 1726-2012. The analysis of frequencies and amplitudes was carried out by using Fast Fourier Transformation (FFT) upon the recorded data of the building in terms of velocity or acceleration. For a quick assessment purposes, ambient noise vibrations were measured on the building of Kinanti and Sendowo dormitories on 2016, [8–10] and were analysed using Fast Fourier Transform and averaging technique. These analyses approved that the dormitory buildings should be strengthen against Earthquake as required by SNI 1726-2012. Such a technique also applied on Ambarrukmo Hotel for liability assessment purpose since this building had exceeded the designated building life time. Another research was carried out to

find the capability of low rise buildings against Earthquake shake that are usually used by engineers. A square masonry wall of $2 \times 2 \text{ m}^2$ with surrounded reinforced columns and beams was tested in plane and was measured its vibration characteristics in stages [10]. An experimental study was carried out on buildings throughout the city of Surabaya in the region, representing the one-story buildings, governmental buildings, historical buildings and public buildings. This study investigated the interaction between natural frequencies of soil and structures upon it, using H/V spectral ratio. This study concluded that the closer the natural frequency of structure to the natural frequency of soil the higher the vulnerability indices of the structure against Earthquake shake [11]. Effect of strengthening of modern, historical and monumental buildings was studied on the natural frequencies of the building, using H/V spectral ratio of ambient noise vibration in the cities of Chania, Rethymno and Heraklion of Crete [12]. The result showed that soil types underneath the building were highly affected to the vibration response of the structure.

This research aims to identify the performance (vulnerability and capability) of the Building Materials Laboratory of the Department of Civil and Environmental Engineering of UGM (see Fig. 1) under horizontal peak ground acceleration originated from earthquake shake using Nakamura proposed theory [1, 3]. The site vibration measurement is very simple and the related analysis can be performed in very short time. For reliable results, a numerical model is set up using SAP 2000 and simulation is carried out by adjusting damping factor and natural frequency obtained from the site measurement data. Simplification is carried out by assuming that the building moves horizontally in the North-South (N-S) and East West (E-W) directions. Two *PCB-Piezotronics* sensors were used, one was placed on the bottom end of column on the ground floor and the other was on the bottom end of column of every floor. The data were recorded simultaneously, in pair and in every direction. From the vibration recordings, the first natural frequency in every direction may be obtained, and so do the amplification factor, the level of structural vulnerability, and the maximum acceleration of the building structure.

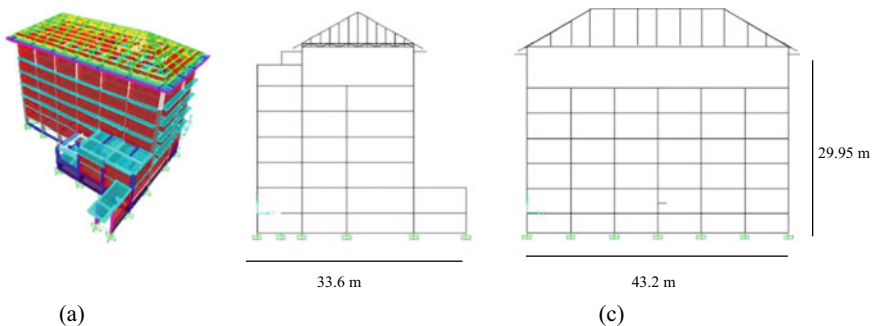


Fig. 1 a 3D image of building, b lateral section, c longitudinal section

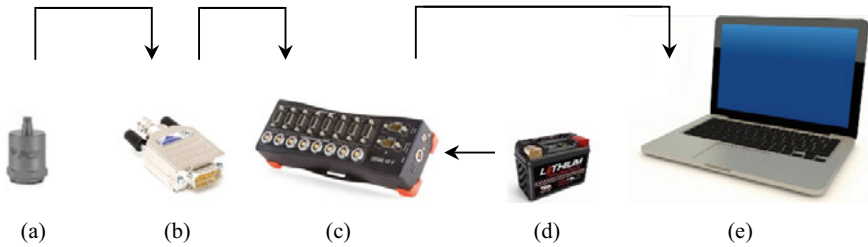


Fig. 2 a Accelerometer PCB 393B05, b adapter MSI BR ACC, c analog to digital converter (DEWE 43A), d battery, and e laptop

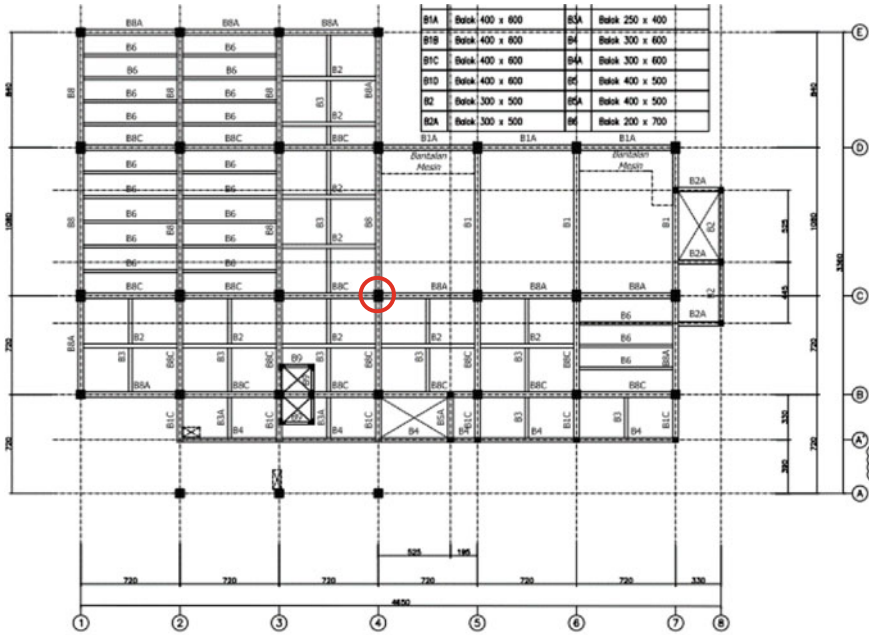
2 Research Method

2.1 Devices

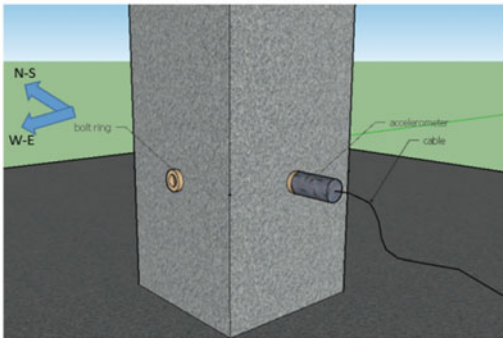
The accelerometers (*PCB Piezotronics*) with sensitivity of 10.270 and 10.300 V/g were elaborated. These sensors serve to record vibrations experienced by the structure in the horizontal direction, namely X and Y (N-S and E-W). The output signal was pre conditioned using signal adapter of MSI BR ACC and was sent to the Conditioner (*DEWE 43A*) which was functioned to filter (low pass, high pass, band stop, band pass) and to convert analog signal into digital signal for further analyses using available programs (*DEWESoft X1 SP7*). The digital data were kept in the computer memory for further analyses (see Fig. 2).

2.2 Site Measurement Procedures

This research used accelerometer sensors, namely *PCB Piezotronics* that can record vibrations in the horizontal direction (N-S and E-W). One sensor was placed close to bottom end of column of the ground floor at about the center of the gravity of the building at column C-4 (see Fig. 3a). The other sensor was placed on the bottom end of column of the top story and sequentially down to the first floor (see Fig. 3b, c). In every floor the micro vibration signal was recorded horizontally in N-S and E-W directions. Vibration signals in both sensors were recorded simultaneously. Sampling rate was set at 100 Hz since the frequency of interest is below 50 Hz. An amount of 1024 data was transformed by FFT program and 25 spectra were averaged to eliminate unwanted noises. For this study, therefore 5 min recording was needed for every direction per floor. To avoid rigorous and noisy data, a recording time was chosen at 05:00 a.m.



(a)



(b)



(c)

Fig. 3 a Point of measurement on the layout of building, b 3D sketch of measurement on bottom end of column, c site experiments

2.3 Signal Processing and FFT

Signal processing is a must since very low vibration concerned which aims, amongst other, to convert time domain data into frequency domain data by means of FFT method and to eliminate noises by averaging technique. Since noise is defined as random signals then by the averaging technique to as many as spectra will eliminate the noise [8]. To choose the number of spectra for noise elimination this

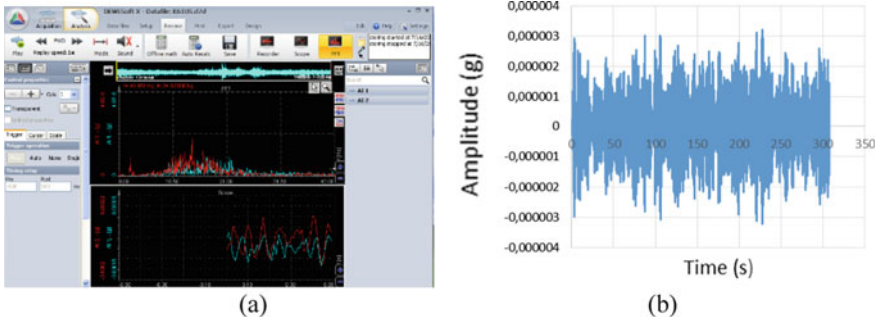


Fig. 4 **a** Display of DeweSoft-X1 program in binary format, **b** time history in *.csv format

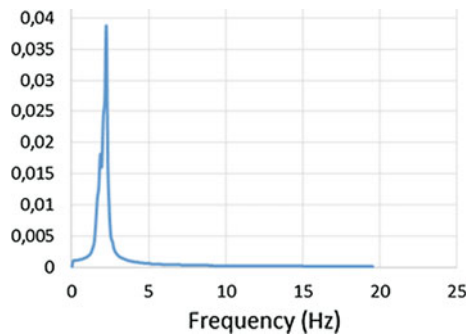
research followed the suggestion as proposed by Ramirez [8] which was 20–30 spectra. Channel-1 contained the vibration signal recorded on the ground floor, and channel-2 was from any upper floors which was recorded in pair.

The recorded data of the micro vibration was picked up and stored using the DeweSoft X-1 program in the form of binary format (see Fig. 4a). For further analyses, by self-made program namely FFTDEWE.exe, the data was downloaded from DeweSoft X-1 memory and was changed into excel format (*.xls). Since the FFTDEWE.exe required *comma separated value format* (*.csv) therefore the data shall be restored again using available (*.csv) extension (see Fig. 3b).

Results of DeweSoft-X1 in binary and excel format are shown in Fig. 4a which the frequency and amplitude are not quite clear. To eliminate noises around the frequency of interest, the binary format can be converted into *.xls format using DeweSoft-X1 and is restored again to obtain data in *.csv format as shown in Fig. 4b. This data is then cut into 25 set of 1024 digital data, and is transformed into frequency domain to provide 25 set of spectrum using FFTDEWE.exe. These spectra are then averaged to eliminate noises.

Result of averaging process is shown in Fig. 5 which indicates that the resonance frequency of the structure is at 2.149 Hz with the peak amplitude of acceleration

Fig. 5 The spectrum of microtremor of the building after signal averaging



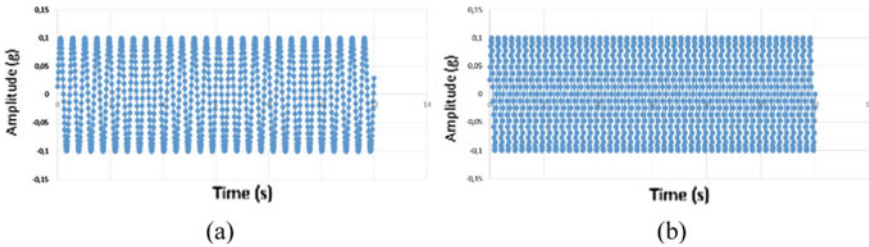


Fig. 6 a Sinusoidal vibrations at $f = 2.1705$ Hz, b sinusoidal vibrations at $f = 4$ Hz

of $0.038/50,000$ (g). From sets of recording, the amplification factors (ratio of horizontal amplitude of a certain floor to the horizontal amplitude of the ground floor at resonance frequency) may be defined in E-W and N-S directions. Results of those amplification factors and the inter story drifts may be drawn graphically and defined respectively. Applying standard of drift ratio as defined in SNI 1726-2012 for certain condition of building after earthquake, the predicted allowable ground acceleration on every floor may be defined.

2.4 Numerical Modeling

The numerical modeling was set up using SAP 2000 in such a way that the dynamic properties were similar to the prototype (building materials laboratory). The damping factor and the first natural frequency of the model were taken from the prototype (site measurement) in the direction of N-S and E-W. The model was then horizontally excited on the ground floor using sinusoidal time history with a frequency of the same as the natural frequency of the model, that is 2.1705 Hz (see Fig. 6a, b) and the amplitude of vibration was arbitrarily set as close as to recorded signal. Another sinusoidal time history of 4 Hz was also applied to study the effect of non-resonant frequency signal on the prediction of the allowable peak ground acceleration.

3 Theoretical Basis

3.1 Amplification Factor and Storey Drift

Based on Nakamura proposed theory [1] the amplification factor (A_{sj}) can be calculated using Eq. (1) by dividing the horizontal amplitude depicted from response spectrum of the floor- j (α_{sj}) by the horizontal amplitude depicted from the response of the ground floor (α_g).

$$A_{sj} = \frac{\alpha_{sj}}{\alpha_g} \tag{1}$$

where,

- A_{sj} amplification factor
- α_{sj} horizontal amplitude of the floor- j (cm/s²)
- α_g horizontal amplitude of the ground floor (cm/s²).

Storey drift (γ_j) can be calculated using Eq. (2) by dividing the difference between the observed deformation of the floor- j and floor- $(j - 1) = (\delta_j - \delta_{j-1})$ by the height between the floors being reviewed (h_j).

$$\gamma_j = \frac{\delta_j - \delta_{j-1}}{h_j} \tag{2}$$

where,

- γ_j story drift
- $\delta_j - \delta_{j-1}$ difference between the observed deformation of the floor- j and floor- $(j - 1)$ (mm)
- h_j height between floors being reviewed (mm).

3.2 Vulnerability Index

Vulnerability index is defined as an index showing the potency of a structure to be collapse [3]. Equation (3) shows the equation for calculating the vulnerability index, K_{Tj} .

$$K_{Tj} = 10^4 \frac{A_{sj} - A_{sj-1}}{4\pi^2 F_s^2 h_j} \tag{3}$$

where,

- K_{Tj} vulnerability index (1/Gal)
- $A_{sj} - A_{sj-1}$ difference of the amplification factors between floors being reviewed
- F_s natural frequency of structure (Hz)
- h_j structure height between floors being reviewed (m).

3.3 The Maximum Allowable Ground Acceleration

The maximum allowable ground acceleration of a structure (α_{baj}) can be calculated using Eq. (4). From this equation, the maximum allowable ground acceleration, α_{baj} is influenced by the square of the frequency (F_s), drift angle (γ_{aj}), and inversely to

the difference between the amplification factors of the floors being reviewed ($A_{sj} - A_{sj-1}$).

$$\alpha_{baj} = 10^4 \frac{4\pi^2 F_s^2 h_j}{A_{sj} - A_{sj-1}} \gamma_{aj} \tag{4}$$

where,

- α_{baj} maximum allowable ground acceleration of structure (Gal or cm/s^2)
- F_s natural frequency of structure (Hz)
- h_j column height between floors being reviewed (m)
- $A_{sj} - A_{sj-1}$ amplification factor difference between floors being reviewed
- γ_{aj} drift angle limit (SNI 1726-2012 clause 7.12.1).

3.4 Dynamic Magnification Ratio (DMF)

It is written in many literatures that amplitude of vibration (x) depends linearly on the static displacement, $\{F(0)/k\} \sin(\omega t - \theta)$ and the dynamic magnification factor (*DMF*). The DMF relates inversely to the root of the damping factor, ξ and to the squared of frequency ratio, $r = \omega/p$ (ω : excitation frequency and p : natural frequency of structure) as shown in Eqs. (5) and (6). The DMF will be maximum when frequency ratio, r is close to unity (1). In such a case the structure is called resonant. Therefore, the amplitude of vibration will much depend on the damping factor as well as on the frequency ratio (see Fig. 7).

$$x = \left\{ \frac{F(0) \sin(\omega t - \theta)}{k} \right\} \frac{1}{\sqrt{(1 - r^2)^2 + (2 \cdot \xi \cdot r)^2}} \tag{5}$$

$$DMF = \frac{1}{\sqrt{(1 - r^2)^2 + (2 \cdot \xi \cdot r)^2}} \tag{6}$$

Fig. 7 The dynamic magnification factor (*DMF*) for different damping factor, ξ

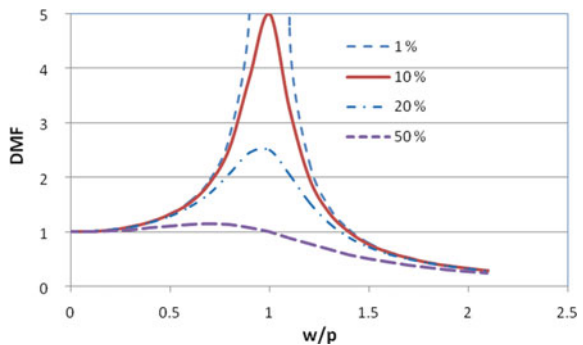
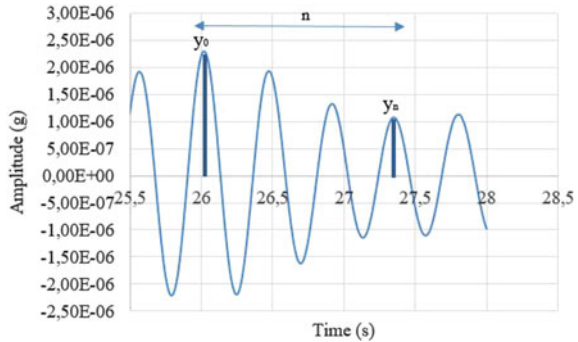


Fig. 8 Free vibration signal in the N-S direction



3.5 Damping Ratio

The damping ratio (ξ) can be calculated using Eq. (7). From this equation, the value of damping ratio is influenced by the number of cycles (n), initial amplitude (y_0), and final amplitude (y_n). Figure 8 is a cut of vibration recording data on the 1st floor for the N-S direction to determine the damping ratio. Obtained a damping ratio of 4.54% from the calculation, then input the data into SAP2000.

$$\xi = \frac{1}{2 \cdot \pi \cdot N} \ln \frac{y_0}{y_n} \tag{7}$$

where,

- ξ damping factor
- N number of cycle between initial and final amplitudes
- y_0 initial amplitude (g)
- y_n final amplitude (g).

4 Results and Discussion

4.1 Stiffness and Damping Ratio

Before applying the structural model, the stiffness of the model was adjusted by modifying modulus of elasticity of concrete which was set to 23,453 MPa, but the concrete strength, f_c' was kept as concrete strength design i.e. 24.9 MPa. Furthermore, the participation of light weight masonry wall was also modelled as shell with modulus of elasticity of 2034 MPa. The damping factor was calculated from cut of time history of the micro vibration, recorded in the N-S direction. Apparent beating phenomenon may be due to the close first natural frequencies in the N-S and E-W direction. The amplitudes at the first peak, y_0 and the n th peak, y_n are respectively

of $2.3 \cdot 10^{-6}$ g and $0.978 \cdot 10^{-6}$ g. The n th peak was selected in such that this peak was about half of the first peak (at $n = 3$). Substituting those data into Eq. (7), the damping factor, ζ was obtained i.e. 4.54% at frequency of 2.31 Hz (see Fig. 8).

5 Prediction of Maximum Allowable Ground Acceleration

Figure 9a indicates that both amplification factors at resonance resulting from site measurement and sinusoidal function ($f = 2.17$ Hz) using numerical analysis are almost the same, but it is not for sinusoidal function at non-resonant frequency ($f = 4$ Hz). The similar behavior of the amplification factors approves that the numerical modelling is appropriate for further simulation. The amplification factor of the non-resonant sinusoidal frequency ($f = 4$ Hz) results in less story drift ratios (see Fig. 9b), therefore, analogically, it requires a larger force of excitation to achieve similar story drift ratio as by the sinusoidal excitation at resonant frequency (2.1705 Hz). Similar phenomenon also occurs in the E-W direction (see Fig. 10a, b).

In anyway, the drift ratios can indicate the position of the most vulnerable column. Figure 9b show that the inter-story drifts for the numerical models, resulting from sinusoidal vibrations at frequency 2.1705 Hz and from site measurement in the direction of N-S can indicate the position of the failure, but it is not for the drift ratios at non-resonant frequency. Such a condition also occurs in the direction of E-W (see Fig. 10b). The possible failure can occur at the 4th story (between the 4th and the 5th floors) in the N-S direction and in the 3rd story (between the 3rd and the 4th floors).

Vulnerability index is inversely proportional to the acceleration (1/Gal) at resonance which can be determined from Eq. (3). The higher the stiffness of a story as indicated by the higher natural frequency, the lower the vulnerability index will be and vice versa. Moreover, the higher the column between floors, the vulnerability index (K_{Tj}) will also be higher and vice versa. In Fig. 11a, the structural vulnerability

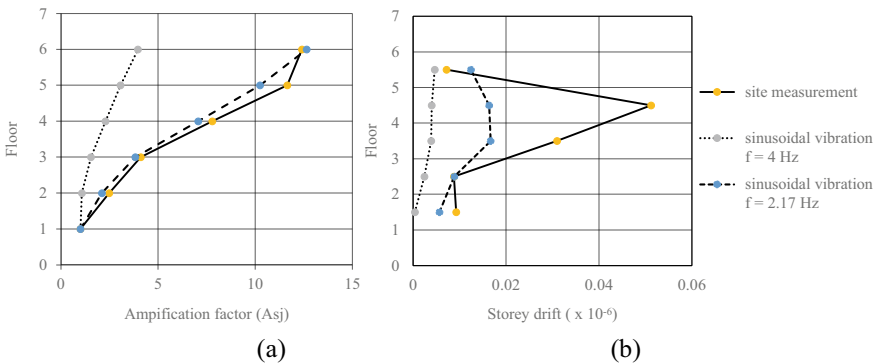


Fig. 9 a Amplification factors in N-S direction, b story drift in N-S direction

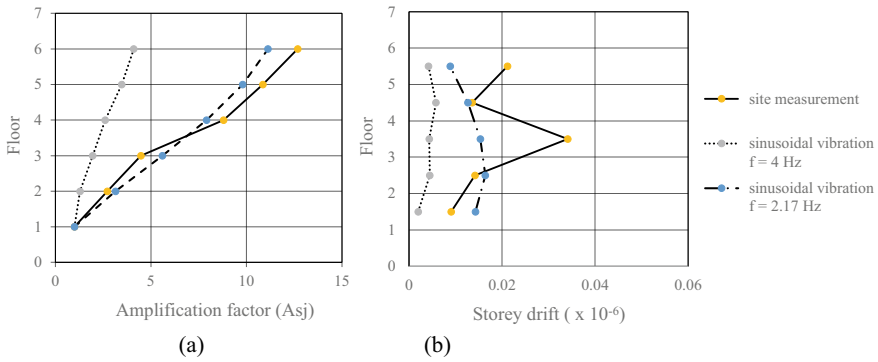


Fig. 10 a Amplification factors in E-W direction, b storey drift in E-W direction

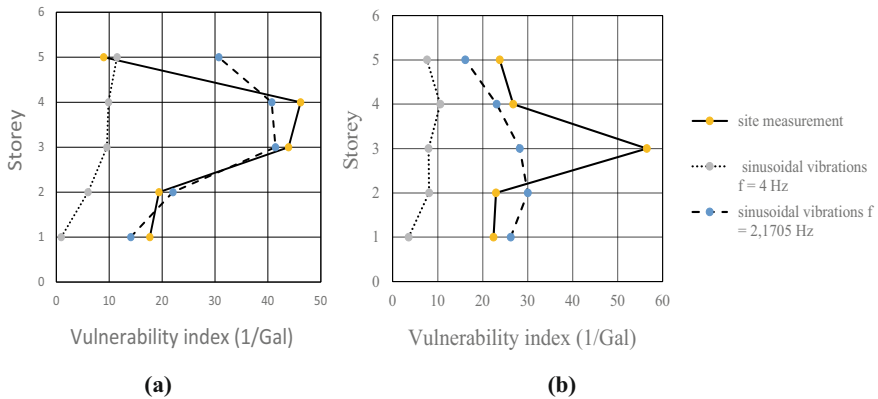


Fig. 11 a Vulnerability index in N-S direction, b in E-W direction

index (K_{Tj}), in the N-S direction resulting from the site measurement at 2.1705 Hz, occurs at the 4th story, with a value of 46.17 (1/Gal). Figure 11a also implies that numerical model in the N-S direction results in almost similar vulnerable position to the site measurement, though it is at the 3rd story with a value of 41.43 (1/Gal), but numerical model with sinusoidal vibration at frequency of 4 Hz (non-resonant frequency) results in a very low vulnerability index i.e. 11.47 (1/Gal).

The highest structural vulnerability index (K_{Tj}) resulting from the site measurement, in E-W direction, occurs at the 3rd story with a value of 56.48 (1/Gal). Figure 11b also implies that numerical model using sinusoidal at frequency of 2.1705 Hz in the E-W direction results in almost similar vulnerable position to the site measurement, though it occurs at the 2nd story with a value of 30.02 (1/Gal). The numerical model with sinusoidal vibration at frequency of 4 Hz (non-resonant frequency) results in a very low vulnerability index i.e. 10.59 (1/Gal).

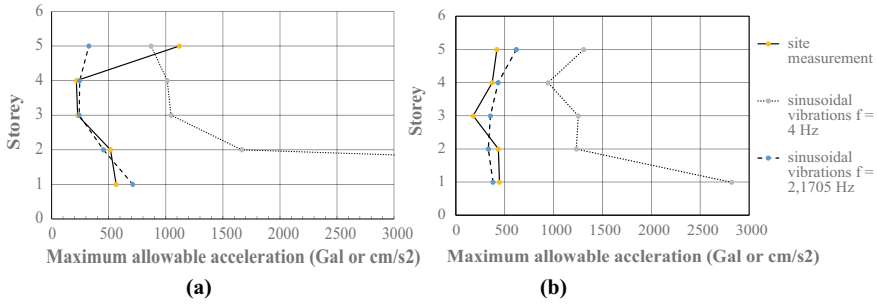


Fig. 12 a The maximum allowable acceleration in N-S direction, b in E-W direction

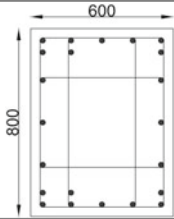
Figure 12a, b show that the maximum allowable ground acceleration at inter-story drift of 1% from site measurement in the N-S and E-W directions (as indicated by the smallest values) are respectively 216.57 cm/s² (at the 4th story) and 177.037 cm/s² (at the 3rd story). Whereas maximum allowable ground accelerations from the numerical model using sinusoidal vibration at frequency of 2.1705 Hz in the N-S and E-W directions are respectively 241.33 cm/s² (at the 3rd story) and 333.06 cm/s² (at the 2nd story) (see Fig. 12a, b).

The maximum allowable ground acceleration (indicated by the smallest acceleration values) of the model using sinusoidal vibration at non-resonant frequency of 4 Hz results in 871.09 cm/s² (at the 5th story) and 943.62 cm/s² (at 4th story) respectively in the N-S and E-W directions. Such different results are due to the fact that non-resonant frequency affects amplification factors and does the dynamic magnification factors, since the dynamic magnification factors are influenced by frequency ratio, $r = f_i/f_n$, see Eq. (5) (where f_i : frequency of excitation and f_n : natural frequency of structure). Thus, Nakamura proposed theory predicts lower maximum allowable ground acceleration, since its prediction relies on the resonant frequency and the related resonant amplitude. It reflects that the worst condition of the building may occur when the time history frequency of earthquake is similar or close to the natural frequency of the building. Instead, the maximum allowable ground acceleration may be very much higher than the prediction of Nakamura theorem.

In general, this discussion concludes that vulnerability index of numerical model resulting from vibration at resonant frequency is almost similar in position and value to the vulnerability index from site measurement. But, when the building is excited by earthquake vibration at frequencies other than resonant frequencies, it will result in less vulnerable structure.

Therefore, since the first resonant frequency of the building is very easy to record using available advanced sensor, the prediction of the maximum allowable ground acceleration using linear analysis will occur when the building is excited by earthquake containing frequency and amplitude as predicted from the site measurement. This prediction assumes that the stiffness as well as the damping factor do not change with time during earthquake excitation and is defined by the inter story drift ratio. At the defined drift ratio, the structure does not necessary fail but partially damage.

Table 1 Details of column reinforcement

Data	K1
Section	
Reinforcement	22D22
Stirrups	4D13 - 100
$f_{c'}$	25 MPa
$f_y, P < 10 \text{ mm}$	240 MPa
$f_y, D > 10 \text{ mm}$	390 MPa

5.1 Strength of Columns

The interaction diagrams of vulnerable columns of K1 at 4th and 3rd stories are created on the basis of existing data (see Table 1) as portrayed in Figs. 13, 14, 15 and 16. A comparison study is carried out to verify the capability of columns K1 against earthquake load using response spectra analysis as required by SNI 1726:2012, as well as against a sinusoidal vibration at frequency of 2.1705 Hz with amplitudes of vibration in the N-S direction of 216.57 cm/s² (Gal) and 490.5 cm/s² (Gal). In the E-W direction the sinusoidal amplitudes are 177.037 cm/s² (Gal) and 490 cm/s² (Gal). Factored axial forces (P_u) and associated factored bending moments (M_u), obtained from many combinations of Dead Load and Live Load as required by SNI 2487:2013 as well as by sinusoidal vibration at 216.57 Gal and 490.5 Ga, are plotted in the interaction diagrams.

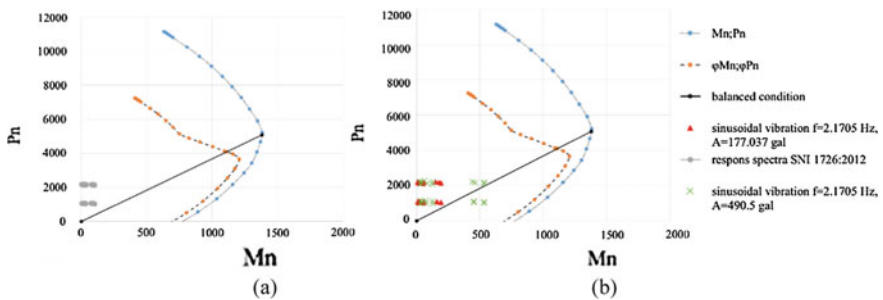


Fig. 13 Interaction diagram of column K1 at the 3rd story in N-S direction: **a** under response spectra analysis as required by SNI 2497:2013, **b** under sinusoidal vibration at frequency of 2.1705 Hz and amplitude of 216.57 cm/s² (Gal) and 490.5 cm/s² (Gal)

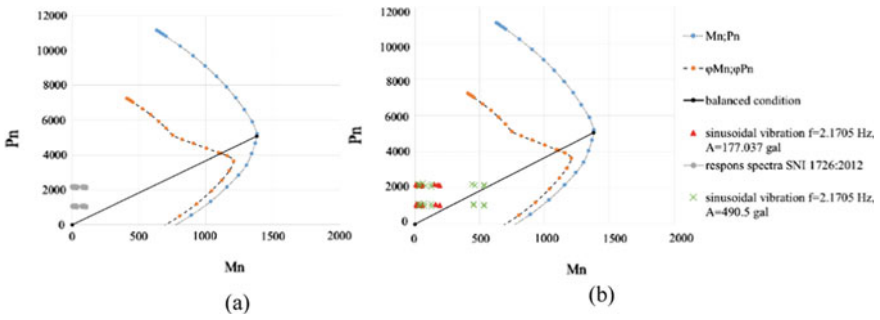


Fig. 14 Interaction diagram of column K1 at the 3rd story in E-W direction: **a** under spectrum response analysis as required by SNI 2497:2013, **b** under sinusoidal vibration at frequency of 2.1705 Hz and amplitude of 177.037 cm/s² and of 490.5 cm/s² (Gal)

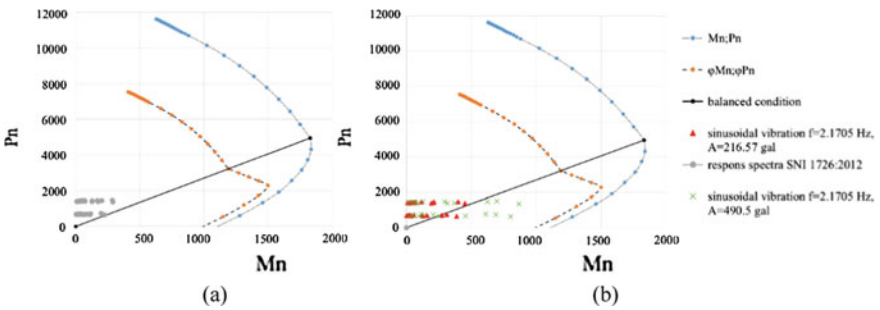


Fig. 15 a Interaction diagram of column K1 at the 4th story in N-S direction, under spectrum response analysis as required by SNI 2497:2013, **b** under sinusoidal vibration at frequency of 2.1705 Hz and amplitude of 216.57 cm/s² and of 490.5 cm/s² (Gal)

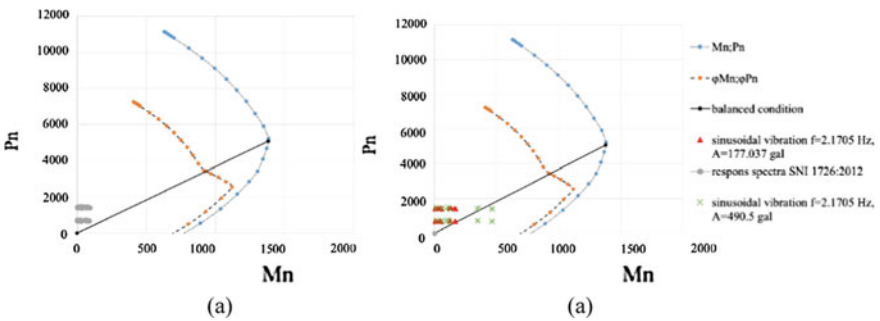


Fig. 16 a Interaction diagram of column K1 at the 4th story in E-W direction, under spectrum response analysis as required by SNI 2497:2013, **b** under sinusoidal vibration at frequency of 2.1705 Hz and amplitude of 177.037 cm/s² and of 490.5 cm/s² (Gal)

Figure 13a (N-S) and Fig. 14a (E-W) indicate that under response spectra (SNI 1726:2012) the resulting factored moments with many combinations of load are still safe since these moments are within the factored moment capacity curve of column K1. Figure 13b (N-S) indicates that due to sinusoidal vibration at resonance with predicted maximum allowable ground acceleration of 216.57 Gal, the several factored moments are about half of its capacity, but using sinusoidal vibration at 490.5 Gal the factored moments are close to its capacity. Figure 14b portrays the behavior of column K1 under sinusoidal vibration at resonance in E-W direction with peak ground acceleration amplitude of 177.037 Gal. The factored moments due many lateral load combinations have still been accommodated by the column capacity. On the other hand, taking account into the biaxial capacity analysis, the sinusoidal vibration at resonance and at amplitude of 216.57 and 490.5 Gal the column capacity of K1 is exceeded (see Table 2).

Table 2 The biaxial column at the 3rd storey

Type of load	P _{uy} (kN)	M _{uy} (kNm)	P _{ux} (kN)	M _{ux} (kNm)	Biaxial (Bresler)	Note
Response spectra SNI 1726:2012 (N-S)	2778.4932	373.51027	2817.369	68.94046	0.43398	<1, safe
Response spectra SNI 1726:2012 (E-W)	2764.4891	287.16118	2802.0875	109.88555	0.50432	<1, safe
Sinusoidal vibration f = 2.1705 Hz, A = 216.57 gal (N-S)	2877.4703	653.03106	2817.4805	115.25126	1.03149	>1, not safe
Sinusoidal vibration f = 2.1705 Hz, A = 177.037 gal (E-W)	2762.9493	357.65564	2803.6324	210.73154	0.69143	<1, safe
Sinusoidal vibration f = 2.1705 Hz, A = 490.5 gal (N-S)	2922.3998	1666.566	2862.41	289.4143	32.1093	>1, not safe
Sinusoidal vibration f = 2.1705 Hz, A = 490.5 gal (E-W)	2894.9598	763.97214	2834.97	574.00098	1.47634	>1, not safe

Figure 15a (N-S) and Fig. 16a (E-W) indicate the interaction diagram of column K1 at the 4th story under SNI 1726:2012 using response spectra. The resulting factored moments with many combinations of load are safe since moments are within the maximum factored moment capacity of column K1. Figure 15b (N-S) indicates that due to sinusoidal vibration at resonance with predicted maximum allowable ground acceleration at 216.57 and 490.5 Gal, the several factored moments are about half of its capacity. Taking account of biaxial capacity analysis, the sinusoidal vibration of resonance at amplitude of 216.57 Gal has caused the column capacity to exceed (see Table 3).

Those above examples conclude that response spectrum method for the earthquake resistance design as required by SNI 1726-2012 provides adequate safety against earthquake load, since no resonance to occur during earthquake shake. The combined axial factored forces and their related factored moments resulting from earthquake response spectrum as required by SNI 1726:2012 are generally lower than that from

Table 3 The strength acceptability by biaxial at the 4th storey

Type of load	P_{uy} (kN)	M_{uy} (kNm)	P_{ux} (kN)	M_{ux} (kNm)	Biaxial (Bresler)	Note
Response spectra SNI 1726:2012 (N-S)	1810.8641	339.60533	1810.8641	59.80904	0.53812	<1, safe
Response spectra SNI 1726:2012 (E-W)	1907.4268	285.66888	1817.4203	101.75171	0.49522	<1, safe
Sinusoidal vibration $f = 2.1705$ Hz, $A = 216.57$ gal (N-S)	1805.4893	508.68552	1805.4893	112.82942	0.82325	<1, safe
Sinusoidal vibration $f = 2.1705$ Hz, $A = 177.037$ gal (E-W)	1907.7927	330.03349	1817.0582	191.73874	0.63570	<1, safe
Sinusoidal vibration $f = 2.1705$ Hz, $A = 490.5$ gal (N-S)	1770.1993	962.29747	1770.1993	271.2155	3.57176	>1, not safe
Sinusoidal vibration $f = 2.1705$ Hz, $A = 490.5$ gal (E-W)	1793.5674	575.33187	1793.5674	509.25939	0.86574	<1, safe

sinusoidal vibration at resonant frequency at predicted ground acceleration amplitude when they are uni-axially analyzed, but may some time they do not so in bi-axial analysis.

This means that Nakamura theorem based on resonant amplitude and natural frequency is proper enough to predict possible failure position and maximum allowable peak ground acceleration. If no resonance to occur, the maximum allowable peak ground acceleration can be much higher.

6 Conclusion

This research discussed the dynamic characteristics of building structures using site measurement data using Nakamura proposed theory, and the effect of resonant and non-resonant frequencies of sinusoidal excitation on the amplification factors, vulnerability indices and predicted maximum allowable ground acceleration numerically. The research concludes:

1. The first natural frequency of the building can be identified by analysing its micro vibration analysis. Moreover, the vulnerable position of damage and the maximum allowable ground acceleration can also be determined.
2. The Nakamura theorem [1] can be employed to detect the vulnerable position of damage at a given inter story drift ratio, the maximum allowable peak ground acceleration.
3. Numerical verification by exciting sinusoidal vibration at resonance to the model has approved the validity of the Nakamura theorem [1] within elastic region (assuming no change of damping factor and stiffness of the structure along with the earthquake shake).
4. In general the building of Material Laboratory is vulnerable to damage at the 4th story or at the 3rd story if ground acceleration goes in N-S direction and in E-W direction respectively.
5. The highest structural vulnerability index (KT_j) resulting from numerical modeling with sinusoidal vibration at frequency of 2.1705 Hz and at out of resonant frequency of 4 Hz, in the direction of N-S are respectively at the 3rd story and the 5th story, but in the E-W direction such a vulnerability index are respectively at 2nd story and 4th story.
6. The maximum allowable ground acceleration on the basis of site measurement data in the N-S and E-W directions are limited by the inter story drift ratio of 1% that occurs at the 4th and the 3rd story, which are 216.576 cm/s² and 177.037 cm/s² respectively.
7. Using sinusoidal vibration at resonant frequency of 2.1705 Hz, the numerical modeling results in the maximum allowable ground acceleration is of 241.33 cm/s² in the N-S direction at 4th storey, which is close to site measurement results.

8. Using numerical modeling and sinusoidal ground vibration at out of resonant frequency of 4 Hz, results in quite high prediction of maximum allowable ground accelerations. This confirms that resonant frequency will highly reduce the maximum allowable ground acceleration.
9. When resonant frequency does not occur along with earthquake shake, the response spectra analysis on the building as required by SNI 1726-2012, clause 6.7.3, is adequate for the design criteria.
10. The bi-axial analysis on column K1 at 4th and 3rd story approves that the column cannot withstand peak ground acceleration at resonance with amplitude of 216.576 cm/s^2 (gal).

Acknowledgements We wish to thank you to the Structure Laboratory of the Department of Civil and Environmental Engineering, Faculty of Engineering, Universitas Gadjah Mada for granting permission to use the dynamic testing devices and also we thanks to the Procurement and Logistics Center of Universitas Gadjah Mada for granting permission to conduct testing in the Building Materials and Environmental Engineering Laboratory of DTSL UGM. A great gratitude also goes to the competitive reasearch grant, held by the Universitas Gadjah Mada (Riset Tugas Akhir) for granting registration fee for the 5th International SCESCM Seminar.

References

1. Nakamura Y (2000) Clear identification of fundamental idea of Nakamura's technique and its applications. In: Proceedings of XII world conference, earthquake engineering, New Zealand paper no. 2656
2. Nakamura Y, Gurler ED, Saita J, Rovelli A, Donati S (2000) Vulnerability investigation of Roman Colosseum using microtremor. Prepared for 12th WCEE 2000 in Auckland, NZ. 2660/6/A
3. Nakamura Y (1997) Seismic vulnerability indices for ground and structures using microtremor. In: World congress on railway research, Florence, Nov 1997
4. Halisa, Priyosulistyo H (2011) The structural dynamic behavior of building with asymmetric plan and dilatation by means of microtremor analysis. In: Proceedings of the 4th ASEAN civil engineering conference, Yogyakarta, 22–23 Nov 2011
5. Priyosulistyo H, Atika UJ, Halisa, Widowati AC (2012) Effect of change of stiffness and damping on the strength prediction of reinforced concrete building structures using microtremor analysis. In: Proceeding seminar, on the 1st international conference on sustainable civil engineering structures and construction materials (SCESCM), Yogyakarta, 11–13 Sept 2012
6. Priyosulistyo H, Widowati AC, Atika UJ (2008) Prediction of strength and structural behaviour of asymmetric buildings using microtremor—learning from vulnerability indices. In: Proceeding seminar on the two year reconstruction of Bantul earthquake, Civil Engineering Department of UII, Yogyakarta
7. Priyosulistyo H (2010) Prediction of strength and structural behaviour of asymmetric buildings using microtremor—learning from vulnerability indices. In: Proceeding seminar on the 3rd ACEC seminar, AUN SEED NET, Manila
8. Afriandini B (2016) Analisis Respon Dinamik Getaran Mikro Gedung Asrama Mahasiswa Kinanti UGM. Master thesis, Department of Civil and Environmental Engineering, Faculty of Engineering, Universitas Gadjah Mada, Yogyakarta

9. Ariyani I (2016) Analisis Mikrotremor Gedung Asrama Sendowo (Prediksi Ketahanan Struktur Terhadap Beban Gempa). Master thesis, Department of Civil and Environmental Engineering, Faculty of Engineering, Universitas Gadjah Mada, Yogyakarta
10. Prayuda H, Zega BC, Priyosulistyo H (2017) Prediction of allowable lateral ground acceleration (in-plane direction) of confined masonry walls using ambient vibration (microtremor) analysis. *Procedia Eng* 171:1194–1203
11. Bahri AS, Utama W, Aini DN, Lutfie MN (2016) Valuation of building strength against earthquake vibrations using microtremor analysis (case study: the city of Surabaya). *IOP Conf Ser Earth Environ Sci* 29:012018. <https://doi.org/10.1088/1755-1315/29/1/012018>
12. Margarita M, Filippou V (2017) Microtremors for seismic response assessments of important modern and historical structures of Crete. *AIP Conf Proc* 1918:020013 (2017)
13. Nakamura Y (2008) Characteristics of H/V spectrum, system and data research. Tokyo
14. Apriansyah R (2010) Karakteristik Dinamik Hotel Ambarukmo Menggunakan Data Seismometer. Master thesis, Department of Civil and Environmental Engineering, Faculty of Engineering, Universitas Gadjah Mada, Yogyakarta
15. Timur E, Ozicer S, Sari C, Uyanik O (2015) Determination of buildings period and vulnerability index using microtremor measurement. In: The 8th congress of the Balkan geophysical society, Chania, 5–8 Oct 2015
16. Sasongko DP, Yuliyanto G, Arifin Z (2019) Vibration vulnerability identification in Kota Lama Semarang using microtremor method. *Indones J Appl Phys* 9(2):105
17. Badan Standarisasi Nasional (1989) SNI 03-1727-1989 Pedoman Perencanaan Pembebanan Untuk Rumah dan Gedung. BSN, Jakarta
18. Badan Standarisasi Nasional (2012) SNI 1726:2012 Tata Cara Perencanaan Ketahanan Gempa Untuk Struktur Bangunan Gedung dan Non gedung. BSN, Jakarta
19. Badan Standarisasi Nasional (2013) SNI 1727:2013 Beban Minimum Untuk Perancangan Bangunan Gedung dan Struktur Lain. BSN, Jakarta
20. Ramirez R (1985) *The FFT fundamentals and concepts*. Prentice-Hall Inc., New Jersey

The Bond Strength and Damping Properties of Mortar Joint Using Rubber Tire Crumbs



Restu Faizah, Henricus Priyosulistyo, and Akhmad Aminullah

Abstract Recently, the utilization of rubber from used car tires known as rubber tire crumbs (RTC) was an interesting discussion in the world. Many researchers have studied the utilization of RTC in Civil Engineering field, which is the RTC as a substitute material for the sand part in concrete or mortar mixtures. The mortar using RTC (RTC-mortar) was also proposed to apply as a mortar joint on masonry walls. The strength of the bond between the mortar and the brick is needed to withstand the in-plane loads, such as shear strength, ductility, and damping capacity. This study investigated the bond strength, shear modulus, stiffness, and damping properties of the RTC-mortar joint due to horizontal cyclic load due to earthquake in-plane load. Mortar specimens consisted of normal mortar (0% RTC) and RTC-mortar with 20%, 40% and 60% RTC contents. This study results in the prediction of the optimum content of rubber tire crumbs (RTC) in a mortar mixture to be applied as a mortar joint on a masonry wall, which is 20% of sand volume. Mortar joint using 20% RTC content have the bond strength of 0.361 MPa and a damping ratio of 14.9%. Based on previous research, the use of mortar containing 20% RTC as a mortar joint of masonry wall also meets the strength requirements, where the compressive strength of mortar joint must exceed the compressive strength of the brick unit.

Keywords Bond strength · Damping ratio · Rubber tire crumb · Mortar joint · Masonry wall

R. Faizah · H. Priyosulistyo (✉) · A. Aminullah
Department of Civil and Environmental Engineering, Universitas Gadjah Mada, Yogyakarta, Indonesia
e-mail: priyo_ugm@ugm.ac.id

R. Faizah
e-mail: restu.faizah@umy.ac.id

A. Aminullah
e-mail: akhmadaminullah@ugm.ac.id

R. Faizah
Department of Civil Engineering, Universitas Muhammadiyah Yogyakarta, Yogyakarta, Indonesia

1 Introduction

Rubber tire crumbs (RTC) is a waste material made of used shredded rubber tire of car using a machine. Recently, the used car tires cause environmental problems because of its abundant amount, while its utilization is very limited. Many researchers have exposed the application of RTC to civil engineering field, such as a replacement material of sand or gravel in asphalt, soil, concrete, and mortar mixture. Rubber tires have specific properties, such as having lightweight, elastic, and great stretching ability. Used rubber tire has an average density of 1100 kg/m^3 , slightly higher than water density but much lower than sand and cement density. Hence, replacing the part of sand in mortar mixture with RTC can reduce the density of mortar. Even at certain RTC contents, a lightweight mortar with density of less than 1850 kg/m^3 can be obtained [1–4]. The elastic property of rubber tires is detected from its low hardness of around 57–69 (shore A) and great elongation of up to 300%. Elastic material is defined as a good ability to turn back into its original shape after unloading, so the addition of RTC in the mortar mixture can increase the ductility of mortar. The properties of 4 brands of used rubber tire are shown in Table 1 [5].

RTC-mortar is one of the utilization of RTC as a replacement material for the sand portion in the mortar mixture. The addition of RTC in the mortar is known to affect the physical, mechanical and damping properties of the mortar. Mechanical properties of mortar, including compressive strength, tensile strength, and flexural strength decrease as the increase of RTC contents in the mortar mixture [6–10]. Increased RTC contents present more porous mortar, resulting in reduced density, and then decrease the compressive strength of RTC-mortar [2]. The low strength of RTC-mortar is caused by the nature of rubber particles that have low adhesion with cement paste and cannot be distributed in a mortar mixture homogeneously [7].

Due to the low properties on mechanical strength, some researchers suggested that the RTC-mortar may apply as a material in non-structural buildings. Jevtic et al. [11] predicted that the RTC-mortar can be successfully applied in lightweight cement-based composites (such as insulating, soundproofing or repair mortars), while Fiore et al. [2], proposed RTC mortar for non-load bearing purposes as in the case of the application of roadway, paving slabs, flow-able and trench fills, insulating barriers,

Table 1 Properties of used rubber tire [5]

No	The properties	Rubber tire brands code			
		A	B	C	D
1	Density (kg/m^3)	1112	1090	1120	1136
2	Tensile strength (MPa)	10.64	14.36	11.90	11.80
3	Hardness (shore A)	57.90	68.74	66.98	67.60
4	Elongation (%)	296	271	238	244
5	Elastic modulus, E (MPa)	1.85	2.09	2.61	2.49
6	Shear modulus, G (MPa)	0.92	1.23	1.77	1.36

and curtain walls. It is also useful for architectural applications such as nailing mortar, false facades, stone backing, and interior construction.

On the other hand, Faizah et al. [12] reported that RTC-mortar has a high potential to be used as a replacement material in the mortar bed joint to increase the ductility of masonry. Masonry walls are non-structural elements which do not bear vertical axial loads but must be able to withstand horizontal forces either in-plane or out-of-plane load during an earthquake. The strength and stiffness of masonry wall resulted from a combination of strength and stiffness of brick and mortar [13]. In order to meet the requirement of the mortar joints of masonry, the RTC content should not be more than 60% of the sand volume replaced. In the masonry wall structure, the in-plane load is resisted by the bond between the bricks and mortar. Therefore, the strength of the bond between the mortar and the brick is needed to withstand the in-plane loads, such as shear strength, ductility, and damping capacity [14]. The adhesion between mortar and brick has a great contribution in resisting the shear load on masonry walls [14].

This study investigated the bond strength, shear modulus, stiffness, and damping properties of the RTC-mortar joint due to horizontal cyclic load that represents an earthquake in-plane load. Mortar specimens consisted of normal mortar (0% RTC) and RTC-mortar with 20%, 40% and 60% RTC contents. The purpose of this study was to compare the bond strength and damping properties of RTC-mortar which had various RTC contents. The results of this study expect information on the optimum of RTC-content for the use of mortar bed joint of the masonry wall structure.

2 Experimental Method

2.1 Materials and Specimen Preparation

The specimens in this study represent a pair of bricks bound by mortar joints but the bricks were replaced by wooden blocks (see Fig. 1). Replacement of bricks with

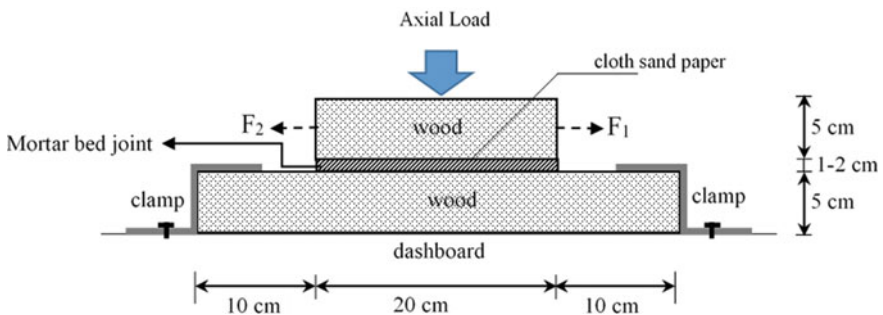


Fig. 1 The experimental configuration

Fig. 2 Rubber tire crumbs (RTC)



Table 2 The specific gravity and density of materials

Properties	Unit	Water	Cement	Sand	RTC #4
Specific gravity	–	1	3.15	2.73	1.14
Density	kg/m ³	1000	1250	1566	421.3

wooden blocks is intended to get the mortar-failure after loading. This is based on the results of a preliminary study which took a pair of bricks bound by a mortar joint to be a specimen. The results show that the specimen has a brick failure, not a mortar failure.

The size of the top wood-block was similar to the size of a normal brick that is $20 \times 10 \times 5$ cm, while the lower part is longer, that is $40 \times 10 \times 5$ cm, for the purpose of binding the beams on the dashboard. The surface of the wooden block attached to the mortar was made rough using cloth sandpaper. The mortar bed joint was placed between the top and bottom of the wooden blocks having a thickness of 20 ± 1.5 mm. There were 4 types of mortar, namely normal mortar (without containing RTC), and RTC mortar with the RTC content of 20%, 40%, and 60%. The number of each type of mortar is 3 units to come up 12 units in total.

The material for making specimens consisted of water, Portland cement type I, and sand from Progo River. The RTC have dimensions of passing #4 (4.75 mm) as shown in Fig. 2. The specific gravity and density of the materials are presented in Table 2. The mortar mixture had a water-cement ratio of 0.6 and a cement-sand ratio of 1:3. The weights of cement, sand, water, and RTC to make 1 m³ of fresh mortar are shown in Table 3. The specimens were tested after 28 days of age.

2.2 Test Procedure

This experiment applied 2 loading methods, which were monotonic and cyclic loads. Monotonic loading was applied to investigate the bond strength, while cyclic loading was carried out to analyze the damping capacity of the mortar joint. The damping ratio was determined based on the hysteretic loop method resulted from the cyclic

Table 3 Mix design for 1 m³ of fresh mortar

Type of mortar	Weight (kg)			
	Cement	Sand	Water	RTC #4
Normal mortar	433.9	1641.4	260.3	0
RTC-mortar 20%	453.5	1372.3	272.1	92.5
RTC-mortar 40%	476.1	1073.7	285.7	194.3
RTC-mortar 60%	499.3	750.7	299.6	305.7

loading test. The experimental setup is shown in Fig. 3. The specimen was clamped to a rigid dashboard to ensure that it remained in position when the top wood was pulled or pushed. The pull or push force was generated by a hydraulic jack that was pumped using double acting hydraulic jack (Enerpac), where the lateral force was measured using Dewe-43 equipment from a load cell connected to the arm of the hydraulic jack.

Overall, the experiment consisted of 2 stages. In the first stage, the specimen is pulled gradually in a horizontal direction until failure. The tests were carried out on 4 sets of the specimen, each set consisted of 2 specimens. In the second stage, the specimen was laterally loaded in 3 cycles. The maximum lateral force was 200 kg (1962 N) in both pulls and push horizontal directions. Each specimen was laterally loaded in two conditions, i.e. with a vertical load of 50 kg (AF-50) and without any vertical load (AF-0) on the top of wooden block. The first stage produced a force–displacement curve that can be used to determine the value of bond strength and shear modulus of the mortar joint. The second stage produced a hysteretic loop

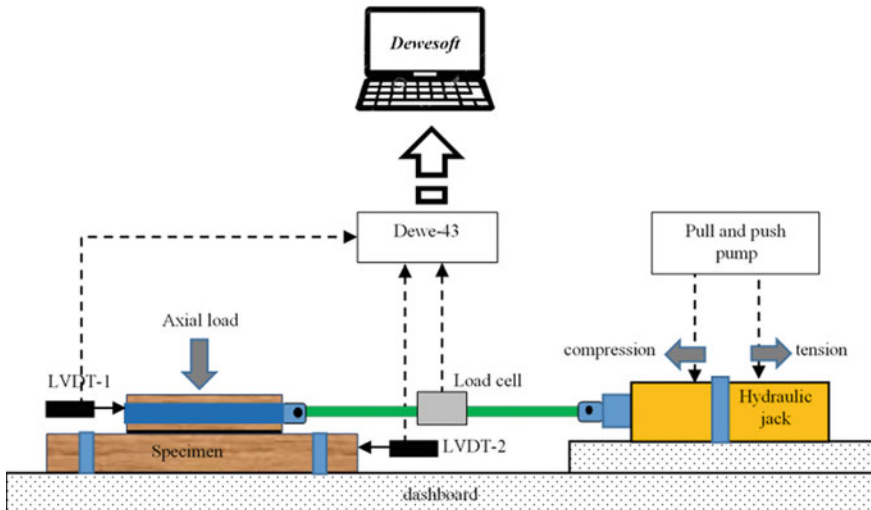


Fig. 3 Experimental setup

curve from cyclic loading that can be used to determine the stiffness and damping ratio of the mortar joint.

2.3 Bond Strength and Damping Analysis

In the first stage, specimen was pulled gradually until failure. Shear strength (γ) was determined using the Eq. 1, with γ , F_p , and A_s are the bond strength (MPa), peak force (N), and effective shear area, respectively.

$$\gamma = \frac{F_p}{A_s} \tag{1}$$

In the second stage, the experiment resulted in a relationship curve between force and displacement in all cycles which is known by a hysteretic loop curve. Furthermore, the damping ratio and stiffness was determined using the hysteretic loop method, as described in Fig. 4. In this case, the energy dissipated was equal to the area enclosed in the loop (E_D), while the maximum energy stored was equal to the triangular area corresponding to a half of Δ_{max} multiplied by F at Δ_{max} , with Δ_{max} is the maximum displacement and F is a lateral cyclic force. Furthermore, the amount of equivalent viscous damping (ξ_{eq}) was evaluated by Eq. 2. E_D represents energy dissipated in 1 cycle, and E_{So} is maximum energy stored [15]. Stiffness can also be determined from the hysteretic curve, which was tangential of the slope of the line connecting to the peak force and displacement as shown in Fig. 5 and calculated by Eq. 3.

$$\xi_{eq} = \frac{1}{4\pi} \frac{E_D}{E_{So}} \tag{2}$$

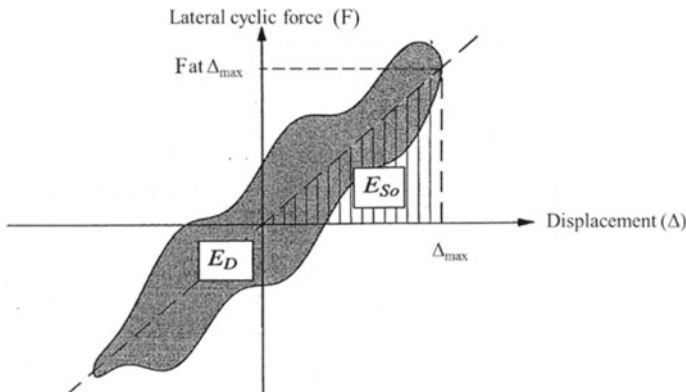
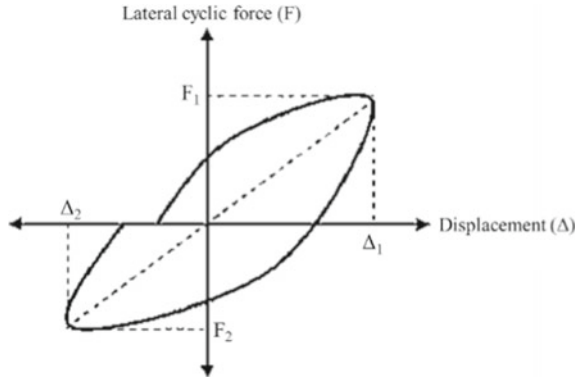


Fig. 4 Hysteretic loop resulted from the cyclic experiment [15]

Fig. 5 Hysteretic loop curve to determine the stiffness



$$K = \left[\left(\frac{F_1}{\Delta_1} \right) + \left(\frac{F_2}{\Delta_2} \right) \right] \times 0.5 \tag{3}$$

where,

Δ_1 : Maximum displacement (+) (mm)

Δ_2 : Minimum displacement (-) (mm)

P_1 : Lateral cyclic force at Δ_1 (kN)

P_2 : Lateral cyclic force at Δ_2 (kN)

3 Result and Discussion

Figure 6 shows the experimental set-up of the 2 conditions, AF-0 and AF-50. The analysis of the test results included bond strength, shear modulus, damping ratio, and stiffness. The 50 kg of the vertical load in AF-50 condition was defined from the assumption that the height of masonry wall above the specimen unit was about 1 m, thus the total vertical load above the specimen unit will be about $250 \text{ kg/m}^2 \times 1 \text{ m} \times 0.2 \text{ m} = 50 \text{ kg}$.

3.1 Bond Strength and Shear Modulus

In the first stage, the specimen was pulled until it was ruptured and then the history of force and displacement was recorded. The type of damage was also observed. There are two types of damage, namely damage on the bond between the mortar and wood and damage on the mortar joint (broken mortar). Figure 7 shows that all

Fig. 6 Two conditions of the experiment, AF-0 and AF-50

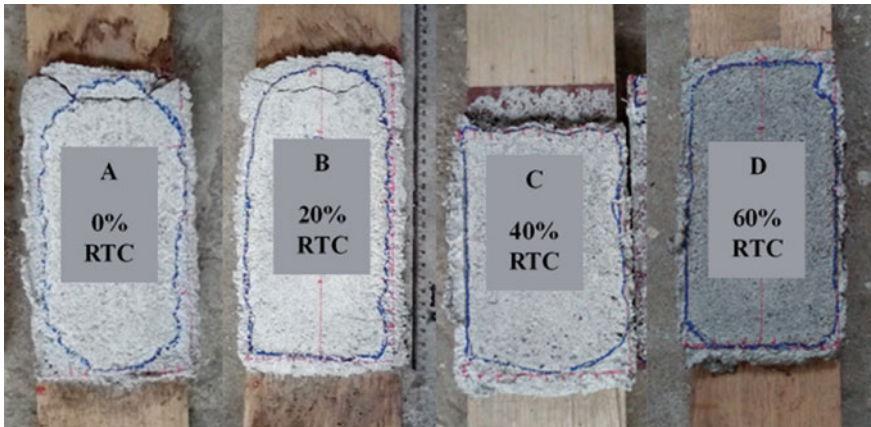


Fig. 7 Damage types of specimens

specimens broke except the specimens with 60% RTC content. The Mortar joint of the specimen with 60% RTC content was not damaged, but the bond between the mortar and the wooden block was perfectly separated. This damage type indicated that bonding between mortar and wood was poor, but the damage type of the other specimens showed a strong bonding [16]. Referring to Mutar et al. [7], it was said that the cohesion between rubber and sand was bad, thus the more rubber content in the mortar will produced the lower bond. Based on these results, it can be predicted that RTC mortar with 60% RTC content has a poor bond, so it is not recommended

to be used as a mortar joint in a masonry wall structure. Maybe the wood has not the same characteristics with the brick in term of bonding with mortar, but this result can reflect the bonding comparison between some mortar having various RTC content.

The curve of force–displacement relationship for all specimens are given in Fig. 8. It can be seen that the slope of the curve for normal mortar was more step than the RTC mortar. This fact shows that the shear modulus of normal mortar is greater than the RTC mortar. From Fig. 8, it can also be observed that the ability to stretch before experiencing failure of RTC-mortar is better than normal mortar. In this experiment, the specimen with 20% RTC content showed the highest stretching ability, which could stretch more than 3 mm from its initial condition. The lowest stretching ability was possessed by specimen with 60% RTC content. This may be due to the weak bond between the mortar joint and the wooden block in accordance with the previous statement which said that RTC mortar with 60% RTC content had a poor bond.

The results of bond strength and shear modulus analysis is given in Table 4, and a comparison between them is presented in Fig. 9. The addition of RTC to the mortar mixture resulted in a decrease in shear modulus. RTC-mortar with 20%, 40% and 60%

Fig. 8 Effect of RTC percentage on force–displacement relationship

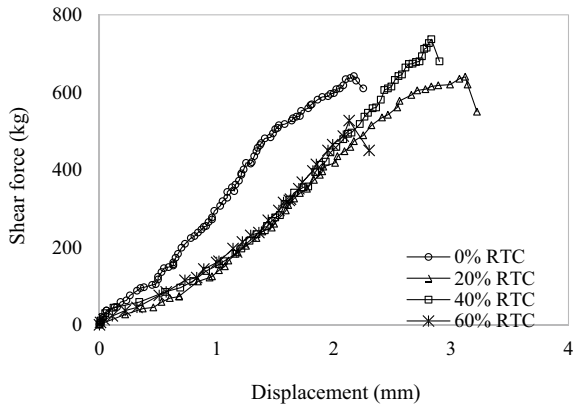
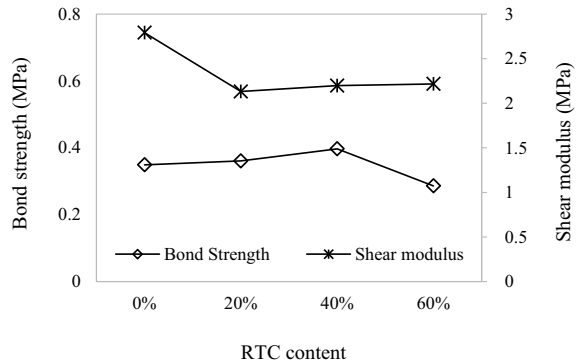


Table 4 The results of bond strength and shear modulus analysis

Item	Unit	RTC content on the specimens			
		(0%)	(20%)	(40%)	(60%)
Shear force	N	6298.02	6278.4	7229.97	5169.87
Maximum of displacement	mm	2.17	3.12	2.83	2.13
Effective shear area (A)	mm ²	18,037.1	17,402.68	18,209.66	18,067.33
Thick of mortar joint (h)	mm	17	16.75	16	16.5
Maximum shear stress	MPa	0.349	0.361	0.397	0.286
Maximum shear strain	–	0.128	0.186	0.177	0.129
Bond strength	MPa	0.349	0.361	0.397	0.286
Shear modulus	MPa	2.791	2.132	2.197	2.217

Fig. 9 A comparison between bond strength and shear modulus



RTC content experienced a decrease in shear modulus of around 21–24% compared to the normal mortar. Although the shear modulus decreased, the addition of 20% and 40% RTC content could increase the bond strength. However, at 60% RTC content, the bond strength of the mortar decreased, even below the bond of normal mortar. The increase in bond strength was considered to be caused by the presence of RTC in the mortar as an elastic fiber that could inhibit damage propagation and prevented sudden rupture of the mortar. However, for RTC-mortar with 60% RTC content, its bond strength decreased due to the poor bond of mortar cohesion (see the analysis of damage type of mortar).

Based on these results, the use of 60% RTC content was considered unfavorable in the application of RTC-mortar as a mortar joint because the bond strength of 60% RTC-mortar is lower than normal mortar. Bond strength can be increased by increasing brick roughness [16] or providing pre-treatment for RTC before use [17].

3.2 Damping Ratio and Stiffness

In the second stage, the specimen was loaded by lateral cyclic forces in the horizontal direction. The peak load was 200 kg (1962 N) in the push and pull directions and was repeated for 3 cycles for each specimen. Figure 10 shows the hysteretic loop curve of the cyclic test results. Each specimen was tested in 2 conditions, AF-50 and AF-0. From the hysteretic curve in Fig. 10 the damping ratio and the stiffness can be analyzed as explained in Eq. 2. The results of this analysis are described in Fig. 11 and shown in Table 5.

Figure 11 shows that the addition of 20% RTC can increase the damping ratio of RTC-mortar as much as 1.24 times than the specimen with no RTC content, but an increase of 40% and 60% RTC respectively results in a decrease in damping. This damping behavior matches with the elastic properties of RTC-mortar that was detected from the stretching ability and shear modulus presented in Table 4. It can be seen that 20% RTC-mortar had the greatest maximum displacement but the lowest

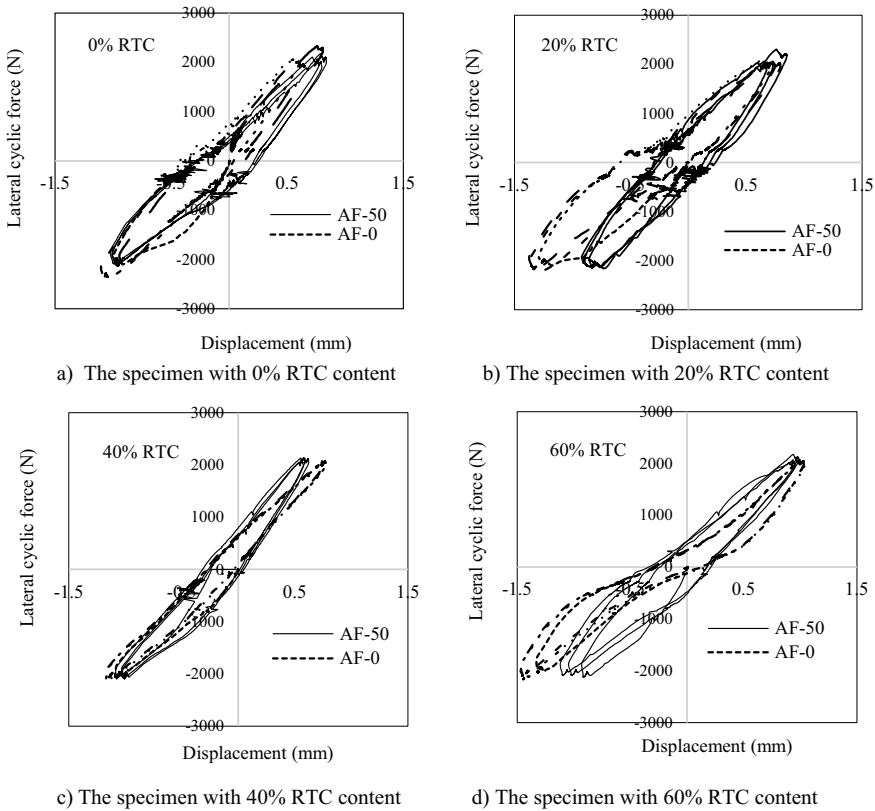


Fig. 10 The hysteretic loop curve of the cyclic test results. **a** The specimen with 0% RTC content. **b** The specimen with 20% RTC content. **c** The specimen with 40% RTC content. **d** The specimen with 60% RTC content

shear modulus. It means that 20% RTC-mortar had better ductility and tended to have good damping. These results seem to indicate that 20% is the optimum content of RTC in the mortar that produces the highest damping ratio. Based on the damping ratio investigated, the use of RTC-mortar as a mortar joint of masonry wall is recommended to have an RTC content of no more than 20% of the sand volume.

From Fig. 11, it can also be seen that the RTC-mortar damping in the AF-50 conditions was higher than in the AF-0 conditions for each RTC content, but the trend of damping behavior of the two conditions was the same. An axial load of 50 kg can increase the damping ratio up to 32%. The damping ratio has an opportunity to increase if the axial force is increased. This phenomenon proves that the structural damping ratio is not only determined by the damping ratio of its component materials but is also strongly influenced by the existing vertical loading conditions.

The stiffness behavior as shown in Fig. 11 had different tendencies with damping behavior. It seems that stiffness will increase if damping decreases, and so does the

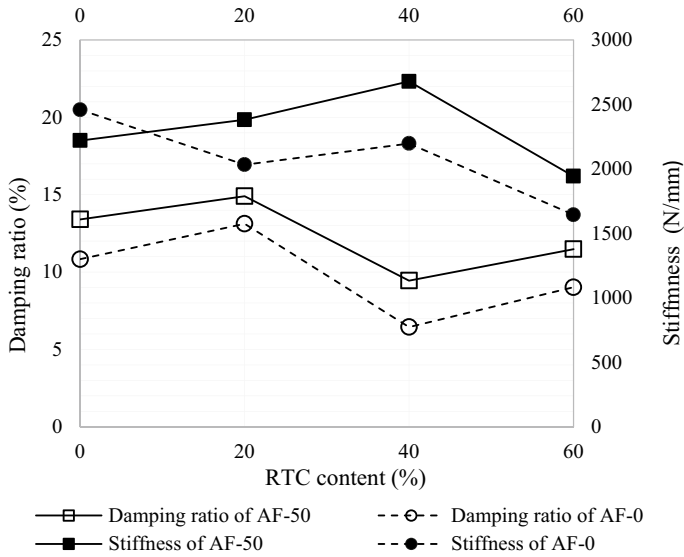


Fig.11 The damping ratio and stiffness of specimens

Table 5 The result analysis of damping ratio and stiffness

Axial force condition	RTC content (%)	Damping ratio (%)	Stiffness (N/mm)
AF-50	0	13.402	2219.677
	20	14.903	2381.370
	40	9.447	2678.119
	60	11.481	1943.467
AF-0	0	10.833	2458.269
	20	13.122	2032.295
	40	6.449	2196.790
	60	9.528	2087.533

vis-versa. This may be due to the fact that the RTC can increase the presence of void in the mortar mixture which causes the mortar to become more porous. The stiffness of the mortar will be lower if the mortar is more porous. However, this void will cause friction that can increase the damping properties. On the other hand, the void in the mortar mixture will reduce the strength of the mortar. Based on this fact, the application of RTC-mortar not only meets the damping ratio but also their strength requirements.

The compressive strength of mortar joint of a masonry wall is required to be greater than the compressive strength of the brick unit, but it is not required to use excessive strength of the mortar joint. This is by reason of the use of high-strength of mortar sometimes not profitable, because if the brick unit is damaged, the masonry

walls will also be damaged [18]. The results of previous research indicated that the compressive strength of mortar with 20% RTC was more than 7 MPa, while the compressive strength of local clay brick unit is around of 5 MPa. It means that using RTC containing 20% RTC as a mortar joint of masonry wall met the requirement [7, 8, 18, 19].

4 Conclusion

In this study, investigations of bond strength and damping ratio of the mortar joint using rubber tire crumb (RTC) were carried out. The bond strength of mortar with 20% and 40% RTC content of sand volume is greater than normal mortar, but the use of 60% RTC content is lower than normal mortar. The RTC mortar with 20% RTC content has good bond strength and high damping ratio, but for 40% RTC content, the damping ratio is low even though the bond strength is good. These results indicate that 20% is the optimum RTC content in the application of RTC-mortar which can increase their damping ratio as much as 1.24 times than mortar with no RTC. The optimum RTC content in the application of RTC-mortar as a mortar joint on the masonry wall is 20%, to get the bond strength of 0.361 MPa and a damping ratio of 14.9% under AF-50 condition. Based on previous research, the use of mortar containing 20% RTC as a mortar joint of masonry wall also meets the strength requirements, where the compressive strength of mortar joint must exceed the compressive strength of the brick unit.

Acknowledgements The authors express their gratitude and high appreciation to the Research Directory of Gadjah Mada University through the Rekognisi Tugas Akhir (RTA) which has sponsored this research.

References

1. Faizah R, Priyosulistyo H, Aminullah A (2019) An investigation on mechanical properties and damping behaviour of hardened mortar with rubber tire crumbs (RTC). MATEC Web Conf 258:05002. <https://doi.org/10.1051/mateconf/201925805002>
2. Fiore A, Marano GC, Marti C, Molfetta M (2014) On the fresh/hardened properties of cement composites incorporating rubber particles from recycled tires. Adv Civ Eng 2014:1–12. <https://doi.org/10.1155/2014/876158>
3. Sadek DM, El-Attar MM (2015) Structural behavior of rubberized masonry walls. J Clean Prod 89:174–186. <https://doi.org/10.1016/j.jclepro.2014.10.098>
4. Sofi A (2018) Effect of waste tyre rubber on mechanical and durability properties of concrete—a review. Ain Shams Eng J 9(4):2691–2700. <https://doi.org/10.1016/j.asej.2017.08.007>
5. Faizah R, Priyosulistyo H, Aminullah A (2019) The properties of waste rubber tires in increasing the damping of masonry wall structure. IOP Conf Ser Mater Sci Eng Universitas Tarumanegara Jakarta 650:012041. <https://doi.org/10.1088/1757-899X/650/1/012041>

6. Aliabdo AA, Abd Elmoaty AEM, Abd Elbaset MM (2015) Utilization of waste rubber in non-structural applications. *Constr Build Mater* 91:195–207. <https://doi.org/10.1016/j.conbuildmat.2015.05.080>
7. Mutar MA, Hussein TS, Malik SH (2018) Effect of crumb rubber aggregates on the characteristics of cement concrete as partial replacement. *Int J Mech Prod Eng Res Dev (IJMPERD)* 8(1):11
8. Samuel A (2013) Mechanical strength of concrete with crumb and shredded tyre as aggregate replacement. *Int J Eng* 3(2):4
9. Wakchaure MR, Channa SS (2018) crumb rubber in concrete: static and dynamic evaluation. *Int Res J Eng Technol (IRJET)* 5(10):520–524
10. Wang Z, Hu H, Hajirasouliha I, Guadagnini M, Pilakoutas K (2020) Tensile stress-strain characteristics of rubberised concrete from flexural tests. *Constr Build Mater* 236:117591. <https://doi.org/10.1016/j.conbuildmat.2019.117591>
11. Jevtic D, Zakic D, Savic A (2012) Investigation of cement based composites made with recycled rubber aggregate. *Hemijaska industrija* 66(4):609–617. <https://doi.org/10.2298/HEMIND111203010J>
12. Faizah R, Satyarno I, Priyosulistyo H, Aminullah A (2018) Improving the masonry brick ductility using mortar bed joint from rubber tire crumbs: a review. *JPS* 29(Supp. 2):117–132. <https://doi.org/10.21315/jps2018.29.s2.9>
13. Paulay T, Priestley MJN (1992) *Seismic design of reinforced concrete and masonry buildings*. John Wiley & Sons, Inc.
14. Lavado L, Gallardo J (2019) Shear strength of brick mortar interface for masonry in Lima City. *Tecnia* 29(2):59–64. <https://doi.org/10.21754/Tecnia.v29i2.707>
15. Chopra AK (2007) *Dynamics of structures: theory and applications to earthquake engineering*, 3rd edn. Upper Saddle River, Pearson Education, Inc., NJ
16. Singh SB, Munjal P (2017) Bond strength and compressive stress-strain characteristics of brick masonry. *J Build Eng* 9:10–16. <https://doi.org/10.1016/j.jobbe.2016.11.006>
17. Christy CF, Shanthi RM, Tensing D (2012) Bond strength of the brick masonry. *Int J Civ Eng Technol (IJCIET)* 3(2):7
18. Wisnumurti, Dewi SM, Soehardjono A (2011) Masonry behavior of local brick from east-java Indonesia. *J Appl Sci Res* 7(6):849–852
19. Nasution M (2019) The experimental investigation of mechanical properties of mortar containing rubber tire crumbs on various percentages (in Bahasa). Thesis, Universitas Gadjah Mada, Yogyakarta

Using Calcium Oxide and Accelerator to Control the Initial Setting Time of Mortar in 3D Concrete Printing



Antoni Antoni , David Christian Widjaya,
Alexander Ricardo Koentjoro Wibowo, Jimmy Chandra ,
Pamuda Pudjisuryadi , and Djwantoro Hardjito 

Abstract In recent years, 3D printing has attracted a lot of attention in the construction industry. Compared with general concrete construction, 3D concrete printing has higher flexibility in creating concrete's shape and design. 3D concrete printing requires the precise control of fresh concrete properties such as flowability, extrudability, and resistance to segregation during printing process. The initial setting time of the concrete also needs to be controlled as it needs to adhere to the next layer and then harden rapidly in order to support the upper layer. This study proposes a method to control the initial setting time of the concrete for the 3D printing process by using a mixture of calcium oxide powder and accelerators. The study showed that using 5–10% calcium oxide and 2–4% accelerator by mass of cement, the initial setting of the concrete can be varied. It is also shown that adding only accelerator prolongs the setting time of the mixture due to the plasticizer contained therein. By using calcium oxide powder, the initial setting time of the concrete can be hastened and the combination of calcium oxide powder and accelerator can reduce the initial setting time while maintaining good workability of the mixture. The addition of accelerator also increases the early compressive strength of the concrete mixture.

Keywords 3D concrete print · Calcium oxide · Accelerator · Initial setting time · Compressive strength

1 Introduction

Three-dimensional (3D) printing, also known as “additive manufacturing,” is an advanced manufacturing process that can automatically generate complex geometric shapes from a computer-assisted model [1, 2]. Currently, limited forms of building structures are available due to restricted shapes of formwork but with 3D concrete printing method various complex shapes can be constructed [3]. The 3D concrete printing construction method still faces many challenges that need to be address

A. Antoni (✉) · D. C. Widjaya · A. R. K. Wibowo · J. Chandra · P. Pudjisuryadi · D. Hardjito
Civil Engineering Department, Petra Christian University, Surabaya 60236, Indonesia
e-mail: antoni@petra.ac.id

© The Author(s), under exclusive license to Springer Nature Singapore Pte Ltd. 2022
S. Belayutham et al. (eds.), *Proceedings of the 5th International Conference on Sustainable Civil Engineering Structures and Construction Materials*, Lecture Notes in Civil Engineering 215, https://doi.org/10.1007/978-981-16-7924-7_56

simultaneously [4], from the construction process [5–8], printing machines and its precision and tolerance [9, 10], design and structural modelling [11, 12], and the hardened properties of the fabricated member [13–15]. The material used in 3D printing has several factors that need to be considered, including extrudability, shape retention, thixotropy, and buildability [16–18].

In 3D concrete printing, extrudability can be defined as the ability of a material to be pumped out through the extruder or nozzle without any interference/blockage in the pipe [19]. Like extrudability, shape retention is also an important factor for 3D concrete printing. After extrusion, the material must retain its shape according to the dimensions of the extruder. Thixotropy can be defined as the time interval during which the material loses its extrudability; for 3D printing concrete, this is always earlier than the setting time [16].

In 3D printing, buildability is a challenging problem. To overcome this, the material that has been extruded must produce sufficient viscosity and yield stress before the second layer begins to fall on it [20, 21]. The main challenge is to determine the best mix of materials to be able to flow out from the printing nozzle smoothly as well as to make a mortar that does not experience slump or sagging and self-compaction after extrusion [22, 23]. Although these two requirements contradict each other, they can be achieved by successively separate processes. First, the material must be extrudable and maintain its shape when applied to a printing bed. Second, the layer that has been applied must not sag with the application of the layer above it. Finally, the material must have good bonding between layers in order to achieve better rigidity and strength. Therefore, materials that have high yield stress and low viscosity are the best materials for this method [24, 25].

The exact composition of the binder and aggregate, and the particle size distribution should be designed carefully for better printability of different construction designs [26–28]. Various additives, such as superplasticizer, retarder, and accelerators, can be used to increase the strength of the printed material. An accelerator is not sufficient to produce such material if the ratio is not adjusted correctly while an inadequate retarder does not allow the material to be pumped through hoses, which can damage the pump and the distribution system [25].

One behavior of the fresh concrete properties that also influence the buildability is the windows of time for the best printing result [29, 30]. After the addition of water into the mixture, certain time need to be elapsed for the chemical reaction to proceed before the fresh concrete exhibit a suitable yield stress and viscosity for the printing process. This behavior further complicated the printing process and the material need to be precisely controlled for the optimum results. The optimum period is closely related to the initial setting time of the mortar, as it is varied with the mixture composition of the fresh mortar.

This study explores the use of local sand and cement as the material for the 3D concrete printing process and calcium oxide powder and accelerator to control the initial setting time of the mortar mixture. The high content of calcium oxide in cementitious mixture is known to cause flash setting in concrete [31], and adding small amount of it can hasten the setting time of the concrete and give the concrete structural strength to sustain the following layer. To modify the yield stress and

viscosity of the mortar matrix, accelerator with plasticizer effect is also added in to the mixture. By adding or reducing the amount of the admixture, the setting time hence the printing time can be controlled. Such a parametric material study can show the behavior of the additive and can be used as a guide to modify the mix design to comply with machine and design requirements. The evaluated fresh and hardened mortar properties include workability, initial setting time, and compressive strength.

2 Experimental Study

2.1 Materials and Mix Design

The fresh and hardened behavior of 3D-printed concrete is studied by investigating the mortar mixture with various admixture. The fine aggregate was sourced from Lumajang quarry in East Java, the cement used was Ordinary Portland cement from Semen Indonesia, the calcium oxide (CaO) powder was obtained from a local producer, and the accelerator used was Sikacim from SIKA. The fine aggregate was graded before mixing to ensure uniform consistency. The Fineness Modulus of the sand used was kept at 2.19. CaO was selected to increase the strength and to speed up the initial setting time and accelerator was added to improve the workability and early age strength of the mortar. Before deciding on the mix design for this study, several preliminary tests were conducted to investigate the dosage required for each parameter, additional admixture such as super-plasticizer and calcium hydroxide was also considered as the potential candidate to accelerate the initial setting time, however the effect was found to be reversed, i.e. the initial setting time of the mixture was prolonged.

The mix design for 3D concrete printing was compiled from other studies where the mass ratio of sand to cement can be varied from 0 to 2.5. Adding more sand can increase the yield stress but susceptible to bleeding occurrence, while the addition of fine powder such as fly ash, nano silica, or nano clay can improve the cohesion of the mixture [16, 27, 32]. Hence for the current study, the ratio of sand to cement was selected at 0.5 to reduce the need of other fine powder material in the mixture. The high amount of cement in the mixture also can provide a high strength buffer due to the imperfect condition of the printing process, the bond between layers, and uncertainty in the mortar compaction. Water to cement ratio was kept at 0.3 from the preliminary trial that give the optimum workability. The resulting mix designs investigated in this study are shown in Table 1.

Table 1 Mixture codes and mix design of the mortar

Mix code	w/c	Water (gr)	Cement (gr)	Sand (gr)	CaO (gr)	Accelerator (gr)
C	0.3	60	200	100	–	–
CA2					–	4
CA4					–	8
CCo5	0.3	60	200	100	10	–
CCo5A2					10	4
CCo5A4					10	8
CCo10	0.3	60	200	100	20	–
CCo10A2					20	4
CCo10A4					20	8

2.2 Specimen Preparation and Testing

Materials and equipment were prepared according to the mix design. Mixing was done by dry mixing cement and sand evenly before pouring water into the mixture. The accelerator was then slowly added while stirring followed by the CaO powder. After the mixture was uniform, it was poured into the flow table cone to measure its flow diameter in the flow table test according to ASTM C230 [33]. The test was carried out at room temperature ranging from 28 to 30 °C and at a relative humidity of 78–80%. The target flow diameter can be correlated with the yield stress of the mortar, and the flow diameter of 13–23 cm is suitable to be used as the printing material for the 3D concrete printing process, with the optimum value at 15–19 cm, according to Tay et al. [29].

The mixture was then cast into 5 cm cube formworks for compressive strength test and filled halfway into 15 cm cube molds for the setting time test. The setting time test was done using a mortar penetrometer and the penetration stress recorded in correlation with time since the addition of water. The mortar penetrometer test was conducted in according to ASTM C403 [34].

The compressive strength specimens were cured in water at room temperature until one day before the compressive strength test. The compressive strength test is conducted at 3, 7, 14, and 28 days from casting, with three replications using universal testing machine.

3 Results and Discussion

3.1 Preliminary Study

A preliminary study is needed to determine the material variables that would be used as the boundary condition in this study. The change of initial setting time is an

essential factor in 3D concrete printing and the dosage of admixtures that influence the change is still unknown.

The materials considered as the admixture were calcium oxide, calcium hydroxide, accelerator, and super-plasticizer. It was observed that each admixture has a different effect on the initial setting time. The addition of super-plasticizer always causes longer initial setting time because the water to cement ratio was kept constant for all mix designs. Combination of super-plasticizer and calcium oxide or calcium hydroxide always resulted in longer setting time than the control (cement only) mixture. Adding calcium hydroxide only also has a slower initial setting time than the control mixture, similar to the super-plasticizer, even though it is combined with an accelerator.

Meanwhile, the accelerator has a similar initial setting time with the control mixture and the addition of calcium oxide powder always produced a mixture with faster initial setting time.

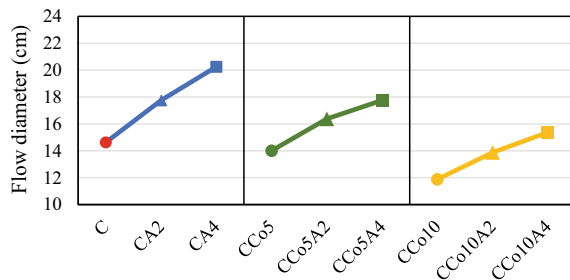
After conducting a preliminary test, super-plasticizer and calcium hydroxide were not used because they did not accelerate the initial setting time. When a longer initial setting time is needed, for example, with long printing cycle time, these admixtures can be considered. Accelerator, when combined with calcium oxide, produced faster initial setting time than the mix design control. The CaO powder dosage used was 5% and 10% of the cement mass and the accelerator was used at 2% and 4% of the cement mass; thus, their combined effect on the initial setting time could be observed. The maximum limit for CaO was set at 10% due to possible flash setting and low workability at higher CaO dosage.

3.2 Workability Control

The flow diameter measures mortar workability in the flow table test. The accelerator dosage is limited to 4% because the initial setting time can be extended further when adding dosage beyond that, as the accelerator chosen in this research also contain some plasticizer. The result of the flow diameter of the mixture is shown in Fig. 1.

Adding CaO to the mortar mixture reduced the workability slightly while the accelerator produced a larger flow diameter. Addition of CaO at 5% and 10% reduced

Fig. 1 Flow diameter of the fresh mortar with variations of additive



the flow diameter from 14.6 cm to 14 cm and 11.8 cm, respectively. The addition of 2% and 4% accelerator, by mass of cement, increased the mixture flow to a pumpable condition. This result showed that CaO and accelerator could be added together to control the initial setting time and workability of the mortar mixture.

The mixture composition of the mortar still need to be adjusted with the parameters of the printing machine, thus the optimization process of the mix design still excluded the addition of supplementary cementitious materials into the concrete mixture. Furthermore, to control the consistency of the mixture, viscosity modifying agent (VMA) can also be added into the mixture when the flow diameter is too high [35].

3.3 Initial Setting Time

The initial setting time test was carried out using the mortar penetrometer at 15 min intervals for all of the mixtures. The initial setting time is defined as the time needed until the penetration pressure reached 500 psi, however the changes of the penetration resistance can give the indication of the hardening process in the mortar mixture. Higher penetration resistance showed increase of stiffness and strength to sustain the upper layer in the 3D printing process. This hardening process is essential in reducing the elastic buckling and plastic collapse at high upper layer count [36].

The change in the mortar's hardening process can be observed by its initial setting time as seen in Fig. 2. The solid red line was the control mixture without any admixture. It can be seen that the time needed to reach the initial setting time decreases with increasing CaO dosage. The reduction of setting time was shown to progress at exponential rate with the increase of CaO dosage. At 5% dosage, the setting time was reduced 21 min, while from 5 to 10% dosage, the initial setting time reduction was 40 min. A faster setting time occurred when adding CaO mostly because of the increase of temperature due to the exothermic reaction of the CaO. At higher CaO

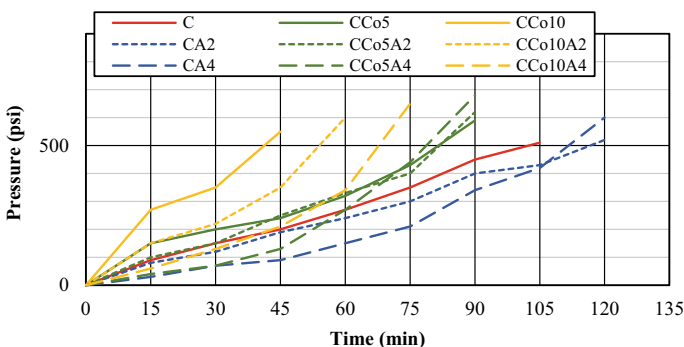


Fig. 2 Penetration pressure into the fresh mortar to measure the hardening process with time

dosage the mixture could cause very rapid setting even flash setting and could reduce the workability of the mixture.

On the contrary to the CaO, the initial setting time increased with increasing accelerator dosage. The mortar mixture with addition of accelerator only have longer initial setting time compared to the control mixture, however the benefit of adding accelerator is found on the increase of workability and the early strength of the mortar. The combination of CaO and accelerator changed the initial setting time at a different rate and can be utilized to control the behavior of the fresh concrete in the 3D printing process.

3.4 Compressive Strength

The compressive strength test was carried out to examine the effect of adding CaO and accelerator on the mortar strength. The concrete compressive strength test was carried for each variable at 3, 7, 14, and 28 days. The results of the mortar compressive strength test are shown in Fig. 3.

The compressive strength of the mortar was very high due to the low sand to cement ratio and low water to cement ratio. The high cement content also aimed to cause a faster initial setting time and increase the cohesion of the mixture. The use of accelerator was also found to increase the early strength and later strength of the mortar mixture. Adding 5% CaO did not have any detrimental effect on the compressive strength. At 10% CaO, there was a reduction in the compressive strength of the mortar. However, with the addition of accelerator, the final strength of the mixture for each CaO series can be increased and is higher than the control mortar.

The effect of using an accelerator on the initial setting time tends to be less beneficial but not detrimental because it does not slow down the initial setting time. However, when considering its benefit to increase the compressive strength, it is more beneficial because the accelerator increases the initial and final compressive

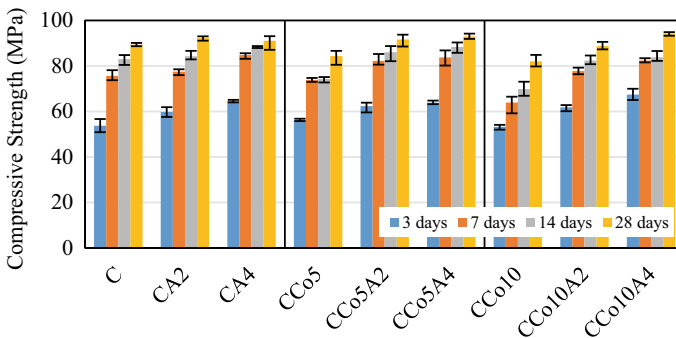


Fig. 3 Increase of compressive strength of the mortar specimen with age

strength. This is shown by the CA4 mixture strength at 3 days of 64.6 MPa while the 28-day compressive strength was 91.1 MPa.

Using only CaO reduced the initial and final strength of the mortar with a higher strength loss at higher CaO dosage. The CCo10 achieved a 3-day strength of 53.3 MPa and 28-day strength of 82.0 MPa, and lower than that of the control mortar. The best combination of faster initial setting time and compressive strength was found with the CCa10A4 mixture with an initial setting time of 60–90 min and the highest 28-day compressive strength of 94.3 MPa.

4 Conclusions

The results of this research lead to the following conclusions:

1. The combination of calcium oxide and accelerator as an additive can control the initial setting time of the concrete material needed in the 3D concrete printing process. Calcium oxide can cause a higher reaction rate in the concrete while the accelerator can control the concrete flowability and increase the compressive strength.
2. Calcium oxide can hasten the initial setting time of the concrete; however, the dosage should be limited to 10% to avoid possible flash setting or rapid hardening at higher dosage.
3. Mortar workability needs to be increased by the use of accelerator as the calcium oxide tends to reduce the workability. The target flow diameter should be greater than 13 cm in the flow table test to ensure a good extrusion process.
4. By changing the CaO and accelerators dosage, the optimum printing window can be adjusted to achieve the best rheological properties of the fresh concrete. However the optimum dosage need to be determined to comply with the printing machine parameter and concrete mixture.

Acknowledgements The authors are thankful for the funding provided by the Deputy for Research Empowerment and Development, Ministry of Research and Technology/National Research and Innovation Centre, Republic of Indonesia under PDUPT scheme no. 002/SP2H/LT-MULTI/LL7/2020.

References

1. Tay YWD, Panda B, Paul SC, Noor Mohamed NA, Tan MJ, Leong KF (2017) 3D printing trends in building and construction industry: a review. *Virtual Phys Prototyp* 12:261–276
2. De Schutter G, Lesage K, Mechtcherine V, Nerella VN, Habert G, Agusti-Juan I (2018) Vision of 3D printing with concrete—technical, economic and environmental potentials. *Cem Concr Res* 112:25–36

3. Bos F, Wolfs R, Ahmed Z, Salet T (2016) Additive manufacturing of concrete in construction: potentials and challenges of 3D concrete printing. *Virtual Phys Prototyp* 11:209–225
4. Buswell RA, Leal de Silva WR, Jones SZ, Dirrenberger J (2018) 3D printing using concrete extrusion: a roadmap for research. *Cem Concr Res* 112:37–49
5. Zhang J, Wang J, Dong S, Yu X, Han B (2019) A review of the current progress and application of 3D printed concrete. *Compos Part A Appl Sci Manuf* 125:105533
6. Gosselin C, Duballet R, Roux P, Gaudillière N, Dirrenberger J, Morel P (2016) Large-scale 3D printing of ultra-high performance concrete—a new processing route for architects and builders. *Mater Des* 100:102–109
7. Duballet R, Baverel O, Dirrenberger J (2017) Classification of building systems for concrete 3D printing. *Autom Constr* 83:247–258
8. Casagrande L, Esposito L, Menna C, Asprone D, Auricchio F (2020) Effect of testing procedures on build ability properties of 3D-printable concrete. *Constr Build Mater* 245:118286
9. Xu J, Buswell RA, Kinnell P, Biro I, Hodgson J, Konstantinidis N, Ding L (2020) Inspecting manufacturing precision of 3D printed concrete parts based on geometric dimensioning and tolerancing. *Autom Constr* 117:103233
10. Kruger J, Cho S, Zeranka S, Viljoen C, van Zijl G (2020) 3D concrete printer parameter optimisation for high rate digital construction avoiding plastic collapse. *Compos Part B Eng* 183:107660
11. Heras Murcia D, Genedy M, Reda Taha MM (2020) Examining the significance of infill printing pattern on the anisotropy of 3D printed concrete. *Constr Build Mater* 262:120559
12. Souza MT, Ferreira IM, Guzi de Moraes E, Senff L, Novaes de Oliveira AP (2020) 3D printed concrete for large-scale buildings: an overview of rheology, printing parameters, chemical admixtures, reinforcements, and economic and environmental prospects. *J Build Eng* 32
13. Rahul AV, Santhanam M, Meena H, Ghani Z (2019) Mechanical characterization of 3D printable concrete. *Constr Build Mater* 227:116710
14. Ding T, Xiao J, Zou S, Zhou X (2020) Anisotropic behavior in bending of 3D printed concrete reinforced with fibers. *Compos Struct* 254:112808
15. Wolfs RJM, Bos FP, Salet TAM (2019) Triaxial compression testing on early age concrete for numerical analysis of 3D concrete printing. *Cem Concr Compos* 104:103344
16. Zhang Y, Zhang Y, Liu G, Yang Y, Wu M, Pang B (2018) Fresh properties of a novel 3D printing concrete ink. *Constr Build Mater* 174:263–271
17. Papachristoforou M, Mitsopoulos V, Stefanidou M (2018) Evaluation of workability parameters in 3D printing concrete. *Proc Struct Integr* 10:155–162
18. Zhang Y, Zhang Y, She W, Yang L, Liu G, Yang Y (2019) Rheological and harden properties of the high-thixotropy 3D printing concrete. *Constr Build Mater* 201:278–285
19. Ma G, Li Z, Wang L (2018) Printable properties of cementitious material containing copper tailings for extrusion based 3D printing. *Constr Build Mater* 162:613–627
20. Paul SC, Tay YWD, Panda B, Tan MJ (2018) Fresh and hardened properties of 3D printable cementitious materials for building and construction. *Arch Civ Mech Eng* 18:311–319
21. Malaeb Z, Hachem H, Tourbah A, Hamzeh F, Maalouf T (2015) 3D concrete printing: machine and mix design. *Int J Civ Eng Technol* 6:14–22
22. Jayathilakage R, Rajeev P, Sanjayan J (2020) Yield stress criteria to assess the build ability of 3D concrete printing. *Constr Build Mater* 240:117989
23. Nerella VN, Hempel S, Mechtcherine V (2019) Effects of layer-interface properties on mechanical performance of concrete elements produced by extrusion-based 3D-printing. *Constr Build Mater* 205:586–601
24. Panda B, Tan MJ (2018) Experimental study on mix proportion and fresh properties of fly ash based geopolymer for 3D concrete printing. *Ceram Int* 44:10258–10265
25. Panda B, Mohamed NAN, Paul SC, Singh GVPB, Tan MJ, Šavija B (2019) The effect of material fresh properties and process parameters on build ability and interlayer adhesion of 3D printed concrete. *Materials (Basel)* 12
26. Manikandan K, Wi K, Zhang X, Wang K, Qin H (2020) Characterizing cement mixtures for concrete 3D printing. *Manuf Lett* 24:33–37

27. Khan MA (2020) Mix suitable for concrete 3D printing: a review. *Mater Today Proc*
28. Zhang C, Hou Z, Chen C, Zhang Y, Mechtcherine V, Sun Z (2019) Design of 3D printable concrete based on the relationship between flowability of cement paste and optimum aggregate content. *Cem Concr Compos* 104:103406
29. Tay YWD, Qian Y, Tan MJ (2019) Printability region for 3D concrete printing using slump and slump flow test. *Compos Part B Eng* 174:106968
30. Diggs-McGee BN, Kreiger EL, Kreiger MA, Case MP (2019) Print time versus elapsed time: a temporal analysis of a continuous printing operation for additive constructed concrete. *Addit Manuf* 28:205–214
31. Antoni A, Purwanto AAT, Suyanto WSPD, Hardjito D (2019) Fresh and hardened properties of high calcium fly ash-based geopolymer matrix with high dosage of borax. *Iran J Sci Technol Trans Civ Eng*
32. Weng Y, Li M, Tan MJ, Qian S (2018) Design 3D printing cementitious materials via fuller Thompson theory and Marson-Percy model. *Constr Build Mater* 163:600–610
33. ASTM C230 Standard specification for flow table for use in tests of hydraulic cement; ASTM International: West Conshohocken, PA, 2010
34. ASTM C403 Standard test method for time of setting of concrete mixtures by penetration resistance; ASTM International: West Conshohocken, PA, 2016
35. Antoni A, Andreas A, Christian E, Hardjito D (2019) Using viscosity-modifying admixture to increase the cohesion of low-cement concrete mixture. *IOP Conf Ser Mater Sci Eng* 615
36. Suiker ASJ, Wolfs RJM, Lucas SM, Salet TAM (2020) Elastic buckling and plastic collapse during 3D concrete printing. *Cem Concr Res* 135:106016

Numerical Simulation of Spalling and Moisture Evaporation in Concrete Tunnel Linings Exposed to Fire



Zobaer Saleheen and Renga Rao Krishnamoorthy

Abstract The modern feat of concrete tunnel construction can be owed to the longest rail tunnel, Gotthard Bass Tunnel and to the longest road tunnel, Laerdal Tunnel. Nevertheless, most concrete tunnels are subject to the rigorous understanding and assessment for the behavior of concrete tunnel lining in the event of an accidental explosion. Due to the rapid heating rate of tunnel fires, capillary and chemically bound water of concrete tunnel lining starts to evaporate and therefore increased pore pressure of water vapor leads to spalling of concrete tunnel linings. Conventional FE (finite element) simulation of heat transfer of concrete tunnel linings does not consider this spalling phenomena. As a result, prediction of temperatures inside tunnel lining by traditional heat transfer methods are remarkably underestimated. Therefore, for this study a numerical simulation was performed by eliminating the elements exceeding a critical temperature to incorporate the spalling of concrete during fire. Abaqus CAE was used as the finite element tool for this study. Existing experimental test results of similar fire exposure (*Richtlinien für die Ausstattung und den Betrieb von Straßentunneln/RABT*) were used to validate the Abaqus FE simulations. After comparing results of traditional analysis method and Abaqus EDM (element deletion method) with experimental data, the authors concluded this study with the finding that contrary to conventional analysis, Abaqus EDM results showed very good correlation with experimental results.

Keywords Tunnel fire · Heat transfer · Abaqus · Element deletion method · Fire induced spalling · Moisture vaporization

Z. Saleheen

School of Civil Engineering, College of Engineering, Universiti Teknologi MARA (UiTM), Shah Alam, Malaysia

R. R. Krishnamoorthy (✉)

Smart Manufacturing Research Institute, Universiti Teknologi MARA, Shah Alam, Malaysia
e-mail: rao@uitm.edu.my

1 Introduction

As mass transit trains have the capacity to transport up to several hundred passengers in such short time, railway has become a very popular mode of mass transportation over the past few decades. Speedy fire escalation and greater convective heating due to small cross-sectional dimension of railway tunnels along with lesser auspicious escape opportunities can cause catastrophic loss of human life and materials during fire. The consequences of railway tunnel fire on loss of human life was observed when nearly 200 people died in both South Korean tunnel fire in 2003 and Azerbaijan tunnel fire in 1995 [1]. The Channel Tunnel connecting UK with European mainland has suffered three major fire incidents over the last couple of years. In 1996, the fire was caused by one of the HGVs (Heavy Good Vehicle) on board an HGV carrier which later on spread into ten HGVs. The fire started off at 1.5 MW but ultimately reached as high as 350 MW which lasted over 7 h and the maximum ceiling temperature was found to be around 1100 °C [1–3]. During this fire, 100 mm to 200 mm of the total 450 mm thick precast RC tunnel lining suffered severe spalling, which ceased all travel and commerce activity of that tunnel for nearly six months [3, 4]. Even though research on influence of fires in concrete structures started as early as 1920, Channel Tunnel fire (1996), Mont Blanc Tunnel fire (1999) and Lainzer tunnel fire (1999) have shown that fires in tunnel quickly rises to the peak temperature and withstands longer than building fires [2, 5]. Therefore, in the recent years many researchers [6–10] have studied the fire safety and behavior of concrete tunnel linings under severe fire scenarios like RWS, RABT and Hydrocarbon fire curve. The focus of these researches can be broadly categorized into three areas such as (a) fire resistance of concrete tunnel linings, (b) material degradation during fire and (c) spalling of concrete.

Currently, three methods are being used by the researchers to evaluate fire resistance of concrete tunnels. The three methods are namely, (i) conducting experimental fire tests, (ii) prescriptive methods and (iii) performance-based approach. FE simulations falls in to the third category. Although researchers like Yasuda et al. [10], Lai et al. [9] and Cavdar [7] have taken the experimental approach to investigate fire induced spalling, numerical simulations done by Kodur and Dwaikat [11] and Caner et al. [12] were focused on degradation of thermal and mechanical properties of concrete and reinforcement due to fire. Savov et al. [4] were among the first ones to evaluate structural loss due to spalling in a FE simulation. The tunnel lining comprised of layered finite beam elements which got deactivated following a predefined spalling scenario. Four spalling depths of 0 mm, 100 mm, 200 mm and 300 mm was considered to occur linearly from 5 to 30 min of fire exposure. However, rather than considering convection and radiation from the heat source, temperature history of the fire exposed surface was used for conduction of the heat inside the tunnel lining.

Fire induced spalling can be characterized as the breaking up of layers or pieces of concrete when it is subjected to a rapid rate (typically 20–30 °C/min) of heating [5]. When concrete gets heated beyond 100 °C, the free water in concrete starts to

evaporate. For smaller concrete elements, by the time concrete reaches 100 °C most of the capillary water gets evaporated. However, for larger concrete elements the process might not be rapid enough thus some moisture gets driven along the lower temperature gradient of the concrete. The chemically bound water from the CSH (Calcium Silicate Hydrate) starts to get released at around 80 °C and at about 110 °C the dehydration becomes significant. Calcium hydroxide starts to dissociate at about 400 °C and dehydration takes place around 500 °C [5, 13]. Evaporation of capillary water along with the chemically bound water results in an additional pore pressure due to water vapor which triggers the spalling of concrete. It can happen either during early exposure of fire or in later stage of fire when the concrete has lost significant portion of its strength on account of being exposed to high temperature for long time [14].

Previously, compressive strength of concrete being used in the construction industry was around 20–50 MPa, which is designated as Normal Strength Concrete (NSC). In the recent years, demand for High Strength Concrete (HSC) of 50–120 MPa has increased at a rapid pace [14]. Although these concretes have a lot of advantages, HSC and UHPC (compressive strength > 120 MPa) are more prone to spalling during fire due to their lower water cement ratio and lower permeability than NSC. Apart from the loss of stability and structural integrity, inner layers of concrete get exposed to the fire temperature as a consequence of spalling. Thence, this paper intends to investigate the effect of spalling and moisture evaporation in heat transfer of concrete tunnel by performing a FE simulation of a segment of concrete tunnel lining subjected to RABT fire scenario. Element deletion feature of commercial FE package Abaqus was used to incorporate the spalling behavior of concrete.

2 Experimental Setup

The experimental test data used in this study was conducted by Choi et al. [15, 16] as a part of their Strategic Research Project grant which was funded by Korean Institute of Civil Engineering and Building Technology. As shown in Fig. 1, the furnace used to simulate the RABT fire scenario had two main and two pilot burners which had the maximum capacity of 580,000 kcal/hr. The internal size of the furnace was 1100 mm × 700 mm × 600 mm. A Programmable Logic Controller (PLC) along with an R type thermocouple was used to maintain the temperature of the furnace with an accuracy of ± 0.25%.

Two reinforced and one unreinforced concrete sample of 1400 mm × 1100 mm × 500 mm size was prepared for the test. Owing to the size of the samples, these concrete specimens were suitable for positioning over the furnace.

28-day Design strength for one reinforced concrete and the unreinforced concrete were 24 MPa, the other reinforced concrete was of 40 MPa strength. Moisture content of all specimens was measured with portable concrete moisture tester before every fire test, which was found to be around 3% on average. In order to keep moisture



Fig. 1 Furnace used by Choi et al. [15] to imitate the RABT fire scenario

content of the samples below TNO [17] recommendation of 4%, the samples were cured and kept indoors for 28 days before testing.

As shown in Fig. 2, seven K type sheathed thermocouples of 6.4 mm diameter were installed inside the sample before pouring of concrete. Outer layer of the thermocouples was insulated with SUS316 stainless steel and magnesium oxide (MgO) to cover the internal wire which was used to measure the temperature inside different depths of concrete samples during fire. Figure 3 shows that seven thermocouples (TC1–TC7) were placed at 50 mm, 100 mm, 150 mm, 200 mm, 250 mm, 300 mm

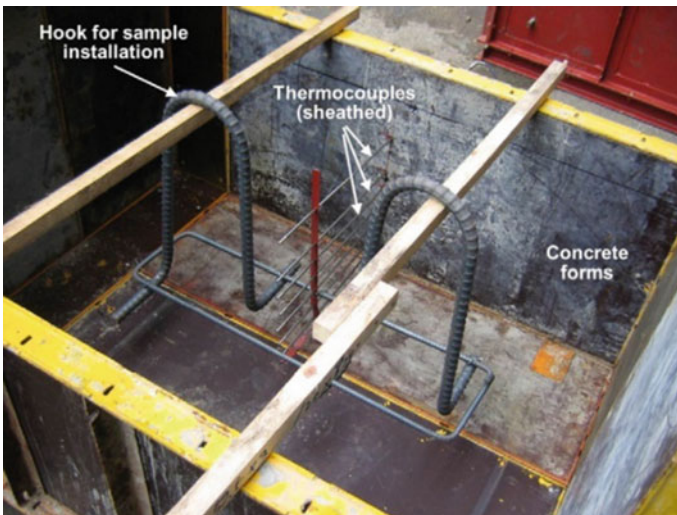


Fig. 2 Unreinforced concrete sample before casting [15]

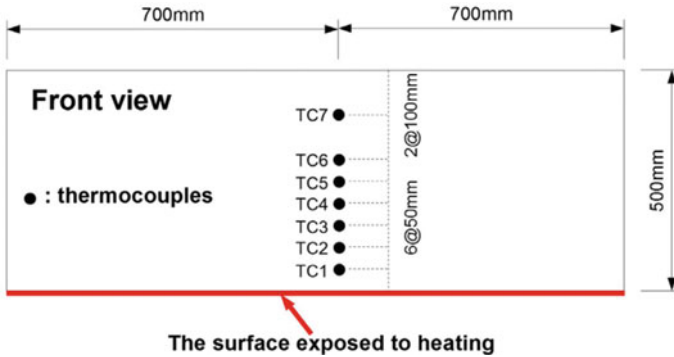


Fig. 3 Location of thermocouples [16]

and 400 mm respectively from the surface exposed to fire. Thermocouples used for this study could measure up to 1370 °C temperature with $\pm 0.75\%$ accuracy.

3 FE Modelling Parameters

The input parameters including RABT fire curve, temperature dependent thermal properties of concrete, critical temperature for spalling and moisture incorporation for finite element modelling of concrete in Abaqus are discussed in the following subsections of this article.

3.1 RABT Fire Curve

Tunnel fire curves (e.g. RWS, HC, RABT-ZTV etc.) were established to simulate fires caused by hazardous good vehicles carrying different types of fuels. RABT/ZTV (*Richtlinien für die Ausstattung und den Betrieb von Straßentunneln*) fire curve was primarily established by the German Ministry of Transportation as a part of the Eureka project [18]. German authorities provided different RABT curves for both road and railway tunnel fires.

Figure 4 shows the RABT curve for railway tunnel fires, which was used in this study. Initial temperature of RABT fire curve is 15 °C, which rises by approximately 240 °C/min temperature gradient for 5 min until it reaches 1200 °C, which is the highest temperature of RABT fire scenario. Peak temperature (1200 °C) of this curve remains same till 60 min then it starts cooling for 110 min, until temperature descend to 15 °C.

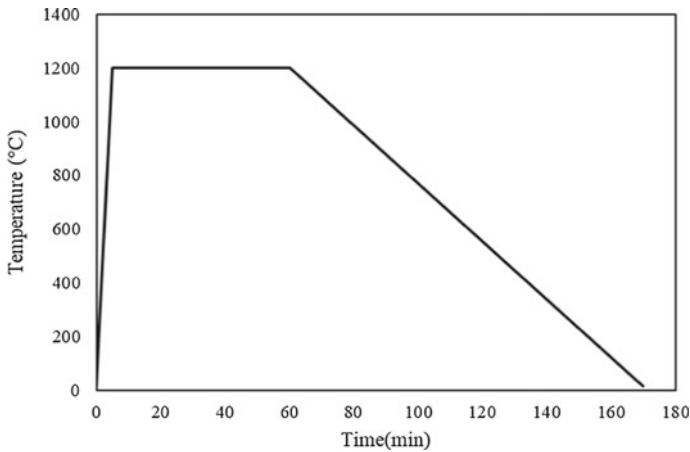


Fig. 4 RABT/ZTV fire curve

3.2 Thermal Properties of Concrete

Specific Heat Specific heat is defined as the amount of heat needed for per mass of the material to increase temperature by 1 °C. Density, moisture content and type of aggregate being used in the concrete has noteworthy impact on its specific heat [14, 19]. Specific heat of concrete ranges from 840 to 1800 J/kg K depending on the type of aggregate being used in concrete [19]. Specific Heat is also susceptible to variation during the physio chemical changes (e.g. evaporation of capillary water, disintegration of calcium hydroxide into CaO and H₂O, quartz transformation of aggregates) occur in concrete during fire. For this study, specific heat given for siliceous aggregate concrete of Eurocode 2 [20] was used after incorporating moisture evaporation during fire (refer to Fig. 5).

Thermal Conductivity Thermal conductivity refers to the rate at which heat gets transferred inside a material. Conductivity of concrete can vary from 1.4 to 3.6 W/m K at room temperature and normally decreases with increasing temperature which is susceptible to variation with moisture and permeability [14]. As shown in Fig. 6, upper bound values of Eurocode [20] for siliceous aggregate concrete was used for this study.

3.3 Critical Temperature for Spalling

Khoury [5] stated that strength loss of siliceous aggregate concrete initiates at 300 °C, but it can occur at lesser temperatures for flint aggregates and at higher temperatures for granite aggregates. Portland cement based concrete loses almost all of its load

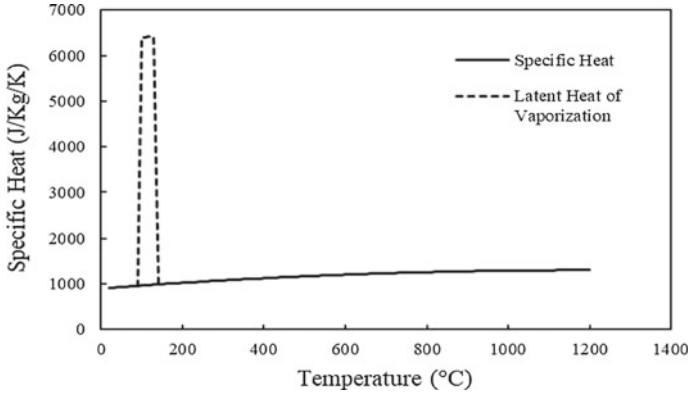


Fig. 5 Specific heat of concrete as per Eurocode 2 [20]

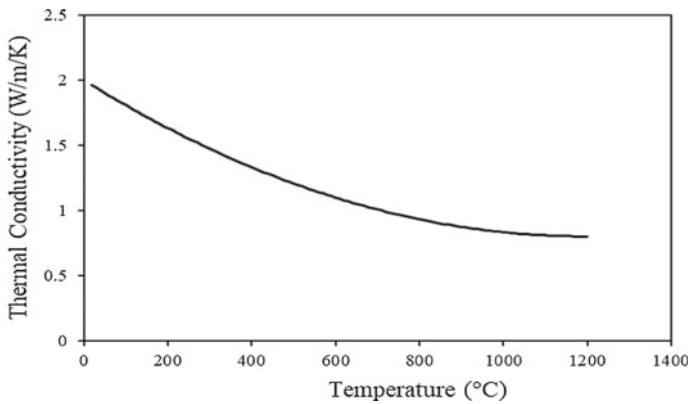


Fig. 6 Thermal conductivity of concrete as per Eurocode 2 [20]

bearing capacity by the time it reaches 550–600 °C temperature [5]. Although previously done experimental studies has shown that fire induced spalling in concrete occurs in the range of 250–420 °C [21, 22], it may deviate for numerical simulations due to its varying parameters. If thermomechanical failure of concrete is simulated in terms of structural loss during a FE analysis, meshed element size and critical temperature for null elements plays a vital role. Choi et al. [15] employed the element elimination technique in Visual FEA to characterize thermomechanical damage of concrete in terms of structural loss due to fire induced spalling. While doing so, they conducted a parametric study for different critical temperatures (500, 600 and 700 °C) and different element sizes (10, 25 and 50 mm). They concluded the study by showing that selecting 600 °C as critical temperature for element size

of 25 mm showed best correlation with their experimental data [15]. However, additional energy required for moisture vaporization was not taken into account in the aforementioned model.

3.4 Moisture Evaporation

When the temperature of concrete rises around 100 °C, capillary water starts evaporating which absorbs a certain amount of energy, as a result heat transfer process gets hindered. Due to this phenomenon, inconsistencies between experiment and simulation results are observed in 100–200 °C range [13], which can be avoided by inducing proper assimilation of moisture vaporization in the model. Hence, for this study, energy required for evaporation was calculated by incorporating latent energy of evaporation into heat capacity of the material, Davies and Wang's [23] stated that capillary water of concrete evaporates within 100–130 °C, so for that interval, additional heat required for moisture evaporation is calculated using latent heat of vaporization for water. Figure 5 shows the specific heat given by Eurocode 2 [20] after the inclusion of latent heat of moisture evaporation given by Davies and Wang [23].

$$DC_p = 2.25 \times 10^6 \times e \times \Delta / DT \quad (\text{J/kg K}) \quad (1)$$

In Eq. (1), DC_p = additional specific heat for moisture evaporation, e = moisture content as a fraction of concrete weight, DT = given temperature interval, from the previous studies, it was observed that conventional latent heat of vaporization, expressed as 2.25×10^6 J/Kg markedly undervalues the extra energy demand for moisture vaporization. Thus, a factor $\Delta > 1$ was proposed in Eq. (1) [23].

4 Thermal FE Analysis Using Abaqus

In order to validate the experimental works done by Choi et al. [15] and evaluate the effects spalling and moisture vaporization in heat transfer of concrete tunnel linings, two separate FE models were prepared using a commercial finite element tool Abaqus CAE. The process of Heat transfer in concrete is governed by three major modes, namely radiation, convection and conduction. For this study, heat transfer from fire to exposed concrete surface was simulated by convection and radiation and thereafter conductivity was used to propagate the heat from fire exposed surface to inner material. For both FE models in Abaqus, convection coefficient of 25 W/m K, radiation coefficient of 0.7 along with temperature dependent conductivity (refer to Fig. 6) was used. Concrete was modelled as C3D8T, an eight node thermally coupled three dimensional solid brick, meshed element size of which was kept as 25 mm for

both models. Among the two FE models, Conventional thermal model was prepared without taking into account of moisture vaporization and spalling.

However, for the EDM (element deletion method) model, spalling behavior of concrete was incorporated by setting a predefined critical temperature. During the analysis, when center of an element reached the critical temperature, computations were stopped and all of the elements exceeding critical temperature were deleted using “model change” feature of Abaqus. Finally, analysis was resumed after applying heat flux on outer boundary of the remaining elements. This process was repeated until full spalling depth of experiment was attained.

5 Discussion of Experimental and Numerical Results

In the fire tests conducted by Choi et al. [15], total spalling depth was close to 100 mm which occurred within first 20 min of fire exposure. For this study, the authors primarily selected a critical temperature and element size based on previous researchers’ recommendation, then a trial and error method was adopted to find the best fit for this simulation. When critical temperature of 550 °C was adapted for 25 mm elements in Abaqus EDM model, spalling started at 8 min of fire exposure and by 21 min, 100 mm concrete was damaged (Fig. 7). Owing to the similar trend of experimental scenario and analogous outcome of previous researches [5, 15, 16], aforementioned values for critical temperature and element size were used for Abaqus EDM model of this study.

Figures 8, 9, 10, 11, 12 and 13 shows comparison of temperature history of concrete at seven thermocouple locations between experimental (Exp), Abaqus conventional thermal analysis (Convn) and Abaqus element deletion method (EDM) results. From experimental results it can be seen that temperature rises steadily for 10 min and 20 min respectively at 50 mm (refer to Fig. 8) and 100 mm (refer to Fig. 9) depth followed by an instantaneous upsurge which takes the temperatures to 1200 °C. Figure 8 shows that, at around 16 min after fire exposer, temperature history curve of Abaqus EDM at 50 mm depth terminates due to spalling, but the results of experimental curve continues further that point because even after spalling of concrete, the thermocouple at that point still gives outputs. Whereas, Abaqus EDM method was able so simulate the temperature trend proximately for both depths (50 and 100 mm), Abaqus conventional analysis reached only 480 °C in 105 min at 50 mm and 280 °C in 160 min.



Fig. 7 Concrete before spalling (left) and after spalling (right)

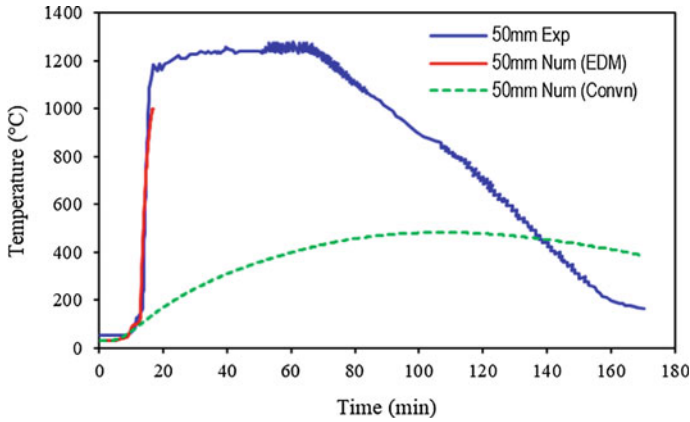


Fig. 8 Temperature history of concrete at 50 mm depth

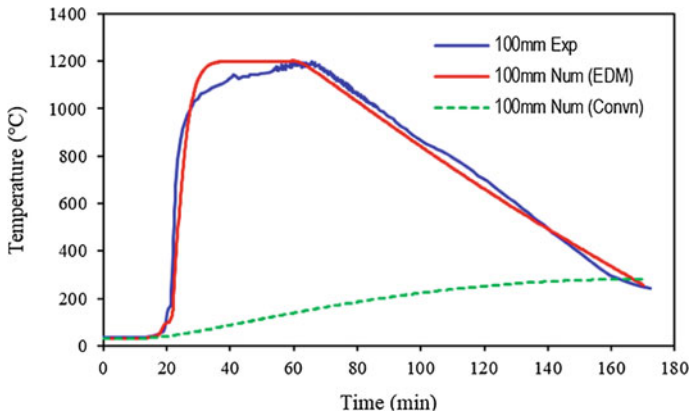


Fig. 9 Temperature history of concrete at 100 mm depth

As shown in Fig. 10, temperature of concrete test sample at 150 mm depth showed a flat plateau after 100 °C due to moisture evaporation which was closely represented in Abaqus EDM curve by employing latent heat of vaporization. By virtue of that, temperature curve of experimental and Abaqus EDM model showed similar trend. Though maximum temperature of experimental result (360 °C) was slightly exaggerated by Abaqus EDM model (380 °C), temperature of Abaqus conventional analysis result (115 °C) was found to be extremely underrated.

Maximum temperature values at 200 mm for test sample (Exp), Abaqus EDM and Abaqus Convsn was found to be adjacent, which are 155 °C, 145 °C and 110 °C respectively. Nevertheless, for concrete test sample (Exp) a distinct temperature gradient was noticed from 40 to 50 min which appeared 10 min later for Abaqus EDM model.

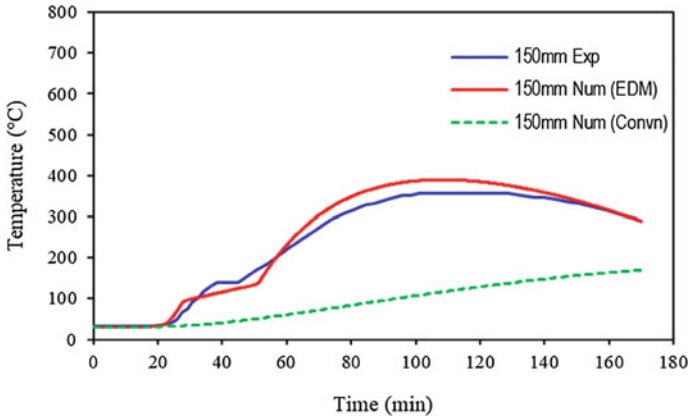


Fig. 10 Temperature history of concrete at 150 mm depth

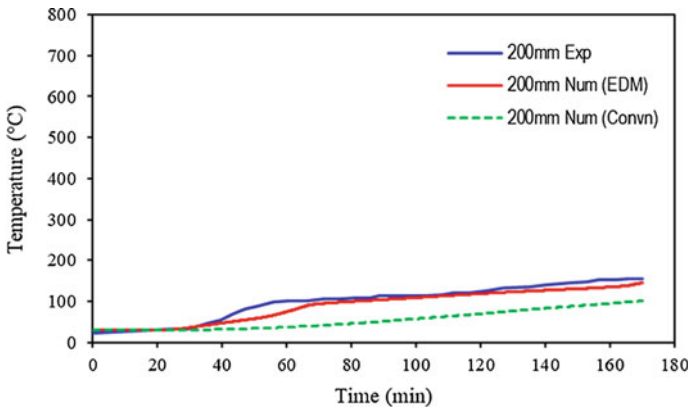


Fig. 11 Temperature history of concrete at 200 mm depth

However, apart from the regular temperature ascending slope, no discernable sharp gradient was found on conventional analysis (Conv) temperature curve.

Abaqus EDM and experimental temperature history curve for 250, 300 and 400 mm concrete depth followed similar course and attained adjacent maximum temperature. However, previously mentioned distinct temperature gradient was observed for experimental temperature curves of 250 and 300 mm concrete depth. Contrary to the previous results, temperature prediction of conventional analysis method (Conv) for these three depths were slightly under estimated than Abaqus EDM results.

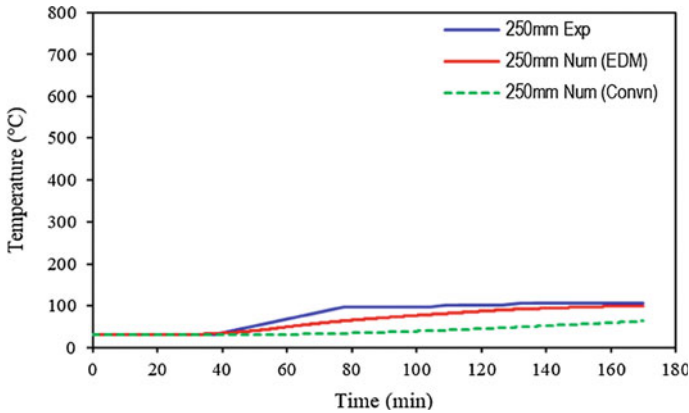


Fig. 12 Temperature history of concrete at 250 mm depth

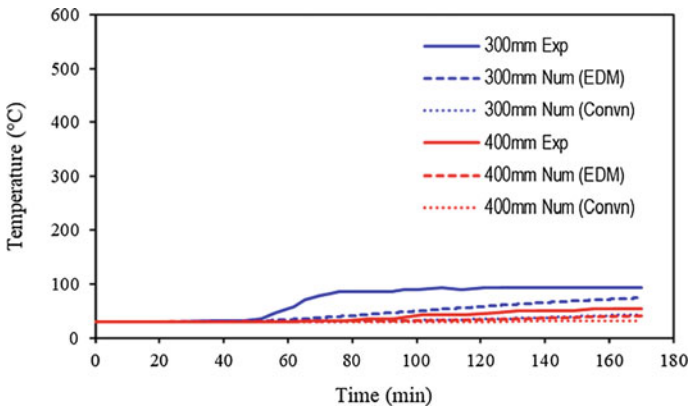


Fig. 13 Temperature history of concrete at 300 and 400 mm depth

6 Conclusion

The authors concluded this study with two prime findings. Firstly, owing to the rapid heating rate and higher peak temperature of tunnel fire curves, tunnel linings are more susceptible to fire induced spalling. Apart from loss of concrete section, spalling also plays a vital role in thermal analysis of concrete tunnel linings. Moreover, when spalling behavior was not incorporated in numerical simulations, temperature predictions of conventional thermal analysis methods were found to be severely underestimated. On the other hand, proper integration of spalling behavior in numerical simulations resulted in reasonably accurate depiction of temperature profile and distribution in concrete tunnel lining.

Secondly, in the experimental results it was observed that around 100–130 °C heat transfer process gets retarded. After thorough investigation, the authors concluded that the flat plateau of temperature history curves were caused by additional energy absorbed by moisture evaporation. Inclusion of latent heat of vaporization in FE simulation resulted in close characterization of experimental scenario. A simplified method of moisture modelling was adapted for this study which was limited to moisture vaporization only but did not take into account of the moisture migration that occurs in heated concrete. On account of that, several minor anomalies in temperature history were detected in the furthest regions from fire exposed surface.

On a final note, the authors would like to add that although incorporation of moisture evaporation energy had shown significant improvement on FE simulation results, comprehensive moisture modelling can result in enhanced understanding of fire performance of concrete.

References

1. Beard A, Carvel R (eds) (2005) Handbook of tunnel fire safety, 2nd edn. ICE Publishing
2. Qiao R, Shao Z, Liu F, Wei W (2019) Damage evolution and safety assessment of tunnel lining subjected to long-duration fire. *Tunn Undergr Space Technol* 83(January):354–363
3. Khorasani NE, Billittier J, Stavridis A (2018) Structural performance of a railway tunnel under different fire scenarios. In: 2018 Joint rail conference, JRC 2018, pp 1–8
4. Savov K, Lackner R, Mang HA (2005) Stability assessment of shallow tunnels subjected to fire load. *Fire Saf J* 40(8):745–763
5. Khoury GA (2000) Effect of fire on concrete and concrete structures. *Prog Struct Eng Mater* 2(4):429–447
6. Gawin D, Pesavento F, Schre BA (2002) Simulation of damage—permeability coupling in hygro-thermo-mechanical analysis of concrete at high temperature. *Commun Numer Methods Eng* 18(2):113–119
7. Çavdar A (2012) A study on the effects of high temperature on mechanical properties of fiber reinforced cementitious composites. *Compos Part B Eng* 43(5):2452–2463
8. Qiao R, Shao Z, Wei W, Zhang Y (2018) Theoretical investigation into the thermo-mechanical behaviours of tunnel lining during RABT fire development. *Arab J Sci Eng* 44:4807–4818
9. Lai H, Wang S, Xie Y (2014) experimental research on temperature field and structure performance under different lining water contents in road tunnel fire. *Tunn Undergr Space Technol* 43:327–335
10. Yasuda F, Ono K, Otsuka T (2004) Fire protection for TBM shield tunnel lining. *Tunn Undergr Space Technol* 19(4–5):317
11. Kodur VKR, Dwaikat M (2008) A numerical model for predicting the fire resistance of reinforced concrete beams. *Cem Concr Compos* 30(5):431–443
12. Caner A, Zlatanic S, Munfah N (2005) Structural fire performance of concrete and shotcrete tunnel liners. *J Struct Eng* 131(12):1920–1925
13. Khoury GA, Majorana CE, Pesavento F, Schrefler BA (2002) Modelling of heated concrete. *Mag Concr Res* 54(2):77–101
14. Kodur VKR (2014) Properties of concrete at elevated temperatures. *ISRN Civ Eng* 2014:429–432
15. Choi SW, Lee J, Chang SH (2013) A holistic numerical approach to simulating the thermal and mechanical behaviour of a tunnel lining subject to fire. *Tunn Undergr Space Technol* 35:122–134

16. Chang SH, Choi SW, Lee J (2016) Determination of the combined heat transfer coefficient to simulate the fire-induced damage of a concrete tunnel lining under a severe fire condition. *Tunn Undergr Space Technol* 54:1–12
17. TNO (Netherlands Organization for Applied Scientific Research) (1998) Fire protection for tunnel (Part1: Fire test procedure). TNO Report 1998-CVB-R1161 (rev.1)
18. Kim S, Shim J, Rhee JY, Jung D, Park C (2019) Temperature distribution characteristics of concrete during fire occurrence in a tunnel. *Appl Sci* 9
19. Harmathy TZ (1970) Thermal properties of concrete at elevated temperatures. *ASTM J Mater* 5(1):47–74
20. Eurocode 2 (1996) EN1992-1-2 design of concrete structures Part 1.2—General Rules-Structural Fire Design
21. Connolly RJ (1995) Spalling of concrete in fires. Doctoral Thesis, Aston University
22. Akhtaruzaman AA, Sullivan PJ (1970) Explosive spalling of concrete exposed to high temperature. Concrete Structures and Technology Research Report, Imperial College, London
23. Davies JM, Wang H (1994) Numerical temperature calculation for composite deck slabs exposed to fire. *Trans Eng Sci* 5:331–338

Optimization on Geometry Design of Double-Layer Space Trusses



Yazmin Sahol Hamid and Nurul Najihah Abd Rahim

Abstract Double-layer space truss (DLST) is widely known by the square-on-square configuration system. This study is conducted to find the optimum design between the other configuration such as diagonal-on-square (DOS), square-on-diagonal (SOD), and triangle-on-triangle (TOT). As designers need to be competitive in the industry, they need to come out with creative design using minimal materials while achieving adequate strength. Thus, they need to have guidelines to use other geometry configuration. Optimum design in this study includes section size diameter, minimal materials consumption with adequate strength. Structural analysis software, SAP2000, is used in finding the optimum section diameter by optimization techniques. Then, stress capacity check will be conducted to understand the behaviour of each member. DLST is commonly subjected to progressive collapse cause of failure of buckling member. Thus, it is crucial to understand the behaviour and the vulnerability of the structure. To achieve optimum design, strength to weight ratio comparison of DLST is done to find the most lightweight structure with adequate strength. Comparison between all the DLSTs is made and DOS is the most optimum design based on section size, minimal materials and adequate in strength. However, DOS have the highest DCR value member and the most vulnerable among all DLSTs. Thus, DOS is more suitable to be used for light loads and moderate span structure and is proved to be economic. TOT is the least optimum in section size diameter and the least vulnerable among all DLSTs. This indicates that the optimization technique will assist designers to design new configuration forms instead of the conventional system.

Keywords Finite element analysis · Double-layer space trusses

Y. Sahol Hamid (✉) · N. N. Abd Rahim
School of Civil Engineering, College of Engineering, Universiti Teknologi MARA (UiTM),
40450 Shah Alam, Malaysia
e-mail: yazminsaoh@uitm.edu.my

1 Introduction

In the past two decades, space structures are attracting widespread interest in the construction industry especially for double-layer grids. Due to its properties to withstand loads on the long span with few intermediate columns, it offers a great advantage for engineers in modern construction. Double-layer grids are made from two layers of the parallel plane grid, consist of upper and lower chords connected with the diagonal member. It is widely used in roof construction such as sports halls, shopping malls, airport hangar, swimming pools and stadiums. Space structures is aesthetically pleasing due to its open ceilings and minimal use of column plus there has been a growing interest in space structures especially in the heart of architects.

When a space roof truss is an open ceiling concept, it allows the space grid to be seen by occupants passing by the building. Currently, the same type of space roof truss configuration is used nowadays which is a square-on square DLST system that is considered safe and economical. This type of arrangement has started to bore not only the architects but other passage by as it's a common shape seen everywhere. Venturing into new forms and configurations is still lacking in our society due to the client's budget to save cost. This study focusses on finding the optimum design of other types of arrangements as guidelines to help designers and meanwhile preserving the structure's strength to weight ratio to save construction cost.

1.1 Configuration of Double-Layer Space Truss

There are two different types of double-layer grids known as lattice grids and space grids. The difference of these grids is two layer of lattice grid is set on parallel while one of space grid layer is arranged as offset producing different type of spatial shape such as tetrahedra and half octahedra. Grid patterns are in form of squares, diagonals, triangles and combination of these for upper and lower planes. Double-layer space grids or known as double-layer space truss (DLST) has various configurations depending on design. However, the most popular arrangement used in construction is square-on-square offset (SOS) due to its low cost, simplicity of design and erection compared to other shape configurations. Previous study by Al Sulayfani and Saaed [1] focused on optimize design of SOS DLST by using STAAD PRO software to analysis and design the structure. Salajagheh et al. [2] also conducted a study to find optimum shape design of SOS configuration by Genetic Algorithm. Selvam and Divyameena [3] studied on optimization of space truss by varying the depth of SOS DLST. Only a few researchers focus on the design of different type of configurations such as diagonal-on-square (DOS), square-on-diagonal (SOD) and triangle-on-triangle (TOT) DLST. To remain competitive in the engineering sector, designers need to be innovative and creative in producing designs while ensuring sufficient strength and minimal materials used. Therefore, there is a need to study the optimum design of other type's configurations and produce guidelines to help

engineers in designing DLST. Numerous types of space structures can be produced in regular or irregular geometry design. Figure 1 shows the configuration of common DLST [4].

DLST consists of upper and lower chord members parallel to each other, connected by vertical or inclined members as shown in Fig. 2. DLST can be divided into lattice grids and space grids. Top and bottom members of lattice grids are arranged in the perpendicular of the same plane in Fig. 3a. In contrast space grids are made

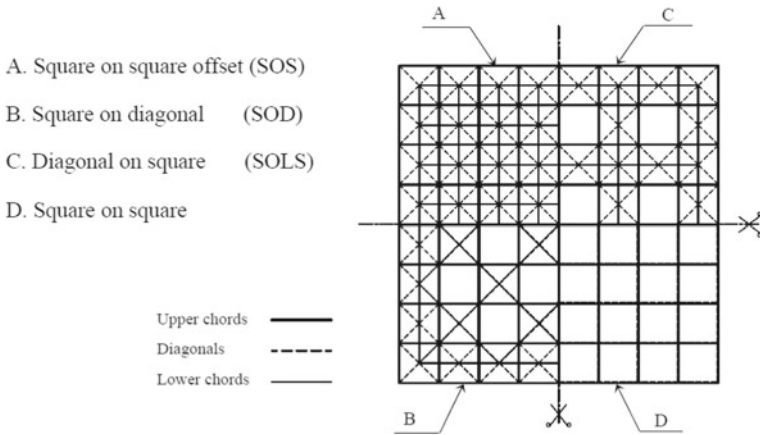


Fig. 1 Most common double layer space truss [4]

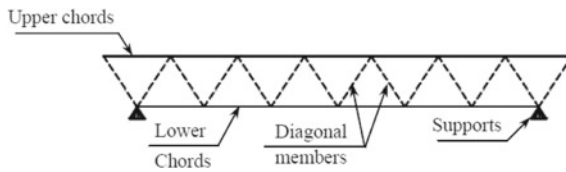


Fig. 2 Component of double-layer space truss [4]

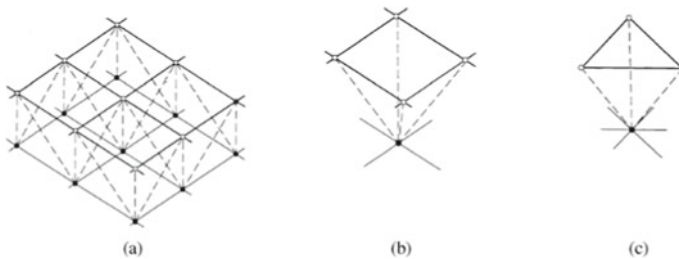


Fig. 3 Elements of double-layer space truss [5]

Table 1 Member size and depth of grid [7]

Span = s (m)	Member = a (m)	Depth = h (m)
Up to 15	2–3	Up to 1.5
15–27.5	2.4–3	1.5–2.1
27.5–36	2.4–3.6	2.1–2.5
36–50	3.6–4.8	2.5–4.0
50–100	4.8–6	3.6–4.8

of prefabricated half octahedra (Fig. 3b) and tetrahedra (Fig. 3c) joined by node connectors or continuous member to form a space frame.

1.2 Structural Size Conditions

For an economical solution, the maximum length of span to width ratio is 1.5:1.0 while the depth of DLST should be ranging between 0.04–0.08 of the span lengths [6]. However, Table 1 can be used for guidance of span, member length and depth of the grid.

1.3 Demand Capacity Ratio (DCR)

In the planning design stage of DLST, software structure is used to design and analyze linear static analysis. Loading is applied to the structure to examine the internal forces among the structural member. DCR is a ratio to indicate the actual internal forces over the design capacity. Allowable DCR value is to be less than 1.0 which exhibits the member to be under stressed, whereas if the amount exceeds 1.0, the member is said to be “overstressed” which can cause to the failure of structure [8].

1.4 Space Configuration

Much research in recent years has focused on the same shape configuration for double layer space truss. Square-on-square shape is well-known for the design of double layer space truss because it is simple, cost-effective and easy in erection. However, a few other shape configurations need to be given attention because of the greater strength and rigidity it produced. Studies done by [9] found that square-on-diagonal indicate more even stress distribution and minimum reduction compared to diagonal-on-square grid. Square-on-diagonal and diagonal-on-square have the same value on slenderness ratios of compressive members, both grids exhibit different

buckling behavior. Boundary members on diagonal-on-square are more effective in controlling buckling than square-on-diagonal [10].

2 Methodology

Finite Element Software is widely used to analyze and design the complex behavior of Double-Layer Space Trusses (DLSTs). In this study, SAP2000 version 20 is used to design four different types of space structure geometry configuration labelled as SOS, DOS, SOD and TOT for square-on-square, diagonal-on-square, square-on-diagonal and triangle-on-triangle respectively. An analysis is performed using this software to perform optimization of the size of members and also to check the stress capacity of each member using Demand Capacity Ratio (DCR). The value of DCR must not be more than one as it will cause the member to be overstressed. Once analysis and stress capacity check has passed, DCR mean and standard deviation is produce in graph to understand the vulnerability index of each DLST. Then, strength to weight ratio of the four configuration is calculated to compare the lightness and strength of each DLST.

2.1 Demand Capacity Ratio (DCR)

In the planning design stage of DLST, software structure is used to design and analyse linear static analysis. Loading is applied to the structure to examine the internal forces among the structural member. DCR is a ratio to indicate the actual internal forces over the design capacity. Allowable DCR value is to be less than 1.0 which exhibits the member to be under stressed, whereas if the amount exceeds 1.0, the member is said to be “overstressed” which can cause to the failure of structure [8]. Manual calculations are made based on “Eurocode 3-2005” [BS EN1993-1-1]. The following Eq. (1) is used to calculate the DCR value of a member.

$$DCR = \frac{Q_{UD}}{Q_{CE}} \quad (1)$$

where,

Q_{UD} = Internal force occurring in a member.

Q_{CE} = Expected design capacity of the member.

DLST scale size and dimension of members are determined complying with the design requirements and it is designed using SAP2000 Version 20. Table 2 shows the design geometry of SOS, DOS, SOD and TOT DLST with joint labels. In this section, all purple line indicates the top member of the DLST, blue line as bottom

Table 2 Dimension and member size of DLSTs

Configuration		SOS	DOS	SOD	TOT
Size dimension (m)		21 × 21	21 × 21	21 × 21	21 × 19.6
Depth (m)		1.5	1.5	1.5	2.5
Member length (m)	Top	3	$3\sqrt{2}$	3	3
	Web	2.6	2.6	2.6	3
	Bottom	3	4.2	$3\sqrt{2}$	3

member and orange line as web member respectively. The complete geometry design of all DLST is shown in Fig. 5.

2.2 Material Properties

Material properties used for this analysis is steel from Eurocode3 for design steel structure. Based on the Eurocode3, the values taken for all members are 7850 kg/m³ for mass density, 210 GPa for modulus of elasticity, 0.3 for Poisson’s ratio and 355 MPa for minimum yield stress.

2.3 Boundary Conditions

X and Y are horizontal axis and Z is the vertical axis in SAP2000 as shown in Fig. 4. Supports for SOS, DOS, SOD, and TOT DLST are situated along the perimeter including at the corners using restraints shown in Table 3 while joints are labelled as in Fig. 5(i)–(iv) respectively.

Fig. 4 X, Y, Z axis

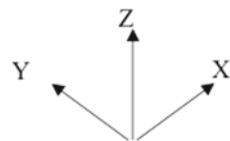


Table 3 Boundary conditions of DLSTs

Joint labels				Translation		
SOS	DOS	SOD	TOT	Ux	Uy	Uz
1	1	1	1	0	0	0
7	5	7	7	Free	0	0
43	21	30	66	0	Free	0
49	25	36	71	Free	Free	0

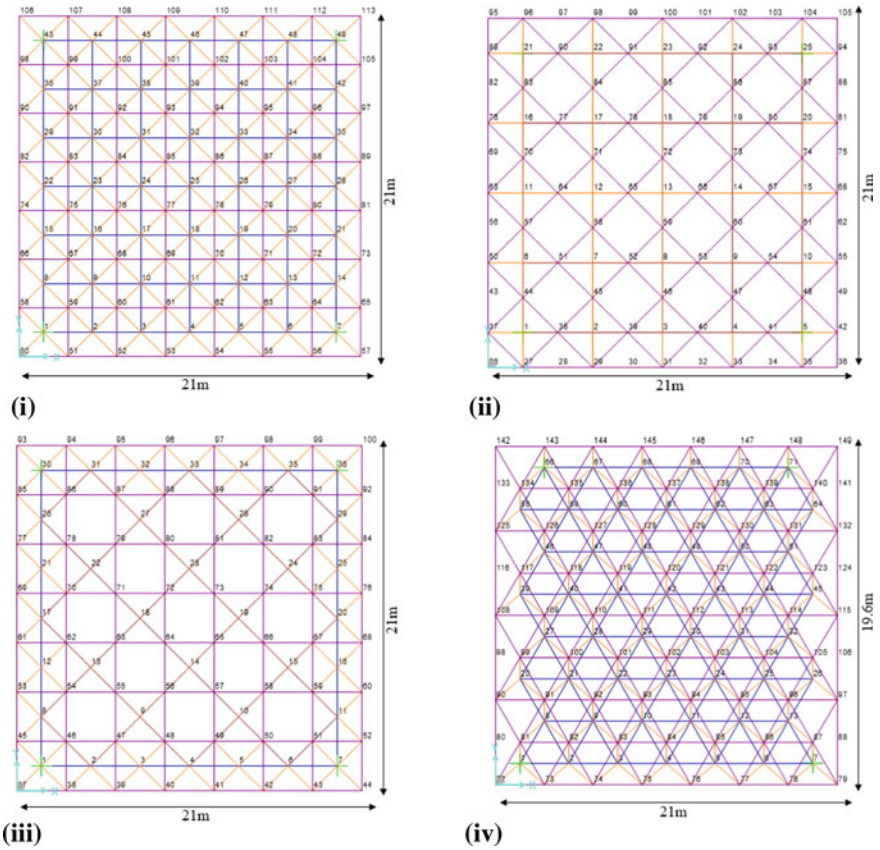


Fig. 5 Plan view with joint labels, (i) SOS DLST, (ii) DOS DLST, (iii) SOD DLST, (iv) TOT DLST

2.4 Loading Conditions

In this study the load used for DLST analysis is the most common load for roof structure design. All DLST models are assigned the same live loads and superimposed permanent dead loads. In SAP2000, self-weight of roof is automatically calculated. Table 4 shows the roof loading used for this analysis.

Permanent action of 0.55 kN per square meter and variable action 0.6 kN per square meter are applied which are distributed vertically as point loads at each joint of the top grid members. The following shows example calculation for model SOS (see Fig. 6).

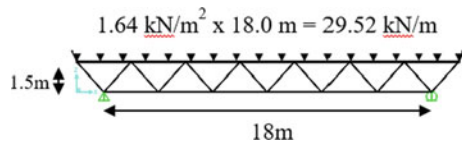
Where,

- $W = 29.52 \text{ kN/m}$
- Length = 18 m
- $N_{top} = 7 \text{ members}$

Table 4 Roof loading

Actions	Design load (kN/m ²)
Permanent actions	Roof and insulation = 0.35 Purlins = 0.05 Services = 0.15 gk = 0.35 + 0.05 + 0.15 = 0.55
Variable actions	Imposed load = 0.6 qk = 0.6
Combination of actions	Permanent action = 0.55 Variable action = 0.6 Using expression 6.10 as in BS EN 1990; Load = 1.35DL + 1.5LL Load = 1.35 × 0.55 + 1.5 × 0.6 = 1.64

Fig. 6 Example for model SOS



N_{bottom} = 6 members

Ratio of $\frac{Length}{Depth}$ is from 10 to 24

Selecting $\frac{Length}{Depth} = 12$, therefore Depth = 1.5 m

Moment, $M = \frac{WL^2}{8}$

Moment, $M = \frac{29.52 \frac{kN}{m} \times (18 \times 18)m^2}{8} = 1195.6 \text{ kN m}$

Force = $\frac{Moment}{Depth} = \frac{1195.6}{1.5} = 797.04 \text{ kN}$

Force for top layer members;

Force = $\frac{Moment}{N_{top}} = \frac{797.04}{7} = 113.9 \text{ kN}$

Force for bottom layer members;

Force = $\frac{Moment}{N_{bottom}} = \frac{797.04}{6} = 132.8 \text{ kN}$

Force for top member layer is 113.9 kN and bottom layer member is 132.8 kN. According to BS EN 10,210-2:1997, outer diameter size of 60.3 mm can be used to start the analysis. This value is obtained from comparing with the moment capacity values. However, one outer size higher that is 76.1 mm is chosen to start the analysis. This is because, the diameter size does not include the self-weight of the member.

2.5 Size Optimization for Double-Layer Space Truss

Optimization of geometry design is the method of finding the optimum section size for each DLST system member. Size optimization method is conducted to find the member size with minimum weight, size and thickness that does not exceed the DCR value limit. 'Auto Section List' provided in SAP2000 are used to group a list of size range that can be assigned to DLST members. Calculation from loading is used to estimate the size range. Section properties must first be defined before using 'Auto Selection List'. Pipe sections are selected for cross sections of DLST members and diameter and thickness of Circular Hollow Hot Rolled Finishes (CHHF) is chosen to be used in 'Auto Selection List'.

After the section diameter range has been selected for DLST design, the selection is then assigned as outer diameter of top layer (D_{top}) member, bottom layer (D_{bottom}) member, and web layer (D_{web}) member. D_{top} member need to be larger than D_{web} and D_{bottom} , while D_{web} can be the same or larger than D_{bottom} . Thickness of members can differ from each other, but diameter of member needs to be the same for every member. Then, DLST model is run in SAP2000 to execute two types of test which is analysis and design match and stress capacity test. The software will run analysis several times to automatically assigned different thickness of member when the analysis and design until the results show that the analysis and design matches. Then, stress capacity of member is checked to make sure DCR value is less than 1.0 for every member and at least one member with DCR value of ≥ 0.9 . This process is repeated for all configurations.

Vulnerability Index

Vulnerability index is used to evaluate the sensitivity of structure upon damage events. It can be quantified by using a probabilistic approach. Using mean and standard deviation distribution of DCR, the vulnerability index of a structure can be compared. DCR mean and standard deviation of each DLST is calculated by using the formula below. Then distribution data of DCR using normal distribution graph is created using Microsoft Excel.

$$\sigma = \sqrt{\frac{\sum(x_i - \mu)^2}{N}} \quad (2)$$

where;

σ = DCR standard deviation

N = Total of members

x_i = DCR value

μ = DCR mean

2.6 Strength to Weight Ratio

Strength to weight ratio is a measure of efficiency of structure to withstand the load applied. Greater value of strength to weight ratio shows the most lightweight structure with the best strength. Strength to weight ratio is measured using the equation below:

$$Ratio = \frac{PL}{W\delta} \quad (3)$$

where;

P = Load applied (kN)

L = Length of span between two supports (m)

W = Self-weight of DLST (kN)

δ = Deflection (m)

3 Results and Discussion

This chapter focuses on achieving optimization geometry design between different type of DLST. There are four types of DLST configuration studied in this chapter which is Square-on-Square (SOS), Diagonal-on-Square (DOS), Square-on-Diagonal (SOD), and Triangle-on-Triangle (TOT).

3.1 Optimization of Geometry Design

In designing DLST structure, various member sizes can be used. However, to achieve economical design, the size must not be too large or too small that will exceed the stress limit. The study explains the size optimization method used in SAP2000 to find the economic member size of DLST structure. Optimization of geometry design is a process of finding the optimum section size for each member of the DLST system. Section diameter 76.1 mm, 60.3 mm, 48.3 mm, is assigned to the DLST members every member at top, web and bottom layer respectively. The analysis is rerun until there is no member with DCR value ≥ 1.0 and at least one member with value ≥ 0.9 . The minimum section diameter is chosen before there is overstressed member. Table 5 shows the diameter optimization result of SOS, DOS, SOD and TOT DLST.

After the optimum size of SOS, DOS, SOD and TOT are achieved, the section size is labelled using the following section label in Table 6. The results of section diameter optimization for SOS, DOS, SOD and TOT are shown in Fig. 7. Since the design of DLST is symmetry, the quarter section label for top, web and bottom

Table 5 Section diameter optimization result, (i) SOS, (ii) DOS, (iii) SOD, (iv) TOT

(i)	Configuration		SOS		
	Analysis run		run #1	run #2	run #3
	Diameter (mm)	Dtop	76.1	76.1	60.3
		Dweb	60.3	60.3	48.3
		Dbottom	48.3	26.9	42.4
Overstressed member		–	–	12 (top) 8 (web)	
(ii)	Configuration		DOS		
	Analysis run		run #1	run #2	run #3
	Diameter (mm)	Dtop	76.1	60.3	60.3
		Dweb	60.3	48.3	42.4
		Dbottom	48.3	26.9	42.4
Overstressed member		–	–	8 (top)	
(iii)	Configuration		SOD		
	Analysis run		run #1	run #2	run #3
	Diameter (mm)	Dtop	76.1	60.3	60.3
		Dweb	60.3	48.3	48.3
		Dbottom	48.3	48.3	42.4
Overstressed member		–	–	8 (bottom)	
(iv)	Configuration		TOT		
	Analysis run		run #1	run #2	run #3
	Diameter (mm)	Dtop	76.1	76.1	76.1
		Dweb	60.3	76.1	60.3
		Dbottom	48.3	60.3	60.3
Overstressed member		2:web 3:bottom	–	–	

Table 6 Section size label

Section label	Section size (mm)	Section label	Section size (mm)
R1	26.9 × 3.2	R7	60.3 × 4
R2	48.3 × 3	R8	60.3 × 5
R3	48.3 × 3.2	R9	76.1 × 3
R4	48.3 × 4	R10	76.1 × 3.2
R5	60.3 × 3	R11	76.1 × 3.6
R6	60.3 × 3.6	R12	76.1 × 5

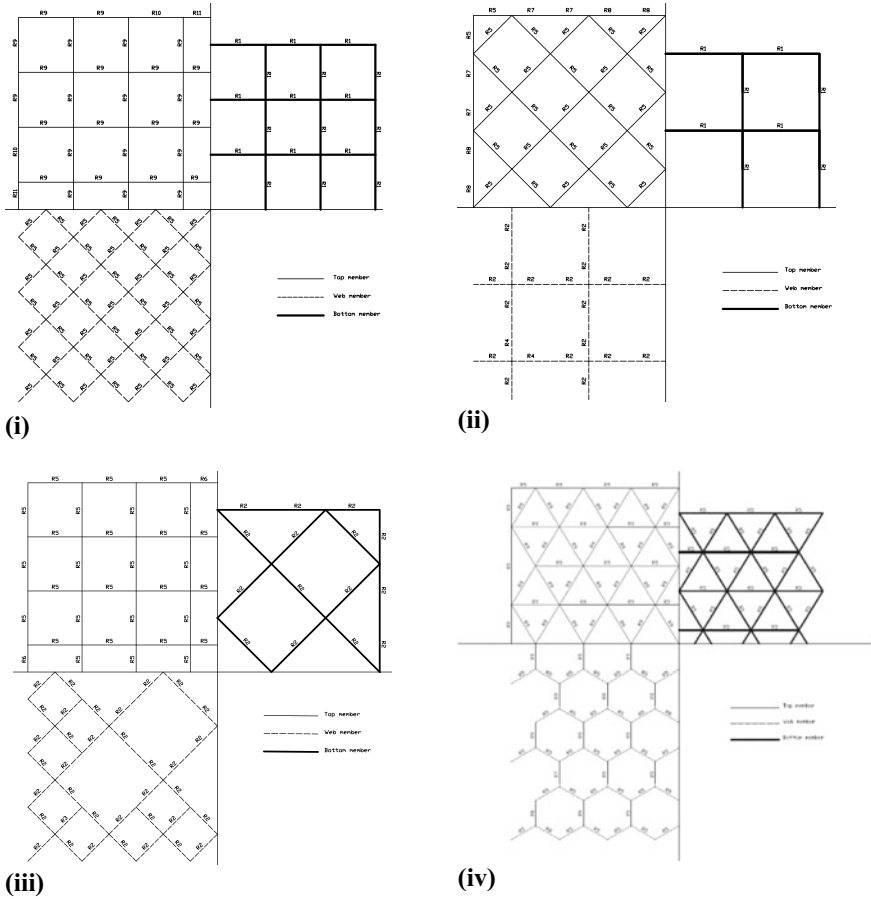


Fig. 7 Section label, (i) SOS, (ii) DOS, (iii) SOD, (iv) TOT DLST

member can represent all the section diameter in the design. This process is repeated for all configurations.

3.2 Analysis of Demand Capacity Ratio

DCR range value is indicated by color shown in Table 7. DCR with red color index or value ≥ 1.0 indicates an overstressed member. To achieve optimum section diameter, there must be at least one member with DCR orange color index or value ≥ 0.9 in DLST. Figure 8 shows the optimum section diameter result of stress capacity check indicated by DCR color index for each DLST.

Table 7 Color index for DCR range value

DCR Range Value	Color Index
$DCR \geq 1.0$	Red
$0.9 \leq DCR < 1.0$	Orange
$0.7 \leq DCR < 0.9$	Yellow
$0.5 \leq DCR < 0.7$	Green
$DCR < 0.5$	Blue

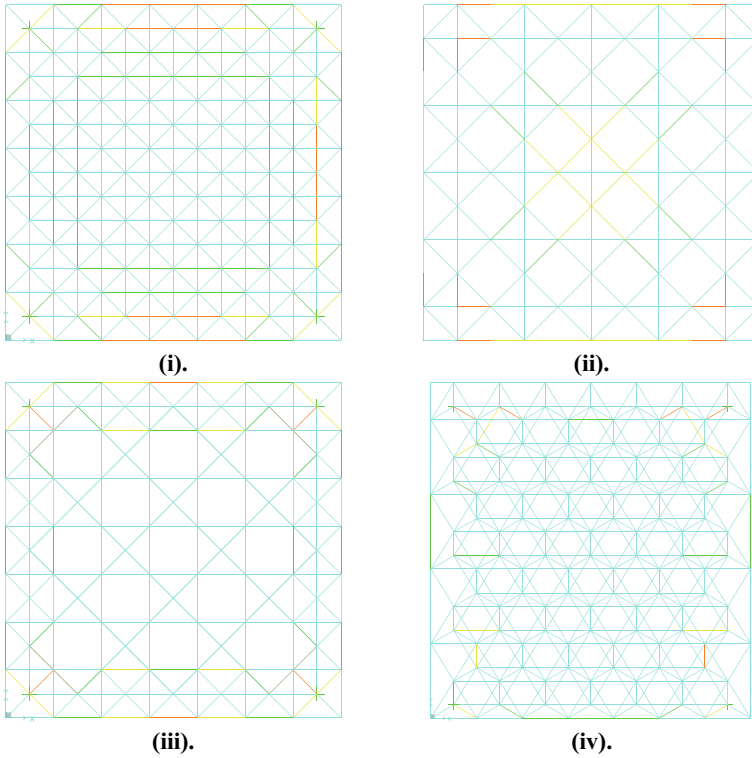


Fig. 8 DCR color contour, (i) SOS, (ii) DOS, (iii) SOD, (iv) TOT DLST

TOT has the highest DCR value followed by DOS. However, there is only one member with highest DCR value for TOT, compared to DOS that have the greatest number of highest DCR value. This shows the most optimize section size and most economical DLST. Due to that, the self-weight of DOS is 28.38 kN which is much smaller than the rest of DLST types. Since SOS are the common DLST type, the weight ratios of other types DLST are compared with SOS (Table 8).

Table 8 DCR value comparison for different DLSTs

Configuration	SOS	DOS	SOD	TOT
Highest DCR value < 1	0.92674	0.941988	0.935607	0.945514
Member with highest DCR	3, 4, 33, 39, 46, 52, 81, 82	144, 145, 146, 147, 187, 198, 199, 210, 211, 222, 223, 234, 274, 275, 276, 277	208, 257, 264, 313	161
Self-weight member (kN)	43.804	28.381	33.763	72.21
Weight ratios	1	0.65	0.77	1.65

3.3 Vulnerability Index of DLSTs

DLST is a very stable form structure since it is a highly indeterminate structural system. However, the instability of the system needs to be analyzed in order to compare the most vulnerable structure between the four configurations. Using a probabilistic approach, the value of DCR mean and standard deviation of each DLST is shown in Table 9. Distribution data of DCR is represented in Fig. 9. TOT has the least DCR_{mean} and DCR_{SD} which DCR values are closed to the mean value that makes it more robust. While DOS has the highest DCR_{mean} and DCR_{SD} that make it the least robust as the DCR value is distributed in large range of values as shown in the graph. Percentage difference of DCR_{mean} and DCR_{SD} is compared to SOS as

Table 9 DCR mean and standard deviation value

Configuration	SOS	DOS	SOD	TOT
DCR_{mean}	0.27	0.358	0.27	0.212
DCR_{SD}	0.259	0.302	0.254	0.1
% DCR_{mean}	0	-32.6	-0.1	21.5
% DCR_{SD}	0	-16.8	1.9	61.2

Fig. 9 Vulnerability index of SOS, DOS, SOD and TOT DLST

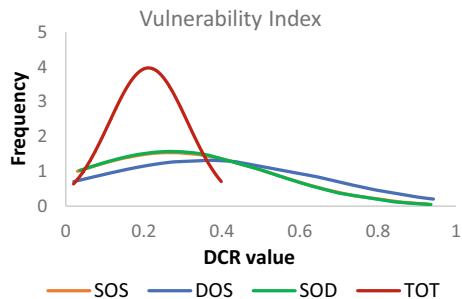
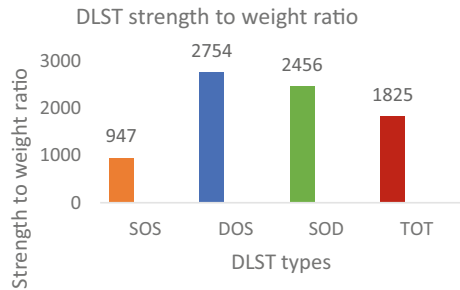


Table 10 Strength to weight ratio

Configuration	SOS	DOS	SOD	TOT
Joint number	64	80	64	84
Load applied (kN)	105.1	131.4	105.12	137.97
Span length (m)	18	18	18	18
Total self-weight (kN)	43.8	28.381	33.763	72.21
Deflection (m)	0.045	0.03	0.023	0.019
Strength to weight ratio	946.9	2754.1	2456.4	1825.5

Fig. 10 Comparison of strength to weight ratio of SOS, DOS, SOD and TOT DLST



it is the most common DLST type. DOS has $\%DCR_{mean} = -32.6$ and $DCR_{SD} = -16.8$. These values show that DOS is more vulnerable than SOS.

3.4 Comparison of Strength to Weight Ratio

To achieve the lowest cost in a DLST design, a minimum amount of material need to be used while ensuring adequate strength for DLST. Table 10 shows the comparison of strength to weight ratio between the four configurations of DLST. DLST with the highest ratio shows the lightest and robust in design. The highest value of strength to weight ratio is 2754 from DOS as represented in Fig. 10 which means the lightest in weight and most significant in strength among all four.

4 Conclusion

Different geometry configuration of double-layer space truss (DLST) gives different section diameter optimization result. Diagonal-on-Square (DOS) shows the most optimize section diameter compared to Square-on-Square (SOS), Square-on-Diagonal (SOD) and Triangle-on Triangle (TOT). This is because DOS has the smallest section diameter and the lightest in self-weight. Demand Capacity Ratio

(DCR) value of SOS, DOS, and SOD is distributed evenly on one-fourth of the member as it is symmetry in configuration and support condition except for TOT as the shape configuration is not symmetry. TOT has the highest DCR value compared to the other three configurations. However, there only one member of TOT with the highest DCR value. Meanwhile, DOS has the highest number of members with highest DCR value compared to the other configurations. This means that DOS is more economical than TOT. Vulnerability index for progressive collapse of DLST is determined based on DCR value of members. DOS has the highest value of DCR mean and standard deviation while TOT has the lowest value of DCR mean and standard deviation. This makes DOS as the most vulnerable and TOT as the least vulnerable and more robust than DOS. DOS has the highest value of strength to weight ratio compared to the other configuration. This means that it is the most lightweight with the most significant strength DLST among all four configurations. For a conclusion, DOS is the most optimum configuration of DLST in terms of geometry design, minimal materials and strength to weight ratio. However, it is also the most vulnerable among all the configurations. Thus, DOS is good for light loads and moderate span structure and is proved to be economic. While TOT are the least optimum in section size diameter and the least vulnerable among all DLSTs.

Acknowledgements The authors would like to acknowledge The Institute of Research Management and Innovation (IRMI) UiTM, Shah Alam, Selangor, Malaysia and Ministry of Higher Education (MOHE) for the financial support of this research. This research is supported by MOHE under the Fundamental Research Grant Scheme (FRGS) with project code: FRGS/1/2018/TK01/UITM/02/28.

References

1. Al Sulayfani B, Saaed T (2008) Optimization of space frame design
2. Salajagheh E, Mashayekhi M, Khatibinia M, Kaykha M (2009) Optimum shape design of space structures by genetic algorithm. *Int J Space Struct* 24
3. Selvam K, Divyameena R (2016) Influence of depth parameter in a plane space truss
4. Elabd M, M A-H (2010) Effect of composite action on the dynamic behaviour of space structures. (Doctor of Philosophy), University of Dundee, UK
5. Lan TT (1999) Space frame structures. In: *Structural engineering handbook*
6. Cuoco DA (1997) Guidelines for the design of double-layer grids. ASCE Publications
7. Mero-Raumstruktur GC (1980) Space frames—the applications of nature’s laws to modern architecture. Germany
8. Hamid YS (2015) Progressive collapse of double layer space trusses. (Degree of Doctor of Philosophy), Universiti of Surrey
9. Lee HG, Makowski ZS (1977) Study of factors affecting stress distribution on double layer grids of the square and diagonal type. *Archit Sci Rev* 20(4):90–102
10. Saka T, Taniguchi Y (1994) Buckling behavior of square-and-diagonal double-layer grid. *J Struct Eng* 120(4):1088–1102. [https://doi.org/10.1061/\(ASCE\)0733-9445\(1994\)120:4\(1088\)](https://doi.org/10.1061/(ASCE)0733-9445(1994)120:4(1088))

Numerical Investigation of Structural Behavior of Timber-Glass Composite Wall Panel



M. A. N. Abuzaid, M. K. Kamarudin, and M. Yussof

Abstract This paper presents the numerical investigation of adhesively timber-glass composite wall panel. The main focus considered on the different geometrical dimensions of the adhesively timber-glass composite wall panel under horizontal load conditions. The analysis was done by using the nonlinear finite element method to obtain the in-plane normal stress and stress distribution of timber-glass wall panel. The analysis was extended with modelling glass as brittle material in order to determine the crack pattern of the glass pane using the commercial software called Abaqus. The results showed that the Abaqus/Standard is capable of modelling the structures of the composite timber-glass wall panel. In terms of different geometrical dimensions, it can be concluded that the in-plane stress distribution is presented in the glass pane due to increased aspect ratios which exceeded glass capacity limitation however timber frame loses its capacity when geometrical parameters are lower. For dynamic analysis, results showed positive signs to some extent to the experimental results. However, using the simplify method in the analysis significantly gives acceptable results in predicting the behavior of the glass pane due to the horizontal loads. In addition, timber and glass composite can be studied further by using finite element tool to visualize the behavior of the structure under dynamic loading.

Keywords Timber-glass · Nonlinear analysis · Brittle cracking · Epoxy adhesive

1 Introduction

The design of structures has been improved and turned to sustainable and translucent structures that can both maintain the environment and create more aesthetics for the building. Recently, the demand for large glass sizes with timber structures has

M. A. N. Abuzaid (✉) · M. Yussof
School of Civil Engineering, College of Engineering, Universiti Teknologi MARA (UiTM),
40450 Shah Alam, Malaysia

M. K. Kamarudin
School of Civil Engineering, Universiti Sains Malaysia, 14300 Nibong Tebal, Pulau Pinang,
Malaysia

greatly increased due to the improvement of the physical properties of glass and the positive influence on the energy efficiency and visual comfort of buildings [1]. From the perspective of ecological impact and energy efficiency, timber and glass are ideal building materials because of low heat transfer, can store carbon dioxide CO₂, and require little or no energy for processing [1]. More in-depth, using timber and glass as alternative structure components represents a potential development of environmentally friendly and energy-efficient buildings [2]. Structurally, the concept of combining two or more materials with different characteristics is to make the overall performance of the composite materials better than a single component [1]. Moreover, a combination of timber and glass in such a way to get a proper load-bearing element where glass has good resistance to pressure while timber has good tensile properties [3, 4].

Be that as it may, the utilization of the two materials in a composite manner can be or maybe confounded, from both the constructional perspective as well as from the part of energy effectiveness. These weaknesses are intricate and still a troublesome undertaking until the present time which has direct impacts on the structure and may lead the structure to loss its load-bearing capacity and causes failure. Most concerns are going to the long-term performance and deformation of the main structural elements. In the use of glass for structural purposes, Ber et al. [3] pointed out that the latest technology in the field of the timber structure is very conservative, mainly due to the lack of research and guidance on the design of glass and glass composite structures. As well, the report of the European Commission, “Guidelines for the European Structural Design of Glass Components” states that the glass standard does not contain any rules or guidelines regarding the use of shear wall panels as the main load bearing element. Only when wall panels loaded perpendicular to their plane are reported the criteria for the use of minor elements [5]. Researches and tests in the area of structural timber-glass elements have been performed in the past twenty years were generally focused on the most important parameters influencing the load-bearing capacity e.g. timber-glass with the in-plane and out-plane loads [3, 6, 7].

The key inference to be drawn from the experimental works is that glass functions as a structural strengthening of the sub-structure of the timber. Test results showed excellent structural efficiency of the composite panel when used as a slab, with an improvement in the overall load obtained of more than 30% compared to the panel without glass [1]. For a structural wall structure tested under vertical load, the contribution of glass became even more apparent: the results showed a strong improvement in the stiffness and resistance of the glass relative to the bare timber frame without glass [1]. Furthermore, failure force values have been remarkably high and can be contrasted with previous laboratory studies using fibre plaster sheathing boards and (FPB) oriented strand boards (OSB) [3].

So, a special motivation for finding missing answers on this topic is encouraged. Therefore, we conducted a research on the elements of timber-glass composite wall panel bonded with epoxy adhesive using different geometrical dimensions in order to obtain the in-plane normal load stresses and stress distributions under large load conditions that relay on nonlinear finite element methods. Also, the study was

extended to the dynamic analysis using finite element software, ABAQUS/Explicit to investigate the crack pattern of the glass when exposed to horizontal loads. The goal of this study is to show that ABAQUS/CAE 6.14 can be used a guideline for structural engineers to predict structural behavior of timber-glass composite structures, thereby save time, money and achieving more designs economically.

2 Methodology

2.1 Experimental Set Up

This section is presented the experimental test setup of the timber-glass composite that was done by Ber et al. [3]. The preparation and the assembly of the timber-glass composite was done in two stages. The first stage is the preparation of the timber frame elements (studs and girders) by joining them together using self-tapping screw at the corners. Hence, the screws do not function for load-bearing but only for keeping timber frame in its place. Then, the epoxy adhesive was applied into the empty slot between the timber frame and the glass pane using a pneumatic gun. Finally, the glass was manually mounted into the center of the timber frame. During the experimental test, one corner is was connected onto the vertical steel profile of the testing machine with three steel bolts where the other was connected by two steel bolts as a pinned support. For the corner under the applied load, moveable supports were added to prevent the specimen of out-plane displacement (see Fig. 1). Eventually, a horizontal static load was applied to the specimen's tests, ranging from point 0 to the failure point by the load protocol of EN594 [8] with a load rate on the panels was 8 N/s from 0 to 10 kN and 10 N/s therefore.

2.2 Three-Dimensional Finite Element Modelling

Finite element method using the commercial software ABAQUS/CAE 6.14 was used in this research in order to study the behavior of timber-glass composite wall panels bonded with epoxy adhesive. More attention is considered on the in-plane stresses and stress distribution of the timber-glass wall panel under horizontal static loads using different aspect ratios. In addition, the study was extended to the dynamic analysis using ABAQUS/EXPLICIT to get the crack pattern of the glass pane. The research is carried out in three main groups particularly Timber-Glass (TG-1, TG-2, and TG-3) (see Table 1).

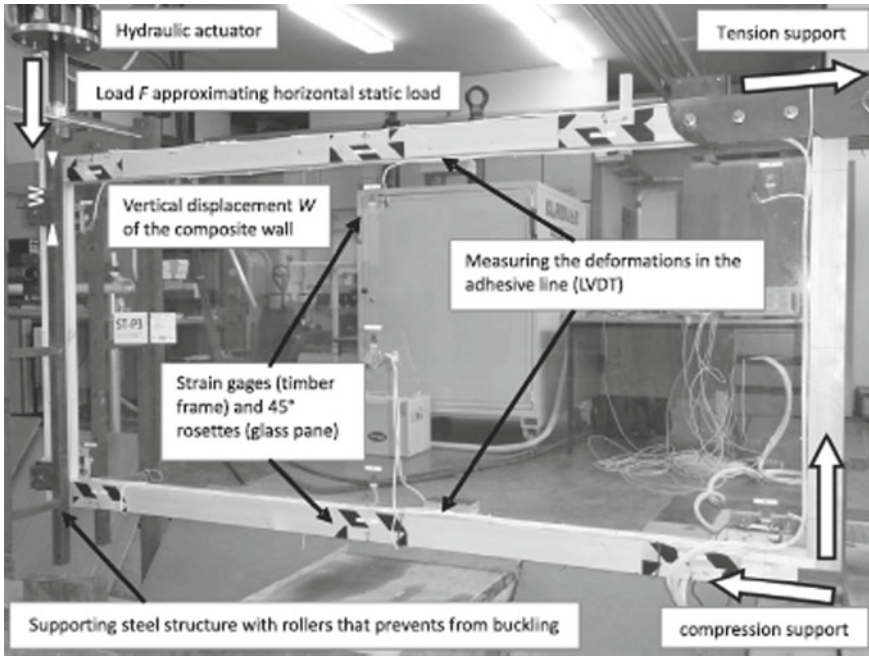


Fig. 1 Test setup [3]

Table 1 Dimensions of models used in the simulation

Group name	Model name	Timber dimension (mm)		Glass dimension (mm)	Epoxy thickness (mm)
		Girder	Stud		
TG-1	TG-1	90 × 80	90 × 90	1100 × 2510 × 10	0.5
TG-2	M-1	90 × 80	90 × 90	1100 × 1100 × 10	0.5
	M-2	90 × 80	90 × 90	1100 × 1650 × 10	0.5
	M-3	90 × 80	90 × 90	1100 × 2200 × 10	0.5
	M-4	90 × 80	90 × 90	1100 × 2750 × 10	0.5
	M-5	90 × 80	90 × 90	1100 × 3300 × 10	0.5
TG-3	TG-3	90 × 80	90 × 90	1100 × 2510 × 10	0.5

Structural Model Geometry

The primary step of this study is to create the geometric structure of the timber-glass composite that will be simulated. The first phase of modelling is defining the geometries. Three groups (TG-1, TG-2, and TG-3) were simulated with different geometrical parameters using numerical modeler ABAQUS/CAE 6.14. A 3D deformable

part, with a solid and extruded base feature was created for all groups. The geometry of (TG-1 and TG-3) was taken based on the previous constructed timber-glass composite wall panel bonded with epoxy resin done by Ber et al. [3] (see Fig. 2). The dimensions of models are based on Table 1. However, in the case of (TG-2), the specimens were modelled with different five aspect ratios 1:1, 1:1.5, 1:2, 1:2.5, and 1:3 categorized as M1, M2, M3, M4, and M5 respectively. The dimensions of models are listed in Table 1.

Material Properties

The second step in developing the model is identifying and assigning the specimens to the material properties and section properties. Timber is classified as non-homogenous materials in three mutually perpendicular directions, namely longitudinal, radial, and tangential, which pose different behaviors. Therefore, a model of engineering constants material in linear-elastic was used to properly describe the timber. The mechanical properties of the used spruce GL24h were extracted from experimental tests [3, 9] as shown in Table 2. Hyperelasticity is the characteristic that rubber and other materials exhibit elastic response under high strain. This behavior

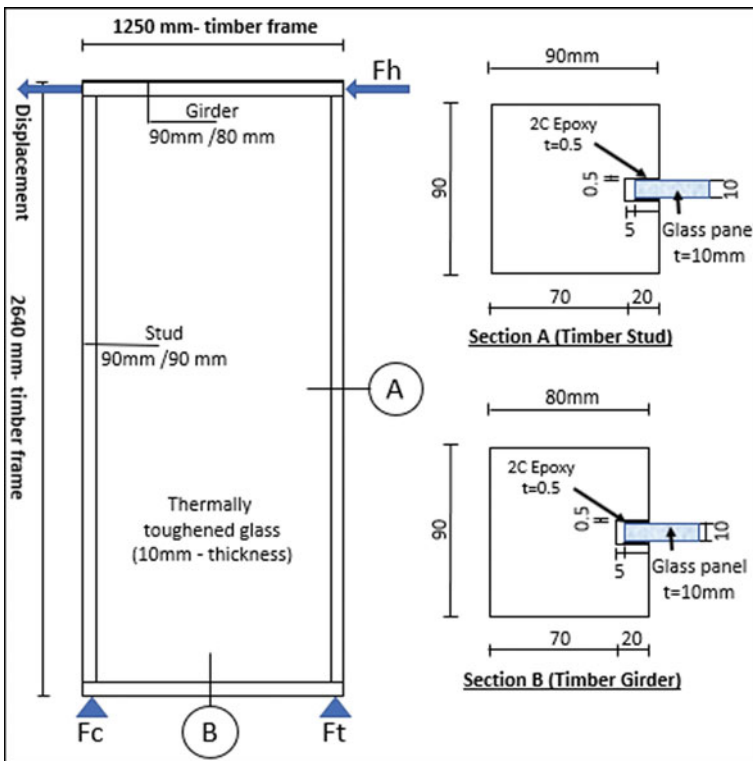


Fig. 2 Experimental test standard dimensions [3]

Table 2 Mechanical properties of timber used [3, 9]

Material	$E_{0(X)}$ (MPa)	$E_{90(Y)}$ (MPa)	$E_{90(Z)}$ (MPa)	ν_{XY}	ν_{YZ}	ν_{XZ}	G_{XY} (MPa)	G_{YZ} (MPa)	G_{XZ} (MPa)	ρ (kg/m ³)
GL24h	11,600	700	700	0.42	0.242	0.42	720	35	720	380

Table 3 Mechanical properties of the material used [3, 11]

Material	ρ (kg/m ³)	f_c (MPa)	f_t (MPa)	ν	E (MPa)
Therm. toughened glass	2500	500	45	0.19	70,000
Epoxy	1500	1500	28	0.45	2800

was also observed when testing and using adhesives. In order to determine the superelastic response of the epoxy resin, the selected strain energy function is the Mooney-Rivlin strain energy function used, see Abaqus [10]. The input source data to define the material is based on the uniaxial tensile test data obtained from experimental test based on Ber et al. [3]. The mechanical properties of adhesive used is presented in Table 3. In the case of TG-1 and TG-2, the interest of the glass simulation was on the linear behaviour, thus the glass was modelled to respond elastically. The performance of glass under increasing load is linearly elastic up to an immediate brittle failure. Young's modulus of the material was taken as 70,000 MPa and the Poisson's ratio was 0.19. However, in the case of TG-3 the focus was on the crack models where the glass is simulated as brittle material. The maximum stress after cracking is set as 14 MPa [3] where the strain and retention factor were assumed. The mechanical properties of the glass used was taken from Ber et al. [3] as listed in Table 2.

Sensitivity Mesh Analysis

For this research, the sensitivity mesh analysis is used to obtain the optimum mesh density. In this study, seventeen models with different mesh sizes, mesh sensitivity analysis was performed to obtain the optimum mesh size which will provide a good balance between accuracy, processor time, and storage load by using the ABAQUS/CAE 6.14 software. For a successive analysis, the mesh density is then controlled by setting the approximate element size, maximum deviation factor, and element shape to hexahedral finite element. The accuracy is improved after a certain mesh density. In order to predict the consistency of the analysis results, the author tried to use several approximate element sizes. All results of mesh are compared with stress and displacement of the experimental test done by Ber et al. [3]. From the seventeen models of mesh sizes used in the analysis, the model with a close value to the experimental test was selected for this study which is 35×35 for timber frame, 6×6 for epoxy adhesive, and 80×80 for glass pane (see Fig. 3). The validation shows 3.4% increase in the finite element model compared to empirical result. This mesh size selection process is a crucial step in validation of the finite element model and ensure the validity and reliability of the software.

Interaction

The interaction conditions and the interaction properties were defined for the part surfaces. To obtain the interaction between selected parts, first defined the surfaces of the wanted parts by creating constraints tool. The type of interaction used is "Tie constraint" which is used as a restriction against both translational degrees of freedom (x, y and z-axis) and rotational degrees of freedom (rotations in all directions) in the

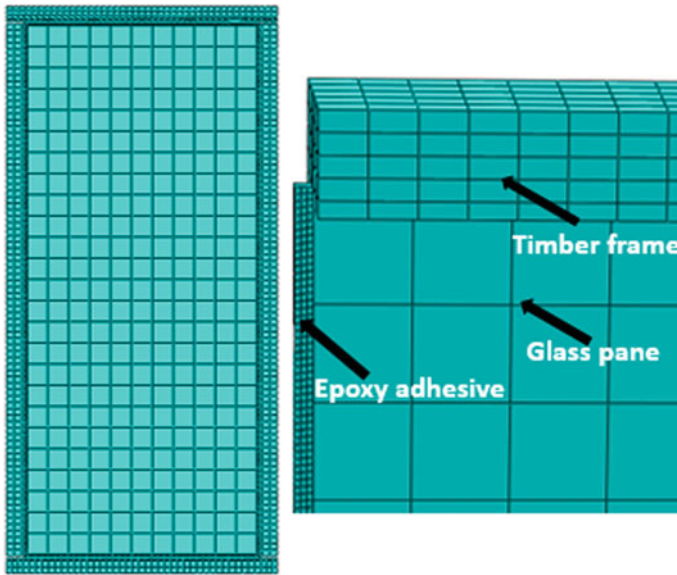


Fig. 3 Mesh details of timber, glass, epoxy adhesive

contact area between parts. In different word, the “Tie constraint” is occupation as a fixed boundary condition in all directions.

Step

Step option defined the analysis technique, period time and increments, and other parameters which program must be run the simulation according to them. After creating the assembly, the author arranged the analysis by starting to define the analysis step based on the selected concepts. TG-1 and TG-2 were performed using non-linear analysis by using Newton–Raphson approach, which is one of Abaqus’/Regular Software Solvers. ABAQUS/Standard typically uses Newton’s approach as a computational technique for solving the equations of nonlinear equilibrium. The Newton–Raphson approach assesses the unbalanced load vector before each solution, which is the difference between the restorative force (the load corresponding to the stress of the element) and the load applied. Therefore, a single static, general step for this simulation was defined. In the “Edit step”, the author set the increment size as initial 0.08, minimum 0.00005, and the maximum as one. However, the time period was set as default. For this module, the output requests in the “Edit Field Output Request” was edited by a selection of the results wanted in the output file and defined interval and the frequency of saving.

For TG-3 modelling dynamic explicit is used to predict the glass model’s crack mode. Abaqus/Explicit is a dedicated finite element analyzer that uses an explicit integration scheme to solve highly nonlinear systems in transient state with several complex series connections. It can be used in a wide variety of applications including

vulnerable structures. As engineers, we have faced the most complicated numerical problems, concerning the material's structure, load and characteristics, and it is hard to obtain results through analysis. Finite Element Method (FEM) can be defined as a method to divide a very complex and enormous geometric problem into small elements where one element is used to analyze the whole problem. The author used finite element analysis (FEA), using the finite element method to analyze the stress and crack patterns on the element based on the geometry, load, and material properties of the element. The Abaqus/Explicit results can be used in Abaqus/Standard as the starting conditions for the continued development. Similarly, the analysis starting with Abaqus/Standard continues in Abaqus/Explicit.

Load and Boundary Conditions

In structural research, glass-timber wall 3D models were placed and supported in the same manner as in the laboratory study. Ideally, this simulation study used two separate types of supports, fixed end supports and movable end supports. At the fixed end, the timber-glass wall was simulated as a cantilever where it supported by tension and compression fixed-fixed end supports at the bottom corners of the timber frame as shown in Fig. 4. The translational (U_1 , U_2 , U_3) as well as rotational (θ_1 , θ_2 , θ_3) degrees of freedom were controlled to be zero. At the movable end, in order to prevent the model of buckling and allowing only in-plane displacement at the free end of the model, movable supports were added along the top timber frame (see Fig. 4). The translational degrees of freedom in Z direction (U_3) as well as rotational degrees of freedom in Z direction (θ_3) were controlled to be zero. The horizontal load F_h , was applied to the upper edge of the wall panel (see Fig. 4). The load increase rate on the wall element was based on the experimental test data [3].

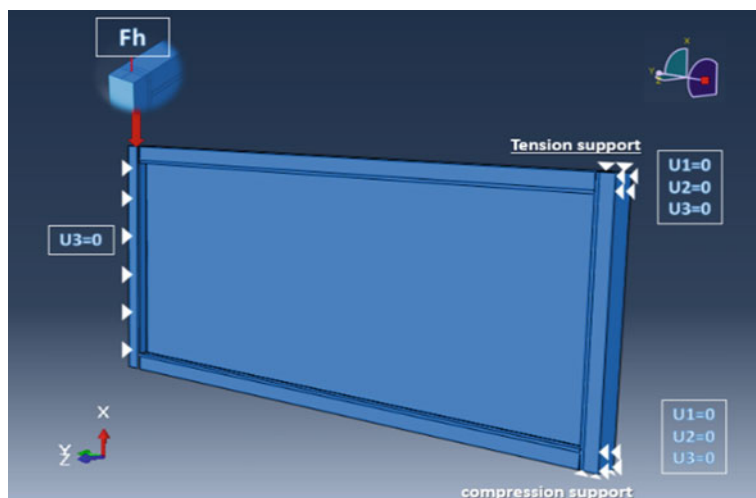


Fig. 4 Boundary conditions and load applied evaluated

3 Analysis Results and Discussion

3.1 *Non-linear Analysis Result Validation and Comparison*

The validation of numerical studies is vital to ensure that any simplifications and assumptions made are appropriate within study. Comparisons between the simulations and the actual experimental results done by Ber et al. [3] are made to ensure the adequacy of the model used as input into the structural analysis. The validation of the numerical study and experimental tests are discussed in terms of the in-plane stress and axial displacement as the following sections.

In-Plane Normal Stress

The in-plane normal stress of the timber-glass wall panel was determined by (FE) analysis using Abaqus/Standard. In this case, the simulation was done based on the experimental data done by Ber et al. [3]. The comparison of the numerical result and the experimental result [3] is shown in Fig. 5 and listed in Table 4.

Displacement

Displacement also presents a very important factor that can show the behavior of the timber-glass composite wall structure. Figure 6 notes the numerical investigation load–displacement curve along with the calculated master curve of the individual specimen investigated experimentally. Also, the results of experimental and numerical specimens are summarized in Table 5 where the normalized values of the vertical displacement (U) relative to force (Fh) are presented.

3.2 *Non-linear Analysis Results for Different Aspect Ratios*

The main objective is to examine the effect of the timber-glass wall panel in terms of different aspect ratios by FE analysis (non-linear analysis) using Abaqus/Standard. Thus, timber-glass composite wall panels were constituent of five models with different aspect ratio (diameter), 1:1, 1:1.5, 1:2, 1:2.5, 1:3 categorized into M1, M2, M3, M4, and M5. The length, a changed whereas the width (b) was kept constant. All models' properties are keyed in with unchanged their properties. The results of the numerical tests are presented by the in-plane stress distribution with the maximum and minimum in-plane stress loads in Figs. 7 and 8, separately for each Model. In addition, Fig. 9 presents the maximum in-plane stress versus aspect ratios.

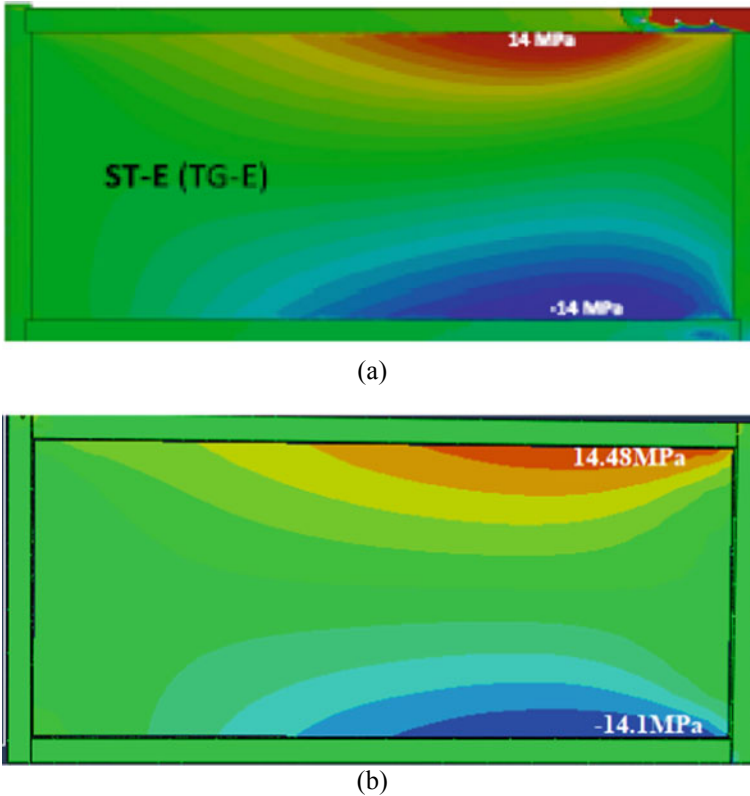


Fig. 5 In-plane normal stresses comparison of **a** experimental test [3], and **b** numerically simulation

Table 4 Max and min in-plane stress result of timber-glass wall panel

Model	Max. in-plane stress (MPa)	Min. in-plane stress (MPa)
Experimental test	14	-14
FE analysis (TG-1)	14.48	-14.1

3.3 Brittle Cracking Explicit Analysis Result

In this case, finite element analysis (FEM) by dynamic analysis using Abaqus/Explicit was conducted. The timber-glass wall panel bonded epoxy adhesive was simulated. The glass panel is defined as a brittle material in which to investigate the crack pattern of the glass pane under static load conditions comparing to the experimental test crack pattern. Figure 10 presents the crack pattern of glass pane numerically and experimentally [3].

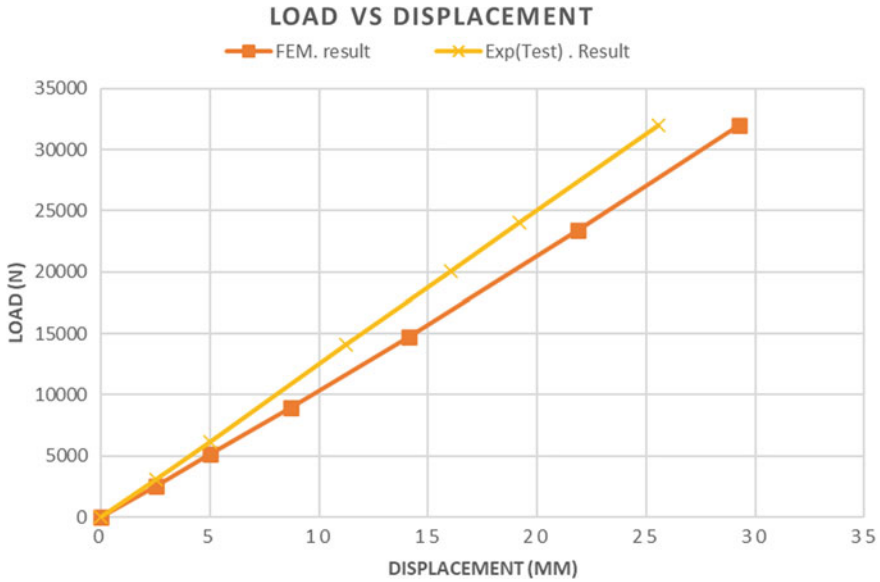


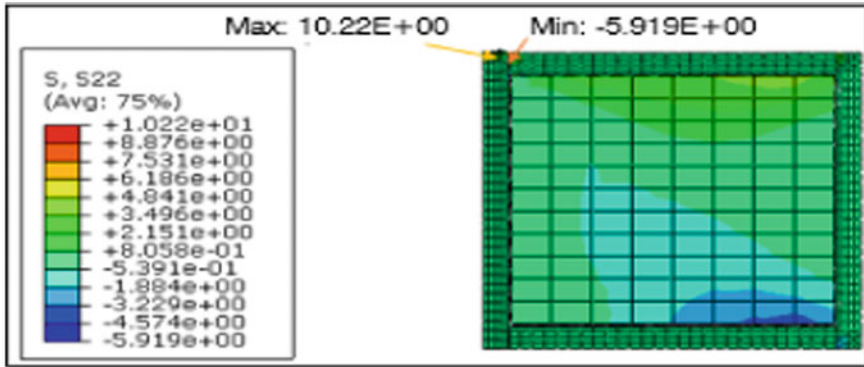
Fig. 6 The vertical displacement relative to the vertical load results for the experimental test [3] and FEM model

Table 5 Summary of the experimental [3] and numerical results of TG-1 model

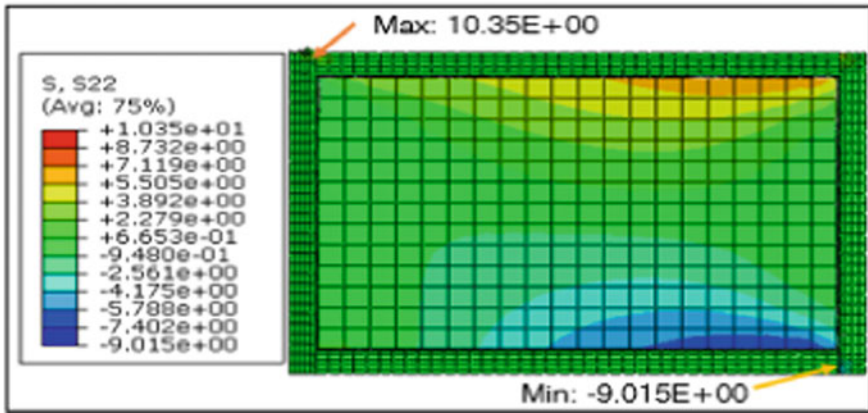
Model	F_h (KN)	U (mm)
Experimental test	32	25.58
Numerical (TG-1)	32	29.2

3.4 Discussion

The in-plane stress load and axial displacement of the numerical investigation show a close agreement to the experimental study. The timber-glass wall panel was modelled with the same dimensions, material properties, and boundary conditions of the experimental test [3] as shown in Fig. 2. In terms of the in-plane normal stress, the experimental test witnessed a linear behavior that culminated in an instant fracture at the tension zone (top right side) in the glass pane. The glass failed at a maximum in-plane tensile stress value of 14 MPa [3] (see Fig. 5a). However, in the numerical analysis model, the in-plane normal stress distribution is observed at the top right side (tension zone) in the glass pane (see Fig. 5b), with a maximum in-plane stress value of 14.48 MPa which presents a fair good agreement with the mechanical test. In terms of axial displacement, both specimens experimental and numerical undergo linear behaviour. It observed that the numerical model displacement proceeded the experimental test with 12.39%. In more detail, the experimental specimen got failed under a maximum applied load 32 kN with a maximum displacement value of 25.58 mm [3] (see Fig. 6). However, the numerical model observed that the model



(1)

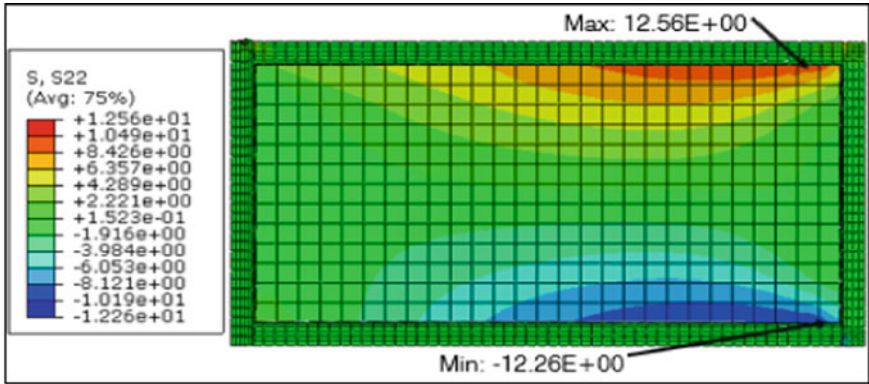


(2)

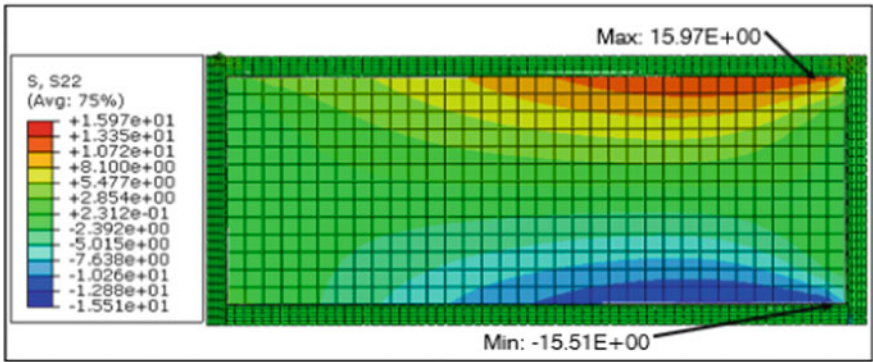
Fig. 7 Maximum and minimum values of in-plane normal stress for (1) M1, (2) M2

failed with a maximum displacement value of 29.2 mm. In light of this, a distinction between experimental and numerical outcomes is much better. The explanation for this disparity can be attributed to timber properties inhomogeneities that cannot be precisely modelled. The latter can be explained with a more detailed description of orthotropy, i.e., distinguishing between radius direction and tangentiality.

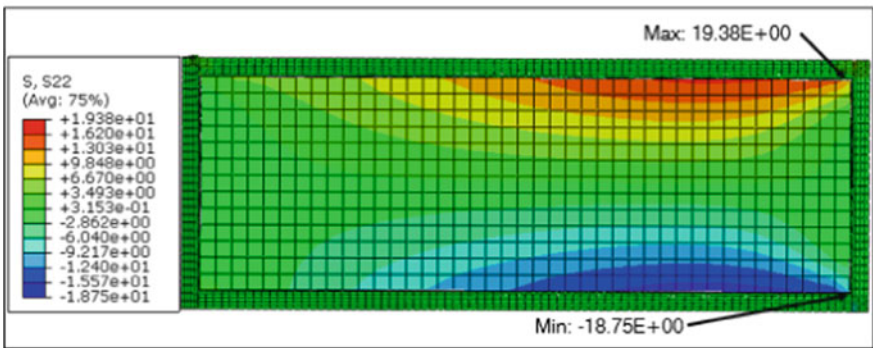
However, in our case, it was not feasible because the timber-glass walls had timber elements that were guided at random. A parametric study on the in-plane stress of the timber-glass composite wall panel bonded with epoxy adhesive. The study carried out five models with different geometrical dimensions (see Table 1). The result of the numerical investigation presented that the glass panel loss its bearing capacity with increase the aspect ratio where timber and epoxy adhesive are intact. More n depth, in Fig. 7, the maximum normal stress is noticed at the lift-side of the timber frame with values of 10.25 MPa and 10.35 MPa for both M1 and M2 respectively where



(a)



(b)



(c)

Fig. 8 Maximum and minimum values of in-plane normal stress for a M3, b M4, c M5

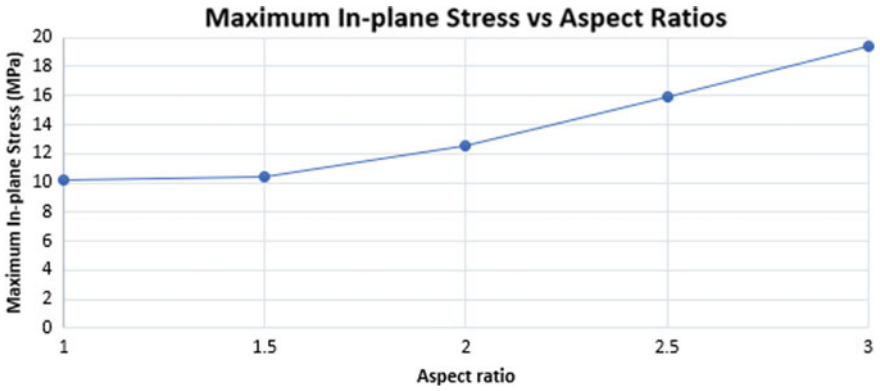


Fig. 9 Maximum in-plane stress versus aspect ratio

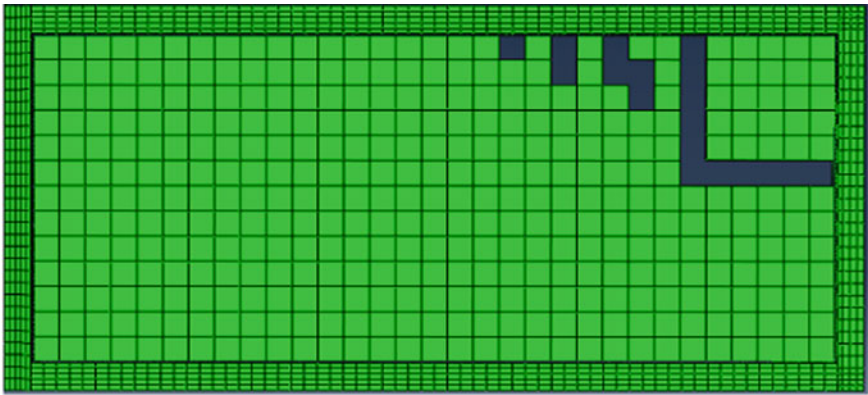


Fig. 10 Crack pattern for glass pane, a numerical test crack pattern, b experimental test crack pattern [3]

Table 6 Summary of the experimental [3] and numerical results of TG-3 model

Model	Maximum in-plane stress (MPa)
Experimental	14
Numerical (TG-3)	13.73

the glass pane stayed intact. However, in Fig. 8a–c, the maximum and minimum in-plane normal stress are observed in the glass panel with of numerical models M3, M4, and M5. The maximum in-plane stress is presented at the tension zone (top right side) of the glass panel. The maximum normal stress values of M3, M4, and M5 are 12.59 MPa, 15.97 MPa, and 19.38 MPa respectively. However, with a simple comparing it is clear that the maximum in-plane stress is increased by approximately $23 \approx 27\%$ within increased aspect ratio of the timber-glass wall panel which means by having a larger glass aspect ratio, more distribution of stresses exerted in the glass pane would be occurred (see Fig. 9). More in depth, lower aspect ratio tends to limit the glass capacity to resist loads while grater aspect ratio dictates the structural load bearing capacity of the glass.

In addition, the crack pattern of the numerical investigation is in line with the related experimental test [3]. The model was simulated with the same dimensions, material properties, and boundary conditions of the experimental test [3]. However, the glass panel only was defined as a brittle material. According to the experimental test, as shown in Fig. 10b, an initial crack was observed in the tensile region of the glass, which resulted in the destruction of the glass plate, and the numerical simulation in the tensile region failed as well, see Fig. 10a. It observes that the final failure of the experimental test specimen is due to the failure of the glass panel in the tensile region with the maximum in-plane stress value of 14 MPa.

However, the numerical analysis of the final failure is due to the maximum failure of the glass with an in-plane stress value of 13.73 MPa, please refer to Table 6. Comparing to the experimental results [3], the maximum in-plane stress of the numerical test that caused the glass to break was reduced by about 2%. Despite the geometrical and mechanical simplification of the implemented FE model. This is under the crack occurred and it is just a justification.

4 Conclusions

In this research, the structural behaviour of the timber-glass wall panel bonded with epoxy adhesive was studied. The studies evolve around the idea of carrying out numerical work on timber-glass wall panel bonded with epoxy resin to investigate the load–displacement failure, in-plane normal stress, and cracking pattern. The objectives of this study are as follows: To simulate the structural behaviour of the timber-glass wall panel based on the experimental data [3] using non-linear analysis ABAQUS/Standard, to examine the stress distribution effect of timber-glass wall panel in terms of different aspect ratios using non-linear analysis ABAQUS/Standard,

and to investigate the crack behaviour of glass by using brittle cracking analysis using ABAQUS/Explicit. Based on the numerical study, the outcomes are summarized below.

1. The timber-glass wall panel bonded with epoxy adhesive is well-produced, which is in good agreement with the experimental data. The geometry and material properties of timber, glass, and epoxy are precisely presented in the numerical simulation modelling. The methodology proposed for simulation is confirmed. The values of vertical-displacement and in-plane stress can be compared to the measured one. The load-axial displacement relationships indicate a model's linear behaviour with instant failure without plastic deformation. And in-plane stress presented a close distribution. Comparison of the data obtained from both numerical simulation and experimental data shows that Abaqus/Standard is capable of modelling the structures of the composite timber-glass wall panel and that Abaqus/Standard is easy to use for its simple control system and that almost no cost is involved in the simulation execution if not for the good machine.
2. The numerical modelling with five different geometrical parameters were done using non-linear Abaqus/standard to get the in-plane normal stress distribution exerted in the composite wall panels. Based on the numerical results, it can be concluded that the in-plane stress distribution is presented in the glass pane due to increased aspect ratios which exceeded glass capacity limitation however timber frame loses its capacity when geometrical parameters are lower.
3. ABAQUS/Explicit has been chosen as the finite element analysis program of choice due to its capability of simulating several physical phenomena concurrently. A simplified approach of analysis has been used when modelling the specimen to obtain numerical results to be compared to the experimental result [3]. The glass is defined as a brittle cracking material. The comparison results showed positive signs to some extent, as the crack pattern was close to the experimental results. However, using the simplify method in the analysis significantly gives acceptable results in predicting the behaviour of the glass due to the horizontal loads.

5 Recommendations

Based on this study's findings, account should be taken of the following recommendations to improve the future work of this study. These are as follows;

- i. It is recommended to use different parameters to study the simulation of timber-glass wall panel in the future, such as the adhesive thickness or the thickness of the glass plate, which can affect the stiffness and bearing capacity of the wall panel.
- ii It is recommended to perform this research by taking different of glass position, i.e. positioning the glass on the outer of the timber frame by using double glass panes.

- iii. It is recommended to consider the porosity in the study and study the effect of load on the structure.
- iv. It is also recommended to conduct laboratory experiments to depict timber-glass composite materials varying their geometry, and then perform numerical simulations to further improve this study.
- v. Because the uncertainty of material behaviour may lead to deviations in the results, it is advisable to attend probabilistic FE simulation for more precise comparison as future studies.

References

1. Alessandra T (2017) Engineered wood glass combination innovative glazing façade system. KTH Royal Institute of Technology
2. Rosliakova V, Nicklisch F, Weller B (2015) A review of possibilities to integrate photovoltaic in a load-bearing timber-glass façade. In: Conference: advanced building skins, Dresden, pp 1–10. <https://doi.org/10.13140/RG.2.1.2920.9681>
3. Ber B, Premrov M, Štrukelj A, Kuhta M (2014) Experimental investigations of timber-glass composite wall panels. *Constr Build Mater* 66:235–246. <https://doi.org/10.1016/j.conbuildmat.2014.05.044>
4. Nicklisch F, Giese-Hinz J, Weller B (2016) Experimental and numerical study on glass stresses and shear deformation of long adhesive joints in timber-glass composites. *Challenging glass 5: conference on architectural and structural applications of glass*, vol 62, no 1, pp 295–304
5. Feldmann M, Kasper R (2014) Guidance for European structural design of glass components. EUR 26439, JRC86637. Publications Office of the European Union, Luxembourg
6. Ber B, Šusteršič I, Premrov M, Štrukelj A, Dujic B (2015) Testing of timber-glass composite walls. *Proc Inst Civ Eng Struct Build* 168(7):500–513. <https://doi.org/10.1680/stbu.13.00105>
7. Kozłowski M, Dorn M, Serrano E (2015) Experimental testing of load-bearing timber-glass composite shear walls and beams. *Wood Mater Sci Eng* 10(3):276–286. <https://doi.org/10.1080/17480272.2015.1061>
8. EN594 (2011) Timber structures—test methods—racking strength and stiffness of timber frame wall panels. European Committee for Standardization, British Standards Institution
9. Ber B, Premrov M, Sustersic I, Dujic B (2013) Innovative earthquake resistant timber-glass buildings. *Nat Sci* 05(08):63–71
10. ABAQUS (2014) Analysis user's guide: Abaqus 6.14, 6.14
11. Kamarudin MK, Yusoff MM, Disney P, Parke GAR (2018) Experimental and numerical investigation of the buckling performance of tubular glass columns under compression. *Structures* 15:355–369. <https://doi.org/10.1016/j.istruc.2018.08.002>

Effect of Palm Oil Bottom Ash (POBA) on Concrete Mechanical Properties of Fresh and Hardened Ultra High Performance Concrete (UHPC)



Izzani Farhana Baharudin, Nurul Huda Suliman, Sakhiah Abdul Kudus, and Nuradila Izzaty Halim

Abstract The rapid development of building construction requires innovation in the improvement of the material properties of the concrete as well as in the finding of a solution to reduce the dependence on the raw materials currently used. In the meantime, the biggest environmental problem that typically causes pollution usually comes from waste disposal. One of the wastes that has been discovered is the bottom ash of palm oil (POBA). Bottom ash is a domestic waste that could be found in a disposal site consisting of silica and alumina. Both silica and alumina are additional cement-based materials that provide cementing properties that can enhance concrete strength due to pozzolanic reactions with the presence of water. This research aims to recycle POBA waste by adding it as an additive to ultra-high-performance concrete (UHPC) mixtures. The composition of 5, 10 and 15% of the bottom ash was used to determine the optimum design. Workability and compressive capacity of 100 mm³ UHPC cubes were observed on the mixing day, 3rd, 7th, 14th and 28th days after day of casting. The research results show that the addition of POBA has had an impact on the workability and compressive strength of the UHPC and that the optimum percentage of the POBA composition is 15%.

Keywords Palm oil bottom ash · Ultra high performance concrete · Superplasticizer · Workability · Compressive strength

1 Introduction

The progress of construction industry in the twenty-first century is leading to growth in recent years. In 2006, 7.5 km² of concrete were produced annually where the concrete consumption can be estimated about 1 m³ per capita [1]. As a result, concrete has become the world's second-largest item needed by humans after their critical water needs [2].

I. F. Baharudin · N. H. Suliman (✉) · S. Abdul Kudus · N. I. Halim
School of Civil Engineering, College of Engineering, Universiti Teknologi MARA (UiTM),
40450 Shah Alam, Selangor, Malaysia
e-mail: nurul_huda@uitm.edu.my

The standard concrete mixture consists of ordinary Portland cement, sand, coarse aggregates and water with a density of about 2400 kg/m^3 . It has excellent compressive strength but comparatively poor tensile strength and, as such, is typically reinforced with a tension-strong material. Shortly thereafter, the launch of concrete technology in ultra high performance concrete (UHPC) attracted construction players' attention. UHPC is suitable to be used in various countries with different climates especially for outdoor and exposed conditions. This concrete product also has greater strength and durability effect than traditional concrete. The utilization of UHPC for bridges and various structures can be seen in various countries including Australia, Austria, Canada, China, Czech Republic, France, Germany, Italy, Japan, Malaysia, Netherlands, New Zealand, Slovenia, South Korea, Switzerland and the United States (US). Later on, the usage of the material for the outdoor and exposed environment of UHPC seems to be the potential for many further applications [3].

Recently, high industrial waste has become the key human and environmental problem. Therefore, to create a safer and greener environment, it is a world subject to discovering such friendly solutions and ways to ensure safe disposal of industrial waste by product. Malaysia is the world's second largest palm oil producer after Indonesia, according to the Malaysian Palm Oil Board (MPOB). The stockpiles grew to 1.73 million tonnes in March 2020 where 8.4% increase from February 2020 [4]. The nation's palm oil industry produces about 90 million tons of lignocellulosic biomass, including empty packets, palm oil trunks, palm oil foliage and palm oil plant effluent (POME). Besides palm oil, most palm kernel shells also produce waste from palm oil agronomy.

Organic commodity shell and fiber are reused as ignition material for boiler and furnace to form various types of waste such as palm oil fly ash (POFA) and palm oil bottom ash (POBA). At the end of the boiling process, landfill has disposed of the boiler clinker in recent years, causing soil contamination and affecting groundwater source. Therefore, POBA was used in this research to reduce waste from dumped into landfill. A research verified that the silica content in POBA is very high which determined using X-Ray Fluorescence (XRF) test. XRF results showed that the silica content in POBA is 40.6 wt% [5].

The chemical compound of silica in bottom ash can possibly supplant concrete or as an added substance to be mixed with concrete. Silica content material from the bottom ash of the palm oil was expected that it can react with slaked lime to produce hydration among water and concrete and so, substance of hydraulic lime paste is formed and set the concrete. However, to obtain data and information regarding UHPC properties a lot of study need to be done such as proposing the bottom ash of palm oil to be utilize as alternative material to replace cement, fine aggregate, sand and etc. Hence, this research is important to discover and analyse how effective the idea of using bottom ash as additive material in the concrete structure.

2 Experimental Program

2.1 Materials Preparation

Palm oil bottom ash (POBA) is a by-product which have continually generated by using local palm oil mill in a large amount. These by-products waste is also typically disposed of as profitless and considered a nuisance to the environment. It consists of an inorganic and incombustible matter which present in the coal. For this research, POBA originated from United Palm Oil, Nibong Tebal, Penang. It was possibly a lump of coal with uneven thickness. To obtain a good concrete mixture, POBA were grinded 8–12 h to ensure it pass a 212 μm sieve. Also involved in concrete mixture were sand and aggregates. To achieve high strength, sand was sieved to pass 2 mm mesh. For coarse aggregates, however, it is usually more than 4.75 mm of particulate matter therefore 10 mm coarse aggregates were used for this study.

A crucial step in high-quality UHPC development is the selection and use of a superplasticizer. Superplasticizer is an additive known as high-range water reducers used to make high-strength concrete. For a constant workability the reduction of water may be up to 30% by using the superplasticizer. The standard water-to-binder ratio ranges from 0.45 to 0.60, while UHPC ranges from 0.14 to 0.20. This research used MasterGlenium ACE 8538 because of its advantages that it can reduce high water content with high flowability and efficient workability, avoid hydration delays and increase early strength development.

2.2 Specimens Design and Casting

In this study, 4 sets of concrete mixture were mixed with 0% (control), 5, 10 and 15% of POBA composition that gave 48 pieces of concrete cube specimens in total as shown in Table 1. While Table 2 displays the mixing design and the quantity of each concrete material used to produce 100 \times 100 \times 100 mm UHPC cubes as per standard BS EN 12390-1 [6]. Each mixture was specifically designed for 12 cubes, splitting 3 cubes for 4 compressive strength test cycles on days 3, 7, 14 and 28. The

Table 1 Number of specimens

Number of concrete cubes 100 \times 100 \times 100 mm					
Bottom ash	3 days	7 days	14 days	28 days	Total
UHPC (C)	3	3	3	3	12
UHPC (5)	3	3	3	3	12
UHPC (10)	3	3	3	3	12
UHPC (15)	3	3	3	3	12
Total					48

Table 2 Design mix proportion

Materials	UHPC (C) (kg)	UHPC (5) (kg)	UHPC (10) (kg)	UHPC (15) (kg)
Cement (800 kg/m ³)	7.92	9.36	9.36	9.36
Fine (433 kg/m ³)	4.29	5.07	5.07	5.07
Coarse (800 kg/m ³)	7.92	9.36	9.36	9.36
Water (160 kg/m ³)	1.58	1.87	1.87	1.87
Admixture (16 kg/m ³)	0.16	0.19	0.19	0.19
POBA	–	0.47	0.94	1.40

water-to-cement ratio is kept stable at 0.20 and the additional POBA ranges from 5 to 15%.

To facilitate testing performance, all types of specimens have been named with one nomenclature such as UHPC (C) for control while UHPC (5), UHPC (10) and UHPC (15) respectively for UHPC which has been modified with an addition of 5%, 10% and 15% POBA.

2.3 Concrete Testing

In this research, two tests were performed, specifically a slump test to determine fresh concrete properties and a compressive strength test as an indicator of incompatible mix design. The slump test is the most common test use in construction filed due to its simplicity of apparatus and procedures. The procedures of slump test were referred to the BS EN 12350-2 [7]. It is an observational test that measures the ease of workability of fresh concrete. To be precise, the consistency between batches and its stiffness is measured and slump classes can be determined as tabulated in Table 3.

While compression test is a test where a material experiences forces that push inside upon the sample from opposing sides or else compressed, squeeze, flattened or crushed by using compressing machine. There is various type of concrete sample dimension such as cylinder, cube and rectangular. In this research, 100 mm³ size of cube is used. The cubes cast is cured until 28 days and the compressive strength of cube is determined at day 3rd, 7th, 14th and 28th. The objective of compression test

Table 3 Slump classes

Slump classes	Slump in mm
S 1 Dry (kerb backing, dry fill and sloping slabs etc.)	10–40
S 2 Standard (foundations, slabs and other general structures)	50–90
S 3 Wet (foundations, slabs, pumping concrete)	100–150
S 4 Very wet (foundations, slabs, pumping and piling concretes)	160–210
S 5 Self leveling (foundations, slabs, pumping and piling concretes)	≥220

is to point out the material's behaviours while it encounters a compressive load by identify is strain, stress, and deformation. By testing a material in the compressive quality, yield strength, ultimate strength, elastic limit, and the elastic modulus among different parameters may all be determined. The compressive strength test procedures were followed the EN12350-3 standard [8]. All cubes were cured according to standard BS EN 12390-2 and tested for their density according to standard BS EN 12390-7 before compressive strength test was carried out [9, 10].

3 Result and Discussion

3.1 Workability of Ultra High Performance Concrete (UHPC)

Workability of mix were observed by undergo a slump test. As soon as the concrete is mixed slump test take place and a visual comparison by naked eye is reached before the concrete is poured into the mould. As in general, the increase of slump value will increase the workability. UHPC is a type of concrete called self-compacting concrete (SCC), which has the ability to self-flow and self-compact and gives relatively high slump test value. It is also categorised as high-fluidity concrete, self-levelling concrete and self-consolidating concrete. It has an excellent ability to travel inside the formwork, which is confirmed by the equally homogeneous gravity effect [11].

The result obtained shows that all UHPC have the slump value of 290 mm. According to BS EN 206-1:2000, the workability of UHPC categorised under the class S5 (≥ 220 mm), which is high workability and self-levelling [12]. While the modified UHPC with POBA, it reveals that by adding POBA it improves concrete workability from 250 to 290 mm. The effect of silica fume on UHPC was fairly complex (Table 4).

According to previous studies, some researchers found that UHPC's workability could increase with the presence of silica fume, while some researchers claim that silica fume may diminish UHPC's workability. According to previous research [13], the workability of green ultra high performance fiber reinforced cementitious composites (UHPRCCs) increases as ultrafine palm oil ash composition increases. This provides the highest diameter flow compared to other blends, which is more

Table 4 Slump for UHPC

Specimens	Slump value (mm)
UHPC (C)	250
UHPC (5)	290
UHPC (10)	290
UHPC (15)	290

than 195 mm. This effect can be explained by lower ignition loss (LOI), lower carbon content in palm oil ash, and lower binder content in UHPFRCC.

Meanwhile, the research findings from [14] shows that the slump values decreased around 55–90 mm when the quantity of silica fume rises from 5 to 15% composition. This occurred when the water in the concrete mix was absorbed due to high surface area of silica fume and induced a decrease in slump value, thereby shifting the properties from plastic to stiff-plastic.

3.2 Density of UHPC

Concrete density is a concrete solidity from concrete mass. Typically, to form a higher or lower density of concrete, the technique of mixing concrete can be modified. A denser concrete produces stronger strength and less voids and porosity. The lower the number of voids in concrete, the lower the permeability to water and soluble elements. Therefore, water absorption will also be reduced and better resilience is expected.

Figure 1 shows the density values for all specimens which have slightly differences from the day 3 to day 28. At day 28, all UHPC specimens reached their maximum density where the UHPC (C) achieved the highest density with 2547 kg/m³ followed by UHPC (15) with 2497 kg/m³. While UHPC (5) and UHPC (10) is 2490 kg/m³ and 2373 kg/m³, respectively.

Nonetheless, UHPC (10) reveals a significantly lower density value. It may be because certain factors that influenced the value such as the amount of silica products

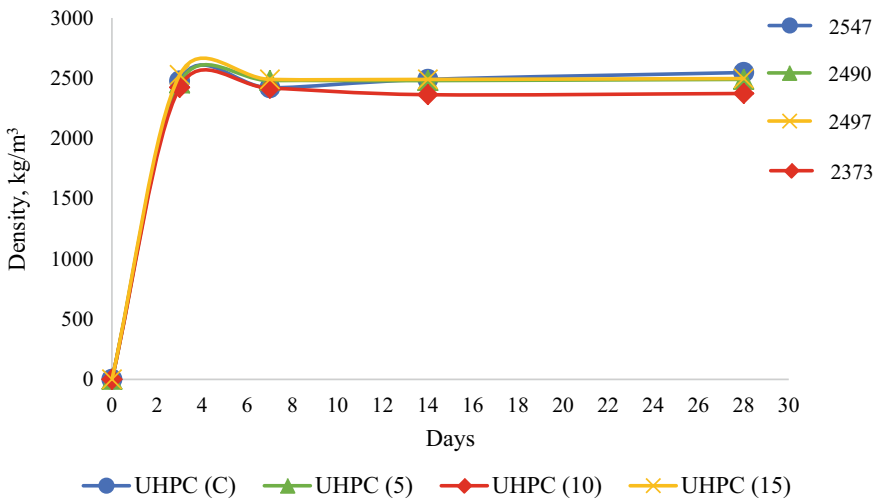


Fig. 1 Density of UHPC

in the mixing concrete is slightly lower or poor handling during concrete mixing, starting from the preparation of materials to the curing process. However, all the specimen density values are acceptable and within the UHPC density requirement range of 2200–2800 kg/m³ [15].

Furthermore, the graph also shows at 7 days the density of the control sample drops about 2.3% from 2477 to 2420 kg/m³, and shortly after that, it began to increase again until it reached 2547 kg/m³. As density and strength are correlate to each other, therefore the compressive strength result for all specimens is observed and it is believed that the density value tends to exhibit their compressive strength.

3.3 Compressive Strength of UHPC

Figure 2 shows the progress of compressive strength of UHPC from day 3, 7, 14 and 28. It has been established that a concrete will acquire 90% of their compressive strength at age 28 days. As to compare, the highest compressive strength at 28 days achieved by UHPC (15) with 86.28 MPa followed by UHPC (C) with 80.32 MPa. This has proven that with the addition of 15% POBA into the UHPC mixture has improved concrete strength by as much 7.4%. While the compressive strength for UHPC (5) and UHPC (10) are 76.74 MPa and 70.14 MPa, respectively.

From the data collected also, it has been indicated that the compressive strength of all UHPC specimens is lower than UHPC’s minimum requirement. According to previous research [16–21], the minimum compressive strength for UHPC is 120 MPa. However, the strength can be affected vapor pressure, sample size, load rate and also

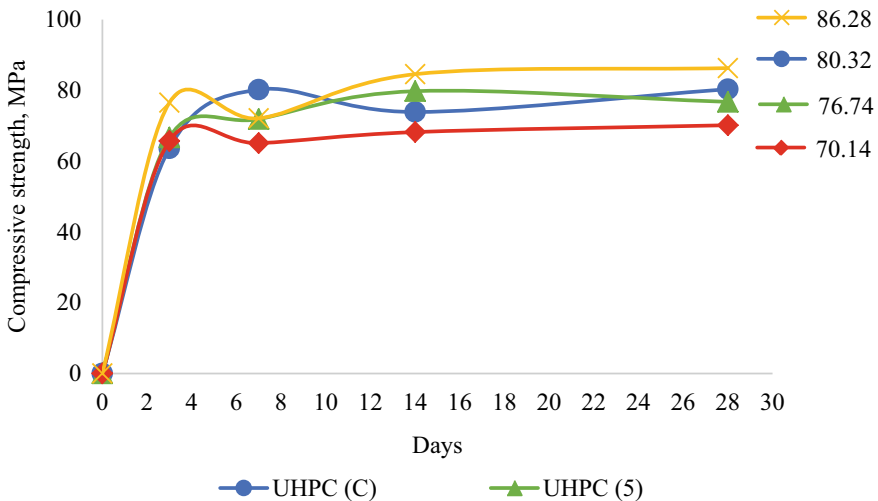


Fig. 2 Compressive strength of UHPC

fiber quality. The most important factor that might affect the value of compressive strength are the type of curing regime. Many researchers have proven that steam curing is one of the best methods of curing to enhance the UHPC strength properties.

Several studies have shown that steam curing is one of the effective curing methods to improve UHPC strength properties. By using 24-h steam curing or 8-h autoclave curing, the compressive strength at 28 days will 20–34% higher than normal curing, which can achieve up to 180–200 MPa [15]. High-temperature curing also useful for the pozzolanic reaction between CH from concrete hydration and reinforcing cemented materials, such as silica fume, which strengthens the micro-structure and gives higher efficiency. This also constructs C–S–H's chain length [22].

The other considerations are fiber quality, where the steel fiber has significantly contributed to the improvement of UHPC's compressive strength. Since tensile and flexural measurements were not performed in this research study, therefore steel fibers were excluded. Some studies have shown that compressive strength increased about 7.7% for UHPC with steel fibers compared to UHPC without steel fibers [23].

Figure 2 also shows an increase and reduction at early compressive strength test, particularly on day 7. That can be clarified by unbalance dilution effect during the pozzolanic reaction. The pozzolanic reaction is a process whereby siliceous or aluminium content contained in POBA is finely divided and, in the presence of moisture, chemically reacts with calcium hydroxide $\text{Ca}(\text{OH})_2$ to create compounds carrying hydraulic cementitious properties. This dilution is are relevant at 2–7 days [23]. Therefore, an early dilution effect will decrease the compressive strength of UHPC. However, at later ages the pozzolanic action will continue to increase strength, this is due to an increase in the interfacial transition zone acts as nucleating sites to react with Calcium Silicate Hydrate (C–S–H) releasing lime [22].

The argument from the previous study also confirmed in this study as compressive strength of UHPC with POBA shows an increment more than 6.91% compared to the control. This is due to the high composition of silica in POBA. In addition, there are other factors that lead to increase the compressive strength such as suffusion contact between cement, silica fume and aggregates which significantly enhance the silica fume. Third, the micro-fine silica particles adequately spread around the cement grain [24].

4 Analysis of Results

4.1 Compressive Strength–Slump Relationship

From the data in Fig. 3, the result shows that at a 15% addition of POBA it can enhance both the workability and compressive strength properties of the UHPC. At the same time, even though both 5 and 10% composition having the same value of slump the value of strength is slightly drop compared to control. However, the results are still acceptable for UHPC research. This is because as referred to [25], UHPC

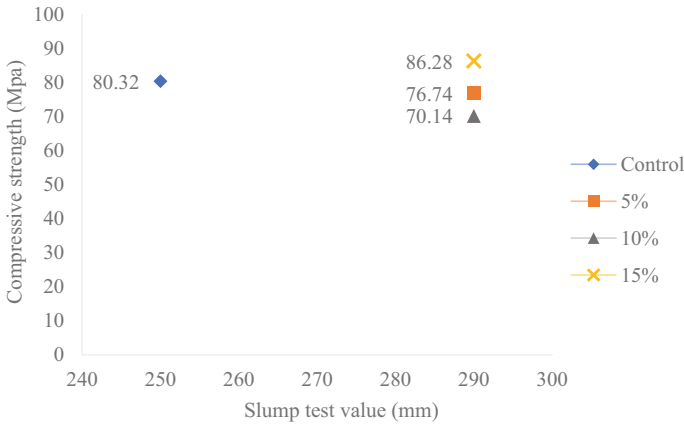


Fig. 3 Compressive strength–slump relationship

mix having slump value between 230 and 405 mm mix and exhibited amazingly high workability which is similar to those of common self-consolidating concrete. Furthermore, unlike the normal concrete, usually excessive slump values can result in aggregate segregation and a serious loss of strength.

4.2 Compressive Strength–Concrete Density Relationship

Concrete solidity can be measure from the density of concrete. Typically, to form a higher or lower density of concrete, the technique of mixing concrete can be modified. Typically, a denser concrete provides good strength and a smaller number of voids and porosity. The lower the number of voids in concrete, the lower the permeability to water and soluble elements. Therefore, water absorption will also be reduced, and better resilience is expected.

As density and strength are correlate to each other, the compressive strength versus density is observed. From the result shows in Fig. 4, all the specimens have a slightly different value of concrete density from day 3 until day 28. The highest density of concrete is at Day 28 with 15% POBA which is 2547 kg/m³ while the lowest density is at Day 14 with 10% POBA which is 2363 kg/m³. However, a high density of UHPC can be improved using well-graded fine sand, quartz sand and silica fume, which can reduce the porosity of the UHPC [26]. The increment in concrete density can be caused by the persistent hydration in the cement compound such as silicates and aluminates releasing hydroxide hydrate (CH) to become calcium hydroxide hydrate (CSH). Then, the CHS will act to fill up the voids and the water will be removed. Therefore, it will increase the bulk density and reduced the pore volume.

Nevertheless, from the bar graph 10% of POBA shows a slightly lower value of density. This might because some factors could affect the density of the concrete

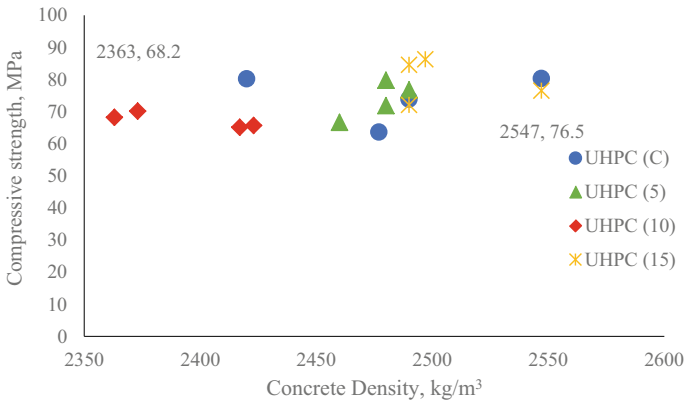


Fig. 4 Compressive strength–concrete density relationship

such as the amount of silica properties in the mixing concrete is slightly lower or improper handling during concrete mixing from preparing the materials until the curing process. However, all the value of the specimen density is reasonable and within the range of requirement of UHPC density value which is from 2200 to 2800 kg/m³ [3].

5 Conclusion

This research was conducted to investigate mechanical properties; UHPC compressive strength and workability with addition of POBA, and to assess the optimum percentage of POBA applied to UHPC mixture. The following points highlighting the main conclusions.

1. The compressive strength obtained with POBA is about 65–86 MPa in a typical room curing regime. Adding POBA at 15% composition has shown to increase the power of UHPC by up to 6.9%.
2. Slump values is from 250 to 290 mm with water cement ratio 0.20. The test demonstrates appropriate and practicable workability for UHPC mixes. It means that the superplasticizer was specifically built and applicable to mixes. Also, the use of POBA addition may significantly affect the fresh concrete that tends to make the fresh properties mix improve its workability and self-flow.
3. 15% POBA addition produces higher and better results at 28 days compared to 5 and 10% POBA compression test results. It appears, therefore, that 15% is similar to the optimal degree of addition appropriate for UHPC.
4. Raw materials, preparation process and curing schemes have a complete effect on UHPC properties and characteristics. Also, the fineness of materials may offer a significant impact that acts as a filler to fill a void between particles,

thereby achieving denser concrete. Therefore, high strength growth may occur due to higher particle surface area affecting pozzolanic activity and energy.

Acknowledgements The authors would like to acknowledge Malaysian Ministry of Higher Education for funding this study under the grant FRGS/1/2018/TK01/UiTM/03/3, 281801180008 and Faculty of Civil Engineering, Universiti Teknologi MARA, Shah Alam, Selangor, Malaysia.

References

1. Soofinajafi M, Shafiq P, Akashah F, Bin Mahmud H (2016) Mechanical properties of high strength concrete containing coal bottom ash and oil-palm boiler clinker as fine aggregates. *MATEC Web Conf* 66:00034
2. Gagg C (2014) Cement and concrete as an engineering material: an historic appraisal and case study analysis. *Eng Fail Anal* 40:114–140
3. Azmee N, Shafiq N (2018) Ultra-high-performance concrete: from fundamental to applications. *Case Stud Constr Mater* 9:e00197
4. The Star (Reuters) (2020) Plantations: Malaysia March palm oil stocks up 1.7% to 1.73 tonnes, says MPOB. <https://www.thestar.com.my/business/business-news/2020/04/10/malaysia-march-palm-oil-stocks-up-17-to-173m-tonnes-says-mpob>. Accessed 25 Aug 2020
5. Yahya Z et al (2015) Effect of solids-to-liquids, Na₂SiO₃-to-NaOH and curing temperature on the palm oil boiler ash (Si+Ca) geopolymerisation system. *Materials* 8:2227–2242. <https://doi.org/10.3390/ma8052227>
6. BS EN 12390-1:2012 (2012) Testing hardened concrete—shape, dimensions and other requirements for specimens and moulds. British Standard Institution
7. BS EN 12350-2:2019 (2019) Testing fresh concrete—slump test. British Standard Institution
8. BS EN 12390-3:2019 (2019) Testing hardened concrete—compressive strength of test specimens. British Standard Institution
9. BS EN 12390-2:2019 (2019) Testing hardened concrete—making and curing specimens for strength tests. British Standard Institution
10. BS EN 12390-7:2019 (2019) Testing hardened concrete—density of hardened concrete. British Standard Institution
11. Ujianto M, Ardiansyah E, Ilokana G, Falah M (2018) Optimization of superplasticizer Master-Glenium SKY 8614 with added materials fly ash, steel slag, and silica fume for high strength concrete. *IOP Conf Ser Mater Sci Eng* 403:012026
12. BS EN 206:1992 (2000) Concrete. Performance, production, placing and compliance criteria. British Standard Institution
13. Aldahdooh M, Muhammad Bunnori N, Megat Johari M (2020) Development of green ultra-high performance fiber reinforced concrete containing ultrafine palm oil fuel ash. *Constr Build Mater* 48(2013):379–389
14. Shihada S, Arafa M (2010) Effects of silica fume, ultrafine and mixing sequences on properties of ultra high performance concrete. *Asian J Mater Sci* 2(3):137–146
15. Azmee N, Shafiq N (2018) Ultra-high performance concrete: from fundamental to applications. *Case Stud Constr Mater* 9:e00197
16. Wang D, Shi C, Wu Z, Xiao J, Huang Z, Fang Z (2015) A review on ultra high performance concrete: part II. Hydration, microstructure and properties. *Constr Build Mater* 96:368–377
17. Liu J, Jin H, Zhao X, Wang C (2019) Effect of multi-walled carbon nanotubes on improving the toughness of reactive powder concrete. *Materials* 12:2625
18. Yu KQ, Lu ZD, Dai JG, Shah SP (2019) Direct tensile properties and stress–strain model of UHP-ECC. *J Mater Civ Eng* 32:04019334

19. Sharma R, Bansal PP (2019) Efficacy of supplementary cementitious material and hybrid fiber to develop the ultra high performance hybrid fiber reinforced concrete. *Adv Concr Constr* 8:21–31
20. Erdogdu S, Kandil U, Nayir S (2019) Effects of cement dosage and steel fiber ratio on the mechanical properties of reactive powder concrete. *Adv Concr Constr* 8:139–144
21. Wan L, Wendner R, Liang B, Cusatis G (2016) Analysis of the behavior of ultra high performance concrete at early age. *Cem Concr Compos* 74:120–135
22. Shi C, Wu Z, Xiao J, Wang D, Huang Z, Fang Z (2015) A review on ultra high performance concrete: part I. Raw materials and mixture design. *Constr Build Mater* 101:741–751
23. El-Din HKS, Mohamed HA, Khater MAE, Ahmed S (2016) Effect of steel fibers on behavior of ultra high performance concrete. In: First international interactive symposium on UHPC
24. Tironi A, Scian AN, Irassar EF (2017) Blended cements with limestone filler and kaolinitic calcined clay: filler and pozzolanic effects. *J Mater Civ Eng* 29(9)
25. Arora A, Yao Y, Mobasher B, Neithalath N (2019) Fundamental insights into the compressive and flexural response of binder- and aggregate-optimized ultra-high performance concrete (UHPC). *Cem Concr Compos* 98:1–13
26. Zhou M, Lu W, Song J, Lee G (2018) Application of ultra-high performance concrete in bridge engineering. *Constr Build Mater* 186:1256–1267

Impacts of Steel LNG Tank Aspect Ratio on Seismic Vulnerability Subjected to Near-Field Earthquakes



N. Sharari, B. Fatahi, A. Hokmabadi, and R. Xu

Abstract Liquefied Natural Gas (LNG) tanks seismic design is critically important considering the high consequences of failure given the hazardous nature of the stored product. The LNG tanks aspect ratio (H/D), as decided at the design stage based on several considerations, can impact its dynamic characteristic and in turn the seismic performance of the tank under the design earthquakes. In this paper, the seismic vulnerability of the inner steel LNG tanks with varying height (H) to diameter (D) aspect ratios is investigated. Dynamic fluid–structure interaction is captured using the added-mass method and tank walls are modelled using general-purpose finite element software ABAQUS considering the material and geometric nonlinearities. Adopting time-history analysis, deformation and stresses developed in the tank subjected to two large near-field earthquakes namely 1994 Northridge and 1995 Kobe earthquakes are assessed. The results demonstrate that the tank aspect ratio (H/D) plays an important role in the modes of failure, where increasing the aspect ratio (tall tanks) initiates the elephant’s foot buckling mode of failure. The selection of optimum aspect ratio can lead to a safe and economic seismic design.

Keywords LNG tank · Nickel steel · Near-field earthquake · Finite element · Seismic response · ABAQUS

N. Sharari · B. Fatahi (✉)

School of Civil and Environmental Engineering, University of Technology Sydney, Sydney, Australia

e-mail: Behzad.Fatahi@uts.edu.au

N. Sharari

e-mail: Noor.Sharari@student.uts.edu.au

A. Hokmabadi · R. Xu

Arup, Sydney Office, Sydney, Australia

e-mail: Aslan.S-Hokmabadi@arup.com

R. Xu

e-mail: Ruoshi.Xu@arup.com

1 Introduction

The global demand for the Liquefied Natural Gas (LNG) has been continuously increasing with average yearly growth of approximately 6.6% in the last twenty years. Several factors derive the demand expansion globally including conversion to cleaner and cheaper fuels for power generation as compared to coal and fuel oil. This leads to an increasing need for smart and affordable storage solutions. Full-containment above-ground LNG tanks have been one of the most common storage options. A full-containment LNG tank consists of (i) an inner cylindrical tank normally open-top steel tank made of cryogenic steel (9% Ni) to fulfill ductility requirements at the operating temperature and (ii) an outer reinforced concrete tank to ensure structural resistance to withstand the external hazards.

The fundamental period range for common LNG tanks are usually between 0.1 and 0.5 s which coincides with the peak of the design response spectrum for most of earthquake ground motions. As such, LNG tanks can absorb significant energy during earthquake events. The safety of these tanks against earthquake excitations is crucial as the environment and economic losses can be significant in case of any damage or failure.

The seismic design of the LNG tanks normally follows the similar standpoint to the nuclear power plants by implementing the two earthquake level scenarios, namely the Operating Basis Earthquake (OBE) and Safe Shutdown Earthquake (SSE) scenarios with no leakage permitted at SSE level [1]. The main difference between the seismic design of the liquid storage tanks and other civil structures is the hydrodynamic loadings and interaction between the tank structure and the contained liquid which makes tanks [2], particularly inner steel tanks with relatively thin walls, vulnerable to failure or damage (e.g. the thin-walled buckling failure mode).

Dynamic buckling phenomenon in steel tanks under seismic effect is generally identified as elastic or elastic–plastic buckling. Many studies showed the elastic–plastic buckling as an outward bulge close to the tank base when the axial compression due to overturning moment and the circumferential hoop stresses, which results from both the hydrostatic and hydrodynamic pressures at the bottom of the tank, exceed the yield limit. This outward bulging occurs at tank base identified as elephant’s foot buckling mode. Indeed, the diamond-shaped buckling mode, which is an elastic buckling happens usually at small values of hoop stresses, as the inward hydrodynamic suction at the base level of the tank wall or at upper level of the tank wall (i.e. secondary diamond shape buckling mode) goes beyond the outward hydrostatic pressure [3].

The fluid–structure interaction concept has been studied by several researchers such as [4, 5] where the hydrodynamic pressure from the liquid was deemed to be decomposed of impulsive and convective liquid mode. The impulsive portion is due to the liquid coincidentally vibrating with the tank wall, while the convective portion is due to the upper portion of liquid sloshing as waves at the surface of liquid. These two forces can be combined in a simple mechanical model to represent the dynamic response of liquid storage tanks as reported by [6, 7].

Several research studies and experiments have been carried out on the dynamic behaviour of liquid storage tanks, some of these studies have been conducted on the inner steel LNG tank to assess the effect of the hydrodynamic forces and enhance their seismic performance. For example, compared the seismic behaviour of the LNG tank using the finite element analysis (FEA) method and the simplified mechanical model, usually used for preliminary seismic analysis and design of liquid storage tank. The results demonstrated that the mechanical models could be used with confidence for the preliminary analysis and design of conventional and isolated LNG tanks [8]. In addition, [9] investigated the effects of base isolation on the seismic response of LNG tanks with different filling liquid levels using finite element analysis (FEA) technique, and their numerical results shown that the lead rubber bearings were very effective in avoiding the significant portion of seismic forces transferring to the tanks and thus enhancing the seismic responses of the LNG tanks.

This study investigates the impact of the aspect ratio (i.e. tank height to diameter H/D) on the seismic response of the 9% Ni steel inner LNG tank under near-field earthquake excitations. For this purpose, three-dimensional finite element simulation using ABAQUS software, capturing material and geometric nonlinearities, were adopted. The fluid–structure interaction effect was considered utilizing the added-mass technique. The seismic response of different tanks is presented and discussed.

2 Details of Adopted Storage Tanks

To demonstrate the height to diameter (H/D) aspect ratio effect on the seismic response of the inner 9% Ni steel LNG tank, three geometric configurations were used in this study (see Fig. 1). The considered tanks were anchored vertical cylindrical ground supported tanks, with the constant diameter of 30.5 m (representing typical modular inner LNG tank size), and different H/D ratios of 0.95 (Tank A), 0.63 (Tank B), and 0.40 (Tank C) corresponding to tall, medium and broad tanks as classified by [10], respectively. The filling level of the LNG liquid height was considered to be 90% of each tank height, which represent the full condition with 10% of freeboard. The structural design of tanks (i.e. wall thicknesses) follows API-650 (American Petroleum Institute) [11] fulfilling the seismic design requirements for fully anchored tanks in high seismic regions.

3 Fluid–Structure Interaction Effects

The seismic analysis of liquid storage tanks generally should capture the hydrodynamic forces exerted on the tank wall by the filling liquid. Evaluation of hydrodynamic forces, given the complex nature of the fluid–structure interaction phenomenon, have been previously investigated via simplified mechanical models,

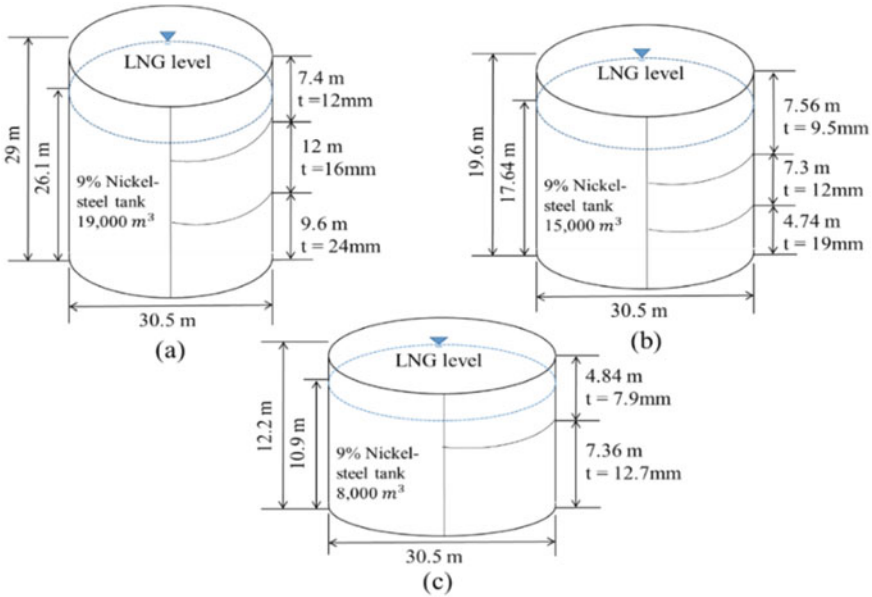


Fig. 1 The considered tank models, **a** tall Tank A with $H/D = 0.95$, **b** medium Tank B with $H/D = 0.63$, and **c** broad Tank C with $H/D = 0.40$

which assume that the loads applied from the liquid to the storage tank walls can be represented in two parts, namely the convective and impulsive forces. The convective component (sloshing mode) relates to the oscillation in the higher region of the stored liquid, while the impulsive component (rigid movement of liquid) corresponds to the dynamic pressure of the coincidental movement of the liquid and tank walls subject to dynamic loadings.

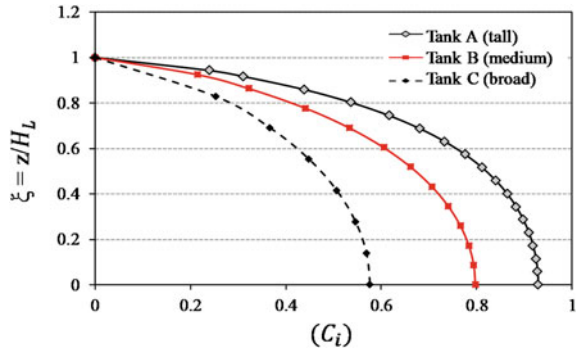
According to Eurocode-8 [12], the spatial-temporal distribution of the rigid impulsive component of the hydrodynamic pressure (p_i) can be given by the following expressions:

$$p_i(\xi, \zeta, \theta, t) = C_i(\xi, \zeta) \rho R \times A_g(t) \tag{1}$$

$$C_i(\xi, \zeta) = 2\gamma \sum_{n=0}^{\infty} \frac{(-1)^n}{\left(\dot{I}_1\left(\frac{v_n}{\gamma}\right)\right) v_n^2} \cos(v_n \zeta) I_1\left(\frac{v_n}{\gamma} \xi\right) \tag{2}$$

where $\xi = r/R$ and $\zeta = z/H_L$ are the non-dimensional coordinates; R is the radius of the tank; r, θ, z are components of cylindrical coordinates with origin at the center of the tank while the z axis is vertical; t is time; C_i is impulsive pressure distribution coefficient; $v_n = ((2n + 1)/1) \pi$; $\gamma = H_L/R$; I_1, \dot{I}_1 are the modified Bessel functions of order 1 and its derivative, respectively; $A_g(t)$ is the horizontal ground acceleration time-history in the free-field; ρ is the mass density of the fluid.

Fig. 2 Impulsive pressure coefficient for the tank-liquid systems



The pressure distribution coefficients defined in Eq. (2) for each of the tank models for $\theta = 0^\circ$ are presented in Fig. 2. To find the overall seismic response of the storage tanks, including the fluid–structure interaction, only the impulsive portion of the liquid is considered in the current study, as this portion is the major component which moves with the tank wall and generates the hydrodynamic forces as reported by previous studies (e.g. [10, 13]).

4 Finite Element Model of the Tank-Liquid System

The nonlinear dynamic analysis of the LNG tank-liquid system carried out using the finite element analysis software ABAQUS (version 2018). The inner steel tank was modelled using shell elements (S4R) with four-nodes, doubly curved quadrilateral and reduced integration finite membrane strain formulations, which has both membrane and bending capabilities suitable for the nonlinear analysis [14]. The 9% Ni steel material which is recognized by the ASTM A36 [15] for cryogenic service temperatures, with the yield stress (f_y) and ultimate strength (f_{ult}) of 245 and 360 MPa, respectively, was used in this study. Additionally, elastic modulus and the strain hardening modulus were considered to be 205 GPa and 3888 MPa, respectively. The 9% Ni steel material behavior was modelled using the kinematic hardening rule with Von Mises yield criteria to capture the metal inelastic behavior under seismic loading.

The LNG liquid was modelled using the lumped added-mass method for the dynamic analysis. In which impulsive portion of the liquid can simultaneously accelerate or decelerate with a tank wall, which reproduces the impulsive pressure. The adopted added-mass technique in this study is a comprehensive alternative to [4] traditional method of the single masses mechanical model used for dynamic analysis for liquid storage tanks. Accordingly, the impulsive hydrodynamic pressure was modelled using a series of added masses attached to the tank nodes via rigid springs. Each lumped mass m_i calculated from the pressure defined using Eq. (1) at each node, where the height of the cylinder was divided into several segments and the

area of the pressure below the curve for each segment was divided by the normal acceleration of the rigid wall $A_g(t)$. The lumped masses are in same vertical distribution as the impulsive pressure (Fig. 3a), and they have a uniform distribution around the circumference (Fig. 3b) same procedure proposed by [10].

The attached masses in ABAQUS were modelled using specific connector elements named MPC type LINK, which simulates a unidirectional rigid spring between two nodes. This assumes zero accelerations in both vertical and tangential directions along the tank wall, while the springs provide radial added inertia effects perpendicular to shell surface. In addition, all the nodes at tank base are restrained in both horizontal and vertical directions to represent fixed base condition.

Figure 4 illustrates the developed finite element models for different tank aspect ratios. The finite element analysis was conducted for each tank in three steps; the

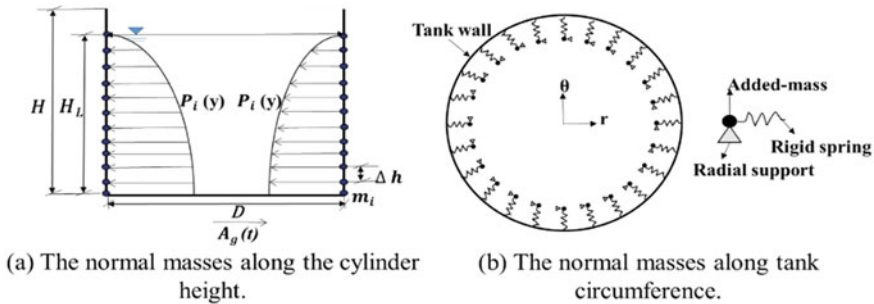


Fig. 3 Mass-spring modelling technique used in this study to capture impulsive fluid–structure interaction, the normal masses **a** along the cylinder height, **b** along tank circumference

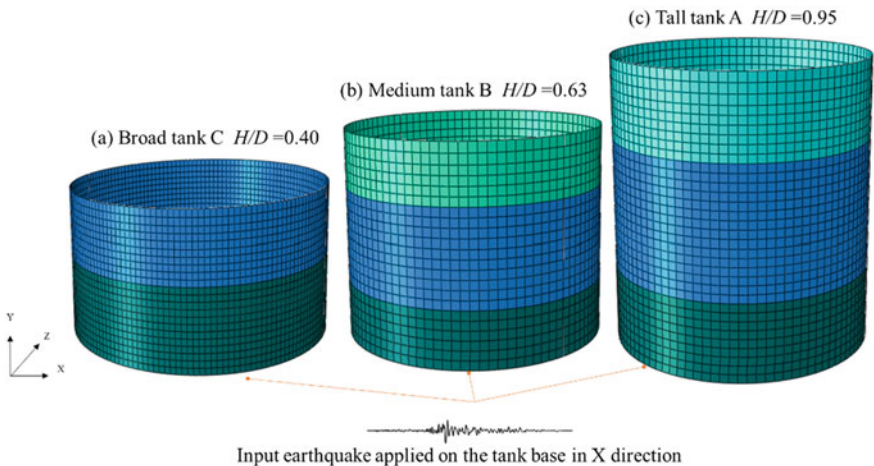


Fig. 4 Finite element models for different tanks adopted in this study **a** broad Tank C, **b** medium Tank B, and **c** tall Tank A

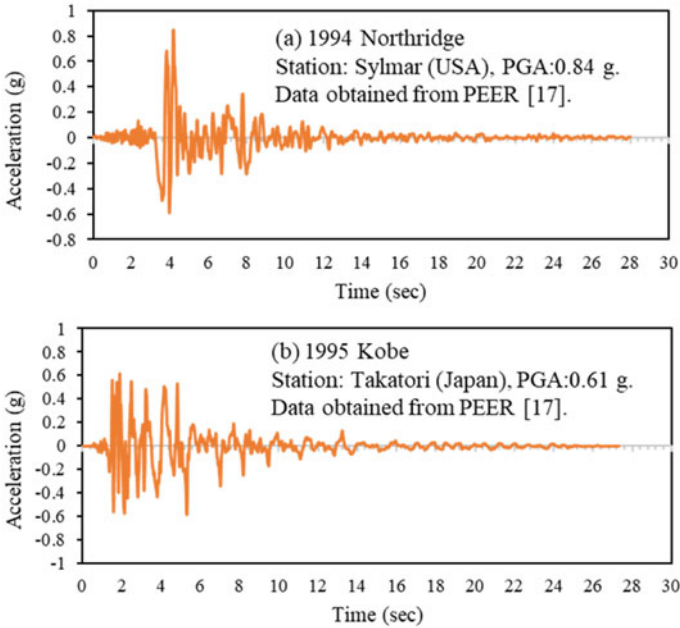


Fig. 5 Adopted earthquake time histories of the ground accelerations, **a** 1994 Northridge earthquake and **b** 1995 Kobe earthquake

first step was the modal analysis to obtain the natural frequency and compare it with the analytical formulations available in API-650. The second step was to establish the initial equilibrium under the gravity load including the hydrostatic load on the tank wall and base. Finally, the earthquake excitation was applied at the tank base in one horizontal direction (no vertical ground motion was considered) to conduct the non-linear dynamic time-history analysis capturing both material and geometric nonlinearities. It is assumed that the LNG tank was sitting on competent hard rock site, and two benchmark near-field earthquake records were selected in this study, these earthquakes selected by several researchers (e.g. [16]) to represent maximum considered level of earthquakes. Namely the 1994 Northridge and 1995 Kobe earthquakes, were used in this study as shown in Fig. 5 [17]. Each running analysis took around 8 h to complete with model size (10 Gb), therefore, fast computation facilities were used to conduct this time-history analysis.

5 Results and Discussion

The results of free vibration analysis and nonlinear time-history analysis for three adopted LNG tanks aspect ratios under 1994 Northridge and 1995 Kobe Earthquake records are presented below.

5.1 Free Vibration Analysis

Modal analysis was performed on the three tanks models Type A (tall), Type B (medium) and Type C (broad) to find the fundamental impulsive period of each tank. Then the natural period obtained from the FEA was compared with the analytical solution presented in API-650 for the fundamental natural period of the impulsive mode as in Eq. (6):

$$T_i = C_l \frac{H_L}{\sqrt{2000 \frac{t_u}{D}}} \sqrt{\frac{\rho}{E}} \tag{6}$$

where, C_l is the coefficient for determining the impulsive period of tank system which depends on the H/D ratio, and could be obtained from API-650; t_u is the equivalent uniform thickness of the tank wall in mm; H_L is the fluid design level in meter; D is the diameter of the tank in meter; E is the modulus of elasticity of the tank in MPa; ρ is the fluid density in kg/m^3 , which was assumed to be 490 kg/m^3 for LNG. In Table 1, the results of FEA computed by eigenvalue modal analysis using Block Lanczos algorithm is compared with those obtained from API-650 code. The results show that the natural period calculated by FEA is in a good agreement (less than 3% difference) with the analytical formulations confirming the reliability of the adopted numerical model with spring-added mass technique to simulate the liquid–tank interaction.

Figure 6 summarises the schematic deformed shapes of tanks corresponding to the fundamental modes of vibration. It can be noticed that for tall Tank A (with $H/D = 0.95$) the fundamental impulsive mode is comparable with a bending mode of a cantilever beam. However, for medium Tank B and broad Tank C ($H/D = 0.63$ and 0.40 , respectively) the bulge shape deformation near the mid-height of the wall is apparent. Which implies that the cross-section area at the tank mid-height is vulnerable to higher deformation during horizontal excitation due to impulsive mass effect.

Table 1 Comparison between fundamental periods of vibration (T_i) for filled tank obtained from FEA and API-650

Tank model	T_i (s)—3D FEA	T_i (s)—API 650
Tall Tank A ($H/D = 0.95$)	0.217	0.220
Medium Tank B ($H/D = 0.63$)	0.145	0.150
Broad Tank C ($H/D = 0.40$)	0.098	0.096

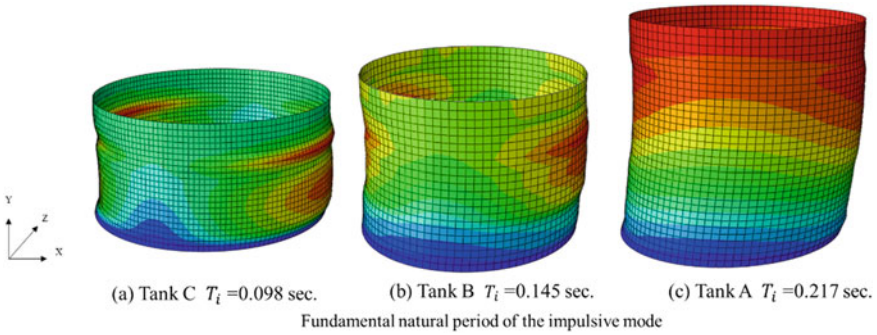


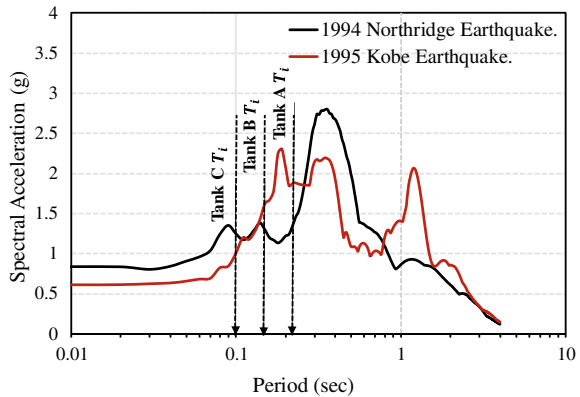
Fig. 6 Fundamental natural period of the impulsive mode for **a** tall Tank A, **b** medium Tank B, and **c** broad Tank C

5.2 Non-linear Dynamic Time-History Analysis

The nonlinear time-history analysis was performed on the LNG inner steel tank with different aspect ratios, subjected to two near-field earthquakes namely 1994 Northridge and 1995 Kobe earthquakes. Figure 7 shows the acceleration response spectra of these earthquakes, as well as the fundamental periods of vibration for three tanks used. The acceleration response spectra is communally used in the seismic analysis as it is interrelated to the maximum superstructure response under the earthquake load [18]. As evident, the fundamental periods of vibration for all selected tanks are located in the short period range of the response spectrum.

To verify the accuracy of the nonlinear time-history analysis employing three-dimensional finite element modelling, the seismic response for these tanks were compared with Eurocode-8 (2006) formulations. In particular, the base shear forces and the overturning moments were computed and compared. According to Eurocode-8 (2006), the base shear force (Q) and bending moment (M) for the liquid storage

Fig. 7 Acceleration response spectra for the selected earthquakes



tank considering impulsive liquid–wall interaction only, can be calculated using the following equations:

$$Q = (m_i + m_w) \times S_a(T_{imp}) \tag{7}$$

$$M = (m_i \times h_i + m_w h_w) \times S_a(T_{imp}) \tag{8}$$

where, m_i is the impulsive mass component; h_i is the height where the impulsive hydrodynamic wall pressure was applied; m_w is the tank wall mass; h_w is the height of the centre gravity of tank wall; $S_a(T_{imp})$ is the impulsive spectral acceleration obtained from the acceleration response spectrum (i.e. Fig. 7). Figures 8 and 9 present the maximum base shear forces and bending moments obtained from the analytical solution and the FEA predictions having reasonable agreement (less than 16% difference). However, it is obvious that increasing the aspect ratio H/D from 0.63 to 0.95 (medium tank to tall tank) increase the base shear forces significantly,

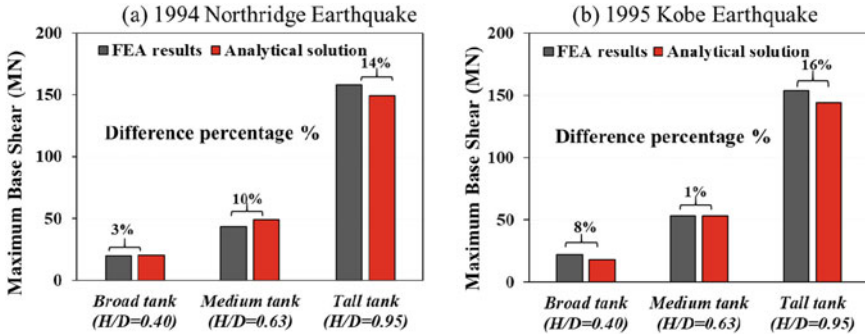


Fig. 8 The maximum base shear force obtained from the analytical solution and 3D FEA, a 1994 Northridge earthquake and b 1995 Kobe earthquake

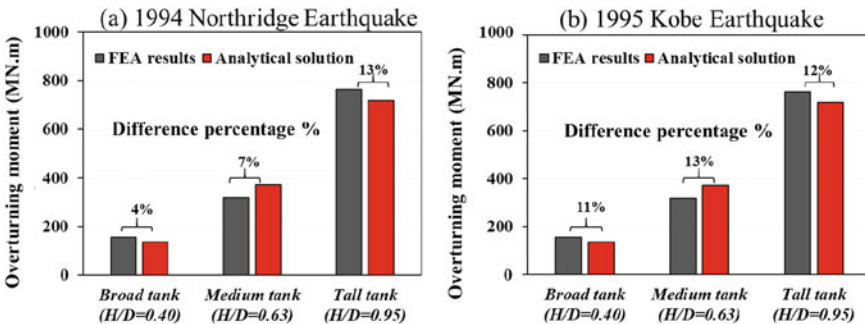


Fig. 9 The maximum overturning moment obtained from the analytical solution and 3D FEA, a 1994 Northridge earthquake and b 1995 Kobe earthquake

which correspond to 72% and 58% increases for the 1994 Northridge and the 1995 Kobe earthquakes, respectively. Furthermore, as a result of increasing the H/D from 0.63 to 0.95 (medium tank to tall tank), overturning moments increased by 58% and 52% under the effects of the 1994 Northridge and the 1995 Kobe earthquakes, respectively.

The conducted nonlinear time-history analysis allows for seismic response comparison of the LNG inner tanks with different aspect ratios. The maximum structural response of the LNG tank walls under the applied earthquakes was reported and compared. The axial force (F_{11}) and the hoop force (F_{22}) for circumferential unit width of the tank (Fig. 10) and radial displacements of the wall are of particular interest and discussed below.

Figure 11 shows distribution of maximum hoop forces for tall, medium and broad tanks under 1994 Northridge and 1995 Kobe earthquakes. For the sake of more meaningful comparison, the hoop forces were plotted against the normalized liquid level (i.e. z/H_L , where z is the elevation measured from the tank bottom and H_L is the Liquid height). The maximum hoop forces were observed at polar coordinate $\theta = 0^\circ$ on the X-axis of the tanks and occurred at $t = 4.2$ s under 1994 Northridge and $t = 5.8$ s under 1995 Kobe earthquake. It can be seen that, irrespective of the tank aspect ratio, the maximum hoop forces were all located at the bottom section of the wall, which shows the higher tendency of the lower levels of the tank wall experiencing bulge if the stresses exceed the yield stress limit. Referring to Fig. 11, the maximum hoop forces increased with increasing aspect ratio, with approximately 20% increase when H/D increased from 0.40 to 0.63, and 25% when H/D increased from 0.63 to 0.95. This is due to the fact that both impulsive hydrodynamic force and hydrostatic force increases with the tank height.

Similar observations could be made for the maximum axial forces, which occurred at $\theta = 0^\circ$ on the X-axis for all tanks (Fig. 12). However, in comparison to hoop forces, the axial forces show more consistent incrementation pattern from the liquid level to the tank base. Referring to Fig. 12, the maximum axial forces increased with the aspect ratio (or the tank height), where 31% and 64% increase was observed when H/D increased from 0.40 to 0.63, and from 0.63 to 0.95, under the 1994

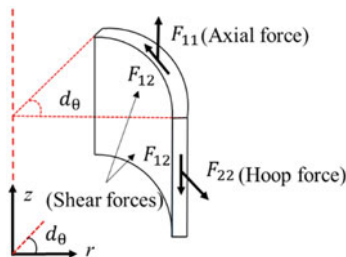


Fig. 10 Illustration of different force components in the LNG tank wall

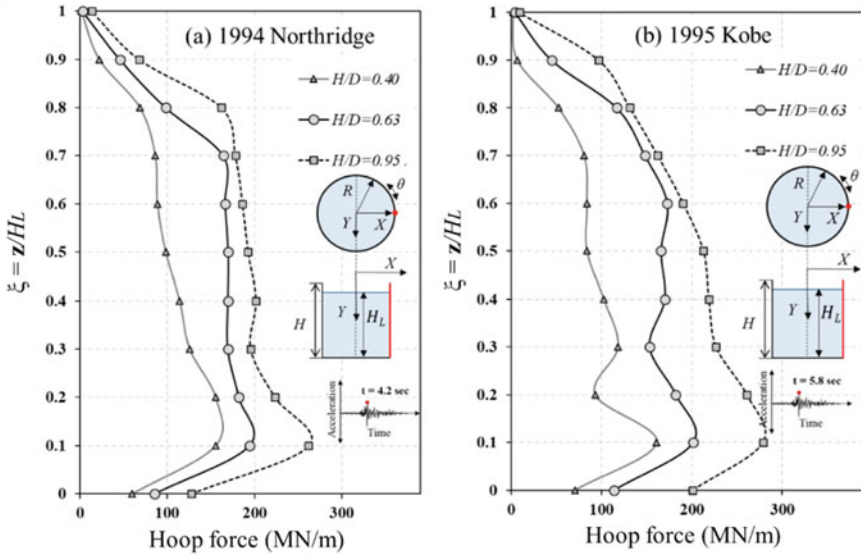


Fig. 11 Distribution of hoop forces in the tank wall at $\theta = 0^\circ$, **a** 1994 Northridge earthquake and **b** 1995 Kobe earthquake

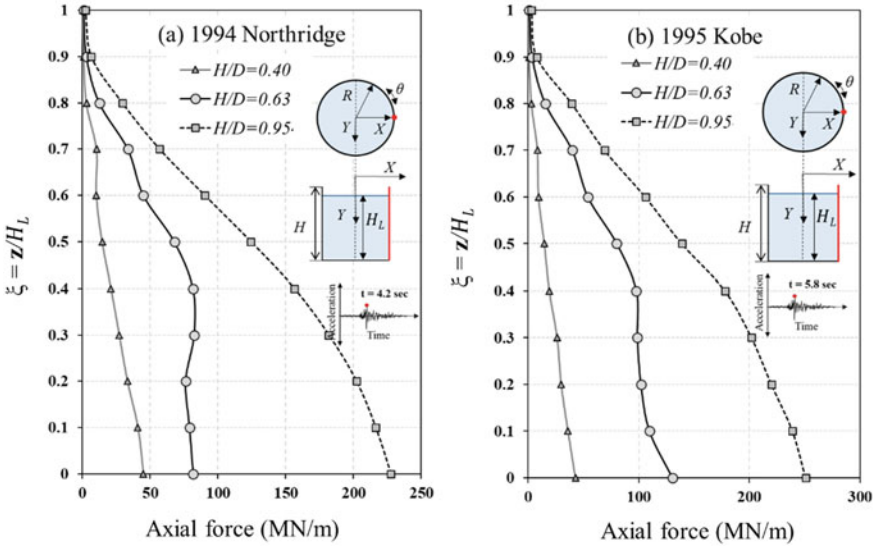


Fig. 12 Distribution of the axial forces in the tank wall at $\theta = 0^\circ$, **a** 1994 Northridge earthquake, **b** 1995 Kobe earthquake

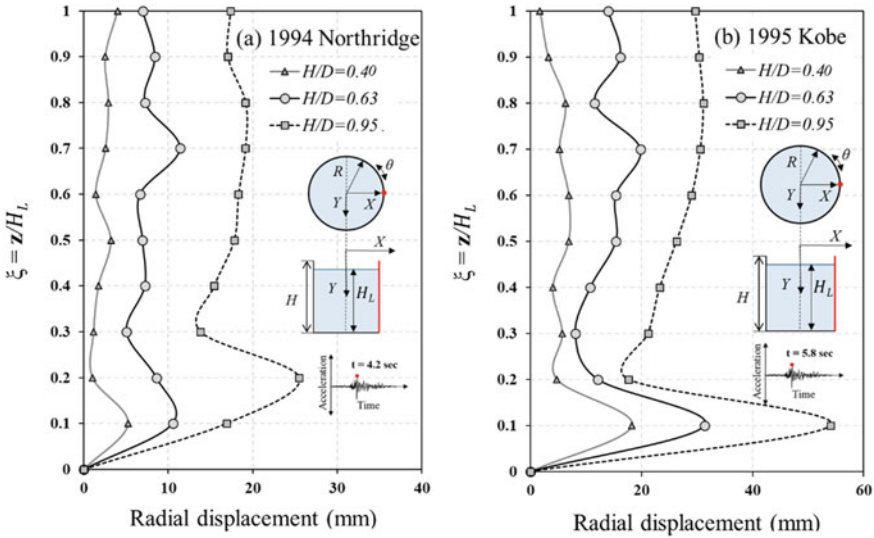


Fig. 13 Distribution of the radial displacement along the normalized liquid height level of the three aspect ratio tank walls at $\theta = 0^\circ$ for **a** 1994 Northridge earthquake, **b** 1995 Kobe earthquake

Northridge, respectively. It can be noted that the corresponding observed amplifications in the maximum axial forces under the 1995 Kobe earthquake were 50% and 60%, respectively.

The combined effects of the axial and hoop forces on the tank response can be observed in the radial displacements predicted along the tanks wall. Figure 13 shows the radial displacement of the wall subjected to adopted earthquake records. In general, the peak radial deformations were observed at the bottom portion of the tanks, while relatively smaller variations at the middle and upper portions of the tanks were observed. These observations are in line with other researchers (e.g. [3]) findings on elephant’s foot buckling failure mode development for tanks. Furthermore, referring to Fig. 13, it can be noted that Tank B with $H/D = 0.63$ showed another peak at the upper portion which could potentially impose the risk of local buckling. This observation is aligned with the reported deformation shape from modal analysis (Fig. 6b) showing bulge shape deformation near the mid-height of the wall.

Interrogating the nonlinear time-history numerical analysis results showed that the developed stresses in board and medium LNG tanks remained below the yield stress limit at all locations under both the 1994 Northridge and the 1995 Kobe earthquakes meaning no plastic buckling. Referring to Fig. 14b, elastic buckling was observed for medium Tank B ($H/D = 0.63$) with inward buckling at the upper portion of the tank walls, which corresponds to the secondary diamond buckling mode. Increasing the H/D ratio to 0.95 (tall tank) raised the damage and failure risk. Referring to Fig. 14c, the Von Mises stresses on the tall Tank A exceed the yield stress limit and the elastic–plastic outward shell bulging at the lower portion of the tank wall (i.e. elephant’s foot buckling) occurred. Figure 15 shows the distribution of the Von Mises

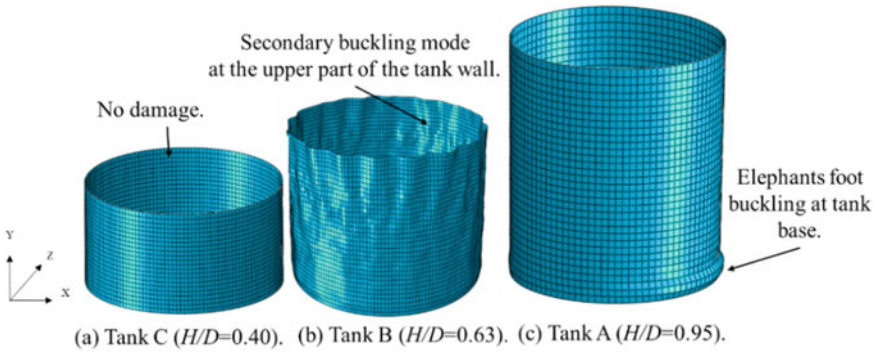


Fig. 14 Damage extend to the LNG tanks, **a** broad Tank C (no damage), **b** medium Tank B (secondary elastic buckling mode), and **c** tall Tank A (elephant’s foot buckling)

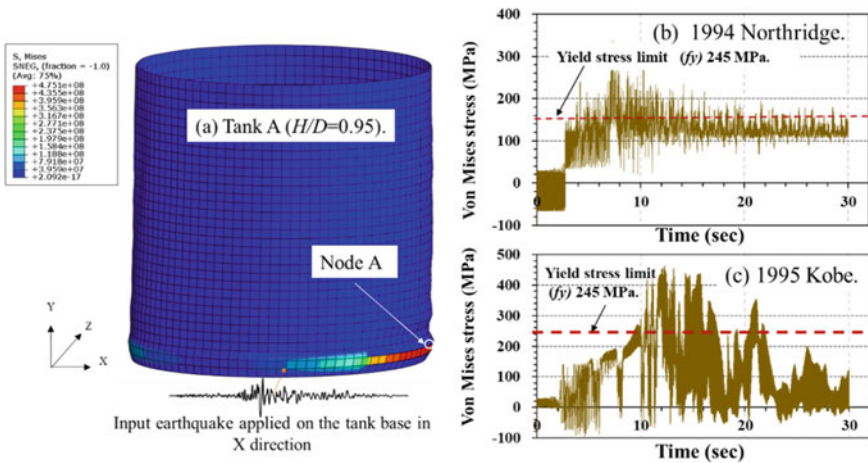


Fig. 15 Formation of the elephant’s foot buckling in tall Tank A ($H/D = 0.95$): **a** distribution of the Von Mises stresses exceeding the yield stress limit near the tank base (i.e. node A), **b** Von Mises stresses (Pa) at node A under 1994 Northridge earthquake and **c** Von Mises stresses at node A under 1995 Kobe earthquake

stresses at the tall Tank A wall together with the time variation of Von Mises stresses for the selected node A near the tank base level, which resulted in the elephant’s foot buckling for tall Tank A.

6 Conclusions

In this paper, the seismic performance of a broad, medium and tall 9% Ni steel LNG tanks with different aspect ratios (H/D) under two strong near-field earthquake ground motions (1994 Northridge and 1995 Kobe earthquakes) were investigated. The modal analysis showed that the deformed shape associated with fundamental mode of tall tank ($H/D = 0.95$) is comparable with a bending mode of a cantilever beam, while for medium Tank ($H/D = 0.63$) the deformed shape captured a bulge formed near the mid-height of the wall. The nonlinear time-history analysis results predicted elastic secondary buckling for the medium tank at the upper portion of the tank wall. The Von Mises stresses exceeded the stress yield limit at the tank base level for the tall tank and elephant's foot buckling (i.e. elastic-plastic buckling) was observed. No damage observed for the broad tank ($H/D = 0.40$).

For the investigated cases, increasing the tank aspect ratio (H/D) from 0.63 to 0.95 (i.e. medium to tall tank) can offer around 20% more storage capacity; however, it increases the base shear forces by 60% and the overturning moments by 50% meaning thicker tank walls are required to meet the design safety requirements (i.e. avoid buckling). The selection of optimum tank ratio particularly in areas with moderate to high seismicity is critical for a safe and economic seismic design.

References

1. Willford M, Sturt R, Huang Y, Almufti I, Duan X (2010) Recent advances in nonlinear soil-structure interaction analysis using LS-DYNA. In: Proceedings of the NEA-SSI workshop, Ottawa, 6–8 Oct 2010
2. Hokmabadi AS, Fatahi B, Samali B (2014) Assessment of soil-pile-structure interaction influencing seismic response of mid-rise buildings sitting on floating pile foundations. *Comput Geotech* 55:172–186
3. Brunesi E, Nascimbene R, Pagani M, Beilic D (2015) Seismic performance of storage steel tanks during the May 2012 Emilia, Italy, earthquakes. *J Perform Constr Facil* 29:04014137
4. Housner GW (1957) Dynamic pressures on accelerated fluid containers. *Bull Seismol Soc Am* 47:15–35
5. Veletsos AS, Yang JY (1977) Earthquake response of liquid storage tank. In: Proceeding of the second engineering mechanics speciality conference. ASCE, Raleigh, pp 1–24
6. Haroun MA, Housner GW (1981) Earthquake response of deformable liquid storage tanks. *J Appl Mech* 48:411–418
7. Malhotra PK, Wenk T, Wieland M (2000) Simple procedure for seismic analysis of liquid-storage tanks. *Struct Eng Int* 10:197–201
8. Christovasilis IP, Whittaker AS (2008) Seismic analysis of conventional and isolated LNG tanks using mechanical analogs. *Earthq Spectra* 24:599–616
9. Zhou Y, Li X, Chen Z (2018) Seismic responses analysis of base-isolated LNG storage tank. In: GeoShanghai international conference. Springer, pp 331–339
10. Virella J, Godoy L, Suárez L (2006) Dynamic buckling of anchored steel tanks subjected to horizontal earthquake excitation. *J Constr Steel Res* 62:521–531
11. American Petroleum Institute (API) (2007) Welded steel tanks for oil storage, API-650. Washington

12. Eurocode-8 (2006) Design of structures for earthquake resistance, part 4: silos, tanks and pipelines. In: European committee for standardization, Brussels, BS EN 1998-4
13. Buratti N, Tavano M (2014) Dynamic buckling and seismic fragility of anchored steel tanks by the added mass method. *Earthq Eng Struct Dyn* 43:1–21
14. Fatahi B, Van Nguyen Q, Xu R, Sun WJ (2018) Three-dimensional response of neighboring buildings sitting on pile foundations to seismic pounding. *Int J Geomech* 18(4):04018007
15. ASTM A36, A19 (2018) Standard specification for carbon structural steel. ASTM International, West Conshohocken, PA
16. Xu R, Fatahi B (2019) Novel application of geosynthetics to reduce residual drifts of midrise buildings after earthquakes. *Soil Dyn Earthq Eng* 116:331–344
17. PEER (2014) NGA-West2 data base. Pacific Earthquake Engineering Research (PEER), University of California. Retrieved from <http://ngawest2.berkeley.edu/>
18. Xu R, Fatahi B (2018) Influence of geotextile arrangement on seismic performance of mid-rise buildings subjected to MCE shaking. *Geotext Geomembr* 46:511–528

Load–Displacement Behavior of Soil–Pile Interaction Under Lateral Action



Thevaneyan K. David and Renga Rao Krishnamoorty

Abstract The usage of pile is very common and in high demand in construction world. However, the cost of design and built of this pile is high. The understanding of the state-of-art of the pile behavior is yet to be fully substantiated especially when the pile interacts with surrounding soil. Substantiating the behavior of soil–pile interaction through fieldwork or laboratory experiment may found to be uneconomical. Therefore, an effort was made to use finite element method to study the behavior of pile interacting with sand and clay. In this study, PLAXIS has been used to study the behavior of soil–pile interaction under lateral load. A 2D finite element analysis was performed on a pile and surrounding soil. The primary objective of this study is to model the soil–pile interaction and to identify the lateral displacement of pile with different types of soils using finite element method. Parametric analysis were attempted to study the effect of varying diameter of pile and soil parameters on the displacement behavior of pile under lateral action. The result shows that indirectly proportionate correlation may exist between the soil physical and pile geometric parameters to the displacements of pile. The result of this study also shows similar effect on the pile displacements qualitatively but varies quantitatively for both sand and clay for various diameters of pile. Stress behavior of the soils interacting with structure was also studied and it yields well with expected behavior.

Keywords Soil–pile interaction · Finite element analysis · PLAXIS · Soil constitutive model · Lateral load

1 Introduction

Deep foundation is an important element that needs careful consideration in designing as well as in construction stages, especially in sand and clay. This type of foundation allows structure to be built upon the soil surface layer and the load was transferred

T. K. David (✉) · R. R. Krishnamoorty
School of Civil Engineering, College of Engineering, Universiti Teknologi MARA (UiTM), Shah Alam, Malaysia
e-mail: tkrishta@uitm.edu.my

from the foundations to a firm deeper soil layer. There are some varieties of deep foundations available such as drilled shaft, driven pile and also caissons. In order to select an appropriate type of foundations; type of soils, expected load effect and ground water level need to be considered. The usage of pile is very common and in high demand in construction world. However, the cost of design and built of this pile is high. Soils are different in their strength and stiffness and its behavior depends on the effective stresses. In this study, single pile foundations with different types of backfill soils were used to substantiate the soil–pile interaction. Substantiating the behavior of soil–pile interaction through fieldwork or laboratory experiment may found to be uneconomical. Therefore, an effort was made to use finite element method to study the behavior of pile interacting with sand and clay. In this study, PLAXIS has been used to study the behavior of soil–pile interaction under lateral load.

While structures are usually satisfactorily modelled with linearly elastic, homogeneous and isotropic materials, modelling of soils is extremely complex as its heterogeneous, anisotropic and nonlinear force–displacement characteristics [1] need to be accounted for. Jaafar et al. [2] has highlighted the need for appropriate material and structural modelling especially for soil–structure interaction of integral bridges (which is a classic case of soil–structure interaction). The finite element method program, PLAXIS, was used in this study as it is known for its advantages which are [3]:

1. Its ability to deal with pore pressure where it used to calculate plastic in undrained soil.
2. Soil–pile interaction where interface stimulate between soil and pile with the friction angle and adhesion different with the friction angle and cohesion of the soil.
3. Better finite element method with soil–structure interaction.
4. Uses advanced constitutive soil models for simulation of its non-linear behavior.

A 2D finite element analysis was performed on a pile and surrounding soil. The primary objective of this study is to model the soil–pile interaction and to identify the lateral displacement of pile with different types of soils using finite element method. Parametric analysis was attempted to study the effect of varying diameter of pile and soil parameters on the displacement behavior of pile under lateral action.

2 Literature Review

The relationship between pile and backfill soil in term of interaction or interface of soil pile is important to be given good considerations. Mohr–Coulomb and Duncan–Chang Hyperbolic models are two soil constitutive models generally used to replicate the soil behavior in numerical models. These two Mohr–Coulomb and Duncan–Chang hyperbolic models can be incorporated with finite element method through PLAXIS 2D Element. The interaction of pile and soil medium is believed to have

Table 1 Parameters of soil and pile in Mohr–Coulomb model [3]

Permeability (m/day)	Friction angle	Cohesion (kPa)	Poisson ratio	Young modulus (MPa)	Density (kNm^{-3})	Model	Material
0.0864	35	1	0.2	90	21	Mohr–Coulomb	Sand
			0.3	20,000	25	Linear elastic	Pile

pertinent effect to the behavior of the structure. The soil properties are very important to be considered in order to gain a good or better analysis result [4].

2.1 Mohr–Coulomb Model

The Mohr–Coulomb model is an elastic-perfectly plastic model and has a fixed yield surface [3], which is the most used constitutive model used in soil medium modeling [5]. It is linearly in the plastic range for the stress strain. This model has five parameters, that is, E and ν for soil elasticity, the friction angle ϕ and the cohesion c for the soil plasticity and the angle of dilatancy ψ [3]. The failure criteria depend most to friction angle and soil cohesion. For the first analysis in the problem, this model is recommended to use because it is a good first order model and trusted into the problem [3]. Moreover, Mohr–Coulomb can be computed practical support pressure for tunnel faces, ultimate load for footings. Table 1 show the general parameters used in Mohr–Coulomb Model.

2.2 Duncan–Chang Model

Duncan–Chang model also known as hyperbolic model is one of the most popular constitutive models used in order to model soil behavior. It is a stress-dependent model where it indicates the nonlinear behavior of soil [6]. This model is able to explain the nonlinearity, inelastic behavior and the stress-dependent of the both cohesive and cohesion less soil. Normally the parameters of the soil are easily obtained from standard tri-axial test [6]. Table 2 show the general parameters used in Duncan–Chang Model.

2.3 Static Analysis

The previous study [6] showed that the Finite Element Method is an appropriate method in order to determine the interface of soil and pile. As the result of the static analysis of FEM, the more accurately model for the interface coefficient showed by

Table 2 Parameters of soil and pile in Duncan–Chang model [3]

Permeability (m/day)	Friction angle	Cohesion (kPa)	Poisson ratio	E_{ref} (MPa)	E_{50} (MPa)	E_{ur} (MPa)	E_{oed} (MPa)	Density (kNm^{-3})	Model	Material
0.0864	35	1	0.2	30,000	45	135	45	21	Hard soil	Sand
			0.2					25	Linear elastic	Pile

Mohr–coulomb Model compared to Hardening-Soil. It is because of the reference graph of Vesic and Meyerhof at the end of the loading where the final extremity of the graph was very closer to the horizontal level and the horizontal settlement can be measure precisely [3].

2.4 Soil Deformation Pattern

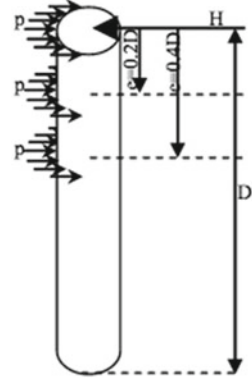
If the bearing capacity is too low, shallow foundation is not capable to use it. Piles should be used to build deep foundations [7]. Applied load on piles can be in the form of axial or lateral load. Most of piles are subjected to lateral load. However, there is also need to assess the behavior piles under simultaneous vertical and horizontal loadings because piles are commonly carried both vertical-horizontal loads [8]. The horizontal displacement of soil in front of laterally load piles has been studied by [8]. As conclusion, they obtained that the horizontal displacement is generally larger than the vertical displacement and these two values decreases rapidly as the distance between piles and soil surface increases. The failure zone is extended and the volume and angle of failure zone increase as the pile loading level increased, but there an ultimate value exist at some loading stages. The sizes of the failure zone decrease as the increases of the ground depth along the pile and the shape of this failure zone is almost conical in three dimensions [9]. However, in this study, lateral load is been considered for a 2D plain strain analysis.

2.5 Lateral Soil Pressure

The most critical part of pile when lateral load applied is the upper part of pile [9] because of its greater deflection and ability of pile to carry higher lateral loads rather than the lower part of piles where carry fewer lateral loads. The lateral soil resistance distributes uniformly between two pile sides in the opposite part of lateral load [10] as shown in Fig. 1.

It is important to study the lateral soil pressure along the pile depth in order to understand and predict which part of piles will carry large soil pressure to prevent from the pile to collapse. Chik et al. [8] studied that the pressure increased with depth in the four condition of soil where the highest value was at the base under dry soil condition. Hajialilue-Bonab et al. [7] stated that they observed the soil particles are located far away from the pile head do not move. It means that the displacement from head of the pile is considers to be decreased as the depth increases. In addition, they observed that the soil grains trail of the pile moves downwards, while the soil grain located in front of the pile move upwards but with small angles. Hajialilue-Bonab et al. [7] concluded that as the depths of pile increases, the displacement at the bottom of the pile can be neglected.

Fig. 1 Distribution of earth pressure subjected to lateral load (after [10])



3 Finite Element Model, Geometric and Material Properties

The interaction between the structures, especially foundation and soil medium is potential to alter the actual behavior of any structure considerably compared to the structure alone. These interactions have been studied using finite element analyses with PLAXIS in an attempt to improve the understanding of the behavior of soil–pile interactions. Modeling techniques and approaches for soil–structure interactions has been vastly discussed by many researchers [4, 6, 11, 12]. In general, the soil behaves as an elastic–plastic material, i.e. initial deformation behavior is elastic deformation and followed by behavior of materials which undergo irreversible plastic deformation without fracture or damage. Soil deformations are basically inelastic since upon load removal, unloading follows an entirely different path from that followed by loading.

Therefore, the choice of soil constitutive model should take into consideration the simplicity and (reliably) realistic representation of real soil behavior. In this study, Duncan–Chang hyperbolic soil constitutive model or hardening soil models were used to replicate the real behavior of soil behind the structure. The Duncan–Chang hyperbolic soil model is incorporated with PLAXIS finite element model. This study is limited to lateral loading analysis only. 2D finite element analyses were performed on the pile structure to investigate the interaction that exists between soil and pile. The interaction between soil and pile was modelled using node to node interaction [10]. The finite element mesh used in the analyses is as shown in Fig. 2.

Since the primary purpose of this study was to understand the state-of-art of the pile behavior and evaluate a conceptual theory, a single type of soil condition was chosen for simplicity. As to eliminate variations in analysis some soil parameters were assumed to be constant. The soil up to 100 m in length on both sides and 30 m in depth was considered and the pile was of 15 m depth with 1 m diameter as shown in Fig. 3. The model was developed after much deliberation and consideration given to convergence and sensitivity study as shown in Fig. 4. This model was then validated qualitatively and quantitatively as shown in Fig. 5 with published works [4, 13].

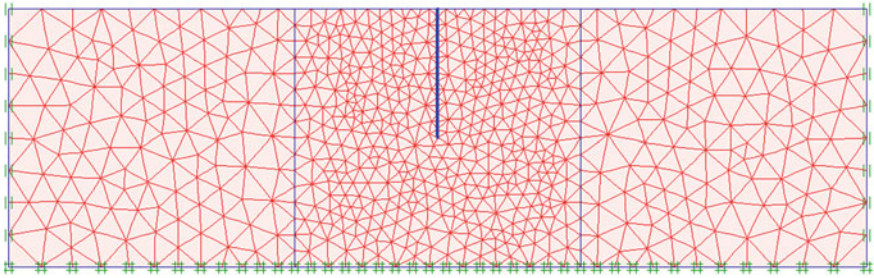


Fig. 2 2D plain strain finite element model meshing

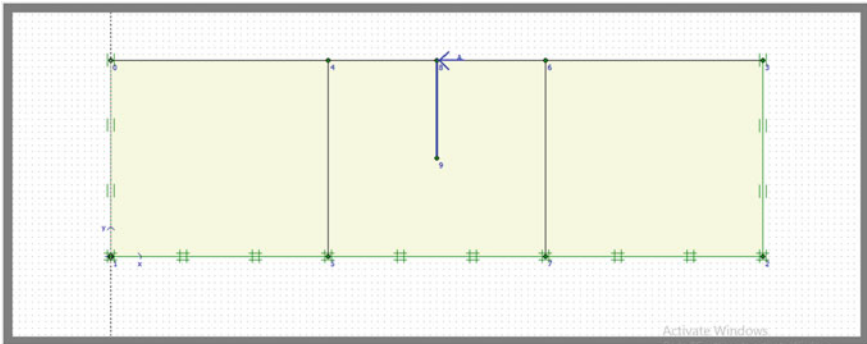


Fig. 3 The size of soil model, pile and lateral load drawn

Fig. 4 Convergence test

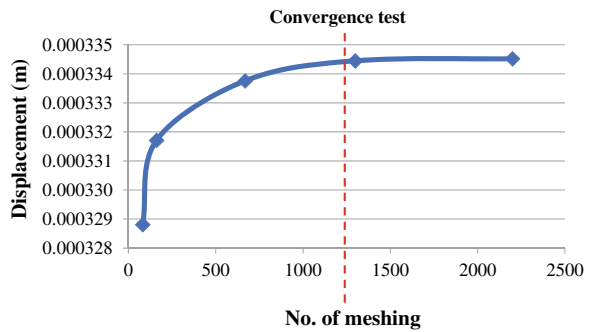


Fig. 5 Load-lateral displacement validation

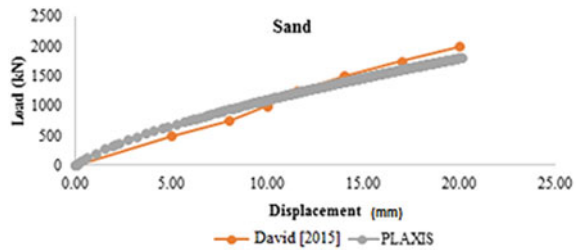


Table 3 Soil and pile properties from previous study [4]

Element			Soil
Material			Sand
Material properties	Linear properties	E (kN/m ²)	50,000
		v	0.35
		n	0.9
	Non-linear properties	P _{am}	101
		E _t	230
		R _f	0.875
		C	21
		φ	19
Element	Properties		
	Modulus of elasticity, E (GN/m ²)	Poison ratio, v	
Concrete pile	35	0.3	

The material properties used for validation purpose was based on previous study [4] and is shown in Tables 3 and 4. Typical structural material was used in this study to replicate the structural behavior of the pile. Table 5 summarizes the soil properties. For validation, finite element model and analysis approach adopted by [7] who investigated pile-backfill soil relationship in stub-type integral abutment bridge was referred. The previous analysis was validated with field test results, investigated by [11, 13].

In [4] analysis, the maximum loading was predetermined and applied in 10 increments. However, in this study the increment of loading was recorded for a predetermined displacement of 20 mm. The load–displacement behavior of the pile was recorded at several intervals. The result of numerical analysis of this study was plotted for load–displacement behavior and compared with the previous study [4] as shown in Fig. 5. The finite element model developed for this study shows a reasonably acceptable result compared to the previous study.

4 Load–Displacement Behavior for Different Types of Soil

In general, the effects of two different types of soils on the pile displacement were studied. Table 5 shows the properties of clay and sand used in this study.

Figure 6 shows the load–displacement behavior of sand and clay. The result indicates that the load–displacement behavior of the soil–pile interaction may be influenced by the stiffness’s of soil. The result shows that sand has higher stiffness than clay where the pile in clay started to fail at less than 850 kN load with 13.6 mm displacement, while sand recorded a displacement of 7.85 mm for 850 kN of load.

Table 4 Clean sand properties used for validating

γ_{unsat} (kN/m ³)	γ_{sat} (kN/m ³)	kx (m/day)	ky (m/day)	E_{50} (kN/m ²)	E_{oed} (kN/m ²)	E_{ur} (kN/m ²)	c_{ref} (kN/m ²)	ϕ (phi) (°)	ψ (psi) (°)
18.4	20	1.0	1.0	50,000	50,000	150,000	3.83	39	9

Table 5 Properties of soils

Properties	γ_{unsat} (kN/m ³)	γ_{sat} (kN/m ³)	kx (m/day)	ky (m/day)	E ₅₀ (kN/m ²)	E _{oed} (kN/m ²)	E _{ur} (kN/m ²)	c _{ref} (kN/m ²)	ϕ (phi) (°)	ψ (psi) (°)
Clean sand	18.4	20	1.0	1.0	50,000	50,000	150,000	3.83	39	9
Clay	15	15	0	0	25,000	25,000	75,000	12	40	10

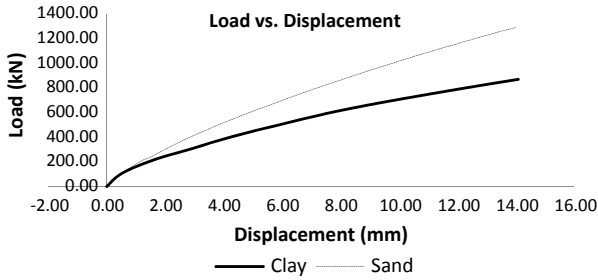


Fig. 6 Load–displacement curve of clay and sand

Maximum loading of 1350 kN was observed for sand at 15 mm displacement rate compared to 850 kN of loading for clay at same displacement rate.

Generally, soil with higher stiffness will exhibit higher strength. Soil with high strength may sustain higher load and increase the capacity of the pile. This can be observed as the lateral load being applied, the pile moves towards the soil, causing an interaction between the pile and the soil, the foundation soil and pile. The piles may move in the same direction or resist the movement. If the foundation soil acts in the direction of the pile movement, it would be beneficial as far as the pile stresses are concerned. The types of foundation soil and the interaction between the piles are important factors affecting the pile stresses.

5 Parametric Analysis

Parametric analysis were attempted to study the effect of varying diameter of pile and soil parameters on the displacement behavior of pile under lateral action. Constant lateral load was applied to the pile to determine the displacement of pile for sand and clay soil condition. Figure 7 directly compares the displacement of pile with diameters of 1.0, 1.1, 1.2, 1.3 and 1.4 m. In general, displacements of pile that computed with different diameters of pile were found to be in good agreement qualitatively despite some numerical error in the analyses. The soil models show similar respond. The load–displacement was recorded at several intervals for predetermined actions of 2100 kN. It was noted that with the 1.0 m diameter of pile records 14.0 mm of displacement at 1300 kN load.

Table 6 shows that the maximum displacement of pile with various diameter for sand and clay soils. It was observed that, pile with 1.4 m diameter shows the smallest displacement comparatively as expected. The maximum loading for diameter of 1.1 m pile falls below 1400 kN load. Zero displacement point falls within the range of 7–8 m from the top of the pile which has a 15 m overall depth.

Displacement of pile in sand records a decrease up to 46% for an increment of 40% in pile diameter. Where else, for clay, pile displacement recorded a decrease up to 55% for the same increment of 40% in pile diameter. This may indicate the

Fig. 7 a Load–displacement curve for pile diameter of 1.0 m in two type of soil. **b** Load–displacement curve for pile diameter of 1.1 m in two type of soil. **c** Load–displacement curve for pile diameter of 1.2 m in two type of soil. **d** Load–displacement curve for pile diameter of 1.3 m in two type of soil. **e** Load–displacement curve for pile diameter of 1.4 m in two type of soil

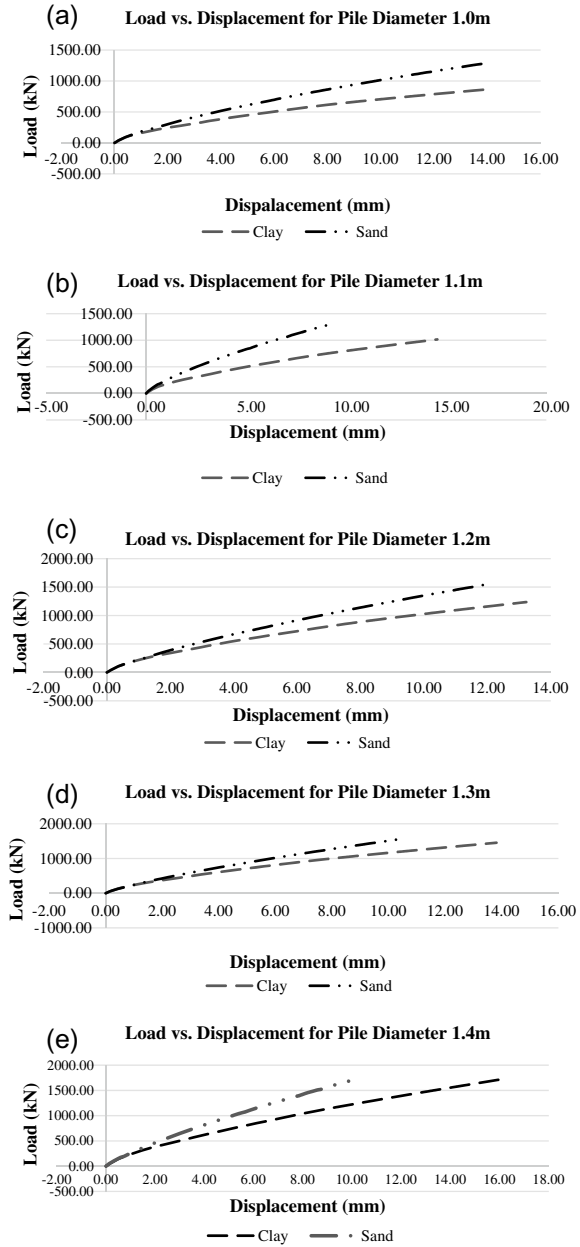


Table 6 Displacement of model at top of the 15 m overall depth pile

Diameter of pile (m)	Displacement of pile	
	Sand	Clay
1.0	7.85	13.60
1.1	5.19	11.00
1.2	5.45	7.48
1.3	4.77	6.36
1.4	4.20	6.10

existence of a correlation between the soil and pile physical properties and diameter of the pile to the displacement of the pile. It may be concluded that the displacement in pile head is influenced by the diameter of pile.

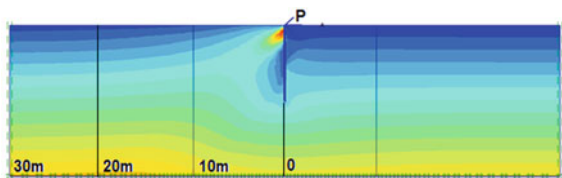
6 Effective Stress Formation

Principal direction or principal stresses represented the effective stresses which are Mean stresses (p') or Relative shear stress. Principle effective stresses are plotted as crosses in the element stress points. In this study, 15-node element been used and be displayed three stress point per element. In this case, the effective stress is equal to the total stress as the water table was not included in this study. Therefore, there was no pore water pressure in the soil geometry model. For this study, the mean shading had been selected as to determine the effective stress in sand as shown in Fig. 8.

The pattern of stresses at different sections were observed for sand; which were at $x = 0$, $x = 10$, $x = 20$ and $x = 30$. Based on Fig. 9, the effective stress at the starting point was higher at the top of the pile. This was because of the force made by the pile cause of lateral load applied. Figure shows the pattern of effective stress as it goes further from the pile. The stress in soil becomes higher at the bottom of the soil as follow the principle stress of the soil. Increase in stresses over the depth is in agreement with general stress behavior of soil. Maximum stress was observed between 0.5 and 2.5 m depth from the surface soil at the face of pile structure. This observation is agreement with the findings of [7, 14].

Generally, the effective stresses are forces that hold the particles in rigid formation. The effective stress of the soil or sand become greater as it goes deeper ground but

Fig. 8 Mean shading of effective stress



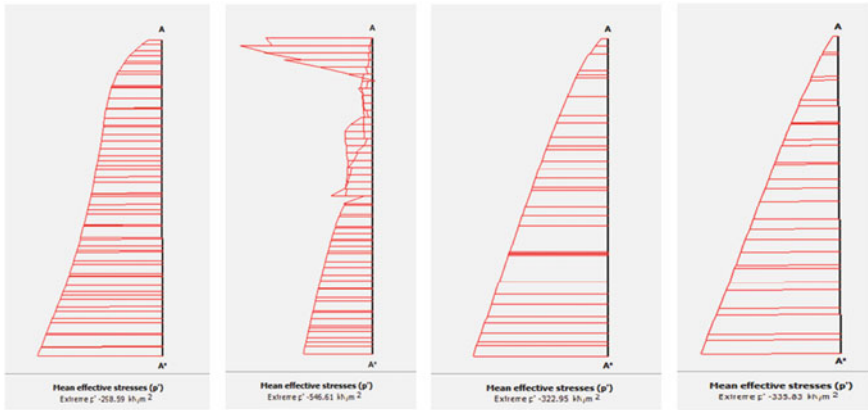


Fig. 9 Section of effective stress at a distance from middle of pile

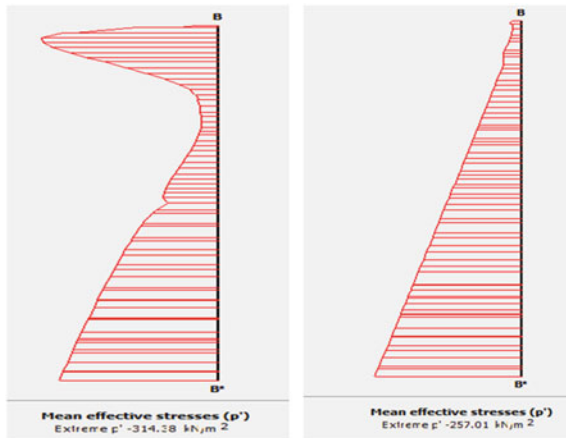
when the forces come from structure, the stress principle will be difference due to the stresses applied to the soil.

6.1 Mean Effective Stress in Sand and Clay

In this case, the effective stress was measured at the surface of the pile where $x = 0$. The result showed for sand and for clay in Fig. 10.

Generally, the pattern of effective stress in both soils; sand and clay shows some good agreement despite the different in mean effective stress quantitatively. In fact, as the depth of pile increases, the stresses increase as well. Therefore, increase in the

Fig. 10 Mean effective stress



diameter of pile may decrease the effective stress of the soil. Simplification in the model developed and no consideration of axial and bending moment in the model may have implication on the results presented here. Therefore, it is recommended that a thorough study considering the axial load and bending moment shall be carried out to further comprehend the stress behavior of soil–pile interactions.

7 Conclusion and Recommendation

The understanding of the state-of-art of the pile behavior is yet to be fully substantiated especially when the pile interacts with surrounding soil. The primary objective of this study is to model the soil–pile interaction and to identify the lateral displacement of pile with different types of soils using finite element method. The soil used in this study was sand and clay which are common in Malaysia geo soil. The geometry model had been made by using finite element software, PLAXIS. The behavior of foundation soil–pile interaction was investigated for lateral loading. The results may indicate that soil with higher stiffness will exhibit higher strength and may sustain higher load by increasing the capacity of the pile by limiting the displacements. Observation on the stress distribution was done to understand the stress behavior of pile. The observation shows that maximum stresses in pile developed at the depth of between 0.5 and 2.5 m from the surface which is in agreement with published works.

There are a few recommendations that could be considered for further studies:

- i. In this study only one constitutive model had been used which was Hardening soil model. Therefore, an advance study can be made as to compare the outcome of other relevant constitutive soil models i.e. soft soil model, modified cam clay model or soft soil creep model.
- ii. In this study, only single pile was analyzed for its load–displacement behavior, this study may further for pile group.
- iii. The effect of cyclic lateral loading on pile displacement can be considered by comparing results of first cycle with several consecutive cycles.
- iv. The seismic load can also be considered for an extensive modeling and analyses.

Acknowledgements The completion of this study would have been not possible if not dependent on the support of my undergraduate students Ahmad Faris Syakirin b. Ahmad Shakiron from the Faculty of Civil Engineering, Universiti Teknologi MARA, Shah Alam. He hence paid equal contribution to the study for which I always feel profound gratitude in my heart.

References

1. Sekhar CD, Roy R (2001) A critical review on idealization and modeling for interaction among soil foundation-structure system. *Comput Struct* 80:1579–1594

2. Jaafar MS, Noorzaei J, Thanoon W (2003) Integral and jointless bridges consideration for secondary effects. In: Seminar on design and construction of integral bridges. Jabatan Kerja Raya, Kuala Lumpur
3. Mahdi Jalali M, Hasan Golmaei S, Reza Jalali S, Borthwick A, Khalegh Ziatabar Ahmadi M, Moradi R (2012) Using finite element method for pile-soil interface (through PLAXIS and ANSYS). *J Civ Eng Constr Technol* 3(10)
4. David TK, Krishnamoorthy RR, Jais IBM (2015) Finite element modeling of soil structure interaction. *J Teknol* 76(8):59–63
5. David TK, Forth JP (2015) Integral pile-backfill soil relationship in stub-type integral abutment. *J Appl Mech Mater* 699:388–394
6. David TK, Forth JP (2011) Modelling of soil structure interaction of integral abutment bridges. *J World Acad Sci Eng Technol*
7. Hajjalilue-Bonab M, Azarnya-Shahgoli H, Sojoudi Y (2011) Soil deformation pattern around laterally loaded piles. *Int J Phys Model Geotech* 11(3)
8. Chik ZH, Abbas JM, Raihan Taha M, Mohammed Shafiqu QS (2009) Lateral behavior of single pile in cohesionless soil subjected both vertical and horizontal loads. *Eur J Sci Res* 29(2)
9. Otani J, Pham K, Sano J (2006) Investigation of failure patterns in sand due to laterally loaded pile using X-ray CT. *Soils Found* 46(4):529–535
10. Zhang L, Silva F, Grismala R (2005) Ultimate lateral resistance to pile in cohesionless soils. *J Geotech Geoenviron Eng ASCE* 131(1):78–83
11. Shamsabadi A, Rollins M, Kapuskar M (2007) Nonlinear soil-abutment-bridge structure interaction for seismic performance based design. *J Geotech Geoenviron Eng* 133(6):707–720
12. Boulanger RW, Curras CJ, Kutter BL, Wilson DW, Abghari A (1999) Seismic soil pile-structure interaction experiments and analyses. *J Geotech Geoenviron Eng* 125(9):750–759. [https://doi.org/10.1061/\(asce\)1090-0241\(1999\)125:9\(750\)](https://doi.org/10.1061/(asce)1090-0241(1999)125:9(750))
13. Rollins KD, Cole RT (2006) Cyclic lateral load behavior of a pile cap and backfill. *J Geotech Geoenviron Eng*
14. Murugan M, Natarajan C, Muthukkumaran K (2011) Behavior of laterally loaded piles in cohesionless soils. *Int J Earth Sci Eng*

Shear Failure of Pile in Clay Due to Soil–Structure Interaction



Thevaneyan Krishta David, Syahrie Safri Peter,
and Renga Rao Krishnamoorthy

Abstract The complex behavior of soil due to its heterogeneous, anisotropic and non-linear in force–displacement interacting with structures, namely pile has complicated the understanding of soil–pile interaction behavior. Efforts have been initiated substantially to fully capture the state-of-art of the soil–structure interaction behavior especially under lateral cyclic actions using finite element modeling and analysis approach. This is an initiative to model the soil pile interaction in clay. Modelling of pile is rather simple and straightforward because of its homogenous properties compared to soil. However, in this study a simplified approach has been taken in modelling both the structure (pile) and soil. A model of a single pile embedded within three layers of clay soil using Mohr–Coulomb soil constitutive model subjected to seismic action is investigated. The objectives of this study are to analyze the embedded pile behavior subjected to standard seismic action and to identify the shear mode failure for pile in clay subjected to seismic action using 2D ABAQUS finite element model approach.

Keywords Soil–structure interaction · Finite element model · ABAQUS · Soil constitutive model

1 Introduction

Strong ground motion due to seismic excitation or so-called earthquake may have great impact on structures and human lives. It originated from beneath the earth and travel to the surface through mediums like soil or rocks. The energy transferred is greater in dense medium compared to less dense medium, in example soil transfer the energy better compared to water. As structures stand on solid ground, it would also experience great deal of seismic wave which may found to be critical and affecting overall performance and sustainability of the structures. These structures tend to

T. K. David (✉) · S. S. Peter · R. R. Krishnamoorthy
School of Civil Engineering, College of Engineering, Universiti Teknologi MARA (UiTM),
40400 Shah Alam, Selangor, Malaysia
e-mail: thevaneyan@uitm.edu.my

fail if the design of the structures were not done considering appropriate and suitable seismic codes of practice. There are some reasons on why the structures are practically vulnerable during this seismic excitation especially during earthquakes. They are such as inadequacy of non-seismic design code and guidelines, low standards of construction due to inattention to local detailing and quality control with high variation in material properties [4]. This have been found to be the problems of structure failures such as schools during Ranau (Malaysia) earthquake in 2015. Structures were design without considering seismic load which lead to failure during the earthquake. After forensic study have been done to study the post-earthquake on the structures, segregation of the concrete and uneven spacing between stirrups were found to be happened in the columns of the school which also proved the lack of quality control during the construction [20].

Consideration of seismic actions in design practices of structures and substructures in Malaysia were not a general choice until the adaptation of Eurocodes as design code of practice. Non-seismic resistance structures/substructures are known to be prone to failure if they were subjected to seismic action. This has been proved occasionally by earthquake events in neighboring country around Malaysia i.e. Indonesia. Up to 2016, there were no significant needs for Malaysia to include seismic action in design consideration, but the damages caused by a minor earthquake in Sabah have changed the perspectives of structure designers. However, there are not enough data regarding seismic activities in Malaysia, especially on how the structures/substructures would behave under seismic excitations, especially with respect to the soil–structure interaction [20].

As been said by Krishta and Forth [14], the interaction between soil–structures, especially foundation pile and soil medium can provide an insight on the actual behavior compared to an independent analysis. Behavior of structures (linear) can be contradicted with soil (non-linear) depending on the loads applied and this create interesting problem to solve since soil and structures are having interdependent relationship [15].

However, attempts to study different parts of soil–structure interactions independently requires considerable assumption and approximation [16]. Therefore, it is necessary to understand the relationship between soil and the most important structural element in such as foundation pile. Efforts have been initiated substantially to fully capture the state-of-art of the soil–structure interaction behavior especially under lateral cyclic actions using finite element modeling and analysis approach on a 1 m diameter pile embedded up to 25 m depth within 3 different properties of clay soil ranging from very soft to very stiff. The material properties were assumed to be homogenous in all direction and parameter of Mohr–Coulomb soil constitutive model being considered. The objectives of this study are to analyze the embedded pile behavior subjected to standard seismic action and to identify the shear mode failure for pile in clay subjected to seismic action.

This study may contribute towards the design consideration using available seismic code of practice. It may also serve as a guideline for retrofitting of an existing structure based on the shear failure mode of pile embedded in soil, generally.

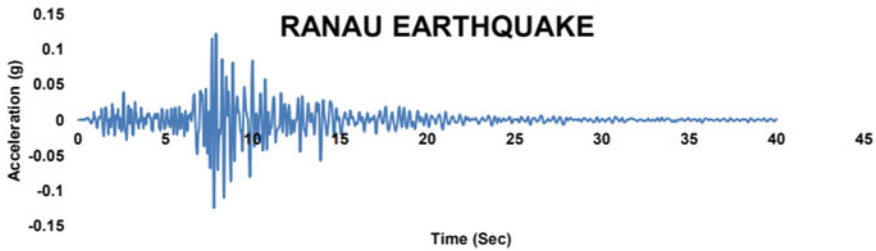


Fig. 1 Time history of Ranau earthquake (2015)

2 Literature Review

2.1 Seismic Hazard

Seismic Hazard Analysis is the process to assess the design parameters of earthquake ground motion at certain location which is peak ground acceleration. The main purpose of Seismic Hazard Analysis is to predict the peak ground acceleration (PGA) and spectral acceleration of bedrock in Malaysia. Recent earthquake of magnitude 6.0 which hit Ranau, Sabah is widely referred. That earthquake has cost several damages to the building surrounding and one of it is a school. The performance of the structures during earthquakes is largely a function of design rather than the material used to construct the structure [18]. Piles is the most common deep foundation found in construction industry of Malaysia. The shear failure mode of pile is to be investigated in this study.

According to the Harith and Adnan [8], the peak ground acceleration (PGA) was predicted 10–2% probability of exceed in 50-year exposure time on bedrock were 0.140 and 0.220 g. The time-history of Ranau earthquake in 2015 in Fig. 1 shows the value of peak ground acceleration during the event is 0.12 g. In more recent study by Harith and Adnan [8], the estimation of the ground motion parameters is based on ground motion prediction equation on rock sites. The estimation done were depending on the shape of seismic source zone and potential. It was concluded that peak ground acceleration at 2% probability of exceedance in 50-years is expected to be at 220 cm/s^2 . Therefore, this study will be using a previous earthquake event that has the same value as recommended.

2.2 Factor Affecting Soil Behavior

The information on the ability of soil to accommodate stress with strains under loading is essential in predicting the behavior of the soil. There is several factors influence the response of a soil element to stress. Some of them are total stress, stress

ratio, pre-water pressure and effective stress, the elasticity, the stiffness, temperature, soil component reaction etc.

There are two categories of main factor that affect the behavior of foundation soil and backfilled materials which are material dependent factors or state dependent factors [1]. The material dependent factors are determined by the nature of the material content, while the state dependent factors are determined by the present and historic state of the effective stress, total stress and pore pressure. Other factors may be considered as secondary factors that affect the behavior of all soil under cyclic loading, which controlled by the main factors identified earlier. Some of the secondary factors identified are as follow;

- i. The amplitude and frequency of the loading
- ii. The rate and magnitude of soil displacement or shear strain
- iii. The rate of pore water dissipating during loading
- iv. The degree of saturation of the soil
- v. The number of total cycles
- vi. The initial state of stress in the soil.

In geotechnical engineering, bearing capacity is the capacity of soil to support the loads applied to the ground. The bearing capacity of soil is the maximum average contact pressure between the foundation and the soil which should not produce shear failure in the soil. Ultimate bearing capacity (Q_f) is the theoretical maximum pressure which can be supported without failure; allowable bearing capacity (Q_a) is the ultimate bearing capacity divided by a factor of safety. Sometimes, on soft soil sites, large settlements may occur under loaded foundations without actual shear failure occurring; in such cases, the allowable bearing capacity is based on the maximum allowable settlement.

2.3 Shear Behavior of Soil

Studies [8] have indicated that when the soil will fail in shear if the footing reaches its ultimate bearing capacity. There are 3 modes of failure namely General Shear Failure (Fig. 2a), Local Shear Failure (Fig. 2b) and Punching Shear Failure (Fig. 2c).

General Shear Failure

Experimental studies have indicated that stiff clay having relative density greater than 70% will have general shear failure [21]. The soil fails after it reaches its peak value (Fig. 2a) and the settlement increases considerably fast. It can be seen by the bulging of sheared soil at the side of the foundation.

Local Shear Failure

Local shear failure occurs more frequently on soft clay because settlement increases with increase in the load value. It commonly happens on soils that have relative density of 35–70%. Figure 2b explains that the failure happens below the toe and

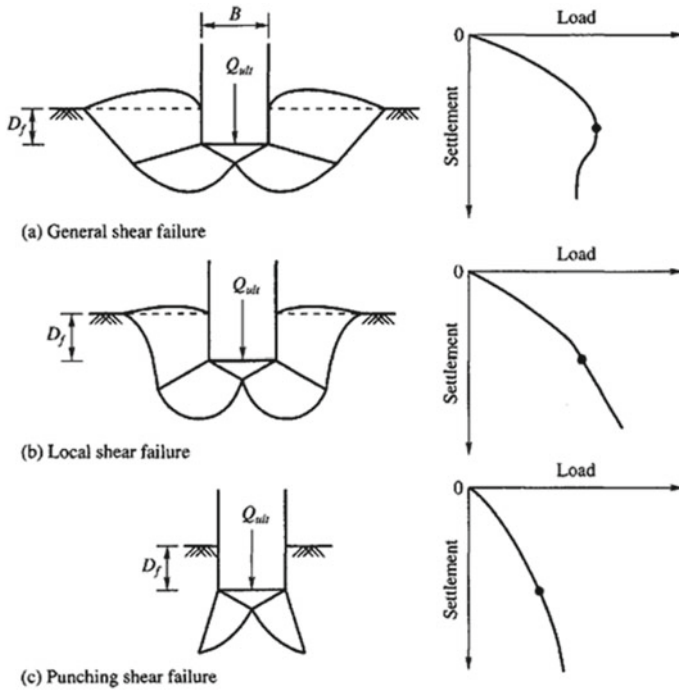


Fig. 2 Mode of shear failure [21]

there is some sign of soil bulging at the surface. The load intensity settlements relationship up to this point is nonlinear.

Punching Shear Failure

For soils that have relative density less than 35%, it has tendency to experiencing punching shear failure. The foundation will consistently penetrate soil without having any displace of soil to the side. The failure surface in soil will not extend to the ground surface. As can be observed in Fig. 2c, the load-settlement shows a nonlinear behavior.

Although vast research works had been done in the last decades, there are some important relationships between variables and factors such as pile size, pile length, soil characteristics and seismic magnitude are still not fully understood [3]. This create a gap that need to be fill especially in Malaysia where in recent years recent seismic activity was detected [20]. Therefore, in this research the correlation between pile, soil characteristics and seismic load are to be investigated.

3 Methodology

3.1 Modelling and Material Parameters

With the advancement of technology, investigation of soil–structure interaction behavior is now possible, and it is an alternative way for investigating the soil–pile relationship. The cost and duration of fieldwork research has led to finding alternative methods that can show good result and help understanding the structure behavior even further [10, 11]. In nineteenth century Jorgenson had proposed a 2D linear frame model [2] and the soil was the treated as linear spring while soil–structure interaction was not considered. The research was further developed by Greimann et al. [6] using 2D frame model with incorporating soil–pile interaction.

A well-defined finite element model is needed to obtain realistic results on the behavior and response of the pile. Although, some aspects need to be simplified or assumed to make this research achievable. Two-dimensional plain strain deformable finite element model was selected in developing this model. This was selected so that it can represent the real situation of the soil–pile interaction. Dimension and model properties are as shown in Fig. 3.

The required materials properties are based on the conversion of SPT N-value to Mohr–Coulomb parameters representing the soil constitutive model and concrete are tabulated in Table 1.

In this study, a typical bored pile having diameter of 1 m and depth of 25 m below the ground level (GL) as shown in Fig. 4 is being modeled. In this study the bored pile is assumed to be vertically perfect and have two-dimensional geometric shape.

Fig. 3 Soil–pile interaction model

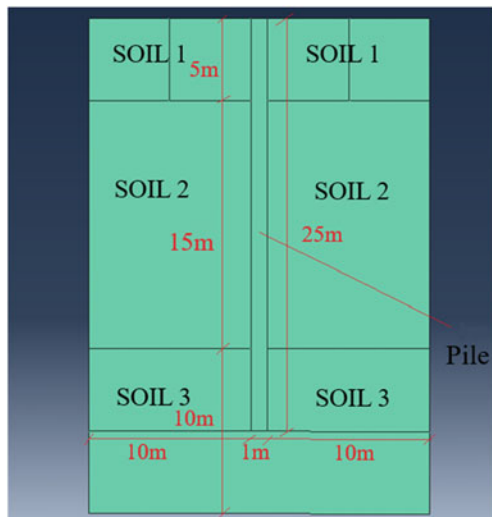


Table 1 Parameters of materials

Parameters	Pile	Soil 1	Soil 2	Soil 3
Density (kg/m ³)	2500	1538	1586	1674
Young’s modulus (kN/m ²)	33,000,000	5000	50,000	100,000
Poisson’s ratio (ν)	0.3	0.2	0.3	0.4
Cohesion (kPa)	–	12	100	192

Fig. 4 Dimension of pile

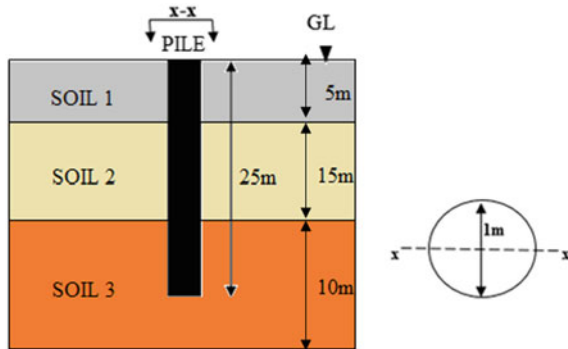


Table 2 Soil parameters

Soil profile	Type of soil	Depth (m)	SPT value
1	Very soft clay	5	0–10
2	Soft clay	15	11–49
3	Stiff clay	10	50 +

Three layers of soil to be considered in this study as shown in Table 2. These soil profiles are adopted from a Malaysia Geotechnical contractor’s bore log report (refer Appendix). These soils are the common type of soil located in Malaysia. The soil profile is to be considered having linear property to simplify this study.

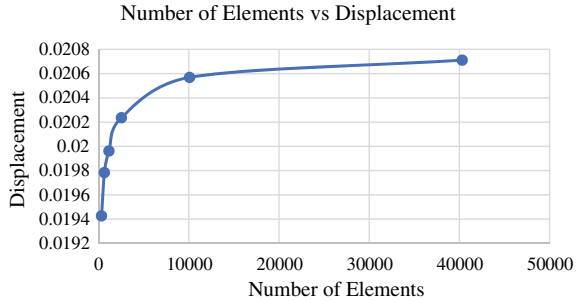
3.2 Convergence Test

There are 2 type of geometric order for meshing and the one been use in this model is 32 quadratics. Quadratic gives less margin of error compare to linear in complex model. The meshing control are structured and having element shape of quad dominated. The mesh was done by planting local seeds size method at edges with several sizing control (Table 3). It is important to find the suitable finite element mesh density for numerical analysis in finite element modelling [17] and it can be done by convergence test. A converged solution is when the increasing number of elements in finite

Table 3 Meshing control

Sizing control value	Number of elements	Displacement
2	315	0.0194
1	630	0.0198
0.75	1147	0.0200
0.5	2520	0.0202
0.25	10,080	0.0205
0.125	40,320	0.0207

Fig. 5 Number of element versus displacement graph



element mesh have insignificant or negligible effect on the results [9]. A very coarse mesh with only 315 number elements and up to a finer mesh with 10,080 elements as shown in Table 3 were tested to find a converging solution. It was observed that, at 10,080 elements and above, the displacement result at pile toe shows insignificant or negligible changes as shown in Fig. 5.

3.3 Dynamics Implicit

Dynamic Implicit procedure was used to find the pile response in soil subjected to seismic action. In this procedure density of each material for gravity load (Table 1) and amplitude of an earthquake are used. The selection of the seismic action was based on Harith and Adnan [8] recommendation with earthquake of 80–140 cm/s² peak acceleration. Therefore, Vrancea earthquake 1940 that meet the recommendation is adopted. The accelerograph record of Vrancea earthquake is shown in Fig. 6 which obtained from European Strong Motion Database [5].

Fig. 6 Accelerograph record of Vrancea earthquake (1940)

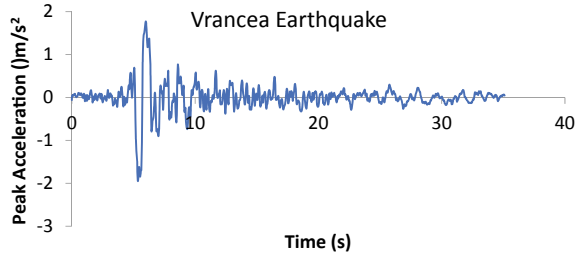


Table 4 Type of boundary condition

Boundary condition	Type
Bottom of the model	Displacement/rotation ($U1 = U2 = 0$)
Left side of the model	Displacement/rotation ($U1 = 0$)
Right side of the model	Displacement/rotation ($U1 = 0$)
Pile settlement	Displacement/rotation ($U2 = 0.025$)
Seismic	Acceleration/angular acceleration ($A1 = 1$)

3.4 Boundary Condition

Boundary condition sets are as stated in Table 4. Default setting (tie) was used for the interaction between soil and pile. This is to represent the sticky behavior of clay soil and as well to enhance the visual shear failure in this model. It may not represent the real pile–interaction; however, it was felt that this would not detract the solution from achieving the objectives of this study.

4 Result and Discussion

For validation of the result, the model was run in static general mode for the settlement of 25 mm to generate the maximum bearing load the soil can sustain with 3 is the value for the factor of safety, and compared with the manual calculation of the pile capacity. For a pile in fine soil the capacity of a single pile can be calculated using the following formula:

Ultimate bearing capacity,

$$Q_{ult} = Q_b + Q_s \tag{4.1}$$

End-bearing capacity,

$$Q_b = c_u N_c A_b \tag{4.2}$$

Shaft resistance capacity,

$$Q_s = \sum \alpha c_u \Delta A_s \tag{4.3}$$

where

$$\text{For clay } N_c = 9, \tag{4.4}$$

$$\Delta A_s = \text{Shaft area} \tag{4.5}$$

α is taken as 0.45 but may vary from 1.0 for soft clay and 0.3 for over consolidated clay (Table 5).

Therefore,

$$\text{Ultimate bearing capacity} = 192 \times 9 + (12 \times 5 \times 1 \times 2) + (100 \times 15 \times 0.47 \times 2) + (192 \times 0.33 \times 5 \times 2) = \mathbf{3891.6 \text{ kN}}.$$

This value is to be compared with action gained from static general procedure at 25 mm of settlement with multiplication factor of safety.

Figure 7 indicates that at a settlement of 25 mm at pile toe, the load is 1567 kN. This value was gained by dividing maximum soil bearing load with factor of safety (2.5) that is normally used in design calculation. Ultimate bearing capacity of the soil is 3917.5 kN. The value from manual calculation and the Abaqus software is not varies thus validating the model.

As for the mode of failure, Fig. 8 shows that this pile is having punching shear failure. This punching shear happens at pile toe. While along the side of the pile, there is some deformation of the soil that increase as it goes to the surface of the

Table 5 Value for α

Pile type	Soil consistency	Undrained shear strength (kPa)	α
Timber and concrete piles	Very soft	0–12	1.00
	Soft	12–24	1.00–0.96
	Medium stiff	24–48	0.96–0.75
	Stiff	48–96	0.75–0.48
	Very stiff	96–192	0.48–0.33
Steel piles	Very soft	0–12	1.00
	Soft	12–24	1.00–0.92
	Medium stiff	24–48	0.92–0.7
	Stiff	48–96	0.70–0.36
	Very stiff	96–192	0.36–0.019

Source Wrana (2015)

Fig. 7 Load against displacement for static general

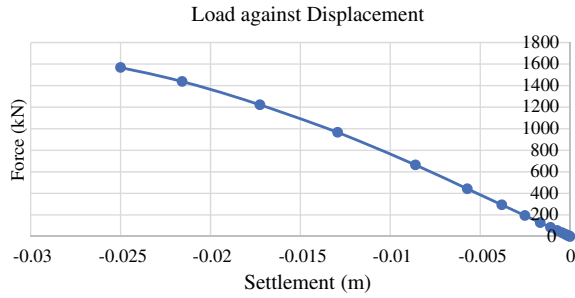
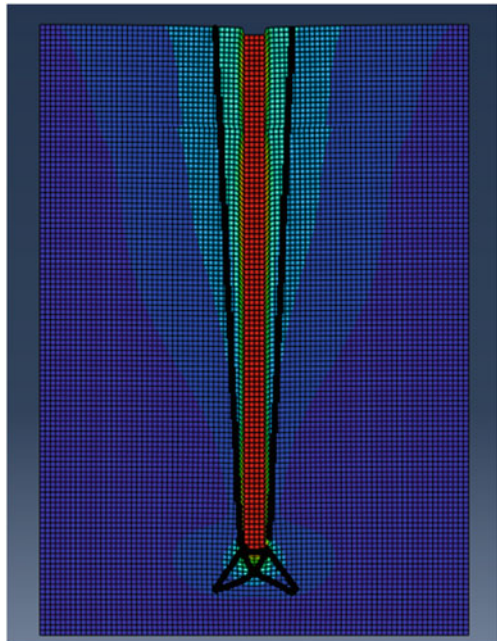


Fig. 8 Deformation of the model in static general



earth. This may indicate that shear failure also happens at the side of the pile and it reduces as it reaches pile toe.

It can be seen in Fig. 9 that the bearing load of the soil does not vary with seismic action. The action with allowable 25 mm settlement is also 1567 kN. This may conclude that soil has insignificant loss of bearing capacity due to the considered seismic action.

Figure 10 shows deformations that represent a bigger scale of general shear failure. More deformation happens on the side of the pile compare to the bottom. This happens because of the push and pulls action of the seismic. The pile propagates to the right and left while subjected to seismic thus create lateral action to the soil. This may create a gap between the pile and soil. With the gap happens, the pile will not have

Fig. 9 Load against displacement for dynamic implicit

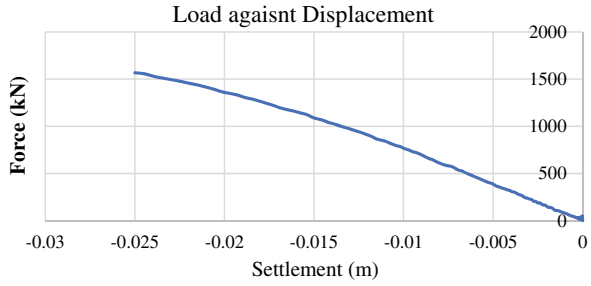
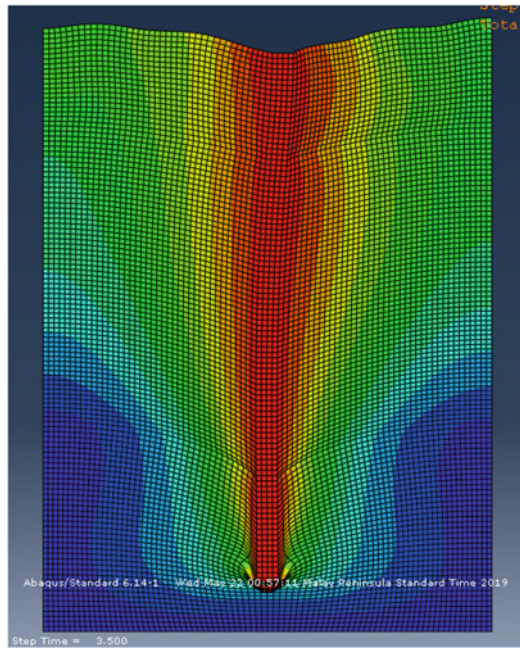


Fig. 10 Deformation of the model in dynamic implicit



friction force to resist the load. This may cause serious damage for friction pile as it depends of the soil friction to sustain action. However, this need to be substantiated with further studies.

5 Conclusion and Recommendations

A simplified yet comprehensive soil–pile interaction model was developed in this study by finite element analysis method approach using ABAQUS software version 6.14. The developed model has produced good result that agrees well with the theoretical formulation of end bearing capacity. The establishment of this model helps to overcome the challenges of determining the behavior of a pile embedded in multilayer

clay. Those challenges were substantiated by producing a result that can represent the real soil–pile interaction behaviors. However, as mentioned earlier, this may find true for clay but extensive further studies may need to be conducted for other soil types.

Parametric studies were carried out by various researchers [1–3] in order to determine the soil–pile behavior and its capacity. This includes several types of soil, different diameter, depth of pile type of loads etc. Not to mention various types of soil model used such as Mohr–Coulomb soil model and Duncan–Chang soil model. Mohr–Coulomb soil model were used to investigate the effect seismic load the behavior of embedded pile in three layers of soil. It can be concluded that the soil end bearing capacity of the pile does not affected by the seismic load.

The result analysis from the model shows a realistic behavior of the pile in the soil. The deformation of soil having pile vertically loaded will only displace downward and having minimal soil displacement to the side of the pile. This shows that pile will have punching shear failure at the pile toe if there is no seismic load applied. The deformation of the soil will change with the introduction of seismic load. From the result it shows that soil will have more sideways deformation compare to vertical displacement. It can be concluded that shear mode failure of the pile having seismic load is similar to local shear failure according to Terzaghi's shear mode failure [19]. Although there are certain aspects that are not included in Mohr–Coulomb soil model i.e. effect of pore water pressure. With this some recommendation that help to understand soil–pile interaction better can be drawn. There is a lot of factor affecting soil behavior such as pore pressure and temperature that are not considered in this study. Each of this factor may give significant impact toward the behavior of the pile. Thus, more research needs to be done to understand soil–pile relationship better. Those conclusions lead to these recommendations;

1. Seismic Condition—Although Malaysia is not yet considered as a country with major earthquake, an extensive study on seismic activity need to be done in the purpose of preparation for any possible occurrence in the future. This research study the behavior of single bored pile in multilayered soil subjecting to seismic loading without considering the moment from structure above. An extensive study can be made with the inclusion of high moment condition from the structure above.
2. Soil Profile—The considered layer of soil in this model are only 3 layers of clay ranging from very soft to very stiff. In real situation, the soil profile a very much varies and may have more than 4 layers and sometimes the arrangement of the soil stiffness is not linear. The soil properties are varying according to the geological place and history. Therefore, soil properties are manipulated variable that enable us to understand deeply about soil to structure relationship.
3. Pile—Pile having different diameter and depth shall be considered. This is due to the loads it carries and the location of sufficient end bearing soil capacity. This research only studies 1 pile size that is 1 m of diameter having 25 m of depth. There may be a significant improvement given by a bigger and longer size of pile. This is because of damping factor can theoretically be produce by it that reduces the seismic wave.

References

1. Anoosh S, Rollins K, Kapuskar M (2007) Nonlinear soil-abutment-bridge structure interaction for seismic performance based design. *J Geotech Geoenviron Eng* 707–720
2. Arsoy S (2000) Experimental and analytical investigations of piles and abutments of integral bridges. Faculty of the Virginia Polytechnic Institute and State University
3. Arockiasamy M, Butrieng N, Munuswamy S (2004) State of the art of integral abutment bridges: design and practice. *J Bridge Eng* 9(5)
4. Cosgun C (2013) Analysis of building damage caused by earthquakes in Eastern Turkey. *Gravevinar* 4:743–752
5. ESD. http://www.isesd.hi.is/ESD_Local/frameset.htm. Accessed 2019/07/11
6. Greimann L, Wolde-Tinse A, Yang P (1987) Finite element model for soil-pile interaction in integral abutment bridges. *Comput Geotech* 127–149
7. Haldar S, Babu GS (2010) Failure mechanism of pile foundations in liquefiable soil: parametric study. *Int J Geomech* 10(2):74–84
8. Harith NSH, Adnan A (2017) Estimation of peak ground acceleration of Ranau based on recent earthquake database. *Malays J Geosci* 1(2):6–9. <https://doi.org/10.26480/mjg.02.2017.06.09>
9. Kachlakev D, Miller T, Yim S (2001) Finite element modeling of reinforced concrete structures strengthened with FRP laminates. Final report SPR 316, Washington, DC
10. Karol RH (1960) *Soils and soil engineering*. Prentice Hall, Englewood Cliffs
11. Kim W, Laman JA (2012) Seven-year field monitoring of four integral abutment bridges. *J Perform Constr Facil* 26(1):54–64
12. Krishta TD, Forth JP (2011a) Modelling of soil structure interaction of integral abutment bridges. *World Acad Sci Eng Technol* 54:769–774
13. Krishta TD, Forth JP (2011b) Soil-structure interaction of integral abutment bridge. In: *Proceedings of international conference on structural engineering construction and management 2011*. ICSEM, Sri Lanka, pp 9–20
14. Krishta TD, Forth JP (2014) Integral pile-backfill soil relationship in stub-type integral abutment bridge. *Appl Mech Mater* 699:388–394. <https://doi.org/10.4028/www.scientific.net/AMM.699.388>
15. Krishta TD, Renga Rao K, Ismachyabadi (2015) Finite element modelling of soil-structure interaction. *J Teknol* 76(8). <https://doi.org/10.11113/jt.v76.5625>
16. Lock RJ (2002) *Integral bridge abutments*. M. Eng. project report, June 2002, London
17. Melosh RJ (1990) *Structural engineering analysis by finite element*. Prentice Hall International, US
18. Skokie (2005) Which is the better material? Concrete or steel? *Building Magazine*. Retrieved from http://www.buildings.com/DesktopModules/BB_ArticleMax. Earthquake-resistant design. *Soil Dyn Earthq Eng* 119:499–507
19. Terzaghi K, Peck RB (1967) *Soil mechanics in engineering practice*, 2nd edn. Wiley, New York
20. Tongkul F (2017) The 2015 Ranau earthquake: cause and impact. *Sabah Soc J* 32(2015):1–28
21. Whitlow R (2004) *Basic soil mechanics*, 4th edn. Pearson Prentice Hall, Singapore

RC Beams Strengthened with Near Surface Mounted Carbon Fiber Reinforced Polymer Plate at Short Term Saltwater Exposure



Amiruddin Mishad, Mohd Hisbany Mohd Hashim, Azmi Ibrahim, Mohammad Hazizi Jamal, and Dicken Anak Baboh

Abstract Fiber Reinforced Polymer (FRP) becomes very popular in construction industry for repairing and strengthening structure because it has high tensile strength, long lasting, high durability, high corrosion resistance, low maintenance and lighter weight. The main objective of the research is to investigate the flexural performance of reinforced concrete beams strengthened with Carbon FRP plate using Near Surface Method (NSM) approach. Three number of specimens of beam with dimension of 125 mm × 300 mm x 1800 mm were prepared and mark as control beam, second beam and third beam. Control beam and second beam were cured at normal environment condition for 28 days, while third beam cured in saltwater solution for 28 days. The second and third beams were strengthened with CFRP plate using near surface mounted (NSM) method All beams were tested up to failure under four-point bending test. 30% of maximum load from control beam were applied to second and third beams to determine the pre-crack for the beams. It has been found that the flexural strength of concrete beam strengthened with NSM by means of CFRP increase by 5–10% and immersing pre-cracked beam in as saltwater affected the strength.

Keywords NSM · CFRP · Flexural performance

1 Introduction

Fiber Reinforced Polymer (FRP) is defined as a composite material made of a polymer matrix reinforced with fibers. The synthetic based FRP is usually made of glass, carbon, aramid, or basalt fibers. Natural fibers extracted from plants or wood such as coconut fibers and jute are also being used as fiber composite. Historically, Bakelite

A. Mishad (✉) · M. H. M. Hashim · A. Ibrahim · D. A. Baboh
School of Civil Engineering, College of Engineering, Universiti Teknologi MARA (UiTM),
40450 Shah Alam, Malaysia
e-mail: amiruddinmishad@uitm.edu.my

M. H. Jamal
Faculty of Engineering, Universiti Teknologi MARA Johor Kampus Pasir Gudang, Jalan
Purnama, Bandar Seri Alam, 81750 Masai, Johor, Malaysia

© The Author(s), under exclusive license to Springer Nature Singapore Pte Ltd. 2022
S. Belayutham et al. (eds.), *Proceedings of the 5th International Conference on Sustainable Civil Engineering Structures and Construction Materials*, Lecture Notes in Civil Engineering 215, https://doi.org/10.1007/978-981-16-7924-7_64

987

was the first fiber-reinforced plastic (FRP) being produced and it was developed by Belgian-born chemist Leo Baekeland in New York in 1907 [1]. Nowadays, Fiber Reinforced Polymer (FRP) becomes very popular in construction industry because it has high tensile strength, long lasting, high durability, high corrosion resistance, low maintenance and lighter weight. Compare to steel reinforcement bar, fiber reinforced polymer has high tensile strength and suitable for repair and strengthening new and old structures.

Uncertain weather and harsh effect from tropical climate may cause the deterioration to the concrete surface. According to [2] due to climate effect such as differences in temperature, water and polluted particle that brought by wind causes the deterioration on building surface. Reinforce concrete surface will deteriorate forming cracks and eventually affect the steel inside it. Besides that, climate change has potential of causing underperformance of a structure and it will lead to failure in the structure, thus it not safe for the user. So, using FRP materials are the alternative way to solve this problem because it can stand under harsh effect of nature and it also not corrodes easily. Carbon fiber reinforced polymer (CFRP) is a composite material that contains various carbon fibers in specific direction and thermosetting resins. CFRP is one of the types of high-performance fiber available for civil engineering application. It has been manufactured by controlled pyrolysis and crystallization of organic precursors at temperatures above 2000 °C.

According to [3] corrosion due to chloride is not suitable for 'Patch repair' technique for treating corrosion because to remove all the penetrated chloride is costly and difficult. Furthermore, chloride that remains on the adjacent side of the affected area will initiate new corrosion circuit. Consequently, cracks on the concrete cover are formed as the steel reinforcement is corroded and swells. Due to this effect, the introduction of FRP in the industry is very worthy of consideration to solve the problem owing to FRP ability to resist corrosion and enhance the performance of the structure. This can give an advantage to the client since the cost of repair and maintenance can be reduced in the long term. Numerous numbers of research are conducted on the use FRP in the structural element such as beam and column to study the advantages of the application especially in the application of Near Surface Mounted (NSM) method [3–9]. Constructed buildings and infrastructures facilities are subjected to deterioration due to many reasons that will result in the long-term effect as the strength decreases over time. Having sustainable construction in mind for the long-term effect, Near Surface Mounted (NSM) method can be used to strengthen the reinforced concrete (RC) members. This will help to ensure that a structure can continuously function for its intended purpose as this method is believed to increase the durability of rehabilitated RC members.

CFRP materials have been known and used worldwide for repair and strengthening deficient and old structure such as bridge and buildings [10]. CFRP is also used in industries such as aerospace, automotive and civil engineering and sports goods. CFRP is also an alternative material used to replace steel reinforcement bar in strengthening and enhance structure such as bridge and building. Compare to steel material, CFRP give more benefit to the structure in term of strength, durability, shear and weight and corrosion resistance. Hence, CFRP become the potential solution to

the problem related to the structure and widely used in strengthening reinforced concrete structures.

Researchers have shown that varying amount of the carbon fiber reinforced polymer (CFRP) was used to strengthen the beams in flexure and control the mid span deflection. CFRP plates or bar is more effective to strengthening of RC beams and by doubling the amount of CFRP content, load carrying capacity can be increased by 97–162% compared to strengthened RC beam [11]. Steel reinforcement bar will loss in strength under excessive loading and adverse environment, which lead to beam failure. Besides that, CFRP can increase shear strength in reinforced concrete. Many existing reinforced concrete members have lack in shear strength and need to be repaired. This happen due to insufficient shear reinforcement in steel area because of corrosion, excessive service load and defect from construction. According to [12], CFRP can improve or increase the load-carrying capacity in shear of RC beam. CFRP is good in shear strength compared to steel and can increase the shear strength of concrete beam.

Corrosion of reinforcing steel causes many structures in adverse environment to experience unacceptable loss in serviceability or safety far earlier than expected and need replacement, repair, and rehabilitation. Uncertain weather and harsh effect from tropical climate may cause the deterioration to the concrete surface. Consequently, if the steel reinforcement bar inside the beam is being exposed through cracks opening, it will eventually corrode and the strength decrease. In addition, crack width of beam will increase the corrosion rate of the steel reinforcement bar in concrete beam. CFRP plate or bar can reduce the problem of corrosion, thus can increase strength and stiffness of the beam [10].

Structural members subjected to harsh environment such as high temperature, wet and dry condition, high humidity, and salt water can reduce the durability of the structure. CFRP have a good long term durability performance in water immersion environments [13]. It means, when CFRP in wet dry cycle condition, the tensile strength and elongation of CFRP does not reduced. According to research done by [14], the flexural strength of beam with CFRP increase significantly when subjected to harsh environment condition such as cycle wet and dry using salt water. Thus, CFRP has higher environmental durability and it suitable to improve the durability performance of the structure.

1.1 Near Surface Mounted (NSM)

This paper focuses on investigating the flexural performance of NSM method for strengthening RC beams that was subjected to saltwater exposure. NSM is a method used for strengthening the flexural members by installing FRP composite materials into the concrete cover in a longitudinal position in a provided groove. CFRP plate is used as the main material for strengthening purposes is the Carbon Fiber Reinforced Polymer (CFRP) plate. NSM method is becoming popular in worldwide application in the where it is commonly used in strengthening the building, car park decks, jetties

and dock-side structures. This method is also widely used in various countries such as north America such as USA, Canada as indicated in Concrete Society design guidelines [4], and Europe [5]. Imjai et al. [6] has shown that pre-cracked beams strengthened with a NSM at the side demonstrated higher capacity at 55%, ductility and energy absorption compared to the control beam. These results indicate an additional flexural reinforcement provided by the SNSM strengthening approach, and to an enhancement of energy absorption capacity in the post-cracking stage. The results also shows that the pre-cracked beam strengthened with SNSM at the tension side of the section shows superior performance over the beam strengthened with SNSM at the compression side.

According to [6, 7], in most cases of studies of NSM, CFRP has been the popular choices used to strengthen concrete structures. Meanwhile, Glass FRP (GFRP) has been used in most applications of the NSM method to masonry and timber structures. FRPs are proven to have great potential for continual application into strengthening of RC structures for its superior properties to be employed in a variety of construction applications. The limitation of FRP composite can be further explored using various new technique such as NSM [7].

The contribution of NSM-FRP in improving the load carrying capacity has been demonstrated in statically indeterminate two-span RC beams was limited by the debonding of the FRP bars at the intermediate support or by the peeling-off of the concrete covers. The improvement of the load carrying capacity for various beam configurations can be seen between 33 and 63% when compared to control beam that is strengthened. However, according to [9] in any strengthening method applied, either internally or externally, high consideration must be given on the durability of the FRP-concrete bond system with epoxy resin under a chloride environment, including its influence on the following components of the system which are epoxy resin, FRP composite and FRP-concrete interface. The study indicated that the tensile strength of FRP may increase after a short-term exposure due to post-curing of the matrix, however, the tensile strength can experience a general decreasing trend when the exposure time is above certain threshold values.

2 Methodology

2.1 Flexural Performance Test

For this research, the flexural strength test is based on [15] that specified on testing flexural strength of hardened concrete specimens. The test only focuses on concrete beam to overcome failure in bending. Flexural bending test are the ability of materials to sustain apply load that is usually applied perpendicular to the axis of the beam until the structure fails or yield is shown in Fig. 1. Three beams were prepared in this investigation which are control beam, NSM strengthened beam cured at room temperature and NSM strengthened beam cured under saltwater for 28 days for

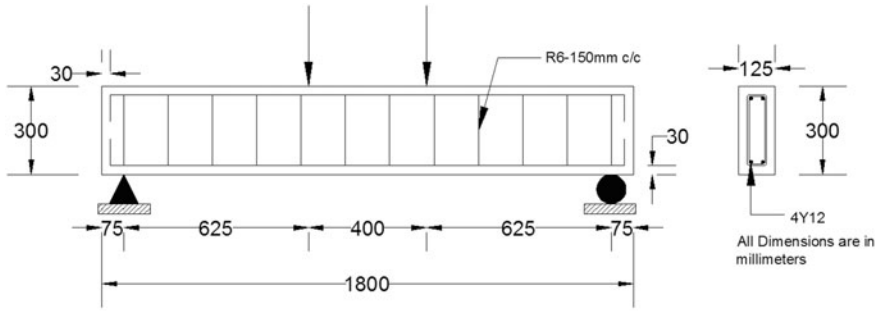


Fig. 1 Four point bending test setup—schematic (above) and actual (below)

all specimens. One (1) litre of water is mixed with forty (40) grams of salt. The purpose of this solution is to simulate a salt water which represents the conditioning of reinforced concrete when immersed into the sea water.

2.2 CFRP Plate Bonded Specimen and Configuration

Carbon fiber reinforced polymer (CFRP) has properties of light weight, high modulus elasticity, high durability, and high strength. Thus, the carbon fiber reinforced polymer plates were used in this experiment to strengthen the reinforced concrete beam. The carbon fiber reinforced polymer (CFRP) plate used has cross-section of 1.2 mm thickness, 50 mm width and 1500 mm length for the size of beam of 125 mm × 300 mm × 1800 mm. The CFRP plates were installed horizontally on the tension side the two specimens of RC beams using near surface mounted (NSM) method. The CFRP strengthened beams were grooved using cutter machined before installing the CFRP plate in the beam. Figure 2 shows the cross-sectional area and dimensional of CFRP plate. Epoxy adhesive was used to glue the CFRP to concrete. The epoxy used as the strengthening material to the grooved concrete surface has a tensile strength of 30 MPa and 2 GPa modulus of elasticity. Adhesive is important bonding material to ensure that the beam bonded system will achieve a perfect bonding.

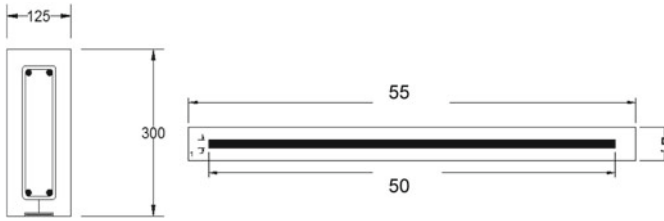


Fig. 2 Cross-sectional area and dimension of CFRP plate

In addition, strain gauges were installed at selected surfaces of the RC beam to determine the strain of concrete, steel and CFRP plate during at application of load to the specimen. Five numbers of strain gauges were used for control beam and eight numbers of specimens used for second and third beam specimens (see Fig. 3). Three strain gauges were installed at the concrete for all beam specimens. The strain gauges located at the center of the beam are associated to deflection at mid span of the beams. Besides that, two strain gauges were installed at the reinforcement bar and located at center of the reinforcement bar. The purpose is to determine the ductility of the steel reinforcement bar in beam specimens. While three strain gauge were installed at CFRP plate for second and third beam specimens to determine the bond strength between concrete and CFRP plate. The reinforcement steel consists of the main and transverse reinforcement with a tensile strength of 460 MPa and 250 MPa respectively. The modulus of elasticity for both reinforcement steel is 200GPa. The

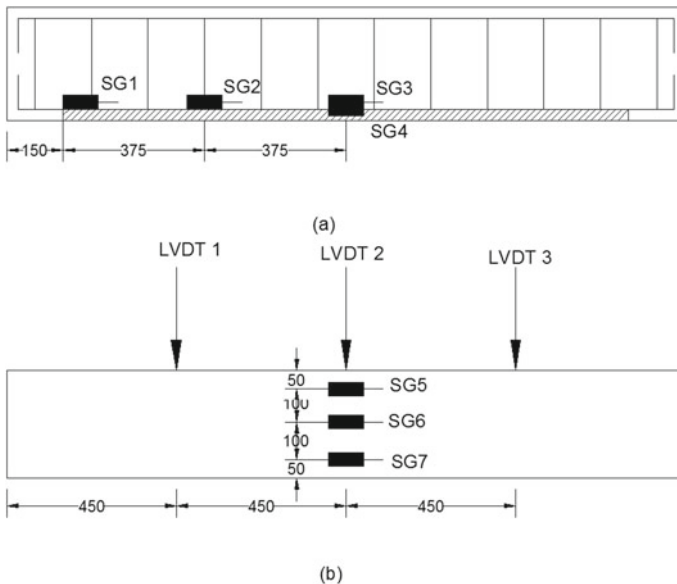


Fig. 3 Arrangement for Strain gauge and LVDT position for experimental setup

longitudinal reinforcement bar used is 12 mm in diameter and the shear reinforcement link is 6 mm @ 150 c/c diameter of steel bar. The CFRP plate used as the strengthening material has a tensile strength of 3000 MPa and 165 GPa modulus of elasticity.

In this study, four numbers of a Linear Variable Displacement Transducer (LVDT) are needed for every test conducted. Three LVDT were placed at bottom of the beam and one LVDT at the center of the top beams. LVDT was used to measure the displacement of specimens during testing. Lastly, LVDT, load cell, and strain gauge were connected to data logger for collecting the result.

3 Results and Discussion

3.1 Ultimate Load Capacity

Three specimens of beam were subjected to four-point bending test as already discuss in previous section. Figure 4 shows the ultimate load capacity of control beam and two beam specimens that strengthened with CFRP plate. In this research, the second beam recorded the highest ultimate load of 126.55 kN, followed by third beam and control beam with 188.84 kN and 113.14 kN respectively.

Strengthening of beam using CFRP plate shows the increment in ultimate load that is 11.85% for second beam that is cured at normal environment condition, while 5% increment of ultimate load for third beam that immersed into saltwater solution. The significant increase in ultimate load shows that strengthening beam using CFRP plate can increase their ultimate load. Thus, it also indicates that CFRP plate can improve the flexural performance of the beam.

Different of curing method also affect the ultimate load for the beam. Second beam that cured at normal environment condition shows higher ultimate load (126.55 kN) compare to the third beam that curing into saltwater solution (118.84 kN). The

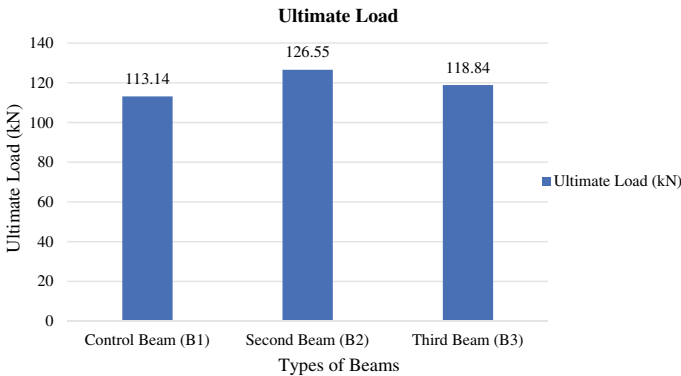


Fig. 4 Ultimate load for beam specimen

different in ultimate load for second and third beam is about 6.5% although both beam were strengthened using CFRP plate. The different can be due to the presence of saltwater that can cause reduction in the tensile strength of steel reinforcement in third beam. Thus, this indicate that saltwater caused corrosion in the steel reinforcement inside the beam that can affect the strength of the beam as whole by means of chloride ingressin.

This results also shows that CFRP plate can increase the load carrying capacity of RC beam after exposure to normal environment condition or saltwater. Besides that, curing method also affect the load carrying capacity of beam. So, CFRP plate can improve the flexural resistance capacity of the strengthened RC beam.

3.2 Load Versus Displacement

Figure 5 shows the results of the load versus displacement. In this study, control beam recorded the highest displacement with 12.52 mm, followed by third and second beam with 9.67 mm and 8.35 mm, respectively. Beam strengthened using CFRP plate shows a reduction in strain that is 33% for second beam that is cured at normal environment condition, while 23% increment of ultimate load for third beam that immersed into saltwater solution. The displacement of the RC beam increase when the load applied increase until the maximum load (peak load) that RC beam can sustain. Although the second and third beam have highest ultimate load compare to control beam, the displacement were smaller compared to control beam because it was affected by the resistance of CFRP plate on the tension zone.

The beam that was cured with saltwater has higher displacement about 14% compared to beam that was cured at normal environment condition. Although normal environment beam has higher ultimate load, the displacement is lesser compared to third beam because the strength of third RC beam been reduced due to the effect

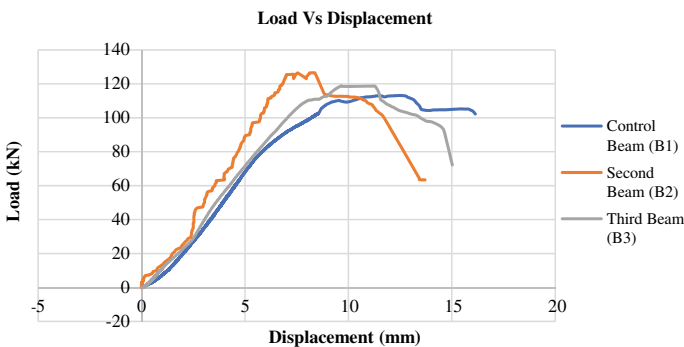


Fig. 5 Load versus displacement distribution

of saltwater to the steel reinforcement. The steel reinforcement was deteriorated by corrosion when exposed to saltwater and it cannot sustain load applied.

The load versus displacement as shown in Fig. 5 indicates that, all the beams behave in elastic state at beginning before the present of micro crack at bottom of beam especially at mid span. Increase of applied load cause the micro crack form into larger crack and when reach maximum load (peak point) the RC beam will fail completely. After reaching peak point, the beam behaved in plastic state until it reaches breaking point.

On the overall, based on relationship between loads versus displacement, the result showed that the increase in strengthening capacity was also associated with an improvement in displacement capacity. The improvement in displacement capacity indicates an increase in stiffness of the strengthening and exposed beam by using CFRP plate compared to the control beam without strengthening. According to research done by [16], the beam strengthened using carbon fiber reinforced polymer (CFRP) showed higher stiffness compared to control beams. The higher the stiffness of the beam, the lower its displacement. Both beams strengthened with CFRP with NSM show lowest displacement, so it means the beams have high stiffness compared to control beam.

3.3 Mode of Failure

All the beam specimens nearly experienced nearly same mode of failure and the types of failure that always occurs on RC beam such as flexural and shear failure. Figures 6, 7 and 8 shows the failure mode of beam specimens.

Flexural failures for the beam always occur at the mid span of the beam. Flexural cracks on the sides of a beam start at the tension face and will extend, at most, up to the neutral axis. For this experiment, the first crack occurred at mid span of the beam before developing and moving further towards the support. Crack widths were greatest at the tension face and was reduce with distance from that face. The flexural failure for second and third beam occurs when less bond between CFRP plate and concrete.



Fig. 6 Failure mode of the control beam

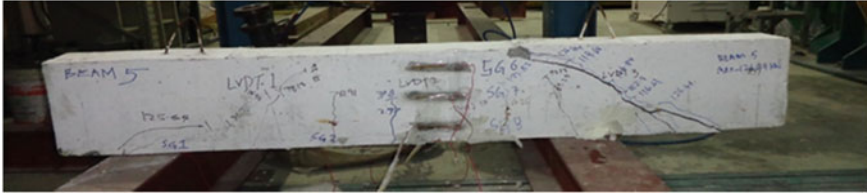


Fig. 7 Failure mode of second beam at normal environment condition

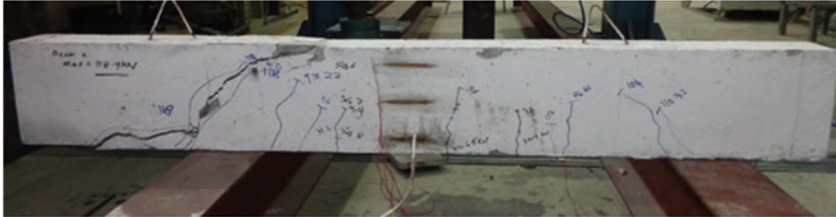


Fig. 8 Failure mode of third beam in saltwater solution

Shear failure occurrence of RC beam more properly called “diagonal tension failure’. In this experiment, shear failure will occur when the beam reach near failure load. When the load applied increase, the micro crack will increase in size and form large crack. Shear cracks occur from the support and move upward to the loading point at the top of the beam. For the second and third beam, shear failure happens when the debonding between CFRP plate and concrete occurred before the beam achieve the failure mode.

From this experiment, control beam showed large crack on the beam upon reaching maximum load compared to second and third beam. Besides that, flexural failure firstly occurred on the beam and when nearly reach failure load, shear failure will form. The presence of CFRP plate in second and third beam delayed the formation of crack on the bonded beams. So, application of CFRP plate through NSM can also enhance the performance the RC beam at tension zone in which meaning that it can improve the structural performance of the RC beam strengthened with CFRP.

4 Conclusion

In this investigation, beam specimens internally bonded with CFRP by NSM were tested using four-point bending test to determine the maximum flexural strength. The maximum flexural load obtained from the experiment for control beam is 113.14 kN, while for second beam is 126.55 kN and the third beam is 118.84 kN. From the result of flexural strength obtained, the beam which is strengthened using NSM and cured at normal temperature shows the highest maximum flexural strength compared to the

control beam and the beam which is NSM strengthened and exposed to saltwater. The beam strengthening with CFRP plate also show higher value of flexural loading capacity compared to beam not strengthened with CFRP plate. Mode of failure that occurs in all beam specimens are flexural and shear failure. The flexural failure occurs at mid span of the beam, while the shear failure happens at the support of the beam. So, it can be concluded that the flexural strength for the beam is different due to curing method and uses of CFRP plate in strengthening of the beam. The present of saltwater also can affect the flexural strength of the beam. Furthermore, application of CFRP plate for strengthening the beam can improve the flexural performance of the old and crack building.

Acknowledgements This work was supported in part by LESTARI under Grant Nos. 600-RMI/DANA 5/3/LESTARI (2/2016). The authors wish to express their appreciation to Universiti Teknologi MARA for providing the facilities and assistance for the successful accomplishment of this research.

References

1. Chandrasekaran (2017) C. 14—Technoeconomic aspects of nonrubber linings—glass, FRP, and lead. In: Chandrasekaran C (ed) Anticorrosive rubber lining. William Andrew Publishing, pp 115–127
2. Hashim MHM, Sam ARM, Hussin MW (2011) The future of external application of fibre reinforced polymer in civil infrastructure for tropical climates region. *Int J Mech Mater Eng* 6(2):147–159
3. Suki N, Hashim MHM, Bakar AA (2014) Flexural performance of RC beams under tropical climate effects. In: Proceedings of international structural engineering and construction: theme: sustainable solutions in structural engineering and construction, Bangkok, Thailand. ISEC Press, pp 9–11
4. Concrete Society (2004) Design guidance for strengthening concrete structures using fibre composite materials. Concrete Society, Camberley, Technical Report 55
5. De Lorenzis L, Teng JG (2007) Near-surface mounted FRP reinforcement: an emerging technique for strengthening structures. *Compos B Eng* 38(2):119–143
6. Imjai T, Setkit M, Garcia R, Figueiredo FP (2020) Strengthening of damaged low strength concrete beams using PTMS or NSM techniques. *Case Stud Constr Mater* 13:e00403
7. Naser MZ, Hawileh RA, Abdalla JA (2019) Fiber-reinforced polymer composites in strengthening reinforced concrete structures: a critical review. *Eng Struct* 198:109542
8. Abdallah M, Al Mahmoud F, Khelil A, Mercier J, Almassri B (2020) Assessment of the flexural behavior of continuous RC beams strengthened with NSM-FRP bars, experimental and analytical study. *Compos Struct* 242:112127
9. Li J, Xie J, Liu F, Lu Z (2019) A critical review and assessment for FRP-concrete bond systems with epoxy resin exposed to chloride environments. *Compos Struct* 220:11372
10. Grace NF, Singh SB (2005) Durability evaluation of carbon fiber-reinforced polymer strengthened concrete beams: experimental study and design. *ACI Struct J* 102(1)
11. Saeed A, Shah A, Nada RA (2006) Strengthening and rehabilitation of concrete structures with carbon fiber reinforced polymers (CFRP). *Earth Space*:1–8
12. Zhang Z, Hsu CTT (2005) Shear strengthening of reinforced concrete beams using carbon-fiber-reinforced polymer laminates. *J Compos Constr* 9(2):158–169

13. Sleeper B, Arnold S, Carr H, Pridmore A (2010) Carbon fiber reinforced polymer (CFRP) as a long-term repair solution. In: Pipelines 2010@ climbing new peaks to infrastructure reliability: renew, rehab, and reinvest. ASCE, pp 1133–1142
14. Toutanji HA, Gomez W (1997) Durability characteristics of concrete beams externally bonded with FRP composite sheets. *Cem Concr Compos* 19(4):351–358
15. BS EN 12390-5 (2009) Testing hardened concrete. Flexural strength of test specimens. Standard by British-Adopted European Standard
16. Barros JA, Fortes AS (2005) Flexural strengthening of concrete beams with CFRP laminates bonded into slits. *Cem Concr Compos* 27(4):471–480

Assessment on Bonding Strength of Cross Laminated Timber Made from Light Red Meranti Manufactured by Vacuum Press Method



M. S. Nordin, M. B. Norshariza, W. C. Lum, N. S. Zainal, and Z. Ahmad

Abstract Cross laminated timber (CLT) is acknowledged to be a high-performance composite material used in the construction industry. The manufacturing of CLT in temperate countries is well established and has been proven to have high mechanical properties compared to solid wood. However, to date, the production of CLT from tropical hardwood is still not available. There are a lot more studies that need to be done particularly regarding bonding quality which contribute to the strength performance of CLT. High temperature and humidity as well as the uniqueness of the tropical hardwood anatomic structure greatly affects adhesion and the mechanical properties of the CLT panels. Thus, the aim of this study is to assess the bonding strength of the CLT panels made in an industrial-scale from tropical hardwood namely, Light Red Meranti. In this study, three and five layer CLT panels with dimensions of 6.5 m length \times 2.2 m width were manufactured by the vacuum press method in accordance with EN 16351. In order to assess the bonding strength, 340 pieces of block samples were taken at various locations from these two panels to represent the entire CLT panel. These block samples were examined under dry and wet conditions in accordance with EN 16351 and EN 14374, respectively. The characteristic value of shear strength was determined based on EN 14358 and wood failure percentage (WFP) was observed and recorded for each block sample. The results show that the bonding performance of five layers CLT was good in dry condition and met the requirement stated in EN 16351 since the characteristic shear strength is ≥ 1.25 N/mm² and the average of WFP is $\geq 70\%$.

M. S. Nordin (✉)

Malaysian Timber Industry Board, Level 13-17, Menara PGRM, No 8, Jalan Pudu Ulu, 56100 Cheras, Kuala Lumpur, Malaysia
e-mail: shaiful.nordin@mtib.gov.my

M. B. Norshariza · W. C. Lum

Institute for Infrastructure Engineering and Sustainable Management, Universiti Teknologi MARA Malaysia, 40450 Shah Alam, Selangor, Malaysia

M. S. Nordin · M. B. Norshariza · N. S. Zainal · Z. Ahmad

School of Civil Engineering, College of Engineering, Universiti Teknologi MARA (UiTM), 40450 Shah Alam, Selangor, Malaysia

Keywords Bonding quality · Cross laminated timber · Tropical hardwood · Vacuum press method

1 Introduction

Utilization of green and sustainable materials in the construction industry has become a global issue. Timber as the oldest construction material fulfils these green and sustainable criteria. However, the scarcity of good quality timber coupled with less timber supply especially from natural forest species results in increasing timber log prices. These factors initiated the Malaysian government through the Malaysian Timber Industry Board (MTIB) to shift from the application of conventional timber structure to the utilization of Engineered Timber Product (ETP). One of the ETP introduced by this body and has the potential to be commercialized in and outside Malaysia is cross laminated timber (CLT).

CLT is a prefabricated multi-layer (at least three layers) engineered panel timber product. The timber grains of each layer are orientated perpendicular to the timber grains of the other layers. The layers are bonded by gluing their surfaces together with an adhesive under pressure for a period of time [1]. These layers' orientation coupled with the appropriate manufacturing process according to relevant standard make this product stronger and provide good rigidity and stability. CLT is used as a load-bearing panel for walls and floors. These panels are easily assembled on site to form multi-story buildings, improving construction and project delivery time, reducing costs, and maximizing efficiency on all levels.

Generally, two manufacturing methods are used to produce CLT which are hydraulic and vacuum press method [2]. The suitability of manufacturing method selection depends on the bonding pressure required for that particular CLT timber species [3]. The hydraulic press method is able to provide higher bonding pressures between 0.10 and 1.00 N/mm² or greater. Meanwhile, the vacuum press provides slightly lower bonding pressures within ranges of 0.05–0.10 N/mm² [4].

In CLT production, the suitable bonding pressure is an important parameter which affects the bonding integrity, aside from timber density, type, and quantity of adhesive applied. Bonding integrity between laminations constitutes a basic prerequisite to the compound effect of the assembly, and also produces better strength of the CLT panel [5]. In the case of one or more weak bonds or even delamination, the load capacity of the assembly drops to a fraction of the intact cross-section. Some locally weak bond-lines may be tolerable for spacious plate-type products. However, the highest degree of bond performance is required throughout to ensure the short and long-term safety and serviceability level [6].

Several studies have been conducted to assess the bonding performance due to durability under serviceability level [7, 8]. Limited information on bonding performance has been reported under dry and wet conditions for CLT and other laminate products. According to Gong et al. [8] the block shear strength of CLT was higher in dry condition compared than that in wet condition. The strength of wood decreased

under higher moisture content which is located below the fibre saturation point. In terms of the wood failure percentage (WFP) assessment, the higher percentage is present in wood categorized under the dry condition. Davalos et al. [7] reported the similar findings in their study for other lamination product.

Different standard testing procedures for determining the bonding integrity between the laminations have been established based on the determination of local shear strength and wood failure percentage (WFP) according to the standards such as [9–13]. In [12], the requirement value for bonding integrity is set as the characteristic shear strength and must be $\geq 1.25 \text{ N/mm}^2$, where the shear strength of each glue line is at least 1 N/mm^2 . However, WFP for the bonding strength of glue lines between crosswise bonded layers is not mentioned in this standard. Hence, in this paper, the requirement value for WFP is referred in accordance to [14] which states the average of WFP must be $\geq 70\%$.

The bonding integrity of the CLT panels made from Malaysia timbers is less known since this product is relatively new in Malaysia. To date, the application of CLT as a structural building produce has not yet been reported and remains in the beginning phase. Few researchers [15, 16] have studied the mechanical properties of CLT using Malaysian tropical timbers namely Sesendok (*Endospermum* spp.) and plantation timber namely *Acacia mangium*. However, both productions are based on laboratory scale testing and provide limited data on the bonding performance.

In order to commercialize the CLT panel using Malaysian tropical hardwood, the manufacturing process must comply with manufacturing standards. Bonding integrity is the first property to be measured for this material as it will affect other strength characteristics such as bending, compression and tension. Therefore, this paper focuses on the bonding integrity of CLT panels made from tropical hardwood, namely Light Red Meranti (*Shorea* spp.) which is categorized under Light Hardwood in *100 Malaysian Timber* [17] and Strength Group 6 (SG6) in the Malaysian Standard [18]. The CLT panels were produced using the vacuum press method since the density of this timber species is considerably low. In addition, to incentivize the production of CLT in Malaysia, the vacuum press method is seen as more suitable and viable since the operation cost is rather affordable compared to the hydraulic press method. The shear strength and WFP values for this CLT were assessed by the block shear test under two different serviceability level which are dry and wet.

2 Materials and Method

2.1 Materials

Light Red Meranti (LRM) with the air-dry density of $385\text{--}755 \text{ kg/m}^3$ has been chosen to manufacture the CLT panel with two different layers (3 layers and 5 layers). These panels were produced in industrial-scale at the CLT factory in Italy with the dimension of $6.5 \text{ m length} \times 2.2 \text{ m width}$ using One-part Polyurethane (1K-PUR) adhesive. This

study focused on the bonding performance of CLT using block shear test under two different conditions which are dry and wet.

2.2 Production of CLT Panel

Solid sawn timbers made from LRM were prepared with the size of 135 mm width \times 35 mm depth \times 1500 mm length. The solid sawn timbers were then graded visually in accordance with [19], Specification for visual strength grading of tropical hardwood timber under Hardwood Structural Grade (HSG). Finger joints were profiled in a clear wood area with approximately 20 mm finger lengths. The joints were then applied with the one component Polyurethane (1K-PUR) adhesive. Finger joints in these sawn timbers were aligned and suitable pressure was applied at the joints to produce lamella. After that, this lamella was cut into approximately 6 m lengths and stacked prior to the planing process. Lamellas were planed into 130 mm width \times 33 mm depth \times 1500 mm length. The planing process was conducted on all four sides of the lamella in order to provide a smooth timber surface for better bonding. The moisture content of the lamella was measured and recorded in between 8 and 13%. For the vacuum pressure method, a groove is required at every lamella and located at the soffit of the layer. This groove is provided in order to reduce the cupping and cracking at the lamella during manufacturing processes. For LRM CLT, the groove geometry provided in lamella is 3 mm width \times 6 mm depth.

The first layer for the panel was arranged in the longitudinal direction from a single lamella without edge bonding. This assembly was conducted on a vacuum pressure bed. The first layer of the panel was applied with the Polyurethane adhesive at one side surface. The second layer was assembled in the transverse direction after the first layer was applied with adhesive. A similar process was repeated in order to obtain 3 and 5 layers of LRM CLT panel. The panel was pressed using vacuum pressure machine within the suitable time period. The CLT panel was conveyed to a machining station where a multi axis numerically-control machine cuts out an opening for windows, doors, splices and other required parts. Figures 1, 2, 3 4 and 5 show the manufacturing of CLT made from LRM.

Fig. 1 Finger-jointing



Fig. 2 Lamella assembly
(longitudinal)



Fig. 3 Adhesive spread

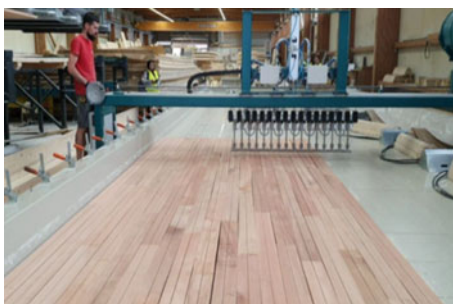


Fig. 4 Lamella assembly
(cross-layer)

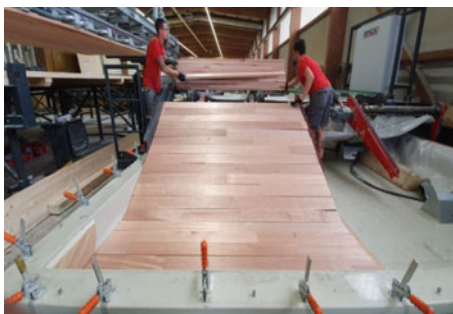
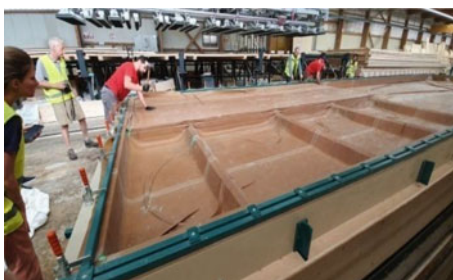


Fig. 5 Vacuum press
method



2.3 Block Shear Test

Samples were prepared according to [12]. Samples with 40 mm width and length were taken from the full thickness of the CLT panel. Samples for this study were cut to represent the entire CLT panel which were located at the top, middle, bottom, left and right of the panel. The sample was then placed in the shearing tool and the glue lines were loaded by self-adjusting bearings in the direction of the timber grain. Two different service conditions were applied in this study (dry and wet condition).

The treatment for block shear under the wet condition was conducted in accordance with [14]. The specimen was submerged in boiling water for 4 h and dried in a ventilated drying oven for 16 h at a temperature of 60 °C. The process followed by immersing the sample again for 4 h in the boiling water before being cooled by room temperature water for 2 h prior to testing.

The evaluation of the shear strength value was more complex for the specimens produced from the vacuum press method, wherein the individual grooves might cross in a bonding line. According to [12], the shear force must be applied in the direction of the bonding line. However, if there was a groove or a butt joint in the bonding line, an effective width was determined by subtracting the cavity width, which results in an effective shear strength. Figures 6, 7 and 8 presents the test preparation for block shear.

The shear strength was determined using Eq. 1. For the characteristic strength value, $f_{v,k}$, the value was calculated according to [20].

$$f_v = k \frac{F_u}{A} \quad (1)$$

where;

- F_u is the ultimate load (in N).
- $A = bt$ is the sheared area (in mm²).
- b is the width (in mm).

Fig. 6 Measuring the sample

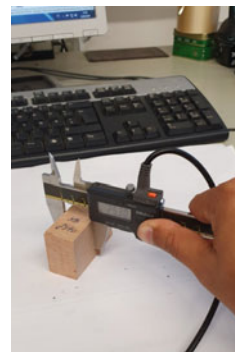


Fig. 7 Sample position during testing



Fig. 8 Sample after block shear test

k factor, $k = 0.78 + 0.0044t$. k modifies the shear strength for sample in the case of length in the grain direction of sheared area is less than 50 mm.

Besides the shear strength, the WFP was determined by visual assessment. In this assessment, a rough surface determined by higher amounts timber fibre on the glue line translates to a higher WFP. Additionally, in cases where the surface appears white in colour (due to the PUR adhesive used), the glue line is recorded as failure of the adhesive. The value of WFP was determined by estimating the area of timber fibre or adhesive marked from the illustrated grid lines on the timber surface (Figs. 10 and 11). Figures 9, 10 and 11 shows the visual assessment of wood failure percentage for 3 layered of LRM CLT panel.



Fig. 9 Dry sample for a 3 layered of LRM CLT

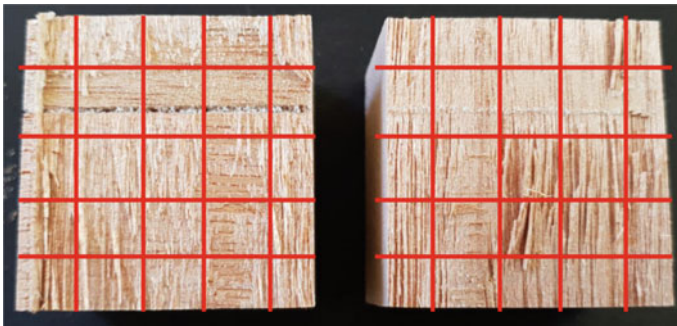


Fig. 10 Wood failure percentage was estimated as 70% at the 1st layer of the sample



Fig. 11 Wood failure percentage was estimated as 10% at the 2nd layer of the sample

3 Results and Discussion

3.1 Shear Strength Properties

The data obtained from the tests were used to calculate the characteristic values of every sample. The mean value, standard deviation, coefficient of variation, and minimum values are summarised in Table 1.

Table 1 shows the shear strength between CLT comprised of 3 and 5 layers. The mean shear values of all the tested samples range from 1.88 to 2.89 N/mm². The mean shear values obtained in this study are comparable to those values reported by [21] which found out that the mean shear strength of Spanish Radiata Pine (*Pinus radiata* D. Don.) ranged from 1.81 to 2.05 N/mm². The mean shear strength of 3 layers CLT is slightly lower compared to 5 layers in both serviceability level of dry and wet. In dry condition, the percentage of difference in between 3 and 5 layers is 13%. Meanwhile, for wet condition, the percentage of difference is presented as 9.6%. In the comparison in between dry and wet condition for 3 and 5 layers, dry condition shows a better result with the percentage of difference 25% and 28%, respectively. The result is similar as the study reported by [22] where the samples with 1k-PUR in dry condition showed a good performance in shear. Coefficient of variance (CoV) for all samples ranges from 21 to 32% which are moderate to high but still considerably acceptable since timber itself has a wide range of variance. Besides that, the testing condition (dry and wet) and number of layer (3 layers and 5 layers) also further increase the heterogeneity of the tested samples.

Based on the requirement stated on [12], the shear strength (f_v) of each glue line must be at least 1 N/mm². In this study, the minimum shear strength of 3 and 5 layers CLT for a dry sample has complied with the requirement set by the standard with a shear strength value of 1.11 N/mm² for 3 layers and 1.36 N/mm² for 5 layers. Although the minimum shear strength value for wet condition did not meet the requirement stipulated in the standard, the mean shear strength value for wet condition exceeds the required value. The characteristic shear strength ($f_{v,k}$) derived from [20],

Table 1 Statistical evaluation of the shear strength results for the for the Light Red Meranti panel from industrial vacuum press

Item	3 layer		5 layer	
	Dry	Wet	Dry	Wet
Number of specimens	11	7	89	63
Mean value [N/mm ²]	2.51	1.88	2.89	2.08
Standard deviation [N/mm ²]	0.79	0.434	0.61	0.54
Coefficient of variation [%]	31.6	23.1	21.0	26.0
Minimum value [N/mm ²]	1.11	0.94	1.36	0.35
Characteristics value according to EN 14358 (2016) [N/mm ²]	1.22	1.09	1.93	1.03

Table 2 Statistical evaluation of the effective shear strength results for the for the Light Red Meranti panel from industrial vacuum press

Item	3 layer		5 layer	
	Dry	Wet	Dry	Wet
Number of specimens	11	7	89	63
Eff. mean value [N/mm ²]	2.59	1.92	2.99	2.15
Eff. standard deviation [N/mm ²]	0.81	0.45	0.64	0.57
Eff. coefficient of variation [%]	31.4	23.6	21.4	26.3
Eff. minimum value [N/mm ²]	1.15	1.00	1.36	0.35
Eff. characteristics value according to EN 14358 (2016) [N/mm ²]	1.27	1.12	1.97	1.06

shows that only dry sample of 5 layers CLT (1.93 N/mm²) has complied with the requirements stated in the standard with the $f_{v,k} \geq 1.25$ N/mm².

Table 2 shows the effective shear strength between 3 and 5 layers CLT. The effective mean shear strength of the CLT demonstrates a similar trend as in Table 1 where 3 layers CLT is slightly lower compared to 5 layers in both wet and dry serviceability levels. In the dry condition, the percentage of difference in between 3 and 5 layers is 13%. Meanwhile, for wet condition, the percentage of difference is presented as 11%. In the comparison between dry and wet condition for 3 and 5 layers, the dry condition shows a better result with the percentage of difference of 26% and 28%, respectively.

Based on the requirement stated on [12], the shear strength (f_v) of each glue line must be at least 1 N/mm². The result shows the effective minimum shear strength of 3 and 5 layers CLT met the requirements of the standard except for the case of the 5 layer wet sample which achieved an effective shear strength value of 0.35 N/mm². Although the shear strength value was 0.35 N/mm², which is less than the minimum requirement given in [12], the overall performance of the CLT panel still fulfilled the requirement as stated in the standard as the mean value for the panel was 2.15 N/mm². The effective characteristic shear strength ($f_{v,k}$) derived from [20], shows a dry sample of CLT 3 layers with a value of 1.27 N/mm² and a wet sample of CLT 5 layers with a value of 1.97 N/mm² and complied with the requirements of the standard which the $f_{v,k} \geq 1.25$ N/mm².

3.2 Relationship of Shear Strength Properties and Wood Failure Percentage

The requirement of shear strength (f_v) stated on [12] for each glue line is at least 1 N/mm², though, no requirement for WFP was stated. In this particular case, the WFP was referred to [14] which is intended to assess the bonding integrity of structural laminated veneer lumber (LVL). The WFP of the specimens must be greater than 70% as stated in the standard.

In order to determine the relationship of shear strength properties and WFP, a graph based on both requirements of the standard [12, 14] was drawn and illustrated as in Figs. 12, 13, 14 and 15. Figures 12 and 13 show that the first lamination of the 3 layer CLT has good bonding performance since most of the samples obtain more than 70% of WFP. While 5 layer CLT as illustrated in Figs. 14 and 15 has good bonding performance quality in the first, second, and third laminations for the dry condition. In wet conditions, 5 layer CLT has a good bonding performance for the first and

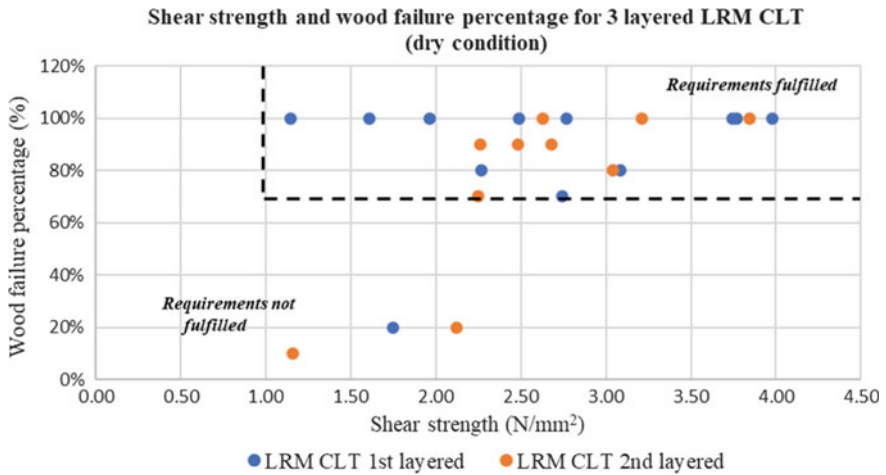


Fig. 12 Relationship of shear strength properties and wood failure percentage for light red Meranti CLT for a dry condition

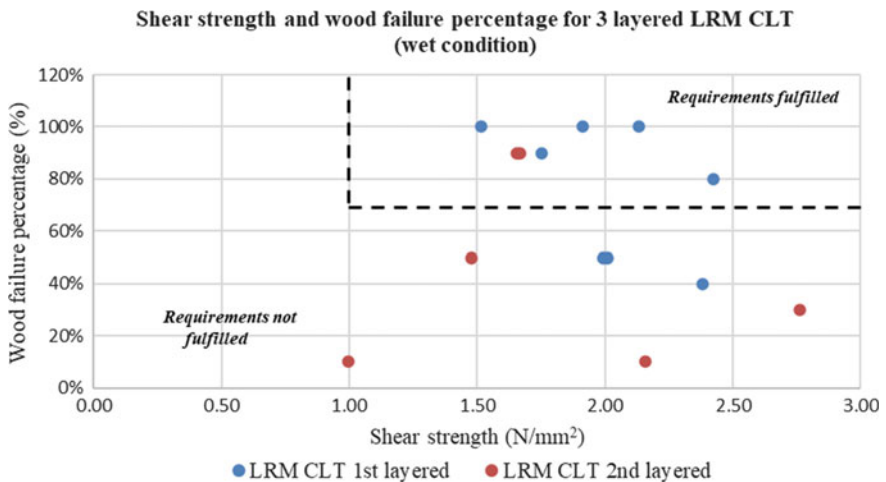


Fig. 13 Relationship of shear strength properties and wood failure percentage for light red Meranti CLT for a wet condition

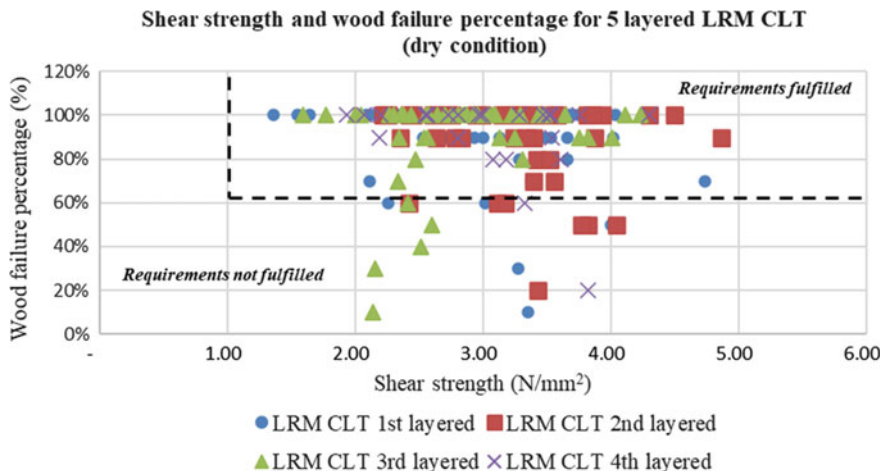


Fig. 14 Relationship of shear strength properties and wood failure percentage for light Red Meranti CLT for a wet condition

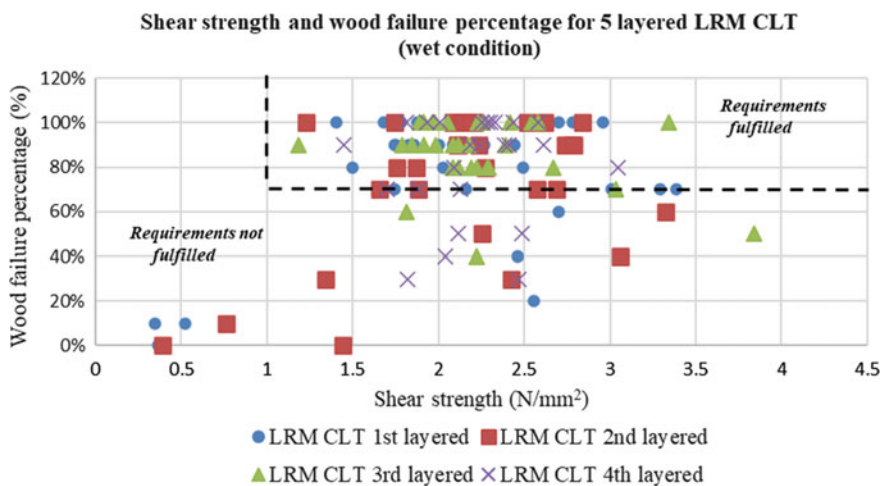


Fig. 15 Relationship of shear strength properties and wood failure percentage for light red Meranti CLT for a wet condition

third laminations. Generally, from the results, there is no correlation between shear strength and WFP. The similar trend is also reported by [23] for European Beech timber.

Overall, in this study, the shear strength and WFP results fulfil the requirements in almost all cases, and only 10% of total samples (340 samples) did not comply with the requirements. However, this result is based on one type of species and adhesive. A further study is recommended since the bonding performance of CLT is

also influenced by other factors including types of adhesive, compression pressure, the grain direction of the face layers, and wood adhesive compatibility [15].

4 Conclusion

Shear strength, characteristic shear strength and wood failure percentage of CLT manufactured from LRM was determined according to [12, 14, 20].

1. The mean shear strength value of 5 layers CLT is greater than 3 layers CLT. In terms of service condition, dry condition presents the better results compared to wet condition. The similar trend is also found for effective mean shear strength values.
2. The characteristic shear strength for 5 layers CLT in dry condition complied with [12]. For effective characteristic shear strength value, 3 and 5 layers CLT in dry condition are compliant.
3. Although some of the results for characteristic shear strength did not comply with the required value in [12], the percentage difference of this value is not significant and still acceptable (less than 18%).
4. No correlation value shows for the relationship of shear strength value and WFP.

Acknowledgements Malaysia Timber Industry Board (MTIB) financially supported the work reported here under national grant RMI/20171212016. We wish to thank the Material Testing Institute (MPA), University of Stuttgart, Germany and CLT factory in Italy for their assistance and support.

References

1. Sikora KS, Harte AM, Mcpolin DO (2014) Durability of adhesive bonds in cross-laminated timber (CLT) panels manufactured using Irish Sitka spruce. In: Proceedings of the 57th international convention of society of wood science and technology, Zvolen, SLOVAKIA, 2014, pp 1–8
2. Karacabeyli K, Gagnon S (2019) Canadian CLT handbook
3. Brandner R, Flatscher G, Ringhofer A, Schickhofer G, Thiel A (2016) Cross laminated timber (CLT): overview and development. *Euro J Wood Wood Prod* 74:331–351. <https://doi.org/10.1007/s00107-015-0999-5>
4. Kairi M (2002) Chapter 4.4: glued/screwed joints/screw glued wooden structures, 2nd edn. In: Johansson CJ, Pizzi T, Leemput MV (eds) COST action E13 ‘wood adhesion and glued products, working group 2: glued wood products: state of the art report
5. Song YJ, Hong SI (2016) Evaluation of bonding strength of larch cross-laminated timber. *J Korean Wood Sci Technol* 44(4):607–615. <https://doi.org/10.5658/WOOD.2016.44.4.607>
6. Aicher S, Ahmad Z, Hirsch M (2018) Bondline shear strength and wood failure of European and tropical hardwood glulam. *Euro J Wood Wood Prod* 76(4):1205–1222. <https://doi.org/10.1007/s00107-018-1305-0>

7. Davalos JF, Qiao P, Trimble BS (2000) Fiber-reinforced composite and wood bonded interfaces: part 1. Durability and shear strength. *J Compos Technol Res* 22(4):224–231. <https://doi.org/10.1520/CTR10544J>
8. Gong Y, Wu G, Ren H (2016) Block shear strength and delamination of cross-laminated timber fabricated with Japanese Larch. *BioResources* 11(4):10240–10250. <https://doi.org/10.15376/biores.11.4.10240-10250>
9. Adhesives for load-bearing timber structures—test methods—part 1: determination of longitudinal tensile shear strength, BS EN 302-1 (2013)
10. Glued laminated timber. Shear test of glue lines, BS EN 392 (1995)
11. Standard test method for strength properties of adhesive bonds in shear by compression loading. ASTM D905–08 (2013)
12. Timber structures. Cross laminated timber. Requirements, BS EN 16351 (2015)
13. Sikora KS, McPolin DO, Harte AM (2016) Shear strength and durability testing of adhesive bonds in cross-laminated timber. *J Adhesion* 92(7–9):758–777. <https://doi.org/10.1080/00218464.2015.1094391>
14. Timber structures. Structural laminated veneer lumber. Requirements, BS EN 14374 (2004)
15. Hamdan H et al (2017) Cross laminated timber (CLT) structure: the first in Malaysia. *Timber Technol Bullet* 70. <https://info.frim.gov.my/infocenter/booksonline/ttb/TTB70.pdf>
16. Mohd Yusof N, Md Tahir P, Lee SH, Khan MA, Mohammad Suffian James R (2019) Mechanical and physical properties of cross-laminated timber made from *Acacia mangium* wood as function of adhesive types. *J Wood Sci* 20. <https://doi.org/10.1186/s10086-019-1799-z>
17. Malaysian Timber Industry Board (MTIB) (2010) 100 Malaysian timbers. Kuala Lumpur
18. Code of practice for structural use of timber—permissible stress design of solid timber, MS 544: Part 2 (2001)
19. Specification for visual strength grading of tropical hardwood timber, MS 1714 (2003)
20. Timber structures. Calculation and verification of characteristic values, BS EN 14358 (2016)
21. Luengo E, Hermoso E, Cabrero JC, Arriaga F (2017) Bonding strength test method assessment for cross-laminated timber derived stressed-skin panels (CLT SSP). *Mater Struct* 50(4):204. <https://doi.org/10.1617/s11527-017-1069-8>
22. Bockel S et al (2020) Characterization of wood-adhesive bonds in wet conditions by means of nanoindentation and tensile shear strength. *European J Wood Wood Products* 78(3):449–459. <https://doi.org/10.1007/s00107-020-01520-1>
23. Aicher S, Ohnesorge D (2010) Shear strength of glued laminated timber made from European beech timber. *Euro J Wood Wood Prod* 69:143–154. <https://doi.org/10.1007/s00107-009-0399-9>

Effect of Kenaf Core to the Physical Properties of Cement-Sand Brick for Non-load Bearing Walls



Mohd Fadzil Arshad, Nurul Aini Salehuddin, Zakiah Ahmad,
Mohd Zaim Mohd Nor, and Abdul Hadi Hassan

Abstract In this study, the effect of replacing the river sand with industrial waste and cellulosic waste is investigated. The cellulosic waste selected for this study is kenaf core, while the industrial waste use in this study is quarry dust. The mortar formulation is adjusted with a different percentage of kenaf core. While the quarry dust is fixed at 75% replacement level. The water-cement ratio set for the formulation varies based on the cement-sand ratio. The physical properties are measured through compressive strength, density, water absorption, and porosity at 28 days. The result shows that the maximum percentages of kenaf core to be used in brick was made by using 25% of kenaf core for a cement-sand ratio of 1:6. The strength achieved at 28 days is 8.46 N/mm², while the density is 1782 kg/m³ at 28 days. However, the optimal percentage of kenaf core which can be used for a cement-sand ratio of 1:8 was 15%. The strength achieved at 28 days is 7.1 N/mm² with a density of 1797 kg/m³. It is observed that the bricks have sufficient strength which also has met the minimum requirement of non-load bearing strength in accordance with the Public Works Department, where the minimum requirement is 5.2 N/mm². The water absorption also below 21% as commonly used. All results show that kenaf core has the potential to be used as lightweight fine aggregate. But it needs to be combined with other materials which contribute to the strength.

Keywords Kenaf core · Cement-sand brick · Quarry dust · Physical properties · Cellulosic waste · Industrial waste

M. F. Arshad (✉) · N. A. Salehuddin · Z. Ahmad
School of Civil Engineering, College of Engineering, Universiti Teknologi MARA (UiTM) Shah Alam, Selangor, Malaysia

M. Z. M. Nor · A. H. Hassan
National Kenaf and Tobacco Board Malaysia, Pahang and Southern Region, Kota Bharu, Malaysia

1 Introduction

After several studies, Malaysia has identified the potential raw fibre to substitute tobacco and it is known as kenaf plant. The scientific name for kenaf is *Hibiscus Cannabinus* L. Kenaf also suitable for commercial-scale production due to the climate in Malaysia. It also introduces a new renewable resource for several industrial purposes. Besides that, kenaf is known as a traditional third-world crop after wood and bamboo for economic development. However, agricultural wastes from kenaf commercialization activity are unavoidable. This lignocellulose plant produces 20% of commercial fibre and 80% of lignocellulose waste or also known as kenaf core. The generation of this waste poses a major disposal problem now since burning is being actively discouraged by the Department of Environment of Malaysia [1].

Webber et al. [2] stated that the kenaf core bulk density is ranging from 100 to 200 kg/m³ and having a porous structure. It can also be grinded or crushed to smaller particle sizes. With these properties, the kenaf core is suitable to be applied in the product as a lightweight material. Even though it is expected that when used, kenaf core does not improve its strength properties when applied as construction materials, kenaf core can give an advantage by reducing the weight and improve the thermal conductivity. This may also be one of the suitable solutions to replace natural sand.

Natural sand that is normally used in Malaysia as a construction material is river sand. The use of this natural sand is costly due to high demand and fewer dragging areas that lead to a shortage in supply. High consumption of natural sand also impacts the environment negatively. Some waste or by-product materials have already been used as a replacement of natural sand such as bottom-ash, quarry waste or limestone or granite dust and siliceous stone powder, filtered sand, copper slag in cement related product such as concrete and mortar mixtures to replace natural sand partially or fully as an alternative to reduce these impacts [3]. The quarry dust is known to be able to replace natural sand. However, a combination of quarry dust and kenaf core where it is a waste to both industries and used as the construction material might become the solution to overcome the disadvantage of natural sand [4].

Nevertheless, there is limited research on the effects of combining two materials such as quarry dust and kenaf core as a sand replacement material in brick on the compressive strength, density, water absorption, and porosity test. In this study, the cement-sand brick containing quarry dust and kenaf core is cast as a composite to determine the optimum percentages of kenaf brick mixture. This research also only focuses on replacing sand in brick production that is used as a non-load bearing wall.

Table 1 Chemical and physical properties of OPC

Reference	OPC (%)
CaO	63.00
SiO ₂	20.00
Al ₂ O ₃	5.70
MgO	0.99
Fe ₂ O ₃	2.90
SO ₃	3.50
K ₂ O	1.20
LOI	2.80
SG	3.00
Surface area (cm ² /g)	11 823
Passing 45 μm (%)	100

2 Materials and Methods

2.1 Materials Preparation and Properties

Ordinary Portland Cement (OPC) was used as the basic cementitious material. The cement binder used was type CEM 1 42, R agreeing to the BS EN 197-1:2000 [5]. The chemical properties of OPC are shown in Table 1. The OPC was supplied by Tasek Cement Bhd. Quarry dust was collected from the factory at Innovative Precast Builder Sdn Bhd and kenaf core was collected from Lembaga Kenaf dan Tembakau Negara (LKTN). The materials were stored in the concrete laboratory. To produce a quality brick, river sand passing the 4.8 mm sieve pan was used. This requirement is outlined in the JKR Standard Specification [6]. There is no further treatment applied to the quarry dust such as sieving before being included in the mixes. Moreover, kenaf core used in this study was ground to 3 mm in size before being applied in the mixes and no sieving was performed. Sieve analysis of all fine aggregate used is shown in Table 2.

2.2 Mix Design

Building works in Malaysia require that the guidelines proposed by the Department of Public Works be followed and fulfilled. JKR 20800-0183-14 [6] stated that the minimum cement to sand ratio is 1:6. Therefore, the mix design or mix proportion of brick in this study was started with the lowest mix ratio of cement to sand which is 1:6. The quantity of quarry dust in the specimen is already set at 75% of the fine aggregate components based on the preliminary study. Sand will be replaced by a fixed amount of 75% quarry dust in each mix and the remaining 25% of sand will be

Table 2 Sieve analysis of quarry dust (QD), kenaf core (KC), and natural sand

BS test sieve	Percentage passing by weight (%)		
	Quarry dust	Kenaf core	Natural sand
10 mm	100.00	100.00	100.00
5 mm	93.69	99.20	99.91
2 mm	55.21	41.54	63.11
1.18 mm	42.56	26.33	45.00
600 μm	29.11	13.31	25.30
425 μm	24.87	10.51	18.24
300 μm	24.24	10.01	17.73
212 μm	12.72	5.51	5.39
150 μm	12.40	5.21	4.87
63 μm	7.67	2.70	1.92
Pan	0.00	0.00	0.00

progressively replaced by kenaf core as stated until the amount of sand is zero. The replacement method for quarry dust is replaced by weight. While the replacement of river sand by kenaf core was done by volumetric means. Since the first trial using 1:6 showed that the kenaf core was able to be replaced until zero sand, the second batch of mix proportion was designed using a 1:8 cement-sand ratio. This mix proportion is designed with the intention of increasing the kenaf core content in the brick with similar cement content by increasing the fine aggregate. Table 3 shows the mix proportion that was selected to obtain the optimal mix design. The water-cement ratio selected is 0.6 and remains fixed for all mixes.

2.3 Specimen Preparation

The preparation of samples involved the process of mixing, casting, and curing. The mixing procedure of the brick followed the procedure stated in the BS EN 771-3: 2011 + A1:2015 [7] and BS EN 772-1:2011 + A1:2015 [8] using the mechanical mixer for mortar. The mould size used in this study is 220 mm \times 100 mm \times 65 mm. This size of brick was used for all tests of brick. The hydraulic pressure method is used to cast the brick. The pressure used in this research is 550 psi and used throughout the research. The specimens were tested for water compressive strength, density, water absorption, and porosity at the age of dry curing, 3, 7, and 28 days.

Table 3 Mix proportion for composite brick that contains three types of fine aggregate

Mix designation	Constituent materials (%)		
	Natural sand	Quarry dust	Kenaf core
<i>Bricks 1:6</i>			
M1	100	0	0
M2	25.0	75	0
M3	0	0	100
M4	22.5	75	2.5
M5	20.0	75	5.0
M6	17.5	75	7.5
M7	15.0	75	10.0
M8	12.5	75	12.5
M9	10.0	75	15.0
M10	7.5	75	17.5
M11	5.0	75	20.0
M12	2.5	75	22.5
M13	0	75	25.0
<i>Bricks 1:8</i>			
M21	100	0	0
M22	25.0	75	0
M23	22.5	75	2.5
M24	20.0	75	5.0
M25	17.5	75	7.5
M26	15.0	75	10.0
M27	12.5	75	12.5
M28	10.0	75	15.0
M29	7.5	75	17.5
M30	5.0	75	20.0
M31	2.5	75	22.5
M32	0	75	25.0
M33	0	0	100

2.4 Compressive Strength Test

This test is prescribed by BS EN 772-1:2011 + A1:2015: Determination of compressive strength [8]. The compressive strength of the bricks is determined at 3, 7, and 28 days for methods of air curing. Universal Testing Machine (UTM-1000) that available at the faculty laboratory in UiTM Shah Alam is used to determine the compressive strength of the bricks.

2.5 Density Test

The density test will be carried out to determine the effect of every material that replaces sand on the properties of brick. Different compositions of every material will differentiate the ability of the materials to make the brick lightweight. BS EN 772-13:2000 [9] will be used as a guideline to conduct the test. All the values measured in the test were used to obtain the density value of the bricks.

2.6 Water Absorption and Porosity Test

The determination of water absorption and porosity are another common test to measure the performance of brick. The total absorption and porosity of brick can be measured by a few methods [10]. Water absorption and porosity are constantly influenced by the density of brick [11]. However, it was affected indirectly by the material used in the mixes [12, 13]. In this study, vacuum saturation was selected as a method to measure both properties. The procedure was conducted following RILEM CP 11.3: Absorption of water by concrete by immersion under vacuum [14].

3 Result and Discussion

3.1 Compressive Strength

The compressive strength development is achieved from the laboratory measurement as illustrated in Fig. 1. The compressive strength development from 3 to 28 days shows the positive effect where the line graph trend for all mixes is similar. The strength development of all the mixes does not show any depleting of strength achieved from days 3 to days 28. However, the inclusion of kenaf core is seen to reduce the strength of brick in every replacement.

A similar trend of strength development was also detected in the bricks made of a 1:8 cement-sand ratio. Figure 2 distinctly shows that kenaf core inclusion in the bricks designed using 1:8 ratio, decreased the strength achieved from 3 days up to 28 days. A similar effect with bricks 1:6 can be observed.

Based on Figs. 1 and 2, the specimen which achieved and maintained the highest strength are M1 and M22 which are the control specimens made with conventional material which is river sand. The lowest strength achieved by the bricks were with those made of 100% kenaf core (M3, M33). It also shows that the strength of M3 and M33 also does not increase significantly from 3 to 28 days. However, the combination of kenaf core with cement does not diminish the function of cement as kenaf core is able to create bonding with the cement and give strength even lowered. This

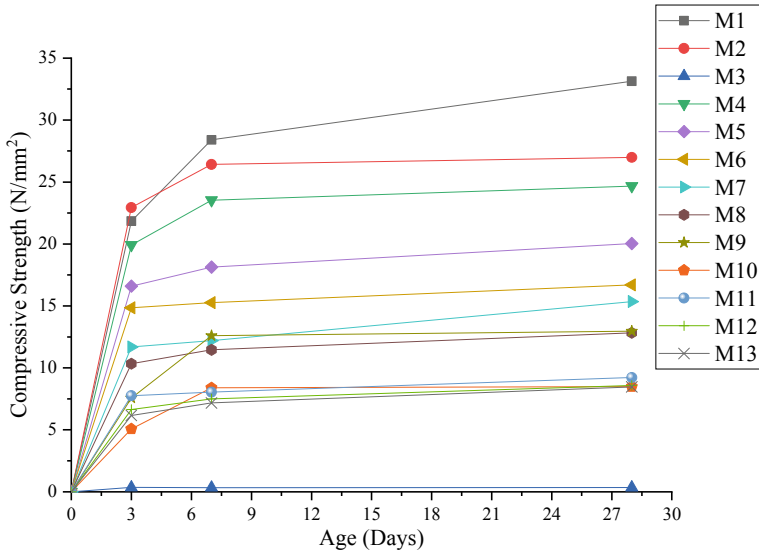


Fig. 1 Compressive strength development of brick with different replacement levels for cement-sand ratio 1:6

condition is also shown by other types of cellulosic waste, where the binding ability of cellulosic waste such as kenaf not as good as natural fine aggregate [15–17].

However, for building works in Malaysia, Department of Public Works have its guideline that needs to be followed and fulfilled. JKR 20800-0183-14 [6] stated the composition, material used, and construction of brickwork need to follow the JKR 20800-0183-14. This standard specification also highlighted that the minimum permissible average compressive strength at 28 days shall be 5.2 N/mm² for bricks and 2.8 N/mm² for hollow blocks. This minimum strength stated is also the minimum strength set for brick that will be used in a non-load bearing wall. The limitation value of compressive strength set by the Public Works Department of Malaysia makes all the mix proportion that contained kenaf core for 1:6 cement-sand brick (M4-M13) produced adequate bricks except for specimen M3. This limitation and strength at 28 days are shown in Fig. 3. While the cement-sand brick 1:8 shows that the optimum level of replacement of kenaf core is only up to 17.5%, the limitation set by JKR 20800-0183-14 has shown that M30–M33 is not suitable to be used as a brick. Even though M30 shows value within limitation, the strength achieved was not significant where it falls within 10% of the significant value set in this research. This is shown in Fig. 4.

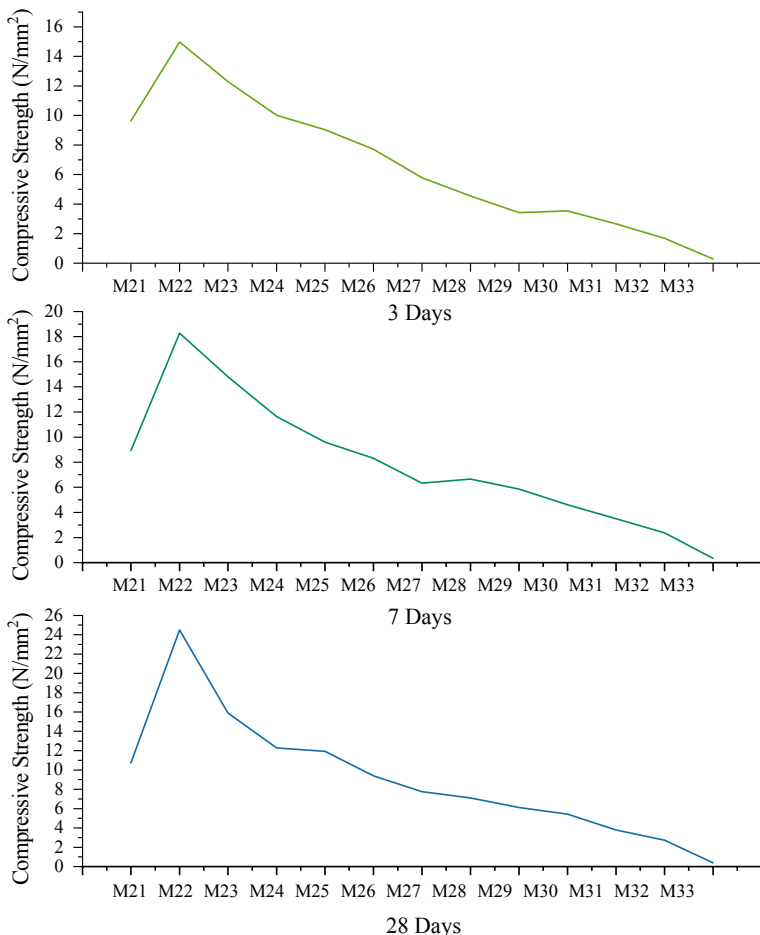


Fig. 2 Compressive strength development of brick with different replacement levels for cement-sand ratio 1:8

3.2 Density

The results for the density value of bricks made of 1:6 cement-sand ratio is presented in Fig. 5. From the figure, M2 is the brick that contains only quarry dust and sand as fine aggregate, has the highest density with a value of 2065 kg/m³ at 28 days. When kenaf core replaces the sand portion, the density of bricks reduces when compared with M2. Bricks with every replacement level show a similar effect, where the higher the kenaf core in the brick portion, the lower the density achieved regardless of the age of curing. The density value in the figure also increases when approaching 28 days from 3 days. However, contradicting results are shown by bricks made of 100% kenaf

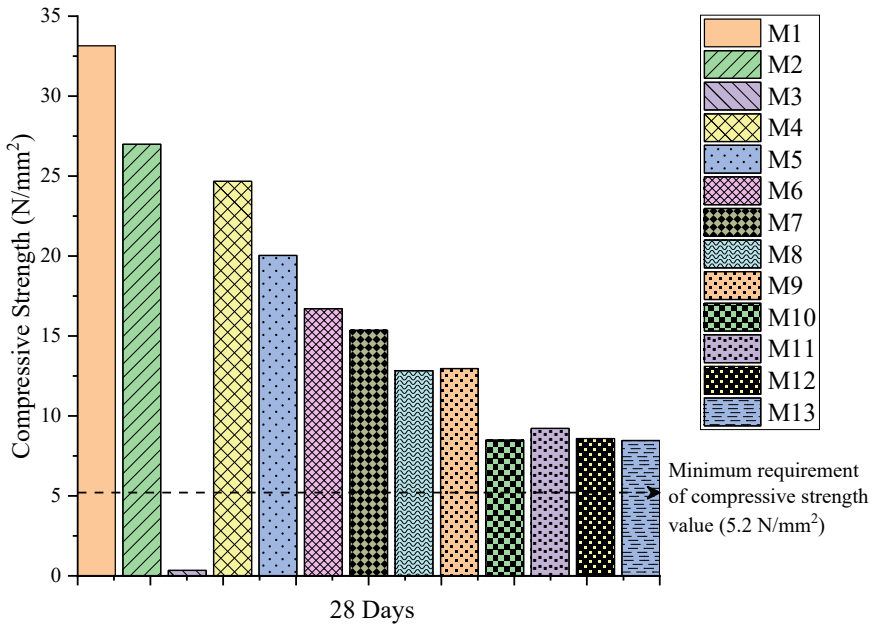


Fig. 3 Effect of fine aggregate replacement to the compressive strength at 28 days for cement-sand brick 1:6 and the limitation by JKR 20800-0183-14

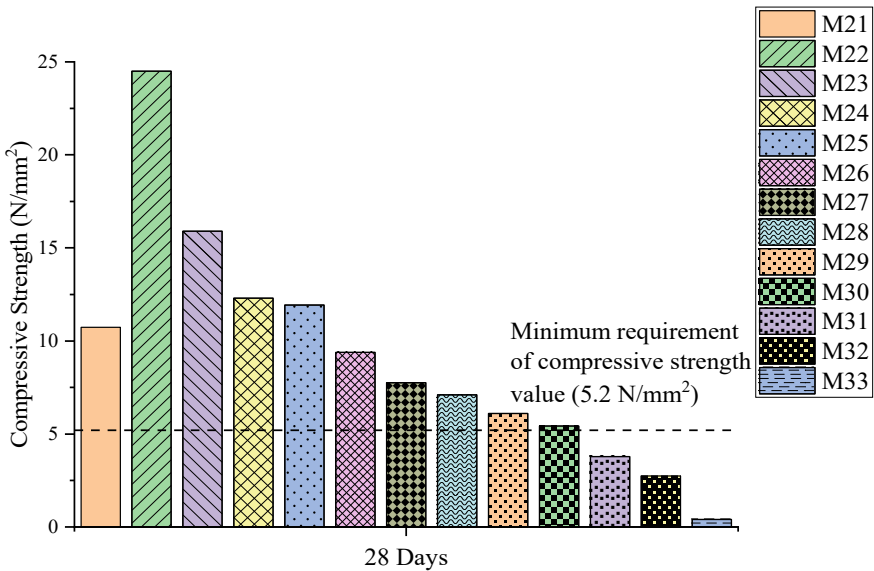


Fig. 4 Effect of fine aggregate replacement to the compressive strength at 28 days for cement-sand brick 1:8 and the limitation by JKR 20800-0183-14

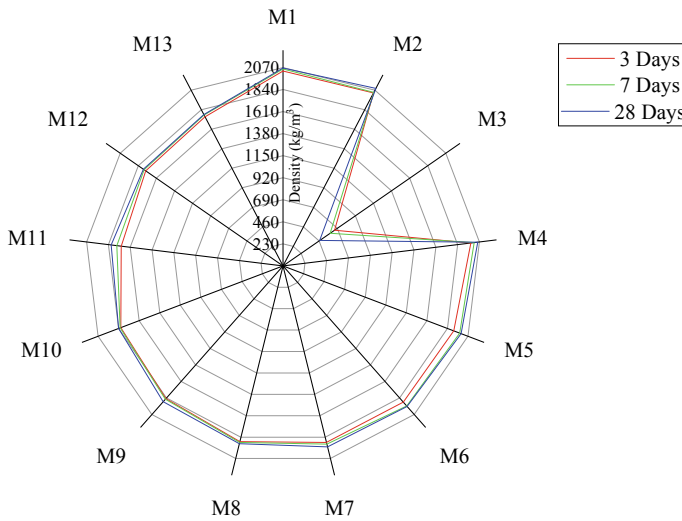


Fig. 5 The density of 1:6 bricks at 3–28 days

core (M3) when approaching 28 days from 3 days. The density is reduced and has the lowest density value of 654 kg/m^3 at 3 days– 457 kg/m^3 at 28 days.

The density values of 1:8 cement-sand brick is shown in Fig. 6. A similar trend of results is also observed for bricks made with cement-sand ratio 1:8 when compared

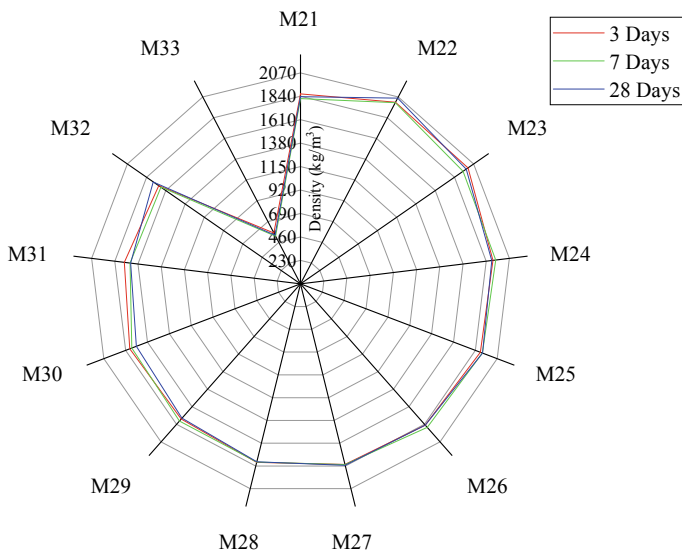


Fig. 6 The density of 1:8 bricks at 3–28 days

with cement-sand ratio 1:6. The increasing amount of kenaf core reduces its density value. As mentioned earlier, the cement-sand 1:8 was designed to increase the kenaf core portion in the brick with similar cement content. However, only M1 shows a significant difference in density value from 2065 to 1835 kg/m³ when fine aggregate was increased when compared between 1:6 and 1:8 bricks. It shows that normal sand needs cement as a filler and binder to make the bricks denser and strong, while quarry dust has the ability to act as a filler which helps in sustaining the density and strength. When the kenaf core was replaced with sand, no significant difference in density between 1:8 and 1:6 bricks was observed.

Both Figs. 5 and 6 shows that the inclusion of kenaf core reduces the density of brick at every replacement level when compared with control brick M2 and M22. However, when considering the compressive strength value, the higher amount of kenaf core with suitable strength value has a density of 1782 kg/m³ (M13) and 1759 kg/m³ (M29). The common density of cement brick used in the non-load bearing wall in Malaysia was having a density of 1800–1900 kg/m³ with a strength value of 2–5 N/mm² [18]. Therefore, this shows that brick with kenaf core has a low density with much higher strength than common bricks available in Malaysia.

Kenaf core also is known as lightweight materials as it has a density between 100 and 200 kg/m³. It is an advantage to use kenaf core to produce a lightweight product such as lightweight brick. The classification of lightweight cement and concrete related product was set with a maximum density of 1840 kg/m³ [19]. It indicates that any bricks that fall below the maximum density can be categorized as lightweight. It also indicates that kenaf core bricks M13 and M29 can be classified as lightweight bricks. Lightweight brick that is used in a non-load bearing wall can be an advantage towards the dead load applied to the main structure such as slab and beam [20].

3.3 *Water Absorption and Porosity*

Table 4 shows the water absorption and porosity value achieved by cement-sand brick 1:6 and cement-sand brick 1:8 at 28 days. Bricks 1:8 have much higher water absorption and porosity values when compared with 1:6. This condition occurred with an increased amount of fine aggregate. When the effect of kenaf core was observed, the increasing amount of kenaf core does increase the water absorption and porosity for both classes of brick.

In general, porosity values are directly related to density and water absorption, where a higher porosity of bricks equates to, lower density, and higher porosity translates to higher water absorption values. This align with the previously discussed effect of the increasing amount of kenaf core resulting in increased porosity and it is proved by the density value achieved earlier. Khalid et al. [21] suggested that one of the reasons for the brick to have a higher porosity value is due to fine aggregate size distribution and shape that are coarser and much random when compared to natural sand. Where it also leads to less packing effect to the brick mixture which caused the density to be lower. This is also supported by the sieve analysis data presented in

Table 4 Water absorption and porosity value of 1:6 and 1:8 bricks at 28 days

Mix designation	Percentage (%)		Mix designation	Percentage (%)	
	Water absorption	Porosity		Water absorption	Porosity
<i>Bricks 1:6</i>			<i>Bricks 1:8</i>		
M1	9.11	18.54	M21	12.01	22.73
M2	7.67	16.19	M22	10.06	20.20
M3	122.11	70.74	M23	9.65	19.36
M4	7.72	17.89	M24	9.91	19.63
M5	7.95	18.03	M25	10.35	20.73
M6	8.08	18.52	M26	11.42	21.81
M7	8.47	19.15	M27	13.16	24.37
M8	9.31	19.82	M28	14.09	24.80
M9	10.75	20.45	M29	14.27	25.10
M10	11.93	22.39	M30	16.57	28.11
M11	13.22	24.01	M31	17.24	29.01
M12	13.69	24.83	M32	19.46	30.30
M13	15.95	28.27	M33	178.51	75.62

Sect. 2 where the kenaf core has a coarser particle size when compared with natural sand. The particle size of the kenaf core is also random as shown in Fig. 7.

Maximum water absorption values were not highlighted in any standard requirement. However, it is usually accepted to use the maximum limit of water absorption for brick as 21%. From the results, all types of bricks satisfied this requirement except M3 and M33 that made of 100% kenaf core. However, kenaf core does affect the water absorption value. The higher the kenaf core the higher the water absorption obtained. Kenaf core is known as lignocelluloses materials. When working with lignocelluloses materials, it often considers porous and at the surface is consider hydrophilic due to the polymer component in lignocelluloses will create hydrogen bonding with water [22]. Therefore, this character of kenaf core needs to be taken as a precaution to avoid it becoming a hindrance towards the brick properties. However,

Fig. 7 Kenaf core was used in this study



the cement-sand brick made with kenaf core in this study was able to overcome this disadvantage and shows an acceptable value of water absorption.

4 Conclusions

Findings obtained from compressive strength, density, water absorption, and porosity, show that the kenaf core affects the properties of brick. The main factors that influence the properties are the porous structure of the kenaf core and its low density. However, all the properties measured were accepted when the kenaf core was included in the cement-sand brick.

The findings from the properties show that specimens M13 and M29 satisfied all the limitations outlined in the standard requirement and standard practice for compressive strength, density, and water absorption. It also shows that in terms of compressive strength and water absorption, M13 and M29 are comparable with the existing product. The utilization of industrial waste such as quarry dust and kenaf core in the M13 and M29 brick shows a positive impact on the brick properties and the practical approach to using this product is in the non-load bearing application such as infill masonry wall.

Acknowledgements The authors would like to express the greatest appreciation and gratitude to the National Kenaf and Tobacco Board Malaysia (NKTB) for assisting and funding this study. This appreciation also extends to the Research Management Institute and Universiti Teknologi MARA of Malaysia for assisting and providing the facility which enables the study to be conducted.

References

1. Zafar S (2011) Renewable energy in Southeast Asia: agricultural biomass waste. *Renewable energy in Southeast Asia: agricultural biomass waste*
2. Webber CL III, Bledsoe VK, Bledsoe RE (2002) Kenaf harvesting and processing. *Trends New Crops New Uses* 9:340–347
3. Sukesh C, Krishna KB, Teja PSL, Rao SK (2013) Partial replacement of sand with quarry dust in concrete. *Int J Innov Technol Explor Eng (IJITEE)* 2(6):254–258
4. Hameed MS, Sekar ASS (2009) Properties of green concrete containing quarry rock dust and marble sludge powder as fine aggregate. *ARPJ J Eng Appl Sci* 4(4):83–89
5. EN BS (2000) 197-1, cement-part 1: composition, specifications, and conformity criteria for common cement. British Standards Institution
6. Jabatan Kerja Raya Malaysia, JKR 20800-0183-14 (2014) Standard specifications for building works
7. EN BS (2011) 771-3: 2011 + A1: 2015 Specification for masonry unit: aggregates concrete masonry units (dense and lightweight aggregates)
8. EN BS (2011) 772-1: 2011 + A1: 2015 method of test for masonry unit: part 1: determination of compressive strength
9. EN BS (2000) 772-13: 2000 method of test for masonry unit: part 13: determination of net and gross dry density of masonry units (except for natural stone)

10. Wilson MA, Carter MA, Hoff WD (1999) British Standard and RILEM water absorption tests: a critical evaluation. *Mater Struct* 32(8):571–578
11. Kearsley EP, Wainwright PJ (2001) Porosity and permeability of foamed concrete. *Cem Concr Res* 31(5):805–812
12. Shimizu T, Matsuura K, Furue H, Matsuzak K (2013) Thermal conductivity of high porosity alumina refractory bricks made by a slurry gelation and foaming method. *J Eur Ceram Soc* 33(15–16):3429–3435
13. Kim Y, Lee Y, Kim M, Park H (2019) Preparation of high porosity bricks by utilizing red mud and mine tailing. *J Clean Prod* 207:490–497
14. Rilem C (1984) 11.3. Absorption of water by immersion under vacuum. *Mater Struct* 17(101):391–394
15. Mostefai N, Hamzaoui R, Guessasma S, Aw A, Nouri H (2015) Microstructure and mechanical performance of modified hemp fibre and shiv mortars: discovering the optimal formulation. *Mater Des* 84:359–371
16. Akkaoui A, Caré S, Vandamme M (2017) Experimental and micromechanical analysis of the elastic properties of wood-aggregate concrete. *Constr Build Mater* 134:346–357
17. Mahzuz HMA, Ahmed M, Hossain MM, Islam MM, Alam MK (2016) Evaluation of strength of mortar using different saw waste with sand and model development. *KSCE J Civ Eng* 20(7):2822–2831
18. Ibrahim WMW, Abdullah MAB, Sandu AV, Hussin K, Sandu IG, Ismail KN, Kadir AA, Binhussain M (2014) Processing and characterization of fly ash-based geopolymer bricks. *Rev Chim* 65:1340–1345
19. Widodo S, Satyarno I, Tudjono S (2014) Experimental study on the potential use of pumice breccia as coarse aggregate in structural lightweight concrete. *Int J Sustain Constr Eng Technol* 5(1):1–8
20. Gündüz L (2008) Use of quartet blends containing fly ash, scoria, perlitic pumice, and cement to produce cellular hollow lightweight masonry blocks for non-load bearing walls. *Constr Build Mater* 22(5):747–754
21. Khalid FS, Herman HS, Azmi NB, Juki MI (2017) Sand cement brick containing recycled concrete aggregate as fine-aggregate replacement. *MATEC Web Conf* 103:01016
22. Nozahic V, Amziane S (2012) Influence of sunflower aggregates surface treatments on physical properties and adhesion with a mineral binder. *Compos A Appl Sci Manuf* 43(11):1837–1849

Bond Strength of Different Mechanically Rebar-Spliced Embedded in Concrete Under Pull Out Test



Nursafarina Ahmad, Nur Fitriah Mohd Rohzi,
N. S. N. Ain Fatimah Nik Mahmood, and M. Hadri Hamidun

Abstract The connection of reinforcement rebars for concrete supersized structure is important for simplifying field work and reducing construction time. On site, mechanical splices are widely used to link two steel reinforcement bars. Since there are several different kinds of mechanical couplers on the market, it is critical to assess the grip between the mechanical coupler and the concrete. The effectiveness of the grip between steel and concrete (bond strength) is a key issue for assessing the overall behavior of reinforced concrete structures. This factor is very crucial since it disrupts the composite action if the bond resistance is inadequate between the concrete and steel. Therefore, this study aims to determine the bond behavior of mechanically spliced steel rebar. The mechanical spliced bond behavior embedded in structural concrete was tested using the pull-out test on cylindrical specimens of 155 mm diameter with 500 mm length. Considering the effect of different mechanical coupler types, Moment Bolt Coupler (MBC) and Half Grout coupler, and steel reinforcing bars of 16, 20, and 25 mm diameter were cast with 30 MPa compressive strength concrete. Furthermore, this study has compared experimental results with bond equations to report the efficiency of the couplers. The findings of the experiments demonstrated that using both mechanical couplers to link two steel reinforcing bars significantly affected on the ultimate resistance, bond strength, and slip as opposed to normal lapping reinforcement.

Keywords Mechanical splice · Bond strength · Reinforcement splice · Pull out test

1 Introduction

In concrete construction, lapping is the preferred method for splicing the rebars together. Lapping in reinforced concrete (RC) is the least costly and mostly accepted

N. Ahmad (✉) · N. F. M. Rohzi · N. S. N. Ain Fatimah Nik Mahmood · M. Hadri Hamidun
School of Civil Engineering, College of Engineering, Universiti Teknologi MARA (UiTM),
40450 Shah Alam, Selangor, Malaysia
e-mail: nursafarina1131@uitm.edu.my

practice. However, this approach can contribute to various issues such as congestion of reinforcement bars inside the sealed lapping joint of the section that can lead to cracking of concrete due to stress localization, resulting in the non-ductile response [1–3]. It is also a waste of steel reinforcing bars due to lapping specifications (i.e., 40D), high costs in the procurement of steel material, and the need for expertise in the tie-up for the connection between the lapping bars. To prevent complications, construction practitioners advocate the use of mechanical splicing to link reinforcement bars as a replacement to the lapping process.

The mechanical splice has been extensively used and is an effective way to splice rebars since it is more practical for site installation and has more advantages in civil infrastructure. Furthermore, the mechanical couplers can ensure consistency of structural continuity between steel rebars, thus providing higher performance. The significant benefits of mechanical splicing couplers are reduced congestion issues in the sections' steel, the capability to connect bars of any length and diameter, and the distribution of concrete cracking can be controlled [4, 5].

There are different forms of couplings available on the market to accommodate the construction purpose, such as Upset Headed Couplers (UHC), Swaged couplers (SWC), shear bolt lock couplers (BLC), and Grouted sleeve couplers (GSC). Each mechanical connector has an intricate form design and advanced molding techniques for manufacturing. Therefore, each connector produces different results on their performance. The mechanical coupler installation is often more straightforward since the bar can be quickly attached manually without any special equipment. This process of utilizing mechanical linking is more precise and time-consuming than the lapping of the reinforcing bars.

The potential inferiority of these mechanical spliced systemic performance criteria under static, dynamic, and cyclic tests in terms of strength, fatigue, and elastic slip under experimental investigation and computational modeling has been performed by numerous scholars [5–12]. However, researchers currently have limited data for exploratory analysis on bond stress between different mechanical splicing with concrete. It is essential to understand and evaluate their bond behavior because the mechanical coupler has more advantages than standard splice lapping.

Bond strength, also known as bond stress, can be defined as measuring the effectiveness of the grip between concrete and steel which can affect the reinforced concrete's performance. Bond stress between steel reinforcement and concrete plays a key role in providing a secure transmission of force from the reinforcement to the underlying concrete [13]. This transmission of force is regarded as bond and is idealized in the immediate vicinity of the interface of steel concrete for a continuous stress region. It is the function that helps straight reinforced bars to be anchored and affects certain additional main features including crack control and segment rigidity of the structural concrete [14]. Besides that, the bond stress is influenced by various factors like chemical adhesion between steel and concrete, reinforcement yield, reinforcement diameter, the roughness of steel bar, the spacing of bars, and the type of aggregate used in concrete [15].

Therefore, the primary research objective is to investigate the bond performance between the mechanical coupler and concrete with different diameters of steel

reinforcement. In this article, two types of tension–compression couplers, namely Moment Bolt Coupler (MBC) and Moment Half Grout Coupler (MHGC) with 16, 20, and 25 mm reinforcement bar diameters were chosen for thorough evaluation and compared with lapped splice specimens.

2 Experimental Investigation

A thorough comparative pull-out test for in-air and embedded coupler in concrete evaluation has been carried out on two different mechanical coupler types of Moment Bolt Coupler, MBC and Moment Half Grout Coupler, MHGC. The efficiency in terms of strength and bond stress and compared with lapped spliced specimens have been evaluated for three diameter size of reinforcement. An Overview of materials, specimens, test plan and setup will be explained in the following sub-sections.

2.1 Materials and Test Specimens

The experimental program is comprised of two stages. In the first stage, a standard lapping specimen is prepared where two reinforcement steel bars are tied to 10d of lapping length. The MBC and MHGC couplers are used to connect 450 N/mm² high strength steel reinforcement bars of 16, 20, and 25 mm diameters. The mechanical coupler has been provided by Leviat A CRH Company, Halfen-Moment product [16], and the details of couplers are as illustrated in Fig. 1. Table 1 gives the specification of the MBC and MHGC that has been used in this study. From Table 1, it can be seen that different sizes of diameter rebars correlate to an extra length of mechanical coupler. The total number of bolts for MBC depends on the size diameter rebar, while MCHG has a different minimum insertion length of the bar.

Figure 2 shows the installation of mechanical splice for MBC and MHGC. The installation method of the spliced MBC is convenient and straightforward. The lock shear bolts were strengthened as the rebars were installed using a nut runner to pull the heads off with ample load. Then, leaving the top of the mounting bolt as the tension of the bolts was hit. As the preset tightening torque is met for the bolts, the heads are sheared off, making the bolt top a little proud of the coupler. Thus, it provides an instant visual confirmation of proper installation. For the MHGC, the end of the steel rebar must be threaded to fit loosely through the one-sided coupling. The grout was then placed into another end coupling and adequately rested to enable the grout to harden.

During the second step, the embedded in-concrete specimens were prepared using PVC cylinders of 155 mm diameter × 500 mm long with different mechanical couplers in the middle. Before the standard lapping and couplers are integrated into the center of the cylinder concrete tubes, the same installation method was used for connecting the couplers with steel rebar as in the first stage. The normal lapping

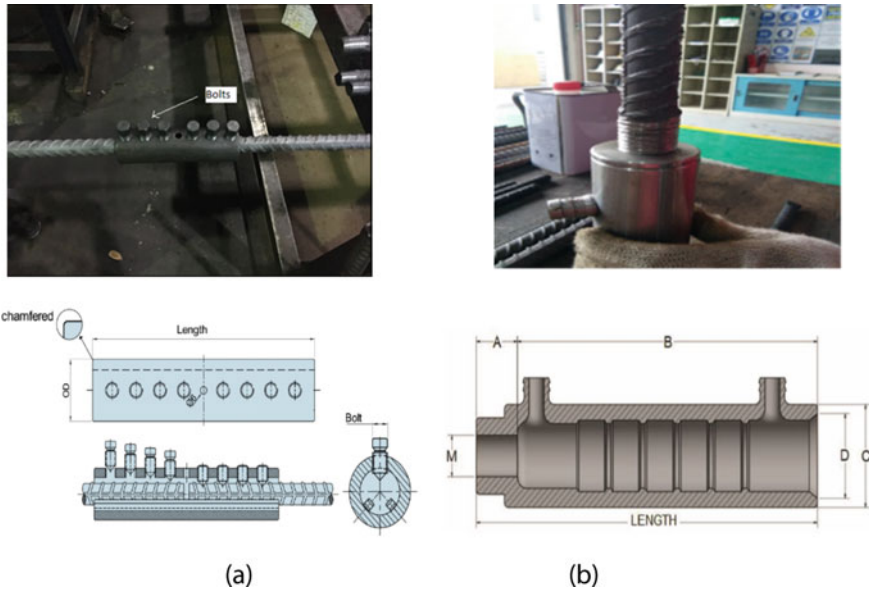


Fig. 1 Mechanical coupler systems **a** moment bolt coupler (MBC), **b** moment coupler half grout (MCHG)

Table 1 Detail specification of standard lapping, MBC, and MCHG

Specimen	Diameter rebar (mm)	Lapping length, 10d (mm)	Length of coupler, <i>a</i> (mm)	External Diameter, <i>b</i> (mm)	Total number of bolts	Minimum insertion (mm)
NL16	16	160	–	–	–	–
NL20	20	200	–	–	–	–
NL25	25	250	–	–	–	–
MBC16	16	–	116	36	6	–
MBC20	20	–	160	42	8	–
MBC25	25	–	175	50	8	–
MCHG16	16	–	168	40	–	128
MCHG20	20	–	205	46	–	160
MCHG25	25	–	250	55	–	200

and couplers were embedded precisely in the concrete with the 150 mm embedded length from the cylinder top to the couplers' end top. Figure 3 illustrates the dimension of the tested specimen for embedded coupler in-concrete. The 30 MPa concrete compressive strength was used for all in-concrete samples. A summary of the test data average for the measured compressive strength of materials is presented in Table 2.

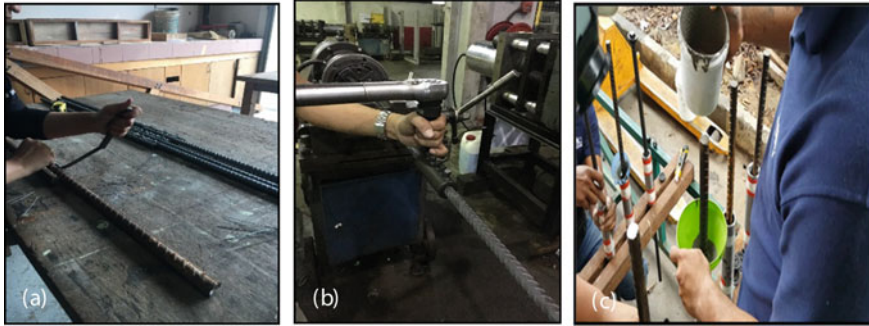


Fig. 2 Installation of stage 1 **a** lap splice with 10d lapping length, **b** tightened the bolt of MBC, **c** pour the grout into the one side of MCHG

Fig. 3 The dimension of tested specimen for in-concrete pull out specimen

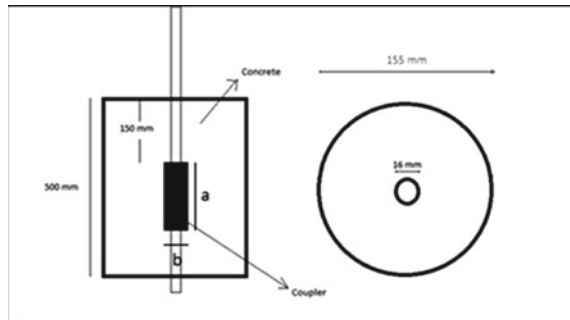


Table 2 Concrete compressive strength, MPa

Test	Cube 1 (MPa)	Cube 2 (MPa)	Cube 3 (MPa)	Average
7 days	30.9	30.40	28.31	29.87
28 days	37.75	36.84	36.54	37 0.04

The concrete was directly transferred into cylinder molds for embedded mechanical in-concrete samples. A square plate with a hole in the middle was mounted to hold the compliance bar in a vertical position rigidly. The mold's interior was filled with an oil film to allow the disassembly of concrete cylinders more accessible for the next day. The standard concrete samples with mechanical couplers are shown in Fig. 4. All these specimens were carefully stored for 28 days under curing treatment before the test date.

Fig. 4 In-concrete specimen after de-molded



2.2 Test Plan and Setup

All samples in-air and embedded mechanical couplers in-concrete were tested under pull-out subjected to a static increasing axial displacement until failure. For in-air mechanical coupler specimens the ends of the steel rebar were inserted into the high-pressure grip jaws of the universal testing machine (UTM) with a capacity of 1000 kN. The grip was tightened to clamp the rebar region to ensure there is no slippage. However, in the case of embedded mechanical coupler samples, one side of the reinforcing bar was gripped, and the bottom of the specimen was tightened to withstand the cylinder's weight. A Linear Variable Differential Transformer (LVDT) was placed under the reinforcement bar at the bottom part to determine the slip of specimens.

The UTM machine was set to pull the in-air samples and embedded mechanical couplers at a 5 mm/minute rate until the specimen failed. The pull-out test was continued until failure occurs to identify the mode failure, either the bar's yielding or loss due to slippage at the coupler. The ultimate tensile stress value, bond intensity, and slip displacement can be established from test results. Figure 5 shows the pull-out test setup for in-air and embedded mechanical coupler in concrete samples.

3 Experimental Results and Observation

The comparative result of different mechanical splices under pull out-static loading was tested for two types of specimens such as (i) in-air mechanical coupler and (ii) embedded mechanical coupler in concrete with three different diameters of rebars.

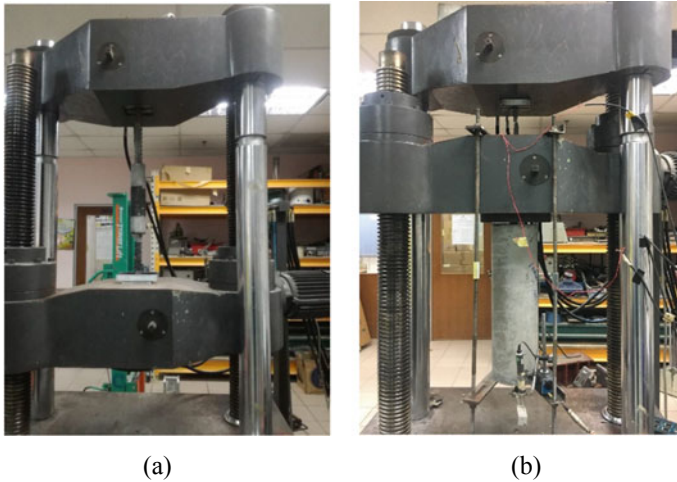


Fig. 5 Universal testing machine with **a** in-air mechanical coupler sample, **b** embedded mechanical coupler in the concrete sample

3.1 In-Air Mechanical Coupler

Each test results reflect three specimens on the average for different MBC and MHGC connected with a diameter of 16, 20, and 25 mm of reinforcement. It is observed that all the specimens failed due to the bar yield, not the coupler failure, as shown in Fig. 6. This indicates the mechanical couplers can withstand more significant loads and provide sufficient ductility to permit the maximum full yield intensity and ultimate strength than the standard lapping steel reinforcement. However, only the MBC16 specimens failed at the coupler due to the screw bolts sheared off the surface of the steel rebar. Table 3 shows the average test result for the in-air pull-out test for both mechanical couplers.

All samples are analyzed for different mechanical splicing having a yield stress of at least 500 MPa and maximum tensile stress of at least 580 MPa. The yield stress and ultimate stress for MBC20 and MBC25 achieved similar values as reported by



Fig. 6 Failure pattern for MBC and MHGC

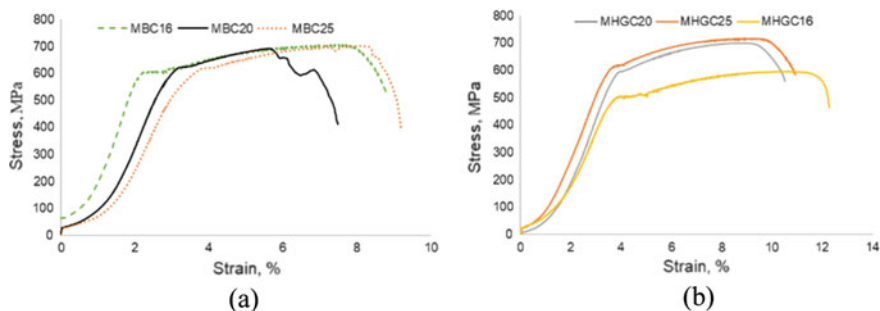
Table 3 Average test result for in-air mechanical couplers

Specimen	Ultimate load (kN)	Ultimate stress (MPa)	Yield load (kN)	Yield stress (MPa)	Failure mode
MBC16	221	621	151	598	Coupler
MBC20	273	657	253	615	Yielding of Bar
MBC25	332	711	306	625	Yielding of bar
MHGC16	162	635	121	498	Yielding of bar
MHGC20	278	680	278	588	Yielding of bar
MHG25	351	726	330	628	Yielding of bar

Chiari and Moreno Junior [5]. As for the in-air tests for the MBC 16 shown in Table 2, the yield load and ultimate load are 151 kN and 221 kN, respectively. There is an increase of 23.5 and 50.2% of maximum strength in MBC20 and MBC25. This is indicated that the increased diameter of steel rebar significantly increases the ultimate strength of splicing reinforcement with mechanical couplers. As expected from the results obtained, it can be inferred that the MHGC specimens demonstrated better performance in terms of load resistance and ductility compared to MBC specimens. However, the MHGC16 has a slightly lower performance from MBC 16 for ultimate and yield loads.

Figure 7 illustrates the typical stress–strain relationship of the pull-out test for in-air mechanical MBC and MHGC specimens. As observed in Fig. 7, the stress–strain curves for all the samples show a similar tendency. It can be seen that the load gradually rises after the point of yield has been reached, up to the point of rupture. The pull-out experiment revealed that the ultimate strain, ϵ_u , between the mechanical coupler MBC and MHGC types specimens is decreased by 26%.

The static pull-out test illustrated in Fig. 7a shows that the comparison yield stress ϵ_y was 2% (MBC16), 3.1% (MBC20), and 3.7% (MBC25), respectively. However, the MBC20 shows a lower ϵ_u with 5.5% compared to the other two MBC specimens. As shown in curves Fig. 7b, the responses for MHGC 20 and MHGC25 show almost identical curves, in which the ultimate strain, ϵ_u , is within similar ranges of 9.4–9.7%.

**Fig. 7** Stress–strain relationships for in-air mechanical coupler pull out tests: **a** MBC, **b** MHGC

MHGC16 show the highest ultimate strain, ε_u around 10% despite having lower yield stress, σ_y compared to the MHGC20 and MHG25.

3.2 *Embedded Mechanical Coupler in Concrete*

For the case of embedded mechanical couplers in concrete, the bond resistance of concrete and mechanical couplers is measured using ultimate load results from the pull-out test to calculate the force required for pulling the steel rod embedded in the concrete specimen. The bond strength is obtained by using the following equation:

$$\tau = F / \pi d_b L_e \quad (1)$$

where:

- τ the bond strength, MPa.
- F the ultimate axial tensile force, kN.
- d_b the nominal diameter bar, mm.
- L_e the embedded length, mm.

In this study, the embedded length is defined as the length lapping for standard lapping and the coupler length for both mechanical couplers to determine the bond strength between concrete and mechanical couplers. Besides that, the normalized bond strength has been obtained by using the following formula:

$$\tau_{nom} = \tau / \sqrt{f c'} \quad (2)$$

where:

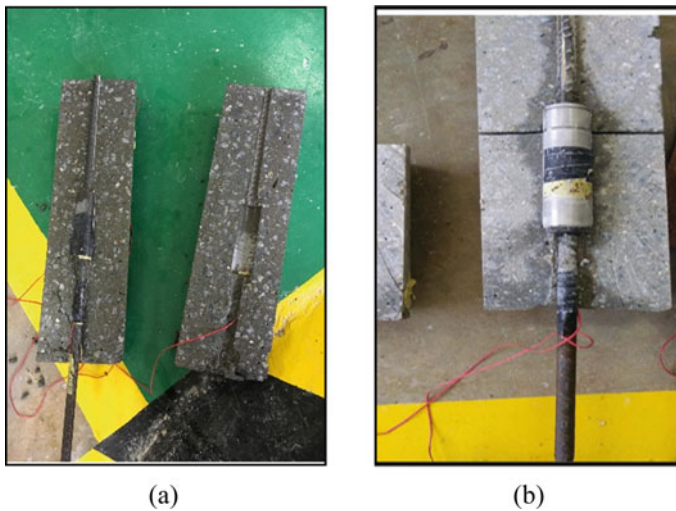
- τ_{nom} normalized bond strength, MPa.
- τ experimental bond strength, MPa.
- $\sqrt{f c'}$ concrete compressive strength.

The main findings for this study in terms of ultimate load, bond strength, and normalize bond strength from pull-out tests on average results of different mechanical couples are given in Table 4. Meanwhile, Fig. 8 shows the internal section after pull-out testing for MBC and MHGC specimens. It is identified that the dominant failure mode was due to bar fracture for all specimens. It also shows that the reinforcement and coupler embedded in the concrete are not affected by the pull-out testing after the concrete is extracted.

According to the tabulation of Table 4, the average value for the maximum axial load for Normal Lapping for diameter 16 mm, 20 mm, and 25 mm are 111.9 kN, 120.1 kN, and 130.2 kN, respectively. It shows that the ultimate axial load increased for specimens with couplers MBC and MCHG compared to standard lapping. For example, the maximum load rises by 12 and 18% as the diameter of reinforcement

Table 4 Average test results for embedded couplers in concrete

Specimen	Embedded length, L_e (mm)	Ultimate load (kN)	Bond strength (MPa)	Normalized bond strength (MPa)	Bar slip (mm)
NL16	160	111.9	13.19	2.17	5.09
NL20	200	120.1	9.56	1.57	4.53
NL25	250	130.2	6.63	1.09	2.67
MBC16	116	125.6	21.5	3.53	4.79
MBC20	160	133.4	13.3	2.19	3.61
MBC25	175	145.6	10.57	1.74	2.32
MHGC16	168	131.8	15.61	2.57	3.79
MHGC20	205	142.1	11.03	1.81	2.16
MHG25	250	150.2	7.64	1.26	1.79

**Fig. 8** The internal section after embedded mechanical couplers pull-out testing for **a** MBC, **b** MHGC specimens

increase from 16 to 25 mm. Thus, the different mechanical coupler significantly affects the ultimate load, which has the same results as the in-air pull-out test. This agreement is similar to previous research by Hamdan and Rahman [17], in which the mechanical coupler withstands more tensile load than lapped bars. The influence of different mechanical couplers and the yield strength of the diameter reinforcement significantly increase the ultimate load.

From Table 4, it can be observed that the bond strength for each specimen of the mechanical coupler has a higher value than normal lapping specimens for the same compressive strength. Utilizing a mechanical coupling is the key explanation of

why the bond intensity between the reinforcing bar and the concrete has improved. This is because the contribution from grout filled coupler in the MHGC significantly enhances the ultimate strength. Meanwhile, the bolt from the MBC coupler contributes to a stronger connection, which resists higher loads. Thus, bond strength improvement increases cohesion, friction, and bearing strength between different mechanical couplers with concrete.

However, the 16 mm diameter for both couplers gives more value to bond strength. The highest intensity can be seen for mechanical couplers with 16 mm diameter, which offers 21.5 MPa for MBC and 15.61 MPa for MCHG, respectively. This can be seen that the bond intensity significantly influences based on the assumption parameter of embedded length for calculation of bond strength between coupler and concrete. Moreover, the MBC moment coupler have more higher value of bond compared to MCHG specimens.

The bond-slip reduces about 5–25% between both MBC and MHGC specimens compared to normal lapping specimens. All the MHGC samples show lesser slip compare to the MBC specimen. The ultimate slip is 4.79 mm, 3.61 mm and 2.32 mm for MBC16, MBC20, and MBC25, respectively. Meanwhile, the maximum slip for MHGC16, MHGC20, and MHGC25 are 3.79 mm, 2.16 mm, and 1.79 mm, respectively. The measured slip between the MBC specimens with normal lapping shows a significant decrease although MBC specimens show lesser maximum slip than MHGC. This is due to the friction between the shear bolt and the reinforcement inside the coupler. It can be concluded that the grout inside the coupler in one end and a threaded bar on the other side affected the slip for MCHG, which has the ability to hold incredibly heavy loads. According to manufacturer Leviat A CRH Company, Halfen-Moment product [16], this mechanical coupler provides seismic resistance and can meet seismic requirements when used along with 100 MPa grout. Therefore, it can be concluded that the ultimate slip is improved when the mechanical coupler is introduced as a method of splicing between two reinforcements.

3.3 Effect of Parameters

Effects of Diameters and Embedded Lengths on The Bond Strength and Slip

The influence of the bar diameters and embedment lengths on the ultimate tensile bond intensity and the maximum slip for embedded mechanical coupler pull-out tests are illustrated in Figs. 9 and 10. It can be seen in Fig. 9 that the bond strength declines and the resulting decrease in ultimate slip as the bar diameters rise from 16 to 25 mm. The ultimate bond strength increases by 8 MPa for MBC16 compared with NL16. However, only an approximate 4 MPa bond strength increase for MBC20 and MBC25 is observed. It is indicated that the influence of bond intensity affected the ultimate slip between mechanical coupler and concrete.

It is found that the ultimate bond strength showed reduction and a resulting drop in the ultimate slip with the increase of embedded length (Fig. 10). There is a negative

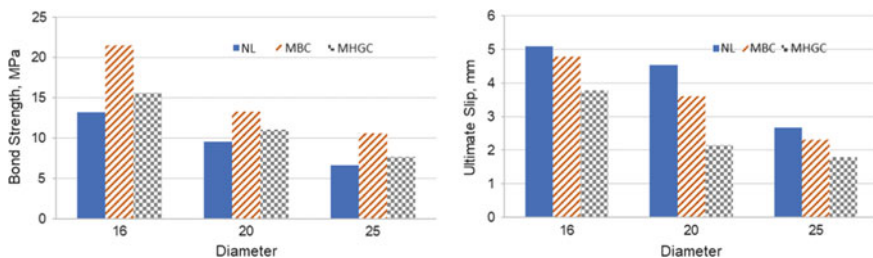


Fig. 9 Effects of diameter on ultimate bond strength and slip for embedded specimens of normal lapping, MBC and MHGC

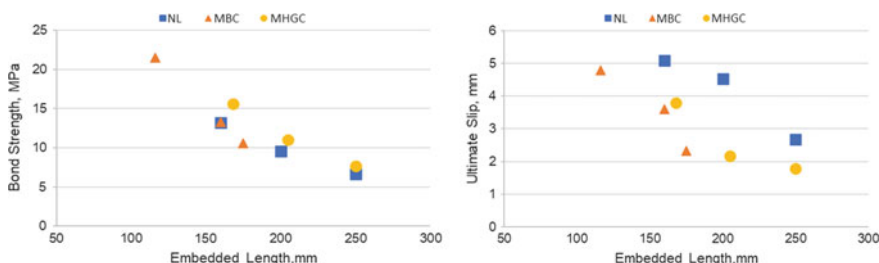


Fig. 10 Effects of mechanical couplers embedded length on ultimate bond strength and slip for embedded specimens of normal lapping, MBC and MHGC

linear downward trend for bond strength for all specimens as the embedded length of couplers increases. As shows in Fig. 10, the normal lapping for 16 mm and 25 mm diameter has a similar embedded length for MBC20 and MHGC25, giving almost an equal bond intensity by 13 MPa and 7 MPa, respectively. As the development of embedded length increases from 160 to 250 mm, the slip decreases by 46%, 50% and 53% for NL, MBC, and MHGC specimens, respectively.

Comparison of the Experimental Bond Strength with Other Equations of Bond Intensity

Several previous researchers have attempted to formulate equations for the relation between the reinforcing bars and the concrete. In this study, the bond strength’s experimental outcomes are compared with the predicted ultimate bond intensity equations from Oragun et al. [18]. Below are the proposed equations:

$$\tau_u = 0.083045/\sqrt{f'c}[1.2 + 3(c/d_b) + 50(d_b/L_d)] \tag{3}$$

where

- c* the concrete cover, mm.
- f'c* the concrete compressive strength MPa,
- d_b* the diameter of reinforcement, mm.
- L_d* the length development, mm.

Table 5 Comparison of the experimental bond strength with other equations of bond intensity

Specimen	Experimental bond strength (MPa)	Orangun et al. [18]	Experiment test bond strength/prediction equations of the bond intensity ratio
NL16	13.19	14.78	0.89
NL20	9.56	11.85	0.81
NL25	6.63	9.50	0.70
MBC16	21.5	15.36	1.40
MBC20	13.3	12.33	1.08
MBC25	10.57	10.58	1.00
MHGC16	15.61	14.65	1.07
MHGC20	11.03	11.33	0.97
MHGC25	7.64	9.19	0.83

Table 5 and Fig. 4 describe the comparison of experimental bond strength with predicted bond equation from Orangun et al. [18]. In this study, the predicted bond equation has been selected since the parameters involved in the equation can be used for calculating bond strength. Based on the predicted equation, the length of development, L_d is assumed to be the coupler's embedded length. Meanwhile, for concrete cover, c is defined as the cover between couplers.

It can be seen from Table 5, the comparison between the predicted equation and experimental bond test result provides the best match. The ultimate bond strength obtained from the experimental work for MBC20, MBC25, MHGC16, and MHGC20 agreed quite well with the predicted equation with the mean ratio being the closest to 1.00, is 1.08, 1.00, 1.07, and 0.97, respectively. Meanwhile, the predicted equation gives an overestimated mean ratio for all standard lapping specimens with a ratio of 0.89, 0.81, and 0.70, respectively. The predicted equation also gives an overestimated mean ratio of 0.83 for MHGC25. A greater or equal to one ratio indicates that the experimental results are more likely to occur at a strength greater than the predicted equation. Meanwhile, the ratio less than one means that the predicted equation not suitable to calculate the related experimental specimens as they are unconservative. The test result from the experimental work for specimen MBC16 provides a higher value than the one predicted. It is evident from Fig. 11 that the results from the experimental show the higher bond intensity than 5 MPa than the predicted equation, which recorded the mean ratio of 1.40.

4 Conclusion

This paper presented in-air and embedded mechanical coupler in-concrete experimental investigation for the different reinforcement coupling systems, accompanied by a discussion of their main performance parameters in terms of strength and

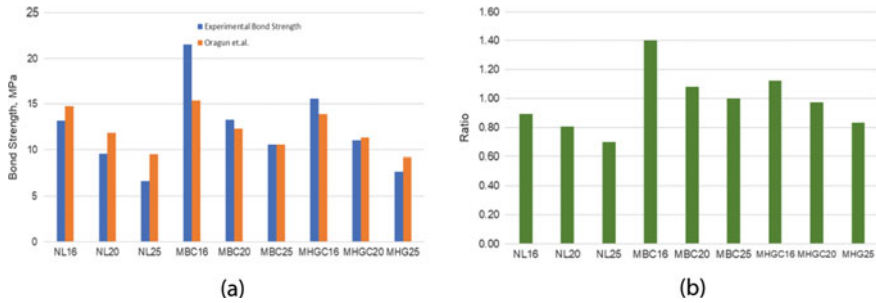


Fig. 11 **a** The experimental and predicted bond strength, **b** ratio between experimental results with the predicted bond equation for different rebar and mechanical couplers

bond stress. Based on the experimental results, the following main conclusions are highlighted.

1. The mechanical couplers MBC and MCHG significantly increase its ultimate load (without embedded in concrete) and the bond strength of the concrete with embedded mechanical coupler through pull-out tests.
2. All specimens for the in-air pull-out test failed due to bar yield. However, only MBC16 failed at the coupler due to the screw bolts off the surface of the reinforcement.
3. The bond-slip result reduces about 5–25% for both mechanical coupler specimens compared with normal lapping specimens.
4. The friction between the shear bolt and the reinforcement inside the coupler enhances the ultimate slip of MBC specimens.
5. The MHGC provides good ultimate slip resistance that would lead to seismic-resistant properties which can hold high load
6. The ultimate slip was improved when the mechanical coupler was introduced as a method of splicing between two reinforcement bars.
7. The bar diameter has significantly affected the bond strength and ultimate slip. When the diameter of couplers increases, the bond and slip decrease.
8. As the development of embedded length from 160 to 250 mm, MHGC give the best results for bond intensity.
9. The ultimate bond strength for the samples embedded mechanical couplers from the experimental works agreed quite well with the predicted equation derived from the previous researchers.

Acknowledgements The study discussed in this paper is funded by the Lestari grant 600-IRMI 5/3/LESTARI (045/2019), Universiti Teknologi MARA (UiTM). Special thanks to Structure Laboratory's technical staff at the Faculty of Civil Engineering, Universiti Teknologi MARA, Shah Alam, Malaysia, for assisting with instrumentation and data collection. The support of the mechanical coupler from the Leviat A CRH Company, Halfen-Moment product is also gratefully acknowledged.

References

1. Bompa DV, Elghazouli AY (2018) Monotonic and cyclic performance of threaded reinforcement splices. *Structure* 16:358–372
2. Aaleti S, Brueggen BL, Johnson B, French CE, Sritharan S (2012) Cyclic response of reinforced concrete walls with different anchorage details: experimental investigation. *J Struct Eng* 139(7):1181–1191. [https://doi.org/10.1061/\(ASCE\)ST.1943-541X.0000732](https://doi.org/10.1061/(ASCE)ST.1943-541X.0000732)
3. Lee SJ, Lee DH, Kim KS, Oh JY, Park MK, Yang IS (2013) Seismic performances of RC columns reinforced with screw ribbed reinforcements connected by mechanical splice. *Comput Concr* 12(2):131–134. <https://doi.org/10.12989/cac.2013.12.2.131>
4. Singh R, Himanshu SK, Bhalla N (2013) Reinforcement couplers as an alternative to lap splices: a case study. *Int J Eng Res Technol* 2(2):6
5. Chiari VG, Moreno JAL (2018) Experimental evaluation of coupler behavior for mechanical rebar splices in reinforced concrete structures. *Revista IBRACON de Estruturas e Materiais* 11(6):1326–1353. <https://doi.org/10.1590/s1983-41952018000600009>
6. Ng PL, Guan GX, Kwan AKH (2017) Role of reinforcement couplers in serviceability performance of concrete members. *IOP Conf Ser Mater Sci Eng* 251:012103. <https://doi.org/10.1088/1757-899X/251/1/012103>
7. Ling JH, Rahman ABA, Ibrahim IS, Hamid ZA (2012) Behaviour of grouted pipe splice under incremental tensile load. *Constr Build Mater* 33:90–98
8. Ling JH, Rahman ABA, Ibrahim IS (2014) Feasibility study of grouted splice connector under tensile load. *Constr Build Mater* 50:530–539
9. Rahman ABA, Yoon LH, Ibrahim IS, Mohamed RN, Mohammad S, Saim AA (2015) Performance of grouted splice sleeves with tapered bars under axial tension. *Appl Mech Mater* 789–790:1176–1180
10. Haber ZB, Saiidi MS, Sanders DH (2014) Seismic performance of precast columns with mechanically spliced column-footing connections. *ACI Struct J* 111(3):639–650
11. Phuong ND, Mutsuyoshi H (2015) Experimental study on performance of mechanical splices in reinforced concrete beams. *ACI Struct J* 112(6):749–760
12. Jokūbaitis V, Juknevičius L (2010) Influence of reinforcement couplers on the cracking of reinforced concrete members. In: Vainiūnas P, Zavadskas EK (eds) *Proceedings of 10th international conference of modern building materials, structures and techniques*. Technika, Vilnius, Lithuania, pp 646–650
13. Long X, Wang C-Y, Zhao P-Z, Kang S-B (2020) Bond strength of steel reinforcement under different loading rates. *Constr Build Mater* 238:117749. <https://doi.org/10.1016/j.conbuildmat.2019.117749>
14. Bilek V, Bonczková S, Hurta J, Pytlík D, Mrovec M (2017) Bond strength between reinforcing steel and different types of concrete. *Proc Eng* 190:243–247
15. Alhawat M, Ashour A (2019) Bond strength between corroded steel reinforcement and recycled aggregate concrete. *Structures* 369–385. <https://doi.org/10.1016/j.istruc.2019.02.001>
16. Leviať A CRH Company (2020) Moment product SLEVIAT 2020—moment coupler brochure DRAFT 3.2. <https://www.leviat.com/our-brands/moment>
17. Hamdan N, Rahman AB (2016) Bond strength between steel reinforcement and grouted splice sleeve connector. <https://www.semanticscholar.org/paper/Bond-Strength-between-Steel-Reinforcement-and-Hamdan-Rahman/e0b459d7b2a60f4d2858541a7604029fb4438139>
18. Orangun CO, Jirsa IO, Breen JE (1977) A re-evaluation of the test data on the development length and splices. *ACI J* 74(3):114–122

Construction Management

Construction Supply Chains for Strategic Materials of Building Contractors in the Greater Bandung Areas



I. Made Bhisma Pranandya, F. S. C. S. Maisarah, and Muhamad Abduh

Abstract Building contractors in the Greater Bandung areas has been facing challenges due to the economic growth of in the tourism sector. Private buildings such as residential, hotel and apartment have been developed to support the growth. Building contractors should have some strategies in doing their business, one of the important strategies is purchasing strategy in construction materials. However, to manage the purchasing efficiently and effectively, the supply chain of strategic construction materials should be mastered by each contractor. Therefore, a study on the supply chain of strategic materials of the building projects in the Greater Bandung areas is needed. The paper discusses a study to identify the construction supply chain of building contractors, i.e., the structure and behaviour of the supply chain, in the Greater Bandung areas, Indonesia. The study uses a survey method to 17 building contractors in the Greater Bandung areas as a start point to further look for the suppliers of their strategic construction materials and their supply chain's structure and behaviour. The coverage of the structure of the construction supply chain is its channels, number suppliers involved for each strategic material and suppliers' capacities. The behaviour includes the relationships between suppliers and how they set up the prices. Another result from the study explain the practices of material and purchasing management by the building contractors in the area of Greater Bandung.

Keywords Behaviour · Building contractors · Logistics · Materials · Structure · Supply chains

1 Introduction

One of the parts about expenses by contractors is cost utilization for material purchase. Purchasing construction materials involve many parties. In the amount

I. Made Bhisma Pranandya (✉) · F. S. C. S. Maisarah · M. Abduh
Faculty of Civil and Environmental Engineering, Institut Teknologi Bandung, Bandung, Indonesia

M. Abduh
e-mail: abduh@itb.ac.id

of 60–80% from all the operations in construction projects is processes of material purchase and services from the suppliers or subcontractors. Those percentages cause the part of the material supply chain gives impacts against the construction project's performance [1]. Kraljic [2] asserts that purchasing gives about 40–80% contribution to the total of company costs, so if the contractors have contracts with suppliers who are not capable or qualified, it will make the contractors become a loss.

Purchasing has a purpose which is buying materials with the right quality, right quantity, right place, right time, and the right price. Based on the purpose of purchasing, so the contractors need a purchasing strategy which has factors. For example, the factors like the quantity of supply segment to buy, a quantity of supplier's option, the type of cooperative relationship between contractors and suppliers, the type of contracts that appropriate, and the appropriate of procurement operational strategy. From the purposes of material purchasing, gives us the perception of purchasing strategy that efficient and effective. The way to get an efficient and effective purchasing strategy is the contractors need to master the supply chain of the strategic materials. If the contractors could take control of the supply chain, then they will make the construction process more efficient and more effective.

The aim of this study is mapping the structure and finding the behaviour of materials construction's supply chain in Indonesia, with the special case the Greater Bandung areas in West Java. In west Java, there are 8.895 contractors with small-sized. The number of contractors with small-sized is dominant in West Java [3]. For the Greater Bandung areas, there are 2.216 small-sized contractors, and they are about 83.7% of the population of contractors. Four cities included in Greater Bandung areas are Cimahi City, Bandung City, Bandung District, and West Bandung District.

Some strategic materials become necessary for construction projects. For the building contractors in Greater Bandung that minor classified, there are bricks, cement, concrete, reinforcing steel, glass, and coarse. The strategic materials give an effective amount of 49.78% to construction material purchasing and 31.06% from the total of cost construction [4]. Most small-sized contractors in Greater Bandung makes this situation become a priority in a supply chain system.

There are two research objectives of this study. First, acquiring the illustration of the supply chain structure for strategic materials of building contractors in Greater Bandung areas. Secondly, identifying the conduct of supply chain parties for strategic material of building contractors in Greater Bandung areas.

2 Structure and Behaviour of Supply Chain

The concept of a supply chain is generally referred to as the alignment of firms that bring products or services to market [5]. Manufacturer, suppliers, transporters, warehouses, wholesalers, retailers, and even customers are included in the supply chain. Chen and Paulraj [6] stated that a typical supply chain is a network of materials, information and services processing links with the characteristics of supply, transformation and demand. There is an internal supply chain between suppliers and

customers. The internal supply chain consists of three different parts. The three parts are purchasing, production, and distribution.

Mentzer et al. [7] define that supply chain as a set of entities (organizations or individuals) directly involved in the supply and distribution flows of goods, services, finances, and information from a source to a destination (customer). There is three degrees of supply chain complexity: a “direct supply chain”, an “extended supply chain”, and an “ultimate supply chain” (see Fig. 1). The direct supply chain consists of a central organization, its suppliers and its customers. The extended supply chain includes suppliers of the immediate suppliers and customers of the immediate customer. The ultimate supply chain includes all organizations that are involved in all flows of products, services, finance, and information from the suppliers until the customers.

The supply chain can have different degrees of complexity depending on the numbers of members and the variety of business process, but there is always a central organization. This central organization can manage the entire supply chain or not and even the supply chain is not managed [7].

An integrated supply chain can generally contain three interrelated flows: material flows (purchasing, transformation, and distribution), informational flows (electronic data exchange or website linkages), and the financial flows (the payment to suppliers for the goods and services and the payment by the customer to the retailer for the final product) [8]. The flows direction in the supply chain is not only one way (to forwarding), from the first supplier to the final customer. Goods can flow back up the supply chain for different reasons such as service or repair, recycling or disposal. The reverse chain can play an important role in areas such as customer satisfaction, recycling and environmental protection. The supply chain has multiple linked suppliers. There are many different configurations for the supply chain. Some of the supply chains are very short and simple but some of the supply chains are long and complicated.

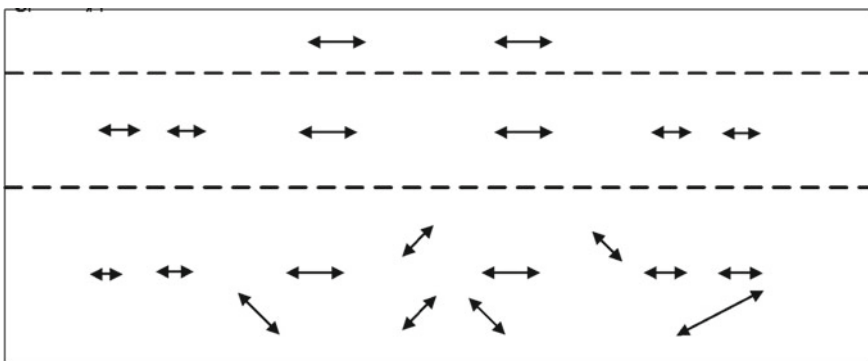


Fig. 1 Types of channel relationships [7]

Lambert, Cooper and Pugh [9] provide insights for mapping supply chain structure through three primary attributes: members of the supply chain, structural dimensions, types of process links; indicating the structure of different supply chains and the interconnection between several focal organizations' supply chains and the resultant *networks of supply*. An early exploratory study using Lambert et al.'s conceptual mapping as a starting point by London and Kenley [10] reported largely on simple descriptions of horizontal and vertical structure, i.e. 'who' supplies to 'whom' along the supply chain and potential numbers of alternative suppliers within the tiers.

Figure 2 describes the contractual relationships between firms in the supply chain that are inveterate within markets. There are several approaches to consider when exploring the nexus between industrial organization economics and analytical modelling. Figure 2 is largely focused upon bringing the industrial organization model closer to the strategic procurement environment for an individual firm. The fundamental assumption in this model is that the supply chain in this instance is 'owned' by the client, who is the focal supply chain organisation.

For the conduct of supply chain parties, it will be examined about marketing strategy. The marketing strategy is about networking between suppliers and customers. Marketing involves several activities. To begin with, an organization may decide on its target customers to be served. If the target had been decided, the product is to be placed in the market by providing the appropriate product, price, distribution and promotional efforts.

These are to be combined or mixed in an appropriate proportion to achieve the marketing goal. Such a mix of product, price, distribution and promotional efforts

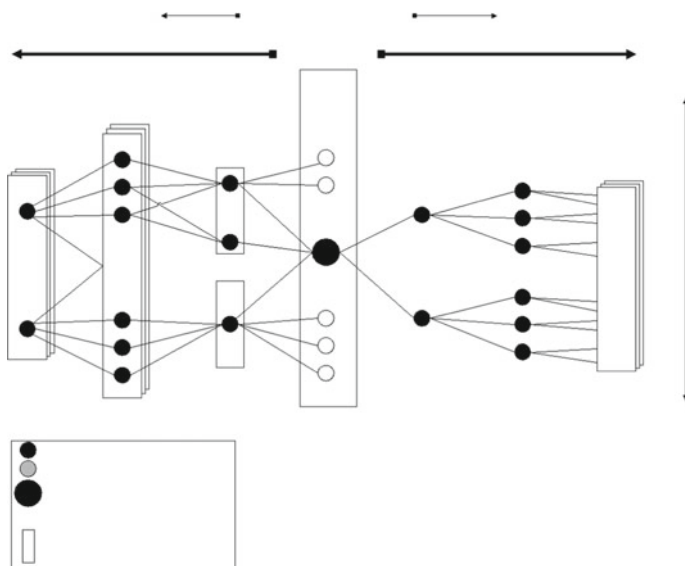


Fig. 2 Construction project supply chain structure from an industrial organization perspective (London et al. [10] after Lambert et al. [5])

is known as “Marketing Mix”. Kotler [11] says that the marketing mix is the set controllable variables that the firm can use to influence the buyer’s responsibility. The controllable variables are referred to as the 4 ‘P’ (product, price, place, and promotion). Each firm strives to build up a composition of 4 ‘P’ that can create the highest level of consumer satisfaction and the organisational objectives.

Table 1 4 ‘P’ marketing mix (source Kotler [11])

No.	Variables	Sub-variables	No	Variables	Sub-variables
1	Product	Variety	3	Place	Channels
		Design			Coverage
		Quality			Locations
		Features			Inventory
		Brand name			Transportation
		Packaging			Logistics
		Services			
2	Price	List price	4	Promotion	Advertising
		Discounts			Personal selling
		Allowances			Sales promotion
		Payment period			Public relations
		Credit terms			

1. **Product:** product refers to the goods and services offered by the organization. In simple words, the product can be described as a bundle of benefits which a marketer offers to the consumer for a price
2. **Price:** Price is the amount charged for a product or services. Pricing is a very crucial decision area as it affects demand for the product and also on the profitability of the firm.
3. **Place:** goods are produced to be sold to consumers. They must be made available to consumers at a place where they can conveniently make a purchase.
4. **Promotion:** If the product is manufactured keeping the consumer needs in mind, is rightly priced and made available at outlets convenient to them but the consumer is not made aware about its price, features, availability, its marketing effort may not be successful.

3 Strategic Commodities

A strategic commodity is a commodity that is considered to be of utmost importance to the economy of a nation, usually to the extent that if the open trading of the commodity is disrupted in some manner the economy will suffer severely. Beside strategic commodities, there are some strategic materials in the construction industry. Strategic materials are defined as key resources that transcend individual industries

in their application. Strategic materials are obtained from several primary resources: the extraction of natural materials from domestic or foreign sources and the creation and production materials from domestic or foreign resources. Kraljic [2] strategic materials are defined as commodities that have high value and in a long-term way, the availability weighs to the production process.

In this research depends on Irfianto et al. [4] research, seven materials become the strategic materials for building contractors in Greater Bandung areas, namely Bricks, Cement, Concrete, Reinforcing steel, Glass, Lumber, and Coarse.

4 Research Methodology

The methodology section describes actions to be taken to investigate a research problem and the rationale for the application of specific procedures or techniques used to identify, select, process, and analyse information applied to understanding the problem, thereby, allowing the reader to critically evaluate a study's overall validity and reliability [12].

4.1 Data Collection Method

The data collection method is the process of gathering and measuring information on variables of interest, in an established systematic fashion that enables one to answer stated research questions, test hypotheses, and evaluate outcomes. The goal for all data collection is to capture quality evidence that then translates to rich data analysis and allows the building of a convincing and credible answer to questions that have been posted [13].

In this research, there are two types of data: primary data and secondary data. The primary data obtained from the questionnaire and direct interviews with the respondents. The secondary data obtained from the literature related to supply chain structure and conduct of supply chain parties. The techniques of data collection are starting to do direct interviews from the small-sized contractors in Greater Bandung areas. After that, the direct interviews will continue to the suppliers of strategic materials. The direct interviews technique will get the illustration of supply chain structure.

For the conduct of supply chain parties, there are some variables from the marketing mix theory. There is an instrument likes questionnaire that will help to get conduct of supply chain parties.

Table 2 shows the variables that will be an instrument to collect primary data from small-sized contractors in the Greater Bandung areas. This instrument is like guidelines to help the process of direct interview with the respondent. In this research, there are two types of respondent. The first is small-sized contractors as the final customer of the construction materials supply chain and the second is suppliers of construction materials.

Table 2 Variables of research instrument for respondents

No	Main variable	Categories	Code
<i>A. Respondent profile</i>			
1	Respondent information	Name	A.1.1
		Position	A.1.2
2	Company's information	Company's name	A.2.1
		Address	A.2.2
		Company's qualification	A.2.3
<i>B. Supply chain structure</i>			
3	Supplier's information	Supplier's name	B.3.1
		Supplier's address	B.3.2
<i>C. Conduct of supply chain parties</i>			
4	Price	Supplier selection based on price aspects	C.4.1
5	Promotion	Supplier selection techniques	C.5.1
6	Place	Supplier selection based on location aspects	C.6.1
		Delivery transportation	C.6.2
7	Product	Supplier selection based on quality and quantity aspects	C.7.1
		Supplier Selection based on services	C.7.2

Descriptive data collection means the data collected are in the form of words and sentences. Such data often capture feelings, emotions, or subjective perceptions of something. This approach aims to address the ‘how’ and ‘why’ of a program and tends to use unstructured methods of data collection to fully explore the topic. These data collection methods include focus groups, group discussions and interviews. This approach is good for further exploring the effects and unintended consequences of a program [13].

4.2 Data Analysis Method

Comparative research is the act of comparing two or more things to discover something about one or all of the things being compared. This technique often utilizes multiple disciplines in one study. When it comes to method, the majority agreement is that there is no methodology peculiar to comparative research [14]. The data in this research will be analysed with the comparative method. The data will be compared between one data to other data. The comparative method can also be done between the primary data and literature that appertain with supply chain structure and conduct of supply chain parties. After collecting data, there is an analysis process that will calculate the value of the mode of each sub-variable. After that, the value of the mode will be categorised to Table 3.

Table 3 Interpretation criteria of the modes sub-variables

The modes (%)	Interpretation criteria
0–20	Never, unimportant
21–40	Rarely, secondary
41–60	Often enough, quite important
61–80	Often, important
81–100	Always, very important

5 Results

The results found a mapping of structure and behaviour of materials construction supply chain from data survey. The survey involved 17 respondents of small-sized contractors and 30 suppliers in the Greater Bandung areas. The supply chain structure is mapping the parties from the downstream until upstream of the supply chain. The conduct of supply chain parties is identified from the analysis of price, promotion, place, and product aspects.

5.1 Supply Chain Structure

The illustrations of supply chain structure are on data tabulation. The primary data form respondent is categorized based on the tiers and identities on the supply chain structure. The identification of supply chain structure must reach to the upstream of the supply chain. In the Table 4 there are some of supply chain structure that has already reached the upstream. For example, on the concrete materials, the identification process reached the batching plant in the Greater Bandung areas. The factories and the quarries have been identified. Four factories become cement suppliers to the batching plant. For the quarries, there are two types of quarries. The coarse quarry with one respondent and the gravel's quarry with three respondents.

From reinforcing steel materials, the supply chain structure has reached the reinforcing steel factories. The contractors have two options for the suppliers of reinforcing steel. The supply can be from the retails that also sell another strategic material. The second option is supplied form steel retails that only sell one type of strategic materials. The distributor of reinforcing steel is the location outside the Greater Bandung areas, and also the factories. The illustration supply chain structure of reinforcing steel has similarities with the illustration supply chain structure of glass. The similarities are the number of tiers is 5 tiers, there are tiers after retails that have been identified as retailers that sell specific materials.

There are third parties on the supply chain structure of bricks and coarse. The third parties are companies or individuals that give transportation services for those strategic materials. The third parties just give services to customers. Small-sized contractors cannot make direct orders to the first tier, they have used the third parties.

Table 4 Supply chain structure for strategic materials

Coarse			
4th tier	3rd tier	2nd tier	1st tier
Final costumer	Retail	Third parties	Quarry
K1		TP1	Q1, Q2
K2	R1	TP10	
	R2		
K3		TP2	
K4	R4	TP3	
K5		TP4	
K6		TP5	
K7	R5	TP6	
K8	R6	TP7	
K9	R7	TP9	
	R8		
	R9		
K10		TP8	
Bricks			
4th tier	3rd tier	2nd tier	1st tier
Final costumer	Retail	Third parties	Home industry
K1		B1	Hn
K2	R1	B8	
	R2		
K3	R10	B2	
K4	R11	B3	
K5	R12	B4	
K6	R13	B9	
	R14	B10	
K7		B5	
K8	R15	B6	
K9	R7		
Cement			
4th tier	3rd tier	2nd tier	1st tier
Final costumer	Retail	Distributor	Factory
K1	R16	C2, C3	F1, T2, T3, F4
	R17	C1, C4	
	R18	C4	
	R19	C1	

(continued)

Table 4 (continued)

Cement			
4th tier	3rd tier	2nd tier	1st tier
Final costumer	Retail	Distributor	Factory
K2	R1	C3, C4, C5	
	R2	C3, C4	
K3	R10	C1, C4	
K4	R20	C1	
	R21	C1	
	R22	C4	
K5	R23	C1, C4	
	R24	C1, C4	
	R12	C1	
K6	R13	C1	
	R14	C1, C4	
K7	R2	C3, C4	
K8	R25	C2, C3	
	R15	C4	
K9	R7	C1, C4	
	R26	C1, C2, C4	
K10	R21	C1	
	R27	C1, C5	
	R28	C4	
Concrete			
4th tier	3rd tier	2nd tier	1st tier
Final costumer	Batching plant	Factory	Quarry
K1	BP1	F1	Q1, QG1, QG2, QG3
K2	BP2	F1	
K3	BP1	F1	
	BP2	F1	
	BP3	F2	
K4	BP1	F1	
	BP2	F1	
K5	BP1	F1	
	BP4	F3	
K6	BP1	F1	

(continued)

Table 4 (continued)

Concrete				
4th tier	3rd tier	2nd tier	1st tier	
Final costumer	Batching plant	Factory	Quarry	
K7	BPS	F4		
	BP2	F1		
	BP3	F2		
K8	BP6	F2, F3		
	BP1	F1		
K9	BP2	F1		
	BP1	F1		
K10	BP4	F3		
	BP1	F1		
K10	BP7	F1		
Reinforcing steel				
5th tier	4th tier	3rd tier	2nd tier	1st tier
Final costumer	Retail	Steel retail	Distributor	Factory
K1	R29	S1	DR3	FS1, FS2
		S1	DR3	
		S2	DR1	
K2	R1		DR1	
	R2		DR2	
K3	R10	S3	DR4	
K4	R11	S3	DR4	
			DR2	
K5		S4	DR6, DR7	
		S5	DR5	
		S6	DR3	
K6	R14		DR1	
K7	R2		DR2	
K8		S7	DR4, DR7	
K9	R7	S3	DR4	
K10		S4	DR6, DR7	
		S5	DR5	
		S6	DR3	

(continued)

Table 4 (continued)

Lumber				
5th tier	4th tier	3rd tier	2nd tier	1st tier
Final costumer	Retail	Distributor	Factory	Cut block
K1		D1	FL1, FL2, FL3, FL4	CBn
K2	R1			
	R2			
K3	R10			
K4	R20			
K5	R21	D2		
	R22			
	R23	D2		
	R24			
K6	R12			
	R13			
	R14	D3		
K7	R2			
K8	R25			
	R15			
K9	R7	D2		
	R26	D1		
K10	R21			
	R27	D1		
	R28	D3		
Glass				
5th tier	4th tier	3rd tier	2nd tier	1st tier
Final costumer	Retail	Class retail	Distributor	Factory
K1		G1	DG1	FGn
		G2	DG1, DG2	
K2	R1		DG1	
	R2		DG2	
K3			DG3	
K4		G3	DG1	
K5	R21		DG2	

(continued)

Table 4 (continued)

Glass				
5th tier	4th tier	3rd tier	2nd tier	1st tier
Final costumer	Retail	Class retail	Distributor	Factory
	R22		DG1	
	R23		DG2	
K6	R13		DG2	
	R14		DG1, DG2	
K7	R2		DG1	
K8		G4	DG1, DG2	
	R25		DG2	
K9	R7		DG1	
K10	R28		DG1	
Legends				
Kn	Small sized contractors	Dn	Lumber distributor	
Kn	Retailers	FLn	Lumber factory	
TPn	Third parties of coarse	CBn	Cut block	
Qn	Quarry of coarse	DRn	Reinforcing steel distributor	
Bn	Third parties of bricks	FSn	Reinforcing steel factory	
Hn	Home industry of bricks	Gn	Glass retailer	
Cn	Cement distributor	DGn	Glass distributor	
Fn	Cement Factory	FGn	Glass factory	
QGn	Quarry of gravel			

The last strategic material is lumber. Lumber material has been identified until the upstream of the supply chain. Cut Block is upstream of lumber supply chain structure. The factory of lumber is depend-on the types of lumber. The local lumber is still in the Greater Bandung areas, but lumber with the greater quality is produced outside the Greater Bandung areas.

5.2 Conduct of Supply Chain Parties

The conduct of supply chain parties is on tabulation data. The process of tabulation data is starting from calculating the mode from each of the variables. The calculating of the mode is an ordinary statistic. After the calculating process, the mode will describe the conduct of supply chain parties. In Table 5 Describe the modes on every variable. The conduct in Table 5 is a relationship between building contractors and suppliers. There are four main variables from marketing mix theory: Price, Promotion, Place, and Product. From the main variables will describe the conduct

Table 5 The conducts of contractors based on marketing mix variables

No.	Main variables	Sub-variables	Percentage (%)	Criteria
1	Price	Supplier selection based on price aspects	96	Appropriateness of price with the quality offered
			73	The cheapest price
			69	Discounts
2	Promotion	Supplier selection techniques	85	Material price survey
			39	Without price survey
			49	Sales marketing come to offer products
			41	Based on electronics
			73	Based on kinship
			64	Get from the advertisements or the internet
			25	Subsidiary
3	Place	Delivery transportation	94	Material delivered by the suppliers
			44	The contractors takes itself
			36	Used third party
4	Product	Supplier selection based on quality and quantity aspects	96	Material compatibility with agreed specifications
			91	Supply of materials without defects
			94	Consistency of quality
			99	Provide according to the order quantity
			83	Ease of payment method
			95	On time delivery
			90	Good respond to order materials
		Supplier selection based on services	86	Good respond to complaints
			96	Ease of communication
			54	Free delivery cost
			90	Clarity of information and easy to understand
			76	Distance to supplier's

(continued)

Table 5 (continued)

No.	Main variables	Sub-variables	Percentage (%)	Criteria
				warehouse

of contractors building. For example, the small-sized building contractors in Greater Bandung will evaluate the suppliers from the price aspect about the appropriateness of price with the quality offered. There are three criteria from supplier selection based on price aspects of sub-variables.

From promotion variables, the building contractors will do direct procurement with the suppliers, but the building contractors will conduct a material price survey first. From the place variables, there are delivery transportation sub-variables of the place is transportation. Transportation is delivery services which are provided by suppliers. Even if sometimes the building contractors just pick up from the retails immediately, because of the urgent situation in the project site.

From the product variables there are also two categories, first is supplier selection based on quality and quantity aspects. From those categories, based on the results of modes calculations, materials should be compatible with the specification that has been agreed.

From the quantity aspects, the building contractors emphasize that the quantity must be accorded to the order. The last categories are supplier selection based on the services aspect. The modes calculation shows that ease of communication and on-time delivery are the most important variables for the building contractors to do supplier selection.

Table 6 gives information about the modes from retailer respondents. This information describes the conduct of retailers from marketing mix variables. From price variables, appropriateness of price with the quality offered is important variables. From the promotion aspect, the retailers have the technique to do supplier selection. The retailers will survey the price first from marketing sales that come to their store. The retailers will compare the price and quality and evaluate from other aspects. The transportation for material delivery is provided by their suppliers. The last main variable is the product that has two different categories. The first category is supplier selection based on quality and quantity. The retailers will evaluate the quality of materials and compare with the specification that has been required. The quantity should be consistent with the ordering. The retailers are considered the suppliers from their services. The services are about ease of payment method and delivery should be on time to their store.

For distributors that become supply chain parties, the process of supplier selection is rarely happening. This situation happened because the distributors have few suppliers. Sometimes they only have one supplier, because the suppliers are direct to the factory of the materials. For example, the distributors of cement materials supply their needs directly to factories depending on their products. This conduct also happens in other materials like lumber, glass, and reinforcing steel.

Table 6 The conducts of retailers based on marketing mix variables

No.	Main variables	Sub-variables	Percentage (%)	Criteria
1	Price	Supplier selection based on price aspects	95	Appropriateness of price with the quality offered
			94	The cheapest price
			66	Discounts
2	Promotion	Supplier selection technique	88	Material price survey
			43	Without price survey
			89	Sales marketing come to offer products
			22	Based on electronics
			26	Based on kinship
			31	Get from the advertisements or the internet
			22	Subsidiary
			3	Place
45	The contractors takes itself			
25	Used third party			
4	Product	Supplier selection based on quality and quantity aspects	97	Material compatibility with agreed specifications
			94	Supply of materials without defects
			94	Consistency of quality
			97	Provide according to the order quantity
			94	Ease of payment method
			94	On time delivery
		Supplier selection based on services	87	Good respond to order materials
			86	Good respond to complaints
			84	Ease of communication
			66	Free delivery cost
			83	Clarity of information and easy to understand
			60	Distance to supplier's warehouse

6 Conclusions

The study of structure and behaviour of construction materials supply chain from the small-sized approach conclude two main aspects. First, the supply chain's structure gives information that the small-sized building contractors in Greater Bandung areas have path choices to fulfil their material needs. For bricks materials, there are three option paths (retailers, third parties, and direct to home industry). The cement materials have two path options (retailers and distributor). Reinforcing steel has two option paths (retailers and steel retailers). For concrete materials, the contractors only have one stripe and it is direct to the batching plant. The lumber materials have two option paths (retailers and distributors), the glass materials have three option paths (retailers, glass retailers, and distributors). The coarse material also has three option paths (retailers, third party and direct to the quarry). Secondly, the conduct of supply chain parties based on price aspects are the appropriateness of price with the quality offered. From the quality and quantity aspects, material compatibility with agreed specifications and according to the order quantity are the most important criteria. From the services aspects, on-time delivery is the most important criteria for supplier selection. The supplier selection technique is a material price survey. The transportation is always provided by the material suppliers.

References

1. Dubois A, Gadde L-E (2002) The construction industry as a loosely coupled system: implications for productivity and innovation. *Constr Manag Econ* 20(7):621–631
2. Kraljic P (1983) Purchasing must become supply management. *Harvard Business Review*
3. Central Bureau of Statistics (BPS) of West Java (2018) *Konstruksi Dalam Angka Provinsi Jawa Barat 2017*. Central Bureau of Statistics, Bandung
4. Irfanto R, Maisarah FSCS, Abduh M (2019) Purchasing strategy of small-sized contractors for building projects in the Greater Bandung Areas. *IOP Conf Ser Mater Sci Eng* 650(1):012004. <https://doi.org/10.1088/1757-899X/650/1/012004>
5. Lambert DM, Stock JR, Ellram LM (1998) *Fundamentals of logistics management*. Irwin/McGraw-Hill, Boston
6. Chen IJ, Paulraj A (2004) Towards a theory of supply chain management: the constructs and measurements. *J Oper Manage* 22(2):119–150
7. Mentzer JT, DeWitt W, Keebler JS, Min S, Nix NW, Smith CD, Zacharia ZG (2001) Defining supply chain management. *J Bus Logist* 22(2):1–25
8. Waller DL (2003) *Operations management: a supply chain approach*, 2nd edn. Thomson Learning
9. Lambert DM, Cooper MC, Pagh JD (1998) Supply chain management implementation issues and research opportunities. *Int J Logist Manage* 11(1):1–17
10. London K, Kenley R (2000) Mapping construction supply chains: widening the traditional perspective of the industry. In: *Proceedings 7th annual European association of research in industrial economic EARIE conference*, Switzerland
11. Kotler P, Amstrong G (2004) *Principles of marketing*, 10th edn. Prentice Hall Inc., Englewood Cliffs, New Jersey
12. Kallet RH (2004) How to write the methods section of a research paper. *Respir Care* 49:1229–1232

13. Kabir SM (2016) Methods of data collection, pp 201–275
14. Heidenheimer A, Hecló H, Adams C (1983) Comparative public policy: the politics of social choice in Europe and America:505

Social Sustainability in Education: An Insight into the Civil Engineering Curricular



Nurul Elma Kordi, Sheila Belayutham, Che Khairil Izam Che Ibrahim,
and Nur Shuhada Nor Shahrudin

Abstract Social sustainability is one of the essential elements in construction towards achieving sustainable construction. Education plays a vital role in expanding the notion of sustainability. However, the education system has often overlooked the dimension of social sustainability, particularly in civil engineering (CE) curricular. The CE curricular in previous studies have shown limited depth and lack of explicit discussion on the implementation of social sustainability in construction. Therefore, this study explores the incorporation of the social dimension in the CE curricula of an undergraduate program as part of a pilot study in distinguishing the state of social sustainability studies in the CE curricular. This study has employed the questionnaire survey to gather responses from both students and lecturers of a selected organisation, with 320 total respondents for students and four lecturers. The findings show that students and lecturers struggle to understand the concept of social sustainability. Even though the Program Outcome (PO) already stated on social sustainability, however, the implementation still lacking. The findings indicate that social sustainability education needs to be built on a theoretical foundation. It is envisaged that the results from this study would be able to highlight the current contents of social sustainability that have been incorporated in the CE curricular. This would further distinguish whether the current education system is on a similar pathway along with the industry towards sustainable construction.

Keywords Engineering education · Social dimension · Sustainable development · Teaching methods

1 Introduction

Sustainable development was officially defined by the World Commission on Environment and Development (WCED) as “meeting the needs of the present without

N. E. Kordi (✉) · S. Belayutham · C. K. I. Che Ibrahim · N. S. Nor Shahrudin
School of Civil Engineering, College of Engineering, Universiti Teknologi MARA (UiTM), Shah Alam, Selangor, Malaysia
e-mail: elma8207@uitm.edu.my

compromising the ability of future generations to meet their needs” [1]. The term “development” includes various activities across different industry sectors. The construction industry’s response to sustainable development is ‘sustainable construction’ [2]. In construction, sustainable construction of projects incorporates key sustainability principles in terms of social, environmental and economic [3]. However, this focus overlooks the social sustainability dimension, which is also important to the well-being of the projects’ users. Therefore, a civil engineer is the chosen person to affect these three aspects given by their broad roles, ranging from designing to deconstructing the built environment [4]. Indeed, with their technical backgrounds and training, a civil engineer is better prepared to understand and contribute to sustainability construction. One of the main attributes of social sustainability is stakeholder engagement, where it involves communication [5]. Thus, engagement and communication are crucial where they should be emphasised in the early stage, which is at the education level.

As engineers of projects that will have lasting economic, environmental and social impacts, it is vital to ensure the students are equipped with the requisite conceptual skills to involve in sustainable design. Reforms in engineering education are needed to ensure the content of sustainability is included in undergraduate curricula. Students as future infrastructure engineers who will have immediate and long-term impacts on the nation are particularly poised to contribute to a sustainable future. Nevertheless, for engineers to positively impact sustainable development, efforts are required to change both the curricular content of undergraduate curricula and the approaches used to promote student learning [6].

In Faculty of Civil Engineering (FCE) UiTM Malaysia, requires engineering education in program EC220 to meet a set of learning outcomes focused on sustainable development. The program of EC220 follows the twelve Washington Accord (WA) characteristics, as shown in Table 1. The WA is an international accreditation agreement for professional engineering academic degrees between the bodies responsible for accreditation in their signatory countries [7].

In FCE, significant efforts have been made in recent years to integrate sustainable development in the university’s Bachelor’s and Master’s degree programs. For example, five POs (PO3, PO6, PO7, PO8 and PO10) are related to social sustainability. These five POs means the subjects should have elements of social sustainability.

Currently, more development in research, education and collaboration on sustainability. Researches start initiated several projects that aim to support sustainability education at the university. However, the awareness, the approachable, and the effectiveness of the social sustainability attribute need to be embedded into the subject still vague and considerable confusion. These findings are in line with the internationally recognised status of social sustainability in engineering education. The engineering curriculum has traditionally been dominated by sustainability considerations of an economic kind, such as maintaining economic efficiency and long-term profitability [8].

Table 1 Washington Accord (WA)—program outcome

Attributes (PO)	Keywords	Washington Accord (WA)—characteristic (with reference WA attribute)
PO1	Engineering knowledge	Apply knowledge of mathematics, natural science, engineering fundamentals and an engineering specialisation to the solution of complex engineering problems
PO2	Problem analysis	Identify, formulate, conduct research literature and analyse complex engineering problems reaching substantiated conclusions using first principles of mathematics, natural sciences and engineering sciences
PO3	Design/development of solutions	Design solutions for complex engineering problems and design systems, components or processes that meet specified needs with appropriate consideration for public health and safety, cultural, societal, and environmental considerations
PO4	Investigation	Conduct investigation of complex engineering problems using research-based knowledge and research methods including design of experiments, analysis and interpretation of data, and synthesis of the information to provide valid conclusions
PO5	Modern tool usage	Select and apply appropriate techniques, resources, and modern engineering and IT tools, including prediction and modelling, to evaluate complex engineering problems, with an understanding of the limitations
PO6	The engineer and society	Apply reasoning informed by the contextual knowledge to assess societal, health, safety, legal and cultural issues and the consequent responsibilities relevant to professional engineering practice and solutions to complex engineering problems
PO7	Environment and sustainability	Evaluate the sustainability and impact of professional engineering work in the solutions of complex engineering problems in societal and environmental contexts
PO8	Ethics	Apply ethical principles and commit to professional ethics and responsibilities and norms of engineering practice

(continued)

Table 1 (continued)

Attributes (PO)	Keywords	Washington Accord (WA)—characteristic (with reference WA attribute)
PO9	Individual and teamwork	Function effectively as an individual, and as a member or leader in diverse teams and in multidisciplinary settings
PO10	Communication	Communicate effectively on complex engineering activities with the engineering community and society
PO11	Project management and finance	Apply knowledge of engineering management principles and economic decision making in one's own work, as a member and leader in a team, to manage projects in multidisciplinary environments
PO12	Lifelong learning	Recognise the need for and have the preparation and ability to engage in independent and life-long learning in the broadest context of technological change

To improve teaching and learning on sustainability at universities, it is crucial to understand the perceived challenges of integrating social sustainability into the engineering curriculum. Against this backdrop, this study aims to develop an integrated framework for a better future lesson plan. This study's specific objectives are given as follows: (i) to define the understanding of social sustainability among students and lecturers in UiTM Shah Alam, and (ii) to determine the current status of social sustainability in civil engineering education.

2 Literature Review

2.1 Sustainable Construction

Sustainable construction defined as a building process that integrates the basic theme of sustainable development. Such a construction process will benefit society in general, such as environmental responsibility, social awareness and economic benefits [9]. The concept of sustainable construction is to give or comfort, whether economic, environmental and social. As for economic, it needs to provide a good service while for the environment, it needs to give safe protection of the integrity and surroundings. Meanwhile, for social, they have a good relationship with human society [10].

2.2 Social Sustainability

In construction practice, the economic and environmental elements of the project have been extensively explored, but the social dimensions of sustainability require further expansion [11, 12]. Social sustainability is close to human needs. Social sustainability, which is the most important objective of sustainable development, focuses on certain fundamental rights, and freedom relates only to human beings [13]. Intergenerational similarities and balance are the most common fundamental rights and freedoms. The current definition focuses more on the attributes that should be seen [14]. They accepted that social sustainability is ‘linked to health, safety, human rights, child labour, labour problems, community initiatives and job benefits’. Study by Wang et al. [15] also agreed that “management practises that could benefit current and future stakeholders by providing a set of social outcomes, such as health, safety, self-identification, ease of access and sense of belonging”. Health and safety are the main attributes that should be focused on social sustainability. In this regard, early education is important. The subjects taught in CE education should meet the sustainability criteria.

2.3 Education in Sustainability Development (ESD)

Early education in civil engineering (CE) discipline primarily forms the requirements for today’s constructions and societies. Education is characterised as a fundamental right, a bad situation for sustainable development and an essential tool for good governance and decision-making in line with democracy. UNECE Member States are encouraged to incorporate ESD into their formal education system in all their related disciplines and non-formal and informal education. Through ESD, people develop strong sustainable development skills, become more confident and act with their nature and passion for social values, gender equality and cultural diversity for a positive and healthier life. The key theme of the ESD-referred to in the UNECE Strategy for EDD-includes: protection, ethics, transparency (local and global), democracy and governance, poverty control, nationality obligations, civil responsibility, justice, security, human rights, health, gender equality, cultural diversity, rural and urban growth, economics, production and consumption models, natural resource [16]. Engineering education practitioners walk new ground while entering a transdisciplinary approach, including perspectives on social sciences and humanities [17].

Education plays a significant role in making such changes happen. Education needs such a change to give everyone access to knowledge, skills and values that extend their rights and the ability to contribute to sustainable development and action for the sake of preservation, greening the economy and creating a just and equitable society [16]. According to the investigation board, the lack of communication resulted in undetected problems during redesign and reconstruction, including undersigned gusset plates and excessive weight of construction equipment and materials on the bridge [18].

3 Methods

Civil engineering is a fast-moving, thrilling, well-paid career. Civil engineers are responsible for the imagery, design, development and maintenance of the physical infrastructure on which our global economy is centred. The Bachelor's degree in Civil Engineering (EC220) was chosen for this study. This course is intended to prepare students for a career that creates the very fabric of our society. Students will be able to develop science, architecture, human resources and management skills, acquire sound knowledge of engineering concepts, and apply them to practical challenges. The rationality behind this approach in relation to the programme is developing an integrated curriculum in which discipline-led and problem-led/project-led learning is combined to develop engineering skills. The curriculum was considered to constitute a representative sample of UiTM engineering education. The research was divided into three phases:

- i. Identify and select the sample of the Bachelor's Degree in Civil Engineering students and lecturers in FCE UiTM Shah Alam.
- ii. Questionnaire survey
- iii. Analyse the related content in the syllabi EC220 programs and develop an integrated framework of social sustainability attribute over the lesson plan of EC220.

3.1 Data Collection

The focus of this study is on how sustainability integrates into education at the undergraduate level. This largely relies on the developed syllabus for the EC220 program. Consequently, this study also uses a systematic review of the literature and data from faculty websites as secondary data to create the questionnaire. The questionnaire is designed to evaluate the current status of incorporating the social dimension of sustainability construction in CE education. A Likert-scale questionnaire was designed to collect the students and lecturers' opinions in the sample since these scales have been shown to be a very useful tool in previous papers on prevention through design [19]. The template consisted of questions on (i) participant's background, (ii) concept of social sustainability and (iii) the current status of social sustainability in subjects, curriculum integration (or teaching methods) and the opportunities and difficulties associated with the integration of social sustainability in the program.

Respondents were asked to evaluate each item from 1 [strongly disagree] to 5 [strongly agree]. The scale concentrated on whether the responding firms consider the core social sustainability issues in their construction projects on a 1–5-point Likert scale. The range of response includes 1 = not at all, to 5 = completely true.

The targeted respondents are chosen among students from the first semester to the end of the semester and lecturers at FCE UiTM Shah Alam to achieve the objectives

Table 2 Sample size (N = 320)

Semester	Number of students	Sample (N)
1	211	40
2	57	40
3	452	40
4	110	40
5	353	40
6	46	40
7	417	40
8	58	40
Total students	1704	320

of this study. The main reason for targeting students and lecturers is that in the social dimension of sustainability construction, civil engineering students are somewhat left behind. To determine their understanding of the social dimension in sustainability construction, the results will be compared between semesters. Table 2 shows the total students of each semester for the semester September-January 2019. There are 1704 students in total numbers of CE students.

A Raosoft online sample size calculator was used to determine the sample size with a 5% margin of error and a 95% confidence interval. The total number of students is 1704; however, based on the described criteria, 314 respondents is the minimum required for the sample size. Incomplete responses were excluded from the statistical analysis. SPSS version 21 was used to analyse data and to produce descriptive statistics. Since the total number of students each semester is different, the questionnaire will be distributed randomly to 40 students for each semester. Therefore, the total size is 320 students. The researchers personally administered the questionnaires to 320 students for eight weeks. All 320 usable questionnaire copies were returned and analysed.

4 Result and Discussion

The determination of the understanding of social sustainability and the current status of social sustainability in civil engineering subjects will be determined using the Relative Importance Index (RII). The relative index technique has been widely used in construction research for measuring attitudes for surveyed variables. Likert scale was used for ranking questions that have an agreement level. The respondents were required to rate the importance of each factor on a 5-point Likert scale using 1 for strongly disagree, 2 for disagree, 3 for neither agree nor disagree, 4 for agree and 5 for strongly agree [20]. Then, the relative importance index was computed using the following equation:

$$\begin{aligned} \text{Relative Importance Index Percentage) } &= \frac{\sum w}{AN} \\ &= \frac{5n5 + 4n4 + 3n3 + 2n2 + 1n1}{5N} \times 100 \end{aligned}$$

where:

- W weighting given to each factor by the respondent, ranges from 1 to 5;
- n1 the number of respondents for strongly disagree;
- n2 the number of respondents for disagreeing;
- n3 the number of respondents for neither disagree or nor agree;
- n4 the number of respondents for agreeing; and
- n5 the number of respondents for strongly agree.

Note: A is the highest weight (i.e., 5 in the study), and N is the total number of samples. The relative importance index ranges from 1 to 100 [21].

4.1 Questionnaire

The survey found that the most significant proportion of the students' respondent is female (69%), while 31% are male. In terms of educational background, most of the respondents (47%) are from the Diploma. Meanwhile, those from Matrics made up the percentage of 41% and the remaining 12% of the respondents from Polytechnics (see Table 3). The questionnaire was also distributed among lecturers in FCE. Four lecturers have answered the questionnaire. They are from the department Construction Business and Project Management (CBPM) (n = 2), Structure and

Table 3 Profile of respondents

Sem.	Age		Gender		Education qualification		
			Male	Female	Diploma	Polytechnics	Matrics
1	19–20 years old	40	15	25	–	–	40
2	19–20 years old	40	18	22	–	–	40
3	21–23 years old	40	15	25	30	5	5
4	21–23 years old	40	5	35	32	8	–
5	21–23 years old	40	10	30	20	15	5
6	21–23 years old	40	9	31	–	–	40
7	21–23 years old	28	11	29	30	10	–
	24 years old and above	12					
8	24 years old and above	40	17	23	38	2	–
Total			100	220	150	40	130

Materials (STRUCM) (n = 1) and Water and Environment (WRES) (n = 1). Three of the respondents have a Master qualification, and one has PhD qualification.

4.2 The Understanding of Social Sustainability Among Respondents

Based on the result of the questionnaire, as shown in Fig. 1, most respondents vote for ‘Maybe’ to understand social sustainability as they are not taking a subject related to social sustainability from semester one to semester three. The subject for semester one until semester three is mainly associated with fundamental science and mathematics and basic engineering such as statics, calculus for engineers, engineering drawing, survey, soil mechanics, hydraulics and others. The students find it challenging to provide a precise meaning of ‘social sustainability’. Sustainability, in general, and social sustainability, in particular, are seen as complex concepts to elucidate and grasp.

For semester four to semester eight, most respondents voted for ‘Agree’ to understand social sustainability as they are taking a subject related to social sustainability. The subjects related to this include ethnic relations, environmental and sustainability, technology entrepreneurship, and engineering for society. Students are more exposed to the industry and society for these subjects. Thus, students have more understanding of the element that should be embedded for the career.

For the interview’s lecturers session, the participants had worked as lecturers and program leaders at UiTM for between 5 and 10 years. All had been actively involved in the integration of sustainable development in their programs; however, only one had been engaged in research directly related to sustainable development. The lecturers were actively involved in sustainability teaching through courses, which had an explicit focus on sustainable development or whose content had a clear connection with sustainability. These included courses that have PO3, PO6, PO7, PO8 and PO10.

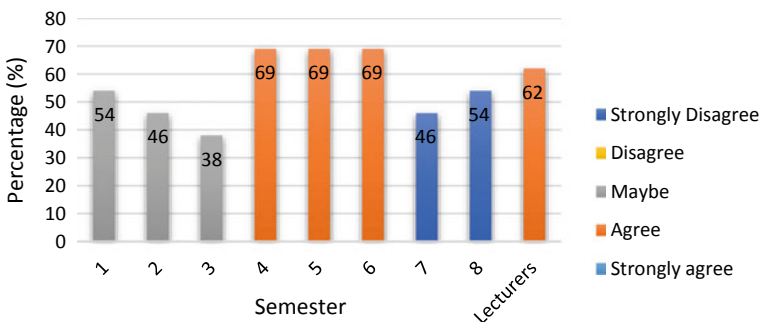


Fig. 1 The understanding on social sustainability among civil engineering students and lecturers

4.3 The Current Status of Social Sustainability in Subjects

Based on Fig. 2, the RII on the questions on section B (current status on social sustainability in their subjects) drops at ‘Maybe’ for students from semester one until semester three. This is because there are no subjects that are specifically about sustainability in their subjects. Students may be thinking that social sustainability subjects are not as important as other subjects such as structural, water, etc. For semester four until semester six, there are ‘Agree’ with the statements in the questionnaire. Students mostly agree about the question related to Course Outcome (CO) and Program Outcome (PO) in subjects. They have some knowledge of COPO. However, most of the students agree that there is rarely access to MyCOPO applications. This is maybe because there is no detailed explanation about that application.

For the students in Semester seven and eight, students mostly ‘Strongly Agree’ with the current status of social sustainability in their subjects. This is because students from this semester have been exposed to social sustainability in their subjects. The result shows ‘strongly agree’ that sustainability construction’s social dimension is vital for improving students’ attitudes while working.

Social sustainability dimensions are not often specified explicitly as a learning objective in the course syllabus. However, participants recognise social dimensions as implicit in many of the courses; therefore, they regard them as being dealt with at least to some degree within their programs. When asked what sustainability knowledge and skills students should possess when they graduate from UiTM, the participants emphasise the importance of attitude change and adopting a thoughtful, holistic way of thinking. Learning activities could be used to train students to reflect on social sustainability, and the lecturer agreed to mention role play, study visits, seminars and project-based learning activities. Allocation of resources in assisted peer discussions and supplementary sustainability training for the lecturer was also factors identified by the participants as crucial to the successful integration of social sustainability education at FCE.

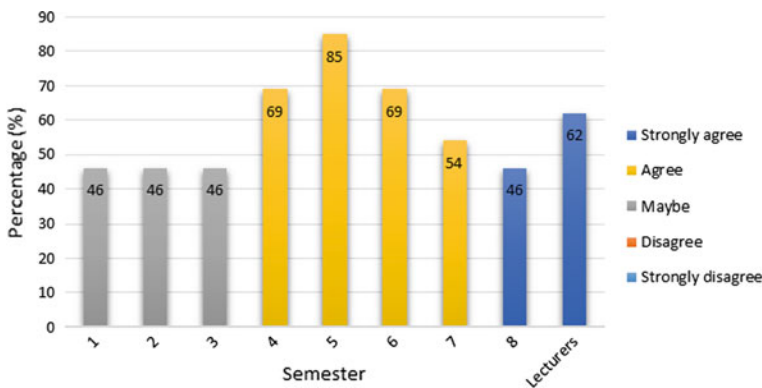


Fig. 2 The current status on SS in civil engineering subjects

Further measures are needed to support faculty members in becoming skilled social sustainability educators, most notably, a theoretical foundation on which social sustainability education can build. As noted above, the challenges associated with integrating social sustainability can be partly attributed to the perceived vague nature of the concept of social sustainability.

4.4 An Integrated Framework of Social Sustainability Attribute Over the Lesson Plan of Civil Engineering Education

The focus of this study is on teaching and course development. The statements presented to us give an insight into the realities that constitute these students' understanding of social sustainability education. The POs have clearly stated that on each subject. Even though there have eight POs related to social sustainability (PO1, PO3, PO6, PO7, PO8, PO9, PO10 and PO12), the implementation of social sustainability on the subjects associated is not emphasised.

The study shows a need to understand why teaching social sustainability in engineering education is perceived as problematic by some faculty members. The lack of any clear definition of social sustainability creates uncertainty. The responsibility for what content to include and what content to leave out ultimately falls on the individual lecturer—a commitment that not all lecturers are confident with and prepared to take on.

Although the need to incorporate sustainability into engineering education has been widely recognised, there are no unique topics on education that concentrate on social sustainability. The emphasis is more applicable to elective subjects, depending on the teaching plan offered by the faculty. Some causes affect the education of the social dimension in sustainability construction. As far as the issue is concerned, students are generally aware of CO and PO in all fields. However, students still do not understand the significance of each CO and PO. The lecturers firmly agree on the result obtained. The lecturer also admitted that social sustainability is not relevant to other subjects, such as water structure, highway, geotechnical, and that it is difficult to refer to the manual and other material education related to social sustainability. The lecturer may feel a lack of desire to alter existing subjects, as so many subjects would be taken in each semester to overwhelm students.

More research is required to obtain a solid fundamental basis for creating understanding work on social sustainability. The potential challenge, for example, is to explore the needs and aspirations of students and industry in the area of social sustainability in the construction sector. Students' social sustainability awareness and skills are required to be learned during their engineering studies at FCE. They envisage the demands and desires of their potential employers should be integrated with the education/early stage of the learning process. All essential skills, particularly communication skills, must be strongly developed for students.

5 Conclusion and Suggestions for Further Development

There is a notable lack of empirical research on how high-level management incorporates social sustainability into the engineering education curriculum. The study explains how students and lecturers identify and operate the social sustainability component of sustainable development in engineering curricula. In general, social sustainability is primarily about individuals themselves, their well-being and their justice in their relationship with each other in an environment in which imbalances between nature and culture can contribute to social stability. Students are expected to have a previous understanding of the CE curriculum and applications from a general sustainability perspective and grasp the basic principles of sustainability. Education can therefore be applied at any stage to achieve social sustainability among learners. Training is crucial as it relates to interaction and thus leads to the broader dissemination of information. Future civil engineers need to create sustainable solutions that satisfy technological, economic and environmental criteria and take into account the social aspects of sustainability in education.

Teaching about social sustainability in the context of engineering education must be closely linked to technology. Project-based learning activities are highlighted as an effective means of achieving learning goals related to sustainable development. Although significant efforts have been made to integrate sustainable development in EC220 programs, it is clear from data analysis that social sustainability remains a less visible topic in engineering education.

Study visits and role play are among the participants' tools as being the most effective in integrating social sustainability into the engineering curriculum. However, no research (UiTM case study) has yet been carried out to investigate how, or the extent to which, these favoured tools are effective in helping students reach the sustainable development learning objectives specified.

Further research is needed to draw more general conclusions as this study is based on case study data from a program (EC220) in UiTM only. However, some tentative conclusions and suggestions can be made for development and further research based on the collected data. To broaden the knowledge and explore the possible solutions to social sustainability in education, this study should extend to other universities to compare the similarities and differences in the way social dimension of sustainability construction is included and taught in other universities.

References

1. World Commission on Environment and Development (1987) Report of the World Commission on Environment and Development
2. Chiang YH, Tao L, Wong FKW (2015) Causal relationship between construction activities, employment and GDP: the case of Hong Kong. *Habitat Int*
3. Abdel-Raheem M, Ramsbottom C (2016) Factors affecting social sustainability in highway projects in Missouri. *Proc Eng* 145:548–555

4. Valdes-Vasquez R, Klotz LE (2013) Social sustainability considerations during planning and design: framework of processes for construction projects. *J Constr Eng Manage* 139(1):80–89
5. Kordi NE, Belayutham S, Ibrahim CKIC, Zulkifli AR (2019) The attributes of social sustainability in construction: a theoretical exploration. In: Association of Research Construction Management ARCOM 2019—Proceedings of 35th Annual Conference, Sept, pp 629–638
6. Watson MK, Pelkey J, Noyes C, Rodgers M (2016) Assessing impacts of a learning-cycle-based module on students' conceptual sustainability knowledge using concept maps and surveys. *J Clean Prod*
7. Ru WW (2017) Outcome-Based Education (OBE)
8. Shields D, Verga F, Blengini GA (2014) Integrating social sustainability in engineering education at the KTH Royal Institute of Technology. *Int J Sustain High Educ* 15(4):390–403
9. Ametepey O, Aigbavboa C, Anshah K (2015) Barriers to successful implementation of sustainable construction in the Ghanaian construction industry. *Proc Manuf*
10. Said I, Osman O, Shafiei M (2009) Sustainability in the housing development among construction industry players in Malaysia. *J Glob*
11. Kaminsky J, Javernick-Will A (2015) Theorising the internal social sustainability of sanitation organisations. *J Constr Eng Manage* 141(2):1–10
12. Jafari A, Valentin V, Bogus SM (2019) Identification of social sustainability criteria in building energy retrofit projects. *J Constr Eng Manage* 145(2):1–11
13. Yilmaz M, Yildiz S, Zorlu F (2021) The importance of occupational health and safety (OHS) and OHS budgeting in terms of social sustainability in construction sector. *J Build Mater Sci* 2(1)
14. Popovic T, Barbosa-Póvoa A, Kraslawski A, Carvalho A (2018) Quantitative indicators for social sustainability assessment of supply chains. *J Clean Prod*
15. Wang H, Zhang X, Lu W (2018) Improving social sustainability in construction: conceptual framework based on social network analysis. *J Manage Eng* 34(6):1–9
16. Nasibulina A (2017) Education for sustainable development. *Adv Intell Syst Comput*
17. Liwång H (2020) Safety management module to create social sustainability skills. *Int J Sustain High Educ* 21(4):717–732
18. National Transportation Safety Board (NTSB) (2007) Collapse of I-35W highway bridge Minneapolis, Minnesota. *Highw Accid Rep*
19. López-Arquillos A, Rubio-Romero JC, Martínez-Aires MD (2015) Prevention through design (PtD). The importance of the concept in engineering and architecture university courses. *Saf Sci* 73:8–14
20. Likert R (1932) A technique for the measurement of attitudes. *Arch Psychol*
21. Le KN, Tam VWY (2007) A survey on effective assessment methods to enhance student learning. *Australas J Eng Educ*

Legacy of the Games: Portable Architecture Transforming the Host City—The Pre-game, Game and Post-game Phase



Shivangi Varma and Himanshu Sanghani

Abstract The Olympics and its contemporaries are world-scale events that aim to promote talent in the field of sports and athletics. These games attract large-scale investments and architecture novelties that represent the modernity of the host city. Detailed schemes and innovative technologies are devised to gain profitable returns; however, a methodical approach is overlooked for the post-event phase. These games leave behind a legacy of neglected structures that require additional funds for sustenance. The critical points for discussion are the high investments, abandoned architecture and debts faced by the country for years post the event. The research aims at challenging the capitalist approach towards developing these sporting arenas and prepare a more sustainable scheme. The study differentiates the pre-event planning and post-event usage phase to understand the financial, technological and architectural stands for space. It emphasises on the ambitious plan of government bodies in strategizing such events, on the pretext of urban renewal and development. Thus, this research explores the addition of sustainable values in the existing technologies; and whether providing flexibility in the architecture could modify its financial implications and successfully steer the legacy phase of the games.

Keywords Olympics · Legacy · Neglected structures · Sporting arenas · Sustainable · Urban renewal · Flexibility in architecture

1 Introduction

The Olympic Games has stimulated the popularity of modern sports and athletics in the past two centuries. This has led to the birth of several other tournaments at a global scale; including the Commonwealth Games, the Asian Games and the FIFA

S. Varma (✉) · H. Sanghani
Sushant School of Art and Architecture, Ansal University, Sector 55, Gurugram,
Haryana 122003, India

H. Sanghani
e-mail: sanghani@ansaluniversity.edu.in

tournaments. These international events simultaneously bring changes in the social, economic as well as the physical state of the city.

Hosting these Games necessitates the regeneration of a city at three fronts. The first front—**technology/infrastructure/sustainability**—drives architects and planners to create innovative, flexible and environmentally responsive buildings. The second front—**economy/investments**—identifies the financial capacity of a city for such events, charting its legacy path and the strategy for its payback. The third and crucial front—**policy and schemes**—endorses what is necessary post-closure of such events. The fate of the *Legacy of the Games*, perhaps, lies within these three fronts but most importantly the ineffective post-event planning schemes and the subsequent decrease in interest in sports, especially amongst the youth. The prevention of such contingencies must be addressed by the government, the sports authorities and committees, and the planners and architects. However, these post-event planning schemes have prerequisites that need to be in favour, for even implementation.

Brazil spent more than USD 3 billion on developing their stadiums, which lie dormant a year after the 2016 Olympiad [1]. The Maracanã Stadium in Rio served as a venue for the 2007 Pan American Games. Deserted for over five years, it was refurbished for the 2014 FIFA World Cup at a cost of USD 500 million [2]. Post its use for the 2016 Olympic Games, the stadium circled back to its initial state of dismal and decay. This questions the ability to generate revenue post these events and their maintenance strategy to recover the cost. The history of these Games reveals the need for the architecture to be versatile and adaptable to several functions, with the technology to dismantle, re-assemble and re-use the structure and materials. The legacy plan will then be a success, both in terms of the policy framework and post-event closure.

The focus of this research is to identify ideal design strategies and technological advancements that could help revamp architecture for such large-scale events. Therefore, it is necessary to recognize the role of these games as an urban catalyst and understand the post-event programme of their legacy. This will assist in identifying loopholes in the planning strategies that can be bridged with architectural solutions. The findings and discussion lead to developing a framework of these schemes and technologies that could be utilized to retrofit and/or construct future examples and subsequently, break the dismal cycle of the architecture and the Games.

2 Goals, Objectives and Research Question

The goal of this research is to investigate design strategies and propose recommendations that could minimize the dismal fate of sporting venues post the event. This is achieved by analysing design ideas that would facilitate maintenance and utilisation of the architecture of the Games. Therefore, it is crucial to study the scope of the existing technology and its application in different scenarios.

This will further lead to drawing a framework to identify gaps in the planning and architectural strategies for the existing case. Thus, it is essential to develop a

table of post-events utilisation and analyse their success and/or failure. This requires a matrix enlisting the technology and design ideologies that could restore the legacy of these games. The research tries to determine the ideal strategy for construction and planning that could be incorporated for new projects by means of comparison between the existing technologies and financial schemes. This would assist in strategizing for gaining profitable returns from the previous as well as upcoming sporting events. But can technology-based design strategies minimize the ill-fate of the sporting events? What are the correct technologies? What kind of architecture is suitable for maintaining the legacy of the games? Can a portable and flexible architecture indicate avant-garde?

3 Approach and Methodology

The research is approached with the three major areas of concern: technology and architectural innovations, the financial capacity of the host city and its planning schemes. This has led to an understanding of the cities' reactions and/or effects of the urban transformation. The union of these three areas will determine the success or failure of the schemes to prevent similar occurrences in the future. In order to strengthen the approach, the research studies the three stages of the Games: the planning, the construction and the post-game legacy phase, which are assessed using distinctive examples. Through the paper, a comparison of the different layout of the built environment is prepared to determine whether the cost and planning of such large-scale construction projects boost or exacerbate the city's development goals. Several countries of varying economies have been analysed with a summary of the financial consequences. The primary case studies include the Asian Games 1982 and Commonwealth Games 2010 in Delhi, while secondary case studies discuss the Olympic Games across London, Rio and Sydney for their ambitious planning and investments, and poor post-phase schemes. Analysing post-game planning strategies by these different authorities and the factors affecting their success or failure helped in preparing an alternative scheme. Additionally, the example of the upcoming FIFA World Cup 2022 in Qatar helps as a prospective case study for reviewing its various architectural innovations, which aided in developing a design ideology. Thus, the outcome of this research is a probable model for the future to prevent discrepancies in the planning and construction of the structures (see Fig. 1).

4 Limitations

The information with respect to worldwide examples throughout the study is based on secondary data. Hence, the analytical approach may differ from research done by experts. The primary research study has been conducted independently and at an elementary level. The lack of support from government agencies and authorities



Fig. 1 Methodology

to conduct an in-depth survey fragmented the research with regard to its situation. The research team could not get first-hand drawings to understand the planning and aesthetical sense of the building and had to rely on the pre-documented rudimentary information. The resultant outcome is, thus, restricted to the form of recommended design principles and planning schemes, not providing a detailed design scheme or framework.

5 Hosting the Games: The Money Involved

It is easier to select bids from those developed and prosperous nations which have the existing infrastructure and financial capabilities to host these monumental games. For the Olympics, the committee decided on a fixed amount of USD 150,000 as the candidature acceptance fee for phase one, and an additional USD 500,000 for phase two, both non-refundable. This is done to provide a glimpse of the expenses pertaining to hosting the Games [3]. Once selected, it becomes imperative to plan the city and rejuvenate the urban areas to produce a world-class venue.

These planning investments can be divided into operational and non-operational costs (see Fig. 2). The Government procures the invested amount through a revenue earning model from the developed infrastructure and utilisation of the facilities provided.

There have been several host cities that have spent double or more than the estimated amount on these games. Figure 3 shows the investment amount for different Olympic Games over the years and their cost overrun. While all the enlisted examples have suffered financial damages, the percentage varies determining the success of the planning schemes of the organising committees. Therefore, such large investments emphasize on the importance of a Post-Game Planning Scheme for regaining the

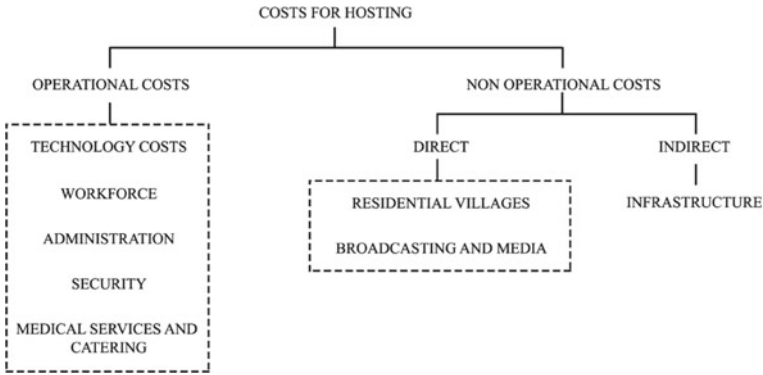


Fig. 2 Costs for hosting [4]

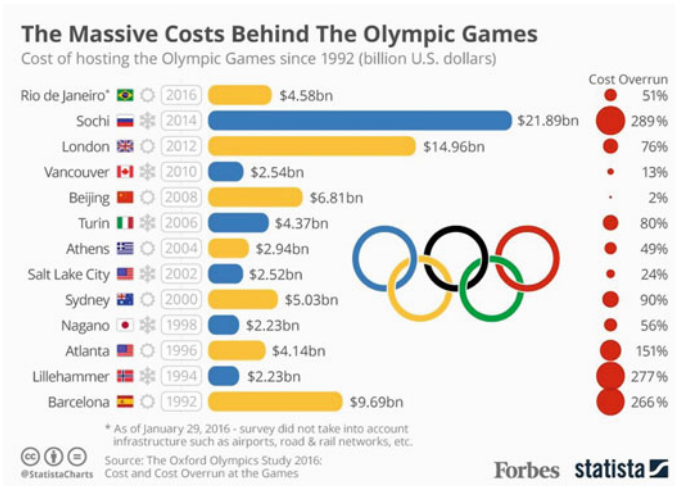


Fig. 3 Graph comparing the cost of various Olympic Games over the years [5]

invested amount with a reasonable profit margin, pulling the economy out of a long spur of debt.

The cost of the London Olympiad in 2012 increased from an estimated USD 5 billion to 18 billion and suffered debt till 2017, five years post the Olympiad [6]. The Rio Olympics of 2016 exceeded its budget of USD 14 billion, leaving the city with a whopping debt of USD 40 million post the closing of the event [7]. The Maracanã Stadium remains non-operational with an overdue of electricity bill of USD 1 million [8] (see Table 1).

Table 1 Debt incurred by host countries post the events

Event	Final cost of hosting	Debt Incurred
London Olympics 2012	USD 18 billion [6]	USD 2.9 million for Olympic Park [9]
Rio Olympics 2016	USD 20 billion [6]	USD 159 million [10]
Delhi CW Games 2010	USD 7.5 billion [11]	USD 80 million [12]
Sydney Olympics 2000	USD 6.9 billion [6]	USD 30 million p.a. for stadium maintenance [13]
Turin Winter Games 2006	USD 4.5 billion [6]	USD 195 million [14]

6 Pre-game Planning Phase: Role of the Government and Planning Schemes

Post winning the bid, committees are formed to devise planning strategies for the events. This opportunity helps evaluate the assets that a city has for its smooth operation. However, the reliance on the existing infrastructure is often insufficient, leading to renovations and construction of new state-of-the-art structures.

6.1 *Delhi—Post Asian Games of 1982, Commonwealth Games 2010*

The Sports Authority of India (SAI) was founded post the Asian Games of 1982, with the objective of maintaining and utilising its built structures. These included the iconic Jawaharlal Nehru Stadium and the Indira Gandhi Stadium among others. For hosting the 2010 Commonwealth Games, the immediate action was to restore and repurpose these sporting arenas (see Table 2).

A total of USD 875 million were estimated for the above-mentioned renovations, including their operational costs during the Games [16]. A new housing facility was additionally built for the participants on the banks of river Yamuna. The Metro rail network was improved, roads were widened, new flyovers were constructed and adequate means of public transport system was developed to connect the various venues. Basic civic services such as power supply and water supply were also reformed in order to create a clean and green city.

6.2 *London Olympic Games of 2012*

Olympic Delivery Authority (ODA), developed for the 2012 Games in London, worked alongside the London Organising Committee of the Olympic and Paralympic Games (LOCOG) to sanction the development of 200 ha of land, waterways, rail

Table 2 Renovation of existing venues for the Delhi Commonwealth Games, 2010 [15]

Venue	Condition before the games	Renovation required
Talkatora Swimming Pool	Roof was in a bad state	Upgradation of the pool, air-conditioning and increase in seating
Major Dhyan Chand Hockey Stadium	Not used post Asian Games	Seating redesigned, a new warm up pitch, Hostel-cum-media centre
Indira Gandhi Stadium	Technological problems and leaking roofs	Existing roof replaced, a new warm up hall and a multi-purpose hall
Nehru Stadium	Not many sporting events took place	Partially open roof, bucket seats instead of concrete, link to metro line
Wrestling Hall	New construction	5000 seating capacity
Karni Singh Shooting Range	Used as a training ground	A new 300 m range

lines, roads, tunnels, bridges, new parklands and 14 new permanent and temporary sporting venues [17].

The venues used for the Olympic Games were divided into three main zones within Greater London: the Olympic Park Zone (see Table 3), the River Zone (see Table 4) and the Central Zone (see Table 5).

In addition to the above, it was planned to upgrade The Docklands Light Railway and provide new high-speed rail service. Transport for London also developed a cable car system, costing USD 78.7 million, to link the Olympic Venues across river Thames [18]. A network of roads was defined with an Olympic Lane, reserved for the athletes and officials.

Post the Games, the authority focused on constructing new facilities and venues, and removing the temporary structures to modify the Olympic Park. In 2013 and 2014, the priority of the ODA was to complete the transformation of the Olympic

Table 3 List of sporting venues within the Olympic Park, London

Venue	Permanent/Temporary	Sports facility for the Olympics
Aquatics Centre	Permanent	Swimming
Basketball Arena	Temporary	Basketball, Handball
BMX Track	Permanent	Cycling
Eton Manor	Permanent	Hockey
Copper Box	Permanent	Handball, Fencing
Velodrome	Permanent	Cycling
Riverbank Arena	Temporary	Field Hockey
Olympic Stadium	Permanent	Athletics, Ceremonies
Water Polo Arena	Temporary	Water Polo

Table 4 List of sporting venues within the River Zone, London

Venue	Sports facility for the Olympics
ExCel	Boxing, Fencing, Judo, Table Tennis, Taekwondo, Weightlifting, Wrestling
Greenwich Park	Equestrian, Modern Pentathlon
North Greenwich Arena	Basketball, Gymnastics
Royal Artillery Arena	Shooting

Table 5 List of sporting venues within the Central Zone, London

Venue	Sports facility for the Olympics
All England Lawn Tennis Club and Croquet Club	Tennis
Earls Court Exhibition Centre	Volleyball (indoor)
Lord's Cricket Ground	Archery
Hyde Park	Swimming
Wembley Arena	Badminton, Gymnastics
Wembley Stadium	Football

Village by installing new kitchens and removing temporary floors and partitions, with the development of a school and health facilities as part of their post legacy phase.

6.3 *Rio Olympics of 2016*

The Brazilian Olympic Committee was developed to prepare sport development strategies in the country, with the aim of achieving social inclusion through sport. For the Rio Olympics in 2016, events took place at eighteen existing venues, most of which required renovation. Nine new venues were constructed and seven temporary structures were built to be removed post the Games (see Table 6). These venues were located across four different regions in the city: Barra, Copacabana, Deodoro and Maracanã (see Fig. 4).

Most of these venues are situated in the Barra Olympic Park, with the athletes' village the largest ever constructed for any Olympic Games. Additionally, Rio underwent urban revitalisation with waterfront development projects, layout of an upgraded transport network including roads, tunnels and sidewalks, and infrastructure development including water supply, sanitation and drainage. The Barra and Deodoro zones were linked by a new highway "TransOlimpica", and a Bus Rapid Transit line.

Table 6 List of a few sporting venues for Rio Olympics 2016

Venue	Existing/New permanent/New temporary	Sports facility for the Olympics
Olympic Aquatics Stadium	New permanent	Swimming and Water Polo
Olympic BMX Centre	New permanent	Cycling (BMX)
Rio Olympic Velodrome	New permanent	Cycling (Track)
Maracanã Stadium	Existing	Ceremonies and Football
Rio Olympic Arena	Existing	Gymnastics
Copacabana Stadium	Temporary	Beach Volleyball
Future Arena	Temporary	Handball



Fig. 4 Map of Rio showing the location of the Olympic Venues spread across Barra, Copacabana, Maracanã and Deodoro [19]

Different official bodies though distinct in their operations and projects work towards the same objective: the urban renewal of the host city. Each city requires different scales of development in terms of the built environment, basic infrastructure, transportation facilities and adequate housing. Therefore, it is crucial to plan out the basic demands of each city and implement these efficiently for the smooth execution of these world-scale events.

7 The Construction Phase

The construction activity involves the development of infrastructure and architectural projects necessary for the functioning of the events. The success of this phase is linked to the status, position and capability of the nation as perceived worldwide. Architects and planners come together to innovate with designs to enhance the cityscape for greater returns. However, these proposals come with their own financial and environmental consequences.

7.1 *Building Typologies*

The architectural projects constructed are set to depict the grandeur of the Games and serve as landmarks of the city. Varying in form, function and services, these can be broadly categorised into:

Sporting Venues. Stadiums and Arenas are the primary category of buildings constructed for the Games and serve as venues for the sporting events and ceremonies.

Accommodation Facilities and Villages. Though constructed to provide accommodation to the athletes during the Games, the biggest concern while designing these structures is their post-game usage and adaptability. These usually form a part of an entire Games Village among other typologies, for localised access to the participants.

Infrastructural Projects. These projects aim at fulfilling two aspects; (a) revitalising the urban core and (b) creating an iconic city. However, there is no deliberation on the impact of their construction process on the city. Examples of these include The Olympic Arch of Turin, constructed to connect the two parts of a city separated by a railway line (see Fig. 5), and the Commonwealth Twin Bridges, built for access to the JLN stadium from the parking across the road (see Fig. 6). Both were major development projects during the respective Games, serving as permanent infrastructural solutions. While the Arch of Turin is identified as an icon for the Olympics, still facilitating pedestrian access, the Commonwealth Bridges have lost their functionality post the Games, leaving a white elephant in the capital city.

7.2 *Light, Sound and Physical Infrastructure*

The additional equipment required for the Games include the light, sound and other physical infrastructure including furniture, escalators, elevators etc. These are more flexible in comparison and thus, can be portable and re-utilised post the events.



Fig. 5 The Olympic Arch of Turin, 2006 [20]



Fig. 6 The Commonwealth Twin Bridges, 2010 [21]

7.3 Technological Innovations

In the spur of creating an iconic city and revitalising the urban areas, technological advancements play an important part in framing the two aspects. The economic wheel and the environmental and societal aspects drive these architectural innovations. Therefore, it is crucial to adhere to the standards of sustainability and passive design strategies. Selective examples show the necessary design ideologies adopted for creating minimum environmental damage as well as a successful game and legacy phase:

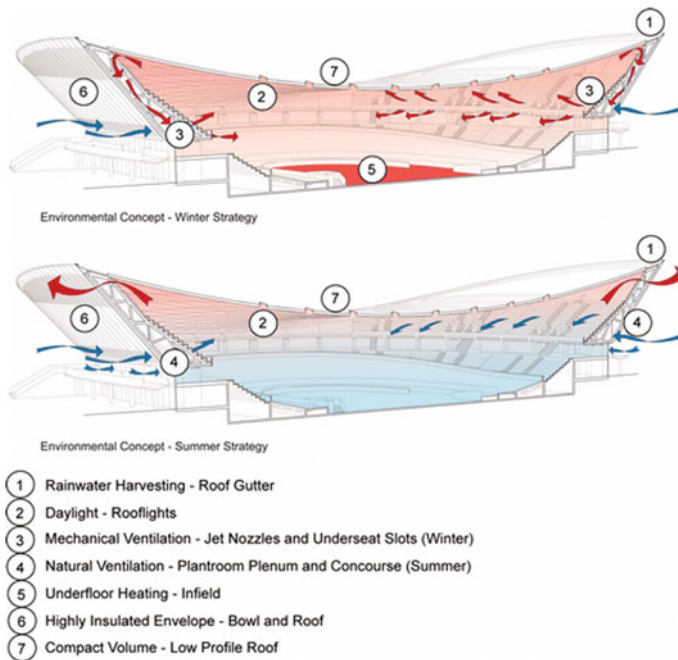


Fig. 7 The Velodrome, London Olympics, 2012 [22]

The Velodrome, London Olympics, 2012. The Velodrome was designed as a sustainable stadium, generating 100% natural ventilation. The structure is clad with FSC-approved, reclaimed Western Red Cedar which forms a perforated skin, allowing convective airflow through the building top, replaced by cool, fresh air from below [22] (see Fig. 7).

The Copper Box, London Olympics, 2012. This multi-sport venue is clad with a maintenance-free, non-corrosive skin of recycled copper. The lightweight insulated roof structure holds rain collectors and 88 sun pipes, allowing natural light into the venue. In addition to saving forty per cent of its annual water and energy usage, the stadium is also deemed sustainable due to the daylight control sensors that are activated where there is no sunlight [22] (see Fig. 8).

London Olympic Stadium, 2012. The main Olympic Stadium was designed with the priority of its post-game usage. The structure incorporates “adaptable architecture” such that the various layers of the stadium can be removed and reused for various purposes depending on the kind of event and the size of the audience (see Fig. 9).

Rio Olympic Stadia, 2016. The Rio committee took a novel approach to move, revamp and recycle its built structures post the Games, to be relocated to schools, community spaces and for housing. The aim was to provide better standards of living

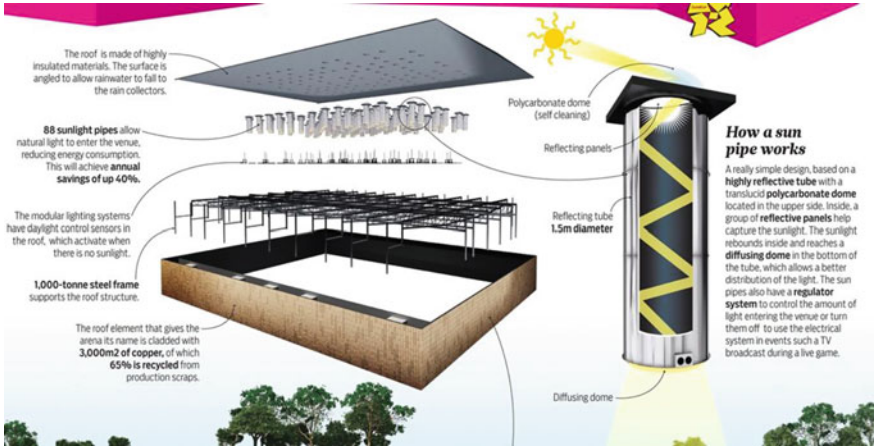
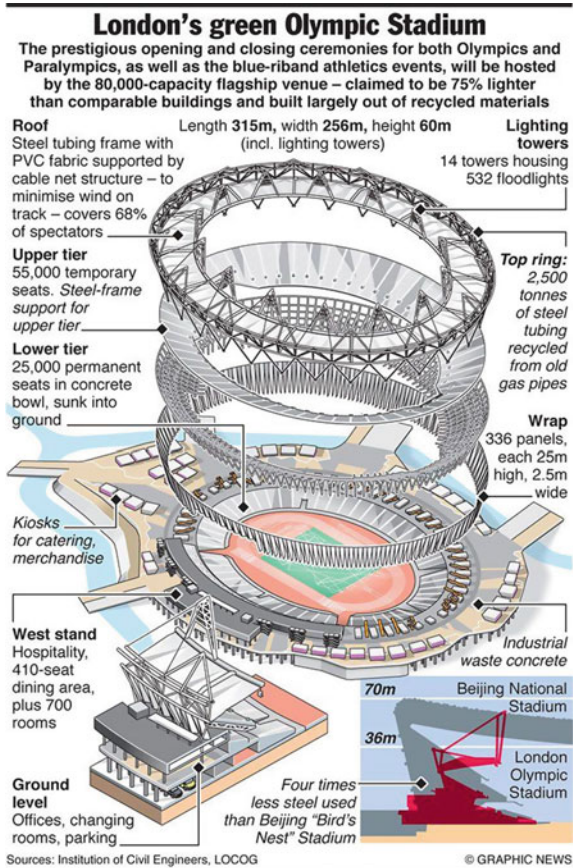


Fig. 8 The Copper Box Arena, London Olympics, 2012 [22]

Fig. 9 The Olympic Stadium, London Olympics, 2012 [23]



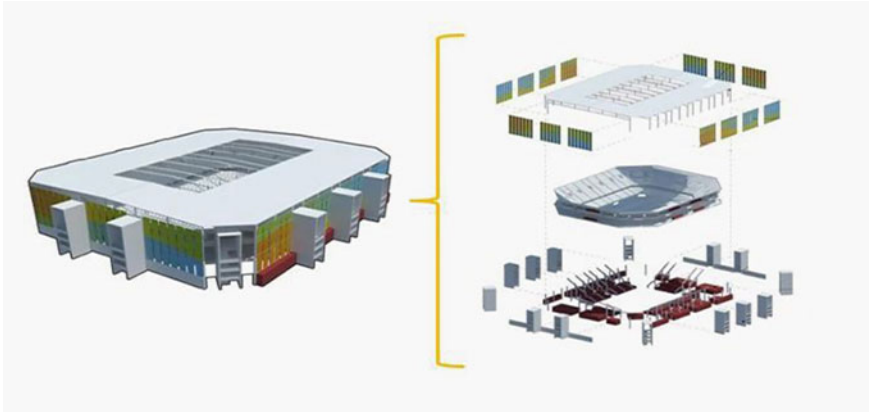


Fig. 10 AECOM's concept for the Nomadic Stadia of Rio [24]

and boost urban development in the city. The designs incorporate elements of prefabrication and use of lightweight materials, shaping the term 'nomadic architecture'. The Aquatics Stadium could be broken down to create two smaller pools while the Future arena, made of modular units, could be dismantled and rearranged across the city, alongside its roof, the panels of the facade, and vertical columns (see Fig. 10).

Ras Abu Aboud Stadium, Qatar 2022. This temporary stadium, under construction, consists of a fully modular, demountable and transportable layout. While the main structure consists of a steel frame, the building blocks are composed of shipping containers. With benefits of negligible time and waste generation during construction, these prefabricated modules are portable and can be reused as smaller venues post the World Cup. The stadium will then be converted into retail and a public park with waterfront development as part of the urban regeneration scheme of Doha, leaving behind a minimal post-game legacy of the Games (see Fig. 11).

8 Post-game Planning Schemes

The technological innovations often lose their magnificence post the events, with the built environment turning into white elephants. Therefore, the execution of the post-game planning schemes is as essential as the design strategies for the post-event operation of the structures.



Fig. 11 Shipping Containers for Temporary Ras Abu About Stadium, Qatar FIFA World Cup 2022 [25]

8.1 The Commonwealth Games, Delhi, 2010

Private Partnership. During the preparation of the commonwealth games, SAI hired a transaction adviser for developing a revenue model to maintain the stadiums after the games. The authority initially ventured with three ideas:

- (a) A revenue-sharing model between the authority and the private company.
- (b) Handing over the stadiums to a private company on a five-to-30-year lease for annual rent.
- (c) One-time rent for a similar lease to a private company.

The scheme also included commercial utilization of the stadiums such as leasing them to companies and health clubs for hosting entertainment events. However, each stadium ended up preparing its own legacy plan with approval from the SAI [26].

Utilisation by Schools, Colleges and Sports Federations. In 2011, the Sports Minister unveiled the “Come and Play” scheme. This opened the three SAI-owned stadia in the city for school children, students, sportspersons as well as common people with a fixed rate of 14 USD per day usage. Additionally, the National Sports Federations were charged 70 USD for holding competitions in these stadia. The SAI appointed 70 coaches to provide coaching for various sports with the motive to keep the stadia occupied and accessible to the general public and sportspersons.

Post the “Come and Play” programme, the Delhi Development Authority (DDA) too introduced the “Pay and Play” Policy in 2015, which opened the DDA owned facilities for use by the general public as well.

However, from an expected 70,000–80,000 people, the ‘Come and Play Scheme’ saw only 18,000 till June 2013, resulting in the subsequent failure of both the

programmes. This was due to the limited access to the stadiums to the majority of the population. As a result, the investment for the maintenance of these venues was higher than the revenue generated. Lack of accommodation and office facilities also prevented the implementation of these schemes thoroughly. Therefore, the SAI had to rely on the ministry for a total of 6.3 million USD to maintain the stadiums [26].

8.2 *The Olympic Games, London, 2012*

The 10-Point Legacy Plan. The ODA developed a 10-point Legacy Plan with the objective of reaching out to the youth and increasing interest in sports. The plan includes:

1. £125m p.a. (USD 163m) funding for elite sport for four years till Rio 2016.
2. £300m (USD 392m) investment on Queen Elizabeth Olympic Park and open it to the public.
3. Bringing 20 major sporting events to the UK by 2019, with more bids in progress.
4. Sport England's £135m (USD 176m) "Places People Play" legacy programme to fund new facilities, volunteering and participation.
5. £1bn (USD 1.3b) investment over the five years following the Games in the Youth Sport Strategy, linking schools with sports clubs and encouraging sporting habits for life.
6. Government support for the "Join-In programme" to build on the spirit of volunteering at local sports club.
7. Introduction of the School Games programme sponsored by Sainsbury's to boost schools sport and county sports festivals.
8. Ensuring PE in schools is available to all.
9. £1.5m (USD 1.9m) funding to the English Federation of Disability Sport to increase participation in sports by disabled people.
10. Continue funding for International Inspiration, the UK's international sports development programme, to 2014 [27].

9 Legacy of the Games

Maracanã Stadium. Built in the 1950s, this Rio stadium was renovated for the 2016 Olympic Games. However, a few months after the event, the stadium became home to vandalism and crime due to its distance from the urban centre. 7800 seats have been stolen and unpaid bills led to a shortage of electricity in the stadium. The grass on the field has not been maintained, which led to the field becoming dry and filled with holes [8] (see Fig. 12).



Fig. 12 State of despair for the Maracanã Stadium, Rio [28]



Fig. 13 Aquatics Centre, Rio [30]

Aquatics Centre, Rio. Though this newly constructed structure incorporated nomadic architecture in its design scheme, its legacy programme failed at the administration level. Due to the large debts looming over the city post the Games, this USD 50 million dollar project was unable to generate any revenue and provide funds for maintenance [29]. Consequently, the pool is filled with mud and dead insects and the tapestry of the facade has been torn (see Fig. 13).

Jawaharlal Nehru Stadium, Delhi. This landmark stadium complex in the capital city is one of the venues for the SAI “Come and Play Scheme”. However, due to the policy’s failure, the stadium is incapable of generating enough revenue for its maintenance. While the stadium complex is home to several annual food festivals and marathons, the structure within remains empty and unusable. The grass field has now become unlevelled with worn-out tracks clogged with rainwater. The chairs are broken, fire-fighting equipment reeks of rust and the electrical fittings have been stolen [31] (see Fig. 14).



Fig. 14 Jawaharlal Nehru Stadium, Delhi [31]

10 Inference: Success and Failure of Legacy Phase

Every city has developed a unique legacy plan to utilise the structures in the post-game phase. However, not all strategies have been deemed successful resulting in the dismal state of the structures and their inability to gain revenue. Table 7 enlists the post-event utilisation of the structures, collected through primary and secondary case studies, which lead to the analysis of their Legacy Plans and the framework that guides their success.

The success of any Legacy Plan depends on the enlisted aspects of the framework:

Table 7 Post events utilisation of structures

Structure	Post events utilisation
<i>Delhi CWG and Asian Games</i>	
Jawaharlal Nehru Stadium	Football Tournaments, Cricket One-Day Internationals, Food Festivals, Marathons Training under ‘Come and Play’ Scheme
Talkatora Indoor Stadium	Indoor Sports Tournaments, Cultural, Religious, Political Events
<i>London Olympics</i>	
Olympic Stadium	Tenancy Programme: home to the West Ham United
Aquatic Centre	Sponsorship
<i>Sydney Olympics</i>	
Olympic Stadium	Rugby, Soccer, Cricket Leagues
<i>Rio Olympics</i>	
Olympic Stadium	–
Aquatics Centre	–

10.1 Technological Innovations

The examples discussed through the paper show the inventive measures taken in the construction techniques and choice of materials. While most structures are designed to ease the functioning of the Games, many ignore to inculcate the post-event usage in their design strategies (see Table 8). These structures are left behind as perma-

Table 8 Matrix of technology used

Venue	Sustainability incorporated in design	Materials used	Legacy strategy incorporated in design
<i>Delhi CWG 2010</i>			
Jawaharlal Nehru Stadium	Low air conditioning dependency	Teflon membrane, steel compression ring, folded plate cladding	–
Talkatora Indoor Stadium	Solar and automated lighting, rainwater harvesting, heat insulation	Recycled materials, fly ash, reflective glass	–
<i>London Olympics 2012</i>			
Velodrome	Natural ventilation and daylight, rainwater harvesting	FSC-approved, reclaimed Western Red Cedar	–
Olympic Stadium	Recycled tubing, minimising wind on track	Steel tubing frame PVC fabric	Adaptable architecture for different uses of the stadium
The Copper Box	Insulated roof, natural lighting, rainwater collectors, energy and light usage savings	Recycled copper cladding, Steel frame for roof structure, polycarbonate dome with highly reflective tube, insulated materials	–
<i>Rio Olympics 2016</i>			
Future Arena	Prefabrication, lightweight structures, rainscreens	Horizontal wooden slats as façade and steel structural frame	Nomadic architecture for relocating venues
Aquatics Centre	Anti UV panels reducing temperature gain, natural ventilation	Portuguese tiling, tapestry as facade	Nomadic architecture for relocating venues
<i>Qatar FIFA World Cup 2022</i>			
Ras Abu Aboud Stadium	Portable shipping containers, minimal construction time and low waste generated	Steel structure, shipping containers	Temporary and portable architecture

ment “white elephants” that require additional investments as well as other favorable factors for the success of the legacy schemes developed by the government.

In Delhi, the SAI “Come and Play” Scheme failed as only 3–4% of the population had access to the venues. Despite a developed transport network, lack of accommodation restricted people to travel from outside the city to utilise the facilities [26]. In Rio, The Maracanã Stadium became home to vandalism and crime due to its isolation from the city center. Therefore, accessibility and adaptability become essential for the re-utilisation of the stadiums and must be considered in the pre-game design strategies.

The London Olympic Stadium incorporated movable elements and retrofitting that allowed it to morph into the desired structure to serve different purposes. Similarly, the Rio Aquatics Centre was designed using concepts of Nomadic Architecture that allowed it to be repurposed into community swimming centres.

11 Flexibility in Architecture

The failure of any legacy plan is derived from its defined use of space and structure. This rigidity in a stadium prevents it from being used beyond specific functions and gain revenue besides certain events. The built environment thus can be modified to accommodate various functions and provide adaptable spaces. This persistent transformation of the structure can be achieved through flexibility in architecture.

Flexibility in architecture is feasible in terms of materials and finishes, external facade, structural members as well as design elements, the advantages of which are manifold:

1. It allows restructuring of the built form.
2. It allows adaptability of spaces.
3. It allows segmentation of the built form resulting in modularity.
4. This modularity facilitates varying use of the structures, providing various facilities.
5. It also facilitates reaching out to the people, increasing its accessibility.
6. This results in a significant increase in its usability and thus, increase in revenue generation (see Fig. 15).

The success of any form of architecture lies in its ability to have an open and free interaction among its users. Thus, the ideal design strategy for the architecture of the Games results from a form that is transformable, adaptable, interactive as well as movable. These four characteristics form the basis of Portable Architecture, serving as primary requirements for the revitalisation of the legacy of the Games.

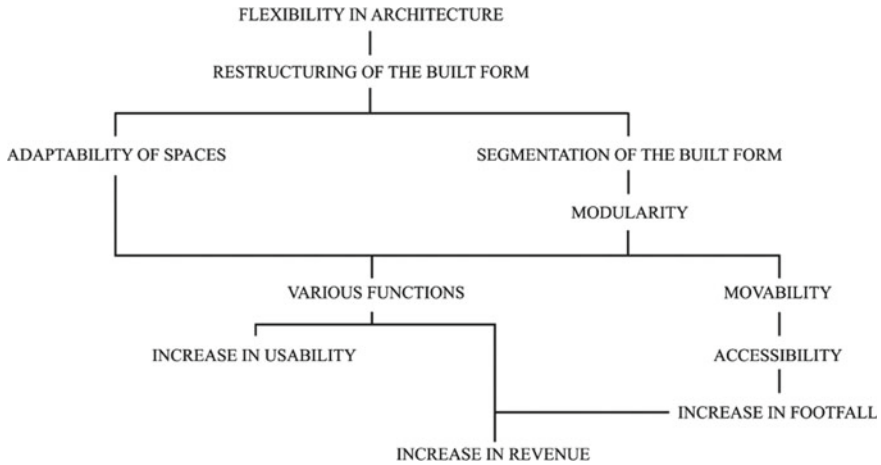


Fig. 15 Advantages of flexibility in stadium architecture

11.1 Portability in Architecture

International recognition, economic growth, high living standards and re-framing the urban core of the city become a significant agenda for the Olympics or its contemporaries. For this, the built environment and its technological innovations play a significant role. But can architecture alleviate the weaker sections of the society? It is understood that providing basic facilities and services within the structure can increase its footfall. However, when the structure becomes flexible, can it contribute to the city’s economic growth?

Adaptability in the architecture of the games allows the site and venue to be re-used for different needs, functions and operations, serving as a sustainable solution. The role of architecture then becomes of prime importance as it re-invents the space, expanding its utility for higher gains. Thus, as the legacy plan succeeds in generating revenue, the initial investment is regained, the country is laid off its debt and a subsequent increase in economic growth takes place. As a result, the tourism industry boosts with an increase in employment and interest in sports, with the Games leaving behind no “white elephants”.

Portable architecture aims to embrace the changes and challenges of the modern dynamic world. Different situations, functions, patterns of use, individual users’ requirements for the present and the future are the main criteria that outline the design for portability. There are five key factors that characterise Portable Architecture [32].

Adaptability. In the built environment, adaptability is gauged with tendencies of different functions following different requirements, adhering to multiple users and their needs.

Transformation. Adaptability of a structure is followed by its transformative technology through flexible materials that allow movement and change in form. Therefore, this mechanism must be easy to operate and require minimum maintenance.

Mobility. Mobility aids in relocating the structure for more accessibility. The advantage of this lies in the capacity of these temporary buildings to be non-disposable. This recycling potential helps build structures which are low in cost but maintain standards.

Interaction. Interactive architecture aims at merging the physical and the natural environment emphasising on the user's needs. For e.g. facades that are programmed for change help create dynamic spaces that can open up to create larger, visually and mentally stimulating spaces within the same structure.

Sustainability. Preservation and adaptive reuse of a building instead of demolition contribute significantly to its environmental sustainability. Such buildings use less energy, offer more occupant comfort, and feature better overall space efficiency than contemporary buildings. Further, the use of recyclable and low-cost materials adds to its energy and economic benefits.

11.2 Roof Structure

Roof frames made out of steel tubes should either be recycled or upcycled from its discarded purpose. These can be used for temporary housing, mobile schools for under-privileged or night-shelters post the events. The roofing panels could be either PVC fabric or any other recyclable material that could act as a building façade after being brought into nomadic nature. The structure should be majorly pre-fabricated in order to repurpose its function post the events.

11.3 Structure and Seats

The column structure to support the main ring and panels should be retractable portal frames which could be repurposed, for e.g. factory shed, school building, warehouse. The seat rows attached must be foldable to be easily removed and stored. An example is the Bluecube-Nomad (see Fig. 16), designed specifically for temporary structures. With a simplistic aluminum design, its advantages include an anti-tamper fixing system and removable magnetic seat numbering, while proving to be more comfortable than permanent seating [33].



Fig. 16 Nomad by Bluecube [33]

11.4 Lights

The London Olympic Stadium has 14 lighting towers around the roof structure, each reaching 70 m above the sports field and supporting 532 individual halogen lights in total [34]. With the heavy requirement of light and energy systems required in every event, it is essential to install a sustainable and energy-efficient system. Thus, portable lighting and LED portable beacon tower lights would serve beneficial in these large-scale events with easy assembly and dismantling.

11.5 Tracks and Grass

Track and grass field stadiums serve a limited purpose, restricted to certain outdoor games and events. Using artificial turf and race-tracks allow the field to be used for multiple functions. These can be laid on an existing ground with low maintenance and can be removed and stored post the Games.

12 Discussion and Findings

The principles of Portable Architecture, in the case of sporting events, contribute significantly to the generation of revenues and use of the built environment (see Table 9).

Flexible Technology. The flexibility of portable architecture puts behind obsolete technology and incorporates innovations that can be modified depending upon the need of the user. This means transformability of the structure and use of recyclable materials keeps the structure low on investment.

Additional Facilities. The structure can be repurposed to provide additional facilities for varying functions. As a result, the structure can be used for indoor as well as outdoor sporting events and public spaces for large gatherings.

High Revenue Generation. With the stadium being able to host all kinds of events and providing additional facilities, larger audience will be attracted, increasing the footfall and thus, generating greater revenue. This revenue could be further utilised for advertisements and bigger events that would further increase the expected footfall. Therefore, a virtuous circle is developed forming a successful Legacy Plan for the Games.

Increased Use of Structures. Portable architecture allows the ability to transform, move, and adapt and interact with the surrounding environment. This is capable of facilitating multi-purpose use for the stadiums that can act as sporting and non-sporting events.

Accessibility. The mobility of the structure allows the architecture to reach out to the audience rather than waiting for the audience to visit the stadiums. Thus, facilitating accessibility to the stadiums.

Maintenance. The problem of maintaining the structures will be reduced with the use of recyclable materials that prove to be cost-effective and energy-efficient. In

Table 9 Principles of portable architecture utilized as solutions to the games

Problems persisting in the games	Characteristics of portable architecture suitable for the solution
Obsolete technology	Use of recyclable materials
Inadequate facilities	Repurposing of structure according to the user’s needs
Low revenue generation	Interaction with the environment attracting more audience
Restricted use of structure	Ability of transformation and adaptation to the user’s needs
Accessibility	Mobility of structure
Poor maintenance	Cost-efficient, recyclable materials that do not require high maintenance
High cost of investment	Low cost of construction and materials used

addition, specific facilities can be provided only when required, lowering their need for maintenance.

Low Cost of Investment. Portable structures are cost-effective and energy-efficient, achieving sustainability measures while providing architectural masterpieces that can be effectively used for multi-purposes. Portable structures can be utilised for all building typologies: stadiums, housing, infrastructure, public spaces etc.

With the above-mentioned qualities and specific strategies of portability in architecture, the post-event plans and schemes can succeed in their implementation without additional strategies. Following recommendations, if incorporated in the planning of these monumental structures, would lead to an effective legacy phase:

1. The stadiums could be retrofitted with re-usable models. These could be transformed for indoor sports, outdoor field games, and track events.
2. In order to attract audiences of all kinds, the stadium should be able to host cultural events and gatherings, with the pitch of the stadium being repurposed for acoustic needs.
3. The stadium could provide portable outdoor eating facilities, thus facilitating its use only when occupied.
4. The roofing system could incorporate automation technology that could open and close depending on the time of the day, the weather conditions and the lighting requirements.
5. The lighting of the stadium could be versatile, changing with the requirements: vibrant for concerts and cultural performances, and dim for sporting events.
6. Extensions to the stadium could be constructed using portable design characteristics allowing sections to be removed to increase gathering spaces and provide interaction between the built enclosure and the surrounding complex.
7. This extension could be moved to open grounds to provide an interactive space for public gatherings. For e.g. museums, seating, or even landscape elements.
8. Use of recyclable materials with low maintenance further reduces the investment in sustenance.
9. Portability facilitates the preparation of the stadium to host future world-scale events. Therefore, investment in the construction of new structures and development of new technology is reduced by a vast amount.
10. The pitch itself could be made movable, pre-fabricated to reach out to people in different parts of the city. Thus, acting as training grounds, these could be spread across the city enabling a larger portion of the public making use of the services.
11. The facilities can also be rented out to schools and universities for their individual events, government schools in particular, where adequate sports facilities and equipment is hard to find.

Assumptions made:

1. The Government is willing to invest an additional amount to incorporate these design strategies with the incentive of receiving increased revenue in the long-run.

2. The authority of each portable module remains with the government body itself. Thus, in times of events at the stadium complex, the modules are rearranged and re-fabricated according to the particular functions and needs.
3. The additional cost of transportation of the modules and its revamping is compensated by the revenues gained with a profitable margin.

13 Conclusion

Architecture of the Games plays a vital role in determining its success or failure. The economic and social aspects are all interlinked with the architecture as the primary feature, capable of altering the fate of the Games. Thus, incorporating a design solution that would serve various purposes and cater to different sections of the society will prove beneficial in the urban restoration of the city as well as in the development of an efficient Legacy Plan.

The essential measures that are required for a successful implementation of any planning strategy include:

1. Identifying the needs of the Public
2. Catering to all kinds of requirements
3. Providing basic facilities and amenities to the users
4. Enabling the stadium to function according to the requirements of the different events, technologically, spatially and socially
5. Implementing a strategy to attract the attention of larger portions of the public through advertisements as well as offering interesting spatial experiences
6. Facilitating the accessibility of the public to the built environment
7. Lessening monetary dependency through green and energy-efficient strategies.

Portable Architecture is the answer to address all the above factors. The positive impacts of portability in architecture are numerous in comparison to conventional methods (see Fig. 17). The world is slowly moving ahead with time, with development in technology, altering the needs of the people and the environment they live in. As humans go back to their roots, becoming more nomadic with time, Portable Architecture is the solution to serve the inevitable dynamism of human life in sports.

Temporary buildings have half the carbon footprint of conventional buildings, and can cost up to 80% less than permanent traditional builds...

—Verne Hills

14 Recommendation for Future Research

The research provides a path towards a design solution for the legacy of the games and its planning schemes; however, further study on the architectural front and in-depth research on the three fronts are required. Technology and architecture go hand

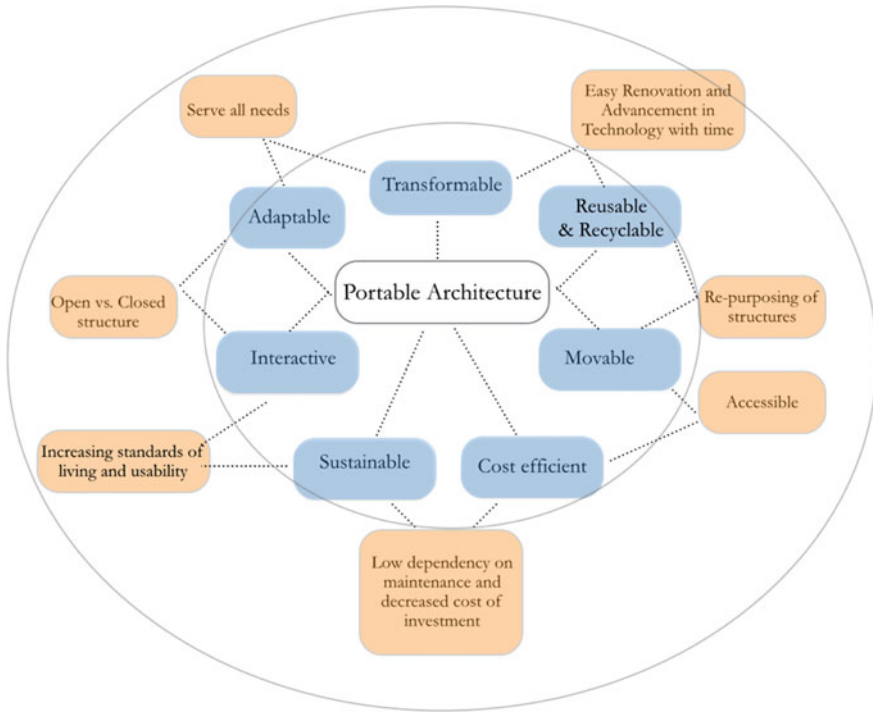


Fig. 17 Benefits of portability in architecture

in hand, the finer research in these two realms will validate the sustainable financing and payback period. Thus, it is important to gain knowledge and understanding in the following architectural schemes:

1. Finer details of the various structural and architectural components of a stadium
2. Prototyping modules
3. Assembly of various systems
4. Flexible and adaptable materials
5. Various services that would be associated with portability
6. Flexibility in different programs and spaces

References

1. Manfred T (2015) Brazil's \$3 billion World Cup stadiums are becoming white elephants a year later. Business Insider, 13 May 2015. [Online]. Available: <https://www.businessinsider.in/sports/brazils-3-billion-world-cup-stadiums-are-becoming-white-elephants-a-year-later/articleshow/47272959.cms>. Accessed 13 Jan 2020

2. Shedrofsky K (2017) Brazil: millions overbilled in Maracana Stadium renovation. Organised crime and corruption reporting project, 14 Mar 2017. [Online]. Available: <https://www.occrp.org/en/daily/6198-brazil-millions-over-billed-in-maracana-stadium-renovation>. Accessed 8 Jan 2020
3. Mobilian ZE (2015) The economics of hosting the olympic games: the miscalculation of cost-benefit analyses and why cities continue to Bid. Claremont McKenna College, Claremont
4. Pareek A (2015) Slideshare, 8 Sept 2015. [Online]. Available: <https://www.slideshare.net/anshulpareek22/cost-of-olympics-52532683>. Accessed 21 Dec 2019
5. McCarthy N (2016) The massive cost of hosting the Olympic games. Forbes, 4 Aug 2016. [Online]. Available: <https://www.forbes.com/sites/niallmccarthy/2016/08/04/the-massive-cost-of-hosting-the-olympic-games-infographic/#6e975492e385>. Accessed 22 Dec 2019
6. McBride J (2018) The economics of hosting the Olympic games. Council on Foreign Relations, 19 Jan 2018. [Online]. Available: <https://www.cfr.org/backgrounder/economics-hosting-olympic-games>. Accessed 13 Jan 2020
7. Wade S (2017) IOC balks at helping Rio with \$35 million-\$40 million Olympic debt. Chicago Tribune, 9 July 2017. [Online]. Available: <https://www.chicagotribune.com/sports/olympics/ct-olympics-rio-debt-20170709-story.html>. Accessed 11 Dec 2019
8. Charner F, Darlington S (2017) Why the legendary Maracana now looks like a ghost stadium. CNN, 2 Feb 2017. [Online]. Available: <https://edition.cnn.com/2017/02/01/football/maracana-stadium-rio-2016-olympics/index.html>. Accessed 17 Dec 2019
9. Magnay J (2011) Olympic Park debts of £229m to burden London's taxpayers. The Telegraph, 17 Nov 2011. [Online]. Available: <https://www.telegraph.co.uk/sport/olympics/8897244/Olympic-Park-debts-of-229m-to-burden-Londons-taxpayers.html>. Accessed 11 Dec 2019
10. Otto T (2019) Cruel cost of Rio Olympics still crippling Organising Committee. news.com.au, 13 Feb 2019. [Online]. Available: <https://www.news.com.au/sport/sports-life/cruel-cost-of-rio-olympics-still-crippling-organising-committee/news-story/db4f6f1518abf418453f35a740780a10>. Accessed 17 Dec 2019
11. Madhavan N (2012) Unlike Delhi CWG, London Olympics well within budget. Business Today, 25 Oct 2012. [Online]. Available: <https://www.businesstoday.in/opinion/perspective/unlike-delhi-cwg-london-olympics-well-within-budget/story/189362.html>. Accessed 11 Dec 2019
12. India's Commonwealth Games bills still not paid (2011) BBC, 13 Oct 2011. [Online]. Available: <https://www.bbc.co.uk/news/magazine-15279279>. Accessed 11 Dec 2019
13. Wills J (2019) The economic impact of hosting the olympics. Investopedia, 25 June 2019. [Online]. Available: <https://www.investopedia.com/articles/markets-economy/092416/what-economic-impact-hosting-olympics.asp>. Accessed 29 Dec 2019
14. Nguyen L (2009) Olympic debt left over. BCBusiness, 1 Mar 2009. [Online]. Available: <https://www.bcbusiness.ca/olympic-debt-left-over>. Accessed 8 Jan 2020
15. Sharma M (2009) Commonwealth Games 2010 and Use of the facilities after the Games. Centre for Civil Society, New Delhi
16. Deshpande R, Singh MK (2010) Rising cost: Commonwealth Games to get Rs 700 crore more Read more at: https://economictimes.indiatimes.com/news/politics-and-nation/rising-cost-commonwealth-games-to-get-rs-700-crore-more/articleshow/5700111.cms?utm_source=contentofinterest&utm_medium=. The Economic Times, 19 Mar 2010. [Online]. Available: <https://economictimes.indiatimes.com/news/politics-and-nation/rising-cost-commonwealth-games-to-get-rs-700-crore-more/articleshow/5700111.cms>. Accessed 11 Dec 2019
17. The Legacy of London 2012 has come to life at Queen Elizabeth Olympic Park (2018) Queen Elizabeth Olympic Park, 27 July 2018. [Online]. Available: <https://www.queenelizabetholympicpark.co.uk/news/news-articles/2018/07/the-legacy-of-london-2012-has-come-to-life-at-queen-elizabeth-olympic-park>. Accessed 20 Dec 2019
18. Schittich C (2013) Cable cars in the city—large-scale aerial urban circulation systems. In: Designing circulation areas. Institut für internationale Architektur-Dokumentation GmbH & Co., Munich, p 50

19. Menegaz F (2016) Is it possible to fit all of Brazil's woes in a single article? Slate, 3 Aug 2016. [Online]. Available: <https://slate.com/culture/2016/08/everything-thats-gone-wrong-in-brazil-in-the-runup-to-the-2016-rio-olympics.html>. Accessed 11 Jan 2020
20. Goujon (2016) The best olympic architecture. Architectural Digest, 18 July 2016. [Online]. Available: <https://www.architecturaldigest.com/gallery/best-olympic-architecture-beijing-athens-barcelona-slideshow>. Accessed 21 Dec 2019
21. Reuters (2010) Commonwealth games bridge rebuilt in record time. The Telegraph, 2 Oct 2010. [Online]. Available: <https://www.telegraph.co.uk/sport/othersports/commonwealthgames/8038393/Commonwealth-Games-bridge-rebuilt-in-record-time.html>. Accessed 25 Dec 2019
22. Winkelmann A (2016) Deconstructing olympic architecture. Humphries Poli Architects P.C. and Ratio Architects, 20 July 2016. [Online]. Available: <http://hparch.com/deconstructing-olympic-architecture/>. Accessed 12 Dec 2019
23. Rogers S (2012) Olympics 2012 in infographics: logistics. The Guardian, 25 June 2012. [Online]. Available: <https://www.theguardian.com/sport/datablog/gallery/2012/jun/25/olympics-infographics-logistics>. Accessed 22 Dec 2019
24. AECOM (2016) After the games, Rio's stadiums won't rot—they'll transform. Wired, 8 Jan 2016. [Online]. Available: <https://www.wired.com/2016/08/games-rios-stadiums-wont-rot-the-yll-transform/>. Accessed 21 Dec 2019
25. Planell J (2018) Ras Abu About Stadium: Fenwick Iribarren Architects. Fenwick Iribarren Architects, 5 Apr 2018. [Online]. Available: <http://www.fenwickiribarren.com/en/proyecto/rasabuabout.html>. Accessed 10 Jan 2020
26. Dey A (2012) Maximising the potential of stadiums in Indian cities. Dissertation in Architecture, Sushant School of Art and Architecture, New Delhi
27. London 2012 legacy plan published (2012) BBC, 18 September 2012. Available: <https://www.bbc.com/news/uk-politics-19638262>. Accessed 12 Dec 2019
28. Moreto G (2017) Left to rot: Maracana in a state of ruin as Brazil's authorities leave ground to rot after lining their pockets. The Sun, 10 Jan 2017. [Online]. Available: <https://www.thesun.co.uk/sport/football/2576924/maracana-in-a-state-of-ruin-as-brazils-authorities-leave-ground-to-rot/>. Accessed 17 Dec 2019
29. Otto T (2017) Rio's olympic aquatic centre left in ruins after grand promises. news.com.au, 8 Feb 2017. [Online]. Available: <https://www.news.com.au/sport/sports-life/rios-olympic-aquatic-centre-left-in-ruins-after-grand-promises/news-story/f0d7a5aedfd314c41ae42f66b98d5ca3>. Accessed 12 Dec 2019
30. "Rio's olympic venues, six months on—in pictures (2017) The Guardian, 10 Feb 2017. [Online]. Available: <https://www.theguardian.com/sport/gallery/2017/feb/10/rios-olympic-venues-six-months-on-in-pictures>. Accessed 12 Dec 2019
31. Vikram K (2016) Worn-out tracks, unlevelled ground and poor upkeep of Delhi's Jawaharlal Nehru Stadium reflects the state of sports facilities offered in India. Daily Mail, 21 Aug 2016. [Online]. Available: <https://www.dailymail.co.uk/indiahome/indianews/article-3750817/Worn-tracks-unlevelled-ground-poor-upkeep-Delhi-s-Jawaharlal-Nehru-Stadium-reflects-state-sports-facilities-offered-India.html>. Accessed 13 Dec 2019
32. Bharatkumar A (2013) Flexible architecture: what value does flexible architecture add to dwellings? Dissertation in Architecture, School of Planning and Architecture, New Delhi
33. Nomad (2019) bluecube, [Online]. Available: <https://www.bluecubeseating.com/portfolio/nomad/>. Accessed 20 Dec 2019
34. Bushby H, Heald C (2012) London 2012: ten facts about the Olympic Stadium. BBC, 4 May 2012. [Online]. Available: <https://www.bbc.com/news/uk-17905304>. Accessed 20 Dec 2019

Cost Structure Identification for Third-Party Logistics Services in Construction Projects



Fauziah S. C. S. Maisarah and Muhamad Abduh

Abstract The third-party logistics services have been applied to some large-scale construction projects in several countries and research regarding this has been published in the last five years. However, a review of the cost structure for these services is still rarely done. The previous research has been done provides an overview of the potential value of third-party logistics services to support the logistics activities of small-sized contractors which can occupy an interface space between the supply chain of materials and construction projects in Indonesia. Therefore, a study on the cost structure of third-party logistics services will be conducted to complete the model. This paper presents a comprehensive study within a literature review and survey to identify the cost structure of the third-party logistics services to support strategic commodities of small-sized contractor in building construction and road projects. The activity-based costing approach is used to set out the cost structure. In general, the cost structure incurred on third-party logistics services consists of the direct cost of the commodities, transportation costs, costs, storage costs, administrative costs, and supporting service costs. The cost formulation of the third-party logistics service provider should be defined with counting analysis of the resources consumed for all activities and it will be a further study of this research. The result of this study will be used to assess the feasibility of the third-party logistics business model for small-sized contractors in Indonesia.

Keywords Cost structure · Activity-based costing · Third-party logistics

F. S. C. S. Maisarah (✉) · M. Abduh
Faculty of Civil and Environmental Engineering, Institut Teknologi Bandung, Bandung, Indonesia
e-mail: f_fadjar@students.itb.ac.id

M. Abduh
e-mail: abduh@itb.ac.id

1 Introduction

In the process of implementing a construction project, the costs incurred in the process of material flow from suppliers to the project site, i.e. logistical costs. Logistics costs generally consist of transportation costs, storage costs, ordering costs, material production costs, and other costs that rising in the process. Logistics costs will be affected by the type of logistics method that the project used. Therefore, the project leader should select a suitable type of logistics method for each project.

The selection of logistic models to be implemented in a project must carefully consider the market analysis of suppliers, the structure of material usage, accurate planning of material usage, and the minimum costs incurred due to the logistics process [1]. Therefore, the contractor as the executor of project implementation must invest, in terms of time and system, so that the implementation of material logistics activities can support project performance. Implementing the third-party logistics services, some or even all of the material logistics activities can be outsourced to the service providers so that the contractor might focus on its construction operations. The process of selecting a logistics method, whether it will be done by the contractor or outsourced, will be easier if it can be converted in the amount of cost.

In common, contractors have human resources who can manage the logistics of the materials however, some studies have reviewed the potential of implementation outsourcing logistics in construction projects [2–6]. Logistics costs using the method of outsourcing logistics have been simulated by Sobotka and Czarnigowska [1], and the results are stated to reduce costs. The context of the logistics cost simulation studied was carried out using an approach to market conditions found in Poland. Component costs incurred for material logistics activities in construction projects that occur are booking costs, internal and external transportation costs, capital costs, inventory costs, penalty fees due to shipping delays.

Fang and Ng [7] use an activity-based costing approach to analyse logistics costs. By using this approach, the resources used can be traced back to the activities that use these resources, especially the cost components. By simulating the activities carried out, it can help the authorities to choose the appropriate logistics scenario. The basic logistics cost elements from the results of Fang and Ng's study [7] include inventory costs, transportation costs, warehouse costs, and procurement costs.

This paper will discuss the cost structure identification for third-party logistics services for supporting strategic construction material procurement of small-sized contractors in accordance with the results of previous studies [8, 9].

2 Activity-Based Costing

Activity-based costing is an approach to determining the cost of a product (goods or services) based on the cost of consuming resources from the activities that produce the product. Comparing with the conventional approach in cost analysis, activity-based

costing approach is more detail in giving information by supply chain management context [7]. Information relating to costs can be given in more detail so that the cost calculation becomes more accurate. The difference between activity-based costing and traditional approach in calculation costs is on determining its overhead cost and the excess of the capacity of production [10].

The activity-based costing in financing system is based on the costs incurred in the activities that encourage the creation of a product or service, for example, the overhead cost in production and distribution of a product or service. Production costs and overhead costs incurred are determined from each activity involved, so in this case, the overhead costs incurred can be more than one type of overhead. Whereas traditional financing systems are only based on the calculation of production costs for each unit of product or service, while overhead costs are based on working hours of work or machinery based on a certain production volume.

Despite activity-based costing, the approach gives more accurate cost analysis, however, its application is more complicated. The stages of implementing activity-based costing method in determining a service or product are by classifying overhead costs into homogeneous cost groups, depending on the cost driver that is causing it and allocating certain overhead costs.

3 Research Method

The research was conducted with literature studies and some surveys. Figure 1 is the methodology of this research. A qualitative approach was taken to find out the logistical problems experienced by contractors in the perspective of construction practitioners. Explorative descriptive method is a method that can provide an initial

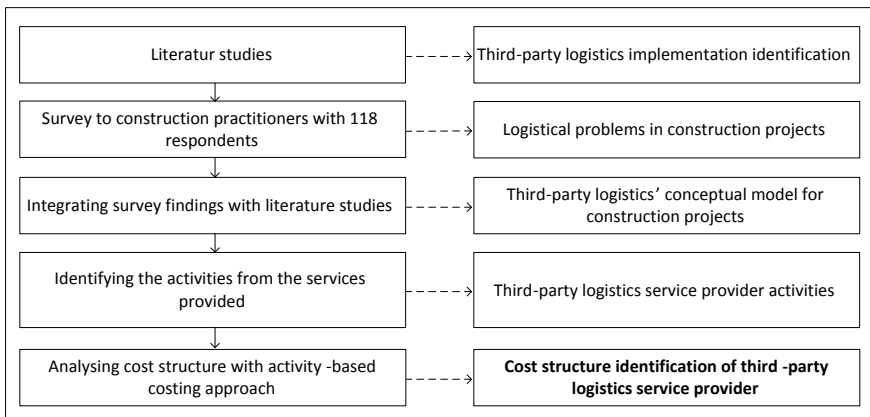


Fig. 1 Research methodology

description of a phenomenon based on the understanding of a group of individuals who are units of analysis.

The data collection method is carried out by distributing online questionnaires to construction practitioners who have work experience in construction companies (contractors). The results of data collection using an online questionnaire obtained as many as 118 respondents and spread from 75 construction companies in Indonesia, with a variety of work experience. The number of respondents, almost 90% have work experience of more than 1 year, it is assumed that respondents have able to disclose data on logistical activities in projects that they often work on.

4 Third-Party Logistics Services for Construction Projects

The third-party logistics services provider is a common entity in the manufacturing industry to increase productivity, nevertheless, in construction it is rarely implemented. There are some terms for third-party logistics, i.e. logistics outsourcing, logistics alliances, contract logistics, and contract distribution [11] even in this paper the term used is third-party logistics.

According to Ekeskär and Rudberg [2], third-party logistics is an effective tool for the logistics process in construction projects and can be used as a link between project sites and the upstream domain of the construction materials supply chain. This is in accordance with the role of supply chain management (SCM), which is as part of the connection between the project location and its supply chain (Role 1) which has been declared by Vrijhoef and Koskela [12]. Therefore, Abduh [8, 9] proposing a conceptual business model for third-party logistics as a potential entity as a connection between construction materials supply chain and construction projects. The application of third-party logistics needs to be explored further so that in preparing the model business, some logistical problems in the contractor perspective were done by Maisarah and Abduh [13].

Robbins [14] explains that logistics for construction is different from logistics for other industries. The main objective of logistics is to ensure efficient management related to transportation, storage and distribution of materials and equipment at the project site. Logistics in construction also provides support for project locations, such as security, cleaning, safety and welfare (accommodation on the ground), community relations, evacuation in emergencies, and first aid [15]. Browne [16] states that three things pose challenges in logistical problems in construction, namely place, complexity, and achieving a higher level in the aspect of sustainability. These three challenges require good logistics management in construction.

Activities in construction projects consist of planning construction materials related to the needs of the quantity, specifications, and schedule of the arrival of materials at the project site, procurement of materials, in the form of supplier selection and payment methods, as well as management of materials available at the project warehouse, including structuring materials that facilitate material handling and the goods in and out and inventory management, applied. These activities require human

resources who have good competence in logistics and adequate equipment and material storage (warehouse). Logistics activities and production control in construction operations will be able to improve project performance, this is related to planning procurement of construction materials that can determine the distance of transportation and transportation costs charged. Material requirements planning and arrival schedule can also increase labour productivity in the field because it can reduce unproductive waiting times.

Manufacturing or construction systems make a change from input to output with the help of transformation utility and adding value so that the shape or size of the success of the manufacturing and construction process is when the output value is greater than the input. This is very different from the logistics system, the output value should not be different from the input, so what is used is the time and place utility. The output should not change from the input, which changes only the time and place, in this case changing ownership, in a different time and location dimensions. The logistics system involves 2 points, namely the origin and destination, and involves 3 streams, namely products, information and money.

Lundesjö [15] explains that professionals from various industries will define the term logistics as a method and system for delivering products or materials to the right location at the right time and with the right amount and quality at the lowest cost. Some people say that logistics relates to the transportation, storage, and handling of a product through the supply chain from raw materials to the process of adding a certain value to the end-user. Christopher [17] states that logistics is a strategic process in terms of managing procurement, movement and storage of materials, spare parts, and inventory of goods (and information flow) through the organization and its marketing channels in such a way as to obtain benefits in a cost-effective manner to meet customer requests.

In construction projects, logistics activities become very important because, with good logistics activities, the construction implementation process will have the potential to succeed. Therefore, the strategy in managing logistics activities for construction projects is very important to do [25]. The strategy of implementing logistical functions in a construction project can be carried out with the strategy of using the logistics centre (LC) function. Some logistics centre approach for supporting construction project are *construction consolidation centre* [15, 18], *construction logistics consolidation centre* [19], *logistics outsourcing* [4], *logistics central* [20], *third party logistics* [2; 3], *coordinated construction logistics* [21], *construction logistics solution* [6], *third party logistics* [5], dan *construction consolidation centre* [22].

This paper is supported by the data of the previous studies which are conducted from the author's team. The data in the previous survey involving 118 practitioners as respondents provide an overview of the logistical problems based-on they experience in the logistics process in projects. Table 1 provides logistical problems in construction projects.

Based on the survey, problems No. 1 to 10 and problems No. 13 are the basic problems from the logistics process, that is transportation and distribution construction materials from a supplier. The problems related to how to order the materials

Table 1 Logistical problems in construction projects

No.	Logistical problems	Percentage
1	Guarantee of delivery time	43
2	Accuracy in quantity, specifications, and quality of material delivered	17
3	Guarantee of material availability	13
4	Material prices are not in accordance with the initial agreement with suppliers	6
5	Scope of delivery place for service area	5
6	Commitment of suppliers	4
7	Complexity about the administration of material procurement	2
8	Tracking of delivery	2
9	Material handling in the site from logistics vehicle	2
10	Flexibility in the payment method	2
11	Lack of ability for logistics planning	2
12	RL (Reverse logistics) for material waste	1
13	Lack of information about the material specification	1

from suppliers and ensure the material delivered to the construction site. The problems No. 11 show that some contractors require assistance in logistics planning. Besides, problem No. 12 is related to environmental needs for green construction requirements.

If a third-party logistics service wants to be an entity involved in the construction supply chain as a link between the material supply chain and the project, then it must be able to be a solution to the logistical problems experienced by practitioners. The top three of the problems are a guarantee of delivery time, material availability, and the accuracy in quantity, specifications, and quality of material delivered, which are very common problems in the logistics process. Therefore, the third-party logistics provider should be focussing on them.

As a result of the construction logistics problems, the main service of third-party logistics for the construction supply chain is to supply and deliver construction materials from suppliers to sites. The support services are to respond to problem No. 11 and 12. The reverse logistics for material waste and consultation in terms of logistics planning such as calculating materials needed and adjusting with construction operation schedule. Figure 2 is a conceptual model of third-party logistics provider with its services and accompanying activities.

Subsequently defining the service to be provided by third-party logistics, the process and activities that must be carried out to realize the service can be identified. From the analysis of the survey result, third-party logistics should be providing three services to support a construction project in providing construction materials. The first and main service is supplying materials to sites (S1). The second service is assisting contractors in consultation logistics planning (S2) in terms of the material needs and scheduling materials arrival to sites so that to minimise waste of materials

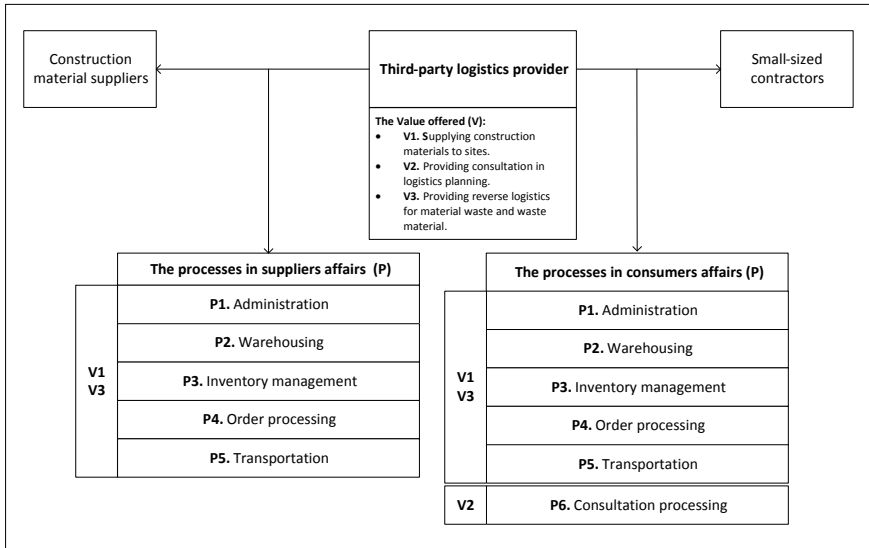


Fig. 2 The conceptual model for third-party logistics services

and other resources such as materials cumulation in the stockyard and traffic congestion from logistics vehicles arriving in the site. The last service is providing reverse logistics for material waste to the disposal area and waste material to a third-party logistics warehouse (S3). Based on the three services the process of them could be defined as seen in Table 2.

After defining the activities, the next step is identifying the resources which are needed. Maisarah and Abduh [23] conduct a focus group discussion with contractors, suppliers, and government agencies to validate third-party logistics entity models and discuss the resources needed for it. The result of discussion found that the resources must be owned by logistics service providers in addition to competent human resources, and also require adequate information technology networks and facilities that support logistics services, whether transportation facilities, warehousing, and information technology infrastructure. Strong financial support is also one of the things that logistical service providers must have to be able to provide services to their customers.

Figure 3 describes the breakdown activities based on the services that have been identified earlier.

5 The Cost Structure of a Third-Party Logistics Provider

Sobotka and Czarnigowska [1], give two examples of analysis of the calculation of logistics costs for two supply models. The first example is, using the standard logistics

Table 2 Third-party logistics services activities

Values (V)	Processes (P)	Activities (A)
V1, V3	P1. Administration	A1.1. Payment and administration
		A.1.2. Customers service activities
V1, V3	P2. Warehousing	A2.1. Receiving materials
		A2.2. Storage activities
		A2.3. Packing materials
V1, V3	P3. Inventory management	A3.1. Forecasting
		A3.2. Analyse suppliers
		A3.3. Analyse costumers needs
V1, V2, V3	P4. Order processing	A4.1. Order to suppliers
		A4.2. Process costumers order
V1, V3	P5. Transportation	A5.1. Transport materials
		A5.2. Tracking materials delivery
		A5.3. Handling materials
V2	P6. Consultation process	A6.1. Quantity surveyor activities
		A6.2. Report documents

cost model that applies to Poland. This cost component is the cost of purchase and overhead costs. Purchase costs consist of the cost of material transportation and material unloading costs. These two costs are generally calculated based on the presentation of total material costs. Overhead costs consist of administrative costs and indirect costs for projects that are special or specific in nature.

The concept of calculating costs for material supply is based on the use of large amounts of material, carried out regularly or routinely, and is ongoing or over a long period. This assumption is given with consideration that it will reduce total costs. The basis for calculating costs is to consider the schedule of work implementation and the use of materials in a project. Therefore, the material delivery activity is adjusted to the schedule. With this assumption, we will get three supply models to be analysed, namely:

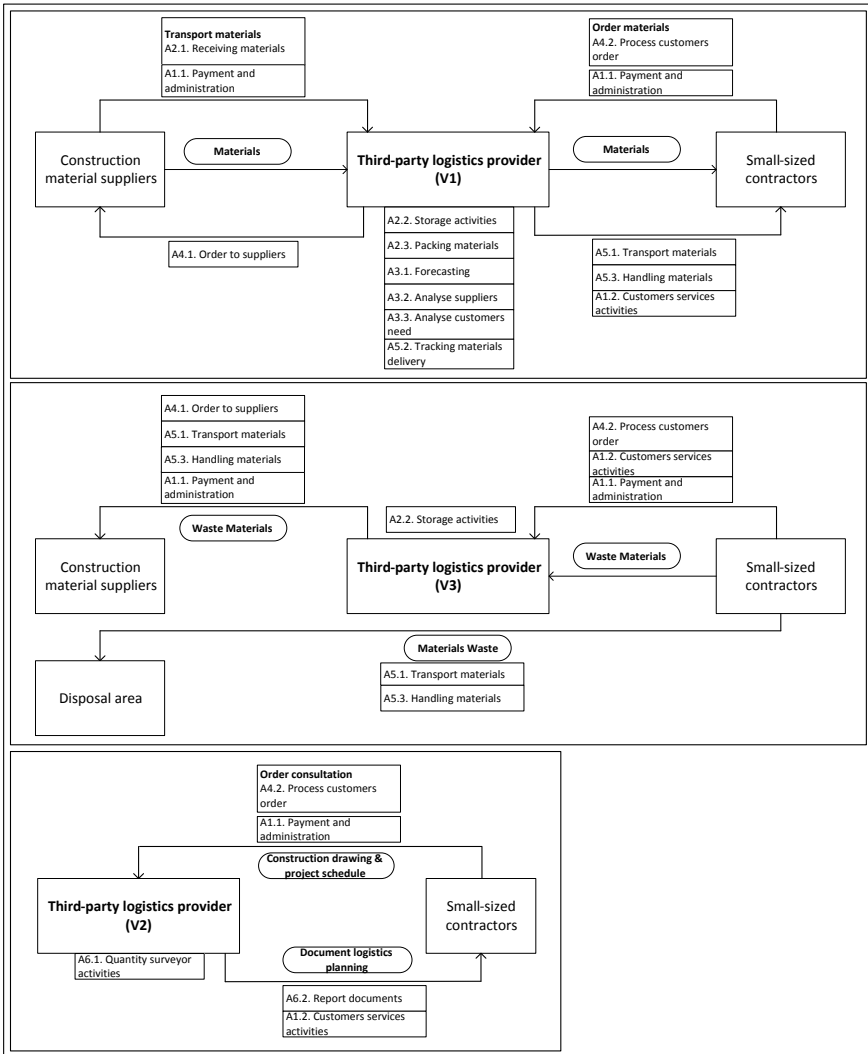


Fig. 3 The conceptual model for third-party logistics activities

1. Delivery directly to the project site and the size of the shipment is calculated by the concept of an economical number of orders with consideration of logistics vehicle capacity.
2. Delivery directly to the project site and the size of the shipment is determined based on the planned use of the material.
3. Delivery to specific locations (auxiliary stacking yards) and the size of deliveries to the project site is carried out regularly.

Cost calculation for construction logistics centre needs a model of process and activities of the services offered. The reliable information from partners in the construction supply chain area is needed to formulate the detailed cost of services [24].

The logistics process in a construction project starts from the process of purchasing material before the material is used in a project. Therefore, determining the logistics costs for construction projects with an activity-based costing approach is very helpful as a system in calculating the costs of various activities to produce a product or activity [7].

Implementing third-party logistics in a construction project will reduce is expected to improve project efficiency, because contractors can save time in selecting suppliers. The availability of appropriate materials during the implementation of construction operations can also increase construction productivity. Moreover, the benefit of this will be better if third-party logistics can provide just-in-time services so that the contractor does not need to think about storing material at the project site [24].

However, the cost incurred in implementing third-party logistics service providers is still being analysed. Based on the activity model of the third-party logistics service provider as shown in Fig. 3. The activity-based costing should be defined not only from the activities but also from the resource consumed. Nevertheless, from the activities that identified we could formulate the basic cost. The basic cost is the cost that occurred for the main activity, i.e. transportation and warehousing. The cost of transportation will be more efficient because the third-party logistics can coordinate many suppliers and select the most suitable supplier from the location aspect.

The storage cost of third-party logistics will be more efficient because of the economies of scale from the amount aspect if comparing every project build their storage in sites. The supporting cost occurred for the administration and customer services activities.

6 Conclusion

In this paper, a literature review and survey about implementation logistics outsourcing models for construction projects conducted by small-sized construction companies give some insight into what kind of their services and activities to occur. Three services should be provided by a third-party logistics services provider, i.e., supplying construction materials to the site, providing consultancy in logistics planning, and picking reverse logistics for material waste and waste materials.

The cost structures based on activities of the services consist of transportation costs, storage costs, administrative costs, and supporting service costs. The cost formulation of third-party logistics should be defined with counting analysis of the resources consumed for all the activities and will be a further study of this research. Moreover, the result will be used to assess the feasibility of the third-party logistics business model for small-sized contractors in Indonesia.

References

1. Sobotka A, dan Czarnigowska A (2005) Analysis of supply system models for planning construction project logistics. *J Civil Eng Manag* 11(1):73–82
2. Eksekär A, Rudberg M (2015) Third-party logistics in construction: perspective from supplier and transport providers. In: 22nd International annual EurOMA conference. Switzerland
3. Ekeskär A, Rudberg M (2016) Third-party logistics in construction: the case of a large hospital project. *Constr Manag Econ* 34(3):174–191. <https://doi.org/10.1080/01446193.2016.1186809>
4. Wanyonyi AN (2014) Logistics outsourcing and performance of road construction projects in Nairobi Country. Research Project, University of Nairobi
5. Vrijhoef R (2018) Improving efficiency and environmental impact applying JIT logistics and transport consolidation in urban construction projects. In: Proceedings of the creative construction conference
6. Janné M (2018) Construction logistics solutions in urban areas. Thesis for: Licentiate of Engineering. <https://doi.org/10.3384/lic.diva-147536>
7. Fang Y, Ng TS (2011) Applying an activity-based costing approach for construction logistics cost analysis. *Constr Innov* 11(3):259–281
8. Abduh M (2017) Kebutuhan layanan logistik strategis untuk pemberdayaan kontraktor kecil di Indonesia. In: University Network for Indonesia Infrastruktur Development (UNIID 2017). Palembang, 19–20 Sept 2017
9. Abduh M (2018) Conceptual business models of strategic logistics services for small-sized contractors. In: The fourth Australasia and South-East Asia structural engineering and construction conference University of Southern Queensland, Springfield Campus, Brisbane. ISBN: 978-0-9960437-7-9
10. Griful-Miquela C (2001) Activity-based costing methodology for third-party logistics companies. *Int Adv Econ Res* 7:133–146
11. Selviaridis K, Spring M (2007) Third-party logistics: a literature review and research agenda. *Int J Logist Manag* 10(1):25–150
12. Vrijhoef R, dan Lauri K (2000) The four roles of supply chain management in construction. *Eur J Purchasing Supply Manag*
13. Maisarah FSCS, Kusuma H, Abduh M (2019) Persepsi praktisi konstruksi terhadap layanan logistik pihak ketiga. In: Prosiding Konferensi Nasional Teknik Sipil 13, Banda Aceh, 19–21 Sept 2019
14. Robbins S (2015) Effective management of construction project supply chain, 62–76. In: Lundesjö G (ed) Supply chain management and logistics in construction: delivering tomorrow's build environment. Kogan Page Limited, London
15. Lundesjö G (2015) Consolidation centres in construction logistics. In: Lundesjö G (ed) Supply chain management and logistics in construction: delivering tomorrow's build environment. Kogan Page Limited, London
16. Browne M (2015) The challenge of construction logistics. In: Lundesjö G (ed) Supply chain management and logistics in construction: delivering tomorrow's build environment. Kogan Page Limited, London
17. Christopher M (2011) Logistics and supply chain management, 3rd ed. Pearson Education Limited, London
18. Lundesjö G (2011) Guidance: construction logistics. The Logistics Business. The United Kingdom
19. Shigute SA, Nasirian A (2014) The future of construction logistics consolidation centers in construction. Master of Science Thesis in The Master Program Design and Construction Project Management Chalmers University of Technology Sweden
20. Samuelsson S, Ahmetasevic M (2014) Management of construction logistics in Stockholm: Identifying ways of improvement for construction logistics within the inner city of Stockholm. Independent thesis in The Faculty for Technology, Applied Mechanics, Construction Engineering, Uppsala University

21. Bengtsson SH (2018) Construction client collaboration for inter-organizational innovation. Licentiate thesis, School of Architecture and the Built Environment (ABE), Real Estate and Construction Management, Project Communication, KTH University
22. Navarro-Correcher C, Pérez-Cervera C, Sanz-Argent J, Furió-Pruñonosa S (2018) Business models analysis of Construction Consolidation Centres. In: Proceedings of 7th Transport Research Arena TRA 2018, April 16–19, Vienna, Austria
23. Maisarah FSCS, Abduh M (2018) Parameter penentuan potensi entitas penyedia layanan logistik strategis untuk kontraktor kecil di Indonesia. In: Prosiding Seminar Nasional Infrastruktur Berkelanjutan 2018, Institut Teknologi Nasional (ITN) Malang, 28–29 Nov 2018
24. Janné M, Fredriksson A (2018) Cost modelling construction logistics centres. In: The 30th NOFOMA Conference, University of Southern Denmark
25. Ala-Riksu T, Karkkainen M (2006) Material delivery problems in construction projects: a possible solution. *Int J Prod Econ* 104:19–29

Constraint and Fault Tree Analysis in Safety Construction System Integration



N. Fitri, A. Bhaskara, and A. Purbiantoro

Abstract Construction projects is an activity contains many elements of hazard and causes a poor record in terms of occupational safety. Therefore, occupational safety is always an aspect that have to be regenerated, caused by the problem complexities which includes issues in terms of humanity, legal aspects, accountability and the image of the organization. This research aims to determine the level of accuracy in the field of the application of occupational safety management systems based on engineering judgement, identify and analyze the potential risk of loss/work accident using the Fault Tree Analysis (FTA) method and plan mitigation to reduce the scope of construction work in progress. This research is a quantitative analysis which is done by collecting primary data through interviews and observations and secondary data in the form of data from the construction project. FTA used to investigate potential work accidents by analyzing the direct causes to the underlying causes of the accident. The results show the level of implementation accuracy of the Occupational Safety Management System that has been applied obtained an assessment rate of 97.29% and included in the satisfactory rating level, however after a probability assessment based on engineering judgement there are indications of doubts of 23.37% of the results. The FTA causality results found several events tendencies potentially lead to loss, events such as workers not using personal protective equipment, workers acting carelessly, and lack of work experience are events that often occur in FTA basic events.

Keywords Audit · Causalities · Constraint · FTA · Safety construction system

N. Fitri

Universitas Islam Indonesia, KM 14, 5 Kaliurang Street, Yogyakarta, Indonesia
e-mail: fitri.nugraheni@uii.ac.id

A. Bhaskara (✉) · A. Purbiantoro (✉)

Universitas Teknologi Yogyakarta, No. 63 Glagahsari Street, Yogyakarta, Indonesia
e-mail: adwitya.bhaskara@staff.uty.ac.id

1 Introduction

Work safety means how someone protecting themselves or others. Because of work-load happening in construction sites require a worker to get the protection so that they could work maximally. Work safety is the most crucial factor in achieving the project's goals. The maximum performance of triple constrains (cost, quality and time) is meaningless if the rate of occupational safety is being ignored.

Construction is an event with a high-risk for an accident. Therefore, the service providers are required to apply the management system of work safety as an action for resolving the accident risk that might occur. Concerning guidance to apply the management system of occupational safety and health in Indonesia, one of them is based on Indonesian Government Regulation No. 50 the year 2012 [1].

The regulation mentioned specific terms and conditions that every company employing worker above or 100 (a hundred) people or has a high level of potential dangers is required to apply The Management System of Occupational Health and Safety or Occupational Health and Safety Assessment Series (OHSAS 18001:2007) which integrated by Company Management System [2]. The requirement is including Company investment due to an obligation arranged in the Law of The Republic of Indonesia.

Through the implementation of the Management System of Work Safety, it is expected that the company is able to have a Safety, healthy, efficient, and productive environment. Further, the implementation of management system of work safety also helps the owner of Company to execute the standard of Occupational health and Safety which also became a public guide both nationally and internationally.

2 Literature Review

Constraint and fault tree analysis in this research is an integration system between audit and causalities structure for find out the basis trigger which cause of construction accident by fault tree analysis method. There are two basic influential literature used in this research.

2.1 *Domino Theory*

Construction accidents can be prevented just by identifying the root causes of accidents, which is possible by accident investigation techniques such as theories of accident causation and human errors. Accident prevention has been defined by Heinrich as 'An integrated program', a series of coordinated activities, directed to the control of unsafe personal performance and unsafe mechanical conditions, and based on certain knowledge, attitudes, and abilities. Some other synonyms for accident

prevention have been emerged later such as loss prevention, loss control, total loss control, safety management, incidence loss control [3] Heinrich was the pioneer in the Accident causation theories. He described the accidents causation theory, man and machine relationship, frequency and severity relation, unsafe acts reasons, management role in accident prevention, costs of accidents and the impact of safety on efficiency [4]. Heinrich's domino theory has been modified and updated over the years with greater emphasis on management as an original cause of accidents. The management-based theories define management as responsible for causing accidents, and they attempt to recognize failures within the management system [5].

The sequential domino representation was continued by Bird and Germain (1985) who acknowledge that the Heinrich's domino sequence had underpinned safety thinking for over 30 years. They recognized the need for management to prevent and control accidents in what were fast becoming highly complex situations due to advances in technology. They developed an updated domino model which they considered reflected the direct management relationship with the causes and effect of accident loss and incorporated arrows to show the multilinear interaction of the cause-and-effect sequence. This model became known as the *Loss Causation Model* and was again represented by line of five dominos, linked to each other in a linear sequence [6]. The updated and modified sequence of events is [7]:

- (a) Lack of control/management (inadequate program, inadequate program standard, inadequate compliance to standard)
- (b) Basic causes/origins (basic causes: (1) personal factors, (2) job factors)
- (c) Immediate causes/Symptoms (sub-standard act and condition)
- (d) Incident (contact with energy and substance)
- (e) Loss (property, people, process)

2.2 *Fault Tree Analysis*

A fault tree analysis can be simply described as an analytical technique, whereby an undesired state of the system is specified (usually a state that is critical from a safety standpoint), and the system is then analyzed in the context of its environment and operation to find all credible ways in which the undesired event can occur [8].

As deductive approach, FTA starts with an undesired event, such as failure of main engine, and the determines (deduces) it causing systematic, backward stepping process. In the determining the cause fault tree is constructed as a logical illustration of the events and their relationships that are necessary and sufficient result in the undesired event, or top event [9].

2.3 Assessment

Main indicator for assessment in this research is based on Government Regulation of Indonesia Republic Number 50 Year 2012 about Application System of Occupational Safety and Health is basic. Determination of audit criteria are divided into three level as follows.

1. Initial Level Assessment
Assessment of Management System of Occupational Health and Safety for 64 criteria's
2. Transition Level Assessment
Assessment of Management System of Occupational Health and Safety for 122 criteria's
3. Advance Level Assessment
Assessment of Management System of Occupational Health and Safety for 166 criteria's

3 Research Method

The method used in this research is quantitative which is systematic, planned, and structured from the preliminary to its design. Primary data was obtained from the interview and observation focused on the work process and site condition which potential of an accident. The first step, data analyzed by audit assessment and the result is specified detailly by FTA to find out the basic potential accident in construction work on progress. Mind mapping of this research presented as follows (Fig. 1).

3.1 Research Instrument

The research instrument refers to the Application of Management System of Occupational Health and Safety, and Indonesian Government Regulation No. 50 the Year 2012 appendix II, also the integration of OHSAS 18001. The following is a broad line research instrument submitted to the resource person (Table 1).

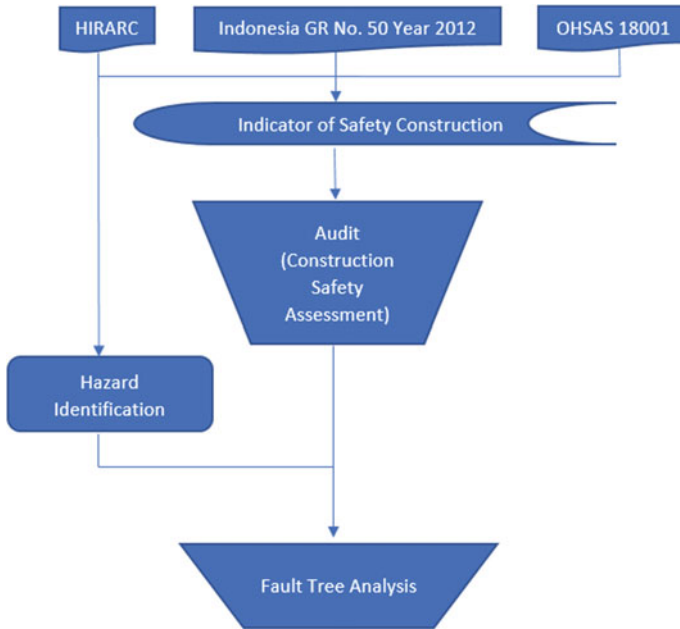


Fig. 1 Mind mapping (outcome flowchart)

Table 1 Research instrument grids

Element criteria	Sub element	Total
Development and commitment maintenance	1.1.1–1.4.10	25
Creation and documentation of occupational health and safety plan	2.1.1–2.4.1	13
Planning control and contract review	3.1.1–3.2.4	8
Document control	4.1.1–4.2.3	7
Work secure based on occupational health and safety	5.1.1–5.9.1	53
Monitoring standard	6.1.1–6.4.5	22
Report and deficiencies correction	7.1.1–7.3.6	9
Management and material loading	8.1.1–8.2.3	7
Collection and data usage	9.1.1–9.2.2	5
Occupational health and safety usage	10.1.1–10.1.3	3
Skill and abilities development	11.1.1–11.5.1	14
Grand total		166

4 Result and Discussion

Output Mapping of this study is as follows:

4.1 Data Collection Results

The percentage level of the implementation of the work safety management system which has been applied by the service provider for the building project of hospital service is (Table 2):

$$\frac{(\text{Critical Category} \times 0) + (\text{Major Category} \times 50) + (\text{Minor Category} \times 100)}{\text{Total Audit Criteria}} \times 100$$

$$\frac{(0 \times 0) + (9 \times 50) + (157 \times 100)}{166} \times 100$$

$$= 97.29\%$$

Classification of Assessment Colour

See Fig. 2.

Description:

- a. Critical Sub
 - Not applying criteria
 - There are findings that result in a fatality
- b. Major Sub
 - Unqualified for laws and regulation
 - Neglecting one of Occupational Health and Safety principals; and
 - There is minor for an audit category in some sections.
- c. Minor Sub
 - Consistent to comply with the requirements of the standard of laws and regulations, handbook, and some other references
 - The Implementation of Occupational Health and Safety is qualified

Probability and Possibility Analysis

The probability number of the research instrument is obtained from the discussion group between the writer and the people involved in construction project whereas the possibility number is several engineering judgments of the writer based on direct observation in each project site. The average of the probability and the possibility will

Table 2 Research instrument grids

Criteria number	Score	Type	Criteria number	Score	Type
1			5.7		
1.1			5.7.1–5.7.7	100	Minor (Green)
1.1.1–1.1.5	100	Minor (Green)	5.8		
1.2			5.8.1–5.8.2	100	Minor (Green)
1.2.1–1.2.6	100	Minor (Green)	5.9		
1.3			5.9.1	100	Minor (Green)
1.3.1–1.3.3	100	Minor (Green)	6		
1.4			6.1		
1.4.1–1.4.10	100	Minor (Green)	6.1.1–6.1.7	100	Minor (Green)
2			6.2.1–6.2.8	100	Minor (Green)
2.1.1–2.1.5	100	Minor (Green)	6.3		
2.1.5	50	Major (Yellow)	6.3.1–6.3.2	100	Minor (Green)
2.2			6.4		
2.2.1–2.2.3	100	Minor (Green)	6.4.1–6.4.5	100	Minor (Green)
2.3			7		
2.3.1–2.3.4	100	Minor (Green)	7.1		
2.4			7.1.1	100	Minor (Green)
2.4.1	100	Minor (Green)	7.2		
3			7.2.1	100	Minor (Green)
3.1			7.3		
3.1.1–3.1.4	100	Minor (Green)	7.3.1–7.3.4	100	Minor (Green)
3.2			7.3.5–7.3.6	50	Major (Yellow)
3.2.1–3.2.4	100	Minor (Green)	7.4		
4			7.4.1	100	Minor (Green)
4.1			8		
4.1.1	100	Minor (Green)	8.1.1–8.1.4	100	Minor (Green)
4.1.2	50	Major (Yellow)	8.2		
4.1.3–4.1.4	100	Minor (Green)	8.2.1–8.2.3	100	Minor (Green)
4.2			9		
4.2.1–4.2.3	100	Minor (Green)	9.1		
5			9.1.1–9.1.3	100	Minor (Green)
5.1			9.2		
5.1.1–5.1.8	100	Minor (Green)	9.2.1–9.2.2	100	Minor (Green)
5.1.9	50	Major (Yellow)	10		
5.1.10–5.1.11	100		10.1		
5.1.12	50	Major (Yellow)	10.1.1–10.1.3	100	Minor (Green)

(continued)

Table 2 (continued)

Criteria number	Score	Type	Criteria number	Score	Type
5.1.13	100	Minor (Green)	11.1		
5.1.14	50	Major (Yellow)	11.1.1–11.1.7	100	Minor (Green)
5.1.15	100	Minor (Green)	11.2		
5.1.16–5.1.18	100	Minor (Green)	11.2.1–11.2.2	100	Minor (Green)
5.1.19	50	Major (Yellow)	11.3		
5.1.20–5.1.23	100	Minor (Green)	11.3.1–11.3.2	100	Minor (Green)
5.2			11.3.3	50	Major (Yellow)
5.2.1–5.2.4	100	Minor (Green)	11.4		
5.3			11.4.1	100	Minor (Green)
5.3.1–5.3.2	100	Minor (Green)	11.5		
5.4			11.5.1	100	Minor (Green)
5.4.1–5.4.4	100	Minor (Green)			
5.5					
5.5.1–5.5.8	100	Minor (Green)			
5.6					
5.6.1–5.6.2	100	Minor (Green)			

After the audit of 166 advanced criteria level, the results are:

- (1) Critical category (Score = 0), there is 0 criteria
- (2) Major category (Score = 50), there are 9 criteria
- (3) Minor category (Score = 100), there are 157 criteria

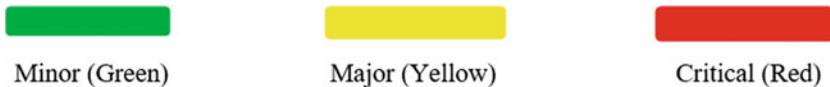


Fig. 2 Classification of Assessment Colour

be taken as the determinant number which is used to determine the average number in each element. In this case, both the probability and the possibility are divided into three rating scale 0–3, 4–6, 7–9 [10].

After the analysis of probability and possibility, obtained a result for the percentage level of the implementation of the work safety management system which has been applied by the service provider about 74.60%. The result is lower 23.37% than Survey data Collection which shows 97.29% due to the service provider unable to showing the evidence that they already applied the principal or the criteria of the implementation of Management System of Occupational Health and Safety Indonesian Government Regulation No. 50 the Year 2012 Appendix II integrated by OHSAS 18001. The comparison results between survey data and probability and possibility analysis based on engineering judgment are shown at Fig. 3.

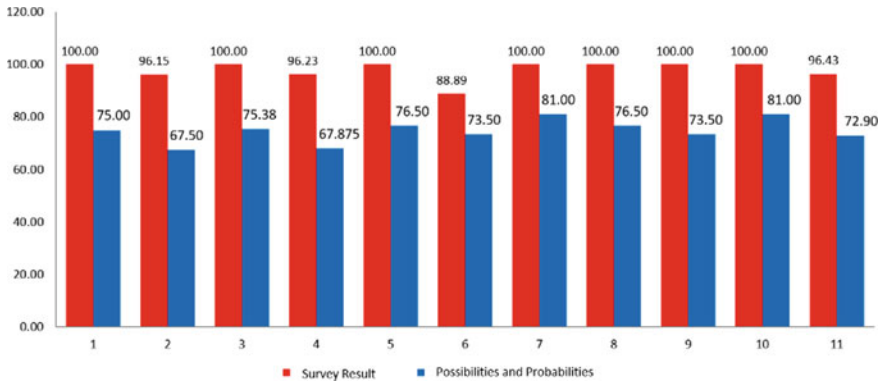


Fig. 3 Probability and possibility and survey result chart

4.2 Constraint Analysis by FTA

Based on the Domino theory in this study, figuring FTA for a basic event is an unsafe act or unsafe condition event, so that the basic event can be eliminated by performing cut set ranking with Boolean algebra for simplifying/reducing so the accident events and injury would not occur. Here are an FTA depiction and a discussion of potential work accidents on the scope of construction in progress.

Potential Hazards of Tower Crane Operation (TC)

The result of Modeling Fault Tree Analysis (FTA) of Potential Hazard of Tower Crane Operation (Fig. 4).

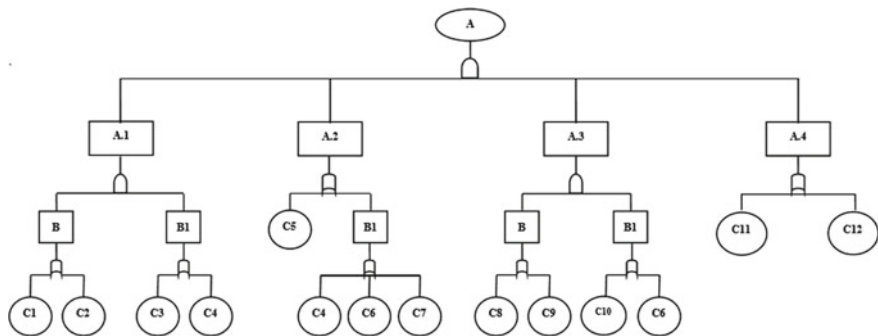


Fig. 4 FTA Graphic model of potential hazard in Tower Crane Operation

Table 3 The event description on the graphical model of the tower crane operation

No.	Symbol	Description	No.	Symbol	Description
1	A	The potential hazard on tower crane operation (TC)	11	C.4	Workers act recklessly such as joking, smoking and working out of procedure
2	A.1	Falling worker or workers hit by falling objects when the erection	12	C.5	The rotation portion and the height of the tower crane does not match to the field
3	A.2	Striking the surrounding building	13	C.6	Lack of experience/the expertise is not suitable
4	A.3	The broken sling rope	14	C.7	There is no communication between TC operator and the foreman
5	A.4	Struck by lightning	15	C.8	The absence of danger sign
6	B	Technique factors	16	C.9	There is no inspection of work equipment or routine checks before the operation
7	B.1	Workers factor	17	C.10	Working out of procedure
8	C1	Less socialization of Occupational Health and Safety officer	18	C.11	The absence of lighting rod at the top of Tower Crane (TC)
9	C2	Absence of danger sign around Tower Crane area	19	C.12	Operate during heavy rain
10	C.3	Not using the personal protective equipment			

Description:
See Table 3.

FTA Data Analysis:

The next step after creating the FTA graphic model is further analyzing the basic event that leads to the top event by looking for a minimal cut set obtained from analysis results using the Boolean algebra of distributive law. Operator notation of Boolean logic used for OR gate is an addition symbolized by (+) whereas for AND gate is a multiplication symbolized by (·)

A	= A1 . A2 . A3 . A4	B	= C1 + C2
A1	= B . B1	B1	= C3 + C4
A2	= C5 + B1	B1	= C4 + C6 + C7
A3	= B . B1	B	= C8 + C9
A4	= C11 + C12	B1	= C10 + C6

From the Boolean algebra shown above, then a minimum cut set is sought to find a combination of several events until the results no longer to be reduced/simplified. The results of the combination of these events are called the cause of the peak event.

A =	$A1 \cdot A2 \cdot A3 \cdot A4$
=	$(B \cdot B1) \cdot (C5 + B1) \cdot (B \cdot B1) \cdot (C11 + C12)$
=	$((C1 + C2) \cdot (C3 + C4)) \cdot (C5 + (C4 + C6 + C7)) \cdot ((C8 + C9) + (C10 + C6)) \cdot (C11 + C12)$
=	$(C1 + C2 + C3 + C4) \cdot (C5 + C4 + C6 + C7) \cdot (C8 + C9 + C10 + C6) \cdot (C11 + C12)$

From the results of the analysis using boolean algebra, there are 4 minimum cut sets, which are the combination of basic events that can cause the potential of a hazards accident in tower crane operation. The following are basic events that probably cause the potential accident in tower crane operation along with a discussion of risk that can be applied (Table 4).

Potential Hazards of the Formwork

The results of the Fault Tree Analysis (FTA) depiction of the potential dangers of the formwork (Fig. 5).

Description:
See Table 5.

FTA data Analysis:

Minimal Cut set using algebra Boolean law:

A	= $B1 \cdot B2 \cdot B3$	C2	= $D3 + D4$
B1	= $C1 \cdot C2$	C1	= $D5 + D6 + D7$
B2	= $C3 \cdot C4$	C2	= $D8 + D3$
B3	= $C1 \cdot C2 \cdot C3$	C1	= $D5 + D1 + D9$
C1	= $D1 + D2$	C2	= $D10 + D11 + D4 + D8$
		C3	= $D12 + D13 + D14$

Event Combination result:

A	= $B1 + B2 + B3$
	= $(C1 \cdot C2) + (C1 \cdot C2) + (C1 \cdot C2 \cdot C3)$
	= $((D1 + D2) \cdot (D3 + D4)) + ((D5 + D6 + D7) \cdot (D8 + D3)) + ((D5 + D1 + D9) \cdot (D10 + D11 + D4 + D8)) \cdot (D12 + D13 + 14)$
	= $(D1 + D2 + D3 + D4) + (D5 + D6 + D7 + D8 + D3) + (D5 + D1 + 9 + D10 + D11 + D14 + D18 + D12 + D13 + D14)$

Table 4 Results of Boolean algebra analysis and risk control

No.	Basic event combination	Combination description	Risk control
1	C1, C2, C3, C4	The operation of tower crane has the potential to cause the risk of falling worker/hit by a falling object accident. This incident able to occur due to 4 (factors) which are the lack of OHS socialization or the lack of supervision from OHS officers, the absence of danger sign around crane tower operations, workers do not use the personal protective equipment and workers act recklessly	<ul style="list-style-type: none"> • Implementation of morning safety talks before starting work • Socialization of occupational health and safety program • Provide personal protective equipment (PPE) for workers • Conduct supervision of workers to comply by prescribed procedures) • Installation of falling hazards sign and prohibition to drop object around the tower crane operation site
2	C5, C4, C6, C7	Tower crane operation could potentially lead to the tower crane incident hitting the building around. The incident can appear if the rotation area and the height of tower crane does not match to the field, recklessness of worker, and the cut of communication between TC operator and foreman	<ul style="list-style-type: none"> • Engaging the expert/tower crane operator who owns the “Work Permit” of relevant agencies • Supervise the workers to work in accordance with the prescribed procedures • Provide HT for communication tools used between operator and foreman
3	C8, C9, C10, C6	Tower crane operation has the potential to break its sling ropes during the operation. The incident can occur due to the absence of warning signs and no inspection of work equipment or routine checks is carried out, working out of procedure/working with unsuitable expertise	<ul style="list-style-type: none"> • Routine inspection of construction tools and ensuring everything has been running as procedure that have been applied before starting work • Installing a warning sign (ADJUST LIFT CAPACITY)
4	C11, C12	Tower crane operation has the potential to cause tower crane events to be struck by lightning. The event can occur due to the absence of a lightning rod at the top of tower crane or occurs because tower Crane continues to operate during heavy rains	<ul style="list-style-type: none"> • Installing the lightning rod at the top of tower crane • Prohibit the operation of tower crane when the weather is raining heavily, and the strong wind

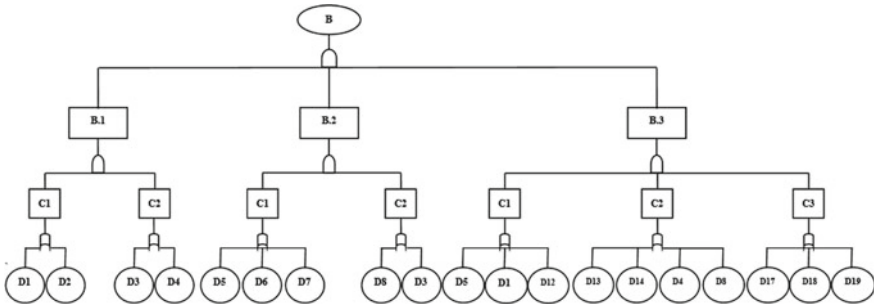


Fig. 5 The FTA graphic model of the potential dangers of the formwork

Table 5 The event description on the graphical model of the formwork

No	Symbol	Description	No.	Symbol	Description
1	B	Potential dangers of formwork	12	D.5	The absence of a warning sign
2	B.1	The collapse of the formwork	13	D.6	An error in lifting materials/equipment to a higher place
3	B.2	workers hit by falling objects and exposed to sharp instruments	14	D.7	Storing materials that are out of place
4	B.3	Falling at height	15	D.8	Workers do not use PPE
5	C1	Technical factors	16	D.9	Production pressure
6	C2	Worker factors	17	D.10	Lack of experience
7	C3	Environmental factors	18	D.11	Worker Fatigue
8	D.1	Lack of supervision from the officer	19	D.12	Poor lighting in the workplace
9	D.2	An error when assembling the completeness of reinforcement	20	D.13	Slippery work floor
10	D.3	Recklessness of the workers	21	D.14	Disregarded safety sign in construction sites
11	D.4	Performing without complying with the prescribed procedures (Joking, smoking, etc.)			

From the result of the analysis using the Boolean algebra, it is obtained 3 minimum cut sets taken from a combination of basic events. Here is the basic event tendency cause a potential accident in formwork installation along with a discussion of its risk control that able be applied (Table 6).

Table 6 The results of Boolean algebra analysis and risk control

No.	Basic event combination	Combination description	Risk control
1	D1, D2, D3, D4	Collapsed formwork events can occur due to several factors such as the absence of supervision while operation, an error when assembling the completeness of reinforcement and worker's faults	<ul style="list-style-type: none"> • Implementation of morning safety talk before starting work • Perform installation inspection of the work equipment such as: cross bracing, scour, ties, base mount clamp, scaffolding, etc. to ensure if it is installed correctly or not a ll • Inspect the installation of work equipment such as: cross bracing, scour, ties, • Supervise the workers to work in accordance with the standard operating procedures
2	D5, D6, D7, D8, D9	The incidence of workers hit by a falling object and exposed to a sharp instrument could occur due to the absence of warning sign, an error in lifting material/equipment to a higher place, the position of the object or equipment that is not in its place, workers do not use PPE while working, or occur due to recklessness of the workers	<ul style="list-style-type: none"> • Installation warning signs of falling object and prohibition to drop object • Supervise the workers to work in accordance with the standard operating procedures • Require all workers to use APD/PPE
3	D10, D11, D12, D13, D14, D15, D16, D3, D4	The incidence of workers falling from the height could be occur when the worker works inadequate to their expertise, fatigue workers, workers do not use PPE, Poor lighting in the worksite, Slippery work floor, and workers neglect Occupational Health and Safety signs	<ul style="list-style-type: none"> • Socialization of Occupational, health and safety program • Provide personal protective equipment (PPE) for workers • Require all workers to use adequate PPE around the worksite • Held the <i>Safety Induction</i> when welcoming new workers

Potential Hazards of The Reinforcement Work

The results of the Fault Tree Analysis (FTA) depiction of the potential dangers in reinforcement work (Fig. 6).

Description:
See Table 7.

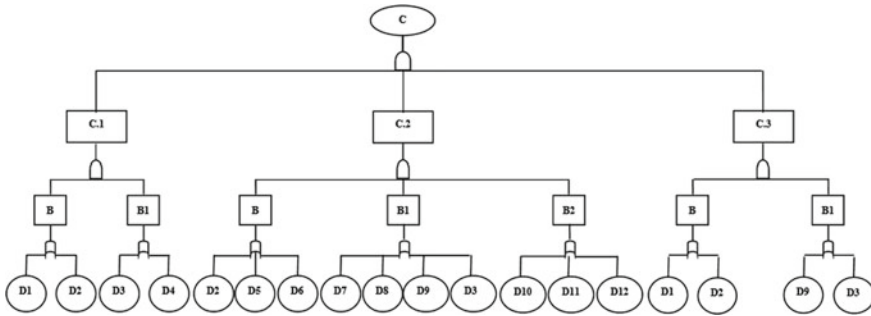


Fig. 6 The FTA graphic model of potential dangers in the reinforcement work

Table 7 The event description on the graphical model of the reinforcement work

No.	Symbol	Description	No.	Symbol	Description
1	C	Potential dangers of reinforcement work (assembly/fabrication)	11	D5	Lack of supervision
2	C.1	workers hit by a falling object, exposed to a sharp instrument, being caught in or between objects	12	D6	Production pressure
3	C.2	Worker falls on the installation of column reinforcement	13	D6	Production pressure
4	B	Technical factors	14	D7	Lack of experience
5	B1	Worker factors	15	D8	Fatigue worker
6	B2	Environment factors	16	D9	Performing without complying with the prescribed procedures (Joking, smoking, etc.)
7	D1	Lack of socialization of occupational health and safety	17	D10	Poor lighting in the workplace
8	D2	The absence of warning sign	18	D11	Slippery work floor
9	D3	Worker do not use ADP/PPE equipment	19	D12	Disregarding occupational health and safety sign in the workplace
10	D4	The recklessness of the workers			

FTA data Analysis:

Minimum Cut set using Boolean algebra law:

C	= C1 . C2 . C3	B	= D2 + D5 + D6
C1	= B1 . B2	B1	= D7 + D8 + D9 + D3
C2	= B . B1 . B2	B2	= D10 + D11 + D12
C3	= B1 . B2	B	= D1 + D2
C1	= D1 + D2	B1	= D9 + D3
B	= D1 + D2		
B1	= D3 + D4		

Event Combination Result:

C	= C1 + C2 + C3
	= (B . B1) + (B . B1 . B2) + (B . B1)
	= ((D1 + D2) . (D3 + D4)) + ((D2 + D5 + D6) . (D7 + D8 + D9 + D3) . (D10 + D11 + D12)) + ((D1 + D2) . (D9 + D3))
	= (D1 + D2 + D3 + D4) + (D2 + D5 + D6 + D7 + D8 + D9 + D3 + D10 + D11 + D12) + (D1 + D2 + D9 + D3)

From the result of the analysis using the Boolean algebra, it is obtained 3 minimum cut sets taken from a combination of basic events. Here are the basic event that can cause a potential accident in reinforcement work along with a discussion of its risk control that can be applied (Table 8).

5 Conclusion

Based on audit results then its unable to depend 100% to justify the safety construction climate on construction sites, need to be supported by other justification such as FTA approach for specified causations. The conclusion results from both of approach as follows.

1. The percentage level of implementation of occupational safety management system that has been applied by the service provider based on the result of the survey obtained a valuation rate of 97,29%, but after the probability assessment based on engineering judgment, researchers have doubts of 23,37% of the results.
2. Through the analysis using the Fault Tree Method, there are several events that could potentially lead to work accident on the scope of operating tower crane, formwork and reinforcement work. Events such as workers do not use APD (personal protective equipment), recklessness of worker, the absence of supervision from the officer and not working according to their expertise/lack

Table 8 Results of Boolean algebra analysis and risk control

No.	Basic event combination	Combination description	Risk control
1	D1, D2, D3, D4	The incidence of workers hit by a falling object and exposed to sharp objects in the reinforcement work could occur due to lack of socialization of Occupational Health And Safety, the absence of warning sign, workers do not use PPE while working, or occur due to negligence of the workers such as dispose of an object from a higher place	<ul style="list-style-type: none"> • Implementation of safety talk morning before starting the work • Supervise the workers to work in accordance with the standard operating procedures • Require all workers to use adequate PPE in the construction sites • Installing of warning signs of falling object and prohibition to drop object
2	D2, D5, D6, D7, D8, D9, D3, D10, D11, D12	The incidence of workers falling from the height when working on reinforcing steel able to occur due to the absence of warning sign, poor of supervision, high pressure of production, worker works not suitable to his expertise, fatigue worker, workers do not use PPE, poor lighting in the workplace, slippery work floor, and workers neglect safety signs around the worksite	<ul style="list-style-type: none"> • Installing the safety sign of falling hazard • Held safety induction when welcoming a new worker
3	D1, D2, D9, D3	The incidence of worker pinched by bar cutter and bar bender occur due to lack of supervision from officer, the absence of warning sign, performing without complying with the prescribed procedures or working without using PPE	<ul style="list-style-type: none"> • Socializing the safety program • The machine must be provided with a safety cap • Requiring all workers to use the adequate PPE (gloves, helmet & safety shoes • Held safety induction every welcoming a new worker • Installing the warning sign of pinched hazard

if work experience are the most common events in basic event Fault Tree Analysis. To anticipate the events, the company carries out risk control by holding safety induction to new workers, requiring workers to always use PPE during activities, socializing the Health and Safety program, and asking all workers to participate in the Occupational Safety Program that has been designed to allow the company’s target regarding work safety known as zero accident able be realized.

References

1. Government Regulation Number 50 Year (2012) The implementation of management system of occupational health and safety. Jakarta
2. OHSAS 18001 (2007) Occupational health and safety management system—requirements
3. Abdelhamid TS, Everett JG (2000) Identifying root causes of construction accidents. *J Constr Eng Manag* 126(1):52–60
4. Hagan PE, Montgomery JF, O'Reilly JT (2001) Accident prevention manual for business & industry administration & programs, 12th edn. Occupational safety and health series. The National Safety Council Press, Itasca
5. Liska RW, Goodloe D, Sen R (1993) Zero accident techniques. Clemson University, Clemson, South Carolina
6. OHSBOK (2012) Model causation: safety. tullmarine, Victoria, Australia
7. Lingard H, Rowlinson S (2005) Occupational health and safety in construction project
8. Nasa Office Of Safety and Mission Assurance (1981) Fault tree handbook with aerospace applications. Washington, DC
9. Nasa Office Of Safety and Mission Assurance (2002) Fault tree handbook with aerospace applications. Washington, DC
10. Rusand M, Barros A, Hoyland A (2005) System reliability theory: model, statistical method, and application, 2nd edn. Wiley, New Jersey

Identifying Competency of Housing Construction Personnel in Indonesia



Albani Musyafa', Dhanoe Seto Nugroho, and Nelly Buldan Afifa Hidayati

Abstract House is one of the main human needs, and the Government must guarantee the fulfilment of these rights. However, at present, Indonesia is experiencing a backlog that is the lack of descents houses for the Indonesian society and this continues to grow as population growth with insufficient housing supply. Increasing the capacity of descent houses production can overcome the backlog in Indonesia so that this problem does not worsen. To increase the capacity of house production, supporting factors must be prepared. These factors include the human resources, especially construction executor who have positions as leaders. The objective of this paper is to determine the critical competencies that must be mastered by the construction executor of house construction. This is useful for improving the education and training for the construction executor. In this study, the method used includes two main steps, first is data collection methods and data processing methods. Data collection was carried out by interviewing and giving questionnaires to those who have knowledge of the construction executor of houses construction work. Data processing is carried out by sorting the mean rank of competencies so that it can be seen the important sequence of competencies that must be owned by the construction executor in the construction of houses. The results of this study get the most important types of competencies for construction executor, namely: competence in reinforcement work, concrete mix work, measurement work, painting work, easel work, and roof covering work.

Keywords Competence · Construction · Descent house

A. Musyafa' · D. S. Nugroho (✉) · N. B. A. Hidayati
Civil Engineering, Universitas Islam Indonesia, Jl. Kaliurang KM 14.5, Sleman, Yogyakarta
55582, Indonesia
e-mail: 17511193@students.uii.ac.id

A. Musyafa'
e-mail: 955110102@uui.ac.id

N. B. A. Hidayati
e-mail: 17511211@students.uii.ac.id

1 Introduction

Currently Indonesia undergoes a great backlog of decent residential houses. Census 2019 shows that almost seventy percent of the residential house in Indonesia is in the category of houses that are not worth of live from its sanitary aspect [1]

If other aspects are taken into account, the backlog has reached more than 7 million housing units. This number continues to grow along with population growth and the quantity/quality of inadequate supply of houses. As a result of population growth, housing needs reach around 500,000 to 700,000 housing units per year [1, 2]. Meanwhile, housing production from official developers is only around 1 million houses per year [3]. Although housing construction has increased, it is not enough due to less land and increasing population growth. The shortage of housing supply is met by the independent house constructions whose quality is difficult to control.

Often those who have positions or jobs as executors or executors on a project do not pay attention to the ability that must be had to maximize their work. The executor of the project itself is the executor of a construction in general or housing construction project, has an understanding of a person or body that receives or carries out construction work according to the costs provided and carries out in accordance with the rules and conditions and drawings of a predetermined plan, in general called a contractor.

The executor can be in the form of an individual body or company that is a legal entity or a legal entity that is engaged in carrying out construction work. The main task of the executor is the business entity or person appointed by the project owner to carry out the physical work of the project in accordance with the design made by the Planning Consultant in the plan drawing.

In order to become an executor, specific skills are needed to be able to run a project. In general, the capabilities possessed by project executors are the same, but it will be different if the projects carried out are also different. In accordance with the rules that a construction executor must have the ability to work in the field. Therefore, a clear capability standard is needed so that the implementation of housing construction is not constrained in terms of the ability of the housing project executor. Thus, the Indonesian people need to build better quality housing units to overcome the backlog. One of the efforts in meeting the needs of the settlement is housing. One of the efforts to meet the residential need is housing.

In accordance with the government's program to increase the production of liveable houses, human resources (HR) in the housing industry must also be prepared. One of the important human resources is the expert in implementing housing construction. The housing executor must have the competencies needed so that housing has decent quality, however, the price is affordable, and the construction duration is shorter so that the backlog can be overcome in a relatively short time.

However, at present the education institution/training to produce housing construction experts has not worked as expected [4]. Therefore, support for this institution needs to be given. One way is to find out the competencies needed by these experts.

2 Purpose and Objective

The purpose of this paper is to determine the critical competencies that must be mastered by a building construction executor. This is very useful for improving education and training for construction executors in housing construction in Yogyakarta in particular and in Indonesia in general.

This critical competency sequence is used to determine the priority of education and training for the construction executor. The education and training need to be done to print more implementing experts that are needed to overcome the backlog of liveable homes in Indonesia. This education and training are needed to produce more competent human resources especially construction executors to overcome backlog problems in Indonesia.

3 Literature Review

Research on human resource competencies in the field of construction needs to be encouraged. This is because the applicable regulations require that every worker has a certificate of expertise or work skills which include Construction executor or labour qualifications and other classifications [5]. This certification must go through a series of education, training and competency tests including in the field of housing construction.

A decent house is the right of every Indonesian. At present, Indonesian people lack a very large liveable house (backlog) [2]. This backlog will be difficult to overcome without the implementation of good housing construction due to increased demand for housing due to population growth and the quality of home products is still low. Therefore, Indonesia needs a very large workforce in the housing sector, including the experts.

3.1 *Experts Executor*

Experts. Are individuals who have special expertise in providing services based on their expertise and are not bound by work relations (doing free work/providing professional services), for example accountants, doctors, lawyers, notaries, actuaries, tax consultants, architects, designers and so on.

Executor. Is the person (committee, organization, etc.) working or executing (design and so on).

3.2 Construction Executor

Construction. Construction is an activity to build facilities and infrastructure. In civil engineering, a construction is also known as a building or infrastructure unit in an area or in several areas. In summary construction is defined as the object of the whole building (an) which consists of parts of the structure. For example, Building Structure Construction is the overall shape/shape of the building structure. Other examples: Road Construction, Bridge Construction, Ship Construction, etc.

Construction Executor. Is a classification of workers who work at the construction stage to realize the plans that have been made previously. The main task of the executor in the field of housing construction is to realize buildings that meet the specified quality, time and cost plans. For this reason, executors must develop methods of construction that are appropriate to the conditions, efficient and easy. The implementation can be divided into pre-construction and construction stages [6]. Therefore, the role of the executor is very influential on the quality and cost of implementing residential buildings. This role is increasingly important in large-scale projects such as the current handling of the housing backlog.

3.3 Housing

Housing is a group of houses or other buildings that are built together as a single development. The shape varies in any country. Housing is usually built by a living contractor with only a few styles of house or building design, so that the appearance is uniform.

3.4 Building

Buildings are man-made structures consisting of walls and roofs that are permanently erect somewhere. Buildings are also commonly referred to as houses and buildings, which are all means, infrastructure or infrastructure in culture or human life in building their civilization.

3.5 Residential Building

Judging from its structure, residential buildings can be divided into three main parts namely the foundation, walls and roof. In general, building houses in housing complexes are made of brick, especially on the walls [7]. This structure must be strong enough so that it is not easily damaged/collapsed by common events. The

foundation parts are a structure that supports a building and distributes its load to the earth. The implementation of this section requires building design skills learned in civil engineering.

The wall and roof are generally equipped with facilities for ventilation, natural lighting/artificial and so forth. The interior of the house building is typically divided into several sections, such as a bedroom, kitchen-dining room, bathroom, toilet, laundry and washing place, prayer room, family room, living room, study room, patio, garage and so forth. Meanwhile, the exterior of the building needs to be equipped with a front yard, backyard, garden, carport and others. The houses generally also need utilities such as power cables, communication cables, water pipes, sewage pipes, sewage treatment/trash. However, part of the foundation, walls, roof, interior and exterior home building requires good execution in order to house more secure, convenient, beautiful and can improve the productivity of its occupants. It can be said that a decent residential building has specifications that must meet both its structure, interior, exterior and utilities. The building plan was made by consultant planners. This plan includes pictures, look, cut and detail. Implementing work on the plan. However, in implementation, procedures and methods of implementation should be developed.

3.6 Public Facilities and Social Amenities

Housing requires public facilities and social facilities to support the activities of its citizens. These include public roads, pedestrian street, drainage systems, public lighting, sewerage/water pipes, duct/pipe dirty water, a business centre, health/fitness, parks, games, school buildings, telephone lines, gas pipelines, processing residential waste, security systems, transportation and so forth. The facility should be well planned so that it is safe, orderly, beautiful and easy to maintain. This facility was planned by consultant planners. However, in implementation, procedures and methods of implementation should be developed.

Competency of Executor based on the description, then the housing executor should have the competence to develop creative ideas for the realization of a plan into a real building. An executor housing must be able to translate these plans into operational measures both before construction and during construction [8]. Given the extent of the executor job, these competencies are divided into the pre-construction and construction phase. In the pre-construction stage, the housing executor must be able to develop creative, effective and efficient ideas for the construction and put it in the construction plan. While at the construction stage, the housing executor should be able to realize, correct and improve the initial idea so that the construction process can work well [6].

Based on the study and interview with the interviewees, the competence of the executors in the pre-construction stage are:

1. Budgeting/scheduling

2. Site plan planning for construction
3. Making shop drawings
4. Location mapping
5. Preparation of work contract agreements
6. Anticipating problems occupational Health and Safety
7. Planning of labour

While the executive competence of the construction phase are:

1. Method of implementation of the roof frame
2. The method of implementation of the beam-column reinforcement plate
3. The method of implementation of scaffolding and formwork
4. The method of concreting
5. Electrical work and plumbing jobs
6. Control of materials and equipment
7. Control of time and quality

4 Research Method

The research methods used in this paper includes two main methods, there are data collection and data processing methods. The following is an explanation of the used research methods.

4.1 Data Collection Method

Data was collected by interview and questionnaire. The interview is intended to identify the types of competence while a questionnaire intended to determine the level of importance of these competencies.

Respondents in this study are taken from samples randomly selected from developers who have worked on housing construction in the Yogyakarta region in recent years. This research was conducted by taking the primary data. Thirty samples in this study were people who were leaders of the housing implementation team. They met at the construction site of homes scattered in the Yogyakarta area. Their participation is voluntary.

4.2 Data Processing Method

The main data from this study are tabulated by scoring as Table 1. The score shows the important level in five levels, namely very important, important, doubt, not important, very unimportant. From the table it appears that the data of this study are ordinal or

Table 1 Scoring data

Answer	Score
Very unimportant	1
Not important	2
Doubt	3
important	4
Very important	5

non-parametric [9]. Data processing is intended to rank in order to know the order of importance of competencies that should be owned by the housing executors in carrying out their work. Ranking obtained from the sample data is validated with statistical probability of obtaining a valid generalization [10].

The technique used to obtain the order based on the ranking is the mean rank analysis [10]. Validation test rankings are calculated by using Kendal-W (Kendall's Coefficient of Concordance) which the formula is shown in Eqs. 1 and 2 [10].

$$W = \frac{12 \sum R_i^2 - 3\pi^2 k(k + 1)^2}{\pi^2 k(k - 1)^2} \tag{1}$$

$$x^2 = m(k - 1)W \tag{2}$$

With:

- W Kendall's Coefficient of Concordance
- K Census variable
- N Census sample
- R_i Chi Square

4.3 Description Data

Because there are 14 main questions for 30 respondents, the respondent's answer forms a matrix of 30 × 14. The data are described in Table 2, which shows each question answered by the respondents so that there are no empty variable values. In addition, standard deviation, minimum and maximum values, as well as the average value of each score in variable are also known.

Some of these mean have the same value as happened to competency variables no. 1 and 8 or competency variables no. V3 and V7 and V10 or V8. However, the variables that have the same mean value have a different implementation group. Because ranking is made for each group of stages, this does not matter. Therefore, the order of competence variables can be based on the mean value or mean rank [9]. Appropriate determination of the score, the higher the rank, the more important mean competence. The results of the ranking analysis construction executor competence housing

Table 2 Description data and executor competence

No.	Pre-construction stage competencies	N	Min	Max	Mean	Std. deviation
V1	Budgeting/Scheduling	30	4	5	4.9	0.305
V2	Site plan for construction planning	30	4	5	4.97	0.183
V3	Making shop drawings	30	5	5	5	0.000
V4	Location mapping	30	4	4	4	0.000
V5	Preparation of employment contract agreement	30	3	4	3.53	0.507
V6	Anticipating health and safety issues	30	3	4	3.83	0.379
V7	Workforce planning	30	4	5	4.83	0.379
No.	Construction stage competencies	N	Min	Max	Mean	Std. deviation
V8	Roof truss Implementation methods	30	4	5	4.83	0.379
V9	Beam, column, and plate reinforcing method	30	4	5	4.9	0.305
V10	Scaffolding and formwork implementation methods	30	5	5	5	0.000
V11	Concreting method	30	4	5	4.8	0.407
V12	Electricity and plumbing work	30	4	5	4.47	0.507
V13	Material and equipment control	30	4	5	4.13	0.346
V14	Time and quality control	30	4	5	4.5	0.509

construction executive at pre-construction stage show that sequentially, expert executors of residential buildings have to master the following 7 competencies: Preparation of shop drawings, site plan for construction planning, budgeting, scheduling, workforce planning, locations mapping, anticipation occupational health and safety issues, as well as preparation of contractual agreements. In general, the competencies required in the pre-construction phase have been studied in the course of civil engineering. However, its application in the field of housing still needs to be provided through training especially regarding technical application. Whereas at the construction stage, housing construction executor must master the following 7 competencies: Scaffolding and formwork implementation methods; beam, column, and plate reinforcing method; roof truss implementation methods; concreting method; electricity and plumbing work; time and quality control; as well as material and equipment control.

5 Result and Analysis

Data analysis is intended to obtain a ranking of the types of competencies that are considered important to master by experts in housing construction executives. These competencies are divided into two groups, namely the competence of the pre-construction and construction phase. Based on the competence division, an important level of competence in each stage of the work can be seen in Tables 3 and 4.

According to the score determination, the higher the mean rank value, the more important the competence is. The results of the competency ranking analysis of the experts in the implementation of housing construction at the pre-construction stage show that in sequence, the experts implementing the housing construction must master the following 7 competencies: Making shop drawings, Planning site plans for construction, Budgeting, Scheduling, Workforce planning, Mapping locations, Anticipating occupational health and safety issues, and Preparation of work contract agreements. In general, competencies at the pre-construction stage have been studied in Civil Engineering college, but in terms of implementation, good practice and experience is needed so that application in the housing sector is still needed for training on these competencies, especially regarding technical applications. Whereas in the

Table 3 Important sequence of competencies in pre-construction stage

No.	Pre-construction stage competencies	Mean Rank	Ranking	Description
V1	Budgeting/Scheduling	4.9	3	
V2	Site plan for construction planning	4.97	2	
V3	Making shop drawings	5	1	Most Important
V4	Location mapping	4	5	
V5	Preparation of employment contract agreement	3.53	7	
V6	Anticipating health and safety issues	3.83	6	
V7	Workforce planning	4.83	4	

Table 4 Important Sequence of Competencies in Pre-Construction Stage

No.	Construction stage competencies	Mean rank	Ranking	Description
V8	Roof truss implementation methods	4.83	3	
V9	Beam, column, and plate reinforcing method	4.9	2	
V10	Scaffolding and formwork implementation methods	5	1	Most important
V11	Concreting method	4.8	4	
V12	Electricity and plumbing work	4.47	6	
V13	Material and equipment control	4.13	7	
V14	Time and quality control	4.5	5	

Table 5 Kendall's W test result

Item	Important sequences	
	Pre-construction stage competencies	Construction stage competencies
Number of sample	30	30
Kendall's coefficient of concordance	0.872	0.432
Chi-square	156.898	77.693
Df	6	6
Significance	0.000	0.000
Description	Valid	Valid

construction stage, housing construction experts must master the following 7 competencies: Scaffolding and formwork implementation methods; beam, column, and plate reinforcing method; roof truss implementation methods; concreting method; electricity and plumbing work; time and quality control; as well as material and equipment control. In general, the competencies needed at the construction stage have been studied in the civil engineering study program too. However, competence at the construction implementation stage has also been studied in civil engineering college, but in this case the main milestone is how the ability of the executors to apply the competencies that have been previously learned which greatly determines the performance of the workforce and the results of the work. To determine the effect of the addition of respondents (if done) then the sequence is tested by Kendall's W or the Coefficient of Concordance [9]. The test results can be seen in Table 5.

From the test, it is known that the significance number of the competency sequences is less than 0.05. This means that the competencies sequence in both pre-construction and construction stages are valid [10].

6 Discussion

To overcome the backlog that occurs in Indonesia, it is very dependent on the construction executors and the competencies they have, but many construction executors do not know what competencies are needed and need to be improved. Most assume that management expertise is needed, but not only that expertise is needed there are many more skills needed and need to be improved. For discussion, these competencies are compared with those developed in the study program which are relatively close to the housing sector, namely civil engineering. As shown by Table 3, in the pre-construction stage, there are seven most important competencies that must be possessed by experts implementing housing construction. Of the seven competencies, there are three competencies that should receive more attention for

civil engineering graduates who want to become experts in implementing housing construction, namely making shop drawings, planning site plans for construction, and preparing work contract agreements.

The first competency is the ability of executors to plan and make a good site plan so that the circulation of work does not interfere with each other, with the arranged circulation of work, the work will be more efficient and quickly completed. The second competency is the ability to draw pictures of the housing plan that will be implemented, in accordance with the plan and the description given. The third competency is the ability to make employment contracts agreement. The work contract is used if a field executor gets a job as an executor in the auction model with the housing developer, to avoid fraud that harms the field executor.

Meanwhile, at the construction stage, of the seven competencies that must be mastered, three competencies that need more attention from civil engineering graduates who want to become experts are the scaffolding and formwork implementation method, the roof truss implementation method, as well as the electrical work and pipeline. These competencies are centred on the ability of the executor to properly direct and supervise the work, including in choosing what method to use in carrying out the construction in accordance with the situation and conditions so that the work can run smoothly, safely, and on time.

7 Conclusion

This research resulted in two groups of competencies that must be mastered by experts in the field, namely: pre-construction stage competencies and construction stage competencies.

The important sequence of competencies in the group is as follows. In the pre-construction stage, housing construction experts must master: Preparation of shop drawings, site plan for construction planning, budgeting, scheduling, workforce planning, locations mapping, anticipation occupational health and safety issues, and as well as preparation of contractual agreements. In general, competencies at the pre-construction stage have been studied in Civil Engineering college, but in terms of implementation, good practice and experience is needed so that application in the housing sector is still needed for training on these competencies, especially regarding technical applications.

Whereas in the construction phase, housing construction experts must master: Method of scaffolding and formwork implementation, Method of reinforcing plate column reinforcement, Method of roof truss implementation, Concrete method, Time and quality control, Electrical work and plumbing, Material and equipment control. In general, the competencies needed at the construction stage have been studied in the civil engineering study program too. However, competence at the construction implementation stage has also been studied in civil engineering college, but in this case the main milestone is how the ability of the executors to apply the competencies

that have been previously learned which greatly determines the performance of the workforce and the results of the work.

It is recommended for graduates of educational and training institutions to add and deepen these competencies so that the alumni have the competencies needed to become experts in implementing housing construction which are much needed. Working as a field executor of a housing project is not an easy job, where a career is at stake in the results of the housing construction. The better the results achieved, the greater the opportunity to continue working in the field of building construction, especially housing. When becoming a field executor of a housing development project, it is expected to master the skills needed to work. It is expected that with the high skills acquired as executors can help overcome the existing backlog more efficiently.

8 Research Limitation

Limitations need to be made for this broad scope of research. These limits are:

1. Housing is housing with a land area of more than 1 ha;
2. Respondents in this study are housing developers who have carried out housing construction of an area of more than 1 ha;
3. The house construction under review is to have a reinforced concrete beam-column structure and brick wall
4. Data collection was conducted in 2019 in the Yogyakarta region.

References

1. BPS (2019) *Presentase Rumah Tangga menurut Provinsi, Tipe Daerah dan Sanitasi Layak 2009–2019*
2. Prabowo D, Tinggi KM (2020) Program Sejuta Rumah Berlanjut Dua Periode. <https://properti.kompas.com/read/2019/08/07/210000521/kebutuhan-masih-tinggi-program-sejuta-rumah-berlanjut-dua-periode>. Last accessed 2020/09/22
3. Husaini A (2019) Kementerian PUPR: Jumlah backlog rumah capai 7,6 juta unit per 8 Maret 2019. <https://industri.kontan.co.id/news/kementerian-pupr-jumlah-backlog-rumah-capai-76-juta-unit-per-8-maret-2019>. Last accessed 2020/09/19
4. Tribunjogja (2015) REI-DIY: Awas Banyak Developer Oportunis. <https://issuu.com/tribunjogja/docs/tribunjogja-14-02-2015>. Last accessed 2020/09/19
5. LL-SETNEG (2017) *Undang –Undang Republik Indonesia No 2 Tahun 2017 Tentang Jasa Konstruksi*, Jakarta
6. Imam S (1999) *Manajemen Proyek: dari Konseptual sampai Operasional*. 1st edn. Penerbit Erlangga, Jakarta Pusat
7. CEVEDS-International (2007) *The reports of dissemination and training of BARRATAGA (Bangunan Rumah Rakyat Tahan Gempa – Earthquake Resistant People House) to The Government Officers of Construction Agency, CEEDEDS UII in collaboration with ARPRO*, Yogyakarta

8. Kemnakertrans (2009) Penetapan SKKNI Sektor Konstruksi Bidang Konstruksi Gedung dan Bangunan Sipil Sub Bidang Konstruksi Gedung Jabatan Kerja Ahli Geodesi dan Bangunan Gedung, Kementerian Tenaga Kerja dan Transmigrasi Republik Indonesia, Jakarta
9. Sugiyono (2008) Statistik Nonparametris, 1st edn. Alabeta, Bandung
10. Singgih S (2000) Buku Latihan SPSS: Statistik Parametrik, 1st edn. Elex media Komputindo, Jakarta

Experiment to Determine Worker Needs Index in Brick Work with Space Mold Tools



Albani Musyafa', Irsyad Hanif Ansori, and Muchammad Rizky Anugrah

Abstract Indonesian people are experiencing a huge backlog of decent housing. The data shows that almost a third of the houses in Indonesia are categorized as unfit for housing. This means the backlog can reach 22 million homes. This number continues to grow along with population growth and insufficient supply of livable homes. With these conditions, Indonesian people must increase the construction of livable homes. Brick wall houses are increasingly in demand by the community. Based on the government's program to increase the production of livable homes, the productivity of works in the construction of these houses must also be increased. One way to increase productivity is to use equipment that can speed up the process of installing spaces (mortar). For this reason, it is necessary to experiment with the use of these spacing molds in brick work. The purpose of this research was to determine the worker's need on the work of masonry wall with mortar spacing molds. The benefit that can be taken from this research is that the results can be used as a reference for construction services in estimating the productivity of laborers. With the increased productivity of this work, it is expected to help overcome the problem of the backlog. The experimental research object is the labor productivity of the couple's brick work. The research sample is a worker who works on residential development in Sleman, Yogyakarta. The data of this research are the results of the total time and effective time of the work of masonry performed by 18 masons. The calculation of work time is expressed in units of seconds. The production unit takes 70 bricks which is equivalent to 1 m². In conclusion, the index of need for workers on brick wall pair work is 0.7. The need was validated by t-test which showed that the use of this mortar spacing tool significantly increased productivity. Therefore, to

A. Musyafa' (✉) · I. H. Ansori · M. R. Anugrah
Civil Engineering, Universitas Islam Indonesia, JL. Kaliurang KM 14.5, Sleman Yogyakarta
55582, Indonesia
e-mail: 955110102@uui.ac.id

I. H. Ansori
e-mail: 17511078@students.uui.ac.id

M. R. Anugrah
e-mail: 17511213@students.uui.ac.id

improve the productivity of masons in the work of masonry spaced molding tools should be used.

Keywords Productivity · Worker index · Masonry work · Space mold · Housing

1 Background

Shortage of appropriate housing in Indonesia today is still very large. Taking into account the rate of population growth and demolishing, the shortfall can be overcome if the production of livable homes in Indonesia reaches 2 million units per year over the next 25 years [1].

Because of the great need for the house, in 2015 the government launched a project of 1 million homes each year. However, to be able to meet the house production target that can be categorized as a high amount like that, we need a high amount of production. Therefore, it is necessary to increase production capacity. These efforts, one of which is the selection of work implementation methods that can produce material efficiency. These efficiency efforts must be developed in the process of building houses in Indonesia, from the beginning to the end of the process, as well as in small and large scope [2].

As the construction process in general, in the construction of houses, there is also material left over because it is wasted. In the work of masonry for walls, a lot of wasted material is mortar. This is due to the installation of mortar on the brick freely or does not have a mortar retaining system that allows the mortar not to fall. In reality, many of the fallen mortars were not taken any more so they were wasted. Mortar is composed of PC cement and tidal sand so that it has a significant value. In fact, the weight of this wall work is about 20% of the total construction cost [3].

Moreover, many workers do the work without using tools other than petting, resulting in widespread inefficiency of the mortar material. The volume of falling mortar can be reduced if the mortar installation is assisted by a mold that can withstand the fall of the mortar. This mortar mold has the function to form a species with a thickness and width as needed. In addition, this mold must be light enough so that it can be operated by a handyman. The significance of the use of these molds to reduce the volume of wasted mortar needs to be examined.

2 Purpose and Objective

The purpose of this study was to determine the efficiency of mortar requirements in the work of masonry walls using special molds.

3 Benefit

The results of this study can be used by implementers as information in determining the index of mortar needs in brickwork. In addition, the results of this study can also be used by related parties to persuade the public to do efficiency in the work of masonry pairs.

4 Literature Review

4.1 House Backlog

House backlog is one of the indicators used by the Government as stated in Rencana Strategis (Renstra) or strategic plan as well as Rencana Pembangunan Jangka Menengah (RPJMN) or Medium-term Development Plan related to the housing sector to measure the number of housing needs in Indonesia. House backlog can be measured from two perspectives, from the residential and ownership aspects.

House backlog from the perspective of occupancy is calculated by referring to the ideal calculation concept: 1 family occupies 1 house. The formula used to calculate a house backlog from an occupancy perspective is:

$$\text{Backlog} = \sum \text{Family} - \sum \text{House}$$

In the attachment of Book 1 of the Republic of Indonesia's Presidential Regulation Number 2 of 2015 concerning the 2015–2019 National Mid-Term Development Plan (RPJMN), the baseline backlog of residential homes in Indonesia in 2014 was 7.6 million.

The concept of inhabiting in the calculation of the backlog represents that each family is not required to have a house, but the Government facilitates/encourages every family, especially those who belong to Low Income Communities (MBR) can inhabit a decent home, either by leasing/contracting, buying/inhabiting their own home, or living in a house owned by relatives/family as long as the certainty of living (secure tenure).

Ownership backlog is calculated based on the home ownership rate/percentage of households (households) occupying their own home. The basic data source used in this calculation is sourced from BPS data.

In the context of utilizing data and information to support the implementation of the task of channeling and managing funds the FLPP (Fasilitas Likuiditas Pembiayaan Perumahan) or Housing Financing Liquidity Facility, PPDPP (Pusat Pengelolaan Dana Pembiayaan Perumahan) or Center for Housing Financing Management continue to utilize various strategic housing data. Please note that the first paragraph

of a section or subsection is not indented. The first paragraphs that follows a table, figure, equation etc. does not have an indent, either.

4.2 Brick Work

Basically, there are two building blocks for bricks, namely bricks and mortar. Brick is a building material in the form of blocks, generally measuring about $5 \times 11 \times 22$ cm, which is made from soil that is burned in high temperatures so that it has a certain strength and is not easily destroyed.

Mortar is a mixture of cement, sand and water with a certain composition with the function as a binding agent between bricks. When still wet, the mortar is soft, but after the binding process by the PC, the mortar will harden so that it has a certain compressive strength. Therefore, the mortar must have a certain thickness, dry time, and strength so that it is expected that the mortar holding the compressive force due to the load acting on it is not destroyed. There are 3 main constituents of mortar, namely cement, fine aggregate (sand) and water.

In accordance with practice in the field, there are several types of brick wall installation, one of which is a pair of $\frac{1}{2}$ stone, namely lengthwise brick installation with red brick width as the wall thickness. This type of couple is often found in residential construction.

Efforts for cost efficiency in the construction of residential houses can be done on brickwork. The work of brick masons has a significant weight on the construction of these houses.

Theoretically, the need for mortar is the specific volume between bricks in a masonry wall. The volume of this space can be calculated by the surface area of the space on the wall multiplied by the thickness of the wall or brick. Basically, the surface area of the wall consists of brick side and spaced surfaces. Thus, if in 1 square meter the walls are 70 pieces of brick size $5 \times 11 \times 22$ [4], then the volume of spacing is: $23,0001 \text{ cm}^3$. This means that the thickness of the space is approximately 1 cm in both horizontal and vertical spaces. Proportionally, if the spacing is 1.5 cm thick, the volume of spacing is $34,500 \text{ cm}^3$ or 0.0345 m^3 . However, this volume is a theoretical requirement. This need will be noted in experiments.

To achieve these research objectives, first look for the value of mortar needs in brick masonry work with methods that use spacing molds and methods that do not use spacing molds. From these two values, the efficiency of mortar requirements is determined.

4.3 Space Mold

In the field of construction, many tools are created or developed to make work more efficient. Efficiency can be obtained in terms of time, cost and quality [5]. In

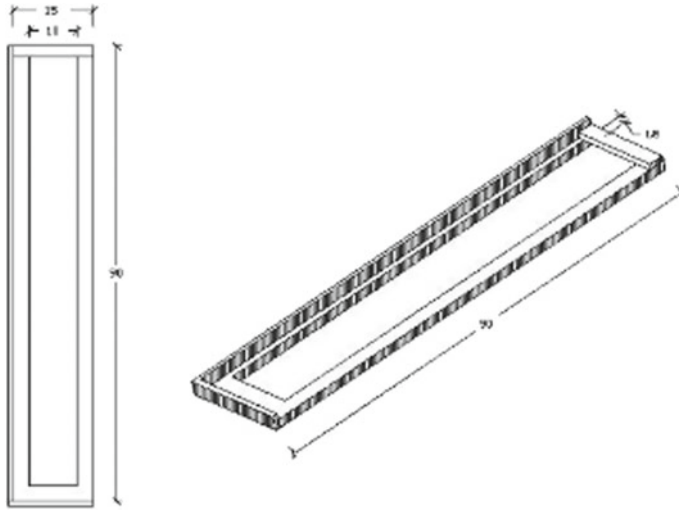


Fig. 1 Spacing mold

brickwork, a tool that can be used is a space mold. Besides making it tidier and easier to install mortar on bricks with mold aids can save the use of mortar because there's not that many mortars falling and is wasted.

Savings or efficiency in the use of mortar materials are the focus of this study. This efficiency means that by using this tool, the same volume of work can be achieved with less mortar [6]. In other words, with a smaller amount of mortar, will produce a product with the same volume.

The spacing tool used in this study is shown in Fig. 1. The way this tool works is: put the mold under the row of bricks to be installed; fill the mold with mortar; The mortar is lifted or moved; then the brick is placed on the printed mortar. This tool is made of wood with a size as shown in the picture.

4.4 Construction Worker

Explicitly, there is no definition of construction worker in the Law on Construction Services or PP on Business and the Role of the Construction Services Community. However, there is a requirement for Construction Workers as stipulated in Article 70 paragraph 1 of the UUK: "Every construction worker working in the Construction Services field must have a Work Competency Certificate."

In the 2017 UUK it is not explicitly mentioned who is included in the construction workforce. In fact, in the 1999 UUK there is information about who must have a work competency certificate (article 9).

Construction workers have certain classifications and qualifications. Construction workers are classified based on scientific fields related to construction services, namely:

- Architecture
- Civil
- Mechanical
- Environmental governance
- Implementation management

Construction workers are qualified in positions:

- Operator
- Technician or analyst
- Expert

Each qualification position is still divided into levels/levels according to their abilities and experience.

4.5 Productivity

Productivity is the ratio between the results of activities (outputs) and all the sacrifices (costs) to realize these results (inputs) [7]. Inputs can include production costs and equipment costs. While output can consist of sales, earnings (income), market share, and damage (defects) [8].

Many studies have shown that productivity is strongly influenced by factors: knowledge, skills, abilities, attitudes, and behaviors of workers in the organization so that many productivity improvement programs put these as basic assumptions [8].

Increasing productivity can be achieved by minimizing all kinds of costs including in utilizing human resources (do the right thing) and increasing output as much as possible (do the thing right) [9]. In other words that productivity is a reflection of the level of efficiency and total work effectiveness [10].

In general productivity is defined as the relationship between real and physical results (goods or services) with the actual entry [11]. Productivity is also defined as the level of efficiency in producing goods or services. Productivity is also interpreted as:

- (a) Comparison of price measures for inputs and results
- (b) The difference between a collection of total expenditure and inputs expressed in general units.

The best-known measure of productivity is related to labor which can be calculated by dividing expenditure by the amount used or the hours worked by people.

5 Method

This type of research is an experiment, namely by testing the two methods, namely using and not using a space print. Of the two types of methods tested, the volume of mortar data is used.

The steps in the research are as follows. Determine the size of the brick used is $5 \times 11 \times 22$ [4]. Determine the space between the bricks that is 1.5 cm both for vertical and horizontal. Determine the size of the wall area as an experimental cycle of 1 m^2 , half a stone thick, consisting of 70 bricks [4] with 4 layers of brick or horizontal spaces. Determine the composition of the ingredients making up mortar 1PC:8PP. Prepare sufficient mortar, determine the craftsman who will do the experiment, which consists of 7 workers who each do 3 times of experiment so that there are 21 times of experiment in each method. So that in total in this study there were 42 experiments. Then, record the need for mortar material for each experiment.

Data processing is done by comparing the average value of mortar use for each method. Validation is done by t test two related samples [12]. Experiments carried out in the area of Caturharjo, Sleman, Yogyakarta.

6 Result and Analysis

The results of 42 experiments, carried out in each method of implementation, can be seen in Table 1. The experiment was carried out by 7 workers, so each worker conducted 6 experiments with details of 3 experiments with mold equipment and 3 experiments without mold equipment.

Table 1 shows the volume of mortar needed in each experiment, whether or not using a spacebar. The volume of the mortar is calculated by reducing the volume of the mortar before installation with the volume of the remaining mortar. In this experiment mortar that fell in the installation process was not taken.

In general, the experiments carried out in this study went according to plan. Workers as an important part of the research instrument seems to be doing their job well. The experiment was considered to be going well because the standard deviations of the duration of the 2 methods were not too different i.e. 203,719 and 207,703. In addition, the duration of the implementation of the two experimental methods by workers has a correlation of 0.951 which can be interpreted that the workers perform two ways of carrying out experiments with the same conditions.

Theoretically, Table 2 shows that the amount of wasted mortar will be lowered if the brickwork is done with mold equipment. If using a spacing mold, the wasted mortar is 0.004 m^3 , whereas if without the mold, the wasted mortar is 0.0156 m^3 . The use of this mold can reduce wasted mortar by 0.152 per m^2 masonry. The table also shows that the use of molding tools in brick wall installation can save about 23% of the volume of mortar. These savings are proven to be consistent from the results of the t-test of two related samples [13].

Table 1 Mortar needs data for 1 m³ bricks

Sample	Production time with mold (s)	With mold (m ³)	Production time without mold (s)	Without mold (m ³)
1	1697	0.0416	1458	0.0523
2	1633	0.0403	1532	0.0502
3	1553	0.0396	1547	0.0530
4	1451	0.0396	1275	0.0502
5	1388	0.0406	1264	0.0495
6	1402	0.0396	1304	0.0516
7	1501	0.0374	1306	0.0516
8	1433	0.0385	1324	0.0502
9	1368	0.0388	1295	0.0502
10	1262	0.0353	986	0.0487
11	1187	0.0364	954	0.0195
12	1205	0.0346	1012	0.0480
13	1843	0.0360	1613	0.0495
14	1869	0.0364	1642	0.0484
15	1835	0.0360	1623	0.0487
16	1562	0.0410	1380	0.0480
17	1527	0.0381	1361	030,484
18	1495	0.0392	1327	0.0491
19	1314	0.0385	1154	0.0509
20	1291	0.0410	1097	0.0519
21	1298	0.0374	1126	0.0516
Total	31,114	0.8059	27,580	1.0515
Average	1482	0.0384	1313	0.0501

Table 2 Primary data description

Data	Minimum	Maximum	Mean	Standard deviation
Work duration with mold	1187	1869	1481.62	203.719
M ³ mortar with mold	0.0346	0.0416	0.038376	0.0020371
Work duration without mold	954	1642	1313.33	207.703
M ³ mortar without mold	0.0480	0.0530	0.050071	0.0014917

As is known that the composition of the mortar is cement and sand with a ratio of 1:8. To find out the efficiency of the ingredients of mortar, which is cement and sand, the volume of each ingredient needs to be calculated. The calculation is based on the index of material needs.

Table 3 Table of material needs index

Material needs	Unit	Index
Red brick	Piece	70
PC	Kg	6.5
PP	M3	0.05

Table 4 Material requirements in brickwork work according to experiments

Material	With mold		Without mold	
	Cement	Sand	Cement	Sand
Volume	4.992 kg	0.0384 m ³	6.5 kg	0.05 m ³
Price (IDR)	1275	115,000	1275	115,000
Cost (IDR)	6364.8	4416	8287.5	5750
Total (IDR)	10,780.8		14,037.5	

Material requirements for installing 1 m² of red brick walls measuring 5 × 11 × 22 cm ½ brick thick, mixed species 1 PC:8 PP is as shown in Table 3 [4]. Please note that, the composition of 6.5 kg PC and 0.05 m³ of sand will form 1PC: 8 PS mortar of 0.05 m³ as well. This is because the grains of cement only fill cavities between the grains of sand. Therefore, the material requirements for brickwork in accordance with the specifications in this experiment can be determined according to Table 4.

The table shows the average value of the required volume of cement and sand material in each method of carrying out the work in the experiment. The cost for these ingredients can be determined by multiplying the volume of the material and the unit price of the material. Although, the price of the work unit consists of 3 (three) components, i.e.: unit price of material/material, unit price of labor wages, unit price of equipment [4], in this discussion only alludes to the cost component that comes from the material.

The cost of the couple's work can be seen in Table 4. Cost savings derived from materials obtained by using these spaced molding tools alone reach more than 23%. If the cost of the masonry work can be saved 23% and the cost of wall installation is 11% of the whole building [3], then the use of this tool alone can save costs about 2.5% of the total cost of home construction. By using this tool, the brickwork process is expected to be able to save more material needs. This is because the species mold tool is able to minimize wasting mortar. Even if it is carried out by skilled workers, this special molding tool is able to reduce the duration of the brickwork.

7 Conclusion and Suggestion

Based on the analysis and discussion that has been done, it can be concluded that the influence of the use of spaced molding tools on brickwork can save mortar by 23%,

or can save costs by 23.2% if using a mixture of 1PC: 8 PP. Besides saving material, the spacing molding tool also results in a tidier job. Therefore, to the construction implementer to be able to use the spacing molding tool in brickwork.

On a national scale, these savings will definitely be very meaningful. Moreover, the Indonesian people now still need the construction of millions of housing units each year [1]. The success of this development program is influenced by effective and efficient implementation methods. Therefore, the results of this study are expected to contribute to the success of the development program. Besides that, with the spaces mold, the results of the work should be tidier. This tidiness adds to the quality of construction results. Besides that, the tidiness also had a positive impact on the plastering work [6].

References

1. Musyafa A (2014) Balancing supply-demand of livable house in Indonesia based on demography backlog and demolishing (A model for the acceleration of appropriate housing provision based on demographics, backlog and demolishing)
2. Sastra MS, Marlina E (2006) *Perencanaan dan Pengembangan Perumahan*. Yogyakarta
3. Musyafa A (2013) *Komposisi Harga Jual Rumah Tinggal Layak Huni di Yogyakarta: Studi Kasus Pembangunan Rumah Tipe 90/115 di Luar Kompleks Perumahan*
4. Standar Nasional Indonesia and Badan Standardisasi Nasional (2008) *Tata cara perhitungan harga satuan pekerjaan besi dan aluminium untuk konstruksi bangunan gedung dan perumahan*
5. Soeharto L (1995) *Manajemen Proyek: dari Konseptual sampai Operasional*. Erlangga, Jakarta
6. Musyafa A (2015) *Eksperimen Untuk Menentukan Indeks Kebutuhan Tukang Pada Pekerjaan Pasangan Dinding Bata Dengan Alat Cetakan Spasi*
7. Kussriyanto B (1984) *Meningkatkan Produktivitas Karyawan*. Gramedia, Jakarta
8. Gomes FC (1995) *Manajemen Sumber Daya Manusia*. Andi Offset, Yogyakarta
9. Manuaba A (1992) *Pengaruh Ergonomi Terhadap Produktivitas*
10. Tarwaka, Solichul H, Bakri, Sudiajeng L (2004) *Ergonomi untuk Keselamatan, Kesehatan Kerja, dan Produktivitas*. Surakarta: UNIBA PRESS
11. Sinungan M (2003) *Produktivitas, Apa dan Bagaimana*. Bumi Aksara, Bandung
12. Walpole RE, Raymond M (1996) *Ilmu Peluang dan Statistika untuk Insinyur dan Ilmuwan (Terjemahan)*. Bandung
13. Santoso S (2000) *Buku Latihan SPSS Statistik Parametrik*. Elex Media Komputindo, Jakarta

Development of Entry Mode Assessment Criteria (EMAC) Model for Malaysian Construction Companies to Sustain in International Operations



Norizzati Ibrahim and Che Maznah Mat Isa

Abstract Many Malaysian construction companies are looking for opportunities to generate revenues through international projects. However, not many of the previous studies examined the companies' strengths related to entry mode decision to sustain in international markets. It is important for construction companies to make the right decision in selecting the right entry mode before operating worldwide. Therefore, this study examines the strength factors for companies to sustain in international operations focusing on evaluating the strength factors that enable construction companies to survive and sustain in foreign countries. A quantitative method using questionnaire survey is adopted to get feedbacks on company's strength factors from 30 managers involved in international projects. This paper presents the Entry Mode Assessment Criteria (EMAC) Model that has been developed as a diagnostic instrument to measure various dimensions of strength factors to assist the companies in the selection of entry mode to operate projects abroad. In addition, the Internal Readiness Test (IRT) has been used in the EMAC models to test whether the company is capable or fit to operate in international market. The EMAC formula was developed through the Hierarchical Analytical (AHP) process and the improved Delphi study by adding analysis applied to construction companies in Malaysia. Results from the EMAC formula indicate that the companies with the highest ranking (value of 633.2) used a wide variety of entry modes including Intermediary and Exporting entry modes to obtain technology resources, expertise and manpower to carry out construction activities abroad. This study will guide the construction companies that are interested in exploring foreign business opportunities based on analysis of the companies' strength before expanding into international markets.

Keywords International construction markets · Readiness · Strength Factor · Sustained Operations

N. Ibrahim (✉) · C. M. M. Isa
School of Civil Engineering, College of Engineering, Universiti Teknologi MARA (UiTM),
40450 Shah Alam, Selangor, Malaysia

1 Introduction

The Malaysian government encourages local contractors to participate in projects in regional and global markets based on their expertise and experience in the areas of infrastructure projects, port and airport construction, highways and building construction [1]. Three critical decisions need to be made before entering foreign markets are: when to enter (timing), where to enter (location) and how to enter (mode, scale, strategy) [2, 3]. Generally, there are two main variables (internal and external) factors that drive companies' internationalization [2]. A strategic location offers cheap and available workforce for construction work which will give impact the cost of the project [4]. Entering developed countries such as Germany and Japan require sophisticated technology in construction activities that relates on financial strength of the companies. According to Gunhan and Arditi [5], companies need to be highly knowledgeable about international business and the factors that are responsible for failure before entering the international market. While Hastak and Shaked [6] argue that financial resources and the ability to produce high quality products are also very important to consider in the international market. This paper focuses on the construction companies' readiness based on company's strength based on Delphi-AHP method and their decision on entry mode to carry out international operations in both ASEAN and non-ASEAN countries.

2 Literature Review

2.1 *International Markets for Construction Companies*

Many construction firms look for opportunities to expand their business operation internationally, however there are many obstacles that need to be considered before entering the overseas market such as technology risk, political risk, social risk and economic risk [1]. The Construction Industry Development Board (CIDB), Malaysia reported that the value of international contracts awarded to Malaysian contractors has decreased from 5,881.42 factories in 2006 to just RM 124.85 in 2017 [7]. According to [8], a lack of in-depth knowledge of overseas markets and international experience has been a major catalyst for local companies not entering the international market. According to [6], before a company enters the international market, it is important to make strategic mode selection to ensure the company's sustainability in international markets.

2.2 *AHP Model*

This study used a combination of AHP and Delphi methods based on a study by [5]. Saaty [9] stated that the AHP techniques are based on a combination of respondents' information and experience in determining ratio scales key factors through continuous paired comparisons. AHPs are very helpful in making decisions for many factors that are studied simultaneously and complicated. This method is used because it is an altruistic approach to problem solving through a systematic approach to decision making [10]. According to Gunhan and Arditi [5], the Delphi Method is based on the arguments given by experts through a conference or debate. Experts will provide feedback and opinion on the problems faced by several groups of individuals [5]. The AHP method will compare every major factor. Whereas experts will give their opinion on a scale of 1–9 through the Delphi Method where “1” means very important factors and “9” means one of the most important factors compared to other factors [10].

2.3 *Entry Mode Decisions*

Even though many previous studies have been carried out on the choice of entry modes, most of these studies focused only on two types of modes which are: (1) equity mode such as joint ventures or wholly owned subsidiaries, and (2) non-equity modes such as direct and indirect exporters and contractual agreements [2, 8, 11, 12]. However, there is a lack of focus on entry mode strategies in terms of assessment criteria based on intermediate mode (IM), hierarchical entry mode (HE) and export mode (EE). Therefore, this study builds on theoretical framework based on three types of entry modes (IM, HE and EE) to contribute to the empirical aspects of market entry strategies towards the development of entry mode assessment criteria (EMAC) model that will provide guidance especially to the interested local construction companies to explore foreign investment opportunities and also to international construction companies to sustain their international operation.

2.4 *International Entry Decision Model (IEDM)*

In this study, an IEDM model adopted from Gunhan and Arditi [5], that consists of formulas, is used on companies to assess their decisions to expand their businesses to the international markets into specific locations or countries through testing of the company's strengths.

Figure 1 shows the modified IEDM model that consists of two main tasks: (1) Tasks performed in developing the model and (2) Tasks performed when using the developed model. In the first step, an internal Readiness Test study will be performed

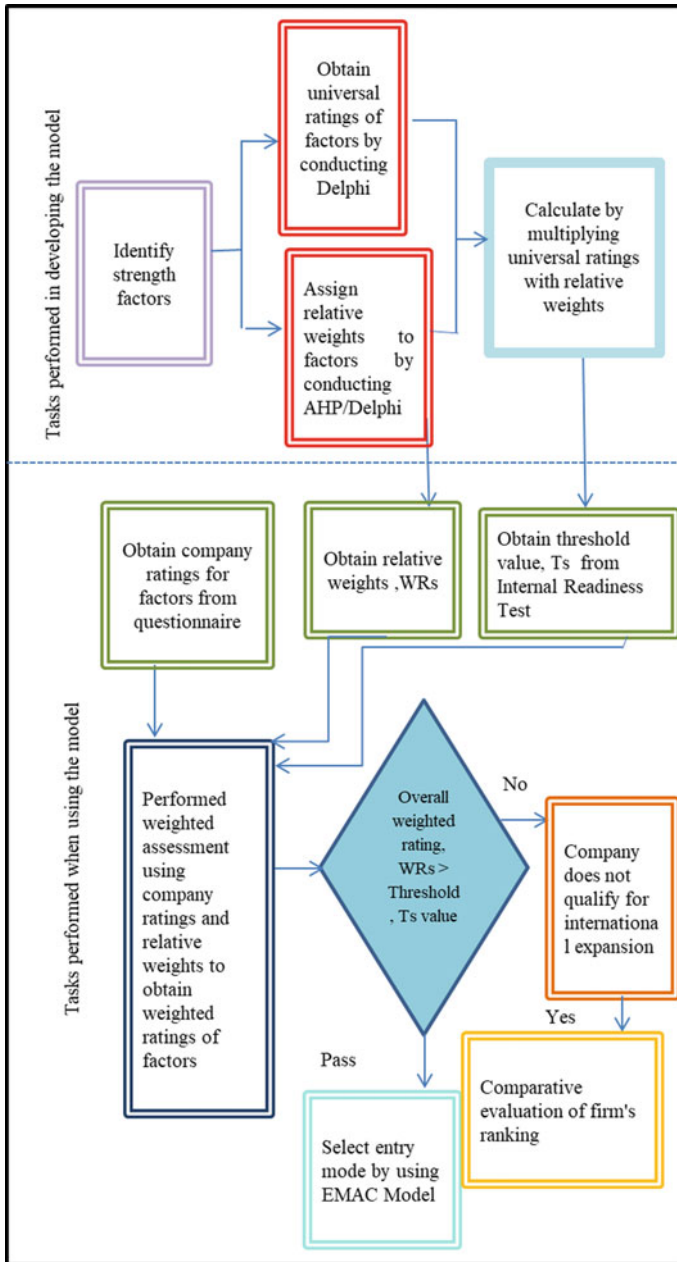


Fig. 1 Development of international entry decision model (IEDM). Adopted from Gunhan and Arditi [5]

Table 1 Country classification

No.	Country classification based on name of country where the companies are located
1	ASEAN: Brunei, Cambodia, Indonesia, Laos, Malaysia, Myanmar, Philippines, Singapore, Thailand, and Vietnam
2	Non-ASEAN: Canada; Australia, South Africa, Mexico, Brazil, Turkey, USA, UK, Netherlands, United Arab Emirates, India, China, Macau, Hong Kong, South Korea, Maldives, Papua New Guinea, Solomon Islands, New Caledonia, Japan, North Korea, Taiwan, Nepal, Pakistan, Russia, Mauritius, Saudi Arabia, Bahrain, Ireland

where the Threshold value, T_s will be tested using Eq. 1. Next, the assessment of relative weight (W_{si}) for the strength factor used in this study is based on the values of the AHP and the Delphi method adapted from Demirbag, Tatoglu and Glaister [8], whereby the information generated is based on the information provided by experts in the construction industry. Gunhan and Arditi [5], studied the relative comparisons between pairs of factors using a scale of 1–9 where 1 indicated that the factor pairs had similar meanings while 9 meant that one factor was more important than the other. The Delphi process is very useful in obtaining information on the pairwise comparisons required by AHP. As a result, the total value of the strength rating (WRs) is derived from multiplication of the rating value from the respondents from scale 1–5, R_s and the value of W_{Si} (relative weighted valuation) as shown in Eq. 2. If the results show that the value of WRs exceeds the value of Threshold, then the company is eligible to enter the international market. Then, comparisons of the company's positions will be made using the EMAC model.

2.5 Country Classification

ASEAN is categorized as a rapidly developing country by [13]. There are ten (10) countries in ASEAN including Malaysia, which are Brunei, Cambodia, Indonesia, Laos, Myanmar, Philippines, Singapore, Thailand, and Vietnam. Hence, for this study the company's location is categorized into ASEAN and non-ASEAN countries as tabulated in Table 1.

3 Methodology

3.1 Research Approach

A quantitative approach is adopted using a survey questionnaire administered to 30 managers from construction companies with international experience. This preliminary study is part of an on-going research work to develop an international entry

Table 2 Construction companies' strength factors related to international construction

Strength	Definition
S1: project management capability	Companies can follow the standard quality and can complete the projects as in contract
S2: financial	Companies have a strong financial background to carry out construction projects
S3: specialist expertise	Companies acquired competitive advantages as specialists
S3: international network	Companies have established good relations with foreign countries
S4: track record/international experience	Companies have vast experience in completing projects in the past
S5: technological advancement	Companies have the expertise and knowledge of projects using advanced technology
S6: sufficient resources	Companies have enough resources in terms of materials, labors and equipment

decision model (IEDM) to assist companies to make effective decisions to sustain in international markets.

This paper focuses on the construction companies' readiness based on companies' strength and their decision on entry mode and entry location to carry out international operations. The company's strengths considered in this study are shown in Table 2.

Descriptive analysis was carried on the respondents' feedbacks on their company's strength. Majority of respondents agreed that these strength attributes have contributed to their sustained international operations. The feedbacks given by the respondents are further used to carry out the readiness test for construction companies as discussed in the following sub-section.

Development of Entry Mode Assessment Criteria (EMAC) Model

The EMAC model is developed to rank international companies based on the entry mode choices and company's strength factors that lead to sustainable operations in international markets and to assist other companies to make decision to enter the international markets using suitable entry modes. Figure 2 shows how the Eq. (1) is developed.

In this study, the entry modes are categorized into three (3) namely; Intermediate Entry Mode (IEM), Hierarchical Entry Mode (HEM) and Exporting Entry Modes (EEM) as tabulated in Table 3.

The EMAC equation as shown in Eq. 1 is a combination of weightage values (WE_i) from the results of [8], as well as the ranking value of PROMETHEE II method by Cristian, Zhang and Salifou [4].

$$\text{EMAC Model} = 10 \text{ IEM} + 6 \text{ HEM} + 4 \text{ EEM} \quad (1)$$

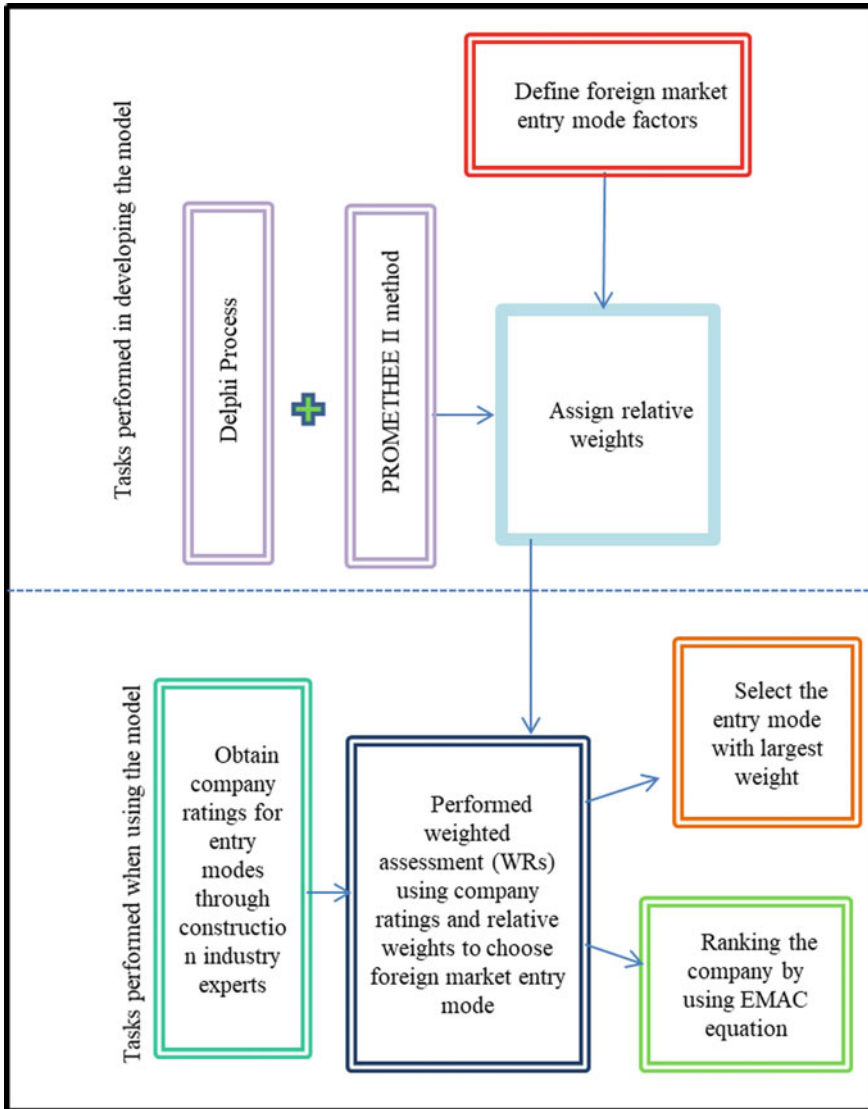


Fig. 2 Process in selection of entry mode and ranking the company by using EMAC Model

Furthermore, the rating of each mode (R_{si}) selected was measured by respondents using a likert scale of 1–5 to obtain the total weightage of entry mode (WR_m) as in Eq. (2) The total weightage of entry mode (WR_m) is measured as a result of the rating value (R_{si}) multiplied by the EMAC coefficient, W_{mi} value as mentioned in Table 3.

Table 3 Weightage of entry mode

Delphi method and AHP method		PROMETHEE II method (ranking of entry mode)	EMAC model		
Entry mode	Weightage, W_{Ei}		Entry mode	Category of mode	EMAC coefficient, WM_i
Joint venture	63.70	1	Intermediate entry mode (IEM)	<ul style="list-style-type: none"> • Franchising (IEM1) • Licensing (IEM2) • Joint venture or strategic alliance (IEM3) • Contract manufacturing (IEM4) • Turnkey contract (IEM5) • Manufacturing contract (IEM6) • Strategic Alliances (IEM7) 	10
Wholly owned subsidiary	25.80	2	Hierarchical entry mode (HEM)	<ul style="list-style-type: none"> • Acquisitions (HEM1) • Wholly owned subsidiaries (HEM2) • Sole Venture Company (HEM3) 	6
Lone operation	10.50	3	Exporting entry modes (EEM)	<ul style="list-style-type: none"> • Direct export (EEM1) • Indirect export (EEM2) • Built, Operate, Transfer (BOT) (EEM3) • Representative Office (EEM4) • Branch Office/Company 	4
Total weight of international market entry mode	100.00				

$$WR_m = \sum(R_{si} \times W_{Mi}) \quad i = 1 \quad (2)$$

As a result, the total weightage (WR_m) to be obtained is 100 if all the ratings obtained from the respondents are 5 as in the example below:

$$\text{EMAC Model, } WR_m = 10(5) + 6(5) + 4(5) = 100$$

3.2 *Internal Readiness Test*

Another test used in this study is an internal readiness test (IRT) which is adopted based on a model developed by Demirbag et al. [8], who used analytic hierarchy process (AHP) to study the relationships between multiple factors simultaneously and by using ratio from both comparative and continuous comparisons. Demirbag et al. [8] studied the relative comparisons between pairs of factors using a scale of 1–9 where 1 indicated that the factor pairs had similar meanings while 9 meant that one factor was more important than the other. For validation purpose, a Delphi method is used through information provided by experts in international construction. The Delphi process is very useful in obtaining information on the pairwise comparisons required by AHP.

First, this study identifies and analyses the strength factors to determine the company's potential to expand into international markets based on threshold value in the test. Companies that pass the threshold value indicate they have the potential to enter international markets. Gunhan and Arditi [5] introduced internal readiness test as respondents need to make an assessment on a scale of 1–5 using Delphi process, where 1 refer not important and 5 very high important due to social, political and economic factors. The "mean universal rating (URs)" will be derived from the Delphi process, which is the result of the median value for each factor and is used to calculate threshold values through internal readiness tests. Companies need to pass internal readiness tests threshold is the value at which companies must pass minimum values. Threshold (Ts) value generated from resulting from the multiplier between the mean universal rating (URs) and the factors' relative weight (Ws) as shown in Eq. (3) below:

$$T_s = \sum(UR_{si} \times W_{si}) \quad i = 1 \quad (3)$$

Next, the rating of each factor was measured by the respondents using a likert scale to obtain the total rating of strengths (WRs). The total weighted rating of strength (Wrs_i) are measured by multiplying the value of rating (Rs) with the respective relative weighted rating (Ws_i) as shown in Eq. (4).

$$WR_s = \sum(R_{si} \times W_{si}) \quad i = 1 \quad (4)$$

Then, the total WRs for the strength factor will be compared to the Threshold values as in Eq. (5). In order for a company to pass an internal readiness test, the total strength factor must be greater than the threshold value. If the company meets the requirements of the internal readiness test, the test of the company’s strength is tested through the IEDM formula.

$$WRs \geq \Sigma Ts \tag{5}$$

4 Analysis and Discussions

This section presents the analysis based on the internal readiness test using the modified model and equations explained in the previous section.

4.1 Internal Readiness Test Based on Strength Factors

Therefore, a company’s score can be measured by the amount of this weighted assessment. Then, the WRs value must be more than the Ts value via the readiness test. If the company successfully passes the internal readiness test, the IEDM formula will be used to determine IEDM formulas will be used to compare companies based on strategic location selection factors as well as company’s strength factors as tabulated in Table 4.

Table 4 shows the values based on the strength factors for forming IEDM formulas as shown in formula 3. According to [8], Wsi value is 11.50 and urs (mean) is 3.7 used in Internal Readiness test.

Equation (6) is based on weightage factor of strength according Table 4.

$$\begin{aligned} \text{Total strength} = & 16.9 S1 + 19.4 S2 + 11.5 S3 + 7.3 S4 \\ & + 8.1 S5 + 13.0 S6 + 23.8 S7 \end{aligned} \tag{6}$$

Table 4 Relative weighted rating (Wsi) for strength factors

Strength factors	Wsi
Project management capability	16.9
Financial strength	19.4
Specialist expertise	11.50
International network	7.3
Track record/international experience	8.1
Technology advancement	13.0
Sufficient resources	23.8
	100.00

4.2 Internal Readiness Test Based on Location

The model developed in this study is tested on the Malaysian construction companies operating in various countries in international markets namely ASEAN and Non-ASEAN regions. Table 5 shows the results from the internal readiness test (IRT) carried out on 30 construction companies.

The results from the IRT show that the highest value of company's strength, WR (WRs = 57.5). This value is higher than the threshold value ($T = 42.55$) which indicates that the company sustains its business in international markets. As shown in Fig. 3, 53% companies with WR values greater than T value can be considered as passing the test and while 47% failed the test.

4.3 Entry Location Analysis

Next, studies on construction projects in foreign countries have been conducted on companies that have successfully passed the Internal Readiness test (Fig. 4). The majority of companies that sustained in foreign country (53.33%) carry out construction projects in the ASEAN countries, the rest (41.67%) in both countries and 17% in non-ASEAN countries.

4.4 Strength Analysis

The strength of the company is tested using Eq. (6) where the company's position in terms of strength factors is obtained as shown in Table 6. The results also show that there are five (5) companies that are ranked the highest as highlighted in grey colour with a total strength value of 476.2.

Figure 5 shows the most effective strength factor used by companies that have successfully carried out construction activities abroad. In addition, the major causes of the strengths that make these companies successful in the international market are the S2 (financial strength) factor; followed by S7 (equipment, material, labor support); S1 (project management capability); S6 (Technology level); S5 (track record/international experience) and S3 (specialist expertise). The results of the analysis mean that once a company has financial strength, it is easy for the company to obtain international projects that require expertise and skills as well as the use of the latest technology.

Table 5 Internal readiness test on 30 construction companies operating in international markets

Companies	Location	Classification of the country (number)	WRS	TS	Passed/failed IRT
1	Singapore	ASEAN (1)	46	42.55	Passed
2	Cambodia	Non-ASEAN (1)	34.5	42.55	
3	Indonesia, Thailand	ASEAN	46	42.55	Passed
4	Indonesia	ASEAN	34.5	42.55	
5	UAE	Non-ASEAN	57.5	42.55	Passed
6	Singapore	Asean	46	42.55	Passed
7	China	Non-ASEAN	23	42.55	
8	Japan	Non-ASEAN	57.5	42.55	Passed
9	Indonesia	ASEAN	46	42.55	Passed
10	India, Myanmar, Thailand	ASEAN (2), Non-ASEAN (1)	57.5	42.55	Passed
11	Indonesia	ASEAN	23	42.55	
12	Indonesia, Sudan	ASEAN	57.5	42.55	Passed
13	Indonesia	ASEAN	34.5	42.55	
14	Australia, Bangladesh, Hong Kong, Indonesia, India, Singapore, Vietnam	Non-ASEAN, non-ASEAN, non-ASEAN, ASEAN, non-ASEAN, non-ASEAN, ASEAN, ASEAN	57.5	42.55	Passed
15	China, Qatar	Non-ASEAN, non-ASEAN	23	42.55	
16	Singapore	ASEAN	46	42.55	Passed
17	China, Myanmar, Thailand, Uzbekistan	Non-ASEAN, ASEAN, ASEAN, non-ASEAN	34.5	42.55	
18	China, Myanmar, Thailand, Uzbekistan	Non-ASEAN, ASEAN, ASEAN, non-ASEAN	34.5	42.55	
19	Myanmar, Sudan	ASEAN, non-ASEAN	57.5	42.55	Passed
20	Australia, Bangladesh, Pakistan	Non-ASEAN, non-ASEAN, non-ASEAN	34.5	42.55	
21	Indonesia	ASEAN	23	42.55	
22	Indonesia, Maldives	ASEAN, non-ASEAN	34.5	42.55	

(continued)

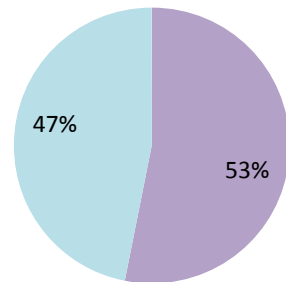
Table 5 (continued)

Companies	Location	Classification of the country (number)	WRS	TS	Passed/failed IRT
23	ssAustralia, Philippines, UAE	ASEAN, non-ASEAN	57.5	42.55	Passed
24	Australia, Philippines, UAE	ASEAN, non-ASEAN	57.5	42.55	Passed
25	Indonesia, India, Saudi Arabia	ASEAN, non-ASEAN	57.5	42.55	Passed
26	Cambodia, Indonesia, Pakistan, Saudi Arabia	ASEAN, non-ASEAN	34.5	42.55	
27	Myanmar	ASEAN	57.5	42.55	Passed
28	China	ASEAN, non-ASEAN	57.5	42.55	Passed
29	China, Indonesia, Thailand	ASEAN, non-ASEAN	23	42.55	
30	Japan	ASEAN, non-ASEAN	57.5	42.55	Passed

Fig. 3 Internal readiness test

Internal readiness test

- firms passed internal readiness test
- firms failed internal readiness test



4.5 Entry Mode Analysis

First, the entry mode chosen will be labelled based on the EMAC coefficient, WMi shown in Table 3. Where, intermediate entry mode (IM) is divided into franchising (IM1), licensing (IM2), joint venture or strategic alliance (IM3), contract manufacturing (IM4), turnkey contract (IM5), manufacturing contract (IM6) and Strategic Alliances (IM7). While Hierarchical Entry Mode (HE) consists of acquisitions (HE1), wholly owned subsidiaries (HE2) and sole venture company (HE3). Exporting entry

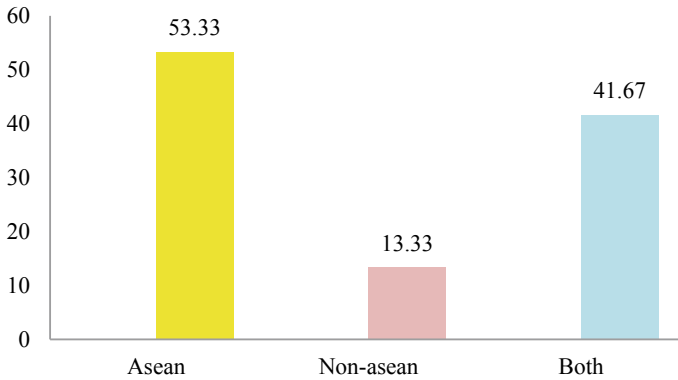


Fig. 4 Entry location analysis

modes (EE) is divided into direct export (EE1), indirect export (EE2); built, operate and transfer (BOT) (EE3); representative office (EE4) and branch office/company. Second, the weightage of entry mode selection by the company is based on Eq. (1). Third, the comparison of company position as shown in Table 7 will be obtained as a result of total strength based on total weightage mode, WR_m by using Eq. (2).

Based on the analysis in Table 7, it was found that the companies that achieved the highest level of weightage utilized multiple modes including three number of Intermediary Mode and one of Exporting Entry mode compared to other companies which enabled the company to compete internationally. The findings also found that companies with the lowest rankings used only exporting entry mode to expand their business in the international market.

5 Conclusion

This study adopted a quantitative approach using a questionnaire survey administered to 30 managers with international experience from construction companies in Malaysia. This study applied the weightage value of the AHP and Delphi Method combined with the weightage of the EMAC model to obtain the company's strength and position in the international market. The EMAC formula was developed as a result of the approach using AHP and the Delphi method as well as PROMETHEE II method. In order to assess the companies' potential to enter international markets, they need to pass the Internal Readiness. Using the Internal Readiness Test, only 53% of the companies passed the test. The study also found that majority of the companies that passed the test carried out construction projects in ASEAN countries only. The company's strength analysis indicates five (5) companies are ranked higher than other companies. These companies achieved the highest rating for entry mode

Table 6 Ranking of the companies through strength analysis

Companies	Wsi = 16.90	Wsi = 19.40	Wsi = 11.50	Wsi = 7.30	Wsi = 8.10	Wsi = 13.0	Wsi = 23.80	Total strength value	Ranking
WRS	S1	S2	S3	S4	S5	S6	S7		
8	84.5	97	57.5	36.5	40.5	65	95.2	476.2	1
10	84.5	97	57.5	36.5	40.5	65	95.2	476.2	1
14	84.5	97	57.5	36.5	40.5	65	95.2	476.2	1
23	84.5	97	57.5	36.5	40.5	65	95.2	476.2	1
24	84.5	97	57.5	36.5	40.5	65	95.2	476.2	1
5	84.5	97	57.5	36.5	40.5	52	95.2	463.2	2
6	84.5	97	46	29.2	40.5	65	95.2	457.4	3
27	84.5	77.6	57.5	36.5	40.5	65	95.2	456.8	4
12	84.5	97	57.5	36.5	40.5	39	95.2	450.2	5
1	84.5	97	46	29.2	40.5	52	95.2	444.4	6
25	84.5	58.2	57.5	36.5	40.5	65	95.2	437.4	7
19	84.5	77.6	57.5	36.5	40.5	39	95.2	430.8	8
9	84.5	58.2	46	29.2	40.5	52	95.2	405.6	9
16	67.6	77.6	46	29.2	32.4	52	95.2	400	10
3	67.6	77.6	46	29.2	32.4	52	95.2	400	10
28	50.7	58.2	34.5	21.9	24.3	39	95.2	323.8	11
30	50.7	58.2	34.5	21.9	24.3	26	95.2	310.8	12

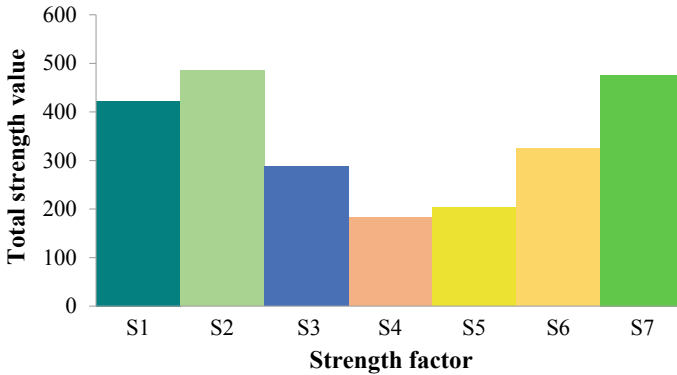


Fig. 5 Companies' strength factors based on calculated strength values

Table 7 Ranking of the company based on total weightage of entry mode and total strength value

Company No.	Entry mode choice in international market and weightage coefficient (WMi)	Total weightage of entry mode, WRm	Total strength value	Total WRm + total strength value	Ranking
5	Strategic alliance (10), joint venture company (10), joint venture project (10), build-operate-transfer (BOT) (4)	170	463.2	633.2	1
24	Joint venture company (10), joint venture project (10), sole venture project (6)	130	476.2	606.2	2
14	Licensing (10), branch office/company (4)	70	476.2	546.2	3
10	Strategic alliance (10), branch office/company (4)	70	476.2	546.2	3
25	Licensing (10), joint venture company (10)	100	437.4	537.4	4
1	Joint venture company (10), branch office/company (4), representative office(4)	90	444.4	534.4	5
8	Joint venture project (10)	50	476.2	526.2	6
23	Joint venture company (10)	50	476.2	526.2	7

(continued)

Table 7 (continued)

Company No.	Entry mode choice in international market and weightage coefficient (W _{Mi})	Total weightage of entry mode, W _{Rm}	Total strength value	Total W _{Rm} + total strength value	Ranking
6	Licensing (10)	50	457.4	507.4	8
12	Joint venture company (10)	50	450.2	500.2	9
19	Joint venture company (10)	50	430.8	480.8	10
27	Representative office(4)	20	456.8	476.8	11
16	Joint venture company (10), branch office/company (4)	70	400	470	12
9	Joint venture company (10)	50	405.6	455.6	13
3	Licensing (10)	50	400	450	14
28	Representative office (4)	20	323.8	343.8	15
30	Local agent (4)	20	310.8	330.8	16

assessment had sufficient resources and expertise to carry out construction activities in international markets. Despite lack of financial resources, they were able to sustain their operations in international markets through business network with other companies in the host country. In addition, the company utilizes technology resources from international companies as result of intermediate entry mode (IEM) such as Joint Venture with other companies in overseas. Therefore, the companies also need to use multi-entry modes to increase the company's strength in the international market. This strategy may help the companies understand the factors such as lack of resources, insufficient financial, technology advancement that may cause companies' failure in carrying out international construction projects. It is envisaged that the developed EMAC model to be very useful for a company seeking to operate in the international markets by identifying the company's strength factors and selecting the right modes together with the right locations.

References

1. Adnan H (2009) An assessment of risk management in joint venture projects (JV) in Malaysia. *Asian Soc Sci* 4(6):99–106. <https://doi.org/10.5539/ass.v4n6p99>
2. Asgari M, Ahmad SZ (2010) Internationalization of Malaysian service firms: business strategy and choice of foreign market entry mode, vol 1. In: International conference on business, economics and tourism management (CBETM 2010), pp 1–6

3. National Research Council (1988) Technological advances in the construction sector. Globalization of technology: international perspectives. The National Academies Press, Washington, DC. <https://doi.org/10.17226/1101>
4. Cristian AV, Zhang Y, Salifou C (2016) Application of PROMETHEE-GAIA method in the entry mode selection process in international market expansion. *Open J Bus Manage* 4:238–250
5. Gunhan S, Arditi D (2005) International expansion decision for construction companies. *J Constr Eng Manage* 131(8):928–937
6. Hastak M, Shaked A (2000) ICRAM-1: model for international construction risk assessment. *J Manage Eng* 16(1):59–69
7. Construction Industry Transformation Plan: 2016–2020 (2019) Construction Industry Development Board Malaysia
8. Demirbag M, Tatoglu E, Glaister KW (2009) Equity-based entry modes of emerging country multinationals: lessons from Turkey. *J World Bus* 44:445–462
9. Saaty T (1994) The analytic hierarchy process series. Fundamentals of decision making, vol 6. RWS, Pittsburgh
10. Saaty T (1999) Decision making for leaders: the analytic hierarchy process for decisions in a complex world. RWS, Pittsburgh
11. Erramilli MK, Agarwal S, Dev CS (2002) Choice between non-equity entry modes: an organizational capability perspective. *J Int Bus Stud*. <https://doi.org/10.1057/palgrave.jibs.8491014>
12. Hollender L, Zapkau FB, Schwens C (2017) SME foreign market entry mode choice and foreign venture performance: the moderating effect of international experience and product adaptation. *Int Bus Rev* 26:250–263. <https://doi.org/10.1016/j.ibusrev.2016.07.003>
13. Chen C (2005) Entry strategies for international construction markets. The Pennsylvania State University. Published degree thesis

Development of Automated Web-Based Condition Survey System for Heritage Monuments Using Deep Learning



Lukman E. Mansuri and D. A. Patel

Abstract Heritage is the identity of any society, and it should be conserved for the coming generations. Heritage monuments and buildings are seriously threatened by environmental agencies such as moisture, intense solar radiation, prevailing winds, and rain, changing their physical attributes. These environmental agencies cause various defects like spalling, abrasion, cracks, stains, and fungal growth in the heritage monuments. Detection and documentation of these defects are processes of the condition survey, which should be required just before the commencement of repair and maintenance of any structure. Traditionally, these defects are detected and documented by experts on the field using paper-based surveys. However, these methods are time-consuming and require immense expertise and cost. This paper presents the novel approach of condition survey by automated defect detection system to overcome these limitations. The automated defect detection system is developed using the Faster R-CNN (Region-based Convolutional Neural Network) to detect multiple types of defects from the heritage monument photos. Moreover, the web-based interface is developed to run the automated condition survey system. Types and number of defects and the position of defects are the output of the developed condition survey system. The system is demonstrated for the national heritage monument located in Surat city to check the developed system's effectiveness and field application. The proposed system is automatic, fast, and reliable for a condition survey of heritage monuments. This system will be useful for conservation, preservation, and maintenance management of heritage monuments.

Keywords Condition survey · Automatic defect detection · Heritage monuments · Deep learning · Faster R-CNN

L. E. Mansuri (✉) · D. A. Patel
Department of Civil Engineering, Sardar Vallabhbhai National Institute of Technology, Surat
395007, India

1 Introduction

Heritage is the identity of any society and it is passed down from one generation to another. The heritage buildings have high historical, architectural, spiritual, social, political and economic values. Heritage buildings differ from modern buildings in the sense that they are anticipated to last permanently. In order to pass on these values of heritage to future generations, good practices for preservation and conservation of heritage monuments prevents them from deterioration and extends their life and basic function.

India is enriched with the richest and diversity of cultural and architectural heritage. India has many heritage monuments and sites, in which the protected 36 monuments are declared as the World Heritage Monuments by UNESCO, and about 3650 monuments in the custody of Archaeological Survey of India (ASI) are declared as monuments of national importance. Still many heritage buildings are in the custody of religious trusts, archaeology departments of state governments and private owners [1]. Heritage conservation is a global challenge [2]. In fact, heritage buildings are seriously threatened by environmental agencies such as moisture, intense solar radiation and prevailing winds which change their physical attributes. The major adverse effects due to these environmental agencies include discoloration, abrasion, spalling, cracks, stains and fungal growth. Without proper understanding of heritage structures, their present condition and defects, the preservation of heritage values has become a challenging and difficult task. Manual visual inspection is conventional practice that is used for primary condition survey of the current state for heritage structures. However, this procedure is laborious and time-consuming as it requires high experience and specialized knowledge of inspection to assess the conditions based on the visual appearance of structures. Moreover, the manual condition survey cannot be done frequently due to high labor and manpower cost and being prone to human errors. More often the sites cannot be easily inspected because many areas of the structure are inaccessible and unsafe.

Recently deep learning is the emerging area of artificial intelligence (AI) which is successfully used for inspection and condition survey of infrastructures by many researchers. Deep learning is the computer vision-based object detection and classification by deep convolutional neural network (CNN) [3]. It is successfully applied for detection of defects from concrete structures and road pavements by various researchers. Also, artificial intelligence tools are one of the emerging digital technologies for the preservation and conservation of cultural heritage [4].

In this connection, this research intends to address the issues of manual condition survey, and to develop image based automated, fast and cost-effective primary condition survey systems for heritage monuments using deep learning methodology. To achieve the goal of development of an automated condition survey system, the objectives of this study are to: (i) develop an automated defect detection system using Faster R-CNN and (ii) build up a web-based interface for primary condition assessment of heritage monuments. The content of this paper is organized as follows: Sect. 2 describes the background of various defect detection systems. Section 3

provides the overview of methodology used for this study. Section 4 describes the Faster R-CNN model in detail. Section 5 provides the details of the dataset used for this study. Section 6 describes the experiment of an automated defect detection system. Section 7 presents the developed web-based condition survey system and lastly Sect. 8 concludes this work.

2 Background

The surface defect detection and condition survey is generally carried out by the extensive equipment [5–8]. These high-scale condition survey procedures are time-consuming and insufficient [9, 10]. Later stage, the data processing and analysis requires high skill professionals and extensive software which is laborious and prone to computational errors [11]. Thus, these methods and techniques are incapable for rapid and robust condition survey of heritage structures. The other method of condition survey is based on sensor-based defect detection in heritage structures [12, 13]. Sensor-based data collection and health monitoring of heritage structures require less time but large expenditure and it also requires professionals to install and operate the instruments. It is very difficult to install in large structures and generally it is not the cost-effective solution for condition survey. There are some other vision-based techniques being used for defect detection and condition surveys like, digital image processing (DIP) and digital image correlation (DIC) [14–16]. DIC techniques require manual feature extraction and it is highly sensitive to noise, and lacking with optimal solution.

With the advanced development in the field of artificial intelligence (AI) especially deep learning techniques can be helpful to overcome the above limitations. The convolutional neural network (CNN)—based on deep learning does not require any manual feature extraction. In recent time, a variety of CNNs have emerged with a high accuracy of recognition, detection and classification [17]. Deep learning has been widely used in medical diagnoses [18–21] and achieved remarkable benchmarks. Moreover, many studies applied deep learning techniques to defect detection such as automated crack detection in concrete and road surfaces [22–25]. Cha et al. [26] used region-based deep learning to detect five-category damage to steel, concrete and bolts [26]. Beckman et al. [26] developed a system for automatic volumetric damage quantification of concrete spalling using deep learning [27]. Wang et al. [17] developed automated damage detection in historic brick masonry walls by mobile deep learning and focused on the detection of two categories of defects [17]. In this line, this study outlines the methodology to achieve the objectives in the next section.

3 Methodology

As discussed in previous sections, this research intends to develop automated, fast and cost-effective primary condition survey systems using deep learning techniques and based on advanced object detection models.

The selection of an object detection model is important for development of an effective defect detection system. Most common and widely used object detection models are SSD (Single shot multibox detector) [28], R-FCN (region-based fully convolutional networks) [29] and Faster R-CNN (faster region-based convolutional networks) [30].

The properties of these object detection models are based on the COCO (common objects in context) mAP (mean average precision) and output type as shown in Table 1. The speed of SSD is more than R-FCN and Faster R-CNN but the training mAP is lower. The precision of training of R-FCN is more than SSD and less than Faster R-CNN. Thus, considering the speed and accuracy of these models, Faster R-CNN inception resnet v2 has been selected to develop an automated defect detection system in this study.

The defect detection classifier was trained with the use of TensorFlow object detection API (application programming interface) released by Google. The trained classifier was successfully applied to develop the automated web-based condition survey system.

Figure 1 shows the methodology adopted to achieve the objectives of study. The image dataset was collected using a digital camera from the English cemetery (national heritage site located in Surat, India). The collected images are then resized and augmented to create a dataset for training, validation and testing. Labeling of images is done on the whole dataset to support the training process. Then the dataset has been trained on the deep learning model, Faster R-CNN inception v2 using Google Colab cloud GPU. Automated defect detection systems are developed using trained classifiers. This system is applied to develop the web-based condition survey system.

Table 1 Widely used object detection models

Model	COCO mAP	Output
ssd_mobilenet_v1_coco	21	Bounding box
ssd_inception_v2_coco	24	Bounding box
rfcn_resnet101_coco	30	Bounding box
faster_rcnn_resnet101_coco	32	Bounding box
faster_rcnn_inception_resnet_v2_coco	37	Bounding box

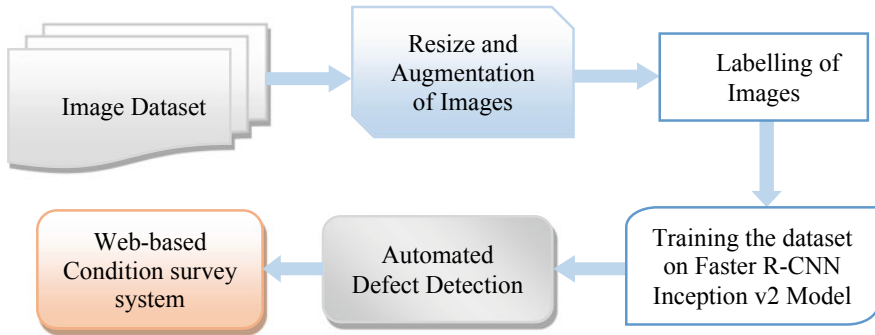


Fig. 1 Methodology

4 Faster R-CNN

Faster R-CNN is a widely used model for object detection. It proposes a way to speed up the calculation of region proposals by establishing a Region Proposal Network (RPN). The RPN is a fully connected convolutional network that trains high-quality region proposals by an end-to-end manner. Trained convolution features by RPN are then shared with Fast R-CNN. The conceptual architecture of Faster R-CNN is illustrated in Fig. 2. Faster R-CNN mainly composed by two stages, (i) RPN boxes extraction, and (ii) Fast R-CNN detection.

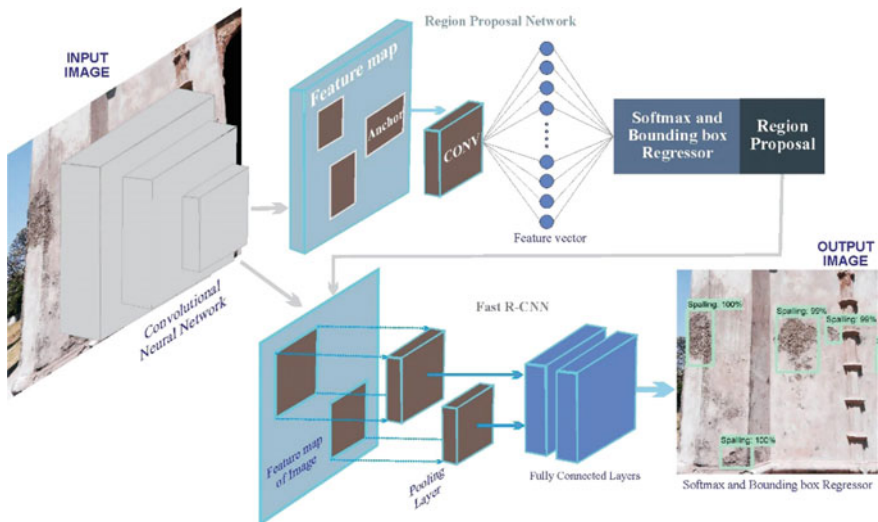


Fig. 2 Conceptual architecture of Faster R-CNN

Bounding boxes are extracted by using RPN which is a fully convolutional neural network, then, object proposal is detected and identified by Fast R-CNN based on extracted proposal by RPN.

The Faster R-CNN is principally divided into four major components as follows,

- (1) Convolution layers: Faster R-CNN is using a set of basic convolutional layers, ReLU (rectified linear unit) function for activation and pooling layers for extraction of feature maps in image. Feature maps are shared with subsequent fully connected and RPN layers.
- (2) Region proposal networks (RPN): generation of region proposals are done by region proposal networks. SoftMax regression is used by this layer to determine the foreground or background anchors and uses bounding box regression by correcting the anchors to get accurate proposals.
- (3) Region of Interest (RoI) pooling: Input feature maps and proposals are collected by this layer. It extracts the feature maps after synthesizing the information and sending it to a related fully connected layer for determining the object categories.
- (4) Classification: The classification of proposals is calculated using proposal feature maps in Faster R-CNN and parallel it uses the bounding box regression to obtain coordinates of detection boxes precisely.

5 Dataset Preparation

For any image-based deep learning system, a good image dataset is a primary need. The image dataset for this study was taken from the English Cemetery, also known as British Cemetery (as shown in Fig. 3), located in Katargam, Surat, India, a protected national heritage site of Archeological Survey of India (ASI). The English cemetery site consists of various monumental structures in the form of tombs over the graves. These monuments were constructed by English factory owners during 1649–1811 AD. All the monuments were constructed by plastered brick masonry. A primary investigation has been done to identify the most common type of surface defects in the monuments. Two major and most common surface defects have been identified in the primary investigation. These two surface defects are *spalling* of plaster and *cracks* in the plaster. Thus, this study is focusing on the automated detection of these two surface defects by using site images.

Total 260 images of 3648×2736 pixels were captured by digital cameras. The images were taken in such a way that it creates a variety of dataset in terms of different backgrounds, various lighting conditions, and different distances from the camera to identify defects from various angles. Moreover, some of the images were captured from very close to defects and some were away from defects in order to get the different backgrounds. Different backgrounds in the dataset is required for better detection of defects in various conditions. These 260 original images were then resized to smaller size of 800×600 pixels for reducing the training time. To develop the main database, augmentation was applied to 260 images and a total of



Fig. 3 Monuments at English cemetery, Surat, India

500 images of 800×600 pixels were created by horizontal flipping and brightness changing. 80% of images were taken for training and 10% for validation and 10% for testing. Thus, from the dataset of total 500 images, 400 images were selected for training, 50 for validation and 50 images for testing.

For training of the defect detection system, the defect present in the image should be manually identified first. The manual identification serves as ground truth images that are used to learn defects from images. The labelling (annotation of defects) is done in all images manually. Example of labelling is shown in Fig. 4. Annotation includes identifying all features and information in images and drawing a rectangular box around each target feature (defect).

These images are then labelled for defect types in two types of defects, spalling and cracks. Labelling of images is done by free labelling software tool LabelImg [31]. The labelling tool allows easy labelling of images by interactive interface. The output of the labelling tool is into extensible markup language (XML) file corresponding to labelled image in the pascal visual object classes (PascalVOC) format. The XML file of each image contains information about the image such as name, size and bounding box coordinates.



Fig. 4 Labelling of image dataset

6 Experiment

The experiment was conducted using the open-source Faster R-CNN model [30] on Google Colab cloud GPU. Object detection training consists of three steps: (1) Performing forward pass, (2) Calculating loss, and (3) Weight updating of network.

In forward pass, a training image which is annotated by ground truth is passed through the model, and output results are calculated. These outputs are compared with ground truth to calculate loss. The main goal of training is to minimize the loss. The training step is to be continued until the loss is minimum and almost constant. Training steps are the important hyper-parameter which directly affect training time and precision of detection. With less number of iteration, the training time is short but the defect detection precision is very low and training loss cannot be done minimum. Training loss can be minimized and stabled with more number of training steps.

In this study, the optimum number of training steps has been found by trial-and-error method with the training steps 1000–40,000. The corresponding loss at every thousand steps is shown in Fig. 5. The minimum loss was recorded on 36,000 steps. Thus, the final training of the whole dataset is done on 36,000 steps which have taken 5 h of training time.

To determine the accuracy of detection, intersection over union (IoU) matrix has been used for this study. The IoU is the measure of degree of overlap between ground truth and detected bounding box. The threshold value of IoU is selected as 0.50 for experiment in this study.

The testing is done on the test dataset to check the accuracy of the defect detection. 0.87 mAP is recorded as the accuracy of defect detection. Figures 6 and 7 show the detected defects on various site images. Figure 6 illustrates the output of automated

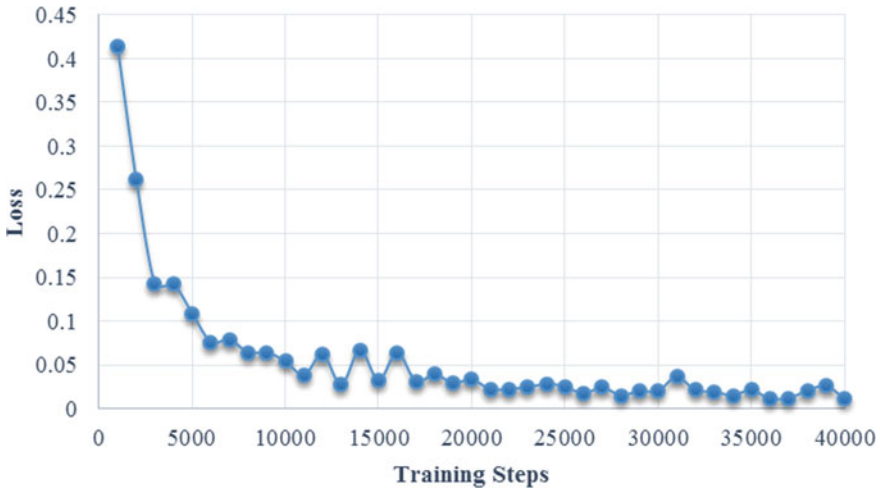


Fig. 5 Loss on different number of training steps



Fig. 6 Detected defects—*spalling*

detected spalling and Fig. 7 illustrates the output of automated detected cracks in site images. The automated defect detection system maps (by bounding box) the defects on the input images. This automated system is further used to develop the web-based condition survey system.

7 Web-Based Condition Survey System

Preservation of heritage monuments in its original form and structure is the aim of any maintenance, repair and rehabilitation system. For making the decision of



Fig. 7 Detected defects—crack

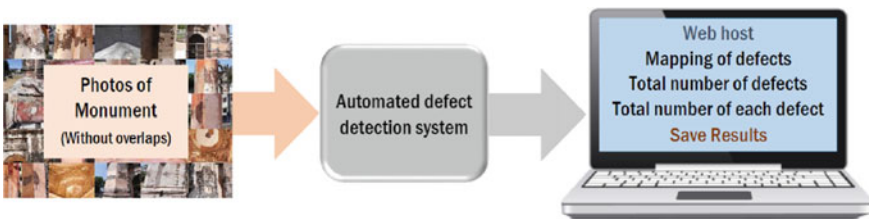


Fig. 8 Web-based condition survey system

repair and maintenance requires the detailed condition survey of the monument. The detailed condition survey requires highly skilled and experienced experts. These experts need time and financial resources for detailed condition surveys. To overcome this limitation and to make this process fast and cost effective, the primary condition survey system is developed and presented here (see Fig. 8). This primary condition survey system will be helpful for knowing the condition of heritage monuments in terms of numbers and types of defects. This primary condition survey system will become the base for taking decisions of doing detailed condition assessment and various on-field testing.

Automated mapping (detection) of defects is the main output of the above developed system. This system is made more insightful by incorporating the counts of defects. The primary web-based condition survey system gives the count of total and individual defects, which can be used for decision making of further maintenance management.

Figure 9 shows the interface of a developed web-based condition survey system which is hosted in a local computer system. This system can be hosted by the heritage conservation authority which can be accessed from anywhere through the web. For condition survey, the photos of monuments have to be captured with no overlap. The captured photos are submitted to the system to get the mapping, number and types of defects.

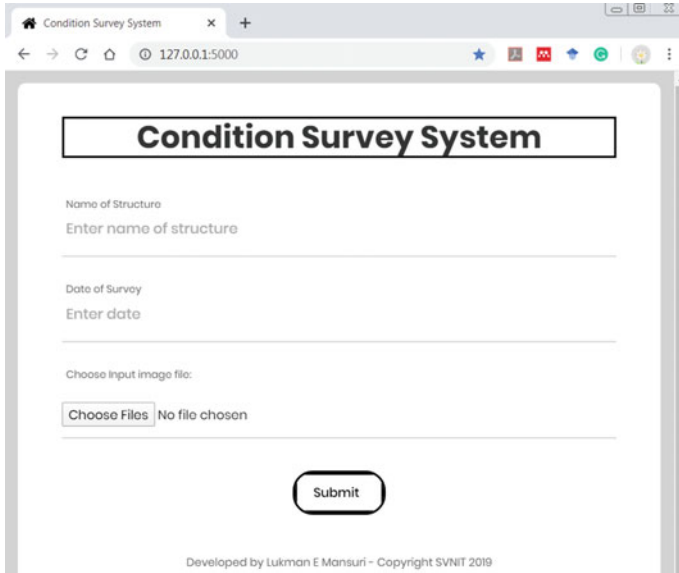


Fig. 9 Interface of web-based condition survey system

The system is demonstrated and validated for one monument of English Cemetery, Surat. Total 15 photos were captured by a digital camera. These photos were then submitted to a web-based system for primary condition survey. The result for this monument is shown in Fig. 10 as the output of the system. The monument has a total of 40 defects among which spalling is detected at 28 places and 12 cracks are detected. Moreover, the mapping is also saved automatically in the computer folder as shown in Figs. 6 and 7. Validation with the site is also given the same numbers of defects and their positions.

The system acts as the primary condition survey for heritage monuments. By capturing photos of monuments, the decision maker can take decisions based on this system. The system is providing mapping (position) of defects and their quantity (numbers), this will help in decision making for detailed condition survey and structural testing. The output data (mapping, number and type of defects) will also be helpful for quantification of damages and estimate the cost of repair and maintenance of the monument.

8 Conclusion

Automated defect detection and web-based primary condition survey method are presented in this paper. The system is developed using the Faster R-CNN model of deep learning. The system detects two types of defects in the heritage brick masonry

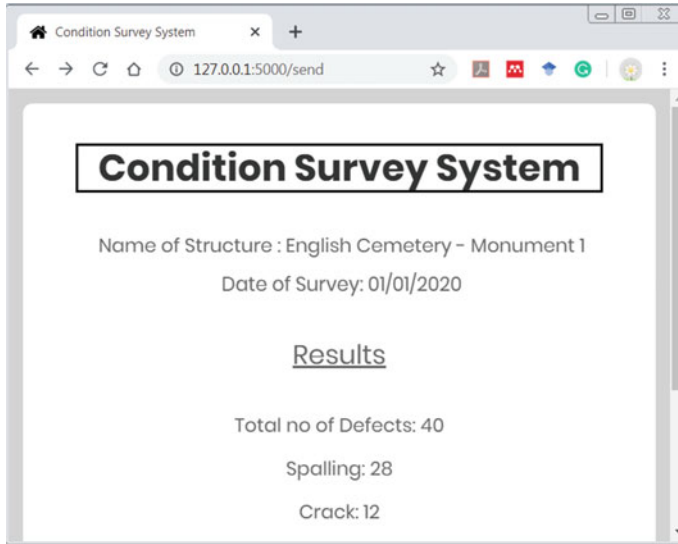


Fig. 10 Output of web-based condition survey system

monuments: ‘*spalling*’ and ‘*crack*’. The dataset of 500 images containing two types of surface defects were labeled and used for this study. To find the optimum number of steps for training a dataset, the trial-and-error method is adopted. The minimum loss was recorded on 36,000 training steps. Then the model is tested for accuracy of detection. The model was found accurate in the detection of two categories of surface defects. The model is also validated for different background conditions and photos taken from different angles. A web-based primary condition survey system is developed using an automated detection system. Mapping of defects, types, and a number of defects are the output of a web-based condition survey system. The developed system is also demonstrated and presented for one monument of English cemetery, Surat.

The developed web-based system can be useful for the primary condition survey of the heritage monuments. The system is web-based, so it can be hosted by the conservation authority, which can then be used anywhere through the web. The developed system will reduce the cost, time, and other efforts of the primary condition survey. The web-based condition survey can become the base for detailed investigation, testing, and maintenance management. The system will further be developed for achieving higher accuracy and automated quantification of detected damages. The system can be embedded with heritage building information modelling (HBIM) to develop a BIM-Based heritage management system.

Acknowledgements The authors are thankful to the Archaeological Survey of India (ASI) Vadodara Circle for permitting data collection for this work. The first author is thankful to the Ministry of Education (MoE), Government of India, and SVNIT Surat for providing fellowship of full-time Ph.D. research.

References

1. Menon A (2014) Heritage conservation in India: challenges and new paradigms. In: SAHC2014—9th international conference on structural analysis of historical constructions, Mexico City, Mexico, pp 14–17
2. Udeaja C, Trillo C, Awuah KGB, Makore BCN, Patel DA, Mansuri LE, Jha KN (2020) Urban heritage conservation and rapid urbanization: insights from Surat, India. *Sustainability* 12:2172. <https://doi.org/10.3390/su12062172>
3. Rawat W, Wang Z (2017) Deep convolutional neural networks for image classification: a comprehensive review. *Neural Comput* 29:2352–2449
4. Mansuri L, Udeaja C, Trillo C, Kwasi G, Patel D, Jha K, Makore CB, Gupta S (2019) Scientometric analysis and mapping of digital technologies used in cultural heritage field. In: Association of researchers in construction management, ARCOM 2019—proceedings of the 35th annual conference, pp 255–264
5. Flores-Colen I, de Brito J, de Freitas V (2009) Expected render performance assessment based on impact resistance in situ determination. *Constr Build Mater* 23:2997–3004
6. Gattulli V, Chiamonte L (2005) Condition assessment by visual inspection for a bridge management system. *Comput Civ Infrastruct Eng* 20:95–107
7. O'Byrne M, Schoefs F, Ghosh B, Pakrashi V (2013) Texture analysis based damage detection of ageing infrastructural elements. *Comput Civ Infrastruct Eng* 28:162–177
8. Reyno T, Marsden C, Wovk D (2018) Surface damage evaluation of honeycomb sandwich aircraft panels using 3D scanning technology. *NDT E Int* 97:11–19
9. Barreira E, de Freitas VP (2007) Evaluation of building materials using infrared thermography. *Constr Build Mater* 21:218–224
10. Flores-Colen I, Manuel Calico Lopes de Brito J, Peixoto de Freitas V (2011) On-site performance assessment of rendering façades for predictive maintenance. *Struct Surv* 29:133–146
11. Huang J, Liu W, Sun X (2014) A pavement crack detection method combining 2D with 3D information based on Dempster-Shafer theory. *Comput Ci. Infrastruct Eng* 29:299–313
12. Boscolo G, Russo S, Ceravolo R, Fragonara LZ (2015) Global sensitivity-based model updating for heritage structures. *Comput Civ Infrastruct Eng* 30:620–635
13. Gentile C, Gallino N (2008) Condition assessment and dynamic system identification of a historic suspension footbridge. *Struct Control Health Monit Off J Int Assoc* 15:369–388
14. Yeum CM, Dyke SJ (2015) Vision-based automated crack detection for bridge inspection. *Comput Civ Infrastruct Eng* 30:759–770
15. Salman M, Mathavan S, Kamal K, Rahman M (2013) Pavement crack detection using the Gabor filter. In: 16th international IEEE conference on intelligent transportation system (ITSC 2013), pp 2039–2044. <https://doi.org/10.1109/ITSC.2013.6728529>
16. Nishikawa T, Yoshida J, Sugiyama T, Fujino Y (2012) Concrete crack detection by multiple sequential image filtering. *Comput Civ Infrastruct Eng* 27:29–47
17. Wang N, Zhao X, Zhao P, Zhang Y, Zou Z, Ou J (2019) Automatic damage detection of historic masonry buildings based on mobile deep learning. *Autom Constr* 103:53–66. <https://doi.org/10.1016/j.autcon.2019.03.003>
18. Ramcharan A, Baranowski K, McCloskey P, Ahmed B, Legg J, Hughes DP (2017) Deep learning for image-based cassava disease detection 8:1–7. <https://doi.org/10.3389/fpls.2017.01852>
19. Thobogang B, Wannous M (2018) Design of plant disease detection system : a transfer learning approach work in progress. In: 2018 IEEE international conference on application system invented, pp 158–161. <https://doi.org/10.1109/ICASI.2018.8394556>
20. Goncharov P, Ososkov G, Nechaevskiy A, Uzhinskiy A, Nestsiaerenia I (2019) Disease detection on the plant leaves by deep learning: selected papers from the XX international conference on neuroinformatics, Oct 8–12, 2018, disease detection on the plant leaves by deep learning. Springer International Publishing. <https://doi.org/10.1007/978-3-030-01328-8>
21. Mohanty SP, Hughes DP, Salathé M (2016) Using deep learning for image-based plant disease detection 7:1–10. <https://doi.org/10.3389/fpls.2016.01419>

22. Jahanshahi MR, Masri SF, Padgett CW, Sukhatme GS (2013) An innovative methodology for detection and quantification of cracks through incorporation of depth perception. *Mach Vis Appl* 24:227–241. <https://doi.org/10.1007/s00138-011-0394-0>
23. Sánchez L, Bairán García JM (2016) Crack detection in concrete elements from RGB pictures using modified line detection kernels 16
24. Fan X, Wu J, Shi P, Zhang X, Xie Y (2018) A novel automatic dam crack detection algorithm based on local-global clustering
25. Dung CV (2019) Autonomous concrete crack detection using deep fully convolutional neural network. *Autom Constr* 99:52–58
26. Cha YJ, Choi W, Suh G, Mahmoudkhani S, Büyüköztürk O (2018) Autonomous structural visual inspection using region-based deep learning for detecting multiple damage types. *Comput Civ Infrastruct Eng* 33:731–747. <https://doi.org/10.1111/mice.12334>
27. Beckman GH, Polyzois D, Cha Y-J (2019) Deep learning-based automatic volumetric damage quantification using depth camera. *Autom Constr* 99:114–124
28. Liu W, Anguelov D, Erhan D, Szegedy C, Reed S, Fu C-Y, Berg AC (2016) SSD: single shot multibox detector. In: *European conference on computer vision*. Springer, pp 21–37
29. Dai J, Li Y, He K, Sun J (2016) R-FCN: object detection via region-based fully convolutional networks. In: *Advances in neural information processing systems*, pp 379–387
30. Ren S, He K, Girshick R, Sun J (2015) Faster R-CNN: towards real-time object detection with region proposal networks. In: *Advances in neural information processing systems*, pp 91–99
31. Tzualin: LabelImg. <https://github.com/tzualin/labelImg>. Last accessed 2018/12/03

Developing Indicators of Green Operation and Maintenance of Green Supply Chain Management in Construction Industry



Mochamad Agung Wibowo, Naniek Utami Handayani, and Nur Farida

Abstract Operation and maintenance (O&M) is the last phase of Project Life Cycle (PLC) that focused on releasing the final deliverables to the customer and followed by the use of facilities and the maintenance of the whole building. This phase is the longest phase because it covers the entire lifetime of the building. The building that is operated and maintained using the green principles will contribute to sustainability by reducing energy and resource emissions by ensuring the building facilities' durability and availability. Green Operation and Maintenance (GOM) programs as part of Green Supply Chain Management (GSCM) in the construction process consist of work implementation and control to conserve 'green' materials according to environmental needs in the project. GOM concept is important because O&M phase is the determinant of whether the building that have been initiated, designed and built with green processes can be maintained to keep contributing positively to the environment. To ensure that the O&M phase is run on the green principle, it is necessary to conduct a study to develop factors that can support the application of GSCM in the O&M phase. The aim of this study is to improve the GOM concept indicators as part of the GSCM construction. The model developed has two dimensions, 12 components, and 18 indicators for the implementation of GOM.

Keywords Green operation and maintenance · Green supply chain management · Project life cycle

1 Introduction

Construction industry in developing countries has several characteristics including, first, construction has typically contributed to an average GDP of 5–9%. Second, the

M. A. Wibowo (✉)

Department of Civil Engineering, Diponegoro University, Semarang, Indonesia 50275

e-mail: agung.wibowo@ft.undip.ac.id

N. U. Handayani · N. Farida

Department of Industrial Engineering, Diponegoro University, Semarang, Indonesia 50275

impact of construction affects the value of the distribution of construction materials and labor absorption, which reaches 5% of the total workforce and often work in this sector is a stepping stone for the manufacturing industry. Third, the impact of construction business is quite extensive, built from small companies that generate entrepreneurial opportunities in small businesses and play an important role for income distribution [1].

The construction industry is widely considered to have a high degree of waste in spite of its significant contributions. Waste consists of material waste at the project site in the construction industry and is often related to various activities such as overproduction, waiting time, shipment of materials, inventory, and labor movement. Rework/repair, defects, waste in the form of materials, delays, waiting, allocation of material that is not suitable, and excessive transfer of material can be defined as the main categories of waste during the construction process [2]. The performance of this industry is also influenced by the characteristics of the construction industry, such as the high complexity and volatility, the temporary structure of the supply chain, the high degree of consumer control on the final product, the disjointed processes, and the complexity of stakeholder linkages [3].

It is possible to suggest implementing the Green Supply Chain Management System to form a productive and environmentally friendly construction industry. In every step throughout the Project Life Cycle (PLC), the initiation, design, construction, and operation and maintenance phase, this implementation is intended to bring the notion of eco-friendly [4].

In general, the commissioning and closure of a green building project are more complex than traditional projects. This is especially valid when developers or owners choose to receive Green Building Certification from third parties. The Green Building is the basis of an environmentally friendly and resource-efficient structure over the life cycle. It is also the task of current facility management teams and end-users to deliver an awareness of the green building system to maintain sustainability [5]. The commissioning process is part of the last stage of the PLC, the service and maintenance phase. The operation and maintenance process centered on the release to the customer of the final deliverables, the handing over of project documents, the termination of supplier contracts, the release of project resources, and the notification to all stakeholders of the project's closure [6]. This phase also focused on the use of facilities and the maintenance of the whole building. In general, the Operation and maintenance phase forms the major part of the life cycle [7].

Previous research on GSCM in the construction industry has established a framework consisting of five principles for GSCM implementation, i.e. Green Initiation, Green Product Design, Green Material Management, Green Construction, and Green Operation and Maintenance [8]. This framework represents all stages in PLC. Detailed indicator of every concept has been developed in previous research about Green Initiation and Green Design [9], Green Material Management [10], and Green Construction [11]. As a continuation of previous studies, this study aims to classify the Green Operation and Maintenance indicators as part of the GSCM in construction.

2 Literature Review

2.1 *Project Life Cycle*

Construction projects are some activities that have multipart and various properties. The project follows a flow of stages, known as Project Life Cycle (PLC). In common, PLC involves several stages, i.e. initiation/conceptualization, planning/design, implementation/construction, and operation and maintenance [9, 12, 13]. All of the PLC phases are less synchronized with one another in the conventional management model. This is what causes the fragmentation of construction projects. The initiation phase is related to the owner as key stakeholders in the process. Data collection, surveys, and feasibility studies are usually conducted in the initiation phase. Feasibility studies are taken to decide whether a project is feasible and also to determine alternative possibilities that can be taken as a consideration in decision making. A project document that will be used as a reference to the next step is the production from the initiation stage [9].

The project planning documents are produced at the planning phase. These documents consist of Detail Engineering Design (DED), Gantt Chart (PERT), Work Breakdown Structure (WBS), and other planning documents (i.e. specification/quality and risk management). The construction phase is the process of executing the planning that has been generated from the previous phase. This process includes execution of plans, project resource management, monitoring, and reporting. The last phase is the operation and maintenance phase that consists of handover project results and maintenance period. This phase can show the success of the project by conducting evaluation and assessment after completion of the project [9, 12, 13].

2.2 *Green Supply Chain Management in Construction*

Green supply chain management (GSCM) is a framework that assimilates environmental deliberation into supply chain management. There is some research that examines to adopt GSCM in manufacture to be applied in the construction industry. The GSCM structure in the construction industry, which includes five principles, is one of the researches that is the key reference of this report, i.e. green initiation, green design, green material management, green construction, and green operation and maintenance [8].

This research is part of the overall framework for applying GSCM to the construction industry based on PLC. The previous research stated that there is GSCM in manufacture industry that could be applied in the construction industry [8]. The roadmap of this research described in Fig. 1.

Each of the research mentioned in Fig. 1 contains detailed concepts, dimensions, elements, and indicators of each concept that corresponds to the PLC stage. First and second stage of PLC corresponds to the research about developing indicators

**Framework for Implementing Green Supply Chain Management
in The Construction Industry based on Project Life Cycle**





Project Life Cycle	Initiation Phase	Design Phase	Construction Phase		Operation & Maintenance Phase
Green Supply Chain Management	 Developing Indicators of <u>Green Initiation</u> and <u>Green Design</u> of Green Supply Chain Management in Construction Industry: A Literature Review <u>Published on 2019</u>	 Developing Indicators of <u>Green Initiation</u> and <u>Green Design</u> of Green Supply Chain Management in Construction Industry: A Literature Review <u>Published on 2019</u>	 Developing Indicators to Implementing <u>Green Material Management</u> in Construction Industry: A Literature Review <u>Published on 2018</u>	 Developing Indicators of <u>Green Construction</u> of Green Supply Chain Management in Construction Industry: A Literature Review <u>Published on 2019</u>	<u>This Research</u> Developing Indicators of <u>Green Operation & Maintenance</u> of Green Supply Chain Management in Construction Industry: A Literature Review

Fig. 1 Roadmap research framework for implementing GSCM to the construction industry based on project life cycle

of green initiation and green design. Green initiation is related to project owner commitment and feasibility of development project. Owner commitment is the most essential thing to realize a sustainable project in the construction industry, because owners are the decision maker who can determine every step towards a sustainable project [9, 14]. Table 1 contains the translation of one of the dimensions in the Green Initiation concept to the indicator level [9].

Green design, that corresponds to the design stage in the PLC, is the most important phase because every choice that is made in the design phase will have an impact on the lifespan of the project system. Design should become a main consideration for detecting the environmental impacts of project activities [9, 14]. Green design concept is translated into five dimensions, i.e. design, innovation capability, product safety, environmental control, and building and environment management [8, 9]. Table 2 contains the translation of one of the dimensions in the Green Design concept to the indicator level [9].

Green material management is a concept that covers two stages of PLC, i.e. planning/design phase and implementation/construction phase. This concept is about how to take out hazardous material or harmful activities then replace them with less harmful ones. Green material management concept is translated into five dimensions, i.e. material planning, packaging, green transportation, material storage, and material handling [8, 10]. Table 3 contains the translation of one of the dimensions in the Green Material Management concept to the indicator level [10].

The implementation/construction stage on the PLC is represented by the Green construction concept. This concept consists of process engineering to diminish the use of resources and energy. This reduction aims to diminish total waste produced during the construction phase. There are four dimensions which are derived from

Table 1 The example of translation the Green Initiation indicators

No.	Dimensions	Elements	Indicators
1	Environment conscious design	Project owner commitment	Educating project team participants to achieve sustainable construction and building concepts
			Provide vision statement on the reason to develop GSCM project
			Facilitating the integration of other project participants
			Introducing green intention early
		Feasibility study	Perform area, demographic, and neighborhood analysis
			Perform site review analysis that evaluate the size, topography, amenities, and Governmental impacts
			Perform market analysis
			Perform financial analysis
			Perform valuation analysis of propose development in project that calculated through a discounted cash flow

Table 2 The example of translation the green design indicators

No.	Dimensions	Elements	Indicators
1	Innovation capability	Resource conservation	Using non-toxic or less toxic materials in design specification
			Consider material durability in design specification
		Design support for waste management implementation	Make coordination design to minimize excess cutting and jointing of materials
			Make design with standard material dimension
			Building element and material design easily disassembled
		Appropriate site development	Percentage of basic green area
			Placing sustainable building project within easy access of public facilities

Table 3 The example of translation the green material management indicators

No.	Dimensions	Elements	Indicators
1	Material planning	Using material that environmental friendly	Percentage utilization of recyclable construction material
			Percentage utilization of hazardous material
		Contract with supplier	Percentage of contract with suppliers
		Select supplier with ISO 14001 certificate	Percentage of suppliers with ISO 14001 certificate
		Quality control of material	Percentage of good material that received in site

green construction, i.e. on-site management and planning, site operation, environment society, and reverse logistics [8, 11]. Table 4 contains the translation of one of the dimensions in the Green Construction concept to the indicator level [11].

The last concept, green operation and maintenance corresponds to the last phase of PLC, operation and maintenance. Green operations and maintenance consist of strategy about work practices and material observation in a project with environmental concern so that the green concept can still be applied during the operational phase of the building [8, 12]. This concept is closely related to the practice of green building principles.

BREEM (UK), LEED (US), BEAM (Hong Kong), CASBEE (Japan) and EDGE (UK) are the various Green Building Rating System (GBRS) that have been developed around the world. The Green Building Rating Systems could help building

Table 4 The example of translation the green construction indicators

No.	Dimensions	Elements	Indicators
1	Site operation	Accidents due to negligence	Number of work accident during a project
		Equipment malfunction	Amount of broken equipment
			There is equipment maintenance schedule
			There is equipment calibration schedule
		Use of wrong materials resulting in their disposal	Percentage of waste that caused by use of wrong material
		Time pressure	There is countdown timer equipment for reminder project schedule
Poor work ethic	All work result meet the specification that has been stated in contract document		

owners in some concerns, which are base lining (i.e., establishing an initial measurement against which to calibrate future performance), benchmarking (i.e., presenting a basis for comparison with competitor), decision making (i.e., creating a basis to select among different solutions), documentation (i.e., to capture evidence to fulfill the rules and regulations). According to the review, the most essential evaluation criteria in the various of GBRs are energy, water, material, indoor environment, site, land and outdoor environment, and innovation [5].

3 Research Methodology

This research is a descriptive study that develops a structure for green operation and maintenance implementation as part of the green supply chain management. The concept, dimensions, elements, and indicators consist of this framework. Data accumulated by observation through the execution of a literature review and interview with researcher, practitioner, and ministry experts. The literature review covered the project life cycle, the management of the green supply chain in the construction industry, and some prior studies on organizational and maintenance issues. The experts who become respondents are composed of four academic experts, two practitioner experts, and one Ministry of Public Work specialist. The goal of the interview is to compare the indicators established with the condition of the sector.

The previous study about issues in operation and maintenance phase are listed in Table 5.

A previous study by Zainol et al. [15] and Asmone et al. [16] has identified the factors and indicators that need to be considered to support the development of a sustainable O&M phase. From the previous stage of PLC, some of the factors and indicators, such as “technical defects,” “construction quality,” “building and construction standards,” and “maintainability design,” must be decided. It shows the interrelationship between phases in the PLC and a holistic approach is needed to ensure the achievement of sustainability throughout the PLC. This vision is in line with the research vision of Wibowo et al. [8] that carries the GSCM concept to try to solve the problem of waste and inefficiency in the construction industry with the aim of sustainable construction.

In a previous study conducted by Zainol et al. [15], Asmone et al. [16], and Wibowo et al. [8], the model developed still did not provide the indicators that could be measured directly in the project. This GOM study is the continuation of study that has been conducted by Wibowo et al. [8]. So, based on this main reference and supported by factors that exist in previous studies, this study will develop the indicators of green operation and maintenance as part of GSCM in construction. Indicator generation is carried out by tracing other studies that have addressed related topics with the critical reference model elements. While the GBRs that stated in Hwang research [5] will be used as additional reference and will be compared in the discussion section.

Table 5 The previous study about issues in operation and maintenance phase

No.	Title and Authors	Objectives	Methods	Result
1	Critical Factors that Lead to Green Building Operations and Maintenance Problems in Malaysia: A Preliminary Study Zainol et al. [15]	Identify the factors that lead to green buildings operation and maintenance problems in Malaysia	Literature review, questionnaire survey	There are five factors that lead to green building O&M problems, in succession, i.e. technical defects, managerial problems, social and cultural problems, political and legal factors, environmental and biological effects These five factors are described in more detail into 15 sub factors that stated in the paper
2	Green Maintainability Performance Indicators for Highly Sustainable and Maintainable Building Asmone et al. [16]	Propose a set of critical green maintainability performance indicators for building projects	Literature review, expert interviews, DEMATEL	The indicators of green maintainability are 13 indicators with 22 sub indicators that stated in the paper The critical indicators of green maintainability are green procurement, construction quality, building and construction standards, design for maintainability, and sustainable facilities management
3	Factors for Implementing Green Supply Chain Management in the Construction Industry Wibowo et al. [8]	Elaborate the concepts, dimensions, and elements of Green supply chain management (GSCM) and develop the framework for implementing GSCM in the construction industry	Literature review, Delphi method	The framework for implementing GSCM consist of five concepts, 22 dimensions, and 82 elements Green operation and maintenance concept consist of 2 dimensions and 13 elements The indicators is not yet developed

(continued)

Table 5 (continued)

No.	Title and Authors	Objectives	Methods	Result
4	Performance and Improvement of Green Construction Projects—Management Strategies and Innovation Hwang [5]	Identify and compare the various of green building rating system that have been developed around the world to determine the most essential evaluation criteria in the various of GBRS	Literature review, questionnaire survey, interviews, statistical analysis methods, fuzzy synthetic evaluation approach, risk criticality index	The most essential evaluation criteria in the various of GBRS are energy, water, material, indoor environment, site, land and outdoor environment, and innovation

4 Result and Discussion

4.1 *Developing Indicators of Green Operation and Maintenance as Part of GSCM in Construction*

Green Operation and Maintenance (GOM) concept in Wibowo et al. [8] consists of two dimensions and 13 elements. The dimensions are “Green Building” that breakdown to 9 elements and “Green Management Policy” that breakdown to 4 elements. The result of literature studies and interviews conducted with expert respondents are the indicators of GOM. Literature studies are conducted first, while interviews with experts are done as verification of the suitability of the literature study results with field conditions. The questionnaire was used as a tool to simplify the interview process. The indicators of Green Operation and Maintenance as part of GSCM in construction are listed in Table 6.

4.2 *Discussion*

Green operation and maintenance related with operation and maintenance phase in Project Life Cycle (PLC). This phase has the longest period in PLC that covered the entire building lifetime. From the description of the indicators above, most of the indicators at first dimensions i.e. Green Building refer to GREENSHIP rating tools as a model that is well known in Indonesia. The indicators referred to are indicators related to the building operational process. These indicators can still be continuously improved during the O&M phase, such as water infiltration and retention, daily energy conservation, water conservation, CO₂ emission reduction, and sewage and waste disposal facility improvement. However, success in improving these indicators greatly depends on the application of green in the previous PLC phase. Thus, the GOM indicators cannot stand alone, but rather as a series of the entire GSCM framework.

Table 6 The indicators of green operation and maintenance

No.	Element	Indicator	References
Dimension: Green Building			
1	Greenery (vegetation planning)	Percentage of basic green area	[5, 17]
2	Water infiltration and retention	Provide rainwater harvesting installation equipment	[5, 17]
		Use water from alternative resource to sanitation and irrigation activity	[5, 17]
3	Daily energy conservation	Measure energy used as a baseline for application better energy management	[5, 17]
		Doing OTTV (overall thermal transmittance value) calculation	[5, 17, 18]
		Amount of energy savings in building installed	[5, 17]
4	Water conservation	Measure water used as a baseline for application better water management	[5, 17]
		Amount of water savings in building installed	[5, 17]
5	CO ₂ emission reduction	Using high efficiency lighting	[19, 20]
		Using solar thermal water heater	
6	Construction waste reduction	Using concrete residual to make nonstructural component (example: cansteen/curb and car stopper)	[21]
		Using ceramics cutting residual to filling floor pattern or decoration	
7	Sewage and waste disposal facility improvement	There are on site wastewater treatment system facility	[5, 17, 22]
		Perform organic waste processing (on site or third party cooperation)	[5, 17]
		Perform an-organic waste processing (on site or third party cooperation)	[5, 17]
8	Biodiversity	Percentage of vegetation landscape (include garden above basement, roof garden, terrace garden and wall garden)	[5, 17]
9	Indoor environmental quality	Indoor air quality meet the specification threshold (CO ₂ = 530–1500 ppm; CO = 10–100.000 µg/m ³ ; NO ₂ = 40–5600 µg/m ³ ; SO ₂ = 20–5200 µg/m ³ ; ammonia = 17.000 µg/m ³)	[23]

(continued)

Table 6 (continued)

No.	Element	Indicator	References
<i>Dimension: green management policy</i>			
10	Green corporate social responsibility	Number of company regulation that support green concept	[24, 25]
11	Green customer education	Publish the sustainability report company that extensively accessible	[26, 27]
12	Green image promotion	Installation green slogan board in project site	[21, 26]
13	Certificate of building proper function	Building has certificate of building proper function	[28]

Concepts that are technically related with the GOM concept are Green Design (GD), Green Material Management (GMM), and Green Construction (GC). The GD elements that greatly influence the GOM are resource conservation, appropriate site development, occupational health and safety, indoor health and comfort, design support for energy conservation, design support for water conservation, and environment assessment [9]. All decisions about these elements will determine success in carrying out the GOM indicators.

The GMM elements that directly influence the GOM are using materials that are environmentally friendly, select suppliers with ISO14001 certificate, and quality control of material [10]. The GC elements that directly influence the GOM are pollution control and quality control [11]. While GI became the basis for the implementation of all GSCM practices in the PLC, especially for the element of project owner commitment [9].

The second dimension of the GOM concept is Green Management Policy which means effort to improve the foundation of environment management by building personal responsibility for eco-friendly activities and also modifying the policies, practices, and principles of management system [29]. This dimension is complementary to the first dimension, i.e. Green Building, where the elements in green building provide technical guidance, while elements in green management policy consist of decisions at managerial level that can support the achievement of a sustainable O&M phase.

This study has differences compared to studies conducted by Zainol et al. [15], Asmone et al. [16], and Wibowo et al. [8]. First, in terms of concept, this study is a unity in a series of GSCM implementation models in the construction industry, which has integrated PLC into the model. This integration is expected to form a continuous model and represent all stakeholders involved in the PLC. In addition, this study has been able to present models up to the indicator level that can be implemented or measured in a project.

In the past two decades, they were a rapid establishment of green building rating systems. The GBRSS is a systematic system built to assess and check the sustainability

Table 7 The comparison of the prevailing GBRs and green operation and maintenance

No.	Prevailing GBRs (BREEAM, LEED, CASBEE, GM)	Green operation and maintenance	
	Aspects most considered	Dimension: green building	Dimension: green management policy
1	Energy	Daily energy conservation	
2	Site	Sewage and waste disposal facility improvement	
3	Indoor Environment	Indoor environment quality	
4	Land and Outdoor Environment	Biodiversity	
5	Material	Construction waste reduction	
6	Water	Water infiltration and retention	
7	Innovation		Green corporate social responsibility Green customer education Green image promotion Certificate of building proper function

and greenness of buildings by construction authorities, foreign organizations, or private consulting companies [5].

Today, numerous GBRs have been developed around the world to assess the sustainability of buildings. Most GBRs are specifically adapted to suit the country's building industry in which they are built and to meet the unique needs of the buildings of that country. The GBRs announces that a building is eco-friendly and environmentally safe, reflecting what widespread green components have been implemented and describes the sustainable values and practices used [5]. The comparison of the prevailing GBRs evaluation criteria and Green operation and maintenance element stated in Table 7.

It can be seen that the prevailing GBRs which are the most considered are also mentioned as indicators in Green Operation and Management. The dimension of Green Building has five aspects that are similar to the prevailing GBRs that are energy, site, indoor environment, land and outdoor environment, material, water, and innovation. Moreover, the dimension of Green Management Policy has indicators that are green corporate social responsibility, green customer education, green image promotion, and certificate of building proper function are considered as "innovation" in the prevailing GBRs. This research is in line with some previous research by Hwang [5].

5 Conclusion

The structure for the implementation of Green Operation and Maintenance as part of GSCM in construction consists of two dimensions, i.e. Green building and Green management policy. These dimensions are translated into 13 elements that consist of 9 elements of green building dimensions (Greenery (vegetation planning), Water infiltration and retention, Daily energy conservation, Water conservation, CO₂ emission reduction, Construction waste reduction, Sewage and waste disposal facility improvement, Biodiversity, and Indoor environmental quality. While the other 4 are the elements of Green management policy, i.e. Green Corporate Social Responsibility, Green Customer Education, Green Image Promotion, and Certificate of Building Proper Function. These elements are translated into 21 indicators that consist of 17 indicators of Green building dimensions and 4 indicators of Green management policy.

These indicators are ways to keep the building or deliverables environmentally friendly during the O&M phase. Compared with other previous research, this study is in unity with the framework of GSCM implementation in the construction industry, which has integrated PLC into the model. This research also presents a structured model from concept, dimensions, elements, and indicators. Further research could develop the detailed measurement scale to complete the measurement tools. Furthermore, the research can also be done by conducting empirical studies in construction projects to validate the indicators and measurement tools.

Acknowledgements This research is partially funded by the Indonesian Ministry of Education and Culture under the Basic Research of Higher Education Excellence Program, managed by Diponegoro University.

References

1. Hermawan F (2014) Kapabilitas Dinamik Sektor Konstruksi Gedung di Daerah Menuju Keberlanjutan Pembangunan yang Realistis: Pendekatan Studi Kasus Kegagalan Konstruksi dan Bangunan di Jawa. In: Kumpulan Tulisan #UntukIndonesia. PPI UK, United Kingdom
2. Alwi S, Keith H, Mohamed S (2002) Non-value adding activities: a comparative study of Indonesian and Australian construction project. In: Proceedings IGLC-10, Gramado
3. Aloini A, Dulmin R, Mininno V, Ponticelli S (2012) A conceptual model for construction supply chain management implementation. In: Smith SD (ed) Proceedings of 28th Annual ARCOM conference. Edinburgh, Association of Researchers in Construction Management, pp 675–685
4. Beamon BM (1999) Designing the green supply chain. *Logist Inf Manage* 12(4):332–342
5. Hwang BG (2018) Performance and improvement of green construction projects—management strategies and innovations, 1st edn. Elsevier Inc., United Kingdom
6. Watt A (2014) Project management. Creative Commons Attribution
7. Hoerber JG, Alsem DM, Willems PH (2015) The management of information over the life cycle of a construction project using open-standard BIM. In: Proceedings of the 32nd CIB W78 conference, Eindhoven

8. Wibowo MA, Handayani NU, Mustikasari A (2018) Factors for implementing green supply chain management in the construction industry. *J Ind Eng Manage* 11(4):73–89
9. Wibowo MA, Handayani NU, Farida N, Nurdiana A (2019) Developing indicators of green initiation and green design of green supply chain management in construction industry. *E3S Web Conf* 115:02006
10. Farida N, Handayani NU, Wibowo MA (2018) Developing indicators to implementing green material management in construction industry: a literature review. *E3S Web Conf* 73:08009
11. Farida N, Handayani NU, Wibowo MA (2019) Developing indicators of green construction of green supply chain management in construction industry. *IOP Conf Ser Mater Sci Eng* 598:01201
12. Kartam NA (1996) Making effective use of construction lessons learned in project life cycle. *J Constr Eng Manage* 122(1):14–21
13. Oberlender GD (2000) *Project management for engineering and construction*, 2nd edn. McGraw-Hill, New York
14. Olanipekun AO, Chan APC, Xia B, Ameyaw EE (2016) Indicators of owner commitment for successful delivery of green building projects. *Ecol Ind* 72:268–277
15. Zainol NN, Mohammad IS, Baba M (2014) Critical factors that lead to green building operations and maintenance problems in Malaysia: a preliminary study. *Adv Mater Res* 935:23–26
16. Asmone AS, Conejos S, Chew MYL (2019) Green maintainability performance indicators for highly sustainable and maintainable building. *Build Environ* 163:106315
17. Green Building Council Indonesia (2013) *GREENSHIP Untuk Bangunan Baru Versi 1.2*
18. Chan ALS, Chow TT (2013) Evaluation of overall thermal transfer value (OTTV) for commercial buildings constructed with green roof. *Appl Energy* 107:10–24
19. Ng ST, Wong JM, Skitmore S, Alin V (2012) Carbon dioxide reduction in the building life cycle: a critical review. In: *Proceedings of the institution of civil engineers-engineering sustainability*
20. Levine M, Ürge-Vorsatz D, Blok K, Geng L (2007) Residential and commercial buildings. In: *Fourth assessment report of the intergovernmental panel on climate change*, Cambridge, United Kingdom and New York
21. Umum KP. Deskripsi Gedung Utama Kementrian Pekerjaan Umum
22. Kautz JL (2015) Green building with onsite wastewater treatment systems
23. Wei W, Ramalho O, Mandin C (2015) Indoor air quality requirements in green building certifications. *Build Environ* 92:10–19
24. Brown JD (2012) Corporate responsibility in the UK construction industry: a study of activities and reporting. Thesis. University of Nottingham
25. Zhao ZY, Zhao XJ, Davidson K, Zuo J (2012) A corporate social responsibility indicator system for construction enterprises. *J Clean Prod* 29–30:277–289
26. Solvalier I (2010) Green marketing strategies—case study about ICA group AB. Thesis. Karlstad University—Karlstad Business School
27. PT PP (Persero Tbk.) (2011) Green building for better living—Pembangunan Berwawasan Lingkungan untuk Kehidupan yang Lebih Baik. *Sustain Rep*
28. Umum Nomor PMP (2007) 25/PRT/M/2007 Tanggal 9 Agustus 2007 Tentang Pedoman Sertifikat Laik Fungsi Bangunan Gedung
29. Tam H, Taruna (2016) Green management, road to sustainability and corporate efficiency. *Int J Appl Res* 2 (1):586–590

Proposed Workflow of 3D Modelling Conversion and Enhancement in Quantity Surveying Profession



Lam Tatt Soon, Hasnanywati Hassan, Nazirah Zainul Abidin,
Myzatul Aishah Kamarazaly, Boon Tik Leong, and Kenn Jhun Kam

Abstract The three-dimensional (3D) models created by BIM modellers have limitations in providing accurate quantities following the standard method of measurement for a bill of quantities preparation. This creates problems for QS in preparing cost estimation, taking off and bill of quantities. Several QSs in Malaysia create a 3D model internally for quantities and costing purposes using QS software without further enhancing the 3D model owing to a software limitation. Therefore, this research aims to propose a workflow of 3D modelling conversion and enhancement in the quantity surveying profession to promote proactiveness for QS in enhancing their competitiveness in developing a data-rich 3D model based on designers' drawings and specifications. To achieve this aim, a case study has been conducted on a 25-storey condominium project in Malaysia to validate the proposed workflow. The 3D model created by a quantity surveying firm has been exported to an Industry Foundation Classes (IFC) file and hence has been enhanced in BIM modeller software. This research will serve as a guidance to QS to strengthen their competencies in developing a data-rich 3D model in implementing BIM in future.

Keywords 3D modelling · Quantity surveying · Workflow · Conversion · Enhancement

1 Introduction

The Malaysian government encourages construction players such as design consultants and QSs to apply Building Information Modelling (BIM) to construction projects to reduce construction projects problems and disputes [10]. The Eleventh Malaysia Plan (2016–2020) clearly emphasises that the use of technology, such

L. T. Soon (✉) · M. A. Kamarazaly · B. T. Leong · K. J. Kam
Taylor's University, No 1, Jalan Taylors, 47500, Subang Jaya, Selangor, Malaysia
e-mail: Lamtatt.soon@taylors.edu.my

L. T. Soon · H. Hassan · N. Z. Abidin
Universiti Sains Malaysia, 11800, Gelugor, Penang, Malaysia

© The Author(s), under exclusive license to Springer Nature Singapore Pte Ltd. 2022
S. Belayutham et al. (eds.), *Proceedings of the 5th International Conference on Sustainable Civil Engineering Structures and Construction Materials*, Lecture Notes in Civil Engineering 215, https://doi.org/10.1007/978-981-16-7924-7_78

1207

as building information modelling (BIM) is crucial in improving the efficiency of construction project implementation. Additionally, the Fourth Industrial Revolution (4IR) has introduced digital technologies to the construction industry, where BIM has become the central repository for collating digital information about a construction project [13]. Moreover, the Construction Industry Development Board (CIDB) developed the Malaysian BIM roadmap for the development of a Malaysian BIM strategic implementation plan [8]. In short, the Malaysian government is putting efforts to improve the AEC industry, and information technology has become significant in recent years.

In BIM implementation, the client is the critical player for BIM implementation, initiating a management team to handle the BIM collaboration among all team members in the current practice. Architects, engineers, QSs, and other consultant team members collaborate in preparing a BIM which is suitable for 4D scheduling and 5D costing. However, the BIM environment in Malaysia is slightly different. Most of the construction projects in Malaysia is currently implementing design-bid-build procurement. The design-bid-build procurement is ineffective in BIM due to the high separation and fragmentation in the construction supply chain, which brings ineffectiveness of the project management and control [6]. Despite the many years of criticism over this separation of design and construction, the fragmentation and poor project coordination are challenging the productivity of BIM [1]. With this constraint of BIM, even though the Malaysian government is putting efforts to improve BIM in the construction industry, the BIM implementation in Malaysia is still in the infancy stage.

Other than collaborating with designers to prepare a BIM model, several quantity surveying firms develop 3D model individually in a quantity surveying software for taking-off and cost estimation preparation following the standard method of measurement [5, 7]. This approach allows quantity surveyors (QSs) to reduce the time spent on measurement and giving consultants more time to analyse data against benchmark information to provide valuable feedback to the design team on building efficiencies [16]. Through the automatic quantification, human error and inaccurate drawing interpretation during measurement will be eliminated. This function is subtly increasing the efficiency as it will avoid the time consuming and duplicate process of quantification [17]. The new technologies have the potential to provide competitive advantages in increasing opportunities and lowering costs [15].

Unfortunately, the developed 3D model is not further enhanced to obtain the benefits of BIM. The developed 3D model cannot be shared directly with other construction players owing to the technical issues of the file conversion. In other words, solving the 3D modelling conversion from the quantity surveying software may allow construction players to take advantage of BIM in Malaysia. In short, Quantity Surveying firms require a transformation to sustain in the changing environment to convert the 3D model into a BIM model to obtain the benefits of the BIM.

Therefore, this research focuses on creating a workflow to guide QSs in converting and enhancing the 3D model prepared for cost estimation purposes in BIM software

after receiving the construction data from the designers such as architects and engineers. QS can serve the data-rich 3D model as a speciality competency service for developers to preserve the cost data.

2 The Workflow of 3D Modelling Conversion and Enhancement

In a conventional BIM implementation, QSs use different systems which may be cumbersome in mapping the quantities generated from the BIM model into the current bill of quantities format, since each of the elements or measurements is defined differently [14]. Most BIM designers' tools can perform quantity abstraction, but these applications lack the functions in cost estimation. Additionally, the accuracy of quantities take-off is highly dependent on the BIM model designed by the designers [11]. QSs extract the quantities from the 3D Model and produce cost estimation accordingly [11]. It is difficult to find a clear-cut job scope on the responsibilities of quantity accuracy when errors occur because both QS and designer contributed to the quantities.

In Malaysia, several QSs create 3D models based on local standards of measurement and prepare the bill of quantities directly after the quantities have been generated from the 3D model. This 3D modelling and bill of quantities preparation process involves the set-up of the project information, import and calibrate the two-dimensional computer-aided design (CAD) drawings, build a 3D model based on designers' CAD drawings, followed by extracting and classifying building quantities for a bill of quantities preparation [19]. This workflow is different compared to BIM and traditional quantities take-off and bill of quantities preparation process. Through this 3D modelling approach, the 3D model and quantities created and generated by QSs manage to avoid software interoperability issue and conflicts between consultants. However, this 3D model is hardly shared with others owing to the technical concerns on file conversion.

In order to solve the technical concerns of 3D modelling conversion from the quantity surveying software, this research aims to create a workflow to guide QSs in converting and enhancing the 3D model prepared for cost estimation purposes. The workflow of the 3D modelling conversion and enhancement process consists of 3 main stages, notably stage 1: developing a 3D model, stage 2: 3D model conversion and stage 3: 3D model enhancement.

2.1 Stage 1: Developing a 3D Model

In the first stage of the workflow for the conversion and enhancement process, all inputs and namely 2D conceptual drawings, 2D building plans, CAD/Portable

Document Format (Pdf). Tender drawings and construction information has to be transformed in creating a 3D model. Quantity Surveying firms need to solve people constraints for their staff (input), as well as process and technological constraints for computer hardware and software application.

Quantity surveying firms will be able to create a 3D model which is suitable for costing and crash detection purposes by collecting the inputs from other designers and consultants. The QSs create the 3D model based on designer CAD drawings (tender drawings) following the standard method of measurement (SMM2) in Malaysia. QSs can auto-generate quantities from the 3D model which according to the standard method of measurement (SMM2) for measurement for a bill of quantities preparation purposes.

2.2 Stage 2: 3D Model Conversion

In the second stage of a proposed workflow for the conversion process, the QS needs to convert the 3D model into an openBIM (IFC) file after the 3D model is developed in the quantity surveying software. Next, the 3D model is imported into the designer software for further enhancement to develop a BIM model. BuildingSMART certified software which supports the import and export of IFC2x3 files are recommended for this approach on data-rich 3D modelling implementation. All of the errors in the 3D model conversion must be solved.

2.3 Stage 3: 3D Model Enhancement

In the third stage, a further enhancement process is required after the 3D model has been successfully imported and converted into the designer software to enhance the 3D model. Building components and objects, specifications, cost data, etc. can be inserted into the converted 3D model. In the 3D modelling enhancement, functional attributes such as installation durations, construction costs and objects' information can be added in the BIM software to improve the 3D model [18]. This enhancement enables users to integrate and reuse building information through the lifecycle of a building since data-rich 3D modelling is currently the most common denomination for a new way of approaching the construction and maintenance of buildings [3, 12]. Additionally, QSs can use the BIM software to simulate the behaviour or performance of the enhanced 3D model within a computer system before the physical construction of the building [2]. All of these benefits of BIM allow QSs to extend their potential competencies in providing clients with better service with reasonable professional costs compared to the employment cost of a new BIM expert externally. Figure 1 summaries the whole process of the proposed workflow in three stages for 3D conversion and enhancement based on current QS practice.

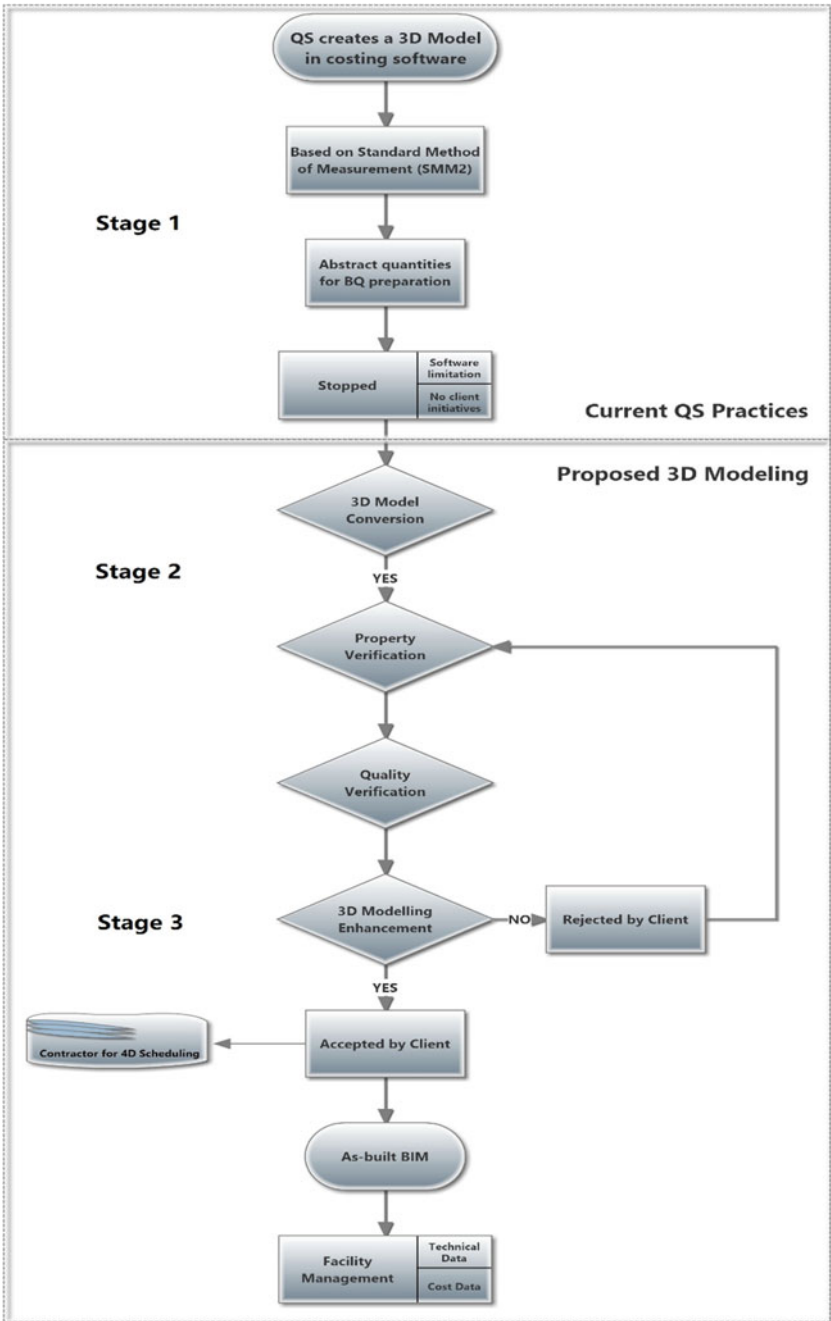


Fig. 1 Proposed three stages of a 3D modelling conversion and enhancement workflow based on QS workflow

3 Research Methodology

This 3D modelling conversion and enhancement process has two stages: conversion and enhancement. Conversion refers to file format conversion from one software to another, followed by the scrutiny process, notably property and quality verification, to ensure the accuracy of the 3D model and to examine any data loss in the conversion process. Property verification involves the process of checking the number of building components, while the quality verification focuses on examining the accuracy of the 3D model. The QS shall prepare a checklist for the 3D model property verification process such as checking the number of building components notably columns, beams, slabs, doors, windows, finishes and so on, followed by the quality verification process which examine the scale of building components in the designer BIM software and components quantities etc. In the conversion phase, the 3D model created by QS is exported into the OpenBIM (IFC format) and then imported into the designer BIM software for enhancement purposes to develop a BIM 3D model. Open BIM (IFC format) is selected in this research because it is a standard established by the BuildingSMART to allow for model exchange between various commercial BIM software vendors. The open BIM concept can rationalise the whole AEC process and make it more cost-effective [9].

Enhancement refers to the additional BIM components input, technical data and cost information. At this stage, some building components such as doors, windows, landscaping, road work and pavement, and other product details can be improved and added into the 3D model in the designer BIM platform. The enhancement of the model is in the form of specification of the building components, the brand of materials and cost data for the building materials, which can be inserted into the 3D model components' properties to enhance the information of the 3D model and make it an enhanced 3D model.

The overall conversion and enhancement process proposes that the QS prepare a 3D model based on CAD drawings followed by abstracting the quantities for cost estimation purposes. Next, the conversion process takes place, followed by the process of scrutiny, which includes property verification and quality verification. Finally, the 3D model enhancement process shall take place to enhance the BIM 3D model.

The interaction between the BIM and the cost estimation software is often ensured via IFC which does not perform flawlessly as there is a loss of information with each import–export process [14]. With the proposed workflow, these issues can be reduced or resolved to develop a data-rich BIM model.

3.1 Data Collection

The research concept had been explained to the construction players and one of the quantity surveying firms agreed to collaborate in this analysis. A 25-storey apartment

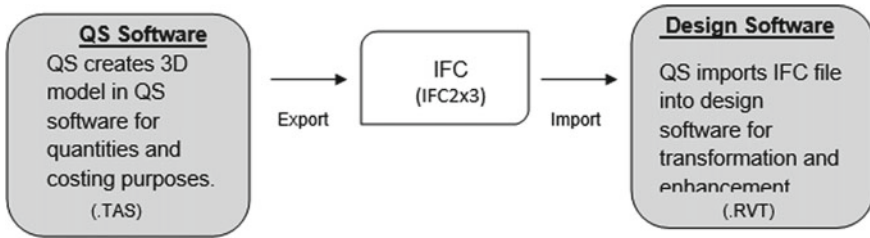


Fig. 2 IFC conversion and enhancement process and files formats

building in Malaysia which had been created by the QS was exported to an IFC file. This 25-storey apartment building is an on-going project; hence the quantities of building components are not allowed to be recorded in this research due to the private and confidential circumstances.

Project Details:

- Type of project: Private Residential Project.
- Building Type: Apartment.
- No of storey: 25 storey.
- Location: Malaysia.

This 25-storey apartment was exported into an IfC file from the QS software by the quantity surveying firm. Next, the IfC file was imported and converted into the design BIM Software. Figure 2 summaries IfC conversion and enhancement process and files formats.

4 Analysis

For the 3D model conversion and enhancement proposed between two different BIM software, the exported IFC file from the 3D model prepared by QSs is imported into a designer BIM software for conversion and enhancement purposes. A QS is suggested to prepare a bulk checklist for the IFC file verification, such as checking the scale of components in the BIM software, pilot checking for components quantities etc. Due to the QS software limitation, some BIM components have to be improved and added in the designer BIM software to enhance the model presentation and components details such as landscaping, road work and pavement, product details etc. Last but not least, the enhanced 3D model can be used for project scheduling (4D) and maintenance purposes (Fig. 3).



Fig. 3 File conversion and data lost correction process in BIM software

4.1 File Conversion and Data Lost Correction in BIM Software

A 25-storey apartment building IFC model was successfully converted into the designer’s BIM software, and the scale of the whole model is absolutely correct. The majority of the components can be converted into the BIM software notably beams, walls, floors, railings, door and window openings etc. However, some components such as finishes etc. cannot be converted into the BIM software, notably wall finishes, floor finishes and ceiling finishes. This building is using load-bearing walls; hence the column is not a significant component in this building. Next, all the errors and data lost mentioned in the BIM software have to be solved and improved to produce a data-rich 3D model.

The 3D model is successfully converted into a designer BIM software through an IFC file conversion process. However, several errors are detected by the designer’s software (Table 1).

Based on the errors detected by the software, the majority of the errors include primary wall and floor Slab with 125 mm thickness (S-125 mm). To clarify the errors of the IFC conversion, the errors have been sent to the trainer of the Certified Software training company in Malaysia (Table 2).

The feedback from the software’s expert mentioned that 3 out of 5 errors could be ignored. Three errors on Floor S-125 mm and one error on the basic wall are needed to be rectified. This serves as good guidance for BIM model quality checking process while basic walls and 125 mm thick floors are essential factors in this model which affect the quality of this 3D model.

Error 2: Highlighted floors overlap (Fig. 4).

There is a duplicated line within the two-floor slabs in the floor plan and the ‘Edit Boundary’ function in the BIM software allows the user to change the boundary line

Table 1 IFC conversion errors

No.	IFC conversion errors
1	Cannot keep elements joined
2	Highlighted floors overlap
3	IfcProfileDef ## has a very short segment that can’t be fixed
4	Line in sketch is slightly off axis and may cause inaccuracies
5	Highlighted walls overlap. One of them may be ignored when Revit finds room boundaries. Use cut geometry to embed one wall within the other

Table 2 IFC conversion errors explanations and decisions

IFC conversion errors	Decisions
(1) It is usually because the element failed to join. This sometimes can be ignored, but if affects the aesthetic of the design, then something will need to be fixed	Ignored
(2) There's a duplicated floor within the boundary sketch	Edit boundary
(3) It seems like it could be ignored	Ignored
(4) This is probably the line was not really 90° from the adjacent line. It could have been like 90.002°. However, sometimes it could be ignored if it is not that significant	Ifc components are replaced in the BIM software
(5) Two walls would have been placed in the same place, or even one of them was extruding partially into the other one. This needs to be looked into. You can click on show element and it will highlight to you where it is	Trim/extend to corner function to join the walls

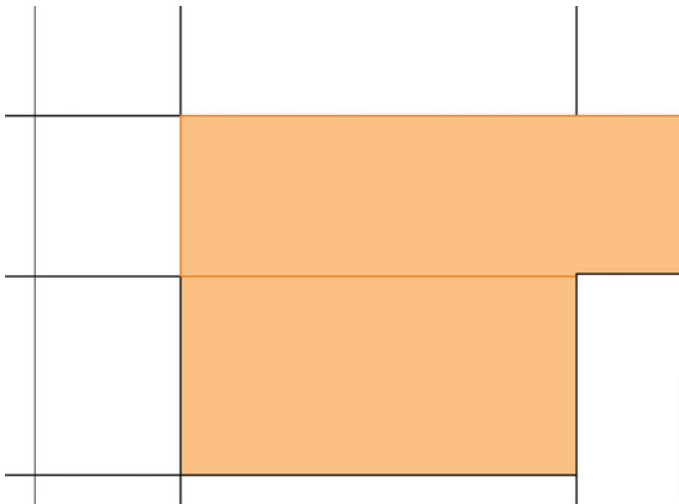


Fig. 4 Highlighted floors overlap

of two-floor slab individually. QS has to edit the boundary of each floor slab to solve this error manually (Fig. 5).

Error 4: Line in Sketch is slightly off axis and may cause inaccuracies (Fig. 6).

The Ifc Opening elements for lift core walls are detected slightly off axis. The ifc opening elements are deleted and replaced with BIM software opening elements at the same dimension. In general, these errors can be ignored since these do not significantly affect the 3D model and quantities (Fig. 7).

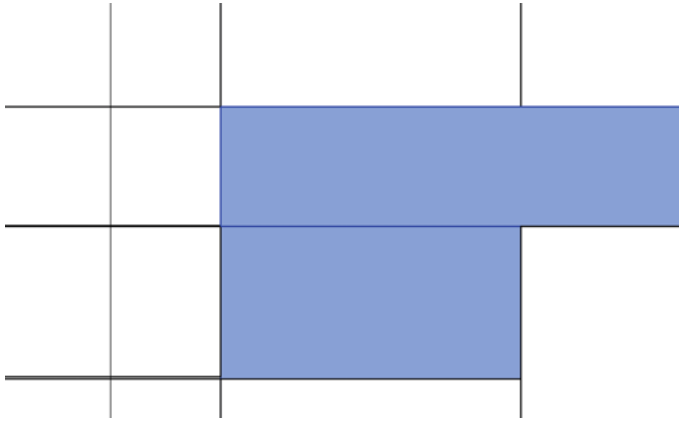


Fig. 5 The corrected boundary of two slabs

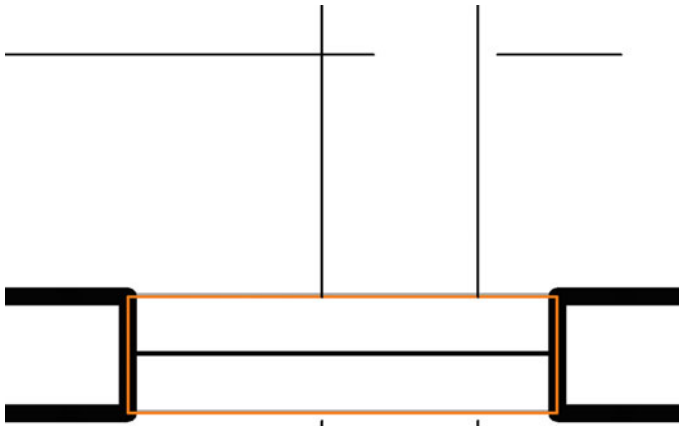


Fig. 6 Line in sketch is slightly off axis and may cause inaccuracies

Error 5: Highlighted walls overlap (Fig. 8).

Based on the BIM software auto identification, the software shows the highlighted overlapping walls in the floor plan. One of the walls is extruding partially into the other one. Trim/extend to corner function in the BIM software can solve this error while QS has to identify each overlapping wall and combine all the walls based on the floor plan (Fig. 9).

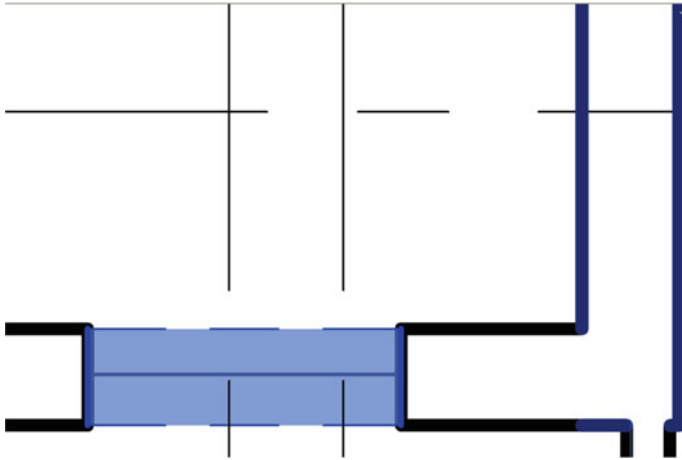
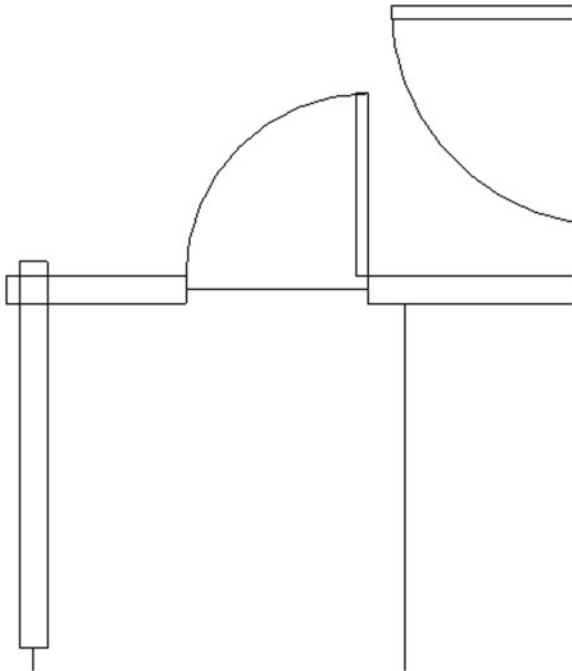


Fig. 7 The ifc opening element is replaced by a new BIM software opening

Fig. 8 Highlighted walls overlap



4.2 3D Model Component Enhancement in BIM Software

Next, several enhancements for the IFC conversion are prepared after the IFC conversion. First, all doors and windows are inserted into the 3D model based on the

Fig. 9 Combined overlapping walls

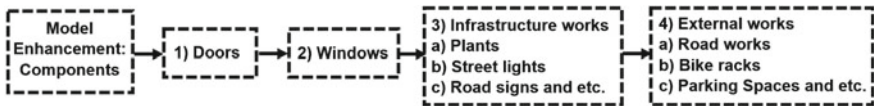
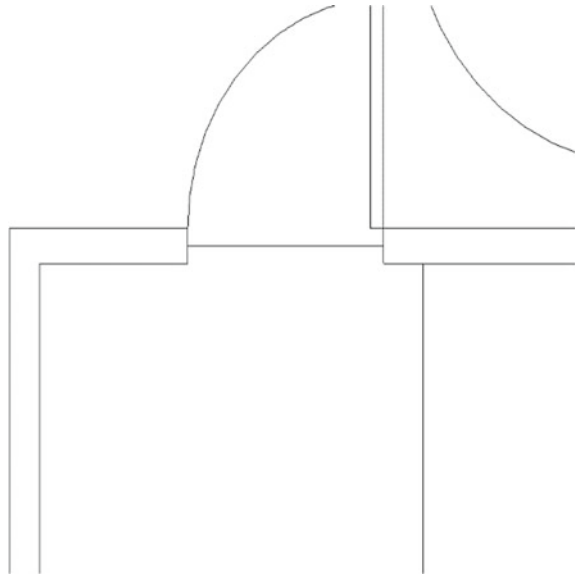


Fig. 10 The BIM model component enhancement process in the designer BIM software

windows and doors names stated in the opening. IFC files converted from 3D modelling software have limitations on doors and windows which are needed to be enhanced in the BIM software (Fig. 10).

Ground-level of the building, infrastructure work and external work elements notably plants, street lights, road work, bike rack, parking space, road sign etc. are created for the 3D model in the BIM software. These approaches manage to enrich the project components of the 3D model as well as improve the overall presentation of the 3D model.

4.3 3D Model Description Enhancement in BIM Software

Last but not least, the specification of the building components, the brand of materials, and cost data for the building materials are inserted into the 3D model components' properties in the BIM software to enhance the information of the 3D model for management and maintenance purposes (Fig. 11).

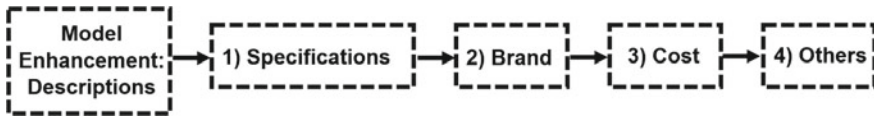


Fig. 11 3D model description enhancement process in BIM software

Additionally, this 3D model is successfully converted and enhanced in the BIM software, hence, other information such as building life cycle information, green building information, and waste management information is recommended to be inserted into the 3D model in future to serve the different purposes of building management and maintenance in 3D modelling.

For traditional BIM quantity take-off (QTO), the QTO process consists of four steps: BIM modelling, physical quality verification, property verification and quantity take-off. [4]. However, 3D modelling is implementing the reverse approach which comprises four steps: quantity take-off, property verification, physical quality verification and BIM modelling. In conversion BIM implementation, QS has to prepare the quality verification and adjustment based on the standard method of measurement before the quantity take-off on the BIM designed by architect and engineers. In short, the implementation of conventional BIM entirely depends on construction designers' initiatives.

However, QS manages to take the initiative in 3D modelling implementation to prepare the quantities take-off and IFC model, followed by the IFC conversion and quality verification. However, IFC conversion and quality verification are optional competencies for QS. In short, this proposed workflow extends QS competencies which allows QS to enhance the 3D model into a data-rich 3D model. Additionally, contractors can further improve the data-rich 3D model in BIM software prepared by QS for as-built BIM in 6D BIM preparation.

5 Conclusion

In summary, the proposed workflow of 3D modelling conversion and enhancement process in the quantity surveying profession is expected to promote the proactiveness of QS in enhancing their competitiveness in developing a data-rich 3D model. A 25-storey apartment building IFC model is successfully converted into the BIM software, and the scale of the whole model is absolutely correct. The majority of the components can be converted into the BIM software notably beams, walls, floors, railings, door and window openings etc. All the errors and data lost mentioned in the BIM software are solved, and the 3D model is successfully converted into the designer BIM software.

Next, several enhancements for the IFC transformation are prepared after the IFC conversion. First, all doors and windows are inserted into the 3D model based on the windows and doors names stated in the opening. Ground-level of the building,

infrastructure work and external work elements are created for the 3D model in the BIM software to enrich the project components of the 3D model as well as improve the overall presentation of the 3D model. Last but not least, the specification of the building components, the brand of materials, and cost data for the building materials are inserted into the 3D model components' properties in the designer BIM software to enhance the information of the 3D model for management and maintenance purposes. A future study is recommended to enlarge the study to quantity surveying firms oversea notably Hong Kong since quantity take-off or measurement is also part of the significant QSs' tasks there. This future study manages to strengthen the QSs' initiatives in 3D modelling implementation, conversion and enhancement.

References

1. Aibinu A, Papadonikolaki E (2016) BIM implementation and project coordination in design-build procurement. In: Proceedings of the 32nd annual ARCOM conference, Association of Researchers in Construction Management, pp 15–24
2. Bazjanac V (2004, Oct) Virtual building environments (VBE)-applying information modeling to buildings. In: EWork and EBusiness in architecture, engineering and construction: proceedings of the 5th European conference on product and process modelling in the building and construction industry: ECPPM 2004, 8–10 Sept 2004x. Taylor & Francis, Istanbul, Turkey, p 41
3. Bryde D, Broquetas M, Volm JM (2013) The project benefits of building information modelling (BIM). *Int J Project Manage* 31(7):971–980
4. Choi J, Kim H, Kim I (2015) Open BIM-based quantity take-off system for schematic estimation of building frame in early design stage. *J Computational Des Eng* 2(1):16–25
5. Derrick (2018) Inspiring careers, Perunding Kos PKT&K. <http://www.quantitiesurveyorsmalaysia.com/careers/>. Accessed 5 Nov 2018
6. Forgues D, Lejeune A (2015) BIM: in search of the organisational architect. *Int J Project Org Manage* 7(3):270–283
7. Glodon (2018) Our customers—Overesea. <http://www-old.glodon.com/en/ourcustomers.aspx>. Accessed 5 Nov 2018
8. Hadzaman NAH, Takim R, Nawawi AH (2015, Sept) BIM roadmap strategic implementation plan: lesson learnt from Australia, Singapore and Hong Kong. In: Proceedings in 31st annual ARCOM conference, pp 611–620
9. Hallberg D, Tarandi V (2011) On the use of open BIM and 4D visualisation in a predictive life cycle management system for construction works. *J Inf Technol Constr (ITcon)* 16(26):445–466
10. Latiffi AA, Mohd S, Kasim N, Fathi MS (2013) Building information modeling (BIM) application in Malaysian construction industry. *Int J Constr Eng Manage* 2(A):1–6
11. Latiffi AA, Mohd S, Rakiman US (2015) Potential improvement of building information modeling (BIM) implementation in Malaysian construction projects. In: IFIP international conference on product lifecycle management. Springer, Cham, pp 149–158
12. Lee G, Sacks R, Eastman CM (2006) Specifying parametric building object behavior (BOB) for a building information modeling system. *Autom Constr* 15(6):758–776
13. Maskuriy R, Selamat A, Maresova P, Krejcar O, David OO (2019) Industry 4.0 for the construction industry: review of management perspective. *Economies* 7(3):68
14. Monteiro A, Martins JP (2013) A survey on modeling guidelines for quantity takeoff-oriented BIM-based design. *Autom Constr* 35:238–253
15. Olatunji OA, Sher W, Gu N (2010) Building information modeling and quantity surveying practice. *Emirates J Eng Res* 15(1):67–70

16. Orr B, Trotter A (2013) Benefits of BIM: collaborating to improve cost analysis, design build source. *Australian Eng Mach* 14:2013
17. Thurairajah N, Goucher D (2013) Advantages and challenges of using BIM: a cost consultant's perspective. In: 49th ASC annual international conference proceedings. Associated Schools of Construction
18. Volk R, Stengel J, Schultmann F (2014) Building information modeling (BIM) for existing buildings—literature review and future needs. *Autom Constr* 38:109–127
19. Zhao PA, Wang CC (2014) A comparison of using traditional cost estimating software and BIM for construction cost control. In: ICCREM 2014: smart construction and management in the context of new technology, pp 256–264

Industry 4.0 in the Malaysian Construction Industry and Its Adoption Challenges



Mohd Afiq Azinuddin Bin Tayib, Nor Azmi Bakhary,
and Che Khairil Izam Che Ibrahim

Abstract The last few decades have seen an exponential growth in the industrial revolution. At present, many developing countries are trying to adapt themselves to the current trend of Industry 4.0 and this also includes Malaysia. Despite that, there is a lack of attention given towards its application in the construction sector especially for the small and medium-sized enterprise (SMEs). An extensive literature review regarding the current state of the Industry 4.0 concept in Malaysia and the construction industry including the challenges of adopting it was conducted. Only a limited number of documents were found in Malaysia in answering the call for Industry 4.0 such as the ‘Industry 4ward’ policy by the Ministry of International Trade and Industry (MITI) and ‘The Race Towards Industry 4.0’ by the Malaysian Productivity Corporation. The silver lining of this however showed that there is a growing interest in the academia world between the subject of Industry 4.0 and the construction industry over the years. There exist few challenges for the adoption but the main challenges found were lack of resources, market issues and organization issues. Thus, future studies should focus on overcoming these challenges first in order to successfully adopt it to the industry. This could also help in forming up the foundations for the adoption of Industry 4.0 in the construction industry too through a proper framework in the near future.

Keywords Industry 4.0 · SMEs · Construction industry · Challenges

1 Introduction

The first concept of industrial revolution was introduced to the world about 300 years ago. It was the tipping point of industrialization and the creation of the ever-transforming industrial revolution, which has contributed exponentially to the development of today’s technology. During those early times, or to be more precise, the First Industrial Revolution, the power of steam and water were harnessed and used

M. A. A. B. Tayib (✉) · N. A. Bakhary · C. K. I. C. Ibrahim
School of Civil Engineering, College of Engineering, Universiti Teknologi MARA (UiTM), Shah Alam 40450, Selangor, Malaysia

greatly by the agricultural sector in concretizing the country's economic value [1]. This was then followed by the Second Industrial Revolution at around the 1870s which displayed the function of electrical energy in the assembly line creation and during these times as well, it is important to know that the basic output was highly reliant on human capabilities. Then in the 1970s, a transformation which leaned more towards the usage of electronics and IT invention was founded and called as the Third Industrial Revolution [2]. And nowadays, there is a new form of technology that tries to incorporate the innovative change from mechanical devices and analogue electronics into today's digital technology called the Fourth Industrial Revolution. The basic foundation of this concept is the connectivity of people and technology with one another. The summarized development of all of the Industries are displayed in Fig. 1.

This concept of The Fourth Industrial Revolution or in short Industry 4.0 originated from Germany where its main purpose was to create a well-organized policy framework that could help in supporting the governments' industrial processes automation [3, 4]. Industry 4.0 was introduced to the general public as "Industries 4.0" with the general idea of implementing a developmental process of the combination between the exchange of data and automation to its country's manufacturing industries [5]. Some of its other purposes was to highlight the needs to improve the globalization of German industrial competition which is aligned to its 2020 High-Tech Strategy [6].

Hermann et al. [7] mentioned that the main objective of Industry 4.0 relates to the idea of the integration of information technologies and techniques and communications technology with its production processes. It focuses on the individual needs of the customer rather than as a whole when making products. And for that, this will contribute to the uniqueness and high quality of the finished product that can be priced the same as mass-produced goods. In other words, production methods combined with the intelligent digitally connected system makes up the gist of the Industry 4.0 concept.

According to Oztemel and Gursev [8], the relatively new concept of Industry 4.0 is not only well known in academia but also in the industry. In simple definition, Industry 4.0 may refer to the Internet of Things (IoT) and the Internet of Services

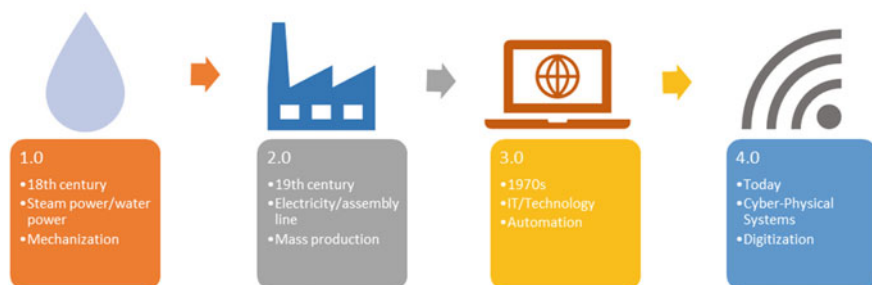


Fig. 1 Industry 4.0 concept development

combined together under the manufacturing ecosystem where all business industries from all over the world can control and connect intelligently with their factories, machineries and warehousing facilities through cyber-physical systems through the sharing of information [9]. Some other synonyms that relate to this concept were cyber-physical systems (CPS), smart factory/manufacturing and Internet of Things [10]. Schmidt et al. [11] defined Industry 4.0 as the superposition of several technological developments that embrace both products and processes and related to the cyber physical systems that describe the integration of digital with physical workflow. In a much simpler definition, Industry 4.0 is the combination of complex physical machinery and devices with networked sensors and software [7].

Companies can gain a lot of benefits by leveraging the current technologies of Industry 4.0. As mentioned by Alcácer and Cruz-Machado [12], the technology of cloud computing can effectively help in cost reduction through the savings gained by removing older IT infrastructures. Cost savings could also be gained through additive manufacturing or 3D-printing since by doing so will reduce the upfront cost due to the fact that there is no need for product specific manufacturing investments [13]. Besides that, operations for the product and time needed to market products would also be reduced at the same time [14].

This advancement in the industry will greatly benefit the small and medium-sized enterprises (SMEs) in their abilities to invest in new technologies and help to connect global development and reduce the impacts which had been produced by the previous industrial revolutions [15]. The concept of Industry 4.0 is one of the major factors of sustainable business performance growth among the SMEs through the elements of big data, Internet of Things, and smart factory [16]. In this paper, a literature review on the current state of Industry 4.0 in Malaysia and the construction industry including the challenges of Industry 4.0 adoption was conducted.

2 Industry 4.0 in the Malaysian Context

The significant value of Industry 4.0 has been acknowledged by the Malaysian government level. The Malaysian Industry and Development Authority (MIDA) has provided tax incentives for the firms that use Industry 4.0. The implementation of Industry 4.0 has also been recognized as a macro strategy to promote economic growth in the RMK11 [17]. In Malaysia, a number of documents had been produced to encourage the usage of Industry 4.0 to the industry [18]. One of them is called the 'Industry 4ward National Policy on Industry 4.0' introduced by the Ministry of International Trade and Industry in 2018. They highlighted that there are three main factors that affect the adoption of Industry 4.0 which are people process and technology. The policy was made to address the ongoing competition of nations and firms, increased regulations and to change the customer behavior [19]. Other than that, the transformation of the manufacturing industry through Industry 4.0 is also in line with the United Nations Sustainable Development Goals (SDGs), especially in support

of Goal #9 and Goal #12 which is about Industry, Innovation and Infrastructure and Responsible Consumption and Production [20].

There seems to be a rise in the agreement about the introduction of Industry 4.0 over the years by the majority of Malaysian executives as compared to their peers in a global context as reported by the “2018 GE Global Innovation Barometer”. China, the U.S. and Japan are the three-leading innovation champions in this concept followed by Germany, Sweden, South Korea but nevertheless, Malaysia has become the leading country globally when it comes to the measurement of innovation based on the GE Global Innovation Barometer 2018 report [21]. This marked a positive start for its implementation in the country, however a report by the GE Global Innovation Barometer showed that the Malaysian businesses is only looking forward to the incremental innovation and internal innovation in terms of their innovation strategy which is once again, varies greatly from their global peers as quoted by the Senior Associate of MIGHT, Dr. Ibrahim Abu Ahmad [22]. The main challenge that still remains in the country is also finding the skills and talent for it. The capabilities of the Malaysian workforce in applying these advanced knowledges, technologies and being innovative in this concept plays a huge role towards the country’s productivity growth in the future [23]. Another good point to add is that to ensure the long-term sustainability of the economic growth and development of the country, the issue of human capital development must be critically resolved first [22].

In Malaysia, the studies that concern with the topic of Industry 4.0 are still somewhat lacking on the governmental, industrial, and educational level. This is needed in order to provide guidance for the industry practitioners and the decision makers in the local government [18]. Malaysia can be considered as a new player of Industry 4.0, in which it has implemented some of the few Industry 4.0 technologies such as automation, IoT, robotics and big data analytics. Nevertheless, the lack of papers that discuss the topic of Industry 4.0 here in Malaysia are still clear. A lot of attention should be given towards the acquaintances and education of this concept to draw the industries and SMEs towards applying it to their businesses [24].

3 Industry 4.0 in the Construction Industry

The rapid growth of the world’s urban population has become a significant factor in the global construction industry [25]. One of these includes the increasing demand for affordable housing [26]. Not only this but most industries have undergone a transformation in incorporating innovation into their products and processes in alignment with their main operations. The application of Industry 4.0 towards the construction industry also plays an important role in the country’s economics. In the report posted by the Department of Statistics Malaysia [27], the value of construction work done in the third quarter 2019 contracted 0.6 per cent year-on-year basis, amounting to RM36.1 billion as compared to the second quarter which amounted up to RM35.9 billion. Based on a study made by Alaloul et al. [28], more than half of the respondents in the study were unaware of the implementation of Industry 4.0 in the construction

industry with only a third of them having been exposed directly to working experiences. Some other issues that exist in the engineering and construction sector is it does not grab a lot of opportunities when it comes to technological advancements and innovations.

The amount of research publications that relates to the topic of Industry 4.0 and construction have grown exponentially over the years and there is currently an active and clear yet unfinished discussion regarding the application of Industry 4.0 in the construction industry [29]. Figure 2 shows the growing annual publication trend when searching for the keyword ‘Industry 4.0’ and ‘construction industry’ using the Scopus and Web of Science online database.

A majority of these publications provide an overview of the capabilities of Industry 4.0 for the construction industry in terms of supply chain and practices. There are currently a lot of exploration and growth opportunities that relate to this concept in the construction industry since the pattern and structure in it are still in their conceptual and infancy stage [30]. However, the limited number of original papers that relate to Industry 4.0 and the construction industry demonstrated that there is still a lack of complete understanding on what Industry 4.0 entails for the construction industry. The current study only focuses on the conceptual part of adopting Industry 4.0 rather than providing the rigid theoretical development aspects of making it real. Other than that, most of the papers only talk about the existing technologies and the ways how these innovations can be used into different industries or sectors.

The introduction of Industry 4.0 is not something which is new to the construction industry. Some of its examples include intelligent machines, smart materials, digital technologies, sensor systems and the central repository for collating digital

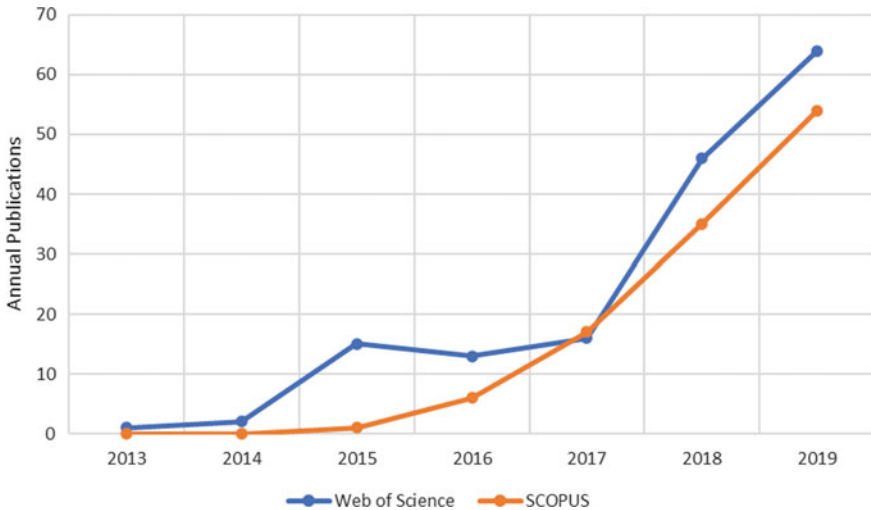


Fig. 2 Annual publications of ‘Industry 4.0’ and ‘construction industry’

information which is mostly being used nowadays which is the Building Information Modeling (BIM) [31]. At present, the construction industry is considered as a major contributor to the employment and economy of various countries [32]. The construction industry has also the highest growth of labor productivity in Malaysia as compared to other sectors such as manufacturing and agriculture in the second quarter of 2019 [27]. This provides a lot of growth opportunities in terms of skills and talents in the construction sector thus improving the country's economic development consequently.

This breakthrough of Industry 4.0 in the construction industry has proven to be a great demonstration that the availability of digital data and online digital access can be beneficial for the construction digitization and used automatically for the processing and gathering of electronic data into the value chain [33]. Even robotic technologies have also been merged with the construction industry and one of those examples is known as the construction automation technologies which produce the building elements, components, and furniture [34]. The combination of BIM into the IT environment and cloud computing has allowed the ease and enhanced decision-making of project deliverability that allows stakeholders to collaborate in different locations at the same time [31]. Some other benefits of the integration between IoT and BIM is it improves security and safety [35], the planning, managing, and monitoring of resources [36].

The adoption of the Industry 4.0 concept in the construction landscape can greatly improve the quality and productivity of construction and attract domestic and even foreign investors since it's capable of automating both the design and manufacturing processes and increase the chances of handling a heterogenous and significant amount of information [29]. The construction industry is significant for the development of social and economic growth of a nation and acts as a driver in producing infrastructures within an economy. Yet the adoption of Industry 4.0 or the latest technology such as Smart Site, simulation and virtualization is still at the infancy stage in which a majority of it is only concentrated on the usage of software [37].

4 Challenges of Implementing Industry 4.0

Industry 4.0 does have its benefits but at the same time, according to Xu et al. [38] it could contribute to a greater inequality and be able to disrupt labor markets in all sectors. The net displacement of human labors by machines might worsen the gap between the returns to capital and labor as humans are being substituted for labor across all industries. In this era driven by digital technologies, the most highly sought resources are not going to be the ordinary labor or capital but instead it will be those that have the capabilities of creating new ideas and innovations. In the near future, talent will become the critical factor of production [39].

The ability for the SMEs to invest in innovative technologies are also limited by the fragile state of the supply chain of the construction industry [40] and also due to the relatively huge gap that exists between the manufacturing and construction even

though both of them are categorized under the same group together [33]. Some other factors that contribute to the slow adoption of Industry 4.0 is the absence of an ideal process change strategy, implementation plan and strategy alignments [29]. A study made by Moeuf et al. [41] had found out that lack of proper expertise in the Industry 4.0 technologies and a short-term strategy mindset are what contributes to the slow adoption of the concept in the industry.

There are also the concerns of cybersecurity, the crimes of hacking and risk assessment as mentioned by [42] in the domain of Industry 4.0. Because through this concept of Industry 4.0, everything will be connected to everything else in the IoT thus this will certainly increase the weaknesses or vulnerabilities of any given network. The need to provide a much better digital security will play an important role because of it. Companies will need to assess all of the risk and create an ideal network which is related to the security [43]. Some of those risks that will be assessed are in terms of accessibility to the systems, threats from internal sources and external sources such as human error and the attack from cyber terrorists or hackers respectively [38]. The uncertainties and profitability that exist in the tendering systems can become a major barrier in introducing Industry 4.0 technologies to the companies [44]. Not only that, organizational resistance can also disrupt the implementation due to the fact that most employees, including the middle managers, are overly concerned about losing their jobs since necessary skills are required in mastering the new technologies. This can adversely impact the social environment within the company [45].

The increasing complexity, uncertainty, the fragmented supply chain, short-term thinking and its working culture [19] has become some of the major factors why the construction sector is in need of Industry 4.0 a new business model [33]. The lack of educational structure and professional level of the employees are one of the major challenges of introducing Industry 4.0 and the inability to see its return of investments had made it much more difficult [46]. Again, seeing it from the construction context, the approaches and innovation of construction automation are still in the infancy stage meaning only certain technologies are currently being used and utilized at the moment [47]. The current technologies that can be applied for the construction industry are still being discovered and investigated based on the increasing interest of the topic over the years.

In recent years, globally, there have been several studies made towards the SMEs in order to identify their state of interest in Industry 4.0. Whether it is the opportunities, benefits, challenges, or the formulation of framework for their adoption, this indicates that SMEs are the target group for the Industry 4.0 adoption. For example, in the UK, Masood and Sonntag [48] made a study of the SMEs there regarding its adoption challenges and benefits, while in Japan, Prause [49] identified the challenges of the Industry 4.0 technology adoption for the SMEs. There is even a study in the same nature about the SMES in Thailand as well by Haseeb et al. [16].

According to Schröder [44] there exists a crucial relationship between how Industry 4.0 is implemented and the size of the company it is being done upon. Large companies have an added advantage such as they are much more advanced in the application of their production plants and IT systems as compared to the SMEs.

Challenges	Authors	Haseeb et al. [16]	Misood & Sornpage [48]	Meunier et al. [41]	Prasse [49]	Schroder [44]	Müller [50]	Matt et al. [3]	Vedhota et al. [46]	Engaldi & Ulewicz [52]	Xu et al. [38]	Dallasega et al. [40]	Mishary et al. [29]	Lambers [42]	Horvath and Szabó [45]	Oesterreich and Feinberg [19]	Foller & Feldmüller [51]
Lack of financial support		x						x	x	x							
Lack of resources		x	x			x	x	x		x		x					
Market issues		x			x		x				x	x					x
Lack of awareness		x															
Knowledge constraints		x				x	x			x							x
Improper strategy				x		x							x				
Low level of standards						x											
Cyber security concern						x					x			x			
Organizational issues			x				x		x						x	x	x

Fig. 3 Challenges of Industry 4.0 adoption from other researchers

A good point to add is that the level on which Industry 4.0 is being distributed in the industry is highly dependent on the size of the enterprise. Large companies will benefit greatly in terms of efficiency when it comes to the usage of Industry 4.0 when compared to SMEs. For the SMEs, the biggest challenges that they have to deal with are the lack of uniform standards and data security, a cost–benefit analysis of the current relevant technologies and the development of an ideal strategy [44, 50]. The SMEs tend to face difficulties in implementing the Industry 4.0 as they are not used to utilizing highly skilled applications and technologies that revolve around the concept. Other than that, the unwillingness of them to invest in the latest technology due to the uncertainty whether it will bring a loss or a profit to their companies has become a major barrier for its introduction [51, 52]. Figure 3 summarizes the list of challenges based on the aforementioned research in the early passage.

Based on the results obtained, one of the most mentioned challenges would be the lack of resources, market issues and organization issues. Organization issues such as the working culture of resisting changes contributes a lot to the slow adoption and since Industry 4.0 requires a certain type of skills, employees which include the middle managers are overly concerned about losing their jobs and being replaced. This result has shown that there are various concerns about implementing the concept to the industry and much focus should be put upon the concern of resources, market competition and working culture since it is the most frequent challenge mentioned by the other researchers.

5 Conclusion and Recommendations

Overall, the current state of the application of Industry 4.0 in the Malaysian construction industry shows a lot of promising opportunities. The interaction between the

SMEs and the concept of Industry 4.0 to the construction industry must be conducted to ensure its successful implementation in the industry. There is also a rising trend towards the interest between the concept of Industry 4.0 and the construction industry. Yet this does not come without its challenges, however. A review of the studies that focuses on the challenges of Industry 4.0 earlier had shown that the main challenges in the adoption are low amount of resources provided to the companies, market issues such as the concern of competitiveness and the organization and work cultural issues ranging from lower and upper management. Despite all of the challenges, the benefits it can provide in return is beneficial for economic growth. Not a lot of academic discussions have been made towards the topic of Industry 4.0 here in Malaysia especially with the construction industry and SMEs. This paper is expected to fill in the gap and will be used in the future studies. Future studies could try to focus on the needs and identify the best approach in adopting the Industry 4.0 concept in the industry especially for the SMEs. A proper framework could greatly help in solving and answering the needs for the SMEs to start shifting from traditional businesses to Industry 4.0 in the near future.

Acknowledgements This research was supported by a fundamental grant scheme (FRGS/1/2019/SS111/UITM/02/10) funded by the Ministry of Higher Education Malaysia (MoHE).

References

1. Ghobakhloo M (2018) The future of manufacturing industry: a strategic roadmap toward Industry 4.0. *J Manuf Technol Manage* 29:910–936
2. Shrouf F, Ordieres-Meré J, Miragliotta G (2014) Smart factories in Industry 4.0: a review of the concept and of energy management approached in production based on the internet of things paradigm, vol 2015
3. Matt DT, Rauch E (2020) SME 4.0: the role of small- and medium-sized enterprises in the digital transformation BT—Industry 4.0 for SMEs: challenges, opportunities and requirements. In: Matt DT, Modrák V, Zsifkovits H (eds). Springer International Publishing, Cham, pp 3–36
4. Bogoviz A, Osipov V, Chistyakova M, Borisov M (2019) Comparative analysis of formation of Industry 4.0 in developed and developing countries. *Stud Syst Dec Control*:155–164
5. Alaloul WS, Liew MS, Wan Abdullah Zawawi NA (2015) The characteristics of coordination process in construction projects. In: 2015 international symposium on technology management and emerging technologies (ISTMET), pp 159–164
6. Marr B (2016) Why everyone must get ready for the 4th industrial revolution. *Forbes*
7. Hermann M, Pentek T, Otto B, Pentek T (2016) Design principles for Industry 4.0 scenarios: a literature review competence center corporate data quality (CC CDQ) view project industrial data space view project design principles for Industry 4.0 scenarios: a literature review. In: 49th Hawaii international conference on system sciences, 16
8. Oztemel E, Gursev S (2020) Literature review of Industry 4.0 and related technologies. *J Intell Manuf* 31:127–182
9. Gilchrist A (2016) Industry 4.0
10. Liao Y, Deschamps F, Loures E de FR, Ramos LFP (2017) Past, present and future of Industry 4.0—a systematic literature review and research agenda proposal. *Int J Prod Res* 55:3609–3329

11. Schmidt R, Möhring M, Härting R-C, Reichstein C, Neumaier P, Jozinović P (2015) Industry 4.0—potentials for creating smart products: empirical research results
12. Alcácer V, Cruz-Machado V (2019) Scanning the Industry 4.0: a literature review on technologies for manufacturing systems. *Eng Sci Technol Int J* 22:899–919
13. Olsen TL, Tomlin B (2019) Industry 4.0: opportunities and challenges for operations management. *Manuf Serv Oper Manage* 22:113–122
14. Fonseca LM (2018) Industry 4.0 and the digital society: concepts, dimensions and envisioned benefits. *Proc Int Conf Bus Excell* 12:386–397
15. Tahmasebinia F, Sepasgozar SME, Shirowzhan S, Niemela M, Tripp A, Nagabhyrava S, Mansuri Z, Ko K, Alonso-Marroquin F (2020) Criteria development for sustainable construction manufacturing in construction Industry 4.0: Theoretical and laboratory investigations. *Constr Innov* 20:379–400
16. Haseeb M, Hussain HI, Ślusarczyk B, Jermisittiparsert K (2019) Industry 4.0: a solution towards technology challenges of sustainable business performance. *Soc Sci* 8
17. National Institute of Public Administration (INTAN) (2015) The eleventh Malaysia plan, 2016–2020
18. Karl S, Nadarajah D (2019) Investigating the relationship between Industry 4.0 and productivity: a conceptual framework for Malaysian manufacturing firms. *Proc Comput Sci* 161:696–706
19. Oesterreich TD, Teuteberg F (2016) Understanding the implications of digitisation and automation in the context of Industry 4.0: a triangulation approach and elements of a research agenda for the construction industry. *Comput Ind* 83:121–139
20. United Nations (2015) About the sustainable development goals. United Nations (UN)
21. Edelman Intelligence (2018) GE global innovation barometer 2018:115
22. Ahmad IA (2016) Is it the dawn of industrial revolution 4.0 in Malaysia? *myForesight* 29
23. Hercko J, Slamkova E, Hnat J (2015) Industry 4.0 as a factor of productivity increase. *Transcom* 2015:1–5
24. Mohamad E, Sukarma L, Mohamad NA, Salleh MR, Rahman MAA, Rahman AAA, Sulaiman MA (2018) Review on implementation of Industry 4.0 globally and preparing Malaysia for fourth industrial revolution. *Proc Des Syst Conf* 28:2203
25. United Nations Department of Economic and Social Affairs (UN DESA) (2018) 68% of the world population projected to live in urban areas by 2050, says. *UN United Nations News*
26. Adabre MA, Chan APC (2019) Critical success factors (CSFs) for sustainable affordable housing. *Build Environ* 156:203–214
27. Department of Statistics Malaysia (DOSM) (2019) Quarterly construction statistics, third quarter 2019
28. Alaloul WS, Liew MS, Zawawi NAWA, Kennedy IB (2019) Industrial revolution 4.0 in the construction industry: challenges and opportunities for stakeholders. *Ain Shams Eng J*
29. Maskuriy R, Selamat A, Ali KN, Maresova P, Krejcar O (2019) Industry 4.0 for the construction industry—how ready is the industry? *Appl Sci* 9:2819
30. Hughes S (2017) Moving to Industry 4.0: a skills revolution. *Mace Gr*:1–11
31. Craveiro F, Duarte JP, Bartolo H, Bartolo PJ (2019) Additive manufacturing as an enabling technology for digital construction: a perspective on construction 4.0. *Autom Constr* 103:251–267
32. Hampson KD, Kraatz JA, Sanchez AX (2014) The global construction industry and R&D. *RD Invest Impact Glob Constr Ind*:4–23
33. Alaloul WS, Liew MS, Zawawi NAWA, Mohammed BS (2018) Industry revolution IR 4.0: future opportunities and challenges in construction industry. *MATEC Web Conf* 203:1–7
34. Bock T (2015) The future of construction automation: technological disruption and the upcoming ubiquity of robotics. *Autom Constr* 59:113–121
35. Li CZ, Hong J, Xue F, Shen GQ, Xu X, Luo L (2016) SWOT analysis and Internet of Things-enabled platform for prefabrication housing production in Hong Kong. *Habitat Int* 57:74–87
36. Fang Y, Cho YK, Zhang S, Perez E (2016) Case study of BIM and cloud-enabled real-time RFID indoor localization for construction management applications. *J Constr Eng Manage* 142

37. Osunsanmi TO, Aigbavboa C, Oke A (2018) Construction 4.0: the future of South Africa construction industry. *Int Sch Sci Res Innov* 12:2017–2018
38. Xu L, Xu E, Li L (2018) Industry 4.0: state of the art and future trends. *Int J Prod Res* 56:1–22
39. Brynjolfsson E, McAfee A (2014) The second machine age: work, progress, and prosperity in a time of brilliant technologies. WW Norton & Company
40. Dallasega P, Rauch E, Linder C (2018) Industry 4.0 as an enabler of proximity for construction supply chains: a systematic literature review. *Comput Ind* 99:205–225
41. Moeuf A, Lamouri S, Pellerin R, Tamayo-Giraldo S, Tobon-Valencia E, Eburdy R (2020) Identification of critical success factors, risks and opportunities of Industry 4.0 in SMEs. *Int J Prod Res* 58:1384–1400
42. Lambert L (2017) The four challenges of the fourth industrial revolution. Mark Mogul
43. Ervural B, Ervural B (2018) Overview of cyber security in the Industry 4.0 era, pp 267–284
44. Schröder C (2016) The challenges of industry 4.0 for small and medium-sized enterprises. Friedrich-Ebert-Stiftung Bonn, Ger
45. Horváth D, Szabó RZ (2019) Driving forces and barriers of Industry 4.0: do multinational and small and medium-sized companies have equal opportunities? *Technol Forecast Soc Change* 146:119–132
46. Vrchota J, Volek T, Novotná M (2019) Factors introducing Industry 4.0 to SMEs. *Soc Sci Res* 8
47. Niu Y, Lu W, Chen K, Huang G, Anumba C (2015) Smart construction objects. *J Comput Civ Eng* 30:4015070
48. Masood T, Sonntag P (2020) Industry 4.0: adoption challenges and benefits for SMEs. *Comput Ind* 121:103261
49. Prause M (2019) Challenges of Industry 4.0 technology adoption for SMEs: the case of Japan. *Sustainability* 11
50. Müller JM, Bulíga O, Voigt KI (2018) Fortune favors the prepared: how SMEs approach business model innovations in Industry 4.0. *Technol Forecast Soc Change* 132:2–17
51. Faller C, Feldmüller D (2015) Industry 4.0 learning factory for regional SMEs. *Proc CIRP* 32:88–91
52. Ingaldi M, Ulewicz R (2020) Problems with the implementation of Industry 4.0 in enterprises from the SME sector. *Sustainability* 12

Customers' Interests in Sustainable Townships and Smart Housing Features in Malaysia



Sahithi Ajjarapu, Che Maznah Mat Isa, Divya Ganesan,
Nur Kamaliah Mustaffa, Ahmad Yazed Yahaya,
and Christopher Nigel Preece

Abstract Sustainable housing design, materials and energy efficiency has been a focus of Malaysian Governments in recent years. Such a focus should improve the quality of the built environment, create better places for people to live and at the same time, improve and protect the environment. However, there are issues pertaining customers' interest on the benefits gained from buying the sustainable township and smart homes. This paper presents the perceptions of customers of the sustainable township and smart housing features in terms of its value, effectiveness, functionality, and practicability towards customer's quality of life. A convenience under non-probability sampling was adopted to obtain customers' feedback based on 144 respondents on 13 statements related to sustainable township and smart housing features. A descriptive analysis using aggregated ranking is derived based on the relative importance index (RII) which resulted in the following rankings: Interest to live in sustainable township with smart housing features, solar system, energy saving appliances, water saving rainwater harvesting system, building arrangements, smart building layout, green areas in township, sustainable township and smart housing features that provide beneficial information, remote monitoring and controlling energy usage through applications, efficient insulation and prepaid option for bill payment. From the environmental perspective, the property development sector has been recognized as a major contributor to the global environmental problem. Thus, the findings from this research may help to determine customers' interest for future property development projects.

S. Ajjarapu · D. Ganesan
Veltech University, Chennai, India

C. M. Mat Isa (✉) · N. K. Mustaffa
School of Civil Engineering, College of Engineering, Universiti Teknologi MARA (UiTM), Shah Alam, Malaysia
e-mail: chema982@uitm.edu.my

A. Y. Yahaya
Sime Darby Property, Petaling Jaya, Malaysia

C. N. Preece
Abu Dhabi University, Abu Dhabi, United Arab Emirates

Keywords Sustainable township · Smart housing features

1 Background of Research

Recently in Malaysia, there has been a greater emphasis from all levels of government, private industry and interest groups associate with the residential property sector on the benefits and importance of sustainable building practices and materials and the need for energy efficiency in housing design and appliances. The residential construction in the Malaysia is going towards the legislative requirements for sustainable and energy efficient homes, as well as the continuing customers' awareness of these issues. Most of the Malaysian developers are making efforts to support the Malaysian Government's effort to engage in sustainability development by incorporating all 17 goals that are either directly or indirectly related to the business value chain. They have incorporated the sustainable features including recyclable roof system, rainwater harvesting system and certified energy efficient appliances in housing development. Such a move would improve the quality of the built environment, create better places for people to live and at the same time, improve and protect the environment. However, issues pertaining to sustainability of housing have been among the major concerns to households, especially those living in major cities. There is a market perception that a buyer has to pay a higher price without having any tangible benefits in order to own a sustainable home. Some of factors identified such as socio-demographic, dwelling, and environmental factors that have the strongest influence on the customer's interest on their daily energy-saving behaviours, the adoption of energy efficient appliances and the energy efficient retrofit investments [1]. Therefore, this research aims to study the perception of customers to the sustainability township and smart housing features based on energy savings in using smart appliances, their functionality, and practicability towards customer's quality of life. The implication of this research is that it may help to set a benchmark in evaluating the sustainable performance level of future property development projects.

2 Literature Review

2.1 Sustainable Development

Sustainable housing design, materials and energy efficiency in housing has been a focus of Malaysian Governments in recent years. In a developing country like Malaysia, the property development sector has grown rapidly as part of a process to support social stability and economic growth of the country. The property development through vibrant activities and sales contribute to the growth and is a catalyst to the economy. A successful contribution of the property development project is when enabled to provide employment opportunities, boost economic activities, reduction

of the poverty level and the scale of serviceability towards communities is high. From the environmental perspective, the property development sector has been recognized as a major contributor to the global environmental problem. The development of property requires large-scale land acquisitions which results in the negative impact on the communities' livelihood and environment.

A study by Trotta [1] identified the socio-demographic, dwelling, and environmental factors that have the strongest influence on the daily energy-saving behaviours, the adoption of energy efficient appliances and the energy efficient retrofit investments in Britain. The results show different household profiles with specific features driving daily energy-saving behaviours and energy efficiency investments. Environmental variables are a good predictor of both energy-saving behaviours and investment in energy efficient appliances but not of energy efficient retrofit measures. By evaluating and understanding the household and dwelling characteristics that affect energy-saving behaviours and energy efficiency investments, it is possible to obtain a clearer idea of where and how energy and emissions savings can be made, and to propose effective and targeted policies that promote energy-responsible lifestyles.

Energy usage and energy efficiency are of increasing concern in Ireland. Regression analyses on a large household micro-dataset reveal that those homes that have more energy-saving features are also likely to have a high 'potential energy use'. Statistically significant dwelling features include location, value and dwelling type, while household features such as income, age, period of residency, social status and tenure type are also important [2]. In addition, energy saving is now an important component of China's energy policy. A study in a municipality of Chongqing, China revealed information about attitudes towards energy and energy saving in the context of household electrical appliances. This study shows that citizens in Chongqing receive relatively little information and guidance on how to save energy in the home and that their stated level of knowledge on this subject is also rather limited. Respondents showed some willingness to save energy as long as this did not reduce their comfort and convenience, and they appeared likely to respond to economic incentives, such as high electricity prices or discounts on appliances. But they seemed to be unaware of the potential for information to help them save energy. The survey also demonstrated a high degree of heterogeneity across society with respect to sources of information and trust in those sources and with respect to attitudes to energy saving at home. These results show that the government needs to substantially adjust its strategies for promoting household energy saving [3].

2.2 *Smart Homes*

Smart homes can be the basic functional component actively contributing to the sustainable townships through its accessibility, e-inclusion, security, connectivity, promotion in education and training, transparency of management, sustainability development etc. [4].

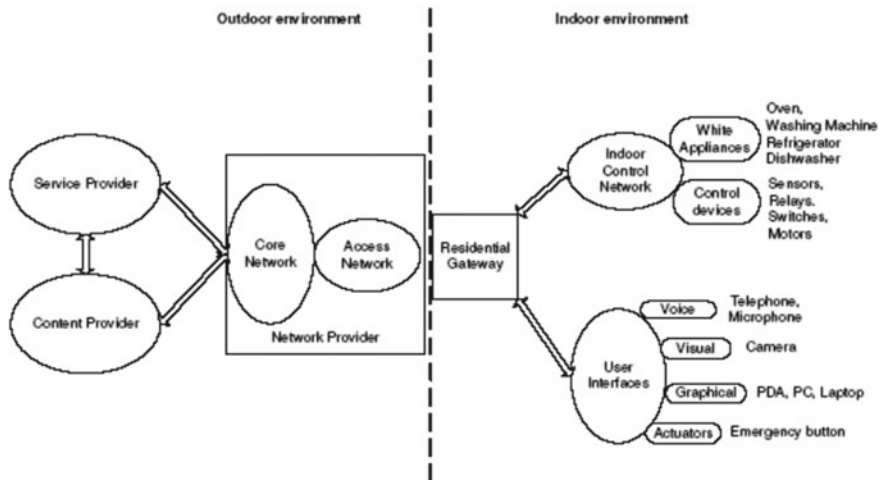


Fig. 1 Smart home concept [6]

In a schematic way, a smart home can be described by a house which is equipped with smart objects, a home network makes it possible to transport information between objects and a residential gateway to connect the smart home to the outside Internet world. Smart objects make it possible to interact with inhabitants or to observe them [5] (Fig. 1).

A study by Wilson et al. [7] indicates the potential benefits of smart home technologies for prospective users are on the aspects of saving energy, time and money, as well as making domestic life less effortful (see Fig. 2).

2.3 Smart Home Features

A smart home consists of four parts: the service platform, smart devices, home gateway, and a home network. In the smart home, many devices are connected and smartly share information using a home network. Consequently, there exists a home gateway that controls the flow of information among smart devices connected to the external network. Service platform uses the services of a service provider that deliver different services to the home network [8].

A smart home is the home or living environment having technology to allow all the household devices/home appliances such as lighting, fan, television, gas outlet etc. to be controlled automatically and be controlled remotely. In Smart homes users can easily monitor and control all home devices/home appliances through the internet. Home appliances connect in predefined proper network architecture and using standard protocols [9]. Basic idea for Smart Homes using IoT is shown in Fig. 3 [10].

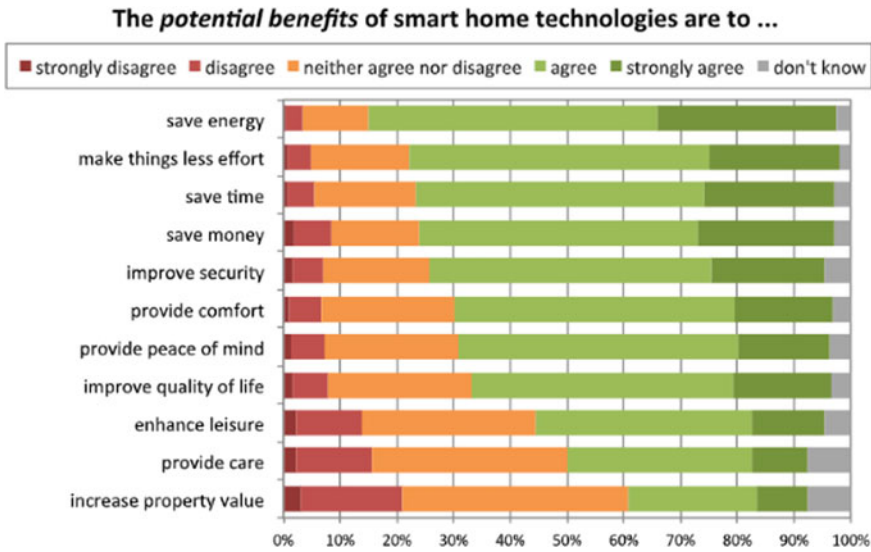
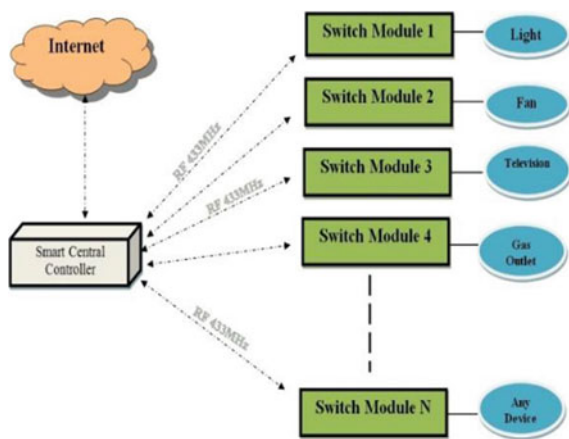


Fig. 2 Benefits of smart home technologies [7]

Fig. 3 Basic idea for smart home system using IoT [10]



Household appliances can be connected to a wired or wireless network via the home gateway. An attack against the home gateway can immediately lead to an attack against the whole household network, as it is the point at which an outside connection can be made as shown in Fig. 4.

There are various smart home features such as prepaid option for bill payment, energy saving or sustainable and smart application of appliances, remote monitoring and controlling of electrical/internet/water appliances, sustainable township and smart housing features like solar system, rainwater harvesting system, efficient insulation and water saving devices, while sustainable township commonly includes,

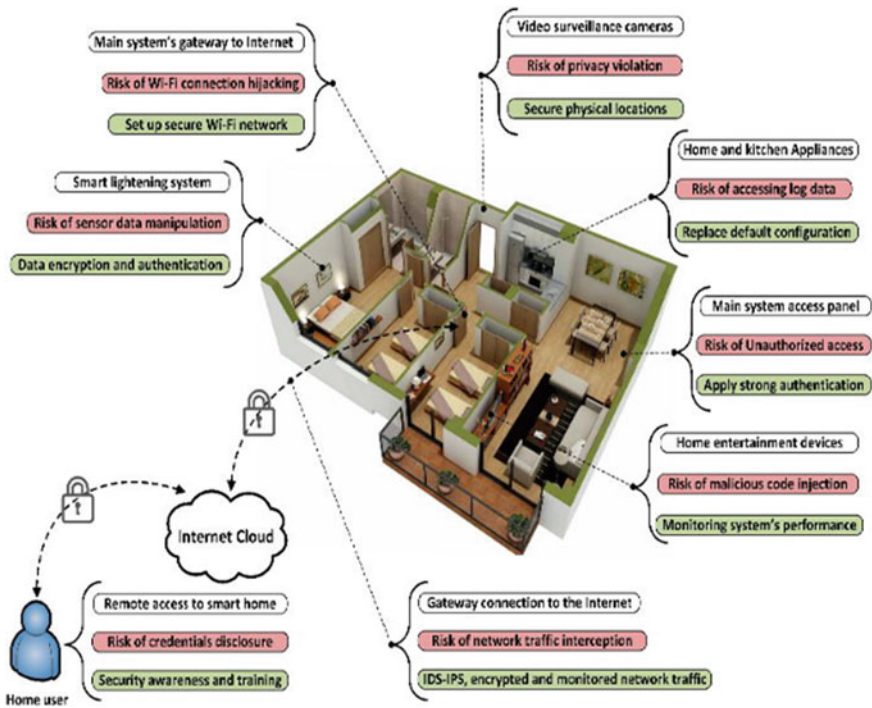


Fig. 4 Security risks and mitigation approaches are pointed to an actual smart home environment. The floor plan was borrowed from amazing architecture [11]

green areas, smart building layout and arrangements. There are many applications to control everything; automatic AC, lights, heating; sound control for the lights; refrigerators can order food automatically; automatically monitor electricity usage; lock home and alarm system; wireless detector to detect who is in your home; an iPad can control the home applications; solar energy roof; home appliances are connected by the wireless network; automatically tell you what is turned on/off by phone” [12]. Water is considered an everlasting free source that can be acquired naturally. Demand for processed supply water is growing higher due to an increasing population. Sustainable use of water could maintain a balance between its demand and supply. Rainwater harvesting (RWH) is the most traditional and sustainable method, which could be easily used for potable and non-potable purposes both in residential and commercial buildings [13].

Research was carried out on the impact of orientation on energy consumption in small-scale construction, and assesses how BIM can be used to facilitate this process. Different building orientations are adopted and their impacts of the whole building energy are investigated. Based on the analysis of the energy consumption corresponding to the different orientations, it emerged that a well-orientated building can save a considerable amount of energy throughout its life cycle [14].

In recent years, the environmental impacts of materials production and processing, particularly those related to energy, are rapidly becoming critical. Material efficiency in terms of longer-lasting products; modularisation and remanufacturing; component reuse; designing products with less material. In industrialised nations there are barriers due to economic, regulatory and social aspects that need to be overcome [15].

Sunlight provides an abundance of energy where a 90 min sunlight that strikes the earth provides the entire planet's energy needs for one year. Solar technology is one of the options being driven by global action to improve energy access and supply security, and to mitigate climate change. Around the world many developing countries like Malaysia are investing in solar generation capacity on various different scales, and, as a consequence, costs continue to fall and technologies improve. There are major solar energy technologies related to solar heating and cooling, photovoltaic and solar thermal electricity, as well as solar fuels [16].

Smart meters are one of the devices that can be used to save energy, money and time. Compared to conventional energy meters, smart meter systems are an enhanced energy meter which comprises smart meters, communication infrastructure and control devices [17]. Other smart devices are remote control, security alarms, sensors that can be integrated in smart home systems which can provide security energy saving and other such smart systems [18].

3 Methodology

A quantitative approach is adopted in this study using a questionnaire survey administered to the customers using a convenience sample. Design of the instrument is based on five (5) sections namely: Section A: Customer's Profile; Section B: Customer Awareness and Knowledge on Sustainable Township and Housing Features; Section C: Customer perception and expectation on sustainable township and smart housing features; Section D: Customer's level of interest on sustainable township and smart housing features and Section E: Customer preferences on sustainable township and smart housing features. This paper only focuses on Sections A and D.

3.1 Data Analysis

A reliability test was carried out on Section D which consists of 13 items resulting in a Cronbach's alpha for the items, which is 0.840 indicating that the instrument is reliable [19].

A normality test using Q-Q Plot was carried out and the graph shows that the data is normal as shown in Fig. 5.

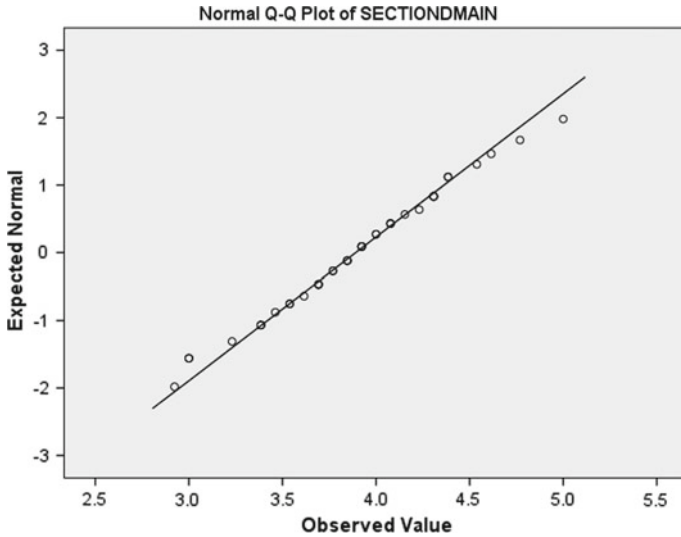


Fig. 5 Normal Q-Q plot for customer’s level of interest in sustainable township and smart home features

3.2 Customers’ Profile

Figure 6 shows that around 56% of the customers are male. More than half of them aged between 24 and 44 years old (see Fig. 7). In terms of education, 44% are with tertiary level and 24% with vocational/technical level (see Fig. 8). Around 68% acquire a monthly household income of RM5000 and below (see Fig. 9) with more than 50% pay an average monthly energy bill between RM400 and RM500 (see Fig. 10).

Fig. 6 Gender

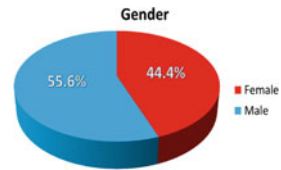


Fig. 7 Age

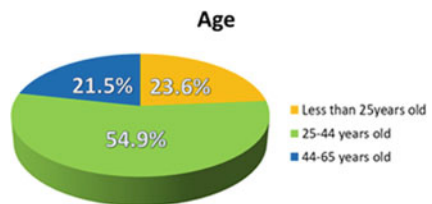


Fig. 8 Qualification

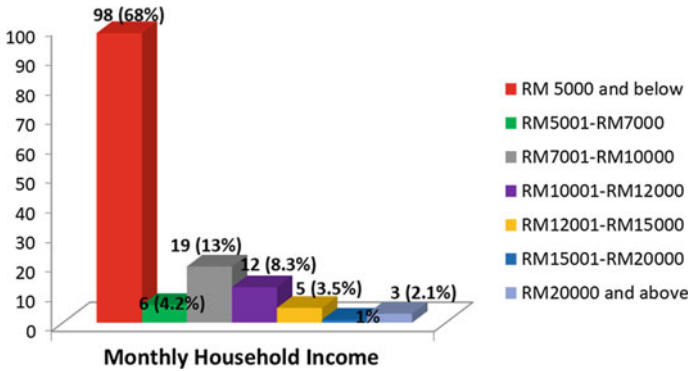
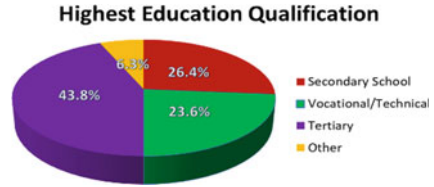


Fig. 9 Monthly household income

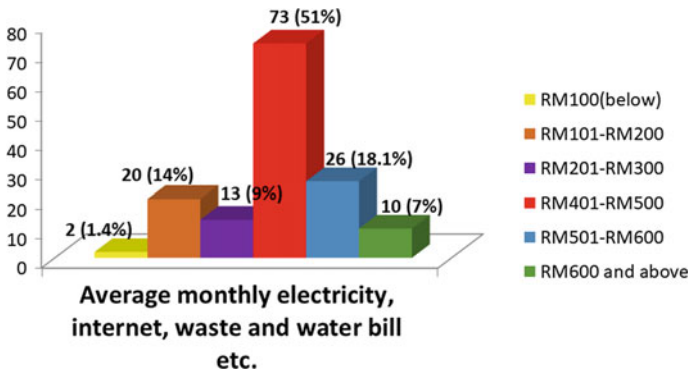


Fig. 10 Average monthly electricity, internet, waste and water bill etc

4 Analysis and Discussions

This section presents the analysis and discussion on 13 statements related to sustainable and smart features of township and housing and the added value services in terms of economic, society and environment. First, all 13 statements are ranked using Relative Important Index as described in the following sub-section.

4.1 Ranking of Customers' Interest

The aggregated ranking is derived based on the relative importance index (RII) using scales which are: 1 (not interested), 2 (Less Interested), 3 (Moderately Interested), 4 (Interested) to 5 (very interested). Table 1 shows the respondents ranking on the relative importance of various aspects of sustainable township and smart housing features. Generally, the statements that are ranked 1–9 show the RII between 0.8 and 1, indicating that the customers are “interested” towards “very interested” in relation to the statement. The last four (4) statements have RII between 0.7 and 0.8 show that the customers are “moderately interested” towards “interested.

Table 1 Ranking of statement on customers' interest related to sustainable township and smart housing features

Ranking (RII)	Statement on customer's level of interest on sustainable township and smart housing features
1 (0.9532)	Interest to live in sustainable township with smart housing features
2 (0.8609)	Solar systems help to reduce dependable energy from power companies and are able to power several electrical appliances
3 (0.8591)	Energy saving appliances based on approved electrical devices by Malaysian government which used less energy
4 (0.8581)	Water saving device to provide approved water reduction device in water system and to promote reduction in water waste
5 (0.8446)	Rainwater harvesting that can help to rescue dependable water from water supplies company
6 (0.8378)	Building arrangements take consideration of wind and sunlight direction which promotes cool air getting into house and reduce surface exposed to sunlight
7 (0.8350)	Smart building layout in the house design to incorporate the used of glass and window which promotes clean and cool air in the house which can help dependable in air conditioner
8 (0.8084)	Green areas in township that provide areas for plantation which reduce heat to environment, area for human activities to improve health and freedom and reduce runoff to minimize flood
9 (0.8027)	Sustainable township and sustainable housing features that provide beneficial information for the purpose of comparison, planning and budgeting of energy/internet/water consumption
10 (0.7893)	Remote monitoring and controlling of electrical/internet/water appliances through applications on smart phones/computers to improve the safety and security
11 (0.7879)	Efficient insulation that provides good and environmental material to promote environmentally friendly product, can be recycle product and last long material
12 (0.7811)	Sustainable and smart application of appliances that can provide current and historical electricity consumption for electricity usage planning and budgeting
13 (0.7310)	Prepaid option for power, internet and water bill payment

4.2 Discussion

The following discussions are presented based on the customers' interest in relation to the economic, society and environment as the main elements in sustainable township and housing features in terms of its value, effectiveness, functionality, and practicability towards customer's quality of life.

"Interest to live in sustainable township with sustainable housing features" is ranked first (RII = 0.9532), followed by "Solar system helps to reduce dependable energy from power company and able to power several electrical appliances such as lighting, water heater and water pump" (RII = 0.8609) and "Energy saving appliances based on approved electrical device by Malaysian government which used less energy" (RII = 0.8591). The fourth ranked feature is "Water saving device to provide approved water reduction device in water system and to promote reduction in water waste" (RII = 0.8581), followed by "Rainwater harvesting that can help to rescue dependable water from water supplies company" (RII = 0.8446) and "Building arrangements take consideration of wind and sunlight direction" (RII = 0.8378). The seventh ranked feature is "Smart building layout in the house design" (RII = 0.8350), followed by "Green areas in township that provide areas for plantation" (RII = 0.8084) and "Sustainable township and sustainable housing features that provide beneficial information" (RII = 0.8027). The tenth ranked feature is "Remote monitoring and controlling of electrical/internet/water appliances through applications" (RII = 0.7893), followed by "Efficient insulation that provides good and environmental material that can be recycled" (RII = 12 (0.7811)). The last ranked statement is "Prepaid option for bill payment" (RII = 0.731) indicating that the respondents were not inclined towards the pre-paid concept.

Based on the ranking, most of the respondents are "very interested" to live in sustainable township and smart housing. However, in terms of value, it was shown that the residential property sector will pay more for an environmentally sustainable township and housing compared to a similarly located residential property that has not been constructed with the same level of environmental sustainability (CIB, 2013).

The second ranked feature chosen by the customers is in terms of environment in the use of solar systems designed based on solar technology. They are aware that solar energy is one of the widely used renewable energy that can be harnessed either by directly or indirectly deriving energy from sunlight. One of the applications of solar energy is to use solar water heating systems based on a study by Jamar et al. [20] the solar collectors, storage tanks and heat transfer fluids are the three core components in solar water heater applications. It is considered as one of the options being driven by global action to improve energy access and supply security, and to mitigate climate change. Even though the solar technology is facing various technical barriers, such as low solar cell efficiencies, low performing balance-of-systems (BOS), economic hindrances (e.g., high upfront costs and a lack of financing mechanisms), and institutional obstacles (e.g., inadequate infrastructure and a shortage of skilled manpower) [21], the customers in Malaysia believed using solar system in

their homes helps to reduce dependable energy from a power company by powering several electrical appliances such as lighting, water heater and water pump.

The third ranked statement is related to the environment using energy saving appliances which was amongst the top preferred sustainable housing features as proven by Trotta [1] that showed environmental variables are good predictors of both energy-saving behaviors and investment in energy efficient appliances. Some examples of these energy saving appliances are smart meter, lighting system, fan, refrigerator and television. However, in Ireland, a study reveals that those homes that have more energy-saving features are also likely to have a high 'potential energy use'. Statistically significant dwelling features include location, value and dwelling type, while household features such as income, age, period of residency, social status and tenure type are also important [2].

The next customers' preferred housing sustainable feature is water saving devices, where it is expected an approved water reduction device in the water system to be provided, to promote reduction in water waste such as dual toilet flush system, shower and pipes for washing machine and dishwasher. In addition, large amounts of heat are wasted during showering processes. A study by Guo et al. [22] that focused on a waste water heat recovery system indicated that more than 50% of the shower waste-water heat can be recycled by the high-performance heat recovery device.

The fifth customers' preferred sustainable housing feature is the rainwater harvesting (RWH) system. Majority of the customers are interested in having a RWH system that can help to rescue dependable water from water supplies companies. This system has the ability to accumulate and collect rain through roof or lawn or open areas around the house and provide alternative sources of water such as grass or plant watering, car wash, toilet flush and any activity with less human body contact. In Malaysia, the use of a rainwater harvesting system is considered as part of the solution proposed by the government to avoid a water crisis. Che-Ani et al. [23] first reviewed the scenario of water shortages in Malaysia even though Malaysia has an ample supply of water due to heavy rains. However, there was increasing water consumption by the industry, agricultural and household users that resulted in limited water supply. Thus, at the user's home level, it was found that rainwater harvesting has become the most suitable solution as suggested by the government with many benefits not just for the users, but also to the government and environment.

The next ranked customers' interests are on the building arrangements, smart building layout, provision of green areas in township, sustainable township and housing features that provide beneficial information. The findings indicate the customers' interest in the design of building arrangements that take into consideration the wind and sunlight direction in order to promote cool air getting into the house and reduce surface exposure to sunlight. Previous studies have shown that the energy consumption corresponding to the different orientations where a well-orientated building can save a considerable amount of energy throughout its life cycle [5]. Based on the analysis of the energy consumption corresponding to the different orientations, it emerged that a well-orientated building can save a considerable amount of energy throughout its life cycle [14]. In addition, it was expected that a smart building layout in the house is designed to incorporate the use of glass and

enough windows to promote clean and cool air in the house which can help depend on the air conditioner. This layout will also promote enough lighting during daytime to reduce use of light. The findings also show that the customers expect that green areas in township are provided for plantation to reduce heat to the environment, areas for human activities to improve health and freedom and at the same time reduce runoff which can reduce flooding. Majority of the customers understood that sustainable township with smart housing features can provide beneficial information that provide information such as real time energy/internet/water consumption and also their usage history on a periodic basis (hourly, daily, weekly and monthly) for the purpose of comparison, planning and budgeting of energy/internet/water consumption.

The tenth ranked statement is the feature in having remote monitoring and controlling of energy appliances to improve the safety and security of homes through smart applications on their smartphones or computers to provide current and historical electricity consumption for their electricity usage planning and budgeting.

The eleventh ranked statement is related to efficient insulation. In recent years, the environmental impacts of materials production and processing, particularly those related to energy, are rapidly becoming critical. The finding shows that the customers are interested to have efficient insulation in order to promotes good and environmental material in construction stage, where material efficiency in terms of longer-lasting products; modularisation and remanufacturing; component reuse; designing products with less material [6], for example of selection of material for roof and wall, selection of paint technology and colour scheme which can reduce heat in the house. Usage of this insulation will promote environmentally friendly products, can be recycled products and longer lasting materials. The twelfth ranked statement is on sustainable and smart application of appliances that can provide current and historical electricity consumption for electricity usage planning and budgeting.

The least preferred feature by the customers is to have the prepaid option for their power/internet/water bill payment. The finding indicates the customers were not inclined towards the pre-paid concept which is not practical anymore due to the current and more popular online banking services.

5 Conclusions

This paper presented the customers' level of interest in sustainable townships and smart housing features based on value, effectiveness, functionality, and practicability towards quality of life. A convenience method based on non-probability sampling was adopted to get the customer's feedback. This paper has given an account of, and the reasons for, the need to have sustainable townships and smart housing. This research would seem to show that the customers generally have awareness of the usage of energy efficient and smart appliances with sustainable features such as solar system, rainwater harvesting system, usage of sustainable environmental materials. This is reflected in their current interest to live in sustainable townships and smart homes. Ranking based on the relative importance index (RII), revealed

that the customers' most preferred sustainable housing features are solar system, energy saving appliances, water saving devices and rainwater harvesting system. In addition, the customers perceived that a sustainable township shall include efficient building arrangements, smart building layout, provision of green areas in township with sustainable and sustainable housing features. They, however, indicated the least interest in the prepaid option concept for bill payment which may be due to convenience in payment using online banking. The evidence from this study suggests that customers are currently aware of sustainable development in Malaysia. From the environmental perspective, the property development sector has been recognized as a major contributor to the global environmental problem. Thus, the findings from this research may help to determine customers' interest for future property development projects and can also provide a valuable reference for future property development projects in order to provide better service based on customer satisfaction and feedback. A limitation of this study is that the numbers of respondents representing the Malaysian customers were relatively small. The study also used a convenience sampling where the selection might be prone to biases, thus the sample may not reflect or be representative of the overall Malaysian customers. Future research may focus on specific developers using a readily available sampling frame to provide a more meaningful and substantial reference for new sustainable townships and smart homes.

References

1. Trotta G (2018) Factors affecting energy-saving behaviours and energy efficiency investments in British households. *Energy Policy*. <https://doi.org/10.1016/j.enpol.2017.12.042>
2. O'Doherty J, Lyons S, Tol RSJ (2008) Energy-using appliances and energy-saving features: determinants of ownership in Ireland. *Appl Energy*. <https://doi.org/10.1016/j.apenergy.2008.01.001>
3. Ma G, Andrews-Speed P, Zhang J (2013) Chinese consumer attitudes towards energy saving: the case of household electrical appliances in Chongqing. *Energy Policy*. <https://doi.org/10.1016/j.enpol.2013.01.024>
4. He X (2018) Smart home—from A concept
5. Ricquebourg V, Menga D, Durand D, Marhic B, Delahoche L (2007) The smart home concept: our immediate future the smart home concept : our immediate future. <https://doi.org/10.1109/ICELIE.2006.347206>
6. Dermosoniadis V, Philippopoulos P, Georgopoulos C (2003) Georgopoulos smart homes: a user perspective. In: 19th International Symposium on Human Factors in Telecommunication
7. Wilson C, Hargreaves T, Hauxwell-Baldwin R (2017) Benefits and risks of smart home technologies. *Energy Policy* 103:72–83
8. Shouran Z, Ashari A (2019) Internet of Things (IoT) of smart home: privacy and security Internet of Things (IoT) of smart home: privacy and security. *Int J Comput Appl* 182(39):3–8. <https://doi.org/10.5120/ijca2019918450>
9. Gabhane JP, Thakare MS, Craig MM (2017) Smart homes system using Internet-of-Things: issues, solutions and recent research directions. *IJRET* 4(5):1965–1969
10. Wang M, Zhang G, Zhang C, Zhang J, Li C (2013) An IoT-based appliance control system for smart homes. In: Proceedings of the 2013 international conference on intelligent control and information processing, ICICIP 2013. <https://doi.org/10.1109/ICICIP.2013.6568171>

11. Ali B, Awad AI (2018) Cyber and physical security vulnerability assessment for IoT-based smart homes. *Sensors* (Switzerland). <https://doi.org/10.3390/s18030817>
12. Zhai Y, Liu Y, Yang M, Long F, Virkki J (2014) A survey study of the usefulness and concerns about smart home applications from the human perspective, pp 119–126
13. Rahman S, Khan MTR, Akib S, Din NBC, Biswas SK, Shirazi SM (2014) Sustainability of rainwater harvesting system in terms of water quality. *Sci World J*. <https://doi.org/10.1155/2014/721357>
14. Abanda FH, Byers L (2016) An investigation of the impact of building orientation on energy consumption in a domestic building using emerging BIM (building information modelling). *Energy*. <https://doi.org/10.1016/j.energy.2015.12.135>
15. Allwood JM, Ashby MF, Gutowski TG, Worrell E (2011) Material efficiency: a white paper. *Resour Conserv Recycl*. <https://doi.org/10.1016/j.resconrec.2010.11.002>
16. Solar energy perspectives (2011)
17. Tenaga Nasional Berhad (TNB) (2015) Customer survey on the deployment of TNB smart meter/advanced metering infrastructure (AMI)
18. Kadam R, Mahamuni P, Parikh Y (2015) Smart home system. *Int J Innov Res Adv Eng* 2(1):81–86
19. Nunally JC (1970) Introduction to psychological measurement
20. Jamar A, Majid ZAA, Azmi WH, Norhafana M, Razak AA (2016) A review of water heating system for solar energy applications. *Int Commun Heat Mass Transf* 76. <https://doi.org/10.1016/j.icheatmasstransfer.2016.05.028>
21. Kabir E, Kumar P, Kumar S, Adelodun AA, Kim KH (2018) Solar energy: potential and future prospects. *Renew Sustain Energy Rev*. <https://doi.org/10.1016/j.rser.2017.09.094>
22. Guo YX, Cai YL, Liang SQ, Chen W (2012) Experimental study on a shower waste water heat recovery device in buildings. *Appl Mech Mater*. <https://doi.org/10.4028/www.scientific.net/AMM.226-228.2402>
23. Che-Ani AI, Shaari N, Sairi A, Zain MFM, Tahir MM (2009) Rainwater harvesting as an alternative water supply in the future. *Eur J Sci Res*

Technology? Financial Viability or What? Challenges and Benefits of Eco and Reflective Roof in Malaysia



Boon Tik Leong, Cheng Fern Tey, Lam Tatt Soon, Kenn Jhun Kam, and Fuey Lin Ang

Abstract Adopt eco roof or reflective roof on the building consider one of the methods to reduce Urban Heat Island (UHI) effect and global warming from getting crucial as well as improve ecological and environmental quality. However, the awareness and application of eco roof and reflective roof are still considered low in Malaysia and the roofing technologies used are not advanced if compared to other Asian countries such as Singapore, Japan and Hong Kong. Aim of this research is to identify the challenges and benefits of eco roof and reflective roof to developers and seek for developers' level of awareness on eco roof and reflective roof. Quantitative method and Central Limit Theorem are applied in this research for data collection and analysis purposes. It is found that eco roof and reflective roof do bring benefits to nature and society. Government play vital role in bringing awareness and encouragement in improving the usage of eco roof and reflective roof.

Keywords Eco roof · Reflective roof · Malaysia

1 Introduction

Climate change, a global calamity environmental issue resulted by extreme human activities [1] caused observable, unpredictable and unprecedented effects either on a local or a global scale [2]. A Human Development Report published by the United Nations Development Programme (UNDP) in 2007 revealed Malaysia released 177.5 million ton of carbon dioxide (CO₂) in 2004 which occupied 0.6% of the global total amount. High levels of carbon dioxide emission led to temperature rise and cause energy demand of cooling loads become higher and electricity bills become more expensive.

To maintain indoor temperature within comfort level, usage of HVAC systems will increase and consumption of air-conditioning energy in urban buildings is 13%

B. T. Leong (✉) · C. F. Tey · L. T. Soon · K. J. Kam · F. L. Ang
Taylor's University, No. 1, Jalan Taylors, Selangor, 47500 Subang Jaya, Malaysia
e-mail: boontik.leong@taylors.edu.my
URL: <https://university.taylors.edu.my/en.html>

Table 1 Solar heat gains in typical Malaysian housing from (PAM CPD Seminar 14/02/2009)

	Single storey terrace	Double storey terrace	Five storey flats	Eight storey flats
Roof/building envelope area (%)	68	45	30	18
Floor/building envelope area (%)	32	55	70	82

higher compared to non-urban buildings [3]. Malaysia relies on energy extract from natural gas, coal, crude oil and other fossil resources to generate electricity. The stronger the dependency on fossil fuels resources, the higher the amount of CO₂ emissions released to the atmosphere [4, 5]. Once the situation of exhaustible natural resources occurs, it causes an inevitable harm to the environment [6]. Roof trusted to be one of the methods to solve the issue of reducing energy consumption [7]. Roof accounts nearly 20 to 25% of urban space areas [8]. Eco and reflective roofs are suggested being use in order to reduce carbon emission and develop a greener environment for younger generation. According to Chan [9], roof surface receives highest solar radiation through a whole day and roof insulation is vital to reduce air-conditioning load. Green Building Index-MS1525 published on CDP Seminar stated typical roof surface of terraced house in Malaysia gained highest amount of sunlight (Table 1).

2 Literature Review

Eco roof widely known as green roof or rooftop garden. It is a modern energy efficient construction technology with vegetation planted on top of growth medium in an open space without using additional land with various benefits such as enhance heat transfer, improve thermal insulation of a building and absorb rainwater fall [10]. Department of Planning and Local Government of South Australia [11] identified green roof system consists of vegetation, filter layer, drainage material, insulation, substrate, water-proofing membrane and root barrier.

Types of eco roof used in current market can classified into 3 categories: extensive eco roof, intensive eco roof and semi-intensive eco roof. Extensive green roof has thinner layer of substrates and lighter loading aspects compared to intensive green roof. It requires minor maintenance and irrigation with limit selection of vegetation and has limited accessibility [12]. Extensive green roof is more suitable for retrofitting building as it is lightweight and minimize increasing structural load on the existing roof [13].

Intensive green roof consists of a thick growing medium layer wherein can support wide varieties of plants, trees and shrubs. It requires maintenance and it is accessible to public. This system requires specific and additional structural support from the building due to heavyweight of substrate [14, 15]. Researches carried out by

Berardi [16], Luo [17] stated semi-intensive green roof demonstrated as a combination of intensive and at least 25% of extensive green roof. According to the United Kingdom's Green Roof Organization (GRO) code 2011, it requires lower additional structural support and maintenance than intensive green roof (Tables 2 and 3).

Doulos [18] defined reflective roof is a roofing system use natural white materials or artificial white paint on the roof surface to reflect incoming solar heat and decrease net radiation within the building. It provides atmospheric heating and enhances building energy savings [19]. It does not provide any additional waste and occupy

Table 2 List of building adopt eco roof (International project and Malaysia project)

Building with eco roof	Types	Type of building	Year	Location
8 House, Copenhagen, Denmark	Extensive	Multi-use building	2010	International project
ACROS Fukuoka Prefectural International Hall, Fukuoka, Japan	Intensive	Commercial building	1994	International project
California Academy of Science, San Francisco, California	Extensive	Office, museum, research facility	2008	International project
Chicago City Hall, Illinois	Semi-intensive	Municipal/Government building	2001	International project
Dani Ridge House, Carmel, California	Extensive	Architecture firm	2006	International project
Cada Desa Condominium, Taman Desa, Kuala Lumpur	Intensive	Condominium	2008	Malaysia project
Hilton and Le Meridien, Jalan Stesen Sentral, Kuala Lumpur	Intensive	Hotel	2003	Malaysia project
Idaman Residence, Jalan P. Ramlee, Kuala Lumpur	Extensive	Condominium	2008	Malaysia project
Islamic Art Museum, Tasik Perdana, Kuala Lumpur	Extensive	Museum	1998	Malaysia project
Kiara 9, Mont Kiara, Kuala Lumpur	Intensive	Condominium	2011	Malaysia project

Table 3 5-Point Likert scale used in questionnaire survey form

Measurement scale	1	2	3	4	5
Level of awareness	Unaware	Partially aware	Neutral	Informed	Well informed
Challenges/benefit factors	Strongly disagree	Moderately disagree	Neutral	Moderately agree	Strongly agree

characteristics of high solar reflectance and thermal emittance [20]. Coatings can be applied both on existing or new roofs of flat roof, low-sloped roof and steep-sloped roof.

Challenges of eco roof agreed by most of researchers are it involves high maintenance cost and investment cost [21–23], limited expertise and inexperienced professionals, lack of relevant scientific data or research of this technology in the construction industry [1, 24, 25] and government constraints such as lack of promotion, subsidies or statutory mandate [26, 27]. Challenges of reflective roof from Synnefa and Santomouris [28] and Revel et al. [29] findings are it easily lose reflectivity owing to the accumulation of dirt and weathering condition and the site topography and building regulations can limit the application of reflective roof.

Main benefits of eco roof are reduce Urban Heat Island effect [30–32], energy consumption by decreasing cooling and heating load of HVAC system [33] and mitigate stormwater runoff [34, 35].

Benefits of reflective roof such as improved indoor and outdoor thermal comfort [36, 37], increase energy saving potential [19, 37–39] and decrease greenhouse gases emission [28, 40, 41].

From Rahman's [42] finding, 94% of respondents agree green roof have potential and they agree cases of green roof increase in Malaysia. Awareness from Malaysian society towards implementing green project is still at very low level even though their importance had been proven by experts. In European countries, 48% of public thinks cool roof technology is still new and not tested enough whereas 32% of them uncertain about cool roof's benefit [28].

In view of the potential of eco roof and reflective roof, there is no comprehensive research that identify the challenges and the perceived benefits of eco roof and reflective roof in Malaysia context.

This paper aims to investigate Developers' awareness level on eco roof and reflective roof and finds the main challenges and benefits of those roofing technologies to Developers.

3 Methodology

Developer registered under REDHA Malaysia, Sabah REDHA and Sarawak REDHA set as target population of this research. Developers were selected as they are the key player in the construction industry and they obtain the right to make final decision

in deciding types of building element or structure that they wish to implement. Total 1548 developers found from the member listing, however only 593 of the developers provide company email address and 513 email are valid. Data collection method used are literature review and questionnaire survey form.

Survey form sub-divided into 3 parts: Section A to collect respondent’s information whereas Section B and Section C aim to collect respondent’s knowledge on eco roof and reflective roof. Example of challenges and benefits questioned in survey were summarized from other researchers’ findings. Formula of Relative Important Index (RII) used for data analysis purpose to identify the ranking of challenges and benefits of eco roof and reflective roof. 5-point Likert scale adopted for respondents show their level of agreement with given statement or items on a metric scale from strongly disagree to strongly agree or from unaware to well informed.

4 Result and Discussion

As the responses rate lower than 30%, therefore Central Limit Theorem (CLT) applied in this study. Findings of [43] stated collect element from all populations requires considerable effort and is often impossible to reach the target. Therefore, a subset of sample regarding to population can be used as a sample of sufficient size which random selected from certain large population. Total 32 responses received from developers in different states. Table 4 shown result of respondents’ awareness level

Table 4 Level of awareness on eco roof and reflective roof

Question 1: Rate your level of awareness on eco roof and reflective roof				
Awareness level	Eco roof		Reflective roof	
	Respondents (n)	Percentage (%)	Respondents (n)	Percentage (%)
Unaware	3	9.38	5	15.63
Partially aware	11	34.38	14	43.75
Neutral	12	37.50	9	28.13
Informed	6	18.75	4	12.50
Well informed	0	0	0	0
Total	32	100.00	32	100.00
Question 2: Do you think eco roof/reflective roof bring benefit and contribute to environment?				
Agreement	Eco roof		Reflective roof	
	Respondents (n)	Percentage (%)	Respondents (n)	Percentage (%)
Yes	21	65.63	7	21.88
No	1	3.13	6	18.75
Maybe	10	31.25	19	59.38
Total	32	100.00	32	100.00

Table 5 RII ranking for benefits of eco roof and reflective roof

Question: To what extent would the following factors encourage you to invest in those roofing technologies?

Benefits	Eco roof		Reflective roof	
	RII	RANK	RII	RANK
Reduce building heat gain	0.913	1	0.844	1
Reduce energy consumption and achieve a better energy performance for existing building	0.881	2	0.819	2
Improve occupant's indoor temperature comfort	0.838	3	0.756	4
Increase longevity life span of building roof	0.838	3	0.619	9
Enhancement of biodiversity	0.781	4	0.581	12
Cost saving potential	0.750	5	0.806	3
HVAC equipment saving	0.738	6	0.756	4
Reduce GHGs (greenhouse gases)	0.681	7	0.656	6
Improve microclimate condition	0.673	8	0.694	5
Mitigate UHI (urban heat island) in high populated areas	0.663	9	0.650	7
Increase roof membrane's durability by reducing direct solar exposure	0.650	10	0.644	8
Reduce smog formation	0.631	11	0.569	13
Improve acoustic benefit	0.613	12	0.594	10
Beautification	0.550	13	0.438	14
Flexibility, simplicity and unique in design	0.531	14	0.588	11

on eco roof and reflective roof and Tables 5 and 6 shown RII ranking for benefits and challenges for eco roof and reflective roof.

According to tabulation above, 37.50% of respondents show neutral awareness on eco roof and 21 out of 32 respondents agreed with the statement that eco roof able to bring benefit and contribute to environment. 43.75% of respondents show partial awareness level on reflective roof and 19 out of 32 respondents are uncertain that does reflective roof able make contribution to environment.

Respondents agreed both roofing technologies bring similar benefits which are able to reduce building heat gain and decrease energy consumption to achieve a better energy performance for existing building. Respondents do agree eco roof can improve occupant's indoor temperature comfort and increase longevity life span of building roof. Cost saving potential is another benefit of reflective roof that agreed by respondents.

Respondents have different view and perspective on the challenges of eco roof and reflective roof. Reasons such as the high maintenance and repair cost involved, complex and complicated construction of eco roof and the lack of incentives and subsidies for building owner in industry are the main challenges that limit application of eco roof. Main challenges of reflective roof are lack of subsidies of incentives and

Table 6 RII ranking for challenges of eco roof and reflective roof

Question: To what extent would the following factors discourage you to invest in those roofing technologies?

Challenges	Eco roof		Reflective roof	
	RII	RANK	RII	RANK
High maintenance/repair cost	0.913	1	0.800	4
Complex and complicated construction	0.906	2	0.781	6
Lack of incentives/subsidies for building owner	0.888	3	0.838	1
Economic constraints	0.863	4	0.819	3
Susceptible to mold, weed and algae growth	0.856	5	0.825	2
Outdated laws and regulations	0.825	6	0.788	5
Subject to wear and tear	0.806	7	0.800	4
Limited construction expertise and professionals	0.769	8	0.688	9
Hard to get experienced installer and specialist companies	0.756	9	0.713	8
Lack of communication, distribution and channeling of product data from government among public and private sectors	0.738	10	0.738	7
This application not widely been used due to technology constraint	0.706	11	0.656	10
Outdated technology	0.681	12	0.656	10
Scarcity of material supply	0.663	13	0.638	11
Lack of local research and studies	0.563	14	0.550	12
The product may be visually unattractive or cause visual discomfort and glare	0.519	15	0.550	12

subsidies for building owner, this roofing technology is susceptible to mold, weed and algae growth and the economic constraints.

5 Conclusion

In a nutshell, findings proved eco roof and reflective roof do bring benefits to nature and society. Economic and technical factors are the main hurdle of the implementation of these two types of roofs.

Government should raise public and private society's awareness on eco roof and reflective roof. At the same time, promotion of subsidies, incentives or design guidelines of those roofing technologies do encourage building owners' willingness to adopt those roofing technologies, this will lead to a great possibility of participation from existing market.

The industry players especially green developers should utilize the benefits identified to enhance the marketability of their product at the same time play their role to contribute to the environment especially reduce UHI effect.

References

1. Ismail A, Samad MHA, Rahman AMA, Yeok FS (2012) Cooling potentials and CO₂ uptake of *Ipomoea Pes-caprae* installed on the flat roof of a single storey residential building in Malaysia. *Procedia Social Behav Sci* 35:361–368
2. Begum RA (2017) Tackling climate change and Malaysia's emission reduction target. *Scientific Malaysian*. <http://magazine.scientificmalaysian.com/issue-13-2017/tackling-climate-change-malaysias-emission-reduction-target/>
3. Baniassadi A, Sailor DJ, Crank PJ, Ban-Weiss GA (2018) Direct and indirect effects of high-albedo roofs on energy consumption and thermal comfort of residential buildings. *Energy Build* 178:71–83
4. Chik NA, Rahim KA (2014) Sources of change in CO₂ emissions from energy consumption by industrial sectors in Malaysia. In Proceedings for 9th Malaysian national economic conference (PERKEM). Conference conducted in Terengganu, Malaysia. Available from: http://www.ukm.my/fep/perkem/pdf/perkem2014/PERKEM_2014_1D3.pdf. Last accessed 25 May 2015
5. Indati MS, Bekhet HA (2014) Highlighting of the factors and policies affecting CO₂ emissions level in Malaysian transportation sector. *Int J Environ Earth Sci Eng* 8(1):10–18
6. Grossman GM, Krueger AB (1995) Economic growth and the environment. *Q J Econ* 110(2):353–377
7. Lee SW, Lim CH, Chan SA, Von KL (2017) Techno-economic evaluation of roof thermal insulation for a hypermarket in equatorial climate: Malaysia. *Sustain Cities Soc* 35:209–223
8. Raji B, Tenpierik MJ, Van Den Dobbelen A (2015) The impact of greening systems on building energy performance: a literature review. *Renew Sustain Energy Rev* 45:610–623
9. Chan C (2009) Assessment: reflective journal, assessment resources. HKU, University of Hongkong. Retrieved 26 Sept 2012
10. VanWoert ND, Rowe DB, Andresen JA, Rugh CL, Fernandez RT, Xiao L (2005) Green roof stormwater retention. *J Environ Qual* 34(3):1036–1044
11. Department of Planning and Local Government (2010) Water sensitive urban design technical manual for the greater Adelaide region. Government of South Australia, Adelaide
12. Nagase A, Dunnett N (2010) Drought tolerance in different vegetation types for extensive green roofs: effects of watering and diversity. *Landscape Urban Plann* 97(4):318–327
13. Ardente F, Beccali M, Cellura M, Mistretta M (2011) Energy and environmental benefits in public buildings as a result of retrofit actions. *Renew Sustain Energy Rev* 15(1):460–470
14. Kosareo L, Ries R (2007) Comparative environmental life cycle assessment of green roofs. *Build Environ* 42(7):2606–2613
15. Peng LL, Jim CY (2015) Economic evaluation of green-roof environmental benefits in the context of climate change: the case of Hong Kong. *Urban For Urban Greening* 14(3):554–561
16. Berardi U, GhaffarianHoseini A (2014) State-of-the-art analysis of the environmental benefits of green roofs. *Appl Energy* 115:411–428
17. Luo H, Huang B, Liu X, Zhang K (2011) Green roof assessment by GIS and google earth. *Procedia Environ Sci* 10:2307–2313
18. Doulos L, Santamouris M, Livada I (2004) Passive cooling of outdoor urban spaces. The role of materials. *Sol Energy* 77(2):231–249
19. Coutts AM, Daly E, Beringer J, Tapper NJ (2013) Assessing practical measures to reduce urban heat: green and cool roofs. *Build Environ* 70:266–276
20. Gartland LM (2012) Heat islands: understanding and mitigating heat in urban areas. Routledge

21. Besir AB, Cuce E (2018) Green roofs and facades: a comprehensive review. *Renew Sustain Energy Rev* 82:915–939
22. Sangkakool T, Techato K, Zaman R, Brudermann T (2018) Prospects of green roofs in urban Thailand—a multi-criteria decision analysis. *J Cleaner Prod* 196:400–410
23. Shafique M, Kim R, Rafiq M (2018) Green roof benefits, opportunities and challenges—a review. *Renew Sustain Energy Rev* 90:757–773
24. Chow MF, Bakar MA, Deck R (2016) A review on the development and challenges of green roof systems in Malaysia. *Int J Civ Environ Struct Constr Architectural Eng* 10(1):16–20
25. Irga PJ, Braun JT, Douglas ANJ, Pettit T, Fujiwara S, Burchett MD, Torpy FR (2017) The distribution of green walls and green roofs throughout Australia: do policy instruments influence the frequency of projects? *Urban For Urban Greening* 24:164–174
26. Brudermann T, Sangkakool T (2017) Green roofs in temperate climate cities in Europe—an analysis of key decision factors. *Urban For Urban Greening* 21:224–234
27. Ismail WZW, Abdullah MN, Hashim H, Rani WSW (2018) An overview of green roof development in Malaysia and a way forward. In: AIP conference proceedings, vol 2016, no 1, p 020058. AIP Publishing
28. Synnefa A, Santamouris M (2012) Advances on technical, policy and market aspects of cool roof technology in Europe: the cool roofs project. *Energy Build* 55:35–41
29. Revel GM, Martarelli M, Emiliani M, Celotti L, Nadalini R, De Ferrari A, Hermanns S, Beckers E (2014) Cool products for building envelope—Part II: experimental and numerical evaluation of thermal performances. *Sol Energy* 105:780–791
30. Abbass OA, Sailor DJ, Gall ET (2018) Ozone removal efficiency and surface analysis of green and white roof HVAC filters. *Build Environ* 136:118–127
31. Cascone S, Catania F, Gagliano A, Sciuto G (2018) A comprehensive study on green roof performance for retrofitting existing buildings. *Build Environ* 136:227–239
32. Rowe DB (2011) Green roofs as a means of pollution abatement. *Environ Pollut* 159(8–9):2100–2110
33. Ziogou I, Michopoulos A, Voulgari V, Zachariadis T (2018) Implementation of green roof technology in residential buildings and neighborhoods of Cyprus. *Sustain Cities Soc* 40:233–243
34. Fauzi MA, Malek NA, Othman J (2013) Evaluation of green roof system for green building projects in Malaysia. *World Acad Sci Eng Technol* 74:124–130
35. Korol E, Shushunova N (2016) Benefits of a modular green roof technology. *Procedia Eng* 161:1820–1826
36. Al-Obaidi KM, Ismail M, Rahman AMA (2014) Passive cooling techniques through reflective and radiative roofs in tropical houses in Southeast Asia: a literature review. *Front Architectural Res* 3(3):283–297
37. Zinzi M, Carnielo E, Agnoli S (2012) Characterization and assessment of cool coloured solar protection devices for Mediterranean residential buildings application. *Energy Build* 50:111–119
38. Alchapar NL, Correa EN (2016) Aging of roof coatings. Solar reflectance stability according to their morphological characteristics. *Constr Build Mater* 102:297–305
39. Gao Y, Xu J, Yang S, Tang X, Zhou Q, Ge J, Xu T, Levinson R (2014) Cool roofs in China: policy review, building simulations, and proof-of-concept experiments. *Energy Policy* 74:190–214
40. Boixo S, Diaz-Vicente M, Colmenar A, Castro MA (2012) Potential energy savings from cool roofs in Spain and Andalusia. *Energy* 38(1):425–438
41. Hosseini M, Akbari H (2016) Effect of cool roofs on commercial buildings energy use in cold climates. *Energy Build* 114:143–155
42. Rahman SR, Ahmad H, Rosley MS (2013) Green roof: its awareness among professionals and potential in Malaysian market. *Procedia Soc Behav Sci* 85:443–453
43. Kwak SG, Kim JH (2017) Central limit theorem: the cornerstone of modern statistics. *Korean J Anesthesiol* 70(2):144

Reviewing Quality Control Management of Road Construction Projects



Debby Willar, Anak Agung Diah Parami Dewi, and Febriane P. Makalew

Abstract Along with the pace of development of road infrastructure in Indonesia, improving the quality of road construction project execution is becoming a concern of the government and related stakeholders. The poor project execution process of national road construction certainly has an impact on the failure of the construction products as well as the increase in work accident rates. This paper reviews the government regulation on the practices of quality control procedures and quality assurance system, and safety control, to provide an evaluation and then a recommendation for stakeholders on the effective implementation of quality control management in road construction projects. Quality documentations must be available, containing quality targets to be achieved throughout the construction process. Quality control and safety control must ensure that all components of road construction are thoroughly secured to meet the specified quality and safety requirements. Far fewer demands are made on the quality assurance system, which both the government and construction companies must develop to ensure that the quality control and safety control processes are sufficiently targeted and effective. The results of the review can be used to stimulate the implementation of quality control and quality assurance of road construction projects integrated with occupational health and safety in order to build qualified road infrastructure projects, which function according to their life span. The review's significance contributes to the knowledge in the area of quality control management of construction projects. The review will help improve awareness among the policymakers and construction practitioners to enable them to be consistent in achieving the quality-safety of infrastructure project delivery.

Keywords Quality control · Quality assurance · Safety control

D. Willar (✉) · F. P. Makalew
Manado State Polytechnic, Manado, Indonesia

A. A. D. P. Dewi
Udayana University, Denpasar, Indonesia

1 Introduction

Public infrastructure, particularly road infrastructure, has a strong linkage with the economic growth of a nation. Road construction is vital as the primary support of dynamic economic activity at both the central and local levels. In Indonesia, as in all other countries around the world, the possession of a good road network is necessary to support growth in both the central and regional levels. Road infrastructure has become a crucial part of daily life. Individual road users, logistic firms, and public transportation agencies expect reliable and safe road infrastructure for traveling from one location to another and transporting goods and people. Road agencies need to properly plan, build, maintain, and operate road infrastructure in order for it to create value for road users [1]. This is associated with the quality of the road.

The quality of roads in Indonesia is still not optimal. Based on the Global Competitiveness Index report, the quality of roads in Indonesia ranks 75. This position is below Singapore (1), Malaysia (20), Brunei Darussalam (32), and Thailand (55). The competitiveness of road infrastructure in Indonesia is still below that of Singapore, Malaysia, and Thailand [2, 3]. The quality of the road, both concrete and asphalt, does not seem to be able to last 5–10 years. Recently, it has been discovered that there are roads that have been damaged in the second year and some after even 10 days. In addition, the growth of new road construction has been slow. Such a worrying condition is compounded by the fact that many of the roads that are in poor condition are located in provincial and rural areas. Given the critical role of road infrastructure in supporting economic development, there is an urgent need for the Indonesian Government to improve the quality of road infrastructure [4]. The success of road infrastructure development is measured in terms of physical construction and its performance, which includes the functioning of the road according to its life span.

The government has enacted main policies on construction services, i.e., UU No. 2/2017, which state that service providers and or sub-service providers are required to submit the results of their construction products right cost, right quality and right time according to the construction contract. In addition, the government also requires that both service users and service providers meet the security, safety, health and sustainability standards in using materials, tools, and practicing occupational, health and safety (OHS). However, there are still poor project execution processes of national road construction that impact the failure of the construction products and the increase in work accident rates. In doing so, the Ministry of Public Works and Housing has set out in more detail several policies focusing on quality control and quality assurance in the management of road construction projects, with the involvement of both private and public sectors. This concern has been studied by Meijer and Visscher [5] regarding the quality control of constructions in seven European countries, which shows that quality control has become more privatized and implemented throughout the construction process with the focus on safety aspects. Using Indonesian regulatory and the review of current practices as the secondary data, this paper aims to review the practices of quality control management of road construction projects, particularly in terms of quality control and quality assurance procedures, and safety control.

The results of the review serve as an overview to stimulate the implementation of quality control and quality assurance of road construction projects integrated with occupational health and safety in order to build qualified road infrastructure projects, which function according to their life span. The review will also help improve awareness among the policymakers and construction practitioners to enable them to be consistent in achieving the quality-safety of infrastructure project delivery.

2 Methodology

The reviews of quality control management of road construction projects are undertaken using Indonesian government regulations on the practices of quality control procedures and quality assurance system, and safety control, together with the relevant literature in the area of quality and construction project management. The first stage of the review is to select the materials. The main consideration in selecting proper materials is the topic's key ideas [6]. The review aims to provide an evaluation and then a recommendation for road construction projects' stakeholders on the practical implementation of quality control and quality assurance integrated with occupational health and safety, hence will help improve awareness among them to be consistent in achieving the quality-safety of infrastructure project delivery.

The second stage is to analyze the materials. One of the three functions in doing the literature reviews is identifying and discussing others' works and then using the reviews to solve similar problems [7]. These reviews consist of four parts. The first part is a review of the importance of quality documentation that must be developed by both the service users and the service providers. The second one is a review of the importance of quality control in securing the execution of road construction projects to meet the specified quality requirements. Furthermore, the review covers quality assurance, which is the process to ensure whether the quality control process is sufficiently targeted and effective. The last part is a review of the importance of safety control in implementing road construction projects. Premised on these reviews, the quality control management of road construction projects in Indonesia are identified and discussed.

3 Quality in Project Management Processes of Road Infrastructure

Project management is the application of knowledge, skills, tools and techniques to project activities to meet the project requirements [8]. PMI's A Guide to the Project Management Body of Knowledge has identified the project management processes consisting of (1) initiating, (2) planning, (3) executing, (4) monitoring and controlling, and (5) closing. Further, the PMBOK Guide identifies one of the

project management knowledge areas as quality. These two elements synergize with the dynamic characteristics of construction work that require an integrated, precise and safe management in the execution of projects in order to achieve final results of construction products that meet the performance target of both the project owner and the construction service providers. By focusing on the performance of targeted construction products, quality is a must throughout the project management processes.

The performance of construction works is generally measured by the satisfaction of the project stakeholders within the constraints of cost, quality, and time [9, 10]. Subsequently, the development of construction works performance expands into health and safety and environmentally friendly construction [11, 12], project team level of effectiveness [13], sustainable construction [14–16], and human resource competence [17]. These performance indicators determine the process of fulfilling the quality assurance of public road construction works throughout the project management processes of road infrastructure.

Road infrastructure conditions that have not been optimal may be caused by problems in the project management processes of road infrastructure projects, especially in terms of quality during the execution phase. The quality of road infrastructure in Indonesia has been subject to debate. The government's road-building program has often been hampered by quality issues. Handling construction quality problems in government projects has been regulated by the Ministry of Public Works No. 04/PRT/M/2009 about the Quality Management System (QMS), and by the Ministry of Public Works and Housing regulation No.31/PRT/M/2015 about Procurement of Construction Works and Consultancy Services, and by The Ministry of Public Works and Housing regulation No. 02/PRT/M/2018 about Occupational Health and Safety. These regulations are intended to lead the construction service providers to the project management processes, for the achievement of performance based on their QMS and OHS policies, which is integrated accordingly with the quality policy specified in the Ministry of Public Works and Housing.

Since the project management processes of road infrastructure involve various parties, the quality aspect should rely on both technical and non-technical aspects. There are technical standards and specifications for road construction that the contractors must follow. On the other hand, several non-technical aspects may impact the weak implementation of quality in project management processes of road infrastructure. Such weak implementation is often caused by several factors, such as managerial, organization, communication, finance, culture, education and auditing [18]. The weakness of managerial factors lies in the difficulty of mobilizing interactions between the production department and the quality department, and the difficulty in carrying out quality control in every department.

Moreover, there are traits within construction organizations that support the quality implementation in project management processes, which is generally bounded in the form of organizational quality culture. In the case of improving the quality performance of Indonesian transport infrastructure projects, Agustiawan et al. [19] found that there is a need for the project stakeholders to be more integrative, cooperative, flexible and focused on being goal-oriented and people-oriented.

Organizational culture developed by every organization of project stakeholders will benefit in developing a quality relationship and communication between project parties, which will, in turn, contribute to better project performance [19]. In addition, studies show that organizational culture influences the quality performance of Indonesian construction companies in undertaking projects, and, hence, improves their business performances [20, 21]. The paradigm in managing projects has moved from traditional patterns to a more relationship-based approach [19]. One example of the conflict that occurs, primarily during the project execution phase, is usually due to the difficulty of the contractor organization in controlling sub-contractors. A better practical collaboration impacts trust, which propagates in face-to-face communication, team building, and information sharing, which are all essential traits to perform quality project management processes [22].

4 Quality Control Management of Road Construction Projects

The lack of understanding of the benefits of QMS possessed by the individual contractor, as well as how the QMS can be applied together between service providers and construction project owners, can hamper internal improvement in the quality and performance of the organization against the effectiveness of QMS implementation in construction. If the stakeholders of infrastructure projects understand and consolidate each other to implement a quality control and quality assurance system during the project execution phase, then the final product performance of road infrastructure construction can be ensured to be effective, qualified and safe.

In general, the quality aspect consists of three parts, namely quality planning, quality assurance, and quality control [23, 24]. Quality planning is used for setting quality objectives and required planning resources for meeting quality requirements. Quality control supports preventing and correcting defects in pre-production, production, and post-production stages. Quality assurance focuses on assuring that prerequisites (e.g., work-force, technologies, materials) of providing/creating a high-quality service or product are available. Currently, the concept of quality planning and quality assurance has been relatively good with a numerous variety of existing policies. However, the application of quality control often causes problems or quality issues under the project management practices of the construction phase. The quality of government projects is often seen in terms of product results and the function of the infrastructure products. On the other hand, quality has two complementary forms, including (1) qualities of processes and (2) qualities of products [25–28].

As stated above, the quality context may cause a problem of project management practices in road infrastructure. Even though there are several regulations associated with quality, it can be found that some conditions of road infrastructure have deteriorated. In the Indonesian context, there are several essential functions of quality control management in road infrastructure projects, namely.

4.1 Quality Documentations

The necessary quality documentation is a quality policy developed by both the service users and the service providers. In the case of the Indonesian road construction projects, the service user is the Ministry of Public Works and Housing, while the service providers are contractors, sub-contractors and suppliers. The quality policy is an effort to guarantee the availability of reliable infrastructure for the community with the principle of being efficient and effective as well as improve the quality of activities sustainably [23, 24]. Another quality documentation required to start undertaking a project construction is a contract quality plan. This document is prepared in the initial process at the pre-construction stage. The contract quality plan is a QMS document prepared by the construction services providers for each contract of work in order to guarantee quality. The contract quality plan contains quality targets, which describe measurable quality achievement targets by following the project specification.

Ensuring that the quality of the road infrastructure can be improved, the fundamental aspects of quality related to the project management have to be fulfilled under the responsibility of a technical director and quality controller, as stated in several quality plans and quality procedures documentations. Quality plan and quality procedures documentations are methods and guidelines that explain the work processes to be undertaken by following the requirements and specifications to be achieved. Subsequently are the quality assurance and quality control. These are carried out during the process of executing, controlling and monitoring the road infrastructure project.

4.2 Quality Control

Quality control secures all components thoroughly and in detail (not randomly) to meet the specified quality requirements, and always has a checklist of what will be inspected. This is a way whereby there is a global growth in demand for improvement of road infrastructure in Indonesia as a developing country to improve quality. Quality control in construction projects can be defined as a procedure that monitors specific project outcomes to define whether they conform to specifications, and identify ways to disregard the causes of poor results [29]. A true reflection of critical risks of developing countries' infrastructure projects delivery is improper quality control [30].

The rationale behind quality control is that it involves a monitoring action, but is also concerned with finding and eliminating causes of quality problems, so that the necessities of the customer are determinedly met [31]. From a construction project perspective, quality control includes observing or measuring actual performance remedial actions to determine whether there are deviations [32]. Quality control conveys with it a general framework for quality management and is essentially the actions and systems applied to attain and sustain the quality of a product or service

[33]. The quality control activities should describe, but not necessarily be limited to, defining and implementing a measurement system and measuring the selected parameters, for instance, weight and temperature [32]. Juran and Gryna [34] state that quality controllers should be experts in the fields of project and statistical quality control, sampling and probability, and must be able to measure quality outputs. Often these control processes include the monitoring of actual project results to evaluate compliance with quality standards and to eradicate poor performance, developments, and products [29, 35, 36]. The quality of construction depends mostly upon the control of construction, which is the critical concern of the contractor [37].

In addition to supervision, quality control issues are also governed by organizational aspects. It can be given that roads in Indonesia consist of national roads, provincial roads and regency roads. In this road division, there are three levels in management, namely top, middle, and bottom level. At the top is management, and at the bottom is the field—the men who work on the grade. In between is a large group of dedicated people in the central office, in the laboratory and in the district offices who constitute the backbone of the department (administration).

4.3 *Quality Assurance*

Quality assurance (QA), is a systematic and planned activity determined in the quality system to ensure whether the quality control process is sufficiently targeted and effective enough. In this process, quality is also expected to be achieved by following the quality plan. Quality assurance is a system whereby the government, as an agency or owner in place, monitors the quality control efforts of the contractor. In contrast, quality control is generally the contractors' system in place during the construction to manage, control and document activities in order to comply with contract requirements.

The government plays an essential role in assuring the quality of road construction projects meet the standard of infrastructure facilities as the primary support of dynamic economic activity at both the central and local levels. The government, therefore, must ensure that the adoption of quality standard policy and regulation by the service providers—as their partners—are based on true motivations to enhance quality in the construction of road infrastructure projects. It is true that in assuring the quality of construction projects, both internal and external motivation [38] and the commitment to comply with the regulations [5], are found to be significant factors perceived by the contractors to enhance a quality assurance program for the construction industry.

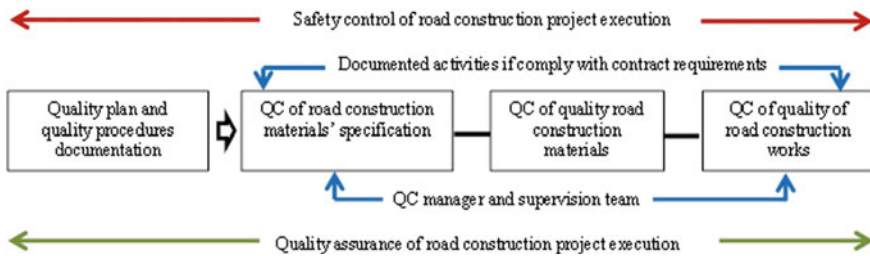


Fig. 1 A framework of quality control management practices in road construction projects

4.4 Safety Control

Safety control technically secures the work structure and should be emphasized in all processes involved. The current issue is the importance of safety control in the implementation of road construction projects. In Indonesia, safety is regulated in the current regulations; however, the implementation is not optimally implemented. Research results on the adoption barriers of the engineering construction standards by Wang et al. [39] found policy barriers due to lack of improper guidance and imperfect standard legal systems. The Indonesian government, as an agency or project owner, needs to pay more attention to the barriers that the Indonesian service providers face and be firm in implementing this rule by providing more technical guidelines.

It is also necessary to conduct periodic observation to make the project run according to the quality plan and policy as well as safety regulations. The stages of quality management in road infrastructure projects are explicitly written. However, all these stages have not been able to run well from the pre-construction to post-construction stages. There are still obstacles in achieving the project objectives, both from the quality plan stage to the periodic observation stage. Quality and safety issues in service organizations are inseparable [40]. The imperfect implementation process of national road construction certainly has an impact on the failure of the construction process and products, as well as the increase in work accident rates. Nevertheless, all parties have to be aware of and not to be shy to admit their mistakes. Love and Smith [41] stated that construction enterprises' board of management should open horizons by 'learning from errors' in order to enhance quality and safety performance.

A specific framework has been developed to simplify understanding the identified quality control management practices in road construction projects (see Fig. 1).

5 Conclusion

The quality of road infrastructure in Indonesia has been subject to debate since the government's road-building program has often been hampered by quality issues. The poor quality of roads can be seen by the damage that still occurs on the road. Based on

the literature and regulation reviews, problems that may cause poor road infrastructure products are identified as problems in the project management processes, especially in terms of quality implementation during the execution phase concerning non-technical aspects, such as lack of interaction amongst departments and cooperation between parent contractors and sub-contractors.

This study also evaluates the practices of quality control procedures and quality assurance system and safety control of road construction projects. The availability of quality policy, quality plan and quality procedures are the first steps in explaining the quality work processes to be undertaken and, hence, the quality performance of road infrastructure to be achieved. Subsequently are the quality control and safety control. Through these activities, all components of road construction are thoroughly secured to meet the specified quality and safety requirements. Last but not least, there is a quality assurance system that both the government as owner and service user and construction companies as service providers must develop to ensure whether the quality and safety control and processes are sufficiently targeted and effective. The results of the study have helped to enhance the implementation of quality control management of road construction projects that the stakeholders face.

Acknowledgements This study was supported by the Ministry of Research and Technology/National Research and Innovation Agency of Indonesia through the 2020 Fundamental Research Scheme. The authors also thank Associate Professor Bambang Trigunaryah of RMIT University, Australia, for his assistance throughout the study.

References

1. Hartmann A, Ling FYY (2016) Value creation of road infrastructure networks: a structural equation approach. *J Traffic Transp Eng (English Edition)* 3(1):28–36
2. PUPR (2019) Pengawasan mutu pekerjaan jalan (quality control of road constructions). Bina Marga Report of the Ministry of Public Works and Housing
3. World Bank (2019) Global competitiveness index. World Bank Report
4. Dewi AP (2014) Framework for implementing design build project delivery system in road infrastructure projects in Indonesia. PhD thesis, Queensland University of Technology, Brisbane
5. Meijer F, Visscher H (2017) Quality control of constructions: European trends and developments. *Int J Law Built Environ* 9(2):143–161
6. Machi LA, McEvoy BT (2009) *The literature review*. Corwin Press, Thousand Oaks
7. Evans D, Gruba P (2009) *How to write a better thesis*, 2nd edn. Melbourne University Press, Carlton
8. Project Management Institute (PMI) (2017) *A guide to the project management body of knowledge (PMBOK Guide)*, 6th edn. PMI, Pennsylvania
9. Zhang L, Fan W (2013) Improving performance of construction projects. *Eng Constr Architectural Manag* 20(2):195–207
10. El-Sawalhi NI, Hammad S (2015) Factors affecting stakeholder management in construction projects in the Gaza strip. *Int J Constr Manag* 15(2):157–169
11. Lam EWM, Chan APC, Chan DWM (2010) Benchmarking success of building maintenance projects. *Facilities* 28(5/6):290–305

12. Zanjirchi SM, Moradi M (2012) Construction project success analysis from stakeholders' theory perspective. *Afr J Bus Manag* 6(15):5218–5225
13. Frödell M, Josephson PE, Lindahl G (2008) Swedish construction clients' views on project success and measuring performance. *J Eng Des Technol* 6(1):21–32
14. Zabihi H, Habib F, Mirsaeedie L (2012) Sustainability in building and construction: revising definitions and concepts. *Int J Emerg Sci* 2(4):570–578
15. Rafindadi AD, Mikić M, Kovačić I, Cekić Z (2014) Global perception of sustainable construction project risks. *Procedia Soc Behav Sci* 119:456–465
16. Yu W, Cheng S, Ho W, Chang Y (2018) Measuring the sustainability of construction projects throughout their lifecycle: a Taiwan lesson. *Sustainability* 10(15):23
17. Yong YC, Mustaffa NE (2012) Analysis of factors critical to construction project success in Malaysia. *Eng Constr Architectural Manag* 19(5):543–556
18. Ahmed MA, Xia B, Coffey V (2017) The requirements of developing a framework for successful adoption of quality management systems in the construction industry. *Int J Soc Behav Educ Econ Bus Ind Eng* 11(1):189–197
19. Agustawan Y, Coffey V, Lamari F (2019) Improving relationship quality between main contractors and sub-contractors in Indonesian infrastructure projects. In: ICAnCEE 2018, MATEC web of conferences, vol 276, pp 1–9
20. Willar D, Trigunaryah B, Coffey V (2016) Organisational culture and quality management system implementation in Indonesian construction companies. *Eng Constr Architectural Manag* 23(2):114–133
21. Mubin CH, Latief Y (2019) Organizational culture influence on implementation of knowledge management and quality management system for improving Indonesian construction companies' performances. *IOP Conf Ser Mater Sci Eng* 508:012037
22. Zuppa D, Olbina S, Issa R (2016) Perceptions of trust in the US construction industry. *Eng Constr Architectural Manag* 23(2):211–236
23. Abdirad H, Nazari A (2015) Barriers to effective implementation of quality management systems in public design projects in Iran. *J Architectural Eng Des Manag* 11(6):457–474
24. Rivelino R, Soekiman A (2016) Kajian pengendalian mutu konstruksi pada pengawasan pelaksanaan pembangunan jaringan irigasi studi kasus: Pembangunan jaringan irigasi di Leuwigoong (a study of construction quality control in the supervision of irrigation network development: the case study of irrigation networks development in Leuwigoong). *Jurnal Konstruksia* 8(1):1–16
25. Blyth A, Worthington J (2000) *Managing the brief for better design*. Taylor & Francis, London
26. Prasad S (2004) Inclusive maps. In: Macmillan S (ed) *Designing better buildings*. Spon Press, London
27. Sebastian R (2005) The interface between design and management. *Des Issues* 21(1):81–93
28. Volker L (2010) *Deciding about design quality*. Sidestone Press, Leiden
29. Cooke B, Williams P (2004) *Construction planning programming and control*. Wiley-Blackwell
30. Babatunde SO, Perera S, Adeniyi O (2019) Identification of critical risk factors in public-private partnership project phases in developing countries: a case of Nigeria. *Benchmarking Int J* 26(2):334–355
31. Foster ST (2001) *Managing quality: an integrative approach*. Prentice-Hall, Upper Saddle River, New Jersey
32. Forman RT, Sperling D, Bissonette JA, Clevenger AP (2003) *Road ecology: science and solutions*. Island Press, Washington D.C.
33. Bowen PA, Edwards PJ, Cattell K (2012) Corruption in the South African construction industry: a thematic analysis of verbatim comments from survey participants. *Constr Manag Econ* 30(10):885–901
34. Juran JM, Gryna FM (1993) *Quality planning and analysis*, 3rd edn. McGraw-Hill College, New York City
35. Oakland J, Marosszeky M (2006) *Total quality in the construction supply chain*. Butterworth-Heinemann, London
36. Kerzner HR (2013) *Project management: a systems approach to planning, scheduling, and controlling*. Wiley, New Jersey

37. Turner JR (2003) Contracting for project management. Gower Publishing Ltd., Surrey
38. Kam KJH, Hamid AHA (2015) The true motives behind the adoption of QCLASSIC-CIS 7: 2006: as a quality assurance initiative in construction industry. *Int J Qual Reliab Manag* 32(6):603–616
39. Wang W, Zhang S, King AP (2016) Research on the adoption barriers of the engineering construction standards in China. *Struct Surv* 34(4/5):367–378
40. Odigie ME, Badar MA, Sinn JW, Moayed F, Shahhosseini AM (2017) An optimal integrated QSMS model from cluster analysis. *TQM J* 29(3):438–466
41. Love PED, Smith J (2016) Error management: implications for construction. *Constr Innov* 16(4):418–424

Review of Previous Research Methods in Evaluating BIM Investments in the AEC Industry



Jeri Adin Ardani, Christiono Utomo, Yani Rahmawati,
and Cahyono Bintang Nurcahyo

Abstract Building Information Modeling (BIM) provides many recognized benefits and becomes the most promising technology in the AEC industry. However, many construction companies are still hesitant to invest in this technology. The lack of information about the financial benefits of BIM implementation against the high cost of investment incurred is one of the obstacles in BIM practice. Therefore, stakeholders need to be encouraged by empirical evidence regarding the financial benefits that BIM presents. Over the last ten years (2010–2020) identified there were 16 studies on the topic of BIM investment. This study using the literature review method aims to review and map the methods used in the studies. The results of this study show that quantitative research with secondary data, case studies, and Return on Investment (ROI) is the most widely used method. However, ROI is still considered incapable of capturing the overall costs and benefits. Therefore, Cost benefit analysis (CBA) becomes the solution to the gap because it can measure intangible benefits and indirect costs as well as a combination with systems dynamic that can be modeling the financial implications arising from BIM investment. The confidentiality of construction cost data and the lack of ability to track BIM project data are among the obstacles when conducting CBA. Therefore, to address the problem two recent studies published in 2020 propose predictive methods using artificial intelligence (AI) approaches to predict the net costs and benefits of BIM implementation. The findings of this study can be used as a guideline for further research methodologies in evaluating and justifying BIM investment to encourage greater adoption of technology in the AEC industry.

Keywords Building information modeling (BIM) · Investment · Project finance

J. A. Ardani (✉) · C. Utomo · C. B. Nurcahyo
Department of Civil Engineering, Institut Teknologi Sepuluh Nopember, Sukolilo, Surabaya
60111, Indonesia
e-mail: jeriارداني.19031@mhs.its.ac.id

Y. Rahmawati
Department of Architecture Engineering and Planning, Universitas Gadjah Mada, Yogyakarta
55281, Indonesia
e-mail: yani.rahmawati@ugm.ac.id

1 Introduction

The Architecture, Engineering, and Construction (AEC) industry are rated poor productivity with low efficiency due to their fragmented processes [1, 2]. Due to the high competitiveness of the construction industry, construction companies must be highly competitive and innovative in making substantial progress and success. In the era of industrial revolution 4.0, digitization technologies that optimize processes in the entire construction value chain are being promoted [3]. Building Information Modelling (BIM) is one of the main technologies for digitizing the construction process and BIM is recognized as being able to enhance collaboration between participants involved [4–7], conduct simulation processes [8, 9], digital asset management practices [10], etc. BIM can assist architects, engineers, and constructors in visualizing what will be built to identify building design, construction, or operational issues, and can drive the role of all stakeholders because with BIM technology accurate virtual building models can be created [11]. With many benefits provided, it makes BIM one of the most promising technological developments in the AEC industry [3].

Despite the fact that BIM delivers many recognized benefits and becomes the most promising technology in the AEC industry, there are still many construction companies that are still hesitant to invest in this technology [12]. Some of the causes for such doubt are investment uncertainty [13], lack of clearly defined financial implications [3] high initial investment costs [3, 14, 15], and lack of financial benefits information from the implementation of BIM [16, 17]. According to [18] the effect of BIM implementation in order to be widespread depends on how the industry can benefit from the adoption and implementation of BIM [18]. Also stated that the companies need to be driven by empirical evidence and investors also need to evaluate to justify the decisions that have been taken to invest in BIM. Therefore, evaluating and justifying the financial benefits of BIM investment is indispensable.

Over the past ten years (2010–2020) there have been 16 identified studies discussing BIM investment evaluations, among them [3, 12–16, 19–28]. Therefore, the purpose of this study is to review and mapping the methods used in such studies. This research using literature review methods with research published in reputable journals in the last ten years, with the scope of BIM investment research topics in understanding and evaluating the feasibility of implementing BIM in the construction industry. The findings of this study can be used as a methodology guideline for future research in evaluating or justifying investment from BIM to encourage greater adoption of technology in the AEC industry.

2 Conceptual Background

2.1 *Benefits of BIM Investment*

Benefits are the positive result of an activity, benefits can be defined as an increase in a measure arising from a particular program or project [29]. BIM is identified from several studies in addition to having tangible and intangible costs, as well as having tangible and intangible benefits. Tangible benefits according to [26] relate to financial benefits such as increased labour productivity and processes, reduction of construction periods, etc. While intangible benefits are defined as non-financial improvements such as the brand value of superior companies, improved corporate image, etc.

2.2 *Evaluation of BIM Investment*

The purpose of evaluating benefits is to justify a decision such as an investment that has already been made, compare and rank and target success as a benchmark [30]. BIM is the latest technology development in the AEC industry that has been recognized as being related to productivity improvement [30]. Therefore, stakeholders need to be encouraged by empirical evidence regarding the financial benefits that BIM presents and stakeholders who have adopted and implemented BIM need to evaluate the benefits and costs to justify their investment [18].

2.3 *Methods of Previous Research*

Research Philosophy. In general, research can be divided into two types, namely quantitative and qualitative research. Quantitative research is a study involving statistical analysis figures and has strict research design standards developed before actual research. While qualitative research uses data collection and analysis that does not involve numbers and describes the realities in life according to respondents [31]. In a study requiring data and data to be obtained from a source, the data source is usually divided into two secondary and primary data. Secondary data is obtained from archiving organizational data or historical data obtained from books, library materials, literature, previous research, and so on. Primary data was obtained from informants by researchers who conducted the survey [31].

Research Methods. The following are some of the data analysis methods used in previous studies to understand and evaluate the feasibility of BIM investment in the AEC Industry.

Return on Investment (ROI). Comparing potential return on investment with the cost. ROI can be estimated in several ways including improving project results, such as through 3D visualization can detect clashes before work starts, reduce RFI, and field coordination problems, better communication, increase productivity and positively impact projects [15]. ROI is usually presented in percentages e.g. in research [12] resulting in a return of 42% of the standard cost, 50% reduced RFI per assembly, and a 67% reduction in duration from the initial duration of the project. The evaluation of the benefits of BIM investment with ROI approach has been widely studied by several studies including [12, 14–16, 19, 23, 26] using ROI from an Ex-post perspective to evaluate the current conditions of decisions that have been taken in the past to invest in BIM.

Benefit Realization Management (BRM). It is a process of managing and organizing so that the maximum benefits arising from investment decisions can be realized [29]. BRM was developed in the 1980s and 1990s as a solution to the existing gap in understanding the return on investment from investment in IT systems [32]. The BRM application to evaluate BIM investment is used by [21] to ensure that the owner gets value from investing in BIM as an effort to answer doubts from owners who are considered still skeptical of BIM investments.

Cost Benefit Analysis (CBA). It is a systematic method used to analyze decisions that have been taken in business by comparing the costs and benefits of an investment [33]. The application of CBA methods to evaluate information and IT system investments is quite common, as is done by [3] implementing CBA as a method for financial assessment of BIM investments at the company level as a solution to the gap from ROI in assessing the benefits and costs of BIM investments, which in general the benefits of BIM are not all quantitatively measurable. Thus CBA became the solution to the gap [3].

System Dynamic (SD). It was developed in 1950 by Prof. JW Forrester with a view to analyzing complex behaviors in social sciences, particularly in management through computer simulations [34]. In practice [3] it using System Dynamic to model the complexity of causal relationships arising from the financial impact of BIM investments. With System Dynamic simulation the implications arising from an activity can be simulated without disturbing the system being run.

Success Level Assessment Model (SLAM BIM). Is a method based on two principles, the first principle is that clearly defined goals play an important role in the success of the BIM project. The second principle is that key performance indicator (KPI) data must be collected continuously. SLAM BIM is in practice used for the purpose of evaluating the success of BIM projects on an ongoing basis, this method is based on the thought that the success of a project cannot be evaluated without first identifying its clear objectives. Therefore, key performance indicators (KPIs) may vary according to the project objective [24]. In practice, SLAM BIM is used by [24] to assess the success of bim projects reviewed through five stages of steps including (1) BIM goal, (2) BIM use, (3) BIM KPI, (4) Unit measurement, (5) Collection form.

Statistical Analysis with ANOVA [13]. A statistical test of Analysis of Variance (ANOVA) to examine respondents' perceptions of BIM investments, related to investment focus areas, expected returns from BIM investments, methods to increase returns from using BIM, and risks in implementing BIM. Thus, the application of ANOVA is recommended as a technique to examine differences in perceptions between three or more sample groups involved.

Artificial Neural Network (ANN). Is a computational model or machine learning method for information processing techniques that work by imitating the workings of the human nervous system and brain, with the aim of solving complex and non-linear problems [35]. ANN began to be studied in the 1940s [36], the application of ANN is currently very developed, including in information applications, medicine, economics, control applications, technology applications, psychology [36], and for economic analysis [37]. ANN application for BIM investment analysis is one of them carried out by [28] who proposed an ex-ante evaluation with the ANN approach to forecasting future impacts related to decision making for BIM investment to be taken, by estimating the costs and benefits associated with implementing BIM in the company.

Random Forest (RF). Designed by Breiman in the early 2000s [38], RF is a machine learning algorithm based on artificial intelligence (AI) as a fast and cost-effective solution to improve accuracy in complex problem solving. RF is very popular and widely used in resolving classification and regression problems. Reference [27] it using this method to predict and evaluate BIM labor costs, as in practice a simple linear regression used by project managers to predict BIM labor costs is potentially error-prone and high-risk to projects with BIM practices. At its core from research conducted by [27], RF is the best option for predicting and justifying labor costs in BIM practice compared to simple linear regression by simply multiplying the gross floor area by factors estimated from previous experience.

3 Result and Discussion

3.1 Methodology

The first step in this study is to identify previous research that has the topic of BIM investment in understanding and evaluating the feasibility of implementing BIM in the construction industry, with the maximum limit published in the last ten years (2010–2020) in reputable journals or at least Q2. Using search engines including Web of Science (WoS), Scopus, Science Direct, ASCE, Springer, Emerald, MDPI, Taylor and Francis, and Google Scholar, the keywords using are “BIM investment”, “ROI BIM”, “evaluation of BIM investment”, “The influence of BIM on project finance”. The results of the investigation found 16 previous studies from selected

Table 1 The quality level of the selected journals and the number of papers

Name of journal	SJR	Q category	Number of papers
Automation in Construction	1.69	Q1 Building and Construction, Civil and Structural Engineering, Control and System Engineering	7
Journal of Construction Engineering and Management	1.039	Q1 Building and Construction, Civil and Structural Engineering, Industrial relations, Strategy and Management	2
Sustainability	0.581	Q2 Energy Engineering and Poer Technology, Environmental Science, Geography, Planning and Development, Management Energy, Sustainability and the Environment	2
Building and Environment	1.871	Q1 Building and Construction, Civil and Structural Engineering, Environmental Engineering, Geography, Planning and Development	1
Computers in Industry	1.007	Q1 Computer Science, Engineering	1
Journal of Computing in Civil Engineering	0.951	Q1 Civil and Structural Engineering, Computer Science Application	1
Journal of Asian Architecture and Building Engineering	0.239	Q2 Architecture, Arts and Humanities (Miscellaneous), Q3 Building and Construction, Civil and Structural Engineering, Q1 Central Studies	1
Practice periodical on structural design and construction	0.232	Q2 Arts and Humanities, Q3 Building and Construction, Civil and Structural Engineering	1

journals. Table 1 presents the quality level of selected journals, it is known that most research on BIM investment is published in the journal Automation in Construction.

3.2 Result

Santos et al. [39] Conducted research with a bibliometric analysis of BIM literature published between 2005 and 2015. From the results of the study [39] found there are 5 studies related to BIM investments namely [12, 15, 19–21]. Then the research conducted by [39] was developed until 2020 and it was found there were 11 relevant studies [3, 13, 14, 16, 22–28]. This study refers only to previous studies that only

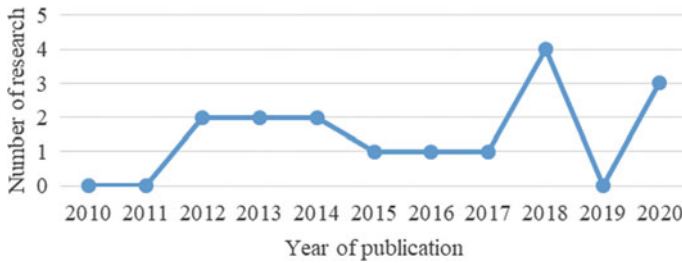


Fig. 1 Number and year of publication

discussed BIM investment in terms of understanding and evaluating the feasibility of implementing BIM in the construction industry and its impact on project finance or companies. Because basically, the purpose of this research is to provide encouragement for stakeholders to apply BIM to their projects or companies through the encouragement of empirical evidence. The results of the literature review obtained 16 relevant studies from the last ten years. Figure 1 presents a curve showing the number and year of publication of these 16 studies.

Research conducted by [40–45] is not included in the category of the 16 studies, because it only discusses the benefits of BIM without evaluating the investment-related costs and benefits to project or company finance. While the research conducted by [11, 46] although it has a topic of discussion that is relevant to this research, it is not included in this category, because the two studies are not published in a journal with a reputation of at least Q2. Table 2 presents the research objectives, perspectives, and levels of the 16 studies that fall into this research category.

Based on Table 2 it can be identified that ex-ante evaluation as stated in the studies [3, 28] is still rarely discussed. Ex-ante evaluations are carried out to predict before the action of a decision is taken and can be evaluated in advance of the impact of future investments, while ex-post evaluations to assess the current conditions of investment decisions taken in the past. The ex-post BIM evaluation has been studied by many researchers. From the literature review conducted, the theoretical mapping techniques from previous research on BIM investment can be seen in Table 3. Literature reviews and theoretical mapping from previous research.

From Table 3 it can be identified that there are 5 techniques used in previous research, namely literature review, interview, case study, workshop, and questionnaire survey. In this context, research techniques through case studies are the most popular. Furthermore, the data analysis techniques used by previous research were identified and found that there were 8 analysis techniques including Return on Investment (ROI), Cost Benefit Analysis (CBA), System Dynamic, Benefit Realization Management (BRM), Success Level Assessment Model (SLAM BIM), Statistical Analysis, Artificial Neural Network (ANN), and Random Forest (RF). Figure 2 maps the methodology of previous research, from the mapping it can be identified that quantitative research with secondary data is the method most used by previous

Table 2 Literature review

Author	Year of publication	Research purpose	Perspective		Level	
			Ex-ante	Ex-post	Project	Corporate
Barlish and Sullivan [12]	2012	Calculate ROI from BIM		✓	✓	
Lee et al. [19]	2012	Propose a method for analyzing BIM ROI based on the cost of avoiding rework from design errors		✓	✓	
Love et al. [20]	2013	The benefits evaluative framework that presents the benefits of intangible BIM and indirect costs		✓		✓
Giel and Issa [15]	2013	Measuring financial savings from the adoption of BIM		✓	✓	
Love et al. [21]	2014	Propose a framework for getting value from BIM investments		✓	✓	
Lu et al. [22]	2014	Develop analytical models to measure the real and intangible costs and benefits of BIM		✓	✓	
Stowe et al. [23]	2015	Assess the ROI and benefits of using BIM on the project		✓	✓	
Won and Lee [24]	2016	Identify the application of the SLAM BIM method to evaluate the success of the BIM project		✓	✓	

(continued)

Table 2 (continued)

Author	Year of publication	Research purpose	Perspective		Level	
			Ex-ante	Ex-post	Project	Corporate
Jin et al. [13]	2017	Identify the focus investments, returns, ways to increase returns, and risks associated with implementing BIM		✓	✓	✓
Ham et al. [14]	2018	Assess the potential costs of design errors and financial benefits provided by BIM		✓	✓	
Shin et al. [25]	2018	Assess the financial benefits of BIM on infrastructure projects		✓	✓	
Reizgevičius et al. [25]	2018	Evaluate the quantitative and qualitative benefits from BIM		✓		✓
Oesterreich and Teuteberg [3]	2018	Assess the economic effects arising from BIM investments at the company level	✓			✓
Kim et al. [26]	2020	Propose the BIM performance evaluation method to review the cost effectiveness of BIM investments		✓	✓	
Huang and Hsieh [27]	2020	Estimating BIM labor costs before starting the project	✓		✓	
Hong et al. [28]	2020	Predict the net cost of implementing BIM	✓			✓

Table 3 Literature review and theoretical mapping of previous research

Author	Types research		Data sources		Methods
	Quantitative	Qualitative	Primary	Secondary	
Barlish and Sullivan [12]	✓			✓	Case study, interview, ROI
Lee et al. [19]	✓			✓	Case study, ROI
Love et al. [20]		✓		✓	Literature review
Giel and Issa [15]	✓			✓	Case study, ROI
Love et al. [21]		✓		✓	Literature review, BRM
Lu et al. [22]	✓			✓	Case study, CBA
Stowe et al. [23]		✓		✓	Workshop, interview, case study, ROI
Won and Lee [24]	✓			✓	Case study, SLAM BIM
Jin et al. [13]		✓	✓		Questionnaire survey, ANOVA
Ham et al. [14]	✓			✓	Case study, ROI
Shin et al. [25]	✓			✓	Case study, survey, interview, CBA
Reizgevičius et al. [16]	✓	✓		✓	Literature review, interview, ROI, regresi exponensial
Oesterreich and Teuteberg [3]	✓			✓	Literature review, case study, CBA, system dynamic
Kim et al. [26]	✓			✓	Case study, ROI
Huang and Hsieh [27]	✓			✓	Case study, random forest, linier regresion
Hong et al. [28]	✓			✓	Case study, questionnaire survey, ANN

studies in the context of BIM investment research in terms of understanding and evaluating the feasibility of implementing BIM.

3.3 Discussion

From Table 2 it can be identified that many studies on BIM investment viewed from an ex-post perspective at the project level include [12–16, 19, 21–26] where investment is evaluated after the investment is made. However, the three most recent studies published in the last three years recognized the drawbacks of previous studies from

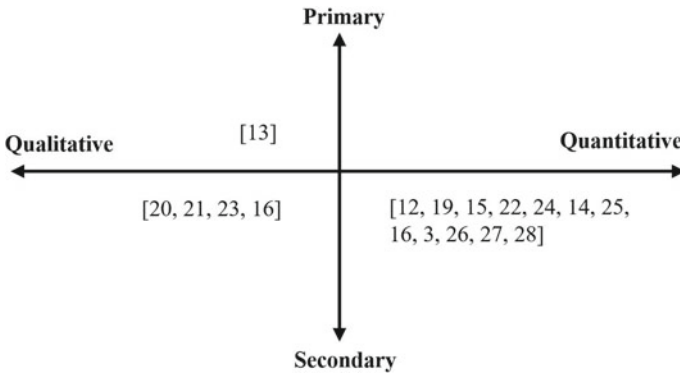


Fig. 2 Mapping diagram previous studies

an ex-post perspective. Therefore, [3, 27, 28] reviewed it from an ex-ante perspective by predicting costs and benefits before investment decisions are taken.

From Table 3, mapped the research methods used in previous research, from the results of the literature review identified 5 research techniques including literature review, interview, case study, workshop, and questionnaire survey. In this context, research techniques through case studies are the most popular. Figure 2 the mapping of research types and data sources consisting of horizontal lines shows the qualitative and quantitative research methods, while the vertical lines show the data sources used in the study, namely primary and secondary data.

From the theoretical mapping, it can be known that quantitative research with secondary data is the most widely used method by previous researchers in the context of BIM investments including adalah [3, 12, 14–16, 19, 22, 24–28]. Furthermore, data analysis techniques used by previous research were identified and obtained 8 analytical techniques including Return on Investment (ROI), Cost Benefit Analysis (CBA), System Dynamic, Benefit Realization Management (BRM), Success Level Assessment Model (SLAM BIM), Statistical Analysis, Random Forest (RF). From the identification, results can be known that ROI is the investment evaluation technique most widely used by previous research.

Evaluation of BIM investment with ROI has been widely applied in previous studies including [12, 14–16, 19, 23] using the ROI approach to identify the value of BIM investment, which is indicated by the percentage of cost savings provided by BIM on the project. ROI is the most popular data analysis technique although according to [20] ROI does not reflect the overall benefits. Therefore, a study published in 2018 by [3] attempted to address this gap by using the CBA to identify indirect costs and intangible benefits that ROI cannot, then in combination with a dynamic system that can be used to assess and model financial implications arising from the implementation of BIM at the company level. However, it was found that the constraints related to the confidentiality of construction cost data are one of the biggest challenges in conducting a cost benefit analysis of BIM implementation [15, 28]. Two recent studies published in 2020 proposed a predictive method using an

artificial intelligence (AI) approach to estimate the net costs of implementing BIM [28] and the labor costs of BIM projects [27]. Among them are the Artificial Neural Network (ANN) method [28], and Random Forest [27].

4 Conclusion

Various research methods used in previous studies on BIM investment have been identified. The research published in the last ten years reviewed in this study mostly use quantitative methods with secondary data. Case studies are the most widely used technique and ROI is the most widely used method of data analysis although it is still considered to have drawbacks i.e. not being able to capture the benefits and costs as a whole [3, 20]. Research conducted by [3] proposes the use of CBA to fill such gap. However, there are constraints related to data confidentiality, construction costs, and the lack of the ability to track BIM project data when performing a cost benefit analysis of BIM implementation [15, 28]. Therefore, to address this problem, two recent studies published in 2020 proposed a predictive method using an artificial intelligence (AI) approach that is faster and more cost-effective to estimate the net cost of implementing BIM [27, 28]. The results of this study are expected to be useful in further research, especially in determining the research methods and data used in this research area to evaluate and justify BIM investment as a driver of greater adoption of technology in the AEC industry. In addition, further research can also use the approach produced in this paper in terms of the number of papers and time spans to gain a better understanding of future research methods in the field of BIM investment, and their effect on project financing.

References

1. Ma X, Chan APC, Li Y, Zhang B, Xiong F (2020) Critical strategies for enhancing BIM implementation in AEC projects: perspectives from Chinese practitioners. *J Constr Eng Manag* 146(2)
2. Elmualim A, Gilder J (2014) BIM: innovation in design management, influence and challenges of implementation. *Architectural Eng Des Manag* 10(3–4):183–199
3. Oesterreich TD, Teuteberg F (2018) Looking at the big picture of IS investment appraisal through the lens of systems theory: a system dynamics approach for understanding the economic impact of BIM. *Comput Ind* 99:262–281
4. Edwards G, Li H, Wang B (2015) BIM based collaborative and interactive design process using computer game engine for general end-users. *Vis Eng* 3(1):4
5. Liu Y, van Nederveen S, Hertogh M (2017) Understanding effects of BIM on collaborative design and construction: an empirical study in China. *Int J Proj Manag* 35(4):686–698
6. Oh M, Lee J, Hong SW, Jeong Y (2015) Integrated system for BIM-based collaborative design. *Autom Constr* 58:196–206
7. Petri I, Alhamami A, Rezgui Y, Kubicki S (2018) A virtual collaborative platform to support building information modeling implementation for energy efficiency. in collaborative networks of cognitive systems. In: Camarinha-Matos LM, Afsarmanesh H, Rezgui Y (eds) IFIP advances

- in information and communication technology, vol 534. Springer International Publishing, Cham, pp 539–550
8. Kim J-U, Hadadi O, Kim H, Kim J (2018) Development of a BIM-based maintenance decision-making framework for the optimization between energy efficiency and investment costs. *Sustainability* 10(7):2480
 9. Amoroso F, Dietrich U, Schuetze T (2018) Development of a building information modeling-parametric workflow based renovation strategy for an exemplary apartment building in Seoul, Korea. *Sustainability* 10(12):4494
 10. Re Cecconi F, Dejaco MC, Moretti N, Mannino A, Blanco Cadena JD (2020) Digital asset management. In: Daniotti B, Gianinetto M, Della Torre S (eds) *Digital transformation of the design, construction and management processes of the built environment*. Research for development. Springer International Publishing, Cham, pp 243–253
 11. Azhar S (2011) Building information modeling (BIM): trends, benefits, risks, and challenges for the AEC industry. *Leadersh Manag Eng* 11(3):241–252
 12. Barlish K, Sullivan K (2012) How to measure the benefits of BIM—a case study approach. *Autom Constr* 24:149–159
 13. Jin R, Hancock CM, Tang L, Wanatowski D (2017) BIM investment, returns, and risks in China's AEC industries. *J Constr Eng Manag* 143(12):04017089
 14. Ham N, Moon S, Kim J-H, Kim J-J (2018) Economic analysis of design errors in BIM-based high-rise construction projects: case study of Haeundae L project. *J Constr Eng Manag* 144(6)
 15. Giel BK, Issa RRA (2013) Return on investment analysis of using building information modeling in construction. *J Comput Civ Eng* 27(5):511–521
 16. Reizzevičius M, Ustinovičius L, Cibulskienė D, Kutut V, Nazarko L (2018) Promoting sustainability through investment in building information modeling (BIM) technologies: a design company perspective. *Sustainability* 10(3):600
 17. Reza Hosseini M, Pärn EA, Edwards DJ, Papadonikolaki E, Oraee M (2018) Roadmap to mature BIM use in Australian SMEs: competitive dynamics perspective. *J Manag Eng* 34(5)
 18. Lu W, Peng Y, Shen Q, Li H (2013) Generic model for measuring benefits of BIM as a learning tool in construction tasks. *J Constr Eng Manag* 139(2):195–203
 19. Lee G, Park HK, Won J (2012) D3 city project—economic impact of BIM-assisted design validation. *Autom Constr* 22:577–586
 20. Love PED, Simpson I, Hill A, Standing C (2013) From justification to evaluation: building information modeling for asset owners. *Autom Constr* 35:208–216
 21. Love PED, Matthews J, Simpson I, Hill A, Olatunji OA (2014) A Benefits realization management building information modeling framework for asset owners. *Autom Constr* 37:1–10
 22. Lu W, Fung A, Peng Y, Liang C, Rowlinson S (2014) Cost-benefit analysis of building information modeling implementation in building projects through demystification of time-effort distribution curves. *Build Environ* 82:317–327
 23. Stowe K, Zhang S, Teizer J, Jaselskis EJ (2015) Capturing the return on investment of all-in building information modeling: structured approach. *Pract Period Struct Des Constr* 20(1)
 24. Won J, Lee G (2016) How to tell if a BIM project is successful: a goal-driven approach. *Autom Constr* 69:34–43
 25. Shin M, Lee H, Kim H (2018) Benefit–cost analysis of building information modeling (BIM) in a railway site. *Sustainability* 10(11):4303
 26. Kim H-S, Kim S-K, Kang L-S (2020) BIM performance assessment system using a K-means clustering algorithm. *J Asian Archit Build Eng* 1–10
 27. Huang C-H, Hsieh S-H (2020) Predicting BIM labor cost with random forest and simple linear regression. *Autom Constr* 118:103280
 28. Hong Y, Hammad AWA, Akbarnezhad A, Arashpour M (2020) A neural network approach to predicting the net costs associated with BIM adoption. *Autom Constr* 119
 29. Bradley G (2010) *Benefit realisation management: a practical guide to achieving benefits through change*, 2nd edn. Gower Publication, Farnham, Surrey, England, Burlington
 30. Sanchez A (2016) *Delivering value with BIM: a whole-of-life approach*, 1st edn. Routledge

31. Adams J, Khan HTA, Raeside R, White D (2007) Research methods for graduate business and social science students, SAGE Publications India Pvt Ltd.: B-42, Panchsheel Enclave, New Delhi
32. Breese R (2012) Benefits realisation management: panacea or false dawn? *Int J Proj Manag* 30(3):341–351
33. Maresova P, Sobeslav V, Krejcar O (2017) Cost–benefit analysis—evaluation model of cloud computing deployment for use in companies. *Appl Econ* 49(6):521–533
34. Ahmad S, Mat Tahar R, Muhammad-Sukki F, Munir AB, Abdul Rahim R (2016) Application of system dynamics approach in electricity sector modelling: a review. *Renew Sustain Energy Rev* 56:29–37
35. Boussabaine AH (1996) The use of artificial neural networks in construction management: a review. *Constr Manag Econ* 14(5):427–436
36. Wu Y, Feng J (2018) Development and application of artificial neural network. *Wireless Pers Commun* 102(2):1645–1656
37. Bruneckiene J, Jucevicius R, Zykiene I, Rapsikevicius J, Lukauskas M (2019) Assessment of investment attractiveness in European countries by artificial neural networks: what competences are needed to make a decision on collective well-being? *Sustainability* 11(24):6892
38. Breiman L (2001) Random forests. *Mach Learn* 45(1):5–32
39. Santos R, Costa AA, Grilo A (2017) Bibliometric analysis and review of building information modelling literature published between 2005 and 2015. *Autom Constr* 80:118–136
40. Al-Ashmori YY, Othman I, Rahmawati Y, Amran YHM, Sabah SHA, Rafindadi AD, Mikić M (2020) BIM benefits and its influence on the BIM implementation in Malaysia. *Ain Shams Eng J*
41. Ghaffarianhoseini A, Tookey J, Ghaffarianhoseini A, Naismith N, Azhar S, Efimova O, Raahemifar K (2017) Building information modelling (BIM) uptake: clear benefits, understanding its implementation, risks and challenges. *Renew Sustain Energy Rev* 75:1046–1053
42. Georgiadou MC (2019) An overview of benefits and challenges of building information modelling (BIM) adoption UK residential projects. *Const Innov* 19(3):298–320
43. Bryde D, Broquetas M, Volm JM (2013) The project benefits of building information modelling (BIM). *Int J Proj Manag* 31(7):971–980
44. Yang J-B, Chou H-Y (2019) Subjective benefit evaluation model for immature BIM-enabled stakeholders. *Autom Constr* 106
45. Olawumi TO, Chan DWM (2019) An empirical survey of the perceived benefits of executing BIM and sustainability practices in the built environment. *Constr Innov* 19(3):321–342
46. Walasek D, Barszcz A (2017) Analysis of the adoption rate of building information modeling [BIM] and its return on investment [ROI]. *Procedia Eng* 172:1227–1234

Sustainable Built Environment

Seismic Performance Evaluation of Horseshoe Tunnel on Weathered-Sedimentary Rock Formation



J. R. K. Nur Aji, A. S. Fajar, T. F. Fathani, and W. Wilopo

Abstract The railway in Indonesia is in the development phase, which began with the construction of new railway lines including railway tunnels. On the other hand, Indonesia is located at the “ring of fire” zone with dense geological structures due to the subduction process. The subduction process increases seismic and volcanic activity. This becomes a hindrance for tunnel construction. Seismic activity has the potential to form geological structures while volcanic activity affects the formation of sedimentary rock mass properties. Both of these processes affect rock mass qualities which are described by the RMR parameters. The geological structures in the sedimentary rock will accelerate the weathering process. Weathered rock layers and minor fault appearance are important issues to be considered in the constructions of railway tunnel. This research aims to simulate a horseshoe tunnel model that considers dynamic load on weathered rocks in evaluating tunnel stability and durability. The dynamic load from the subduction zone is calculated using the point source method to estimate the dynamic load affecting the tunnel. In this study, the model uses plain strain idealization with numerical methods to yield a real condition approach. The model analysis is made with Rocscience software by taking into account weathered rock and arching effect. The result shows that subduction activity increases the dynamic load on weathered rocks that will affect tunnel stability and durability. This seismic performance evaluation is an essential study in tunnel construction performance in the future.

Keywords Horseshoe tunnel · Weathered-sedimentary rock · Numerical simulation

J. R. K. Nur Aji · A. S. Fajar (✉)

Department of Civil and Environmental Engineering, Faculty of Engineering, Universitas Gadjah Mada, Yogyakarta, Indonesia
e-mail: angga.fajar.s@ugm.ac.id

T. F. Fathani · W. Wilopo

Center for Disaster Mitigation and Technological Innovation, Universitas Gadjah Mada (GAMA-InaTEK), Yogyakarta, Indonesia

1 Introduction

In general, underground structures such as tunnels more firm than upper structures such as buildings and bridges during an earthquake. There are several factors why underground structures show a better firm. First, the tunnel structure which has an underground location will experience small seismic amplitude of the ground motion, because the amplification of ground motion has not occurred significantly. Second, tunnels are surrounded by the ground and thus, the structure is rigid and does not experience excitation independently from the ground or experience vibration amplification such as inertia responses from buildings during an earthquake [1].

However, Jaramillo (2017) previous research discussed the impact of seismic design for tunnels in rocks, which was designed for small earthquakes ($PGA < 0,2 g$) to be considered for big earthquakes ($PGA > 0,2 g$). The previous research was based on the increasing number of tunnel incidents that were caused by earthquakes. Accordingly, a reanalysis of entranceway stability was carried out on the increasing of the seismic loads. The previous research shows that the entranceway was still in a stable condition for small earthquakes yet the support system failed to protect from big earthquake incidents [2].

Therefore, a study was conducted to investigate the influence of poor rock formation, which is near to the ground and has $PGA > 0,37 g$ to investigate the seismic tunnel response against artificial time history of shallow earthquake and subduction earthquake.

2 Horseshoe Tunnel and Geotechnical Properties

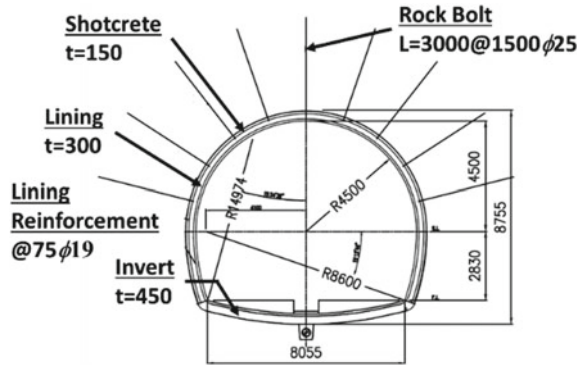
2.1 Horseshoe Tunnel

A railway tunnel was constructed on the Southern coast of Java island which is located 14 km from the seashore of the South Java sea. This tunnel was breaking through a hill named *Bukit Ijo* of 500 m long and 47 m above the sea level. It is a single tunnel that resembles the geometry (see Table 1) of horseshoe tunnel in which the main support system is concrete using single layer reinforcement (see Fig. 1). Two tunnel components in the main support system is lining and invert system where both are reinforced concrete structure that have the same concrete strength.

Table 1 Tunnel reinforcement geometry

Reinforcement	Radius 1 (m)	Radius 2 (m)	Thickness (m)
Shotcrete	4,8	8,9	0,15
Lining	4,5	8,6	0,3
Invert	14,974	–	0,45

Fig. 1 Final tunnel support structure



The train tunnel is constructed to connect Kroya station and Kutoarjo station with double track railway, therefore, the geometry of the tunnel cross-sectional shape is designed to accommodate 2 trains at the same time. New Austrian tunneling method or sequential excavation method is employed to excavate the tunnel. As the tunneling employs New Austrian tunneling method, shotcrete, fore poling, and rock bolt are used as temporary pre-support system to prevent wall collapse caused by ground vibration due to the tunnel excavation. The tunnel cross section that was investigated used rockbolt with a diameter of 25 mm and shotcrete of 150 mm thick for the temporary pre-support system. 3 m long rockbolt with additional grouting was planted and spread on the rock wall with 1.5 m gap. The shotcrete layer sprayed on the rock surface after the installation of rock bolt was modelled as plain concrete in the numerical model.

During the tunnel excavation, several groundwater seepages from the gaps between rock bolt and rocks were found. As a consequence, waterproofing was then applied to protect the main support system from water. To prevent the leakage from spreading to other areas in the tunnel, the water flowing in the waterproofing system is collected in the drainage system and then sent to the drainage channel located in the middle of the invert.

This railway tunnel is located under the hill with an average overburden height of 25 m and a maximum of 38 m or three times bigger than the diameter of the tunnel and is classified as a deep tunnel. Materials used for the tunnel support structures (see Table 2) took into account the presence of waterproofing as it makes discontinuity between rock and the main support system [3].

The tunnel structure located underground will experience three mode deformations during its response to an earthquake. They are axial deformations, curvature deformations, and ovaling or racking (see Fig. 2). The three mode deformations are caused by the wave that propagates at the longitudinal direction of the tunnel and the perpendicular direction of the tunnel. The longitudinal wave will induce the axial and curvature deformations, while the perpendicular wave will induce the ovaling or racking deformation [4].

Table 2 Tunnel reinforcement properties

Support layer	Strength (MPa)	Inertia (m ⁴)	Elastic modulus (MPa)
Rockbolt	240	$1,92 \times 10^{-8}$	200,000
Shotcrete	18	$2,81 \times 10^{-4}$	22,353
Waterproof	—	$8,33 \times 10^{-8}$	1000
Lining concrete	21	$2,25 \times 10^{-3}$	21,538
Invert concrete	21	$7,59 \times 10^{-3}$	21,538

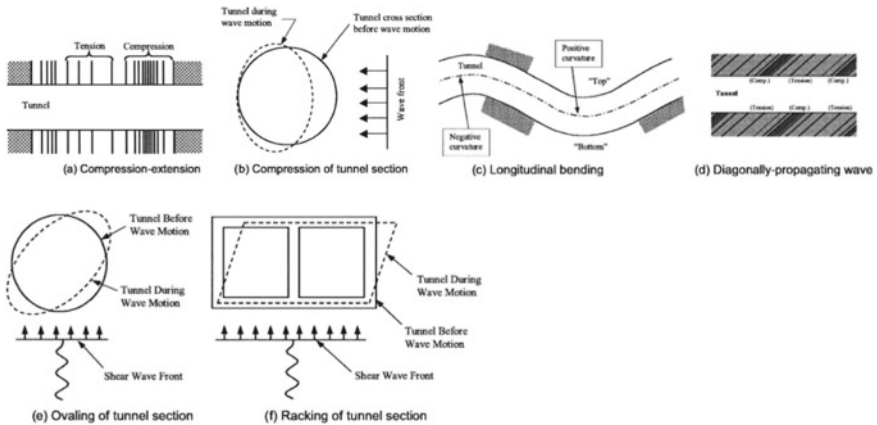


Fig. 2 Deformation modes of tunnels due to seismic waves (4)

Deformed shape of circular and box tunnel have standard forms in response to shocks, different from horseshoe tunnel where the deformation form will be affected by the geometry of tunnel sections.

2.2 Geotechnical Properties

The critical condition of the tunnel sections in which the section has maximum overburden needs careful consideration in choosing a geotechnical properties model. The maximum overburden is frequently a result of weathered rock, which has a poor category according to RMR. Using the analytical analysis (see Fig. 5), it generated maximum overburden load on STA 400 to 450 (see Fig. 3), which was used to make a critical weathered tunnel in the rock model.

Bukit Ijo consists of weak rocks, which is categorized mostly as poor although the geological structure is not found in it. The measurement result of RQD (see Fig. 4) from 360 m core drilling shows that 49,7% rock has less than 50% score. Low RQD

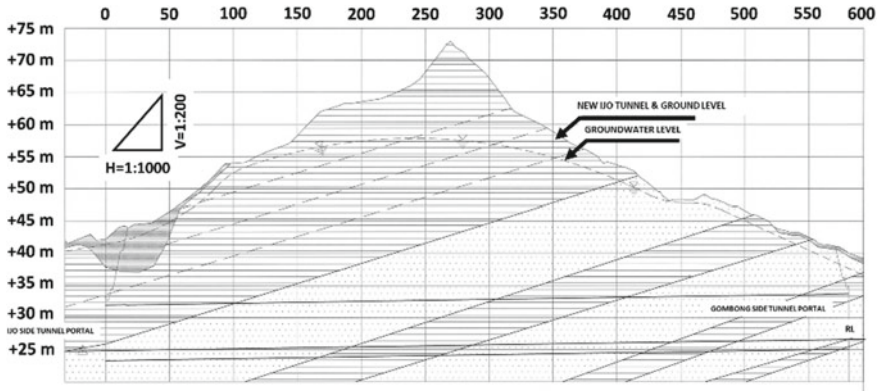
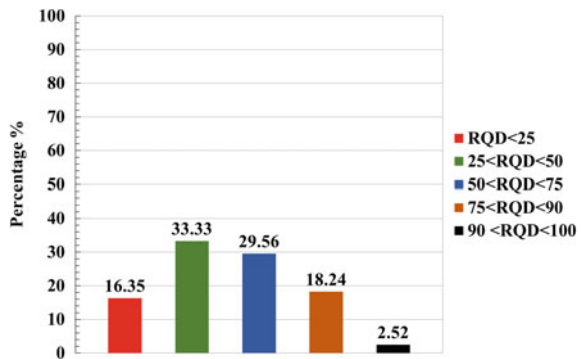


Fig. 3 New Bukit Ijo tunnel geological profile

Fig. 4 RQD measurement histogram for 12 observation points in Bukit Ijo

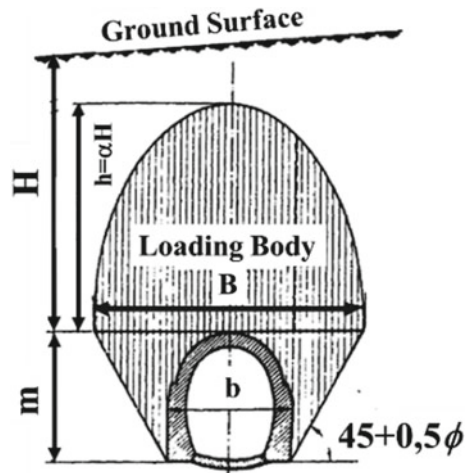


value will yield low RMR value, whereas RMR value is the determinant of rock mechanic parameter value in Eqs. 1 and 2. Consequently, low RQD value obtained from core drilling shows that almost all of the hill rocks have poor quality.

The rocks parameter, which is used in the model analysis, is based on Hoek–Brown criteria and Mohr–Coulomb criteria as those two criteria have been used for deep tunnel construction solutions. Rocks parameter conversion, which refers to the equation relationship of Hoek–Brown dan Mohr–Coulomb criteria, is performed to achieve the Mohr–Coulomb parameter in determining the dimension of the external boundary (see Fig. 5).

$$\phi' = \sin^{-1} \left[\frac{6am_b(s + m_b\sigma'_{3n})^{a-1}}{2(1+a)(2+a) + 6am_b(s + m_b\sigma'_{3n})^{a-1}} \right] \tag{1}$$

Fig. 5 Rock pressure bulb after Bierbäumer (7)



$$c' = \frac{\sigma_{ci} [(1 + 2a)s + (1 - a)m_b \sigma'_{3n}] (s + m_b \sigma'_{3n})^{a-1}}{(1 + a)(2 + a) \sqrt{1 + (6am_b (s + m_b \sigma'_{3n})^{a-1}) / ((1 + a)(2 + a))}} \quad (2)$$

where $\sigma_{3n} = \sigma'_{3\max} / \sigma_{ci}$.

According to the rock facies classification (see Fig. 3), Bukit Ijo rock is classified into seven types of rocks, which are based on the field investigation. The rock mass quality is shown in Fig. 4. The rock-mass can be classified as isotropic materials when the geology structures cannot be used as tunnel control failure and the model fits the Hoek–Brown failure criteria [5]. This research focuses on the tunnel section of STA 400–450 which analyzes using two-dimensional plain strain models in Rocscience 2D (RS2). After that, the static and dynamic condition is discussed. Geotechnical properties for the rock mass model are shown in Table 3.

Table 3 Rock parameters in the Hoek–Brown and Mohr–Coulomb relationships

Layer	σ_{ci} (MPa)	Mb	s	a	Erm (GPa)	GSI	c'	ϕ'
Tuff-breccia	1,82	1,28	0,00,029	0,512	0,535	38	5,95	32
Siltstone	2,22	1,25	0,00,056	0,509	0,783	43	7,29	11
Tuff-breccia	3,57	0,63	0,00,044	0,51	0,895	42	11,69	38,4
Siltstone	3,57	0,66	0,0005	0,509	0,948	43	11,69	38,4
Tuff-breccia	5,57	0,33	0,00,034	0,511	0,996	40	18,28	12

3 Numerical Analysis

Understanding the tunnel's structure condition is a must before calculating the stability and failure of the model. In the previous discussion, it is mentioned that only one tunnel is considered to be a deep tunnel. Besides, the materials surrounding the tunnel are isotropic. Based on the prior condition previously mentioned, this analysis of the research uses a numerical modeling approach, with dynamic time history analysis in a two-dimensional continuum method. To prevent wave energy from returning in the model, special energy-absorbing boundaries at bedrock was incorporated into the model (see Fig. 8). Lining or liner in the numerical model has to discretize become segmented by angles subtended dimension that produces acceptable moment. The minimum subtended angle dimension has been set to $60/R$ to perform an acceptable moment, where R is the radius of the tunnel in feet [6]. Based on the discretization rules, the lining and invert component were discretized into small segment joints with maximum length of 0.5 m.

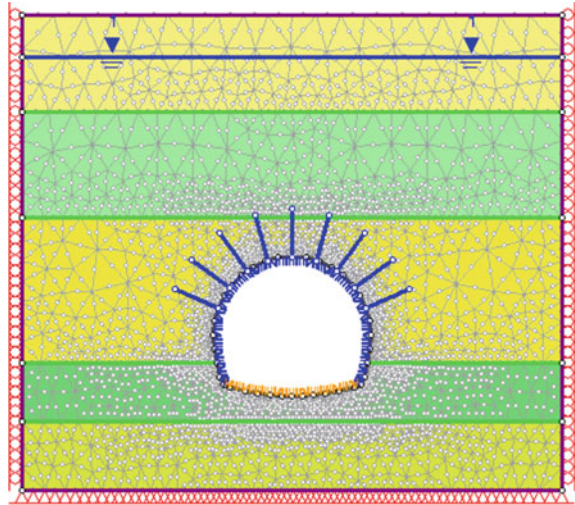
RS2 software will help the numerical modeling approach using a two-dimensional model that analyzes using the finite element method (FEM). The model is run to analyze the stability and support capacity of the tunnel in static and dynamic conditions. On the dynamic condition, RS2 can calculate 2D FEM for each node mesh model and have the ability to analyze dynamic conditions by using the acceleration-time record. The reference to predict the minimum dimension of the external boundary model is Bierbäumer's Theory (1913) which was proposed by Bierbäumer (see Fig. 5) to analyze a tunnel in rock [7]. The vertical dimension of the external boundary is determined to be from the bedrock until exceeding the value of $E + h$ from the rock pressure bulb model. Meanwhile, the horizontal dimension is determined to be from the tunnel axis until exceeding $0.5 B$ from the model rock pressure bulb. The dimensions of the external boundary based on the rock pressure bulb is determined so that the static model loading is closed to the real rock load condition and can be a good initial condition for a dynamic model.

3.1 Static Analysis

The static analysis model of the tunnel in rock is made with no dynamic load on the model except pore water pressure and the weight of material structure, rock and water. Static models allow settlement due to the weight of the soil and rock materials. Hence, the vertical side boundary is restrained only in x-axis which is conditioned to only move vertically, and the bedrock are restrained on the x-axis and y-axis (see Fig. 6). Rock bolt without tensioning is considered in the model because this support acts as a spring in collaboration with other support systems [8].

The result of the internal force lining concrete from the static analysis (see Fig. 11) shows that the critical load lining for the static load happened around 60° and 300° angle. Further, the displacement maximum took place in y-axis at the tunnel's crown.

Fig. 6 Static model finite element analysis



The same behavior also happened during the analytical analysis using the beam spring model [9], which happened at the angle of 60° and 300° . The critical internal forces and same distribution internal forces pattern also happened but with different values, the numerical analysis generates bigger internal forces than the analytical analysis. The different results of analysis between FEM and analytical presumably happened because there is an assumption that cannot be fulfilled in the analytical analysis. For instance, there is no consideration for discontinuity plane in the support system as a consequence from waterproofing and rock pressure calculation which is still conservative because of simplification of rock layers into one layer in bulb form. In addition, if the FEM model has a good meshing quality, the meshing element's weight will be distributed evenly to the tunnel lining structure.

3.2 Dynamic Analysis

In the dynamic system, the fluctuation takes place, which will gradually lose its kinetic energy until it reaches its static condition. Losing kinetic energy is related to the damping rate in the system. The attenuation of Rayleigh is a way to determine dynamic system attenuation, which connects mass and stiffness. Therefore, attenuation matrix becomes proportional to mass (m) dan stiffness (k) in the system:

$$C = \alpha_m \times m + \beta_k \times k \quad (3)$$

In Eq. (3), α_m and β_k are the constants with s^{-1} and s as the unit.

The system will have much natural frequency when the model has many degrees of freedom. The level of attenuation for always being constant in all frequencies

is not possible. Therefore, the model needs to decide two constant frequency and attenuation ratio which is related. There are possibilities to calculate the value of alpha and beta. Meanwhile, a range of frequency between two constants frequency usually has an attenuation ratio under the attenuation score, which is chosen. Besides, frequency outside the range will get dumping stronger. On the other hand, the alpha and beta value can be determined explicitly. Zero in alpha and beta causes the system undamped as a result of the temporary response from the system never disappears.

In a dynamic numerical analysis from the geotechnics system, model boundaries can be made into fictitious boundaries. Even though there are no fictitious boundaries physically, but it is used to approach unlimited volume. Furthermore, those boundaries also use to prevent wave reflection inside the model. Dynamic boundary inside a model can use absorbing condition, transmitting, damper, nodal mass, tied and hydro mass, which depend upon the condition needed (Fig. 7).

The dynamic boundary on the model analysis in this research is made using absorb and transmit condition. This boundary condition tries to make fictitious boundary behavior from soil and stone. Those two dumpings are used to make boundaries in each external border in which the direction of the dumpings is perpendicular to each other. The magnitude of the attenuation coefficient is equal to wave velocity. The wave velocity can be calculated using the viscous boundary condition equation which was proposed by Lysmer and Kohlmeyer (1969) in Eqs. 4–7 [10].

Fig. 7 Viscous boundary by Lysmer and Kuhlemeyer (10)

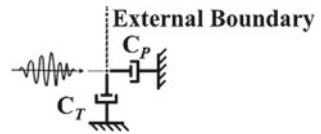
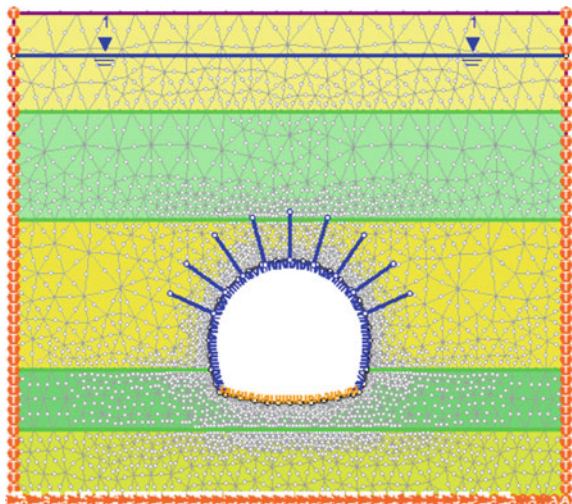


Fig. 8 The boundary condition of the dynamic model



$$C_p = \rho \cdot l_0 \cdot V_p \quad (4)$$

$$C_T = \rho \cdot l_0 \cdot V_s \quad (5)$$

$$V_s = \sqrt{\frac{E}{2(1+v)\rho}} \quad (6)$$

$$V_p = \sqrt{\frac{E(1+v)}{\rho(1+v)(1-2v)}} \quad (7)$$

where E is Young's modulus, v is the Poisson ratio, ρ is rock density, and l_0 is the length of the boundary.

Research on the seismic tunnel performance during an earthquake needs to be done since there are earthquake potentials in a subduction zone that possibly happen. Numerical dynamic analysis using Newmark integration is carried out to learn more about tunnel stability and lining reinforcement capacity. Because the dominant earthquake happens on the horizontal axis, the artificial time history (see Fig. 9) from a shallow earthquake, subduction earthquake, and recorded ground motion in the x-axis model (see Fig. 8) was used.

The attenuation of Rayleigh for tunnel model is determined. Thus, the average damping rate for all-natural frequency in range ω_1 until ω_2 is 5%. ω_1 is the first and foremost of the structure because it frequently makes critical conditions or even collapses. The ratio equation of the mode's damping (ξ_i) can be used to achieve and value, which produces individual attenuation value that is approaching 5%.

$$\xi_i = \frac{1}{2\omega_1} \alpha_M + \frac{\omega_i}{2} \beta_k \quad (8)$$

where ω_i is the natural frequency (rad/s) of mode i .

The seismic performance of the elastic tunnel under an earthquake, will be interpreted from displacement and internal force along the lining and invert concrete. The critical deformed shape of lining concrete for each earthquake (see Fig. 10b) shows horseshoe tunnel behavior in response to vibrations. Each node in the lining concrete (see Fig. 10a) is observed to know the maximum displacement during an earthquake. The result is shown in Table 4. Since a tunnel is an underground structure and experiences motion with soil when an earthquake hits, almost all of the nodes in the numerical models also move when loaded with artificial time history. Accordingly, the maximum displacement value can be obtained from the relative displacement value of each node to node 1 which is placed in the middle of invert (see Fig. 10a).

The maximum displacement value of lining concrete during an earthquake shows when a maximum displacement in the horseshoe tunnel inside the weathered rock

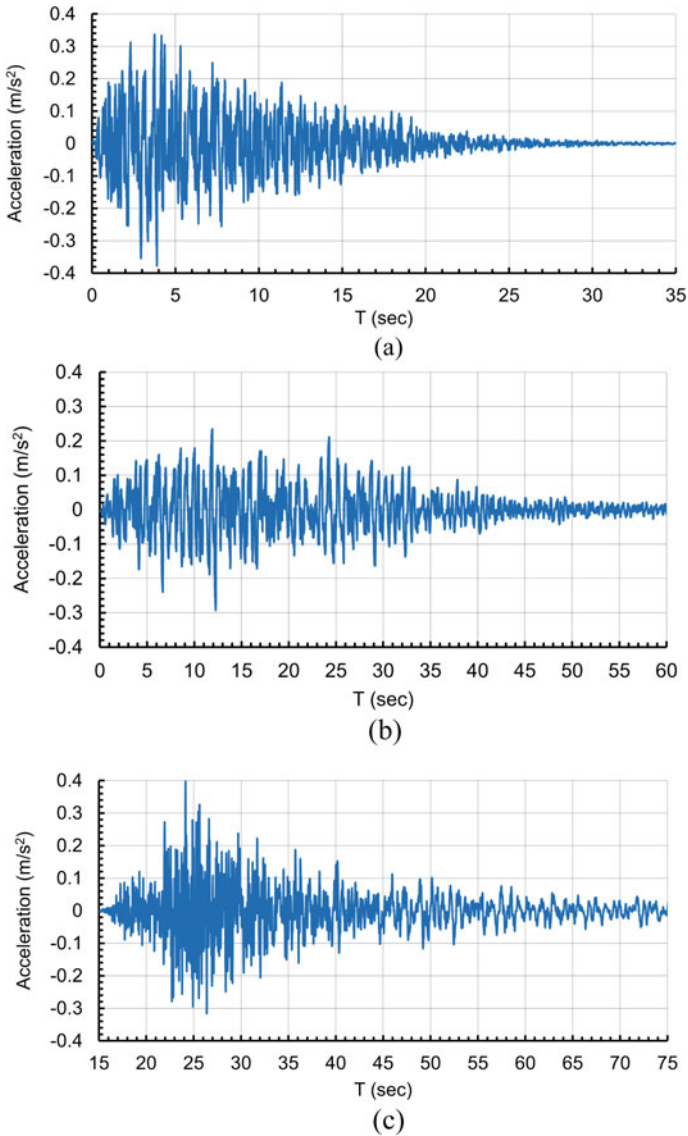


Fig. 9 Artificial time history **a** shallow earthquake; **b** subduction earthquake; **c** recorded earthquake

does not happen at the peak acceleration of ground motion but after that. From the response of the tunnel displacement lining, it can be seen that ground motion with high acceleration may not result in maximum response of tunnel lining structure, such as a shallow and recorded earthquake whereas ground motion with constant acceleration will result in maximum response of tunnel lining structure such as a subduction earthquake. Those things possibly happen because a moderate earthquake

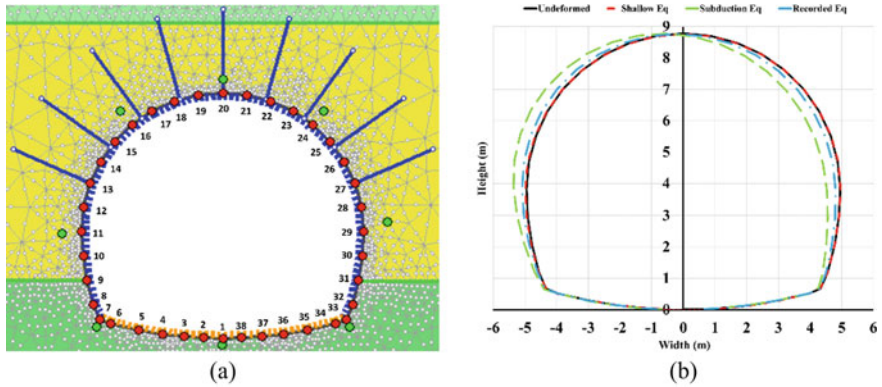


Fig. 10 a Green nodes of query time in tunnel lining; b maximum displacement of the lining during an earthquake

Table 4 The maximum displacement of lining concrete nodes

Load	Nodes	δx -axis (mm)	δy -axis (mm)	Time (s)
Shallow EQ	19	21	-5	7.170
Subduction EQ	20	112	-5	36.901
Recorded EQ	21	-16	-4	49.156
Static load	20	0	-5	-

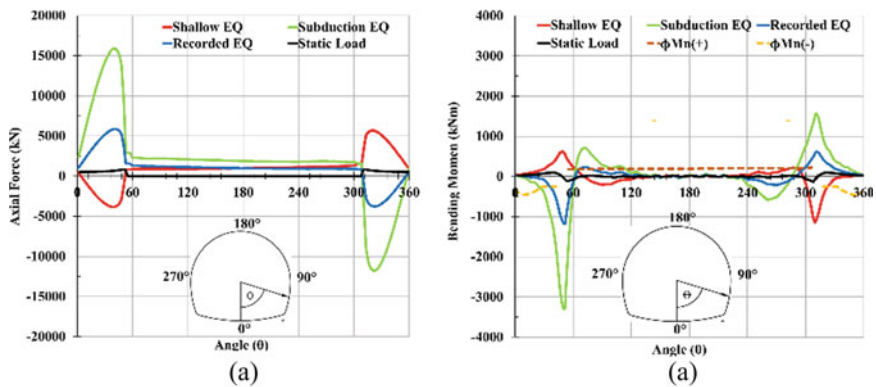


Fig. 11 Lining internal force in dynamic and static load a bending moment; b axial force

with a long duration can lead to a worse impact on the structure. After all, it can reach to its natural frequency.

The maximum internal force will occur at maximum lateral or vertical lining displacement. The reason is maximum displacement can induct tensile stress or maximum compressive stress [11]. As with a typical arch structure with a static

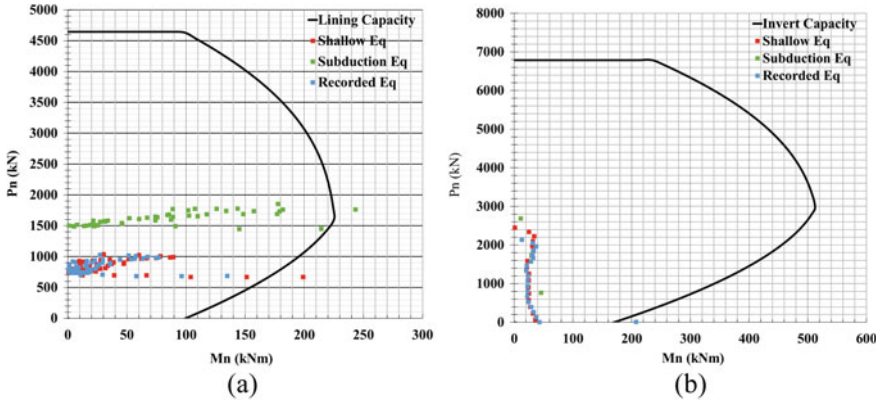


Fig. 12 The capacity of support system versus axial-moment load **a** lining concrete using a single layer of reinforcement **b** inverts concrete using a single layer of reinforcement

load, horseshoe tunnel will act similarly as column element where shear force and combined axial force and bending moment is the determining factor of failure. As increasing shear capacity is easier, lining capacity analysis will be focused on combining axial force and bending moment (see Fig. 12). The moment change of the lining concrete from positive to negative (see Fig. 11b) or vice versa during an earthquake caused the lining concrete to need double reinforcement. As a result, the tensile stress movement on the two sides of the concrete surface can be accommodated. It can be concluded that using single layer reinforcement on one side of the lining concrete is not a wise decision to obtain good seismic performance as when it is seen from the static deformation itself, tensile stress can exist on two different sides of the lining concrete.

The earthquake load from the artificial subduction time history gives the least severe impact in the lining of horseshoe tunnel, particularly at the part of the lining-invert concrete connection. In the lining angle between 120° and 240° , internal forces experience relatively small internal force's enhancement compare with the connection part. Meanwhile, in the tunnel's crown 180° , lining concrete experiences relatively small enhancement of internal forces compared to any other location. The small changing of the internal forces in the tunnel's crown can be affected by the ground motion direction source which has perpendicular direction with dominant vertical load at crown.

In the critical part of the tunnel (in the angle 45° – 60°), when an earthquake strikes, strengthen can be performed. It is suggested to add more reinforcement than thickness. It is because increase in stiffness can increase the dynamic response on the critical part [12]. Reinforcement is considered more effective to add the stiffness as the elasticity modulus of steel materials to concrete material is bigger than the elasticity modulus of concrete to steel.

4 Conclusion

This paper presents the result of the study on the effect of artificial time history in the subduction zone to the stability and durability weathered tunnel in a rock by dynamic time history, Newmark and dynamic numerical method. Besides, it explains some of the complexities in accomplishing and interpreting the results in dynamic analysis of weathered tunnel in the rock. Dynamic time history revealed that the final tunnel support structure is unstable against the design earthquake and has a high probability of failure. Artificial time history of shallow EQ, subduction EQ and recorded EQ was used to perform more elaborate analytical methods. The Newmark analysis demonstrated an approximately ten-millimeter displacement to occur in the final tunnel support structure and a large failing region to form in the case of the design earthquake.

A dynamic numerical analysis was performed on STA 400–450 to further study the stability condition against the design earthquake. According to the calculation of the 2D numerical approach, the study of the seismic performance evaluation of horseshoe tunnel concludes several things as follows:

1. The tunnel maximum displacement during an earthquake (ground motion only in x-axis) often happened in the horizontal direction (x-axis) in the tunnel crown part. As a consequence, the tensile stress at the part of the lining invert connection increases. Further, for the horseshoe tunnel design that considers earthquakes can strengthen, lining-invert connections so that the stability structure is safe.
2. A moderate earthquake with constant and long duration ground motion acceleration (subduction earthquake) will give worse impact to the tunnel support system compared to an earthquake with high (recorded earthquake) but less constant ground motion acceleration or high ground motion acceleration with short duration (shallow earthquake). It is important to consider the earthquake load with a long duration which may be caused by the subduction movement in the horseshoe tunnel plan design in South Java.
3. Single-layer reinforcement cannot be applied in the lining and invert concrete for a horseshoe tunnel with overburden weathered rock especially in lining-invert connections (critical section in the angle 45° – 60°), which has moderate ground acceleration ($>0,2$ g). Double-layer reinforcement is recommended for tunnel lining structure constructed in weathered rock with earthquake load being an important consideration in the design.

References

1. Kampas G, Knappett JA et al (2019) The effect of tunnel lining modelling approaches on the seismic response of sprayed concrete tunnels in coarse-grained soils. *Soil Dyn Earthq Eng* 117:122–137

2. Jaramillo CA (2017) Impact of seismic design on tunnels in rock—case histories. *Undergr Space* 2(2):106–114
3. Jacob JBE, George MF, Duncan JM (2001) Constitutive behavior of geosynthetic interfaces. *J Geotech Geoenviron Eng* 127(10):834–840
4. Hashash YM, Hook JJ, Schmidt B, Yao JI-C (2001) Seismic design and analysis of underground structures. *Tunn Undergr Space Technol* 16(4):247–293
5. Hoek E (2000) *Practical Rock Engineering*
6. Federal Highway Administration (FHWA) (2009) Technical manual for design and construction of road tunnels—civil elements, Tech. rep., Report N° FHWA-NHI-10–034
7. Ponnuswamy S, Victor DJ (2017) *Transportation tunnels*
8. Hoek E (2001) Big tunnels in bad rock 2000 terzaghi lecture. *ASCE J Geotech Geoenviron Eng* 127(9)
9. Elefterija Z, Vlatko S, Dragon CL, Aleksandar P, Marina TM (2017) Tunnel-ground interaction analysis: discrete beam-spring vs continuous FE model. *Tech Gaz* 24(1):61–69
10. Rocscience Inc. (2019). <https://www.rocscience.com/> (2019/12/10)
11. Siew CL, Mohd AMI, Soon MN (2012) The evaluation of tunnel behaviors under high rock stress using numerical analysis method. *EJGE* 17
12. Navid H, Kazem O, Mehran G (2010) Seismic analysis of horseshoe tunnels under dynamic loads duet o earthquakes. In: Coal operator’s conference, Australia

Sustainable Construction and Its Challenges



Adhilla Ainun Musir, Siti Rashidah Mohd Nasir, Siti Hafizan Hassan,
Nur Farah Asyikin Abdul Rahim, and Nurul Farah Afiqah Harun

Abstract Construction projects in Malaysia are currently facing various problems on sustainability due to the negative perception of construction activity widely spread among stakeholders. In addition, there is a gap of knowledge and awareness on sustainable construction and its practices. This led to the concerns of government and private sectors to be more proactive in minimising this problem without restraining the need for development. This study reviewed the challenges of sustainable construction from many parts of the world through various previous studies. The thematic review process was adopted as methodology of this study. The findings of this study identified the main challenges of sustainable construction which consisted of four main themes namely cost and finance; cultural and knowledge; professional and capacity; and design and technologies. These main themes are essential to the stakeholders in the implementation of sustainable construction.

Keywords Sustainable construction · Cost · Finance · Cultural · Knowledge · Professional · Capacity · Design and technologies

1 Introduction

During this twenty-first century, urbanization was closely connected to the construction sector because of its related projects such as housing and infrastructure [1]. Other than that, refer to [2] stated that environmental planning and the construction industry have merged in the sense of urbanization, which is heavily influenced by climate change policies. Besides, based on [3] also pointed out that the shift of the construction industry from the conventional model to sustainable development in the form of ‘sustainable construction’ had received close global attention. Sustainable

A. Ainun Musir (✉) · S. H. Hassan · N. F. A. Abdul Rahim · N. F. A. Harun
Civil Engineering Studies, Universiti Teknologi MARA, Cawangan Pulau Pinang, Permatang
Pauh Campus, 13500 Pulau Pinang, Malaysia

S. R. Mohd Nasir
School of Civil Engineering, College of Engineering, Universiti Teknologi MARA (UiTM),
40450 Shah Alam, Selangor, Malaysia

construction can be defined as “the creation and responsible management of a healthy built environment based on the prudent use of resources and ecological principles” [4]. As there were an increase in the sustainable construction movement’s growth rate throughout the world. Nonetheless, a sustainable solution and green building have a long story of being developed because of the energy crisis and the campaign to protect the environment. Thus, Malaysian construction has put a rapid process and change of interest in sustainable construction.

Construction projects in Malaysia are being criticised for the low productivity and failure to meet client’s satisfaction [5]. Due to these reasons, Malaysian government has introduced the Green Growth concept to promote sustainable development for public projects and Value Management (VM) to improve the projects’ value for money [5]. Hence, based on a study [6], construction industry is urged to move from traditional, labour consuming, energy inefficient and waste generated method of construction to more environmentally friendly, energy efficient and less waste generation of the construction environment. Reference [6] also stated that Malaysian projects in the last decade, especially the magnificent monuments, were not cost and function effective. On certain construction projects, the budgets were overstepped, took longer construction period and quality of the end products were poor. With those issues, Malaysian government came out with an effort to manage our natural resources and conserve the environment while mitigating the effects of climate change by implementing a Green Growth strategy under the 11th Malaysia Plan in Sustainable Development Goal 2030.

Sustainability has been defined as economic development that meets the current generation’s needs without compromising the opportunity and ability for future generation’s need (WCE 1987). Based on a study [7], construction industry sector is the main reason of accruing the depletion of natural resources and triggering the acceleration of climate change. The issue is worsen by having each of the construction activities including demolition and disposal which create a significant environment burden that varies considerably depending on the type and location of each building [8].

With these issues, it led the authorities, organisations, professionals, and citizens to call for a sustainable construction industry that can address the health and environmental problems which arise from buildings in order to reduce the impact of the industry on the environment and people [9] and to reduce the environmental footprint of the built environment [10]. Hence, these triple bottom line approaches (environmental, social and economic) form the framework for sustainable development.

2 Methodology

2.1 Thematic Review Process

Thematic review process [11] was adopted in this study to select appropriate and relevant articles. This approach consists of three stages which are identification, screening and eligibility [11]. In addition, manual searching method was also conducted using established peer reviewed sources such as Scopus and Web of Science (WOS). The three stages of the process are further elaborated as follows:

Identification

Identification is the method to find articles in established sources. Identification is the first stage where the identification of keywords is determined. Besides that, similar word and related keywords are identified by using dictionary and thesaurus.

Screening

Screening is the process of eliminating the unrelated articles within the study. All the unrelated articles or exclusion criteria are removed in this second stage. The most related articles based on the selection of criteria of the study are selected and reviewed.

Eligibility

Eligibility is the final stage of the thematic review process. At this stage, on a more important note, the titles, abstracts and the main content for this study are examined to ensure that they fulfil the inclusion criteria and fit to be employed in the present study in order to achieve the objectives of the current research. The articles are selected based on the criteria of the content. Finally, a total of nine most relevant of empirical data are analysed. The inclusion and exclusion criteria are stated in Table 1.

Table 1 The inclusion and exclusion criteria

Criterion	Eligibility	Exclusion
Literature type	Research articles	Book series, book, chapter in book, conference proceedings
Language	English	Non-English
Subject area	Engineering, social science, environmental	Other than engineering, social science and environment

3 Review Process

3.1 *Thematic Review Process*

Extensive literature search was conducted using the thematic review process where all challenges were identified and tabulated in Table 1 according to the number of frequencies of the challenges. As a result, four main themes namely cost and finance; cultural and knowledge; professional and capacity; and design and technology for challenges of sustainable construction were identified. Table 2 shows the main themes and sub-themes of reviewed articles.

The literature search on the challenges of sustainable construction was conducted from seven previous studies which focused on cost and finance [4, 12–17], while nine studies contributed to culture and knowledge [4, 12, 13, 15–20]. Meanwhile, for the professional and capacities, eight of the studies contributed to this theme [4, 12–18], followed by six previous studies on design and technologies [4, 12, 13, 16, 17, 19].

3.2 *Identify the Main Challenges*

In this section, the discussion on the challenges of sustainable construction revolves around four main themes namely cost and finance; culture and knowledge; professional and capacity and design and technologies along with the emerging 16 sub-themes (refer Table 2).

Cost and Finance

Cost and finance is one of the challenges that contributed to the neglected implementation of sustainable construction. In particular, these challenges include economy conditions of the contractors and perception of higher cost of using sustainable concept. In this theme, a total of seven previous studies were found particularly for economic conditions [4, 12, 13, 16, 17, 19] and higher cost of sustainable concept [4, 13, 15–17, 19] with economy conditions [12] being under this theme too.

Economy Conditions (EC)

Based on reference [12], contractors usually focus on the short-term economic conditions which are the benefits of sustainable construction. They [12] are reluctant to increase their inputs of green element in their project [8] because of inadequate access to green technologies. Moreover, there is a wide gap of knowledge and awareness on sustainable practices, but the stakeholders mainly consider economic as the main issue rather taking a serious effect on economic, environmental and social sustainability [12].

Table 2 The main themes and the sub-themes

Authors	Cost and finance		Culture and knowledge							Professional and capacity					Design and technologies		
	EC	HC	RI	LB	LD	WC	C	LA	G	LP	LS	LC	PB	DT	T	MT	
Shaikha Al Sanad (2015)			/	/	/	/	/	/		/							
Serdar Durdyev et al. (2018)		/					/	/									
M. Khufallah, I. S. Ibrahim and F. Moayedi (2019)	/			/			/	/	/	/				/	/		
L. S. Ng, L. W. Tan, T. W. Seow (2018)		/		/		/	/	/	/	/	/	/	/	/	/		
Wenxin Shen et al. (2018)		/							/					/	/		
Ofori Ametepey, Clinton Aigbavboa and Kwame Ansah (2015)		/		/			/	/		/			/	/			
Susan Dzifa Djokoto, John Dadzie and Eric Ohemeng-Ababio (2014)		/			/	/				/	/					/	
Krishna P. Dhakal, Lizette R. Chevalier (2017)						/				/	/	/	/	/		/	

(continued)

Table 2 (continued)

Authors	Cost and finance		Culture and knowledge					Professional and capacity					Design and technologies			
	EC	HC	RI	LB	LD	WC	C	LA	G	LP	LS	LC	PB	DT	T	MT
B. Williams et al. (2019)		/		/	/	/		/		/	/			/	/	

EC Economy condition, *HC* Higher cost, *R* Risk, *LB* Lack of benefit, *LD* Lack of demand, *WC* Willingness to change, *C* Capability, *LA* Lack of awareness, *G* Guided, *NP* No policy/rules, *LS* Lack of support, *LC* Lack of capacity, *PB* Political barrier, *DT* Design/technical, *T* Technologies, *MT* Materials and tools

Higher Cost (HC)

The challengers toward sustainability seems to be related to the perception of higher cost of sustainable building-options and construction. Based on [16], the cost of building option is the highest and significant among others. The industry and the key players affirmed that the element of bias perception in sustainable construction practices instead of clear evidence of sustainable building or construction was significantly higher at initial cost which was proven by previous studies worldwide [16, 21, 22]. Study by reference [16] stated that the barrier of sustainable concept like green building arises from financial pressure. This is mainly due to the lack of government support, higher cost in preparing documentation, and the lack of training and education in the industry as key players.

Culture and Knowledge

Cultural and knowledge is the resistance and difficulty to adapt the changes on sustainable construction. It is due to the lack of knowledge which leads to lack of demand in the construction sector [4].

Risk of Implementation (RI)

The lack of understanding on the concept of sustainability leads to a small number of contractors and key players having the interest to be involved in sustainable construction. Besides that, it has caused inadequate access for international experts to explore sustainable construction [16]. Furthermore, most of the contractors are willing to adopt on the easier approach but not willing to take risk [15]. Based on study [13], the contractors are afraid to invest higher initial cost and they fear long return period.

Lack of Benefit (LB)

Most of the implementors such as designers and contractors are unaware on the benefit of sustainable construction. This is due to the lack of motivation from the government to provide rewards for those who had applied sustainable concept in the construction [12]. Thus, there is a need of policy and regulation on incentives given by the government with regard to green issues [12].

Lack of Demand (LD)

Lack of advertisement and market information related to sustainable construction project leads to the lack of demand from the key players to be involved in this type of project [12]. The poor demand for green buildings or sustainable concept is also due to lack of credible research on the benefits of green construction [18].

Willing to Change (WC)

This describes the willingness of the key players in adapting and adopting the new way of construction method and changes of technology. As much as the government has put the efforts towards the sustainable construction, it is unfortunate that most of the contractors still prefer the traditional method of construction instead of slowly

moving to apply sustainable concept. It is clear that there is a lack of effort from the practitioner and negative attitudes towards sustainable [15].

Capability (C)

The capability is the ability of the contractors or any other key players to implement sustainability. Based on a study [18], there is inadequate access to the employee's training and learning experience of implementing sustainable concepts. Besides that, the lack of most professionals and designers in taking part in sustainability is considered as the most significant barrier to the adoption of sustainability [16]. In addition, the professionals are also unfamiliar with the implementation and practices [16].

Lack of Awareness (LA)

Furthermore, it has been reported that there is a lack of understanding and awareness among professionals of the key players towards sustainable construction [12]. In addition, a study [16] found that the awareness and knowledge of sustainable construction are relatively low. Based on the study [12], the awareness among respondents only ranged from 5 to 23%. The data represented the level of implementation of sustainable construction in his country. Reference [18] identified that the lack of knowledge and awareness is the one of the factors which hinders sustainable construction in the country.

Guided (G)

There is not much accessible information on the construction industry which relates information database of product's emission; for example, to the sustainable construction of key players [12]. The involvement of professionals is needed not only in terms of knowledge but also as a team member to promote sustainable construction. Together, they can act as training providers to address the current situation and future environment in order to promote sustainable development [12].

Professional and Capacity

Professional and capacity is the most critical barrier of sustainable construction. This is due to the lack of capacity in construction sector to implement sustainable practices which will lead to the failure of sustainability [4].

Lack of Policy/Rules (LP)

Reference [18] stated that the government should introduce standard or rules related to enforcement of sustainability concept. By the enforcement, it will raise and encourage the key players to be involved in this construction industry. It was found that the citizens give little attention or ignore the rules if it is not mandatory to force them to do it [16]. It is more practical if the government enforces the standards for the sustainable concept in construction industry [18]. By implementing the rules, it will develop the belief and trust from the stakeholders which are based on the serious commitment of the government [16]. Government plays an important role in persuading stakeholders towards sustainable practices. If the government does not

play their part, it will demotivate the stakeholders to be involved in this sector. Therefore, it is important for the authorities to realize the importance of sustainability and green concept.

Lack of Support (LS)

This refers to the inadequate access of green technologies and lack of support from top management [15]. The government should offer incentives or bonus to the stakeholders who implement and contribute towards sustainability [18]. The effort from the government and the management will lead to the desires of contractors to be involved in this kind of construction. The construction industry including individual organization plays a major role in achieving successful implementation of sustainable construction [12].

Lack of Capacity (LC)

Effective implementation of sustainable construction is related to the coordination and cooperation between local, national, private and government sectors. This is because the strong support from the key players produces an awareness among them which encourages them to be involved in sustainable construction [15]. Lack of cooperation resulted into lack of knowledge transfer from policy maker to the implementors. Based on a study [14], lack of government incentive has made the key players being dare to take the challenge in the adaptation of sustainable construction.

Political Barrier (PB)

The effects of political barriers also influence the success of sustainable construction [13]. This is also related to the policy maker in which the government places legislation that requires corporate policies to be parallel with the development of various policy documents to enforce sustainability [16]. This includes changing the building codes and improving the sustainability codes. The success of sustainable construction relies on the commitment from the government with the formation of legislation [13].

Professional and Capacity

Professional and capacity is referred to as the capability of the technical part in implementing sustainable construction. It includes the designer to design, the contractors to construct, and the government to be policy maker.

Design/Technical (DT)

The lack of familiarity of sustainable concepts is the one factors of slower implementation of sustainable construction [16]. It resulted into the poor of design due to the lack of appropriate guidance to assist the designers. Therefore, it is important that technical information on sustainable construction is made in proper format and easy to access since it will lead the contractors to fulfill the sustainable design and be responsible with their works [16].

Technologies (T)

Reference [16] illustrated that the challenges on the technologies part is the most direct failure of sustainable construction. It is because most of the components contribute to the effects. The lack of environmentally materials, lack of sustainability measuring tools, lack of example of 'demonstration project', lack of technical ability in terms of design and construction and lack of skills labour are the causes of slower application of sustainability concept. These challenges are considered as technical failure because they have direct impact on the success of sustainable construction principles [16]. In terms of design, the designers have low confident in designing sustainable application into the structures. It shows that the professionals need to have very strong fundamentals of sustainable principle in order to make sure the contractors follow and fulfill all of the requirements.

Materials/Tools (MT)

Another challenge that usually arises is the difficulty in finding the resources of materials and tools. Reference [20] stated that insufficient sustainable materials leads to discouraging involvement of the stakeholders. The proper tools to produce sustainable materials are also limited. Therefore, it resulted into lack of workmanship in the construction part that contributes to the poor quality [18]. Besides that, the slow progress of construction resulted from the difficulties to get the materials locally [18]. Sometimes the materials need to be imported from elsewhere which show the lack of appropriate guidance as one of the resources challenges [18].

4 Analysis and Result

Figure 1 shows the main challenges in implementing sustainable construction. The highest percentage is cultural and knowledge theme with 39.1%. Secondly, it is professional and capacity theme with 31.25% followed by design and technologies, and cost and finance theme with 18.75 and 10.9% respectively. It shows that culture and knowledge is the main challenge in implementing sustainable construction. It consists of 7 sub-themes that contributed to the result.

This is due to the lack of benefit, lack of willingness to change and lack of awareness that give impact to cultural and knowledge. This is supported by reference [16] which stated there is a lack of benefit given to the contractors whom implement sustainable construction such as green building. Based on study [13], the main barriers in the implementation of sustainable construction is cultural change resistance. This is because of the key players' lack of willingness or effort in trying new method, new material and new tools [13].

Another main challenge in implementing sustainable construction is the professional and capacity issue. This is due to the lack of regulation and policy which is not mandatory to all key players. Currently, adopting sustainable construction is only considered as an optional instead of mandatory to the key players [8]. Furthermore,

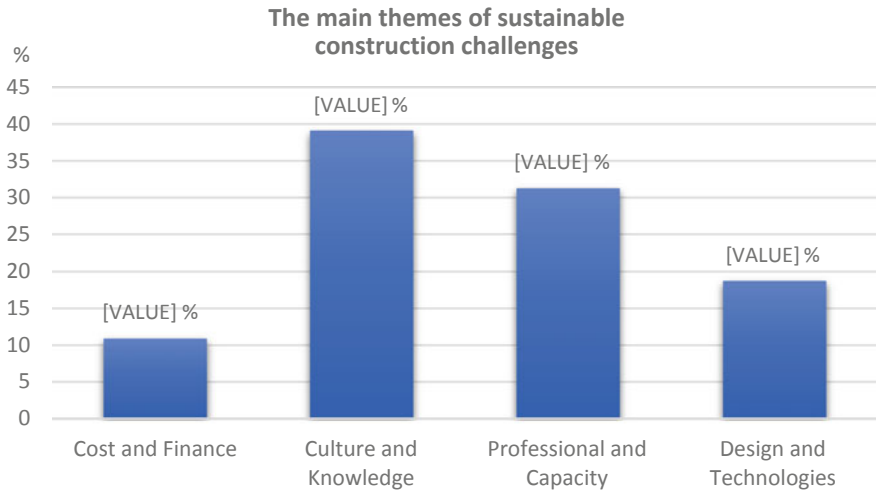


Fig. 1 The main themes of sustainable challenges

the lack of support from the government is also considered as the cause of challenges to implement sustainable construction [12].

The lack of awareness on design and technology [12] is the third challenge that causes the barrier in the implementation of sustainable construction. Besides that, a study [19] stated that there is inadequate promotion of strategies from the government to boost green building in developing countries. This also includes the lack of emphasizing technical skills in sustainable building, the use of materials and the familiarity with the sustainable rating tool or system [19]. Therefore, the demand for extension of time to prepare a design and specifications for sustainable construction projects is required. According to [23] the designers and builders are trying to find a "balance point" that bridges cost with environmental benefits. Still, these rigorous assessments and fees have made it hard to be implemented. As the design was more complicated, they required more professional with extensive knowledge in sustainable design. However, the cost to establish the expertise and hiring more professionals has become a burden to the companies.

As for cost and finance theme, a study [14] stated that the challenge is due to the current economy conditions which lead to the financial pressure of the key players. This statement is also supported by another previous finding [10] in which constructing sustainable building leads to higher project cost [16], higher cost of sustainable building option [14] and higher cost of implementation [17]. Furthermore, the higher cost for technologies, higher cost for material and too many assessment and fee are the reason to avoid sustainable construction.

This finding provides insight in developing the hypothesis of the future study. Thus, the hypothesis can be developed as below:

Hypothesis 1, H_1 : The stringent policy made by the government, the more involvement in implementing sustainable construction.

Hypothesis 2, H_0 : The more awareness and knowledge transfer, the more action will be taken by the key players to embrace sustainable construction.

5 Conclusion

The findings of this study highlighted four main challenges in implementing sustainable constructions. The need of implementing sustainable construction is essential to Malaysian construction industry in order to achieve the objectives of Sustainable Development Goal 2030. The lack of knowledgeable among the key players requires training programs in addressing the current and future environmental concerns within the construction industry. The attitudes among the contractors need to be changed as they are required to adapt with the new technology.

References

1. Shi L, Ye K, Lu W, Hu X (2014) Improving the competence of construction management consultants to underpin sustainable construction in China. *Habitat Int.* <https://doi.org/10.1016/j.habitatint.2013.08.002>
2. Kocabas A (2013) The transition to low carbon urbanization in Turkey: emerging policies and initial action. *Habitat Int.* <https://doi.org/10.1016/j.habitatint.2011.12.016>
3. Gan X, Zuo J, Ye K, Skitmore M, Xiong B (2015) Why sustainable construction? Why not? An owner's perspective. *Habitat Int.* <https://doi.org/10.1016/j.habitatint.2015.01.005>
4. Djokoto SD, Dadzie J, Ohemeng-Ababio E (2014) Barriers to sustainable construction in the Ghanaian construction industry: Consultants perspectives. *J Sustain Dev* 7(1):134–143. <https://doi.org/10.5539/j.s.d.v7n1p134>
5. Abidin Nazirah NZ (2010) Investigating the awareness and application of sustainable construction concept by Malaysian developers. *Habitat Int* 34(4):421–426. <https://doi.org/10.1016/j.habitatint.2009.11.011>
6. Marhani MA, Jaapar A, Bari NAA (2012) Lean construction: towards enhancing sustainable construction in Malaysia. *Procedia Soc Behav Sci* 68:87–98. <https://doi.org/10.1016/j.sbspro.2012.12.209>
7. Díaz López C, Carpio M, Martín-Morales M, Zamorano M (2019) A comparative analysis of sustainable building assessment methods. *Sustain Cities Soc* 49:101611. <https://doi.org/10.1016/j.scs.2019.101611>
8. Sandanayake M, Zhang G, Setunge S (2018) A comparative method of air emission impact assessment for building construction activities. *Environ Impact Assess Rev* 68(December 2016):1–9. <https://doi.org/10.1016/j.eiar.2017.09.003>
9. Doan DT, Ghaffarianhoseini A, Naismith N, Zhang T, Ghaffarianhoseini A, Tookey J (2017) A critical comparison of green building rating systems. *Build Environ* 123:243–260. <https://doi.org/10.1016/j.buildenv.2017.07.007>
10. Dong YH, Ng ST (2015) A life cycle assessment model for evaluating the environmental impacts of building construction in Hong Kong. *Build Environ* 89:183–191. <https://doi.org/10.1016/j.buildenv.2015.02.020>

11. Mohamed Shaffril HA, Samah AA, Samsuddin SF, Ali Z (2019) Mirror-mirror on the wall, what climate change adaptation strategies are practiced by the Asian's fishermen of all? *J Clean Prod* 232:104–117. <https://doi.org/10.1016/j.jclepro.2019.05.262>
12. Science E (2019) Sustainable practices barriers towards green projects in. *IOP Conf Ser: Earth Environ Sci*. <https://doi.org/10.1088/1755-1315/220/1/012053>
13. Ametepey O, Aigbavboa C, Ansah K (2015) Barriers to successful implementation of sustainable construction in the Ghanaian Construction Industry. *Procedia Manuf* 3(Ahfe):1682–1689. <https://doi.org/10.1016/j.promfg.2015.07.988>
14. Durdyyev S, Zavadskas EK, Thurnell D, Banaitis A, Ihtiyar A (2018) Sustainable construction industry in Cambodia: awareness, drivers and barriers. *Sustain* 10(2):1–19. <https://doi.org/10.3390/su10020392>
15. Science E (2018) Constraints to 3R construction waste reduction among contractors in Penang
Constraints to 3R construction waste reduction among contractors in Penang
16. Science E et al (2018) Sustainable construction industry in Cambodia: awareness, drivers and barriers. *Sustain* 10(2):1–19. <https://doi.org/10.3390/su10020392>
17. Williams JB, Jose R, Moobela C, Hutchinson DJ, Wise R, Gaterell M (2019) Residents' perceptions of sustainable drainage systems as highly functional blue green infrastructure. *Landsc Urban Plan* 190(July):103610. <https://doi.org/10.1016/j.landurbplan.2019.103610>
18. Alsanad S (2015) Awareness, drivers, actions, and barriers of sustainable construction in Kuwait. *Procedia Eng* 118:969–983. <https://doi.org/10.1016/j.proeng.2015.08.538>
19. Shen W, Tang W, Siripanan A, Lei Z, Duffield CF, Peng Hui FK (2018) Understanding the green technical capabilities and barriers to green buildings in developing countries: a case study of Thailand. *Sustain* 10(10). <https://doi.org/10.3390/su10103585>
20. Dhakal KP, Chevalier LR (2017) Managing urban stormwater for urban sustainability: barriers and policy solutions for green infrastructure application. *J Environ Manage* 203:171–181. <https://doi.org/10.1016/j.jenvman.2017.07.065>
21. Shafii F (2006) Achieving sustainable construction, pp 5–6
22. Ahn YH et al (2013) Drivers and barriers of sustainable design and construction : the perception of green building experience. *Int J Sustain Build Technol* 7628(November 2016). <https://doi.org/10.1080/2093761X.2012.759887>
23. Govindan K, Khodaverdi R, Jafarian A (2013) A fuzzy multi criteria approach for measuring sustainability performance of a supplier based on triple bottom line approach. *J Clean Prod*. <https://doi.org/10.1016/j.jclepro.2012.04.014>

Removal of Nutrients, Organic Matter and Total Suspended Solids from River Water by Adsorption on Chicken Eggshell



Wen-Pei Low, Fung-Lung Chang, and Shwu Ying Loo

Abstract Due to the abundant source of chicken eggshell, the eggshell waste is assessed to convert it to a green adsorbent for the purpose of water decontamination. This study proposes the application of chicken eggshell with different pre-treatment methods (Untreated chicken eggshell (UTCE) and vinegar-treated chicken eggshell (VTCE)) to remove nutrients, organic matters and total suspended solids present in the river. The contaminated river water sample used in this study was circulated in a prototype to pass through the UTCE and VTCE for five consecutive days respectively. The water parameters were tested in accordance with the APHA method, which was later analysed and compared by evaluating the adsorption capacity, percentage removal of each pollutants and kinetic order reactions. The result showed that UTCE able to remove 35.63% of total phosphorus (TP), 44.69% of total nitrogen (TN) and 69.74% of total suspended solid (TSS) from contaminated river. As for VTCE experiment, the percentage of Biochemical Oxygen Demand (BOD), Chemical Oxygen Demand (COD), TN and TSS eliminated were 28.57, 17.5, 47.21 and 91.67% respectively. The analysis also found that The kinetic adsorption follows the pseudo second order model for both UTCE and VTCE adsorbent which the highest regression coefficient is 0.9033 and 0.9898 respectively. The adsorption isotherm for both UTCE and VTCE is more satisfactorily fitted with Freundlich model respectively with maximum correlation coefficients of 0.9939 and 0.996 respectively. The study demonstrated the efficacy of CE and proved that it as VTCE as viable cost effective adsorbent than UTCE for river water decontamination.

Keywords Eggshell · Organic matter · Nutrients · Total suspended solids · Kinetic order reactions

W.-P. Low (✉) · F.-L. Chang · S. Y. Loo
Department of Civil Engineering, Faculty of Engineering and Quantity Surveying, INTI
International University Nilai, Negeri Sembilan, Malaysia
e-mail: wenpei.low@newinti.edu.my

© The Author(s), under exclusive license to Springer Nature Singapore Pte Ltd. 2022
S. Belayutham et al. (eds.), *Proceedings of the 5th International Conference on Sustainable Civil Engineering Structures and Construction Materials*, Lecture Notes in Civil Engineering 215, https://doi.org/10.1007/978-981-16-7924-7_86

1319

1 Introduction

Without a doubt, water pollution is a significant global crisis that humanity is encountered in the twenty-first century and is undesirable to the sustainability of water resources [1]. The widespread industrialization, the increasing population density, the rapid urbanization and the developing agriculture result in the heavy demand of water resources, in the meantime lower the availability of clean, healthy and good quality water due to the escalating of waste generated. In Malaysia, about 98% of the water requirements of nation are provided by river water [2]. Therefore, it is important to avoid contaminated river water by the untreated discharges or any hazardous solid waste.

There are many treatment techniques available in the market for removing the pollutants in organic or inorganic matters forms from polluted water streams. Typical treatment methods are such as chemical precipitation, ultrafiltration, and reverse osmosis. However, those methods are required high cost but not satisfied performance due to complicated operation, high-energy consumption, expensive chemical reagents and proper disposal of toxic waste disposal [3]. Hence, adsorption process using solid adsorbents has become the alternative practice due to low cost, eco-friendly, ease in complicated operation and undesirable by products [4, 5].

Coal-based activated carbon (AC) is the one of the common adsorbent used to remove various type of water pollutants especially for the heavy metal ions removal. Despite on the excellent adsorption ability of the AC, yet it is still prohibited and discouraged mainly because of it is costly and the preparation and regeneration of AC are tedious which may also contribute to environmental issues [6]. As mentioned in one of the study done by Hjaila et al. in the year 2013, the production of AC has create global warming potential, whereby producing 1 kg of AC from olive-waste cakes emitted 11.096 kg of carbon dioxide (CO₂) into the atmosphere [7].

The utilization of natural waste materials as optional adsorbent has gain great interest in removing contaminants from polluted water sources due to their availability, eco friendliness and affordability. A low cost adsorbent only requires little processing, plenty in nature or a by-product or waste materials resulting from another industry [8]. Pino et al. deduced that the coconut shell exhibit good sorption properties towards heavy metals due to the polar functional groups in the cellulose as it had a high adsorption of cadmium metal ions which was 285.7 mg/g and it potential range of concentration for removal of cadmium ion was from 20 to 1000 mg/L [9]. The employment of spent tea leaves as adsorbent in treating tannery wastewater was investigated by Nur-E-Alam et al. The maximum BOD reduction was achieved in time of 120 min at the dose of 5 g/L which was about 85.88% [10].

As worldwide egg consumption is high, there are thousands tonnes of eggshells are produced everyday around the world thus the eggshell disposal will escalate the landfill problem as well as give rise to critical environmental issue. There are about total 18 billion eggshells and roughly, 113,398,093 kg of annual waste load are generated from the breaking operations [11]. Chicken eggshell are one of the



Fig. 1 The UTCE (right) and VTCE (left) after sieving through a No.30 mesh

abundance waste materials that are readily available, so it can be reutilized as a low-cost and environmental friendly method to treat the contaminated river water.

As described by Stadelman [12] and Rahmi and Lelifajri [13], the eggshell is made up by 94% calcium carbonate, 1% magnesium carbonate, 1% calcium phosphate and about 4% organic matter. Eggshell possesses vesicular and cellulosic structures [14, 15]. Taking into account the distinctive properties of eggshell waste such as porous and cellulosic structures, large surface areas, high swelling capacities and excellent mechanical strengths thus make it a suitable adsorbent for water and wastewater decontamination [15].

2 Methodology

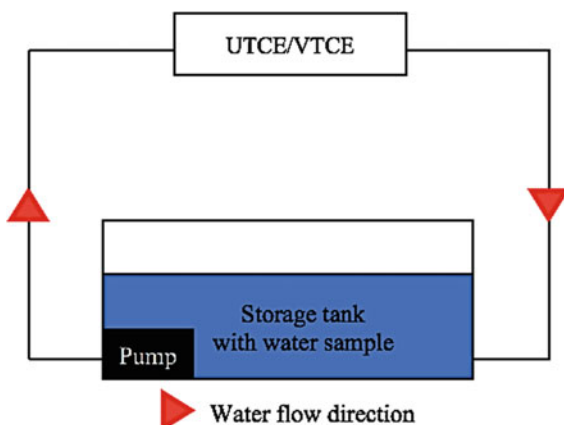
2.1 Preparation of Adsorbent

Chicken eggshells were washed thoroughly to remove the impurities. For UTCE preparation, the eggshells were oven-dried at 100 °C for 24 h to remove the moisture content. For VTCE preparation, the eggshells were washed and soaked in diluted vinegar for 24 h, then further rinsed and oven-dried for another 24 h at 100 °C. The dried UTCE and VTCE were crushed and sieved through a No. 30 mesh (as shown in Fig. 1). Both materials were kept in an airtight plastic container for further use.

2.2 Sampling

The sampling location was at Batang Labu River which located within Kampung Tanjung, Nilai. The water samples were collected directly in the middle of river. Water samples was collected thrice since three batches of experiment were conducted

Fig. 2 Diagram on the concept of how the treatment process functions



in the different time and each set of water sample used was collected on the first day of experiment.

2.3 Adsorption Studies

Three groups of experiments were conducted which included controlled sample without the presence of adsorbent, water sample treated with UTCE and water sample underwent adsorption with VTCE. Each batch of experiment was left to run for five consecutive days. A 35 L of collected water sample was used for each batch of the experiment and 2 g/L of adsorbent was employed for each UTCE and VTCE experiment. The concept of this adsorption process was adsorbent as filtration media whereby water was regularly circulated and passed through the adsorbent throughout the treatment process. Figure 2 shows the diagram on the concept of the treatment process functions.

2.4 Standard Test Methods

The testing for the controlled water sample as well as treated water samples with and without adsorbents for five tested parameters included TN, TP, BOD, COD and TSS was carried out per day in order to observe the changes in the concentration of pollutant for determining the percentage of removal of pollutant. The initial concentration of water sample for each group of the experiment was tested on the same day of sampling to reflect the pollutant level of Batang Labu River. The standard test methods implemented in this study were based on American Public

Table 1 Standard method for each water parameters according to APHA [16]

Water parameters	Standard method used
Biochemical oxygen demand (BOD)	APHA 5210 B
Chemical oxygen demand (COD)	APHA 5220 C
Total nitrogen (TN)	APHA 4500 N _{org} B
Total phosphorus (TP)	APHA 4500 P
Total suspended solid (TSS)	APHA 2540D

Health Association (APHA). Table 1 shows the standard method used for each water parameters.

2.5 Analytical Method

The effectiveness of the chicken eggshell with different pre-treatment method was identified through removal percentage from Eq. 1 and adsorption capacity from Eq. 2 [17].

$$R = \frac{C_i - C_f}{C_i} \times 100 \quad (1)$$

$$q = \frac{(C_i - C_f) \times V}{m} \quad (2)$$

where C_i is the initial concentration of pollutant in river water (mg/L), C_f is the final concentration of pollutant in river water (mg/L), R is the percentage of pollutants removed (%), Q is the amount of pollutant adsorbed (mg/g), V is the volume of water sample (L) and m is the mass of adsorbent (g).

In order to describe the adsorption mechanism of pollutants onto chicken eggshell, the kinetics of each water parameter adsorption on chicken eggshells were evaluated using pseudo-first order [18] as expressed in Eq. 3 and pseudo-second order models [19] as indicated in Eq. 4.

$$\log(q_e - q_t) = \log q_e - \left(\frac{k_1}{2.303} \right) t \quad (3)$$

$$\frac{t}{q_t} = \left(\frac{1}{k_2 q_e^2} \right) + \left(\frac{1}{q_e} \right) t \quad (4)$$

where q_e is the amount of pollutant adsorbed at equilibrium (mg/g), q_t is the amount of contaminant adsorbed at time t (mg/g), k_1 is the rate constant of pseudo first order adsorption (min^{-1}), k_2 is the rate constant of pseudo second order adsorption ($\text{mg} \cdot \text{mg}^{-1} \cdot \text{min}^{-1}$).

The equilibrium between adsorbent and adsorbate were examined using two isotherms including Langmuir [20] and Freundlich [21] from Eqs. 5 and 6 respectively.

$$\frac{1}{q_e} = \frac{1}{q_m} + \left(\frac{1}{k_L q_m} \right) \frac{1}{C_e} \quad (5)$$

$$\ln q_e = \ln k_F - \frac{1}{n} \log C_e \quad (6)$$

where q_e is the equilibrium capacity (mg/g), q_m is the maximum adsorption capacity (mg/g), k_L is the Langmuir constant related to the energy of adsorption (L/mg), k_F is the Freundlich constant related to adsorption capacity, n is the Freundlich constant related to adsorption intensity and C_e is the equilibrium concentration (mg/L).

The quality water samples before and after adsorption were categorized based on the concentration. BOD, COD and TSS were classified according to Interim National Water Quality Standard for Malaysia (INWQS) as presented in Table 2 whereas TN and TP were grouped with reference to Chemical water quality classification for nutrients developed by Working Group of the Federal States on Water Issues as displayed in Table 3.

Table 2 INQWS for Malaysia [22]

Classes	Unit	Parameters		
		BOD	COD	TSS
I	mg/L	< 1	< 10	< 25
IIA	mg/L	3	25	50
IIB	mg/L	3	25	50
III	mg/L	3–6	25–50	50–150
IV	mg/L	6–12	50–100	150–300
V	mg/L	> 12	> 100	> 300

Table 3 Chemical water quality classification for nutrients developed by working group of the federal states on water issues [23]

Classes	Unit	Parameter	
		TN	TP
I	mg/L	≤ 1	≤ 0.05
I–II	mg/L	≤ 1.5	≤ 0.08
II	mg/L	≤ 3	≤ 0.15
II–III	mg/L	≤ 6	≤ 0.3
III	mg/L	≤ 12	≤ 0.6
III–IV	mg/L	≤ 24	≤ 1.2
IV	mg/L	> 24	> 1.2

3 Result and Discussion

3.1 Adsorption Performance

Overall, decrement in concentration of TN and TSS were noticed in both UTCE and VTCE experiment in comparison to control experiment after the adsorption process. Figures 3 and 4 presented the removal percentage of contaminants in UTCE and VTCE experiment respectively.

In accordance with Fig. 3, the results disclosed that the percentage removal of TN, TP and TSS were 44.69, 35.63 and 69.74% respectively. In the presence of UTCE in the treatment process, 2.48 mg/g of TN, 0.29 mg/g of TP as well as 17.75 mg/g of TSS were being held by the adsorbent. The UTCE also showed the greatest adsorption capacity on TSS. According to Fig. 3 and their adsorption capacity, it can be observed that the removal percentage of contaminants and the number of pollutants adsorbed by UTCE in ascending order was TP followed by TN and TSS. This indicated that the effectiveness of pollutants removal by UTCE performed the best on TSS then TN and TP. Only BOD and COD did not show increment in the concentration level. The initial and final concentration levels of TN were lower than 12 mg/L thus both cases were categorized as Class III in EPA. In spite of no improvement in classes, yet there was still 44.69% of removal involved where from the upper limit of Class III to

Fig. 3 Removal percentage of pollutants in UTCE experiment

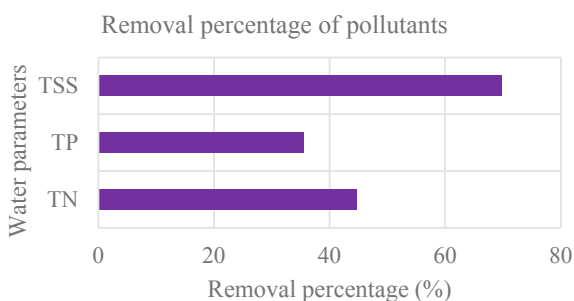
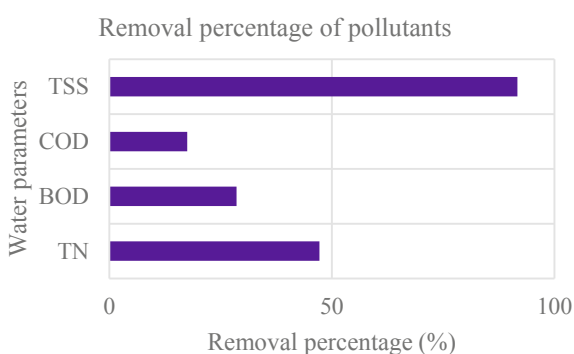


Fig. 4 Removal percentage of pollutants in VTCE experiment



the lowest limit of Class III. As for TP, its level on day one and day five exceeded the maximum concentration of Class IV which was 1.2 mg/L but there was 35.63% of pollutants been removed. Therefore, TP was sorted into Class IV which indicated the water body was excessively polluted. On the other hand, the BOD level had dropped from Class II to Class III as its first concentration was measured at 2 mg/L and the last concentration was recorded at 4 mg/L. This still needs extensive treatment for drinking purpose but fits for livestock drinking for Class III water quality [22]. The concentration of COD before and after the treatment process was found to be less than 25 mg/L so it was placed under Class II in both circumstances. This indicated that perhaps the increment in COD has less impact since it was still in the same class. For the TSS, the level was decreased from 49.2 to 17.4 mg/L after the adsorption experiment so it changed from Class III to Class I. TSS was the water parameter that had been eliminated the most from the polluted water sample.

Through the result, it revealed that UTCE did not perform well in reducing BOD and COD. This is probably because of the decomposition of chicken eggshell as eggshell contained organic matter [12, 13]. As the microorganism present in the collected river water will break down the organic matter which then results in the increment of BOD and COD level. Besides, the chicken eggshell used was crushed into fine particles so this allowed eggshells to decompose much faster as eggshells have a very high surface area to volume ratio [24]. On top of that, water circulation would enhance the biodegradability of organic matter in contaminated water [25].

On the other hand, the VTCE seems to be keen in removing the water parameters such as TN, BOD, COD, and TSS as these parameters had a reduction in the concentration level. The results showed that TN had been removed by 47.21%, BOD had been eliminated by 28.57%, COD had been got rid by 17.5% and TSS had been cleared away by 91.67% according to Fig. 4. The removal of contaminants by VTCE was arranged in order from lowest to the highest which was COD followed by BOD then TN and TSS. Therefore, it can be deduced that the removal capability of VTCE for TSS is the most effective followed by TN, BOD and COD. With the aid of VTCE as treatment medium, TN was adsorbed by 2.78 mg/g, BOD was taking up to 1 mg/g, COD was adsorbed by 3.5 mg/g and TSS was adsorbed by 18.15 mg/g. On the basis of Table 3, the TN level at the beginning and end of experiment were both found to be lower than 12 mg/L thus it was classified as Class III in both scenarios but there was 47.21% of pollutant been eliminated. The BOD level decreased from 7 to 5 mg/L that results in transition of classes from Class IV to Class III. This water quality was suitable for irrigation purpose as the water source contains organic substrate that can bring microbial regrowth [26]. As for COD, its class remains unchanged which was Class III before and after adsorption process because its concentration level in both cases were within the range of Class III. However, there was still 17.5% of removal involved. Improvement in concentration of TSS can be observed as its level was declined from 33.6 to 3.3 mg/L. Hence, it was grouped in Class II at first and Class I at last. Again, the result showed that the TSS had the greatest amount of contaminants adsorbed by VTCE among five parameters.

In fact, for TN and TSS, it was found to be larger in the VTCE experiment compared to the UTCE experiment. In the meantime, the result also revealed that

TN and TSS in UTCE treated water sample was lesser than that in VTCE treated water sample in terms of the adsorption capacity. Cho and Seo stated that the acid treatment of eggshell able to remove the dense cuticle layer of eggshell thereby increasing its Brunauer–Emmett–Teller (BET) surface area as well as total pore volume [27]. Therefore, the uptake of contaminants by VTCE was greater than UTCE as more molecules can be adsorbed by the acid-treated adsorbent. It was observed that when the water samples regularly pumped through both types of treatment medium, it enhanced the percentage of TN eliminated by 44.69 and 47.21% for UTCE and VTCE respectively. This situation can be explained through the chemical adsorption, in which the chemisorbed species were bounded to the solid surface, and they will not readily desorb due to the monolayer coverage and stronger forces at stake [28, 29]. In line with Bhaumik et al., the total available adsorption sites are limited for a fixed adsorbent dose so the adsorbent will become saturated at a certain concentration of adsorbate [20]. However, it still showed a reduction in pollutant TN for overall performance. The percentage removal of TSS was measured lower in the UTCE experiment with 69.74% but higher in the VTCE experiment with 91.67%. This process might be reversible which means the molecules can be removed from the surface of adsorbent since the interaction between the solid surface and the adsorbed molecules was weak as the adsorbate was held to the surface by weak Van Der Waals forces [17].

On the other hand, the VTCE experiment showed a reduction in BOD and COD levels. This can be explained by the antibacterial and antimicrobial action of the vinegar. The acetic acid in the vinegar will chemically change the proteins and fats that make up microorganisms and penetrate the cell membrane of bacteria so prompting a release of the proton which causes the cell to die [30, 31]. Vinegar can tackle microbes such as salmonella, Escherichia coli, pseudomonas aeruginosa that can be found in river water [32]. In other words, vinegar able to kill microorganisms by destroying the cell structure which then reduces the microorganisms feeds on eggshell thus decrease the decomposition of eggshell. As the break down activity was lowered then lead to reduction of BOD and COD level in the treated sample.

3.2 Adsorption Kinetic Studies

In order to examine the reaction pathways of the adsorption process, the kinetics characteristics between adsorbent and adsorbate were analysed which two kinetic isotherms models including pseudo first order and pseudo second order were recommended to fit the experimental data. The parameters for the proposed kinetic models that derived from experimental data which utilizing UTCE and VTCE adsorbent was summarized in Tables 4 and 5 respectively. The tables comprise of the rate constant of pseudo first order, k_1 and rate constant of pseudo second orders, k_2 which was obtained through the slope of plotted graph, the amount of contaminant adsorbed at

Table 4 Parameters for pseudo first order and pseudo second order models for UTCE adsorbent

Water parameters	Models			
	Pseudo 1st order		Pseudo 2nd order	
	Parameter	Value	Parameter	Value
TN	k_1	-0.3747	k_2	0.4279
	$q_e(\text{theo})$	2.1968	$q_e(\text{theo})$	2.8337
	R^2	0.7576	R^2	0.7276
TP	k_1	-0.0592	k_2	-10.849
	$q_e(\text{theo})$	0.4896	$q_e(\text{theo})$	0.3316
	R^2	0.0526	R^2	0.7978
TSS	k_1	-0.7204	k_2	-2.0038
	$q_e(\text{theo})$	22.846	$q_e(\text{theo})$	1.6284
	R^2	0.7569	R^2	0.9033

Table 5 Parameters for pseudo first order and pseudo second order models for VTCE adsorbent

Water parameter	Models			
	Pseudo 1st order		Pseudo 2nd order	
	Parameter	Value	Parameter	Value
TN	k_1	-0.2308	k_2	-0.7525
	$q_e(\text{theo})$	4.2815	$q_e(\text{theo})$	3.4399
	R^2	0.8373	R^2	0.8168
BOD	k_1	0.0953	k_2	6.05
	$q_e(\text{theo})$	1.7746	$q_e(\text{theo})$	0.9091
	R^2	0.1747	R^2	0.7463
COD	k_1	-0.2383	k_2	-0.5868
	$q_e(\text{theo})$	6.6359	$q_e(\text{theo})$	3.6403
	R^2	0.5508	R^2	0.8543
TSS	k_1	-1.2859	k_2	0.2665
	$q_e(\text{theo})$	18.8712	$q_e(\text{theo})$	18.7266
	R^2	0.9916	R^2	0.9898

equilibrium, q_e which was determined from the intercept of plotted graph, the regression coefficient, R^2 that denoted the conformity between model predicted values and experimental data.

With reference to Table 4, it was cleared from the result that the reaction for UTCE treatment media was not likely to be pseudo first order as the correlation coefficient for most water parameters in pseudo first order model was relatively lower compared to pseudo second order model except for the TN removal. The application of the pseudo first order and second order model showed similar regression coefficients.

The results obtained with the pseudo second order were in good agreement with the experimental data as most of the correlation coefficients were close to unity which is one as displayed in Table. A fairly large value of the regression coefficient showed that the model successfully depicted the kinetics of experimental data [17]. With regard to this, the maximum regression coefficient was 0.9033 in TSS. Therefore, it can be concluded that the adsorption mechanism of UTCE adsorbent followed well with pseudo second order kinetics. Pseudo second order kinetic model was applicable to chemical adsorption in liquid media [33].

For Table 5 the regression coefficient obtained for the BOD and COD corresponding to pseudo second order were greater than those corresponding to pseudo first order thus the pseudo second order model was found to be explained the adsorption kinetics more effectively. While, the application of the pseudo first order and second order model showed similar regression coefficients for both TN and TSS. On top of that, the maximum regression coefficients recorded was approximately one, which was 0.9898. The very high regression coefficient confirmed the applicability of the model. Accordingly, as reflected with higher regression coefficient values in pseudo second order, the reaction between VTCE adsorbent and contaminants was controlled by chemical adsorption. The equilibrium adsorption capacity was arranged in order from lowest to highest which was BOD with 0.9091 mg/L, TN with 3.4399 mg/L, COD with 3.6403 mg/L and TSS with 18.7266 mg/L. In comparison with UTCE, for pseudo second order model, the maximum amount of TN, BOD, COD and TSS adsorbed by VTCE were higher which indicated that modification of eggshell with acetic acid was more feasible for the removal of respective parameters from contaminated water source.

3.3 Adsorption Isotherm

In order to describe the interaction between adsorbent and adsorbate, two commonly applied isotherms models including Langmuir and Freundlich to fit the experimental data modeled adsorption. The parameters for the proposed isotherm models utilizing UTCE and VTCE adsorbent was expressed in Tables 6 and 7 respectively. The tables consists of the Langmuir constant pertained to energy of adsorption, k_L and Freundlich constant associated to adsorption capacity, k_F , which were defined through the slope of plotted graph, the maximum adsorption capacity, q_m and the degree of non-linearity between adsorption and concentration of solution, n which were calculated from the intercept of plotted graph, the regression coefficient, R^2 . In line with Desta, if “ n ” equal to one, adsorption is linear whereas if “ n ” was smaller than one, the process is chemical adsorption and if “ n ” was greater than one, the process is physical adsorption [21].

Application of Langmuir and Freundlich models to the adsorption isotherm, isotherm result revealed that the Freundlich isotherm offered good satisfactory with high regression coefficient value that close to one compared to Langmuir isotherm in accordance to Table 6. Excellent linearity with high regression coefficient of 0.9939,

Table 6 Parameters for Langmuir and Freundlich isotherm for UTCE adsorbent

Water parameters	Models			
	Langmuir		Freundlich	
	Parameters	Value	Parameters	Value
TN	k_L	-0.2281	k_F	15,559.65
	q_m	0.63723	n	0.54585
	R^2	0.9774	R^2	0.9939
TP	k_L	-4.9044	k_F	0.03443
	q_m	0.158	n	1.14929
	R^2	0.4037	R^2	0.7723
TSS	k_L	-0.0566	k_F	80,849
	q_m	1.43328	n	0.43531
	R^2	0.7641	R^2	0.8791

Table 7 Parameters for Langmuir and Freundlich isotherm for VTCE adsorbent

Water parameters	Models			
	Langmuir		Freundlich	
	Parameters	Value	Parameters	Value
TN	k_L	-0.3869	k_F	804.27
	q_m	0.96237	n	0.84846
	R^2	0.6269	R^2	0.8855
BOD	k_L	-0.3889	k_F	617.87
	q_m	0.34285	n	0.53743
	R^2	0.75	R^2	0.9303
COD	k_L	-0.0315	k_F	6.17×10^{11}
	q_m	-0.3561	n	0.33242
	R^2	0.6132	R^2	0.996
TSS	k_L	-0.9257	k_F	1563.87
	q_m	12.7389	n	4.3649
	R^2	0.8322	R^2	0.9557

0.7723, and 0.8971 in TN, TP, and TSS were obtained. It can be deduced that the Freundlich was the best fitting model for the isotherm data. This is because Langmuir isotherm interpreted the adsorption process at lower concentration while Freundlich isotherm defined adsorption behaviour at higher concentration [34].

As the adsorption data followed Freundlich model so this model suggested that removal of TN, TP and TSS from UTCE mechanism took place by means of chemical and physical interaction between adsorbent and adsorbate. Based on Table 6,

the “n” value of TP was greater than one which interpreted to mean that the pollutants adsorption on VTCE adsorbent were all multilayer coverage on heterogeneous surface (physical adsorption) whereas TN and TSS had “n” value smaller than one which indicated monolayer adsorption on homogeneous surface (chemical adsorption) [21, 33]. A maximum 80,849 mg/g of k_f was recorded in TSS which implied that TSS can be easily adsorbed by VTCE from the polluted water.

As observed from the isotherm data obtained for the removal of TN, BOD, COD and TSS by VTCE in adsorption process, the regression coefficients in Freundlich isotherm were greater compared to Langmuir isotherm which proved that the Freundlich model was more appropriate to describe the adsorptive behaviour of surface of VTCE to uptake the contaminants. Isotherm results revealed that the adsorption data fitted to Freundlich isotherm better than Langmuir model which yielded linear regression coefficients approximately to one with a large regression coefficient value of 0.8855, 0.9303, 0.996 and 0.9557 in TN, BOD, COD and TSS. According to Table 7, with regression coefficient more than 0.93, Freundlich model presented a better-fitted adsorption mechanism of VTCE towards removal of BOD, COD and TSS.

On the basis of regression coefficient, the adsorption data showed a good compliance with Freundlich model which this was an indicative of both chemical as well as physical adsorption [33]. The “n” value in the Freundlich equation was recorded between 0.33 and 4.36 as demonstrated in Table 7. From Table 7, the “n” value of TN, BOD and COD was less than one, which implied chemical adsorption while TSS had “n” value larger than one, which indicated physical adsorption.

The greater value of k_f represented easy uptake of contaminants from the water source with high adsorptive capacity of adsorbent [35]. The COD has the maximum k_f of 6.17×10^{11} mg/g which means COD can be easily removed by the VTCE from the aqueous solution and COD had the largest adsorption capability on VTCE [36].

4 Conclusion and Recommendations

In this study, UTCE had a significant effect on TN, TP and TSS removal whereas VTCE was more appropriate for the removal of TN, TSS, organic matter such as COD, BOD. VTCE was favourable to be employed as a treatment media in adsorption process for the removal of TN, BOD, COD and TSS from contaminated water stream owing to the increasing of number of pores on eggshell surface by acetic acid.

According to the regressive coefficient that above 0.98, the adsorption of pollutants by VTCE followed a pseudo second order pathway and an equilibrium adsorption capacity of 18.7266 mg/L was attained. The kinetic adsorption of UTCE fitted well by the pseudo second order model and reached an equilibrium adsorption capacity of 2.8337 mg/L.

For the adsorption isotherm models of VTCE, the Freundlich equation agreed with the experimental data which the adsorption mechanism as chemical adsorption for TN, BOD and COD and physical adsorption for TSS. As for adsorption on UTCE,

the adsorption data showed a good compliance with the Freundlich equation as well which adsorption behaviour for TN and TSS was chemical adsorption whereas for TP was physical adsorption. Thus, it can be concluded that VTCE was the suitable material for the treatment of organic matter and nutrients in the polluted river water.

References

1. Afroz R, Rahman A (2017) Health impact of river water pollution in Malaysia. *Int J Adv Appl Sci* 4(5):78–85
2. Basheer AO, Hanafiah MM, Abdulhasan MJ (2017) A study on water quality from Langat River, Selangor. *Acta Scientifica Malaysia* 1(2):1–4
3. Gupta VK, Ali I, Saleh TA, Nayak A, Agarwal S (2012) Chemical treatment technologies for waste-water recycling—an overview. *RSC Adv* 2(16):6380–6388
4. Mittal A, Teotia M, Soni RK, Mittal J (2016) Applications of egg shell and egg shell membrane as adsorbents: a review. *J Mol Liq* 223:376–387
5. Ahmaruzzaman M (2011) Industrial wastes as low-cost potential adsorbents for the treatment of wastewater laden with heavy metals. *Adv Coll Interface Sci* 166(1–2):36–59
6. Deliyanni EA, Kyzas GZ, Triantafyllidis KS, Matis KA (2015) Activated carbons for the removal of heavy metal ions: a systematic review of recent literature focused on lead and arsenic ions. *Open Chem* 13(1):699–708
7. Hjaila K, Baccar R, Sarrà M, Gasol CM, Blázquez P (2013) Environmental impact associated with activated carbon preparation from olive-waste cake via life cycle assessment. *J Environ Manage* 130:242–247
8. Bailey SE, Olin TJ, Bricka RM, Adrian DD (1999) A review of potentially low-cost sorbents for heavy metals. *Water Res* 33(11):2469–2479
9. Pino GH, de Mesquita LMS, Torem ML, Pinto GAS (2006) Biosorption of cadmium by green coconut shell powder. *Miner Eng* 19(5):380–387
10. Nur-E-Alam M, Mia MAS, Chowdhury MJ (2017) BOD reduction using spent tea waste from Tannery wastewater. *J Sci Innov Res* 6(2):58–62
11. Poland AL, Sheldon BW (2001) Altering the thermal resistance of foodborne bacterial pathogens with an eggshell membrane waste by-product. *J Food Prot* 64(4):486–492
12. Stadelman WJ (2000) Eggs and egg products. In: Francis FJ (ed) *Encyclopedia of food science and technology*. Wiley, New York, pp 593–599
13. Rahmi and Lelifajri (2017) Influence of heat treatment on eggshell particles as low cost adsorbent for methylene blue removal from aqueous solution. *Rasayan J Chem* 10(2):634–642
14. Yari AR, Majidi G, Reshvanloo MT, Nazari S, Emami Kale Sar M, Khazaei M, Tabatabai-Majd MS (2015) Using eggshell in acid orange 2 dye removal from aqueous solution. *Iranian J Health Sci* 3(2):38–45
15. Stevens M, Batlokwa B (2017) Removal of Nickel (II) and Cobalt (II) from wastewater using vinegar-treated eggshell waste biomass. *J Water Resour Prot* 9(8):931–944
16. APHA (2012) *Standard methods for the examination of water and wastewater*. American Public Health Association, Washington, DC
17. Ribeiro A, Vilarinho C, Araújo J, Carvalho J (2014) Development of an integrated process for eggshell valorization. In: ASME 2014 international mechanical engineering congress and exposition. American Society of Mechanical Engineers, pp V014T11A024-V014T11A024
18. Ho YS (2004) Citation review of Lagergren kinetic rate equation on. *Scientometrics* 59(1):171–177
19. Ho YS (2003) Removal of metal ions from sodium arsenate solution using tree fern. *Process Saf Environ Prot* 81(5):352–356

20. Bhaumik R, Mondal NK, Das B, Roy P, Pal KC, Das C, Baneerjee A (2012) Eggshell powder as an adsorbent for removal of fluoride from aqueous solution: equilibrium, kinetic and thermodynamic studies. *J Chem* 9(3):1457–1480
21. Desta MB (2013) Batch sorption experiments: Langmuir and Freundlich isotherm studies for the adsorption of textile metal ions onto teff straw (*Eragrostis tef*) agricultural waste. *J Thermodyn*
22. Department of Environment (DOE) Malaysia (2007) Malaysia environmental quality report 2006. Sasyaz Holdings Sdn Bhd, p 72
23. German Environment Agency (2014) Chemical Quality Standards and Assessment. <https://www.umweltbundesamt.de/en/topics/water/rivers/assessment-of-watercourses/chemical-quality-standards-assessment%20#textpart-1>. 6th Nov 2018
24. Townsend E (2015) Using eggshells in the garden. <https://www.gardeningatleisure.co.za/gardening/using-eggshells-in-the-garden/>. 1st Apr 2019
25. Low WP, Fadhil Md Din M, Ponraj M, Ali Fulazzaky M, Iwao K, Rahman Songip A, Chellipapan S (2015) Application of low-cost fabricated column model for the adsorption analysis of pollutants from river water using coconut coir. *Desalination Water Treat* 53(5):1342–1351
26. Lenntech (1998) Irrigation water quality. <https://www.lenntech.com/applications/irrigation/quality/irrigation-water-quality.htm>. 10th Apr 2019
27. Cho YB, Seo G (2010) High activity of acid-treated quail eggshell catalysts in the transesterification of palm oil with methanol. *Biores Technol* 101(22):8515–8519
28. Mathew BB, Jaishankar M, Biju VG, Beeregowda KN (2016) Role of bioadsorbents in reducing toxic metals. *J Toxicol*
29. Lofrano G (ed) (2012) Emerging compounds removal from wastewater: natural and solar based treatments. Springer Science & Business Media
30. David Suzuki Foundation (2019) Does vinegar kill germs? <https://david Suzuki.org/queen-of-green/does-vinegar-kill-germs/>. 1st Apr 2019
31. Evangeli A, Ai Tong T (2018) Does vinegar really kill household germs? <https://www.abc.net.au/news/health/2018-01-12/does-vinegar-really-kill-household-germs/8806878>. 1st Apr 2019
32. Minnesota Pollution Control Agency (2008) Bacteria: sources, types, impact on water quality 3(20)
33. Contreras Rodríguez AR (2015) Removal of cadmium (II), lead (II) and chromium (VI) in water with nanomaterials
34. Ramadoss R, Subramaniam D (2018) Adsorption of chromium using blue green algae-modeling and application of various isotherms. *Int J Chem Technol* 10:1–22
35. Weber WJ, Borchardt JA (1972) Physicochemical processes for water quality control, vol 640. Wiley-Interscience, New York
36. Guo Z, Li J, Guo Z, Guo Q, Zhu B (2017) Phosphorus removal from aqueous solution in parent and aluminum-modified eggshells: thermodynamics and kinetics, adsorption mechanism, and diffusion process. *Environ Sci Pollut Res* 24(16):14525–14536

Effect of Roofing Material on the Quality of Harvested Rainwater



Nordila Ahmad, Muhammad Faiz, Zuliziana Suif, Maidiana Othman,
and Siti Khadijah Che Osmi

Abstract Due to the catchment surface, water absorption of the roof and the runoff coefficient of the roof, different roof styles can influence the quality and quantity of rainwater. Six roof models with different roofing materials (i.e., concrete tiles, color bond steel, bituminous, corrugated galvanized, vegetated and gravel) were installed in a field. In order to obtain the parameter value of water quality and rainwater quantity and roof efficiency, physical and chemical tests were performed. Measuring pH, turbidity, total suspended solid (TSS), total dissolved solid (TDS), temperature and metal testing are part of the laboratory work (Aluminium, Zinc, Lead, Copper). The findings obtained were compared to the water quality requirements set out in the National Drinking Water Quality Standards of Malaysia. It was found that the green roof (vegetated) are highly effective at volume reduction of rainwater. The average runoff coefficient for vegetated roofing is 0.349. For green roof materials, the relation between rainfall depth and runoff coefficient is not directly proportional. The green roof is ideal for the high yield of the rainwater field, although it is dependent on quantity assessment. The study reveals that the green roof materials perform in terms of heat reflector, but further treatment is required to achieve the high efficiency of rainwater storage quantity.

Keywords Roofing material · Harvested rainwater · Water quality

N. Ahmad (✉) · M. Faiz · Z. Suif · M. Othman · S. K. Che Osmi
Engineering Faculty, National Defence University, Sg. Besi Camp, Kuala Lumpur, Malaysia
e-mail: nordila@upnm.edu.my

Z. Suif
e-mail: zuliziana@upnm.edu.my

M. Othman
e-mail: maidiana@upnm.edu.my

S. K. Che Osmi
e-mail: sitikhadijah@upnm.edu.my

1 Introduction

Recently, water shortages have been felt at one time or another throughout the world. This is a regional issue and will soon deteriorate into a national problem. Water supply systems have strengthened, but because of population growth and development, demand is growing. The uniform temperature, plentiful rainfall and high humidity are the climate of Malaysia. However, for different reasons, it is possible to face water shortages in the future. In Malaysia, the total population was 32.6 million in 2019 and 29.2 million in 2012, rising 11.64 percent over the last seven years (Department of Statistics Malaysia 2020). This indicates that Malaysia's demand and availability of water is increasing over the year. As the population grows, so is the demand for clean water. Dams and water treatment plants have to be designed to meet the needs of the people in order to cater for the rising demand. Inevitably, the demand will surpass the supply and this situation will cause the country's water shortage.

Urbanization has led to increased pollution of surface runoff and flooding of runoff in recent years. Collected rainwater is one of the best available strategies in urban developments to create sustainable water cycles [1–4, 13, 14]. To meet the increasing demand for good quality water in adequate quantities in urban areas experiencing urban stream depletion and water scarcity, successful collected rainwater strategies are essential [5–9]. In addition, due to the roughness of the roof surface, the water absorption of the roof and the runoff coefficient of the roof, different types of roof can influence the quantity of rainwater storage [15]. It is critical that rainwater harvesting systems are properly built or constructed in order to collect the high quantity and quality of rainwater for adequate water reuse [16]. Therefore, more research on the performance of rainwater qualitatively and quantitatively by differential type roof material to increase the potential reuse of storage water is considered essential. The purpose of this study was to evaluate the quality and quantity of rainwater harvested and to determine the coefficient of runoff from the materials of the roof selected.

2 Materials and Methodology

This research was performed on a model that was built to determine the water quality and quantity of rainwater harvested using various roof materials. The selected roof material was concrete tile (F), colour bond steel (E), galvanised corrugated steel (D), vegetated steel (A), gravel (B) and bituminous steel (B) (C). Such chosen materials are widely used as building roofs, such as residential, factory, industrial, etc. The roof models are flat, about 20 degrees from the horizontal, in slope. For the collection of rainwater from March 2018 to April 2018, ten rainfall events were selected. The laboratory test was performed to obtain the water quality parameter value, rainwater storage quantity and roof efficiency as well. The obtained parameters of water quality were split into physical and chemical parameters. The tests for physical parameters

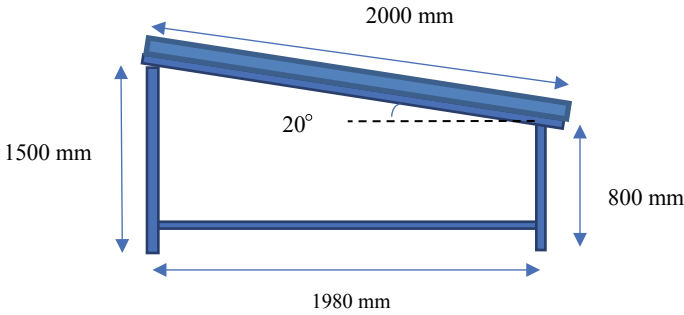


Fig. 1 Side view of experimental model

were turbidity, total solid suspended, total solid dissolved, total coliform, and temperature. Although the tests for chemical parameters were pH, heavy metals (Zinc, Lead and Copper). In order to verify the quality difference between untreated and treated rainwater, the results obtained were compared with the water quality requirements enforced in the National Drinking Water Quality Standard (NDWQS) Guidelines of Malaysia. The raingauge was mounted to track the rainfall depth for each rainfall event near the study location. The rainfall intensity was calculated by using the Logical Method to calculate the runoff coefficient for each type of roof. The angle of the roof is set at 20 ± 2 degrees and the roof catchment dimension is 2 m (L) and 1 m (L) (W). The perforated edge for the planned drainage at the bottom of the roof catchment is built to regulate the discharge of rainwater. The modal experiment is shown in Fig. 1.

3 Results and Analyses

3.1 Quantity of Rainwater

Relationship between rainfall depth and volume of rainwater

The relationship between volume and rainfall depth is shown in Fig. 2 for all types of roofs where A (vegetated roof), B (gravel), C (bituminous), D (corrugated galvanised), E (coloured steel) and F (coloured steel) are used (concrete tile). The vegetated roof (A) absorbs the lowest amount of rainwater relative to all forms of roof, as shown in Fig. 2. Next is the gravel roof, followed by (B). Both roofs were listed as green roofs. The findings also showed that almost more than half of storm water was preserved for all activities by vegetated and gravel roof. This may be due to the rainwater being well absorbed by the soil in the vegetated roof. For the vegetated roof, the infiltration process often helps to minimise surface runoff. Meanwhile, there is no penetration mechanism for the gravel roof, but gravel raises the surface area of the rainwater to block the movement of rainwater through the gutter. In addition, the

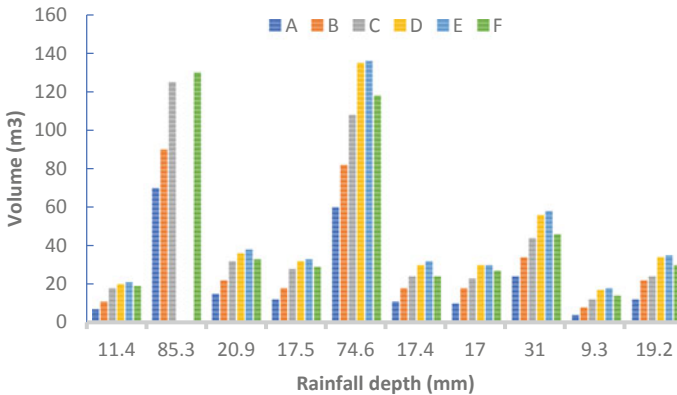


Fig. 2 Volume of rainwater versus rainfall depth

voids between the gravel permit the absorption of rainwater within the gravel. The overall green roof thus showed a successful result in storm water volume reduction.

The relation between the intensity of rainfall and the coefficient of runoff was discussed in this section. A dimensionless factor which is used to convert the rainfall amounts to runoff is the runoff coefficient. The runoff coefficient equation has been updated in this analysis and is presented in Eq. 1.

$$C = V/d_i A \tag{1}$$

where

- C runoff coefficient
- V volume of rainwater
- d_i rainfall depth
- A catchment area

Relationship between rainfall intensity and runoff coefficient

Figure 3 shows the relationship between rainfall intensity and the coefficient of runoff. The findings show that the vegetated roof (model A) has always displayed the lowest values with a range of 0.27–0.412 relative to the other runoff coefficient. 0.349 is the average runoff coefficient. Although the average runoff coefficient values were 0.539, 0.742, 0.888, 0.912 and 0.773 for gravel (modal B), bituminous (modal C), corrugated galvanised (modal D), colourbond steel (modal E) and concrete tile (F) respectively. The highest runoff coefficient value is shown by the corrugated galvanised, while bituminous and concrete tiles forecast near C values between each other. Next, the second lowest runoff coefficient was the gravel roof and this shows that the green roof still shows a low runoff coefficient and hence predicts low storage volumes and rainwater discharge.

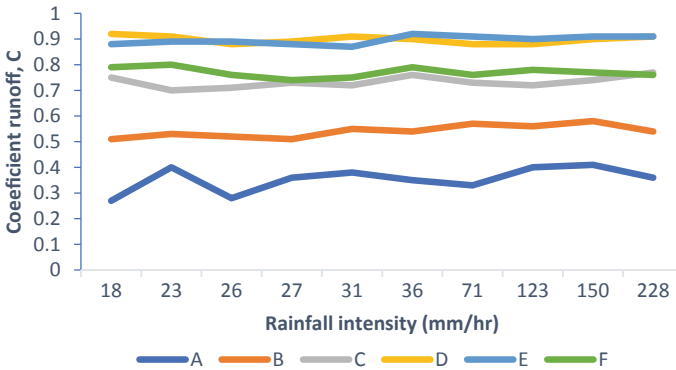


Fig. 3 Relationship between rainfall intensity with runoff coefficient

3.2 Quality of Rainwater

Next, by performing physical and chemical parameter monitoring, quality evaluation was performed. These findings were compared with six different types of materials for the roof. Turbidity, total solid (total suspended solid and total dissolved solid) and total coliform are included in the physical parameter measures. While pH tests and heavy metal tests consist of chemical parameters (Zinc, Lead and Copper). The findings were contrasted with the Interim National Water Quality Standard (INWQS) to determine the quality of water related to drinking water, human contact protection and ecosystem health. The laboratory experiments were performed in compliance with the normal operation and procedure, Standard Water and Wastewater Monitoring.

Physical parameter

Sight, smell, senses of touch and taste decide the physical features of rainwater. Basically, because of the various kinds of roof materials, the physical parameter for rainwater is distinct. There are also strong effects on the chemical calculation of physical parameters. Therefore, the rainwater physical parameter test had to be conducted to assess the effect of roof materials. The findings on turbidity versus rainfall intensity for all roof materials are shown in Fig. 4. Compared to the other five roofs with a range of 88–204 mg/l, the vegetated roof (A) offers a high turbidity value. In relation to the rainfall rate, the turbidity value was not consistent. The average turbidity is 141.5 mg/l for the vegetated roof. This finding suggests that the rise in the amount of rainfall intensity did not affect the rising value of turbidity. The vegetated roof contains higher turbidity from observations since the highest substances from the soil are used. The remaining roof materials are graded as low turbidity. Between the five roof products, the average turbidity values were just 2994 mg/l. However, the average turbidity is 1.845, 1.393, 1.54, 1.186 and 0.9 mg/l for gravel roof (B), bituminous roof (C), corrugated galvanised roof (D), colourbond steel (E) and concrete tiles (F). The four different materials in question do not exceed

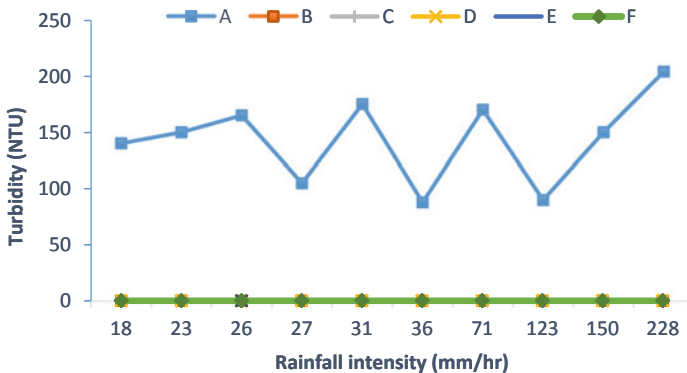


Fig. 4 Average turbidity for all roof types

2 mg/l. It indicates that the gravel roof was significantly larger than the four styles of materials used for the roof. The key explanation for this is that the gravel has been replaced with sandy soil. It was washed by rainwater during the rainy day, and the sandy soil was moved to the storage tank. Other roof materials such as bituminous roof, corrugated galvanised roof, colourbond steel and concrete tile, however, show less turbidity results and are only affected by air emissions before the series of rainfall events.

Next, a complete suspended solids (TSS) test was carried out. The goal is to determine the quantity of filterable solids in a sample of rainwater. For each rainfall occurrence, there were three rainwater samples prepared from the same form of roof material. The particles suspended in water that do not move through the filter paper are included in the TSS. The relationship between the strength of rainfall and the sum of total suspended solids for each type of roof material is shown in Fig. 5. The rainfall strength value does not impact the appearance of total suspended solids on the basis of the results. The average vegetated roof TSS value is 130 mg/l, which is the highest TSS value among all styles of roof. The second highest one was followed by a 50 mg/l gravel roof. In addition, with values of 20 mg/l (bituminous), 25 mg/l (corrugated galvanised), 30 mg/l (corrugated galvanised), the TSS results for bituminous, corrugated galvanised and concrete tile roofs are similar to each other (concrete tile). Colourbond steel with 10 mg/l recorded the lowest TSS. Because of the soil and gravel in the model, the green roof is predicted to have more suspended solids, according to the findings. More particles were introduced to the rainwater storage by the rainwater infiltrating into the soil.

Complete dissolved solids (TDS) are those solids with a pore size of 2.0 microns or smaller that move through a filter. There are solids that are non-filterable and smaller than suspended solids. The previous portion is the measurement of rainwater suspended solids. However, some of the minerals, salts or others are dissolved in invisible rainwater. The dissolved solid test is then followed by one of the rainwater assessment measures. Similar to the TSS test, three samples of rainwater were prepared at each rainfall event from all roof materials. In Fig. 6, all the results have

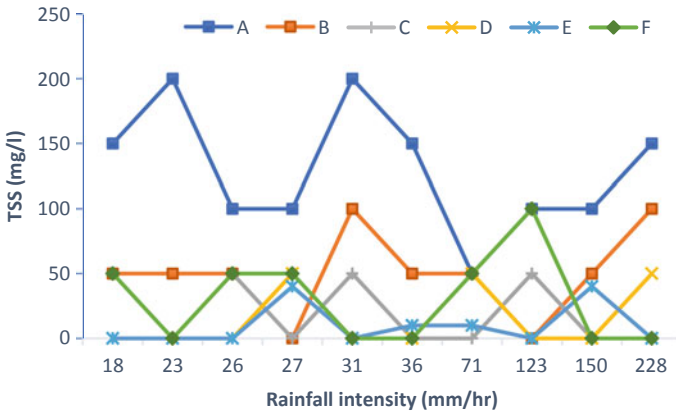


Fig. 5 Average TSS versus rainfall intensity

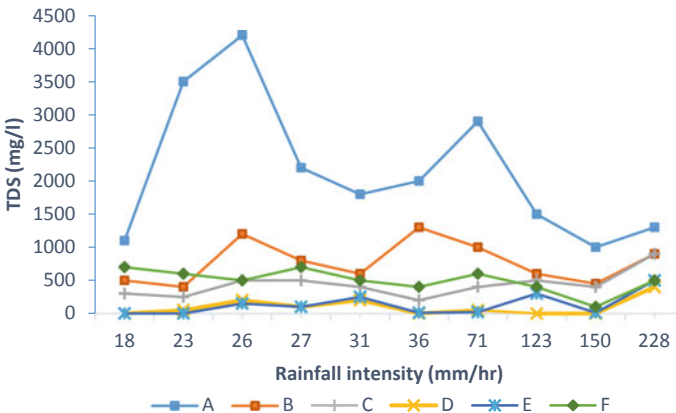


Fig. 6 Average total dissolved solid for all roof type at different rainfall intensity

been plotted. The rainwater obtained by the vegetated roof from the graph contained the highest TDS value, ranging from 1050 to 4150 mg/l. Second, the gravel roof with a value of 790 mg/l was the second highest TDS level. However, other roofs (bituminous, colourbond steel and galvanised corrugated steel) recorded small TDS values of an average of 1240 mg/l. Due to the smooth surface of the roof material, corrugated galvanized and colourbond steel have the lowest TDS values.

The final physical parameter was total coliform. To calculate the total coliform of rainwater, the membrane filtration method is used since this method is ideal for estimating bacterial communities in low turbidity water. The main aim of this experiment is to indicate the difference between all roof materials in the number of coliforms. Figure 7 shows the cumulative coliform obtained from all six types of roof material in the rainwater storage age at ten rainfall events. The rainwater obtained by the

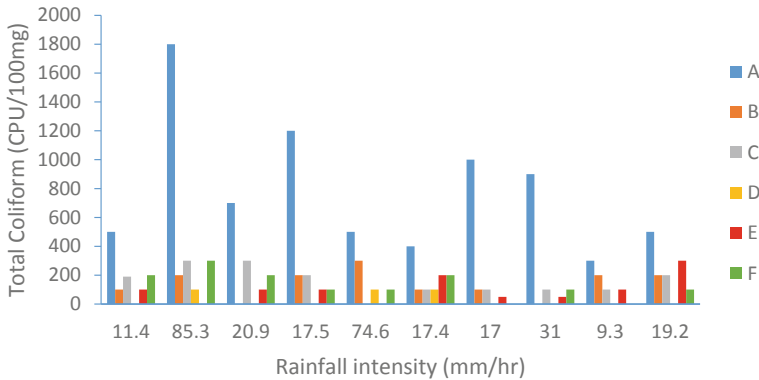


Fig. 7 Total coliform at different types of roof material for ten intensity of rainfall events

vegetated roof (A) displays the highest total coliform concentration according to the graph, where it ranges from 400 to 1800 CFU/100 ml. However, low data values for 140 CFU/100 ml (B), 160 CFU/100 ml (C), 30 CFU/100 ml (D), 100 CFU/100 ml (E) and 130 CFU/100 ml (E) were predicted for the mean total coliform for other roof types (F). Coliform bacteria are a widely used sanitary food and water quality bacterial predictor. It is also present in soil, plants and aquatic environments. This will also check that the vegetated roof displays the largest coliform quantity relative to other roofs. In addition, for the corrugated galvanised roof (D), the gross coliform concentration was almost undetectable. Just 100 CFU/100 ml in three rainfall events were detected out of ten rainfall events. This indicates that the galvanised corrugated material is not ideal for the growth of bacteria. Overall, apart from vegetated roof, all roof material has less coliform concentration.

One of the variables that will influence the quality and quantity of rainwater is roof temperature. Studies on heat transfer from various roof materials are crucial. The temperature of the roof varies according to the ambient temperature, time, climate, etc. During the peak time of sunshine, which is about 12 pm–2 pm, the calculation of roof temperature was therefore carried out. Before the rain event began, the day-time roof temperature was registered. The goal of this test is to determine the effectiveness of roofing materials in reducing heat transfer and how the quality and quantity of storage of rainwater is affected. The temperature of various roof materials relative to rainfall events is shown in Fig. 8. The corrugated galvanised roof (D) has been found to show the highest temperature, with the exception of 6 April 2018. The temperature range was within the range of 33.54–35.28 °C. Next, the colourbond steel roof was the second highest roof temperature, followed by roof C, where the value was within 33.2–34.72 °C.

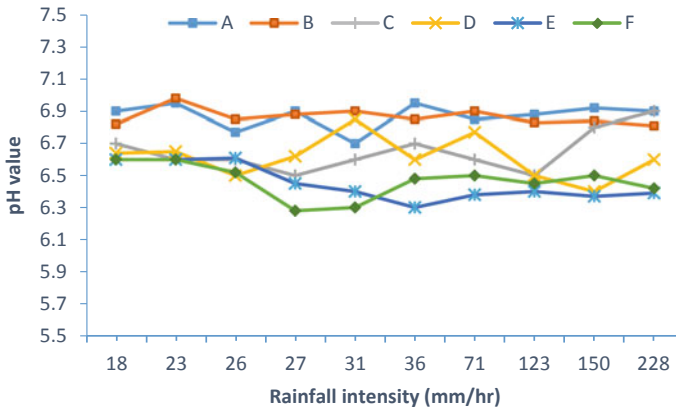


Fig. 8 Average pH for all rainfall events

Chemical parameter

Chemical parameters are important rainwater quality indicators [10, 11]. Aesthetic characteristics such as the look of water, smells and tastes may be affected by rain-water attributes. Only pH has been tested in this research. At ten rainfall events, three rainwater samples are prepared from each roof material type. The results in Fig. 8 were plotted. Both samples of rainwater display pH values below 7, where it can be labelled as acidic. Both pH values from rainwater samples were detected at pH 6–7. The highest pH value of the gravel roof was recorded, with an average of 6.87. With a mean of 6.86, 6.7, 6.57, 6.48 and 6.45 respectively, followed by vegetated roofing, corrugated galvanised, bituminous, concrete tiles and the lowest pH value of colourbond steel. Since the pH value was not very different between the six forms of roof, it can be inferred that the pH of rainwater was not affected much by the rusted region of any roof. Somehow, as shown in Fig. 8, the pH value trend towards acid is only slightly modified. This may also be an explanation why rain-water obtained by colourbond steel was the lowest pH in this test where for a long period of time the roof was exposed to oxygen and moisture and created a rusted component on the colourbond steel roof and thus rendered the pH value low.

Heavy metal test

Rainwater usually includes metal substances due to variations in the content of the roof [12]. This research uses the technique of atomic absorption spectroscopy (AAS). In order to assess the heavy metal concentration in rainwater, the heavy metals selected in this study were zinc, lead and copper. The results of metal concentration for six rainwater samples in various roof types are shown in Table 1.

The findings show that in all samples with concentrations ranging from 0.5441 to 3.2081 mg/l, zinc was detected. However, the normative range was surpassed by the rainwater sample for roof C, D and E. Corrugated galvanised and colourbond steel may have been given a high zinc concentration value due to the corrosive portion of the

Table 1 Heavy metal results in rainwater samples

Rainwater samples	Heavy metals concentrations (mg/l)		
	Zinc	Copper	Lead
Vegetated roof, A	0.5441	0.0156	0.1010
Gravel roof, B	0.696	0.0138	0.1104
Bituminous, C	2.7182	0.0122	0.1109
Corrugated galvanized, D	2.6097	0.0101	0.0855
Colourbond steel, E	3.2081	0.0114	0.0532
Concrete Tile F	0.7283	0.0136	0.0814

roof. Consequently, only styles A, B and F of the roof were within the range of normal samples. Next, on all roofs with concentrations from 0.0101 to 0.0156 mg/l, copper was found. Copper's normal range is 0.025–1.00 mg/l. It is found that green roof rainwater samples suggest high copper concentrations of 0.0156 and 0.0135 mg/l. However, all of the values were lower than the normal values. First, bituminous roof (C) findings indicate the highest lead concentration (0.1109 mg/l), followed by tests of gravel roof rainwater (B) and vegetated roof (A) of 0.1104 and 0.1010 mg/l respectively. For rainwater samples D, E and F, the lead concentration findings are beyond the normal range of 0.1–7 mg/l. These three materials are significantly lower than the results of the regular exam. This may be because the concentration of lead is influenced by heat absorption. Overall, the order of total heavy metal concentration is $Zn > Pb > Cu$ based on results.

4 Conclusions and Recommendation

One factor affecting the quantity and efficiency of rain-water storage is the roof content. There was a small amount of rainwater obtained from the green roof (vegetated and gravel roof). The average runoff coefficient is 0.349 for the vegetated roof and 0.539 for the gravel roof. The green roof is extremely effective at minimising the amount of rainwater. The rainwater acted as runoff and the water was absorbed into the soil, so the process of infiltration took place through the soil and gravel.

The effect of the rainfall depth and runoff coefficient relationship between green roof materials was not directly proportional. Green roof still displays a low coefficient of runoff and thus forecasts low storage volume and rainwater discharge. Green roof area ideal for high yield of rainwater area construction based on quantity assessment. It helps to mitigate the effect of erosion during the heavy downpour of rain on the drainage system.

Both physical and chemical characteristics of the rainwater samples were evaluated in the quality assessment and compared with the Malaysia National Drinking Water Quality Standard (NDWQS). Except for the vegetated roof, the turbidity of rainwater storage for all forms of roof content was lower than 5 NTU. The result

for total suspended solid (TSS) and total dissolved solid (TDS) was also found to contain the highest quantity of total solid in the vegetated roof and thus to provide the highest turbidity value for rainwater. The high total coliform value was observed in a vegetated roof rainwater sample with an average of 780 CFU/100 ml. However, the pH of the roof materials was approximately the same value, so it can be assumed that the increasing number of total coliforms did not affect the pH. The pH values for all rainwater samples are within pH 6–7, as shown in the analyses, where the NDWQS requirement except for rainwater obtained by concrete tiles and colourbond steel has been fulfilled. Rusted also roof did not have an effect on the values of Ph. Although the results of the heavy metal test suggest that the heavy metal concentration order was $Zn > Pb > Cu$.

In conclusion, each type of roof has had various effects on the quality and quantity of storage of rainwater. Corrugated galvanised and colour-bond steel are recommended for the consistency and quantity of rainwater storage. However, as a good heat reflector, the green roof materials were performed, but further treatment is required to perform the high efficiency on the amount of rainwater storage.

References

1. Pazwash H, Boswell S (1997) Management of roof runoff conservation and reuse. In: Proceedings of 24th ASCE water resources planning and management annual conference, Aesthetics on the Constructed Environment, Houston, TX, p 784
2. Kim R-H, Lee S, Lee J-H, Kim Y-M, Suh J-Y (2005) Developing technologies for rainwater utilization in urbanized area. *J Environ Technol* 26(4)
3. Lye Dennis J (2009) Rooftop Runoff as a source of contamination: a review. *Sci Total Environ* 407(21):5429–5434
4. Lee JY, Bak G, Han M (2012) Quality of roof-harvested rainwater e comparison of different roofing materials. *Environ Pollut* 162(2012):422–429
5. Van Roon M (2007) Testing and refining a policy and methods framework for water sensitive urban design. In: *Rainwater and urban design 2007*. A.C.T., Barton. Engineers Australia, pp 1142–1149
6. Farreny R, Gabarrell X, Rieradevall J (2011) Resources cost-efficiency of rainwater harvesting strategies in dense mediterranean neighborhoods. *Conserv Recycl* 55:686–694
7. Förster J (1998) The influence of location and season on the concentrations of macroions and organic trace pollutants in roof runoff. *Water Sci Technol* 38(10):83–99
8. Fletcher TD, Deletic A, Mitchell V, Hatt BE (2008) Reuse of urban runoff—a review of recent Australian advances and remaining challenges. *J Environ Qual* 37:116–127
9. Olaoye RA, Olaniyan OS (2012) Quality of rainwater from different roof material. *Int J Eng Technol* 2(8) (2012)
10. Hani RA, Saad A, Shdeifat A (2018) Harvested rain water quality of different roofing material types in water harvesting system at al Al-Bayt University/Jordan. *Jordan J Civil Eng* 12(2):228–244
11. Farreny R (2011) Roof selection for rainwater harvesting: quantity and quality assessments in Spain. *Water Res* 45:3245–3254
12. Mendez CB, Brandon Klenzendorf J, Afshar BR, Simmons MT, Barrett ME, Kinney KA, Kirisits MJ (2013) The effect of roofing material on the quality of harvested rainwater. *Water Res* 45(5):2049–2059

13. Bae S, Maestre JP, Kinney KA, Kirisits MJ (2019) An examination of the microbial community and occurrence of potential human pathogens in rainwater harvested from different roofing materials. *Water Res* 1591:406–413
14. Zhang Q, Wang X, Hou P, Wan W, Ouyang Z (2014) Quality and seasonal variation of rainwater harvested from concrete, asphalt, ceramic tile and green roofs in Chongqing, China. *J Environ Manage* 132:178–187
15. Nalwanga R, Muyanja CK, McGuigan KG, Quilty B (2018) A study of the bacteriological quality of roof-harvested rainwater and an evaluation of SODIS as a suitable treatment technology in rural Sub-Saharan Africa. *J Environ Chem Eng* 6(3):3648–3655
16. Sánchez AS, Cohim E, Kalid RA (2015) A review on physicochemical and microbiological contamination of roof-harvested rainwater in urban areas. *Sustain Water Qual Ecol* 6:119–137

Impact of Proposed Bus Rapid Transit (BRT) Peshawar on Modal Shares of Private Modes



Jawad Mehmood, Sameer-Ud-Din, Muhammad Jawed Iqbal, and Nasir Ali

Abstract Peshawar has an importance that would serve as transit routes and central figure of enormous business activities between central Asian states to Asian countries in the China Pakistan Economic Corridor (CPEC) project. A city having geographical and strategic importance of providing a gateway to Afghanistan for supplies of North Atlantic Treaty Organization (NATO), with a population of approximately 4.26 million. Over the last decade, this city has been faced with numerous terrific challenges, and the most critical one is traffic congestion. The Government has invested and planned a megaproject of Bus Rapid Transit (BRT) for the public that will assist in improving road traffic conditions by offering them an alternative and economical way of transportation. The sustainable objectives cannot be achieved from any scheme until and unless it has proven as value to money, and for that, the operational performance has to be vetted with an evaluation process determining its acceptance among commuters. In this study, we have evaluated the said scheme to determine barriers/attributes influencing the model shift. Revealed and stated preference approach models has adopted to carryout survey covering socio-economic characteristics (age, gender, the purpose of the trip), current-mode choice, travel time, and speed cycles. This dataset leads us to develop a binary logit model explaining the model shift behavior from private towards proposed BRT on attributes of travel time, speed cycles, and vehicle operating cost. Our model predicts that the vehicle operating cost is a leading factor in inflecting car users to shift on BRT for a city with quite different demographic and social norms as of other developed and developing countries. These findings would be fruitful in estimating the acceptance of the public in owning schemes. Subsequently, assist policymakers and operating agencies in

J. Mehmood · Sameer-Ud-Din (✉)
National University of Science and Technology (NUST), Islamabad, Pakistan
e-mail: sameeruddin@nit.nust.edu.pk

M. Jawed Iqbal
Military College of Engineering, Risalpur, Pakistan
e-mail: drjawediqbal@scee.nust.edu.pk

N. Ali
Università degli Studi di Palermo, Palermo, Italy
e-mail: nasir.ali@unipa.it

scheme planning and strategies about possible outcomes that their initiatives could impose as a value of money or vice versa.

Keywords Modal shifts · Bus rapid transit (BRT) · Congestion · Binary logit model · Transport planning and strategy

1 Introduction

The effects of urban transportation systems cannot be neglected on the way people travel; it can reshape the mobility of people. There are many big cities, where the development of public transport has been ignored, and mobility requirements are utterly dependent on private vehicles. Due to the fast growth of population and economy in the developing countries, there is a dire need of effective, cost-efficient and environmentally friendly urban transportation systems keeping in consideration of transport demand and travel pattern. Howsoever, lack of pertinent execution of planning control will lead to superfluous cost for infrastructure and its operation, and also the disastrous impacts on many environments, economics, and social life [1]. Bus Rapid Transit (BRT) has turned into a conjoint globally transit mode, predominantly in America, Europe, and chiefly in Asia, due to its worth for money, capacity, low on the pocket, comparative flexibility as compare to other modes of transportation, and large network coverage [2]. A lot of case studies have been done that shows that BRT is cost-effective mode to provide an effective and efficient transport mode. Many developing Asian cities also cogitate BRT in the planning of public transportation as of its benefits of low investment and easy execution over rail systems [3]. For the development of efficient urban transportation systems the key factor is to understand the attitude, travel behavior, and the mobility needs. BRT system is normally built in areas where there is problem of traffic congestion or it may likely to occur in the near future. Bus, private cars, rickshaws are the main transport mode used in Pakistan and insufficient capacity and management and operational problems causing falling level of service. In nonexistence of appropriate and effective bus rapid transit service, the bus users now are using private transport such as Cars, Motor bikes, Rickshaws impacting huge on their pockets as well as creating problems of traffic safety and hazardous environmental emissions [4].

2 Past Studies of Modal Shift to BRT

The development of BRT is foreseen to raise the appeal of transport and influence modular shift from private vehicles. Data is supportive that the light rail and BRT are similar in performance in the opinion of the public. A study has been conducted in Jakarta, Indonesia to record the opinions of public transport users towards the development of a new transportation system. The new BRT systems were proposed

under the different scenarios with and without feeder routes and with various fare options. The study concluded that difference of opinions and probability is observed among the public transport users to shift towards the better transportation service [5]. In another study conducted by Currie, trip attribute approach was used to evaluate the relative passenger attraction of BRT systems equalled to other transit modes. This study explained that passenger preferences in different countries towards the on a street bus, BRT and light rail based on trip attributes. The study concluded that the passengers valued trip attributes for BRT and rail modes in a broadly similar manner. The study also revealed that BRT are cost-effective as compared to a rail system, the lower cost of BRT systems as compared to rail systems have strengthened this claim [6]. In a survey conducted in Jakarta, Indonesia to assess the modal shift from private vehicles to the BRT systems in its first month of operation, and the results show that there is significant change of mode from private vehicles to BRT i.e. 14% of private cars and 6% motorcycle users have changed their mode of travel [7].

Albeit numerous examinations affirm that BRT is alluring to passengers, still the degree of modal shift is questionable. In this regard Levinson et al. conducted a review regarding the BRT studies conducted around the world and findings shows that 72% of BRT passengers in Houston were originally using private cars and in Vancouver, 20% of BRT passengers were previously using private cars [8]. In France the mode shift of the BRT Buses with High Level of Service was 29% from private cars [9]. In Los Angeles 18% BRT passengers were previously using private cars. The main reason of this was bus way was built in a poorly served area [10]. In a study conducted about the case study of Beijing, China bus rapid transit 12.4% of passengers were shifted from the privately owned cars [11]. The difference in result in all the case studies is because of the difference in the passengers' choice, passengers' perception, performance and characteristics of system. In a study conducted in Dublin, Ireland. Specify that people are keen to pay handsome amount towards the improved bus journey in term of comfort and travel time [12], In an another study conducted in Malaysia to assess the policies to boost public transport use in, and established that age, gender, cost, income ownership are also play an important role in individual's modal shift instead of relying only on travel time. However, the most important policies are based on the travel time of trip and cost of trip [13].

In another study conducted by McDonnell in which he evaluated the efficiency of different BRT schemes under different several situations focused with and without BRT, and the sharing policies, separate bus lane, ticket machines, bus stops and improved bus frequency. The results depict that all combined actions can attain up to 50% of bus share, while bus share was only 20% for the case of bus with separate bus lane. The modal shift is rather high but for this result it should be kept in mind that travel time of bus is considerable lower than travel time by car under all scenarios. But here there arise a question that how many travelers would change their mode of travel to BRT if travel time of private vehicles were lower than or equal to travel time of BRT [14].

3 Case Study Area

Peshawar is the capital of Khyber Pakhtunkhwa and among the biggest cities of Pakistan with a population of 4.26 million in the 2017 census [15]. It assumes an important geographical location in Central Asia as the main business hub of China Pakistan Economic Corridor (CPEC) and is also a gateway to Afghanistan for North Atlantic Treaty Organization (NATO) supplies [16]. During the last few years, the city is facing the problem of traffic congestion, carbon footprints, and road safety (accidents/fatalities) due to exponentially increase in private motorization. Modal shares of public modes are on drop e.g., private cars are increased by 229%, which has compromised the, road capacity, safety and environmental aspects of the city [17–19]. There are several factors behind this drop e.g., inefficient policies and strategies, inconvenient services, lack of adherence to plan which has forced many to shift towards private modes (car, motorcycles, taxi, etc.). Thus, there is a dire need that all stakeholders including policymakers should sit together, and observe strategies, policies, and interventions related to public transport in Peshawar to have sustainable urban development.

Urban transportation projects like Bus Rapid Transit (BRT) are considered as the most efficient and economical solution which recompenses for traffic congestion, environmental pollution, and safety issues to have a sustainable urban transportation system. BRT projects have been upheld effectively in different parts of the world which abridged costs of travel, travel time, traffic casualties, and environmental pollution [20, 21]. It is found to be a low carbon target for Asian countries which will emit low carbon dioxide (CO₂) by compelling users toward it [22, 23]. The effectiveness of BRT has envisioned the government of KPK to initiate construction of the BRT Peshawar project in 2017. It has a 26 km long corridor having 31 stations at an average distance of 850 m. An at-grade section consists of 15 km and a flyover consists of an 8 km section while the remaining 3 km section constitutes of underpass [24] (Fig. 1).

Valuation of urban transportation schemes is vital to weigh the performance and operations as well as to conclude the acceptance of such scheme over the daily commuters. It is apprehensive to determine that either the service bears the magnitude and potential to gratify commuters from private modes by providing reliable and quality service or not. The second is to ascertain the service attributes which will be upsetting the shift of private and public modes that will have an impact on road network parallel to the BRT project by reducing traffic congestion, environmental pollution, and traffic accident issues. These factors provide the basis to conduct this study that will help to identify the barriers for shifts between modes and evaluate the potential of BRT Peshawar to attract commuters on private modes.

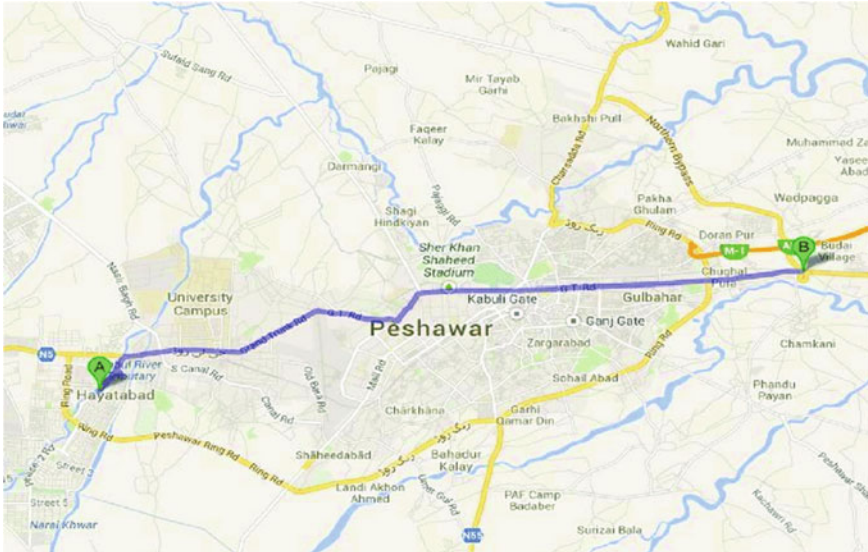


Fig. 1 Peshawar bus rapid transit route [25, 26]

4 Methodology

To carry out the study, a questionnaire survey was performed from daily commuters about different transportation modes centered on two approaches: revealed and stated preference approach [2]. In the revealed preference survey, respondents were asked about socioeconomic characteristics (age, gender, and purpose of the trip), current-mode choice, travel time, and speed cycles while in the stated preference survey, commuters were presented choices where they have to choose among present transportation modes and proposed BRT.

The data has been collected from six sections that run parallel to the BRT Peshawar corridor. The sections include Karkhano Station to PDA Station, Tatara Park Station to Board Bazar Station, Board Bazar Station to Peshawar University Station, University Town Station to Tehkal Station, Tehkal Station to Saddar Station, Malik Saad Station to Old Haji Camp Station. The data is composed of 420 samples for owned car modes, collected in the desired sections. The data of speed cycles were acquired from drivers of the mode, and the vehicle operating cost is calculated using the Hepburn model from known speed [27].

A significant part of discrete choice and logistic regression is the logit function. Because of their ability to reflect complex aspects of people’s travel decisions by adding large demographic and policy-sensitive explanatory variables, Logit models were implemented for logistic regression analysis. In the relations between the independent and width, it does not presume linearity [28].

Binary logit models have been used to carry out the analysis that explains the modal shift behavior of commuters about current private modes towards proposed BRT Peshawar. The utility function is defined as a result of a binary logit model based on three service attributes (travel time, speed cycles, and vehicle operating cost) which will predict the modal shifts between the current mode of travel and proposed BRT. Binary logit function is given in Eq. (1) while utility function is given in Eq. (2) [27]

$$P_{BRT} = e^{U_{BRT}} / (e^{U_{BRT}} + e^{U_{car}}) = 1 / (1 + e^{U_{car} - U_{BRT}}) \quad (1)$$

$$U_{car} - U_{BRT} = \Delta\beta_0 + \beta_1(t_{car} - t_{BRT}) + \beta_2(SC_{car} - SC_{BRT}) + \beta_3(VOC_{car} - VOC_{BRT}) \quad (2)$$

Equation (2) can be simplified as shown in Eq. (3)

$$\Delta U = \Delta\beta_0 + \beta_1 \Delta t + \beta_2 \Delta SC + \beta_3 \Delta VOC \quad (3)$$

In the equations mentioned above, U_{car} is the utility or satisfaction of car mode, U_{BRT} is explaining the utility or satisfaction of bus rapid transit. P_{BRT} describes the modal shift towards bus rapid transit Peshawar from private car mode. t_{car} explains the travel time by car in minutes per kilometre whereas t_{BRT} corresponds to the travel time of bus rapid transit in minutes per kilometre. SC_{car} is for speed cycles of private car per kilometer and SC_{BRT} represents the speed cycles of bus rapid transit per kilometre. VOC_{car} shows the vehicle operating cost of car in cents per vehicle per kilometer and VOC_{BRT} represents the vehicle operating cost of bus rapid transit in cents per bus per kilometer. Whereas, $\beta_0, \beta_1, \beta_2, \beta_3$ represents the Coefficients of service attributes.

5 Results

The results show that the BRT Peshawar has performed well in various elements that affect the performance, ride quality, and the ability to attract users towards it. It has dedicated right of way, appropriate alignment, platform level entering for passengers, improved infrastructure, and positive impacts on hazardous environmental emissions, high pavement class, and appropriate stations which makes the service more efficient and suitable for public transport. Safety features are the key of any urban transportation project and are incorporated in the aforesaid project with the aid of pedestrian bridges and dedicated corridor which improves the quality as well as safety of the service. However, few improvements are desired in the areas of service planning, infrastructure, passing lanes, and bicycle sharing to escalate ridership, quality, and steadiness of service to lead to sustainable transportation.

This research study has introduced the logit model to conduct the study on modal shift analysis between owned cars and BRT Peshawar modes. The binary logit model was engendered in between private mode (car) and proposed BRT Peshawar. The results depict that coefficients of all three service attributes have exhibited negative signs in the binary logit model of car and BRT Peshawar which specifies the direct relationship between service attributes and modal shifts. It illustrates that change in utility (ΔU) value will be decreased by increasing the values of service attributes (travel time, speed cycles, and vehicle operating cost) of car mode which will shift the users toward BRT. The calibrated model predicts that vehicle operating cost is the primary factor as compared to other service attributes (speed cycles and travel time) that will influence the shifts of car and BRT. The traffic congestion on the main road of Peshawar has been increased to such an extent that the road network is often blocked with increased travel time that has significantly increased the vehicle operating cost. Therefore, users consider vehicle operating cost as the leading factor that will compel them towards BRT which is well predicted by the model. The second service attribute that affects the shift proportion of both modes is the speed cycle which spectacles that the increase in the vehicle operating cost and speed cycles of the car will induce more commuters to make a journey by BRT. The analysis revealed that the users of owned cars have shown a significant willingness of 33.8% towards BRT Peshawar which will significantly reduce traffic congestion, environmental pollution and will improve traffic safety that will lead towards efficient transportation in Peshawar city. The results are presented in Table 1.

Model statistics foresees that the model of car and BRT is well calibrated and infers rightly about the modal shifts. The statistics for binary logit model including standard deviation, p value, R^2 , and t-statistic are calculated. It shows that all constants and attributes have of t-statistic greater than 1.96 which contributes to the significance of model having no significant difference from average. The p-value is less than 0.05 which describes the correctness of the model [29]. The estimate of coefficient of determination (R^2) for the model is greater than 0.9 which reveals the goodness of fit in the model that correctly predicts the results.

Table 1 Car versus BRT Peshawar model estimations

	Coefficient	t Stat	P-value
Intercept	0.91	2.76	0.02
Δt	-0.0061	-1.98	0.05
ΔSC	-0.105	-2.39	0.03
ΔVOC	-0.22	-3.47	0.01
Multiple R	0.99		
R square	0.98		
Adjusted R square	0.964		
Standard error	0.124		
Observations	420		

6 Conclusion

1. The study is concluded with the help of a stated and revealed preference survey to assess the commuter's current modal choices and their potential to shift towards proposed BRT Peshawar. The data is comprised of socio-economic characteristics of respondents (gender, age, and trip purpose), travel time, speed cycles, vehicle operating cost, current modal choice, and preferred mode when BRT Peshawar becomes operational.
2. The binary logit model is used for modeling commuter's modal shifts from owned cars towards BRT Peshawar which is based on three service attributes (travel time, speed cycles, and vehicle operating cost) that explain variation in modal shifts.
3. The calibrated model represents that the vehicle operating cost is the main factor that is influencing the shifts of car and BRT Peshawar modes. The road networks of Peshawar city are frequently blocked due to traffic congestion with a reduced level of service of roads resulted in high vehicle operating costs. Therefore, vehicle operating cost is the main governing factor that will influence them to use BRT as trip making which is well represented by the model. The car users have shown a willingness of 33.8 percent to shift towards BRT Peshawar which will have a positive impact on road safety, carbon footprints, and traffic congestion issues.
4. The findings are quite supportive in determining that the BRT Peshawar can provide safe, comfortable, high quality and reliable service to passengers, and have great potential to attract commuters of owned cars that will significantly reduce the current traffic-related problems. This study will assist the relevant agencies in planning and developing strategies to improve the quality and ridership of the BRT Peshawar by appealing to a significant fraction of users from current private modes to have sustainable development.
5. These research findings would be helpful for BRT planning in other congested urban communities as of Peshawar, Pakistan, which experience a high level of private vehicle share along with the same demographic features. The BRT framework has high potential in pulling in private vehicle users. So, the fundamental worries in arranging a BRT framework ought to give a huge diminishing in travel time and minimal effects on the pocket of low and middle income people.

References

1. Patankar VM, Kumar R, Tiwari G (2007) Impacts of bus rapid transit lanes on traffic and commuter mobility. *J Urb Plan Dev* 133(2):99–106
2. Satiennam T, Jaensirisak S, Satiennam W, Detdamrong S (2016) Potential for modal shift by passenger car and motorcycle users towards Bus Rapid Transit (BRT) in an Asian developing city. *IATSS Res* 39(2):121–129

3. Jaensirisak S, Klungboonkrong P (2009) Why bus rapid transit (BRT) is interested by transport planners and travellers in Thailand. In: Proceedings of the Eastern Asia Society for transportation studies, vol 7. The 8th international conference of eastern Asia Society for transportation studies, 2009, pp 266–266. Eastern Asia Society for Transportation Studies
4. Hossain M (2006) The issues and realities of BRT planning initiatives in developing Asian cities. *J Public Transp* 9(3):4
5. Soehodho S, Nainggolan PJ (2005) Public transport user attitude based on choice model parameter characteristics (case study: Jakarta busway system). *J Eastern Asia Soc Transport Stud* 6:480–491
6. Currie G (2005) The demand performance of bus rapid transit. *J Public Transp* 8(1):3
7. Ernst JP (2005) Initiating bus rapid transit in Jakarta, Indonesia. *Transp Res Rec* 1903(1):20–26
8. Levinson H, Zimmerman S, Clinger J, Rutherford S, Smith RL, Cracknell J, Soberman R (2003) Transit cooperative research program (TCRP) Report 90, bus rapid transit: case studies in bus rapid transit. Transportation Research Board, Washington, DC, p 1
9. Rabuel S (2010) Buses with a high level of services: choosing and implementing the right system. Certu, Lyon
10. Callaghan L, Vincent W (2007) Preliminary evaluation of metro orange line bus rapid transit project. *Transp Res Rec* 2034(1):37–44
11. Deng T, Nelson JD (2012) The perception of bus rapid transit: a passenger survey from Beijing Southern Axis BRT Line 1. *Transp Plan Technol* 35(2):201–219
12. McDonnell S, Ferreira S, Convery F (2009) Impact of modal change and residential location on WTP for bus priority provisions: evidence from a stated choice survey of catchment area residents in Ireland. *JTEP* 43(2):213–235
13. Nurdden A, Rahmat RAOK, Ismail A (2007) Effect of transportation policies on modal shift from private car to public transport in Malaysia. *J Appl Sci* 7(7):1013–1018
14. McDonnell S, Zellner M (2011) Exploring the effectiveness of bus rapid transit a prototype agent-based model of commuting behavior. *Transp Policy* 18(6):825–835
15. Pakistan Bureau of Statistics (2017) Province wise results of census 2017. Available from: http://www.pbs.gov.pk/sites/default/files/PAKISTAN%20TEHSIL%20WISE%20FOR%20WEB%20CENSUS_2017.pdf
16. Farooq A, Javaid A, Karl A (2015) Peshawar local public transport strategy and organization. *Int J Eng Dev Res* 2321–9939(3):1–7
17. Ali Z, Shah S, Hussain A (2012) Growing traffic in Peshawar: an analysis of causes and impacts. *South Asian Stud* 27(2):1026–678X
18. Khan A, Arshad MA (2015) Study of various mass transit options for Peshawar city by life cycle cost analysis
19. Ullah I, Liu K, Vanduy T (2019) Examining Travelers' acceptance towards car sharing systems—Peshawar City, Pakistan. *Sustainability* 11(3):808
20. Carrigan A et al (2013) Social, environmental and economic impacts of BRT systems. *Bus Rapid Transit Case Stud Around World* 151
21. Bel G, Holst M (2018) Evaluation of the impact of bus rapid transit on air pollution in Mexico City. *Transp Policy* 63:209–220
22. Kikuchi H et al (2013) Possibility to Realiza low carbon city in medium-sized city of Asia: case study in Khon Kaen city, Thailand. In: Proceedings of the Eastern Asia Society for transportation studies
23. Satiennam T et al (2013) A potential study of Bus Rapid Transit (BRT) supporting low carbon Asian developing city. In: Proceedings of the Eastern Asia Society for transportation studies
24. TransPeshawar. BRT features. Available from: <https://transpeshawar.pk/brt-features/>
25. Ahmad SF, Ahmad SI (2019) Should we build mega transport project in cities? The case of TransPeshawar Pakistan. *Int J Exp Learn Case Stud* 4(1):63–73
26. BRT Peshawar Maps and Bus Stations available from: <https://www.politicpk.com/brt-peshawar-metrobus-route-map-bus-stations/>

27. Sinha KC, Labi S (2011) *Transportation decision making: principles of project evaluation and programming*. Wiley, Hoboken
28. Anwar AM, Yang J (2017) Examining the effects of transport policy on modal shift from private car to public bus. *Procedia Eng* 180:1413–1422
29. Rumsey DJ (2015) *U Can: statistics for dummies*. Wiley, Hoboken

Design of Groundwater Filter Media Using Activated Carbon for Emergency Purpose



Zuliziana Suif, Siti Khadijah Che Osmi, Maidiana Othman, Nordila Ahmad, and Adam Muhammad Ezzat Aripin

Abstract The water used for drinking must be clean, safe and not have contaminants. In previous, activated carbon (AC) was proved as an important element in water filtration system because it acts as an absorbent of pollutant or organic matter and effectively removes the unwanted substances from water. Thus, the main objectives of this study is to design the filter media using produced AC from coconut shell and to evaluate performance of produced AC in groundwater treatment based on most effective percentage removal of a parameter tested. The process of carbonised was done at temperature of 600 °C in 2 h under pure nitrogen gas with a heating rate of 10° C/min. The zinc chloride was used as an activating agent at a fixed activation time and temperature. The physical and chemical characteristics of activated carbon produced was examined by adsorption capacity using Freundlich Adsorption Isotherm. The characteristics of water quality were analyzed by raw water testing are consist of turbidity, pH, total solid suspended (TSS), dissolved oxygen (DO), Biochemical Oxygen Demand (BOD), ammonia (NH₃-N) and temperature. The result shows that the using of AC applied as layer in groundwater filtration removed BOD, TSS, turbidity and NH₃-N and achieved the standard of water quality. Overall, the removal of parameters in groundwater filtration is more effective by using size of powder than using AC in granular size.

Keywords Groundwater · Filter media · Activated carbon · Filtration system

1 Introduction

Water is very important not only in human life but also for all creatures especially for emergency purpose. The water used for drinking must be clean, safe and free from contaminants. Several potential sources of pollution of groundwater are related to land use within the catchment areas. The activities such as industry, agricultural

Z. Suif (✉) · S. K. Che Osmi · M. Othman · N. Ahmad · A. M. Ezzat Aripin
Department of Civil Engineering, Faculty of Engineering, National Defence University of Malaysia, Sg. Besi Camp, 57000 Kuala Lumpur, Malaysia
e-mail: zuliziana@upnm.edu.my

activities, and other human based activities from commercial and residential areas are contribution sources of contamination.

A system used to make water more suitable for a desired end use is defined in water treatment. Usage as drinking water, industrial processes, medical and many other uses may infer these. It is the removal and improving of current components in water for eventual application in all water treatment processes. Without adverse environmental effects, treated water may be released into the natural environment. Instead, activated carbon is one of the platforms that could be used. Activated carbon, which has high surface area and adsorption ability, is the most prospective adsorbent for adsorption.

The chemical process industry (CPI) faces many of the same problems as the drinking water industry in the treatment of groundwater for use, where small quantities of chlorinated aliphatic and aromatic solvents, generally referred to as Volatile Organic Pollutants (VOCs), have been found in drinking water aquifers 9 [1]. The EPA is to produce Maximum Contaminant Levels (MCLs) for 83 particular pollutants by 1989, under the 1986 Amendments to the Safe Drinking Water Act (SDWA). VOCs are all of these unique pollutants. For eight such substances, limits have already been given. For drinking water, these compounds are particularly regulated. Many of the VOCs mentioned, which are now detected in almost 20 percent of the supply of potable groundwater [1], may be harmful to processes and products generated by the CPI.

On behalf of the Third National Agricultural Policy (NAP3), the evolving economic needs, notably acute labour shortages, limited availability of suitable land, increasing production costs, declines in exchange rates, the development of the World Trade Organization (WTO) and the rapid liberalisation of agricultural trade, have produced new problems and challenges in the agricultural sector. In view of the above-mentioned challenges, the Ministry of Agriculture stated that the NAP3 was formulated with the overarching objective of optimising revenue through the efficient use of sectoral resources and using natural resources on a sustainable basis, such as the production of activated carbon for groundwater treatment.

Activated carbon (AC) is the common term used for a group of crystalline form absorbing substances with large internal pore structures that make the carbon more absorbent [2]. AC is useful in drinking water treatment because the property of it acts as an adsorbent, so that can most effectively remove particles and organics from water. The AC used as water filter layer give the most contribution in reducing pollution in water. Pollutants were eliminated by adsorption at suitable bases from product and AC. The suitable AC was supported for reduction of specific pollutants.

One of the most environmentally friendly solutions is the processing of activated carbon from local agricultural waste, by converting negative useful waste into usable materials. The main objectives of this study is to design a filter media using activated carbon and to evaluate performance of produced activated carbon in groundwater treatment based on most effective percentage removal of a parameter tested.

2 Materials and Methods

To achieve the objectives of this research, the selected agricultural waste had been converted to activated carbon through a chemical activation method with fixed time of 2 h at 600 °C burning temperature. After the activated carbon produced, sieve analysis test is conducted to separate the activated carbon into two different of sizes which is granular and powder. Other than that, the characteristics of activated carbon also has been determined using adsorption test. Then, the water filter media system has been designed to fulfill the second objectives. A good filtration process had been able to produce a good quality of water. For this research, specifically, one filter was designed. The filters consist with sand, fine gravel and coarse gravel apart from activated carbon as the main media component in the filter.

2.1 Production of Activated Carbon

The production of activated carbon (AC) by coconut shells (CS) using chemical activation was conducted at Fabrication Laboratory of Universiti Pertahanan Nasional Malaysia (UPNM). The CS was scratched off to remove coconut meat. The coconut shell was washed carefully with distilled water to remove adhering soil and clay and then dried in air at 110 °C in an oven for 24 h. The coconut shell crushed and then passed through different sieves. The particle size between 500–250 μm was selected for further pretreatment. Sieve analysis process was done to separate the AC into two different size that were powder (PAC) and granular (GAC) for adsorption test. Laboratory test for determining performance characteristics and performances of AC were done using adsorption test. The test was conducted at Biology Laboratory of UPNM.

The zink chloride (ZnCl_2) activating agent from CS was carried out by refluxed the coconut shell with a 1 M sodium hydroxide (NaOH) solution for an hour to reduce the ash content in the sample. The CS was impregnated with ZnCl_2 and water at various ratios. The impregnation ratio that mass of the activating agent compared to the mass of the dried coconut shell (wt/wt) varying from 1/1 to 2/1 for ZnCl_2 respectively. The mixture was heated under pure nitrogen gas with a heating rate of 10 °C/min in Heat Treatment Furnace. The temperature used was 600 °C for 2 h fixed time until the furnace shows the reading in room temperature about 28 °C. Then, acid washing produces with a 3 M hydrochloride acid (HCl) solution with pH 6.70 until 7.00. Then, the mixture was dried in oven at room temperature for 24 h.

2.2 Adsorption Measurement

This calculation involves the number of iodine (in mg) adsorbed by 1 g of AC filtration below an assign setting [3]. Good signs of an AC filter to discard organic composites were measured on number of iodine.

The test was done to determine the maximum wavelength and most effective of contact time. Batch adsorptions were performed in 5 sets of 250 ml conical flask where 0.1 g powder of methalyne blue in addition with 1000 ml of distilled water and the 200 ml of 0.1 g/L methalyne blue solution were placed in each of flask. The 0.1 g of activated carbon, with particle size of 200 μm was added to flask and kept in an isothermal shaker of 120 rpm at 30 °C until equilibrium was reached. The samples were agitated with times of 10, 20, 30, 60 and 120 min. Aqueous samples were taken from the solutions and then were analyzed. All samples were filtered orderly to minimize intervention of the carbon fines during the analysis. Concentration Methalyne blue in the solutions before and after adsorption were measured using a double beam UV–vis spectrophotometer (UV-1601 Shimadzu, Japan) at its maximal wavelength of 565 nm and most effective of contact time at 120 min.

2.3 Adsorption Isotherm

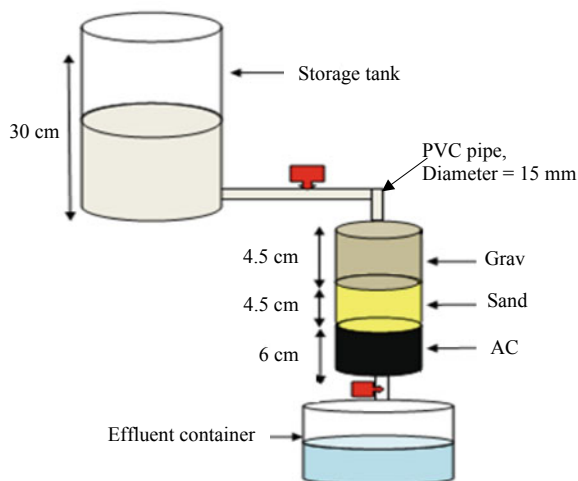
Application of Langmuir isotherm is the mass action law leading to the thermodynamic equilibrium constant [4]. The free sites concentration with the adsorbate concentration in the solution and complex sites concentration at the adsorbent surface are links [4]. Instead, the empirical Freundlich equation is the vital and frequently used for expressing multilayer adsorption [5]. The saturated adsorption has no value and commonly used in chemical and physical adsorptions, additionally in solution adsorption. The Freundlich equation are commonly used in explain for isotherms in liquid condition. The empirical Freundlich adsorption isotherm also applied to connect the number of impurities in the solution condition to the impurities in the adsorbed condition given as [6].

$$x/m = kc^{\frac{1}{n}} \quad (1)$$

Equation 1 is the concentration of the adsorbed state where x/m . x is the amount of impurity adsorbed at equilibrium, m is the weight of carbon applied and c is the impurities concentration present in the water, k is the capacity of adsorption as unit (mg/g) (L/mg) 0.5. k is derived from the intercept of a linear plot of $\log(x/m)$ versus $\log(C)$ and $1/n$ (dimensionless value) is allied to the gradient of the graph. Giving the logarithm of both sides produces:

$$\log(x/m) = \log k + 1/n \log C \quad (2)$$

Fig. 1 Water filter media consists gravel, sand and activated carbon of layers



The amount of carbon applied was measured by fractioning the number of impurity discard by the carbon loading (x/m).

2.4 Design Filter

The model filter consisted of a 15 mm diameter PVC connection pipe, 6 L water bottle with 15 cm diameter, 1.5 L container with 15 cm diameter (for effluent retainer) and 10 L of water bottle with 15 cm diameter (for storage water). There have two of valve between storage tank with filter and between filter with effluent container. The cylindrical filter had a combination of filter pads consists three layers. The designed filter has granular AC filled in a plastic vessel at the entering. The collector is mounted at the reservoir for an accessible to water. Figure 1 showed the filter media model system consists gravel, sand and activated carbon of layers.

2.5 Laboratory Test

In this study, laboratory testing was conducted before and after filtration with or without AC with raw water testing. The purpose of raw water testing was to determine the characteristics of water sample prior to treatment for domestic purpose such as drinking water. For the testing, it may consist with physical and chemical. In this paper, the water testing was consisted turbidity, pH, total solid suspended (TSS), Biological Oxygen Demand (BOD), ammonia ($\text{NH}_3\text{-N}$) and Dissolved Oxygen (DO).

The BOD, DO, NH₃-N, TSS and pH were analyzed in behalf on the standard method procedures. The effluent and influent from the filters have been compared and interpreted based on the result of all parameters test in order to obtain the highest percentage removal and the most effective filtration system.

3 Results and Analysis

3.1 Efficiency of Carbon Sources

The two activated carbons PAC and GAC were loaded into different filter cartridges. Carbon PAC was accomplished carbon for the total impurity concentration absorbed. From the absorbance analysis results exhibit that, using PAC in removed the unwanted particles in water is more efficient than GAC. The importance characteristics in choosing types of carbon are particle size, total surface area, voids space between particles and pore structure [7]. The PAC has a smaller particle size than GAC. The PAC also have larger surface area, more voids space between particles and more pore structure than has in GAC. So, the PAC had higher adsorption capacity than GAC.

The equation method described the relationship between amounts of impurity adsorbed at equilibrium, x/m against the impurity concentration, C . The $\log(x/m)$ plot versus $\log C$ in Eq. (2) provides the effects of the isothermal plots shown in Fig. 2. Carbon loading (x/m) differed linearly with the impurity concentration by the isotherm plots. The constants, k and $1/n$ were get from the graph where n was linked to the gradient of the graph given as an outlined in Table 1. The k was linked

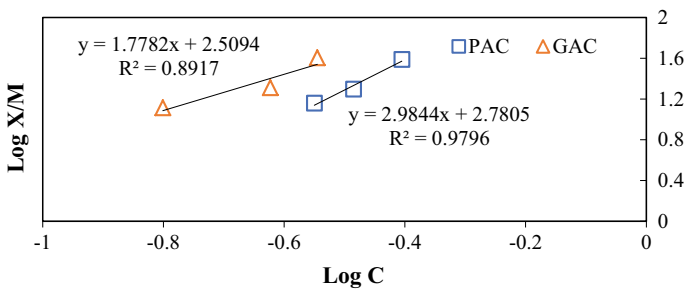


Fig. 2 The plot of impurities discard versus impurities present

Table 1 Results from isotherm plots

Carbon type	Adsorbent capacity, n	Strength of adsorption, k
GAC	1.918	2.509
PAC	2.959	2.781

to the intercept on the x/m -axis which generated 2.509 and 2.781 for carbon GAC and PAC respectively. The k value is linked to the capacity of adsorbent. Whereas the value of n is linked to the adsorption strength [6]. The adsorbate mass per dry unit weight of carbon (x/m) (mg/g) leans on instantaneously on k and exponentially on n . The values defined by n and k (Table 1) have shown a remarkable contrast in the absorption capacity of the carbon size. PAC has an excessive adsorbent capacity as differentiate to the GAC.

In the Freundlich Adsorption Isotherms [8], the slope and points of the isotherm outlines show sufficiently works on one carbon respective to the others carbon. Moreover, the present impurities by the isotherm outlines (Fig. 2) lessen for carbon PAC as contrast to Carbon GAC. This leveled Carbon PAC for an excellent strength of adsorptive apart from carbon GAC.

Specifically, a practically vertical isotherm outline presents bad adsorptive characteristics at bottom impurity concentrations. Besides several testing using the ACs filled in the filters on the treated water, the impurity levels were decreased substantially with produced AC powder apart from produced for granular size. This could be as an outcome of excessive adsorption AC capacity produced from powder than granular.

3.2 Water Filtration System Design

From the physicals and chemicals parameters tests carried out for groundwater samples collected. The influent water sample is that passing through a filter is being treated with the mediums.

Biochemical Oxygen Demand (BOD)

The result for BOD parameter were presented in Fig. 3. According to the result, it shows that the decreasing value of BOD in the effluent compare to influent by used AC as layer in filter media. After filtration, the used of AC decreased the initial BOD concentration from 1.60 to 0.29 mg/L until 0.09 mg/L or 81.88–94.38%. In previous study, it was proved that using of AC can remove the parameters of BOD. Phillips and Shell [9] presented a study of the effectiveness of granular AC and other general contaminants in removing BOD and seem that BOD removal by the AC averaged 33%.

Dissolved Oxygen (DO)

Figure 4 provide the result for DO parameter. Based on the result, the filtered water using AC as medium layer shows the decreasing initial DO concentration from 6.43 to 5.42 mg/L until 5.42 mg/L or 13.06 to 15.71% in percentage removal.

The amount of DO in the water sample depends on the temperature of the water, the amount of sediment in the water sample, the amount of oxygen extracted from the environment by breathing and decaying species, and the amount of oxygen returned

Fig. 3 BOD test on groundwater using AC

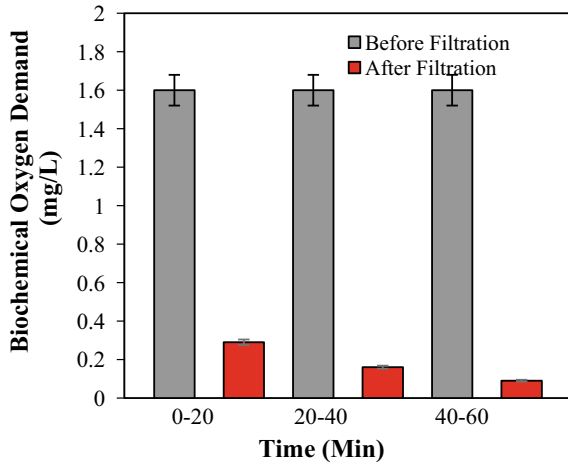
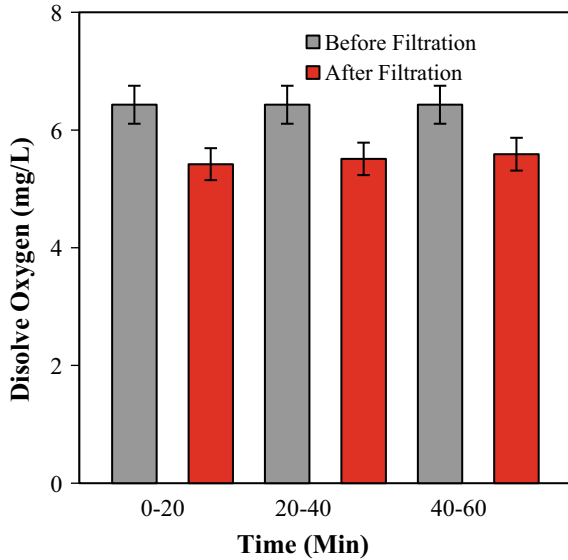


Fig. 4 DO test on groundwater using AC

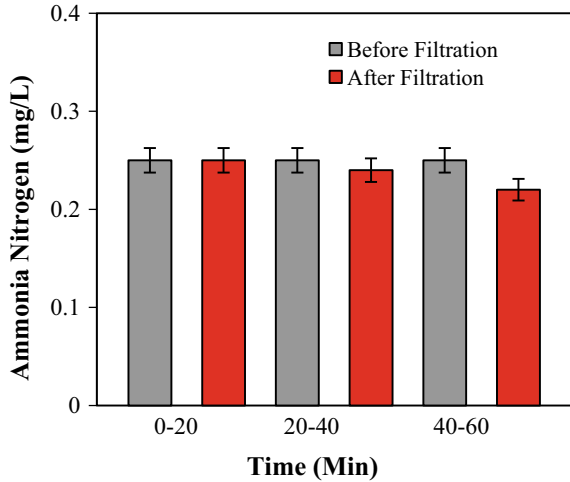


to the environment by photosynthesizing plants. The unwanted particles or microorganisms in sand, gravel and AC layer had influenced the decreased of DO in groundwater. The temperature factor also become affects the amount of DO in groundwater. When temperature rises, less gas is being dissolved.

Ammoniacal Nitrogen (NH₃-N)

Figure 5 showed the result for NH₃-N parameter. According to the result, the parameter ammonia of water filtered is decreased. The used of AC not change the initial

Fig. 5 NH₃-N test on groundwater using AC



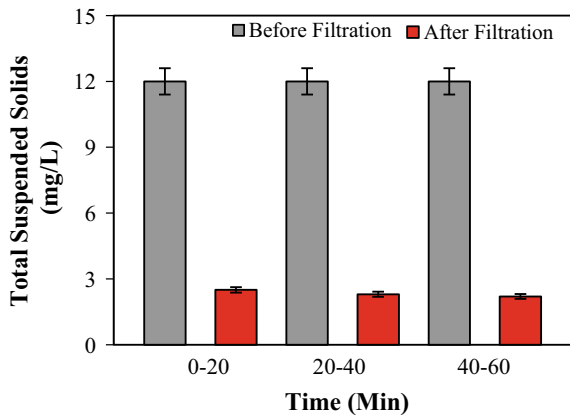
NH₃-N concentration of 0.25 mg/L at 20 min interval time. The used of AC was achieved the objective at 40 and 60 min with removed the initial NH₃-N concentration to 0.22 mg/L until 0.24 mg/L or percent of removal of 4% until 12%. The result of less removal of NH₃-N based on effect of pH. The adsorption of NH₃-N was highest at pH = 9 and lowest or not removed at pH = 5 The AC after washed in pH 6 until pH = 7. So, the removal of NH₃-N used AC give less of value.

Total Suspended Solid (TSS)

The result for TSS parameter were presented in Fig. 6. The result shows that used of AC as layer in filter media successful removed the TSS parameter.

After filtration, the used of AC decreased the initial TSS concentration from 12 to 2.2 mg/L until 2.5 mg/L or 79.17% until 81.67%. In previous study, the using of AC

Fig. 6 TSS test on groundwater using AC



can remove the parameters of TSS. Phillips and Shell [9] stated that the effectiveness of granular AC in removing solid suspended and seem that solid suspended removal by the AC in averaged 25%.

Turbidity

The result in Fig. 7 shows for turbidity parameter. The used of AC as layer in filter media decreased the turbidity parameter at 60 min retention time. After filtration, the used of AC decreased the initial turbidity concentration from 7.93 to 2.96 mg/L until 3.05 mg/L or 61.54% until 62.67%. It was higher than not used AC in filtration that increased 9.97% until 11.1% with different between highest or lowest percent removal of turbidity after filtration of using AC with lowest reading of percent removal of turbidity after filtration of not used AC. Berg [10] stated that AC had replaced sand in filtration and final effluent in range less than 0.1 NTU.

pH

Figure 8 shows the result for pH parameter. According to the result, water filtered used of AC as layer in filter media were increased the pH parameter at 60 min retention times. After filtration, the used of AC decreased the initial pH concentration from 6.26 to 5.83 until 6.13 or 2.08% until 6.87%. It was lower than not used AC in filtration that decreased 3.68% until 8.47% with different between highest or lowest percent increment of pH after filtration of using AC with lowest reading of percent increment of pH after filtration of not used AC. The washed of AC after heated in high temperature was difficult to achieve close pH 6.70 until 7.00. The characteristic of AC in acidic was effected the pH of construction water after filtration.

Fig. 7 Turbidity test on groundwater using AC

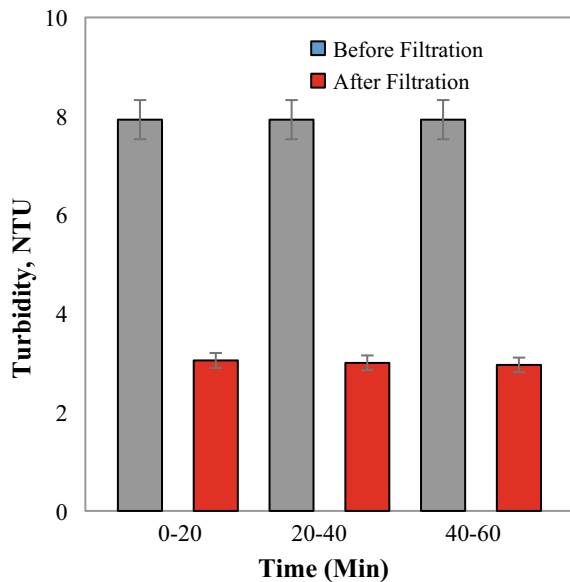
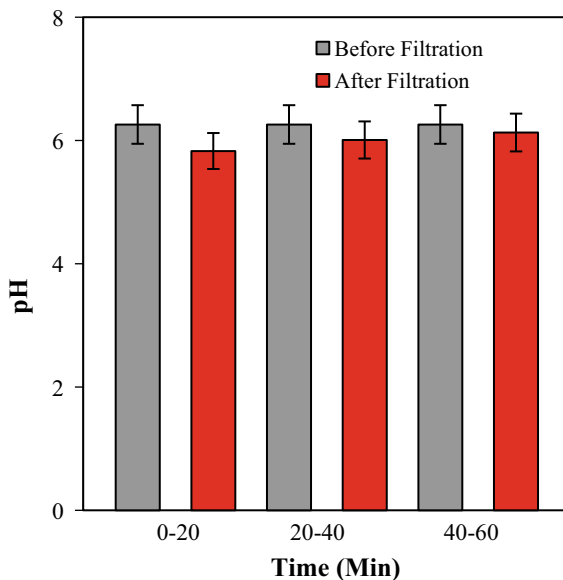


Fig. 8 pH test on groundwater using AC



4 Conclusion

Laboratory adsorption testing was the tool used for this study to assess the effectiveness of the AC produced from coconut shells of varying sizes (powder and granular) in the purification process. In a laboratory scale plant, preparation of activated carbon from pyrolyzed coconut shell waste was conducted. The adsorption ability of the AC produced in powder size was higher than that produced in granular size.

However, the AC in powder size had a critical capacity for adsorption than the granular size. The results show a substantial difference between them. The outcome of the test is statistically significant and the difference in their mean percentage impurity removal rate is very small and can be excluded as such.

The adsorption of methylene blue means that the AC was found to be much stronger. The AC from the coconut shells was successful in removing water turbidity. One choice that people who have problems with quality drinking water frequently use is home water purification using AC filters. For treating such organic components, AC is considered the best home technique. However, AC filter have a short lifespan. Eventually, adsorbed contaminants will saturate the surface of the AC and no further purification will occur.

AC filter are not recommended for metals and other ions that may also be prevalent in drinking water pollutants. These are obviously some of the obstacles to be further explored. The selection of an AC filter should be based upon, water analysis and a detailed evaluation of the individual homeowner's experience. The suitable filter depth depends on the water flow rate through the filter. The slower the rate of flow, the better the removal is. The poor output of the filter may be due to pores being

blocked by the AC and possibly due to inappropriate filter depth. In addition to the complex matrix/structural network, the remarkable properties of AC allow poisons, creosotes, heavy metals, insecticides, bad odours and tastes, chemical substances and impurities or undesirable substances to be trapped in both liquid and gases.

The AC operates when a specific material cannot be isolated by ordinary physical filtering (using a sieve, filter paper and filter sheets, and sand). AC operates by adsorbing impurities into its pores. Adsorption occurs by collaboration between the enormous adsorptive surface of the carbon, including its weak electrostatic charges (known as the forces of Van der Waals), the distribution of pores and the construction of pores. The carbon pores become saturated with impurities, binding them even to the outside of the carbon.

It should be noted here that all pollutants in water cannot be regulated by any one piece of treatment equipment. Both types of care have drawbacks of their own. In order to efficiently treat water for human use, an integration of treatment processes is necessary. Different forms of carbon filters can be said to remove different pollutants. For example, AC filters and other compounds, are unable to remove microbial contaminants (bacteria and viruses), calcium and magnesium (hard water minerals) and fluoride nitrate. Therefore, the method of sedimentation is first and foremost suggested to minimise turbidity before adding water into a filter. This is because surface water requires pre-treatment to decrease turbidity, and this is an additional benefit in that the filter saturation / life cycle would be extended.

Acknowledgements A part of this research work was supported by Short Term Grant of Universiti Pertahanan Nasional Malaysia under grant UPNM/2019/GPJP/TK/9.

References

1. Love OT Jr, Eilers RG (1986) Report finds only 50 drinking water plants able to remove organics, groundwater monitor. *J Am Water Wks Assoc* 74(8)
2. Tadda MA, Ahsan A, Shitu A, ElSergany M, Arunkumar T, Bipin J, Abdur Razzaque M, Nik Daud NN (2016) A review on activated carbon: process, application and prospects. *J Adv Civil Eng Pract Res* 2(1):7–13
3. Bruce ID, Sharon OS (2013) Drinking water treatment: activated carbon filtration, revise version. University of Nebraska Lincoln, NebGuid 1489
4. Dang D, Ding W, Cheng A, Liu S, Zhang X (2011) Isotherm equation study of F adsorbed from water solution by $\text{Fe}_2(\text{SO}_4)_3$ modified granular activated alumina. *Separat Sci Eng. Chinese J Chem Eng* 19(4):581–585
5. Violante A, Huang PM, Gadd GM (2008) Biophysico chemical processes of heavy metals and metalloids in soil environments. Wiley Interscience, America, p 217
6. Weber WJ Jr (1972) Physicochemical processes for water quality control. Wiley Interscience, Wiley, New York
7. Clark RM (1989) Granular activated carbon: design, operation, and cost. Lewis Publishers
8. Davis J, Robert L (2002) Engineering in emergencies: a practical guide for relief workers, 2nd edn. RedR/ITDG Publishing, Warwickshire

9. Phillips WJ, Shell GL (1969) Pilot plant studies of effluent reclamation. *Water Wastes Eng* 6(11):38-41
10. Berg G (1996) Virus transmission by the water vehicle. *Virus Removal by Sewage Treat Proced* 3(2):90-100

Prediction of HMA Mixture Performance from Rheological and Rutting Evaluation of Nanopolymer Asphalt Binder



Ekazarizan Shaffie, Ahmad Kamil Arshad, Juraidah Ahmad, Wardati Hashim, Ramadhansyah Putra Jaya, Khairil Azman Masri, Mohd Amin Shafii, and Haryati Yacoob

Abstract Recently, the interest among researchers in nanopolymers used in modified binders has increased in order to achieve high performance of the bituminous mixture. This work presents a study on HMA with different nanopolymer proportions and different mix gradation types conducted to evaluate the rheological performance of asphalt binder and HMA mixtures. The design method of the Marshall mix was used to achieve an optimal asphalt binder content with a different proportion of nanopolymer polymer modifiers. The resilient modulus test was conducted to measure the stiffness of the HMA mixtures, while the dynamic shear rheometer test with a short-term aging technique was used to evaluate the rutting of the asphalt binder. The regression analysis was used to test the performance of the nanopolymer rheological asphalt binder and HMA asphalt mixture. Empirical and predicted data from experimental research have been used to construct and validate regression models. The rheological asphalt binder has been shown to have a significant effect on the performance of the HMA asphalt mixture. This result has shown that the finding provides guidance for predicting the performance of HMA asphalt mixtures with

E. Shaffie (✉) · A. Kamil Arshad · J. Ahmad · W. Hashim
Institute for Infrastructure Engineering and Sustainability Management (IIESM), Universiti Teknologi MARA (UiTM), 40450 Shah Alam, Selangor, Malaysia
e-mail: eka@uitm.edu.my

E. Shaffie · A. Kamil Arshad
School of Civil Engineering, College of Engineering, Universiti Teknologi MARA (UiTM), 40450 Shah Alam, Selangor, Malaysia

R. Putra Jaya · K. Azman Masri
Department of Civil Engineering, College of Engineering, Universiti Malaysia Pahang (UMP), Lebuhraya Tun Razak, 26300 Kuantan, Pahang, Malaysia

M. Amin Shafii
Centre of Geotechnics, Faculty of Engineering and The Built Environment, SEGi University, 47810 Kota Damansara Petaling Jaya, Selangor, Malaysia

H. Yacoob
Faculty of Engineering, School of Civil Engineering, Universiti Teknologi Malaysia, 81310 Johor Bahru, Malaysia

respect to the performance of the rutting asphalt binder and, as a result, nanopolymer can be used as an asphalt modifier in road construction.

Keywords Nanopolymer · Asphalt binder · Rheological properties · Hot mix asphalt · Rutting · Resilient modulus

1 Introduction

Through the years, conventional HMA mixtures have had a strong impact on the road pavement. Nevertheless, the demand for bitumen has increased rapidly in the last few years, with the increase in pavement failures due to permanent deformation or pavement surface rutting. Therefore, it is important for the Malaysian authority to provide good quality of asphalt binder to reduce cost of maintenance and improve pavement performance. Polymer-modified asphalt binder has been found to enhance several asphalt mix properties, such as fatigue life, susceptibility to temperature, and resistance to permanent deformation [1–3]. The polymer in the modified binder (PMB) should not be too viscous at mixing temperature or too brittle at low temperatures. In addition, PMB must have good stability during storage and transportation to ensure better mechanical strength performance than conventional asphalt. Styrene-butadiene-styrene (SBS), styrene-butadiene rubber (SBR), Elvaloy, rubber, ethylene vinyl acetate (EVA), polyethylene, and others are polymers that are commonly used for asphalt modification [3–5]. It is evident from previous studies that polymers are the appropriate material for the modification of asphalt, which in turn increases (a) the high temperature stiffness, (b) reduces the low temperature stiffness, (c) improves fatigue resistance, (d) improves age hardening resistance, (e) facilitates the preparation of stiffer hot-mixes as compared to conventional asphalt. The associated benefits of improving these properties are: (a) resistance to rutting, bleeding and flushing, (b) prevention of thermal cracking, (c) prevention of ravelling and crippling, (d) increase in durability and (e) possibility of thinner lifts [2–4]. Analytical methods to better characterize a PMB are not well established yet and many of them have been employed by several authors [6]. In addition to the reviewed advantages, researchers have also faced various challenges, including high costs, high temperature sensitivity of some PMBs, low aging resistance, poor storage stability and limited improvement in elasticity. The poor storage stability of some PMBs is usually due to the poor compatibility of polymer modifiers and bitumen controlled by the various properties of polymers and bitumen, such as density, molecular weight, polarity and solubility [5]. Some bitumen polymer modification issues are still not well understood. More efforts are expected to be made to encourage further development [6].

Although a common technique used for pavement improvement is the polymer modified asphalt binder, it will be of interest to experts and engineers to investigate the efficiency of pavement performances ranging from macro and meso scales to nanoscales. Nanomaterials for asphalt mixtures are becoming particularly interesting in the field of pavement engineering. Several studies have reported that nanomaterials

have an excellent potential to improve the quality of asphalt binders and mixtures. This may improve the properties of the asphalt pavement. The most common materials used were several good asphalt modifiers, such as carbon nanofiber, carbon nanotube, nanoclay, and nanosilica, based on previous research and development [7–9]. Yusoff's study of the potential benefits of nanosilica particles in asphalt mixtures concluded that asphalt mixture modified by 4% nanosilica increased fatigue and rutting resistance and appears to have the greatest potential for beneficial binder modification [10]. Yao reported that the addition of nanoclay and carbon microfiber improves the stripping performance of mixtures or reduces the potential for moisture damage [11]. Research conducted by Li et al. [12] indicated that the addition of SBR/nanoclay improves the viscoelastic properties, resulting in enhancing its resistance to rutting at high temperature. On the other hand, the addition of carbon nanotubes contributes to the improvement of rutting resistance at higher performance temperatures and increases the failure temperature, viscosity and elastic modulus when modified with any supplied virgin binders [12]. Although nanomaterial binders have been studied by several researchers, conclusive results have yet to be established; however, there is a broad agreement on the use of nanomaterials as a potential modifier in asphalt binders [13]. The need to evaluate nanopolymer asphalt binders has therefore been explored to enhance rutting and permanent deformation resistance. In this study, nanopolyacrylate (NP) and composite nanopolyacrylate with natural rubber latex (NC) were used.

An important phenomenon for determining the overall performance of the modified asphalt binder is the study of the rheological properties of the asphalt binder. In the Superpave performance grade asphalt binder specification, the rolling thin film oven, pressure ageing vessel and dynamic shear rheometer are used to characterise the viscous and elastic behaviour of asphalt binders at high and intermediate service temperatures. The rheological testing such as dynamic shear rheometer (DSR) measures the complex shear modulus (G^*) and phase angle (δ) of the binder which is used to determine the relationship between asphalt binder stiffness and the type of deformation. The $G^*/\sin\delta$ relationship is used to determine the asphalt binder's rutting at high-performance temperature as an indicator [14, 15]. It is important to understand this relationship to ensure stable and durable asphalt pavement. The regression analysis was conducted to evaluate the nanopolymer rheological asphalt binder and the performance of HMA mixture. Alternatively, predicting the rutting performance of the HMA mixture based on the rheological properties of the asphalt binder is very useful in describing the performance of the HMA. Several published works have applied regression analysis in pavement material modeling for its excellent ability to describe the correlation between dependent variables and a particular response. Recently, the use of regression analysis in pavement engineering has been increasingly recognized [16, 17]. Regression analysis is a statistical and mathematical technique that uses numerical and graphical representations to develop models between responses and one or more independent variables [18]. Regression analysis is mainly used for experimental design, modeling and optimization in a few experimental runs [16]. Regression analysis has been applied in various areas, such as mechanical engineering, biomass science and concrete materials. The present

study aims to develop models for predicting the performance of HMA mixtures from rheological and rutting evaluation of nanopolymer asphalt binder.

1.1 Materials

In this study, granite aggregates from Blacktop Quarry, penetration grade bitumen (PEN) 80/100 and performance grade (PG 76) were used to produce AC14 and SMA14 HMA mix designs. Both types of asphalt binders were supplied by SHELL, Malaysia. In this study, two modifiers were used: nanopolyacrylate (NP) and a composite polymer of natural rubber latex (NC) nanopolyacrylate. Nanopolyacrylate has been obtained from the Nan Pao Resins Chemical CO., Taiwan. While the ACP-DMT, Klang supplied the natural rubber latex.

1.2 Preparation of Modified Asphalt Binders

Nanopolymer modified asphalt binders were prepared by adding a different proportion of nanopolyacrylate and natural rubber latex. The Penetration Grade 80/100 asphalt binder was heated to 160 °C in the oven. Nanopolyacrylate and natural rubber latex were slowly added to the liquid asphalt binder and sheared using a mechanical stirrer attached to the propeller mixer. When the mixing temperature of 160 °C was reached, the mixing cycle began at an increased speed of up to 1000 rpm for 60 min [19]. The modified asphalt mixtures were carefully stored prior to further testing.

1.3 Dynamic Shear Rheometer (DSR) Test

Dynamic Shear Rheometer (DSR) test was performed in accordance with ASTM D7175. This test is used in the Superpave performance grade asphalt binder specification to characterize the viscous and elastic behaviour of asphalt binders at high and intermediate service temperatures. At the desired temperature and frequency of loading, the DSR evaluates the complex shear modulus (G^*) and phase angle (δ) of asphalt binders. The complex modulus (G^*) can be considered to be the total resistance of the deformation of the sample when sheared repeatedly and the phase angle (δ) is the lag between the shear stress applied and the resulting shear strain. The results of G^* and δ are generally used as indicators of HMA rutting and fatigue cracking [16]. Rutting and fatigue cracking are the greatest concern in the early and later stage of a pavement life. The rutting of the asphalt binder can be measured by the $G^*/\sin\delta$ ratio at a high-performance temperature. This relationship was used as an indicator to determine the performance of the asphalt binder [20]. An asphalt

Fig. 1 The RTFO machine

binder with a high G^* value is considered to be stiffer, which increases its deformation resistance, and an asphalt binder with a low $\sin\delta$ value is considered to be more elastic, and the ability to recover part of the deformation is increased [21]. The asphalt binder sample was aged through a rolling thin film oven (RTFO) to simulate the short-term aging of bitumen during the asphalt mixture mixing and compaction process. The RTFO test is conducted using RTFO Model N759, SEM, Pty. Ltd., Australia as shown in Fig. 1. The asphalt binder samples were poured into glass containers for this process and placed in the RTFO carriage with the opening of the glass containers in the chamber facing the jet air. With a carriage rotation speed of 15 rpm, the ageing process continues for 85 min at 163 °C. While the pressure ageing vessel (PAV) as shown in Fig. 2 is used to simulate the aging of the asphalt binder that occurs during 5–10 years of HMA pavement service. There are few advantages to the pressure ageing of the asphalt binder, such as: limited loss of volatiles, accelerated oxidation without high temperatures, an adequate amount of asphalt binder may be aged for further testing at one time, and the test is practical for routine laboratory testing. The PAV is used to age RTFO residues which provide simulated long-term aging of the asphalt binder in the HMA pavement.

1.4 Resilient Modulus Test

Resilient modulus of HMA mixture is used to evaluate the elastic properties. This test shall be carried out in accordance with ASTM D 4123 [22]. It is measured in indirect tensile mode using the Universal Testing Machine (UTM-5P) at controlled

Fig. 2 The PAV machine

temperatures of 25 and 40 °C (± 1 °C) as shown in Fig. 3. The pulse repetition period of 1000, 2000 and 3000 ms was used to distinguish between different modes of loading of samples. The standard peak load of 900 N was selected and applied vertically to the diametrical plane of the cylindrical specimen and the horizontal

Fig. 3 Resilient modulus test (UTM-5P machine)

deformation was measured. The result is presented through a graph and the average resilient modulus is calculated.

1.5 Development of Resilient Modulus Model from Rutting, $G^*/\sin\delta$ of Asphalt Binder ($M_R - G^*/\sin\delta$)

Resilient Modulus Model was predicted using Rutting, $G^*/\sin\delta$ of Asphalt Binder. Several processes such as data collection and screening outliers, descriptive statistics, correlation analysis, modeling of selected variables and model validation are required to develop a regression model. To provide a meaningful model for a better understanding of the strength of the relationship between dependent and independent variables, multi-regression was performed with a confidence level of 95%. In this study, the resilient modulus, M_R (40 °C) was assigned as dependent variables while temperature, mix design, asphalt binder type, percent asphalt binder, modifier and viscosity were assigned as independent variables. Model validation begins for all model variables with basic descriptive statistics. The relationship between actual or empirical values with the predicted values is then examined using a scatter plot. The scatter plots will show how the value of the scatter point is closer to a straight line of 45° between the empirical values and the values predicted. To check and compare the discrepancies or variations of the developed models, Root Mean Squared Error (RMSE), Mean Absolute Error (MAE) and Mean Absolute Percentage Error (MAPE) are then used. In addition, to check the validity of the models, a paired t-test is performed. A multiple regression model was finally developed.

2 Results and Discussions

2.1 Statistical and ANOVA Analysis

Table 1 shows the statistical and ANOVA values between asphalt binders (independent variables, X-Rutting, $G^*/\sin\delta$) and HMA mixtures (independent variables, Y- M_R (40 °C)). Correlation findings show a fair coefficient of determination (R^2) which indicates a close relationship between the 40 °C resilient modulus and the

Table 1 Statistical and ANOVA analysis between asphalt binders and HMA mixtures

Mixture types	Equation	R^2
AC-NP	$Y = 0.3672X - 1254.3$	0.9
SMA-NP	$Y = 0.1017X + 211.92$	0.7
AC-NC	$y = 0.0501x + 320.45$	0.9
SMA-NC	$y = 0.0271x + 588.55$	0.7

40 °C $G^*/\sin\delta$ asphalt binder for each asphalt binder type and HMA mixture type. The NP and NC modified asphalt binders and HMA mixtures, AC14 and SMA14 are clearly affected by the resilient modulus. Effective prediction models of resilient modulus from rutting, $G^*/\sin\delta$ asphalt binder ($MR - G^*/\sin\delta$) have therefore been developed.

2.2 Prediction Resilient Modulus Model

The resilient modulus model was predicted using the 95% confidence level of multi-regression to provide a significant model. Resilient modulus factor, M_R (40 °C) was assigned as dependent variables while temperature, mix design, asphalt binder type, percent asphalt binder type, modifier and viscosity were assigned as independent variables. Table 2 provided a statistical analysis summarizing the value of the standard error mean, the standard deviation, the minimum value, the median value, the maximum value, skewness and kurtosis of screening.

Potential relationships between dependent and independent variables for regression models have been established through a correlation analysis. Based on the results obtained in Table 3, the temperature has a high correlation with the Resilient Modulus (r -value = 0.902). While the other variables, such as mix design, binder type, percent

Table 2 Descriptive statistic for resilient modulus model

Variable	Mean	StDev	Minimum	Median	Maximum	Skewness	Kurtosis
Resilient modulus	1418.3	758.9	467.0	977.0	3207.0	-0.42	-1.36
Temperature	1.5000	0.5007	1.0000	1.5000	2.0000	-0.00	-2.01
Mix design	1.5000	0.5007	1.0000	1.5000	2.0000	0.00	-2.01
Asphalt binder type	2.2857	0.7009	1.0000	2.0000	3.0000	-0.46	-0.89
% Asphalt binder type	2.7143	1.0317	1.0000	3.0000	4.0000	-0.19	-1.14
Modifier	7.500	4.037	1.0000	7.5000	14.000	0.00	-1.21
Rutting, $G^*/\sin\delta$	6622	1896	4849	5343	9899	0.75	-1.14

Table 3 The correlation matrix among variables

Variable	Resilient modulus	
	R value	P value
Temperature	0.902	0.000
Mix design	0.156	0.004
Binder type	0.204	0.000
% Binder type	0.256	0.000
Modifier	0.264	0.000
$G^*/\sin\delta$	0.219	0.000

Table 4 Multi linear regression for the $M_R - G^*/\sin\delta$ model

Predictor	Coef	P
Constant	480.49	0.000
Binder type	0.04	0.005
% Binder type	52.067	0.000
Rutting	0.011904	0.003
log mixdes \times modifier	19.955	0.000

$S = 63.4$ $R-Sq = 62.6\%$

Table 5 Analysis of variance for $M_R - G^*/\sin\delta$ model

C	DF	SS	MS	F	P
Regression	4	718,599	179,650	44.76	0.000
Error	107	429,501	4014		
Total	111	1,148,100			

binder type and rutting $G^*/\sin\delta$, display a weak correlation with the resilient modulus (r -value < 0.4). Nevertheless, because the p -value was less than 0.05 (p -value < 0.05), both variables were significant.

The second model of multiple linear regressions was used to classify the predictor potential in the $G^*/\sin\delta$ model. Based on the result obtained in Table 4, all variables were significant where the p -value for multiple linear regression was less than 0.05 (p -value < 0.05). As a result, these predictors can be used in the model to predict the resilient modulus of the $G^*/\sin\delta$ asphalt binder. The R^2 value for the model was 62.6% of the variations, which indicates that the linear relationship between the response and the predictor fits well with the data.

The potential M_R model to be used for prediction was then analyzed using further variance analysis (ANOVA). The outcome of ANOVA in Table 5 indicates that the p -value was less than the 0.05 suggesting that the regression model was significant. This could be used to predict the resilient modulus of the $G^*/\sin\delta$ of asphalt binder. As a consequence, the resilient modulus equation ($M_R - G^*/\sin\delta$) for predicting this model was developed as shown in Eq. 1. This finding showed that the coefficient of the type of binder for this model had a positive indication that an increase in the percentage of the type of binder would lead to an increase in the rutting, i.e. $G^*/\sin\delta$. In addition, the positive sign for the percent of binder type also indicates that an increase in this factor will lead to an increase in the rutting $G^*/\sin\delta$.

$$\begin{aligned} \text{Resilient Modulus} = & 480 + 0.01 \text{ Binder Type} + 52.1\% \text{ Binder Type} \\ & + 0.0119 \text{ Rutting} + 20.0 \text{ log mix design} \times \text{modifier} \end{aligned} \tag{1}$$

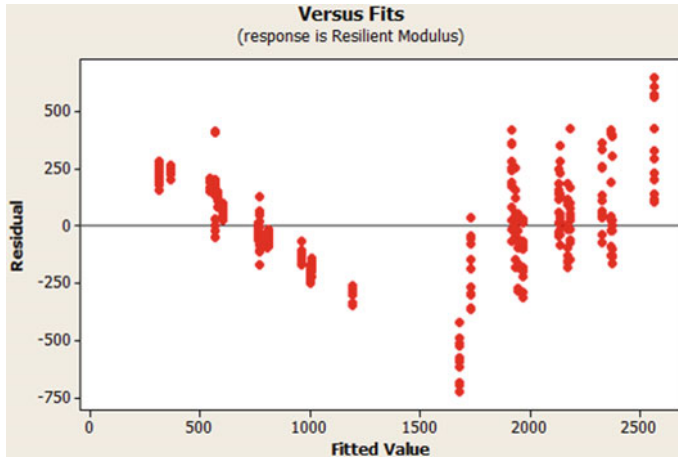


Fig. 4 Graph of residual versus fitted values for $M_R - G^*/\sin\delta$ model

2.3 Justification of the Regression Model Assumptions

Justifications for regression model assumptions are evaluated using a regression analysis. The regression analysis was used to model and determine the relationship between the response variable and one or more predictors. Figure 4 shows the residuals versus the fitted values plot for the resilient modulus with the $M_R - G^*/\sin\delta$ of asphalt binder. The results show a rather random scatter along the horizontal line with zero residual. Therefore, the model was adequate and the regression assumptions were met.

2.4 Normality Test for Residuals

Normality test used to determine if the data set is modelled for normal distribution using the Kolmogorov–smirnov test. The P-value of the Kolmogorov–smirnov test must be greater than 0.150, suggesting that the model was normally distributed. The result obtained in Fig. 5 did not satisfy the criterion, which indicates that the p-value was less than 0.01. The initial data for model development was transformed (Fig. 6) and the result of the P-value for the transformed data was greater than 0.150. Accordingly, this finding implies that the data was normally distributed after transformation and can therefore be accepted for model development.

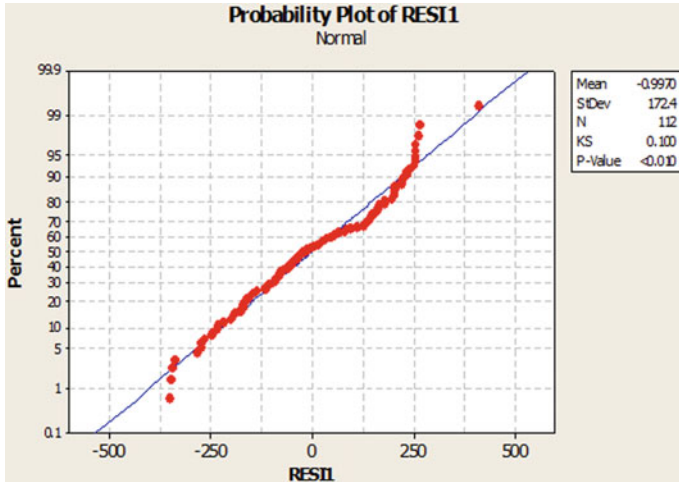


Fig. 5 Probability plot before data transform

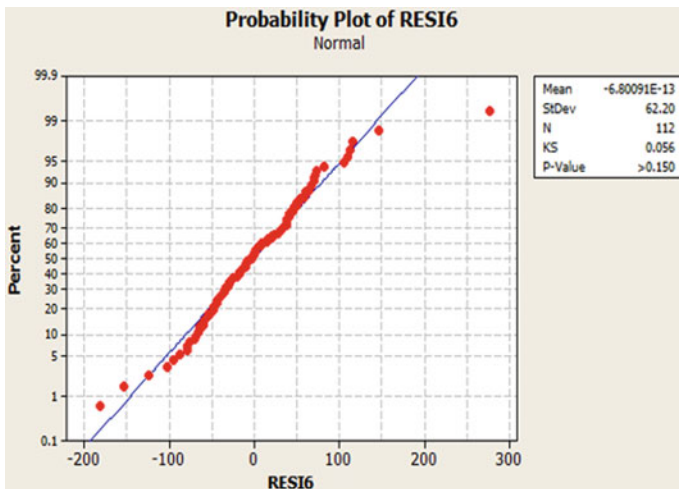


Fig. 6 Probability plot after data transform

2.5 Model Validation of $M_R - G^*/\sin\delta$

Validation of the model is carried out to assess the accuracy of the models developed against the independent data set. Figure 7 shows the scatter plot of the $M_R - G^*/\sin\delta$ model which represents the relationship between the empirical $M_R - G^*/\sin\delta$ and predicted $M_R - G^*/\sin\delta$. The point plots are scattered closely to the line of linearity

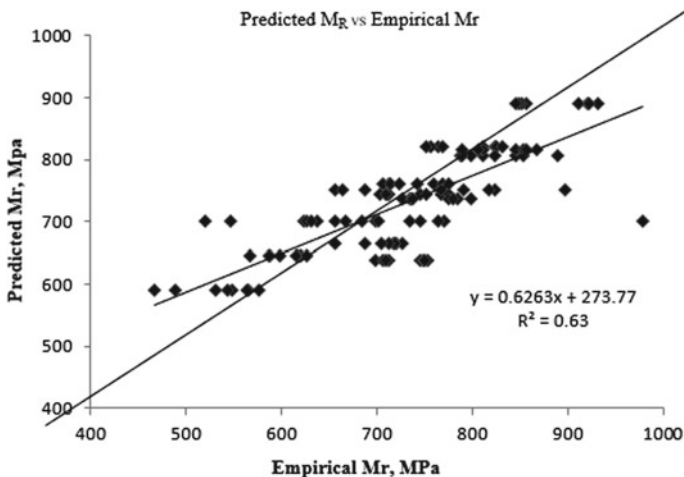


Fig. 7 Predicted $M_R - G^*/\sin\delta$ versus empirical $M_R - G^*/\sin\delta$

Table 6 MSE, MAE, and MAPE for $M_R - G^*/\sin\delta$ model

Model	RMSE (MPa)	MAE (MPa)	MAPE (%)
$M_R - G^*/\sin\delta$	16.93	7.01	6.71

for both models with the coefficient of determination, $R^2 = 0.63$. Therefore, the observed model can be successfully used to predict the independent dataset.

Model validation shall be performed to evaluate the accuracy of the models developed against an independent data set. Figure 5 displays the scatter plot of the $M_R - G^*/\sin\delta$ model, which represents the relationship between the empirical $M_R - G^*/\sin\delta$ and the predicted $M_R - G^*/\sin\delta$. Point plots are scattered closely to the linearity line for both models with a coefficient of determination, $R^2 = 0.63$. The observed model can therefore be used successfully to predict an independent dataset.

For the accuracy of the results, the findings obtained (Table 6) from the empirical value of the predicted $M_R - G^*/\sin\delta$ are 16.93 MPa for RMSE, 7.01 MPa for MAE and 6.71% for MAPE. The findings reveal a small discrepancy between the RMSE, MAE and MAPE values. This results indicate that the $M_R - G^*/\sin\delta$ model can be used and that it is acceptable to predict $G^*/\sin\delta$.

A comparison of the means was made for the paired t-Test between the predicted $M_R - G^*/\sin\delta$ and the measured $M_R - G^*/\sin\delta$. Table 7 shows the results of the validation analysis for $M_R - G^*/\sin\delta$ model. This result shows that the P-value

Table 7 Validation analysis result for $M_R - G^*/\sin\delta$ model

Test	Value
t-statistic	-0.07
p-value	0.944

is 0.944, which is greater than 0.05. It therefore indicates that the predicted $M_R - G^*/\sin\delta$ predicted model did not differ significantly from the $M_R - G^*/\sin\delta$ empirical values. Model was validated and the model predicted almost fit with the empirical data obtained. In conclusion, the model was successfully developed and validated.

3 Conclusions

From the study, on the basis of the results and analyses, the following conclusions can be highlighted:

1. Resilient Module at 40 °C showed a significant relationship with viscosity and $G^*/\sin\delta$ asphalt mixtures made with both mixtures and the modified type of binder.
2. The proposed ($M_R - G^*/\sin\delta$) model is.
3. Resilient Modulus = 480 + 0.01 Binder Type + 52.1% Binder Type + 0.0119 Rutting + 20.0 log mix design X modifier.
4. Based on the empirical data and the predicted data, this model has been successfully developed and validated, showing that the findings of the dependent and independent variables selected can affect each other in terms of pavement performance.
5. It could therefore be concluded that the use of NP and NC polymers as an asphalt modifier is feasible and the findings are expected to provide a starting point for the development of a national standard for the prediction of the performance of the HMA mixture with regard to the asphalt binder performance.

Acknowledgements Special thanks to the Research Management Institute (RMI) of Universiti Teknologi MARA for providing the financial support (600-IRMI/FRGS 5/3 (379/2019)). The authors would like to thank the Faculty of Civil Engineering, Universiti Teknologi MARA Malaysia for providing the experimental facilities and to all technicians at Highway and Traffic Engineering Laboratory.

References

1. Yusoff NIM, Breem AAS, Alattug HNMM, Hamim A, Ahmad J (2014) The effects of moisture susceptibility and ageing conditions on nano-silica/polymer-modified asphalt mixtures. *Constr Build Mater* 72:139–147
2. Yildirim Y (2007) Polymer modified asphalt binders. *Constr Build Mater* 21(1):66–72
3. Al-Khateeb GG, Ramadan KZ (2014) Investigation of the effect of rubber on rheological properties of asphalt binders using superpave DSR. *KSCE J Civ Eng* 19:127–135
4. Galooyak SS, Dabir B, Nazarbeygi AE, Moeini A (2010) Rheological properties and storage stability of bitumen/SBS/montmorillonite composites. *Constr Build Mater* 24(3):300–307
5. Zhu J, Birgisson B, Kringos N (2014) Polymer modification of bitumen: advances and challenges. *Eur Polym J* 54:18–38

6. Da Silva L (2004) Study of rheological properties of pure and polymer-modified Brazilian asphalt binders. *J Mater* 9:539–546
7. Forms C (2009) Nanomaterials, nanotechnologies and design, pp 403–465
8. Khattak MJ, Khattab A, Rizvi HR, Zhang P (2012) The impact of carbon nano-fiber modification on asphalt binder rheology. *Constr Build Mater* 30:257–264
9. Jamal Khattak M, Khattab A, Rizvi HR (2013) Characterization of carbon nano-fiber modified hot mix asphalt mixtures. *Constr Build Mater* 40:738–745
10. Sanchez F, Sobolev K (2010) Nanotechnology in concrete—a review. *Constr Build Mater* 24(11):2060–2071
11. Yao H et al (2013) Rheological properties and chemical analysis of nanoclay and carbon microfiber modified asphalt with Fourier transform infrared spectroscopy. *Constr Build Mater* 38:327–337
12. Li R, Xiao F, Amir Khanian S, You Z, Huang J (2017) Developments of nano materials and technologies on asphalt materials—a review. *Constr Build Mater* 143:633–648
13. Shan G, Yan S, Tyagi RD, Surampalli RY, Zhang TC (2009) Applications of nanomaterials in environmental science and engineering: review, pp 110–119 (2009)
14. Shaffie E, Ahmad J, Arshad AK, Kamarun D (2015) Empirical and rheological properties evaluation of modified asphalt binder containing nanopolyacrylate polymer modifier. *J Teknol* 76(9):85–89
15. Joshi C, Archana PM, Amarnath M (2013) Determining the rheological properties of asphalt binder using dynamic Shear Rheometer (Dsr) for selected pavement. *Ijret Org*, pp 192–196
16. Md Diah J, Ahmad J, Mukri M (2013) The methodology on statistical analysis of data transformation for model development. *Int J Stat Appl* 2(6):94–100
17. Diaz LG (2016) Creep performance evaluation of cold mix asphalt patching mixes. *Int J Pavement Res Technol* 9(2):149–158
18. Arshad AK, Shaffie E, Binti Z, Rahman A (2018) Asphaltic concrete evaluation for mechanistic pavement design
19. Shaffie E et al (2018) Effect of mixing variables on physical properties of modified bitumen using natural rubber latex. *Int J Civ Eng Technol* 9(7):1812–1821
20. Shaffie E, Ahmad J, Arshad AK (2015) Empirical and rheological properties evaluation of modified asphalt binder containing nanopolyacrylate polymer modifier. *J Teknol* 76(9)
21. Joshi C, Patted A, Archana M, Amarnath M (2013) Determining the rheological properties of asphalt binder using dynamic shear rheometer (Dsr) for selected pavement. *IJRET Int J Res Eng Technol* 2:192–196
22. American Society for Testing and Materials (ASTM) (1995) Standard test method for indirect tension test for resilient modulus of bituminous mixtures. Washington, ASTM D4123–82

Study on Nitrogen Removal Capability of Selected Regional Sewage Treatment Plants in Klang Valley, Malaysia



Suzana Ramli, Jurina Jaafar, and Raja Baharudin Raja Mohamad

Abstract A laboratory-based study was undertaken on the capability of nitrogen removal and other pollutants for selected public sewage treatment plants operated by Indah Water Konsortium (IWK) in Malaysia namely Cyberjaya Sewage Treatment Plant (STP), in Selangor, Bandar Tun Razak STP and Pantai STP both located in Kuala Lumpur. The sewage treatment plants utilize extended aeration system (EA), sequencing batch reactor (SBR), and advanced conventional activated sludge (CAS) respectively. The new regulation of Environmental Quality Act, Environmental Quality (Sewage) Effluent Regulation 2009 was enacted on 10th December 2009. All the selected STPs are subjected to EQA Standard B and they were constructed way before the new regulation is enforced. The new regulation requires all effluent discharges from sewage treatment plants to comply with effluent discharges not only on carbon organic pollutants but also on the nutrient pollutants for examples nitrogen and phosphorus. All the selected STPs were found to be very efficient in removing the organic carbon such as BOD, SS and COD, oil and grease. The effluent released to the water body was found to be satisfactory and complied to the new effluent standard. Laboratory test and data sampling collected showed similarity in term of patterns and values of the influent and effluent concentrations. The concentration of influent was found to be below the recommended design influent values. Since the selected STP are equipped with nitrogen removal facilities, there are some reductions or removal of nitrogen contents in effluent found in the samples.

Keywords Biological nutrient removal · Nitrification · Denitrification · Nitrogen

1 Introduction

Nitrogen and phosphorus are essential nutrients to the growth of living organisms. Even though some other nutrients such as iron are necessary for growth but nitrogen

S. Ramli (✉) · J. Jaafar · R. B. R. Mohamad
School of Civil Engineering, College of Engineering, Universiti Teknologi MARA (UiTM),
40450 Shah Alam, Selangor, Malaysia
e-mail: suzana799@uitm.edu.my

and phosphorus are more important to living organisms [1]. Removal or reduction of nitrogen in wastewater prior to discharge to receiving water may be desirable. High nitrogen contents in wastewater, the discharge of $\text{NO}_3\text{-N}$ would cause problems. The excessive and continuous discharge of nutrients such as nitrogen and phosphorus to the receiving waters may pose the ecological problems which can affect the health of aquatic life and consequently affect humans and animals. The major affects related to excessive and continues discharge of nutrients to receiving waters are eutrophication, ammonia toxicity and contamination of nitrate in ground water [2].

Department of Environment Malaysia, reported that the major pollutants discovered from River Water Quality Monitoring programs in 2007 and 2008 were BOD, $\text{NH}_3\text{-N}$ and SS. Water Quality Monitoring program is to detect river water quality and to identify pollutant sources. Department of Environment (DOE) [3] found that high BOD can be attributed to discharges of untreated or partially treated sewage and the discharges from agro-based and industrial manufacturing whilst the sources of SS were from earthwork and land clearing activities. The main sources of $\text{NH}_3\text{-N}$ were from livestock farming and domestic sewage discharges. Based on $\text{NH}_3\text{-N}$ and results of monitoring program in 2008, out of these 143 river basins or 1063 monitoring stations, 33 river basins were categorized as polluted, 38 river basins were categorized as slightly polluted and 72 river basins as clean. Almost half (50%) of the river basins were in category polluted and slightly polluted due to $\text{NH}_3\text{-N}$. In 2008, 17,633 water pollution point sources were recorded [4]. Out of these 9524 numbers from STPs includes of 688 Network Pumping Stations which contributed about 54.01% as major water pollution point sources in Malaysia.

Treatment of wastewater in Malaysia has entered the new dimension where not only organic carbon removal to be considered and addressed but removal of nutrient (nitrogen and phosphorus) in wastewater effluent also now becomes necessary. This is due to more stringent new requirements by The Malaysian Government toward protecting of water quality of rivers, lakes, coastal and environment. This indirectly will improve the quality of life of the people. The issue now is the problems with older STP constructed prior to new requirement of removal of nitrogen and phosphorus. Most of the old STPs are designed and built without nutrient removal facilities.

1.1 Nitrogen Removal

Nitrates are a form of nitrogen found in several difference forms in global and aquatic ecosystems. Nitrite and nitrate are produced during nitrification process through ammonia utilization by nitrifying bacteria. Nitrite nitrogen is relatively unstable and is easily oxidized to the nitrate form. It always found that concentration of nitrite in wastewater is very low. It is seldom exceed 1 mg/L in wastewater and 0.1 mg/L in surface water. Nitrite can be very important in wastewater even though in low concentration because it is extremely toxic to most of the fish and can increase the chlorine dosage requirement and indirectly increase the cost of disinfection in water supply.

Nitrate nitrogen is the most highly oxidized form of nitrogen found in wastewater. The nitrate concentration is important where the secondary effluent discharge to be reclaimed and used for ground water recharge. Concentration of nitrate in wastewater effluent may vary from 0 to 20 mg/L as N. A typical range of ammonia nitrogen is from 15 to 20 mg/L as N [5]. Department of Environment (DOE) [4] specifies maximum limit set under EQA for nitrate nitrogen ($\text{NO}_3\text{-N}$) is 50 mg/L and 10 mg/L for standard B where the effluent discharges to the enclosed water body and river respectively. According to IWK [6] nitrate level in public water supplies must be less than 10 mg/L of $\text{NO}_3\text{-N}$ (maximum contaminant level) and 1 mg/L for $\text{NO}_2\text{-N}$ for regulated public water. Ministry of Health Malaysia (MOH) [7] indicates that maximum acceptable value of the Malaysia Drinking Water Quality Standards for ammonia nitrogen and nitrate nitrogen are 1.5 mg/L and 10 mg/L respectively. Reference [1] revealed that more than 0.05 mg/L of organic form of nitrogen such as ammonia-nitrogen and nitrate-nitrogen may enhance algae growth. More than 0.2 mg/L of molecular or free un-ionized ammonia can be toxic to certain species of fish.

The biological nitrogen removal from wastewater can be achieved by designing the wastewater system to provide anoxic and aerobic or oxic environment for nitrification and denitrification condition. Nitrogen removal is achieved by aerobic nitrification and anoxic denitrification using autotrophic nitrifying and heterotrophic denitrifying bacteria. There are more stringent effluent limits on nitrogen as the increase of importance to control the nutrients release with effluent and more impaired watercourse due to enrichment of nutrients. The conventional treatment cannot remove or reduce the nitrogen compounds especially Ammonia nitrogen ($\text{NH}_3\text{-N}$), Nitrite Nitrogen ($\text{NO}_2\text{-N}$) and Nitrate Nitrogen ($\text{NO}_3\text{-N}$) as shown in Table 1.

Peavy et al. [8] stated that test for nitrogen forms in wastewater usually include analysis for ammonia including both ammonia and ammonium, nitrate and organic nitrogen. The results of the analyses are generally expressed as mg/L of the particular species as nitrogen.

Table 1 Nitrogen concentration and removals during treatment of municipal wastewater

Nitrogen form	Raw wastewater	Primary effluent		Secondary effluent (without nitrification)	
	mg/L	mg/L	% removal	mg/L	% removal
Organic nitrogen	10–25	7–20	10–40	3–6	50–80
Dissolved	4–15	4–15	0	1–3	50–80
Suspended	4–15	2–9	40–70	1–5	50–80
Ammonia nitrogen	10–30	10–30	0	10–30	0
Nitrite nitrogen	0–0.1	0–0.1	0	0–0.1	0
Nitrate nitrogen	0–0.5	0–0.5	0	0–0.5	0

1.2 Malaysia Effluent Standard

The Environmental Quality Act (EQA) 1974 specified two standards of STP effluent discharge namely Standard A and Standard B. Standard A is designed for upstream discharge of any raw water intake or within water catchment. While for Standard B is for effluent discharge downstream of any raw water intake points. Suruhanjaya Perkhidmatan Air Negara or SPAN and [9] recommends all STPs should be designed to be able to produce final effluent free from BOD, suspended Solids (SS), COD, Ammoniacal nitrogen (AMN), Nitrite Nitrogen, Total Phosphorus as well as oil and grease according to standards required. In 2009, Department of Environment (DOE) [9] set new absolute limit for the effluent quality of various parameters for wastewater treatment plant. To achieve Standard A requirements, Ammoniacal Nitrogen for enclosed water body and river should be less or equal to 5.0 mg/L and 10.0 mg/L respectively. For nitrite nitrogen for river, the limit is set to be 10.0 mg/L while for enclosed water body the limit is 20 mg/L. This limit however differs from new sewage treatment plant and the existing plants. For old treatment plant (built before 2009), the requirement for nitrogen removal for both Standard A and B is 50 mg/L.

1.3 System in Selected Sewage Treatment Plant (Extended Aeration with Anoxic Tank, Sequencing Batch Reactor and Conventional Activated Sludge System)

Extended Aeration Systems (FBDAEA) are mechanical secondary treatment systems. FBDAEA systems are robust and can withstand surges in hydraulic or organic load. To breakdown the organic material in sewage, bacteria require oxygen. This may be introduced by agitation (using surface aerators) or by submerged “diffusers”. Sewage entering a plant in passed through primary treatment where coarse material and grit is removed. The sewage then passes to secondary treatment in the form of any aeration tank where it is injected with fine bubbles of air from submerged diffusers. The effluent with suspended material is then passed into a “clarifier” (sedimentation tank) where the material settles as a sludge. The sludge is drawn off with some being returned to the aeration tank to ensure enough bacteria are present in the tank to continue the process of breaking down newly introduced sewage. This system can consistently produce a high quantity effluent. By monitoring the influent and effluent, the activity in the aeration tank can be adjusted to cater for variations in hydraulic or organic load. These plants only require moderate areas of land.

SBR is utilized for small communities that have traditionally faced the problems of high per capital costs, limited finances and limited operation and maintenance budgets for sewage treatment [10]. Where populations are less dense, the receiving environment is able to cope with lesser level of treatment, often only primary treatment will be provided. However, as population increases, these primary treatment

systems must be replaced with secondary treatment systems. Sequencing batch reactors or sequential batch reactors are a type of activated sludge process for the treatment of wastewater. SBR reactors treat wastewater such as sewage or output from anaerobic digesters or mechanical biological treatment facilities. The advantage of SBR is that the system is easily adjustable that enhance the flexibility on the operation cycle in order achieve targeted effluent quality.

The activated sludge process is a conventional biological process that is used for reduction of organic matter present in the wastewater [11]. It basically involves the oxidation of carbonaceous biological matter, for reduction of the organic pollutants. A Conventional Activated Sludge (CAS) system commonly include an aeration tank, which is used for biological degradation, and a secondary clarifier (sedimentation tank), where the sludge is separated from the treated wastewater (refer to process flow diagram). The first step of a CAS system is the aeration tank, where the wastewater is mixed with air to activate micro-organisms. While digesting the wastewater, the organisms collide with each other, forming larger particles called flocs, which have a larger capacity to degrade the biological components of the wastewater. CAS was found to be efficient in achieving and complying the required effluents standards.

2 Methodology

Samples were taken from 3 sewage treatment plants namely Cyberjaya STP, Selangor, Bandar Tun Razak STP and Pantai STP both in Kuala Lumpur. Samples were taken at incoming (influent) just before it entered into first unit process in STP and effluent (treated sewage) just before being discharged into stream or at effluent channel. All samples were taken in same day. Total of 4 sampling events from January to March 2011 were taken for the purpose of this study. 1.5 L plastic bottles were used for sample collection. The onsite measurement of dissolve oxygen (DO), pH and temperature were carried out using the handheld portable multi parameters meter (model: Ponsel ACTEON 3000) Reading and time of those measurements carried out were also recorded.

Data available from data collections from IWK and laboratory testing are BOD, SS, COD, O&G, AMN (NH₃-N) and NO₃-N. Since total ammonium nitrogen is toxic to aquatic organisms and is the major component of nitrogen in raw sewage. It was chosen as the parameter for assessment of efficiency of nitrogen removal [12]. Tables 2 and 3 show the instruments and method for effluent quality parameters and the analysis techniques used in this study.

Determination of percentage removal to total ammonium nitrogen and other parameter are achieved by comparing it concentration in waste water for before (influent) and after (effluent) the treatment. The inferential statistic is the process of to make judgment of the probability observed in the study [13]. In this study involves determining whether or not there is a significant difference between the data obtained from IWK and laboratory result with the EQA effluent standard B. The hypothesis testing was used for decision on this study. The inferential statistic is

Table 2 Instruments and Methods for Water Quality Parameters

Measurement	Parameter	Instrument and method
On site	DO	<ul style="list-style-type: none"> • Handheld portable multi • Parameters meter probe (model: Ponsel ACTEON 3000)
	pH	
	Temperature	
Laboratory	BOD	<ul style="list-style-type: none"> • BOD apparatus • Standard method part 2130B
	COD	<ul style="list-style-type: none"> • HACH 2500 spectrophotometer • HACH COD reactor • Reactor digestion method • Method 8000—water and wastewater • 26,811–26,812 (1980)
	SS	<ul style="list-style-type: none"> • HACH 2500 spectrophotometer • Photometric method • Method 8006—water and wastewater • 31, 1159 (1959)
	AMN	<ul style="list-style-type: none"> • HACH 2500 spectrophotometer • Nessler method • Method 8038—water, wastewater and sea water
	NO ₃	<ul style="list-style-type: none"> • HACH 2500 spectrophotometer • Cadmium reduction method • Method 8171—water, wastewater and sea water

Table 3 The analysis techniques for the study

Objectives	Analysis techniques
1. To determine profile of all parameters results	Descriptive statistics such as frequency distribution, percentages, mean, standard deviation and charts (SPSS 16.0)
2. To determine the relationship between actual influent and recommended influent design value	One sample T test (SPSS 16.0)
3. To determine the compliance effluent and EQA Standard B	One sample T test (SPSS 16.0)

related to hypothesis testing. The hypothesis testing is used of statistical technique to determine the probability that gives hypothesis is true. The process of the hypothesis testing is described as follows [13]:

1. Formation of the null hypothesis or H_0 and the alternative hypothesis H_A . A null hypothesis is a statistical that is tested for possible rejection under the assumption that it is true.
2. An appropriate a test statistic to be used is identified and select for assesses the truth of the null hypothesis. For this study, one sample test statistic for tests of hypothesis was used.

3. The probability value or P-value is computed which is the probability that a test statistic at least as significant as the observed assuming that null hypothesis were true. The smaller the P-value the stronger evidence against the null hypothesis. P-value is used to decide whether we have enough evidence to reject the null hypothesis and the study is supported by the experiment results as primary data and secondary data collected.

3 Results and Analysis

All the selected STPs were designed to meet Standard B of the discharged effluent. It was observed that the overall removal of main parameters such as BOD, COD, SS, oil and grease were good for most of the STPs. However, the removal of ammoniacal nitrogen and nitrite nitrogen were low compared to other parameters. Results from statistical test also showed the same findings. From the hypothesis test carried out, it was found that the values of actual influent parameters were less compared to design values. For effluent discharges, all the values were complied to new EQA Standard B requirements. Measurement of physical parameters such as temperature, DO and pH were performed at preliminary treatment just before fine screens for influent and at final effluent channel for effluent. Figure 1 shows the results of onsite measurement of influent for temperature, DO and pH of all selected sites.

An average of raw sewage's temperature for all sites was almost the same at around 27 °C. Influent from Pantai STP recorded the highest temperature of 27.99 °C and Cyberjaya STP recorded same average of pH value at 6.48. From Fig. 1, it shows that Bandar Tun Razak STP getting the highest average DO of 2.4 mg/L. This is due to the velocity of the influent at location of sample taken at the incoming channel before drum fine screens.

The results of onsite measurement of effluent for temperature, DO and pH of all selected STPs are shown in Fig. 2. From the result, an average of treated effluent's temperature for all sites was almost the same at around 27.7 °C. The effluent's pH for all STPs were at an average of pH 6.5 and Cyberjaya STP witnessed the highest average DO for effluent reading at 4.10 mg/L. The results were influenced by the flow velocity at sampling point in this case at effluent channel.

All the effluent result (as in Fig. 3) values were less than EQA effluent standard B at 20 mg/L. Once again, Cyberjaya STP showed the lowest concentration of both influent and effluent AMN. Pantai STP demonstrates the efficient removal of AMN at above 80% removal rate based on data from IWK and laboratory test results. Bandar Tun Razak STP recorded the lowest removal rate for $\text{NH}_3\text{-N}$ at 32% and 20% based on IWK records and laboratory test results respectively.

There were no available data of $\text{NO}_3^-\text{-N}$ from IWK for Bandar Tun Razak STP for both influent and effluent $\text{NO}_3^-\text{-N}$ concentration since there was no monitoring of $\text{NO}_3^-\text{-N}$ for Bandar Tun Razak STP. Cyberjaya STP. From Figs. 4 and 5, it can be observed that the $\text{NO}_3^-\text{-N}$ concentrations both for influent and effluent were below than EQA Standard B. Based on the laboratory test results, it shows that Pantai

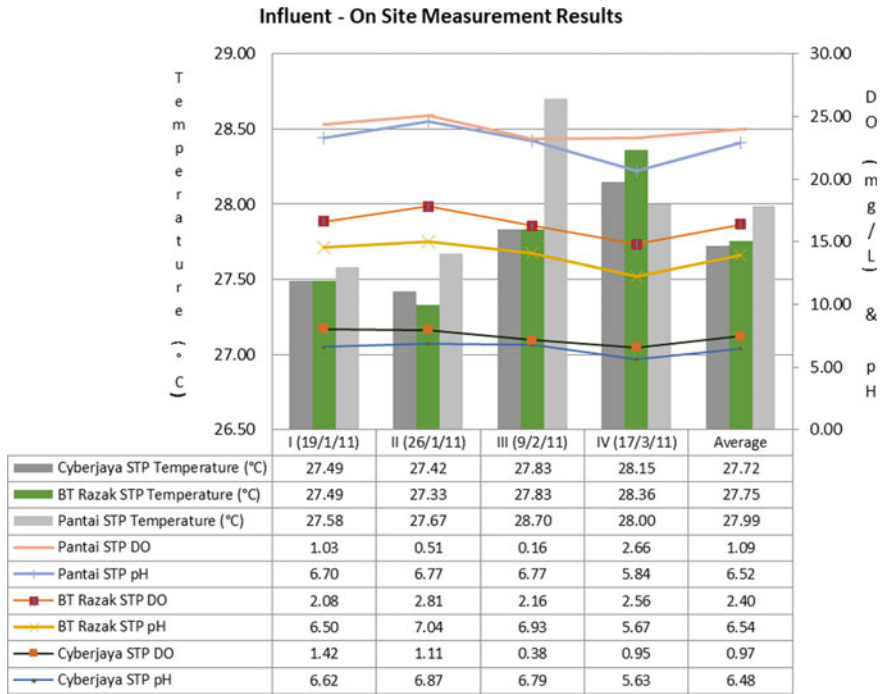


Fig. 1 Influent results of On Site measurement

STP has achieved significant reduction on $\text{NO}_3^- - \text{N}$ concentration in effluent. Once again, Bandar Tun Razak STP shows less efficient in removal of $\text{NO}_3^- - \text{N}$. Overall performance, it was recorded that $\text{NO}_3^- - \text{N}$ removal rate at more than 73% as shown in both Figs. 4 and 5. All the selected STPs were designed to meet Standard B of the discharge effluent. It is observed that the overall removal rate for most of the parameters namely BOD, COD, SS O&G were good for all of the STPs. On the other hand, the removal of $\text{NH}_3 - \text{N}$ and $\text{NO}_3 - \text{N}$ were recorded lower than selected parameters.

4 Conclusion and Recommendations

Results from the statistical test shows that the similar results as discussed before. From the hypothesis test carried out, it was found that the values of actual influent parameters (BOD5, COD, SS, O&G, $\text{NH}_3 - \text{N}$ and $\text{NO}_3 - \text{N}$) that enter the STPs were less than the design influent values and the value of actual effluent parameters (BOD5, COD, SS, O&G, $\text{NH}_3 - \text{N}$ and $\text{NO}_3 - \text{N}$) were less than the EQA Standard B. In other words, the effluent discharges from STPs were compiled to the new EQA Standard B effluent discharge. Based on the analysis, we can conclude that:

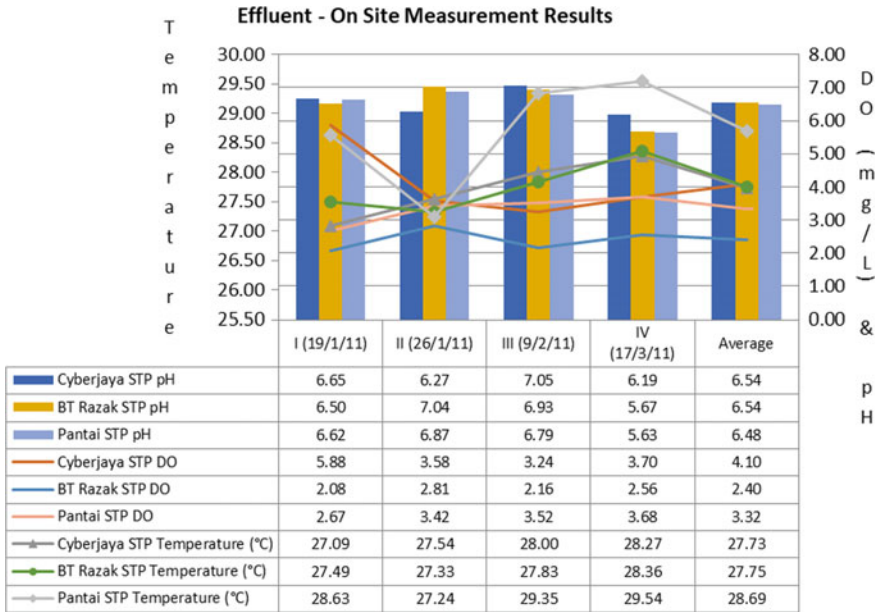


Fig. 2 Effluent results of On Site measurement

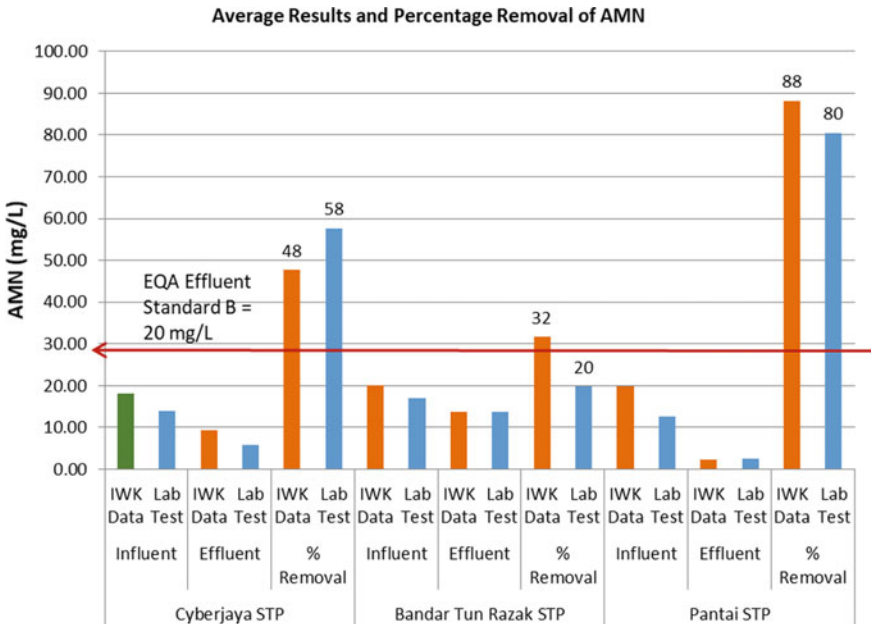


Fig. 3 Percentage removal of NH₃-N

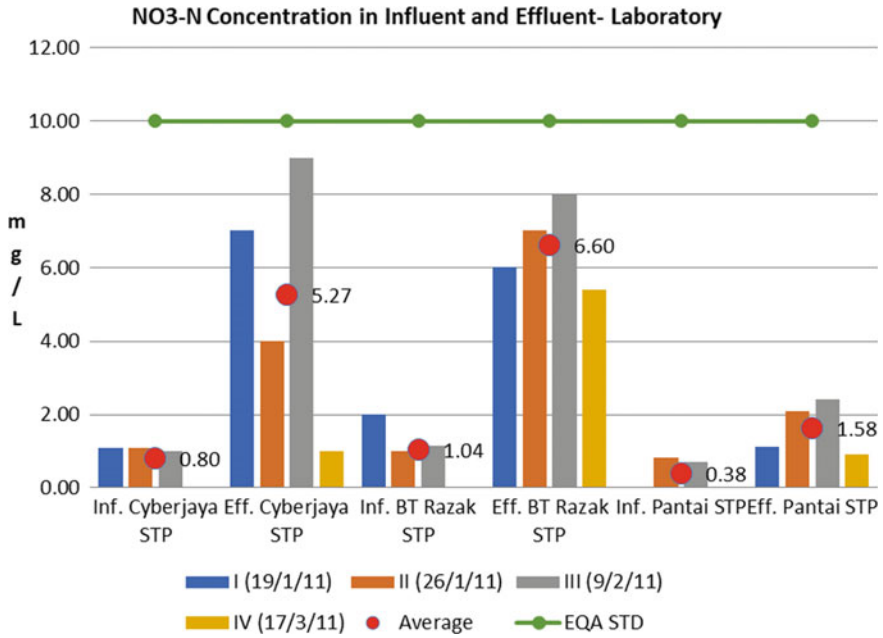


Fig. 4 NO₃-N concentration in influent and effluent (test results)

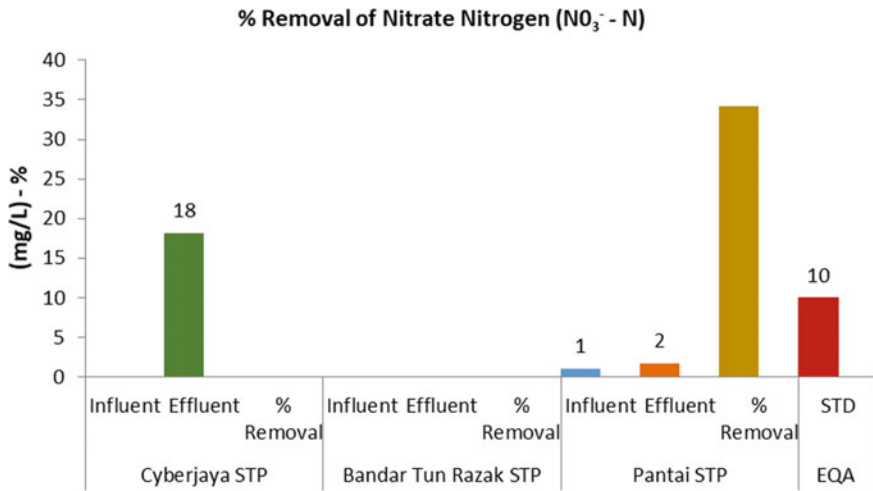


Fig. 5 NO₃⁻-N concentration in effluent and influent (IWK data)

1. For all STPs, it was found that the concentration of raw sewage enters STP was low. The actual characteristics of measured parameters were below the recommended influent design value by Gray [14].
2. All STPs are complied with the new EQA effluent Standard B discharge to river or stream.
3. All the systems, extended aeration with anoxic zone, SBR and step feed activated sludge system are able to remove nitrogen from wastewater especially $\text{NH}_3\text{-N}$ and $\text{NO}_3\text{-N}$.
4. The selected STPs are able to remove nitrogen with the conditions; they must operate and maintain the STP according to what the STP design for.
5. There are selections of the BNR configuration available depending on the requirement and the quality of effluent limit to be achieved.

Since all the selected STPs are required to produce only standard B effluent and the final discharge is not to enclosed water body, the obligation to observe and monitor the phosphorus concentration is not compulsory. It is suggested that further study on phosphorus substance and their consequences to the environment. In order to study on phosphorus, it is recommended that STP located upstream of raw water supply intake point or within the water catchment area and effluent discharge to stagnant water such as lakes, is selected for the future study. This STP is subjected to EQA Standard A effluent discharge to stagnant water body. Their effects to water supply quality also can be assessed. Recommended future research would include cost evaluation related capital cost, operation and maintenance of STP with BNR facilities. The cost assessment could determine cost analysis of development for BNR plant and could also determine cost to performance ratio. Comparisons should be made to different types of configuration of BNR processes.

In addition, the future research could also be performed in the laboratory scales by using actual sewage flows to determine the actual or more exact value to be used for future standard and design value of BNR plant in Malaysia.

References

1. Water Environmental Federation (WEF) and American Society of Civil Engineer (ASCE)/Environmental and water Resources Institute (EWRI) (2006) Biological nutrient removal (BNR) operation in wastewater treatment plants. McGraw-Hill, New York
2. Hassan R (1999) Ammonia nitrogen determination in a POME receiving stream. *J Inst Eng Malaysia* 60(3):21–36
3. Department of Environment (DOE) (2006) Impak Issue 3, Department of Environment, Ministry of Natural Resources and Environment Malaysia, Putrajaya Malaysia
4. Department of Environment (DOE) (2011) Environmental Quality Act, 1974, Department of Environment, Ministry of Natural Resources and Environment Malaysia, Putrajaya Malaysia. <http://www.doe.gov.my/en/content/environmental-quality-act-1974>. Accessed 12 Jan 2011
5. Metcalf and Eddy, Inc. (2003) Wastewater engineering: treatment and reuse, 4th edn., revised by Tchobanoglous G, Burton FL, Stensil HD. McGraw Hill Company Inc., New York
6. IWK (2011) Public Sewage Treatment Plants in Malaysia. https://www.iwk.com.my/cms/upload_files/resource/sustainabilityreport/SustainabilityReport2011.pdf

7. Ministry of Health Malaysia (MOH) (2004) National Standard for Drinking Water Quality, Ministry of Health, Malaysia
8. Peavy HS, Rowe DR, Tchobanoglous G (1985) Environmental engineering. McGraw-Hill Inc., Singapore
9. Department of Environment (DOE) (2009) Malaysia Environmental Quality Report 2008 Department of Environment, Ministry of Natural Resources and Environment Malaysia, Putrajaya Malaysia
10. Jeyanayagam S (2005) True confessions of the biological nutrient removal process. Florida Water Resour J 37–44
11. Gray NF (2004) Biology of wastewater treatments, 2nd edn. Imperial College Press, London
12. Lai PCC, Lam PKS (1997) Major pathways for nitrogen removal in waste water stabilization ponds. Water Air Soil Pollut J 94:125–136
13. Mason RR (1976) Essentials of statistics. Prentice- Hall Inc., New Jersey
14. SPAN (2009) Malaysian Sewerage Industrial Guidelines

Sustainable Use of Plastic Waste on Laterite Soil as Stabilizer



Nurul Ain Binti Ibrahim, Tan Jia Jun, Muhammad Irfan Shahrin,
and Nur'Ain Mat Yusof

Abstract Plastic has been widely used in many fields due to its lightweight, strength, durability, and capable of being moulded in any form. However, plastic pollution has become one of the major threats to the world since plastic waste is non-biodegradable and composed of higher toxic pollutants that may harm the environment significantly. Therefore, recycle and reuse of plastic waste can be one effective way to reduce the risk of plastic pollution. With the rapid growth of cities, one of the main constraints in the construction industry is the availability of land with allowable soil settlement and sufficient bearing capacity. Therefore, the engineers need to find alternative solutions to make use of the land area even though with weak soil properties. One of the effective and low-cost ways is to reinforce the soil strength using plastic waste. This research was conducted to study the effect of using plastic waste as soil reinforcement in laterite soil. Variations in compaction characteristics and unconfined compressive strength of laterite soil for different plastic waste content and dimension were investigated. The results obtained were compared with untreated laterite soil. The optimum percentage and dimension of plastic waste needed to increase the soil strength were obtained from the results. The soil strength reinforced with plastic waste can be reduced as the percentage and dimension of plastic waste exceed certain proportions and sizes.

N. A. B. Ibrahim (✉) · T. J. Jun

Department of Civil Engineering, Faculty of Engineering and Quantity Surveying, INTI International University, Nilai, Negeri Sembilan, Malaysia

e-mail: nurulain.ibrahim@newinti.edu.my

M. I. Shahrin

Department of Geotechnics and Transportation, School of Civil Engineering, Faculty of Engineering, Universiti Teknologi Malaysia, Johor, Malaysia

e-mail: muhammadirfan.s@utm.my

N. Mat Yusof

School of Civil Engineering, College of Engineering, University Teknologi MARA, Pahang Branch, Bandar Tun Abdul Razak, 26400 Jengka, Pahang, Malaysia

e-mail: nurainyusof@uitm.edu.my

Keywords Plastic waste · Soil stabilization · Compaction characteristic · Unconfined compressive strength · Laterite soil

1 Introduction

In construction, the underlain soil's stability to sustain the loading is among the most important factors that the engineer needs to consider. The types of construction carried out are very much rely on the soil's capability to support the load. Suppose the construction takes place on the weak soil without improving the soil's engineering properties after a certain period. In that case, it may lead the soil to consolidate and cause a differential settlement of soil to occur [1]. Insufficient bearing capacity of soil to sustain the loading may provide high risk of settlement to occur, reduce the structure service lifetime, and worst case scenario may cause structural failure. According to Ozdemir [2], construction that underlain by weak soil is not recommended due to its poor engineering properties such as low shear strength, high plasticity, undesirable of soil grading, risk of soil settlement, and the tendency for the soil to shrink and swell due to the effect of moisture content in the soil. Laterite soil is known as the soil which has undergone the weathering process in a long period. Laterite soil is formed when the temperature is high enough and there are heavy rainfalls with alternating wet and dry periods, which lead to soil leaching, leaving only iron and aluminium oxides [3]. Laterite formation is the repeated cycle of wet and dry seasons. Rainwater moisturizes the laterite soil and allows the surface to be touched by leached ions. Laterite forms in the low area in the topography and in the plateau, which prevents soil erosion. The reaction zone where rocks are in contact with water from the lowest to the highest level of the water tables is gradually reduced by the quickly leached sodium, potassium, calcium, and magnesium ions [4].

Soil engineering properties can be enhanced by stabilising certain poor soils with suitable agents. Improving the soil's carrying potential or consistency by compaction, mixing proportion, or incorporation of admixture is the authentic sense of soil enhancement. Babitharani et al. [5] mentioned that soil stabilization is altering some soil properties by different methods, mechanical or chemical to produce an improved soil material with all the desired engineering properties. There are various methods to stabilize the soil, which should be verified in the laboratory with the soil material before applying it to the field. The key to improving soil is to evaluate soil's physical properties and the insufficient property to enable us to choose the best approach to improve the soil strength of locally available soils [6].

Construction costs and the amount of material used are the central problems for a project. The cost of introducing additives to the soil for soil improvement has also increased in recent years, which opened the door widely to develop other soil additives such as plastics and bamboo. Nowadays, human beings' lifestyle that uses plastic day to day leads to augmenting environmental risk issues due to improper plastic waste management. This may cause harmful gas produced by plastic waste to lead to a health-related problems. Thus, utilization of plastic waste as to reinforce

the soil strength can be one of the effective solutions both for environmental and economic benefit since good quality soil is scarce for road embankments, provide good soil bearing capacity to support the foundation and provide a stronger base for the upper pavement structure respectively. This leads to a reduction of the budget for construction and, at the same time, can save the environment by reuse plastic waste since plastic is non-biodegradable and non-useful materials [7].

In the developing country, economic growth has led to a significant increment in plastic usage and, as a result, cause plastic pollution to occur. Lack of awareness on the importance of recycling plastic waste and lack of technological support causes the waste to be disposed of in landfills, washed away by the river, and burned in incinerators. These phenomena bring hazards to the environment, which causes pollution to occur, contamination of the food chain, and biodiversity breakdown, respectively [8]. One of the most effective methods to reduce plastic waste disposal is by using plastic waste as a construction material, which allows us to dispose of the plastic waste as non-useful material becomes useful material. Plastic waste management institute in 2002 reported about 55% of waste plastic being used for recycling and reuse. Recycling plastics made from more than one type of polymers, such as heterogeneous characters or some fibres may increase soil performance. The mentioned criterion is essential for soil improvement to enhance the soil's physical and mechanical properties [6].

In this project, plastic waste is used as a sustainable material to be reinforced with laterite soil in order to improve the engineering properties of laterite soil. This soil reinforcement using plastic waste can be used to meet society's challenges, lower down the amount of waste, and provide the potential of unwanted material become wanted material in engineering application. Thus, more comprehensive research is needed for this study to ensure that the use of plastic waste as a construction material can be implemented.

1.1 Literature Review

Compaction characteristic

The advantages of utilizing plastic waste as stabilizer were to enhance soil properties, reduce construction costs, and reduce plastic pollution, promoting sustainable development. Compaction involves the procedure in which the soil mass is being densified and as a result, it may lower the air voids in the soil under dynamic loading. This test is important to identify the maximum dry density and optimum soil moisture content [9]. According to Peddaiah et al. [10] research, effect of 0.2%, 0.4%, 0.6% and 0.8% of plastic waste was investigated on the compaction characteristic of soil. A series of standard proctor test was carried out following (IS-2720 Part-VII) procedure to identify the compaction characteristic of soil reinforced with plastic waste. The results indicated that the soil achieves the soil's optimum compaction characteristics with further inclusion of 0.4% of plastic waste in the soil. For the laterite soil, Salleh et al. [11] stated that only a small increment was observed in soil compaction

Width	10mm				15mm			
Length	20mm		40mm		20mm		40mm	
Proportion	OMC	MDD	OMC	MDD	OMC	MDD	OMC	MDD
0%	20.05	1.53	20.05	1.53	20.05	1.53	20.05	1.53
0.15%	23.93	1.514	18.48	1.559	19.11	1.589	22.18	1.523
0.30%	11.4	1.667	23.05	1.529	20.75	1.502	23.22	1.524
0.45%	19.17	1.551	19.25	1.535	18.30	1.594	23.62	1.519
0.60%	22.01	1.521	18.5	1.557	20.00	1.572	24.11	1.502

Fig. 1 Standard Proctor Test Result [12]

characteristic when being reinforced with an additive that allowed soil particles to be compacted into a denser state. Hence, it improved the soil compaction characteristic. Based on Fig. 1, Hansaraj [12] found that the optimum content of plastic waste needed as a soil stabilizer was 0.30%, with dimensions at 10 mm × 40 mm and 15 mm × 40 mm, respectively. This is because the optimum moisture content and maximum dry density achieved were the highest compared to other plastic fibre content used with respect to a different dimension.

Unconfined compressive strength

According to Dikkar [12], research showed that the unconfined compressive test of plastic waste size 10 mm × 20 mm with 0.3% of plastic waste added with Black Cotton clayey soil would reach the optimum UCS = 10.75 kg/cm² in 21 days. However, further with plastic waste that exceeded 0.3% cause unconfined compressive strength of the soil decreases. According to Peddaiah et al. [10], research showed that 0.4% content of plastic waste with sizes 15 mm × 15 mm reinforced with silty sand is the optimum content that gives the compressive strength of 11 kg/cm². This is because the further addition of the plastic fibre that exceeded 0.4% will gradually decrease the compressive strength of the soil.

2 Experimental Methods

2.1 Laboratory Works

Laterite soil was used in this study in which the soil was collected near the Sepang area where the soil is rusty red which also an indication of high iron oxide content. The sample was collected at a depth of approximately 1 m below the ground surface. Plastic waste was used to reinforce the laterite soil. Several laboratory tests were carried out on the soil sample in accordance with BS 1377: Part 2: 1990 [13]. The laboratory tests include moisture content test, dry sieve test, Atterberg Limit tests, standard proctor test, and unconfined compressive strength test to obtain the soil's physical and mechanical properties. The effect of plastic waste was studied on compaction characteristic and unconfined compressive strength of soil at 0.15%, 0.30%, 0.45%, and 0.60% by soil weight. Plastic waste will be selected into two different sizes with a dimension of 10 mm × 10 mm and 15 mm × 15 mm mixed with the laterite soil. The mode of failure of the soil was observed and studied. Waste plastic bag collected in this study (Fig. 2) was categorized as class 4 low-density polyethylene (LDPE), which can be recycled, safe and healthy plastics such as bottles and grocery bags as according to Fig. 3.

Fig. 2 Cut plastic bag



Fig. 3 Plastic classification [14]

3 Result and Discussion

3.1 Moisture Content Test

The natural moisture content of the soil sample collected was tested on the day of soil collection to ensure no moisture content loss due to the surrounding temperature. After 24 h of the oven drying process, three laterite soil samples' average moisture content was 15.49%. According to Chow et al. [8] research, the moisture content result of laterite soil founded in India was 12%. According to Mohd Yusoff et al. [15] research, the moisture content of laterite soil founded in Batu Pahat was 22.54%, with 1.5 m below the ground surface. Based on past research results, even though it is not mandatory to meet those requirements, natural moisture content values are not too distinct. Another factor that affects the result of natural moisture content is clay content, as high clay content will have a high density of particle arrangement and fewer pores within the particle. According to Yahaya et al. [16] research stated, soil's natural moisture content produces greater influence than clay content toward corrosion occurrence at most of the site, which can be an important process in fine-grained soils.

3.2 Particle Size Distribution Test

Based on Fig. 4, the curve shape indicates a good gradation of laterite soil collected as the soil particles are varying from gravel to silt and clay sizes. There was 13.4% of gravel retained on no. #4. This shows that the laterite soil is occupied with high fine grain and lack of course grain. Hence, this clearly shows that laterite soil does not consist of the same size grains due to the fraction pass through sieve no. #4 exceeded

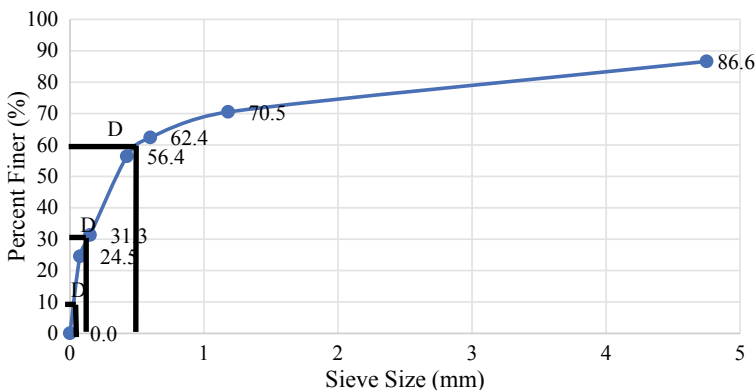


Fig. 4 Particle size distribution curve

Table 1 Particle size classification and analysis

Soil component (%)	Percentage retained (%)
Gravel (76.2–4.75 mm)	13.4
Sand (4.75–0.075 mm)	62.1
Silt and Clay (<0.075 mm)	24.5

50%. Percentage retained on each sieve size for gravel, sand, silt, and clay as listed in Table 1. It shows that the highest percentage of soil composition is sandy soil.

Figure 4 showed that $D_{10} = 0.04$, $D_{30} = 0.16$ and $D_{60} = 0.4$ in result of $C_u = 12.5$ and $C_c = 1.28$. C_u is greater than six, which shows that the laterite soil sample is well-graded and consists of a large range of particle sizes in the soil. However, due to $C_c = 1.28$, laterite soil was classified as well as graded soil because the result of C_c was within 1–3. A similar result was achieved by [15] research, where the C_u of laterite soil is 15.26 and C_c of 0.213. Similar result for [7] research, particle size distribution results showed that percentage retained for gravel = 12%, sand = 53.2%, silt and clay = 34.8%, $C_u = 9$ and $C_c = 0.8$ which had well graded on soil sample.

3.3 Atterberg Limit Test

This test has been conducted in order to determine the consistency of fine-grained soil. Cone penetration method was used to ascertain the plastic limit, liquid limit, and plasticity index of the soil samples. The result analysed shows that the plastic limit obtained was 21.72%. Based on Fig. 4, the best-fit equation of the graph was $0.6701x - 2.413$. From the equation found, the liquid limit was 33.45%. This value was the moisture content value obtained from Fig. 5, which corresponds to the 20 mm of cone penetration.

The plasticity index obtained in this study was 11.72%. Based on Fig. 6, the Casagrande Plasticity Chart shows that the soil was categorized above “A-line” based on the plasticity index and liquid limit obtained. Therefore, the soil sample can be classified as low plasticity of clay with the symbol (CL).

According to Mohd Yusoff et al. [15] research, atterberg limit results were $LL = 54\%$, $PL = 23.1\%$, $PI = 30.9\%$ which classified the soil as CL by following USCS classification. According to Ashraf et al. [7] research, atterberg limit results were $LL = 45\%$, $PL = 18.3\%$, $PI = 26.7\%$ which classified as CL by following USCS classification. Based on previous research results presented, all LL , PL , and PI values were varying slightly with respect to a different location, climate, and country. The main reason was due to the variety of formation of mineral constituents of laterite soil, which solely depends on the climatic conditions. However, most of the laterite soil plasticity index plots above the A-line which classified as CL. CL indicates the soil is low plasticity of clay.

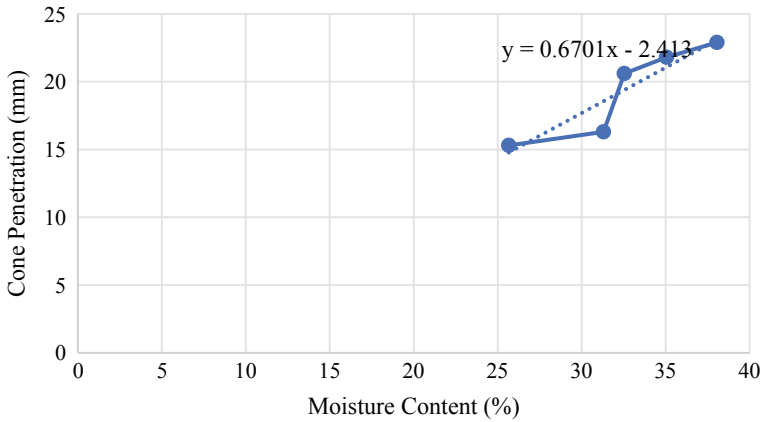


Fig. 5 Liquid limit

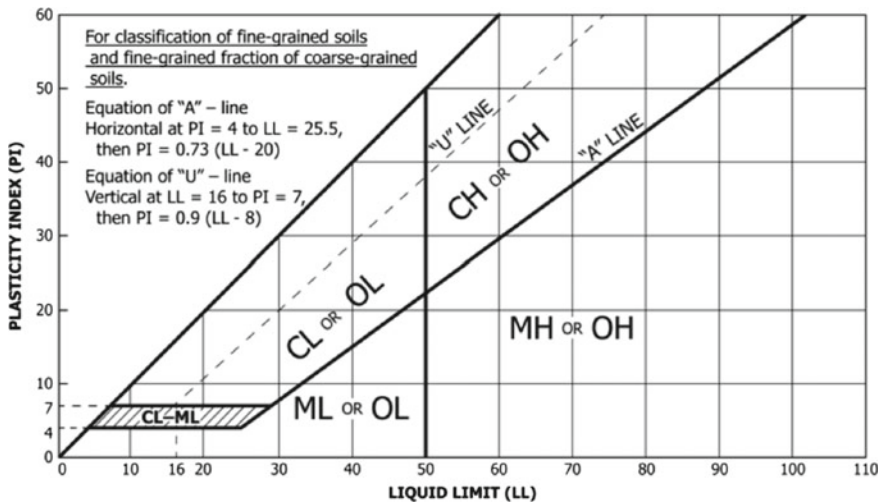


Fig. 6 Plasticity chart

3.4 Standard Proctor Test

Based on Fig. 7 and Table 2, the untreated laterite soil optimum moisture content was 16%, and the maximum dry density was 1.89 g/cm³. From Fig. 7, it was observed that there is a decrease in dry unit weight with the increase of moisture content for a soil reached a limit value in which the further addition of water to the soil will result in dry density reduction.

Based on Table 2, a different proportion of plastic waste was used to stabilize laterite soil, and the results had shown in the table. The table observed that for 10 mm

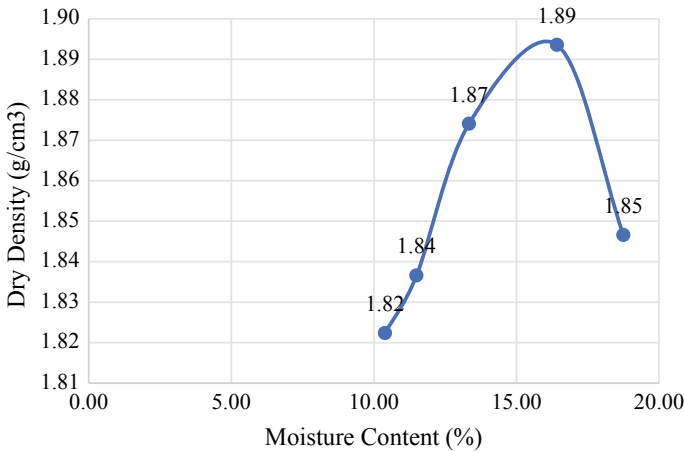


Fig. 7 Compaction curve of untreated laterite soil

Table 2 Compaction characteristic of untreated and treated laterite soil

Dimension	10 mm × 10 mm		15 mm × 15 mm	
	OMC (%)	MDD (g/cm³)	OMC (%)	MDD (g/cm³)
0	16	1.89	16	1.89
0.15	16	1.90	17	1.88
0.30	17	1.86	17	1.88
0.45	17	1.90	17	1.90
0.60	17	1.90	17	1.91

× 10 mm, the proportion of plastic waste increase as optimum moisture content and maximum dry density increase, but in 0.30%, the dry density had decreased and continued by 0.45% and 0.60% the maximum dry density had increased. For dimension 15 mm × 15 mm, the proportion of plastic waste increase as optimum moisture content increase and maximum dry density decrease for 0.15% and 0.30% but increase in 0.45% and remain unchanged in 0.60%. From Table 2, the optimum proportion of plastic waste added as a stabilizer was 0.45% by the weight of soil as optimum moisture content increases and maximum dry density increases.

According to Dikkar [12] research, the result shows that a proportion of plastic waste increases, optimum moisture content, and maximum dry density increase. The optimum moisture content increased by 1–2%, and the maximum dry density increased by around 0.02–0.1 g/cm³. The optimum percentage of plastic waste added was 0.30%, with dimensions 10 mm × 40 mm and 15 mm × 40 mm. The improvement in the maximum dry density of the soil as the plastic fibre content increases is due to the reduction in the voids and pore space between the soil particles, which as

a result it gives effective compaction and increases in the soil cohesion, respectively [17].

3.5 Unconfined Compressive Strength Test

The effect of plastic fibre with a variation of fibre content and a variety of fibre sizes reinforced with the laterite soil is extended to study the reinforced soil's behavior on unconfined compressive strength. The soil sample was prepared with 0.15%, 0.30%, 0.45% and 0.60% plastic content by mass of soil and plastic fibre with a dimension of 10 mm × 10 mm and 15 mm × 15 mm respectively. Untreated soil is acting as the control variable.

Figures 8 and 9 shows the stress-strain characteristics of plastic fibre reinforced with laterite soil. The result shows that unconfined compressive strength for untreated

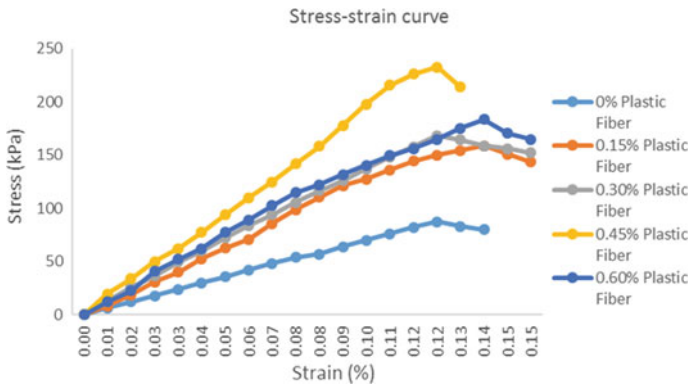


Fig. 8 Stress-strain curve with varying plastic fibre content at 10 mm × 10 mm size

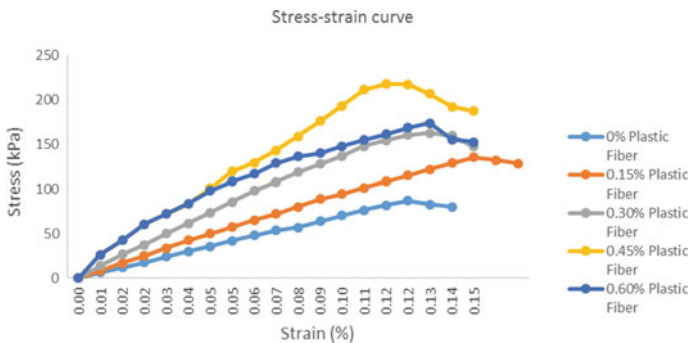


Fig. 9 Stress-strain curve with varying plastic fibre content at 15 mm × 15 mm size

laterite soil is 87.28 kN/m^2 . Based on these two figures, it can be seen that different plastic fibre size does not give a significant difference in the unconfined compressive strength of the soil. Instead, unconfined compressive strength slightly decreases as the size increases from $10 \text{ mm} \times 10 \text{ mm}$ to $15 \text{ mm} \times 15 \text{ mm}$. Similar results obtained by Alshkane [18] in which the research study shows that the sand reinforced with the short plastic fibre give slightly higher strength than long fibre. The increase in fibre size gives a non-uniform distribution of plastic fibre inside the soil mass. Besides, it also shows that the laterite soil reinforced with $10 \text{ mm} \times 10 \text{ mm}$ of plastic fibre mobilizes the highest stiffness of soil plastic matrix, increasing the soil strength [10].

It is also observed that both figures show that addition of plastic fibre in percentages increases the unconfined compressive strength of the soil. For example, for laterite soil reinforced with $10 \text{ mm} \times 10 \text{ mm}$ size of plastic fiber, unconfined compressive strength of the soil increases from 87.28 kN/m^2 (untreated soil) to 158.52 kN/m^2 (for 0.15% plastic fiber content), 168.21 kN/m^2 (for 0.30% plastic fiber content) and 232.51 kN/m^2 (for 0.45% plastic fiber content). However, with further addition of 0.6% plastic fiber content, UCS value start showing decreasing pattern which is from 232.51 kN/m^2 (for 0.45% plastic fiber content) to 183.61 kN/m^2 (for 0.60% plastic fiber content). A similar pattern can be seen on Fig. 9 where the UCS of the soil increases gradually from 0% of plastic fibre content up to 0.45% plastic fibre content, but UCS starts to drop as the plastic fibre content increases to 0.6% by soil mass. Thus, it can be concluded that the reinforcing effect of plastic fibre on the compressive strength of the laterite soil reduced at 0.6% of plastic fibre content. In addition, 0.45% of plastic fibre reinforcement resulted in optimum percentage by soil mass since the UCS of the laterite soil is at the highest regardless of the plastic fibre dimension used. According to Dikkar [12] research, the optimum percentage of plastic waste obtained was 0.45% in which the unconfined compressive strength of soil had increased by approximately 800 kN/m^2 as compared to untreated soil and the UCS of soil had remained unchanged with the further addition of 0.60% plastic fibre content.

Recycling plastics mostly consist of more than one type of polymers such as heterogeneous character or some fibres to increase their strength and elasticity. The above characteristic is useful for soil improvement to increase the geotechnical properties of soil. Based on the UCS results obtained, clearly showed that by adding plastic waste as the stabilizer can increase the unconfined compressive strength and enhanced the geotechnical properties of the soil.

4 Conclusion and Recommendation

From the research, it can be concluded that recycling plastic waste is possible. The engineering properties of the laterite soil can be enhanced by using plastic fibre as soil reinforcement. The result observed that the laterite soil is classified as Sandy Clay (SC) with low plasticity of clay according to American Society and Testing Material (ASTM). The results show that using plastic fibre enhanced the soil's compaction

characteristic as it increases the maximum dry density of the soil. Besides, it can be observed that a 0.45% percentage by soil mass is the optimum content of plastic waste that can be used to enhance the strength of laterite soil significantly. Also, this research concludes that although there is only a slight difference on the UCS of soil for both plastic fibre size 10 mm × 10 mm and 15 mm × 15 mm tested, still the highest compressive strength achieved was 232.51 kN/m² by using 10 mm × 10 mm which is at 0.45% plastic content. Thus, it is recommended to use plastic fibre with size 10 mm × 10 mm and a 0.45% content to reinforce the laterite soil strength. Thus, it is proven that plastic waste can be recycled as sustainable material to be used as soil reinforcement where it can reduce the impact of environmental hazards, more economical as it helps to reduce the cost for the plastic waste disposal and reduce the construction cost, especially when dealing with a weak soil on-site project. Future research is recommended to study the effect of plastic waste on various types of soil and study the effect of plastic waste mixed with any other stabilizer to enhance the soil strength, which can further be used as for pavement construction.

References

1. Brahmachary TK (2017) Soil stabilization using fly ash and cotton fiber. *Int J Trend Sci Res Dev (IJTSRD)* 1173–1181
2. Ozdemir MA (2016) Improvement in bearing capacity of a soft soil by addition of fly ash. *Procedia Eng* 143(Ictg):498–505
3. Dwevedi A, Kumar P, Kumar P, Kumar Y, Sharma YK, Kayastha AM (2017) Soil sensors: detailed insight into research updates, significance, and future prospects, October
4. Yamaguchi, Frontier Research on Earth Evolution in JAMSTEC (2003–2004)
5. Babitharani H, Ashwini DG, Pavan SKC, Dimple B, Koushik B, Sindhu S (2017) Soil stabilization using plastic. *IJETS* 4(9):557–572
6. Patil A (2016) Experimental review for utilisation of waste plastic bottles in soil improvement techniques. *Int J Eng Res* 5:8–9. ISSN: 2319-6890
7. Ashraf A, Sunil A, Dhanya J, Joseph M, Varghese M, Veena M (2011) Soil stabilisation using raw plastic bottles, no December
8. Chow C-F, So W-MW, Cheung T-Y, Yeung S-KD (2017) Plastic waste problem and education for plastic waste management. In: *Emerging practices in scholarship of learning and teaching in a digital era*, pp 125–140
9. Patle D, Burike M, Madavi SD, Raut S (2017) Soil stabilization using plastic waste. *IJRIS* 58–68
10. Peddaiah S, Burman A, Sreedeeep S (2018) Experimental study on effect of waste plastic bottle strips in soil improvement. *Geotech Geol Eng* 36(5):2907–2920
11. Salleh NM, Odimegwu TC, Raja TA (2014) International conference on engineering, information technology and science (ICEITS), vol 2, no 1, pp 1–19
12. Dikkar H (2017) Improvement of soil properties by using waste plastic. *Int Res J Eng Technol* 4(4):3383–3388
13. BS 1377: Part 2:1990, Methods of test for soils for civil engineering purposed, British Standard
14. Pavani P, Rajeswari TR (2014) Impact of heavy metals on environmental pollution. *J Chem Pharm Sci* 94(3):87–93
15. Mohd Yusoff SAN, Bakar I, Wijeyesekera DC, Zainorabidin A, Madun A (2015) Comparison of geotechnical properties of laterite, kaolin and peat. *Appl Mech Mater* 773–774:1438–1442

16. Yahaya N, Lim KS, Noor NM, Othman SR, Abdullah A (2011) Effects of clay and moisture content on soil-corrosion dynamic. *Malaysian J Civ Eng* 23(1):24–32
17. Kalliyath JV, Joy JT, Paul JM, Vadakkal AM (2016) Soil stabilization using plastic waste. *Int J Sci Technol Eng* 2(12):484–487
18. Alshkane Y (2017) Reinforcement of sandy soil using plastic fibres made from waste plastic bottles, 1(December)

Exploration of Palm Kernel Use in Construction: A Review



Donald Kwabena Dadzie, A. K. Kaliluthin, and D. Raj Kumar

Abstract In Ghana and other developing tropical countries in the world, oil palm is noted to be one of the most sustainable cash crops due to its versatility. The entire palm tree apart from the root, is useable for one or more products. The stem can be used as timber; the branches and leaves as baskets; the fruit bunches as palm oil and soap; the nut as palm kernel oil; and the kernel shell being waste as a potential construction material. Depletion of natural resources coupled with the environmental degradation caused by the extraction of natural resources such as sand and crushed rocks, have necessitated the need for researchers in the construction industry to explore more sustainable alternative materials such as palm kernel shell (PKS) for construction. Previous studies conducted on PKS centered more on the properties of the PKS as aggregate to replace conventional natural resource aggregates, and also the behaviour of composite materials produced with partially replaced PKS as aggregated such as PKS blocks, concrete, mortar and terrazzo finishing. To some extent, professionals in the construction industry are convinced that these much-reported proofs about PKS exploitation as potential construction material. Further studies have indicated that, the use of PKS results in affordable products. To some extent, this might be true, but very little is reported on this claim as empirical evidence. To this end, further studies with emphasis on the application of PKS products to construct building elements are required. These when supported with empirical evidence of cost-reduction and behavioural checked by appropriate design standards and code of practices, will to a large extent, boost stakeholders' and professionals' interest in adopting PKS material for construction.

D. K. Dadzie (✉) · A. K. Kaliluthin
Department of Civil Engineering, B.S. Abdur Rahman Crescent Institute of Science and Technology, Chennai, India
e-mail: dadzie_civil_2019@crecident.education

A. K. Kaliluthin
e-mail: kalil@crecident.education

D. Raj Kumar
Department of Civil Engineering, University College of Engineering Tindivanam, Tindivanam, India

Keywords Palm oil · Palm kernel shell · Aggregate · Affordable material · Sustainability

1 Introduction

The vision of this study is geared towards assessing by way of undertaking an analytical academic journey into reviewing the feasibilities in the exploration of palm kernel use in the construction industry. Inferring from the study of Oti et al. [1], there is the need to alleviate the constant increment in demand for minimum cost and environmental friendly construction materials. This according to the authors comes together with the quest to reinforcing economic growth and competitiveness. In order to accomplish these assertions, the researchers postulate that agricultural wastes could serve as a feasible substitute material in the construction industry, with particular reference to nations where abundant agricultural wastes are discharged. The production of palm oil for example, result in various waste product materials such as empty fruit bunches, palm kernel ash and palm kernel shells. The use of Palm Kernel Shell (PKS) in construction cannot be overemphasised. Many empirical and experiential findings have affirmed the PKS as an agriculture organic waste sourced from oil mills. Evidence in the study of Itam et al. [2] establishes that Palm Kernel Shell (PKS) is an unwanted material gotten during the action of crushing palm nuts in the palm oil mills. To this effect, the authors aver that it is for the purpose of extracting palm oil. Consequently, Ikumapayi and Akinlabi [3] elaborate that PKS may also be referred to as Oil Palm Kernel (OPKS) and consist of great lignocellulosic biogenic unwanted obtained from the activity of crude palm oil processing. In throwing more light on the contentions of [3, 4] advance that the PKS is the tough part that encompasses the nut of the fruit that contains the palm kernel seed of the palm tree. Further to that, Okpala [5] observes that the PKS is one of the greatest quantitative unwanted materials produced in the South East part of Asia. In corroboration to this stand, Zafar [6] opines that the Palm Oil industry in Southeast Asia and Africa produces enormous quantity of biomass wastes whereby its disposal poses much of a challenge. More so, the work of Sylvester and Lukuman [7] reveal that the disposal of the PKS waste has been a major challenge to the palm oil producers on the basis that large volumes of such waste are generated daily due to the booming of the palm oil market. Studies shows that without sustainable utilisation of the PKS waste, the material will continue to impact negatively to the surrounding environment. Substantiation in support for the latter is observed in the work of Ahmad et al. [8] where they establish that the Palm Kernel Shell has demonstrated in being the topmost choice of biomass waste. This according Rahman et al. [9] is followed by sawdust pellet and shredded EFB. For this reason, Shafiqh et al. [10] share the view that the utilisation of PKS would go a long way to enforce minimum construction costs in comparison to other waste materials not limited to plastic waste, rubber crump and others. In light of their contentions, they opine that with the appropriate mix design, Palm Kernel Shell could be employed in the development of standard strength concrete, which

may vary from 20 to 30 MPa. In corroboration to the foregoing, Itam et al. [2] assert that palm nut shell could be employed as material for construction when it comes to low-cost buildings. Implicit in their assertion, they attribute their reason to the fact that it could reach a compressive strength of 18 N/mm^2 . These statistics according to the authors could have an indirect impact in facilitating waste reduction. Construction researchers have taken kind interest in assisting to solve this canker by utilising the PKS waste in construction. This is also in a way helping to solve depleting of natural resource materials such as sand and crushed rocks currently confronting the construction industry.

2 Generation of Palm Kernel Shell

Palm kernel shell (PKS) is an agriculture organic waste by product which according to studies, it is generated in large quantities from oil palm mills [7, 11]. The source of PKS comes from the extraction of oil from the palm fruit (c). After extraction of first oil usually called palm oil (red colour), a nut with hard endocarp outer layer known as palm kernel (d) is obtained. The palm kernel when further crushed, separate the endocarp (shell) from the nut. This gives two products, thus the palm nut (f) and palm kernel shell (e). The palm nut is used to produce second oil known as palm nut oil (g), whereas the PKS is discarded as waste.

3 Sustainability and Environmental Effects of Palm Kernel Shell

These wastes according to Maghfouri et al. [12] constitute about 5.5% of harvested bunch of fresh fruit (Fig. 1b) with over 4million tonnes annual generation globally. A global report by Global Palm Oil Market Forecast [13] shows an incremental projection of palm oil market value from 65.73 billion in 2015 to 92.84 billion by 2021. One key reason cited for this high growth rate is that, the oil from palm exhibits small amount of cholesterol as compared to most edible oils in the oil market. This gives clear evidence that demand for oil palm keeps increasing. The motivation is therefore there for individuals and industries and even developing countries in tropical climates such as Ghana to venture into palm oil businesses. Ideally, the booming of the palm oil market should not jeopardise or have negative impact on the environment. On the contrary, this is not the case. Recent studies still indicate more PKS wastes are generated since the demand for palm oil products continues to increase [11, 14]. The PKS until recent was widely used as below for melting iron and gold, fuel for domestic use, filling material for road [7, 15]. However, Bediako et al. [11] and Abdullah and Sulaiman [16] has reported that, the PKS wastes still stands underutilized since the current usage both domestically and industrially cannot by



(a) Bunches on palm tree



(b) Harvested Bunch



(c) Oil from palm fruit



(d) Palm kernel



(e) Palm kernel shell



(f) Palm kernel nut



(g) Oil from palm kernel nut

Fig. 1 Oil extraction from palm

far get closer to the large volumes generated annually. These therefore confirms the existence of large quantities of unused PKS dumped around the oil mills as waste, creating pollution and causing significant degradation to the environment due to difficulty in disposing the PKS wastes including challenges of land availability to stockpile the PKS wastes [14, 17].

One major way of sustainably reducing these environmental effects is seeking alternative use of the PKS wastes, for example as material in the construction industry.

Currently, there exist two major challenges on the construction industry thus: (a) To solicit for sustainable construction materials to replace depleting natural resources mostly sand and crushed rocks [12]. (b) To reduce CO₂ emission into the environment by incorporating environmentally friendly materials in construction elements and products [18].

The positive impact of the construction industry to mankind cannot be exaggerated. The industry apart from offering human beings with building and facilities, also provide employment both directly and indirectly to individuals and other related industries [19]. The construction industry is therefore noted to play a major role in almost every country's urbanization. Contrary to these positive impacts, the industry is noted to possess negatives impact to same mankind, more especially the environment. Typical example mostly experienced during construction is the waste disposal, dust, traffic congestion and noise which mostly affect the comfort of mankind [19].

In addition to the aforementioned environmental effect experienced from construction, the provision of building requires the use of materials. Maghfouri et al. [12], indicated that concrete the most widely used construction products, consumes over 12 billion tonnes of natural aggregates annually. Furthermore, Azunna [17] hints that there exists high demand for concrete for construction. As the demand for construction products increases, so is the consumption of the natural resources until sustainable materials are found as replacement [12]. The extraction of these natural resources apart from its environmental issues such as damaging and disturbing of the ecosystem, are also getting depleted [11, 12, 17, 20]. According to Muntohar and Muhammadiyah [21], building and construction activities produce about 36% of carbon dioxide (CO₂) emissions. By same report, the construction industry has been task to intensify measures to reduce the CO₂ emission to 30% by the year 2030. In summary, two major challenges are imposed on the construction industry thus:

1. To solicit for sustainable construction materials to replace depleting natural resources mostly sand and crushed rocks [11, 12, 17].
2. To reduce CO₂ emission into the environment by incorporating environmentally friendly materials in construction elements and products [21].

4 Palm Kernel Shell as Sustainable Construction Material

The PKS wastes according to Shafigh et al. [10] was since 1980s identified as potential waste material for construction, and as such more studies have been conducted to proof the PKS as sustainable construction materials.

4.1 Palm Kernel Shell as Aggregates for Construction Works

The properties of PKS as an aggregated to substitute both fine and coarse aggregate in concrete production have long been studied. Usman et al. [15] studied the use of

sawdust and PKS as substitute for fine and coarse aggregates in concrete with the main aim of reducing the cost of construction in developing countries. At 25% replacement, the resulting concrete was found suitable for the construction of partitions and panel walls in framed buildings. The researchers further conducted a study aimed at determining the effect of PKS aggregate on the physical and mechanical properties of normal weight concrete (NWC) and reported that PKS aggregates can replace more than 40% of conventional aggregates for lightweight concrete. Usman et al. [15] examined the Effects of Palm Kernel Shells Sizes and Mix Ratios on Lightweight Concrete. Findings indicates that PKS concrete of sizes 5–15 mm in ratio 1:1.5:3 satisfied strength requirement for lightweight reinforced concrete whereas PKS sizes 5–15 mm concrete in mix ratio 1:2:4 meets the minimum strength for plain concrete structures. Comparative study of the physical properties of PKS Concrete and Normal weight concrete in Ghana was studied by Usman et al. [15]. Though results from the study indicates weak bond between the PKS aggregates and the cement matrix due to smooth convex surface of the PKS aggregates, however, an appreciable compressive strength was recorded which makes the PKS concrete to some extent possible to be used as structural lightweight concrete for the construction of low-cost housing. Fono-Tamo et al. [22] undertook a study to determine the effect of varying PKS sizes and mix ratio on the physical and mechanical properties of the OPKS blocks. The density, flexural and compressive strengths of the PKS block (shellcrete), was noted to maximize better CO₂ emission reduction without compromising the mechanical properties required, the mix design of 1:1:2 was noted to be the best hence recommended ratio for the production of shellcrete for lightweight masonry construction. The extent to which the results on the shellcrete study satisfy BS and IS masonry units couple with the need to further examine the shellcrete characteristics in terms of, fire resistance, thermal and sound insulation and durability is anticipated.

4.2 The Use of Palm Kernel Shell and Ash for Concrete Production

Oti et al. [1] investigated the potentials of using PKS and ash as a partial replacement for coarse aggregate and Portland cement (PC) for mortar and concrete improvement. PK ash produced at temperature (350–750 °C) were used to replace OPC up to 50% to produce PK ash aggregate mortar and PKS coarse aggregate up to 100% replacement to produce PKS concrete. Test on physical properties of the materials including compressive strength, tensile splitting strength, and chemical durability properties in aggressive environment exposure were carried out. The PK ash and shell as from the results obtained has the potential to replace OPC and normal granite coarse aggregate up to 50% at 750 °C and 25%. Report on the durability performance of improved PKS mortar for masonry works will be much appreciated.

4.3 Experimental Investigation on the Properties of Lightweight Concrete Containing Waste Oil Palm Shell Aggregate

Hung et al. [14] carried out an experimental research to compare the mechanical, permeation and structural properties between OPSC and NWC of similar compressive strength. Through trial mix, 30 MPa OPS concrete was prepared using OP cement, GGBS, OPS as coarse aggregate and manufactured sand as fine aggregate including superplasticizer under water-binder-ratio of 0.33. NWC was also prepared with PC as the only binder in water-binder-ratio of 0.625 by same trial mix. Grade 30 NWC obtained from local ready-mix plant used to cast reinforced concrete beam specimens also for the study. Finding from the test result indicates that, the NWC had a little high splitting tensile strength and modulus of elasticity than the OPSC whose initial water absorption and sorptivity test results were lower than the corresponding NWC. Also, the bond strength result of the OPSC was about twice better than the NWC, hence the OPSC resulted to smaller cracking spacing. In-depth durability study on the GGBS-blended OPSC is required to complement the study.

4.4 Development of Pulverized Palm Kernel Shells Based Particle Board

Adewole [23] analysed the performance of pulverized PKS based particleboard. In the composite development stage, the pulverized PKS was mixed to together with materials such as saw dust and adhesive. PKS–wood-based particleboard was produced with PKS, saw dust and top board and subject to bending strength, dimensional changes, thermal and mechanical properties. In conclusion, it was noticed that the PKS wood based particleboard can perform better when its strength is improved and the composite of the PKS with saw dust and binder are properly combined. However, further studies on the fire resistance, thermal resistance, sound resistance and water absorption properties were recommended to complement the study.

4.5 The Feasibility of Palm Kernel Shell as Replacement for Coarse Aggregate in Lightweight Concrete

Itam et al. [2] conducted a study to determine the possibility of substituting PKS aggregates in lightweight concrete as an effort to improve the compressive strength, workability, water absorption and density of PKS concrete. By DOE method of mix design, sample concrete was prepared using PKS, crushed granite rocks, natural sand and OPC Type 1 including 15% silica fume. Test result shows that concrete

produced with PKS aggregates as substitute exhibits characteristics such as reduction in strength and workability, but increased water absorption capacity. The study confirms that PKS aggregates possess the properties to be used as lightweight concrete material, however 50% replacement was recommended to be the limit.

4.6 Development of Palm Kernel Shell Lightweight Masonry Mortar

Noor et al. [24] piloted a study aimed at coming out with PKS lightweight mortar for masonry wall construction. In the study, the PKS masonry mortar (PKSMM) and normal weight river sand mortar cubes were prepared with Plotland limestone cement and crushed PKS fine aggregate to a ratio of 1:3, 1:4 and 1:5 and tested for density and compressive strength at 28 days curing period. It was concluded that, PKS fine aggregates of ratio 1:3 can be used for the production of lightweight PKS masonry mortar and further to bond masonry unit even in sever exposure conditions such as external walls of building. Further research works included on construction of PKS masonry blockwall bonded with improved PKS cement mortar; Plastering/rendering PKS masonry blockwall using improved PKS cement mortar and assessment of the properties and performance of PKS masonry wall in terms of compressive strength (F_k), fire resistance, thermal and sound insulation, waster absorption and durability.

4.7 The Effect of Palm Kernel Powder on Compressive Strength and Absorption of Portland Cement Mortar

Yalley [25] researched in to the effects of Palm Oil Fibre (POF) on the compressive and flexural strength of the PKS concrete. In the study, PKS was used to replace the coarse aggregate in 0%, 25%, 50% and 75% palm oil fibre (POF) as additive cured for 28 days and tested for compression strength, flexural and water absorption. The addition of PKS aggregate increases the porosity of the concrete, while no significant improvement of the flexural strength was achieved, though the compression strength obtained at 25% PKS with POF replacement qualifies it to be use for lightweight structural concrete. PKS powder do not exhibit the character of binding material hence doubt it use as substitute for sulphate resistance cement powder rather than as fine aggregates in the mortar mix. The low compressive strength recorded might be the reduction of the cement content by the PKS power hence re-assessment of the effect of PKS powder on compressive strength Cement and Sand Mortar is recommended.

4.8 Use of Palm Kernel Shells as a Partial Replacement of Chippings in Terrazzo Floor Finish

Abolagba and Osuji [26] performed a study to determine the effects of replacing terrazzo chippings with PKS on hardened properties of terrazzo finishes. The Density, water absorption, abrasion resistance, compressive strength of PKS terrazzo floor finish was determined at the harden stage and compared to the conventional terrazzo chippings floor finish. ANOVA (Pearson correlation) was used to determine the impacts of the PKS replacement on the properties of the terrazzo finish. All the tested properties of the PKS terrazzo floor finish resulted in to poor performance as the PKS aggregates replacement increases. However, at 45% PKS replacement, the results were within the minimum recommended by ASTM C109/C 109M standards.

4.9 Assessment of Manufactured Sand in Concrete Produced with Palm Kernel Shells as Coarse Aggregate

Al-Majeed et al. [27] determined the extent to which the use of manufactured sand in mixes affects the density and compressive strength. British building Research (BRE) method was adopted to produced lightweight concrete (LC) class 22 and 38, batched by volume using natural sand of 25% interval to till 100% to replace the manufactured sand and 100% use of PKS aggregates. The lightweight concrete (LC) 22 gave maximum compressive strength at 28 days of 16.1 N/mm² and at 90 days of 18.22 N/mm², whereas for LC38, 19 N/mm² and 20.3 N/mm² was obtained at 28 days and 90 days all at safe manufactured sand as fine aggregate replacement of 32%.

4.10 The Effect of Palm Kernel Powder on Compressive Strength and Absorption of Portland Cement Mortar

Reference [27] performed a study aimed to determine the effects that palm kernel powder used as partial replacement for cement has on compressive strength and water absorption properties of cement and sand mortar. In the methodology, PKSs were grinded into powder and used to replace the sulphate resistance cement powder in the proportion of 0%, 5%, 10%, and 15% by weight measurement to a ratio of 1:3. Concrete cubes were prepared, kept in 3% NaCl and 3% HCl solutions for 7 and 28 days, and subject to water absorption and compressive strength tests. It was deduced for the study that, the presence of PKS powder in the mortar makes it a lightweight, and also as the PKS replacement increases, the water absorption of the mortar also increases. However, on the opposite, the compressive strength of the mortar reduces as the PKS content increases in the mix. Furthermore, in comparing

the effect of the NaCl and HCl solutions on the compressive strength of the mortar, the results showed that the NaCl is more harmful on the compressive strength than the HCl.

4.11 Investigation of the Properties of Self-compacting Concrete with Palm Kernel Shell Ash as Mineral Additives

Sylvester and Lukuman [7] undertook a study on the properties in terms of workability and compressive strength of self-compacting concrete (SCC) produced with cement partially replaced with PKS aggregate mineral additives. OPC grade 42.5, PKS ash incinerated at about 420 °C, super plasticizer, portable water, 10.5 mm crushed granite stones as coarse aggregates and fine aggregate of maximum size not more than 3.35 were used to produce SCC 0%, 10%, 15%, 20% and 25% PKS ash replacement. The SCC was tested for workability using slump flow, L Box and V Funnel test apparatus and strength using compressive strength testing machine at 7, 14, 21 and 28 days curing period. The results after testing showed that at 25% PKS aggregates replacement for cement, the self-compacting concrete achieved an acceptable workability and compressive strength.

4.12 Compressive Strength of Concrete with Palm Kernel Shell as a Partial Replacement for Coarse Aggregate

Azunna [17] studied the properties of PKS at different percentage substitutes for coarse aggregate, and also to determine the specific areas in civil engineering where PKS can efficiently perform concrete when applied. A ratio of 1:2:4 was adopted to produce PKS concrete specimens and tested for water absorption capacity, workability and the compressive strength, and results were compared with concrete produced from normal aggregates. PKS in general was noted to have good potentials as coarse aggregate in producing lightweight structural and even moderate strength application. However, the compressive strength of the concrete with above 25% replacement of PKS do not meet structural lightweight concrete. Notwithstanding, the water absorption capacity obtained for the concrete is within the range for normal concrete specification. However, same tests could be repeated on PKS aggregate batched by volume and results duly compared to values from this study, including use of other mix ratios is recommended for assessment in future research works. In addition to future works, the addition of additives to improve the PKS aggregate concrete properties to satisfy structural lightweight concrete is further required. Typical PKS lightweight concrete structural member should be designed according to IS standard code of practice and further subject to various design test requirement will furthermore boost acceptance of the PKS as lightweight structural material.

5 Future Exploitation of Palm Kernel Shell

Making substantive inferences from the literature herein, the study of Usman et al. [15] establishes that at 25% replacement of sawdust and PKS, the resulting concrete was found suitable for the construction of partitions and panel walls in framed buildings. But findings from Usman et al. [15] shows that PKS aggregates possess the properties to be used as lightweight concrete material, with 50% replacement as recommended limit. Regardless, even though these researchers assert that PKS concrete of sizes 5–15 mm in ratio 1:1.5:3 satisfied strength requirement for lightweight reinforced concrete, Itam et al. [2] shows that concrete produced with PKS aggregates as substitute exhibits characteristics such as reduction in strength and workability but showed increased water absorption capacity. On the contrary the study of Fono-Tamo et al. [22] establishes that the mix design of 1:1:2 was noted to be the best hence recommended ratio for the production of shellcrete for lightweight masonry construction. The density, flexural and compressive strengths of the PKS block (shellcrete), was noted by Fono-Tamo et al. [22] to maximize better CO₂ emission reduction without compromising the mechanical properties required however, Oti et al. [1] report that the durability performance of improved PKS mortar for masonry works will be much appreciated in this discourse.

Interestingly, all these past studies conducted on PKS as epitomised in this study cantered more on the properties of the PKS as aggregate to replace conventional natural resource aggregates, and the behaviour of composite materials produced with partially replaced PKS as aggregated such as PKS blocks, concrete, mortar and terrazzo finishing. To some extent, Professionals in the construction industry are convinced about these much-reported proofs on PKS exploitation as potential construction material. Furthermore, additional studies have indicated the use of PKS results in affordable products mostly in tropical countries like Ghana, where this oil palm grows better, hence serving as local available material and relatively cheaper to be obtained. Though this might be true to some extent, however, very little is reported on this claim as empirical evidence. Future studies with emphasis on the application of PKS products such as for lightly loaded walls and slabs improved with polymers, fibres, hydraulic cement and admixtures, supported with empirical evidence of cost-reduction and behavioural checked would much be appreciated and adopted for construction.

References

1. Oti JE, Kinuthia JM, Robinson R, Davies P (2015) The use of palm kernel shell and ash for concrete production. *Int Sci Index Civ Environ Eng* 9(1):263–270. Available at: <https://waset.org/publications/10000699/the-use-of-palm-kernel-shell-and-ash-for-concrete-production>
2. Itam Z, Beddu S, Mohd Kamal NL, Alam MA, Ayash UI (2016) The feasibility of palm kernel shell as a replacement for coarse aggregate in lightweight concrete. *IOP Conf Ser: Earth Environ Sci* 32(1):012040. <https://doi.org/10.1088/1755-1315/32/1/012040>

3. Ikumapayi OM, Akinlabi ET (2018) Composition, characteristics and socioeconomic benefits of Parlm kernel shell exploitation: an overview. *J Environ Sci Technol* 11:220–232
4. Yusuf IT, Jimoh YA (2012) Palm kernel shell waste recycled concrete road as cheap and environmental friendly freeway on very poor subgrades. *Sci J Civ Eng Architect* 2012
5. Okpala DC (1990) Palm kernel shell as a lightweight aggregate in concrete. *Build Environ* 25(4):291–296
6. Zafar S (2020) Energy potential palm kernel shell. Retrieved on 27/07/2020 from <https://www.bioenergyconsult.com/palm-kernel-shells/>
7. Sylvester OO, Lukuman BI (2018) Investigation of the properties of self-compacting concrete with palm kernel shell ash as mineral additive. *J Civ Eng Constr Technol* 9(April):11–18. <https://doi.org/10.5897/JCECT2017.0473>
8. Ahmad RN, Hamidin N, Ali UFM, Abidin CZA (2014) Characterisation of bio-oil from palm kernel shell pyrolysis. *J Mech Eng Sci* 7:1134–1140
9. Rahman AA, Sulaiman F, Abdullah N (2016) Influence of washing medium pre-treatment on PYrolysis yields and product characteristics of palm kernel shell. *J Phys Sci* 27:53–75
10. Shafigh P, Jumaat MZ, Mahmud H (2011) Oil palm shell as a lightweight aggregate for ProductionHigh strength lightweight concrete. *Constr Build Mater* 25:1848–1853
11. Bediako M, Gawu SK, Adjattor AA, Ankrah JS, Atiemu E (2016) ‘Case studies in construction materials analysis of co-fi red clay and palm kernel shells as a cementitious material in Ghana’, *Case Studies in Construction Materials*. Elsevier Ltd 5:46–52. <https://doi.org/10.1016/j.cscm.2016.06.001>
12. Maghfouri M, Shafigh P, Aslam M (2018) Optimum oil palm shell content as coarse aggregate in concrete based on mechanical and durability properties
13. Global Palm Oil Market Forecast (2010) *Food Australia* 62(9):398
14. Hung K, Alengaram UJ, Zamin M (2014) Experimental investigation on the properties of lightweight concrete containing waste oil palm shell aggregate. *Procedia Eng* 125:587–593. <https://doi.org/10.1016/j.proeng.2015.11.065>
15. Usman ND, Idusuyi FI, Ojo EB, Simon B (2012) The use of sawdust and palm kernel shell as substitute for fine and coarse aggregates in concrete construction in developing countries. *J Chem Mech Eng Pract* 2(3):51–62. Available at: https://www.academia.edu/5974657/The_Use_of_Sawdust_and_Palm_kernel_Shell_as_Substitute_for_Fine_and_Coarse_Aggregates_in_Concrete_Construction_in_Developing_Countries
16. Abdullah N, Sulaiman F (2013) The oil palm wastes in Malaysia, biomass now-sustainable growth and use. *Biomass now—sustainable growth and use*, pp 75–100. <https://doi.org/10.5772/55302>
17. Azunna SU (2019) Compressive strength of concrete with palm kernel shell as a partial replacement for coarse aggregate. *SN Appl Sci* 1(4):1–10. <https://doi.org/10.1007/s42452-019-0334-6>
18. Dean B, Dulac J, Petrichenko K, Graham P (2016) Towards a zero-emission, efficient, and resilient buildings and construction sector. *Global Status Report*. Available at: [https://www.worldgbc.org/sites/default/files/UNEP188_GABC_en\(web\).pdf](https://www.worldgbc.org/sites/default/files/UNEP188_GABC_en(web).pdf)
19. Oyejobi DO et al (2012) Effects of palm kernel shells sizes and mix ratios on lightweight concrete, 9(2)
20. UN Global Status Report (2017) Towards a zero-emission, efficient and resilient buildings and construction sector. Retrieved on 11/03/2021 from https://www.worldgbc.org/sites/default/files/UNEP%20188_GABC_en%20%28web%29.pdf
21. Muntohar A, Muhammadiyah U (2014) Lightweight masonry block from oil palm kernel shell, (MARCH). <https://doi.org/10.1016/j.conbuildmat.2013.12.087>
22. Fono-Tamo RS, Idowu OO, Koya FO (2014) Development of pulverized palm kernel shells based particleboard. *Int J Mater Mech Eng* 3(3):54. <https://doi.org/10.14355/ijmme.2014.0303.01>
23. Adewole KK (2016) Development of palm kernel shell lightweight masonry mortar, 10(9):1241–1244

24. Noor NMD, Xiang-ONG J, Noh HM, Hamid NAA, Kuzaiman S, Ali A (2017) Compressive strength, flexural strength and water absorption of concrete containing palm oil kernel shell. IOP Conf Ser: Mater Sci Eng 271(1):012073. <https://doi.org/10.1088/1757-899X/271/1/012073>
25. Yalley PP (2018) Use of palm kernel shells as a partial replacement of chippings in Terrazzo Floor Finish. © Research India Publications <http://www.ripublication.com>, 9(1), pp. 35–47
26. Abolagba IO, Osuji SO (2018) Assessment of manufactured sand in concrete produced with palm kernel shells as coarse aggregate. Int J Sci Res (IJSR) 7(3):23–27
27. Al-Majeed EA, Hameed DH, Mohnia MSA (2018) The effect of palm kernel powder on compressive strength and absorption of Portland cement mortar. Int J Civ Eng Technol 9(10):213–223. <http://www.iaeme.com/IJCIET/issues.asp?JType=IJCIET&VType=9&IType=10>

Evaluation of the Physical and Mechanical Properties of Concrete with Partial Replacement of Coarse Aggregates with Epoxy-Based E-Waste (EBEW)



Joseph Berlin Juanzon and Jaime Aquino

Abstract Electronic waste or e-waste refers to electronic products that are no longer of use to the original purchaser. It is an evolving issue that causes serious environmental pollution problems. E-waste in the concrete industry is considered to be one of the most practical applications for the solution of large quantities of e-waste material. In this research study, e-waste was used as a partial replacement for the coarse aggregate. Replacement of the coarse aggregate with Epoxy based e-waste (EBEW) in the range of 0, 5, 10 and 15% was used. A total of 36 samples were tested for the physical and mechanical properties of the concrete mix specimens with partial replacement of the Epoxy-base e-waste and compared to the control concrete mix with a target mix of 3000 psi (20.7 MPa). Test results for the physical properties of EBEW showed a favourable decrease in density and water absorption of test samples with 15% partial replacement of EBEW. Mechanical properties showed a very significant increase of 47.88% in compressive strength of 26.53 MPa, a 41.35% increase in flexural strength of 5.64 MPa and a 131.12% increase in pull-out strength of 11.63 MPa for all specimens with a 15% partial replacement of EBEW. This is very positive implication that reuse of EBEW will result in waste reduction and improve the structural integrity of building structures including cost reductions.

Keywords Epoxy based e-waste · Compressive strength · Flexural strength · Pullout strength test · Density

J. B. Juanzon (✉)
Pamantasan ng Lungsod ng Maynila, Intramuros, Manila, Philippines
e-mail: jbjuanzon@plm.edu.ph

J. Aquino
Commission on Higher Education, Quezon City, Philippines

1 Introduction

1.1 Background

Technology certainly provides our everyday lives with ease, and has become an integral part of life. Technology innovation has improved the communications, medicine, transportation, entertainment, education, agriculture, tourism, infrastructure and many more sectors; but, as technology continues to progress, it has also created a ballooning issue that threatens human and environmental health, the so called Electronic waste (e-waste).

E-waste is a term used to describe both electrical and electronic equipment (EEE) products and their parts that have been discarded by their owners; waste not intended for re-use. E-waste or waste electrical and electronic equipment (WEEE) is a diverse and rapidly increasing waste stream covering a wide variety of items, including computers, fluorescent lamps, microwave ovens, televisions, refrigerators [1, 2].

In recent years, due to the high rate at which it is produced and the dangerous substances found in e-waste, the e-waste issue has been gaining growing attention. Rapid technological changes create new product models which accelerate obsolescence and lead to the discarding of electronic equipment before even the end of their useful life [3]. Such discarded products contain hundreds of toxic materials to be disposed of which can cause significant contamination and harm to health and the environment. Even in developed countries recycling and disposal of e-waste can pose major risks to staff and communities and great care must be taken to prevent dangerous access to recycling operations and the leakage of materials such as heavy metals from landfills and incinerator ashes [4].

Global environmental activities developing with expansion of living and non-living resources and related social activities. The connection of environmental issues with the electronic and electrical industries begin with the generation of E-waste and therefore the pollution possibilities [5]. Waste Electronic and Electrical Equipment (WEEE) is complex in terms of materials and components and is sophisticated. In fact, it's due to the manufacturing cycle. Exposition of this waste stream is of vital importance in the creation of an effective and environmentally sustainable recycling program for profit [6].

According to a report by international organization Environment Protection Agency (UNEP) titled, "Recycling from E-waste to resource", estimates that 20–25 million loads of electronic waste are generated worldwide once a year. Globally one billion mobile phones were sold in 2007, up from 896 million in 2006. The report assesses current policies, skills, waste collection networks and informal recycling in 11 representative developing economies in America, Africa and Asia. According to the studies conducted within the EU, e-waste is growing at a rate of 3–5% once a year or approximately thrice faster than other individual waste streams within the solid waste sector [7, 8]. The rapid adoption of information technology around the

world combined with the introduction of new design and development in the electronic field at regular intervals is causing the early obsolescence of many electronic products used today around the world [9].

According to Raju [10], concrete is important material for all civil works consisting of cement, fine and coarse aggregates. Nowadays it is becoming impossible to move sand from natural river beds and aggregates due to environmental clearances. It is highly desirable to substitute the fine aggregate or coarse aggregates in concrete cement with any industrial by-product. It makes an appealing alternative because of its lower cost, if sufficient output can be obtained.

Not only does electronic waste have an advantage in making it used in concrete, cement and other construction materials, it also helps in reducing the cost of cement and concrete processing. The use of e-waste in cement has many indirect benefits, such as minimizing the cost of landfill, saving power and electricity and protecting the environment from potential pollution effects. In the concrete sector, attempts have been made to use non-biodegradable electronic waste components as a partial replacement of the coarse or fine aggregates [11].

In a study conducted by Kang et al. [12], they discussed the trends in existing e-waste recycling programs, collection methods, etc., the various recovery and recycling technologies for glass, plastics and metals found in e-waste are discussed in detail. The authors highlighted the plastic recycling processes involving shredding, separation and palletizing techniques. The recycling techniques discussed for plastics have been adopted as the basic process for this research work. There are reported to be three primary purposes for size reduction. The first is the generation of particles that can be handled more easily than bulky parts. Second is the generation of uniformly sized and shaped particles that can be effectively separated in downstream processes. Third, the liberation of dissimilar materials from one another.

In another study on the replacement of coarse aggregates with e-waste in concrete. The disposal of a large quantity of e-waste materials, the re-use of e-waste in the concrete industry is considered to be the most feasible application. Due to an increase in the cost of normal gross aggregates, civil engineers are tasked with finding suitable alternatives. E-waste is used as one of these alternatives for coarse aggregates. Due to the scarcity of the coarse aggregate for the preparation of concrete, a partial replacement of the e-waste with the coarse aggregate was attempted [13].

Akram et al. [14], who studied e-waste management through the use of e-plastic particles in concrete, tested the feasibility of using shredded e-plastic particles as a partial replacement for coarse aggregates. It was observed that when e-plastic alone was used, there was a decrease in strength, but when 10% fly ash was added, results compared to control specimen is very evident for 15% proportion of e-waste. They suggested that the use of this e-waste in concrete would reduce the requirement for conventional large aggregates, resulting in the conservation of natural resources.

Experimental study was also conducted on the utilization of e-waste particles as fine aggregates in concrete with a percentage replacement ranging from 0 to 21.5% i.e. (7.5, 15 and 21.5%) on the strength criteria of M30 Concrete. Compressive strength of concrete with and without e-waste plastic as aggregates was observed, and exhibits an effective strength. The feasibility of using e-waste plastic particles as

a partial replacement of the fine aggregate has been presented. It was also observed that the compressive strength of the concrete was found to be optimal when the fine aggregate was replaced by 7.5% with electronic waste. Beyond that, the compressive strength of concrete decreases. The compressive strength of concrete will gradually decrease when the fine aggregate is replaced by Electronic waste in excess of 15%. From this study, the authors were able to identify that Electronic waste is also a good replacement for fine aggregates at 15% partial replacement [15].

A further study was also conducted on the use of non-metallic e-waste as a coarse aggregate in concrete. The result shows an analysis of the compressive strength of the grades M20 and M25 of concrete by replacing the coarse aggregate with the addition of non-metallic e-waste at 0–20%. According to their study up to 5–6% replacement of e-waste is suitable to use up to (G + 2) building construction, road construction. More than 10% is not considerably useful for construction field because of strength decreases [16].

Prasanna [17] presented the results of the investigation to study the performance of e-waste-prepared concrete as part of the coarse aggregate. Their experimental study was carried out by preparing specimens using e-waste particles as coarse aggregates in concrete with a percentage change from 0 to 20% i.e. (5, 10, 15, and 20%). And Conventional specimens are also prepared for M30 grade Concrete without using e-waste aggregates. By comparing the results with conventional concrete at 28 days strength it was observed that the strength of concrete was reduced by 33.7% when coarse aggregate is replaced by 20% of e-waste. And it was reduced by 16.86% when coarse aggregate is replaced by 20% of e-waste plus 10% fly ash.

In a recent experimental study by Saranya [18], coarse aggregates were partially replaced by e-waste at 0, 32, 34, 36, 38, 38%, and were tested for compression and split tensile strength at 7, 14 and 28 days. Results shows that 34% partial replacement of coarse aggregates registered the highest compressive strength of 25.3 MPa which is only slightly higher than the control sample with 25.10 MPa compressive strength at 28 days. The split tensile test shows a decreased in strength from 5.58 to 4.88 MPa for 34% partial replacement of coarse aggregates.

The main objective of this study is to test the viability of utilizing an Epoxy Based e-waste (EBEW) as coarse aggregate blended in concrete, as a waste reduction measure and as an economic alternative for coarse aggregate. Specifically, the research determines the physical properties of the concrete such as density, water absorption and percent voids, with partial replacement of coarse aggregates with epoxy-based e-waste of 0, 5, 10, and 15%. And determine the mechanical properties of the concrete such as compressive, flexural and pullout capacity with partial replacement of coarse aggregates with epoxy-based e-waste with the same percent replacement with the physical properties.

2 Methodology

2.1 Specimen Preparation

Epoxy based e-waste will be collected from local body of electronics and electrical appliances which was discarded in scrap as shown in Fig. 1.

This epoxy-based e-waste were cut in 4.75 mm, 12.5 mm, and 19.0 mm sizes using the side cutter plier and long nose plier (Fig. 2).

The concrete mix design was prepared in the form of concrete test cylinders, beams and cast in place concrete base anchored by 12 mm \varnothing \times 600 mm deformed bars with hexagonal nut insert head. The insert head should be embedded into the fresh concrete to ensure that a uniform embedment depth and a plane surface perpendicular to the axis of the insert shaft.

Fig. 1 Epoxy based E-waste (EBEW)



Fig. 2 Cut/crushed epoxy based E-waste as coarse aggregate replacement

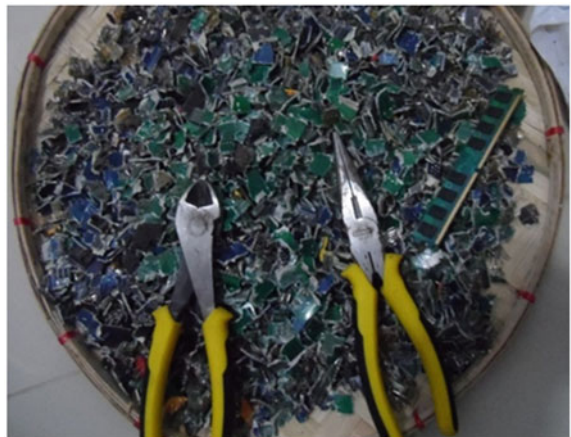


Table 1 Proportions and weight of each mix material

Mix specification	Control mix	Modified mix 1	Modified mix 2	Modified mix 3
Proportion of (EBEW) added (%)	0	5	10	15
Cement	297.1	297.1	297.1	297.1
Fine Aggregates	658.9	658.9	658.9	658.9
Coarse Aggregates	1184	1124.8	1065.6	1006.4
EBEW	0	59.2	118.4	177.6
Water-Cement ratio	222.11	222.11	222.11	222.11

These concrete test cylinders, beams and concrete base will be used for compressive, flexural, pull-out strength testing and will also be used for the determination of density, water absorption and percent of hardened concrete voids.

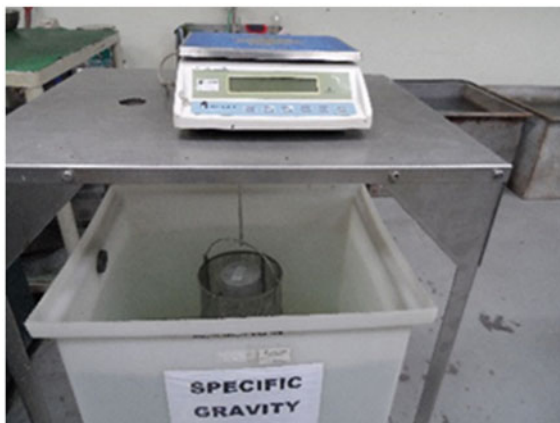
The mix proportion used was 1:2.22:4 ratio (1 part of cement, 2.22 parts of sand, and 4 parts of coarse aggregates) with water-cement ratio of 0.75 (0.75 unit of water for every unit mass of cement). Table 1 show the proportion and weight of each materials in kg/cum. It was the concrete mix design used by the researcher based on the computations using the software for Concrete Mix Design Weight Method SI Units Non-air entrained.

2.2 Physical Properties Test

Testing of physical properties of hardened concrete is usually scheduled so that the boiling of the samples takes place when the sample is between 21 and 22 days of age. Each specimen was placed directly on the oven rack, and dried the sample specimens at a temperature of 100–110 °C as per ASTM C-642 for about 8 h. Each specimen was removed from the oven to cool it in dry air at a temperature of 20–25 °C and determined the mass of each dried specimen using the calibrated LNWH30K weighing scale with a capacity of 30 kg [19].

After final drying, cooling and determination of mass the dried specimens were immersed in water at approximately 21 °C for not less than 48 h. Surface-dry the specimen by removing surface moisture with a towel, and determine the mass. The specimen was placed in a suitable receptacle, covered with tap water, and boiled for 2–5 h. And it was cooled by natural loss of heat for not less than 14 h to a final temperature of 20–25 °C. The surface moisture of the specimen was removed with a towel and the mass of the specimen was determined. The specimen was suspended after immersion and boiling, by a wire and bucket and determine its apparent mass in water as shown in Fig. 3 [20].

Fig. 3 Determination of mass in water



2.3 Mechanical Properties of Concrete

After 28 days, the 100 × 200 mm cylindrical concrete, the 100 × 100 × 300 mm concrete beam and the 150 × 150 × 100 mm cast-in-place concrete base anchored by 12 mmØ × 600 mm deformed bar with hexagonal nut insert head specimens were tested using the Universal Testing Machine (UTM) having a loading capacity of 1000 kN.

The compressive, flexural and pull-out strength test of modified mixtures and control mix have been tested for comparison. Four (4) concrete mixtures with varying content of partial replacement of coarse aggregates with epoxy based e-waste have been produced. Of these, four varying percentages of partial replacement of coarse aggregates with epoxy based e-waste of 0, 5, 10 and 15% of hardened concrete properties have been tested in accordance with the ASTM C-39, ASTM C-293 and ASTM C-900 respectively [21, 22].

3 Results and Discussion

3.1 Physical Properties

After weighing of the concrete specimens an analysis was made on the densities, percent absorptions and percent voids of 100 × 200 mm concrete cylinder, 100 × 100 × 300 mm concrete beam and 150 × 150 × 100 mm concrete base containing 0, 5, 10 and 15% Epoxy Based E-Waste added in concrete was implemented to check the difference in significance. Table 2 shows the Bulk Density of the specimen samples.

Table 2 Bulk density, dry (Mg/m^3) = g1

Sample	0%	5%	10%	15%
Sample 1	2.3342	2.3257	2.3223	2.2725
Sample 2	2.3395	2.3284	2.307	2.2717
Sample 3	2.3391	2.3307	2.3216	2.267
Mean	2.3376	2.3283	2.317	2.2704

Table 3 F-value of the physical properties of 100×200 mm concrete cylinder specimen

Physical properties	F-value		F-critical	Significant difference
1. Bulk density, dry	108.32	>	4.07	Yes
2. Bulk density after immersion	11.62	>	4.07	Yes
3. Bulk density after immersion and boiling	116.51	>	4.07	Yes
4. Apparent density	102.57	>	4.07	Yes
5. Absorption after immersion	15.14	>	4.07	Yes
6. Absorption after immersion and boiling	18.88	>	4.07	Yes
7. Volume of permeable voids	22.54	>	4.07	Yes

Comparison between the control mix and the modified mixtures were evaluated and determined for any statistical significance between them. One-way ANOVA with a 0.05 level of significance was used for the statistical evaluation part of the data analysis.

The data gathered in the control and modified mixtures such as densities, percent absorptions and percent voids of 100×200 mm cylinder specimen were statistically checked if it will be significant in the research, as shown in Table 3. All the F-values for the Physical Properties of 100×200 mm concrete cylinder are greater than the F-critical which means that there is significant difference between the control and the modified mixtures specimens, meaning, the Physical Properties of control mix (0% EBEW) are not the same with those of the Modified mixtures (5, 10 and 15% EBEW). It is clear that the Densities, Percent Absorptions, and Percent Voids of $100 \text{ mm} \times 200 \text{ mm}$ concrete cylinder goes on decreasing with increase in percentage of Epoxy Based E-waste (EBEW) added in concrete.

3.2 Mechanical Properties

Compressive Strength. The results of compressive strength were presented in Table 3. The test was carried out to obtain compressive strength of concrete at the age 28 days. The cylinder were tested using Universal Testing Machine (UTM)

with a capacity of 1000 KN. Figure 4a–d, shows failure modes of concrete cylinder samples at 0, 5, 10 and 15% partial replacement of coarse aggregates with EBEW.

As shown in Table 4 the mean compressive strength of the modified mixtures were increased by 10.58%, 14.17%, and 41.38% respectively compared to the control

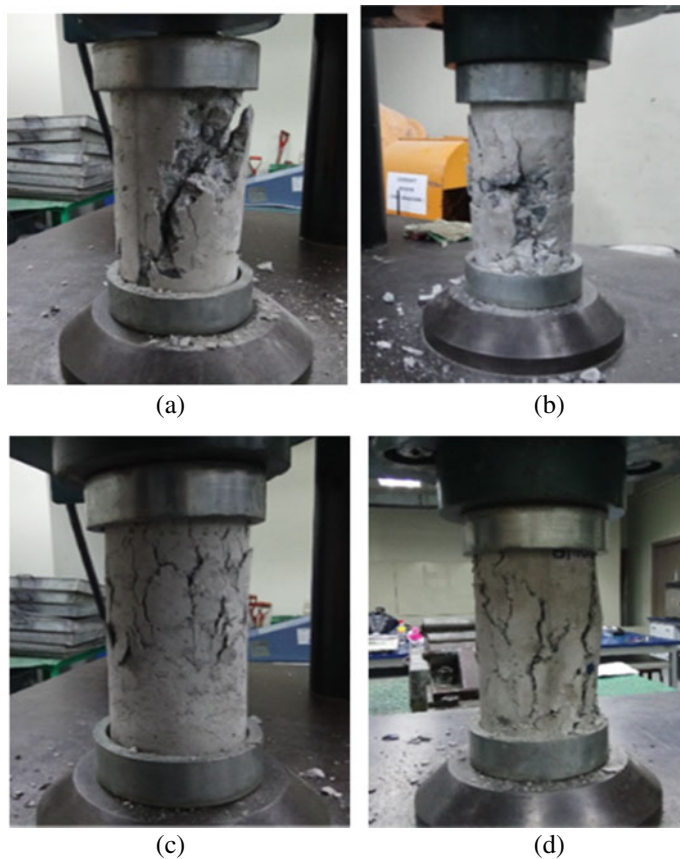
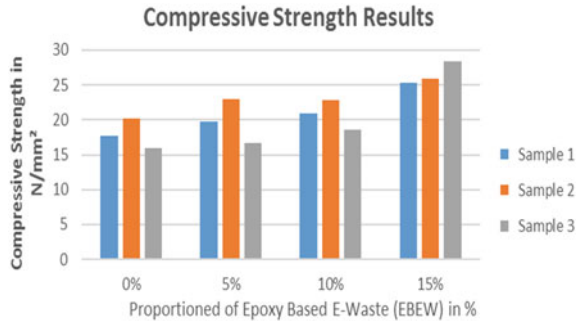


Fig. 4 Cylindrical samples compressive test failure

Table 4 Compressive strength test results in N/mm²

Proportion of (EBEW)	Control mix	Modified mix 1	Modified mix 2	Modified mix 3
	0%	5%	10%	15%
Sample 1	17.66	19.81	20.86	25.33
Sample 2	20.21	23.01	22.78	25.94
Sample 3	15.96	16.71	18.63	28.33
Mean	17.94	19.84	20.76	26.53

Fig. 5 Compressive test results



mixture when coarse aggregate is replaced by 5, 10, and 15% of Epoxy Based E-Waste (EBEW). The addition of Epoxy Based E-Waste (EBEW) shows increase in compressive strength gradually.

And also this may be one of the economical ways for the disposal of E-waste without creating any environmental issues.

Figure 5 shows the graphical presentation of the compressive strength of the three (3) test samples on each 0, 5, 10 and 15% replacement of coarse aggregates by EBEW.

Flexural Strength. The flexural strength of normal concrete and partial replacement of coarse aggregate with EBEW were tested on the 28th days. Figure 7a, b shows failure mode for 0 and 5%, while Fig. 6a, b, and shows the failure mode in concrete beam sample for 10% and 15% respectively.

As presented in Table 5 the mean flexural strength of $100 \times 100 \times 300$ mm concrete beam were increased by 22.81%, 23.56% and 41.35% respectively when coarse aggregate were replaced by 5, 10, and 15% of Epoxy Based E-Waste (EBEW) as compared to 0% EBEW. However, by comparing the F-value and F-critical results presented in Table 6 using one-way Analysis of Variance (ANOVA) with 0.05 level of significance, it is observed that the F-value are less than the F-critical which means that there is no significant difference between the control mix and the modified mixtures for the Flexural strength of $100 \times 100 \times 300$ mm concrete beam specimens in spite of the mean flexural strength are increasing gradually.

Figure 7 shows the graphical presentation of the flexural strength of the three (3) test samples on each 0, 5, 10 and 15% replacement of coarse aggregates by EBEW.

Pull-out Strength. The pullout strength of control specimens and experimental specimens were tested on the 28th days. Figure 8a–d shows failure mode of pull-out strength samples for 0, 5, 10 and 15% replacement of coarse aggregate with EBEW.

As presented in Table 6 the mean pullout strength of $150 \times 150 \times 100$ mm concrete base were increased by 44.93%, 87.67% and 131.21% respectively when coarse aggregates were replaced by 5, 10, and 15% of Epoxy Based E-Waste (EBEW) as compared to 0% EBEW.

Figure 9 shows the graphical presentation of the pull-out strength of the three (3) test samples on each 0, 5, 10 and 15% replacement of coarse aggregates by EBEW.

As shown in Table 7 the computed F-value was 33.90 compared to the F-critical of 4.07, which means that there is a significant difference between the control mix

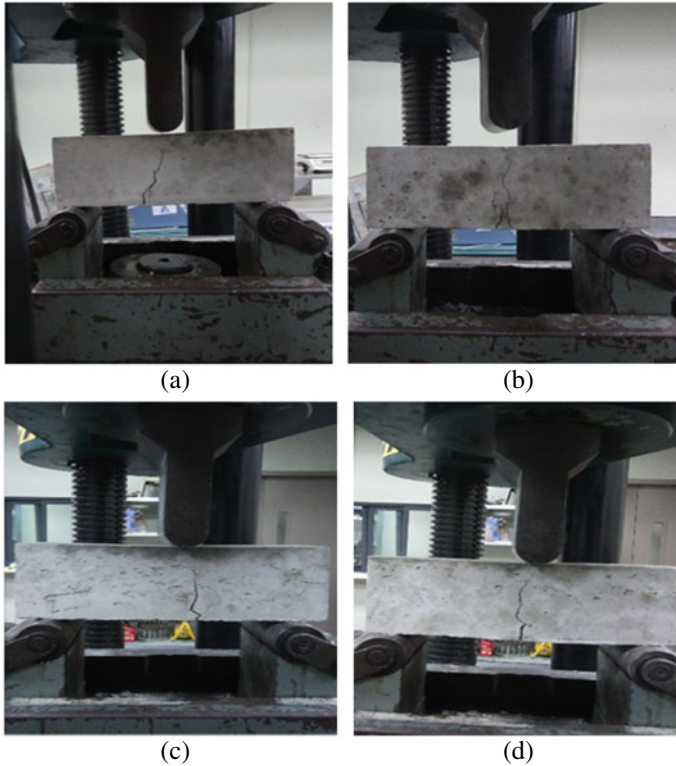
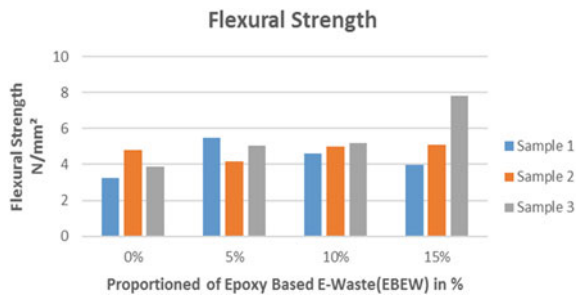


Fig. 6 Flexural test on beam sample

Fig. 7 Flexural test results



and the modified mixtures for the Pull-out strength, and F-value for compressive strength is greater than the F-critical which also means that there is a significant difference between the control mix and modified mixtures for compressive strength. However, the computed F-value is greater than that of the F-critical, which means that there is no significant difference in the control mix and modified mixtures for flexural strength.

Table 5 Flexural strength test results in N/mm^2

Proportion of (EBEW)	Control mix	Modified mix 1	Modified mix 2	Modified mix 3
	0%	5%	10%	15%
Sample 1	3.26	5.47	4.6	3.99
Sample 2	4.82	4.17	5	5.08
Sample 3	3.89	5.06	5.18	7.84
Mean	3.99	4.9	4.93	5.64

Table 6 Pullout strength test results in N/mm^2

Proportion of (EBEW)	Control mix	Modified mix 1	Modified mix 2	Modified mix 3
	0%	5%	10%	15%
Sample 1	4.78	7.63	10.29	12.97
Sample 2	4.81	6.5	9.59	10.89
Sample 3	5.49	7.73	8.45	11.03
Mean	5.03	7.29	9.44	11.63

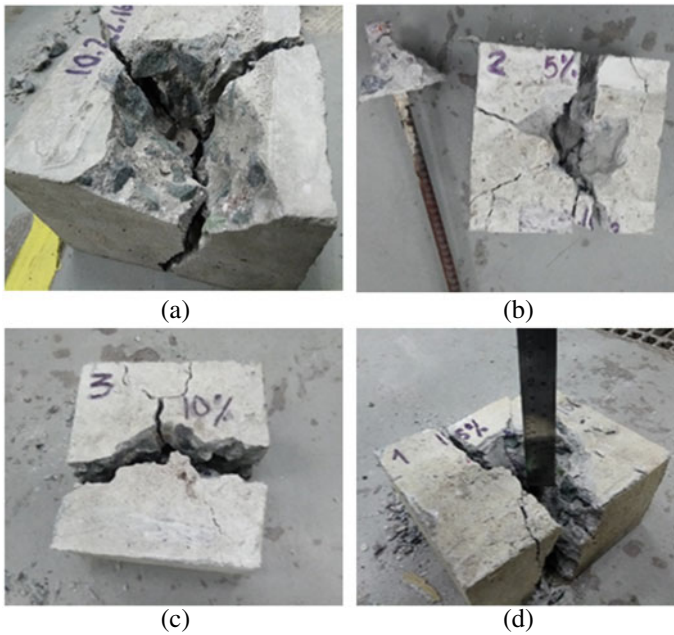


Fig. 8 Pull-out test failure for 0, 5, 10 and 15%

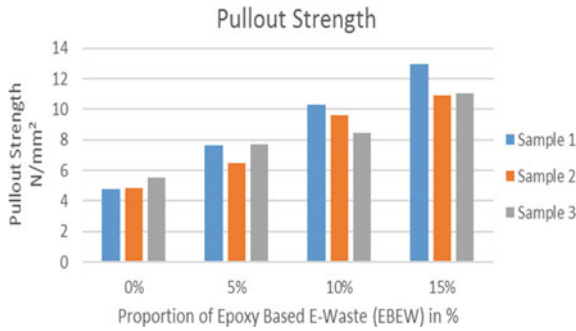


Fig. 9 Pull-out test results

Table 7 F-value of the mechanical properties of concrete

Mechanical properties	F-value		F-critical	Significant difference
1. Compressive Strength	7.71	>	4.07	Yes
2. Flexural strength	1.07	<	4.07	No
3. Pull-out Strength	33.9	>	4.07	Yes

4 Conclusion

It can be concluded that the partial replacement of the coarse aggregate will not only solve the waste disposal problem, but also result in a very positive outcome as an alternative material for the coarse aggregate in concrete.

Based on the results of the Physical Properties of concrete, it is concluded in this investigation that the density decreases when 5, 10, and 15% of EBEW materials were added in concrete as compared to the control (0% EBEW) concrete specimens, and according to the test results obtained from the percent absorption and permeable voids of concrete cylinder, concrete beam and concrete base specimens compared to the experimental specimens the results also shows a decreasing pattern.

It can also be concluded that the use of Epoxy Based e-Waste (EBEW) in concrete can increase the compressive strength of concrete by up to 47.88%, with the 15% replacement obtained the highest compressive strength of 26.53 MPa which is slightly higher than the result of previous study of Saranja [16] with a compressive strength of 25.3 MPa with 34% replacement of coarse aggregates.

Based on the results of the pull-out test, it is concluded in this investigation that adding Epoxy Based e-Waste (EBEW) of 5, 10 and 15% in concrete will gradually increase as compared to that of the 0% EBEW as shown in Table 5.

From the above discussions, it was identified that the use of EBEW in concrete can possibly improve its mechanical properties and can also be one of the economical ways for their proper disposal in an environment friendly manner.

5 Recommendation

Based on the results of the compressive, flexural and pull-out test, the concrete with partial replacement of coarse aggregates with EBEW registered its maximum strength at 15% partial replacement, therefore, it is recommended for further studies that partial replacement of coarse aggregates by EBEW be tested on percentage replacement higher than 15% until optimum partial replacement that will yield better results is reached.

Acknowledgements The authors would like to acknowledge the assistance of Engr. Juan F. Puriran, Jr. Chief Administrative Officer, GSD-AFMS office of the Commission of Higher Education Central Office, for allowing the researchers to conduct the experiment inside the CHED-CO motor pool area.

References

- Balde CP, Wang F, Kuehr R, Huisman J (2015) *The global E-waste monitor 2014: quantities, flows and resources*. United Nations University, Tokyo and Bonn
- Veglio F, Birloaga I (2018) *Waste electrical and electronic equipment recycling-aqueous recovery methods*. Woodhead Publishing Series in Electronic and Optical Materials, UK
- Peralta GL, Fontanos PM (2006) E-waste issues and measures in the Philippines. *J Mater Cycles Waste Manage* 8:34–39
- Ashwini Manjunath BT (2016) Partial replacement of E-plastic waste as coarse-aggregate in concrete. *Procedia Environ Sci* 35
- Wang J, Li Y, Song J, He M, Xia K (2015) Recycling of acrylonitrilebutadiene styrene (ABS) copolymers from waste electrical and electronic equipment (WEEE), through using an epoxy-based chain extender. *Polym Degrad Stabil* 112
- Balakrishnan R, Babu A, Kuber P, Chiya, Ahmed B (2007) Electrical and electronic waste: a global environmental problem. *Waste Manage Res*
- Heart S, Agamuthu P (2012) E-waste: a problem or an opportunity? Review of issues, challenges and solutions in Asian countries. *Waste Manage Res* 30(11):1113–1129
- Cui F, Forssberg E (2003) Mechanical recycling of waste electric and electronic equipment: a review. *J Hazard Mater* 99:243–263
- Bhutta MKS, Omar A, Yang X (2011) Electronic waste: a growing concern in today's environment. *Econ Res Int*
- Raju CR (2014) An experimental study on strength behavior of cement concrete with use of plastic fibre. *Int J Eng Res Appl*
- Nagan S, Lakshmi R (2010) Studies on concrete containing E-plastic waste. *Int J Environ Sci* 1
- Kang HY, Schoenung JM (2005) Electronic waste recycling; a review of U.S. infrastructure and technology options. *J Resour Constr Recycl*
- Suchitra S, Manoj K, Indu VS (2015) Study on replacement of coarse aggregate by E-waste in concrete. *Int J Tech Appl* 3:226–270
- Akram A, Sasidhar C, Dasha KM (2015) E-waste management by utilization of E-plastics in concrete mixture as coarse aggregate replacement. *Int J Innov Res Sci Eng Technol*
- Damal VS, Londhe SS, Mane AB (2015) Utilization of electronic waste plastic in concrete. *Int J Eng Res Appl*

16. Deshmukh GP, Manaktar PA (2015) Use of non-metallic E-waste as coarse aggregate in a concrete. IJRET: Int J Res Eng Technol
17. Prasanna PK, Rao MK (2014) Strength variations in concrete by using E-waste as coarse aggregate. IJEAR 4
18. Saranya K, Muthuswamy V, Sathiyaraj R, Sudharsan A (2017) An experimental study on partial replacement for coarse aggregate by E-waste in concrete. Int J Innov Sci Eng Technol 4
19. Standard Test Method for Density, Absorption, and Voids in Hardened Concrete, C-642. Annual Book of ASTM Standards, **4.02**
20. Standard Practice for Making and Curing Concrete Test Specimens in the Field, C-31. Annual Book of ASTM Standards, **4.01**
21. Standard Test Method for Compressive Strength of Cylindrical Concrete Specimens, C-39. Annual Book of ASTM Standards, **4.02**
22. Standard Test Method for Flexural Strength of Concrete (Using Simple Beam with Center-Point Loading), C-293. Annual Book of ASTM Standards, 4.02

The Potential of Plastic Waste as Building Material



Chong Lih Yen, Myzatul Aishah Kamarazaly, Soon Lam Tatt, Nurulhuda Hashim, Shirley Chin Ai Ling, and Azrina Md. Yaakob

Abstract Building a home can be very costly due to the actual production cost (including the material cost) and the compliant cost. High cost as a primary requirement for constructing houses is forming a significant problem for people who suffers from poverty especially in developing countries. In the past recent years, many studies regarding the possibility of recycling and reusing solid waste product such as plastic bottle has as building material have been done to reduce the cost of the overall construction project. On the other hand, the increase of solid waste product has been steadily increasing for the past few years. Over the years, plastic derived waste has been exponentially increasing due to the substantial quantities of plastic consumption around the world. Plastic bottles being the second leading plastic waste generated in abundance, can be used as a sustainable building material in the construction industry to potentially reduce the number of plastic waste generated each year. In the past recent years, studies have invented the ‘bottle brick’ as a waste reduction strategy due to its non-biodegradable nature. Among a variety of plastic bottle grades, polyethylene terephthalate (PETE) plastic bottles is mainly discussed in this paper as an implementation in the Malaysian construction industry. This paper also provides a comparison between PETE plastic bottles with the conventional materials. With the comparison between different building materials, a cost analysis on constructing a house using plastic bottle will be provided.

Keywords PETE plastic bottles bricks · Building material · Plastic bottle construction · Plastic waste · Plastic bottles

C. L. Yen · M. A. Kamarazaly (✉) · S. L. Tatt · N. Hashim · S. C. A. Ling · A. Md. Yaakob
1, Jalan Taylors, 47500 Subang Jaya, Selangor, Malaysia

© The Author(s), under exclusive license to Springer Nature Singapore Pte Ltd. 2022
S. Belayutham et al. (eds.), *Proceedings of the 5th International Conference on Sustainable Civil Engineering Structures and Construction Materials*, Lecture Notes in Civil Engineering 215, https://doi.org/10.1007/978-981-16-7924-7_95

1441

1 Introduction






1.1 Research Background

“Population, urbanisation and economic growth, in addition to increasingly unsustainable consumer behaviour, have caused rates of waste generation to rise exponentially in recent decades” [1]. Plastic, considered as a very common material, has been widely used and can be easily obtainable by everyone in the world [2]. A study carried out by Jalaluddin [3], stated that plastic has the insolubility of approximately 300 years in nature where plastic is considered as a sustainable waste and environmental pollutant. Reusing or recycling plastics can effectively mitigate the environmental impacts that has resulted by plastic pollutions. However, due to its properties, plastics can be challenging to recycle as they contain additives and a range of different plastic blends [4]. One of the strategies implicated by the World Bank is that they finance and advises on solid waste management project using vast products and services to address the entire lifecycle of waste—from generation to collection and transportation, and finally treatment and disposal [5]. Today, plastics waste disposal has become a major global environmental problem. Disposal of these plastic wastes in either to the ocean or landfill is considered as non-sustainable from the environmental point of view as the disposal of plastics to landfill sites has caused the landfill capacity to decrease rapidly [6]. In year 2018, Malaysia has become the leading alternative destination for plastic scarp after China banned imports of such waste [7]. Among those scarp, studies have proven that plastic bottles are the second leading plastic waste generated in abundance throughout the world. Plastic bottles can be categorised based on several grades as shown in the Table 1.

2 Issue

“Plastic pollution has grown as the use of flexible, lightweight and readily available materials has become an integral part of economic activity across the world. It is indeed impossible now to imagine life without plastics” [8]. As well as the shocking scale of waste dumping into the oceans, the management of solid waste and proper dispose still remain as one of the largest and fastest growing sustainability issues emerging alongside global development [1]. Few years back, past research regarding the alternatives of replacing conventional building materials such as clay bricks have been done with direct inclusion of polyethylene or plastic fibre, polyethylene terephthalate (PETE) bottles in shredded form, chemically treated polyethylene fibre, crushed forms and PETE in aggregate form by replacing natural coarse aggregate [2]. The increase in popularity of using environmental friendly, lightweight and flexible construction material has brought the need to investigate how it can be implemented in Malaysia by reducing environmental impact while maintaining the material requirements which meets the building standards.

Table 1 Plastic bottle grade [9]

Grade	Material	Properties	Application
	Polyethylene Terephthalate	Clarity, barrier to gas and moisture, heat resistant, toughness	Clear soft drink and beverage bottles, food packaging, fibres, drink bottles
	High Density Polyethylene	Toughness, resistance to moisture and chemicals, ease of processing	Bottles (food products and cosmetics), industrial wrapping and film, plastic bags, pallets
	Polyvinyl Chloride	Versatility, toughness, resistance to grease, oil and chemicals	Bottles, packaging film, credit card, water container, pipes, packaging plastics
	Low Density Polyethylene	Toughness, flexibility, ease of sealing, barrier to moisture	Cling film, plastic bag, flexible containers and food wraps, dispensing bottles
	Polypropylene	Strength, toughness, versatility, barrier to moisture	Packaging, margarine pots, yoghurt container, beer crates, industrial fibres, pots
	Polystyrene	Versatility, insulation, clarity, easily formed	Disposal hot or cold drink cups and plates, dairy product containers, pots, tubs, trays
	All other resins and multi-materials not otherwise defined	Properties dependent on chemical makeup	Baby bottles, CDs, other resins, complex composites and laminates, car parts, pallets

Based on a study conducted by Wahid et al. [2], it is stated that brick is one of the most accommodating masonry units as a building material due to its properties. For the past few years, many attempts have been made to incorporate waste in the production of bricks, for example: using paper processing residues, sludge, polystyrene foam, plastic fibre and many more. Thus, many invention of bricks incorporating wastes have been produced. Among those successful invention, the most notifiable creation such as paper bricks, eco-bricks and Polli-bricks have been successfully implemented in some countries. However, there is hardly any implementation of these bricks in the Malaysian construction industry.

3 Challenges

3.1 *Increasing of Plastic Waste*

Since 1980, global plastic production has increased by 5% where 85% of the plastics are incinerated, dumped into landfills or ends up in the ocean [8]. A plastic campaigner at Manila, Beau Bacongus, stated that these plastic wastes have been contributing to the increase of floods by clogging drains, causing respiratory issues when burned, shortening animal lifespans when consumed and contaminating water when dumped into canals and oceans. Relating to the statement made by Bacongus, this issue has lead the management of plastic waste to become one of the largest and fastest growing sustainability challenges emerging alongside the global development. “Despite the fact of the alarming rate of plastic waste, the mechanism that the society have put in place to properly manage and dispose plastic waste have not grown or evolved in tandem” [1]. As the population grows across the world, the rise of plastic waste has become known; but the problem now is how to reduce the plastic wastes?

3.2 *High Recycling Cost*

The most common solution that have been practiced and implemented across the world for years is the 3R programme which are, reduce, reuse and recycling. For the past few years, the battle to reduce plastic waste have become a quarter of a billion dollars more expensive every year as the cost of recycled plastic soars [10]. Consequently, the local authority has started to cut plastic recycling services. Taking UK as an example, plastic recycling waste has been building up since China introduced importing restrictions last year. The situation has become so bad that the local authority can no longer afford to send it to be recycled [11]. Neil Clarke, managing director at Recycling UK, said: “Everyone is told to recycle, and it’s the right thing to, but it will not work if the end market is not there. There are concerns that plastics that are hard to recycle are actually going into landfill.” [11]. Thus, there is a call for an industrial land collection system of plastic products for recycling and circular economy is introduced to the market [12]. Circular economy is an economic system aimed to eliminate waste with continual use of resources [12].

Plastic bottle waste that is initially considered as rubbish, evidently could be cleaned and processed into a new product that has money value [13]. For instance, building homes with plastic bottles in developing country or even incorporating plastic strips into bricks and concrete blocks as a new hybrid building material. “The aim here is to collect every single bottle and put them back in the market.” said by the chairman of Waste Management Association of Malaysia, Ho De Leong. In a way, circular economy helps to close loops on plastic production and encouraged innovative use. The problem underlying for the need of study is to innovate the use of plastic bottles into the construction industry.

3.3 Sustainability Challenges

According to a study conducted by Shoubi et al. [14], recycling needs additional energy to treat the materials to produce something usable. The recycling process is considered unsustainable as it produces wastewater and air pollutants. Hence, the best solution is to reuse as no additional energy is required [14]. Since plastic bottles are considered as a sustainable waste which is proven as an innovative building materials, it can be a proper solution for replacing conventional materials [15]. However, there are challenges to be faced while implementing it to the construction industry.

It is never easy for new sustainable products to enter a new market where nobody has used it yet. According the Associate Principal of Green Living, Yellamraju, a developer may not be interested in paying for sustainable materials or 'green' features when the benefit will be passed on to the new owners or tenants, unless he is able to recoup the additional cost of the sustainable material. Same goes to the plastic bottle construction, if the return costing is not great, it is highly unlikely that the developer or architect to design such building by using plastic bottles as they could not see the benefits. Furthermore, consumers also tend to have low confidence level towards new product as they could not see the value of the sustainable products where its future implications are still unknown.

4 Research Objective

The study aims to achieve the following objectives:

1. To compare between different type of PETE plastic bottles bricks as building material.
2. Reliability of different type of plastic bottle bricks in the construction industry.
3. To provide a general idea on economic perception of plastic bottle bricks.

5 Need for Study

In recent years, several waste reduction strategies have been invented and implemented throughout the world. The 'bottle brick' is one such invention that can be used as a substitute for conventional materials such as bricks which I believed would be more and more popular in the future construction industry.

"With the increasing population growth today, the need of building has increased, and to respond to this demand, the countries tend to use the industrial building materials and decline the use of indigenous and traditional materials in construction." says Rawat and Kansal. Furthermore, the Binastra Land project director Steven Ooi commented that the production cost including the building materials and the foreign labour costs have gone up in the recent years [16]. These factors not only increase

the energy consumption and producing carbon footprints, they can also raise the cost for homes. In recent times, construction developers have been seeking for broader sources of building material alternatives with lower price, while trying to minimize the wastes produced from site to create a more sustainable environment. Therefore, there is a need to conduct a cost analysis to see how plastic bottle construction can save cost.

Controversially, since developing countries such as Malaysia, generate medium-low to higher income, it will most probably become a burden to handle the high waste management cost. Certainly, converting plastic wastes such as plastic bottles into buildable houses can fulfil the demand on building as the population increase while saving cost; is a win-win situation where the country can save cost from waste management and use it at a more appropriate place which increases the country's income in a long-term basis. Either way, it is still crucial for the country to implement effective waste management system and to not leave the problem hanging despite the cost.

6 Research Methodology

This is a conceptual paper which is based solely on a review and analysis of research and data from the literature. Several methods were used to collect and analyse the literature. Further future research method adopted will be a mixed method of case study and qualitative method which involves questionnaire and surveys covering the possibility of implementing plastic bottle construction in Malaysia. The targeted respondents are the plastic bottle supplier and construction developers. The research findings will assist developers on the implementation of plastic bottle construction in the Malaysian construction industry through better understanding of the comparison of different building materials.

6.1 Methods for Collecting and Analysing Literature

Firstly, the research was conducted using the Google search engine. Terms such as 'eco-bricks' and 'plastic bottle construction' were used, but only limited amount of information was found. Literature from the experiment on compressive strength of bottle bricks by Muyen et al. [17], was used to further the research on the comparison of the compressive strength of different types of plastic bottle bricks with the conventional bricks. The most helpful piece of literature was the research conducted by Taaffe et al., *Experimental Characterisation of PETE Bottle Eco-Bricks*, that contained accurate results of experiments while providing a general idea on the cost of plastic bottle construction.

Next, the literature review on journals are conducted mainly with three databases pertaining to construction and plastic waste. The databases were Elsevier, Isurv, and

ResearchGate. All articles that were deemed to be relevant to the main keywords such as ‘plastic bottle construction’ and ‘PETE plastic bottle bricks’ in this conceptual paper were retrieved and reviewed. Few other keywords were searched and sorted in the same manner. Thirdly, books on the topic for this conceptual paper were searched using Taylor’s Library catalogue. The same terms used in the database search was used to find books related to the topic. However, none of the books were deemed useful as this research topic is considered relatively new to the industry.

6.2 Data Collection and Data Sources for Future Research

For future research a mixture of qualitative and case study would be conducted to obtain data on the developer’s and architect’s perception of plastic bottle construction.

The procedures for conducting the research would be to conduct a semi-structured interview session obtain professional opinions and perceptions towards plastic bottle construction in the Malaysian construction industry. The expected targets of the interview sessions are predetermined by the needs of research information, which include experts from the construction industry including developers and architects who have handled with new building material or professionals who have worked on sustainable projects. Additionally, it is best to conduct a case study based on existing buildings that have been using plastic bottle as a building material. This sampling strategy are best positioned to receive information, comments and voices from different parties, thus, enabling the studies to provide with comprehensive and significant information while providing necessary recommendation for this study.

6.3 Research Framework

The research framework demonstrates on the issue, impact and reason of conducting this research. The framework further proposed a practical framework to implement plastic bottle construction in the Malaysian construction industry. For the ease of understanding, the research framework summarises the key content of the paper. This paper serves as the starting point of discussion of the current issue on plastic waste and the solution to it where plastic bottle construction is introduced (Fig. 1).

7 Literature Review

“Urbanization has caused a vast and rapid growth of construction industries which requires a lot of building materials that utilizes natural resources either in their production plant or as the materials itself.” [18]. In recent years, the demand for sustainable construction materials and the rate of production of plastic has been

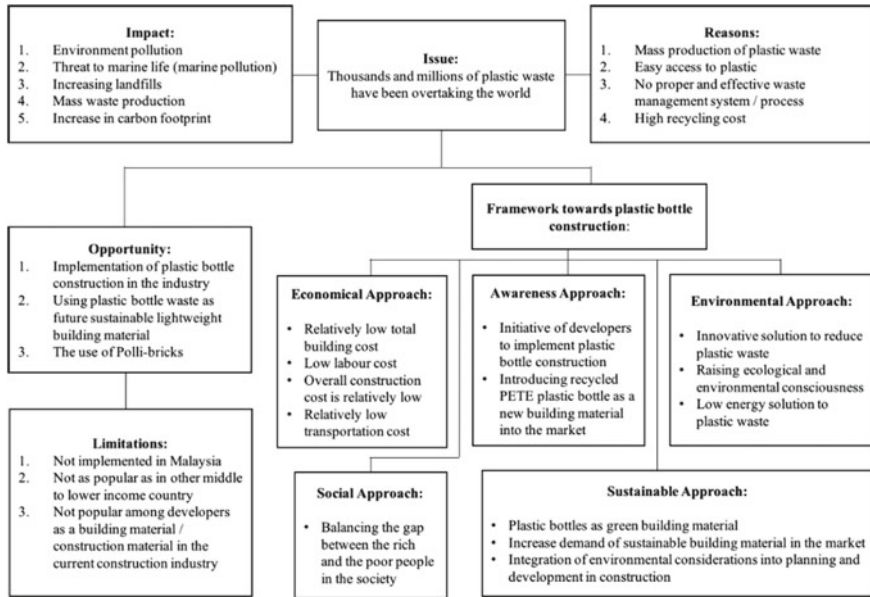


Fig. 1 Research framework

increasing steadily yearly. The demand of both the construction industry and the plastic production industry had been the major contributor in the growth of municipal solid waste around the world. As a society, thinking holistically about the products used along with their impacts is crucial to come out with alternatives [19]. Hence, utilizing plastic wastes as a construction material especially in brick production can solve both the municipal solid waste and demands for sustainable construction materials creatively. In a way, it also helps to provide more homes to the middle-low income society while helping the younger generations such as the fresh graduates and alumni as they do not have much income yet.

7.1 Overview of Plastic Bottle Bricks

Since most of the construction are made up of conventional materials such as bricks and mortar which contributed to global warming due to the emission of carbon dioxide, the best solution to overcome these issues is by replacing conventional bricks with plastic bottle bricks [20]. Due to its physical property, plastic bottle bricks posts as a great community project uplift that focuses on redirecting the life cycle of non-recyclable materials [21]. Plastics, being a non-renewable source, can serve as innovative building materials which can be effectual in mitigating environmental

impacts. Soon, the replacement of conventional building materials with plastic bottles will become a future trend in the construction industry.

Plastic bottle bricks involves the use of disposable PETE bottles, debris and earth as raw material for construction [17]. Over the years, a few other options of plastic bottle bricks have been developed and implemented in several countries which are sand-filled plastic bottle bricks, plastic-filled plastic bottle bricks and engineered Polli-bricks. These plastic bottles are very durable and have minimal chances of breaking down, making these plastic bottle bricks an ideal building material which are starting to be spread and used around the world especially in developing countries to construct houses and even water tanks [22].

Raut et al. [12] concluded that plastic bottle bricks can be a better building material as compared to conventional building material such as bricks, concrete and ceramic blocks in a way such as time of execution, load capacity, flexibility, waste and cost reduction, and energy efficiency. This can be further supported as reported by Mojtaba in their studies, reusing plastic bottles as a building material can have substantial effects on saving the building embodied energy as compared to conventional building material such as bricks by reducing carbon dioxide emission in the manufacturing process of cement and the percentage of cement used. In addition to that, Pakrashi et al. [23] reviewed that plastic bottles are viable resource for construction purposes with a series of possible application as plastic bottle bricks are relatively easy to manufacture.

7.2 *Sustainable Development*

Sustainable Development (SD) is defined as the development which meets the needs of the present without compromising the needs of future generations [24]. In the International Journal of Science, Engineering and Technology Research, Shoubi, Shoubi and Barough reviewed some purposes of SD as follows:

- **Resource Conservation:** To conserve non-renewable resources such as fuel and minerals to ensure there are sufficient supply for the present and future generations.
- **Built Development:** Integration of environmental considerations into planning and development to respect the natural environment.
- **Environmental Quality:** To prevent or reduce processes such as landfilling that leads to environment degradation and develop the culture of reusing and recycling process.
- **Social Equity:** To impede development that increases the gap between the rich and the poor and to encourage for reach to the social equality.

SD is presented as a more or less a clean break from other modes of development on both a worldwide and local scale. In order to achieve sustainable, the development must include three main pillars of sustainability namely: environmental, social and economical [25].

Economic Sustainability. Human communities across the globe are able to maintain their independence and have access to the resources that they require, financial and other, to meet their needs [26]. As such, economic exists within the society as all parts of human economy are achieved via interaction among people [14].

Environmental Sustainability. The economy and society depends on the environmental sustainability as they are inter-related to each other [14]. Natural resources within the earth's environmental system are consumed by humans at a rate where they are able to replenish themselves [26].

Social Sustainability. Universal human rights and basic necessities are attainable by all people, who have access to enough resources in order to keep their families and communities healthy and secure [26]. When the society is affected, sustainable development would be hard to achieve as it would be uneconomical [14].

Plastic bottle bricks are considered as a sustainable material which can help in achieving SD as it can abstain from resource depletion, assist in protecting the environment; prevent or reduce the environmental degradation process such as landfilling through and it can assist to obtain a social equity by closing the gap between the rich and the poor people in the society [14].

7.3 *Sustainable Material*

With the aim of mitigating environmental impacts where non-biodegradable plastic waste was reused, plastic wastes are regarded as a long lasting and durable material [27]. It addresses sustainable site planning, energy efficiency, conservation of material and resources by using renewable resources as well as recycling and reusing [14]. The sustainability of plastic bottle bricks as a sustainable material is shown as follows:

- Keeping plastic out of the ecosystem while preventing the contamination of plastic degradation to the environment [28].
- Redirecting the lifecycle of non-recyclable material [21].
- Reduce natural resource consumption while managing plastic wastes.
- Promote sustainable building material that is cost effective as plastic can be turned into useful building materials.

Briefly, the whole idea of plastic bottle bricks is to promote it as a future sustainable building material. Building material play an essential role in enhancing the overall building performances. Without proper waste management, it could lead to environmental, social and economic impacts as the construction industry is one of the major waste generators. According to Napier [29], responsible waste management is an essential aspect of sustainable building where managing waste means eliminating waste where possible; minimizing waste where feasible; and reusing materials which might become waste.

Table 2 Criteria of sustainable building material [30]

Manufacturing process (MP)	Building operations (BO)	Waste management (WM)
Waste reduction (WR)	Energy efficiency (EE)	Biodegradable (B)
Pollution prevention (P2)	Waste treatment and Conservation (WTC)	Recyclable (R)
Recycled (RC)	Nontoxic (NT)	Reusable (RU)
Embodied energy (EER)	Renewable energy source (RES)	Others (O)
Natural materials (NM)	Longer life (LL)	

The essential of sustainable management of resources is by practicing reduction, recycling and reuse of wastes [29]. Waste takes the form of spent or unwanted materials generated from construction and demolition process. Being a non-brittle material, plastic bottle bricks produces much less construction waste compared to conventional bricks [17]. In a way, using plastic bottle bricks can reduce the construction waste generated as the plastic bottle bricks itself is part of the solid waste which means that there is no need to generate new resources for the purposes of building material which makes the plastic bottle bricks a sustainable building material. The sustainability of a building material can be determined by the selection criteria, grouped by the affected building life-cycle phase as shown as Table 2 [30].

7.4 Plastic Bottle Bricks as Building Material

Plastic bottles have slow disintegration process. Thus, reusing plastic can be the best possible solution to municipal waste where disposable plastic bottles are used to replace bricks in the construction industry as they benefit in good construction ability in terms of buildability, strength, physical properties [14]. Based on the study Yahaya Ahmed from Nigeria’s Development Association for Renewable Energies, it is proven that the resistance of each plastic bottle bricks against the load is 20 times higher as compared to bricks. Apart from that, the compressed filling materials inside the plastic bottle bricks makes the plastic bottle bricks a bulletproof shelter, where they can absorb abrupt shock loads [17]. Furthermore, plastic bottle bricks are also ideal for wall as it has a self-supporting property supported by cross-shaped cables at the front and back of the bottle which causes the cable to create equal force against each other [14]. It is believed that the future trend of sustainable building material in the construction industry will be moving towards plastic bottle bricks especially in developing countries (Figs. 2 and 3).



Fig. 2 Self-supporting property [31]



Fig. 3 Supporting material: cross-shaped cable (green wires) [31]

8 Key Findings on Literature Review Related to Objective 1

Eco-Bricks

Eco-brick is a building block made entirely from unrecyclable plastics which can be used in all sorts of sustainable building projects. It is created by filling PETE plastic bottles with un-recyclable plastics such as food wrappers, plastic bags, plastic food containers or Styrofoam [22]. The fillings may vary from plastic filled to sand filled, gravels, cork or even wood particles [17]. Creating eco-bricks is not a simple process as the plastics has to be cleaned and dried; and is best to cut up into smaller pieces in order to be packed tightly into the bottles.

Other than that, there is also a minimum weight requirement to ensure the eco-bricks are sturdy enough to build with where the minimum density is 0.33 g per ml. For example, a 600 ml bottle should weigh at least 200 g whilst a 1.5 L bottle needs to weight around 500 g. Eco-bricks may appear strong, but they can deform under pressure and collapse when it does not meet the minimum weight requirement; while unclean or damp plastic fillings may cause mold and methane formation inside the eco-bricks [32]. Two major type of eco-bricks namely sand filled plastic bottle bricks and plastic filled plastic bottle bricks (eco-brick) that has been practiced in some of the developing country will be reviewed further.

8.1 Sand Filled Plastic Bottle Bricks

In the study of Muyen et al. [17], waste PETE bottles of different sizes were collected and washed. Fine sands were filled in to the dried bottles in three layers where each layer are compacted with 20 blows by using the tamping rod. A Digital Display Compression testing machine was used to carry out their test on the compression strength where the sand filled plastic bottle bricks were placed between the loading of the machine. The process is repeated with increasing load until there is a sudden drop of force in the reading and is recorded as the maximum load (Figs. 4 and 5).

Different sizes of sand filled plastic bottle are then tested subsequently with the same process mentioned. In their findings, the sand filled plastic bottle bricks did not break. However, there is deformation of the bricks. Thus, Muyen et al. [17] concluded that the compressive strength of the sand filled plastic bottle bricks increases with the size of the bottle as shown in Fig. 6. Table 3 shows the results of the compression test carried out by the authors.

8.2 Plastic Filled Plastic Bottle Bricks

Plastic filled bottle bricks, also known as the eco-bricks, are formed by compacting waste plastic bags within the PETE bottles (Fig. 7). In the study of Taaffe et al. [23],



Fig. 4 Sand filled plastic bottle bricks [33]



Fig. 5 Sand compaction [33]

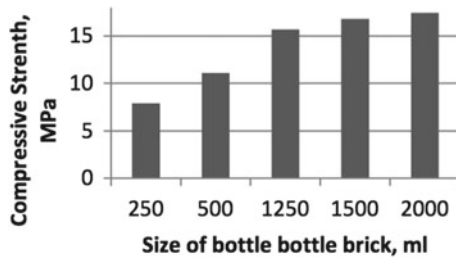


Fig. 6 Compressive strength of different sized sand-filled bottle bricks [17]

Table 3 Compressive strength of 1000 ml sand-filled bottle bricks [17]

Curing period (days)	Size of bottle brick (ml)	Compressive strength (MPa)
3	1000	10.0
7	1000	12.4
8	1000	19.9

Fig. 7 Plastic filled plastic bottle bricks [34]

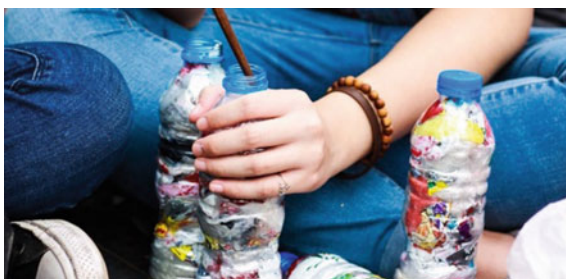


a few sizes of plastic bottle ranging from 500 ml to 2 l are considered, but only the 500 ml plastic bottles are used to carried out the compression test as it is quite a challenge to manually compact the plastics compared to sand fillings in larger bottles. A specific requirement stated by the authors is that the plastic that enters the bottle must be clean and dry. A metal rod of diameter around 12–16 mm and 350–500 mm length is recommended by the author to compact the plastic fillings for a 500 ml bottle by taps.

4–6 taps are required to compress the plastic into the bottles, more taps may be required as the subsections increases [23]. While compacting with the stick, the bottle needs to be rotated while applying force to ensure the plastic wastes are evenly compacted and to avoid voids (Fig. 8). The completed bottles should weigh no less than 220 g after packing. A Denison compressive testing machine is use by the authors in their studies for the compression test. The process of the compression test is similar to the sand filled plastic bottle compression test but with an additional platen which was added to allow for smaller specimens in the test.

The plastic filled plastic bottle bricks were placed in the centre of the machine where an initial preload of 5 kN is applied. The process is repeated by increasing the load until there is a sudden drop of force which stops the machine. The reading is then recorded as the maximum load. In Taaffe et al. [23] findings, failure is not complete as the specimen is did not break. However, there is deformation of the bricks is detected which concluded that plastic filled bottle bricks have good resistance to the compressive force applied. Briefly, the compressive strength of the plastic filled plastic bottle bricks increases with the size of the bottle as shown in Fig. 9.

Fig. 8 Plastic compaction [35]



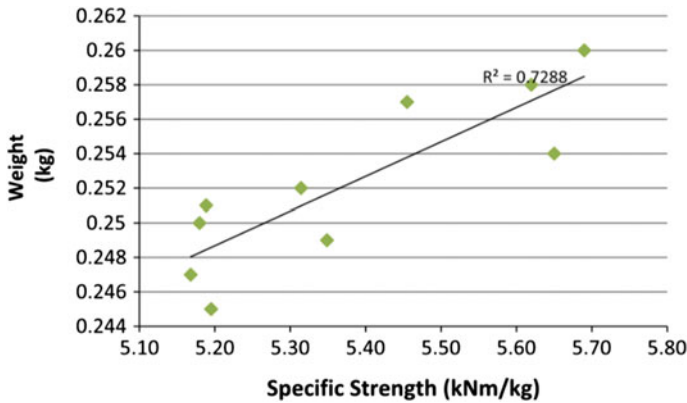


Fig. 9 Compressive strength of different weight plastic filled bottle bricks [23]

Table 4 Compressive strength of 500 ml plastic-filled bottle bricks [23]

Size of bottle brick (ml)	Weight of bottle brick (g)	Compressive strength (MPa)
500	25	2.80
500	26	2.90
500	27	2.96

In short, it can be concluded that sand filled eco bricks can withstand stronger compressive strength as compared to plastic filled eco bricks which means sand filled eco bricks may be a more suitable option to be used as a building material (Table 4).

Engineered-Bricks

The engineered plastic bottle bricks involve the process of holistic thinking where the recycled plastic bottles collected are melted and reformed to a standardized size [36]. One of the examples of these engineered bricks are Polli-bricks which is invented by Arthur Huang, founder of Miniwiz.

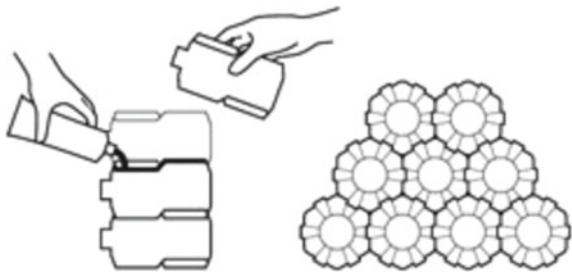
8.3 Polli-Bricks

Polli-bricks (Fig. 10) are recycled polymer bottle that can be interlocked to build incredible structures. Polli-bricks are made entirely from PETE bottles which are collected locally where the recycled PETE bottles are melted and formed [38]. According to Property Report [38], it is said that buildings constructed with polli-bricks are able to withstand 130 kph blast of wind, guarding it against typhoons. The origin of polli-bricks are actually from Taiwan, where 4.5 millions of PETE bottles are consumed every year. Over the years, they have acquired the skills to process plastic bottles into useful building material, helping to dispose a great number of



Fig. 10 Polli-bricks [37]

Fig. 11 Self-interlocking System of Polli-Bricks [39]



plastics [38]. The founding Architect of Miniwiz, Arthur Huang and his team were able to formulate a hollow building block called as polli-brick which is derived from molten PETE.

The Property Report [38] also reviewed that polli-bricks are engineered in a way with fire resistant and water resistant coating where they can interlock into each other like LEGO building blocks. Each interlocking bricks are created from around 4 recycled PETE plastic bottles. The purpose of these interlocking system is used for the solidifying of structural steel frame, making the entire system sturdier while minimizing the use of silicone sealant. The shape design of the bricks incorporates a great deal of air which in a way providing thermal and sound insulation to the entire building. Furthermore, the strength to weight ratio of the polli-brick is also impressive thanks to its honeycomb geometry that is combined with reinforced wall thickness (Figs. 11 and 12).

8.4 Summary: The Reliability of Plastic Bottle Bricks

Engineered plastic bottle bricks as a building material are more reliable as compared to eco bricks in terms of strength, durability and in design. The engineered plastic

Fig. 12 Design of Polli-Bricks [40]



bottle brick, Polli-Bricks, are the most reliable among the 3 type of plastic bottle bricks as discussed previously. It is more suitable to be used in constructing medium to high structures and buildings. Based on the result of compressive strength test from different type of eco bricks, sand-filled eco bricks are more reliable as it can withstand greater strength and pressure. On the other hand, eco bricks such as plastic filled plastic bottle bricks are more suitable to be used as a decorative façade or for building furniture such as benches while sand-filled plastic bottle bricks which have higher compressive strength durability is more suitable to be used for short rises building that carries lighter load or with minimal compressive strength.

9 International Example

9.1 *EcoARK Pavilion, Taiwan*

This project is originally designed by Miniwiz Sustainable Energy Development, a Taiwanese agency, founded by Arthur Huang; with a purpose to address the great disparity between sustainability, recycling and eco-consciousness and the bleak market reality around its lack of financially feasible applications [42] (Fig. 13).

Aside from that, Miniwiz also focuses on turning post-consumer waste into high performance materials which enables the movement into the circular economy. It is their top priority to show the world the unlimited potential of trash by taking the recycled material to the highest form of product engineering where they can demonstrate financial feasibility of environmentally serving technologies that can compete and outcompete the traditional and far less sustainable technologies [42].

The EcoARK Pavilion in Taiwan is the first every building in the world that is fully constructed with polli-bricks, the hexagonal building bricks that fits together perfectly on such scale. The use of polli-bricks ensures the building to be perfectly watertight and sturdy enough to withstand earthquakes and strong winds up to 130 km/h [43]. Furthermore, the insulating properties of polli-bricks makes it even more suitable



Fig. 13 EcoARK Pavilion, Taiwan [41]

material for all climates. However, it is not intended for buildings subjected to extreme temperatures [43] (Figs. 14 and 15).

The EcoArk Pavilion is built using 1.5 million polli-bricks bottles which provides natural ventilation and lighting during the day as the plastic lets the light through while in the evening, 40,000 electroluminescent diodes are used to light up the entire



Fig. 14 Interior of EcoARK Pavilion, Taiwan [42]



Fig. 15 Exterior of EcoARK Pavilion [42]

building. It is also stated by Miniwiz that polli-bricks can reduce the amount of carbon dioxide given away during construction [43].

10 Economic Perception

A study conducted by Shoubi et al. [14] stated that constructing a house by plastic bottles used for the walls, joist ceiling and concrete column offers diminution of 45% in the final cost. Furthermore, this can be supported by the studies of Yahaya Ahmed where separation of various components of cost shows that the use of local manpower in making bottle panels can lead to cost reduction up to 75% as compared to building the walls using conventional building materials such as bricks and concrete blocks.

10.1 Construction Cost

As a result of positive impact on the environment, social and economic issues, sustainability has in recent times attained much acceptance. Nevertheless, the price of sustainable construction materials is too high to be affordable in developing countries. Thus, the invention of plastic bottle bricks would be the best solution to affordable, cost effective, and sustainable building material in developing countries.

Previous studies had proven that plastic bottle bricks are low cost sustainable alternatives where the construction costs can be saved in many factors. Since plastic bottle bricks are made entirely from PETE recycled bottles, which can be collected

locally in large quantities, it can avoid the costs and impacts of transporting these building material for example from one region to another [43].

Furthermore, as reviewed in the article of Plastic eMag [43], the plastic bottle bricks are generally much more lighter than conventional bricks which means, it can save cost on fuel for transporting heavy building materials. It must be noted that sophisticated manpower can lead to reducing the construction time where the relative costs become lower [14].

However, the construction cost of plastic bottle building still varies on many different factors. For example, the average plastic bottle costs around \$7000 per classroom, which is 100–200% cheaper than the average school that is built using cinder-blocks based on the plastic bottle brick project in Guatemala [44]. Since the plastic wastes is naturally available in large quantities, hence the cost factor will decrease which is economical [20].

11 Conclusion

In short, plastic bottle bricks can be seen as the future sustainable building material which brings benefits from alleviating pressure from landfills while creating buildings that are cost efficient. Considering the strength of plastic bottle bricks and relatively low cost of construction, they can be the next construction material of choice in the Malaysian construction industry. As their popularity are increasing among lower to middle income countries, there would be a positive change in the urban fringe and slums area. It is a win-win invention where the streets in townships are cleaned up while educating the community that the wastes littering their streets actually hold value [21].

Gradually, plastic bottle construction will catch the attention of the developers and architecture in the construction industry. Thus, there is a need to evaluate and analyse plastic bottle construction in the Malaysian construction industry while providing a detailed comparison between PETE plastic bottle as a building material with the conventional building material and to provide a detailed cost analysis on the plastic bottle brick construction. By doing this, I hope that this research could help people all around the world that are in need of these cheaper alternative construction material for building affordable houses while achieving social equity.

12 Future Prospect

Based on the literature, the following recommendations for future research are as the following:

Recommendation 1: Further research should be conducted to forecast the service life of plastic bottle construction and the use of plastic waste in concrete structures.

Recommendation 2: Further research should be conducted on the strategies to promote the application and implementation of plastic bottle bricks in the Malaysian construction industry.

Recommendation 3: Further research should be conducted on the buildability of plastic bottle construction in terms of the construction technology and method used.

Recommendation 4: Future studies should focus on analysing the cost of using PETE plastic bottle bricks.

Recommendation 5: Further research should be conducted on the perception of the construction players on implementing plastic bottle construction and ranking the suitability of implementing different types of plastic bottle bricks in the Malaysian Construction Industry.

References

- Nichols S, Smith N (2019) Waste Generation and Recycling Indices 2019: Overview and findings. Bath, England: Verisk Maplecroft
- Wahid SA, Rawi SM, Desa NM (2015) Utilization of plastic bottle waste in sand bricks. *J Basic Appl Sci Res* 5(1):35–44
- Jalaluddin M (2017) Use of plastic waste in civil constructions and innovative decorative material (eco-friendly). *MOJ Civ Eng* 3(5):1–10
- Ritchie H, Roser M (2020) Our World in Data. Plastic Pollution. <https://ourworldindata.org/plastic-pollution>. Last accessed 2020/03/19
- The World Bank (2020) Solid Waste Management. <https://www.worldbank.org/en/topic/urbandevelopment/brief/solid-waste-management>. Last accessed 2020/03/19
- Abdel-Shafy HI, Mansour MSM (2018) Solid waste issue: sources, composition, disposal, recycling, and valorization. *Egypt J Pet* 27(4):1275–1290
- New Straits Time (2020) Malaysia, flooded with plastic waste, to send back some scrap to source. <https://www.nst.com.my/news/nation/2019/05/490387/malaysia-flooded-plastic-waste-send-back-some-scrap-source>. Last accessed 2020/04/05
- Financial Times (2020) How to meet the challenge of plastic waste. <https://www.ft.com/content/be1461ec-7718-11e9-bbad-7c18c0ea0201>. Last accessed 2020/03/22
- PLASgran (2020) PLASgran guide to plastic recycling grades. <https://plasgranltd.co.uk/sell-your-plastic-waste/guide-to-plastic-recycling-grades/>. Last accessed 2020/04/05
- Ambrose J (2020) War on plastic waste faces setback as cost of recycled material soars. <https://www.theguardian.com/environment/2019/oct/13/war-on-plastic-waste-faces-setback-as-cost-of-recycled-material-soars>. Last accessed 2020/03/05
- The Telegraph (2020) Plastic becoming too expensive to recycle, council say, as giant waste mountain is discovered. <https://www.telegraph.co.uk/news/2018/10/19/plastic-becoming-expensive-recycle-councils-say-giant-waste/>. Last accessed 2020/06/29
- The Star Online (2020) ‘Solution must go beyond recycling’. <https://www.thestar.com.my/metro/metro-news/2019/08/21/solution-must-go-beyond-recycling>. Last accessed 2020/03/05
- Kristina HJ, Christiani A, Jobilion E (2018) The prospects and challenges of plastic bottle waste recycling in Indonesia. In: The 2nd international conference on eco engineering development 2018, Indonesia, 2018. IOP Publishing Ltd., Tangerang
- Shoubi MV, Shoubi MV, Barough AS (2013) Investigating the application of plastic bottle as a sustainable material in the building construction. *Int J Sci Eng Technol Res* 2(1):28–32
- Pandey SP, Gotmare S, Wankhade SA (2017) Waste plastic bottle as construction material. *Int Adv Res J Sci Eng Technol* 4(3):1–6

16. New Straits Times (2020) Rising house price: 'don't blame developers'. New Straits Times. <https://www.nst.com.my/property/2017/09/277126/rising-house-prices-dont-blame-developers>. Last accessed 2020/03/19
17. Muyen Z, Barna TN, Hoque MN (2016) Strength properties of plastic bottle bricks and their suitability as construction materials in Bangladesh. *Progress Agric* 27:362
18. Amir SN, Yusof NZ (2018) Plastic in brick application. *Trends Civ Eng Arch* 4(1):341–344
19. World Resources Institute (2020) Banning straws and bags won't solve our plastic problem. <https://www.wri.org/blog/2018/08/banning-straws-and-bags-wont-solve-our-plastic-problem>. Last accessed 2020/03/22
20. Niranjana D, Rushikesh P, Sahil J, Omkar P (2018) Plastic bottles used in construction. *Sci J Impact Factor (SJIF)* 5(4):1–4
21. Yuppiefchef (2020) What is an ecobrick and why are we making them? <https://www.yuppiefchef.com/spatula/what-is-an-eco-brick-and-why-were-making-them/>. Last accessed 2020/05/15
22. Ecotricity (2020) What is an ecobrick? <https://www.ecotricity.co.uk/news/news-archive/2019/what-is-an-ecobrick>. Last accessed 2020/03/19
23. Taaffe J, O'Sullivan S, Rahman ME, Pakrashi V (2014) Experimental characterization of polyethylene terephthalate (PET) bottle eco-bricks. *J Mater Des* 60:50–56
24. United Nations General Assembly (1987) Report of the world commission on environment and development: our common future. United Nations General Assembly, Development and International Co-operation: Environment, Oslo
25. Legrand (2020) Sustainable development description. <https://www.legrandgroup.com/en/sustainable-development-description>. Last accessed 2020/05/15
26. University of Alberta (2020) What is Sustainability? <https://www.mcgill.ca/sustainability/files/sustainability/what-is-sustainability.pdf>. Last accessed 2020/03/19
27. The Sustainability Project. Ecobricks: Plastic Solved. <https://thesustainabilityproject.life/blog/2018/10/07/ecobricks-plastic-solved/> last accessed 2020/03/19
28. Bocadillos (2020) Eco bricks—why everyone should have an eco-brick in their kitchen. <http://www.bocadillos.co.za/ecobricks/>. Last accessed 2020/03/19
29. Whole Building Design Guide (2020) Construction Waste Management. <https://www.wbdg.org/resources/construction-waste-management>. Last accessed 2020/03/05
30. Kim J, Rigdon B (1998) Sustainable architecture module: introduction to sustainable design. National Pollution Prevention Center for Higher Education, 430 E. University Ave., Ann Arbor, MI 48109-1115734.764.1412
31. African Impact (2020) Environment Conservation & Ecobricking. [Photograph]. <https://africanimpact.com/volunteer/conservation/environmental-sustainability/environmental-conservation-ecobricking-zambia/>. Last accessed 2020/06/29
32. Quora (2020) What are the advantages and disadvantages of plastic bricks? <https://www.quora.com/What-are-the-advantages-and-disadvantages-of-plastic-bricks>. Last accessed 2020/03/19
33. S.E.A. Build a House Out of Plastic (2020) Fire-Proof, Bullet-Proof, and Well-Insulated. [Photograph]. <https://www.spiritearthawakening.com/science-tech/technology/useful-resources/build-house-plastic-fire-proof-bullet-proof-well-insulated>. Last accessed 2020/03/05
34. The Bogota Post (2020) Patent helps accelerate student eco-brick project in Medellin. [Photograph]. <https://thebogotapost.com/eco-brick-patent-medellin/24831/>. Last accessed 2020/06/29
35. Vietnamnet (2020) High school students make ecobricks. [Photograph]. <https://english.vietnamnet.vn/fms/education/213198/high-school-students-make-ecobricks.html>. Last accessed 2020/03/21
36. Ramaraj BA, Nagammal JB (2014) Exploring the current practices of post consumer PET bottles and the innovative applications as a sustainable building material—a way ahead. In: The 30th international plea conference, 2014, Ahmedabad, 2014. Plea 2014 Publishing Ltd., Ahmedabad
37. Archi Expo (2020) Panel Curtain Wall/Recycled Plastic/Durable. [Photograph]. <https://www.archiexpo.com/prod/miniwiz-sed-co-ltd/product-64621-1814532.html>. Last accessed 2020/03/22

38. Property Report (2020) This building made from plastic bottles can survive earthquakes and typhoons. <http://www.property-report.com/detail/-/blogs/this-building-made-from-plastic-bottles-can-survive-earthquakes-and-typhoons>. Last accessed 2020/03/22
39. Bekeken A (2020) Polli-Brick EcoARK; building with recycled plastic bottles. [Photograph]. <https://www.stichtingmilieunet.nl/andersbekekenblog/afval/polli-brick-bouwen-met-gerecycelde-pet-flessen.html>. Last accessed 2020/03/22
40. Green J (2020) Interlocking Polli-Brick used for EcoARK. [Photograph]. <https://www.jetsongreen.com/2010/04/interlocking-polli-brick-used-for-ecoark.html>. Last accessed 2020/05/15
41. Wang L (2020) Amazing building made from 1.5 million plastic bottles withstands fires and earthquakes. [Photograph]. <https://inhabitat.com/amazing-plastic-bottle-architecture-wit-hstands-earthquakes-in-taipei/>. Last accessed 2020/05/15
42. Miniwiz (2020) About Miniwiz. <http://www.miniwiz.com/about.php>. Last accessed 2020/05/15
43. Plastic eMag (2020) Exotic formula: plastic bricks. <http://plastics-themag.com/Polli-brick-a-revolutionary-high-tech-process>. Last accessed 2020/05/15
44. Hug it Forward (2020) Flor de Paraxchaj. [Photograph]. <https://hugitforward.org/flor-de-paraxchaj/>. Last accessed 2020/03/22

Identification Characteristic of Energy Efficient Timber House



Febriane Paulina Makalew, Rilya Rumbayan, and Novatus Senduk

Abstract The energy efficient house principle is to minimize the use of energy for household and daily activity. Timber house is the potential in saving energy due to its characteristics. Effort in saving energy for the building has been done, such as the use of supporting energy save including solar panel and design house to circulate air and heat in a passive house. The aim of this paper is to identify the potential of energy efficient in a timber house and it's characteristic. The methodology used is survey data on traditional timber houses in Woloan village, North Sulawesi. The result shows that there is limited implementation of energy efficient timber houses in Woloan village. The characteristic of energy efficient timber house is construction on floor, wall, roof and opening with treatment to safe energy passively and the use of the solar panel. There is potential in improving the quality of timber houses to be energy efficient buildings. The use of solar panels for timber houses based on order has been recognized, although the construction is conducted by the solar panel company. Moreover, the construction and lay out of the house is dominant by natural ventilation and adequate opening for natural light. There is a need for further research to evaluate the amount of energy efficient in a different type of timber house as well as the mixed construction of timber and other construction material.

Keywords Timber house · Energy efficient · Passive house · Solar panel

1 Introduction

The material of timber has been used for many constructions including house construction. Timber has been acknowledged as safer energy material due to its characteristics. The characteristic of timber is a good thermal insulator. Wood is a material that cannot transfer heat therefore the internal house does not receive heat from outside. Timber house can be found in many areas including in North Sulawesi, Indonesia. The traditional house of Minahasa, one of the ethnic in North

F. P. Makalew (✉) · R. Rumbayan · N. Senduk
Manado State Polytechnic, Manado, North Sulawesi Indonesia, Indonesia
e-mail: febrianne.makalew@sipil.polimdo.ac.id

© The Author(s), under exclusive license to Springer Nature Singapore Pte Ltd. 2022
S. Belayutham et al. (eds.), *Proceedings of the 5th International Conference on Sustainable Civil Engineering Structures and Construction Materials*, Lecture Notes in Civil Engineering 215, https://doi.org/10.1007/978-981-16-7924-7_96

1465

Sulawesi, is dominant using timber for construction material. In designing energy efficient buildings, the use of wood as the main material for timber houses give an impact on indoor temperature to be more comfortable for people. However, there is a need to considered other parts of house construction. The use of material glass on the window of timber house for the purpose of increasing natural light on the other hand can increase the temperature of the internal house. The characteristic of glass is transparent and as the best transmission of heat.

The concept of energy efficient building has been widespread with many terms. The consideration of environment quality is an approach for better building construction such as green building, environmentally friendly construction and passive house. GBCI [1] for example, established criteria for the green building including energy efficiency and conservation which consist of electricity, passive design analysis, artificial lighting, thermal condition, heat reduction, energy efficient home appliances and renewable energy sources. In terms of material resource and cycle, environmentally friendly material and certified wood are criteria that need to consider (ibid). For indoor health and comfort the criteria including fresh air circulation and natural light. Azizah et al. [2], evaluate the standard of greenhouse to a number of dwelling in the urban area. The standard green house of selected dwelling with vary functions can be improved through the use of renewable energy and lighting device. Using the standard ASHRAE (American Society of Heating, Refrigeration, Air conditioning Engineering), the timber house in the coastal and hill area is measured [3]. The timber house in the coastal area is more comfortable than the coastal area based on AMV value.

A passive house is one of the house designs types to improve the quality of energy efficient houses. The concept of a passive house is started in 1983 in Germany and has been developed ever since in many countries [4]. A good ventilation system in the passive house should overcome more than 75% heat in the house which is lower 90% than the conventionally built house (ibid). Therefore, the design for energy efficient timber houses should implement the concept of the passive house through house construction and material (ibid). The standard of a passive house is based on the use of energy at a low level [5]. The criteria for the assessment of a passive house is including heating, cooling, air tightness and renewable primary energy (ibid). Whilst the criteria for building components are including insulation on the ground, exterior and interior and construction of window and ventilation (ibid). In terms of renewable energy, the type used for passive houses such as solar panel system, the PV system and renewable energy plants (ibid).

Considering the advantage in applied passive house concept, [6] evaluate the development in using the passive house as a system in recently and future. Such a system has been used by the client and industry in which the regulation is the second leading (ibid). The implementation of a passive house could be improved by adequate information, skilled and stakeholder involvement. However, the process of reaching the optimum benefit of the passive house should be followed with good quality control. The climate change has led to research on passive house evaluation in which the majority house fails to circulate the heat in the peak temperature [7]. Problems found in the ventilation system that is inadequate. The passive house in the

rural area helps the community to live with energy efficient dwelling and in a comfort area (ibid). However, a passive house system can be failed if the daily activity has not followed the rule of its system (ibid).

Different type of timber house has been developed from traditional to modern house. Moreover, the house also creates energy efficient house whether it's naturally constructed such as for a traditional house or adding energy efficient devices such as for a modern house. The traditional timber construction of Kaili ethnic in Central Sulawesi Indonesia for example, is evaluated as an energy efficient house [8]. The energy efficient can be seen in the construction of houses including roof, floor, window, ventilation, wall and vegetation (ibid). Interestingly, the floor board use for the house has a gap that allows air circulation to the indoor building and creates a comfort room (ibid). Traditional house multi-storey is focusing on the part of the building, material, construction system, opening and ornament [9].

The design and construction of timber houses have been developed to protect the environment from degradation. The implementation of the solar panel to block based construction for a residential house in western China is aimed to protect the environment in a rural area [10]. The system is divided into three categories including solar energy, green technology and standard. For the solar energy category, the block is including passive and active solar energy (ibid). Result suggests that the house in the rural area should face the solar path and living area on the opposite site to block the heat movement (ibid). This type of house is not just energy efficient but also environmentally friendly due to its design and function. Moreover, Lazarevica et al. [11] create an innovation system on multi-storey wood-frame. The part of the building is a building frame with the material of wood. Emphasis on its components, building materials, construction systems, ornaments, opening's treatment, environment, and its spatial organization (ibid). The recent development on frame timber house has led to prefabrication house structure with 3D analysis of modular built in [12]. The type of house is multi-storey and multifamily building.

Furthermore, the development of construction material in a creative way has been done to support the timber house in achieving energy efficient buildings. Part of building construction material as main or supporting material help reduce the indoor heat and safe more energy. The use of wood as a building material is to reduce carbon emission [13]. This is to encourage the use of wood as construction material in an innovative way (ibid). Lianto [14], using material glass for the window can give adequate light for the indoor house as well as the impact on the increasing of room temperature. The type of glass should be properly chosen to avoid excessive heat to the indoor house such as RayBan glass and adding material to the surface using plastic film (ibid).

The criteria of energy efficient houses also vary from the stages of construction preparation to the treatment approach. Natural wood house stages are started from log cutting to waste treatment as life cycle assessment [15]. The life cycle CO₂ emission with natural material is lower than another source which is including energy consumption from the household (ibid). In terms of aspects that support energy efficient building Baboli et al. [16] evaluate that the design of houses considering a moderate climate with orientation based on maximum natural light and available

courtyard. Moreover, design an environmentally friendly house is a mixed approach to interior and exterior treatment [17]. Such treatment is related to air circulation and light intake including building orientation, vegetation, type of window and roof (ibid).

Therefore, identify the characteristic of energy efficient for timber houses could help in creating and developing an optimum design and construction of the house.

2 Design and Construction of Timber House

In designing a timber house, the approach for the concept should be established since the beginning of the process. Energy efficient building approach supports a good quality of the environment. The occupant of the timber house could get benefit from their daily activity including low spending on energy needs as well as having a comfortable room. With the creativity of the designer in considering occupant needs, the building design is attractive as well as energy efficient is achieved. The construction of timber houses originally follows the principle of building strength and characteristic of wood as the main material.

Timber house design and construction has been developed in considering the characteristic of location including weather and geography local condition, the material available, man power resource and local culture. The development of traditional timber houses to a modern timber house can be found in many places including Tomohon city and Woloan village. The timber house traditionally was only one floor placed in the high level around 3 m-high from the ground. The house is supported by a structural column made by the high quality of wood. The foundation was made by the original stone.

Traditional timber house in Minahasa, North Sulawesi has been built by the ancestor since the beginning of the tribe community. A number of original timber houses can be found in North Sulawesi such as in Tomohon city and Woloan village. This area is an old area for traditional culture and house. The characteristic of traditional timber house is as shown in Table 1.

The example of a traditional timber house can be seen in the Fig. 1.

From Fig. 1, there are differences between traditional timber houses and modern timber houses. The original timber house is made of wood for all parts of the building construction. The main difference can be seen in the building structure where the column on the first floor uses high quality of wood. Traditional timber house only has a floor plan on the second floor. The first storey is an open plan design with stairs as access to the second floor. Traditionally this design aims to protect the occupant from a wild animal therefore there is no room for activity on the first floor. The example of a timber house in Fig. 1a is one of the original houses left in the area. The area is the city of Tomohon known as having a number of original traditional timber houses.

The evaluation for the traditional timber house can be divided into different aspects including the type of material, construction, quality of the material. In terms of the type of material used, the traditional house originally uses wood for the whole

Table 1 Characteristic of energy efficient timber house

No.	Part of house construction	Characteristic
1	Foundation	Material stone Place on the ground Develop into concrete with stone and concrete
2	Column	Material wood High quality of wood for structure The first floor developed into reinforcing concrete Second floor high quality of wood
3	Beam	Material wood High quality of wood for construction
4	Wall	Material wood Type of board with 30 cm wide Developed into “lammersering” smaller type of board with 10 cm wide
5	Ceiling	Material wood Type of board with 30 cm wide Developed into “lammersering” smaller type of board with 10 cm wide and gypsum
6	Roof frame	Material wood Developed into light steel
7	Roof cover	Material palm fiber, zinc board Developed into tile roof and concrete
8	Window	Material wood and glass for opening Wood for frame Developed into the glass for thermal protection For frame developed into light steel material
9	Door	Material wood for frame and opening



a



b

Fig. 1 The example of the traditional timber house. **a** Traditional house. **b** Modern timber house

construction and structure. Moreover, for the roof cover material, the original material use is made of sago palm leaves or Rumbia. The development of the traditional house is the change of material used such as the use of zinc board for the roof covered. The level of the traditional building is placed on the high area around 1.5–3 m height. For kitchen and bathroom, originally placed at the backyard separate from the main building.

The modern timber house is varied in terms of design and construction. The example in Fig. 1b is a developed timber house from traditional house design. The floor plan is available for first and second floor building. The first floor made of concrete and brick. The structure is reinforced concrete and the wall is constructed by red brick. The wall plastering with mixed cement and sand and finishing with painting. The function of the first floor is mostly similar to the second floor such as bedroom and living room. For certain function such as kitchen, is placed on the first floor. The bathroom mostly placed on the first floor while some have placed on the second floor with concrete as a construction material.

The concept of the passive house can be implemented in a timber house can be seen in Fig. 2. The main criteria are air circulation and treatment for the construction.

The implementation of the passive house concept can be applied to a different type of timber house. The window needs to be constructed with a wood frame and for opening is using the type of glass with protection from the exceed heat of the sun. Cross ventilation is important in circulating air from room to room. Good quality of window and ventilation construction help to create a comfort room with comfort temperature for the occupant. An additional device such as solar panel and thermal insulation support the energy efficient house. Solar panel contributes to the energy provided by getting energy power from the sun. Thermal insulation is placed in the wall is to protect the room from the heat from outside. The material for building construction should be chosen carefully as some material can increase the temperature of the room.



Fig. 2 Implementation concept of the passive house to timber house

3 Characteristic of Energy Efficient Timber House

The characteristic of energy efficient timber house based on a literature review and preliminary survey can be seen in Table 2.

The type of timber house in Woloan village can be seen in Table 3.

The variation of timber house is caused by the change in occupant needs, development of material and devices. The wood board, for example, has been used originally for the window opening. The change of wood board for opening on the window to the material of glass is to increase the quality of the light in the room. The change of the first floor from an open plan to a floor plan with a number of rooms is considering the need for a place for vary activities of the occupant. This changing should not decrease the quality of air circulation as well as the use of energy. The design for mezzanine in the two storeys of house support the air circulation vertically.




Based on data, the majority timber house in Woloan Village has not fully considered the use of energy efficient construction. The evaluation of energy efficient timber house can be seen in Table 4.

From the sample of a timber house, the design and construction for saving energy in a natural way are implemented due to available opening with glass material and a cross circulation system of air ventilation. The general type of floor plan with cross ventilation and window design in the house is the principle of a passive house. The passive house is a type of design in which the building control its temperature to be comforted for human due to the construction and floor plan create a space that protects the over heat from outside. With this process and supported by cross air circulation and adequate light, the energy used for light and air condition is low.

Table 2 Characteristic of energy efficient timber house

No.	Characteristic	Source
1	Floor construction	[8], traditional Minahasa house
2	Wall construction with insulation	[5]
3	Roof construction	[17]
4	Material use	[9, 11, 13]
5	Supporting appliance and device	[2, 5]
6	Spatial and orientation	[11]
7	Low energy	[10]
8	Natural light, opening	[9, 16]
9	Standard of energy use	[3]
10	Pass certified of saving energy	[1, 5]
11	Environment consideration	[10, 17]

Table 3 Type of timber house

No.	Type	Characteristic
1	Timber house one storey 	New house prefabrication
2	Timber house two storey	New house prefabrication
3	Timber house two storey not full 	New house prefabrication
4	Timber house two storey not full	Old traditional Minahasa house First floor open plan for multi-function
5	Timber house two storey full	Old house
6	Timber house two storey with mezzanine 	New house prefabrication
7	Mixed timber and concrete house	New house The first floor is concrete The second floor is timber
8	Mixed timber and concrete house	Used house The first floor is concrete The second floor is timber

Moreover, the design for the type of two-storey timber house has been developed into a variety of the second floor from a full floor plan similar to the first floor to half floor plan. This design supports natural air circulation floor to floor as well as the distribution of light.

In the design of the passive house, the development of timber construction has not included insulation on the wall and the floor. While the use of a solar panel is limited.

Table 4 Evaluation of energy efficient based on the type of timber house

No.	Type of timber house	Evaluation energy efficient	Natural light	Natural air	Material
1	Traditional timber house	No adding of solar panel	Natural light from opening window glass	Natural air circulation from ventilation with cross type	Material old timber with majority damage due to less maintenance
2	New prefabrication timber house	Adding solar panel with construction by solar panel company	Natural light from opening window glass	Natural air circulation from ventilation with cross type	New timber with vary quality Jati wood and Nantu wood
3	Mixed house of timber and concrete	Electricity power from the national electricity company	Natural light from opening window glass	Natural air circulation from ventilation with cross type	Vary the type of wood for construction First floor with concrete Second floor with timber

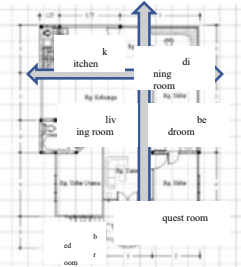
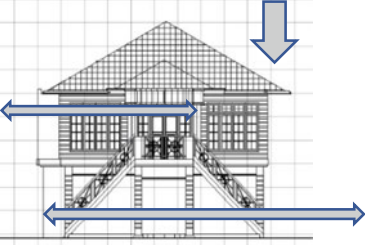
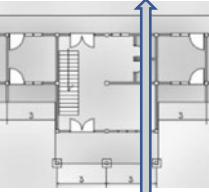

The implementation for timber house to be more energy efficient by using the less additional device and more design on timber construction to adjust the temperature of the house itself, it's crucial to be considered.

The implementation of energy efficient timber houses can be applied by design the floor plan of a timber house with cross air circulation and natural light area. Energy efficient timber houses in a traditional timber house and modern timber house from the sample houses show a different level of implementation. The design for energy timber houses can be seen in Table 5.

4 Conclusion

In conclusion, the characteristic of energy efficient timber houses based on literature study and field study are basically considered air circulation, natural light, material use, additional devices and energy use. The concept of energy efficient houses is developed widely based on consideration of environment impact including green house and passive house. Timber house is using wood as the main material which is a thermal insulator. Wood is an energy efficient material. The use of the material other than wood needs to acknowledge the effect of increasing heat due to the character of material such as glass for the window. The passive house as a concept for energy efficient houses can be applied in a timber house. The main approach is the air need to have good circulation such as the type of cross ventilation. Moreover, the use of insulation on the wall helps to protect the room from excessive heat. Timber house

Table 5 Design for energy efficient timber house

No.	Type of house	Potential energy efficient timber house
1	<p>Traditional timber house The floor plan should have cross ventilation horizontally and vertically if possible</p>  <p>Floor plan</p>	<p>Improve opening and ventilation Construct insulation on the wall Using solar panel Using glass with surface protection</p>  <p>Front view</p>
2	<p>Modern timber house The floor plan should have cross ventilation</p>  <p>Floor plan</p>	<p>Improve opening and ventilation Construct insulation on the wall Using solar panel Using glass with surface protection</p>  <p>Front view</p>

is an example of an energy efficient house. Types of timber houses are vary based on the number of storeys, material use and time of construction. Timber house has been developed from original traditional house to other types including, one storey timber house, full two-storey timber house, half full two storeys of a timber house, two storey timber houses with mezzanine and mixed timber and concrete house. The concept of energy efficient house such as a passive house, need to be maintained and have good quality control. A number of changes recently including weather conditions should be balanced with the improvement of control and standard.

Acknowledgements This research is funded by Indonesia Ministry of Research and Technology, National Research and Innovation Council under the scheme of High Institution Priority Basic Research.

References

1. Green Building Council Indonesia (GBCI) (2014) Greenship rating tools untuk rumah tinggal versi 1.0 greenship homes version 1.0, Direktorat Pengembangan Perangkat Penilaian

2. Azizah R, Wardani ED, Mardikasari, Aryani A (2017) Pengukuran greenship home pada rumah tinggal berkonsep “green” di perkotaan, *J Teknik Sipil Perencanaan* 19(1):17–24
3. Hermawan, Prianto E, Setyowati E (2015) Thermal comfort of wood-wall house in coastal and mountainous region in tropical area. *Proc Eng* 125:725–731
4. Ionescu G-L (2017) Passive house. *J Appl Eng Sci* 7(20):23–27
5. Passive House Institute ((PHI) (2016) Criteria for the passive house. *EnerPHit and PHI Low Energy Building Standard*
6. Pitts A (2017) Passive house and low energy buildings: barriers and opportunities for future development within UK practice. *Sustainability* 9:272. <https://doi.org/10.3390/su9020272>
7. Foster J, Sharpe T, Poston A, Morgan C, Musau F (2016) Scottish passive house: insights into environmental conditions in monitored passive houses. *Sustainability* 8:412. <https://doi.org/10.3390/su8050412>
8. Herniwati A (2008) Penghematan energi pada arsitektur tradisional suku kaili (rumah panggung souraja). *J SMARTek* 6(1):63–70
9. Attia AS (2019) Traditional multi-story house (Tower house) in Sana’a city, Yemen. An example of sustainable architecture. *Alexandria Eng J*
10. Shao J, Chen H, Zhu T (2016) Solar energy block-based residential construction for rural areas in the West of China. *Sustainability* 8:362. <https://doi.org/10.3390/su8040362>
11. Lazarevica D, Kauttob P, Antikainen R (2020) Finland’s wood-frame multi-storey construction innovation system: analysing motors of creative destruction. *For Policy Econ* 110:101861
12. Maleszaa J, Miedziałowski C (2017) Current directions in development of modern wood-framed houses. *Proc Eng* 172(2017):701–705
13. Hildebrandt J, Hagemann N, Thräna D (2017) The contribution of wood-based construction materials for leveraging a low carbon building sector in Europe. *Sustain Cities Soc* 34(2017):405–418
14. Lianto F (2012) Pengaruh beberapa jenis kaca dengan ketebalan tertentu terhadap rambatan panas dari sinar matahari ke dalam ruangan. *J Arsitektur Desain Teori Dan Sains* 3(1)
15. Tonooka Y, Takaguchi H, Koichi Y, Maeda T (2014) Life cycle assessment of a domestic natural materials wood house. *Energy Proc* 61(2014):1634–1637
16. Baboli FBM, Ibrahim N, Sharif DM (2015) Design characteristics and adaptive role of the traditional courtyard houses in the moderate climate of Iran. *Proc—Social Behav Sci* 201:213–223
17. Simbolon H, Nsution IN (2017) Desain rumah tinggal yang ramah lingkungan untuk iklim tropis. *J Educ Build* 3(1)

The Effect of Dominant Rainfall Duration on the Planning of Dimensions of Infiltration Well and the Reduction of Surface Runoff



Sri Amini Yuni Astuti and Dinia Anggraheni

Abstract To overcome the risk of flooding, as well as in the framework of ground-water conservation efforts, many infiltration wells built. The dominant rainfall duration (duration of rains that often occur in an area) is to determine the dimensions and amount of the wells. Thus in this paper will be discussed the influence of the dominant rain duration on the planning of dimensions and the amount of the needed infiltration wells, and which are worthy to be built based on the limitations of existing land. The planning of the infiltration wells used the Sunjoto method. The study location was on the integrated campus UII. Rainfall data was taken from Prumpung station in 1998–2016. The greater the longer the dominant rain duration will require a greater number and dimension of infiltration wells. With the limitations of existing land, the larger the longer the dominant rain duration is used, the reduction of surface runoff is almost the same, not much change.

Keywords Dominant rain duration · Dimensions of infiltration wells · Sunjoto method

1 Introduction

1.1 Background

Water is needed by humans to fulfill various needs of his life, namely: for human needs, industrial, public needs, watering crops, irrigation, toilets, and flushing waste. For the water needs to be fulfilled, the groundwater conservation business must be done. Many buildings are already known for groundwater conservation efforts, including reservoirs, infiltration wells, recharge channels, recharge garden, and biopori.

S. A. Y. Astuti (✉) · D. Anggraheni
Faculty of Civil Engineering and Planning of Islamic, University of Indonesia, Yogyakarta, Indonesia
e-mail: amini_yuni@uii.ac.id

This paper explained the infiltration wells, which is about the influence of the dominant rainfall duration against the dimension of the wells and the runoff of the surface. It is important, because sometimes in an area of unknown data about the rainfall duration that often occur. So this article discussed how far it affected. For the study location, a case of a drainage system was taken at the UII Integrated campus area, which was at the river of Kimpulan.

1.2 The Problem, Objectives and Benefits

From the explanation above, it can be expressed the problem was how big is the influence of the dominant rain that occurred in the campus area integrated UII against the dimension of wells? And how big is the influence of the dominant rain occurring in the campus area integrated UII against the reduction of surface runoff in the area?

This paper was written with the following objectives, those are to know how big the influence of the dominant rainfall occurred in the campus area integrated UII against the dimensions of wells, and to know how big the influence of the dominant rainfall occurred in the campus area integrated UII against the reduction of surface runoff in the area.

The advantage of this paper can know the influence of the dominant rainfall duration on the dimensional planning of the infiltration wells and the reduction of surface runoff occurring in an area, so that if later will plan the dimension of infiltration wells in an area, the capture of the dominant rainfall duration becomes not a problem, if not known data.

2 Previous Research

2.1 Reduction of Drainage Channel Dimension Due to the Existence of Recapan Wells in Maguwoharjo Drainage Network–Wedomartani, Sleman (Purnomo, SN, 2013)

The problem of this research was in the development of developing land, these developments must be followed by the management of integrated drainage of the environment. The concept of drainage planning that removes water immediately from the land can only reduce flooding but does not preserve the preservation of groundwater. Therefore planned infiltration wells a groundwater conservation efforts.

The runoff discharge was sought to use rational methods, while the design of the wells was used Sunjoto method.

The results showed that the discharge of runoff before the presence of infiltration wells ranged from 8 m³/sec to the residential land and 3 m³/sec on the paddy fields and

the moor. After the infiltration well was built, the average runoff discharge reduced to 36%. Then the cross-section of drainage channels on residential land reduced 50%, and on rice fields and the field can reduce 30% [1].

2.2 Diameter Effect on the Number of Infiltration Wells (Case Study on Commercial Buildings on JL Kaliurang Km 12–13) (Astuti and Prasajo)

Excessive groundwater intake resulted in a rapid groundwater drop, which could disrupt the ecosystem balance in the integrated UII campus area. To overcome it should be considered groundwater conservation using infiltration wells. This research aims to analyze the influence of the use of diameter size to the number of needed infiltration wells.

This research used the Sunjoto method. This method took into account the water catchment as an unfixed flow, depending on the height of the face. Calculated the number of wells needed with a diameter of 0.6 m, 0.8 m, 1 m, and 1.2 m, at 5 locations commercial building on JL Kaliurang Km 12 Sleman Jogjakarta.

The results showed the use of smaller diameters would require more amount of wells. The effectiveness of the wells depends on the type of soil (permeability) and the dimensions of wells (diameters). To design the infiltration wells, it is recommended to calculate several possible diameters. Selected diameter with the highest effectiveness value and consider the ability of local conditions [2].

2.3 Planning of Infiltration Wells for Groundwater Conservation in a Residential Area (Case Study in Housing RT. II, III, and IV Perumnas East Circumference of Bengkulu) (Iriani et al. 2013)

Increased development of life facilities in the community triggered the change of land use which caused the reduction of open land as a land of infiltration. This leads to the flow of the surface (runoff) and rainwater absorbed by the soil slightly. For that, it is necessary to make fitting in the form of a recent well that serves to hold the rainwater into the soil slowly. The purpose of this research is to know the amount and construction of the infiltration wells. The research was held in the housing of RT. II, III, and IV Perumnas east of Bengkulu City with a total of 153 units.

This research used a survey method of measurement, questionnaire/interview, and a test of an extension to obtain the required data.

Based on the data and analysis of the calculation by SK SNI 03-2453-2002, can be determined the wells that shape a circle with a diameter of 1 m and a depth of 3 m for individual catchment wells, while communal infiltration wells circle diameter of

1.4 m and a depth of 3 m as many as 92 pieces. Another alternative is rectangular-shaped infiltration wells with a width of 1.2 m and a depth of 1.5 m for individual catchment wells, while communal infiltration wells with a rectangular width of 1.4 m and a depth of 3 m as many as 72 pieces. Construction of appropriate infiltration wells according to the technical directive on the implementation of environmental-oriented drainage in residential areas (2002) was a wall of brick or red bricks without dips and between the pair is given holes [3].

2.4 The Study on Preventing Surface Run off by Using an Infiltration Well (Case Study in the Region of Perumnas Made Lamongan Regency) (Saleh 2011)

The growth of population and the rapid development of civilization causes changes in land use function. Many lands that were originally open land or forest turned into a residential and industrial area. Not only the urban area but has been expanded in cultivated and protected areas, which serve water. The impact of the land-use change will result in an increased risk of flooding. The same thing happened in Perumnas. To prevent this and also to preserve groundwater, this study was conducted. This study aims to reduce the runoff of surfaces and to increase the potential groundwater.

The water building design in this study was an infiltration well of rainwater. The well can accommodate the rain and surface runoff. The infiltration wells in the study designed in each home.

The results of the analysis obtained the total volume of rainfall with a return period of 2 years is $= 2627.468 \text{ m}^3$ while the total volume of wells is 3022.5 m^3 . Designed wells with the radius of a circle from 0.45 to 0.75 m with variations to the depth of the wells ranged from 1.6–2.9 m. So the well is very effective to hold the whole runoff with rain by 2 years of the return period [4].

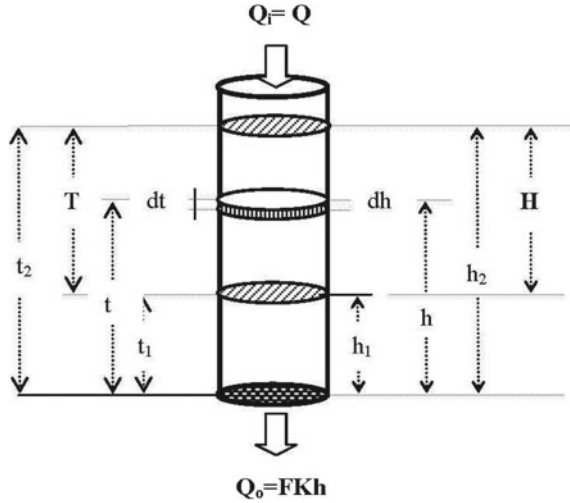
3 Theory

3.1 Infiltration Well

The well is the hole to infiltrate water into the ground, while the well of drinking water serves to take the groundwater to the surface. Thus the construction and depth are different. The wells were dug with the depth above the groundwater, while the wells of drinking water were dug deeper or under the ground waterfront.

The working principle of wells is channeling and accommodating rainwater into a hole or well so that water can be gradually absorbed into the ground. So, the water will go a lot more into the ground and little is flowing as the surface flow (runoff).

Fig. 1 The unsteady flow approach to the infiltration well



Sunjoto in 2011 proposed formula as the basis for calculating the depth of the wells as follows [5]. The rain that falls on the roof of the building will be poured into the infiltration well, then it will seep into the ground. Flow mechanism follows an unsteady flow (Fig. 1).

$$Q_i = \text{discharge due to rain falling on the roof} \\ = Q$$

$$Q_o = \text{discharge which seep in to the ground} \\ = F.K.h$$

There are equation: The volume of water in the well = $(Q_i - Q_o).dt$

$$A_{well}.dh = (Q - F.K.h).dt$$

$$\pi.R^2.dh = (Q - F.K.h).dt$$

$$dt = \frac{\pi.R^2}{(Q - F.K.h)}dh$$

$$\int_{t_1}^{t_2} dt = \int_{h_1}^{h_2} \frac{\pi.R^2}{(Q - F.K.h)}dh$$

$$\int_{t_1}^{t_2} dt = \frac{\pi \cdot R^2}{-F \cdot K} \int_{h_1}^{h_2} \frac{d(Q - F \cdot K \cdot h)}{(Q - F \cdot K \cdot h)}$$

If $t_1 = 0$, $t_2 = T$, $h_1 = 0$ and $h_2 = H$

$$\int_0^T dt = \frac{\pi \cdot R^2}{-F \cdot K} \int_0^H \frac{d(Q - F \cdot K \cdot h)}{(Q - F \cdot K \cdot h)}$$

$$T = \frac{\pi \cdot R^2}{-F \cdot K} [\ln(Q - F \cdot K \cdot H) - \ln Q]$$

$$-\frac{F \cdot K \cdot T}{\pi \cdot R^2} = \ln \frac{(Q - F \cdot K \cdot H)}{Q}$$

$$e^{-\frac{F \cdot K \cdot T}{\pi \cdot R^2}} = 1 - \frac{F \cdot K \cdot H}{Q}$$

$$H = \frac{Q}{F \cdot K} \left(1 - e^{-\frac{F \cdot K \cdot T}{\pi \cdot R^2}}\right) \quad (1)$$

With:

- H is the depth of well
- Q is discharge flow due to rain falling on the roof
- F is the geometry factor
- K is soil permeability
- T is t_d (dominant rain duration)
- R is the radius of the infiltration well

The geometry factor is a value that represents the shape of the well tip, its appearance, radius, wall tightness and its placement in the soil layer. Dominant rain duration is the duration of rain that most often occurs on an area.

Soil permeability coefficient is the ability of soil grain to drain liquids. Permeability expressed as the speed of liquid flowing through an ingredient (soil, rocks). The permeability value can be obtained using measuring in the field namely by using the method of tracer material and 2 test wells to be observed. Or it could also be considered the same as the constant infiltration rate. More details can be found in groundwater hydrology book [6].

The function of the wells is to reduce the runoff of the surface and to raise the face of groundwater or groundwater conservation efforts.

To determine the required number of wells, first determine the discharge capacity of one well, by changing the above equation to be the following.

$$Q_{1well} = \frac{F \cdot K \cdot H_{1well}}{\left(1 - e^{-\frac{F \cdot K \cdot T}{\pi \cdot R^2}}\right)} \tag{2}$$

$$n_{wells} = \frac{Q}{Q_{1well}} \tag{3}$$

3.2 Hydrological Cycles

A hydrological cycle is a process that begins with the evaporation of water by sunlight then if in a condition that allows the moisture to condense, and will be a grain of rainwater that will fall to the Earth. Before reaching the ground, some rainwater will be held in plants and buildings. And some others reach the surface of the ground, some are flowing at the surface of the ground as water runoff and some are pervasive (infiltration) in the soil layer. The magnitude of runoff and infiltration depends on the soil parameters or soil type. The water runoff flows on the ground surface then through the channels, lakes, rivers to the sea. While water infiltration pervasive in the soil layer, it will be the high-level water level of the ground in the soil layer. It also flows in the ground towards the lowest face of the water, eventually also the possibility of arriving at lakes, rivers, and seas. The process will then repeat, starting from the evaporation process and forming a cycle [7].

3.3 Area Rainfall

The rainfall data obtained from rainfall gauge which is measures rainfall occurs only at one place or point only (rainfall station). Given the rain is very varied against the place (space), then for a large area, one of the rainfall gauges cannot yet describe the rain of the region. In this case, it is necessary to rain the area obtained from the average price of rainfall some of the rainfall stations that are in and/or around the area [7].

The method to obtain the area rainfall used in this study was The Thiessen polygon method with the following formula.

$$\bar{p} = \frac{A_1 \cdot p_1 + A_2 \cdot p_2 + A_3 \cdot p_3 + \dots + A_n \cdot p_n}{A_1 + A_2 + A_3 + \dots + A_n} \tag{4}$$

3.4 Frequency Analysis

In hydrology there are several ways of obtaining flood magnitudes, such as empirical means, statistics, and analysis with models [8]. The statistical way is considered best, as it bases the analysis on measured debit data in rivers. It's certainly very dependent on the quality of the data available. The quality of the data is not good cannot be expected results in good analysis. In statistical sciences known several kinds of frequency distribution and four types of distribution are widely used in the field of hydrology is Normal distribution, Log-Normal, Log-Person III, and Gumbel.

3.5 Rational Formula

If the data was available, then design the discharge. One of the ways is used rational formula [9], which is expressed as follows.

$$Q = 0.002778 \times C \times I \times A \quad (5)$$

With:

- Q is discharge runoff due to rain (m^3/s)
- C is the direct runoff coefficient of the roof of the house or another
- I is the rain intensity (mm/h)
- A is the roof area (ha) (for the design of infiltration well)
- A is the catchment area (ha) (for the design of channel capacity)

3.6 Rainfall Intensity

The rain intensity is calculated using the Mononobe formula expressed as follows [9].

$$I = \frac{R_{24}}{24} \left(\frac{24}{t} \right)^{\frac{2}{3}} \quad (6)$$

With:

- I is the rain intensity in mm/h
- R is the design Rain (daily) in mm
- t is t_d (the dominant rain duration (hours)) for the design of discharge wells
- t_c (the concentration–time (hours)) for the design of channel capacity

To estimate the concentration–time can use the equation developed by Kirpich (1940) in [9], which can be written as follows.

$$t_c = \left(\frac{0.87 \times L^2}{1000 \times S_o} \right)^{0.385} \quad (7)$$

With:

t_c concentration Time (hours)

L length of the main channel from upstream to drain (km)

S_o slope of the main channel.

4 Methodology

The research location was at UII campus. Data required in the form of data includes soil permeability coefficient, maximum daily rainfall data from the year 2007–2016 at Prumpung Rainfall Station, coordinate of rainfall station, and topography of UII integrated campus. Here is the flowchart of this study (Fig. 2).

5 Data Analysis

5.1 Data

It is known that the drainage channel system of the integrated campus of UII in the Kimpulan River is as follows (Fig. 3).

The channel condition can be seen in Table 1.

5.2 Discharge of Surface Runoff Without Infiltration Wells

From previous research known R_5 is 122.836 mm. Then rain intensity can be calculated as Table 2.

Subsequently, it can be calculated discharge of the surface runoff without infiltration wells, as Table 3.

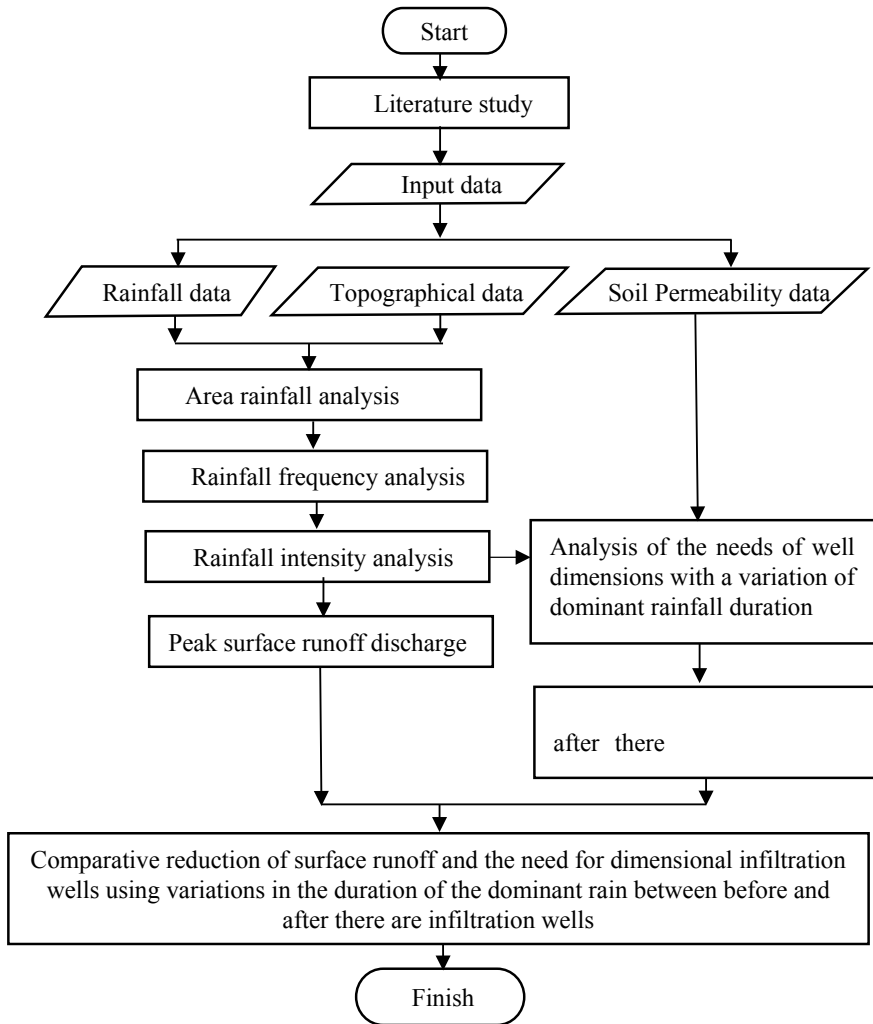


Fig. 2 Flowchart study

5.3 Discharge of Surface Runoff with Infiltration Wells

Can be calculated that for the $t_d = 2$ h, 1.5 h and 1 h, consecutive value of rain intensity (I) is 26.8268, 32.4983, and 42.5849 mm/hour. Then, it can be calculated discharge runoff from the roof, as Table 4.

With the limitations of existing land and with the well-aware value of soil permeability, it can be sought the number of wells and discharge of runoff that can enter the infiltration wells, see Table 5.

Fig. 3 UII campus drainage channel system chart

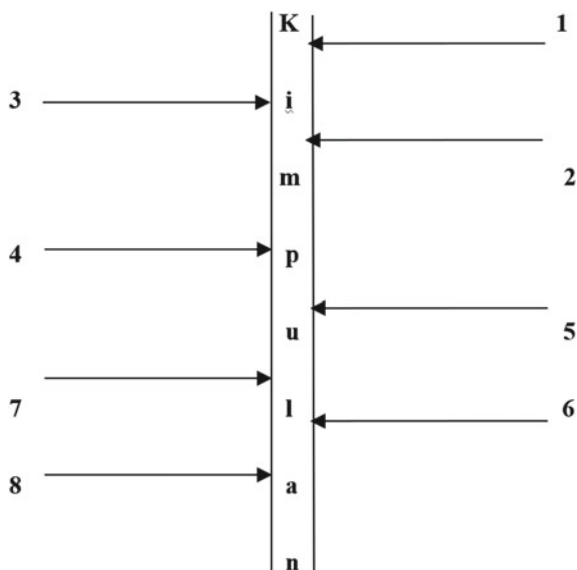


Table 1 The UII campus drainage channel system data

Channel	L (Km)	S	C	A (ha)
1	0.188	0.0102	0.6	0.072
2	0.232	0.0235	0.474	2
3	0.198	0.0223	0.6	0.065
4	0.254	0.0028	0.556	1
5	0.073	0.0122	0.6	0.027
6	0.176	0.0051	0.673	0.477
7	0.227	0.0274	0.6	0.082
8	0.177	0.0315	0.408	0.7

Table 2 Time concentration and rain intensity

Channel	L (Km)	S	t_c (hour)	R_{5th} (mm)	I (mm/hour)
1	0.188	0.0102	0.1070	122.836	188.909
2	0.232	0.0235	0.0913	122.836	210.088
3	0.198	0.0223	0.0824	122.836	224.848
4	0.254	0.0028	0.2220	122.836	116.163
5	0.073	0.0122	0.0482	122.836	321.444
6	0.176	0.0051	0.1328	122.836	163.566
7	0.227	0.0274	0.0846	122.836	220.991
8	0.177	0.0315	0.0662	122.836	260.247

Table 3 Discharge runoff surface without infiltration wells

Channel	C	I (mm/hour)	A (ha)	Q (m ³ /s)
1	0.6	188.908569	0.072	0.0227
2	0.474	210.088475	1.784	0.4935
3	0.6	224.847861	0.065	0.0244
4	0.556	116.163021	1.446	0.2594
5	0.6	321.443957	0.027	0.0145
6	0.673	163.565543	0.477	0.1459
7	0.6	220.991048	0.082	0.0302
8	0.408	260.246807	0.7	0.2065

Table 4 Discharge of surface runoff from a roof

Channel	Building	Roof coef.	Roof area (ha)	Q (m ³ /s) from roof		
				t _d = 2 h	t _d = 1.5 h	t _d = 1 h
1	–			0	0.0000	0.0000
2	Recto-rate	0.9	0.119	0.0080	0.0097	0.0127
	GKU	0.9	0.123	0.0082	0.0100	0.0131
	HI	0.9	0.204	0.0137	0.0166	0.0217
	D3 economic	0.9	0.127	0.0085	0.0103	0.0135
	FIAI (new)	0.9	0.128	0.0086	0.0104	0.0136
3	–			0.0000	0.0000	0.0000
4	TBK laboratory	0.9	0.133	0.0089	0.0108	0.0142
	FPSB and FK	0.9	0.366	0.0245	0.0297	0.0390
5	–			0.0000	0.0000	0.0000
6	Mosque	0.9	0.2	0.0134	0.0163	0.0213
7	–			0.0000	0.0000	0.0000
8	Library	0.9	0.19	0.0127	0.0154	0.0202

When viewed in Table 5, the longer the value of t_d (dominant rainfall duration) tends to be more and more wells needed. It happened because according to the Formula (1), the number and dimensions of the wells are directly proportional to the t_d .

Furthermore, it can be sought to discharge surface runoff with the presence of infiltration wells (Table 6).

Table 5 The number of wells and discharge of runoff that can enter the infiltration wells

Channel	Building	n wells (unit)			Q wells (m ³ /s)		
		t _d = 2 h	t _d = 1.5 h	t _d = 1 h	t _d = 2 h	t _d = 1.5 h	t _d = 1 h
1	–						
2	Recto-rate	6	6	6	0.0080	0.0097	0.0127
	GKU	8	7	7	0.0082	0.0100	0.0131
	HI	13	13	11	0.0136	0.0166	0.0217
	D3 economic	8	8	7	0.0085	0.0103	0.0135
	FIAI (new)	9	8	7	0.0086	0.0104	0.0136
3	–						
4	TBK laboratory	6	6	6	0.0089	0.0108	0.0142
	FPSB and FK	14	14	14	0.0146	0.0192	0.0284
5	–						
6	Mosque	13	12	11	0.0134	0.0163	0.0213
7	–						
8	Library	13	12	10	0.0127	0.0154	0.0202

Table 6 Discharge surface runoff with the presence of infiltration wells (without the rain falling on the roof)

Channel	Building	C	I (mm/hour)	A land area, without roof (ha)	Q surface runoff (m ³ /s)
1	–	0.6	188.9086	0.0720	0.0227
2	Recto-rate	0.188	210.0885	1.0830	0.1188
	GKU				
	HI				
	D3 economic				
	FIAI (new)				
3	–	0.6	224.8479	0.0650	0.0244
4	TBK laboratory	0.374	116.1630	0.9470	0.1143
	FPSB and FK				
5	–	0.6	321.4440	0.0270	0.0145
6	Mosque	0.51	163.5655	0.2770	0.0642
7	–	0.6	220.9910	0.0820	0.0302
8	Library	0.225	260.2468	0.5100	0.0830

5.4 Reduction of Surface Runoff

From Table 7 above, it can be seen that the use of a variation of t_d (dominant rainfall duration) is not so influential on the reduction of surface runoff, the value is almost

Table 7 Reduction of surface runoff without and with presence infiltration wells

Channel	Building	Q discharge surface runoff without infiltration wells (m ³ /s)	Q discharge surface runoff with infiltration wells (m ³ /s)			Reduction of runoff (m ³ /s)		
			t _d = 2 h	t _d = 1.5 h	t _d = 1 h	t _d = 2 h	t _d = 1.5 h	t _d = 1 h
1	–	0.0227	0.0227	0.0227	0.0227	0	0	0
2	Recto-rate	0.4935	0.1189	0.1188	0.1188	0.3746	0.3747	0.3747
	GKU					0	0	0
	HI					0	0	0
	D3 economic					0	0	0
	FIAI (new)					0	0	0
3	–	0.0244	0.0244	0.0244	0.0244	0	0	0
4	TBK laboratory	0.2594	0.1242	0.1248	0.1249	0.1352	0.1346	0.1345
	FPSB and FK					0	0	0
5	–	0.0145	0.0145	0.0145	0.0145	0	0	0
6	Mosque	0.1459	0.0642	0.0642	0.0642	0.0817	0.0817	0.0817
7	–	0.0302	0.0302	0.0302	0.0302	0	0	0
8	Library	0.2065	0.0830	0.0830	0.0830	0.1235	0.1235	0.1235
		1.1970	0.4820	0.4825	0.4826	0.7150	0.7145	0.7144
Reduction of run off (%)						59.73	59.69	59.68

the same. So if in an area there is no data about t_d (dominant rain duration), then used t_d 2 h or 1 h does not matter.

6 Discussion

In previous studies, all of them used t_d = 2 h. This follows the book which says about the Sunjoto method. In the book, it does not say why using t_d = 2 h. Just use the assumption that the rain that often happens is 2 h. So it does not use real dominant rainfall data. Therefore, it is necessary to ask the actual extent of the influence of the dominant rain duration. From the data analysis above, it can be known that the use

of dominant rainfall does not significantly affect the reduction of surface runoff in an area. However, it affects the number and dimensions of infiltration wells.

The greater the t_d value, the greater the dimension of the infiltration well. The number of infiltration wells is determined by the potential land area and the dimensions of one infiltration well. Infiltration wells should be built on land that has a deep enough groundwater level and is not too close to the foundation of a building.

If the available land in an area is limited, not all of the discharge due to rain falling on the roof can be entered into infiltration wells.

The number of infiltration wells is calculated by the load discharge divided by the discharge of one infiltration well. The number of infiltration wells cannot be calculated from the required well depth divided by one well depth, because the infiltration flow approach is an unsteady flow, depending on the elevation of the review point. With the same depth length but with different elevations, the permeate discharge will be different.

7 Conclusions and Suggestions

7.1 Conclusions

From the explanation above, it can be concluded that the longer the value of t_d (dominant rainfall duration) tends to be more and more wells needed and the use of a variation of t_d (dominant rainfall duration) is not so influential on the reduction of surface runoff, the value is almost the same.

7.2 Suggestion

This study can be suggested: if it will design a drainage wells system in an area, then use the t_d (dominant rain duration) data in the area. If the data is not there, then use $t_d = 2$ h or $t_d = 1$ h, no problem.

References

1. Purnomo SN (2013) Dimension reduction of drainage channels due to the existence of infiltration wells in drainage networks. *Dinamika Rekayasa* 9(1):13–19
2. Prasjo RA, Astuti SAY (2015) Comparison of design of rain water infiltration wells using Sunjoto method and SNI 03-2453-2002 in commercial buildings on Jalan Kaliurang Km 12 Sleman. *J Teknisia* XX(2):142–153
3. Iriani K, Gunawan A, Bisperi (2013) Rainwater absorption well planning for groundwater conservation in the Bangkulu circle housing Perumnas. *J Inersia* 5(1)

4. Saleh C (2011) Study of surface runoff management by using infiltration wells (case study in the Perumnas made area of Lamongan regency. *Media Teknik Sipi* 9(2):116–124
5. Sunjoto (2015) Pro-air drainage technique. Gadjah Mada University, Yogyakarta
6. Purnama S (2010) Groundwater hydrology. Publisher Kanisius, Yogyakarta
7. Triatmojo B (2013) Applied hydrology. Beta Offset, Yogyakarta
8. Sri Harto (1985) Applied hydrology. BP KMTS FT UGM, Yogyakarta
9. Suripin (2004) Sustainable Urban drainage system. Andi Offset, Semarang

Evaluation of Hot Mix Asphalt Mixtures Design Modified with Hydrate Lime



Noorfaizah Hamzah, Nur'Ain Mat Yusof, Adnan Derahman,
and Mustaqiim Mohamad

Abstract Most road surfaces are paved with asphalt concrete, but there are frequent occurrences of rutting, cracking and, in particular, stripping of the pavement due to the effects of traffic flow, thermal variation and water erosion caused by rain. In this research, a number of experiments have been conducted to examine the efficacy of anti-stripping fillers, including Hydrate Lime as an additive anti-stripping agent, in a mixture of asphalt concrete. A sample of asphalt concrete is placed in a 1000 ml beaker with approximately 500 ml of water and heated to boil. The 250 g of loose HMA mixture was heated at a maximum temperature of 100 °C (212 °F) but not less than 80 °C (176 °F) and immersed in boiling water for 24 h in order to evaluate the perforation of stripping in these mixtures. The Lottman test is performed to evaluate the effect of moisture with hydrated lime as anti-stripping and to measure the effect of water on the tensile strength of the paving mixture. The Marshall Test is performed to determine the optimum bitumen. The value of the optimum bitumen is important for the design of the mixtures in order to indicate other mix performance tests and to obtain the value of flow, stability, air void and other parameters. Statistical analysis is carried out to evaluate the significance of hydrated lime for the stripping performance of the HMA mixture. The evaluated information indicates that this filler can increase the ability of the asphalt concrete to withstand stripping of the road surface and thus increase durability. The results provide a good reference for road construction with similar regional road characteristics in Malaysia.

Keywords Hot mix asphalt · Hydrate lime · Lottman test · Marshall test

N. Hamzah (✉) · A. Derahman · M. Mohamad
School of Civil Engineering, College of Engineering, Universiti Teknologi MARA (UiTM),
40450 Shah Alam, Selangor, Malaysia
e-mail: noorfaizah1209@uitm.edu.my

N. Mat Yusof
School of Civil Engineering, College of Engineering, Universiti Teknologi MARA Pahang
Branch, 26400 Bandar Tun Abdul Razak, Jengka, Pahang, Malaysia

© The Author(s), under exclusive license to Springer Nature Singapore Pte Ltd. 2022
S. Belayutham et al. (eds.), *Proceedings of the 5th International Conference on Sustainable
Civil Engineering Structures and Construction Materials*, Lecture Notes in Civil
Engineering 215, https://doi.org/10.1007/978-981-16-7924-7_98

1493

1 Introduction

The Public Works Department alone is responsible to the total extend of Malaysia roads network for about 61,075.32 km of paved roads and 18,428.84 km of unpaved roads and the Malaysia government spends on average MYR 950 million in year 2005 for construction, maintenance and rehabilitation (JKR, 2005). Malaysian economic growth in rural areas has been triggered by good and safe roads and highways network system. Highway pavement design in Malaysia has been adopting the Marshall Method of mix design. Unfortunately, this design method does not account for local environment and materials characteristic that contributed to pavement failure on Malaysian roads.

One of the most common problems in flexible pavement in Malaysia is aggregate stripping. Stripping of the pavement has been defined as weakening or eventual loss of the adhesive bond usually in the presence of moisture between the aggregate surface and the asphalt cement in a Hot Mix Asphalt (HMA) pavement or mixture. When a weakening in the bond occurs, loss of strength of the HMA can be sudden. Typically, stripping starts at the bottom of the HMA layer then propagate upward. Stripping is one of the most difficult distresses to identify in HMA pavements from surface examination because the surface appearance can take various forms such as rutting, shoving, raveling, or cracking.

Currently, there are a number of additives that are available that can be added to the HMA mixture as a solution to the stripping problem and hence, create a high-performance pavements characteristic. For many years, polymers are used to modify asphalt cement to increase the high temperature stiffness of the HMA mixture which can reduce the probability of pavement failures. Previous research showed that the incorporation of rubber or polymers to bitumen also has beneficial effects on bitumen binders on road pavement. It would decrease the thermal susceptibility and permanent deformation under load (rutting) and increased the resistance to low temperature cracking [1].

Besides that, hydrated lime in asphalt pavements can reduce stripping, rutting, cracking, and aging. Hydrated lime substantially improves each of these properties when used alone, and works well in conjunction with polymer additives, helping to create pavement systems that will perform to the highest expectations for many years. Typically, the amount of hydrated lime added is 1–2% by weight of the mix, or 10–20% by weight of the liquid asphalt binder. Many states with different climates and road conditions report that modifying hot mix asphalt with hydrated lime will add years to pavement life. Field studies confirm that lime-treated pavements last longer for example, a Nevada study concludes that lime increases pavement life by 38% [1, 2]. Mechanistic-empirical modelling further demonstrates lime's benefits in asphalt. Dynamic modulus (E^*) testing of seventeen different asphalt mixtures based on six different project sites across the United States shows that the addition of hydrated lime increases the dynamic modulus of the HMA mix between 17 and 50% [2].

Several highway agencies have proven the effectiveness of lime with cold-in-place recycled (CIR) mixtures. Lime treatment of the CIR mixtures can increase their initial stability which allows the early opening of the facility to traffic and improves their resistance to moisture damage which significantly extends the useful life of the pavement.

1.1 Stripping Failure in Malaysia

Stripping of aggregate from asphalt binder has been a common problem that results in premature pavement failures in Malaysia. Malaysia being in tropical climate receives a significant amount of rainfall throughout the year. Stripping occurs when the bond between the asphalt cement and the aggregate breaks down due to the presence of moisture, and the binder separates from the aggregate [3]. Certain types of aggregates are particularly susceptible to stripping. In addition to that chemical phenomenon, environmental characteristics such as heat, heavy rains, freeze/thaw cycles, and traffic play a major role in stripping.

The most serious consequence of stripping is the loss of strength and integrity of the pavement. Stripping failures within the asphalt pavement structure can translate into various types of pavement failure such as fatigue cracking, rutting, raveling and potholes. This condition makes driving dangerous, and driving comfort and safety are often compromised. The damage of asphalt pavements due to moisture also can significantly increase the maintenance costs of a pavement and ultimately, reduce the life of the pavement.

Due to these problems, asphaltic concrete can be optimized in many ways to create high performance pavements. Hydrated lime (lime produced by just adding enough water to quicklime to slake it), is one of the modifiers that improves performance of asphaltic pavement to overcome the above short comings. Hydrated lime is the most effective anti-stripping agent available and is universally used to deal with serious stripping problems certain types of aggregates are particularly susceptible to stripping. When lime is added to hot mix, it reacts with aggregates, strengthening the bond between the bitumen and the stone, while it treats the aggregate, lime also reacts with the asphalt itself. Lime reacts with highly polar molecules that can otherwise react in the mix to form water-soluble soaps that promote stripping.

The objective of this research is to evaluate HMA stripping performance, in the mix design; to evaluate the effects of percentage of anti-stripping additive on asphalt mixtures using performance tests; and to determine the suitability of HMA mixture with hydrate lime as additives to address Malaysian condition.

2 Hydrated Lime as Stripping Agent

Hydrated lime has been widely used as an ASA for reducing the moisture susceptibility of HMA. Some other solid ASAs used are Portland cement, fly-ash, flue dust, etc. The liquid ASAs used include liquid amines and diamines, liquid polymers, etc. Addition of lime is the most accepted way to reduce the moisture susceptibility of HMA in many parts of the country. The general practice is to add 1–1.5% of lime by the dry weight of the aggregate to the mix. If the aggregate contains more fines, more lime may be required to be added to the mix due to the increased surface area of the aggregate. Generally, three forms of lime are used in HMA: Hydrated Lime ($\text{Ca}(\text{OH})_2$), Quick Lime (CaO), and Dolomitic Lime [3].

When lime is added to hot mix, it reacts with aggregates, strengthening the bond between the bitumen and the stone. While it treats the aggregate, lime also reacts with the asphalt itself. Lime reacts with highly polar molecules to inhibit formation of water-soluble soaps that promote stripping. When those molecules react with lime, they form insoluble salts that no longer attract water [4]. Rigorous testing designed to simulate long-term performance (e.g., multiple freeze–thaw cycles) can be used to demonstrate lime's superior anti stripping properties. In addition, the dispersion of the tiny hydrated lime particles throughout the mix makes it stiffer and tougher, reducing the likelihood the bond between the asphalt cement and the aggregate will be broken mechanically, even if water is not present [4, 5].

3 Experimental Work

There are two main laboratory testing involves which is The Boiling Water Test (ASTM D 3625) [6] is a subjective test for the effects that moisture has on a particular HMA mix. It is used primarily as an initial screening test of HMA mix and Lottman Test, this test method covers procedures for preparing and testing asphalt concrete specimens for the purpose of measuring the effect of water on the tensile strength of the paving mixture. In addition, Marshall Test also is performed to determine the optimum bitumen.

3.1 Materials

Gradation Selection The gradation is referred from the Standard Specification for Road Works, JKR/SPJ/rev2008. Table 1 shows the gradation limit for Asphalt concrete.

Hydrate Lime The Hydrate Lime were supplied by the UiTM Pavement Laboratory and was sieve until it is passing 75 μm of sieve size. Then the Hydrate Lime was mix together with the Pan as filler in HMA mix design. Every sample of HMA mix design

Table 1 Gradation limit for ACW14

Sieve size	Percentage passing (%)	Percentage retained (%)	Weight (g)	Accumulate weight (g)	Control point
20 mm	100	–	1200	0	100
14 mm	95	5	1140	60	90–100
10 mm	81	14	972	228	76–86
5 mm	56	25	672	528	50–62
3.35 mm	47	9	564	636	40–54
1.18 mm	26	21	312	888	18–34
0.425 mm	18	8	216	984	12–24
0.105 mm	10	8	120	1080	6–14
0.075 mm	6	4	72	1128	4–8
Pan	0	–	1200	72	–

was added with Hydrate Lime and the amount of Hydrate Lime for one sample is 25% from the weight of the aggregate that retain the Pan. The total weight of aggregates and Hydrate Lime is summarized in Table 2.

Binder The amount of the binder is various from 4.0 to 6.0% for ACW 14 JKR Standard, and the percentage of binder is stated in Table 3.

Aggregate Preparation Aggregate was selected, have a suitable shape and cleaned out from dust of other materials. Aggregate was dried to a weight set at a temperature of 105 °C to 110 °C and aggregates are sieve to the respective grades. Next, the weight of each grade of aggregate grading was calculated and the results were recorded.

Mixture Preparation (i) Aggregate grade needed was weight to make a mixture, when compressed in the mould to be 63.5 mm high for Marshall Compaction. (ii) Bitumen was heated to the 110 °C temperature. (iii) Aggregate was heated in oven

Table 2 Total weight of aggregates and hydrate lime filler

Weight of aggregates (g)	Weight of hydrate lime filler (25%) (g)	Total weight (g)
1200	6.5	1206.5

Table 3 Percentage of binder

Percentage of binder (%)	Weight of binder (g)	Total weight (g)
4.0	48	1248
4.5	54	1254
5.0	60	1260
5.5	66	1266
6.0	72	1272

Fig. 1 Aggregate heated in oven



to the 200 °C temperature as shown in Fig. 1. (iv) Separated aggregate was mixed in the fireplace. (v) When the temperature becomes 110 °C, mix the bitumen until it well blended. (vi) The mixture was compacted using 75 blows for both side of sample. (vii) The sample was taken out from mould and leaves it until the next day.

3.2 Marshall Stability Test

The dimension and specifications of the Marshall apparatus are explained in ASTM D1559 [6]. The diameter of the specimen is 101.6 and nominal thickness is 63.5 mm.

The test procedure: (i) Three specimens were prepared according to the Standard are immersed in a water bath for 30 and 40 min or in an oven for 2 h at 60 ± 1.0 °C. (ii) The test testing heads and guide rods are thoroughly cleaned, guide rods lubricated and head maintained at a temperature between 21.1 and 37.8 °C. (iii) A specimen is removed from the water both or oven, placed in the lower jaw and the upper jaw placed in position. The complete assembly is then placed in the Marshall Stability and flow machine and the flow meter is adjusted to zero. (iv) The load is applied to the specimen at a constant strain rate of 50.8 mm/min until the maximum

load is reached. The maximum force and flow at the force are read and recorded. The maximum time that is allowed between removal of the specimens from the water bath and maximum load is 30 s. (v) The applied load must be corrected when thickness specimen is other than 63.5 mm by using the proper multiplying factor.

3.3 The Boiling Water Test (ASTM D 3625)

The boiling water test is a visual rating of the degree of stripping after boiling the loose HMA mixture for 10 min. The boiling water test is extremely simple to perform but appears to have the potential to evaluate the effect of anti-stripping additives in the mixture to minimize the loss of adhesion between aggregate and asphalt binder. Furthermore, this test has also presented a good correlation between laboratory results and field performance [7].

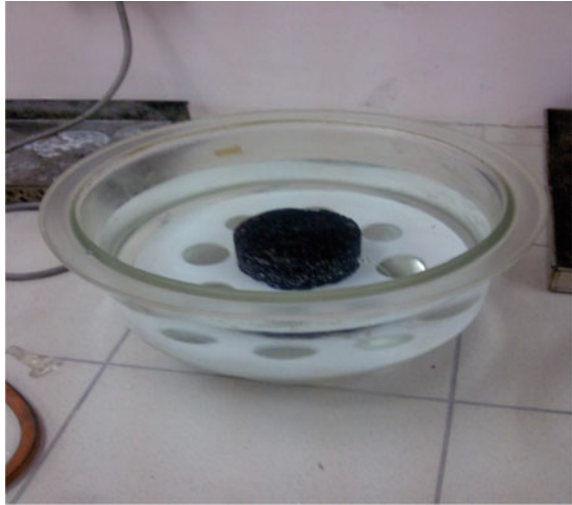
The sample preparation as follow: (i) Placed Approximately 500 ml of water in a 1000 ml beaker and heated to boil. (ii) The 250 g of loose HMA mixture was heated at a maximum temperature of 100 °C (212 °F), but not lower than 80 °C (176 °F), and immersed in the boiling water for 10 min. (iii) The beaker was removed from the heat source and a paper was used to skim off the bitumen on the water surface to prevent recoating. (iv) The water was removed after cooling it to room temperature, and placed the mixture onto a white paper towel to be visually analyzed. (v) The criterion of failure is by visual identification of stripped (uncoated) aggregates.

3.4 Lottman Test

This test method covers procedures for preparing and testing asphalt concrete specimens for the purpose of measuring the effect of water on the tensile strength of the paving mixture. This test method can be used to evaluate the effect of moisture with or without anti stripping additives including liquids and pulverulent solids such as hydrated lime.

Equipment for preparing and compacting specimens from either of the following: AASHTO Test Methods T245 (Marshall). Vacuum Pump with Manometer or Vacuum Gage in accordance with AASHTO Test Method T209: the pump should be capable of evacuating air from the vacuum container to 508 mm (20 inches) Hg. When using the high vacuum pumps associated with the Rice Test (AASHTO T209) the vacuum system should include a regulator connected to the pump with a gauge suitable for controlling and measuring the applied vacuum. The size of the residual pressure manometer generally used in the Rice Test may be too small to measure the partial vacuum of 20 inches. Balance with suspension mechanism and water bath in accordance with AASHTO Test Method. Figure 2 shows the Rice Test Vacuum Container (AASHTO T209).

Fig. 2 Rice test vacuum container (AASHTO T209)



4 Results and Discussion

4.1 *Marshall Stability Test*

The Marshall stability and flow test provides the performance prediction measure for the Marshall mix design method. The stability portion of the test measures the maximum load supported by the test specimen at a loading rate of 50.8 mm/min (2 inches/min). Basically, the load is increased until it reaches a maximum then when the load just begins to decrease, the loading is stopped and the maximum load is recorded. During the loading, an attached dial gauge measures the specimen's plastic flow as a result of the loading. The flow value is recorded in 0.25 mm increments at the same time the maximum load is recorded. The 25% of Hydrate Lime sample and control Sample without additive needs Marshall Test. The results obtained will be used to plotting graph of stability versus binder content and stiffness versus binder content. The results obtained were compared with the parameter which is specified in JKR/SPJ/2005.

4.2 *Optimum Binder*

Optimum binder content mean of bitumen contents that give an optimum value of density, stability and 4% air voids. To determine optimum binder content, certain graph need to be plot referring to Marshall Stability, flow, VMA and VFA. Each of these values against the specification values and if all is with the specification, and then the preceding optimum bender content is satisfactory. If any of this properties

is not specified the standard, the mixture should be redesign. From the calculation, OBC for control sample is 5.6% and for modified sample is 4.6%. There are some values that obtained from graph for determine the optimum binder content for control sample, are:

- (i) The maximum value of stability graph = 4.85%
- (ii) The maximum value of density graph = 6%
- (iii) 70% of VFB graph = 5.75%
- (iv) 5.0% of VTM graph = 5.75%

From the value above: The optimum bitumen content for control mixture = $(4.85 + 6.00 + 5.75 + 5.75)/4 = 5.6\%$.

The values to determine Optimum Binder Content for Hydrate Lime mixture:

- (i) The maximum value of stability graph = 4.6%
- (ii) The maximum value of density graph = 4.7%
- (iii) 70% of VFB graph = 4.6%
- (iv) 5.0% of VTM graph = 4.4%

From the value above: The optimum bitumen content for Hydrate Lime mixture = $(4.6 + 4.7 + 4.6 + 4.4)/4 = 4.6\%$.

4.3 Volumetric Properties

The purpose of conducting Marshall Test is to study the characteristic of the addition of Hydrate Lime in the mixture. All parameters were referred JKR/SPJ/2005 against specification. Table 4 shows values of Marshall Properties including control and modified sample.

The stability of the modified sample is quite higher compared to the control sample according to the JKR standard. It must more than 8000 N and for the modified sample the value is 25500 N for Hydrate Lime sample which is pass because exceed 18,000 N for control sample. The value of air void for Hydrate Lime is 4.4% lower than control sample air void which is equal to 4.7%.

The compacted mix should not have very high air voids, which accelerates the aging process, adequate voids in the total compacted mixture to permit a small

Table 4 Marshall test result for ACW14 for control and modified sample

Marshall properties	JKR/SPJ/2005 specification	Control sample OBC = 5.6%	Remark	Hydrate lime sample OBC = 4.6%	Remark
Stability	> 8000 N	18,000 N	Pass	25,500 N	Pass
Flow	2.0–4.0 mm	3.8	Pass	3.4	Pass
VTM	3.0–5.0%	4.7	Pass	4.4	Pass
VFB	70–80%	71	Pass	70	Pass

amount of compaction when traffic load is applied without bleeding and loss of stability. Density and air void content are directly related. The higher the density, the lower the percentage of air voids in the HMA. The Percentage Voids Filled with Binder (VFB) between control and Hydrate Lime are 71% and 70%. This represents the volume of the effective asphalt content. It can also be described as the percent of the volume of the VMA that is filled with asphalt cement.

4.4 Modified Lottmen Test

This test method covers procedures for preparing and testing asphalt concrete specimens for the purpose of measuring the effect of water on the tensile strength of the paving mixture. This test method can be used to test asphalt concrete mixtures in conjunction with mixture design testing to determine the potential for moisture damage, to determine whether or not an anti-stripping additive is effective and sufficient, and to determine what dosage of an additive is needed to maximize the effectiveness. This test method can also be used to test mixtures produced in field plants and to determine the effectiveness of additives, on the mixture, under the conditions imposed in the field. The results may be used to predict long term stripping susceptibility of bituminous mixtures.

Compaction of Specimens The desired number of blows was determined or revolutions needed to obtain test specimens with approximately 7% air voids. To estimate this number, compacted trial test specimens at varying number of blows for Marshall are 40 blows to 60 blows. After determining the blows or revolutions needed, compact six new test specimens to $7 \pm 1\%$ air voids when using the Marshall apparatus. The values of air void for 40 blows and 60 blows are 7.557 and 5.443. Additional specimens should be prepared at this time. These extra specimens will allow for a better grouping into equal subsets. The bulk specific gravity accordance with Test Method T166 was determined and expresses the volume of the specimen in cubic centimetres. By the plotting the graph, Fig. 3 shows the requirement number of blows is about

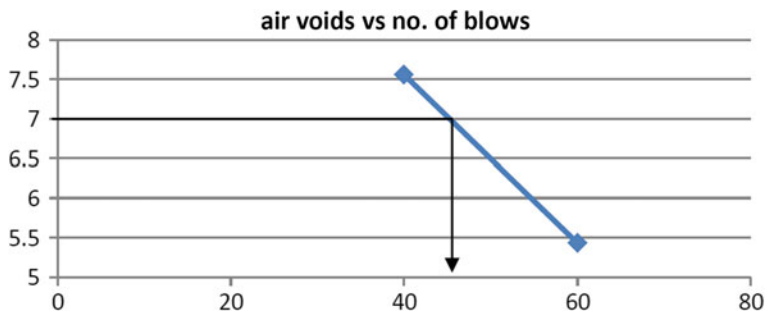


Fig. 3 Requirement number of blow air void versus no. of blows

45 blows in order to achieved $7 \pm 1\%$. This no. of blows was used to compact the samples for purpose of wet and dry testing of stripping performance. Then the term (surface dry weight minus weight in water) is the volume of the specimen in cubic centimetres.

Air Void Parameter T Moisture damage is determined by preparing a set of laboratory-compacted specimens conforming to the job mix formula with an additive. The specimens are compacted to a void content corresponding to void levels expected in the theory, usually in the $7 \pm 1\%$ range. The set is divided into two subsets of approximately equal void content. One subset is maintained dry (unconditioned plugs), while the other subset is partially saturated with water and moisture conditioned (conditioned plugs). The value of air void percentage for conditioned plugs named as S1 (sample 1), S1 (sample 2) and S3 (Sample 3) are 7.25%, 7.17% and 7.12% respectively. Then the air voids for unconditioned plugs are 7.0%, 6.88% and 6.75%. All samples performances are satisfied by the requirement of void level range.

Volume of the Partially Saturated Specimens The diameter, thickness and immersed mass of each specimen was determined, then rolled and surface dry with a damp towel to determine the saturated surface-dry mass. The degree of saturation was determined for individual specimens by dividing the volume of the absorbed water by the volume of air voids, and expresses the result as a percentage. Percentage of saturation row indicated by S1, S2 and S3 are 71.4, 73.5 and 72.4 respectively. If the volume of water is between 60.0 and 80.0%, therefore it is suggested target is 70–80% of the volume of air, proceed to the next step of conditioning, if the volume of water is less than 60.0% repeat the partial saturation procedure for another 5 s period and if the volume of water is more than 80.0%, the specimen has been damaged and must be discarded.

Conditioned Plugs Testing For conditioned plugs, after the 24 h moisture-conditioning period, the temperature was adjusted of the subset by conditioned Plugs soaking them in a water bath for 2 h at $(25 \pm 1.0 \text{ }^\circ\text{C})$. Placed specimens into the loading apparatus and position the loading strips so that they are parallel and centered on the vertical diametrical plane. The maximum load in pounds (N) for S1, S2, and S3 are 6230, 6371 and 6441 respectively.

Unconditioned Plugs Testing Before placed a specimen into the loading apparatus and positioned the loading strips so that they are parallel and centered on the vertical diametrical plane, measured diameter, thickness, and also Dry mass (g), Mass in water (g) and SSD mass (g) for each sample. The length of the loading strips must exceed the specimen's thickness. Apply a diametral load at 2 mm/min (50.8 mm/min) until the maximum load is reached. Table 5 shows the maximum load in Newton (N) for each sample.

Interpreting Result of Tensile Strength The potential for moisture damage is indicated by the ratio of the tensile strength of the wet subset to that of the dry subset.

Table 5 Maximum load unconditioned plugs (N)

Sample 1	Sample 2	Sample 3
6896	6939	6875

Table 6 Average tensile strength

Average dry strength (kPa)	Average wet strength (kPa)
2776	2547

Table 6 shows the average indirect tensile strength of conditioned and unconditioned, the value of tensile strength ratio is 91.8% is pass because exceed the acceptable resistance to moisture damage which is tensile strength ratio must more and equal to 80% where average wet strength (kPa) divided by average dry strength (kPa) in order to get value of tensile strength ratio.

5 Conclusion

Hydrated lime in hot mix asphalt (HMA) creates multiple benefits, hydrated lime's ability to control water sensitivity and well accepted ability as an anti-stripping to reduce moisture damage. Through laboratory testing results the hydrated lime in HMA enhances the bitumen aggregate bond and improves the resistance of the bitumen itself to water induced damage based on modified Lottman test data. Hydrated lime is not simply filler but reacts with the bitumen. The lime particles adsorb polar components of the bitumen. This adsorbed inter layer makes hydrated lime a very effective additive. The level of the bitumen lime reaction was found to be bitumen dependent. In terms of optimum binder content, modified sample by Hydrate Lime was required less bitumen rather than control sample that was mean cost can be reduced. From the result obtained, the bitumen content of control sample is 5.6% and modified sample is 4.6%. The "active" filler effect has graduated temperature sensitivity. At high temperatures the filler effect is most pronounced it is considerably less at temperatures near the glass transition of the bitumen. Furthermore, volumetric properties result shows value of stability for Hydrate Lime sample is high than control sample and passed JKR specification. It is means that the roads can cater more loads compared to the control mixtures.

In other words, the use of Hydrate Lime gave low flow compared to the control mixtures. The value of low flow was resulted in high stiffness. Besides, the Hydrate Lime as additive in HMA mitigates moisture sensitivity, improving both adhesive and cohesive properties of the mixture. Even as it stiffens asphalt mixtures hydrated lime improves fatigue life through "crack pinning". From the laboratory test, the value of tensile strength ratio is 91.8% which has exceeded the acceptable resistance to moisture damage that indicate the tensile strength ratio is more than 80%. It can be

deduced that Hydrate Lime can be used as an additive to mitigate stripping problem on roads especially in Malaysia.

References

1. Hicks RG, Scholz TV (2001) Life cycle costs for lime in hot mix asphalt. Report and Software, Highway and Traffic Engineering Notes, Shah Alam
2. Bari J (2005) Evaluation of the effect of lime medications on the dynamic modulus stiffness of HMA use with the new mechanistic-empirical pavement design guide. TRRTRB 1929:10–19
3. Hunter ER, Ksaibati K (2002) Evaluating moisture susceptibility of asphalt mixes. Department Civil and Architectural Engineering University of Wyoming P.O. Box 3295, Laramie, WY 82071-3295
4. Petersen JC, Plancher H, Harnsbergen PM (1998) Lime treatment of asphalt to reduce age hardening and improve flow properties. In: Proceedings, AAPT, vol 56
5. Petersen JC, Dorrence SM, Ensley EK, Barbour FA, Barbour RV (1974) Paving asphalt, chemical composition, oxidation weathering, and asphalt aggregate interactions, (PB Rep., No. 238956/7GA. Avail: NTIS from Gov Rep Announce Index (U.S.) 1975, 75(8):154 (Eng)
6. Association of State Highway and Transportation Officials (AASHTO) (2013) Standard specifications for transportation materials and methods of sampling and testing. In: AASHTO, vol 265. Washington DC, pp 245–199
7. Parker DC, Frazier JR, Wilson T, Michael S (1986) Evaluation of boiling and stress pedestal tests for assessing stripping potential of Alabama asphalt concrete mixtures, (Cir Eng Dep Auburn Univ AL 36849–5501, USA). TransD Res Rec 1096 (Asphalt Anal Sulfur Mixes Seal Coats), pp 90–100

Effectiveness of Waste Glass as Filler in Hot Mix Asphalt



Noorfaizah Hamzah, Nur'Ain Mat Yusof, Adnan Derahman,
and Ahmad Hafizi Rosely

Abstract Unwanted or unusable materials such as waste glass are the result of any facet of society. However, problems continue due to inadequate disposal capacity and restricted recycling options. The climatic aspect, such as the temperature and moisture, also significantly affects the longevity of Hot Mix Asphalt (HMA) pavements, other than high traffic effect stress. The effectiveness of a modified HMA pavement is measured by its stability, flow and stripping resistance, which have been tested by using Marshall Test apparatus. It was found that the best performance was obtained by adding 25% of the waste glass as filler in the modified HMA pavement. The modified Lottman test is also conducted to ensure of the ability of an additives to perform when conditions are imposed in the field and to evaluate long term stripping susceptibility of bituminous mixtures. The longevity and moisture resistance are higher than unmodified binder mixes. In general, the stability, flow and stripping resistance are found to be very effective in all mixes with the addition of waste glass as filler in HMA.

Keywords Hot mix Asphalt · Waste glass · Marshall test · Modified Lottman test

1 Introduction

There have been tremendous increases of road and highways to suit the users need in Malaysia. However, there are problems arising such as the durability of roads due to traffic impact stress and climatic factors. These cause discomfort and promote hazards to road users. One of the problems that exist is stripping problem. Stripping

N. Hamzah (✉) · A. Derahman · A. H. Rosely
School of Civil Engineering, College of Engineering, Universiti Teknologi MARA (UiTM),
40450 Shah Alam, Selangor, Malaysia
e-mail: noorfaizah1209@uitm.edu.my

N. Mat Yusof
School of Civil Engineering, College of Engineering, Universiti Teknologi MARA Pahang
Branch, 26400 Bandar Tun Abdul Razak, Jengka, Pahang, Malaysia

can be defined as the loss of bond between aggregates. Asphalt binder usually starts at the bottom of the Hot Mix Asphalt (HMA) layer and progresses upward.

Ravelling is also one type of stripping but it starts from the surface and progresses to downward. The main cause of the stripping is water. Water will reduce the displacement of asphalt on the aggregate particle surface. Usually, some aggregates have an affinity for water over asphalt (hydrophilic). These types of aggregates are more acidic and tend to be stripping after exposure to water on the road. There are many ways to reduce or overcome these problems. The used of many types of additive materials such as fly ash, glass, steel slag, fine crumb rubber and other material especially waste material to reduce the rutting problem and increase the strength of the pavement surface by using Marshall Method.

According to Tarek et al. [1], traditionally, glass recycling process has involved the collection and sorting of glass by color for use in the manufacture of new glass containers. Recycling postconsumer glass from the municipal solid waste stream for the use as a raw material in new glass products is limited, high cost due to collection and processing (hand sorting) of waste glass, and specifications that limit impurities in the glass production process. In addition, during collection and handling of glass, high percentages of glass breakage can actually be recovered using hand-sorting practices. Given these limitations, traditional glass recycling rates have been relatively low.

Many solutions that had been produce to reuse all these glass for example as an alternative an additive in making concrete and it is suitable as stabilizer in road work. The used of waste glass as filler in HMA will replace the used of the cement. The comparison between samples of the bitumen based on Marshall Mix Design was conducted. The stability and flow tests were conducted to figure out the strength, the Lottman modified tests also were conducted to determine the stripping problem against modified mix of the sample.

In this study, the material of waste glass has been chosen to be used as filler in the mix design to improve the quality of the road. There are many advantages of using these waste materials. The advantage can reduce the cost of material to be used in pavement of road.

2 Literature Review

Waste materials are generated increasingly with the continuous growth in the economy and as consumption increases. The growing quantities of waste materials, lack of natural resources and shortage of landfill spaces represent the importance of finding innovative ways of reusing and recycling waste materials [2]. Today, many waste materials such as tyres, plastics, waste glass, etc. are used for construction of different layers of pavements including the asphalt surface layer [3]. High performance and environment friendly roads can be constructed by the use of many waste materials in bituminous paving mixes [4]. Accordingly, many researchers [5, 6] have studied the utilization of glass as aggregate for asphalt mixtures. Asphalt pavements

are composite materials consisting of interspersed aggregates, asphalt binder, and air voids. Its constitutive behavior is defined by interaction of these constituents. The load-carrying behavior and resulting failure of such materials depends on many mechanisms that occur at the constituent level [7]. Flexible pavement consists of unbound compacted stone under a bituminous surfacing. Flexible pavement consists of three layers, sub-base, base and bituminous surfacing [8]. To create a flexible pavement, crush up the small stone pieces either pressed together and mixed with a glue-like material known as bitumen to form bituminous layer but the bitumen needs to be heated first about 300 degrees Fahrenheit (150 °C) and then stone is added. Machines then lay the mixture onto the road, creating the pavement the cars drive on.

Flexible pavement has a lot of advantages in terms of initial cost, availability of material locally, construction machinery and labour, construction and upgrading work and also timing open to traffic. By using flexible pavement, it is lower initial cost, easy and cheap to get material, easy to upgrade and also can be open to traffic once ready [8]. But flexible pavements also have their own problem such as stripping problem. During the past several years many states experienced problems with amount and severity of permanent deformation in HMA pavements. This problem with permanent deformation, or rutting, was attributed to an increase in truck tire pressures, axle loads, and volume of traffic [7, 9].

2.1 Hot Mix Asphalt

Asphalt pavements typically provide excellent performance and value. Asphalt pavements are smooth, quiet, and durable. It does not require long construction times and they are easy to maintain resulting in minimal traffic delays [10]. Therefore, by careful selection of asphalt binder and aggregate combination helped in providing optimum performing HMA pavement. Figure 1 shows the sample of HMA production.

HMA is the most popular mix around the world and widely used. It is composed of the combination of fine and coarse aggregate in different sizes and asphalt cement which binds together with bitumen acting as binder. It is also produced by heating the asphalt binder to decrease its viscosity and drying the aggregate to remove moisture from it prior to mixing. The components are heated and mixed at a central plant and placed on the road using an asphalt spreader.

2.2 Aggregates

“Aggregates” is a collective term for the mineral materials such as sand, gravel and crushed stone that are used with a binding such as water, bitumen, Portland cement, lime and others to form compound materials such as asphalt concrete and Portland



Fig. 1 Hot mix Asphalt production

cement concrete [11]. Aggregate are an important ingredient of the materials used in highway construction. They constitute 80% by weight Portland cement concrete (PCC) and HMA. In term of volume, the corresponding ratios are 75% for PCC and 85% for HMA, respectively [12]. Therefore, the physical mechanical and chemical properties of aggregates play an important role in the performance in flexible pavement. Aggregates can either be natural or manufactured. Natural aggregates are normally extracted from larger rock formation through an excavation from the quarry. Manufactured aggregate is often the by product or other manufacturing industries [11, 12].

Aggregates derived from the natural rocks can be classified on the basics size as crushed stone, sand, or gravel. Crushed stone refers to the different rock type and size that are come from blasting and crushing. Sand and gravel comprise any clean mixture of aggregate sizes found in natural deposits, such as steam channels [12].

According to Jabatan Kerja Raya (JKR) [13], aggregate for the asphaltic concrete shall be a mixture of coarse and fine aggregate and mineral filler. Course aggregate shall be screened crushed hard rock, angular in shape and free from dust, clay vegetative and other organic matter. The coarse aggregate conformed to physical and mechanical quality requirement which are: (i) The Los Angeles abrasion test shall not be more than 25% (ASTMC 131); (ii) the weight average loss of weight in the magnesium sulphate soundness test of five cycles shall not be more that 18% (AASHTO T104); (iii) the flakiness index shall not more that 25% (MS 30); (iv) the water absorption shall not more that 2% (MS 30); (iv) the polished stone value shall not be less that 40% for only applicable to aggregate for wearing course (MS 30). Figure 2 shows the samples of aggregates used in HMA.

Fine aggregate shall be clean screened quarry dusts. It shall be non-plastic and free from clay, loam, aggregation of material, vegetation and other organic matter, and other deleterious substance. The fine aggregate conformed to physical and mechanical quality requirement which are: (i) the sand equivalent of aggregate fraction passing the no. 4 (4.75 mm) sieve shall not be less than 45% (ASTM d 2419); (ii) the



Fig. 2 Samples of aggregates

fine aggregate angularity shall not be less than 45% (ASTM 1252); (iii) the methylene blue value shall not more than 10 mg/g; (iv) the weight average loss of weight in the magnesium sulphate soundness test of five cycles shall not more than 20% (AASHTO T104); (v) the water absorption shall not be exceeding 2% (MS 30).

The physical properties of aggregates are those that refer to the physical structure of the particles that make up the aggregate. The aggregate must be hot, dry and clean and the mixture also must be well-compacted, densely-graded, densely graded, asphalt concrete and place it directly on a properly prepared stone base. The compaction must be hard and tough. To minimize its effects, the design of asphalt must be proper planning and immediate diagnosis (Asphalt Stripping) as shows in Fig. 3.

2.3 Asphalt Binder

The asphalt binder component of an asphalt pavement typically makes up about 4–6% of the total asphalt mixture, and coats and binds the aggregate particles together. Asphalt cement is used in hot mix asphalt. Liquid asphalt, which is asphalt cement dispersed in water with the aid of an emulsifying agent or solvent, is used as the binder in surface treatments and cold mix asphalt pavements. The properties of binders are often improved or enhanced by using additives or modifiers to



Fig. 3 Stripping occurs in the surface and subsurface pavement structure

improve adhesion, flow, oxidation characteristic, and elasticity. Modifier includes oil, filler, powders, fibers, wax, solvents, emulsifiers, wetting agents, as well as other proprietary additive (AASTHO, 1993).

2.4 Mineral Filler

In order to improve the density and strength of the mixture, the mineral filler is added with the HMA. It shall be incorporated as part of the combined aggregate gradation and it shall be of finely divided mineral matter of limestone such as limestone dust or hydrated lime. Not less than 70% by weight shall pass 0.0075 mm sieve.

By weight, the ratio of the combined coarse aggregate, fine aggregate and mineral filler of final gradation that passing 0.0075 mm sieve shall be in the range of 0.6–1.2. The mineral filler shall also be treated as an anti-stripping agent [13].

2.5 Gradation Specification for Asphaltic Concrete

One of the most influential characteristic in characterizing the soil is by gradation. In hot mix asphalt, gradation helps determine almost every important property including stiffness, stability, durability, permeability, workability, fatigue resistance, friction resistance and resistance to moisture damage [14, 15].

Gradation usually measured by a sieve analysis. In a sieve analysis, a sample of dry aggregate of known weight is separated through a series of sieve with progressively smaller openings. One separated, the weight of particles retained on each sieve measured and compared to the total sample weight. The information in the table below indicates that gradation limit for the asphaltic concrete [13].

2.6 Waste Material

Numerous waste materials result from manufacturing operations, service industries, sewage treatment plants, households and mining. Legislation has been enacted by several states in recent years to either mandate the use of some waste materials or to examine the feasibility of such usage. The hot mix asphalt (HMA) industry has been pressured in recent years to incorporate a wide variety of waste materials into HMA pavements. This has raised the following legitimate concerns: (i) engineering concerns such as effect on the engineering properties (for example, strength and durability), impact on production, and future recyclability; (ii) environmental concerns such as emissions, fumes, odor, leaching, and handling and processing procedures; (iii) economic concerns such as life cycle costs, salvage value, and lack of monetary incentives. The waste materials can broadly be categorized as: (a) industrial wastes such as cellulose wastes, wood lignins, bottom ash and fly ash; (b) municipal/domestic wastes such as incinerator residue, scrap rubber, waste glass and roofing shingles; (c) mining wastes such as coal mine refuse.

2.7 Properties of HMA

Since the waste material were replaced and/or modified the properties of asphalt cement binder and/or HMA, it has affect the engineering properties (such as strength and durability). Therefore, the HMA containing the waste material must be reevaluated thoroughly and carefully both in the laboratory and the field [16].

2.8 Waste Glass

Among many wastes, the glass waste population is dramatically increasing. In geotechnical engineering, the application of glass wastes is used as an additive to different soils for subgrade improvement. Besides, it is mainly limited to road pavement. Since it is chemically inert, glass has high instric strength and low gas permeability. Therefore, it can be deduced that waste glass is one of an attractive recycling option as a replacement of aggregates in construction or road pavement.

When manufactured by humans, glass is a mixture of silica, soda, and lime. Other materials are sometimes added to the mixture to “frost” or cloud the glass or to add colour. The elements of glass are heated to 1800° Fahrenheit (982 °C). The resulting fused liquid can be poured into moulds or blown into various shapes, and when cooled, glass is a strong, minimally conducting substance that will not interact with materials stored inside. As a result, glass is frequently used in scientific laboratories to minimize inadvertent chemical reactions and to insulate power lines.

Glass is a strange substance, defying easy scientific categorization. It is not a solid, not a gas, and not quite a liquid either. Generally, it is classified as a rigid liquid, maintaining liquid properties while acting like a solid. Heat can return the glass to a liquid and workable form, making it easy to reuse and recycle. Many solutions that had been produce to reuse all these glass for example as an alternative as an additive in concrete making and suitable for being stabilizer in road work. This entire waste glass was used in pavement design to overcome stripping and defect problem by using Marshall Method.

3 Methodology

Marshall test was used to determine the stability and amount of flow of the sample base on the Marshall test analysis, the optimum binder content can be calculated. Marshall test needs to be conducted for both control and modified. The results obtained are used to plotting graph of stability versus binder content and stiffness versus binder content. The results obtained were compared with the parameter which is specified in JKR/SPJ/2005 [13].

3.1 Sieve Analysis

A gradation test or sieve analysis used to separate particles of different sizes. assess the particle size distribution of a granular material. In civil engineering, this technique can be performed on any type of non-organic or organic granular materials including sands, crushed rock, clays, granite, feldspars, coal, and soil. This is an effective method to determine the size distribution of particles.

3.2 Crushing and Sieve Waste Glass

Waste glass which is collected from plant, restaurant and others were crushed into very fine particle so that it passed 75 μm of sieve size. Then the fine particles of waste glass were mixed together with the pan size particles as filler in mix design. The amount of waste glass need to be added into one sample is 2% from the weight of the total weight of aggregate.

3.3 Calculation for Binder Content

$$\text{Weight of binder content} = (A/(100 - A)) \times B. \quad (1)$$

where,

A = Percentage of binder content.

B = Total weight of aggregate + filler.

3.4 Gradation Selection

The process of proportioning the aggregates or also known as aggregate blending used to obtain the desired gradation that were well within the gradation limit. The gradation limits for the mixes that were prepare as specified by JKR [13]. For this study, the mix prepared is a combination of coarse aggregate, fine aggregate and waste glass as filler which known as ACW14. The gradation limits is taken from the median of the specified gradation limits. Referring to the calculation, which is base on the gradation limit, each weight for particular size is determined. The different size of aggregate were weighted and mix with the gradation calculated earlier. Then, the sample is packed into tray and labeled and ready to be used. Table 1 shows the various gradation limits for Asphaltic Concrete [13]. Figure 4 shows the aggregates gradation for the Marshall specimens.

Table 1 Gradation limit for ACW14

BS sieve size (mm)	28.8	20.0	14.0	10.0	5.0	3.35	1.18	0.425	0.150	0.075
Percentage passing	0	100	90–100	76–86	50–62	40–54	18–34	12–24	6–14	4–8

Fig. 4 Aggregates gradation



3.5 Preparation of Compacted Specimen

Procedures for preparation of compacted specimen are: (i) the aggregates (1200 g) graded according to the ASTM standard are over dried at 170–180 °C (not more than 280 °C). Table 2 shows the weight of the gradation aggregates; (ii) the required quantity of asphalt is weighted out and heated to a minimum temperature of about 135 °C (max \pm 160 °C \pm 5 °C); (iii) the thoroughly cleaned mould is heated on a hot plate or in oven to a temperature 135–150 °C. The mould is 101.6 mm diameter by 76.2 mm high and provided with a base plate and extension collar; (iv) a crater is formed in the aggregates, the binder poured in and mixing carried out until the aggregates is coated. The mixing temperature shall be within the limit set for the binder temperature. Figure 5 shows the mixing of the aggregates and bitumen.

A piece of filter paper is fitted in the bottom of the mould and the whole mix poured in three layers. The mix is then vigorously trowel 15 times round the perimeter and 10 times in the center leaving a slightly rounded surface. The mould is placed on the Marshall Compacter with 75 blows. After compaction the base plate is removed and the same blows are compacted to the bottom of the sample that has been turned around. The specimen is then carefully removed from the mould and then marked. Figure 6 shows the Marshall Compacter machine.

Table 2 Total weight of the mix specimen

Percentage of binder (%)	Weight of binder (g)	Total weight (g)
4.0	51.0	1275.0
4.5	57.7	1281.7
5.0	64.4	1288.4
5.5	71.2	1295.2
6.0	78.1	1302.1

Fig. 5 The mixing process



Fig. 6 Marshall Compacter machine



3.6 Determination of Bulk Specific Gravity of the Specimen

This test covers the determination of bulks specific gravity of the samples which only can be used for a specimen that does not absorb more than 2% of water by volume. The density (unit weight) and percentage of air void of compacted mixers was calculated based on the results obtained. The bulk specific gravity was determine using water displacement method where specimen was weighted in three conditions (in air when submerged in water and saturated dry surface condition). The apparatus used for the tests are balance and water bath.

Procedures for the determination of bulk specific gravity of the specimen: (i) the specimen is cooled to a room temperature at 25 ± 1 °C and the dry mass is recorded (A); (ii) the specimen is immersed in a 25 ± 1 °C water bath and saturated at 4 ± 1 °C min; (iii) the specimen is then, placed in a basket and its mass is determined to nearest 0.1 g while immersed in water in a 25 ± 1 °C (C). The immersed saturated specimen is removed from the water bath and damp dried with the damp absorbent cloth as quickly as possible. The specimen is the weighted (B). Any water that seeps from the specimen during the weighting operation is considered as part of saturated specimens. The bulk specific gravity can be calculated by using the following equations:

$$\text{Bulk specific gravity} = (A/B - C) \quad (2)$$

where;

A = mass of specimen in air (g).

B = saturated surface dry (SSD) mass (g).

C = mass of specimen in water (g).

3.7 *Marshall Stability and Flow Test*

The most widely used method of asphalt mixing design in the Marshall Method for the determination of stability and flow, density and voids filled with binders with varying binder contents. It is also intended to determine the optimum for stability, durability, flexibility, fatigue and others.

The mechanism of failure in the Marshall Test apparatus complex but it is essentially a type of unconfined compression test. This has limited correlation with deformation in a pavement where the material is confined by the tire, the base and the surrounding surfacing. Wheel tracking test have shown that resistance to plastic flow increases with reducing binder content whereas Marshall stability's decrease. Improvement on the assessment, based on stability, is possible by considering flow and most and most agencies (e.g. Asphalt Institute of JKR Malaysia) set minimum for stability and maximum flow for various purposes (roads, airport). In addition to binder content, stability and flow are the primary variables in asphalt sample performance, binder type, aggregate grading, particle shape, parent rock geology (most importantly, porosity), compaction degree, also contribute as significant factors.

The dimension and specifications of the Marshall apparatus are explained in ASTM D1559. The diameter of the specimen is 101.6 mm and nominal thickness is 63.55 mm. In order to conduct the Marshall Stability and Flow Test, three specimens, prepared referring to the Standard are immersed in a water bath for 30 and 40 min or in an oven for 2 h at 60 ± 1.0 °C.

The testing heads and guide rods are thoroughly cleaned, guide rods lubricated and head maintained at a temperature in between 21.1 and 37.8 °C. Then, the specimen is placed in the lower jaw and the upper jaw placed in position. The complete assembly is then placed in then Marshall Stability and flow machine and the flow meter adjusted zero. The load is applied to the specimen at a constant strain rate of 50.8 mm/min until the maximum load reached. The maximum force and flow are recorded. The maximum time that's allowed between removals of the specimens from the water bath maximum load is 30 s. The applied load must be corrected when thickness of specimen is other than (2 ½ in.) or 63.5 mm by using the proper multiplying factor. Figure 7 shows the Marshall stability and Flow test apparatus.

Fig. 7 Marshall stability and Flow test apparatus



3.8 Evaluating of Stripping Performance Using Modified Lottman Test

Modified Lottman Test is a combination of the Lottman Test, and the Tunnicliff and Root Test which accepted by AASHTO T-283. Six specimens are produced with air voids between six percent and eight percent. The higher percentage of air voids will led to more moisture damage on the cores.

Number of blows and percentage of air voids for stripping test. To determine air voids in samples at 7%, first two samples was tried by 40 no. of blows and 60 no. of blows. Then the sample was mix and compacted by the specified no. of blows. The samples were cooled at room temperature and find the bulk specific gravity of the sample both. To determine air voids:

$$A_v = 100 - 100 (G_{mb}/G_{mm}) \quad (3)$$

where:

G_{mb} = Bulk specific gravity of the samples.

G_{mm} = Theretical maximum density of the sample.

3.9 Preparation for AASHTO T-283 Test

Sample preparation in AASHTO T-283 was prepared using Marshall Impact compaction. As for compaction effort, to achieve the required $7 \pm 1\%$ air voids,

the specimens was compacted at the design asphalt content where two (2) specimens are subjected to 40 and 60 blow compactive efforts, respectively. After an overnight room temperature curing, bulk specific gravity was determined referring to ASTM D2726. Graph of air voids versus number of blows was established to get the compactive effort that achieve $7 \pm 1\%$ air void content in sample.

After that, six (6) samples weight of 1200 g was prepared. An aggregate and bitumen was mix together. Then, loose mixtures are put into a $60\text{ }^{\circ}\text{C}$ oven for 16 h. The mixes were heated to $135\text{ }^{\circ}\text{C}$ for 2 ± 0.5 h. In purpose to achieve an air void of $7 \pm 1\%$, the sample is compacted using Marshall compacter with the required number of blows.

The compacted specimen was store at room temperature for 3–4 days before testing. Two (2) additional specimens were prepared to ensure there would be at least six specimens to satisfy the air voids requirement. The extra samples were used to determine the required time for vacuum saturation.

Testing of samples

For testing, two (2) groups of three (3) specimens was used which one (1) set of three (3) was subjected to cycles of wetting, thawing and hot water curing. These conditions are utilized to accelerate environmental effects on the asphalt mixture. The wetting involves 55–80% saturation by applying 10–26 in. Hg vacuum, followed by soaking in water for 24 ± 1 h at $60 \pm 1\text{ }^{\circ}\text{C}$, and conditioning in water for two hours at $25 \pm 0.5\text{ }^{\circ}\text{C}$ before testing.

The indirect tensile stress was conducted on the condition and unconditioned set of specimens. The steel loading strips was used to apply a load along the diameter of the specimen. Loading rate was controlled to a vertical deformation of 50.8 mm/min [17]. The minimum acceptable TSR used is 0.7 [11, 18, 19]. Figure 8 shows the process of the testing samples.

The maximum force was recorded and converted into the tensile strength of the samples as follows:

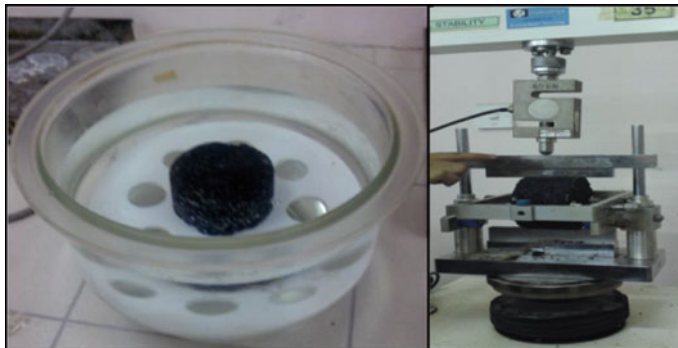


Fig. 8 Vacuum to achieve 70–80% saturation

$$St = 2P/(\pi tD) \quad (4)$$

where:

St = tensile strength.

P = maximum load.

t = specimen thickness.

D = diameter specimen (102 mm).

The tensile strength ratio (TSR) is calculated as follows:

$$\text{TSR} = (S1/S2) \times 100 \quad (5)$$

where;

$S1$ = average tensile strength for conditioned subset.

$S2$ = average tensile strength of dry subset.

If the value of TSR > 80%, it is good again stripping resistance. If the value of TSR < 80%, it is not good again resistance and not susceptible to moisture.

4 Results and Discussion

4.1 Sieve Analysis and Aggregate Distribution

In order to prepare the sample of marshal mix design, the various gradation of aggregates need to be weigh by using sieve shaker. Actually, there are two types of sieve analysis which are dry sieve analysis and wash sieve analysis. The size of aggregates for the ACW14 are 14, 10, 5, 3.35, 1.18, 0.425, 0.15, 0.075 mm, and tray (pan).

Wash sieve analysis was conducted to find out the value of dust coated the aggregate. According to the test, the amount of the total pan that needs to mix inside the sample can be determined. The pan or filler is the aggregates dust that is passing 0.075 mm. the weight of the pan divide by the percentage of waste glass which is 25% and pan 75%. If wash sieving are not conducted, the value of pan that obtain from dry sieve are high. During conducting wash sieve analysis, the amount of pan is reducing half of dry sieve analysis.

4.2 Aggregate Bulk Specific Gravity

Bulk specific gravity of course and fine aggregate was determined before mixing the specimen. The purpose of this test is to determine the exact value of specific gravity. The aggregate was combining by calculating the percentage of separate fraction between course aggregate, fine aggregate and filler by using volumetric properties

Table 3 Theoretical maximum density (Gmm) for both mixtures

Bitumen content (%)	Control (0% of waste glass)	Modified (25% of waste glass)
4.0	2.492	2.466
4.5	2.474	2.448
5.0	2.456	2.431
5.5	2.438	2.413
6.0	2.429	2.396

analysis. The sizes of course aggregate are in between 14 and 5 mm and the size of fine aggregate in between 3.35 mm until 0.075 mm.

The test of fine and course aggregate was conducted separately, and the value of specific gravity course aggregate is 2.611 and fine aggregate is 2.707 mm. The Ordinary Portland Cement was added in the mix of aggregate as filler as specified in JKR [13]. This test can also reveal apparent specific gravity and percentage of water absorption.

4.3 Theoretical Maximum Density

The purpose of conducting this test is to determine the density and theoretical maximum density of loose sample Hot Mix Asphalt after mixed the specimen. By conducting this test, the average effective specific gravity is 2.623. Theoretical maximum density, Gmm can be determined by using formulae and the value is different regarding to the binder content. Table 3 shows the Theoretical Maximum Density (Gmm) for both mixtures.

4.4 Optimum Binder Content

Optimum binder content (OBC) of bitumen contents that give an optimum value of density, stability and 4% air voids. To determine optimum binder content, certain graphs need to be plot referring to Marshall Stability, flow, VMA and VFA. Each of these values against the specification values and if all is with the specification, and then the preceding optimum bender content is satisfactory. If any of this properties is not specified the standard, the mixture should be redesign. From the calculation at below, OBC for control sample is 5.6% and for modified sample is 4.76%. There are some values that obtained from graph in Figs. 9, 10, 11, 12, 13, 14 for determination of the optimum binder content for control sample. The summary of optimum binder content (OBC) for both mixtures are tabulated as in Table 4.

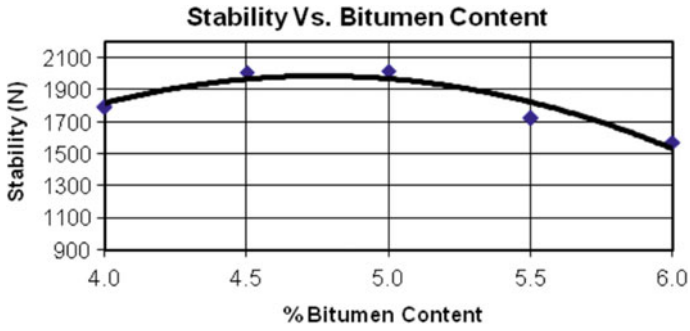


Fig. 9 Stability versus bitumen content

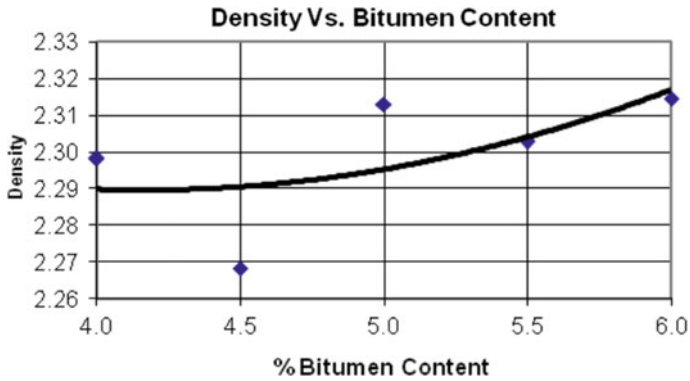


Fig. 10 Density versus bitumen content

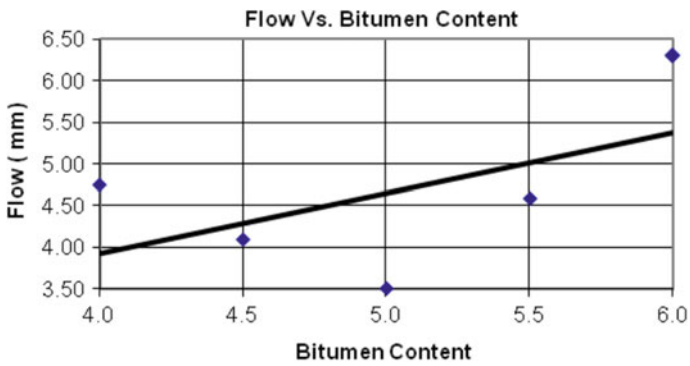


Fig. 11 Flow versus bitumen content

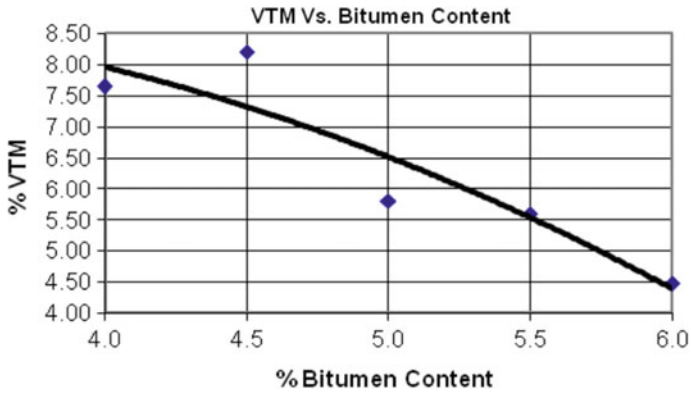


Fig. 12 VTM versus bitumen content

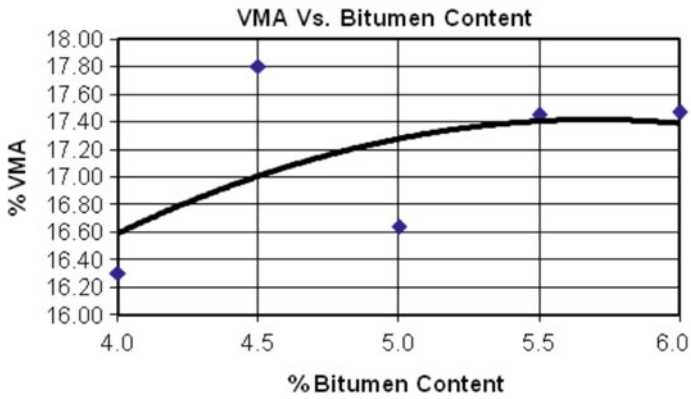


Fig. 13 VMA versus bitumen content

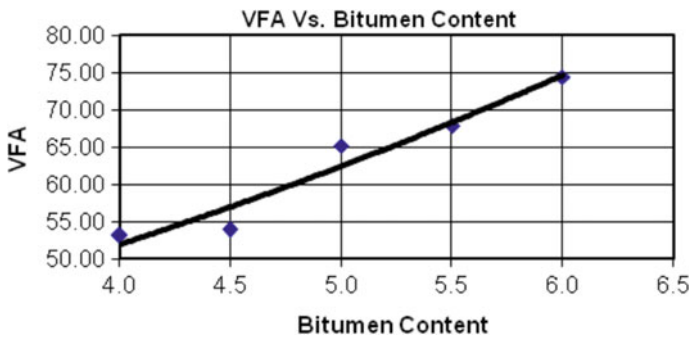


Fig. 14 VFA versus bitumen content

Table 4 Summary of optimum binder content (OBC) for both mixtures

Parameters	Control (0% of waste glass)	Modified (25% of waste glass)
The maximum value of stability graph (%)	4.85	5.25
The maximum value of density graph (%)	6	5.00
70% of Void fill with bitumen (VFB) graph (%)	5.75	4.52
5.0% of Void in total mix (VTM) graph (%)	5.75	4.25
Optimum bitumen content (%)	5.6	4.76

4.5 Volumetric Properties

The purpose of conducting Marshall Test is to study the characteristic of the addition of waste glass in the mixture. All parameters were referred JKR/SPJ/2005 against specification. Table 5 shows the values of Marshall test properties including control and modified sample.

According to the value obtained from the laboratory test, the stability of the modified sample is higher compared to the control sample according to the JKR standard. JKR standard states that the value of the stability must more than 8000 N. The stability value for modified samples is 21,500 N which is passing the specification requirement 18,000 N.

The next properties that are concern in this research are flow value of the samples. The standard range of the flow value is 2.0–4.0 mm. The actual value of flow which is the control samples is 3.8 mm, compared with the modified sample is lower than the control sample which is 3.63 mm. The result shows that the waste glass added inside the modified samples are improving the flow of the pavement which is good. When flows lower, that means the flexibility increase. Usually the stability increased, the flow will reduce.

VTM means void in total mix. The value of VTM shows the increasing of voids or pore space in the sample. Value that provide by JKR Standard is between 3 and 5%. Base on the result obtained, the value of VTM where 3.8% is lower than control sample, 4.7%. This shows that the void in modified sample is less than control sample. Voids allow moisture and air creep into the bonding between aggregate and binder

Table 5 Marshall Test result for ACW14 for control and modified sample

Marshall properties	JKR/SPJ/2005 specification	Control Sample OBC = 5.6%	Remark	Modified Sample OBC = 4.76%	Remark
Stability	>8000 N	18,000 N	Pass	24,600 N	Pass
Flow	2.0–4.0 mm	3.8	Pass	3.63	Pass
VTM	3.0–5.0%	4.7	Pass	3.75	Pass
VFB	70–80%	71	Pass	70	Pass

thus reduces the durability of the pavement structure. According on these two values, it can be conclude that modified sample is good in durability compared to control sample when added waste glass into it.

Lastly is VFB, void filled with bitumen. Based ok JKR Standard, VFB must within the range of 70–80%. For modified sample, the range is within the standard but the value is less a little bit than control sample which is 1%. That’s means control sample is coated more aggregate rather than modified sample but still acceptable because within the JKR standard.

4.6 Stripping Performance

Number of blows for 7% of air voids is determined before mixing procedure. Two modified samples are compacted with 40 and 60 number of blows each. After the compaction process, the specific gravity of samples is determined. Table 6 shows result for air voids analysis for stripping test. Figure 15 shows the air voids versus no. of blow graph.

Table 6 Result of air voids analysis for stripping test

For 40 no. of blows		For 60 no. of blows	
Weight in air (g)	1203	Weight in air (g)	1184.6
Weight in water (g)	684	Weight in water (g)	679.4
SSD (g)	1215.7	SSD (g)	1191
Gmb	2.263	Gmb	2.315
Gmm	2.448	Gmm	2.448
Average	7.557	Average	5.433

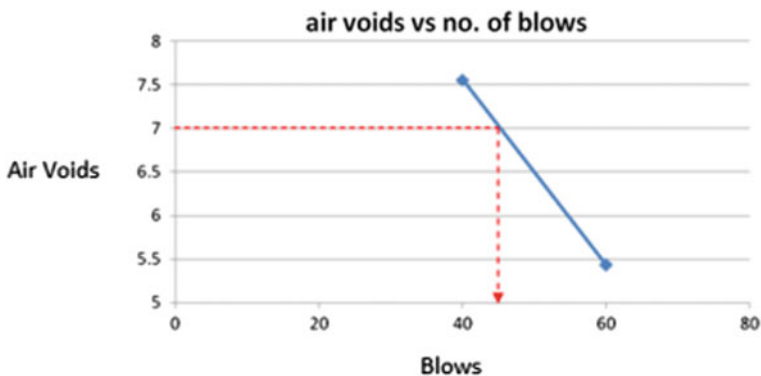


Fig. 15 Air voids versus no. of blows

Table 7 Average tensile strength

Average dry strength (N)	Average wet strength (N)
6918	6350

From the graph, the number of blows required to meet 7% air voids is 45. The number of blows is used to compact the samples for the purpose of wet and dry testing of stripping performance.

4.7 Modified Lottman Test

The test is to measure the effect of water on the tensile strength of the paving mixture. This test can be used to determine the effect of moisture with or without anti-stripping additives. This test method can be applied to asphalt concrete mixture to find the potential for moisture damage, to evaluate whether the additives add in mix is appropriate or not and also can measure the amount or dosage that need to be add into mixture hence give better result. This test also measure the ability of an additives to perform when conditions is imposed in the field. The result is used to evaluate long term stripping susceptibility of bituminous mixtures.

Tensile Strength Ratio (TSR). After the data for the stripping test collected, the Tensile Strength Ratio (TSR) can be determine by divided the average value of the wet samples with the dry samples. Table 7 shows average loading for the wet and dry sample.

$$\begin{aligned}
 \text{TSR} &= \text{Average load of wet samples} / \text{average load of dry samples} \times 100\% \\
 &= 6350 / 6918 \times 100\% \text{ (4.1)} \\
 &= 91.8\% \geq 80\%.
 \end{aligned}$$

According to the data obtained during the test, the value of the loading gain for the both dry and wet samples needs to be calculated and analysis for the TSR value. The TSR value for the stripping test is 91.8%. According to the ASTM, the actual values that need to be passing are 80%. So as the conclusion, by adding waste glass as the additive inside the pavement structure is acceptable against stripping defect.

5 Conclusion

Based on the data obtained from the study, it is clearly shown that the performance of the pavement improves by applying 25% of waste glass as filler inside the pavement structure. Compared to the control pavement, performance increases. In order to

determine the improvement between the both samples, several factors assessed which are the stability and flow result, percentage of OBC, and stripping defect test.

By replacing the 25% of the filler with the waste glass, it gives total impact to road pavement characteristics. Generally, the glass itself is made and produced by using fine aggregates. After the process, the fine aggregates transform into the glass and used for the multipurpose used. The result is therefore logically acceptable. In addition, through use of 52 waste glass produced a low flow compared to the control mixtures. Low-flow value resulted in high stiffness.

Optimum binder content is a very important element in order to produce a good road pavement. The OBC value for the modified sample is 4.76% which is lower compared with the OBC for the control sample is 5.6%. It shows that by replacing the waste glass, the OBC content will reduce in order to construct proper road pavement for the road user. Besides that, the price also decreases due to the lower OBC content. In fact, waste glass is a recycle material which is easy to found and cheap in the market.

In terms of stripping performance, by replacing the waste glass in the mix, it gives high ratio of dry test against wet test. The result is satisfied if the wet test sample divide by wet test sample is achieve more than 80%. Based on the Modified Lottman Test, the result of stripping performance of modified sample is more than 91.5% which is good. Therefore it can be deduced that, by adding waste glass as filler was produced long life span and also optimum the cost of maintenance work on the road.

As the conclusion, by replacing the waste glass as filler in pavement structure has provided a lot of advantages and benefits in terms of stability and flow, OBC, and stripping performance. Therefore, the used of waste glass is suitable and acceptable to be used as filler in the Hot Mix Asphalt.

References

1. Tarek AK, Bernd RTS, Kenneth JW (2005) Recycling solid waste as road construction materials. An environmentally sustainable approach, Chap 2. Springer, Hiedelberg
2. Tahmoorian F, Samali B, Yeaman J Crabb R (2018) The use of glass to optimize bitumen absorption of hot mix asphalt containing recycled construction aggregates. *Materials* 11(7). <https://doi.org/10.3390/ma11071053>
3. Chandh KA, Akhila S (2016) A laboratory study on effect of plastic on Bitumen. *Int J Sci Res* 5:1406–1409
4. Merrin B et al. (2017) Laboratory study on using waste glass as filler in bituminous mixes. *Int Res J Eng Technol (IRJET)* 04(07):1333–1337
5. Androjic I, Dimter S (2016) Properties of hot mix asphalt with substituted waste glass. *J Mater Struct* 49:249–259
6. Issa Y (2016) Effect of adding crushed glass to asphalt mix. *Arch Civ Eng* 2016:LXII
7. Brown ER, Cross SA (1992) Aggregate properties and the performance of super pave design in hot mix asphalt. Transportation Research Board of the National Academic
8. Pavement materials: aggregates (2010) Lecture notes in transportation systems engineering. Retrieved 03 Dec 2011. http://www.civil.iitb.ac.in/~vmtom/1100_LnTse
9. Brown SF (1991) Application of new concepts in asphalt mix design. Association of Asphalt Paving Technologies

10. Civil Engineering Portal (2018) Retrieved 12 01, 2020, from Aggregate Impact Value. <http://www.engineeringcivil.com/aggregate-impact-value.html>
11. Robert et al (1996) Asphalt cement modifiers. Retrieved 13 Mar 2011, from <http://www.NEW/modifiers-filler.htm>
12. Papagiannakis M (2007) Pavement design and materials
13. Jabatan Kerja Raya (2005) Standard specification for road works (JKR/SPJ/rev2005). Kementerian Kerja Raya, Kuala Lumpur
14. Ekarizan S (2008) Stripping performance of hot mix asphalt (HMA) using polymer and hydrated lime as additives. Universiti Teknologi MARA
15. Day DE, Schaffer R (1975) Glasphalt paving handbook. Recycled glass in asphalt. University of Missouri-Rolla
16. Kandhal SP (1992) Waste materials in hot mix asphalt. National Center for Asphalt Technology
17. Mathew TV (2007) Pavement design. Civil Engineering Department Indian Institute Technologies, Mumbai, p 55
18. Ksaibati K (2002) Evaluation of bottom ash asphalt mixes. Department of Civil & Architectural Engineering, University of Wyoming
19. Ksaibati ER (2002) An assessment of regional road user needs in three rural states. Department of Civil and Architectural Engineering, University of Wyoming

Evaluating the Impact of Junction Type on Emissions Level



Masria Mustafa and Nur Amirah Mohammad Noor

Abstract The objectives of this study were to determine vehicle's emissions level at different junction type (signalised intersection and roundabout) and to evaluate the most efficient type of junction to be implemented in the city for better traffic environment. The value of carbon monoxide (CO), carbon dioxide (CO₂), hydrocarbon (HC), and nitrogen oxide (NO_x) for vehicular traffic were evaluated for both morning and afternoon peak periods at both junction types by using SIDRA software. The results indicate that replacing the traffic signal with the roundabout tends to reduce level of emissions. This type of study is very important in terms of environmental and economic considerations. The result of this study will help to enable the policy maker in strategizing the best solutions of mitigating pollutant level in the country, which will also improve the resident's safety for better and sustainable transport.

Keywords Emission · Junction type · SIDRA

1 Introduction

Table 1 shows the lists summary of new passenger and commercial vehicles registered in Malaysia for the year 1980 to September 2018. Traffic volume is growing due to the increased of the local population and economic growth. Continuous growth of the traffic volume will lead to traffic congestion. As depicted in Fig. 1 the number of person's daily trip is increasing in line with GDP. The mobility trend increased from 13 million trips in 1990 to 40 million trips in 2010. It was projected that 131 million trips will be generated in 2030. Increase of delay will increase the travel period, which will also reduce the capability of the road to cater the high traffic demand. Besides, with the increasing of vehicle delay, the vehicle fuel consumption will also increase which eventually contribute to high emissions levels. The high demands of mobility resulted in an increase of cars in contrast to growth. The emission of

M. Mustafa (✉) · N. A. M. Noor
School of Civil Engineering, College of Engineering, Universiti Teknologi MARA (UiTM),
40450 Shah Alam, Selangor, Malaysia
e-mail: masria@salam.uitm.edu.my

Table 1 Summary of new passenger and commercial vehicles registered in Malaysia for the year 2000 to September 2020

Year	Passenger car	Commercial vehicles	Total (p car and com veh)
2010	543,594	61,562	605,156
2011	535,113	65,010	600,123
2012	552,158	75,575	627,733
2013	576,640	79,104	655,744
2014	588,348	78,139	666,487
2015	591,275	75,402	666,677
2016	514,594	65,491	580,085
2017	514,675	61,950	576,625
2018	533,202	65,512	598,714
2019	550,179	54,108	604,287
Sept 2020	310,008	31,481	341,489

Source http://www.maa.org.my/info_summary.htm

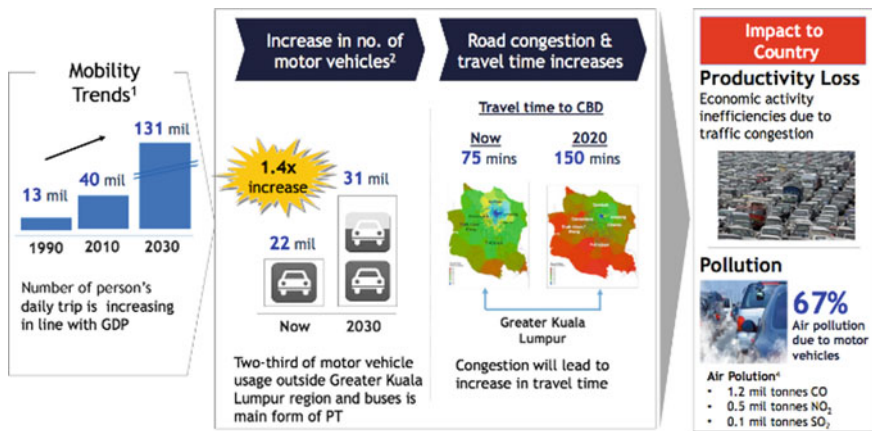


Fig. 1 The rapid growth in mobility trends over the years [1]

pollutants to the atmosphere in 2017 were from motor vehicles (70.4%) followed by power plant (24.5%), industrial (2.9%) and others (2.1%).

Motor vehicle emissions pollute the atmosphere covering 70% (3,070,182 tonnes) of the total emission [2]. The pollution amount is much greater as compared to those generated from power plant, industrial and other sources, which contribute to 24.3%, 2.8% and 2.9% respectively. According to [3], the CO₂ emission from transportation sector in Malaysia increased from 15 million metric tons in early nineties to 42.43 million metric tons in 2012. Figure 2 depicts the emissions to the atmosphere by different sources.

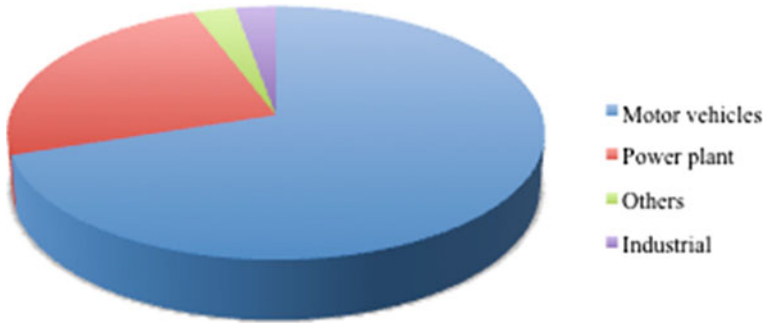


Fig. 2 Emissions different sources [2]

Air pollution has contributed to many serious health and environmental problem including forming of acid rain, ozone pollutants and greenhouse effect. Besides, the vehicles emissions give impact on the economy and society and become threats to all living species, especially human beings [3]. There are several factors that contribute to the increment of vehicles emissions including intersection control type, vehicular characteristics, traffic volume and driving pattern. At the intersection, the drivers tend either to slow down or completely stop in order to secure acceptable gap to enter the existing traffic flow [4]. Therefore, the vehicle is required to reduce their speed and stop in variable patterns of interruption and proceed with constant traffic flow at an ideal speed. Ultimately, the longer the stops period, vehicular emissions will be increased as more fuel is consumed.

This study is essential because the traffic volume is growing due to the increased of the local population and economic growth. Continuous growth of the traffic volume will lead to traffic congestion as the available lanes on road are remaining fixed. Increasing of delay will increase the travel period, which will also reduce the proficiency of the junction to cater the overflow of traffic. Besides, with the increasing of vehicle delay, the vehicle fuel consumption will also increase which eventually contribute to high emissions levels. A comparison of the combined air pollutant emission load in 2014 and 2015 is shown in Fig. 3. In 2015 the combined air pollutant emission load accumulated to 2,001,195 metric tonnes of carbon monoxide (CO), 927 metric tonnes of nitrogen oxides (NO₂), 209,156 metric tonnes of sulphur dioxide (SO₂) and 23,904 metric tonnes of particulate matter (PM) was estimated. The same trend was also observed in 2014 where 1,941,039 metric tonnes of carbon monoxide (CO) was recorded which contribute to the highest amount of emission loading. This study was conducted to determine the emission level at different junction type (signalized intersection and roundabout) and to evaluate the most efficient junction types in term of emissions level.

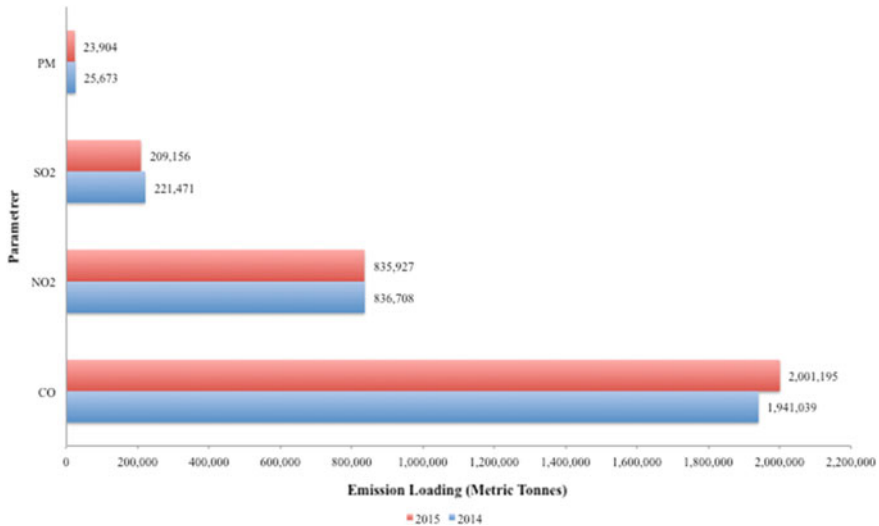


Fig. 3 Air pollutant emission load from all sources, 2014–2015

2 Literature Review

2.1 Studies on Vehicles Emissions

High traffic volume is one of the main causes for serious traffic congestion especially during peak-hour [4]. The vehicle emissions produced are depending on several factors such as traffic pattern, vehicles characteristic and street configurations [5]. Besides, the vehicle emissions are depending on fuel consumption, vehicle type, traffic volume, and driving pattern. Vehicle's engine operating modes, temperatures, speeds, accelerations and decelerations are included under travel-related factors [6]. A study was carried by [4] out to assess the effect of traffic volume and their compositions on carbon emissions at junction by developing mathematical models to predict the CO emissions. Their results show that traffic volumes and their compositions were found to be major causes that affecting emissions of carbon monoxide (CO) at the junction. One reason is because more fuel is consumed when the traffic congestion is increased and more emissions are emitted at the same time. Moreover, the repeated stop and go circumstances had caused more emissions to be released during traffic congestion. Besides, a study by [7] had also evaluated and compared the vehicle emissions at roundabout and cross road for two different scenarios, congested and uncongested conditions. Their interesting results indicated that the emissions levels at roundabout are lesser than the cross road for both conditions, congested and uncongested. As expected, the emissions emitted by vehicles during congested condition are greater than uncongested condition. Higher speed variations and regular stops that occur due to congestion, resulted in the increment of emissions levels. Conversely,

a study conducted by [8] shows different results whereas traffic volumes increase, the efficiency of a roundabout in decreasing the traffic delay at intersection are low. Therefore, the signalized intersection was proven to produce low emissions.

According to [9], types of intersection control is one of the factors that may influence the vehicular emissions level. Several studies were conducted to evaluate the emissions at traffic junction in many countries. A study conducted by [10] emphasized on a comparison of the performance of All Way Stop Control (AWSC) intersection and smart roundabout. They concluded that there was a statistically significant of reduction in delay, queuing and stopping after the modern roundabout was installed. As a result, the emissions level proved to be lower at smart roundabout as compared to All Way Stop Control (AWSC). Besides, intersections are critical elements of road networks in terms of emission impact since their control type and geometric configuration can affect the vehicular emissions [11]. All different level of vehicle movement at the junction contributes to pollutant emissions [12]. Vehicle movements at signalised intersection are controlled by traffic signals. When the signal turns green, vehicles will accelerate and enter the junction. Meanwhile the incoming vehicles will enter the junction at cruising speed while the signal is green. However, vehicles will decelerate and come to a complete stop when the signal turns red. Kumra et al. [5] claimed that the drivers will normally keep the engines on at the intersection which resulted in extra fuel consumption and finally contribute to great emissions emitted at the junctions. For roundabout, a study conducted by [13] demonstrates the effectiveness of modern roundabout in reducing the emissions level when replacing the all way stop control (AWSC). The result of this study shows a statistically significant decrease in terms of average delay and queue length after the AWSC was replaced with roundabout. Besides, [14] conducted a comparative study on emissions level at roundabout, free-flow slip lane and signalised intersection by using SIDRA and MOVES2010b. Their results reveal that the roundabout with a free-flow slip lane significantly decreases pollutant emissions compared to all-way stop-controlled intersection. The results indicate that roundabouts with slip lanes reduce 27% of CO₂ emissions and 17% of CO emissions compared to an all-way stop-controlled intersection. Besides, [7] indicated that the roundabout produces a positive effect on the environment since it is a practical alternative to reducing emissions level. The emission for CO₂, NO_x and CO at roundabout are 19.03%, 37.69% and 45.65% less than crossroad for uncongested cases while 34.29%, 95.18% and 55.12% less for congested cases respectively. In contrast, a study conducted by [8] revealed that roundabout does not essentially lead to a reduction in emissions levels. The roundabout contributed to a high level of emission levels compared to a two-way stop control type. While some studies investigate the effect of geometric design of the signal control, [15] investigate the errors that static modelling outputs introduce in the emission estimation process and suggest improvements in the modelling process.

2.2 *Using Simulation for Vehicle Emission Studies*

SIDRA is well known to have better efficiency of comparisons between different types of junction over other software models [9]. SIDRA method highlights the consistency of capacity and performance analysis methods for sign-controlled, roundabouts and signalised intersections through the use of an integrated modelling framework. According to [4], SIDRA emission estimates are derived from traffic flow parameters, traffic volume, compositions, speeds, turning movements and road geometry. SIDRA uses a four-mode drive cycle model (idling, acceleration, deceleration, and cruise) for estimating fuel consumption, pollutant emissions and operating cost for all types of traffic facilities. Other simulation methods can also be used to access the emissions level at various junction types. Onga et al. [16] has conducted a study to calculate emissions from road transport in Malaysia by using COPERT 4. Their results indicated that the CO₂ become main source of Greenhouse gases (GHG) pollution which contribute to 71% of the total CO₂ corresponding emissions, followed by NO_x at 21%. Passenger cars contributed the highest source of direct GHG pollutants, CO, NO_x and Non-methane volatile organic compounds (NMVOC). A study by [11] used a traffic microsimulation tool (S-Paramics) together with emission estimator (AIRE) to evaluate the emissions levels at roundabout and fixed-time signal control. Results from their study have indicated that a roundabout can cut pollutants more than a fixed-time signal control. Besides, noteworthy studies of [17] had used MOVES and CMEM software together with the Paramics microsimulation model to compare CO and NO_x emissions level. They concluded that MOVES and CMEM produce similar level of NO_x, but varies in the estimations of CO. CO estimations from CMEM are 4–6 times greater than those from MOVES while NO_x estimations in CMEM are lower than those generated by the MOVES. Meanwhile, [18] used (Vehicle Specific Power) VSP model in their study which is based on a real case study working under saturation level. The model assessed CO₂, CO, NO_x and HC emissions which are based on the speed and acceleration of vehicles and the road grade, by using data transferred from the microsimulation software AIMSUN.

From the literatures, we can conclude that the type of junction gives impact to emissions level. In most study, vehicular emissions contain a wide variety of pollutants such as carbon dioxide (CO₂), carbon monoxide (CO), oxides of nitrogen (NO_x), particulate matter (PM10) and hydrocarbons (HC). In this study, all of these emissions are considered except particulate matter and SIDRA was used as a test bed for creating the test environment.

3 Methodology

Signalized intersection site chosen for this study was a four-leg signalised intersection located at Section 7, Shah Alam, Selangor, Malaysia. It is located in front of second main gate of Universiti Teknologi MARA (UiTM). The junction is connected to

Persiaran Kayangan and Persiaran Permai. Persiaran Permai is located at the east-west direction while Persiaran Kayangan is located at the south-north direction as depicted in Fig. 4. Two types of data had been collected for this study which are traffic data and geometric parameters of the junction. Traffic volume, movement of vehicles, vehicles' speed as well as geometric parameters including the number of lane, width of lane and traffic control signal timing were collected. The data was used as input data to analyse the emissions level at different junction type by using SIDRA software. The data was collected during normal day with no adverse weather and any external factor(s), such as special events in the nearby locality of the study junction. The data collection starting from 7.00 a.m. to 8.00 a.m. for morning session and 5.30 p.m. to 6.30 p.m. for evening session.

Traffic Volume

The traffic volumes and traffic movements at junction were collected by using video recorder. Video recording method for data collection was used as the recorded data can be accessed and retrieved at any time later. All recorded information can be accessed for evaluation purposes and also for re-verification of data, or reuse for other purposes. The traffic volume from the junction was recorded for one-hour for each peak hour. Traffic volumes were collected and classified into 15-min periods according to movement and types of vehicles such as passenger car, light vans and medium lorries, heavy lorries, buses and motorcycles.



Fig. 4 Satellite image of study location

Vehicles Speeds

The data for speed of vehicles was collected for the purpose of calibration in SIDRA Software. The speed data was collected for every approach by using radar speed meter (radar gun). The sample speeds of approximately 100 vehicles were measured at each of the approach to determine the mean speeds of the vehicles travel at the junction. The mean speed obtained was then transferred to SIDRA as an input before simulation process begin.

Road Geometric

The road geometric data of the junction that had been considered in this study were number of lane, lane width, width of slip lane, and traffic signal control. The number of lane was observed and recorded for every approach and the width of the lane and slip lane for every approach was measured too. The cycle length for each phase of traffic signal control was recorded manually by using stop watch and the data was then transferred to SIDRA software to simulate the signalised intersection.

Model Calibration and Validation

The validation process was then executed in order to verify the results. Besides, validation process is necessary to ensure that the parameters used in the simulation matched with local condition. In this study, the validation process was carried out by using flow rate data for morning period at signalised intersection. The result was validated by using the GEH Static equation [19] and Table 2 presents a different of GEH values as an indication of a goodness of fit.

$$GEH = \sqrt{\frac{(M - O)^2}{0.5(M + O)}} \quad (1)$$

where

M Simulated flow

O Observed flow.

The simulation of signalised intersection was performed by using the field data collected such as geometric data and traffic data. Table 3 shows the parameter value of geometry data that used for simulation of signalised intersection while Table 4 indicates the value of geometry parameter that applied to modelled roundabout.

Table 2 Description for varies of GEH value [19]

Value	Description
$GEH < 5$	Flows can be considered a good fit
$5 < GEH < 10$	Flows may require further investigation
$10 < GEH$	Flows cannot be considered to be a good fit

Table 3 Geometry data used for simulation of signalised intersection

Approach	1 (south)	2 (north)	3 (west)	4 (east)
Number of lane	4	4	2	1
Lane width (m)	3.2	3.2	3.5	3.5
Slip lane width (m)	5.5	4.2	5.5	4.2

Table 4 Geometry parameter used for modelled roundabout

Element	Value
Island diameter (m)	100
Number of circular lane	2
Circulating lane width (m)	8.5
Entry radius (m)	20
Entry angle (°)	30
Lane width (m)	3.5
Slip lane width (m)	5.5

4 Results and Discussions

4.1 General

In order to achieve the objectives of this study, analysis was carried out once the simulation and modelling process were performed. The simulation and modelling was executed by using the field data collected. Table 5 lists the data of traffic volume for morning and evening peak hour. As the objective of this study is to analyse the most efficient types of junctions in terms of emissions level, thus, the results of the emissions level from intersection and roundabout were analysed. The percentage difference on level of emissions between roundabout and signalised intersection is summarize in Table 6 for morning and evening peak hour respectively.

Table 5 Traffic volume data for morning peak hour





Direction	Approach				Approach			
	a.m.				p.m.			
	1 (south)	1 (south)	1 (south)	1 (south)	1 (south)	2 (north)	3 (west)	4 (east)
	313	313	313	313	962	263	262	909
	1012	1012	1012	1012	916	940	252	371
	828	828	828	828	349	476	794	123
	167	167	167	167	162	121	280	-

Table 6 Comparison of emissions levels between roundabout and signalised intersection for morning peak hour

Emissions types	a.m.			p.m.		
	Roundabout	Signalised intersection	% difference	Roundabout	Signalised intersection	% difference
Carbon dioxide (CO ₂)	2791.9 kg/h	3248.6 kg/h	-14.06%	2431.9 kg/h	2806 kg/h	-13.33%
Carbon monoxide (CO)	1.655 kg/h	12.02 kg/h	-86.23%	1.391 kg/h	10.433 kg/h	-86.67%
Hydrocarbon (HC)	0.259 kg/h	2.371 kg/h	-89.08%	0.208 kg/h	2.03 kg/h	-89.75%
Nitrogen oxide (NO _x)	1.369 kg/h	1.57 kg/h	-12.80%	1.168 kg/h	1.333 kg/h	-12.38%

The result shows that the roundabout is able to reduce CO₂ and NO_x about 14.06% and 12.80% respectively. Besides, replacing the signalised intersection with roundabout had shown great reduction of HC and CO as it able to reduce up to 86.23% and 89.08% respectively for morning peak hour. The same pattern of reduction is shows on the result of evening peak hour as it able to cut the emissions levels to 13.33%, 86.67%, 89.75%, and 12.38% for CO₂, CO, HC and NO_x respectively. This contrasts with [20] who found that the signal control outperformed the roundabout in the range of 37–43% reduction in emissions. Many authors have stressed the roundabout is the most efficient type of junction in terms of emissions level [21]. The average delay and queuing are greater at signalised junctions since the vehicles are required to queue at a red of traffic signals even if the delay are equivalent to roundabout [13]. Moreover, most of the drivers keep their vehicles on during their waiting time at the traffic light. It caused activities of fuel combustion keep continue even when their vehicles are at stop which then contribute to risen of emission level at particular junction. Thus, the emissions levels are commonly larger at signalised junction compared to roundabout. Besides that, at signalised intersection there is high tendency for the vehicles to have longer waiting period due to traffic signal control as compared to roundabout. At the roundabout, waiting time to enter the junction is lower as compared to signalised intersection because the driver is only required to slow down and stop if needed in order to find the acceptable gap of acceptance to allow them to enter the circulating lane or any approach without having long waiting time. Another contributing factors include fuel used, technology of engine combustion, exhaust after treatment devices and vehicle characteristics [16].

Table 7 Varies percentage of vehicles volumes

Percentage of volume	Descriptions
50%	The field volume data was reduced to 50%
75%	The field volume data was reduced to 25%
100%	The field volume data obtained from fieldwork
125%	The field volume data was increased to 25%
150%	The field volume data was increased to 50%

4.2 Emission Level at Different Percentage of Volumes

Vehicle volumes at the junction affect the emissions level at the particular junction. This is because the volumes will affect the traffic delay. The junctions will become congested when the volume is high and the delay is increase because the waiting time for the driver to enter the junction is longer. Moreover, higher vehicles volumes will lead to higher fuel consumptions. For this part of analysis, we vary the traffic volume to see the effect of different traffic delay at the junction. Several percentage of volumes were applied as data input for both, roundabout and signalised intersection. Table 7 shows various percentage of volume which represent the level of congestion for the network.

Figures 5, 6, 7 and 8 depict the relationship between the percentage volume and emissions level by using morning peak hour (a.m.) dataset. The graphs show strong positive correlation with R^2 values are closer to 1. As the traffic volume increase, the emissions level increase since the delays are longer. According to [13], the greater average delays at roundabouts will caused the emissions to be equivalent and even larger than signalised intersection. In contrast, during uncongested situation,

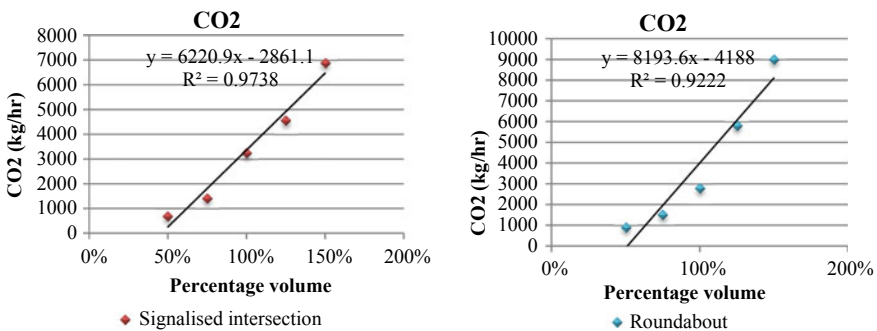


Fig. 5 Relationship of CO₂ and percentage volume for signalised intersection and roundabout

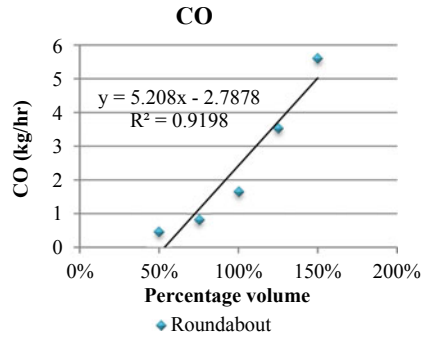
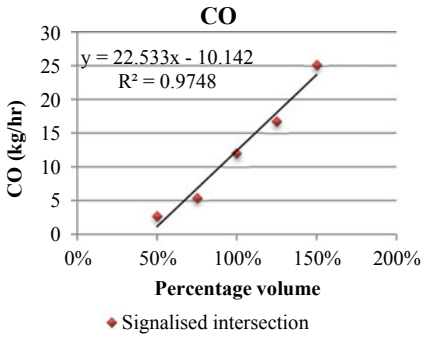


Fig. 6 Relationship of CO and percentage volume for signalised intersection and roundabout

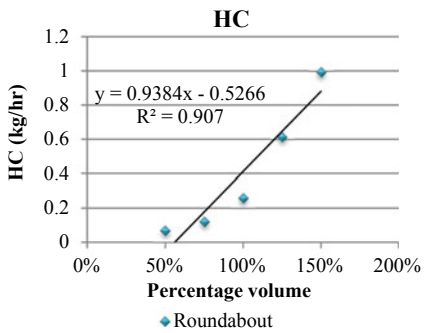
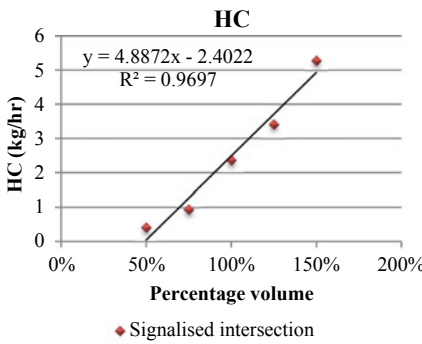


Fig. 7 Relationship of HC and percentage volume for signalised intersection and roundabout

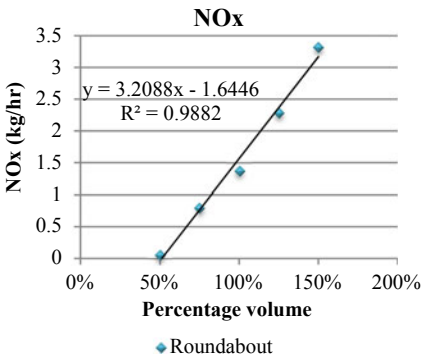
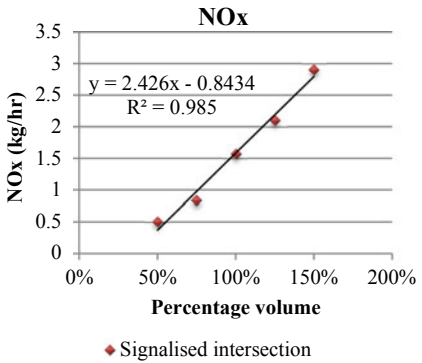


Fig. 8 Relationship of NO_x and percentage volume for signalised intersection and roundabout

vehicles are rarely stops at a roundabout which then cause the queue length and delay become low and eventually the emissions produced are lesser. Besides, there also others factors that contribute to emissions level such as fuel used, technology of engine combustion, exhaust after treatment devices and vehicle characteristics [16]. In addition, a recent study by [22] revealed that in case for signalized intersection, an increase in the green signal ratio and the vehicle road section speed within a specified range has a positive significance for reducing the CO₂, CO, HC, and NO_x emissions of vehicles. Additional support for this explanation comes from [21] as the maximum instantaneous emissions were produced during acceleration driving mode and the minimum during idle mode.

The emissions emitted by the vehicles are mainly affected from the type of fuel consume as the emissions are produced based on the chemical and properties of the fuel used. Due to this, as a mitigation action in reducing the air pollution from transportation, the European system is applied for regulation standard on vehicle emission [23]. Fuel regulation and emission standard EURO 4 is currently applied in Malaysia as the replacement of previous standard of EURO 2 regulation standards [16]. This is the standard applied for fuel consumed in order to control the level of gas emissions from the vehicles. Furthermore, Malaysia also enforced a regulation on emission standard of pollutants under Environmental Quality (Control of Emission from Diesel Engines) Regulations 1996. This regulation is enforced under Environmental Quality Act 1974 [Act 127] where a heavy-duty diesel engine for a vehicle with a Gross Vehicle Weight (“GVW”) of over 3.5 tonnes, shall not exceed the standard of the emission of the gaseous pollutant of CO, HC and NO_x as listed in Table 8.

5 Conclusions

This study was carried out to evaluate the effect of junctions’ type towards vehicles emissions level by using SIDRA software. Carbon dioxide (CO₂), Carbon monoxide (CO), Hydrocarbon (HC) and Nitrogen oxide (NO_x) were assessed in case for signalised intersection and roundabout. The field data was collected and used as data input in simulation. Our results show that roundabout tends to reduce the emissions levels efficiently even in variety of traffic condition level. Findings reported in this study could be extended by analysing emissions at various types of junction such as smart roundabout, signalised roundabout, roundabout without slip lane and signalised intersection or using additional sites with varying geometric features, vehicular traffic level and compositions. This type of study is very important in terms of environmental and economic considerations.

Table 8 Standard of emission and Gaseous emission limit for motorcycle engines and light vehicles

Standard of emission of the gaseous pollutant of CO, HC and NO_x (“Environmental Quality Act 1974 [Act 127]”)			
Mass of carbon monoxide (CO) gram per kWh	Mass of hydrocarbons (HC) gram per kWh	Mass of oxides of nitrogen (NO _x) gram per kWh	Mass of particulates (PT) gram per kWh
4.5	1.1	8.0	0.36
Gaseous emission limit for motorcycle engines (“Environmental Quality Act 1974 [Act 127]”, 2003)			
Engine type	CO (g/km)	HC (g/km)	NO _x (g/km)
2 strokes	8	4	0.1
4 strokes	13	3	0.3
Gaseous emission limit for light vehicles (“Environment Quality Act 1974 [Act 127]”)			
Vehicle type	Reference mass (kg)	CO (g/km)	HC + NO _x (g/km)
Total mass < 2.5 tonnes		2.2	0.5
Petrol engine used for carrying goods and having a maximum weight not exceeding 3.5 tonnes	≤ 1250	2.72	0.97
	1250 < RM ≤ 1700	5.17	1.40
	1700 < RM	6.90	1.70

Acknowledgements The authors wish to thank Universiti Teknologi MARA (UiTM) for funding the research.

References

- Nun N (2016) Transforming greater KL and beyond. In: Greater KL and smarty city summit 2016, Kuala Lumpur
- Compedium of Environment Statistics 2016 (2016) Department of Statistics Malaysia
- Azadeh Ghadimzadeh AAM, Hosea MK, Asgari N, Shamsipour R, Askari A, Narany TS (2015) Review on CO₂ emission from transportation sector. *Malays J Environ Sci Toxicol Food Technol (IOSR-JESTFT)* 9(5):61–70
- Puan OC, Nabay MM, Ibrahim MN (2014) Effect of vehicular traffic volume and composition on carbon emission. *J Teknol* 70:17–20
- Kumar R, Parida P, Tiwari D, Gangopadhyay S (2013) Idling emission at intersection and exploring suitable mitigation measures. *J Traffic Logistics Eng* 1(2)
- Noceraa S, Bassoa M, Cavallaroa F (2016) Micro and Macro modelling approaches for the evaluation of the carbon impacts of transportation. *Transp Res Procedia* 24:146–154
- Boubaker S, Rehim F, Kalboussi A (2016) Impact of intersection type and a vehicular fleet’s hybridization level on energy consumption and emissions. *J Traffic Transp Eng* 3(3):253–261
- Ahn K, Kronprasert N, Rakha H (2009) Energy and environmental assessment of high speed roundabouts. *J Transp Res Board* 1–19
- Ranjitkar P, Shahin A, Shirwali F (2014) Evaluating operational performance of intersections using SIDRA. *Open Transp J* 8:50–61

10. Alkhaledi K (2015) Evaluating the operational and environmental benefits of a smart roundabout. *S Afr J Ind Eng* 26(2):191–202
11. Gastaldi M, Meneguzzo C, Rossi R, Lucia LD, Gecchele G (2014) Evaluation of air pollution impacts of a signal control to roundabout conversion using microsimulation. *Transp Res Procedia* 3:1031–1040
12. Hashim W, Ibrahim W, Ramli NA (2009) A case study of mitigating air pollution emissions at traffic light junctions. In: Sasser S (ed) *Human settlement development*
13. Mandavilli S, Russell ER, Rys MJ (2003) Impact of modern roundabouts on vehicular emissions
14. Al-Ghandour M (2013) Experimental analysis of single-lane roundabout slip lanes: fuel consumption and emissions. In: *Green streets, highways, and development conference*, Austin, Texas, United States
15. Tsanakas N, Ekström J, Olstam J (2020) Estimating emissions from static traffic models: problems and solutions. *J Adv Transp* 2020:5401792
16. Onga HC, Mahlia TMI, Masjukia HH (2011) A review on emissions and mitigation strategies for road transport in Malaysia, vol 15. Elsevier, pp 3516–3522
17. Chamberlin R, Swanson B, Talbot E, Dumont J, Pesci S (2011) Analysis of MOVES and CMEM for evaluating the emissions impacts of an intersection control change. In: *Transportation research board 90th annual meeting*, Washington DC, United States
18. Vasconcelos L, Silva AB, Seco AM, Fernandes P, Coelho MC (2013) Turbo roundabouts: multicriterion assessment on intersection capacity, safety, and emissions. In: *93rd Annual meeting of the transportation research board 2013*, Washington DC, United States
19. Oketch T, Delsey M, Robertson D (2004) Evaluation of performance of modern roundabouts using paramics micro-simulation model. TSH Associates, p 13
20. Shaaban K, Abou-Senna H, Elnashar D, Radwan E (2019) Assessing the impact of converting roundabouts to traffic signals on vehicle emissions along an urban arterial corridor in Qatar. *J Air Waste Manag Assoc* 69(2):178–191
21. Meneguzzo C, Gastaldi M, Rossi R, Gecchele G, Prati MV (2017) Comparison of exhaust emissions at intersections under traffic signal versus roundabout control using an instrumented vehicle. *Transp Res Procedia* 25:1597–1609
22. Zhao H, He R, Jia X (2019) Estimation and analysis of vehicle exhaust emissions at signalized intersections using a car-following model. *Sustainability* 11:3992
23. Owen AD, Tao JY (2015) International best practice for emissions and fuel standards: implementation possibilities for ASEAN. *ABE Res House* 2(1):7–16